

Consultative Committee for Space Data Systems

**REPORT CONCERNING
CCSDS RADIO FREQUENCY AND MODULATION**

PROCEEDINGS OF THE CCSDS RF AND MODULATION SUBPANEL 1E ON BANDWIDTH- EFFICIENT MODULATIONS

CCSDS B20.0-Y-2

YELLOW BOOK

JUNE 2001



AUTHORITY

Issue:	Yellow Book, Issue 2
Date:	June 2001
Location:	Oxfordshire, U.K.

This document has been approved for publication by the Management Council of the Consultative Committee for Space Data Systems (CCSDS) and represents the consensus technical agreement of the participating CCSDS Member Agencies. The procedure for review and authorization of CCSDS Reports and the record of Agency participation in the authorization of this document can be obtained from the CCSDS Secretariat at the address below.

This Report is published and maintained by:

CCSDS Secretariat
Program Integration Division (Code M-3)
National Aeronautics and Space Administration
Washington, DC 20546, USA

FOREWORD

This document consists of comparative and technical studies presented at the May 2001 CCSDS Subpanel 1E meeting concerning bandwidth-efficient modulations. These studies were conducted to evaluate existing and new technologies in an effort to improve RF communication channel efficiencies.

At time of publication, the active Member and Observer Agencies of the CCSDS were

Member Agencies

- Agenzia Spaziale Italiana (ASI)/Italy.
- British National Space Centre (BNSC)/United Kingdom.
- Canadian Space Agency (CSA)/Canada.
- Central Research Institute of Machine Building (TsNIIMash)/Russian Federation.
- Centre National d'Etudes Spatiales (CNES)/France.
- Deutsches Zentrum für Luft- und Raumfahrt e.V. (DLR)/Germany.
- European Space Agency (ESA)/Europe.
- Instituto Nacional de Pesquisas Espaciais (INPE)/Brazil.
- National Aeronautics and Space Administration (NASA HQ)/USA.
- National Space Development Agency of Japan (NASDA)/Japan.

Observer Agencies

- Austrian Space Agency (ASA)/Austria.
- Central Research Institute of Machine Building (TsNIIMash)/Russian Federation.
- Centro Tecnico Aeroespacial (CTA)/Brazil.
- Chinese Academy of Space Technology (CAST)/China.
- Commonwealth Scientific and Industrial Research Organization (CSIRO)/Australia.
- Communications Research Centre (CRC)/Canada.
- Communications Research Laboratory (CRL)/Japan.
- Danish Space Research Institute (DSRI)/Denmark.
- European Organization for the Exploitation of Meteorological Satellites (EUMETSAT)/Europe.
- European Telecommunications Satellite Organization (EUTELSAT)/Europe.
- Federal Service of Scientific, Technical & Cultural Affairs (FSST&CA)/Belgium.
- Hellenic National Space Committee (HNSC)/Greece.
- Indian Space Research Organization (ISRO)/India.
- Institute of Space and Astronautical Science (ISAS)/Japan.
- Institute of Space Research (IKI)/Russian Federation.
- KFKI Research Institute for Particle & Nuclear Physics (KFKI)/Hungary.
- MIKOMTEK: CSIR (CSIR)/Republic of South Africa.
- Korea Aerospace Research Institute (KARI)/Korea.
- Ministry of Communications (MOC)/Israel.
- National Oceanic & Atmospheric Administration (NOAA)/USA.
- National Space Program Office (NSPO)/Taipei.
- Swedish Space Corporation (SSC)/Sweden.
- United States Geological Survey (USGS)/USA.

DOCUMENT CONTROL

Document	Title and Issue	Date	Status
CCSDS B20.0-Y-2	Proceedings of the CCSDS RF and Modulation Subpanel 1E on Bandwidth-Efficient Modulations	June 2001	Current Issue

CONTENTS

<u>Section</u>	<u>Page</u>
1 GENERAL COMPARATIVE STUDIES	
1-01 Efficient Modulation Methods Study—A Comparison of Modulation Schemes—Phase 1: Bandwidth Utilisation (W. Martin and T. Nguyen)	1-1
1-02 Efficient Modulation Methods Study—A Comparison of Modulation Schemes—Phase 2: Spectrum Shaping (W. Martin and T. Nguyen).....	1-29
1-03 CCSDS Efficient Modulation Study—A Comparison of Modulation Schemes—Phase 3: End-to-End System Performance. (W. Martin, L.Lam, T. Yan, and S.Million).....	1-91
1-04 Comparison of ESA and NASA Interference Susceptibility Analysis Attachment: CCSDS-SFCG—Efficient Modulation Methods Study at NASA/JPL—Phase 4: Interference Susceptibility (W. Martin and T. Yan).....	1-171
1-05 End-to-End Losses of Selected Bandwidth Efficient Modulation Schemes (E.Vassallo)	1-213
1-06 End-to-End Losses of Selected BW-Efficient Modulations—Part.2: Coded Channel Performance (E.Vassallo)	1-231
1-07 NASA GSFC Efficient Spectrum Utilisation Analysis (B.Younes)	1-257
1-08 Advanced Spectrum Shaping for Efficient Bandwidth Utilisation (G.Block, A.Southern, M.Otter, and M.Reichel)	1-401
1-09 Interference Susceptibility of Selected Bandwidth-Efficient Modulations (E. Vassallo).....	1-473
1-10 Advanced Modulation Schemes for Future ESA Standards (E. Vassallo)	1-493
1-11 On the Introduction of Bandwidth-Efficient Modulation Methods on Telemetry Links (J.Gerner)	1-761
1-12 Performance of Selected Bandwidth-Efficient Modulations (T. Yan).....	1-779
1-13 Comparison of RFI Susceptibility Results – the BPSK Case (E.Vassallo)	1-799
1-14 Coded Bit Error Performance of Selected Bandwidth Efficient Modulations (D. Lee and T. Yan).....	1-835

CONTENTS (continued)

<u>Section</u>	<u>Page</u>
2 GMSK & FQPSK	
2-01 Selected Laboratory Measurements and Results of FQPSK Modems (L. Lam).....	2-1
2-02 Preliminary Results on GMSK Modulation: Spectral Analysis, Error Rates and Synchronization (L. Lam).....	2-25
2-03 Questions on GMSK Performances (E. Vassallo).....	2-43
2-04 GMSK Status Report (D. Olsen)	2-47
2-05 Simulated Performance of FQPSK-1 & FQPSK-KF (or XPSK) Modulation (A. Ribes)	2-55
2-06 Performance Evaluation & Interpretation of Unfiltered FQPSK (M. Simon and T. Yan)	2-79
2-07 Improved GMSK ($B_{Th}=0.25$) Demodulation Performance (A. Ribes)	2-109
2-08 Coded Bit Error Performance of FQPSK and GMSK with Combined Trellis Decoding (E. Vassallo)	2-117
2-09 NASA GSFC BW Efficient Modulation Studies: Response to May, 2000 CCSDS P1E AIs Including a Report on Testing of FQPSK through NASA's TDRSS (D. Lee and T. Yan)	2-127
2-10 Studies and Simulation Results on a Coherent GMSK Demodulator (B. Younes, J. Brase, and M. Burns)	2-141
3 FILTERED/SHAPED OQPSK	
3-01 Comparison of Results on Losses of SRRC-OQPSK in a Non-Linear Channel (E. Vassallo).....	3-1
3-02 Non-Linearity Effect on Raised Cosine Power Spectrum (T. Eng)	3-9
3-03 NASA GSFC Bandwidth Efficient Modulation and Coding Study QPSK with Square Root Raised Cosine Filtering Evaluation (D. Zillig, J. Brase, and M. Burns)	3-19

CONTENTS (continued)

<u>Section</u>	<u>Page</u>
3-04 Bandwidth Efficient Modulation-QPSK (K. Nakada).....	3-27
3-05 An Assessment of Shaped Offset QPSK for Use in NASA Space Network and Ground Network Systems (B. Younes, J. Brase, C. Patel, and J. Wesdock).....	3-35
4 TRELLIS OQPSK	
4-01 Trellis-Coded QPSK with Variable Overlapped Raised-Cosine Pulse Shaping (M. Simon, P. Arabshahi, M. Srinivasan, and T. Yan).....	4-1
5 8/16 PSK	
5-01 PSK Multi-D Trellis-Coded Modulation (A. Ribes)	5-1
5-02 Performance Comparison of 4D-8PSK TCM and FQPSK-B in a Non-Linear Satellite Channel (D. Lee, T. Yan, and W. Martin)	5-43
5-03 NASA GSFC Bandwidth Efficient Modulation and Coding Study Monodimensional 8PSK TCM Evaluation (D. Zillig, J. Brase, and M. Burns)	5-57
5-04 Proposal for 4D-8PSK Treillis Coded Modulation for Medium and High Data Rate Links: Treillis Coding Aspects, Spectrum Occupancy, BER Performances (viewgraphs) (A. Ribes).....	5-67
5-05 Spectral Regrowth Test Data for SRRC 8-PSK Modulation Passed through a SSPA in Saturation (May 2000) (D. Olsen and J. Michaelson).....	5-109
5-06 Spectral Regrowth Test Data for SRRC 8PSK Modulation Passed through an SSPA in Saturation (Oct 2000) (D. Olsen, A. Leong, and W. Johnson)	5-131
6 TECHNICAL STUDIES – RECEIVERS/TRANSMITTERS DESIGN	
6-01 Acquisition Performance Comparison of the Generalized MAP Symbol Synchronizer versus the Data-Transition Tracking Loop (T. Yan)	6-1
6-02 MAP-Motivated Carrier Synchronization of GMSK Based on the Laurent AMP Representation (T. Yan).....	6-15
6-03 On the Feasibility of Using the BLOCK V Receiver to Support 8-PSK Modulation Scheme (H. Tsou and C. Racho)	6-31

CONTENTS (continued)

<u>Section</u>	<u>Page</u>
6-04 Power Spectrum of MSK-Type Modulations in the Presence of Data Imbalance (M. Simon, P. Arabshahi, L. Lam, and T. Yan).....	6-39
6-05 Selected Laboratory Measurements of the MAP Symbol Synchronizer (A. Gray, L. Lam, T. Yan, W. Martin).....	6-59
6-06 Occupied Bandwidth of MSK & GMSK in the Presence of Data Imbalance (T. Yan)	6-67
6-07 GMSK Modulator Design for Onboard Applications (Study of GMSK Modulator) (J. Gerner).....	6-83
6-08 Performance of Near-Optimal and Simplified FQPSK-B Receivers (D. Lee, M. Simon, and T. Yan)	6-105
6-09 Prototyping Parallel Algorithms for High Rate FQPSK Waveforms (E. Kang, D. Lee, N. Lay).....	6-117
6-10 An Off-Line Coherent FQPSK-B Software Reference Receiver (H. Tsou, S. Darden, and T. Yan)	6-125
6-11 BER Performance of GMSK, FQPSK-B, SRRC OQPSK and Butterworth OQPSK with Block V Receiver (D. Lee, J. Weese, W. Martin, and T. Yan)	6-137
6-12 NASA GSFC Study on the Impact of SFCG REC 17-2R1 Spectrum Mask on Space Science Services Space-to-Earth Links (M. Burns)	6-157

AUTHORITY

Issue:	Yellow Book, Issue 2
Date:	June 2001
Location:	Oxfordshire, U.K.

This document has been approved for publication by the Management Council of the Consultative Committee for Space Data Systems (CCSDS) and represents the consensus technical agreement of the participating CCSDS Member Agencies. The procedure for review and authorization of CCSDS Reports and the record of Agency participation in the authorization of this document can be obtained from the CCSDS Secretariat at the address below.

This Report is published and maintained by:

CCSDS Secretariat
Program Integration Division (Code M-3)
National Aeronautics and Space Administration
Washington, DC 20546, USA

FOREWORD

This document consists of comparative and technical studies presented at the May 2001 CCSDS Subpanel 1E meeting concerning bandwidth-efficient modulations. These studies were conducted to evaluate existing and new technologies in an effort to improve RF communication channel efficiencies.

At time of publication, the active Member and Observer Agencies of the CCSDS were

Member Agencies

- Agenzia Spaziale Italiana (ASI)/Italy.
- British National Space Centre (BNSC)/United Kingdom.
- Canadian Space Agency (CSA)/Canada.
- Central Research Institute of Machine Building (TsNIIMash)/Russian Federation.
- Centre National d'Etudes Spatiales (CNES)/France.
- Deutsches Zentrum für Luft- und Raumfahrt e.V. (DLR)/Germany.
- European Space Agency (ESA)/Europe.
- Instituto Nacional de Pesquisas Espaciais (INPE)/Brazil.
- National Aeronautics and Space Administration (NASA HQ)/USA.
- National Space Development Agency of Japan (NASDA)/Japan.

Observer Agencies

- Austrian Space Agency (ASA)/Austria.
- Central Research Institute of Machine Building (TsNIIMash)/Russian Federation.
- Centro Tecnico Aeroespacial (CTA)/Brazil.
- Chinese Academy of Space Technology (CAST)/China.
- Commonwealth Scientific and Industrial Research Organization (CSIRO)/Australia.
- Communications Research Centre (CRC)/Canada.
- Communications Research Laboratory (CRL)/Japan.
- Danish Space Research Institute (DSRI)/Denmark.
- European Organization for the Exploitation of Meteorological Satellites (EUMETSAT)/Europe.
- European Telecommunications Satellite Organization (EUTELSAT)/Europe.
- Federal Service of Scientific, Technical & Cultural Affairs (FSST&CA)/Belgium.
- Hellenic National Space Committee (HNSC)/Greece.
- Indian Space Research Organization (ISRO)/India.
- Institute of Space and Astronautical Science (ISAS)/Japan.
- Institute of Space Research (IKI)/Russian Federation.
- KFKI Research Institute for Particle & Nuclear Physics (KFKI)/Hungary.
- MIKOMTEK: CSIR (CSIR)/Republic of South Africa.
- Korea Aerospace Research Institute (KARI)/Korea.
- Ministry of Communications (MOC)/Israel.
- National Oceanic & Atmospheric Administration (NOAA)/USA.
- National Space Program Office (NSPO)/Taipei.
- Swedish Space Corporation (SSC)/Sweden.
- United States Geological Survey (USGS)/USA.

DOCUMENT CONTROL

Document	Title and Issue	Date	Status
CCSDS B20.0-Y-2	Proceedings of the CCSDS RF and Modulation Subpanel 1E Meeting of May 2001 Concerning Bandwidth-Efficient Modulations	June 2001	Current Issue

CONTENTS

<u>Section</u>	<u>Page</u>
1 GENERAL COMPARATIVE STUDIES	
1-01 Efficient Modulation Methods Study—A Comparison of Modulation Schemes—Phase 1: Bandwidth Utilisation (W. Martin and T. Nguyen).....	1-1
1-02 Efficient Modulation Methods Study—A Comparison of Modulation Schemes—Phase 2: Spectrum Shaping (W. Martin and T. Nguyen).....	1-29
1-03 CCSDS Efficient Modulation Study—A Comparison of Modulation Schemes—Phase 3: End-to-End System Performance. (W. Martin, L.Lam, T. Yan, and S.Million).....	1-91
1-04 Comparison of ESA and NASA Interference Susceptibility Analysis Attachment: CCSDS-SFCG—Efficient Modulation Methods Study at NASA/JPL—Phase 4: Interference Susceptibility (W. Martin and T. Yan).....	1-171
1-05 End-to-End Losses of Selected Bandwidth Efficient Modulation Schemes (E.Vassallo, G. Povero, M.Visintin)	1-213
1-06 End-to-End Losses of Selected BW-Efficient Modulations—Part.2: Coded Channel Performance (E.Vassallo, G. Povero, M.Visintin)	1-231
1-07 NASA GSFC Efficient Spectrum Utilisation Analysis (B.Younes)	1-257
1-08 Advanced Spectrum Shaping for Efficient Bandwidth Utilisation (G.Block, A.Southern, M.Otter, and M.Reichel)	1-401
1-09 Interference Susceptibility of Selected Bandwidth-Efficient Modulations (E. Vassallo, G. Povero, M.Visintin)	1-473
1-10 Advanced Modulation Schemes for Future ESA Standards (N.A. D’Andrea, M. Luise, U. Mengali, and R. Reggiannini).....	1-493
1-11 On the Introduction of Bandwidth-Efficient Modulation Methods on Telemetry Links (J.Gerner)	1-761
1-12 Performance of Selected Bandwidth-Efficient Modulations (D. Lee and T. Yan).1-	779
1-13 Comparison of RFI Susceptibility Results – the BPSK Case (E.Vassallo, G. Povero, M.Visintin)	1-799
1-14 Coded Bit Error Performance of Selected Bandwidth Efficient Modulations (D. Lee and T. Yan)	1-835

CONTENTS (continued)

<u>Section</u>	<u>Page</u>
2 GMSK & FQPSK	
2-01 Selected Laboratory Measurements and Results of FQPSK Modems (J. Weese and L. Lam)	2-1
2-02 Preliminary Results on GMSK Modulation: Spectral Analysis, Error Rates and Synchronization (P. Arabshahi and L. Lam)	2-7
2-03 Questions on GMSK Performances (M. Luise and E. Vassallo).....	2-25
2-04 GMSK Status Report (D. Olsen)	2-29
2-05 Simulated Performance of FQPSK-1 & FQPSK-KF (or XPSK) Modulation (A. Ribes).....	2-37
2-06 Performance Evaluation & Interpretation of Unfiltered FQPSK (M. Simon and T. Yan).....	2-61
2-07 Improved GMSK ($B_{Th}=0.25$) Demodulation Performance (E. Vassallo and M. Visintin)	2-91
2-08 Coded Bit Error Performance of FQPSK and GMSK with Combined Trellis Decoding (D. Lee and T. Yan).....	2-99
2-09 NASA GSFC BW Efficient Modulation Studies: Response to May, 2000 CCSDS P1E AIs Including a Report on Testing of FQPSK through NASA's TDRSS (B. Younes, J. Brase, and M. Burns)	2-109
2-10 Studies and Simulation Results on a Coherent GMSK Demodulator (E. Bouisson and A. Ribes)	2-123
3 FILTERED/SHAPED OQPSK	
3-01 Comparison of Results on Losses of SRRC-OQPSK in a Non-Linear Channel (E. Vassallo).....	3-1
3-02 Non-Linearity Effect on Raised Cosine Power Spectrum (T. Eng)	3-9
3-03 NASA GSFC Bandwidth Efficient Modulation and Coding Study QPSK with Square Root Raised Cosine Filtering Evaluation (D. Zillig, J. Brase, and M. Burns)	3-19

CONTENTS (continued)

<u>Section</u>	<u>Page</u>
3-04 Bandwidth Efficient Modulation-QPSK (K. Nakada)	3-27
3-05 An Assessment of Shaped Offset QPSK for Use in NASA Space Network and Ground Network Systems (B. Younes, J. Brase, C. Patel, and J.Wesdock)	3-35
4 TRELLIS OQPSK	
4-01 Trellis-Coded QPSK with Variable Overlapped Raised-Cosine Pulse Shaping (M. Simon, P. Arabshahi, and M. Srinivasan)	4-1
5 8/16 PSK	
5-01 PSK Multi-D Trellis-Coded Modulation (A. Ribes).....	5-1
5-02 Performance Comparison of 4D-8PSK TCM and FQPSK-B in a Non-Linear Satellite Channel (D. Lee, T. Yan, and W. Martin).....	5-43
5-03 NASA GSFC Bandwidth Efficient Modulation and Coding Study Monodimensional 8PSK TCM Evaluation (D. Zillig, J. Brase, and M. Burns)	5-57
5-04 Proposal for 4D-8PSK Treillis Coded Modulation for Medium and High Data Rate Links: Treillis Coding Aspects, Spectrum Occupancy, BER Performances (viewgraphs) (A. Ribes)	5-67
5-05 Spectral Regrowth Test Data for SRRC 8-PSK Modulation Passed through a SSPA in Saturation (May 2000) (D. Olsen and J.Michaelson)	5-109
5-06 Spectral Regrowth Test Data for SRRC 8PSK Modulation Passed through an SSPA in Saturation (Oct 2000) (D. Olsen, A.Leong, and W.Johnson)	5-131
6 TECHNICAL STUDIES – RECEIVERS/TRANSMITTERS DESIGN	
6-01 Acquisition Performance Comparison of the Generalized MAP Symbol Synchronizer versus the Data-Transition Tracking Loop (T. Yan)	6-1
6-02 MAP-Motivated Carrier Synchronization of GMSK Based on the Laurent AMP Representation (T. Yan)	6-15
6-03 On the Feasibility of Using the BLOCK V Receiver to Support 8-PSK Modulation Scheme (H. Tsou and C. Racho)	6-31

CONTENTS (continued)

<u>Section</u>	<u>Page</u>
6-04 Power Spectrum of MSK-Type Modulations in the Presence of Data Imbalance (M. Simon, P. Arabshahi, L. Lam, and T. Yan).....	6-39
6-05 Selected Laboratory Measurements of the MAP Symbol Synchronizer (A. Gray, L. Lam, T. Yan, W. Martin).....	6-59
6-06 Occupied Bandwidth of MSK & GMSK in the Presence of Data Imbalance (D. Lee)	6-67
6-07 GMSK Modulator Design for Onboard Applications (Study of GMSK Modulator) (C. Barrieres).....	6-83
6-08 Performance of Near-Optimal and Simplified FQPSK-B Receivers (D. Lee, M. Simon, and T. Yan)	6-105
6-09 Prototyping Parallel Algorithms for High Rate FQPSK Waveforms (E. Kang, D. Lee, N. Lay).....	6-117
6-10 An Off-Line Coherent FQPSK-B Software Reference Receiver (H. Tsou, S. Darden, and T. Yan)	6-125
6-11 BER Performance of GMSK, FQPSK-B, SRRC OQPSK and Butterworth OQPSK with Block V Receiver (D. Lee, J. Weese, W. Martin, and T. Yan)	6-137
6-12 NASA GSFC Study on the Impact of SFCG REC 17-2R1 Spectrum Mask on Space Science Services Space-to-Earth Links (M. Burns)	6-157

SFCG-13
Ottawa, Canada
13-21 October 1993

SF-13/40/D

CCSDS - SFCG EFFICIENT MODULATION METHODS STUDY

A COMPARISON OF MODULATION SCHEMES

PHASE 1: BANDWIDTH UTILIZATION

(Response to SFCG Action Item 12/32)

**Warren L. Martin
Tien M. Nguyen**

Members, CCSDS Subpanel 1E, (RF and Modulation)

24 September 1993

CCSDS RF AND MODULATION STUDY

A COMPARISON OF MODULATION SCHEMES

1.0 INTRODUCTION

At its 12th annual meeting the Space Frequency Coordination Group, SFCG-12, held during November 1992 in Australia, the SFCG requested the CCSDS RF and Modulation Subpanel to study and compare various modulation schemes (SFCG Action Item 12-32). Further explanation and clarification of this request was provided by the SFCG's representative to Subpanel 1E during the CCSDS RF and Modulation meeting at JPL from 8-12 February 1993. Several attributes such as bandwidth needed, power efficiency, spurious emissions, and interference susceptibility were the benchmarks suggested for comparing the several modulation schemes.

As the presently allocated frequency bands become more congested, it is imperative that the most bandwidth-efficient communication methods be utilized. Additionally, space agencies are under constant pressure to reduce costs. Budget constraints result in simpler spacecraft carrying less communications capability as well as reduced staffing at the earth stations used to capture the data. Therefore, the power-efficiency of each modulation scheme becomes an important discriminator in the evaluation process.

The following paper explores both those modulation schemes which have been traditionally employed by space agencies together with newer techniques promising significantly improved communications channel efficiencies. This paper represents an interim report to the SFCG since modulation schemes such as QPSK, OQPSK, and MSK have not yet been studied. Supporting analysis for the information contained in this paper was by Tien M. Nguyen and can be found in References 1, 2, 3, and 5.

2.0 BANDWIDTH MEASUREMENT

2.1 Traditional Modulation Methods

Traditionally, space agencies have employed subcarriers for both telecommand and telemetry data transmissions. Subcarriers provided a simple method for separating different types of data as well as ensuring no overlap between the modulated data's frequency spectra and the RF carrier. It was not uncommon for early spacecraft to have two or more subcarriers.

Subcarrier modulation suffers the disadvantages of greater spacecraft complexity, additional losses in the modulation/demodulation process, and a large occupied bandwidth. An effort was made to mitigate the latter effect by specifying that Category A missions utilize sinewave subcarriers while Category B missions should use squarewave subcarriers (CCSDS Recommendation 401 (2.4.5) B-1). Although requiring more bandwidth, square wave subcarriers were found to be acceptable for deep space missions because the weaker signals from such spacecraft, together with the separately allocated frequency bands, ensured that spacecraft transmissions would not interfere with one another. They offered the advantage of being less susceptible to in-band interference.

In the 1960s and 1970s, when data rates were low and only 2 or 3 channels required, the added complexity and spectrum utilization required when using subcarriers could be tolerated. Since then, missions have become more complex, technology has matured, and the radio frequency spectrum has become more congested. Greater data rates require higher frequency subcarriers which expand the occupied bandwidth increasing the likelihood of overlapping downlinks from different spacecraft which could interfere with one another.

CCSDS RF AND MODULATION STUDY

A COMPARISON OF MODULATION SCHEMES

Fortunately, new modulation techniques and improved data formatting can significantly reduce the amount of bandwidth needed to transmit information. Reference 4 describes a Packet Telemetry data format recommended by the Consultative Committee for Space Data Systems (CCSDS). These formats include a Transfer Frame into which Data Packets are placed. Three bits in the header of each Transfer Frame can be set by the user to indicate the type of data in that frame. Thus, the CCSDS *Packet Telemetry* system can provide up to eight separate and independent virtual channels.

The eight virtual channels are equivalent to eight separate, but simultaneous, data streams from the spacecraft. But, rather than employing eight subcarriers, these Transfer Frames (channels) are transmitted consecutively in a single data stream. By combining the CCSDS *Packet Telemetry* format with one of the direct modulation schemes discussed in this paper, and applying some judicious spectrum shaping, it is now possible to transmit messages at a high rate while using a comparatively small bandwidth. Before describing these alternative modulation systems, a reference for bandwidth measurement must be established.

2.2 Occupied Bandwidth

Several years ago the International Telecommunications Union (ITU) established criteria for quantifying the bandwidth used by a telecommunications system. Termed *Occupied Bandwidth*, RR-147, of the ITU's *Radio Regulations* defined the term as:

Occupied Bandwidth: The width of a frequency band such that, below the lower and above the upper frequency limits, the mean power emitted are each equal to a specified percentage $\beta/2$ of the total mean power of a given emission.

Unless otherwise specified by the CCIR for the appropriate class of emission, the value of $\beta/2$ should be taken as 0.5%.

Under the ITU definition, the *Occupied Bandwidth* is that span of frequencies which contains 99% of the emitted power. Where digital communications are concerned, *Occupied Bandwidths* of unfiltered signals tend to be very large. Some people believe that *Occupied Bandwidth* is not a useful concept for digital communications systems absent some degree of filtering.

The ITU *Radio Regulations* also contain an alternative definition called *Necessary Bandwidth*. RR-146 defines *Necessary Bandwidth* as:

Necessary Bandwidth: For a given class of emission, the width of the frequency band which is just sufficient to ensure the transmission of information at the rate and with the quality required under the specified conditions.

Here, the problem is one of uncertainty. To a large extent "quality" is a subjective concept. Using *Necessary Bandwidth* definition is difficult without a specific standard. Moreover, no attention is paid to power efficiency which would satisfy the requirements of both space and terrestrial communications systems. Generally, *Necessary Bandwidth* is not deemed to be a useful measure for space communications systems.

CCSDS RF AND MODULATION STUDY

A COMPARISON OF MODULATION SCHEMES

2.3 Required Bandwidth

Given the problems with both the *Occupied Bandwidth* and the *Necessary Bandwidth* notions, this paper proposes a new measure called *Required Bandwidth*. For the most part, the definition of *Required Bandwidth* is the same as that for *Occupied Bandwidth*. The principal difference is that a more realistic value for the percentage of power is selected. The proposed definition is:

Required Bandwidth: For a specific type of modulation, the width of the frequency band such that, below the lower and above the upper frequency limits, the mean power emitted are each equal to 2.5 percent of the total unfiltered, ideally modulated digital data spectrum, using the same modulation scheme.

Note that this definition is not referenced to 99% of the power in the transmitted spectrum as is the one for *Occupied Bandwidth*. That is because spectrum control is inherent in the concept of *Required Bandwidth*. In simple terms, *Required Bandwidth* is that bandwidth needed to complete a communication with an acceptable amount of power loss. For example, a 5% decrease in power corresponds to -0.2 dB. Such a reduction should be acceptable to most space missions. Yet, the bandwidth required to send identical messages over two channels, one using the *Occupied Bandwidth* definition and the other employing the new *Required Bandwidth* definition, will be several times less in the latter channel when compared to the former. As will be demonstrated in the remainder of this paper, accepting a small loss in the system's performance, dramatically reduces the amount of bandwidth needed to complete the communication.

It is assumed that some spectrum shaping will be employed at an appropriate location in the information transmission system so that *only the Required Bandwidth is transmitted from the spacecraft*. Figure 2-1 is a simplified block diagram of a spacecraft Radio Frequency Subsystem (RFS). Note that spectrum shaping can be located in the ranging channel, at the input to the modulator, and at the output of the power amplifier. Spectrum shaping is found on most current spacecraft. All of the spectrum shaping devices shown in Figure 2-1 may not be required. The actual number and their locations will depend upon the specific RFS design and the linearity of the multiplier and the power amplifier. Obviously, it is desirable to avoid spectrum shaping at the output of the power amplifier because of the RF power loss and increased weight. If the spectrum shaping is done at an earlier point, then the losses resulting from spectrum shaping at the transmitter's output can be largely avoided.

Coherent turnaround and one-way ranging signals present unique problems in *Required Bandwidth* systems. To achieve the desired measurement accuracy, ranging tones sometimes have frequency components, and hence *Required Bandwidths*, which are larger than those needed for telemetry and telecommand operations. Since many space missions need all of these services, the RFS depicted in Figure 2-1 must accommodate the separate spectral requirements imposed by the different services. Clearly, the mechanization of the flight radio system may depend upon a mission's specific requirements.

Fortunately, the system depicted in Figure 2-1 should permit the flexibility to meet the needs of all services. Moreover, even if the *Necessary Bandwidth* increases during ranging operations, these sessions are usually concluded quickly so that the increased bandwidth requirement is of short duration.

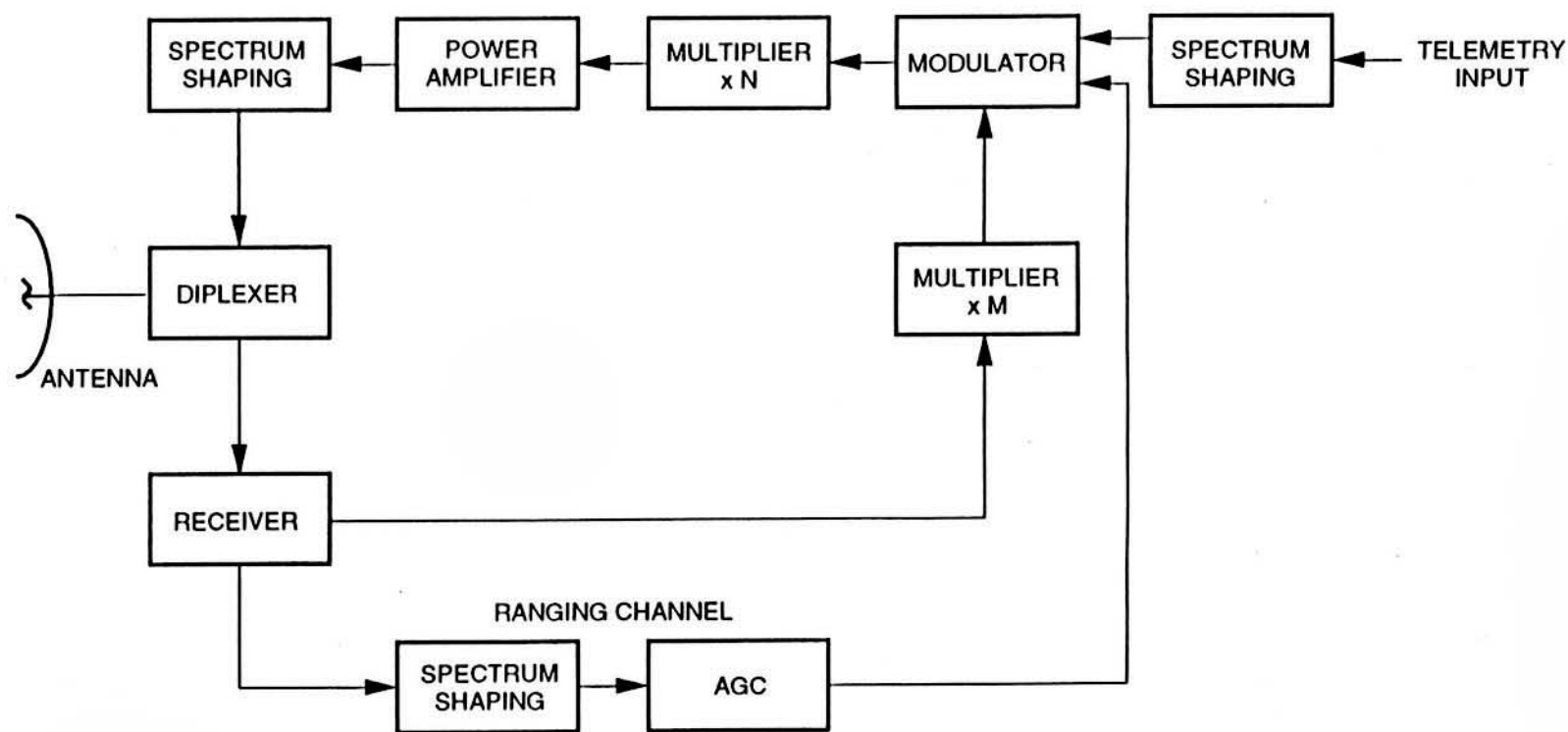
CCSDS RF AND MODULATION STUDY
COMPARISON OF MODULATION SCHEMES

Figure 2-1. Simplified Block Diagram of Spacecraft Radio Frequency Subsystem

CCSDS RF AND MODULATION STUDY

A COMPARISON OF MODULATION SCHEMES

3.0 COMPARISON OF MODULATION SCHEMES

Modulation schemes listed in Table 1 were investigated in Reference 1 and are compared in this paper. Because this is an interim report, QPSK, OQPSK, and MSK (including GMSK), have not been studied yet and will be included in the final report. Modulation methods listed below are shown in the order of increasing bandwidth efficiency (diminishing *Required Bandwidth*).

TABLE 3-1: INVESTIGATED MODULATION SCHEMES

Modulation Type	Description
PCM/PSK/PM squarewave	NRZ data is PSK modulated on a squarewave subcarrier which is then phase modulated on a residual RF carrier.
PCM/PSK/PM sinewave	NRZ data is PSK modulated on a sinewave subcarrier which is then phase modulated on a residual RF carrier.
PCM/PM/Bi- ϕ	Data is Bi-Phase (Manchester) modulated directly on a residual RF carrier.
PCM/PM/NRZ	NRZ data is phase modulated directly on a residual RF carrier.
BPSK/Bi- ϕ	Data is Bi-Phase (Manchester) modulated on an RF carrier fully suppressing it.
BPSK/NRZ	NRZ data is phase modulated directly on an RF carrier fully suppressing it.

To compare the *Required Bandwidths* for the several modulation schemes, power transfer efficiencies of 90% and 95% are used. As noted above, these correspond to power losses of 0.45 dB and 0.2 dB respectively. For each modulation type the bandwidth needed to convey 90% and 95% of the modulated signal will be computed. Bandwidths will be normalized to the data Symbol Rate, R_s , so that the various types can be compared. Additionally, an RF carrier modulation index of 1.2 radians, a value typical for primary telemetry channels having reasonable data rates, was used for evaluating all modulation schemes.

Figure 3-1 shows the frequency spectrum of each of the several modulation schemes shown in Table 3-1. One need look no further than this figure to see that there is a very large disparity in the bandwidths used by the several schemes.

3.1 Subcarrier Modulation Schemes

Subcarriers were routinely used for telemetry channels. Not only did they facilitate separation of different data types, but also they served to separate the data's transmitted spectrum from the RF carrier. Spectral separation was particularly important in the early days of the space program when data rates were low and the data sidebands were frequently indistinguishable from the carrier.

CCSDS RF AND MODULATION STUDY COMPARISON OF MODULATION SCHEMES

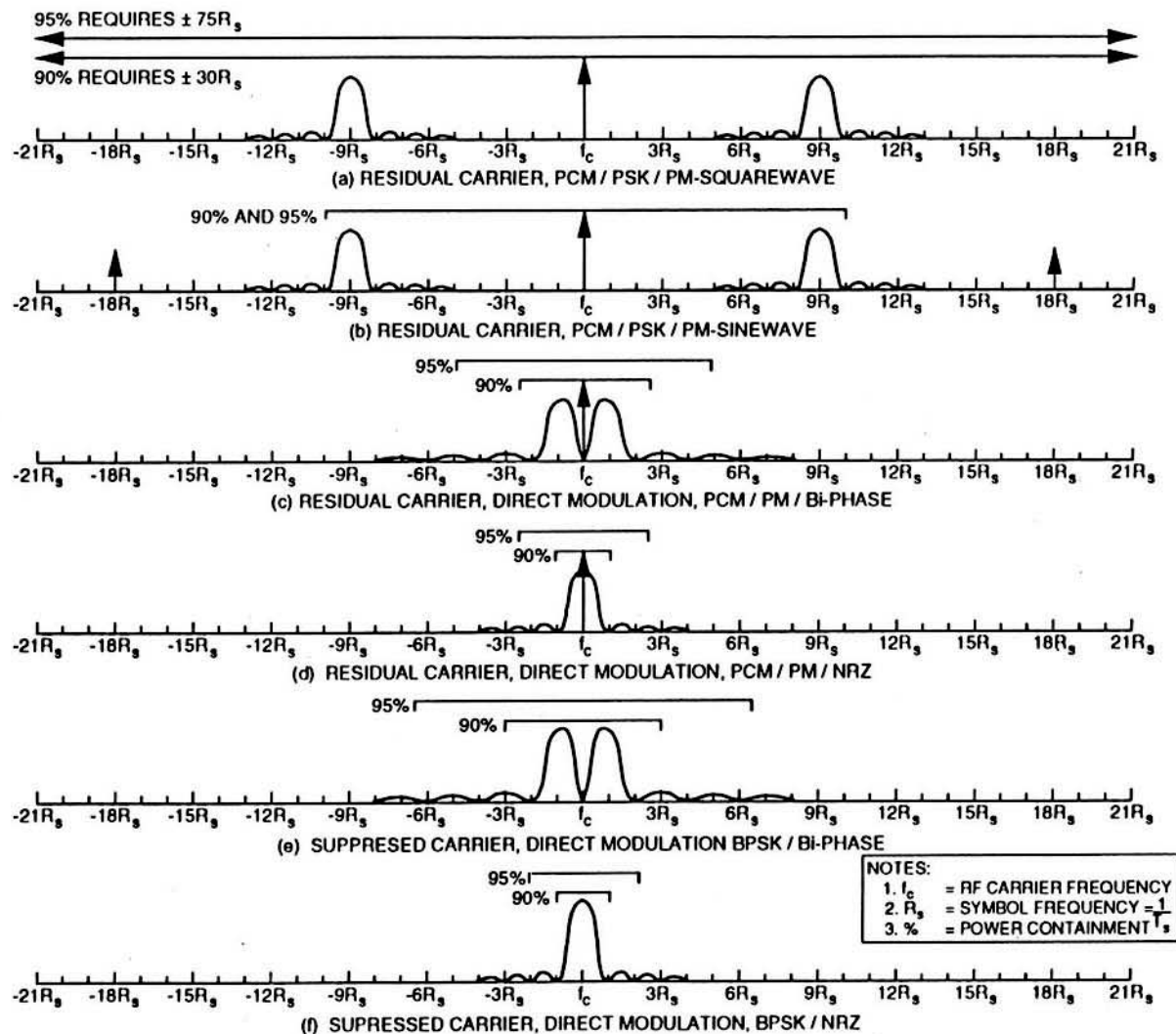


Figure 3-1. Spectra of Various Modulation Methods

CCSDS RF AND MODULATION STUDY

A COMPARISON OF MODULATION SCHEMES

In this analysis, both sinewave and squarewave subcarriers will be examined to determine their effect upon the *Required Bandwidth*.

3.1.1 Squarewave Subcarriers

CCSDS Recommendation 401 (2.4.5) B-1 states that Category B missions should employ squarewave subcarriers. Although requiring a larger bandwidth than sinewave subcarrier modulation schemes, use of squarewave subcarriers does provide slightly better performance at high modulation indices than do sinewave subcarrier systems. This is so because, if the receiver's bandwidth is sufficient, high order harmonics are recoverable whereas the high order Bessel functions, present with sinewave subcarriers at high modulation indices, are not. Figure 3-1 (a) shows the frequency spectrum of a system employing a single squarewave subcarrier. Limited space restricted the ability to show the full spectrum. Odd harmonics of the subcarrier's frequency, each with data sidebands, will be present with diminishing amplitude as the order increases.

Figure 3-2 shows the spectrum bandwidth needed for data systems employing squarewave subcarriers. All plots in this paper normalize the spectrum bandwidth to the data Symbol Rate¹, R_s (e.g., BW/R_s). Bandwidth is also dependent upon the ratio between the subcarrier's frequency and the symbol rate, as well as the RF carrier's modulation index. The reason for the former should be obvious while the latter is because, at lower modulation indices, a greater percentage of the transmitted power will be found in the carrier's comparatively narrow frequency band.

Three values for Subcarrier Frequency/Symbol Rate (n) corresponding to 3, 9, and 15 were evaluated. While these represent the minimum and maximum ratios generally used, some missions have been known to fly ratios as high as 1,000. A brief glance at Figure 3-2 will clearly show the effect of these high ratios on the *Required Bandwidth*.

For comparative purposes, the same reference points are used for evaluating both squarewave and sinewave subcarrier modulation methods (e.g., modulation index (m) = 1.2 radians and subcarrier frequency-to-symbol rate ratio (n) = 9). From Figure 3-2, it is clear that the *Required Bandwidth* is quite large for either 90% or 95% power efficiencies. Approximately $30 R_s$ and $75 R_s$ are required for the respective efficiencies. A summary of the results will be found in columns 2 and 3 of Table 3-2 at the end of this section.

As will be shown in 3.1.2, squarewave subcarriers consume substantially more bandwidth than do sinewave subcarriers. Although the modulation/demodulation losses are likely to be greater than for direct modulation schemes, most of the transmitted power is recoverable when using squarewave subcarriers, provided that the earth station receiver's bandwidth is sufficiently wide.

Squarewave subcarriers may still find application in some Category B missions where the data's symbol rate is low and significant data sideband power will fall into the RF carrier phase locked loop's bandwidth if a direct modulation scheme is used.

¹ Symbol Rate is equal to the data rate for uncoded transmissions and the encoded bit rate for coded transmissions.

CCSDS RF AND MODULATION STUDY COMPARISON OF MODULATION SCHEMES

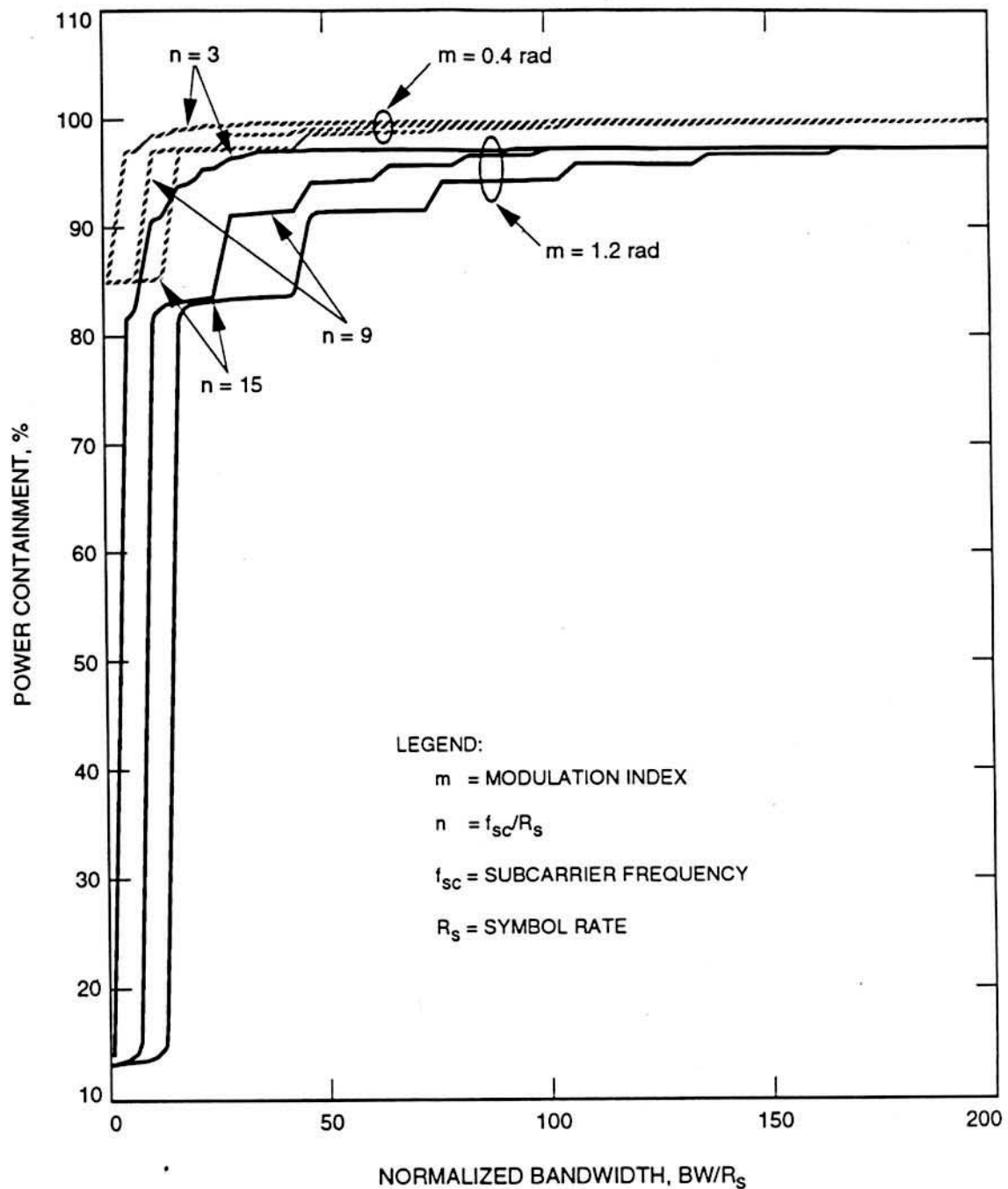


Figure 3-2. Bandwidth Needed for PCM/PSK/PM-Squarewave

CCSDS RF AND MODULATION STUDY

A COMPARISON OF MODULATION SCHEMES

3.1.2 Sinewave Subcarriers

CCSDS Recommendation 401 (2.4.5) B-1 states that Category A missions should employ sinewave subcarriers. Congestion in the 2 GHz band, combined with the comparatively strong signals from Category A spacecraft, constrain each user to the minimum amount of spectrum necessary for his communication. Sinewave subcarriers require less spectrum bandwidth than do squarewave subcarriers. Although sinewave subcarriers have greater losses, and therefore are less efficient than squarewave subcarriers at high RF modulation indices, the stronger signals from Category A missions largely offset this disadvantage.

Figure 3-1 (b) depicts the frequency spectrum of a system utilizing a single sinewave subcarrier. Unlike the squarewave subcarrier's frequency spectrum, a sinewave subcarrier will have energy at the even harmonics in the form of a Delta function. The Delta function's amplitude will depend upon the RF carrier's modulation index. It is this energy that is lost during the demodulation process and which accounts for the lower efficiency of sinewave subcarrier systems.

Figure 3-3 shows the spectrum bandwidth for data systems using sinewave subcarriers. As with the squarewave subcarrier plot, the figure normalizes bandwidth to the data Symbol Rate, R_s (e.g., BW/R_s) and utilizes a subcarrier frequency-to-symbol rate ratio of 9. Some missions have flown ratios as high as 1,000. A brief glance at Figure 3-3 will clearly show the effect of these high ratios on the *Required Bandwidth*.

For a mid-range value of $n = 9$ and a typical modulation index of 1.2 radians, the *Required Bandwidth* is about 10 times the Symbol Rate, R_s , for both the 90% and 95% Power Containments². Note that a bandwidth approximately 30 times the Symbol Rate is required if the ITU's *Occupied Bandwidth* computation is used. Results of these computations will be found in columns 2 and 3 of Table 3-2.

Although using less bandwidth than squarewave subcarriers, the use of sinewave subcarriers does introduce greater losses than other modulation methods because of the high order Bessel functions which become prominent at high modulation indices. Nevertheless, sinewave subcarriers may still find application in some Category A mission designs where the data's symbol rate is low and significant data sideband power will fall into the RF carrier phase locked loop's bandwidth.

² Power Containment is that percentage of the total modulated data's power contained in the indicated *Required Bandwidth* for each specific modulation index and subcarrier frequency-to-symbol rate ratio.

CCSDS RF AND MODULATION STUDY COMPARISON OF MODULATION SCHEMES

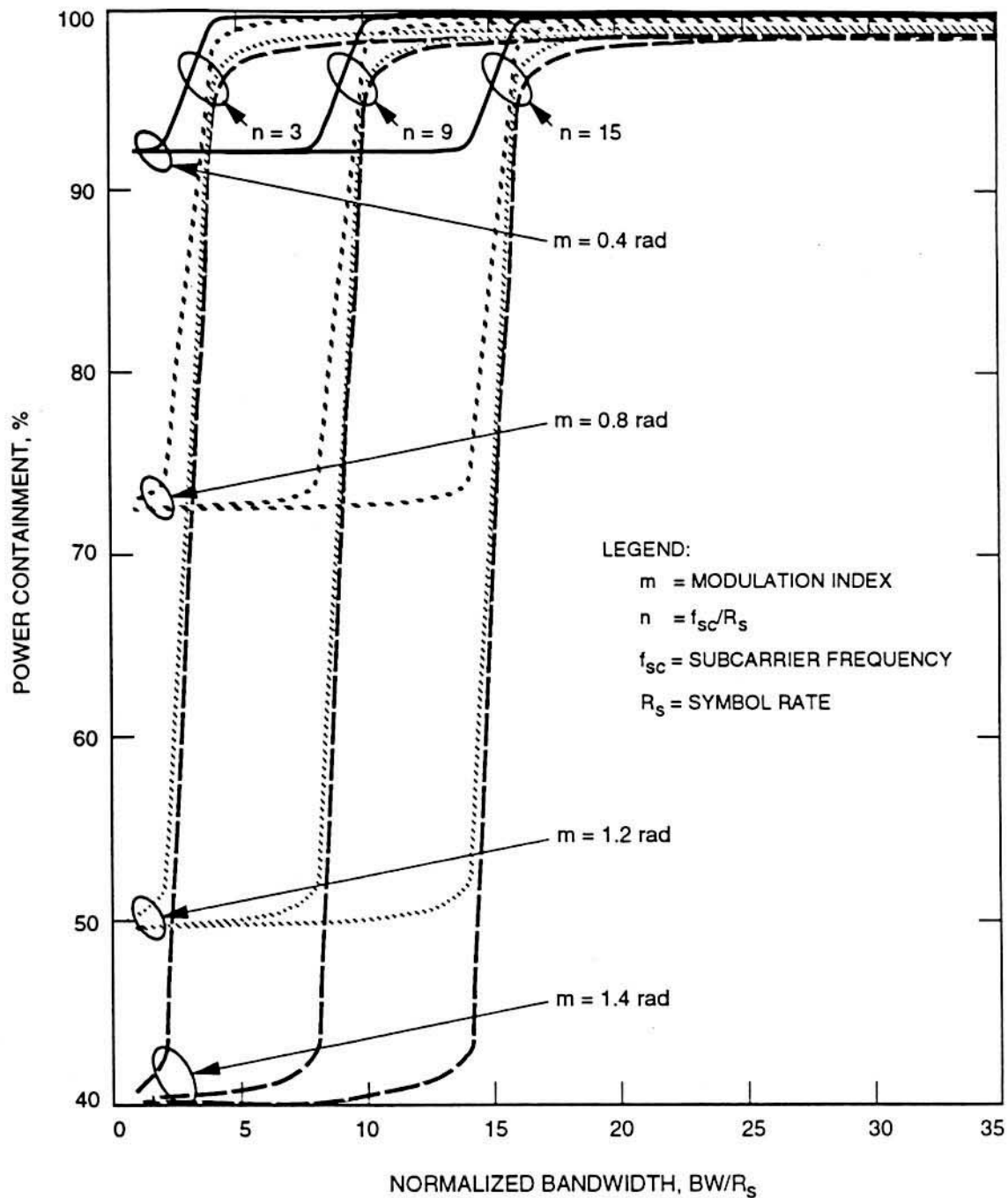


Figure 3-3. Bandwidth Needed for PCM/PSK/PM-Sinewave

CCSDS RF AND MODULATION STUDY

A COMPARISON OF MODULATION SCHEMES

3.2 Direct Modulation Schemes

As indicated in Table 3-1, several direct modulation schemes were considered. Historically, space agencies used residual carrier systems³. This provided a stable reference frequency at the earth station which was used to demodulate the data from the carrier. Alternative, suppressed carrier systems, will be considered following a discussion of traditional residual carrier systems. None of the modulation schemes considered in this section employ subcarriers.

Direct modulation schemes are inherently more bandwidth efficient than those employing subcarriers. This is due, in part, to the way that the ITU defined *Occupied Bandwidth* to be that span of frequencies, covered by the modulated signal, which excludes only the lower 0.5% and the upper 0.5% of the transmitted power. Thus, large frequency gaps between the RF carrier and the subcarrier are included in the *Occupied Bandwidth* calculation despite the fact that there is no significant modulation sideband energy in large portions of these frequency gaps.

3.2.1 Direct Modulation, Residual Carrier, Bi- ϕ

From a spectrum bandwidth perspective, direct modulation with a Bi- ϕ format is a compromise between direct modulation with an NRZ format and a conventional subcarrier telemetry system. It places the modulated data sidebands closer to the RF carrier while providing a null in the data's frequency spectrum at the RF carrier's frequency. Figure 3-1 (c) shows the PCM/PM/ Bi- ϕ spectrum which ensures that the carrier will be easily distinguishable from the surrounding data sidebands. The bandwidth advantage of direct modulation schemes is readily apparent in this figure.

Sometimes called Manchester modulation, a Bi- ϕ format is formed by the modulo-2 addition of each data symbol with a squarewave clock whose period is equal to that of a data symbol. In addition to moving the data's spectrum away from the RF carrier's frequency, Bi- ϕ modulation also ensures RF carrier phase transitions during each data symbol.

With random data, this modulation scheme produces a spectrum with a clearly discernable RF carrier component and a $[(\sin^4 x)/(x)^2]$ distribution with peaks at about $\pm 0.75 R_s$ (R_s = symbol frequency, f_s) due to the modulation. A null in the data's spectrum will lie at the RF carrier's frequency, f_c . Additional nulls, on either side of f_c will lie at $\pm 2 f_s$, $\pm 4 f_s$, $\pm 6 f_s$, etc. Figure 3-4 shows the spectrum bandwidth at various levels of power containment. For a modulation index, m , of 1.2 radians, *Required Bandwidths* of $2.5 R_s$ and $5 R_s$ are needed for 90% and 95% power containment respectively. A summary of the findings will be found in Table 3-2, columns 2 and 3.

Direct Bi- ϕ modulation is useful when bandwidth conservation is important and the modulated symbol rate is sufficient to ensure that the level of data sideband power, falling in the phase locked loop's bandwidth, is sufficiently low. This modulation scheme should find broad application in future missions having low or moderate data rates or where a stable carrier reference frequency is required.

³ Residual Carrier System is one in which the modulation index is less than ± 90 degrees so that a small percentage of the total transmitted power remains at the RF carrier frequency.

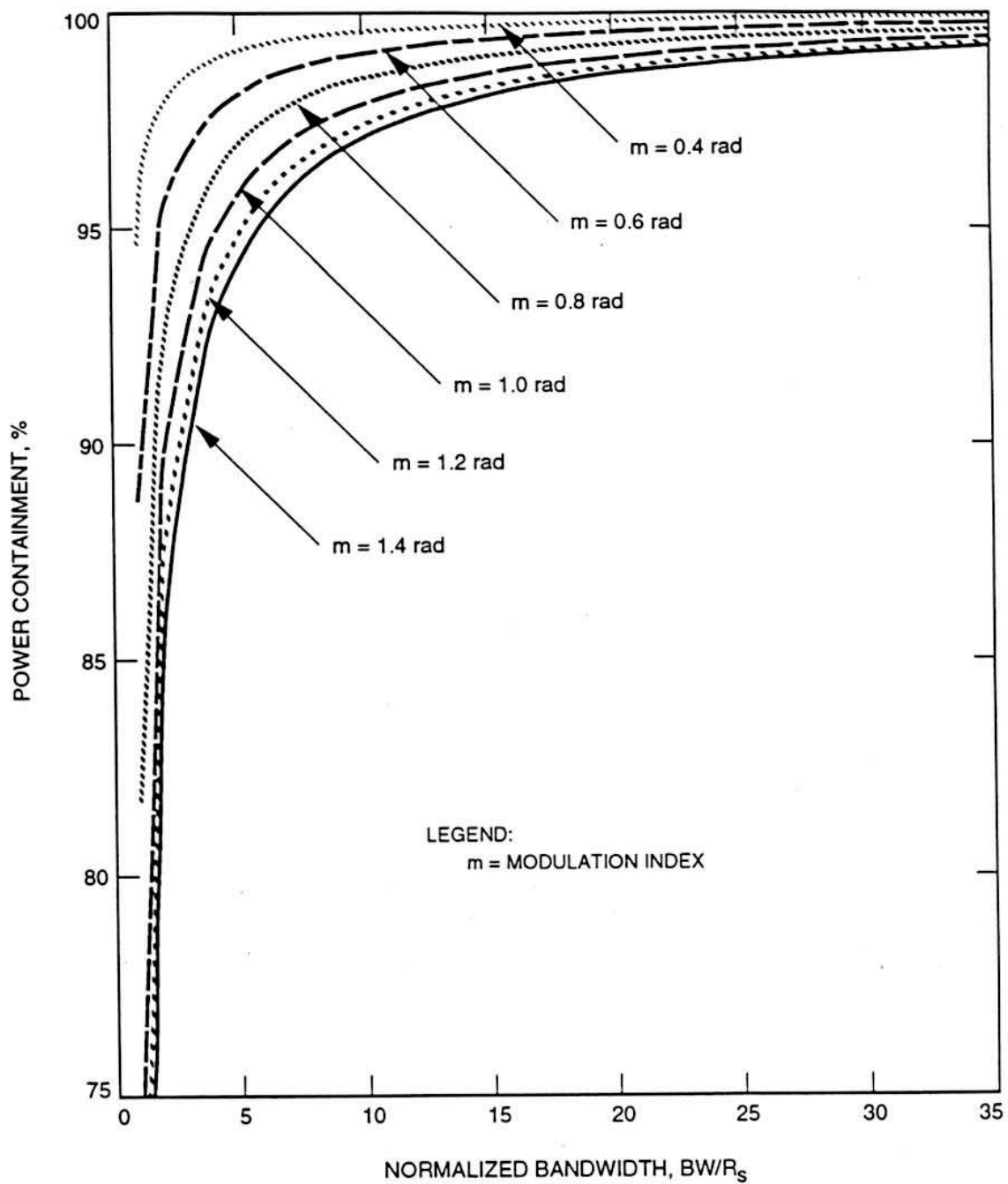
CCSDS RF AND MODULATION STUDY
COMPARISON OF MODULATION SCHEMES

Figure 3-4. Bandwidth Needed for PCM/PM/Bi-Phase

CCSDS RF AND MODULATION STUDY

A COMPARISON OF MODULATION SCHEMES

3.2.2 Direct Modulation, Residual Carrier, NRZ

Direct NRZ differs from Direct Bi- ϕ modulation in that the double frequency clock component is absent in the former modulation type. Here, the modulated telemetry data's frequency spectrum is discernably narrower than the one for Bi- ϕ modulation. The RF frequency spectrum for this modulation type will be found in Figure 3-2 (d). For random telemetry data, the power spectrum is described by $[(\sin x/x)^2]$. The peak of the spectrum occurs at the RF carrier's frequency, f_c , and the nulls are at $f_c \pm 1 f_s, \pm 2 f_s, \pm 3 f_s$, etc.

Clearly, the advantage of direct NRZ modulation is the substantially reduced bandwidth needed for communications as compared to the modulation types discussed above. Figure 3-5 shows the spectrum bandwidth for several levels of power containment. This is the most bandwidth efficient modulation method considered so far. Table 3-2, columns 2 and 3 list the *Required Bandwidths* for 90% and 95% power containments respectively.

PCM/PM/NRZ modulation suffers the disadvantage of placing the peak of the data's frequency spectrum at the RF residual carrier's frequency. Unless the data symbol rate is comparatively high, so as to spread the data sideband's power over a relatively broad frequency range, the RF carrier may be difficult to detect. Additionally, the presence of data power within the earth station's phase locked loop's bandwidth can introduce RF carrier interference with the result that the loop's phase jitter is increased.

PCM/PM/NRZ also suffers a second disadvantage. Data streams containing significant imbalances in 1s and 0s (imbalance in Mark-to-Space ratio) can adversely affect the performance of a PCM/PM/NRZ system (Reference 5). Figure 3-6 shows the effect upon Signal-to-Noise Ratio (SNR) in the residual carrier's Phase-Locked-Loop resulting from an imbalanced data stream. Here, a $p = 0.5$ means that a 1 (Mark) or a 0 (Space) are equally likely. System performance was evaluated at an RF modulation index of 1.25 radians and a Phase-Locked-Loop Bandwidth/Telemetry Symbol Frequency Span ratio of 0.001. A Phase-Locked-Loop SNR of 23 dB for balanced data (e.g., $p = 0.5$), will be degraded by more than 15 dB when the probability of a Mark (or a Space) is reduced from 0.5 to 0.4.

At high modulation indices, little power is left in the residual carrier. Imbalances in the Mark-to-Space ratio of the modulated NRZ data produce a component at the RF carrier's frequency which has a randomly varying phase with respect to that RF carrier. This "*dc-component*" results in interference to the residual RF carrier which has the effect of lowering the SNR in the carrier tracking loop, particularly as the imbalance increases and the "*dc-component*" becomes significant with respect to the carrier component's amplitude. As the carrier Phase-Locked-Loop's phase jitter increases, data demodulation efficiency drops. This "Radio Loss" or "Phase Jitter" loss must be assessed to accurately predict the telecommunications channel's performance. Demodulation efficiency resulted in the CCSDS Recommending a minimum carrier tracking loop SNR of 15 dB at high modulation indices.

The resulting degradation to the telemetry data channel's performance for large Mark-to-Space ratio imbalances in a PCM/PM/NRZ system is clearly evident in Figure 3-7. This figure shows the effect upon Symbol Error Rate (SER) and Symbol Signal-to-Noise Ratio (SNR) as the Probability of a Mark is reduced. Modulation indices and bandwidth ratios are identical to those used for the analysis of the carrier tracking loop above.

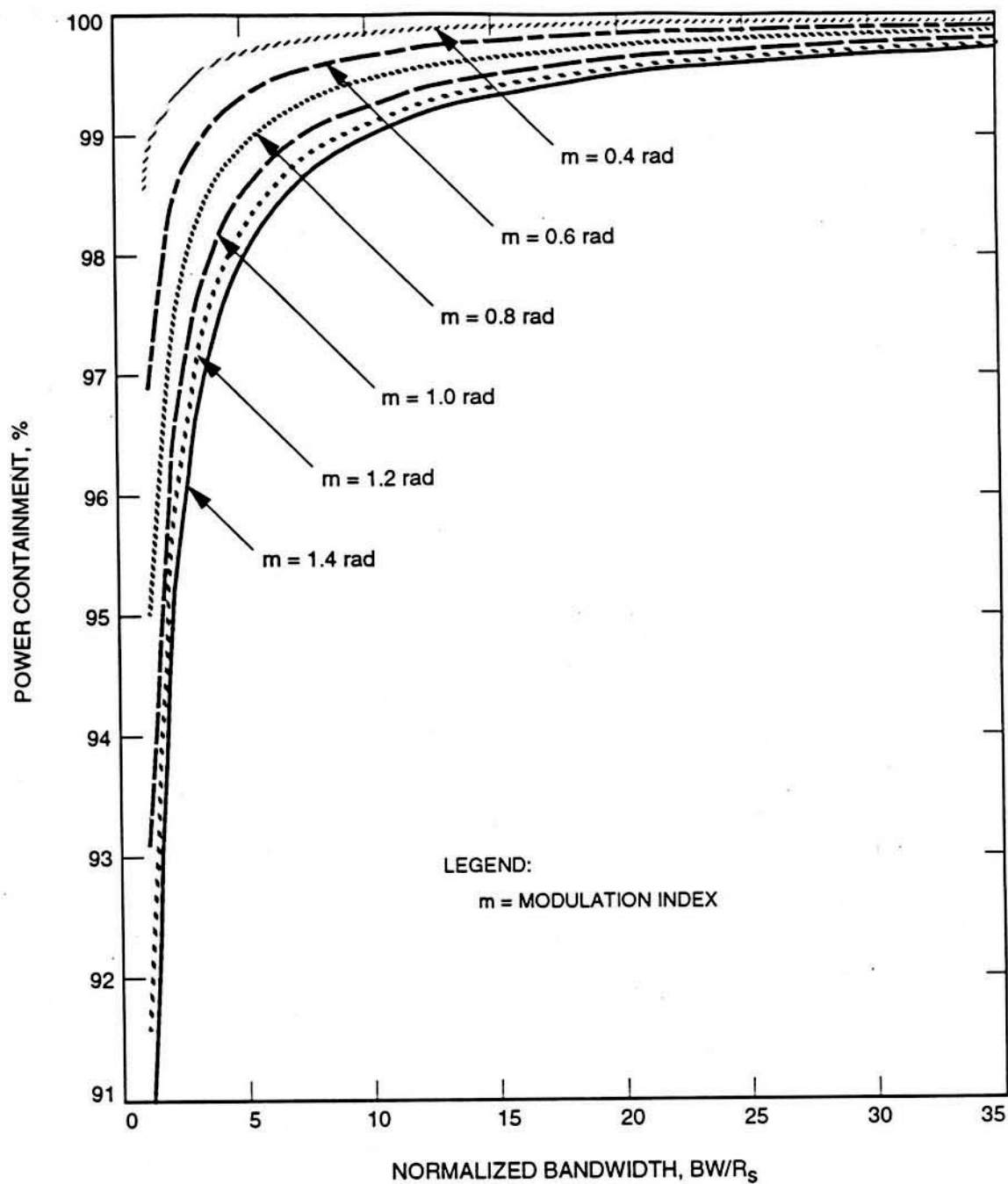
**CCSDS RF AND MODULATION STUDY
COMPARISON OF MODULATION SCHEMES**

Figure 3-5. Bandwidth Needed for PCM/PM/NRZ

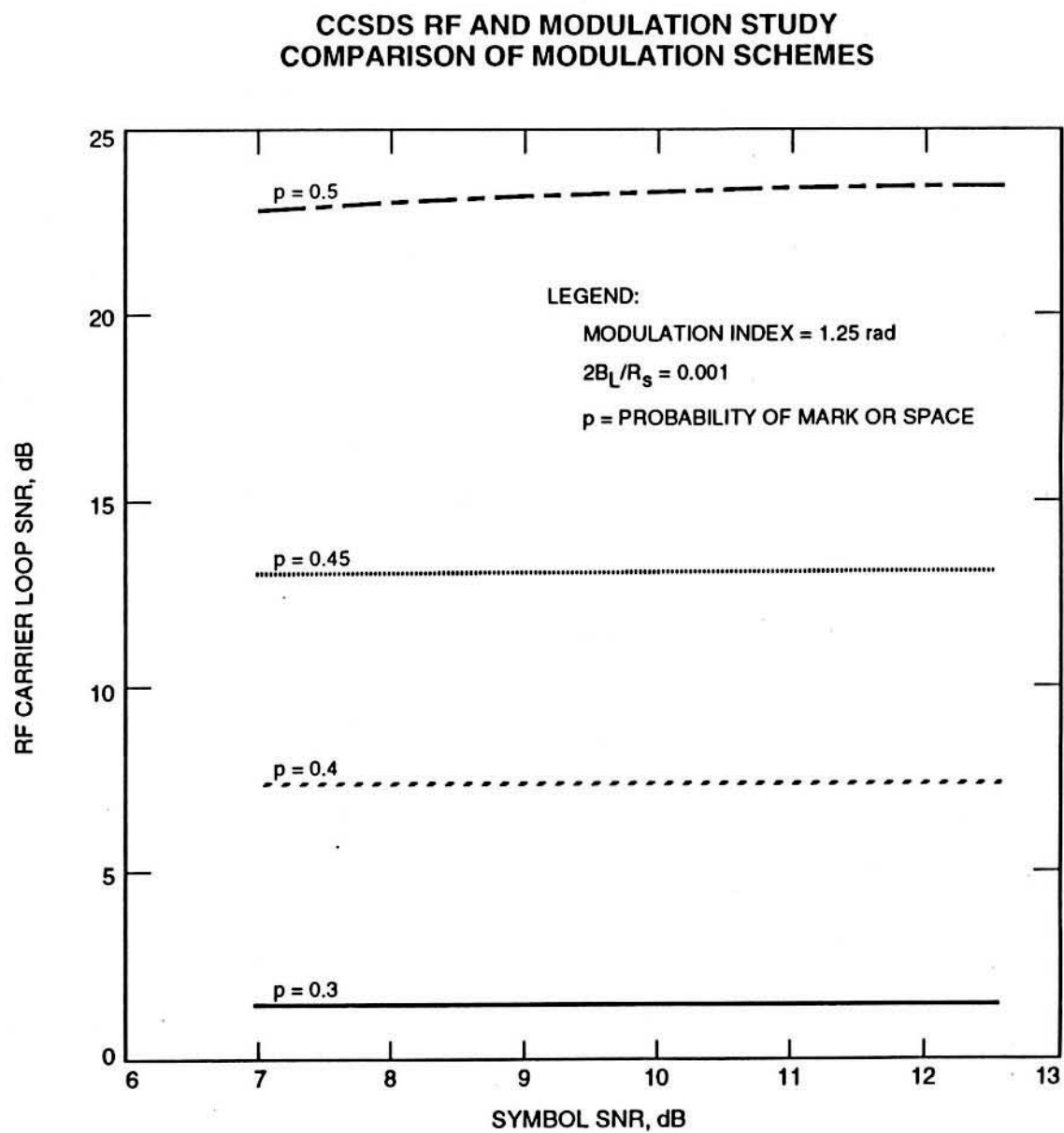


Figure 3-6. Effect of Unbalanced Data on RF Carrier Loop SNR for PCM/PM/NRZ Modulation

CCSDS RF AND MODULATION STUDY COMPARISON OF MODULATION SCHEMES

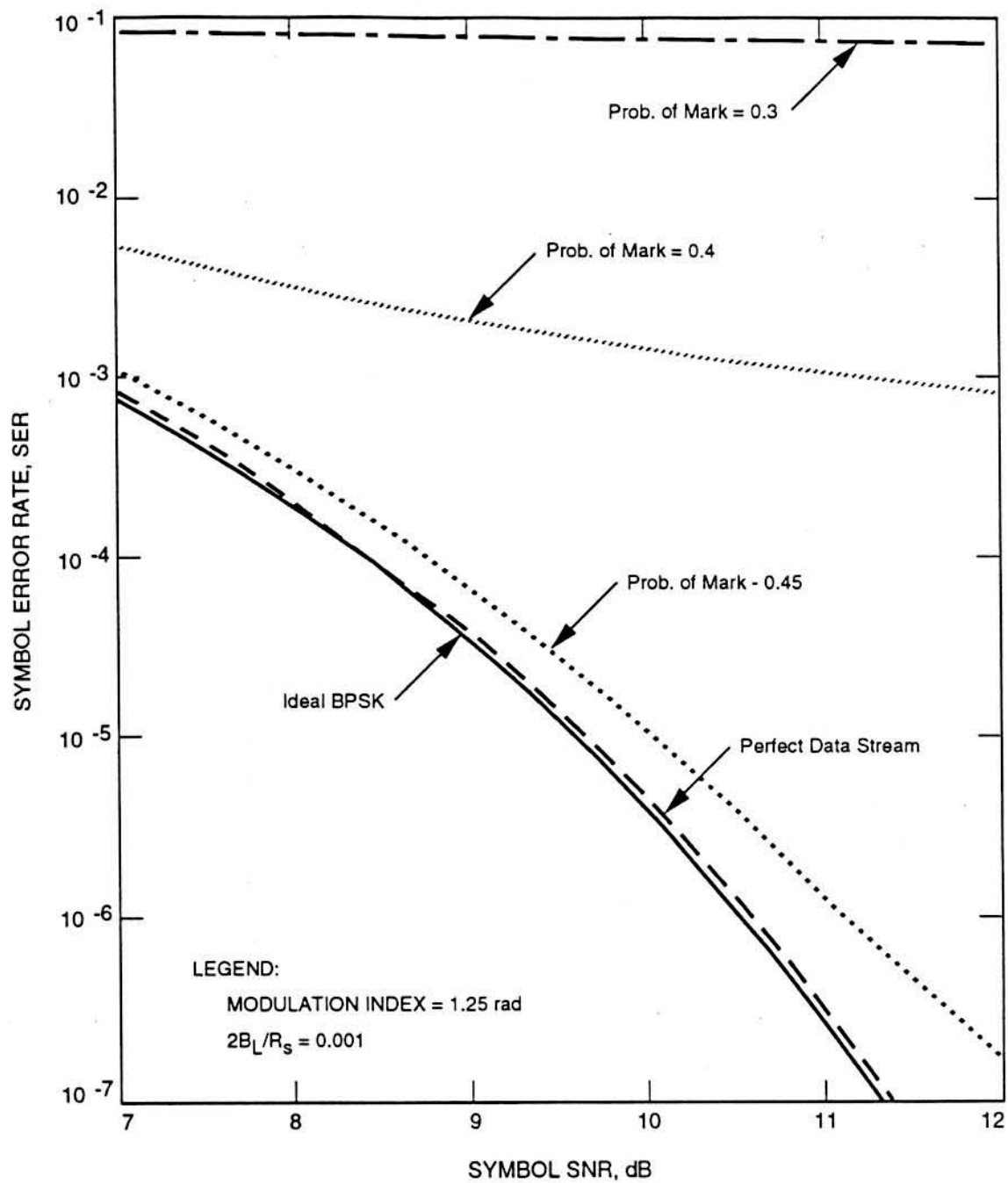


Figure 3-7. Effect of Unbalanced Data on Telemetry Symbol Error Rate for PCM/PM/NRZ Modulation

CCSDS RF AND MODULATION STUDY

A COMPARISON OF MODULATION SCHEMES

With a probability of Mark-to-Space = 0.45 the telemetry data system experiences a loss of about 0.3 dB when compared to a perfect data stream. But, a Mark-to-Space = 0.4 produces a several dB loss. Additionally, the Symbol Error Rate becomes substantially invariant with Symbol SNR.

Figure 3-8 shows that a PCM/PM/NRZ system's performance is particularly sensitive to modulation index. Specifically, Mark-to-Space ratio imbalances result in significantly greater system losses at high modulation indices than at low ones. This result follows from the fact that, at low modulation indices, significantly more power is retained in the residual RF carrier so that the SNR degradation, resulting from the "dc-component" produced by imbalanced data, is lower. Therefore, if the Mark-to-Space ratio falls to 0.4, then modulation indices should be kept at or below 1 radian.

This sensitivity of PCM/PM/NRZ modulation to data imbalances means that it should be used with extreme care to ensure that the system is operating in a region where the losses due to telemetry data imbalances are acceptable. Convolutional coding will help to restore a balance between 1s and 0s, but if such coding is inadequate, due to the nature of the raw telemetry data, then a data randomizer, such as the one recommended by the CCSDS, or some other means to reduce the effects of data imbalances should be employed (Reference 6).

Direct NRZ modulation should find application to residual carrier systems where minimum bandwidth utilization is important, when the data rates are moderate to high, and when there is a good balance between 1s and 0s in the modulated telemetry data stream. When using this modulation type, care must be exercised to ensure that the carrier is sufficiently distinguishable for RF carrier acquisition at the earth station's receiver. Some earth stations may prefer that the telemetry modulation be turned off during the acquisition process. Other earth stations, using a spectrum analyzer in their receiver acquisition system, may experience no difficulty in acquiring the RF carrier with telemetry modulation turned on.

One of NASA's International Solar Terrestrial Physics (ISTP) program's spacecraft named Polar uses this modulation scheme. Polar is an earth orbiter, has a residual carrier, and a data rate of 500 kb/s. A rate $\frac{1}{2}$, constraint length 7 convolutional code concatenated with a Reed-Solomon code increases the symbol rate to slightly above 1 Ms/s. This spacecraft will be launched in mid 1994.

CCSDS RF AND MODULATION STUDY COMPARISON OF MODULATION SCHEMES

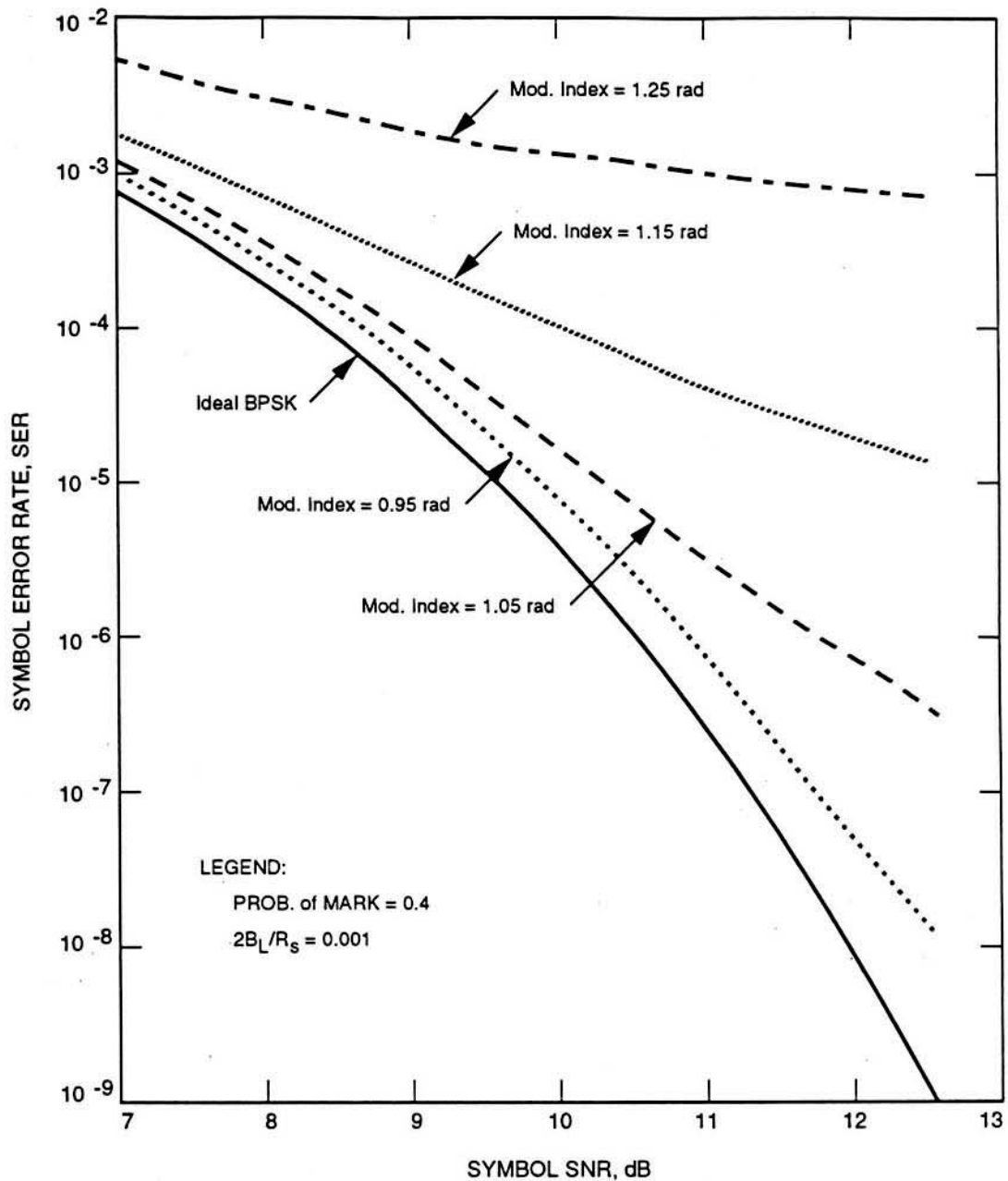


Figure 3-8. Effect of Modulation Index on Symbol Error Rate with Unbalanced Data for PCM/PM/NRZ Modulation

CCSDS RF AND MODULATION STUDY

A COMPARISON OF MODULATION SCHEMES

3.2.3 Suppressed Carrier, Bi-Phase Shift Keyed (BPSK/Bi- ϕ)

BPSK/Bi- ϕ modulation fully suppresses the RF carrier by modulo-2 adding the telemetry data to a squarewave clock at twice the telemetry symbol's frequency and modulating the RF carrier with and index of ± 90 degrees. In this regard, the system is similar to the one described in section 3.2.1 above. Like that modulation scheme, the data's spectrum will follow a $[(\sin^2 x)/(x)^2]$ distribution with peaks at $\pm 2 f_s$, $\pm 4 f_s$, $\pm 6 f_s$, etc. and a null at the carrier's frequency. However, unlike direct residual carrier Bi- ϕ modulation, there will be no residual RF carrier component. The BPSK/Bi- ϕ spectrum is shown in Figure 3-2 (e).

A carrier component is reestablished within the earth station receiver's Costas or Squaring Loop. The result is that all of the transmitted power is placed in the data's sidebands. Since the RF carrier is reconstructed from the data sidebands, virtually all of the transmitted power is available for this purpose as well.

Costas Loops regenerate the RF carrier by combining signals detected in a reference and a quadrature channel. Noise, as well as signal is present in both channels and both are combined. As a consequence, it is important to have a sufficient Signal-to-Noise Ratio (SNR) in the loop. A minimum SNR of 12 - 15 dB is recommended for such loops.

Figure 3-9 shows the spectrum bandwidth as a function of power containment. Note that the *Required Bandwidth* is slightly greater for this modulation type than for the residual carrier PCM/PM/Bi- ϕ owing to the lack of RF carrier. This slightly larger *Required Bandwidth* appears in Table 3-2.

BPSK/Bi- ϕ modulation will find application in high data rate systems where conservation of bandwidth is important and where maximum system performance is required. Some comparatively low rate missions (Galileo-S-Band, Pluto Flyby, and MESUR) are considering the use of BPSK modulation.

3.2.4 Direct Modulation, Suppressed Carrier, NRZ (BPSK/NRZ)

Like direct residual carrier modulation, BPSK/NRZ differs from BPSK/Bi- ϕ in that the double frequency clock component is absent in the former modulation type. In all other respects, BPSK/NRZ is the same as BPSK/Bi- ϕ discussed above. The modulated signal's frequency spectrum is shown in Figure 3-2 (f). It reflects the bandwidth conserving nature of NRZ modulation. Figure 3-9 demonstrates the bandwidth efficiency of BPSK/NRZ modulation as compared with BPSK/Bi- ϕ modulation.

Given the sensitivity of a PCM/PM/NRZ system's performance to imbalances between 1s and 0s in the data stream, a question arises as to whether BPSK/NRZ systems have the same problem. Studies are underway to analyze and simulate the performance of these systems in the presence of imbalanced data.

BPSK/NRZ modulation will find application in moderate to high data rate telemetry data systems where bandwidth conservation is of importance, where there is a possibility that the modulated data symbols may contain an imbalance between 1s and 0s, and where the complexities of QPSK and N-PSK modulation methods are to be avoided.

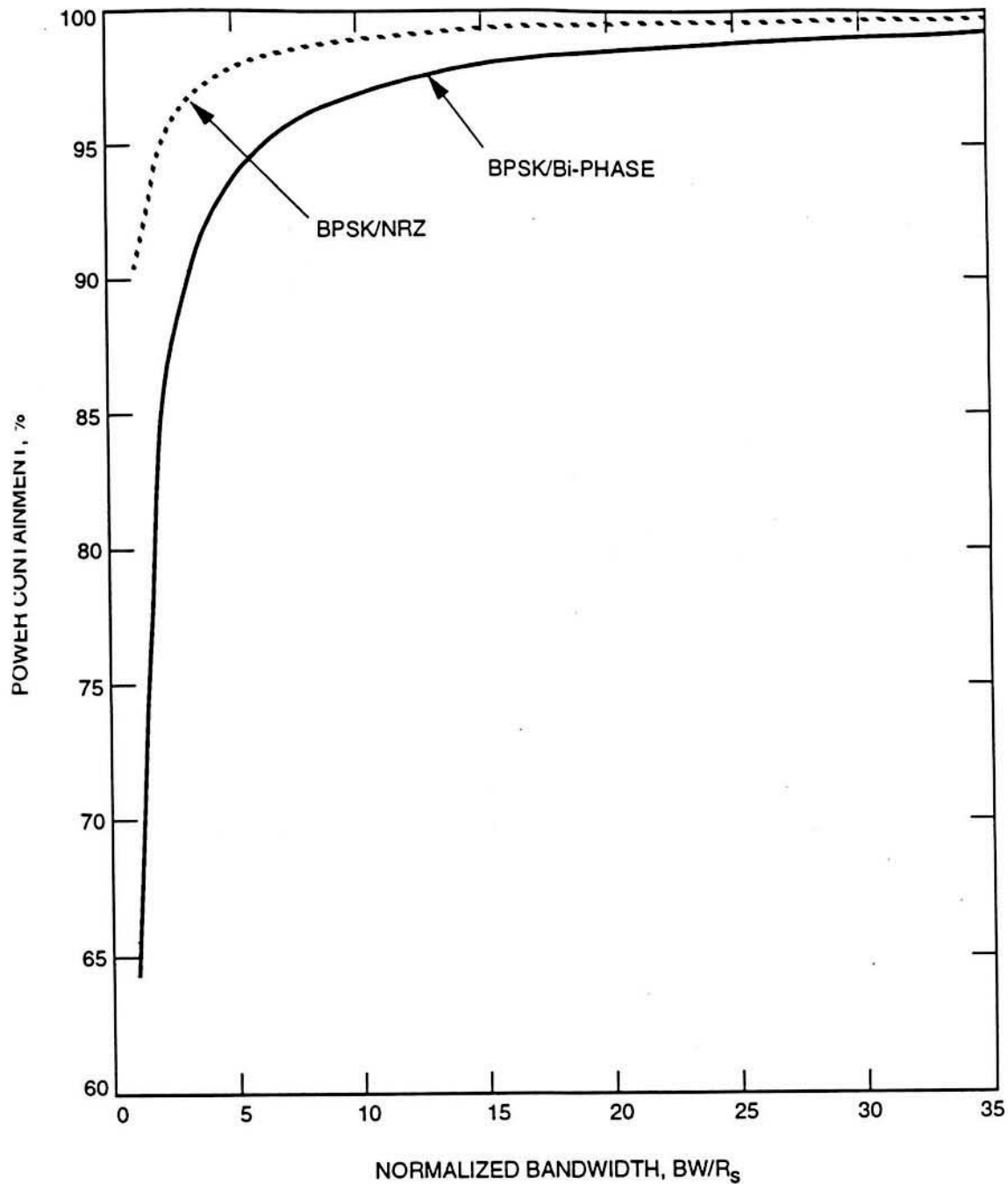
**CCSDS RF AND MODULATION STUDY
COMPARISON OF MODULATION SCHEMES**

Figure 3-9. Bandwidth Needed for BPSK Signals

CCSDS - SFCG STUDY COMPARISON OF MODULATION SCHEMES

TABLE 3-2: PERFORMANCE SUMMARIES OF MODULATION SCHEMES

Modulation Type	90% Power Containment	95% Power Containment	ISI SNR Reduction dB	ISI SNR Reduction dB	ISI SNR Reduction dB	In-Band Interference Susceptibility
PCM/PSK/PM (Sq) $n = 9, m = 1.2 \text{ rad.}$	$\pm 30 R_s$	$\pm 75 R_s$	0.75 @ $\pm 10 R_s$	0.15 @ $\pm 20 R_s$	0.01 dB @ $\pm 50 R_s$	Less susceptible than PCM/PSK/PM sine by about 4 dB. Susceptible to Out-of-Band interference.
PCM/PSK/PM (Sine) $n = 9, m = 1.2 \text{ rad.}$	$\pm 10 R_s$	$\pm 10 R_s$	0.75 @ $\pm 10 R_s$	0.18 @ $\pm 20 R_s$	0.04 dB @ $\pm 50 R_s$	More susceptible than PCM/PSK/PM square.
PCM/PM/Bi- ϕ $m = 1.2 \text{ rad.}$	$\pm 2.5 R_s$	$\pm 5 R_s$	6.3 @ $\pm 1 R_s$	0.34 @ $\pm 2 R_s$	0.20 dB @ $\pm 5 R_s$	No information available.
PCM/PM/NRZ $m = 1.2 \text{ rad.}$	$\pm 1.2 R_s$	$\pm 2.5 R_s$	0.85 @ $\pm 1 R_s$	0.21 @ $\pm 2 R_s$	0.01 dB @ $\pm 5 R_s$	No information available.
BPSK/Bi- ϕ $m = \pm 90 \text{ deg.}$	$\pm 3 R_s$	$\pm 6.5 R_s$	6.3 @ $\pm 1 R_s$	0.29 @ $\pm 2 R_s$	0.15 dB @ $\pm 5 R_s$	Less susceptible than QPSK. No information available comparing to modulation types listed above.
BPSK/NRZ $m = \pm 90 \text{ deg.}$	$\pm 1 R_s$	$\pm 2 R_s$	0.74 @ $\pm 1 R_s$	0.17 @ $\pm 2 R_s$	0.04 dB @ $\pm 5 R_s$	Likely to be more sensitive than BPSK/Bi- ϕ . No information available as to other modulation types.

CCSDS - SFCG STUDY COMPARISON OF MODULATION SCHEMES

4.0 EFFECT OF SPECTRUM SHAPING

Spectrum shaping of the radiated signal is implicit in the notion of *Required Bandwidth*. Depending upon the flight radio system's architecture, the suggested concept may introduce a small loss in transmitted power in order to obtain a significant saving in bandwidth. Spectrum shaping should be accomplished so as to minimize the size, weight, and power losses due to any additional components. Options for spectrum shaping were shown in Figure 2-1.

If bandwidth restriction becomes excessive, whether at the transmitter or receiver, additional losses can be introduced. When the bandwidth is restricted to less than the main lobe of the transmitted data's frequency spectrum, then the shape of the transmitted pulse is changed. Symbols are elongated with the result that one symbol will begin to overlay the following symbol (Reference 1). Termed Intersymbol Interference (ISI), the effect is a loss in symbol energy resulting in a reduced telemetry SNR.

ISI was evaluated for three bandwidths equivalent to $\pm 1 R_s$, $\pm 2 R_s$, and $\pm 5 R_s$ (Reference 1). The results will be found in columns 4, 5, and 6 of Table 3-2. Since all spectrum shaping was assumed to be at the spacecraft, actual bandwidth, sufficient to handle one, two, or five times the main spectral lobe(s) were used. Transmitter bandwidths are listed below the losses in the ISI columns of Table 3-2. These filter bandwidths also provide an easy method for comparing the *Required Bandwidths* of the several modulation methods.

5.0 SUSCEPTIBILITY TO INTERFERENCE

Reference 3 reviewed the literature to determine whether any comparative studies of susceptibility to interference could be found. Very little information was discovered. The data that was found tended to compare the susceptibility of similar systems rather than different modulation schemes. Results are summarized in column 7 of Table 3-2. For example, data was found comparing squarewave and sinewave subcarrier systems. Another study measured the relative performance of BPSK and QPSK systems. None were located which contrasted subcarrier and direct modulation methods.

Despite this lack of information, some simple observations can be made. Generally, the larger the frequency spectrum's width, the less the susceptibility to in-band interference. This results from the logical assumption that individual interference bursts tend to be concentrated in narrow frequency ranges. Therefore, the larger the width of the transmitted data's frequency spectrum, the less susceptible it is to interference in a portion of that band.

This "rule" is one reason why squarewave subcarriers have a distinct advantage over some of the other modulation techniques. Of course, other methods such as high rate convolutional coding and spread spectrum modulation can be used to achieve the same result with any of the direct modulation methods. However, the important point is that restricting the frequency spectrum's width increases the susceptibility to in-band interference.

CCSDS - SFCG STUDY COMPARISON OF MODULATION SCHEMES

6.0 CONCLUSIONS AND RECOMMENDATIONS

Because of the difficulties with the ITU definitions for *Occupied Bandwidth* and *Necessary Bandwidth*, it is recommended that both the CCSDS and SFCG adopt a new definition for *Required Bandwidth* based upon the proposal in Section 2.3. Because spectrum shaping is intrinsic in the concept of *Required Bandwidth*, the definition should specify the percentage of power containment (acceptable loss). A suggested level of 95% (-0.2 dB) is recommended for *Required Bandwidth*.

With regard to modulation schemes, it is recommended that subcarriers should be eliminated from flight systems except in those unusual cases where they are required for some valid technical reason. The excessive amount of bandwidth required by subcarrier modulation systems is graphically summarized in Figure 6-1. Instead, one of the direct modulation schemes described above, together with CCSDS recommended Virtual Channels (Reference 4) should be used to separate the data streams. The CCSDS and SFCG should immediately consider limiting the use of subcarrier modulation schemes, except in specified circumstances.

Where bandwidth conservation is important, and particularly in high data rate systems, special consideration should be given to PCM/PM/NRZ and BPSK/NRZ formats⁴. *Required Bandwidths* for the several direct, residual carrier, modulation schemes are shown in Figure 6-2. If spectral spreading is needed to meet PFD limitations, then consideration should be given to reducing the transmitter's power and using convolutional encoding to compensate for the diminished power and to spread the spectrum.

After the study of all candidate modulation schemes are completed (including QPSK, OQPSK, and MSK), both the CCSDS and SFCG should coordinate and consider adopting Recommendations favoring specific direct modulation methods. It is likely that the recommended types of modulation will be a function of mission design and data rate.

⁴ Provided that there is a good balance in the modulated data stream's 1s and 0s (Mark-to-Space ratio).

CCSDS RF AND MODULATION STUDY COMPARISON OF MODULATION SCHEMES

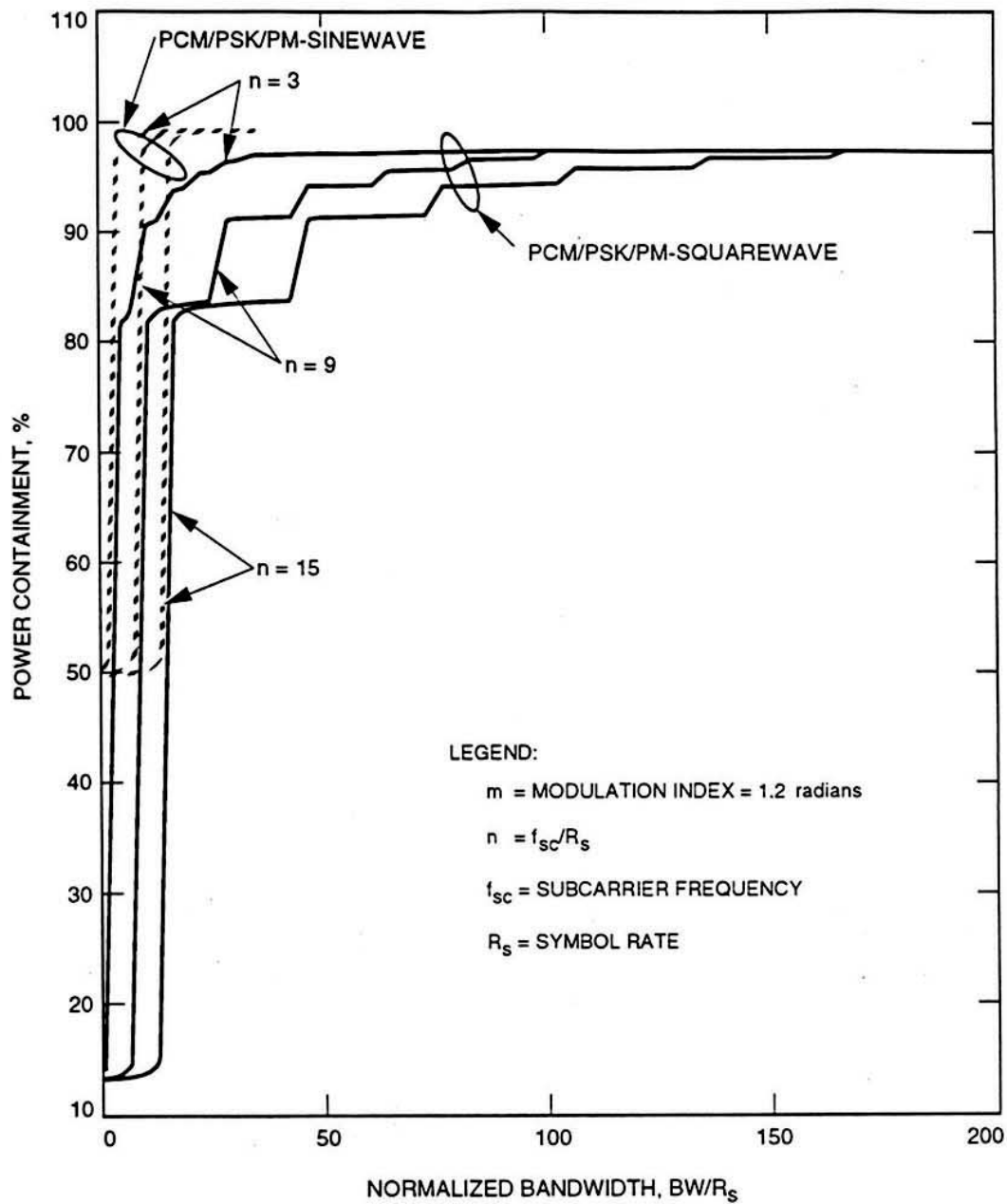


Figure 6-1. Comparison of PCM/PSK/PM Modulation Types

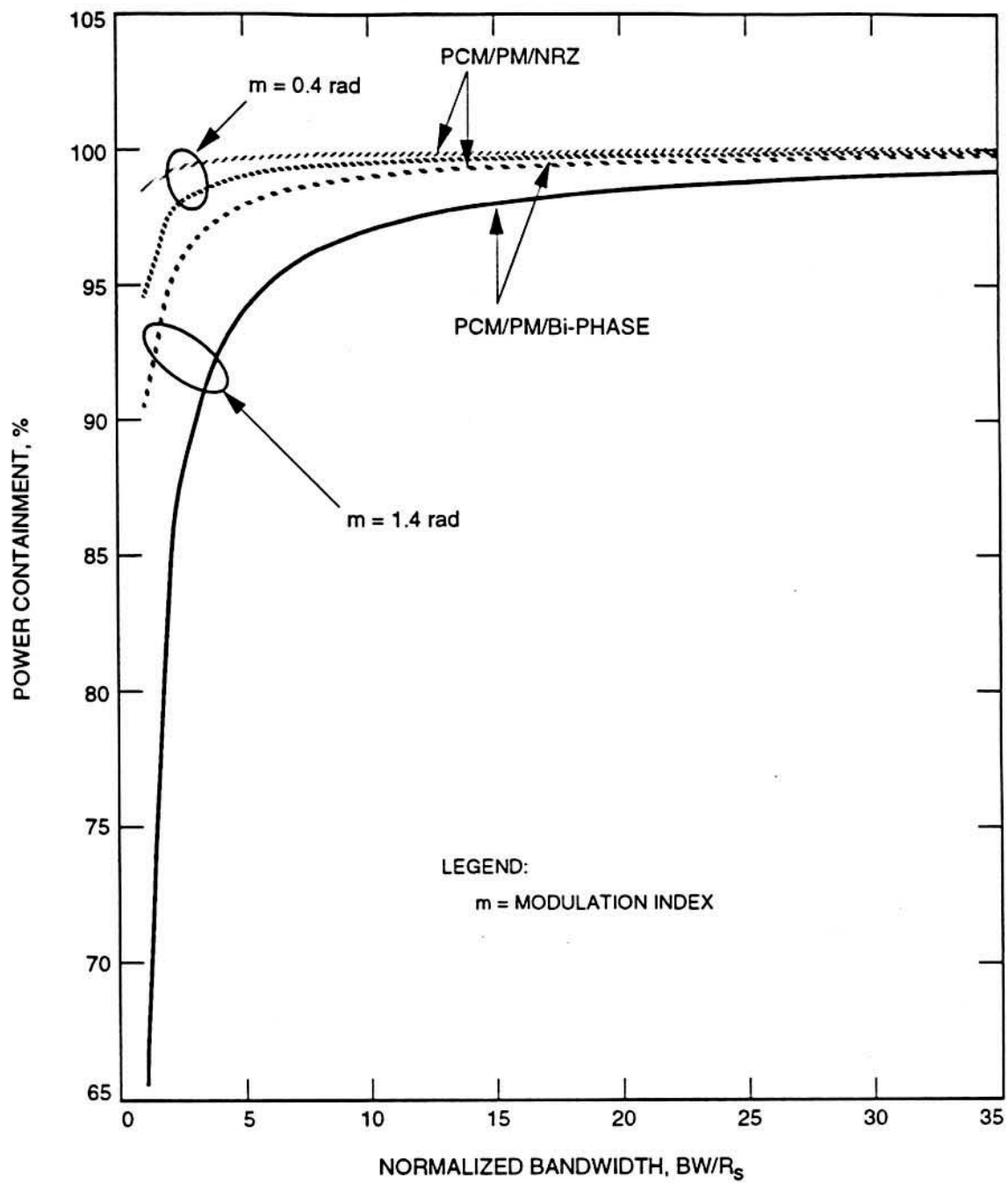
**CCSDS RF AND MODULATION STUDY
COMPARISON OF MODULATION SCHEMES**

Figure 6-2. Comparison of PCM/PM Modulation Types

**CCSDS - SFCG STUDY
COMPARISON OF MODULATION SCHEMES**

REFERENCES

1. *Required Bandwidths and Unwanted Emissions for Residual and Suppressed Carrier Systems*, Tien M. Nguyen, Jet Propulsion Laboratory, September 1993.
2. *Crosstalks in QPSK Communications Systems*, Tien M. Nguyen, Jet Propulsion Laboratory, September 1993.
3. *A Review of the Current Available Studies for the Interference Susceptibility of Various Modulation Schemes*, Tien M. Nguyen, Jet Propulsion Laboratory, September 1993.
4. Consultative Committee for Space Data Systems, Recommendations for Space Data System Standards, *Packet Telemetry*, CCSDS 102.0-B-2, January 1987.
5. *Behavior of PCM/PM Receivers in Non-Ideal Channels; Part 1: Separate Effects of Imperfect Data Streams and Bandlimiting Channels on Performance*, Tien M. Nguyen, Jet Propulsion Laboratory, September 1993.
6. *Unbalanced Data Compensation Techniques for PCM/PM Receivers*, Tien M. Nguyen and Sami M. Hinedi, Jet Propulsion Laboratory, February 1993.

[This page intentionally left blank.]

**SFCG Meeting
Rothenburg, Germany
14-23 September 1994**

CCSDS - SFCG EFFICIENT MODULATION METHODS STUDY

A COMPARISON OF MODULATION SCHEMES

PHASE 2: SPECTRUM SHAPING

(Response to SFCG Action Item 12/32)

**Warren L. Martin
Tien M. Nguyen**

Members, CCSDS Subpanel 1E, (RF and Modulation)

August 1994

CCSDS - SFCG EFFICIENT MODULATION METHODS STUDY
Phase 2: Spectrum Shaping

ACKNOWLEDGMENTS

The authors wish to thank Dr. Sami Hinedi of the Communications Research Section at the Jet Propulsion Laboratory for his invaluable council, suggestions, and discussion of the concepts presented in this paper and for his careful review of the simulation process. Additionally, the authors are in debt to Aseel Anabtawi and Loc Lam for their dedicated effort in preparing the many spectrum plots contained in the following pages and which are the basis for the conclusions reached in this phase of the CCSDS-SFCG Efficient Modulation Methods Study.

The authors convey their special gratitude to Tony Sedor and the other personnel in the Telecommunications and Mission Operations Graphic Arts Department for their heroic efforts in producing all of the drawings, spectra, and other plots contained in this report. Without the dedicated efforts of all of these people this study could not have been completed.

CCSDS - SFCG EFFICIENT MODULATION METHODS STUDY
Phase 2: Spectrum Shaping

TABLE OF CONTENTS

1.0	INTRODUCTION	1
2.0	OPTIMIZING BANDWIDTH EFFICIENCY	3
2.1	RF Spectrum Management	3
2.1.1	Modulation Schemes	3
2.1.2	Spectrum Shaping	3
2.2	Evaluation of Alternative Systems	4
2.2.1	Simulator Problems	7
2.2.2	Simulation Conditions	7
2.3	Selection of Filter Locations	8
2.4	Optimum Filter Types	10
2.5	Simulation Tests	10
3.0	SIMULATION RESULTS	13
3.1	Reference Data	13
3.2	Filtered Data	15
3.2.1	Butterworth Filter, 5 th Order	15
3.2.2	Bessel Filter, 3 rd Order	20
3.2.3	Raised Cosine Filters	20
3.2.3.1	Raised Cosine Filter ($\alpha = 0.25$), NRZ-L	25
3.2.3.2	Raised Cosine Filter ($\alpha = 0.5$), NRZ-L	25
3.2.3.3	Raised Cosine Filter ($\alpha = 1$), NRZ-L	25
3.2.3.4	Square Root Raised Cosine Filter ($\alpha = 1$), NRZ-L	25
3.2.3.5	Raised Cosine Filter ($\alpha = 1$), Sampled	34
3.2.3.6	Square Root Raised Cosine Filter ($\alpha = 1$), Sampled	34
3.3	Summary of Filter Simulations	35
4.0	SYSTEM CONSIDERATIONS	41
4.1	Filter Amplitude Response	41
4.1.1	5 th Order Butterworth Filter Response	42
4.1.2	3 rd Order Bessel Filter Response	42
4.1.3	Raised Cosine Filter Response ($\alpha = 1$), NRZ-L	42
4.1.4	Square Root Raised Cosine Filter Response ($\alpha = 1$), NRZ-L	43
4.1.5	Raised Cosine Filter Response ($\alpha = 1$), Sampled Data	43
4.1.6	Square Root Raised Cosine Filter Response ($\alpha = 1$), Sampled Data	44
4.1.7	Summary of Filter Output Amplitude Variation Study	44

CCSDS - SFCG EFFICIENT MODULATION METHODS STUDY
Phase 2: Spectrum Shaping

TABLE OF CONTENTS (Continued)

4.2	Inter-Symbol Interference (ISI)	46
4.2.1	Raised Cosine and Square Root Raised Cosine Filter Eye Diagrams									
	NRZ-L Data	47
4.2.2	Raised Cosine and Square Root Raised Cosine Filter Eye Diagrams									
	Sampled Data	47
4.2.3	Summary of ISI Studies	50
5.0	PHASE 2 SUMMARY	51
6.0	PHASE 3	53
	REFERENCES	55

CCSDS - SFCG EFFICIENT MODULATION METHODS STUDY
Phase 2: Spectrum Shaping

LIST OF TABLES

1-1	Performance Summaries of Modulation Schemes	2
2-1	Comparison of Theoretical and Simulated Amplitudes	6
2-2	Simulations	11
3-1a	Spectrum Levels Relative to First Data Sideband (Ideal Data)	40
3-1-b	Spectrum Levels Relative to First Data Sideband (Non-Ideal Data)	40
4-1	Filter Amplitude Variation to Random NRZ-L Data Pattern	44
4-2	Inter-Symbol Interference for Filter Pairs	50
5-1	Summary Utilization Ratio Improvement	52

LIST OF FIGURES

2-1	Simplified Spacecraft RFS Block Diagram	5
2-2	Frequency Spectra of Random Digital Data	6
2-3	Comparison of Traveling Wave Tube and Solid State Amplifiers (Ideal Data)	9
3-1	Spacecraft Configuration for Evaluating Alternative Modulation Methods	14
3-2	Unfiltered Baseband NRZ-L Data Spectra (Ideal Data)	16
3-3	Unfiltered Baseband NRZ-L Data Spectra (Non-Ideal Data)	17
3-4	Baseband 5 th Order Butterworth Filtered NRZ-L Data Spectra (Ideal Data)	18
3-5	Baseband 5 th Order Butterworth Filtered NRZ-L Data Spectra (Non-Ideal Data)	19
3-6	Baseband 3 rd Order Bessel Filtered NRZ-L Data Spectra (Ideal Data)	22
3-7	Baseband 3 rd Order Bessel Filtered NRZ-L Data Spectra (Non-Ideal Data)	23
3-8	Amplitude Responses for Raised Cosine Filters	24
3-9	Baseband Raised Cosine ($\alpha = 0.25$) Filtered NRZ-L Data Spectra (Ideal Data)	26
3-10	Baseband Raised Cosine ($\alpha = 0.25$) Filtered NRZ-L Data Spectra (Non-Ideal Data)	27

CCSDS - SFCG EFFICIENT MODULATION METHODS STUDY
Phase 2: Spectrum Shaping

LIST OF FIGURES (Continued)

3-11	Baseband Raised Cosine ($\alpha = 0.5$) Filtered NRZ-L Data Spectra (Ideal Data)	28
3-12	Baseband Raised Cosine ($\alpha = 0.5$) Filtered NRZ-L Data Spectra (Non-Ideal Data)	29
3-13	Baseband Raised Cosine ($\alpha = 1$) Filtered NRZ-L Data Spectra (Ideal Data)	30
3-14	Baseband Raised Cosine ($\alpha = 1$) Filtered NRZ-L Data Spectra (Non-Ideal Data)	31
3-15	Baseband Square Root Raised Cosine ($\alpha = 1$) Filtered NRZ-L Data Spectra (Ideal Data)	32
3-16	Baseband Square Root Raised Cosine ($\alpha = 1$) Filtered NRZ-L Data Spectra (Non-Ideal Data)	33
3-17	Baseband Raised Cosine ($\alpha = 1$) Filtered Sampled Data Spectra (Ideal Data)	36
3-18	Baseband Raised Cosine ($\alpha = 1$) Filtered Sampled Data Spectra (Non-Ideal Data)	37
3-19	Baseband Square Root Raised Cosine ($\alpha = 1$) Filtered Sampled Data Spectra (Ideal Data)	38
3-20	Baseband Square Root Raised Cosine ($\alpha = 1$) Filtered Sampled Data Spectra (Non-Ideal Data)	39
4-1	Filter Amplitude Responses to a Random NRZ-L Data Pattern	45
4-2	Eye Diagrams for Raised Cosine ($\alpha = 1$) Filters, NRZ-L Data in a Non-Linear Channel	48
4-3	Eye Diagrams for Raised Cosine ($\alpha = 1$) Filters, Sampled Data in a Non-Linear Channel	49

CCSDS - SFCG EFFICIENT MODULATION METHODS STUDY

Phase 2: Spectrum Shaping

1.0 INTRODUCTION

At the 12th annual meeting of the Space Frequency Coordination Group (SFCG-12), held during November 1992 in Australia, the SFCG requested the CCSDS RF and Modulation Subpanel to study and compare various modulation schemes (SFCG Action Item 12-32). Preliminary findings were discussed at last year's NASA-ESA Frequency Coordination meeting. The first published report was presented at the CCSDS Subpanel 1E and SFCG meetings in September 1993.

The initial paper considered six modulation schemes including PCM/PSK/PM Square, PCM/PSK/PM Sine, PCM/PM/NRZ, PCM/PM/Bi- ϕ , BPSK/NRZ, and BPSK/Bi- ϕ (Reference 1). It was shown that telemetry subcarriers (PCM/PSK/PM Square or Sine) tend to require an excessive amount of the frequency spectrum. Conversely, PCM/PM/NRZ and BPSK/NRZ are the most spectrum efficient and require the minimum hardware modifications to existing earth station receivers.

While PCM/PM/NRZ and BPSK/NRZ modulation are the most bandwidth efficient, they are sensitive to data imbalance. Therefore, unless convolutional coding is used, care must be exercised to ensure that data balance is maintained [Reference 7]. Modulation systems employing subcarriers were found to be the least efficient and it was concluded that their use should be avoided absent circumstances compelling their use. In fact, based upon that report, the CCSDS has adopted a Blue Recommendation and the SFCG has approved a provisional Recommendation discouraging the use of telemetry subcarriers.

Reference 2 completed Phase 1 of the CCSDS modulation study by reporting the equivalent bandwidth and Inter-Symbol Interference (ISI) results for QPSK, OQPSK, and GMSK modulation. Table 1-1 summarizes the results of the Phase 1 study reported in References 1, 2, and 8.

This paper is concerned with Phase 2 of the *CCSDS - SFCG Efficient Modulation Methods Study* and explores the benefits accruing from spectrum shaping of the transmitted signal. Several alternative filter types and locations are considered and the results are compared. An estimate of the increased spectrum utilization, resulting from the application of the proper modulation and spectrum shaping methods, is provided. It is shown that spectrum shaping, in combination with an efficient modulation type, has the potential for increasing frequency band utilization by several times.

CCSDS - SFCG EFFICIENT MODULATION METHODS STUDY
Phase 2: Spectrum Shaping

TABLE 1-1: PERFORMANCE SUMMARIES OF MODULATION SCHEMES

Modulation Type	90% Power Containment	95% Power Containment	ISI SNR Reduction dB	ISI SNR Reduction dB	ISI SNR Reduction dB	In-Band Interference Susceptibility
PCM/PSK/PM (Sq) ¹ n = 9, m = 1.2 rad.	$\pm 30 R_B$	$\pm 75 R_B$	0.75 @ $\pm 10 R_B$	0.15 @ $\pm 20 R_B$	0.01 dB @ $\pm 50 R_B$	Less susceptible than PCM/PSK/PM sine by about 4 dB. Susceptible to Out-of-Band interference.
PCM/PSK/PM (Sine) ¹ n = 9, m = 1.2 rad.	$\pm 10 R_B$	$\pm 10 R_B$	0.75 @ $\pm 10 R_B$	0.18 @ $\pm 20 R_B$	0.04 dB @ $\pm 50 R_B$	More susceptible than PCM/PSK/PM square.
PCM/PM/Bi- ϕ ¹ m = 1.2 rad.	$\pm 2.9 R_B$	$\pm 5.1 R_B$	6.3 @ $\pm 1 R_B$	0.34 @ $\pm 2 R_B$	0.20 dB @ $\pm 5 R_B$	No information available.
PCM/PM/NRZ ¹ m = 1.2 rad.	$\pm 0.7 R_B$	$\pm 1.2 R_B$	0.85 @ $\pm 1 R_B$	0.21 @ $\pm 2 R_B$	0.01 dB @ $\pm 5 R_B$	No information available.
BPSK/Bi- ϕ m = ± 90 deg.	$\pm 3.1 R_B$	$\pm 6.5 R_B$	6.3 @ $\pm 1 R_B$	0.29 @ $\pm 2 R_B$	0.15 dB @ $\pm 5 R_B$	Less susceptible than QPSK. No information available comparing to modulation types listed above.
BPSK/NRZ m = ± 90 deg.	$\pm 1 R_B$	$\pm 2 R_B$	0.74 @ $\pm 1 R_B$	0.17 @ $\pm 2 R_B$	0.04 dB @ $\pm 5 R_B$	Likely to be more sensitive than BPSK/Bi- ϕ . No information available as to other modulation types.
QPSK	$\pm 0.5 R_B$	$\pm 1.0 R_B$	0.35 @ $\pm 0.5 R_B$	0.2 @ $\pm 1.0 R_B$	-	More sensitive than BPSK/NRZ due to crosstalk and phase distinguishability.
OQPSK	$\pm 0.5 R_B$	$\pm 1.0 R_B$	0.15 2 $\pm 0.5 R_B$	0.1 @ $\pm 1.0 R_B$	-	More sensitive than BPSK/NRZ due to crosstalk and phase distinguishability.
GMSK	$\pm 0.4 R_B$	$\pm 0.5 R_B$	0.35 @ $\pm 0.4 R_B$	0.2 @ $\pm 0.5 R_B$	-	Similar to MSK [Ref. 8] (i.e., less sensitive than BPSK/NRZ.

NOTES:

- 13.1 % of power contained within residual carrier.
- R_b is the frequency span occupied by each data bit, given the data bit rate (R_b is the same as R_s in Phase 1).

CCSDS - SFCG EFFICIENT MODULATION METHODS STUDY**Phase 2: Spectrum Shaping****2.0 OPTIMIZING BANDWIDTH EFFICIENCY**

This paper documents the work completed since the SFCG meeting in late September 1993. At the conclusion of these modulation studies, Recommendations will be drafted by the CCSDS and SFCG endorsing specific modulation types and spectrum shaping depending upon mission conditions.

2.1 RF Spectrum Management

From the Phase 1 findings, it became obvious that careful selection of the modulation type, together with some spectrum shaping, will be required to achieve bandwidth efficient communications.

2.1.1 Modulation Schemes

Phase 1 concluded that spectrum utilization is very dependent upon modulation type (References 1 and 2). With these studies, nine modulation schemes were investigated and their characteristics are summarized in Table 1-1. It was shown that telemetry subcarriers (PCM/PSK/PM Square or Sine) tend to require an excessive amount of the frequency spectrum. Conversely, GMSK, OQPSK, QPSK, BPSK/NRZ, and PCM/PM/NRZ are the most spectrum efficient. GMSK is clearly the most bandwidth efficient modulation method although the remaining four modulation types listed above produce acceptable Inter-Symbol-Interference (ISI) levels when band limited to $\pm 2 \times$ Data Rate (R_b). (R_b is the frequency span occupied by one bit given the data rate and is equivalent to R_s in the Phase 1 paper.)

2.1.2 Spectrum Shaping

Judicious filtering can also assist in reducing spectrum utilization. When used in conjunction with a spectrum efficient modulation, the result can be a significant savings in the *Required Bandwidth*. The issue becomes one of selecting the proper filter type and location.

Spectrum shaping increases the risk of Inter-Symbol Interference (ISI). Band-limiting caused by the filter distorts the symbol's waveform so that successive symbols begin to overlap one another resulting in ISI [Reference 9]. It is not sufficient to shape the spacecraft's transmitted spectrum such that it requires only a small portion of the RF frequency band if the result significantly increases the ISI. ISI appears as a telemetry data system loss and should be accounted for under *Waveform Loss* on page 4 of the CCSDS Link Design Control Table (DCT).

Accordingly, any spectrum shaping investigation must consider the additional losses due to ISI for it is a major parameter establishing the utility of each modulation scheme. Furthermore, nonlinearities found in the spacecraft's modulator, multiplier and power amplifier, along with imperfect data, can introduce additional spurious emissions, including in-band components, into the transmission. These factors must also be considered in order to obtain a reasonable evaluation of the overall system. This study's objective is to provide the most realistic estimate of actual system performance possible without building and testing real hardware.

CCSDS - SFCG EFFICIENT MODULATION METHODS STUDY

Phase 2: Spectrum Shaping

Figure 2-1 is a simplified block diagram of a Spacecraft Radio Frequency Subsystem (RFS). It identifies three locations where spectrum shaping can occur (shaded boxes) which will limit the *Required Bandwidth* of the transmitted signal. These are: 1) At the input to the spacecraft's modulator, 2) At the output of the multiplier, and 3) At the output of the power amplifier. Baseband filtering is always used in the turnaround transponder's ranging channel so there will be no further consideration of its characteristics. The following Sections discuss the merits of placing the filters at these three locations.

2.2 Evaluation of Alternative Systems

Evaluating alternative implementation approaches, using only analytical methods, is probably an exercise in futility. Unless one assumes virtually perfect conditions (e.g., data and hardware), the number of factors to be considered becomes unmanageable. Ideally, one would build the required hardware and make actual measurements on each of the several systems. However, this approach is clearly impractical from both a cost and time approach.

Thus, it was decided to utilize a communications system simulator. While not a perfect emulator of a real system, it does provide a close approximation permitting the comparative studies to be completed in a finite amount of time. Its accuracy should be far greater than a purely analytical approach, particularly if care is exercised in modeling the several system elements.

The system utilized was a Signal Processing Worksystem (SPW) marketed by COMDISCO Systems, Foster City, California. This software is installed on a SPARC-10 Sun Workstation. COMDISCO has a library of communications system components. For this study, JPL spacecraft modulator and frequency multiplier models were employed. These two models are based upon specifications and information describing the same components found in the NASA Standard Transponder.

Simulations were completed using ideal and non-ideal data. Ideal data exhibits perfect symmetry and data balance while non-ideal data conforms to the CCSDS Recommendations 401 (2.4.8) B-1 for asymmetry and to Recommendation 401.0 (X.X.X) B-1 for data imbalance. The CCSDS limits data asymmetry (ratio of time duration of a 1 to time duration of a 0) to $\pm 2\%$ and data imbalance (probability of a 1 vs probability of a 0 [mark-to-space ratio]) to 0.45. Except for the Raised Cosine and Square Root Raised Cosine filters ($\alpha = 1$) which received both NRZ-L and Sampled data inputs, all simulations used NRZ-L inputs since most spacecraft data systems produce that format.

Non-ideal data was used so that the simulation results would more accurately predict actual hardware performance. Stray capacitance in spacecraft wiring can increase the data asymmetry while the random data can produce long runs of 1s or 0s (data imbalance). Data imbalance will not pose a problem with PCM/PM/Bi- ϕ modulation, since each data symbol will have both states (1 and 0). However, for PCM/PM/NRZ modulation, data imbalance is a significant concern [Ref. 7].

Initially, concern was expressed regarding the accuracy of the COMDISCO simulator. Users of different software had discovered that their simulations contained errors in the amplitude of the modulation sidelobes which were several R_B away from the carrier. It was reported that the COMDISCO simulation of ideal data could be 5 dB below the correct level at $f_c \pm 10 R_B$.

To calibrate the accuracy of the COMDISCO system, a frequency spectrum of ideal, random data was made. Figure 2-2 and Table 2-1 contain the results of both theoretically computed and simulated amplitudes. Note the good agreement indicating that COMDISCO accurately simulates frequency spectra amplitudes.

CCSDS - SFCG EFFICIENT MODULATION METHODS STUDY
Phase 2: Spectrum Shaping

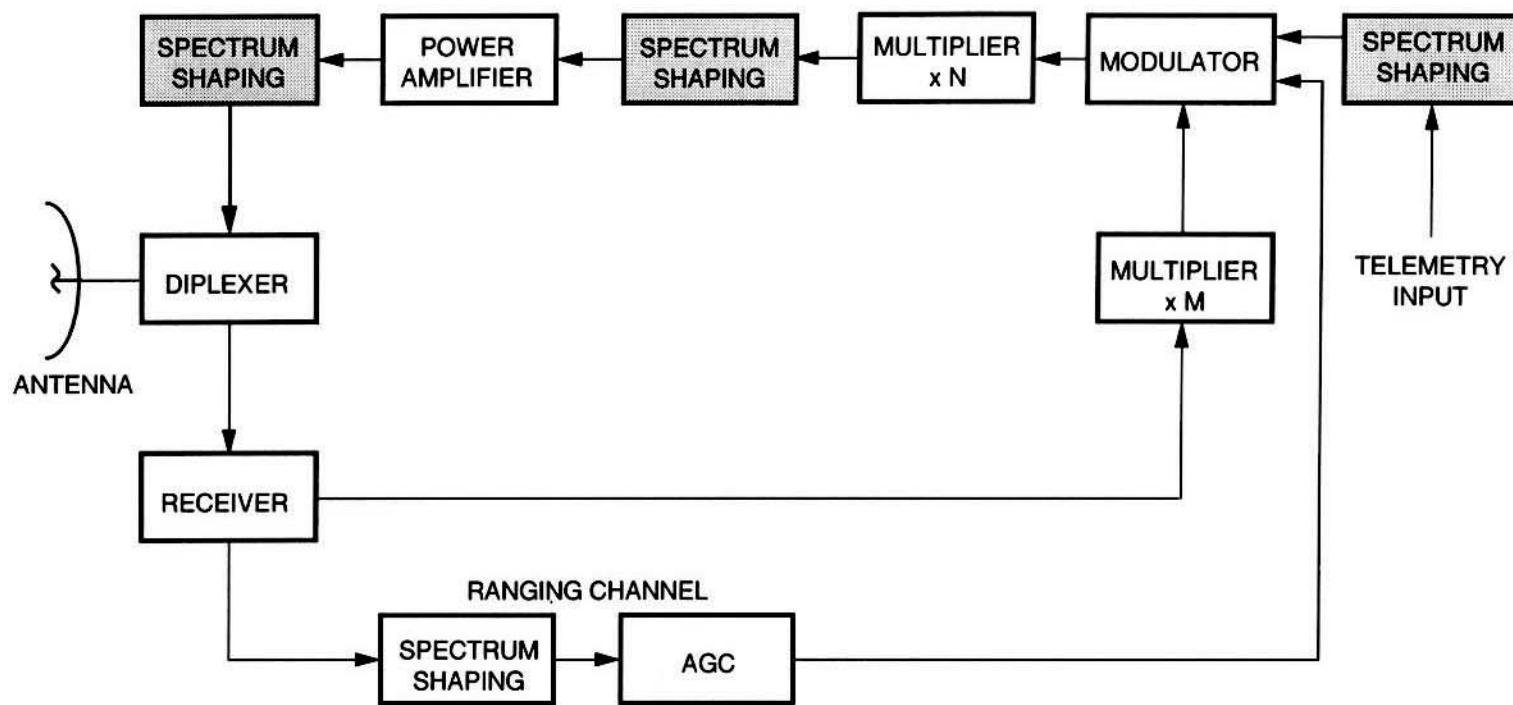


Figure 2-1. Simplified Spacecraft RFS Block Diagram

CCSDS - SFCG EFFICIENT MODULATION METHODS STUDY
Phase 2: Spectrum Shaping

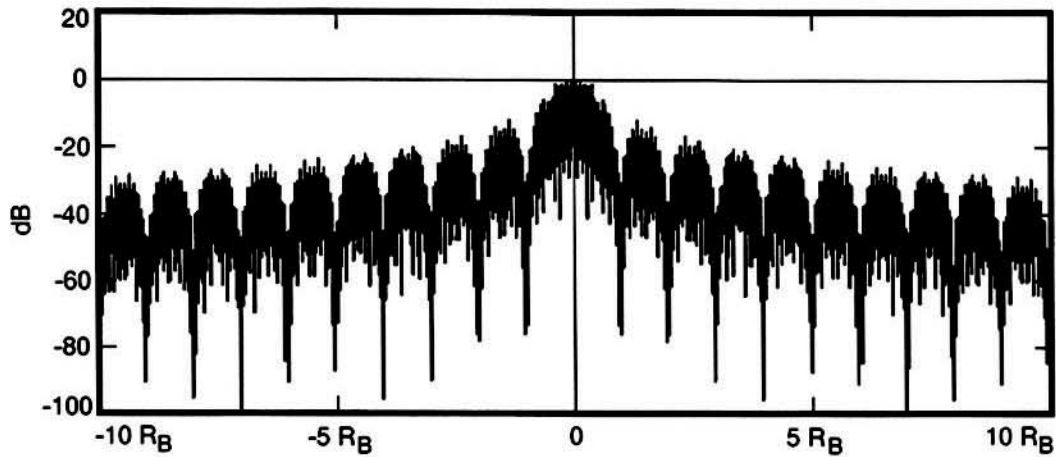


Figure 2-2. Frequency Spectrum of Random Digital Data (Ideal Data)

Table 2-1. Comparison of Theoretical and Simulated Amplitudes

Offset from Center Frequency ($\pm R_B$)	Theoretical Amplitude (dB)	Simulated Amplitude (dB)
0	0	0
1.5	-13.46	-13.5
2.5	-17.90	-18
3.5	-20.82	-21
4.5	-23.01	-23
5.5	-24.75	-25
6.5	-26.20	-27
7.5	-27.44	-27.5
8.5	-28.53	-29
9.5	-29.50	-29.5

Figure 2-2 and Table 2-1. COMDISCO Simulation of Random Data Spectrum

CCSDS - SFCG EFFICIENT MODULATION METHODS STUDY

Phase 2: Spectrum Shaping

2.2.1 Simulator Problems

COMDISCO's simulation software used in JPL's Communications Research Section (331) contains models for a modulator, a multiplier, a TWT power amplifier, and now, a solid state power amplifier. All models emulate real equipment and contain the nonlinearities and imperfections found in the actual hardware.

The modulator and multiplier models were designed by JPL and are based upon characteristics of corresponding elements found in NASA's standard deep space transponder. COMDISCO provided the model for the TWT which replicates a Hughes TWT Model 275H. JPL implemented the Solid State Power Amplifier (SSPA) model which is based upon specifications provided by the European Space Agency (ESA) for their 10 Watt, solid state, S-band power amplifier.

Some problems arose during the simulations due to differing conventions. COMDISCO designed their model of the Hughes 275H TWT to operate with a baseband complex envelope input/output and then be translated to the RF carrier frequency. Their reasoning was simple. Computers function slowly and have limited capacity. By operating at baseband, the *sample rate-to-modulation data rate* ratio, and hence the resolution, can be greatly increased over that which would be possible at the full RF frequency. All imperfections and nonlinearities found in the actual TWT have been translated to baseband and are included in the model.

Conversely, the modulator and multiplier models were designed to operate at the full RF frequency so that a complete RF simulation could be obtained, although at a lower resolution. When this difference was discovered, models for the modulator, multiplier and new solid state power amplifier were translated to also operate at baseband. Like the TWT, all imperfections inherent in the actual hardware operating at RF frequencies are retained in the revised models.

All simulations utilize both ideal and non-ideal NRZ-L and Sampled data as defined in Section 2.2. Additionally, a non-ideal modulator, multiplier, and 10 Watt solid state S-band amplifier were employed to ensure that the results represent actual system performance. Simulations were made at baseband and translated to the RF operating frequency.

2.2.2 Simulation Conditions

Because of the large number of simulations required, it was decided to focus on a single modulation scheme for Phase 2. Although not the most bandwidth efficient, PCM/PM/NRZ modulation was selected because most space agencies still use residual carrier communications systems. While implemented only occasionally, the bandwidth efficiency of PCM/PM/NRZ makes it attractive for evaluating filter efficacy.

Efficient spectrum utilization is most important for Category A missions where their larger numbers, stronger signals, and higher data rates exacerbate the frequency band congestion. Therefore, where possible, Phase 2 focused on these systems rather than on those used for Category B missions where congestion is less of a problem. Consequently, all simulations employed the ESA 10 Watt solid state power amplifier and a 4th Order Butterworth bandpass second harmonic filter, with a $\pm 20 R_b$ cutoff frequency, following the power amplifier (Figure 2-1). (R_b is the frequency spectrum width required by a single data bit).

CCSDS - SFCG EFFICIENT MODULATION METHODS STUDY

Phase 2: Spectrum Shaping

For comparative purposes, spectra for both the Hughes TWT Model 275H and the European Space Agency's 10 Watt Solid State S-band power amplifiers are provided in Figure 2-3 using a spectrum width of $f_c \pm 20 R_b$. Both amplifiers were operating in full saturation. Spectra for the two amplifier types, using non-ideal data, showed no discernable differences. Accordingly, the following results are believed to be equally applicable to both TWTs and solid state amplifiers, operating in a fully saturated mode.

As noted, models for a non-ideal modulator and multiplier were also utilized. These models are estimates of the modulator and multiplier found in the NASA standard transponder and are based on published specifications. When combined with non-ideal data, the simulation should represent actual spacecraft telemetry system performance reasonably well.

2.3 Selection of Filter Locations

Figure 2-1 shows that filters can be placed at the modulator's input, the multiplier's output, and/or the power amplifier's output. Clearly, from a spectrum management viewpoint, the most effective filter location is following the power amplifier. Such a filter will attenuate spurious emissions resulting from nonlinearities in the modulator, multiplier, and power amplifier. Moreover, all spacecraft should have 2nd harmonic filters to reduce unwanted emissions in other bands.

However, from a spacecraft construction and operations perspective, spectrum shaping following the power amplifier is undesirable. Not only do such filters have to carry the full transmitted power which tends to make them large and heavy, but also, output filtering may not be compatible with some mission operations requirements.

For example, unless the telemetry symbol rate is equal to, or greater than, the ranging code rate, the filter's bandwidth will be a compromise either partially attenuating the ranging signal and/or permitting far too many telemetry data sidebands to be transmitted defeating the objective of limiting the telemetry spectrum. Such a filter is likely to preclude Δ DOR measurements.

There is yet a third disadvantage to an output filter. An output filter can significantly reduce the high order data sidebands together with any spurious emissions that may be present. However, a portion of the transmitted power is contained within the data sidebands and their elimination translates into a power loss. In the past, a 5% loss (-0.2 dB) was considered to be acceptable.

Some filtering at the power amplifier's output will be required to eliminate the second, and higher order harmonics generated by the nonlinearities present in the power amplifier. Perhaps in some cases, this filter can also be used to partially filter the data sidebands. However, it should be expected that such sideband filtering will be modest.

Therefore, other filter locations should be considered. Again, from a spectrum management viewpoint, the second most desirable location is following the multiplier and just prior to the power amplifier. This is so because artifacts resulting from nonlinearities in the modulator and multiplier will be reduced even if those from the power amplifier will not. Spectrum shaping at the multiplier or power amplifier input may be necessary in BPSK and/or QPSK systems using "switched modulators" where baseband filtering is not feasible (see page 10 and Section 4.1.3). With suppressed carrier modulation, ranging and Δ DOR tones are unlikely to pose problems and these filter locations should be acceptable. To obtain the same performance measured for the baseband filters, the bandpass characteristics should produce same transmitted RF spectrum characteristics discussed on the following pages.

CCSDS - SFCG EFFICIENT MODULATION METHODS STUDY
Phase 2: Spectrum Shaping

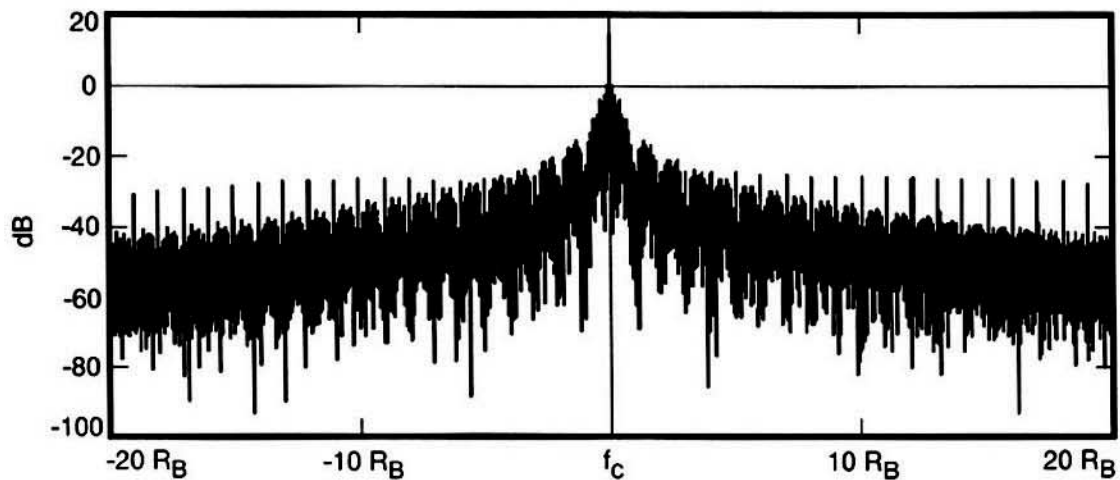


Figure 2-3a. Solid State Power Amplifier (SSPA) Spectrum (Non-Ideal Data)

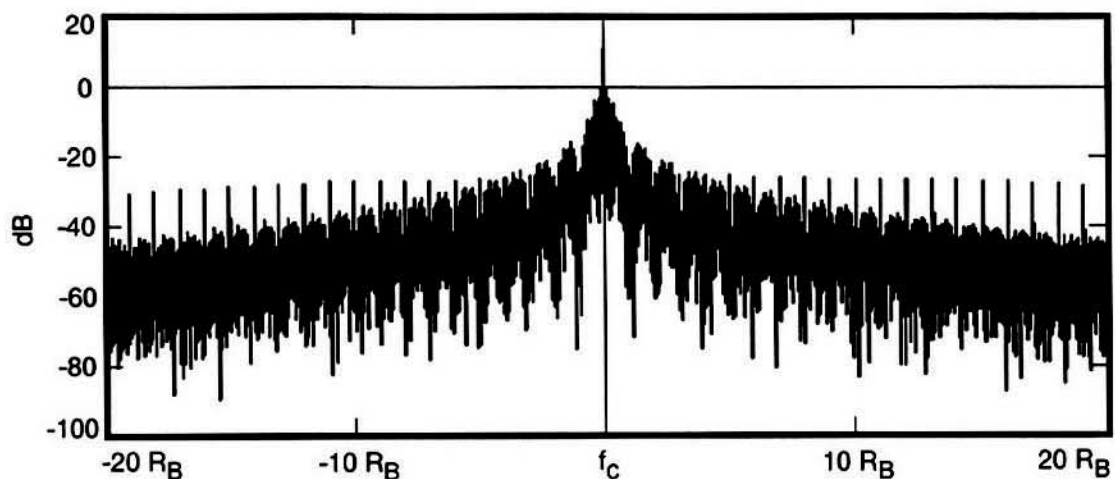


Figure 2-3b. Traveling Wave Tube (TWT) Spectrum (Non-Ideal Data)

Figure 2-3. Comparison of Traveling Wave Tube and Solid State Power Amplifiers (Non-Ideal Data)

CCSDS - SFCG EFFICIENT MODULATION METHODS STUDY

Phase 2: Spectrum Shaping

Baseband filtering remains as the single, most advantageous, alternative to post power amplifier filtering for residual carrier modulation. Virtually all of the disadvantages listed above for the post power amplifier filter are eliminated. The filter can be small, lightweight, and consume very little power. Moreover, such a filter location is compatible with simultaneous telemetry, ranging, and Δ DOR tones since they can have separate, unfiltered, modulator inputs.

However, baseband filtering may be incompatible with some suppressed carrier modulators. If the BPSK or QPSK modulator is linear so that its output phase shift is a linear function of input voltage, then baseband filtering is feasible. Conversely, if the modulator is "switched" so that the output phase has 2 (BPSK) or 4 (QPSK) discrete phases which occur when the input voltage passes certain thresholds, or if a digital input is required, then baseband filtering will not be effective.

Baseband filtering suffers from one other significant disadvantage. Irrespective of how well the input data has been filtered, nonlinearities found in the modulator, multiplier and solid state power amplifier will have a tendency to reestablish the data sidebands that the filter was intended to eliminate. Nevertheless, because of its simplicity, an investigation of baseband filtering is worthwhile to quantify the benefits which can be obtained.

2.4 Optimum Filter Types

Given that baseband filtering is the most practical choice, one must select the optimum filter type for this location. This selection is especially critical because of the several nonlinear elements following the filter. As noted above, each of these elements has a tendency to restore some of the frequency components that the filter removed. Moreover, some filters exhibit ringing at the cut-off frequency which wreaks havoc when passed through non-linear system components.

Here, the approach was to simulate the system's performance using the equipment described in Section 2.2.2 which included models of a non-ideal modulator, multiplier, and power amplifier. Four filter types were selected for comparison. These were: a 5th Order Butterworth filter, a 3rd Order Bessel filter, Raised Cosine filters with $\alpha = 0.25, 0.5$, and 1, and a Square Root Raised Cosine filter with $\alpha = 1$.

Note: The purpose of these simulations was to establish the effect of baseband filtering on the transmitted data's spectrum. Accordingly, narrow bandpass filters were used with cut-off frequencies of $\pm 1 R_B$. ($1 R_B$ is the span of a single data bit in the frequency domain, e.g., for random data, spectral nulls occur at $\pm 1 R_B, \pm 2 R_B, \dots, \pm n R_B$).

One might expect that the Inter-Symbol Interference (ISI), resulting from such a narrow baseband filter, might be high. In Phase 1 of this study, it was found that filter bandwidths of at least $\pm 2 R_s$ [$\pm 2 R_s = \pm 2 R_B$] were required to ensure that the ISI was held to an acceptable value.

2.5 Simulation Tests

Table 2-2 contains a list of the simulations undertaken for this study. Because of time constraints, all simulations employed a PCM/PM/NRZ modulation format. The first two simulations, without any baseband filtering, were intended to serve as references with which to compare subsequent simulations employing a variety of baseband filters. Each of the reference spectrum plots should be compared with the corresponding plots for the filtered data in order to evaluate the benefits of baseband filtering. These first two cases utilize ideal data (no data asymmetry nor any data imbalance) and non-ideal data (corresponding to characteristics set forth in Section 2.2 respectively).

CCSDS - SFCG EFFICIENT MODULATION METHODS STUDY

Phase 2: Spectrum Shaping

Table 2-2: SIMULATIONS

Sim No.	Modulation Type	Filter Location	Filter Type	Filter Char	Data Char.	Spectrum Plots	Plot Locations	Test Purpose
1	None (Baseband)	None	None	None	Ideal NRZ-L	$\pm 10 R_B$, $\pm 200 R_B$	Mod, PA, PA Unfil.	Unfiltered NRZ-L data spectrum reference.
2	None (Baseband)	None	None	None	Non-Ideal NRZ-L	$\pm 10 R_B$, $\pm 200 R_B$	Mod, PA, PA Unfil.	Unfiltered NRZ-L data spectrum reference.
3	PCM/PM/NRZ	Baseband	Butterworth	5 th Order	Ideal NRZ-L	$\pm 10 R_B$, $\pm 200 R_B$	Mod, PA, 2 nd Har Fil	Evaluation of Butterworth filter, ideal NRZ-L data.
4	PCM/PM/NRZ	Baseband	Butterworth	5 th Order	Non-Ideal NRZ-L	$\pm 10 R_B$, $\pm 200 R_B$	Mod, PA, 2 nd Har Fil	Evaluation of Butterworth filter, non-ideal NRZ-L data.
5	PCM/PM/NRZ	Baseband	Bessel	3 rd Order	Ideal NRZ-L	$\pm 10 R_B$, $\pm 200 R_B$	Mod, PA, 2 nd Har Fil	Evaluation of Bessel filter, ideal NRZ-L data.
6	PCM/PM/NRZ	Baseband	Bessel	3 rd Order	Non-Ideal NRZ-L	$\pm 10 R_B$, $\pm 200 R_B$	Mod, PA, 2 nd Har Fil	Evaluation of Bessel filter, non-ideal NRZ-L data.
7	PCM/PM/NRZ	Baseband	Raised Cosine	$\alpha = 0.25$	Ideal NRZ-L	$\pm 10 R_B$, $\pm 200 R_B$	Mod, PA, 2 nd Har Fil	Evaluation of Raised Cosine filter ($\alpha = 0.25$), ideal NRZ-L data.
8	PCM/PM/NRZ	Baseband	Raised Cosine	$\alpha = 0.25$	Non-Ideal NRZ-L	$\pm 10 R_B$, $\pm 200 R_B$	Mod, PA, 2 nd Har Fil	Evaluation of Raised Cosine filter ($\alpha = 0.25$), non-ideal NRZ-L data.
9	PCM/PM/NRZ	Baseband	Raised Cosine	$\alpha = 0.5$	Ideal NRZ-L	$\pm 10 R_B$, $\pm 200 R_B$	Mod, PA, 2 nd Har Fil	Evaluation of Raised Cosine filter ($\alpha = 0.5$), ideal NRZ-L data.
10	PCM/PM/NRZ	Baseband	Raised Cosine	$\alpha = 0.5$	Non-Ideal NRZ-L	$\pm 10 R_B$, $\pm 200 R_B$	Mod, PA, 2 nd Har Fil	Evaluation of Raised Cosine filter ($\alpha = 0.5$), non-ideal NRZ-L data.
11	PCM/PM/NRZ	Baseband	Raised Cosine	$\alpha = 1$	Ideal NRZ-L	$\pm 10 R_B$, $\pm 200 R_B$	Mod, PA, 2 nd Har Fil	Evaluation of Raised Cosine filter ($\alpha = 1$), ideal NRZ-L data.
12	PCM/PM/NRZ	Baseband	Raised Cosine	$\alpha = 1$	Non-Ideal NRZ-L	$\pm 10 R_B$, $\pm 200 R_B$	Mod, PA, 2 nd Har Fil	Evaluation of Raised Cosine filter ($\alpha = 1$), non-ideal NRZ-L data.
13	PCM/PM/NRZ	Baseband	Sq Root Raised Cosine	$\alpha = 1$	Ideal NRZ-L	$\pm 10 R_B$, $\pm 200 R_B$	Mod, PA, 2 nd Har Fil	Evaluation of Square Root Raised Cosine filter ($\alpha = 1$), ideal NRZ-L data.
14	PCM/PM/NRZ	Baseband	Sq Root Raised Cosine	$\alpha = 1$	Non-Ideal NRZ-L	$\pm 10 R_B$, $\pm 200 R_B$	Mod, PA, 2 nd Har Fil	Evaluation of Square Root Raised Cosine filter ($\alpha = 1$), non-ideal NRZ-L data.
15	PCM/PM/NRZ	Baseband	Raised Cosine	$\alpha = 1$	Ideal Sampled	$\pm 10 R_B$, $\pm 200 R_B$	Mod, PA, 2 nd Har Fil	Evaluation of Raised Cosine filter ($\alpha = 1$), ideal Sampled data.
16	PCM/PM/NRZ	Baseband	Raised Cosine	$\alpha = 1$	Non-Ideal Sampled	$\pm 10 R_B$, $\pm 200 R_B$	Mod, PA, 2 nd Har Fil	Evaluation of Raised Cosine filter ($\alpha = 1$), non-ideal Sampled data.
17	PCM/PM/NRZ	Baseband	Sq Root Raised Cosine	$\alpha = 1$	Ideal Sampled	$\pm 10 R_B$, $\pm 200 R_B$	Mod, PA, 2 nd Har Fil	Evaluation of Square Root Raised Cosine filter ($\alpha = 1$), ideal Sampled data.
18	PCM/PM/NRZ	Baseband	Sq Root Raised Cosine	$\alpha = 1$	Non-Ideal Sampled	$\pm 10 R_B$, $\pm 200 R_B$	Mod, PA, 2 nd Har Fil	Evaluation of Square Root Raised Cosine filter ($\alpha = 1$), non-ideal Sampled data.

CCSDS - SFCG EFFICIENT MODULATION METHODS STUDY
Phase 2: Spectrum Shaping

This Page is
initially left blank.

CCSDS - SFCG EFFICIENT MODULATION METHODS STUDY

Phase 2: Spectrum Shaping

3.0 SIMULATION RESULTS

Simulations were completed for each case listed in Table 2-2. Simulation modeling estimated the performance of actual hardware (non-ideal modulator, multiplier, and power amplifier) using both ideal and non-ideal data sources for all cases. The objective was to ensure that simulation results accurately predicted true hardware performance. Figure 3-1 is a block diagram of the flight system, showing filter locations and alternative study conditions.

For each of the cases listed in Table 2-2, individual spectra were simulated and plotted for: (1) the data source, either the data itself where no filter is present or at the filter's output if one was used, (2) at the output of the power amplifier (prior to the 2nd harmonic filter), and (3) at the output of the 2nd harmonic filter.

Different spectrum widths and resolutions were used depending upon the point being investigated. All spectral frequency axes are labeled in terms of R_b , where R_b is the normalized spectral frequency occupied by a single bit in the telemetry data stream. This generalized labeling permits the reader to scale the results of these simulations to any desired data rate.

At baseband, filtered and unfiltered data spectrum plots have a width of $f_0 \pm 10 R_b$. The power amplifier's output is also plotted $f_c \pm 10 R_b$, where f_c is the residual carrier's frequency. These two comparatively high resolution (resolution = 8 Hz) plots permit examination of the transmitted signal's fine structure for accurate determination of the filter's attenuation. A 4th Order Butterworth bandpass filter with a cutoff frequency of $f_c \pm 20 R_b$, which does not affect the baseband filtering, follows the power amplifier. Its purpose is to simulate a 2nd harmonic filter frequently used following power amplifiers to protect users of other bands. So that a large part of the frequency band will be visible, these plots cover a range of $f_c \pm 200 R_b$ with a resolution of 11 Hz.

3.1 Reference Data

Simulations were made using unfiltered data (Table 2-2, Case Nos. 1 and 2) to establish a benchmark for comparing the several filter types. Figure 3-2 contains a series of plots for ideal data while Figure 3-3 contains equivalent plots but for non-ideal data. Comparing Figure 3-2a with Figure 3-3a clearly demonstrates the difference in the baseband frequency spectrum for ideal and non-ideal data. Note the significantly increased spurious emissions, including in-band components, present in the non-ideal data.

When unfiltered NRZ-L data is modulated, multiplied and amplified using imperfect system components in a PCM/PM/NRZ format, the results appear in Figures 3-2b and 3-3b. Spurious emissions with in-band components present in the baseband data, also appear at the output of the power amplifier. This spectrum plot represents the power amplifier's output prior to the 2nd harmonic filter so that readers can see the full effect of both baseband and post power amplifier filtering used in subsequent cases.

From Figure 3-3b, it can be seen that the peak level of the third data sideband (e.g., at $f_c \pm 3 R_b$) is approximately 21 dB below the peak level of the 1st data sideband and the fifth data sideband (e.g., at $f_c \pm 5 R_b$) is about 25 dB below the peak level of the 1st data sideband. These levels can serve as references for comparing the various filter options. For a non-ideal data source, the spurious emissions extend well beyond the *Necessary Bandwidth*. Note: while spectra for ideal data is included in this paper, performance comparisons will be made using spectra for non-ideal data because they should better represent actual operating hardware.

CCSDS - SFCG EFFICIENT MODULATION METHODS STUDY
Phase 2: Spectrum Shaping

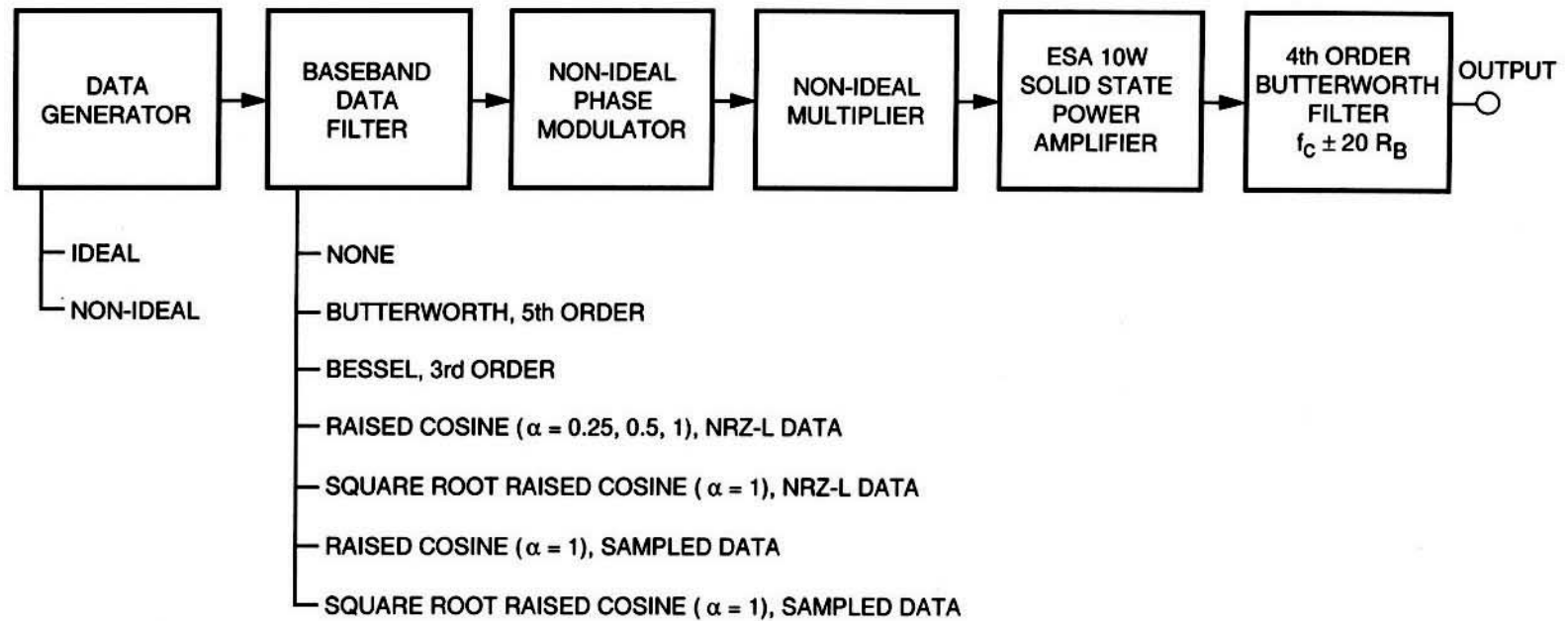


Figure 3-1. Spacecraft Configuration for Evaluating Alternative Modulation Methods

CCSDS - SFCG EFFICIENT MODULATION METHODS STUDY

Phase 2: Spectrum Shaping

3.2 Filtered Data

Figures 3-2 and 3-3, showing spectra of unfiltered data, can serve as references with which to compare spectra using different types of baseband filters. Because of their large number, only a limited number of plots could be included and discussed in this paper. For the filtered cases, spectra will be provided at the output of: the baseband filter, the power amplifier, and the 2nd harmonic filter. Furthermore, because the unfiltered baseband reference data (Figures 3-2 and 3-3) applies to each of the cases, it will not be repeated for each filter studied. Readers are referred to the corresponding unfiltered case in order to determine the effect of various filter types on the baseband and transmitted spectra.

For purposes of determining filter efficacy, the only meaningful data is the frequency spectrum that is actually transmitted. Accordingly, the transmitted spectra resulting from unfiltered and filtered data must be compared at the power amplifier's output and at the 2nd harmonic filter's output. These data should provide the most accurate estimate of a real flight hardware system's performance. Results of all simulations for the power amplifier's output are summarized in Table 3-1 for filtered and unfiltered, ideal and non-ideal, data. As with the unfiltered data, three plots are provided for each of the filtered cases corresponding to: (1) the baseband filter's output, (2) the power amplifier's output, and (3) the output of the 4th Order Butterworth 2nd harmonic filter with a bandwidth of $\pm 20 R_b$.

3.2.1 Butterworth Filter; 5th Order

From Table 2-2, the first filter to be considered is the 5th Order Butterworth. The BT product for this filter was set to 1.0 and the bandwidth to R_b . Figures 3-4 and 3-5 depict system's performance using this filter for ideal and non-ideal NRZ-L data respectively. Figures 3-4a and 3-5a should be compared to Figures 3-2a and 3-3a for the ideal and non-ideal data cases respectively. At $\pm 2 R_b$, the filter attenuates the baseband data sidebands by 40 dB, using a non-ideal data source. However, note the ringing at the knee of the curve which is probably the result of the filter's high (5th) Order. The effect of this ringing will become apparent as the signal passes through additional non-linear elements.

Figures 3-4b and 3-5b show the spectrum at the power amplifier's output. Note the spurious emissions, with in-band components, at frequency intervals of R_b which probably result from filter ringing, non-ideal components, and perhaps the ISI. The large spurious signals are present for both ideal and non-ideal data but additional, lower level spurious emissions can be seen in the frequency spectrum using non-ideal data. Figures 3-4b and 3-5b should be compared with Figures 3-2b and 3-3b respectively. Spurious emissions, with in-band components, are very evident in Figure 3-3b where no baseband filtering was used and are clearly the result of non-ideal data. Thus, both the Butterworth baseband filter and non-ideal data are seen to introduce in-band spurious emissions which represent non-recoverable data power. However, comparing Figures 3-3b and 3-5b reveals that the filtering significantly reduces the spurious emission level.

Figures 3-4c and 3-5c are the frequency spectra at the output of the 4th Order Butterworth 2nd harmonic bandpass filter which follows the power amplifier. Initially, this filter had a cut-off frequency of $f_c \pm 150 R_b$ and was intended to reduce the second harmonic emission. However, the non-linear transmitting system produced both odd and even harmonics with the result that significant emissions are present at $f_c \pm 50 R_b$, $\pm 100 R_b$, etc. Therefore, these simulations used a second harmonic filter bandwidth of $f_c \pm 20 R_b$.

CCSDS - SFCG EFFICIENT MODULATION METHODS STUDY
Phase 2: Spectrum Shaping

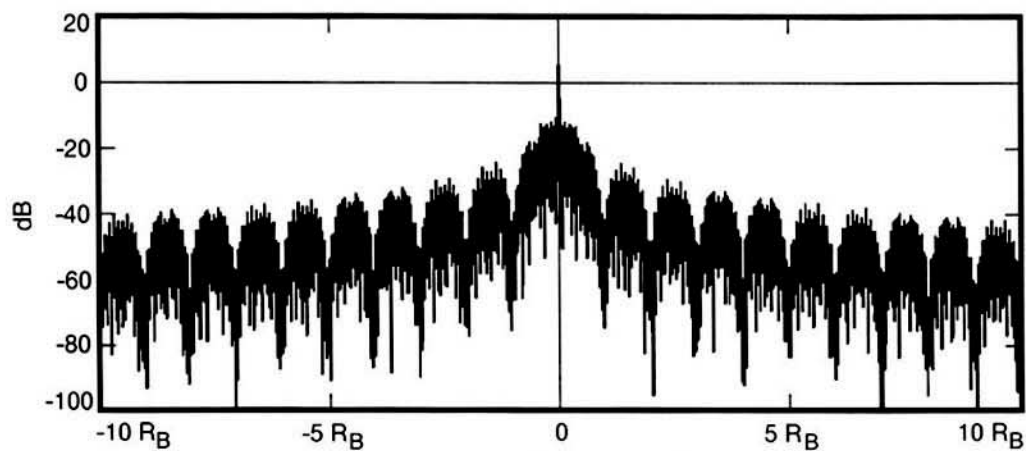


Figure 3-2a. Unfiltered Baseband Data

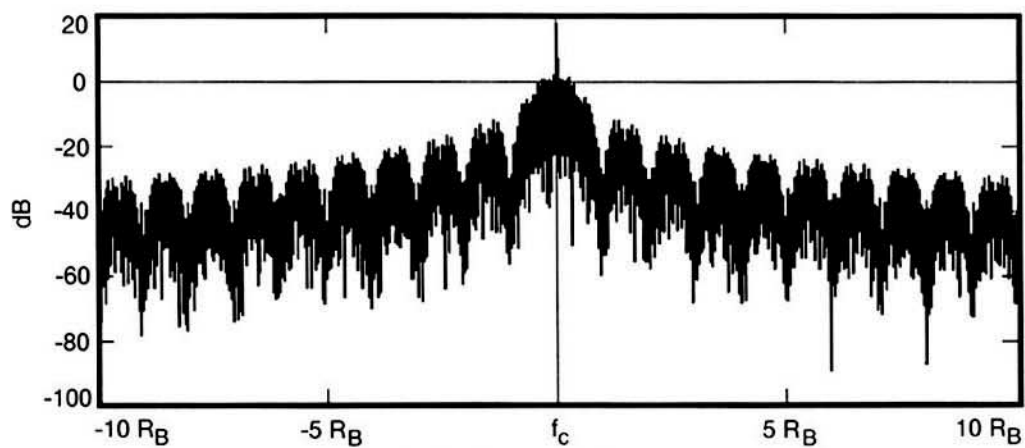
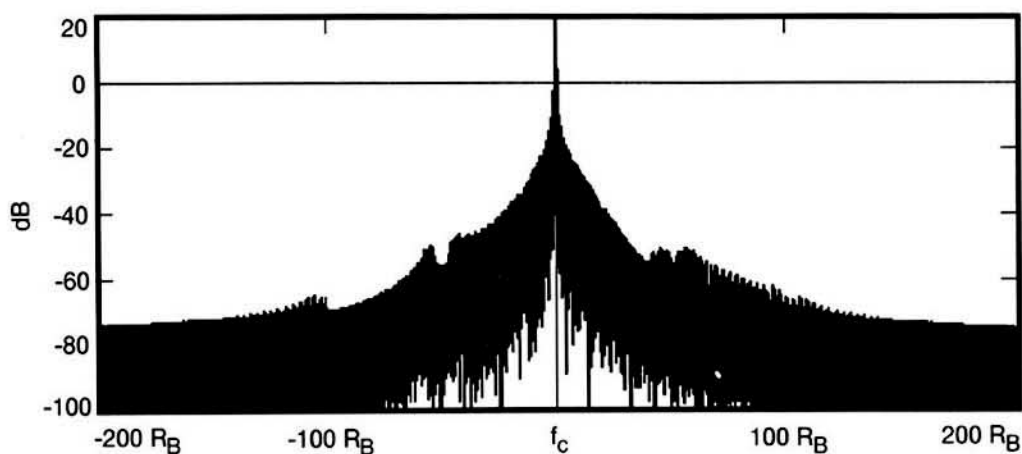


Figure 3-2b. Output of Power Amplifier

Figure 3-2c. Output of Second Harmonic Filter ($\pm 20 R_B$)**Figure 3-2. Unfiltered Baseband NRZ-L Data Spectra (Ideal Data)**

CCSDS - SFCG EFFICIENT MODULATION METHODS STUDY
Phase 2: Spectrum Shaping

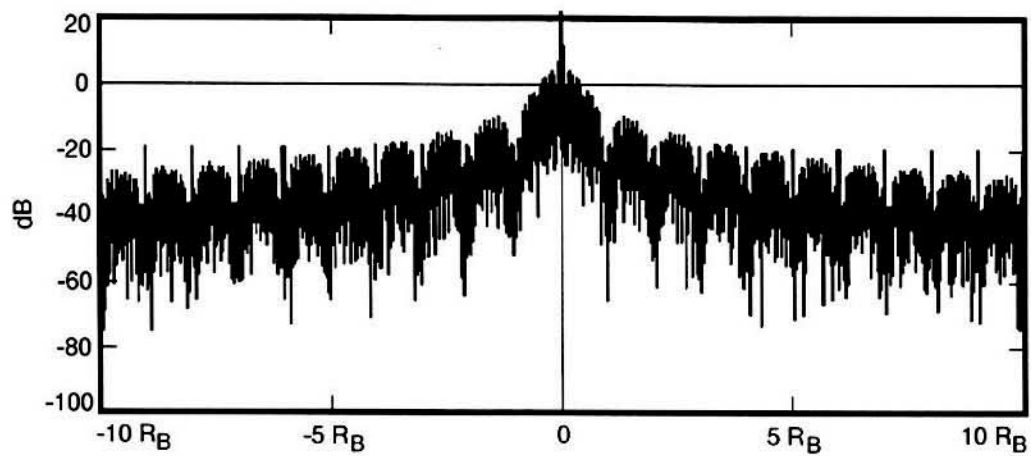


Figure 3-3a. Unfiltered Baseband Data

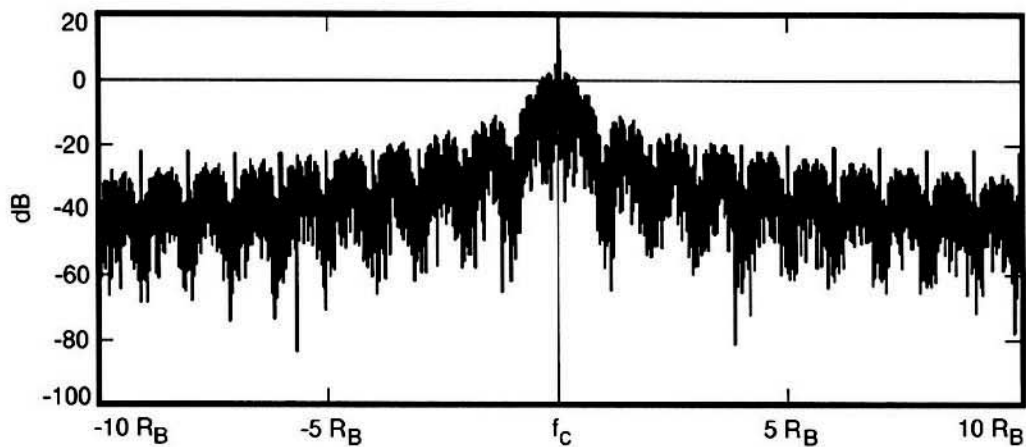


Figure 3-3b. Output of Power Amplifier

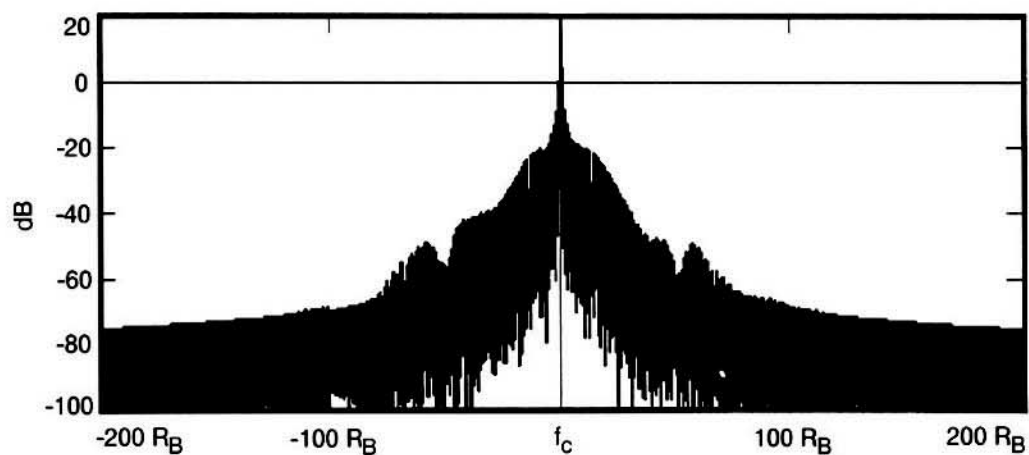


Figure 3-3c. Output of Second Harmonic Filter ($\pm 20 R_B$)

Figure 3-3. Unfiltered Baseband NRZ-L Data Spectra (Non-Ideal Data)

CCSDS - SFCG EFFICIENT MODULATION METHODS STUDY
Phase 2: Spectrum Shaping

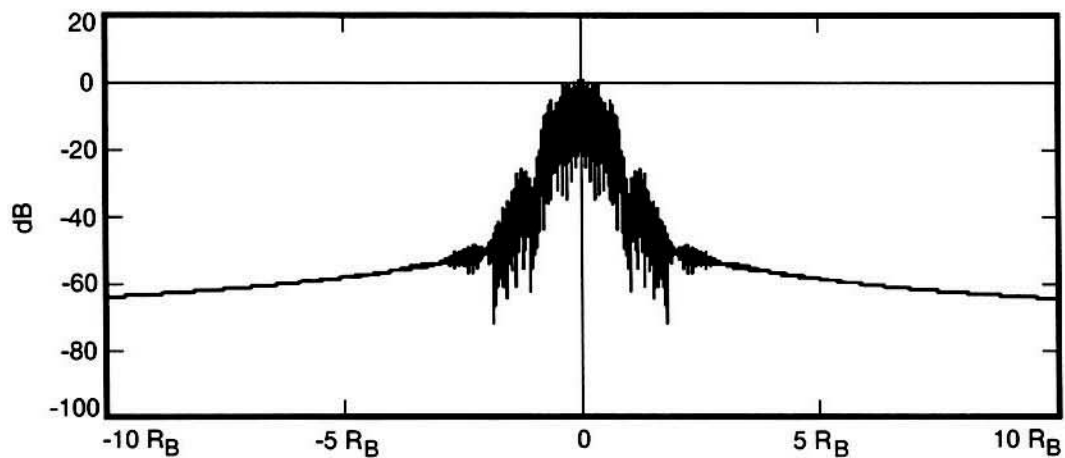


Figure 3-4a. Output from Butterworth Filter (5th Order)

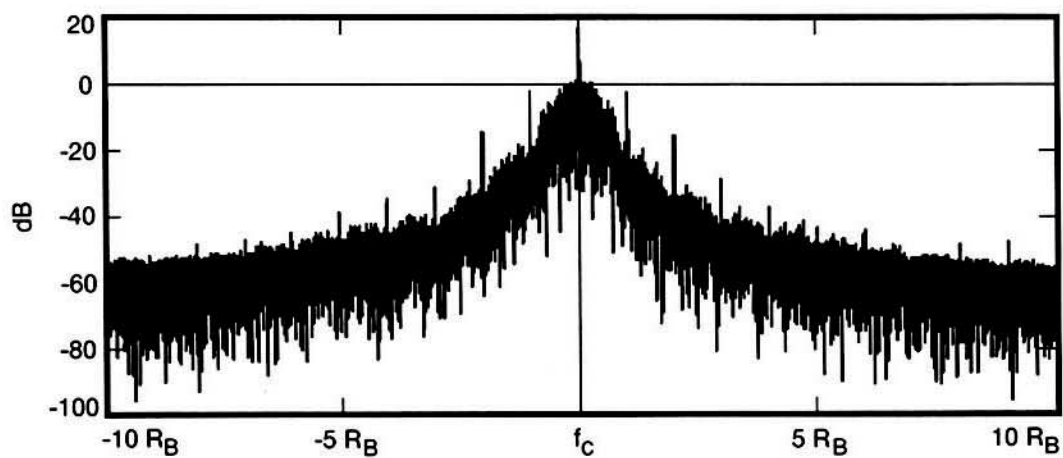


Figure 3-4b. Output of Power Amplifier

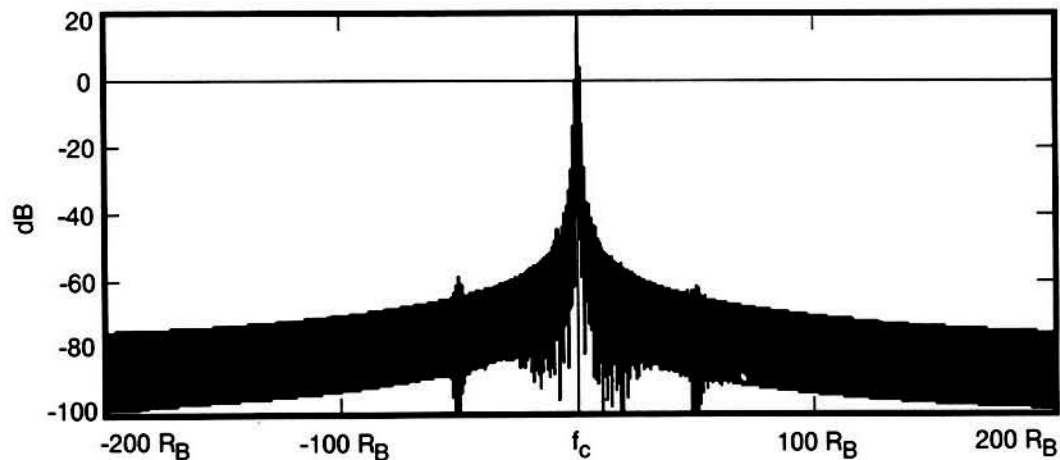


Figure 3-4c. Output of Second Harmonic Filter ($\pm 20 R_B$)

**Figure 3-4. Baseband 5th Order Butterworth Filtered NRZ-L Data Spectra
(Ideal Data)**

CCSDS - EFFICIENT MODULATION METHODS STUDY
Phase 2: Spectrum Shaping

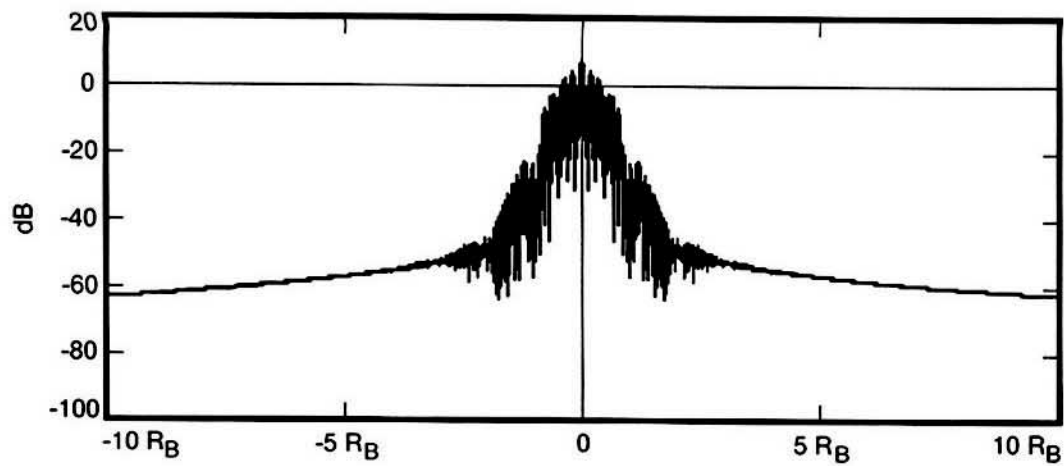


Figure 3-5a. Output from Butterworth Filter (5th Order)

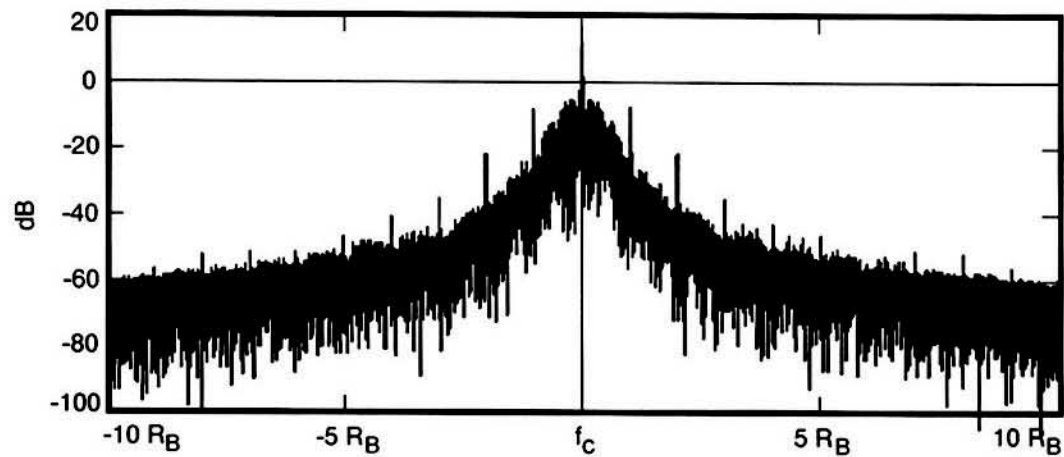


Figure 3-5b. Output of Power Amplifier

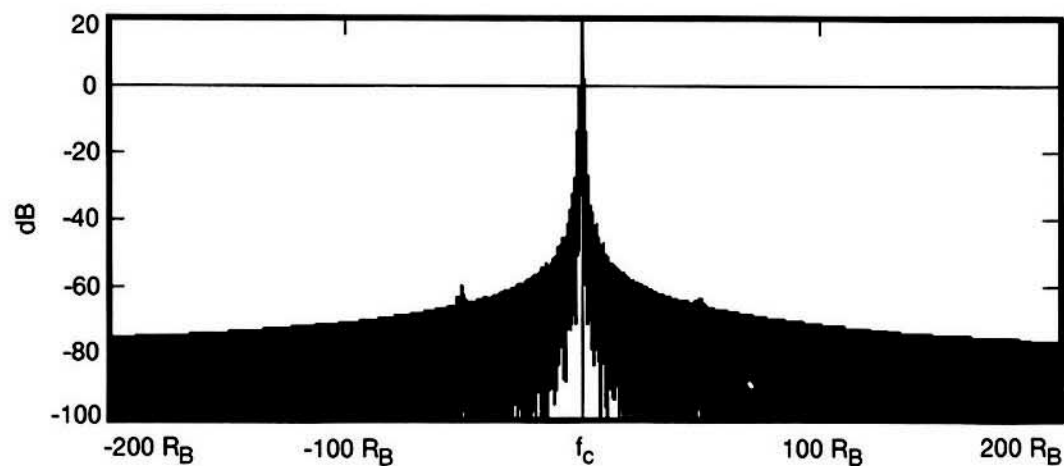


Figure 3-5c. Output of Second Harmonic Filter ($\pm 20 R_B$)

**Figure 3-5. Baseband 5th Order Butterworth Filtered NRZ-L Data Spectra
 (Non-Ideal Data)**

CCSDS - SFCG EFFICIENT MODULATION METHODS STUDY

Phase 2: Spectrum Shaping

From a Frequency Manager's perspective, the important result from baseband filtering can be seen when comparing Figures 3-3c and 3-5c. At $f_c \pm 5 R_b$, the Butterworth filter attenuates the sidebands by an additional 22 dB, placing the absolute level of sidebands beyond $\pm 5 R_b$ at 47 dB, or more, below the peak of the main data lobe. Whether this additional attenuation is sufficient to greatly increase band utilization is discussed in Section 5. A summary of the attenuation provided by each filter type will be found in Table 3-1.

The in-band spurious emissions are a cause of concern for Butterworth filters. Initially, it was thought that these spurious signals could be the result of Inter-Symbol Interference (ISI). To investigate this possibility, the Butterworth filter's bandwidth was widened from approximately $1 R_b$ to about $5 R_b$. The result was a reduction in the amplitude of the in-band spurious signal near the carrier but an increase in these same emissions at and around $\pm 5 R_b$. No significant benefit was obtained by widening the Butterworth filter's bandwidth.

3.2.2 Bessel Filter

A 3rd Order Bessel filter is an alternative to the Butterworth filter. For consistency, a BT product of 1.0 and a bandwidth of R_b were selected. Some writers suggest that Bessel filters are superior to Butterworth filters when applied to baseband signals. Spectra for this filter appear in Figures 3-6 and 3-7 and should be compared with Figures 3-4 and 3-5 respectively.

Comparing Figures 3-5b and 3-7b (power amplifier outputs) reveals that the modulated and amplified spectra are virtually identical for the two filters. Both exhibit a significant number of in-band spurious emissions. Likewise, comparing Figures 3-5c and 3-7c (2nd harmonic filter output) shows that the transmitted spectra are substantially indistinguishable from one another. Attenuation values contained in Table 3-1 show the Butterworth filter to be superior. The Bessel filter's poorer attenuation is probably due to its comparatively low Order. Like Butterworth filters, there is some concern regarding the use of Bessel filters because of the in-band spurious emissions.

3.2.3 Raised Cosine Filters

Raised Cosine filters were selected for evaluation because the linearity of their phase-frequency relationship should help to eliminate the ringing found in Butterworth filters at the cutoff frequency. Their comparatively narrow bandwidth, combined with a smooth response, should provide a signal which concentrates most of the data sideband energy in or near the main lobe significantly attenuating the sidebands. Such filters are commonly employed to pack a multiplicity of signals in a confined frequency band.

Raised Cosine filters accept two types of input signals: non-sampled and sampled. With non-sampled input signals like NRZ-L, $d(t)$, the Raised Cosine filter behaves in a manner similar to a passive filter with a transfer function, $X(f)$, having a Raised Cosine shape (Reference 10). Here, the filter's output is the convolution of the input signal $d(t)$ with $x(t)$ where $x(t)$ is the inverse Fourier transform of $X(f)$. Conversely, when the input signal is sampled (e.g., a pulse of short duration with an amplitude of + 1 representing a "1" and a similar pulse of short duration with an amplitude of - 1 representing a "0"), the Raised Cosine filter acts like a waveform generator producing a true Raised Cosine shape of $X(f)$ in the frequency domain. In practice, one can obtain a Raised Cosine waveform using a non-Sampled data input by cascading the Raised Cosine filter and a 1/Sinc filter. Note that $\text{Sinc}(t)$ is defined as $\sin(t)/t$.

CCSDS - SFCG EFFICIENT MODULATION METHODS STUDY

Phase 2: Spectrum Shaping

Maximizing data transmission efficiency requires the receiver have a filter matching the one at the transmitter. For linear channels (e.g., channels without AM-AM and AM-PM conversions), placing a Raised Cosine or Square Root Raised Cosine filter at the transmitter requires installing the same filter at the receiver. The result is a system transfer function approximating a $[\text{Raised Cosine}]^2$ or a Raised Cosine function respectively. With this implementation, one can obtain ISI-free sample points for optimum data detection (see Figures 4-2a and 4-2c).

However, for non-linear channels, such as those considered here, the principle is no longer applicable because of the distortion introduced by the system. With such channels, ISI-free sample points no longer exist as shown in Figures 4-2b and 4-2d. The objective of this study is not only to find a bandwidth efficient communications system which can increase frequency band utilization, but also, to identify an implementation that can be realized. Accordingly, detection and ISI will be discussed in greater detail in Section 4.

The "bandwidth" of a Raised Cosine filter is determined by a parameter termed α which can be varied from 0 to 1. For $\alpha = 0$, the filter's transfer function approximates that of a "Brick Wall" filter with bandwidth T while an $\alpha = 1$ yields a sinusoidal transfer function having a total width of $2T$. Figure 3-8a depicts the amplitude responses in the frequency domain for a Raised Cosine filter while Figure 3-8b does the same of a Square Root Raised Cosine filter.

As described above, if Sampled data is fed to a Raised Cosine filter, the resulting waveform will be a pure Raised Cosine function rather than the convolution of the inverse Fourier transform with an NRZ-L function. To generate a true Raised Cosine waveform, a Sampled data input rather than a NRZ-L data input is required. Sampled data is produced by generating a pulse, of short duration, having a $+1$ amplitude representing each "1" and a pulse of the same duration but having a -1 amplitude to representing each "0".

To determine if the filter's performance is significantly affected, spectra for both NRZ-L and Sampled data are analyzed. A Sampled data waveform requires modifications to existing spacecraft hardware. However, if the bandwidth reduction resulting from this data type is large, then such alterations may be desirable and worth the expenditure.

In the following sections, spectra for both Raised Cosine and Square Root Raised Cosine filters with NRZ-L and Sampled data inputs are provided. Both filter types have advantages and disadvantages with respect to each other as well as with regard to Butterworth and Bessel filters which can only be illuminated by comparing the several types. To make this comparison it is necessary to examine the transmitted spectra for the several Raised Cosine and Square Root Raised Cosine filters. Spectra for Raised Cosine filters with an NRZ-L input and $\alpha = 0.25, 0.5$, and 1 are provided to demonstrate the effect of this parameter. However, Raised Cosine filters for Sampled data and all Square Root Raised Cosine filters are only evaluated at $\alpha = 1$.

CCSDS - SFCG EFFICIENT MODULATION METHODS STUDY
Phase 2: Spectrum Shaping

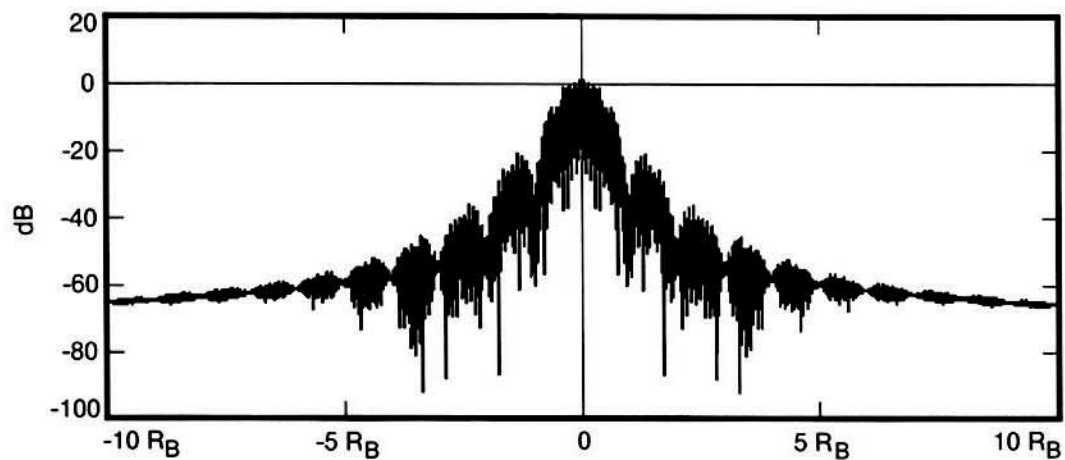


Figure 3-6a. Output from Bessel Filter (3rd Order)

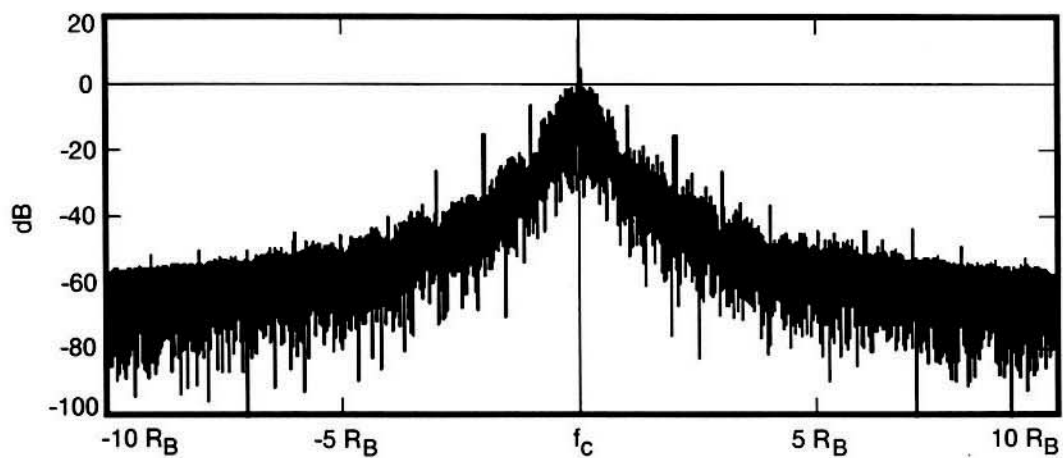


Figure 3-6b. Output of Power Amplifier

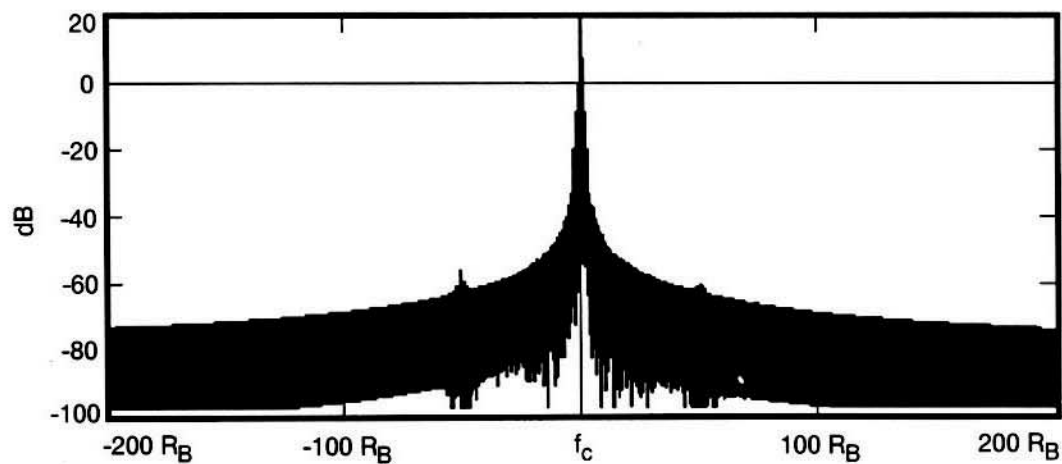


Figure 3-6c. Output of Second Harmonic Filter ($\pm 20 R_B$)

**Figure 3-6. Baseband 3rd Order Bessel Filtered NRZ-L Data Spectra
(Ideal Data)**

CCSDS - SFCG EFFICIENT MODULATION METHODS STUDY
Phase 2: Spectrum Shaping

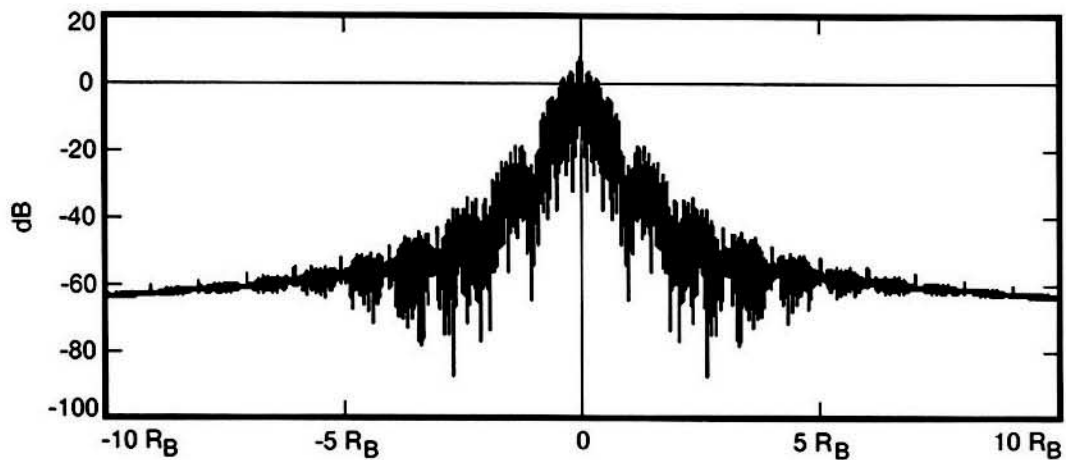


Figure 3-7a. Output from Bessel Filter (3rd Order)

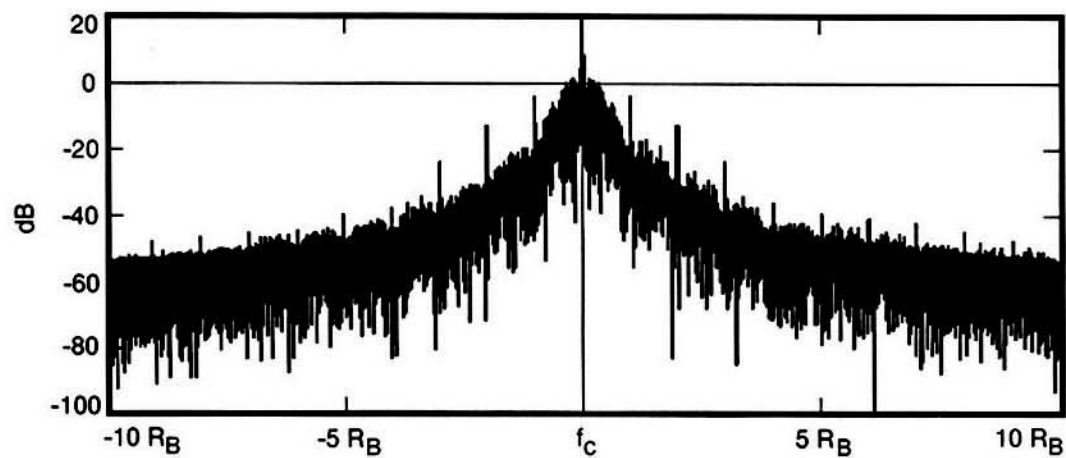


Figure 3-7b. Output of Power Amplifier

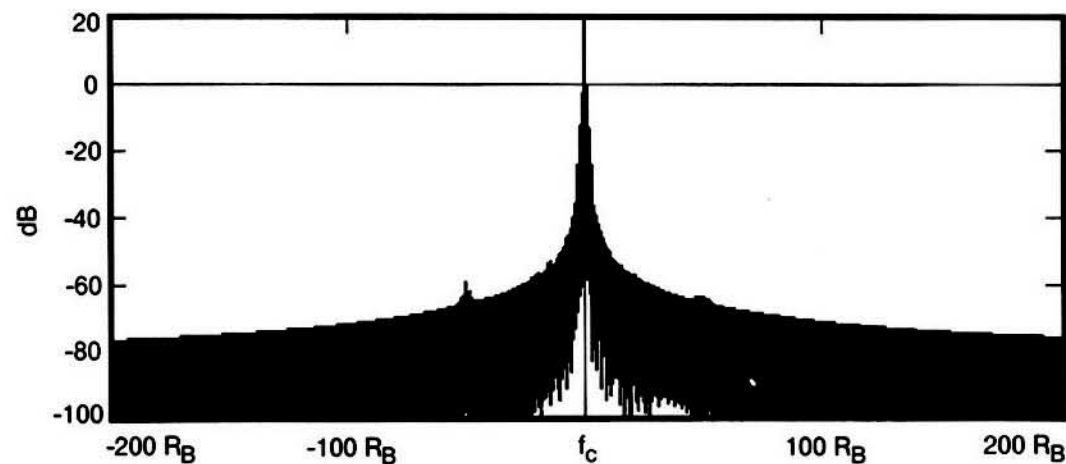


Figure 3-7c. Output of Second Harmonic Filter ($\pm 20 R_B$)

**Figure 3-7. Baseband 3rd Order Bessel Filtered NRZ-L Data Spectra
 (Non-Ideal Data)**

CCSDS - SFCG EFFICIENT MODULATION METHODS STUDY
Phase 2: Spectrum Shaping

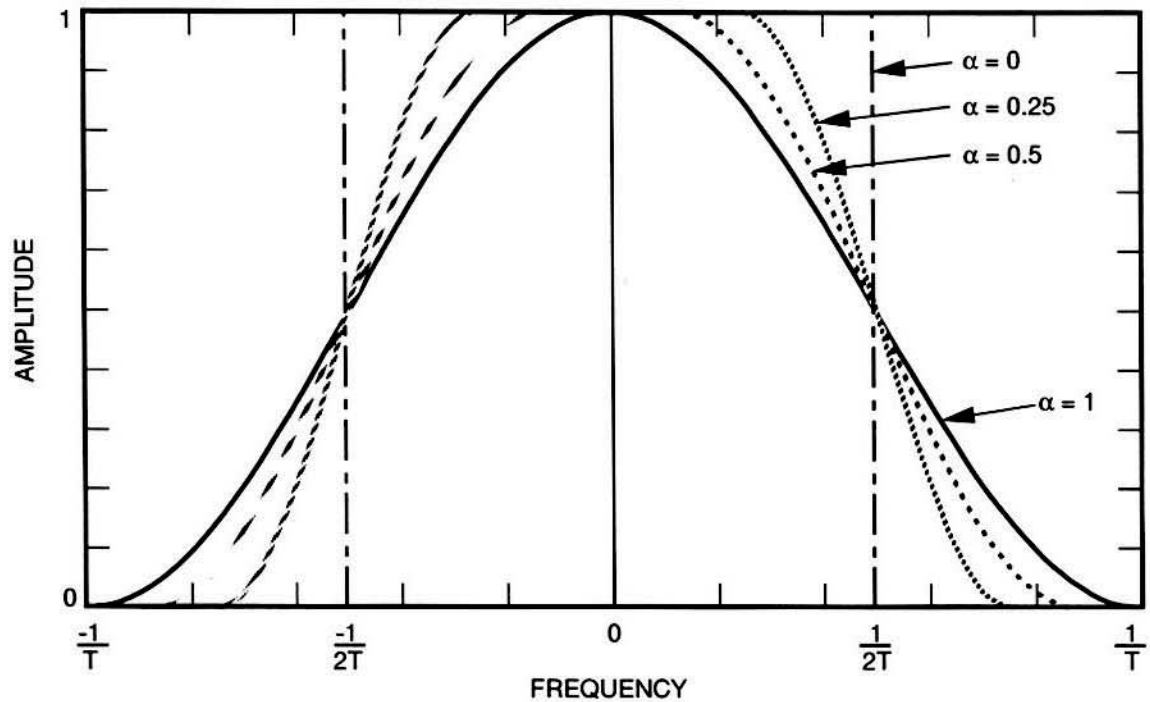


Figure 3-8a. Amplitude Response of a Raised Cosine Filter

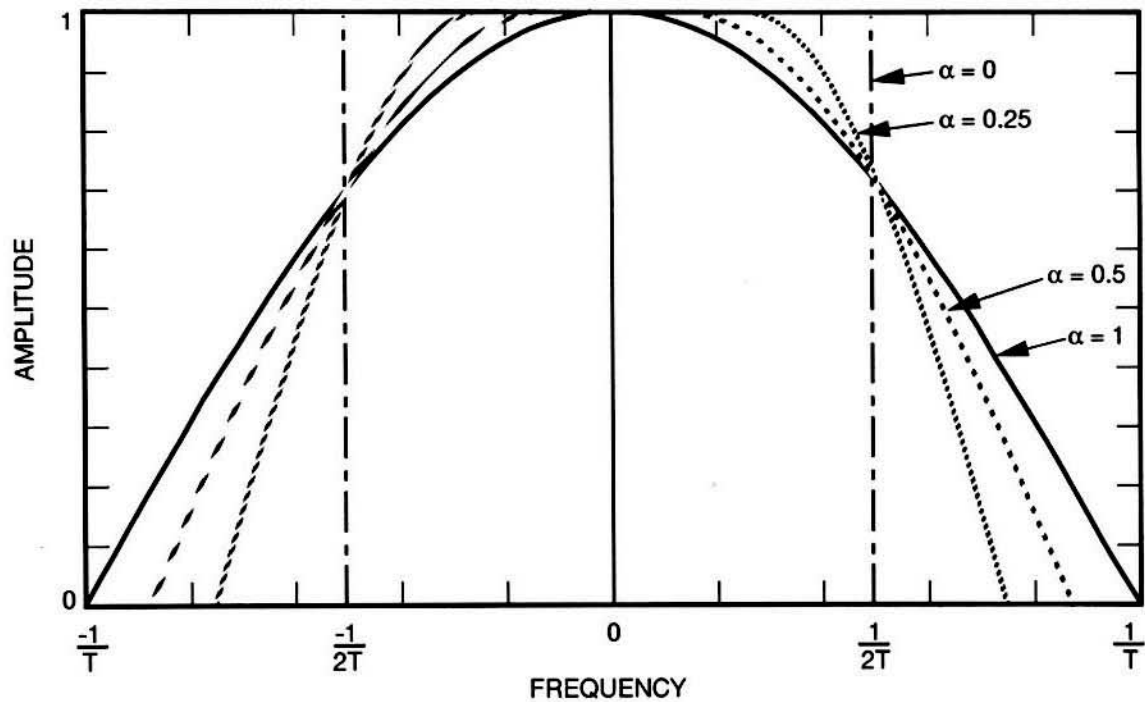


Figure 3-8b. Amplitude Response of a Square Root Raised Cosine Filter

Figure 3-8. Amplitude Responses for Raised Cosine Filters

CCSDS - SFCG EFFICIENT MODULATION METHODS STUDY

Phase 2: Spectrum Shaping

3.2.3.1 Raised Cosine Filter ($\alpha = 0.25$), NRZ-L Data

Comparing Figures 3-9a and 3-10a for a Raised Cosine ($\alpha = 0.25$) filter with Figures 3-4a and 3-5a for Butterworth and Figures 3-6a and 3-7a for Bessel filters shows that the former offers a significant advantage over both of the latter filter types. Despite some evidence of higher order sidebands, the spectrum is narrower, cleaner, better defined, than the spectra for other filter types. Moreover, the attenuation at $\pm 5 R_B$ is significantly greater than that for the Butterworth or Bessel filters. In-band spurious emissions are absent, even for non-ideal data. The reason why Raised Cosine filters are frequently chosen to separate signal sources operating in the same band is clearly obvious from Figures 3-9a and 3-10a. With $\alpha = 0.25$, this is the narrowest bandwidth Raised Cosine filter to be considered in this study.

Outputs from the power amplifier are also comparatively uniform although the greatly attenuated higher order data sidebands are clearly visible in Figures 3-9b and 3-10b for ideal and non-ideal data respectively. Unfortunately, the nonlinearities of the modulator, multiplier, and power amplifier cause a significant increase in amplitude in the 2 to 7 R_B region. Nevertheless, with non-ideal data, the transmitted signal levels are 40 dB below the main lobe at $\pm 3 R_B$ and 53 dB below the main lobe at $\pm 5 R_B$.

3.2.3.2 Raised Cosine Filter ($\alpha = 0.5$), NRZ-L Data

Similar RF frequency spectrum levels, using non-ideal data, are found with a Raised Cosine ($\alpha = 0.5$) filter (Figure 3-12b). This filter provides a transmitted data spectrum which is 43 dB below the main data lobe at $\pm 3 R_B$ and 52 dB below the main lobe at $\pm 5 R_B$.

As with the previous filter, the transmitted RF spectrum (Figure 3-12c) is comparatively smooth and free of in-band spurious emissions, even for non-ideal data. Since there appears to be no significant difference in the spectra using the two filters, the selection must depend upon other factors such as ISI, implementation complexity, etc.

3.2.3.3 Raised Cosine Filter ($\alpha = 1$), NRZ-L Data

Because a Raised Cosine filter with an $\alpha = 1$ has a larger bandwidth than filters with smaller values of α , the baseband data spectrum using non-ideal data (Figure 3-14a) is wider than those described above. However, the higher order data sidebands seen in the previous cases are clearly absent.

At the power amplifier's output (Figure 3-15b), the spectrum is characterized by a smooth roll-off with no in-band spurious emissions evident. Due to this filter's wider bandwidth, the attenuation at $\pm 5 R_B$ is slightly less than that for filters with smaller values of α . At $\pm 5 R_B$, the signal level is 51 dB below the main lobe rather than 52 or 53 dB.

3.2.3.4 Square Root Raised Cosine Filter ($\alpha = 1$), NRZ-L Data

To obtain two ISI-free sample points, a Square Root Raised Cosine filter was evaluated. Only a single filter with $\alpha = 1$ was analyzed. Results are shown in Figures 3-15 and 3-16 for ideal and non-ideal data respectively. Like the full Raised Cosine filters, the Square Root Raised Cosine filter was supplied with NRZ-L data.

CCSDS - SFCG EFFICIENT MODULATION METHODS STUDY
Phase 2: Spectrum Shaping

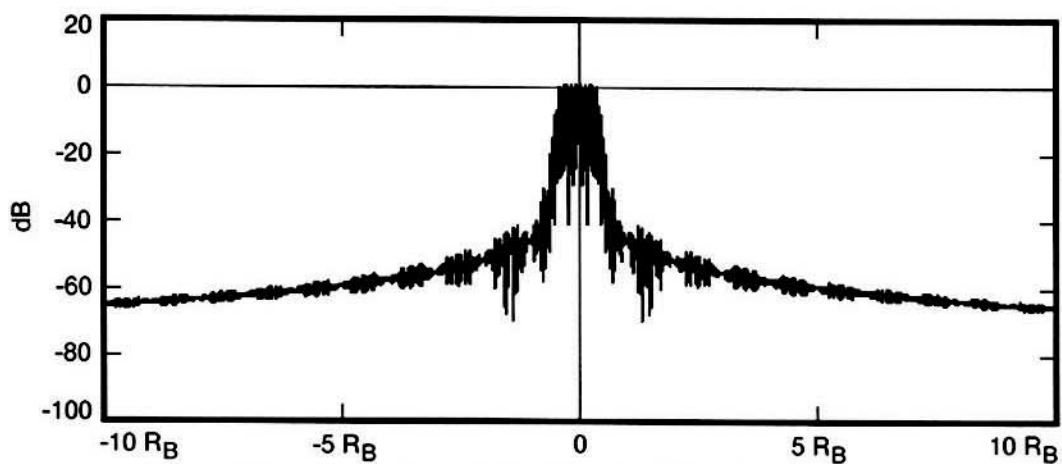


Figure 3-9a. Output from Raised Cosine Filter ($\alpha = 0.25$; 2000 Taps)

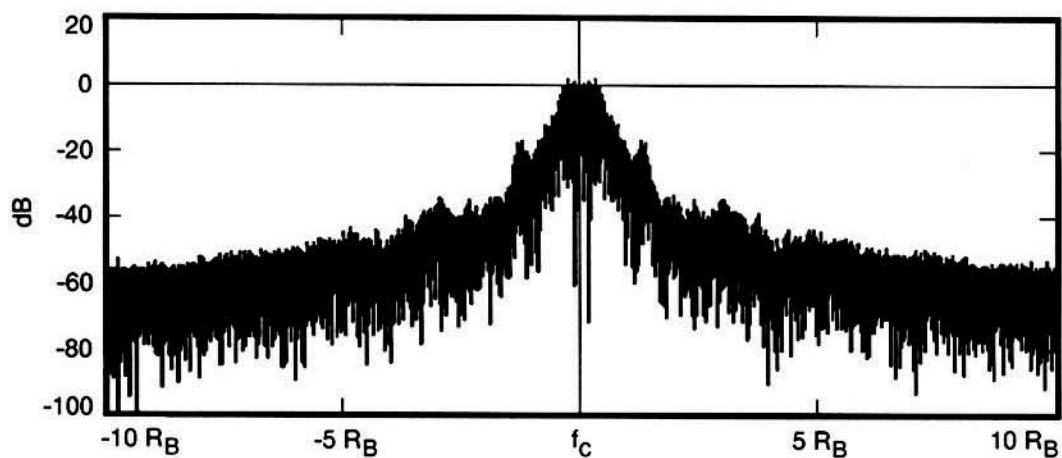


Figure 3-9b. Output of Power Amplifier

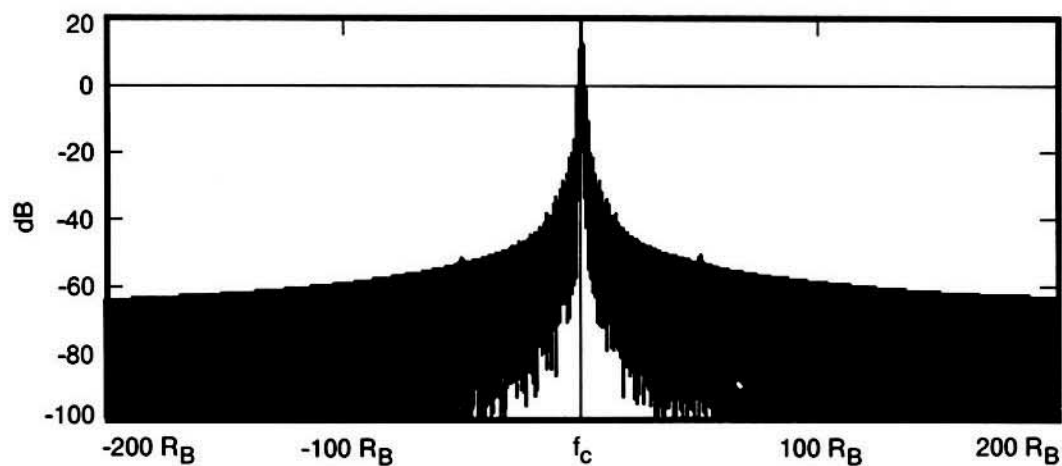


Figure 3-9c. Output of Second Harmonic Filter ($\pm 20 R_B$)

**Figure 3-9. Baseband Raised Cosine Filtered NRZ-L Data Spectra, $\alpha = 0.25$
(Ideal Data)**

CCSDS- SFCG EFFICIENT MODULATION METHODS STUDY
Phase 2: Spectrum Shaping

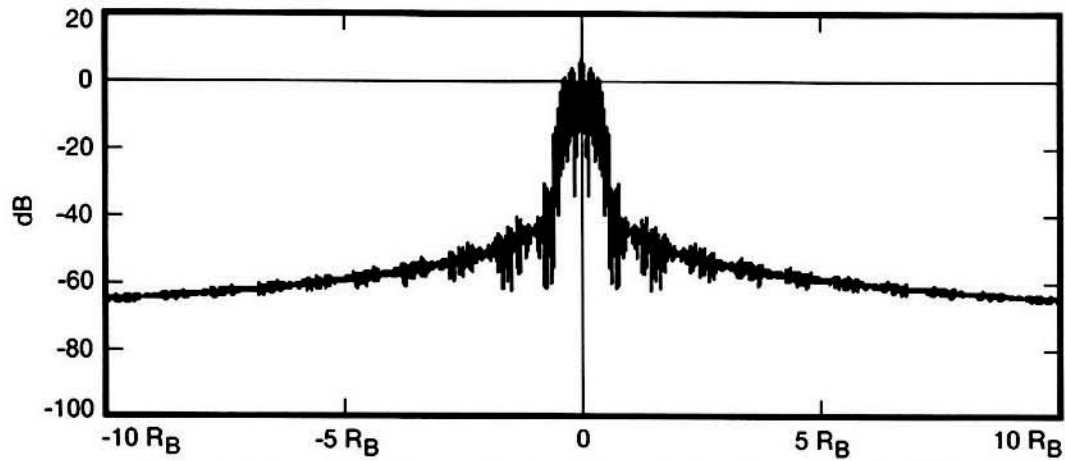


Figure 3-10a. Output from Raised Cosine Filter ($\alpha = 0.25$; 2000 Taps)

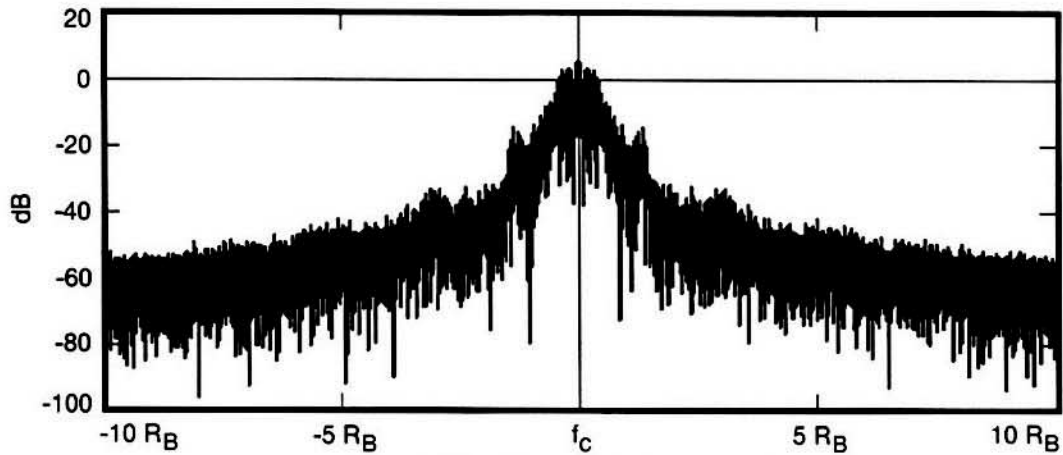


Figure 3-10b. Output of Power Amplifier

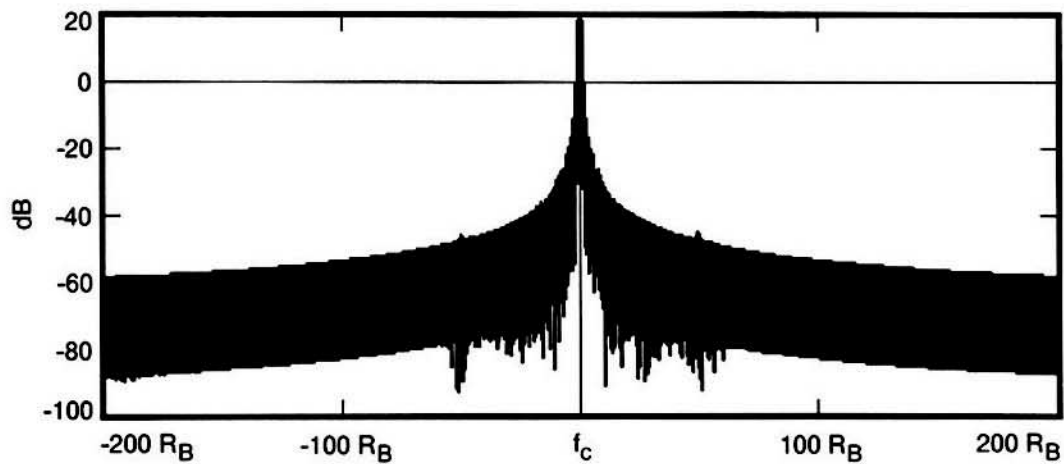


Figure 3-10c. Output of Second Harmonic Filter ($\pm 20 R_B$)

**Figure 3-10. Baseband Raised Cosine Filtered NRZ-L Data Spectra, $\alpha = 0.25$
 (Non-Ideal Data)**

CCSDS - SCFG EFFICIENT MODULATION METHODS STUDY
Phase 2: Spectrum Shaping

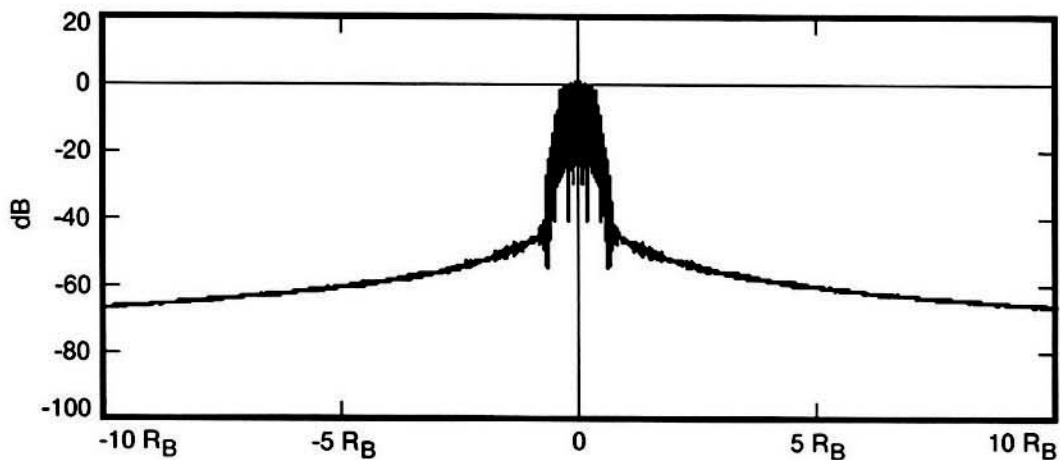


Figure 3-11a. Output from Raised Cosine Filter ($\alpha = 0.5$; 2000 Taps)

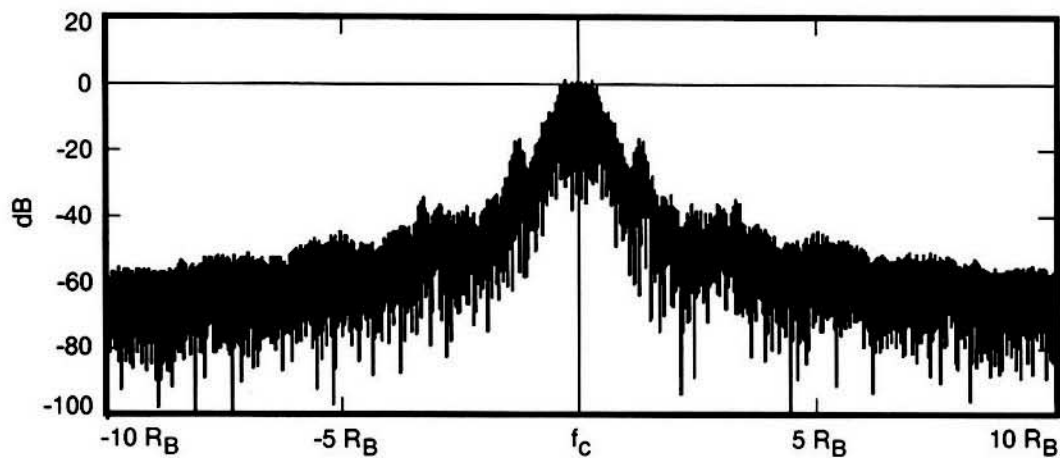


Figure 3-11b. Output of Power Amplifier

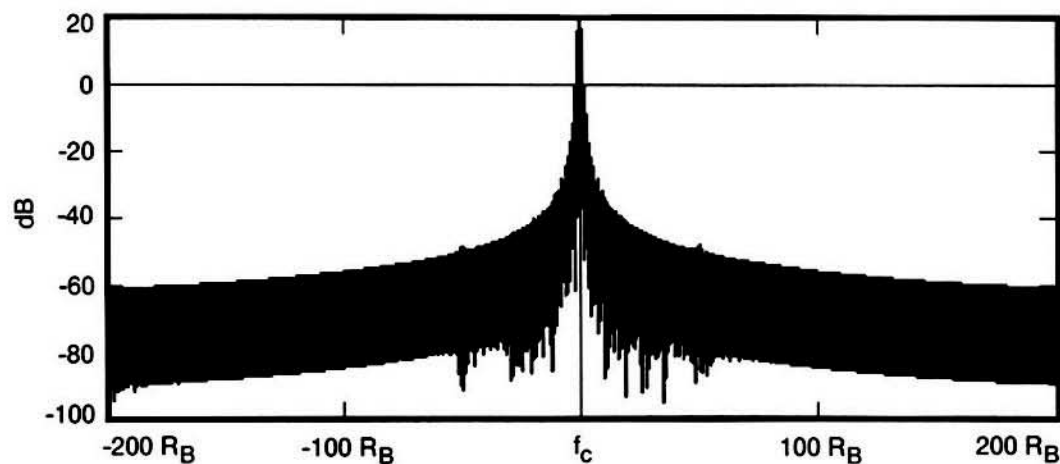


Figure 3-11c. Output of Second Harmonic Filter ($\pm 20 R_B$)

Figure 3-11. Baseband Raised Cosine Filtered NRZ-L Data Spectra, $\alpha = 0.5$
(Ideal Data)

CCSDS - SFCG EFFICIENT MODULATION METHODS STUDY
Phase 2: Spectrum Shaping

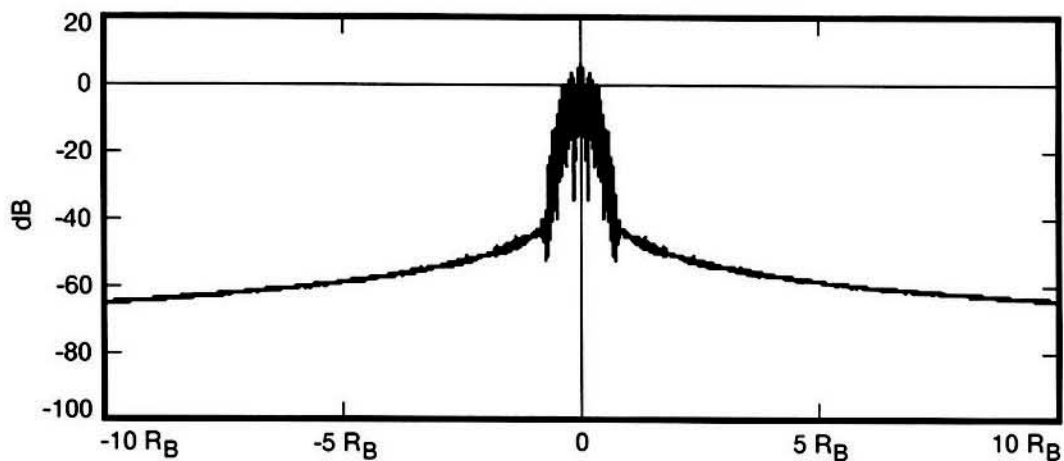


Figure 3-12a. Output from Raised Cosine Filter ($\alpha = 0.5$; 2000 Taps)

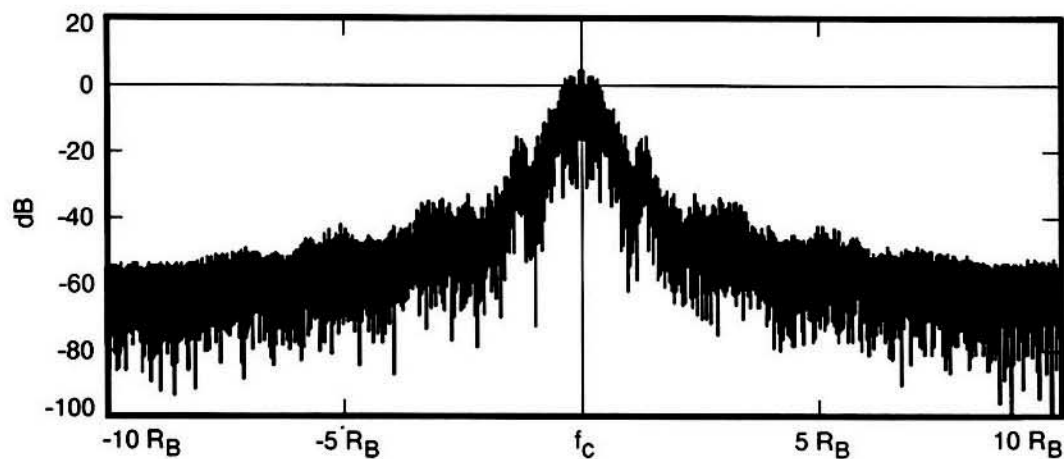


Figure 3-12b. Output of Power Amplifier

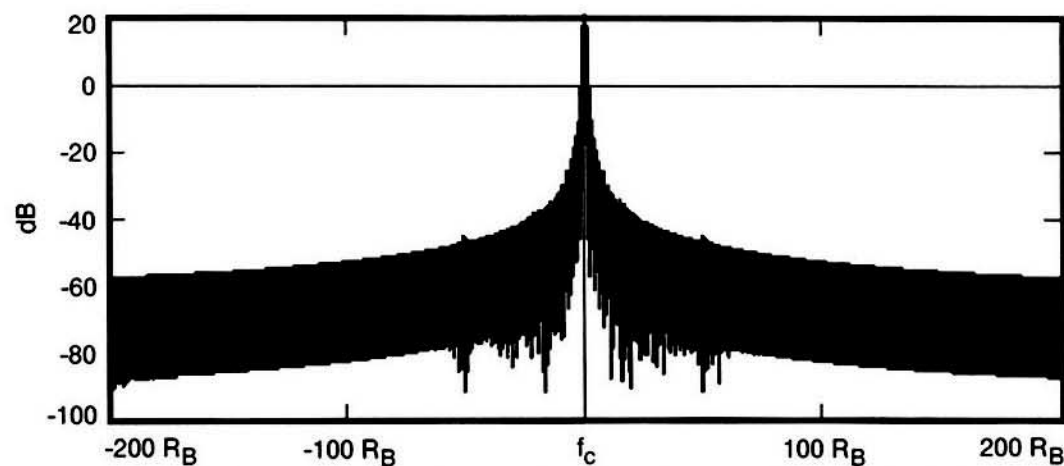


Figure 3-12c. Output of Second Harmonic Filter ($\pm 20 R_B$)

**Figure 3-12. Baseband Raised Cosine Filtered NRZ-L Data Spectra, $\alpha = 0.5$
(Non-Ideal Data)**

CCSDS - SFCG EFFICIENT MODULATION METHODS STUDY
Phase 2: Spectrum Shaping

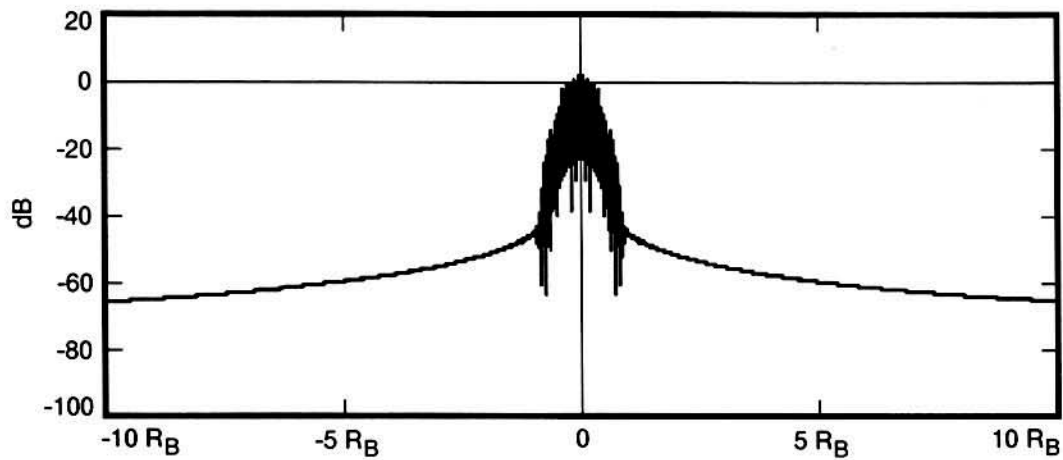


Figure 3-13a. Output from Raised Cosine Filter ($\alpha = 1$; 2000 Taps)

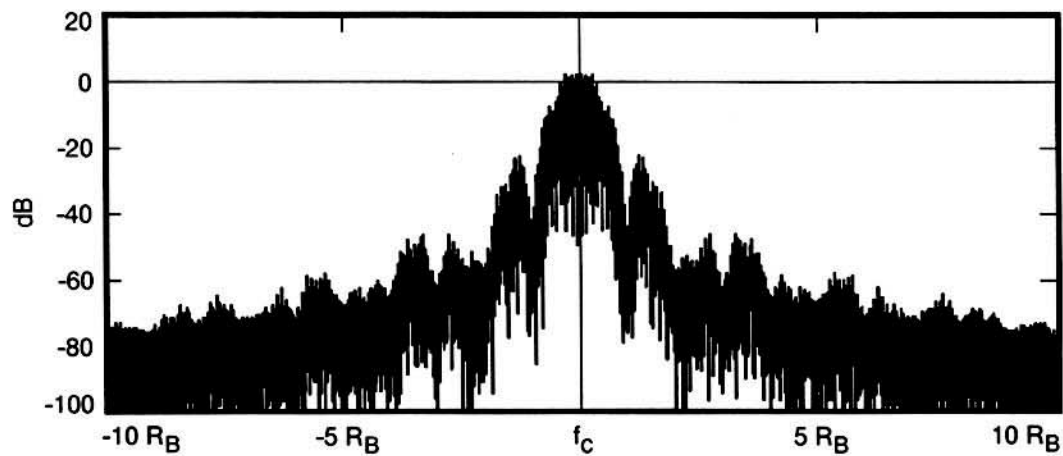


Figure 3-13b. Output of Power Amplifier

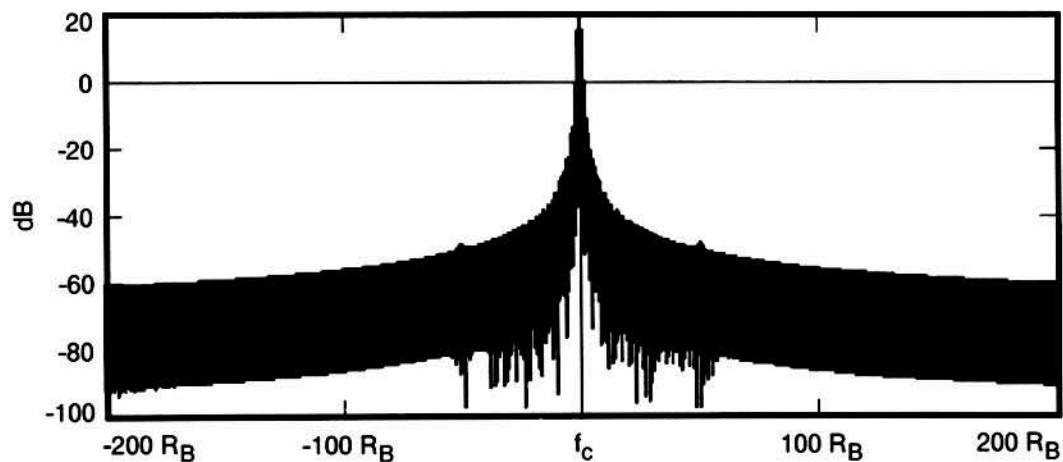


Figure 3-13c. Output of Second Harmonic Filter ($\pm 20 R_B$)

**Figure 3-13. Baseband Raised Cosine Filtered NRZ-L Data Spectra, $\alpha = 1$
 (Ideal Data)**

CCSDS - SFCG EFFICIENT MODULATION METHODS STUDY
Phase 2: Spectrum Shaping

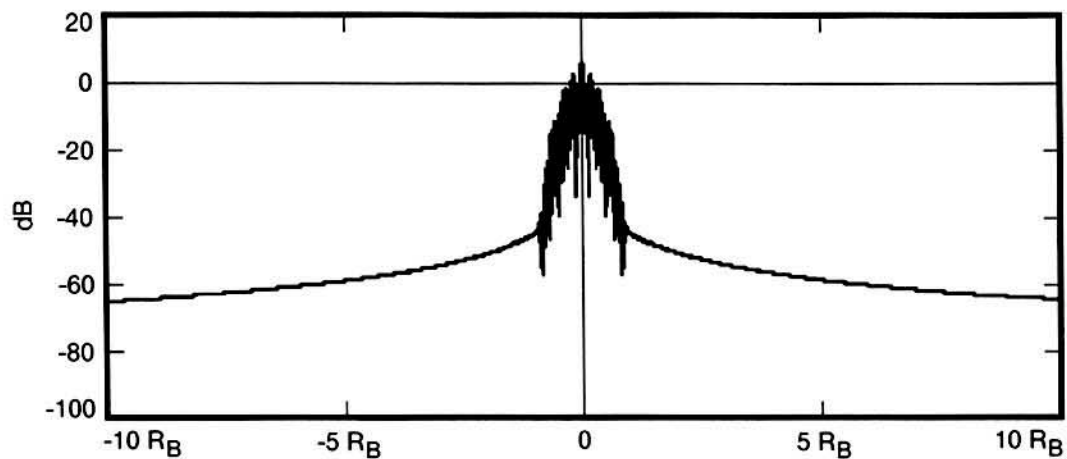


Figure 3-14a. Output from Raised Cosine Filter ($\alpha = 1$; 2000 Taps)

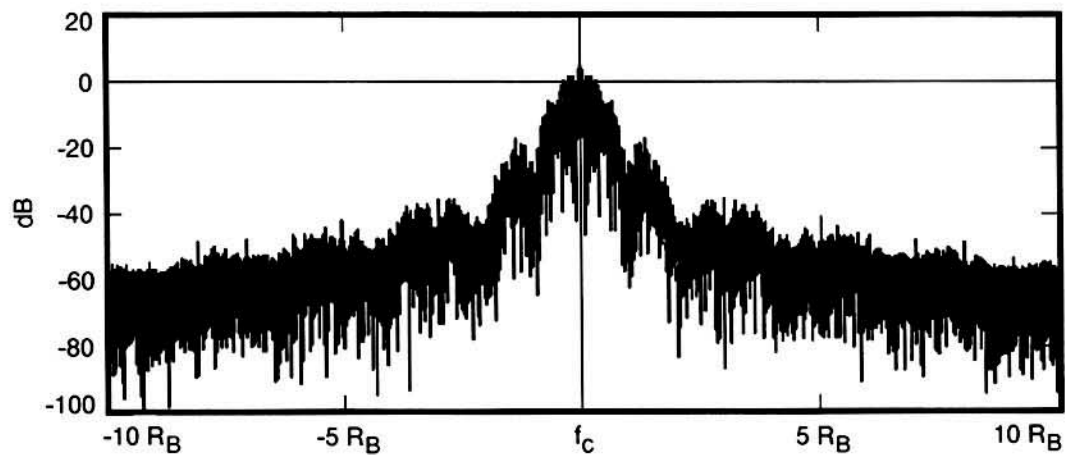


Figure 3-14b. Output of Power Amplifier

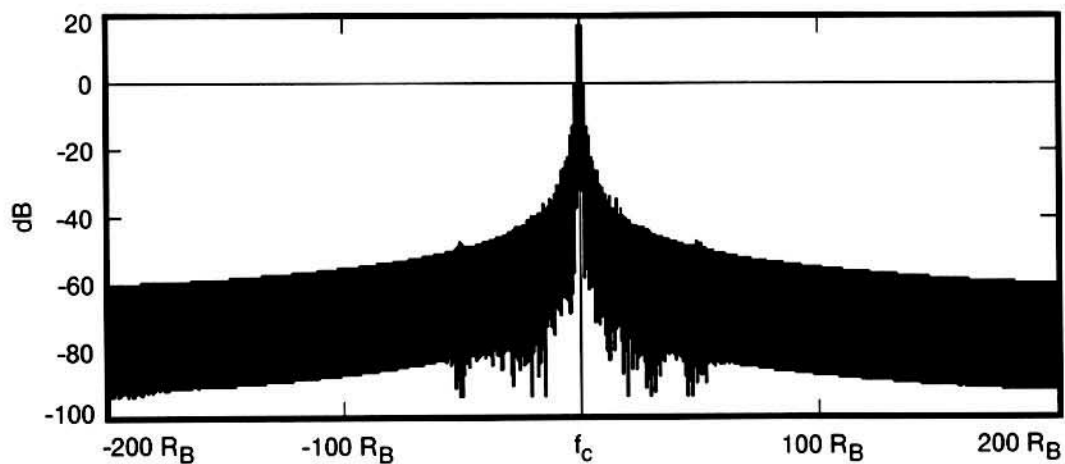


Figure 3-14c. Output of Second Harmonic Filter ($\pm 20 R_B$)

**Figure 3-14. Baseband Raised Cosine Filtered NRZ-L Data Spectra, $\alpha = 1$
 (Non-Ideal Data)**

CCSDS - SFCG EFFICIENT MODULATION METHODS STUDY
Phase 2: Spectrum Shaping

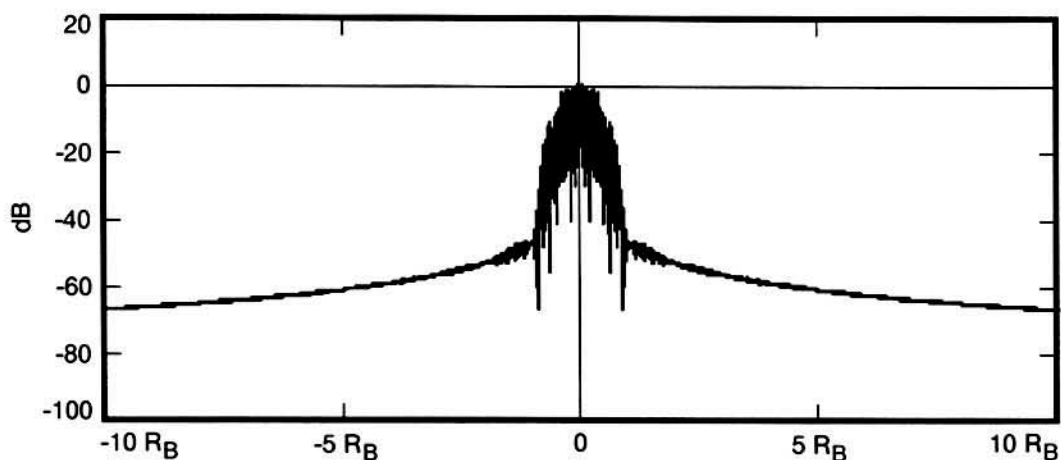


Figure 3-15a. Output from Square Root Raised Cosine Filter ($\alpha = 1$; 2000 Taps)

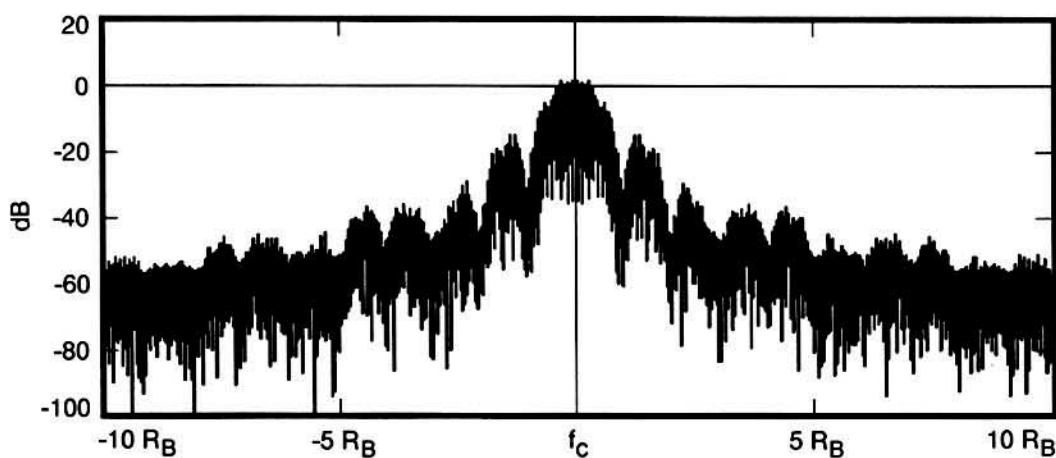


Figure 3-15b. Output of Power Amplifier

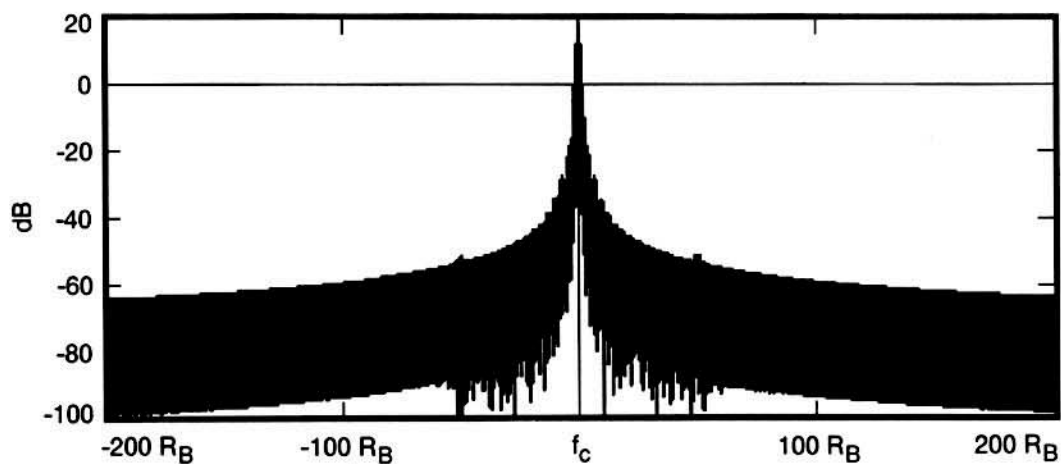


Figure 3-15c. Output of Second Harmonic Filter ($\pm 20 R_B$)

Figure 3-15. Baseband Square Root Raised Cosine Filtered NRZ-L Data Spectra, $\alpha = 1$ (Ideal Data)

CCSDS - SFCG EFFICIENT MODULATION METHODS STUDY
Phase 2: Spectrum Shaping

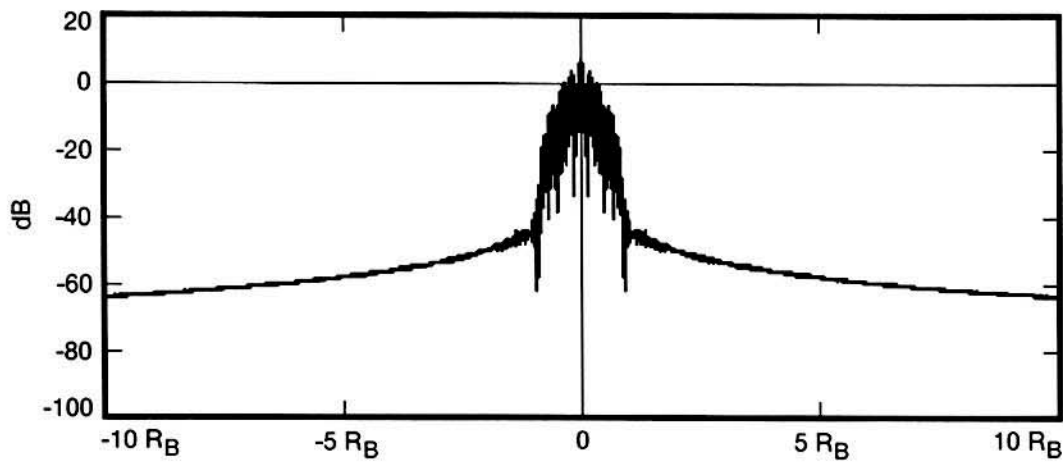


Figure 3-16a. Output from Square Root Raised Cosine Filter ($\alpha = 1$; 2000 Taps)

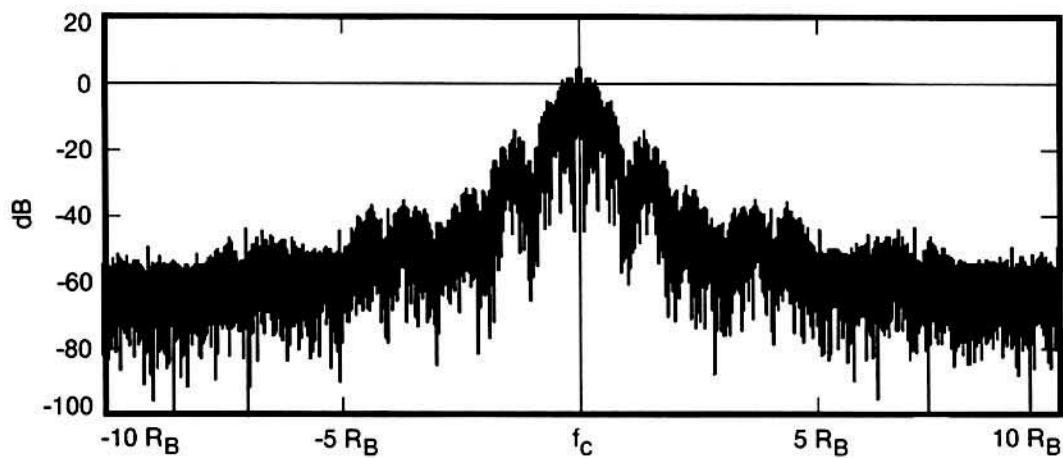


Figure 3-16b. Output of Power Amplifier.

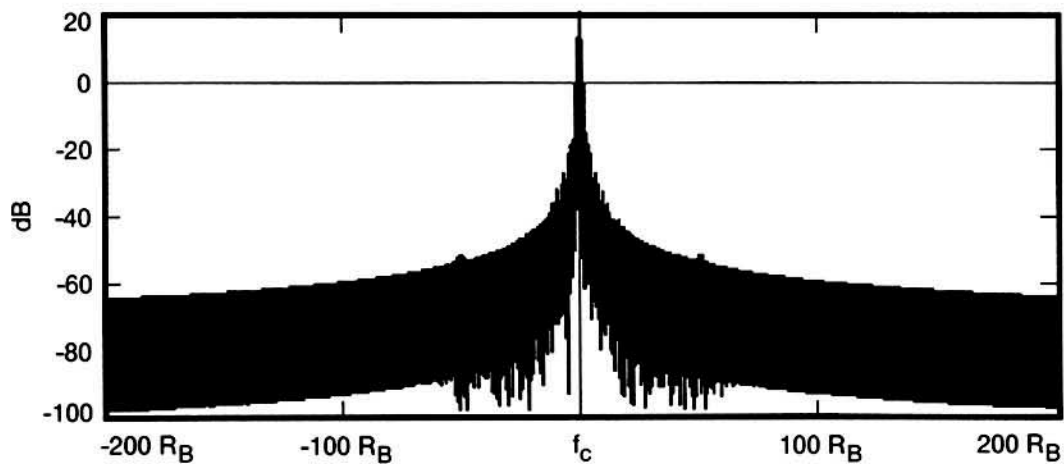


Figure 3-16c. Output of Second Harmonic Filter ($\pm 20 R_B$)

Figure 3-16. Baseband Square Root Raised Cosine Filtered NRZ-L Data Spectra, $\alpha = 1$ (Non-Ideal Data)

CCSDS - SFCG EFFICIENT MODULATION METHODS STUDY

Phase 2: Spectrum Shaping

3.2.3.4 Square Root Raised Cosine Filter ($\alpha = 1$), NRZ-L (Continued)

Figures 3-16b and 3-16c, for the power amplifier and second harmonic filter outputs respectively, also show a smooth roll-off and no spurious emissions, even using non-ideal data. Excellent attenuation was obtained with the signal level at $\pm 5 R_b$ falling to 53 dB below the level of the main data lobe. This is better performance than was obtained with any of the full Raised Cosine, Butterworth, or Bessel filters. The Square Root Raised Cosine filter appears to be a strong candidate for the optimum baseband filter type.

3.2.3.5 Raised Cosine Filter ($\alpha = 1$), Sampled Data

Since Raised Cosine filters only produce a true Raised Cosine function with Sampled data inputs as described in Section 3.2.3 above, simulations using Sampled data were made to determine whether the resulting spectra offered significant advantages over those produced by NRZ-L data. Figures 3-17a and 3-18a, for ideal and non-ideal data respectively, show the filter's output for Sampled data. The effects of sampling are evident from the small spikes seen in the Figures, particularly for the non-ideal data case.

These spikes are also clearly evident in Figures 3-17b and 3-18b representing the power amplifier's output. With a Sampled data input, the spectra for a Raised Cosine ($\alpha = 1$) filter begins to resemble those of the Butterworth and Bessel filters.

Following the second harmonic filter ($f_c \pm 20 R_b$), Figures 3-17c and 3-18c, the spectrum appears to be similar to that for a Raised Cosine filter ($\alpha = 1$) with an NRZ-L input. However, measurements made with COMDISCO to determine the point where the frequency spectrum falls to a level 50 dB below the main data lobe show the performance with Sampled data is poorer than with NRZ-L data (see Tables 3-1a and 3-1b). This degraded performance results from the spikes generated by the data sampling process.

While it may be possible to reduce the amplitude or eliminate these emissions by a post filter signal processor, there is no evidence that the resulting spectrum would be better than a Raised Cosine filter with an NRZ-L input. However, amplitude studies discussed in Section 4 show that a Raised Cosine filter, with a Sampled data input, has a significantly more uniform output than one with an NRZ-L data input. Therefore, despite their poorer sideband attenuation, Raised Cosine filters with Sampled inputs may be useful in an operational system.

3.2.3.6 Square Root Raised Cosine Filter ($\alpha = 1$), Sampled Data

Figures 3-19a and 3-20a show the output of a Square Root Raised Cosine filter ($\alpha = 1$) with Sampled ideal and non-ideal data inputs respectively. Here the sampling effect is very evident and can be seen as a series of amplitude changes at intervals of approximately $0.1 R_b$. These additional low level "spurious emissions" are likely the result of the Square Root Raised Cosine filter's wider bandwidth.

The power amplifier's output is shown in Figures 3-19b and 3-20b. Both exhibit significant levels of in-band spurious emissions with the result that they perform much like systems with Butterworth and Bessel filters.

CCSDS - SFCG EFFICIENT MODULATION METHODS STUDY**Phase 2: Spectrum Shaping**

Spurious emissions are clearly evident in the broadband spectrum ($f_c \pm 200 R_b$) measured at the output of the second harmonic filter (Figures 3-19c and 3-20c). The effect of these emissions is obvious in Tables 3-1a and 3-1b, for ideal and non-ideal data respectively, where the data sideband attenuation at $\pm 5 R_b$ is 14-16 dB less using a Sampled data input than is the case for an NRZ-L data input. Given the amplitude variations found for a Square Root Raised Cosine filter using a Sampled data input (see Section 4), it is questionable whether or not this filter with a Sampled data input will be useful.

3.3 Summary of Baseband Filter Simulations

Four filter types, seven different baseband filters, and four types of input data were studied to determine their effect in limiting the transmitted telemetry data spectrum's width. Most space agency's data systems produce an NRZ-L baseband format so it was selected as the primary input to the filters. However, because of their design, both the Raised Cosine and Square Root Raised Cosine filters were also evaluated using Sampled data inputs. To obtain the most realistic results, all simulations were performed with a non-ideal modulator, frequency multiplier, and solid state power amplifier. For completeness, filters were tested using both ideal and non-ideal data as defined in Section 2.2.

A summary of the sideband levels for no baseband filtering and for the several baseband filter types appears in Tables 3-1a and 3-1b for ideal and non-ideal data respectively. Numbers in these Tables represent the highest signal levels, relative to the first (main) data lobe, found at the named (or greater) frequency on either side of the RF carrier. The attenuation provided by each filter can be found by subtracting the value in the first row, representing the unfiltered case, from the value for the desired filter at the same frequency. Numbers in these Tables were obtained from the COMDISCO simulator by positioning a cursor on the frequency spectrum at each of the specified frequency offsets and reading the amplitude directly from a digital representation on the screen. Accuracy of the measurement is believed to be within ± 2 dB.

Having completed the performance survey of the several filter types, the task becomes one of building a flight system. The most effective filter in the world, which produces the most compact RF spectrum, will be useless if flight and ground systems using the filter cannot be easily implemented. The characteristics of the several filters, as they relate to actual systems, is the subject of the next Section.

CCSDS - SFCG EFFICIENT MODULATION METHODS STUDY
Phase 2: Spectrum Shaping

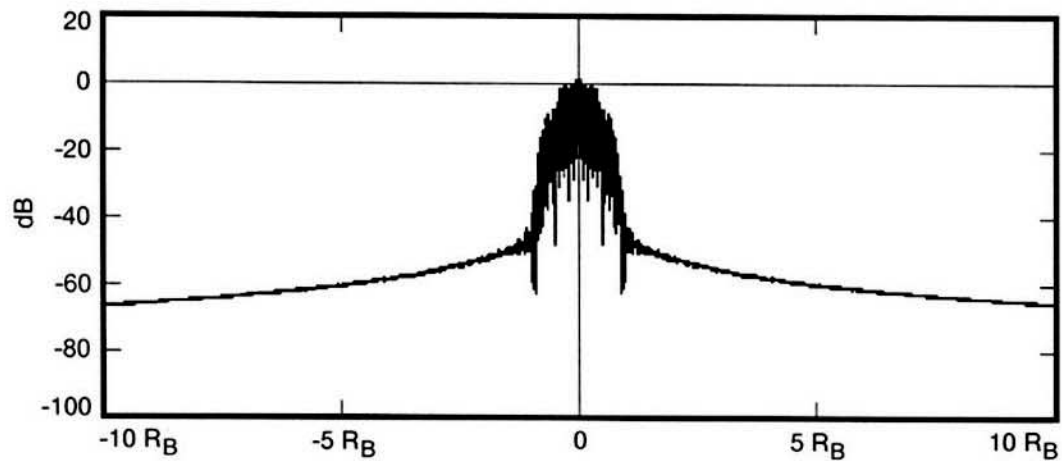


Figure 3-17a. Output from Raised Cosine Filter, $\alpha = 1$

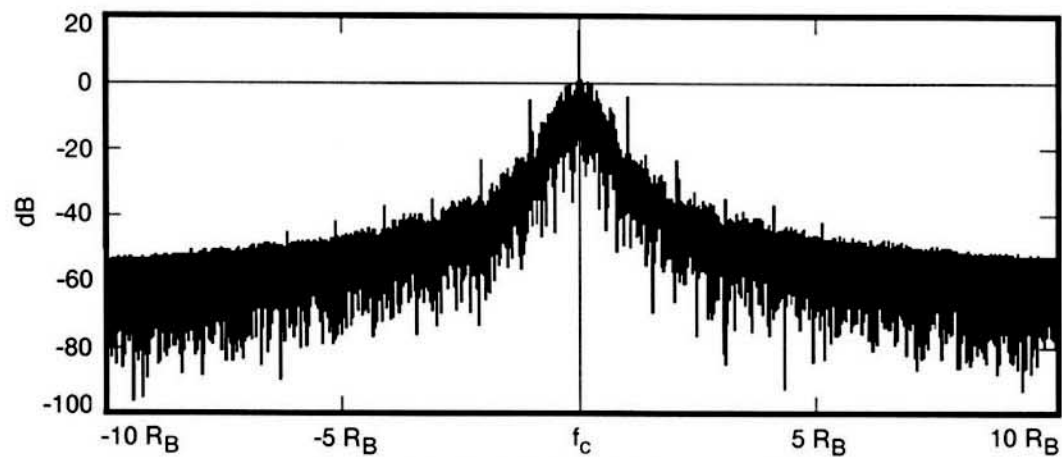


Figure 3-17b. Output of Power Amplifier

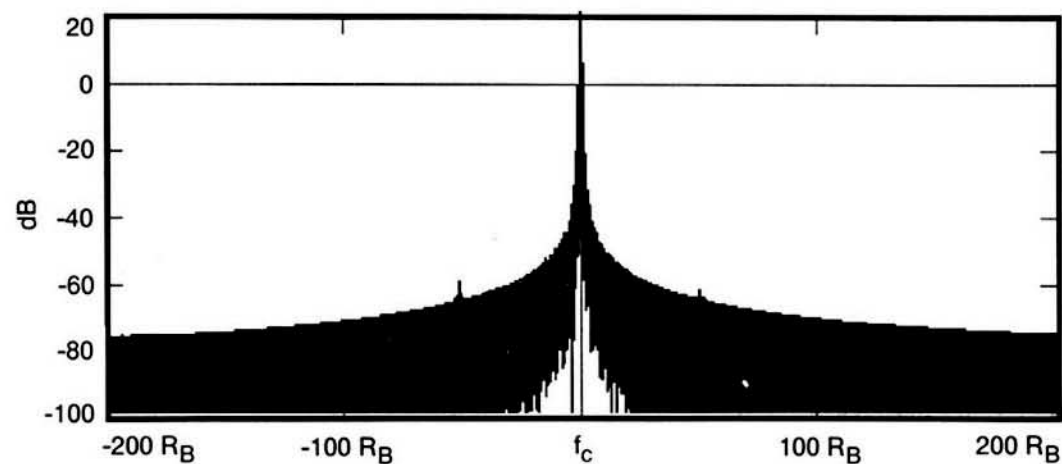


Figure 3-17c. Output of Second Harmonic Filter ($\pm 20 R_B$)

Figure 3-17. Baseband Raised Cosine Filtered Sampled Data Spectra, $\alpha = 1$
(Ideal Data)

CCSDS - SFCG EFFICIENT MODULATION METHODS STUDY
Phase 2: Spectrum Shaping

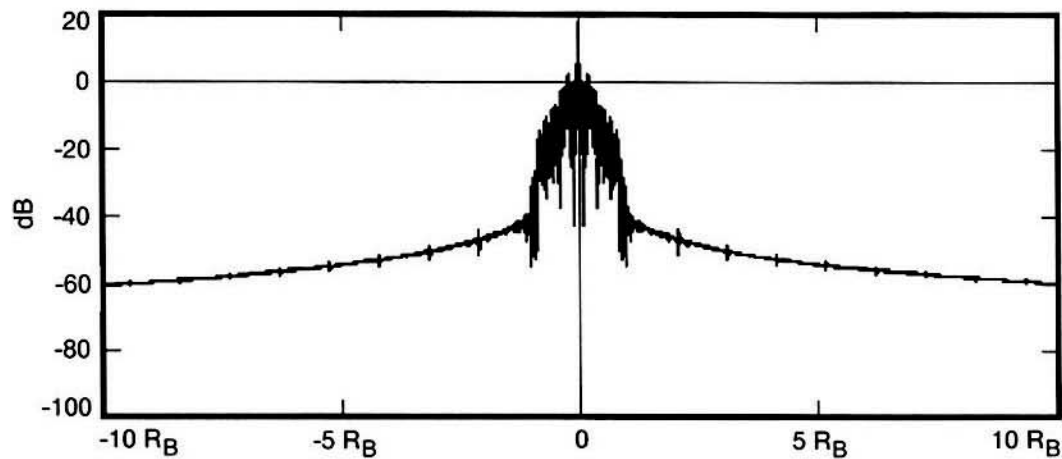


Figure 3-18a. Output from Raised Cosine Filter, $\alpha = 1$

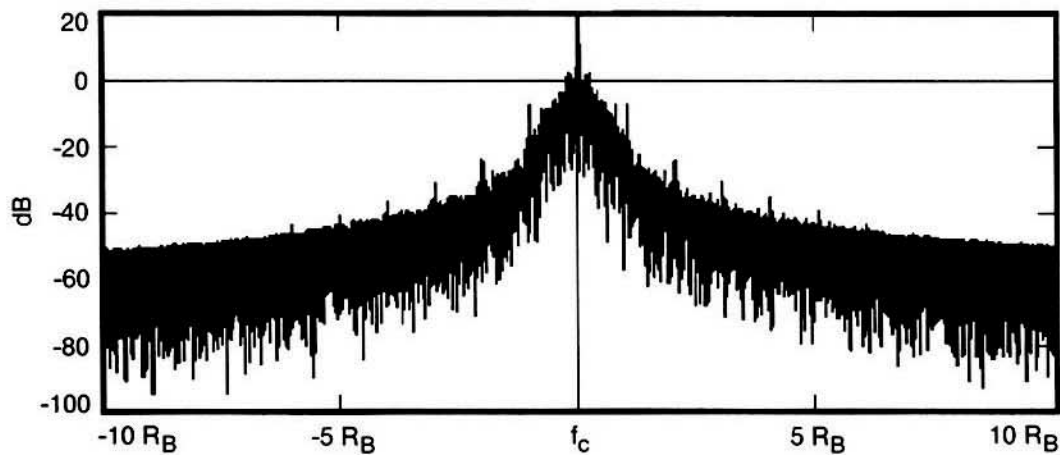


Figure 3-18b. Output of Power Amplifier

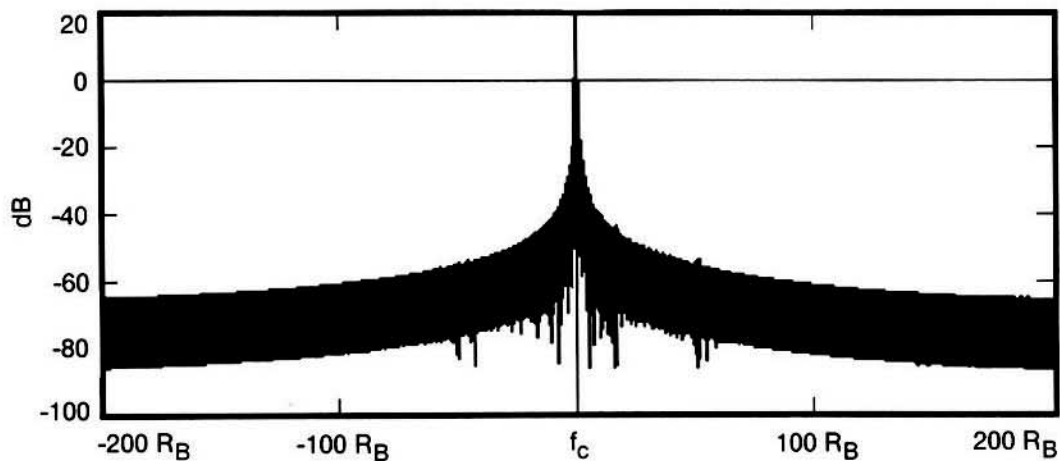


Figure 3-18c. Output of Second Harmonic Filter ($\pm 20 R_B$)

**Figure 3-18. Baseband Raised Cosine Filtered Sampled Data Spectra, $\alpha = 1$
 (Non-Ideal Data)**

CCSDS - SFCG EFFICIENT MODULATION METHODS STUDY
Phase 2: Spectrum Shaping

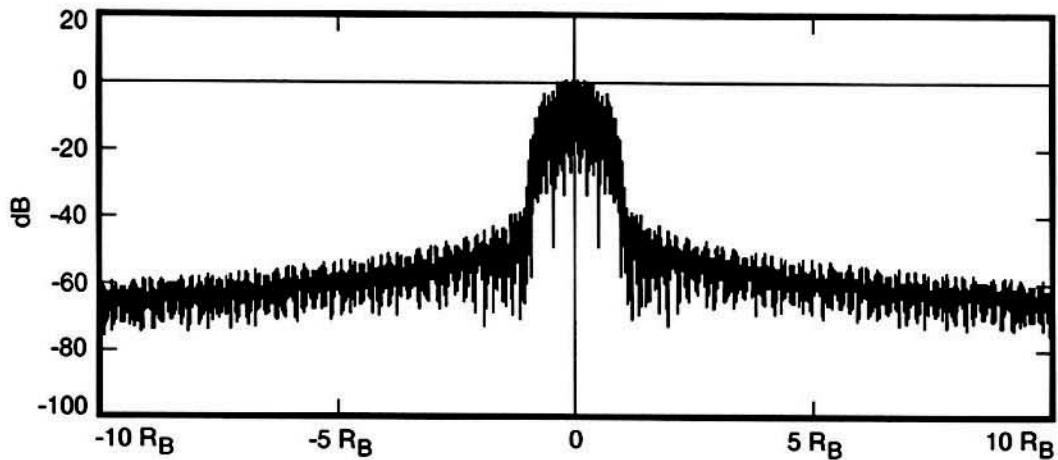


Figure 3-19a. Output from Square Root Raised Cosine Filter, $\alpha = 1$

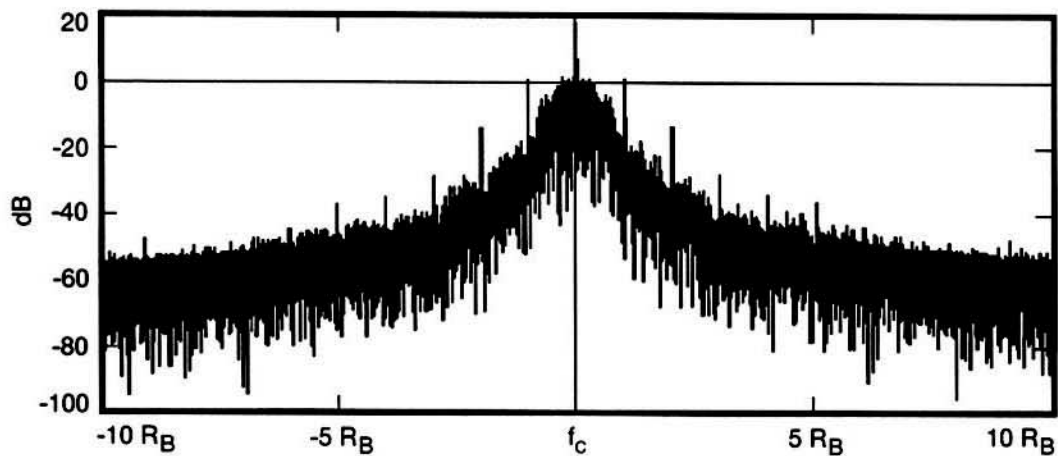


Figure 3-19b. Output of Power Amplifier

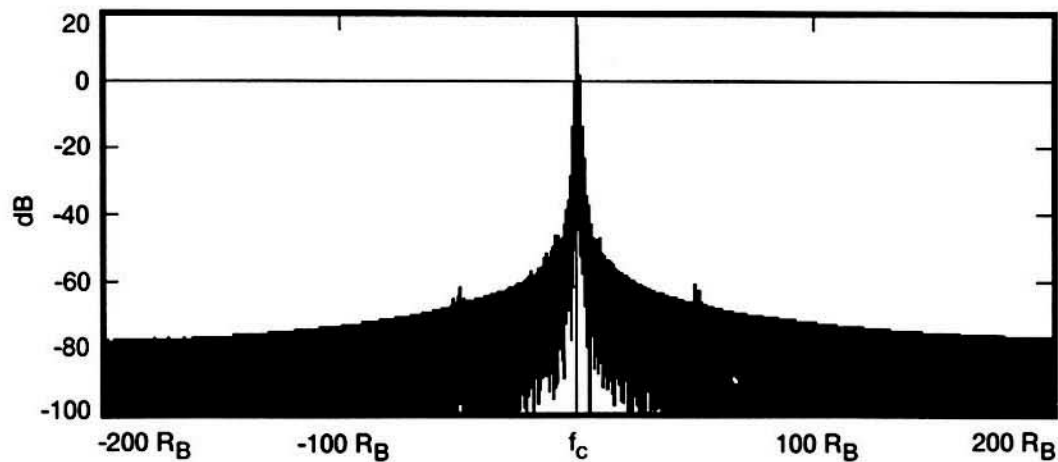


Figure 3-19c. Output of Second Harmonic Filter ($\pm 20 R_B$)

**Figure 3-19. Baseband Square Root Raised Cosine Filtered Sampled Data Spectra, $\alpha = 1$
 (Ideal Data)**

CCSDS - SFCG EFFICIENT MODULATION METHODS STUDY
Phase 2: Spectrum Shaping

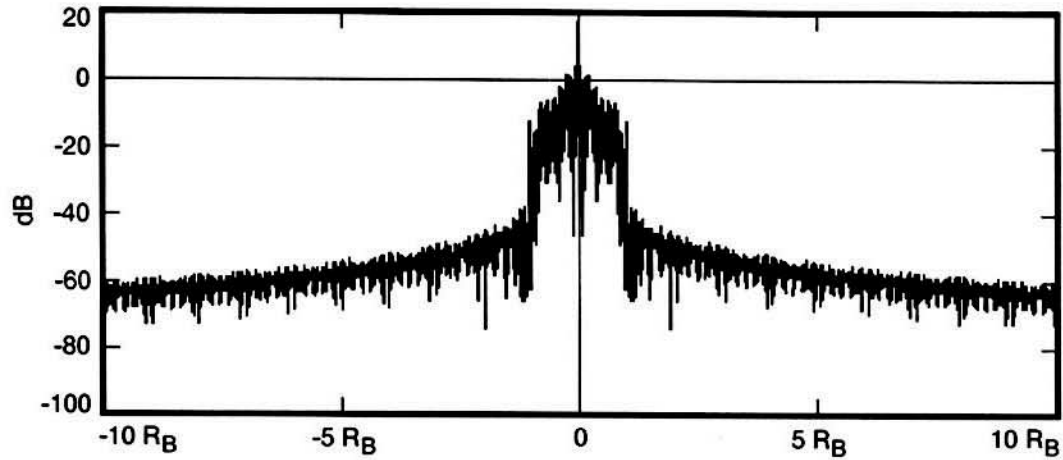


Figure 3-20a. Output from Square Root Raised Cosine Filter, $\alpha = 1$

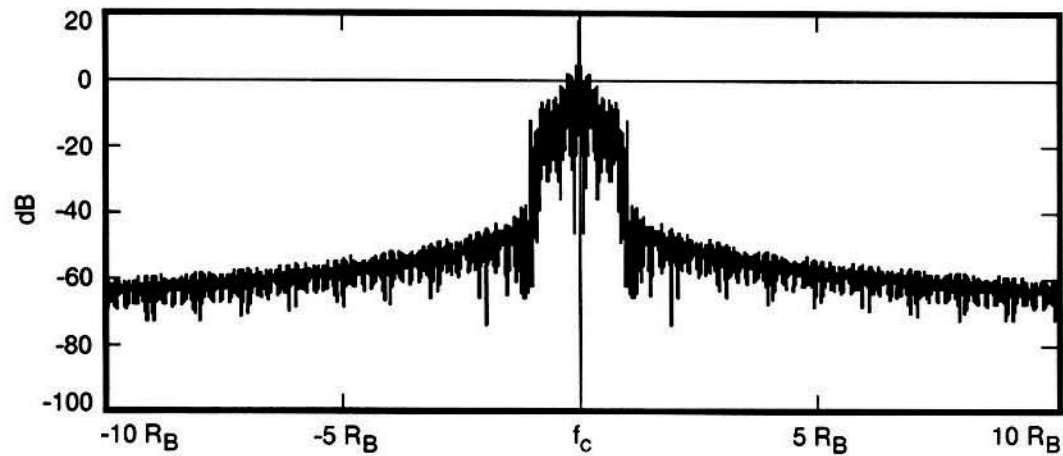


Figure 3-20b. Output of Power Amplifier

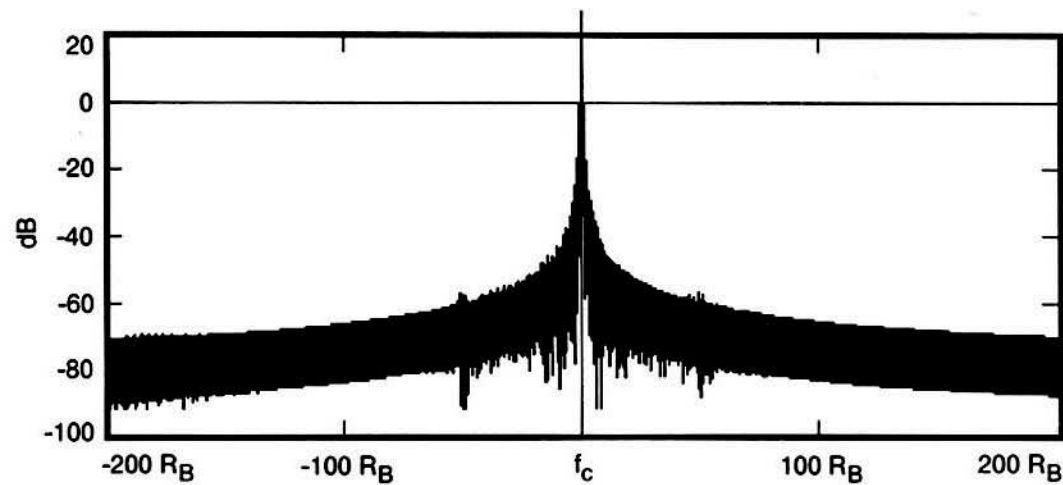


Figure 3-20c. Output of Second Harmonic Filter ($\pm 20 R_B$)

**Figure 3-20. Baseband Square Root Raised Cosine Filtered Sampled Data Spectra, $\alpha = 1$
 (Non-Ideal Data)**

CCSDS - SFCG EFFICIENT MODULATION METHODS STUDY
Phase 2: Spectrum Shaping

Table 3-1a. Spectrum Levels Relative to First Data Sideband (Ideal Data)

Filter Type	$\pm 0 R_b$ dB	$\pm 5 R_b$ dB	$\pm 10 R_b$ dB	$\pm 20 R_b$ dB
None, Unfiltered Data (Reference)	0	- 35	- 39	- 39
Butterworth, 5 th Order	0	- 45	- 62	- 65
Bessel, 3 rd Order	0	- 47	- 58	- 62
Raised Cosine ($\alpha = 0.25$), NRZ-L Data	0	- 54	- 58	- 64
Raised Cosine ($\alpha = 0.5$), NRZ-L Data	0	- 52	- 59	- 67
Raised Cosine ($\alpha = 1$), NRZ-L Data	0	- 52	- 61	- 66
Square Root Raised Cosine ($\alpha = 1$), NRZ-L Data	0	- 55	- 59	- 68
Raised Cosine ($\alpha = 1$), Sampled Data	0	- 49	- 57	- 63
Square Root Raised Cosine ($\alpha = 1$), Sampled Data	0	- 39	- 54	- 62

Table 3-1b. Spectrum Levels Relative to First Data Sideband (Non-Ideal Data)

Filter Type	$\pm 0 R_b$ dB	$\pm 5 R_b$ dB	$\pm 10 R_b$ dB	$\pm 20 R_b$ dB
None, Unfiltered Data (Reference)	0	- 25	- 26	- 29
Butterworth, 5 th Order	0	- 47	- 61	- 69
Bessel, 3 rd Order	0	- 45	- 54	- 62
Raised Cosine ($\alpha = 0.25$), NRZ-L Data	0	- 53	- 59	- 68
Raised Cosine ($\alpha = 0.5$), NRZ-L Data	0	- 52	- 62	- 69
Raised Cosine ($\alpha = 1$), NRZ-L Data	0	- 51	- 63	- 70
Square Root Raised Cosine ($\alpha = 1$), NRZ-L Data	0	- 53	- 66	- 71
Raised Cosine Filter ($\alpha = 1$), Sampled Data	0	- 43	- 54	- 60
Square Root Raised Cosine ($\alpha = 1$), Sampled Data	0	- 39	- 52	- 59

CCSDS - SFCG EFFICIENT MODULATION METHODS STUDY

Phase 2: Spectrum Shaping

4.0 SYSTEM CONSIDERATIONS

From Section 3 and Table 3-1b for non-ideal data, Raised Cosine and Square Root Raised Cosine filters appear to have a distinct advantages over the other types. Not only do they exhibit a smooth roll-off characteristic and have no discernable in-band spurious emissions, but also, the data sideband attenuation is greater than for Butterworth or Bessel baseband filters. Thus, the issue is one of determining whether these filter types are suitable for integration into space agencies' space-to-earth communications systems. This Section examines the practical application of the filters.

Two areas must be investigated to ascertain if these filters are useful in space telemetry systems. First, the filter's amplitude response to a random data pattern must be studied to determine its uniformity. Second, the Inter-Symbol Interference (ISI) must be measured to ensure that the losses are not excessive. Only if a filter provides acceptable performance in both of these areas should it be considered for a real communications system.

4.1 Filter Amplitude Response

Space agencies commonly employ phase modulation on their space-to-earth RF links. To minimize spacecraft telecommunications system redesign, each of the filters considered in Section 3 must be evaluated to determine whether or not it operates properly with existing spacecraft phase modulators. Between certain limits, a typical phase modulator in a residual carrier system will have a linear input voltage-to-output phase relationship. Thus, a linear change in input voltage will produce a linear change in RF phase at the output of the modulator. Generally, the linear region lies between approximately 0.1 to 1.4 radians of output phase shift.

Suppressed carrier modulators may be different. If the modulator's output phase is a nearly linear function of input voltage then the suppressed carrier and residual carrier systems will operate similarly. However, if the suppressed carrier modulator is switched (e.g., the output phase has only two [BPSK] or four [QPSK] discrete states which are largely independent of input voltage) then baseband filtering will not work because the output phase switches in 90 or 180 degree steps.

All filters studied in Section 3 were fed the same random NRZ-L or Sampled data. This test consisted of a 50-bit random NRZ-L data pattern, having differing run lengths of 1s and 0s, which was applied to each filter's input. Note that sometimes transitions occur at every bit-time.

[Bit Pattern = 111111111000000000010101010100010000100101111011]

Here, the objective was to measure each filter's amplitude response to this bit pattern in order to judge whether or not a particular filter type produced an output which was suitable for a spacecraft communications system. The output amplitude for each filter type, resulting from the random bit pattern, was plotted and variations in that amplitude were measured using COMDISCO in much the same way that the attenuation provided by each baseband filter was measured (see Section 3.3).

Each filter is considered in order and plots of its output amplitude appear in Figure 4-1. Amplitude variations were measured and are listed in Table 4-1 and represent the difference between the maximum and minimum values obtained at each filter's output from the random data pattern. Variations (% and dB) are referenced to the steady state value and show the amount of data sideband power deviation resulting from changes in data transition density. The large power variations found in the right-most column of Table 4-1 are because low transition density data approximates a squarewave while high transition density data is virtually a sinewave.

CCSDS - SFCG EFFICIENT MODULATION METHODS STUDY

Phase 2: Spectrum Shaping

The random data pattern applied to all filters appears in Figure 4-1a and serves as a reference for subsequent filter evaluations. Ideally, a filter affects only the waveform and not the amplitude. Changes in amplitude are translated linearly into variations in phase angle by the modulator. Therefore, non-uniformity in input amplitude is translated into a change in data sideband power.

4.1.1 5th Order Butterworth Filter Response

Figure 4-1b shows the amplitude response of a 5th Order Butterworth filter to the random data pattern of Figure 4-1a. The filter's output is characterized by an overshoot at transitions which is probably the result of the filter's high Order (5th). Adjustment of the BT product may correct this overshoot. Variations between steady state (minimum) and peak (maximum overshoot) values can be as much as 26%.

Because of the complex waveform, it is difficult to compute the precise sideband power change as a function of transition density. However, an estimate of this power variation can be obtained by assuming that a long run of 1s or 0s (2 or more 1s or 0s) produces a squarewave modulating signal while transitions at every bit-time, passing through a filter with a BT product of 1.0, result in a waveform approximating a sine wave.

Using the CCSDS Link Design Control Table (DCT), the data sideband power was computed and noted for a squarewave modulating signal assuming that the peak of the squarewave data waveform corresponds to a modulation index of 1.2 radians. Thereafter, the DCT was reset for sinewave modulation and a new modulation index, corresponding to the peak of the overshoot (e.g., $1.26 \times 1.2 \text{ radians} = 1.51 \text{ radians}$), was entered. The new data sideband power was calculated and recorded. The power change between high and low transition density data was obtained by differencing the two computed sideband powers. **Note: this method is intended as an approximation of the total difference between steady state high and low transition density data and is not purported to be a precise measure.**

For the Butterworth filter, a power reduction of 1.4 dB for high transition density data was computed. Even with the overshoot at transitions, the high transition density data produced a somewhat lower transmitted sideband power because of its sinusoidal shape.

4.1.2 3rd Order Bessel Filter Response

Figure 4.1c depicts the output from a 3rd Order Bessel filter to the random data pattern. Here, the output is far more uniform than that of the 5th Order Butterworth filter. Measurements made using COMDISCO show that the variation is only 1.0%. Using the same technique described above, and assuming a 1.2 radian modulation index for the squarewave peak, the power decrease for high transition density data is 2.5 dB.

4.1.3 Raised Cosine Filter Response ($\alpha = 1$), NRZ-L Data

Full Raised Cosine ($\alpha = 1$) filters did poorly in this test (Figure 4d). Although the filter produced excellent waveforms, when the run-length of 1s or 0s exceeded 2, the amplitude variations for input data having transitions every bit-time are significant. COMDISCO measurements show the peak amplitude of high transition density data to be only 62% of the steady state amplitude. Using the same measurement method described above, and assigning a modulation index of 1.2 radians to the squarewave peak, the transmitted data sideband power is found to drop by 5.6 dB for high transition density data.

CCSDS - SFCG EFFICIENT MODULATION METHODS STUDY

Phase 2: Spectrum Shaping

Amplitude variations cause two problems. First, the received E_b/N_0 will be a function of data transition density. A significantly larger telemetry margin will be required for such systems to ensure that the Bit-Error-Rate (BER) does not increase to intolerable levels when long runs of alternating 1s and 0s occur.

Second, amplitude variations probably render Raised Cosine filters, with an NRZ-L input, useless in suppressed carrier systems. Assuming that the suppressed carrier system's modulator is linear and not switched (see Section 4.1), then it can be set to produce a uniform ± 90 degree peak modulation index for long runs (2 or more) of 1s or 0s.

However, when data transitions occur at each bit-time, the reduced amplitude at the filter's output results in a smaller modulation angle. Changing modulation angles, caused by varying data transition densities, produce a continually shifting reference phase in the receiver's Costas Loop. The result is a misalignment between the received signal's phase and the receiver's reference phase which manifests itself as a data detection loss.

4.1.4 Square Root Raised Cosine Filter Response ($\alpha = 1$), NRZ-L Data

Figure 4.1e shows the amplitude response for a Square Root Raised Cosine ($\alpha = 1$) filter. The amplitude decline for high transition density data is far less prominent than that for a full Raised Cosine filter but it still falls to 86% of the steady state value. Using a modulation index of 1.2 radians for the squarewave peak value, the data sideband power decline for high transition density data is calculated to be 3.3 dB.

4.1.5 Raised Cosine Filter Response ($\alpha = 1$), Sampled Data

To complete the investigation of Raised Cosine filters, output amplitude changes were investigated using a Sampled data input. Figure 4-1f shows the filter's output response to a Sampled data pattern corresponding to the NRZ-L pattern in Figure 4-1a. Recall that for Sampled data, a pulse of short duration and an amplitude of + 1 represents a "1" while an equally short pulse with an amplitude of - 1 represents a "0".

Comparing Figures 4-1f and 4-1d reveals that Sampled data greatly reduces the amplitude variation between high and low transition density data. Whereas an NRZ-L input causes amplitude changes of 38%, Sampled data reduces the difference to only 6% (see Table 4-1). Recall that the power variations in the right-most column of Table 4-1 are largely because low transition density data approximates a squarewave while high transition density data is virtually a sinewave having a lower RMS power than a squarewave.

In Section 4.1.3 it was concluded that the amplitude variation from a Raised Cosine filter using an NRZ-L input was too large to make this filter type suitable in most systems, particularly where suppressed carrier modulation is employed. Using a Sampled data input, most of the amplitude changes disappear which may make this type of filter useable in some applications. However, spectrum studies in Section 3, using non-ideal data, determined that the sideband attenuation for a Raised Cosine filter with a Sampled data input was 8 dB poorer at $\pm 5 R_b$ than was the case for a Raised Cosine Filter with an NRZ-L data input. In fact, its performance was 2 and 4 dB poorer than the Bessel and Butterworth filters respectively making its value doubtful (see Table 3-1b).

CCSDS - SFCG EFFICIENT MODULATION METHODS STUDY

Phase 2: Spectrum Shaping

4.1.6 Square Root Raised Cosine Filter Response ($\alpha = 1$), Sampled Data

Figure 4-1g shows the amplitude response of a Square Root Raised Cosine ($\alpha = 1$) filter to Sampled data. At first, the filter seems unusable due to the large amplitude variations (22%) and the presence of the individual pulses comprising each bit. But note that the high transition density data has a greater amplitude than does the low transition density data. Applying the power measurement technique used for the other filters and recalling that low transition density data is similar to a squarewave while high transition density data approximates a sinewave, the data sideband power change was found to be only 1.3 dB.

Nevertheless, the issue is whether a Square Root Raised Cosine filter with a Sampled data input is useful in a real space communications system. Returning to Table 3-1b for non-ideal data, the sideband attenuation at $\pm 5 R_b$ is found to be 14 dB poorer when Sampled data, rather than NRZ-L data, is used. Both the Butterworth and Bessel filters perform substantially better in both sideband attenuation and uniformity of output than does a Square Root Raised Cosine ($\alpha = 1$) filter using Sampled data.

4.1.7 Summary of Filter Output Amplitude Variation Study

Amplitude variation measurements are summarized in Table 4-1 for each of the filters. While the power changes appear to be excessive, the computational method is likely to represent a "worst case" and most of the variation is due the squarewave to sinewave conversion. No attempt was made to "optimize" any of the filters and doing so may improve the amplitude uniformity. Additionally, amplitude changes become irrelevant if the data transition density becomes constant as would be the case with Bi- ϕ modulation. Furthermore, convolutional encoding and/or data randomization will increase the data transition density although it cannot assure a uniform density. Further study is required to determine which filters, if any, are useful in suppressed carrier systems.

As discussed in Section 4.1.5, the amplitude changes found with Raised Cosine filters can be substantially eliminated by employing a sampling technique. Amplitude plots for such filters are very similar to that for a Bessel filter in which the peak amplitude is independent of transition density.

Table 4-1. Filter Amplitude Variation to Random Data Pattern

Filter Type	Maximum Value	Minimum Value	Variation %	Variation dB
5 th Order Butterworth, NRZ-L	± 1.26	± 1.0	21	1.4
3 rd Order Bessel, NRZ-L	± 1.02	± 1.01	1	2.5
Raised Cosine ($\alpha = 1$), NRZ-L	± 1.02	± 0.63	38	5.6
Square Root Raised Cosine ($\alpha = 1$), NRZ-L	± 1.04	± 0.90	13	3.3
Raised Cosine ($\alpha = 1$), Sampled	± 1.07	± 1.0	6	2.8
Square Root Raised Cosine ($\alpha = 1$), Sampled	± 1.47	± 1.15	22	1.3

CCSDS - SFCG EFFICIENT MODULATION METHODS STUDY
Phase 2: Spectrum Shaping

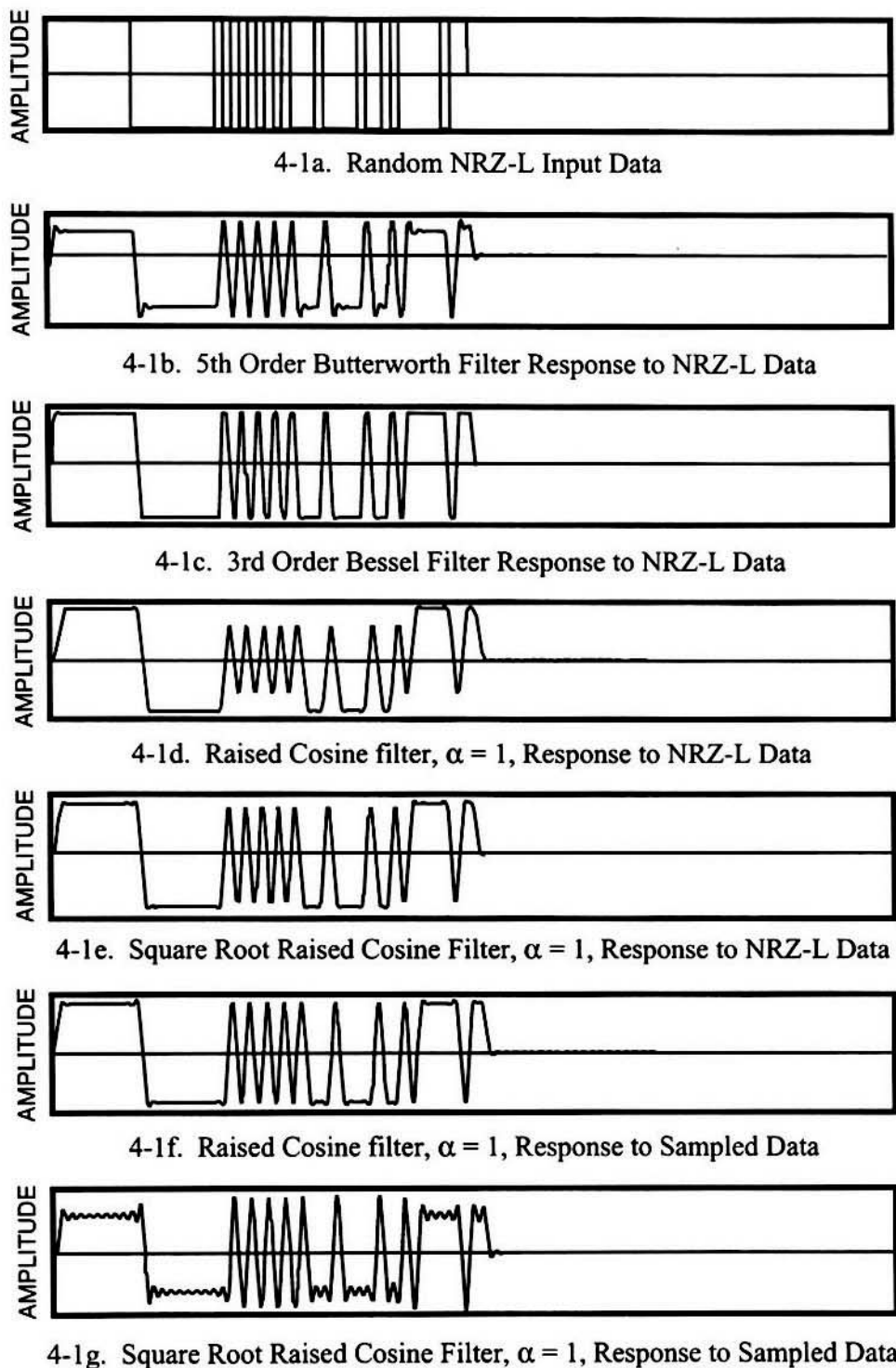


Figure 4-1. Filter Amplitude Responses to Random NRZ-L and Sampled Data

CCSDS - SFCG EFFICIENT MODULATION METHODS STUDY

Phase 2: Spectrum Shaping

4.2 Inter-Symbol Interference (ISI)

A filter may be very effective in limiting the transmitted data spectrum and yet render the communications system useless if the Inter-Symbol Interference (ISI) is too high. As noted in Section 4.1, inserting a baseband data filter affects the transmitted data symbol's waveform. For ideal data, what was once a perfect pulse (e.g., zero rise and fall times and complete data symmetry) will begin to exhibit longer and longer data symbol rise and fall times as the baseband filter's bandwidth is narrowed. A well designed filter should not introduce data asymmetry but the data symbol will begin to approximate a sinewave as the higher order harmonics are attenuated by the filter. Eliminating the high order data harmonics is the principal reason that the bandwidth of the transmitted data spectrum is reduced as the filtering is increased.

Some filters elongate the data symbol. When that happens, the trailing edge of one symbol begins to overlap the leading edge of the following symbol. The interference resulting from this Inter-Symbol Interference (ISI) produces a loss because the distinguishability of individual symbols has been reduced. Such loss must be accounted for in the Link Design Control Table (DCT) since it adversely affects the data channel's capacity. For example, ISI losses occurring in the telemetry system would be entered at line 75 of the CCSDS DCT.

Calculations of the ISI were made for each of the passive filters included in this study. As stated above, both the Butterworth and Bessel filter's bandwidths were set at $\pm 1 R_b$ and the BT product was equal to 1.0 in order to compare the transmitted data spectra from these filters with those from the Raised Cosine and Square Root Raised Cosine filters. Such narrow filtering most certainly increases the ISI for those two filter types shown in Table 4-2 below. However, even with the narrow Butterworth and Bessel filter bandwidths, the transmitted data spectra obtained with Raised Cosine and Square Root Raised Cosine ($\alpha = 1$) filters, using NRZ-L inputs, are materially better than the former types (see Table 4-1).

NOTE: The ISI losses reported in Table 4-2 for the Butterworth and Bessel cases are for two filters only, one at the transmit end and one matched filter at the receive end. Effects of the modulator, multiplier, power amplifier, and other system components have not been included. Since only the effects of the filters are being investigated, Ideal Data is used for this part of the study.

Determining the ISI for Raised Cosine and Square Root Raised Cosine filters requires an examination of the Eye Diagrams for each of the filters. An Eye diagram is constructed by overlaying a digital data stream, which has undergone filtering, on a single amplitude plot whose time scale covers interval: $-T < t < T$. An ISI-free sample point exists where all lines, representing the data symbols, cross one another simultaneously.

Theoretically, a pair of Raised Cosine filters ($\alpha = 1$), operating in a linear communications system with one filter at the transmitting end and the other at the receiving end, will exhibit at least one ISI-free sample point. A pair of Square Root Raised Cosine filters, similarly located and operating under the same conditions, will exhibit at least two ISI-free sample points.

Figures 4-2 and 4-3 are eye diagrams for Raised Cosine and Square Root Raised Cosine ($\alpha = 1$) filters using NRZ-L and Sampled data respectively. Two eye diagrams, generated with ideal data, are presented for each case. The first represents the output of the spacecraft's baseband filter while the second depicts the output of a second, identical filter after the signal has passed through the solid state power amplifier. Since modulator and multiplier nonlinearities can be controlled, they were not included in these simulations.

CCSDS - SFCG EFFICIENT MODULATION METHODS STUDY

Phase 2: Spectrum Shaping

4.2.1 Raised Cosine and Square Root Raised Cosine Filter Eye Diagrams, NRZ-L Data

Figure 4-2 contains eye diagrams for Raised Cosine and Square Root Raised Cosine filters using NRZ-L data inputs. Figure 4-2a shows the eye diagram at the data source for a Raised Cosine ($\alpha = 1$) filter output over an interval of $2T$. Note the existence of a single ISI-free sample point per symbol at $0.5T$ where all lines converge.

Figure 4-2b represents the output of the second Raised Cosine ($\alpha = 1$) filter after the signal has passed through the nonlinear power amplifier. Here there are no ISI-free sample points. In fact, the comparative chaos of the diagram suggests that the nonlinearities may introduce a substantial amount of ISI. While it has not been possible to measure the ISI level at this writing, the diagram suggests that an alternative filtering and detection system at the receiving end should be investigated.

Similar results were found for the Square Root Raised Cosine ($\alpha = 1$) filter using NRZ-L data. Figure 4-2c showing the baseband filter output on the data source side has two ISI-free sample points per symbol at $0.25T$ and $0.75T$. Conversely, Figure 4-2d depicts the output of the second Square Root Raised Cosine ($\alpha = 1$) filter after the signal has passed through the nonlinear power amplifier. Again, no ISI-free sample points exist. However, this diagram is less chaotic than Figure 4-2b suggesting that the ISI level may be lower for this filter combination than is the case for the two Raised Cosine filters.

4.2.2 Raised Cosine and Square Root Raised Cosine Filter Eye Diagrams, Sampled Data

Figure 4-3 contains eye diagrams for both Raised Cosine and Square Root Raised Cosine filters using Sampled data. As does Figure 4-2a, Figure 4-3a represents the spacecraft's Raised Cosine ($\alpha = 1$) baseband filter output. It exhibits a single ISI-free sample point per symbol at $0.5T$. Figure 4-3b depicting the output of the second, identical Raised Cosine filter following the power amplifier has no ISI-free sample points. However, like the previous case, the comparative order of the diagram may suggest lower ISI levels than is the case with the same filter receiving NRZ-L data.

Figure 4-3c shows the output of a Square Root Raised Cosine ($\alpha = 1$) filter with a Sampled data source. Like Figure 4-2c, two ISI-free points per symbol are present at $0.25T$ and $0.75T$. However, Figure 4-3d, depicting the second Square Root Raised Cosine ($\alpha = 1$) filter's output following power amplification, is more chaotic than that for the Raised Cosine filter. It is unclear, from an ISI point of view, whether Square Root Raised Cosine filters will fair better with NRZ-L or Sampled data inputs. Further study is necessary to make this determination as well as to compute the actual ISI levels.

CCSDS - SFCG EFFICIENT MODULATION METHODS STUDY
Phase 2: Spectrum Shaping

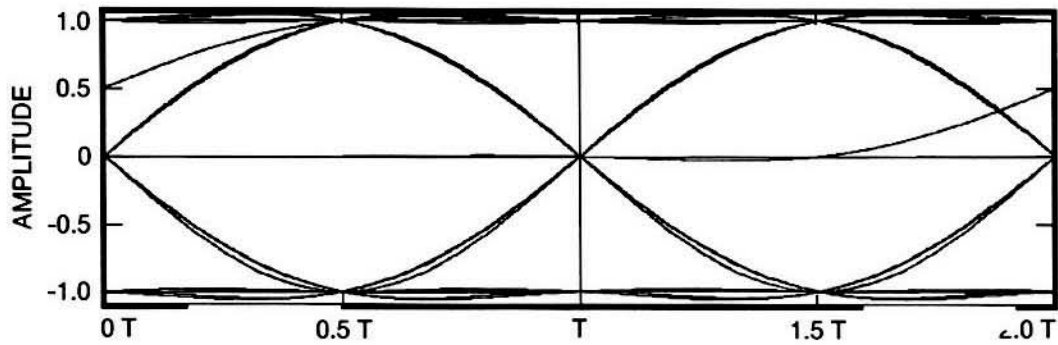


Figure 4-2a. Baseband Filter Output, Single Raised Cosine Filter ($\alpha = 1$)

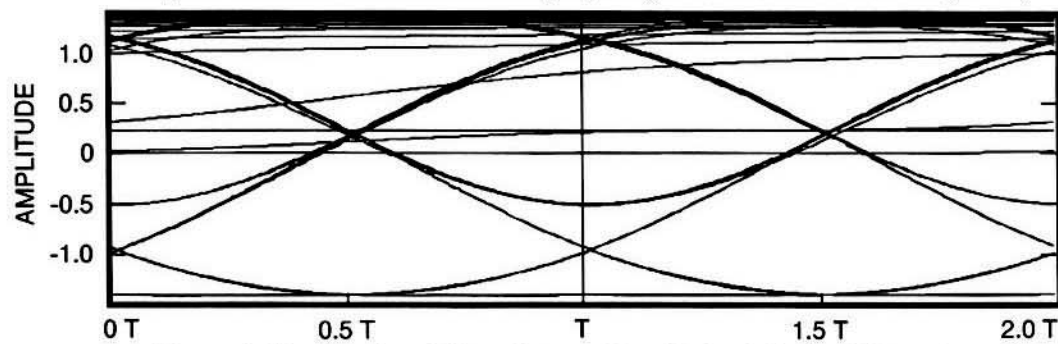


Figure 4-2b. Receiver Filter Output, Two Raised Cosine Filters ($\alpha = 1$)

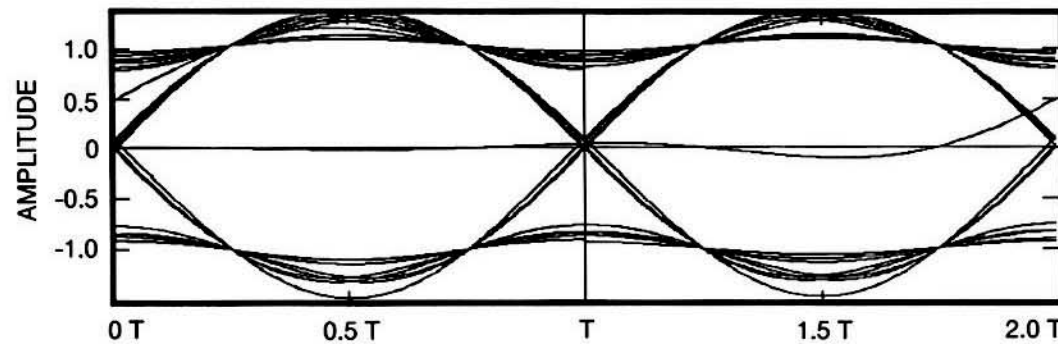


Figure 4-2c. Baseband Filter Output, Single Square Root Raised Cosine Filter ($\alpha = 1$)

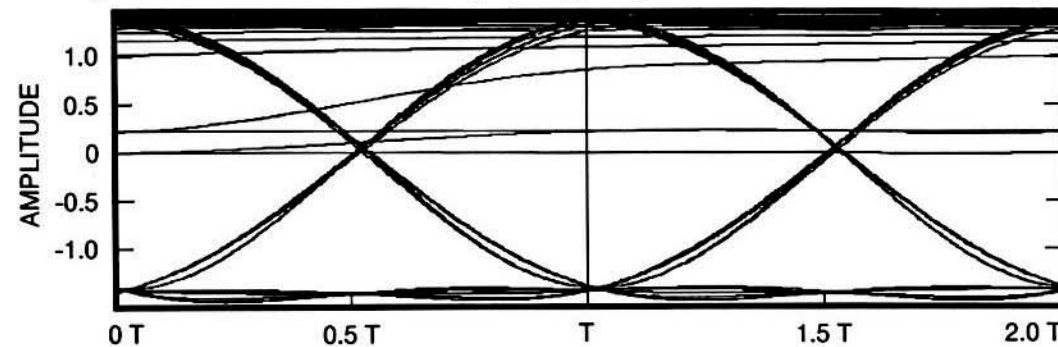


Figure 4-2d. Receiver Filter Output, Two Square Root Raised Cosine Filters ($\alpha = 1$)

Figure 4-2. Eye Diagrams for Raised Cosine Filters ($\alpha = 1$), Ideal NRZ-L Data in a Non-Linear Channel

CCSDS - SFCG EFFICIENT MODULATION METHODS STUDY
Phase 2: Spectrum Shaping

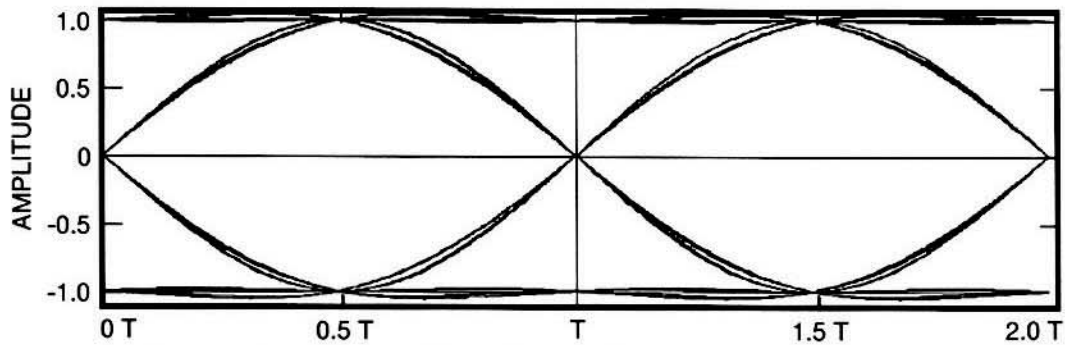


Figure 4-3a. Baseband Filter Output, Single Raised Cosine Filter ($\alpha = 1$)

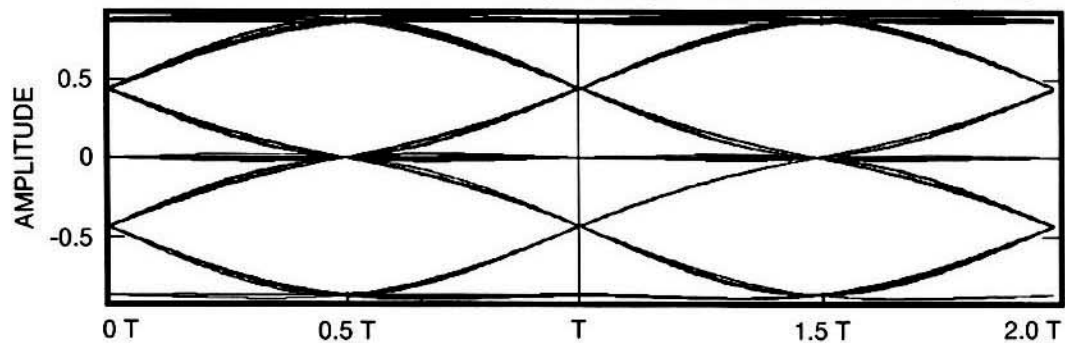


Figure 4-3b. Receiver Filter Output, Two Raised Cosine Filters ($\alpha = 1$)

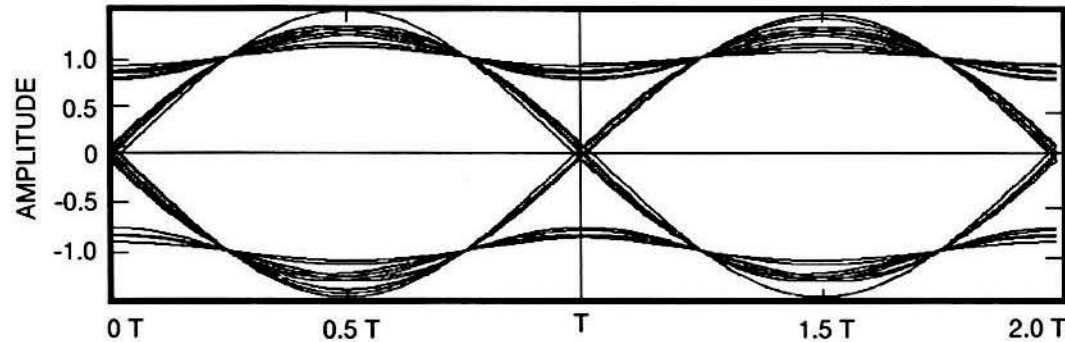


Figure 4-3c. Baseband Filter Output, Single Square Root Raised Cosine Filter ($\alpha = 1$)

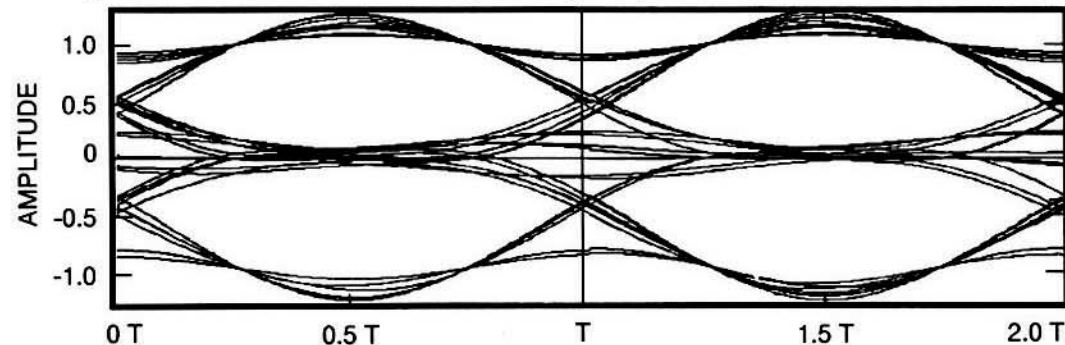


Figure 4-3d. Receiver Filter Output, Two Square Root Raised Cosine Filters ($\alpha = 1$)

Figure 4-3. Eye Diagrams for Raised Cosine Filters ($\alpha = 1$), Ideal Sampled Data in a Non-Linear Channel

CCSDS - SFCG EFFICIENT MODULATION METHODS STUDY**Phase 2: Spectrum Shaping****4.2.3 Summary of ISI Studies**

For passive filters such as the Butterworth and Bessel types, bandwidths greater than $1 R_b$ will be required to achieve reasonable ISI levels. While this will increase the transmitted frequency spectrum's width, their simplicity and comparatively good performance makes them candidates worth considering.

Raised Cosine and Square Root Raised Cosine filters pose more of a problem. The lack of any ISI-Free sample points, after the signal has passed through nonlinear system elements, makes their application questionable. However, the superior sideband attenuation of a Square Root Raised Cosine ($\alpha = 1$) filter using NRZ-L data makes it a very attractive candidate.

Perhaps alternative filtering and sampling techniques can be found which will permit using Square Root Raised Cosine filters while obtaining reasonable ISI levels. Further studies in Phase 3 will be needed to determine whether or not a viable system design using Square Root Raised Cosine filters is feasible.

TABLE 4-2: INTER SYMBOL INTERFERENCE FOR FILTER PAIRS
(Ideal Data and Components)

BASEBAND FILTER TYPE	ISI @ $\pm 1 R_b$ dB	ISI @ $\pm 2 R_b$ dB	ISI @ $\pm 5 R_b$ dB
Unfiltered Baseband NRZ-L Data, Reference	0	0	0
Butterworth Baseband Filter, 5 th Order, NRZ-L Data	- 0.85	- 0.47	- 0.23
Bessel Baseband Filter, 3 rd Order, NRZ-L Data	- 1.51	- 0.61	- 0.24
Raised Cosine Baseband Filter ($\alpha = 1$), NRZ-L Data	TBD	TBD	TBD
Square Root Raised Cosine Baseband Filter ($\alpha = 1$), NRZ-L Data	TBD	TBD	TBD
Raised Cosine Baseband Filter ($\alpha = 1$), Sampled Data	TBD	TBD	TBD
Square Root Raised Cosine Baseband Filter ($\alpha = 1$), Sampled Data	TBD	TBD	TBD

NOTE:

TBD ISI values for Raised Cosine and Square Root Raised Cosine filters have not been computed at this time. Further investigation will be necessary in Phase 3 to determine their behavior in nonlinear channels and to design the optimum filtering and detection system.

CCSDS - SFCG EFFICIENT MODULATION METHODS STUDY**Phase 2: Spectrum Shaping****5.0 PHASE 2 SUMMARY**

This investigation of baseband filters and their effect on the transmitted telemetry data's spectrum shows that such filters can significantly narrow the transmitted RF bandwidth. Data sideband power reductions from 22 - 28 dB at $\pm 5 R_b$ and 29 - 41 dB at $\pm 10 R_b$ appear to be feasible using the filters described in this paper. These reductions were obtained with non-ideal data and hardware and with no effort devoted to filter optimization. With some effort, greater attenuations may be obtainable.

At this juncture, the real issues are:

1. *Can the number of spacecraft using a specific frequency band be increased if baseband filtering is employed?*
2. *If the number of spacecraft using a specific frequency band can be increased, how many more can be accommodated than would be the case if no filtering is used?*

To estimate the value of baseband filtering, one can compare the number of missions with filtering which will fit into a frequency allocation to the number fitting into the same allocation but which do not have such filtering. This frequency band *Utilization Ratio* (ρ) is found from the relationship:

$$\rho = \frac{\text{Number of Spacecraft with Filtering Accommodated in Frequency Band}}{\text{Number of Spacecraft without Filtering Accommodated in Frequency Band}}$$

Finding this ratio requires making certain assumptions. Foremost among these is the acceptable interference level from spacecraft operating on adjacent channels. Such a calculation is complicated by the fact that each spacecraft has a unique data rate and power spectral density which affects the frequency separation required to avoid interference. Additional frequency separation will be needed because of each spacecraft's Doppler frequency shifts.

However, guard-bands to provide RF isolation between several missions exhibiting differing characteristics will be required irrespective of whether or not baseband filtering is utilized. If the allocated frequency band is sufficiently large to accommodate many spacecraft, and the guard bands are assumed to be small compared to the missions' assigned [noticed] bandwidths, then the existence of these guard bands will not have a large effect on the *Utilization Ratio*.

An estimate of the increased spectrum utilization can be obtained by making a few additional simplifying assumptions:

1. All spacecraft have the same data rate with identical EIRPs and PFDs.
2. Spectra from spacecraft in adjacent channels will be permitted to overlap one another provided that, at the frequency where the overlap occurs, the signals are at least 50 dB below that of the main telemetry lobe (1st data sideband).

Here, the 50 dB is an arbitrary value and the reader can substitute any other desired number. Like the frequency guard band between adjacent spacecraft, the level selected where spectral overlap is permitted will not make a first order change in the *Utilization Ratio*. Only the total number of spacecraft which can be placed in the allocated frequency band will vary.

CCSDS - SFCG EFFICIENT MODULATION METHODS STUDY
Phase 2: Spectrum Shaping

COMDISCO measurements were made using unfiltered ideal and non-ideal data, with the second harmonic filter removed, to determine the frequency at which the data spectrum was 50 dB below the main lobe. Spectra for each of the filter types in Section 3 was used to determine the frequency at which total data power fell to 50 dB below the main data lobe. Using the two numbers, the *Utilization Ratio* was computed using the relationship above. Table 5-1 summarizes the results.

TABLE 5-1. SUMMARY OF UTILIZATION RATIO IMPROVEMENT

Filter Type	Ideal Data - 50 dB Pt.	Ideal Data Util. Ratio (ρ)	Non-Ideal Data - 50 dB Pt.	Non-Ideal Data Util. Ratio (ρ)
Unfiltered, Reference	35 R_B	-	51 R_B	-
Butterworth, 5 th Order	6 R_B	5.8	5.7 R_B	8.9
Bessel, 3 rd Order	6 R_B	5.8	6 R_B	8.5
Raised Cosine ($\alpha=1$), NRZ-L	4.9 R_B	7.1	4.9 R_B	10.4
Sq Rt Raised Cosine ($\alpha=1$), NRZ-L	4.6 R_B	7.6	4.7 R_B	10.8
Filter Averages, NRZ-L Data:	5.4 R_B	6.6	5.3 R_B	9.6
Raised Cosine ($\alpha=1$), Sampled Data	5.6 R_B	6.2	6 R_B	8.5
Sq Rt Raised Cosine ($\alpha=1$), Samp. Data	6.8 R_B	5.1	6.3 R_B	8.1
Filter Averages, Sampled Data:	6.2 R_B	5.6	6.2 R_B	8.3

From the averages, is clear that baseband filtering offers a significant potential for increasing the number of spacecraft operating in a given frequency band, particularly if there is data asymmetry. Bandwidth utilization can potentially increase from 6 to 10 times, compared to unfiltered data, depending upon the data's condition, baseband filter type, and data type (NRZ-L or Sampled).

The importance of this finding is best illustrated with an example. If baseband filtering is applied in the present 90 MHz wide Category A 2 GHz band, the potential increased utilization is equivalent to obtaining 6 to 10 additional 90 MHz wide frequency allocations in that same band. While these ratios may represent upper bounds, it is clear that a significant increase in spectrum utilization is potentially possible using baseband filtering, even if the ratios are only 3 or 4 to 1. Judging by the auctions now underway in several countries, such additional frequency spectrum will be worth a small fortune and should easily justify expenditures necessary to develop any new filters and/or earth station equipment.

However, baseband filtering is not without problems. Amplitude variations, resulting from data transition density changes found at the output of some of the better performing filters, may make their use difficult with certain modulation types. These variations can be eliminated if Bi- ϕ modulation is used but the required frequency spectrum is increased. Amplitude variations resulting from the use of baseband filters, may make their use in BPSK/NRZ, QPSK/NRZ, and OQPSK/NRZ systems difficult or impossible, even if these systems have linear modulators. If switched modulators are employed, baseband filtering may not be possible and RF or IF filters will be needed. Further study is required to determine if the amplitude variations can be reduced and to measure their effect on the performance of systems built using each of the modulation methods.

CCSDS - SFCG EFFICIENT MODULATION METHODS STUDY

Phase 2: Spectrum Shaping

6.0 PHASE 3

Given that baseband filtering has been found to improve the frequency band *Utilization Ratio*, the next step is to apply this technique to each of the modulation schemes identified in Phase 1. New plots, similar to those used in Phase 1, showing *Power Containment* vs. R_b will be generated for comparison with those of Phase 1. At the conclusion of Phase 3, the modulation techniques providing the most efficient frequency spectrum utilization should become clear and the CCSDS and SFCG should be in a position to select preferred methods.

Baseband filter construction will also be considered in greater depth to ensure that the preferred filters can be implemented in a real flight system. Given the apparently superior performance of Raised Cosine filters, further study will be devoted their design, implementation, and performance in a space data system. Compromises in filter design, needed to construct the filters for flight applications, will also be considered.

Earth station detection of the filtered telemetry signal must be investigated to determine the effect of filtering on the telemetry system's performance. While some increase in spacecraft transmitter power might be justified to obtain a significant bandwidth reduction, the extent of such a penalty if it exists, must be computed. Accordingly, end-to-end system performance, including the Inter-Symbol Interference and the Bit-Error-Rate (BER) as a function of E_b/N_0 will be estimated using either actual hardware or by COMDISCO simulation. Strawman designs for the filter, symbol synchronizer, and data detection equipment will be needed.

CCSDS - SFCG EFFICIENT MODULATION METHODS STUDY
Phase 2: Spectrum Shaping

This Page is
initially left blank.

CCSDS - SFCG EFFICIENT MODULATION METHODS STUDY
Phase 2: Spectrum Shaping

REFERENCES

1. Martin, W. L. and Tien M. Nguyen, *CCSDS RF and Modulation (Subpanel 1E) Study, A Comparison of Modulation Schemes*, Jet Propulsion Laboratory, Pasadena, California, 24 September 1993.
2. Otter, Manfred, *A Comparison of QPSK, OQPSK, BPSK, and GMSK Modulation Schemes*, European Space Agency, European Space Operations Center, Darmstadt, Germany, June 1994.
3. McGregor, D. N., et. al., *Spectral Characteristics of Digital Phase Modulated Signals*, National Telecommunications Conference, November 1975.
4. Saleh, A. M., *Frequency Independent and Frequency Dependent Nonlinear Models of TWT Amplifiers*, IEEE Transactions on Communications, Vol. COM-29, No. 11, November 1981.
5. Saleh, A. M., *Intermodulation Analysis of FDMA Satellite Systems Employing Compensated and Uncompensated TWTs*, IEEE Transactions on Communications, Vol COM-30, No. 5, May 1982.
6. De Gaudenzie, Riccardo *QPSK, OQPSK, MSK, GMSK - A Comparative Performance Evaluation for Space Data Transmission Applications*, Consultative Committee for Space Data Systems, Report of the Proceedings of the RF and Modulation Subpanel 1E Meeting at the Ames Research Center, April 11-20, 1989, CCSDS 421.0-G-1, September 1989, p 25.
7. Nguyen, Tien M. and Sami M. Hinedi, *Unbalanced Data Compensation Technique for PCM/PM Receivers*, NASA Tech Brief [to be published].
8. Nguyen, Tien M., *A Review of Current Available Studies for the Interference Susceptibility of Various Modulation Schemes*, "Report of the Proceedings of the RF and Modulation Subpanel 1E Meeting at the GSOC", September 20-24 1993, (Yellow Book) CCSDS B20.0-Y-1, February 1994.
9. Lucky, R. W., J. Salz, and E. J. Walker Jr., *Principles of Data Communication*, New York: Mc Graw-Hill, 1968, pp 63-65.
10. Proakis, John G., *Digital Communications*, 2nd Edition, New York: Mc Graw-Hill, 1989, pp 528-546.

[This page intentionally left blank.]

**SFCG Meeting
Galveston, Texas
16-25 September 1997**

**SF17 - 28/D
Revised: 9-5-97**

**CCSDS - SFCG
EFFICIENT MODULATION METHODS STUDY
AT NASA/JPL
PHASE 3: END-TO-END SYSTEM PERFORMANCE**

**Warren L. Martin
Tsun-Yee Yan
Loc V. Lam**

September 1997

EFFICIENT MODULATION METHODS STUDY AT NASA/JPL

**SFCG Meeting
Galveston, Texas
16-25 September 1997**

SF17 - 28/D

Revised: 9-5-97

CCSDS - SFCG

EFFICIENT MODULATION METHODS STUDY

AT NASA/JPL

PHASE 3: END-TO-END SYSTEM PERFORMANCE

Warren L. Martin^{*}
Tsun-Yee Yan^{*}
Loc V. Lam^{*}

September 1997

*** Staff Members of the Jet Propulsion Laboratory, California Institute of Technology**

EFFICIENT MODULATION METHODS STUDY AT NASA/JPL**SUMMARY**

This report contains results from Phase 3 of the *CCSDS - SFCG Efficient Modulation Methods Study* conducted at the Jet Propulsion Laboratory (JPL). Simulations were used to measure the end-to-end performance of a telemetry data transmission and capture system for Category A missions. Included in the document are descriptions of the simulation system (Section 2), system performance measurements (Section 3), and the conclusions and recommendations (Section 4).

With increasing RF spectrum congestion, it is imperative that users take immediate steps to minimize their data transmission bandwidth. This implies filtering signals prior to radiation. After reviewing several filtering locations, JPL concluded that baseband filtering was the only practical method. However, baseband filtering of a phase modulated signal introduces discrete components into the RF spectra. Phase 3 study results demonstrate that a significant increase in RF spectrum efficiency can be obtained using baseband filtering if these spectral spikes can be tolerated.

All system performance data in Section 3 are obtained by simulating a complete data transmitting and receiving system. Bit-Error-Rate, RF Spectra, and Power Containment plots are provided. Non-ideal data and system parameters are included in simulation models to make the results as realistic as possible.

In addition to the traditional phase modulation methods, MSK, GMSK, and FQPSK modulation types are investigated. FQPSK-B is a proprietary modulation technique of Dr. Kamilo Feher. GMSK and FQPSK are significantly more bandwidth-efficient than any of the traditional phase modulation methods and are the recommended types for high data rate systems. FQPSK and GMSK both employ baseband filtering.

This report concludes by developing five separate mission classifications. Missions are assigned to a class depending upon their requirements. A modulation method is recommended for each class. Recommended modulation types are the *most bandwidth-efficient feasible*, given the class's requirements.

Readers interested solely in Phase 3 study results can skip directly to Section 4.

EFFICIENT MODULATION METHODS STUDY AT NASA/JPL

ACKNOWLEDGMENTS

This document could not have been published without the heroic efforts of three persons: Ann [Nancy] Schweiner, Anthony [Tony] Sedor and Roy Halton.

Tony and Roy spent countless hours preparing the diagrams and plots found in this report. As professional graphic artists, their high standards are reflected in the many figures contained in the document.

A very special thanks is due Nancy for her professionalism, patience, and quality standards. In addition to proofreading this Phase 3 report, Nancy edited each figure and translated it from a graphics application to this word processing program. Anyone who has attempted such a chore will immediately understand the task's magnitude and the frustration which most certainly follow. It was an ordeal. Whatever else can be said about modern computer application programs, *they are not friendly*.

The authors would also like to thank Dan Bathker, Franz Borncamp, Robert Petrie, and many others for their constructive suggestions and ideas. In the end, this document represents the work of many people.

The research described in this paper was carried out by the Jet Propulsion Laboratory, California Institute of Technology under a contract with the National Aeronautics and Space Administration.

EFFICIENT MODULATION METHODS STUDY AT NASA/JPL**TABLE OF CONTENTS**

SECTION	TITLE	
1.0	INTRODUCTION	1
1.1	PRIOR STUDIES	1
1.2	PHASE 3 OBJECTIVES	2
1.3	PHASE 3 SCOPE OF WORK	2
1.4	PHASE 3 MODULATION TYPES	3
1.5	PHASE 3 STUDY APPROACH	3
1.5.1	Simulated Measurements	4
1.5.2	Evaluation Criteria	4
1.6	REPORT ORGANIZATION	4
2.0	SYSTEM CONFIGURATION	5
2.1	SIMULATION SYSTEM	5
2.1.1	Data Source	6
2.1.2	Filtering	7
2.1.2.1	Filtering After Power Amplification	7
2.1.2.2	Filtering at a Transponder Intermediate Frequency (i.f.)	7
2.1.2.3	Filtering at Baseband	8
2.1.2.4	Baseband Filter Optimization	9
2.1.2.5	Spectral Spikes	10
2.1.3	Modulator Design	10
2.1.3.1	Universal Phase Modulator	10
2.1.4	Power Amplifier	12
2.1.5	ARX II Receiver	12
2.1.5.1	Symbol Synchronizer	12
2.2	MSK, GMSK, AND FQPSK MODULATION SIMULATIONS	13
3.0	SIMULATION RESULTS	14
3.1	REFERENCE MODULATION	14
3.2	PCM / PM / NRZ MODULATION	17
3.2.1	PCM / PM / NRZ Modulation Bit-Error-Rate	17
3.2.2	PCM / PM / NRZ Modulation Spectra	19
3.2.3	PCM / PM / NRZ Modulation Power Containment	19
3.2.4	PCM / PM / NRZ Modulation Study Conclusions	19
3.3	PCM / PM / Bi- ϕ MODULATION	21
3.3.1	PCM / PM / Bi- ϕ Modulation Bit-Error-Rate	22
3.3.2	PCM / PM / Bi- ϕ Modulation Spectra	22
3.3.3	PCM / PM / Bi- ϕ Modulation Power Containment	25
3.3.4	PCM / PM / Bi- ϕ Modulation Study Conclusions	26
3.4	BPSK / NRZ MODULATION	26
3.4.1	BPSK / NRZ Modulation Bit-Error-Rate	26
3.4.2	BPSK / NRZ Modulation Spectra	26
3.4.3	BPSK / NRZ Modulation Power Containment	29
3.4.4	BPSK / NRZ Modulation Study Conclusions	29

EFFICIENT MODULATION METHODS STUDY AT NASA/JPL**TABLE OF CONTENTS (Continued)**

SECTION	TITLE	
3.5	BPSK / Bi- ϕ MODULATION	30
3.5.1	BPSK / Bi- ϕ Modulation Bit-Error-Rate	30
3.5.2	BPSK / Bi- ϕ Modulation Spectra	32
3.5.3	BPSK / Bi- ϕ Modulation Power Containment	32
3.5.4	BPSK / Bi- ϕ Modulation Study Conclusions	32
3.6	QPSK MODULATION	34
3.6.1	QPSK Modulation Bit-Error-Rate	35
3.6.2	QPSK Modulation Spectra	35
3.6.3	QPSK Modulation Power Containment	38
3.6.4	QPSK Modulation Study Conclusions	38
3.7	OQPSK MODULATION	39
3.7.1	OQPSK Modulation Bit-Error-Rate	39
3.7.2	OQPSK Modulation Spectra	39
3.7.3	OQPSK Modulation Power Containment	42
3.7.4	OQPSK Modulation Study Conclusions	42
3.8	CONTINUOUS PHASE MODULATION	43
3.8.1	MSK and GMSK Modulation Bit-Error-Rate	43
3.8.2	MSK and GMSK Modulation Spectra	43
3.8.3	MSK and GMSK Modulation Power Containment	44
3.8.4	MSK and GMSK Modulation Study Conclusions	44
3.9	8-PHASE SHIFT KEYED (8-PSK) MODULATION	46
3.9.1	8-PSK Modulation Bit-Error-Rate	47
3.9.2	8-PSK Modulation Spectra	47
3.9.3	8-PSK Modulation Power Containment	47
3.9.4	8-PSK Modulation Study Conclusions	47
3.10	FQPSK-B MODULATION	50
3.10.1	FQPSK-B Modulation Bit-Error-Rate	51
3.10.2	FQPSK-B Modulation Spectra	52
3.10.2.1	Hardware Spectrum Measurements	52
3.10.3	FQPSK-B Modulation Power Containment	53
3.10.4	FQPSK-B Modulation Study Conclusions	53
4.0	SUMMARY, CONCLUSIONS, AND RECOMMENDATIONS	57
4.1	SUMMARY	57
4.1.1	Summary of Losses	57
4.1.2	RF Spectrum Efficiency	57
4.2	CONCLUSIONS	63
4.2.1	Filtering Conclusions	63
4.2.2	Loss Conclusions	63
4.2.3	Modulation Methods Conclusions	64
4.2.4	Spectrum Improvement Conclusions	65

EFFICIENT MODULATION METHODS STUDY AT NASA/JPL**TABLE OF CONTENTS (Continued)**

SECTION	TITLE	
4.3	RECOMMENDATIONS	65
4.3.1	Mission Classification	65
4.3.1.1	Low Data Rate (10 s/s - 20 ks/s)	65
4.3.1.2	Modest Data Rate (20 ks/s - 200 ks/s)	65
4.3.1.3	Medium Data Rate (200 ks/s - 2 Ms/s)	66
4.3.1.4	High Data Rate (2 Ms/s - 20 Ms/s)	66
4.3.1.5	Very High Data Rate (20 Ms/s - and Above)	66
GLOSSARY		68
REFERENCES		69

EFFICIENT MODULATION METHODS STUDY AT NASA/JPL**TABLE OF FIGURES**

FIGURE	TITLE	
2.1-1	Simulated System Block Diagram	5
2.1-2	Universal Phase Modulator in Transmitting System	11
2.1-3	Universal Phase Modulator Characteristics	11
2.1-4	ARX II Receiver Modifications	13
3.1-1	Unfiltered BPSK/NRZ Reference Modulation Spectra with Non-Ideal Data	15
3.2-1	PCM / PM / NRZ Modulation Bit-Error-Rate	18
3.2-2	PCM / PM / NRZ Modulation Spectra	20
3.2-3	PCM / PM / NRZ Modulation Power Containment	21
3.3-1	PCM / PM / Bi- ϕ Modulation Bit-Error-Rate	23
3.3-2	PCM / PM / Bi- ϕ Modulation Spectra	24
3.3-3	PCM / PM / Bi- ϕ Modulation Power Containment	25
3.4-1	BPSK / NRZ Modulation Bit-Error-Rate	27
3.4-2	BPSK / NRZ Modulation Spectra	28
3.4-3	BPSK / NRZ Modulation Power Containment	30
3.5-1	BPSK / Bi- ϕ Modulation Bit-Error-Rate	31
3.5-2	BPSK / Bi- ϕ Modulation Spectra	33
3.5-3	BPSK / Bi- ϕ Modulation Power Containment	34
3.6-1	QPSK Modulation Bit-Error-Rate	36
3.6-2	QPSK Modulation Spectra	37
3.6-3	QPSK Modulation Power Containment	38
3.7-1	OQPSK Modulation Bit-Error-Rate	40
3.7-2	OQPSK Modulation Spectra	41
3.7-3	OQPSK Modulation Power Containment	42
3.8-1	MSK / GMSK Modulation Bit-Error-Rate	44
3.8-2	MSK / GMSK Modulation Spectra	45
3.8-3	MSK / GMSK Modulation Power Containment	46
3.9-1	8-PSK Modulation Bit-Error-Rate	48
3.9-2	8-PSK Modulation Spectra	49
3.9-3	8-PSK Modulation Power Containment	50
3.10-1	FQPSK-B Modulation Bit-Error-Rate	51
3.10-2	FQPSK-B Modulation Spectra	53
3.10-3	FQPSK-B Hardware Generated FQPSK-B Modulation Spectrum	54
3.10-4	FQPSK-B Modulation Power Containment (0 - 20 R_B)	55
3.10-5	FQPSK-B Modulation Power Containment (0 - 2 R_B)	56
4.1-1	Spectral Efficiency Relative to Unfiltered BPSK / NRZ	61
4.1-2	Two-sided Required Bandwidth	62

EFFICIENT MODULATION METHODS STUDY AT NASA/JPL**LIST OF TABLES**

TABLE	TITLE	
1.4-1	Phase 3 Modulation Types	3
2.2-1	Optimized Baseband Filter Characteristics	9
3.1-1	Summary of Reference Modulation Measurements	16
3.6-1	QPSK Input Data - RF Carrier Relationship	35
4.1-1	System Losses	58
4.1-2	Bandwidth Efficiencies	60
4.3-1	Recommended Modulation Methods for Category A Missions	67

EFFICIENT MODULATION METHODS STUDY AT NASA/JPL

1.0 INTRODUCTION

At the 12th annual meeting of the Space Frequency Coordination Group (SFCG-12), held during November 1992 in Australia, the SFCG requested that the Consultative Committee on Space Data Systems (CCSDS) RF and Modulation Subpanel study and compare various modulation schemes (SFCG Action Item 12-32). Since then, representatives from the European Space Agency (ESA), NASA's Goddard Space Flight Center (GSFC), NASA's Jet Propulsion Laboratory (JPL), and New Mexico State University (NMSU) have completed a three-phase study. This document summarizes the results found in Phase 3 of the *CCSDS-SFCG Efficient Modulation Methods Study* [hereinafter termed the *Efficient Modulation Methods Study*] by the JPL team.

This study was motivated by the realization that frequency bands are becoming commodities auctioned to the highest bidder. Additionally, the number of users in bands, traditionally used by space agencies, has burgeoned. The result has been increased congestion and more frequent reports of interference. It is becoming necessary for regulatory organizations to scrutinize requests for frequency *Assignments* carefully to ensure that only those systems designed to use the minimum *necessary* bandwidth are granted protection or licenses. This study was intended to determine the minimum RF bandwidth *required* for a space data system transmitting digital data. The Phase 3 study objective is to *pack many more users in a frequency band, particularly at 2 and 8 GHz*, while avoiding mutual interference between spacecraft operating on adjacent frequencies.

Given the existing set of frequency allocations, the potential for interference increases directly with the data rate and the number of such missions flying. It was shown during Phases 1 and 2 that, absent bandwidth control, spacecraft transmitting high telemetry rates require RF bandwidths many times their data rates. Expanded frequency allocations are unlikely in the foreseeable future. Therefore, filtering to restrict RF spectrum utilization is becoming mandatory. But, the losses incident to such filtering and the susceptibility to interference resulting from band limiting are also important. Phase 3 of the *Efficient Modulation Methods Study* seeks to minimize the transmitted RF bandwidth while maintaining acceptable system losses and reasonable interference immunity.

While these results are generally applicable to all digital communications systems employing the modulation types covered, this study's emphasis was on telemetry transmissions from Category A missions (distance $\leq 2 \times 10^6$ km) and not on deep space (Category B) missions.

1.1 PRIOR STUDIES

Phase 1 and Phase 1b were concerned with identifying the several modulation methods commonly used by space agencies and determining the bandwidth needed by each. The initial two papers¹,² considered nine modulation schemes including:

- PCM/PSK/PM Square
- PCM/PSK/PM Sine
- PCM/PM/NRZ
- PCM/PM/Bi- ϕ
- GMSK
- BPSK/NRZ
- BPSK/Bi- ϕ
- QPSK
- OQPSK

EFFICIENT MODULATION METHODS STUDY AT NASA/JPL

Phase 2³ demonstrated that an unfiltered frequency spectrum rolls off very slowly, particularly with non-ideal data (2% *Data Asymmetry*, 10% *Data Imbalance*). Transmitting systems with asymmetric data and non linear elements (modulators, multipliers, and power amplifiers) distort the signal, exacerbating the problem. Such systems produce a transmitted RF spectrum with significant energy at frequencies many multiples of the data rate (R_B) from the center frequency.

Phase 2 considered the benefits of baseband filtering prior to transmission. Several alternative filter types and locations were considered and the results compared using PCM/PM/NRZ modulation. It was noted that post Power Amplifier (PA) filtering was theoretically the most effective method for limiting unwanted emissions in the RF spectrum. However, such filters suffer from the disadvantages of substantial weight, transmitter power loss, and comparatively high cost. These disadvantages result in a reluctance by flight projects to limit their RF bandwidth requirements. Moreover, post PA filters have to be tailored to the telemetry data rate and the RF frequency of each mission. Similar faults were found with filters placed at some intermediate frequency (i.f.).

Phase 2 concluded⁴ that baseband filtering produced the best compromise between simplicity, flexibility, weight, and cost. Four filter types were investigated using PCM/PM/NRZ modulation: Butterworth, Bessel, Raised Cosine, and Square Root Raised Cosine. Raised Cosine filters were discarded because their output amplitude varied the data's transition density. The remaining filter types survived and were tested again in Phase 3. Square Root Raised Cosine filters produced the best roll-off in the RF spectrum, when compared to the unfiltered case, although both Butterworth and Bessel filters provided reasonable attenuation. It was shown that spectrum shaping, in combination with a bandwidth-efficient modulation type, had the potential for increasing frequency band utilization by several times.

1.2 PHASE 3 OBJECTIVES

Phase 3 is concerned with the space data system's end-to-end performance. Modulation methods and filtering, which significantly reduce RF spectrum requirements, are of little value if captured data contain so many errors that it becomes unusable. Here, the objective is to develop guidelines for digital data transmission/receiving systems producing the minimum RF spectrum width while having reasonable end-to-end losses.

1.3 PHASE 3 SCOPE OF WORK

Phase 3 studies examine modulation types currently used or planned by the international space agencies. It is constrained to minimize changes to transmitting and receiving equipment. Such restrictions undoubtedly limit the performance obtained to sub-optimal. However, the large investment which space agencies have in their current data systems dictates a slow and orderly transition to more sophisticated techniques.

<p>This Phase 3 Study Explores the Feasibility of Baseband Filtering Only.</p>

EFFICIENT MODULATION METHODS STUDY AT NASA/JPL

1.4 PHASE 3 MODULATION TYPES

Phase 2 examined modulation methods currently used or planned by the CCSDS Space Agencies. Except for PCM/PSK/PM *Sine* and PCM/PSK/PM *Square*, all modulation types studied in Phase 2 are retained in this Phase 3 study. The two subcarrier modulation types were dropped because they were not found to be bandwidth-efficient unless the Subcarrier-to-Symbol-Rate ratio was kept at a value of 4 or lower. Frequently, space agencies have used higher Subcarrier-to-Symbol-Rate ratios, some of which exceed a value of 200! Table 1.4-1 lists the Phase 3 modulation types.

Table 1.4-1: Phase 3 Modulation Types

Modulation Name	Modulation Type	Filter Types Used
PCM/PM/NRZ	Phase	Butterworth, Bessel, Square Root Raised Cosine
PCM/PM/Bi- ϕ	Phase	Butterworth, Bessel, Square Root Raised Cosine
BPSK/NRZ	Phase	Butterworth, Bessel, Square Root Raised Cosine
BPSK/Bi- ϕ	Phase	Butterworth, Bessel, Square Root Raised Cosine
QPSK	Phase	Butterworth, Bessel, Square Root Raised Cosine
OQPSK	Phase	Butterworth, Bessel, Square Root Raised Cosine
MSK	Frequency ²	Sinewave Pulse Shaping
GMSK	Frequency ²	Gaussian Pulse Shaping
8-PSK	Phase	Butterworth, Bessel, Square Root Raised Cosine
FQPSK-B	Phase ¹	Proprietary Design

NOTES:

1. Non-Constant Envelope

2. Continuous Phase Modulation

1.5 PHASE 3 STUDY APPROACH

Phase 3 examines the performance of the modulation methods listed in Table 1.4-1 when combined with alternative baseband filtering techniques. Performance was evaluated by measuring the increase in E_b / N_0 required to maintain the data Bit-Error-Rate (BER) at a constant level. Most international space agency missions now adhere to CCSDS Recommendations for Space Data System Standards (Blue Books). This implies a packetized format which must operate at very low BERs ($BER \leq 1 \times 10^{-6}$). Such low BERs require error detecting-correcting codes operating at very low symbol energies. When the received signal's E_s / N_0 falls too low and the Symbol-Error-Rate (SER) rises, the decoder may be incapable of correcting errors resulting in deleted telemetry frames.

For the CCSDS recommended code (convolutional: $R = \frac{1}{2}$, $k = 7$; concatenated with a Reed-Solomon 223/255 block code) the required SER lies between 1×10^{-2} and 1×10^{-3} . Therefore, the criterion applied to Phase 3 is that of the $SER \leq 1 \times 10^{-3}$ which results in a $BER \leq 1 \times 10^{-7}$ when using CCSDS recommended concatenated coding. Phase 3 studies made use of uncoded data.

EFFICIENT MODULATION METHODS STUDY AT NASA/JPL

Phase 3 involved the following steps for the several modulation methods and filter types:

- Determining which transmit system characteristics affect the RF spectrum
- Optimizing each baseband filter's bandwidth
- Measuring the transmitted RF spectrum's width at several levels
- Quantifying end-to-end system losses
- Calculating the increased RF spectrum utilization
- Evaluating modulation types according to interference susceptibility
- Recommending modulation methods and filtering standards to both CCSDS and SFCG

1.5.1 Simulated Measurements

Constructing a real hardware system to make the necessary measurements was too time consuming, expensive, and beyond the scope of this Phase 3 study. As in phase 2, all measurements were made using simulations. FQPSK-B simulations received a cursory hardware validation test.

1.5.2 Evaluation Criteria

Phase 3 searched for those modulation methods and baseband filter combinations providing the narrowest RF spectrum width with acceptable end-to-end losses. Improving the RF bandwidth efficiency of high data rate systems provides the maximum return-on-investment. Therefore, all recommended systems had to be capable of operating at high to very high digital data rates. Moreover, the recommended systems were required to be compatible with existing spacecraft transmitters and earth station receivers.

Evaluation involved studying BER vs E_b / N_0 plots to select a filter bandwidth as narrow as possible while introducing acceptable Filtering Losses (Inter-Symbol Interference [ISI] and Mismatch). Spectra were plotted for the selected filters to assess the improvement in bandwidth efficiency. Finally, Power Containment curves were generated to show occupied bandwidth.

1.6 REPORT ORGANIZATION

This *CCSDS - SFCG Efficient Modulation Methods Study* Phase 3 report is divided into four sections. Following these introductory remarks, Section 2 describes the simulation system used to make end-to-end performance measurements. Section 2 also discusses filter location selection and filter bandwidth optimization. Section 3 contains study results. Bit-Error-Rate (BER) curves, RF spectrum, and Power Containment plots are presented for each modulation type. Section 3 contains the data needed for the conclusions found in Section 4. Section 4 summarizes this study and sets forth both conclusions and recommendations. Persons interested only in the Phase 3 study results need only read Section 4.

EFFICIENT MODULATION METHODS STUDY AT NASA/JPL

2.0 SYSTEM CONFIGURATION

Efficient Modulation Methods Study, Phases 1 and 2 (References 1, 2, and 3), provided several important system configuration results including:

- Subcarrier modulation should be avoided whenever possible.
- Non-ideal data and transmitting system components materially affect the RF spectrum.
- Baseband filtering tends to reduce the detrimental effects of asymmetrical data waveforms.
- Baseband filtering can significantly reduce the transmitted RF spectrum's width.
- Raised cosine baseband filters are not useful with an NRZ digital data source.
- Amplitude modulation is detrimental to the phase modulated RF spectrum's width.

These findings are incorporated in the Phase 3 study. While the Phase 3 transmitting system's block diagram is similar to that in Phase 2, there are significant differences. Additionally, a receiving system was added to complete the end-to-end evaluation. Figure 2.1-1 is a system block diagram. This section summarizes the simulator's and communications system's characteristics.

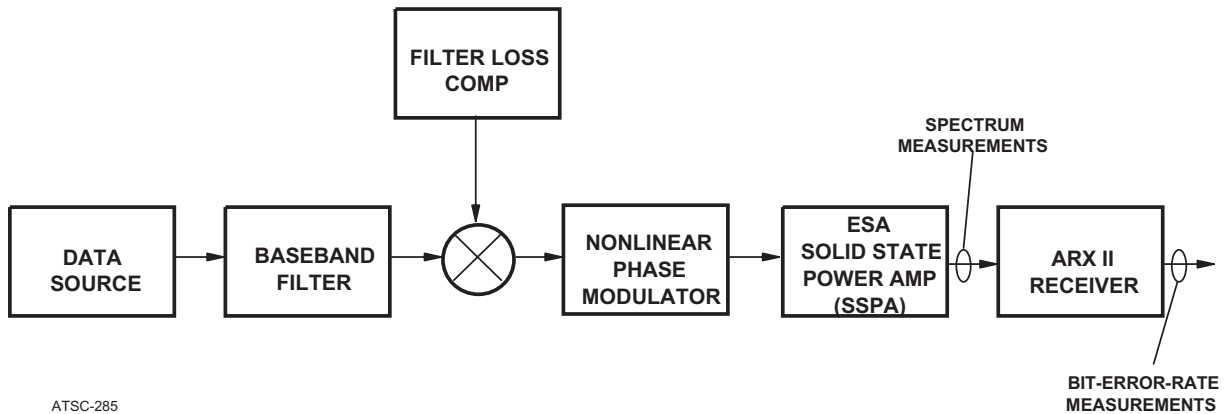


Figure 2.1-1: Simulated System Block Diagram

2.1 SIMULATION SYSTEM

All Phase 3 measurements were made by simulation using Cadence Design Systems Inc. Signal Processing Work system (SPW) running on a Sun Ultra Spark 2, 4-processor, workstation. A study was undertaken to optimize the simulator's operating parameters and a Fast Fourier Transform (FFT) bin size of 1 Hz was selected. The corresponding resolution bandwidth is 1.33 Hz. All spectra contained in this study are plotted at that resolution.

As in Phase 2, the frequency scale is specified in units of baseband data rate, R_B . R_B corresponds to the frequency span, f_s , between RF spectrum nulls resulting from the data bit period, T_B . Thus,

$$f_s = R_B = \frac{1}{T_B} \quad \text{where: } T_B \text{ is the Data Symbol's Bit Period.} \quad 2-1$$

EFFICIENT MODULATION METHODS STUDY AT NASA/JPL

R_B , rather than the R_S , is used to permit easy comparison of the bandwidths required by the several modulation types. No error-detecting error-correcting coding is used in this study so $R_B = R_S$. When comparing spectrum plots for PCM/PM/NRZ and PCM/PM/Bi- ϕ modulation using the same data rate, the latter requires approximately twice the spectrum width of the former. This is so because a Bi- ϕ modulating waveform is created by the modulo-2 addition of a baseband NRZ digital data stream with a synchronous double frequency square wave signal. Thus, each baseband data bit comprises both a +1 and -1 symbol, doubling the rate.

Signal amplitude (power) is measured in dB relative to the data sideband's peak. Modulation types are normalized with respect to the peak data sideband power irrespective of whether they are residual or suppressed carrier systems. Since the required spectral width is determined entirely by the modulation sidebands, the spectrum efficiency of a modulation-filter combination can be determined by measuring sideband power as a function of R_B . Spectrum plots label the carrier frequency f_c as $R_B = 0$.

2.1.1 Data Source

The Data Source is capable of generating either Non-Return-to-Zero (NRZ) or Bi-Phase (Bi- ϕ) data formats. The latter format is often termed *Manchester* coding. Only the NRZ data format was used during Phase 2 to facilitate a simple comparison of baseband filter types. In Phase 3, both types of data formats are employed.

Except for the reference case (Section 3.1) employing both ideal and non-ideal data, all system performance evaluations were made using non-ideal data. In Phase 2, non-ideal data meant:

Data Asymmetry (ratio duration of +1 to duration of -1) = $\pm 2\%$
 Data Imbalance (difference of "+1s" to "-1s", mark-to-space) = 10%

These values represented the maximum deviations from ideal data which technical studies, undertaken by the CCSDS RF and Modulation Subpanel (Subpanel 1E), show should be permitted. They are independent of the duration of the asymmetry or imbalance.

A new modulator was developed for the Phase 3 study. Termed the *Universal Phase Modulator* (UPM), this device embodies a Digital-to-Analog (D/A) converter at its input. The D/A converter contains a 3-bit register to hold the telemetry data. Data is clocked into the register at uniform intervals. Re-clocking at the modulator's input removes *Data Asymmetry* introduced by the stray capacitance and inductance in lines connecting the spacecraft's data system to the modulator. Therefore, the Phase 3 study used the following data characteristics.

- Data Asymmetry (ratio duration of +1 to duration of -1) = $\pm 0\%$
- Data Imbalance (difference of "+1s" to "-1s", mark-to-space) = 10%
 - For this study the Probability of a Mark (P_M) = 0.55

EFFICIENT MODULATION METHODS STUDY AT NASA/JPL

2.1.2 Filtering

Phase 2 demonstrated that significant RF spectrum limiting was obtained using baseband filtering. Except for the Raised Cosine filter whose output amplitude decreased at high transition densities, Phase 3 filter types are identical to those used in Phase 2. Raised Cosine filters were excluded from the Phase 3 study.

During Phase 2, alternative filter locations were considered. These locations included:

- Filtering After Power Amplification (post PA filtering)
- Filtering at a Transponder Intermediate Frequency (i.f.)
- Filtering at Baseband

2.1.2.1 Filtering After Power Amplification

Post Power Amplifier (PA) filtering is very attractive to Spectrum Managers because all unwanted emissions, which are outside the filters passband, will be eliminated. Theoretically, this filter location provides maximum control over emissions. However, it would be difficult for post PA filtering to improve the RF spectrum utilization efficiency of most space missions.

Experts state that either stripline or waveguide bandpass filters are generally used in microwave applications. For reasonable insertion losses (≤ 6 dB), such filters are constrained to bandwidths ranging from 1.5% - 2% of the transmitted frequency. For stripline filters, this corresponds to a *Loaded Q* (Q_L) of 50 - 70. Available materials limit the *Unloaded Q* (Q_U) to values of about 250 resulting in insertion losses on the order of 6 dB! Additional small losses result from filtering modulation sidebands beyond the filter's passband. Similar values of Q_L are obtainable with waveguide filters. While this filter type can have a somewhat lower insertion loss, they tend to be very large and heavy.

Assuming the best case, $Q_L = 70$ and a transmitting frequency of 2250 MHz, the narrowest practicable filter bandwidth would be 32 MHz! With convolutionally encoded data, BPSK/NRZ modulation, and a filter whose symbol Bandwidth - Time product (BT_s), is 2; the *minimum usable data rate* is 4 Mb/s (8 Mb/s if data is not convolutionally encoded). The vast majority of Category A missions which could benefit from filtering have far lower data rates.

JPL personnel concluded that post PA filtering cannot significantly increase the number of Category A missions operating in a frequency band and this study did not include that filtering option.

2.1.2.2 Filtering at a Transponder Intermediate Frequency (i.f.)

Filtering at i.f. is attractive because the filter operates at low power levels, does not reduce transmitted RF power, can be small and lightweight, and does not introduce the spectral spikes inherent in baseband phase domain filtering. However, the feasibility of this option depends upon the transponder's design.

EFFICIENT MODULATION METHODS STUDY AT NASA/JPL

The transponder for JPL's Cassini mission modulates at the RF transmitting frequency (i.e., 8.4 GHz); therefore, the remarks concerning Q_L set forth in Section 2.1.2.1 above apply and i.f. filtering is impractical. If a transponder modulates at lower frequencies and translates the signal to the RF frequency, then some filtering may be possible.

For i.f. frequencies in the 100 MHz range, Surface Acoustic Wave (SAW) filters provide good performance. If a $Q_L = 100$ is achievable with a $BT_s = 2$ and the i.f. frequency is only 100 MHz, then the minimum filter bandpass will be 1 MHz corresponding to an uncoded symbol rate of 250 ks/s. This is probably a sufficiently low data rate if it was the only impediment.

Effective spectrum management requires that the i.f. filter's bandwidth be adjusted to each mission's maximum telemetry data rate. JPL has found that transponder modifications are very expensive and may introduce performance problems. Transponders must be thoroughly tested to ensure that spurs and leakage are controlled and well understood. Failure to do so can result in *lockup*, with the result that all communication to the spacecraft becomes impossible. Modifying an i.f. filter for a new data rate may require full retesting of the transponder.

There is one additional constraint. Many space missions utilize turnaround ranging having code rates higher than the telemetry data rate. In such cases, i.f. filtering requires that the bandwidth be adjusted to the wider bandwidth signal, even if it is only present for a small fraction of the time. This was deemed undesirable from implementation and spectrum management viewpoints.

For all of these reasons, i.f. filtering was not found to significantly increase the number of Category A missions operating in a frequency band and this study does not include an i.f. filtering option.

2.1.2.3 Filtering at Baseband

JPL's *Efficient Modulation Methods Study* was limited to this option. Baseband filtering is attractive because the filters operate at low power, are lightweight, do not reduce transmitted RF power, and are small and simple (lowpass rather than a bandpass). Moreover, since they precede the phase modulation process, a second input bypassing the filter can be provided for the turnaround ranging signal.

Baseband filtering of phase modulated signals suffers from the disadvantage of introducing spikes into the RF spectrum. These spikes are clearly evident in the spectra found in Section 3 of this report. Pre-distorting the modulation waveform can reduce the spike amplitude near f_c ; however, their complete elimination requires use of an alternative modulation method such as Continuous Phase Modulation (CPM) or FQPSK.

Despite this limitation we have concluded that baseband filtering is the only practical method to limit the transmitted RF spectrum for the purpose of improving bandwidth efficiency. The remainder of this report discusses the performance of baseband filtered systems.

EFFICIENT MODULATION METHODS STUDY AT NASA/JPL

2.1.2.4 Baseband Filter Optimization

During Phase 2, no attempt was made to optimize the baseband filters for phase modulated signals. With a $BT_s = 1$, the Butterworth and Bessel filters essentially limited the PCM data to its fundamental frequency component (e.g., the rectangular waveform becomes sinusoidal in appearance). Such bandwidth restriction is likely to result in unacceptable losses.

Phase 3 included a separate study to optimize filter bandwidth. This investigation measured RF spectrum width, system performance, and system losses as a function of each filter type's BT_s product. The following parameters were measured:

- Inter-Symbol Interference (ISI) + Mismatch Losses
- Bit-Error-Rate (BER) vs Bit [Symbol] Signal-to-Noise Ratio (SNR)
- Transmitted RF Spectrum Width

Table 2.2-1 summarizes the findings of the baseband filter study.

Table 2.2-1: Optimized Baseband Filter Characteristics

Filter Type	Characteristics	ISI + Mismatch Losses ¹ (dB)
Butterworth	3-Pole; $BT_s = 2$	0.2 - 1.3
Bessel	3-Pole; $BT_s = 2$	0.1 - 1.0
Square Root Raised Cosine	2000 Taps; $\alpha = 1.0$; NRZ	0.4 - 0.8

NOTES:

1. Inter-symbol interference + mismatch losses for the phase modulation types in Table 1.4-1. Losses evaluated at $BER = 1 \times 10^{-3}$.

Phase 2 studies disclosed that baseband filters materially improve the RF spectrum of an asymmetrical baseband modulating waveform. That is not surprising because elimination of higher order harmonics should reduce RF spectrum's width. To a great extent, baseband filters will correct data asymmetry likely to occur in high data rate systems where re-clocking of the data at the modulator's input is not possible.

Baseband filtering introduces losses from Inter-Symbol Interference (ISI) and lack of an equivalent filter in the receiver (Mismatch Losses). There are additional system losses resulting from imperfect carrier tracking and symbol synchronization. Termed *Filtering Losses* these components are tabulated in Table 4.1-1.

EFFICIENT MODULATION METHODS STUDY AT NASA/JPL

2.1.2.5 Spectral Spikes

Spectral spikes are an inherent result of a filtered waveform which is phase modulated on an RF carrier.⁵ Spikes were evident in all filtered, phase modulated spectra contained in the *Efficient Modulation Methods Study*, Phase 2, report. Spikes can be eliminated by removing the baseband filter, relocating the filter following phase modulation or power amplification, or by selecting a new modulation type such as Continuous Phase Modulation (CPM) or FQPSK. Pre-distorting the modulating waveform can reduce, but not eliminate, spikes close to the center frequency.

2.1.3 Modulator Design

Phase Modulation (PM) is commonly used by the CCSDS Space Agencies for communication with spacecraft. While Frequency Shift Keying (FSK) and Amplitude Modulation (AM) have been used in the past, most of these spacecraft using these older methods are no longer in use. Therefore, neither of these types are considered in this study. Continuous Phase Modulation (CPM) techniques appear to offer some advantages in spectrum efficiency and have been examined as part of this study.

Phase modulators have proven a serious source of difficulty throughout the *Efficient Modulation Methods Study* because of their profound effect upon the width of the transmitted RF spectrum. A study was conducted to measure the extent of these effects.

Modulators containing non-linearities and amplitude modulation can materially increase RF spectrum's width. Every effort was made during the Phase 3 study to ensure that the simulation results accurately reflect the performance of real hardware. In furtherance of that objective, non-ideal data and component hardware models were used. Nevertheless, during Phase 3 when it was discovered that a hardware element's performance could be improved with only a simple change, that modification was incorporated.

The phase modulator is an example. Early in Phase 3, the modulator's simulation model was adopted from the Cassini mission's development program. The model accurately reflects Cassini modulator's real performance. Because Cassini's telecommunications link employs a residual carrier, its modulator operates over a comparatively restricted range. It does not need to maintain perfect phase shift vs. input voltage linearity above approximately ± 80 degrees. Additionally, amplitude variations beyond ± 80 degrees are also unimportant. For other modulation types, both non-linearities can significantly affect the RF spectrum.

2.1.3.1 Universal Phase Modulator

A simple modification to the Cassini modulator substantially eliminates both amplitude and phase non-linearities permitting the modulator to be used in QPSK and 8-PSK applications. Rather than modulating at a transmit frequency $f_T \approx 8.4$ GHz, the modulator operates at $f_T/2 \approx 4.2$ GHz and is followed by a $\times 2$ multiplier. The latter multiplies both the frequency and phase shift by 2 times providing the correct transmitting frequency and permitting the modulator to operate in its linear region. A block diagram of this *Universal Phase Modulator* (UPM) appears in Figure 2.1-2. The modulator is termed *Universal* because it can generate all phase modulation types, save OQPSK, listed in Table 1.4-1. It was used for all spectra in Section 3.

EFFICIENT MODULATION METHODS STUDY AT NASA/JPL

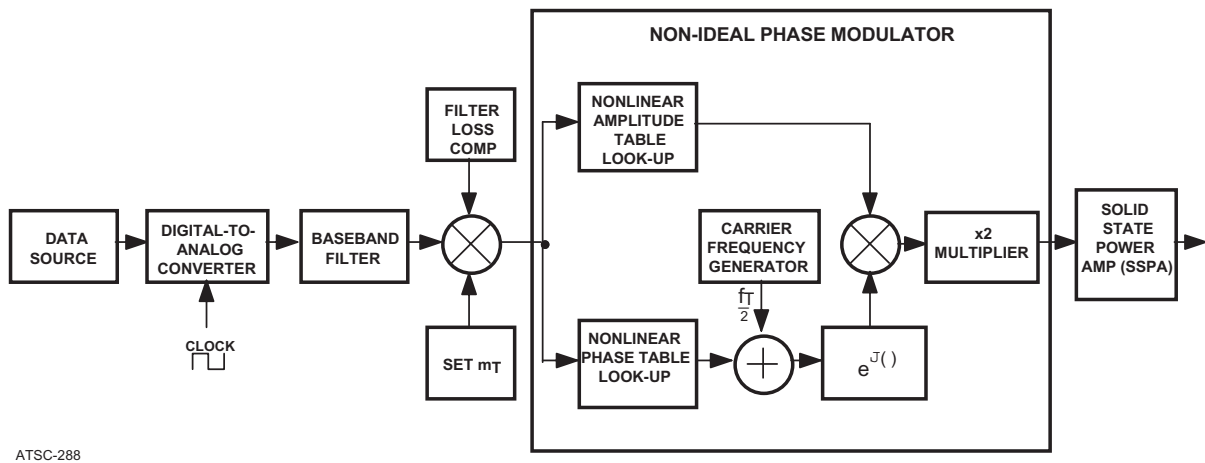


Figure 2.1-2: Universal Phase Modulator in Transmitting System

In Figure 2.1-2, the *Universal Phase Modulator* consists of the Cassini modulator and the associated analog-to-digital converter, baseband filter, summer, and $\times 2$ multiplier. Baseband filtering is accomplished in the phase domain resulting in a constant envelope modulation.

The UPM's characteristics appear in Figure 2.1-3. It shows the UPM's phase shift to be quite linear with input voltage. Amplitude variation is about ± 0.4 dB and is slightly smaller if a frequency multiplier, rather than a squaring circuit, is used for frequency doubling.

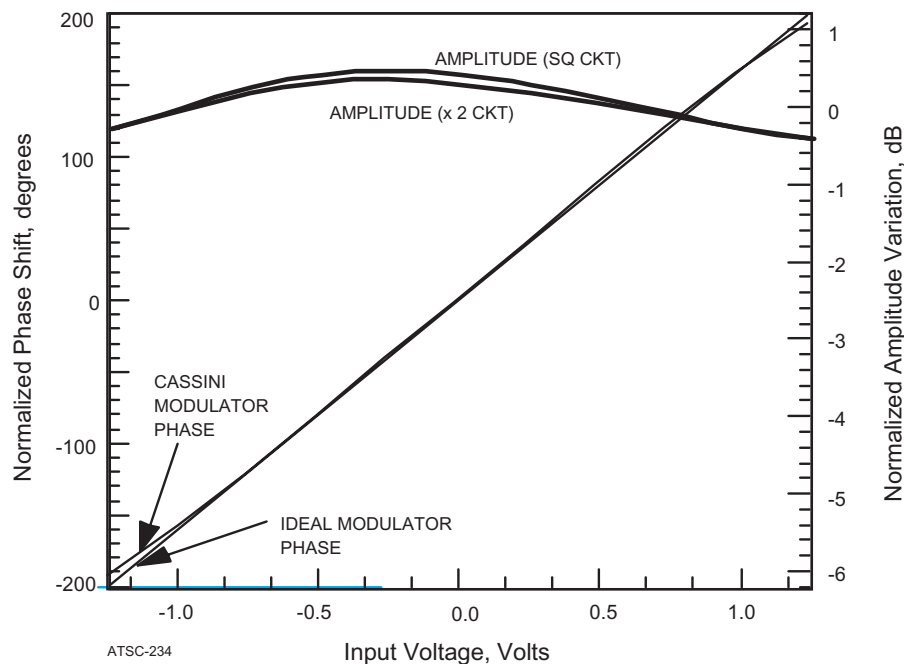


Figure 2.1-3: Universal Phase Modulator Characteristics

EFFICIENT MODULATION METHODS STUDY AT NASA/JPL

2.1.4 Power Amplifier

The power amplifier remains unchanged from that used in the Phase 2 study. Because of spectrum congestion and RF signal levels, the *Efficient Modulation Methods Study* is principally applicable to Category A missions (spacecraft whose distance from Earth is $\leq 2 \times 10^6$ km). Category A missions typically employ Solid State Power Amplifiers (SSPAs). The simulation model embodied the characteristics of the European Space Agency's SSPA.

2.1.5 ARX II Receiver

A receiver is required to complete the communications system. The ARX II was developed by JPL's Communications Systems and Research Section. It was the research and development prototype for the Block V receiver now widely deployed throughout the Deep Space Network (DSN).

Many simulations were run throughout the development cycle of the ARX II. The ARX II simulation model, developed and verified by comparing simulation results to actual receiver measurements, has been used for this Phase 3 study.

By design, the ARX II can handle most of the modulation types shown in Table 1.4-1. Some modifications to the simulator model were required to handle 8-PSK. Since the actual hardware does not currently embody these features, the simulator's performance could not be verified by hardware tests. Figure 2.1-4 shows squaring circuits added to the ARX II receiver model which were necessary to handle 8-PSK modulation.

2.1.5.1 Symbol Synchronizer

The ARX II receiver includes a symbol synchronizer utilizing a Digital Transition Tracking Loop (DTTL). DTTL synchronizers are commonly used by space agencies. Unfortunately, the design suffers from three disadvantages. First, its performance deteriorates below an E_s / N_0 of -7 dB. Second, it has difficulty in obtaining and maintaining symbol synchronization at low symbol transition densities. Third, it does not support modulation types such as 8-PSK, MSK, GMSK, and FQPSK. For this Phase 3 study, it was necessary to employ a different type of device known as a Maximum A Posteriori (MAP) symbol synchronizer.

Preliminary studies show that MAP symbol synchronizers overcome many of the problems found with DTTL devices. Good performance can be obtained down to an $E_s / N_0 = -10$ dB. Synchronization can be maintained, even at low symbol transition densities. Finally, MAP synchronizers can handle MSK, GMSK, an FQPSK signals, as well as those generated by the traditional phase modulation schemes.

A MAP synchronizer was implemented in the SPW simulator for the MSK, GMSK, and FQPSK-B studies. No actual hardware for such a device exists at JPL. Therefore, the SPW model assumed ideal performance (i.e., perfect synchronization). This assumption made it impossible to quantify all of the losses for the phase modulated systems, summarized in Table 4.1-1. Further development of MAP synchronizers is recommended to determine their performance.

EFFICIENT MODULATION METHODS STUDY AT NASA/JPL

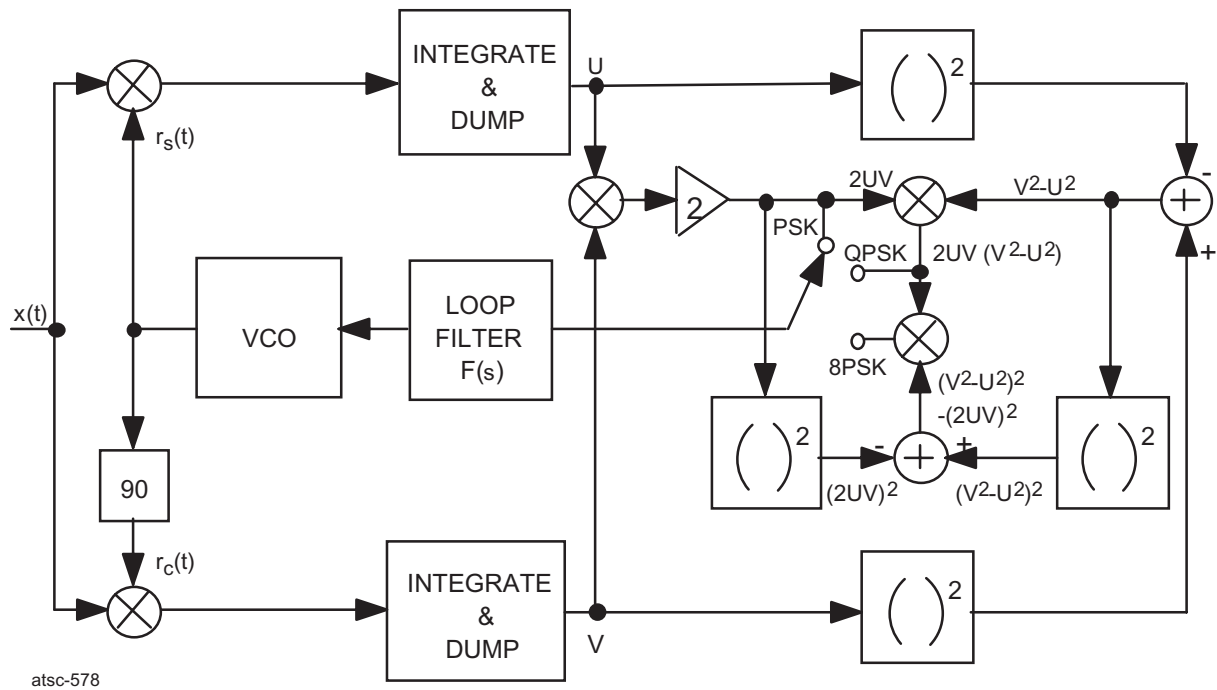


Figure 2.1-4: ARX II Receiver Modifications

2.2 MSK, GMSK, AND FQPSK-B MODULATION SIMULATIONS

Even as modified, the ARX II receiver can not accommodate Continuous Phase Modulation (MSK and GMSK) nor the new Feher QPSK (FQPSK) modulation. Because preliminary studies showed these modulation methods to be very bandwidth-efficient, it was important that they be included in Phase 3 of the *Efficient Modulation Methods Study*.

Phase 3 studies of MSK, GMSK, and FQPSK-B were accomplished assuming an ideal modulator and receiver. The ESA power amplifier described in Section 2.1.4 was used and both system losses and spectra are computed with this non-linear element. However, losses due to modulator non-linearities and imperfect carrier tracking and symbol synchronization are not included.

EFFICIENT MODULATION METHODS STUDY AT NASA/JPL

3.0 SIMULATION RESULTS

A principal Phase 3 study objective was the identification of modulation types having minimal RF spectrum width, reasonable end-to-end losses, and maximum interference immunity. Space missions have differing goals resulting in differing constraints and requirements. CCSDS Subpanel 1E has long suspected that there is not one *best* modulation type for all missions. Rather, there is likely to be a *preferred* modulation type for *each* mission type.

The key is to establish a set of mission categories into which missions having similar characteristics can be assigned. Each category can be examined to determine the best one or two modulation methods for that set. Clearly, the number of separate categories should be the minimum possible. Mission categories and recommended modulation methods are more fully examined in Section 4.3.

This Section contains the results of the Phase 3 *Efficient Modulation Methods Study* conducted at JPL. Following establishment of a *Reference Case*, each modulation method is compared. First, the baseband filter's bandwidth is selected using Bit-Error-Rate (BER) performance curves representing the end-to-end system performance. Second, RF spectra, generated using the selected baseband filter, are examined to find bandwidth efficiency and unwanted emissions. Finally, power containment curves are provided to find the *occupied bandwidth* and to easily compare relative bandwidth efficiencies.

3.1 REFERENCE MODULATION

Determination of bandwidth efficiency requires a comparative reference. In the Phase 2 study, PCM/PM/NRZ was used because it is a residual carrier modulation providing a compact RF spectrum. However, PCM/PM/NRZ modulation suffers from certain disadvantages discussed below and its selection was always controversial. Therefore, the generally accepted BPSK/NRZ was adopted as the reference modulation type for this Phase 3 study.

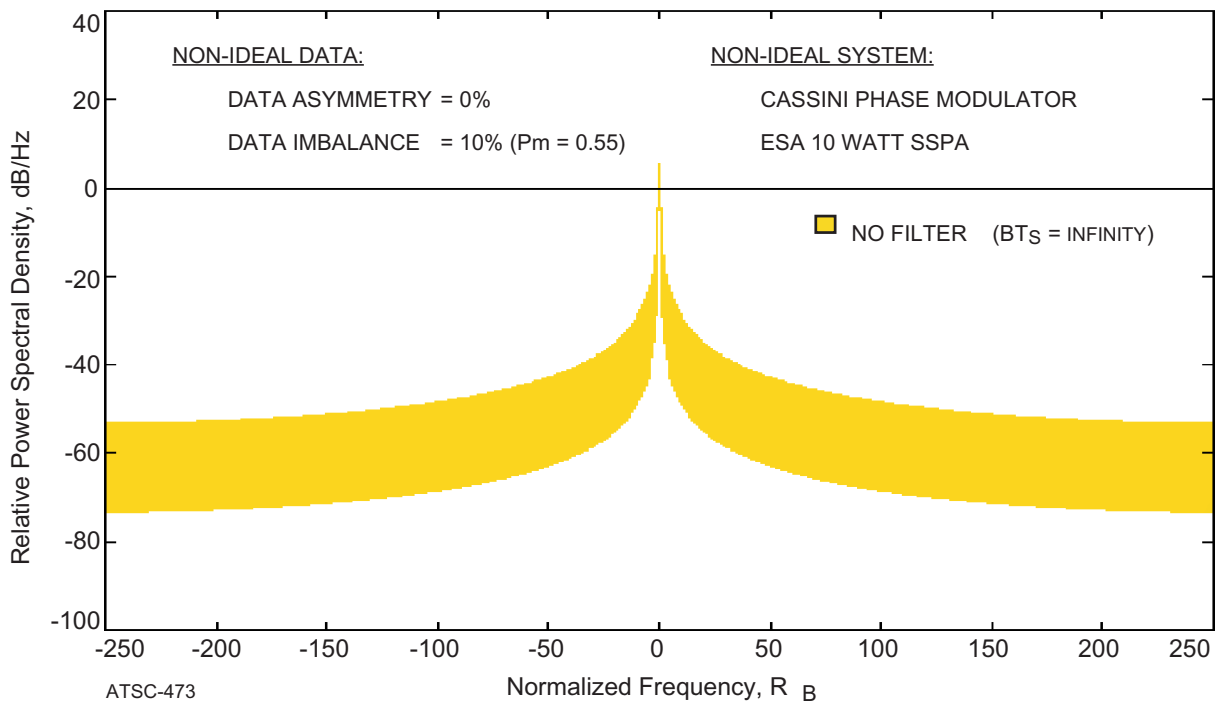
All spectrum plots in Section 3 have a resolution bandwidth of 1.33 Hz. Figure 3.1-1 shows unfiltered BPSK/NRZ spectra using a Cassini modulator and non-ideal data. Figure 3.1-1a incorporates a 10% data imbalance (difference in +1s and -1s) and Figure 3.1-1b adds a 2% data asymmetry (duration of +1 compared to duration of -1) to the 10% data imbalance. Data asymmetry produces spikes substantially increasing the spectrum's width. Spectra are plotted over a frequency interval, $f_c \pm 250 R_B$, making amplitudes beyond this span indeterminate. Table 3.1-1 summarizes the reference case measurements.

Figure 3.1-1 and Table 3.1-1 clearly demonstrate that unfiltered digital data transmission methods are unacceptable, particularly where there is data asymmetry. Data asymmetry (Figure 3.1-1b) introduces spikes into the RF spectrum at multiple $\pm R_B$ intervals increasing the level of *Unwanted Emissions* by 15-18 dB. Nulls in the discrete spectrum occur at:

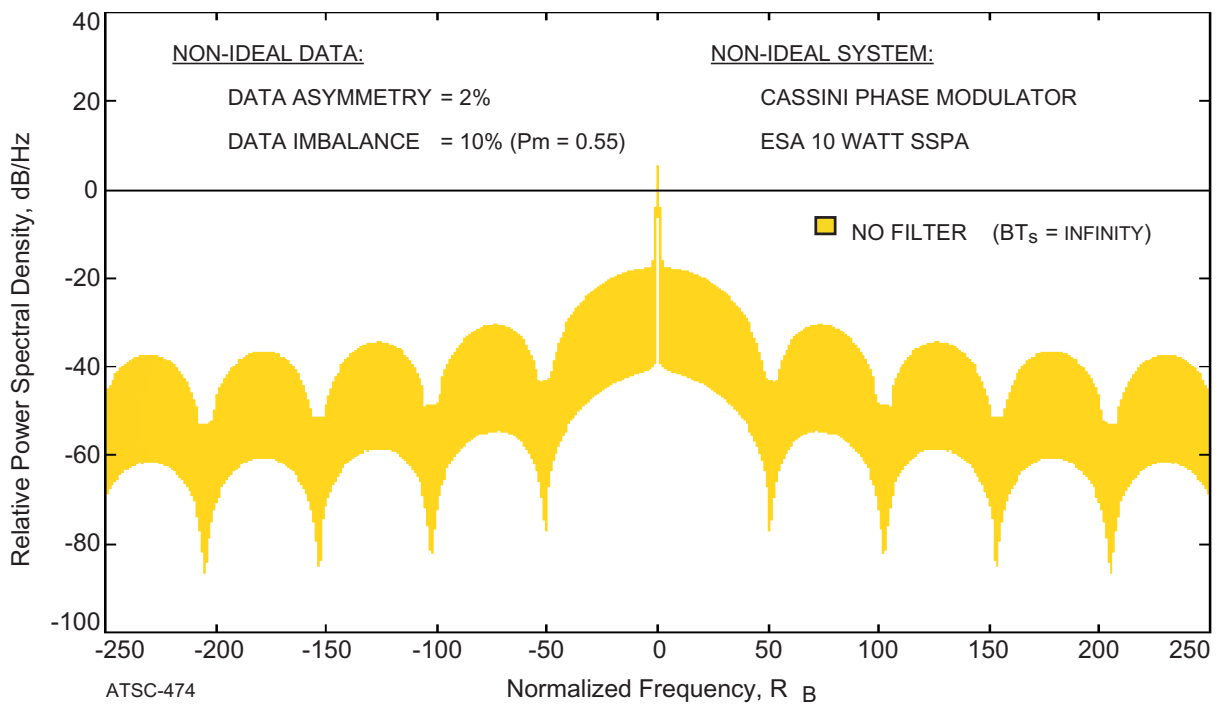
$$R_B / \eta = R_B / 0.02 = 50 R_B$$

where: η = data asymmetry

EFFICIENT MODULATION METHODS STUDY AT NASA/JPL



3.1-1a: 10% Data Imbalance and No Data Asymmetry



3.1-1b: 10% Data Imbalance and 2% Data Asymmetry

Figure 3.1-1: Unfiltered BPSK/NRZ Reference Modulation Spectra with Non-Ideal Data

EFFICIENT MODULATION METHODS STUDY AT NASA/JPL

Table 3.1-1: Summary of Reference Modulation Measurements

Data Imbalance Only (Figure 3-1a)		Data Imbalance and Asymmetry (Figure 3-1b)	
dB Below Sideband Peak	Spectrum Width R_B	dB Below Sideband Peak	Spectrum Width R_B
-20	$\pm 3.6 R_B$	-20	$\pm 19.1 R_B$
-30	$\pm 11.6 R_B$	-30	$\pm 40.1 R_B$
-40	$\pm 74.8 R_B$	-40	$> \pm 250 R_B$
-50	$\pm 130.5 R_B$	-50	$> \pm 250 R_B$
-60	$>> \pm 250 R_B$	-60	$>> \pm 250 R_B$

All modulation methods discussed below, are measured with respect to the unfiltered BPSK/NRZ reference case and the results are summarized in Table 4.1-2. Additionally, each modulation type also includes an unfiltered (i.e., $BT_s = \infty$) spectrum on the same figure for reference purposes. Note: Unfiltered spectra, found on the figures for each modulation method, is for the same modulation method under discussion and not the BPSK/NRZ reference case.

Because the *Universal Phase Modulator*'s sample-and-hold and baseband filter substantially remove all data asymmetry, comparisons to BPSK/NRZ are made with Figure 3-1a (i.e., $\eta = 0$). This represents a *worst case* since spectra with spikes due to filtering are being compared to spectra without spikes resulting from data asymmetry.

All spectrum plots and bandwidth measurements are stated in terms of R_B . This normalized parameter is described in Section 2.1 (equation 2-1) and represents the frequency span occupied by one sidelobe of the modulating signal. Readers can easily convert Section 3 measurements to their desired data rate by multiplying their data rate by the value of R_B .

For example, sidebands of unfiltered BPSK/NRZ modulation, with a 10% data imbalance and a 2% data asymmetry, are 20 dB below the peak at $\pm 19.1 R_B$ (Table 3.1-1). If the modulating data rate is 10 ks/s, then the sidebands will be 20 dB below the peak amplitude at ± 191 kHz away from the center frequency.

All spectra are plotted using a resolution bandwidth of 1.33 Hz. This was the narrowest feasible simulation bandwidth using SPW. It is sufficiently close to 1 Hz so that the continuous and discrete portions of spectra are depicted with the proper relationship to one another. Readers can easily adapt these separate parts of the spectrum for any desired bandwidth by adjusting the continuous portion by the ratio of the new bandwidth to 1 Hz.

EFFICIENT MODULATION METHODS STUDY AT NASA/JPL

3.2 PCM / PM / NRZ MODULATION

Phase modulation techniques are subdivided into two categories: residual carrier and suppressed carrier. The distinction lies in the presence (residual) or absence (suppressed) of an RF carrier component. Traditionally, space agencies employed the former. However, as data rates have increased and Power Flux Density (PFD) became a problem for Earth orbiting spacecraft, many mission designers began using suppressed carrier modulation. For this Phase 3 study, the residual carrier modulation index was 1.2 radians (peak).

Nevertheless, residual carrier systems are still widely used, particularly where simultaneous telemetry and ranging data capture is required. Unbalanced QPSK (UQPSK) is occasionally used in suppressed carrier applications requiring simultaneous telemetry and ranging. However, absent a low rate data type or a realtime reallocation of power, the UQPSK quadrature channel may not be used effectively when ranging is turned off.

Although care must be taken to control data imbalance, PCM/PM/NRZ modulation provides the narrowest RF spectrum of the residual carrier types tested. High levels of data imbalance can result in large end-to-end system losses making this modulation type unsuitable in applications having low telemetry performance margins. Generally, convolutional encoding ensures a sufficient symbol transition density to keep losses at an acceptable level.

PCM/PM/NRZ modulation has been used successfully on NASA's Polar spacecraft and is under consideration for some future missions. Where a remnant carrier is required and convolutional coding is employed, this modulation type deserves serious consideration.

3.2.1 PCM / PM / NRZ Modulation Bit-Error-Rate (BER)

End-to-end system performance measurements were a principal Phase 3 study objective. The best, most compact, RF spectrum is of little value if the Earth station's receiver cannot capture the telemetry signal. BER vs E_B / N_0 plots were created for Butterworth, Bessel, and Square Root Raised Cosine (SRRC) filters. Curves representing Symbol Bandwidth - Time (BT_s) values of 1, 2, and 3 were plotted for the two passive (Butterworth and Bessel) filter types. BER vs E_B / N_0 plots for SRRC filters included a single value $\alpha = 1$ curve.

Figure 3.2-1 contains plots for the three filter types. Inspecting these curves at $BER = 1 \times 10^{-3}$, shows BT_s values of 2 and 3 to be almost identical. Conversely, losses for $BT_s = 1$ are greater increasing the required E_B / N_0 . Applying the criteria set forth in Section 1.5.2, a value of $BT_s = 2$ was selected for Butterworth and Bessel filters. Note that loss increases from $BT_s = \infty$ to $BT_s = 2$ or 3 are insignificant. System losses and its components are summarized in Table 4.1-1.

System losses can be found by subtracting the E_B / N_0 value for Ideal PCM/PM/NRZ from the corresponding E_B / N_0 value for a $BT_s = 2$ or 3 at a $BER = 1 \times 10^{-3}$. Each plot also contains an ideal BPSK/NRZ modulation curve for reference purposes. To a first order, system losses for all three filter types appear to be about the same. Thus, the selection of the best filter depends upon its complexity and the resulting spectrum.

EFFICIENT MODULATION METHODS STUDY AT NASA/JPL

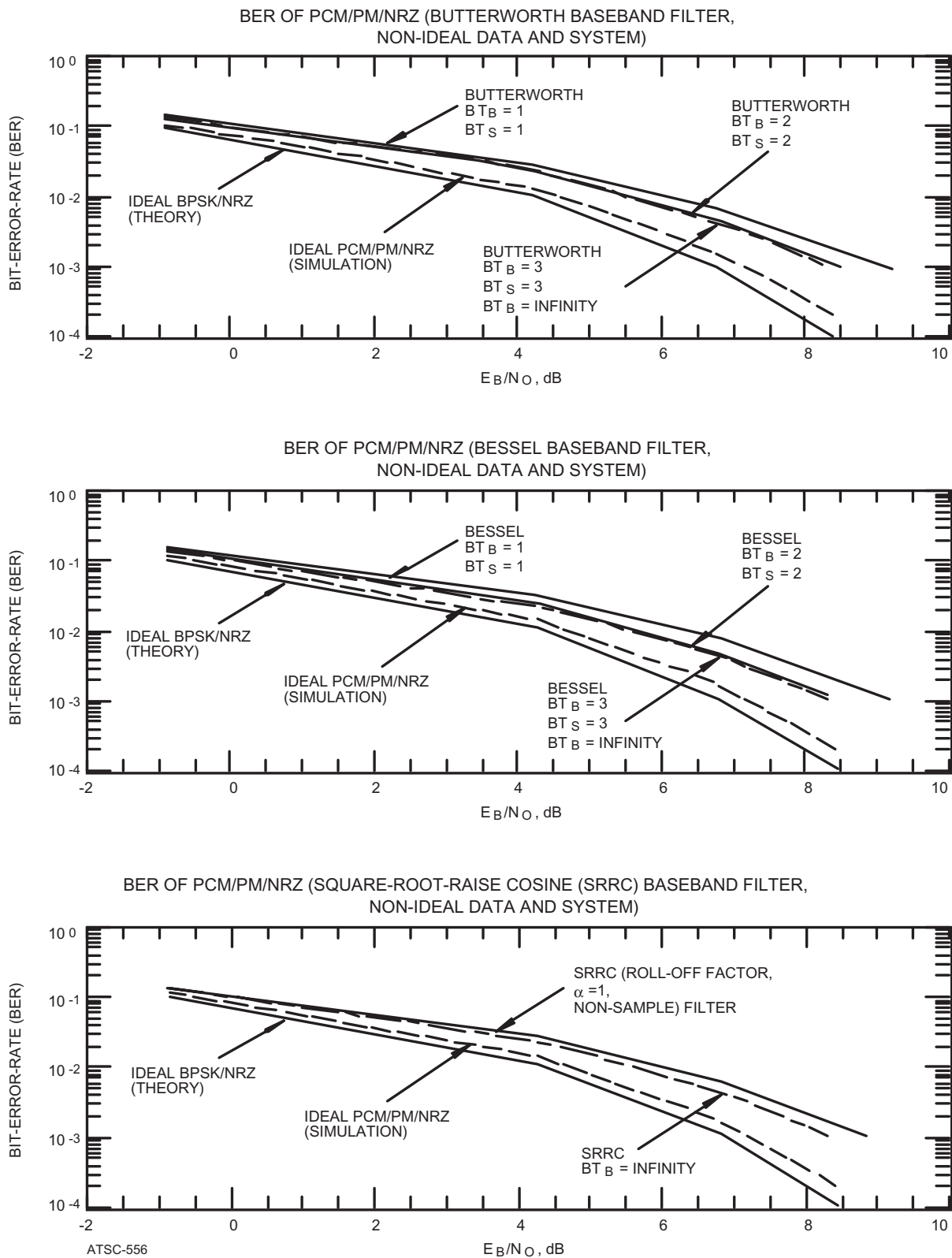


Figure 3.2-1: PCM/PM/NRZ Modulation Bit-Error-Rate

EFFICIENT MODULATION METHODS STUDY AT NASA/JPL

3.2.2 PCM / PM / NRZ Modulation Spectra

Figure 3.2-2 shows PCM/PM/NRZ spectra, measured at the SSPA's output, for span bandwidths of $20 R_B$ (Fine Detail) and $500 R_B$ (Broadband Spectra). Four filter cases appear for each of the modulation types evaluated in Phase 3 representing an unfiltered reference and three baseband filtered cases. The topmost, yellow (or light grey) curve always represents the unfiltered (i.e., $BT_s = \infty$) case of the modulation type under evaluation. It is placed there for comparative purposes.

Because $\eta = 0$ for the unfiltered case, no spikes appear in the spectrum. However, filtering introduces RF spectrum spikes at R_B intervals (Figure 3.2-2a). Note that the amplitude of the spikes drops below that for the unfiltered spectrum at $\pm 7 R_B$, $\pm 6 R_B$, and $\pm 3 R_B$ for the Bessel, Butterworth, and Square Root Raised Cosine filtered cases respectively. The net result of baseband filtering is to widen the spectrum close to the center frequency while significantly restricting its width at larger values of R_B . This effect is clearly evident in Figure 3.2-2b.

Figure 3.2-2b also demonstrates that Butterworth and Square Root Raised Cosine baseband filters are considerably more effective in restricting the RF spectrum's width than is a Bessel baseband filter. Because of its simplicity, the Butterworth filter ($BT_s = 2$) appears to be the best choice for baseband filtering.

3.2.3 PCM / PM / NRZ Modulation Power Containment

Figure 3.2-3 depicts the one-sided bandwidth of a PCM/PM/NRZ signal. Modulation on an RF carrier doubles the one-sided bandwidth. Using a Butterworth $BT_s = 2$ filter, the *occupied bandwidth* is about $\pm 2 R_B$ ($4 R_B$ total spectrum width).

Table 4.1-2 contains the two-sided bandwidth as measured using SPW. $8.2 R_B$ are needed to be 20 dB below the data sideband's peak amplitude. The $4 R_B$ difference between *occupied bandwidth* and the -20 dB point in Table 4.1-2 results from spikes due to baseband filtering. In Table 4.1-2, no spectral components exceed -20 dB beyond a bandwidth of $8.2 R_B$. However, the power contained in the spikes is vanishingly small. Thus, for filtered phase modulated signals, the power containment bandwidth will be substantially smaller than that required for an equivalent sideband attenuation.

3.2.4 PCM / PM / NRZ Modulation Study Conclusions

PCM/PM/NRZ is the most bandwidth-efficient residual carrier modulation method investigated. It should receive serious consideration by projects having moderate data rate requirements (20 ks/s - 2 Ms/s) when a residual carrier is required. Because system losses are very sensitive to data imbalance, some means for ensuring an approximately equal number of +1s and -1s over a time interval of $1/B_L$ must be provided (where B_L is the receiver phase-locked loop's bandwidth expressed in Hz). Convolutional encoding may be sufficient. If not, the CCSDS recommended data randomizer should be used.⁶

EFFICIENT MODULATION METHODS STUDY AT NASA/JPL

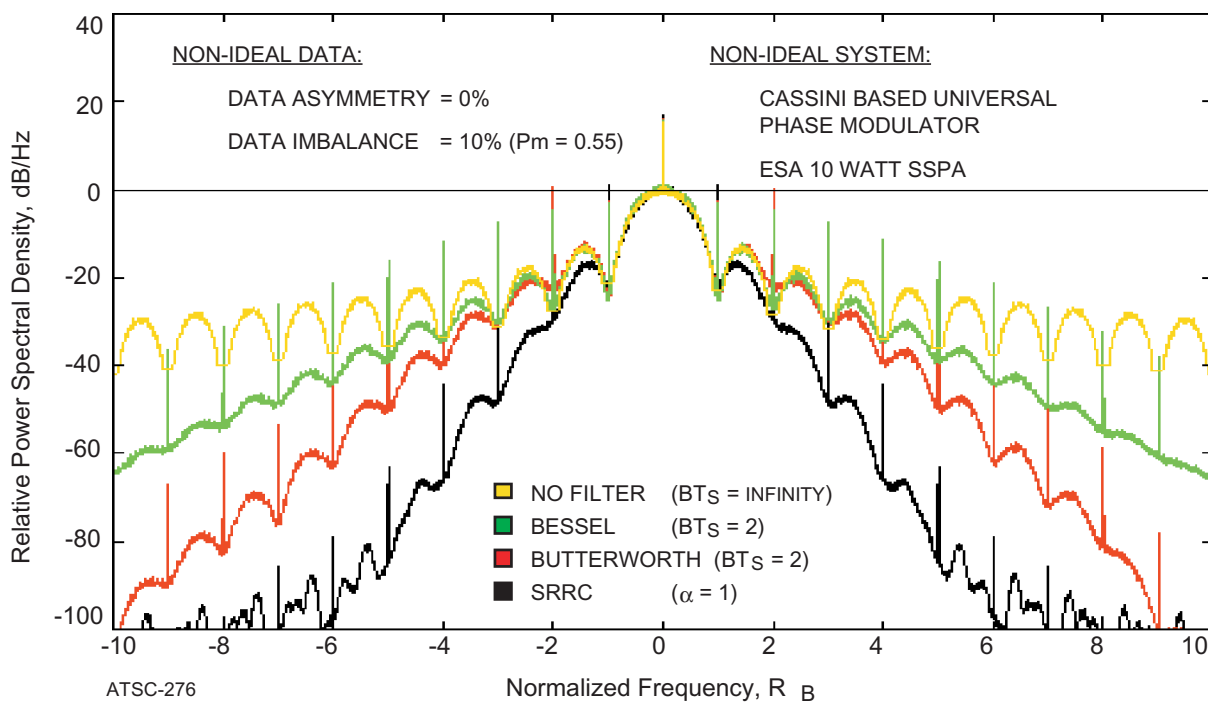
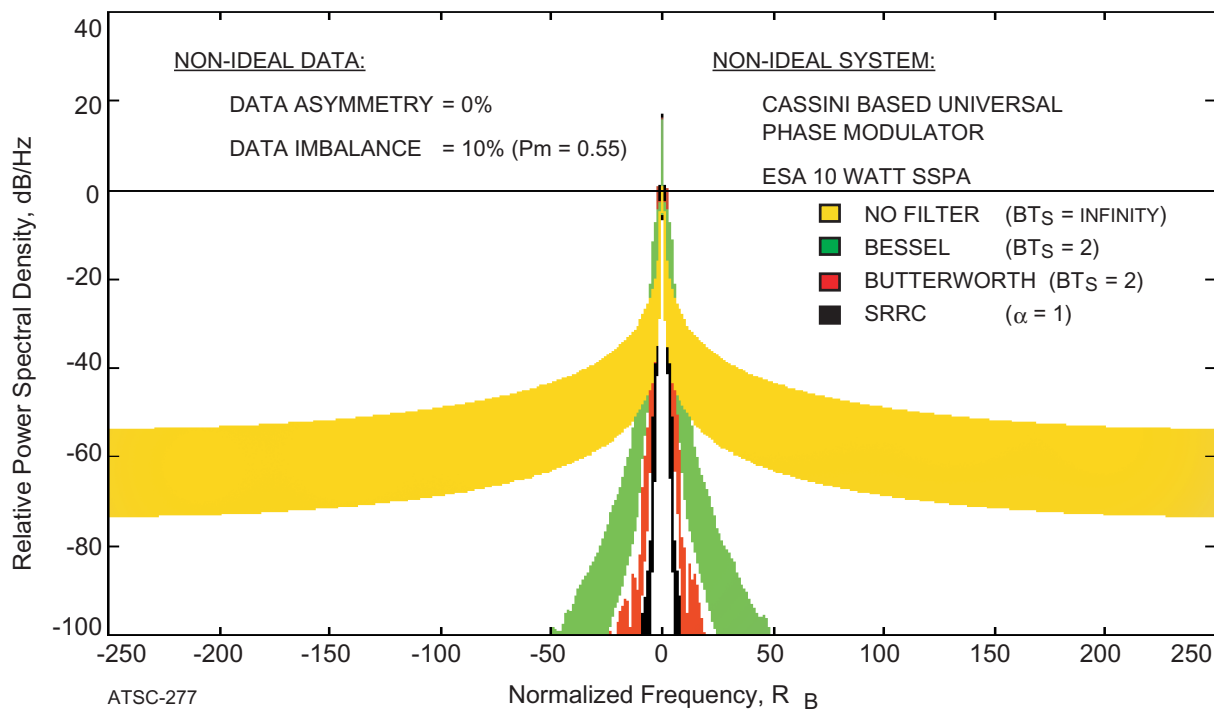
3.2-2a: Fine Detail ($f_C \pm 10 R_B$)3.2-2b: Broadband Spectra ($f_C \pm 250 R_B$)

Figure 3.2-2: PCM/PM/NRZ Modulation Spectra

EFFICIENT MODULATION METHODS STUDY AT NASA/JPL

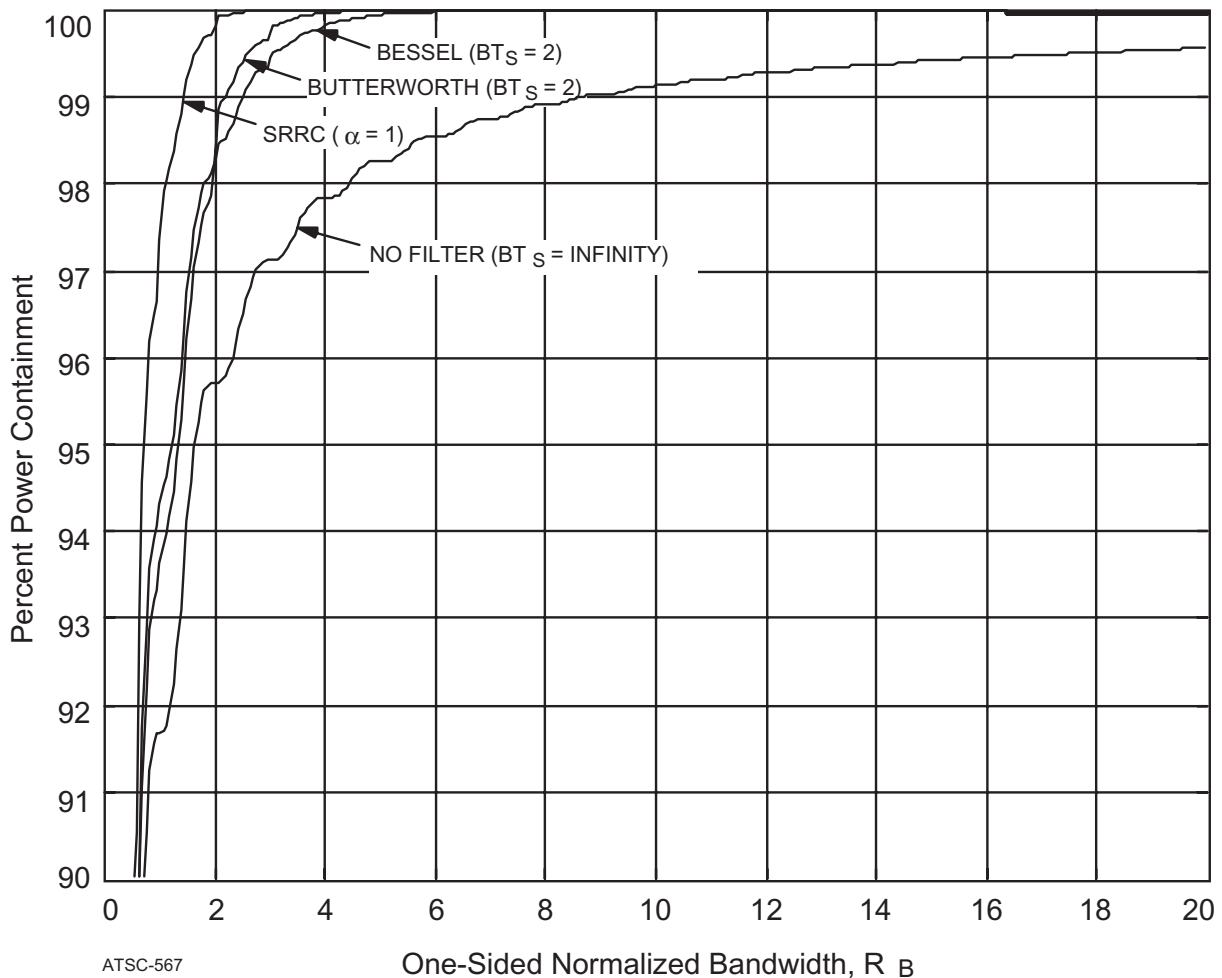


Figure 3.2-3: PCM/PM/NRZ Modulation Power Containment

Additionally, PCM/PM/NRZ modulation requires carrier distinguishability be maintained. Since the data sideband's spectrum peaks at the RF carrier frequency, the data rate must be sufficiently high to ensure that the data's power spectral density does not interfere with carrier detection. With a rate $\frac{1}{2}$ convolutional encoding, a data rate of 10kb/s may not be sufficient for some applications. At such a low symbol rate, the Earth station receiver phase-locked-loop's bandwidth will need to be quite narrow. For low data rate applications, where carrier distinguishability is not sufficient or where interference to the tracking loop may occur, UQPSK modulation may be preferred. Each mission's requirements should be analyzed to ensure proper operation where PCM/PM/NRZ is used.

3.3 PCM / PM / Bi- ϕ MODULATION

Where residual carrier modulation must be used, Manchester encoding is frequently thought to be preferable to PCM/PM/NRZ modulation. This is so because there is a spectral null at the RF carrier frequency increasing its distinguishability. Additionally, data imbalances, which can pose problems for PCM/PM/NRZ modulation, are eliminated.

EFFICIENT MODULATION METHODS STUDY AT NASA/JPL

PCM/PM/Bi- ϕ eliminates data imbalance by the modulo-2 addition of information data with a double-frequency squarewave. Each Manchester encoded information data bit comprises both a +1 and -1 with the result that the number of +1s and -1s are approximately equal over a time interval of $1/B_{LO}$ where B_{LO} is the receiver phase locked loop s bandwidth. However, spectral bandwidth is doubled.

3.3.1 PCM / PM / Bi- ϕ Modulation Bit-Error-Rate (BER)

Figure 3.3-1 displays the BER vs E_B / N_0 plots for the three filter types using PCM/PM/Bi- ϕ modulation. Comparing these curves with those for PCM/PM/NRZ modulation (Figure 3.2-1) reveals that losses for PCM/PM/Bi- ϕ are significantly less than for PCM/PM/NRZ modulation. At a BER = 1×10^{-3} the difference in required E_B / N_0 is about 0.7 dB. Increased losses found with PCM/PM/NRZ result principally from the 10% *data imbalance* included in this study. However, the figure shows a distinct difference between the ideal curve and the reference BPSK/NRZ curve.

The double-frequency squarewave requires the baseband filter s bandwidth be reset. Loss measurements in Phase 2 showed that a $BT_S = 2$ provided the best compromise between system losses and RF spectrum width for PCM/PM/NRZ modulation. With PCM/PM/Bi- ϕ modulation, a $BT_S = 2$ filter bandwidth is retained; however, it is based on the Manchester code s symbol period (BT_S), rather than on BT_B , the information data bit s period. Such a filter would be equivalent to a $BT_B = 4$ for the information data. System losses and its components are summarized in Table 4.1-1

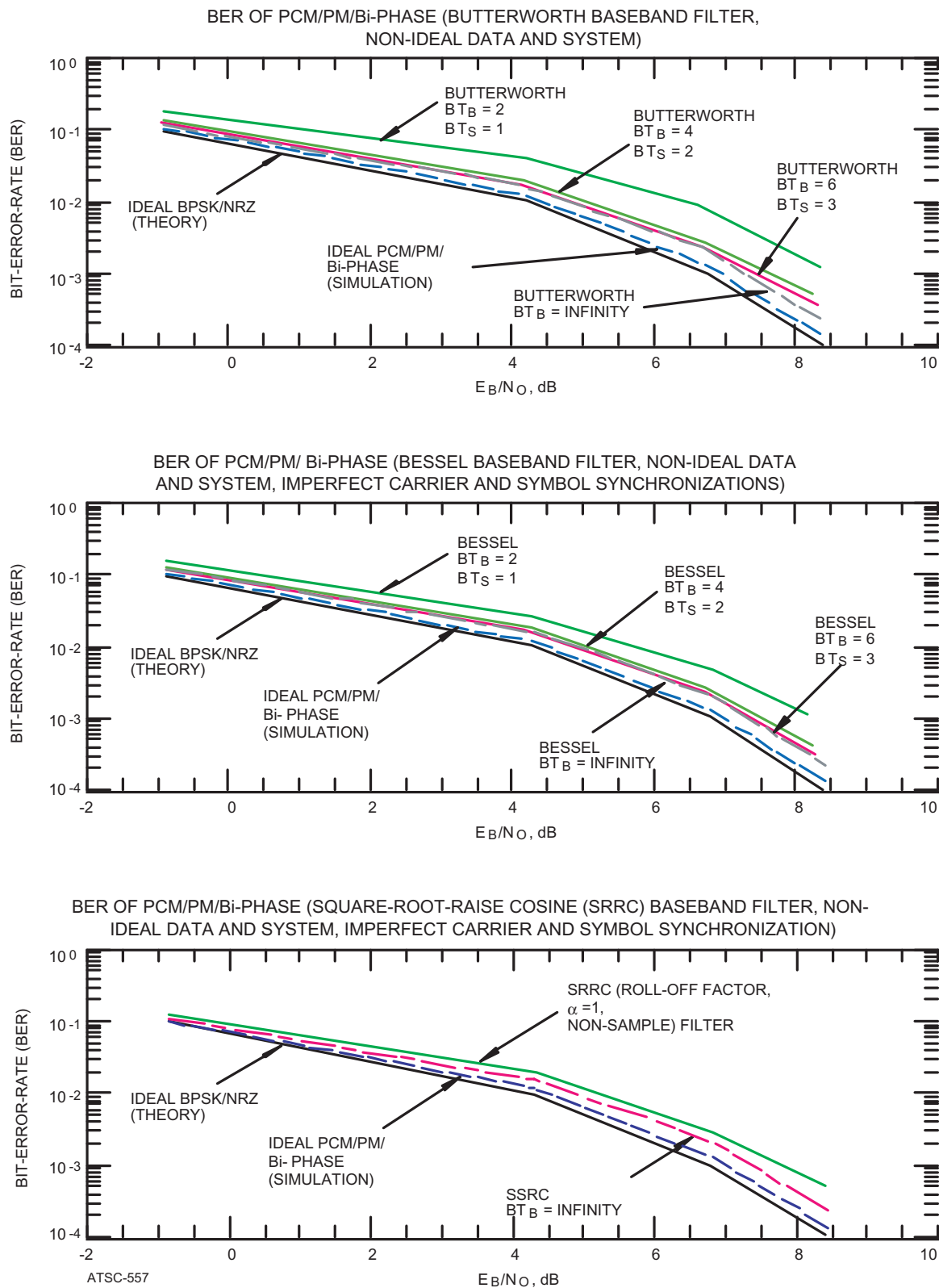
3.3.2 PCM / PM / Bi- ϕ Modulation Spectra

While PCM/PM/Bi- ϕ improves RF carrier detectability over PCM/PM/NRZ modulation, the bandwidth efficiency is substantially reduced. Comparing Figures 3.2-2b and 3.3-2b, for PCM/PM/NRZ and PCM/PM/Bi- ϕ modulations respectively, shows that the -100 dB level is reached at $\pm 50 R_B$ for the former while $\pm 100 R_B$ are required for the latter. One concerned with spectrum efficiency should avoid the use of PCM/PM/Bi- ϕ whenever possible.

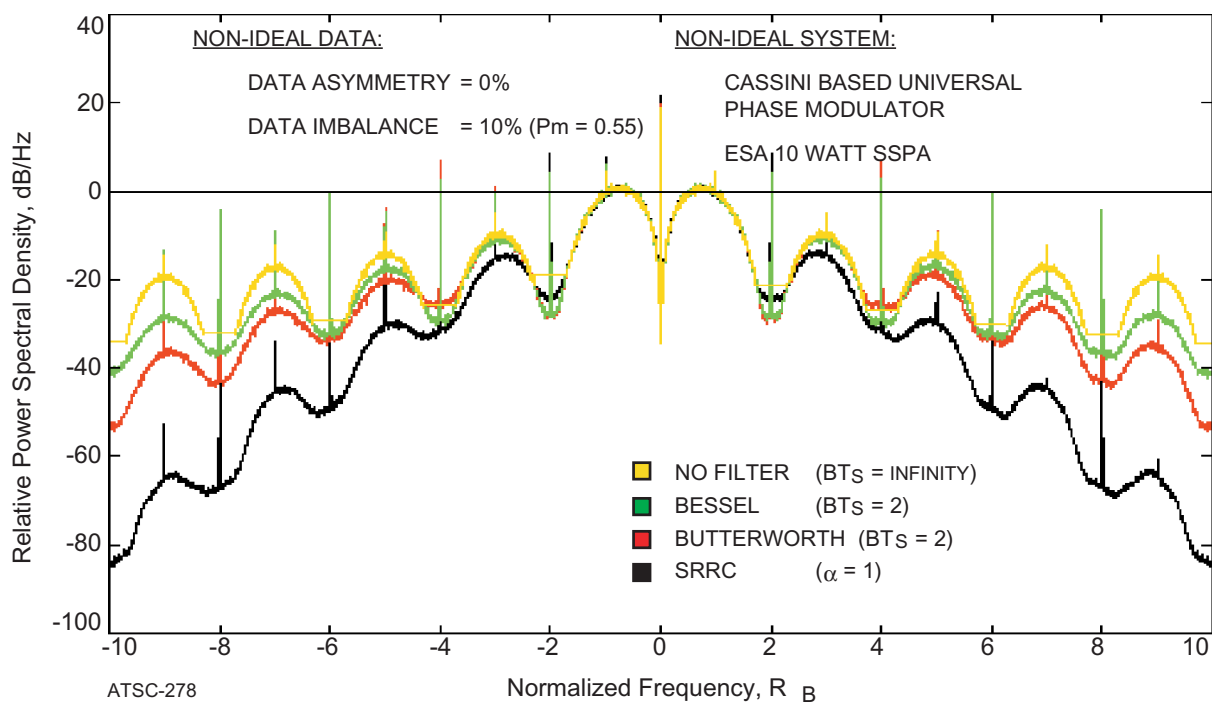
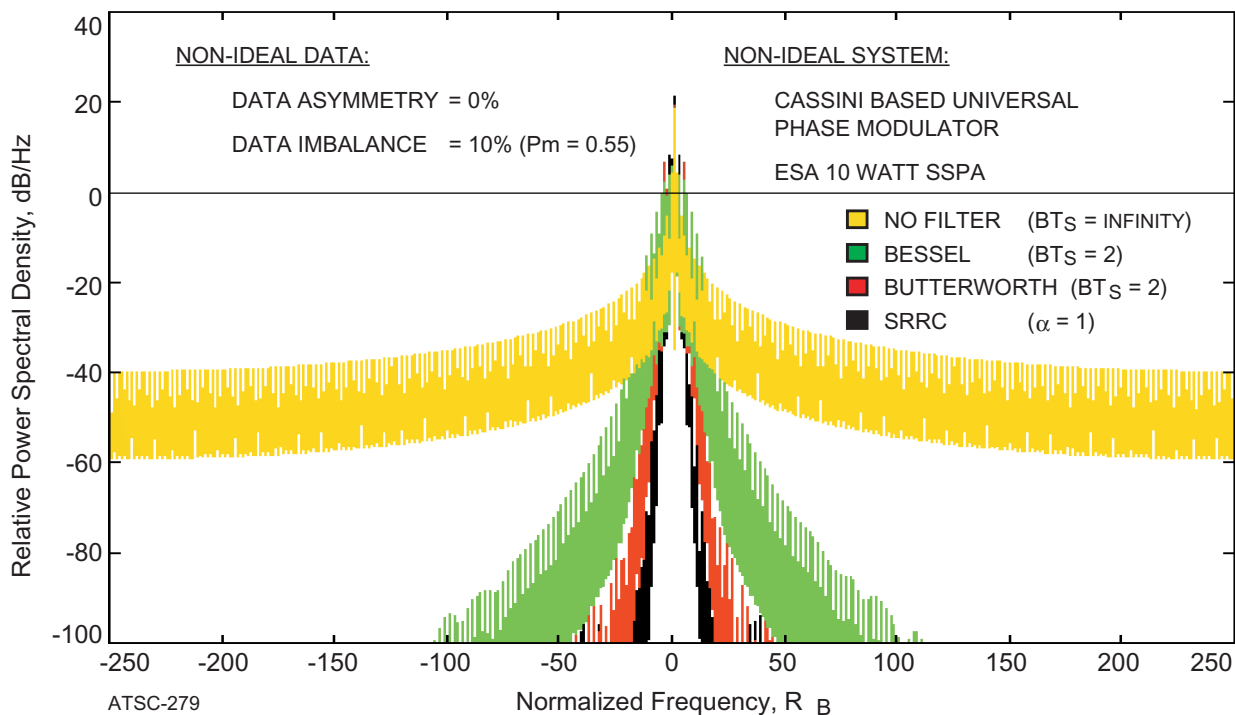
As in the PCM/PM/NRZ case, filtered spectra are actually wider than the unfiltered spectra in the neighborhood of the RF carrier frequency. However by $\pm 12 R_B$ filtered spectra become narrower and remain so thereafter. Filtering substantially improves the bandwidth efficiency as the distance from the RF carrier is increased.

For this study, timing errors between the information data bits and Manchester code symbols were considered negligible. Nevertheless, additional spikes are introduced into the RF spectrum from the 10% data imbalance. With PCM/PM/NRZ modulation, spikes occurred only in the nulls at $\pm R_B$ intervals. For PCM/PM/Bi- ϕ modulation, spikes can be seen in both the nulls and at the peaks of the spectrum (Figure 3.3-2a). *Note: These spikes are present when $\eta = 0$. Spikes due phase domain filtering appear at spectrum nulls while spikes resulting from data imbalance appear at the peaks.*⁷ Since some data imbalance is always likely to be present, this finding suggests that PCM/PM/Bi- ϕ modulation users may have been operating with spectral spikes all along.

EFFICIENT MODULATION METHODS STUDY AT NASA/JPL

Figure 3.3-1: PCM/PM/B- ϕ Bit-Error-Rate

EFFICIENT MODULATION METHODS STUDY AT NASA/JPL

3.3-2a: Fine Detail ($f_C \pm 10 R_B$)3.3-2b: Broadband Spectra ($f_C \pm 250 R_B$)Figure 3.3-2: PCM/PM/Bi- ϕ Modulation Spectra

EFFICIENT MODULATION METHODS STUDY AT NASA/JPL

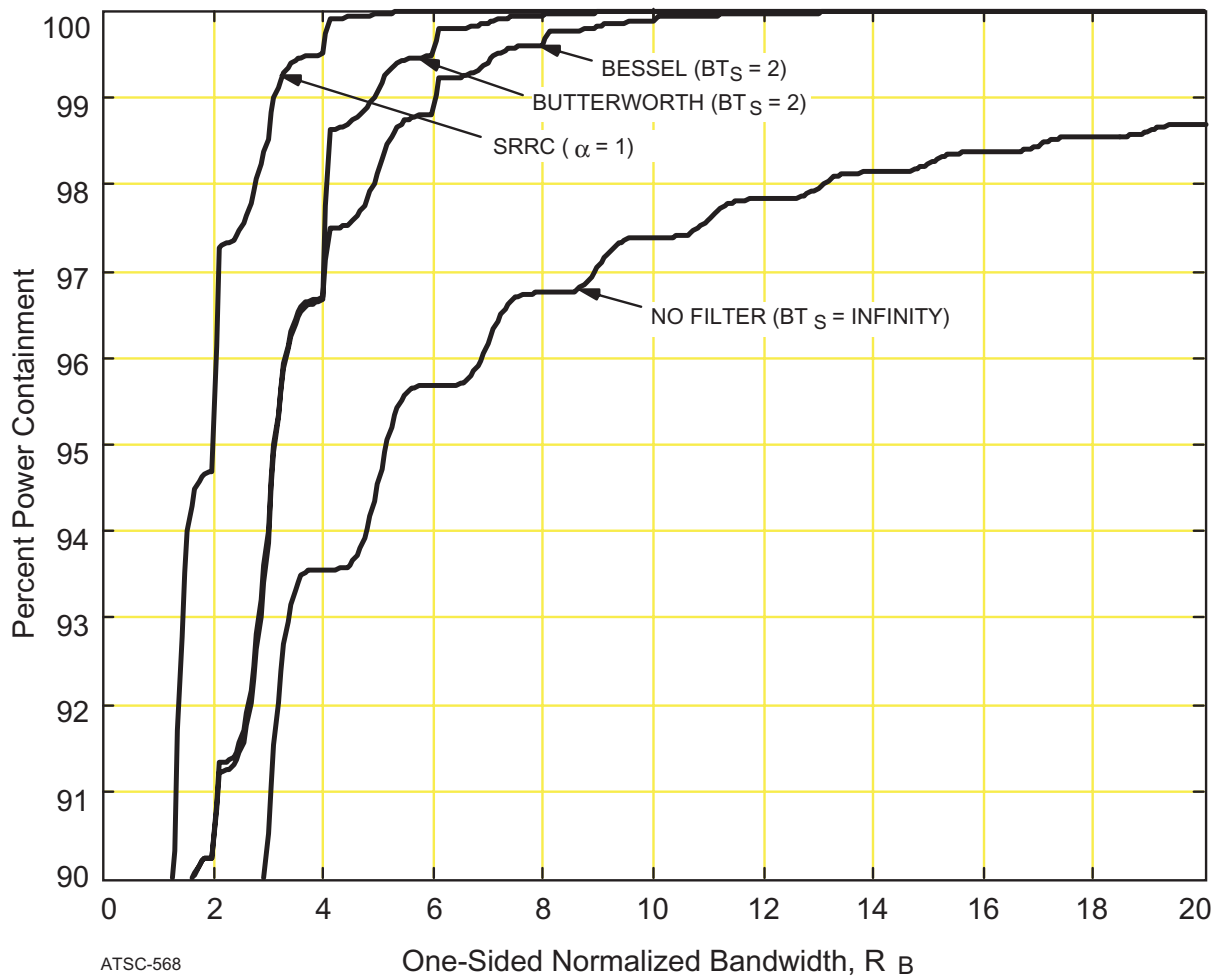


Figure 3.3-3: PCM/PM/Bi-φ Modulation Power Containment

Some *scalloping* is discernable in the darker portion of Figure 3.3-2b. It appears to be periodic at approximately $10 R_B$. Concern was expressed that this may be a result of the Manchester encoding process. To resolve the matter, the original SPW data was expanded in a series of steps so that individual spectral lobes, and spikes, became identifiable. No evidence of a periodic signal was found. The authors have concluded that these variations are an artifact of the graphics presentation process and are not actually present in the RF spectrum.

3.3.3 PCM / PM / Bi-φ Modulation Power Containment

As expected, Figure 3.3-3 shows that power containment for PCM/PM/Bi-φ modulation is twice that of PCM/PM/NRZ. Here the *occupied bandwidth* is approximately $9 R_B$ using a Butterworth, $BT_S = 2$ filter. PCM/PM/Bi-φ modulation was found to be one of the *least* bandwidth-efficient modulation types considered in the Phase 3 study.

EFFICIENT MODULATION METHODS STUDY AT NASA/JPL

3.3.4 PCM / PM / Bi- ϕ Modulation Study Conclusions

If a residual carrier is required and either the data imbalance is greater than 5% (\mathcal{P}_M or $\mathcal{P}_S \geq 0.525$) or the data's symbol rate is so low that RF carrier distinguishability may be impaired, PCM/PM/NRZ may be unsuitable. In such cases, PCM/PM/Bi- ϕ modulation could be considered. RF spectrum efficiency is reduced by half as compared to PCM/PM/NRZ making PCM/PM/Bi- ϕ modulation the least bandwidth-efficient type in this study.

Space agency Spectrum Managers truly concerned about bandwidth efficiency should encourage the use of modulation methods other than PCM/PM/Bi- ϕ , particularly at data rates above 1 Mb/s. Specifically, the need for a residual carrier should be reviewed to ensure that it is absolutely necessary. If not, BPSK, UQPSK, or QPSK modulation should be considered.

3.4 BPSK / NRZ MODULATION

BPSK/NRZ modulation is typically used as a reference for other modulation methods for comparing bandwidth efficiency, Bit-Error-Rate (BER) performance, and system losses. Unlike PCM/PM/NRZ, BPSK/NRZ modulation does not exhibit large system losses at high levels of data imbalance obviating the need for Manchester encoding. Nevertheless, problems can arise in the symbol synchronizer's Digital Transition Tracking Loop (DTTL) at low symbol transition densities where it may experience difficulty in remaining locked. Since symbol synchronizers are commonly implemented using DTTLs, the spacecraft must provide an adequate symbol transition density.

BPSK/NRZ modulation is useful if the symbol transition density is sufficient for the DTTL. Generally, convolutional encoding provides an adequate data transition density. In these cases, it is preferred over Manchester encoded BPSK because of the substantially narrower bandwidth.

3.4.1 BPSK / NRZ Modulation Bit-Error-Rate (BER)

Bit-Error-Rate (BER) plots for the three filter types can be found in Figure 3.4-1. These plots are similar to those for PCM/PM/Bi- ϕ modulation and the E_b / N_0 required for a 1×10^{-3} BER, with a Butterworth ($BT_s = 2$) filter, is within 0.1 - 0.2 dB. System performance differences are so small that BER cannot be used to discriminate between these two modulation types. System losses and its components are summarized in Table 4.1-1.

3.4.2 BPSK / NRZ Modulation Spectra

Figure 3.4-2 shows the RF spectra for this modulation type. Except for the lack of an RF carrier component, these spectra are virtually indistinguishable from those for PCM/PM/NRZ. This is so for both the filtered and unfiltered cases. The apparent RF carrier component, extending above the 0 dB reference line, is actually a dc component introduced by the 10% data imbalance.

EFFICIENT MODULATION METHODS STUDY AT NASA/JPL

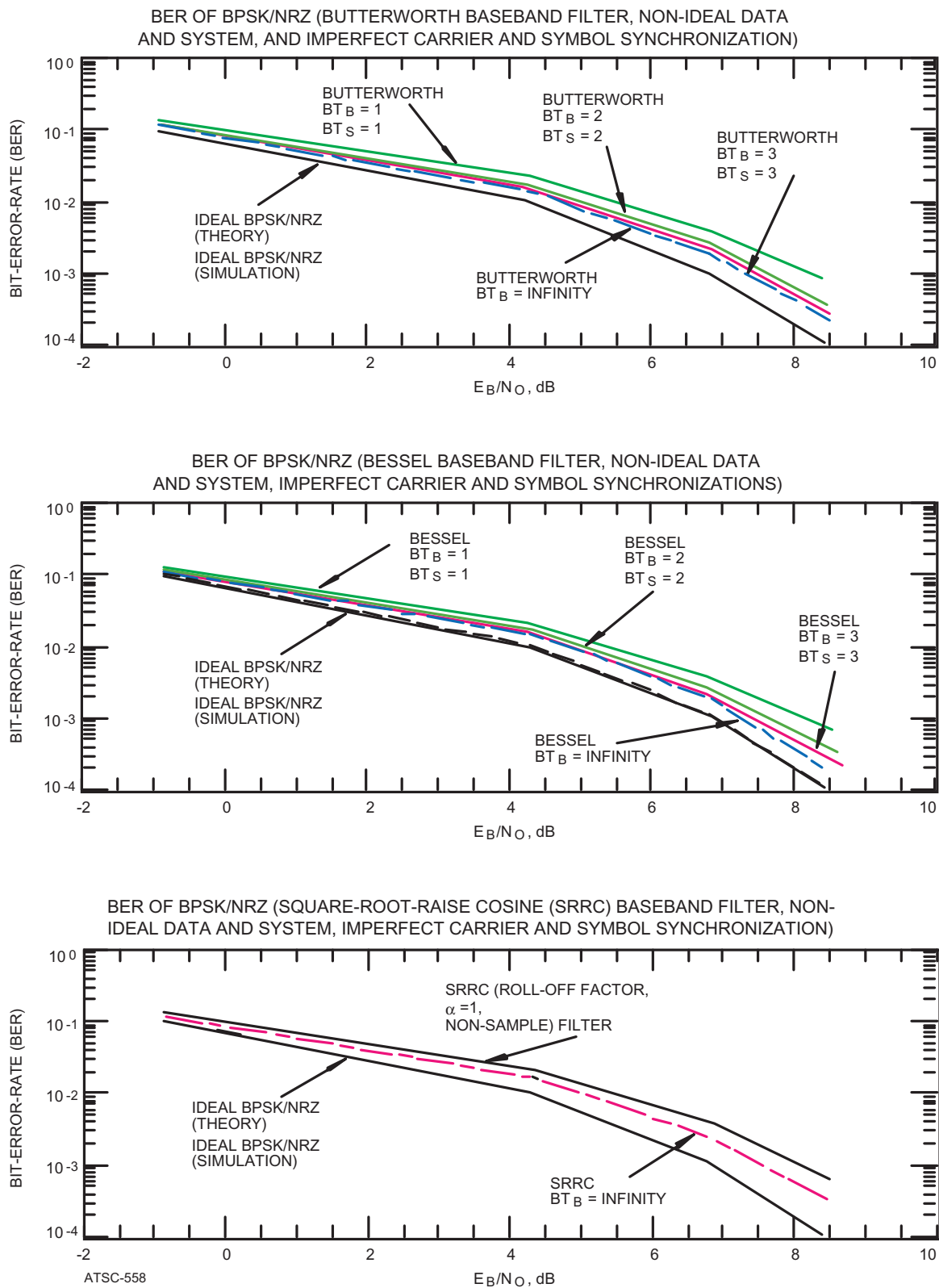


Figure 3.4-1: BPSK/NRZ Modulation Bit-Error-Rate

EFFICIENT MODULATION METHODS STUDY AT NASA/JPL

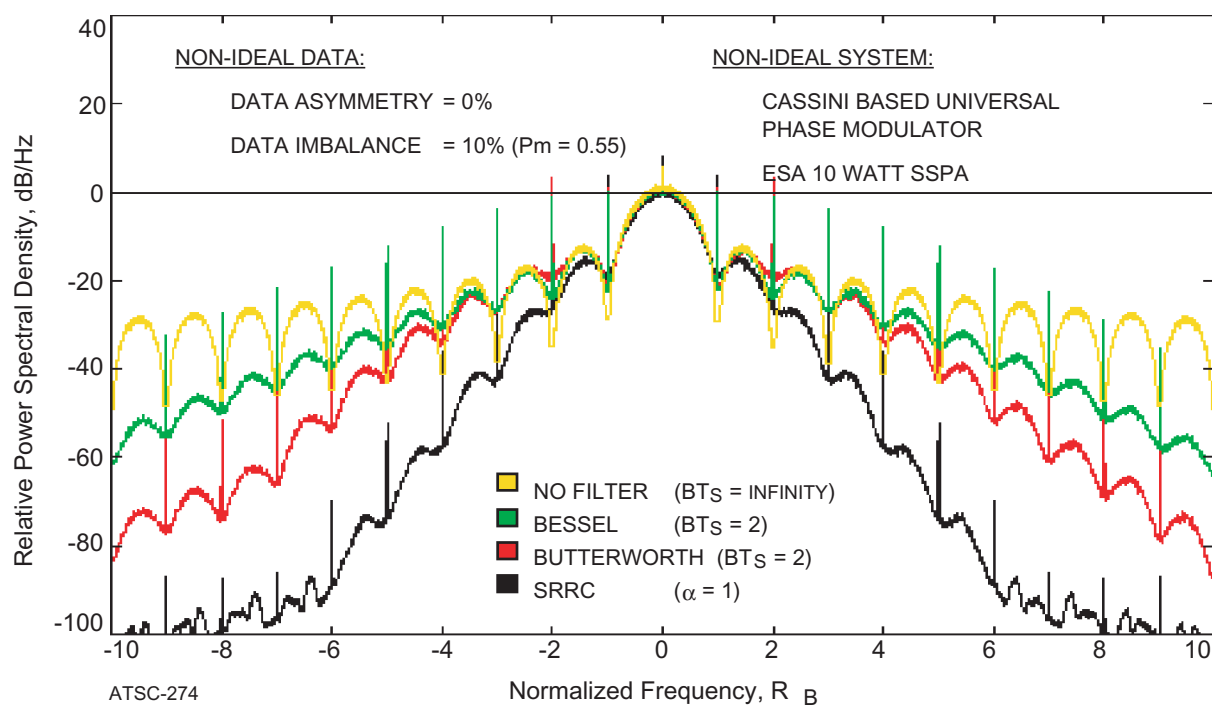
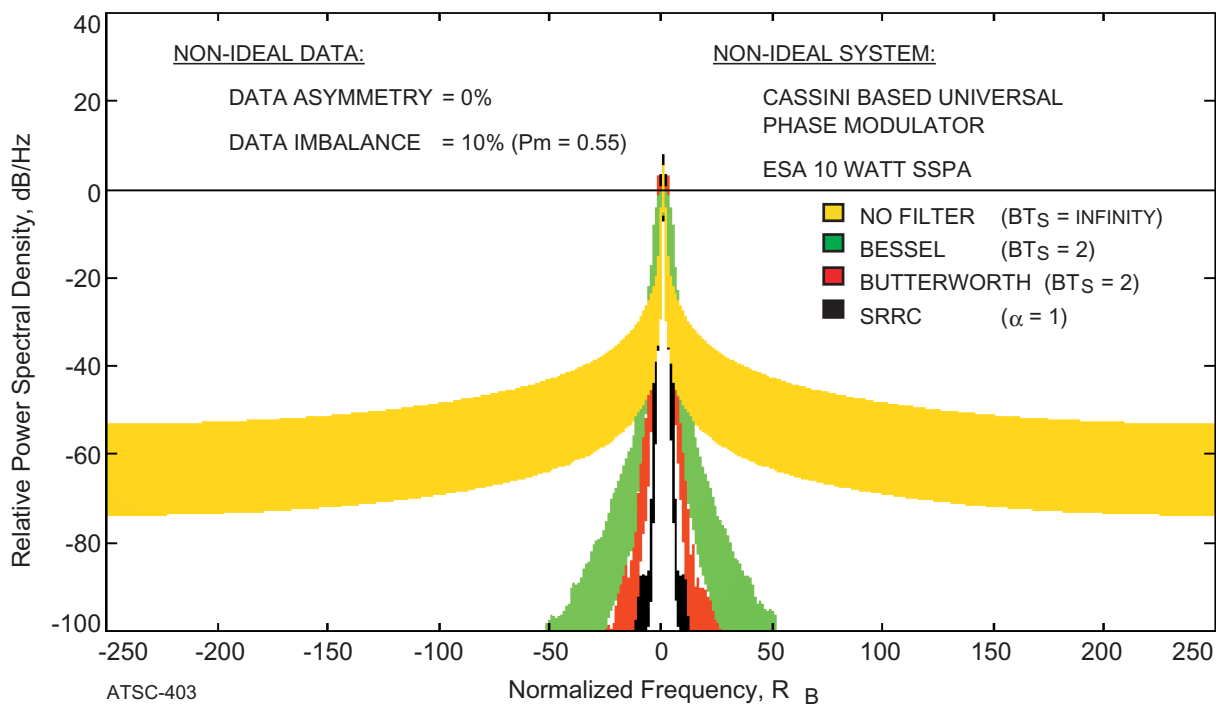
3.4-2a: Fine Detail ($f_c \pm 10 R_B$)3.4-2b: Broadband Spectra ($f_c \pm 250 R_B$)

Figure 3.4-2: BPSK/NRZ Modulation Spectra

EFFICIENT MODULATION METHODS STUDY AT NASA/JPL

Comparing filtered BPSK/NRZ and PCM/PM/NRZ spectra (Figures 3.4-2 and 3.2-2), the former appears to be slightly wider than the latter. This is the result of placing all transmitted power in the BPSK/NRZ modulation sideband. PCM/PM/NRZ modulation does retain a portion of the total power for the residual carrier component lowering the modulation sideband power. To a first order, Figures 3.2-2 and 3.4-2 demonstrate that BPSK/NRZ modulation has no RF bandwidth advantage over PCM/PM/NRZ modulation.

Conversely, BPSK/NRZ has a clear spectral advantage over the PCM/PM/Bi- ϕ modulation (Figure 3.3-2). Absent a high data imbalance level causing symbol synchronization problems, BPSK/NRZ appears to offer the best compromise between system losses and spectral efficiency of the modulation methods considered thus far.

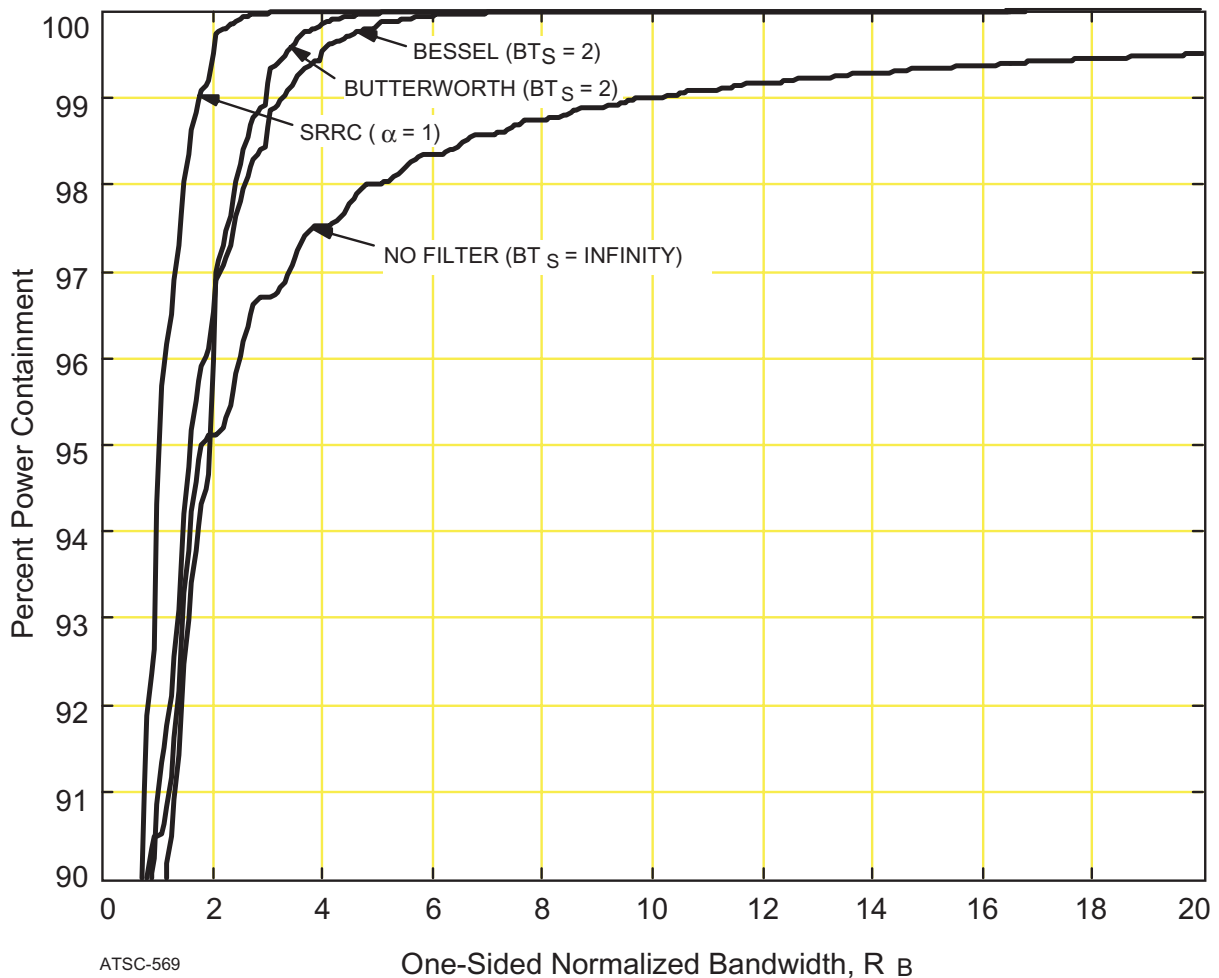
3.4.3 BPSK / NRZ Modulation Power Containmentment

Figure 3.4-3 profiles BPSK/NRZ modulation power containment. Comparing with Figure 3.2-3, BPSK/NRZ can be seen to have an *occupied bandwidth* roughly 50% greater than that of PCM/PM/NRZ, using a 1.2 radian (peak) modulation index, ($6 R_B$ vs $4 R_B$). Nevertheless, BPSK/NRZ is reasonably bandwidth-efficient and deserves consideration for some applications.

3.4.4 BPSK / NRZ Modulation Study Conclusions

Missions not requiring a residual carrier and having modest data rates (20 ks/s - 200 ks/s) should consider BPSK/NRZ modulation first. It provides a good compromise between spectrum efficiency and simplicity of design.

While data imbalance does not result in system losses as in the case of PCM/PM/NRZ modulation, the statistics of each application should be reviewed. Agencies employing a DTTL architecture in their symbol synchronizers, must ensure a sufficient transition density to acquire and maintain synchronization. Manchester encoding prior to BPSK modulation can ensure sufficient transitions. As with PCM/PM/Bi- ϕ modulation, there is a 100% penalty in spectrum efficiency over the NRZ equivalent.

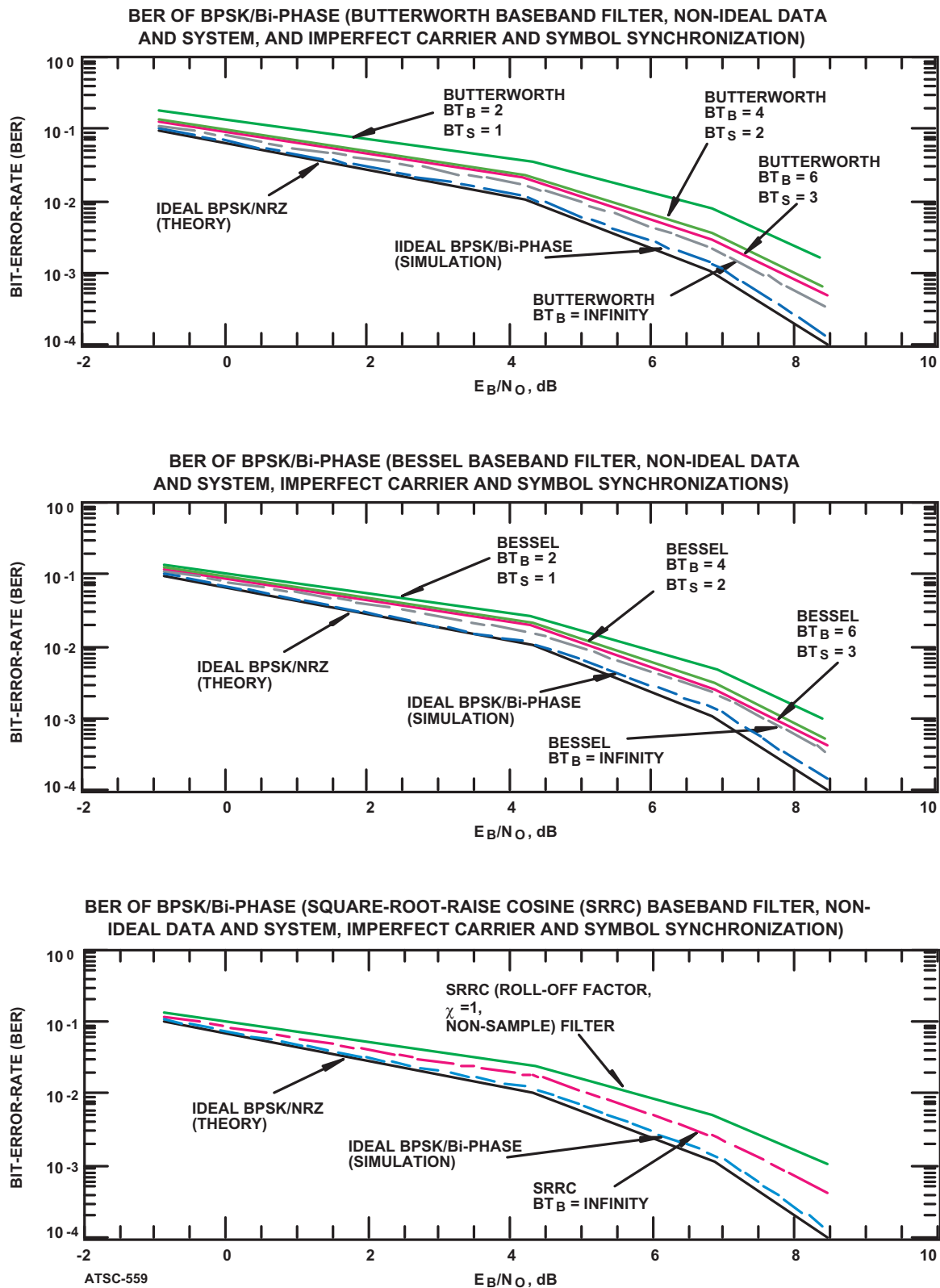
EFFICIENT MODULATION METHODS STUDY AT NASA/JPL**Figure 3.4-3: BPSK/NRZ Modulation Power Containment****3.5 BPSK / Bi- ϕ MODULATION**

This modulation method is useful where the modulating symbol transition density, due to data imbalance, is so low that the DTTL in the symbol synchronizer may lose lock. Its application is likely to be limited because most telemetry links are convolutionally encoded.

3.5.1 BPSK / Bi- ϕ Modulation Bit-Error-Rate (BER)

Figure 3.5-1 provides BER performance for BPSK/Bi- ϕ modulation. With a Butterworth $BT_S = 2$ filter, its performance is similar to, but slightly poorer than, PCM/PM/Bi- ϕ and BPSK/NRZ modulations. BER behavior of BPSK/Bi- ϕ is certainly better than that of PCM/PM/NRZ (Figure 3.2-1). Of course, the 10% data imbalance adversely affected the losses of PCM/PM/NRZ which was not the case with the PCM/PM/Bi- ϕ or BPSK/Bi- ϕ modulation types.

EFFICIENT MODULATION METHODS STUDY AT NASA/JPL

Figure 3.5-1: BPSK/Bi- ϕ Modulation Bit-Error-Rate (BER)

EFFICIENT MODULATION METHODS STUDY AT NASA/JPL

3.5.2 BPSK / Bi- ϕ Modulation Spectra

Figure 3.5-2 contains spectra for this modulation type. As for other modulation types, filtering significantly reduces RF bandwidth requirements. Again the passive Butterworth filter ($BT_s = 2$) appears to offer the best compromise between system complexity and RF bandwidth reduction.

Comparing BPSK/Bi- ϕ and BPSK/NRZ spectra (Figures 3.5-2 and 3.4-2) yields the following observations. First, BPSK/Bi- ϕ modulation approximately doubles the bandwidth. Second, spikes due to phase domain filtering appear at spectrum nulls while spikes resulting from the data imbalance appear at the peaks. Third, baseband filtering also produces a dc component at f_c . Manchester encoding makes it virtually impossible for *data imbalance* to exist making the spike at f_c very small on the unfiltered BPSK/Bi- ϕ curve on Figure 3.5-2. The existence of the small spike at f_c in the unfiltered case results from the use of non-ideal system components.

Contrasting spectra for BPSK/Bi- ϕ modulation (Figure 3.5-2) and PCM/PM/Bi- ϕ modulation (Figure 3.3-2), also shows interesting differences. The broadband residual carrier spectrum is slightly narrower than suppressed carrier spectrum because of the power retained in the RF carrier. Except for the f_c component, the spike amplitudes are approximately the same for the two modulation types.

3.5.3 BPSK / Bi- ϕ Modulation Power Containment

With an *occupied bandwidth* of $12 R_B$ using a Butterworth, $BT_s = 2$ filter, BPSK/Bi- ϕ is the least bandwidth-efficient modulation method in the Phase 3 study. Even with a Square Root Raised Cosine ($\alpha = 1$) filter, the *occupied bandwidth* is $8 R_B$.

3.5.4 BPSK / Bi- ϕ Modulation Study Conclusions

With its comparatively large bandwidth requirements and its poorer BER performance, BPSK/Bi- ϕ modulation is not likely to find wide application. Its use should be limited to circumstances when the data's symbol transition density is so low that the symbol synchronizer may have difficulty in acquiring or maintaining lock or where suppressed carrier modulation is required with very low data symbol rates.

Generally, space agencies interested in maximizing bandwidth efficiency should avoid use of this modulation type whenever possible. Where data symbol transition densities are so low that one of the NRZ modulation formats is unsuitable, use of BPSK/Bi- ϕ modulation may be unavoidable. Alternatively, space agencies could consider using symbol synchronizers which are not based on a Data Transition Tracking Loop (DTTL) architecture. For example, an open loop design such as the Maximum A Posteriori (MAP) symbol synchronizer⁸ will not have difficulty at low transition densities. This alternative symbol synchronizer architecture is particularly attractive for modulation methods such as MSK, GMSK, and FQPSK.

EFFICIENT MODULATION METHODS STUDY AT NASA/JPL

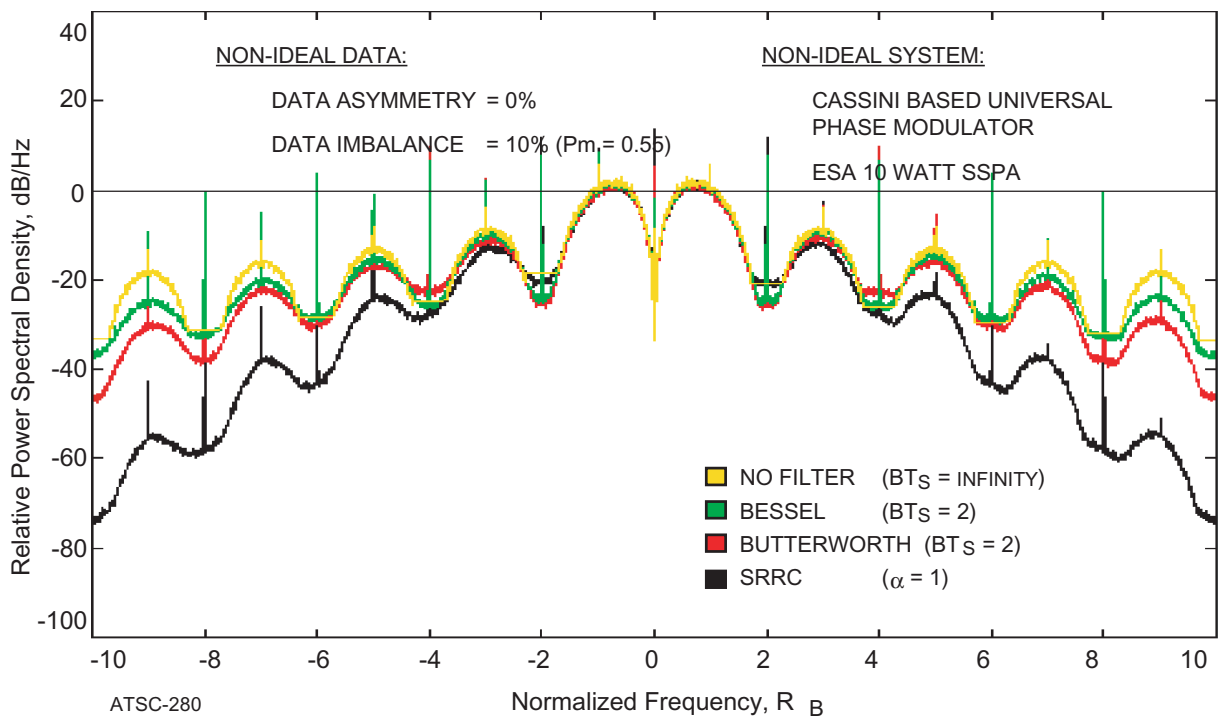
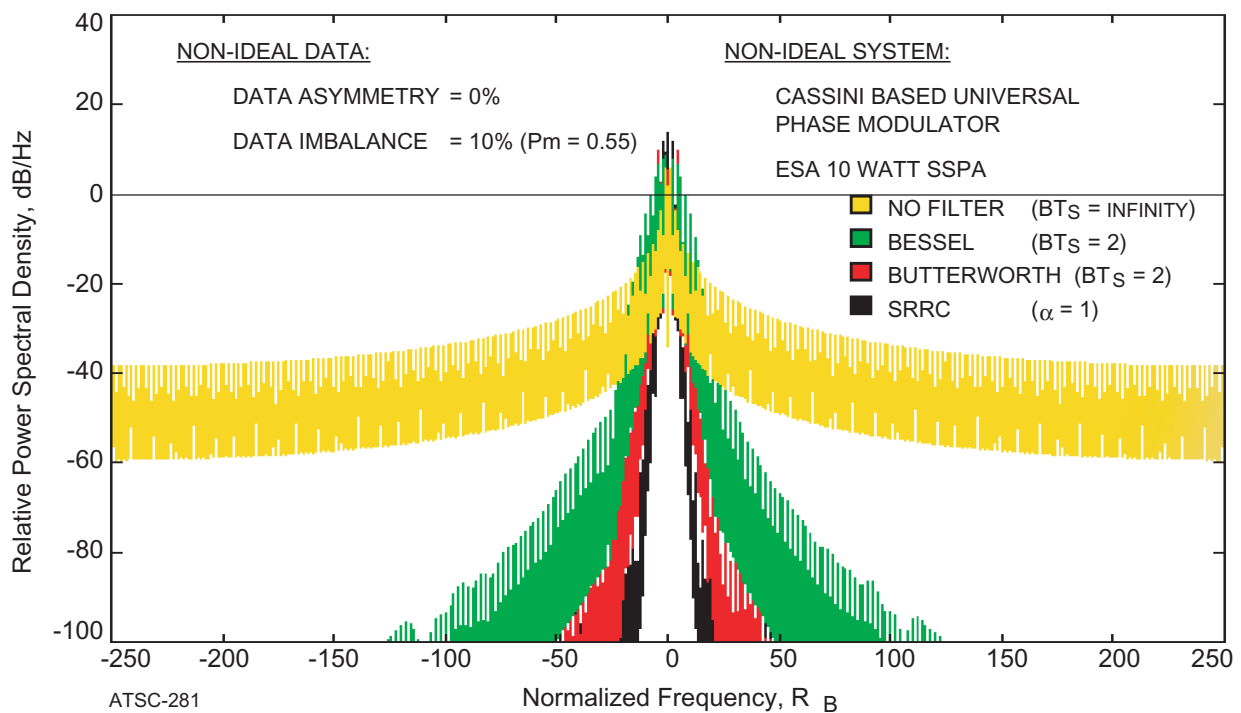
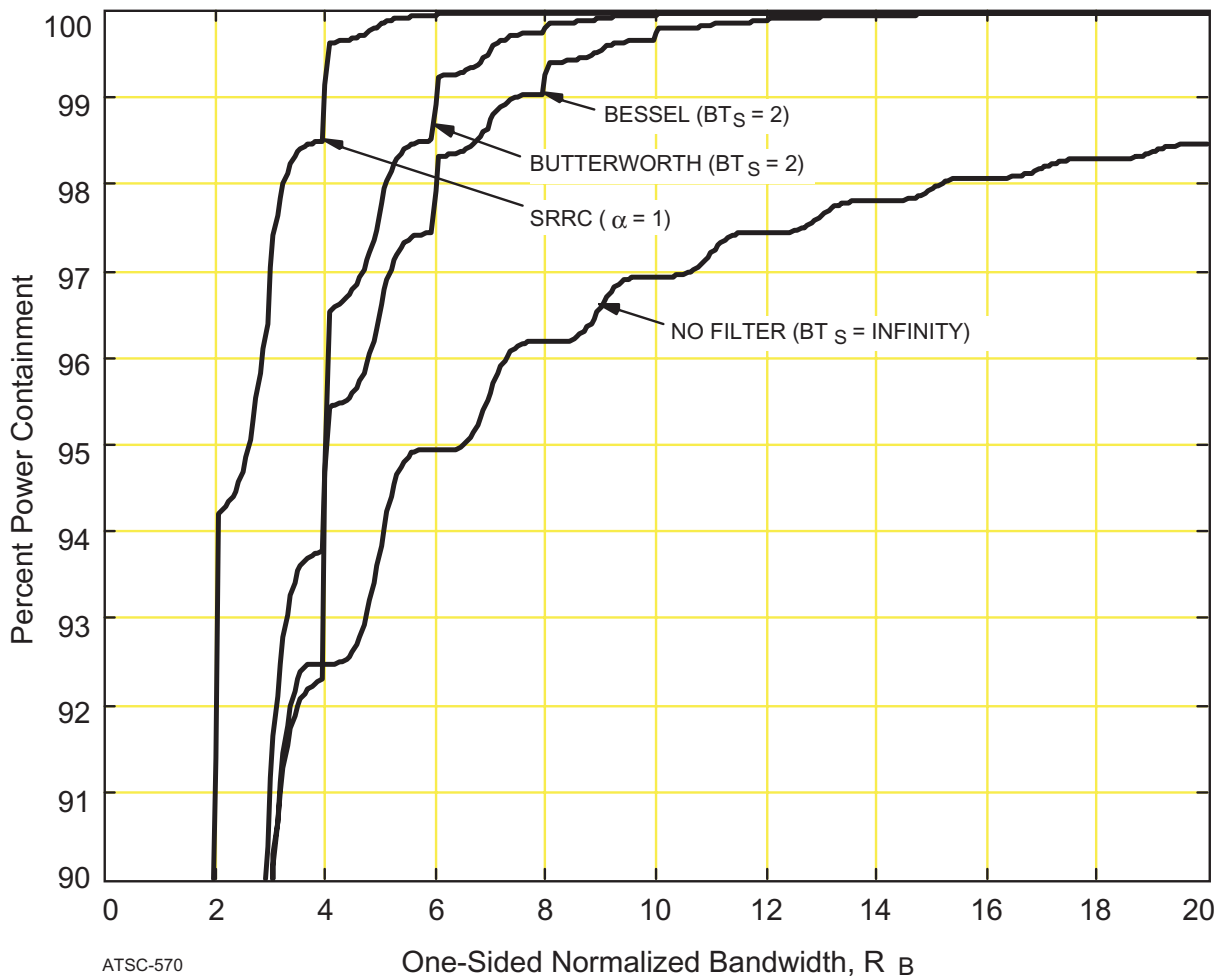
3.5-2a: Fine Detail ($f_C \pm 10 R_B$)3.5-2b: Broadband Spectra ($f_C \pm 250 R_B$)

Figure 3.5-2: BPSK/Bi-φ Modulation Spectra

EFFICIENT MODULATION METHODS STUDY AT NASA/JPL

Figure 3.5-3: BPSK/Bi- ϕ Modulation Power Containment

3.6 QPSK MODULATION

Although found less frequently than the modulation types discussed above, QPSK has been used by many CCSDS Space Agencies. It has often found application in high data rate missions operating in the *Earth Exploration Satellite* and the *Meteorological* services.

QPSK can be visualized as two BPSK/NRZ channels having an orthogonal phase relationship, each containing $P_T/2$ transmit power where P_T is the spacecraft's total transmitted power. The resulting four-phase states represent specific information bit pairs. Table 3.6-1 shows the RF carrier phase shift provided by the Universal Phase Modulator (UPM) for the bit-pair combinations.

EFFICIENT MODULATION METHODS STUDY AT NASA/JPL

Table 3.6-1: QPSK Input Data - RF Carrier Phase Relationship

Input Data (bit- pairs)	RF Carrier Phase (degrees)
00	45
01	-45
10	135
11	-135

3.6.1 QPSK Modulation Bit-Error-Rate (BER)

Figure 3.6-1 contains the QPSK BER vs data bit power relationships for the three filter types. With $P_T/2$ transmit power and a data rate of one-half that in each BPSK/NRZ channel, the received signal-to-noise ratio remains unchanged. That is clearly shown by coincidence in the Ideal BPSK/NRZ and Ideal QPSK curves on Figure 3.6-1 which differ by less than 0.1 dB at a $BER = 1 \times 10^{-3}$.

As the bandwidth is restricted, crosstalk between orthogonal I and Q channels increases, resulting in greater losses. At a $BT_s = 1$, QPSK Filtering Losses become 2.2 to 2.9 dB for Bessel and Butterworth filters respectively. An E_B / N_0 of about 8.3 dB is required to achieve a 1×10^{-3} BER using a Butterworth $BT_s = 2$ filter. BPSK/NRZ modulation achieves the same BER with an E_B / N_0 of only 7.7 dB with a Butterworth ($BT_s = 2$) filter.

3.6.2 QPSK Modulation Spectra

The most obvious difference from BPSK/NRZ appears in the spectra shown on Figure 3.6-2 for QPSK. Filtered QPSK's spectral width is one-half that of BPSK/NRZ (Figure 3.4-2) and one-fourth that of BPSK/Bi- ϕ modulation. Of the traditional phase modulation methods, filtered QPSK is the most bandwidth-efficient.

QPSK is no exception to the general rule that filtering is required. Comparing unfiltered and filtered spectra on Figure 3.6-2b instantly reveals the dramatic increase in bandwidth efficiency from filtering. Square Root raised Cosine filters provide the maximum spectrum efficiency; however, the Butterworth $BT_s = 2$ filter is a close second down to levels 60 dB below the peak sideband amplitude. Considering its simplicity, the passive Butterworth filter is the recommended type.

3.6.3 QPSK Modulation Power Containment

Figure 3.6-3 shows the *occupied bandwidth* of a Butterworth ($BT_s = 2$), filtered signal to be approximately $3.5 R_B$. Even without filtering, it is possible to obtain an *occupied bandwidth* of about $10 R_B$. It is clear from Figure 3.6-3 why QPSK has been the modulation method of choice for medium and high data rate missions. It may still be a good choice for some medium data rate projects.

EFFICIENT MODULATION METHODS STUDY AT NASA/JPL

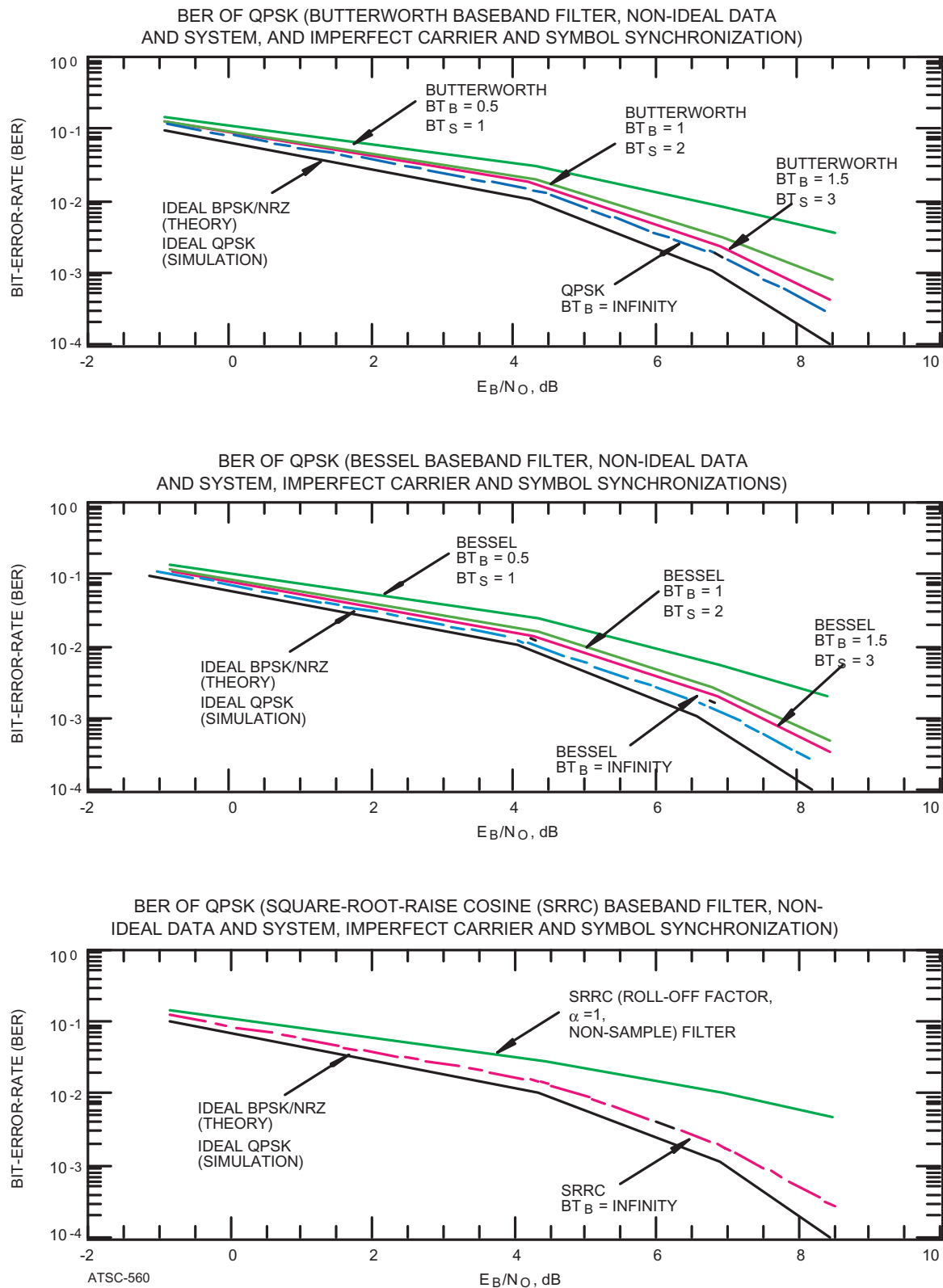


Figure 3.6-1: QPSK Modulation Bit-Error-Rate

EFFICIENT MODULATION METHODS STUDY AT NASA/JPL

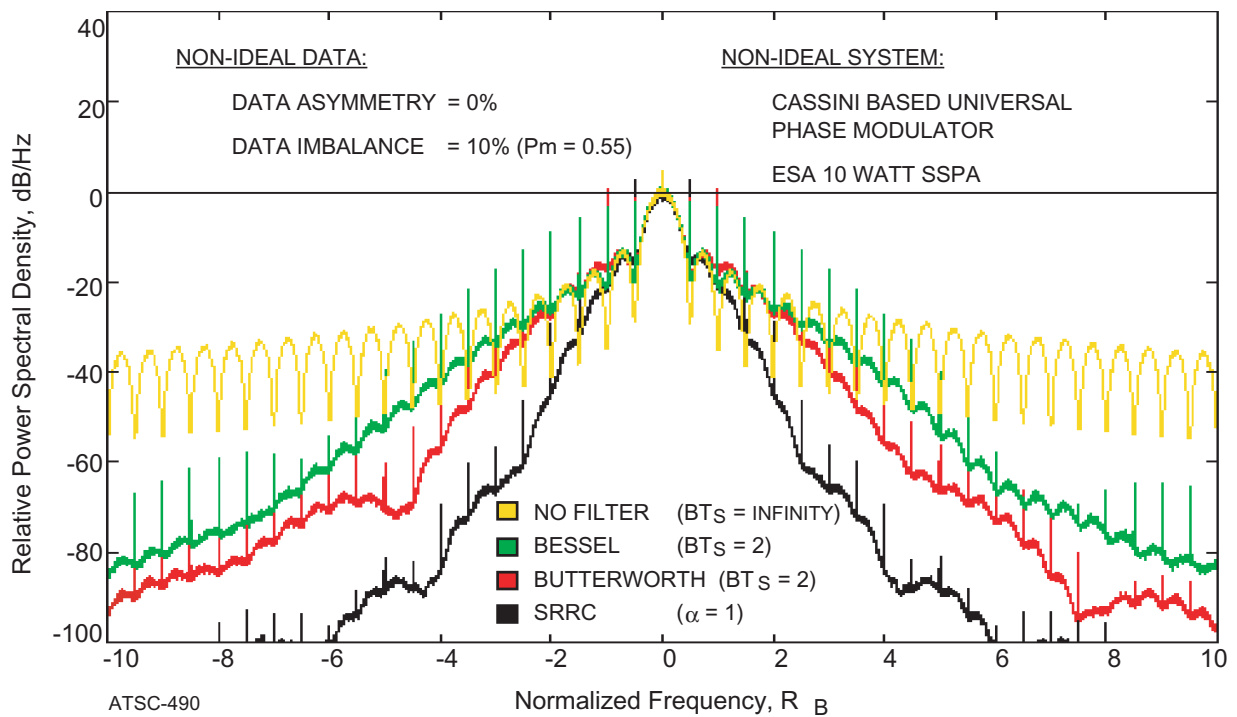
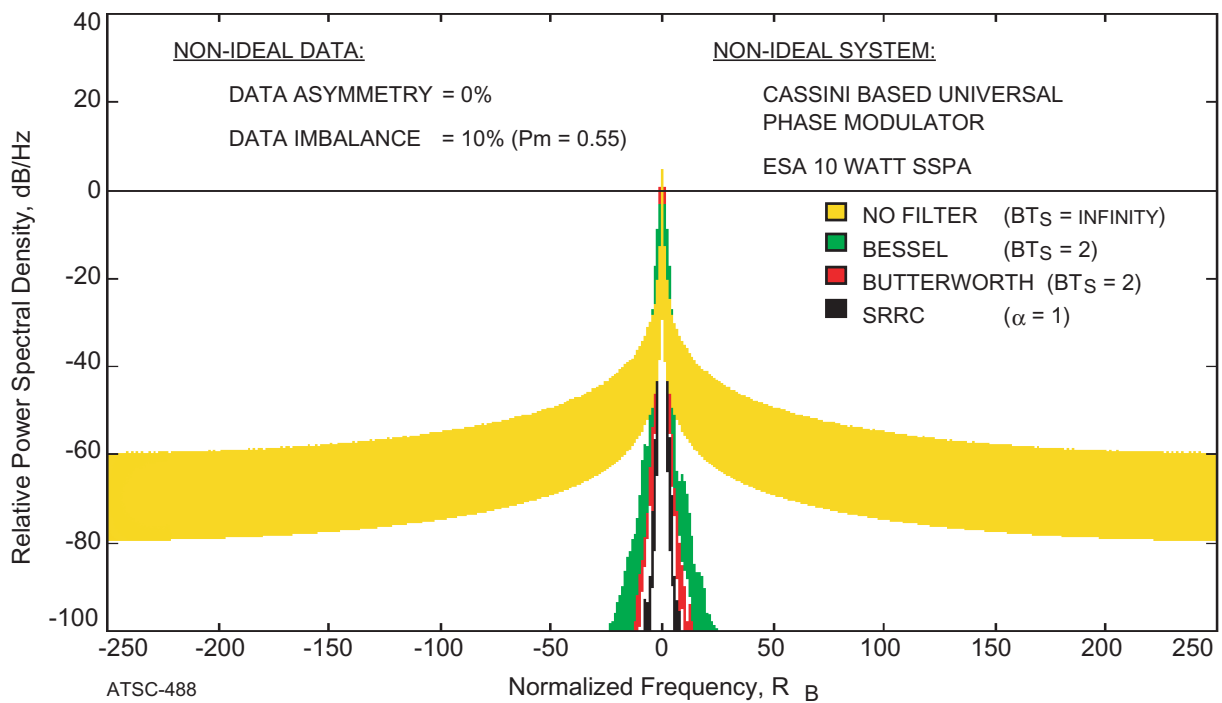
3.6-2a: Fine Detail ($f_c \pm 10 R_B$)3.6-2b: Broadband Spectra ($f_c \pm 250 R_B$)

Figure 3.6-2: QPSK Modulation Spectra

EFFICIENT MODULATION METHODS STUDY AT NASA/JPL

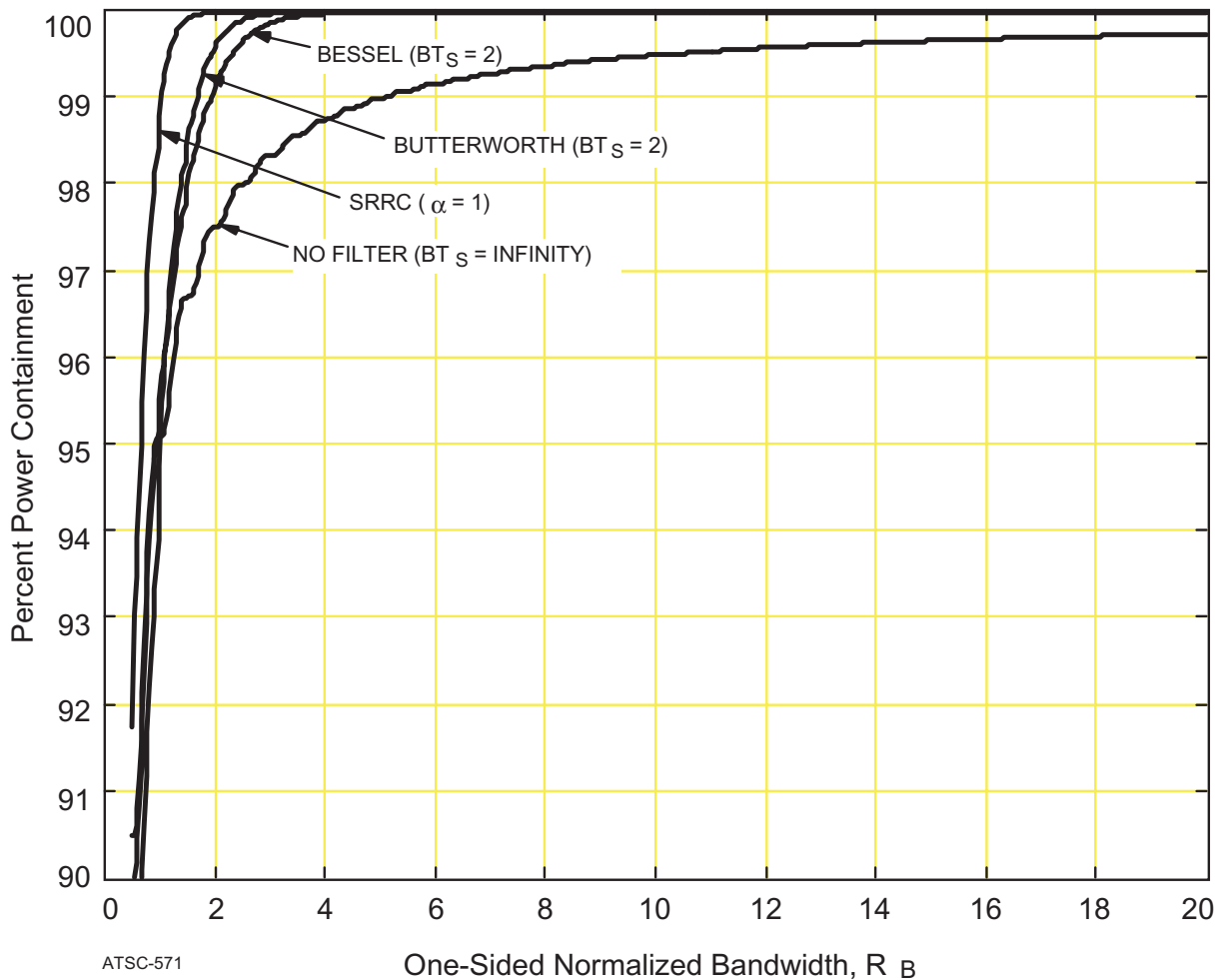


Figure 3.6-3: QPSK Modulation Power Containment

3.6.4 QPSK Modulation Study Conclusions

QPSK modulation has been used in recent years for medium and high telemetry data rate transmissions. Viewed as two orthogonal BPSK/NRZ channels, QPSK bit-error-rate performance is equal to that of BPSK/NRZ with one-half of the data rate on each channel. Like all suppressed carrier systems, a somewhat higher Costas loop Signal-to-Noise Ratio is required for proper operation than is the case for a residual carrier phase-locked loop.

QPSK should receive serious consideration for telemetry systems operating in the 200 ks/s - 2 Ms/s symbol rate range. However, the existence of newer, much more bandwidth-efficient, modulation schemes should relegate QPSK to medium data rate missions, at least in those space agencies truly concerned with minimizing their RF spectrum needs. This is particularly true for missions operating in the *Earth Exploration Satellite* and the *Meteorological* services.

3.7 OQPSK MODULATION

Offset QPSK modulation is purported to generate a more compact spectrum than QPSK in the presence of non-linear amplification. Modulation sidebands are said to decline more rapidly than for QPSK. Absent this non-linearity, OQPSK and QPSK spectra are identical.

I and Q in a OQPSK system are customarily treated as separate, independent channels with a $\frac{1}{2}$ symbol-time offset between the I-channel phase change and the Q-channel phase change. Here, OQPSK is treated as an alternative to QPSK. The simulated transmitting system used the Universal Phase Modulator (UPM).

The UPM's implementation does not permit proper OQPSK operation. Where a 180 degree phase change is occasioned by the data, an intermediate rest level of either ± 90 degrees is established for one-half symbol-time. Restricting the phase change reduces sideband generation in non-linear system elements. To some degree, this pseudo OQPSK modulation system approximates a filtered QPSK modulated system by limiting sequential phase changes to ± 90 degrees.

OQPSK filtering is the same as for QPSK modulation. Butterworth and Bessel filters having $BT_s = 1, 2, \text{ and } 3$ were used. As with the other modulation methods, all spectra are based on a Butterworth $BT_s = 2$ baseband filter. Unfortunately, the results were less than satisfactory.

3.7.1 OQPSK Modulation Bit-Error-Rate (BER)

Figure 3.7-1 contains Bit-Error-Rate (BER) data for OQPSK. With no filtering (i.e., $BT_s = \infty$), the performance is equivalent to that of a QPSK system. However, with the UPM, OQPSK BER performance deteriorates sharply as the filter's bandwidth decreases. With a Butterworth ($BT_s = 2$) filter, an $E_b / N_0 \approx 8.7$ dB is required for a 1×10^{-3} BER. Given the modulator problems, these test data are not sufficient to discriminate between the two modulation types.

3.7.2 OQPSK Modulation Spectra

Determining whether this variant of OQPSK is a viable modulation type is no easier using the spectra shown on Figure 3.7-2. Interestingly, there is virtually no difference between the unfiltered spectra for OQPSK and QPSK (Figure 3.5-2), even with the non-linear power amplifier. The modulator's unsuitability makes it difficult to comment on the spectra.

EFFICIENT MODULATION METHODS STUDY AT NASA/JPL

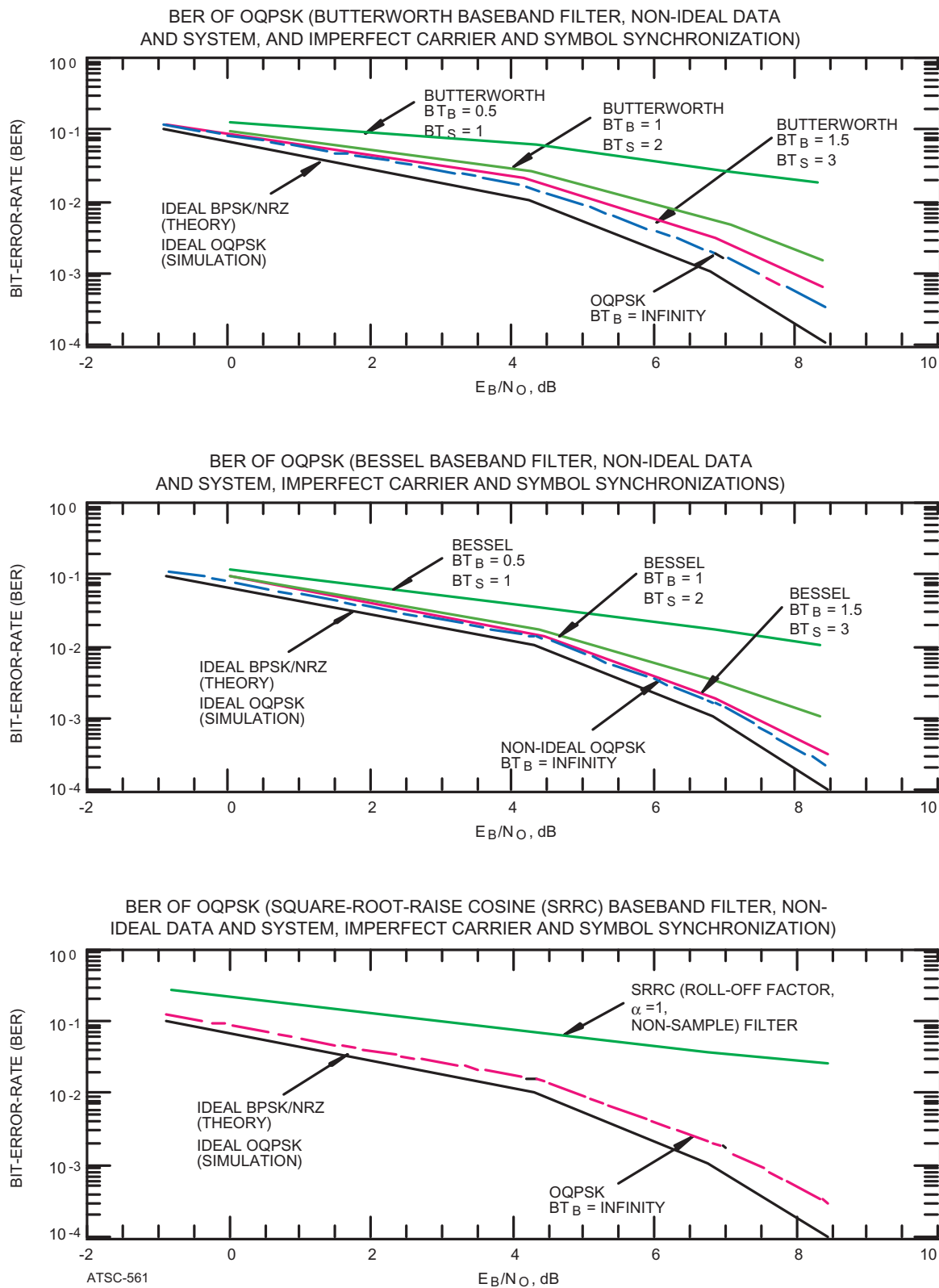


Figure 3.7-1: QPSK Modulation Bit-Error-Rate

EFFICIENT MODULATION METHODS STUDY AT NASA/JPL

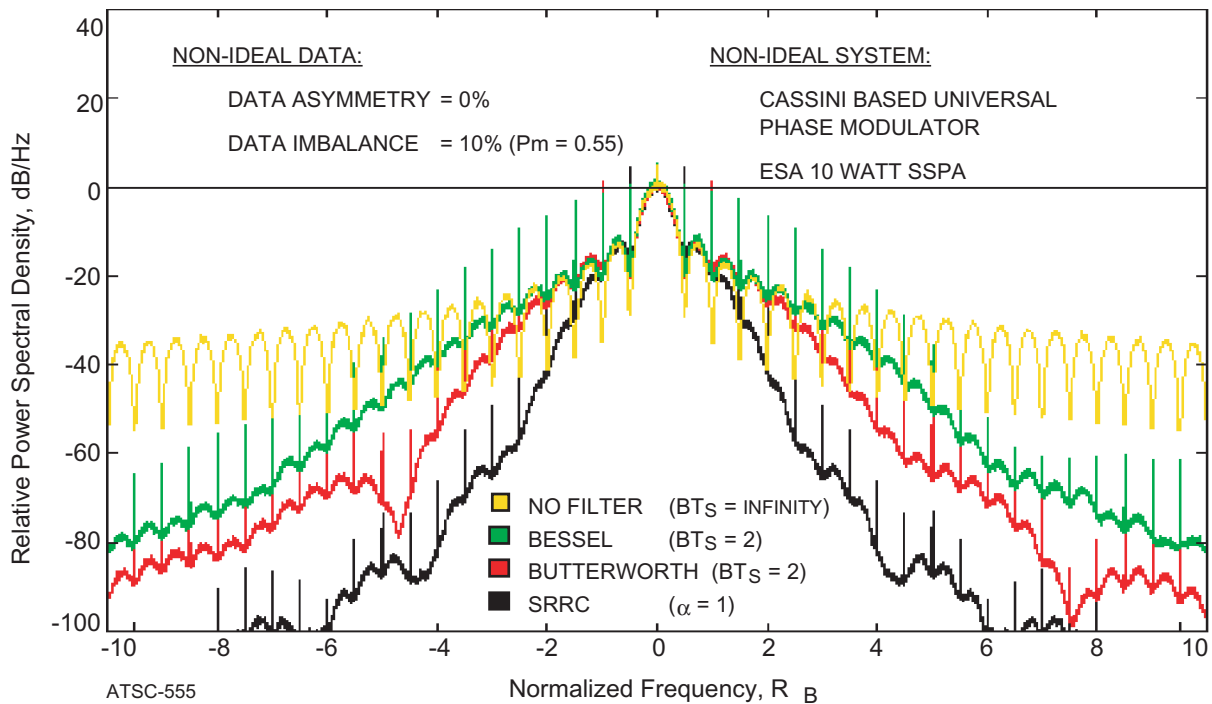
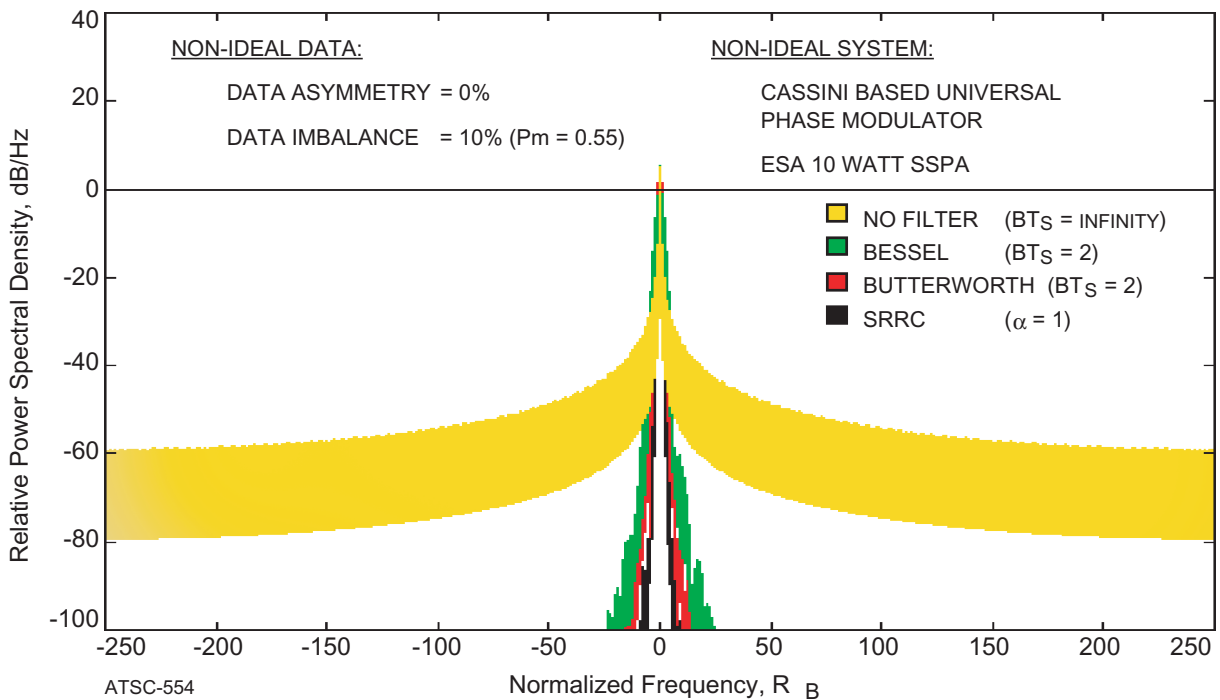
3.7-2a: Fine Detail ($f_c \pm 10 R_B$)3.7-2b: Broadband Spectra ($f_c \pm 250 R_B$)

Figure 3.7-2: OQPSK Modulation Spectra

EFFICIENT MODULATION METHODS STUDY AT NASA/JPL

3.7.3 OQPSK Modulation Power Containment

Power containment, figure 3.7-3 is virtually identical to that for QPSK. With a Butterworth ($BT_S = 2$) filter, the *occupied bandwidth* is about $3.5 R_B$. No power containment differences were found between OQPSK and QPSK.

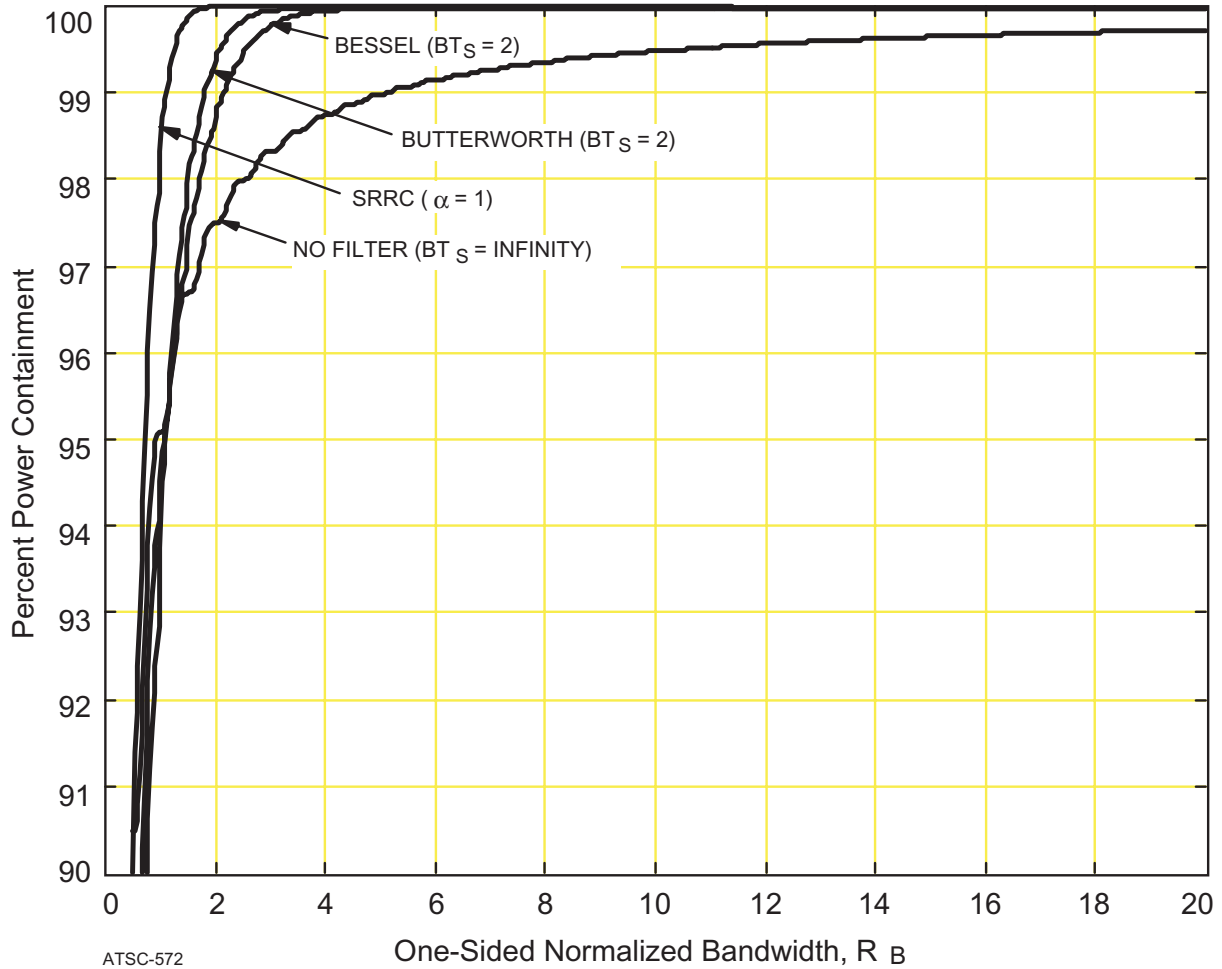


Figure 3.7-3: OQPSK Modulation Power Containment

3.7.4 OQPSK Modulation Study Conclusions

No discernable bandwidth differences between OQPSK and QPSK modulation were found, despite the use of non-linear system elements such as a saturated power amplifier. However, the OQPSK BER performance deteriorates sharply as the filter bandwidth decreases. This finding could be the result of an inadequate phase modulator. With baseband filtering, the UPM's transitions require an excessively long time with an intermediate dwell state. A true OQPSK modulation evaluation requires a different phase modulator design. At this time there is not sufficient extrinsic evidence of OQPSK's superiority to warrant modulator modifications or additional investigations.

EFFICIENT MODULATION METHODS STUDY AT NASA/JPL

3.8 CONTINUOUS PHASE MODULATION (CPM)

Two modulation types, not commonly used by the CCSDS Space Agencies, have been included in Phase 3 for comparative purposes. Both are in a class termed Continuous Phase Modulation (CPM). As the name implies, phase changes are gradual and without discontinuities. The resulting RF spectrum is inherently narrower than that for the unfiltered phase modulation methods discussed above. Two variants of CPM are included in this study: Minimum Shift Keying (MSK) and Gaussian Minimum Shift Keying (GMSK). Neither modulation scheme has been widely used by space agencies. Because they are essentially the same, they are grouped together in this section.

MSK is unfiltered while GMSK adds a baseband Gaussian filter to the modulator. The Universal Phase Modulator (UPM) and the ARX II receiver are not suitable for CPM. Therefore, the simulation system used for CPM studies deviates from that described in Section 2.1 above. Modifications include an ideal frequency modulator from the SPW library and an ideal receiver with perfect carrier tracking and symbol synchronization.

Demodulation was based on a paper showing that GMSK can be decomposed into a series of amplitude pulses.⁹ The Phase 3 study receiver simulation model is predicated on a paper describing how the optimum receiver's four or eight matched filters can be reduced to only two filters, a matched filter followed by a Wiener filter to reduce ISI.¹⁰

3.8.1 MSK and GMSK Modulation Bit-Error-Rate (BER)

Figure 3.8-1 contains Bit-Error-Rate curves for MSK and GMSK. GMSK studies included two separate filters with $BT_s = 0.5$ (equivalent to $BT_B = 0.25$) and $BT_s = 1$ (equivalent to $BT_B = 0.5$). Since these bandwidths are smaller than those for the Butterworth and Bessel filters ($BT_s = 1, 2, 3$), one can anticipate that the end-to-end losses should be higher and the RF spectrum will be narrower.

Unlike previous modulation studies having three plots, one for each filter type, here there is but one. MSK is unfiltered and GMSK includes a Gaussian filter with two bandwidths ($BT_s = 0.5, 1$). For simplicity, these, along with an ideal BPSK/NRZ reference curve, are placed on a single BER graph. Note that the E_b / N_0 required for a 1×10^{-3} BER is 7.3 - 8.2 dB which compares favorably with BPSK/NRZ, even with a Gaussian filter bandwidth $BT_s = 0.5$. Losses can be expected to increase when a non-ideal modulator and receiver are employed; however, Figure 3.8-1 was generated using the ESA power amplifier operating in full saturation.

3.8.2 MSK and GMSK Modulation Spectra

Most MSK and GMSK applications have been in Personal Communication Systems (PCSs). Spacecraft telemetry transmission systems have avoided GMSK because of demodulation and synchronization difficulties. Often termed frequency modulation, MSK and GMSK were included because of their inherently narrow spectral bandwidths. Unlike the other modulation types, MSK is unfiltered and sidelobes are reduced by avoiding phase change discontinuities. Figure 3.8-2 shows spectra for unfiltered, ideal BPSK/NRZ (reference), MSK, and GMSK using the two filter bandwidths. No discrete components are present in MSK or GMSK spectra despite baseband filtering.¹¹

EFFICIENT MODULATION METHODS STUDY AT NASA/JPL

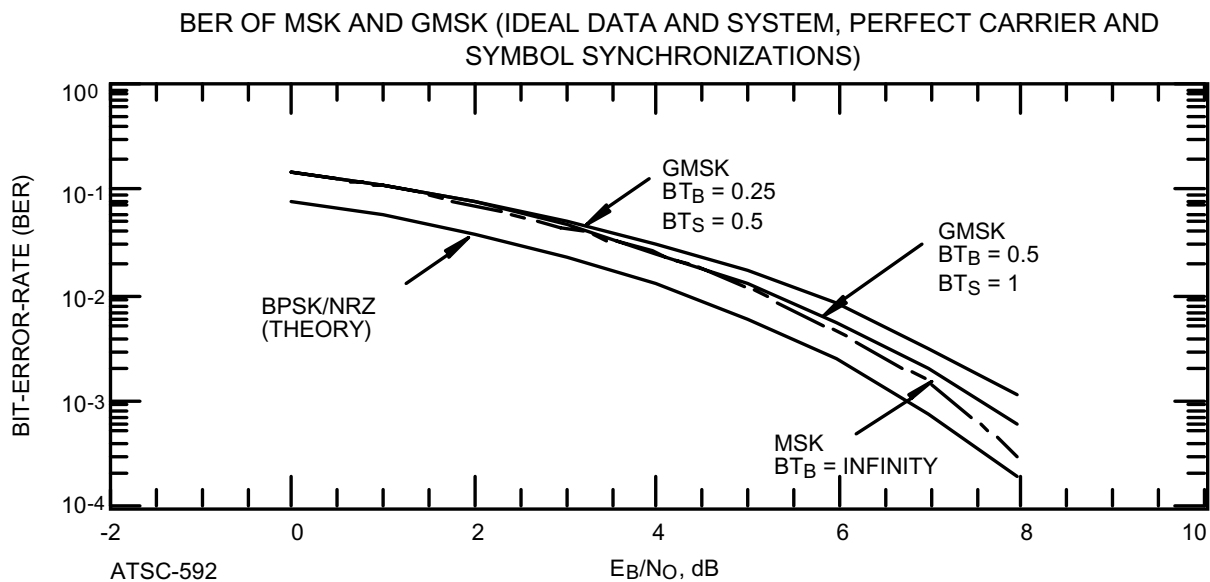


Figure 3.8-1: MSK / GMSK Modulation Bit-Error-Rate (BER)

Figure 3.8-2 shows MSK modulation to be significantly more bandwidth-efficient than the unfiltered BPSK/NRZ reference, reaching a level 60 dB below the peak sideband amplitude at $\pm 8 R_B$. Its lack of discrete spectral components makes it attractive for space telemetry applications.

However, from Figure 3.8-2 it is apparent that MSK modulation is of little interest when compared to GMSK. GMSK modulation is significantly more bandwidth-efficient than any other method considered previously. For example, it is 2 to 6 times more bandwidth-efficient than filtered QPSK modulation, depending upon the specific filter bandwidths selected. When coupled with its BER performance, GMSK should be seriously considered for high and very high data rate missions.

3.8.3 MSK / GMSK Modulation Power Containment

Figure 3.8-3, Power Containment, supports the finding that GMSK has a high bandwidth efficiency. *Occupied bandwidth* is difficult to read, because of its small value, but it appears to be less than $1.2 R_B$ for both filter bandwidths. This represents a 16-times improvement over the unfiltered [reference] BPSK/NRZ modulation and a 5-fold efficiency increase over filtered BPSK/NRZ.

3.8.4 MSK / GMSK Modulation Study Conclusions

Clearly, space agencies interested in RF spectrum efficiency should seriously consider GMSK modulation. This is particularly true for high and very high data rate missions. Unlike the phase modulation types described above, GMSK requires new modulator, demodulator, and symbol synchronizer designs. In that respect, this recommendation departs from one of the *Efficient Modulation Methods Study* guidelines: *that only simple modifications to existing Earth station equipment are permitted for any recommended modulation method*. However, GMSK's bandwidth efficiency is too great to ignore and a departure from the guideline is warranted.

EFFICIENT MODULATION METHODS STUDY AT NASA/JPL

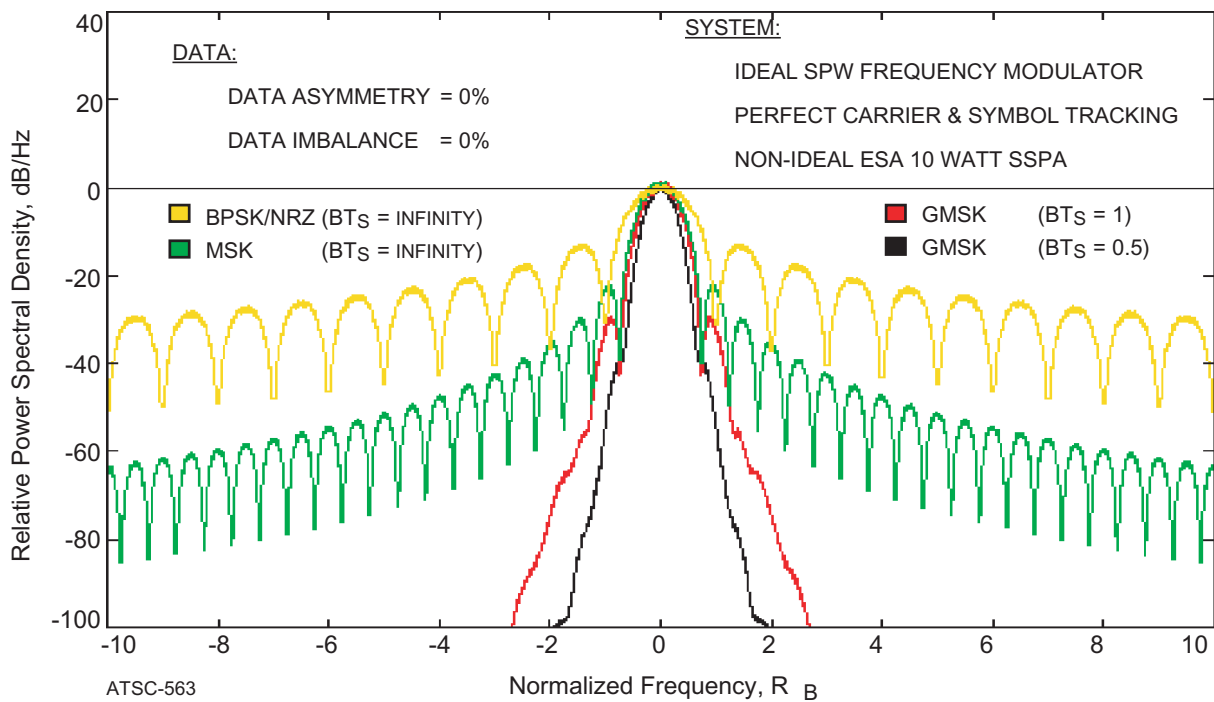
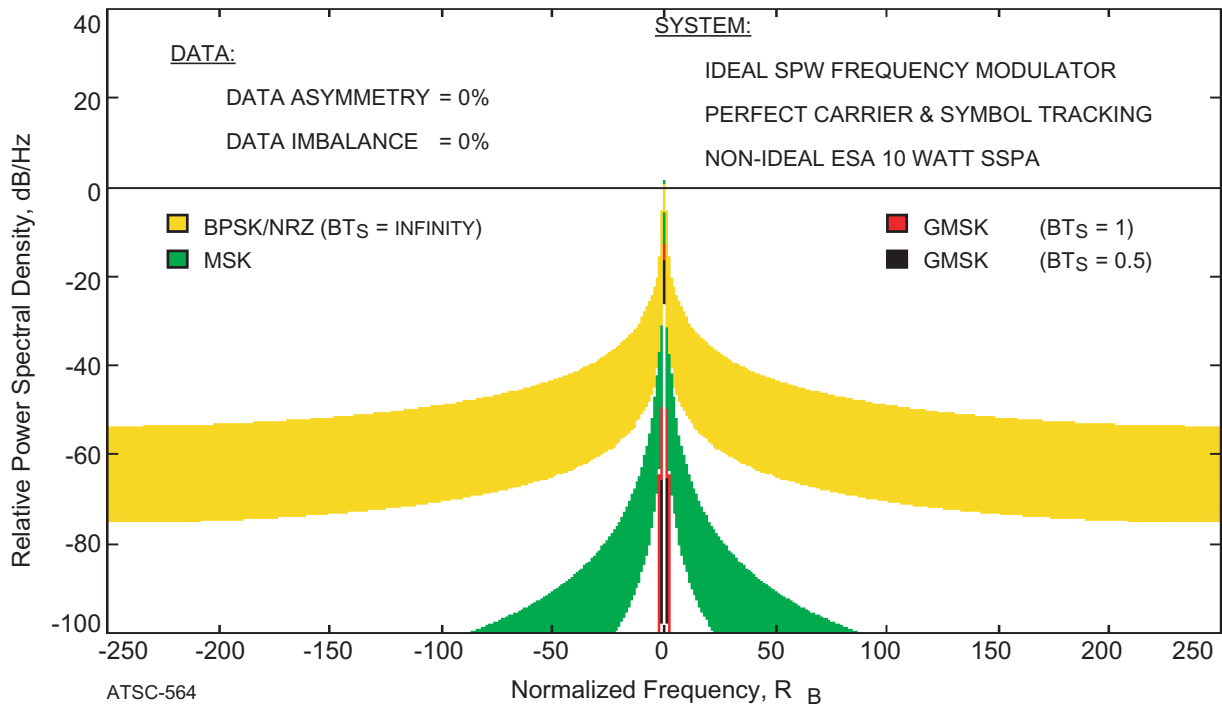
3.8-2a: Fine Detail ($f_c \pm 10 R_B$)3.8-2b: Broadband Spectra ($f_c \pm 250 R_B$)

Figure 3.8-2: MSK / GMSK Modulation Spectra

EFFICIENT MODULATION METHODS STUDY AT NASA/JPL

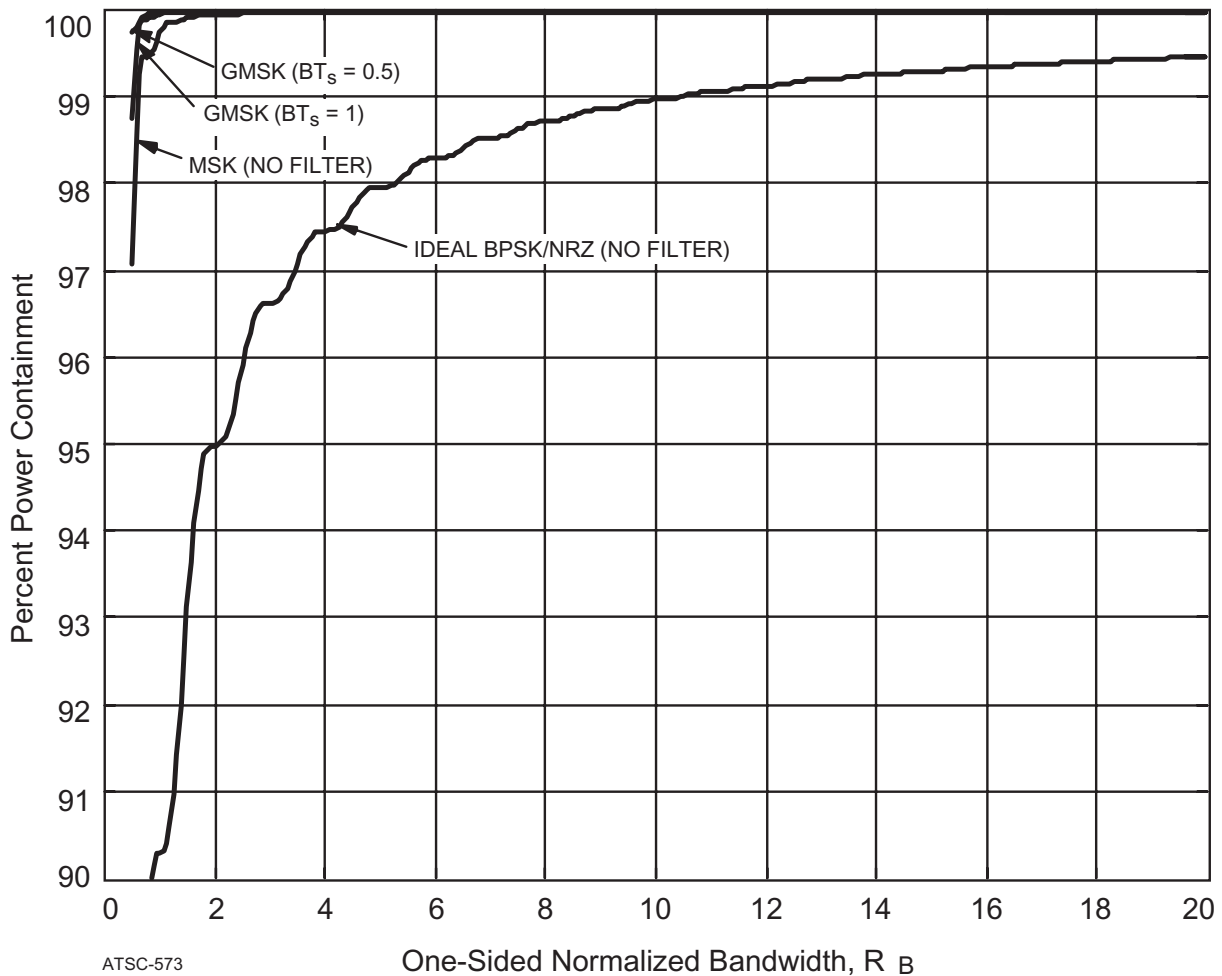


Figure 3.8-3: MSK / GMSK Modulation Power Containment

3.9 8-PHASE SHIFT KEYED (8-PSK) MODULATION

8-PSK modulation is not currently used by CCSDS Space Agencies. NASA Goddard Space Flight Center (GSFC) and their contractor New Mexico State University (NMSU) have devoted a substantial effort to understanding this modulation method.^{12, 13} 8-PSK transmits three data bits simultaneously rather than just two data bits as in QPSK.

For study consistency with other phase modulation studies, a complete transmitting and receiving system needed to be simulated. The Universal Phase Modulator is capable of 8-PSK modulation and the transmitting system, including the ESA power amplifier, was used for this evaluation.

The eight possible state vector phases in 8-PSK modulation cannot be orthogonal as in the case of QPSK. Therefore, the ARX II receiver was modified, as shown in Figure 2.3-2, to demodulate an 8-PSK signal by adding signal squaring circuits to the Costas Loop. These devices also squared the noise compromising the system's performance. Inserting a filter in the modulator further degrades system performance because non-orthogonality increases crosstalk between phase states.

EFFICIENT MODULATION METHODS STUDY AT NASA/JPL

3.9.1 8-PSK Modulation Bit-Error-Rate (BER)

Losses are evident in Figure 3.9-1 showing the Bit-Error-Rate performance for 8-PSK modulation. Relative to ideal BPSK/NRZ modulation, even an ideal (lossless) 8-PSK system imposes heavy performance penalties. Ideal 8-PSK requires an E_B / N_0 of 9.5 - 10 dB to attain a $BER = 1 \times 10^{-3}$. When a Butterworth $BT_s = 3$ filter is added, the required E_B / N_0 rises to 11.5 dB. Compared to the E_B / N_0 of about 8 dB, needed for a filtered non-ideal QPSK system at the same BER, it is clear that 8-PSK is not a useful modulation method in power limited applications. Losses using a Square Root Raised Cosine ($\alpha = 1$) filter were so great that the plot is not even included in this report.

Excessive losses result from the non-orthogonal relationship between phase states. This simulation shows that inherent 8-PSK modulation losses are unlikely to be acceptable in most applications, even without filtering.

NMSU studies found that filtered 8-PSK modulation BER rate performance improved in non-constant amplitude applications. The Universal Phase Modulator produces a nearly constant envelope signal. That characteristic results in the narrowest RF spectrum. Utilizing a non-constant envelope spectrum may improve the BER performance at the expense of spectrum width.

3.9.2 8-PSK Modulation Spectra

Notwithstanding the system losses, spectrum advantages of simultaneously transmitting three data bits is clearly evident in Figure 3.9-2. 8-PSK modulation with a Butterworth filter having a $BT_s = 2$ produces the most compact RF spectrum of any phase modulation method reviewed thus far. A $BT_s = 2$ was used for consistency with studies of the other modulation types.

Figure 3.9-2 also demonstrates that filtering will be needed. The unfiltered spectrum (top) is very similar to that for unfiltered QPSK. 8-PSK provides a 1.8 dB improvement in data rate over QPSK and the spectral improvement appears to be on the same order.

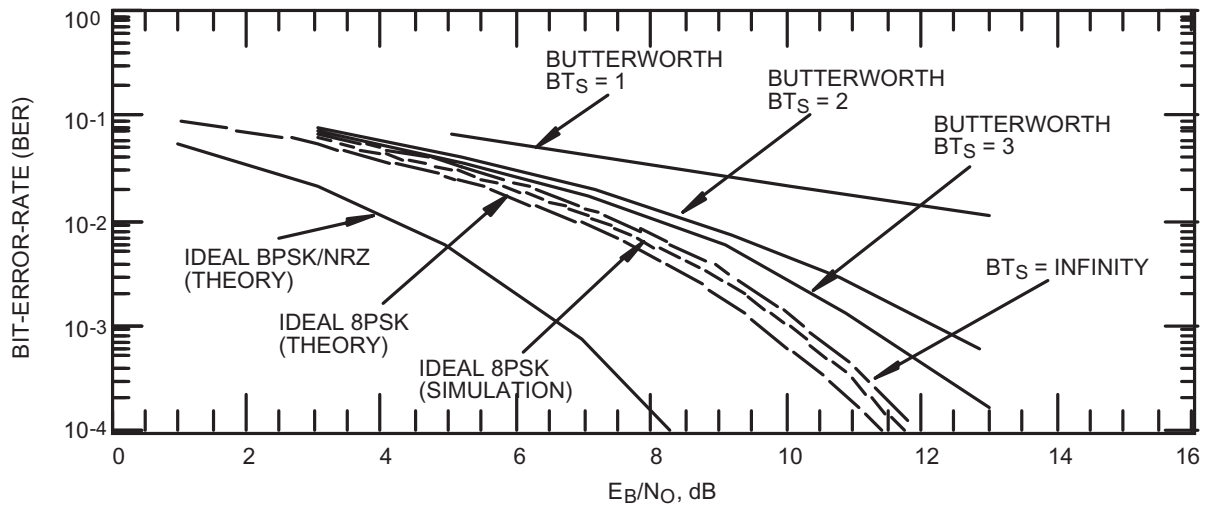
3.9.3 8-PSK Modulation Power Containment

Power Containment curves, Figure 3.9-3, show the *occupied bandwidth* to be about $2.4 R_B$ when using a Butterworth $BT_s = 2$ filter. This bandwidth will increase with a $BT_s = 3$ filter which is required to avoid the additional 1 dB loss.

3.9.4 8-PSK Modulation Study Conclusions

Results of this study show 8-PSK modulation to be of little value for most space telemetry data transmissions. While 8-PSK does provide a marginally narrower spectrum, system losses make the modulation type unsuitable for most Category A missions. 8-PSK modulation may be attractive in strong signal applications where system losses are of little importance.

EFFICIENT MODULATION METHODS STUDY AT NASA/JPL



BER OF 8PSK (BESSEL BASEBAND FILTER, NON-IDEAL DATA AND SYSTEM,

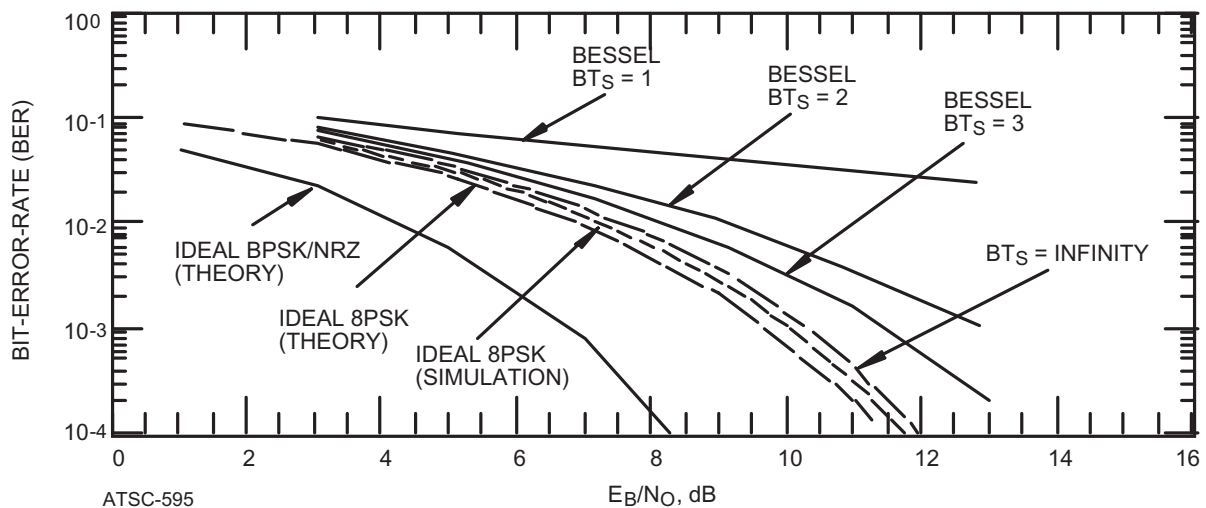


Figure 3.9-1: 8-PSK Modulation Bit-Error-Rate

8-PSK modulation and demodulation can be accomplished by modifying space agencies' existing spacecraft and Earth station hardware. In this regard, 8-PSK modulation does comply with one of the *Efficient Modulation Methods Study* guidelines. However, even if it were possible to construct a lossless receiver, the performance penalty, compared to GMSK and FQPSK-B modulation, is too high to warrant further consideration.

EFFICIENT MODULATION METHODS STUDY AT NASA/JPL

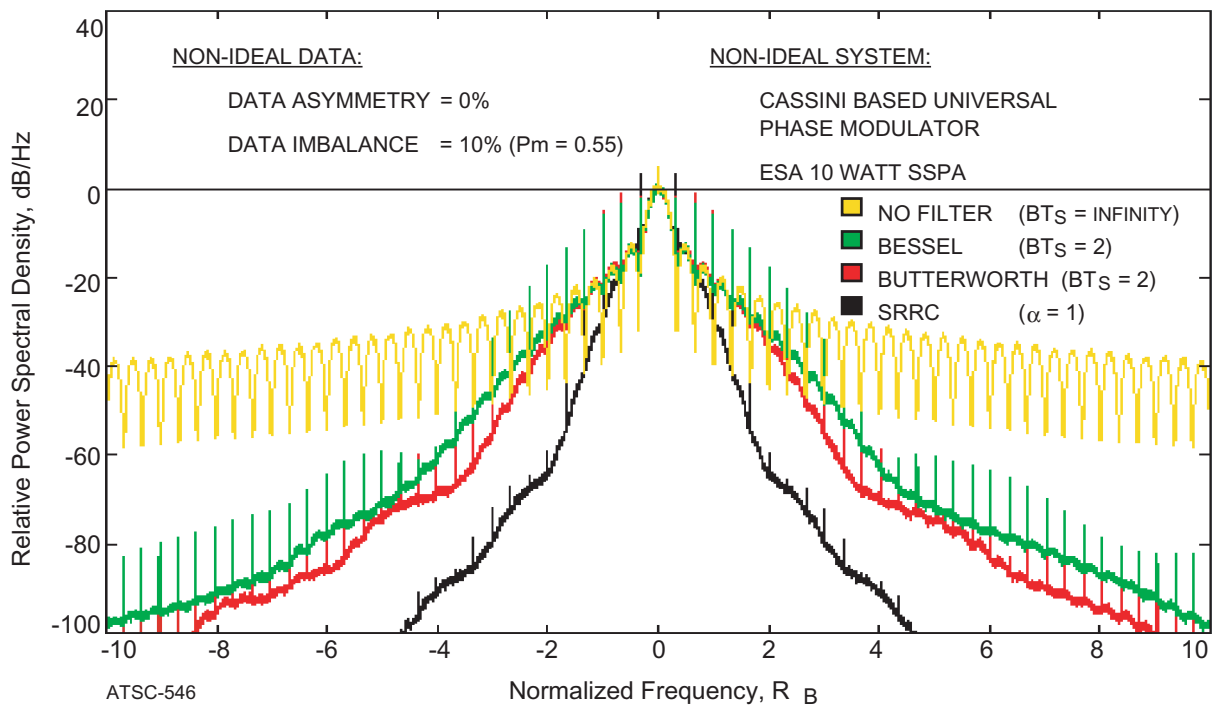
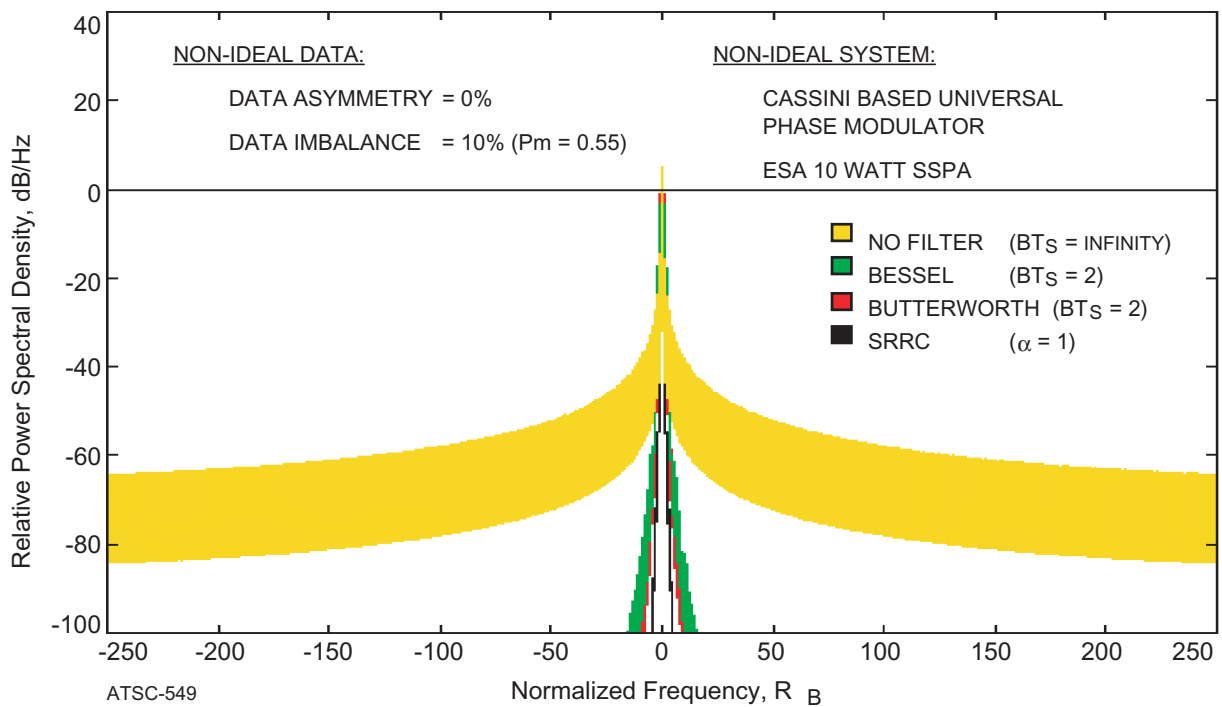
3.9-2a: Fine Detail ($f_C \pm 10 R_B$)3.9-2b: Broadband Spectra ($f_C \pm 250 R_B$)

Figure 3.9-2: 8-PSK Modulation Spectra

EFFICIENT MODULATION METHODS STUDY AT NASA/JPL

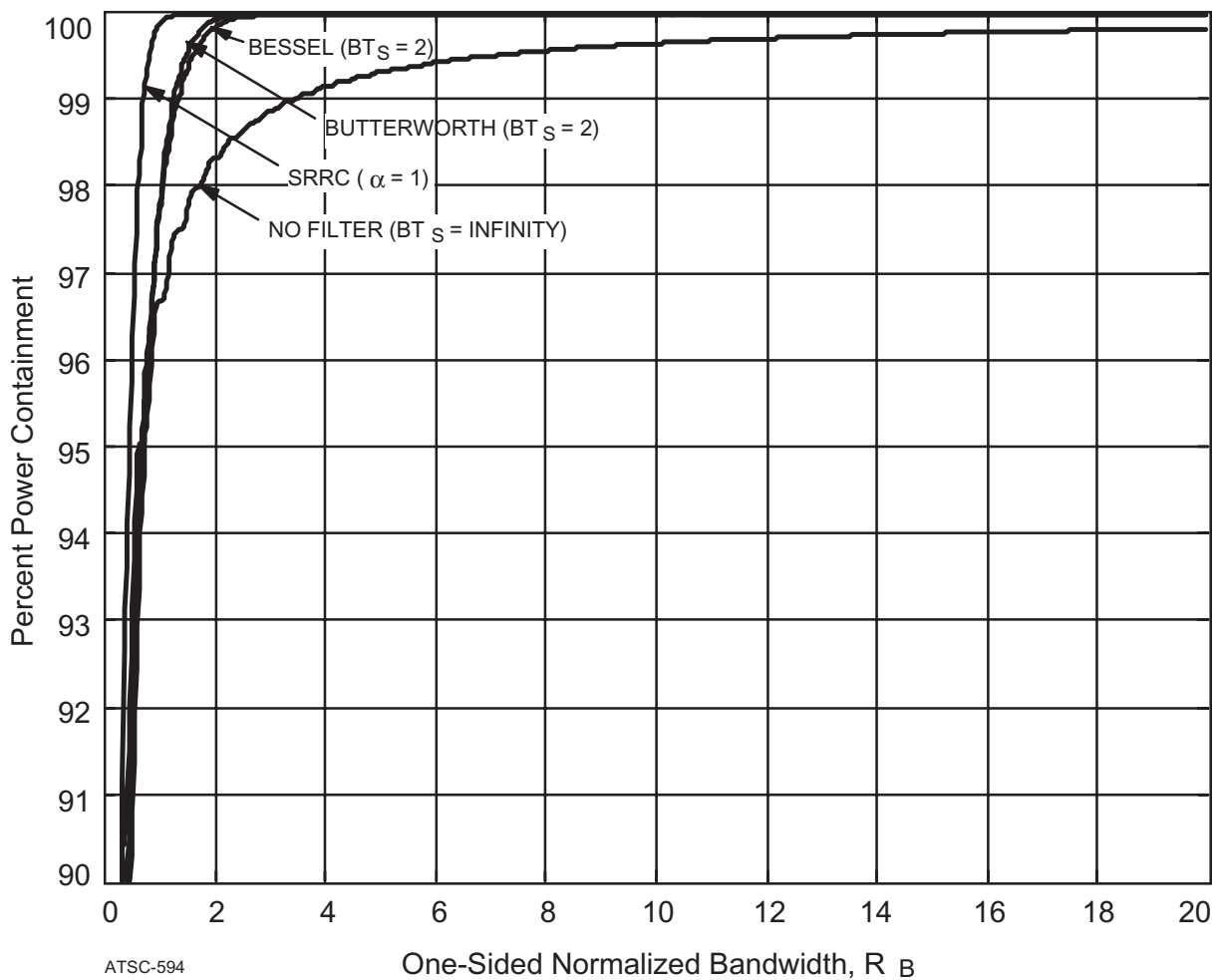


Figure 3.9-3: 8-PSK Modulation Power Containment

3.10 FEHER QPSK (FQPSK)

CCSDS Subpanel 1E (RF and Modulation) became aware of a new modulation type at its Spring 1997 meeting. Named FQPSK for its inventor, Dr. Kamilo Feher, it was reported to have a very narrow RF spectrum and only minimal end-to-end system losses.¹⁴ Test data provided by Dr. Feher showed a spectrum narrower than that of GMSK using a $BT_S = 0.50$ filter. Sideband attenuations were tabulated for the several modulation types studied and it was concluded that FQPSK-B could be a very attractive modulation method.

Subpanel 1E determined that FQPSK deserved further investigation. With Dr. Feher's permission, FQPSK-B, a specific version of FQPSK, was simulated using SPW. Additionally, Mr. Eugene Law of the Naval Air Warfare Center Weapons Division at Point Mugu obtained an FQPSK-B modulator-demodulator (modem) for hardware tests. NASA members of Subpanel 1E witnessed these spectrum tests and obtained copies of the spectra. *Note: This is the only modulation type covered in this report for which there are actual hardware verification tests.* These tests confirm the simulation results reported here.

EFFICIENT MODULATION METHODS STUDY AT NASA/JPL

FQPSK-B modulation is a form of OQPSK modulation in which one of 16 wavelets [waveforms] is selected for transmission on the I-channel and another is chosen for transmission on the Q-channel. Wavelet determination depends on the present and previous data bit pair values for the I and Q channels. There is a $\frac{1}{2}$ -symbol-time offset between I and Q transmissions.^{15, 16} FQPSK-B modulates and filters at baseband. Thereafter, the signal is translated to an i.f. frequency and then translated again to the transmitted RF frequency.

3.10.1 FQPSK-B Modulation Bit-Error-Rate (BER)

Simulations of FQPSK-B were conducted at JPL with the assistance of Dr. Feher. Figure 3.10-1 shows the Bit-Error-Rate (BER) performance. Like MSK and GMSK modulation, existing transmitting and receiving equipment simulation models were unsuitable for FQPSK-B. However, BER performance was measured using ESA's power amplifier operating in full saturation.

Comparing FQPSK-B to ideal BPSK/NRZ shows that an additional E_B / N_0 of 1.7 dB is required to achieve a 1×10^{-3} BER. This is 0.3 dB greater than GMSK with a $BT_s = 0.5$. Dr. Feher commented that additional system optimization might reduce these losses. His suggestions included adding hard limiters to the transmitting system and improving the receiver filter's phase performance.

Supporting his position, Dr. Feher points to BER measurements made at Point Mugu using actual hardware. Dr. Feher's modem, operating with a 1 Watt SSPA in full saturation, produced a 1×10^{-3} BER at an E_B / N_0 of 8 dB, about 1.3 dB more than ideal BPSK/NRZ and 0.1 dB less than GMSK with a $BT_s = 0.5$. However, that modem was designed for relatively fixed signal level applications, such as closed circuit television distribution. It did not provide 60 dB of sideband attenuation. Further BER tests will be required to verify the better E_B / N_0 performance using a modulator capable of a 60 dB sideband attenuation.

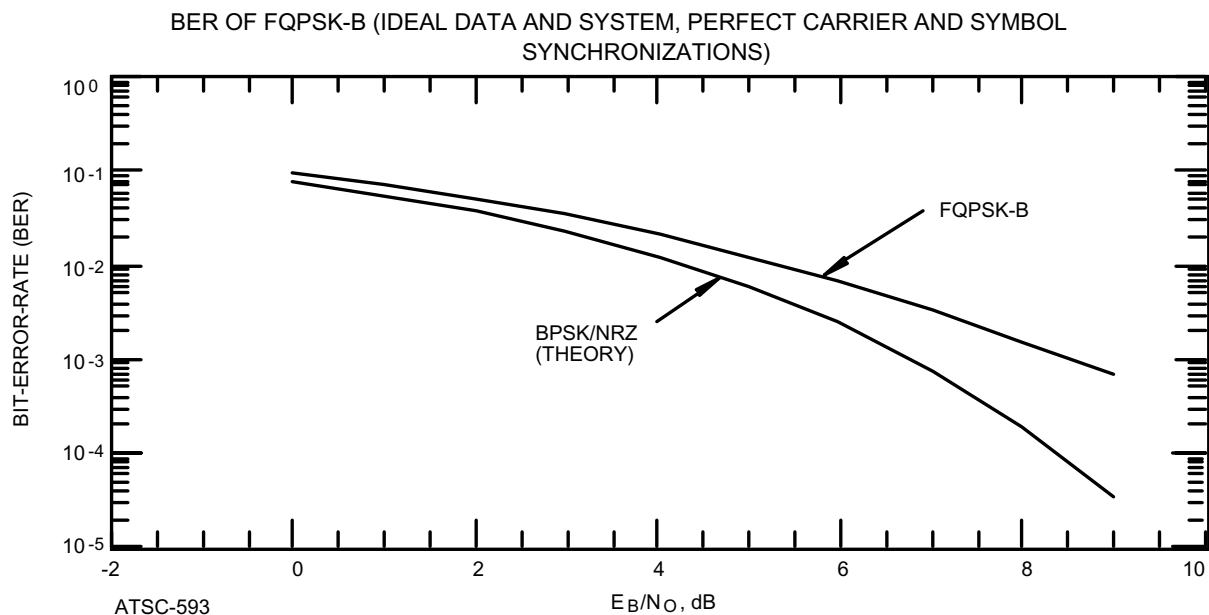


Figure 3.10-1: FQPSK-B Modulation Bit-Error-Rate

EFFICIENT MODULATION METHODS STUDY AT NASA/JPL

3.10.2 FQPSK-B Modulation Spectra

Figure 3.10-2 shows FQPSK-B spectra obtained by simulations. Spectra are obtained using ESA's 10 Watt SSPA operating in full saturation. However, as with the MSK and GMSK simulations, an ideal modulator and receiver were simulated.

FQPSK-B spectra do not have discrete components, giving it a distinct advantage over filtered phase modulation schemes. Sideband attenuation does tend to reach a floor at approximately 75 dB below the peak amplitude where spectral broadening is clearly evident in Figure 3.10-2a. Unlike most of the phase modulation schemes, spectral broadening in the vicinity of f_c does not occur. Rather, Figure 3.10-2a shows the spectrum width around f_c to be significantly narrower than BPSK/NRZ.

FQPSK-B has a very compact, bandwidth-efficient spectrum. Simulations show it to be slightly better than GMSK reaching a level 50 dB below the peak sideband amplitude at a bandwidth of $1.7 R_B$ rather than at $1.9 R_B$ for GMSK with a $BT_s = 0.5$. At a sideband attenuation of 60 dB, FQPSK-B and GMSK are within $0.1 R_B$ of one another.

3.10.2.1 Hardware Spectrum Measurements

FQPSK-B is the only modulation type in the Phase 3 *Efficient Modulation Methods Study* for which there are actual hardware measurements. On 1 July 1997 FQPSK-B hardware tests were conducted at the Naval Air Warfare Center at Point Mugu. Dr. Feher contributed a laboratory model of his FQPSK-B modulator. The test configuration included: a random data generator producing 1 Mb/s, Dr. Feher's FQPSK-B modulator, a Hewlett Packard (HP) Model 8780A Vector Signal Generator for QPSK modulation, a frequency translator, a 1-Watt SSPA, and an HP spectrum analyzer.

Tests were run with the SSPA in full saturation at 2.44 GHz and frequency spectra were plotted by the HP spectrum analyzer. Figure 3.10-3 reproduces the HP analyzer's plot on the same scale as that used for the *Fine Detail* spectra shown in Figure 3.10-2a. Separate figures are provided because the spectrum plotted in Figure 3.10-3 is virtually indistinguishable from the FQPSK-B curve in Figure 3.10-2a, down to a level 55 dB below the peak sideband amplitude. Below the -55 dB point, the hardware generated spectrum in Figure 3.10-3 becomes wider than the SPW computed spectrum in Figure 3.10-2a. Readers should understand that *no attempt was made to optimize* the hardware test configuration at Point Mugu. The test bed was constructed using hardware elements designed for a variety of other uses.

These measurements confirm the bandwidth efficiency of FQPSK-B modulation, as predicted by SPW. Neither a 2 GHz receiver nor an FQPSK-B demodulator-symbol synchronizer were available to measure Bit-Error-Rate. Therefore, system losses calculated by SPW could not be confirmed using this test configuration.

Additional hardware tests were conducted using an FQPSK-B modem provided by Dr. Feher. The test configuration operated at 70 MHz. This inexpensive commercially available modem was designed to operate over a more restrictive set of signal levels than the laboratory modulator described above. It did not provide sideband attenuations much below 40 dB.

EFFICIENT MODULATION METHODS STUDY AT NASA/JPL

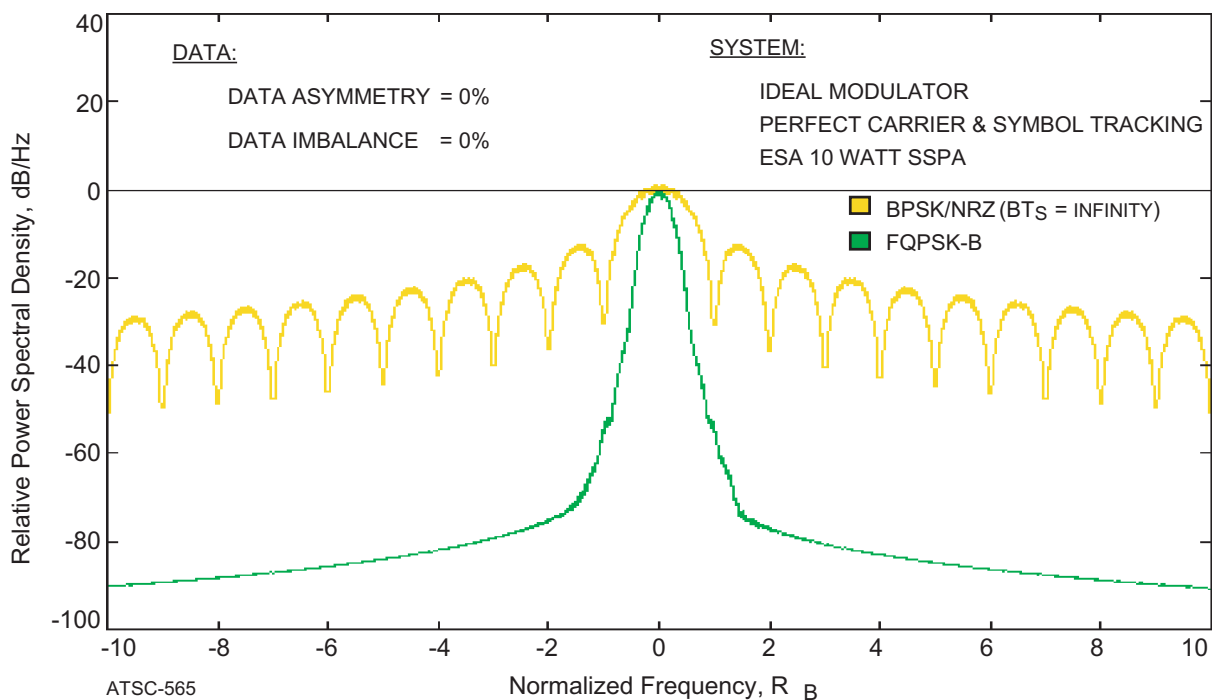
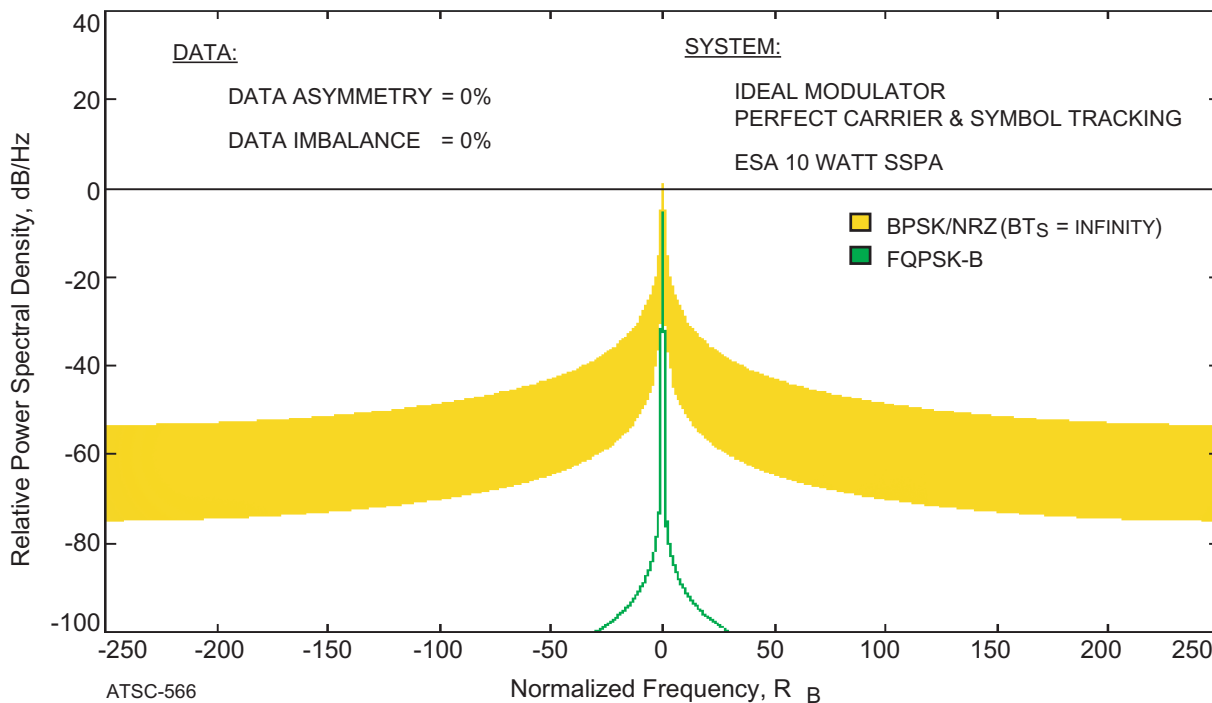
3.10-2a: Fine Detail ($f_C \pm 10 R_B$)3.10-2b: Broadband Spectra ($f_C \pm 250 R_B$)

Figure 3.10-2: FQPSK-B Modulation Spectra

EFFICIENT MODULATION METHODS STUDY AT NASA/JPL

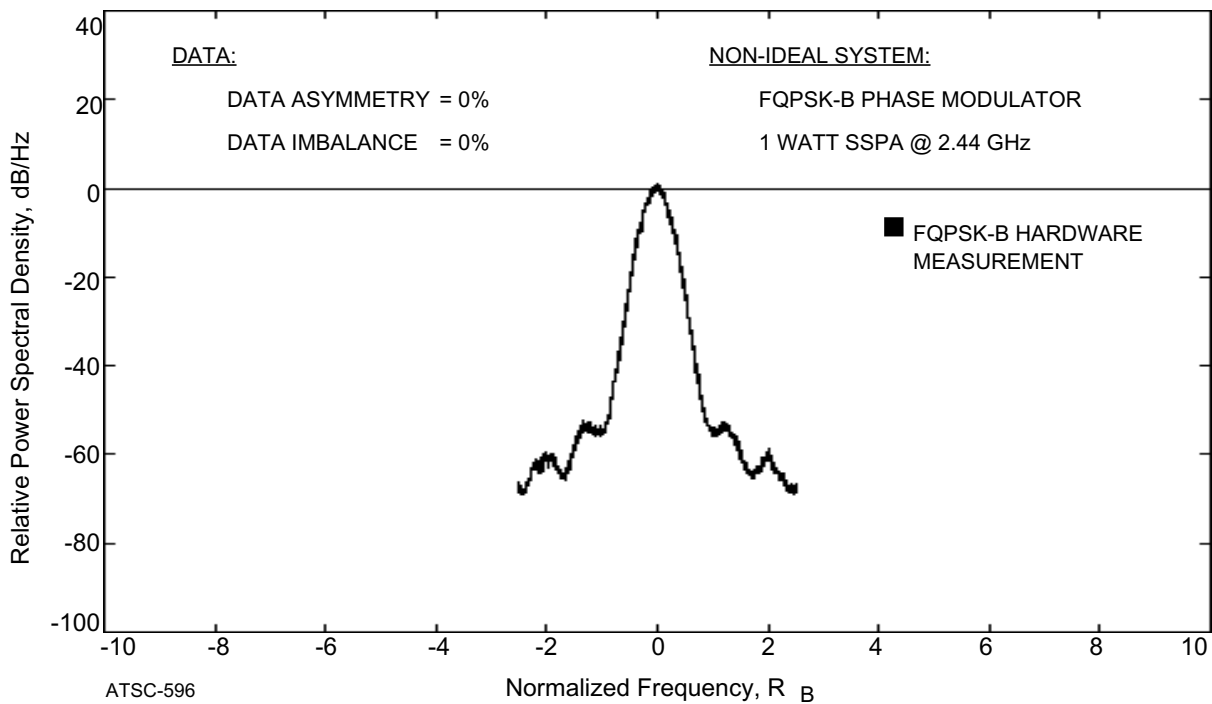


Figure 3.10-3: Hardware Generated FQPSK-B Modulation Spectrum

However, it was possible to make system loss measurements. At a 2×10^{-2} BER, the loss was determined to be about 1.3 dB. This tends to corroborate the 1.7 dB loss, computed by SPW, for the better laboratory modulator which has a more restrictive bandwidth.

3.10.3 FQPSK-B Modulation Power Containment

FQPSK-B frequency spectrum efficiency is so high that two power containment plots are required. Figure 3.10-4 is plotted using a 0 - $20 R_B$ scale for consistency with the other modulation methods. However, virtually all of the transmitted power is contained in such a small bandwidth that Figure 3.10-5 is added. Its scale of 0 - $2 R_B$ clearly shows the *occupied bandwidth* to be only $0.8 R_B$. This is significantly better than the $1.0 R_B$ found with GMSK using a filter bandwidth of $BT_s = 0.5$.

3.10.4 FQPSK-B Modulation Study Conclusions

Although FQPSK-B modulation was only recently added to the *Efficient Modulation Methods Study*, it appears to be one of the most bandwidth-efficient modulation method considered. Because of its proprietary nature¹⁷, some of its parameters are not apparent from published documents. Whether this proprietary nature would serve as an impediment to universal application by space agencies is also not clear.

What is clear is that FQPSK-B modulation must be seriously considered for high and very high data rate missions. With RF spectra valued in the United States at several hundred dollars per Hertz, NASA, and probably all space agencies, have a duty to investigate this modulation type further.

EFFICIENT MODULATION METHODS STUDY AT NASA/JPL

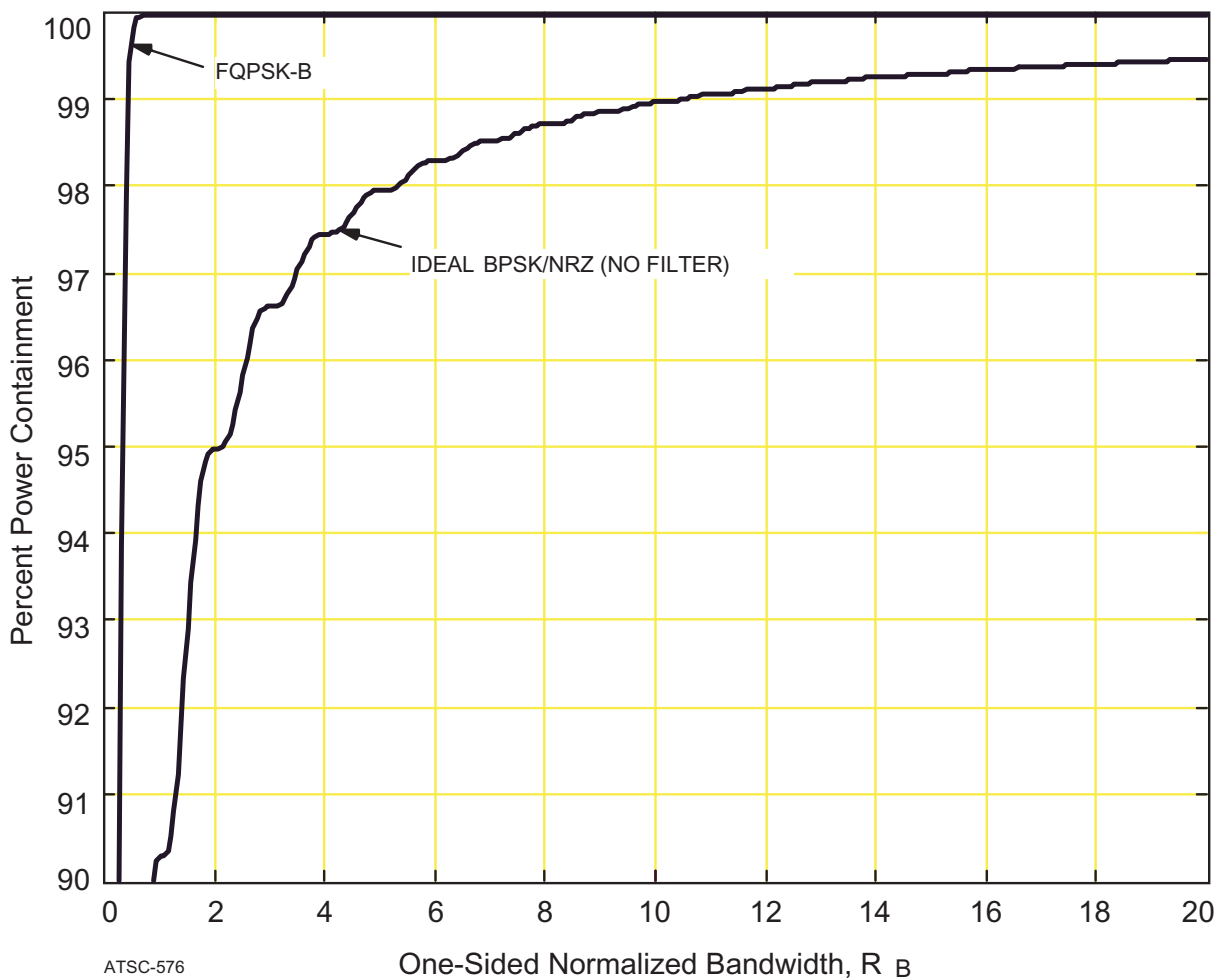
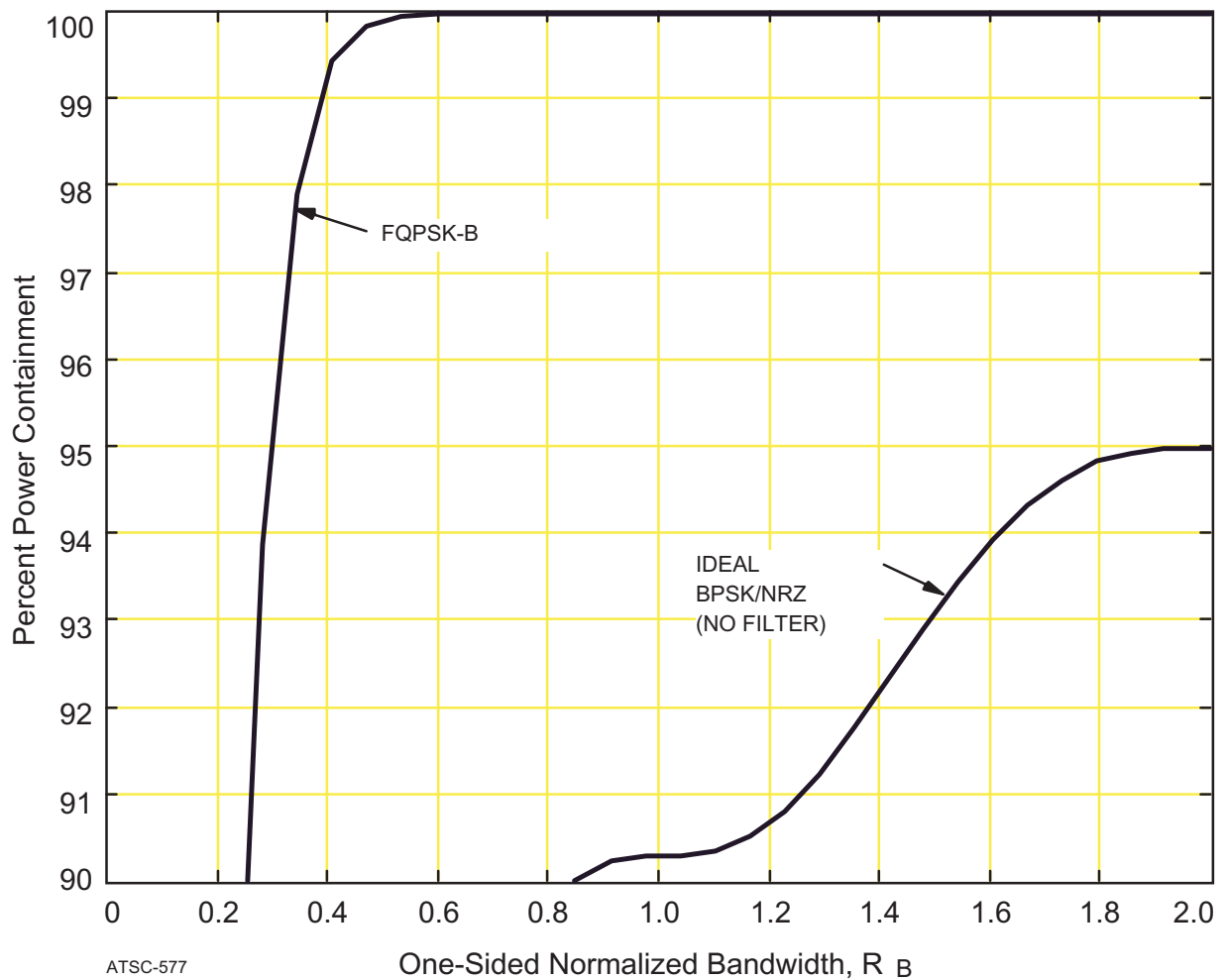


Figure 3.10-4: FQPSK-B Power Containment (0 - 20 R_B)

The authors recommend hardware tests be conducted to verify SPW spectra and BER simulation measurements at the earliest possible time. These tests should include an optimized transmitting and receiving system, capable of measuring both spectra and end-to-end system losses. This test bed should be established in a controlled environment where all parameters can be measured and controlled. If such tests confirm these simulation results, FQPSK-B should be considered as a recommended standard by the CCSDS and SFCG.

EFFICIENT MODULATION METHODS STUDY AT NASA/JPL

**Figure 3.10-5: FQPSK-B Modulation Power Containment (0 - 2 R_B)**

EFFICIENT MODULATION METHODS STUDY AT NASA/JPL

4.0 SUMMARY, CONCLUSIONS, AND RECOMMENDATIONS

The *CCSDS - SFCG Efficient Modulation Methods Study* measured the RF spectrum's width and end-to-end system performance using computer simulations. In compliance with the SFCG's request, the conclusions identify those modulation schemes that are the most bandwidth-efficient and suggest that CCSDS and SFCG Space Agencies adopt recommendations specifying their use.

4.1 SUMMARY

This chapter summarizes the results found in Sections 1, 2 and 3. For each modulation method, it reviews end-to-end system losses, examines RF spectrum bandwidth, and discusses the spectrum improvement factor resulting from baseband filtering.

4.1.1 Summary of Losses

Table 4.1-1 shows system and filtering losses occurring in the end-to-end system for each modulation type. Column 2 contains losses relative to ideal BPSK/NRZ modulation. Recall that ideal BPSK/NRZ assumes: perfect data ($P_m = P_s = 0.5$; $\eta = 0$), an ideal system (perfect carrier tracking and symbol synchronization), and no filtering ($BT = \infty$).

Existing SPW models for the ARX II receiver were unable to handle 8-PSK, MSK, GMSK, and FQPSK modulation. Except for the SSPA, which was identical to that for the other modulation types, ideal system hardware was used for simulating performance making it impossible to determine carrier tracking and synchronization losses. RF spectrum width was measured as were end-to-end losses relative to ideal BPSK/NRZ. Filtering losses, inherent in GMSK and FQPSK-B, are included in leftmost column of Table 4.1-1 containing losses relative to ideal BPSK/NRZ.

NOTE: All modulation types exhibit a loss with respect to ideal BPSK/NRZ. To find the true cost of a modulation method, one should subtract 0.56 dB which is the loss for filtered BPSK. Thus, the true loss for GMSK ($BT_s = 0.5$) is about 0.8 dB and FQPSK-B is about 1.1 dB.

Phase 3 studies employed baseband filtering exclusively. A principal objective was the selection of the proper filter bandwidth. Recall that filter selection criteria required using a filter producing the narrowest RF spectrum while introducing only moderate losses.

From Table 4.1-1, it is clear that filters having a $BT_s = 1$ often exceeded the allowable loss of approximately 1 dB. However, filters having a $BT_s = 2$ generally met the 1 dB loss criterion. 8-PSK was the exception requiring a $BT_s = 3$ filter bandwidth to be acceptable. For the other modulation types, BER curves in Section 3 showed that there was no significant benefit in using a $BT_s = 3$ filter bandwidth. Thus, Butterworth and Bessel baseband filters, with a $BT_s = 2$, were used.

4.1.2 RF Spectrum Efficiency

Another Phase 3 study objective was to determine the RF spectral bandwidth of each modulation type. This was necessary to rank the several modulation methods with respect to one-another. Many Spectrum Managers are concerned principally with *occupied bandwidth* (i.e., 99% power containment). Here, the focus is on many power containment levels.

EFFICIENT MODULATION METHODS STUDY AT NASA/JPL

Table 4.1-1: System Losses

Modulation Type	Losses in dB (Non Ideal Data and System) ¹							
	Loss Relative to Ideal BPSK ²	Butterworth Filter (3 RD Order)			Bessel Filter (3 RD Order)			SRRC Filter
		Filtering Losses ³			Filtering Losses ³			Filtering Loss ³
		BT=1	BT=2	BT=3	BT=1	BT=2	BT=3	$\alpha=1$
PCM/PM/NRZ	-1.52	-0.7	-0.20	-0.01	-0.80	-0.10	-0.01	-0.52
PCM/PM/Bi- ϕ	-0.56	-1.1	-0.34	-0.12	-0.91	-0.16	-0.01	-0.45
BPSK/NRZ	-0.56	-0.9	-0.30	-0.12	-0.70	-0.17	-0.01	-0.57
BPSK/Bi- ϕ	-0.61	-1.0	-0.44	-0.25	-0.87	-0.29	-0.11	-0.79
QPSK/NRZ	-0.64	-2.92	-0.82	-0.37	-2.24	-0.60	-0.20	-3.70
OQPSK/NRZ	-0.65	N/A ⁴	-1.30	-0.37	N/A ⁴	-1.00	-0.23	N/A ⁴
MSK ⁵	-0.5	N/A	N/A	N/A	N/A	N/A	N/A	N/A
GMSK ^{5,6}	-0.8	N/A	N/A	N/A	N/A	N/A	N/A	N/A
GMSK ^{5,7}	-1.4	N/A	N/A	N/A	N/A	N/A	N/A	N/A
8-PSK	-3.4	N/A ⁴	-1.9	-0.9	N/A ⁴	-2.4	-1.0	N/A
FQPSK-B ⁵	-1.7	N/A	N/A	N/A	N/A	N/A	N/A	N/A

NOTES:

1. Losses determined at a Bit-Error-Rate of 1×10^{-3} with $\eta = 0$, $P_m = 0.55$ (negative numbers indicate a loss).
2. System losses were measured relative to ideal BPSK/NRZ (perfect data, lossless equipment).
3. Filtering Losses include: ISI + Mismatch + Imperfect Carrier Tracking & Symbol Synchronization.
4. BER reached a minimum of 1×10^{-2} .
5. Filtering Losses Not Available (N/A) because BER measured with ideal system components.
6. Filter bandwidth $BT_s = 1$ ($BT_b = 0.5$).
7. Filter bandwidth $BT_s = 0.5$ ($BT_b = 0.25$).

The *Efficient Modulation Methods Study* was motivated by a desire to pack a substantially greater number of spacecraft into a given frequency allocation, particularly in the 2 and 8 GHz Category A mission bands. Maximum packing density occurs when spectra from two spacecraft, operating on adjacent frequencies, just begin to overlap at n dB below the peak of the data sideband's spectrum.

This follows from a *worst-case* assumption that the Earth station's antenna is boresighted on both spacecraft simultaneously. Where spacecraft are not coincidently within the Earth station antenna's beamwidth, the interferer's and victim's relative signal strengths will determine the spacial separation necessary to avoid interference. Obviously, even as frequency band usage increases, some spacial separation is expected. This study attempted to determine the value of n .

EFFICIENT MODULATION METHODS STUDY AT NASA/JPL

Views differ regarding the optimal value of n . Some believe that spectra from spacecraft on adjacent frequencies could be permitted to intersect at a level of 20 dB below the peak sideband amplitude. Others believe that the number should be greater or less than 20 dB.

In any event, Category A missions in highly elliptical orbits can undergo signal level changes of 30 dB or more at the Earth's surface. Thus, it would seem prudent to prohibit RF spectra, from spacecraft operating on adjacent frequencies, from intersecting at levels higher than 50 dB below the peak of the data sideband generated by the spacecraft having the stronger signal.

To provide maximum flexibility, RF spectrum bandwidths have been tabulated at values of n from 20 to 60 (dB) below the data sideband's peak. RF spectrum width increases as a function of n and each user must select the proper value. A value of $n = 50$ is recommended for most applications.

For a specific value of n , one can calculate the improvement in spectral efficiency. CCSDS Subpanel 1E concluded that BPSK/NRZ was to be the reference modulation type. A *Spectrum Improvement Factor (SIF)* can be calculated by comparing the bandwidth of unfiltered BPSK/NRZ to the bandwidth of the modulation method under discussion according to the relationship:

$$SIF = \frac{\text{Bandwidth of Unfiltered BPSK/NRZ}}{\text{Bandwidth of Named Modulation Type}} \quad (4-1)$$

Since the bandwidth is a function of n , the SIF will also vary with n . Table 4.1-2 contains the bandwidths and *SIFs* at several values of n for all modulation types covered in this Phase 3 study. Bandwidths for all phase modulation types were evaluated using a Butterworth, $BT_s = 2$ filter.

For symmetrical data ($\eta=0$), no spikes are present in the spectra of unfiltered BPSK/NRZ. All measurements in Table 4.1-2 were made with respect to a continuous unfiltered BPSK/NRZ reference spectrum. Conversely, all phase modulation schemes, which employ baseband filtering, have both continuous and discrete parts to their spectrum.

SIF measurements in Table 4.1-2 were made with respect to the discrete part of the baseband filtered modulation spectrum. This represents a *worst case* bandwidth comparison. Readers should understand that no discrete spectral components exceed the value of n in any of the *SIFs* shown in Table 4.1-2. Since SPW's resolution bandwidth was set to 1.33 Hz, one can conclude that the *SIFs* should be close to those obtained using real hardware viewed on a spectrum analyzer with a 1 Hz resolution.

Preferred modulation types become immediately apparent when *SIFs* are plotted as a function of n as in Figure 4.1-1. Modulation types fall into two distinct groups FQPSK-B / GMSK and everything else. Even 8-PSK is not a competitor for those two types. The message is clear:

If RF bandwidth is important, then the results of this study show that FQPSK-B and GMSK ($BT_s = 0.5$) are the modulation methods of choice.

EFFICIENT MODULATION METHODS STUDY AT NASA/JPL

Table 4.1-2: Bandwidth Efficiencies

Two-Sided Bandwidth, R_B						Spectrum Improvement Factors ²				
Modulation Type	Sideband Attenuation, dB					Sideband Attenuation, dB				
	20	30	40	50	60	20	30	40	50	60
PCM/PM/NRZ ¹	8.2	10.2	10.2	14.2	16.2	1.3	2.3	7.3	18.4	40.2
PCM/PM/Bi- ϕ ¹	16.2	20.2	24.2	28.2	32.2	0.7	1.2	3.1	9.3	20.2
BPSK/NRZ ¹	8.2	10.2	14.2	16.2	18.2	1.3	2.3	5.3	16.1	35.8
BPSK/Bi- ϕ ¹	20.2	24.2	28.2	32.2	40.2	0.5	1.0	2.6	8.1	16.2
QPSK ¹	5.2	6.2	7.2	8.2	12.2	2.1	3.7	10.4	31.8	53.4
OQPSK ¹	5.2	7.2	8.2	10.2	18.2	2.1	3.2	9.1	25.6	35.8
MSK	1.3	3.0	5.1	9.1	19.1	8.3	7.7	14.7	28.7	34.1
GMSK ($BT_s=1$)	1.2	1.9	2.3	2.5	3.0	9.0	12.2	32.5	104.4	217.0
GMSK ($BT_s=0.5$)	1.0	1.2	1.6	1.9	2.1	10.8	19.3	46.8	137.4	310.0
8-PSK ¹	3.6	4.8	5.6	6.8	8.8	3.0	4.8	13.4	38.4	74.0
FQPSK-B	0.9	1.1	1.4	1.7	2.2	12.0	21.1	53.4	153.5	295.9
Average	6.5	8.2	9.8	11.9	15.7	4.2	6.6	16.6	47.6	94.4

NOTES:

1. Measurements of phase modulated spectra are made using Butterworth $BT_s = 2$ filter
2. Measurements show bandwidth improvement compared to unfiltered BPSK/NRZ modulation

Further work is required to determine Filtering Losses of FQPSK-B and GMSK modulation types. Losses should be determined by actual hardware tests rather than by additional simulations. Currently, there is a plan to conduct hardware tests with several modulation types, including FQPSK-B, at ESA/ESTEC in early 1998. Such tests can be used to validate the information contained in this report.

Relative bandwidth efficiencies can also be shown by plotting the Two-Sided Bandwidth (R_B) as a function of Sideband Attenuation (dB). Figure 4.1-2 graphically illustrates the performance of the 10 modulation methods studied. Although less dramatic than Figure 4.1-1, Figure 4.1-2 clearly demonstrates that there are three classes of bandwidth efficiency. Ranked from highest to lowest bandwidth efficiency, these are:

1. FQPSK-B and GMSK
2. BPSK/NRZ, PCM/PM/NRZ, OQPSK, QPSK, MSK and 8-PSK
3. BPSK- ϕ and PCM/PM/Bi- ϕ

EFFICIENT MODULATION METHODS STUDY AT NASA/JPL

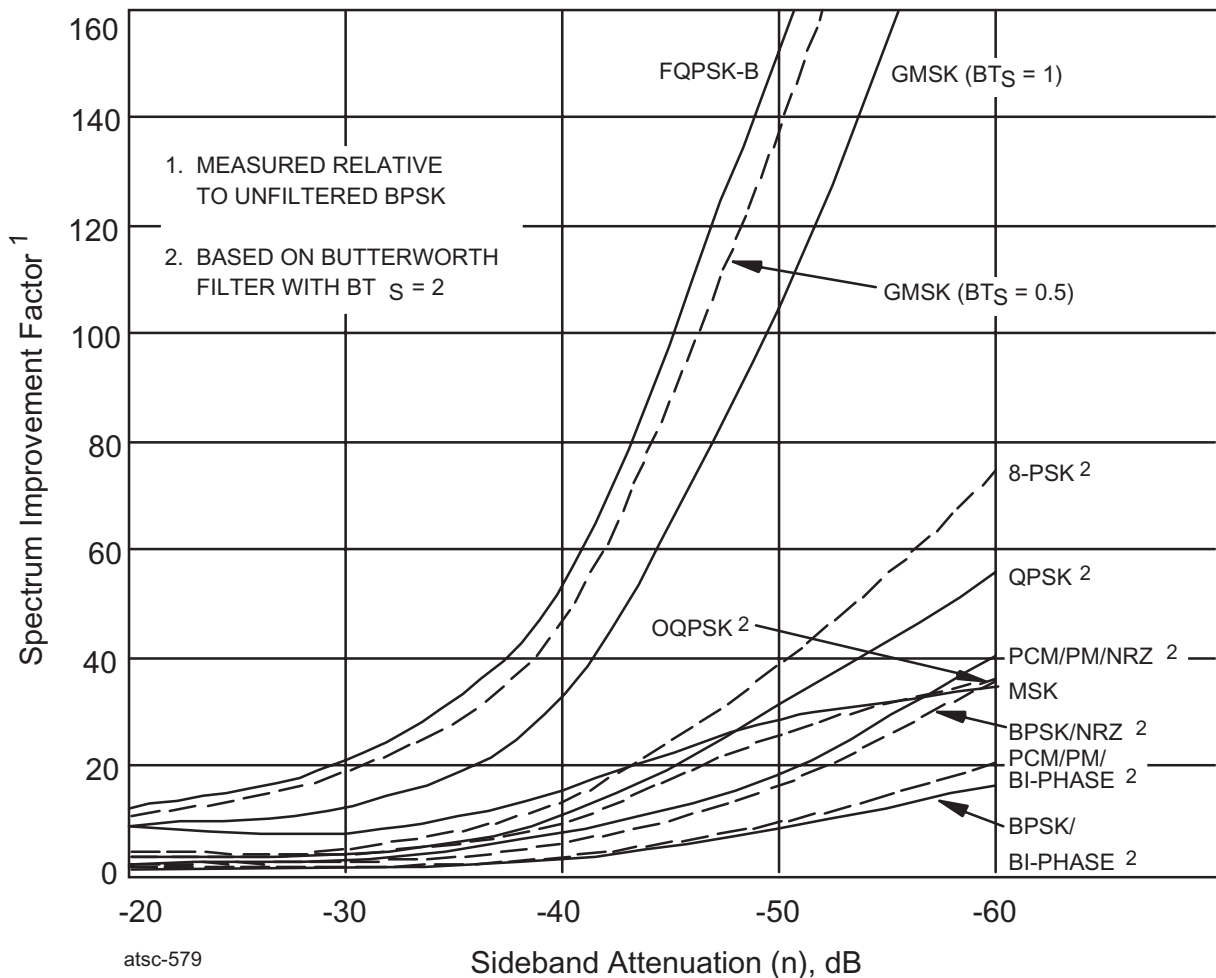


Figure 4.1-1: Spectral Efficiency Relative to Unfiltered BPSK / NRZ

Figure 4.1-1 relates the spectral efficiencies of the several modulation methods investigated in the Phase 3 *Efficient Modulation Methods Study*. *SIF*, as defined in equation 4-1 is plotted as a function of n (number of dB below the peak sideband amplitude). Three classes of bandwidth efficiency are evident: High (FQPSK-B and GMSK); Medium (8-PSK, QPSK/OQPSK, MSK, PCM/PM/NRZ, and BPSK/NRZ); and Low (PCM/PM/Bi- ϕ , BPSK/Bi- ϕ).

All Phase 3 modulation bandwidth measurements are made using a Butterworth 3RD order $BT_S = 2$ filter. MSK has no filtering and GMSK curves are labeled with the Gaussian filter's BT_S factor. FQPSK-B measurements are based on a proprietary filter in FQPSK-B modulation.

EFFICIENT MODULATION METHODS STUDY AT NASA/JPL

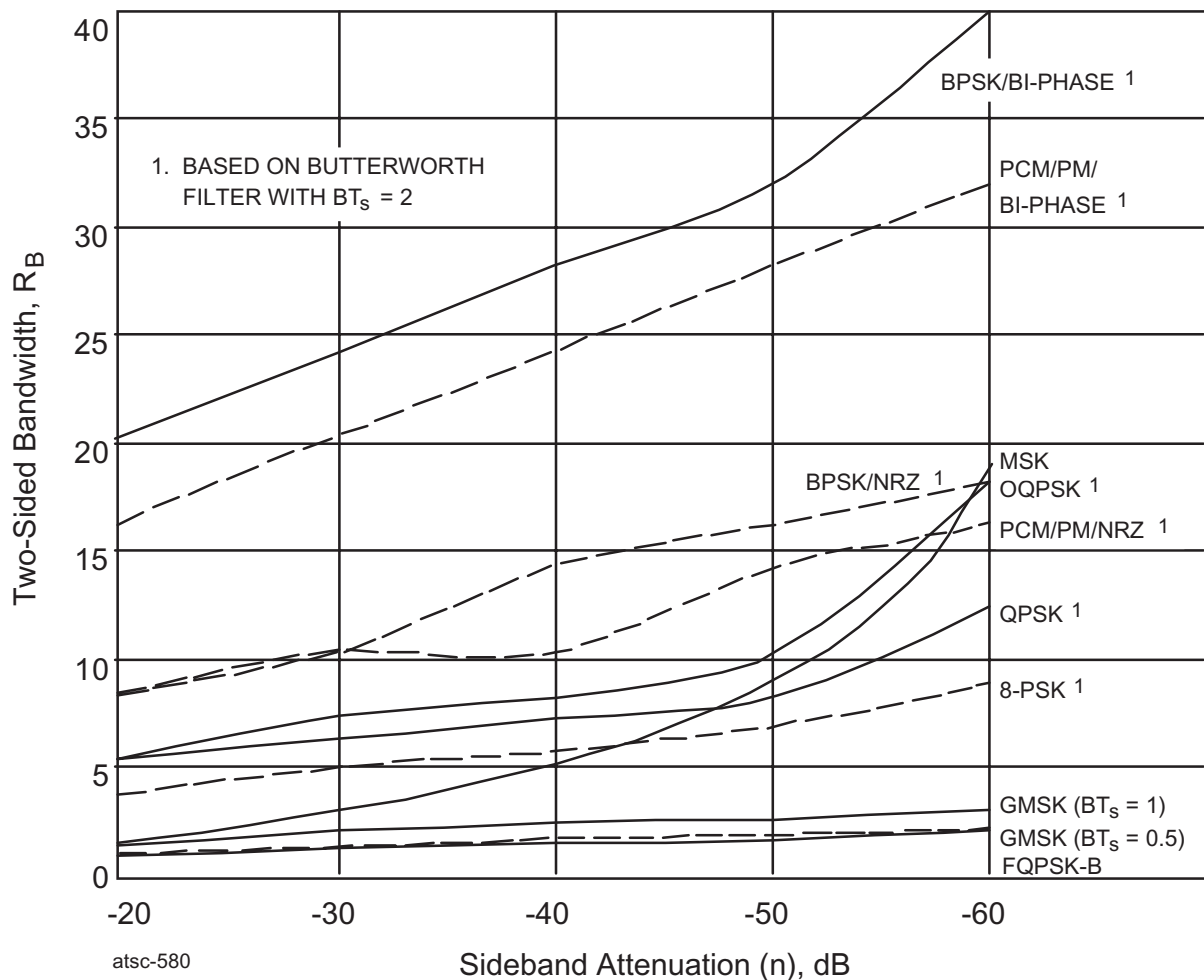


Figure 4.1-2: Two-Sided Required Bandwidth

Figure 4.1-2 depicts modulation efficiency using the Two-Sided Bandwidth as the key parameter. It shows the RF bandwidth *required* by each modulation type to obtain a desired value of n . This Figure can be used to establish the separation between adjacent users operating in the same frequency band, as well as to make a cost comparison between alternative modulation methods.

For example, at $n = -50$ [dB], adjacent users *require* a separation of only 2 times their data bit rate when FQPSK-B modulation is used, whereas a separation of 32 times the data bit rate is *required* when BPSK/Bi- ϕ modulation is employed. The 16-fold difference between the most and least efficient modulation methods facilitates an easy cost-comparison of the several modulation methods in this study.

Costs can be calculated if the spectrum's unit-value (ξ) is known. Auctions of the 900 MHz band, conducted by the Federal Communications Commission several years ago, yielded an average return of $\xi = \$744/\text{Hz}$. Modulation method cost comparisons can be made using the following relationship:

$$\text{Cost} = \xi \cdot \text{Data rate (Hz)} \cdot \text{Required Two-Sided Bandwidth from Figure 4.1-2.} \quad (4-2)$$

EFFICIENT MODULATION METHODS STUDY AT NASA/JPL

4.2 CONCLUSIONS

Conclusions fall into distinct categories relating to filtering methods, losses, modulation types, and *Spectrum Improvement Factors (SIFs)*. Each conclusion is summarized in the subsections below.

4.2.1 Filtering Conclusions

Baseband filtering significantly reduces the transmitted RF spectrum's width. Study conclusions are:

- Filtering of transmitted signals will be required to obtain an acceptably narrow RF spectrum.
- Hardware limitations make post PA filtering impractical at data rates below about 8 Ms/s.
 - Realizable Q s limit the filter's bandwidth to about 1-2% of the transmitted frequency.
 - Filtering power losses may be unacceptable, even at a 1-2% bandwidth.
 - For low data symbol rates, post PA filtering may make turnaround ranging difficult.
- Depending upon its architecture, transponder i.f. filtering may not be practical.
 - Q limitations stated above apply if modulation occurs at the transmitting frequency.
 - Filtering at i.f. requires transponders be modified for each mission.
 - Filtering at i.f. makes data rate changes difficult.
 - For low data symbol rates, i.f. filtering may make turnaround ranging difficult.
 - Filtering within the transponder risks introducing spurious emissions causing *lock-up*.
- Baseband filtering is the only practical alternative to unacceptable post PA and i.f. filtering.
 - Baseband filtering can be accomplished with a simple, passive low-pass filter design.
 - A 3RD order Butterworth filter ($BT_s = 2$) provides the best performance-simplicity ratio.
 - Filtering prior to phase modulation produces undesirable spikes in the RF spectrum.
 - Spikes can only be avoided by using a different modulation method (GMSK, FQPSK).
- Both GMSK and FQPSK-B utilize baseband filtering and do not require i.f. nor post PA filters.

4.2.2 Loss Conclusions

Table 4.1-1 partitions losses into two categories: System (losses relative to ideal BPSK) and Filtering (ISI and Mismatch). One criterion for the Phase 3 study was that end-to-end losses should be *reasonable*. CCSDS Subpanel 1E determined that approximately 1 dB was reasonable. The following conclusions regarding losses were reached:

- High system loss (1.5 dB) found for PCM/PM/NRZ, resulted from a 10% data imbalance.
 - When a $BT_s = 2$ Butterworth filter is used, data imbalance should not exceed 5%.
- 8-PSK modulation exhibits an excessive system loss (3.4 dB).
 - Filtering losses decreased for non-constant envelope modulation.
 - However, spectrum width increased.
 - Losses were not reduced to an acceptable level.
 - High losses make 8-PSK modulation unsuitable for power-limited Category A missions.
- GMSK ($BT_s = 0.5$) also exhibited high (1.4 dB) system losses.
 - Increasing filter bandwidth to $BT_s = 1$ reduced system losses to an acceptable level.
 - Losses were measured with an ideal (lossless) receiver.
- FQPSK-B losses were found to be a high 1.7 dB.
 - Losses were also measured with an ideal (lossless) receiver.

EFFICIENT MODULATION METHODS STUDY AT NASA/JPL

4.2.3 Modulation Methods Conclusions

Figures 4.1-1 and 4.1-2, graphically identify the preferred modulation methods. For the several modulation methods considered, the following conclusions were reached.

- FQPSK-B provides the narrowest RF spectrum of all modulation methods studied.
 - FQPSK-B should be considered for all high and very high data rate missions.
 - Provided that losses are acceptable.
- GMSK, with a filter bandwidth $BT_s = 0.5$, produces virtually equivalent results to FQPSK-B.
 - Further work is required to validate system losses using real hardware.
- 8-PSK, with its high losses, does not appear useful for most Category A missions.
 - Excessive losses and modest performance gains do not provide sufficient advantages.
- QPSK has comparatively poorer bandwidth efficiency than does FQPSK-B and GMSK.
 - Its common usage may dictate its consideration in some applications.
 - Absent spread spectrum, QPSK cannot provide simultaneous telemetry and ranging.
- OQPSK could not be evaluated properly with the UPM.
 - OQPSK should be reserved for applications requiring separate, independent data channels.
 - Orthogonally phased BPSK/NRZ modulators, with a $\frac{1}{2}$ symbol offset should be used.
- BPSK/NRZ has poor bandwidth efficiency and should not be used if bandwidth is important.
 - Bandwidth efficiency is slightly lower than PCM/PM/NRZ modulation.
 - BPSK/NRZ may be an alternative to PCM/PM/NRZ when:
 - A residual carrier is not required.
 - The data imbalance is so great that PCM/PM/NRZ would suffer excessive losses.
- PCM/PM/NRZ has poor bandwidth efficiency, but has best efficiency of residual carrier types.
 - Applications requiring a residual carrier should consider this modulation method.
 - When using PCM/PM/NRZ, care must be taken to ensure proper data balance.
- MSK modulation is not highly spectrum efficient.
 - No specific advantages were found to MSK, save the lack of spectral spikes.
- Bi- ϕ modulation has very poor RF spectrum efficiency.
 - Bi- ϕ modulation should not be used unless the symbol transition density is too low.
 - This conclusion applies to both PCM/PM/Bi- ϕ and BPSK/Bi- ϕ modulations.
- Subcarrier modulation tends to waste spectrum and should be avoided whenever possible.
 - When used, the subcarrier frequency-to-data symbol rate ratio should be low (≤ 4).
 - CCSDS *virtual channels* should be used to separate data types.

4.2.4 Spectrum Improvement Conclusions

The following conclusions were reached regarding RF spectrum efficiency improvement:

- Baseband filtering greatly increases the number of spacecraft operating in a frequency band.
 - Spectrum utilization efficiency can increase by a factor from 2 to more than 100 times.
 - The amount of improvement depends upon modulation method and sideband attenuation.
 - This result attains despite non-linear system elements, non-ideal data, and spectral spikes.
- Modulation method should be selected to maximize the *Spectrum Improvement Factor*.
 - Modulation schemes with low *Spectrum Improvement Factors* should be avoided.
 - Modulation method selection should be based on system capabilities, data rates, and *SIFs*.

EFFICIENT MODULATION METHODS STUDY AT NASA/JPL

4.3 RECOMMENDATIONS

Based upon the results of the Phase 3 *Efficient Modulation Methods Study*, the CCSDS and SFCG are encouraged to create and adopt Recommendations specifying the preferred modulation methods. Because space missions have a broad range of objectives, communication requirements will vary. Some grouping of applications is necessary before assigning a modulation type.

4.3.1 Mission Classification

One method for grouping applications is by specific attributes. Missions sharing those attributes are assigned a classification and a modulation method(s) most appropriate to that group are selected. Where RF spectrum and modulation types are of paramount concern, the telemetry data symbol rate appears to be the best discriminator. The following classifications are recommended:

4.3.1.1 Low Data Rate (10 s/s - 20 ks/s)

This class includes low rate scientific missions as well as the Telemetry, Tracking, and Command (TT&C) services for most missions. Turnaround ranging may be required. If it is, subcarrier modulation may be appropriate (see CCSDS Recommendation 401 (3.3.4) B-1). If ranging is not required, then any appropriate modulation type should be acceptable. All mission types operating in the space services can be found in this class.

4.3.1.2 Modest Data Rate (20 ks/s - 200 ks/s)

Most Category A missions fall in this and the following classification. If space agencies are serious about reducing RF spectrum requirements, they must use appropriate filtering and modulation techniques for spacecraft in these classes. Typical missions operate in the *Space Research* service and include NASA's ISTP Wind and ESA's Integral missions.

The recommended modulation method depends upon whether or not simultaneous telemetry and turnaround ranging signals are required (see CCSDS Recommendation 401 (3.4.1) B-1). If they are, a residual carrier modulation method is suggested because users can independently control the division of power between the carrier, telemetry, and ranging channels. PCM/PM/NRZ is the most bandwidth-efficient residual carrier modulation method and is recommended provided that the telemetry data imbalance is less than 5% during a time interval equal to one time-constant of the Earth station receiver's phase-locked-loop.

At low data symbol rates, care must be taken with PCM/PM/NRZ modulation to ensure that the Earth station's receiver can distinguish between the RF carrier and the spectral components of the data sidebands. The spacecraft's modulation index and the Earth station receiver's phase-locked-loop bandwidth should be adjusted to ensure proper operation.

If simultaneous telemetry and turnaround ranging is required and the data imbalance is greater than 5%, then Unbalanced QPSK (UQPSK) is the recommended modulation type. Within limits, telemetry and ranging powers can be set independently. If simultaneous telemetry and turnaround ranging is not required or where data imbalance exceeds 5%, BPSK/NRZ is recommended.

EFFICIENT MODULATION METHODS STUDY AT NASA/JPL

4.3.1.3 *Medium Data Rate (200 ks/s - 2 Ms/s)*

As noted, most Category A scientific missions fall into this and the prior classification. Generally, such spacecraft operate in the *Space Research* service allocation. Examples include NASA's Polar and ESA's SOHO missions.

Because many of these missions are collecting scientific data, simultaneous turnaround ranging is frequently required. In these cases, PCM/PM/NRZ modulation is recommended, providing the telemetry data symbol imbalance does not exceed 5% in one time-constant of the Earth station receiver's phase-locked-loop. If data imbalance exceeds 5%, then UQPSK can be used.

In this classification, data symbol rates can be as high as 2 Ms/s, so bandwidth conservation is important. If simultaneous turnaround ranging is not required, then QPSK modulation is recommended.

4.3.1.4 *High Data Rate (2 Ms/s - 20 Ms/s)*

Typically, missions with data symbol rates in this range operate in the *Earth Exploration Satellite* service. Examples include NASA's Lewis and the Canadian Space Agency's (CSA's) Radarsat projects. In this and the following classification, RF spectrum limiting becomes imperative. Decreasing bandwidth utilization by a factor of 10 saves considerably more RF spectrum when the data symbol rate is 20 Ms/s than is the case when it is 200 ks/s. Both the CCSDS and SFCG should immediately adopt filtering and modulation Recommendations for these last two classes.

From Figures 4.1-1, 4.1-2, and Table 4.1-1, FQPSK-B or GMSK ($BT_s = 0.5$) modulation are the clear choices if RF spectrum conservation is important. Modulator modifications may be required to provide turnaround ranging with either of these modulation types and the ranging signal will have to be sequential, not simultaneous, with the telemetry data.

4.3.1.5 *Very High Data Rate (20 Ms/s - and Above)*

Missions with data symbol rates in this range operate almost exclusively in the *Earth Exploration Satellite* service. Examples include NASA's Earth Observation Satellite (EOS) and ESA's Earth Resources Satellite (ERS-1). Previous comments regarding bandwidth conservation and modulation methods apply emphatically to this class. FQPSK-B or GMSK ($BT_s = 0.5$) are the recommended modulation methods.

The CCSDS and SFCG are urged to move with all dispatch to obtain the additional system performance information for both FQPSK-B and GMSK modulation types. The authors recommend that tests, using real hardware, be conducted in a carefully controlled environment to validate these simulations and to measure actual system performance. Recommendations, consistent with Table 4.3-1, should be adopted at the earliest possible opportunity.

EFFICIENT MODULATION METHODS STUDY AT NASA/JPL

Table 4.3-1: Recommended Modulation Methods for Category A Missions

No.	Telemetry Classification	Classification Attributes	Example Missions	Recommended Modulation Method
1	Low Data Rate 10 s/s - 20 ks/s	Simultaneous telemetry & ranging <u>may</u> be required.	TT&C, Low Rate Science	PCM/PSK/PM (Sine) Any Appropriate Type
2	Modest Data Rate 20 ks/s - 200 ks/s	Simultaneous telemetry & ranging required Data Imbalance $\leq 5\%$	<i>Space Research</i> NASA/Polar ESA/Integral	PCM/PM/NRZ UQPSK ¹
		Simultaneous telemetry & ranging <u>not</u> required Data Imbalance $\geq 5\%$	<i>Space Research</i> CNES/SPOT-4	BPSK/NRZ
3	Medium Data Rate 200 ks/s - 2 Ms/s	Simultaneous telemetry & ranging required Data Imbalance $\leq 5\%$ (If $\geq 5\%$, use UQPSK)	<i>Space Research</i> NASA/Polar	PCM/PM/NRZ UQPSK ¹
		Simultaneous telemetry & ranging <u>not</u> required	NASA/Image	QPSK
4	High Data Rate 2 Ms/s - 20 Ms/s	Simultaneous telemetry & ranging <u>not</u> required	<i>Space Research</i> NASA/Lewis	FQPSK ² GMSK ²
5	Very High Data Rate 20 Ms/s and Above	Simultaneous telemetry & ranging <u>not</u> required	<i>EES</i> NASA/EOS-AM	FQPSK ² GMSK ²

NOTES:

1. UQPSK should be used where the Data Imbalance $\geq 5\%$ or when data rates are so low that carrier tracking loop interference can occur.
2. Subject to confirmation of reasonable end-to-end system losses.

EFFICIENT MODULATION METHODS STUDY AT NASA/JPL**GLOSSARY**

ARX II	A Research and Development Earth Station Receiver, (Prototype for DSN Block V)
BER	Bit-Error-Rate
Bi- ϕ	Binary-Phase [Manchester] modulation
B_L	Receiver phase-locked-loop's bandwidth, expressed in Hz
BPSK	Bi-Phase Shift Keying [modulation method]
BT_B	Bandwidth - Time Product Based on Bit-Period
BT_S	Bandwidth - Time Product Based on Symbol-Period
Category A	A Space Mission whose distance from Earth is less than $2 \cdot 10^6$ km
CCSDS	Consultative Committee for Space Data Systems
DSN	Deep Space Network
DTTL	Digital Transition Tracking Loop
ESA	European Space Agency
ESOC	ESA Operation Center (Darmstadt, Germany)
ESTEC	ESA Technical Center (Noordwijk, The Netherlands)
FQPSK	Feher QPSK [modulation method]
GMSK	Gaussian Minimum Shift Keying
HP	Hewlett Packard
Hz	Hertz
k	Kilo (1,000)
kb/s	Kilo Bits per Second
kHz	Kilo Hertz
ks/s	Kilo Symbols Per Second
M	Mega (1,000,000)
MHZ	Mega Hertz
MAP	Maximum A Posteriori
MODEM	Modulation-Demodulation
MSK	Minimum Shift Keying
NRZ	Non Return to Zero [format]
OQPSK	Offset QPSK [modulation method]
PA	Power Amplifier
PCS	Personal Communications System
PM	Phase Modulation
PSK	Phase Shift Keying
P_T	Total Power [transmitted]
QPSK	Quadrature Phase Shift Keying [modulation method]
SAW	Surface Acoustic Wave [Filter]
SER	Symbol-Error-Rate
SFCG	Space Frequency Coordination Group
SPW	Cadence Design Systems Inc. Signal Processing Worksystem
SRRC	Square Root Raised Cosine [Filter]
SSPA	Solid State Power Amplifier
Subpanel 1E	CCSDS group concerned with RF and Modulation standards
\mathcal{P}_M	Probability of a Mark [+ 1]
\mathcal{P}_S	Probability of a Space [- 1]

EFFICIENT MODULATION METHODS STUDY AT NASA/JPL**REFERENCES**

1. Martin, W. L. and Tien M. Nguyen, *CCSDS-SFCG Efficient Modulation Methods Study: A Comparison of Modulation Schemes, Part 1: Bandwidth Utilization*, Jet Propulsion Laboratory, Pasadena, California, 24 September 1993.
2. Otter, Manfred, *CCSDS-SFCG Efficient Modulation Methods Study: A Comparison of Modulation Schemes, Phase 1b: A Comparison of QPSK, OQPSK, BPSK, and GMSK*, European Space Agency, June 1994.
3. Martin, Warren L. and Tien M. Nguyen, *CCSDS - SFCG Efficient Modulation Methods Study - A Comparison of Modulation Schemes, Phase 2: Spectrum Shaping*, Jet Propulsion Laboratory, Pasadena, California, August 1994.
4. Ibid.
5. Simon, Marvin K., *On the Power Spectrum of Angle Modulated PSK Signals Corrupted by ISI*, TDA Progress Report 42-130, Jet Propulsion Laboratory, Pasadena, California, 15 August 1997.
6. *Telemetry Channel Coding*, CCSDS 101.0-B-3, May 1992.
7. Simon, Marvin K., *On the Power Spectrum of Angle Modulated PSK Signals Corrupted by ISI*, TDA Progress Report 42-130, Jet Propulsion Laboratory, Pasadena, California, 15 August 1997.
8. Lindsey, William C., and Marvin K. Simon, *Telecommunication Systems Engineering*, Prentice Hall, Englewood Cliffs, New Jersey, 1973.
9. Laurent, P. A., *Exact and Approximate Construction of Digital Phase Modulators by Superposition of Amplitude Modulated Pulses*, IEEE Transactions on Communications, COM 34, pp 150-160, 1986.
10. Ghassan Kaway Kaleh, *Simple Coherent Receivers for Partial Response Continuous Phase Modulation*, IEEE Journal on Selected Areas in Communications, vol. 7, No. 9, December 1989.
11. Simon, Marvin K., *On the Power Spectrum of Digitally Frequency Modulated Signals*, TDA Progress Report 42-130, Jet Propulsion Laboratory, Pasadena, California, 15 August 1997.
12. Tao, Jianping, and Dr. Sheila Horan, *Pulse Shaped Constant Envelope 8-PSK Modulation Study*, New Mexico State University, NMSU-ECE-97-005, March 1997.
13. Horan, Sheila, *Pulse Shaped Non-Constant Envelope 8-PSK Modulation Study in Terms of Bit-Error-Rate*, New Mexico State University, NMSU-ECE-97-004, March 1997.

EFFICIENT MODULATION METHODS STUDY AT NASA/JPL

14. Feher, Dr. Kamilo, *Wireless Digital Communications: Modulation & Spread Spectrum Applications*, Prentice Hall, Upper Saddle River, New Jersey, 1995.
15. Kato, S., and K. Feher, *XPSK: A New Cross-Correlated Phase Shift Keying Modulation Technique*, IEEE Transactions, pp 701-707, May 1983.
16. Feher, K., *Filtering Inventions Enhance Digitally Modulated RF Products*, Microwave and RF, pp. 140-148, April 1995.
17. Kato, S., and K. Feher, *Correlated Signal Processor*, U.S. Patent 4,567,602, issued 28 January 1986, Canada Patent 1211517, issued 16 September 1986.

[This page intentionally left blank.]

**CCSDS Meeting
Noordwijk, The Netherlands
October 18-22, 1999**

CCSDS - SFCG

EFFICIENT MODULATION METHODS STUDY

AT NASA/JPL

PHASE 4: INTERFERENCE SUSCEPTIBILITY

**Warren L. Martin
Tsun-Yee Yan
Andrew Gray
Dennis K. Lee**

September 1999

Issued: 12 October 1999

EFFICIENT MODULATION METHODS - INTERFERENCE SUSCEPTIBILITY**TABLE OF CONTENTS**

Section	Title	Page
1.0	INTRODUCTION	1
	SFCG Workplan AI18-17/2	2
2.0	STUDY DESCRIPTION	3
2.1	Study Approach	3
2.1.1	Transmitting System	3
2.1.1.1	Baseband Filtering	4
2.1.2	Interfering Signal Types	4
2.1.2.1	Case 1: Narrowband Interference Outside Telemetry Bandwidth	5
2.1.2.2	Case 2: Narrowband Interference In Telemetry Bandwidth But Far From f_c	5
2.1.2.3	Case 3: Narrowband Interference In Telemetry Bandwidth and Close to f_c ...	6
2.1.2.4	Case 4: Wideband Interference In Telemetry Bandwidth and Around f_c	6
2.1.3	Receiver Design	7
2.1.4	Theoretical Calculations vs Hardware Simulations	8
2.1.5	Matched Filter	9
3.0	STUDY RESULTS	10
3.1	Unfiltered BPSK (Reference Case)	10
3.2	Filtered OQPSK	14
3.2.1	OQPSK Bit-Error-Rate with an I-Q Modulator	18
3.3	GMSK	21
3.4	FQPSK-B	25
3.4.1	Special FQPSK-B Study	28
3.5	Spread Spectrum	30
3.5.1	DSSS Spectral Efficiency	33
4.0	SUMMARY AND CONCLUSIONS	35
	GLOSSARY	38
	REFERENCES	39

EFFICIENT MODULATION METHODS - INTERFERENCE SUSCEPTIBILITY**TABLE OF CONTENTS (Continued)****LIST OF FIGURES**

No.	Title	Page
1.0-1	SFCG Spectrum Mask	1
2.1-1	Interfering Signals	4
2.1-2	Costas Loop Narrowband Interference Susceptibility (Hardware)	7
2.1-3	Simulated EOS AM-1 Receiver (APRX)	8
3.1-1	Unfiltered BPSK Spectrum	11
3.1-2a	Unfiltered BPSK Susceptibility to Narrowband Interference (Theory)	11
3.1-2b	Unfiltered BPSK Susceptibility to Wideband Interference (Theory)	12
3.1-3	Theoretical vs Actual Losses to an Unfiltered BPSK Victim	13
3.2-1	OQPSK Modulation Spectra with SRRC Filter ($\alpha = 0.5$)	14
3.2-2a	OQPSK (But., $BT_s = 1$) Susceptibility to Narrowband Interference (Theory)	15
3.2-2b	OQPSK (But., $BT_s = 1$) Susceptibility to Narrowband Interference (Hardware)	15
3.2-3	OQPSK (SRRC, $\alpha = 0.5$) Susceptibility to Narrowband Interference (Theory)	16
3.2-4	OQPSK (SRRC, $\alpha = 0.5$) Susceptibility to Wideband Interference (Theory)	18
3.2-5a	OQPSK BER with Butterworth ($BT_s = 1$) Baseband Filter	19
3.2-5b	OQPSK BER with SRRC ($\alpha = 0.5$) Baseband Filter	19
3.3-1a	GMSK ($BT_s = 1$) Susceptibility to Narrowband Interference (Theory)	22
3.3-1b	GMSK ($BT_s = 0.5$) Susceptibility to Narrowband Interference (Theory)	22
3.3-2	GMSK ($BT_s = 0.5, 1$) Spectra	23
3.3-3	GMSK Susceptibility to Wideband Interference (Theory)	24
3.4-1a	FQPSK-B Susceptibility to Narrowband Interference (Theory)	26
3.4-1b	FQPSK-B Susceptibility to Narrowband Interference (Hardware)	26
3.4-2	FQPSK-B Susceptibility to Wideband Interference (Hardware)	27
3.4-3	FQPSK-B Susceptibility to Adjacent Channel Interference (Theory)	28
3.4-4	FQPSK-B Bit-Error-Rate Susceptibility to ACI (Theory)	29
3.5-1	DSSS Bit-Error-Rate Susceptibility to Narrowband Interference	32
3.5-2	DSSS SNR Susceptibility to Wideband Interference	32

List of Tables

No.	Title	Page
3.5-1	Comparison of DSSS and FQPSK-B Channel Capacities for 2 GHz Band	34
4.0-1	Data Degradation From Narrowband Interference of Equal Power (Theory)	35
4.0-2	Data Degradation From Wideband Interference of Equal Power (Theory)	35

EFFICIENT MODULATION METHODS - INTERFERENCE SUSCEPTIBILITY

1.0 INTRODUCTION

At its September 1997 meeting in Galveston, Texas, the Space Frequency Coordination Group (SFCG) adopted provisional Recommendation 17-2 dealing with *Efficient Spectrum Utilization for Space Science Services*. It did so following a five-year study by the Consultative Committee for Space Data Systems (CCSDS) which examined bandwidth efficiencies of modulation schemes which the Space Agencies were using or considering for use (References 1, 2, 3, 4 and 5). This study was begun in 1992 at the request of the SFCG and contributions were provided by: NASA's Jet Propulsion Laboratory (JPL), NASA's Goddard Space Flight Center (GSFC), European Space Agency's (ESA's) European Space Operations Center (ESOC), New Mexico State University, and the Aerospace Corporation. SFCG Provisional Recommendation 17-2 included a spectrum mask regulating unwanted RF emissions. Following a 1-year provisional status, SFCG-18 adopted Rec. 17-2R1 SFCG-18 (Reference 6). Recommendation 17-2R1 includes the spectrum mask shown in Figure 1.0-1 limiting emissions in the 2 and 8 GHz bands.

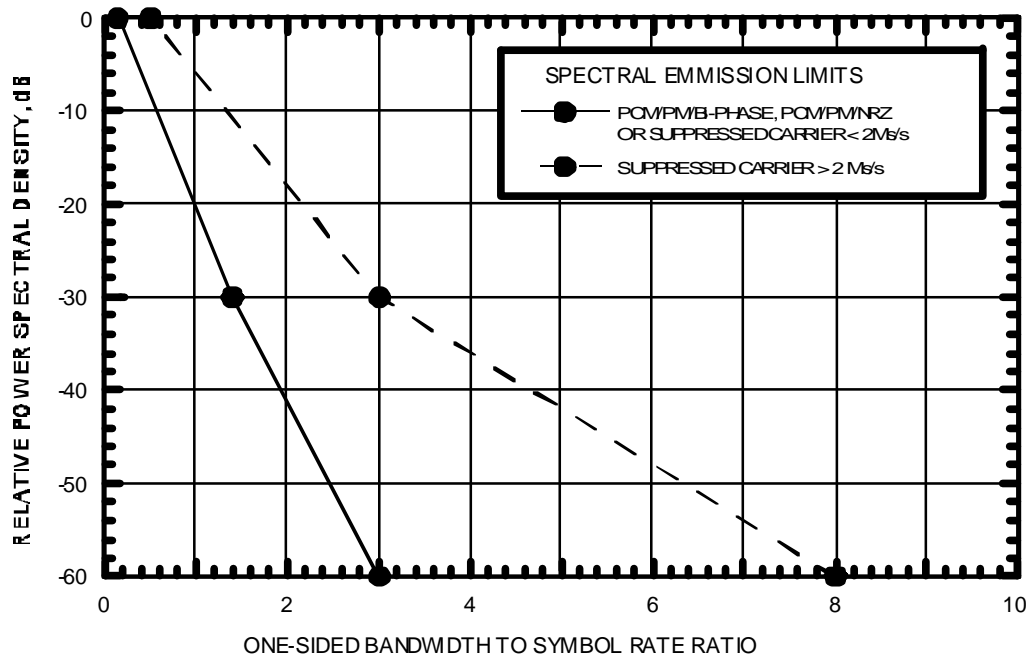


Figure 1.0-1: SFCG Spectrum Mask

This mask partitions missions into two types, those with telemetry data rates greater than 2 Mega symbols per second (Ms/s) and those with rates below 2 Ms/s. The former are constrained to use a suppressed carrier modulation while the latter are permitted to use either suppressed or residual carrier. Spacecraft telemetry systems for missions starting after 2001 should comply with the relevant mask. Some sort of filtering will be required to meet these masks. At SFCG-18, a question arose as to whether narrowing the RF spectral bandwidth will increase the susceptibility to interference. This Phase 4 Efficient Modulation Methods study seeks to determine if that is so.

EFFICIENT MODULATION METHODS - INTERFERENCE SUSCEPTIBILITY

Definition of Interference Susceptibility:

The likelihood that another signal source, operating in the same or other allocated frequency band, will produce an unacceptable degradation to a victim employing bandwidth efficient modulation.

Some SFCG-18 representatives speculated that narrowing the transmitted RF spectrum will increase a modulation type's interference susceptibility. Subsequent to the SFCG's action item, the following Workplan was devised:

"A18-17/2 Workplan: Interference Susceptibility of Bandwidth Efficient Modulation Schemes

The action item consists in determining which is the RFI [Radio Frequency Interference] level that will cause a degradation of 1 dB in link performances. The analysis will be done for two types of radio frequency interferences (RFI):

! A pure carrier (narrow band case)

! A wide band RFI (TBD)

both centred at the useful signal centre frequency and then at 0.5 x symbol rate from the centre frequency.

Modulations to be considered are:

Task 17/2-1: Unfiltered BPSK (benchmark)

Task 17/2-2: GMSK $BT=0.5$

Task 17/2-3: GMSK $BT=1$

Task 17/2-4: OQPSK filtered with a 6-pole Butterworth filter, $BT=1$

Task 17/2-5: OQPSK filtered with a SRRC filter, roll-off factor of 0.5

Task 17/2-6: FQPSK

In all cases, the transmitted signal is passed through a non-linear channel, TWTA with 0 dB backoff.

The report will provide AM/AM and AM/PM characteristics of the TWTA.

It must be noted that the actual performances in the presence of RFI are those of the receiver and may vary a lot with the chosen design. Therefore, the report will also include a description of those features in the receiver design which are influential in RFI susceptibility, e.g., carrier tracking loop, bit synchronizer."

Subsequent Workplan clarification revealed that a Solid State Power Amplifier, not a TWT, should be used in this evaluation. The same amplifier used in Reference 4 was selected for this study.

EFFICIENT MODULATION METHODS - INTERFERENCE SUSCEPTIBILITY

2.0 STUDY DESCRIPTION

Susceptibility to two types of interfering signals was requested by the SFCG: a pure carrier (single frequency tone) and wide-band RFI (characteristics unspecified). Selecting a broad-band interfering signal is difficult because it should represent the types of interference to be found in the space science service bands. Given currently allocated services, such broad-band interference is likely to result from a digitally modulated signal, having a rate of a few megabits per second, and with a power level similar to the victim's. Moreover, the interferer is not likely to employ one of the bandwidth-efficient modulation methods permitting frequency assignments to be made with no spectral overlap between users in their *necessary bandwidths*. Accordingly, the broadband interferer is expected to be something like unfiltered Binary Phase Shift Keyed (BPSK) modulation. That modulation type was used as the broadband interferer for this Phase 4 study.

2.1 Study Approach

This study was based on a dual approach. First, a theoretical analysis was made to determine the modulation type's susceptibility to both narrowband and wideband interference. From this analysis, simulations generated curves showing losses to the victim's received signal resulting from an interferer as its frequency separation from the victim signal changes and its relative power to the victim varies. An analysis was made for each of the modulation types listed in the Workplan.

Where possible, theoretical simulations were verified by simulation of a hardware system. The hardware simulation's sole purpose was to validate the analytical computations by "spot-checking" several points, not to generate complete interference susceptibility curves. Hardware simulations of the Digital Signal Processor (DSP) employ Hardware Description Language (HDL), which has been validated using actual APRX receiver hardware.

2.1.1 Transmitting System

Spectra for the several modulation methods appear in the *CCSDS-SFCG Efficient Modulation Methods Study Phase 3* report (Reference 4). In completing this interference susceptibility analysis, it was desirable to retain the compact spectra measured during that study in order to comply with the spectrum mask contained in SFCG Recommendation 17-2R1. Therefore, an attempt was made to use the same, constant envelope, transmitting system employed in Phase 3.

Phase 3 studies demonstrated that the *Universal Phase Modulator* did well in generating QPSK but poorly with OQPSK. QPSK is not specified in the Workplan and most of the modulation methods identified (OQPSK, GMSK, and FQPSK) require an OQPSK modulator. In Phase 3 it was found that a linear phase modulator, with baseband filtering, produced discrete components within the comparatively narrow RF spectrum. Conversely, baseband filtering with an In-Phase-Quadrature (I-Q) modulator significantly reduced spectral spikes but produced a large amount of Amplitude Modulation (AM) widening the transmitted RF spectrum. Nevertheless, an I-Q phase modulator was determined to be the better choice for Phase 4 (see Section 3.2.1).

EFFICIENT MODULATION METHODS - INTERFERENCE SUSCEPTIBILITY

2.1.1.1 Baseband Filtering

Phase 3 studies concluded that Intermediate Frequency (i.f.) and post power amplifier filtering were impractical for several reasons and such filtering will not be considered further here (Reference 4). There is also a change in the Square Root Raised Cosine (SRRC) filter's design. Phase 3 simulations assumed a spacecraft data system producing an NRZ signal feeding a device approximating an SRRC waveform. This mechanization was selected because the original SFCG study guidelines called for minimum changes to the spacecraft's hardware, mandating an NRZ data source.

A proper system generates an impulse which passes through an SRRC filter producing a true SRRC waveform. While yielding significantly better performance, this method also requires modifications to a spacecraft's data system hardware. Since the Efficient Modulation Methods Study was first begun in the early 1990s, attitudes have changed and hardware modifications are now acceptable. Therefore, this study generates an SRRC filter in the proper manner, significantly improving the system's performance.

2.1.2 Interfering Signal Types

Figure 2.1-1 graphically depicts the different interference types. Consider an FQPSK-B telemetry signal having a spectrum centered at f_c and a width of about $\pm 1 R_B$ at 60 dB below its peak level. The victim's receiver has a matched filter bandwidth corresponding to the transmitted telemetry pulse shape. Additionally, the victim's receiver has a phase-locked-loop whose bandwidth does not vary with signal level. Circled numbers on Figure 2.1-1 identify four interference cases.

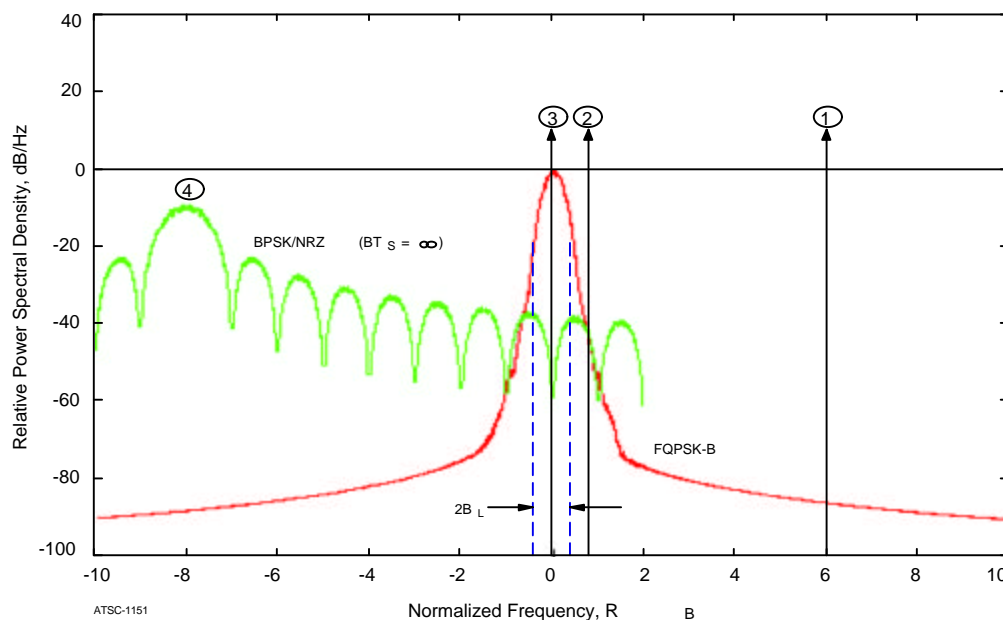


Figure 2.1-1: Interfering Signals

TSC-1151

EFFICIENT MODULATION METHODS - INTERFERENCE SUSCEPTIBILITY

Interference losses are obtained by establishing an initial random phase between the interferer and victim and computing the degradation in E_B/N_0 . One hundred such calculations are made, each with a random initial phase offset, and at the same victim-to-interferer power level. These E_B/N_0 losses are averaged to create a single point. Points are generated for every $0.1 R_B$ offset from f_c . A smooth curve is fitted through these points representing the *average* degradation, or *expected value* of loss, resulting from the two types of interference.

2.1.2.1 Case 1: Narrowband Interference Outside Telemetry Bandwidth

Referring to Figure 2.1-1, Case 1 assumes that signals well outside the main spectral lobe will be substantially attenuated by the receiver's filters. For hardware simulations using the receiver depicted in Figure 2.1-3, a narrowband interferer only affects the receiver's operation if it is of sufficient amplitude to cause non-linear operation (e.g., saturation) of a front-end amplifier whose bandwidth is usually wider than the pre-detection filter. Typically, receiver bandwidths progressively narrow as the signal proceeds through the various i.f. amplifiers.

As the interferer's frequency is moved from a frequency far from f_c toward f_c , it eventually falls within the Low Noise Amplifier's (LNA's) bandwidth. If the interferer's level is sufficient, gain compression can result diminishing amplification of the desired signal. Even if the LNA's amplification does not decrease, the interfering signal's amplitude may be increased by the AGC amplifier's gain following the LNA.

Gains and bandpass filter widths are unique to every receiver and it is impractical to consider all combinations. Given a specific receiver design, out-of-band emissions produce substantially the same effect, whatever modulation method is used.

Case 1 need not be considered further because the receiver's behavior is independent of the modulation type used and the purpose of this study is to compare interference susceptibility of efficient modulation schemes. Items common to all modulation types need not be investigated.

2.1.2.2 Case 2: Narrowband Interference In Telemetry Bandwidth Far From f_c

In this case, the interferer is sufficiently far from the desired signal's center frequency (f_c) so that the receiver filter's roll-off serves as a weighting function attenuating the interfering signal in the same way that noise is reduced. For similar total power levels of desired signal (P_S) and interfering signal (P_I) (i.e., $P_S \approx P_I$), a signal inside the *matched filter's* bandwidth, but comparatively far from f_c , has only a small effect on system's performance.

The amount of the degradation to the desired data signal (S_D) is proportional to power remaining in the interfering signal (P_{TI}), after attenuation by the receiver filter's roll-off characteristic, compared to the total power in the desired signal (P_{TS}) (i.e., $S_D \propto P_{TI} / P_{TS}$).

EFFICIENT MODULATION METHODS - INTERFERENCE SUSCEPTIBILITY

2.1.2.3 Case 3: Narrowband Interference In Telemetry Bandwidth and Close to f_c

Initially, it was postulated that all losses described in Case 2 are present together with an additional loss due to additional losses in the receiver's phase-locked-loop. Since the receiver's Costas Loop reconstructs a *carrier* component at f_c , it was believed that the interfering signal would cause phase jitter in the reconstructed carrier.

Costas Loop losses, due to narrowband interference, were evaluated at three locations: at f_c , within the Costas Loop's bandwidth (at $0.0005 \times$ data rate), and outside the Costas Loop's bandwidth but within the *matched filter's* bandwidth (at $0.008 \times$ data rate). Figure 2.1-2 resulted from simulations made using the receiver in Figure 2.1-3. This figure shows Costas Loop phase jitter losses to be substantially independent of the interfering signal's location but very much a function of the interference-to-signal power ratio.

Although initially surprising, this result could have been anticipated considering the mechanization of a Costas Loop. A reconstructed carrier is generated by controlling an oscillator's phase using an error signal derived from orthogonal I-Q channels. Since the transmitted RF spectrum is generated entirely by the data, it is not surprising that an interfering signal lying anywhere within the *matched filter's* bandwidth affects the loop's performance. The amount of performance degradation depends upon the frequency separation between victim and interferer and the matched filter's roll-off characteristics. The same *matched filter* weighting factor argument, affecting interference susceptibility in Case 2 above, applies here.

Case 2 and Case 3 are combined in this study. A high Costas Loop SNR is assured by the relative small Costas Loop-Data bandwidth.

2.1.2.4 Case 4: Wideband Interference In Telemetry Bandwidth and Around f_c

Wideband interference works in the same ways described above but with the distinction that it arises in all three locations simultaneously. The extent to which it degrades the receiver's performance is determined by:

- ! The characteristics of the interfering signal (i.e., power spectral density).
- ! The ratio of interfering signal power (P_i) within the receiver filter's bandwidth, considering its roll-off characteristics, to the desired signal's power (P_s) in the same bandwidth.

Susceptibility to wideband interference was determined by centering an unfiltered BPSK interferer, having an equal power to the victim's, far from the victim's center frequency (f_c). The interferer's center frequency is then shifted towards (f_c) so that progressively more of the interferer's signal falls into the victim's bandwidth.

EFFICIENT MODULATION METHODS - INTERFERENCE SUSCEPTIBILITY

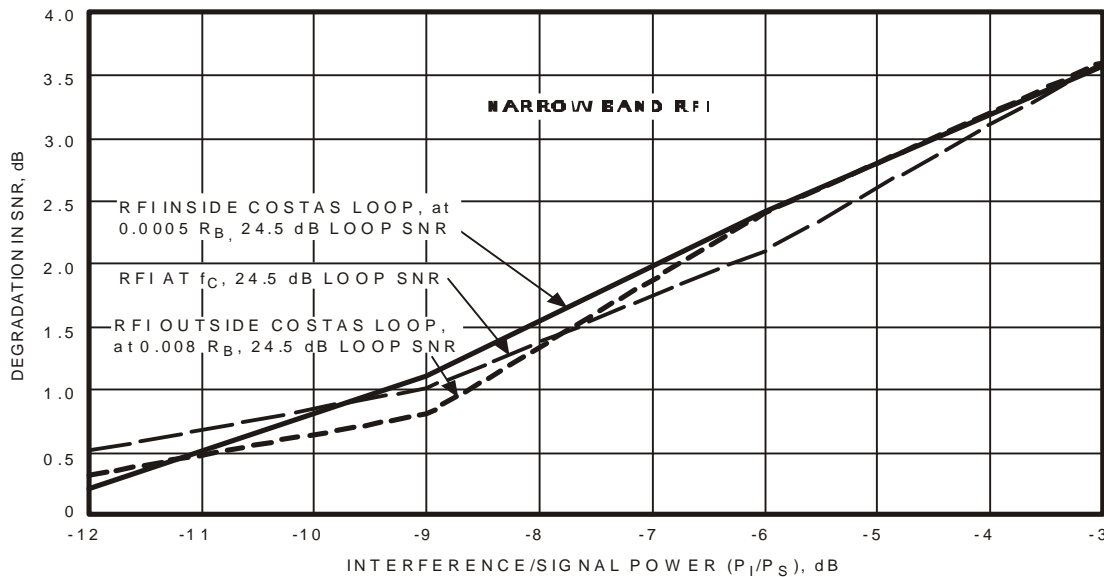


Figure 2.1-2: Costas Loop Narrowband Interference Susceptibility (Hardware)

2.1.3 Receiver Design

The Workplan raises specific questions regarding the receiver's performance in the presence of interference. Degradation due to interference need only be considered in the presence of a receiver. Absent a receiver there will be no interference. How interference affects a receiver depends upon the receiver's design and the position of the interference with respect to the center frequency of the victim signal.

For purposes of this hardware validation, the receiver Phase-Locked-Loop's (PLL's) bandwidth was selected to provide a high Signal-to-Noise-Ratio (SNR) of approximately 25 dB. The telemetry channel employed a Finite Impulse Response (FIR) filter to match the modulated spectrum. For consistency with the Phase 3 study, and for the reasons set forth in Reference 4, all losses were evaluated at a 1×10^{-3} Bit-Error-Rate (BER).

Figure 2.1-3 is a simplified block diagram of the receiver used in the hardware simulations. Named the APRX, it was designed for the EOS AM-1 mission and supports data rates up to 600 Mb/s. Evaluating how interference affects receiver performance requires examining several of its elements. Relevant components will be examined in the sections below discussing different interference types and modulation methods.

EFFICIENT MODULATION METHODS - INTERFERENCE SUSCEPTIBILITY

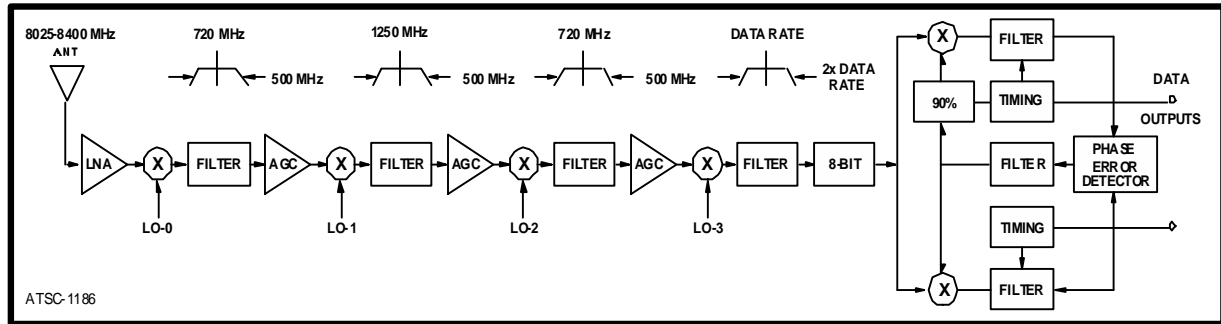


Figure 2.1-3: Simulated EOS AM-1 Receiver (APRX)

In Figure 2.1-3, adjusting the Local Oscillator (LO) frequencies (e.g., LO-0, -1, and -2) shifts the received signal's frequency to first an upper and then a lower filter band edge. Successive filter/amplifier pairs produce a result equivalent to a single pre-detection bandpass filter. Such a design permits fixed bandwidth filters to be used in a receiver which must handle a variety of data rates. A distributed automatic gain control function ensures sufficient signal amplitude while avoiding amplifier saturation. The digital portion of this receiver contains a Costas Loop and a Symbol Tracking Loop capable of handling both BPSK, QPSK, and OQPSK signals.

Unlike the theoretical analysis, the APRX receiver implements an adjustable post detection filter in the digital signal processor limiting the spectrum to the main lobe. This digital detection (*matched*) filter in the APRX is created by the average time-reversed pulse shape of the received waveform. The pulse shapes of approximately 1,000 random bit-times are time-domain averaged. The waveform is then zero-padded and passed through a discrete-time Fourier transform. Frequency domain detection coefficients are programmed into the APRX. These filters remain unchanged for all simulations, irrespective of the modulation type being evaluated.

2.1.4 Theoretical Calculations vs Hardware Simulations

All interference susceptibility calculations are made using a theoretical model. Computations are based on a baseband filter, a lossless I-Q modulator (see Section 2.1.1), ESA's Solid State Power Amplifier (SSPA) operating in full saturation (Reference 4), a lossless receiver having a "matched" filter, and perfect synchronization of both the carrier and symbol tracking loops. Computed interference susceptibility plots have the word (*Theory*) in their title.

Hardware simulations modeled the same transmitting subsystem described above but substituted a simulation model of the receiver (APRX) shown in Figure 2.1-3 for the perfect device used in the theoretical calculations. Synchronization losses are included. Hardware simulations are included, where possible to: 1) validate the theoretical calculations and 2) provide a more realistic measure of system performance with real hardware. All interference susceptibility plots in Section 3 are based on either theoretical calculations, the hardware simulations, or preferably both methods. Plots based on simulations with perfect synchronization are labeled *Theory* while those employing the APRX are marked *Hardware*.

EFFICIENT MODULATION METHODS - INTERFERENCE SUSCEPTIBILITY

2.1.5 Matched Filter

A properly designed *matched filter* optimizes the received signal-to-noise ratio by replicating the pulse shape of the transmitted signal. It attenuates (weights) an interfering signal in the same way that it reduces noise. Absent significant spectral spreading by the SSPA, all of the energy contained in the received spectrum will be recovered while admitting only the minimum amount of noise.

In Phase 4, the focus is on a receiver's interference susceptibility. Consider a congested frequency band, such as 2 GHz, where the likelihood of encountering interference is comparatively high. One can trade power-transfer-efficiency for interference immunity. This is best illustrated with an example.

The *Occupied Bandwidth* (99% power containment) of an unfiltered BPSK/NRZ signal is approximately $\pm 10 R_B$. However, 90% of the same signal is contained in only $\pm 1 R_B$. A receiver filter with a $\pm 10 R_B$ bandwidth will recover virtually all of the received energy in the *occupied bandwidth* but it will also have some interference susceptibility over a span of at least $\pm 10 R_B$.

If the receiver filter's bandwidth is reduced from $\pm 10 R_B$ to $\pm 1 R_B$, then approximately 0.45 dB of the received energy will be lost but the receiver's interference immunity will be increased so that an interfering signal lying between ± 1 and $\pm 10 R_B$ will be significantly attenuated. For equivalent roll-off characteristics, the interference immunity is increased several fold. System losses will result from the discarded received signal energy and an increase in Inter-Symbol Interference (ISI).

Absent low noise and/or i.f. amplifier saturation or gain compression resulting from an interfering signal, a receiver's performance in the presence of an interfering signal is determined entirely by its filters.

EFFICIENT MODULATION METHODS - INTERFERENCE SUSCEPTIBILITY

3.0 STUDY RESULTS

This section summarizes the results found during the *CCSDS-SFCG Efficient Modulation Methods Study at JPL, Phase 4: Interference Susceptibility*. In evaluating filtered OQPSK, the Workplan specifies a 6-pole Butterworth ($BT_s = 1.0$) and a Square Root Raised Cosine (SRRC, $\alpha = 0.5$) bandpass filters. JPL's *Efficient Modulation Methods Study: Phase 3* (Reference 4), addressed only baseband filtering, and utilized 3RD order Butterworth ($BT_s = 2$) and SRRC ($\alpha = 1.0$) low-pass filters. A Butterworth ($BT_s = 2$) filter was selected because losses with a $BT_s = 1$ filter were nearly 3 dB, when using the constant amplitude *Universal Phase Modulator*, well above the 1 dB SFCG guideline. OQPSK losses were even higher and both were deemed unacceptable. Phase 4 employs an I-Q modulator (see Section 2.1.1 above and Section 3.2.1 below). End-to-end losses with the requested filters are evaluated in Section 3.2.1.

Phase 4 investigated the following modulation types:

1. Unfiltered BPSK (Reference Case)
2. OQPSK using a 3RD order Butterworth low-pass filter ($BT_s = 1$)
3. OQPSK using an SSRC low-pass filter ($\alpha = 0.5$)
4. GMSK ($BT_s = 1.0$)
5. GMSK ($BT_s = 0.5$)
6. FQPSK-B
7. Direct Sequence Spread Spectrum / BPSK

The latter modulation type was included because some SFCG representatives speculated that spread spectrum communications are largely immune to interference and may be even more bandwidth efficient than those studied during Phase 3. Their inclusion in this study was an effort to place spread spectrum modulation in their proper perspective with respect to the other types.

3.1 Unfiltered BPSK (Reference Case)

Figure 3.1-1 is the spectrum of an unfiltered BPSK-NRZ signal. It is identical to the one found in Figure 3.4-2 in Reference 4. This spectrum is representative of an unfiltered BPSK signal after amplification by an SSPA operating in full saturation. Clearly, unfiltered BPSK cannot meet the requirements of either spectrum mask shown in Figure 1.0-1.

Figure 3.1-2a shows the degradation to an unfiltered BPSK signal from the first three cases of narrowband interference. Figure 3.1-2b depicts losses from Case 4, wideband interference, described in Section 2.1.2.4 (see Figure 2.2-1). These plots are based on a matched filter receiver. Data channel losses are plotted as a function of the interfering signal's distance (in R_b) from the victim signal's center frequency, f_c . Different power ratios for Interferer-to-Victim Signal (P_i/P_s) are shown. Note the similarity in the BPSK-NRZ modulation frequency spectrum in Figure 3.1-1 and the data loss in Figure 3.1-2a. For a properly designed matched filter, the narrowband interference susceptibility relationship is similar to the transmitted spectrum plot.

EFFICIENT MODULATION METHODS - INTERFERENCE SUSCEPTIBILITY

Note:

The “Degradation in E_b/N_0 ” curves in this section are concerned solely with losses due to interfering signals. A degradation of 0 dB means that there is no loss due to the interfering signal. Typical end-to-end losses for the modulation type still apply.

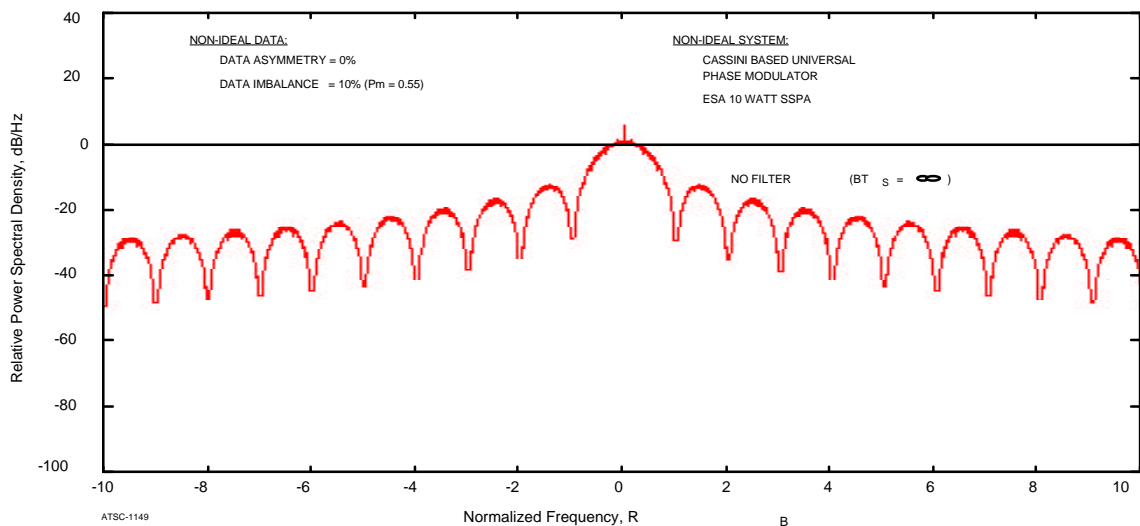


Figure 3.1-1: Unfiltered BPSK Spectrum

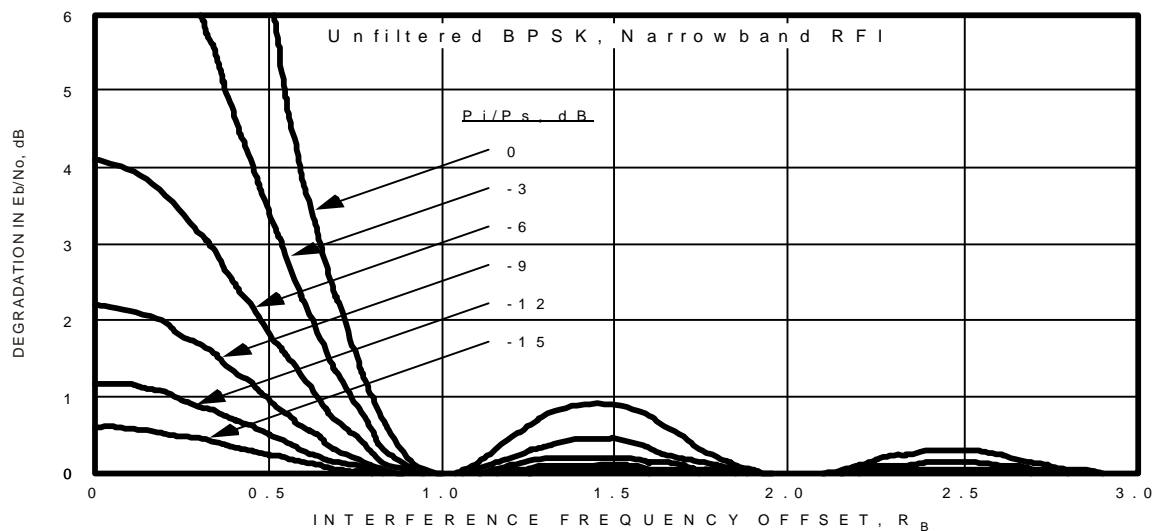


Figure 3.1-2a: Unfiltered BPSK Susceptibility to Narrowband Interference (Theory)

EFFICIENT MODULATION METHODS - INTERFERENCE SUSCEPTIBILITY

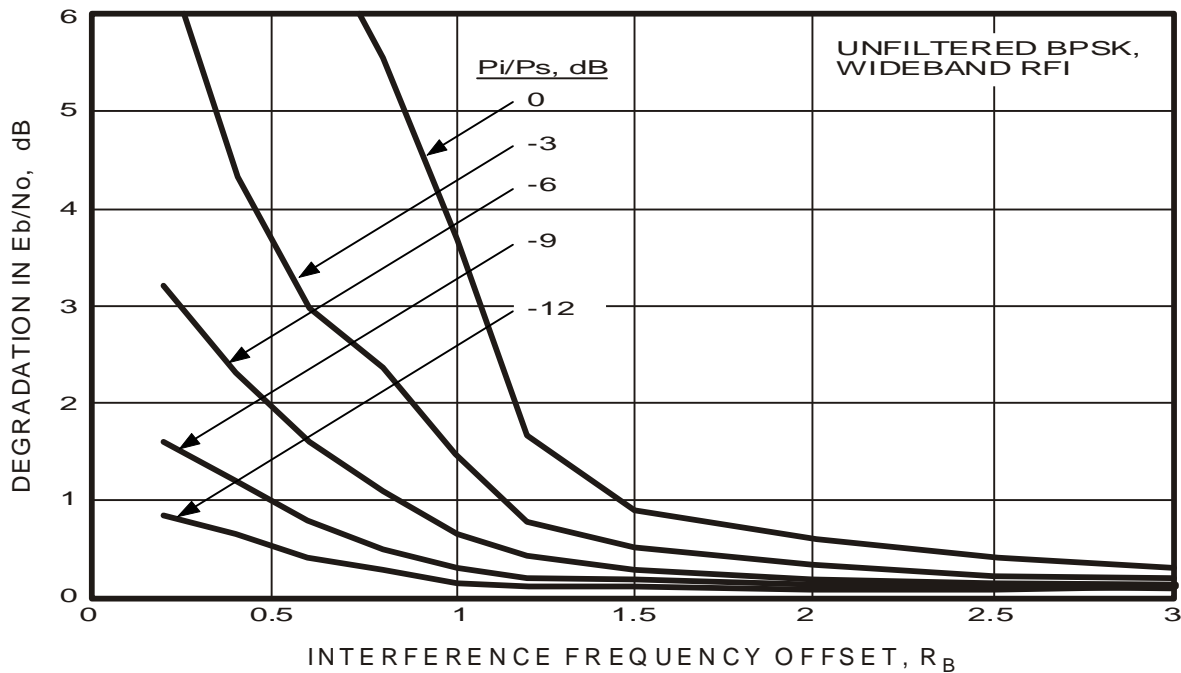


Figure 3.1-2b: Unfiltered BPSK Susceptibility to Wideband Interference (Theory)

First Finding:

To a first order, the receiver's matched filter's characteristics completely determine a modulation method's interference sensitivity function, whether that interference is in-band or out-of-band.

A *matched filter's* characteristics should correspond to the transmitted pulse shape. Consider a victim spacecraft using BPSK modulation at a 2 Msps data rate operating in the 2200-2290 MHz band. Assume further that the victim's antenna is aligned with an interferer transmitting an unmodulated carrier with a power equal to the victim's on a channel 5 MHz away. Figure 3.1-2a shows that the victim's receiver experiences a loss of approximately 0.5 dB.

If the *matched filter's* bandwidth is restricted to $\pm 1 R_B$, it is no longer matched to the transmitted signal and only about 90% of the received signal power is admitted producing a loss of approximately 0.45 dB. But, reducing the bandwidth also substantially eliminates the receiver's interference susceptibility beyond $\pm 1 R_B$. Whether this is a useful tradeoff depends upon the interference environment (density, relative signal strength, etc.).

Second Finding:

To minimize interference susceptibility, a matched filter's bandwidth should be as narrow as possible after accounting for the minimum acceptable power transfer, and the maximum acceptable ISI.

EFFICIENT MODULATION METHODS - INTERFERENCE SUSCEPTIBILITY

Unfiltered BPSK's susceptibility to wideband interference is both different from, yet similar to, that for narrowband interference. Wideband interference susceptibility curves differ from those for narrowband interference which has a shape similar to the RF spectrum. That is expected, since the interfering signal is spread over a wide range of frequencies. The similarity lies in the losses outside the main spectral lobe. For a wideband interferer and victim having equal power, separated in center frequency by $\pm 2.5 R_B$, the victim experiences losses of about 0.5 dB, the same as for the narrowband case. Likewise, for separations of $\pm 1.5 R_B$, there is approximately 1 dB loss in both cases.

Figures 3.1-2a and 3.1-2b are based upon theoretical calculations for unfiltered BPSK and show the losses resulting from both narrowband and wideband interference. For readers skeptical of such methods, actual data was obtained from an operating system in JPL's Telecommunications Development Laboratory (TDL). The configuration consisted of a Pseudo-Noise (PN) sequence, modulated as an unfiltered BPSK signal in a test transponder, transmitted and being captured by a DSN Block V receiver (the receiver found at DSN stations). A tone (CW) signal (interferer), having the same power as the victim, was injected into the Block V receiver at various frequency offsets. The Bit-Error-Rate (BER) performance for the victim is shown in Figure 3.1-3. Good agreement (0.25 dB) was found when comparing the results from the two methods.

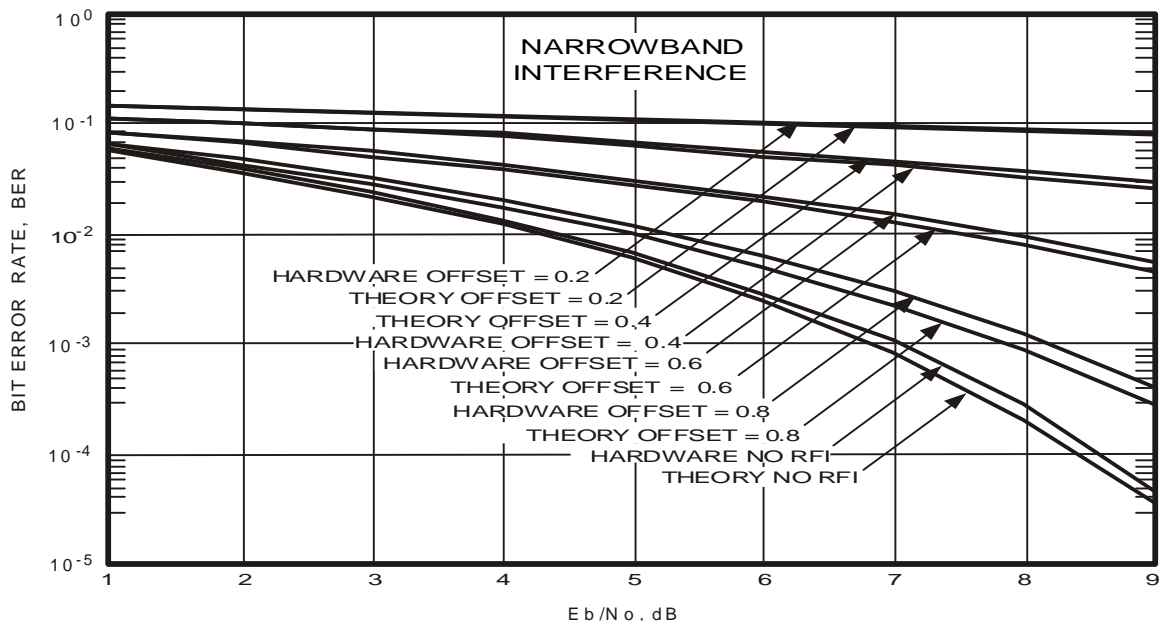


Figure 3.1-3: Theoretical vs Actual Losses to an Unfiltered BPSK Victim

Using the $0.8 R_B$ interferer offset curve in Figure 3.1-3, a BER of 1×10^{-3} (baseline BER for Phase 3) requires an E_B/N_0 of about 8 dB. Comparing with the *No RFI* curve shows that there is approximately a 1 dB loss due to a narrowband interferer, having equal power, $0.8 R_B$ away. Essentially the same value appears in Figure 3.1-2a for the loss at $0.8 R_B$, demonstrating that the theoretical calculations match actual hardware measurements.

EFFICIENT MODULATION METHODS - INTERFERENCE SUSCEPTIBILITY

3.2 Filtered OQPSK

Figure 3.2-1 contains frequency spectra for Offset QPSK (OQPSK) modulation using a baseband SRRC filter ($\alpha = 0.5$), an I-Q modulator (see Section 2.1.1), and ESA's SSPA operating in full saturation. The large Amplitude Modulation (AM) component found in I-Q modulators with baseband filtering eliminates spectral spikes. Bumps in the spectrum result from a 64-tap Finite Impulse Response (FIR) filter in the transmitter. The spectrum appears to satisfy SFCG mask requirements. Note the reduced sidelobes in Figure 3.2-1 as compared to the reference case (Figure 3.1-1).

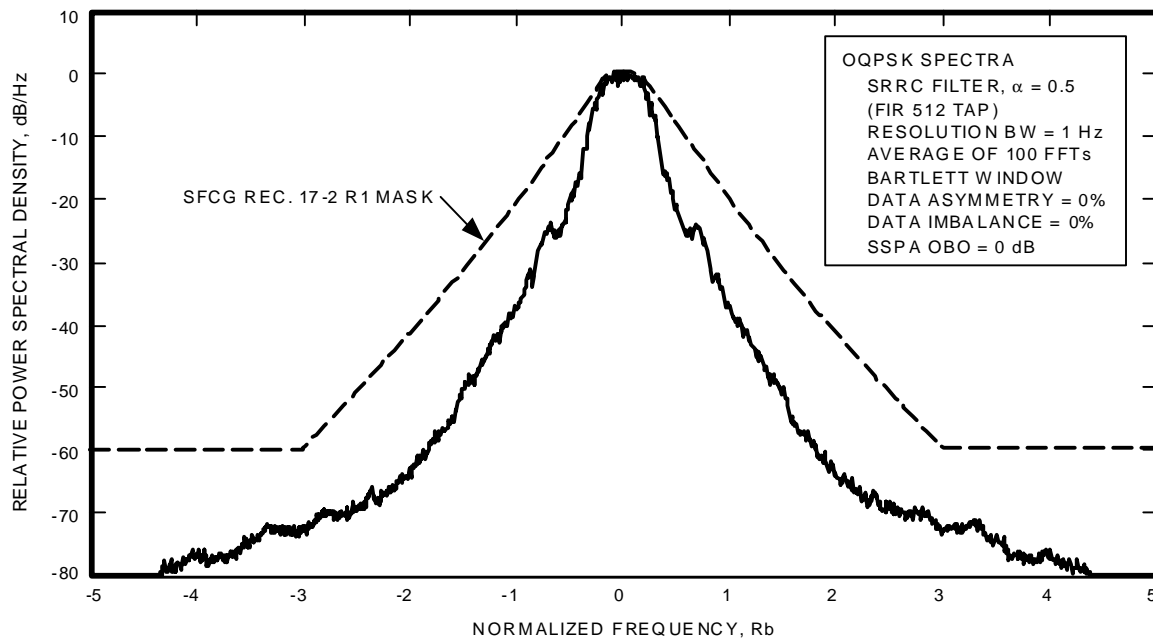


Figure 3.2-1: OQPSK Modulation Spectra with SRRC Filter ($\alpha = 0.5$)

Section 2.1.1.1 described the proper method for generating an SRRC waveform. The RF spectrum shown in Figure 3.2-1 is the product of a correctly generated SRRC waveform and the I-Q modulator described in Section 2.1.1. Spectral spreading, due to the AM component in the I-Q modulator, is clearly evident in Figure 3.2-1.

OQPSK's susceptibility to narrowband interference with Butterworth ($BT_s = 1$) and SRRC ($\alpha = 0.5$) baseband filters is shown in Figures 3.2-2a, 3.2-2b, and 3.2-3. Compared to the susceptibility of the unfiltered BPSK-NRZ reference, it is clear that the interfering signal must be much closer to the desired signal's center frequency, f_c , before significant degradation occurs. With a narrowband interferer of equal power to the victim, unfiltered BPSK suffers degradations of 0.5 and 1 dB at $f_c \pm 2.5 R_B$ and $\pm 1.5 R_B$ respectively, whereas OQPSK, with a Butterworth filter ($BT_s = 1$), only reaches these same levels at $f_c \pm 0.5 R_B$ and $\pm 0.45 R_B$.

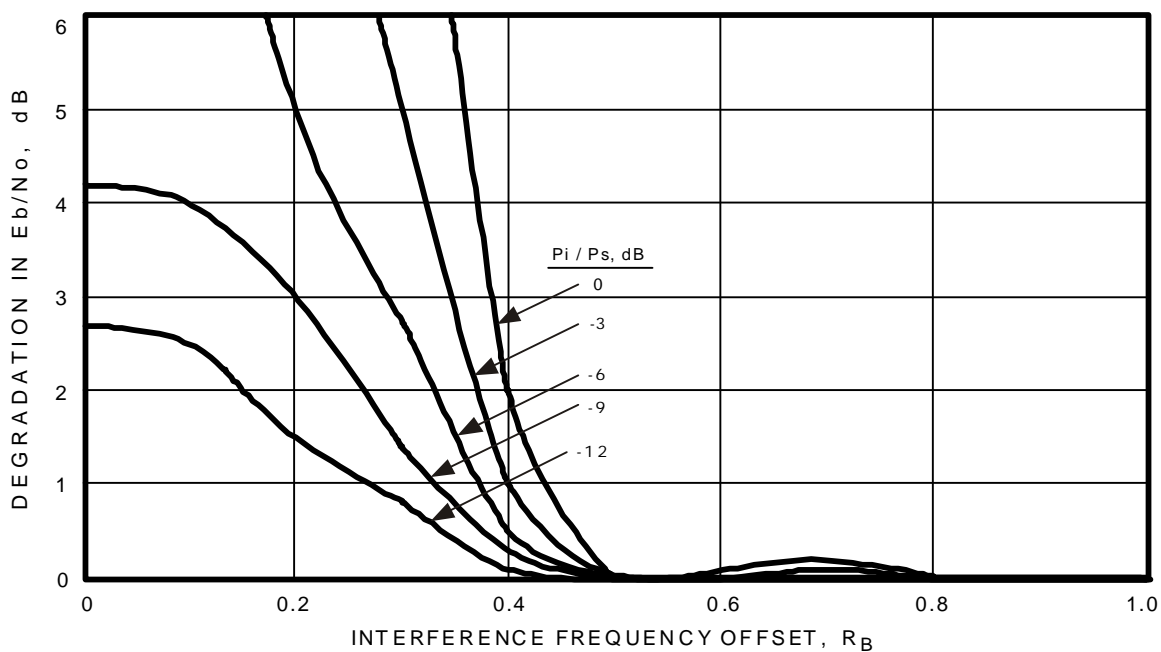
EFFICIENT MODULATION METHODS - INTERFERENCE SUSCEPTIBILITY

Figure 3.2-2a:
OQPSK (Butterworth, $BT_s = 1$) Susceptibility to Narrowband Interference (Theory)

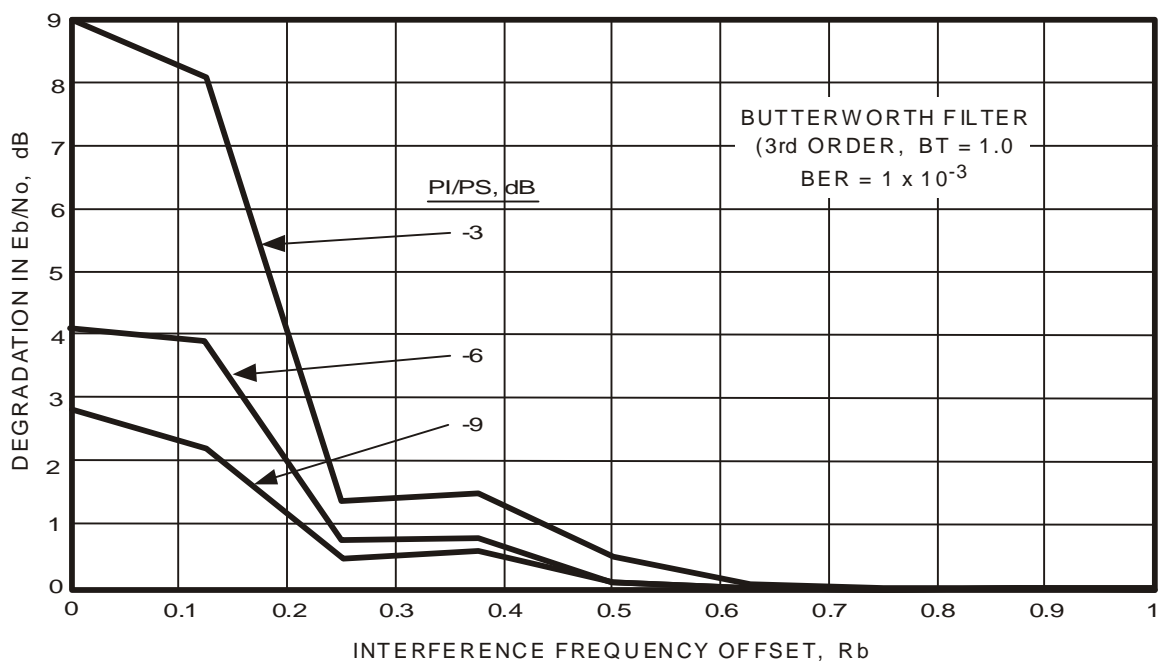


Figure 3.2-2b:
OQPSK (Butterworth, $BT_s = 1$) Susceptibility to Narrowband Interference (Hardware)

EFFICIENT MODULATION METHODS - INTERFERENCE SUSCEPTIBILITY

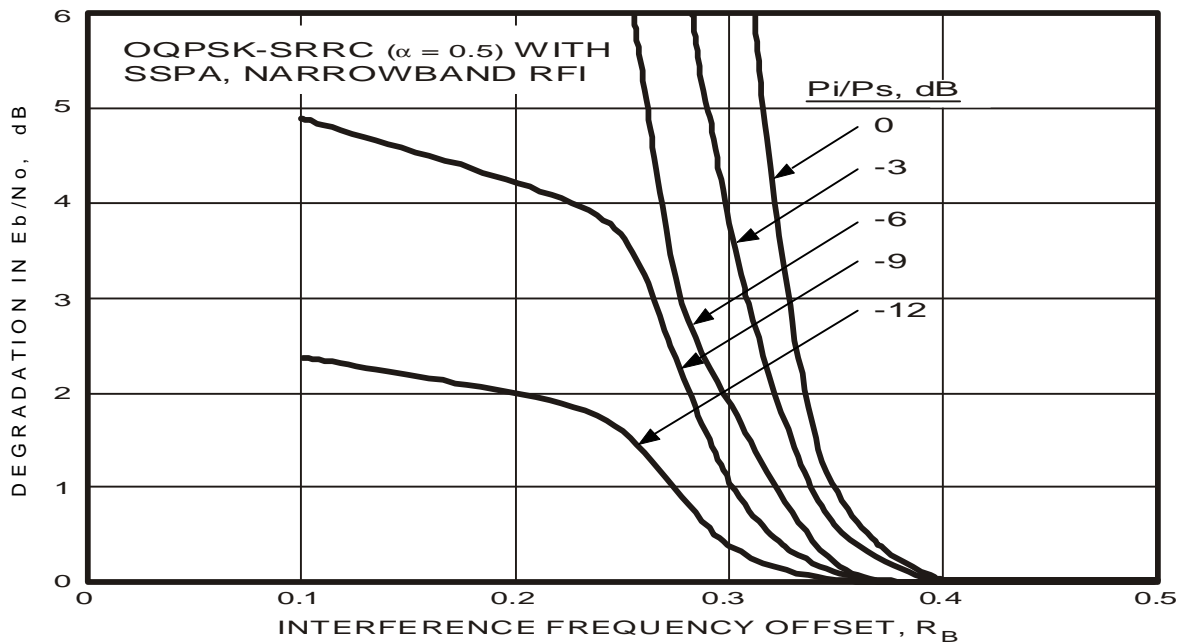


Figure 3.2-3:
OQPSK (SRRC, $\alpha = 0.5$) Susceptibility to Narrowband Interference (Theory)

Substituting a baseband SRRC filter ($\alpha = 0.5$) for the Butterworth reduces interference susceptibility even further. Now, losses of 0.5 and 1 dB occur at approximately $f_c \pm 0.37 R_B$ and $\pm 0.35 R_B$ respectively. These results follow from the facts that:

1. OQPSK's spectrum is more compact than BPSK so the *necessary bandwidth* is reduced.
2. Baseband filtering rapidly attenuates spectral sidelobes with the result that they are outside the *necessary bandwidth* and significant interference will not occur.

Third Finding:

When comparing interference susceptibility of different modulation methods, those with more compact spectra have more interference immunity than modulation types requiring larger bandwidths, provided that the receiver has a properly designed matched filter and the spectral width remains narrower at all levels.

This finding is contrary to the popular belief that the more compact a modulation spectra, the more susceptible it will be to interference. This erroneous idea can probably be traced to the notion that spread spectrum modulation has a high degree of interference immunity because its signal is spread over such a large frequency band that a narrowband interferer has an insignificant effect.

EFFICIENT MODULATION METHODS - INTERFERENCE SUSCEPTIBILITY

That generalization is incorrect because the processes of spread spectrum and bandwidth efficient modulation are entirely different. In spread spectrum modulation, a PN code, having a chip rate much greater than the data rate (100 to 1,000 times), is mixed with the data to spread the transmitted spectra over a broad range of frequencies (100 to 1,000 times the original bandwidth). At the receiver, a local model of the PN code is cross-correlated with the received signal to de-convolve the spectrum into that of the original data. This cross-correlation process causes the narrowband interference to be spread over a broad range of frequencies with the result that it no longer has significant power within the data bandwidth.

Conversely, bandwidth efficient modulation simply uses the power that would have been spread over a larger range of frequencies and concentrates that same transmitted power in a smaller bandwidth. When this occurs two things happen:

Corollary 1 to Third Finding:

The power spectral density of a bandwidth efficient modulated signal is increased with respect to a non-baseband filtered modulation, reducing its susceptibility to a narrowband interferer having the same total transmitting power.

and

Corollary 2 to Third Finding:

If the receiver has a properly designed matched filter, there will be virtually no susceptibility to interference lying outside its bandwidth. Therefore, a narrowband interferer, occurring within the victim's allocated frequency band, has a lower probability of falling within the victim's bandwidth.

Figure 3.2-4 depicts the susceptibility of OQPSK modulation with an SRRC ($\alpha = 0.5$) filter to wideband interference based on a theoretical analysis. Like those for the narrowband interference, degradation in E_B/N_0 is plotted as a function of interferer-victim separation. Seven points were computed and fitted with the curve shown in Figure 3.2-4. As with the other curves in this report, losses were measured at a BER of 1×10^{-3} corresponding to an E_B/N_0 of 8 dB.

Comparing Figures 3.2-3 with 3.2-4 it is clear that a SRRC filtered OQPSK receiver is more susceptible to a wideband interferer of equal power than to narrowband interference at the same power. A wideband interferer produces a 1 dB degradation at $0.9 R_B$, whereas that same loss occurs at $0.35 R_B$ when the interference is from a narrowband source. Why that is so becomes clear when one inspects Figure 3.1-1 showing the spectrum for an unfiltered BPSK signal. The interferer's main spectral lobe overlaps the victim's main spectral lobe so that there will be energy at the victim's f_C . Limiting the degradation to 0.5 dB requires the interferer's center frequency to be at least $1 R_B$ from the victim's.

EFFICIENT MODULATION METHODS - INTERFERENCE SUSCEPTIBILITY

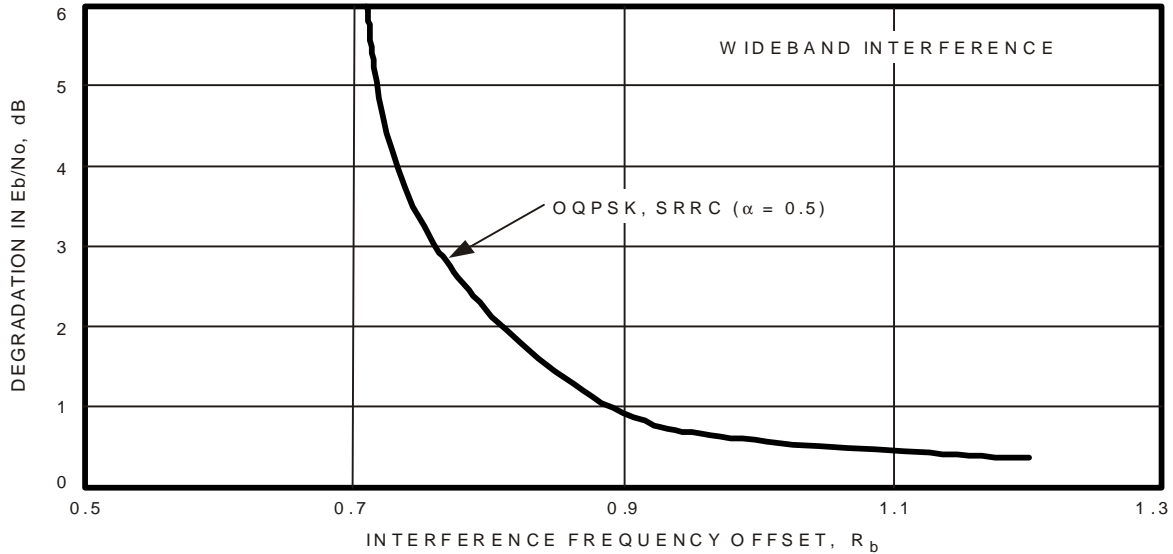


Figure 3.2-4: OQPSK (SRRC, $\alpha = 0.5$) Susceptibility to Wideband Interference (Theory)

3.2.1 OQPSK Bit-Error-Rate With An I-Q Modulator

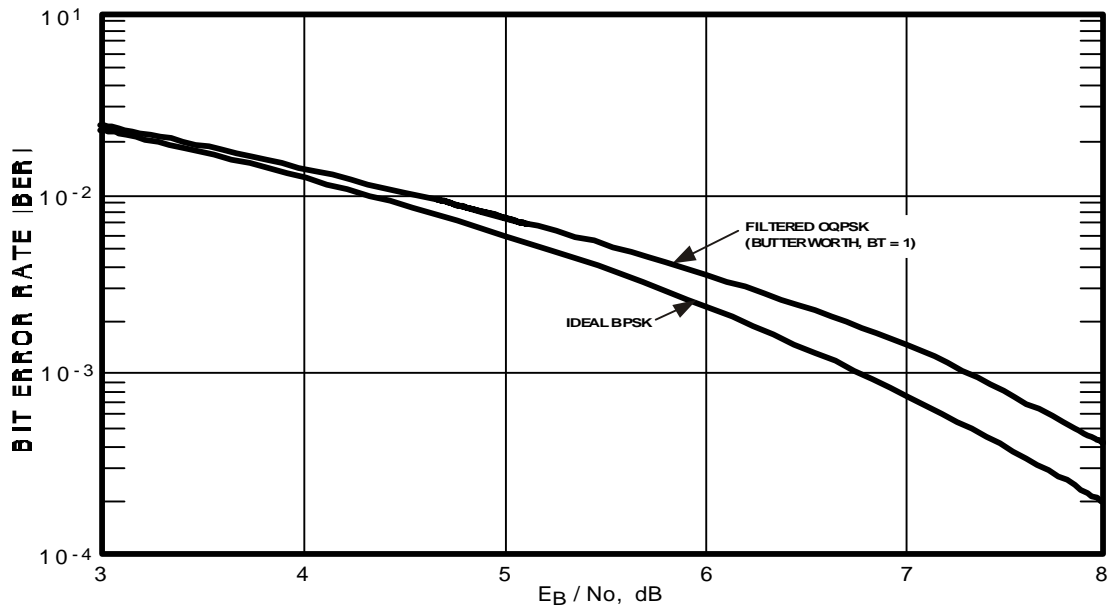
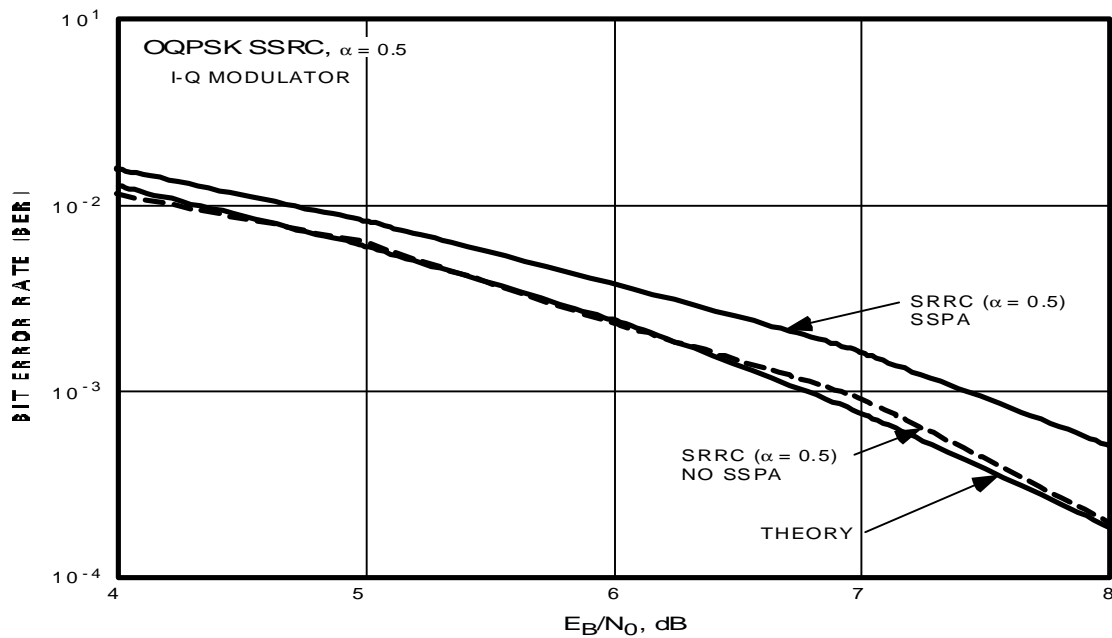
Phase 3 studies demonstrated that the *Universal Phase Modulator* was unsuitable for OQPSK. Phase 4 utilized an I-Q modulator. There was suspicion that this change may have rendered the OQPSK BER measurements in Phase 3 invalid. Therefore, a study was undertaken to reevaluate losses with the specified configuration.

Since the bandwidths of both filters were changed from the values used in Phase 3, new BER curves were generated for a system containing an I-Q modulator and both baseband 3-pole Butterworth ($BT_s = 1$) and SRRC ($\alpha = 0.5$) filters. As before, losses were evaluated at a $BER = 1 \times 10^{-3}$ ensuring virtually error-free channel performance with the CCSDS concatenated code.

Figures 3.2-5a and 3.2-5b depict BER as a function of the received E_b/N_0 for Butterworth ($BT_s = 1$) and SRRC ($\alpha = 0.5$) filters respectively when used in a transmitting system containing an ideal I-Q modulator. An ideal modulator has perfect amplitude and phase balance between the I and Q channels. CCSDS Recommendations 401 (2.4.14a) B-1 and 401 (2.4.14b) B-1 specify a maximum amplitude imbalance of 0.2 dB and a maximum phase imbalance of 2 degrees for an OQPSK modulator. If these *worst case* conditions occur, the degradation in E_b/N_0 will be about 0.8 dB at a $BER = 1 \times 10^{-3}$.

Both Butterworth and SRRC filters produce losses of about 0.6 dB, considerably lower than those found in the Phase 3 study. However, the Phase 3 study included filtering and synchronization losses which are not considered in the Phase 4 study.

EFFICIENT MODULATION METHODS - INTERFERENCE SUSCEPTIBILITY

Figure 3.2-5a: OQPSK BER with Butterworth ($BT = 1$) Baseband FilterFigure 3.2-5b: OQPSK BER with SRRC ($\alpha = 0.5$) Baseband Filter

EFFICIENT MODULATION METHODS - INTERFERENCE SUSCEPTIBILITY

During the Phase 3 study, it was found that end-to-end losses and RF spectrum width are inversely related. The narrowest RF spectrum width was obtained with constant envelope modulation. The Universal Phase Modulator, a linear analog device, has a relatively flat amplitude vs phase shift characteristic producing a very compact RF spectrum. However, the end-to-end losses were found to be ≥ 3 dB for Butterworth ($BT_s = 1$) and SRRC ($\alpha = 1$) filters.

Conversely, I-Q modulators with baseband filtering have significant AM because the phase shift is generated by adding the amplitudes of two signals differing in phase by 90 degrees. With a squarewave input, each leg is either ± 1 at all times. However, narrowband ($BT_s = 1$ or $\alpha = 0.5$) baseband filtering produces a constantly varying amplitude in both legs of the modulator. When multiplied, the result also varies in amplitude. A signal with a large AM component amplified by a non-linear device (SSPA) produces sideband re-growth and the transmitted spectrum is widened. For this reason I-Q modulators were not used in the Phase 3 study.

Spectral broadening at levels lower than 20 dB below the peak can be observed in Figure 3.2-1 which was produced using a SRRC ($\alpha = 0.5$) filter. Broadening is the result of the non-constant envelope modulation and a fully saturated power amplifier. The resulting spectrum appears to comply with the SFCG mask at all levels. ESA's study (Reference 5) places a simple Butterworth ($BT_s = 1.2$) filter at both an intermediate frequency (i.f.) and after power amplification. Their study showed that this configuration also meets the SFCG mask requirements.

EFFICIENT MODULATION METHODS - INTERFERENCE SUSCEPTIBILITY

3.3 GMSK

Gaussian Minimum Shift Keying (GMSK) is widely used in Personal Communications Systems (PCS). However, the characteristics of a PCS system differ from those needed in a *space sciences* application. Generally, PCS are characterized by strong signals which can tolerate relatively large end-to-end losses. The inverse is true for most space missions.

During the Phase 3 *Efficient Modulation Methods Study*, GMSK was found to be one of two modulation types that was significantly more bandwidth efficient than the others. Systems using GMSK were determined to have no difficulty in complying with the SFCG mask.

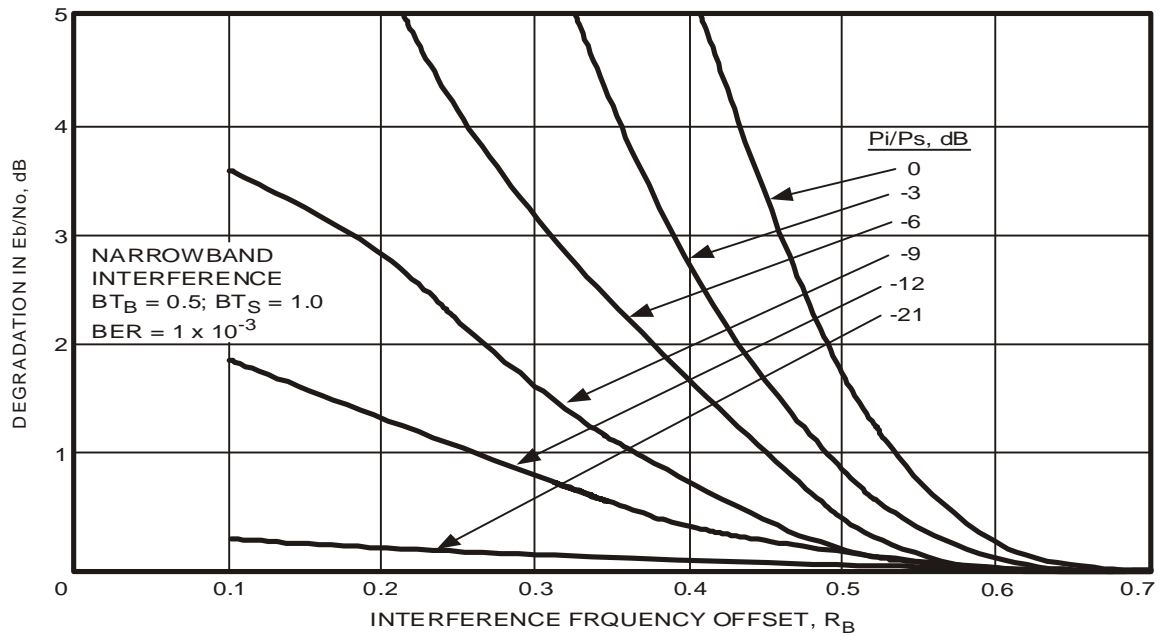
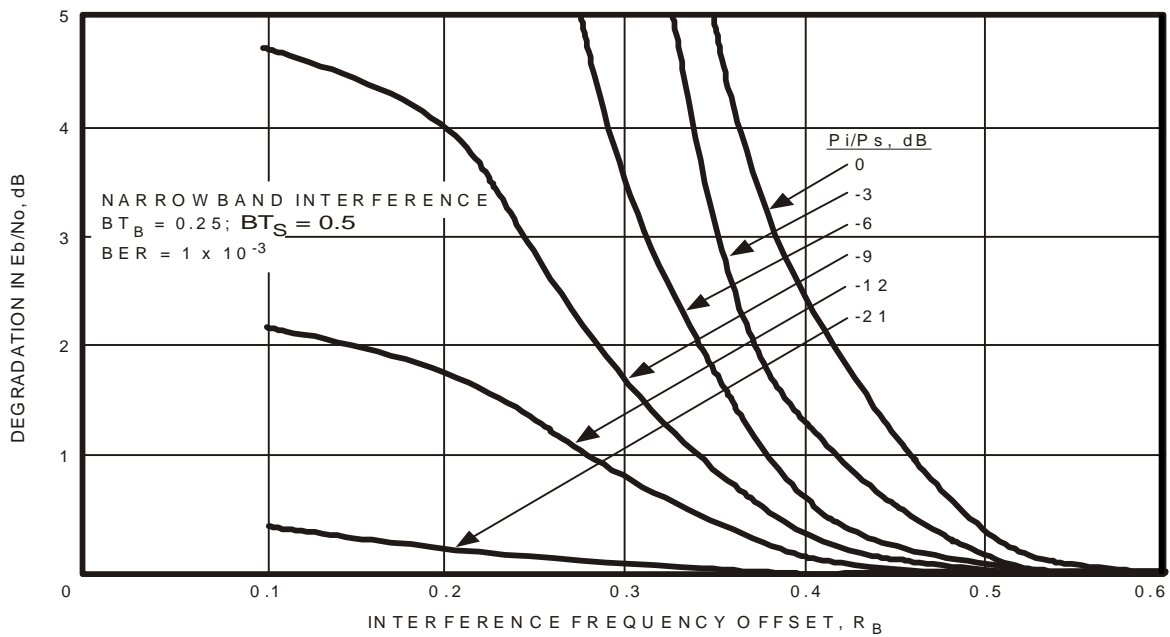
The *Workplan* for the interference susceptibility study requested two GMSK filters be evaluated: $BT_B = 0.5$ and $BT_B = 0.25$. As before, both narrowband and wideband interference susceptibility was evaluated. Figures 3.3-1a and 3.3-1b show the susceptibility of a GMSK system to narrowband interference. These Figures are for filter bandwidths of $BT_B = 1$ and $BT_B = 0.25$ respectively.

Surprisingly, GMSK ($BT_B = 0.25$) is slightly more susceptible to narrowband interference than is OQPSK using an SRRC ($\alpha = 0.5$) filter. That is evident when comparing Figures 3.3-1b and 3.2-3 where interference degrades GMSK's E_B/N_0 by 0.5 dB at $f_c \pm 0.5 R_B$ rather than at $f_c \pm 0.37 R_B$ for the SRRC filtered OQPSK.

Such an unexpected result precipitated an investigation to explain this result. Figure 3.3-2 is the RF spectrum for a GMSK modulated signal measured in Phase 3 (Reference 4). The 2-sided spectral width of SRRC ($\alpha = 0.5$) OQPSK at 60 dB below the peak is $4.8 R_B$ (Figure 3.2-1) compared to only $2 R_B$ for GMSK (Figure 3.3-2). However, at 20 dB below the peak, the respective 2-sided spectrum widths are $0.9 R_B$ and $1.0 R_B$ showing that SRRC filtered OQPSK's spectrum near its peak is slightly narrower than the one for GMSK. It remains narrower at all levels above 20 dB below the peak. This is the region of greatest susceptibility to interference with the result that a narrowband interferer begins to affect GMSK at $\pm 0.55 R_B$, whereas an SRRC filtered OQPSK receiver only detects the same interferer at $\pm 0.4 R_B$.

This finding seems to suggest that SRRC filtered OQPSK modulation is superior to GMSK. That might be so if narrowband interference susceptibility were the only criterion. It is not. The principal motivation for the Efficient Modulation Methods study is to determine how many more spacecraft can operate in currently allocated frequency bands without causing mutual interference. It has been established that an Earth orbiting spacecraft's telemetry signal, received at a ground station, can undergo 40 dB of variation in telemetry signal level between its apogee at 1.8×10^6 km (approximately L_1) and its perigee at 18,000 km ($2.6 R_E$). ICE (formerly ISEE-3) has undergone even greater variations upon its return to Earth from deep space.

EFFICIENT MODULATION METHODS - INTERFERENCE SUSCEPTIBILITY

Figure 3.3-1a: GMSK ($BT_B = 0.5$) Susceptibility to Narrowband Interference (Theory)Figure 3.3-1b: GMSK ($BT_B = 0.25$) Susceptibility to Narrowband Interference (Theory)

EFFICIENT MODULATION METHODS - INTERFERENCE SUSCEPTIBILITY

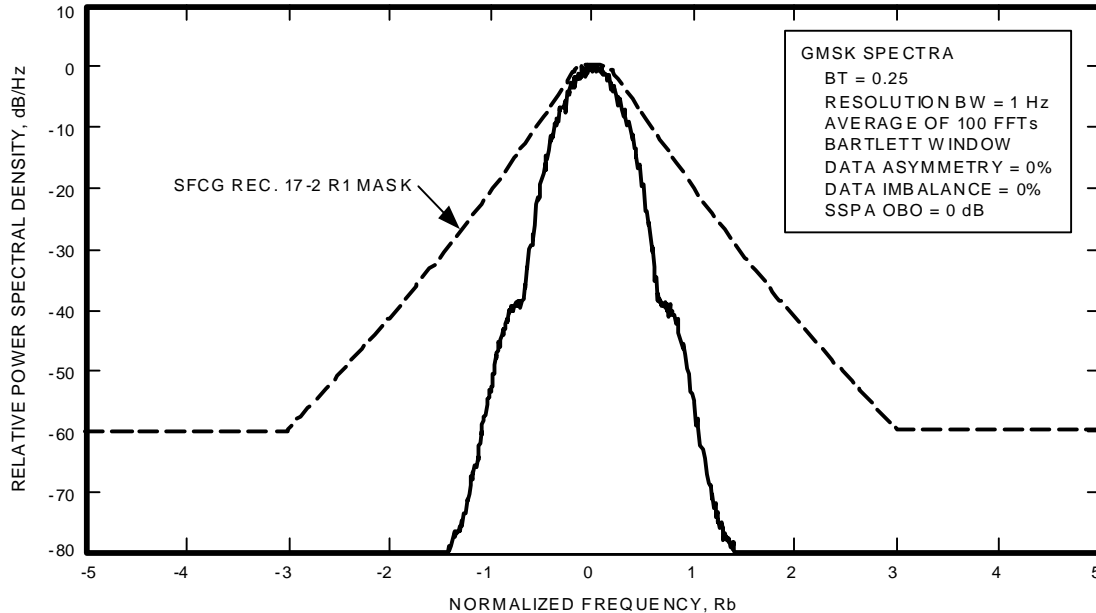


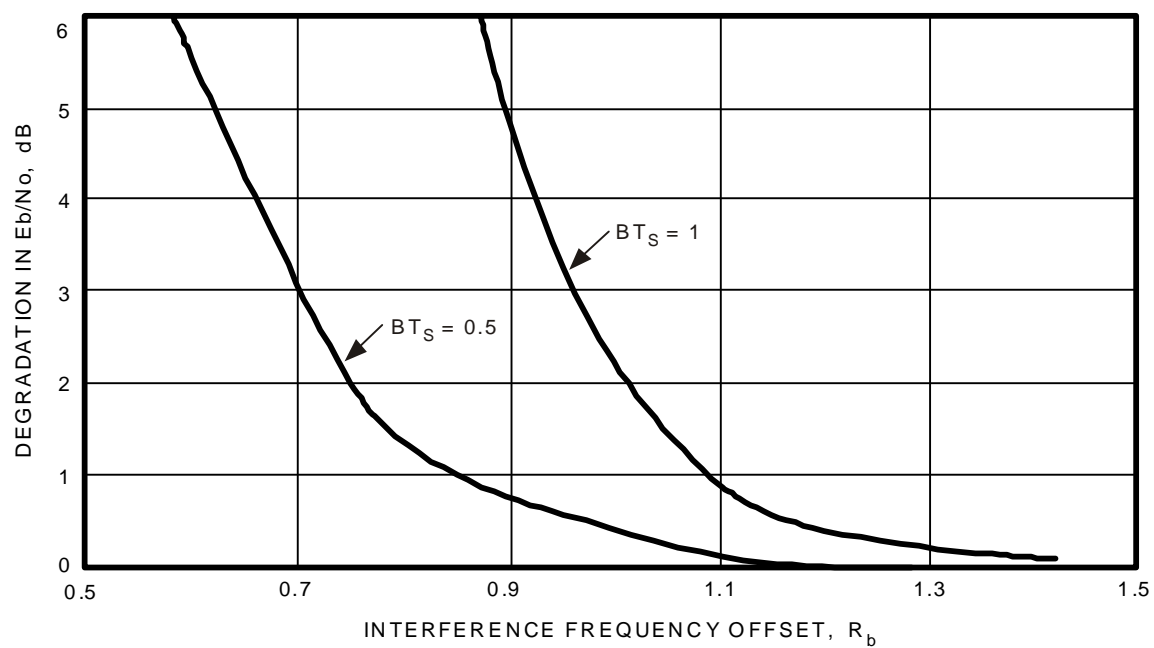
Figure 3.3-2: GMSK ($BT_B = 0.25, 0.5$) Spectra

For an interference-free environment, RF spectra of two spacecraft on adjacent frequencies should not overlap at levels above 20 dB below their peak. Reference 4 showed that some spacecraft signal levels, received at an Earth station, vary by as much as 30 dB from apogee to perigee. Reference 8 notes that space agencies frequently change data rates without adjusting their transmitter power causing the telemetry data's signal to vary by as much as 30-40 dB (see Figure A1-2)! Therefore, adjacent users should be separated in frequency by one-half of the sum of their respective spectra's width, measured at a level 80-90 dB (20 dB + 30 dB + 40 dB) below the peak. That is clearly impractical and Reference 4 suggests the spacing be set by the spectral width 60 dB below the peak.

GMSK has a spectral width of $2 R_B$ at 60 dB below the peak whereas SRRC filtered OQPSK is $4.8 R_B$ at the same level. Thus, GMSK permits more than 2.4 times as many spacecraft in a given bandwidth than does SRRC filtered OQPSK with but a minor increase in interference susceptibility.

Comparing Figure 3.3-3 for GMSK ($BT_B = 0.25$) with Figure 3.2-4 for SRRC ($\alpha = 0.5$) filtered OQPSK shows that they exhibit about the same degradation to wideband interference. Both have about a 1 dB loss at a $1 R_B$ separation.

In summary, interference immunity is only one term in the equation for selecting the best modulation method. That determination must consider a multiplicity of factors while focusing on the central objective of the Efficient Modulation methods study - *packing the maximum number of users in a frequency band having fixed edges* while maintaining mutual interference immunity. Highest RF spectrum utilization will be obtained using modulation types with very narrow spectra at 60 dB below their peak (see Table 3.5-1 below).

EFFICIENT MODULATION METHODS - INTERFERENCE SUSCEPTIBILITY**Figure 3.3-3: GMSK Susceptibility to Wideband Interference (Theory)**

EFFICIENT MODULATION METHODS - INTERFERENCE SUSCEPTIBILITY

3.4 FQPSK-B

In the Phase 3 *Efficient Modulation Methods Study*, Feher Quadrature Phase Shift Keying (FQPSK) modulation, a.k.a. Feher patented OPSK, was found to be the most bandwidth efficient modulation tested. It was better than GMSK ($BT_B = 0.25$). A patent for FQPSK-B and other modulation schemes is held by Dr. Kamilo Feher and Digcom Inc., El Macero, California.

Pursuant to a Technology Cooperation Agreement between Digcom and JPL and Non-Disclosure Agreements between Digcom and several persons at JPL, Dr. Feher provided the authors with key proprietary parameters for analyzing the performance of FQPSK-B. A commercially manufactured FQPSK-B modem was also furnished by Digcom permitting the authors to verify their simulation results. FQPSK-B was the only modulation type studied where simulations could be validated using actual hardware.

Figures 3.4-1a and 3.4-1b show FQPSK-B's narrowband interference susceptibility based on theoretical computations and hardware simulations respectively. Like the GMSK ($BT_B = 0.25$), the theoretical performance of FQPSK-B in the presence of narrowband interference (Figure 3.4-1a) shows its susceptibility to narrowband interference starts at $f_C \pm 0.55 R_B$. For an interferer having equal power to the victims, a 0.5 dB degradation is reached at $f_C \pm 0.5 R_B$ and a 1 dB loss occurs at $f_C \pm 0.45 R_B$. FQPSK-B's susceptibility to narrowband interference is about the same as that for GMSK ($BT_B = 0.25$) which experiences a degradation in E_b/N_0 of 0.5 and 1 dB at $\pm 0.49 R_B$ and $\pm 0.47 R_B$ respectively. Neither are quite as good as SRRC ($\alpha = 0.5$) filtered OQPSK where the corresponding points occur at $0.37R_B$ and $0.35 R_B$. FQPSK-B's slightly greater narrowband interference susceptibility than that for SRRC filtered OQPSK is likely due to a slightly broader spectrum in the vicinity of f_C . Please refer to Section 3.3 for the explanation.

Caution:

These comparisons are based on theoretical calculations and the investigators' best estimates of actual system performance. The differences noted are second order and well within the uncertainties of the analytical techniques employed. Readers should treat OQPSK, GMSK, and FQPSK-B as having approximately equal narrowband interference susceptibility.

Figure 3.4-1b shows FQPSK-B's narrowband interference susceptibility based on hardware simulations. Hardware simulations are made at specific points and the straight lines connecting those are not representative of actual system performance between discrete points. Comparing the theoretical computations with the hardware simulations produces some interesting observations:

1. The effects of narrowband interference begin at $f_C \pm 0.5 R_B$.
2. At a $P_I/P_S = -3$ dB, hardware interference susceptibility is greater than predicted by theory.
3. At a $P_I/P_S = -6$ dB, hardware interference susceptibility is lower than theory.
4. At a $P_I/P_S = -9$ dB and below, hardware interference matched theory.

EFFICIENT MODULATION METHODS - INTERFERENCE SUSCEPTIBILITY

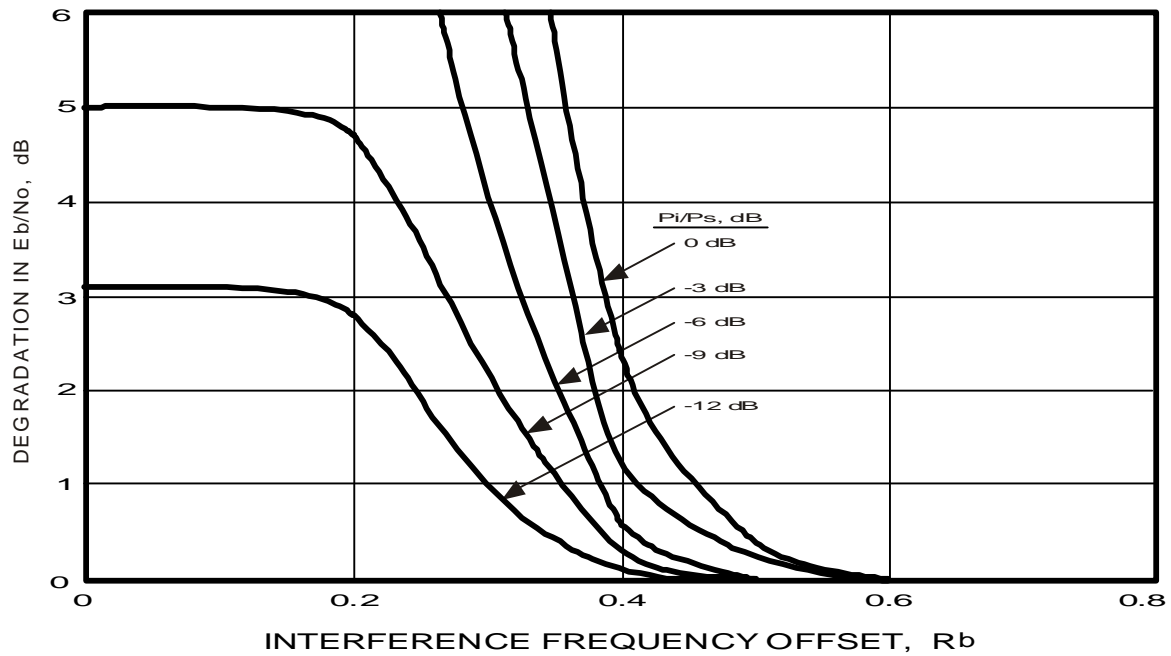


Figure 3.4-1a: FQPSK-B Susceptibility to Narrowband Interference (Theory)

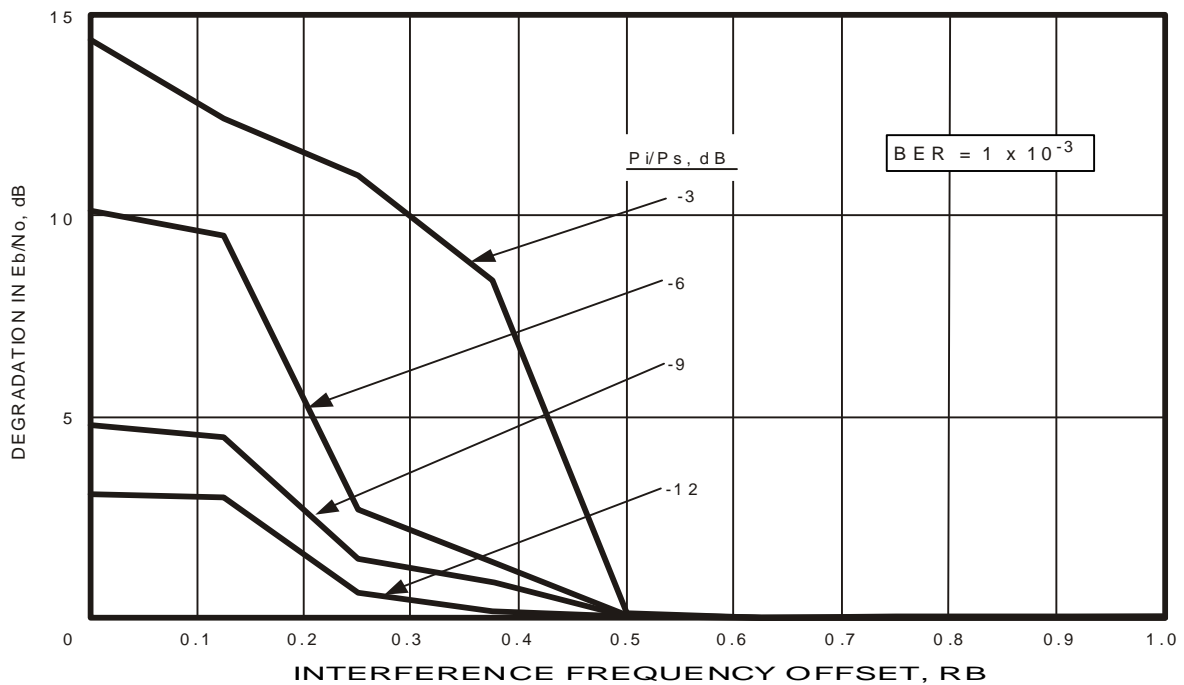


Figure 3.4-1b: FQPSK-B Susceptibility to Narrowband Interference (Hardware)

EFFICIENT MODULATION METHODS - INTERFERENCE SUSCEPTIBILITY

These observations require an explanation. First, hardware simulations corroborate that narrowband interference first affects FQPSK-B around $f_c \pm 0.55 R_b$. At greater separations an interferer with equal power will not affect the receiver provided it includes a proper filter.

Second, the poorer performance shown by the hardware simulations, when compared with theoretical calculations at a $P_I/P_S = -3$ dB (and above), is most likely due to synchronization failure. Recall that theoretical computations assume ideal synchronization whereas hardware simulations are based upon the APRX receiver shown in Figure 2.1-1 which does include synchronization losses. At high interference levels, synchronization losses can be expected to increase significantly. Some of this loss may result from the filtering used in the receiver which was optimized for Butterworth filtered OQPSK but not for FQPSK-B.

Third, the more interesting case is the better performance shown by the hardware simulations at a $P_I/P_S = -6$ dB and below as compared with theoretical computations. Again one must examine the filtering in the APRX. This filter matches an *average* of the transmitted spectrum and is narrower than the "matched" filter used in the theoretical simulations. While narrowband interference susceptibility is reduced, the end-to-end losses are increased and were not measured for this study. Essentially, the filter built into the APRX is filtering the signal as well as the interference.

Figure 3.4-2 compares FQPSK-B's susceptibility to wideband interference with Butterworth filtered OQPSK. They are based on hardware simulations. FQPSK-B is always better than OQPSK, by as much as 3 dB at low values of P_I/P_S . Moreover, FQPSK-B experiences a loss of approximately 10 dB for a $P_I/P_S = -5$ dB which corresponds to the value found in the narrowband interference case.

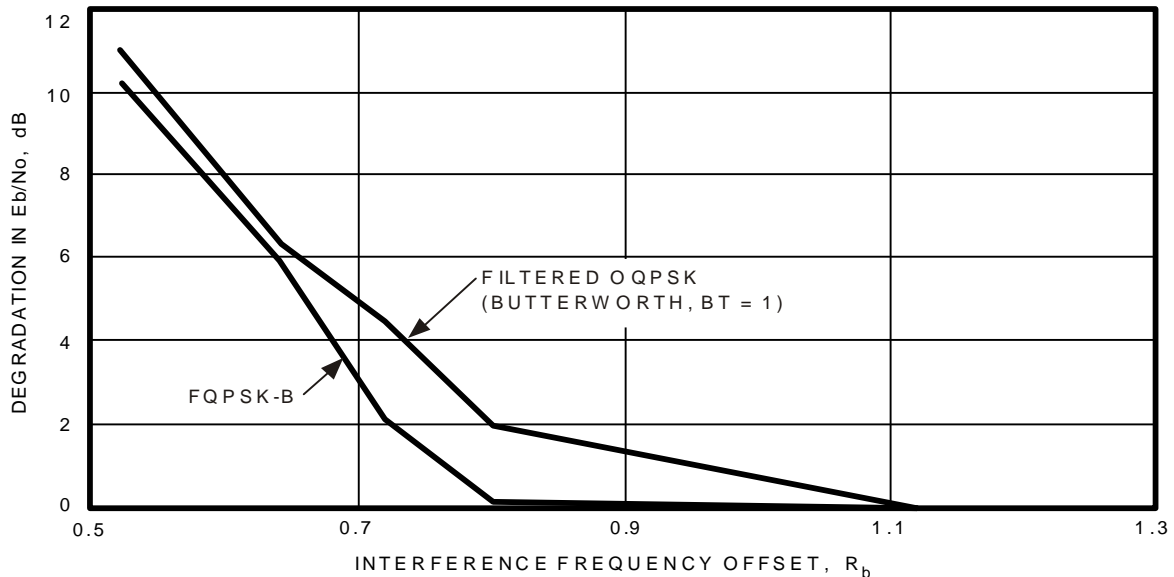


Figure 3.4-2: FQPSK-B Susceptibility to Wideband Interference (Hardware)

EFFICIENT MODULATION METHODS - INTERFERENCE SUSCEPTIBILITY

3.4.1 Special FQPSK-B Study

A special JPL study was undertaken in support of the Advance Range Telemetry (ARTM) Project at Edwards Air Force Base (EAFB). Personnel designing this new missile range telemetry system were interested in FQPSK-B because it permits more users to operate in the allocated band than is possible with their present modulation method. One of their principal concerns was Adjacent Channel Interference (ACI). Although the report describing the study results is not public because it contains proprietary Digcom information, it is possible to provide some of the findings from that independent study.

ARTM's goals are similar to those of the *CCSDS-SFCG Efficient Modulation Methods Study*: *how can more independent users be packed into a given bandwidth without sacrificing interference immunity?* ARTM personnel believed that Adjacent Channel Interference (ACI) is the key parameter for determining a modulation type's susceptibility to interference from another signal. This study also addressed that question. ACI implies another user, transmitting data on an adjacent RF frequency. If the frequency separation is insufficient, there will be interference degrading the victim's telemetry performance.

There is a key difference between this study and the one for ARTM. This Phase 4 study uses unfiltered BPSK as the wideband interferer while the one for ARTM used a like signal. Thus, the ARTM study used adjacent FQPSK-B signals to determine the minimum separation between two users transmitting the same data rate.

Figure 3.4-3 shows the ACI (in dB) as a function of signal separation for two receiver filters having different roll-off characteristics. Since actual FQPSK-B filter parameters are Digcom proprietary, the complete set of characteristics cannot be listed. It is sufficient to note that the sharper the roll-off, the lower the ACI. For two FQPSK-B signals of equal power spaced $1 R_B$ apart, a receiver having the filter with the more gradual roll-off only permits 1/10,000th of the adjacent channel's power to enter the victim's receiver.

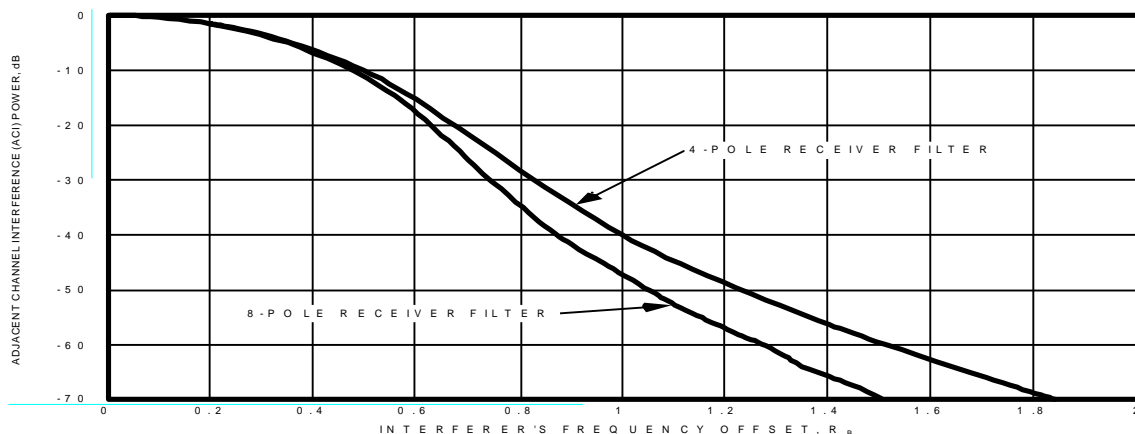


Figure 3.4-3: FQPSK-B Susceptibility to Adjacent Channel Interference (Theory)

EFFICIENT MODULATION METHODS - INTERFERENCE SUSCEPTIBILITY

A more dramatic picture of interference immunity is shown in Figure 3.4-4. Bit-Error-Rate (BER) is plotted as a function of received signal power (E_B/N_0) for two FQPSK-B signals placed $1 R_B$ apart. Here, the interferer's signal power is 20 dB stronger than the victim's. Referring to the line representing a BER 1×10^{-3} , it can be seen that the victim suffers only about a 1.1 dB loss in a receiver having a 4-Pole filter and approximately a 0.9 dB loss if the receiver has an 8-Pole filter with a sharper roll-off. There is no doubt this is due to the very steep attenuation of the FQPSK-B spectrum.

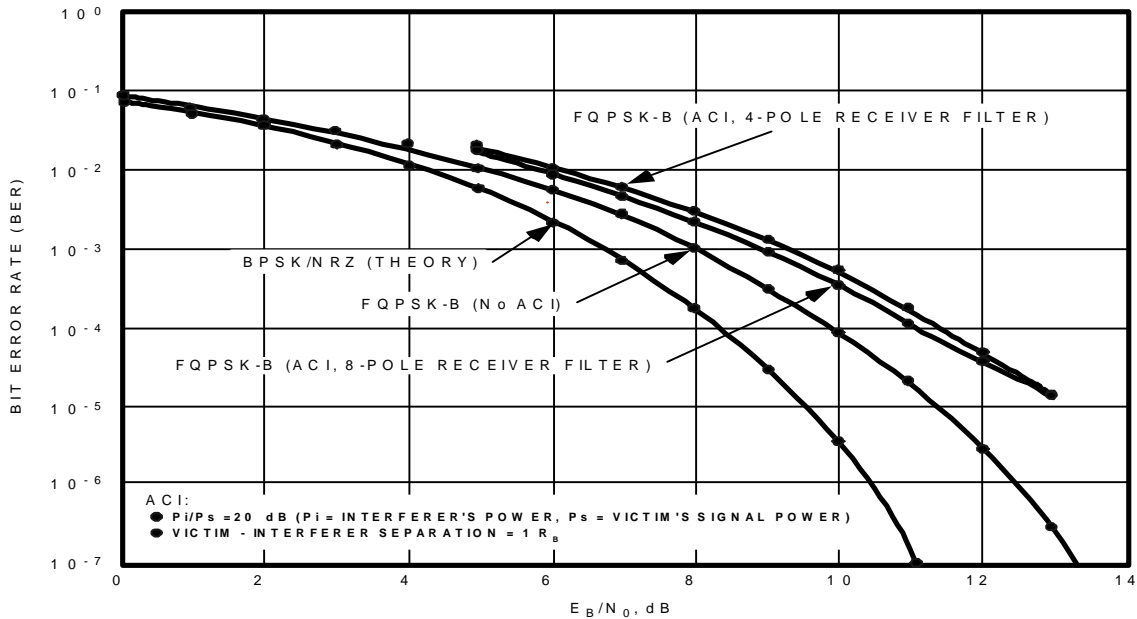


Figure 3.4-4: FQPSK-B Bit-Error-Rate Susceptibility to ACI (Theory)

EFFICIENT MODULATION METHODS - INTERFERENCE SUSCEPTIBILITY

3.5 Spread Spectrum

Although not a part of the Workplan (see Section 1), a cursory look at spread spectrum communications is included in this Phase 4 report. It is included because some members of the SFCG speculated that the properties of spread spectrum modulation are superior to those of bandwidth limited modulation. One representative to SFCG-18 expressed the opinion that spread spectrum communications could actually be “more bandwidth efficient” than the modulation types studied by the CCSDS in their Phase 3 report.

The principal focus of this Phase 4 study is interference susceptibility; however, as noted in Section 3.3, this is but one consideration. The better question is: Which modulation type permits the maximum number of users in a frequency band having fixed edges while providing mutual interference immunity? The following information addresses some of these issues.

A Direct Sequence Spread Spectrum (DSSS) signal is generated by mixing a Pseudo Noise (PN) code with the data. In the receiver, the inverse process occurs when a local model of the PN code is cross-correlated with the received signal. After the local model’s PN code phase is aligned with that in the received signal, the spread spectrum is de-convolved to that of the original data.

Theoretically, multiple spread spectrum signals can be overlain, provided that the PN codes are mutually orthogonal so that their cross-correlation is 0. Individual receivers perform the cross-correlation process described above with result that several channels can all occupy the same frequency spectrum.

A PN code’s bit rate is termed the chip rate and the information data-to-chip rate ratio is an important parameter. Termed the *processing gain*, this parameter determines the amount of spectral spreading that occurs. Typical values lie between 100 and 1,000. The higher the processing gain, the greater the immunity to interference but the wider the *necessary* bandwidth. DSSS binary phase shift keyed modulation’s spectra will have the familiar Sin x/x form with nulls at 1/chip period and lines spaced at 1/chip repetition period.

Assuming that spread spectrum transmissions must lie within the allocated frequency band and that filtering is employed to limit the transmitted spectrum to only the main lobe, maximum permitted symbol rates for a spread spectrum system can be computed using the relationship:

$$\text{Data Rate} = \left[\frac{\text{Allocated Bandwidth}}{\text{Processing Gain}} \right] \times \left[\frac{2 \text{ for OQPSK}}{2 \text{ for sidebands}} \right]$$

If a rate ½ convolutional code is used, the information data rate will be reduced by half. Moreover, these values assume a single user is permitted to spread his signal over the entire 90 MHz bandwidth when operating in the 2 GHz band and over the entire 50 MHz bandwidth when in the 8 GHz band.

EFFICIENT MODULATION METHODS - INTERFERENCE SUSCEPTIBILITY

When multiple spread spectrum channels are “stacked”, signals with orthogonal cross-correlation properties appear as noise in other than the intended receivers. This has the effect of degrading the Signal-to-Noise-Ratio (SNR). The amount of degradation depends upon the spread spectrum signal’s power spectral density and the victim receiver’s system noise temperature and explains why larger processing gains are preferred. Accordingly, there is a limit to the number of spread spectrum signals that can overlay each other.

Fourth Finding:

As a practical matter for a processing gain of 1,023, about 300 Direct Sequence Spread Spectrum signals can overlay one another before the additive noise level in a victim receiver, operating at an 8 dB SNR, becomes excessive (Reference 7).

This comparatively small number appears to be inconsistent with the PCS industry’s experience. But, there are two differences. First, cell phones have a comparatively low information data rate so that, even when their signals are spread, a single user’s signal does not require the entire allocated band. Cell phone users can be stacked side-by-side as well as vertically. Second, spacial diversity makes it unlikely that more than the acceptable number of users will be attempting to reuse the same frequency in the same cell at the same time.

Figure 3.5-1 shows a DSSS system’s BER as a function of received signal strength (E_B/N_0), in the presence of narrowband RFI, for three different processing gains: 31, 127, and 1023. The interferer is spaced $1 R_B$ from center frequency of the DSSS system and has equal power.

Two points are worth noting. First, a DSSS system’s performance in the presence of narrowband interference is very much a function of its processing gain, the higher the better. Second, the figure suggests that a minimum processing gain of 100 is required unless larger losses from interference and fewer independent channels can be tolerated.

This finding is corroborated by Figure 3.5-2 which shows the degradation in E_B/N_0 as a function of separation between interferer and victim for wideband RFI. Degradation is independent of the separation (see explanation in Section 3.2) and is essentially 0 dB for a processing gain of 1023, 0.5 dB for a gain of 127, and 1.3 dB for a gain of 31. A curve for unfiltered, ideal BPSK is included for reference purposes and is equivalent to the 0 dB curve in Figure 3.1-2b.

Comparing Figure 3.5-1 with Figure 3.2-2b for SRRC filtered OQPSK, in the presence of a narrowband interferer having equal power, yields an interesting finding. For a narrowband interferer and a 1×10^{-3} BER, a DSSS system, with a processing gain of 127 or lower, will equal or exceed a 0.5 dB loss at any frequency separation between victim and interferer. A filtered OQPSK system is only susceptible when the narrowband interferer is within $0.5 R_B$.

EFFICIENT MODULATION METHODS - INTERFERENCE SUSCEPTIBILITY

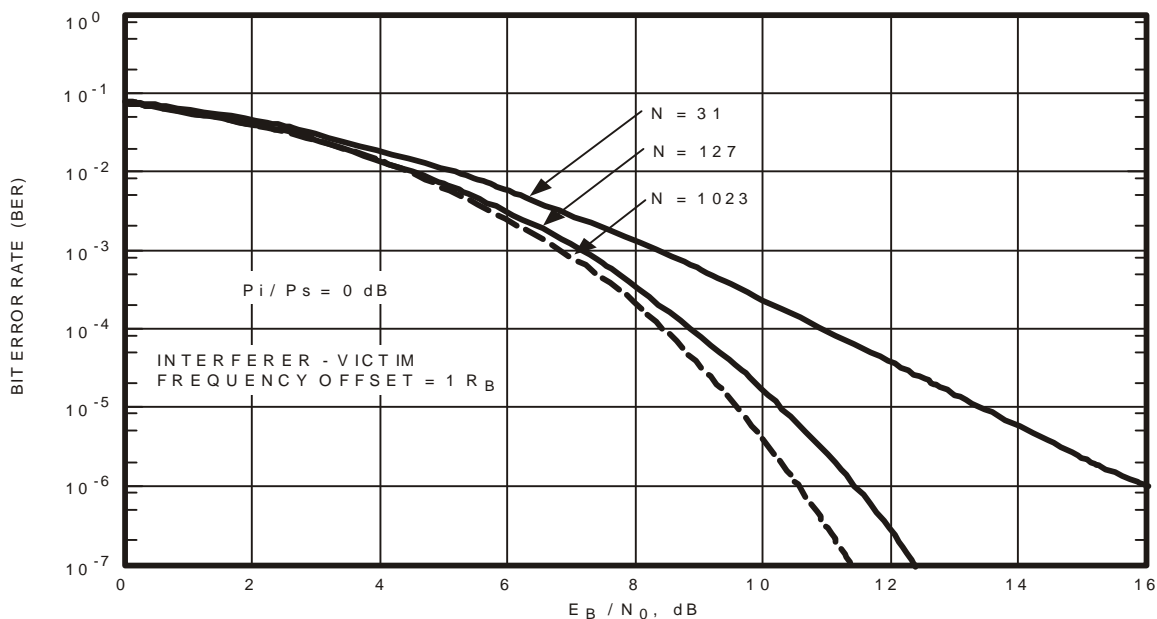


Figure 3.5-1: DSSS Bit-Error-Rate Susceptibility to Narrowband Interference

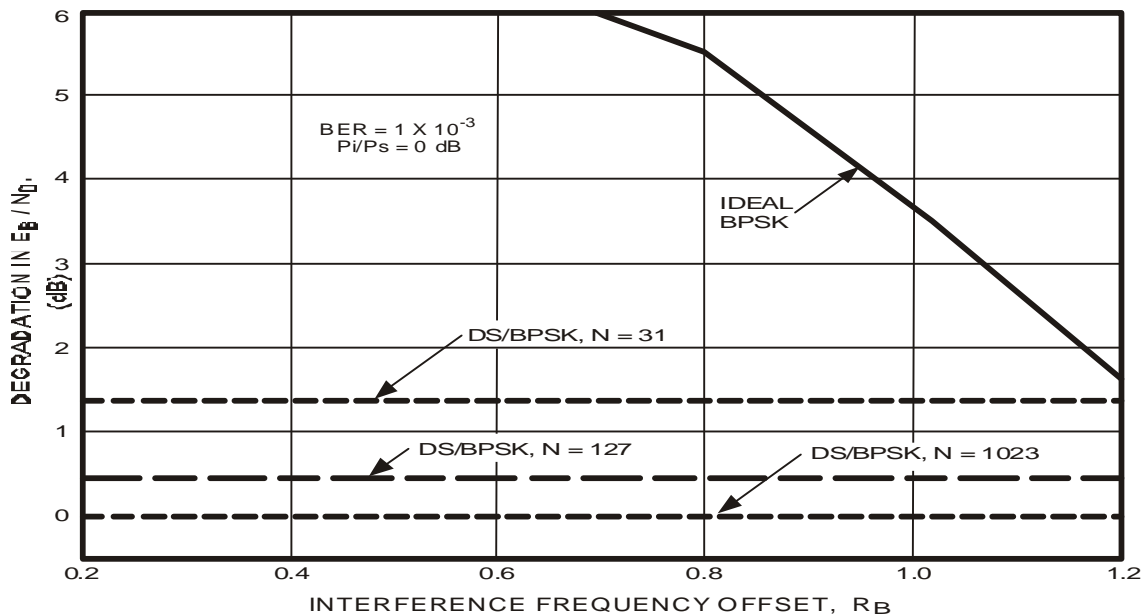


Figure 3.5-2: DSSS SNR Susceptibility to Wideband Interference

EFFICIENT MODULATION METHODS - INTERFERENCE SUSCEPTIBILITY

3.5.1 DSSS Spectral Efficiency

The principal purpose behind the *Efficient Modulation Methods Study* was to identify those modulation methods permitting the maximum number of independent users to operate simultaneously in a specified bandwidth. Given the speculations put forth in SFCG-18, it would be interesting to compare DSSS systems with one of the more bandwidth efficient modulation schemes studied in Phase 3. This analysis of the two systems compares two parameters:

1. The maximum number of users that can simultaneously operate in a fixed bandwidth.
2. The maximum number of bits per second that can be returned on the link.

The study also includes the following assumptions:

1. Users operate in the Category A mission 2 GHz band allocated to the *Space Research* service.
2. All spectral emissions must be within the 90 MHz allocated band but may use the entire band.
 - a) DSSS users must filter to transmit only main spectral lobe.
 - b) FQPSK-B users are packed side-by-side at $1 R_B$ with no additional filtering.
3. The maximum bit-rate for the DSSS system is given by:

$$[(\text{Allocated Bandwidth} / \text{Processing Gain}) \times (2 \text{ for OQPSK} / 2 \text{ for sidebands})].$$

$$= \text{Allocated Bandwidth} / \text{Processing Gain}.$$

$$= 708,661 \text{ bps for a processing gain of 127.}$$

$$= 87,977 \text{ bps for a processing gain of 1023.}$$
4. The maximum number of equal power DSSS users that can be “overlaid” is (Reference 7):
 - a) 37 for a Processing Gain of 127.
 - b) 75 for a Processing Gain of 255.
 - c) 150 for a Processing Gain of 511.
 - d) 300 for a Processing Gain of 1023.
5. Maximum number of simultaneous independent FQPSK-B users is given by:

$$[(\text{Allocated Bandwidth} / \text{Data Rate}) \times (2 \text{ for OQPSK} / 2 \text{ for sidebands})]$$

$$= \text{Allocated Bandwidth} / \text{Data Rate}$$
6. Evaluations made at a $\text{BER} = 1 \times 10^{-3}$.
7. Adjacent channel interference shall not exceed 1 dB.

Study results for a DSSS system operating in the 2 and 8 GHz bands *Space Research* (SR) and *Earth Exploration Satellite* (EES) services are summarized in Table 3.5-1. Several observations can be made regarding a DSSS system’s application to a space science mission:

1. DSSS systems are useable only at low data rates and have a:
 - a) Maximum data rate of 709 kbps in 2 GHz *Space Research* service allocation.
 - b) Maximum data rate of 394 kbps in 8 GHz *Space Research* service allocation.
 - c) Maximum data rate of 2.95 Mbps in 8 GHz *EES* service allocation.

EFFICIENT MODULATION METHODS - INTERFERENCE SUSCEPTIBILITY

Table 3.5-1: Comparison of DSSS and FQPSK-B Channel Capacities

Band (GHz)	ITU Allocated Service ₁	Allocated Bandwidth (MHz)	DSSS Processing Gain	Max. DSSS Data Rate (kbps)	Max. Simul. DSSS Users (No.) ₂	Max. DSSS Band Cap. (Mbps)	Max No. FQPSK-B Users	Max. FQPSK-B Band Cap. (Mbps)	FQPSK/DSSS Band Cap Ratio
2	SR	90	127	709	37	26	127	90	3.4
2	SR	90	255	353	75	26	255	90	3.4
2	SR	90	512	176	150	26	512	90	3.4
2	SR	90	1023	88	300	26	1023	90	3.4
8	SR	50	127	394	37	15	127	50	3.4
8	SR	50	255	196	75	15	255	50	3.4
8	SR	50	512	98	150	15	512	50	3.4
8	SR	50	1023	49	300	15	1023	50	3.4
8	EES	375	127	2,953	37	109	127	375	3.4
8	EES	375	255	1,471	75	110	255	375	3.4
8	EES	375	512	732	150	110	512	375	3.4
8	EES	375	1023	367	300	110	1023	375	3.4

Notes:

1. SR = *Space Research* service; EES = *Earth Exploration Satellite* service.

2. Based on a 8 dB SNR; BER = 1 E-3 (Reference 7)

- 2) DSSS systems are not very user efficient. At a 1×10^{-3} BER, there can be nearly 3½ times as many users in an allocated band if they use FQPSK-B rather than DSSS modulation.
- 3) DSSS systems are not very bandwidth efficient. At a 1×10^{-3} BER, an FQPSK-B system can move nearly 3½ times more bits in a fixed bandwidth per unit time than can a DSSS system.

From these observations, it is clear that DSSS systems may have application in spreading the spectrum to meet Power Flux Density (PFD) requirements, but only if bandwidth efficiency and data transfer efficiency are not top priorities. Generally, PFD will only be a concern on space-to-Earth links when residual carrier systems are used. SFCG Recommendation 17-2R1 requires users of data symbol rates above 2 Msps to use suppressed carrier modulation. Data rates typically found in suppressed carrier modulation systems are very unlikely to exceed PFD limits, even when they employ bandwidth efficient modulation methods.

Fifth Finding:

DSSS modulation is not appropriate for any space mission transmitting a telemetry data rate in excess of 2 Msps and which is covered by SFCG Recommendation 17-2R1.

EFFICIENT MODULATION METHODS - INTERFERENCE SUSCEPTIBILITY

4.0 SUMMARY AND CONCLUSIONS

As requested in the Workplan contained in Section 1, this study has examined the several modulation methods for their susceptibility to both narrowband and wideband interference. Pursuant to a request in the Workplan, narrowband and wideband interference susceptibilities were determined by analysis and simulation. Where possible, they were confirmed by hardware simulations or actual measurements. Table 4.0-1 summarizes the narrowband interference susceptibility for several losses from 0.25 to 1.0 dB. Table 4.0-2 provides the equivalent values for wideband interference.

Table 4.0-1: Data Degradation From Narrowband Interference of Equal Power (Theory)

Modulation Type	Minimum Interference Offset from f_c for Specified Data Loss ¹			
	0.25 dB Loss	0.50 dB Loss	0.75 dB Loss	1.00 dB Loss
Unfiltered BPSK-NRZ	$\pm 2.5 R_B$	$\pm 1.7 R_B$	$\pm 1.6 R_B$	$\pm 1.5 R_B$
OQPSK (BW, $BT_s = 1$)	$\pm 0.7 R_B$	$\pm 0.47 R_B$	$\pm 0.45 R_B$	$\pm 0.43 R_B$
OQPSK (SRRC, $\alpha = 0.5$)	$\pm 0.38 R_B$	$\pm 0.37 R_B$	$\pm 0.36 R_B$	$\pm 0.35 R_B$
GMSK ($BT_B = 0.5$)	$\pm 0.6 R_B$	$\pm 0.58 R_B$	$\pm 0.5 R_B$	$\pm 0.53 R_B$
GMSK ($BT_B = 0.25$)	$\pm 0.52 R_B$	$\pm 0.49 R_B$	$\pm 0.47 R_B$	$\pm 0.46 R_B$
FQPSK-B	$\pm 0.52 R_B$	$\pm 0.49 R_B$	$\pm 0.46 R_B$	$\pm 0.42 R_B$
Spread Spectrum ²	Never	Never	Never	Never

NOTE: 1. Based upon equal powers in interfering and desired signals.
2. Based on a Processing Gain of 1023.

Table 4.0-2: Data Degradation From Wideband Interference of Equal Power (Theory)

Modulation Type	Minimum Interference Offset from f_c for Specified Data Loss ¹			
	0.25 dB Loss	0.50 dB Loss	0.75 dB Loss	1.00 dB Loss
Unfiltered BPSK-NRZ	$\pm >3 R_B$	$\pm 2.5 R_B$	$\pm 2.4 R_B$	$\pm 1.8 R_B$
OQPSK (BW, $BT_s = 1$)	$\pm 1.05 R_B$	$\pm 0.96 R_B$	$\pm 0.88 R_B$	$\pm 0.8 R_B$
OQPSK (SRRC, $\alpha = 0.5$) ²	$\pm 1.3 R_B$	$\pm 1.0 R_B$	$\pm 0.93 R_B$	$\pm 0.9 R_B$
GMSK ($BT_B = 0.5$)	$\pm 1.3 R_B$	$\pm 1.18 R_B$	$\pm 1.12 R_B$	$\pm 1.09 R_B$
GMSK ($BT_B = 0.25$)	$\pm 1.06 R_B$	$\pm 0.98 R_B$	$\pm 0.90 R_B$	$\pm 0.85 R_B$
FQPSK-B ²	$\pm 0.79 R_B$	$\pm 0.77 R_B$	$\pm 0.75 R_B$	$\pm 0.72 R_B$
Spread Spectrum ³	Never	Never	Never	Never

NOTE: 1. Based upon equal powers in interfering and desired signals.
2. Based on hardware simulation.
3. Based on a Processing Gain of 1023.

EFFICIENT MODULATION METHODS - INTERFERENCE SUSCEPTIBILITY

Susceptibility of a victim receiver to narrowband interference of equal power is approximately the same for all filtered modulation types save SRRC ($\alpha = 0.5$) OQPSK (Table 4.0-1). OQPSK appears better for an interferer of equal power to the victim because OQPSK's main spectral lobe is somewhat narrower than either GMSK's or FQPSK's down to a level of 20 dB below the peak. Thereafter, it becomes much wider than either GMSK or FQPSK-B. Section 3.3 explains why this apparent advantage is not useful for space science missions.

The susceptibility of filtered modulations to wideband interference also tends to be grouped with FQPSK-B being slightly better than the others. It remains to be demonstrated whether that advantage results from hardware simulations rather than a theoretical computation. A somewhat similar result was found for hardware simulations of Butterworth ($BT_s = 1$) filtered OQPSK and it appears slightly better than SRRC ($\alpha = 0.5$) filtered OQPSK. It is likely that all are quite similar.

Spread spectrum modulation has virtual immunity to narrowband and wideband interference provided the processing gain is high (1023). At lower processing gains (31) the interference susceptibility of spread spectrum modulation to either narrowband or wideband interference increases sharply.

All filtered modulation types have less susceptibility to interference than does unfiltered BPSK. That disparity becomes ever more evident as the interferer's power increases with respect to the victim's. Considering the space science applications described in Section 3.3 and Reference 4, approximately 2.4 times as many FQPSK-B (or GMSK) users can be packed into an allocated frequency band than is possible with either SRRC ($\alpha = 0.5$) OQPSK or DSSS modulation, without any concern about mutual interference (Table 3.5-1).

Several other observations were made throughout the several sections of this report. They are repeated here for the convenience of the reader.

1. Definition of Interference Susceptibility: The likelihood that another signal source, operating in the same or other allocated frequency band, will produce an unacceptable degradation in E_B/N_0 to a victim employing bandwidth efficient modulation.
2. The amount of the degradation to the desired data signal (S_D) is proportional to power remaining in the interfering signal (P_I), after attenuation by the receiver filter's roll-off characteristic, compared to the total power in the desired signal (P_{TS}). ($S_D \propto P_I / P_{TS}$).
3. Absent low noise and/or i.f. amplifier saturation or gain compression resulting from an interfering signal, a receiver's performance in the presence of an interfering signal is determined entirely by its filters.
4. To a first order, the receiver's matched filter's characteristics completely determine a modulation method's interference sensitivity function, whether that interference is in-band or out-of-band.

EFFICIENT MODULATION METHODS - INTERFERENCE SUSCEPTIBILITY

5. To minimize interference susceptibility, a matched filter's bandwidth should be as narrow as possible after accounting for the minimum acceptable power transfer, and the maximum acceptable ISI.
6. When comparing interference susceptibility of different modulation methods, those with more compact spectra (smaller necessary bandwidths) have more interference immunity than modulation types requiring larger bandwidths, provided that the receiver has a properly matched filter.
7. The power spectral density of a bandwidth efficient modulated signal is increased with respect to a non-baseband filtered modulation, reducing its susceptibility to a narrowband interferer having the same total transmitting power.
8. If the receiver has a properly designed matched filter, there will be virtually no susceptibility to interference lying outside its bandwidth. Therefore, a narrowband interferer, occurring within the victim's allocated frequency band, has a lower probability of falling within the victim's narrower bandwidth.
9. For equally received power from interferer and victim, SRRC ($\alpha = 0.5$) OQPSK permits slightly tighter user packing; however, when distances vary so that the received powers are unequal such as is found in space applications, then about $3\frac{1}{2}$ times more GMSK and/or FQPSK-B users can be placed in a band than is possible with OQPSK modulation.
10. As a practical matter for a processing gain of 1,023, about 300 Direct Sequence Spread Spectrum signals can overlay one another before the additive noise level in a victim receiver, operating at an 8 dB SNR, becomes excessive (Reference 5).
11. DSSS systems are not very user efficient. At a 1×10^{-3} BER, there can be nearly $3\frac{1}{2}$ times as many users in an allocated band if they use FQPSK-B rather than DSSS modulation.
12. DSSS systems are not very bandwidth efficient. At a 1×10^{-3} BER, an FQPSK-B system can move nearly $3\frac{1}{2}$ times more bits in a fixed bandwidth per unit time than can a DSSS system.
13. DSSS modulation is not appropriate for any space mission transmitting a telemetry data rate in excess of 2 Msps, which must operate in the 2 and 8 GHz *Space Research* or *Earth Exploration Satellite* services and which is covered by SFCG Recommendation 17-2R1.

The research described in this paper was carried out by the Jet Propulsion Laboratory, California Institute of Technology, under a contract with the National Aeronautics and Space Administration.

EFFICIENT MODULATION METHODS - INTERFERENCE SUSCEPTIBILITY**GLOSSARY**

BER	Bit-Error-Rate
BPSK	Binary Phase Shift Keyed
BT	Bandwidth-Time (factor specifying filter bandwidth)
CCSDS	Consultative Committee for Space Data Systems
DSN	Deep Space Network
DSP	Digital Signal Processor
DSSS	Direct Sequence Spread Spectrum (modulation)
ESA	European Space Agency
ESOC	European Space Agency Center
f_c	Center (or Carrier) Frequency
FIR	Finite Impulse Response (filter mechanization)
FQPSK	Feher Quadrature Phase Shift Keyed (modulation method)
FQPSK-B	A Special Configuration of FQPSK
GMSK	Gaussian Minimum Shift Keyed
GSFC	Goddard Space Flight Center
HDL	Hardware Description Language
I-Q	In-Phase-Quadrature (modulator mechanization)
ISI	Inter-Symbol Interference
JPL	Jet Propulsion Laboratory
ksps	Kilo-symbols per second (1×10^3 symbols per second)
Mps	Mega-symbols per second (1×10^6 symbols per second)
QPSK	Quadrature Phase Shift Keyed
OQPSK	Offset QPSK ($1/2$ -bit-time offset)
PCS	Personal Communications System
PFD	Power Flux Density
P_I/P_S	Ratio of Interferer's Total Transmitted Power to Victim's Total Transmitted Power
PSD	Power Spectral Density
NASA	National Aeronautics and Space Administration
NRZ	Non Return to Zero
R_B	Frequency Span Corresponding to 1/Data-Bit Period
RFI	Radio Frequency Interference
SFCG	Space Frequency Coordination Group
SRRC	Square Root Raised Cosine [filter]
SSPA	Solid State Power Amplifier
TDL	Telecommunications Development Laboratory (located at JPL)

EFFICIENT MODULATION METHODS - INTERFERENCE SUSCEPTIBILITY

REFERENCES

1. Martin, Warren L. and Tien M. Nguyen, *CCSDS - SFCG Efficient Modulation Methods Study, A Comparison of Modulation Schemes, Phase 1: Bandwidth Utilization*, Jet Propulsion Laboratory, Pasadena, California, 24 September 1993.
2. Otter, Manfred, *CCSDS - SFCG Efficient Modulation Methods Study, A Comparison of Modulation Schemes, Phase 1b: A Comparison of QPSK, OQPSK, BPSK, and GMSK*, European Space Agency Operations Center, Darmstadt, Germany, June 1994.
3. Martin, Warren L. and Tien M. Nguyen, *CCSDS - SFCG Efficient Modulation Methods Study, A Comparison of Modulation Schemes, Phase 2: Spectrum Shaping*, Jet Propulsion Laboratory, Pasadena, California, August 1994.
4. Martin, Warren L., Tsun-Yee Yan, Loc V. Lam, *CCSDS - SFCG Efficient Modulation Methods Study at NASA/JPL, Phase 3: End-to-End System Performance*, Jet Propulsion Laboratory, Pasadena, California, September 1997.
5. Block, Gerhard, Dr. Manfred Otter, and M. Reichel, *Advanced Spectrum Shaping for Efficient Bandwidth Utilisation*, European Space Agency, Paris, France, Contract No. 11605/96, September 1997.
6. *SFCG Recommendation 17-2R1*, SFCG Handbook Published by the SFCG Secretariat, European Space Agency Headquarters, Paris, France, Latest Edition
7. Cooper, G. And R. Nettleton, *A Spread Spectrum Technique for High Capacity Mobile Communications*, IEEE Transactions on Vehicular Technology, Vol 27, pp. 264-275, November 1978.
8. [NASA], *Merits of SFCG Recommendation 17-2R1 Emission Masks in the 2200-2290 MHz and 8025-8400 MHz Bands*, National aeronautics and Space Administration, Paper SF19-15/D, submitted to SFCG 19, 7-15 September 1999, Noordwijk, The Netherlands.

CCSDS Panel 1E
Document 99/45
End-to-End Losses of Selected
Bandwidth-Efficient Modulation Schemes

Gabriella Povero¹ Enrico Vassallo² Monica Visintin³

Abstract

Butterworth and Square-Root-Raised-Cosine (SRRC) filtered OQPSK, and GMSK modulations are compared over AWGN and nonlinear channels. The purpose of this work is to help finding out the most suitable modulation scheme for the increasingly crowded frequency bands available for space research missions. Both end-to-end losses and power spectral density curves will be derived.

1 Introduction

In the frame of the development of a worldwide standard for inter-operable modulation techniques to be used for space missions, a number of suitable modulation schemes are under investigation for possible adoption at CCSDS. Among these, the following modulations have been studied by both ESA and NASA [1], [5], [7], [10]:

- square-root-raised-cosine (SRRC) filtered OQPSK with roll-off factor 0.5
- Butterworth (6-pole) filtered OQPSK with $BT_s=1.0$
- GMSK with $BT_b=0.25$, $BT_b=0.5$ and $BT_b=1.0$

This paper describes the results of the ESA work in determining end-to-end system losses for the above schemes over the non-linear satellite channel. The same nonlinear amplifiers considered in [1] are assumed; moreover, for sake of completeness, also the case of a simple linear AWGN (Additive White Gaussian Noise) is included.

The effect of coding is not addressed in this paper. Work is, however, on progress and the first results of end-to-end losses for a CCSDS encoded channel are planned to be presented at the Spring 2000 meeting of CCSDS P1E.

¹ COREP, Politecnico di Torino

² ESOC, European Space Agency

³ Dipartimento di Elettronica, Politecnico di Torino

2 Transmission schemes

Each of the following subsections describes one of the considered schemes. Valid for all the modulation schemes is the assumption that the receiver carrier and clock recovery subsystems are perfect (synchronized system performance.)

The information bits are generated at rate $1/T_b$ and zeros and ones are equally likely.

The power spectra of the considered modulation in a linear channel are compared in Figure 2.

Unfiltered BPSK (benchmark)

The BPSK (Binary Phase Shift Keying) transmitted signal has complex envelope

$$\tilde{x}(t) = \sqrt{E_b} \sum_{k=-\infty}^{\infty} a_k \psi(t - kT)$$

where $a_k \in \{\pm 1\}$ and $\psi(t) = \sqrt{1/T} u_T(t)$, with $u_T(t) = 1$ for $0 < t < T$, and $u_T(t) = 0$ elsewhere, and E_b is the energy per bit; in this case the symbol interval T (or T_s) is equal to the bit interval T_b .

The receiver generates the complex envelope $\tilde{r}(t)$ of the received signal, passes it through the matched filter with impulse response $\psi(t)$, samples at times $nT + T$, and takes the decision on a_n with a zero-threshold detector.

Butterworth-filtered OQPSK

The OQPSK (Offset Quadrature Phase Shift Keying) transmitted signal has complex envelope

$$\tilde{x}(t) = \sqrt{E_b} \left[\sum_{k=-\infty}^{\infty} a_{k,R} g(t - kT) + j a_{k,I} g(t - kT - T/2) \right]$$

where both $a_{k,R}$ and $a_{k,I}$ take values in $\{\pm 1\}$, $T = T_s = 2T_b$ is the symbol interval, and $g(t)$ is the convolution of $u_T(t)$ and the impulse response of a 6-pole Butterworth filter with 3-dB bandwidth equal to $1/T$.

The received complex envelope is passed through an Integrate and Dump filter with impulse response $\sqrt{1/T}u_T(t)$, the real component is sampled at times $t_0 + nT$, while the imaginary part is sampled at times $t_0 + nT + T/2$, where instant t_0 is that of maximum eye opening. A threshold detector takes the decisions on $a_{n,R}$ and $a_{n,I}$. The eye pattern of the in-phase component of the signal at the output of the receiver filter is shown in Figure 3.

With respect to ideal BPSK, the losses due to intersymbol interference (ISI) in a linear channel are 0.44 dB at $P_b(e)=10^{-1}$, 0.52 dB at $P_b(e)=10^{-2}$, 0.60 dB at $P_b(e)=10^{-3}$.

SRRC-filtered OQPSK

The transmitted signal has complex envelope

$$\tilde{x}(t) = \sqrt{E_b} \left[\sum_{k=-\infty}^{\infty} a_{k,R} \psi(t - kT) + ja_{k,I} \psi(t - kT - T/2) \right]$$

where $a_{k,R}$ and $a_{k,I}$ take both values in $\{\pm 1\}$ and $\psi(t)$ is the impulse response of a square-root-raised cosine (SRRC) filter with roll-off factor 0.5. The transmitted signal power spectrum is shown in Figure 2, and it is apparent that SRRC-filtered OQPSK in a linear channel is the most bandwidth efficient modulation among those considered in this paper.

Two receivers are assumed: the first using the matched filter with impulse response $\psi(t)$ (SRRC-a), the second using an Integrate and Dump filter with impulse response $\sqrt{1/T}u_T(t)$ (SRRC-b).

The sampling is performed at the maximum eye opening and a zero-threshold detector takes the decision. The eye patterns at the output of the receiver filters for the SRRC-a and SRRC-b cases are shown in Figure 4 and Figure 5.

SRRC-a has the same performance as ideal BPSK in terms of bit error rate in a linear channel, while SRRC-b suffers from a loss of 0.59 dB at $P_b(e)=10^{-1}$, 0.61 dB at $P_b(e)=10^{-2}$, 0.65 dB at $P_b(e)=10^{-3}$, due to ISI.

GMSK

Three GMSK (Gaussian Minimum Shift Keying) signals are considered, with normalized bandwidth $BT_b = 0.25$, $BT_b = 0.5$ and $BT_b = 1$.

Their performance is assessed in the presence of two possible coherent receivers, the first based on a 4-state Viterbi detector, the second one on a simple threshold detector. A precoder is used prior to the modulator in both cases ([4]-[5]) to reduce the bit error probability due to the inherent differential encoding of GMSK.

If $d_k \in \{\pm 1\}$ is the k -th symbol to be transmitted, then the precoder outputs $a_k = (-1)^k d_k d_{k-1}$; the resulting GMSK complex signal can be approximated with the first two terms in the Laurent decomposition [2]:

$$\tilde{x}(t) \cong \sqrt{E_b} \left[\sum_{k=-\infty}^{\infty} e^{j\frac{\pi}{2}A_{0,k}} C_0(t - kT_b) + e^{j\frac{\pi}{2}A_{1,k}} C_1(t - kT_b) \right],$$

where

$$A_{0,k} = \sum_{m=-\infty}^k a_m = A_{0,k-1} + a_k,$$

$$A_{1,k} = \sum_{m=-\infty}^k a_m - a_{k-1} = A_{0,k-2} + a_k,$$

$C_0(t)$ and $C_1(t)$ are waveforms of duration $(L + 1)T_b$ and $(L - 1)T_b$, respectively, being $L = 4$ sufficient to make the above approximation very stringent for $BT_b \geq 0.25$. The analytical evaluation of $C_0(t)$ and $C_1(t)$ is treated in [2]. With the use of the following definitions:

$$\begin{aligned} \exp\left[j\frac{\pi}{2}A_{0,2n}\right] &= d_{2n}, \\ -j \exp\left[j\frac{\pi}{2}A_{0,2n+1}\right] &= d_{2n+1}, \end{aligned}$$

we get

$$\begin{aligned} \tilde{x}(t) &\cong \sqrt{E_b} \left[\sum_{n=-\infty}^{\infty} d_{2n} C_0(t - 2nT_b) - j d_{2n-2} d_{2n} d_{2n-1} C_1(t - 2nT_b) \right] + \\ &+ \sqrt{E_b} \left[\sum_{n=-\infty}^{\infty} j d_{2n+1} C_0(t - 2nT_b - T_b) - d_{2n-1} d_{2n} d_{2n+1} C_1(t - 2nT_b - T_b) \right]. \end{aligned}$$

The optimum receiver ([3][4][5]) must find the maximum among the likelihood ratios

$$\lambda = \Re \left\{ \int \tilde{r}(t) \tilde{x}_i^*(t) dt \right\}$$

where $\tilde{r}(t)$ is the complex envelope of the received signal, and $\tilde{x}_i^*(t)$ is the conjugate of the complex envelope of the i -th possible transmitted signal while $\Re \{ \}$ denotes the real part. It can be easily shown that

$$\lambda = \sum_n \lambda_i(n)$$

where

$$\lambda_i(n) = \Re \left\{ \exp \left[-j \frac{\pi}{2} A_{0,n}^{(i)} \right] r_{0,n} + \exp \left[-j \frac{\pi}{2} A_{1,n}^{(i)} \right] r_{1,n} \right\}$$

$$\lambda_i(2n) = d_{2n}^{(i)} \Re \{ r_{0,2n} \} + d_{2n-2}^{(i)} d_{2n-1}^{(i)} d_{2n}^{(i)} \Im \{ r_{1,2n} \}$$

$$\lambda_i(2n+1) = d_{2n+1}^{(i)} \Re \{ r_{0,2n+1} \} + d_{2n-1}^{(i)} d_{2n}^{(i)} d_{2n+1}^{(i)} \Im \{ r_{1,2n+1} \}$$

being

$$r_{0,n} = \int \tilde{r}(t) C_0(t - nT) dt$$

$$r_{1,n} = \int \tilde{r}(t) C_1(t - nT) dt.$$

Thus the receiver is made of two input filters (with impulse responses $C_0(-t)$ and $C_1(-t)$) followed by a sampler at times nT and a Viterbi detector with 4 states and branch metric $\lambda_i(n)$ (see Figure 1), which takes two different expressions on even and odd values of n . In any case, the branch metric evaluation requires a simple addition or subtraction, and the Viterbi detector is very simple and fast.

If the second component $C_1(t)$ is neglected too, $\tilde{x}(t)$ looks like an OQPSK signal with symbol period $T = 2T_b$ and baseband waveform $C_0(t)$; thus a receiver made of a

matched filter with impulse response $C_0(-t)$, a sampler and a threshold detector can be used, as for the OQPSK signals of the previous sections ([4]). Notice that, by neglecting the second component, part of the transmitted energy is lost, and that ISI arises, since $C_0(t)$ does not satisfy the first Nyquist criterion. The eye patterns of the in-phase component of the signals at the output of the matched filters $C_0(-t)$ are shown in Figure 6, Figure 7, and Figure 8 for the cases $BT_b = 0.25, 0.5$, and 1 , respectively. Thus GMSK can be seen either as a CPM binary modulation with symbol interval $T = T_b$, or as a quaternary OQPSK modulation with symbol interval $T = 2T_b$, which generates some confusion. In the following, we will consider $T = T_b$, as in the original definition of GMSK signals [6]; however, in order to avoid confusion, we will use the unambiguous bit interval T_b most of the time.

For **$BT_b = 0.25$** , the error probability evaluated with the threshold detector is higher than that obtained with the Viterbi detector, as shown in Figure 9, due to the presence of strong ISI ($C_0(t)$ alone does not obey the Nyquist criterion) as evidenced in Figure 6. The losses with respect to ideal BPSK are 0.10 dB at $P_b(e)=10^{-1}$, 0.11 dB at $P_b(e)=10^{-2}$, 0.19 dB at $P_b(e)=10^{-3}$ with the Viterbi detector, while they are equal to 0.23 dB at $P_b(e)=10^{-1}$, 0.64 dB at $P_b(e)=10^{-2}$, 1.06 dB at $P_b(e)=10^{-3}$ with the threshold detector. The losses for the Viterbi detector receiver are deemed to be a result of the fact that the Laurent decomposition into only two components may just be at the limit of validity for $BT_b=0.25$. [11]

For **$BT_b = 0.5$** , the error probability evaluated with the threshold detector is substantially equal to that obtained with the Viterbi detector, as shown in Figure 9, at least for BER higher or equal to 10^{-3} . The losses with respect to ideal BPSK are 0.01 dB at $P_b(e)=10^{-1}$, 0.02 dB at $P_b(e)=10^{-2}$, 0.03 dB at $P_b(e)=10^{-3}$.

For **$BT_b = 1$** , the error probabilities are equal for the two receivers and a loss lower than 0.003 dB can be found with respect to ideal BPSK for bit error rates down to 10^{-6} .

Therefore, in the following simulations the receiver for the cases $BT_b=0.5$ and 1 will consist of a filter with impulse response $C_0(-t)$ and a threshold detector, while it will consist of two filters (with impulse responses $C_0(-t)$ and $C_I(-t)$) and a Viterbi detector for the case $BT_b=0.25$. The threshold detector allows for the measurements of

the error probability with the more precise semi-analytical technique, while error counting is necessary for a Viterbi detector. As a consequence, the measured losses for $BT_b=0.25$ case are less accurate than those of the other modulation schemes.

3 Channel models

Two channel models have been considered: the usual AWGN (Additive White Gaussian Noise) channel with noise spectral density $N_0/2$, and a non-linear channel.

The non-linear channel is in turn characterized by two possible amplifiers: a TWTA (Travelling Wave Tube Amplifier) and an SSPA (Solid State Power Amplifier) with AM/AM and AM/PM curves shown in Figure 10 and Figure 11, respectively.

The input backoff was set equal to 0 dB in both TWTA/SSPA cases.

4 Simulation results

Figure 12 and Figure 13 show the power spectra of the considered modulated signals at the output of the TWTA and SSPA amplifiers, respectively.

It is apparent that in a non-linear channel the most bandwidth efficient modulation scheme is GMSK with $BT_b = 0.25$ followed by GMSK with $BT_b = 0.5$.

Moreover, the selected modulation schemes generally meet the power spectral density mask recommended by the Space Frequency Coordination Group (SFCG) in REC 17-2R1 for future Space Science missions. The only exception is for GMSK $BT_b = 1.0$ around the main lobe whereas the far sidelobes requirements are met.

The overall losses of the considered modulations in the non-linear channel with respect to ideal BPSK in a linear channel are given in Table 1.

These losses were measured as the difference between the values $E_{b,sat}/N_0$ (dB) and E_b/N_0 (dB) that cause a given BER when the nonlinear amplifier is present or absent. $E_{b,sat}$ is defined as the energy of the signal at the output of the amplifier driven at 0 dB back-off by an unmodulated carrier, in the time interval T_b .

As stated in section 2, perfect synchronization and ideal data are considered.

It can be seen that, as expected, the simulation results for GMSK end-to-end losses on a non-linear channel are the same as for a linear channel (constant envelope modulation). This is an indication of the simulation accuracy.

The following considerations can be made:

- GMSK losses are negligible for the optimal Laurent-based receiver for the cases $BT_b=1.0$ and $BT_b=0.5$, and are less than 0.2 dB for $BT_b=0.25$ at $P_b(e) = 10^{-3}$;
- SRRC-OQPSK with a matched receiver achieves less than 0.6 dB losses over an SSPA at $P_b(e) = 10^{-3}$;
- SRRC-OQPSK with integrate and dump filter suffers from a loss greater than 1 dB at $P_b(e) = 10^{-3}$;
- Butterworth-filtered OQPSK losses with an integrate and dump filter are around 1 dB at $P_b(e) = 10^{-3}$;
- Butterworth-filtered OQPSK through an SSPA/TWTA channel suffers from just a slight loss increase with respect to the AWGN channel, especially at $P_b(e) = 10^{-1}$ and $P_b(e) = 10^{-2}$;
- The TWTA is more detrimental to filtered OQPSK than SSPA.

The GMSK end-to-end losses results for the $BT_b=0.5$ case are similar to the results of [8]-[9] for a perfectly synchronized system. When practical synchronization systems are considered, document [9] has shown these losses to go up to only 0.2 dB at $P_b(e) = 10^{-3}$.

For a pre-coded GMSK $BT_b=0.5$ modulation, figure 8 in NASA/JPL document [5] indicates about 0.2 dB losses at 10^{-3} ; however, it is not stated if synchronization losses are included.

On the other hand, NASA/JPL document [7] quotes 0.8 dB end-to-end losses for GMSK $BT_b=0.5$ and 1.4 dB losses for GMSK $BT_b=0.25$. Clarification is therefore needed.

OQPSK losses were quoted in NASA/JPL paper [7] to be around 3 dB. This was due to the specific implementation used for the modulator (Universal Phase Modulator). NASA/JPL paper [10] considered instead an I-Q modulator implementation and indicated an end-to-end loss of about 0.5 dB for the Butterworth-filtered OQPSK in a linear channel (we found 0.6 dB, see sect. 2.2.), and a loss of about 0.6 dB for the SRRC-filtered OQPSK in the presence of an SSPA, ideal synchronization and

matched filtering (we found 0.56 dB) both at $P_b(e) = 10^{-3}$. This shows the good agreement between the results found by NASA/JPL and those of the present document.

5 Conclusions

The choice of the bandwidth-efficient modulation scheme to be used for space missions should fall on GMSK, if minimization of the end-to-end losses is the only criterion to be considered. A receiver with a matched filter and a simple threshold detector is adequate for GMSK whenever $BT_b \geq 0.5$, while a receiver with two filters and a Viterbi detector is necessary for $BT_b = 0.25$.

If an even simpler receiver is required to minimize Earth station modifications costs, then a Butterworth-filtered OQPSK or SRRC-OQPSK should be preferred, however, provided that a matched receiver is used.

All modulations considered meet the SFCG proposed spectral emission mask with exception of GMSK $BT_b = 1.0$ around the main lobe.

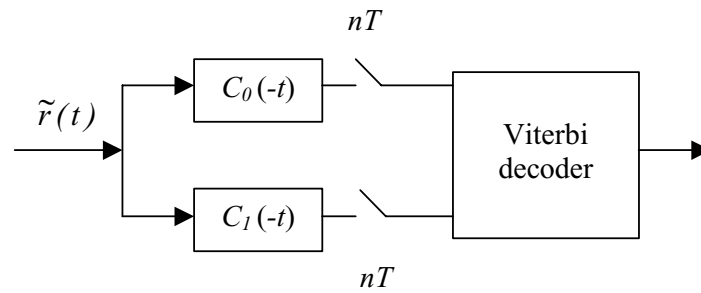


Figure 1: Scheme of the GMSK Viterbi detector

References

- [1] M. Otter, G. Block, Advanced Spectrum Shaping for Efficient Bandwidth Utilisation, Study report on SFCG AI 12/32 "Efficient Modulation Study", ESA, September 1997.
- [2] P.A.Laurent, "Exact and Approximate Construction of Digital Phase Modulations by Superposition of Amplitude Modulated Pulses (AMP)", IEEE Trans. Commun., Vol. COM-34, No. 2, Feb. 1986, pp. 150--160.
- [3] G.K.Kaleh, "Simple Coherent Receivers for Partial Response Continuous Phase Modulation", IEEE JSAC, Vol. 7, No. 9, Dec. 1989, pp. 1427--1436.
- [4] G.L. Lui, "GMSK Modulation: Description of Waveform, Receiver, and Performance", CCSDS Panel 1E, Houston, May 1998.
- [5] P.Arabshahi, L.Lam, "Preliminary Results on Gaussian Minimum Shift Keying Modulation: Spectral Analysis, Error Rates, and Synchronization", CCSDS Panel 1E, Houston, May 1998.
- [6] K. Murota, K. Hirade, "GMSK Modulation for Digital Mobile Radio Telephony", IEEE Transactions on Communications, Vol. COM-29, No. 7, July 1981, pp. 1044-1050.
- [7] W. Martin, T. Yan, L. Lam, "CCSDS Phase 3 Study Update", CCSDS Panel 1E, Houston, May 1998.
- [8] M. Luise, E. Vassallo, "CCSDS Panel 1E AI 99-1E-4, Questions on GMSK Performances", CCSDS Panel 1E, October 1999.
- [9] N. A. D'Andrea, M. Luise, U. Mengali, R. Reggiannini, "Advanced Modulation Schemes for Future ESA Standards", ESA Report, March 1991.
- [10] W. Martin, T. Yan, A. Gray, D. Lee, "CCSDS-SFCG Efficient Modulation Methods Study at NASA/JPL, Phase 4: Inteferece Susceptibility", SF19-1/D, SFCG-19, September 6, 1999.
- [11] M. K. Simon, "MAP-Motivated Carrier Synchronization of GMSK based on the Laurent AMP Representation", CCSDS Panel 1E, Houston, May 1998.

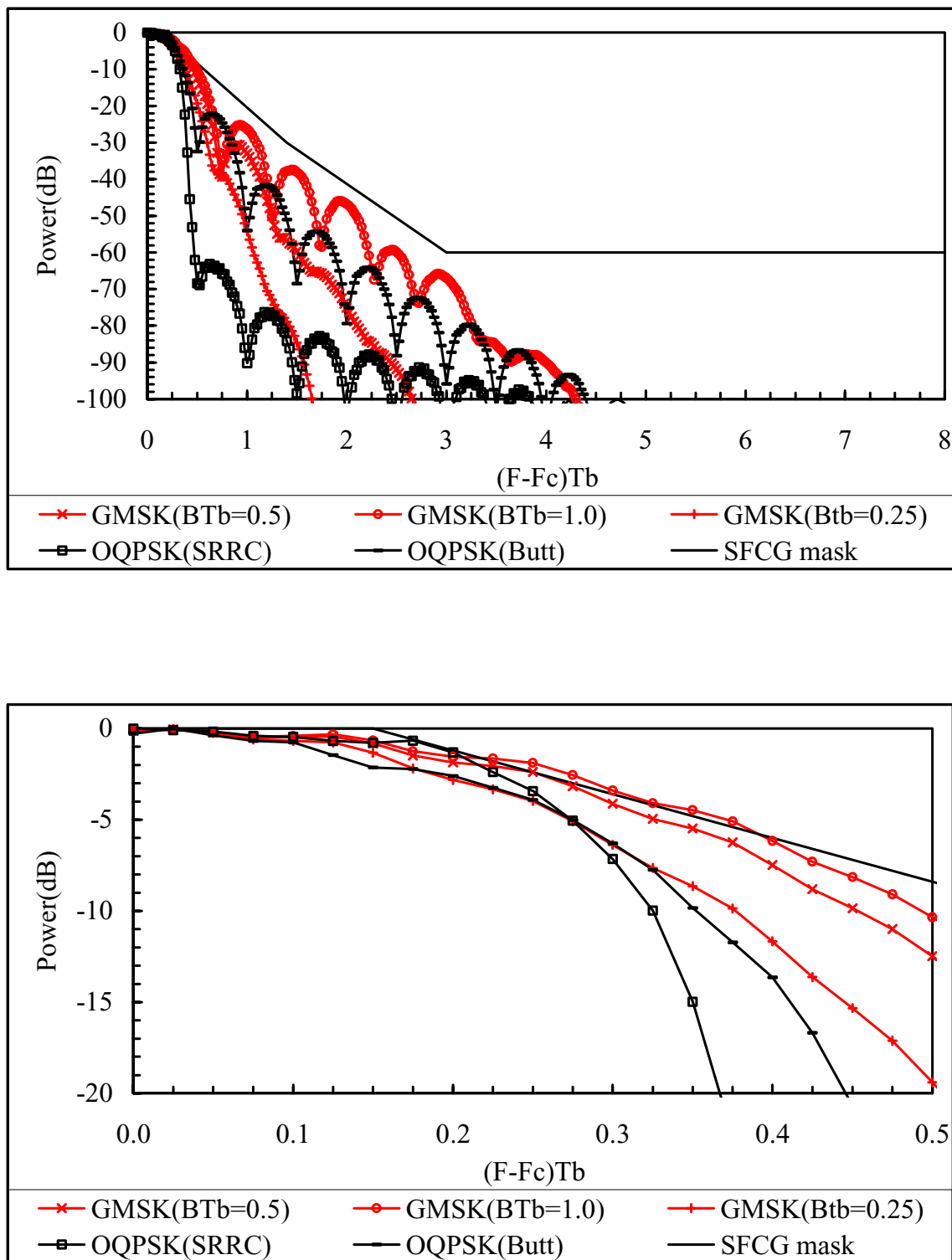


Figure 2: Power spectra of the modulated signals (linear channel).

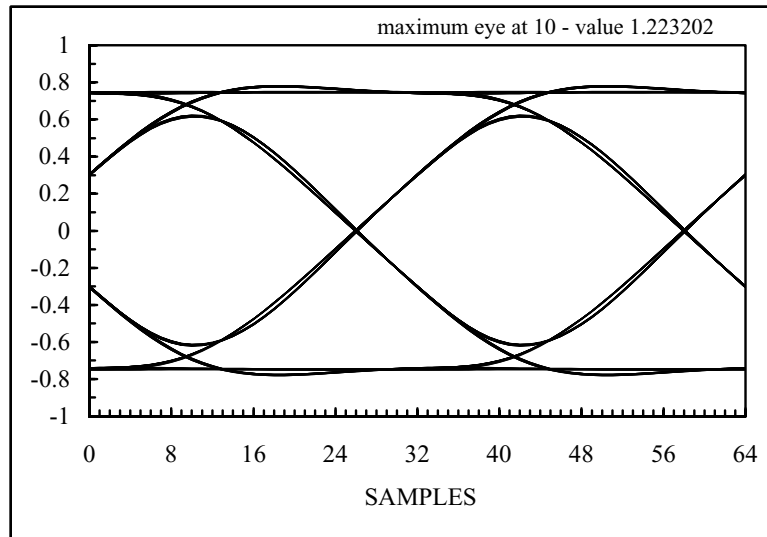


Figure 3: Eye pattern of the in-phase component of the signal at the receiver filter output for Butterworth-filtered OQPSK.

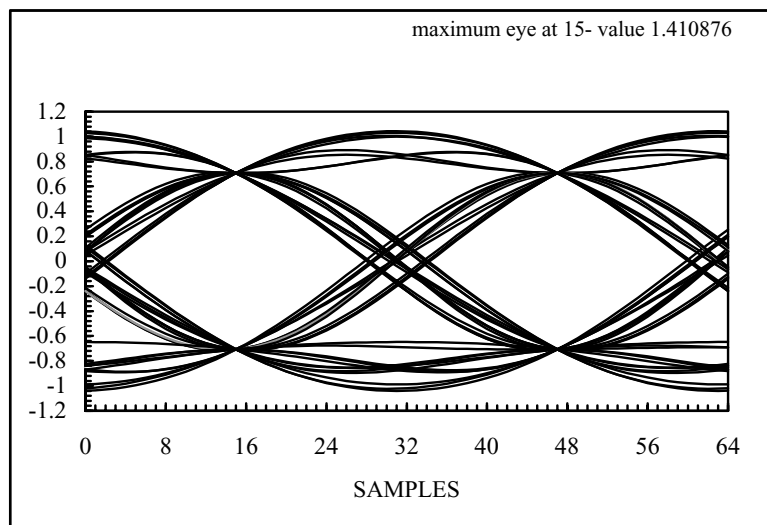


Figure 4: Eye pattern of the in-phase component of the signal at the receiver filter output for SRRC-a filtered OQPSK

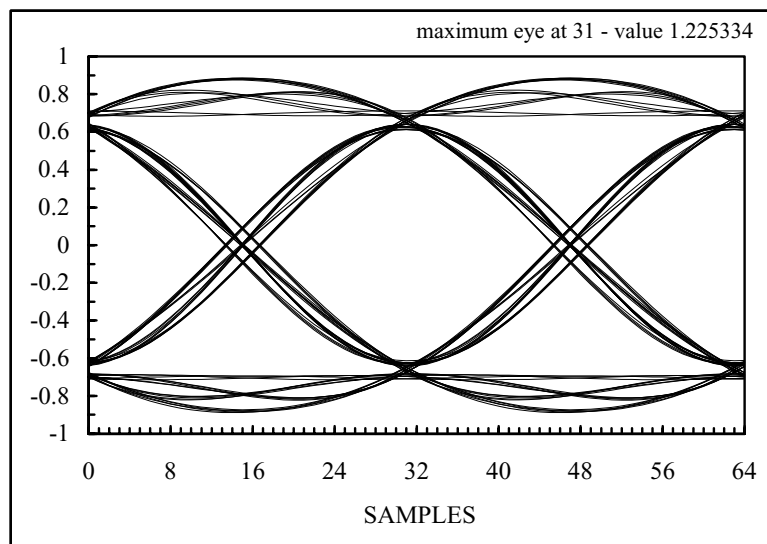


Figure 5: Eye pattern of the in-phase component of the signal at the receiver filter output for SRRC-b filtered OQPSK

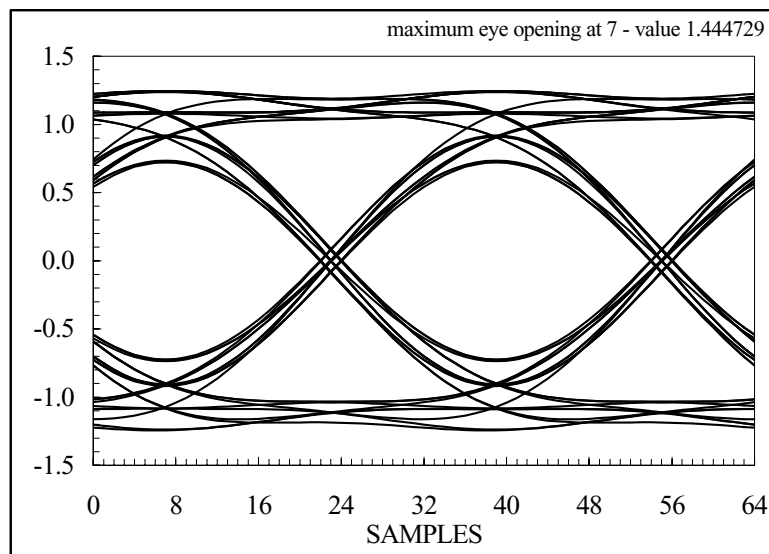


Figure 6: Eye pattern of the in-phase component of the signal at the receiver filter output for GMSK with $BT_b=0.25$

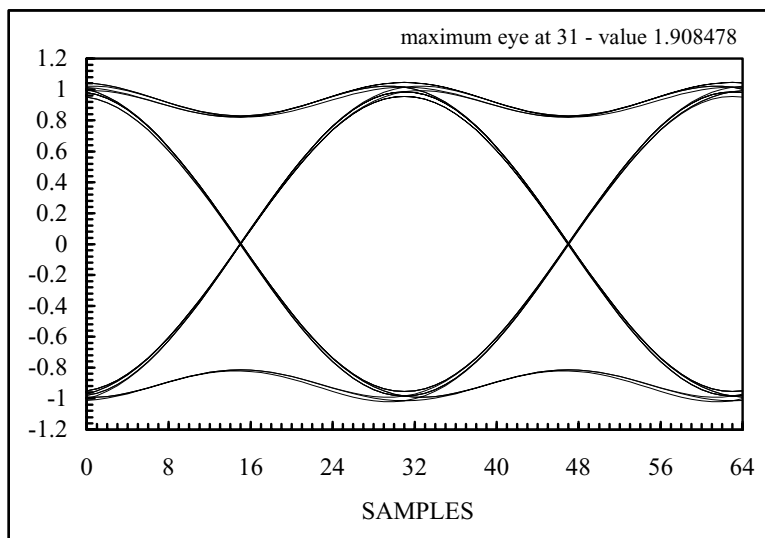


Figure 7: Eye pattern of the in-phase component of the signal at the receiver filter output for GMSK with $BT_b=0.5$

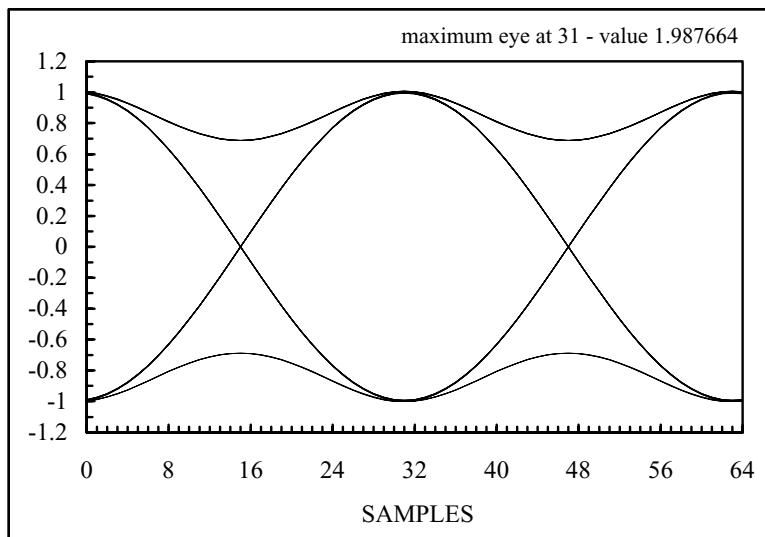


Figure 8: Eye pattern of the in-phase component of the signal at the receiver filter output for GMSK with $BT_b=1$

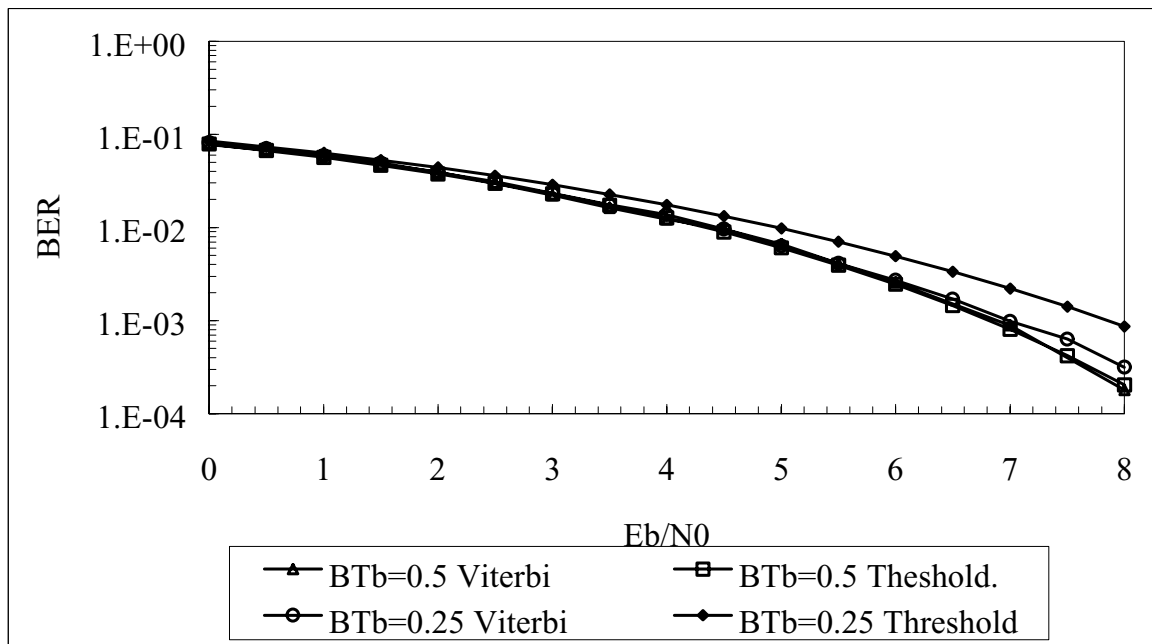


Figure 9: GMSK ($BT_b=0.25, 0.5$) error probabilities obtained with the threshold detector and the Viterbi detector.

modulation format	channel type	loss (dB) at $P_b(e)=10^{-1}$	loss (dB) at $P_b(e)=10^{-2}$	loss (dB) at $P_b(e)=10^{-3}$
Butterworth OQPSK	TWTA	0.51	0.71	0.98
	SSPA	0.44	0.66	0.96
SRRC-a OQPSK	TWTA	0.36	0.55	0.74
	SSPA	0.19	0.38	0.56
SRRC-b OQPSK	TWTA	0.75	0.98	1.31
	SSPA	0.59	0.77	1.07
GMSK $BT_b = 1$	TWTA	0.001	0.001	0.001
	SSPA	0.001	0.001	0.001
GMSK $BT_b = 0.5$	TWTA	0.01	0.02	0.03
	SSPA	0.01	0.02	0.03
GMSK $BT_b = 0.25$	TWTA	0.10	0.11	0.19
	SSPA	0.10	0.11	0.19

Table 1: Non-linear channel end-to-end losses with respect to ideal BPSK (on linear channel)

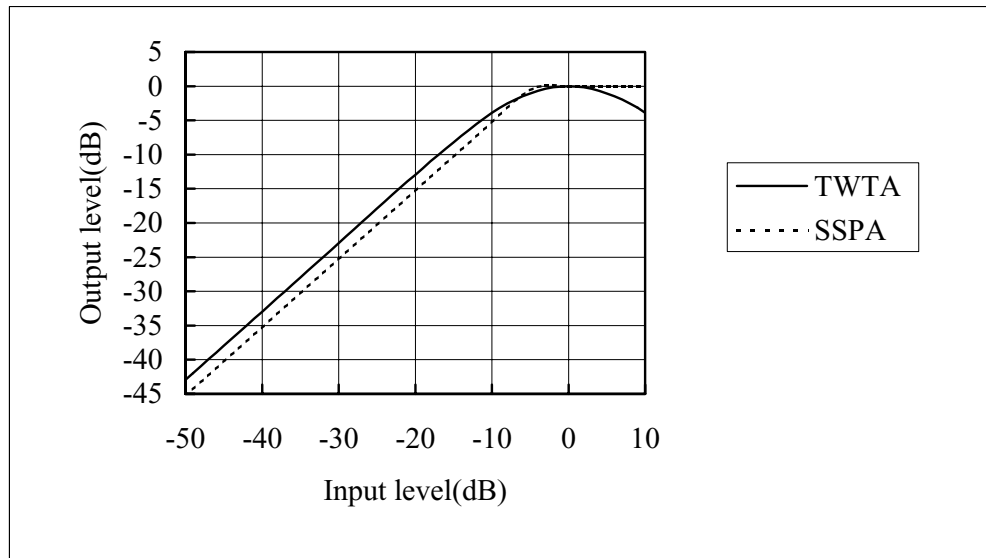


Figure 10: AM/AM characteristic of the assumed non-linear amplifiers

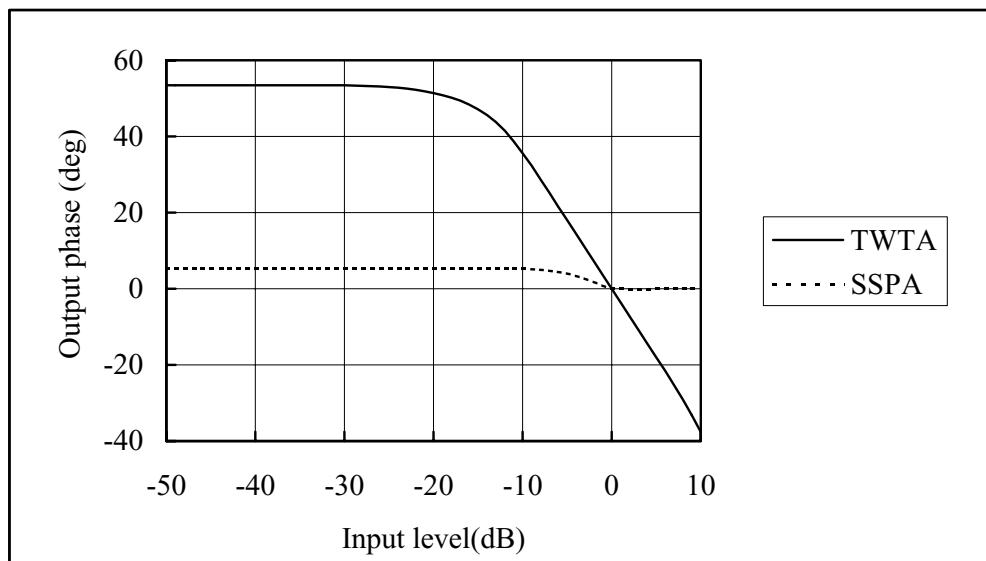


Figure 11: AM/PM characteristics of the assumed non-linear amplifiers

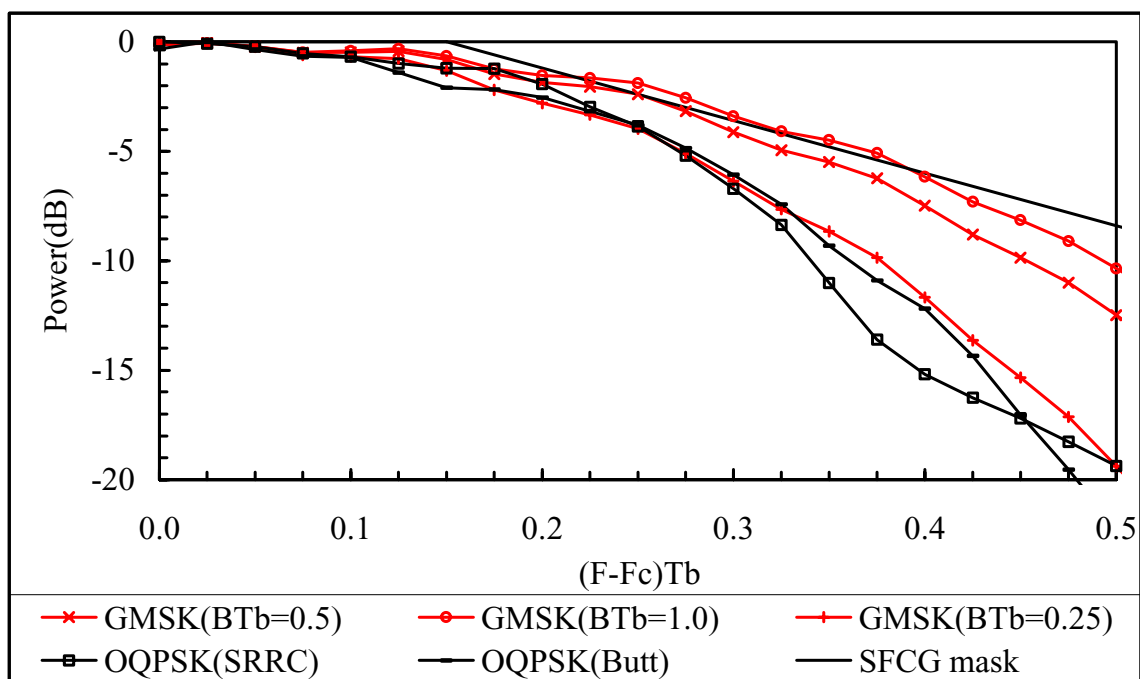
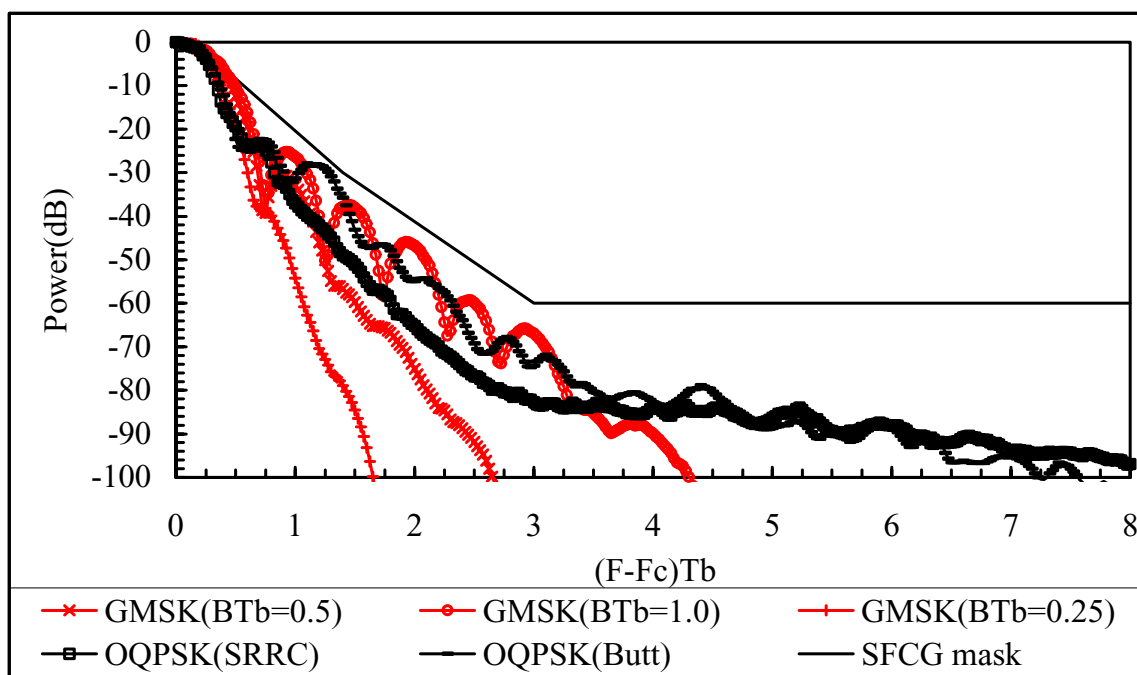


Figure 12: Power spectra of the modulated signals at the output of the TWTA

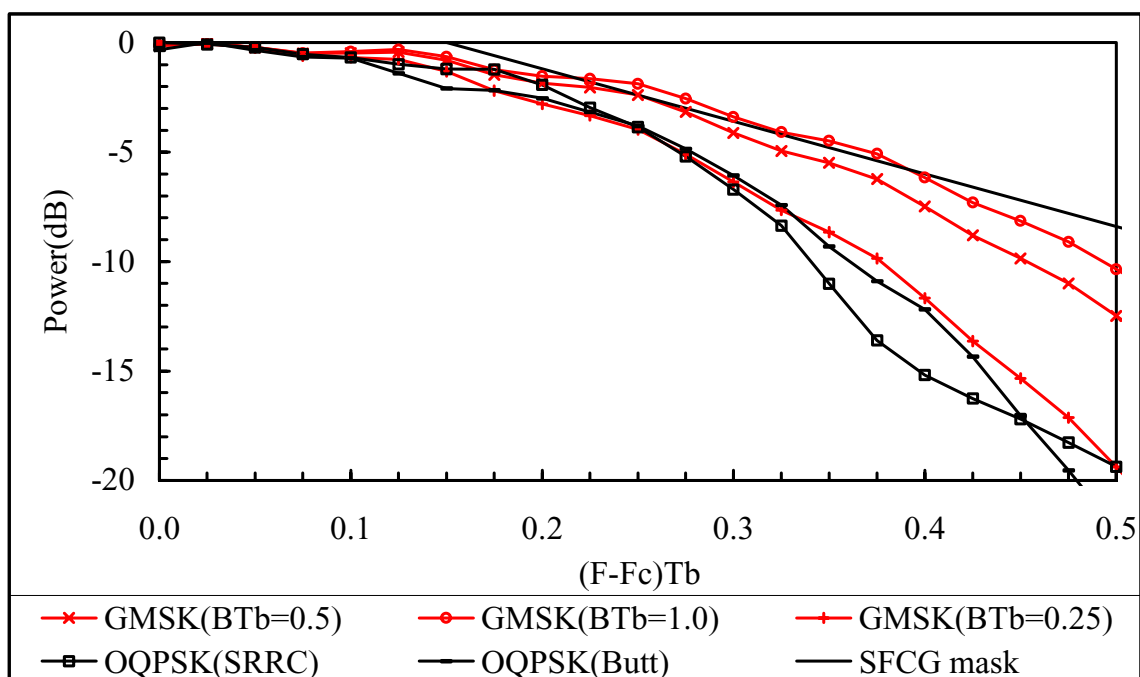
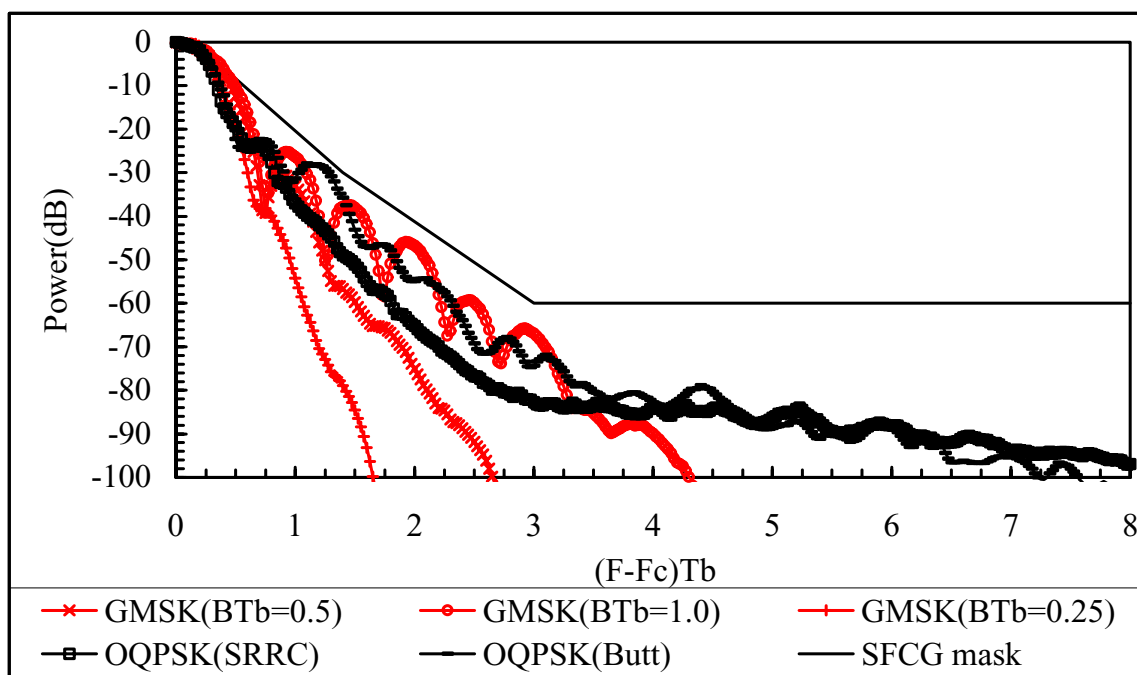


Figure 13: Power spectra of the modulated signals at the output of the SSPA.

CCSDS Panel 1E**Document 00/11****End-to-End Performance of Selected Modulation Schemes****Part II : Coded Channels**Gabriella Povero¹ Enrico Vassallo² Monica Visintin³**Abstract**

Butterworth and Square-Root Raised Cosine (SRRC) filtered OQPSK, and GMSK modulations are compared over a non-linear channel in the presence of the channel co-decoder specified in CCSDS 101.0B-3 Blue Book. No wide-band or narrow-band interfering signals are considered. The signal-to-noise ratio necessary to obtain a bit error rate (BER) equal to 10^{-6} at the output of the channel decoder is measured.

1 Introduction

This paper describes the effect of channel coding on the transmission systems considered in [3]. The encoding scheme is concatenated R-S and convolutional (interleaving depth =5) as recommended in CCSDS 101.0-B-3 Blue Book, and the modulated signal is passed through a nonlinear solid state power (SSP) amplifier. The wide-band and narrow-band interfering signals considered in [3] are not considered here. In particular, the following transmission schemes were studied:

1. Unfiltered BPSK transmitter, SSP amplifier, receiver made of an integrate and dump filter, and a threshold detector (benchmark);
2. GMSK with $BT_b=0.5$ transmitter, SSP amplifier, receiver made of a filter with impulse response $C_0(-t)$ and a threshold detector;
3. GMSK with $BT_b=0.25$ transmitter, SSP amplifier, receiver made of a filter with impulse response $C_0(-t)$, a 3-tap FIR equalizer (Wiener filter), and a threshold detector;
4. SRRC OQPSK (square root raised cosine OQPSK, with a roll-off factor equal to 0.5) transmitter, SSP amplifier, receiver made of a square root raised cosine filter with roll-off factor 0.5, and a threshold detector (case SRCC (a));
5. SRRC OQPSK (square root raised cosine OQPSK, with a roll-off factor equal to 0.5) transmitter, SSP amplifier, receiver made of an integrate and dump filter, and a threshold detector (case SRRC (b));

¹ COREP, Politecnico di Torino

² ESOC, European Space Agency

³ Dipartimento di Eletttronica, Politecnico di Torino

6. Butterworth OQPSK transmitter, SSP amplifier, receiver made of an integrate and dump filter, and a threshold detector.

All simulations were run with ideal carrier and clock synchronizers. The SSP non-linear amplifier is assumed equal to that considered in [3] and is driven at 0 dB back-off.

Aim of the work is the evaluation of the signal to noise ratio $E_{b,sat}/N_0$ (dB) that allows to get a bit error probability (BER) equal to 10^{-6} at the output of the decoder, and consequently the loss with respect to the ideal BPSK system, for each of the 5 systems described above. $E_{b,sat}$ is defined as $P_{sat} \cdot T_b$, being P_{sat} the maximum power at the output of the amplifier and T_b the duration of one information bit. In the following, the short-hand notation E_b/N_0 will be used instead of $E_{b,sat}/N_0$.

The paper is organized as follows: section 2 gives details on the co-decoding scheme and, on the structure of the Viterbi decoder (not specified in the CCSDS Blue Book), section 3 lists the simulation results for each of the considered transmission systems, section 4 includes some considerations on the obtained results, section 5 draws the conclusions.

2 The encoding scheme

According to the CCSDS 101.0-B-3 Blue Book, the transmission system to be considered is made of:

1. a symbol source (equally likely and statistically independent symbols made of $M=8$ bits each);
2. a switch S1 with 1 serial input and $I=5$ parallel outputs; the switch spends one Reed Solomon symbol in each of the 5 positions;
3. $I=5$ parallel Reed Solomon (R-S) encoders with codeword length $N=255$, number of information symbols $K=223$, number of symbols that can be corrected $t = 16$, each;
4. a switch S2, with $I=5$ inputs and 1 output which acts as a frame assembler and which is synchronized with switch S1; at the output of switch S2, a frame of $I \times N$ symbols exists, where the first $I \times K$ symbols exactly correspond to the $I \times K$ symbols generated by the source, and the last $I \times (N-K)$ symbols correspond to the R-S parity check symbols;
5. a rate $1/2$ transparent convolutional encoder with constraint length 7;
6. a digital modulator which transmits an energy equal to E for each input bit; the energy used to transmit an information bit is equal to $E_b=2EN/K$, being $K/(2N)=0.437$ the overall coding rate;
7. an AWGN channel with noise spectral power density $N_0/2$;
8. a digital receiver with 3-bit soft outputs for each channel bit;
9. a Viterbi decoder with $2^6=64$ states;
10. a switch S1 (as in the transmitter side);
11. $I=5$ parallel Reed-Solomon decoders;
12. a switch S2 (as in the transmitter side).

Figure 2.1 and Figure 2.2 depicts the transmission scheme. The convolutional encoder structure is shown in Figure 2.3.

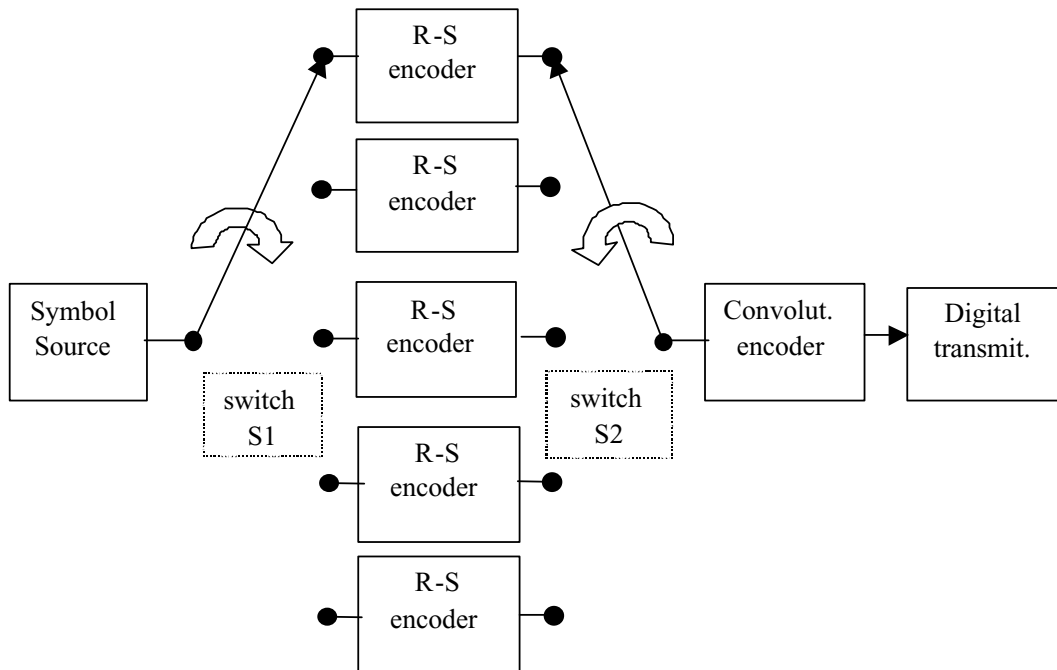


Figure 2.1: Transmission scheme: the transmitter.

The Viterbi decoder observes $2N_d$ 3-bit soft inputs to take the decision on the first bit, using the trace-back technique and starting from the most likely state, and thus introduces a delay equal to N_d R-S encoded bits. The value of N_d is not specified in the CCSDS Blue Book, but the analysis of the system with a BPSK modulator showed that $N_d = 70$ is a good compromise between complexity (delay) and performance. Notice that the recommended value for N_d is generally considered to be 5 times the constraint length (i.e., 35 in this case), which showed instead to be too small for this concatenated encoding scheme. Actually, if $N_d = 35$ is enough to approximately obtain the ideal ($N_d = \infty$) performance of the Viterbi decoder when the convolutional encoder alone is considered, it is true that any reduction in the error probability at the output of the Viterbi decoder is extremely valuable and should not be neglected in the presence of a Reed-Solomon outer encoder. If p is the error probability for a symbol at the input of the Reed Solomon decoder, then the error probability at the output of the R-S decoder reduces approximately to p^{17} ; if p is decreased to $0.9 p$ by increasing the decision depth in the Viterbi decoder, then the output error probability is reduced to $0.16 p^{17}$, i.e. about one order of magnitude is gained from a 10% decrease of p . Thus an almost negligible reduction of the error probability at the output of the convolutional decoder generates a substantial reduction of the error probability at the output of the R-S decoder. A decision depth equal to 100 produced only marginal benefits, so that 70 was considered a correct value for this parameter.

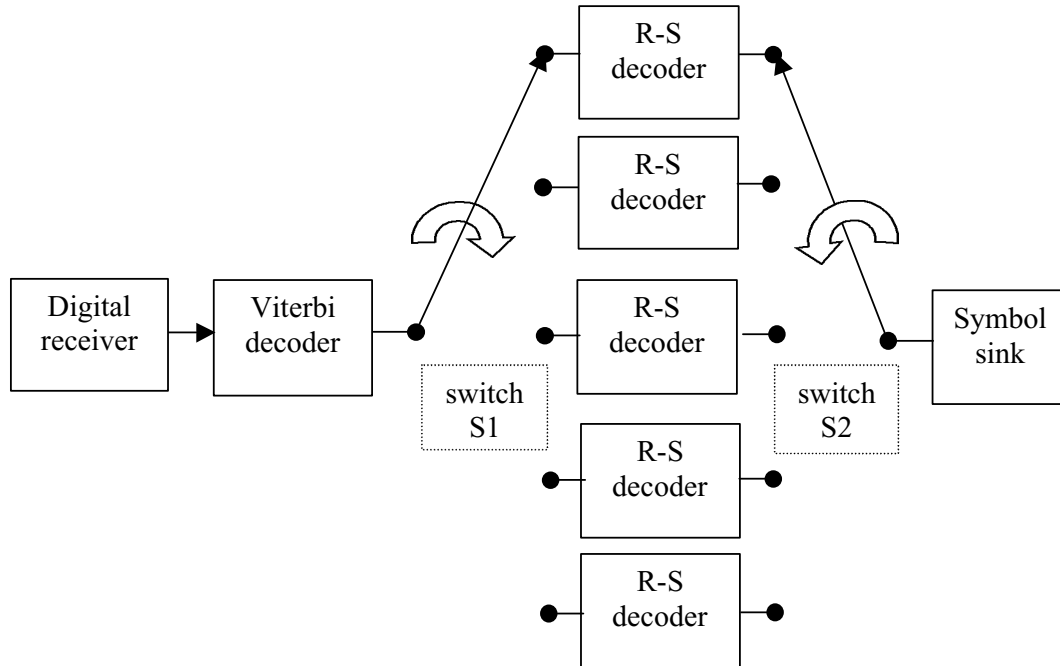


Figure 2.2: Transmission scheme: the receiver

Another question related to the Viterbi decoder is how to set the thresholds at the output of the digital demodulator. The following choices have been considered:

1. The 7 thresholds are set at the following values: $-1, -0.66, -0.33, 0, 0.33, 0.66, 1$; the input signal is multiplied by a constant C so that the root mean square (r.m.s.) of each sample at the input of the quantizer be equal to 0.5 (notice that two 3-bit quantized samples are required for each output bit, so that the overall r.m.s. of the input becomes equal to 1); the value of C depends on the signal to noise ratio; the branch metrics in the Viterbi algorithm are fixed (they do not depend on the signal to noise ratio) and equal to $0, 1, 2, \dots, 7$;
2. the thresholds and the metrics are set as in item 1; the multiplying constant C is set so that the average value of the useful part of each sample at the input of the quantizer be equal to ± 0.707 (thus it does not depend on the noise);
3. the thresholds and the multiplying constant are set as in item 2; the branch metrics in the Viterbi algorithm are computed from the transition matrix of the discrete Gaussian channel, i.e. from the transition probabilities of a channel where the transmitted alphabet is composed of two symbols ($+1$ and -1) and the received one is composed of 8 symbols (the 8 levels at the quantizer output). In particular, called P_{1j} the generic conditional probability that the received sample lies within the j -th interval having transmitted the level $+1$, the associated metric M_{1j} is

$$M_{1j} = \log(P_{11}) - \log(P_{1j})$$

Note that M_{1j} is proportional to the distance between the received signal and the signal associated to the channel branch with conditional probability P_{1j} ; moreover M_{1j} depends on the signal-to-noise ratio. Metrics M_{-1j} are similarly defined.

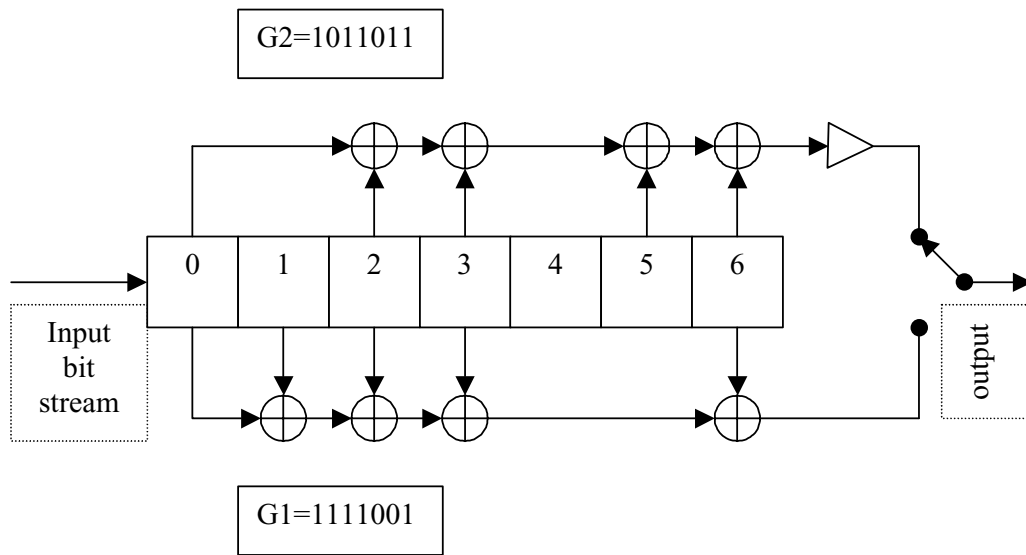


Figure 2.3: The convolutional encoder scheme.

The first strategy is that considered by DTU (Denmark Technical University) [1] and JPL/NASA [2] for the evaluation of the system performance in the presence of an unfiltered BPSK modulator. Politecnico di Torino considered the three strategies, but could not find significant differences among them in terms of BER at the output of the outer (R-S) decoder. Nevertheless, both DTU and JPL measured lower values of BER at small signal to noise ratios, with respect to Politecnico, while the BER values were comparable at higher signal to noise ratios (see Fig. 3.2).

A frame is defined as a block of $I=5$ R-S codewords, and it corresponds to $n=I \times M \times K=8,920$ information bits (the number of transmitted channel bits is instead $2 \times I \times M \times N=20,400$). A received frame is not correct if just one of its information bits is wrong; thus a frame error rate (**FER**) can be measured together with the bit error rate (**BER**). It is also interesting to measure the bit error rate at the output of the Viterbi (**BER_{Vit}**) detector, and that at the output of the digital receiver (**BER_{mod}**). Also of interest is the probability that one R-S symbol is wrong at the output of the R-S decoder (symbol error rate, **SER**).

In order to have a reasonable accuracy of the measured error rates with the counting technique, it is necessary to count at least 20 wrong frames, or about 1000 wrong bits at the sink. The counting of 10 to 20 wrong bits (which is generally considered enough) is not sufficient to have a good estimate of the bit error rate in this case. In fact, if a frame is wrong, it is because at least one R-S codeword is erroneously detected, and this corresponds to more than $t=16$ wrong R-S symbols in the codeword, i.e., more than 16 wrong bits in the frame. Thus either no bits or at least 16 bits are wrong in a simulation. Moreover, if an R-S symbol is wrong, then the actual number of wrong bits is highly variable, and at least 20 error events are needed to have a reasonable estimate of its average number.

3 Performance of the transmission schemes

In this section, the performance of the various modulation schemes is given, with the complete encoding system, in the presence of an SSP amplifier with 0 dB back-off. Since the non-linear amplifier does not affect the constant envelope signals (such as unfiltered BPSK and GMSK), it will not be considered in sections 3.1, 3.2, and 3.3.

3.1 Unfiltered BPSK

The measured error probabilities are listed in Table 3.1, Table 3.2, and Table 3.3 and they are plotted in Figure 3.1 and Figure 3.2, together with analogous measurements obtained by the Denmark Technical University (DTU) [1] and the Jet Propulsion Laboratory (JPL) [2]. Table 3.1 and Table 3.2 include the FER/BER values measured with decoding depths equal to 35 and 70, to show the remarkable advantage of an increased decoding depth. It can be noticed that a substantial agreement exists in terms of frame error rate between Politecnico and DTU, while the bit error rate curve obtained by Politecnico lies above those of DTU and JPL. Politecnico measures a loss with respect to DTU which ranges from 0.1 dB for low signal to noise ratios to ~ 0 dB at $E_b/N_0=2.5$ dB.

E_b/N_0 (dB)	Poli (35)	Poli (70)	DTU
2.00		6.20E-01	5.50E-01
2.10	8.48E-01	2.75E-01	
2.20	5.75E-01	1.10E-01	1.10E-01
2.25	4.18E-01		
2.30	2.73E-01	3.20E-02	2.10E-02
2.35	1.68E-01		
2.40	7.50E-02	5.60E-03	5.00E-03
2.45	4.17E-02		
2.50	1.25E-02	4.76E-04	7.00E-04
2.55	6.00E-03		
2.60	1.88E-03	3.33E-05	4.00E-05

Table 3.1: Measured values for the frame error rate (FER).

E_b/N_0 (dB)	Poli (35)	Poli (70)	JPL (70)	DTU
2.00	4.86E-02	1.87E-02	1.17E-02	1.00E-02
2.10	3.02E-02	7.24E-03	4.11E-03	
2.20	1.54E-02	2.43E-03	1.08E-03	1.30E-03
2.25	9.43E-03			
2.30	5.34E-03	4.84E-04	2.44E-04	2.20E-04
2.35	2.72E-03			
2.40	1.24E-03	7.59E-05	3.32E-05	4.00E-05
2.45	4.73E-04			
2.50	1.45E-04	5.96E-06	3.42E-06	5.00E-06
2.55	5.92E-05			
2.60	1.77E-05	4.07E-07	3.10E-07	3.50E-07

Table 3.2: Measured values for the bit error rate (BER).

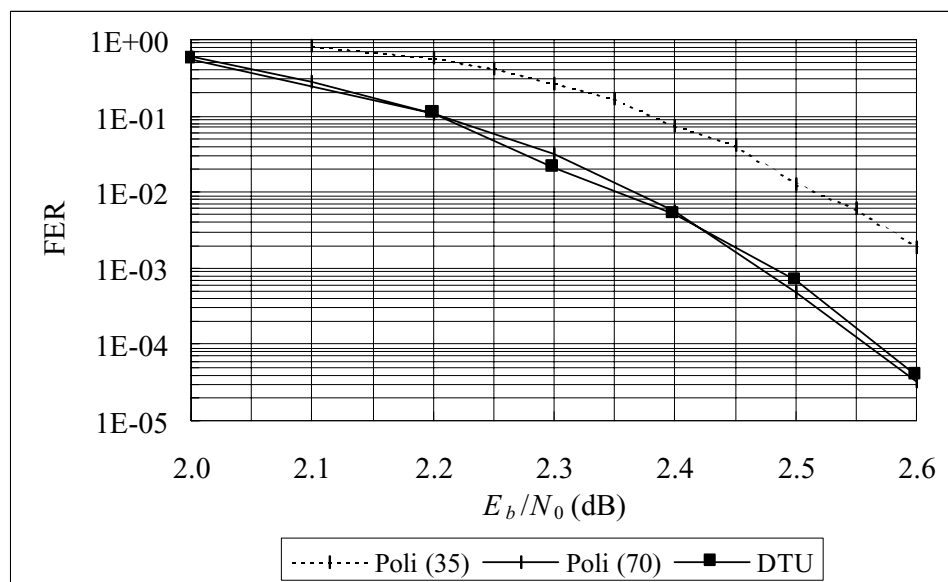


Figure 3.1: Measured values for the frame error rate (FER).

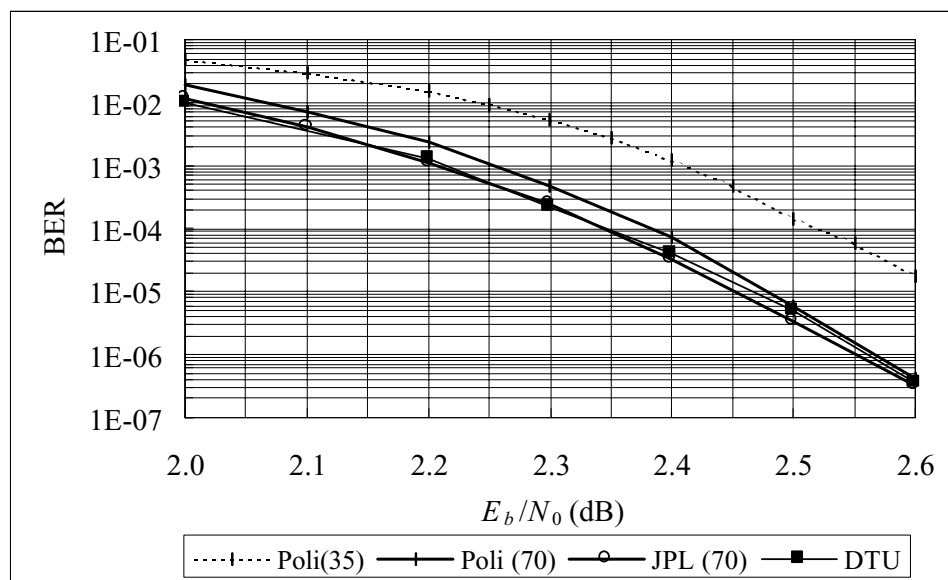
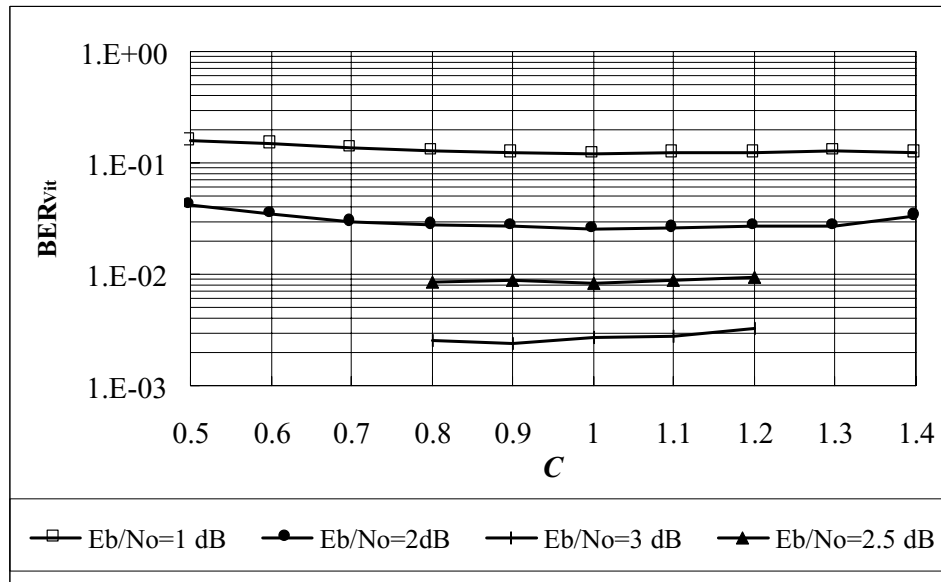


Figure 3.2: Measured values for the bit error rate (BER).

E_b/N_0 (dB)	BER BPSK	SER BPSK	FER BPSK	BER _{Vit} BPSK	BER _{mod} BPSK	BER (JPL)
2.0	1.87E-02	4.10E-02	6.20E-01	2.36E-02	0.120	1.17E-02
2.1	7.24E-03	1.58E-02	2.75E-01	1.93E-02	0.117	4.11E-03
2.2	2.43E-03	5.34E-03	1.10E-01	1.61E-02	0.114	1.08E-03
2.3	4.84E-04	1.07E-03	3.20E-02	1.31E-02	0.111	2.44E-04
2.4	7.59E-05	1.66E-04	5.60E-03	1.05E-02	0.109	3.32E-05
2.5	5.96E-06	1.36E-05	4.76E-04	8.56E-03	0.106	3.42E-06
2.6	4.07E-07	9.27E-07	3.33E-05	6.85E-03	0.104	3.10E-07

Table 3.3: Measured error probabilities for the encoded BPSK system.

In order to correctly compare the results obtained by Politecnico and those obtained by JPL and DTU, Politecnico tried to optimize the value of the samples at the input of the 3-bit quantizer, by multiplying those samples by a constant C . When $C=1$, then the useful part of the sample takes on the two values ± 0.707 , while the noisy part of the sample has a variance that depends on the signal to noise ratio E_b/N_0 (where E_b is the energy necessary to transmit one information bit, including the presence of the R-S code, so that the signal to noise ratio E_b/N_0 corresponds to that of Table 3.1 and Table 3.2, and Figure 3.1 and Figure 3.2). Then the bit error rate at the output of the Viterbi decoder BER_{Vit} was measured, letting the parameter C vary in the nearby of 1. Results are shown in Figure 3.3 and it is apparent that $C=1$ is optimum, and that the variation of BER_{Vit} with respect to C is minimum, especially at $E_b/N_0 = 2$ dB, where the difference in the results obtained by Politecnico and JPL/DTU is maximum. As a consequence, it can be argued that the difference in the results obtained by Politecnico and those obtained by JPL/DTU is not due to a different scaling of the quantizer input signal, but probably on a more subtle different implementation of the Viterbi algorithm. Thus, $C=1$ was kept valid by Politecnico in all the subsequent simulations, with the other modulation systems.

Figure 3.3: Measured BER at the output of the Viterbi decoder as function of parameter C .

3.2 GMSK with $BT_b = 0.5$

The structure of the digital transmitter and receiver is shown in Figure 3.4.

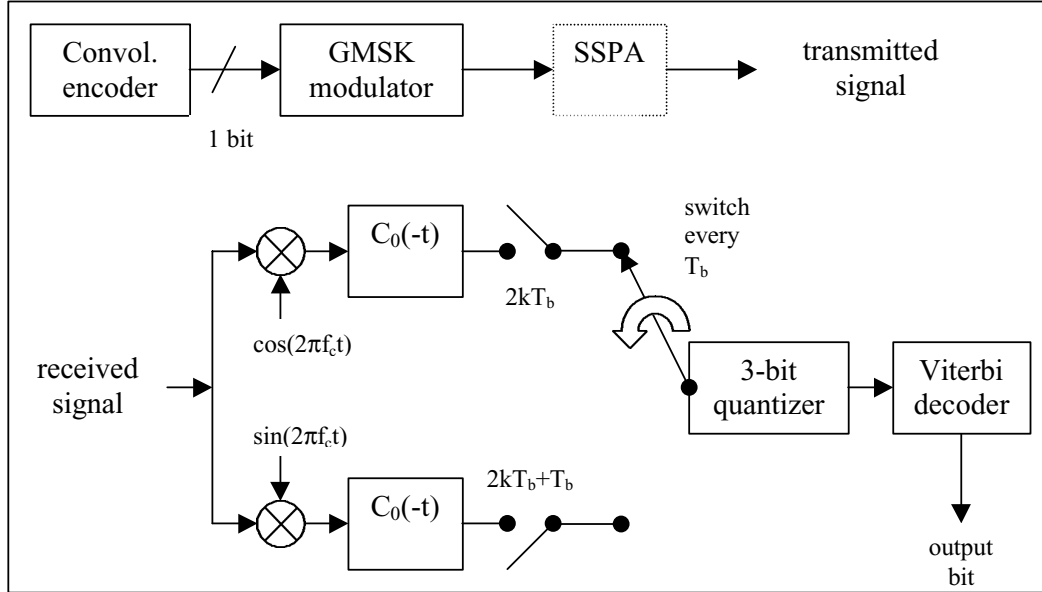


Figure 3.4: Transmitter and receiver structures for the GMSK system with $BT_b=0.5$ (the SSP amplifier can be omitted).

E_b/N_0 (dB)	BER GMSK 0.5	SER GMSK 0.5	FER GMSK 0.5	BER _{vit} GMSK	BER _{mod} GMSK	BER (BPSK)	FER (BPSK)	BER (JPL)
2.0	1.93E-02	4.24E-02	5.95E-01	2.35E-02	0.119	1.87E-02	6.20E-01	1.10E-02
2.1	7.88E-03	1.74E-02	2.90E-01	1.97E-02	0.117	7.24E-03	2.75E-01	5.00E-03
2.2	2.18E-03	4.65E-03	9.50E-02	1.65E-02	0.114	2.43E-03	1.10E-01	1.50E-03
2.3	4.16E-04	9.17E-04	3.25E-02	1.36E-02	0.111	4.84E-04	3.20E-02	3.00E-04
2.4	6.35E-05	1.42E-04	5.00E-03	1.08E-02	0.109	7.59E-05	5.60E-03	4.50E-05
2.5	7.49E-06	1.68E-05	5.00E-04	8.67E-03	0.107	5.96E-06	4.76E-04	5.00E-06
2.6	5.90E-07	1.34E-06	4.57E-05	6.90E-03	0.104	4.07E-07	3.33E-05	

Table 3.4: Measured error probabilities for the encoded GMSK system with $BT_b=0.5$ (the shaded values at $E_b/N_0=2.6$ have been determined using the polynomials given in section 4, on the basis of the measured values of BER_{vit}).

Table 3.4 lists the measured error rates for the case of a GMSK transmission system with $BT_b = 0.5$, while Figure 3.5 and Figure 3.6 plot the BER and FER values as functions of E_b/N_0 , respectively. It turns out that the ratio SER/BER is almost constant in the nearby of 2.2; on the contrary the ratio between the bit error rate at the output of the Viterbi decoder and the bit error rate at the output of the R-S decoder is highly variable. An analysis of the relationship between BER_{vit} and BER will be given in Section 4. The bit error rate at the output of the GMSK receiver BER_{mod} is

practically constant and equal to 0.1. Column BER(JPL) of Table 3.4 lists the BER values measured by JPL with the same transmitting system.

It can be noticed that the GMSK system loss with respect to BPSK is almost negligible at $\text{BER}=10^{-6}$ (0.01 dB); the loss of the uncoded GMSK system with respect to an uncoded BPSK at $\text{BER}_{\text{mod}}=0.1$ was measured to be equal to 0.01 dB.

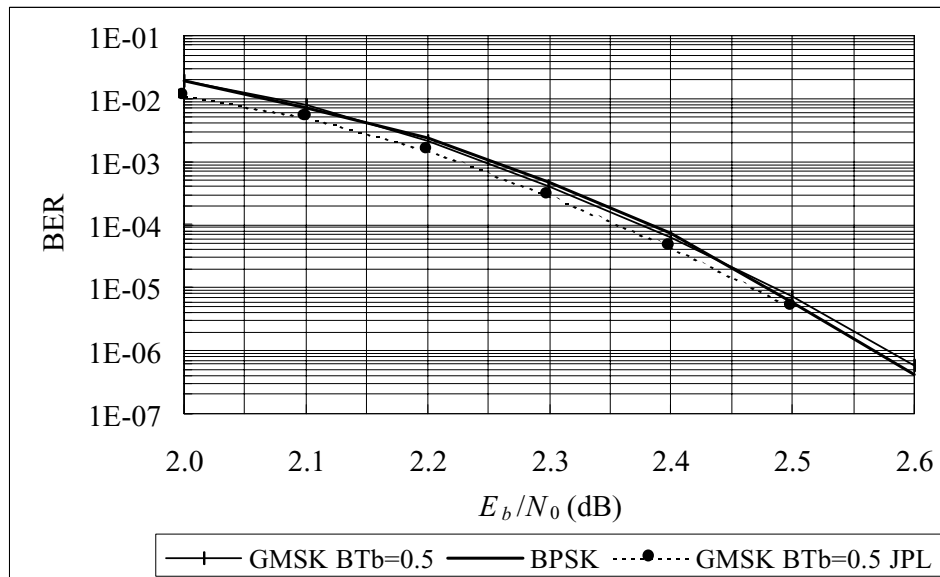


Figure 3.5: Measured values of BER as function of E_b/N_0 for the encoded GMSK system with $BT_b=0.5$.

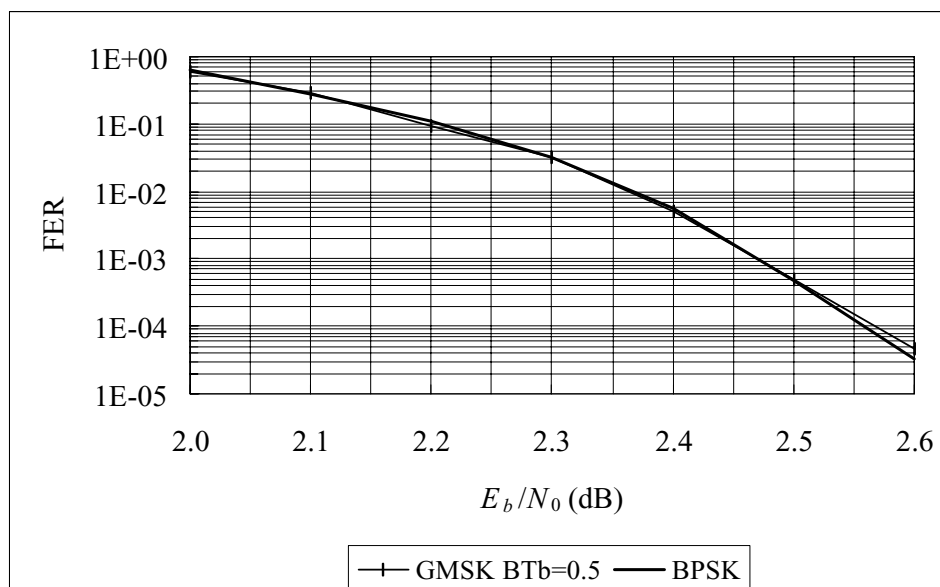


Figure 3.6: Measured values of FER as function of E_b/N_0 for the encoded GMSK system with $BT_b=0.5$.

3.3 GMSK with $BT_b = 0.25$

The structure of the digital transmitter and receiver is shown in Figure 3.7. The equalizer structure is a 3-tap FIR filter with delays equal to $2T_b$ and coefficients $-0.086, 1.012, -0.086$.

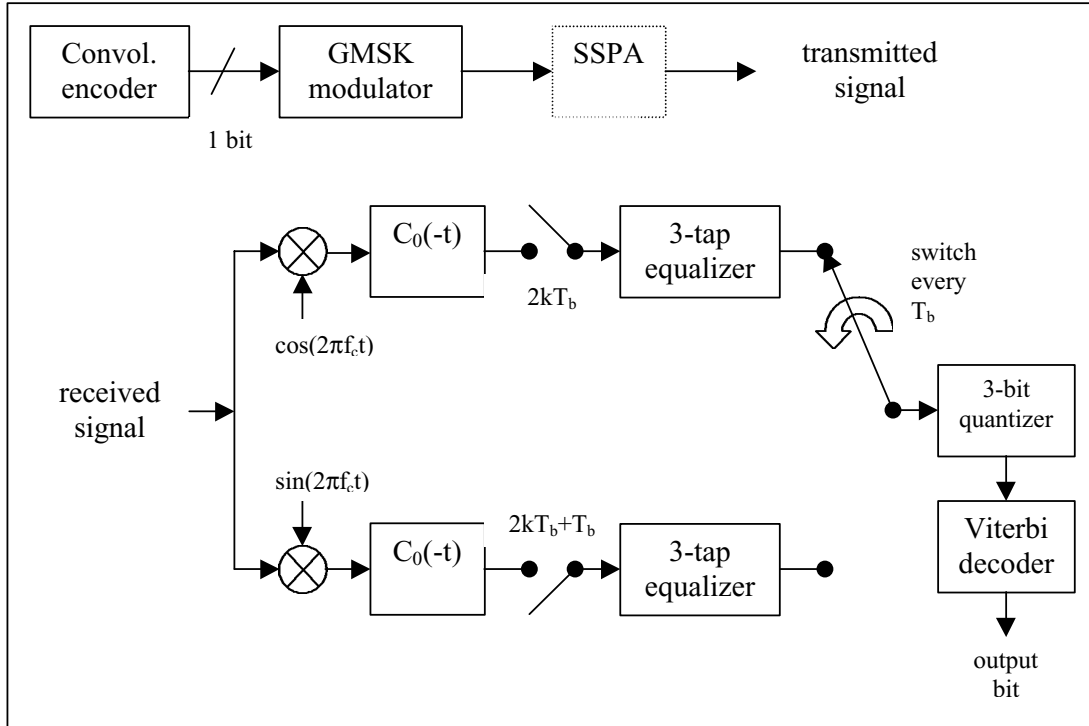


Figure 3.7: Transmitter and receiver structures for the GMSK system with $BT_b=0.25$ (the SSP amplifier can be omitted)

Table 3.5 lists the measured error rates for the case of a GMSK transmission system with $BT_b = 0.25$, while Figure 3.8 and Figure 3.9 plot the BER and FER values as functions of E_b/N_0 . Column BER(JPL) of Table 3.5 lists the BER values measured by JPL with the same transmitting system. It can be noticed that the GMSK system loss with respect to BPSK is of about 0.16 dB at $\text{BER}=10^{-6}$. Again, the ratio SER/BER is almost constant in the nearby of 2.2; the ratio $\text{BER}/\text{BER}_{\text{vit}}$ is again highly variable, while BER_{mod} is practically constant and equal to 0.1. It is interesting to notice that the loss of an uncoded GMSK system with $BT_b = 0.25$ was estimated equal to 0.16 dB at $\text{BER}_{\text{mod}}=0.1$, and this value is coincident with the encoded system loss at $\text{BER}=10^{-6}$.

E_b/N_0 (dB)	BER GMSK 0.25	SER GMSK 0.25	FER GMSK 0.25	BER _{Vit} GMSK	BER _{mod} GMSK	BER (BPSK)	FER (BPSK)	BER (JPL)
2.0	4.50E-02	9.86E-02	8.80E-01	3.10E-02	0.123	1.87E-02	6.20E-01	3.00E-02
2.1	2.77E-02	6.11E-02	7.53E-01	2.59E-02	0.121	7.24E-03	2.75E-01	2.00E-02
2.2	1.28E-02	2.82E-02	4.47E-01	2.13E-02	0.118	2.43E-03	1.10E-01	9.00E-03
2.3	4.02E-03	8.84E-03	1.77E-01	1.79E-02	0.115	4.84E-04	3.20E-02	3.00E-03
2.4	8.13E-04	1.80E-03	4.75E-02	1.45E-02	0.113	7.59E-05	5.60E-03	7.50E-04
2.5	1.65E-04	3.67E-04	1.08E-02	1.19E-02	0.110	5.96E-06	4.76E-04	1.10E-04
2.6	1.65E-05	3.65E-05	1.25E-03	9.60E-03	0.107	4.07E-07	3.33E-05	1.80E-05
2.7	2.15E-06	4.78E-06	1.73E-04	7.79E-03	0.105			2.00E-06
2.75	6.43E-07	1.46E-06	4.99E-05	6.95E-03	0.104			

Table 3.5: Measured error probabilities for the encoded GMSK system with $BT_b=0.25$ (the shaded values have been determined using the polynomials given in section 4, on the basis of the measured values of BER_{Vit}).

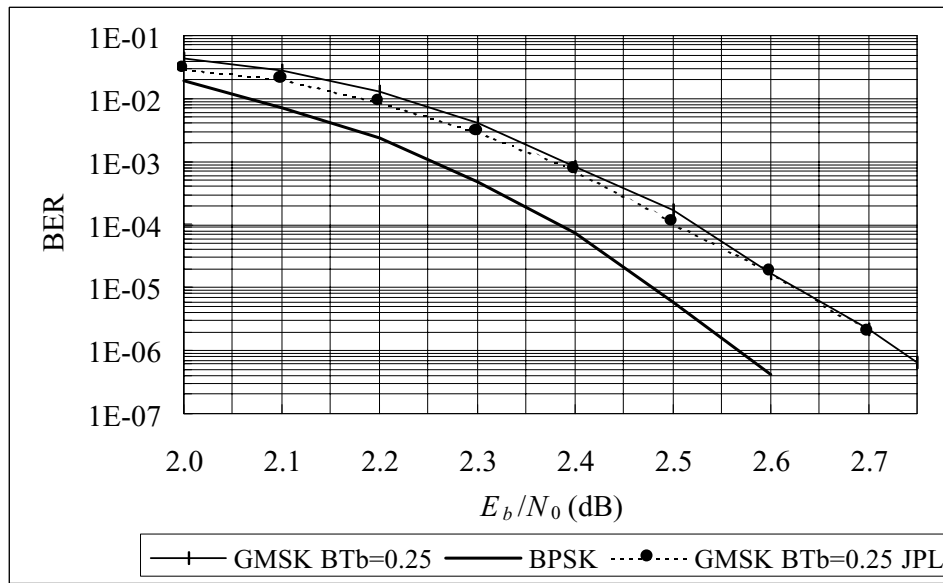


Figure 3.8: Measured values of BER as function of E_b/N_0 for the encoded GMSK system with $BT_b=0.25$.

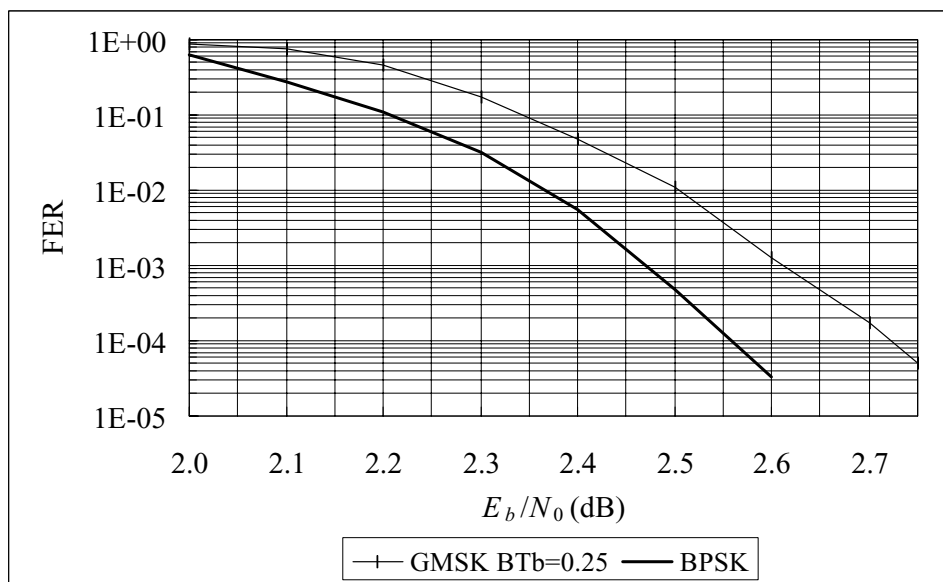


Figure 3.9: Measured values of FER as function of E_b/N_0 for the encoded GMSK system with $BT_b=0.25$.

3.4 SRRC-a OQPSK

The structure of the digital transmitter and receiver is shown in Figure 3.10.

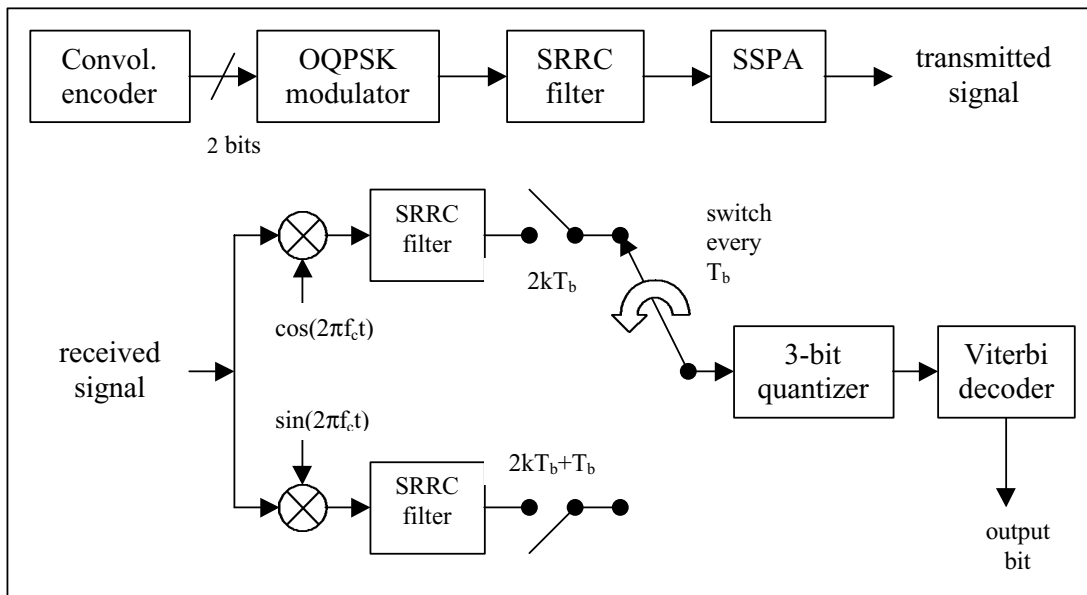


Figure 3.10: Transmitter and receiver structures for the SRRC (a) OQPSK system.

Table 3.6 lists the measured error rates for the case of the SRRC-a OQPSK transmission system, while Figure 3.11 and Figure 3.12 plot the BER and FER values as functions of E_b/N_0 , respectively. Column BER(JPL) of Table 3.6 lists the BER values measured by JPL with the same transmitting system.

Again, the ratio SER/BER is almost constant in the nearby of 2.2 and BER_{mod} is approximately equal to 0.1. It can be noticed that the SRRC-a OQPSK system loss with respect to BPSK is of about 0.18 dB at $\text{BER}=10^{-6}$; the loss of the uncoded SRRC-a OQPSK system with respect to an uncoded BPSK at $\text{BER}_{\text{mod}}=0.1$ was measured to be equal to 0.21 dB.

E_b/N_0 (dB)	BER SRRC-a	SER SRRC-a	FER SRRC-a	BER_{vit} SRRC-a	BER_{mod} SRRC-a	BER (BPSK)	FER (BPSK)	BER (JPL)
2.0	5.17E-02	1.14E-01	9.50E-01	3.36E-02	0.125	1.87E-02	6.20E-01	4.00E-02
2.1	3.49E-02	7.68E-02	7.75E-01	2.77E-02	0.122	7.24E-03	2.75E-01	2.30E-02
2.2	1.88E-02	4.13E-02	5.70E-01	2.32E-02	0.119	2.43E-03	1.10E-01	1.50E-02
2.3	6.44E-03	1.42E-02	2.40E-01	1.91E-02	0.117	4.84E-04	3.20E-02	6.50E-03
2.4	1.89E-03	4.20E-03	1.05E-01	1.58E-02	0.114	7.59E-05	5.60E-03	1.70E-03
2.5	3.75E-04	8.34E-04	2.10E-02	1.30E-02	0.111	5.96E-06	4.76E-04	3.50E-04
2.6	3.75E-05	8.23E-05	2.75E-03	1.03E-02	0.109	4.07E-07	3.33E-05	8.00E-05
2.7	4.78E-06	1.07E-05	3.57E-04	8.16E-03	0.106			1.00E-05
2.75	1.01E-06	2.28E-06	7.87E-05	7.25E-03	0.105			
2.8	3.00E-07	6.89E-07	2.28E-05	6.48E-03	0.103			

Table 3.6: Measured error probabilities for the encoded SRRC-a OQPSK system (the shaded values have been determined using the polynomials given in Section 4, on the basis of the measured values of BER_{vit}).

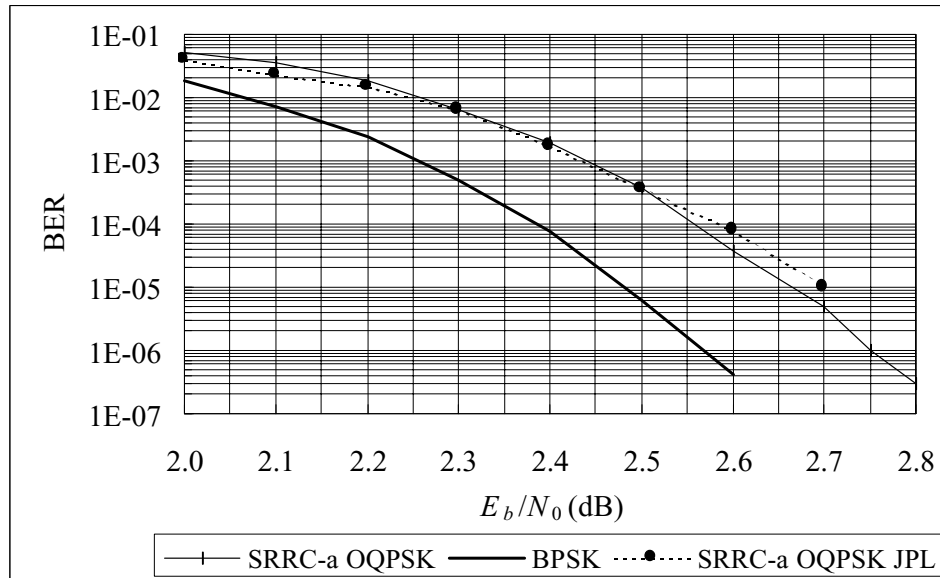


Figure 3.11: Measured values of BER as function of E_b/N_0 for the encoded SRRC-a OQPSK system.

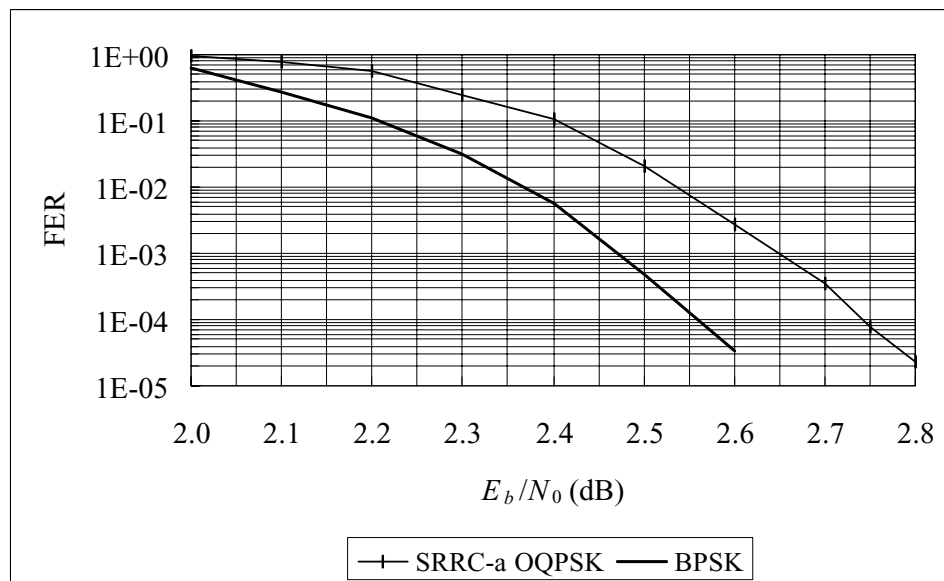


Figure 3.12: Measured values of FER as function of E_b/N_0 for the encoded SRRC-a OQPSK system.

3.5 SRRC-b OQPSK

The structure of the digital transmitter and receiver is shown in Figure 3.13.

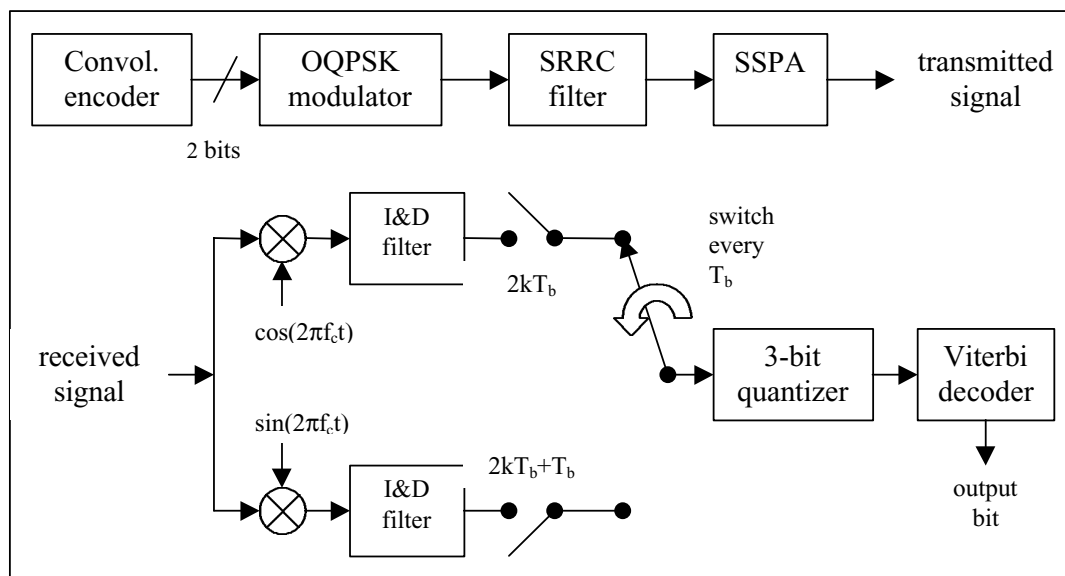


Figure 3.13: Transmitter and receiver structures for the SRRC-b OQPSK system.

Table 3.7 lists the measured error rates for the case of the SRRC-b OQPSK transmission system, while Figure 3.14 and Figure 3.15 plot the BER and FER values as functions of E_b/N_0 , respectively. Again, the ratio SER/BER is almost constant in the nearby of 2.2; the ratio BER/BER_{Vit} is again highly variable (it will be analyzed in Section 4) , while BER_{mod} is approximately equal to 0.1.

It can be noticed that the SRRC-b OQPSK system loss with respect to BPSK is of about 0.57 dB at BER=10⁻⁶; the loss of the uncoded SRRC-b OQPSK system with respect to an uncoded BPSK at BER_{mod}=0.1 was measured to be equal to 0.58 dB.

E_b/N_0 (dB)	BER SRRC-b	SER SRRC-b	FER SRRC-b	BER _{Vit} SRRC-b	BER _{mod} SRRC-b	BER (BPSK)	FER (BPSK)
2	6.82E-02	1.56E-01	1.00E+00	6.22E-02	0.135	1.87E-02	6.20E-01
2.1						7.24E-03	2.75E-01
2.2	6.60E-02	1.46E-01	1.00E+00	4.61E-02	0.129	2.43E-03	1.10E-01
2.3						4.84E-04	3.20E-02
2.4	4.98E-02	1.08E-01	9.10E-01	3.32E-02	0.124	7.59E-05	5.60E-03
2.5						5.96E-06	4.76E-04
2.6	1.49E-02	3.27E-02	4.60E-01	2.23E-02	0.118	4.07E-07	3.33E-05
2.7	4.99E-03	1.10E-02	1.99E-01	1.80E-02	0.116		
2.8	1.14E-03	2.52E-03	6.23E-02	1.48E-02	0.113		
2.9	1.62E-04	3.58E-04	1.08E-02	1.21E-02	0.111		
3.0	3.10E-05	6.99E-05	2.00E-03	9.84E-03	0.108		
3.1	2.72E-06	6.11E-06	2.13E-04	7.95E-03	0.105		
3.2	2.62E-07	6.04E-07	1.99E-05	6.40E-03	0.103		

Table 3.7: Measured error probabilities for the encoded SRRC-b OQPSK system (the shaded values have been determined using the polynomials given in Section 4, on the basis of the measured values of BER_{Vit}).

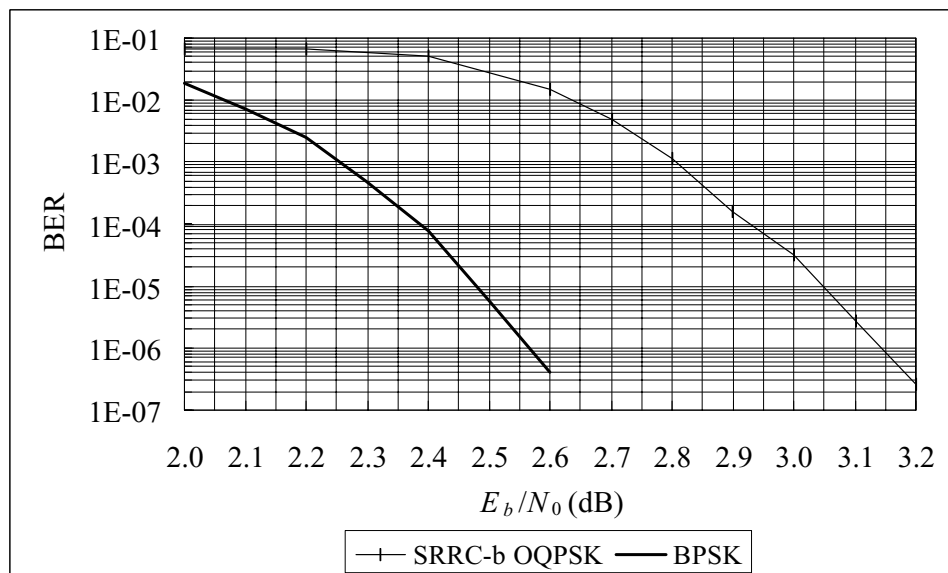


Figure 3.14: Measured values of BER as function of E_b/N_0 for the encoded SRRC-b OQPSK system.

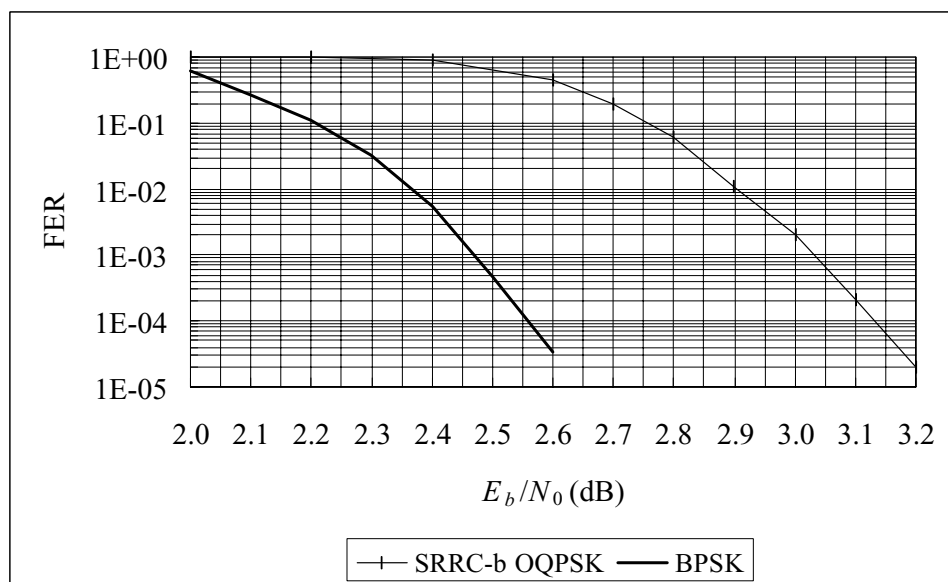


Figure 3.15: Measured values of FER as function of E_b/N_0 for the encoded SRRC-b OQPSK system.

3.6 Butterworth OQPSK

The structure of the digital transmitter and receiver is shown in Figure 3.16.

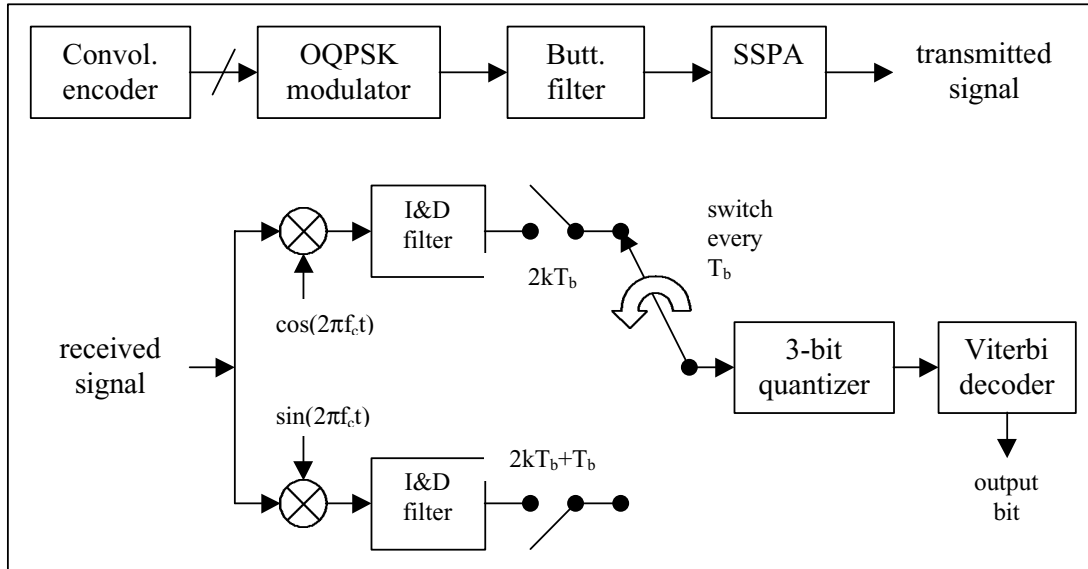


Figure 3.16: Transmitter and receiver structures for the Butterworth-filtered OQPSK system.

Table 3.8 lists the measured BER and FER values for the case of a Butterworth OQPSK transmission system, while Figure 3.17 and Figure 3.18 plot the BER and FER values as functions of E_b/N_0 , respectively.

It can be noticed that the Butterworth OQPSK system loss with respect to BPSK is of about 0.35 dB at $\text{BER}=10^{-6}$; the loss of the uncoded Butterworth OQPSK system with respect to an uncoded BPSK at $\text{BER}_{\text{mod}}=0.1$ was measured to be equal to 0.35 dB. The difference in the results obtained by Politecnico and those found by JPL is due to a different choice of the receiver filter (integrate and dump for Politecnico, matched filter for JPL).

E_b/N_0 (dB)	BER Butt.	SER Butt.	FER Butt.	BER _{vit} Butt.	BER _{mod} Butt.	BER (BPSK)	FER (BPSK)
2	6.03E-02	1.35E-01	1.00E-00	4.54E-02	0.129	1.87E-02	6.20E-01
2.1	5.67E-02	1.26E-01	9.90E-01	3.86E-02	0.126	7.24E-03	2.75E-01
2.2	4.54E-02	1.00E-01	8.90E-01	3.21E-02	0.123	2.43E-03	1.10E-01
2.3	2.77E-02	6.06E-02	6.90E-01	2.60E-02	0.121	4.84E-04	3.20E-02
2.4	1.25E-02	2.79E-02	4.40E-01	2.16E-02	0.118	7.59E-05	5.60E-03
2.5	5.08E-03	1.12E-02	2.10E-01	1.77E-02	0.115	5.96E-06	4.76E-04
2.6	8.02E-04	1.79E-03	5.00E-02	1.44E-02	0.113	4.07E-07	3.33E-05
2.7	1.421E-04	3.20E-04	1.03E-02	1.17E-02	0.110		
2.8	2.07E-05	4.62E-05	1.50E-03	9.32E-03	0.108		
2.9	1.64E-06	3.70E-06	1.29E-04	7.58E-03	0.105		

Table 3.8: Measured error probabilities for the encoded Butterworth-filtered OQPSK system (the shaded values have been determined using the polynomials given in Section 4, on the basis of the measured values of BER_{vit}).

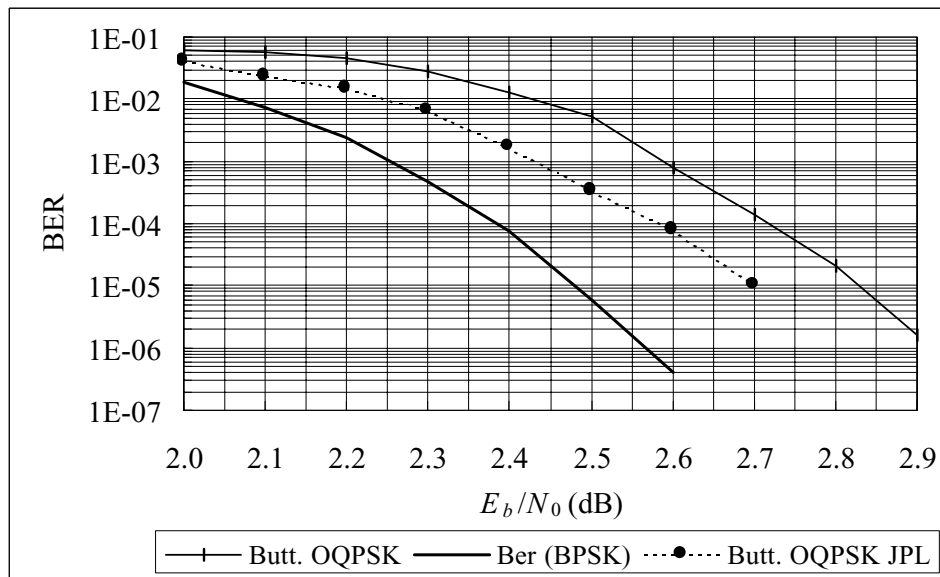


Figure 3.17: Measured values of BER as function of E_b/N_0 for the encoded Butterworth-filtered OQPSK system.

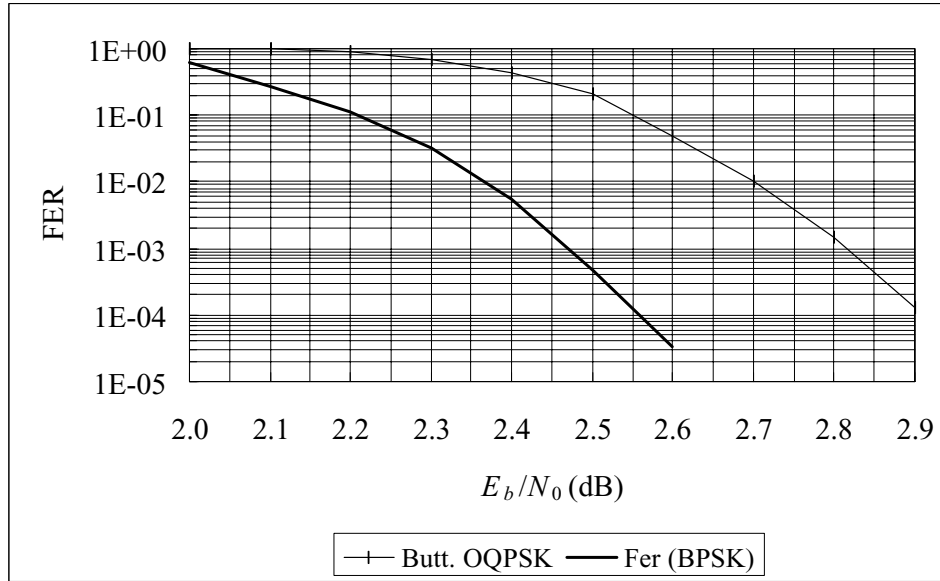


Figure 3.18: Measured values of FER as function of E_b/N_0 for the encoded Butterworth-filtered OQPSK system.

4 BER analysis

This section deals with the analysis of the results found in the previous one.

First of all, it was noticed that the loss of each complete encoded system at $\text{BER}=10^{-6}$ was substantially coincident with the loss of the uncoded system at $\text{BER}_{\text{mod}} = 0.1$ (see Table 4.1 and Table 4.2). Notice that the evaluation of the loss of the uncoded system is much easier and faster, since the semi-analytical technique can be used to quickly estimate its value; however

- the uncoded system BER_{mod} curves are very flat at $\text{BER}_{\text{mod}}=0.1$, and an error margin exists in the measure of the corresponding E_b/N_0 ,
- the value of BER_{mod} for the uncoded system that exactly corresponds to $\text{BER}=1 \cdot 10^{-6}$ at the output of the R-S decoder cannot be determined with precision, since, again, the curve is very flat.

Nonetheless, if the hierarchy alone is required among the various transmission schemes, the analysis of the uncoded systems seems to be adequate, even in the presence of inter-symbol interference due to non-linear amplifiers or to the chosen mo-demodulator structure. On the contrary, if the exact losses are required, then the uncoded system BER cannot be completely relied on (actually, the difference in the losses measured at $\text{BER}=10^{-6}$ and at $\text{BER}_{\text{mod}}=10^{-1}$ is very small for the considered cases).

Second, it was found that, while the bit error rate at the output of the R-S decoder varies from 10^{-2} to 10^{-6} by increasing the value of E_b/N_0 of 0.5 dB (approximately), the bit error rate at the output of the Viterbi decoder reduces from $3 \cdot 10^{-2}$ to $8 \cdot 10^{-3}$

(approximately). The variation of BER_{vit} is thus more remarkable than the variation of BER_{mod} , and it can be successfully used to predict the system loss at an overall BER of 10^{-6} , even if the dependence of BER from BER_{vit} is not linear or easily determined. Figure 4.1 plots BER versus BER_{vit} , for all the considered modulation systems, without distinguishing among them, while Figure 4.2 plots FER versus BER_{vit} . It can be noticed that all the points lie with good approximation on a curve that can be fitted by a polynomial function using the criterion of the minimum square error (for example). The fact that the points $(\text{BER}, \text{BER}_{\text{vit}})$ all lie on a curve, with no dependence from the modulation scheme, suggests that

- the measure of BER_{vit} is sufficient to correctly estimate the value of BER with high precision,
- all the points are reliable (i.e. the simulations were correctly performed).

Again, the measure of BER_{vit} is easier than the measure of BER, due to the higher values of BER_{vit} (even if the semi-analytical technique cannot be used), and due to the fact that it is not necessary to run long simulations to find at least 20 wrong frames (actually, it becomes unnecessary to consider the outer code at all). Moreover, from the value of BER_{vit} , both BER and FER can be estimated at the same time. The use of the polynomial curve allows for the evaluation of the exact BER_{vit} value necessary to obtain $\text{BER}=10^{-6}$.

The 4-th order polynomial functions that approximate BER/SER/FER are the following:

$$\begin{aligned}\log_{10}(\text{BER}) &\approx 6.4564 x^4 + 43.0799 x^3 + 98.8511 x^2 + 95.1233 x + 31.6541 \\ \log_{10}(\text{SER}) &\approx 6.7643 x^4 + 45.1848 x^3 + 104.2506 x^2 + 101.2773 x + 34.6227 \\ \log_{10}(\text{FER}) &\approx 8.5164 x^4 + 59.8761 x^3 + 148.1236 x^2 + 156.1333 x + 59.8646\end{aligned}$$

where x is equal to $\log_{10}(\text{BER}_{\text{vit}})$

A value of BER equal to 10^{-6} is obtained with $\text{BER}_{\text{vit}}=7.246 \cdot 10^{-3}$ (it corresponds to $\text{SER}=2.266 \cdot 10^{-6}$, and $\text{FER}=7.86 \cdot 10^{-5}$); a value of SER equal to 10^{-6} is obtained with $\text{BER}_{\text{vit}}=6.711 \cdot 10^{-3}$ (it corresponds to $\text{BER}=4.367 \cdot 10^{-7}$, and $\text{FER}=3.359 \cdot 10^{-5}$); a value of FER equal to 10^{-4} is obtained with $\text{BER}_{\text{vit}}=7.411 \cdot 10^{-3}$ (it corresponds to $\text{BER}=1.276 \cdot 10^{-6}$, and $\text{SER}=2.884 \cdot 10^{-6}$).

Figure 4.3 and Figure 4.4 summarize the performance of the various considered systems, and Table 4.1 lists their losses at $\text{BER}=1 \cdot 10^{-6}$. It can be noticed that the most advantageous modulation system is GMSK with $BT_b=0.5$, whose loss with respect to BPSK is almost negligible. GMSK with $BT_b=0.25$ comes next, followed by SRRC-a OQPSK, Butterworth-filtered OQPSK, and SRRC-b OQPSK.

Tables 4.2 and 4.3 list the losses of the uncoded systems (with SSPA) at $\text{BER}_{\text{mod}}=10^{-1}$ and $\text{BER}_{\text{mod}}=10^{-3}$, respectively. It can be noticed that the hierarchy of the uncoded systems at $\text{BER}_{\text{mod}}=10^{-3}$ is different from that of the encoded systems, while they are equal at $\text{BER}_{\text{mod}}=10^{-1}$.

modulation scheme	E_b/N_0 at $\text{BER}=10^{-6}$	Loss (dB) at $\text{BER}=10^{-6}$
Unfiltered BPSK	2.57	0.00
Butt. OQPSK	2.92	0.35
SRRC-a OQPSK	2.75	0.18
SRRC-b OQPSK	3.14	0.57
GMSK $BT_b=0.5$	2.58	0.01
GMSK $BT_b=0.25$	2.73	0.16

Table 4.1: Comparison of the encoded systems

modulation scheme	E_b/N_0 at $\text{BER}_{\text{mod}}=10^{-1}$	Loss (dB) at $\text{BER}_{\text{mod}}=10^{-1}$
Unfiltered BPSK	-0.86	0.00
Butt. OQPSK	-0.51	0.35
SRRC-a OQPSK	-0.65	0.21
SRRC-b OQPSK	-0.28	0.58
GMSK $BT_b=0.5$	-0.85	0.01
GMSK $BT_b=0.25$	-0.70	0.16

Table 4.2: Comparison of the uncoded systems at $\text{BER}_{\text{mod}}=10^{-1}$.

modulation scheme	E_b/N_0 at $\text{BER}_{\text{mod}}=10^{-3}$	Loss (dB) at $\text{BER}_{\text{mod}}=10^{-3}$
Unfiltered BPSK	6.78	0.00
Butt. OQPSK	7.34	0.56
SRRC-a OQPSK	7.39	0.61
SRRC-b OQPSK	7.78	1.00
GMSK $BT_b=0.5$	6.82	0.04
GMSK $BT_b=0.25$	7.20	0.41

Table 4.3: Comparison of the uncoded systems at $\text{BER}_{\text{mod}}=10^{-3}$.

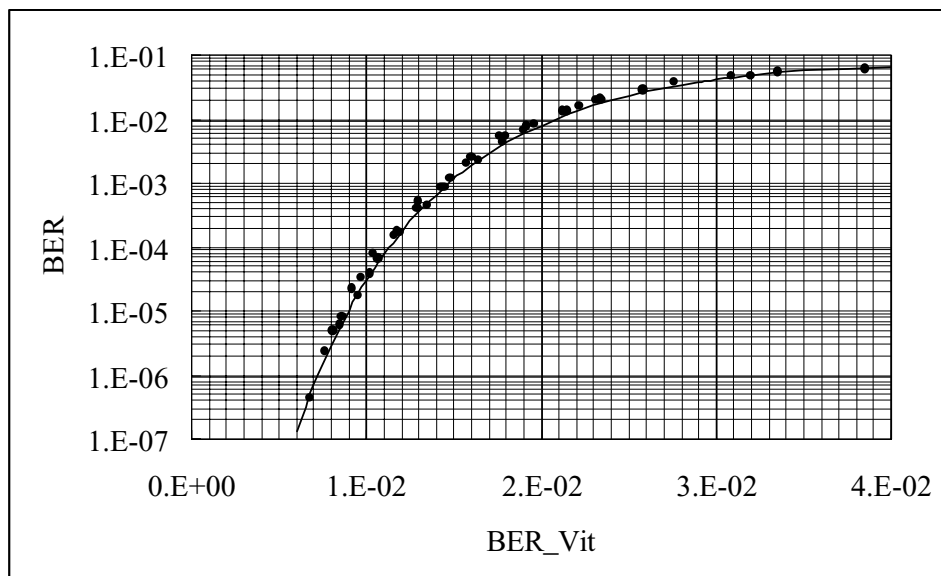


Figure 4.1: BER as a function of BER_{Vit} for all the considered modulation schemes. Measured values are shown with symbols, the interpolating polynomial function with a line.

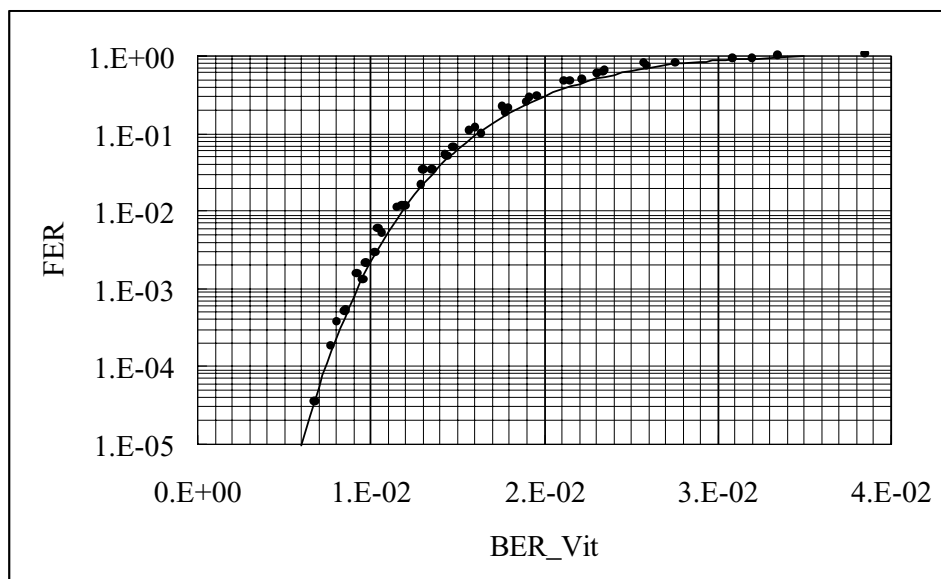


Figure 4.2: FER as a function of BER_{Vit} for all the considered modulation schemes. Measured values are shown with symbols, the interpolating polynomial function with a line.

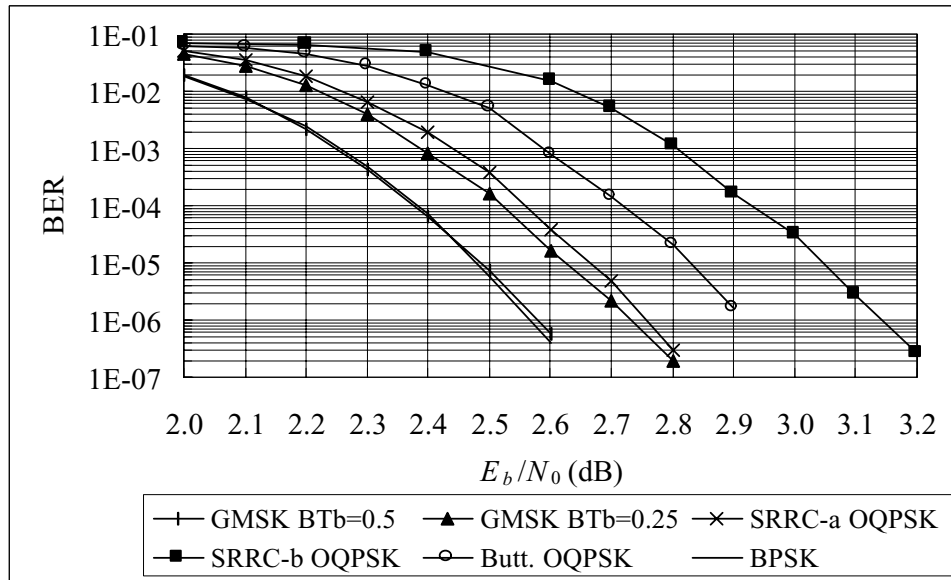


Figure 4.3: Comparison among the considered transmission systems in terms of BER.

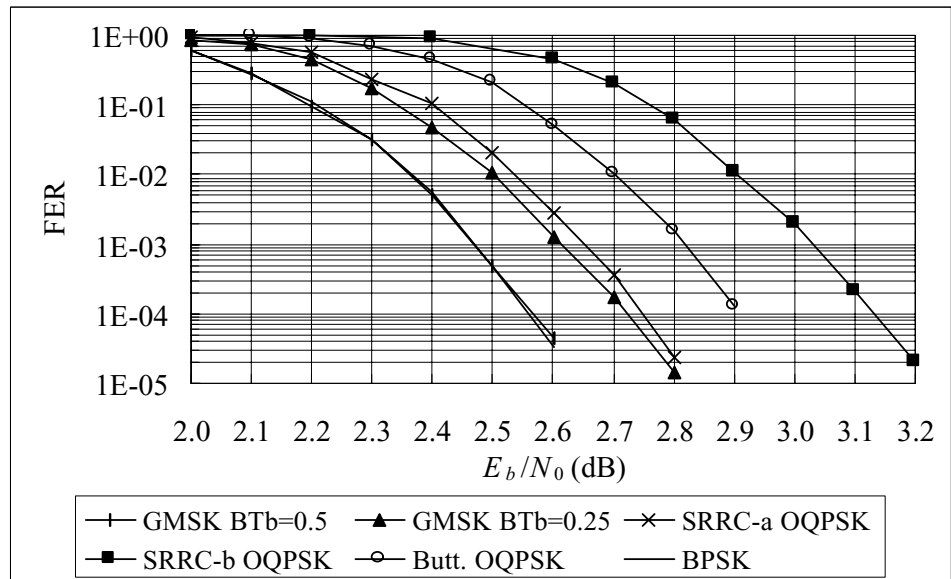


Figure 4.4: Comparison among the considered transmission systems in terms of FER

5 Conclusions

The simulation of the overall encoded transmission system showed that the case of GMSK with $BT_b=0.5$ is the most convenient in terms of signal to noise ratio necessary to obtain an overall BER equal to 10^{-6} . The use of GMSK with $BT_b=0.25$ causes a 0.15 dB higher loss in terms of signal to noise ratio, with an increase in bandwidth efficiency. The SRRC-a OQPSK system is comparable with the GMSK system with $BT_b=0.25$ over the non linear channel considered in this part of the report, but is more affected by wideband and narrowband interference as shown in [3], so that GMSK with $BT_b=0.25$ should be preferred. SRRC-b and Butterworth OQPSK systems suffer from higher losses.

Results obtained by Politecnico are similar to those obtained by JPL (apart from the Butterworth case, for which the results are not comparable) in terms of losses at $BER=10^{-6}$, but they differ for low signal to noise ratios, where, however, the system is not supposed to work.

References

- [1] J. Andersen, J. Justesen, K. Larsen, E. Paaske, "Evaluation of Extended CCSDS Reed-Solomon Codes for Bandwidth Efficiency", ESA/ESOC Contract No. 13441/99/D/CS, Final Report, November 1999
- [2] D. Lee, T.-Y. Yan, "Performance of Selected Bandwidth Efficient Modulations", CCSDS Panel 1E Doc. 99/34, Noordwijk, October 1999
- [3] G.Povero, E.Vassallo, M.Visintin, "End-to-End Losses of Selected Bandwidth-Efficient Modulation Schemes", CCSDS Panel 1E Doc. 99/45, Noordwijk, October 1999.

[This page intentionally left blank.]

NASA GSFC Efficient Spectrum Utilization Analysis

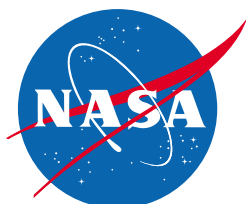
19 April 2000

Prepared For:

**Badri Younes
NASA Goddard Spaceflight Center
Greenbelt, MD, USA**

Prepared By:

**ITT Industries
Advanced Engineering and Sciences
Reston, VA, USA
Under Contract No.: GS-35F-0109J
Task Order No.: S-87070-Y**



PREFACE

This report provides an assessment of several bandwidth efficient modulation schemes for use in GSFC flight projects with regards to compliance with the SFCG spectral mask, link implementation loss and interference susceptibility.

Direct all questions and inquiries to:

Badri Younes

CLASS Project Manager
NASA Goddard Spaceflight Center
Greenbelt, MD 20771 USA

Tel: +1 301 286 5089; Fax: +1 301 286 1724

Email: Badri.younes@gsfc.nasa.gov

REPORT CONCERNING CCSDS RADIO FREQUENCY AND MODULATION

This report is a revision of an earlier report dated 11 June 1999. Several modifications and additions have been made since the earlier report. These are highlighted in the table below.

Item	11 June 1999 Version	This Version
BTs Definition	Product of two-sided filter bandwidth and channel symbol period.	Product of one-sided filter bandwidth and channel symbol period. This is consistent with definition used in other SFCG and CCSDS reports.
Data Asymmetry	PSD plots are generated with 10% data asymmetry but labeled as 5% data asymmetry. Incorrect model produced data asymmetry which is 2x that indicated in the report.	Data Asymmetry model has been corrected and results that are depending on data asymmetry are generated for 6% and 3% data asymmetry.
Transmitter PA models - TWTA-1 - TWTA-2 - ESA SSPA	One TWTA model was used with AM/PM = 12 deg/dB at 1 dB output backoff.	PSD plots are generated using 3 PA models: TWTA -1 (same as used in 6/11/99 report), TWTA-2 (AM/PM reduced to 3 deg/dB) and ESA SSPA.
Method to generate PSD	Single FFT method is used. Plots include FFT result and a frequency domain smoothed plot.	n FFT's are generated. n FFT's are averaged. n=50.
Spectra Filtered OQPSK	Generated using TWTA-1 at different OBO and BTs=0.5, 1.0, and 1.5.	Generated using three different transmitter PA models: TWTA-1, TWTA-2, and ESA SSPA Generated at three different OBO and BTs=0.5, 1.0, and 1.5. Generated for 3% and 6% Data Asymmetry.
Spectra Filtered OQPSK/PM	Generated with Butterworth filter using TWTA-1 at different OBO and BTs=1.0.	Regenerated with Butterworth filter using TWTA-1 at different OBO and BTs=0.5 and 1.0. Generated with Gaussian filter using TWTA -1, at 0dB OBO for BTs=1.0.
Spectra GMSK	Generated using TWTA-1 at different OBO and BT=0.5 and 1.0.	Regenerated using TWTA-1 at different OBO and BT=0.5 and 1.0.
Spectra Enhanced FQPSK	NA	Generated using TWTA-1 at different OBO.

Item	11 June 1999 Version	This Version
BER Plots Filtered OQPSK	Generated using TWTA-1 at different OBO and BTs=0.5, 1.0, and 1.5. Generated using TWTA-1 at 1dB OBO and BTs=1.0 with wideband and narrowband interference.	Generated using Different PA model, at 0dB OBO and BTs=1.0.
BER Plots Filtered OQPSK/PM	Generated using TWTA-1 at 0dB and 1dB OBO and BTs=1.0.	Generated using TWTA-1, at 0dB OBO and BTs=1.0.
BER Plots GMSK	Generated using TWTA-1, at 0dB OBO and BT=0.5 and BT =1.0. Generated Using Linear PA for BT=0.5 and 1.0. Generated using TWTA-1 at 0dB OBO and BT=0.5 with wideband interference.	Regenerated using TWTA-1, at 0dB OBO for BT=0.5 and BT =1.0. Regenerated Using Linear PA for BT=0.5 and 1.0. Will include Appendix to describe theoretical performance for GMSK with Integrate and dump detectors.
BER Plots Enhanced FQPSK	NA	Generated using TWTA-1 at three different OBO.
Base band Filter Response	NA	Provides documentation of the fidelity of the pulse shaping filters used in the study. Impulse Response and Frequency Response are generated for <ul style="list-style-type: none"> - Butterworth Filter - SRRC Filter - Gaussian Filter.

NASA GSFC Efficient Spectrum Utilization Analysis

Section 1	Executive Summary	1-1
1.1	Introduction	1-1
1.2	Results Summary.....	1-2
Section 2	Introduction	2-1
2.1	Objective	2-1
2.2	Scope	2-1
2.3	Approach	2-2
2.4	SFCG Recommendation 17-2R1.....	2-3
Section 3	Simulation Model.....	3-1
3.1	Overview	3-1
3.2	User Transmitter Model	3-1
3.2.1	Data Source	3-4
3.2.2	Modulator	3-5
3.2.3	Amplifier	3-10
3.2.4	RF Transmit Components	3-12
3.3	Ground Terminal Receiver Model	3-13
3.3.1	BPSK/OQPSK Ground Terminal Receiver Model	3-13
3.3.2	GMSK Ground Terminal Receiver Model.....	3-15
3.4	Interference Model	3-18
3.5	End-to-End Link Simulation Model.....	3-21
Section 4	Filtered OQPSK & OQPSK/PM Simulation Results.....	4-1
4.1	Overview	4-1
4.2	Spectra.....	4-1
4.2.1	Filtered OQPSK Spectra	4-2
4.2.2	Filtered OQPSK/PM Spectra	4-19
4.3	Implementation Loss	4-22
4.3.1	OQPSK/PM Implementation Loss	4-28
4.4	Filtered OQPSK Interference Susceptibility	4-29
4.4.1	Approach	4-30
4.4.2	Results	4-33
Section 5	GMSK Simulation Results.....	5-1
5.1	Overview	5-1
5.2	GMSK Spectra	5-1
5.3	GMSK Implementation Loss.....	5-6
5.4	GMSK Interference Susceptibility	5-8
Section 6	Enhanced FQPSK Simulation Results	6-1
6.1	Overview	6-1
6.2	Enhanced FQPSK Spectra.....	6-1
6.3	Enhanced FQPSK Implementation Loss	6-4

Section 7	Conclusions	7-1
7.1	Overview	7-1
7.2	Conclusions	7-1
7.2.1	Summary	7-1
7.2.2	Filtered OQPSK with I/Q Modulator	7-2
7.2.3	Filtered OQPSK with Phase Modulator	7-3
7.2.4	GMSK	7-3
7.2.5	Enhanced FQPSK.....	7-3
Section 8	References	8-1
Appendix A	Interference and Noise Model	A-1
Appendix B	GMSK Carrier Tracking For Transmitted Signal With Data Asymmetry	B-1
Appendix C	Wideband and Narrowband Interference Impact On FOQPSK and GMSK	C-1
Appendix D	Hardware Distortion Parameters	D-1
Appendix E	GMSK Theoretical BER Performance.....	E-1
Appendix F	Baseband Filter Response.....	F-1
Appendix G	Filtered OQPSK, GMSK Power Flux density Analysis.....	G-1
Appendix H	Modulation Scheme Study with TDRS KaSA Return Link.....	H-1

Glossary

AWGN	Additive White Gaussian Noise
BER	Bit Error Rate
BPSK	Binary Phase Shift Keying
FIR	Finite Impulse Response
FQPSK	Feher-patented QPSK
EFQPSK	Enhanced Feher-patented QPSK
GMSK	Gaussian filtered Minimum Shift Keying
GSFC	Goddard Space Flight Center
HDRR	High Data Rate Receiver
IF	Intermediate Frequency
MSK	Minimum Shift Keying
NRZ	Non-Return to Zero data formatting
OBO	Output Back-Off
OQPSK	Offset Quadrature Phase Shift Keying with I/Q modulator
OQPSK/PM	Offset Quadrature Phase Shift Keying with linear phase modulator
PA	Power Amplifier
PCM	Pulse Code Modulation
PM	Phase Modulation
PSD	Power Spectral Density
QPSK	Quadrature Phase Shift Keying
RF	Radio Frequency
SFCG	Space Frequency Coordination Group
SRRC	Square Root Raised Cosine
SSPA	Solid State Power Amplifier
XTCQM	Cross Correlated Trellis Coded Quadrature Modulation

Section 1 Executive Summary

1.1 Introduction

The SFCG has recommended that space science projects starting after the year 2001 comply with an emitted spectrum mask for space-to-earth data transmission in the bands 2200-2290 MHz, 2290-2300 MHz, 8025-8400 MHz, and 8400-8500 MHz (SFCG Rec. 17-2R1). Typically, techniques used to narrow the transmitted spectrum incur a cost of additional transmit power required to achieve the same BER performance.

SFCG has conducted several studies to assess the spectrum and power requirements for several candidate modulation techniques [1, 2, 3]. These studies computed RF transmit spectra and additional transmit power required for each modulation technique but did not include degradations in BER performance due to the transmitter imperfections that are typically specified for GSFC missions.

The purpose of this study is to assess the additional power required for several bandwidth efficient modulation techniques while including distortions caused by the transmitter hardware that are typically specified for GSFC flight project transmitters. The results of this study can then be used to assess the impact of compliance with the SFCG Rec 17-2R1 spectral mask to GSFC missions.

The study addresses filtered OQPSK (using an I/Q modulator), filtered OQPSK/PM (using a linear phase modulator), GMSK modulation, and enhanced FQPSK modulation. Enhanced FQPSK is a form of Feher QPSK modulation proposed by Simon and Yan of NASA/JPL [9]. For filtered OQPSK, two filter types are studied: 6-pole Butterworth and Square Root Raised Cosine (SRRC). For OQPSK/PM the Butterworth filter is studied. The study evaluates performance of these modulation techniques with several different spacecraft transmitter power amplifiers operating with the following three Output Back-Off (OBO) points:

- Saturation (0 dB OBO).
- 1 dB OBO.
- Linear (6.7 dB OBO).

The study evaluates the following performance metrics:

- Transmit signal spectrum.
- Implementation loss (E_b/N_0 vs. BER degradation).
- Interference susceptibility (I/N that causes 1-dB degradation).

This study addresses the following questions for each modulation technique:

- Does the transmitted RF spectrum comply with the SFCG rec. 17-2R1 spectral mask?
- Is the SFCG Rec. 17-2R1 spectral mask a reasonable restriction?
- What is the penalty in transmission power required to achieve BER performance as compared to unfiltered BPSK?
- Is the modulation technique more susceptible to interference than unfiltered BPSK?

1.2 Results Summary

For each modulation technique, the transmitted power spectrum was determined via simulation and compared to the SFCG spectral mask. BER implementation loss was determined via simulation for 10^{-3} and 10^{-5} BER. The results were obtained with three transmitter PA operating points: 6.7-dB Output Back-Off (OBO) that results in a nearly linear amplifier characteristic; 1-dB OBO; 0-dB OBO that represents operating at the saturation point. For the modulation techniques that meet the spectral mask and incurred reasonable implementation loss, interference susceptibility was assessed for wideband and narrowband interference. The results are summarized in Table 1-1.

Observations

The observations that follow are based on Table 1-1 and the results presented in Sections 4, 5, and 6 of this report.

- For filtered OQPSK, BTs of 1.0 is required to comply with the spectral mask and to minimize implementation loss. Implementation loss for BTs = 0.5 is excessive. This would represent a considerable impact to a spacecraft communication system design in terms of size, weight and DC power consumption. The SRRC filter provides better performance than the Butterworth filter although the SRRC performance is 8.2 dB worse than unfiltered BPSK. For BTs=1.0 and BTs=1.5 the implementation loss is 1.0 and 0.5 dB higher than that for BPSK. This is a reasonable cost for compliance with the SFCG recommendation; however, this may not maximize DC power efficiency since this performance is achieved with 1-dB PA output back off. In all cases the 60-dB bandwidth and the implementation loss depend on the power amplifier characteristics.
- For filtered OQPSK/PM with BTs = 1.0, compliance with the spectral mask is achieved with reasonable increase in implementation loss. The 60-dB bandwidth and implementation loss are insensitive to the backoff and performance is adequate with the worst case amplifier characteristics (TWTA-1). This is possible due to the constant envelope of the OQPSK/PM signal. With filtered OQPSK/PM modulation, implementation loss is only 0.6 dB higher than for unfiltered BPSK. OQPSK/PM clearly has a performance advantage over the OQPSK in terms of spectrum and DC power efficiency of the transmitter power amplifier. Spectrum for OQPSK/PM with a Gaussian filter was assessed. Since the Gaussian filter did not show improvement in spectrum performance, it was not assessed further.
- For GMSK, neither the BT = 0.5 or BT=1.0 meet the spectral mask with the PA OBO 1 dB or 0.0 dB. In this case the nonlinear amplifier does not regenerate the sidelobes because the GMSK signal has a constant envelope; but the main lobe of the spectrum is wider than the main lobe for OQPSK and does not comply with the mask specification at $0.15 \times$ symbol rate.
- The simulations show that implementation loss for GMSK is nearly identical for BT=1.0 and BT=0.5 and is approximately 0.6 dB higher than that for BPSK. This result is true for PA operating at 1-dB OBO and at 0-dB OBO. This demonstrates that GMSK is a reasonable technique for reducing the emitted signal bandwidth. By allowing operation at PA saturation, DC power consumption can be minimized.
- For Enhanced FQPSK, the spectrum is compliant with the SFCG mask with the worst case power amplifier characteristics. The implementation loss at 10^{-5} BER is 2.6 dB larger than

for unfiltered BPSK. This result is obtained with a sub optimum receiver structure but represents the QPSK equipment currently used in GSFC ground terminals. The 60-dB bandwidth is actually wider than that for filtered OQPSK/PM.

Table 1-1. Summary of Study Results

Modulation /Pulse Shaping Filter	Amplifier Model	Trans- mitter PA OBO	Two-sided 60dB Bandwidth	Compliance With Rec. 17-2R1 Spectral Mask SR > 2 Msps / SR < 2 Msps	Implementation Loss		Recom- mended
					Relative to BPSK ⁽⁷⁾		
					@BER = 10 ⁻³	@BER = 10 ⁻⁵	
BPSK Unfiltered	TWTA -1	1.0 dB			0.0 dB	0.0 dB	
OQPSK Unfiltered	TWTA -1	1.0 dB	637 x Rb	No/No	0.3 dB	0.3 dB	No
OQPSK Butterworth Filter, BTs=0.5	TWTA -1	1.0 dB	4.2 x Rb	Yes/Yes	12.8 dB ⁽¹⁾	> 14.4 dB ⁽¹⁾	No
	TWTA -1	0.0 dB	5.5 x Rb	Yes/Yes	NA	NA	No
	TWTA -2	0.0 dB	3.4 x Rb	Yes/yes	NA	NA	
	ESA SSPA	0.0 dB	4.8 x Rb	Yes/Yes	NA	NA	
OQPSK Butterworth Filter, BTs=1.0	TWTA -1	1.0 dB	4.8 x Rb	Yes ⁽⁵⁾ /Yes	0.7 dB	1.0 dB	Yes
	TWTA -1	0.0 dB	4.8 x Rb	Yes ⁽⁵⁾ /Yes	1.2 dB	1.8 dB	Yes
	TWTA -2	0.0 dB	4.0 x Rb	Yes/Yes	0.55 dB	0.8 dB	Yes
	ESA SSPA	0.0 dB	3.9 x Rb	Yes/Yes	0.55 dB	0.8 dB	Yes
OQPSK Butterworth Filter, BTs=1.5	TWTA -1	1.0 dB	7.5 x Rb	No/Yes	0.5 dB	0.7 dB	No
	TWTA -1	0.0 dB	7.92 x Rb	No/Yes	NA	NA	No
OQPSK SRRC Filter, BTs=0.5	TWTA -1	1.0 dB	3.7 x Rb	Yes/Yes	4.2 dB	8.2 dB	No
	TWTA -1	0.0 dB	3.8 x Rb	Yes/Yes	NA	NA	No
	TWTA -2	0.0 dB	3.0 x Rb	Yes/Yes	NA	NA	
OQPSK SRRC Filter, BTs=1.0	TWTA -1	1.0 dB	5.0 x Rb	Yes ⁽⁵⁾ /Yes	0.8 dB	1.0 dB	Yes
	TWTA -1	0.0 dB	5.0 x Rb	Yes ⁽⁵⁾ /Yes	1.2 dB	2.7 dB	Yes
	TWTA -2	0.0 dB	4.0 x Rb	Yes/Yes	NA	NA	
OQPSK SRRC Filter, BTs=1.5	TWTA -1	1.0 dB	7.6 x Rb	No/Yes	0.4 dB	0.5 dB	No
	TWTA -1	0.0 dB	7.8 x Rb	No/Yes	NA	NA	No
<div><div><div>1. Not explicitly simulated. Estimated from BER vs. Eb/No curves.</div><div>2. For GMSK, BT is the product of the one-sided bandwidth of the Gaussian filter and the bit duration.</div><div>3. GMSK simulation results for BT=1.0 and BT=0.5 were nearly identical.</div><div>4. NA - Not Analyzed.</div><div>5. The continuous component of the spectrum complies with the mask, but the line components exceed the mask.</div></div><div><div>6. The spectrum complies with the mask outside of the necessary bandwidth ($\pm 0.5 \times \text{SR}$), but exceeds the mask within the necessary bandwidth.</div><div>7. Implementation loss relative to unfiltered BPSK with transmitter distortions and with TWTA-1 operating at 1 dB OBO.</div></div></div>							

Table 1-1. Summary of Study Results (Continued)

Modulation /Pulse Shaping Filter	Amplifier Model	Trans- mitter PA OBO	Two-sided 60dB Bandwidth	Compliance With Rec. 17-2R1 Spectral Mask SR > 2 Msps / SR < 2 Msps	Implementation Loss		Recom- mended
					Relative to BPSK ⁽⁷⁾		
					@BER = 10 ³	@BER = 10 ⁵	
Unfiltered OQPSK/PM	TWTA -1	1.0 dB	637 x Rb	No/No	0.3 dB	0.4 dB	No
OQPSK/PM Butterworth Filter, BTs=1.0	TWTA -1	1.0 dB	3.0 x Rb	Yes/Yes	0.50 dB	0.6 dB ⁽⁴⁾	Yes
	TWTA -1	0.0 dB	3.0 x Rb	Yes/Yes	0.50 dB	0.6 dB ⁽⁴⁾	Yes
OQPSK/PM Gaussian Filter, BTs=1.0	TWTA -1	0.0 dB	4.4 x Rb	Yes/Yes	NA	NA	No ⁽⁸⁾
GMSK, BTs =1.0 (BT = 0.5 ⁽²⁾)	TWTA -1	1.0 dB	3.1 x Rb	Yes ⁽⁶⁾ /Yes	1.1 dB ⁽³⁾	0.6 dB ⁽³⁾	Yes
	TWTA -1	0.0 dB	3.1 x Rb	Yes ⁽⁶⁾ /Yes	1.1 dB ⁽³⁾	0.6 dB ⁽³⁾	Yes
GMSK, BTs = 2.0 (BT=1.0 ⁽²⁾)	TWTA -1	1.0 dB	5.16 x Rb	Yes ⁽⁶⁾ /Yes	1.2 dB ⁽³⁾	0.6 dB ⁽³⁾	Yes
	TWTA -1	0.0 dB	5.16 x Rb	Yes ⁽⁶⁾ /Yes	1.2 dB ⁽³⁾	0.6 dB ⁽³⁾	Yes
Enhanced FQPSK	TWTA -1	1.0 dB	NA	NA	1.4 dB	2.6 2.1 dB ⁽⁴⁾	Yes
	TWTA -1	0.0 dB	3.6 x Rb	Yes/Yes	1.4 dB	2.6 2.1 dB ⁽⁴⁾	Yes
<div><div><div>1. Not explicitly simulated. Estimated from BER vs. Eb/No curves.</div><div>2. For GMSK, BT is the product of the one-sided bandwidth of the Gaussian filter and the bit duration.</div><div>3. GMSK simulation results for BT=1.0 and BT=0.5 were nearly identical.</div><div>4. NA - Not Analyzed.</div><div>5. The continuous component of the spectrum complies with the mask, but the line components exceed the mask.</div></div><div><div>6. The spectrum complies with the mask outside of the necessary bandwidth (± 0.5 x SR), but exceeds the mask within the necessary bandwidth.</div><div>7. Implementation loss relative to unfiltered BPSK with transmitter distortions and with TWTA-1 operating at 1 dB OBO.</div><div>8. Not recommended because BER performance was not assessed. Although BER performance may be better than OQPSK/PM with a Butterworth filter, the Spectrum is wider than OQPSK/PM with a Butterworth filter.</div></div></div>							

Table 1-2. Summary of Study Results

Modulation/ Pulse Shaping Filter	Amplifier Model	Trans- mitter PA OBO	Interference Susceptibility I/N for 1 dB Degradation at BER = 10^{-3}		
			WB	NB (f=0.0)	NB (f=0.5xRs)
Unfiltered OQPSK	TWTA -1	1.0 dB	-5.8 dB ⁽¹⁾	-9.0 dB ⁽¹⁾	-5.0 dB ⁽¹⁾
OQPSK Butterworth Filter, BTs=1.0	TWTA -1	1.0 dB	-5.8 dB	-9.7 dB	-7.5 dB
	TWTA -1	0.0 dB	-5.8 dB	-9.6 dB	-6.7 dB
GMSK, BTs = 1.0 (BT = 0.5 ⁽²⁾)	TWTA -1	0.0 dB	-5.8 dB	-11.3 dB	-7.3 dB
	TWTA -1				
GMSK, BTs = 2.0 (BT=1.0 ⁽²⁾)	TWTA -1	0.0 dB	-5.8 dB	-10.2 dB	-6.6 dB
1. Interference susceptibility for unfiltered OQPSK obtained via closed form analysis using ideal user transmitter. 2. For GMSK, BT is the product of the one-sided bandwidth of the Gaussian filter and the bit duration.					

- Table 1-2 provides an assessment of interference susceptibility for several of the modulation techniques. Interference susceptibility results show that performance degradation due to wideband and narrow band interference is similar for each modulation technique. This is largely due to the fact that in each case an integrate and dump detector is used.

Conclusions

- All of the bandwidth efficient modulation techniques studied are able to meet the SFCG high data rate spectral mask with the exception of GMSK which exceeds the mask slightly near the center frequency.
- Of the modulation techniques studied, OQPSK/PM with BTs=1.0 provides the best combination of spectrum performance and BER implementation loss with a low complexity integrate and dump receiver. This modulation technique allows compliance with the SFCG spectral mask with worst case transmitter PA operating characteristics and has lower 60-dB bandwidth an enhanced FQPSK. Implementation loss for OQPSK/PM modulation technique is 0.6 dB higher than implementation loss for unfiltered BPSK.
- Filtered OQPSK with BTs=1.0 has been verified by simulation to meet the SFCG mask when transmitted via a PA with 1-dB OBO and 0-dB OBO for both Butterworth and SRRC filters. The additional implementation loss incurred due to the filtering is 1.0 dB for both filters,

- when transmitted via a PA with 1-dB OBO. With worst case amplifier characteristics 1.8 to 2.7 dB additional implementation loss is incurred for Butterworth and SRRC, respectively.
- GMSK incurs less than 1.0 dB of additional implementation loss compared to BPSK, even with 0-dB OBO. However, the GMSK spectrum does not meet the spectral mask in the main lobe region of the spectrum because the main lobe is wider than that of OQPSK.
- The modulation techniques together with the integrate and dump receiver studied are not significantly more susceptible to wideband or narrowband interference than unfiltered QPSK. Note that other studies [13] have used a matched filter receiver and have reported some differences in interference susceptibility among modulation methods.
- The use of bandwidth efficient modulation techniques results in an increase in peak power flux density for the modulation methods and integrate and dump receiver addressed in this study. The increase is partly due to higher transmit power spectral density near the center frequency and partly due to the increased EIRP required to compensate for increased BER implementation loss.

Recommendations

- Consider relaxing the portion of the SFCG spectral mask within 1x symbol rate to allow GMSK modulation with transmitter distortions. This may also allow other modulation schemes and may not significantly increase adjacent channel interference. Relaxation of the spectrum within 1x symbol rate ~~to adjacent channel interference~~ has been proposed at the CCSDS Panel 1E meeting held in October 1999 and a draft liaison statement to SFCG was prepared.
- NASA GSFC missions planning to use S-Band or X-band space-ground links and attempting to meet the SFCG spectral mask should consider filtered OQPSK/PM (BTs=1.0) to reduce spectral emissions while also maintaining low BER implementation loss using existing SN and GN ground terminal equipment.
- Further study of the modulation techniques should include assessment of:
 - Sensitivity of system performance to receiver parameters with filtered OQPSK, including carrier tracking loop bandwidth. The current study used fixed carrier tracking loop.
 - Sensitivity of system performance to a non-ideal OQPSK/PM modulator. The modulator used in this study included an ideal phase modulator.
- The cost impacts to existing NASA assets (e.g. ground terminals) should be evaluated and considered prior to selecting a bandwidth efficient modulation scheme.

Section 2 Introduction

2.1 Objective

The SFCG has recommended that space science projects starting after the year 2001 comply with an emitted spectrum mask for space-to-earth data transmission in the bands 2200-2290 MHz, 2290-2300 MHz, 8025-8400 MHz, and 8400-8500 MHz. In order to comply with the recommendation, transmitters must limit out-of-band emissions. Two methods of accomplishing this are post power amplifier output filtering and use of a bandwidth efficient modulation technique. SFCG has conducted several studies to assess the spectrum and power requirements for several candidate modulation methods [1, 2, 3]. In these studies it was determined that post power amplifier output filtering was impractical because of the size and insertion loss associated with RF output filtering. Several bandwidth efficient modulation techniques were studied in [1, 2, 3]. Typically, these techniques allow transmission with a more narrow spectrum at the cost of additional transmit power required to achieve the same BER performance.

At SFCG 18, recommendation 17-2R1 was adopted. Action item 18-17 was assigned to J-L. Gerner of ESA with contributions from NASA and others to perform additional studies on the candidate modulation methods to determine the interference susceptibility. There is also a desire by NASA GSFC to more accurately characterize the power requirements for Earth Science and Space science missions by accounting for the impact of transmitter distortions on end-to-end performance. The purpose of this study is to assess the additional power required for several bandwidth efficient modulations techniques while accounting for distortions caused by the transmitter hardware. The results of this study can then be used to assess the impact of compliance with SFCG Rec 17-2R1 to GSFC missions.

The objective of this study is to assess the implementation loss and interference susceptibility of filtered OQPSK, GMSK, and enhanced FQPSK (per Ref [9]) modulation schemes relative to unfiltered BPSK modulation in the presence of typical transmitter distortions. This assessment will specifically address the following questions for each modulation scheme:

1. Can the transmitted RF spectrum comply with the SFCG rec. 17-2R1 spectral mask?
2. Is the SFCG Rec. 17-2R1 spectral mask a reasonable restriction for GSFC missions?
3. What is the penalty in transmission power required to achieve BER performance as compared to BPSK?
4. What is the impact of bandwidth efficient modulation on compliance with power flux density restrictions?

2.2 Scope

This study will compute the spectrum and implementation loss for filtered OQPSK, GMSK and enhanced FQPSK modulation techniques. The study will compute interference susceptibility for some cases of filtered OQPSK and GMSK. The study will include transmitter distortions typical to X-band and S-band space-to-ground transmitters used for GSFC missions.

Filtered OQPSK modulations will include Butterworth and Square Root Raised Cosine (SRRC) filters with various bandwidths. GMSK modulation will be assessed with $BT = 0.5$ and $BT = 1.0$.

The study will address performance with three different transmitter power amplifiers operating at saturation and at 1-dB output back-off. The power amplifiers represent a TWTA with worst case

AM/PM, a TWTA with reduced AM/PM and the ESA SSPA which has been used in other SFCG studies.

Interference susceptibility will be assessed for narrowband interference centered at two fixed frequencies and wideband interference.

2.3 Approach

The performances of the various modulation schemes are analyzed by simulation using the Signal Processing Worksystem (SPW) software. The simulations will produce power spectral density of the transmitted signals and bit error rate performance in the presence of transmitter distortions, receiver imperfections and interference.

The transmitted power spectrum will be computed for each modulation technique and compared to the SFCG spectral mask. A simulation model of the transmitter will be used to generate a sample of the transmitter output signal. The spectrum of the output signal will be estimated from the sample. The transmitter simulation model will include modulator distortions, linear filter distortions and nonlinear power amplifier distortions. The transmitter distortion parameters and parameter values are listed in Section 3.

BER simulations that include the transmitter model, an additive white Gaussian noise channel and a ground terminal receiver model will determine implementation loss. The simulation will estimate the BER vs. E_b/N_0 performance. The implementation loss is defined as the difference between the E_b/N_0 required for 10^{-3} and 10^{-5} BER in the simulation and the theoretical required E_b/N_0 . The implementation loss translates into additional transmit power required to achieve the desired BER. The difference between the implementation loss for each modulation technique and that for BPSK will demonstrate the link budget cost of compliance with SFCG Rec 17-2R1.

Interference susceptibility will be determined by BER simulations similar to implementation loss simulations with the addition of an interference signal added to the desired signal plus thermal noise. The simulations will determine the interference signal level required to cause an additional 1-dB degradation in BER Vs E_b/N_0 performance. Two types of interference will be analyzed: narrowband, modeled as a tone, and wideband, modeled as bandlimited noise.

The spectrum measurement, implementation loss and interference simulations will be performed with a transmitter that includes various distortions. The objective of the study is to assess performance at X-band and at S-band. Transmitters at these bands may have varying distortion parameter values. The approach here is to use a baseline set of distortion parameters, based on those for existing missions and two alternate sets. This approach allows the results to be applied to both bands.

The end-to-end performance of the modulation techniques will depend on the demodulation and detection method. In this study BPSK, filtered OQPSK and GMSK modulations techniques use coherent detection with integrate and dump detection filters. Coherent detection is currently used for existing missions and provides 3-dB improvement over noncoherent detection. Integrate and dump data detection is optimum for unfiltered BPSK and QPSK in an AWGN channel.

For GMSK, coherent detection with I&D detection filters is used with a modification to support detection of GMSK.

2.4 SFCG Recommendation 17-2R1

The SFCG,

CONSIDERING

- a. that frequency bands allocated to the space science services are becoming more congested as space missions multiply, data rates increase, and other services enter these bands;
- b. that usage of spectrum beyond what is actually required increases the potential for interference to other users and at the same time may result in a higher susceptibility to interference from other users of the band;
- c. that notified bandwidth requirements beyond the amount of spectrum actually required generally increases the coordination burden;
- d. that subcarrier modulation techniques require substantially more spectrum compared to suppressed carrier modulation techniques;
- e. that the required bandwidth with subcarrier modulation is a function of the subcarrier frequency and the subcarrier-to-symbol rate ratio;
- f. That, for telemetry subcarrier frequencies above 60 kHz, a subcarrier frequency-to--highest symbol rate ratio not exceeding 4 (for Cat. A missions) or 5 (for Cat. B missions) is generally sufficient to obtain acceptable performance;
- g. that the presence of telecommand feed-through and/or ranging signals may require the selection of a slightly higher value of subcarrier frequency-to-highest symbol rate ratio;
- h. that subcarriers are not required any longer to separate telemetry data streams because several channels can be present simultaneously on a single RF carrier if virtual channels are used;
- i. that there are no technical reasons which would require the use of subcarrier modulation for symbol rates above approximately 60 kilosymbol/second (Ks/s);
- j. that the use of PCM/PM/Bi-phase or PCM/PM/NRZ modulation is only justified when a distinct carrier component is required and for symbol rates below 2 Ms/s;
- k. that filtered modulation schemes have bandwidth characteristics which generally reduce coordination burdens;
- l. that spectrum shaping can be used to significantly reduce the occupied bandwidth;

RECOMMENDS

1. that, with immediate applicability to all space science service bands, space agencies use the most bandwidth efficient modulation schemes practicable for their missions;
2. that, with immediate applicability to all space science service bands, subcarrier modulation shall not be used except where absolutely required and then only for symbol rates below or equal to 60 Ks/s;

3. that, with immediate applicability to all space science service bands, if a subcarrier is required, it shall comply with the specifications set forth in considering f) and g);
4. that, with immediate applicability to all space science service bands, PCM/PM/Bi-phase or PCM/PM/NRZ modulation shall only be used when a carrier component is technically necessary and for symbol rates below 2 Ms/s;
5. That the emitted spectrum for all Space Science Services projects starting in or after the year 2001, and that will utilize space-to-Earth link frequency assignments in the bands 2200-2290 MHz, 2290-2300 MHz, 8025-8400 MHz, or 8400-8500 MHz, adhere to the spectral emission masks in Figure 2-1.

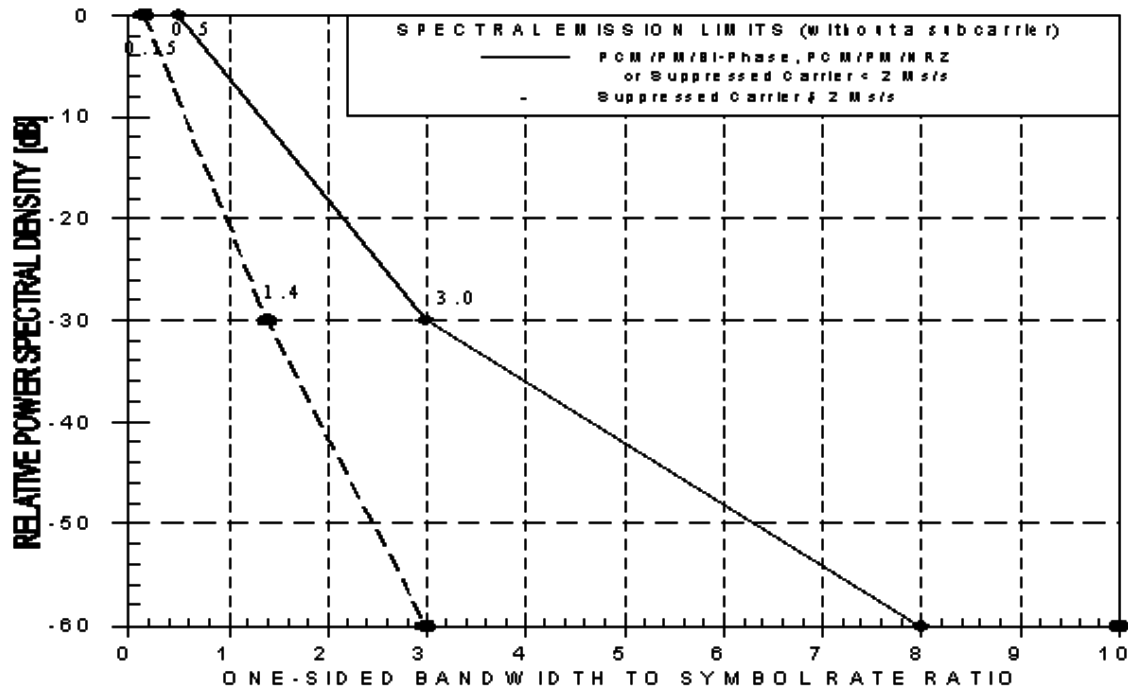


Figure 2-1. SFCG Rec. 17-2R1 Spectral Emission Limits

Notes

1. CCSDS Recommendations 401.0 (2.4.14A)B-1 and 401.0 (2.4.14B)B-1
2. CCSDS Recommendation for Packet Telemetry (CCSDS 102.0-B-2)
3. For purposes of this Recommendation, the symbol rate is defined as the baseband bit rate following error correcting coding (if applicable) and Bi-(encoding (if used) but excluding any other spectrum modifying modulation.
4. Measured relative to the peak of the telemetry spectrum and excluding all spurious emissions

Section 3 Simulation Model

3.1 Overview

Simulation models were developed to assess the implementation loss and interference susceptibility of filtered OQPSK, GMSK and enhanced FQPSK modulation. The goal of the simulation model is to accurately reflect the performance of the user transmitter hardware including linear and nonlinear distortions.

Figure 3-1 shows an overview of the simulation models used in the study. The user transmitter generates the user signal with the specified modulation format and distortions. The space-ground channel adds thermal noise and an interference signal. The ground terminal includes linear distortions due to front end filtering, carrier tracking, and symbol synchronization and data detection. BER is measured by comparing the received data bits with the transmitted data bits. The transmitted signal spectrum is monitored at the user transmitter output.

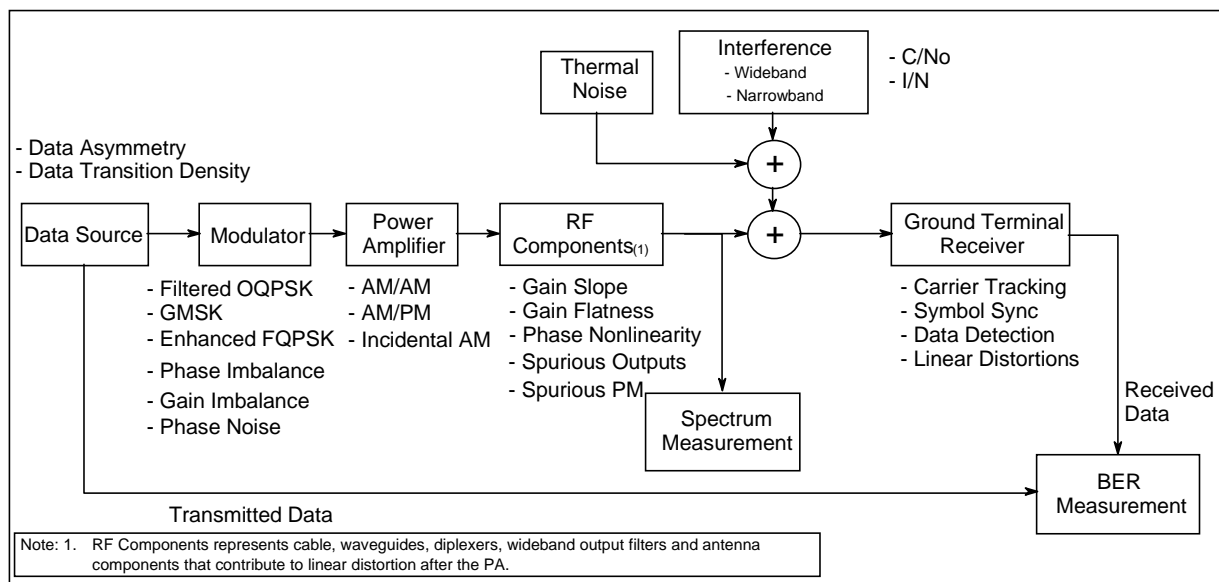


Figure 3-1. Simulation Model

3.2 User Transmitter Model

The user transmitter model is designed to generate signals with the modulation schemes under study, include impairments in the data source and modulator and include linear and nonlinear distortions due to power amplifiers and output filters, waveguides and antennas. By including the transmitter impairments we can more accurately assess the impact of compliance with Rec. 17-2R1.

The sections that follow describe in more detail the following components of the user transmitter model:

- 1 Data source.
- 2 Modulator (Filtered OQPSK, GMSK, Enhanced FQPSK).
- 3 Power Amplifier.
- 4 RF Components.

One objective of this study is to assess the performance of bandwidth efficient modulation schemes in the presence of transmitter hardware distortions that are typical to GSFC flight project transmitters. The transmitter distortion parameters and the associated values listed in Table 3-1 are typically specified for transmitters used in GSFC flight projects with S-Band and X-band communication systems. The goal of the simulation model is to accurately represent the distortion caused by these parameters.

Table 3-1 also shows the parameters used in the Phase 3 study [3]. Many of the parameters listed in Table 3-1 were not addressed in the Phase 3 study. We expect the results of this study to show more degradation than in the Phase 3 study due to the additional distortion effects.

Two of the parameters in Table 3-1 are not included in the simulation: Frequency stability and data bit jitter. Long term frequency stability does not effect BER performance but does effect initial acquisition. Since acquisition is not addressed in this study, frequency stability is not included in the model. Short-term frequency stability is treated as phase noise that is included in the simulation model.

Data bit jitter is caused by clock variation in the spacecraft data system. The receiver symbol synchronizer tracks out low frequency jitter. High frequency jitter causes a mismatch in the integrate and dump detector timing and results in BER degradation. The simulation tools used in this study do not include data bit jitter. Analytic calculations of jitter impact indicate that for bit jitter less than 1.0 %, BER degradation is less than 0.1 dB.

Table 3-1 indicates that several parameters are not used for GMSK since they are not defined for GMSK modulation. Data asymmetry in GMSK causes an average frequency shift and short term frequency variations. This caused problems for the carrier tracking loop simulation. For GMSK BER analysis the data asymmetry is 0 %. This issue is discussed in Appendix B.

Table 3-1. Representative GSFC Flight Project
S-Band and X-Band Transmitter Distortion Parameters

Source	Parameter	Set 1	Set 2	Phase 3 Study [3]
Data Source	Data Transition Density	0.50	0.50	0.45
	Data Asymmetry, % (OQPSK only)	3.0	5.0	0.0
	Data Bit Jitter, %	Not simulated	Not simulated	Not Simulated
Modulator	I/Q Power Ratio (OQPSK only)	1.0:1.0	1.0:1.0	1.0:1.0
	I/Q Data Skew, %	0.0	0.0	0.0
	Frequency Stability, ppm	Not simulated	Not simulated	Not Simulated
	Phase Noise, deg. rms	3.6	3.6	Not Simulated
	Gain Imbalance, dB (OQPSK only)	0.25	0.5	Universal Phase Modulator ⁽²⁾
	Phase Imbalance, deg. (OQPSK only)	± 2.0	± 5.0	Universal Phase Modulator ⁽²⁾
	Data Transition Time, % of symbol duration (OQPSK only)	See Table 3-2 ⁽⁵⁾	See Table 3-2 ⁽⁵⁾	TBD
Power Amplifier	AM/AM, dB/dB	0.9, 0.47, 0.0	0.47, 0.0	ESA SSPA ⁽³⁾
	AM/PM, deg./dB	0.0, 12.0, 15.0	12.0	ESA SSPA ⁽³⁾
	Incidental AM, %	5.0	5.0	Not Simulated
	Data Transition Induced PM, deg. Rms (OQPSK only)	See Table 3-3 ⁽⁵⁾	See Table 3-3 ⁽⁵⁾	Not Simulated
RF Transmit Components	3 dB Bandwidth, MHz	2,000.0 ⁽⁴⁾	2,000.0 ⁽⁴⁾	Not Simulated
	Gain Flatness, dB	± 0.3 over $\pm F$ MHz ⁽¹⁾	± 0.6 over $\pm F$ MHz⁽¹⁾	Not Simulated
	Gain Slope, dB/MHz	0.1	0.1	Not Simulated
	Phase Nonlinearity, deg.	± 3.0 over $\pm F$ MHz ⁽¹⁾	± 6.0 over $\pm F$ MHz⁽¹⁾	Not Simulated
	Spurious PM, deg. rms	2.0	2.0	Not Simulated
	Spurious Outputs (inband), dBc	30	30	Not Simulated

Notes:

1. F is defined as 70% of the first null of the transmitted signal spectral density.
2. Analog phase modulator was used instead of a QPSK modulator. Gain and phase response of the universal phase modulator is provided in ref [3].
3. Characteristics of ESA SSPA operating in saturation were used.
4. Wide bandwidth is used to represent wideband RF transmit components. Typically GSFC flight project transmitters are specified with minimum 3-dB bandwidth of 2x the transmitted symbol rate.
5. Measured from simulation. These parameters are determined by other specified parameters. The filtering in particular will determine the data transition time; therefore, these parameters are a function of the modulation scheme.

Table 3-2. Measurement of OQPSK Data Transition Time (% of symbol duration)

Pulse Shaping Filter	BTs	Linear PA (OBO = 6.7 dB)	PA OBO = 1.0 dB	PA OBO = 0.0 dB
Butterworth Filter	0.5	117.5	136.5	130.8
	1.0	44.8	44.5	38.4
	1.5	29.9	30.4	26.8
SRRC Filter	0.5	97.0	74.2	43.2
	1.0	47.0	43.2	30.3
	1.5	30.3	34.1	22.7

Table 3-3. Measurement of OQPSK Data Transition Induced PM (deg, rms)

Pulse Shaping Filter	BTs	Linear PA (OBO = 6.7 dB)	PA OBO = 1.0 dB	PA OBO = 0.0 dB
Butterworth Filter	0.5	0.0	19.0	33.0
	1.0	0.0	10.0	16.0
	1.5	0.0	11.0	17.0
SRRC Filter	0.5	0.0	17.0	32.0
	1.0	0.0	10.0	16.0
	1.5	0.0	9.0	16.0

3.2.1 Data Source

The data source represents the spacecraft on-board data system, which provides NRZ data to the transmitter. The data source model produces a PCM data stream that will be provided to modulator input. This model generates two data streams (I and Q) using PN sequence generators using NRZ-L, M data format. The PN sequence generators provide a sequence with data transition density of approximately 50% and may include data asymmetry. The data source also provides a reference signal to assist in BER estimation. The reference signal is an undistorted signal that can be used to compare to the received signal in the BER estimator.

The data source includes data asymmetry in the output data streams. Data asymmetry η is defined to be:

$$\eta = (l-s)/(l+s)$$

where l and s are the longest and shortest bit duration data segments following a high to low data transition. Thus the data asymmetry can be introduced in the data stream by extending the high level following a high to low transition. The result of data asymmetry block in Data Source Model is extending the high level k more samples when the high level-following a high to low transition, with

$$k = \eta \times N$$

where, N is the nominal number of samples per symbole in the absense of data asymmetry. For example, for a 5% data asymmetry and $N = 20$ samples per symbol, $k = 1.0$. In SPW

implementation of data asymmetry, k is rounded to nearest integer. See Figure 3-2 for illustration.

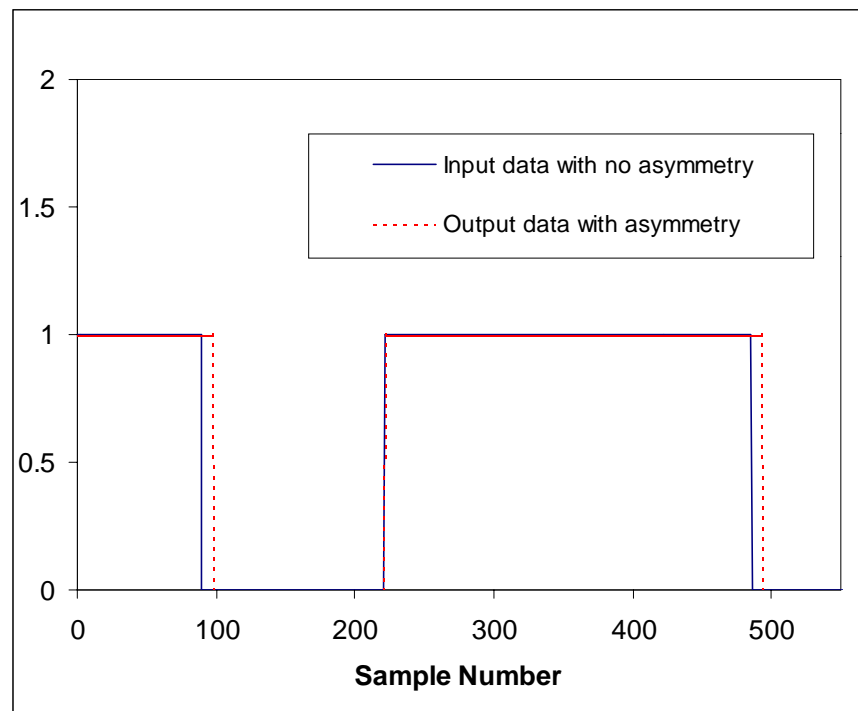


Figure 3-2. Data Stream with Data Asymmetry

3.2.2 Modulator

3.2.2.1 BPSK, QPSK, OQPSK/PM Modulator

The purpose of the BPSK/OQPSK modulator is to simulate a PSK modulator with baseband filtering for pulse shaping and to include distortion due to gain and phase imbalance. The modulator simulates BPSK, QPSK, OQPSK, and OQPSK/PM modulations using one or two streams of baseband input data received from the data source. The baseband pulse-shaping filter is either a Butterworth or Square Root Raised Cosine (SRRC) filter.

The Phase 3 Bandwidth Efficient Modulation study [3] recommended baseband filtering over IF or RF filtering. Two modulator forms are possible in an implementation of baseband filtered OQPSK. The first form uses a phase modulator or pair of phase modulators that phase modulate a carrier with the filtered data stream. This configuration is shown in Figure 3-3.

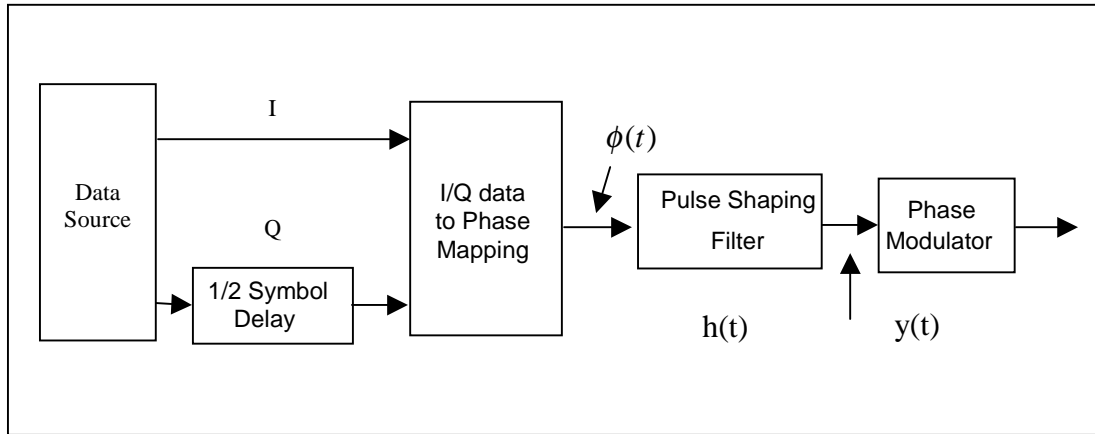


Figure 3-3. Filtered OQPSK With Analog Phase Modulator (OQPSK/PM)

The input to the modulator is the I and Q NRZ data streams. The Q-channel data stream is delayed by $\frac{1}{2}$ symbol to create Offset QPSK. I-Q data is mapped to phase as in Table 3-4.

Table 3-4. I-Q to Phase

I Channel	Q Channel	RF Carrier Phase (degree)
-1	-1	45
-1	1	-45
1	-1	135
1	1	-135

The phase signal goes through the pulse shaping filter, in contrast to filtered OQPSK described in Figure3-4, where the I and Q channel data streams go through the pulse shaping filter. The filtered phase signal is input to a linear phase modulator to produce the modulated output signal. The modulator being used in the model is an ideal linear phase modulator. The output of the modulator is:

$$s(t) = A \cos(\omega_c t + \phi(t) * h(t))$$

where,

ω_c = carrier frequency, rad/s

$\phi(t)$ is the phase output from the I-Q to phase mapping

$h(t)$ is the impulse response of the pulse shaping filter

* denotes convolution

The modulated output has constant envelope, in contrast to the non-constant envelope output of the I/Q modulator. The constant envelope signal will be less effected by the AM/AM and AM/PM distortion of the transmitter power amplifier.

second form of modulator is an I/Q modulator where the in-phase and quadrature carrier signals are amplitude modulated with a filtered NRZ data stream. This implementation is illustrated in Figure 3-4.

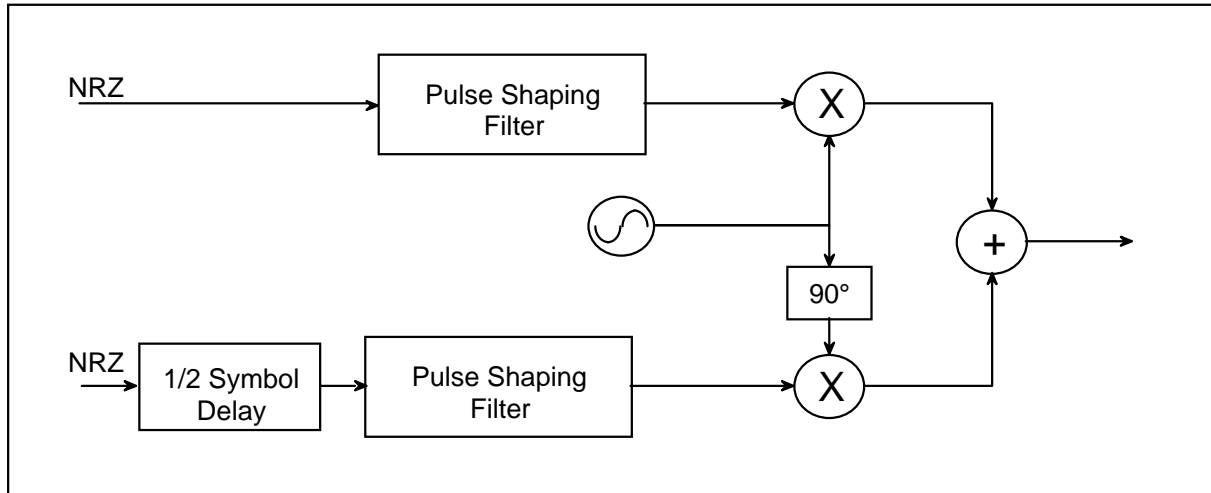


Figure 3-4. Filtered OQPSK With I/Q Modulator

The output of the modulator is:

$$s(t) = y_i(t) \cdot \sin(\omega_c t + \varphi) + y_q(t) \cdot \cos(\omega_c t + \varphi)$$

where, $y_i(t), y_q(t) = \text{filtered NRZ data}$

$\omega_c = \text{carrier frequency, rad/s}$

$\varphi = \text{oscillator phase at } t = 0$

In this implementation the magnitude variations due to filtering are present in the output signal and as a result the output signal does not have a constant envelope. In the absence of filtering, the implementations of Figures 3-3 and 3-4 produce identical output signals.

Pulse shape filtering is performed at the modulator output. This is mathematically equivalent to baseband filtering with an I/Q PSK modulator as shown in Figure 3-4. Note that the model used here does not apply to baseband filtering with a linear phase modulator and therefore may produce different results than those presented in reference [3]. Appendix F provides implementation, Impulse and frequency response of baseband filter.

The study will investigate the three cases of filtering listed below.

1. No filtering.
2. 6th order Butterworth filter (BTs=0.5, 1.0, 1.5).
3. Square Root Raised Cosine (SRRC) filter with roll-off factor = 0.5 (BTs=0.5, 1.0, 1.5).

For the Butterworth filter, B is defined as the one-sided 3-dB bandwidth and Ts is the inverse of the individual I or Q channel symbol rate.

The SRRC filter is typically defined relative to a specified baud rate so that the half power frequency of the filter response occurs at frequency which is $\frac{1}{2}$ of the baud rate. Therefore the SRRC filter is typically specified with $BTs = 0.5$. In this study we use the SRRC filter with $BTs = 0.5, 1.0$ and 1.5 . With these parameters, the half power frequency response of the SRRC filter occurs at $\frac{1}{2}, 1$ and 1.5 times the baud rate, respectively.

3.2.2.2 GMSK Modulator

GMSK is minimum shift keying (MSK) with a pre-modulation Gaussian filter. Figure 3-5 shows the configuration of the GMSK modulator. MSK is binary digital FM with modulation index = 0.5. The pre-modulation Gaussian filter has narrow bandwidth and sharp cutoff, which suppresses high frequency components thereby resulting in a bandwidth efficient modulation. The Gaussian filter also has lower overshoot impulse response that protects against excessive amplitude deviations. Appendix G provides Gaussian filter impulse response.

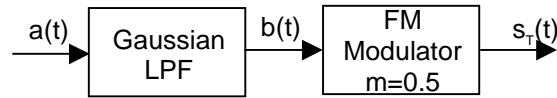


Figure 3-5. Configuration of the GMSK Modulator

When the data sequence is $\{a_n\}$, a waveform of the transmitted bit sequence can be expressed as

$$a(t) = \sum_{k=-\infty}^{\infty} b_k u(t - kT_b)$$

$$b_k = \begin{cases} 1; & a_k = 1 \\ -1; & a_k = 0 \end{cases}$$

$$u(t) = \begin{cases} 1; & 0 \leq t < T_b \\ 0; & \text{otherwise} \end{cases}$$

When $a(t)$ is filtered by a Gaussian LPF with its 3-dB bandwidth of B_b , the filter output is given by

$$b(t) = a(t) \otimes c_b(t)$$

$$c_b(t) = \sqrt{\frac{2\pi}{\ln 2}} B \exp\left(-\frac{2\pi^2}{\ln 2} B_b^2 t^2\right)$$

$b(t)$ is then fed to the FM modulator with its modulation index of 0.5 to obtain the transmitted signal expressed as

$$s_T(t) = A \cdot \cos(2\pi f_c t + \phi(t) + \theta_0)$$

$$\phi(t) = \frac{\pi}{2T_b} \int_{-\infty}^t b(\tau) d\tau$$

Since modulator distortion parameters for GMSK are not defined, gain imbalance and phase imbalance are not included in the model. Data asymmetry was omitted from the GMSK simulations used to obtain BER performance. Data asymmetry at the input to the GMSK modulator causes a frequency shift that is incompatible with the receiver simulation model. This phenomenon is discussed in detail in Appendix B.

3.2.2.3 Enhanced FQPSK Modulator

The definition of this modulation is provided in [9]. The definition is repeated here for completeness. It generates sixteen basis waveforms $s(i)$; $i=0,1,2,\dots,15$ defined over the interval $-T_s/2 \leq t \leq T_s/2$ which collectively form a transmitted signaling set for the I and Q channels. The particular I and Q waveforms chosen for any particular T_s signaling interval on each channel depends on the most recent data transition on that channel as well as the two most recent successive transitions on the other channel. The specific waveforms are as follows.

$$\begin{aligned}
 s_0(t) &= A, & -\frac{T_s}{2} \leq t \leq \frac{T_s}{2}, & \quad s_8(t) = -s_0(t) \\
 s_1(t) &= \begin{cases} A, & -\frac{T_s}{2} \leq t \leq 0 \\ 1 - (1-A)\cos^2 \frac{\pi t}{T_s}, & 0 \leq t \leq \frac{T_s}{2} \end{cases} & \quad s_9(t) = -s_1(t) \\
 s_2(t) &= \begin{cases} 1 - (1-A)\cos^2 \frac{\pi t}{T_s}, & -\frac{T_s}{2} \leq t \leq 0 \\ A, & 0 \leq t \leq \frac{T_s}{2} \end{cases} & \quad s_{10}(t) = -s_2(t) \\
 s_3(t) &= 1 - (1-A)\cos^2 \frac{\pi t}{T_s}, & -\frac{T_s}{2} \leq t \leq \frac{T_s}{2} & \quad s_{11}(t) = -s_3(t) \\
 s_4(t) &= A \sin \frac{\pi t}{T_s}, & -\frac{T_s}{2} \leq t \leq \frac{T_s}{2} & \quad s_{12}(t) = -s_4(t) \\
 s_5(t) &= \begin{cases} \sin \frac{\pi t}{T_s} + (1-A)\sin^2 \frac{\pi t}{T_s}, & -\frac{T_s}{2} \leq t \leq 0 \\ \sin \frac{\pi t}{T_s}, & 0 \leq t \leq \frac{T_s}{2} \end{cases} & \quad s_{13}(t) = -s_5(t)
 \end{aligned}$$

$$s_6(t) = \begin{cases} \sin \frac{\pi t}{T_s}, & -\frac{T_s}{2} \leq t \leq 0 \\ \sin \frac{\pi t}{T_s} - (1-A) \sin^2 \frac{\pi t}{T_s}, & 0 \leq t \leq \frac{T_s}{2} \end{cases} \quad s_{14}(t) = -s_6(t)$$

$$s_7(t) = \sin \frac{\pi t}{T_s}, \quad -\frac{T_s}{2} \leq t \leq \frac{T_s}{2} \quad s_{15}(t) = -s_7(t)$$

As indicated in [9], these basis waveforms exhibit the key Enhanced FQPSK property of having no slope discontinuities anywhere in the time, regardless of the value of A selected. Note that for the evaluations conducted here, a value of $1/\sqrt{2}$ was chosen for A .

The I and Q channel signals are selected according to the BCD code which is determined by the I and Q channel data transitions. The implementation of modulator is illustrated in Figure 3.6.

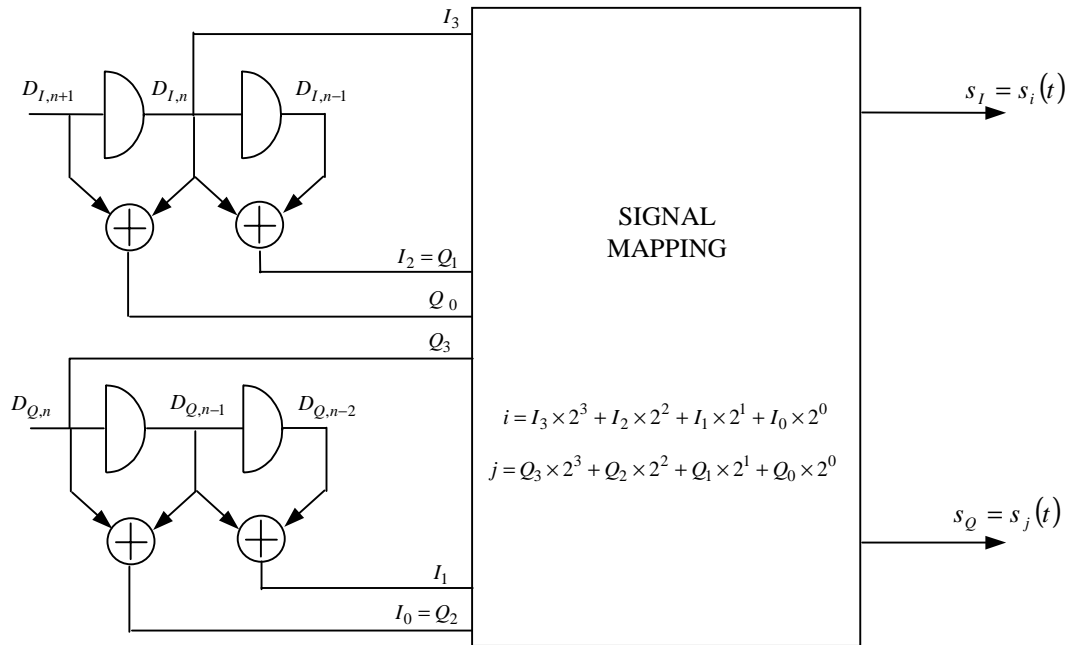


Figure 3.6. Enhanced FQPSK Modulator

3.2.3 Amplifier

The transmitter model includes a non-linear power amplifier. Three models are used in study, TWTA -1, TWTA -2 and ESA SSPA model. The TWTA -1 and TWTA -2 are modeled as AM/AM and AM/PM lookup table with the characteristics shown in Figures 3-7 and 3-8. The gain transfer for TWTA -1 and TWTA -2 are identical and are based on TWTA. The AM/PM

characteristics are parametric and are observed so that TWTA -1 has AM/PM at 12 dg/dB at 1 dB OBO and TWTA -2 has AM/PM at 3 dg/dB at 0 dB OBO. ESA SSPA is taken from [8]. The amplifier is used with three different operation points. The normal operating point is at 1-dB output back off. For linear operation the output back off is 6.7 dB. The linear operating point is used for simulations without transmitter distortions. For operation at saturation, the output back off is 0 dB. Table 3-5 lists the AM/AM and AM/PM for each amplifier at the three operating points.

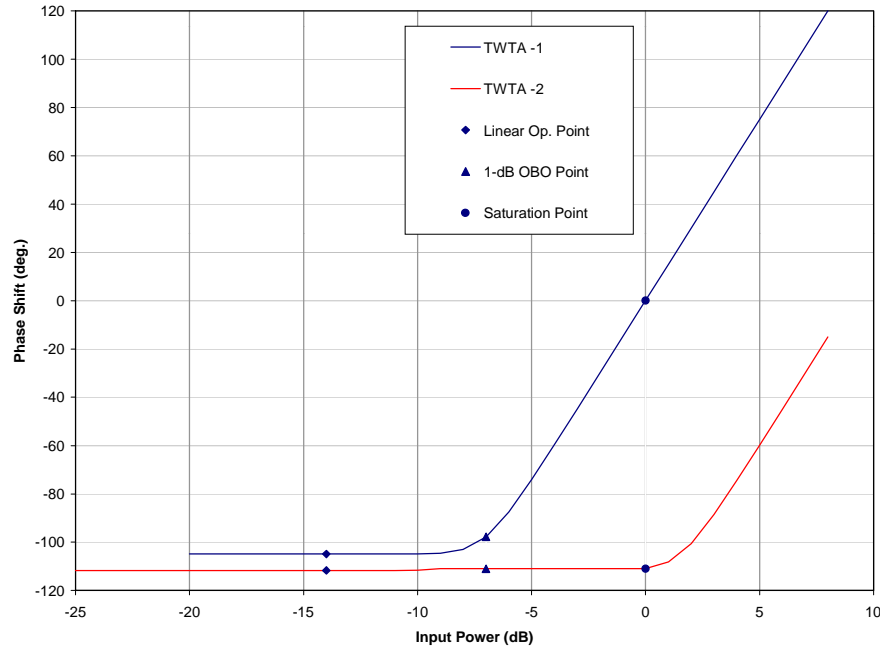


Figure 3-7. TWTA -1 and TWTA -2 Phase Shift vs. Input Power

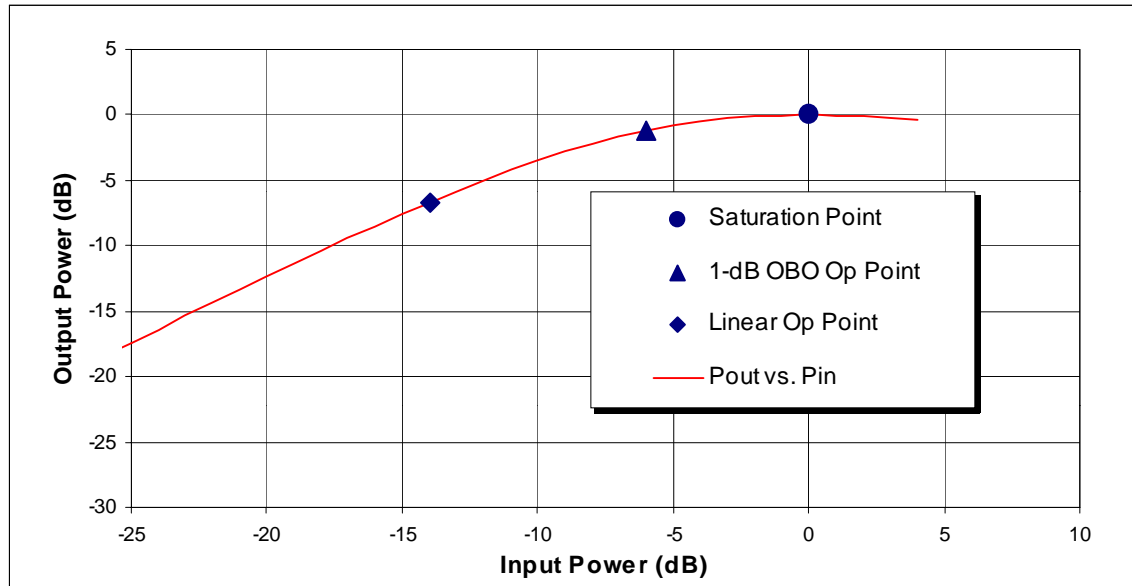


Figure 3-8. TWTA -1 and TWTA -2 Output Power vs. Input Power

Table 3-5. Model and Amplifier Operating Points Used in Simulation

Amplifier Model	Operating Point	Input Back-Off	Output Back-Off	AM/AM	AM/PM
TWTA -1	Linear	14.0 dB	6.7 dB	1.0 dB/dB	0.0 °/dB
	1-dB OBO	6.0 dB	1.0 dB	0.47 dB/dB	12.0 °/dB
	Saturation	0.0 dB	0.0 dB	0.0 dB/dB	15.0 °/dB
TWTA -2	Linear	14.0 dB	6.7 dB	1.0 dB/dB	0.0 °/dB
	1-dB OBO	6.0 dB	1.0 dB	0.47 dB/dB	0.0 °/dB
	Saturation	0.0 dB	0.0 dB	0.0 dB/dB	3.0 °/dB
ESA SSPA	Linear	14.0 dB	6.7 dB	1.0 dB/dB	0.0 °/dB
	1-dB OBO	6.0 dB	1.0 dB	0.7 dB/dB	0.2 °/dB
	Saturation	0.0 dB	0.0 dB	0.0 dB/dB	0.9 °/dB

3.2.4 RF Transmit Components

A linear filter is used to produce gain and phase distortion with the parameters: gain slope gain flatness, phase nonlinearity and 3-dB bandwidth. This filter accounts for linear distortions due to RF transmit components such as: upconverters, output filters, diplexers, waveguide and antenna components. Three parameters are used for the filter: gain flatness, gain slope, phase nonlinearity. The parameter values used in the simulations are listed in Table 3-1.

3.3 Ground Terminal Receiver Model

The ground terminal receiver model includes carrier-tracking loop, symbol synchronizer, data detection and linear distortion due to front-end RF/IF components. By including these receiver functions, the BER performance can be assessed in the presence of phase error due to imperfect carrier tracking and timing error due to imperfect symbol synchronization. The OQPSK receiver is used for filtered OQPSK, filter OQPSK/PM and enhanced FQPSK.

Because of the differences between OQPSK and GMSK modulation, two different ground terminal receiver models are used.

3.3.1 BPSK/OQPSK Ground Terminal Receiver Model

The BPSK/OQPSK ground terminal receiver model performs carrier tracking, symbol timing recovery, demodulation and bit detection for BPSK and OQPSK modulated user signals. The model includes RF/IF components, carrier tracking loop, symbol synchronizer and data detector. The configuration of the ground terminal receiver is shown in Figure 3-9.

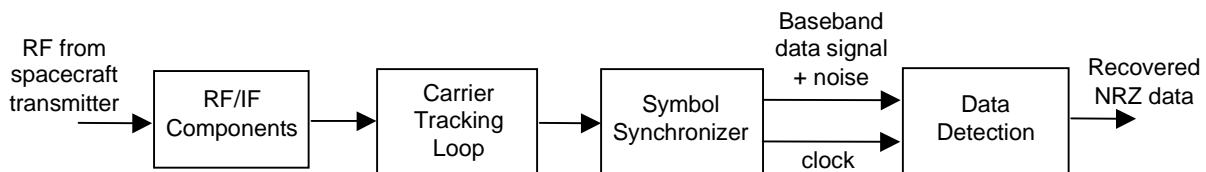


Figure 3-9. BPSK/OQPSK Ground Terminal Receiver Configuration

The signal input to the ground terminal receiver is the RF signal received from the spacecraft transmitter. The recovered NRZ data is provided as an output.

3.3.1.1 RF/IF Components

The RF/IF components consist of the antenna, LNAs, downconverters and connecting cables and waveguides. These components convert the received RF signal to an intermediate frequency suitable to the receiver and provide the signal to the receiver.

The aggregate linear distortions of these components are modeled as a composite linear filter implemented prior to the receiver input. The parameters and values for these distortions are provided in Table 3-6.

Table 3-6. RF/IF Components Linear Distortion Parameters

Parameter	Value
3-dB Bandwidth	3.2 x Symbol Rate
Gain Flatness	0.6 dB (p-p)
Gain Slope	0.1 dB/MHz
Phase Nonlinearity	10°

The Input signal is the modulated RF signal from spacecraft transmitter. The output is the modulated IF signal with additional linear distortion due to the RF/IF components.

3.3.1.2 Carrier Tracking Loop Model

The carrier-tracking loop acquires the carrier, detects and tracks the phase of the signal. The carrier tracking loop model accounts for phase error, which degrades BER performance, due to a non-ideal carrier reference signal used in the coherent detection of BPSK/QPSK signals.

The carrier-tracking loop is a modified second order Costas loop as described in [6] with arm filters turned to the symbol rate. The assumed design is based on the High Data Rate Receiver at NASA's White Sands Complex and is depicted in Figure 3-10 below. This design is optimized for QPSK but is also used for OQPSK.

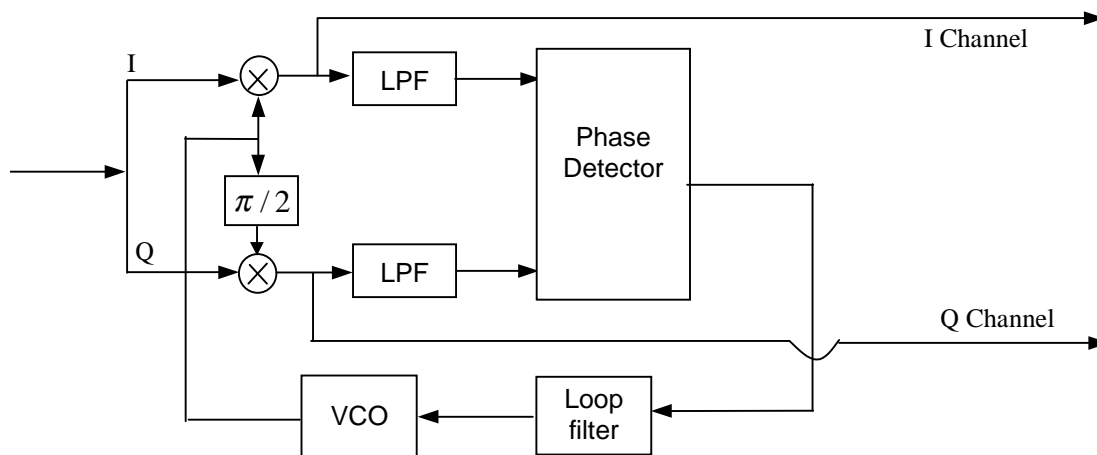


Figure 3-10. Carrier Tracking Loop Configuration

The arm filter is a lowpass filter designed to eliminate the high frequency (RF/IF) component of the input and limit the impact of the thermal noise term. The bandwidth of the arm filter is tuned to the input signal data rate. The output of the arm filter is input to the phase detector.

The parameters for carrier tracking loop include arm filter bandwidth, loop noise bandwidth, and damping factor. The values of these parameters are provided in Table 3-7. The input to the carrier-tracking loop is the modulated IF signal and the output is the demodulated baseband data signal to be sent to symbol synchronizer.

Table 3-7. Carrier Tracking Loop Parameters

Parameter	Value
Arm Filter 3-dB Bandwidth (2-sided)	3.07 x Symbol rate
Closed Loop Bandwidth	1.6x10 ⁻⁵ x Symbol rate
Damping Factor	0.223

3.3.1.3 Symbol Synchronizer Model

The symbol synchronizer recovers the symbol timing of the demodulated signal and provides clock signals synchronized with the data for use in data detection. Due to the additive noise at the input, the symbol synchronizer generates timing error that degrades BER performance.

The symbol synchronizer used in the model is a dual channel data transition tracking loop with a second order closed loop transfer function (refer to [6]). It is based on the dual channel symbol synchronizer in the High Data Rate Receiver at NASA's White Sands Complex.

The parameters and values for symbol synchronizer are provided in Table 3-8.

Table 3-8. Symbol Synchronizer Parameters

Parameter	Value
Loop Noise Bandwidth	$2.03 \times 10^{-4} \times \text{Symbol Rate}$
Damping Factor	0.707

The input is the demodulated signal from carrier tracking loop. The outputs are the PCM baseband signal and clock signal synchronized to the data transitions.

3.3.1.4 Data Detection

The detector, shown in Figure 3-11, provides matched filter hard decision detection for an unfiltered BPSK/QPSK signal. For filtered BPSK/OQPSK, this filter is sub-optimal but is easier to implement and is representative of existing equipment.

The input is PCM baseband signal and clock signal synchronized to the data transitions, and the output is recovered NRZ data.

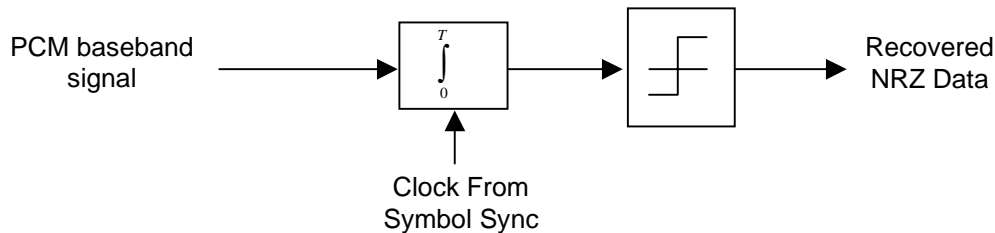


Figure 3-11. BPSK/OQPSK Data Detector

3.3.2 GMSK Ground Terminal Receiver Model

The coherent GMSK receiver performs carrier tracking, symbol timing recovery, demodulation and data detection for GMSK modulated user signal. It includes ground terminal linear distortion due to RF/IF component, carrier tracking loop, symbol synchronizer, and data detector.

The GMSK ground terminal model is similar to the BPSK/OQPSK model except, the data detector is modified to recover GMSK data and the phase detector is modified to correctly form the GMSK phase error. Both the carrier phase detector and the data detector require a clock signal synchronized to the symbol transitions to operate properly. In this simulation model an ideal symbol synchronizer is used to generate a clock signal. The ground terminal receiver receives RF signals from the spacecraft transmitter, and recovers the NRZ data as an output. The configuration of the ground terminal is shown in Figure 3-12.

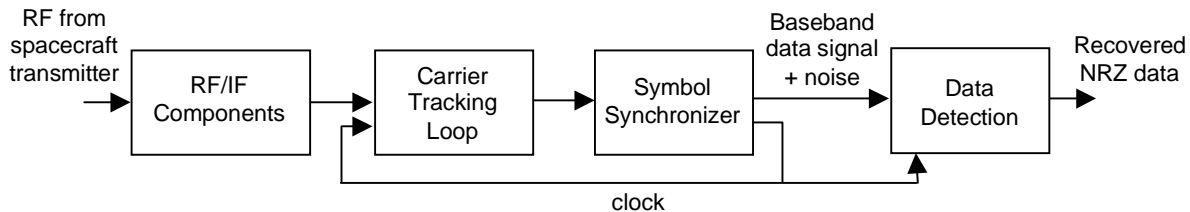


Figure 3-12. GMSK Ground Terminal Configuration

3.3.2.1 RF/IF Components

The RF/IF component model represents linear distortions due to the antenna, LNAs, downconverters and connecting cables and waveguides. The aggregate linear distortions of these components are modeled as a composite linear filter implemented prior to the linear receiver input. The distortions are the same as those for BPSK/OQPSK indicated in Table 3-3.

The input to these components is the RF input signal transmitted from the spacecraft transmitter and the output is an IF signal with additional linear distortions due to the RF/IF ground components.

3.3.2.2 Carrier Tracking Loop Model

The carrier tracking loop model accounts for the effects of a non-ideal carrier reference signal used in the coherent detection of GMSK signals. The carrier-tracking loop is similar to the modified Costas loop used for BPSK/OQPSK except for the phase detector. The phase detector is modified to correctly form the phase locked loop error signal with a GMSK input signal based on reference [5]. In the GMSK loop, proper phase detection requires the symbol synchronizer clock. The phase detector includes a lowpass arm filter tuned to the symbol rate. The configuration of the loop is shown in Figure 3-13. The phase detector, loop filter, and VCO are configured to form a second order phase locked loop.

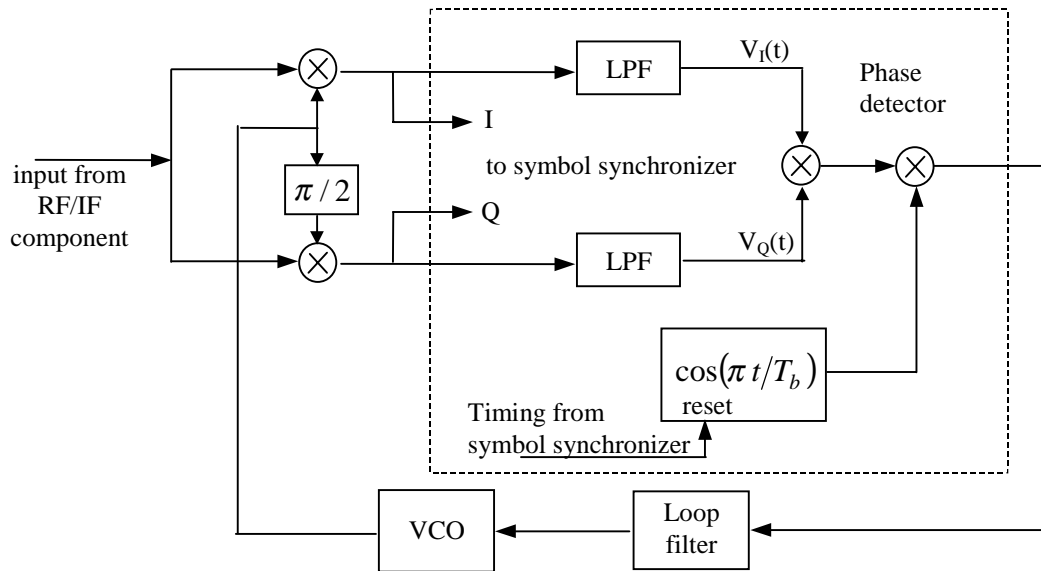


Figure 3-13. Carrier Tracking Loop for GMSK

The carrier-tracking loop has two inputs: the received signal from RF/IF components and the symbol timing clock from the symbol synchronizer. The output is I and Q channel GMSK waveform.

The carrier tracking loop parameters include arm filter bandwidth, loop noise bandwidth, and damping factor. The parameters for the carrier-tracking loop are listed in Table 3-9.

Table 3-9. Carrier Tracking Loop Parameters

Parameter	Value
Arm Filter 3-dB Bandwidth (2-sided)	3.07 x Symbol rate
Closed Loop Bandwidth	1.67×10^{-5} x Symbol rate
Damping Factor	0.25

3.3.2.3 Symbol Synchronizer

The symbol synchronizer recovers the timing of the demodulated signal symbol transitions. The timing signal is used for phase detection in the carrier tracking loop and for data detection in the integrate and dump (I&D) data detector. The symbol synchronizer in this model provides perfect symbol timing to the carrier tracking loop and data detector.

A symbol synchronizer can be implemented for GMSK with DTTL algorithm described in [5]. However, it causes additional performance degradation. The DTTL performance can be improved by optimizing DTTL parameters. Since this study does not focus on imperfect timing, perfect timing is assumed in this study.

The output of the demodulated signal from carrier tracking loop is fed into the symbol synchronizer for transition detection and then sent to data detector. Another output of this block is the perfect timing.

3.3.2.4 Data Detection

Hard decision coherent data detection is used in the simulation model. The coherent data detector has the configuration shown in Figure 3-14. Integrated Dump detector represents minimum complexity. One can use matched filter but it is complex.

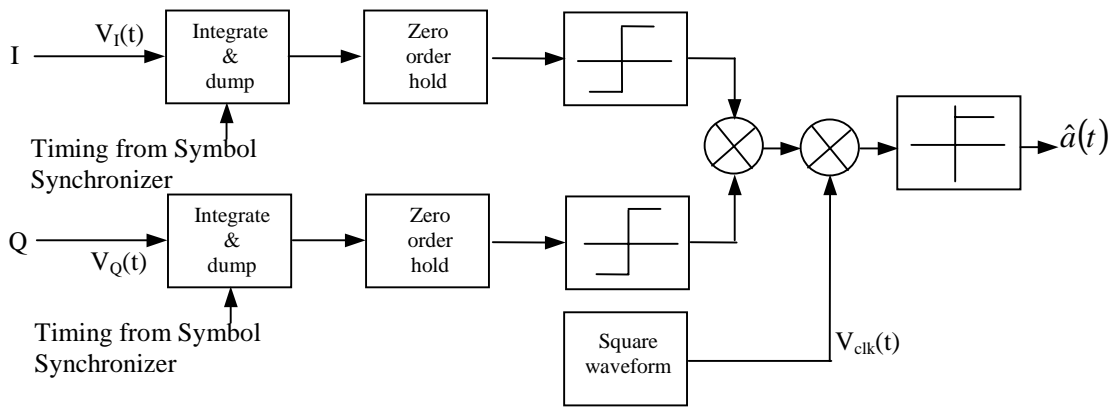


Figure 3-14. GMSK Data Detector

The integrate and dump circuit of data detector is synchronized to the data transitions by the symbol synchronizer. The data detector uses an I&D and limiter for the I&Q channels identical to BPSK/OQPSK, however, additional processing is required to recover the original data sequences for the GMSK modulation. The original data is recovered by multiplying I&Q channel data together with a sequence synchronous to the symbol transition as described in [5]. The data detector receives the baseband GMSK waveform from symbol synchronizer and outputs the recovered data sequences.

3.4 Interference Model

To assess the interference susceptibility of the bandwidth efficient modulation, an interference model is used that adds either a wideband or a narrowband interference signal to the transmitted desired signal. Wideband interference is modeled as Additive White Gaussian Noise (AWGN) spreading over the signal bandwidth and narrowband interference is modeled as a CW tone at a constant frequency.

The interference model generates zero-mean Gaussian noise with the variance required to meet a given C/N or signal-to-noise ratio. It also generated narrow or wide band interference with power required to meet a given I/N as well.

Figure 3-15 provides the block diagram of end-to-end system with white noise and wide band or narrow band (tone) interference.

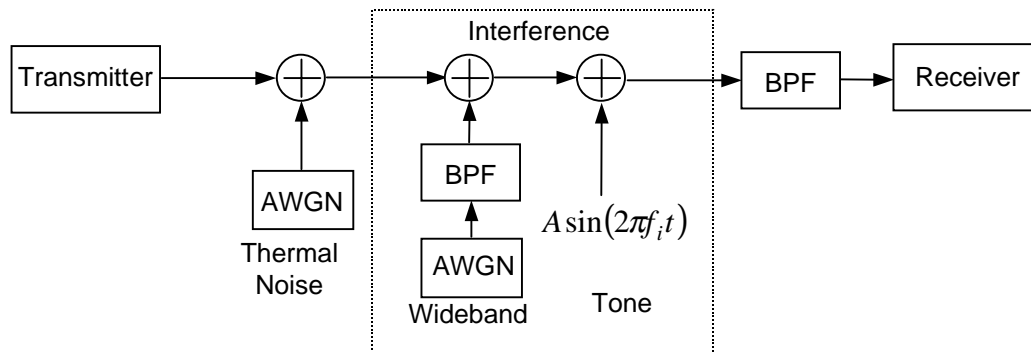


Figure 3-15. End-to-end System with Noise and Interference

The signal received at the ground terminal is:

$$r(t) = s(t) + n_i(t) + n_i(t); \text{ wide - band}$$

$$s(t) + n_i(t) + A \cdot \sin(2\pi \cdot f_i \cdot t); \text{ narrow band}$$

Table 3-10 lists the interference model parameters.

Table 3-10. Interference Model Parameters

Parameter	Parameter Value
Wide-band Interference Bandwidth, BW_i	3.2x Symbol Rate
Narrow-band Interference Frequency, f_i	0 Hz, 0.5 x Symbol Rate
I/N	Varied
Receiver noise bandwidth BW_n	3.2x Symbol Rate

The AWGN (thermal noise) is spread over the entire simulation bandwidth while the wide band interference is over a certain specified bandwidth. As indicated in the diagram, the wide band interference is generated by a white noise signal passing through a BPF. The narrow band interference is modeled as a single tone.

To present the white noise and interference, the following parameters are defined.

BW_n -- Double side receiver noise bandwidth

BW_i -- Double side wide band interference noise bandwidth, approximate to 3-dB bandwidth for the BPF with high order as used in the simulation

\bar{P}_s -- Average signal power

N -- Average thermal noise power over the receiver noise bandwidth BW_n

I -- Average interference power

f_s -- Sampling frequency

f_i -- Interference center frequency

$SNR = C/N$ -- Signal-to-noise ratio in dB

$INR = I/N$ -- Interference-to-noise ratio in dB

A -- Amplitude of narrow band (tone) interference

Appendix A provides the SPW interference model which is implemented by equivalent base band complex signals. The detailed analysis and equation deviation are provided in Appendix A. In the Appendix A, the signal power, noise power and interference power are represented as complex signals while the real signal powers are used in this section. By taking account that the real signal power is half of the complex signal power, the results in Appendix A are summarized as below.

a) Thermal noise with the noise power meeting the required signal-to-noise ratio SNR.

Thermal noise power density is

$$N_0 = \frac{N}{BW_n}$$

with noise power $N = \frac{\bar{P}_s}{10^{(SNR/10)}}$ which is defined over the receiver noise bandwidth BW_n .

The noise variance of the thermal noise is

$$\sigma_t = \sqrt{\frac{f_s \bar{P}_s}{10^{(SNR/10)} \cdot BW_n}}$$

b) Narrow band (tone) interference with required interference-to-noise ratio.

The amplitude A is

$$\frac{1}{2} A^2 = \left(\frac{I}{N} \right) \cdot BW_n \cdot N_0$$

$$A = \sqrt{\frac{2 \cdot 10^{(INR/10)} \bar{P}_s}{10^{(SNR/10)}}}$$

c) Wide-band interference

The power spectral density of wide band interference is

$$I_0 = \left(\frac{I}{N} \right) \cdot \frac{BW_n}{BW_i} \cdot N_0$$

The noise variance of the wide-band interference to bandpass filtering is:

$$\sigma_i = \sqrt{\frac{10^{(INR/10)} f_s \bar{P}_s}{BW_i 10^{(SNR/10)}}}$$

3.5 End-to-End Link Simulation Model

The transmitter, noise, interference and ground terminal models are combined in an end-to-end simulation model. Randomly generated data bits are fed into the transmitter that generates the modulated signal and provides the modulated signal to the ground terminal input. The ground terminal model receives the transmitted signal plus interference and noise, and recovers the original data bits. The recovered data bits are compared to the transmitted bits. A BER estimator is used to estimate the probability of error for the link.

The difference between the measured performance obtained via simulation and the theoretical performance is defined as implementation loss. Results for BPSK and OQPSK without filtering are shown in Figure 3-16. Results for BPSK, OQPSK and OQPSK/PM without distortions are shown in Figure 3-17. Results for GMSK are shown in Figure 3-18. These performance curves serve to validate that the simulation performs as expected. With no distortions, the simulation results are very close to the theoretical performance. With transmitter distortions, some implementation loss is observed. As expected, implementation loss for QPSK is higher than for BPSK.

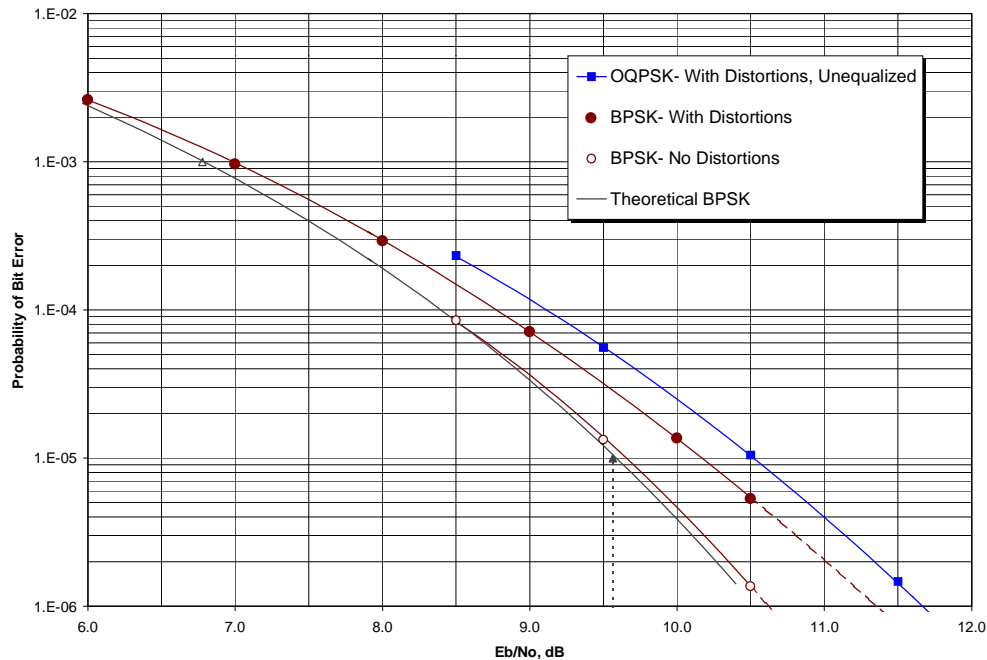


Figure 3-16. BPSK and OQPSK BER Performance Baseline

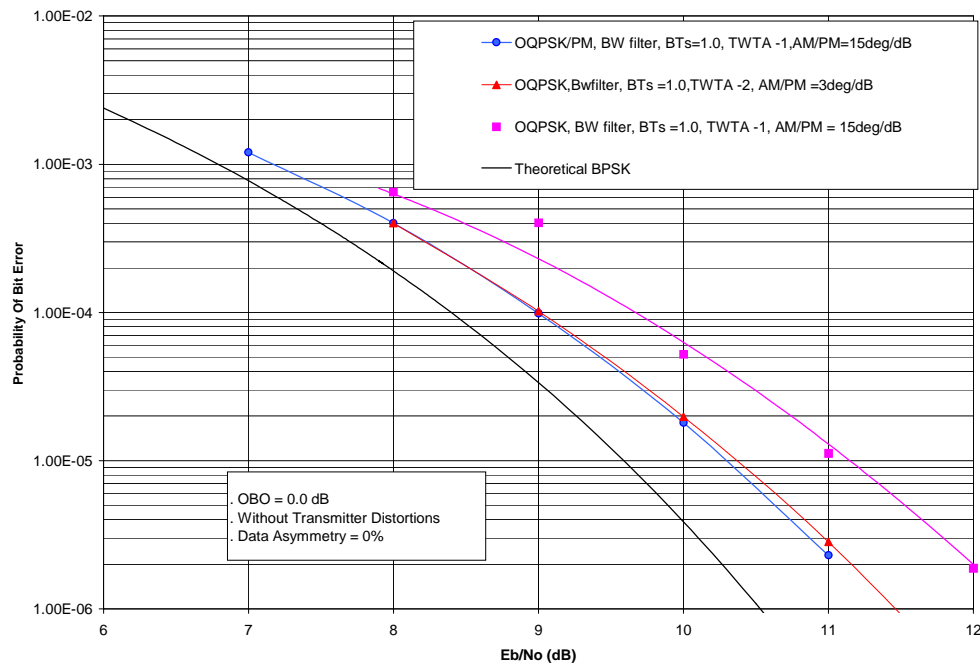


Figure 3-17. BPSK and OQPSK and OQPSK/PM BER Performance Baseline

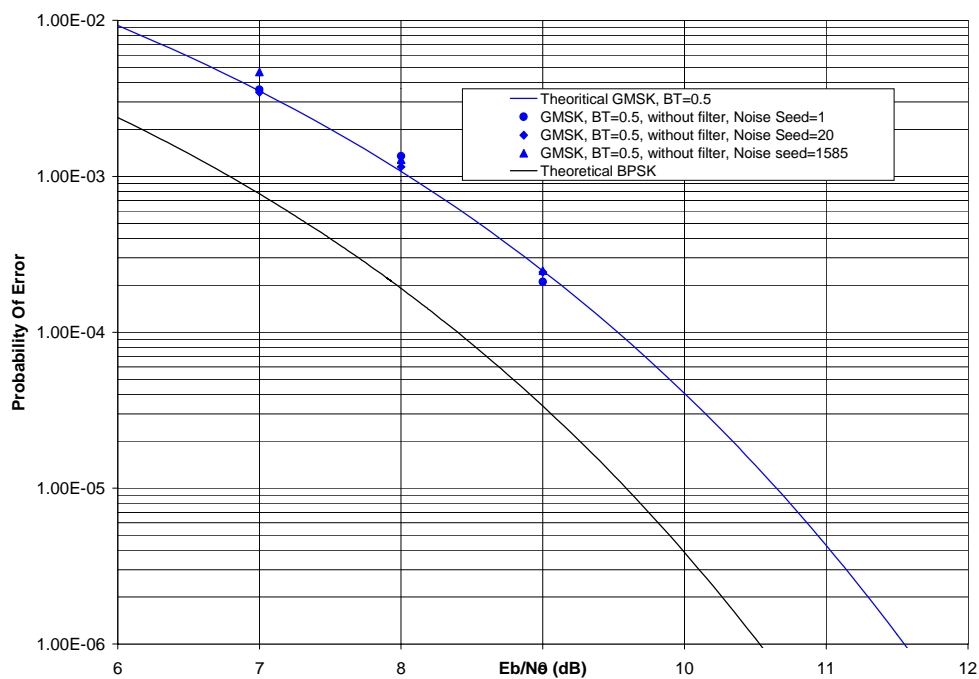


Figure 3-18. GMSK BER Performance Baseline

Section 4 Filtered OQPSK & OQPSK/PM Simulation Results

4.1 Overview

This section presents the simulation results for filtered OQPSK and OQPSK/PM modulations. The results are provided in the form of transmitted signal spectrum compared to the Rec 17-2R1 mask, implementation loss compared to the implementation loss for BPSK and interference susceptibility.

4.2 Spectra

Summary:

The user transmitter simulation model described in Section 3 was used to generate power spectral density plots for unfiltered OQPSK, Butterworth filtered OQPSK, SRRC filtered OQPSK, Butterworth filtered OQPSK/PM, and Gaussian filtered OQPSK/PM. For each modulation, the power spectral density was computed for several amplifier types. Two TWTA's with different AM/PM characteristics were used to assess the sensitivity of the spectrum to AM/PM. The ESA SSPA was also used to allow comparison to other CCSDS and SFCG studies. The power spectral densities for these modulation techniques are shown in Figures 4-1 to 4-32. Also included in the plots are the high data rate and low data rate spectral masks recommended by SFCG Rec 17-2R1. Table 4-1 summarizes compliance of the power spectral densities and the spectral masks recommended by SFCG Rec 17-2R1.

The following observations are made regarding the information in Table 4-1:

- 1 Excluding the linear PA cases, the minimum two-sided 60 dB bandwidth was $3.0 \times R_b$. This was with the SRRC filtered OQPSK, $BT_s = 0.5$ and the Butterworth filtered OQPSK/PM, $BT_s = 1.0$. Note that the two-sided 60 dB bandwidth of the SFCG high data rate spectral mask is $6.0 \times R_b$.
- 2 All cases studied are within the SFCG high data rate spectral mask except for the $BT_s = 1.5$ cases with a nonlinear power amplifier.
- 3 The Butterworth filtered OQPSK/PM, $BT_s = 1.0$ case resulted in two-sided 60 dB bandwidth of $3.0 \times R_b$ for all amplifiers operating at saturation, including the GSFC TWTA-1 with $AM/PM = 15$ deg/dB.

The sections that follow provide the PSD plots for each case considered in this study.

Table 4-1. Filtered OQPSK and OQPSK/PM Spectrum Performance

Modulation/P ulse Shaping Filter	Amplifier Model	PA OBO (dB)	AM/PM (deg /dB)	Data Asym metry	BTs = 0.5 Two-sided 60dB Bandwidth ⁽³⁾	BTs = 1.0 Two-sided 60dB Bandwidth ⁽³⁾	BTs = 1.5 Two-sided 60dB Bandwidth ⁽³⁾
OQPSK Butterworth Filter	Linear PA	NA	0 deg/dB	0.0%	1.1x Rb [2]	1.94 x Rb [12]	
	Linear PA	NA	0 deg/dB	6.0%	-	-	3.32 x Rb [22]
	TWTA-1	0.0dB	15deg/dB	0.0%	5.4 x Rb [3]	4.8x Rb [13]	-
	TWTA-1	1.0 dB	12 deg/dB	6.0%	4.2 x Rb [4]	4.8 x Rb ⁽¹⁾ [14]	7.5 x Rb ⁽²⁾ [23]
	TWTA-1	0.0dB	15 deg/dB	6.0%	5.5 x Rb [5]	4.8 x Rb ⁽¹⁾ [15]	7.92 x Rb ⁽²⁾ [24]
	TWTA-1	0.0 dB	15 deg/dB	3.0%	5.5 x Rb [6]	4.8 x Rb ⁽¹⁾ [16]	-
	TWTA-2	0.0 dB	3 deg/dB	6.0%	3.4x Rb [7]	4.0 x Rb [17]	-
	ESA SSPA	0.0 dB	0.9 deg/dB	6.0%	4.8 x Rb [8]	3.9 x Rb [18]	-
OQPSK SRRC Filter	Linear PA	NA	0 deg/dB	6.0%	-	-	3.56 x Rb [25]
	TWTA-1	1.0 dB	12 deg/dB	6.0%	3.7 x Rb [9]	5.0 x Rb ⁽¹⁾ [19]	7.6 x Rb ⁽²⁾ [26]
	TWTA-1	0.0dB	15 deg/dB	6.0%	3.8 x Rb [10]	5.0 x Rb ⁽¹⁾ [20]	7.8 x Rb ⁽²⁾ [27]
	TWTA-2	0.0dB	3 deg/dB	6.0%	3.0 x Rb [11]	4.0 x Rb [21]	-
OQPSK/PM Butterworth Filter	Linear PA	NA	0 deg/dB	0.0%	-	3.0 x Rb [29]	-
	TWTA-1	1.0 dB	12 deg/dB	6.0%	-	3.0 x Rb [30]	-
	TWTA-1	0.0dB	15 deg/dB	6.0%	-	3.0x Rb [31]	-
OQPSK/PM Gaussian Filter	TWTA-1	0.0dB	15 deg/dB	6.0%	-	4.4 x Rb [32]	-
1. The continuous component of the spectrum complies with the mask, but the line components exceed the mask. 2. The spectrum does not comply with the SFCG Rec 17-2R1 high data rate mask. 3. Number in bracket represents figure number; [2] represents figure 4-2.							

4.2.1 Filtered OQPSK Spectra

Unfiltered OQPSK (Figure 4-1):

For Unfiltered OQPSK, we observe significant sidelobes in the power spectral density. Also, the side lobes exceed the high data rate mask after the 3rd sidelobe. Discrete spectral components due to data asymmetry are present.

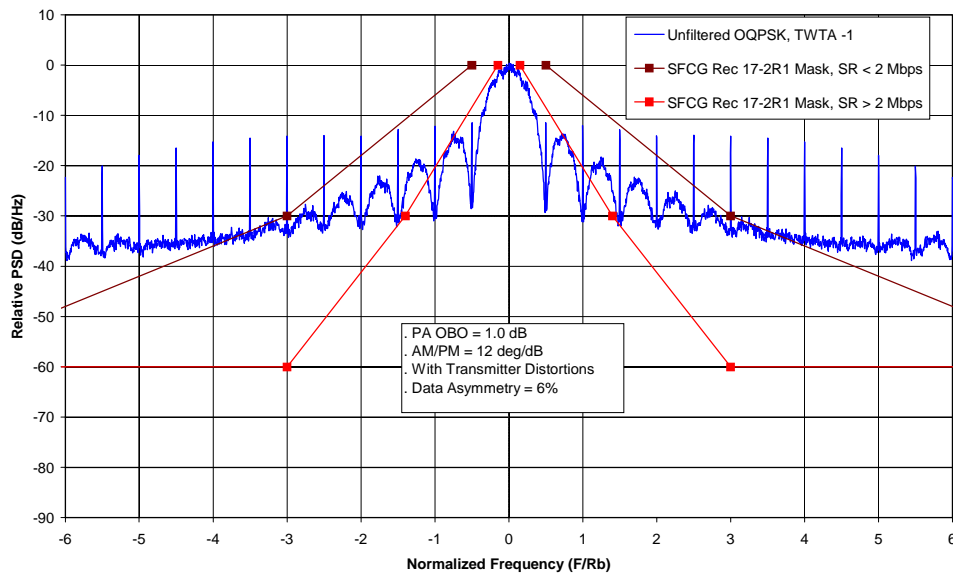


Figure 4-1. Unfiltered OQPSK Spectrum
(TWTA -1, PA OBO = 1.0 dB, AM/PM = 12 deg/dB)

Filtered OQPSK BTs = 0.5 (Figure 4-2 to Figure 4-11):

Figures 4-2 to 4-8 provide the PSD plots for the case of Butterworth filtered OQPSK with BTs = 0.5. Plots are provided for a linear amplifier, TWTA-1, TWTA-2 and the ESA SSPA. For TWTA-1, plots are provided for 0 dB and 1 dB output back off and for different amounts of data asymmetry.

Figure 4-2 shows the ideal spectrum for Butterworth filtered OQPSK with BTs = 0.5. This plot was generated with a linear power amplifier and with no transmitter distortions. The two-sided 60-dB bandwidth is $1.1 \times R_b$ and the spectrum is well within the high data rate mask. Figure 4-3 shows the same case except that the TWTA-1 with 0dB output back off is used. This plot illustrates the effect of the nonlinear amplifier on the spectrum. Figure 4-4 shows the same case as Figure 4-3 but with the TWTA-1 output back off set to 1 dB and with transmitter distortions included; the spectrum is reduced in this case.

Figure 4-5 shows the same case as Figure 4-3 but with transmitter distortions added. In this case data asymmetry is 6 %. Figure 4-5 shows line components in the spectrum due to data asymmetry. Figure 4-6 shows the spectrum for the same case but with the data asymmetry reduced to 3 %. The line components are reduced compared to the 6 % data asymmetry case.

Figure 4-7 and Figure 4-8 shows the spectrum with the TWTA-2 and the ESA SSPA, respectively. In both cases the amplifiers are operating at saturation. The spectrum is significantly reduced as compared to the spectrum with TWTA-1. This illustrates the impact of AM/PM on spectral performance for this modulation.

Figures 4-9 to 4-11 provide the PSD plots for the case of SRRC filtered OQPSK with $BT_s = 0.5$. Plots are provided for TWTA-1 and TWTA-2. For TWTA-1, plots are provided for 0 dB and 1 dB output back off.

Figure 4-9 shows the spectrum for SRRC filtered OQPSK with $BT_s=0.5$. This plot was generated with a TWTA-1 with 1dB output back off. Figure 4-10 shows the same case as Figure 4-9 but output back off set to 0 dB. Figure 4-11 shows the same case as Figure 4-10 but with the TWTA-2; the spectrum is reduced in this case.

Filtered OQPSK $BT_s = 1.0$ (Figure 4-12 to Figure 4-21):

Figures 4-12 to 4-18 provide the PSD plots for the case of Butterworth filtered OQPSK with $BT_s = 1.0$. Plots are provided for a linear amplifier, TWTA-1, TWTA-2 and the ESA SSPA. For TWTA-1, plots are provided for 0 dB and 1 dB output back off and for different amounts of data asymmetry.

Figure 4-12 shows the ideal spectrum for Butterworth filtered OQPSK with $BT_s = 1.0$. This plot was generated with a linear power amplifier and with no transmitter distortions. The two-sided 60-dB bandwidth is $1.94 \times R_b$ and the spectrum is well within the high data rate mask. Figure 4-13 shows the same case except that the TWTA-1 with 0dB output back off is used. This plot illustrates the effect of the nonlinear amplifier on the spectrum. Figure 4-14 shows the same case as Figure 4-13 but with the TWTA-1 output back off set to 1 dB and with transmitter distortions included; line components exceeds the high data rate mask.

Figure 4-15 shows the same case as Figure 4-13 but with transmitter distortions added. In this case data asymmetry is 6 %. Figure 4-15 shows line components in the spectrum due to data asymmetry. Figure 4-16 shows the spectrum for the same case but with the data asymmetry reduced to 3 %. The line components are reduced compared to the 6 % data asymmetry case.

Figure 4-17 and Figure 4-18 shows the spectrum with the TWTA-2 and the ESA SSPA, respectively. In both cases the amplifiers are operating at saturation. The spectrum is significantly reduced as compared to the spectrum with TWTA-1. This illustrates the impact of AM/PM on spectral performance for this modulation.

Figures 4-19 to 4-21 provide the PSD plots for the case of SRRC filtered OQPSK with $BT_s = 1.0$. Plots are provided for TWTA-1 and TWTA-2. For TWTA-1, plots are provided for 0 dB and 1 dB output back off.

Figure 4-19 shows the spectrum for SRRC filtered OQPSK with $BT_s=1.0$. This plot was generated with a TWTA-1 with 1dB output back off. Figure 4-20 shows the same case as Figure 4-19 but output back off set to 0 dB. Figure 4-21 shows the same case as Figure 4-20 but with the TWTA-2.

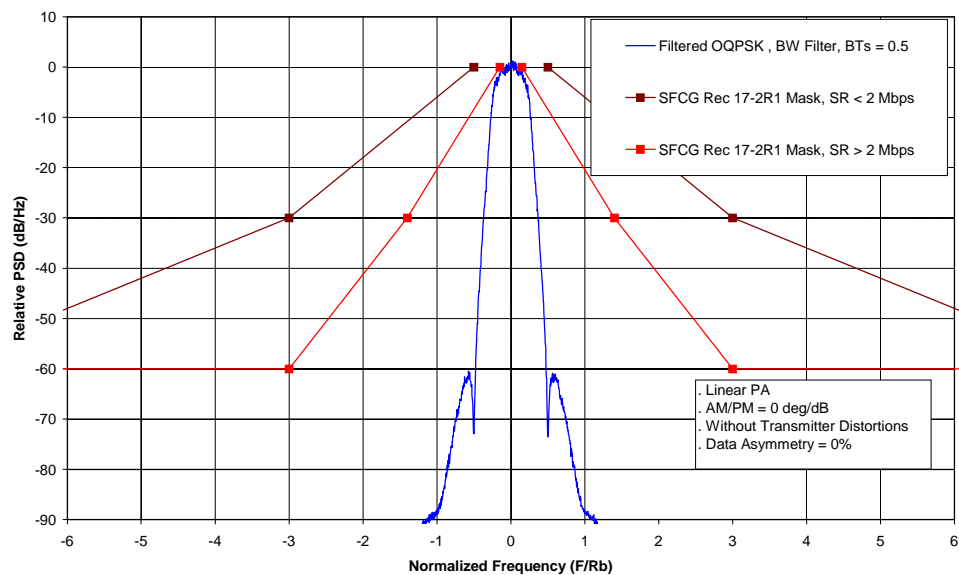


Figure 4-2. Filtered OQPSK Spectrum
(6-Pole Butterworth Filter $BT_s=0.5$, without distortions, Linear PA, AM/PM = 0 deg/dB)

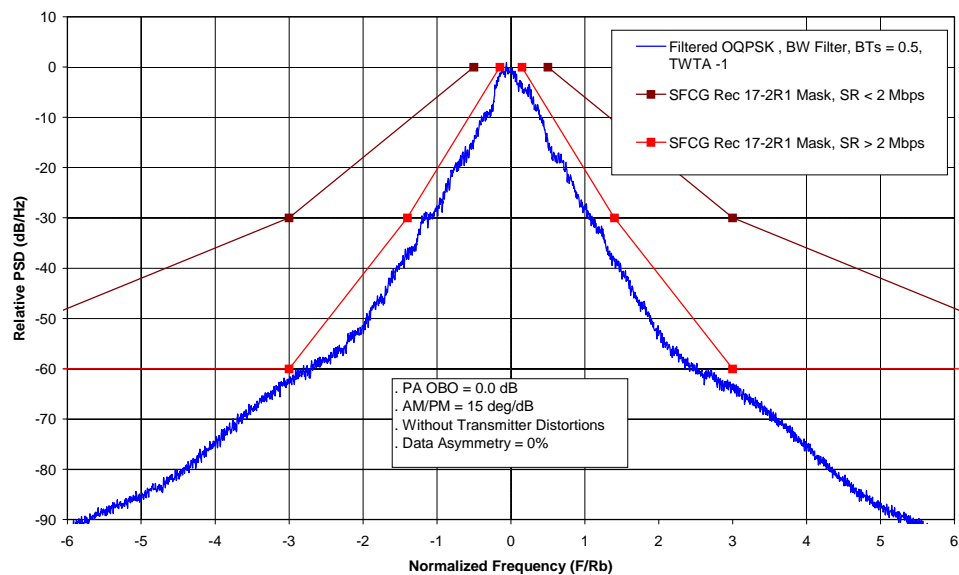


Figure 4-3. Filtered OQPSK Spectrum
(6-Pole Butterworth Filter $BT_s=0.5$, TWTA -1, PA OBO=0.0 dB, AM/PM = 15 deg/dB)

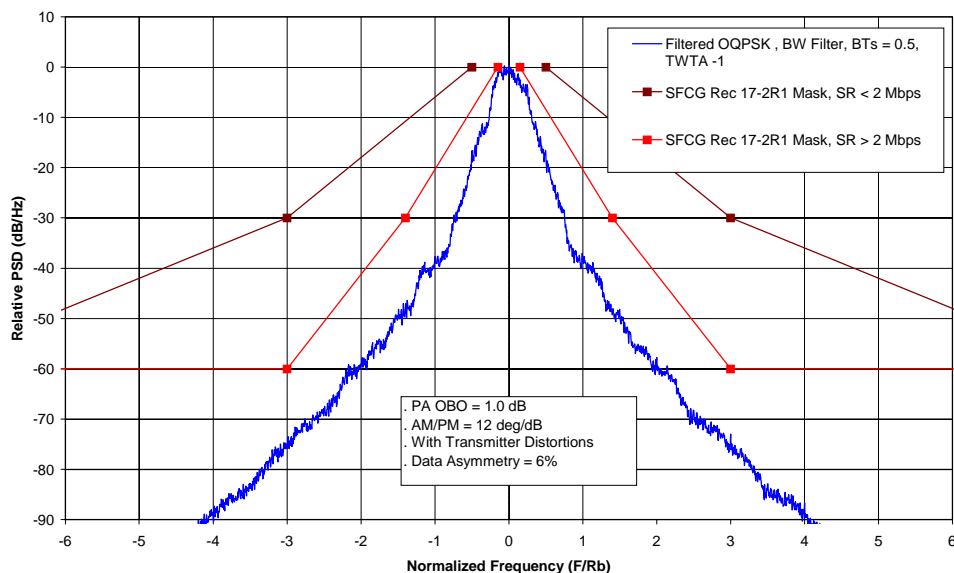


Figure 4-4. Filtered OQPSK Spectrum
 (6-Pole Butterworth Filter $BT_s=0.5$, TWTA -1, PA OBO=1.0 dB, AM/PM = 12 deg/dB, Data Asymmetry =6%)

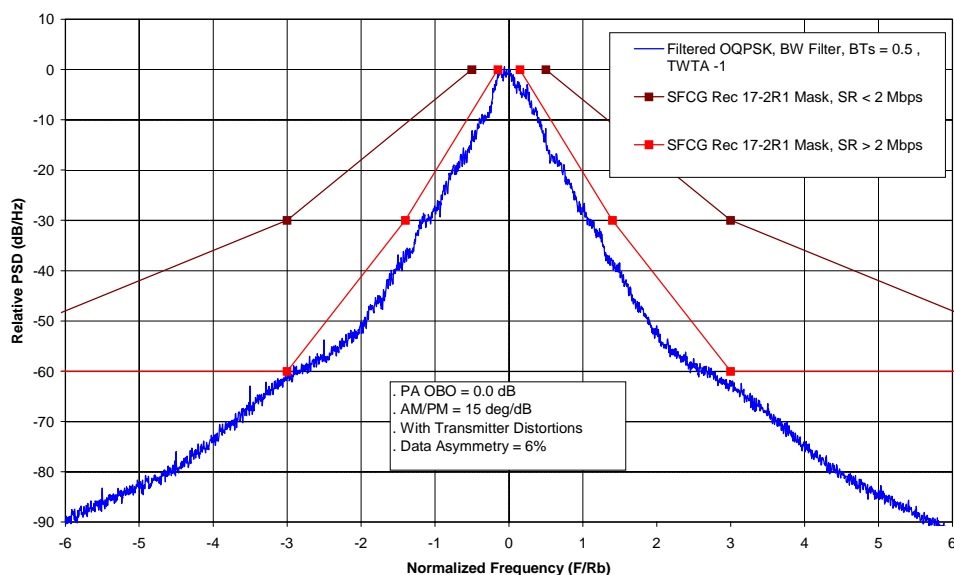


Figure 4-5. Filtered OQPSK Spectrum
 (6-Pole Butterworth Filter $BT_s=0.5$, TWTA -1, PA OBO=0.0 dB, AM/PM = 15 deg/dB, Data Asymmetry = 6%)

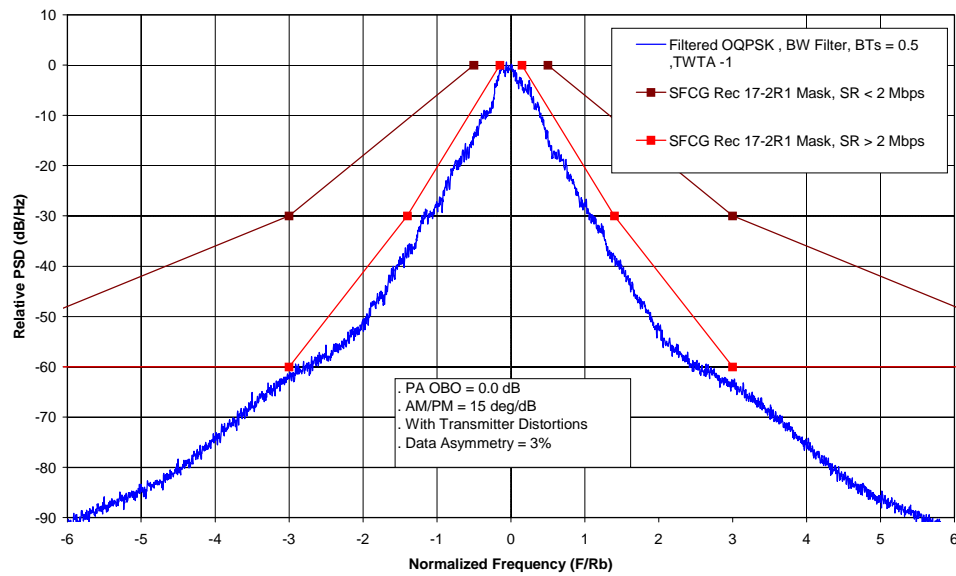


Figure 4-6. Filtered OQPSK Spectrum
(6-Pole Butterworth Filter $BT_s=0.5$, TWTA -1, PA OBO=0.0 dB, AM/PM = 15 deg/dB, Data Asymmetry = 3%)

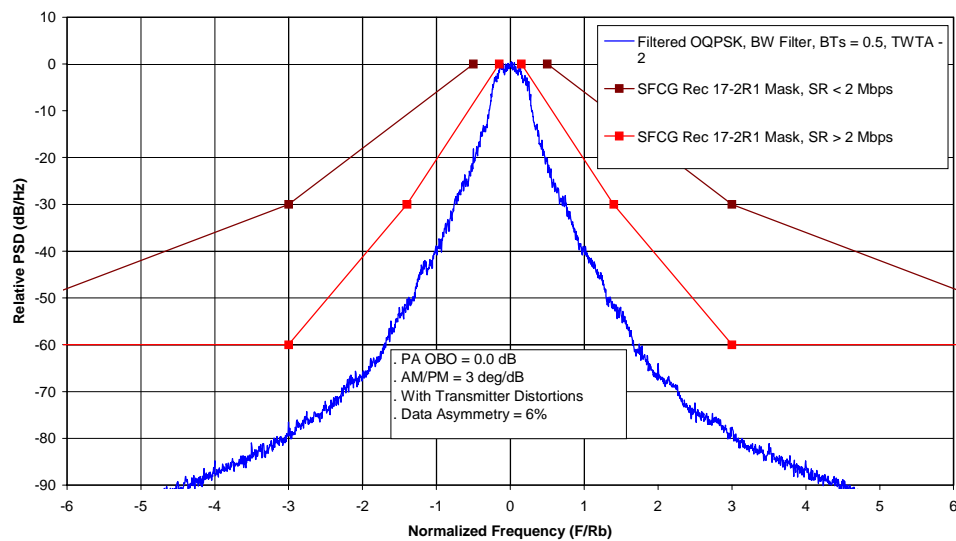


Figure 4-7. Filtered OQPSK Spectrum
(6-Pole Butterworth Filter $BT_s = 0.5$, TWTA -2, PA OBO = 0.0 dB, AM/PM = 3 deg/dB, Data Asymmetry = 6%)

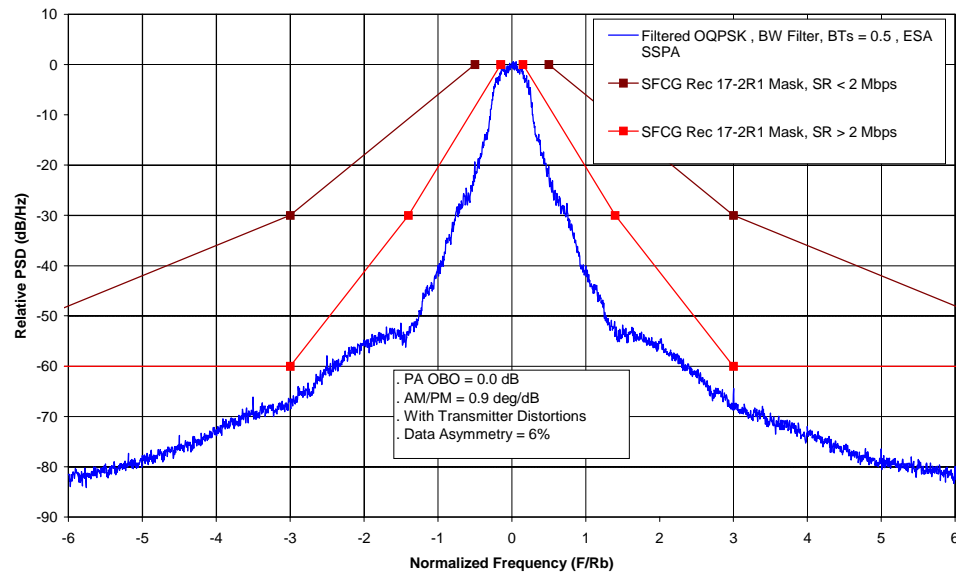


Figure 4-8. Filtered OQPSK Spectrum
(6-Pole Butterworth Filter $BT_s=0.5$, ESA SSPA, PA OBO = 0.0 dB, AM/PM = 0.9deg/dB, Data Asymmetry = 6%)

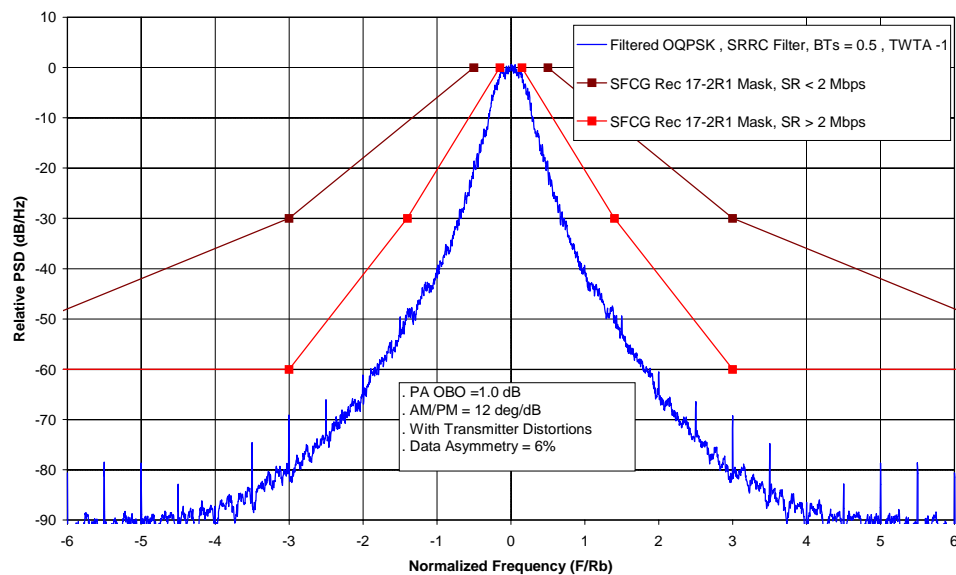


Figure 4-9. Filtered OQPSK Spectrum
(SRRC Filter $BT_s=0.5$, $\alpha=0.5$, TWTA -1, PA OBO=1.0 dB, AM/PM = 12deg/dB, Data Asymmetry = 6%)

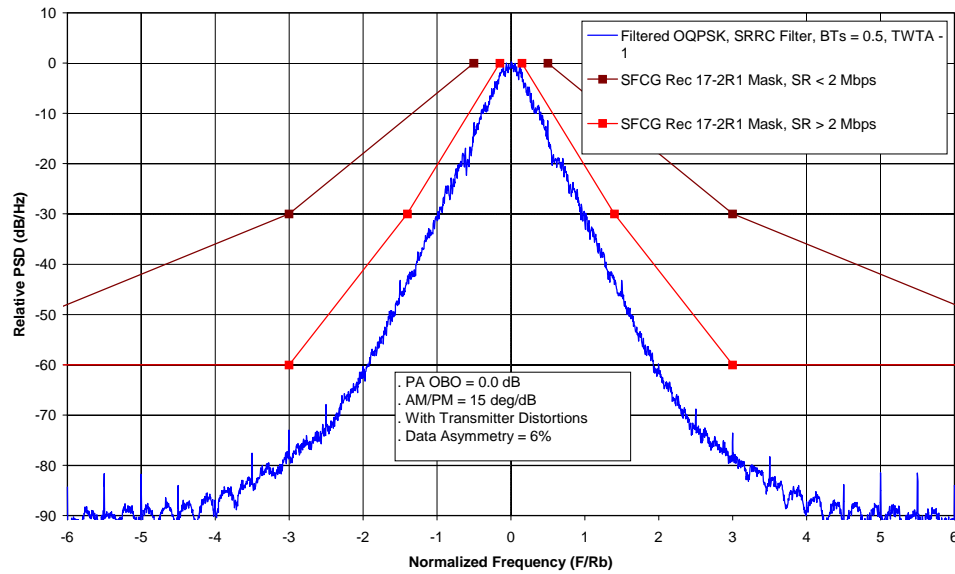


Figure 4-10. Filtered OQPSK Spectrum
(SRRC Filter BTs=0.5 $\alpha=0.5$, TWTA -1, PA OBO=0.0 dB, AM/PM = 15 deg/dB, Data Asymmetry = 6%)

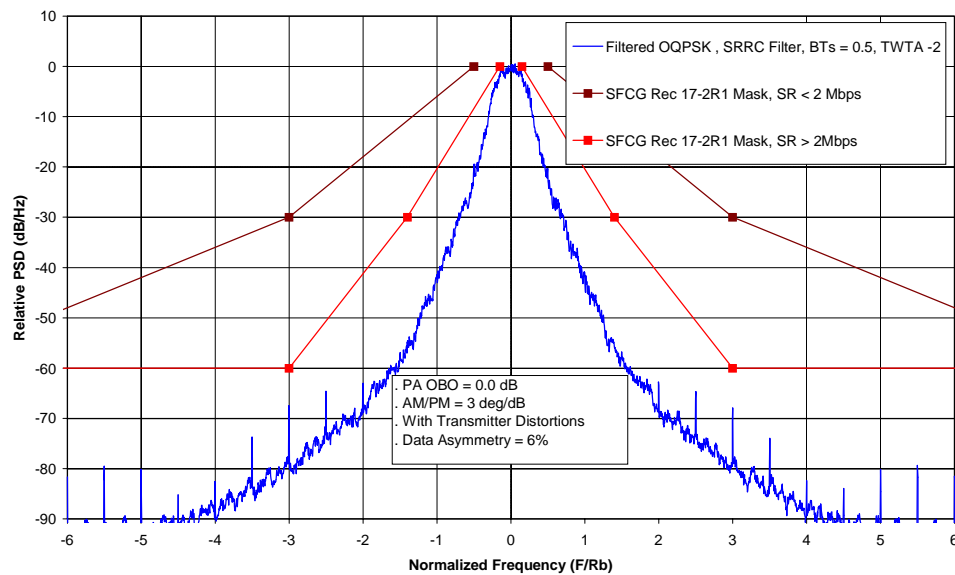


Figure 4-11. Filtered OQPSK Spectrum
(SRRC Filter BTs=0.5 $\alpha=0.5$, TWTA -2, PA OBO=0.0 dB, AM/PM = 3 deg/dB, Data Asymmetry = 6%)

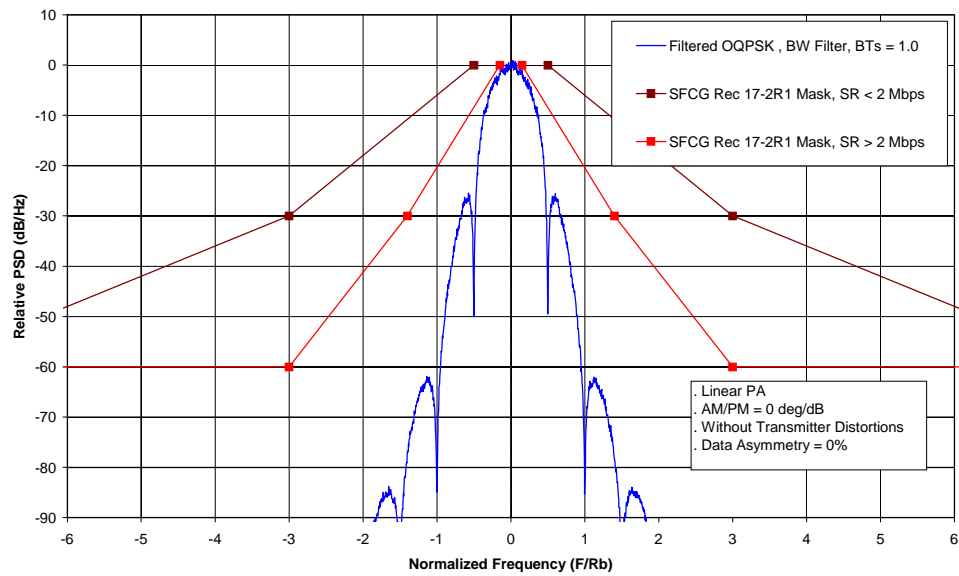


Figure 4-12. Filtered OQPSK Spectrum
(6-Pole Butterworth Filter BTs=1.0, Linear PA, AM/PM = 0deg/dB)

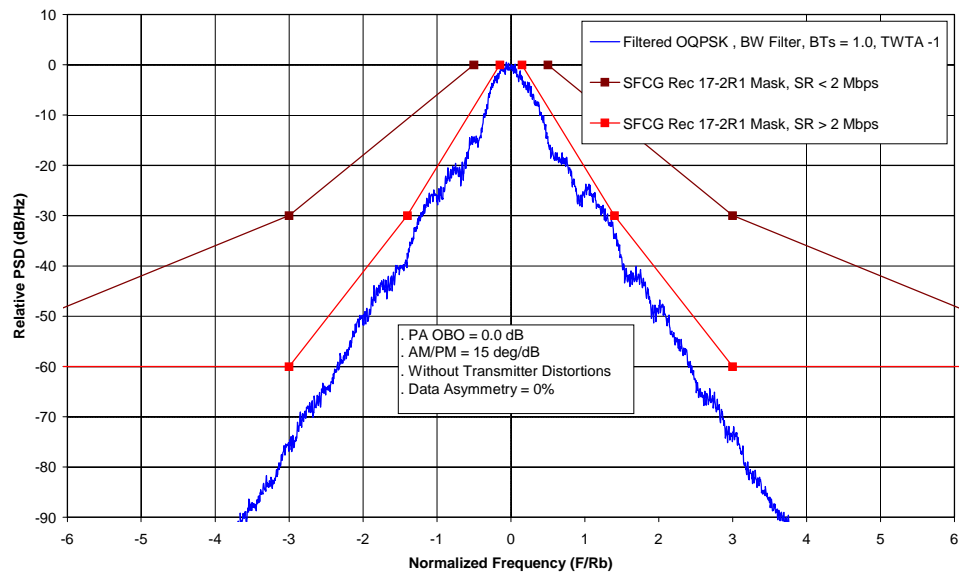


Figure 4-13. Filtered OQPSK Spectrum
(6-Pole Butterworth Filter BTs=1.0, TWTA -1, PA OBO=0.0 dB, AM/PM 15 deg/dB)

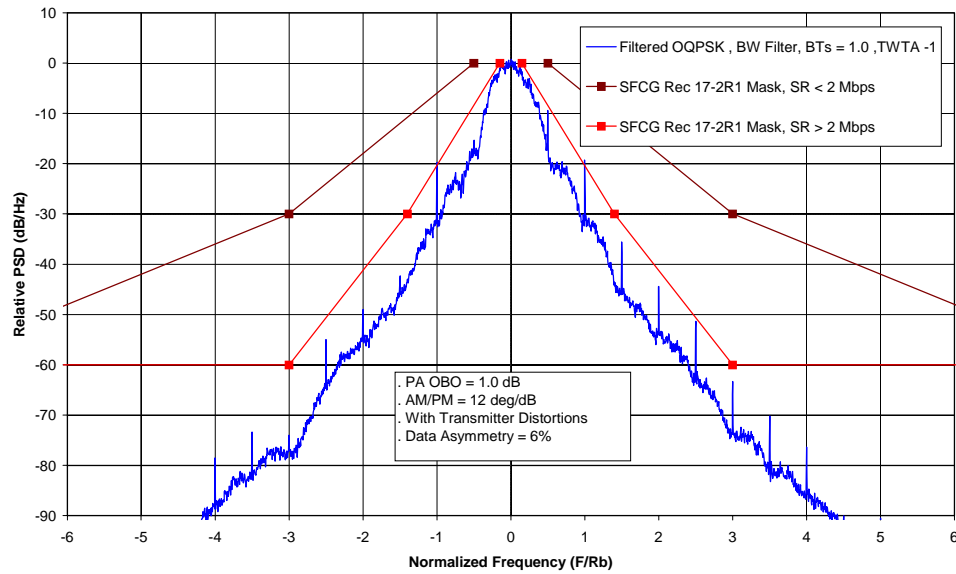


Figure 4-14. Filtered OQPSK Spectrum
(6-Pole Butterworth Filter $BT_s=1.0$, TWTA -1, PA OBO=1.0dB, AM/PM = 12 deg/dB, Data asymmetry =6%)

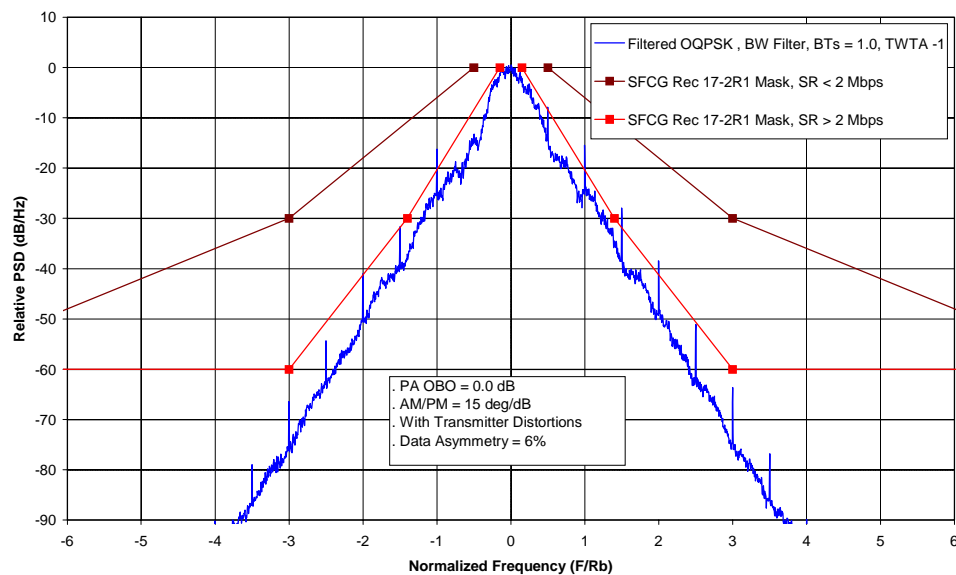


Figure 4-15. Filtered OQPSK Spectrum
(6-Pole Butterworth Filter $BT_s=1.0$, TWTA -1, PA OBO=0.0 dB, AM/PM =15 deg/dB Data Asymmetry = 6%)

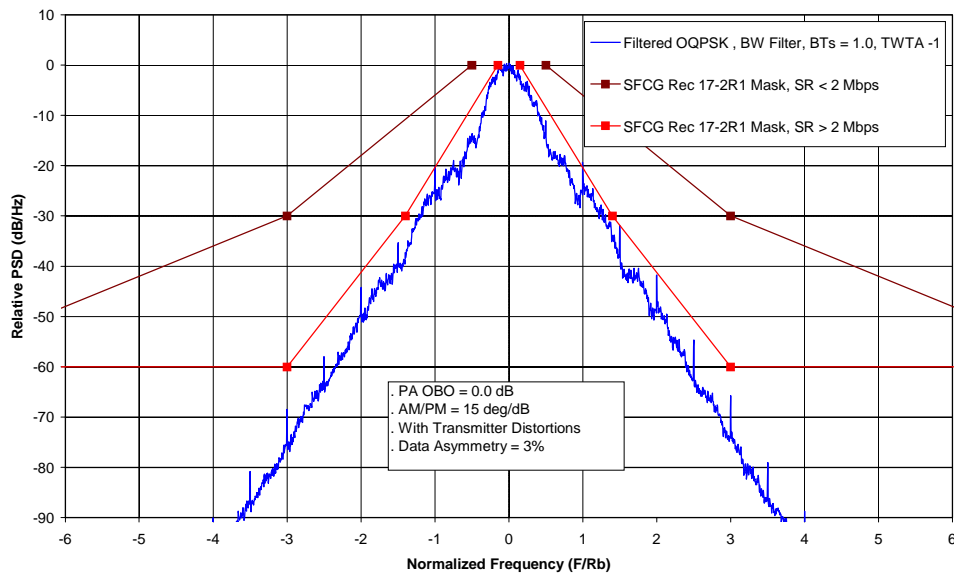


Figure 4-16. Filtered OQPSK Spectrum
(6-Pole Butterworth Filter $BT_s=1.0$, TWTA -1, PA OBO=0.0 dB, AM/PM = 15 deg/dB, Data Asymmetry = 3%)

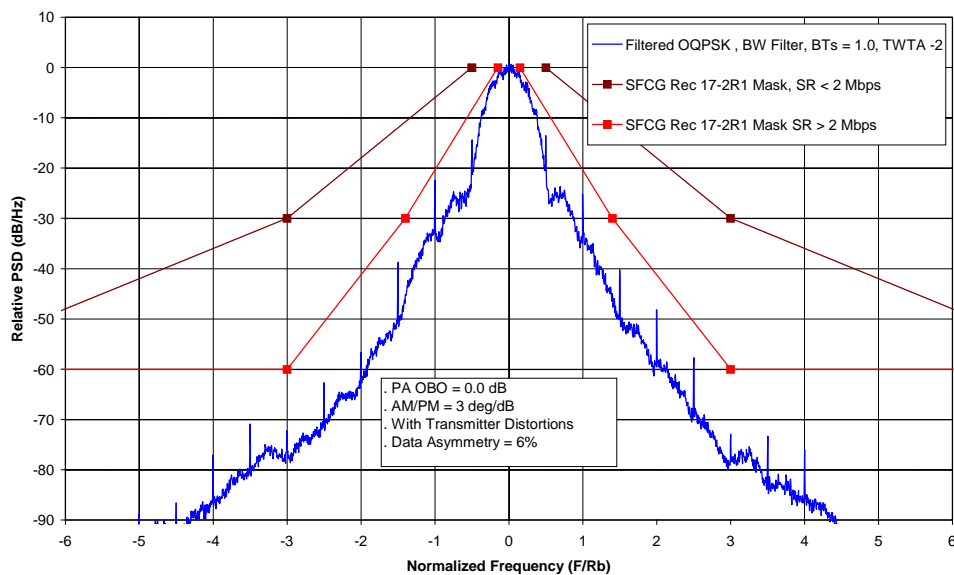


Figure 4-17. Filtered OQPSK Spectrum
(6-Pole Butterworth Filter $BT_s=1.0$, TWTA -2, PA OBO=0.0 dB, AM/PM = 3 deg/dB, Data Asymmetry = 6%)

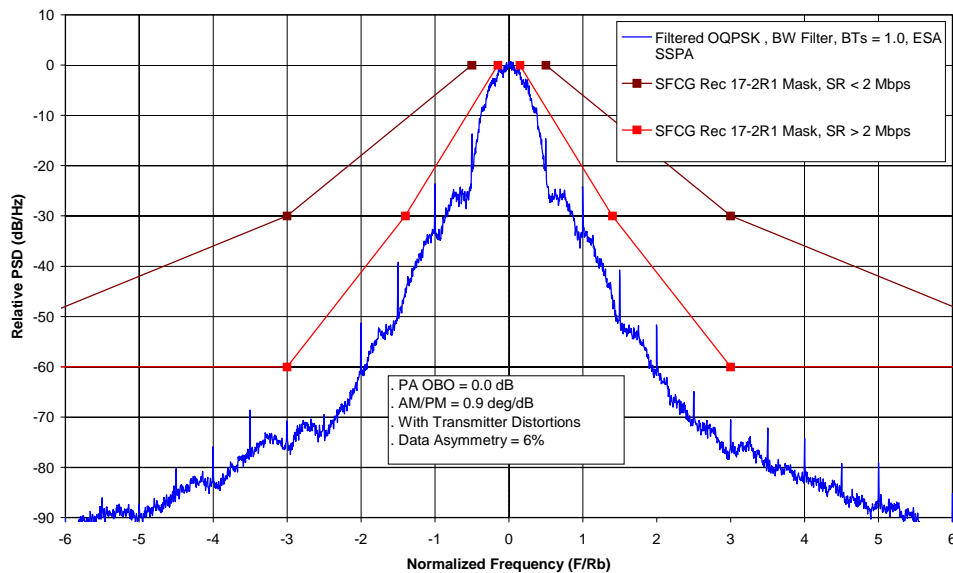


Figure 4-18. Filtered OQPSK Spectrum
(6-Pole Butterworth Filter $BT_s=1.0$, ESA SSPA, PA OBO =0.0 dB, AM/PM =0.9deg/dB, Data Asymmetry = 6%)

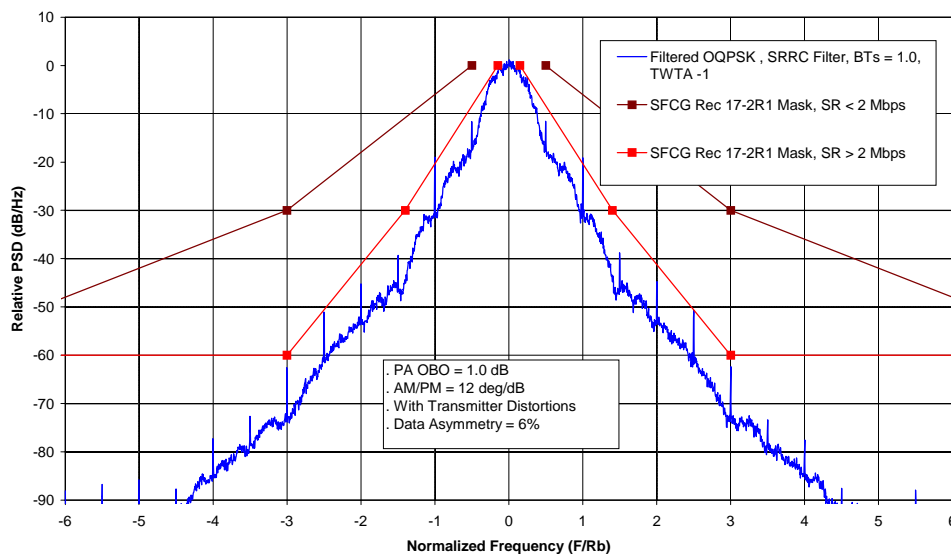


Figure 4-19. Filtered OQPSK Spectrum
(SRRC Filter $BT_s=1.0$ $\alpha=0.5$, TWTA -1, PA OBO=1 dB, AM/PM = 12 deg/dB, Data Asymmetry = 6%)

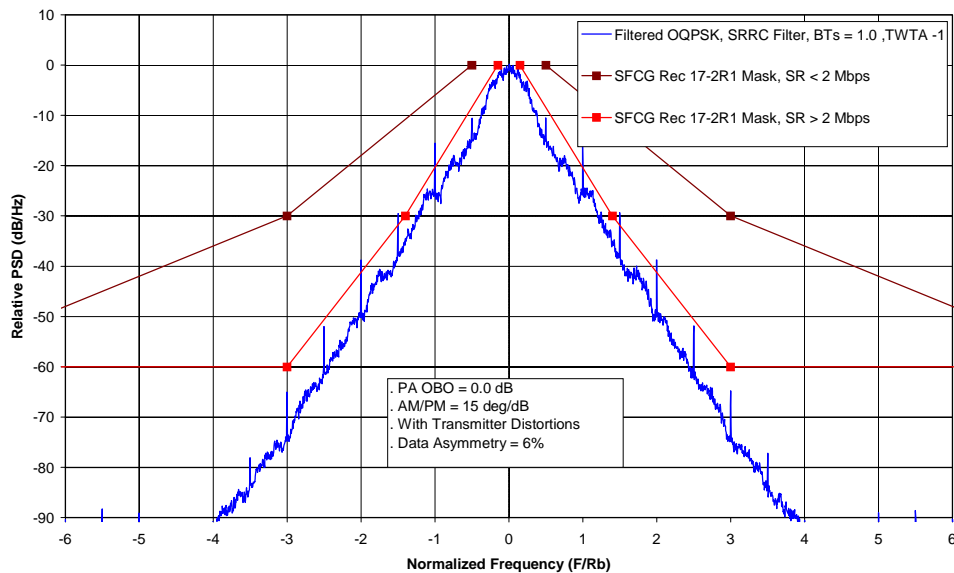


Figure 4-20. Filtered OQPSK Spectrum
(SRRC Filter BTs=1.0 $\alpha=0.5$, TWTA -1, PA OBO=0.0 dB, AM/PM = 15 deg/dB, Data Asymmetry = 6%)

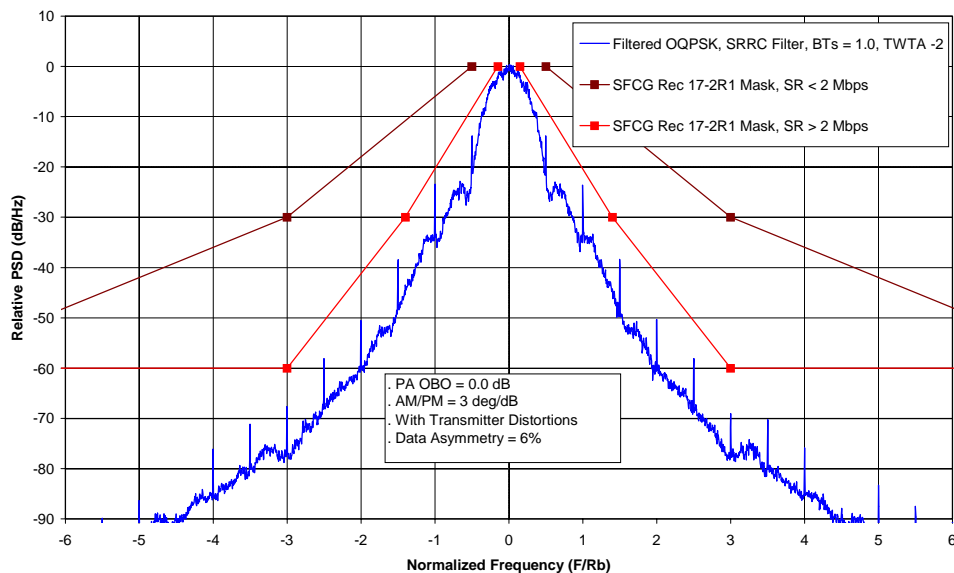


Figure 4-21. Filtered OQPSK Spectrum
(SRRC Filter BTs=2.0 $\alpha=0.5$, TWTA -2, PA OBO=0.0 dB, AM/PM = 3 dg/dB, Data Asymmetry = 6%)

Filtered OQPSK BTs = 1.5 (Figure 4-22 to Figure 4-27):

Figures 4-22 to 4-24 provide the PSD plots for the case of Butterworth filtered OQPSK with BTs = 1.5. Plots are provided for a linear amplifier and TWTA-1. For TWTA-1, plots are provided for 0 dB and 1 dB output back off.

Figure 4-22 shows the spectrum for Butterworth filtered OQPSK with BTs = 1.5. This plot was generated with a linear power amplifier and with transmitter distortions. The two-sided 60-dB bandwidth is $3.32 \times R_b$ and the spectrum is well within the high data rate mask. Figure 4-23 shows the same case except that the TWTA-1 with 1dB output back off is used. This plot illustrates the effect of the nonlinear amplifier on the spectrum; the spectrum does not comply with the high data rate mask. Figure 4-24 shows the same case as Figure 4-23 but with the TWTA-1 output back off set to 0 dB. In both figures, the spectrum does not comply with the high data rate mask.

Figures 4-25 to 4-27 provide the PSD plots for the case of SRRC filtered OQPSK with BTs = 1.5. Plots are provided for a linear amplifier and TWTA-1. For TWTA-1, plots are provided for 0 dB and 1 dB output back off.

Figure 4-25 shows the spectrum for SRRC filtered OQPSK with BTs = 1.5. This plot was generated with a linear power amplifier and with transmitter distortions. The two-sided 60-dB bandwidth is $3.56 \times R_b$ and the spectrum is well within the high data rate mask. Figure 4-26 shows the same case except that the TWTA-1 with 1dB output back off is used. This plot illustrates the effect of the nonlinear amplifier on the spectrum; the spectrum does not comply with the high data rate mask. Figure 4-27 shows the same case as Figure 4-26 but with the TWTA-1 output back off set to 0 dB; the spectrum does not comply with the high data rate mask.

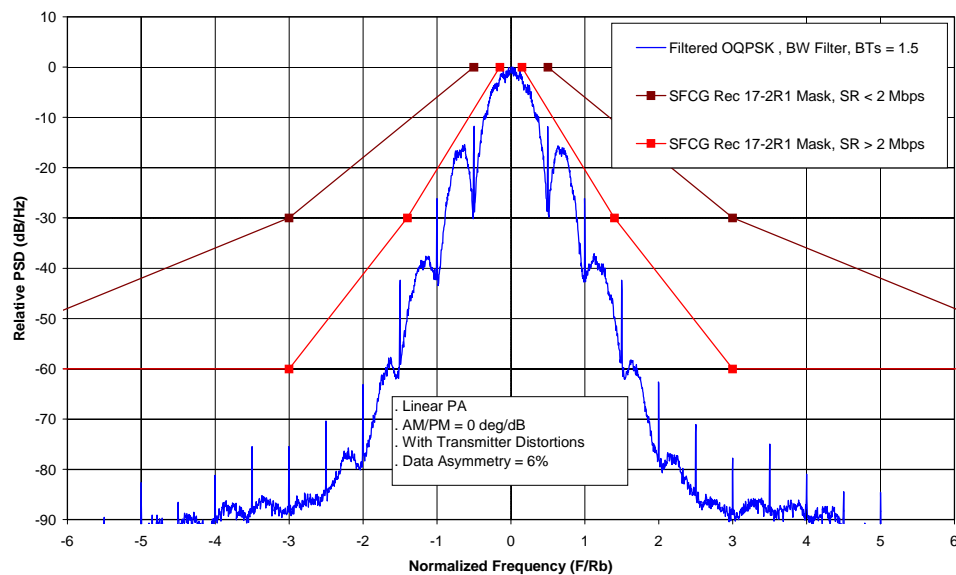


Figure 4-22. Filtered OQPSK Spectrum
(6-Pole Butterworth Filter BTs=1.5, Linear PA, AM/PM = 0 deg/dB, Data Asymmetry = 6%)

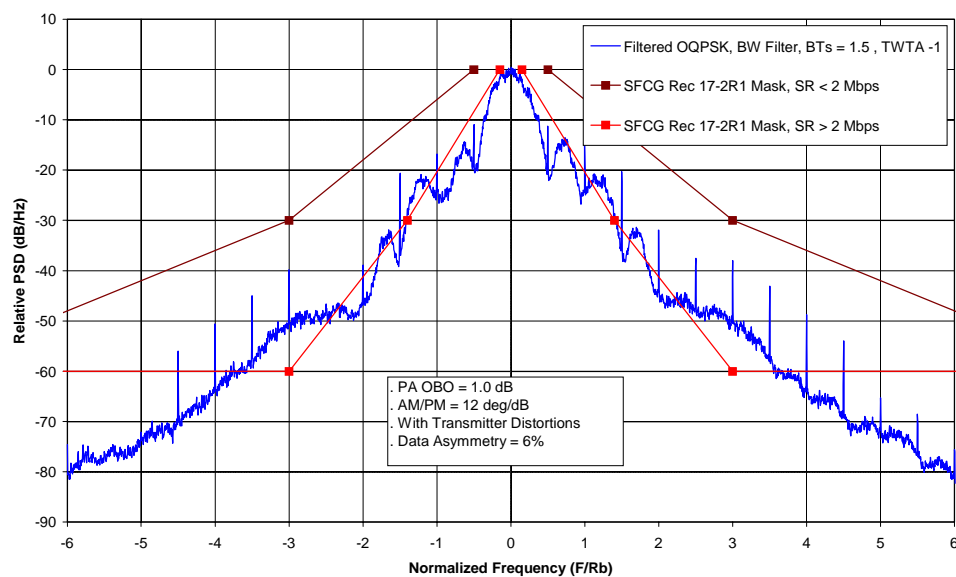


Figure 4-23. Filtered OQPSK Spectrum
(6-Pole Butterworth Filter BTs=1.5, TWTA -1, PA OBO=1.0 dB, AM/PM = 12 deg/dB, Data Asymmetry = 6%)

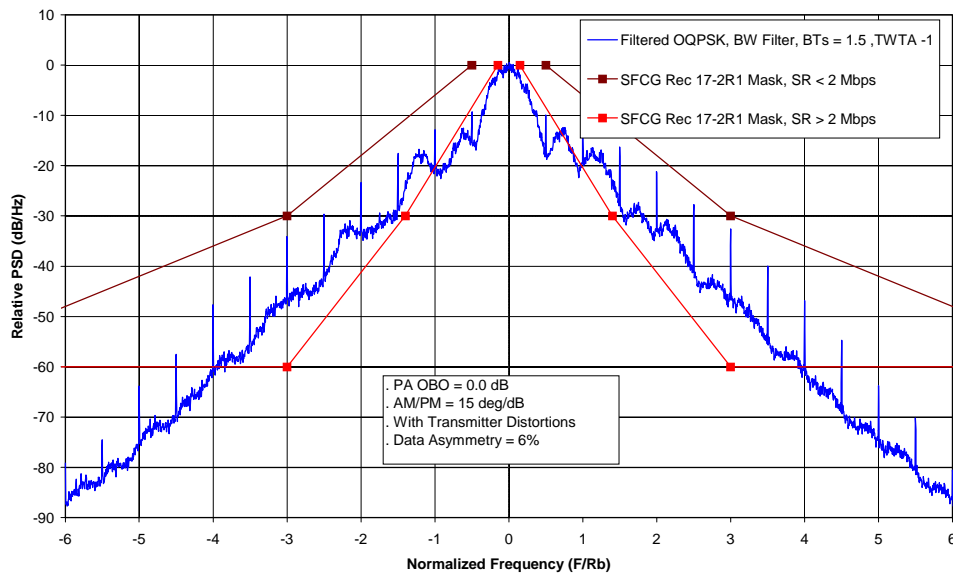


Figure 4-24. Filtered OQPSK Spectrum
(6-Pole Butterworth Filter $BT_s=1.5$, TWTA -1, PA OBO=0.0 dB, AM/PM = 15 deg/dB, Data Asymmetry = 6%)

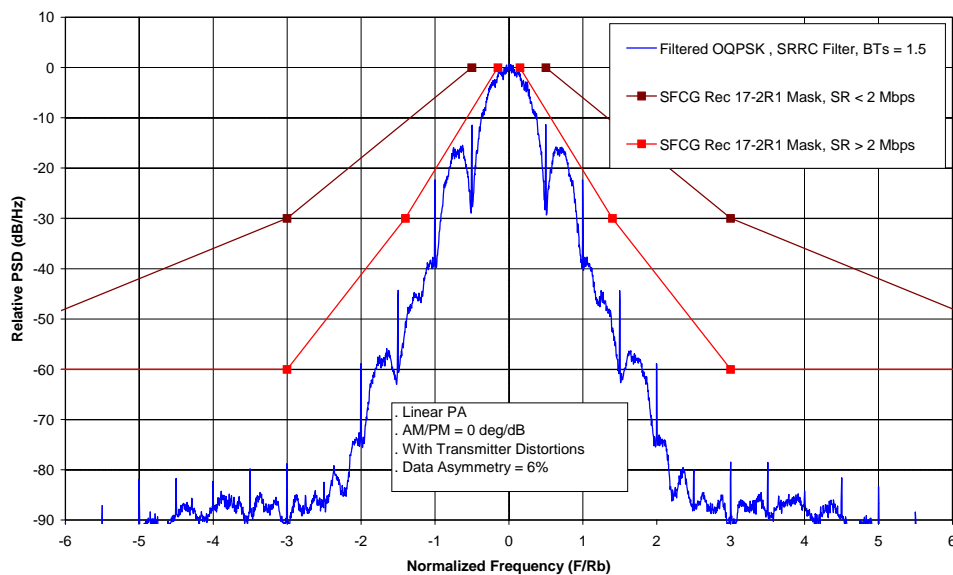


Figure 4-25. Filtered OQPSK Spectrum
(SRRC Filter $BT_s=1.5$ $\alpha=0.5$, Linear PA, AM/PM =0 deg/dB, Data Asymmetry = 6%)

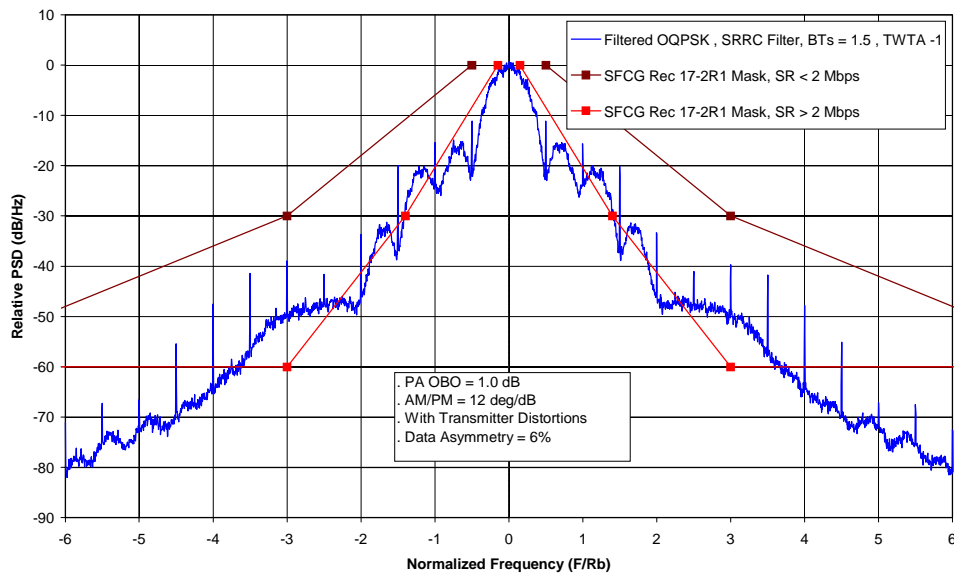


Figure 4-26. Filtered OQPSK Spectrum
(SRRC Filter $BT_s=1.5$, $\alpha=0.5$, TWTA -1, PA OBO =1.0 dB, AM/PM = 12 deg/dB, Data Asymmetry = 6%)

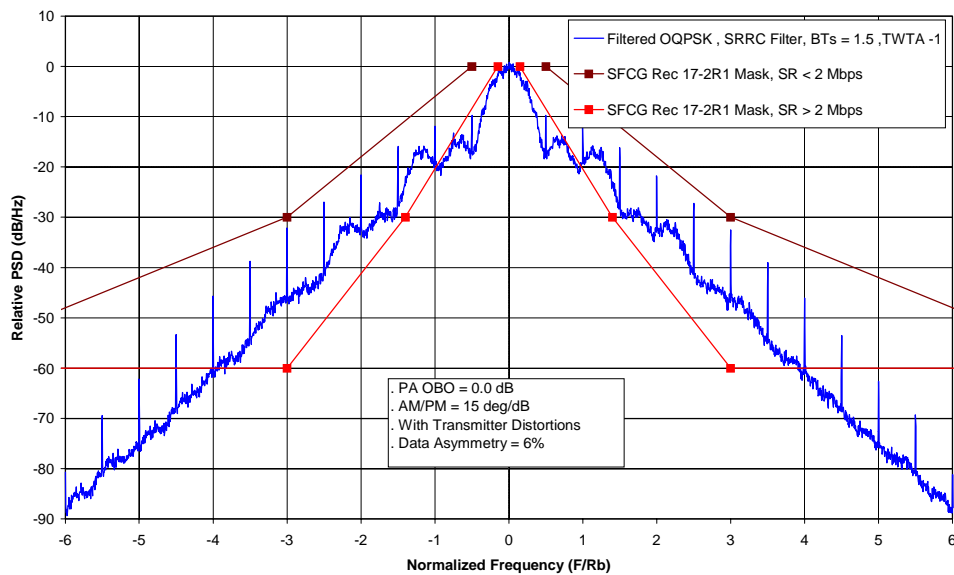


Figure 4-27. Filtered OQPSK Spectrum
(SRRC Filter $BT_s=1.5$, $\alpha=0.5$, TWTA -1, PA OBO=0.0 dB, AM/PM = 15 deg/dB, Data Asymmetry = 6%)

4.2.2 Filtered OQPSK/PM Spectra

Unfiltered OQPSK/PM (Figure 4-28):

PSD plot for unfiltered OQPSK/PM is close to PSD for unfiltered OQPSK shown in Phase 3, except the spikes here were caused by data asymmetry while the spikes in Phase 3 were caused by data imbalance.

Butterworth Filtered OQPSK/PM BTs = 1.0

Figures 4-29 to 4-31 provide the PSD plots for the case of Butterworth filtered OQPSK with BTs = 1.0. Plots are provided for a linear amplifier and GSFC TWTA-1. Plots are provided for 0 dB and 1 dB output back off for a TWTA -1.

Figure 4-29 shows spectrum for Butterworth filtered OQPSK with BTs = 1.0. This plot was generated with a linear power amplifier and with no transmitter distortions. The two-sided 60-dB bandwidth is $3.0 \times R_b$ and the spectrum is well within the high data rate mask. Figure 4-30 shows the same case except that the GSFC TWTA-1 with 1dB output back off and transmitter distortions are included. Figure 4-31 shows the same case as Figure 4-30 but with the TWTA-1 output back off set to 0 dB. PSDs plots for Butterworth filtered OQPSK/PM are very close in the case of OBO = 6.7, OBO = 1 and OBO = 0. For OQPSK/PM modulator, phase passes pulse-shaping filter, AM/AM has little effects on the output from pulse shaping filter when PA OBO changed from 1 to 0. This result will be justified by BER performance described in next subsection.

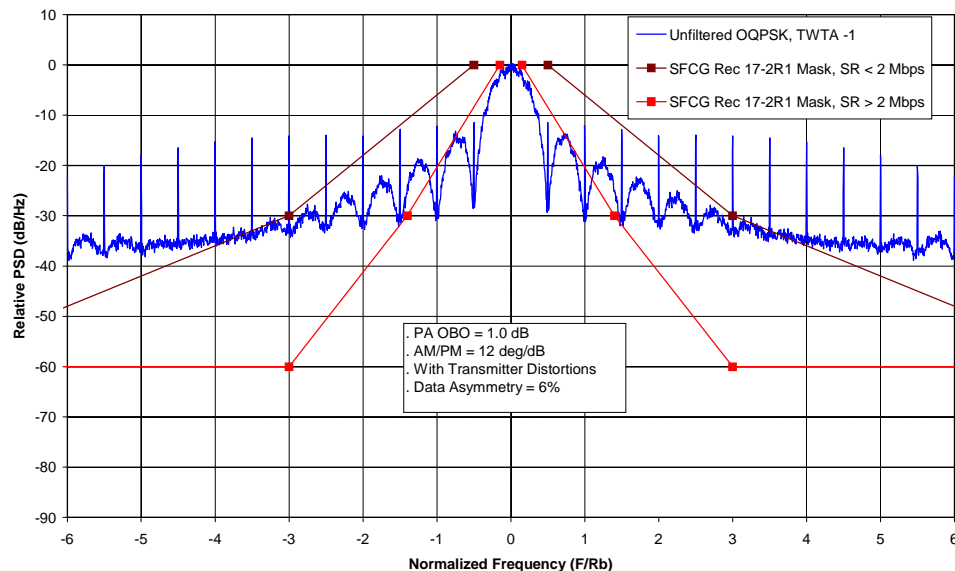


Figure 4-28. Unfiltered OQPSK Spectrum

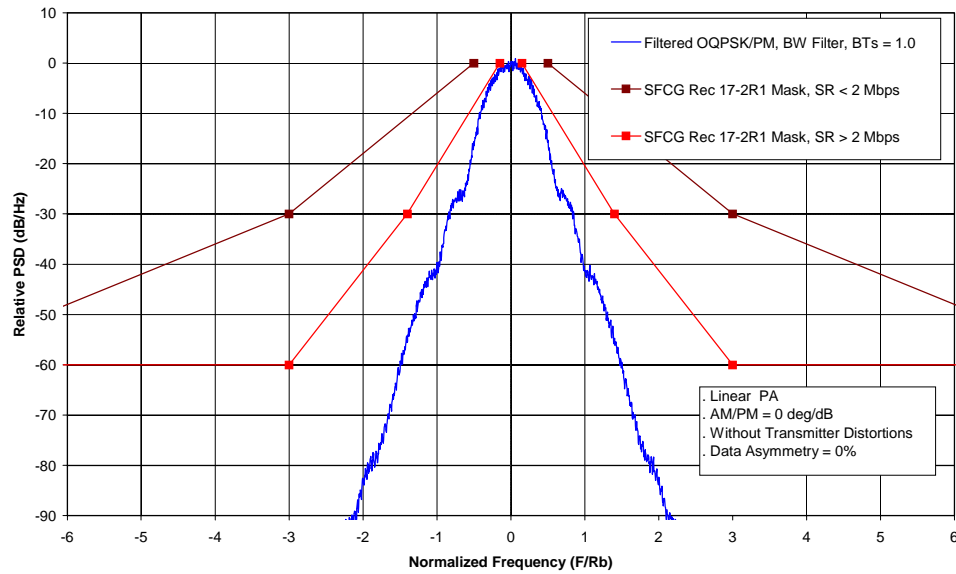


Figure 4-29. Filtered OQPSK/PM Spectrum
(6-Pole Butterworth Filter $BT_s=1.0$, Linear PA, AM/PM = 0 deg/dB, without distortions)

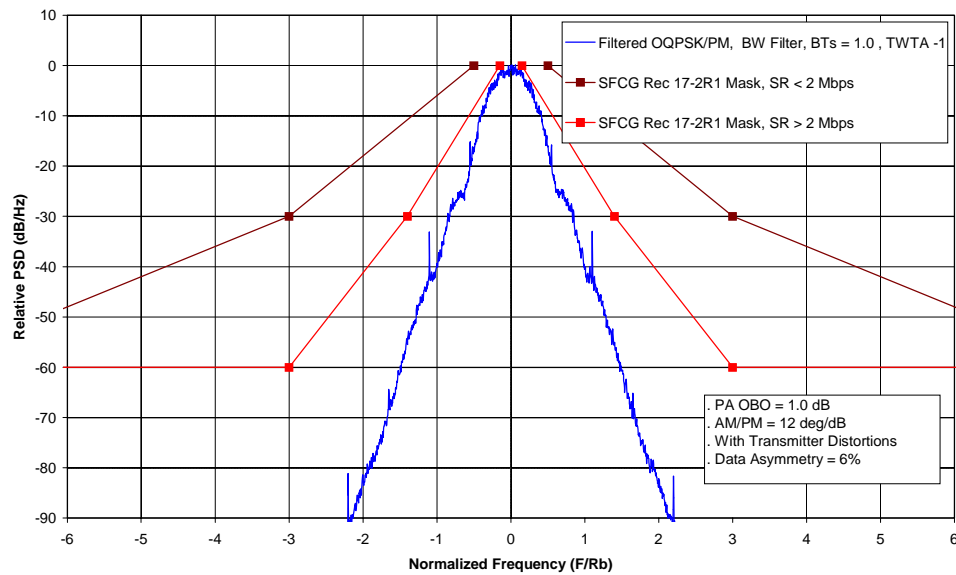


Figure 4-30. Filtered OQPSK/PM Spectrum
(6-Pole Butterworth Filter $BT_s=1.0$, TWTA -1, PA OBO=1.0 dB, AM/PM = 12deg/dB, Data Asymmetry = 6%)

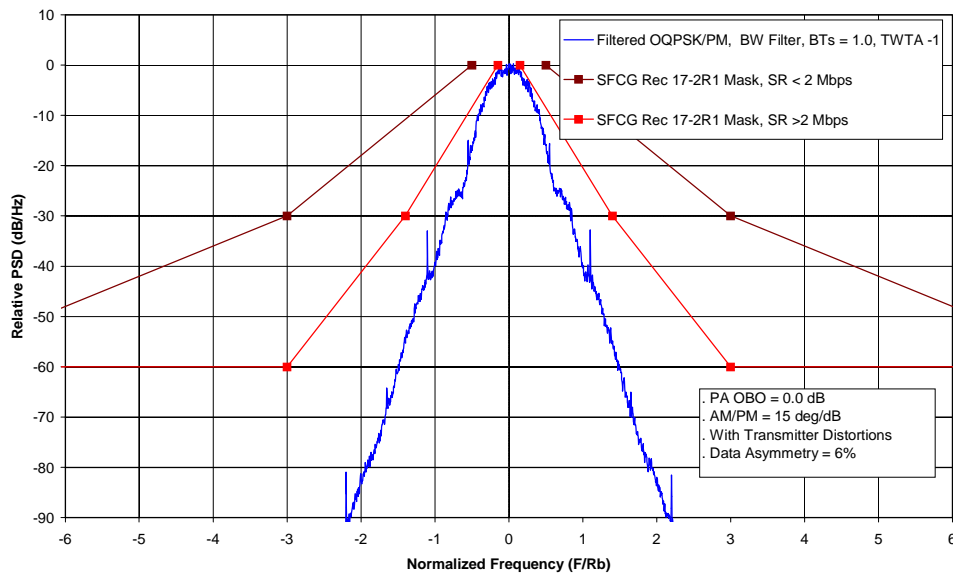


Figure 4-31. Filtered OQPSK/PM Spectrum
(6-Pole Butterworth Filter $BT_s=1.0$, TWTA -1, PA OBO=0.0 dB, AM/PM =15deg/dB, Data Asymmetry = 6%)

Gaussian Filtered OQPSK/PM $BT_s = 1.0$

Figure 4-32 provides the PSD plots for the case of Gaussian filtered OQPSK with $BT_s = 1.0$. This plot was generated with a TWTA -1 output back off set to 0dB and with transmitter distortions. The two-sided 60-dB bandwidth is $4.4 \times R_b$ and the spectrum is within the high data rate mask. The Spectrum is wider than the OQPSK/PM spectrum in Figure 4-31.

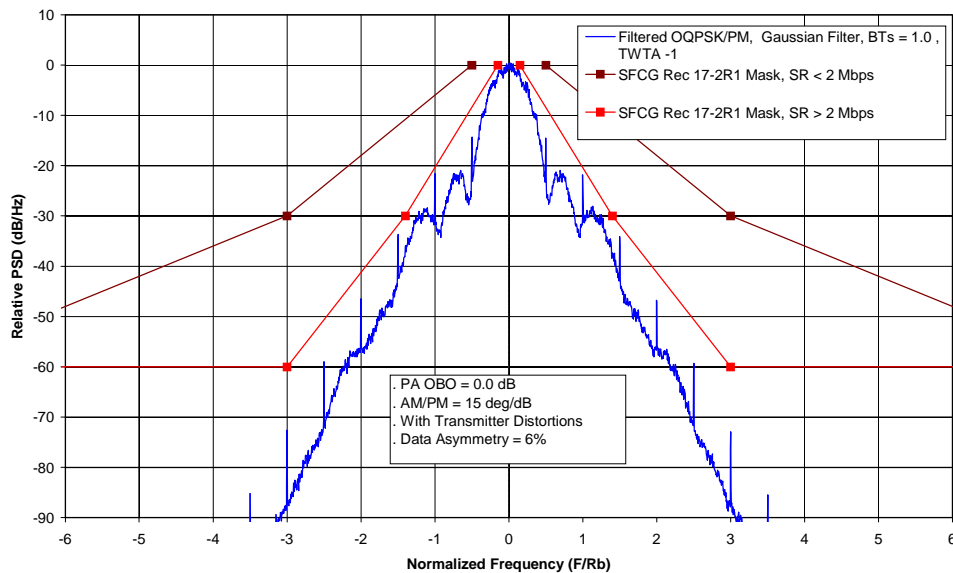


Figure 4-32. Filtered OQPSK/PM Spectrum

(Gaussian Filter, $BT_s=1.0$, TWTA -1, PA OBO=0.0 dB, AM/PM =15deg/dB, Data Asymmetry = 6%)

4.3 Implementation Loss

Summary:

The end-to-end BER simulation model described in Section 3 was used to generate BER vs. E_b/N_0 performance for BPSK, unfiltered OQPSK, filtered OQPSK, unfiltered OQPSK/PM and filtered OQPSK/PM. Note that in all cases integrate and dump data detection is used. Although not optimum for filtered modulations, integrate and dump detection is simple and reflects the capabilities of equipment currently in use by NASA ground terminals. BER curves are provided in Figures 4-33 to 4-38. The implementation loss for each modulation scheme was calculated relative to theoretical BPSK performance. Table 4-2 lists implementation loss relative to theory for a BER of 10^{-3} and 10^{-5} . Table 4-2 also lists implementation loss relative to BPSK with the distortions listed in Section 3. This provides the additional transmit power required for the bandwidth efficient modulation to meet the BER requirement relative to BPSK.

The following observations are made regarding the information in Table 4-2:

- Several bandwidth efficient modulation methods result in a modest increase in implementation loss even though a suboptimum detection is used. These include: Butterworth filtered OQPSK ($BT_s=1.0, 1.5$), SRRC filtered OQPSK ($BT_s = 1.5$) and Butterworth filtered OQPSK/PM ($BT_s = 1.0$).

- For SRRC and Butterworth filtered OQPSK with $BTs = 0.5$, the implementation loss is excessive. It is likely that these can be reduced by using a matched filter rather than the integrate and dump detector.
- For SRRC and Butterworth filtered OQPSK with $BTs = 1.0$, the implementation loss is excessive when the amplifier is operated at saturation. This was found to be true for the TWTA-1. For Butterworth filtered OQPSK, the TWTA-2 and the ESA SSPA were also used at saturation with improved results.
- Butterworth filtered OQPSK/PM provided an increase in implementation loss of only 0.6 dB with the TWTA-1 operating in saturation.

Table 4-2. BPSK, OQPSK and OQPSK/PM Implementation Loss

Modulation	Amplifier Model	PA Output Back-Off	Transmitter Distortions	Implementation Loss			
				Relative to theoretical BPSK		Relative to BPSK ⁽⁴⁾	
				@BER = 10 ⁻³	@BER = 10 ⁻⁵	@BER = 10 ⁻³	@BER = 10 ⁻⁵
BPSK, unfiltered	Linear PA	NA	None	< 0.1 dB	< 0.1 dB	NA	NA
BSPK, unfiltered	TWTA -1	1 dB	Set 1 ⁽²⁾	0.2 dB	0.6 dB	0.0dB	0.0 dB
OQPSK, unfiltered	TWTA -1	1 dB	Set 1 ⁽²⁾	0.5 dB	0.9 dB	0.3 dB	0.3 dB
OQPSK- 6-pole Butterworth Filter (BT=0.5)	TWTA -1	1 dB	Set 1 ⁽²⁾	> 13 dB ⁽¹⁾	> 15 dB ⁽¹⁾	> 12.8 dB ⁽¹⁾	> 14.4 dB ⁽¹⁾
OQPSK- 6-pole Butterworth Filter (BT=1.0)	TWTA -1	1 dB	Set 1 ⁽³⁾	0.9dB	1.6 dB	0.7 dB	1.0 dB
OQPSK- 6-pole Butterworth Filter (BT=1.0)	TWTA -1	0 dB	Set 1 ⁽²⁾	1.4 dB	2.4 dB	1.2 dB	1.8 dB
	TWTA -2	0 dB		0.75 dB	1.4 dB	0.55 dB	0.8 dB
	ESA SSPA	0 dB		0.75 dB	1.4 dB	0.55 dB	0.8 dB
OQPSK- 6-pole Butterworth Filter (BT=1.5)	TWTA -1	1 dB	Set 1 ⁽²⁾	0.7 dB	1.3 dB	0.5 dB	0.7 dB
OQPSK- SRRC Filter (BT=0.5)	TWTA -1	1 dB	Set 1 ⁽²⁾	4.4 dB	8.8 dB ⁽¹⁾	4.2 dB ⁽¹⁾	> 8.2 dB ⁽¹⁾
OQPSK- SRRC Filter (BT=1.0)	TWTA -1	1 dB	Set 1 ⁽³⁾	1.0 dB	1.6 dB	0.8 dB	1.0 dB
OQPSK- SRRC Filter (BT=1.0)	TWTA -1	0dB	Set 1 ⁽²⁾	1.4 dB	3.3 dB	1.2 dB	2.7 dB
OQPSK- SRRC Filter (BT=1.5)	TWTA -1	1 dB	Set 1 ⁽²⁾	0.6 dB	1.1 dB	0.4 dB	0.5 dB
OQPSK/ PM) Unfiltered	TWTA -1	1 dB	Set 1 ⁽²⁾	0.5 dB	1.0 dB	0.3dB	0.4 dB
OQPSK/ PM Butterworth Filter (BT=1.0)	TWTA -1	1 dB	Set 1 ⁽²⁾	0.7 dB	1.2 dB	0.5dB	0.6 dB
OQPSK/ PM Butterworth Filter (BT=1.0)	TWTA -1	0 dB	Set 1 ⁽²⁾	0.7 dB	1.2 dB	0.5dB	0.6 dB
<ol style="list-style-type: none"> Not explicitly simulated. Estimated from BER vs. Eb/No curves The transmitter distortions are same as Set 1, except no phase noise. Set 1 with phase noise 3.6° rms is also simulated, resulted in less than 0.1 dB additional degradation. Implementation loss relative to Unfiltered BPSK with transmitter distortions and with TWTA -1 operating at 1 dB OBO. 							

4.4.1 Filtered OQPSK Implementation Loss

This section provides implementation loss results for filtered OQPSK modulation. Both Butterworth and SRRC filters are addresses.

Baseline Performance

Figure 4-33 shows the BER vs. E_b/N_0 performance for unfiltered BPSK and QPSK modulation. The simulation results for BPSK with no transmitter distortions agree closely with the theoretical results. When distortions are added, the implementation loss increases to 0.6 dB. The loss for QPSK with transmitter distortions is approximately 1.0 dB. The BPSK performance with transmitter distortions will be used as the baseline for comparison in this study.

Butterworth and SRRC Filtered OQPSK

BER vs. E_b/N_0 performance for Butterworth filtered OQPSK is shown in Figure 4-34 for BTs = 0.5, 1.0 and 1.5 with the TWTA-1 amplifier operating with 1-dB output backoff. Similar results for SRRC filtered OQPSK are shown in Figure 4-35. In both cases, BTs=0.5 produces an excessively large implementation loss. This could be reduced by the use of a more complex receiver.

For BTs = 1.0 additional BER simulations were performed with the TWTA-1 amplifier operating with a 0-dB output backoff. Results for Butterworth and SRRC filtered OQPSK are shown in Figure 4-36. In both cases an increase in implementation loss is observed with a slightly larger increase for SRRC filtered OQPSK.

The results presented in Figures 4-33 to 4-36 show performance with the TWTA-1 amplifier and with 6 % data asymmetry. Some additional simulations for Butterworth filtered OQPSK (BTs = 1.0) were performed with different amplifiers operating at saturation and with 3 % data asymmetry. These results are shown in Figure 4-37 and a comparison of implementation loss is summarized in Table 4-3. The decrease in data asymmetry from 6 % to 3 % did not affect the implementation loss results for this case with TWTA-1. A 1-dB improvement is observed through the use of TWTA-2 and the ESA SSPA. Both TWTA-2 and the ESA SSPA have significantly improved AM/PM performance in comparison to TWTA-1.

**Table 4-3. Butterworth Filtered OQPSK (BTs = 1.0)
Implementation Loss**

Amplifier Model	PA Output Back-Off	Implementation Loss @ BER = 10^{-5}	
		6 % Data Asymmetry	3 % Data Asymmetry
TWTA -1	1 dB	1.6 dB	NA
TWTA -1	0 dB	2.4 dB	2.4 dB
TWTA -2	0 dB	NA	1.4 dB
ESA SSPA	0 dB	NA	1.4 dB

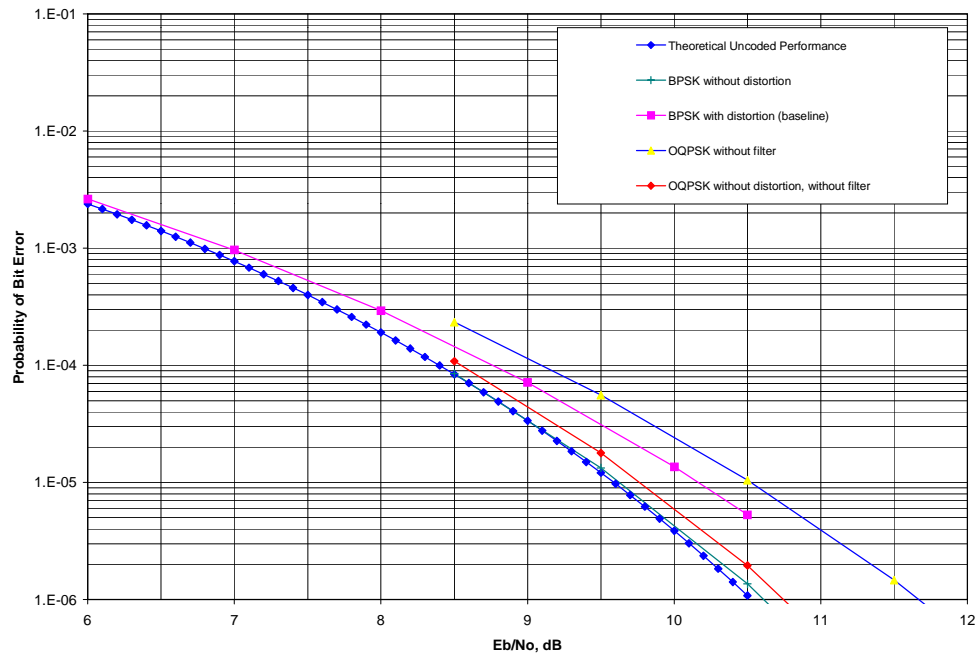


Figure 4-33. Probability of Error vs. E_b/N_0 for BPSK and OQPSK Modulation

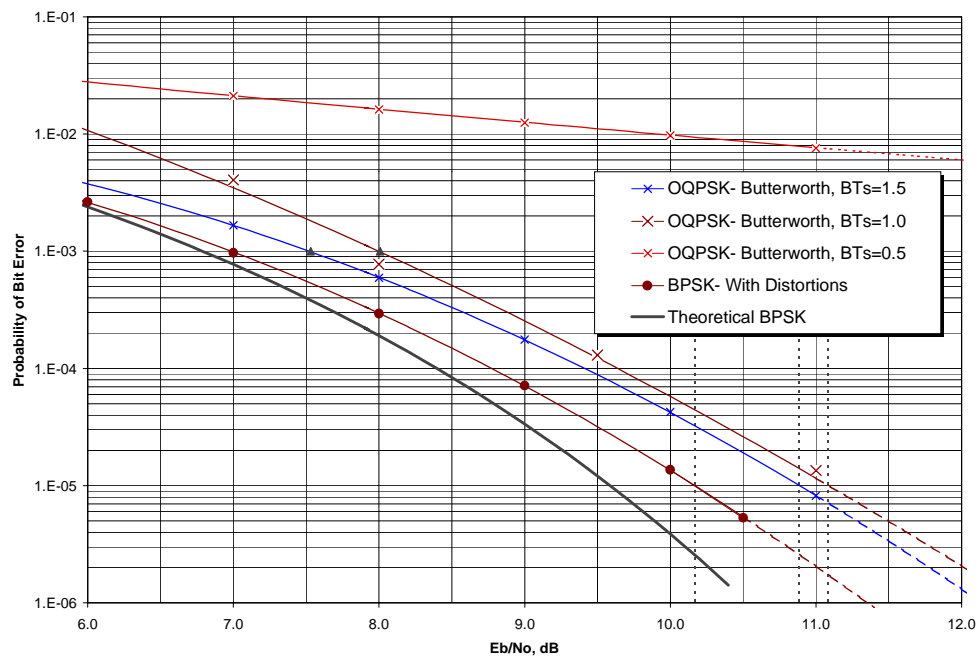


Figure 4-34. Probability of Error vs. E_b/N_0 for BPSK and Filtered OQPSK Modulation, 6-pole Butterworth Filter

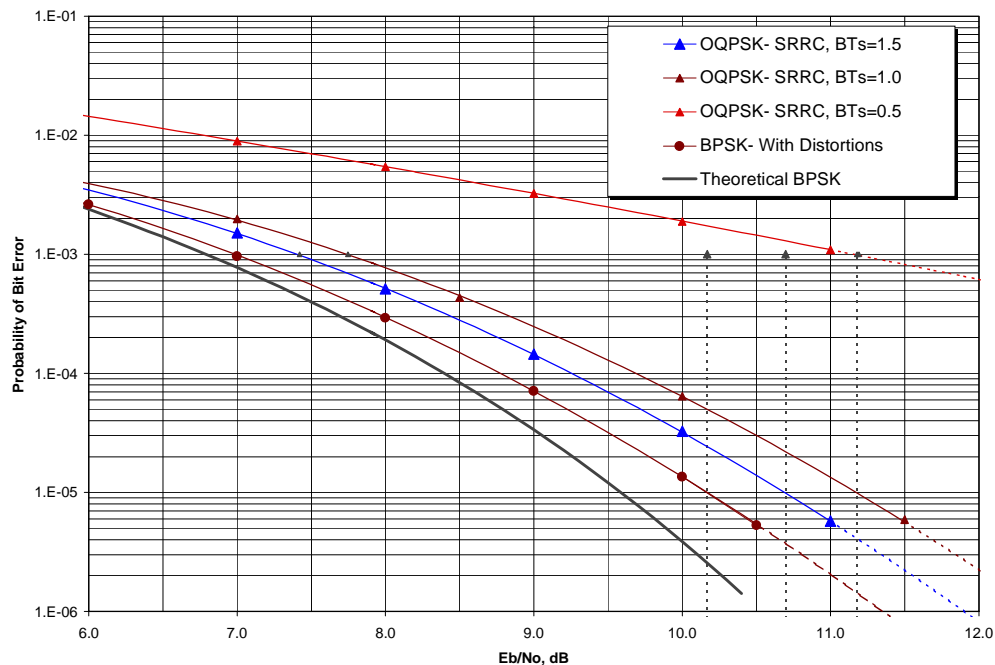


Figure 4-35. Probability of Error vs. E_b/N_0 for BPSK and Filtered OQPSK Modulation – SRRC

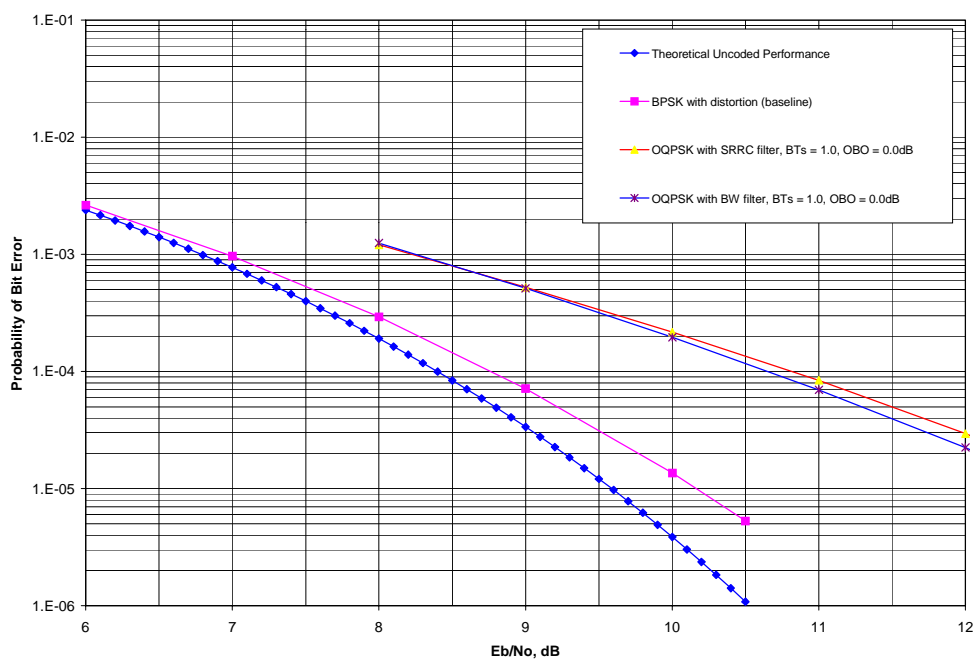


Figure 4-36. Probability of Error vs. E_b/N_0 for BPSK and Filtered OQPSK Modulation, $OBO=0.0$ dB

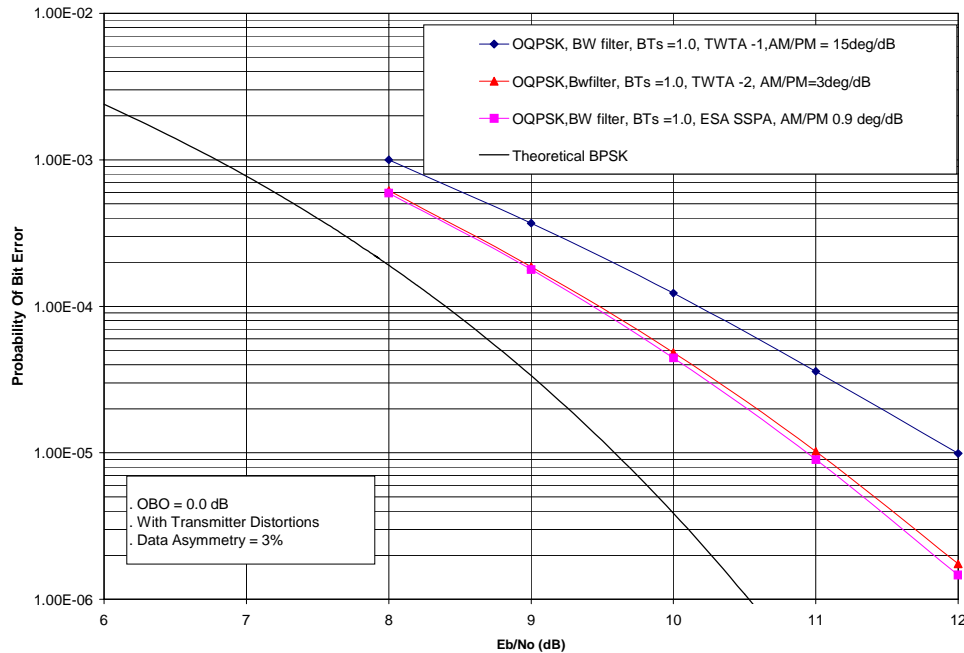


Figure 4-37. Probability of Error vs. E_b/N_0 for BPSK and Filtered OQPSK Modulation, $OBO=0.0$ dB, using different PA model

4.3.1 OQPSK/PM Implementation Loss

This section provides implementation loss results for Butterworth filtered OQPSK/PM modulation. Both and SRRC filters are addresses.

BER vs. E_b/N_0 performance curves are provided in Figure 4-38.

Figure 4-38 shows performance for unfiltered QPSK and QPSK/PM. The results show close agreement between these two cases. This is expected since without filtering, the two implementations of OQPSK produce identical output signals. Differences in the performance curves are within the confidence interval of the simulation.

Figure 4-38 shows that for filtered OQPSK/PM, the results for PA $OBO = 1$ and PA $OBO = 0$ are almost identical. This results is different than that found for OQPSK. Since OQPSK/PM has constant envelope by design, amplitude variations are not present at the input to the power amplifier; therefore, AM/AM and AM/PM effects do not degrade BER performance. For this reason the PSDs for the 1-dB and 0-dB output backoff cases are also almost identical.

The NASA/JPL Phase 3 report [3] analyzes a filtered OQPSK modulator which also used a linear phase modulator. The results are compared here. With the Butterworth filter ($BTs = 1.0$), an $E_b/N_0 = 8.7$ dB is required for a 1×10^{-3} BER (1.9 dB implementation loss) in the NASA/JPL Phase 3 report version of the modulator; the results from Figure 4-38 of this report show E_b/N_0 of 7.5 dB is enough for a 1×10^{-3} BER. Some reasons for the different performance are: different

transmitter distortion parameters, and a different implementation of the transmitter. Reference [3] indicated that the filtered OQPSK modulator used in the study was not a true OQPSK and therefore the results may not be valid.

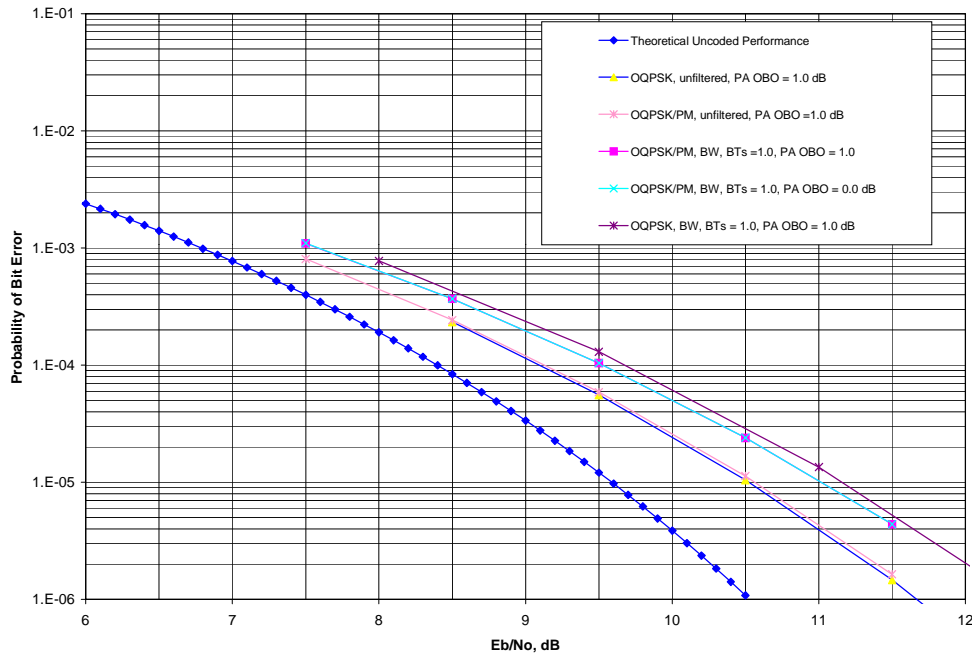


Figure 4-38. Probability of Error vs. E_b/N_o for unfiltered OQPSK and filtered OQPSK/PM with 6-pole Butterworth Filter

4.4 Filtered OQPSK Interference Susceptibility

Summary

The interference model described in Section 3.4 was used to combine the transmitter, noise, and ground terminal models in to an end-to-end simulation model as illustrated in Figure 3-16. The interference is defined by the interference power to noise power ratio (I/N). For narrowband interference, the interference center frequency is also specified. Wideband interference and narrowband interference with center frequencies at 0Hz and 0.5 R_s were used to determine I/N for 1-dB degradation relative to baseline performance (no interference) for the Butterworth pulse shaping filter with $BT_s = 1.0$.

The I/N results for filtered OQPSK end-to-end BER simulations with interference are shown in Table 4-4. The I/N values are for a 1 dB degradation at a BER of 10^{-3} .

Table 4-4. I/N (dB) for 1-dB degradation

Case	Narrowband Interference $f_i = 0\text{Hz}$	Narrowband Interference $f_i = 0.5\text{ Rs}$	Wideband Interference $B_i = 3.2 \times \text{SR}$
BW, BTs=1.0, PA OBO =1	-9.7	-7.5	-5.8
BW, BTs=1.0, PA OBO =0	-9.6	-6.7	-5.8
Note 1: N defined on Bandwidth B_n , $B_n = 3.2 \times \text{SR}$.			

4.4.1 Approach

We investigated wideband interference and narrowband interference with center frequencies at 0Hz and 0.5 Rs. At Probability Bit Error 10^{-3} , I/N was varied to achieve 1 dB degradation relative to the baseline simulation results (no interference). At a Probability of BER of 10^{-5} , 1dB degradation achieved with narrowband interference at 0 Hz frequency for Butterworth filter and SRRC filter PA OBO = 0 dB.

To achieve a 1dB degradation the I/N was varied to obtain a BER curve by the SPW end-to-end simulation, then compute BER degradation by comparing baseline BER curve at 10^{-3} . BER vs. Eb/No curves are shown in Figures 4-39 and 4-40 for a transmitter PA output back off of 1-dB. We plotted BER vs. I/N was plotted for each case. I/N for a 1-dB degradation is obtained by interpolating, as shown in Figure 4-41 and 4-42.

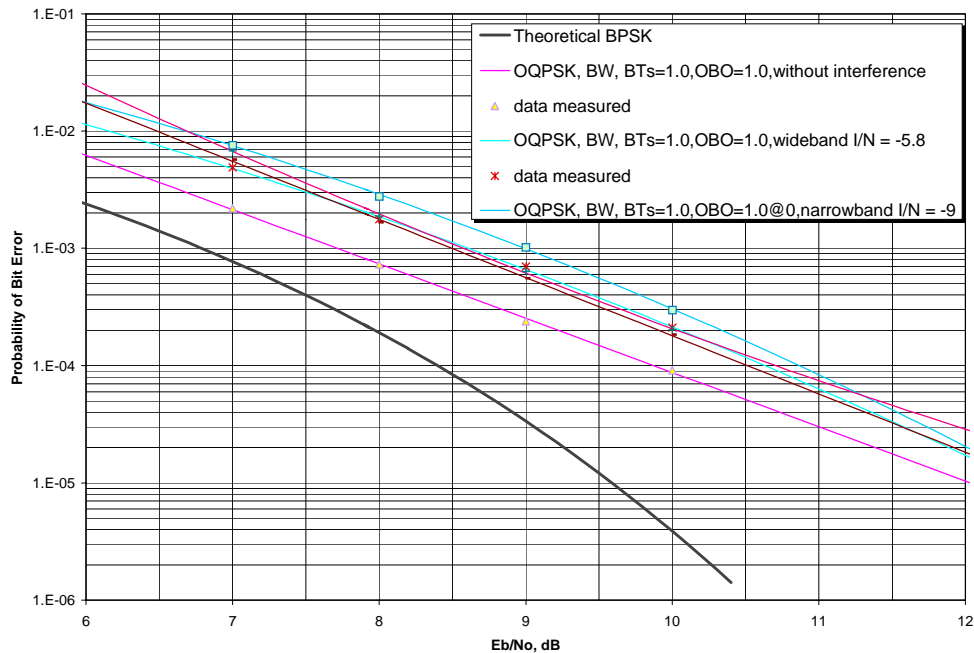


**Figure 4-39. Probability of Error vs. E_b/N_0 for filtered OQPSK
BW filter $BT_s = 1.0$, PA $OBO = 1.0$ dB**

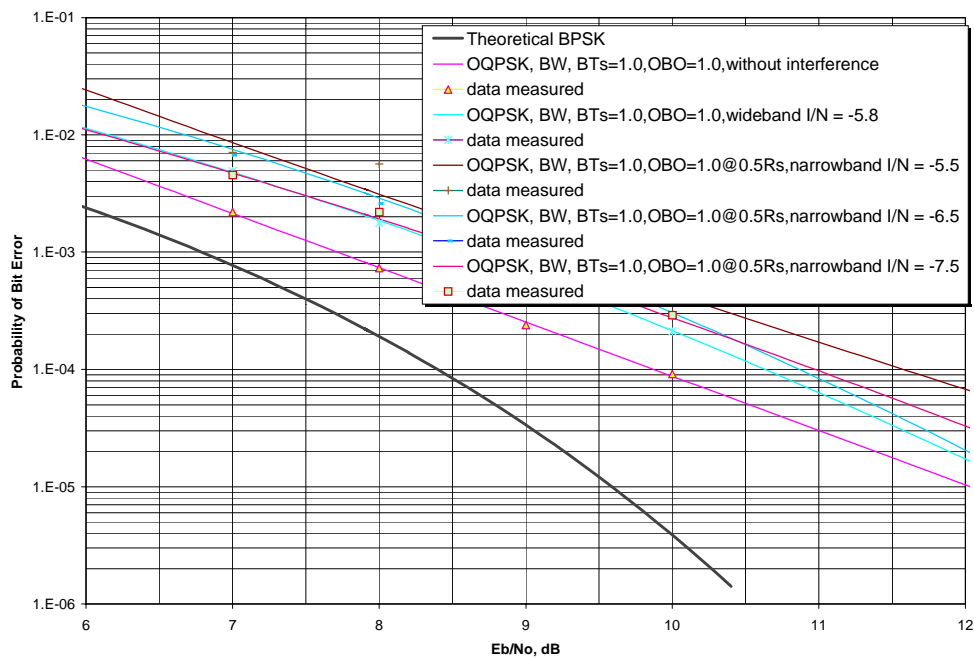


**Figure 4-40. Probability of Error vs. E_b/N_0 for filtered OQPSK
BW filter $BT_s = 1.0$, PA $OBO = 1.0$ dB**

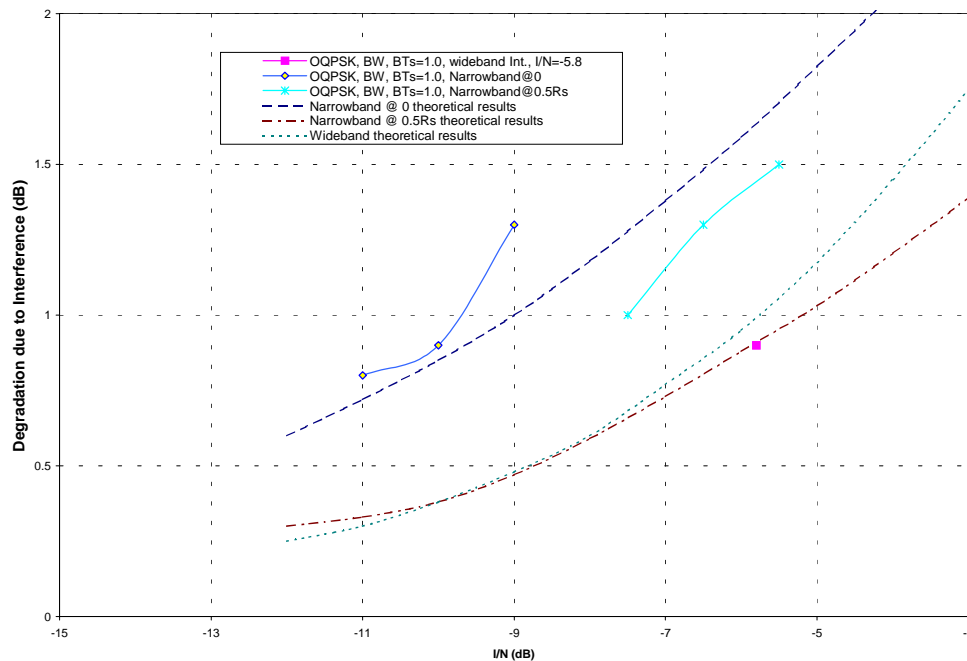


Figure 4-41. Probability of Error vs. I/N , BW, PA OBO = 1.0 dB

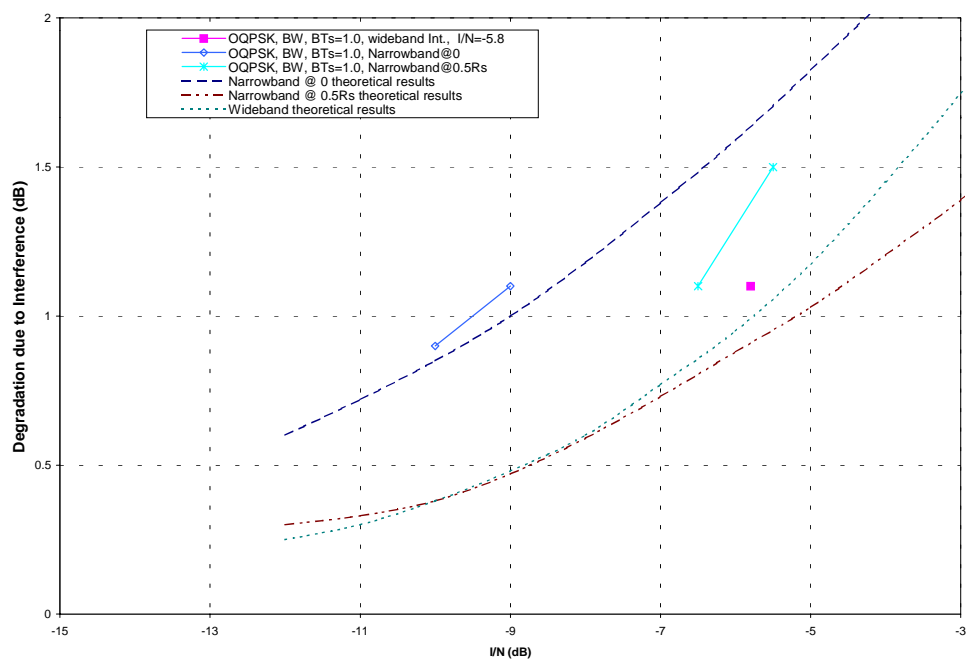


Figure 4-42. Probability of Error vs. I/N , BW, PA OBO = 0.0 dB

4.4.2 Results

Table 4-4 shows I/N values to achieve 1 dB degradation in the presence of interference for wideband and narrowband center frequencies 0 and 0.5 Rs at Probability Bit Error 10^{-3} .

As indicated in Appendix C, in the case of the wideband interference, I/N = -5.8 dB is the value to achieve 1 dB degradation, which is verified by our SPW simulations.

For narrowband interference, frequency at 0 Hz has worse affects on BER than frequency 0.5 Rs, as expected. Narrowband interference has worse effects on BER than wideband interference does. For this reason, we select narrowband frequency at 0Hz to obtain I/N value to achieve 1 dB degradation at Probability Bit Error 10^{-5} .

Section 5 GMSK Simulation Results

5.1 Overview

This section presents the simulation results for GMSK modulation. The results are provided in the form of transmitted signal spectrum compared to the Rec 17-2R1 mask, implementation loss compared to the implementation loss for BPSK modulation and interference susceptibility.

5.2 GMSK Spectra

Summary

The user transmitter simulation model described in Section 3 was used to generate power spectral density plots for GMSK. For this modulation; the power spectral density was computed for nonlinear amplifier and TWTA-1 amplifier. The power spectral densities for GMSK with various setups are shown in Figures 5-1 to 5-6. Also in the plots are the high data rate and low data rate spectral mask recommended by SFCG Rec 17-2R1. Table 5-1 summarizes compliance of the power densities and the spectral masks Recommended by SFCG Rec 17-2 R1 and it is indicated that the PSD does not comply with the mask, as distortions are included.

The following observations are made regarding the information in Table 5-1:

- 1 Excluding the linear PA cases, the minimum two-sided 60 dB bandwidth was $3.1 \times R_b$. This was with $BTs = 0.5$. Note that the two-sided 60 dB bandwidth of the SFCG high data rate spectral mask is $6.0 \times R_b$.
- 2 Excluding the linear PA cases, All cases studied are complies with the SFCG high data rate spectral mask outside the necessary bandwidth ($\pm 0.5 \times SR$). It is recommended to relax the portion of the SFCG spectral mask within $1 \times$ symbol rate.
- 3 The GMSK, $BTs = 1.0$ case resulted in two-sided 60 dB bandwidth of $5.16 \times R_b$ for TWTA -1 operating at saturation and 1 dB back off.
- 4 In Section 4.0, it is indicated that nonlinear PA operating point affects the filtered OQPSK PSD. The lower PA back off results in higher OQPSK PSD sidelobes. Since GMSK has constant envelope, its PSD is barely affected by the PA operating point. This phenomenon is observed in Figures 5-3 to 5-6.

The sections that follow provide the PSD plots for each case considered in this study.

Table 5-1. GMSK Spectrum Performance

Modulation/ Pulse Shaping Filter	Amplifier Model	PA OBO (dB)	AM/PM (deg /dB)	Data Asymmet ry	BT = 0.5 ⁽¹⁾ Two-sided 60dB Bandwidth ⁽³⁾	BT = 1 ⁽¹⁾ Two-sided 60dB Bandwidth ⁽³⁾
GMSK Gaussian Filter	Linear PA	NA	0 deg/dB	0.0%	2.9 x Rb [1]	3.6 x Rb [2]
	TWTA-1	1.0 dB	12 deg/dB	6.0%	3.1 x Rb ⁽²⁾ [3]	5.16 x Rb ⁽²⁾ [5]
	TWTA-1	0.0dB	15 deg/dB	6.0%	3.1 x Rb ⁽²⁾ [4]	5.16 x Rb ⁽²⁾ [6]
1. For GMSK, BT is the product of the one-sided bandwidth of the Gaussian filter and the bit duration. 2. The spectrum complies with the mask outside of the necessary bandwidth ($\pm 0.5 \times \text{SR}$), but exceeds the mask within the necessary bandwidth. 3. Number in bracket represents figure number; [1] represents figure5-1.						

Spectra for Linear PA and No Distortions

Figure 5-1 and 5-2 show the spectrum for GMSK with BTs = 0.5 and BT s=1.0. This plot was generated with a linear power amplifier and with no transmitter distortions. The two-sided 60-dB bandwidth is $2.9 \times R_b$ and $3.6 \times R_b$; the spectrum are well within the high data rate mask for both cases. The spectrum for $BT=1.0$ has higher sidelobes due to the wider Gaussian filter bandwidth. The spectra are very close to the mask near $F/R_b=0.15$.

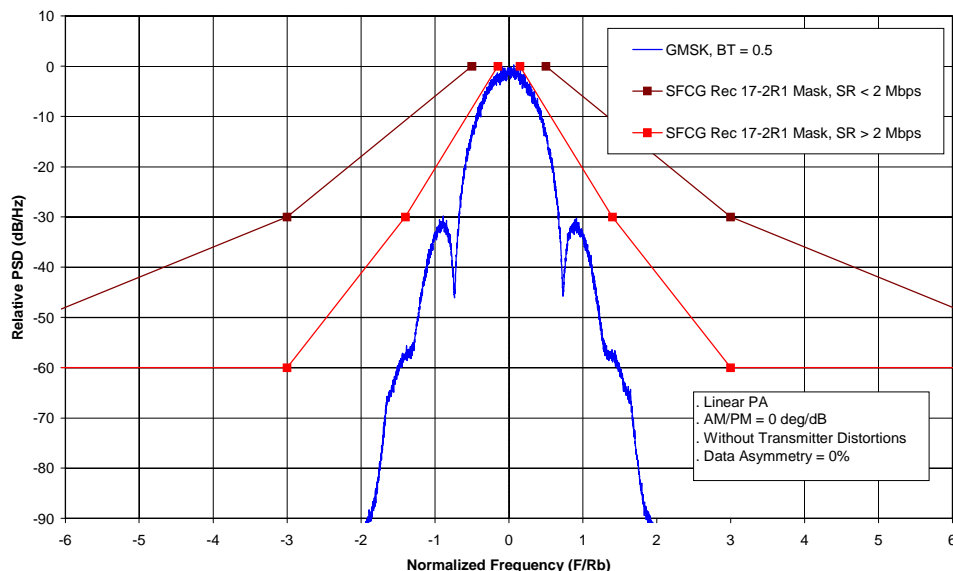


Figure 5-1. GMSK Spectrum (BT=0.5, Linear PA, AM/PM 0 deg/dB, without distortions)

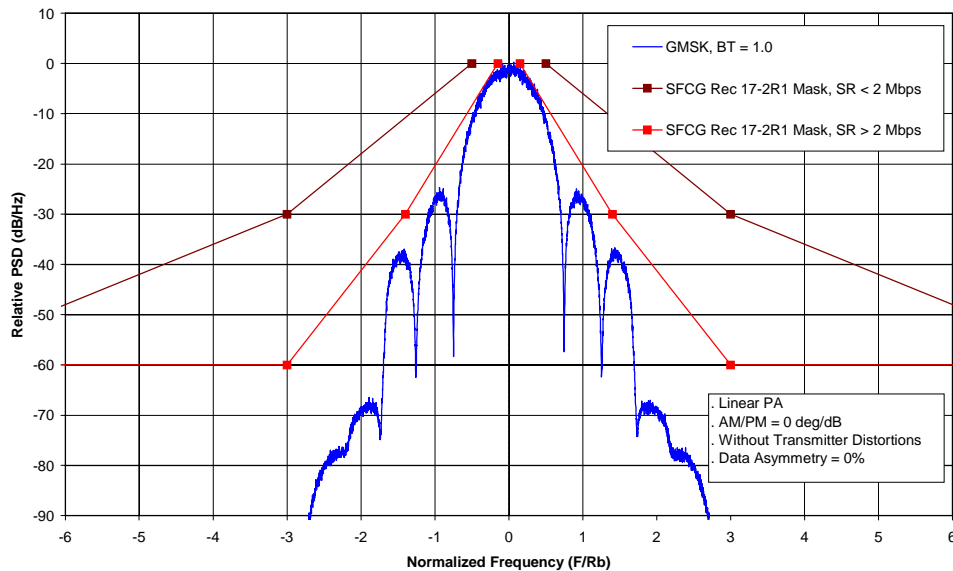


Figure 5-2. GMSK Spectrum ($BT=1.0$, Linear PA, $AM/PM = 0$ deg/dB, without distortions)

Spectra for $BT=0.5$ and Transmitter Distortions

Figure 5-3 and 5-4 provide the PSD plots generated with TWTA -1 with 0dB and 1 dB output back off, with transmitter distortions and $BT=0.5$. Both spectra do not meet the mask near $F/R_b=0.3$. Around $F/R_b=2.0$, there is about 20dB margin. The PA operating point does not significantly affect the PSD due to the GMSK constant envelope. Therefore the PA may operate at saturation point (0dB back off) and reach the highest DC power efficiency.

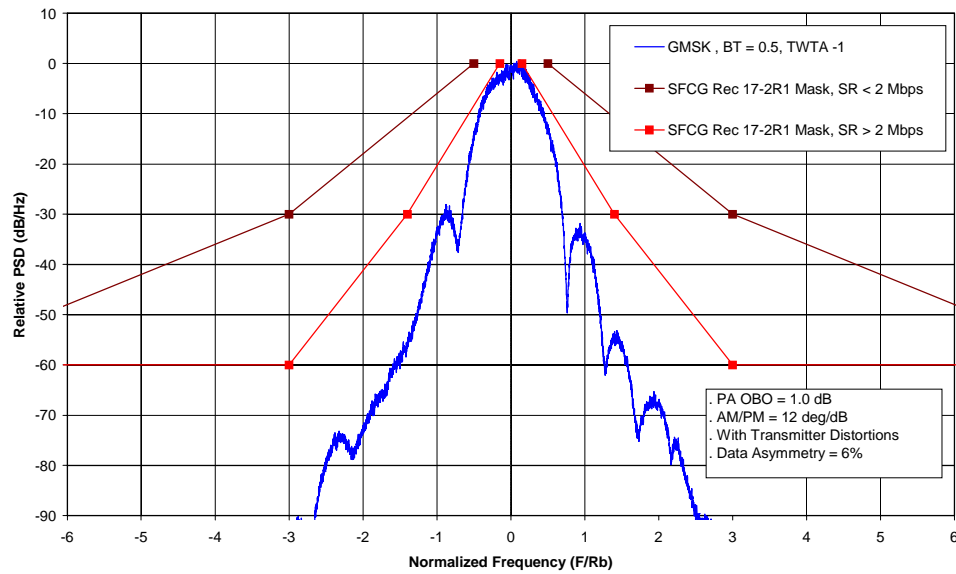


Figure 5-3. GMSK Spectrum (BT=0.5, TWTA -1, PA OBO=1dB, AM/PM = 12dg/dB, Data Asymmetry=6%, with distortions)

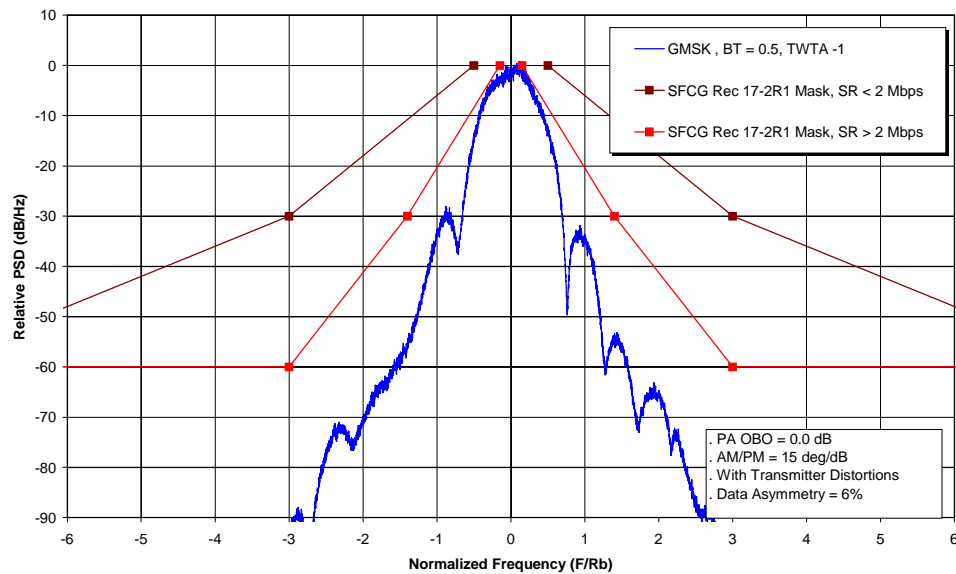


Figure 5-4. GMSK Spectrum (BT=0.5, TWTA -1, PA OBO=0.0dB, AM/PM = 15deg/dB, Data Asymmetry = 6%, with distortions)

Spectra for $BT_s=1.0$ and Transmitter Distortions

Figure 5-5 and 5-6 provide the PSD plots generated with TWTA -1 with 0dB and 1 dB output back off, with transmitter distortions and $BT_s=1.0$. Similar to that of $BT_s=0.5$ Both spectra do not meet the mask near $F/R_b=0.3$. Different from PSD for $BT=0.5$ which has 20dB margin at $F/R_b=2.0$, there is only 5dB margin for $BT_s=1.0$, due to a wider Gaussian filter and thus higher sidelobes. The constant envelope of GMSK modulation allows the use of PAs operating at or near saturation resulting in a high DC power efficiency.

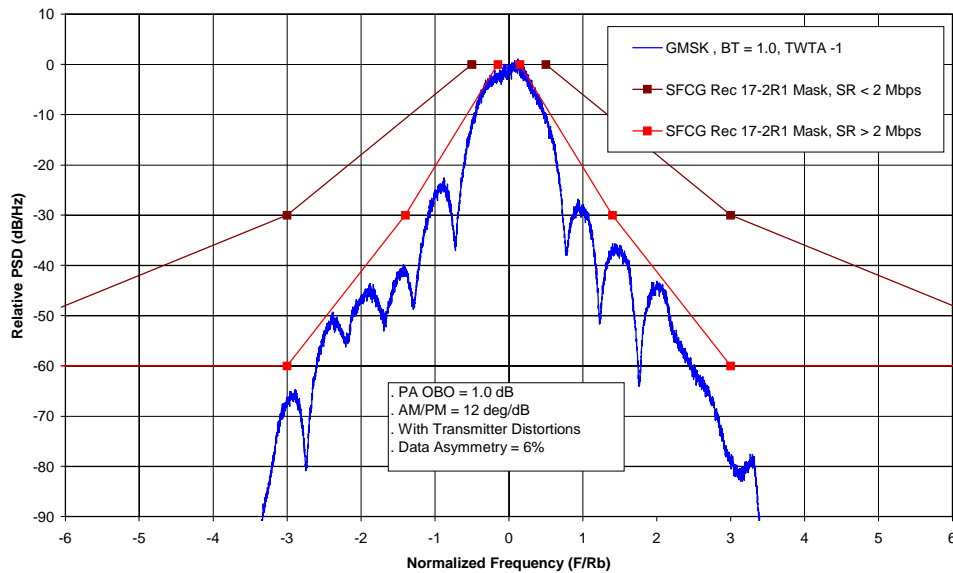


Figure 5-5. GMSK Spectrum ($BT=1.0$, TWTA -1, PA OBO=1.0dB, AM/PM = 12deg/dB, Data Asymmetry = 6%, with transmitter distortions)

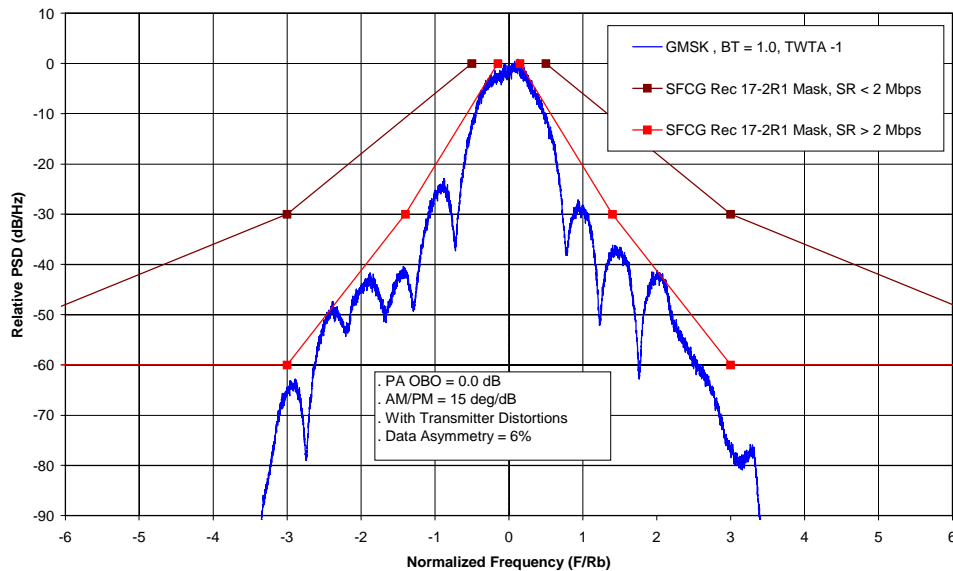


Figure 5-6. GMSK Spectrum (BT=1.0,TWTA -1, PA OBO=0.0dB, AM/PM = 15deg/dB, Data Asymmetry = 6%, with distortions)

5.3 GMSK Implementation Loss

The end-to-end BER simulation model described in Section 3 was used to generate BER vs. E_b/N_0 performance for GMSK. The BER curves are provided in Figure 5-7.

The implementation loss for each case was calculated relative to theoretical BPSK performance and BPSK performance with distortions. Table 5-2 lists implementation loss relative to theory for BER of 10^{-3} and 10^{-5} . Table 5-2 also lists the additional BER degradation relative to BPSK with distortions listed in Section 3. This provides the additional transmit power required for the bandwidth efficient modulation to meet the BER requirement relative to BPSK.

BER vs. E_b/N_0 performance for GMSK is shown in Figure 5-7 for BT = 0.5 and 1.0 with the TWTA-1 amplifier operating with 1-dB and 0dB output backoff. Implementation loss is nearly identical for these four cases. This phenomenon is consistent with the observation in Section 5.2. PA nonlinearity does not affect the constant envelope GMSK signal, and thus does not affect the BER performance.

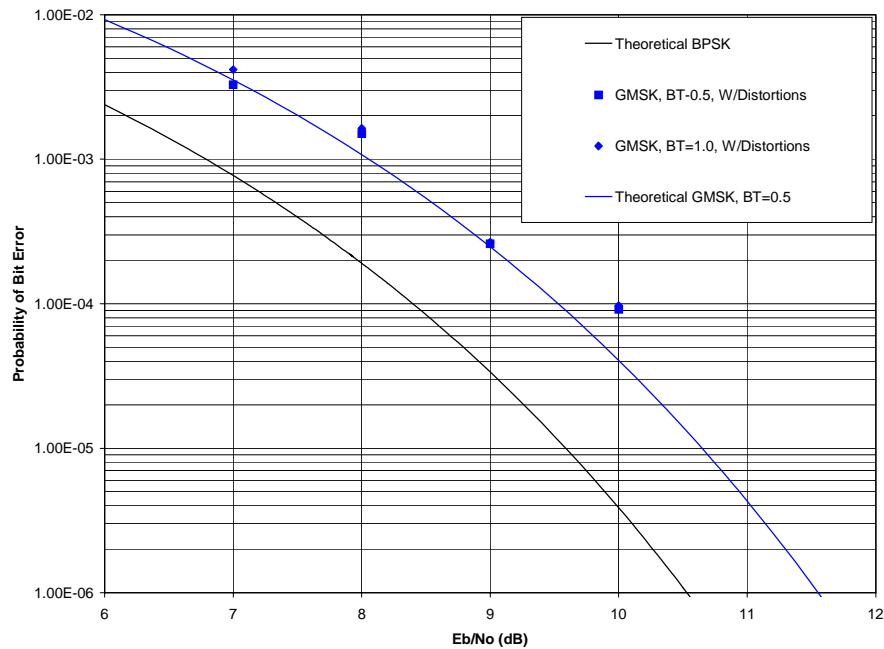


Figure 5-7. Probability of Error vs. E_b/N_o for GMSK (BT=0.5, 1.0, PA OBO=1.0dB, 0.0dB)

Table 5-2. GMSK Implementation Loss

Modulation	Amplifier Model	PA Output Back- Off	Transmi tter Distortio ns	Implementation Loss			
				Relative to theoretical BPSK		Relative to BPSK ⁽³⁾	
				@BER = 10 ⁻³	@BER = 10 ⁻⁵	@BER = 10 ⁻³	@BER = 10 ⁻⁵
BSPK, unfiltered,	TWTA -1	1 dB	Set1 ⁽²⁾	0.2 dB	0.6 dB	0.0 dB	0.0 dB
GMSK, BT = 0.5 ⁽¹⁾	Linear PA	NA	None	1.0 dB	0.8 dB	0.8 dB	0.2 dB
GMSK, BT = 0.5 ⁽¹⁾	TWTA -1	1 dB	Set1 ⁽²⁾	1.3 dB	1.2 dB	1.1 dB	0.6 dB
GMSK, BT = 0.5 ⁽¹⁾	TWTA -1	0 dB	Set1 ⁽²⁾	1.3dB	1.2 dB	1.1 dB	0.6 dB
GMSK, BT = 1.0 ⁽¹⁾	Linear PA	NA	None	1.1 dB	0.8 dB	0.9 dB	0.2 dB
GMSK, BT = 1.0 ⁽¹⁾	TWTA -1	1 dB	Set1 ⁽²⁾	1.4 dB	1.2 dB	1.2 dB	0.6 dB
GMSK, BT = 1.0 ⁽¹⁾	TWTA -1	0 dB	Set1 ⁽²⁾	1.4 dB	1.2 dB	1.2 dB	0.6 dB
1. For GMSK, BT is the product of the one-sided bandwidth of the Gaussian filter and the bit duration. 2. The same as set1 except gain imbalance, phase imbalance and data asymmetry are not defined for GMSK. 3. Implementation loss relative to Unfiltered BPSK with transmitter distortions and with TWTA-1 operating at 1 dB OBO.							

Conclusions

According to Figure 5-7 and Table 5-2, the following conclusions are reached. The simulated BER performance is similar for $BT=0.5$ and $BT=1.0$, because the theoretical difference between these two cases is within 0.2dB which within the simulation accuracy limits. The performance is similar for $OBO=1.0\text{dB}$ and 0.0dB due to the constant envelope GMSK signal. Additional loss of 0.6dB relative to BPSK is reasonable for the 1.0dB and 0 dB OBO cases. It is recommended to study other constant envelope modulation schemes.

5.4 GMSK Interference Susceptibility

Summary

The interference susceptibility assessment includes wideband and narrowband interference. The wideband interference is over the entire signal bandwidth and narrowband interference is modeled as a tone with constant frequency. Interference susceptibility results are provided in this section for wideband interference and narrowband interference results are provided for an interference tone at two offset frequencies 0Hz and 0.5 Rs. Simulations were performed to assess the additional BER performance degradation due to interference. The simulation results are summarized in Table 5-3. It is concluded that the performance is least susceptible to wideband noise and most susceptible to narrowband interference at zero frequency offset from carrier.

Table 5-3. Interference-to-Noise Ratio for 1dB Degradation, GMSK

Case	I/N ⁽¹⁾ (dB) for 1 dB Degradation		
	Narrowband Interference, $f_i=0\text{Hz}$	Narrowband Interference, $f_i=0.5R_s$	Wideband Interference, $BW_i=3.2 R_s$
GMSK BT=0.5	-11.3	-7.3	-5.8
GMSK BT=1.0	-10.2	-6.6	-5.8
Note:			
1. N is defined over the receiver noise bandwidth which is $3.2 R_s$			

Approach

An end-to-end BER simulation model was developed to study interference susceptibility as shown in Figure 3-1. The interference model is described in Section 3.4. User transmitter and GT receiver models are described in Section 3.2 and 3.3. End-to-end BER simulations were performed to assess the additional BER degradation due to interference. The interference power is specified by interference power to noise power ratio (I/N). Where I is the total interference power and N is the noise power over the receiver noise bandwidth. The Simulation obtained a certain I/N which causes a 1dB additional performance degradation at BER=1e-3, and 1e-5 with respect to the baseline performance for GMSK provided in Section 5.3. The additional degradation caused by wideband interference can be predicted analytically and is verified by the simulation.

Two narrowband interference frequencies offset from the carrier are selected at 0 Hz and half of the symbol rate. The phase of the interference signal is varied by slight offset of interference frequency to symbol rate.

In Figure 5-8, the baseline BER vs. E_b/N_0 curves and provided together with BER performance with wideband interference at I/N=-5.8dB. About 1dB additional degradation due to interference at BER=1e-3 is indicated in Figure 5-8. This approach is applied for other cases to obtain the relation between additional degradation and I/N.

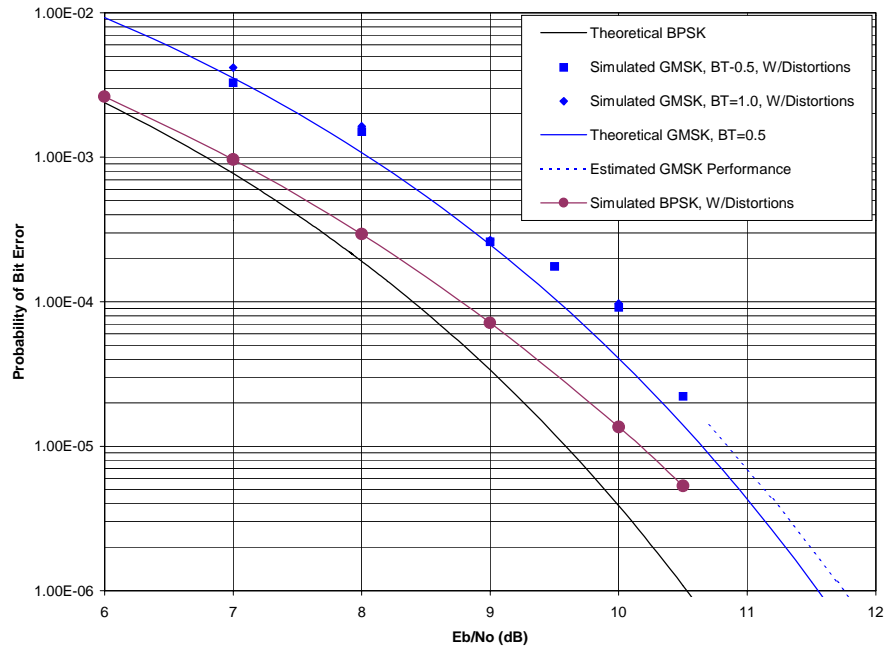


Figure 5-8. Probability of error vs. E_b/N_0 for GMSK (theory, baseline, interference)

Results

By using the above approach, the relation between additional degradation and I/N is obtained by simulation. Degradation vs. I/N curves are provided by Figure 5-9 and Figure 5-10 for BT=0.5 and B=1.0 with various interference.

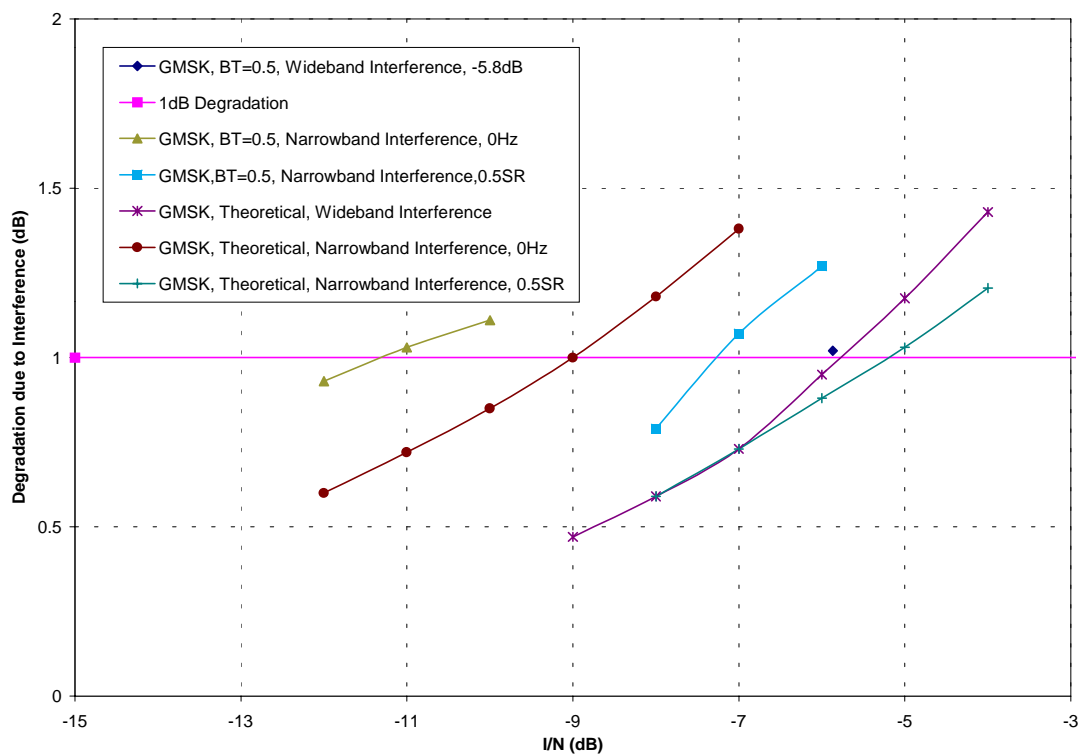


Figure 5-9. Degradation vs. I/N for GMSK BT=0.5

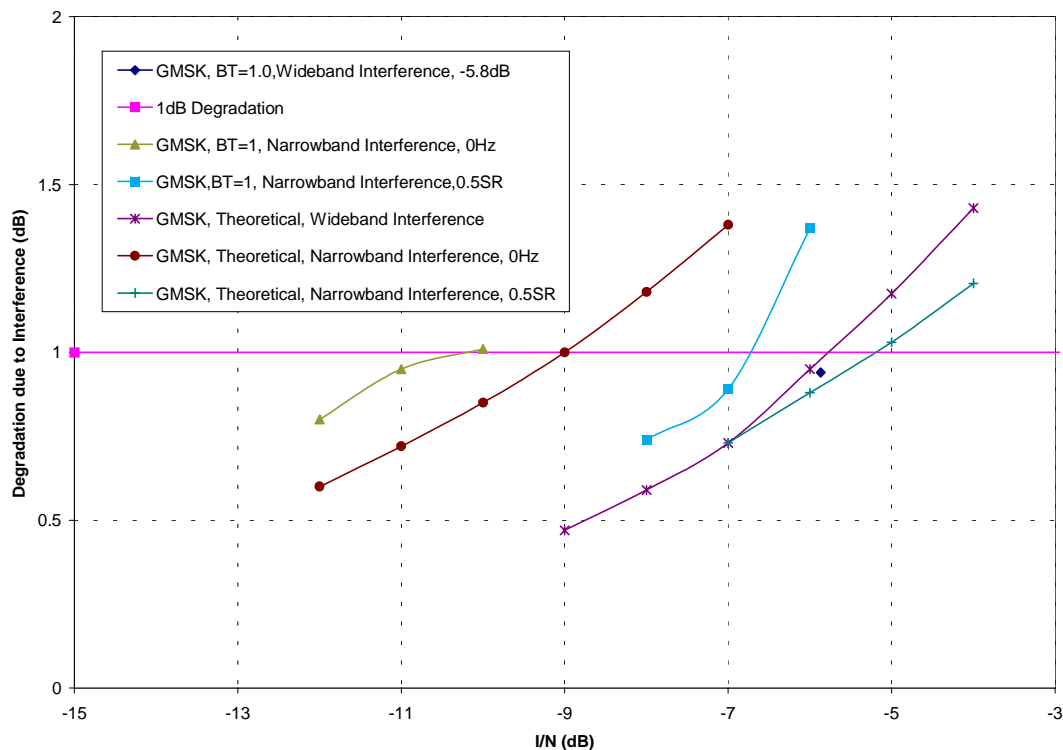


Figure 5-10. Degradation vs. I/N for GMSK BT=1.0

From Figure 5-9, Figure 5-10, the I/N resulting in 1dB BER degradation can be obtained and Table 5-3 summarizes the results. It is concluded that the performance is least susceptible to wideband noise and most susceptible to narrowband interference at zero frequency.

The power of interference at output of integrate & dump is proportional to $\frac{\sin^2(\pi f_i T_s)}{(\pi f_i T_s)^2}$ which has a 3.9dB difference between $f_i = 0$ and $f_i = 0.5R_s = 1/2T_s$. Therefore, 3.9dB difference is expected in I/N between two frequencies offset from carrier. From Table 3-5, I/N differences of 4.0dB and 3.6dB are obtained for BT=0.5 and BT=1.0 respectively. The simulation results agree with the theory.

The theoretical results provided in Appendix C are also presented in Figure 5-9 and Figure 5-10. The wideband interference is equivalent to the white noise and can be treated as an increase in the noise floor. The analytical results for wideband interference agree with the simulation very well. For narrowband interference, the difference between the theoretical results and the simulation are caused by the following reasons. First, the simulated degradation is for BER of 10^{-3} while analysis is based on BER of 10^{-5} . Second, the analysis in Appendix C is based on MSK with unlimited Gaussian filter bandwidth. The analysis is more accurate for higher BT value (e.g., BT=1.0) than lower a BT (e.g., BT=0.5).

Section 6 Enhanced FQPSK Simulation Results

6.1 Overview

This section presents the simulation results for enhanced FQPSK modulations. The results are provided in the form of transmitted signal spectrum compared to the Rec 17-2R1 mask, implementation loss compared to the implementation loss for BPSK.

6.2 Enhanced FQPSK Spectra

Summary

The user transmitter simulation model described in Section 3 was used to generate power spectral density plots for enhanced FQPSK modulation. For this modulation, the power spectral density was computed for nonlinear amplifier and TWTA-1 amplifier. The TWTA-1 amplifier represents worst case performance with AM/PM = 15 deg/dB. The power spectral densities for enhanced FQPSK with various filters and distortions are shown in Figures 6-1 to 6-3. Also in the plots are the high data rate and low data rate spectral mask recommended by SFCG Rec 17-2R1. Table 6-1 summarizes compliance of the power densities and the spectral masks Recommended by SFCG Rec 17-2 R1 and lists the two-sided 60-dB bandwidth.

The following observations are made regarding the information in Table 6-1:

- 1 Excluding the linear PA cases, the minimum two-sided 60 dB bandwidth was $3.52 \times R_b$. Note that the two-sided 60 dB bandwidth of the SFCG high data rate spectral mask is $6.0 \times R_b$.
- 2 In Section 4.0, it is indicated that nonlinear PA operating point affects the filtered OQPSK PSD. The lower PA back off results in higher OQPSK PSD sidelobes. Since Enhanced FQPSK has constant envelope, its PSD is barely affected by the PA operating point. This phenomenon is observed in Figures 6-1 to 6-3.

Table 6-1. Enhanced FQPSK Spectrum Performance

Modulation	Amplifier Model	PA OBO (dB)	AM/PM (deg /dB)	Data Asym-metry	Compliance with SFCG Mask	Two-sided 60dB Bandwidth ⁽¹⁾
Enhanced FQPSK	Linear PA	NA	0 deg/dB	0.0%	Yes	$3.4 \times R_b$ [1]
	TWTA-1	0.0 dB	15 deg/dB	0.0%	Yes	$3.6 \times R_b$ [2]
	TWTA-1	0.0 dB	15 deg/dB	0.0%	Yes	$3.6 \times R_b$ [3]
1. Number in bracket represents figure number; [1] represents figure 6-1.						

Spectra for Linear PA

Figure 6-1 shows the spectrum for Enhanced FQPSK. This plot was generated with a linear power amplifier and with no transmitter distortions. The two-sided 60-dB bandwidth is $3.4 \times R_b$. The spectrum is well within the SFCG high data rate mask.

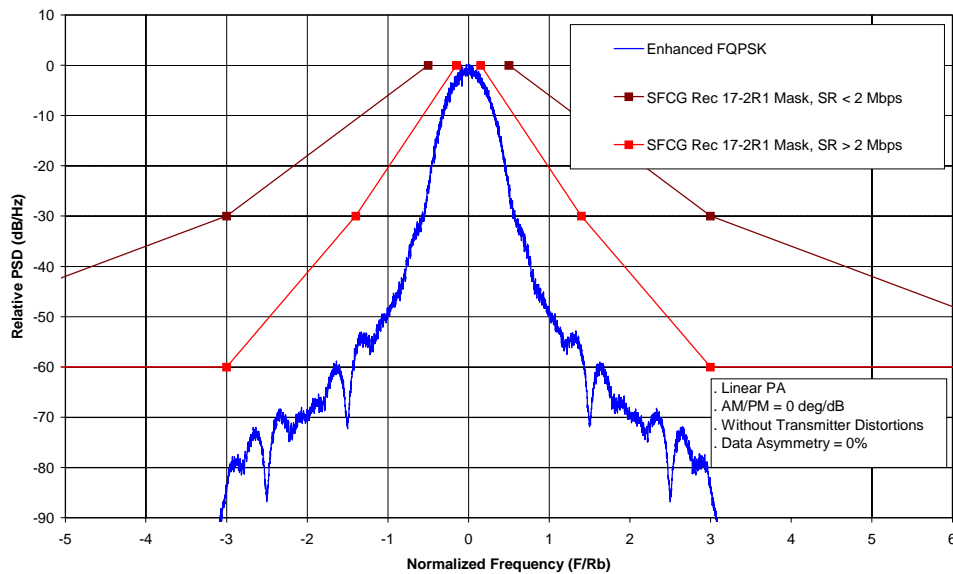


Figure 6-1. Enhanced FQPSK Spectrum (Linear PA, AM/PM = 0 deg/dB without distortions)

Spectra for Nonlinear PA

Figure 6-2 shows the spectrum for Enhanced FQPSK that was generated using a transmitter with TWTA-1 and no other transmitter distortions. The two-sided 60-dB bandwidth is $3.6 \times R_b$. The spectrum is well within the high data rate mask. Figure 6-3 is the same case as 6-2 but with transmitter distortions; spectrum is well within the high data rate mask. In both cases the skirts of the spectrum increase slightly as compared to the spectrum generated with the linear amplifier.

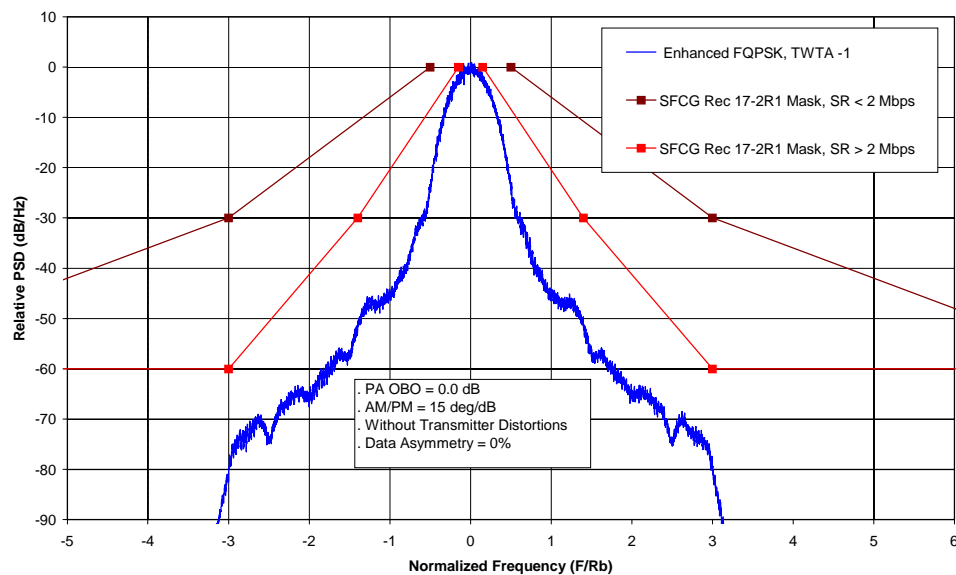


Figure 6-2. Enhanced FQPSK Spectrum (TWTA -1, PA OBO=0.0dB, AM/PM = 15deg/dB, without distortions)

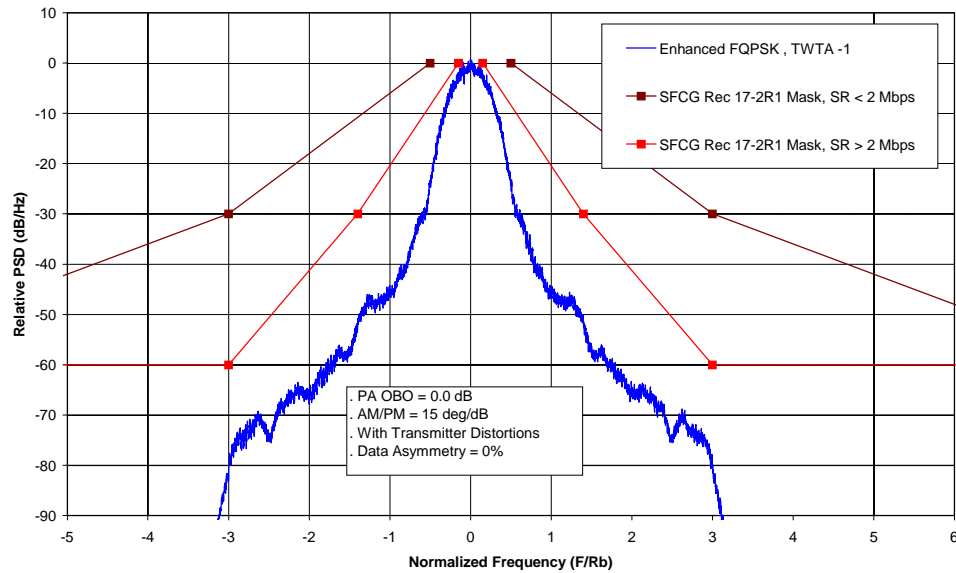


Figure 6-3. Enhanced FQPSK Spectrum (TWTA -1, PA OBO=0.0dB, AM/PM = 15deg/dB, With Transmitter Distortions)

6.3 Enhanced FQPSK Implementation Loss

The end-to-end BER simulation model described in Section 3 was used to measure the BER performance for enhanced FQPSK modulation. The BER curves are provided in Figure 6-4.

The implementation loss for each case was calculated relative to theoretical BPSK performance and BPSK performance with distortions. Table 6-2 lists implementation loss relative to theory for BER of 10^{-3} and 10^{-5} . Table 6-2 also lists the additional BER degradation relative to BPSK with distortions listed in Section 3. This provides the additional transmit power required for the bandwidth efficient modulation to meet the BER requirement relative to BPSK.

Simulations were performed using the worst case TWTA at each of the three operating points with the implementation loss at each point being nearly identical. This result is consistent with the constant envelope property of the enhanced FQPSK signal.

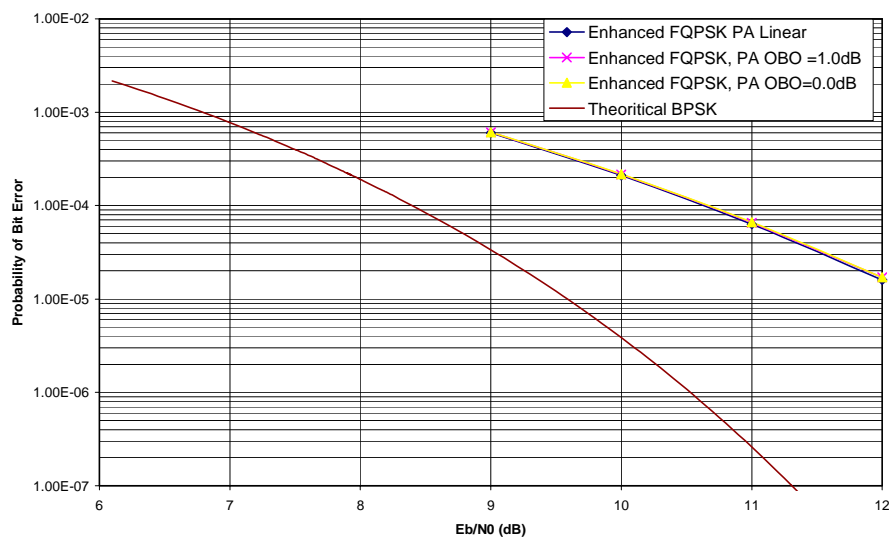


Figure 6-4. Probability of Error vs. E_b/N_0 for EFQPSK (PA OBO=1dB, 0dB, and Linear)

Table6-2. Enhanced FQPSK Implementation Loss

Modulation	Amplifier Model	PA Output Back- Off	Transmi tter Distortio ns	Implementation Loss			
				Relative to theoretical BPSK		Relative to BPSK ⁽²⁾	
				@BER = 10 ⁻³	@BER = 10 ⁻⁵	@BER = 10 ⁻³	@BER = 10 ⁻⁵
BSPK, unfiltered,	TWTA-1	1 dB	Set1 ⁽¹⁾	0.2 dB	0.6 dB	0.0 dB	0.0 dB
FQPSK	Linear PA	NA	Set1 ⁽¹⁾	1.6 dB	3-22.7 dB	1.4 dB	2-62.1 dB
	TWTA-1	1 dB	Set1 ⁽¹⁾	1.6 dB	3-22.7 dB	1.4 dB	2-62.1 dB
	TWTA-1	0 dB	Set1 ⁽¹⁾	1.6 dB	3-32.7 dB	1.4 dB	2-72.1 dB
1. The same as set1 except gain imbalance, phase imbalance, and data asymmetry, which are not defined for Enhanced FQPSK. 2. Implementation loss relative to Unfiltered BPSK with transmitter distortions and with TWTA-1 operating at 1 dB OBO.							

Section 7 Conclusions

7.1 Overview

The SFCG has recommended that space science projects starting after the year 2001 comply with an emitted spectrum mask for space-to-earth data transmission in the bands 2200-2290 MHz, 2290-2300 MHz, 8025-8400 MHz, and 8400-8500 MHz (SFCG Rec. 17-2R1). Typically, techniques used to narrow the transmitted spectrum result in a cost of additional transmit power required to achieve the same BER performance.

This study has assessed the additional transmit power required for Filtered OQPSK, GMSK and enhanced FQPSK modulation techniques while including distortions caused by the transmitter hardware that are typically specified for GSFC flight project transmitters. The transmitted signal spectrum for each modulation technique has been compared with the SFCG Rec 17-2R1 spectral mask. To assess additional transmit power required, BER simulations were performed using a low complexity integrate and dump detection receiver for all modulation techniques. The integrate and dump detection is suboptimum for the modulation techniques studied but it represents a low complexity receiver implementation and in provides good performance for several modulation techniques that meet the SFCG high rate mask. In most cases the BER performance can be improved by the use of a more complex receiver. Examples of a more complex receiver techniques are: use of multiple matched filters, use of a trellis decoder.

Filtered OQPSK and GMSK modulation techniques have also been evaluated for interference susceptibility to determine if they are more susceptible than QPSK to wideband and narrowband interference.

Two implementations of filtered OQPSK were considered: the first uses baseband data filtering followed by an I/Q modulator; the second uses baseband data filtering followed by a phase modulator. Both implementations yield identical OQPSK signals when filtering is removed. With baseband filtering, the I/Q modulator approach causes amplitude variations in the output signal, while the phase modulator approach results in a constant envelope output signal.

For filtered OQPSK, two types of baseband filtering were considered: 6-pole Butterworth and Square Root Raised Cosine. In both cases, several bandwidths were used. For filtered OQPSK/PM, two types of baseband filtering were considered: 6-pole Butterworth and Gaussian.

7.2 Conclusions

7.2.1 Summary

Filtered OQPSK/PM PSD was found to be in compliance with the SFCG Rec 17-2R1 mask. Filtered OQPSK PSD for BTs = 0.5 and 1.0 was found to be in compliance with the SFCG Rec 17-2R1 mask but for BTs = 1.5 the filtered OQPSK PSD exceeds the SFCG Rec 17-2R1 mask. For GMSK with BT = 1.0 and 0.5, out-of-band emissions are well within the SFCG mask but the main lobe of the spectrum does not comply with the SFCG mask specified at 0.15 times the symbol rate. The enhanced FQPSK PSD was found to be in compliance with the SFCG Rec 17-2R1 mask.

Constant envelope modulation with baseband filtering allows the best trade-off of bandwidth occupancy and required power. These include GMSK, filtered OQPSK/PM, enhanced FQPSK and XTCQM. Even with typical GSFC-specified hardware distortions, additional power

required for GMSK and filtered OQPSK/PM relative to unfiltered BPSK was found to be approximately 0.6 dB. Filtered OQPSK/PM has the additional advantage that it can be received with an OQPSK receiver which is an existing capability at NASA SN and GN ground terminals.

The study found that the portion of the spectral mask within 1x symbol rate is overly restrictive. The results of this study show that while the spectrum for GMSK meets this mask in theory, when transmitter distortions are considered, the GMSK spectrum does not comply with the mask. If the mask were relaxed in this area more modulation schemes would be able to comply. It would seem that relaxing the in band portion of the mask would have little impact to adjacent channel interference. A liaison statement from CCSDS Panel 1E to SFCG has been drafted to recommend relaxing the high rate mask within 1x symbol rate.

Interference susceptibility results show that performance degradation due to wideband and narrow band interference is similar for each modulation technique. This is largely due to the fact that in each case an integrate and dump detector is used.

7.2.2 Filtered OQPSK with I/Q Modulator

For filtered OQPSK, compliance with the spectral mask is achieved with BTs of 1.0 or less and with all three PA operating points.

BER performance for filtered OQPSK shows that for BTs=0.5 the implementation loss is significantly higher than for BPSK. This would represent a considerable impact to a spacecraft communication system design in terms of size, weight and DC power consumption. The SRRC filter provides better performance than the Butterworth filter although it is 8.2 dB worse than BPSK. These BER results were obtained with the worst case TWTA and an integrate and dump receiver. Performance could be improved by the use of a power amplifier with lower AM/PM and by the use of a more complex matched filter receiver. These results were not pursued in this study since the BER results for BTs = 1.0 were superior and the spectra for BTs = 1.0 were in compliance with the SFCG high rate mask.

For BTs=1.0, the implementation loss is 1.8 dB and 2.7 dB higher than that for unfiltered BPSK with the worst case TWTA at saturation for the Butterworth and SRRC filtered, respectively. The loss can be reduced to 1.0 dB or lower with a 1-dB backoff of the worst case TWTA or by use of a power amplifier with lower AM/PM. This is a reasonable cost for compliance with the SFCG recommendation.

For BTs = 1.5, BER performance was 0.7 dB and 0.5 dB higher than that for unfiltered BPSK with the worst case TWTA at 1-dB output backoff for the Butterworth and SRRC filtered, respectively. Performance with the TWTA at saturation was not assessed since the spectra for BTs = 1.5 does not comply with the SFCG high rate mask.

For filtered OQPSK, narrowband interference at a 0 Hz frequency offset from the carrier has worse effects on BER than at a 0.5 Rs offset, as expected. Narrowband interference causes more BER degradation than wideband interference. The impact of narrowband and wideband interference is not significantly different than for unfiltered BPSK; this is largely due to the fact that an integrate and dump detection was used in both cases.

7.2.3 Filtered OQPSK with Phase Modulator

An alternate form of filtered OQPSK (OQPSK/PM) has been analyzed with a baseband Butterworth filter with $BT_s = 1.0$. The transmit signal complies with the spectral mask with the transmitter power amplifier in saturation. Implementation loss is approximately 0.6 dB higher than that for unfiltered BPSK using the worst case TWTA in saturation. This approach has significant performance advantages over OQPSK with an I/Q modulator. Both modulations can be received with a standard OQPSK receiver.

Of the modulation methods addressed in this study, filtered OQPSK/PM provided the best combination of spectral efficiency and low implementation loss with a low complexity receiver. Since this modulator produces a constant envelope signal, performance is relatively insensitive to power amplifier characteristics.

Interference susceptibility was not analyzed for this modulation method but the performance is estimated to be similar to that for filtered OQPSK since the same receiver structure is used and the signal structure is similar to filtered OQPSK.

7.2.4 GMSK

GMSK incurs less than 1.0 dB of additional implementation loss compared to BPSK, even with 0-dB OBO. However, the GMSK spectrum does not meet the spectral mask in the main lobe region of the spectrum because the main lobe is wider than that of OQPSK.

For GMSK, neither the $BT = 0.5$ or $BT=1.0$ meet the spectral mask with the PA OBO 1 dB or 0.0 dB. In this case the sidelobes are not regenerated because the GMSK signal has a constant envelope, but the main lobe of the spectrum is wider than the main lobe for OQPSK and does not comply with the mask specification at $0.15 \times$ symbol rate.

The simulations show that implementation loss for GMSK is nearly identical for $BT=1.0$ and $BT=0.5$ and is approximately 1.0 dB higher than that for BPSK. This result is true for PA operating at 1-dB OBO and at 0-dB OBO. This demonstrates that GMSK is a reasonable technique for reducing the emitted signal bandwidth. By allowing operation at PA saturation, DC power consumption can be minimized. The BER results obtained in this study for GMSK used an integrate and dump detector and a modified QPSK receiver. This represents a minimum complexity receiver; however, GMSK is not compatible with existing QPSK receiver equipment.

it is concluded that GMSK modulation, received with an integrate and dump detector, is not significantly more susceptible to interference than unfiltered BPSK.

7.2.5 Enhanced FQPSK

For Enhanced FQPSK, the transmit signal complies with the worst case TWTA in saturation. Since this modulation produces a nearly constant envelope signal, performance is not significantly impacted by the amplifier characteristics.

In evaluation of the measured enhanced FQPSK BER performance, it is important to consider the detection means used. The receiver structure employed for this analysis was based on symbol-by-symbol detection using an integrate-and-dump filter. Although this technique is suboptimal, it most closely represents the existing equipment in use by NASA SN and GN ground stations.

The simulations show that the implementation losses for enhanced FQPSK with symbol-by-symbol integrate and dump detection are approximately 2.7 dB higher than that for BPSK for the worst case TWTA in saturation. Performance is not significantly improved with the amplifier operating with 1-dB backoff.

It is likely that the enhanced FQPSK BER performance could be improved substantially with the use of either a matched filter symbol-by-symbol detector or, better still, a trellis-coded demodulator. Both approaches would require a more complex receiver and associated modifications to existing NASA ground station equipment.

Section 8 References

- [1] CCSDS - SFCG Efficient Modulation Methods Study: A comparison of Modulation Schemes, Phase 1: Bandwidth Utilization, SFCG Action Item 12/32, Warren L. Martin, Tien M. Nguyen, September 1993.
- [2] CCSDS - SFCG Efficient Modulation Methods Study: A Comparison of Modulation Schemes, Phase 2: Spectrum Shaping, SFCG Action Item 12/32, Warren L. Martin, Tien M. Nguyen, August 1994.
- [3] CCSDS - SFCG Efficient Modulation Methods Study at NASA/JPL, Phase 3: End-to-End System Performance, SFCG Action Item 12/32, SF17-28/D, September 1997.
- [4] Efficient Spectrum Utilization for Space Science Services on Space-to-Earth Links, SFCG Recommendation 17-2R1, 17 September, 1998
- [5] Applications of Digital Wireless Technologies to Global Wireless Communications, Seiichi Sampei, Feher/Prentice Hall, 1997
- [6] Telecommunication Systems Engineer, W. Lindsey and M. Simon, Englewood Cliffs, N.J., Prentice-Hall, 1973.
- [7] Study of Narrow Band Interference into Wide band Digital Links, Phase I: Analytic Model Development, T.W. Benjamin, J.A. Gobble, R.A. Combs, M.J. Kelley, Session 14 of Third Ka Band Utilization Conference, September 15-18, 1997, Sorrento, Italy.
- [8] CCSDS Panel 1E, Document 99/45, End-to-End Losses of selected Bandwidth-Efficient Modulation Schemes. Gabriella Povero, Enrico Vassallo, Monica Visntin.
- [9] Performance Evaluation and Interpretation on Unfiltered Feher-Parented Quadrature-Phase-Shift Keying (FQPSK), M. K. Simon and T. Y. Yan, TMO Progress Report 42-137, May 15, 1999.
- [10] Digital Communication, John Proakis, McGraw-Hill, 1989.
- [11] Power Spectrum of MSK-Type Modulation in the Presence of Data Imbalance, M. K. Simon, P. Arabshahi, L. Lam, and T. Y. Yan, TMO Progress report 42-134, August 15, 1998.
- [12] *TDRS H,I,J* Dedicated (225 MHz) and KuSAR End-to-End Link Modeling and Simulation, Technical memo, Stanford Telecom, SNSE-450-98226, 7 July, 1998.
- [13] CCSDS - SFCG Efficient Modulation Methods Study at NASA/JPL, Phase 4: Interference susceptibility, CCSDS Input Paper, 99/35, September 1999.

Appendix A Interference and Noise Model

The link white Gaussian noise and interference model generates zero-mean Gaussian noise with the variance required to meet a given C/N or signal-to-noise ratio at a selected point in the signal path. It also generates narrow or wide band interference with a variance required to meet a given I/N . This block accepts the C/N as an input signal in dB and interference-to-noise ratio I/N is a user defined parameter.

Figure A-1 provides the block diagram of the interference and noise model.

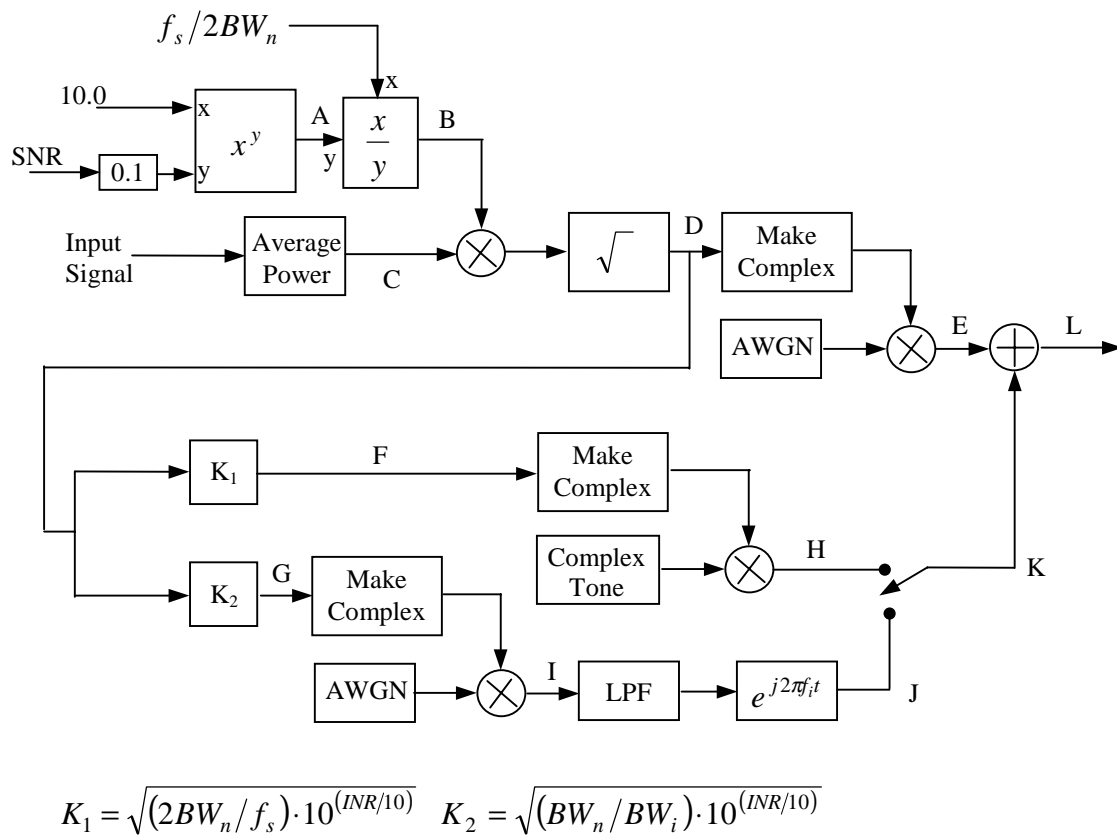


Figure A-1. Noise and Interference Model

The input signals of the model include the transmitted user signal of the required signal-to-noise ratio SNR. The output at node **L** is white Gaussian noise plus a wide band or narrow band (tone) interference.

To analyze the performance of this block, the following parameters are defined.

BW_n -- Double sided channel noise bandwidth

BW_i -- Double sided wide band interference noise bandwidth, approximate to 3-dB bandwidth

\bar{P}_s -- Average complex signal power

\bar{P}_n -- Average complex noise power

\bar{P}_i -- Average complex interference power

f_s -- Sampling frequency

f_i -- Interference center frequency

$SNR = C/N$ -- Signal-to-noise ratio in dB

$INR = I/N$ -- Interference-to-noise ratio in dB

A -- Amplitude of narrow band (tone) interference

The paragraph below show the derivation of white gaussian noise, narrowband tone interference and wideband interference.

- a) Generate white Gaussian noise at node **E**, with the noise power meeting the required signal-to-noise ratio SNR.

Assume the noise at node E is $N_E = N_{Ei} + jN_{Eq}$ with noise density

$$N_{E0i} = N_{E0q} = \frac{N_{E0}}{2}, \text{ and variance } \sigma_{Ei}^2 = \sigma_{Eq}^2 = \sigma_E^2$$

Obviously,

$$\sigma_E^2 = \frac{N_{E0}}{2} f_s \quad (\text{A.1})$$

In order to meet the required SNR, the noise power should be

$$\bar{P}_n = \frac{\bar{P}_s}{10^{(SNR/10)}} \quad (\text{A.2})$$

Noise power can also be represented as

$$\bar{P}_n = BW_n \cdot \frac{N_{E0i}}{2} + BW_n \cdot \frac{N_{E0q}}{2} = BW_n N_{E0} \quad (\text{A.3})$$

From equation (A.1), (A.2), and (A.3), it can be obtained

$$\sigma_E^2 = \frac{f_s \bar{P}_s}{2 \cdot 10^{(SNR/10)} \cdot BW_n} \quad (\text{A.4})$$

From Figure A, the value at node **A** is: $10^{(SNR/10)}$

The value at node **B** is: $\frac{f_s}{2 \cdot BW_n \cdot 10^{(SNR/10)}}$

With the average signal power \bar{P}_s at node **C**, the value at node **D** is

$\sqrt{\frac{f_s \bar{P}_s}{2 \cdot 10^{(SNR/10)} \cdot BW_n}} = \sigma_E$. It is obviously that the required noise is obtained at node **E** by multiplying an unite AWGN with the scale factor at node **D**.

- b) Generate narrow band (tone) interference at node **H** with required interference-to-noise ratio.

Combining equation (A.1) and (A.3), the noise power is

$$\bar{P}_n = \frac{2\sigma_E^2}{f_s} \cdot BW_n \quad (A.5)$$

Therefore, the interference power is

$$\bar{P}_i = \bar{P}_n \cdot 10^{(INR/10)} = \frac{2\sigma_E^2}{f_s} \cdot BW_n \cdot 10^{(INR/10)} \quad (A.6)$$

As narrow band interference is represented as a complex tone with power \bar{P}_i , the amplitude A should be

$$\begin{aligned} A &= \sqrt{\frac{2\sigma_E^2}{f_s} \cdot BW_n \cdot 10^{(INR/10)}} \\ &= \sqrt{\frac{2}{f_s} \cdot BW_n \cdot 10^{(INR/10)}} \cdot \sigma_E \\ &= K_1 \cdot \sigma_E \end{aligned} \quad (A.7)$$

where σ_E is the value at node **D**.

- c) Generate wide band interference at node **I**

Assume the noise at node **I** is $N_I = N_{Ii} + jN_{Iq}$ with noise density $N_{I0i} = N_{I0q} = \frac{N_{I0}}{2}$,

and variance $\sigma_{Ii}^2 = \sigma_{Iq}^2 = \sigma_I^2$

Therefore,
$$\sigma_I^2 = \frac{N_{I0}}{2} f_s \quad (A.8)$$

The power of wide band interference at node **J** can be represented as

$$\bar{P}_i = BW_i \cdot \frac{N_{I0i}}{2} + BW_i \cdot \frac{N_{I0q}}{2} = BW_i N_{I0} \quad (A.9)$$

From equation (A.6), (A.8), and (A.9),

$$\sigma_I^2 = \frac{BW_n \cdot 10^{(INR/10)}}{BW_i} \cdot \sigma_E^2 \quad (\text{A.10})$$

The scale factor at node **G** should be

$$\begin{aligned} \sigma_I &= \sqrt{\frac{BW_n \cdot 10^{(INR/10)}}{BW_i}} \cdot \sigma_E \\ &= K_2 \sigma_E \end{aligned} \quad (\text{A.11})$$

Appendix B GMSK Carrier Tracking for Transmitted Signal with Data Asymmetry

JPL studied the GMSK spectrum and end-to-end performance with various kinds of signal distortions except data asymmetry as signal re-clocking is assumed. Different from other signal distortions such as gain flatness, phase nonlinearity: data asymmetry has specific effects on end-to-end performance. This appendix provides the results of a study on the effect of data asymmetry.

Figure B-1 and B-2 presented the power spectrum density of a GMSK signal with 6% data asymmetry only. Compared with Figure 5-1 to Figure 5-6 which contain the GMSK PSD without and with distortions together with various PA operating points respectively, it is shown that the data asymmetry has more effect on results in a wider bandwidth.

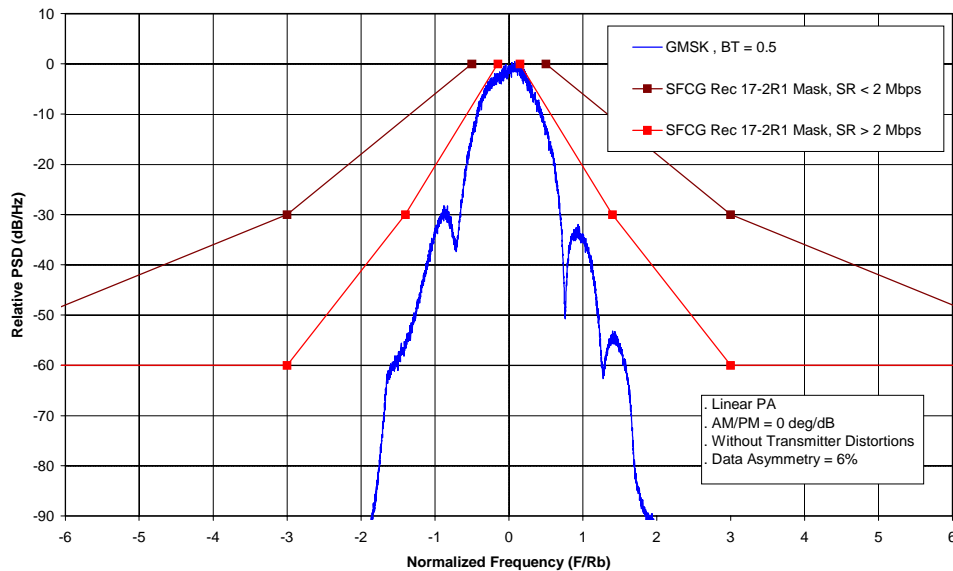


Figure B-1. GMSK Spectrum (BT=0.5, Linear PA, Data Asymmetry=6%, without transmitter distortions)

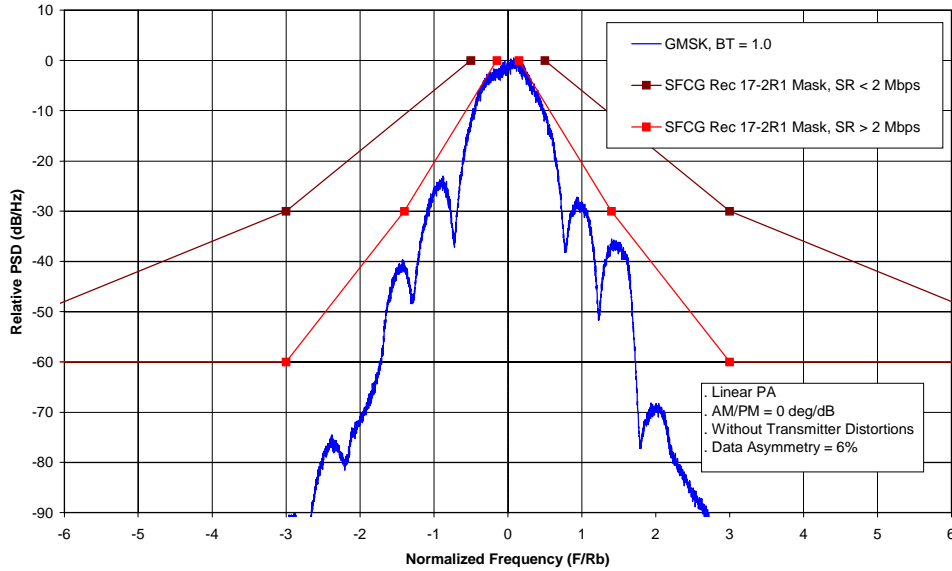


Figure B-2. GMSK Spectrum (BT=1.0, Linear PA, Data Asymmetry =6%, without transmitter distortions)

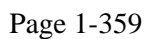
Besides affecting the signal bandwidth, the data asymmetry affects the carrier tracking. In Section 3.2.2.2, the GMSK transmitted signal is represented as

$$s_T(t) = A \cdot \cos(2\pi f_c t + \phi(t) + \theta_0)$$

$$\phi(t) = \frac{\pi}{2T_b} \int_{-\infty}^t b(\tau) d\tau$$

where $b(t)$ is the NRZ data signal. As the +1 and -1 data have the equal probability, it is obvious that the data asymmetry results in a phase accumulation, which is equivalent to carrier frequency offset. In a real system, the accumulated phase is compensated for offsetting the carrier frequency, together with the phase lock loop (PLL). By sweeping carrier frequency, the carrier frequency is offset to cancel most of the phase accumulation, and the residual phase variation is then tracked out by PLL.

The second order PLL block diagram is provided in Figure B-3.



19 April 2000

June 2001

CCSDS B20.0-Y-2

Page 1-359

19 April 2000

June 2001

CCSDS B20.0-Y-2

Page 1-359

Table B-1. PLL Parameters Selection

Parameter setup	ω_n	ζ	K
1	11.313	0.707	1.0
2	5.6565	0.707	2.0
3	2.2627	0.707	2.0
4	1.6971	0.707	6.0
5	1.6971	0.707	4.0
6	1.6971	0.707	2.0
7	1.13137	0.707	2.0

Appendix C Wideband And Narrowband Interference Impact On FOQPSK and GMSK

C.1 Introduction

C.1.1 Objective

The objective of this appendix is to present analytical models for assessing the impact of wideband and narrowband interference on filtered OQPSK and GMSK BER performance. These analytical models are intended to be used to provide verification for the simulation results presented in the main body of the report.

C.1.2 Scope

This appendix derives analytical models for assessing the impact of wideband and narrowband interference on filtered OQPSK and GMSK BER performance. The derivation approach is an extension of the approach used in reference [7] for assessing the impact of wideband and narrowband interference on BPSK BER performance. Since the BPSK analysis of reference [7] is a basis for the filtered OQPSK and GMSK analysis, it is repeated in this appendix for completeness and convenience to the reader.

This appendix also provides BER degradation plots based upon the filtered OQPSK and GMSK interference models. The plots are provided in a variety of formats including BER versus S/I for a constant E_b/N_0 , BER versus E_b/N_0 for a constant I/N, and degradation versus I/N at a BER of 10^{-5} .

C.2 Analytical Models

This section presents the derivation of analytical models for assessing the impact of wideband and narrowband interference on BPSK, filtered OQPSK and GMSK. The analysis for BPSK is presented first as the filtered OQPSK and GMSK analysis builds upon the BPSK analysis.

C.2.1 BPSK

C.2.1.1 Wideband Interferer

This paragraph calculates the probability of error, P_e , for a BPSK system when wideband interference is present. This approach duplicates the BPSK wideband P_e derivation in reference [7]. For BPSK, the desired signal, $s(t)$ is as follows:

$$s(t) = A d(t) \cos(\omega_o t) \quad \text{eq: C.1}$$

Where: A is the signal amplitude
 $d(t)$ is the bit stream and is either +1 or -1

ω_o is the BPSK signal's carrier frequency

The interference signal, $i(t)$, is modeled as AWGN. Figure C-1 depicts the modeling approach.

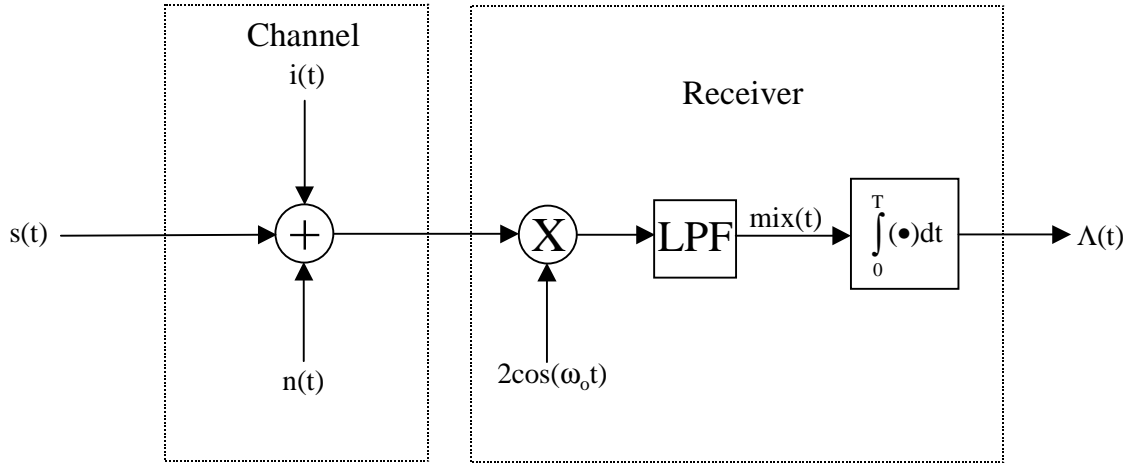


Figure C-1. Interference Model

If the interference is AWGN, then the P_e equation is as follows which is the standard P_e equation for BPSK, except N_o is replaced by $N_o + I_o$:

$$P_e = Q\left(\sqrt{\frac{2E_b}{(N_o + I_o)}}\right) \quad \text{eq: C.2}$$

Where: E_b is the energy per bit for the desired BPSK signal

N_o is the one sided noise power spectral density

I_o is the total interference power averaged over the desired signal's bandwidth.

$$I_o = \frac{I}{B}$$

I is the total interference power. B is the desired signal's bandwidth. For this analysis, the bandwidth, B , is defined as follows:

$$B = \frac{3.2}{T}$$

Where T is the BPSK signal's bit period.

C.2.1.2 Narrowband Interferer

This paragraph calculates the probability of error, P_e , for a BPSK system when narrowband interference is present. This approach duplicates the BPSK narrowband P_e derivation in reference [7]. For BPSK, the desired signal, $s(t)$ is as follows:

$$s(t) = A d(t) \cos(\omega_o t) \quad \text{eq: C.3}$$

Where: A is the amplitude of the signal
 $d(t)$ is the bit stream and is either +1 or -1
 ω_o is the BPSK signal's carrier frequency

The interference CW tone, $i(t)$, is defined as follows:

$$i(t) = A_i \cos(\omega_i t + \theta_i) \quad \text{eq: C.4}$$

Where: A_i is the CW tone's amplitude
 ω_i is the CW tone's frequency
 θ_i is the CW tone's phase at $t=0$ relative to the phase of $s(t)$. θ_i is a uniform random variable with a probability density function (pdf) as follows:

$$f(\theta_i) = \begin{cases} 1/2 & \text{when } 0 \leq \theta \leq 2\pi \\ 0 & \text{otherwise} \end{cases}$$

Reference [7] derives the equation for P_e when the interference is narrowband and the desired signal modulation scheme is BPSK. Figure C.1 again depicts the modeling approach. Reference [7], paragraph 2.2.1 states the following P_e result:

$$\overline{P_e} = \frac{1}{2\pi} \int_0^{2\pi} Q \left\{ \sqrt{\frac{2E_b}{N_o}} \left[1 - \frac{\sqrt{2}}{\sqrt{\frac{S}{I}} \Delta\omega T} \sqrt{1 - \cos(\Delta\omega T)} \cos(\theta) \right] \right\} d\theta \quad \text{eq: C.5}$$

Where; $\overline{P_e}$ is the P_e averaged over all θ .

θ is a random variable with the same pdf as θ_i . θ is a function of θ_i .

E_b is the energy per bit for the desired BPSK signal, $s(t)$

N_o is the one-sided noise power spectral density

S is $s(t)$'s signal power

I is the interference CW tone's power

$\Delta\omega = \omega_o - \omega_i$

We can solve Equation C.5 via Numerical Integration with a computer. We can prove equation C.5 as follows assuming a “-1” bit was transmitted:

$$\text{mix}(t) = -A + A_i \cos[\Delta\omega t + \theta_i] + \text{noise} \quad \text{eq C.6}$$

As shown in Figure C.1, $\text{mix}(t)$ is the baseband signal plus noise. The second term in equation C.6, $A_i \cos[\Delta\omega t + \theta_i]$, is due to the CW tone interferer. The “noise” term is due to $n(t)$.

We can re-write equation C.6 by putting the CW tone term in quadrature form as follows:

$$\text{mix}(t) = -A + A_i \cos(\theta_i) \cos[(\Delta\omega)t] - A_i \sin(\theta_i) \sin[(\Delta\omega)t] + \text{noise}$$

As shown in Figure C.1, $\Lambda(t)$ is the integrator's output.

$$\Lambda(t) = -AT + A_i \cos(\theta_i) \int_0^T \cos[(\Delta\omega)t] dt - A_i \sin(\theta_i) \int_0^T \sin[(\Delta\omega)t] dt + \text{noise}$$

$$\Lambda(t) = -AT + A_i \left\{ \int_0^T \cos[(\Delta\omega)t] dt \cos(\theta_i) - \int_0^T \sin[(\Delta\omega)t] dt \sin(\theta_i) \right\} + \text{noise}$$

We can now use the following trigonometry identity:

$$\gamma \cos(x + \varphi) = A \cos(x) + B \sin(x)$$

Where for our problem:

$$A = \int_0^T \cos(\Delta\omega)t dt = (1/\Delta\omega) \sin[(\Delta\omega)T]$$

$$B = \int_0^T \sin(\Delta\omega)t dt = (1/\Delta\omega) \{ 1 - \cos[(\Delta\omega)T] \}$$

$$x = (\theta_i) \quad \gamma = \sqrt{A^2 + B^2}$$

$$\varphi = \tan^{-1} (B/A)$$

Thus;

$$\Lambda(t) = -AT + A_i [\gamma] \cos(\theta_i + \varphi) + \text{noise}$$

Because θ_i is a random variable, we can set $\theta = \theta_i + \varphi$ where θ is also statistically a random variable with a probability density function as follows:

$$f(\theta) = \begin{cases} 1/2\pi & \text{when } 0 \leq \theta \leq 2\pi \\ 0 & \text{otherwise} \end{cases}$$

Thus,

$$\Lambda(t) = -AT + A_i \gamma \cos(\theta) + \text{noise}$$

We now need to find the P_e formula from $\Lambda(t)$. We will define an $s(t)_{\text{equiv}}$ as the equivalent signal that yields the same $\Lambda(t)$ as $s(t)$, but without a CW tone interferer present. Figure C-2 depicts the equivalent model.

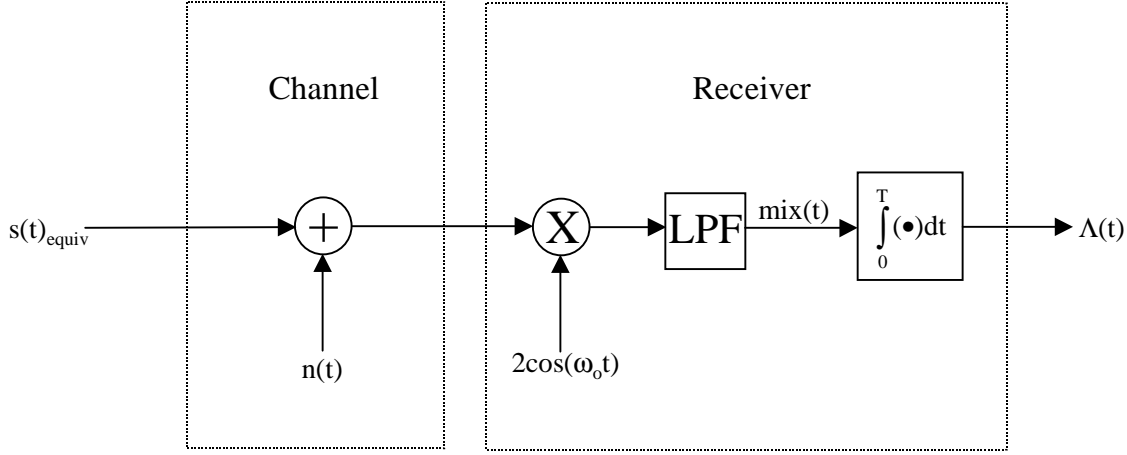


Figure C-2. Equivalent Interference Model

We can write $s(t)_{\text{equiv}}$ as follows:

$$s(t)_{\text{equiv}} = A_{\text{equiv}} \cos(\omega_o t) \quad \text{eq: C.7}$$

From $s(t)_{\text{equiv}}$ and $\Lambda(t)$, we can find an expression for $E_{b_{\text{equiv}}}$ where $E_{b_{\text{equiv}}}$ is the bit energy at the output of the integrator caused by $s(t)_{\text{equiv}}$ when no interference is present. Once we find $E_{b_{\text{equiv}}}$, we can find P_e as follows which comes from the basic P_e formula for BPSK:

$$P_e = \frac{1}{2\pi} \int_0^{2\pi} Q \left\{ \sqrt{\frac{2E_{b_{\text{equiv}}}}{N_o}} \right\} d\theta \quad \text{eq: C.8}$$

A_{equiv} must have a value where $s(t)_{\text{equiv}}$ produces $\Lambda(t)$ at the output of the integrator when no interference is present.

$$A_{\text{equiv}} = (\Lambda(t) - \text{noise})/T = [-AT + A_i \gamma \cos(\theta)]/T$$

$$E_{b_{\text{equiv}}} = (A_{\text{equiv}})^2 T/2$$

$$E_{b_{\text{equiv}}} = [(-AT + A_i \gamma \cos(\theta))/T]^2 T/2$$

$$E_{b_{\text{equiv}}} = A^2 T/2 - AA_i \gamma \cos(\theta) + A_i^2 \gamma^2 \cos^2(\theta)/(2T)$$

Because $E_b = A^2 T/2$, we have the following:

$$E_{b_{\text{equiv}}} = E_b \{ 1 - AA_i \gamma \cos(\theta)/E_b + A_i^2 \gamma^2 \cos^2(\theta)/(2TE_b) \}$$

$$E_{b_{equiv}} = E_b \{ 1 - 2A_i \gamma \cos(\theta) / (A^2 T) + 2A_i^2 \gamma^2 \cos^2(\theta) / (2T^2 A^2) \}$$

$$E_{b_{equiv}} = E_b \left[1 - \frac{2\gamma \cos(\theta)}{\frac{A}{A_i} T} + \frac{\gamma^2 \cos^2(\theta)}{\left(\frac{A}{A_i}\right)^2 T^2} \right]$$

Because $(A/A_i)^2 = S/I$ where S is the power of $s(t)$ and I is the power in $i(t)$, we have the following:

$$E_{b_{equiv}} = E_b \left[1 - \frac{\gamma \cos(\theta)}{\sqrt{S/I} T} \right]^2 \quad \text{eq: C.9}$$

Also, from above;

$$\gamma = \sqrt{\frac{1}{(\Delta\omega)^2} \{ [1 - \cos[(\Delta\omega)T]]^2 + \sin^2[(\Delta\omega)T] \}} = \sqrt{\frac{1}{(\Delta\omega)^2} \{ 2 - 2\cos[(\Delta\omega)T] \}}$$

$$\gamma = (1/\Delta\omega) \sqrt{2} \sqrt{1 - \cos[(\Delta\omega)T]}$$

Thus,

$$E_{b_{equiv}} = E_b \left[1 - \frac{\sqrt{2}}{\sqrt{\frac{S}{I}} (\Delta\omega) T} \sqrt{1 - \cos[(\Delta\omega)T]} \cos(\theta) \right]^2 \quad \text{eq: C.10}$$

The last step is to substitute equation C.10 into equation C.8 which proves equation C.5.

Filtered OQPSK

This section derives the P_e equations for FOQPSK for the following two cases:

Wideband Interference

Narrowband Interference

Wideband Interferer

Because a OQPSK or FOQPSK system can be thought of as just two BPSK systems in quadrature, the P_e for the FOQPSK modulation scheme with wideband interference is exactly the same as equation C.2.

However, for OQPSK and FOQPSK, the energy/bit is 1/2 the energy/bit for BPSK when the desired signal power, S , is the same for both BPSK, OQPSK, and FOQPSK. For example, $s(t)$ for QPSK is as follows:

$$s(t) = \frac{A}{\sqrt{2}} d_1(t) \cos(\omega_o t) + \frac{A}{\sqrt{2}} d_Q(t) \sin(\omega_o t) \quad \text{eq: C.11}$$

where the total power of $s(t)$, S , is the same as the total power for the BPSK signal in equation C.1. But, notice the amplitude in each of the QPSK channels is $\frac{A}{\sqrt{2}}$, not A .

Therefore, the power and energy/bit in each QPSK channel is 1/2 the power and energy/bit in the BPSK system.

The following is the P_e for FOQPSK when the interference is modeled as wideband noise.

$$P_e = Q\left(\sqrt{\frac{2E_b}{N_o + I_o}}\right) \quad \text{eq: C.12}$$

Where: E_b is the energy per bit in each channel

N_o is the one sided noise power spectral density

I_o is the total interference power averaged over the desired signal's bandwidth, B .

The desired signal's bandwidth, B , is the same value as B for BPSK if the FOQPSK data rate is twice the BPSK data rate.

Narrowband Interferer

Because a OQPSK or FOQPSK system can be thought of as just two BPSK systems in quadrature, the P_e for the FOQPSK modulation scheme with narrowband interference is exactly the same as equation C.5, except that the signal power, S , becomes $S/2$. S becomes $S/2$ because half of the signal power is in the I channel and half of the power is in the Q channel. The following is the P_e for FOQPSK when the interference is modeled as a narrowband CW tone:

$$\overline{P_e} = \frac{1}{2\pi} \int_0^{2\pi} Q\left\{\sqrt{\frac{2E_b}{N_o}} \left[1 - \frac{\sqrt{2}}{\sqrt{\frac{S}{2I}} \Delta\omega T} \sqrt{1 - \cos(\Delta\omega T)} \cos(\theta)\right]\right\} d\theta \quad \text{eq. C.13}$$

Where; $\overline{P_e}$ is the P_e averaged over all θ .

θ is a random variable with the same pdf as θ_i . θ is a function of θ_i .

E_b is the energy per bit in each I and Q channel

N_o is the one-sided noise power spectral density

S is $s(t)$'s signal power

I is the interference CW tone's power

$\Delta\omega = \omega_o - \omega_i$

Equation C.11 depicts how the signal power is divided between the I and Q channels which results in the $\sqrt{\frac{S}{2I}}$ term in equation C.13 rather than the $\sqrt{\frac{S}{I}}$ term in equation C.5. Also for FOQPSK, equation C.6 becomes the following:

$$\text{Mix}(t) = \frac{A}{\sqrt{2}} + A_i \cos[\Delta\omega t + \theta_i] + \text{noise}$$

Repeating the narrowband interferer derivation in paragraph C.2.1.2 with the updated mix(t) equation will yield equation C.13.

We can solve Equation C.13 via Numerical Integration with a computer.

C.2.2 GMSK

This section will derive the P_e equations for GMSK for the following two cases:

- a. Wideband Interference
- b. Narrowband Interference

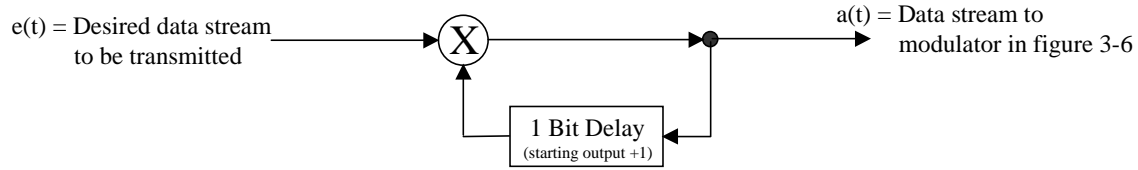
However, before calculating the GMSK P_e for each interference case, it is important to understand how differential encoding/decoding affects the P_e . In order to demodulate the GMSK signal described in section 3.2.2, the GMSK system requires differential encoding in the modulator and differential decoding in the receiver.

C.2.2.1 Background

When a GMSK or MSK signal is modulated as described in section 3.2.2, a differential encoder must be added to the input of the modulator in figure 3-5 and a differential decoder must be added to the output of figure 3-14. Although this differential encoding/decoding eliminates the phase ambiguity in the receiver's reference signal, it would be required even with an unambiguous reference signal. Figures 3-13 and 3-14 depict that prior to the differential decoder, the receiver demodulates the phase during one "bit" interval to being either in the 1st and 3rd quadrants of the phase plane or in the 2nd and 4th quadrants of the phase plane. By looking at the previous bit period's phase, the differential decoder can determine whether the rotating phasor changed directions or remained traveling in the same direction. The change in direction or lack of change yields the bit's absolute value (+1 or -1).

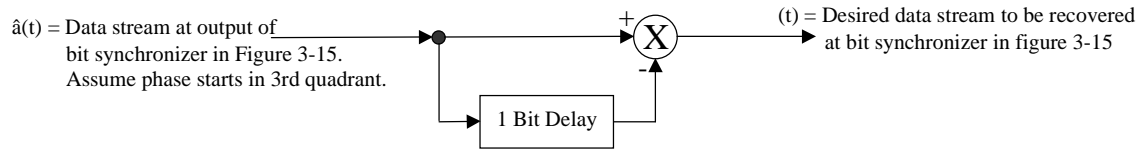
Let us take an example as follows:

The input to the modulator in Figure 3-6 is as follows:



Set: $e(t) = +1 -1 -1 +1 +1 +1 -1 -1 +1 -1 -1 -1 +1 +1 -1 +1$

At the receiver, we will add the following differential decoder to the output of Figure 3-15:



As shown in figures 3-13 and 3-14, $\hat{a}(t) = \text{sgn}(V_i(t)) \cdot \text{sgn}(V_o(t)) \cdot V_{\text{clk}}(t)$ where $V_{\text{clk}}(t)$ has the effect of being a positive square wave pulse which reconstructs the NRZ data stream.

Table C.1 lists the results of the bit sequence at each point along the system. In the table, the ellipses enclose bits that the encoder or decoder multiply together to obtain the output bit to which an arrow points. The FM modulator produces a ω_2 frequency when $a(t)=+1$ and produces a ω_1 frequency when $a(t)=-1$. For this example, we assume that the phase for the first bit, of $\hat{a}(t)$ is in the 3rd quadrant of the phase plane. However, the starting quadrant is unimportant and is a function of the reference carrier, which has a phase ambiguity. The starting quadrant does not affect the results for $\hat{e}(t)$.

Table C-1: Differential Encoding/Decoding Example

$e(t)$	$a(t)$	Modulator Frequency	$\hat{a}(t)$	$\hat{e}(t)$
+1	+1	ω_2	+1 (3rd Quadrant assumed)	C
-1	-1	ω_1	+1	-1
-1	+1	ω_2	+1	-1
+1	+1	ω_2	-1	+1
+1	+1	ω_2	+1	+1
+1	+1	ω_2	-1	+1
-1	-1	ω_1	-1	-1
-1	+1	ω_2	-1	-1
+1	+1	ω_2	+1	+1
-1	-1	ω_1	+1	-1
-1	+1	ω_2	+1	-1
-1	-1	ω_1	+1	-1
-1	+1	ω_2	+1	-1
+1	+1	ω_2	-1	+1
+1	+1	ω_2	+1	+1
-1	-1	ω_1	+1	-1
+1	-1	ω_1	-1	+1

We can now assess the impact of the encoding/decoding process on the P_e . Figure C-3 depicts a new scenario for the receiver. Figure C-3 depicts how an error on the I Channel can affect more than one bit at the input to the decoder. An error on the I channel affects more than one data bit because the bit period of each channel, T , is twice as long as the data rate period, T_b . Because bits 4 and 5 have errors at the input to the decoder, bits 4 and 6 will have errors at the decoder output. Bit 5 of the decoder output will not be in error. Bit 5 at the decoder output is dependent upon bits 4 and 5 at the decoder input. If both bits 4 and 5 are incorrect at the decoder input, then the errors will cancel out at the output of the decoder. Thus, the P_e for GMSK will be about twice the P_e for FOQPSK. The GMSK P_e is not exactly twice the FOQPSK error because there may be adjacent channel bit errors on the I or Q channels that lead to only two output decoder data bit errors rather than four data bit errors. However, for low P_e scenarios, the probability of two adjacent channels bit errors occurring is negligible compared to the probability of single channel bit errors occurring.

We should note that if a non-differential encoder/decoder system is not employed for the BPSK or FOQPSK systems, a phase ambiguity still results. Thus, the P_e for GMSK, BPSK, and QPSK is the same for systems without a phase ambiguity. For the purposes of this paper, a differential encoder/decoder is not required for FOQPSK. Therefore, in this paper, GMSK has a P_e twice that of BPSK and FOQPSK, but the phase ambiguity difference should be noted.

C.2.2.2 Wideband Interferer

Because the GMSK receiver system is the same as the FOQPSK receiver except for the differential decoder as stated in 5.1, the P_e for the GMSK modulation scheme with Wideband interference is exactly the same as equation C.12, except the P_e is double. The P_e equation for GMSK with Wideband interference is as follows:

$$P_e = 2 \cdot Q \left(\sqrt{\frac{2Eb}{N_o + I_o}} \right) \quad \text{eq: C.14}$$

At first, doubling the P_e seems like a large increase, but in terms of power, the increase is small. For example if the $E_b/(N_o + I_o) = 9.7$ dB, then the P_e for equation C.2 is $7.7E-06$. If the $E_b/(N_o + I_o)$ for equation C.13 is 10 dB, then a P_e of $7.7E-06$ is again achieved. Thus, for this case, the doubling of the P_e only means that an additional 0.3 dB of power is required to achieve the same P_e .

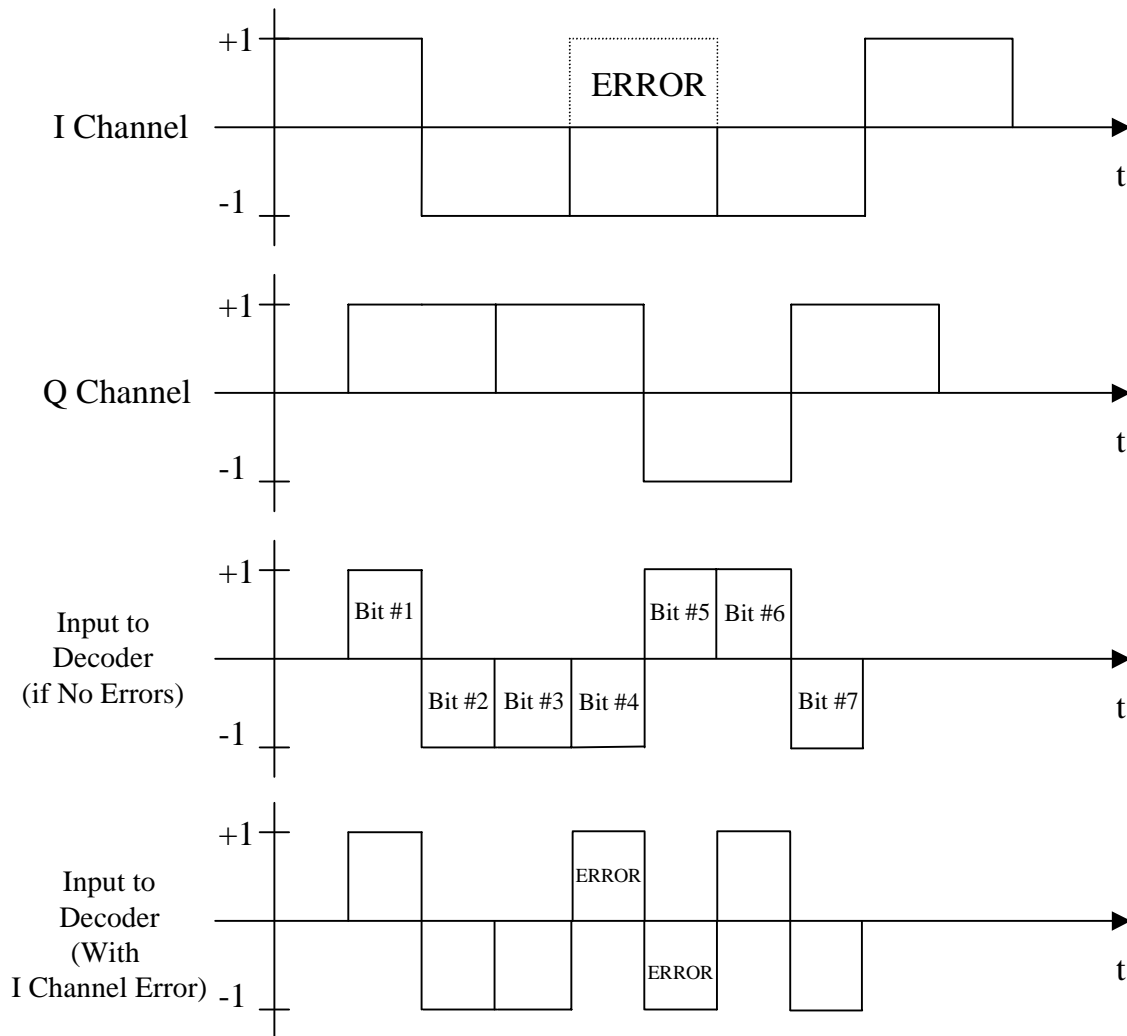


Figure C-3. I Channel Bit Error Example

C.2.2.3 Narrowband Interferer

Because the GMSK receiver system is the same as the FOQPSK receiver system except for the differential decoder as stated in 5.1, the P_e for the GMSK modulation scheme with narrowband interference is exactly the same as equation C.13, except the P_e is double. The P_e equation for GMSK with narrowband interference is as follows:

$$\overline{P_e} = 2 \cdot \frac{1}{2\pi} \int_0^{2\pi} Q \left\{ \sqrt{\frac{2E_b}{N_o}} \left[1 - \frac{\sqrt{2}}{\sqrt{\frac{S}{2I}} \Delta\omega T} \sqrt{1 - \cos(\Delta\omega T)} \cos(\theta) \right] \right\} d\theta \quad \text{eq. C.15}$$

Where; $\overline{P_e}$ is the P_e averaged over all θ .

θ is a random variable with the same pdf as θ_i . θ is a function of θ_i .

E_b is the energy per bit in each I and Q channel

N_o is the one-sided noise power spectral density

S is $s(t)$'s signal power

I is the interference CW tone's power

$\Delta\omega = \omega_o - \omega_i$

We can solve Equation C.15 via Numerical Integration with a computer.

C.3 Results

C.3.1 Filtered OQPSK

This section provides the following plots for FOQPSK with wideband and narrowband interference for the two cases when $\Delta\omega T=0$ and $\Delta\omega T=0.5$:

- Pe versus S/I for a constant $E_b/N_o = 11$ dB
- Pe versus E_b/N_o for a constant $I/N = -5$ dB
- Degradation in Pe versus I/N for a constant Pe of 1×10^{-5}

We will define degradation in Pe as the increase in desired signal power, S , that is required when interference is present to achieve the same Pe as when no interference is present.

Case 1 Parameters ($\Delta\omega T=0$):

- Total Bit Rate = 50 Mbps, thus I Channel Bit Rate = 25 Mbps
- T = Channel Bit Period = $1/(2.5 \times 10^7)$
- $\omega_o = 8$ GHz
- $\omega_i = 8$ GHz - 0 MHz
- $\Delta\omega = 0$ MHz
- $\Delta\omega T = 0.0$

The P_e versus S/I , the P_e versus E_b/N_o , and the Degradation in P_e versus I/N plots for $\Delta\omega T = 0.0$ are shown in Figures C-4, C-5, and C-6, respectively.

Case 2 Parameters ($\Delta\omega T=0.5$):

- a. Total Bit Rate = 50 Mbps, thus I Channel Bit Rate = 25 Mbps
- b. T = Channel Bit Period = $1/(2.5 \times 10^7)$
- c. $\omega_o = 8$ GHz
- d. $\omega_i = 8$ GHz - 12.5 MHz
- e. $\Delta\omega = 12.5$ MHz
- f. $\Delta\omega T = 0.5$

The P_e versus S/I , the P_e versus E_b/N_o , and the Degradation in P_e versus I/N plots for $\Delta\omega T = 0.5$ are shown in Figures C-7, C-8, and C-9, respectively.

When calculating the plots, the “I/N” parameter is a function of the bandwidth, B . As stated in section C.2.1.1, the bandwidth was arbitrarily defined as follows:

$$B = \frac{3.2}{T}$$

Where for FOQPSK and GMSK, T , is the symbol period and R is the total bit rate. The relationship between E_b/N_o and S/N is as follows:

$$\frac{S}{N} = \frac{E_b(R)}{N_o B} = \frac{E_b(2/T)}{N_o (3.2/T)}$$

$$\frac{S}{N} = 0.625 \frac{E_b}{N_o}$$

The relationship between E_b/N_o and S/N affects I/N because the following relationship is also important when calculating the plots:

$$\frac{I}{N} = \frac{S/N}{S/I}$$

Thus, the narrowband curves in Figures C-6 and C-9 will shift right or left, if a bandwidth other than $3.2/T$ is chosen. Also, whether the narrowband interference model yields more degradation or less degradation than the wideband interference model depends upon the bandwidth chosen.

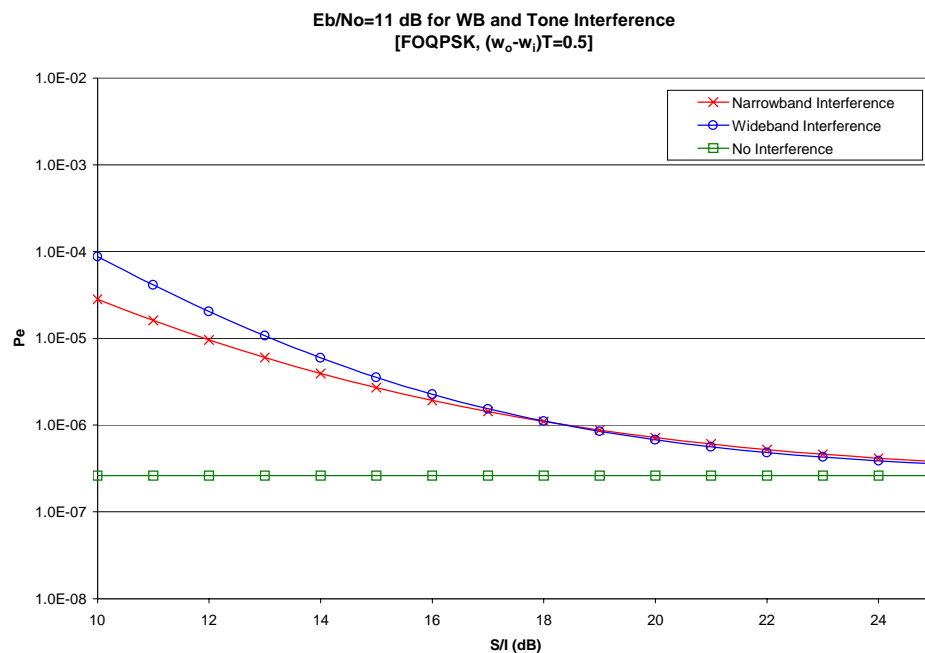


Figure C-4. FOQPSK, $E_b/N_o = 11$ dB, $\Delta\omega T = 0$

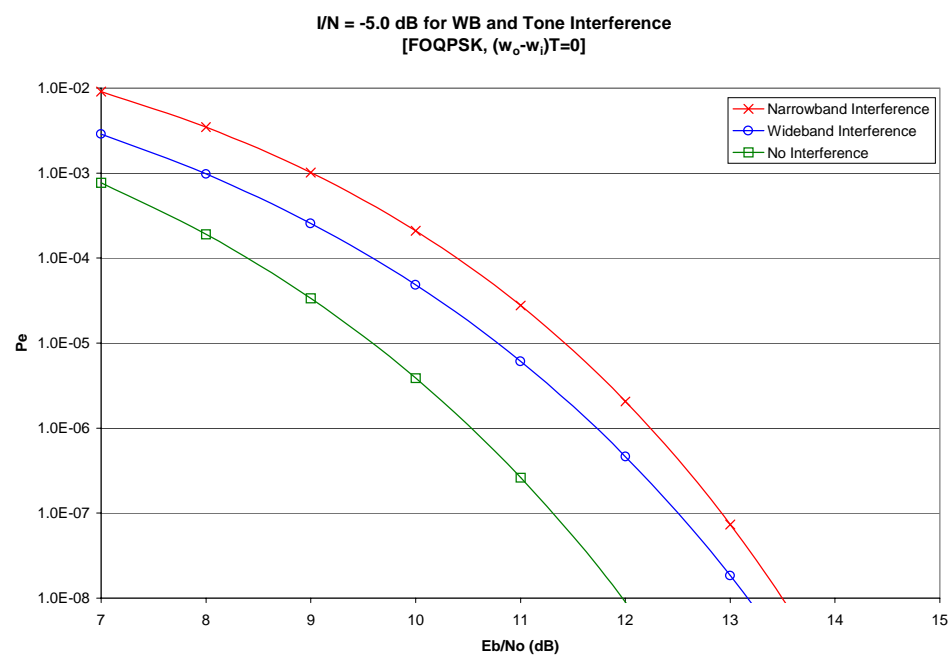


Figure C-5. FOQPSK, $I/N = -5.0$ dB, $\Delta\omega T = 0$

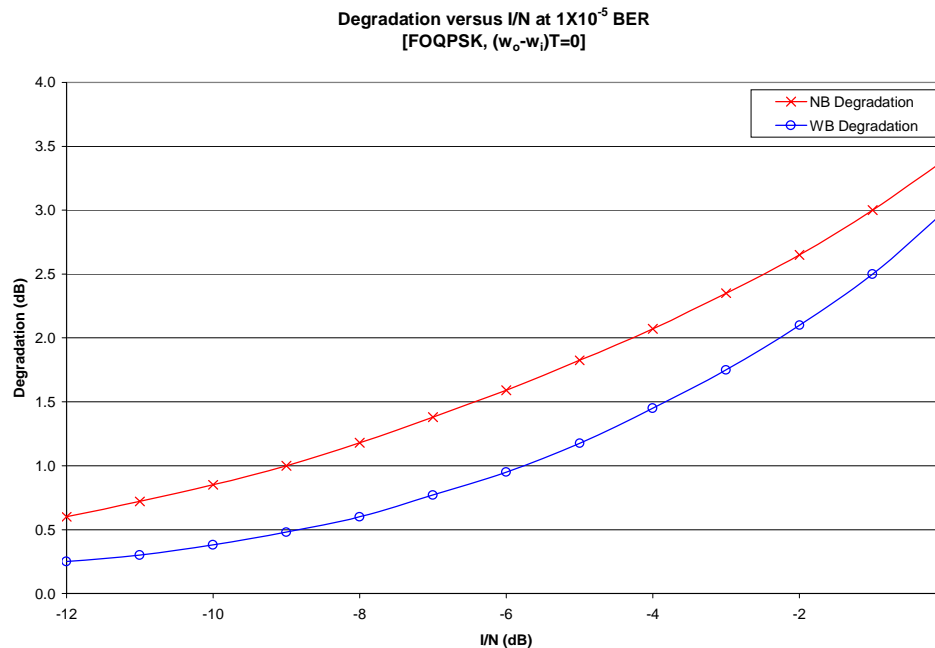


Figure C-6. FOQPSK, $Pe = 1 \times 10^{-5}$, $\Delta\omega T = 0$

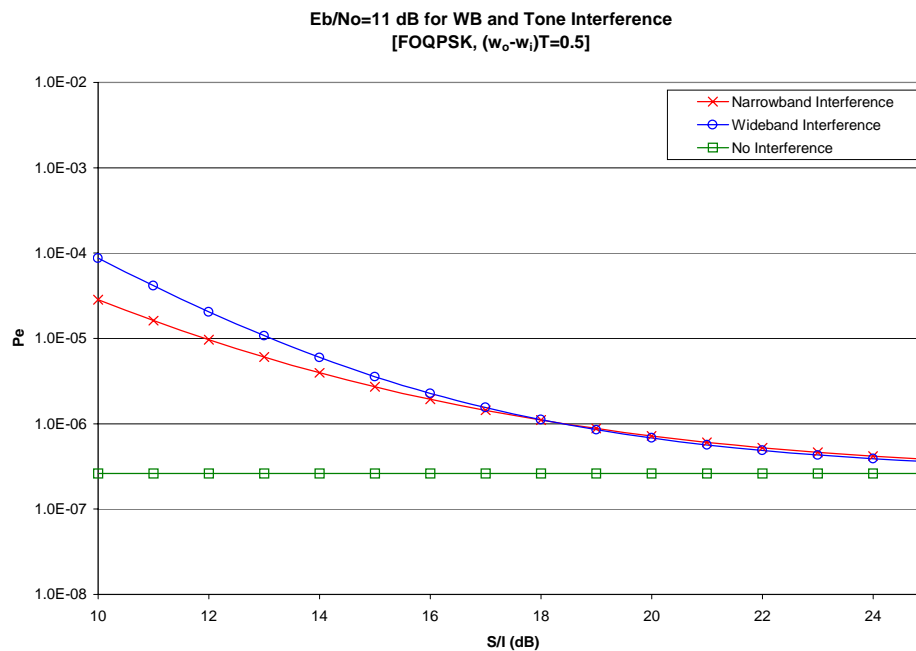


Figure C-7. FOQPSK, $E_b/N_o = 11$ dB, $\Delta\omega T = 0.5$

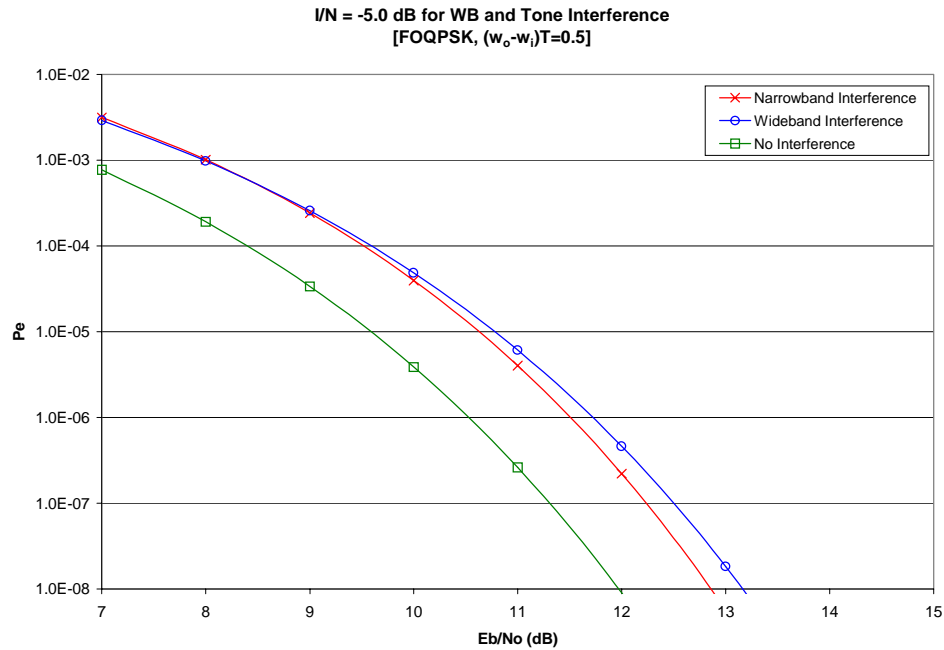


Figure C-8. FOQPSK, $I/N = -5.0$ dB, $\Delta\omega T = 0.5$

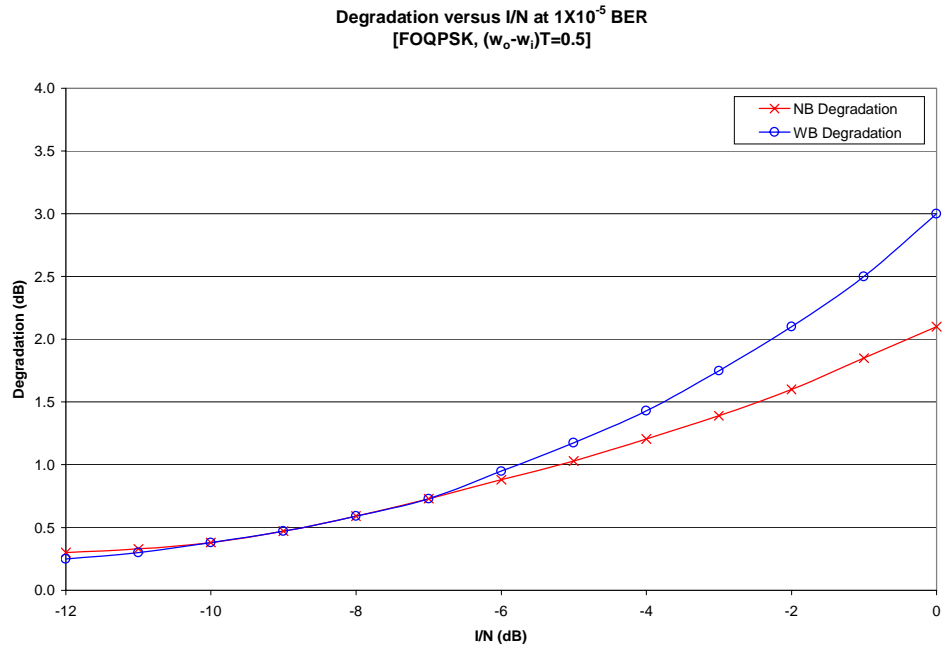


Figure C-9. FOQPSK, $P_e = 1 \times 10^{-5}$, $\Delta\omega T = 0.5$

C.3.2 GMSK

This section provides the following plots for GMSK with wideband and narrowband interference for the two cases when $\Delta\omega T = 0$ and $\Delta\omega T = 0.5$:

Pe versus S/I for a constant Eb/No = 11 dB

Pe versus Eb/No for a constant I/N = -5 dB

Degradation in Pe versus I/N for a constant Pe of 1×10^{-5}

Case 1 Parameters ($\Delta\omega T=0$):

Total Bit Rate = 50 Mbps, thus I Channel Bit Rate = 25 Mbps

$T = \text{Channel Bit Period} = 1/(2.5 \times 10^7)$

$\omega_o = 8 \text{ GHz}$

$\omega_i = 8 \text{ GHz} - 0 \text{ MHz}$

$\Delta\omega = 0 \text{ MHz}$

$\Delta\omega T = 0.0$

The Pe versus S/I, the Pe versus Eb/No, and the Degradation in Pe versus I/N plots for $\Delta\omega T = 0.0$ are shown in figures C.10, C.11, and C.12, respectively.

Case 2 Parameters ($\Delta\omega T=0.5$):

Total Bit Rate = 50 Mbps, thus I Channel Bit Rate = 25 Mbps

$T = \text{Channel Bit Period} = 1/(2.5 \times 10^7)$

$\omega_o = 8 \text{ GHz}$

$\omega_i = 8 \text{ GHz} - 12.5 \text{ MHz}$

$\Delta\omega = 12.5 \text{ MHz}$

$\Delta\omega T = 0.5$

The Pe versus S/I, the Pe versus Eb/No, and the Degradation in Pe versus I/N plots for $\Delta\omega T = 0.5$ are shown in figures C.13, C.14, and C.15, respectively.

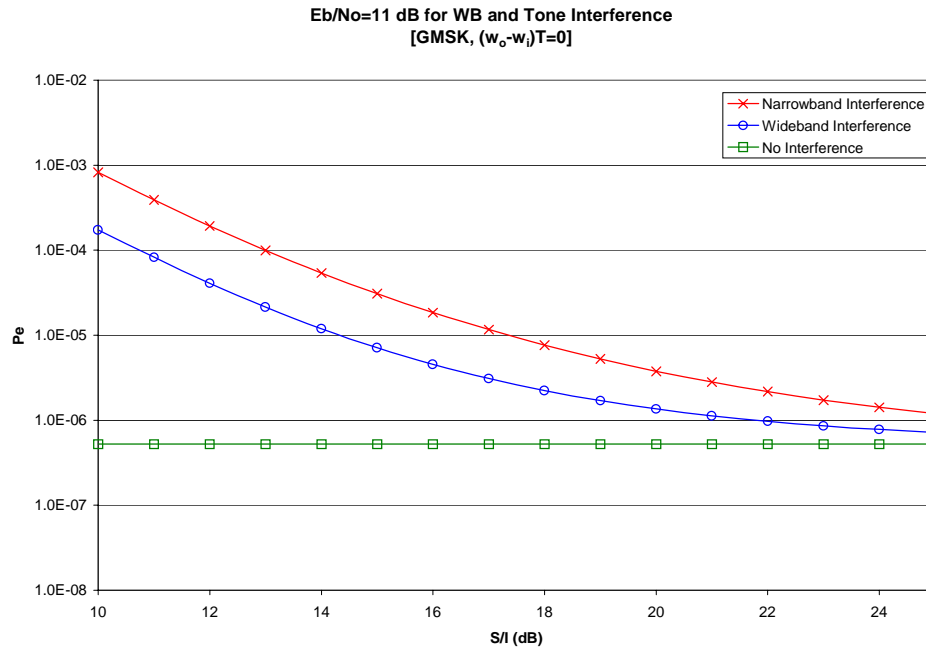


Figure C-10. GMSK, $E_b/N_0 = 11$ dB, $\Delta\omega T=0$

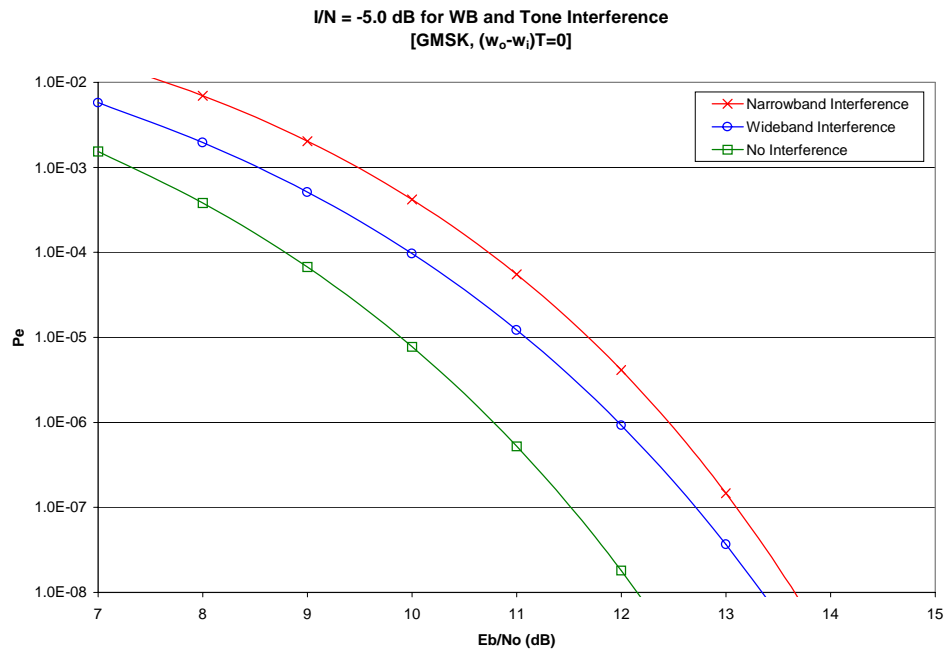


Figure C-11. GMSK, $I/N = -5.0$ dB, $\Delta\omega T=0$

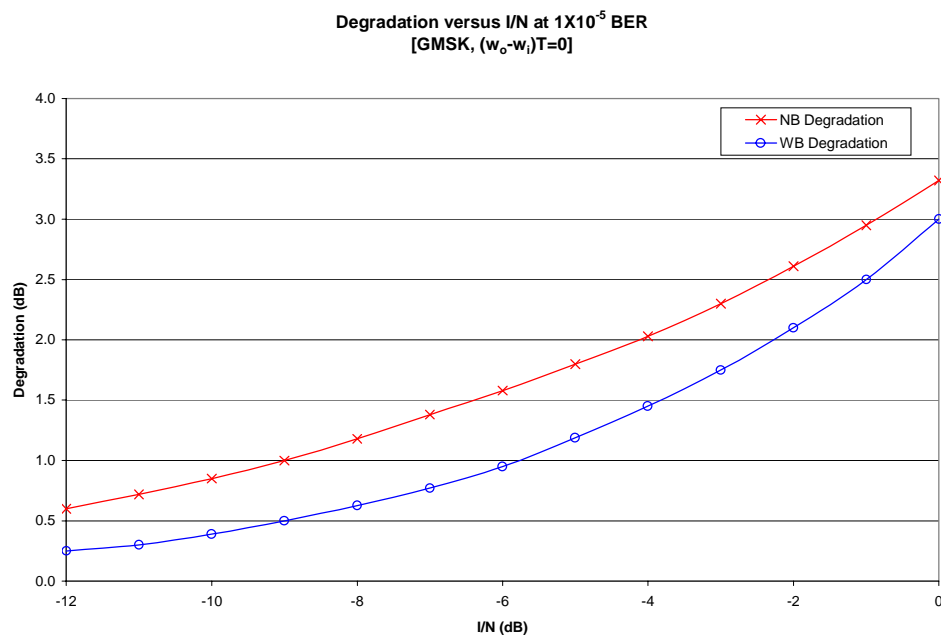


Figure C-12. GMSK, $Pe = 1 \times 10^{-5}$, $\Delta\omega T = 0$

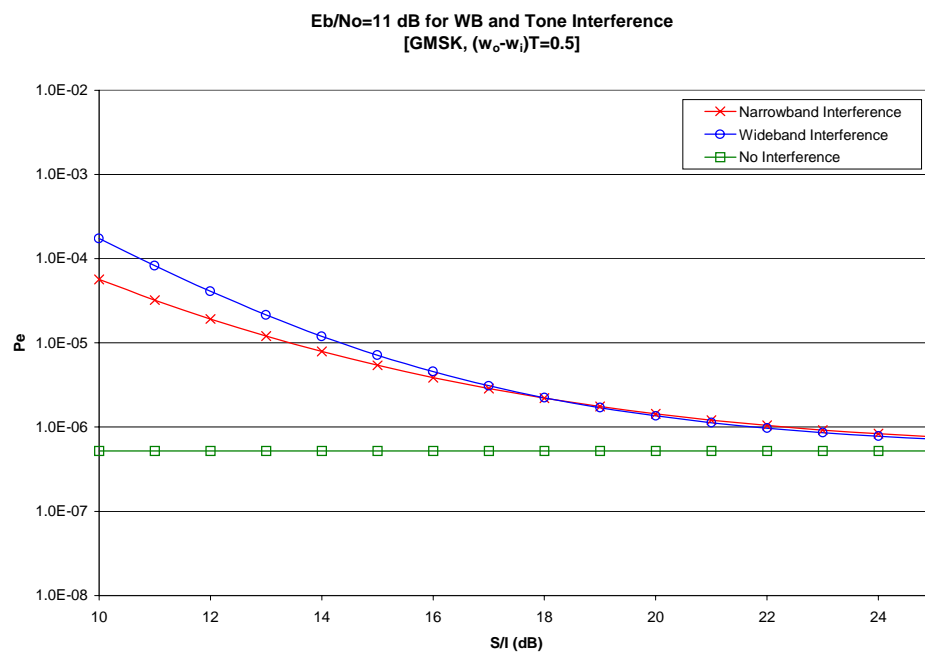


Figure C-13. GMSK, $E_b/N_o = 11$ dB, $\Delta\omega T = 0.5$

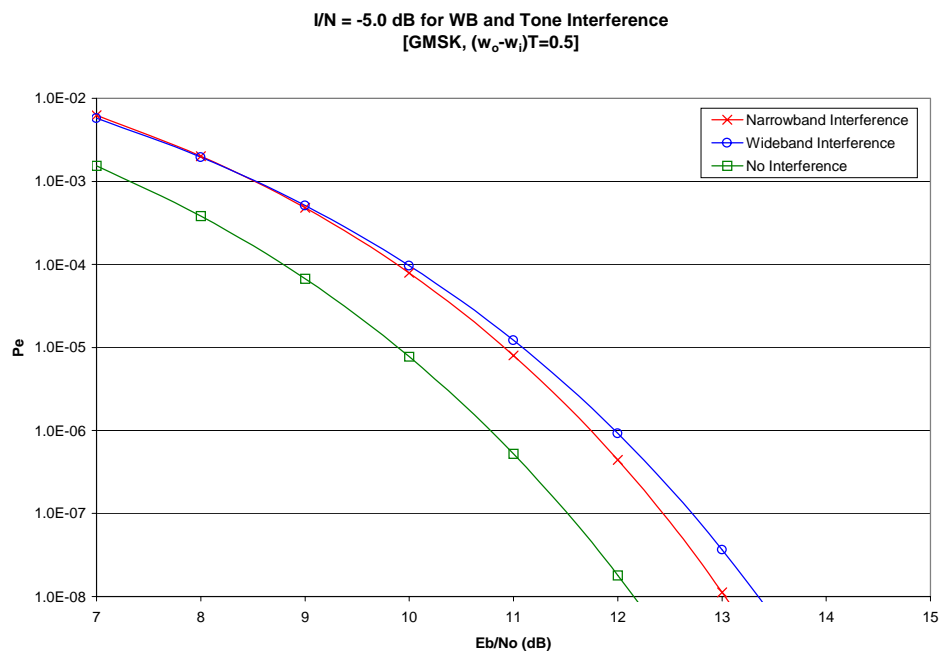


Figure C-14. GMSK, $I/N = -5.0$ dB, $\Delta\omega T = 0.5$

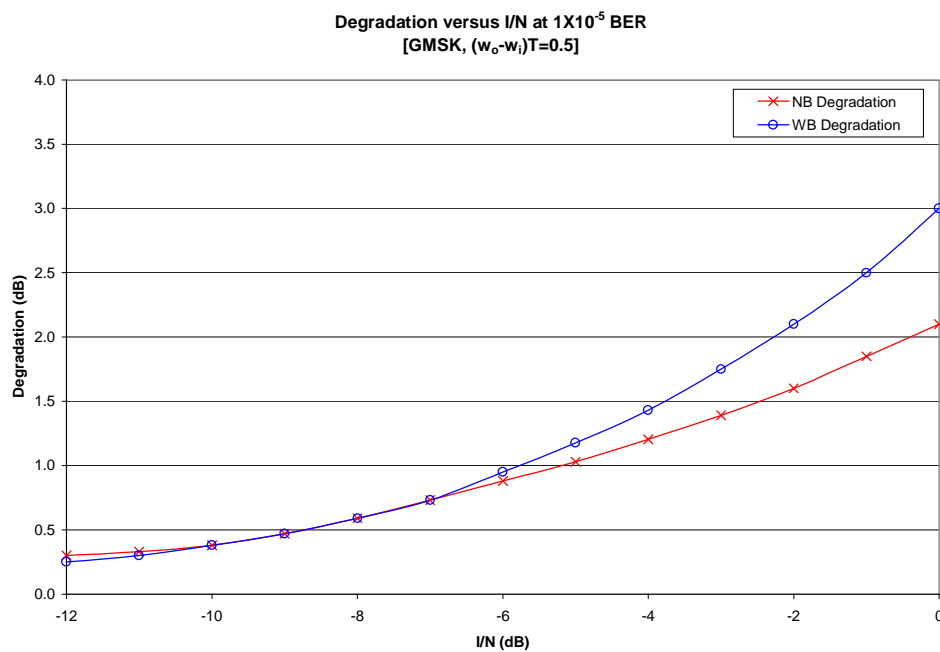


Figure C-15. GMSK, $P_e = 1 \times 10^{-5}$, $\Delta\omega T = 0.5$

Appendix D Hardware Distortion Parameters

This appendix addresses three hardware distortion parameters that are modeled in the simulation results presented in this report. They are incidental AM, spurious PM and spurious outputs. Each distortion is described in this appendix and the parameters are provided in Table 3-1.

D.1 Incidental AM

Incidental AM, which may be introduced by the user transmitter, represents an undesirable sinusoidal AM component superimposed on the desired signal. It is defined as the modulation index of sinusoidal amplitude modulation on the data signal. In this study, one incidental AM component is addressed, the following Figure D-1 provides the diagram for one incidental AM tone.

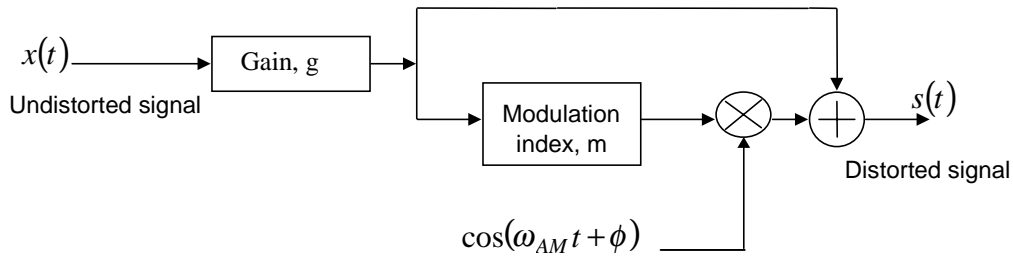


Figure D-1. Block Diagram of Incidental AM

The distorted output signal is

$$s(t) = gx(t)[1 + m \cos(\omega_{AM}t + \phi)]$$

Where m is the incidental AM modulations index, ω_{AM} is the incidental AM radian frequency, and ϕ is an arbitrary phase of incidental AM. Incidental AM is specified by incidental AM modulation index m in percentage, and incidental AM radian frequency ω_{AM} .

There are two kinds of incidental AM. The first assumes that incidental AM does not rob power from the desired signal - i.e., it essentially increases the transponder output power. In this case, the gain g is 1. A more pessimistic assumption treats the incidental AM as robbing power from the desired signal, thus maintaining the overall transponder output power constant. In this case, the gain $g = \sqrt{1/(1 + m^2/2)}$ to keep the overall output power constant. It is this latter assumption that we employ for present purposes.

Incidental AM robs the power from the desired signal and thus degrades the system performance.

D.2 Spurious Phase Modulation (PM)

Unwanted phase modulation to the transmitted signal is composed of continuous phase spectrum components and discrete phase spectrum components. The continuous spectrum is generated by that component of the undesired phase modulation defined as phase noise, while the discrete spectral components are defined as spurious phase modulation (PM). A mathematical model for spurious PM is presented in Figure D-2.

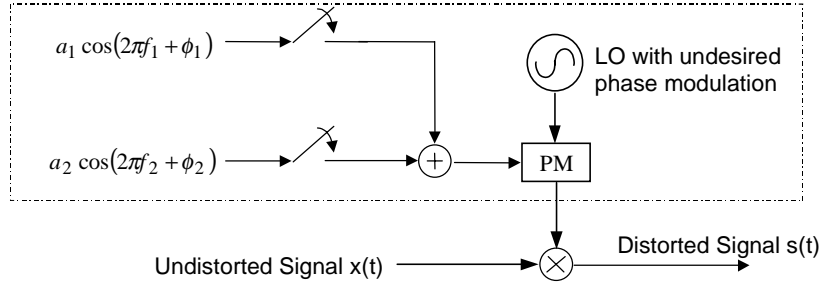


Figure D-2. Block Diagram of Spurious PM

Figure E.2 indicates an IF signal is upconverted by local oscillator which includes undesired phase modulation or spurious PM. The IF signal and distorted RF signal can be represented as

$$x(t) = A \cos(\omega_c t + \phi(t) + \theta)$$

$$s(t) = A \cos\left(\omega_c t + \theta(t) + \phi + \sum_i a_i \cos(2\pi f_i t + \phi_i)\right)$$

where A is the signal magnitude. $\theta(t)$ is the data. ϕ, ϕ_i are arbitrary phase. a_i is the magnitude of each spurious PM.

The rms values of the sinusoid phases and the frequency f_1, f_2 are the parameters specifying spurious PM.

Spurious PM causes cycle slipping and untracked phase error, and thus results in degraded carrier tracking and BER performance.

D.3 Spurious Outputs

Spurious outputs are defined as the sum of the power in all spurs within the specified bandwidth, measured relative to the total signal power. dBc is used to represent the spur power relative to total signal power. Figure D-3 provides the block diagram of two spurs.

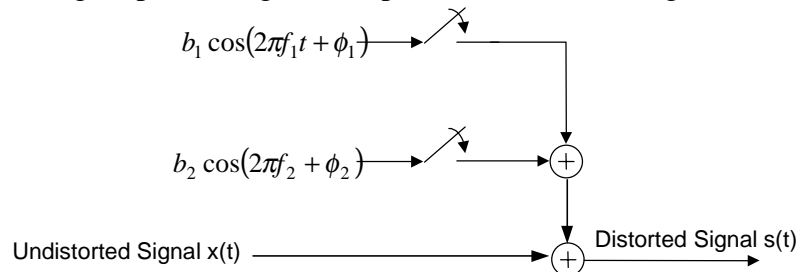


Figure D-3. Block Diagram of Spurious Outputs

The distorted signal is represented as

$$s(t) = x(t) + \sum_i b_i \cos(2\pi f_i t + \phi_i)$$

The spurious outputs is specified by spur frequency f_1, f_2 and the total spur power in dBc, which is relative to the signal power. ϕ_1 and ϕ_2 are the arbitrary phases.

A spurious output has the impact on system performance such as narrow band interference. It results in degraded data detecting and thus BER performance.

Appendix E GMSK Theoretical BER Performance

E.1 Introduction

This appendix provides a theoretical calculation for GMSK BER performance when received with a coherent integrate and dump detector. Since MSK and GMSK modulation includes inherent differential encoding, BER performance can be improved by the use of pre-coding the input sequence. In this appendix the BER is calculated for both with and without pre-coding. The analysis is valid for $BT = 0.5$ and results are calculated for $BT = 0.5$ and $BT = 1.0$. These cases were also investigated via simulation in the body of this report.

E.2 Theoretical BER Calculation

The theoretical BER calculation for GMSK is based the functional model shown in Figure E-1. The modulator receives an NRZ input data stream. The NRZ data stream is integrated which results in a sequence of ramp functions with positive slope for +1 symbol and negative slope for -1 signal. The ramp signal is filtered with the Gaussian filter and input to a phase modulator. The modulation index is set to $\pi/2$ radians so that each NRZ pulse causes either a positive or negative phase trajectory with a magnitude of $\pi/2$ radians.

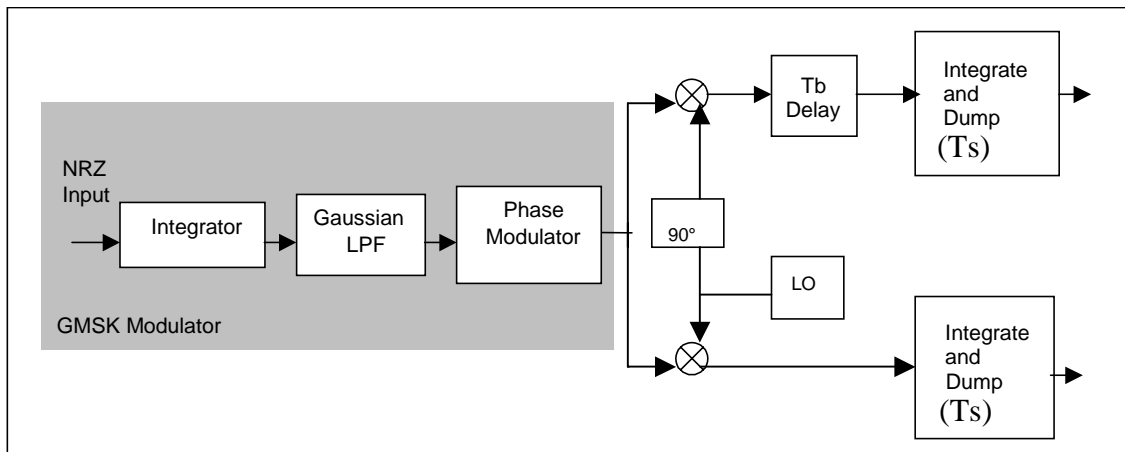


Figure E-1. GMSK Analysis Model

The theoretical performance of GMSK modulation is calculated by computing the transmitter output signal based on a sequence of input bits. The sequence of input bits is long enough so that all possible received signal waveforms are included in the analysis. The waveforms are assumed to be received using coherent detection with integrate and dump detection filters. The output of the integrate and dump detection filters is computed for each of the sequences. Based on the integrate and dump output, a probability of error for a particular bit can be computed conditioned on a particular

sequence. The conditional error probabilities are then averaged over the sequences assuming that all sequences are equally likely.

The probability of error for antipodal signaling schemes is given below. This applies to ideal BPSK and QPSK using integrate and dump detection.

$$P_e = Q\left[\sqrt{2E_b/N_o}\right]$$

For GMSK with integrate and dump detection, the error probability calculation is similar to that for QPSK except that the desired signal component of the output of the integrate and dump filter is reduced and depends on the GMSK waveform and the particular bit sequence. The noise level at the integrate and dump output is unchanged from QPSK. This analysis computes the effective E_b/N_o loss for each bit sequence, compute the probability of error for each sequence and then average the probabilities over the sequences.

The conditional probability of error for each bit sequence is given by :

$$P_{e,i} = Q\left[\sqrt{2E_b/N_o} \cdot \gamma_i\right]$$

The total probability of error is calculated by averaging over all sequences as follows

$$P_e = \sum_{i=1}^N P_{e,i} \cdot P_i$$

Where P_i is the probability of each sequence.

The GMSK modulator output is given by the following equations. The input NRZ data is integrated and then filtered with the Gaussian low pass filter. The resulting signal is normalized so that when it is applied to the phase modulator the phase of the output signal will change by $\pm\pi/2$ at each NRZ data transition.

$$y_i(t) = \int_{-\infty}^t d_i(\tau) d\tau$$

$$x_i(t) = \int_{-\infty}^{\infty} h(t-\tau) \cdot y_i(\tau) dt$$

The phase modulator output signal is given by the following equations. The first equation is a single carrier representation of the signal. The second signal is a quadrature representation of the same signal. The I and Q components of the quadrature representation will be used as inputs to the I and Q integrate and dump detectors.

$$s_i(t) = \sqrt{2P_s} \cos\left[2\pi\omega t + \frac{\pi}{2} \cdot x_i(t)\right]$$

$$s_i(t) = \sqrt{2P_s} \cos\left[\frac{\pi}{2} \cdot x_i(t)\right] \cdot \cos(2\pi\omega t) - \sqrt{2P_s} \sin\left[\frac{\pi}{2} \cdot x_i(t)\right] \cdot \sin(2\pi\omega t)$$

The I and Q components of the modulator output are computed for each of eight possible bit sequences shown in Table 1. For BT values lower than 0.5, the length of the sequences considered would have to be increased.

Table 1. Four-Bit Sequences and Probability

Probability (P_i)	k-1	k	k+1	k+2
0.125	-1	1	-1	-1
0.125	-1	1	-1	1
0.125	-1	1	1	-1
0.125	1	1	-1	-1
0.125	1	1	-1	1
0.125	1	1	1	-1
0.125	1	1	1	1

The output of the integrate and dump detectors is computed by integrating the I and Q components of the transmitted signal over T_s which is 2x the bit duration. The output of the integrate and dump for the Q channel is shown below.

$$\Lambda_i = \frac{\sqrt{2P_s}}{T_s} \int_0^{T_s} \sin\left[\frac{\pi}{2} \cdot x_i(t)\right] dt$$

In the case of MSK, the phase modulator input is a sequence of ramp functions with positive slope for a +1 and a negative slope for a -1. In this case, the integrate and dump output is given by:

$$\Lambda_i = \frac{\sqrt{2P_s}}{T_s} \int_0^{T_s} \sin\left[\frac{\pi}{2} \cdot t/T_s\right] dt = \sqrt{2P_s} \cdot \frac{2}{\pi}$$

The integrate and dump output is normalized by the total power to compute the signal level degradation relative to QPSK.

$$\gamma_i = \frac{\sqrt{2}}{T_s} \int_0^{T_s} \sin\left[\frac{\pi}{2} \cdot x_i(t)\right] dt$$

Values of γ_i calculated for BT = 0.5 and 1.0 are listed in Table 2. For MSK

$$\gamma_i = \frac{\sqrt{2} \cdot 2}{\pi} \approx 0.900.$$

Table 2. Loss Calculation

BTs	γ_1	γ_2	γ_3	γ_4	γ_5	γ_6	γ_7	γ_8
0.5	0.913	0.950	0.974	0.937	0.877	0.913	0.937	0.900
1.0	0.907	0.916	0.920	0.910	0.897	0.907	0.910	0.900

From Table 1, the eighth sequence corresponds to a series of +1's. In this case the GMSK waveform is nearly identical to the MSK waveform. The integrate and dump output for the eighth sequence agrees with that expected for MSK.

E.3 Simulation Results

Simulations of the GMSK system shown in Figure 1 were performed using an ideal transmitter and ideal coherent receiver with integrate and dump detection. Several BER simulations were performed with different noise seeds. The results are compared to the theoretical performance computed above.

Figure E-2 shows BER vs. E_b/N_0 performance for GMSK with $BT = 0.5$. Figure E-3 shows BER vs. E_b/N_0 performance for MSK. In both cases the simulation points are in close agreement with the theoretical results.

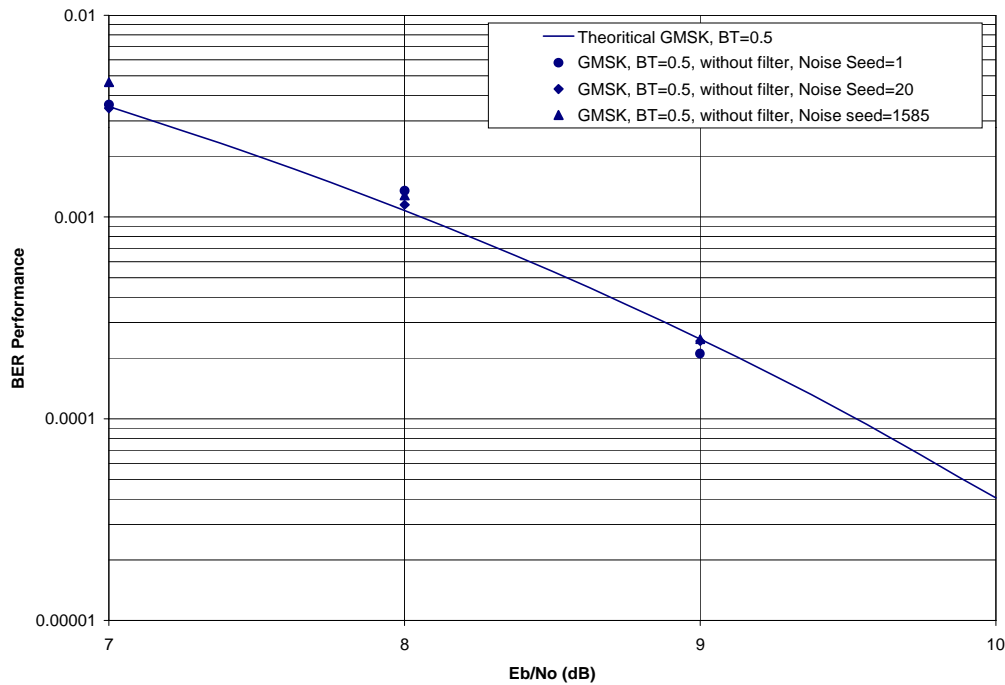


Figure E-2. Probability of Bit Error vs. E_b/N_0 for GMSK with I&D Detection

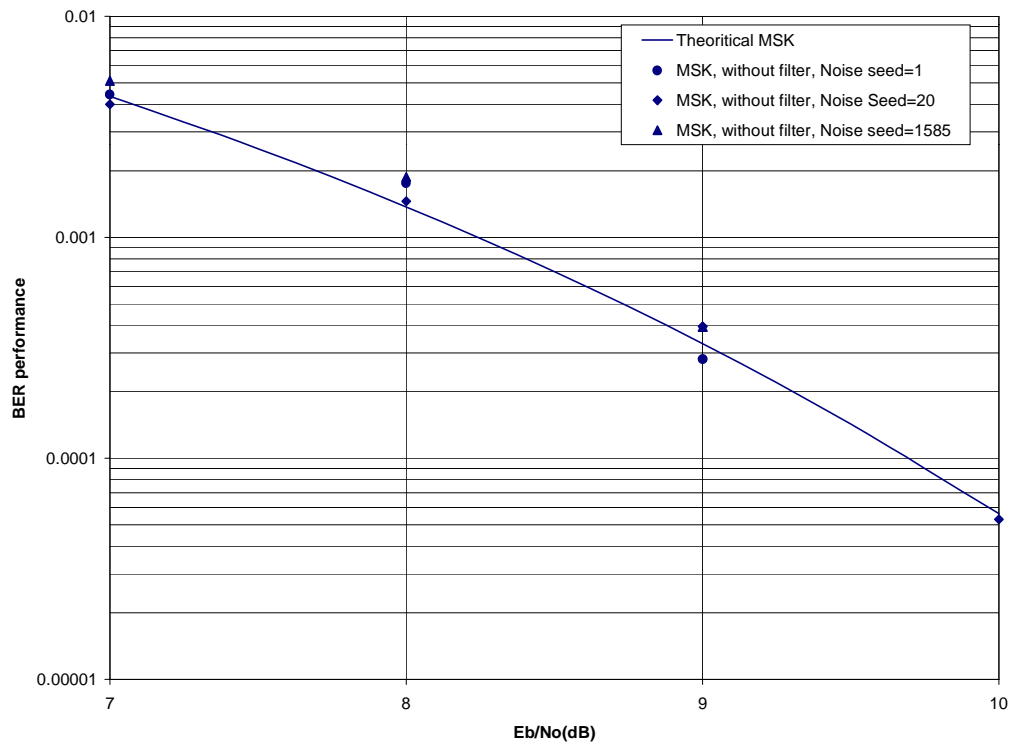


Figure E-3. Probability of Bit Error vs. E_b/N_0 for MSK with I&D Detection

Appendix F Base-band Filter Response

Three types of baseband filters are used in this study for pulse shaping:

Butterworth

Gaussian

Square Root Raised Cosine (SRRC)

The implementation of these filters in a transmitter can impact the spectrum and BER performance. This appendix addresses the fidelity of the filter implementations used in the study.

The Butterworth filter is implemented as an IIR filter and is well-documented in textbooks. The Gaussian and SRRC filters are implemented as transversal FIR filters. The fidelity of the implementation of these filters depends on the length of the filter, the time quantization and the amplitude quantization.

Fig F-1 shows impulse response of gaussian filter. Samples are not quantized in amplitude. 32 points cover the whole impulse response. There are 32 quantization levels and 5 bits per symbols. The distance between two points depends on sampling frequency and baud rate. The distance between two point is 0.1. There are 10 samples per symbols.

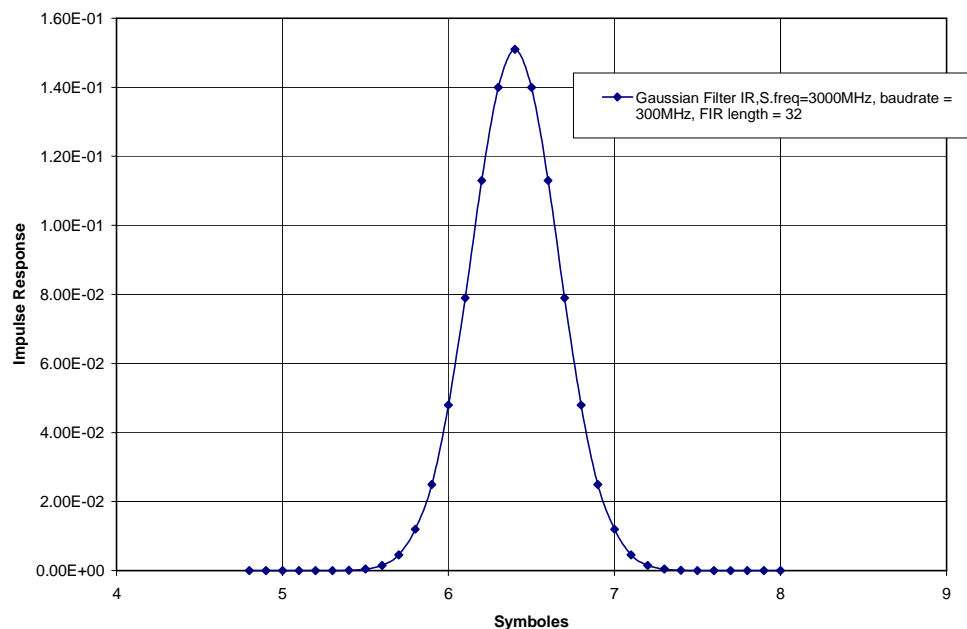


Figure F-1. Impulse response of Gaussian filter

Fig. F-2 shows impulse response of SRRC filter. 256 points covers the whole range of impulse response of SRRC filter. The distance between two points is 0.003. There are 33 samples per symbols.

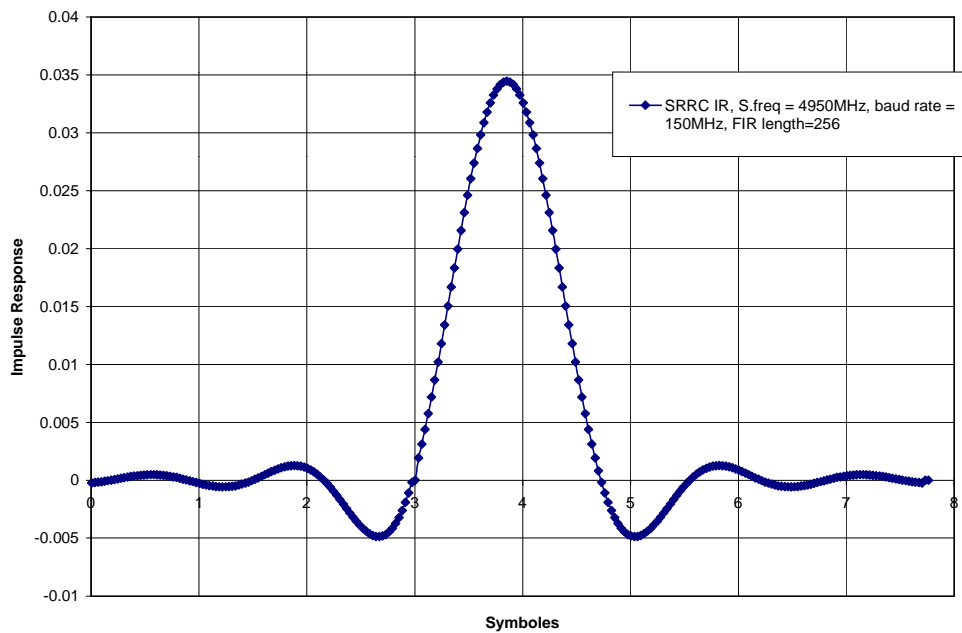


Figure F-2. Impulse response of SRRC filter

Fig.F-3 shows frequency response of Gaussian filter, Butterworth filter and SRRC filter

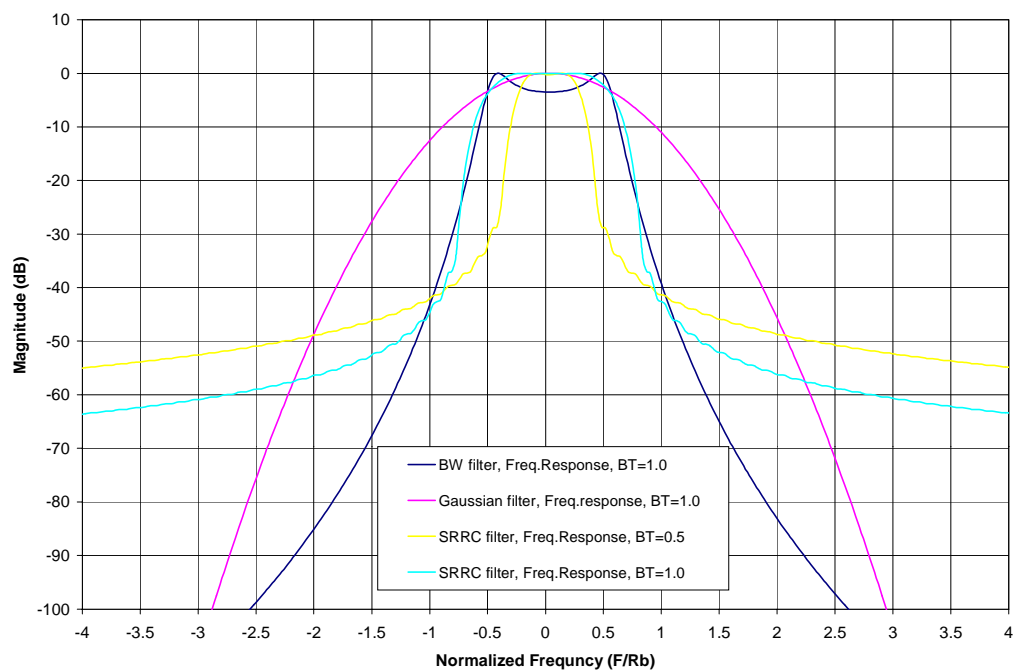


Figure F-3. Frequency response of Butterworth, Gaussian and SRRC filter

Appendix G Filtered OQPSK, GMSK Power Flux Density Analysis

G.1 Summary

This appendix provides an assessment of the increase in Power Flux Density (PFD) of a transmitted signal for filtered OQPSK and GMSK relative to unfiltered OQPSK. Bandwidth efficient modulation techniques tend to concentrate signal power within the necessary bandwidth. This concentration would increase the spectral density of the transmitted signal near the center frequency. Radio regulations impose restrictions on power flux density impinging on the earth. The purpose of this appendix is to quantify the increase in PFD due to the use of bandwidth efficient modulation techniques. Two factors contribute to the increase in power flux density: 1) Power spectral density is more concentrated within the necessary bandwidth. 2) Typically additional EIRP is required to compensate for additional implementation loss due to the use of bandwidth efficient modulation. Section 4 and Section 5 of this report have investigated the additional EIRP required to compensate for increased implementation loss. The required increase in implementation loss is somewhat dependant on the type of receiver. For example, a matched filter receiver will exhibit less loss than an integrate and dump receiver. The analysis here assumes that an integrate and dump receiver is used. This appendix compares the PSD of filtered OQPSK and GMSK with that of unfiltered OQPSK by SPW simulation and analytic methods. The PFD increase due to implementation loss and PSD concentration is summarized in Table G-1.

Table G-1. Total PFD increase due to Implementation Loss and PSD of filtered OQPSK, GMSK (dB)

	Filtered OQPSK (PA OBO =1)		GMSK (PA OBO = 0)	
	Butterworth (BTs=1.0)	SRRC (BTs=1.0)	BT = 0.5	BT = 1.0
Implementation loss	1.6	1.6	1.2	1.2
Loss due to PSD	0.28	0.32	0.58	0.18
Total	1.88	1.92	1.78	1.38

Section 4 and Section 5 of this report evaluate transmit signal spectrum, implementation loss, and interference susceptibility for filtered OQPSK, filtered OQPSK/PM, and GMSK modulation.

G.2 Power Spectral Density Analysis

We investigated the absolute power spectral density of unfiltered OQPSK, filtered OQPSK, MSK and GMSK by SPW simulation and analytic methods. Table G-2 provides a summary of the results.

The SPW simulation results are shown in Table G-2, Column 4. The results were obtained by setting the user transmitter described in Section 3.2 to transmit the desired modulation type, then the periodogram approach was used to estimate the power spectral density of the output of the user transmitter.

For example: for uncoded, unfiltered OQPSK with data rate 150 MHz, the theoretical value of the PSD at the center frequency is -78.76 dB from equation (1) (refer to (3.4.55) [10]), while by SPW simulation it is -78.78 dB (Figure G-1). For MSK with a data rate of 300 Mbps, the theoretical value of the PSD at the center frequency is -76.64 dB from equation (2) (refer to (33) [11]), while by SPW simulation it is -76.64 dB (Figure G-2).

$$\Phi(f) = 2A^2T_b (\sin 2\pi fT_b / 2\pi fT_b)^2 \quad (1)$$

$$\Phi_{MSK}(f) = T_b \frac{16}{\pi^2} \frac{\cos^2 2\pi fT_b}{(1-16f^2T_b^2)^2} \quad (2)$$

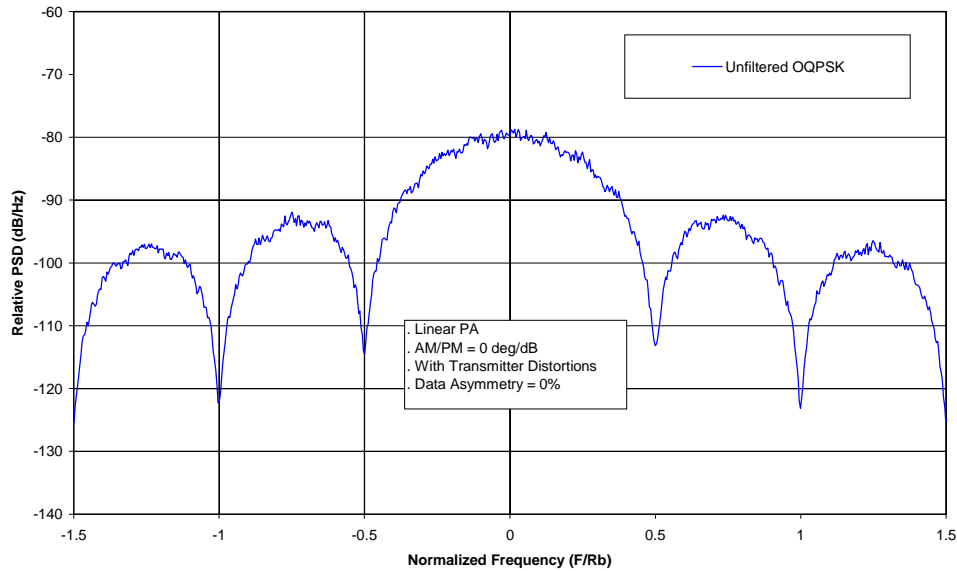


Figure G-1. SPW simulation result of absolute PSD of OQPSK

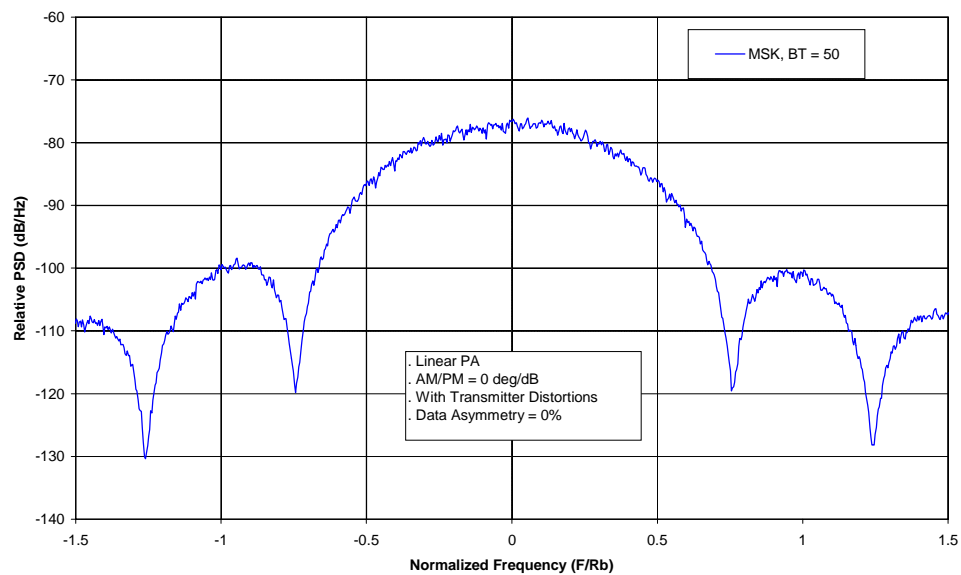


Figure G-2. SPW simulation result of absolute PSD of MSK

Table G-2: Absolute Power Spectral Density Level at the Center Frequency

Modulation	Operating Point	Analytic Result (dB)	Simulation Result (dB)	Simulation Result (dB) Normalized to OQPSK (for filtered OQPSK) or MSK(GMSK)
Unfiltered OQPSK	Linear OBO	-78.76	-78.78	0
	PA OBO = 1		-78.76	0.02
	PA OBO = 0		-78.75	0.03
Filtered OQPSK, with BW, BTs = 1.0	Linear OBO	-78.32	-78.42	0.36
	PA OBO = 1		-78.48	0.30
	PA OBO = 0		-78.56	0.22
Filtered OQPSK, with SRRC, BTs = 1.0	Linear OBO	-78.30	-78.38	0.40
	PA OBO = 1		-78.44	0.34
	PA OBO = 0		-78.60	0.18
MSK	Linear OBO	-76.64	-76.64	0
GMSK, with BT = 1	Linear OBO		-76.46	0.18
	PA OBO = 1		-76.46	0.18
	PA OBO = 0		-76.46	0.18
GMSK, with BT = 0.5	Linear OBO		-76.06	0.58
	PA OBO = 1		-76.06	0.58
	PA OBO = 0		-76.06	0.58

Appendix H Modulation Scheme Study with TDRS KaSA Return Link

SFCG has conducted several studies to assess the spectrum and power requirements for several candidate modulation techniques. These studies computed RF transmit spectra and additional transmit power required for each modulation technique but did not include degradation in BER performance due to the transmitter imperfections that are typically specified for GSFC missions. The study of OQPSK and GMSK modulation schemes documented in Section 4 and Section 5 assessed the additional power required for these modulation techniques while including distortions caused by the transmitter hardware that are typically specified for GSFC flight project transmitter for direct downlinks from user spacecraft to supporting ground terminals. This appendix provides an assessment of the modulation techniques performance while transmitting through a Tracking and Data Relay Satellite (TDRS) at Ka-Band.

A simulation model of the TDRS H, I, J KaSA 225 MHz dedicated return channel was integrated into the OQPSK and GMSK end-to-end simulation models developed and used in Section 4 and Section 5 of this report. Figure H-1 provides the simulation configuration.

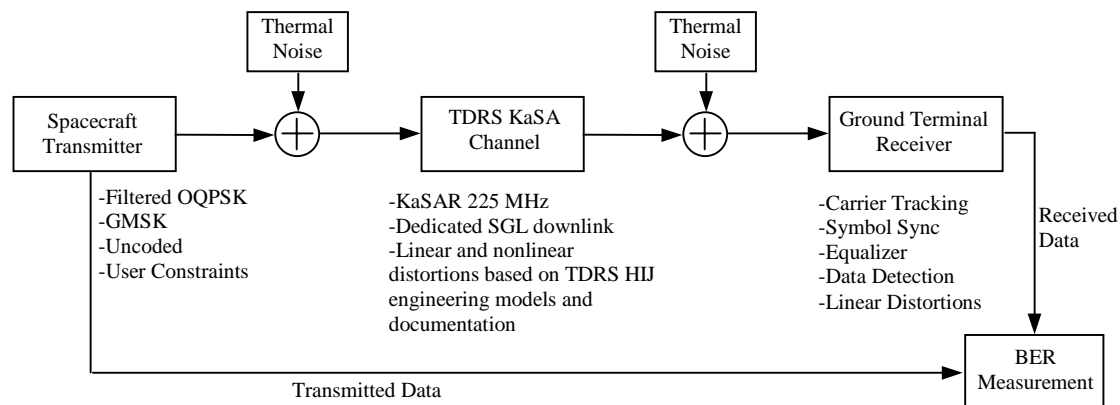


Figure H-1. End-to-end Simulation Configuration

The transmitter and receiver are set with the set 1 transmitter distortion values described in Table 3-1. TDRS H, I, J KaSA 225 MHz dedicated channel was developed based upon unit engineering model test data. A description of the TDRS H, I, J KaSA model can be found in reference [12]. The characteristics of the TDRS H, I, J KaSAR channel model are summarized in Table H-1.

Table H-1. TDRS KaSA 225MHz Dedicated Return Channel Parameters

Parameter		Description
Linear Distortion	Bandwidth, MHz	220.5
	Gain Flatness, dB p-p	1.55
	Gain Slope, dB/MHz	0.1
	Phase Nonlinearity, deg p-p	4.6
Nonlinear Distortion	AM/AM, dB/dB	0.9
	AM/PM, deg/dB	2.5
Simulation Parameters	Sampling Frequency, MHz	3000.0
	Modulation Type	SQPSK
	Data Rate, Mb/sec	300.0
	Code Rate	Uncoded
	SSL C/No, dB-Hz	101.47 ^[1]
	SGL C/No, dB-Hz	Varied to cover desired Eb/No
Notes:		
1. SSL C/No for SQPSK. Value for GMSK is 106.47.		

The simulation configuration shown in Figure H-1 was used to generate BER vs Eb/No performance. The ground terminal receiver includes an equalizer. Figure H-2 and H-3 provides filtered OQPSK BER curves for ground terminal receiver equalizer on and off, respectively.

The implementation losses are summarized in Table H-2.

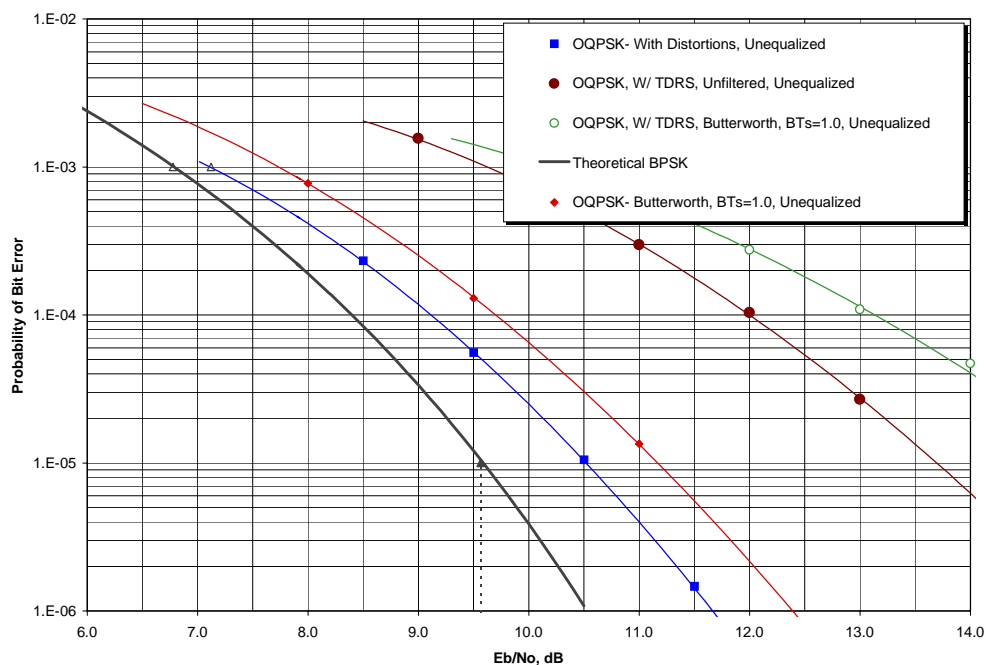


Figure H-2. Probability of Error vs. E_b/N_0 for Filtered OQPSK without Ground Equalizer

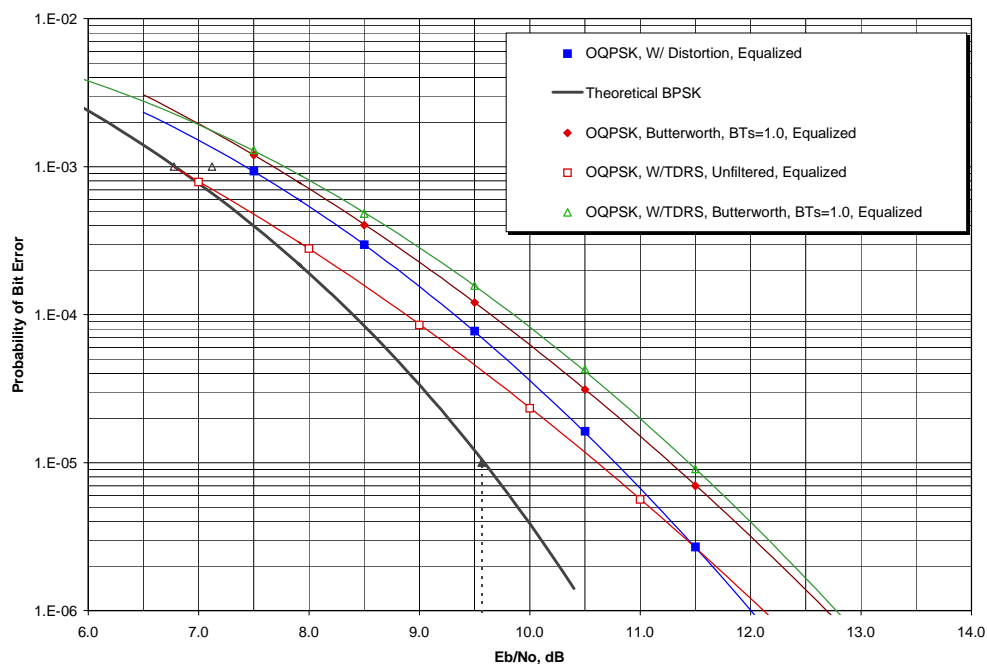


Figure H-3. Probability of Error vs. E_b/N_0 for Filtered OQPSK with Ground Equalizer

Table H-2. Implementation Loss

Modulation	PA Output Back- Off	TDRS Chann el	Equa lizer	Implementation Loss			
				@BER = 10^{-3}	@BER = 10^{-5}	@BER = 10^{-3} (Relative to BPSK)	@BER = 10^{-5} (Relative to BPSK)
BPSK, unfiltered,	1 dB	no	no	0.2 dB	0.6 dB	0.0dB	0.0 dB
OQPSK, unfiltered	1 dB	no	no	0.5 dB	0.9 dB	0.3 dB	0.3 dB
OQPSK, unfiltered	1 dB	yes	no	2.8 dB	4.1 dB	2.6 dB	3.5 dB
OQPSK, unfiltered	1 dB	no	yes	1.2 dB	1.2 dB	1.0 dB	0.6 dB
OQPSK, unfiltered	1 dB	yes	yes	0.0 dB	1.1 dB		0.5 dB
OQPSK, 6- pole Butterworth, BTs=1.0	1 dB	no	no	0.9dB	1.6dB	0.7dB	1.0dB
OQPSK, 6- pole Butterworth, BTs=1.0	1 dB	yes	no	3.5 dB	5.6 dB	3.3 dB	5.0 dB
OQPSK, 6- pole Butterworth, BTs=1.0	1 dB	no	yes	1.0 dB	2.2 dB	0.8 dB	1.6 dB
OQPSK, 6- pole Butterworth, BTs=1.0	1 dB	yes	yes	1.1 dB	1.8 dB	0.9 dB	1.2 dB
GMSK, BT = 0.5	0 dB	no	no	1.3 dB	1.2	1.1 dB	0.6 dB
GMSK, BT = 0.5	0 dB	yes	no				

[This page intentionally left blank.]



ADVANCED SPECTRUM SHAPING

ESA CONTRACT 11605/96/F/TB

ESA Technical Manager: G. Block

FINAL REPORT

September 1997

prepared by: A. Southern, M. Otter, M. Reichel
RSI, Griesheim, Germany

EUROPEAN SPACE AGENCY CONTRACT REPORT

The work described in this report was done under ESA contract. Responsibility for the contents resides in the author or organisation that prepared it.

ESA STUDY CONTRACT REPORT

No ESA Study Contract Report will be accepted unless this sheet is inserted at the beginning of each volume of the Report

ESA CONTRACT NO: 11605/96/F/TB	SUBJECT: ADVANCED SPECTRUM SHAPING FOR EFFICIENT BANDWIDTH UTILISATION		NAME OF CONTRACTOR R S I
* ESA CR() No:	* STAR CODE	No. of Volumes: 1	CONTRACTOR'S REFERENCE RSI/ASS
<p>ABSTRACT:</p> <p>This study covers the investigation of various techniques in order to optimize the use of radio frequency spectrum. Of primary interest are modulation schemes, filter and pulse shaping techniques which allow a significant reduction in occupied bandwidth at the expense of a slight system degradation and a moderate increase of hardware complexity. Radio frequency spectrum is a very limited resource and an allocated bandwidth must often be shared by several services. Of particular interest are frequencies below a few GHz because of favourable propagation conditions and attractive antenna designs.</p> <p>ESA, as well as most other space agencies, depend on a very limited number of useful frequency bands for payload data transmissions, launching and operating its spacecraft. This applies to the support of science, telecomm and Earth observation missions, equally. A number of frequency bands have been identified for the purpose of this study. The available bandwidth in the lower and most heavily used bands is small and has to be shared with an ever increasing number of both inter-service as well as intra-service users. Interference cases with operational impacts have already been encountered and it is evident that the general probability of interference is approaching the limit of acceptability. It is consequently becoming increasingly difficult to identify a quasi interference-free environment for new ESA missions, in particular, if currently used bandwidth-inefficient modulation schemes require coordination of a much wider bandwidth than actually needed. New bandwidth efficient and interference resistant spectrum shaping techniques are consequently required and shall be introduced in ESA as well as in an international environment. This will better protect ESA missions from RFI and reduce the rapidly increasing burden of coordination.</p> <p>An important factor for efficient use of available frequency band are unwanted emissions. These comprise spurious emissions and higher order lobes of the data spectrum, so-called out-of-band emissions. Spectral masks are proposed for out-of-band emissions as well as for spurious emissions. A detailed investigation on the impact of several non-linear high power amplifier implementations has been carried out. Various types of filters with different characteristics have been investigated. All possible locations in the transmission path for placing a spectrum shaping component have been taken into account. The results of the study are reflected in a set of recommendations and spectral masks with the objective to maximize the efficient use of frequency spectrum.</p> <p>The work described in this report was done under ESA contract. Responsibility for the contents resides in the author or organisation that prepared it.</p> <p>Name of authors: A. SOUTHERN, M. OTTER, M. REICHEL</p>			
** NAME OF ESA STUDY MANAGER G.F. BLOCK DIV: FMDIRECTORATE: D/TEL	** ESA BUDGET HEADING 60.512		

* Sections to be completed by ESA

** Information to be provided by ESA Study Manager

ABSTRACT

This study covers the investigation of various techniques in order to optimize the use of radio frequency spectrum. Of primary interest are modulation schemes, filter and pulse shaping techniques which allow a significant reduction in occupied bandwidth at the expense of a slight system degradation and a moderate increase of hardware complexity. Radio frequency spectrum is a very limited resource and an allocated bandwidth must often be shared by several services. It is becoming increasingly difficult to identify a quasi interference-free environment for new ESA missions, in particular, if currently used bandwidth-inefficient modulation schemes require coordination of a much wider bandwidth than actually needed. New bandwidth efficient and interference resistant spectrum shaping techniques are consequently required. This will better protect ESA missions from RFI and reduce the rapidly increasing burden of coordination. An important factor for efficient use of available frequency band are unwanted emissions. These comprise spurious emissions and higher order lobes of the data spectrum, so-called out-of-band emissions. Spectral masks are proposed for out-of-band emissions as well as for spurious emissions. A detailed investigation on the impact of several non-linear high power amplifier implementations has been carried out. Various types of filters, number of poles and bandwidth-time products (BT) have been investigated. All possible locations in the transmission path for placing a spectrum shaping component have been taken into account. The results of the study are reflected in a set of recommendations and spectral masks with the objective to maximize the efficient use of frequency spectrum.

TABLE OF CONTENTS

INTRODUCTION	1
Study Objectives and Background	1
Scope of the Activity	2
SYSTEM CHARACTERISTICS AND TECHNICAL SPECIFICATIONS	3
SELECTION OF SUITABLE SPECTRUM SHAPING TECHNIQUES AND	
DEFINITION OF PERFORMANCE OBJECTIVES	5
Suppressed Carrier Modulation Schemes for Medium to High Data Rate Transmissions	5
Unfiltered Spectra of Suppressed Carrier Modulation Schemes	6
Occupied Bandwidth of Suppressed Carrier Modulation Schemes without Shaping	6
Subcarrier Modulation	7
Conditions Requiring the Use of a Telemetry Subcarrier	8
Occupied Bandwidth of Unfiltered PCM/PM/PSK with Sinewave Subcarriers	12
Recommendations for the Use of Subcarriers	15
Bi- ϕ Modulation on a Residual Subcarrier	18
Occupied Bandwidth Comparison of Modulation Techniques	19
SHAPING TECHNIQUES AND PERFORMANCE ASSESSMENT	20
Investigation of Suitable Shaping Techniques	20
Techniques Applied at RF Level	20
Techniques Applied at IF Level	26
Techniques Applied at Baseband Level	38
Calculation of Overall System Degradation without Performance Optimisation	46
DETAILED OVERALL PERFORMANCE ASSESSMENT AND OPTIMISATION OF	
SELECTED TECHNIQUES	49
Selection of Preferred Shaping Techniques	49
Identification of Suitable Equalisation Techniques in Receiver	49
Calculation of Overall Degradation with System Optimisation	51
Comparison of Hardware Complexity for the Identified Techniques	56
EXTERNAL INTERFERENCE SUSCEPTIBILITY ASSESSMENT	56
Susceptibility to Narrowband RFI	56
Susceptibility to Wideband RFI	57
Susceptibility to Pulsed RFI	57
DEFINITION OF SPECTRAL MASKS FOR UNWANTED EMISSIONS	59
Definition of a Suitable Mask for the Data Spectrum	59
Definition of a Suitable Spectral Mask for Spurious Components	61
Discrete Lines inside the wanted signal	61
Discrete Lines outside the wanted signal	62
RECOMMENDATIONS	65
REFERENCES AND APPLICABLE DOCUMENTS	67

1 INTRODUCTION

1.1 Study Objectives and Background

Radio frequency spectrum is a very limited resource and an allocated bandwidth must often be shared by several services. Of particular interest are frequencies below a few GHz because of favourable propagation conditions and attractive antenna designs. ESA, as well as most other space agencies, depend on a very limited number of useful frequency bands for payload data transmissions, launching and operating its spacecraft. This applies to the support of science, telecomm and Earth observation missions, equally.

The main objective of the proposed study is a comprehensive and detailed investigation of technical means to improve spectrum efficiency without any significant financial or performance burdens. A number of frequency bands have been identified for the purpose of this study. The available bandwidth in the lower and most heavily used bands is small and has to be shared with an ever increasing number of both inter-service as well as intra-service users. Interference cases with operational impacts have already been encountered and it is evident that the general probability of interference is approaching the limit of acceptability. It is consequently becoming increasingly difficult to identify a quasi interference-free environment for new ESA missions, in particular, if currently used bandwidth-inefficient modulation schemes require coordination of a much wider bandwidth than actually needed. New bandwidth efficient and interference resistant spectrum shaping techniques are consequently required and shall be introduced in ESA as well as in an international environment as soon as possible. This will better protect ESA missions from RFI and reduce the rapidly increasing burden of coordination.

An important factor for efficient use of available frequency band are unwanted emissions. These comprise spurious emissions and higher order lobes of the data spectrum, so-called out-of-band emissions. Regarding out-of-band emissions, bandwidth efficient and interference robust spectrum shaping techniques which minimize mutual interference between ESA missions and other users of frequency spectrum have been studied. This comprised an investigation of methods for the reduction of the occupied bandwidth of various modulation and baseband processing techniques. A trade-off regarding the identified techniques versus link performance and implementation complexity has been carried out.

A limited set of spectrum shaping techniques which can meet a spectral mask requirement has been identified during the trade-off analysis. The study results will be internationally promoted in SFCG, CCSDS and ITU with the objective of being adopted by space agencies, as standard techniques for good frequency management on a world wide basis. The study results will demonstrate that the sharing situation can be greatly improved by applying the derived techniques.

The results of this study will be brought to the attention of the above groups in a suitable format. Of particular importance has been the Space Frequency Coordination Group (SFCG) because of its international group of frequency managers with participants from all major space

agencies. The less formal and more flexible environment in the SFCG, as compared to the official organs of the International Telecommunication Union (ITU), appears to be optimum for an initial introduction of the results derived by this study.

1.2 Scope of the Activity

The scope of this activity comprised bandwidth and power efficient as well as interference robust modulation techniques. An assessment of a limited set of spectral shaping techniques has been carried out in detail in terms of occupied bandwidth reduction, performance degradation and implementation complexity. Spectral masks for unwanted emissions have been identified which control both out-of-band and spurious emissions. The study has also taken into account practical aspects such as hardware complexity, operational constraints and technical limitations. A prime task was the definition of a spectral mask for medium to high data rate transmissions and a selection of suitable spectral shaping techniques which can achieve this objective. The mask was defined based on minimum spectral occupation together with reasonable degradation and hardware complexity. The mask and the corresponding shaping techniques are applicable to transmission techniques which typically occupy a bandwidth in excess of several hundred kilohertz.

In view of the difficulty to introduce any limitation on spectral emissions, the study covered a wide range of available techniques and a careful final selection of a subset thereof based on practical and performance justifications.

2 SYSTEM CHARACTERISTICS AND TECHNICAL SPECIFICATIONS

Minimum set of modulation techniques: BPSK, QPSK, OQPSK, GMSK
PCM/PM/PSK, PCM/PM/Bi- ϕ

Data rate range: 10 kb/s to 300 Mb/s

Required bit error rate: $< 10^{-5}$

Acceptable degradation: < 0.5 dB for BPSK (tentative)
 < 0.8 dB for QPSK (tentative)

Spectral density maximum of RF signal: $< 40 - 10 \times \log(\text{symbol rate})$ dBc in any 1 kHz

The identified techniques shall be usable in some or all of the frequency bands listed in Table 1.

Frequency Band (MHz)	Allocated Service	Direction	Allocation Status
2025 - 2110 2110 - 2120	SR, SO, EES SR (DS)	Earth-space Earth-space	PRIMARY PRIMARY
2200 - 2290 2290 - 2300	SR, SO, EES SR (DS)	Space-Earth Space-Earth	PRIMARY PRIMARY
7145 - 7190 7190 - 7235	SR (DS) SR	Earth-space Earth-space	FN (Art.14) FN (Art. 14)
8025 - 8400 8400 - 8450 8450 - 8500	EES SR (DS) SR	Space-Earth Space-Earth Space-Earth	secondary PRIMARY PRIMARY
14000 - 14300 14400 - 14470 14500 - 15350	SR SR SR	Space-Earth Space-Earth Space-Earth	secondary secondary secondary
16600 - 17100	SR	Earth-space	secondary
31800 - 32300 34200 - 34700	SR (DS) SR (DS)	space-Earth Earth-space	PRIMARY PRIMARY
37000 - 38000 40000 - 40500	SR SR	Space-Earth Earth-space	PRIMARY PRIMARY

Table 2 contains the currently specified ESA values for occupied bandwidth for reference with respect to the improvement factor.

Frequency Band (MHz)	Function		Maximum Occupied Bandwidth (kHz)
2025 - 2120	Telecommand (8 kHz subcarrier)	Category A and B	66
	Telecommand (16 kHz subcarrier)		132
2025 - 2110	Ranging Earth-Space (Category A)		1200
2110 - 2120	Ranging Earth-Space (Category B)		2400
2200 - 2290	Telemetry (symbol rate < 8 ksymb/s)		240
and	Telemetry (8 ksymb/s ≤ symb. rate ≤ 60 ksymb/s)		1700
8450 - 8500	Telemetry (symbol rate > 60 ksymb/s)		2000 or 6 × symbol rate, whichever is larger
2200 - 2290 and 8450 - 8500	Ranging Space-Earth (Category A)		1200
2290 - 2300	Ranging Space-Earth (Category B)		3000
8025 - 8400	Telemetry Earth-to-Space (Category A)		TBD
2290 - 2300 and 8400 - 8450	Telemetry Ranging Space-Earth (Category B)		3000

Spurious emissions: < -60 dBc (within a reference bandwidth of 100 Hz)

Symbol clock synchronisation: < ± 2% of the symbol period or 1 nanosecond, (whichever is larger)

Phase noise of the unmodulated carrier: < 2° RMS around 2 GHz
< 6° RMS around 8 GHz
(integrated between 10 Hz and 1 MHz)

3 SELECTION OF SUITABLE SPECTRUM SHAPING TECHNIQUES AND DEFINITION OF PERFORMANCE OBJECTIVES

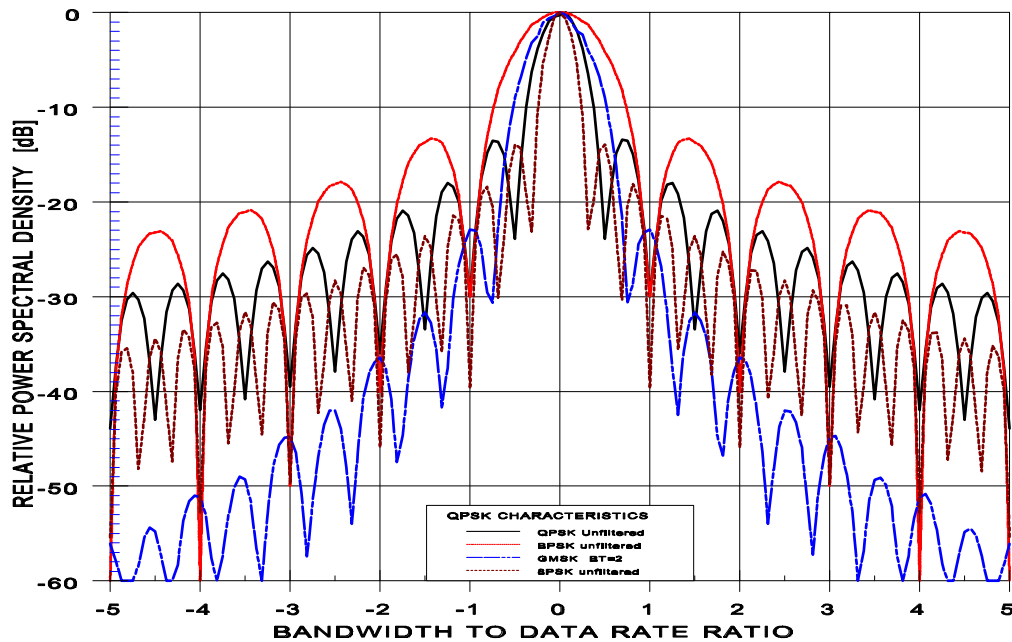
3.1 Suppressed Carrier Modulation Schemes for Medium to High Data Rate Transmissions

As the first activity, a suitable set of modulation schemes has been identified for transmission of data rates typically in excess of 100 kb/s. It has been taken into account that the identified modulation techniques shall also be suitable for transmission down to 10 kb/s. The technical specifications provided by ESA listed a minimum set of techniques to be studied. This list has been amended by one additional modulation schemes which is considered as an attractive candidate. It is referred to as Octal PSK (OPSK), also known as 8-PSK. Other bandwidth efficient modulation techniques have been described in literature. However, for reasons of cost and world wide standardisation, the introduction of entirely new modulation schemes has been found not suitable. After all, enormous investments are effected and the proposed schemes shall be implementable with a minimum of effort.

Many different modulation techniques are in use for various applications. Space services have usually a requirement for data transmissions over long distances in a power limited environment. Modulation techniques that operate satisfactorily at low signal-to-noise ratios are consequently often applied. Such modulation techniques are typically based on Phase Shift Keying (PSK), which is accomplished by switching the phase of a continuous sine wave between opposite states at a frequency proportional to the symbol rate. This signal can then either be amplified and transmitted directly as an RF signal or modulated onto another RF carrier. The former one is called suppressed carrier modulation and the latter is referred to as subcarrier modulation.

The following section covers suppressed carrier modulation schemes of interest to space radio communications. The most promising modulation schemes for a future standard have been selected for this study. These are Quaternary Phase Shift Keying (QPSK), Offset QPSK (OQPSK), 8PSK and Gaussian filtered Minimum Shift Keying (GMSK). Binary Phase Shift Keying (BPSK) has been taken as the reference. Of particular interest are spectral density distribution, cumulative power, inter symbol interference degradation and susceptibility to external interference. The effect of filtering QPSK signals and the impact of a non-linear amplification process are addressed.

Suppressed carrier modulation methods require in general a much smaller bandwidth than subcarrier methods. In addition, any filtering is more effective as there are no gaps between spectral components. The investigated modulation schemes have all in common that the carrier is directly modulated. With ideal data, i.e. no data imbalance and no asymmetry, a continuous spectrum without any individual line components is available. The modulation process is based upon either phase switching in the case of all PSK schemes or a continuous phase transition for GMSK. An intermediate solution is baseband filtering by means of pulse shaping of bits which then enter a linear PSK modulator.



3.1.1 Unfiltered Spectra of Suppressed Carrier Modulation Schemes

The modulation schemes QPSK, OQPSK, 8PSK and GMSK have been identified as candidates for suitable medium to high data rate modulation techniques and have been investigated with respect to their spectral distribution and performance. For comparison, and serving as the reference, BPSK has also been included. PSK techniques are well established and relevant information can be found in many text books. GMSK is a rather new technique. Figure 1 shows a comparative set of unfiltered spectra for BPSK, QPSK, 8PSK and GMSK.

It can be seen that unfiltered PSK rolls off very smoothly. At 10 times the data rate, for example, the spectral density has only decreased by 30 dB and can consequently still create significant interference to other users.

BPSK and conventional QPSK do not have a constant envelope any longer when filtered. A non-linear power amplifier operating close to saturation will restore the filtered part of the spectrum to a significant extent. With QPSK, an additional degradation may occur due to cross talk between the I and Q channels. For design complexity reasons, filtering is often implemented before the high power amplifier, and preferably at IF level. Any kind of continuous phase modulation allows driving a power amplifier in the most efficient operating point. GMSK is a special case of a minimum shift keyed signal with Gaussian shaped baseband pulses.

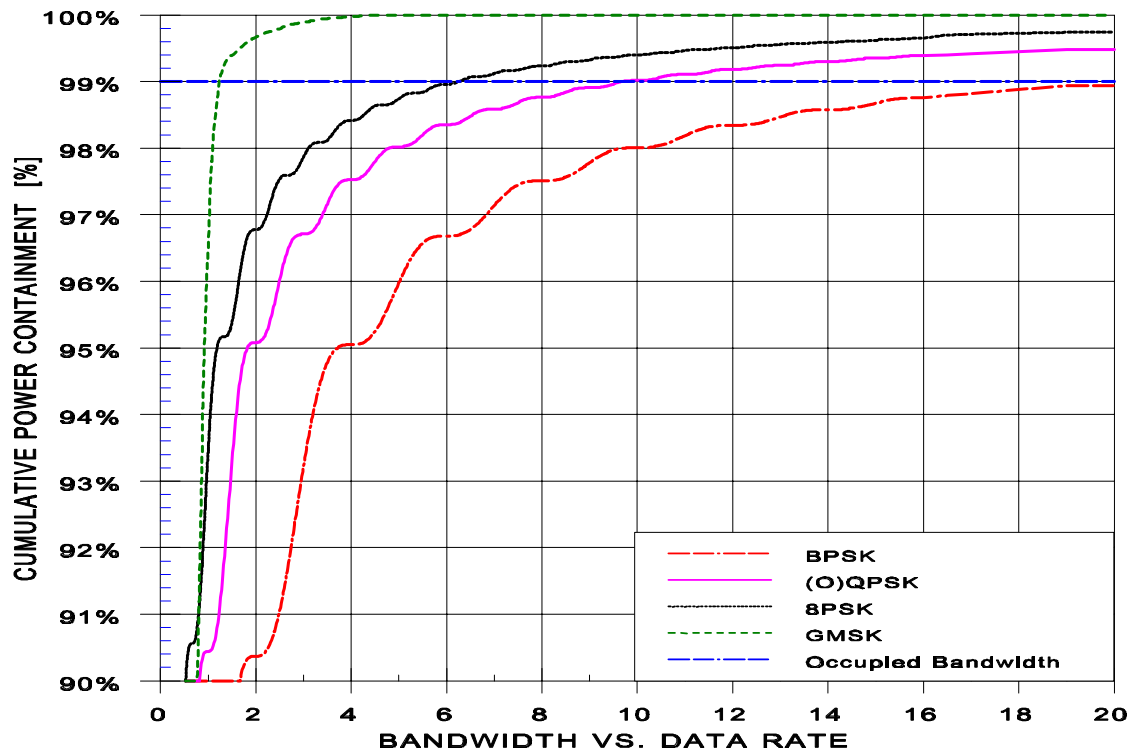
3.1.2 Occupied Bandwidth of Suppressed Carrier Modulation Schemes without Shaping

The occupied bandwidth of the identified set of modulation schemes has been calculated disregarding for the time being spectral shaping techniques. The obtained results provide a relative comparison between the identified techniques and also serve as the baseline for the achievable improvement factor.

Figure 2 shows the cumulative power of BPSK, (O)QPSK, 8PSK and GMSK as a function of the normalized bandwidth. The definition of data rate is in this case the total symbol rate

entering the modulator. The spectrum of QPSK and OQPSK is identical. For GMSK very moderate filtering ($BT=2$) has been applied. It is in fact possible to suppress the side lobes almost entirely when increasing the filtering on the pulses. However, for typical space communication applications, moderate filtering is sufficient.

It is shown that GMSK, with very moderate filtering, concentrates 99% of its energy in the main lobe, whereas (O)QPSK requires 5 times the data rate and BPSK even 10 times the data rate before the 99% power containment is reached.



3.2 Subcarrier Modulation

Subcarrier modulation is a transmission technique which has been used for several decades. The use of subcarrier modulation results often in inefficient use of frequency spectrum if operating parameters are not selected carefully. A careful assessment of technical and operational constraints for the use of subcarrier modulation has been made in this section. The conditions for the use of subcarrier modulation have been investigated and boundaries have been derived with respect to practical limits for subcarrier frequency to symbol rate ratios.

3.2.1 Conditions Requiring the Use of a Telemetry Subcarrier

This section attempts to derive reasonable limits for data rates, above which the use of subcarriers is not required from a technical point of view. The use of subcarrier modulation is in general discouraged as it often results in inefficient use of frequency spectrum. With the rapid increase of radio frequency systems in certain favourable parts of the spectrum, mutual interference is becoming unavoidable and shall be reduced as far as possible. A brief overview of reasons and requirements for using subcarriers is given below and some conclusions are derived as to the use of alternative techniques which are more spectrum efficient.

In the past, a number of technical reasons have lead to the implementation of subcarrier modulation which has been a widely used technique for data transmission up to around 100 kb/s. The main reasons for using a subcarrier have been:

1. To allow adequate power allocation to carrier, telemetry and ranging channels. This is of particular importance for low to medium rate data transmissions where insufficient power for the carrier recovery would be available with suppressed carrier systems. In addition, the data signal must be separated from the carrier in such a way, that it creates negligible interference in the carrier loop bandwidth.
2. To separate the telemetry signal from the telecommand signal on transponders which feed through all signal components within the ranging bandwidth. The telecommand subcarrier frequency is either 8 or 16 kHz with a maximum data rate of 4 kb/s. For ranging, a major tone of 100 kHz is often used. The subcarrier for the telemetry signal must be selected such, that the distance to the ranging and/or telecommand signal is greater than the armfilter bandwidth in the data demodulator.
3. To enable a simple sweep search for the carrier over the full frequency uncertainty range (oscillator instability and Doppler) during the acquisition phase without the risk of locking onto a data sideband. Around 2 GHz a maximum Doppler ± 110 kHz in coherent mode and around ± 100 kHz in non-coherent mode can occur.
4. To separate different types of data by putting them on several subcarriers. Data from different payloads, housekeeping telemetry and ranging signals have often been distinguished by modulating a separate subcarrier.

Regarding telecommand feedthrough, a transponder can in principle be designed in such a way that the telecommand spectrum is filtered out. This requires one additional filter on-board but has also the advantage of slightly improved ranging signal quality.

A carrier search over the full frequency uncertainty range is practically never required as the orbit of a spacecraft is normally known well enough to predict the carrier to within a few kHz. For the initial acquisition in non-coherent mode, some knowledge of the oscillator stability results also in a limited search area. Most receivers are equipped with the capability to search over a specified range around the expected centre frequency which is derived from an orbit generator.

The introduction of virtual channels eliminated the requirement for using separate subcarriers for individual data streams.

Adequate power distribution to the carrier, telemetry and ranging channels is the only reason where physical limitations require the use of a subcarrier. A carrier recovery and tracking loop needs a relatively high signal-to-noise ratio for rapid carrier acquisition and low bit error rate degradation due to phase noise. Required values range typically between 10 and 18 dB, depending mainly if and what kind of channel coding is applied. On the other hand, the same channel coding results in reduced E_b/N_0 requirements ranging typically between 3 and 10 dB. A carrier recovery loop based on a suppressed carrier system would suffer from at least 6 dB squaring loss. The signal-to-noise ratio in the carrier loop is also determined by the loop bandwidth to which limits are set by orbital dynamics. This leads to a situation where data have to be modulated onto a subcarrier depending on data rate and orbital dynamics as otherwise insufficient power will be available in the carrier recovery loop.

The tables below give an idea what typical performance characteristics could be expected for a second order tracking loop. In order to acquire and track a low power signal, the loop bandwidth B_l has to be small. The required loop bandwidth is determined by the signal to noise density ratio S/N_0 , the squaring loss and the required signal to noise ratio in the loop, which is typically 15 dB.

For a second order loop with a damping factor $\xi = 0.7$, the maximum permissible rate of input frequency change (max. tracking rate) is given by [8]:

$$\Delta \dot{f} = 0.57 B_l^2 \text{ [Hz/s]}$$

This parameter determines the maximum sweep rate (typically half of the maximum tracking rate) as well as the maximum frequency rate uncertainty. The latter is determined mainly by the accuracy with which spacecraft velocity and position can be determined. The spacecraft velocity can normally be predicted with an error of better than 1% but the Doppler rate uncertainty can be significantly larger if the spacecraft position is not known within a few seconds.

The lock-in range is the maximum frequency deviation between the loop reference and the actual signal over which the loop will successfully lock. It is given by [9]:

$$\Delta f_m = 0.785 B_l \text{ [Hz]}$$

In ESA, a value of $0.42 B_l$, which is derived from [8], is often used. The acquisition or pull-in time is given by [8]:

$$t_p = 4.2 \frac{\Delta f^2}{B_l^3} [s]$$

Regarding Δf , the oscillator instability is the main source for frequency errors in non-coherent modes. The transmit carrier stability over the full operating range (mainly temperature and lifetime) is typically $\pm 10^{-5}$. A medium term stability of 10^{-6} has been assumed based on some knowledge of the operating temperature and the ageing trend. The resulting frequency offset is normally too large for a direct pull-in so that a sweep over the expected frequency uncertainty will be required. A value corresponding to half of the maximum permissible rate of input frequency change is normally taken for the sweep rate and has been assumed for the calculations. In coherent mode, the Doppler uncertainty is the dominating factor for the frequency offset.

Frequency uncertainties can vary over a wide range depending on the oscillator quality, the type of orbit and the accuracy with which predictions can be made. In general, it can be stated that near earth missions involve typically high frequency uncertainties due to orbit perturbations and high relative velocities. Deep space missions allow often very good frequency predictions due to stable orbits. The frequency uncertainty of geostationary spacecraft is mainly determined by oscillator instabilities.

Tables 3 and 4 give an impression what system characteristics can be expected for uncoded and coded transmissions. A carrier signal-to-noise ratio of 15 dB has been assumed as required. Together with the available E_b/N_0 this leads to the required maximum loop bandwidth. The resulting pull-in range and acquisition times can then be calculated. It can be concluded that the limit for using suppressed carrier modulation and subcarrier modulation is in the area of a few kilohertz. The characteristics used in the calculations are believed to be typical for a wide range of satellite systems. Special cases may occur for which also for higher data rates a subcarrier may be required. The results are intended to give an idea on the conditions which require the use of a telemetry subcarrier.

Figure 3 shows the carrier signal-to-noise ratio versus the symbol rate. Typical carrier loop bandwidths of 10 and 100 Hz have been assumed and the 2 cases of uncoded ($E_b/N_0 = 9.6$ dB) as well as coded ($E_b/N_0 = -1.2$ dB) transmissions have been considered. The coded case (CCSDS standard concatenated code, $K=7$, $R = \frac{1}{2} \cdot 223/255$) is the more critical one because of the reduced power due to the coding gain.

REPORT CONCERNING CCSDS RADIO FREQUENCY AND MODULATION

ADVANCED SPECTRUM SHAPING FOR EFFICIENT BANDWIDTH UTILISATION

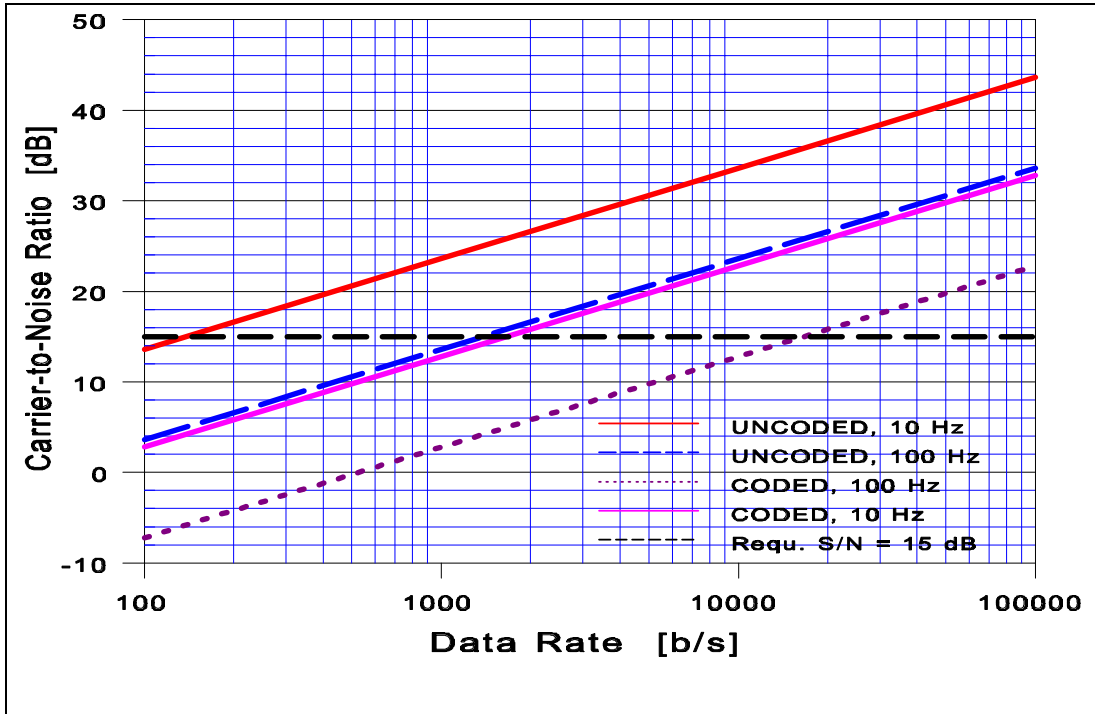
Symbol rate	100	1000	10000	b/s
Energy per symbol, E_s/N_0 (uncoded case)	9.6	9.6	9.6	dB
Signal to noise density ratio, S/N_0	29.6	39.6	49.6	dBHz
Minimum squaring loss	6.0	6.0	6.0	dB
Required S/N in carrier loop	15.0	15.0	15.0	dB
Loop bandwidth to obtain the requ. S/N	7.2	72.4	724.0	Hz
Maximum carrier frequency	2300.0	2300.0	2300.0	MHz
Maximum frequency uncertainty	3000.0	3000.0	3000.0	Hz
Lock-in range (without sweep)	5.7	56.9	569.0	Hz
Max. frequency rate uncertainty (near earth)	500.0	500.0	500.0	Hz/s
Maximum tolerable frequency change rate	29.9	2990.0	299000	Hz/s
Mean acquisition time with sweep	100.3	1.0	0.01	s

Symbol rate	100	1000	10000	b/s
Energy per symbol, E_s/N_0 (coded case)	-1.2	-1.2	-1.2	dB
Signal to noise density ratio, S/N_0	18.8	28.8	38.8	dBHz
Minimum squaring loss	6.0	6.0	6.0	dB
Required S/N in carrier loop	15.0	15.0	15.0	dB
Loop bandwidth to obtain the requ. S/N	0.6	6.0	60.0	Hz
Maximum carrier frequency	2300.0	2300.0	2300.0	MHz
Maximum frequency uncertainty	3000.0	3000.0	3000.0	Hz
Lock-in range (without sweep)	0.5	4.7	47.3	Hz
Max. frequency rate uncertainty (near earth)	500.0	500.0	500.0	Hz/s
Maximum tolerable frequency change rate	0.2	20.7	2070.0	Hz/s
Mean acquisition time with sweep	14500.0	144.9	1.4	s

Due to orbital dynamics, the loop bandwidth for near earth missions is typically rather wide but on the other hand, a high E_b/N_0 is normally available. For deep space missions loop

bandwidths in the order of 1 Hz are often feasible. Bi-phase modulation should always be preferred if the data spectrum falls outside the loop bandwidth.

The fact that subcarrier modulation is in general less power efficient has not been considered. This is due to the presence of 2 signal components and losses associated with the modulation process, in particular for sine wave modulation.



3.2.2 Occupied Bandwidth of Unfiltered PCM/PM/PSK with Sinewave Subcarriers

The occupied bandwidth of an ideal non-filtered PCM/PSK/PM signal modulated onto a sinewave subcarriers is determined by Bessel function components together with the $\{\sin(x)/x\}^2$ distribution of a PSK signal. Both are listed in Appendix A. The power distribution in the spectrum follows the equation:

$$P = \int_{f-f_0}^{f+f_0} [J_0^2(m) + 2\sum J_i^2(m) S_{\theta} + 2\sum J_k^2(m)] df$$

J_i are the odd Bessel components which are multiplied with the frequency shifted spectrum $S_{(f)}$ for PSK/NRZ. J_k are the even Bessel components where the power is contained in a spectral line. A program has been used which can calculate the occupied bandwidth by actually integrating

the spectrum in steps of 0.1 times the symbol rate until the power accumulated exceeds 99% of the total signal power.

Figure 4 shows the calculated occupied bandwidth up to a subcarrier-to-symbolrate ratio of 10. For higher data rates it is desirable to keep the subcarrier-to-symbolrate ratio as small as possible.

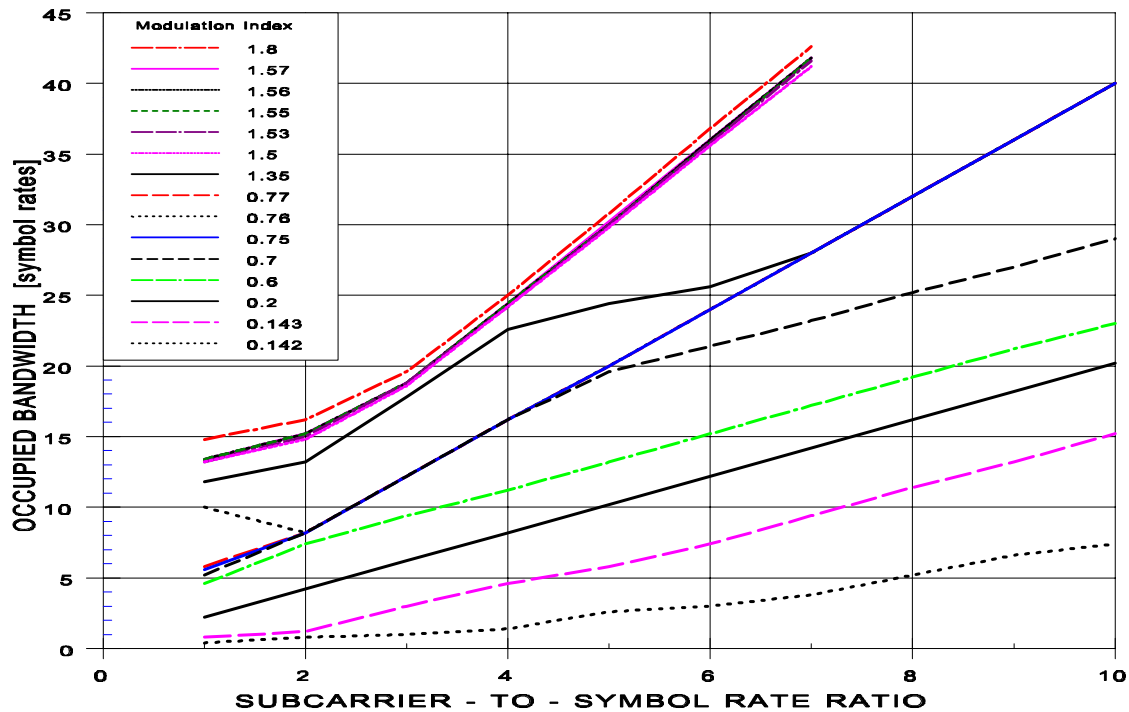
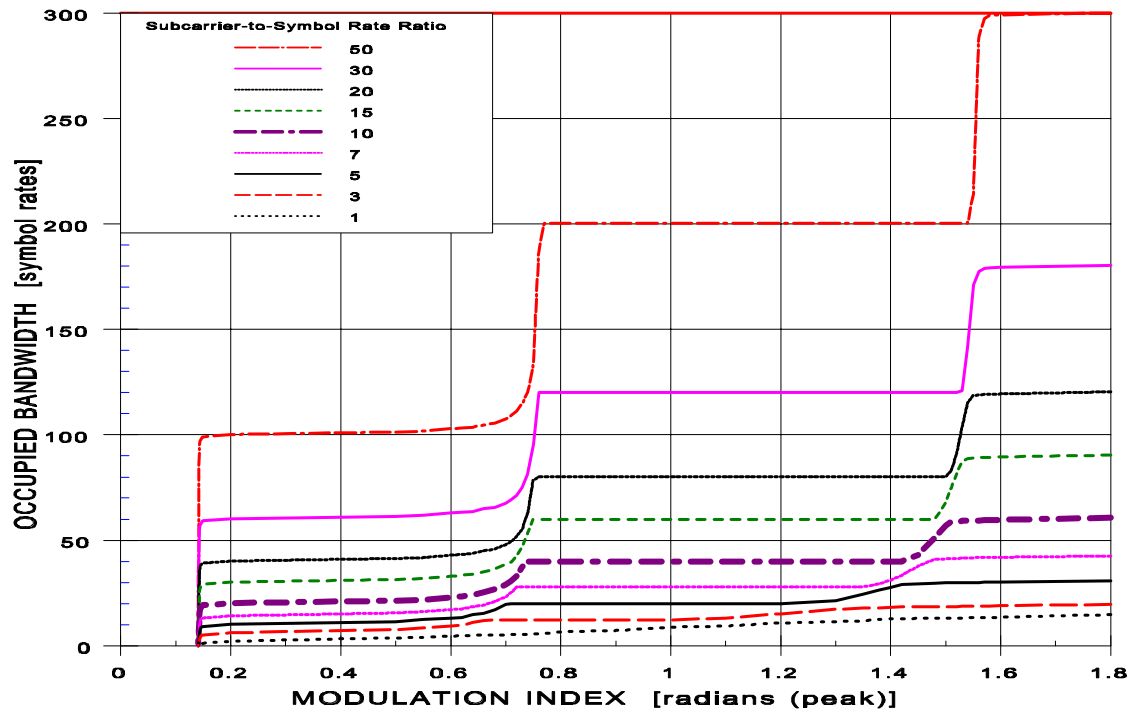


Figure 5 shows the occupied bandwidth versus the modulation index with the subcarrier - to - symbolrate ratio as parameter. As expected from the magnitudes of the Bessel components, the curves clearly show the transition areas where higher order Bessel components start contributing significantly to the total signal power.

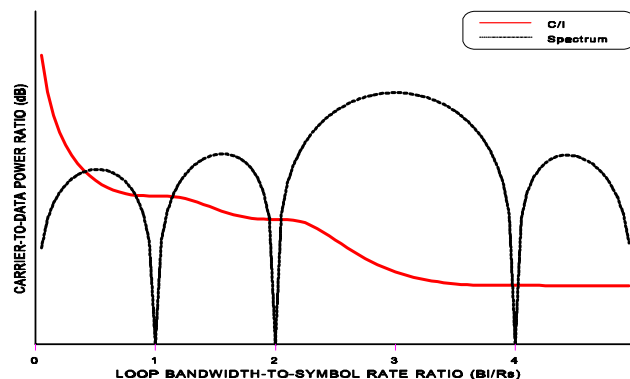
It shall be noted that the calculated bandwidths are theoretical values which may deviate from the real value as in practice a number of bandlimiting effects usually reduce or cut-off high frequency components before the signal is actually emitted.



3.2.3 Recommendations for the Use of Subcarriers

Part of the spectrum of the data modulated onto the subcarrier falls into the carrier tracking loop bandwidth and reduces the carrier-to-noise plus interference ratio $C/(N+I)$. Figure 6 illustrates the variation of the carrier-to-data power ratio versus an increasing loop bandwidth. It can be seen that the C/I reduces the fastest where the spectrum has its maxima. For this example, a sinewave subcarrier with a subcarrier-to-symbol rate ratio of 3 has been selected.

The C/I is not only a function of the loop bandwidth but also of the modulation index and the subcarrier-to-symbol rate ratio. The modulation index and the loop bandwidth are mission dependent and consequently not freely selectable. The subcarrier-to-symbol rate ratio n is the only parameter which can be selected in order to minimize the occupied bandwidth.



Figures 7 and 8 show the C/I versus the bandwidth-to-symbol rate ratio for $n = 4$ and $n = 10$ for a sinewave subcarrier typically employed with Category A missions. The modulation index has been selected as parameter. For Category A, a maximum degradation of 0.3 dB is normally considered acceptable. For uncoded transmissions, the phase noise impact on the data demodulation requires a $C/(N+I)$ of approximately 10 dB to meet this requirement. For concatenated coding in accordance with CCSDS recommendations, a $C/(N+I)$ of 15 dB is required. In order to meet a $C/(N+I)$ of 10 dB and 15 dB, it is suggested that a C/I of 15 dB and 20 dB, respectively, be considered as performance criterion for determining the minimum n . An operational range between 15 and 20 dB has been marked in the figures.

In order to achieve a high C/N with a low power signal, the loop bandwidth B_l shall be small. Orbital dynamics and phase noise set limits to the lower bound of the loop bandwidth. A low Earth orbiter with an orbit height of 300 km can have a worst case frequency change rate of around 5 kHz/s at a transmission frequency of 2290 MHz. This would require a loop bandwidth of around 90 Hz.

An estimation of practical loop bandwidth-to-symbol rate ratios is needed. According to the CCSDS Green Book on Earth station capabilities, loop bandwidths between 30 Hz and 3000 Hz, and symbol rates above 10 s/s can be supported by most agencies. In theory, this may allow high loop bandwidth-to-symbol rate ratios but in practice, such cases are rarely found.

A typical carrier loop bandwidths of 300 Hz for Category A missions has been assumed. Most of these missions operate with symbol rates in excess of 500 b/s and loop bandwidths of less than 300 Hz, so that a loop bandwidth-to-symbol rate ratio of typically less than one will be encountered in practice. In the extremely rare case where a very low bit rate is encountered in connection with a high loop bandwidth, the modulation index has to be selected such, that the carrier power will be significantly higher than the data power, which then automatically results in a lower C/I for a constant n .

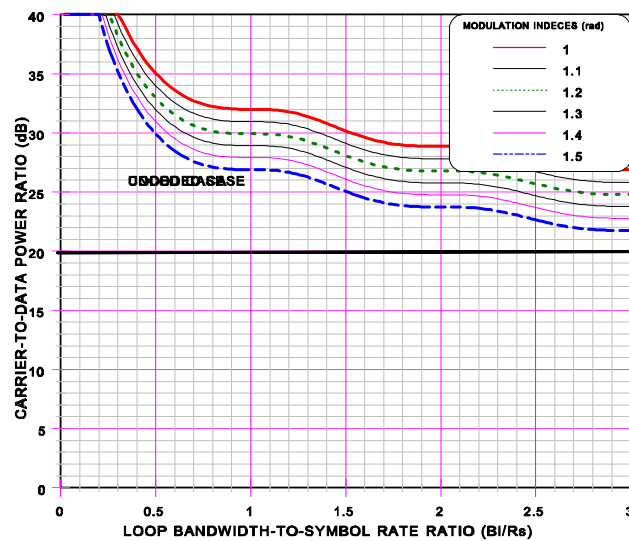
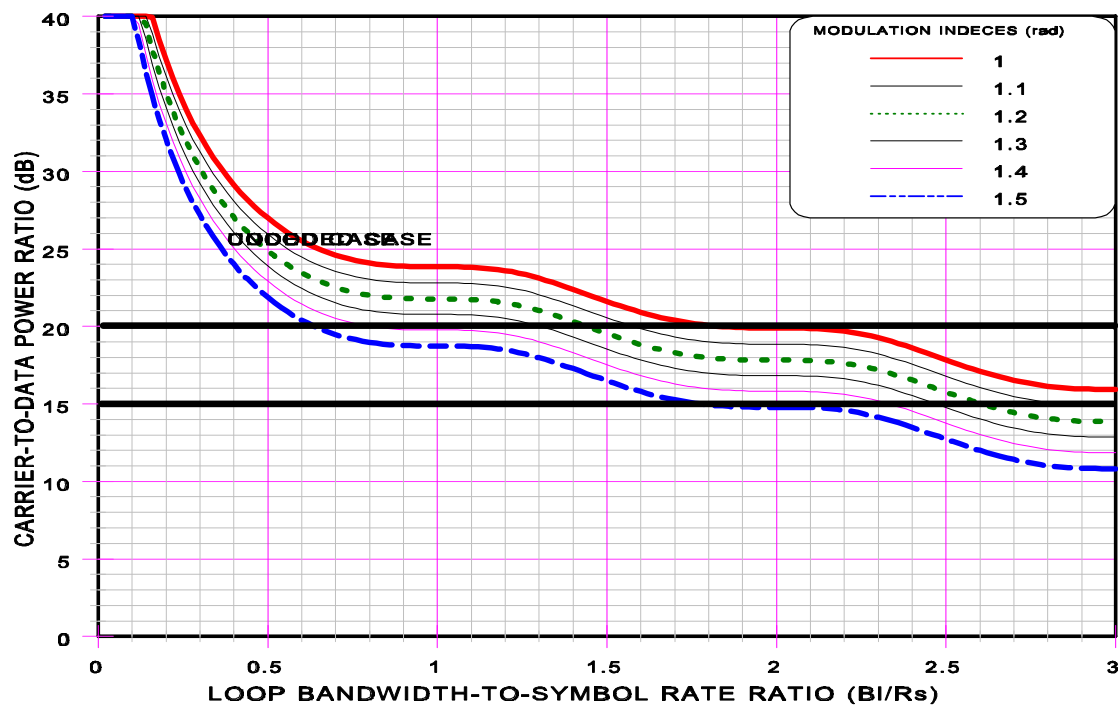
It shall be noted that CCSDS recommendation 2.4.3 specifies a minimum subcarrier frequency of 20 kHz. This will automatically lead to values of n up to 2000 for symbol rates of 10 s/s. However, the required occupied bandwidth is small in absolute terms and a high value of n is of no concern for low symbol rates as long as the subcarrier frequency is limited.

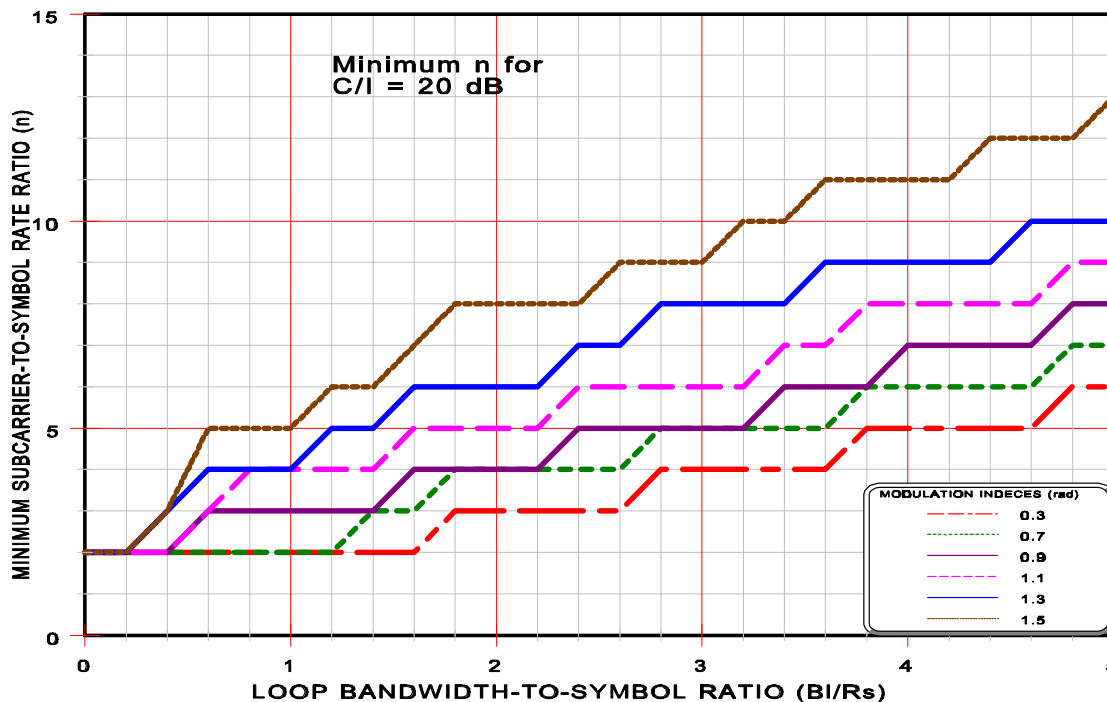
For Category A missions, a PCM/PSK/PM modulation scheme with a sinewave subcarrier is typically employed for transmission of low data rates. The subcarrier frequency-to-symbol rate (R_s) ratio, n , should be minimized to avoid unnecessary occupation of frequency spectrum. The lowest value of n can be determined by the amount of acceptable interference from the data spectrum into the carrier tracking loop bandwidth (B_l). For Category A missions, a degradation of 0.3 dB in the symbol detection process shall not be exceeded, which, for CCSDS recommended coding schemes, requires a $C/(N+I)$ in the carrier tracking loop of 15 dB. The N/I shall be at least 5 dB which would result in an acceptable C/I of around 20 dB.

For rather small ratios of symbol rate to carrier tracking loop bandwidth, the modulation index has to be adjusted accordingly in order to achieve the required loop SNR resulting in a nearly constant C/I versus B_l/R_s . In the presence of a telemetry signal only, a minimum value of $n=4$ is in general sufficient to obtain the required performance under typical operating conditions.

For higher symbol rates, the presence of a telecommand feed-through and/or ranging signal may require the selection of higher values of n . For higher symbol rates, an upper value of $n=10$ can be considered in agreement with good spectrum engineering. CCSDS recommendation 2.4.3 specifies a minimum subcarrier frequency of 20 kHz with a preference around 60 kHz for systems using the standard tone ranging.

The minimum values of n in order to meet the required C/I of 20 dB is shown in figure 9 for Category A missions.



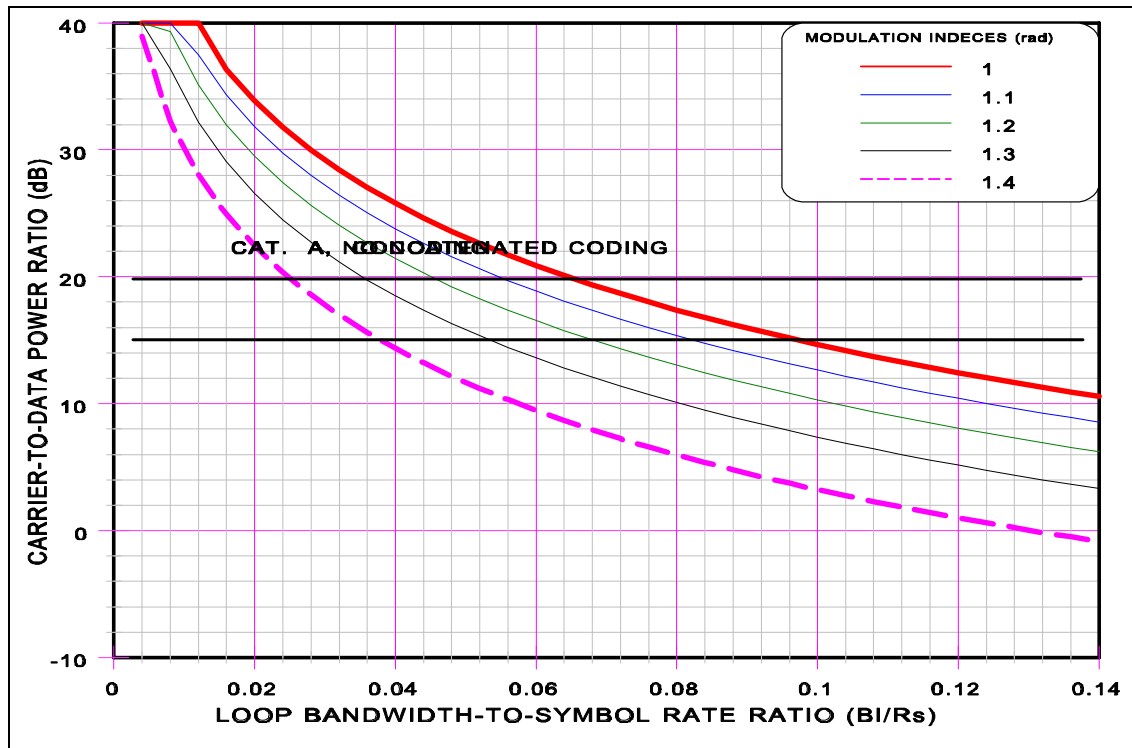


It can be recommended that the subcarrier frequency shall not exceed 60 kHz for symbol rates below 6 ks/s and that a subcarrier frequency-to-symbol rate ratio between 4 and 10 be selected for symbol rates above 6 ks/s. A subcarrier frequency-to-symbol rate ratio of 4 for sinewave subcarriers is sufficient to achieve the required performance in the absence of telecommand feed-through and ranging signals.

3.3 Bi- ϕ Modulation on a Residual Subcarrier

For symbol rates above approximately 50 ks/s, subcarriers shall be dispensed with and replaced by Bi-Phase modulation or suppressed carrier modulation. Figure 10 shows the C/I versus the loop bandwidth-to-symbol rate ratio for Bi-Phase modulation. It can be seen that high modulation indices, which are typical for this type of modulation, as sufficient power is normally available in the residual carrier, require a loop bandwidth-to-symbol rate ratio of around 0.02 in the worst case. For a typical Category A loop bandwidth of 300 to 1000 Hz, this would allow Bi-Phase modulation only for data rates in excess of 15 to 50 ks/s when high performance channel coding is used. Without channel coding, a C/N of around 10 dB and consequently a C/I of around 15 dB would be sufficient.

It is recommended that Figure 10 be taken into account for the operating conditions of PCM/PM/BI-PHASE modulation on a residual RF carrier.



3.4 Occupied Bandwidth Comparison of Modulation Techniques

Figure 11 shows a comparison between various suppressed carrier modulation techniques, subcarrier modulation techniques with various n and Bi-phase modulation. It is interesting to note that for the recommended range $4 \leq n \leq 10$, subcarrier modulation is actually more bandwidth efficient. For the suppressed carrier modulation techniques, the carrier power has been determined by the power that is available in a typical carrier recovery circuit. For BPSK a squaring loss of 6 dB has been assumed and for QPSK a double squaring loop with 12 dB squaring loss. This leads to factors of 0.25 (-6 dB) for BPSK and 0.063 (-12 dB) for QPSK. No representative values are available for 8PSK and GMSK. They have arbitrarily been set to the same value as for QPSK.



4 SHAPING TECHNIQUES AND PERFORMANCE ASSESSMENT

4.1 Investigation of Suitable Shaping Techniques

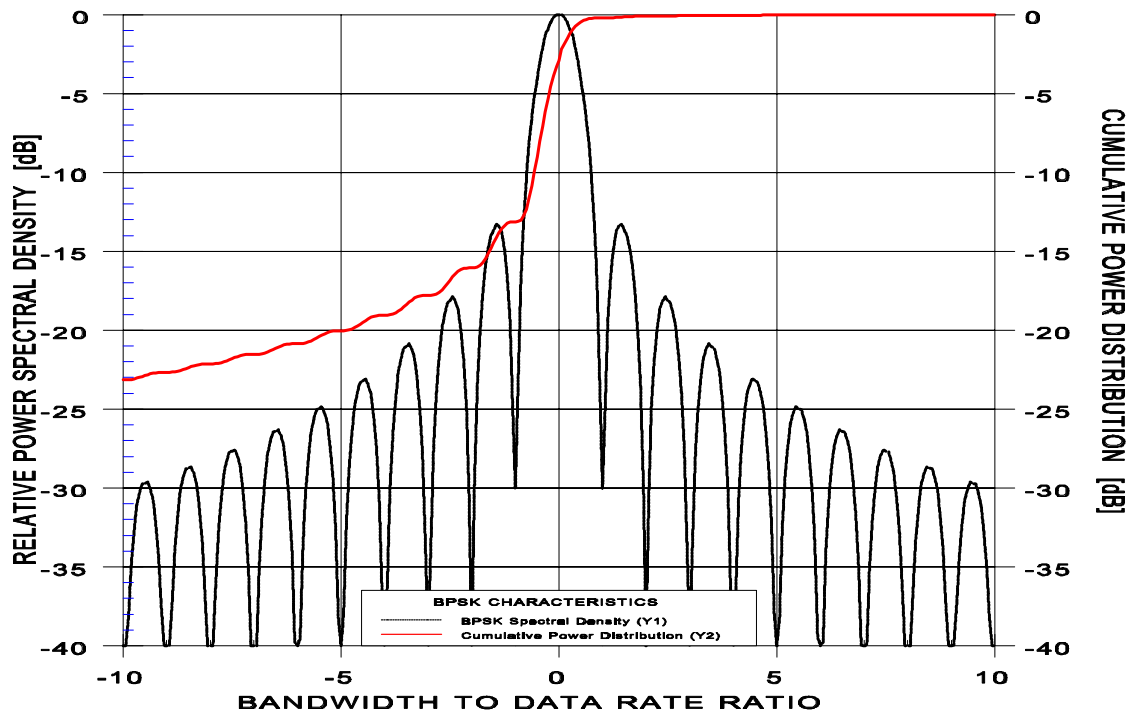
There are several possibilities along the transmission path where signal processing can be applied. Figure 12 shows an overview of a typical transmission system. Four key locations have been selected with appropriate techniques applied at RF level, IF level and baseband level.

4.1.1 Techniques Applied at RF Level

Filtering at radio frequency level can be applied to any modulated signal irrespective of the modulation technique. Where filtering at a low power level is desirable, but where an IF level is not available, for example with direct switched modulation of the carrier frequency, filtering can be applied before the High Power Amplifier (HPA). The higher the ratio between carrier frequency and filter bandwidth, the more difficult the implementation of the filter. If the HPA is operated in a highly non-linear region, the higher order components of a filtered spectrum would be restored to a major extent. In this case, only filtering after the HPA is expected to result in satisfactory performance.

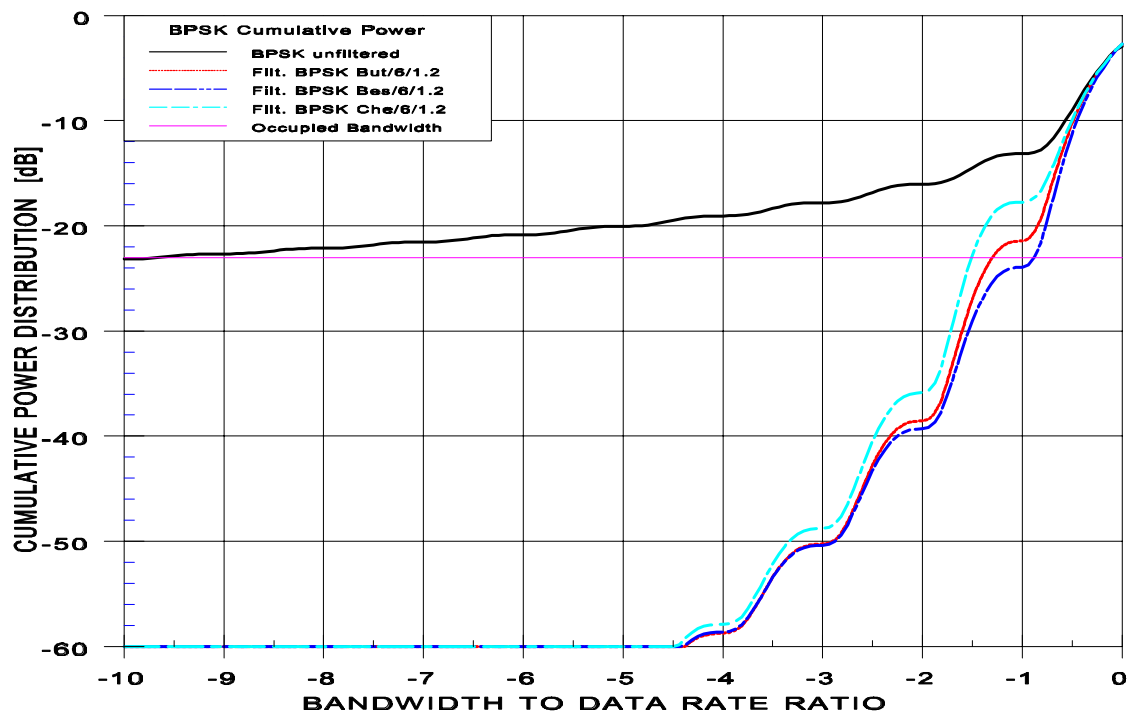
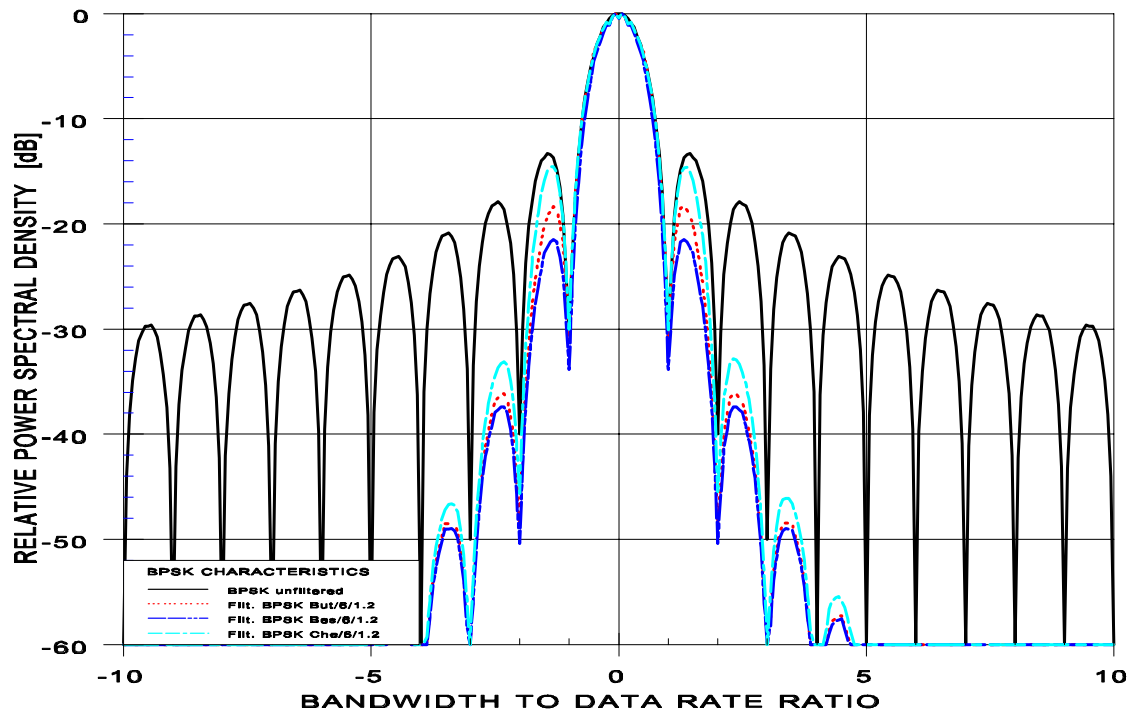
All following figures in this section show spectra of PSK modulated signals where filtering is applied at RF level after the HPA. The occupied bandwidth can be determined from the cumulative power distribution. The point where the cumulative power reaches a value of -23 dB corresponds to a power containment of 0.5%. The occupied bandwidth, assuming a symmetrical spectrum, is consequently twice the normalized data rate. Figure 13 illustrates the dependence of

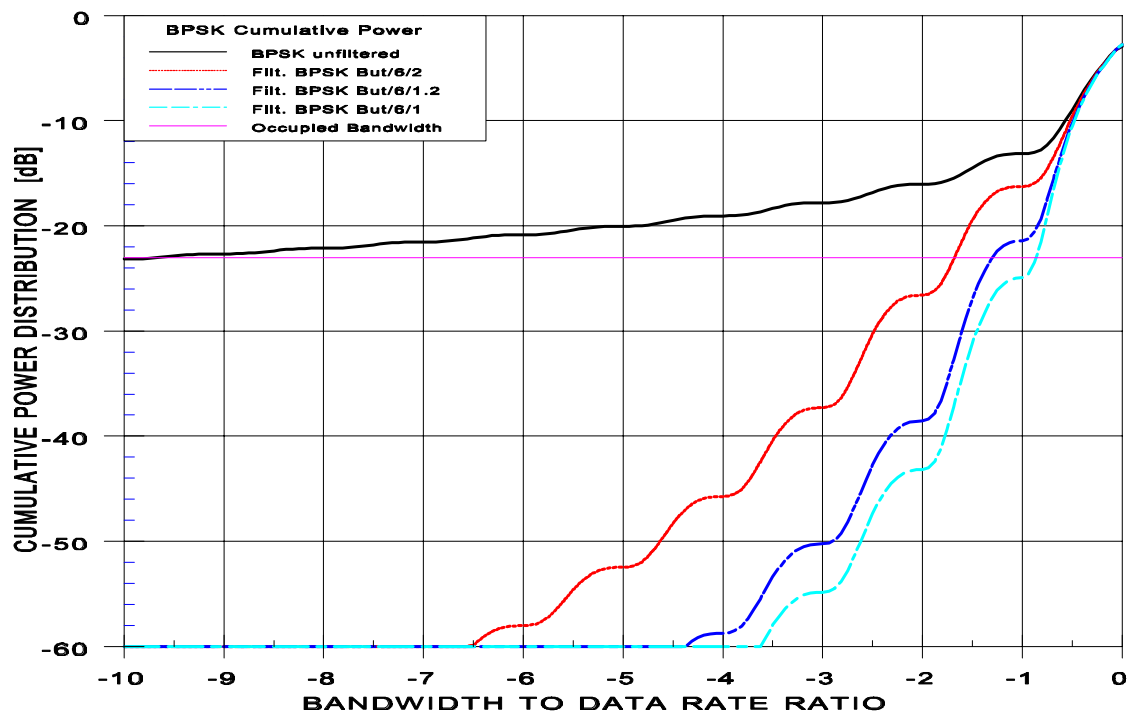
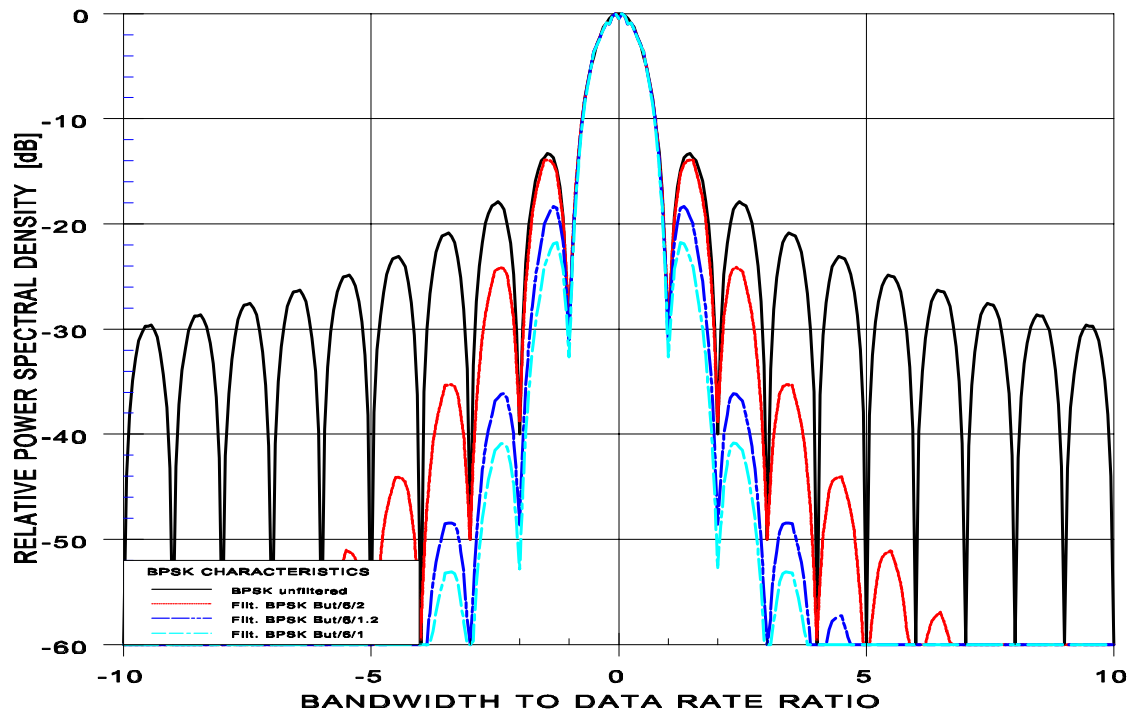
the cumulative power containment versus the spectral distribution. The spectrum is integrated from the lower to the upper frequency limit. In order to improve the clarity of the figures, only the part from the lower frequency limit to the centre frequency is shown except for figure 13.

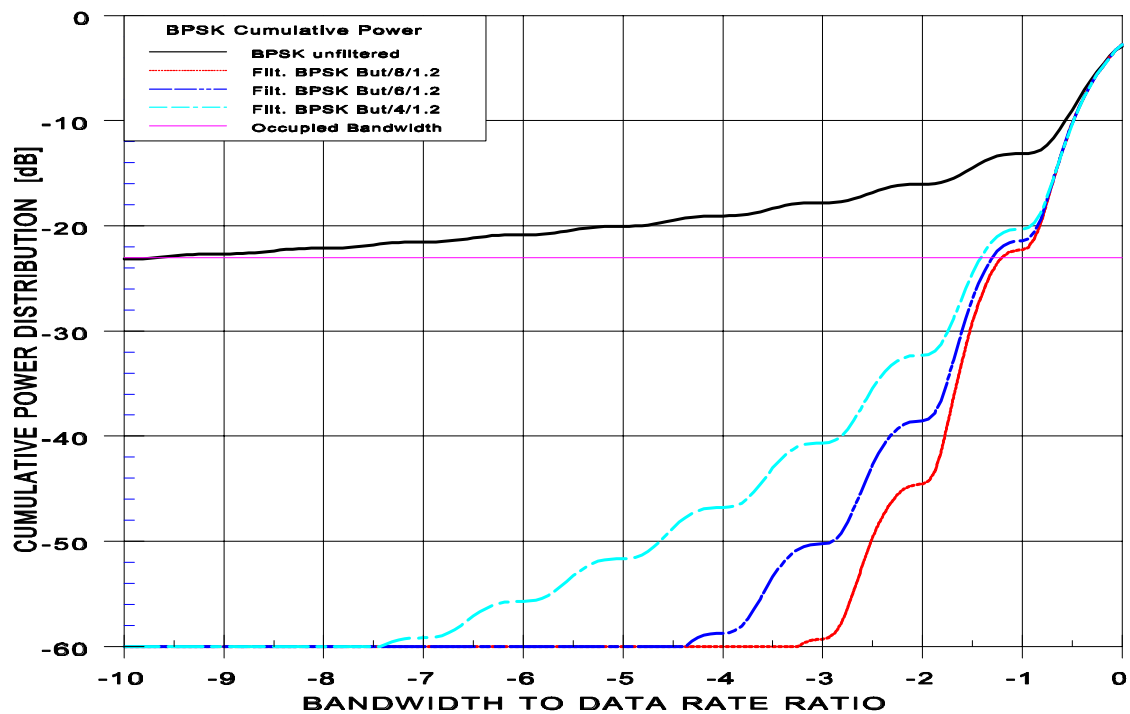
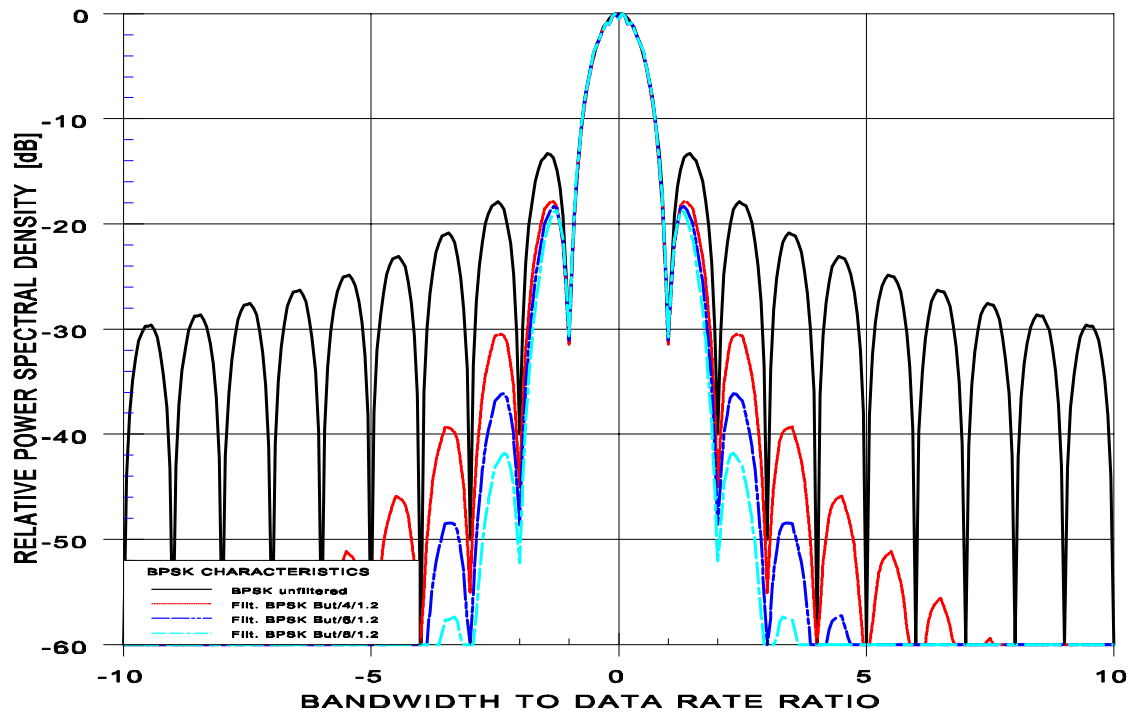


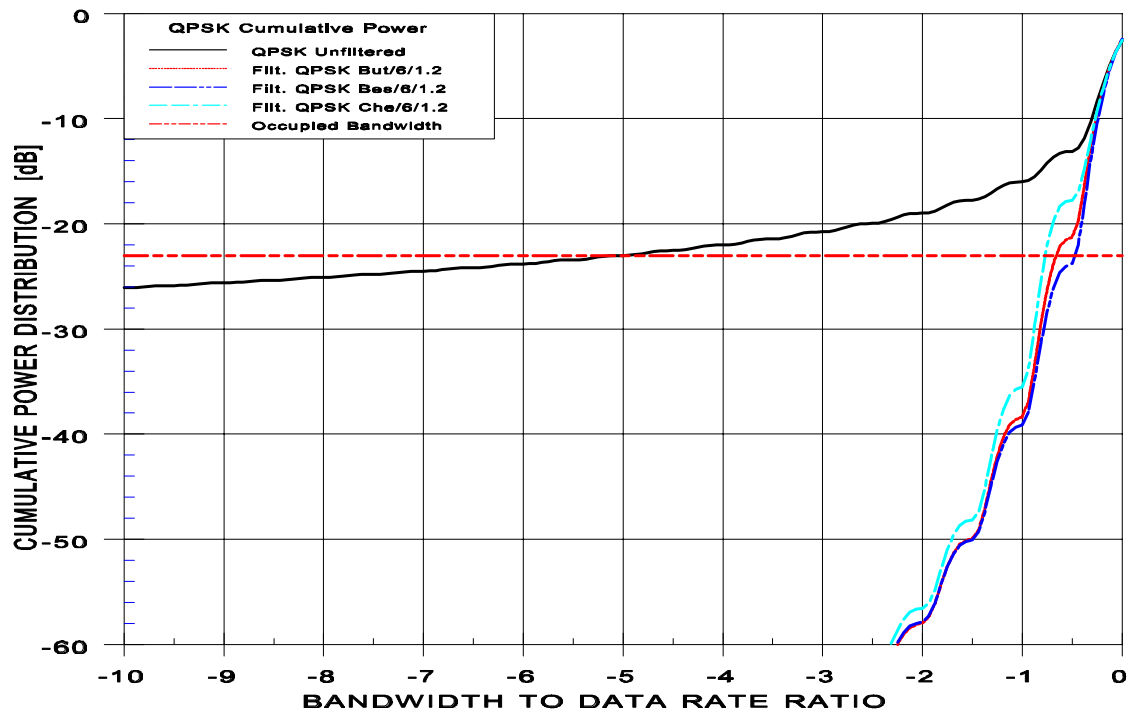
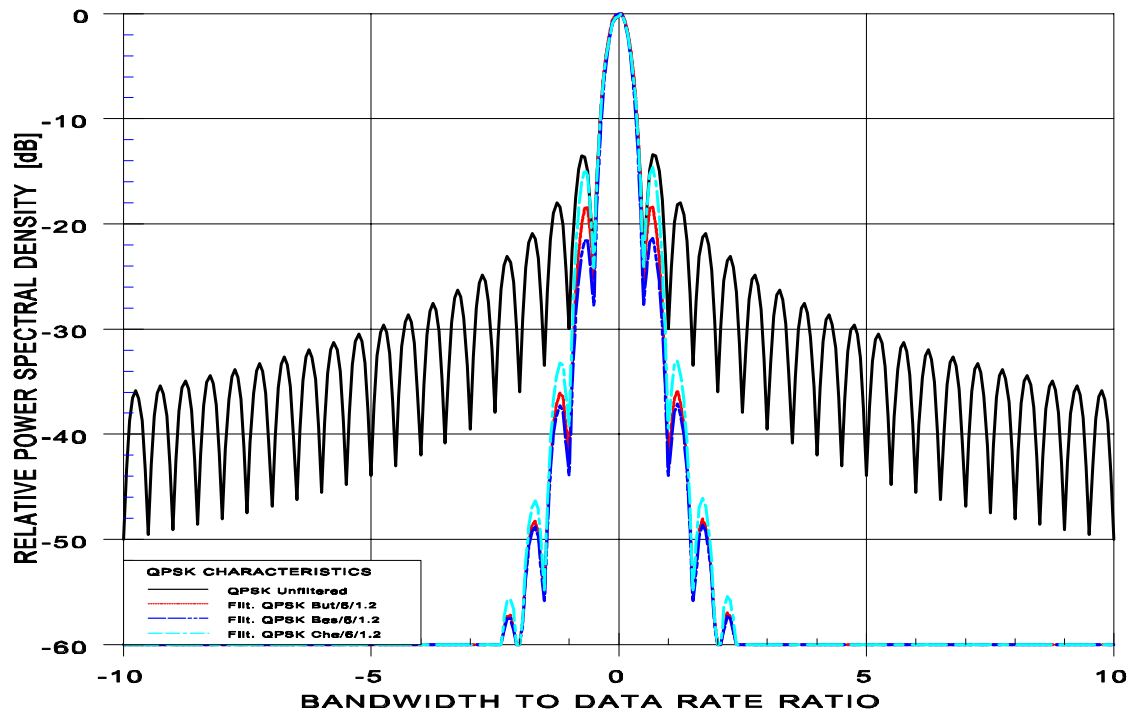
A large number of simulations has been carried out to test the sensitivity of the spectra with respect to modulation technique, filter type, number of poles and impact of the bandwidth-time (BT) product. The complete set of simulations is contained in Appendix B. The following figures are a summary showing the impact of the above parameters.

The types of filters investigated included Butterworth, Bessel and Chebyshev. Figures 14 and 15 show the impact of the filter type. For the same number of poles, the Bessel filter shows the steepest roll-off. Figures 16 and 17 show the impact of the bandwidth-time (BT) product for the Butterworth filter with $N=6$. The impact on the occupied bandwidth is substantial. The difference is nearly a factor of 2 between $BT=1.2$ (nearly identical to $BT=1.0$) and $BT=2$. The impact of the orders of the filters are shown in figures 18 and 19 for a Butterworth filter with $BT=1.2$. The investigated orders of 4, 6 and 8 have little relative influence on the occupied bandwidth but rather on the sidelobe roll-off. Finally, figures 20 and 21 show the spectral distribution and the cumulative power distribution for QPSK and OQPSK modulation. The spectrum is twice as compact as BPSK and there is no difference between QPSK and OQPSK as no non-linear device is involved.









4.1.2 Techniques Applied at IF Level

Phase modulation techniques which are based upon switching the phase of a single frequency between 2 distinct opposite phase states are not suitable for smooth transitions of the control signal. This would, on the contrary, even degrade performance. The higher order spectral components can in this case be reduced by filtering the signal at an intermediate frequency level. Implementation of filters at IF level is normally quite simple as the filter has to handle only low power and can be designed for a relatively high ratio between filter bandwidth versus centre frequency.

Without any non-linear components in the transmission system, the spectra would look the same as in the case of filtering at RF level. However, a typical communication system contains non-linear components which cause in general a distortion of the frequency spectrum. The key non-linear component in the transmission chain is often the High Power Amplifier (HPA). In order to maximize power efficiency, the HPA is normally driven into saturation, with a typically non-linear relation between input power and output power. A signal with varying power level (non constant envelope) will therefore be distorted with the effect that higher order spectral components are restored. Figures 22 and 23 show the amplitude and phase transfer characteristics of two typical high power amplifiers used by ESA. One is a standard Traveling Wave Tube (TWT) amplifier for medium to high power applications and the other is a Solid State Power Amplifier (SSPA) for low to medium power requirements.

The impact of a typical HPA on the filtered spectrum as a function of modulation scheme and the spectrum shaping technique is shown in the following figures. The occupied bandwidth has been calculated for both linear and non-linear cases. In the non-linear case, a back-off of 0 dB and 3 dB has been taken into account. The distortion with the TWT is significantly higher than with the SSPA. Most spectral curves have been simulated with the TWTA which is the more pessimistic case.

The filter parameters have been selected in such a way that the occupied bandwidth would in general lie in the range 1 to 2.5. Butterworth filters have been chosen as the reference case because they are wide-spread and relatively easy to implement.

Figures 24 and 25 show the restored spectra for BPSK with a TWT back-off of 0 and 3 dB, respectively. For comparison, the unfiltered and ideally filtered cases are shown. There is hardly a difference between the two curves.

Figures 26 and 27 show the restored spectra for BPSK with a SSPA back-off of 0 and 3 dB, respectively, in comparison to unfiltered and ideally filtered BPSK. Also in this case, there is hardly a difference between the two curves.

Figures 28 and 29 show a comparison between the TWT and the SSPA effects on the restored spectra for a back-off of 0 dB. It can be seen that beyond the third sidelobe, the SSPA spectrum rolls off significantly faster. The occupied bandwidth is only 6 times the data rate compared to 8 times the data rate with the TWT and 20 times the data rate without any filtering.

Figures 30 and 31 show the restored spectra with QPSK for a back-off of 0 and 3 dB, respectively. It is interesting to note, that the improvement with the 3 dB back-off is not very significant.

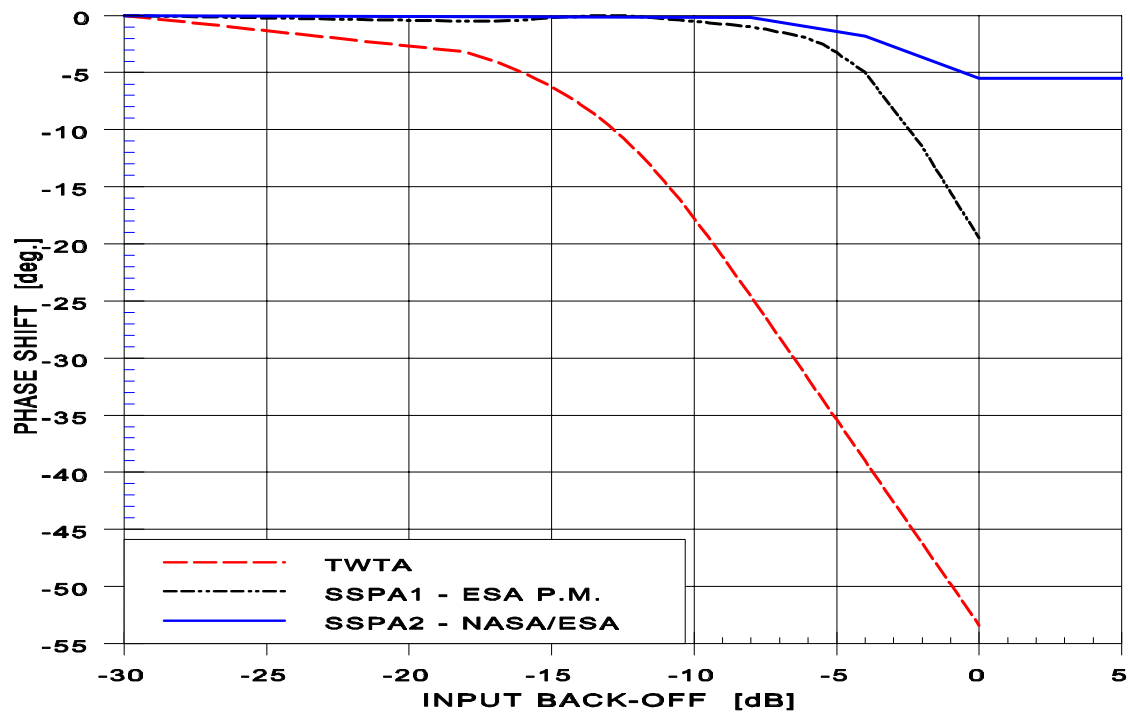
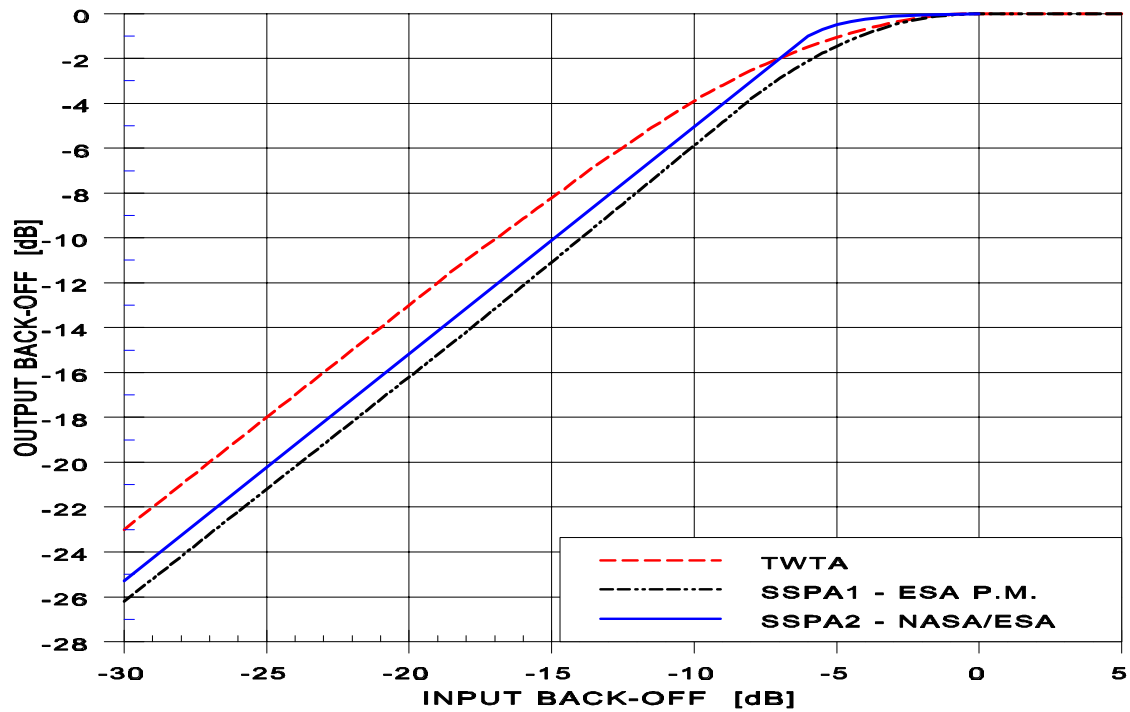
Figures 32 and 33 show the restored spectra with OQPSK for a back-off of 0 and 3 dB, respectively. There is even less difference compared to QPSK and it does not appear attractive from a spectral point of view to back-off the HPA.

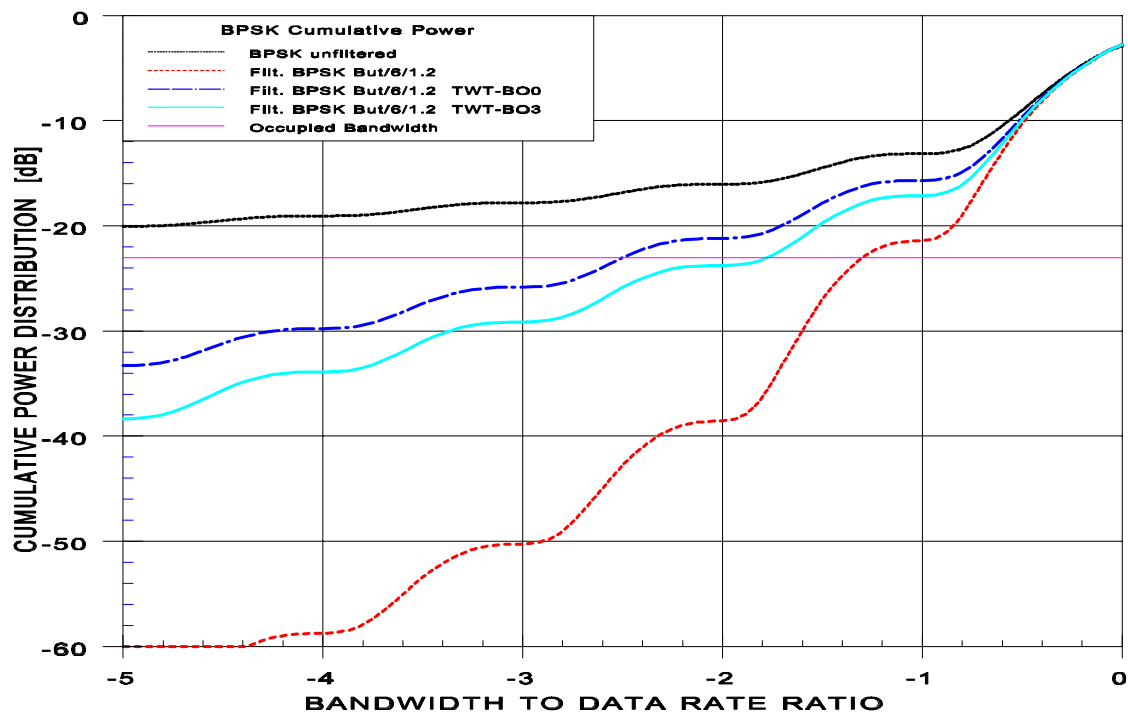
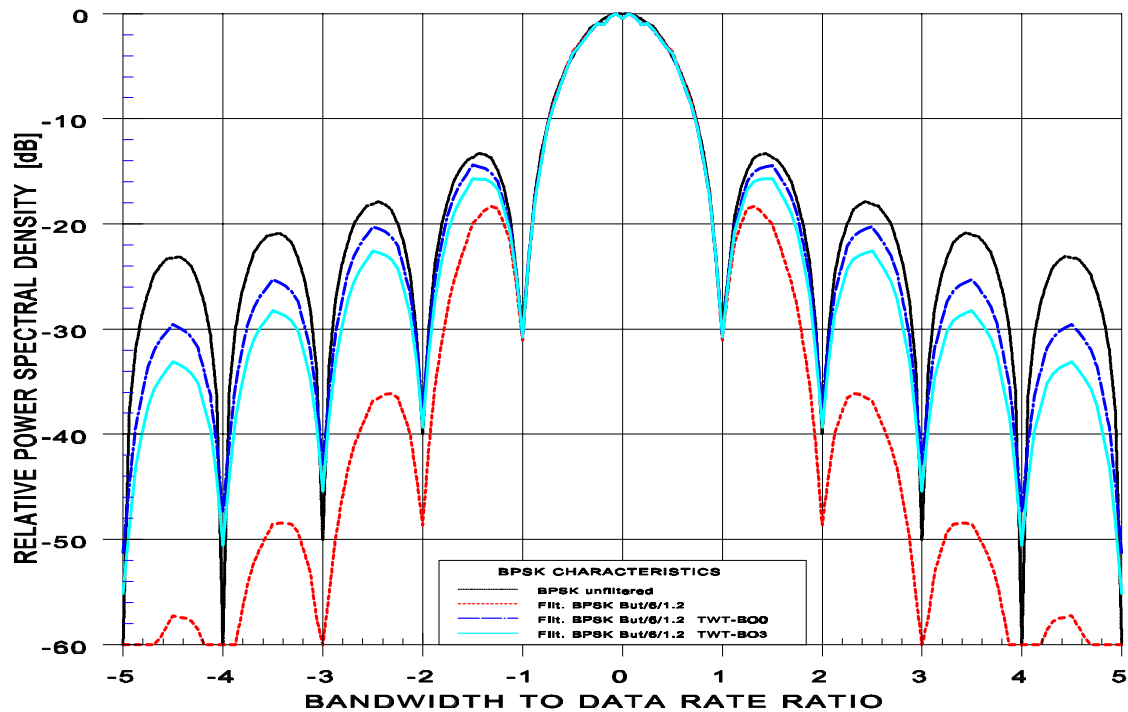
Figures 34 and 35 show the comparison between QPSK and OQPSK modulation for a back-off of 0 dB. It can be seen that the spectrum is far less restored with OQPSK compared to QPSK.

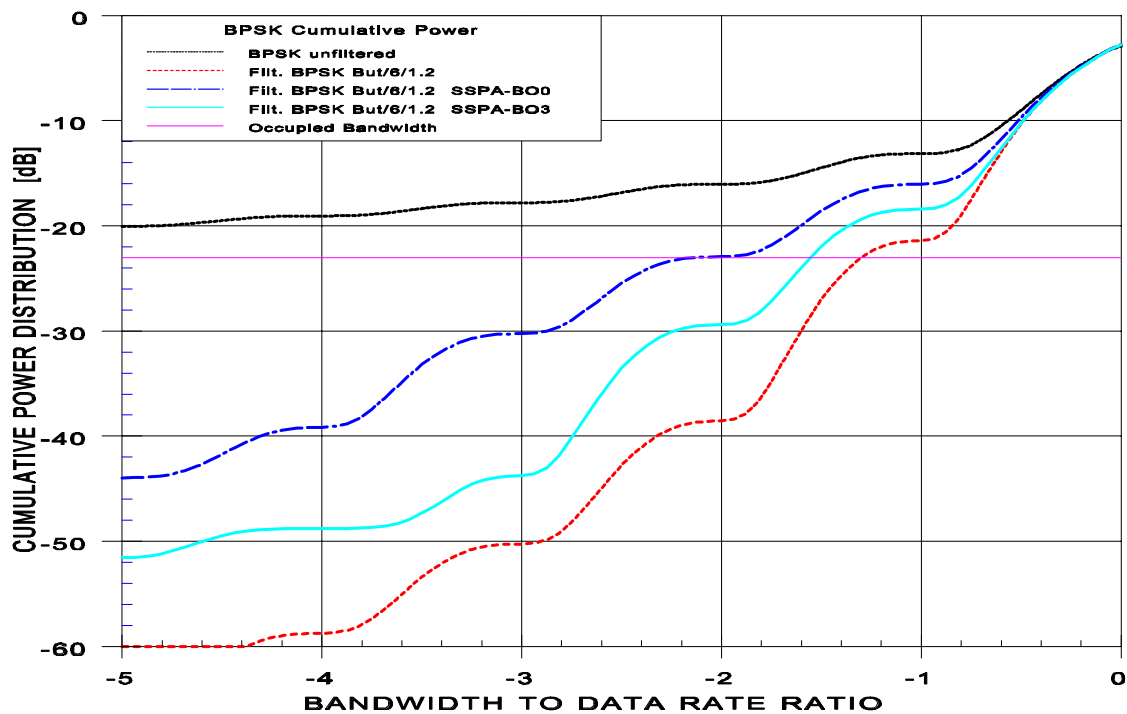
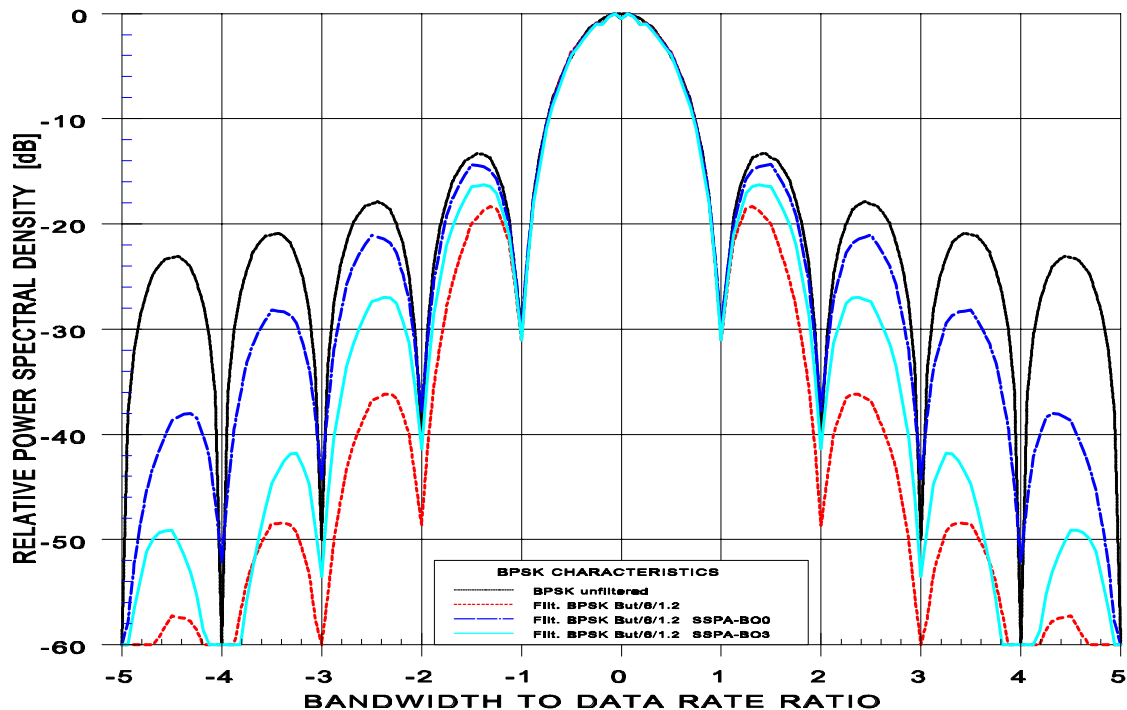
The various cases studied lead to interesting results. It can be concluded that filtering at IF level before the non-linear component does restore the spectrum only to a rather limited extent. The occupied bandwidth is in general still reduced by more than a factor of 4. The best performance is obtained with OQPSK where the improvement factor is in excess of 7.

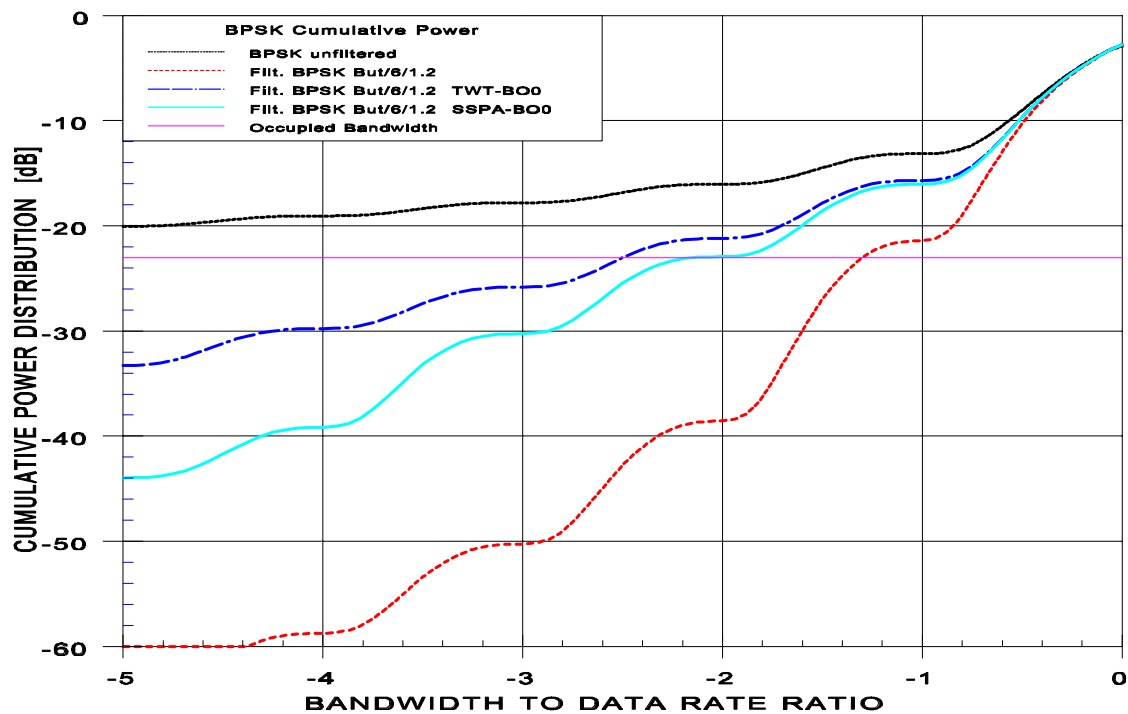
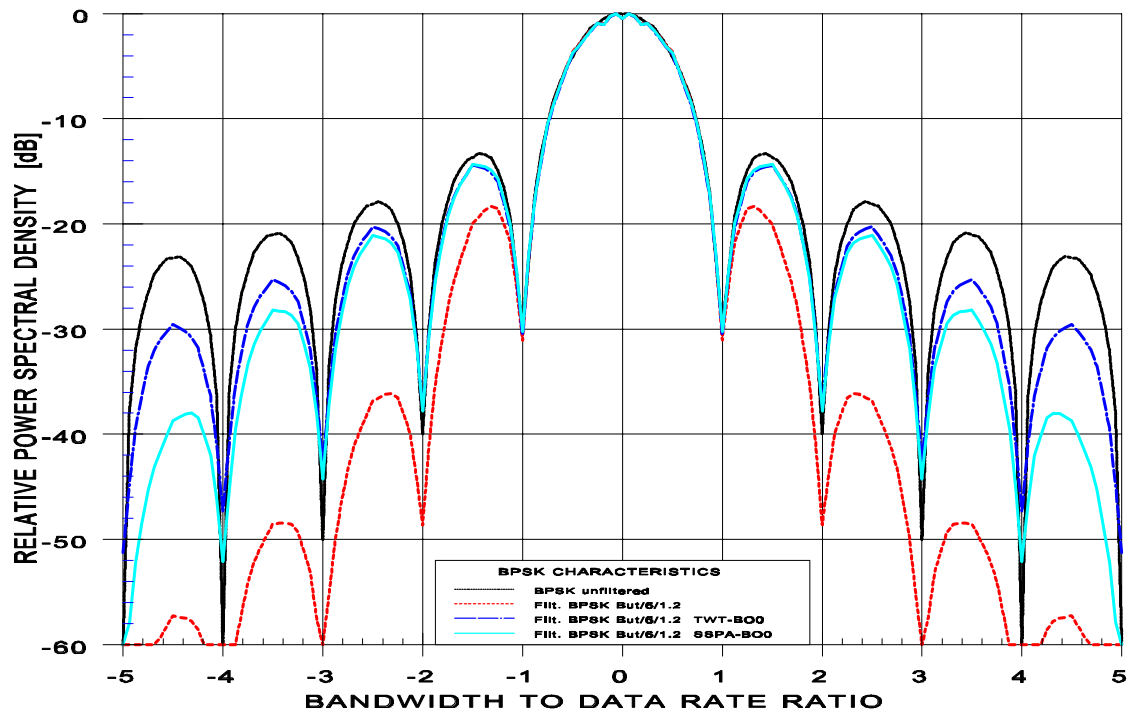
During a CCSDS meeting in spring 1997, it became apparent that several types of different high power amplifiers have been used and it was found interesting to determine their impact on spectra and occupied bandwidth. A standard TWTA was compared with 2 types of SSPAs. The results are shown in figures 36 and 36 for QPSK modulation and 37 and 37 for OQPSK modulation. In all cases a 0 dB back-off as well as a 3 dB back-off have been investigated. It can be seen that there is indeed a significant difference between TWTAs and SSPAs in favour of the latter ones.

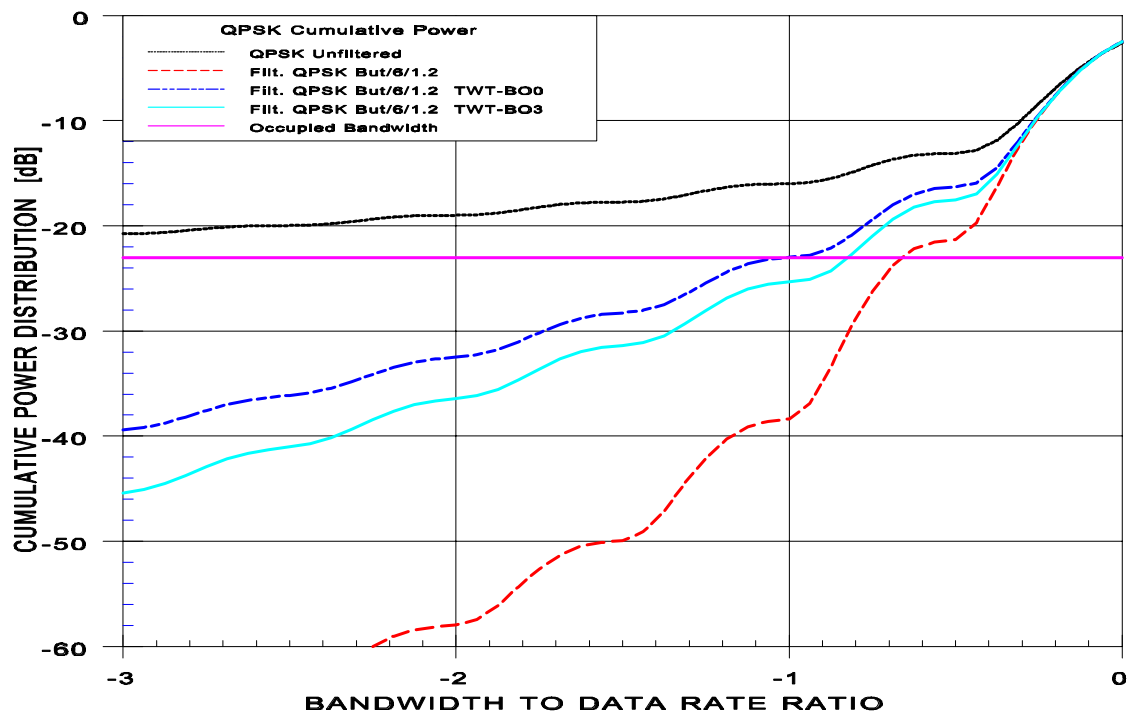
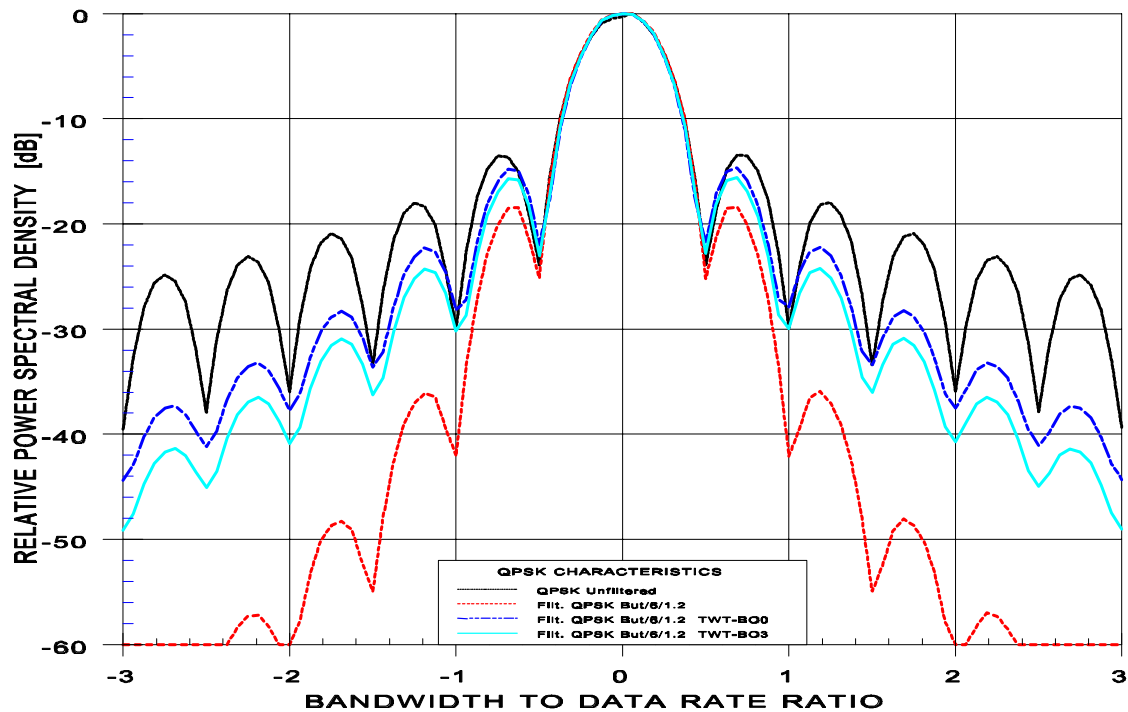
Figures 37 and 38 show the impact of filtering an 8PSK signal with and without a non-linear amplifier. A TWTA has been used in this case as 8PSK is often used with high data rates requiring output power levels which can in many cases only be provided by TWTs. A 0 dB and a 3 dB back-off have been investigated.

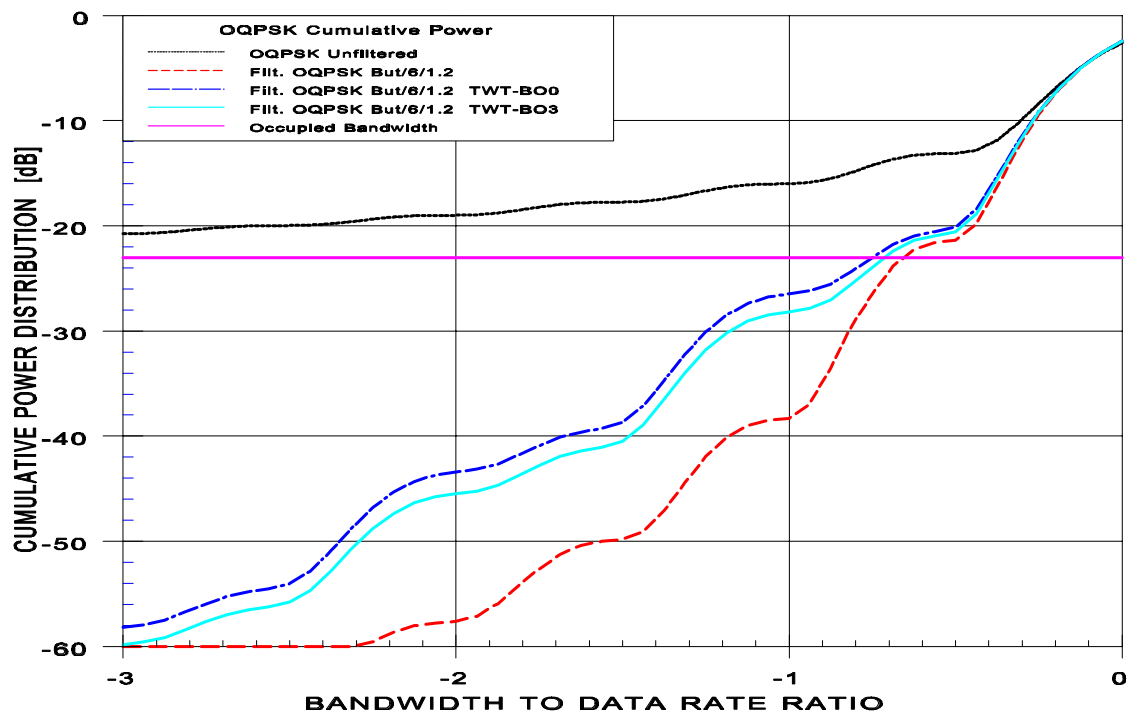
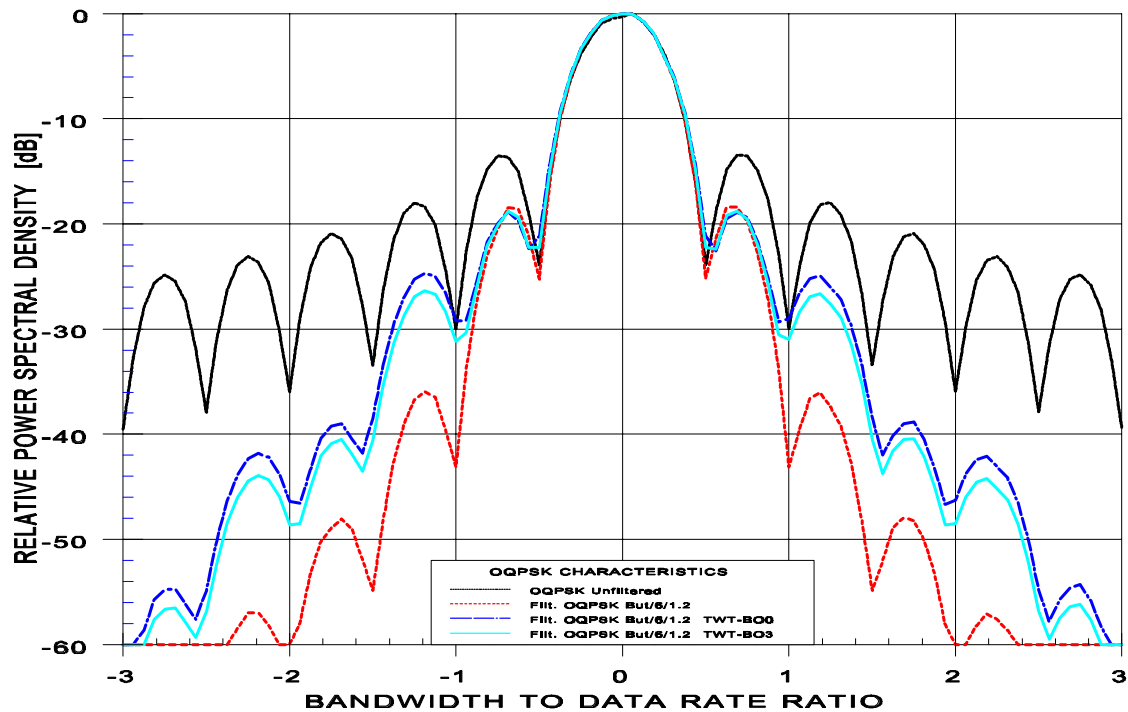


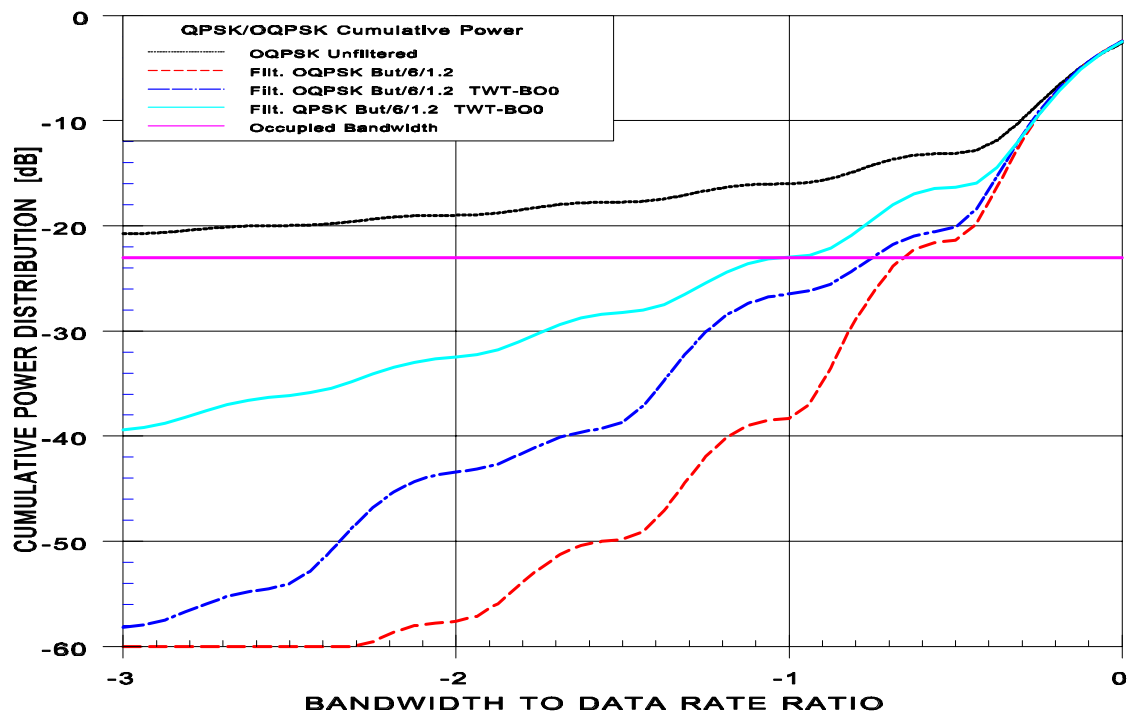
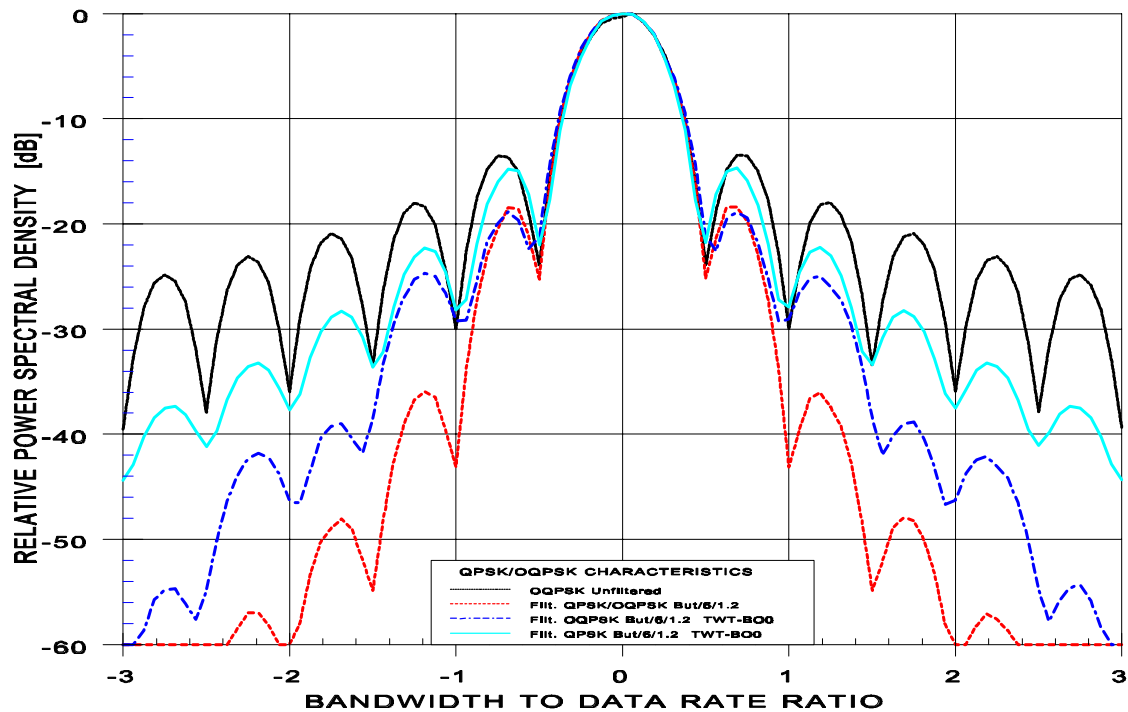


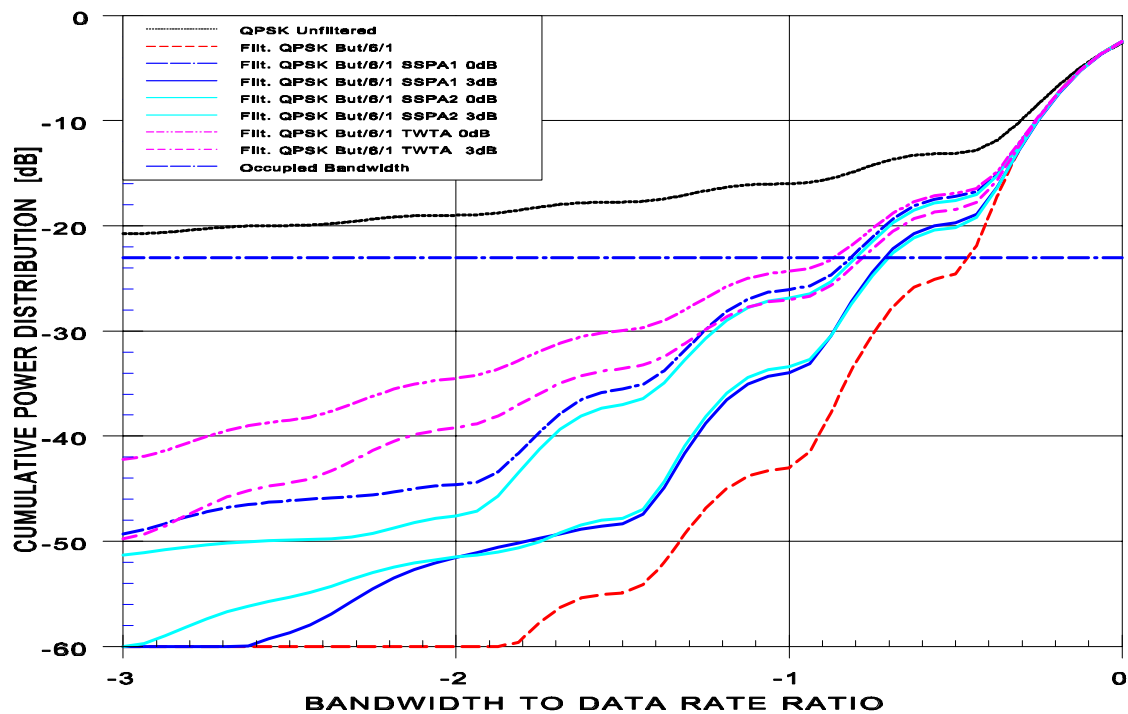
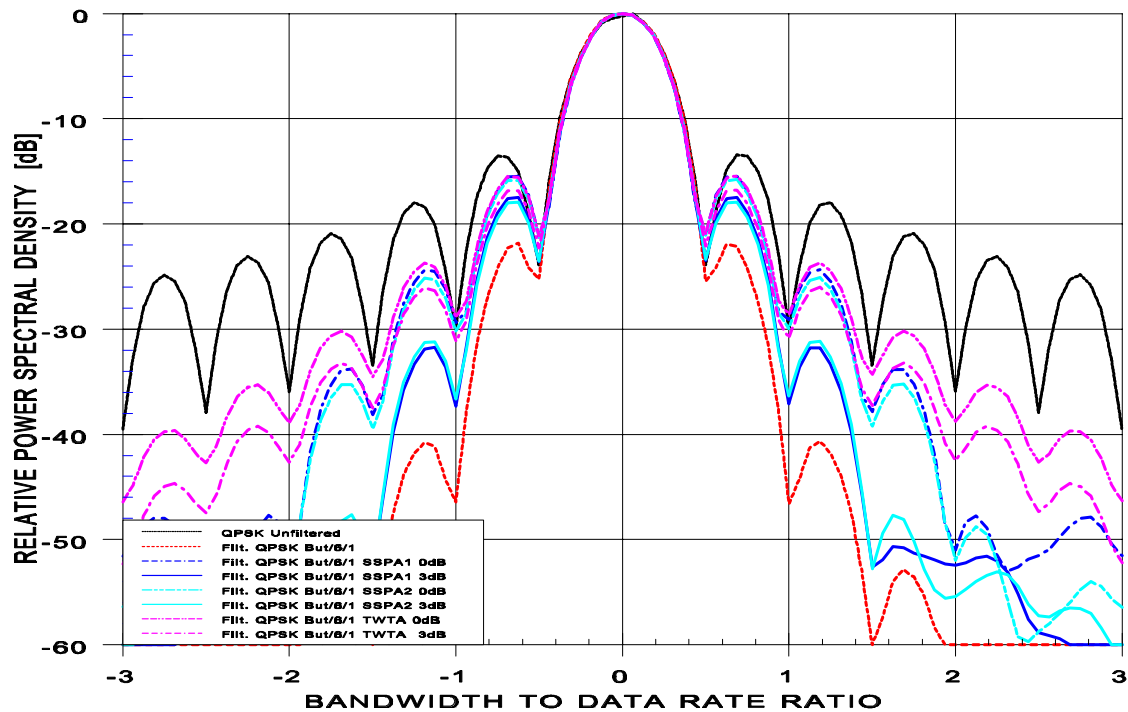


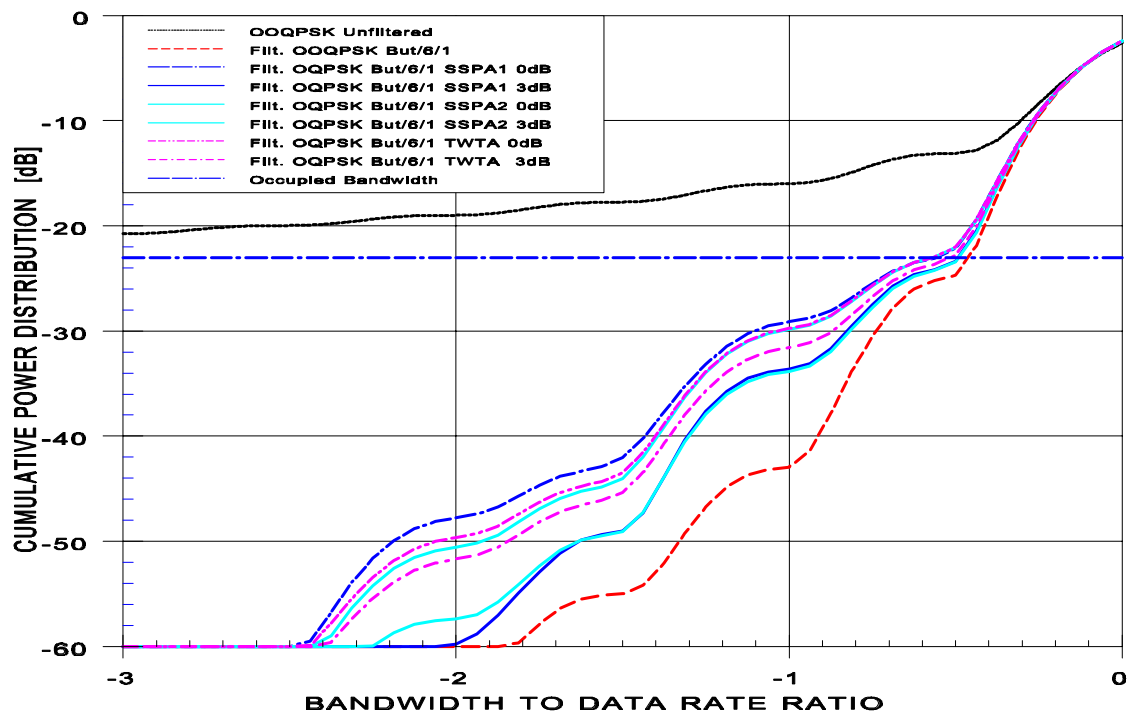
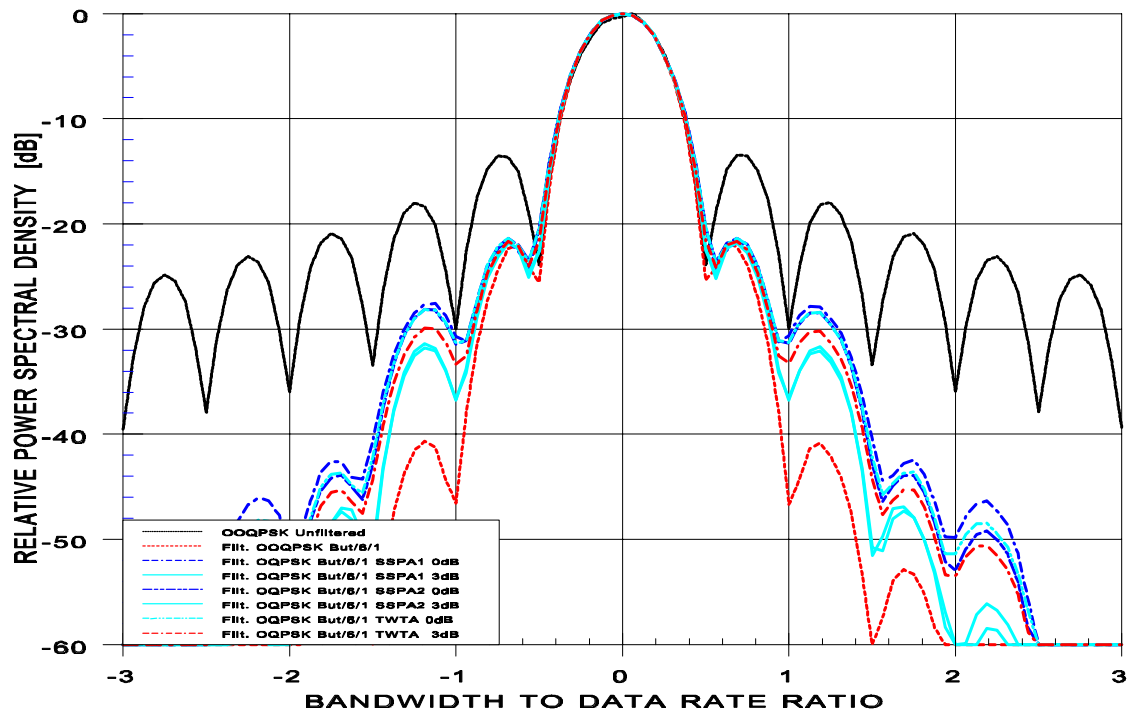


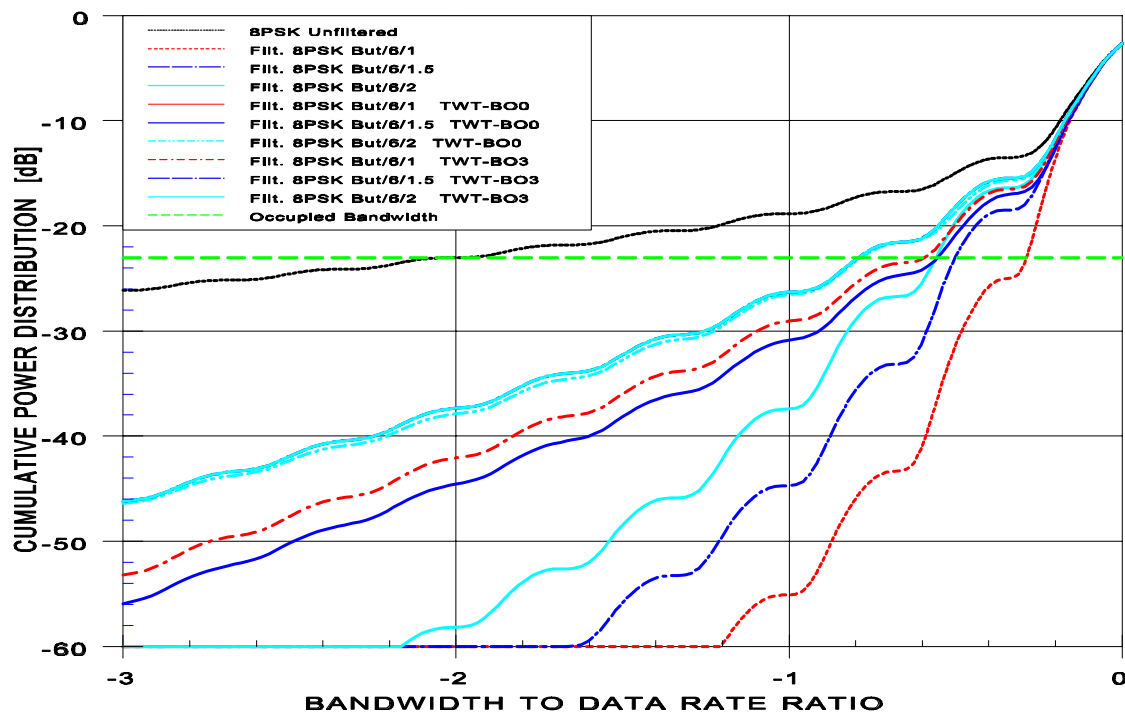
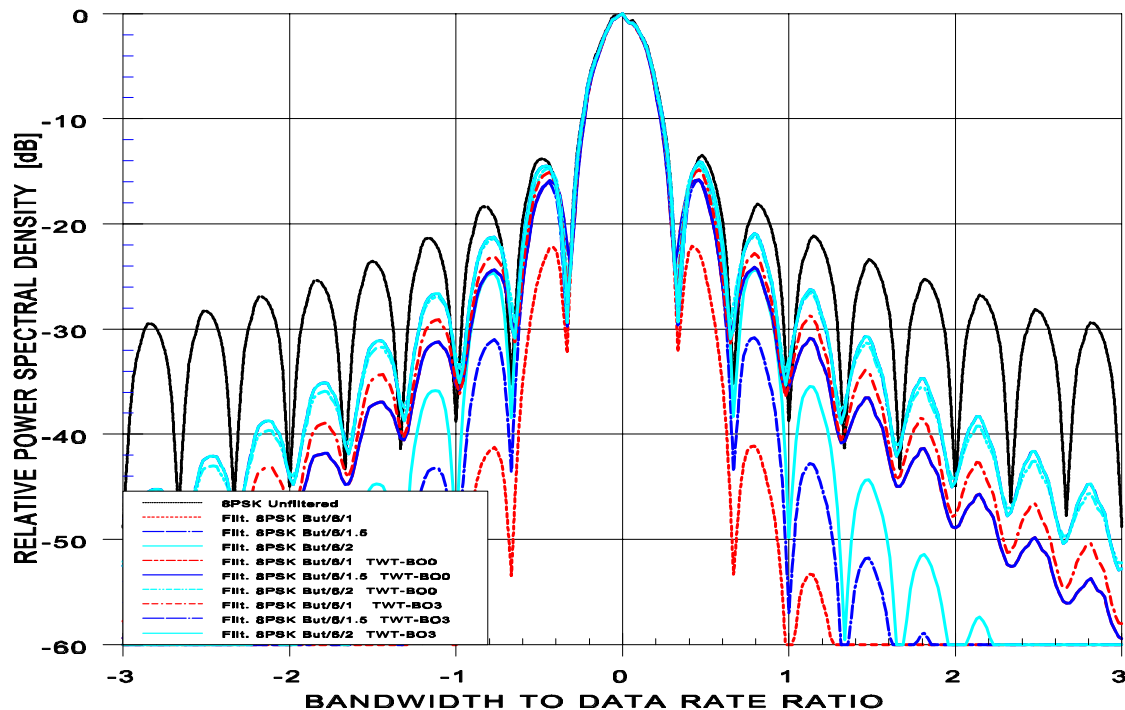












4.1.3 Techniques Applied at Baseband Level

An alternative technique to filtering at IF or RF level is baseband pulse shaping, also referred to as baseband filtering. Phase modulation techniques which are based on a linear relation between the modulation angle and the control signal, so-called linear modulation, allow shaping of the resulting spectra by smoothing the control signal. This basically removes the sharp edges of a digital signal and consequently the higher order components of the spectrum. With PSK techniques, this can be done mildly if a linear modulator is available. Transponders have actually been built in ESA which apply one of this techniques.

Gaussian Minimum Shift Keying (GMSK) and raised cosine filters are known to be suitable for shaping the digital pulses. With GMSK, the baseband pulses are shaped according to the Gaussian distribution function. Additional filtering is not required. As all MSK techniques have constant envelopes, non-linear amplifiers have no effect on the spectral shape. For comparison, also Butterworth and Bessel filters have been looked at as a suitable technique to shape the modulating pulses.

Pulse shaping cannot be applied with purely switching modulators as any smooth pulses without sharp transitions zones will only lead to data asymmetry if the switching levels for the rising and the falling edge are not the same. A linear modulation process is consequently required.

Baseband pulse shaping techniques have the distinct advantage that they can be made independent of the symbol rate and IF frequencies. Their disadvantage lies in the fact, that non-switching modulators must be used.

Figures 42 and 43 show GMSK spectra with a memory length of 1 and a BT products of 1, 2 and 3, respectively. Further spectra showing the impact of memory length on GMSK spectra can be found in Appendix E. No impact is noticeable when the signal is amplified by the TWT. The spectrum efficiency is very good.

Figures 44 and 45 show spectra and cumulative power distribution for a phase domain baseband Butterworth premodulation filter. The 3dB bandwidth has been used as a parameter. Several orders of the filter have been simulated with each of the 3dB bandwidths and an order of 5 has been selected for the plots because it has been proposed by other studies and allows therefore a comparison of the obtained results. The spectrum efficiency is rather limited for the linear case but quite attractive if non-linear devices are involved as the spectrum is not restored. The spikes in the null of the lobes have a critically high power level. The total power containment of the spike is around -16 dB in the first null and -21 dB in the second one.

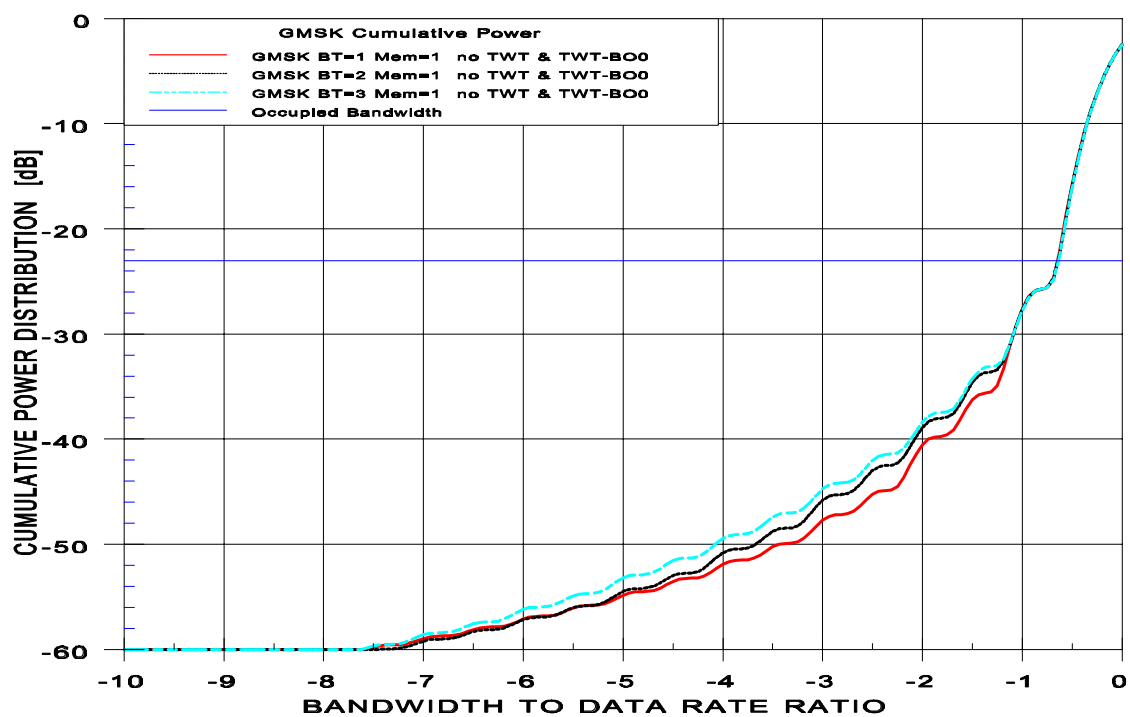
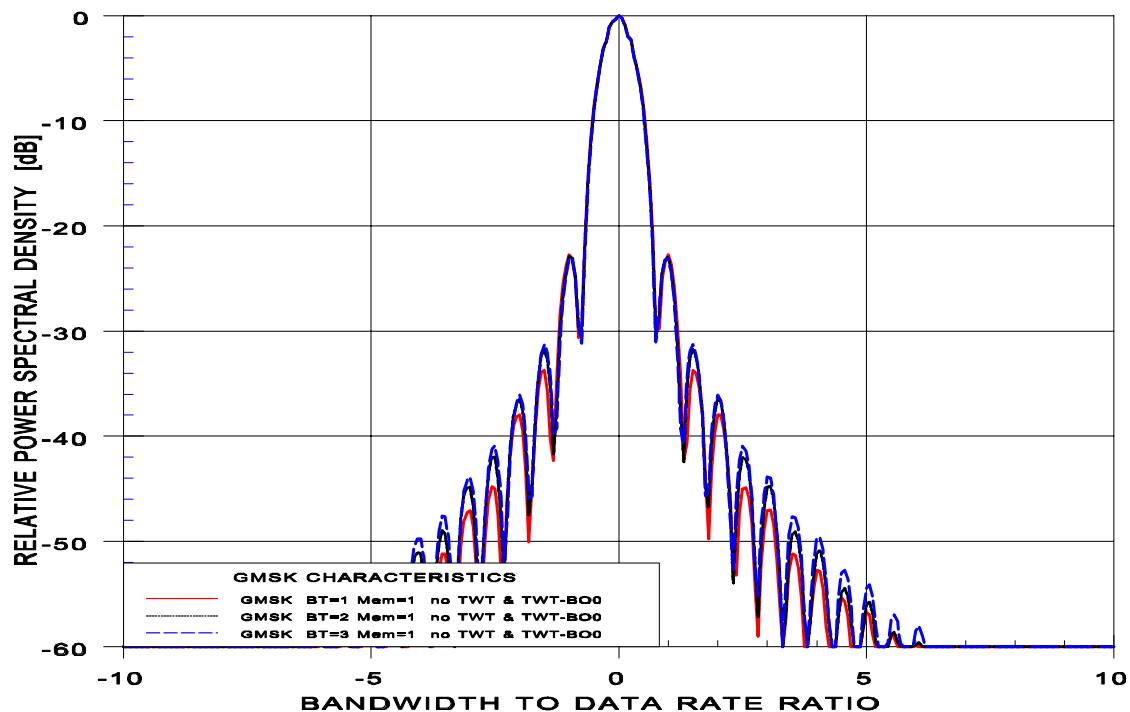
Figures 46 and 47 show spectra and cumulative power distribution for an amplitude domain baseband Butterworth premodulation filter. The 3dB bandwidth has again been used as a parameter. The spectrum efficiency is very good for the linear case but quite poor if non-linear devices are involved as the spectrum is restored to a major extent.

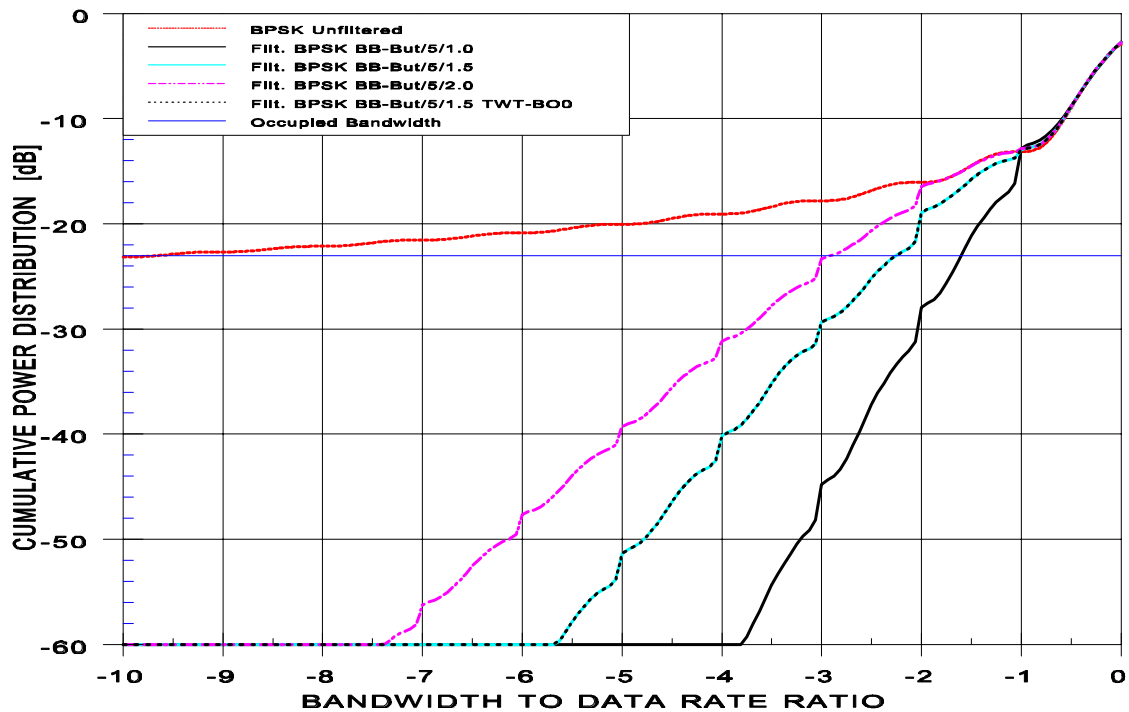
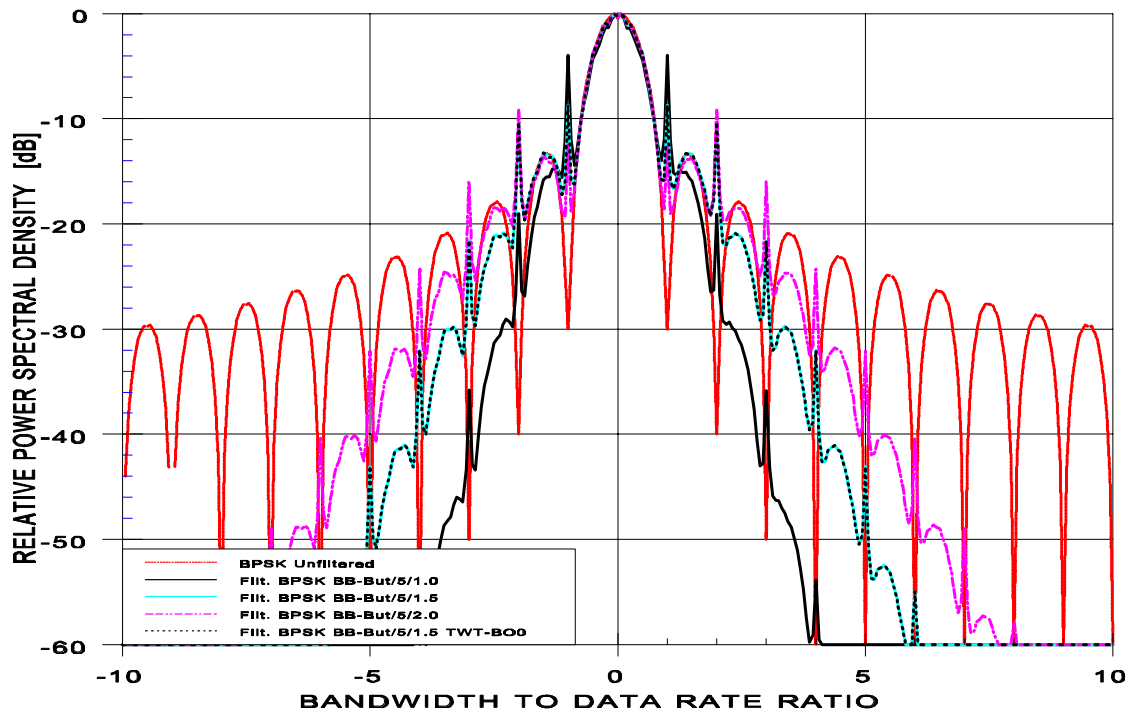
Figures 48 and 49 show spectra and cumulative power distribution for a baseband Bessel premodulation filter in the phase domain. The asymptotic bandwidth has been used as a parameter. Several orders of the filter have been simulated with each of the bandwidths and an order of 3 has been selected for the plots because it has been proposed by other studies and allows therefore a

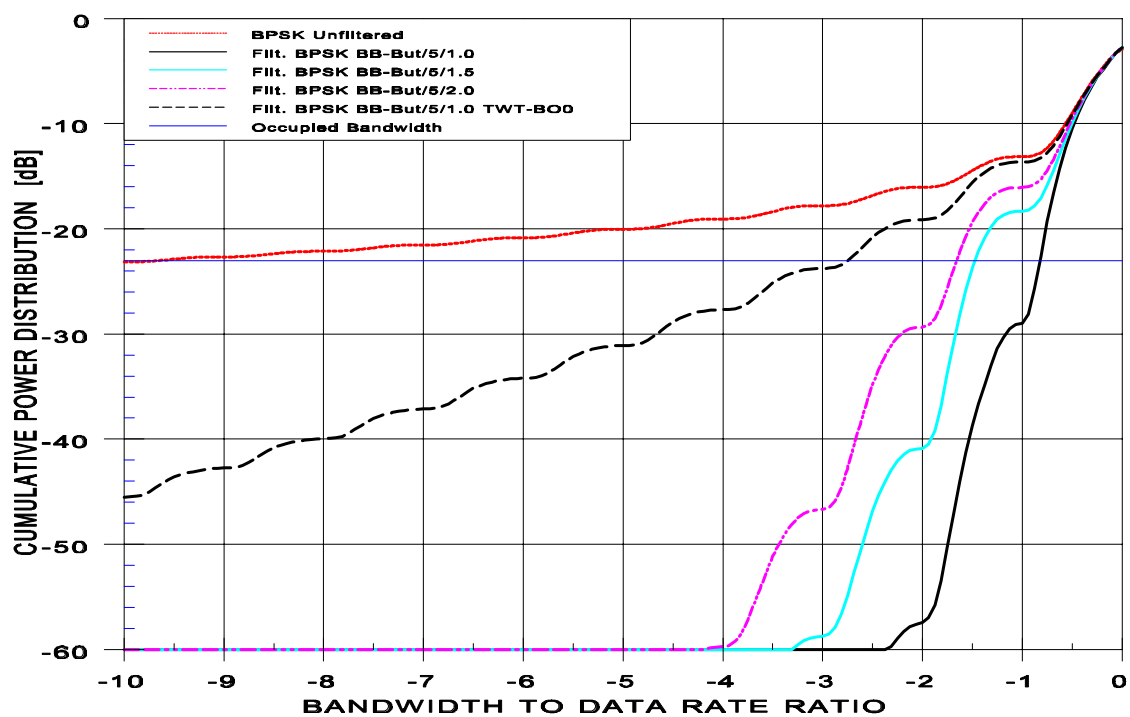
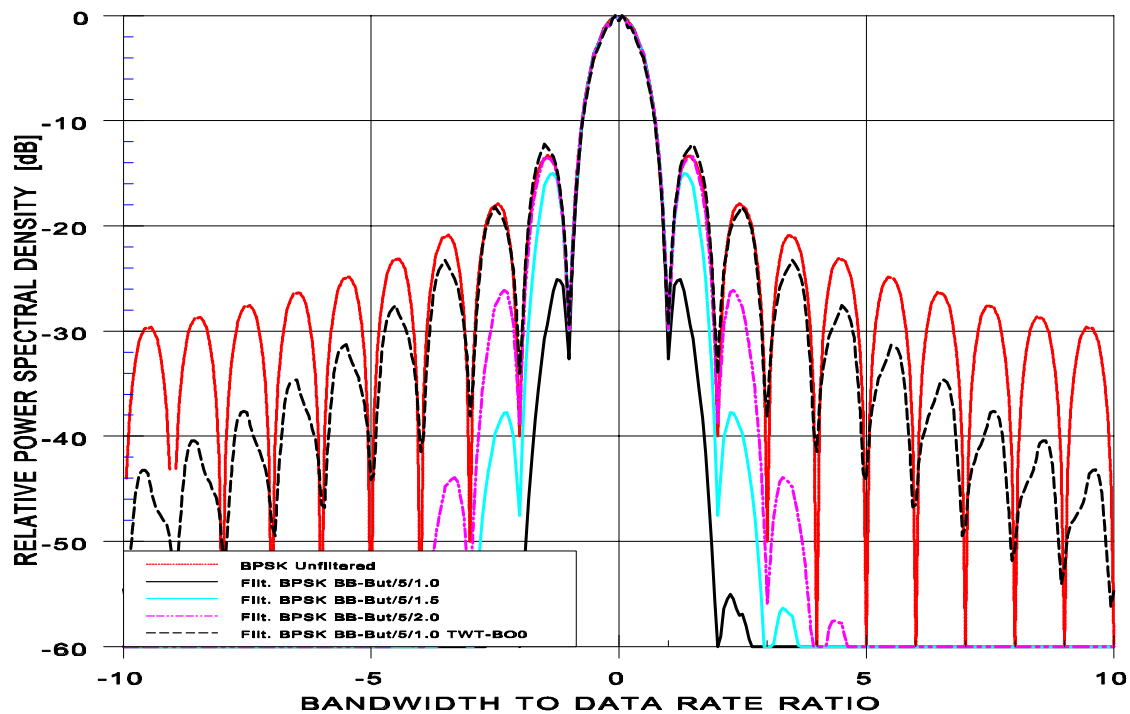
comparison of the obtained results. The spectrum efficiency is also rather limited and comparable to Butterworth filters. This filter would only be attractive for non-linear devices as the spectrum is not restored. The spikes in the null of the lobes are also rather high with a total power containment of around -20 dB in the first null and -25 dB in the second one.

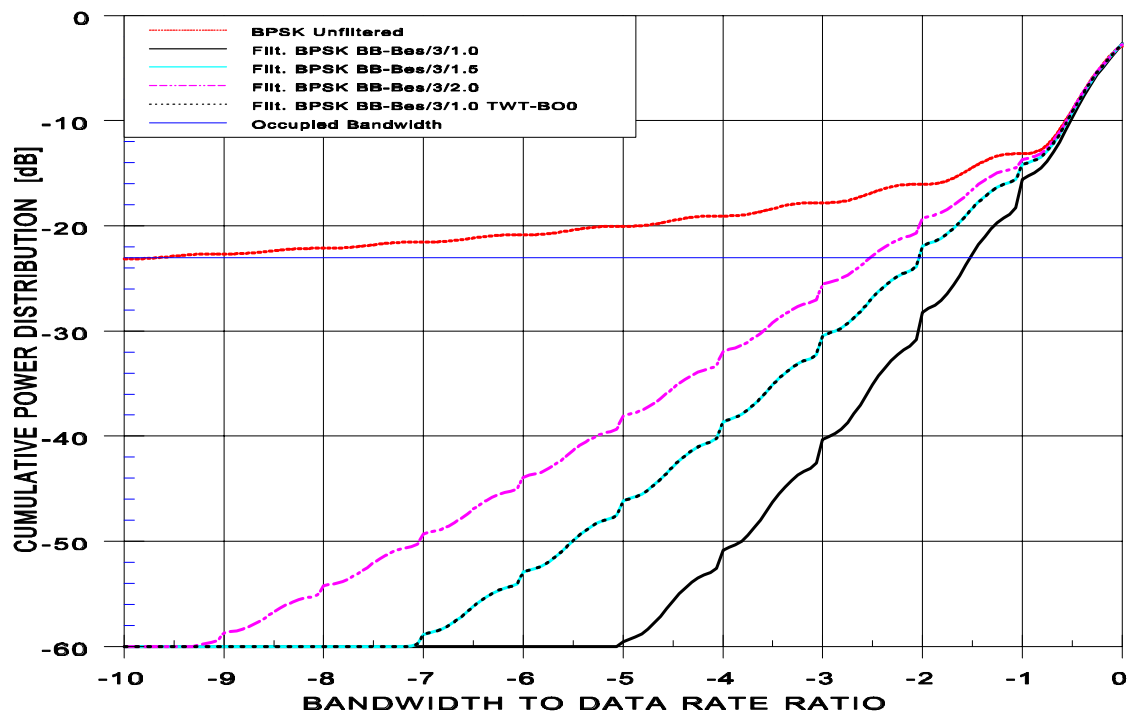
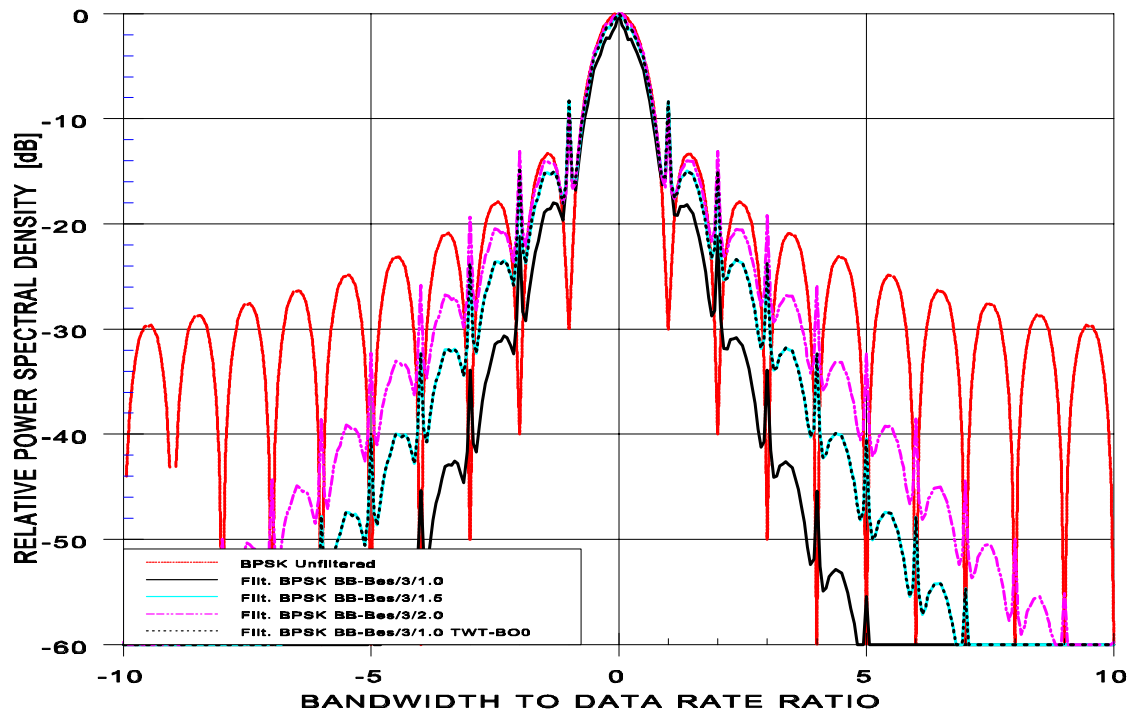
Figures 50 and 51 show spectra and cumulative power distribution for an amplitude domain baseband Bessel premodulation filter. Similar to Butterworth filters, the spectrum efficiency is very good for the linear case but quite poor if non-linear devices are involved as the spectrum is restored to a major extent.

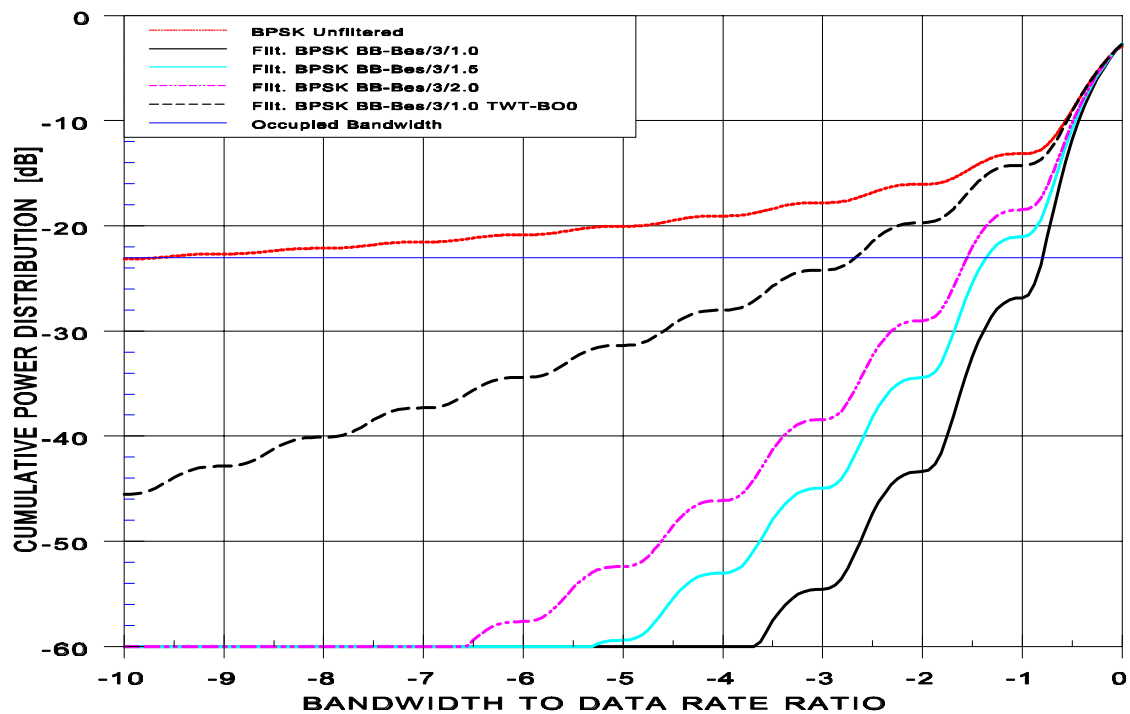
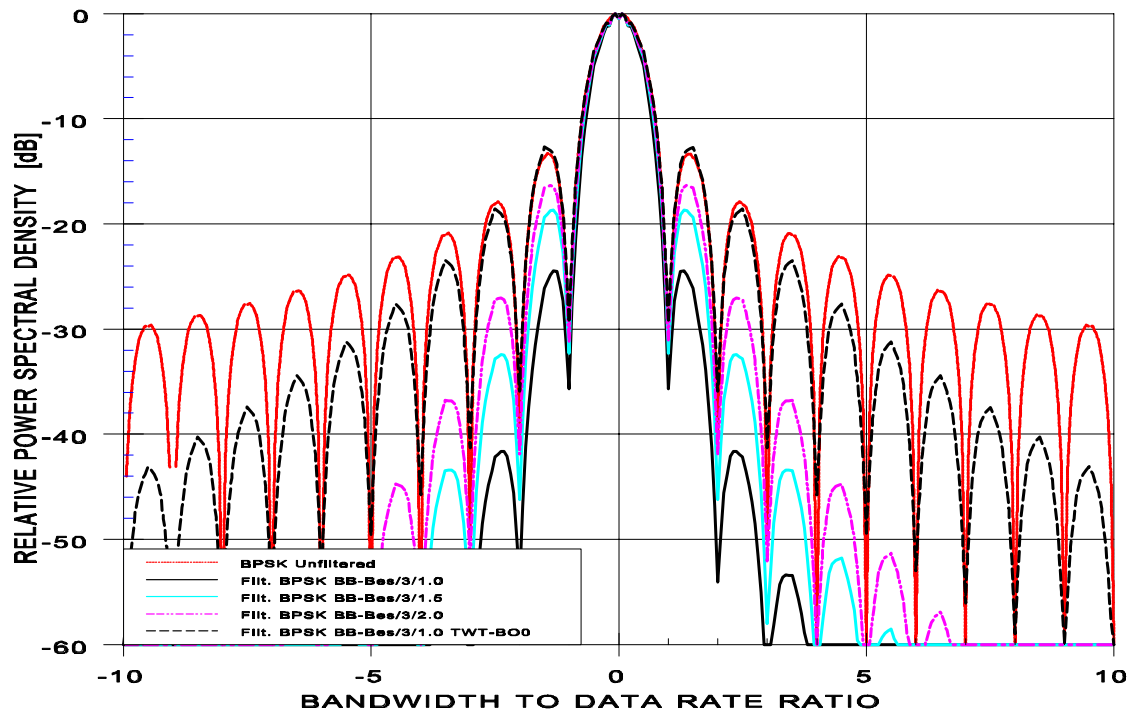
Figures 52 and 53 show spectra and cumulative power distribution for a baseband Square Root Raised Cosine (SRRC) premodulation filter. Roll-off factors of 0.5, 0.8 and 1.0 have been used as parameters. The spectrum efficiency is rather good and comparable to GMSK. The spikes in the null of the lobes have also a critically high power level. The total power containment of the spikes is around -14 dB in the first null but insignificant for any other spikes.

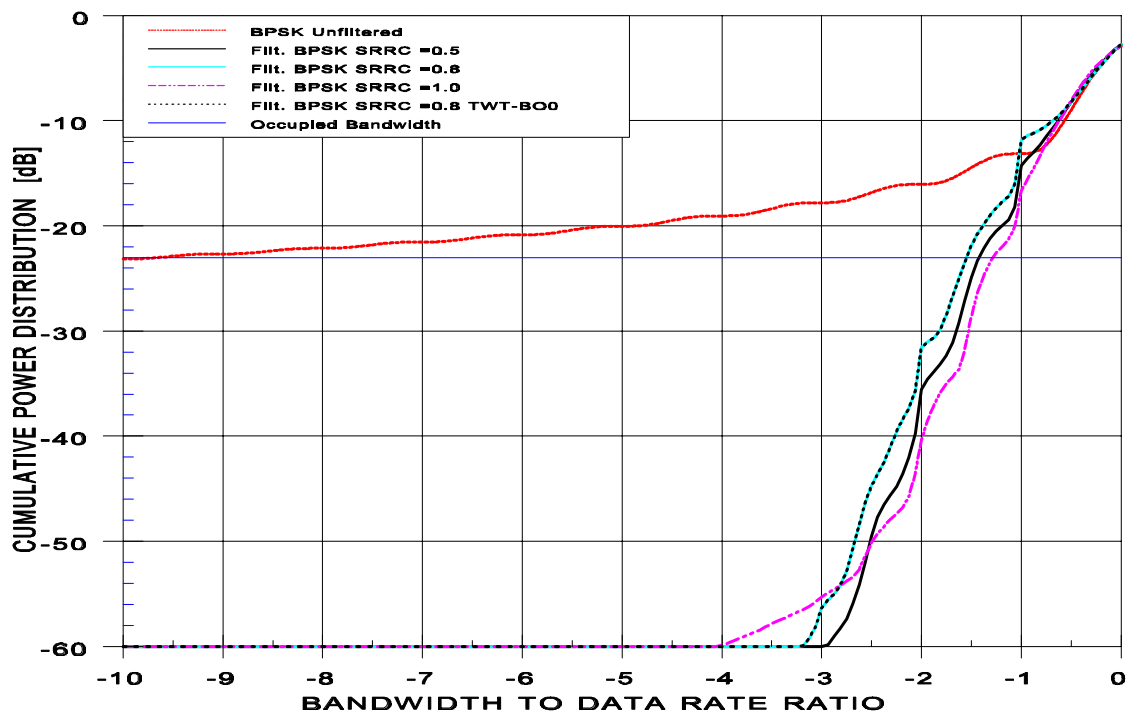
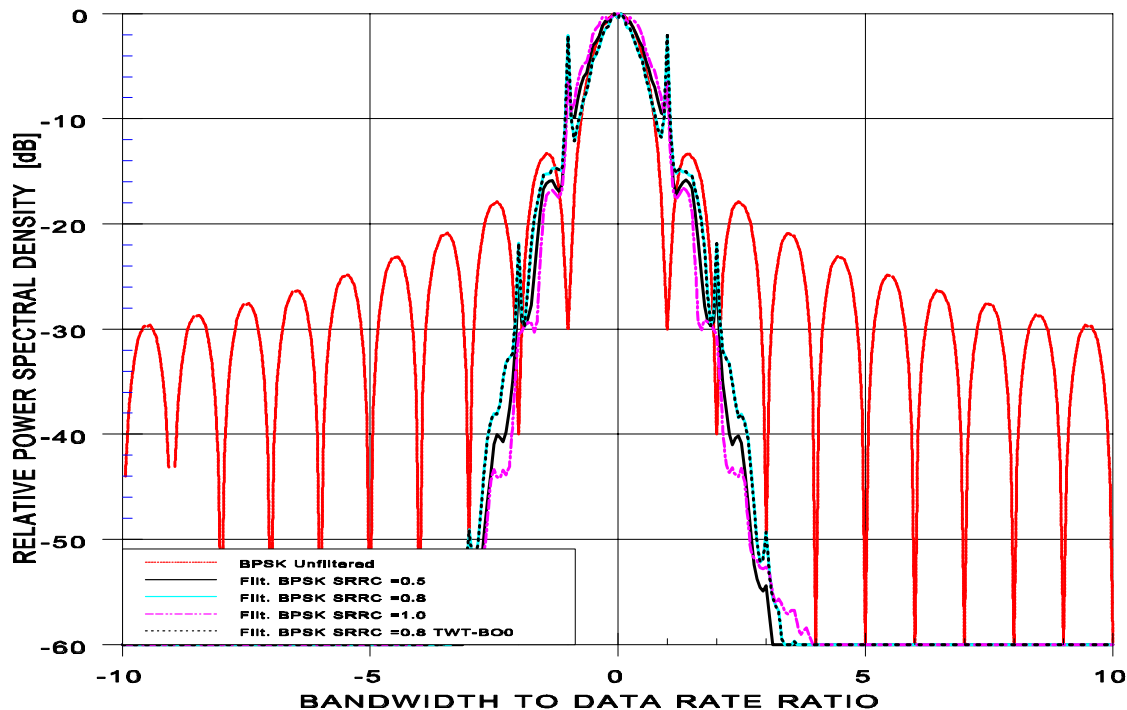












4.2 Calculation of Overall System Degradation without Performance Optimisation

Any kind of signal processing will have an impact on the end-to-end system performance. Some of the various shaping techniques identified in the above sections may result in very good spectral efficiency but at the same time distort the signal to an unacceptable degree. Of equal importance is therefore the assessment of the overall system performance. An summary of the bandwidth efficiency and an estimation of the BER degradation for all candidate schemes is provided below. In this workpackage, typical operating conditions regarding non-linearities in the transmission chain have been taken into account. No pre-demodulation signal processing, e.g. equalisation has been used.

The following table summarizes the occupied bandwidth requirements for the various cases studied. It can be seen that filtering at IF level before the non-linear component does restore the spectrum only to a rather limited extent. The occupied bandwidth is still reduced by more than a factor of 4. The best performance for techniques applied at IF level is obtained with OQPSK where the improvement factor is in excess of 7. It can also be seen that filtering at baseband level does not restore the spectrum if phase domain filtering is used and is thus very suitable for non-linear channels, in particular if several data rates need to be supported. The best performance is obtained with GMSK and square root raised cosine pulse shaping.

It shall be emphasized that the chosen filter characteristics in terms of type, order and 3 dB bandwidth are simply taken as an example to demonstrate that mild filtering already "does the job". Other filter types or different parameters may be equally adequate or even better. Under these conditions it is not reasonable to claim that filtering is too complex and too costly. Filtering can be done either at IF or RF level. Filtering the amplified RF spectrum requires a waveguide filter which often has a non negligible impact on cost and weight. In addition, a few fractions of a dB are lost due to reduced emitted spectral power.

Filtering at RF level before the high power amplifier requires simpler hardware and does not suffer any power losses. For QPSK, the spectrum may, however, be restored to a large extend by a non-linear power amplifier. Filtering at IF is simpler in terms of hardware but can only be applied if the RF carrier is not directly modulated. The spectrum may again be restored for QPSK.

REPORT CONCERNING CCSDS RADIO FREQUENCY AND MODULATION

ADVANCED SPECTRUM SHAPING FOR EFFICIENT BANDWIDTH UTILISATION

Modulation scheme	Filter Parameters	Non-linear Component and back-off	Estimated degradation BER 10^{-5}	Normalized Occupied Bandwidth	Bandwidth Improvement Factor
BPSK	no filter	TWTA 0 dB	0	22	1.00
BPSK	Butterworth N=6, BT=1.2	TWTA 0 dB	0.6	5.0	4.40
BPSK	Butterworth N=6, BT=1.2	TWTA 3 dB	0.6	3.6	6.11
BPSK	Butterworth N=6, BT=1.2	none	0.3	2.6	8.46
QPSK	no filter	TWTA 0 dB	0	11	1.00
QPSK	Butterworth N=6, BT=1.2	TWTA 0 dB	0.9	2.0	5.50
QPSK	Butterworth N=6, BT=1.2	TWTA 3 dB	0.7	1.6	6.88
QPSK	Butterworth N=6, BT=1.2	none	0.3	1.4	7.86
OQPSK	no filter	TWTA 0 dB	0	11	1.00
OQPSK	Butterworth N=6, BT=1.0	TWTA 0 dB	1.3	1.5	7.33
OQPSK	Butterworth N=6, BT=1.0	TWTA 3 dB	0.8	1.4	7.86
OQPSK	Butterworth N=6, BT=1.0	none	0.4	1.3	8.46
GMSK	BT=1, Mem=1	TWTA 0 dB	0.6	1.2	18.33
GMSK	BT=1, Mem=3	TWTA 0 dB	0.6	1.1	20.00
GMSK	BT=2, Mem=1	TWTA 0 dB	0.5	1.2	18.33
GMSK	BT=2, Mem=3	TWTA 0 dB	0.5	1.1	20.00
GMSK	BT=3, Mem=1	TWTA 0 dB	0.5	1.2	18.33
GMSK	BT=3, Mem=3	TWTA 0 dB	0.5	1.1	20.00
BPSK	Butterworth N=5, BT=1.2	TWTA 0 dB	1.2	3.8	5.79
BPSK	Butterworth N=5, BT=2	TWTA 0 dB	1.0	5.8	3.79

REPORT CONCERNING CCSDS RADIO FREQUENCY AND MODULATION

ADVANCED SPECTRUM SHAPING FOR EFFICIENT BANDWIDTH UTILISATION

Modulation scheme	Filter Parameters	Non-linear Component and back-off	Estimated degradation BER 10^{-5}	Normalized Occupied Bandwidth	Bandwidth Improvement Factor
BPSK	Butterworth N=5, BT=3	TWTA 0 dB	0.8	8.0	2.75
BPSK	Bessel N=3, BT=1.2	TWTA 0 dB	1.3	3.4	6.47
BPSK	Bessel N=3, BT=2	TWTA 0 dB	1.1	4.0	5.50
BPSK	Bessel N=3, BT=3	TWTA 0 dB	0.8	5.3	4.15
BPSK	SRRC, $\alpha = 0.5$	TWTA 0 dB	1.3	2.8	7.86
BPSK	SRRC, $\alpha = 0.8$	TWTA 0 dB	1.0	3.0	7.33
BPSK	SRRC, $\alpha = 1.0$	TWTA 0 dB	0.8	3.2	6.88

5 DETAILED OVERALL PERFORMANCE ASSESSMENT AND OPTIMISATION OF SELECTED TECHNIQUES

5.1 Selection of Preferred Shaping Techniques

Based on the results obtained during WP 100 and WP 200, it was found that the following schemes should be considered further as reference candidates for spectrum shaping. It shall be noted that these schemes are not a final selection or recommendation for techniques to be used. Their purpose is merely to serve as representative examples in order to achieve a desired spectral mask without excessive cost or performance burdens. There is a nearly unlimited combination of various filter types and parameters available which lead to similar or better performance, all being a question of trade-off between complexity and system performance.

BPSK with Butterworth filter, $N=6$, $BT=1$, no or a linear amplifier

BPSK with Butterworth filter, $N=6$, $BT=1$, SSPA

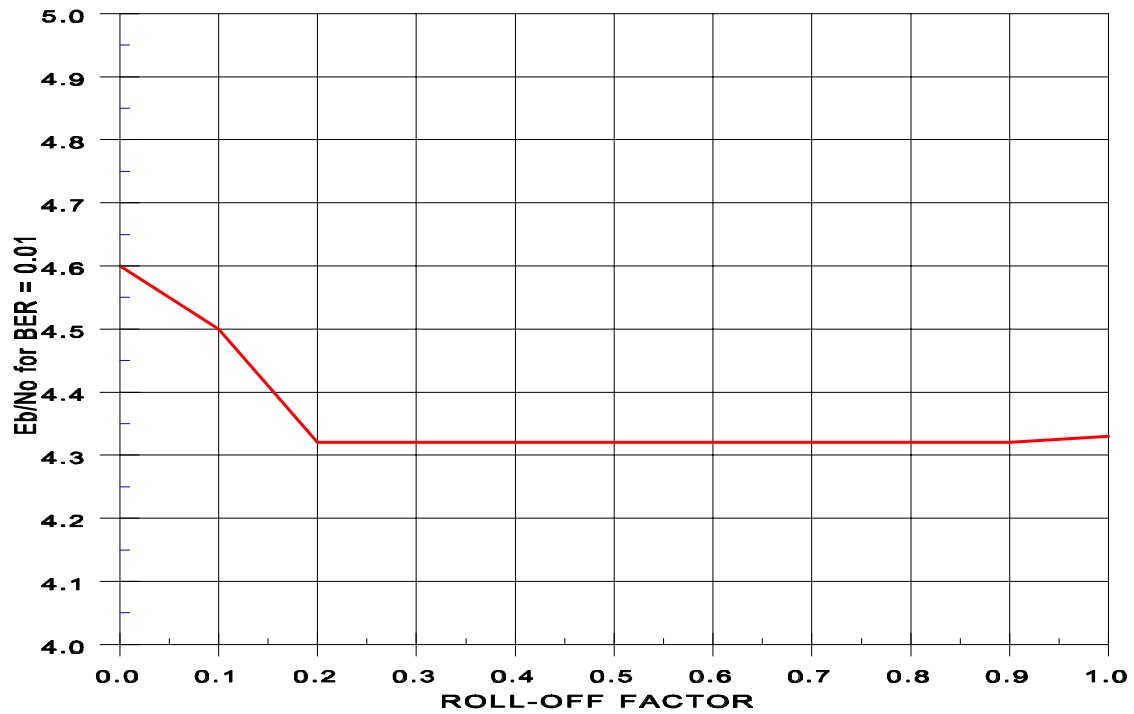
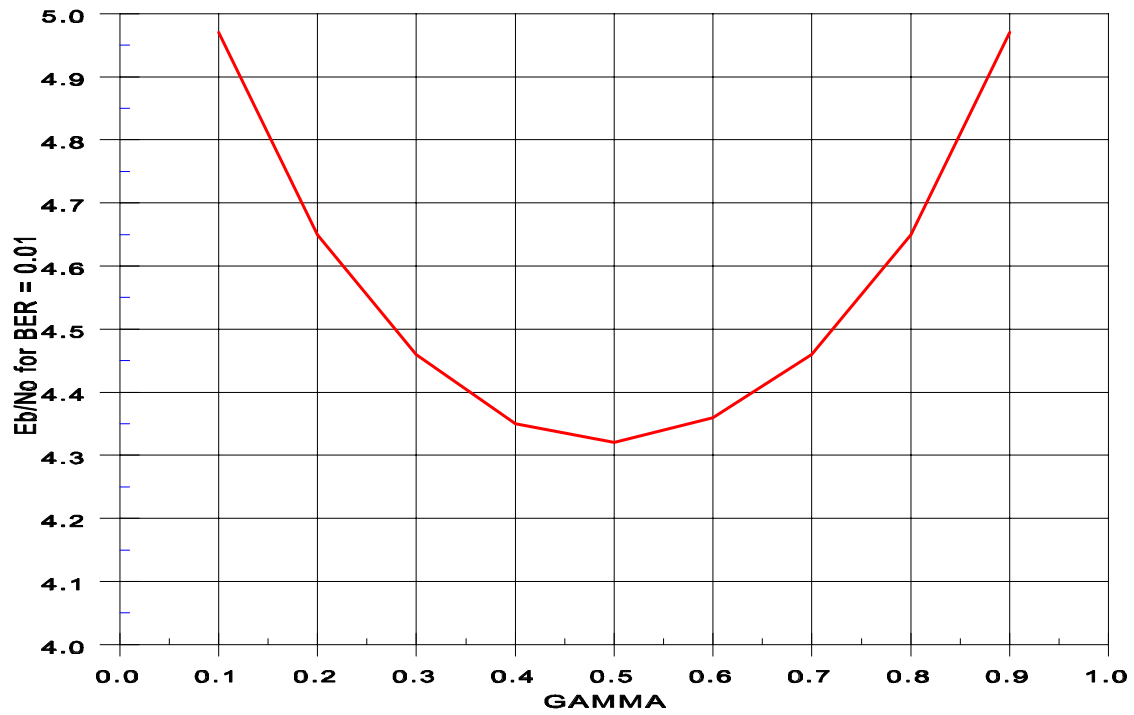
BPSK with SRRC Baseband filter, $\alpha=0.5$, SSPA

OQPSK with Butterworth filter, $N=6$, $BT=1$, SSPA

5.2 Identification of Suitable Equalisation Techniques in Receiver

Equalisation techniques can be applied in order to compensate the effect of signal distortion in equipment and along the transmission path. Any signal processing which removes part of the signal energy or changes the signal from its ideal state will result in an overall system degradation which may be recoverable, at least to some extent. The minimisation of losses will have to be concentrated on matching the detection process to the expected signal. It is obvious that a receiver which expects a rectangular pulse but actually receives a cosine shaped pulse will perform worse than one which can take that into account. This can be accomplished by either using a matched filter with respect to the expected pulse shape or by including a signal equalizer in front of the data detection block.

The optimum combination is a raised cosine filter at either end of the transmission chain. Such a combination will theoretically have no Inter Symbol Interference (ISI). Various parameters can be selected to optimise raised cosine filters, in particular the exponent to which the cosine function is raised (γ) and the roll-off factor of the raised cosine function. Figures 54 and 55 show that optimum performance is achieved if γ is 0.5 and if α is within a range between 0.2 and 0.9.



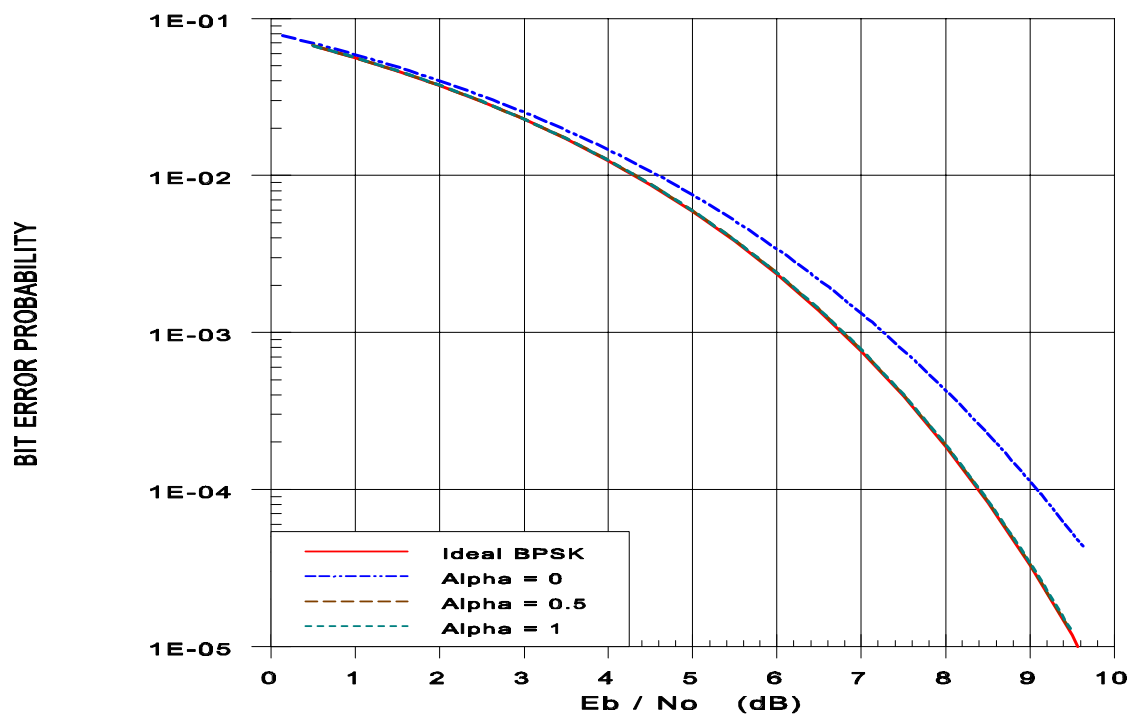
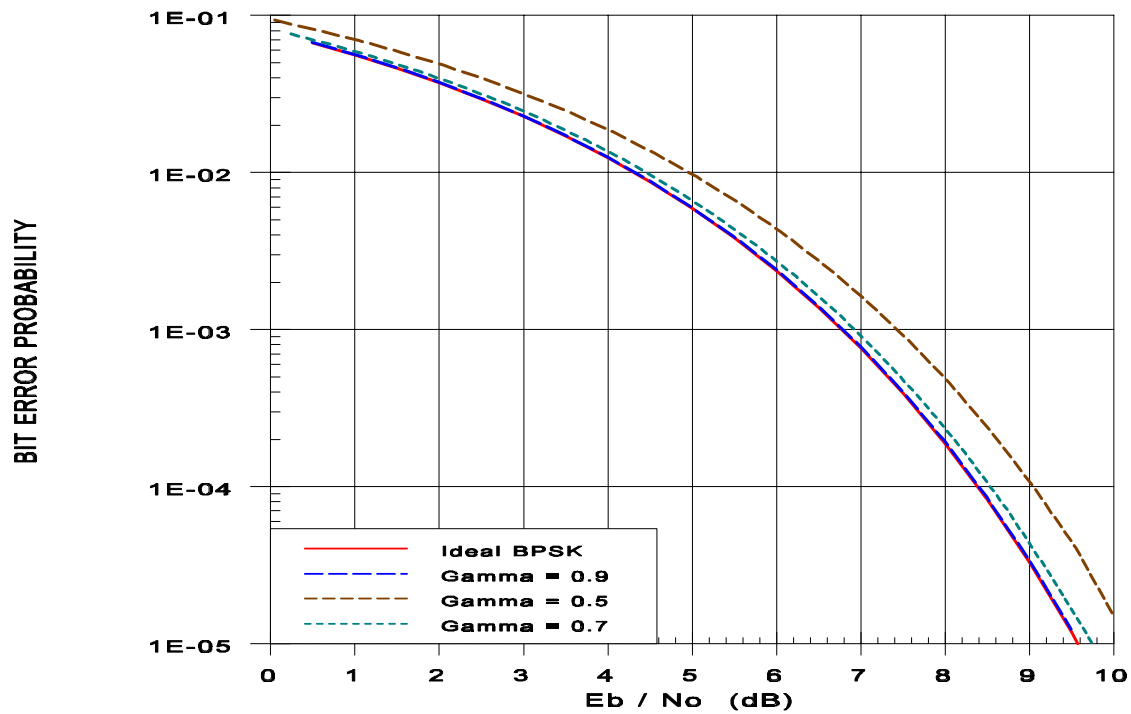
5.3 Calculation of Overall Degradation with System Optimisation

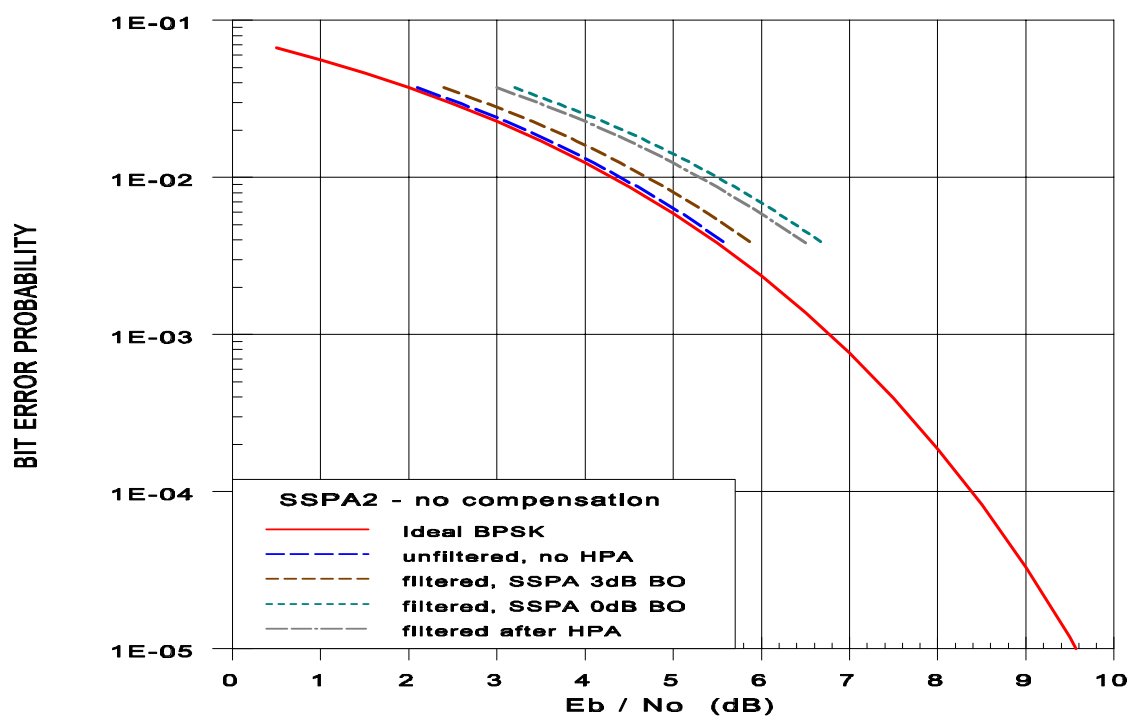
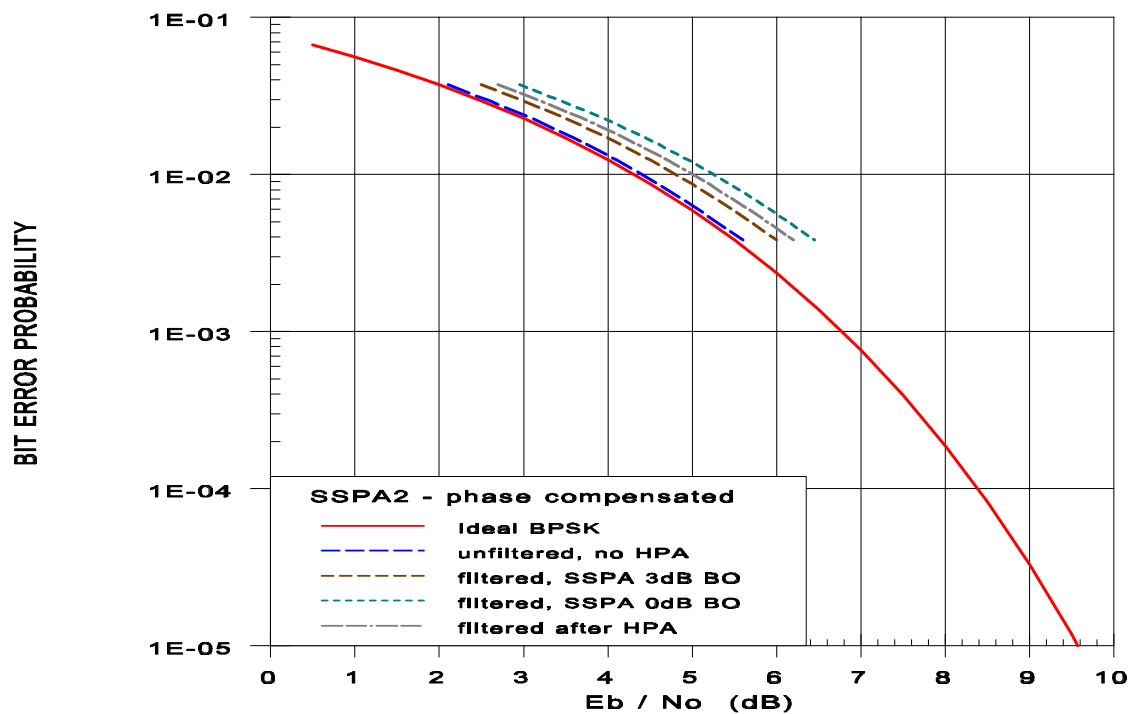
The BER degradation for all selected schemes has been calculated taking into account the above identified equalisation techniques and system non-linearities. The best performance is obtained for raised cosine filtering on the transmit as well as the receive side, but the complexity is also significant. Figures 56 and 57 show the performance obtained for variable gamma and roll-off factor (α). It can be seen that the performance is quasi ideal. The receive filter is matched to the transmit filter and no ISI occurs. An alternative would be a raised cosine filter at the transmitter side and a Butterworth filter at the receiver side. In this case the receive filter is not ideally matched anymore and a degradation of a few tenths of dB will occur.

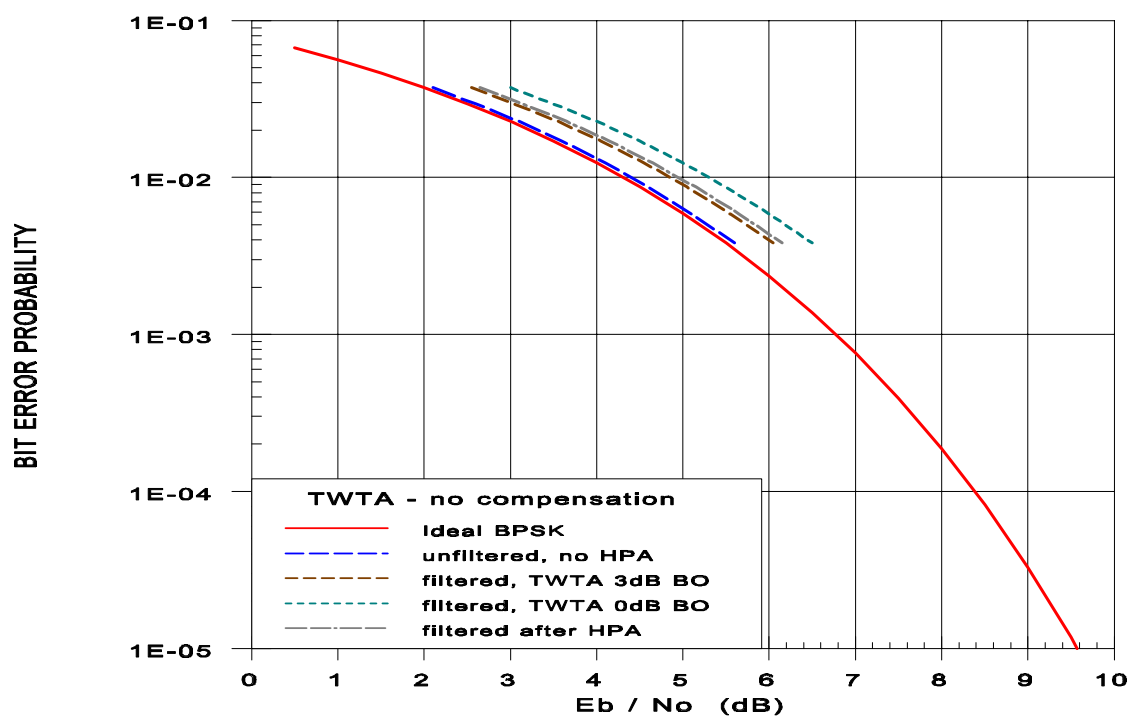
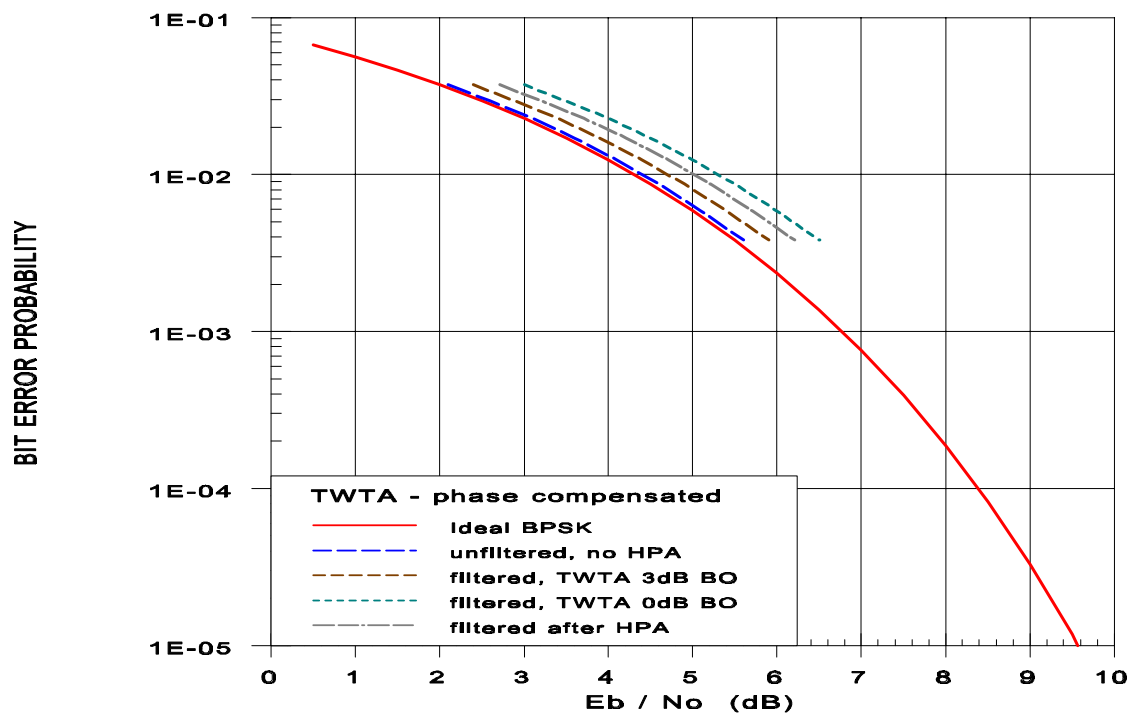
A very interesting aspect is the impact of the non-linearity on the system degradation and it is felt that this may have a bigger impact than the shaping techniques itself. Four cases have been investigated. Two based on an SSPA, one with phase compensation, the other one without, and two based on a TWT, one again with phase compensation, the other one not. Figures 58, 59, 60 and 61 show the comparison of these cases for a constellation with a Butterworth filter (BT=1) at IF level and no back-off. It can be seen that phase compensation can reduce degradation and should therefore be applied whenever possible.

The study also lead to interesting results regarding the different degradation of QPSK and OQPSK in the presence of a non linear amplifier. It was observed that OQPSK had always a larger degradation than QPSK. When investigating the matter further, a distinction was made between degradation caused by AM/AM distortion and AM/PM distortion. While the AM/PM distortion was about the same (but still around twice as much as for BPSK), the AM/AM distortion was around twice as high for OQPSK as compared to QPSK. This is due to the fact that, with OQPSK, the envelope at sampling time is no longer constant. It can vary between the envelope of the sampled channel only, i.e. the quadrature channel has a transition and is zero, or have a maximum of the square root sum of the two components. A non-linear component in the system has therefore a larger impact.

Table 6 contains a summary of the overall system performance for the selected shaping techniques taking into account the above optimisation techniques.







Modulation scheme	Filter Parameters	Non-linear Component and back-off	Estimated degradat. BER 10^{-2}	Estimated degradat. BER 10^{-5}	Normalized Occupied Bandwidth	Bandwidth Improvem. Factor
BPSK	no filter	TWTA 0 dB	0	0	22	1.00
BPSK	Butterworth N=6, BT=1	TWTA 0 dB	0.8	0.9	4.6	4.78
BPSK	Butterworth N=6, BT=1	TWTA 3 dB	0.4	0.55	3.3	6.67
BPSK	Butterworth N=6, BT=1	SSPA 3 dB	0.35	0.5	3.1	7.10
BPSK	Butterworth N=6, BT=1	none	0.6	0.7	1.7	12.94
GMSK	BT=1	TWTA 0 dB	0.6	0.6	1.3	16.92
BPSK	Butterworth N=5, BT=1	TWTA 0 dB	1.0	1.2	3.8	5.79
BPSK	SRRC, $\alpha=0.5$	TWTA 0 dB	0.1	0.1	2.8	7.86
QPSK	no filter	TWTA 0 dB	0	0	11	1.00
QPSK	Butterworth N=6, BT=1	TWTA 0 dB	1.0	1.2	2.0	5.50
QPSK	Butterworth N=6, BT=1	TWTA 3 dB	0.6	0.8	1.6	6.88
QPSK	Butterworth N=6, BT=1	none	0.8	0.9	1.4	7.86
OQPSK	no filter	TWTA 0 dB	0	0	11	1.00
OQPSK	Butterworth N=6, BT=1	TWTA 0 dB	1.2	1.4	1.5	7.33
OQPSK	Butterworth N=6, BT=1	TWTA 3 dB	0.7	0.9	1.4	7.86
8PSK ¹	SRRC, $\alpha=0.5$	SSPA 0 dB	1.6(+3.2)	2.7(+3.2)	1.8 (-50dB)	6.11
FQPSK ²	BT=1	HPA 0dB	1.3 (TBD)	1.7 (TBD)	0.85	25.88

Table 6: PERFORMANCE SUMMARY OF SELECTED SHAPING TECHNIQUES

¹ according to work performed under NASA contract

² according to results presented to CCSDS by Dr. Kamilo Feher

5.4 Comparison of Hardware Complexity for the Identified Techniques

It is evident and well known that for MPSK schemes the complexity increases significantly with M . BPSK modulators and demodulators are simpler than their QPSK counterparts. Of relevance is only the complexity in the demodulator. Whereas a BPSK demodulator requires a single squaring loop for carrier recovery and 2 filter arms for data recovery, twice of these are required for a QPSK demodulator. Although the actual implementation can vary, it may be fair to assume that QPSK modems have nearly twice the complexity of BPSK modems. OQPSK is only slightly more complex than QPSK. In comparison to QPSK schemes, 8PSK is approximately 50% more complex.

The modems are often determined by mission requirements and the deciding factor lies more in the shaping techniques. Filters at baseband are obviously much simpler to implement because the order is half compared to IF level and they can be implemented at very low power levels. They can often be incorporated in the digital signal processing section of the modem. Filters at IF level are simpler to implement than filters at RF level because the ratio between the centre frequency and the passband is in general small compared to RF filters and the power levels are also low. Most complex are filters at RF level after the power amplifier, in particular when the data rate is less than approximately 10^{-3} of the radio centre frequency.

6 EXTERNAL INTERFERENCE SUSCEPTIBILITY ASSESSMENT

It is often not a noise-like environment which has the biggest impact on the end-to-end performance of a communication system. In addition to internal signal distortion caused by non-linearities, hardware imperfections and spectral shaping techniques, external distortion may occur on the receiving side. Most of the bands allocated to and used by the Space Radiocommunication Services are subject to interference from other services with which the bands are shared. In particular the 2 GHz bands are subject to heavy interference from Fixed Service and Mobile Service installations. The increasing number of satellites results also in rapidly growing intra-service interference. It is therefore of interest to investigate the behavior of bandlimited modulation techniques in the presence of external interference. The impact of the following types of interference to the selected modulation techniques has been investigated with spectrum shaping being applied.

6.1 Susceptibility to Narrowband RFI

Narrowband interference originates from unmodulated carriers, remnant carriers and narrowband mobile service applications and is characterised by a strong signal component which can fall into the receiver loop bandwidth or into the arm filters for data recovery. In the first case, the typical impact is tracking of a false carrier or of a combined signal component with varying amplitude and phase. In this case, data can normally not be obtained even if the E_b/N_0 would be sufficiently high.

The second, and more likely case, is a strong narrow signal component falling into the arm filter of the data demodulator. This causes in general a degradation of the E_b/N_0 . It has been assumed that a strong narrowband interference with a power equal to -6 dB compared to the wanted signal falls in the middle of the right part of the spectral main lobe. The corresponding spectra for the wanted and interfering signals are shown in figure 62. The interference centre frequency being thus 0.5 times the data rate away from the centre frequency of the wanted signal. The narrowband characteristics have been simulated by using an interfering signal with approximately 10% of the bandwidth of the wanted signal. The results for BPSK, QPSK and OQPSK modulation are summarized in table 7. It can be seen that OQPSK is the most vulnerable of the 3 modulation schemes but the difference is well within acceptable limits and should thus not be considered a decisive aspect for using this technique.

6.2 Susceptibility to Wideband RFI

Wideband interference originates often from high data rate fixed service and mobile service applications but may also originate from high data rate space science service applications. This type of interference is characterised by a noise like signal component which falls into the receiver loop bandwidth as well as into the arm filters for data recovery. The impact is in general a reduction of the loop signal to noise ratio and the E_b/N_0 . For typical interference constellations, the impact on the data recovery subsystem is more significant than on the carrier recovery loop. Very wideband interference is practically noise-like and is not of interest for simulations. An interesting case appears to be interference with data rates between around 1 and 3 times the data rate of the wanted signal. For the simulations, a factor of 2 has been used. The resulting spectra for wanted and interfering signals are shown in figure 63. The corresponding bit error rates for BPSK, QPSK and OQPSK are shown in table 7. Like with narrowband interference, OQPSK is the most vulnerable one, followed by QPSK. Even though the signal-to-noise ratio is the same for both interference cases, the error rate is lower for wideband interference because only part of it will actually fall into the data recovery subsystem. With narrowband interference, the full amount of energy will be found in the data recovery subsystem.

6.3 Susceptibility to Pulsed RFI

Pulsed interference originates from burst mode operations or radiolocation applications and is characterised by a strong, short duration wideband signal which can fall into the receiver loop bandwidth as well as into the arm filters for data recovery. The simulation model does not have the capability of a burst interference generator. However, the interference impact has been investigated and it has been concluded that pulsed RFI will not have any influence on the shaping technique. The performance of a communication system in the presence of pulsed interference will be mainly determined by time constants of various system components. Two cases can be distinguished. In the first, the interference will be short enough in order not to lose the signal in the tracking and data loops. The degradation will then depend primarily on the capability of the channel coding system to cope with the generated burst of errors. In the second case, the signal will be lost and a complete re-synchronisation process will be required. This will necessitate carrier recovery, bit synchronisation and channel decoder synchronisation, possibly also de-interleaver and frame synchronisation. It is obvious that spectrum shaping techniques do not have an impact on

the above and that for the purpose of this study the cases of narrowband and wideband interference cover also the pulsed RFI case for adequate time periods.

Modulation scheme	Spectrum Shaping Parameters	Non-linear Component and back-off	Bit Error Rate for $E_b/I_o = 6\text{dB}$ with wideband interference	Bit Error Rate for $E_b/I_o = 6\text{dB}$ with narrowband interference
BPSK	Butterworth $N=6$, $BT=1$	SSPA, 3 dB	1.3×10^{-4}	4.5×10^{-3}
QPSK	Butterworth $N=6$, $BT=1$	SSPA, 3 dB	2.1×10^{-4}	6.2×10^{-3}
OQPSK	Butterworth $N=6$, $BT=1$	SSPA, 3 dB	3.2×10^{-4}	8.1×10^{-3}

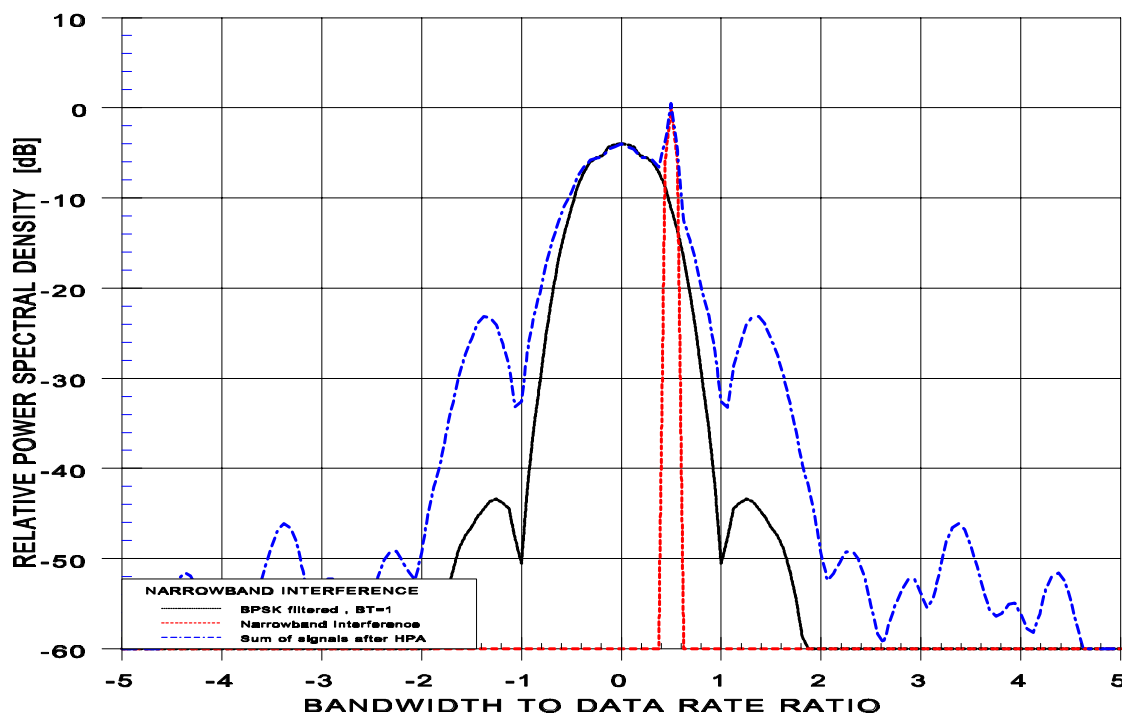
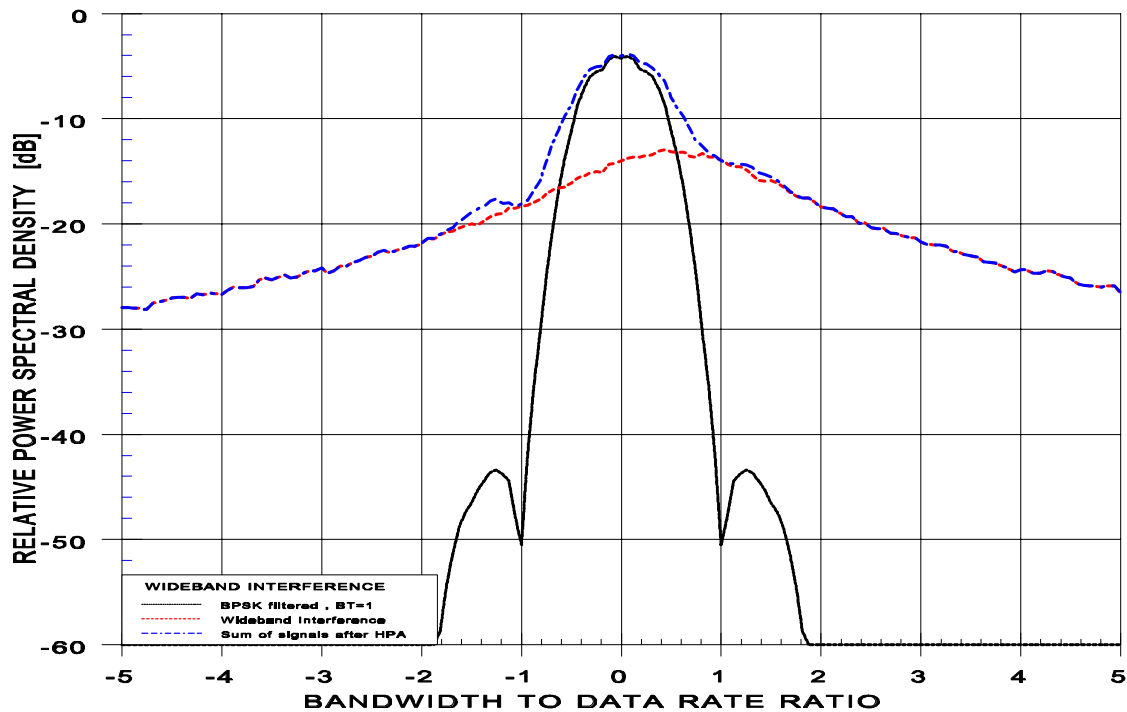


Table 7: PERFORMANCE SUMMARY FOR INTERFERENCE CASES

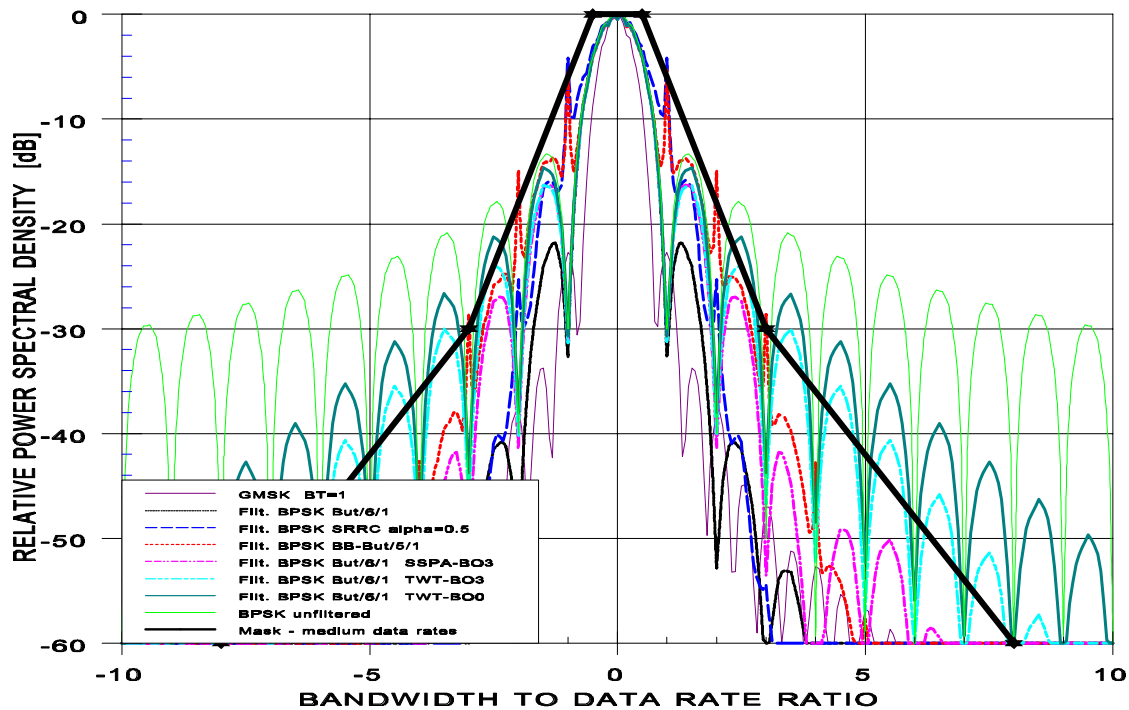
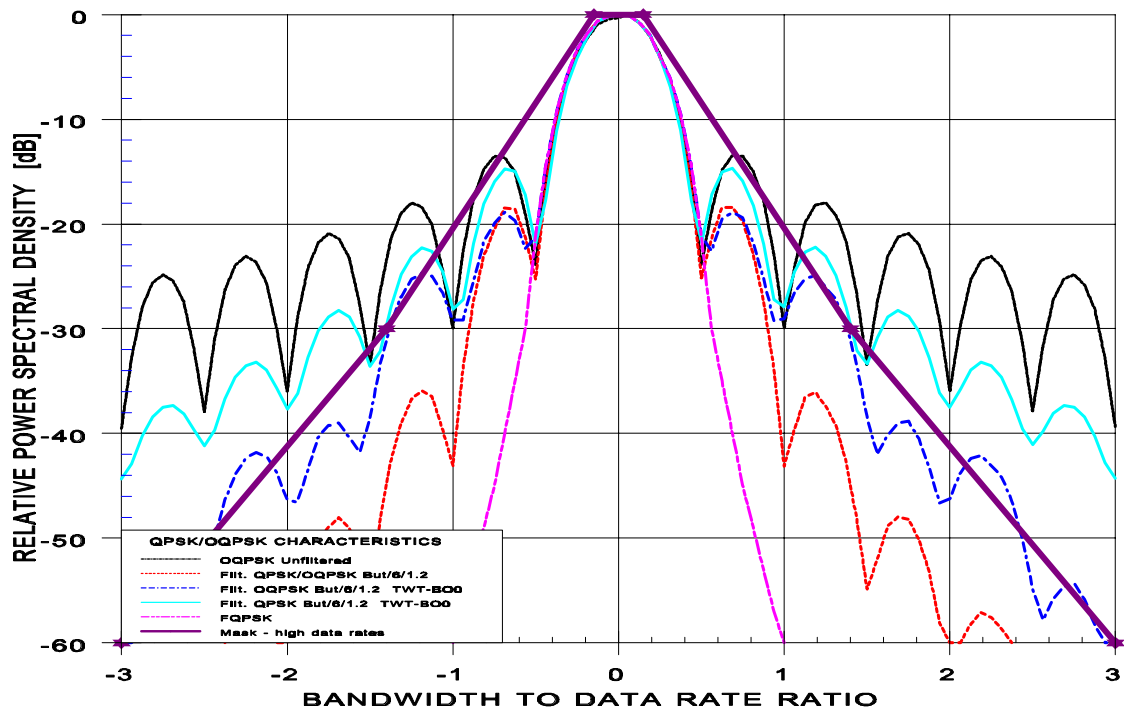


7 DEFINITION OF SPECTRAL MASKS FOR UNWANTED EMISSIONS

7.1 Definition of a Suitable Mask for the Data Spectrum

Based on the obtained results for spectrum efficiency improvement versus performance degradation and hardware complexity, the following masks are considered suitable for limiting the data spectrum. Two masks are proposed because a distinction should be made between high data rate and medium data rate applications. A limit of approximately 10 Mb/s is proposed for the transition between the 2 masks. Most of the identified shaping techniques can meet the masks irrespective of the level where the signal shaping is applied. This allows the user the choice for a preferred technique depending on his specific system requirements.

Figure 64 shows the spectra for the selected spectrum shaping techniques and the proposed mask for high data rate applications in excess of 10 Mb/s. In comparison to BPSK techniques, it is easier to meet a comparatively narrower spectrum because OQPSK can be used. For this technique, the spectrum restoration due to non-linear system components is smaller than for conventional QPSK because the signal envelope is less fluctuating. This is due to bit transitions not occurring at the same time instant as is the case with QPSK. The amplitude of the envelope therefore never goes to zero.



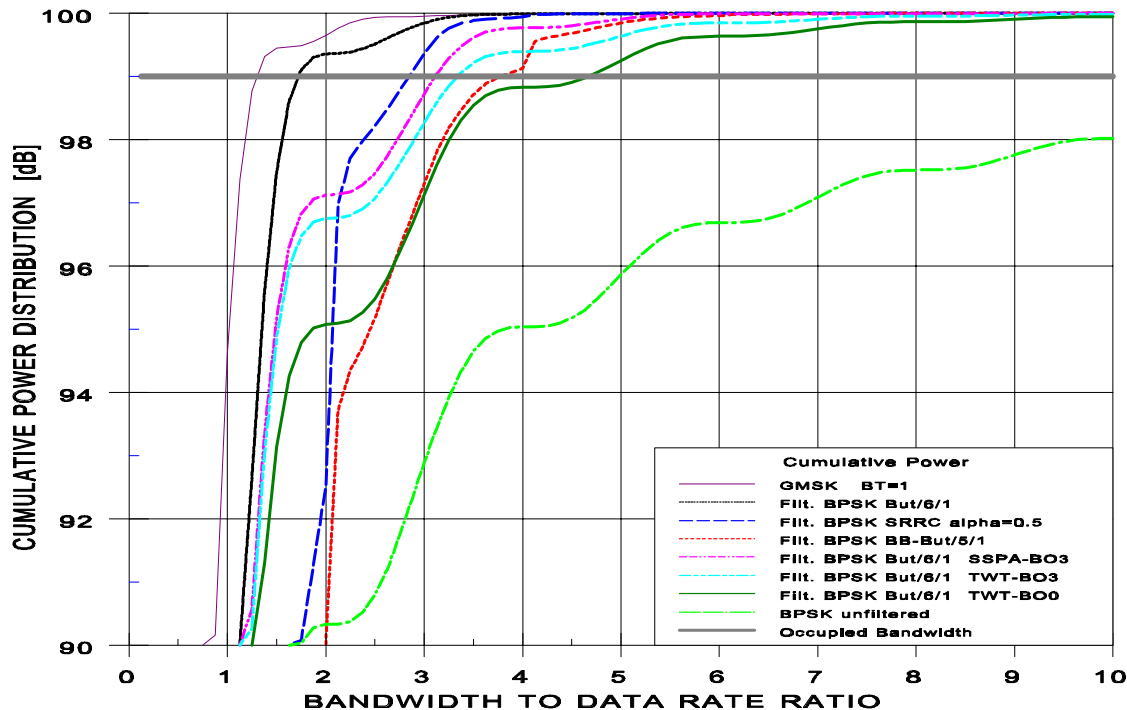


Figure 65 shows spectra of interest and a proposed mask for spectrum shaping based on BPSK schemes. Such a mask could be made applicable to data rates between 50 kb/s and 10 Mb/s. Figure 66 shows the corresponding occupied bandwidth for the selected techniques.

7.2 Definition of a Suitable Spectral Mask for Spurious Components

Various specifications for limits on spurious components can be found in ITU documentation and agency standards. These specifications have been reviewed and the mask in figure 67 is proposed. The definition of discrete lines, or spurious emissions in ITU terms when outside the necessary bandwidth, is an ever challenging subject. There are several different reasons for such specifications.

7.2.1 Discrete Lines inside the wanted signal

An unwanted spectral component inside the arm filter bandwidth of the demodulator will cause interference to the wanted signal and, if strong enough, may even lead to a false signal lock. In the frame of ESA mission support, it has been found that spectral lines in the order of 20 dBc inside the arm filter bandwidth will not cause a significant degradation. In theory, the degradation is only 0.04 dB. A -30 dBc limit can therefore be considered quite adequate. In addition, if high data rates are used in connection with correspondingly high EIRP levels emitted by the spacecraft, PFD limits on the Earth's surface may be exceeded. For example, a 1 Ms/s transmission at PFD limits based on the data spectrum would lead to a PFD excess of 4 dB if a -20 dBc spectral component would be present. A -30 dBc limit would therefore avoid any PFD problems for data rates up to 4 Ms/s in the worst case where the data spectral density corresponds to the PFD limits, which would cover most ESA missions. Higher data rates than 4 Ms/s will require tighter specifications.

From a performance and typical PFD excess point of view, a value of -30 dBc can be considered quite appropriate and is believed to be achievable with reasonable hardware complexity.

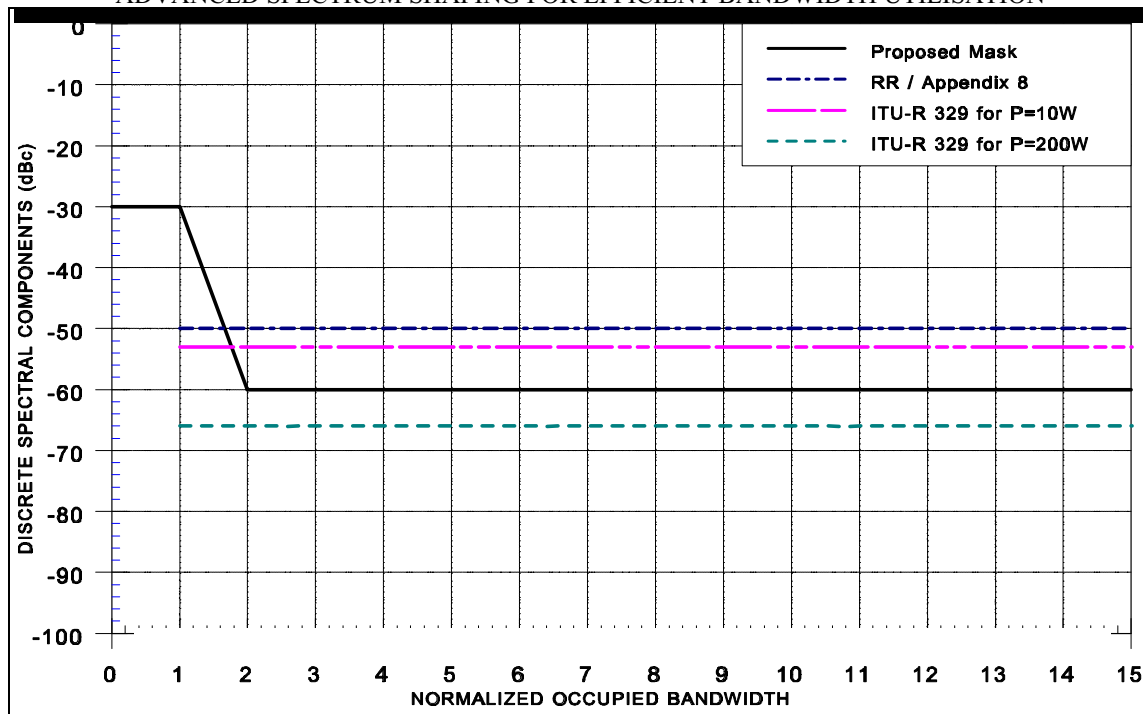
7.2.2 Discrete Lines outside the wanted signal

Unwanted spectral components outside the signal passed through the arm filter (more or less equivalent to spurious emissions as defined by the ITU) may cause harmful interference to other receivers operating in the same band or neighbouring bands. In practice, it is the protection requirements for the deep space service which are the most stringent ones. The corresponding protection levels are given in Table 4.8 and can be as high as -257 dBW/m²/Hz for the largest antennas at 2 GHz. It is obvious that these protection requirements can in most cases not be met by technical specifications. However, it must also be recognized, that the probability of causing harmful interference to deep space stations is typically in the order of 10^{-5} to 10^{-10} . It appears therefore appropriate that a reasonable technical effort shall be made to reduce the potential for interference in the first place and that the remaining interference probability be handled by operational means to be decided by the frequency managers concerned on a case by case basis.

The corresponding requirements for spurious emissions shall therefore be based on reasonable technical specifications rather than specific protection requirements. As a guideline, the ITU Radio Regulations (App. 8) or the proposed modifications by Task Group 1/3 to recommendation ITU-R 329 can be taken into consideration. RR/App. 8 specifies -50 dBc but is not applicable to space stations of space services. Rec. 329 recommends a transmitter power P depended value corresponding to $-43 - 10\log(P)$. Other sources (e.g. PSS-04-109) specify a maximum value of -60 dBc in a 100 Hz bandwidth. Inherent filtering effects or very mild filtering or pulse shaping can be applied which would further reduce the magnitude of the spurious components as a function of the frequency separation from the centre frequency.

Taking into account the various points listed above and trying to merge them into a reasonable technical specification which make the hardware manufacturers and deep space representatives equally unhappy, the following mask for discrete spectral lines is proposed. This mask is applicable to suppressed carrier systems only. It shall be noted that the occupied bandwidth has been used as the reference bandwidth because it is well defined and is normally notified to the ITU as the necessary bandwidth in the corresponding forms. In Figure 67, RR/App. 8 and recommendation ITU-R 329 have been included for reference. A transmitter power value of 10 W may be considered representative for spacecraft. ESTRACK stations operate in most cases with 200 W amplifiers.

ADVANCED SPECTRUM SHAPING FOR EFFICIENT BANDWIDTH UTILISATION



8 CONCLUSIONS

- Relatively simple spectrum shaping results already in substantial occupied bandwidth reductions.
- The filter type and its order are of secondary importance for achieving a similar occupied bandwidth
- Baseband filtering is very attractive with non-linear devices but creates spikes at critical amplitudes in the nulls of the spectrum
- Baseband filtering is very attractive if several data rates are used on one mission
- Filtering at IF or RF before the HPA is in many cases very attractive in particular for very high data rates
- A solid state power amplifier is preferred over a traveling wave tube amplifier

- There is not much difference between no HPA back-off or a few decibels back-off regarding occupied bandwidth
- Phase compensation of the HPA results in performance improvement
- Offset QPSK shall be preferred over regular QPSK on non-linear channels despite slightly higher system losses
- FQPSK may be a very attractive modulation technique on non-linear channels but results in relatively high system losses and requires further study

9 RECOMMENDATIONS

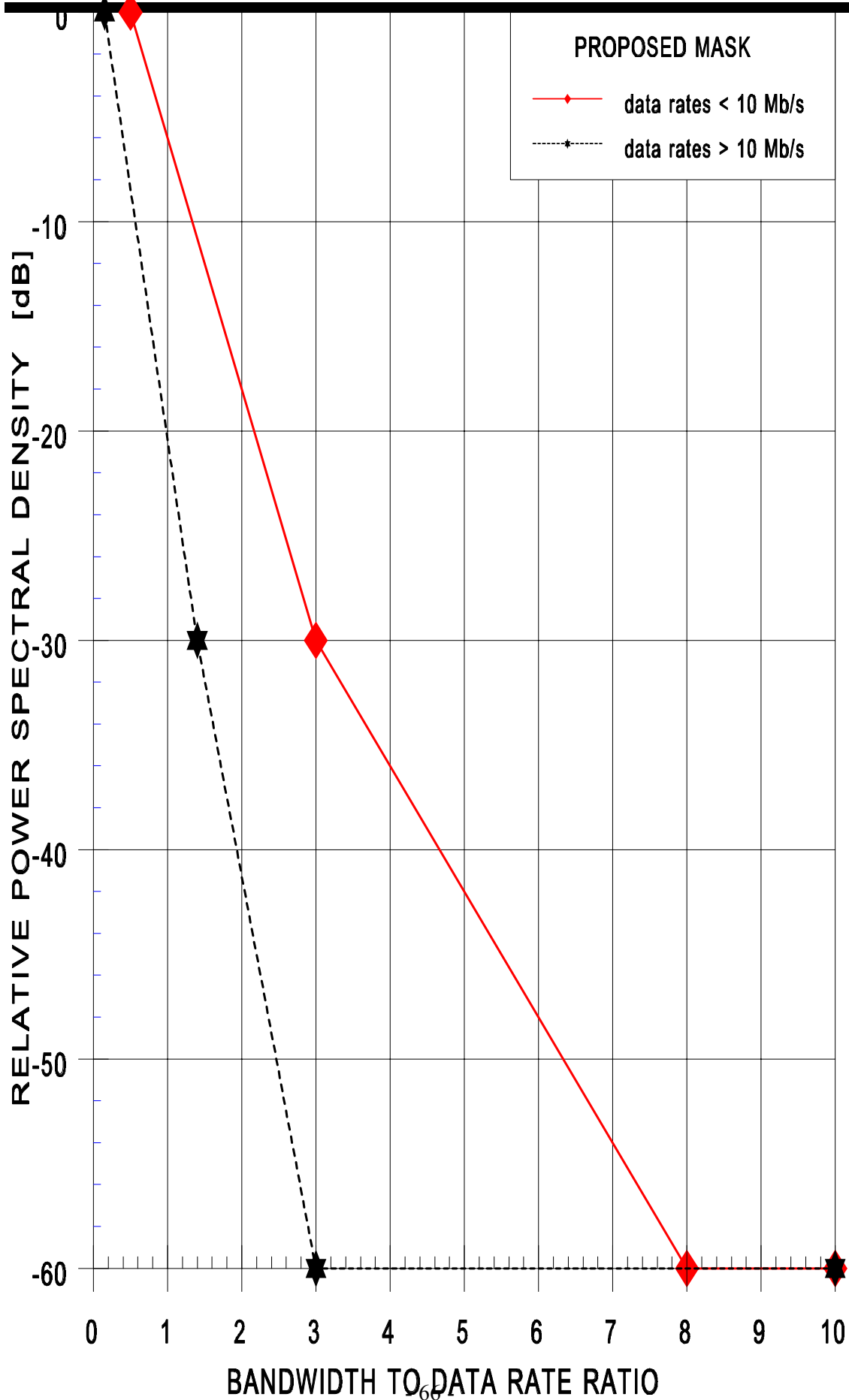
Various considerations have to be taken into account for deriving suitable recommendations resulting from this study. The usage of spectrum beyond what is actually required increases the potential of interference to other users and at the same time results also in a higher susceptibility to interference from other users of the band. Notified bandwidth requirements beyond actually required spectrum increase the coordination burden.

Subcarrier modulation techniques require substantially more spectrum compared to suppressed carrier modulation techniques. The required spectrum with subcarrier modulation is a function of the subcarrier frequency and the subcarrier-to-symbol rate ratio. Subcarrier frequencies are typically 60 kHz or higher, for which a subcarrier-to-symbol rate ratio of 4 is generally sufficient to obtain acceptable performance. There are no technical reasons which would require the use of subcarrier modulation for data rates above 50 ks/s. The use of bi-phase modulation is only justified when a distinct carrier component is required. With unfiltered suppressed carrier modulation schemes, medium to high data rate transmissions have bandwidth requirements which result in increased coordination burdens. Spectrum shaping can be used effectively to reduce the occupied bandwidth by a factor between 5 and 10 for suppressed carrier modulation schemes,

Based on the above and on the detailed study results, the following recommendations are made:

- subcarrier frequency modulation shall not be used except where absolutely required,
- a subcarrier frequency-to-symbol rate ratio of 4 be selected for subcarrier frequencies above 60 kHz unless multi-component signals result in spectral overlaps which require a higher value for sufficient separation of the individual components,
- bi-phase or suppressed carrier modulation shall be used for data rates above 50 ks/s,
- bi-phase modulation shall only be used when a carrier component is absolutely required,
- for suppressed carrier modulation techniques, the mask in figure 68 be used as a guideline for out-of-band emissions

ADVANCED SPECTRUM SHAPING FOR EFFICIENT BANDWIDTH UTILISATION



10 REFERENCES AND APPLICABLE DOCUMENTS

- [1] Handbook of the Space Frequency Coordination Group
December 1995
- [2] CCSDS Recommendations for Radio Frequency and Modulation Systems
Blue Book - Part 1: Earth Stations and Spacecraft
November 1994
- [3] Radio Frequency and Modulation Standard
ESA Document PSS-04-105
December 1989
- [4] Ranging Standard
ESA Document PSS-04-104
March 1991
- [5] ITU Radio Regulations
Edition 1994, Geneva
- [6] ITU RTF, RSA, RRA Series
Science Services
CCIR Recommendations, Geneva 1992
- [7] Gardner F.M., Phase Lock Techniques
John Wiley & Sons, New York
New York, 1966
- [8] Spilker, J.J., Digital Communications by Satellite
Prentice Hall Inc.
New Jersey, 1977
- [9] Feher, K., Wireless Digital Communications
Prentice Hall Inc.
New Jersey, 1995
- [10] Feher, K., Efficient FQPSK Modulation - Integrated Transceiver Developments
Contribution to CCSDS Sub-Panel 1E Meeting, April 1997
- [11] Martin W.L., Yan T.-Y, Lam L.V.
Efficient Modulation Methods Study at NASA/JPL
CCSDS-SFCG, 1997
- [12] Horan S., et al, Pulse Shaped Constant Envelope 8-PSK Modulation
New Mexico State University, March 1997

[This page intentionally left blank.]

CCSDS Panel 1E

SFCG Action Item AI 18-17/2, Tasks 17/2-1 to 17/2-5

Interference Susceptibility of Selected Bandwidth-Efficient Modulation Schemes

Gabriella Povero^{*} Enrico Vassallo[†] Monica Visintin[‡]

Los Angeles, April-May 1999

Abstract

The SFCG-18 recommended that RFI susceptibility studies be performed for the bandwidth-power efficient modulation schemes proposed by CCSDS. In this paper, Butterworth and Square-Root-Raised-Cosine (SRRC) filtered OQPSK, and GMSK with $BT_b = 0.5$ and $BT_b = 1$ are compared in the presence of narrow band and wide band interferers, over AWGN and nonlinear channels. The purpose of this work is to find out the most suitable bandwidth efficient modulation scheme for the increasingly crowded frequency bands available for space missions.

1 Introduction

In the frame of the development of a world-wide standard for the modulation technique to be used for space missions, a deep analysis has been carried out recently, and the results are reported in [1]. The objective there was to study the bandwidth efficiency of several modulation schemes in the presence of a nonlinear channel characterized by either a TWTA (Travelling Wave Tube Amplifier) or an SSPA (Solid State Power Amplifier), both driven at 0 dB backoff. The conclusions were that, depending on the position of filtering inside the modulator, the more suitable schemes are:

baseband filtering: square-root-raised-cosine (SRRC) filtered OQPSK with roll-off factor 0.5, and GMSK

IF or RF filtering: Butterworth filtered OQPSK

However further investigation was required, in order to determine which of these modulation schemes has to be preferred for the overcrowded bands available for space

^{*} COREP, Politecnico di Torino

[†] ESOC, European Space Agency

[‡] Dipartimento di Elettronica, Politecnico di Torino

missions. In particular, it had to be found which one was the most robust against the unavoidable co-channel interference. This paper describes the results of this investigation. Narrow band and wide band interference are considered, the first deriving by data imbalance of co-channel signals or by residual carrier modulations originating from lower rates missions, the other deriving by other missions using the same frequency channel. Moreover the interfering signals can be at the same frequency or with a frequency offset with respect to the wanted signal as happens with present frequency assignments. The same nonlinear amplifiers considered in [1] are assumed, but, for sake of completeness, also the case of a simple linear AWGN (Additive White Gaussian Noise) is included.

The paper is organized as follows: section 2 precisely defines the considered transmission schemes (including the receiver structure), sections 3 and 4 give a detailed description of the nonlinearities and the interferers that have been considered, sections 5 and 6 are used to list the results and draw the conclusions.

2 Transmission schemes

Each of the following subsections describes one of the considered modulators. Valid for all is the assumption that the receiver carrier and clock recovery subsystems are perfect. The information bits are generated at rate $1/T_b$ and zeros and ones are equally likely. The considered modulations are briefly described in the following subsections, while their power spectra are compared in Figure 1. All the simulations were performed with the simulation package TOPSIM-IV.

2.1 Unfiltered BPSK (benchmark)

The BPSK (Binary Phase Shift Keying) transmitted signal has complex envelope

$$\tilde{x}(t) = \sqrt{E_b} \sum_{k=-\infty}^{\infty} a_k \psi(t - kT)$$

where $a_k \in \{\pm 1\}$ and $\psi(t) = \sqrt{1/T} u_T(t)$, with $u_T(t) = 1$ for $0 < t < T$, and $u_T(t) = 0$ elsewhere, and E_b is the energy per bit; in this case the symbol interval T is equal to the bit interval T_b . The receiver generates the complex envelope $\tilde{r}(t)$ of the received signal, passes it through the matched filter with impulse response $\psi(t)$, samples at times $nT + T$, and takes the decision on a_n with a zero-threshold detector.

2.2 Butterworth-filtered OQPSK

The OQPSK (Offset Quadrature Phase Shift Keying) transmitted signal has complex envelope

$$\tilde{x}(t) = \sqrt{E_b} \left[\sum_{k=-\infty}^{\infty} a_{k,R} g(t - kT) + ja_{k,I} g(t - kT - T/2) \right]$$

where both $a_{k,R}$ and $a_{k,I}$ take values in $\{\pm 1\}$, $T = 2T_b$ is the symbol interval, and $g(t)$ is the convolution of $u_T(t)$ and the impulse response of a 6-pole Butterworth filter with 3-dB bandwidth equal to $1/T$. The received complex envelope is passed through a filter with impulse response $\sqrt{1/T}u_T(t)$, the real component is sampled at times $t_0 + nT$, while the imaginary part is sampled at times $t_0 + nT + T/2$, where instant t_0 is that of maximum eye opening. A threshold detector takes the decisions on $a_{n,R}$ and $a_{n,I}$. The eye pattern of the in-phase component of the signal at the output of the receiver filter is shown in Figure 2. With respect to ideal BPSK, the losses due to intersymbol interference (ISI) are 0.44 dB at $P_b(e)=10^{-1}$, 0.52 dB at $P_b(e)=10^{-2}$, 0.60 dB at $P_b(e)=10^{-3}$.

2.3 SRRC-filtered OQPSK

The transmitted signal has complex envelope

$$\tilde{x}(t) = \sqrt{E_b} \left[\sum_{k=-\infty}^{\infty} a_{k,R} \psi(t - kT) + ja_{k,I} \psi(t - kT - T/2) \right]$$

where $a_{k,R}$ and $a_{k,I}$ take both values in $\{\pm 1\}$ and $\psi(t)$ is the impulse response of a square-root-raised cosine (SRRC) filter with roll-off factor 0.5. The transmitted signal power spectrum is shown in Figure 1, and it is apparent that SRRC-filtered OQPSK is the most bandwidth efficient modulation among those considered in this paper.

Two receivers are assumed: the first using the matched filter with impulse response $\psi(t)$ (SRRC-a), the second using a filter with impulse response $\sqrt{1/T}u_T(t)$ (SRRC-b). The sampling is performed at the maximum eye opening and a zero-threshold detector takes the decision. The eye patterns at the output of the receiver filters for the SRRC-a and SRRC-b cases are shown in Figure 3 and Figure 4. SRRC-a has the same performance as ideal BPSK in terms of bit error rate, while SRRC-b suffers from a loss of 0.59 dB at $P_b(e)=10^{-1}$, 0.61 dB at $P_b(e)=10^{-2}$, 0.65 dB at $P_b(e)=10^{-3}$, due to ISI.

2.4 GMSK

Two GMSK (Gaussian Minimum Shift Keying) signals are considered, with normalized bandwidth $BT_b = 0.5$ and $BT_b = 1$. Their performance is assessed in the presence of two possible coherent receivers, the first based on a 4-state Viterbi detector, the second one on a simple threshold detector; a precoder is used prior to the modulator in both cases ([4] [5]). If $d_k \in \{\pm 1\}$ is the k -th symbol to be transmitted, then the precoder outputs $a_k = (-1)^k d_k d_{k-1}$; the resulting GMSK complex signal can be approximated with [2]

$$\tilde{x}(t) \cong \sqrt{E_b} \left[\sum_{k=-\infty}^{\infty} e^{j\frac{\pi}{2}A_{0,k}} C_0(t - kT_b) + e^{j\frac{\pi}{2}A_{1,k}} C_1(t - kT_b) \right]$$

where

$$A_{0,k} = \sum_{m=-\infty}^k a_m = A_{0,k-1} + a_k,$$

$$A_{1,k} = \sum_{m=-\infty}^k a_m - a_{k-1} = A_{0,k-2} + a_k,$$

$C_0(t)$ and $C_1(t)$ are waveforms of duration $(L + 1)T_b$ and $(L - 1)T_b$, respectively, being $L=4$ sufficient to make the above approximation very stringent for $BT_b > 0.25$. The analytical evaluation of $C_0(t)$ and $C_1(t)$ is treated in [2]. With the use of the following definitions:

$$\exp\left[j\frac{\pi}{2}A_{0,2n}\right] = d_{2n},$$

$$-j \exp\left[j\frac{\pi}{2}A_{0,2n+1}\right] = d_{2n+1},$$

we get

$$\tilde{x}(t) \cong \sqrt{E_b} \left[\sum_{n=-\infty}^{\infty} d_{2n} C_0(t - 2nT_b) - j d_{2n-2} d_{2n} d_{2n-1} C_1(t - 2nT_b) \right] +$$

$$+ \sqrt{E_b} \left[\sum_{n=-\infty}^{\infty} j d_{2n+1} C_0(t - 2nT_b - T_b) - d_{2n-1} d_{2n} d_{2n+1} C_1(t - 2nT_b - T_b) \right]$$

The optimum receiver ([3][4][5]) must find the maximum among the likelihood ratios

$$\lambda = \Re \left\{ \int \tilde{r}(t) \tilde{x}_i^*(t) dt \right\}$$

where $\tilde{r}(t)$ is the complex envelop of the received signal, and $\tilde{x}_i^*(t)$ is the conjugate of the complex envelope of the i -th possible transmitted signal. It can be easily shown that

$$\lambda = \sum_n \lambda_i(n)$$

where

$$\lambda_i(n) = \Re \left\{ \exp\left[-j\frac{\pi}{2}A_{0,n}^{(i)}\right] r_{0,n} + \exp\left[-j\frac{\pi}{2}A_{1,n}^{(i)}\right] r_{1,n} \right\}$$

$$\lambda_i(2n) = d_{2n}^{(i)} \Re\{r_{0,2n}\} + d_{2n-2}^{(i)} d_{2n-1}^{(i)} d_{2n}^{(i)} \Im\{r_{1,2n}\}$$

$$\lambda_i(2n+1) = d_{2n+1}^{(i)} \Re\{r_{0,2n+1}\} + d_{2n-1}^{(i)} d_{2n}^{(i)} d_{2n+1}^{(i)} \Im\{r_{1,2n+1}\}$$

being

$$r_{0,n} = \int \tilde{r}(t) C_0(t - nT) dt$$

$$r_{1,n} = \int \tilde{r}(t) C_1(t - nT) dt.$$

Thus the receiver is made of two input filters (with impulse responses $C_0(-t)$ and $C_1(-t)$) followed by a sampler at times nT and a Viterbi detector with 4 states and branch metric $\lambda_i(n)$ which takes two different expressions on even and odd values of n . In any case, the branch metric evaluation requires a simple addition or subtraction, and the Viterbi detector is very simple and fast.

If the second component ($C_1(t)$) is neglected too, $\tilde{x}(t)$ looks like an OQPSK signal with symbol period $T = 2T_b$ and baseband waveform $C_0(t)$; thus a receiver made of a matched filter with impulse response $C_0(t)$, a sampler and a threshold detector is feasible, as for the OQPSK signals of the previous sections ([4]). Notice that, by neglecting the second component, part of the transmitted energy is lost, and that ISI arises, since $C_0(t)$ does not satisfy the first Nyquist criterion. The eye patterns of the in-phase component of the signals at the output of the matched filters are shown in Figure 5 and Figure 6 for the cases $BT_b = 0.5$ and $BT_b = 1$, respectively. Thus GMSK can be seen either as a CPM binary modulation with symbol interval $T = T_b$, or as a quaternary OQPSK modulation with symbol interval $T = 2T_b$, which generates some confusion. In the following, we will consider $T = T_b$, as in the original definition of GMSK signals; however, in order to avoid confusion, we will use the unambiguous bit interval T_b most of the time.

For $BT_b = 0.5$ and $BT_b = 1$, the error probability evaluated with the threshold detector is only slightly different from that obtained with the Viterbi detector, as shown in Table 1. Therefore the threshold detector will be considered in the assessment of the system performance in the presence of interferers, and the Viterbi receiver will be used to check the possible differences. The error probability at the output of the threshold detector is very similar to that of ideal BPSK. In the case $BT_b = 1$, the loss is less than 0.001 dB for bit error rates up to $P_b(e) = 10^{-3}$, while for $BT_b = 0.5$ the losses are 0.01 dB at $P_b(e) = 10^{-1}$, 0.02 dB at $P_b(e) = 10^{-2}$, 0.03 dB at $P_b(e) = 10^{-3}$.

3 Channel models

Two channel models have been considered: the usual AWGN (Additive White Gaussian Noise) channel with noise spectral density $N_0/2$, and a nonlinear channel, characterized by two possible amplifiers: a TWTA (Travelling Wave Tube Amplifier) and an SSPA (Solid State Power Amplifier) with AM/AM and AM/PM curves shown in Figure 7 and Figure 8, respectively. The input backoff was set equal to 0 dB in both cases.

The nonlinear channels have been taken into consideration for the OQPSK modulations only, being unfiltered BPSK and GMSK signals unaffected by the

nonlinearities, due to their constant envelope. Figure 9 and Figure 10 show the power spectra of the considered modulated signals at the output of the TWT and SSP amplifiers, respectively. It is apparent that now the most bandwidth efficient modulation scheme is GMSK with $BT_b = 0.5$.

The overall losses of OQPSK modulations with respect to ideal BPSK are given in Table 2; notice that SRRC-b suffers from a loss greater than 1dB at $P_b(e) = 10^{-3}$, that TWTA is more detrimental than SSPA, and that Butterworth filtered OQPSK has just a slight increase in its losses with respect to the AWGN channel, especially at $P_b(e) = 10^{-1}$ and 10^{-2} . These losses were measured as the difference between the values $E_{b,sat} / N_0$ (dB) and E_b / N_0 (dB) that cause a given BER when the nonlinear amplifier is present or absent. $E_{b,sat}$ is defined as the energy of the signal at the output of the amplifier driven at 0 dB back-off by an unmodulated carrier, in the time interval T_b .

4 Interferers

Two types of interferers are considered:

- narrow band interferer: a pure carrier with center frequency f_c or $f_c + 1/(2T)$, or $f_c + 1/(4T_b)$
- wide band interferer: a signal of the same format as the useful signal and center frequency f_c or $f_c + 1/(2T)$, or $f_c + 1/(4T_b)$

where f_c is the center frequency of the useful signal. The two cases $f_c + 1/(2T)$ and $f_c + 1/(4T_b)$ are equivalent for OQPSK systems, for which $T = 2T_b$, but not for BPSK and GMSK, for which $T = T_b$.

In the case of wide band interference, it is assumed that the interfering signal undergoes the same impairments as the useful signal (i.e. the same filters and nonlinearity), that the carried bits are statistically independent from those of the useful signal, and that a time offset τ exists between the symbol epochs of the useful and the interfering signals. Moreover, for narrow or wide band interference, a phase offset φ exists with respect to the carrier phase of the useful signal. The values of φ and τ were chosen in order to maximize the asymptotic loss due to the presence of interference. For narrow band interferers, it can be shown analytically that $\varphi = 0$ if the interferer is isofrequential, $\varphi = 45^\circ$ for GMSK and BPSK with interference at $f_c + 1/(4T_b)$, and $\varphi = 90^\circ$ when the interferer is centered at $f_c + 1/(2T)$ for all the modulation schemes apart from Butterworth-filtered OQPSK, whose worst case phase is $\varphi = 30^\circ$. In the case of wide band interferers the worst case values of φ and τ were found via simulation, and they are listed in Table 3.

5 Results

For each of the considered modulation schemes, channels, and interferers, the values of the signal to interferer power ratio

$$\eta = \frac{\text{useful signal power}}{\text{interferer power}}$$

that caused a degradation of 1 dB with respect to ideal BPSK at bit error rates equal to 10^{-1} , 10^{-2} , and 10^{-3} was determined. In particular, ideal BPSK (with no interferers) allows to get $P_b(e) = 10^{-1}$ at $E_b/N_0 = -0.8556$ dB, $P_b(e) = 10^{-2}$ at $E_b/N_0 = 4.3232$ dB, and $P_b(e) = 10^{-3}$ at $E_b/N_0 = 6.7895$ dB. Therefore the values of γ that allow to get $P_b(e) = 10^{-1}$ at $E_b/N_0 = 0.1444$ dB, $P_b(e) = 10^{-2}$ at $E_b/N_0 = 5.3232$ dB, and $P_b(e) = 10^{-3}$ at $E_b/N_0 = 7.7895$ dB were measured in all the considered conditions.

The results are shown in Table 5, Table 6, and Table 7 (some results are repeated, in order to ease the comparison; some values are missing since the system loses more than 1 dB even in the absence of interferers). Due to the flatness of the function $P_b(e)$ versus E_b/N_0 , especially at $P_b(e) = 10^{-1}$, the measurements suffer from lack of precision. For example, in the case of SRRC-a OQPSK with AWGN channel and centered narrow band interferer ($\varphi = 0$), $P_b(e)$ can be theoretically found as

$$P_b(e) = \frac{1}{8} \operatorname{erfc} \left[\sqrt{\frac{E_b}{N_0}} (1 + \sqrt{2/\eta}) \right] + \frac{1}{8} \operatorname{erfc} \left[\sqrt{\frac{E_b}{N_0}} (1 - \sqrt{2/\eta}) \right] + \frac{1}{4} \operatorname{erfc} \left[\sqrt{\frac{E_b}{N_0}} \right]$$

At $E_b/N_0 = 0.144$ dB, $P_b(e) = 0.101$ for $\gamma = 8.9$ dB, and $P_b(e) = 0.099$ for $\gamma = 9.3$ dB; thus an error of $\pm 1\%$ in $P_b(e)$ corresponds to an uncertainty of 0.4 dB on γ . At 10^{-2} and 10^{-3} , the uncertainty on γ reduces to 0.14 and 0.09 dB, respectively.

Additional uncertainty must be added when γ is estimated via simulation, even if the more accurate semi-analytical technique is used instead of error counting. In the case of SRRC-a OQPSK with AWGN channel, simulation produced $\gamma = 9.00$ at $P_b(e) = 10^{-1}$ (theoretical value: 9.11), $\gamma = 13.93$ at $P_b(e) = 10^{-2}$ (theoretical value: 13.99), $\gamma = 16.08$ at $P_b(e) = 10^{-3}$ (theoretical value: 16.11).

In the overall, a resolution of about 1 dB, 0.3 dB and 0.2 dB can be considered valid for the values of γ at $P_b(e) = 10^{-1}$, 10^{-2} , and 10^{-3} , respectively. In some cases it seems that the introduction of a nonlinear amplifier increases the robustness against interference, but this is simply due to the measurements errors.

As for the **narrow band interferer** at frequency f_c , it can be noticed that GMSK is the most robust modulation: its performance is comparable to that of BPSK, and its advantage over OQPSK modulations is remarkable in the presence of a nonlinear amplifier. Actually the receiver filter for the GMSK modulation has a gain of 2.67 dB for $BT_b = 0.5$, and 2.27 dB for $BT_b = 1$, while the integrate and dump receiver has a gain of 3 dB (the bit interval is normalized to 1 and the impulse responses of the receiver filters have unitary energy). As a consequence, GMSK with $BT_b = 1$ is more robust against narrow band interference with respect to BPSK, without additional losses, since the intersymbol interference is absolutely negligible. GMSK with $BT_b = 0.5$ has some advantage in terms of narrow band interference with respect to BPSK, but suffers from ISI, and in the overall BPSK performs better. The best OQPSK modulation is SRRC-a (the other two suffer from ISI), but it is inherently worse than BPSK, due to the presence of 4 symbols instead of 2.

When the narrow band interferer has frequency $f_c + 1/(2T)$, GMSK behaves astonishingly better than the other modulations: the reason is that at $f = 1/(2T)$ (with $T=T_b$) the baseband matched filter in the GMSK receiver has an attenuation of 8 dB for $BT_b = 1$ and 9.8 dB for $BT_b = 0.5$, while the filter with impulse response $\sqrt{1/T}u_T(t)$ (with $T = 2T_b$) has an attenuation of just 0.9 dB. On the other hand, when the frequency offset is equal to $1/(4T_b)$ (see Table 7) then the results obtained with GMSK become comparable to those of OQPSK (the attenuations for the GMSK matched filters are equal to 0.13 dB for $BT_b = 0.5$ and 0.02 dB for $BT_b = 1$). Actually, if GMSK is thought of as a special case of OQPSK, this last comparison is the only reasonable one; the results with frequency offset $1/(2T)$ were included for completeness, and to convince of their unfairness. However, even with an interferer at frequency $f_c + 1/(4T_b)$, GMSK keeps on being the best choice among the considered bandwidth efficient modulations (but now, in spite of a greater ISI, $BT_b = 0.5$ is better than $BT_b = 1$, due to the higher attenuation of the receiver filter at frequency $1/(4T_b)$).

The use of a Viterbi detector in the GMSK receiver gave results very similar to those obtained with the simpler threshold detector. For a narrow band interferer the error probabilities measured with the counting technique in the presence of the Viterbi detector are listed in Table 4. Keeping in mind that these measurements are less precise than those obtained with the semi-analytical measurement technique of the threshold detector, the substantial equivalence of the two receivers can be claimed.

In the presence of **wide band interferer**, GMSK keeps on being the best modulation, independently of the frequency offset of the interfering signal, due to a more compact power spectrum. Table 6 and Table 7 show the simulation results, and again the two cases of frequency offset $1/(4T_b)$ and $1/(2T)$ are included for completeness. It is interesting to notice that Butterworth filtered OQPSK has a better performance than SRRC-a OQPSK when an amplifier is present: this is due to the minor impact of the nonlinearity in the first case, as already mentioned.

In the overall, GMSK has to be considered as the less sensitive modulation with respect to narrow or wide band interferers, being most of the times better than BPSK too. The case $BT_b = 0.5$ has to be preferred in the presence of wide band interferers, or narrow band interference with frequency offset, but the difference with respect to the case $BT_b=1$ is substantially negligible. In terms of complexity, GMSK with threshold detector is equivalent to SRRC-a, which has a worse performance in the presence of interference. Butterworth filtered OQPSK has a simpler transmitter than SRRC filtered OQPSK, while its receiver is equal to that of the SRRC-b scheme. Between SRRC-b and Butterworth filtered OQPSK, this last scheme has to be preferred in terms of interference susceptibility, and overall complexity. Between SRRC-a and Butterworth filtered OQPSK, the first scheme is more robust against narrow band interference, but the second one has to be preferred in the presence of wide band interferer and non linear amplifiers.

If the expected bit error rate prior to coding is of the order of magnitude of 10^{-3} , then the advantage of using GMSK is remarkable (it can tolerate interferers with 10 times more power than the other modulation schemes), but it rapidly decreases when higher BER's are considered (at 10^{-1} the interferer power can be 2 times higher).

6 Conclusions

The choice of the modulation scheme to be used for space missions should fall on GMSK, if the interference susceptibility is the only criterion to be considered. A receiver with matched filter and a simple threshold detector is adequate in the GMSK receiver, and no need has been found for the use of a Viterbi detector. If an even simpler integrate and dump receiver is required, then Butterworth filtering should be preferred, resulting in a loss of robustness against interference which ranges from 2-3 dB at $P_b(e) = 10^{-1}$ up to 15-20 dB at $P_b(e) = 10^{-3}$ with respect to GMSK.

References

- [1] M. Otter, G. Block, Advanced Spectrum Shaping for Efficient Bandwidth Utilisation, Study report on SFCG AI 12/32 "Efficient Modulation Study", ESA, September 1997.
- [2] P.A.Laurent, "Exact and Approximate Construction of Digital Phase Modulations by Superposition of Amplitude Modulated Pulses (AMP)", IEEE Trans. Commun., Vol. COM-34, No. 2, Feb. 1986, pp. 150--160.
- [3] G.K.Kaleh, "Simple Coherent Receivers for Partial Response Continuous Phase Modulation", IEEE JSAC, Vol. 7, No. 9, Dec. 1989, pp. 1427--1436.
- [4] G.L. Lui (The Aerospace Corporation), "GMSK Modulation: Description of Waveform, Receiver, and Performance", CCSDS Panel 1E, Houston, May 1998.

- [5] P.Arabshahi, L.Lam, “Preliminary Results on Gaussian Minimum Shift Keying Modulation: Spectral Analysis, Error Rates, and Synchronization”, CCSDS Panel 1E, Houston, May 1998.

E_b/N_0	$P_b(e)$ Viterbi	$P_b(e)$ threshold
0.0	7.74e-2	7.91e-2
0.5	6.76e-2	6.75e-2
1.0	5.94e-2	5.67e-2
1.5	4.80e-2	4.68e-2
2.0	3.92e-2	3.79e-2
2.5	2.98e-2	3.00e-2
3.0	2.22e-2	2.32e-2
3.5	1.62e-2	1.74e-2
4.0	1.22e-2	1.27e-2
4.5	9.60e-3	8.99e-3
5.0	6.60e-3	6.11e-3
5.5	4.10e-3	5.75e-3
6.0	2.56e-3	2.48e-3
7.0	8.90e-4	8.16e-4
8.0	2.80e-4	2.07e-4

Table 1: GMSK error probabilities obtained with the threshold detector and the Viterbi detector.

modulation format	channel type	loss (dB) at $P_b(e)=10^{-1}$	loss (dB) at $P_b(e)=10^{-2}$	loss (dB) at $P_b(e)=10^{-3}$
Butterworth OQPSK	TWTA	0.51	0.71	0.98
	SSPA	0.44	0.66	0.96
SRRC-a OQPSK	TWTA	0.36	0.55	0.74
	SSPA	0.19	0.38	0.56
SRRC-b OQPSK	TWTA	0.75	0.98	1.31
	SSPA	0.57	0.77	1.07

Table 2: Losses of OQPSK modulations with respect to ideal BPSK, due to the presence of a nonlinear amplifier (no interference).

modulation format	channel type	f_c		$f_c + 1/(2T)$		$f_c + 1/(4T_b)$	
		φ		φ		φ	
BPSK	AWGN	0	0	90	0	90	0
Butterworth		45	0	0	$T/4$	0	$T/4$
SRRC-a		45	0	0	0	0	0
SRRC-b		45	$T/4$	0	$T/2$	0	$T/2$
GMSK 0.5		45	0	45	$T_b/2$	45	$T_b/2$
GMSK 1		30	0	45	$T_b/2$	45	$T_b/2$
Butterworth	TWTA	45	0	0	$T/4$	0	$T/4$
SRRC-a		45	0	0	0	0	0
SRRC-b		45	$T/4$	0	$T/2$	0	$T/2$
Butterworth	SSPA	45	0	0	$T/4$	0	$T/4$
SRRC-a		45	0	0	0	0	0
SRRC-b		45	$T/4$	0	$T/2$	0	$T/2$

 Table 3: Worst case values of φ and for wide band interferers.

freq. offset	BT_b	γ	E_b / N_0	BER thr.	BER Vit.
0	1.0	8.95	0.14	1.e-1	9.93e-2
		13.32	5.32	1.e-2	1.07e-2
		15.42	7.79	1.e-3	1.06e-3
	0.5	8.95	0.14	1.e-1	9.95e-2
		13.81	5.32	1.e-2	1.09e-2
		15.99	7.79	1.e-3	1.01e-3
$1/(4T_b)$	1.0	8.91	0.14	1.e-1	1.03e-1
		13.52	5.32	1e-2	1.09e-2
		15.32	7.79	1.e-3	1.12e-3
	0.5	8.81	0.14	1.e-1	1.03e-1
		13.48	5.32	1.e-2	1.15e-2
		15.37	7.79	1.e-3	1.12e-3

 Table 4: GMSK bit error rates measured in the presence of narrow band interferer at frequency f_c and $f_c + 1/(4T_b)$ with the threshold and the four state Viterbi detector.

interference type	channel type	modulation scheme	at BER=10 ⁻¹	at BER=10 ⁻²	at BER=10 ⁻³
narrow f_c	AWGN	BPSK	9.21	13.69	15.45
		Butt.OQPSK	12.38	19.32	24.93
		SRRC-a OQPSK	9.11	13.99	16.11
		SRRC-b OQPSK	12.92	18.38	21.05
		GMSK $BT_b=0.5$	8.95	13.81	15.99
		GMSK $BT_b=1$	8.51	13.32	15.42
	TWTA	BPSK	9.21	13.69	15.45
		Butt.OQPSK	12.30	19.88	34.51
		SRRC-a OQPSK	11.07	17.84	22.82
		SRRC-b OQPSK	15.34	31.46	--
		GMSK $BT_b=0.5$	8.95	13.81	15.99
		GMSK $BT_b=1$	8.51	13.32	15.42
	SSPA	BPSK	9.21	13.69	15.45
		Butt.OQPSK	11.67	19.19	30.94
		SRRC-a OQPSK	9.99	16.29	20.37
		SRRC-b OQPSK	12.84	20.42	--
		GMSK $BT_b=0.5$	8.95	13.81	15.99
		GMSK $BT_b=1$	8.51	13.32	15.42
narrow $f_c + 1/(2T)$	AWGN	BPSK	5.29	9.77	11.53
		Butt.OQPSK	11.56	18.24	23.77
		SRRC-a OQPSK	9.21	13.69	15.45
		SRRC-b OQPSK	12.33	17.48	20.02
		GMSK $BT_b=0.5$	-3.56	1.30	3.47
		GMSK $BT_b=1$	-1.80	2.99	5.09
	TWTA	BPSK	5.29	9.77	11.53
		Butt.OQPSK	11.48	18.82	32.82
		SRRC-a OQPSK	11.35	17.86	22.84
		SRRC-b OQPSK	14.79	31.00	--
		GMSK $BT_b=0.5$	-3.56	1.30	3.47
		GMSK $BT_b=1$	-1.80	2.99	5.09
	SSPA	BPSK	5.29	9.77	11.53
		Butt.OQPSK	10.86	18.11	29.51
		SRRC-a OQPSK	10.28	16.25	20.19
		SRRC-b OQPSK	12.24	20.12	--
		GMSK $BT_b=0.5$	-3.56	1.30	3.47
		GMSK $BT_b=1$	-1.80	2.99	5.09

Table 5: Values of γ that produce a loss of 1 dB with respect to ideal BPSK, in the case of narrow band interferer at frequency f_c and $f_c + 1/(2T)$.

	channel type	modulation scheme	at BER=10 ⁻¹	at BER=10 ⁻²	at BER=10 ⁻³
wide f_c	AWGN	BPSK	9.21	13.69	15.45
		Butt.OQPSK	9.89	15.54	18.61
		SRRC-a OQPSK	8.43	13.41	15.62
		SRRC-b OQPSK	11.67	16.93	19.87
		GMSK $BT_b=0.5$	7.40	12.24	14.39
		GMSK $BT_b=1$	8.28	12.86	14.74
	TWTA	BPSK	9.21	13.69	15.45
		Butt.OQPSK	10.16	16.09	19.62
		SRRC-a OQPSK	10.32	17.21	22.51
		SRRC-b OQPSK	14.42	> 50	--
		GMSK $BT_b=0.5$	7.40	12.24	14.39
		GMSK $BT_b=1$	8.28	12.86	14.74
	SSPA	BPSK	9.21	13.69	15.45
		Butt.OQPSK	9.69	15.50	18.81
		SRRC-a OQPSK	9.39	15.71	19.84
		SRRC-b OQPSK	11.78	20.07	--
		GMSK $BT_b=0.5$	7.40	12.24	14.39
		GMSK $BT_b=1$	8.28	12.86	14.74
wide $f_c + 1/(2T)$	AWGN	BPSK	5.29	9.77	11.53
		Butt.OQPSK	8.39	14.06	17.28
		SRRC-a OQPSK	6.25	11.12	13.36
		SRRC-b OQPSK	9.87	15.22	17.97
		GMSK $BT_b=0.5$	4.38	9.36	11.61
		GMSK $BT_b=1$	5.02	9.93	12.08
	TWTA	BPSK	5.29	9.77	11.53
		Butt.OQPSK	8.15	14.00	17.49
		SRRC-a OQPSK	8.38	15.16	20.43
		SRRC-b OQPSK	12.42	> 50	--
		GMSK $BT_b=0.5$	4.38	9.36	11.61
		GMSK $BT_b=1$	5.02	9.93	12.08
	SSPA	BPSK	5.29	9.77	11.53
		Butt.OQPSK	7.63	13.39	16.69
		SRRC-a OQPSK	7.32	13.63	17.78
		SRRC-b OQPSK	9.69	17.93	--
		GMSK $BT_b=0.5$	4.38	9.36	11.61
		GMSK $BT_b=1$	5.02	9.93	12.08

Table 6: Values of γ that produce a loss of 1 dB with respect to ideal BPSK, in the case of wide band interferer at frequency f_c and $f_c + 1/(2T)$.

interference type	channel type	modulation scheme	at BER=10 ⁻¹	at BER=10 ⁻²	at BER=10 ⁻³
wide $f_c + 1/(4T_b)$	AWGN	BPSK	5.20	10.06	12.19
		Butt.OQPSK	8.39	14.06	17.28
		SRRC-a OQPSK	6.25	11.12	13.36
		SRRC-b OQPSK	9.87	15.22	17.97
		GMSK $BT_b=0.5$	5.55	10.80	13.21
		GMSK $BT_b=1$	5.36	10.53	12.85
	TWTA	BPSK	5.20	10.06	12.19
		Butt.OQPSK	8.15	14.00	17.49
		SRRC-a OQPSK	8.38	15.16	20.43
		SRRC-b OQPSK	12.42	> 50	--
		GMSK $BT_b=0.5$	5.55	10.80	13.21
		GMSK $BT_b=1$	5.36	10.53	12.85
	SSPA	BPSK	5.20	10.06	12.19
		Butt.OQPSK	7.63	13.39	16.69
		SRRC-a OQPSK	7.32	13.63	17.78
		SRRC-b OQPSK	9.69	17.93	--
		GMSK $BT_b=0.5$	5.55	10.80	13.21
		GMSK $BT_b=1$	5.36	10.53	12.85
narrow $f_c + 1/(4T_b)$	AWGN	BPSK	5.20	10.06	12.19
		Butt.OQPSK	11.56	18.24	23.77
		SRRC-a OQPSK	9.21	13.69	15.45
		SRRC-b OQPSK	12.33	17.48	20.02
		GMSK $BT_b=0.5$	8.81	13.48	15.37
		GMSK $BT_b=1$	8.91	13.52	15.32
	TWTA	BPSK	5.20	10.06	12.19
		Butt.OQPSK	11.48	18.82	32.82
		SRRC-a OQPSK	11.35	17.86	22.84
		SRRC-b OQPSK	14.79	31.00	--
		GMSK $BT_b=0.5$	8.81	13.48	15.37
		GMSK $BT_b=1$	8.91	13.52	15.32
	SSPA	BPSK	5.20	10.06	12.19
		Butt.OQPSK	10.86	18.11	29.51
		SRRC-a OQPSK	10.28	16.25	20.19
		SRRC-b OQPSK	12.24	20.12	--
		GMSK $BT_b=0.5$	8.81	13.48	15.37
		GMSK $BT_b=1$	8.91	13.52	15.32

Table 7: Values of γ that produce a loss of 1 dB with respect to ideal BPSK, in the case of narrow and wide band interferer at frequency $f_c + 1/(4T_b)$.

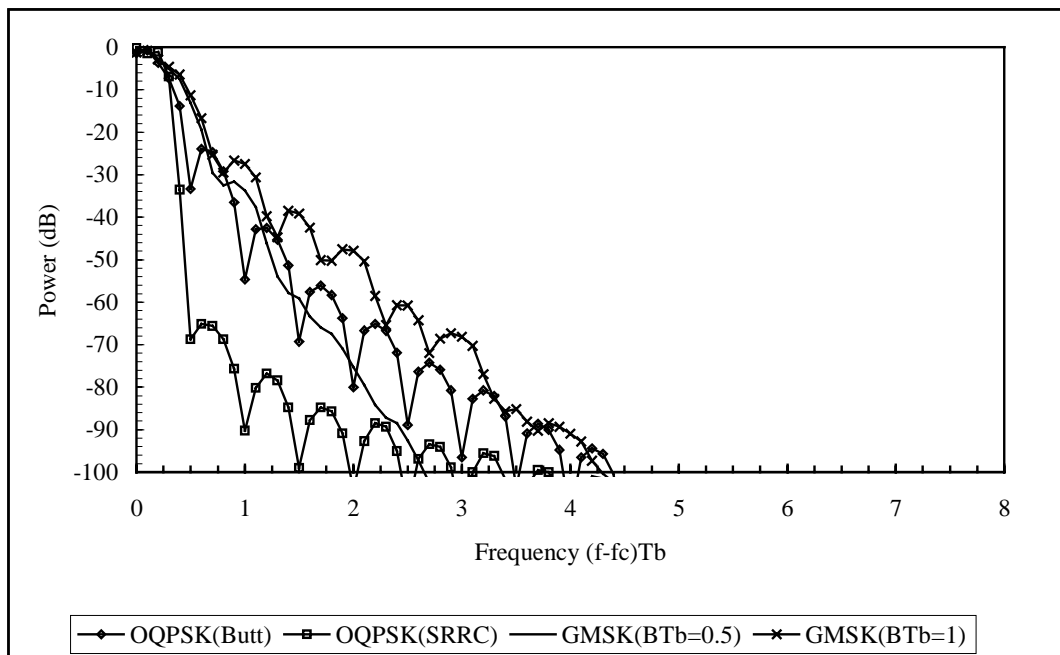


Figure 1: Power spectra of the modulated signals.

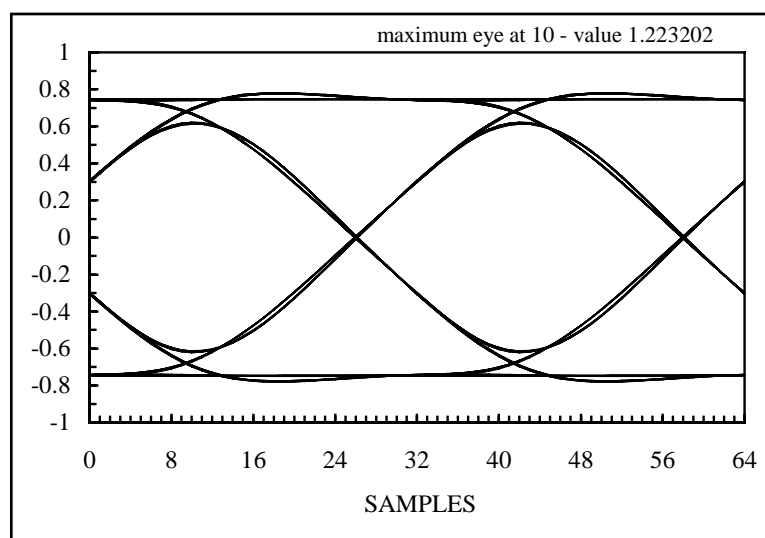
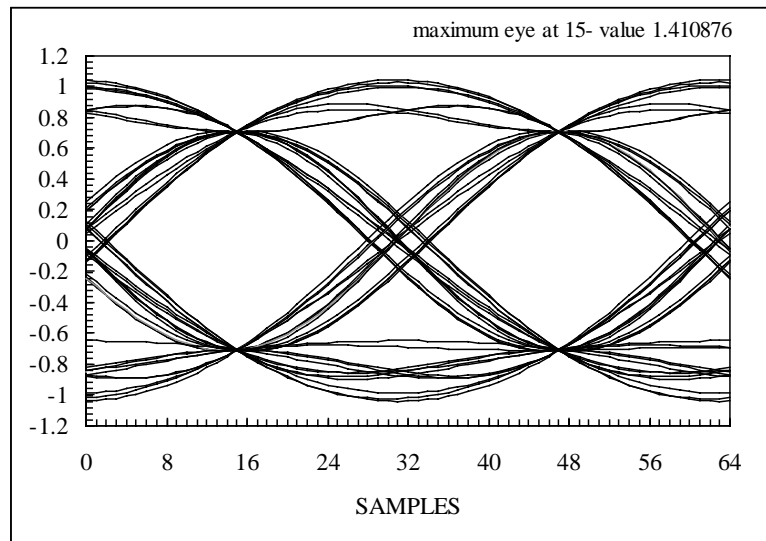
Figure 2: Eye pattern of the in-phase component of the signal at the receiver filter output. Case of Butterworth filtered OQPSK. The sampling interval used in the simulation was $T_b/16$.

Figure 3: Eye pattern of the in-phase component of the signal at the receiver filter



output. Case of SRRC-a filtered OQPSK. The sampling interval used in the simulation was $T_b/16$.

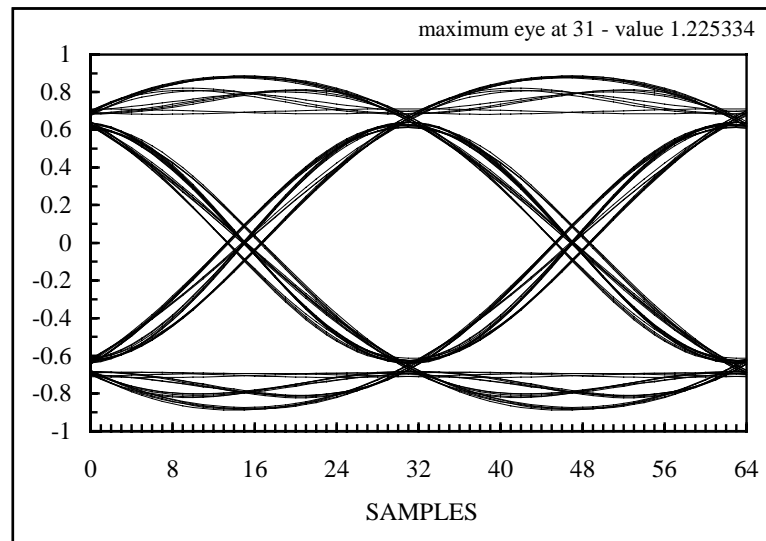


Figure 4: Eye pattern of the in-phase component of the signal at the receiver filter output. Case of SRRC-b filtered OQPSK. The sampling interval used in the simulation was $T_b/16$.

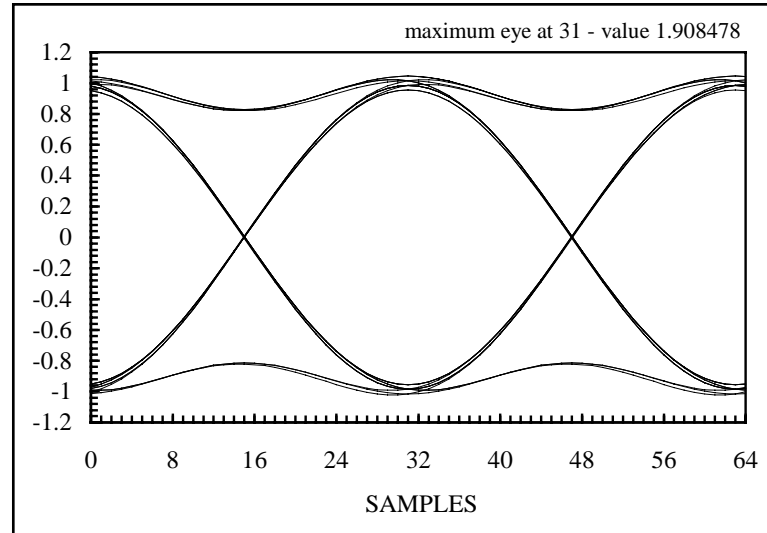


Figure 5: Eye pattern of the in-phase component of the signal at the receiver filter output. Case of GMSK with $BT_b=0.5$. The sampling interval used in the simulation was $T_b/16$.

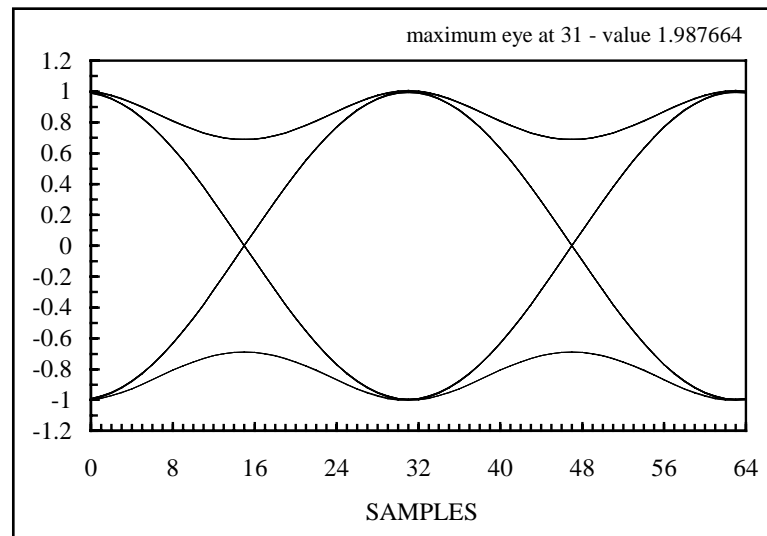


Figure 6: Eye pattern of the in-phase component of the signal at the receiver filter output. Case of GMSK with $BT_b=1$. The sampling interval used in the simulation was $T_b/16$.

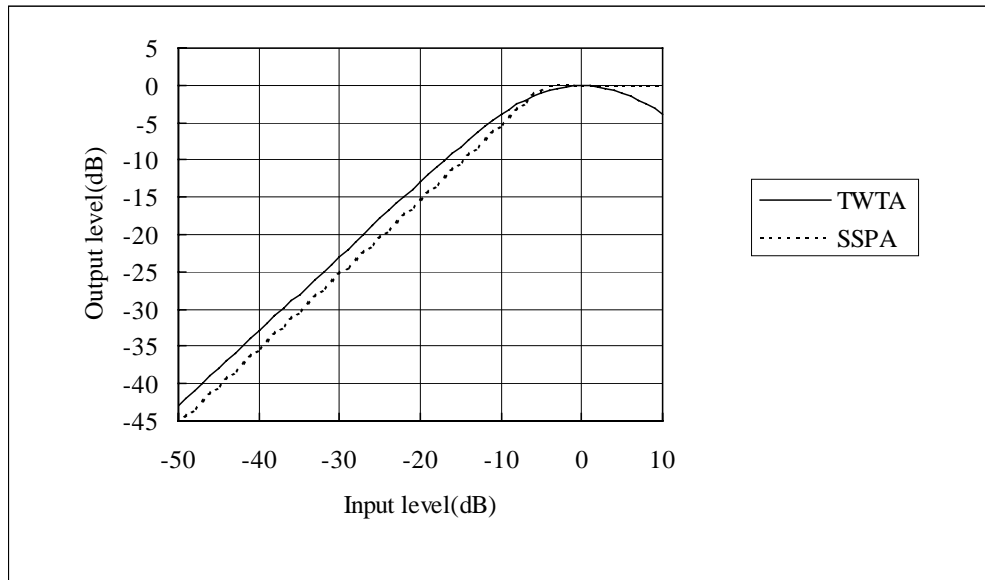


Figure 7: AM/AM characteristic of the non linear amplifiers.

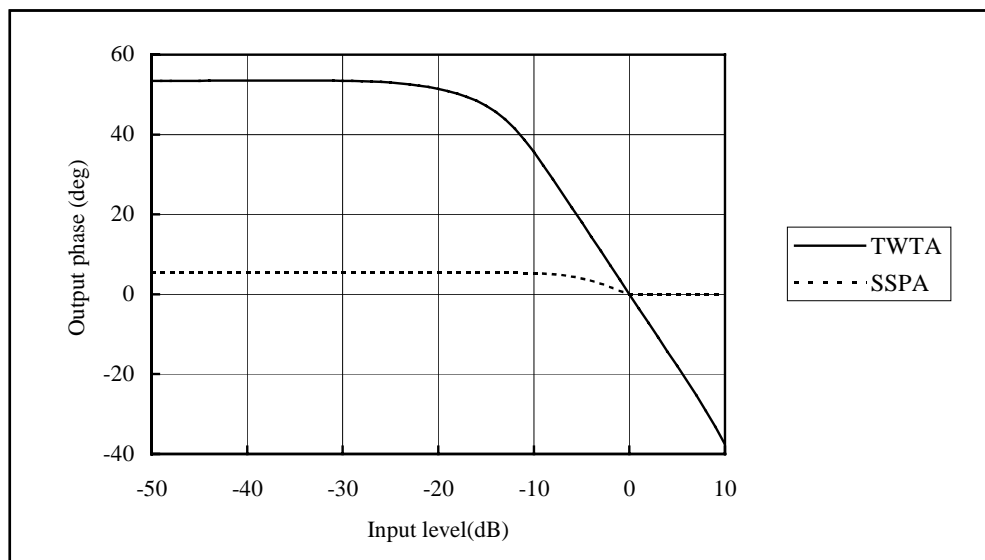


Figure 8: AM/PM characteristics of the non linear amplifiers.

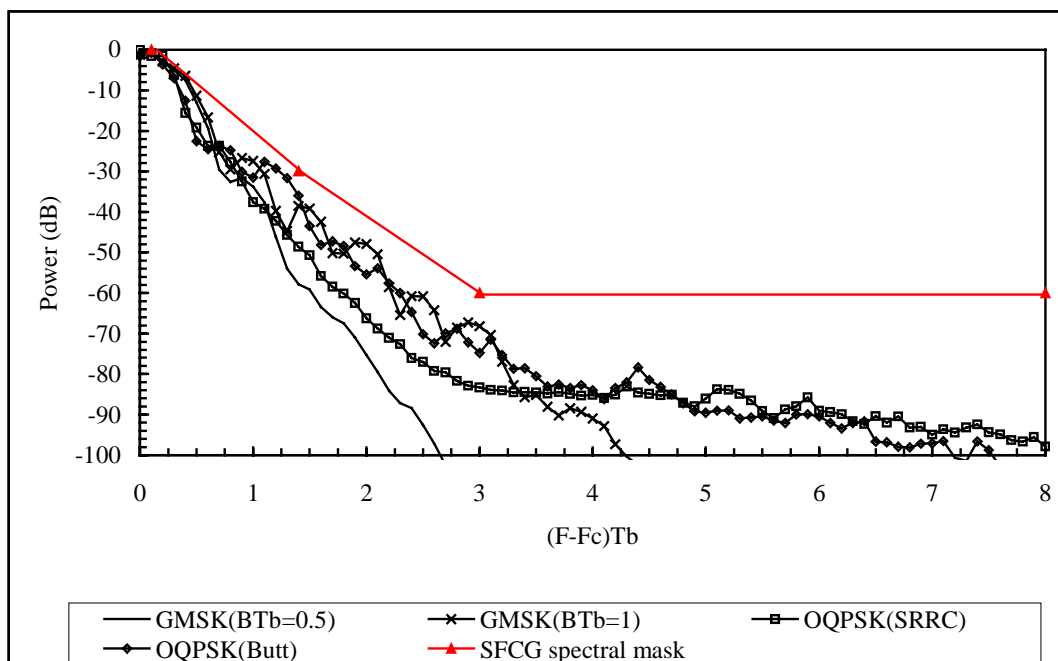


Figure 9: Power spectra of the modulated signals at the output of the TWTA.

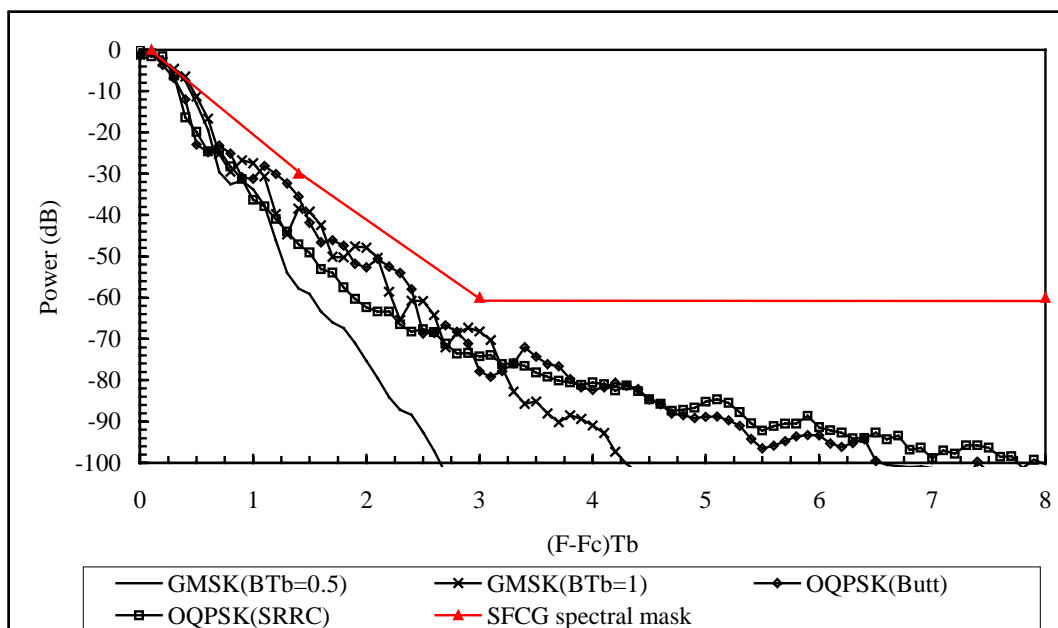
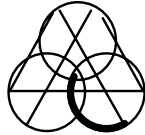


Figure 10: Power spectra of the modulated signals at the output of the SSPA.



consorzio
pisa
ricerche



Istituto
ELETTRONICA
TELECOMUNICAZIONI

ADVANCED MODULATION SCHEMES

FOR FUTURE ESA STANDARDS

ESTEC/Contract # 8565/89/NL/JG

ESA Technical Manager: R. de Gaudenzi

FINAL REPORT

Prepared by:

N. A. D'Andrea, M. Luise, U. Mengali and R. Reggiannini

Istituto di Elettronica e Telecomunicazioni

University of Pisa

Pisa, March 1991

TABLE OF CONTENTS

Introduction & Scope of the Work	1
 I Survey of Efficient Modulation Techniques	
I.1 Power and Bandwidth Efficient Modulations	3
I.2 Staggered Linear I-Q Modulation Techniques (Offset Binary Modulations)	6
I.3 Continuous Phase Modulations	8
 II Pre-Selection of Modulation Techniques	
II.1 Modulation Choice - The Particular Application	12
II.2 OBM's: OQPSK, MSK	18
II.3 CPM's: Generalized MSK, Gaussian MSK (GMSK), 3RC	22
 III Consideration of Simplified Receivers	
III.1 Optimum Receivers for OBM and CPM	27
III.2 The Simplified I-Q Receiver for OBM/CPM	29
III.3 The Problem of Optimal Filtering in I-Q Receivers	34
 IV Build-Up and Testing of the Simulation Program	
IV.1 Block Diagram of the Simulation to be Developed	37
IV.2 Testing: Results from Some Elementary Cases	43
 V Impact of the Synchronization Subsys. upon System Performance	
V.1 Clock Recovery for OBM - The Traditional Approach	50
V.2 A Novel Open-Loop Analog Clock Regenerator	51
V.3 Performance of the Analog Scheme	60
V.4 Clock Recovery for OBM: Closed-Loop Digital Circuits	71
V.5 Performance of the Digital Schemes	79

VI Impact of Carrier Phase Recovery Loop on System Performance

VI.1	Phase Recovery for OBM - An Overview	110
VI.2	Design of a Digital Closed-Loop Algorithm for Phase Recovery	113
VI.3	Open Loop Analysis	117
VI.4	Influence of Clock Jitter on the Phase Loop Behavior	124
VI.5	Closed Loop Performance	129
VI.6	Performance of the Second Order Phase-Recovery Loop	134
VI.7	Performance Degradation due to Joint Phase/Clock Recovery	143

VII Joint Carrier Phase / Frequency Tracking

VII.1	Frequency Recovery Schemes	161
VII.2	BQ Description	162
VII.3	S-Curve and Spectral Analysis	167
VII.4	Numerical Results for an Elementary Case	170
VII.5	BQ Filter Design	173
VII.6	Joint Carrier Frequency and Phase Recovery	176
VII.7	Analysis and Design of the Carrier Phase Recovery Loop	177
VII.8	Choice of the AFC Bandwidth	181
VII.9	The Doppler Effect for LEO Satellites	184
VII.10	Impact of Doppler Shifts on Tracking Subsystem Performance	188
VII.11	Computer Simulation Results	189

VIII Frequency Acquisition

VIII.1	A Simple Solution to Frequency Acquisition	207
VIII.2	Lock Control Analysis and Design	208
VIII.3	Lock Control Testing	211

IX Overall Performance

IX.1	Overall Structure of the Receiver	222
IX.2	Interaction Between Carrier & Clock Recovery Subsystems	227
IX.3	Tracking Performance - No Doppler Effect	228
IX.4	Tracking Performance with Doppler Effect	229

IX.5 Acquisition Samples	236
IX.6 Nonlinear Channels	243
Final Trade-Off	253
References	256
Acknowledgements	263

Introduction & Scope of the Work

In the near future the European Space Agency (ESA) envisages a revision of the *"Radio Frequency and Modulation Standards"*, in order to cope with the requirements of future missions. In particular, ESA is foreseen that the use of suppressed-carrier bandwidth-and-power efficient modulation techniques will be encouraged. The use of power-efficient suppressed carrier modulations is suggested by on-board power limitations and by the demand of high data rates. On the other hand, spectrum efficiency is a strong prerequisite in future applications where multiple telemetry channels and/or low-power service channels will be required.

The current version of the *"Radio Frequency and Modulation Standards"* recommends unfiltered BPSK, QPSK (and possibly UQPSK) as the only applicable suppressed carrier modulations. It is well known that these signals have poor spectrum efficiency, so that (baseband) filtering of the modulated signal is mandatory in the multiple-channel environment cited above. On the other hand, when saturated power amplifiers are employed in the satellite transmitter, the filtered PSK system may experience both power efficiency degradation (due to nonlinear distortion in the power amplifier) and spectrum efficiency degeneration (due to sidelobe regrowth at the amplifier output). Re-consideration of the applicable modulation techniques from the overall system point-of-view is therefore in order.

The presence of strongly nonlinear power amplification suggests the consideration of *Continuous Phase Modulation (CPM)* schemes as candidate modulation techniques for space-to-earth telemetry links. The most important characteristic of these signals is the constant envelope feature which makes them virtually insensitive to the nonlinear AM/AM and AM/PM characteristics of the power amplifier. This allows to set the amplifier operating point at saturation with no performance degradation. Thus, it seems

reasonable to speculate that simple CPM schemes might represent a better trade-off between energy efficiency, power efficiency and hardware complexity when compared to filtered PSK schemes.

In the first part of this work we carry out a comprehensive survey of efficient transmission techniques for satellite applications, and we pre-select three CPM schemes as candidate modulations for the application at hand. Frequency-Raised-Cosine filtered OQPSK is also assumed as a "benchmark modulation" to perform a comparative performance evaluation of CPM schemes.

After this preliminary section on modulation techniques, we approach the key topic of the design of the synchronization subsystems for the CPM and OQPSK receivers. This leads to the design of a complete receiver structure for OQPSK, MSK and GMSK modulation formats. Taking into account the recent advances in VLSI technology both in terms of pure performance and with regards to reliability, particular attention is devoted to the aspect of a full-digital modem implementation.

The performance of the different synchronization algorithms, of the complete receiver structure and also the interaction between the different synchronization subsystems (clock, phase and frequency) are thoroughly examined both by theoretical analysis and by means of extensive computer simulations.

I

Survey of Efficient Modulation Techniques

I.1. Power and Bandwidth Efficient Modulations

The main resources of any communication system are channel bandwidth and available power at the transmitter site. The goal of any communication system is to exploit these two resources in some optimal sense. Based on this observation, any communication link can be roughly classified as *band limited* or *power limited*, depending on the constraints posed on the availability of the cited resources.

In the satellite communication system to be discussed in the following, both bandwidth and power can be considered as scarce resources. Specifically, maximum radiated field intensity is established by the weight and size of the onboard power generating equipment and antennas as well as by the data signalling rate, while a bandwidth constraint, although unusual in telemetering applications, arises from the specification that the system should accommodate multiple telemetering channels, and also that interference on low-power adjacent channels should be reduced to a minimum.

To proceed further on, formal definitions of spectral and power efficiency are required. Let the modulation **spectral efficiency** λ be defined as

$$\lambda \triangleq \frac{R_b}{B} \quad \frac{\text{bit/sec}}{\text{Hz}} \quad (\text{I.1.1})$$

where R_b denotes the transmitted information rate (bit/s), and B is the

modulated signal bandwidth occupancy. The modulation **power efficiency** is defined as *that average energy E_b that must be received for every information bit in order to attain a specified error probability on a Gaussian channel affected by a given noise spectral density N_0 .*

A tradeoff choice between these two efficiency parameters is normally required in system design, since increasing spectral efficiency often degrades power efficiency, and viceversa. For instance, use of multilevel alphabets leads to a better value of λ , but also entails a larger error probability, provided that the energy per bit E_b is left unchanged. On the other hand, use of redundant codes allows for a reduction in error probability, but normally deteriorates the spectral efficiency.

The power and bandwidth efficiencies of any communication scheme can be jointly visualized in the so-called Shannon plane where, for a fixed error probability, each modulation scheme is represented by a point whose coordinates are the energy-per-bit-to-noise-spectral-density ratio, $\varepsilon \triangleq E_b/N_0$, required to achieve a fixed "target" bit error probability, and the spectral efficiency λ , respectively. As is well known [Ben87], Shannon derived a sort of uncertainty principle, stating that the representative point of any modulation format must lie in the plane (ε, λ) below the curve defined by

$$\lambda = \log_2 (1 + \varepsilon \lambda) \quad \text{or, equivalently} \quad \varepsilon = \frac{2^\lambda - 1}{\lambda} , \quad (\text{I.1.2})$$

the latter representing a fundamental bound to the performance of any communication system. The diagram of the above curve is depicted in Fig. I.1, together with the representative points of a number of popular modulations with Nyquist pulse shaping. In the following, a modulation format will be considered *efficient* if its representative point lies closer to the Shannon bound as compared to other conventional modulations.

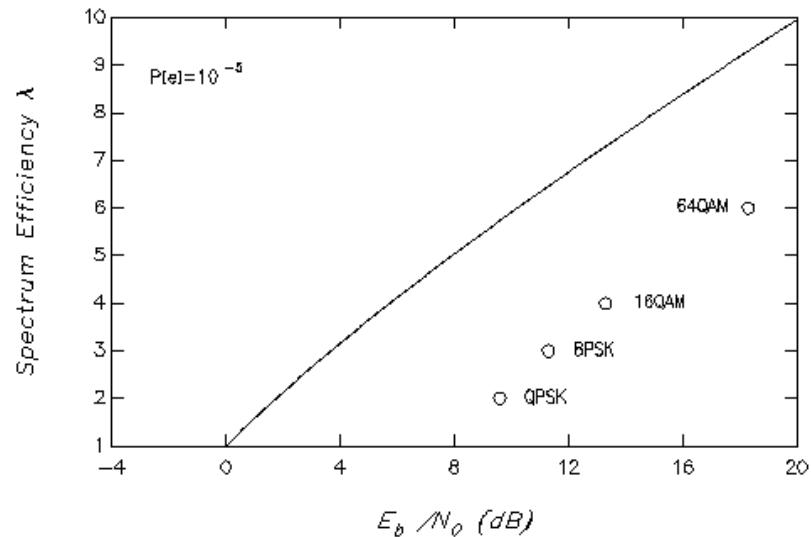


Fig. I.1

For convenience, the efficient modulations to be analyzed in the sequel will be subdivided into two classes, namely, amplitude/phase *linear modulations* and constant-envelope *angle modulations*. Within these classes, of special interest for satellite communications are the binary, staggered-symbol linear modulations (in the sequel referred to as Offset Binary Modulations, OBM), and the Continuous Phase Modulations (CPM). As shown in Fig. I.2, these two groups are not completely disjoint, since a number of modulation techniques, whose most important representative is MSK, may be either qualified as OBM or CPM.

The combined encoding/modulation schemes [Ung87], [And78], [Piz85], [JSAC] will not be considered in the present study because of the complexity of the respective receivers, which has been judged not adequate for the application. Nonetheless convolutional codes possibly concatenated with

block codes might be employed in a similar way as for conventional PSK schemes, to improve energy efficiency.

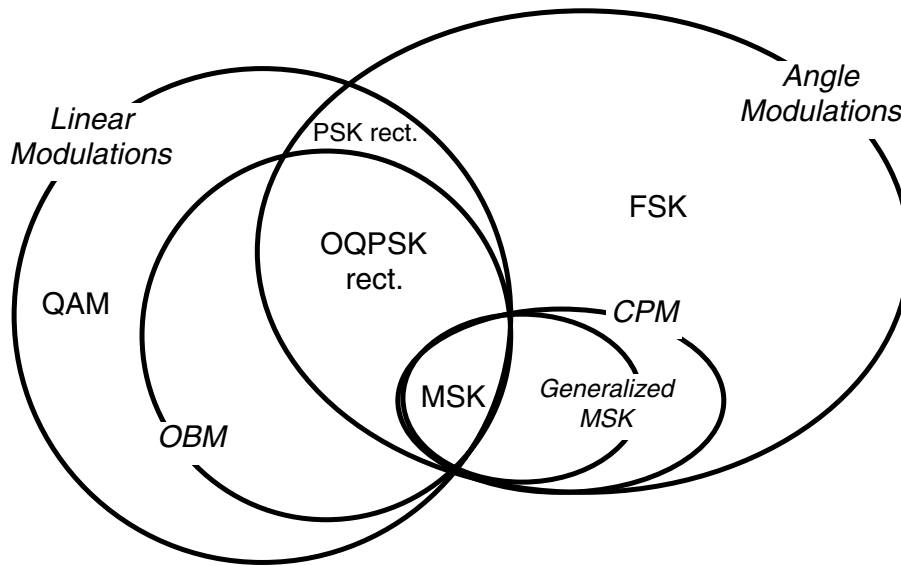


Fig. I.2

I.2. Staggered Linear I-Q Modulation Techniques (OBM)

By definition, the bandpass waveform $s(t)$ is said to belong to the OBM class [Har83] provided that it can be written in the form

$$s(t) = \sum_k a_k p(t-2kT) \cos 2\pi f_0 t - \sum_k b_k p[t-(2k+1)T] \sin 2\pi f_0 t \quad (\text{I.2.1})$$

where a_k and b_k are drawn from the alphabet $\{\pm 1\}$ and $p(t)$ denotes the signalling pulse. The signalling rate is $R=1/2T$ on each arm of the transmitter, whilst the information bit rate R_b equals $1/T$. Using complex envelope notation, we get

$$s(t) = \text{Re}\{\tilde{s}(t) e^{j2\pi f_0 t}\} \quad (\text{I.2.2})$$

where

$$\tilde{s}(t) \triangleq \sum_k a_k p(t-2kT) + j \sum_k b_k p[t-(2k+1)T] \quad (\text{I.2.3})$$

A block diagram of the so-called *parallel* or *I-Q* Offset Binary modulator is sketched in Fig. I.3.

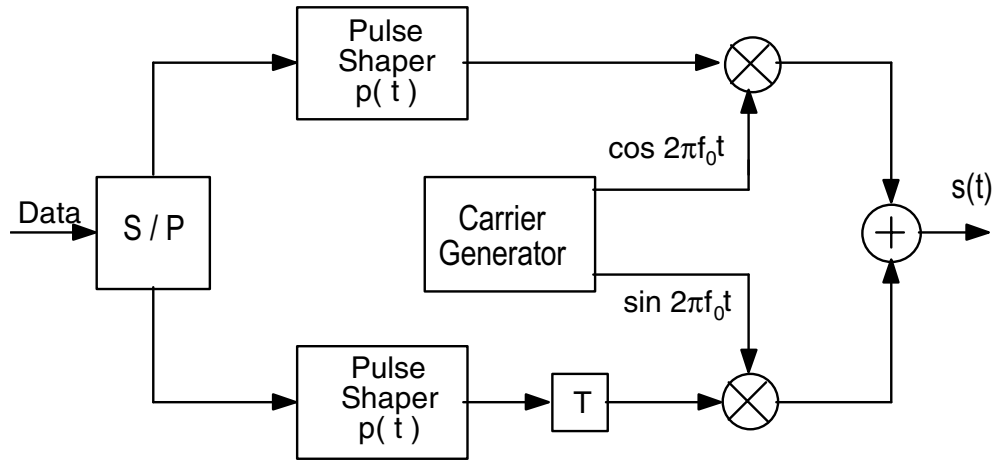


Fig. I.3

Several different shapes have been proposed for the OBM baseband pulse $p(t)$. It can be shown [Feh87] that if the following conditions hold

$$p(t) = p(-t) \quad (\text{I.2.4a})$$

$$p^2(t) + p^2(t-T) = 1 \quad \text{per } 0 \leq |t| \leq \frac{T}{2}, \quad (\text{I.2.4b})$$

then the modulated signal exhibits a constant envelope. As is known, the latter property makes the system insensitive to the nonlinearities of the transmitter amplifier stages. Furthermore, as the power spectral density of the transmitted signal is proportional to $|P(f)|^2$ ($P(f)$ denoting the Fourier transform of $p(t)$), the signal spectrum can easily be shaped through proper pulse design. In this view, a good choice for $p(t)$ is represented by the class of functions satisfying conditions (I.2.4) and having continuous derivatives up to the order N . If these requirements are met, $|P(f)|^2$ rolls off asymptotically as $|f|^{-2(N+2)}$.

I.3. Continuous Phase Modulations

By definition, the bandpass waveform $s(t)$ is said to belong to the CPM class if its complex envelope can be written in the form [And86]

$$\tilde{s}(t) \triangleq \sqrt{2 P_s} \exp\{j2\pi h \sum_i a_i q(t-iT) + \theta_0\} \quad (\text{I.3.1})$$

where

P_s is the average (and instantaneous) received power of $s(t)$.

h is the so-called modulation index, which is usually chosen as $h=m/n$, m and n relatively prime integers.

T is the symbol spacing.

a_i is the i -th symbol, belonging to the M -ary alphabet $\mathcal{A}=\{-(M-1), -(M-3), \dots, -1, 1, \dots, (M-1)\}$. Symbols $\{a_i\}$ are supposed to be independent and identically distributed (IID).

$q(t)$ is the so-called phase response of the CPM modulator, and is constrained as follows: $q(t) = 0$ if $t < 0$, $q(t) = 1/2$ if $t > LT$, where L is an

integer representing the duration of the frequency pulse $g(t)$. The relationship between the frequency pulse $g(t)$ and the phase response $q(t)$ is

$$q(t) = \int_{-\infty}^t g(\tau) d\tau, \text{ i.e. } g(t) = dq(t)/dt \quad (\text{I.3.2})$$

θ_0 is an initial arbitrary phase.

When $L = 1$, the modulation is qualified as *full response*, whereas, if $L > 1$, it is said to be *partial response*. Several different types of CPM modulations can be generated, depending on the possible choices of $g(t)$.

The parameters that directly affect the power-spectral efficiency of the modulation are the modulation index h and the pulse characteristics, such as pulse shape and length [And86]. In particular, if $g(t)$ has continuous derivatives up to the order N , the PSD of $\tilde{s}(t)$ can be shown to roll off asymptotically as $|f|^{-2(N+6)}$, independent of the value of h . As N grows, the bandwidth occupancy of both the main lobe and the first sidelobes (right and left) increases, whereas an increase of L improves both the asymptotic decay and the main lobe/first sidelobes extension. In the latter case, however, more complex receiver structures are commonly required. The role played by the modulation index can be easily understood: the greater is h , the wider will be the bandwidth extension, with an increasing loss in spectral efficiency.

Figures I.4 and I.5 show the functional block diagrams of two possible continuous-phase modulators. The first one (Fig. I.4) was explicitly devised for a digital implementation [Mas85], while the second is suited for implementation with analog technology (Fig. I.5).

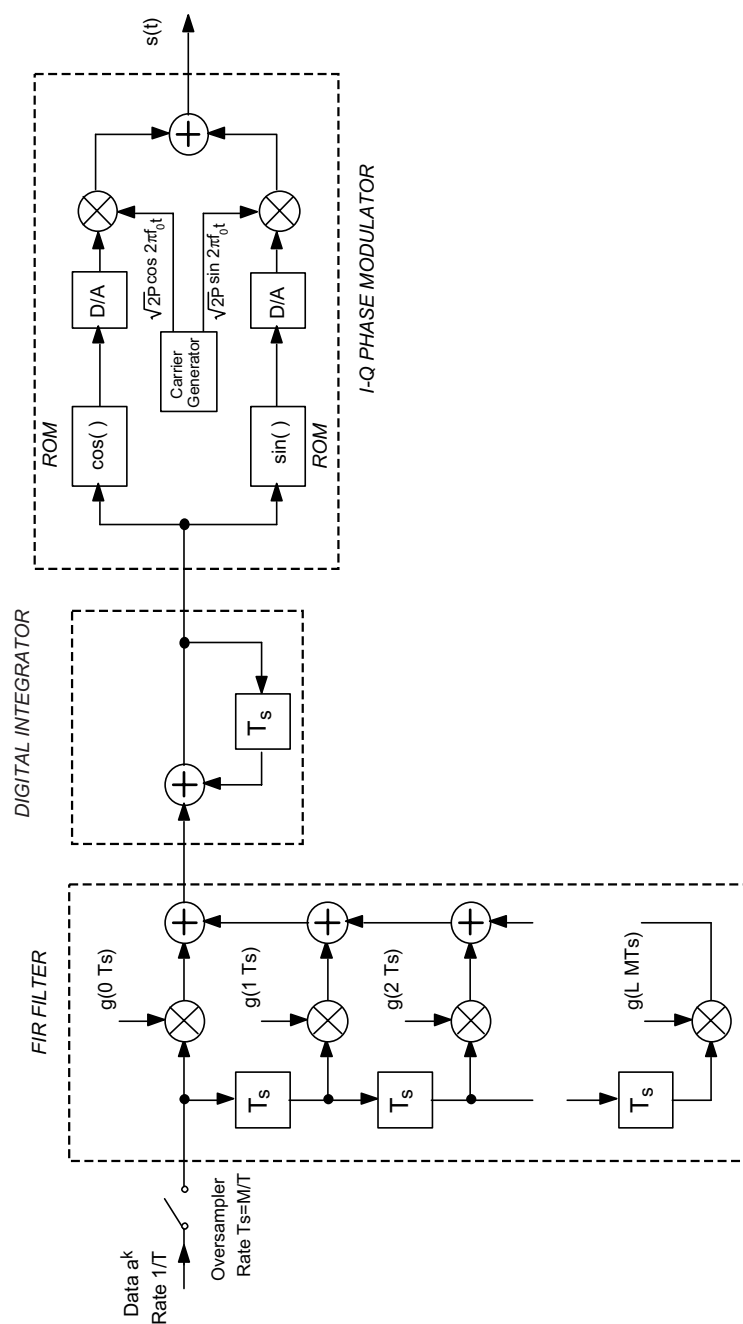


Fig. I.5

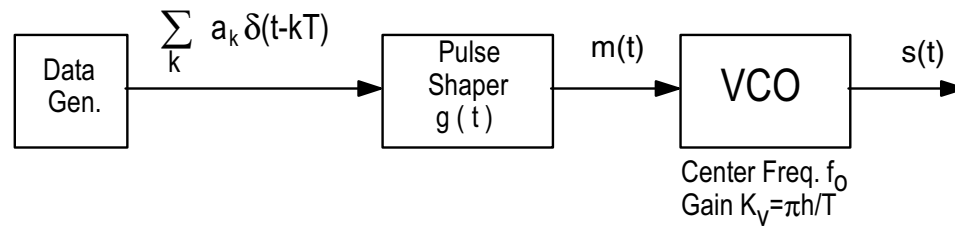


Fig. I.4

To conclude this Section, it is noted that the constant envelope property is a very attractive feature of all angle modulations (such as CPM), since it permits power amplifiers to be operated at a constant power level close to or at saturation with no BER performance impairment and spectral sidelobes regrowth.

(This space is intentionally left blank)

II

Pre-Selection of Modulation Techniques

II.1 Modulation Choice: The Particular Application

Power efficiency is perhaps the main concern in the design of communication systems to be used for telemetering applications. This arises from the severe specifications imposed on minimum power flux density (PFD) to be ensured in the downlink channel, and, to a smaller extent, on the specifications concerning the allowable power expenditure in the uplink channel. In [ESA86], the limiting values of PFD at the ground for the downlink channel, as well as that of the Equivalent Isotropically Radiated Mean Power for the uplink channel, are fixed in accordance with the ITU Radio Regulations. From the above observations, the system at hand can be classified as *power limited*.

As far as bandwidth occupancy is concerned, there are some constraints arising from: co-existence of a number of channels (Multiple Telemetry Channel), necessity to minimize interference on channels used for distance and Doppler measurements, when these channels are spectrally close to telemetry channels [ESA86]. An additional requisite is the safeguard of portions of the available bandwidth, for possible allocation of low-power service channels. The above requirements entail the choice of modulations fitting proper specifications on power spectral density (PSD) and Out-of-Band-Power (OBP). To this aim, it is useful to recall the definition of *bandwidth occupancy* fixed in [ESA86] according to the ITU Radio Regulations:

Let the **bandwidth occupancy** be defined as *that frequency band such*

that the mean powers emitted below the lower and above the upper frequency limits are each equal to a specified percentage $\beta/2$ of the total mean power of a given emission. Unless otherwise specified by the CCIR for the appropriate class of emissions, the value of $\beta/2$ should be taken as 0.5%.

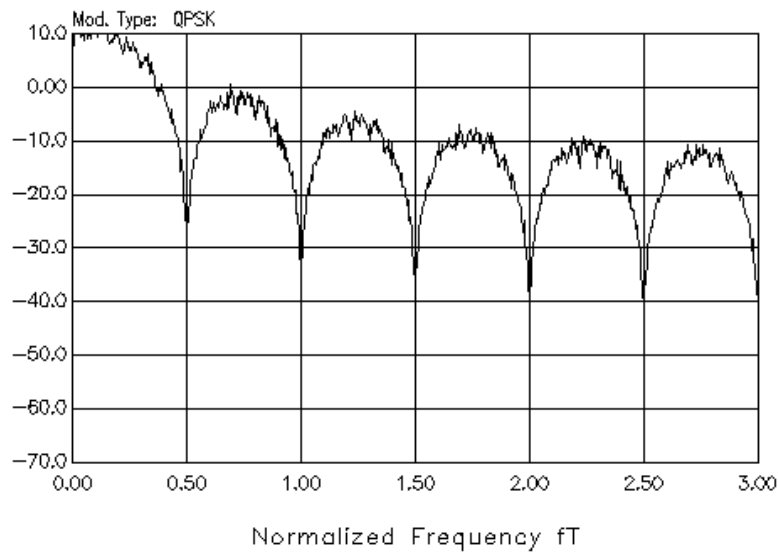


Fig II.1

We also recall that in the document [ESA86] the spectral masks to be met by the modulated signals are specified. Taking the above into account, then, the system to be defined can also be classified as *band limited*. Besides the above recommendations, there are further constraints on system design arising from some channel peculiarities. For instance, high power amplifiers (HPA's) are to be operated at saturation for power efficiency optimization. As a consequence, undesirable AM-to-PM conversion phenomena may arise in signal amplification, with related performance degradation, especially for phase-modulated waveforms.

Neglecting modulations employing subcarriers, that are more commonly encountered in low data rate telemetry applications, the most popular modulations used so far are rectangular-pulse BPSK and QPSK, both featuring a constant envelope. Figure II.1 shows the simulated baseband-converted PSD of the complex envelopes of the cited modulations. Unfortunately, the presence of strong sidelobes in their PSD's makes these modulations hardly applicable in *band limited* channels.

Bandpass filtering prior to power amplification might appear a tempting approach to attain the prescribed signal bandwidth limitation. Inspection of the I-Q diagram of a filtered QPSK signal (Fig. II.2), however, reveals that when a π -rad phase discontinuity occurs, the filtered signal envelope exhibits a 100% fluctuation. When such a waveform is passed through a saturated HPA, the well-known phenomenon of sidelobe regrowth occurs, thus nullifying the filter action [Bha81], [DeG89]. The solution to this problem can neither be sought in a post-HPA filter (presumably rather bulky and difficult to implement in view of the extremely high value of Q required), nor in an increase of the amplifier back-off, which would entail a deterioration of the satellite power efficiency.

In OQPSK modulation, abrupt π -rad phase transitions are avoided by delaying the data stream on one of the branches of the I-Q modulator by half symbol spacing. Maximum allowed phase transitions are now $\pi/2$, and this property considerably reduces spurious AM effects on the filtered waveform, as compared to the previous case. As is seen from the I-Q diagram of Fig. II.3, although the two modulations have exactly the same PSD, the envelope of the filtered signal is far less sensitive to a hard nonlinearity in comparison with the QPSK case. Figures II.4 and II.5 show the (baseband converted) PSD's of a QPSK and an OQPSK waveform, respectively, after power amplification with a 0 dB back-off. The shaping filter is a raised cosine Nyquist-root filter, with rolloff factor 0.5.

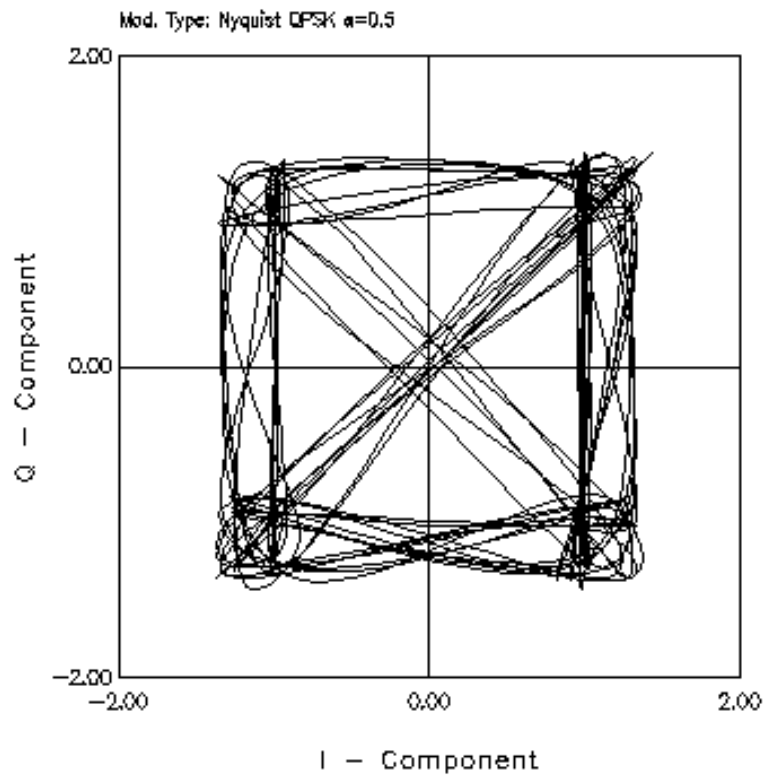


Fig II.2

Recognition that abrupt phase transitions cause the mentioned spectrum broadening of the HPA output draws one's attention onto Continuous Phase Modulations (CPM). The first step towards this goal is consideration of MSK, which can be seen both as a first simple example of CPM and as a half-cosine shaped OQPSK [Pas79]. Thanks to this twofold nature, MSK presents the typical advantages of both CPM (constant-envelope, spectral compactness) and OBM (extreme simplicity of the I-Q receiver implementation).

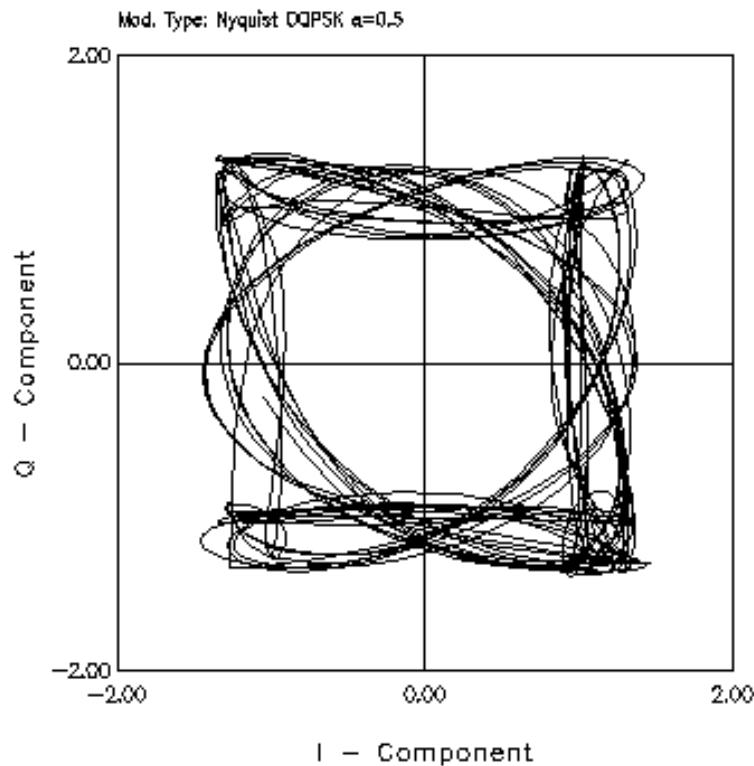


Fig. II.3

The system requirement of a simple receiver structure, together with the consideration that, broadly speaking, the more efficient the modulation is the more challenging synchronization results [D'A87], renders particularly attractive a subset of CPM's called *Generalized Minimum Shift Keying* (GMSK) [Lui90], including Gaussian MSK (GMSK) and L-Raised Cosine (L-RC) CPM. This kind of signals in fact allow for a simple I-Q linear receiver with only a minor degradation with respect to a (far more expensive) MLSE demodulator. A GMSK signal is generated by letting the MSK rectangular frequency pulses pass through a Gaussian-shaped filter, prior to being fed to the FM modulator

(see Fig. I.4). An L-RC signal is generated by letting the modulator frequency response $g(t)$ have a raised cosine shape of length LT , L integer. The spectral compactness provided by both the cited modulations is definitely superior to that exhibited by basic MSK.

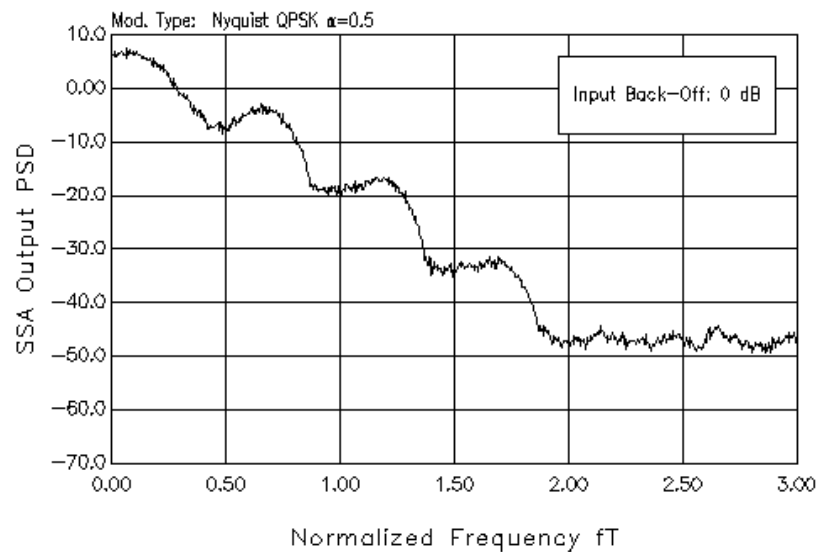


Fig. II.4

Among the mentioned modulations, then, consideration of the Nyquist-root-filtered OQPSK (hereinafter addressed as NYQ-OQPSK) and MSK appears a necessary step, since the former modulation has to be used as a benchmark for performance comparisons, while the latter can be regarded as the workhorse of efficient modulations.

Among Generalized MSK modulations, our choice fell on GMSK and 3RC, since the former has been widely analyzed and tested under various operating conditions, while the other performs closely to MSK and GMSK on the Gaussian channel, in terms of error probability [And86].

To conclude, it is noted that, according to specifications [ESA86], phase modulations are normally to be preferred to OBM, except in those cases wherein use of CPM would cause the specified PFD limits to be exceeded.

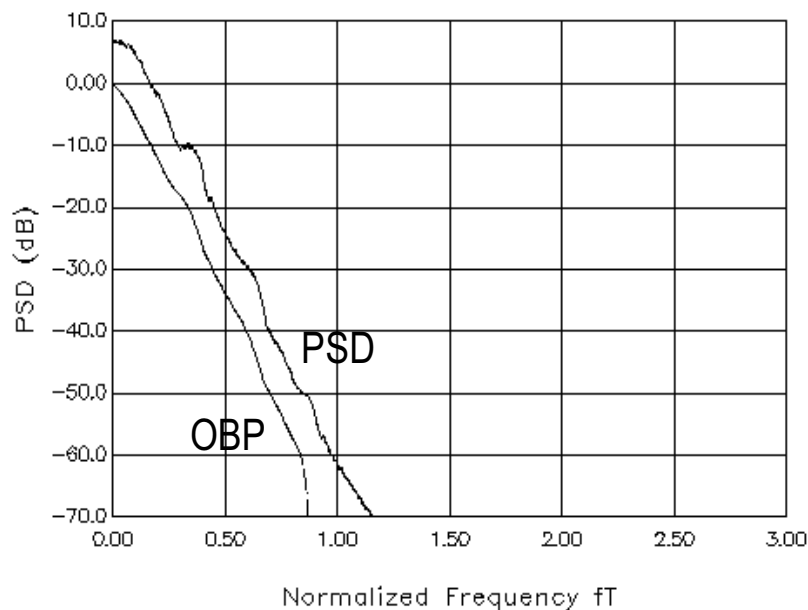


Fig. II.5

II.2 OBM's: OQPSK, MSK

In the following, we will briefly describe the characteristic features of the two abovementioned modulation techniques, referring the reader to [Pas79], [And86] and [Ana87] for more details.

II.2.a: OQPSK

The expression of a Rectangular-pulse OQPSK is obtained from (I.2.1) letting

$$p(t) = r\left(\frac{t}{2T}\right) \quad (\text{II.2.1})$$

where $r(x)$ is the rectangular function equal to 1 for $|x| < 0.5$ and 0 elsewhere. In this case the expression of the normalized Power Spectral Density (PSD) of OQPSK is given by

$$S(f) = \left(\frac{\sin 2\pi fT}{2\pi fT} \right)^2$$

As already mentioned, the spectrum occupancy of such a modulation cannot be considered satisfactory. It was thought then to take into consideration a "bandlimited" OQPSK. In particular, if we introduce the classical raised-cosine Nyquist function $P_N(f)$,

$$P_N(f) = \begin{cases} 1, & 0 < |2fT| \leq \frac{1-\alpha}{2} \\ \cos^2 \left[\frac{\pi}{2\alpha} \left(2fT - \frac{1-\alpha}{2} \right) \right], & \frac{1-\alpha}{2} < |2fT| \leq \frac{1+\alpha}{2} \\ 0, & \text{elsewhere} \end{cases} \quad (\text{II.2.2})$$

then the elementary pulse $p(t)$ will be the inverse-Fourier-transform of $P(f) \triangleq 2T \sqrt{P_N(f)}$, where we assume an equally-splitted filtering between transmitter and receiver. The PSD $S(f)$ of the OQPSK will be proportional to $P_N^2(f)$, and is sketched in Fig. II.6 for a roll-off factor $\alpha=0.5$. Also shown (dashed) is the so-called Out-of-Band Power (OBP) here defined as follows:

$$\text{OBP}(f) \triangleq \frac{\int_{-\infty}^{\infty} S(v) dv}{\int_0^{\infty} S(v) dv} \quad (\text{II.2.3})$$

which can also be expressed in dB units.

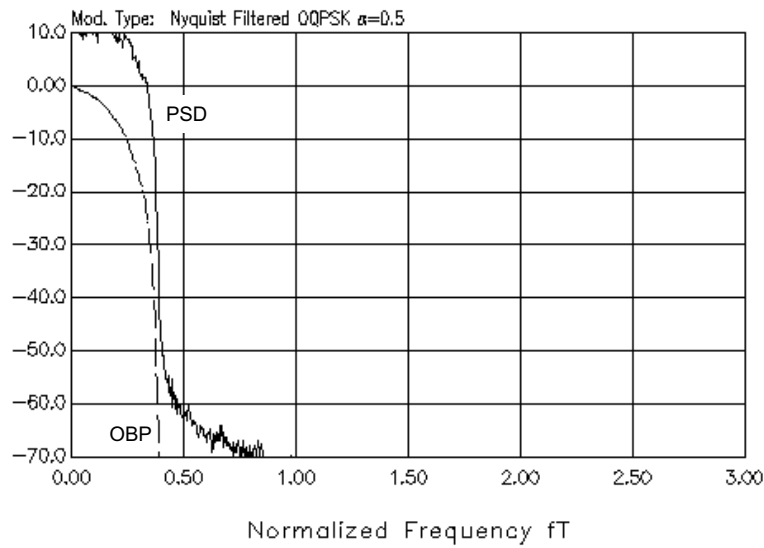


Fig. II.6

II.2.b: MSK

If we choose in (I.2.3)

$$p(t) = r \left(\frac{t}{2T} \right) \cos \left(\frac{\pi t}{2T} \right) \quad (\text{II.2.3})$$

we get an MSK signal. By virtue of the particular half-cosine pulse $p(t)$ of MSK, the modulated signal can be viewed, beside its OBM nature, as a continuous phase FSK with mark and space tones at $f_0 \pm 1/4T$. In fact, the signal $s(t)$ in (I.2.3) can be also expressed as:

$$s(t) = \cos \left[2\pi f_0 t - a_k b_k \frac{\pi t}{2T} + \phi_k \right] \quad (\text{II.2.4})$$

where ϕ_k equals 0 if $a_k = 1$ or equals π if $a_k = -1$. The variable ϕ_k also assures the phase continuity of the FSK signal. Expression (II.2.4) further stresses the constant-envelope feature of MSK.

The PSD of MSK is easily found to be [Bha81]

$$S(f) = \frac{16}{\pi^2} \left(\frac{\cos 2\pi fT}{1-16(fT)^2} \right)^2 \quad (\text{II.2.5})$$

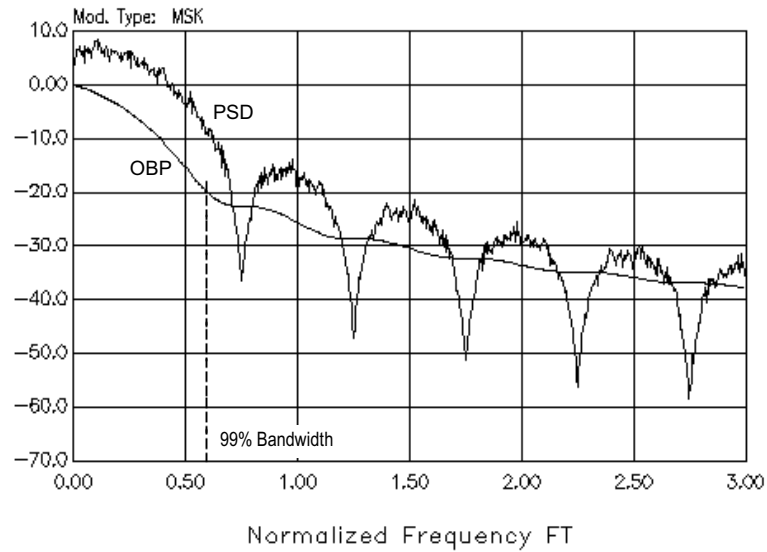


Fig II.7

The first null in the PSD of an MSK-modulated signal takes place at $fT=0.75$ (see the simulated PSD in Fig. II.7), whereas the successive nulls occur at $f_n T = 0.75 + 0.5n$, n an integer. The asymptotic decay of the PSD is proportional to $(fT)^{-4}$ and the 99% of the total signal power is allocated in the interval $|fT|<0.6$ around the carrier frequency (as opposed to $|fT|<4$ for a rectangular-pulse OQPSK).

II.3 CPM' s: Generalized MSK, GMSK, 3RC

In the following we report briefly on the main characteristics of the pre-selected CPM schemes. We only mention that the class "Generalized MSK" is intended to include all those CPM schemes with $h=1/2$ which can be demodulated by means of a linear I-Q receiver (see also [Pas79], [And86], [Lui90] and Chapter III of this report).

II.3.a GMSK

If we let in (I.3.2)

$$g(t) = r\left(\frac{t}{T}\right) \otimes h(t) \quad (\text{II.3.1})$$

where $h(t)$ is the impulse response of a Gaussian filter with bandwidth B_G ,

$$h(t) = \frac{1}{\sigma T \sqrt{2\pi}} \exp\left\{-\frac{t^2}{2\sigma^2 T^2}\right\} \quad (\text{II.3.2.a})$$

$$\sigma \triangleq \frac{\sqrt{\ln 2}}{2\pi B_G T} \quad (\text{II.3.2.b})$$

we get the so-called Gaussian MSK (GMSK) [Hir81]. This modulation scheme has many applications in mobile radio applications (such as the GSM land mobile radio system) due to its constant-envelope and compact-spectrum

features. In particular, the spectral occupancy of the modulated signal can be finely adjusted by varying the parameter B_G [Hir81]. Letting $B_G \rightarrow \infty$, GMSK turns into an MSK signal, as shown in Fig. II.8. Common values for the product $B_G T$ are in the interval $0.25 \div 0.5$. In the following, we will focus upon the case $B_G T = 0.5$, whose PSD and OBP are reported in Fig. II.8.

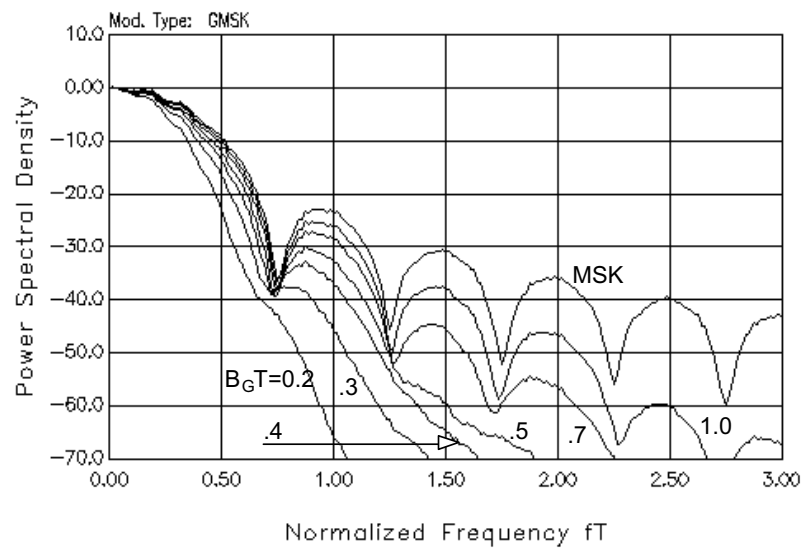


Fig. II.8

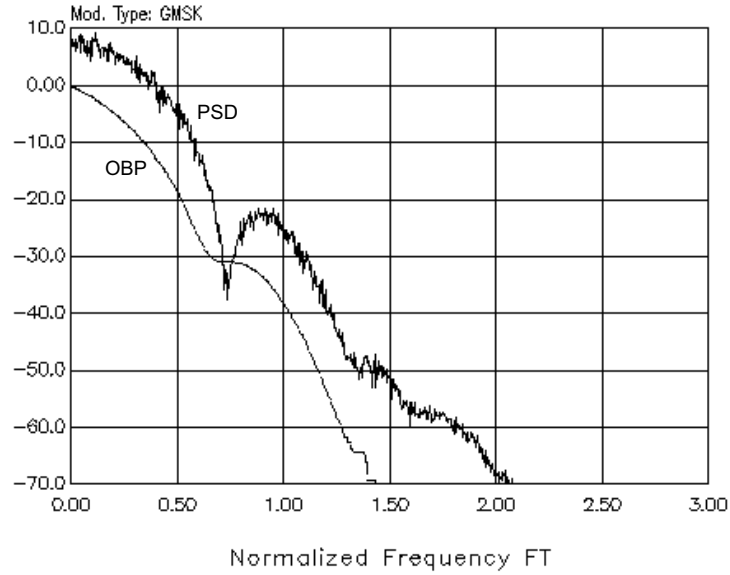


Fig. II.9

II.3.b 3RC

Letting in (I.3.2)

$$g(t) = r \left(\frac{t}{3T} \right) \frac{1 + \cos \left(\frac{2\pi t}{3T} \right)}{2} \quad (\text{II.2.2})$$

we obtain the so-called 3RC CPM, whose important feature is a better spectral behaviour with respect to MSK, as is apparent from the relative PSD and OBP diagrams of Fig. II.10.

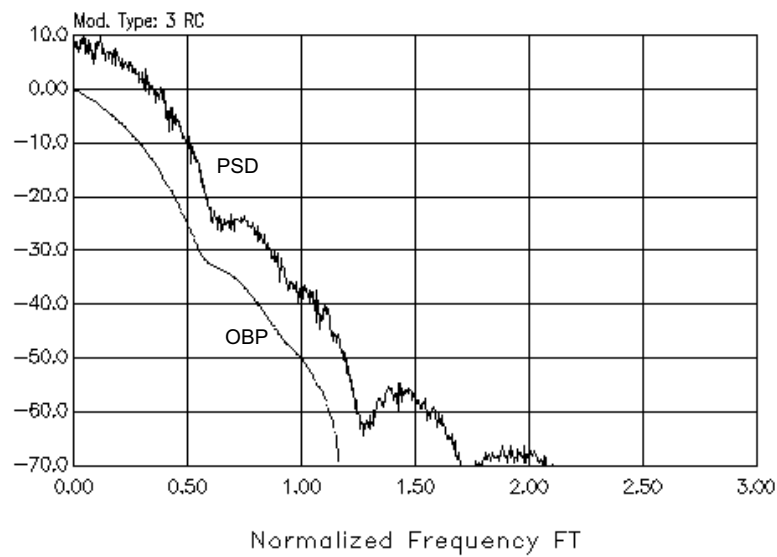


Fig. II.10

To summarize, in Fig. II.11 we report the comparison between the OBP of the four pre-selected modulations, together with the OBP of Rectangular-Pulse OQPSK. It is to be noted that the nonlinear amplifier has no influence upon all constant-envelope modulations (i.e. Rect-Pulse OQPSK, MSK, GMSK, 3RC), so that the relevant OBP curves in Fig. II.11 also apply for the signal at the amplifier output. On the contrary, the OBP curve of the amplifier output for NYQ-OQPSK turns into that already shown in Fig. II.5.

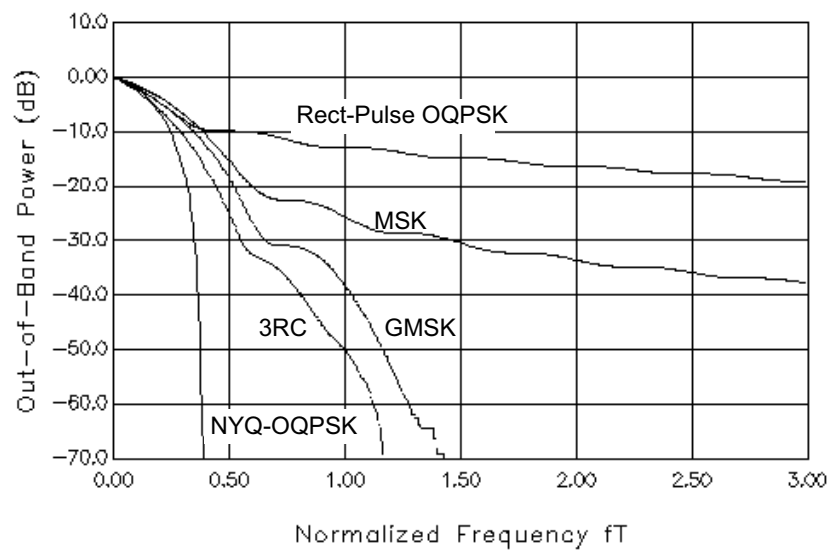


Fig.II.11

(This space is intentionally left blank)

III

Consideration of Simplified Receivers

III.1 Optimum Receivers for OBM and CPM

It is straightforward to derive the structure of the optimum receiver in AWGN for an OBM signal (I.2.1). The resulting scheme is that of a "parallel" I-Q receiver with appropriate staggering of the sampling times on the two arms. Figure III.1 depicts such a scheme, where the blocks labeled MF are demodulation filters matched to the elementary pulse $p(t)$. Further receiver structures can be conceived (like the "serial" demodulator described in [Ana87]), which however will not be considered in the present study.

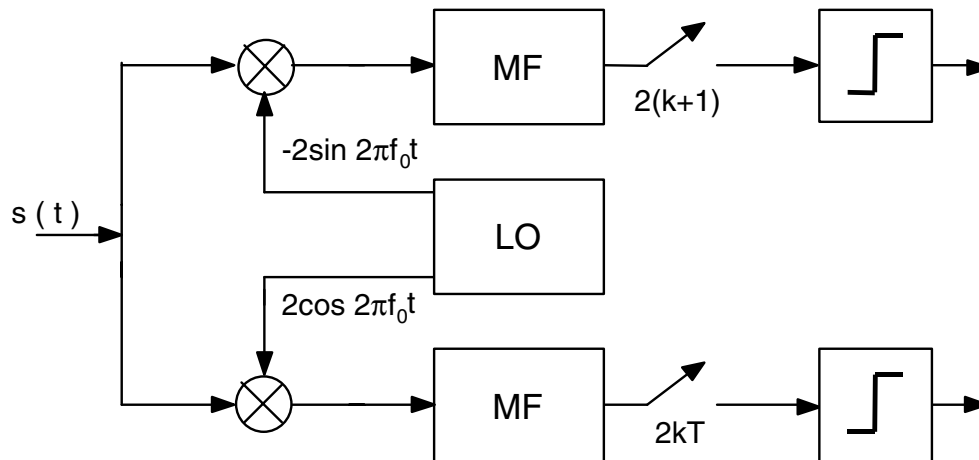


Fig. III.1

We want to explicitly mention here that the I-Q receiver with matched

filtering bears attains minimum BER only when no intersymbol interference is present at the sampling instants. When this condition is not fulfilled, a performance degradation with respect to the "matched filter bound" is to be expected. Moreover, the I-Q receiver is a *coherent* scheme, thus requiring an accurate carrier recovery subsystem. As is often the case in communications, the synchronization aspect turns out to play a crucial role in the system design of the link under examination, as will be seen in the sequel.

Let us now focus our attention upon CPM receivers. To this aim, observe that a CPM signal $\tilde{s}(t)$ as in (I.3.1) can be expressed in the interval $kT \leq t < (k+1)T$ as

$$\tilde{s}(t) = \sqrt{2P_s} \exp \left\{ j \left[2\pi h a_k q(t-kT) + 2\pi h \sum_{i=k-L+1}^{k-1} a_i q(t-iT) + \theta_k \right] \right\} \quad (\text{III.1.1})$$

where

$$\theta_k \triangleq \theta_{k-1} + \pi h a_{k-L} \quad , \quad \theta_0 = 0 \quad (\text{III.1.2})$$

Equation (III.1.1) clearly outlines the infinite memory of previous data peculiar to continuous-phase modulations (via the integration process inherent to the VCO). An optimum CPM receiver cannot thus employ a "symbol-by-symbol" decision strategy, but rather has to perform Maximum Likelihood Sequence Estimation after observation of (theoretically) the entire transmitted signal. Again, such a receiver has a *coherent* structure, with all the relative pros and cons.

A further observation stems from (III.1.1). In the usual hypothesis of a rational modulation index $h=m/n$, it is straightforward to show that the phase angle θ_k is allowed to assume a finite number of values only, namely all the integers multiples of π/n (assuming with no loss of generality $\theta_0=0$). As a consequence, the modulated signal $\tilde{s}(t)$ in the interval $kT \leq t < (k+1)T$ may be

regarded as the output of a finite-state machine whose input is the current data symbol a_k . The modulator determines the value of $\tilde{s}(t)$ on the basis of a_k and of the internal state $\sigma_k \equiv \{ a_{k-L+1}, a_{k-L+2}, \dots, a_{k-1}; \theta_k \}$ and updates its state with a shift of the L past symbols and making use of (II.1.2). After this characterization, it is apparent that the MLSE of data symbols can be carried out recursively by means of the Viterbi Algorithm (VA), after appropriate definition of the branch metrics.

The strict dependence of the signal values from the previous "history" of the modulation process is thus the key to the energy efficiency of CPM. This dependence, for adequately selected modulation indices h and elementary frequency pulses $g(t)$, leads to a growth of the free Euclidean distance between points in the modulated signal space and therefore produces a reduction of the asymptotic (i.e. for high values of E_b/N_0) BER of the receiver.

On the other hand, the implementation of a Viterbi receiver is quite challenging with the present technology, particularly, as regards CPM's, for what concerns the branch metric processor. Some simplified structures for MLSE has been presented, like the so-called M-algorithm [15] or the SA(B) technique [Aul85], with some performance degradations. In this study, the effort of employing MLSE has been judged excessive in the global economy of receiver design, and other simplified receiver structures have been taken into consideration.

III.2 The Simplified I-Q Receiver for OBM/CPM

In the preceding Section we presented the structure of the I-Q receiver for OBM's, and we also stressed the complexity of an optimum MLSE receiver for CPM's. Fortunately, when $h=1/2$ the complexity of the abovementioned CPM demodulator can be circumvented by resorting to a sub-optimum receiver whose structure has been studied for the so-called Generalized MSK

modulations [Lui90], [Tan87], [Gal85]. In this case in fact, the CPM can be thought of as a "distorted" version of an OBM [Lau86] and a linear I-Q OBM receiver can be employed as well for data demodulation [Lui90]. The only condition to the applicability of such a receiver is a sort of "eye-opening" constraint which has to be borne by the phase response $q(t)$ of the CPM:

$$\sum_{m=0}^D |q(mT+\tau)| + \sum_{m=D+1}^{L-1} \left| \frac{1}{2} - q(mT+\tau) \right| < \frac{1}{2} \quad (\text{III.2.1})$$

where τ is the sampling instant and the integer D can be chosen freely in the range $0 \leq D \leq L$. Examples of open-eye diagrams of Generalized MSK are given in Fig. III.2 and III.3 which depict the eye-diagrams of the in-phase component of the transmitted GMSK signal with $B_G T = 0.5$ and of the 3RC signal, respectively.

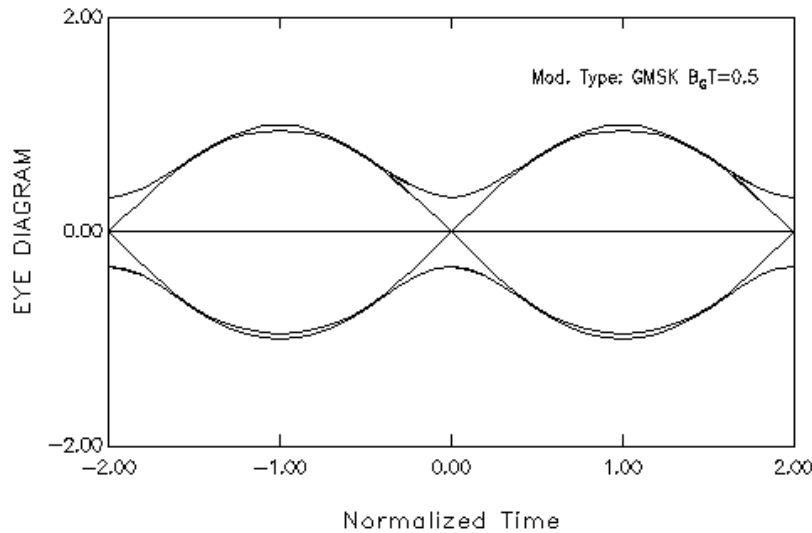


Fig. III.2

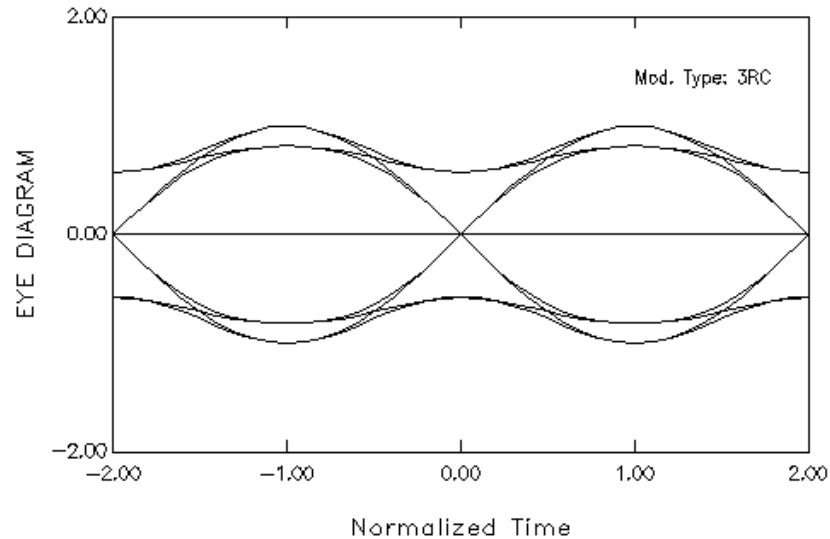


Fig. III.3

The cost of the simplicity of the I-Q receiver for CPM's with respect to a bulky Viterbi demodulator is to be paid for a slight performance degradation. The best we can expect in fact from a "symbol-by-symbol" linear receiver is the matched filter bound, which, in principle, might be improved resorting to multi-symbol MLSE. Moreover, at the output of the arm filters, a sort of "intersymbol interference" is present, due to the non-linearity of the modulation process and the inherent memory of previous data when $L > 1$. Figure III.4 shows the Symbol Error Rate (SER) performance of a GMSK modulation with $B_G T = 0.5$ when the Average Matched Filter (see next Section) is employed, whilst the same applies to Fig. III.5 for 3RC modulation (dashed line=matched filter bound). The degradation at a BER of 10^{-5} is vanishing for GMSK and about 0.5 dB for 3RC with respect to the matched filter bound (which is exactly attained by MSK and NYQ-OQPSK) and can be tolerated in our application.

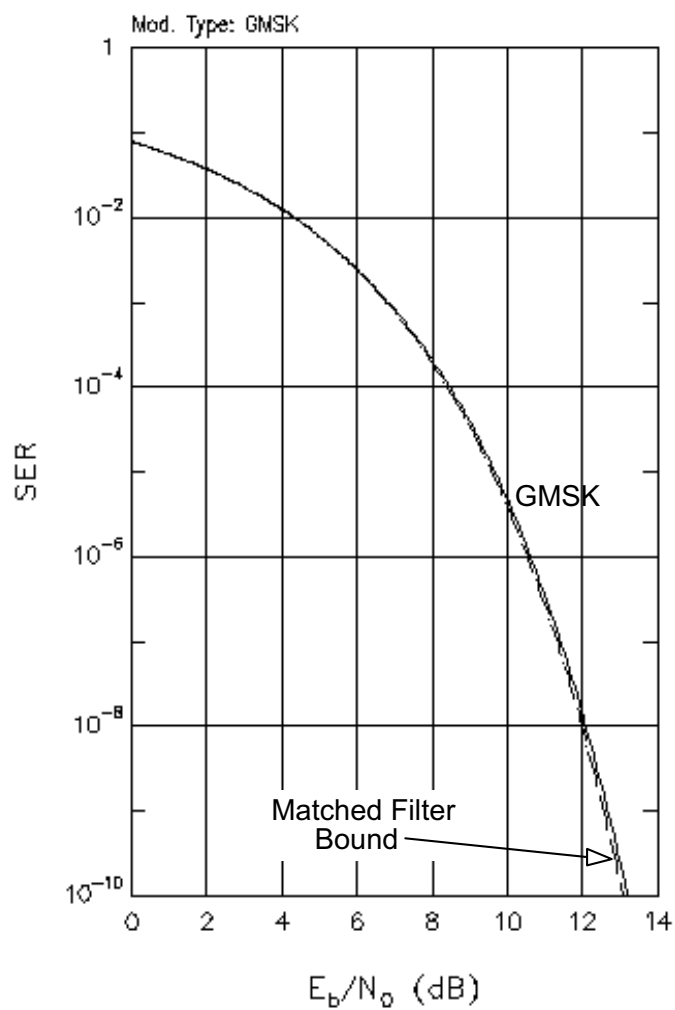


Fig. III.4

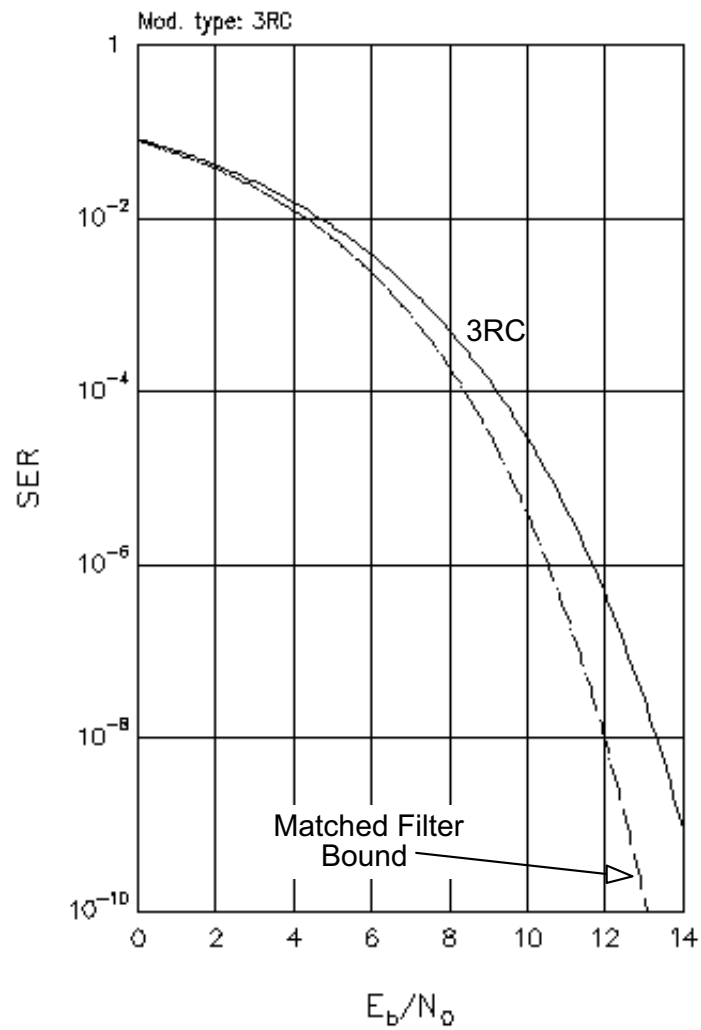


Fig. III.5

III.3 The Problem of Optimal Filtering in I-Q Receivers

In the I-Q receiver for Generalized MSK, the only design aspect to be solved is the appropriate choice of the demodulation filter. Among many other alternatives [Tan87], [Gal85] in this work it was decided to take into consideration only the so-called "Average Matched Filter" [Lui90], which is the optimum filter in conditions of poor SNR. More sophisticated optimal filters [Tan87] were not taken into account due to their design complexity as opposed to only minor performance benefits. For the sake of completeness, we report here the expression of the impulse response of the AMF for a generalized MSK whose phase response is $q(t)$:

$$h_{\text{AMF}}(t) \triangleq \sum_{k=0}^L h_k(t-kT) u(t-kT) \quad (\text{III.3.1})$$

where

$$h_0(t) \triangleq \prod_{i=0}^{L-1} \sin[\pi q(t+iT)] \quad (\text{III.3.2})$$

$$h_L(t) \triangleq \prod_{i=0}^{L-1} \cos[\pi q(t+iT)] \quad (\text{III.3.3})$$

$$h_k(t) \triangleq \left\{ \prod_{i=0}^{k-1} \cos[\pi q(t+iT)] \right\} \left\{ \prod_{i=k}^{L-1} \sin[\pi q(t+iT)] \right\}, \quad k=1,2,\dots,L-1 \quad (\text{III.3.4})$$

Figures III.6 and III.7 show the eye diagrams of the in-phase components of GMSK and 3RC at the output of the respective AMF's. It can also be shown that the AMF for MSK coincides with the usual matched filter $p^*(-t)$. The Eye Diagram of the in-phase component of MSK at the output of such a filter is shown in Fig. III.8

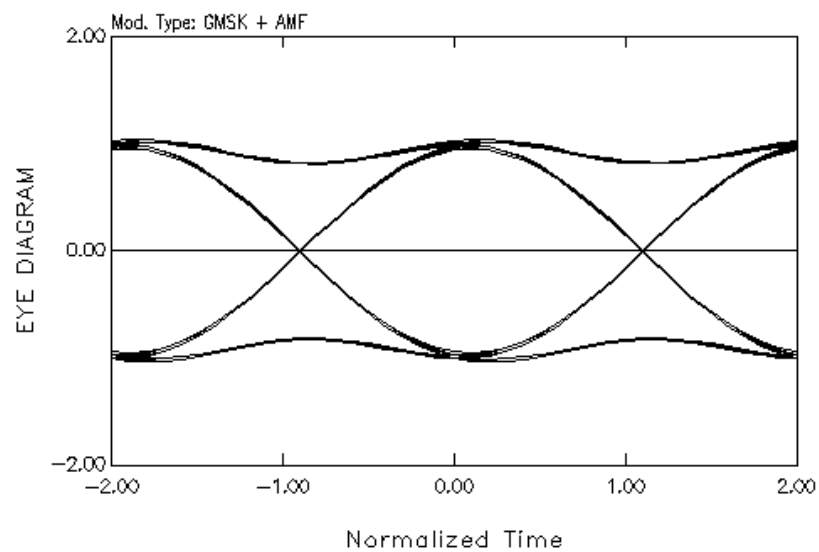


Fig. III.6

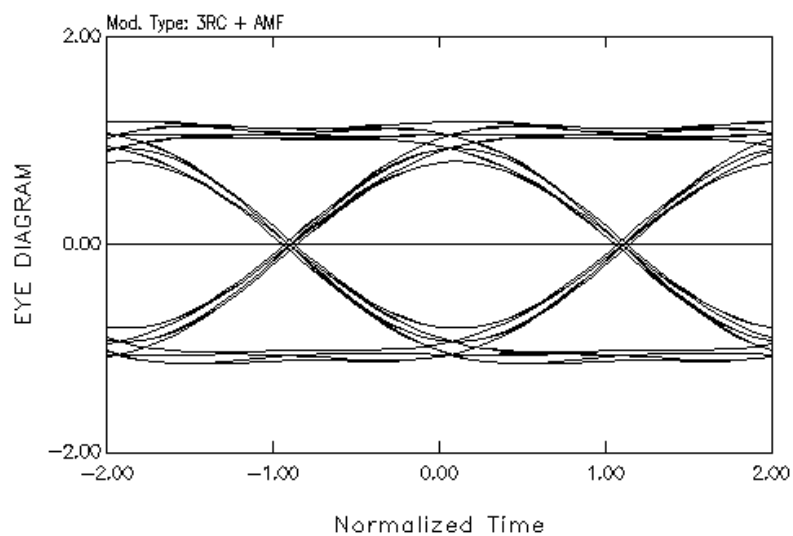


Fig. III.7

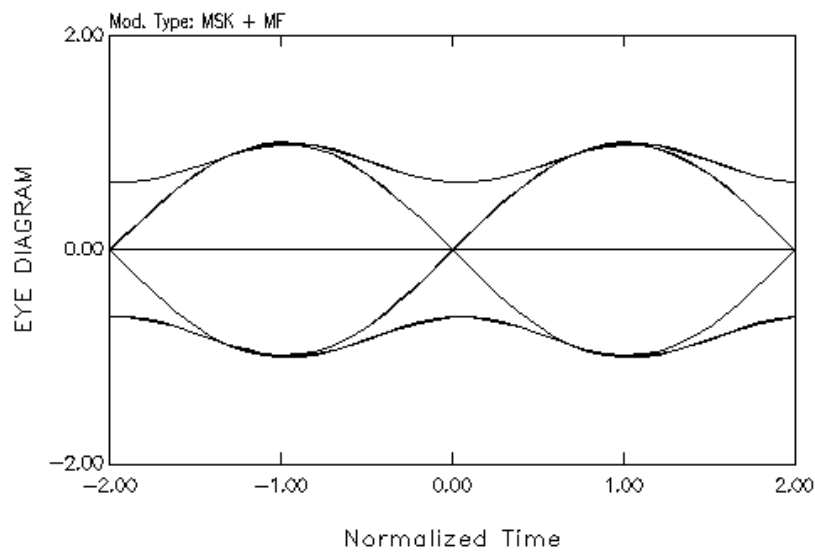


Fig. III.8

(This space is intentionally left blank)

IV Build-Up and Testing of the Simulation Program

IV.1 Block Diagram of the Simulation to be Developed

MODULATORS

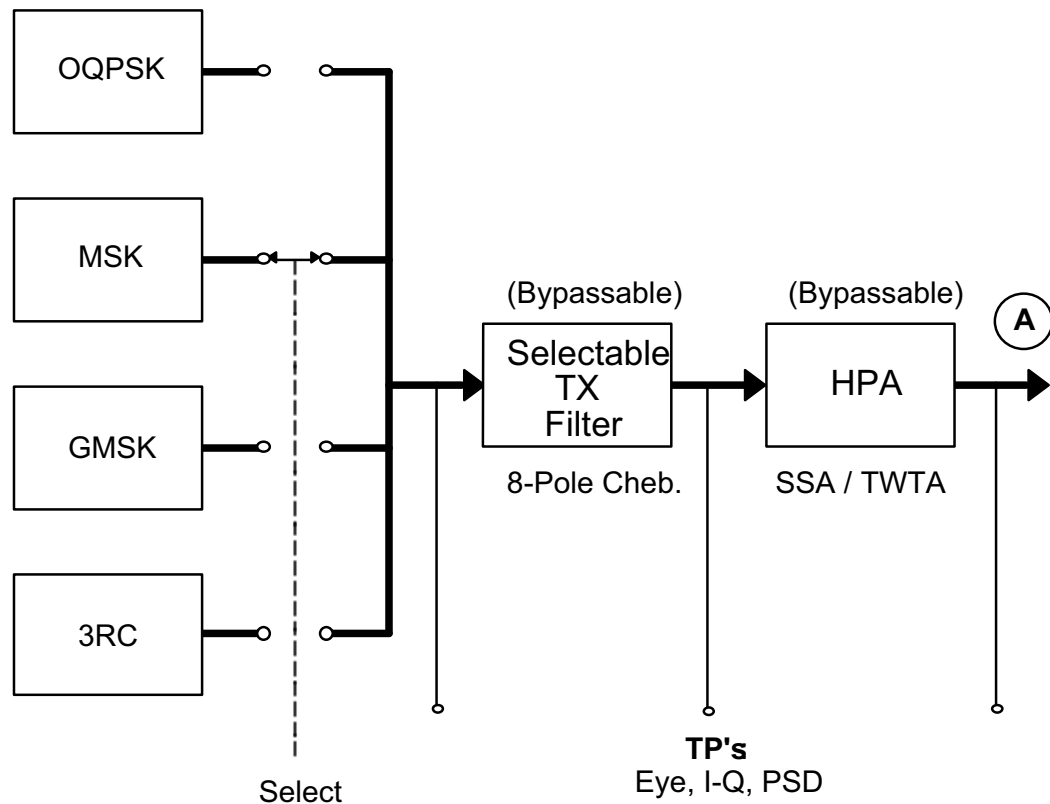


Fig. IV.1

In this Section we report a description of the basic structure of the

simulation program that was developed under this contract. Figure IV.1 depicts the Transmitter block diagram, composed of a selectable data modulator followed by bypassable transmit filter and High Power Amplifier. The AM/AM and AM/PM characteristics of the HPA obtained from the contract Technical Manager are shown in Fig. IV.2 and Fig. IV.3 for a Hughes L-band TWT Amplifier (TWTA) and in Fig. IV.4 and IV.5 for a Solid-State Amplifier (SSA) currently being developed by ANT under the supervision of ESA. For simulation purposes the 0 dB level was normalized to a fictitious unit-power value both for the input and the output signal, so that the saturation point is characterized by 0 dB input and output power.

The Receiver schematic is drawn in Fig. IV.6. The first relevant feature is the doubling of the demodulator chain. In the upper part of the scheme in fact, it is noticed the absence of the AWGN, which is summed at the input of the IF filter in the lower processing chain, instead. This is due to the fact that the upper demodulator is used in the simulation for the semi-analytical SER estimation [Jer84] which does *not* require the simulation of the noise process, but rather that of the overall distortions (ISI, nonlinearities, synch. errors and so on). On the contrary, the second twin demodulator leads to the synchronization subsystems whose behaviour ought to take into account the effect of Gaussian noise too. Note that the demodulation filter can be bypassed because in general it is not an optimum choice as far as the synchronizers are concerned. As will be clear in the next section, two possible bit synchronizer structure, an analog and a digital one, can be selected. The latter requires also an "oversampler" on the demodulated data signal, i.e. a device capable of extracting more than one signal sample per baud period, appropriately driven by a Numerically Controlled Oscillator (NCO). The analog synchronizer generates a timing wave whose zero-crossings are detected (Zero Crossing Detector, ZCD) and serve to drive the signal sampler.

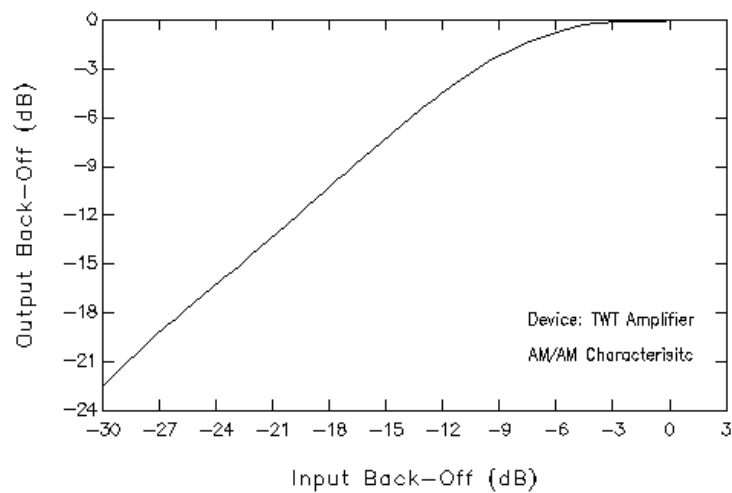


Fig. IV.2

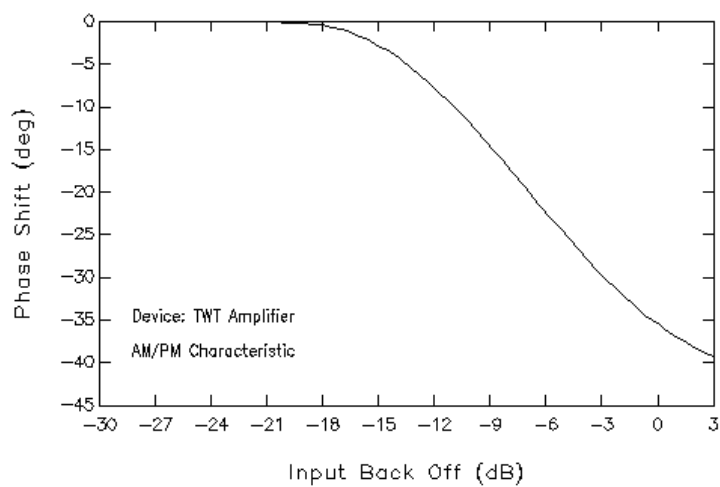


Fig. IV.3

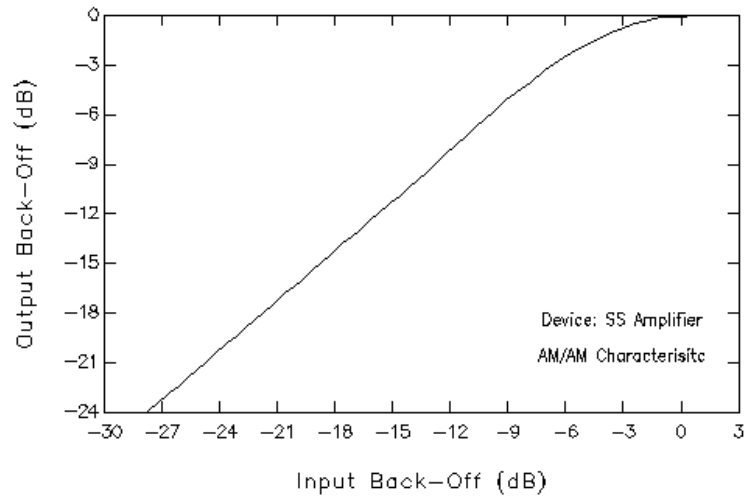


Fig. IV.4

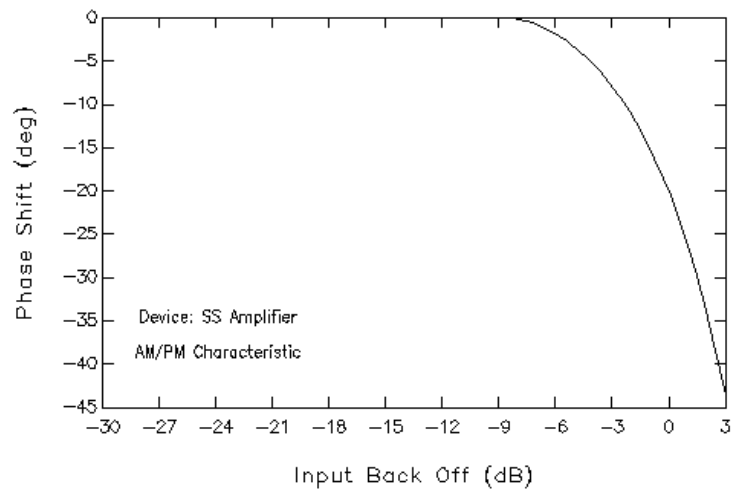


Fig. IV.5

At the so-called "Test Points" **TP** in both Fig. IV.1 and Fig. IV.6 some measurement can be carried out, as is indicated in the schemes. Not shown are the subsystems for carrier acquisition/tracking, whose study will be the subject of the second half of this report.

(This space is intentionally left blank)

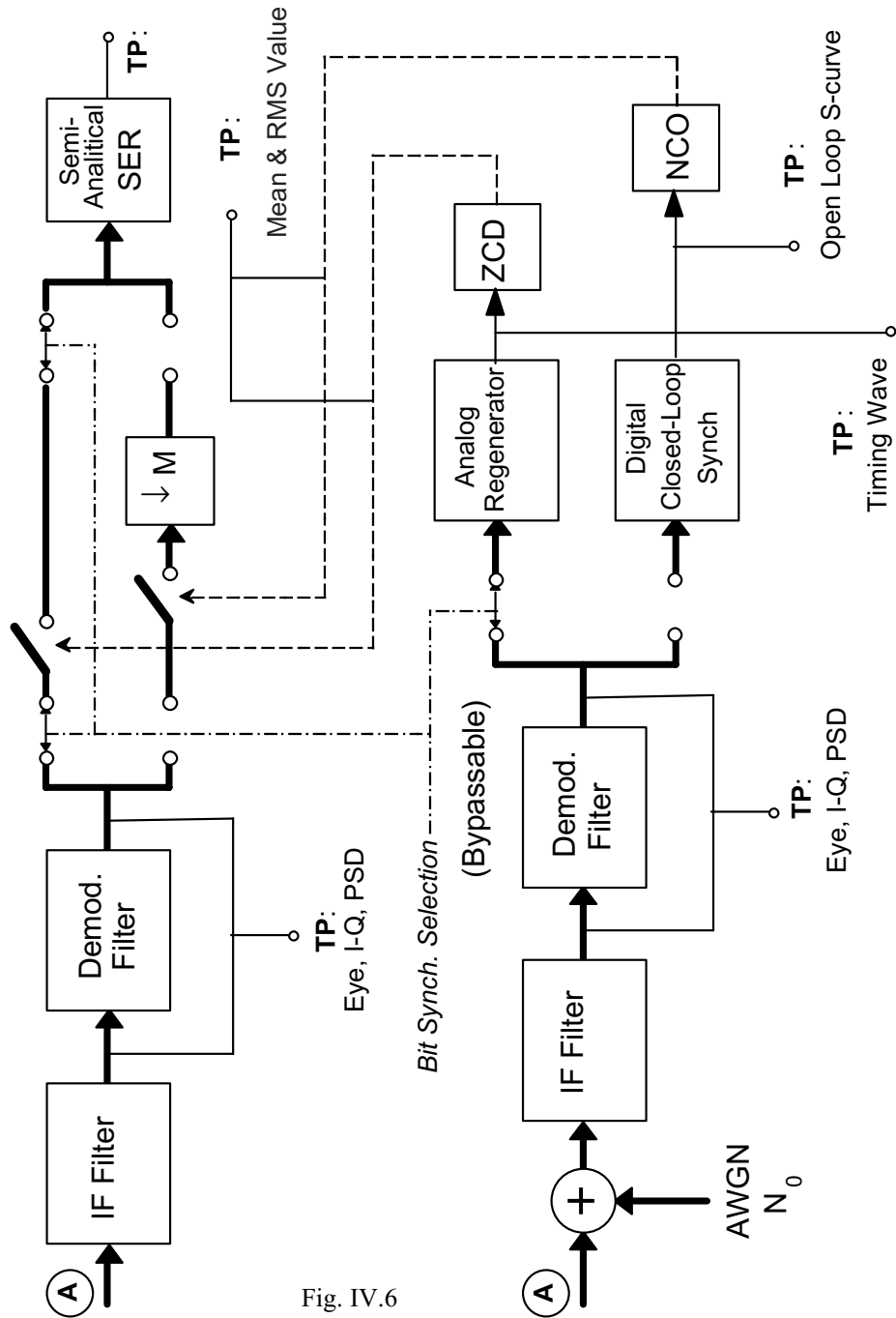


Fig. IV.6

IV.2 Testing: Results from Some Elementary Cases

Examples of results obtained by means of the simulation program has already been presented throughout this report. Nonetheless, in the following we will provide some results in the forms of graphs obtained at the test points **TP** in Fig. IV.1 and IV.6 assuming an MSK transmission (whose results are predictable analytically).

TP @ Modulator Output:

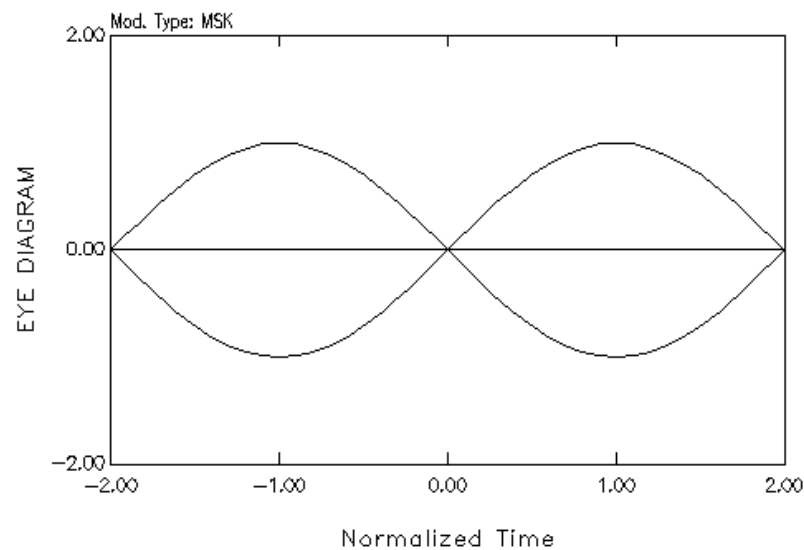


Fig. IV.7a

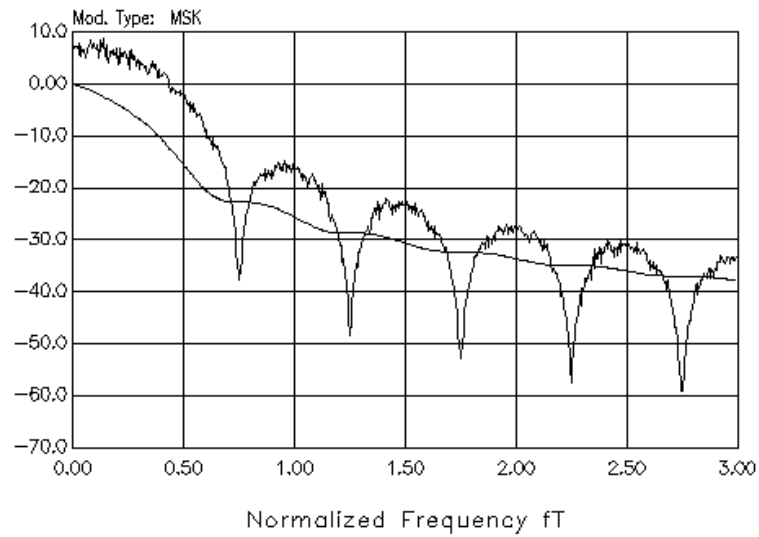


Fig. IV.7b

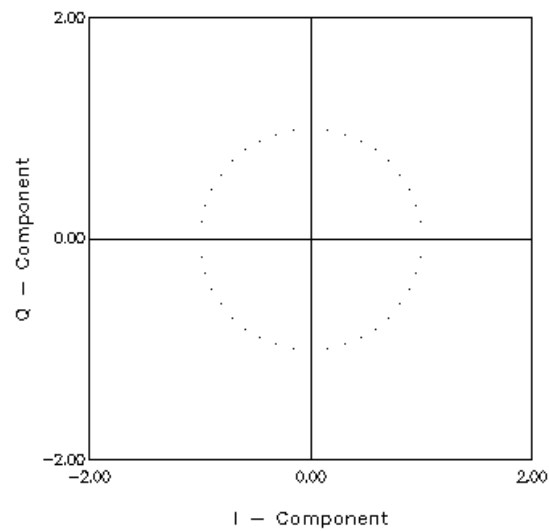


Fig. IV.7c

TP @ SSA Output (0 dB input Back-Off - No TX filtering):

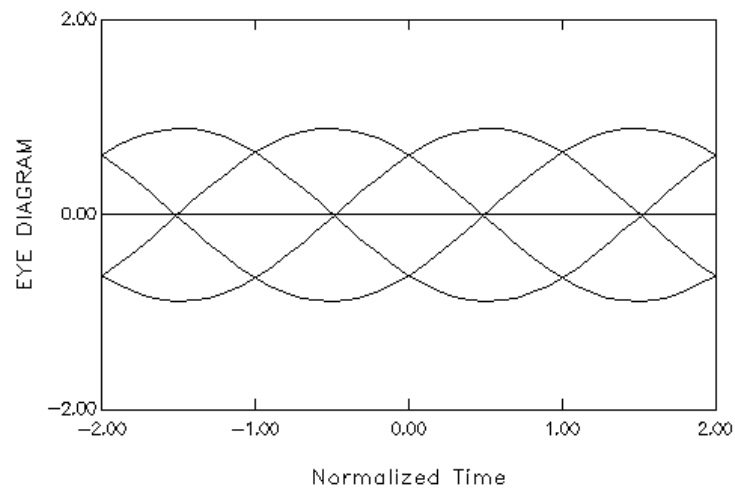


Fig. IV.8a

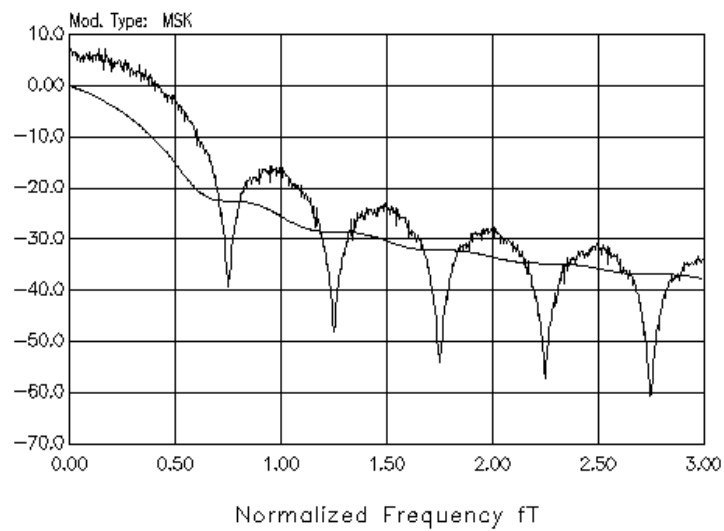


Fig. IV.8b

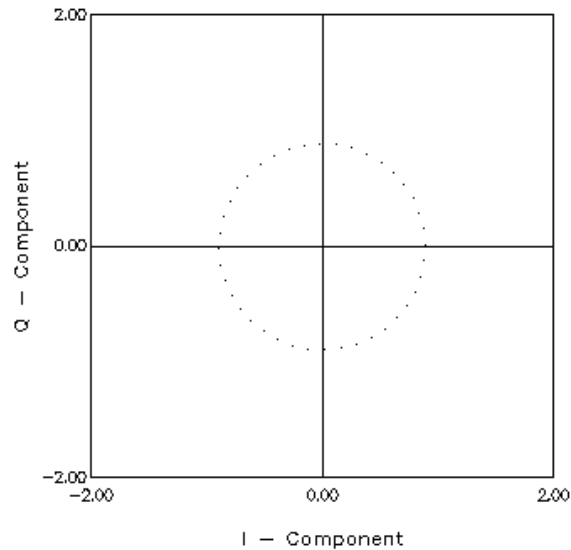


Fig. IV.8c

Some comments relative to this first results are in order. The eye diagram at the output of the SSA (Fig. IV.8a) reveals a phase shift in the transmitted signal with respect to the zero-phase of the reference carrier due to the non-zero phase shift introduced by the HPA (which is driven at saturation, see Fig. IV.5). Nonetheless, due to the constant-envelope feature of MSK stressed by the I-Q diagrams at the input of the HPA (Fig. IV.7c), the PSD of the transmitted signal is unchanged. The envelope of the transmitted signal is also constant (see Fig. IV.8c).

TP @ IF Filter Output - $B_{IF}T=1.5$ (No HPA - No TX filtering):

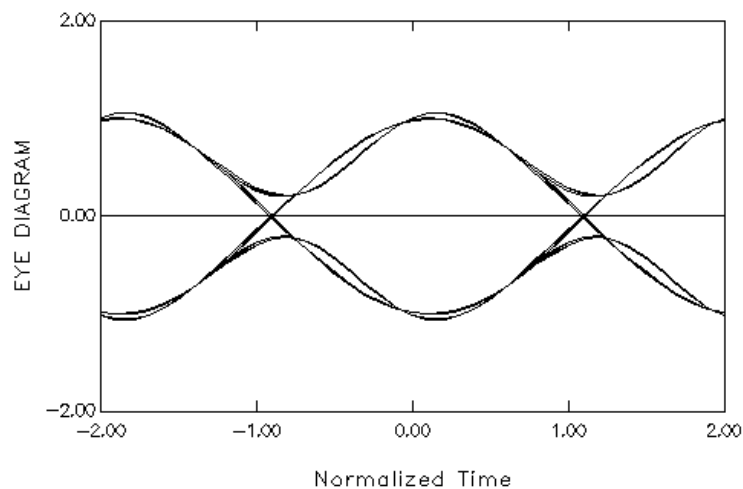


Fig. IV.9

TP @ Matched Filter Output - ($B_{IF}T=1.5$ - No HPA - No TX filtering):

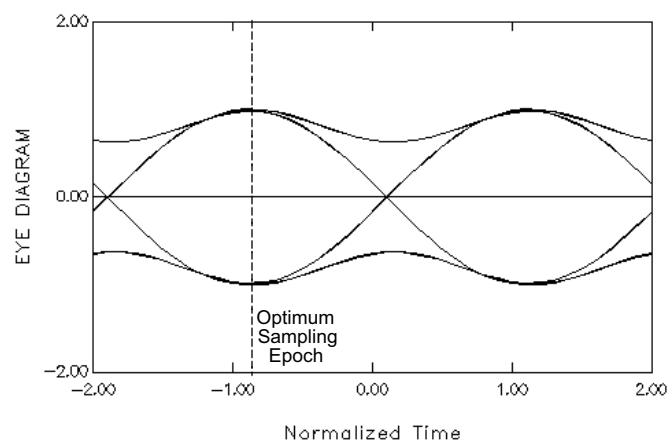


Fig. IV.10

TP @ Analog Regenerator Output $Q=1000$ ($B_{IF}T=1.5$ - No HPA - No TX filtering):

See Fig. V.2

TP @ NCO Output - Algorithm# 2 - $\gamma=5 \cdot 10^{-3}$ - $\tau_0=0.45T$ - $E_b/N_0=\infty$ ($B_{IF}T=1.5$ - No HPA - No TX filtering):

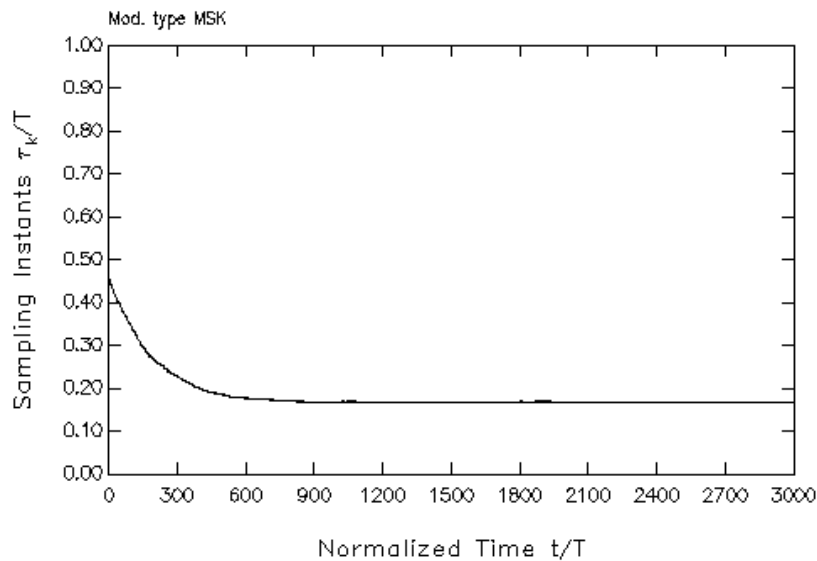


Fig. IV.11

Notice the rapid acquisition of the timing algorithm. As is apparent, the final value of the sampling instant coincides with the "optimum sampling epoch" derived by inspection of Fig. IV.10. Also apparent is the T-delay between Fig. IV.9 and IV.10 introduced by the baseband Matched Filtering.

TP @ Semi-Analytical SER Output - Algorithm# 2 - $\gamma=5 \cdot 10^{-3}$ ($B_{IF}T=1.5$ - No HPA - No TX filtering):

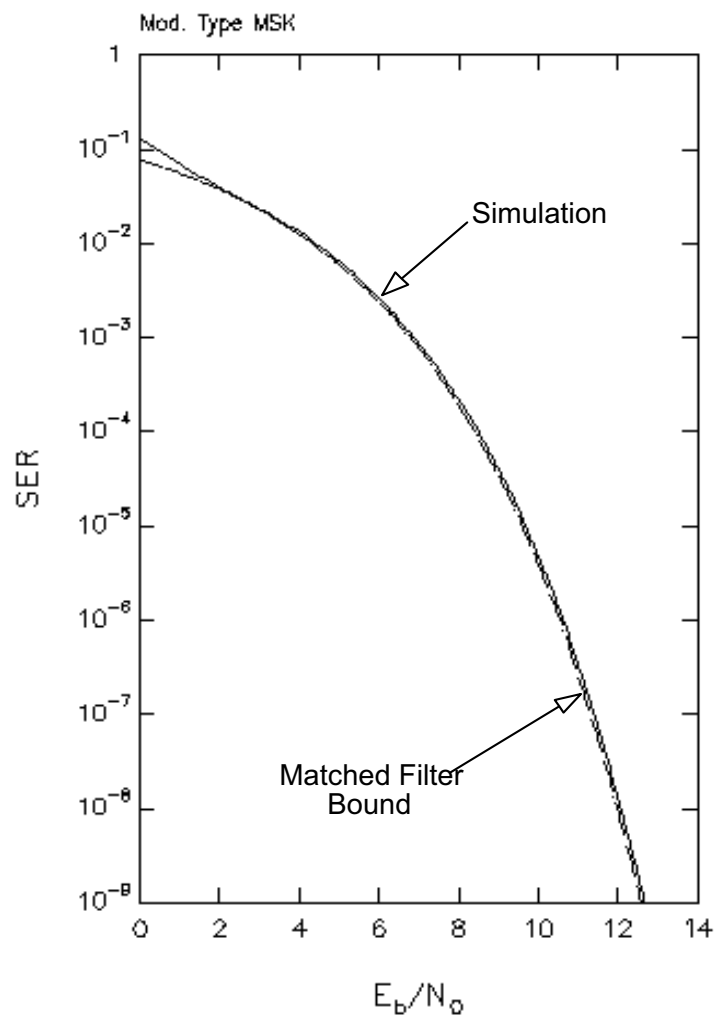


Fig. IV.12

V

Impact of the Synchronization Subsystems upon System Performance

V.1 Clock Recovery for OBM and CPM - The Traditional Approach

Most relevant schemes for clock recovery of MSK-modulated signals can be found in [Boo80], [Boo78], [D'A87]. In [Boo80], a MAP estimation of the sampling instant is performed, leading to the design of a closed-loop tracker. If the tracker is to be implemented with reasonably limited hardware (and without the need of SNR estimation), it results in a decision-aided scheme (obtained by replacing the ideal hyperbolic tangent nonlinearities with hard limiters) which will not be considered for the reasons explained in the following Section. In [Boo78] an ad-hoc baseband synchronizer is described, based on the nonlinearity $r_c^2(t) - r_s^2(t)$ which regenerates a line at frequency $1/T$ in the spectrum of the received signal. r_c and r_s are respectively the in-phase and quadrature components of the incoming signal with respect to the carrier frequency f_0 . This scheme also has to be discarded, since it is easily shown that the amplitude of its timing wave is strongly dependent on a possible phase offset introduced during baseband demodulation. This undesirable feature (as will be clear in the next Section) is a hurdle to fast clock acquisition which we consider a primary goal in the receiver design (especially from a viewpoint of an all-digital implementation of the demodulator). Reference [D'A87] provides a thorough performance analysis of the so-called "deBuda" synchronizer [deB72] described in its original form in [Boo78] too. Later work on this topic showed the delicacy of the double-PLL (or double filter) structure with respect to possible loss of lock (line vanishing) of one of the arms due to non-randomness of transmitted data. Moreover for this scheme it is not possible to

independently adjust the carrier and clock loop noise bandwidths. It was then decided to look for a novel clock synchronization scheme to be implemented at IF.

V.2 A Novel Open-Loop Analog Clock Regenerator

The first approach to the problem of clock synchronization was the design of a suitable recovery scheme to be implemented at IF with analog components, much like the traditional "de Buda" scheme mentioned in the preceding Section, but without those drawbacks related to the double-filtering-plus-mixer structure.

A primary design goal was that of devising a synchronizer insensitive to possible quasi-stationary phase errors introduced in the demodulation process. This feature in fact allows for a prompt clock acquisition, substantially decoupled from the carrier phase acquisition process. Also, we decided to focus upon non-decision-aided (NDA) schemes, sacrificing the favourable tracking performance of decision-aided schemes to the feature of fast acquisition borne by the NDA synchronizers [Gar88]. During acquisition in fact, data decisions are not reliable and the clock loop may dwell in an uncertain state for a long time before lock is acquired (hang-up, [Gar77]).

To further avoid hang-up phenomena related to closed-loop structures, the clock synchronizer was structured as an open-loop regenerator [Mey90] followed by a zero-crossing detector which drives the A/D converter of the baseband part of the receiver.

In Fig. V.1 we show the passband (a) and baseband equivalent (b) (thick lines indicate complex baseband signals) schemes of the clock regenerator, which is based on a delay-and-multiply approach. $r(t)$ is the IF signal and $z(t)$ is the recovered timing wave at frequency $1/T$. As is apparent from scheme (b), the recovered timing wave is insensitive to slowly-varying

phase offsets in the incoming signal (they cancel out in the product $\tilde{r}(t) \tilde{r}^*(t-T)$).

Due to the cyclostationary nature of the data signal $r(t)$, the expected value of the timing wave $z(t)$ is periodic with period T .

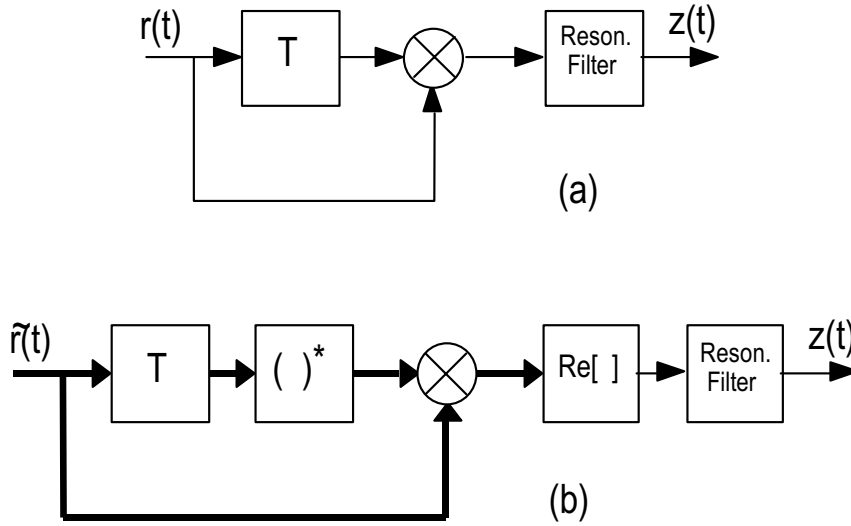


Fig. V.1

The amplitude A of the average timing wave can thus be evaluated as the amplitude of the component at frequency $1/T$ of the Fourier series expansion of $\Re \{E\{\tilde{r}(t) \tilde{r}^*(t-T)\}\}$. Assuming for example an OBM modulation, in the absence of Gaussian noise we have

$$E\{\tilde{r}(t) \tilde{r}^*(t-T)\} = E\left\{\left[\sum_k a_k p(t-2kT) + j \sum_k b_k p(t-(2k+1)T)\right] \times \right. \\ \left. \times \left[\sum_i a_i p(t-2iT-T) - j \sum_i b_i p(t-(2i+1)T-T)\right]\right\} =$$

$$\begin{aligned}
 &= \sum_k p(t-2kT) p(t-2kT-T) + \sum_k p(t-(2k+1)T) p(t-(2k+1)T-T) = \\
 &= \sum_k p(t-kT) p(t-kT-T) = \sum_k \gamma(t-kT) \quad (V.2.1)
 \end{aligned}$$

where

$$\gamma(t) \triangleq p(t) p(t-T) \quad (V.2.2)$$

To obtain the average amplitude of the timing wave, a sort of "oscilloscope display" was simulated by repeatedly representing 4T-long segments of the signal $z(t)$ on the same drawing (just as in the case of the eye diagram of a data-bearing signal). The result of such a procedure, obtained with a resonant filter of unit gain and $Q=1000$ is showed in Fig. V.2. The timing waves obtained in the cases of GMSK and 3RC modulations are also shown in Figs. V.3 and V.4, respectively. These graphs are obtained by simulation when $r(t)$ is a perfect replica of the transmitted signal and in the absence of Gaussian noise.

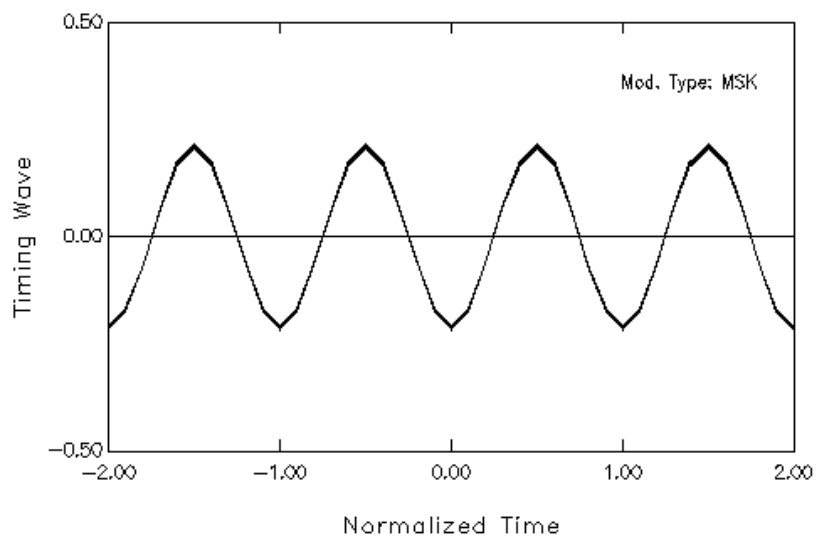


Fig. V.2

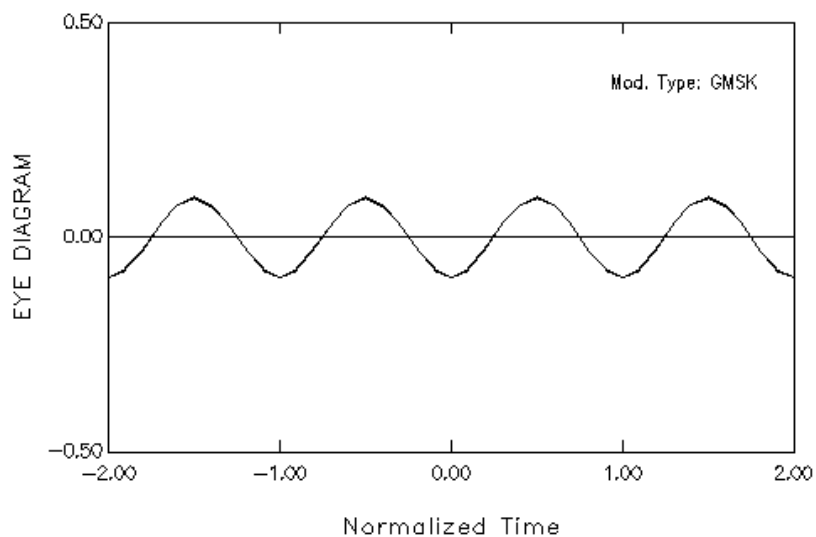


Fig. V.3

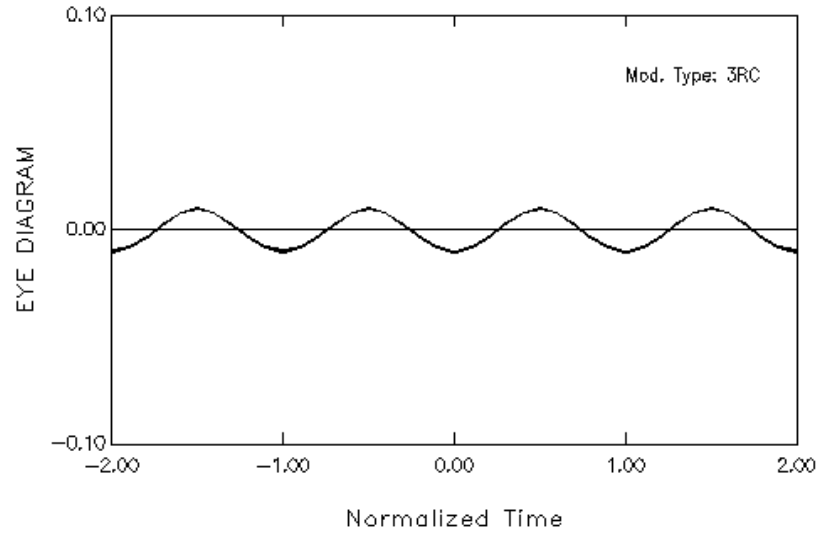


Fig. V.4

For an MSK, $p(t) = \text{rect}(t/2T) \cos(\pi t/2T)$, so that

$$\gamma(t) = 0.5 \text{ rect}\left(\frac{t-T/2}{T}\right) \sin\left(\frac{\pi t}{T}\right) \quad (\text{V.2.3})$$

and

$$A = \frac{2}{T} \int_0^T \gamma(t) \cos \frac{2\pi t}{T} dt = \frac{1}{T} \int_0^T \sin \frac{\pi t}{T} \cos \frac{2\pi t}{T} dt = -2/3\pi \quad (\text{V.2.4})$$

From (V.2.1) for an OBM signal, we have

$$A = 2 \left| \frac{1}{T} \int_{-\infty}^{\infty} p(t) p(t-T) \exp \left\{ -j \frac{2\pi t}{T} \right\} dt \right| =$$

$$= 2 \left| \frac{1}{T} \int_{-\infty}^{\infty} P(f) P^*(f+1/T) \exp \{ -j 2\pi f T \} df \right| \quad (V.2.5)$$

which, for a NYQ-OQPSK yields

$$A = 0 \quad (V.2.6)$$

because filtered OQPSK has a bandwidth less than $1/2T$ (not $1/T$, because the signalling rate on both the in-phase and quadrature arms is $1/2T$). As is apparent from (V.2.5), the proposed algorithm works properly only when the bandwidth of the received signal is greater than $0.5/T$. No useful timing information is obtained if we consider the output of the IF matched filter, either.

A possible alternative structure of baseband bit synchronizer for NYQ-OQPSK is presented in Fig. V.5.

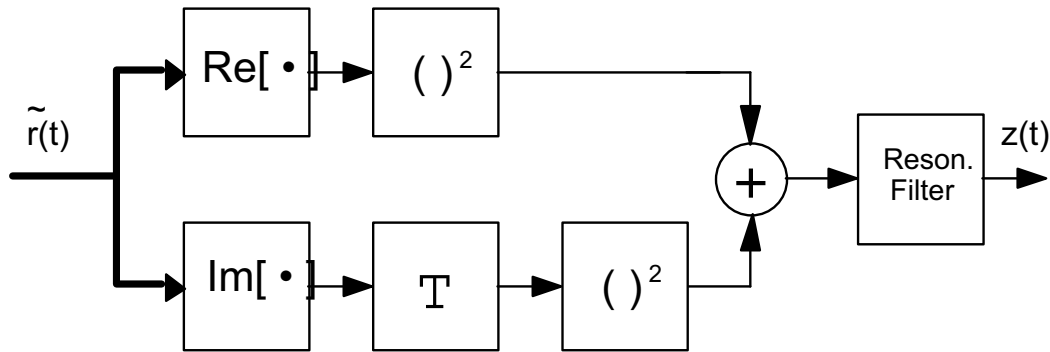


Fig.V.5

The scheme resembles the clock synchronizers employed in QAM systems, the only difference being the presence of the T-delay on the quadrature branch.

The average amplitude of the timing wave can be evaluated as the amplitude of the component at frequency $1/2T$ in the Fourier series expansion of the expected value of $z(t)$. With the usual notation we get

$$\begin{aligned}
 E\{r_c^2(t) r_s^2(t-T)\} &= E\left\{\left[\sum_k a_k p(t-2kT)\right] \left[\sum_j a_j p(t-2jT)\right] + \right. \\
 &\quad \left. + \left[\sum_i b_i p(t-(2i+1)T-T)\right] \left[\sum_q b_q p(t-(2q+1)T-T)\right]\right\} = \\
 &= \sum_k p^2(t-2kT) + \sum_i p^2(t-(2i+1)T-T) = 2 \sum_k p^2(t-2kT) \quad (V.2.7)
 \end{aligned}$$

So that the amplitude A of the useful component is derived as

$$\begin{aligned}
 A &= 4 \left| \frac{1}{2T} \int_{-\infty}^{\infty} p^2(t) \exp\left\{-j \frac{\pi t}{T}\right\} dt \right| = \left| \frac{2}{T} \int_{-\infty}^{\infty} P(f) P^*(f+1/2T) df \right| = \\
 &= \left| \frac{2}{T} \int_{-\infty}^{\infty} P(f) P(f+1/2T) df \right| \quad (V.2.8)
 \end{aligned}$$

Assuming that IF matched filtering has already been performed, $P(f)$ is here coincident with the Nyquist function $P_N(f)$ (II.2.2), so that (V.2.8) can be expressed as

$$\begin{aligned}
 A &= \left| \frac{2}{T} \int_{-\infty}^{\infty} P(f) P(f+1/2T) df \right| \\
 &= \left| 2T \int_0^{\alpha/4T} \left\{1 + \sin\left(\frac{2\pi f T}{\alpha}\right)\right\} \left\{1 - \sin\left(\frac{2\pi f T}{\alpha}\right)\right\} df \right| =
 \end{aligned}$$

$$= \left| 2T \int_0^{\alpha/4T} \left\{ 1 - \sin^2 \left(\frac{2\pi fT}{\alpha} \right) \right\} df \right|$$

$$= \left| 2T \int_0^{\alpha/4T} \cos^2 \left(\frac{2\pi fT}{\alpha} \right) df \right| = \frac{\alpha}{2} \text{ (V.2.10)}$$

In Fig. V.6 we report the timing wave $z(t)$ obtained by simulation with a resonant filter of unit gain and $Q=1000$ and for $\alpha=0.5$.

Unfortunately, a main drawback of this algorithm resides in the strong dependence of the amplitude of the timing wave on possible demodulation phase errors which may occur during baseband conversion. Let in fact θ be the residual static phase error, so that the baseband signal

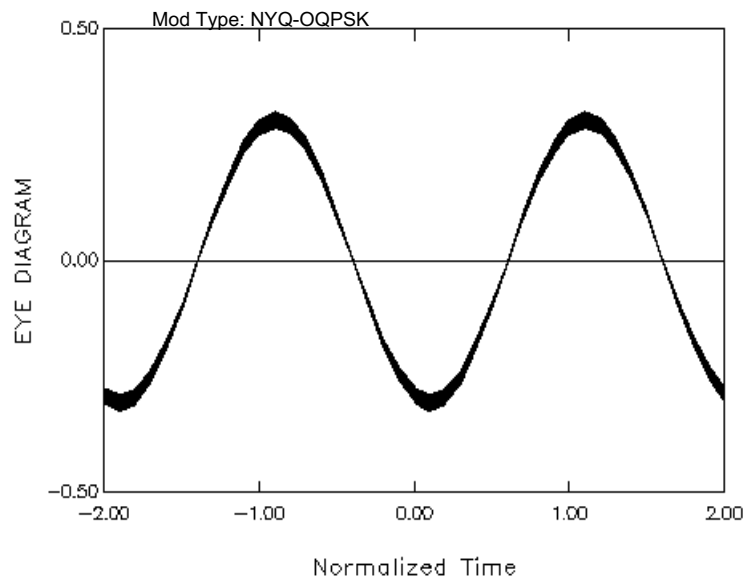


Fig. V.6

can be represented as

$$\tilde{r}_\theta(t) \triangleq \tilde{r}(t) e^{j\theta} \quad (\text{V.2.11})$$

and let $\eta_\theta(t)$ be the expected value of the input of the resonant filter. We get

$$\begin{aligned} \eta_\theta(t) &\triangleq E\{ [r_c(t) \cos\theta - r_s(t) \sin\theta]^2 + [r_c(t-T) \cos\theta - r_s(t-T) \sin\theta]^2 \} = \\ &= \eta(t) \cos^2\theta - \eta(t-T) \sin^2\theta + \eta(t) \cos^2\theta + \eta(t-T) \sin^2\theta \end{aligned} \quad (\text{V.2.12})$$

where $\eta(t) \triangleq \sum_k p^2(t-2kT)$. The phase-dependent amplitude A_θ of the useful component at frequency $1/2T$ can be derived from the following relation:

$$A_\theta \cos\left(\frac{\pi t}{T} + \phi\right) = A \cos\left(\frac{\pi t}{T} + \phi\right) \cos^2\theta + A \cos\left[\frac{\pi(t-T)}{T} + \phi\right] \sin^2\theta \quad (\text{V.2.13})$$

where ϕ is the phase of the amplitude component and A is as in (V.2.10). Finally, from (V.2.13) we get easily

$$A_\theta = A \cos 2\theta. \quad (\text{V.2.14})$$

The variation of the amplitude of the timing wave as a function of the demodulation phase error might reveal a serious hurdle during the acquisition process of the receiver. In fact, the overall design strategy of the demodulator strongly recommends to resort to an all-digital phase recovery algorithm which requires precise knowledge of the optimum sampling instant in order to work properly. On the other side, (V.2.14) stresses the potential inability of the clock synchronizer to provide a useful indication in some initial large-phase-error demodulation conditions. This sort of nasty clock-carrier interaction can be broken only employing a phase-independent clock synchronizer, as mentioned in Sect. V.2.

V.3 Performance of the Analog Scheme

The performance of the analog clock regenerator described in the previous section has been analyzed by simulation. The steady-state performance of the synchronizer has been characterized, as is customary, by computing the variance of the zero-crossings of the regenerated timing wave (which identify the sampling instants of the data-bearing signal). Figures V.7-V.9 show such results for three values of the normalized equivalent noise bandwidth of the resonant filter, namely 10^{-2} , $5 \cdot 10^{-3}$, 10^{-3} .

(This space is intentionally left blank)

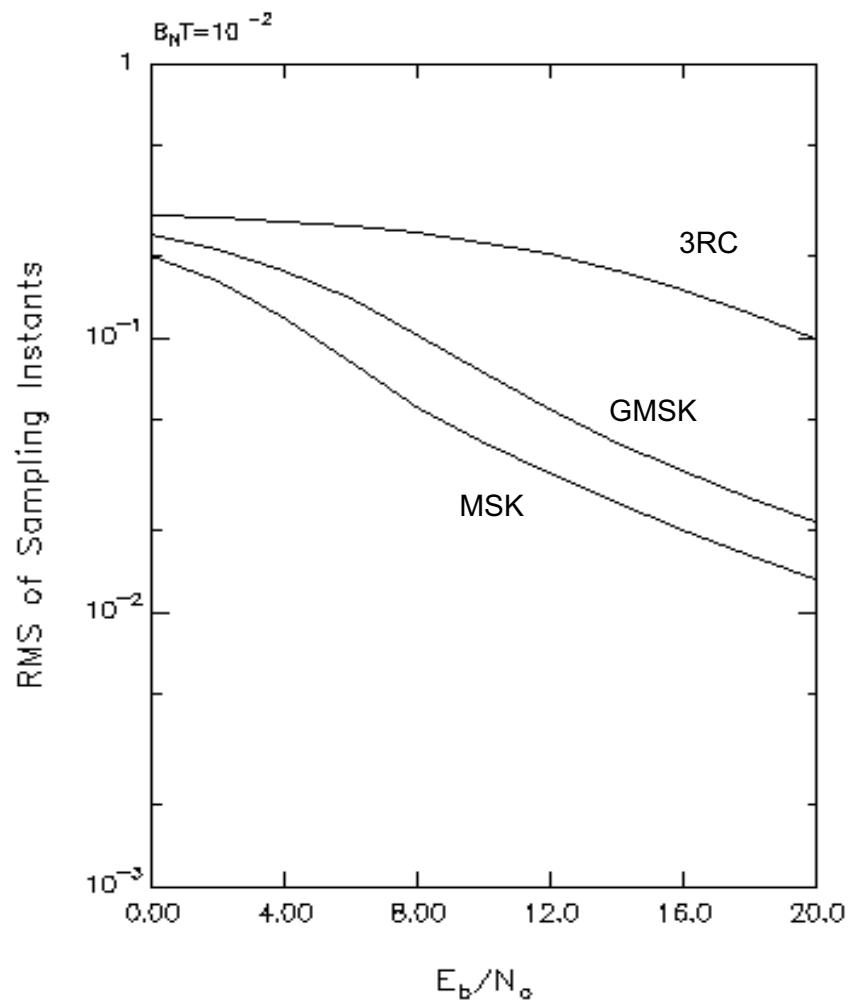


Fig. V.7

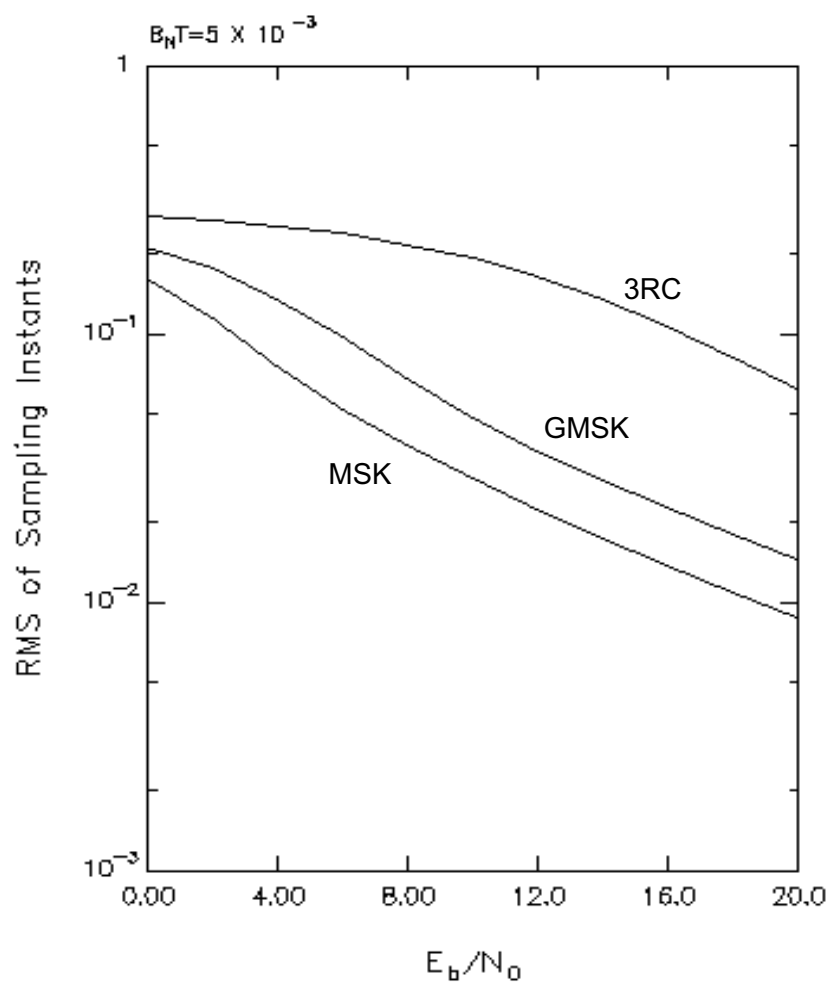


Fig. V.8

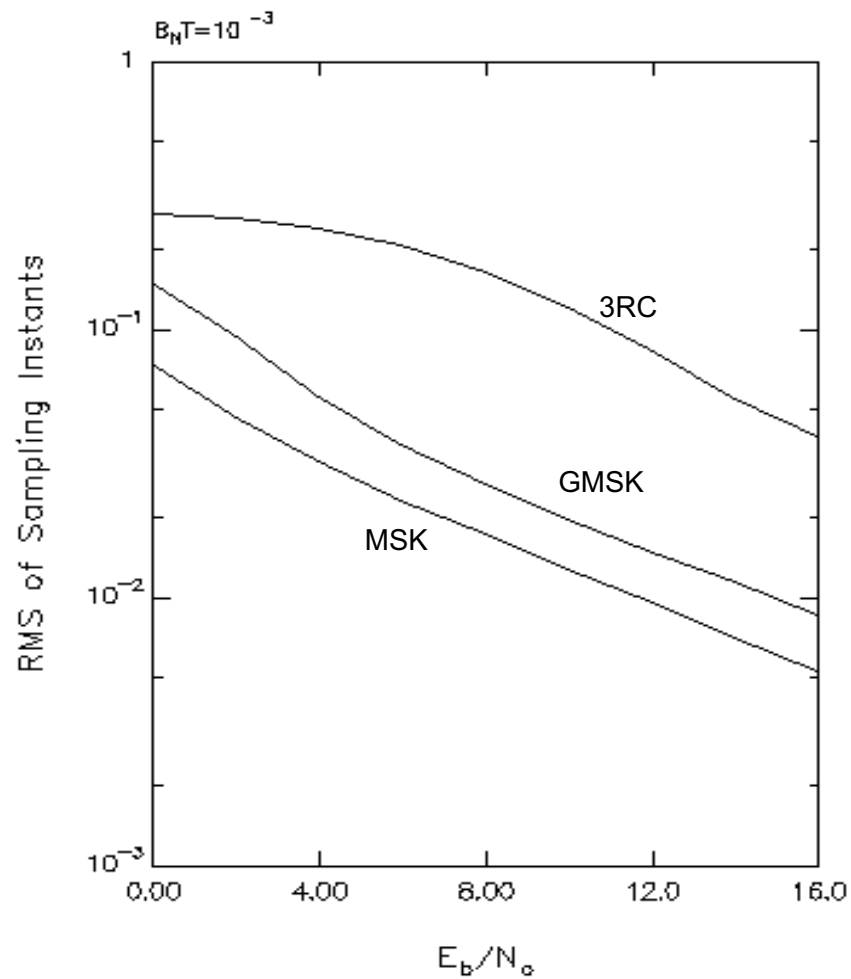


Fig. V.9

The presented algorithm appears quite inadequate with respect to 3RC modulation. Jitter curves for this modulation technique in fact exhibit an early saturation towards the value $1/\sqrt{12}$ corresponding to a uniformly distributed sampling instant over the symbol interval, with no useful timing information. As for the other two modulations, MSK clearly outperforms GMSK, which on the other hand has a sufficiently good performance. In these simulations, the signal input to the synchronizer is the output of the Butterworth IF filter with two-sided bandwidth $B_{IF}T=1.5$

Characterization of the bit synchronizer in a transient regime can be achieved by means of the diagrams in Fig. V.10-V.15 that show the time-evolution of the output of the resonant filter $z(t)$. A rough estimate of the "acquisition time" can be derived for each modulation technique and each filter bandwidth by analyzing the rise of the envelope of the signal $z(t)$.

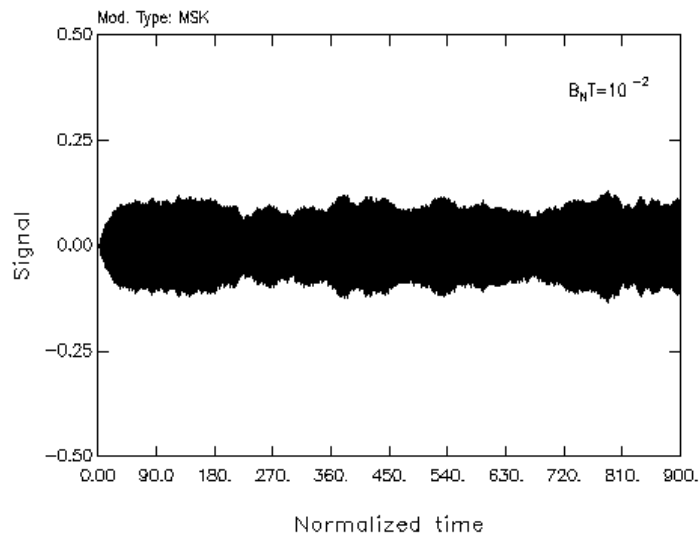


Fig. V.10

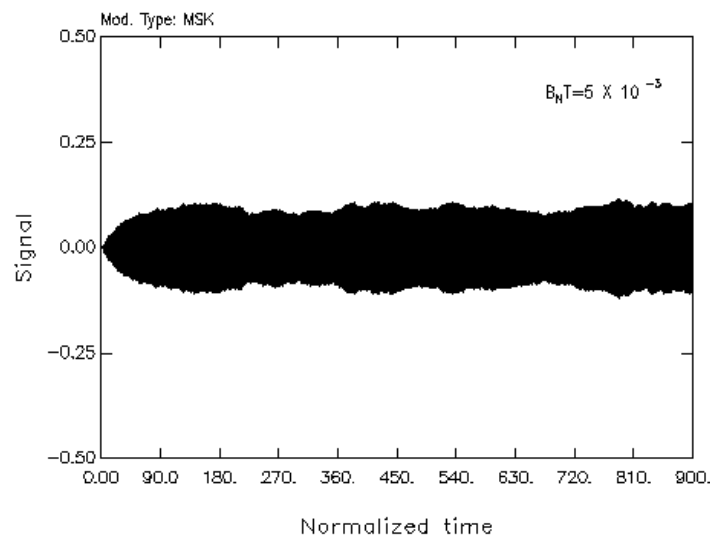


Fig. V.11

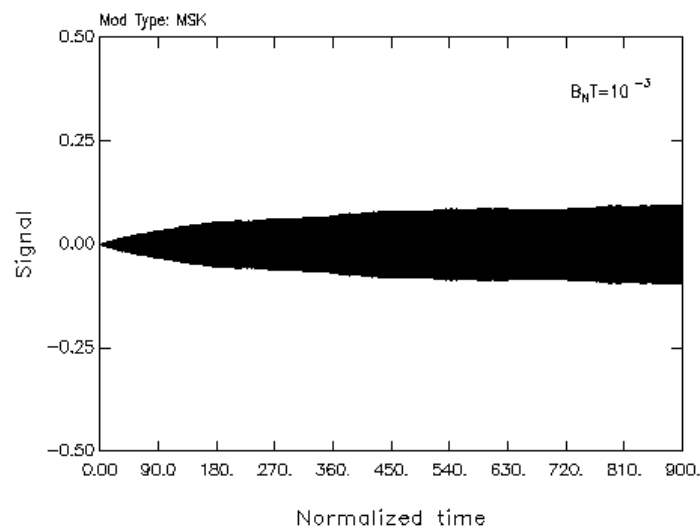


Fig. V.12

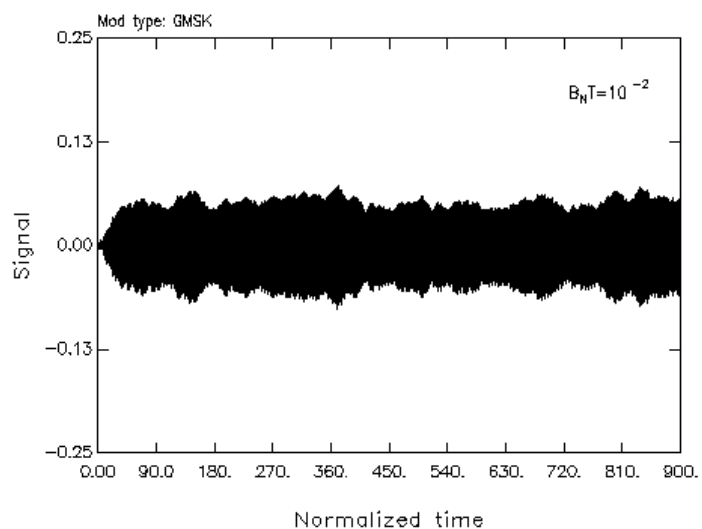


Fig. V.13

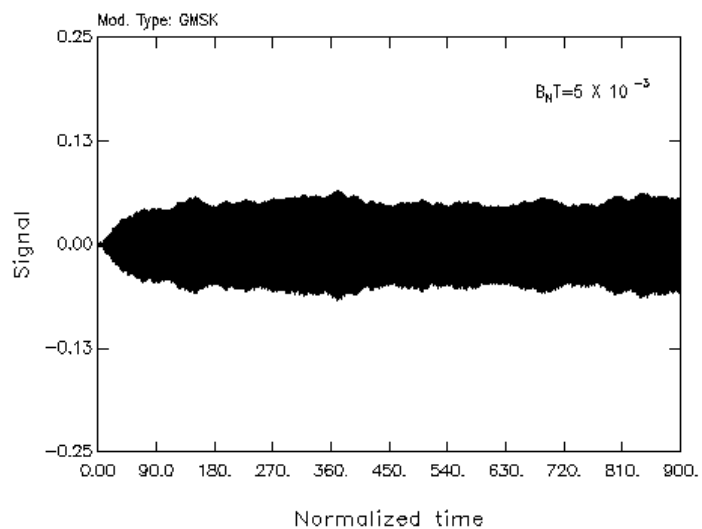


Fig. V.14

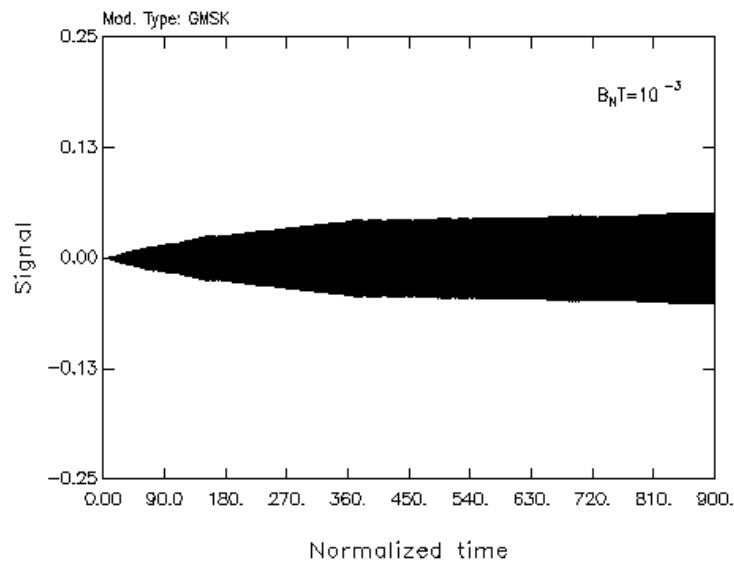


Fig. V.15

Narrower bandwidths of the resonant filter lead to longer acquisition times.

As a final evaluation of the impact of the clock synchronizer upon the receiver performance, in Figs. V.16-V.18 we report the BER curves of the demodulator with the analog clock regenerator previously described, again with filter bandwidths equal to 10^{-2} , $5 \cdot 10^{-3}$, 10^{-3} . The strong correlation between the BER results and the jitter curves of Figs. V.7-V.9 is apparent.

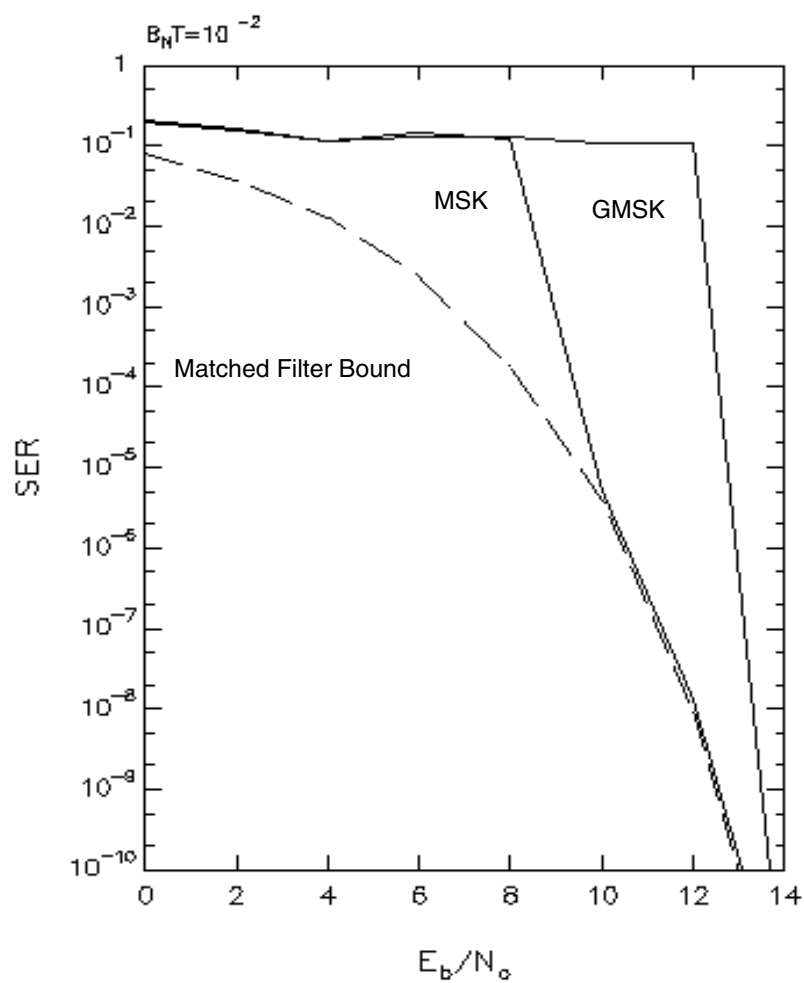


Fig. V.16

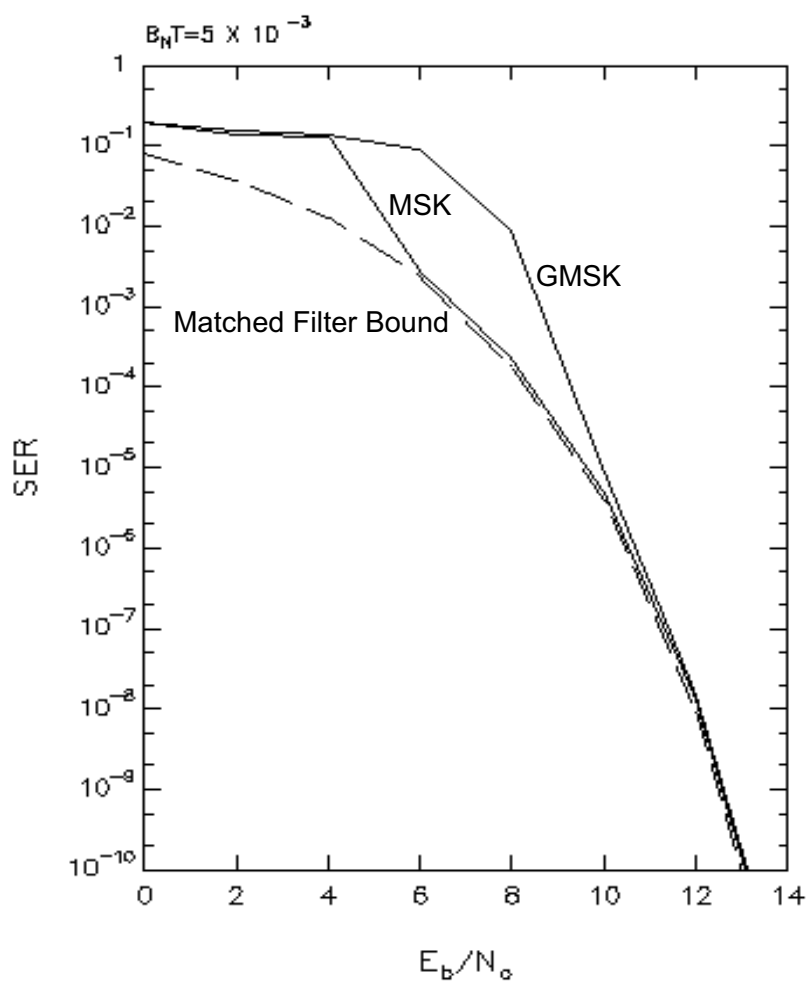


Fig. V.17

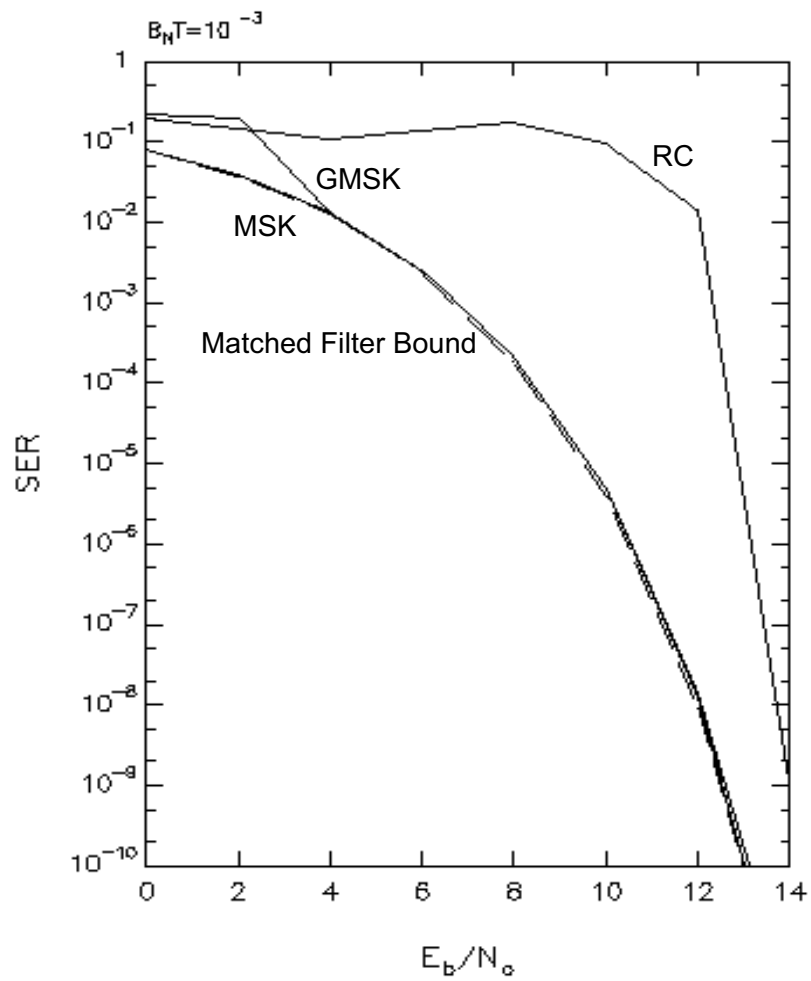


Fig. V.18

V.4 Clock Recovery for OBM: Closed-Loop Digital Circuits

A completely different approach to the problem of clock recovery can be pursued in the context of an all-digital implementation of the receiver. The basic idea is to abandon the open-loop viewpoint and to resort to a closed-loop error-detector-plus-NCO structure such those described in [Gar88] and [Lui88], which is sketched in Fig. V.19.

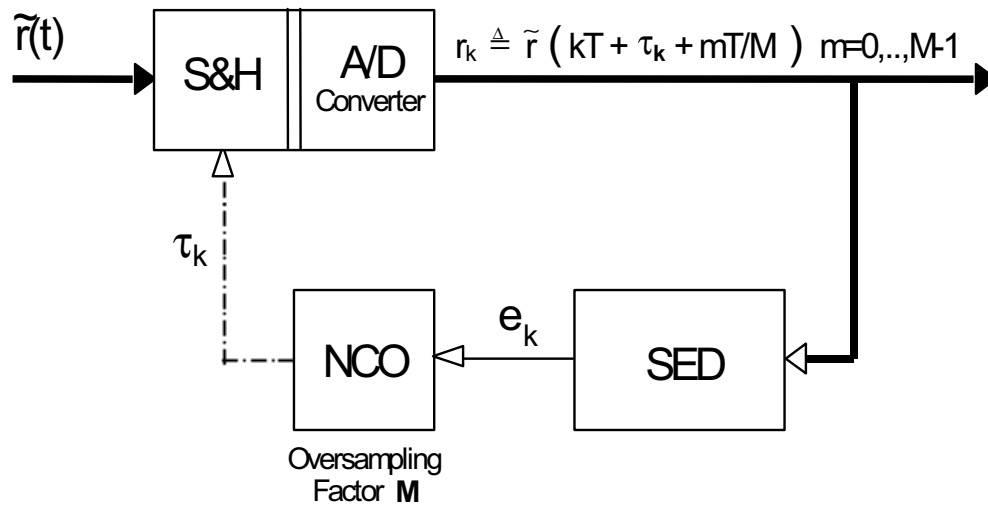


Fig. V.19

The true digital Section of the scheme in Fig. V.19 is the so-called Sampling Error Detector (SED), whilst the Numerically Controlled Oscillator (NCO) is a hybrid component whose task is to drive the A/D converter of the received signal. The SED operates on the signal samples (usually taken with an oversampling factor $M > 1$) so as to provide (on the average) an indication about the offset of the current sampling instant τ_k from the ideal epoch τ . The closed loop structure causes the sampling offset to go to zero in the steady-state. The SED design is strongly dependent on the particular modulation techniques and can be carried out according to various criteria [Gar88], [Mue76], [Gar86], [God78], [Aga85], [Men77], [D'A90]. Two particular design

approach are pursued in the present study. Both of them aim at deriving a Non-Decision-Aided (NDA) SED independent of the demodulation phase offset (as in the analog case).

The first algorithm requires an oversampling factor 4 with respect to the baud rate of the in-phase and quadrature components of the modulated signal (or an oversampling factor $M=2$ with respect to the bit-rate $1/T$). Its structure and working principle is best understood in the case of an MSK modulated signal, and is thoroughly described in [D'A90]. Let us recall here briefly its structure. Assume the baseband oversampled received signal is

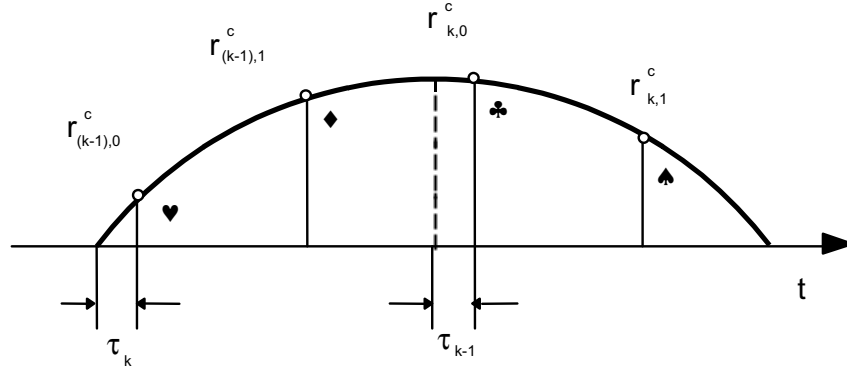
$$\tilde{r}_{k,m} \triangleq \tilde{r}(kT + \tau_k + mT/2) , \quad m=0,1 \quad (V.4.1)$$

where τ_k is the current sampling offset (see Fig V.20 for a visual explanation of this apparently cumbersome notation). Letting

$$\eta_{k,1} \triangleq \Re \left[(\tilde{r}_{k,1} \tilde{r}_{k-1,1}^*)^2 \right] , \quad \eta_{k,0} \triangleq \Re \left[(\tilde{r}_{k,0} \tilde{r}_{k-1,0}^*)^2 \right] \quad (V.4.2)$$

the output of the SED block at the instant $2kT$ is obtained as

$$e_k \Big|_{\text{ALG1}} \triangleq \eta_{k,0} - \eta_{k,1} \quad (V.4.3)$$



Algorithm#1

$$\Re[(\spadesuit \diamond *)^2] - \Re[(\clubsuit \heartsuit *)^2]$$

Algorithm#2

$$\Re[(\spadesuit - \diamond) \clubsuit^*]$$

Fig. V.20

The sampling instant τ_k is updated every $2T$ seconds by the NCO according to the following rule:

$$\tau_k = \tau_{k-1} + \gamma e_k \quad (\text{V.4.4})$$

where γ is the step-size, which is to be determined as a trade-off between the contrasting needs of fast acquisition and small steady-state jitter.

The second algorithm is a generalization of the first [Gar86]. It also requires the same oversampling factor $M=2$ samples/bit. With the same notation as before, we have

$$e_k \big|_{\text{ALG2}} \triangleq \Re \left[(\tilde{r}_{k,1} - \tilde{r}_{k-1,1}) \tilde{r}_{k,0}^* \right] \quad (\text{V.4.5})$$

For a generic OBM signal, let us compute the S-curve of the two algorithms. We recall that the S-curve of the loop is defined as the average value of e_k , computed in open-loop conditions, that is when all τ_k 's are forced to assume a fixed value, say τ :

$$S(\tau) \triangleq E\{ e_k \mid \tau_k \equiv \tau \ \forall k \} . \quad (V.4.6)$$

For further reference we also consider the open-loop RMS jitter, defined as follows:

$$\sigma_{OL}(\tau) \triangleq \sqrt{E\{ [e_k - S(\tau)]^2 \mid \tau_k \equiv \tau \} } \quad (V.4.7)$$

which, in the vicinity of the stable equilibrium point of the loop, gives an idea of the steady-state jitter.

Algorithm#1

The computation of the S-curve, as outlined in [D'A90] is quite cumbersome so that it will not be reported here. We limit ourselves to show some simulation results pertaining to the pre-selected modulation techniques. In Fig. V.21 the S-curve of the Algorithm# 1 is shown for an ideal MSK signal (solid line). Also shown (dashed line) is the RMS jitter in open-loop conditions. It is apparent that this "open loop jitter" is zero at the stable operating point $\tau = -0.25$. It is also noted that the loop equilibrium point (i.e. the null of the S-curve with negative slope) is shifted with respect to the ideal sampling instant $\tau = 0$ of the MSK, so that the indications of the SED have to be "de-biased" by a proper quantity. Figures V.22 and V.23 report the S-curves for GMSK and 3RC respectively.

As is apparent from Fig.V.24, the algorithm does not work with NYQ-OQPSK.

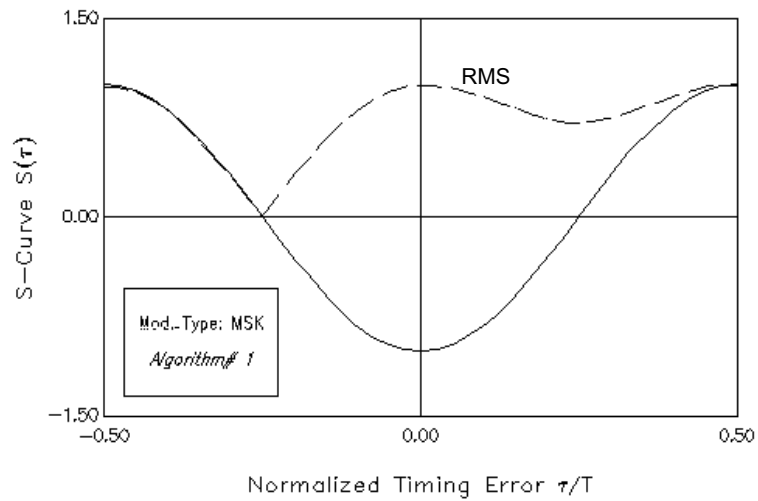


Fig. V.21

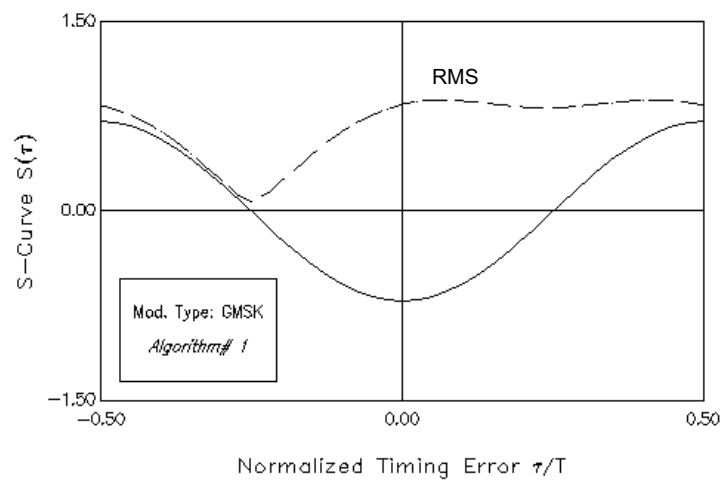


Fig. V.22

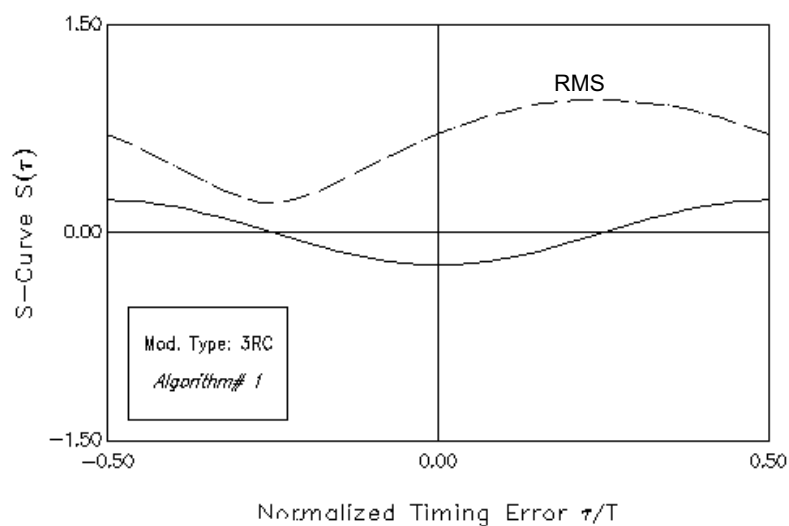


Fig. V.23

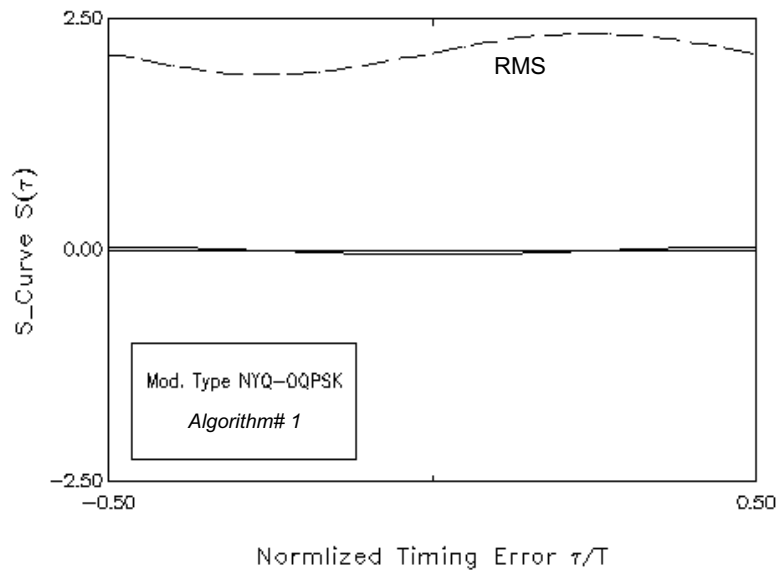


Fig. V.24

Algorithm#2

$$\begin{aligned}
 S_{\text{ALG2}}(\tau) &= E \{ e_k \mid \tau_k \equiv \tau \} = \\
 &= E \left\{ \left(\sum_m a_m [p(kT+\tau+T/2 - 2mT) - p(kT+\tau-T/2 - 2mT)] + \right. \right. \\
 &\quad \left. \left. j b_m [p(kT+\tau+T/2 - 2mT - T) - p(kT+\tau-T/2 - 2mT - T)] \right) \times \right. \\
 &\quad \left. \sum_i [a_i p(kT+\tau - 2iT) - j b_i p(kT+\tau - 2iT - T)] \right\} = \\
 &= \sum_i p(iT+\tau) [p(iT+\tau+T/2) - p(iT+\tau-T/2)] \quad (V.4.5)
 \end{aligned}$$

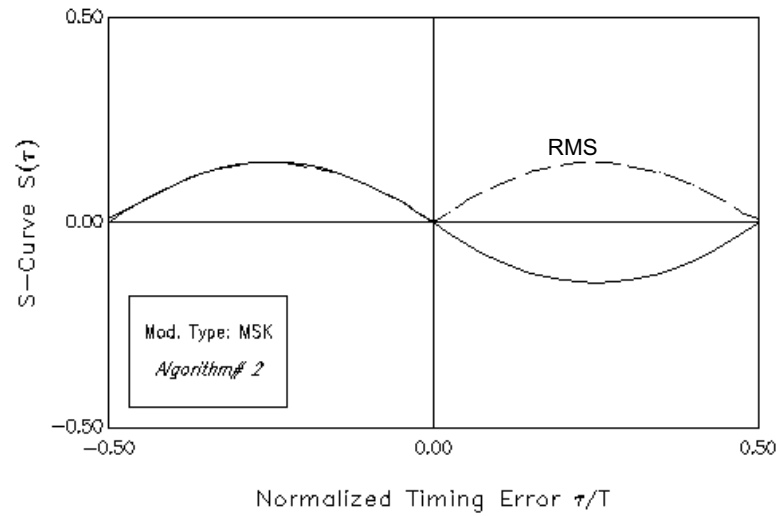


Fig. V.25

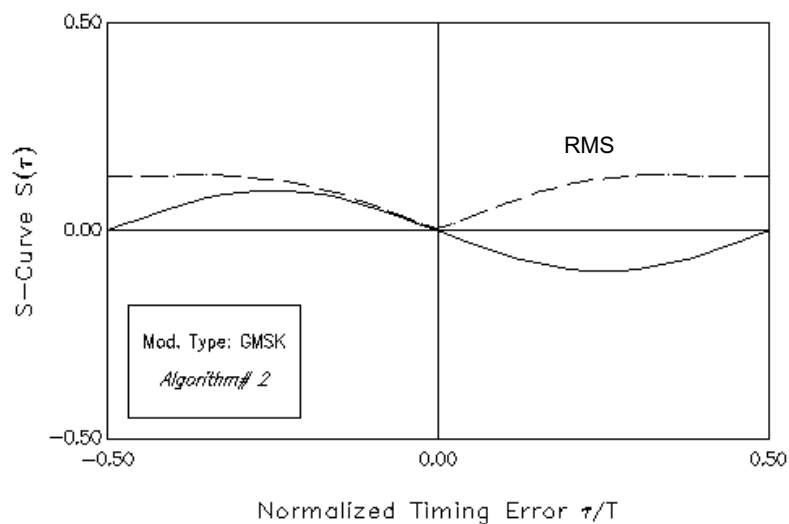


Fig. V.26

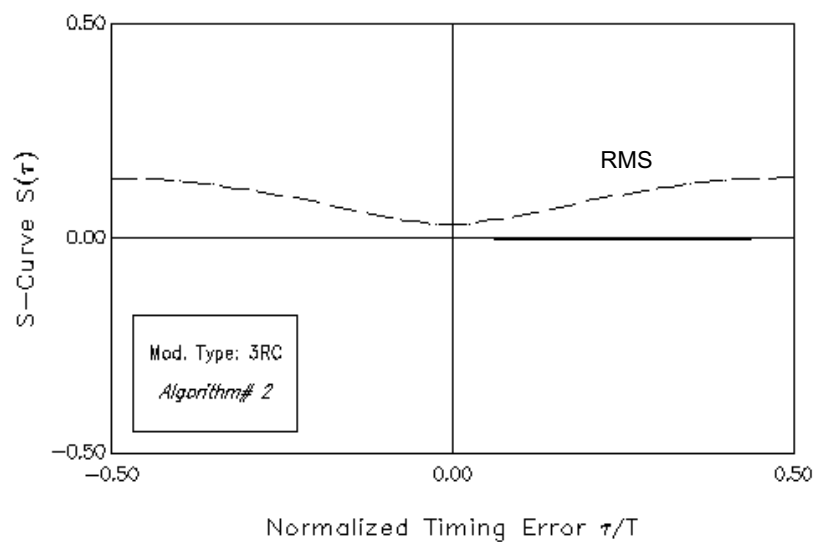


Fig. V.27

For an MSK-modulated signal we get the S-curve shown in Fig. V.25, which is made of the union of two sine-shaped segments. As in the case of the *Algorithm# 1*, the dashed line is the open-loop jitter. In Fig. V.26 and V.27 we report the S-curves, obtained by simulation, for GMSK and 3RC respectively. Again, the algorithm does not work with 3RC or NYQ-OQPSK.

The open-loop performance of the *Algorithm# 2* is particularly unfavourable with compact-spectrum modulations such as 3RC and NYQ-OQPSK. In these cases, the S-curve vanishes, so that the algorithm #2 cannot be employed.

V.5 Performance of the Digital Schemes

In the following we report the results for the two algorithms described above. In particular, we characterize the steady-state performance of such schemes by means of the normalized RMS jitter of the sampling instant. We also provide, as in the case of the analog regenerator, the BER curves of the receiver when the clock recovery loop is employed to derive the data strobe values. Results concerning some typical acquisition phases of the clock recovery loop are also shown.

It is worth noting that the jitter curves appear incomplete with respect to the E_b/N_0 range examined. The reason for this lies in the fact that below the "start" value of E_b/N_0 in the plots, sync losses occur. In this conditions, the jitter measure loses its meaning.

Algorithm #1

The jitter curves relative to the algorithm n. 1 are reported in Figs. V.28-V.30. Notice that no results pertaining to 3RC are reported but for $B_N T = 10^{-3}$, since no reliable lock condition could be attained for larger bandwidths.

The corresponding BER curves are shown in Figs. V.31-V.33. It is apparent that, in order to allow satisfactory operation down to $E_b/N_0=0$ dB, a loop bandwidth less than 10^{-3} is required.

Some typical loop acquisitions are reported in Figs. V.34 to V.42. They show the time-evolution of the normalized sampling instant, starting from that instant corresponding to the unstable null of the S-curve (loop hang-up) and until the steady-state regime is reached. In these figures no thermal noise is assumed. Further acquisition curves are shown in Figs. V.43 to V.45 with $E_b/N_0=5$ dB and $B_N T=10^{-3}$ for the three modulation schemes and in Fig. V.46 for $E_b/N_0=0$ dB and MSK only.

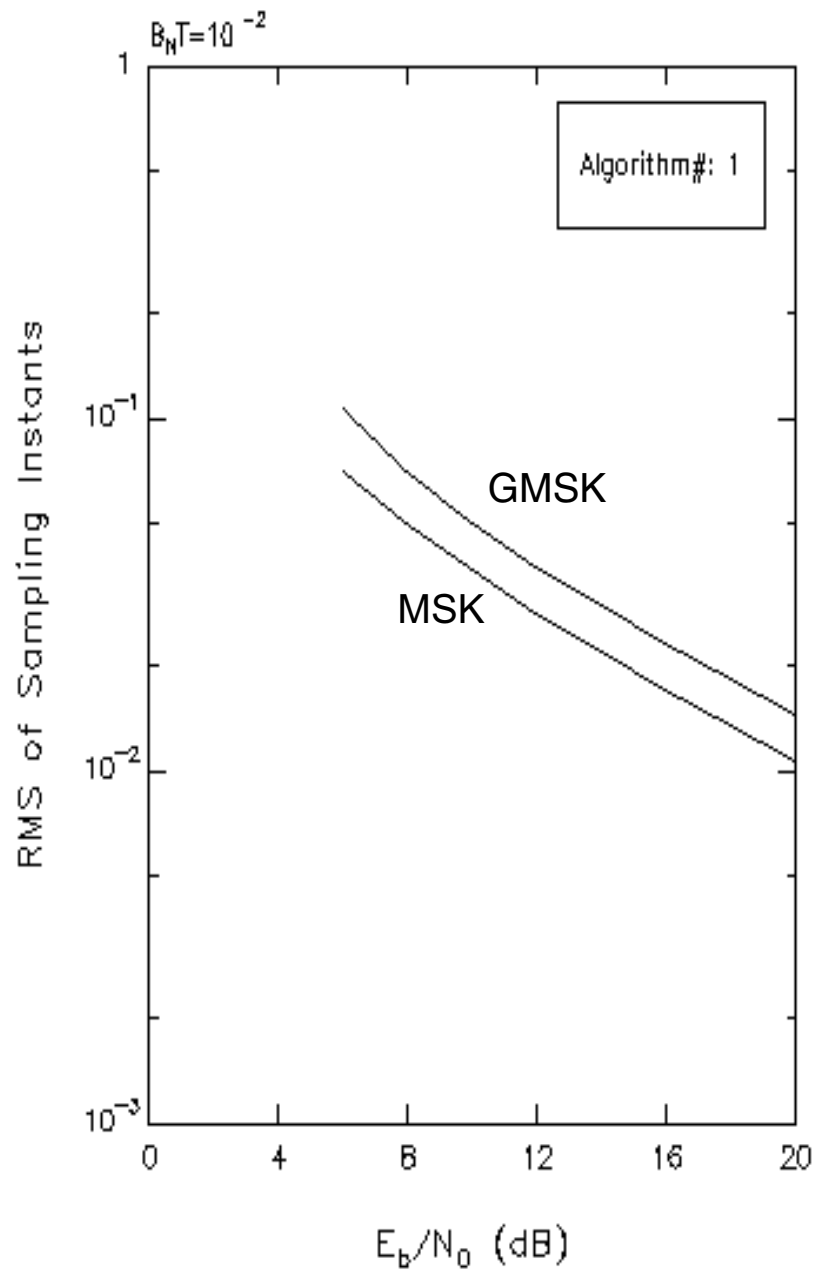


Fig. V.28

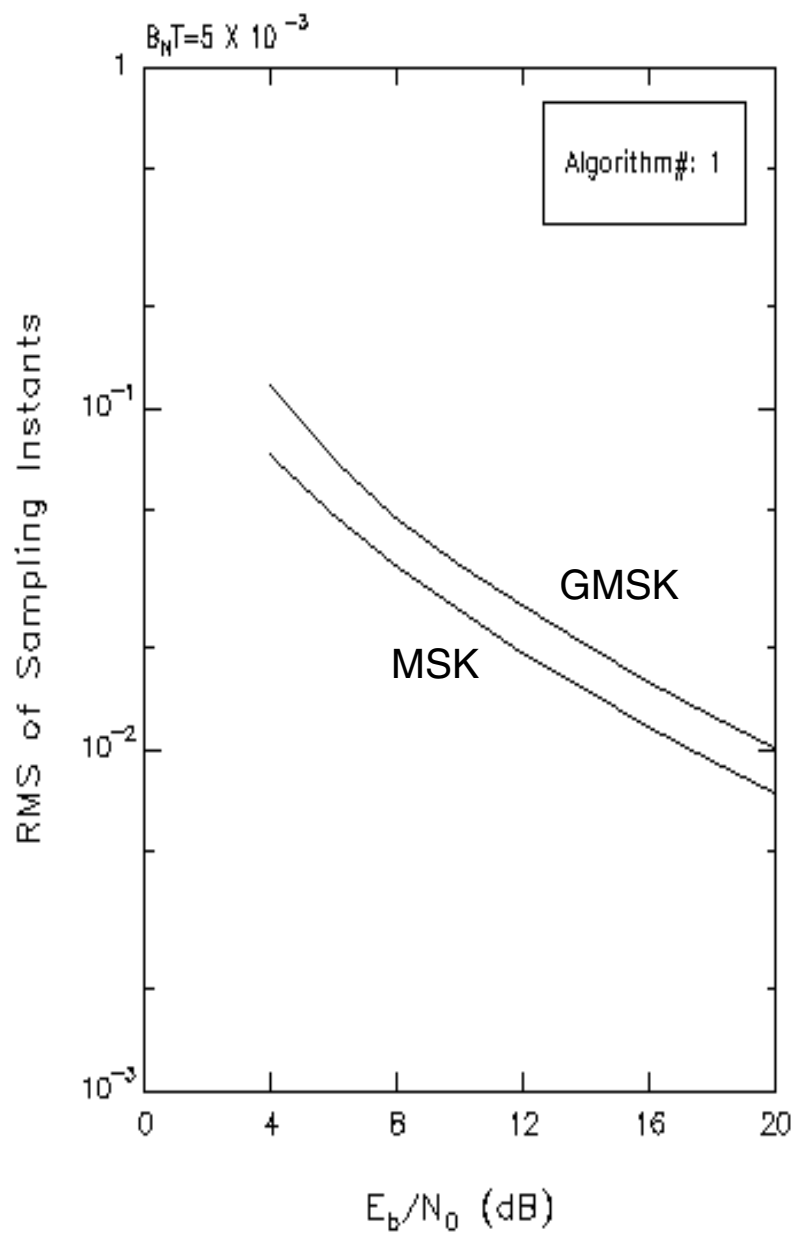


Fig. V.29

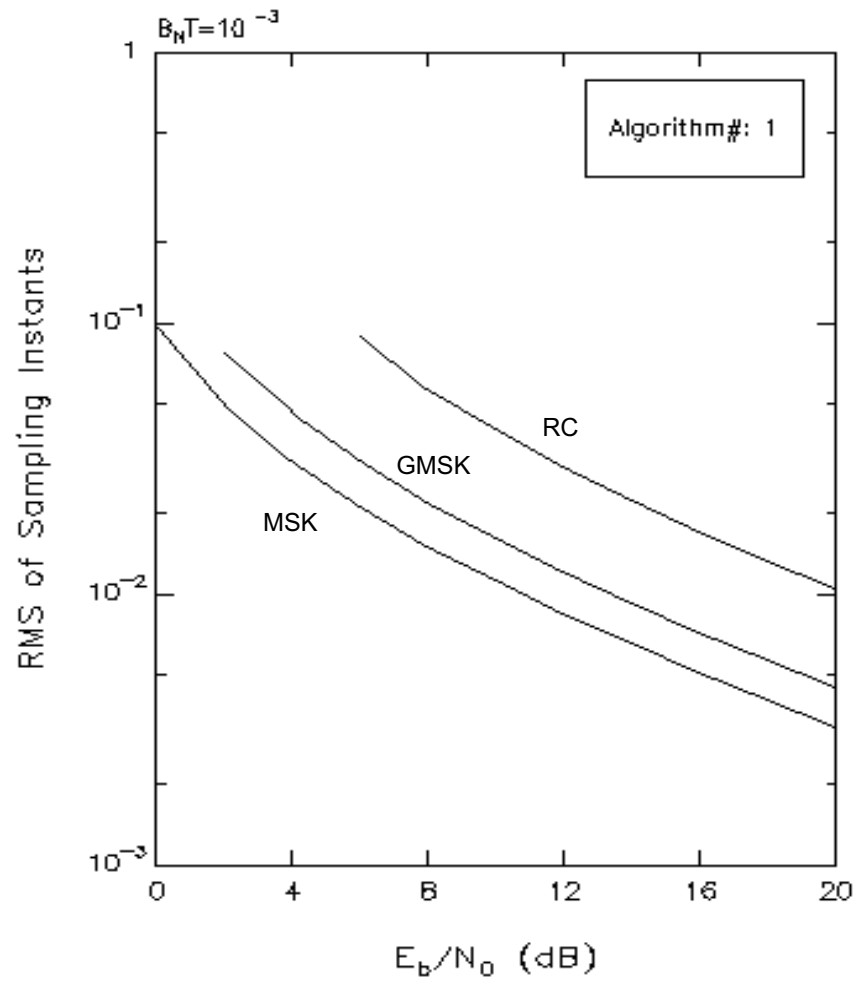


Fig. V.30

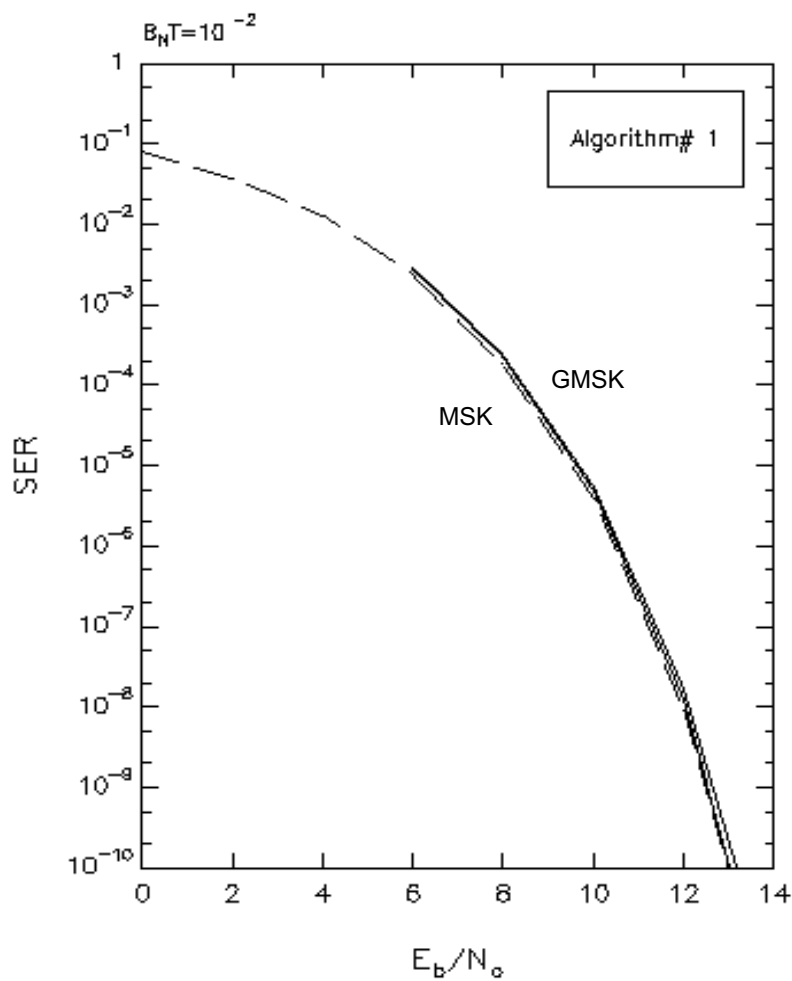


Fig. V.31

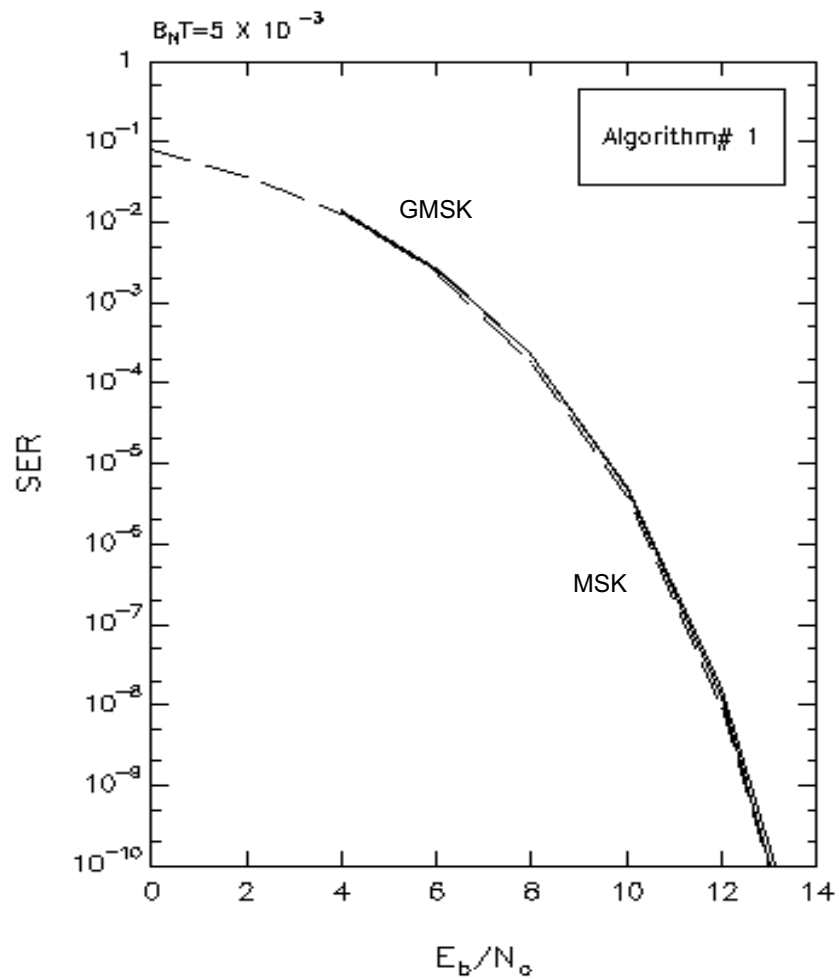


Fig. V.32

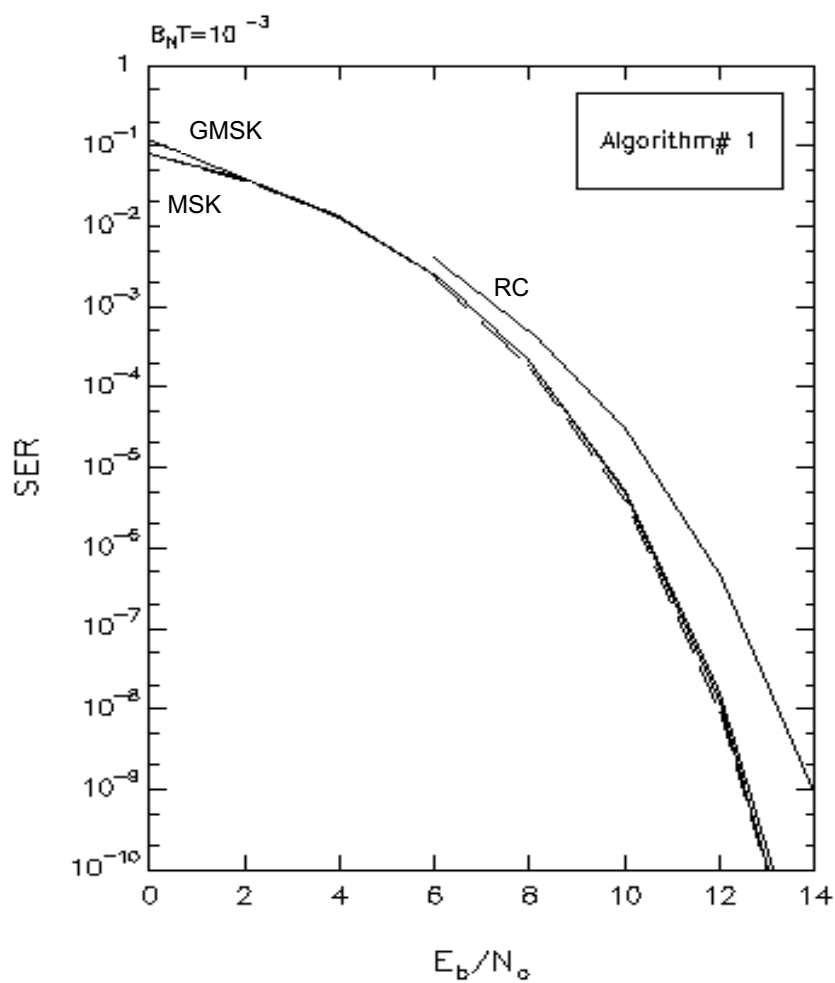


Fig. V.33

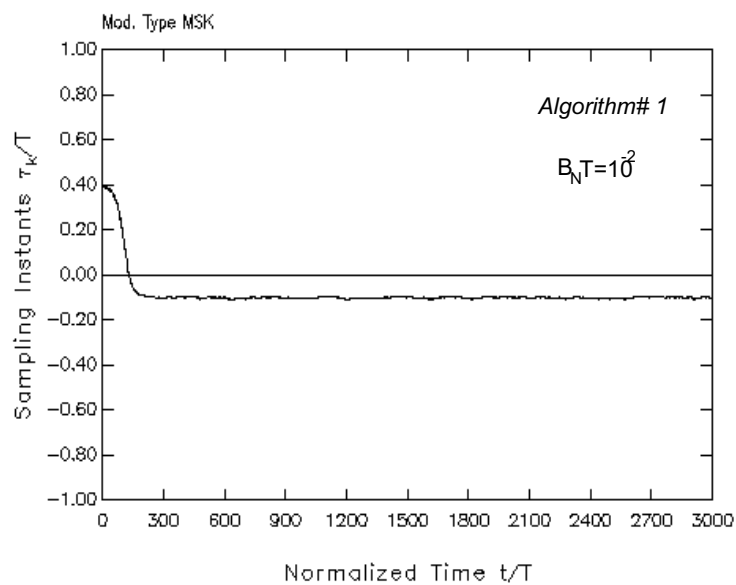


Fig. V.34

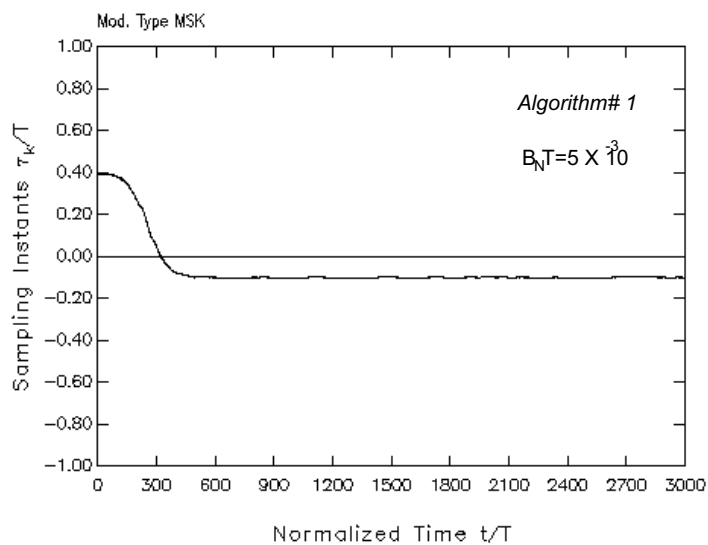


Fig. V.35

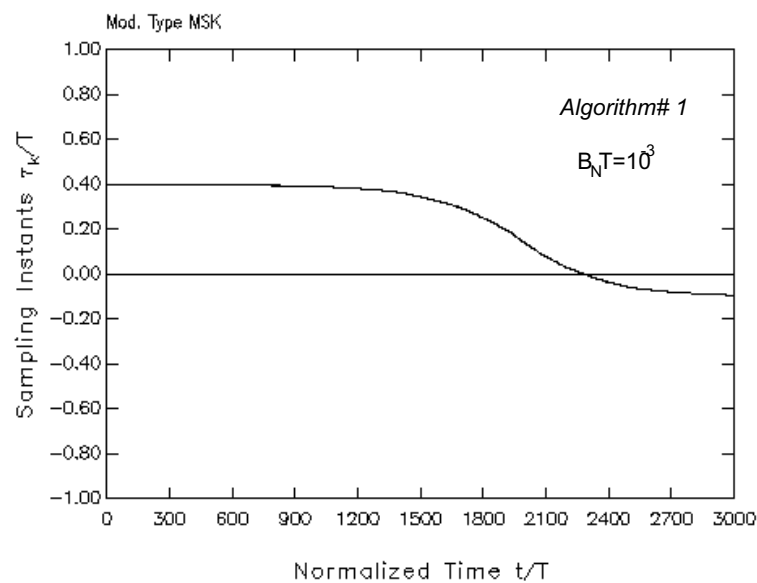


Fig. V.36

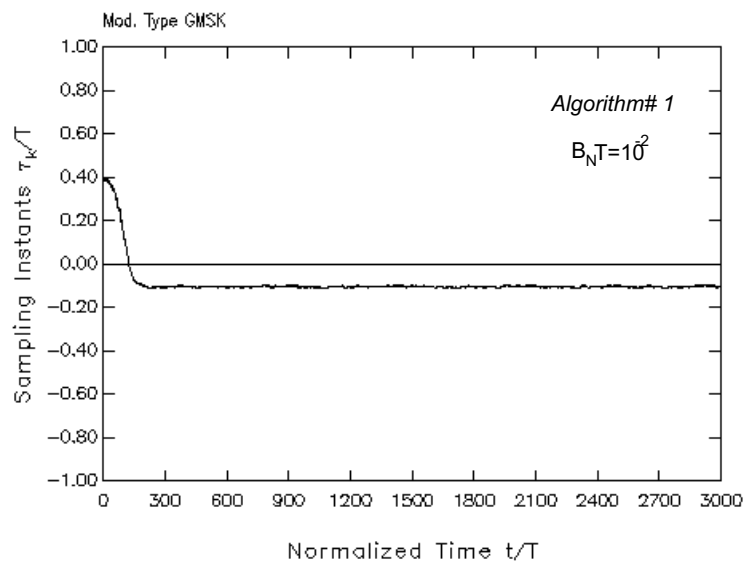


Fig. V.37

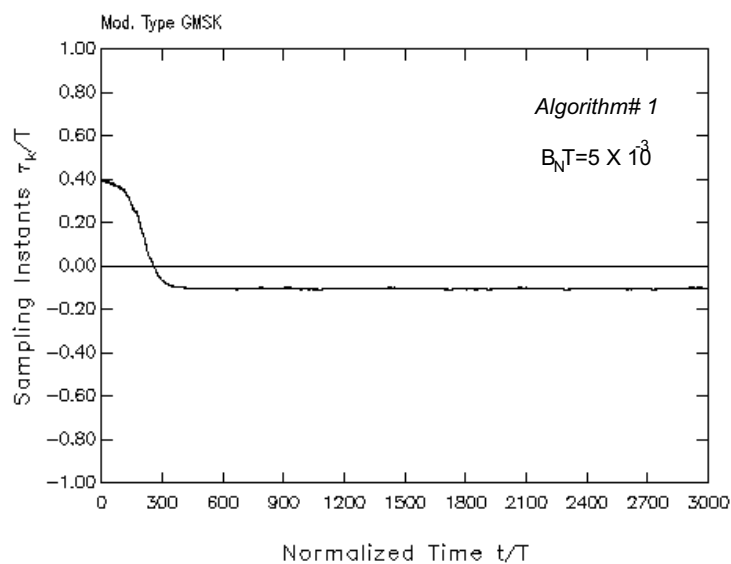


Fig. V.38

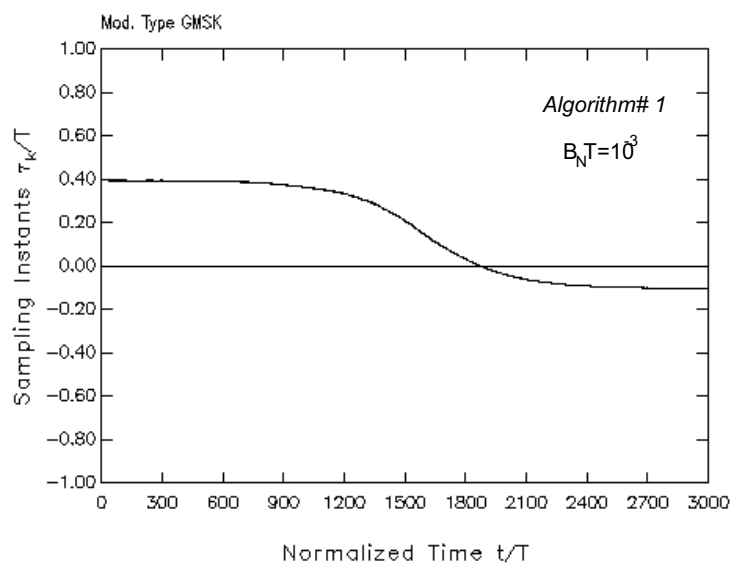


Fig. V.39

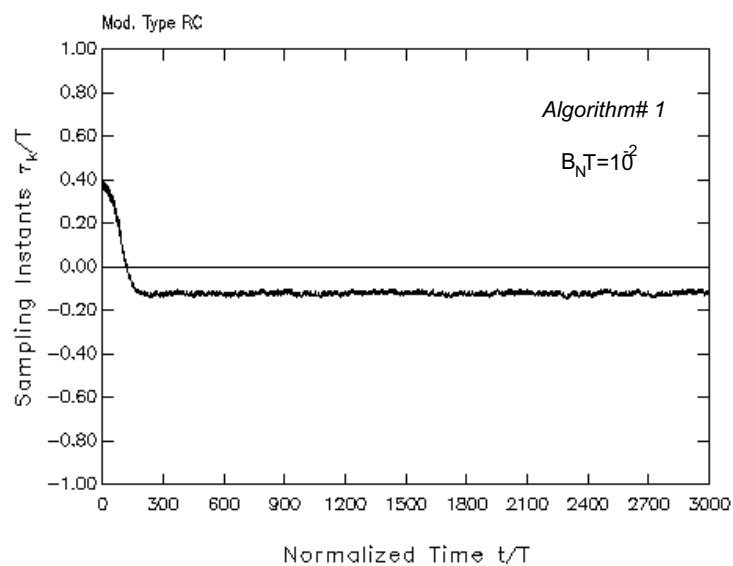


Fig. V.40

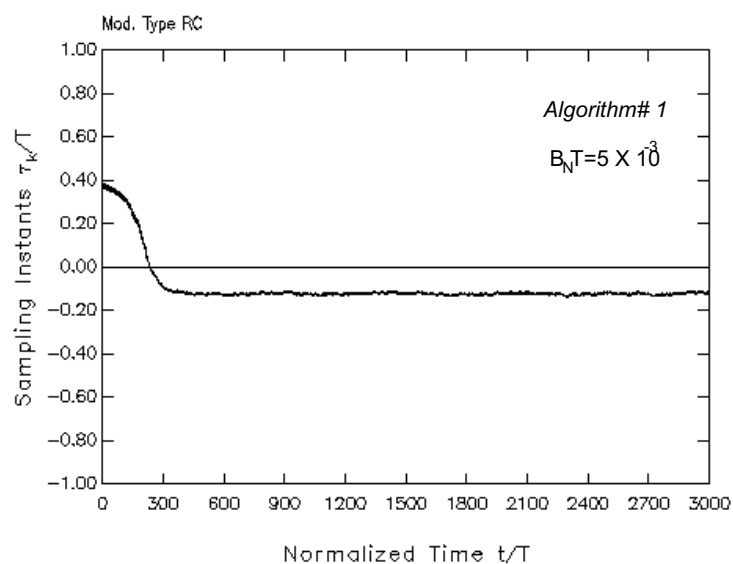


Fig. V.41

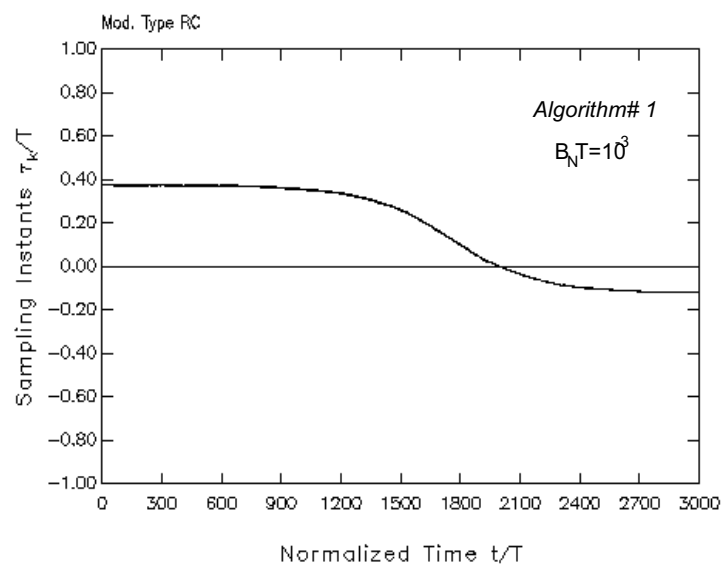


Fig. V.42

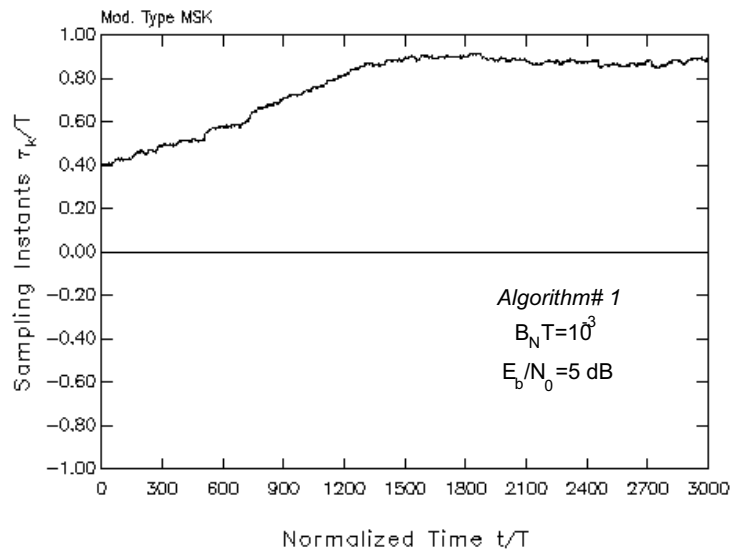


Fig. V.43

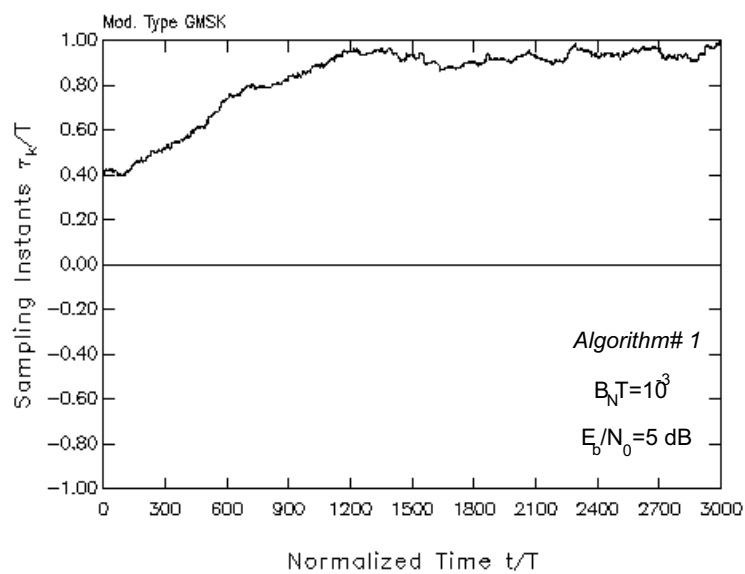


Fig. V.44

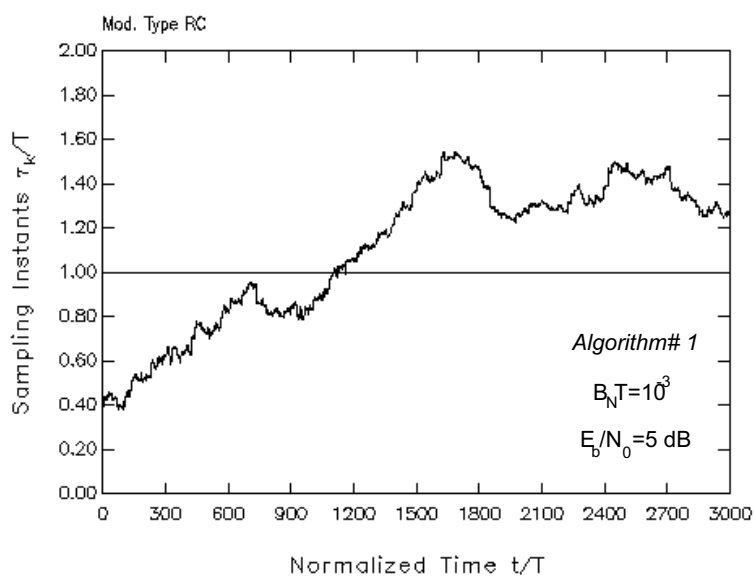


Fig. V.45

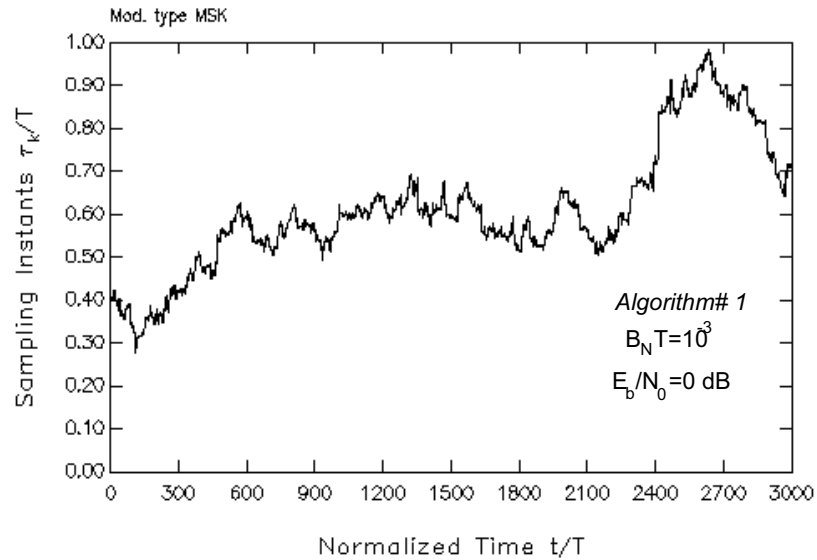


Fig. V.46

Algorithm #2

Jitter and BER curves as in the case of SED #1 are shown in Figs. V.47-V.54 for SED #2, with the addition of the loop bandwidth value $B_N T = 10^{-4}$ for 3RC only. Results pertaining to 3RC in fact are provided in this condition only, since lock losses took place for larger loop bandwidths.

Noiseless acquisition curves are reported in Figs. V.54-V.63 for the modulation types and loop bandwidths indicated in the figures, whilst Figs. V.64-V.67 show acquisitions at 5 dB and 0 dB E_b/N_0 . Notice the typical cycle-slipping behavior of the loop with Algorithm#2 with 3RC and bandwidth $5 \cdot 10^{-3}$ (fig. V.61).

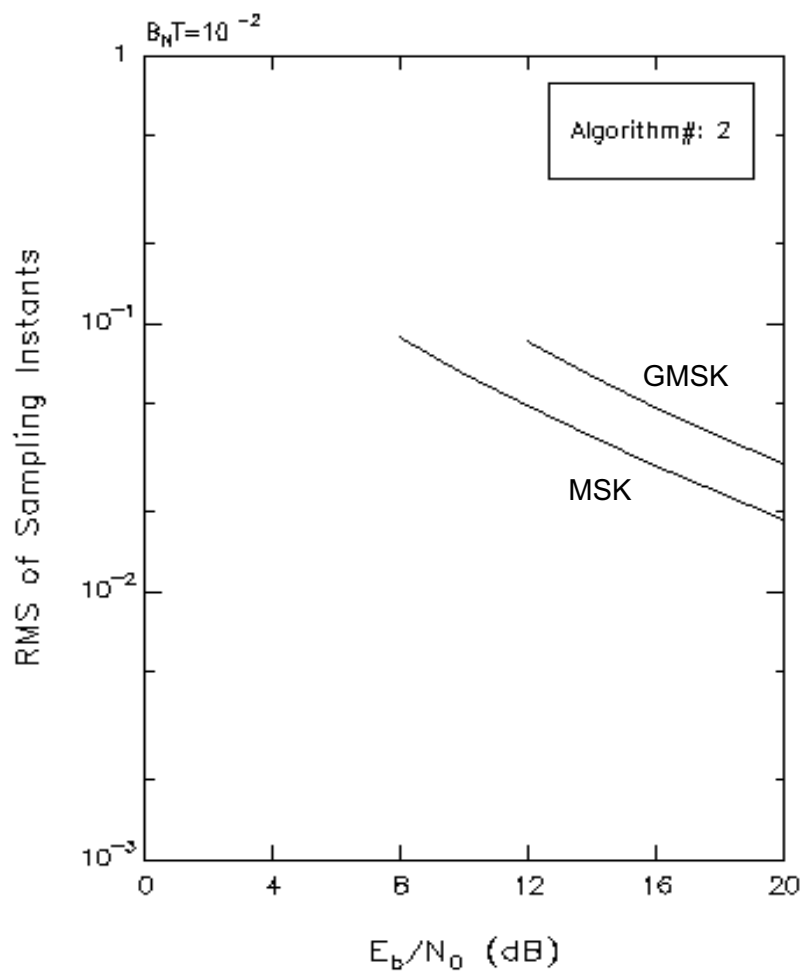


Fig. V.47

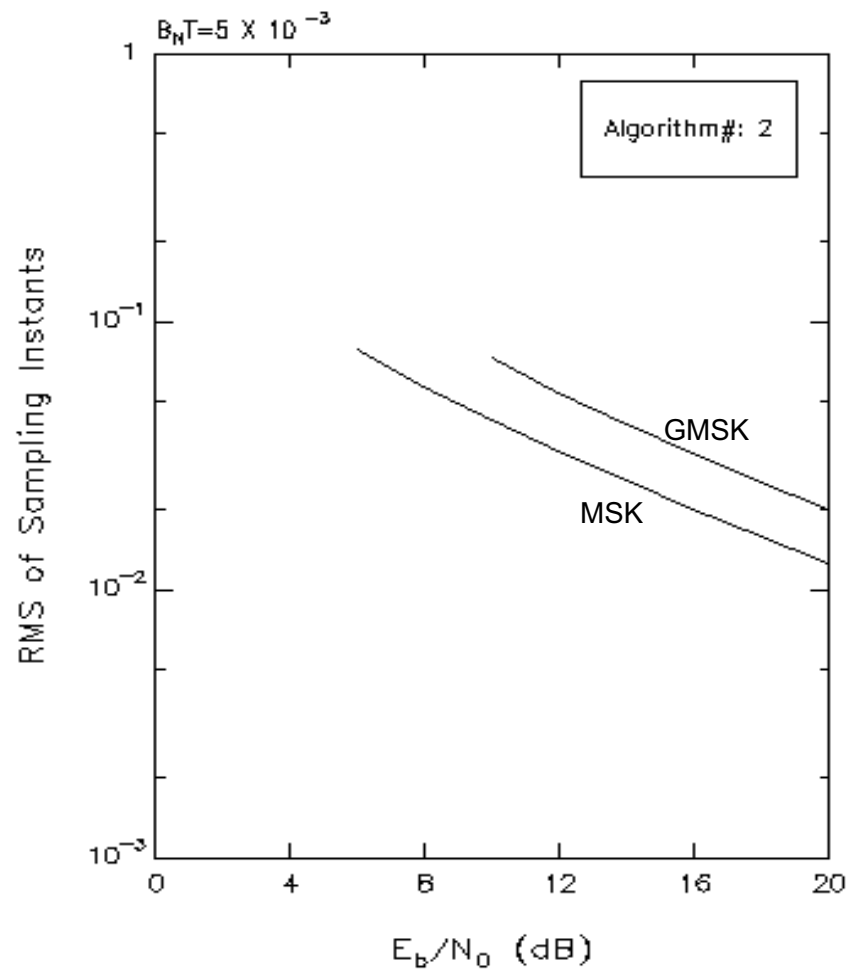


Fig. V.48

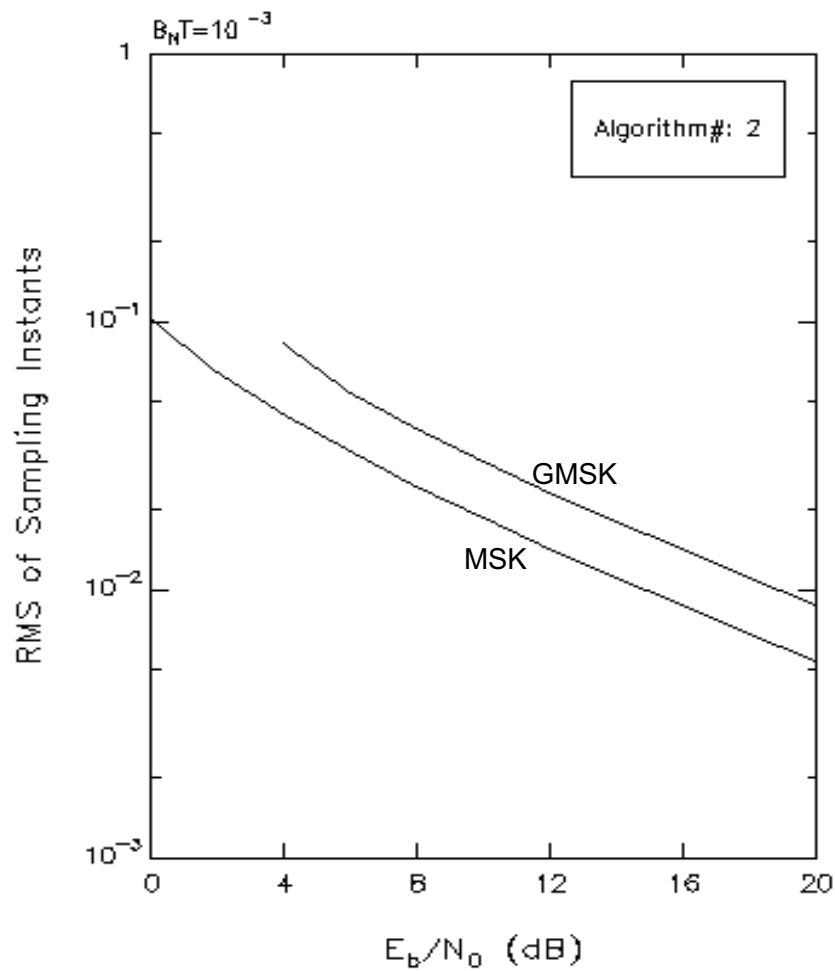


Fig. V.49

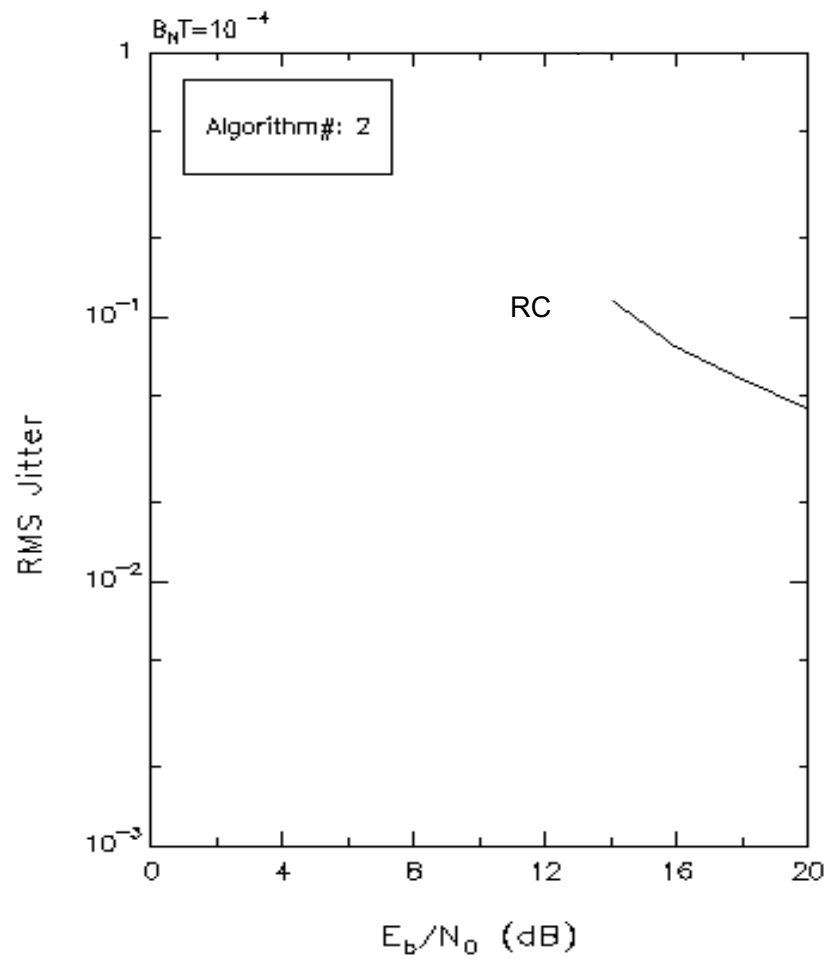


Fig. V.50

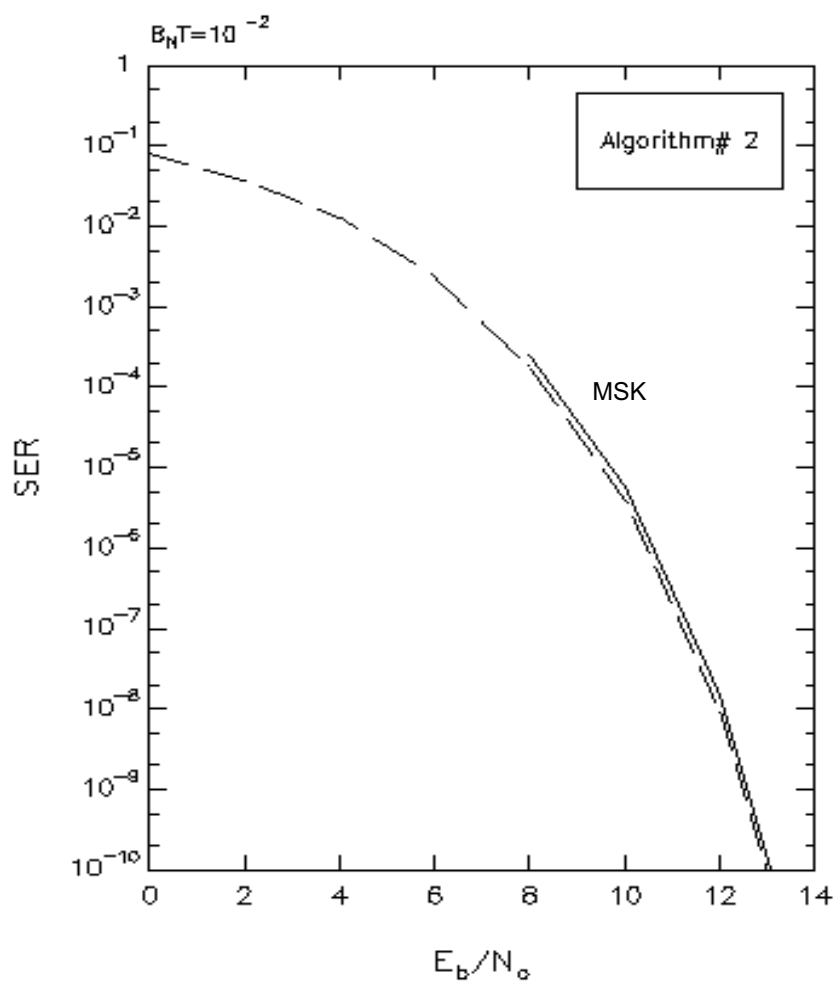


Fig. V.51

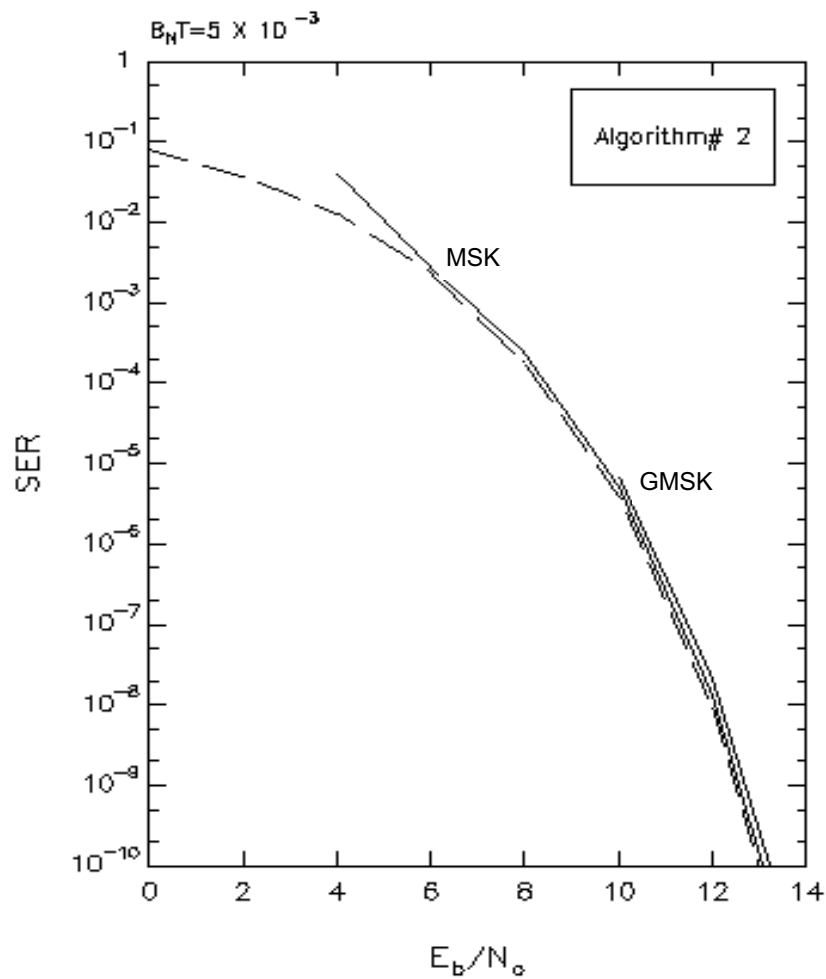


Fig. V.52

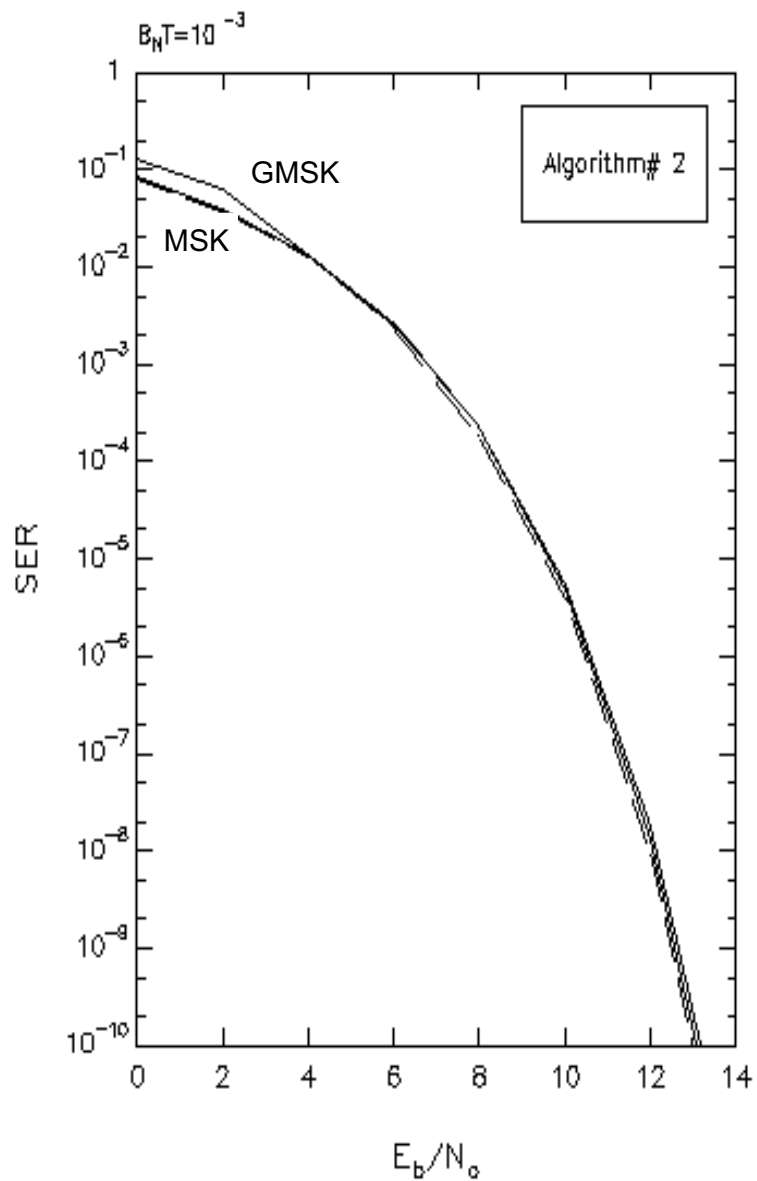


Fig. V.53

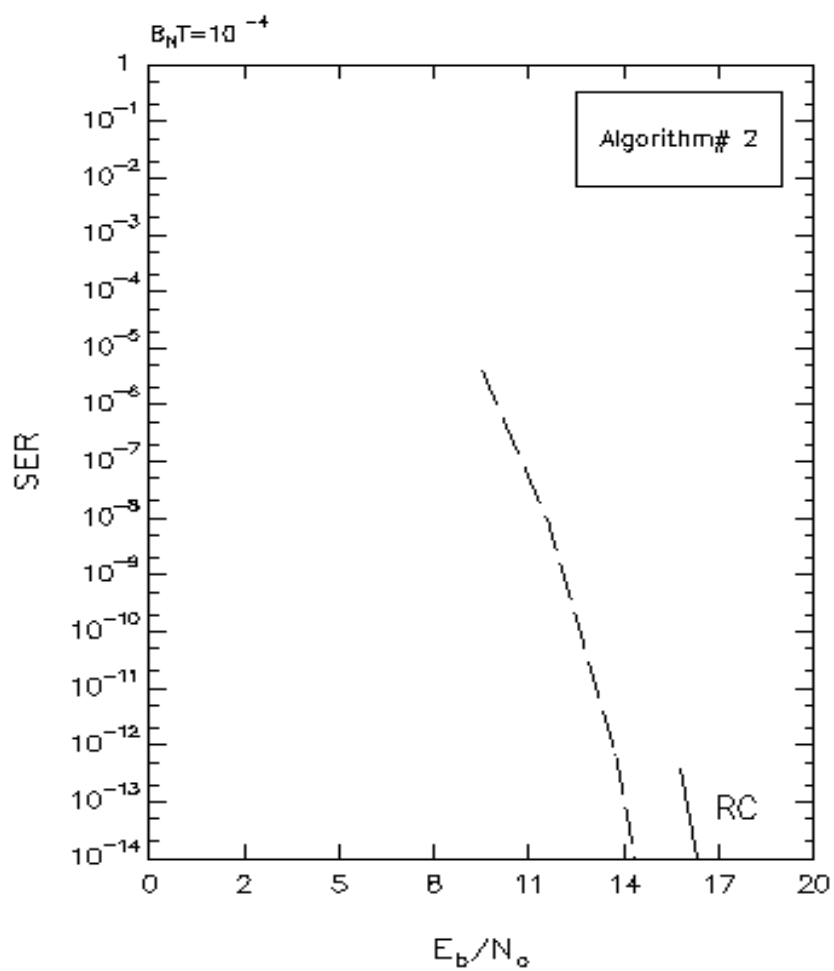


Fig. V.54

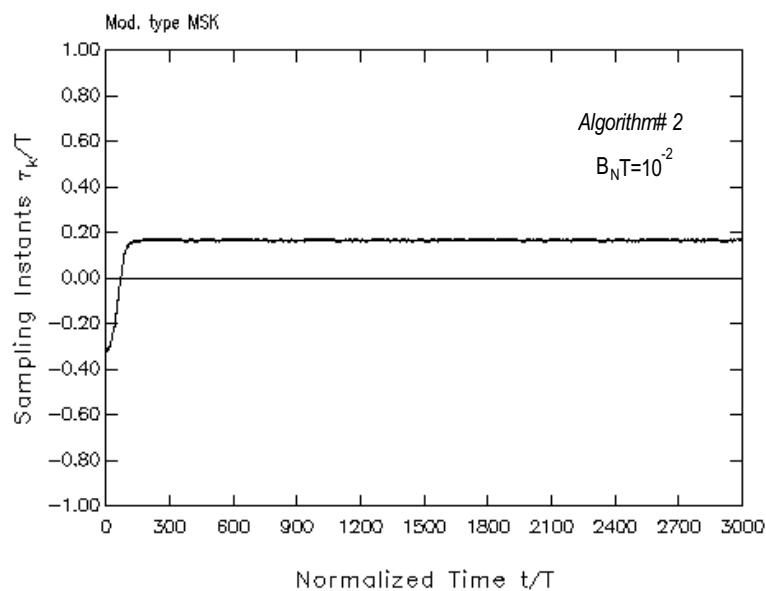


Fig. V.55

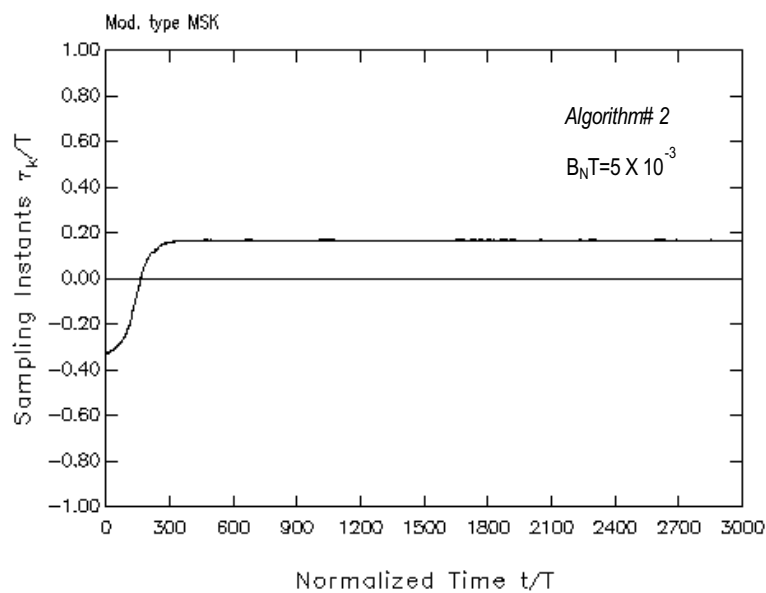


Fig. V.56

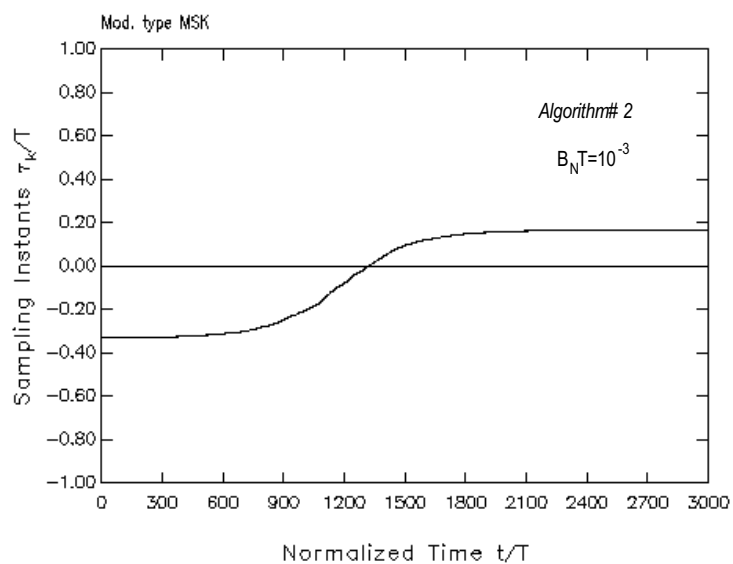


Fig. V.57

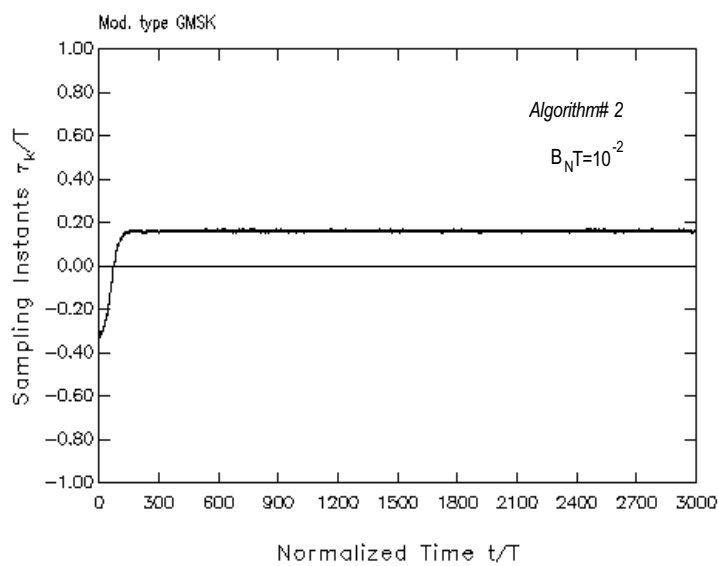


Fig. V.58

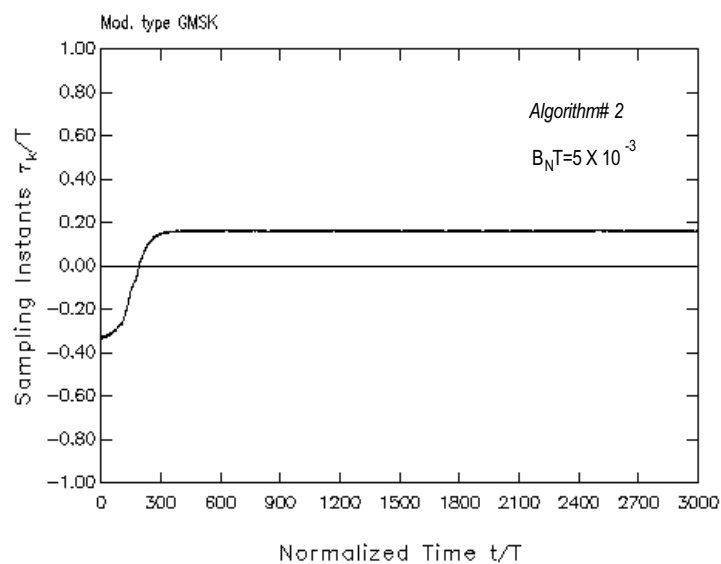


Fig. V.59

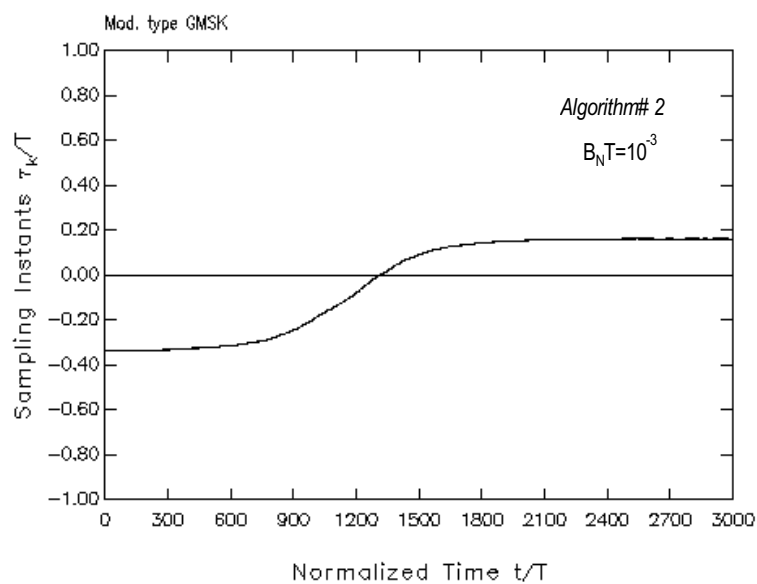


Fig. V.60

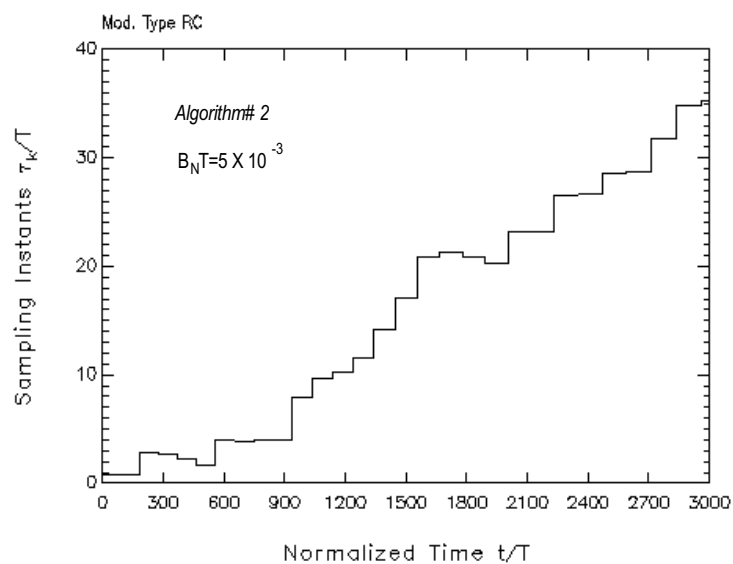


Fig. V.61

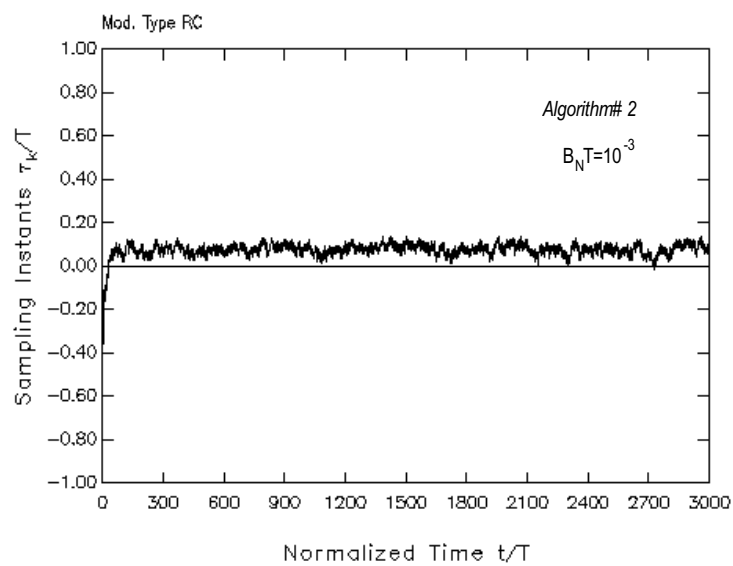


Fig. V.62

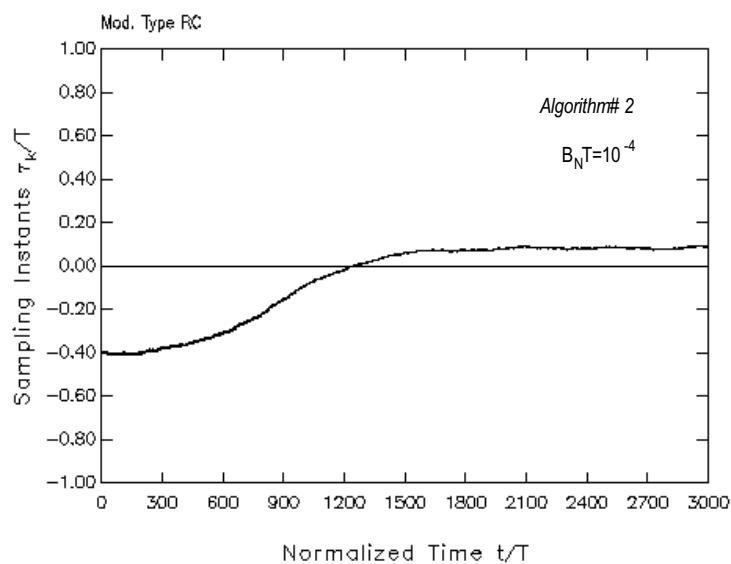


Fig. V.63

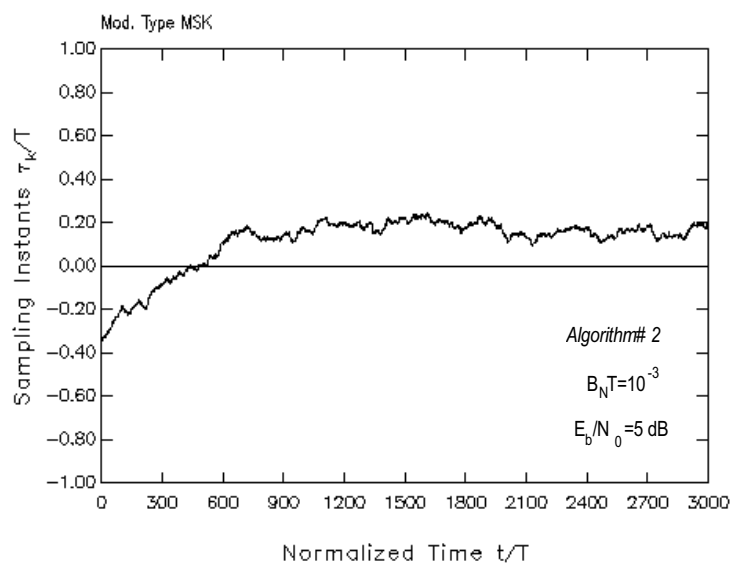


Fig. V.64

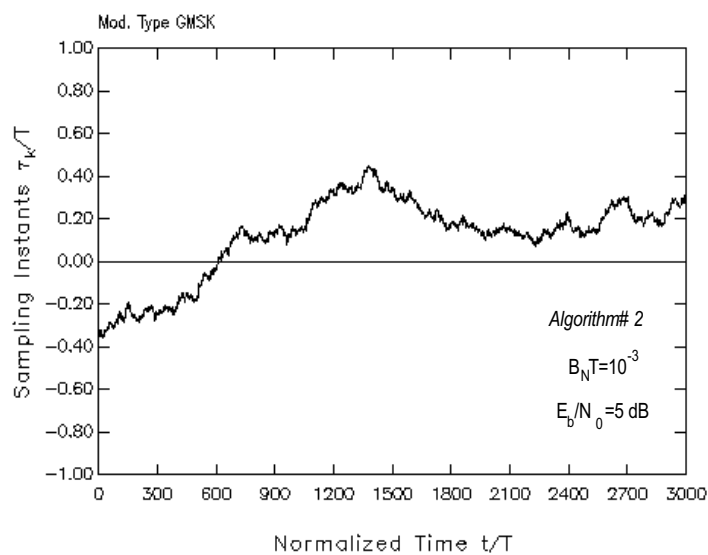


Fig. V.65

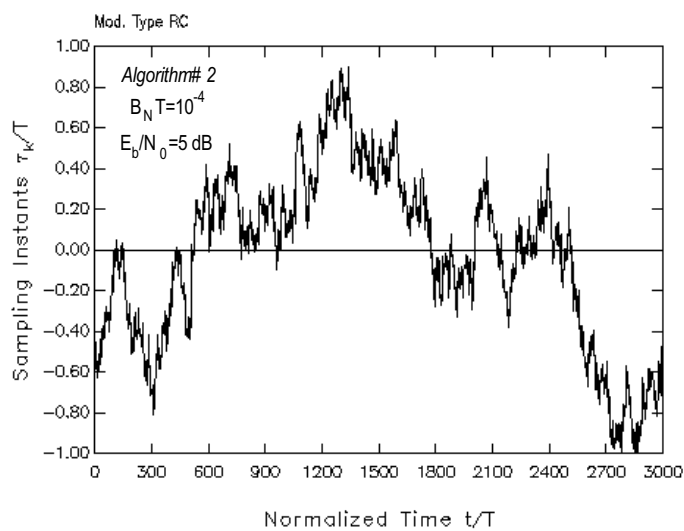


Fig. V.66

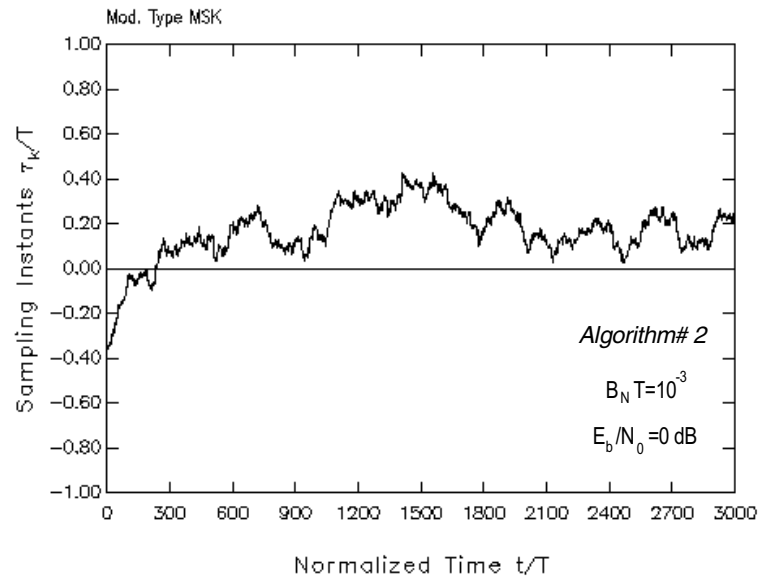


Fig. V.67

Comments and Comparisons

From the above results, some conclusions on the performances of the presented clock recovery schemes can be drawn.

First, the difficulty in extracting a useful clock reference for 3RC modulation is apparent. Rather narrow loop bandwidths are required with such a modulation in order to avoid cycle slipping and to obtain adequate RMS jitter values. Secondly, a slight performance degradation occurs when passing from MSK to its narrow-band counterpart, i.e. GMSK.

As for the comparison between the two algorithms, it is noted that algorithm #1 exhibits smaller steady-state fluctuations. Another favourable feature of Algorithm#1 is its capability of achieving good synchronization also with GMSK. The acquisition plots reveal a slightly greater speed of Algorithm#2. On the other hand, this algorithm exhibits greater sensitivity

both to pattern noise and to thermal noise.

We conclude that Algorithm#1 preferable in our application with respect to Algorithm#2, especially in view of the following two key features:

- *Smaller steady-state timing jitter;*
- *Smaller performance disparity between MSK and GMSK*

A good compromise in the loop design between the contrasting needs of fast acquisition and small jitter may be attained with a loop bandwidth $B_N T = 10^{-3} \div 5 \cdot 10^{-4}$.

(This space is intentionally left blank)

VI Impact of the Carrier Phase Recovery Loop on the System Performance

V I.1 Phase Recovery for OBM - An Overview

The performance of a coherent communication system is affected by the received signal power and by the accuracy of the carrier phase and clock recovery systems. For binary I-Q signalling the requirements on amplitude control are not as critical as those on carrier phase and symbol timing and therefore in the following we will not focus on particular AGC algorithms aimed at adjusting the amplitude of the received signal. A conventional, analog AGC circuitry operating at IF is deemed adequate to reduce signal fluctuations to negligible levels.

The problem of symbol timing extraction was already dealt with in the previous chapters and will not be pursued here further on. Attention will be focused instead on the issue of carrier phase recovery, assuming that carrier frequency acquisition has already been achieved at an appropriate preceding stage.

Assuming that the local oscillator employed for baseband demodulation is affected by a fixed phase offset θ , we may write the complex envelope of the received waveform in the form:

$$\tilde{r}(t) \triangleq [\tilde{s}(t) + \tilde{n}(t)] e^{j\theta} =$$

$$\left\{ \sum_k a_k p(t-2kT) \cos\theta - \sum_k b_k p[t-(2k+1)T] \sin\theta + n_c(t) \right\} \\ + j \left\{ \sum_k a_k p(t-2kT) \sin\theta + \sum_k b_k p[t-(2k+1)T] \cos\theta + n_s(t) \right\} \quad (\text{VI.1.1})$$

where $n_c(t)$ and $n_s(t)$ are independent white Gaussian processes. As is seen from (VI.1.1), a phase error $\theta=\pi/2$ produces a swap between I and Q signal components, while, for $\theta=\pi/4$, the signal and the cross-channel interference have the same level on each branch. In both cases a severe degradation in system performance takes place.

Scanning the literature, a number of carrier phase recovery methods for OBM or CPM systems are found, some suited for analog implementation, as for instance those described in [deB72], [D'A87] and [Boo78], and a few conceived for a digital implementation, like that described in [Gar88].

In the scheme proposed by de Buda in [deB72] and generalized in [D'A87], the incoming signal is passed through a nonlinearity to generate discrete components in the signal spectrum. Two of these tones are then tracked by two PLL's whose outputs, after appropriate mixing and frequency re-scaling, yield the regenerated clock and carrier references.

One major drawback of this scheme is its poor performance in the presence of non-random data patterns, e. g. the trasmission of long strings of "ones" or "zeros". In such a situation, one of the discrete components may vanish so that the corresponding PLL may lose lock, with deleterious effects on the overall system performance [Tan89].

Considering the scheme proposed in [Boo78] for the particular case of MSK, we observe that it is derived following maximum likelihood (ML)

estimation methods. A closed loop structure is used whose aimed at bringing to zero the derivative of the likelihood function [Fra80]. For such a scheme we consider the loop signal error in the limiting case of high signal-to-noise ratio (so that the hyperbolic tangent can be approximated by a binary slicer), and we assume a one-symbol observation interval. Under these hypotheses the following expression for the signal error is found

$$e_k = -\hat{a}_k y_{Q,2k} + \hat{b}_k y_{I,2k+1} \quad (\text{VI.1.2})$$

with

$$y_{I,2k+1} \triangleq \Re\{\tilde{y}[(2k+1)T]\} \quad y_{Q,2k} \triangleq \Im\{\tilde{y}(2kT)\} , \quad (\text{VI.1.3})$$

$$\tilde{y}(t) \triangleq [\tilde{s}(t) + \tilde{n}(t)] \otimes p(-t) e^{j(\theta - \hat{\theta})}. \quad (\text{VI.1.4})$$

In (V.I.2)-(V.I.4), $p(t)$ is the half-cosine-shaped pulse of MSK, \hat{a}_k and \hat{b}_k are the estimated in-phase and quadrature symbols and $\hat{\theta}$ is the estimated carrier phase. The term $\tilde{y}(t)$ can be viewed as the output of a filter matched to the incoming data pulses. From (VI.1.2) it is apparent that the scheme is decision-aided (DA). Notice also that expression (VI.1.2) coincides with that given by Gardner in [Gar88] for the ML estimate of the carrier phase in the more general case of an arbitrary offset linear modulation.

In a closed-loop structure the phase error correction can be performed either by directly modifying the phase of the local oscillator (hybrid loop) or by rotating the complex envelope of the signal after A/D conversion (all-digital scheme). In the first case, attention must be paid to the matched-filter delay within the loop which may impair loop stability. This may occur when the signalling pulse has considerable length as, for instance, with NYQ-OQPSK. To circumvent this shortcoming, in the following we use an all-digital algorithm which avoids the insertion of the matched filter within the loop.

VI.2 Design of a Digital Closed-Loop Algorithm for Phase Recovery

The algorithm is designed starting from the conceptual baseband scheme shown in Fig.VI.1.

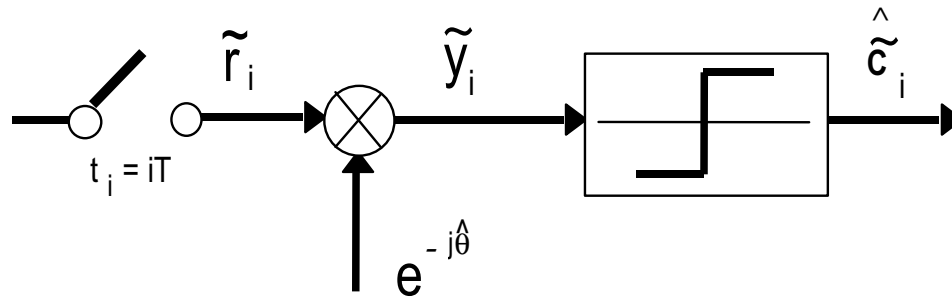


Fig.VI.1

where

$$\begin{aligned} \tilde{r}(t) &\triangleq \left\{ \sum_m a_m p(t-2mT) + j \sum_m b_m p[t-(2m+1)T] \right\} e^{j\theta} + n_c(t) + jn_s(t) = \\ &= \tilde{s}(t) e^{j\theta} + \tilde{n}(t) \end{aligned} \quad (\text{VI.2.1})$$

$$\tilde{r}_i \triangleq \tilde{r}(iT) \quad (\text{VI.2.2})$$

$$\tilde{y}_i \triangleq \tilde{y}(iT) = \tilde{r}(iT) e^{-j\hat{\theta}_i} \quad (\text{VI.2.3})$$

and

$$\tilde{c}_i \triangleq \begin{cases} a_k + j0 & i = 2k \\ 0 + jb_k & i = 2k+1 \end{cases} . \quad (\text{VI.2.4})$$

Our aim is to devise an algorithm that minimizes the mean square error (MSE) between transmitted symbols and corresponding samples at the detector input.

Depending on the definition of the MSE, different algorithms can be envisaged. For ordinary QAM, with no timing offset between I and Q components, it is natural to define the MSE as:

$$\epsilon \triangleq E \left\{ \left| \tilde{y}_i - \tilde{s}_i \right|^2 \right\} \quad (\text{VI.2.5})$$

where $\tilde{s}_i = a_i + jb_i$ is the i -th transmitted symbol.

When the pulses on the I and Q signal components are staggered, other definitions must be used. We may give, for instance, two distinct definitions of the MSE specialized to even and odd indexed instants, as follows:

$$\begin{aligned} \epsilon_c &\triangleq E \left\{ \left| \tilde{y}_{2k} - (a_k + j0) \right|^2 \right\} \\ \epsilon_s &\triangleq E \left\{ \left| \tilde{y}_{2k+1} - (0 + jb_k) \right|^2 \right\} \end{aligned} \quad (\text{VI.2.6})$$

A more comprehensive definition encompassing (VI.2.6) is

$$\epsilon = 0.5 (\epsilon_c + \epsilon_s). \quad (\text{VI.2.7})$$

This definition appears particularly suited for OQPSK and Generalized MSK modulations, since it allows us to take into account the effect of phase errors on *both* branches, not only on the branch currently involved in the decision

process (I-branch for even-numbered instants $2kT$ or Q-branch for odd-numbered ones).

We now look for the value of $\hat{\theta}$ which minimizes (VI.2.7). Recalling that

$$\tilde{y}_{2k} \triangleq \tilde{r}_{2k} e^{j\hat{\theta}}; \quad \tilde{y}_{2k+1} \triangleq \tilde{r}_{2k+1} e^{j\hat{\theta}}, \quad (\text{VI.2.8})$$

and equating to zero the derivative of (VI.2.7) with respect to $\hat{\theta}$ we get

$$\frac{\partial \mathcal{E}}{\partial \hat{\theta}} = -E \left\{ a_k \Im[\tilde{y}_{2k}] - b_k \Re[\tilde{y}_{2k+1}] \right\}. \quad (\text{VI.2.9})$$

The solution to (VI.2.9) is found through the following recursion:

$$\hat{\theta}_{k+1} = \hat{\theta}_k - \gamma e_k \quad (\text{VI.2.10})$$

where e_k is defined as

$$e_k \triangleq - \left\{ a_k \Im\{\tilde{y}_{2k}\} - b_k \Re\{\tilde{y}_{2k+1}\} \right\} \quad (\text{VI.2.11})$$

and γ is the step-size of the recursion.

Recalling (VI.1.2), it is observed that formulation (VI.2.11) of the loop error is formally identical to that obtained in [Boo78] and [Gar88], under the assumption of high signal-to-noise ratio, the sole difference being that matched filtering is not included in our scheme.

The algorithm (VI.2.10) is implemented as indicated in Fig. VII.2. Here the block labeled Phase Error Detector (PED) computes the error signal (VI.2.11) while the blocks "Update algorithm" and "sin/cos ROM" update the phase error estimate and select sin/cos values, respectively.

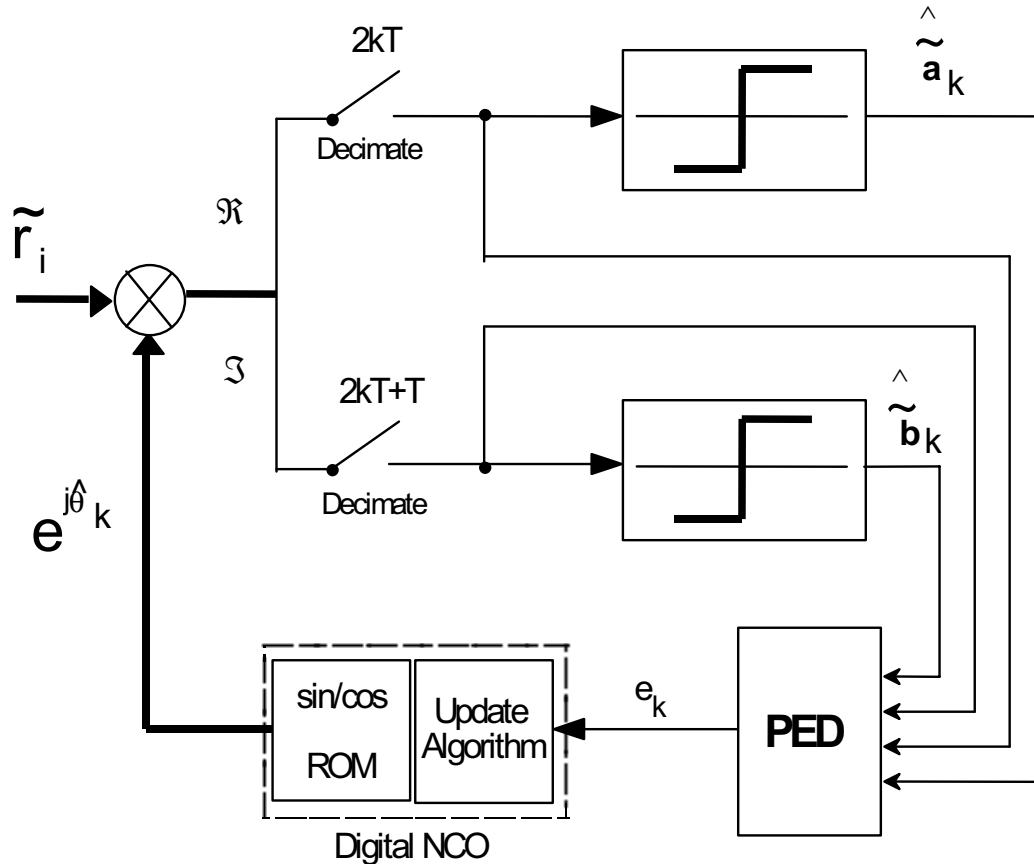


Fig.VI.2

As will be shown later on, for MSK the algorithm (VI.2.10)-(VI.2.11) exhibits a satisfactory performance also when it is fed with the output of the matched filter. This choice is desirable in that the same baud-rate samples (*strokes*) driving the data symbol detector can be employed in the phase-recovery algorithm. Such an option is mandatory for NYQ-OQPSK modulation, since the algorithm does not work properly with a root-raised-cosine shaped pulse.

VI.3 Open Loop Analysis

Denoting by $\theta_e \triangleq \hat{\theta} - \theta$ the *residual phase error*, we now compute the S-curve $S(\theta_e)$ of the phase recovery algorithm

$$S(\theta_e) = E \{ e_k \mid \theta_e \}. \quad (\text{VI.3.1})$$

The derivation of $S(\theta_e)$ is a difficult task because of the dependence of e_k on the estimated symbols \hat{a}_k and \hat{b}_k . To simplify matters, in a first instance the estimated symbols are replaced by transmitted data, i.e. $\hat{a}_k = a_k$ and $\hat{b}_k = b_k$. This approximation is likely to hold true for medium-to-high signal-to-noise ratios. We also assume

$$p(0)=1 \quad \text{and} \quad p(t)=0 \quad |t| \geq T. \quad (\text{VI.3.2})$$

Consider now separately each of the two terms of (VI.2.11). The first term can be written as

$$\begin{aligned} E \left\{ a_k \Im \left[\tilde{y}_{2k} \right] \right\} &= \\ &= E \left\{ a_k \sum_i a_i p(2kT-2iT) \sin \theta_e - a_k \sum_i b_{i+1} p[2kT-(2i+1)T] \cos \theta_e \right\} \end{aligned}$$

Assuming that $E \{ a_i a_j \} = \delta_{ij}$ and $E \{ a_i b_j \} \equiv 0$, we have

$$E \left\{ a_k \Im \left[\tilde{y}_{2i} \right] \right\} = \sin \theta_e.$$

Similarly, the second term of (VI.2.13) yields

$$E \left\{ b_k \Re \left[\tilde{y}_{2i+1} \right] \right\} = - \sin \theta_e,$$

so that

$$S(\theta_e) = 2 \sin\theta_e . \quad (\text{VI.3.3})$$

When the assumption on the time-limited nature of the signalling pulse is dropped, or non-linear modulation techniques such as generalized MSK are considered, an open-loop analysis of the algorithm becomes a formidable task and we are forced to rely on simulation results only.

The hypothesis of correct decisions is likely to fail in the presence of large static phase errors. Therefore, relation (VI.3.3), corresponding to a data-aided (DA) system, is different from the S-curve pertaining to a decision-directed (DD) system $S_{DD}(\theta_e)$. To find an expression for $S_{DD}(\theta_e)$ we relax the assumption of correct decisions. In the hypothesis that conditions (VI.3.2) are still met and that the channel is noiseless, we recognize also that the sample entering the symbol detector is either

$$\tilde{y}_{2k} = a_k \cos\theta_e + j a_k \sin\theta_e$$

or

$$\tilde{y}_{2k+1} = -b_k \sin\theta_e + j b_k \cos\theta_e$$

depending on the sampling instant. Accordingly, the error signal is

$$e_k = \hat{a}_k a_k \sin\theta_e + \hat{b}_k b_k \sin\theta_e. \quad (\text{VI.3.4})$$

Since we are dealing with a binary modulation, the threshold detector operates as follows:

$$\hat{a}_k = \text{sign}[a_k \cos\theta_e] \quad (\text{VI.3.5.a})$$

$$\hat{b}_k = \text{sign}[b_k \cos\theta_e] \quad (\text{VI.3.5.b})$$

Consider now the case $|\theta_e| < \pi/2$ so that $\cos\theta_e > 0$. All decisions are correct and we have

$$S_{DD}(\theta_e) = S(\theta_e) = 2A_2 \sin \theta_e.$$

On the contrary, if $\pi/2 < |\theta_e| < \pi$, we have $\cos \theta < 0$; the decisions are invariably wrong, i. e. $\hat{a}_k = -a_k$ and $\hat{b}_k = -b_k$, yielding

$$S_{DD}(\theta_e) = -S(\theta_e) = -2A_2 \sin \theta_e.$$

The DD version of the S-curve on the interval $\pi/2 < |\theta_e| < \pi$ is thus a reversed-sign version of the data-aided S-curve. For this reason the phase recovery algorithm has an intrinsic phase ambiguity of π radians (sign ambiguity). The value $\theta_e = \pi/2$ is a discontinuity point for $S_{DD}(\theta_e)$ that can be seen as an unstable equilibrium point. Figures VI.3-5 show the DD S-curves for MSK, GMSK and NYQ-OQPSK derived by simulation under the same conditions assumed in the theoretical analysis (i. e. the noiseless received waveform $\tilde{r}(t)$ is unfiltered for MSK and GMSK modulations, whereas it coincides with the matched filter output for NYQ-OQPSK modulation). In all the diagrams, the S-curves are shown over a phase-error range of π radians only, due to the periodicity of $S_{DD}(\theta_e)$.

As already mentioned before, calculations are very cumbersome for GMSK and NYQ-OQPSK modulations, because of the peculiar shape of the signalling pulses. The corresponding S-curves have therefore been evaluated by simulation. In Figs. VI.4-5 the shape of the curves near $\pm\pi/2$ can be ascribed to the fact that, in the presence of intersymbol and/or crosstalk I/Q interference, the detection unit may make wrong decisions even for phase errors less than $\pi/2$. This can happen also with MSK modulation, when the matched filter output is input to the synchronizer (Fig. VI.6). Finally, Fig. VI.7 displays the S-curve for GMSK when the synchronizer is fed by the detection filter output. Figures VI.8-10 correspond to Figs. VI.5-7, with the addition of AWGN. A major difference between the two groups of figures is the absence of sharp corners that are rounded off by the decision errors induced by the noise.

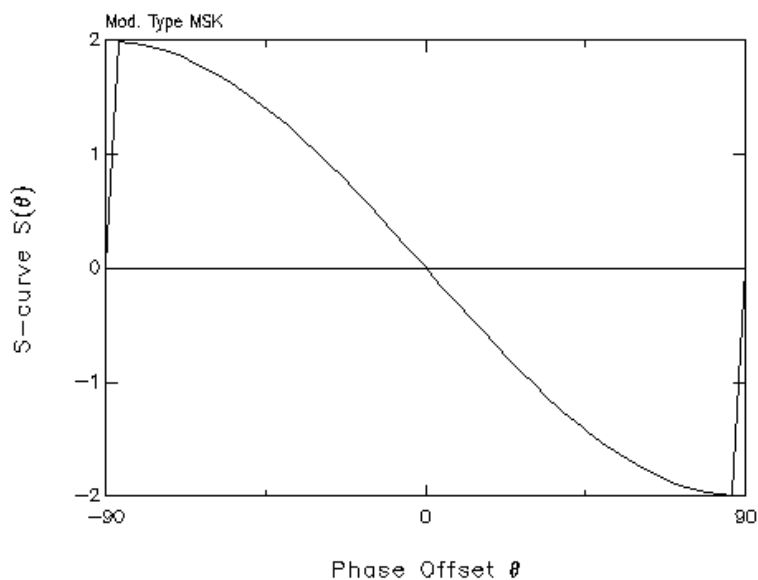


Fig.VI.3

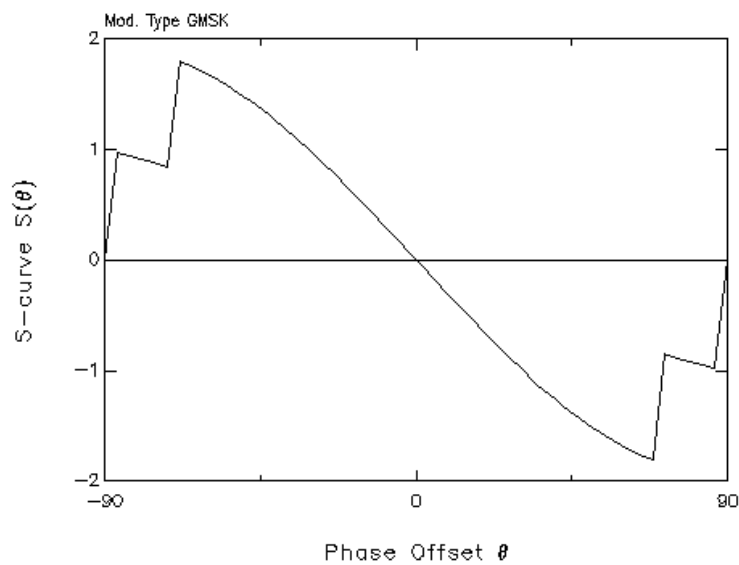


Fig.VI.4

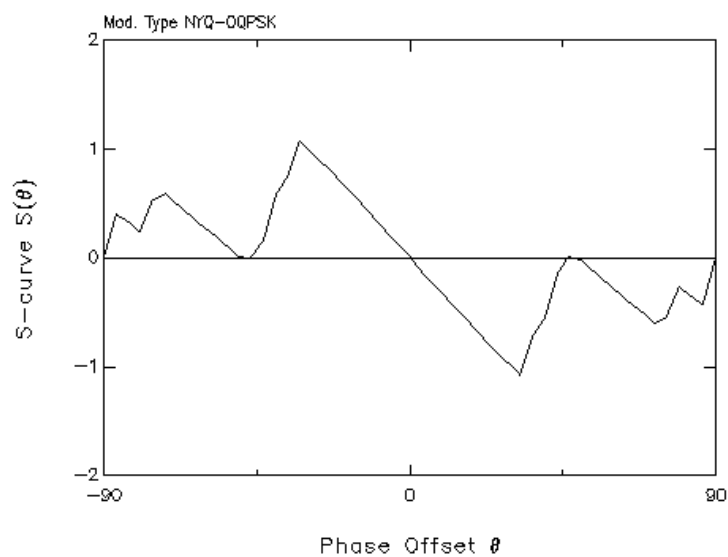


Fig.VI.5

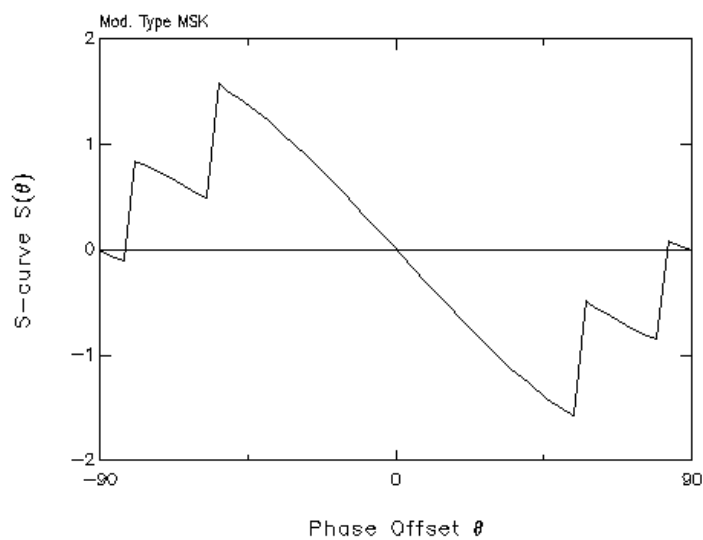


Fig.VI.6

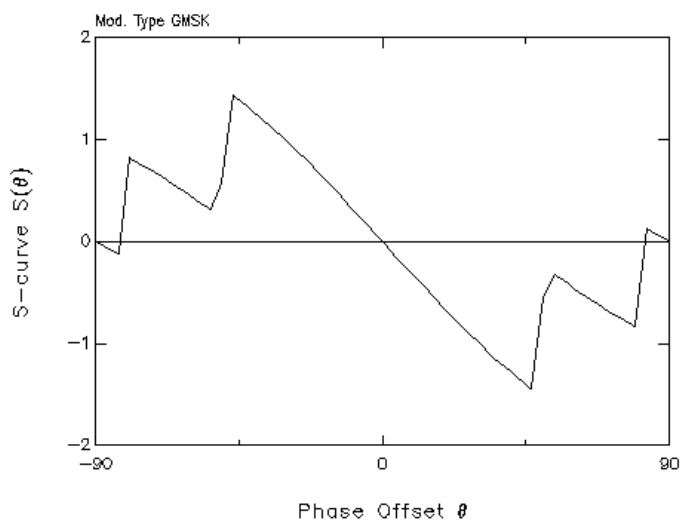


Fig.VI.7

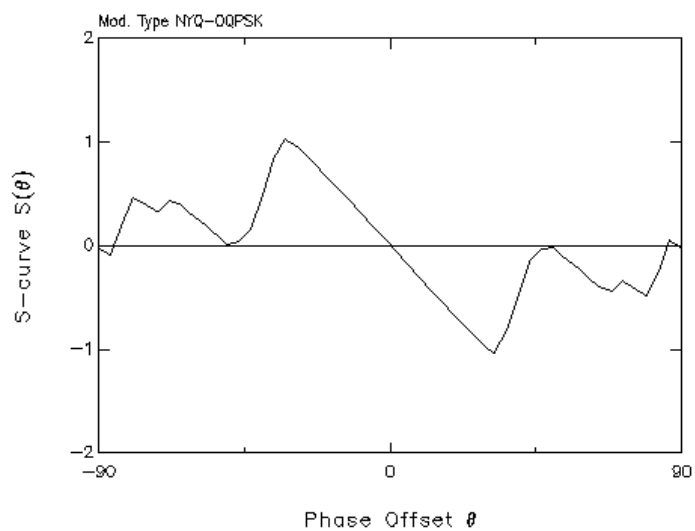


Fig.VI.8

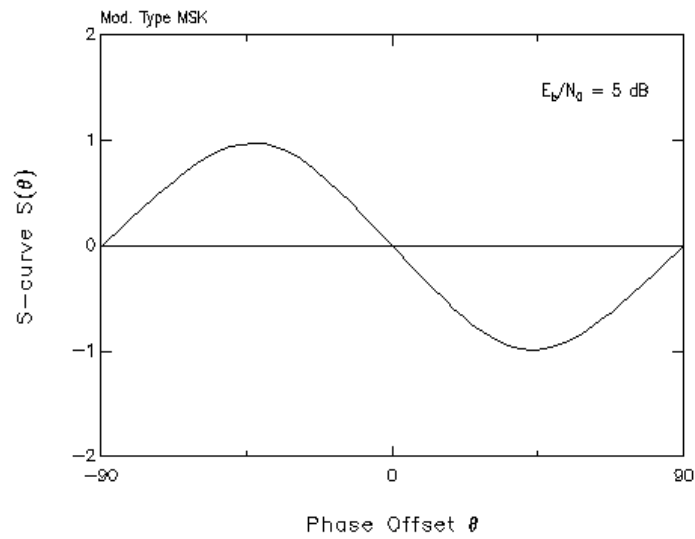


Fig.VI.9

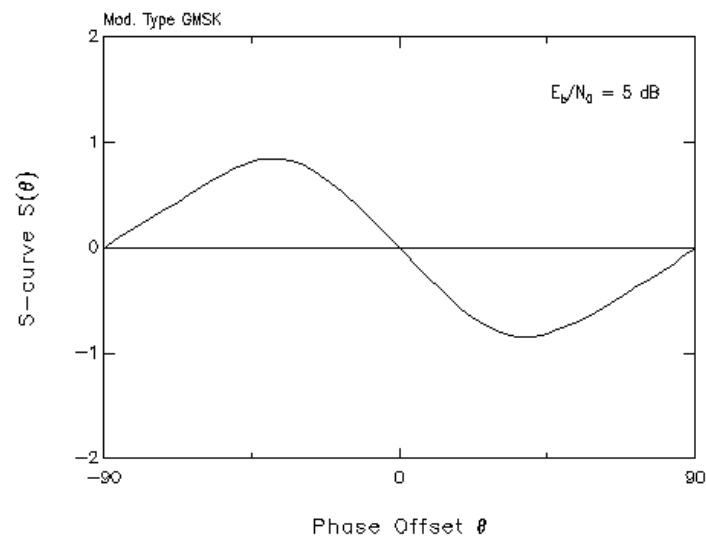


Fig. VI.10

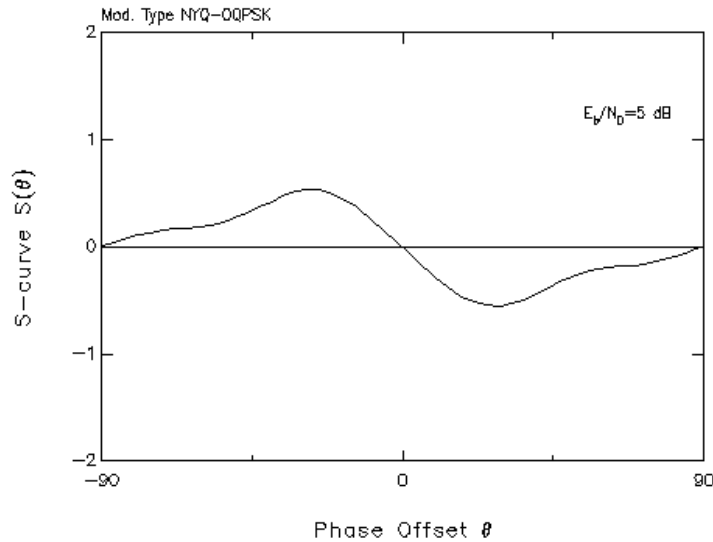


Fig. VI.11

VI.4 Influence of Clock Recovery on Phase Loop Behavior

As already mentioned, the behavior of the phase recovery loop is influenced by timing errors. The reason for this is two-fold: first, the PED relies on estimated data, that may be incorrect if the sampling instant is not adequately chosen; second, proper operation of the PED is achieved only when the sampled signal \tilde{r}_i is taken at the optimum instants.

To see the effect of sampling errors on the S-curve let us assume that the sampling epoch is shifted from its ideal value by a fixed amount τ . In the hypothesis of no thermal noise and correct decisions, we have (using the same notation as in Sect. VI.1):

$$E \left\{ a_k \Im \left\{ \tilde{y}_{2k} \right\} \right\} =$$

$$= \left\{ a_k \sum_i a_{2i} p(2kT - 2iT + \tau) \sin\theta_e - a_k \sum_i b_{2i+1} p[2kT - (2i+1)T + \tau] \cos\theta_e \right\}$$

so that

$$E \left\{ a_k \Im \left\{ \tilde{y}_{2k} \right\} \right\} = A_2 p(\tau) \sin\theta_e .$$

and similarly

$$E \left\{ b_{k+1} \Re \left\{ \tilde{y}_{2k+1} \right\} \right\} = -A_2 p(\tau) \sin\theta_e .$$

The expression of the S-curve is thus

$$S(\theta_e) = 2A_2 p(\tau) \sin\theta_e \quad 0 < |\tau| < T \quad (\text{VI.4.1})$$

and the effect of a sampling offset is solely a reduction in the amplitude of the S-curve..

Taking into account possible decision errors, in the absence of noise we have for MSK, with $0 \leq \tau \leq 0.5T$:

$$\begin{aligned} \tilde{y}_{2k} &= a_k \cos \left[\frac{\pi\tau}{2T} \right] \cos\theta_e - b_{k+1} \cos \left[\frac{\pi(\tau-T)}{2T} \right] \sin\theta_e + \\ &+ ja_k \cos \left[\frac{\pi\tau}{2T} \right] \sin\theta_e + jb_{k+1} \cos \left[\frac{\pi(\tau-T)}{2T} \right] \cos\theta_e \end{aligned} \quad (\text{VI.4.2a})$$

$$\begin{aligned} \tilde{y}_{2k+1} &= a_k \cos \left[\frac{\pi(\tau+T)}{2T} \right] \cos\theta_e - b_{k+1} \cos \left[\frac{\pi\tau}{2T} \right] \sin\theta_e + \\ &+ ja_k \cos \left[\frac{\pi(\tau+T)}{2T} \right] \sin\theta_e + jb_{k+1} \cos \left[\frac{\pi\tau}{2T} \right] \cos\theta_e \end{aligned} \quad (\text{VI.4.2b})$$

so that the output of the PED can be expressed as:

$$\begin{aligned} e_k = \hat{a}_k \left\{ a_k \cos \left[\frac{\pi \tau}{2T} \right] \sin \theta_e + b_{k+1} \cos \left[\frac{\pi(\tau-T)}{2T} \right] \cos \theta_e \right\} - \\ - \hat{b}_{k+1} \left\{ a_k \cos \left[\frac{\pi(\tau+T)}{2T} \right] \cos \theta_e - b_{k+1} \cos \left[\frac{\pi \tau}{2T} \right] \sin \theta_e \right\} . \end{aligned} \quad (VI.4.3)$$

Letting now $\alpha \triangleq \tau/T$, $0 \leq \alpha \leq 0.5$, equations (VI.4.2) can be re-written as

$$\begin{aligned} \tilde{y}_{2k} = a_k \cos \left[\frac{\pi \alpha}{2} \right] \cos \theta_e - b_{k+1} \cos \left[\frac{\pi(\alpha-1)}{2} \right] \sin \theta_e + \\ + j a_k \cos \left[\frac{\pi \alpha}{2} \right] \sin \theta_e + j b_{k+1} \cos \left[\frac{\pi(\alpha-1)}{2} \right] \cos \theta_e \end{aligned} \quad (VI.4.4a)$$

$$\begin{aligned} \tilde{y}_{2k+1} = a_k \cos \left[\frac{\pi(\alpha+1)}{2} \right] \cos \theta_e - b_{k+1} \cos \left[\frac{\pi \alpha}{2} \right] \sin \theta_e + \\ + j a_k \cos \left[\frac{\pi(\alpha+1)}{2} \right] \sin \theta_e + j b_{k+1} \cos \left[\frac{\pi \alpha}{2} \right] \cos \theta_e \end{aligned} \quad (VI.4.4b)$$

$$\begin{aligned} e_k = \hat{a}_k \left\{ a_k \cos \left[\frac{\pi \alpha}{2} \right] \sin \theta_e + b_{k+1} \cos \left[\frac{\pi(\alpha-1)}{2} \right] \cos \theta_e \right\} - \\ - \hat{b}_{k+1} \left\{ a_k \cos \left[\frac{\pi(\alpha+1)}{2} \right] \cos \theta_e - b_{k+1} \cos \left[\frac{\pi \alpha}{2} \right] \sin \theta_e \right\} . \end{aligned} \quad (VI.4.5)$$

Recalling that $\cos \left[\alpha + \frac{\pi}{2} \right] = -\sin \alpha$ and $\cos \left[\alpha - \frac{\pi}{2} \right] = \sin \alpha$, the expression of the estimated symbols \hat{a}_k and \hat{b}_{k+1} turns out to be

$$\hat{a}_k = \text{sgn} \left\{ a_k \cos \left[\frac{\pi \alpha}{2} \right] \cos \theta_e - b_{k+1} \sin \left[\frac{\pi \alpha}{2} \right] \sin \theta_e \right\} \quad (V.I4.6a)$$

$$\hat{b}_{k+1} = \text{sgn} \left\{ a_k \sin \left[\frac{\pi\alpha}{2} \right] \sin\theta_e + b_{k+1} \cos \left[\frac{\pi\alpha}{2} \right] \cos\theta_e \right\} , \quad (\text{VI.4.6b})$$

whereas the error signal takes the form

$$\begin{aligned} e_{k+1} = & \hat{a}_k \left\{ a_k \cos \left[\frac{\pi\alpha}{2} \right] \sin\theta_e + b_{k+1} \sin \left[\frac{\pi\alpha}{2} \right] \cos\theta_e \right\} + \\ & - \hat{b}_k \left\{ a_k \sin \left[\frac{\pi\alpha}{2} \right] \cos\theta_e - b_{k+1} \cos \left[\frac{\pi\alpha}{2} \right] \sin\theta_e \right\} \end{aligned} \quad (\text{VI.4.7})$$

From (VI.4.6) we can partition the (θ_e, α) plane into zones of "correct" and "wrong" decisions. In particular, the "wrong" zone is represented by

$$-\frac{\alpha\pi}{2} \leq \frac{\pi}{2} + \theta_e \leq \frac{\alpha\pi}{2} \quad (\text{VI.4.8})$$

As is apparent, a non-zero sampling offset ($\alpha \neq 0$) induces a non-zero-amplitude range of phases where symbols estimates are always wrong, thus inducing a reshaping of the S-curve. Computation of the Decision-Directed version of the S-curve $S_{DD}(\theta_e)$ is quite cumbersome, so we report only the following simple final result valid for $0 \leq \alpha \leq 0.5$:

$$S_{DD}(\theta_e) = \begin{cases} \sin \left[\frac{\pi\alpha}{2} \right] \cos\theta_e & \theta_e \in \left[\frac{(1-\alpha)\pi}{2}, \frac{(1+\alpha)\pi}{2} \right] \\ \sin\theta_e \text{ sign}[\cos\theta_e] & \text{otherwise} \end{cases} \quad (\text{VI.4.9})$$

The following simulation results show the S-curves for various sampling offsets and confirm the theoretical analysis above. They also reveal that in such conditions, a further stable equilibrium point arises at $\theta_e = \pi/2$.

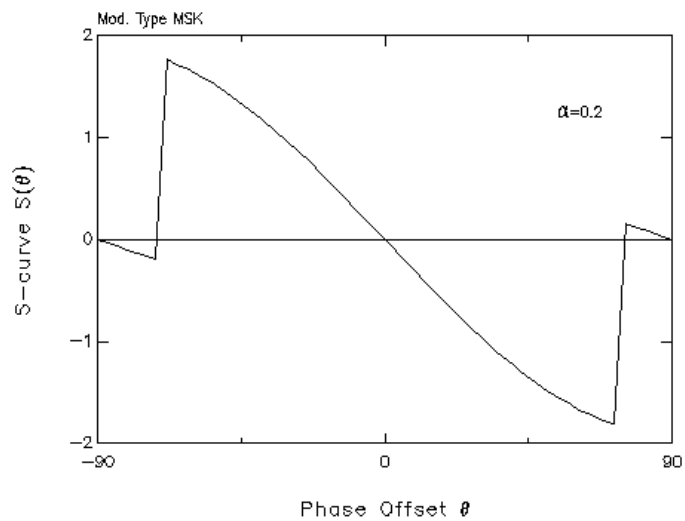


Fig. VI.12

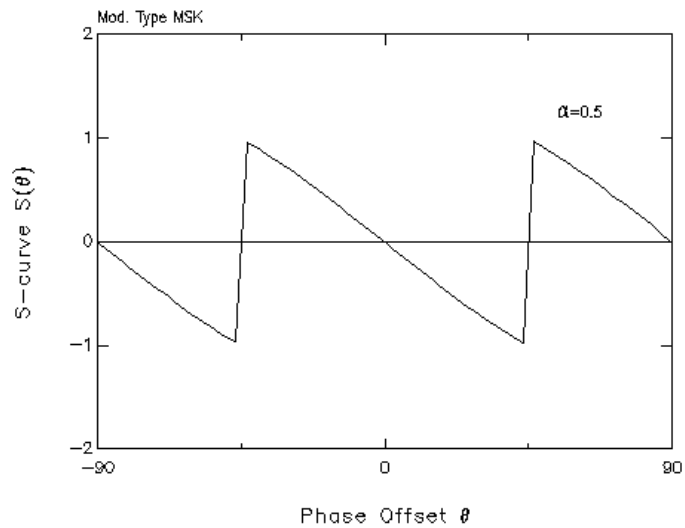


Fig. VI.13

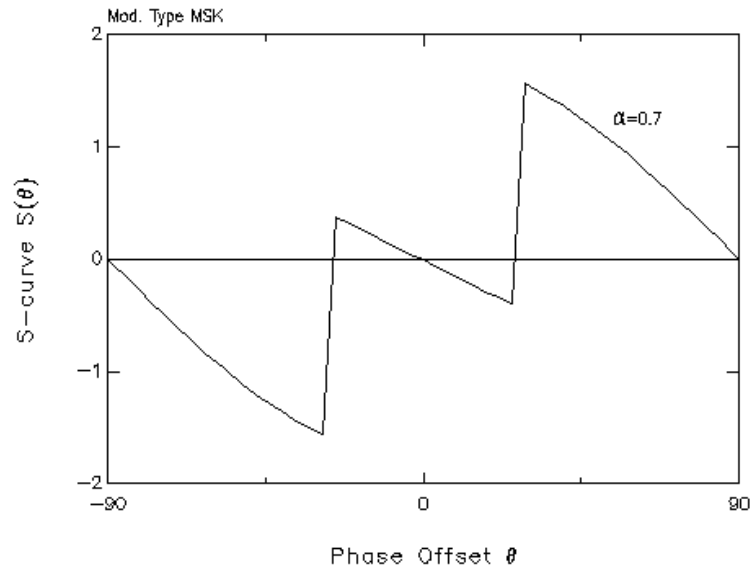


Fig. VI.14

VI.5 Closed-Loop Performance

We now report on some simulation results concerning the performance of the first-order loop depicted in Fig. VI.2, when perfect clock recovery is assumed and the synchronizer is fed with the output of the detection filter. In particular, Fig. VI.15 shows the curves of the RMS phase jitter for MSK and GMSK when the equivalent loop noise bandwidth is set at $B_{N0}T = 4 \cdot 10^{-2}$. Figures VI.16-VI.18 show the phase error during loop acquisition for MSK and the same loop bandwidth as before, for various E_b/N_0 ratios. In figures VI.19-VI.20 analogous results are given for GMSK. As expected, a slight performance degradation compared to MSK is apparent.

We recall here the relationship between the one-sided normalized loop

noise bandwidth $B_{N\theta}T$ and the step-size γ in the stochastic-gradient algorithm (VI.2.10):

$$B_{N\theta}T = \frac{\gamma A}{2(2 - \gamma A)}$$

where A is the slope of $S_{DD}(\theta_e)$ evaluated at the stable equilibrium point (i.e. $\theta_e = 0$).

(This space is intentionally left blank)

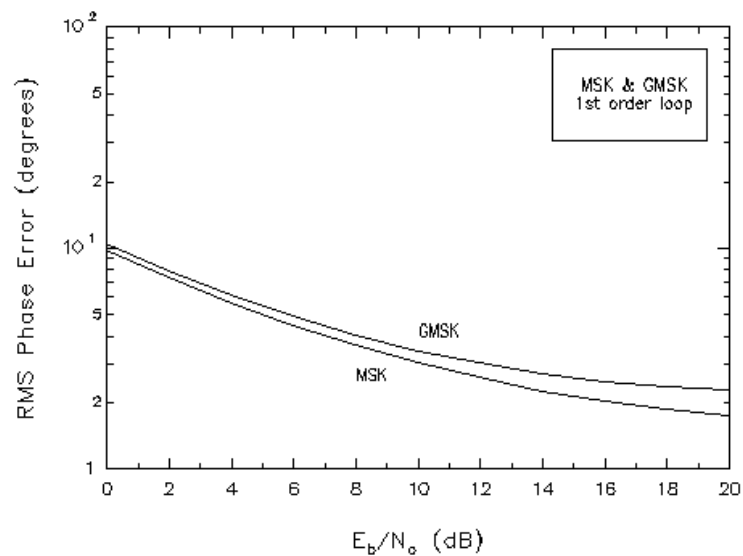


Fig.VI.15

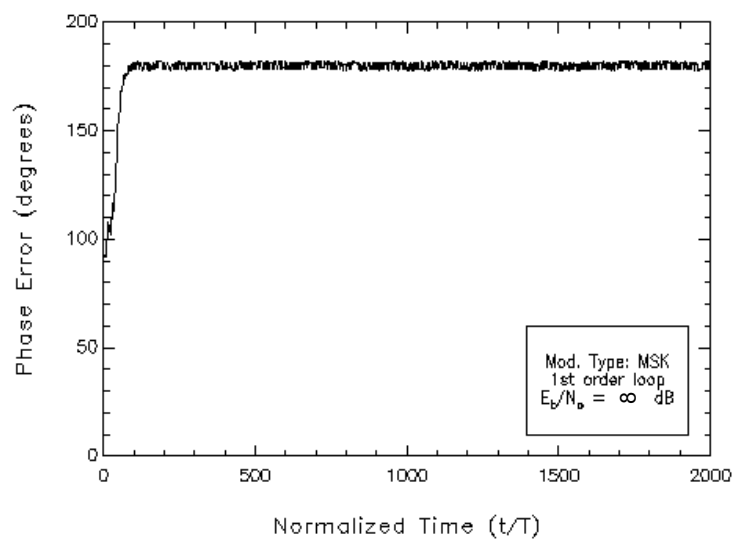


Fig.VI.16

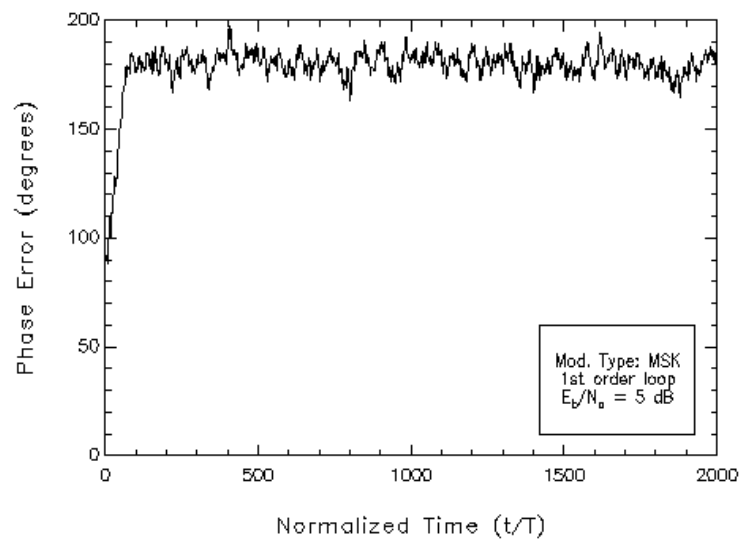


Fig.VI.17

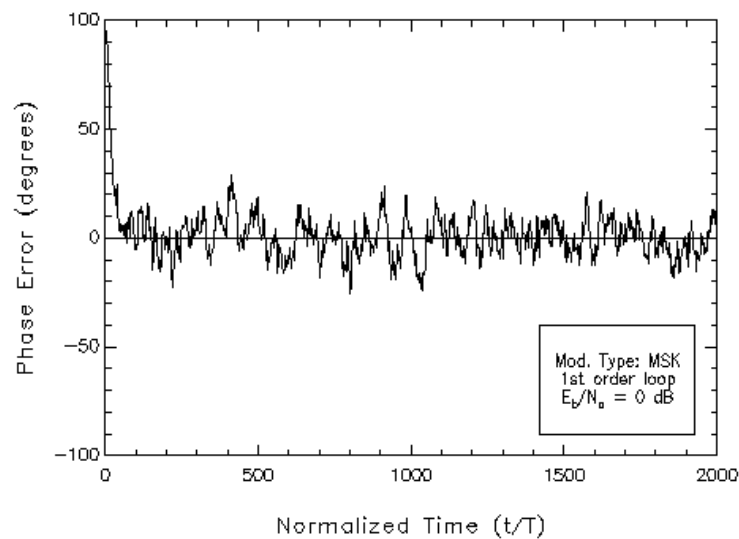


Fig.VI.18

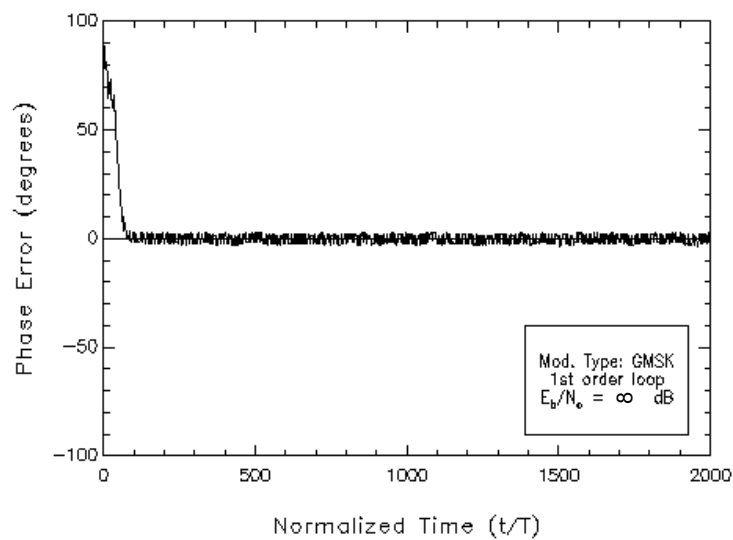


Fig.VI.19

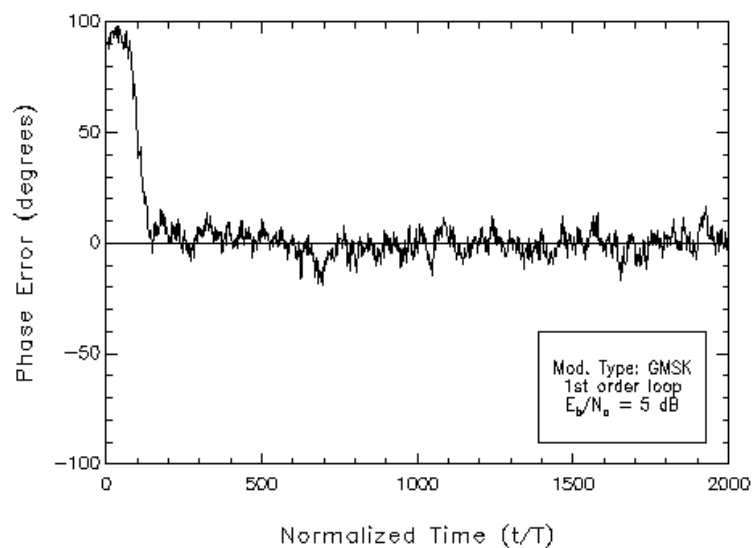


Fig.VI.20

VI.6 Performance of the Second Order Phase-Recovery Loop

In the previous Section we considered the performance of a first-order phase recovery scheme (Fig. VI.2). On the other hand, it is well-known that a first-order loop has an unsatisfactory performance when a residual frequency error affects the received signal [Mey90]. As we will see in the next Chapter (which deals with carrier frequency acquisition and tracking), a small residual time-varying frequency error may still be present even if an Automatic Frequency Control (AFC) is used to track frequency variations due to Doppler shifts.

In such a situation it is mandatory to resort to a second-order loop, which is capable of tracking a constant frequency offset with no steady-state phase error [Mey90]. We do not dwell here on the design of such a loop (see next Chapter for details). We only mention that, among the possible configurations of a second order loop, we chose a structure with two coincident poles.

Figure VI.21 shows the curves of the RMS phase jitter over an E_b/N_0 range from 0 to 20 dB. Again, the loop noise bandwidth is fixed at $4 \cdot 10^{-2}$. The interruption of the OQPSK curve below 4 dB is due to the fact that, in that region, sync losses occur. For the case of OQPSK therefore it is necessary to reduce the loop bandwidth, and in fact the results presented in Fig. VI.22 are for a loop bandwidth $B_{N0}T = 2 \cdot 10^{-2}$.

Some loop acquisitions of the second-order loop are also shown in Figs. VI.23-VI.29 for various modulation schemes. Apart from a small initial phase overshoot, there are no significant differences with respect to the previous Section as far as the acquisition time is concerned.

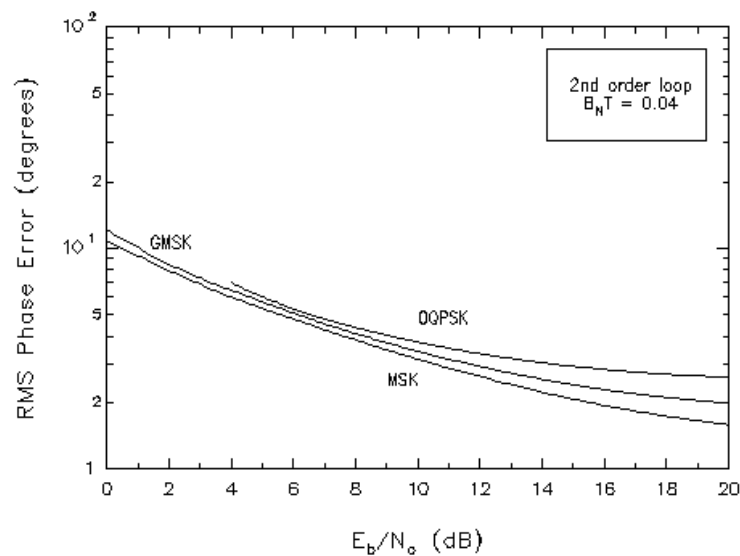


Fig.VI.21

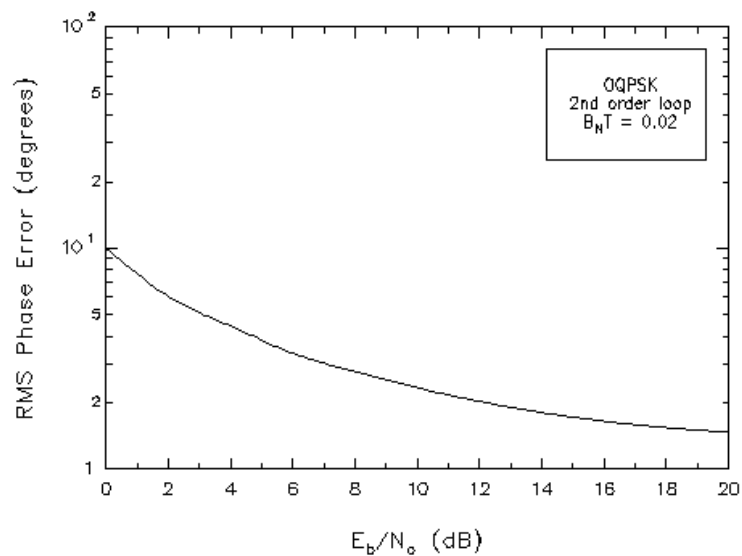


Fig.VI.22

The impact of the phase recovery subsystem (second-order loop) upon the overall system performance can be evaluated from the BER curves in Figs. VI.30-VI.32 . As already mentioned in the previous Chapters, the BER is evaluated over 10^5 symbols by means of the semi-analytic method [Jer84].

At equal loop bandwidth, the usual degradation of GMSK with respect to MSK is apparent. A smaller degradation is incurred by OQPSK due to the narrower loop bandwidth.

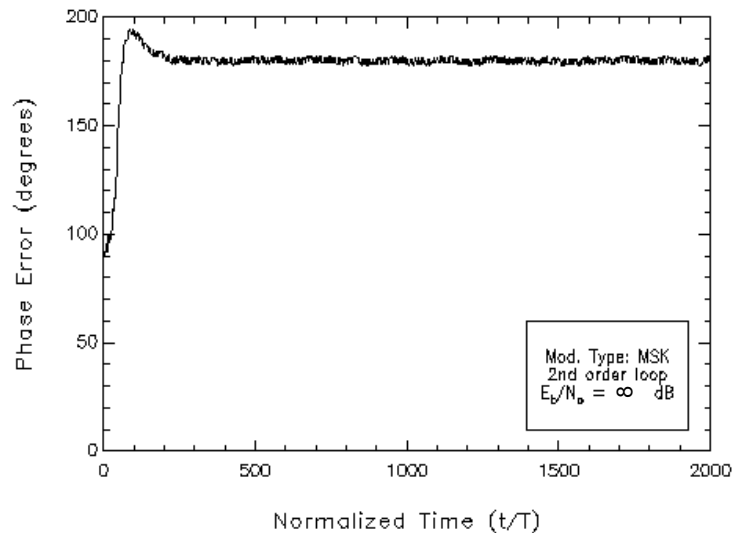


Fig.VI.23

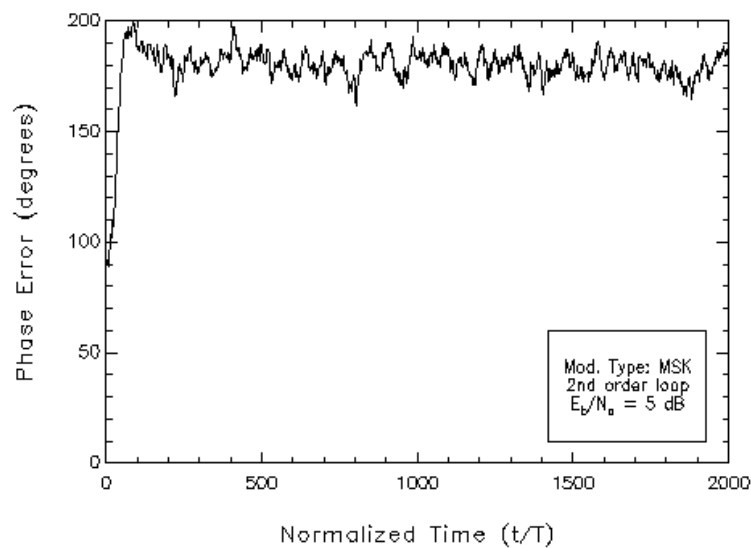


Fig.VI.24

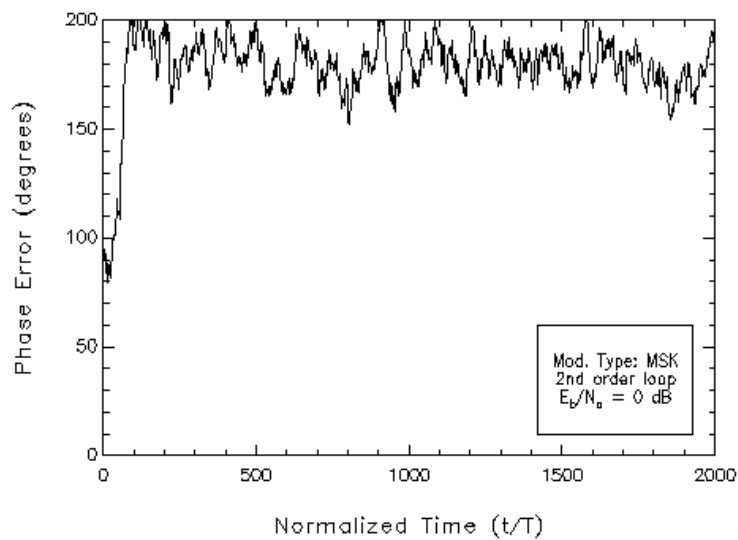


Fig.VI.25

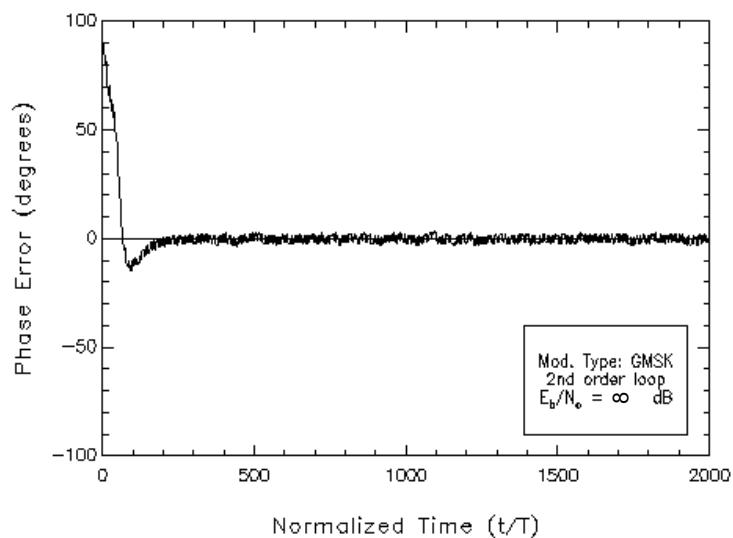


Fig.VI.26

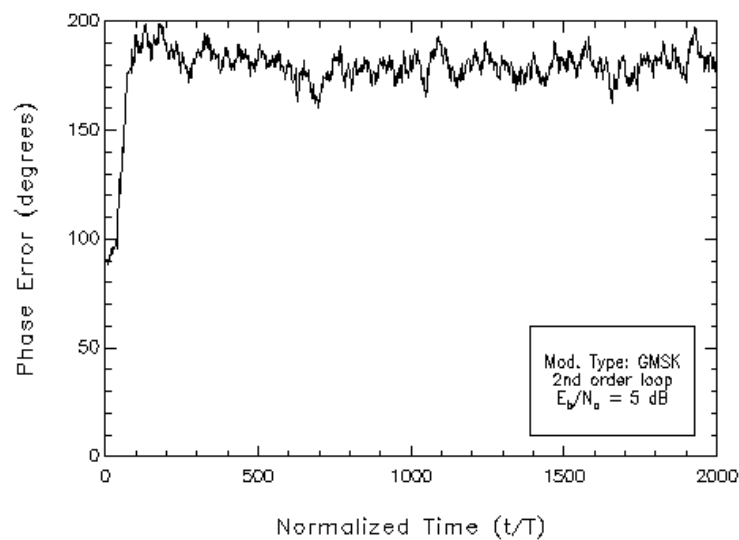


Fig.VI.27

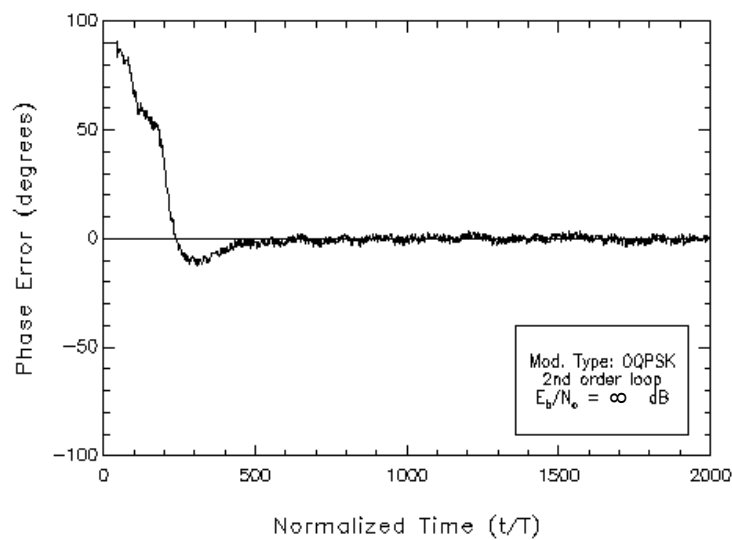


Fig.VI.28

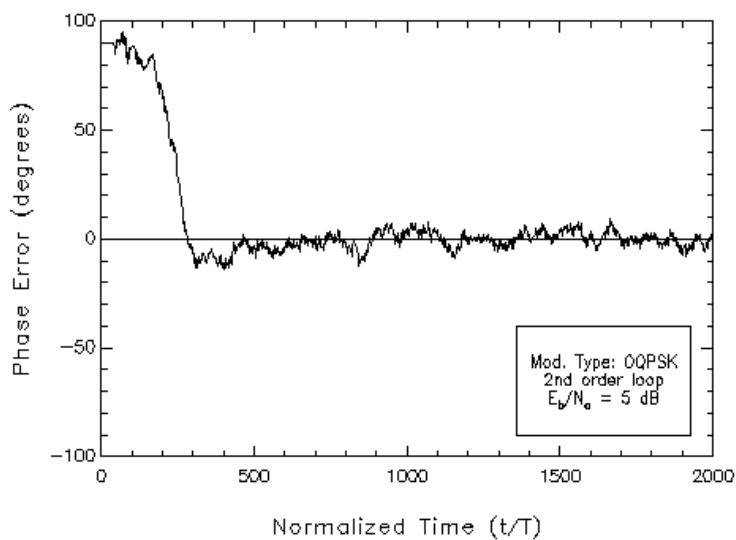


Fig.VI.29

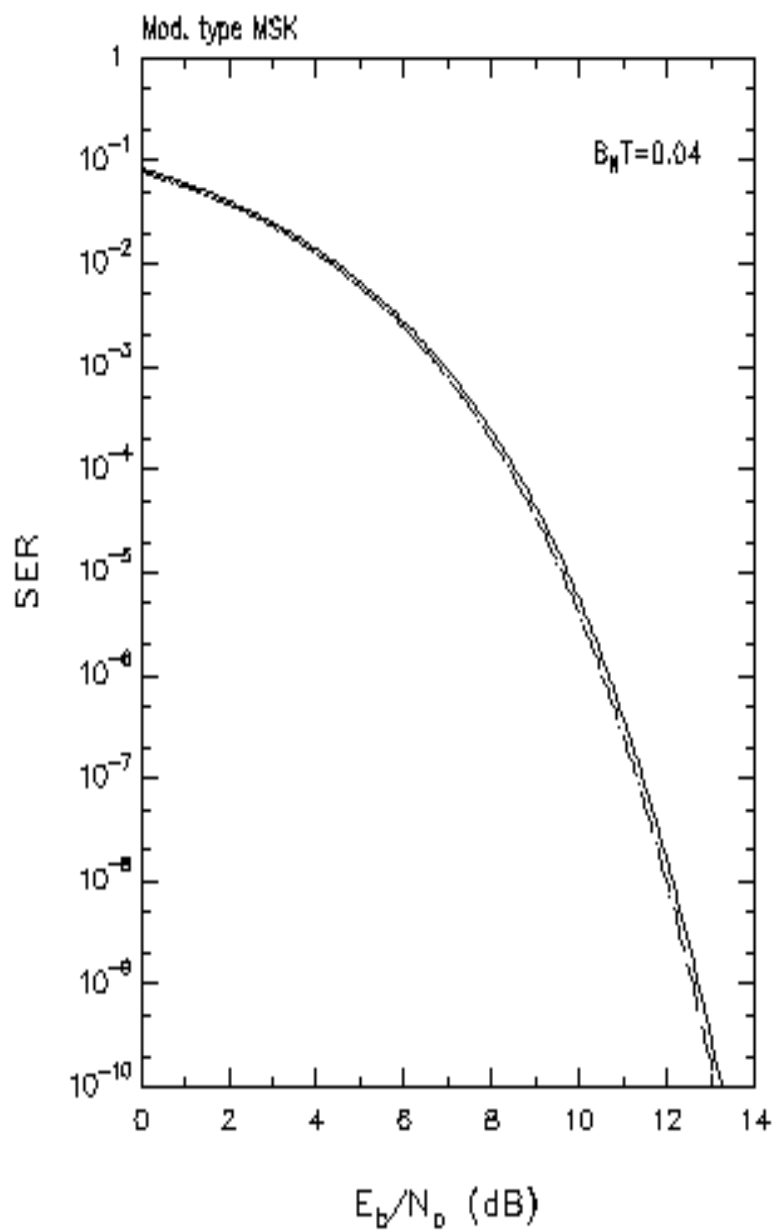


Fig.VI.30

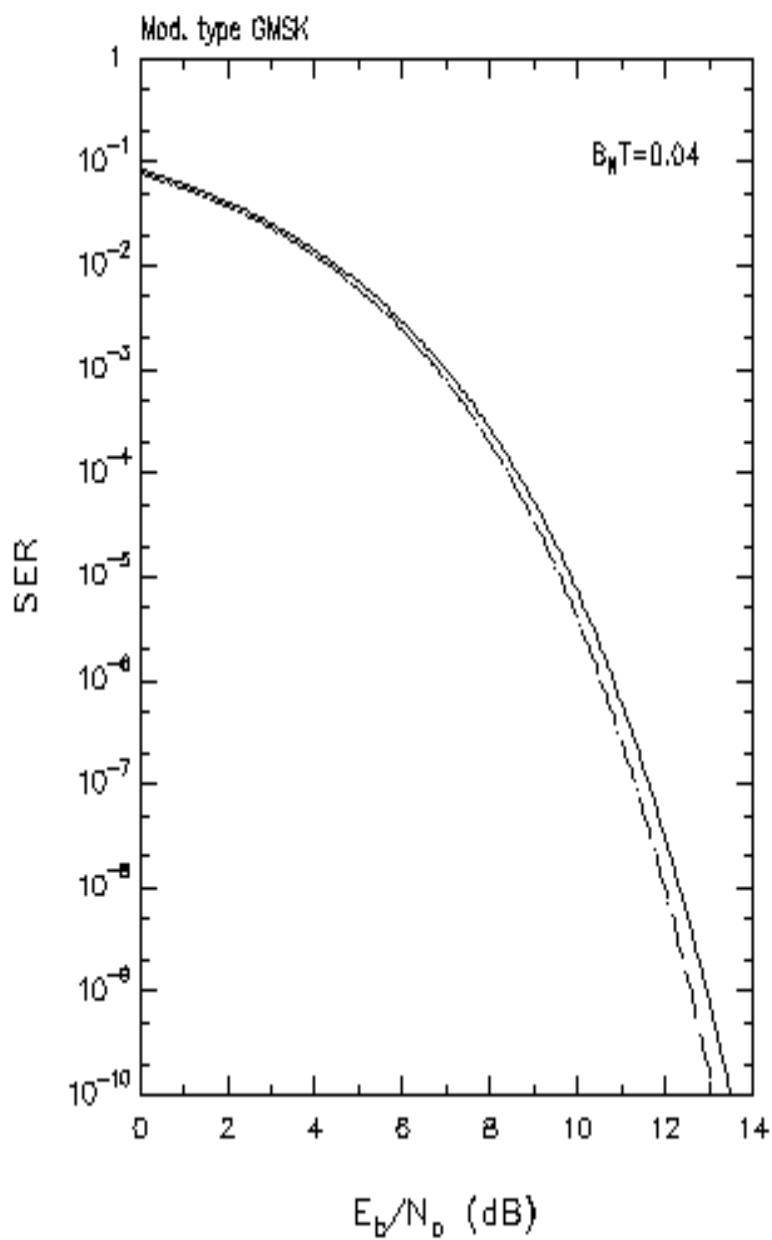


Fig. VI.31

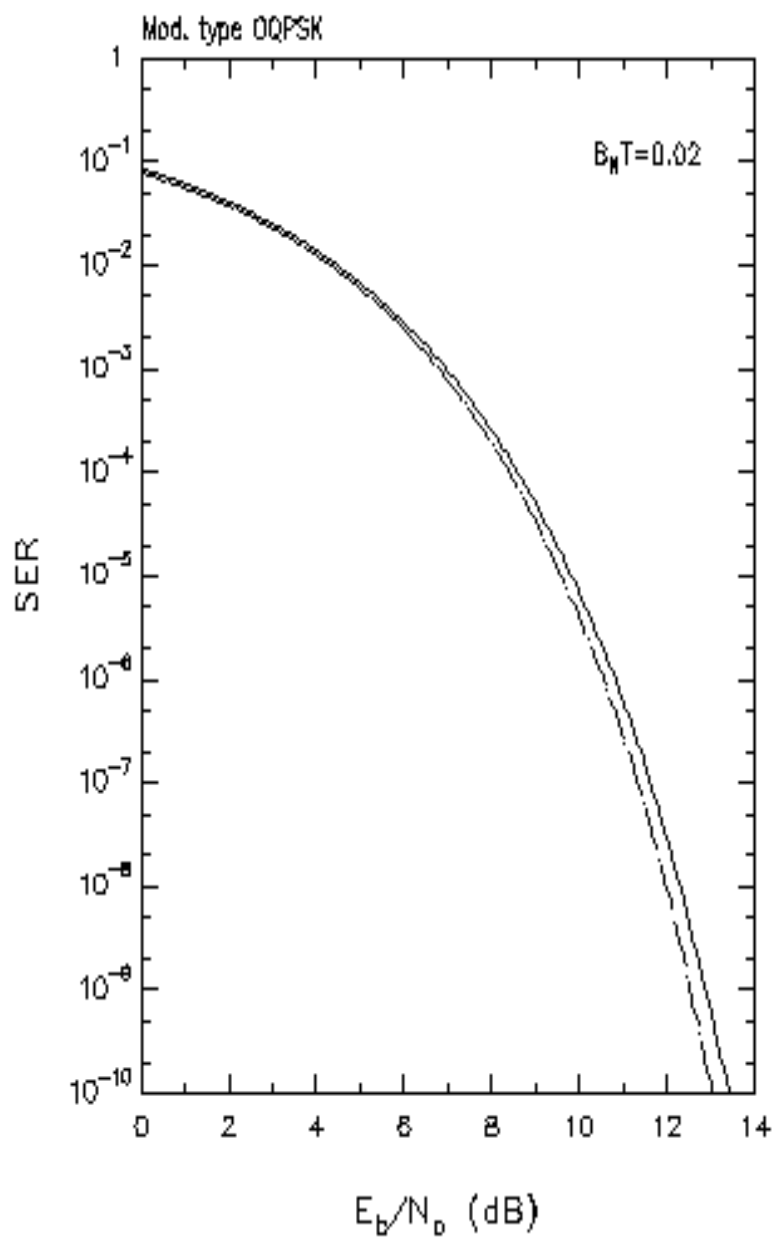


Fig.VI.32

VI.7 Performance Degradation due to Joint Phase/Clock Recovery

Some simulations have been performed to assess the degradation experienced by the receiver when neither clock nor carrier phase are ideal. We examine first the cases of MSK and GMSK and then the NYQ-OQPSK modulation.

•) MSK and GMSK Modulations.

The algorithm # 1 has been used for clock recovery. Figures. VI.33-VI.34 show the curves of the RMS jitter for clock timing and carrier phase (second order loop) over the range 0 to 20 dB. As for phase recovery, we notice a slight increase of the RMS jitter with respect to the case of ideal sampling instant (Fig. VI.15). The noise bandwidths of the loops are $B_{N\theta}T=4\cdot 10^{-2}$ and $B_{N\tau}T=5\cdot 10^{-4}$, for phase and clock recovery, respectively.

(This space is intentionally left blank)

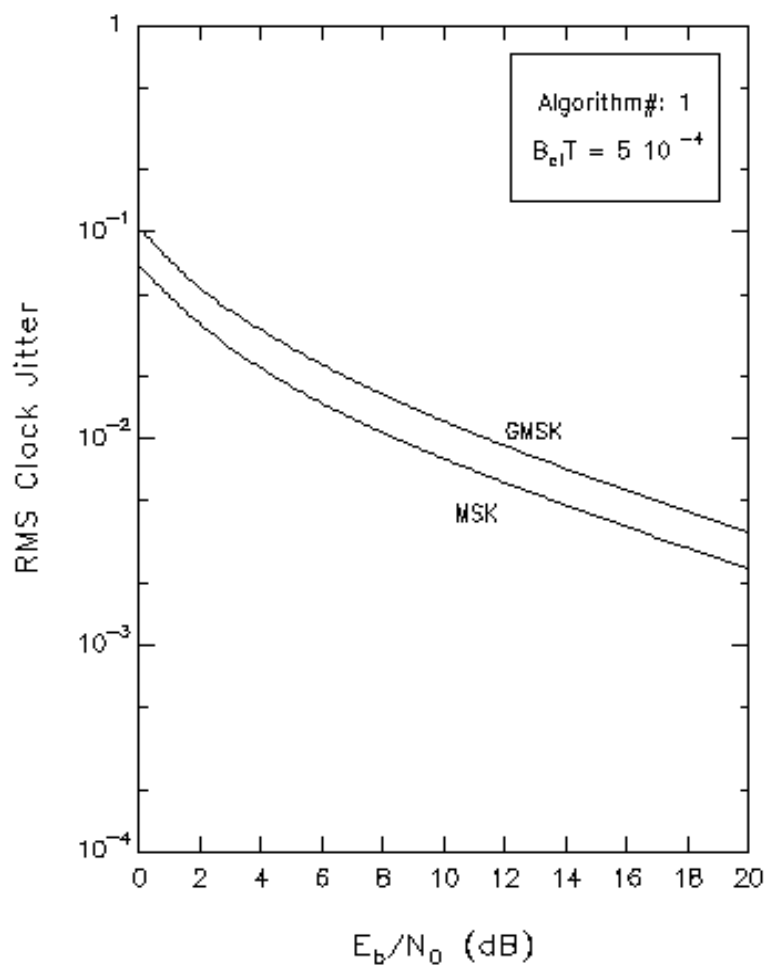


Fig. VI.33

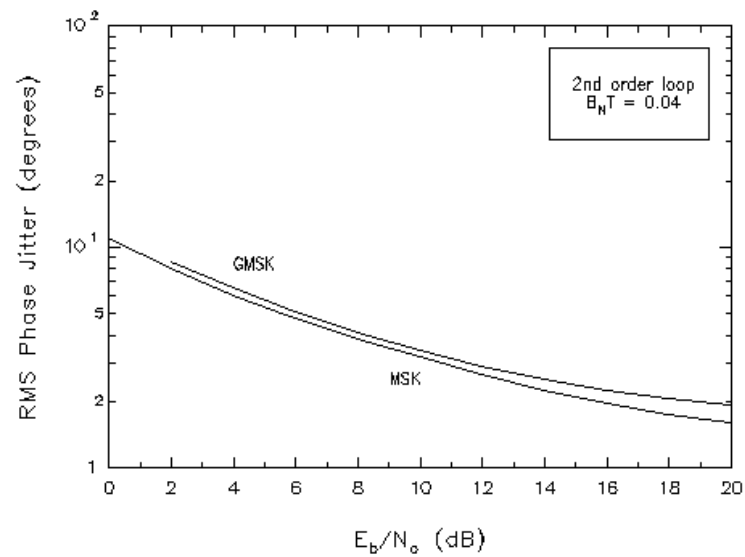


Fig. VI.34

The BER curves are shown in Figs. VI.35-VI.36. Comparison of these results with those pertaining to the ideal sampling case (Figs. VI.30-31) reveals a negligible degradation due to the insertion of clock recovery. It is worth observing that the overall degradation due to phase & clock jitter is limited, with the selected values of loop bandwidths.

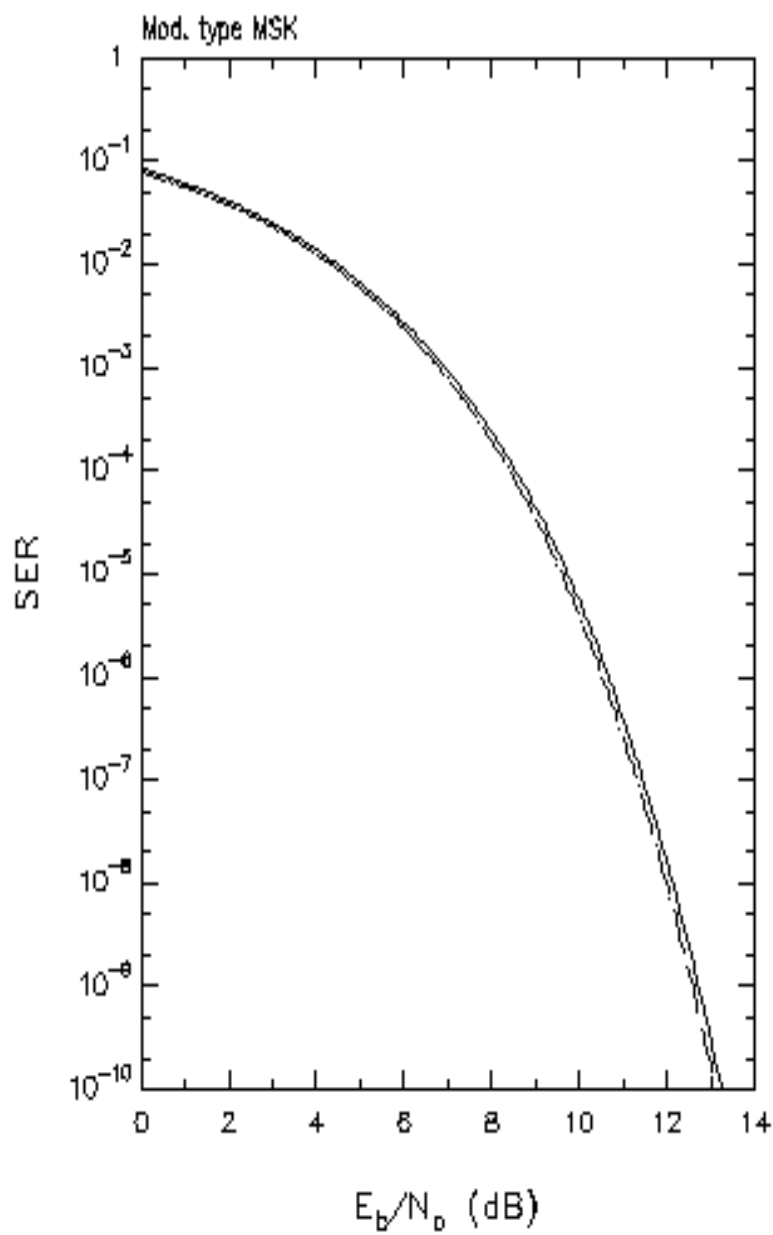


Fig. VI.35

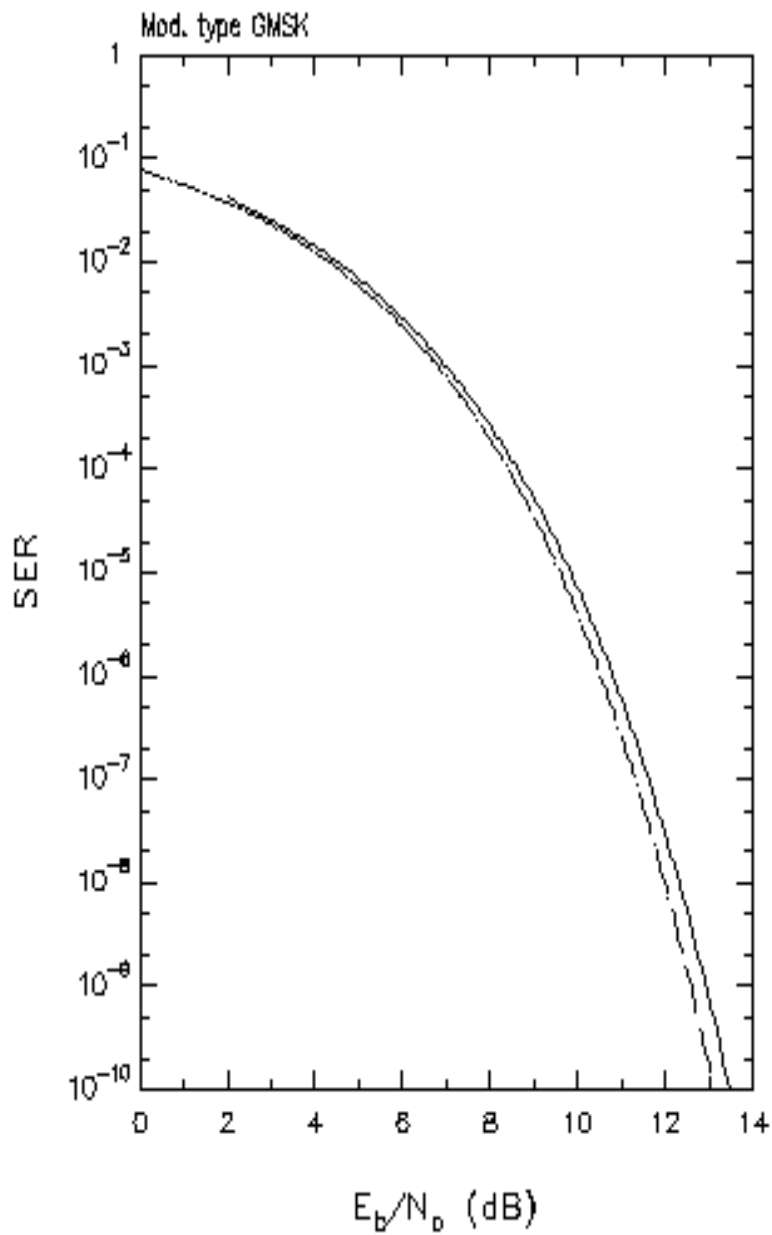


Fig. VI.36

Finally, time diagrams for joint clock/phase acquisition are shown in Figs. VI.37-VI.44. In the absence of noise a fast phase acquisition is apparent, even in the presence of a non-negligible sampling offset.

(This space is intentionally left blank)

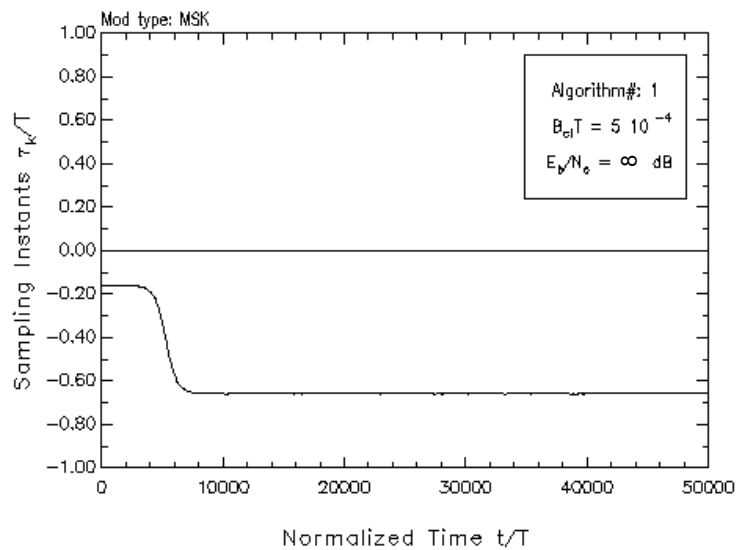


Fig. VI.37

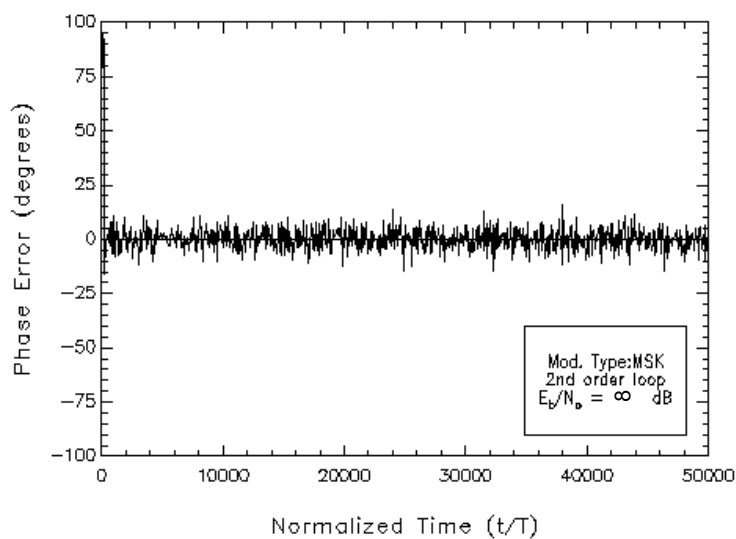


Fig. VI.38

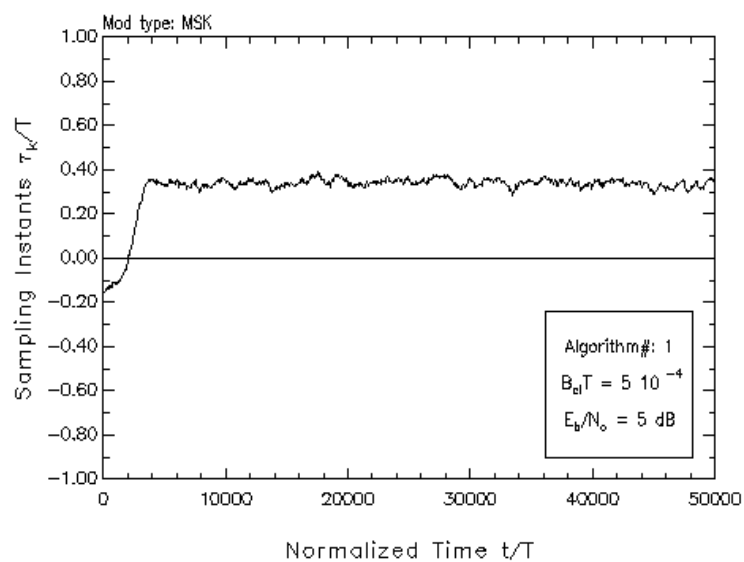


Fig.VI.39

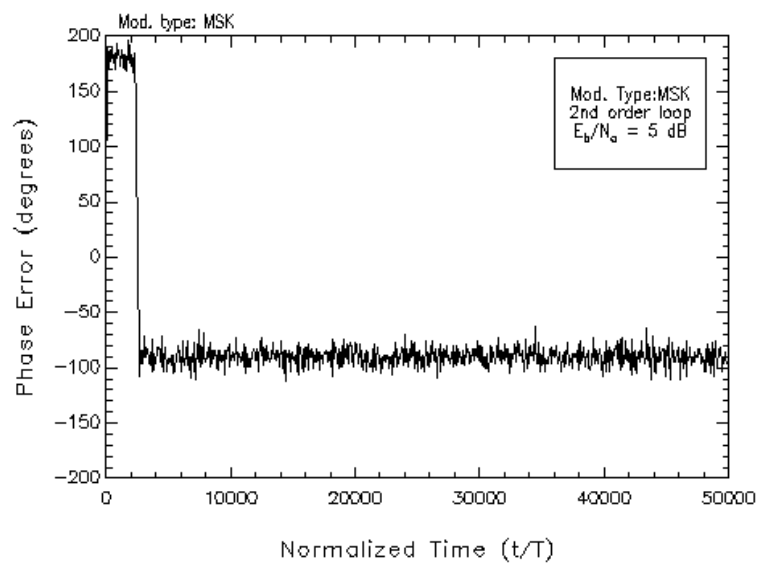


Fig.VI.40

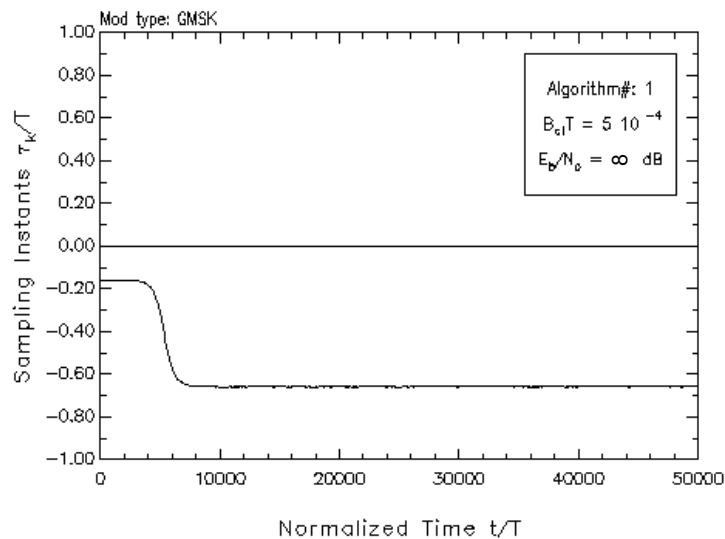


Fig. VI.41

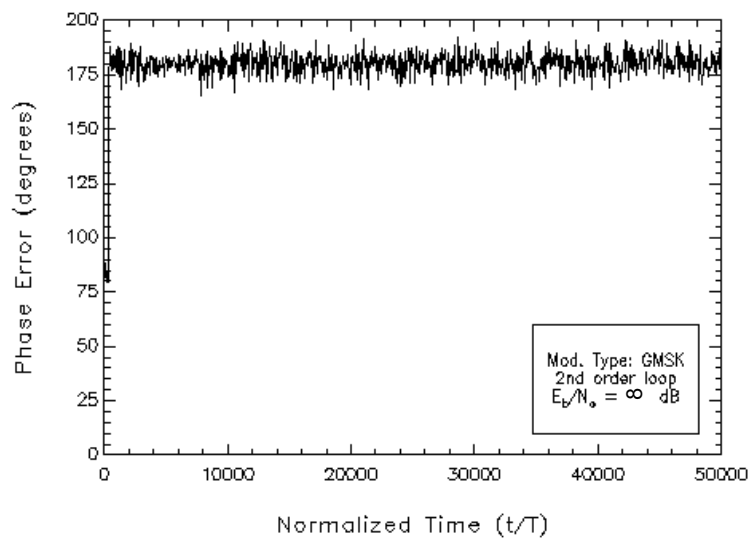


Fig.VI.42

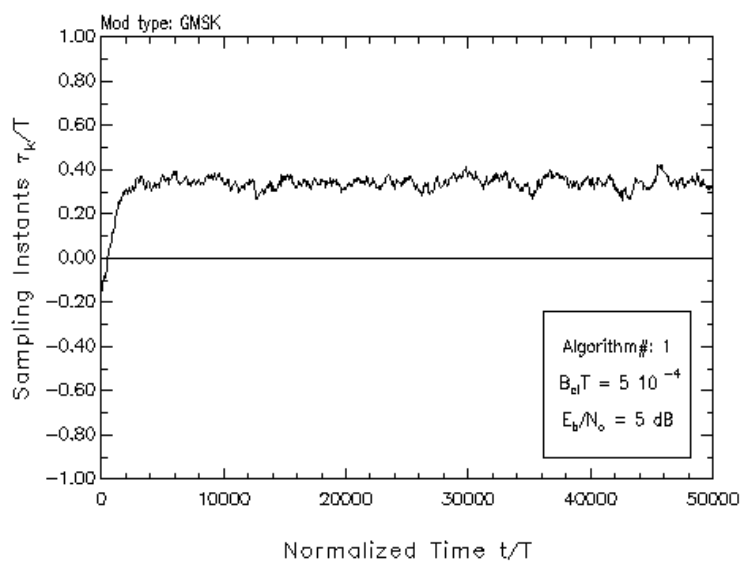


Fig.VI.43

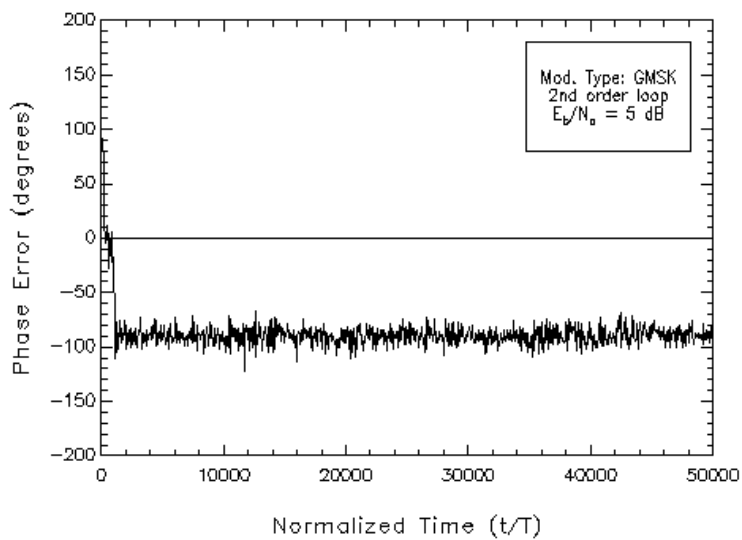


Fig.VI.44

•) OQPSK Modulation

We treat OQPSK as a special case because with this modulation the digital clock algorithm used with MSK and GMSK is no longer applicable. The analog clock regeneration scheme based on separate squaring of the baseband component introduced in the previous report is assumed here. As already stated, this clock synchronizer is sensitive to demodulation phase errors which may cause severe degradations of the amplitude of the regenerated timing wave. It is thus apparent that in this case phase recovery must *precede* clock extraction, so that we must resort to the hybrid phase recovery subsystem shown in Fig. VI.45. The essential difference between this scheme and that employed with MSK/GMSK is that now the loop error signal drives an NCO and the phase error correction occurs in analog form.

The jitter and BER curves for NYQ-OQPSK are reported in Figs. VI.46-47 for a phase loop bandwidth $B_{N0}T=0.02$ and a noise bandwidth of the resonant filter of the clock regenerator $B_{N\tau}T=10^{-3}$.

Figures VI. 48-51 illustrate the joint acquisition of clock and phase recovery systems. As with MSK, phase acquisition is remarkably fast due to the wide loop bandwidth ($B_{N0}T=0.02$). The timing waves in Figs. VI.49 and VI.51 correspond to a time segment of 1000 bit intervals after 9000 transient bits of the regenerated clock reference. The absence of amplitude modulation on the timing waves indicates that acquisition has already occurred.

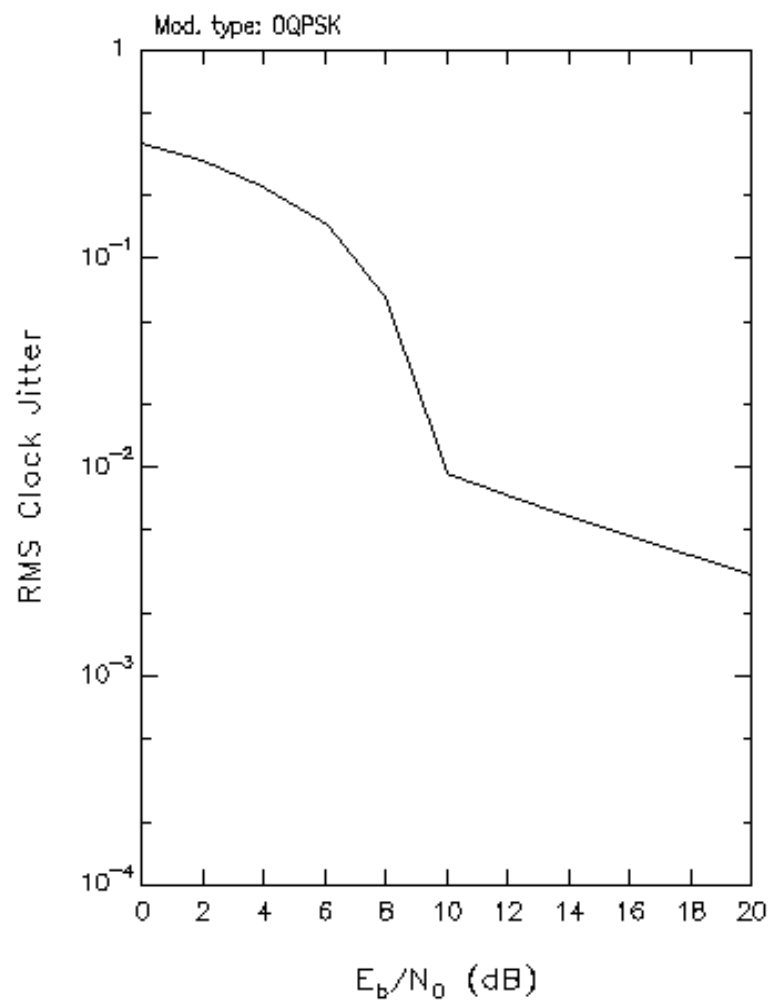


Fig.VI.46a

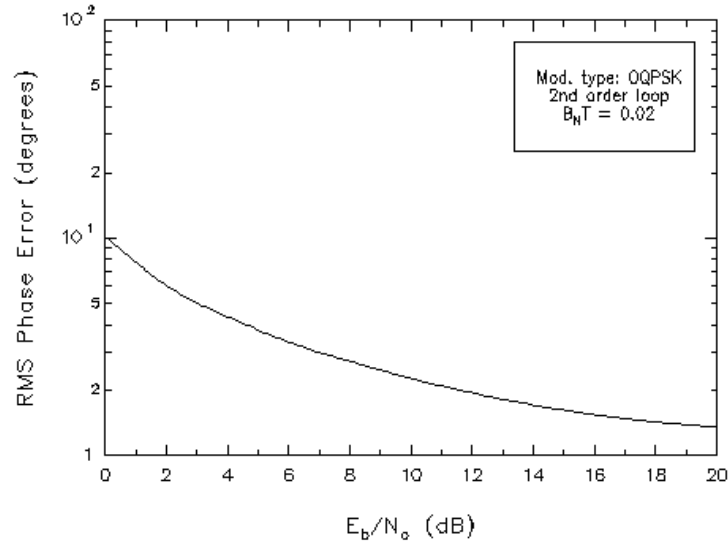


Fig.VI.46b

A further indication of the system performance is the eye diagram on the I/Q signal components. Figure VI.52 shows such a diagram for MSK and a second-order loop with $B_{N0}T=4 \cdot 10^{-2}$. It should be noted that, due to the digital nature of the phase recovery loop, the generic estimate $\hat{\theta}_k$ of the phase is constant over a symbol period. As a consequence, the time-diagram of the residual phase error θ_e is that of a piecewise-constant function with sudden phase jumps at each signaling interval. This may cause small discontinuities in the time-continuous eye diagram of the data signal when a residual frequency error is present, as is the case for Fig. VI.53.

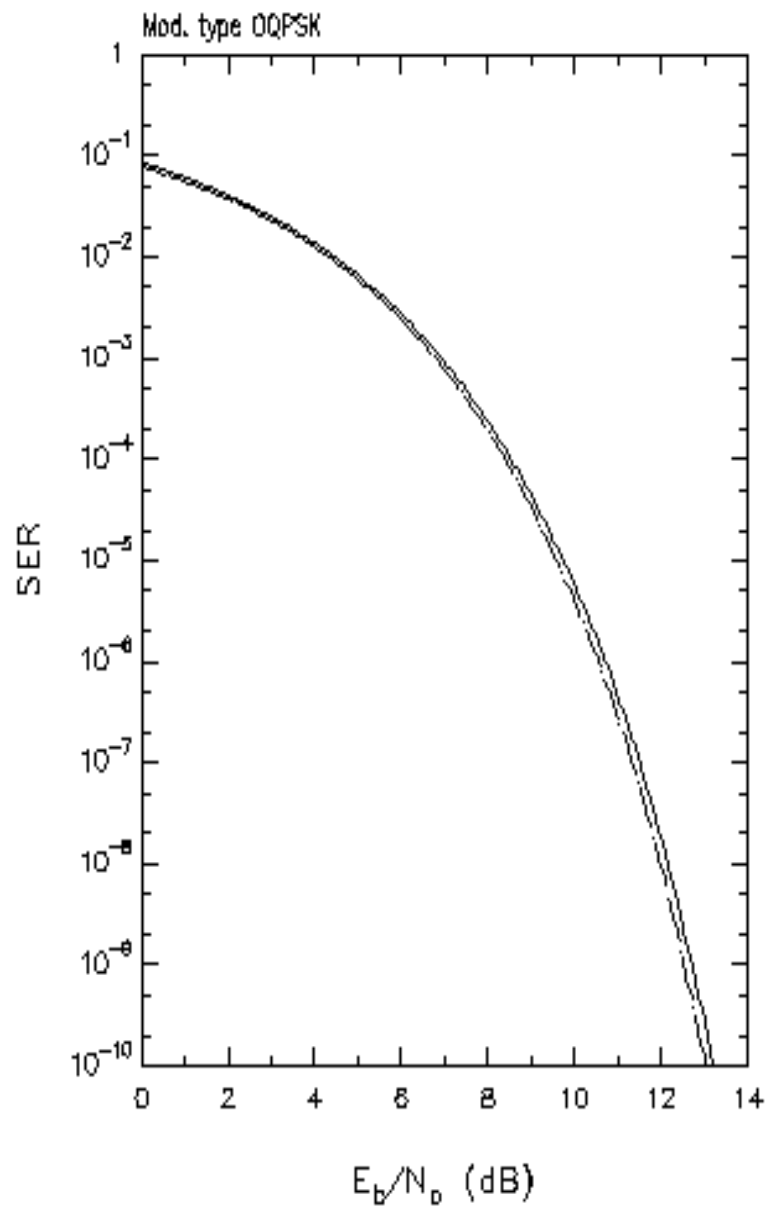


Fig.VI.47

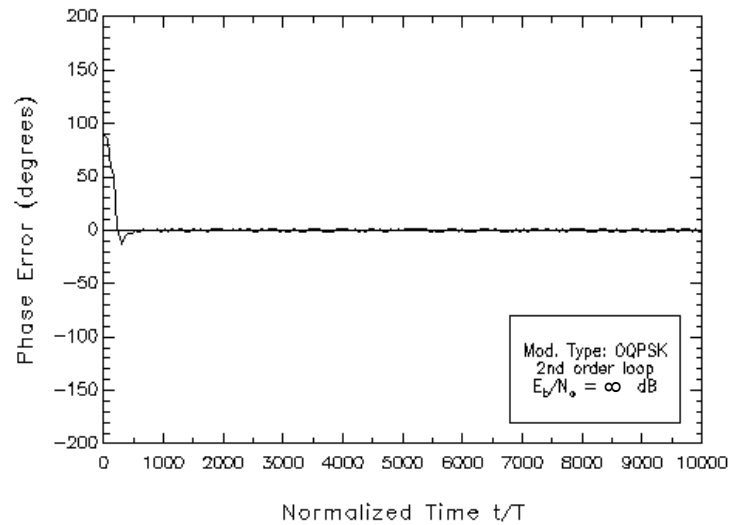


Fig.VI.48

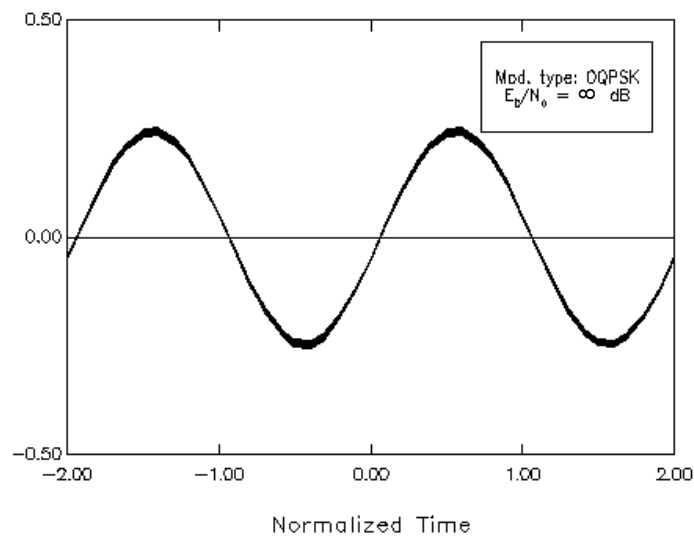


Fig.VI.49

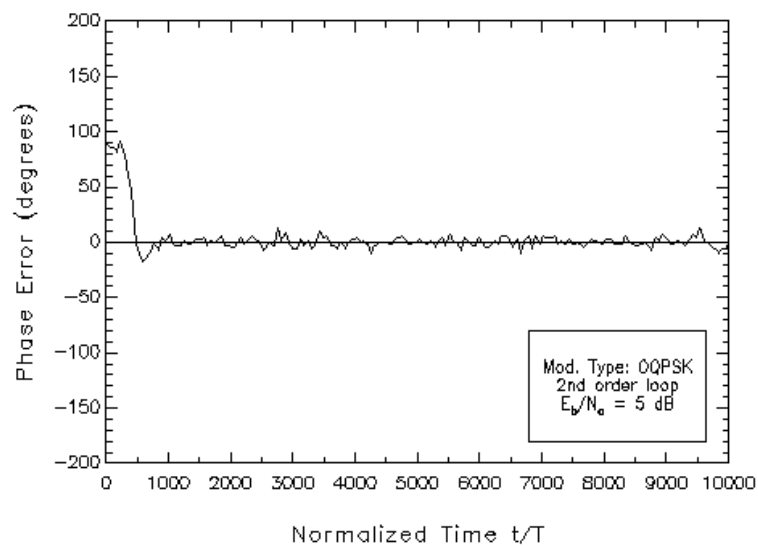


Fig.VI.50

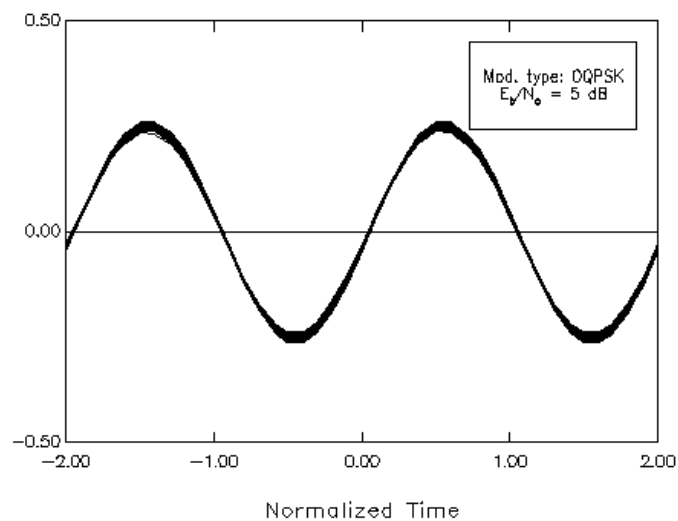


Fig.VI.51

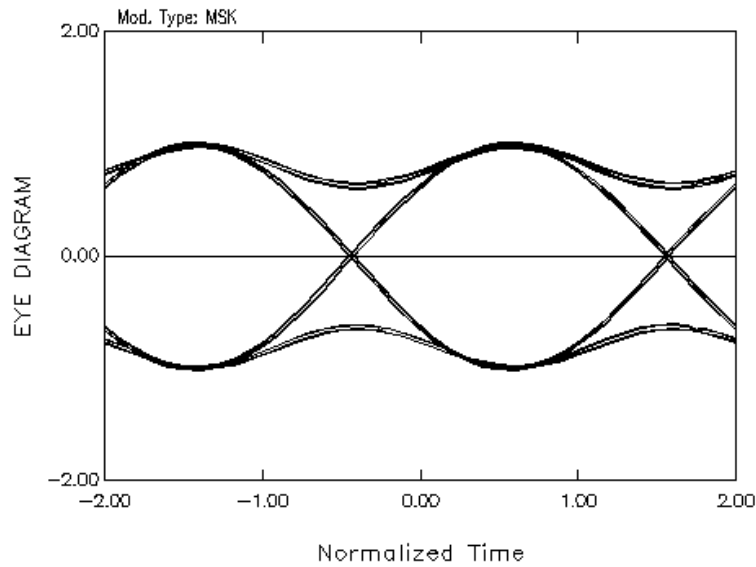


Fig. VI.52

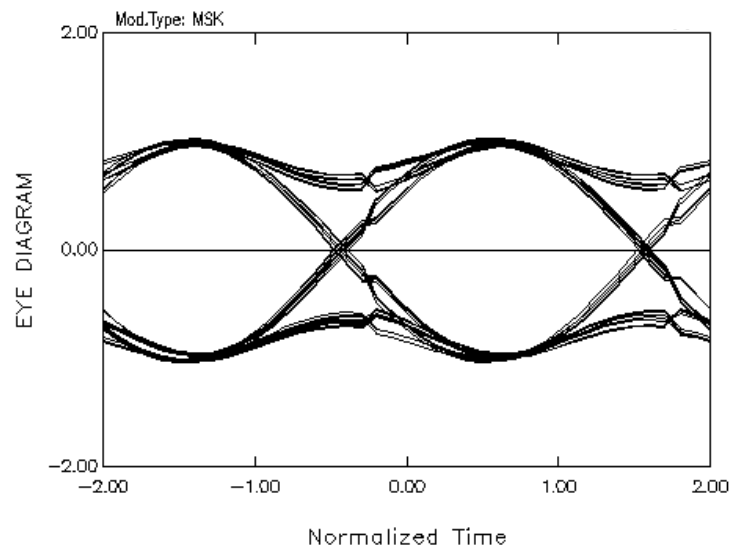


Fig. VI.53

VII

Joint Carrier Phase/Frequency Tracking

VII.1 Frequency Recovery Schemes

Automatic Frequency Control (AFC) loops are often used in receivers for modulated signals either to aid phase-lock loops in acquiring correct carrier frequency or, with differentially coherent receivers, to cope with Doppler shifts and oscillator instabilities. In particular, an AFC capability is required when low-data rate TDMA transmission is used in the presence of strong Doppler effects. The basic configuration of an AFC is shown in Fig. VII.1. The incoming signal is fed together with the VCO output to a frequency difference detector (FDD) so that an error voltage is generated which depends on the frequency difference f_d between the transmission carrier and the local reference. This error is processed in the loop filter and is used to control the VCO in a negative feedback loop.

Several types of FDDs are found in the literature. The rotational frequency detector is a first example [Mes79]. Another familiar FDD is the balanced quadricorrelator [Cah77], [Nat84], [Sim], [Gar83], [Gar85], [D'A90b], [Mey90]. Other schemes are the dual filter detector [Gar88], [Alb89] and a variant of the conventional phase detector [Sar88]. Finally, FDDs based on maximum likelihood estimation methods are studied [Gar90], [Mey90, Chap. 8].

In the following we will be concerned only with FDDs in the form of balanced quadricorrelators (BQs).

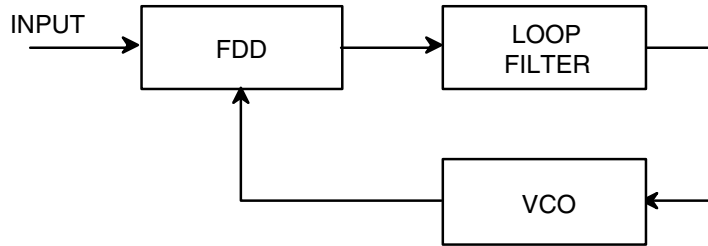


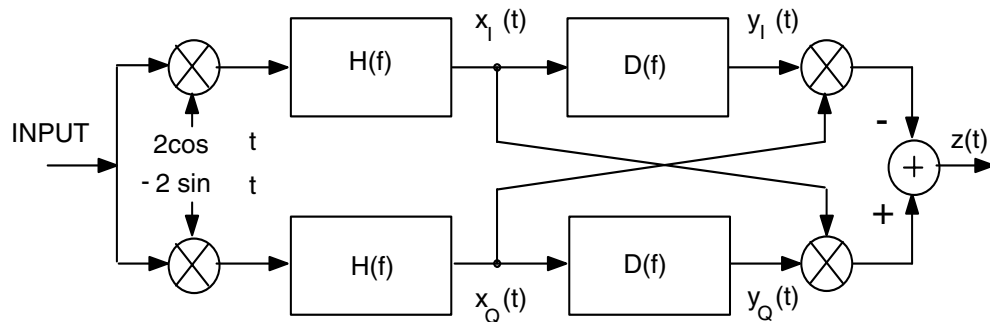
Fig VII.1

VII.2 BQ Description

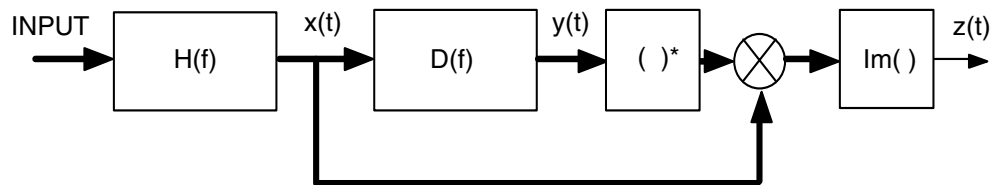
In Fig.VII.2 the passband (a) and the baseband equivalent (b) schemes of a BQ are shown (thick lines indicate complex baseband signals). The input to the circuit is the sum of a digitally modulated carrier plus wide-band Gaussian noise. The complex envelope $r(t)$ of the received signal is composed of AWGN $w(t)$ with PSD equal to N_0 and of a useful component :

$$s(t) = e^{j(\theta + 2\pi f_d t)} \sum_i [a_i g(t - i2T) + jb_i g(t - i2T - \epsilon T)] \quad (\text{VII.2.2})$$

where θ is the carrier phase, $f_d \triangleq f_c - f_0$ is the carrier frequency offset of the VCO, $g(t)$ represents the elementary pulse shape, $2T$ is the reciprocal of the symbol spacing, ϵ denotes the stagger coefficient ($\epsilon=0$ for non-staggered modulation and $\epsilon=1$ for staggered modulation) and finally a_i and b_i are binary data symbols.



(a)



(b)

Fig.VII.2

In the sequel a_i and b_i are modelled as zero-mean random variables with the following second- and fourth-order moments:

$$E\{a_i^2\} = E\{b_i^2\} \triangleq M_2 \quad (\text{VII.2.3})$$

$$E\{a_i^2 b_i^2\} \triangleq M_2^2 \quad (\text{VII.2.4})$$

where M_2 is some positive constant. Note that no specific hypothesis is made

on the coding scheme since the above moments are sufficient in the discussion to follow.

The above signal representation fits conventional QAM or PSK modulations. It also describes exactly linear staggered modulations, such as OQPSK and MSK, while it fits (nonlinear) generalized MSK in an approximate manner only. References [Lau86], [Lui90] indicate how to choose $g(t)$ so as to make (VII.2.2) the best mean-square approximation of a given generalized MSK signal.

The computation of the BQ output is straightforward. With the notations of Fig. VII.2 we define:

$$x(t) \triangleq x_I(t) + jx_Q(t) \quad (\text{VII.2.6})$$

$$y(t) \triangleq y_I(t) + jy_Q(t). \quad (\text{VII.2.7})$$

Then, assuming that sum-frequency components generated by the mixers are effectively suppressed by $H(f)$, one has:

$$x(t) = \sum_i [\tilde{a}_i q_1(t-i2T) + j\tilde{b}_i q_1(t-i2T-\epsilon T)] + w_1(t) \quad (\text{VII.2.8})$$

$$y(t) = \sum_i [\tilde{a}_i q_2(t-i2T) + j\tilde{b}_i q_2(t-i2T-\epsilon T)] + w_2(t) \quad (\text{VII.2.9})$$

where

$$\tilde{a}_i \triangleq a_i e^{j(\theta + 4\pi f_d i T)} \quad (\text{VII.2.10})$$

$$\tilde{b}_i \triangleq b_i e^{j[\theta + 4\pi f_d (i + \epsilon) T]} \quad (\text{VII.2.11})$$

$$q_1(t) \triangleq [g(t) e^{j2\pi f_d t}] \otimes h(t) \quad (\text{VII.2.12})$$

$$q_2(t) \triangleq [g(t) e^{j2\pi f_d t}] \otimes h(t) \otimes d(t) \quad (\text{VII.2.13})$$

$$w_1(t) \triangleq w(t) \otimes h(t) \quad (\text{VII.2.14})$$

$$w_2(t) \triangleq w(t) \otimes h(t) \otimes d(t). \quad (\text{VII.2.15})$$

In (VII.2.12)-(VII.2.15) $h(t)$ and $d(t)$ are the impulse responses of $H(f)$ and $D(f)$. Next it is easily checked that:

$$z(t) = \Im \{x(t) y^*(t)\} \quad (\text{VII.2.16})$$

where $\Im\{\cdot\}$ stays for "imaginary part of". Finally, inserting (VII.2.8)-(VII.2.9) into (VII.2.16) and rearranging yields:

$$z(t) = z_{SS}(t) + z_{SN}(t) + z_{NN}(t) \quad (\text{VII.2.17})$$

with:

$$\begin{aligned} z_{SS}(t) &\triangleq \Im \left\{ \sum_i [\tilde{a}_i q_1(t-i2T) + j\tilde{b}_i q_1(t-i2T-\epsilon T)] \right. \\ &\quad \times \sum_i [\tilde{a}_i^* q_2^*(t-i2T) - j\tilde{b}_i^* q_2^*(t-i2T-\epsilon T)] \left. \right\} \end{aligned} \quad (\text{VII.2.18})$$

$$\begin{aligned} z_{SN}(t) &\triangleq \Im \left\{ w_1(t) \sum_i [\tilde{a}_i^* q_2^*(t-i2T) - j\tilde{b}_i^* q_2^*(t-i2T-\epsilon T)] \right\} \\ &\quad + \Im \left\{ w_2^*(t) \sum_i [\tilde{a}_i q_1(t-i2T) + j\tilde{b}_i q_1(t-i2T-\epsilon T)] \right\} \end{aligned} \quad (\text{VII.2.19})$$

$$z_{NN}(t) \triangleq \Im \left\{ w_1(t) w_2^*(t) \right\}. \quad (\text{VII.2.20})$$

Equation (VII.2.17) emphasizes the fact that $z(t)$ comes from the interaction of signal with itself (S×S), of signal with noise (S×N) and of noise with itself (N×N).

The control signal generated by the BQ is the DC-component of $z(t)$ and is a function of the carrier frequency offset f_d . Such a function, say $S(f_d)$, is the S-curve of the BQ. Superimposed on $S(f_d)$ is a random disturbance

$$n(t) \triangleq z_{SS}(t) + z_{SN}(t) + z_{NN}(t) - S(f_d) \quad (\text{VII.2.21})$$

which affects the performance of the AFC. In the next section we will compute the expression of $S(f_d)$ in terms of the various system parameters.

VII.3 S-Curve and Spectral Analysis

A. S-Curve.

The S-curve is obtained by taking the expectation (over data and noise) of $z(t)$, conditioned on a fixed value of f_d , and then averaging over a symbol period $2T$:

$$S(f_d) = \frac{1}{2T} \int_0^{2T} E\{z(t)|f_d\} dt. \quad (\text{VII.3.1})$$

The operations indicated in (VII.3.1) are straightforward and, after some labour, we get to the following result [D'A90b]:

$$S(f_d) = \frac{M_2}{T} \int_{-\infty}^{+\infty} |G(f)|^2 P(f+f_d) df \quad (\text{VII.3.2})$$

with

$$P(f) \triangleq |H(f)|^2 \Im \{D^*(f)\}. \quad (\text{VII.3.3})$$

Expression (VII.3.2) can be seen as the integral of the baseband data signal spectrum $(M_2/T)|G(f)|^2$ weighed by the function $P(f+f_d)$. The two factors must overlap one another to give a non-zero $S(f_d)$ and, as is apparent from Fig. VII.3, this happens if f_d is less than B_S+B_P in absolute value, B_S being the signal bandwidth and $2B_P$ the width of $P(f)$.

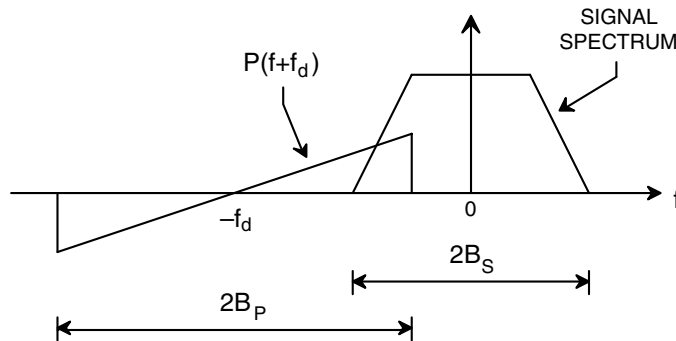


Fig.VII.3

In the sequel, attention will be concentrated on bandlimited signals with B_S on the order of $1/2T$. Also, from tracking performance considerations

[D'A90c] it is possible to show that B_p on the order of $1/2T$ is a suitable choice. In conclusion, for the cases of interest in this report the S-curves extend approximately within $\pm 1/T$ around the origin.

It should be noted that the right-hand side of (VII.3.3) does not depend on the stagger coefficient ε . This means that $S(f_d)$ is the same for staggered or non-staggered signals, provided that they have the same spectrum (i.e. the same elementary pulse shape $g(t)$). Also, it is easily recognized from (VII.3.3) that $P(f)$ is an odd function of frequency and therefore the S-curve vanishes at the origin $f_d=0$ for any signal with a symmetric spectrum around the carrier frequency.

In the vicinity of the origin the S-curve can be approximated by a straight line whose slope A is obtained by taking the derivative of (VII.3.2) with respect to f_d at the origin:

$$A \triangleq \left. \frac{dS(f_d)}{df_d} \right|_{f_d=0} = \frac{M_2}{T} \int_{-\infty}^{+\infty} |G(f)|^2 \dot{P}(f) df. \quad (\text{VII.3.4})$$

where $\dot{P}(f)$ represents the frequency derivative of $P(f)$.

B. Spectral analysis.

When the AFC is operating in the steady state, the VCO frequency undergoes fluctuations $\Delta(t)$ around an average value which equals the incoming carrier frequency. As is known (see e.g. [Mey90], Chap. 8) $\Delta(t)$ is related to the noise $n(t)$ generated by the BQ through $H_{EQ}(f)$, the equivalent transfer function of the loop. In fact $\Delta(t)$ can be seen as the output of $H_{EQ}(f)$ when driven by $n'(t) \triangleq n(t)/A$ and therefore the mean-square value of $\Delta(t)$ is easily computed in terms of $H_{EQ}(f)$ and of the power spectral density of $n'(t)$.

The expression of $H_{EQ}(f)$ is:

$$H_{EQ}(f) \triangleq \frac{AKF(f)}{1 + AKF(f)} \quad (\text{VII.3.5})$$

where K is the gain of the VCO and $F(f)$ represents the transfer function of the loop filter.

The derivation of the spectral density of $n'(t)$ is not straightforward (see [D'A90c] for staggered modulations and [D'A90b] for nonstaggered modulations). We have not pursued this topic further because of overwhelming complexity with respect to our goal. However it is important to point out that high values of self-noise spectrum are associated with staggered modulations [D'A90c]. This agrees with the claim [Gar88]-[Gar90] that frequency tracking with staggered signals is a comparatively difficult task. From now on we shall consider staggered modulations only and therefore we shall always assume a unity value for the stagger coefficient ϵ .

VII.4 Numerical Results for an Elementary Case

Before examining the problem of the BQ filter design, it is instructive to consider an elementary case. Let us assume an MSK modulation format, an ideal low pass filter for $H(f)$ and a delay of T seconds for $D(f)$. The bandwidth of $H(f)$ is taken sufficiently large so that the signal is passed undistorted. We can write the complex envelope of the transmitted signal in the following form :

$$s(t) = e^{j(\theta + 2\pi f_d t)} \sum_i \{a_i g(t - i2T) + jb_i g[t - (2i+1)T]\} \quad (\text{VII.4.1})$$

where

$$g(t) = \text{rect}\left(\frac{t-T}{2T}\right) \cos\left(\frac{\pi t}{2T}\right) \quad (\text{VII.4.2})$$

and a_i and b_i are binary zero-mean random variables whose values are ± 1 . In this simple case it is easily shown that the expectation of $z(t)$ over data and noise, conditioned on a fixed value of f_d , is given by:

$$E\{z(t)|f_d\} = \sin(2\pi f_d t) \sum_i g[t - (2i+1)T] \{g(t - i2T) + g[t - 2(i+1)T]\} \quad (\text{VII.4.3})$$

Inserting (VII.4.3) into (VII.3.1) we obtain, after some labour, the following expression for the S-curve (fig. VII.4):

$$S(f_d) = \frac{1}{\pi} \sin(2\pi f_d T) \quad (\text{VII.4.4})$$

It should be noted that the presence of multiple lock points is due to the assumption that $H(f)$ is broad-band. In fact, if we replace $H(f)$ with a four-pole Butterworth filter with one-sided bandwidth $1/2T$ (leaving $D(f)$ unchanged), the S-curve has only one stable lock point, as shown in Fig. VII.5.

As a matter of fact the S-curve beyond $f_d = \pm 1/T$ vanishes because of narrow-band filtering.

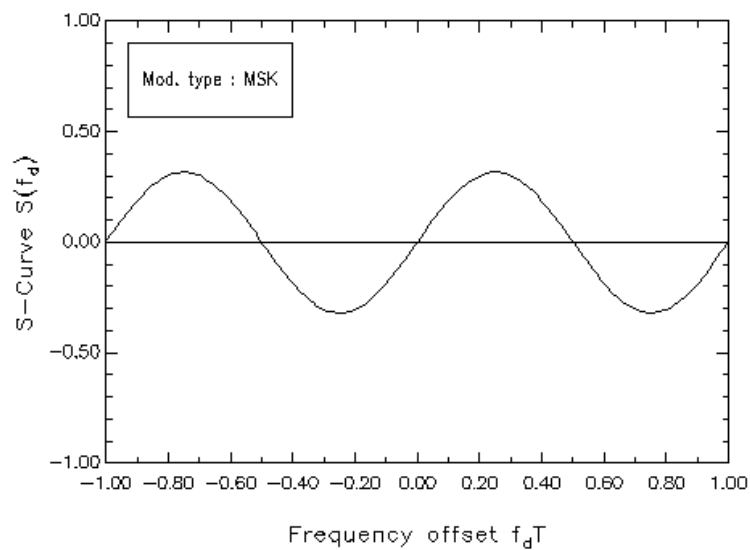


Fig.VII.4

(This space is intentionally left blank)

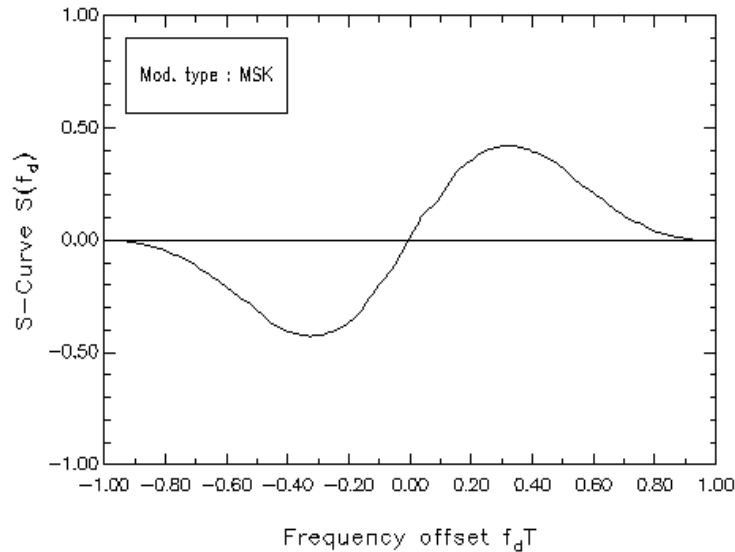


Fig.VII.5

VII.5 BQ Filter Design

It is natural to look for conditions on BQ filters and loop parameters so as to reduce fluctuations in the VCO frequency. It has been shown [D'A90c] and [D'A90b] that, in a frequency tracking loop operating in the steady state, self-noise can be eliminated or greatly reduced by proper design of the BQ filters. This result is valid for both staggered and non-staggered modulations. In the following we give design criteria for the BQ filters that allow substantial self-noise reductions. The results are based on the analysis reported in [D'A90b]-[D'A90c].

A. MSK and GMSK modulation formats

In this case we take $D(f)$ as a delay of T seconds and $H(f)$ as the cascade of a differentiator and a two-pole Butterworth low-pass filter with one sided bandwidth $1/2T$. The corresponding S-curves, obtained by computer

simulations, are shown in Fig.VII.6 and Fig.VII.7.

B. OQPSK modulation format

For this format we take $D(f)$ as a $2T$ delay and $H(f)$ as a two-pole Butterworth bandpass filter with one-sided bandwidth $0.1/T$ and central frequency $0.3/T$. The corresponding S-curve is shown in Fig.VII.8.

Figure VII.9 shows the RMS normalized frequency jitter vs. E_b/N_o for these choices of BQ filters and for a normalized loop noise bandwidth $B_{EQ}T = 10^{-3}$ (frequency normalization is made with respect to $1/T$ so that, if $\Delta(t)$ is the un-normalized frequency jitter, its normalized counterpart is $T\Delta(t)$). These plots are drawn for comparison purpose only, since the final implementation of the AFC in our receiver requires a much narrower loop bandwidth to attain a tolerable residual steady-state frequency jitter.

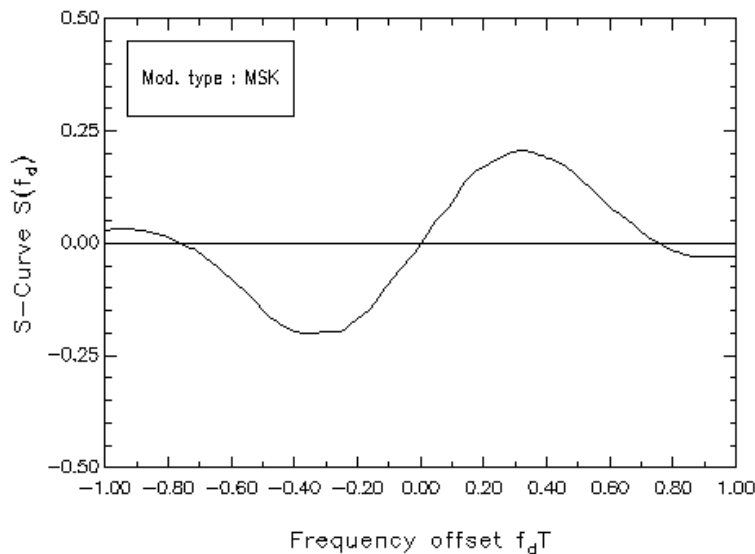


Fig.VII.6

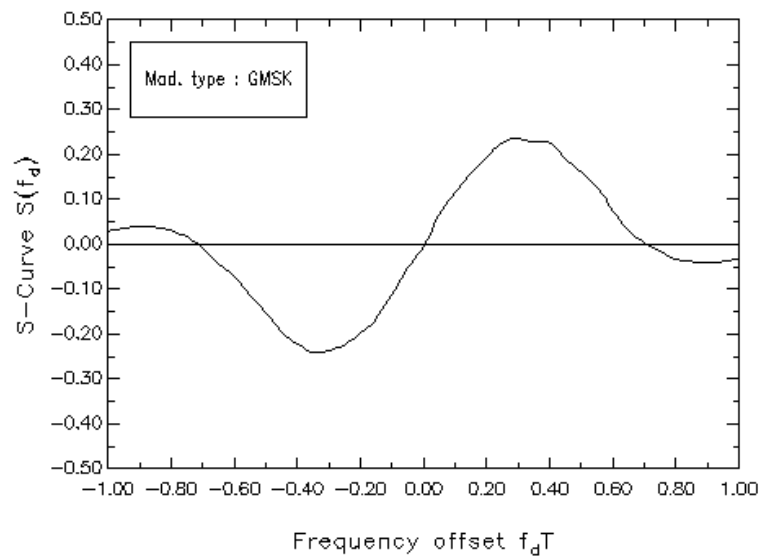
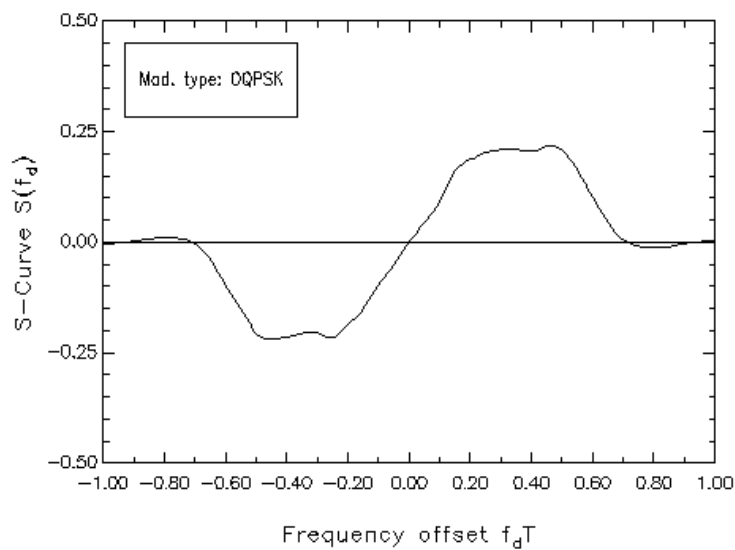
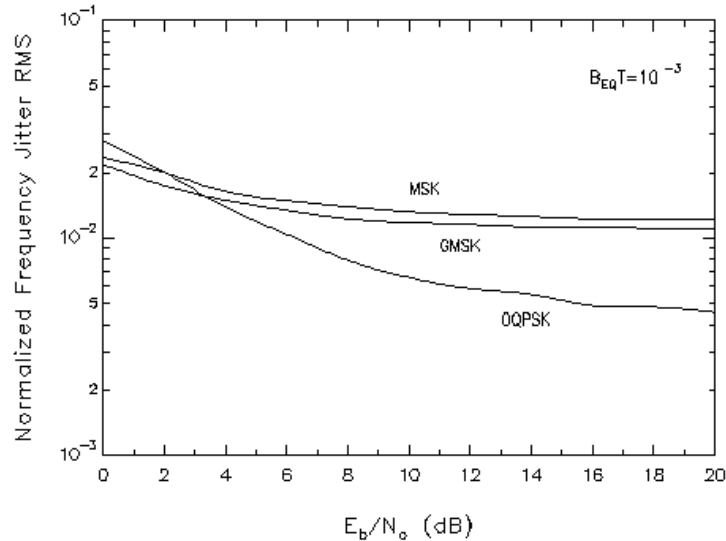


Fig.VII.7



FigVII.8



FigVII.9

VII.6 Joint Frequency and Phase Carrier Recovery

In the second half of the report we concentrated on the carrier acquisition/tracking subsystem. In particular the following two parts have been considered:

- 1] An automatic frequency control loop (AFC).
- 2] A second-order decision-aided carrier phase recovery loop (see also chapter VI).

Notice that the AFC cannot be designed separately from the carrier recovery loop. In the tracking mode, in fact, the AFC adds frequency jitter to the demodulation carrier so that the bandwidths of the AFC and of the phase recovery loop must be jointly chosen. On one side in fact the AFC bandwidth should be kept as narrow as possible so as to limit frequency jitter. At the

same time however it should be wide enough to limit acquisition time after a loss of lock and/or to follow rapid changes in frequency due to Doppler shifts. In its turn the bandwidth of the phase recovery loop must be chosen as a compromise between frequency tracking capability and noise suppression.

VII.7 Analysis and Design of the Carrier Phase Recovery Loop

The carrier phase recovery subsystem implemented in the final version of this study is a decision-directed second-order loop. The importance of the adoption of a second-order loop (instead of a first-order) will be apparent in Section VII.8 when the impact of Doppler shifts on the receiver performance is analyzed in detail. A thorough description of a second-order tracking loop can be found in [Gar83] and a simpler analysis of the linearized loop is reported below.

The scheme of the phase-recovery loop is shown in Fig.VII.10. We assume a small phase error. The PED operates on the signal samples and provides, every T seconds, an indication of the offset between the received signal phase θ_i and the VCO phase θ_0 . Assuming a proportional-plus-integral loop filter

$$F(z) = 1 + \frac{\alpha}{1 - z^{-1}} \quad (\text{VII.7.1})$$

where $\alpha > 0$ is the gain of the integral branch, the loop behavior is described by the following equations:

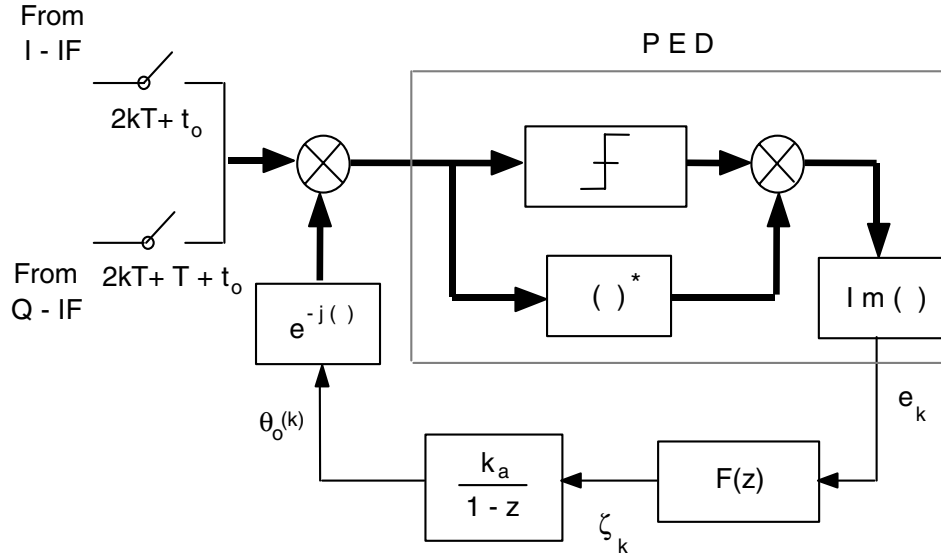


Fig.VII.10

$$e_k = A (\theta_{0k}(k) - \theta_i(k)) \quad (VII.7.2)$$

$$\zeta_k = \zeta_{k-1} + (\alpha + 1) e_k - e_{k-1} \quad (VII.7.3)$$

$$\theta_0(k+1) = \theta_0(k) - K_a \zeta_k \quad (VII.7.4)$$

Let $K \triangleq A K_a$ (A is the slope of the S-curve in the origin) denote the total loop gain. The closed-loop transfer function $H(z)$ can be obtained by Z-transforming equations (VII.6.2), (VII.6.3) and (VII.6.4):

$$H(z) = \frac{\Theta_0(z)}{\Theta_i(z)} = \frac{K[z(1 + \alpha) - 1]}{z^2 + [K(1 + \alpha) - 2]z + (1 - K)} \quad (VII.7.5)$$

The loop has a zero at

$$z_0 = \frac{1}{1+\alpha} , \quad 0 < z_0 < 1 \quad (\text{VII.7.6})$$

and two poles. The plot of the root locus is shown in Fig.VII.11. In this figure the stability boundary is shown as a dashed circle, while the locus is the solid curve. For $K = 0$ the two poles coincide at $z = 1$. As K increases, the poles move on a circle with center at $z = z_0$ and radius $1 - z_0$. When K assumes the value $4z_0(1 - z_0)$, the poles coincide at $z = -1 + 2z_0$, then, for larger values of K , a pole moves on the real axis towards the z_0 , while the other moves on the same axis towards $-\infty$. This latter pole crosses the unit circle for $K = 4z_0/(1+z_0)$ which, therefore, represents the stability limit of the loop.

Our problem is to specify the loop gain K and the zero location so as to obtain adequate noise immunity and a good dynamical behaviour. For a digital transfer function $H(z)$ the (one sided) noise bandwidth B_L is defined as

$$B_L = \frac{1}{2T |H(1)|^2} \int_{-\pi/T}^{\pi/T} |H(e^{j2\pi fT})|^2 df \quad (\text{VII.7.7})$$

Inserting (VII.6.5) into (VII.6.7) does not lead to a simple expression for the noise bandwidth. However the result can be put in a simple form in the special case of coincident poles. This is a practical case because a slight overdamping of the loop is beneficial when Gaussian noise and oscillator flicker noise are the main disturbances [Gar83].

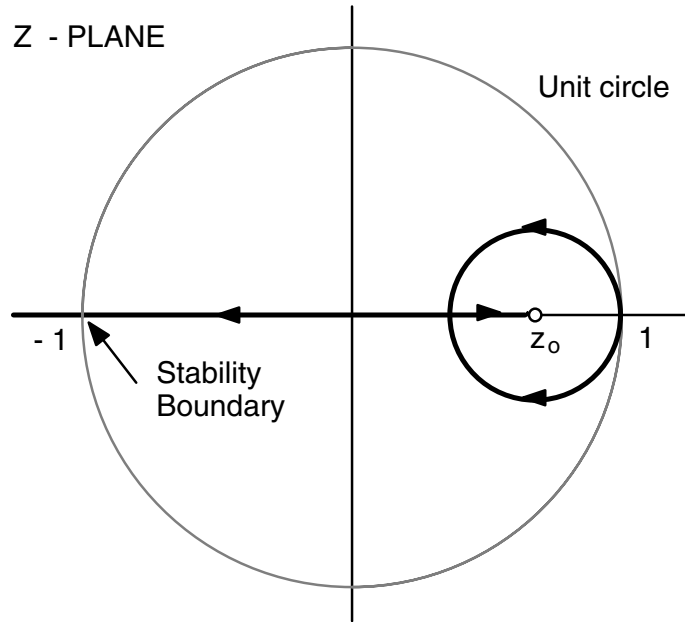


Fig.VII.11

Under the assumption of coincident poles, i.e $K = 4z_0(1-z_0)$, it can be shown [Gar83] that :

$$B_L T = \frac{1}{4} \frac{(1 - z_0) (1 + 2z_0 + 2z_0^2)}{z_0^3} \quad (\text{VII.7.8})$$

From now on we shall always assume $K = 4z_0(1-z_0)$, i.e. coincident poles, and we shall use (VII.6.8) to determine the noise bandwidth.

Next we consider the loop design problem. For $B_L T$ fixed, it is possible to determine the corresponding value of z_0 by means of equation (VII.6.8). Then the corresponding value of α is found from equation (VII.6.6), while K

follows immediately from the condition of pole coincidence.

For each modulation format the normalized noise bandwidth $B_L T$ has been chosen narrow enough so as to determine negligible performance degradation on the bit error rate (BER) curve at some value of the energy per bit to noise spectral density E_b/N_0 and with ideal frequency and clock references. The allowed performance degradation is 0.2 dB while the reference value of E_b/N_0 is 6.8 dB, which corresponds to $BER=10^{-3}$ for ideal matched filter detection.

The values of the normalized noise bandwidth $B_L T$ satisfying the above mentioned criterion have been computed by a trial-and-error method via computer simulation and the corresponding BER degradations have been assessed (using the "worst case bound") from the eye-diagram of the received signal after phase correction. These values of $B_L T$ as well as those of other meaningful parameters are shown in Table I. As an example of our procedure, fig.VII.12 shows the eye diagram of an MSK signal at the output of the matched filter, assuming ideal phase and frequency recovery. Fig.VII.13 shows the same diagram after insertion of the carrier phase recovery with normalized noise bandwidth $B_L T=0.04$. A small decrease in eye-opening is apparent.

VII.8 Choice of the AFC Bandwidth

Having chosen the noise bandwidth of the phase recovery loop, the AFC bandwidth has to be selected next. Our approach consists in designing the AFC so as to limit the amount of frequency jitter in the reference signal. In other words the loop bandwidth has to be chosen narrow enough so as to not affect appreciably the eye-diagram of the received signal.

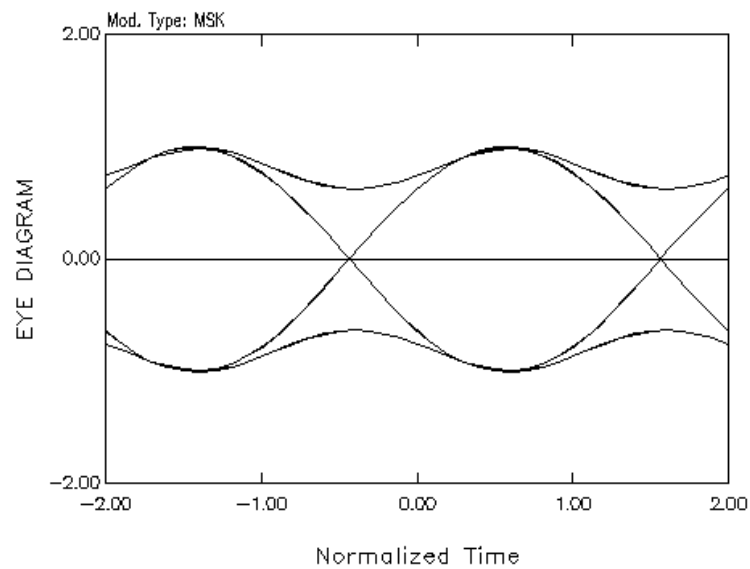


Fig.VII.12

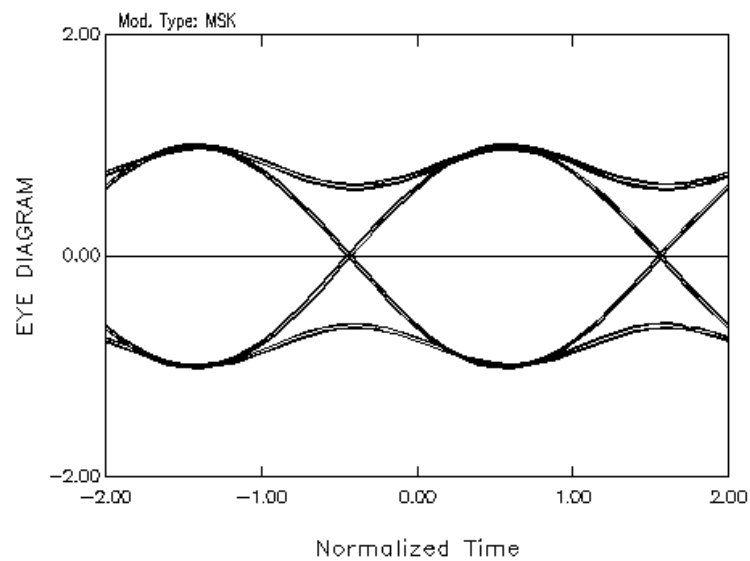


Fig.VII.13

Mod. type	$B_L T$	z_0	α	K_a	K
<i>OQPSK</i>	0.02	0.984	0.0163	0.032	0.065
<i>MSK</i>	0.04	0.969	0.032	0.062	0.128
<i>GMSK*</i>	0.04	0.969	0.032	0.063	0.128

TABLE I

* the normalized modulation filter bandwidth is assumed to be $\beta T=0.5$

The resulting loop bandwidth values are reported in Table II for each modulation format. It should be noted that while this choice ensures good compensation of the frequency jitter, it is not clear at this stage whether the AFC can track the actual Doppler accelerations. This problem will be treated in Section VII.10.

Modulation format	OQPSK	MSK	GMSK
$B_{BQ}T$	$1.25 \cdot 10^{-5}$	$0.625 \cdot 10^{-5}$	$0.52 \cdot 10^{-5}$

TABLE II

VII.9 Doppler Effect for LEO Satellites

A simplified model for the Doppler effect affecting the satellite-to-earth radio link is described in [ESA90]. The results provided in the above reference can be summarized as follows. Let us assume that the orbit of a

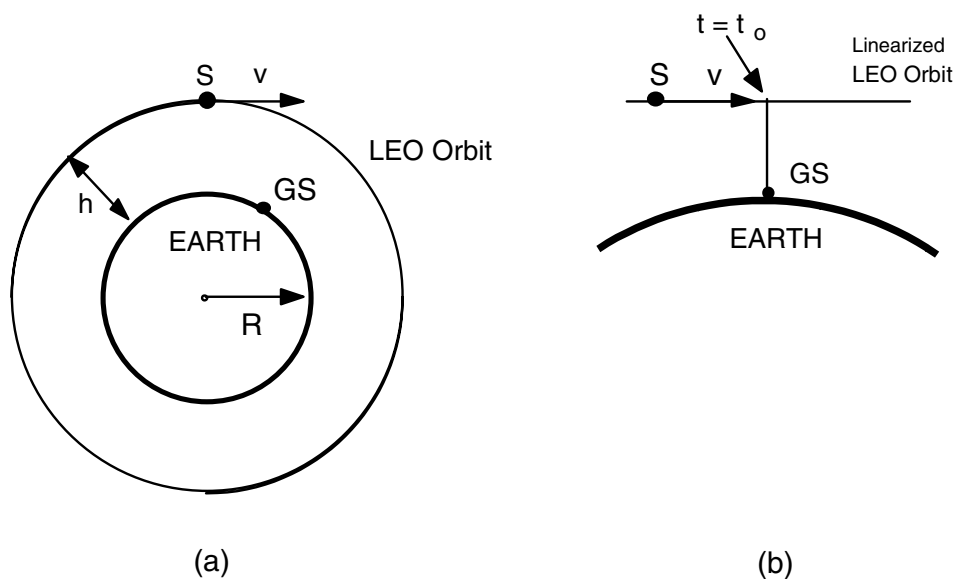


Fig.VII.14

Low Earth Orbit (LEO) satellite can be modelled as shown in Fig.VII.14 (a). The same model is valid for elliptical orbits, at least in the region next to the perigee. We want to compute the satellite (S) carrier frequency received at the ground station (GS) during the revolution of the spacecraft around the earth.

Our aim is to evaluate the maximum Doppler shift and acceleration in the received signal. These are particularly meaningful parameters for the design of the carrier acquisition & tracking subsystems. In fact the carrier acquisition subsystem design must accommodate for maximum frequency shift, while the tracking subsystem is required to work properly even in the presence of worst-case Doppler acceleration. We also suppose that the GS lies in the same plane containing the centre of the earth and the spacecraft and we adopt a linearized model for the satellite orbit like that shown in Fig.VII.14 (b) (which is a good approximation for a LEO). In these conditions it is easily shown [ESA90] that the following relationships hold true:

$$f_c = f_{co} k_d(t) \quad (VII.8.1)$$

$$\alpha_c \triangleq \frac{df_c(t)}{dt} = f_{co} \frac{dk_d(t)}{dt} \quad (VII.8.2)$$

$$k_d(t) \approx 1 - \frac{(t - t_o)^2 v^2}{c \sqrt{h^2 + (t - t_o)^2 v^2}} \quad (VII.8.3)$$

$$\frac{dk_d(t)}{dt} \approx - \frac{(vh)^2}{c [h^2 + (t - t_o)^2 v^2]^{3/2}} \quad (VII.8.4)$$

where f_{co} is the transmitted carrier frequency, α_c is the Doppler acceleration, f_c is the received carrier frequency and f_d is the Doppler shift ($f_d \triangleq f_c - f_{co}$). In these equations c is the light speed, v is the spacecraft speed, h the satellite altitude measured from the earth surface and t_o is the overhead pass epoch. These formulas are valid only in a short time interval centered at t_o when

Doppler frequency acceleration is maximum and thus the carrier tracking subsystem operates in the most critical conditions. In particular, from (VII.8.4) we obtain the following equation for the maximum Doppler acceleration:

$$\alpha_c^M \triangleq f_{co} \frac{dk_d(t_o)}{dt} \simeq -f_{co} \frac{v^2}{ch} \quad (\text{VII.8.5})$$

In the present study we only consider the worst case of a low-orbiting satellite, i.e. a spacecraft operating in the following three scenarios:

- a) $h = 200 \text{ km}, v=10 \text{ km/s}, R = 64 \text{ kb/s}$ (VII.8.6)
- b) $h = 200 \text{ km}, v=10 \text{ km/s}, R = 128 \text{ kb/s}$ (VII.8.6)
- c) $h = 200 \text{ km}, v=2 \text{ km/s}, R = 64 \text{ kb/s}$ (VII.8.6)

Figures VII.15 and VII.16 show the corresponding normalized Doppler shift and the accelerations for the scenarios (a) and (b) computed by means of equations (VII.8.1)-(VII.8.4) (it is assumed $t_o = 0$). The normalization is made with respect to f_{co} for the Doppler shift f_d and with respect to α_c^M for the Doppler acceleration.

In order to ease computer simulations, we adopted a piecewise linear approximation for the curves of fig.VII.15. The result of this approximation can be summarized analytically as follows:

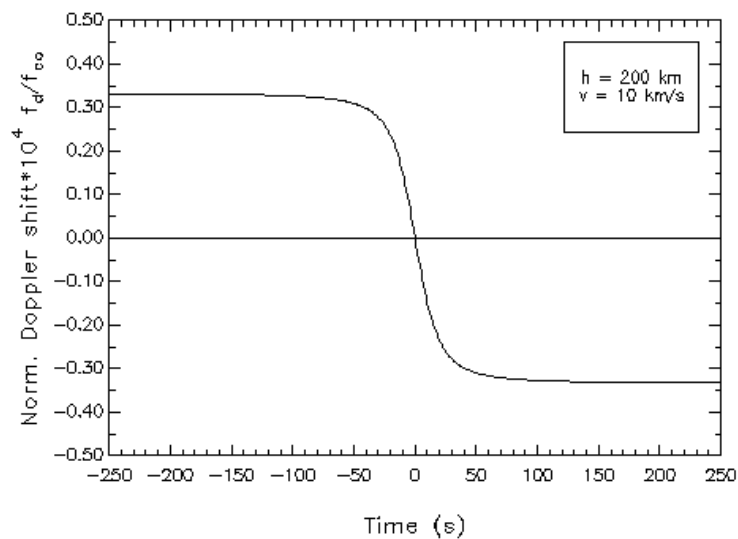


Fig.VII.15

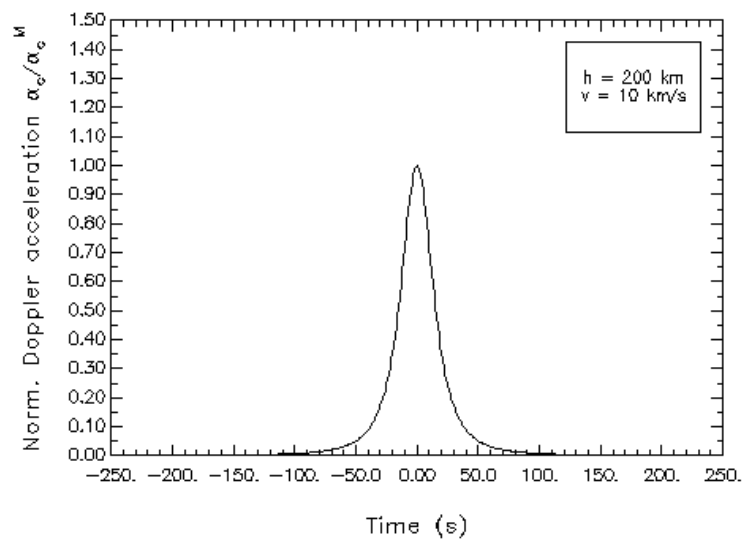


Fig.VII.16

$$f_d / f_{co} = \begin{cases} \alpha_0, & |t| > \tau \\ \alpha_0 \frac{t}{t_o}, & |t| \leq \tau \end{cases} \quad (\text{VII.8.7})$$

$$\frac{1}{\alpha_c^M} \frac{df_c(t)}{dt} = \begin{cases} 0, & |t| > \tau \\ 1, & |t| \leq \tau \end{cases} \quad (\text{VII.8.8})$$

Considering (VII.8.6) we can assume the following values for the parameters τ and α_0 :

$$\tau = 20 \text{ sec}$$

$$\alpha_0 = 3.33 \cdot 10^{-5}$$

for the scenarios (a) and (b), while for the scenario (c) we have

$$\tau = 100 \text{ sec}$$

$$\alpha_0 = 6.67 \cdot 10^{-6}$$

It is apparent that in our approximation the Doppler acceleration remains constant at its maximum value over the time interval $(-\tau, \tau)$. For a carrier frequency at $f_{co} = 2.1 \text{ GHz}$ we have $\alpha_c^M = -3500 \text{ Hz/sec}$ for cases (a) and (b) and $\alpha_c^M = -140 \text{ Hz/sec}$ for the case (c).

VII.10 Impact of Doppler Shifts on Frequency Tracking Subsystem Performance

The presence of large Doppler accelerations represent an important factor in the design of the AFC because small bandwidths in this subsystem may impair its tracking capabilities in the presence of fast carrier frequency

changes. For this reason we have checked the AFC Doppler tracking capability by computer simulation. The results are given in the next section.

VII.11 Computer Simulation Results

In this section we show that the carrier phase and frequency recovery subsystems designed according to the above criteria represent a satisfactory solution for the challenging synchronization problems of LEO satellites. First we study the AFC when the received signal is modulated by an hypothetical Doppler frequency ramp and then we test the system operation when the phase recovery subsystem is inserted. Throughout this Section, ideal clock recovery is assumed.

For each of the selected modulation formats, namely MSK, GMSK and OQPSK, and for each of the cited three scenarios, we monitor the behaviour of the AFC loop when the incoming signal is affected by a piecewise linear Doppler Shift as described in Sect. VII.9. Figures VII.17 -VII.22 show Doppler shift (DS), VCO Frequency (VF) and BQ output (BQo) vs. time for cases (a) and (b). The BQ output is proportional to the residual frequency error (i.e., the difference between the Doppler shift and the VCO frequency). The slope of the "Doppler ramp" is chosen according to the numerical values given in Sect. VII.9 and for a carrier frequency $f_{co} = 2.1$ GHz. The plots prove the tracking capability of the frequency recovery subsystem. They also show that, in the steady state, the AFC follows the frequency ramp with a lag. Nonetheless, this frequency lag is completely recovered by the phase recovery loop as illustrated in figs.VII.23-VII.31 which represent the eye-diagrams after phase correction, for the same modulation formats as in figs.VII.17-VII.22 (the eye diagrams for case (c) were determined with the same criteria as the other two). It should be noted that these diagrams are relevant to a 500-symbol time segment of the received signal, taken after $2.5 \cdot 10^5$ bit periods since transmission start. This corresponds to the midpoint of the frequency ramp,

where the recovery loop has already settled down. A small performance degradation can be inferred from the observation of the slight additional eye-closure in cases (b) and (c). This degradation is confirmed by the symbol error rate (SER) curves derived in the same time interval and reported in Figs. from VII.32 to VII.35.

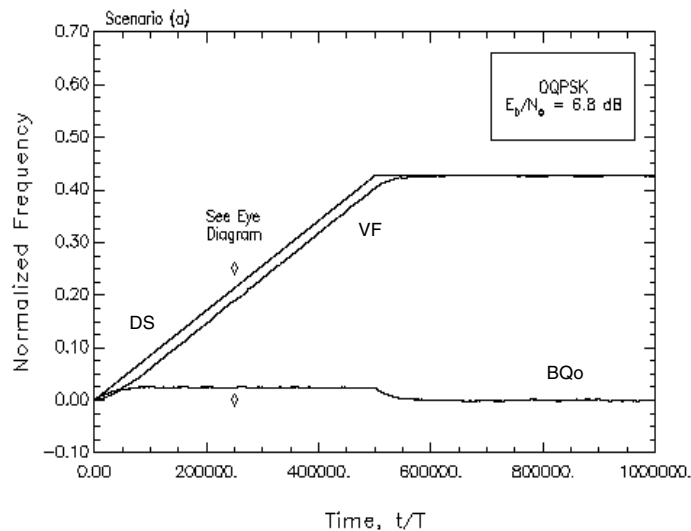


Fig.VII.17

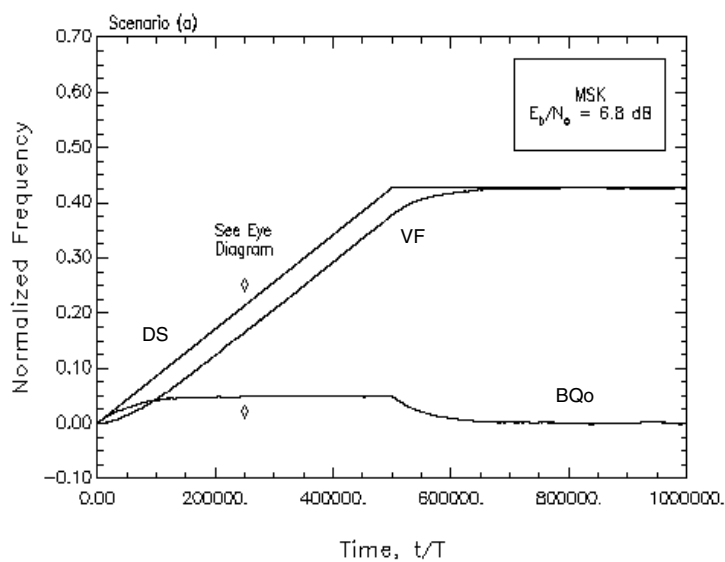


Fig.VII.18

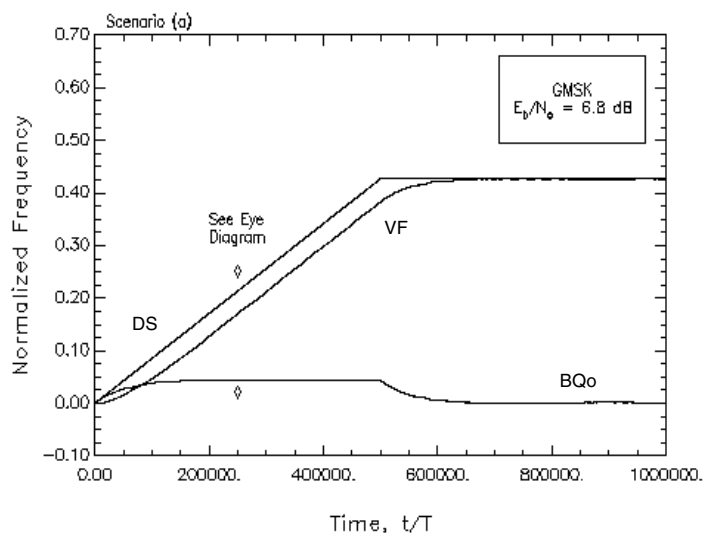


Fig.VII.19

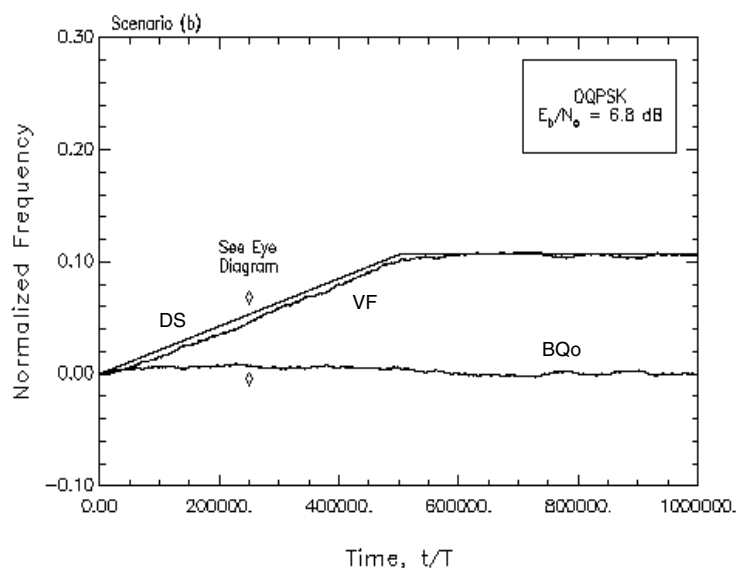


Fig.VII.20

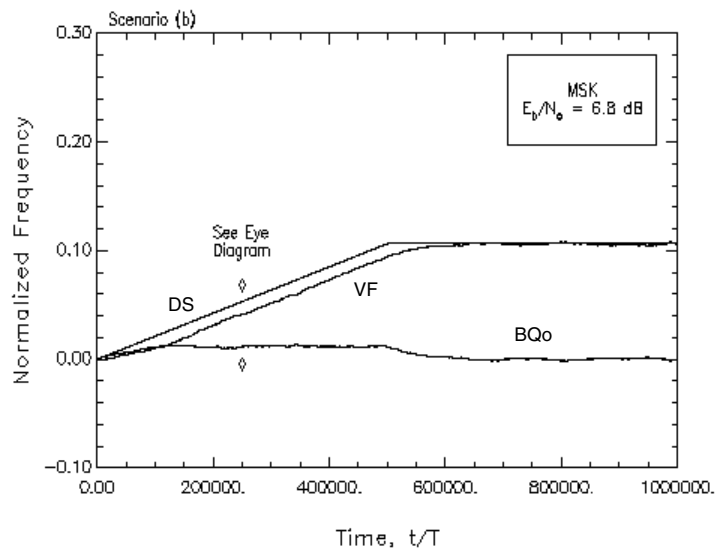


Fig.VII.21

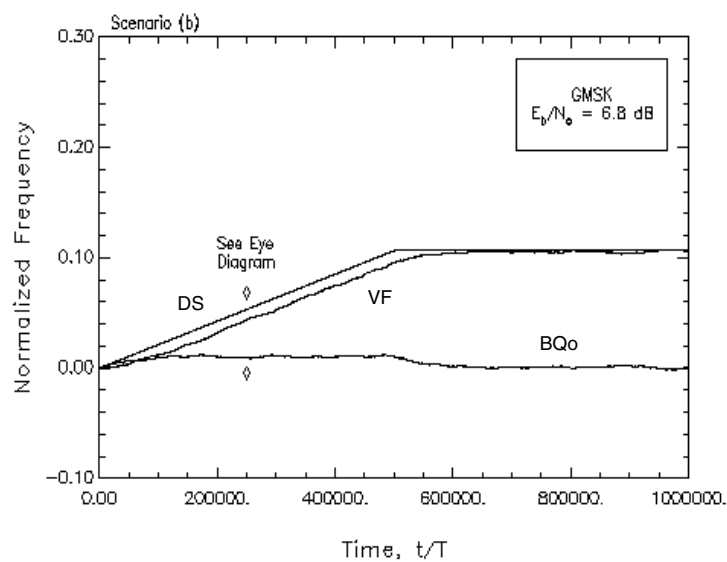


Fig.VII.22

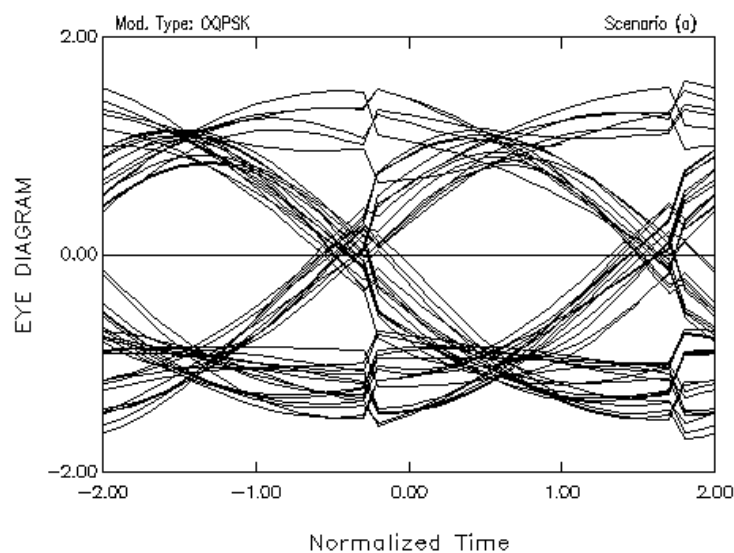


Fig.VII.23

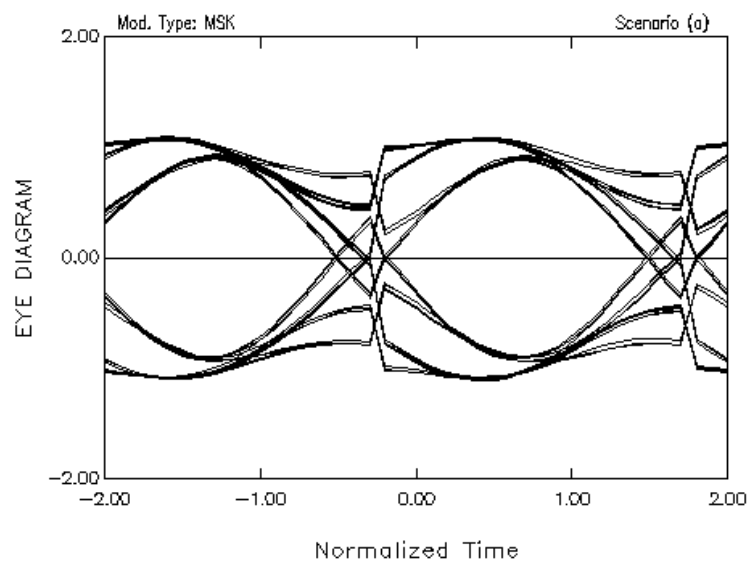


Fig.VII.24

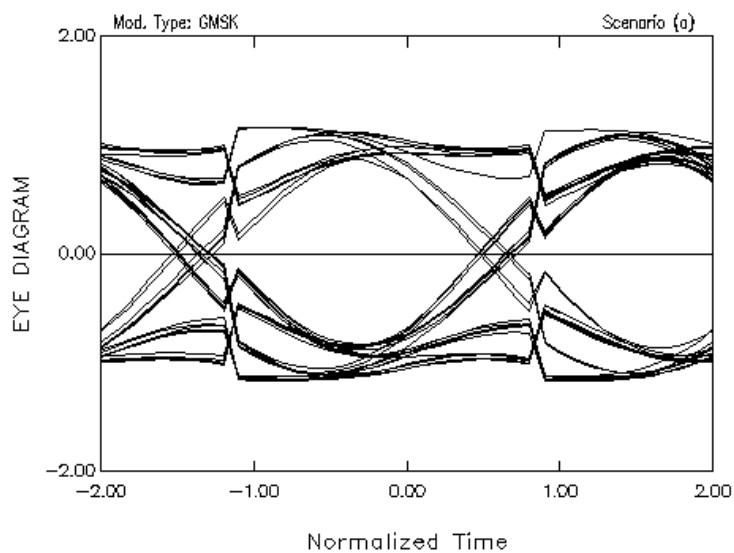


Fig.VII.25

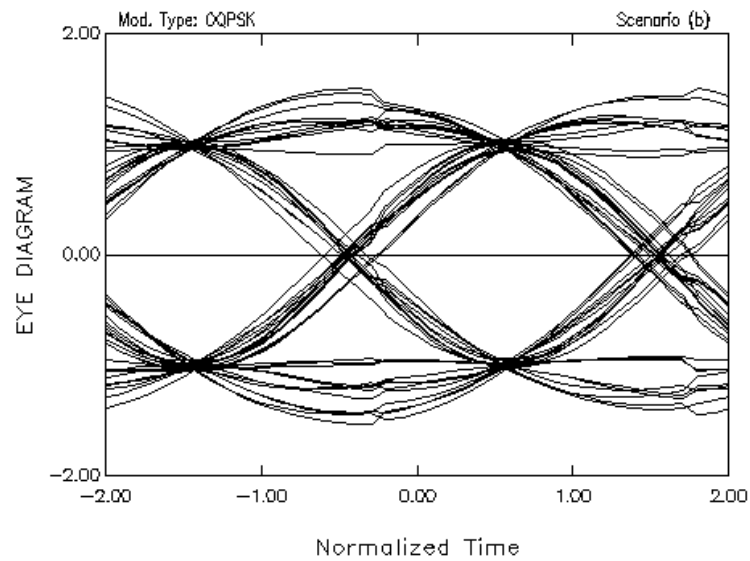


Fig.VII.26

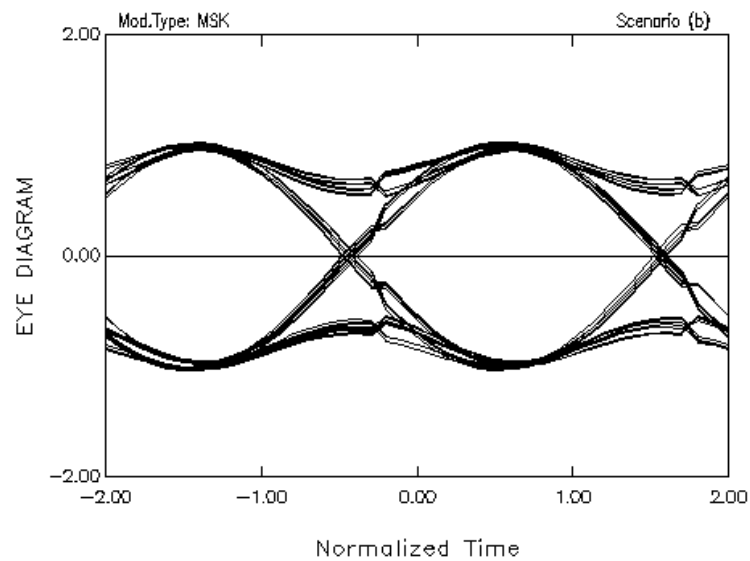
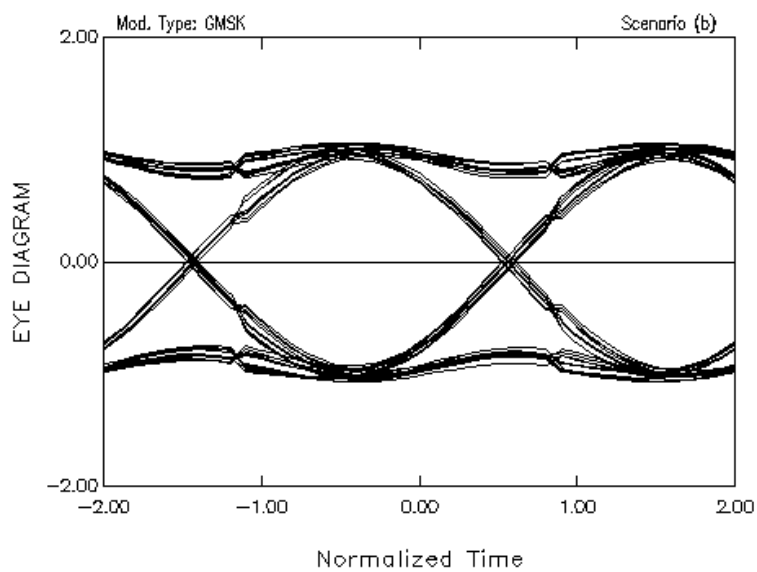


Fig.VII.27



FigVII.28

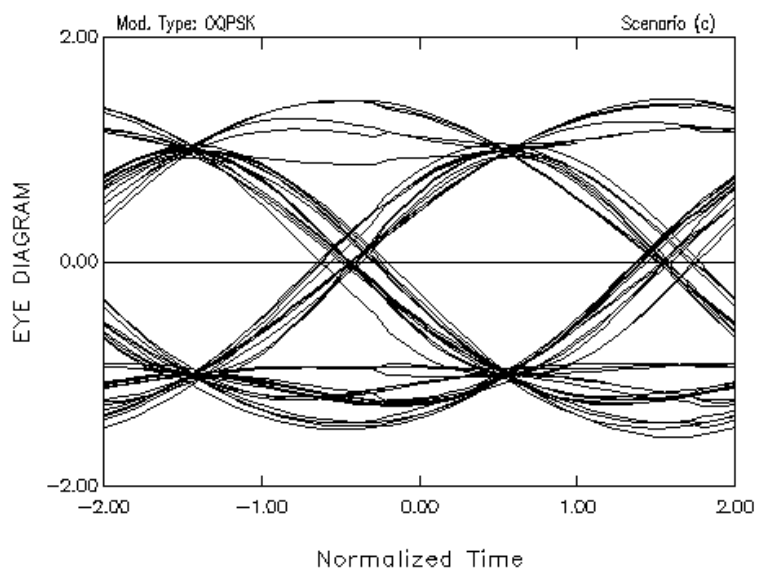


Fig.VII.29

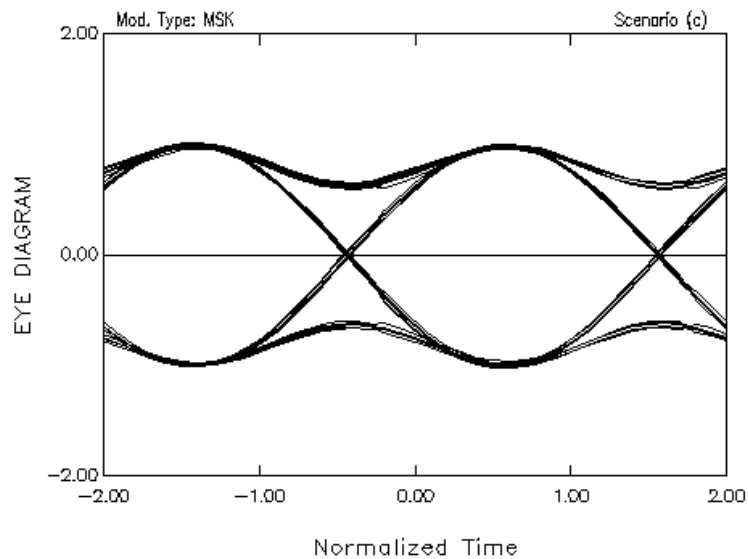


Fig.VII.30

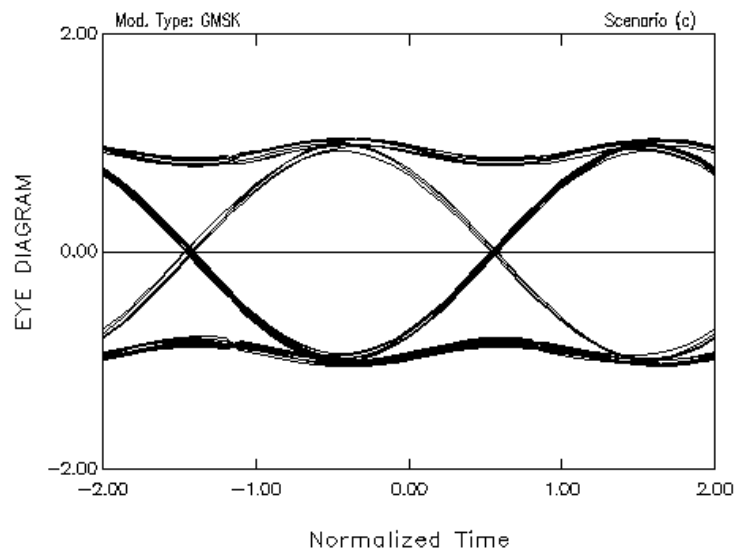


Fig.VII.31

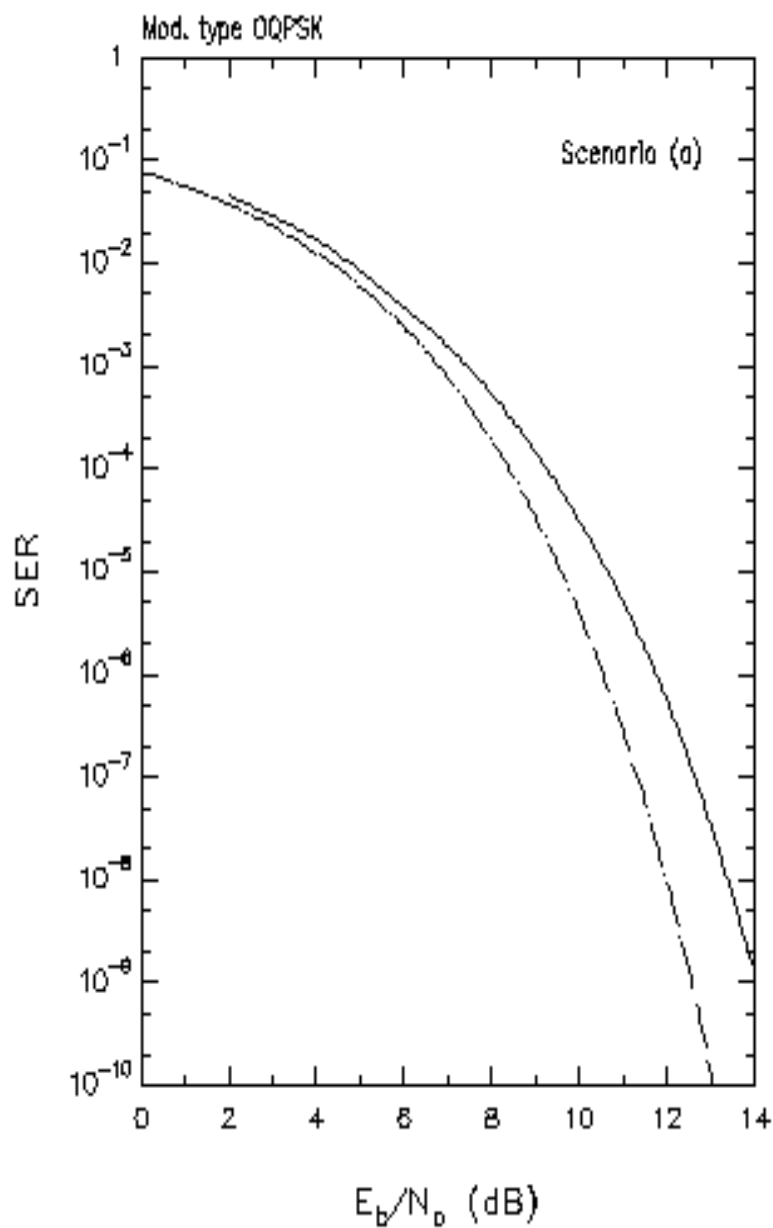


Fig.VII.32

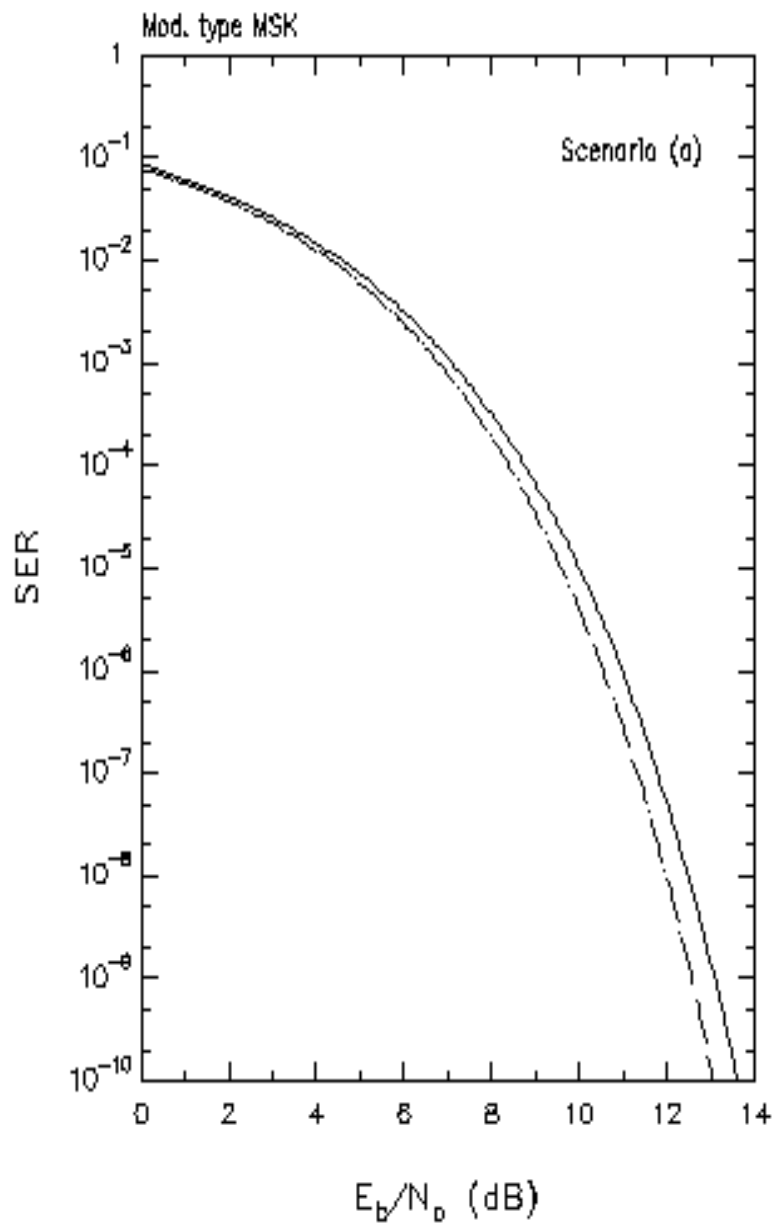


Fig.VII.33

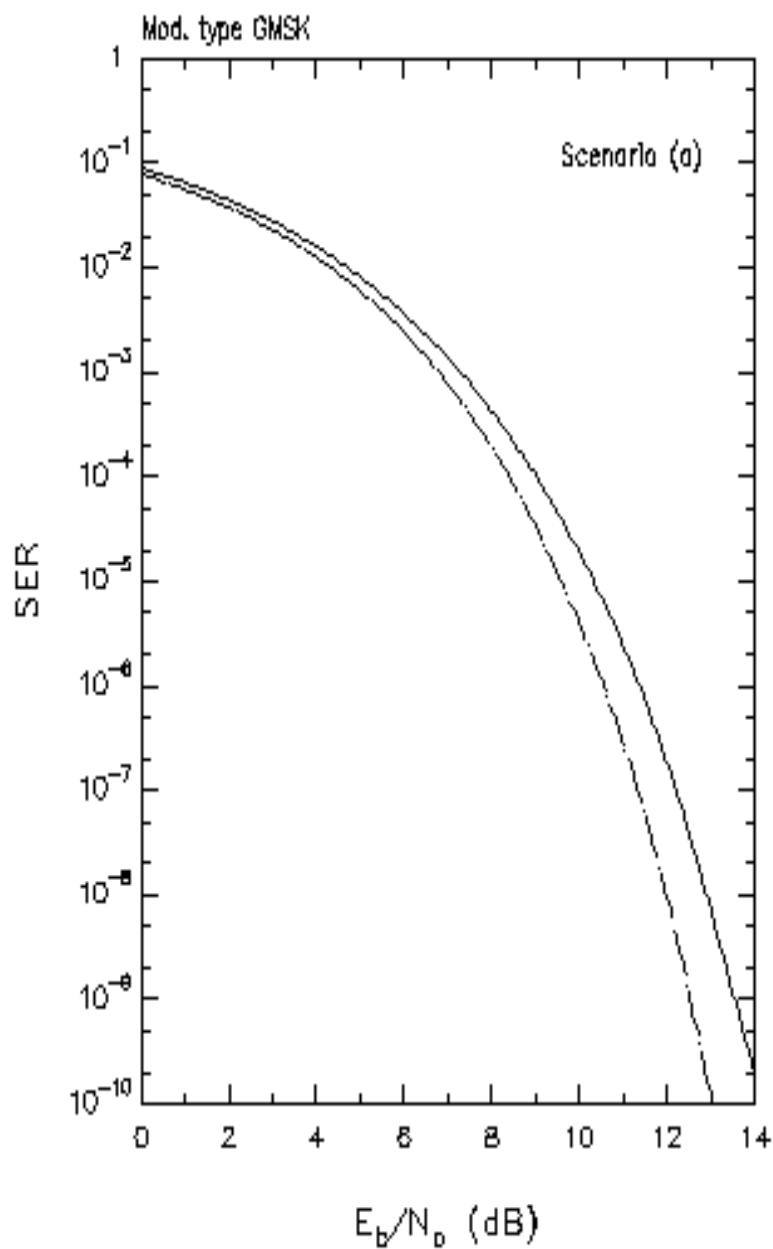


Fig.VII.34

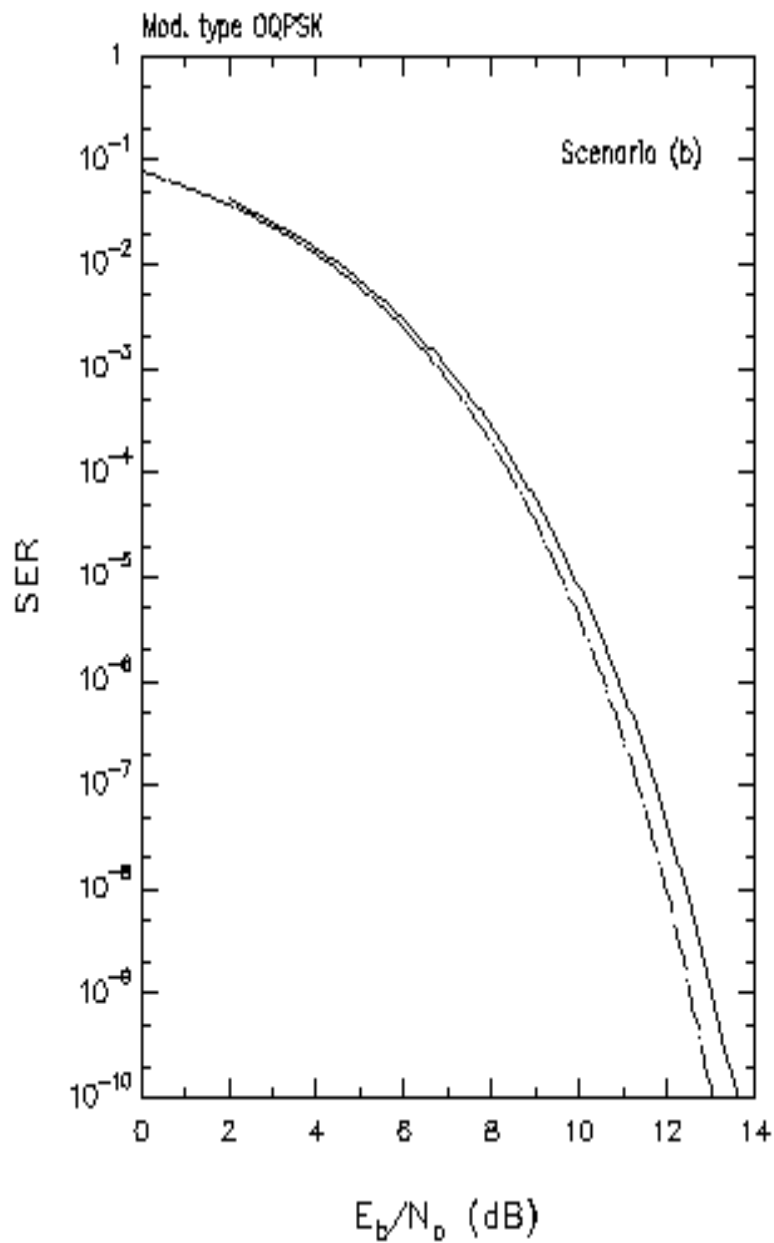


Fig.VII.35

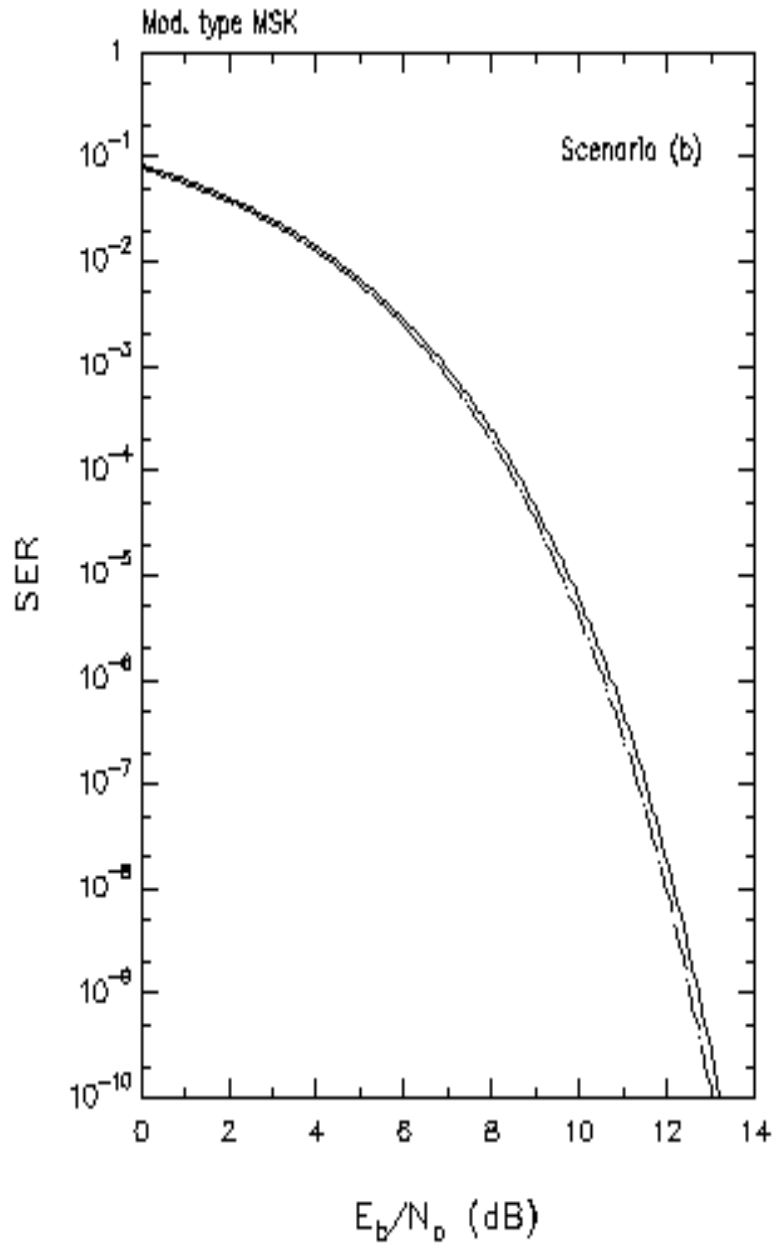


Fig.VII.36

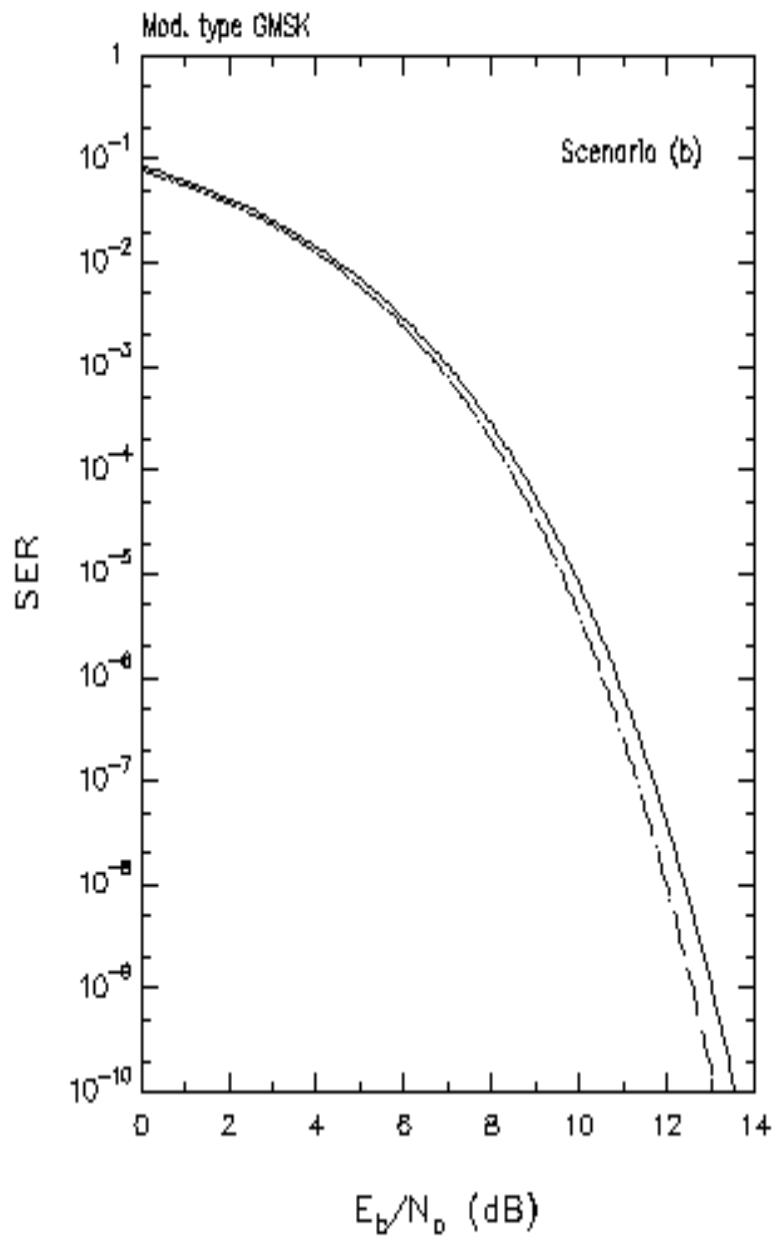


Fig.VII.37

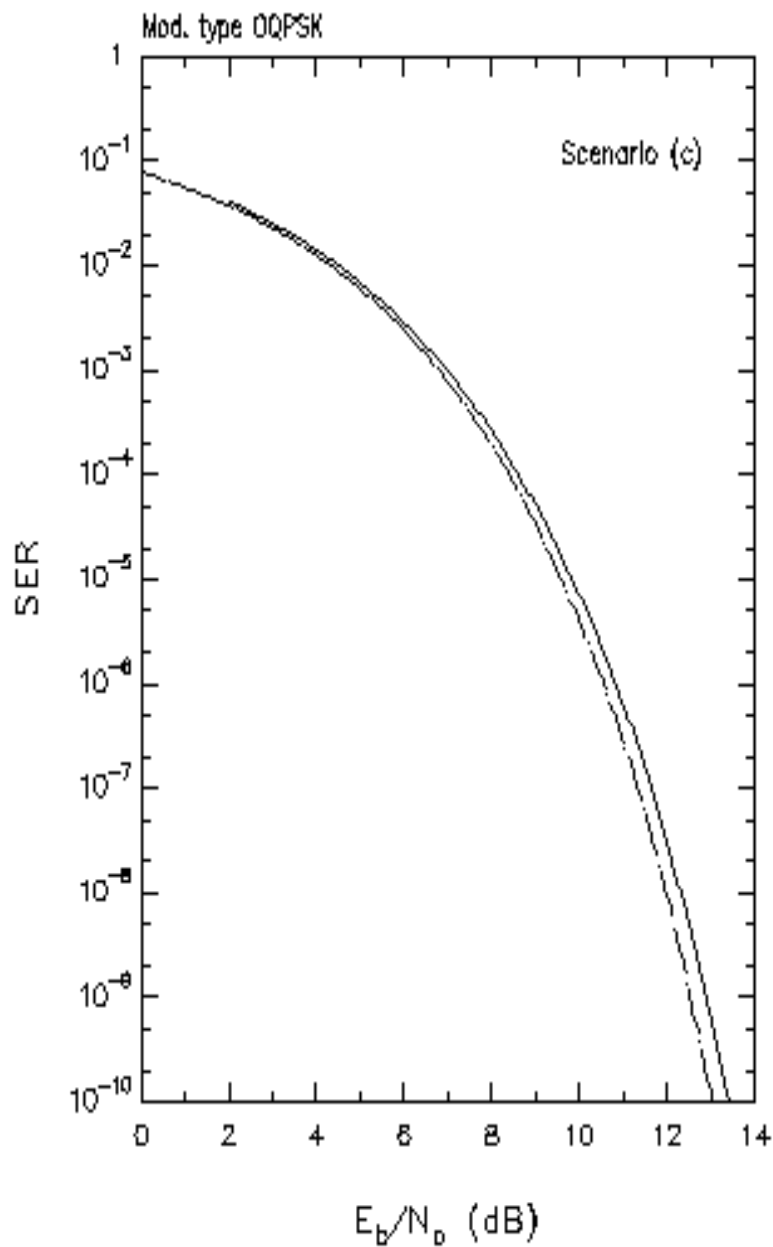


Fig.VII.38

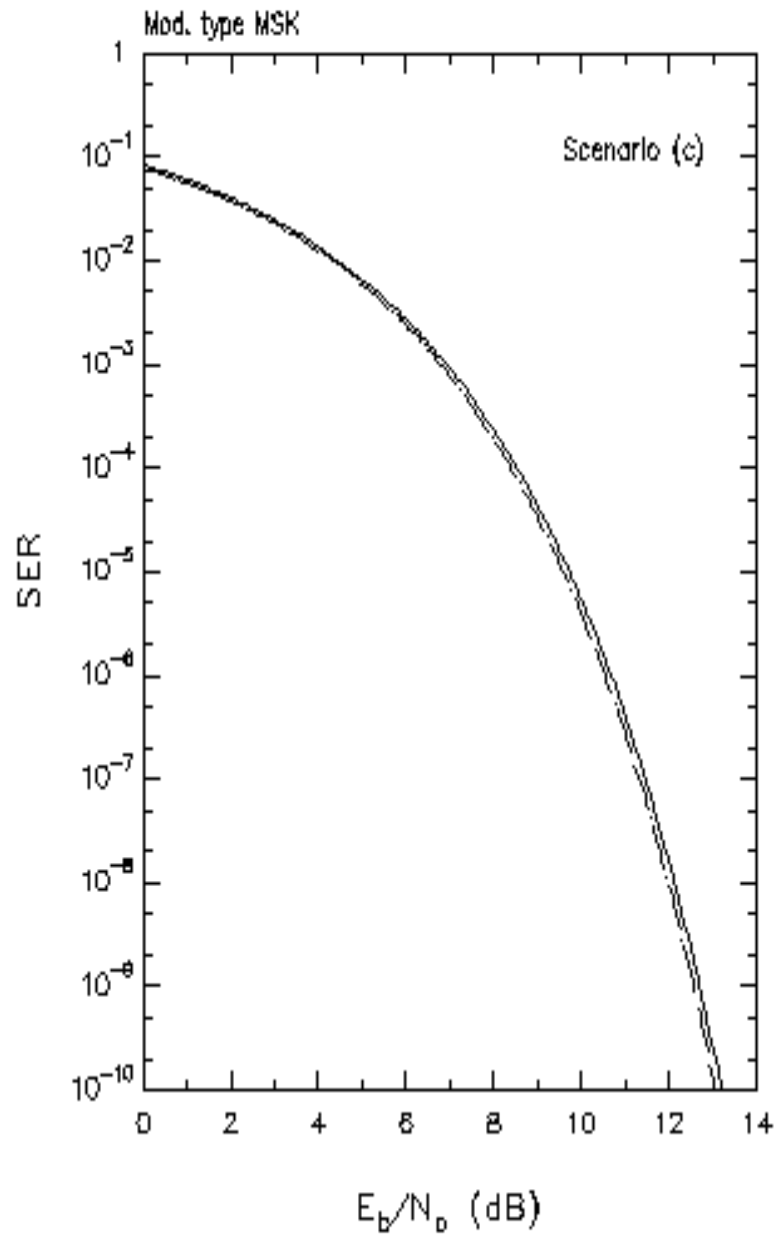


Fig.VII.39

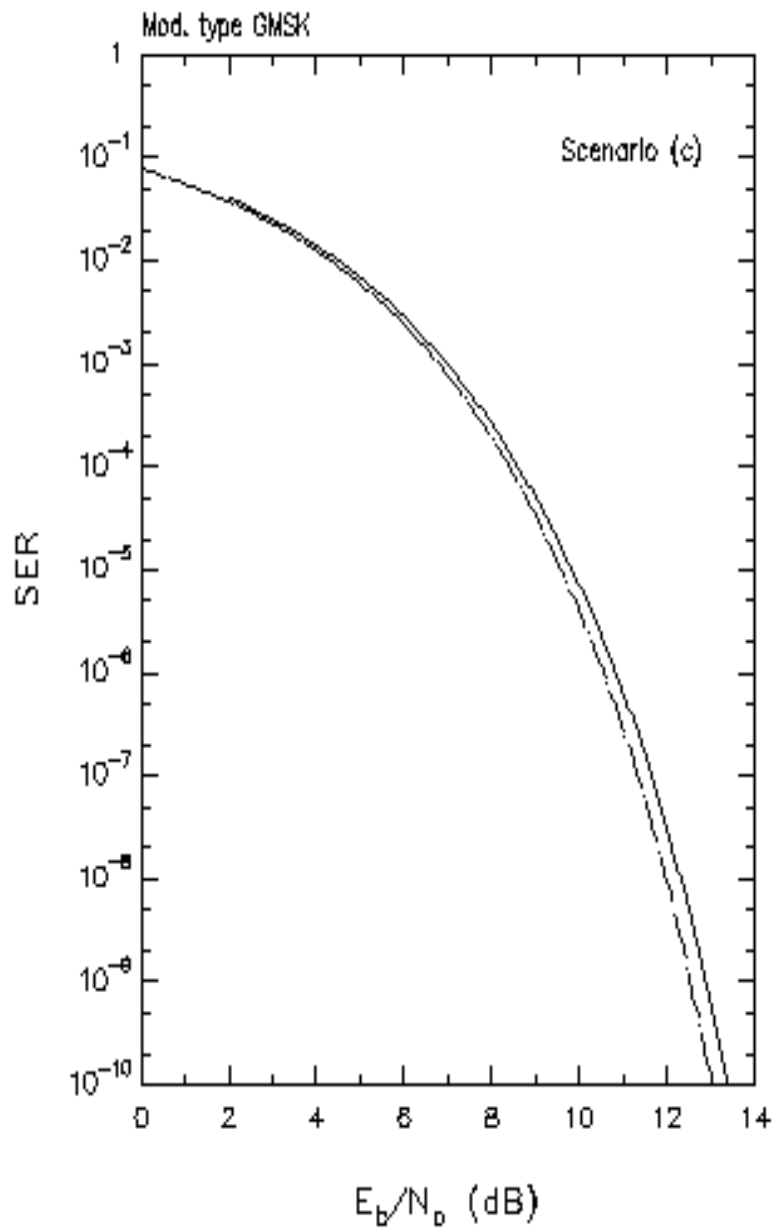


Fig.VII.40

VIII

Frequency Acquisition

VIII .1 A Simple Solution to Frequency Acquisition

During carrier tracking a loss of lock of the synchronization circuitry may accidentally occur. For this reason it is important to provide the receiver with a frequency acquisition subsystem capable to drive the receiver back to its original tracking state. This subsystem is made of three parts:

-) an out-of-lock detector (briefly, lock detector)
-) a staircase generator driving the VCO
-) an auxiliary command unit.

The command unit turns the staircase generator on whenever the lock detector senses a loss of lock. This causes the VCO to generate a sweep scanning the range of possible carrier frequency values. When this search phase is over, lock condition is sustained by applying a proper DC offset to the VCO input. The frequency acquisition/tracking subsystem is shown in fig.VIII.1. The lock control circuit has the task of "freezing" the staircase for a fixed time interval (inhibit time) after loop closure, to prevent unstable behaviour of the overall system. A detailed description of the lock control operation is given in the following section.

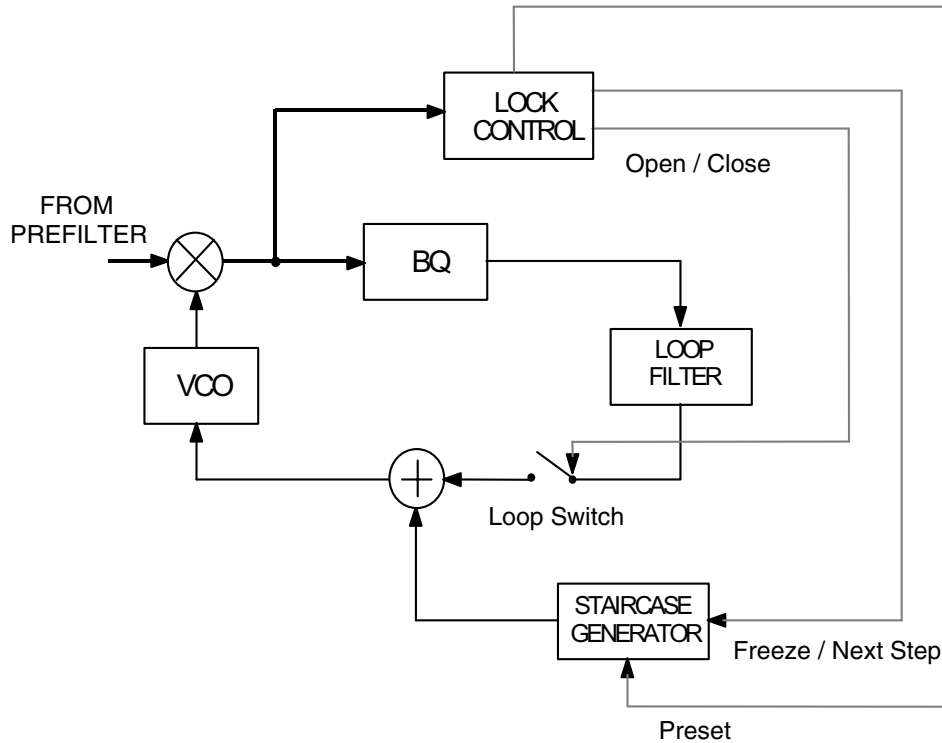


Fig.VIII.1

VIII .2 Lock Control Analysis and Design

The lock control unit is made of a lock detector and a group of logic circuits whose operation is explained below. Figure VIII.2 shows the functional block diagram of the lock detector in baseband equivalent form. Basically, its task is to measure the average signal power at the output of two filters and to compare their ratio with a threshold so as to determine whether the in-lock hypothesis is true. To this aim, the lock detector is provided with two RMS meters which are briefly indicated as LPPM (Low Pass Power Meter) and BPPM (Band Pass Power Meter), whose block diagrams are detailed in fig.VIII.3. The filters required in the cited

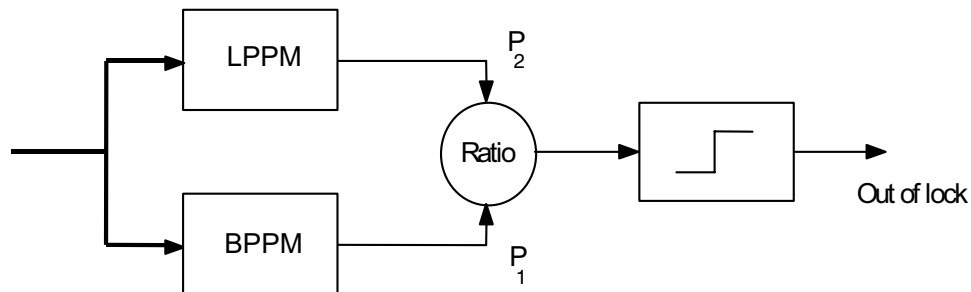
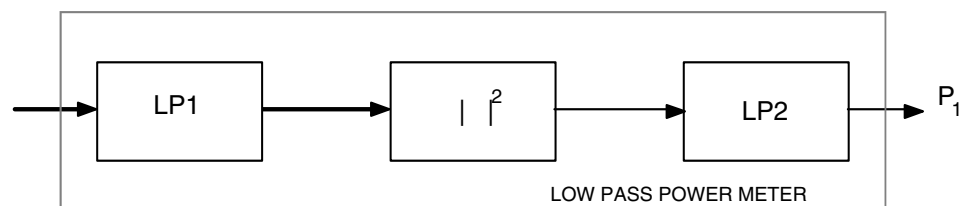
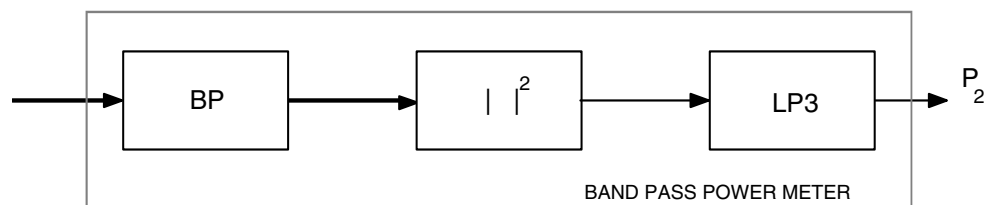


Fig.VIII.2



(a)



(b)

Fig.VIII.3

measuring branches are designed according to the following criteria:

A. LPPM

LP1 is a four-pole Butterworth lowpass filter of bandwidth $0.25/T$, while LP2 is a two-pole Butterworth lowpass filter of bandwidth $10^{-2}/T$.

B. BPPM

LP3 is identical to LP2, while BP is a four-pole Butterworth bandpass filter of two-sided bandwidth $0.25/T$ and central frequency $1/T$.

When the system is in the tracking mode, P_1 gives an estimate of the useful signal power and, at normal E_b/N_o ratios, is much greater than P_2 , the latter being a measure of the noise power in the same bandwidth. The presence of the ratio-computing block renders the system insensitive to residual amplitude fluctuations at the AGC output. When a loss of lock occurs, the ratio $R = P_1/P_2$ rapidly decreases and eventually drops below a threshold Th , thus causing the acquisition phase to restart.

The acquisition subsystem behavior is better described by the state diagram of fig.VIII.4 (Δ denotes the inhibit time). Assume that the system is initially in the tracking state, with the loop switch "closed" and the staircase generator providing some constant output. When the lock detector senses a negative-going crossing of the threshold Th , the system is turned to the acquisition mode. In this state, the staircase generator is reset and starts sweeping the VCO, while the loop switch is kept open. Each step of the frequency sweep lasts D second, while step spacing is H Hz. The acquisition stage is governed by the following algorithm:

-) At the end of each step, the output of LPPM is sampled and stored in memory together with the corresponding VCO input level.
-) After a complete sweep (lasting MD seconds) has been effected, the control logic detects the power sample of maximum value.
-) The VCO control level corresponding to such power sample is applied to the VCO and the loop switch is closed.

Then the acquisition system enters the inhibit mode, allowing the AFC

to take over and the loop equilibrium condition to be restored. After a fixed delay Δ , the system is again in the "tracking mode" condition.

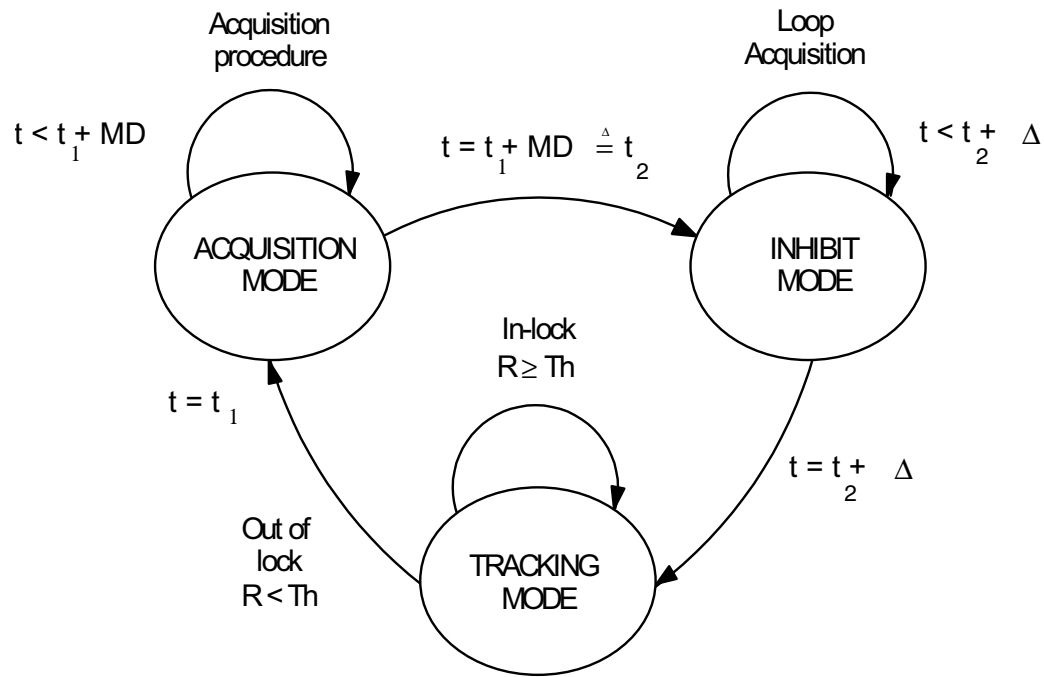


Fig.VIII.4

VIII.3 Lock Control Testing

A number of simulation tests have been carried out to ensure the correct operation of the frequency acquisition system. In all simulation runs, the relevant parameters were fixed as follows:

$$D=10^3 T; \quad M=17; \quad H=0.125/T; \quad \Delta=10^4 T.$$

Computer results show that the carrier acquisition time is strictly related to the AFC bandwidth.

Figures VIII.5-VIII.21 show VCO frequency sweeps and the corresponding sampled values of P_1 for nine acquisition trials, divided into three groups of three trials for each modulation format under study. The sweep speed α_Δ is 1/8 of the bit-rate in 1000 bit periods, i.e. $\alpha_\Delta = 1.25 \cdot 10^{-4} / T^2$. The maximum sweep speed is determined by the duration of each power measurement step, which in turn depends on the bandwidth of the meter low-pass filter LP2. Broadly speaking, the longer a step measurement lasts, the more the measured power is reliable. More specifically, a sort of "threshold value" for the step duration exists below which the measurement is by no means to be regarded as reliable. Our choice $D=1000$ is definitely conservative, in that a reasonable safety threshold is about the value 300 for an output meter bandwidth $B_{LP2}=B_{LP3}=1/100T$.

As specified above, after the research phase, when the VCO is swept by the control signal, the peak value of P_1 is detected, then the VCO input voltage is permanently set at the corresponding level and, finally, the AFC loop is closed. From this instant onwards, the dynamic behaviour of the system is imposed by the AFC bandwidth: a slow acquisition transient is started with the offset frequency approaching zero. Note that this transient is much faster for OQPSK than for MSK and GMSK, since the loop bandwidth for the latter modulations had to be adequately reduced in order to limit the estimated frequency fluctuations in the steady-state.

In the simulations, the normalized VCO sweep $f_d T$ spans the interval (-2.125, 2.125). An inhibit time of 10^4 bit periods is assumed.

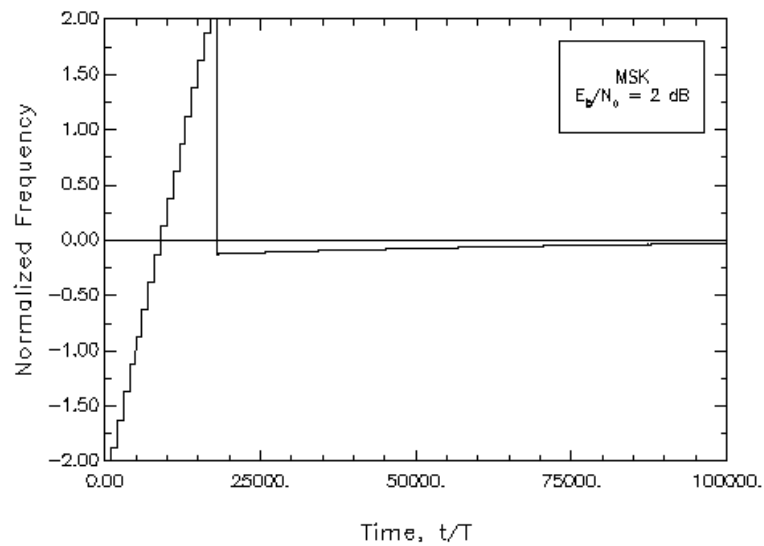


Fig.VIII.5

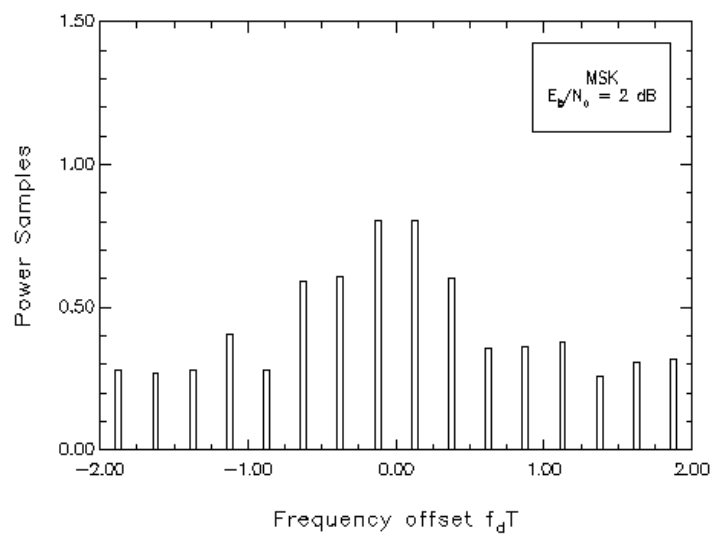
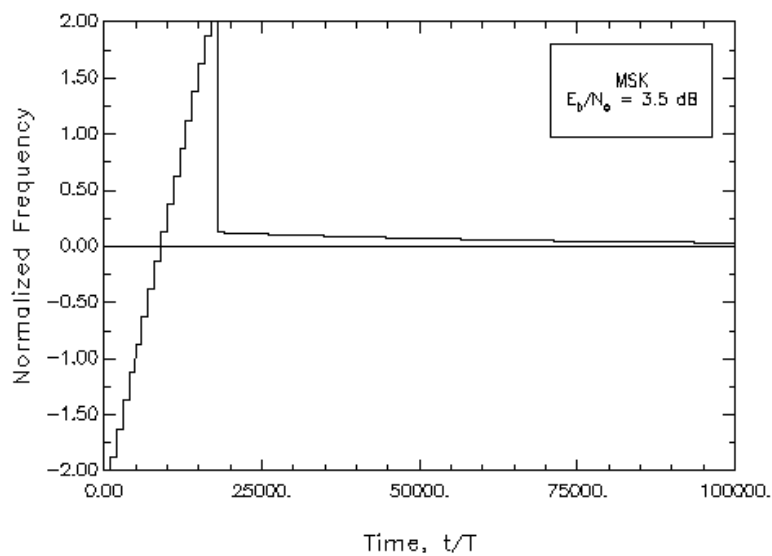


Fig.VIII.6



FigVIII.7

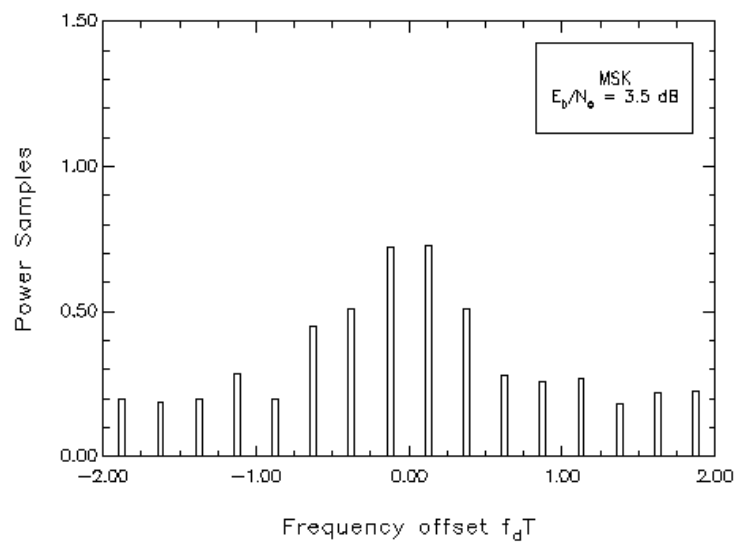


Fig.VIII.8

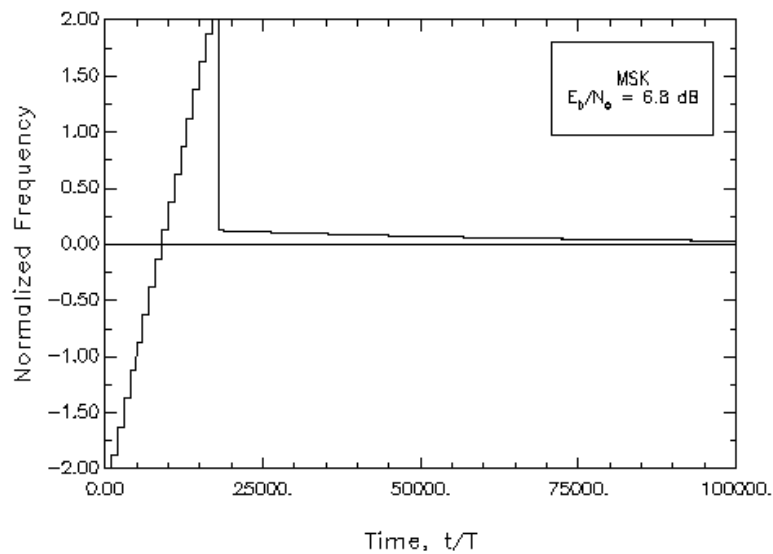


Fig.VIII.9

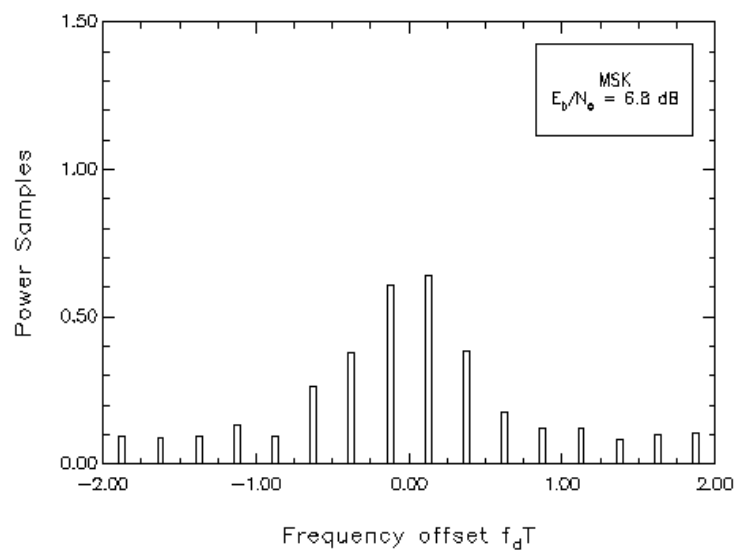


Fig.VIII.10

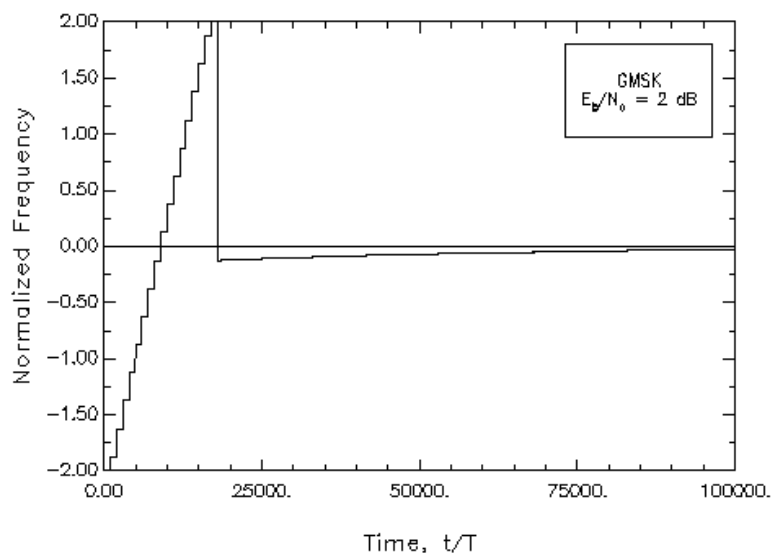


Fig.VIII.11

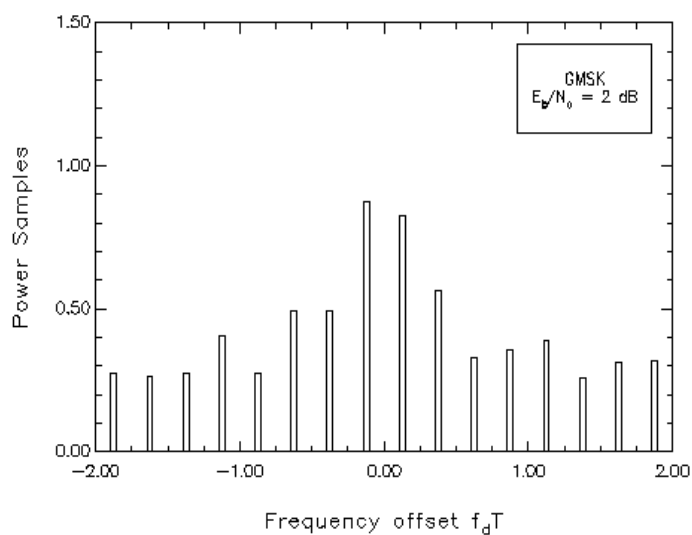


Fig.VIII.12

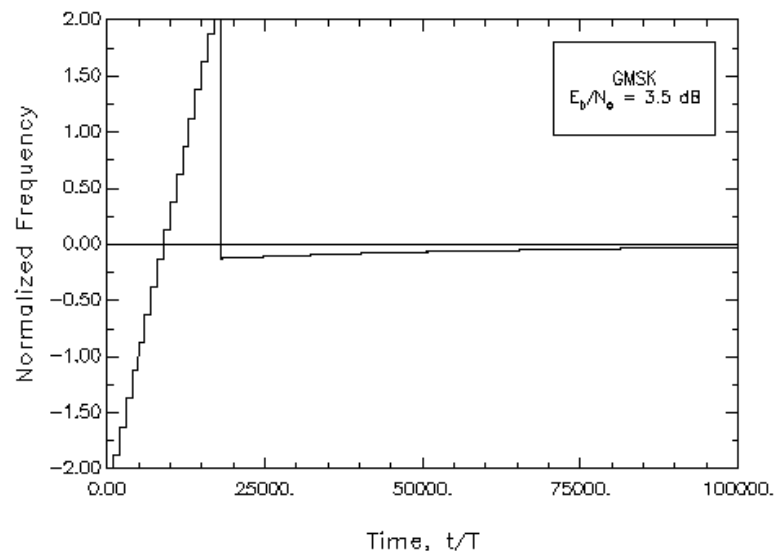


Fig.VIII.13

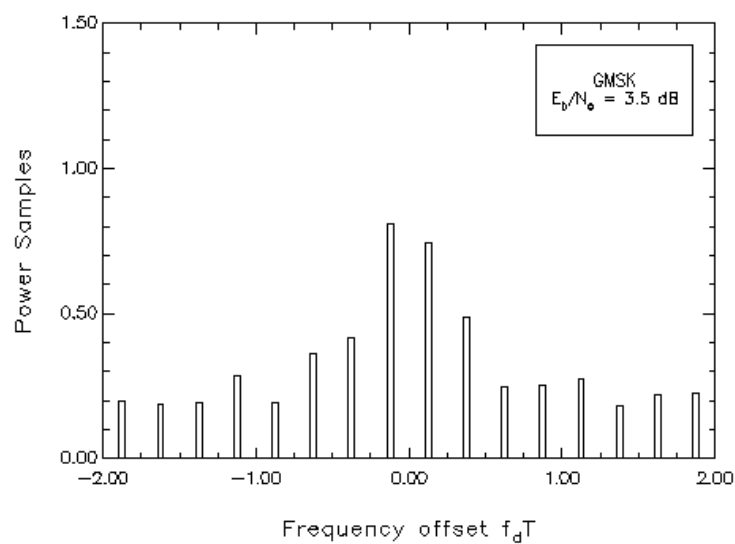


Fig.VIII.14

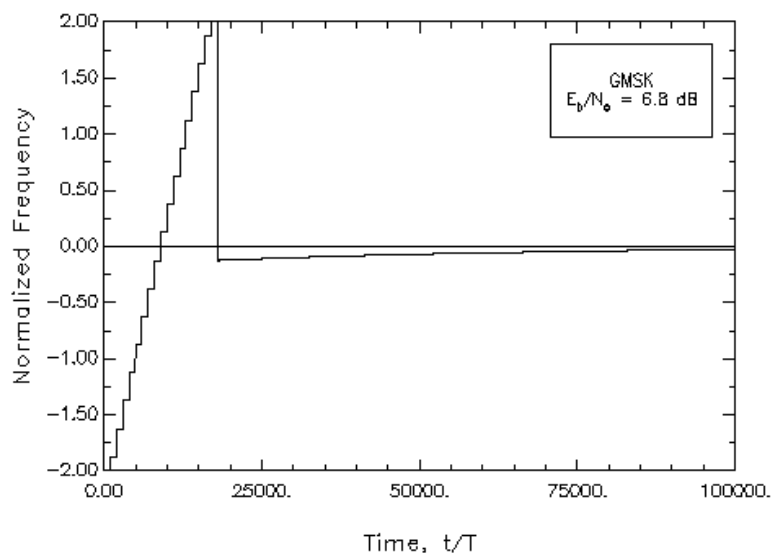


Fig.VIII.15

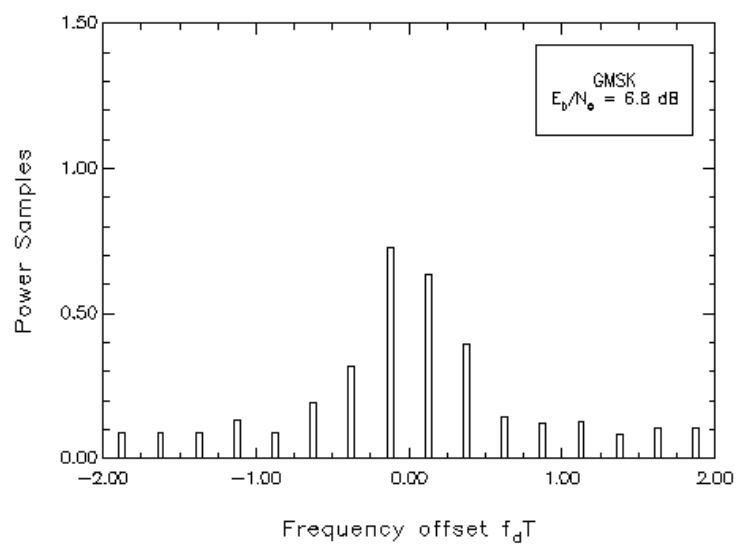


Fig.VIII.16

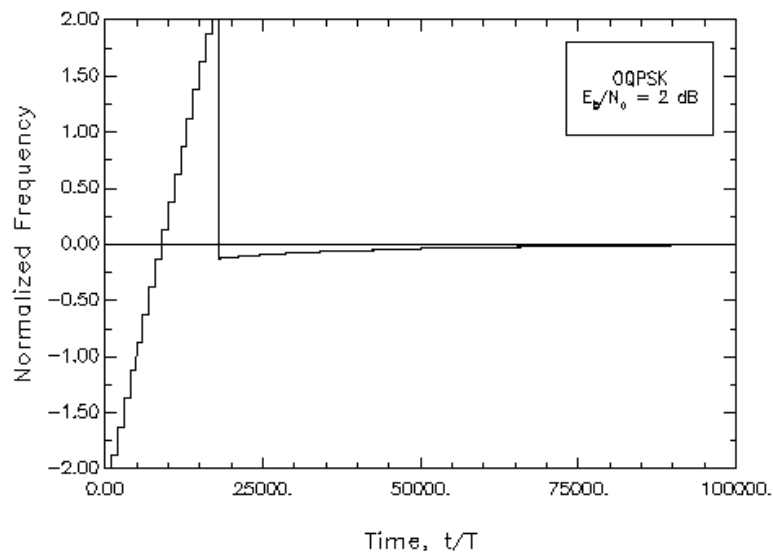


Fig.VIII.17

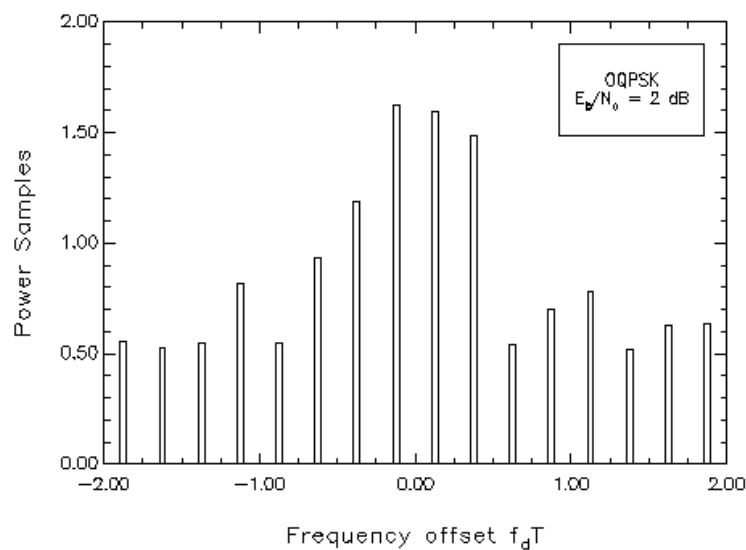


Fig.VIII.18

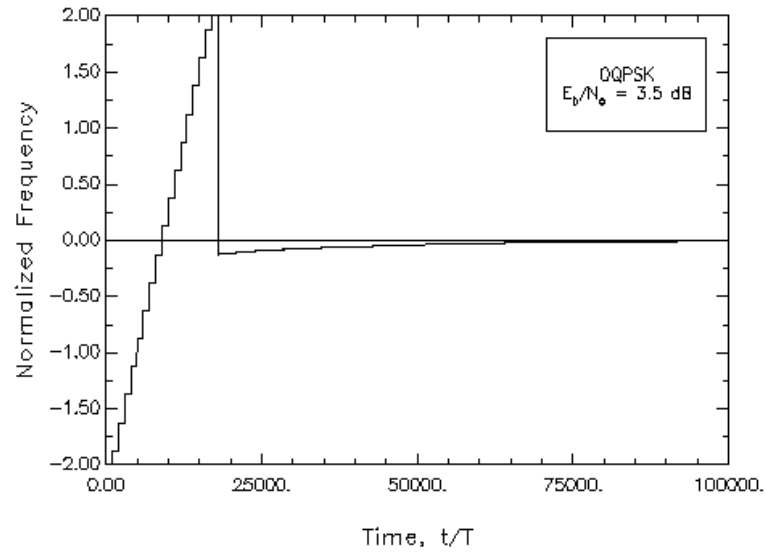


Fig.VIII.19

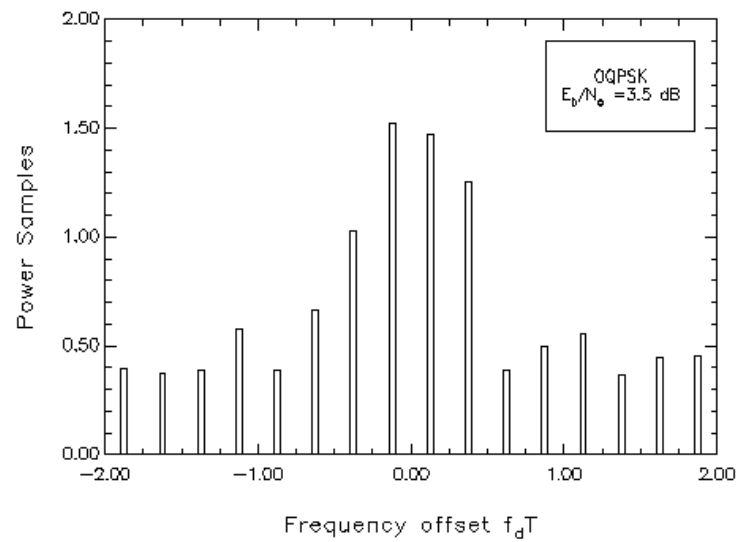


Fig.VIII.20

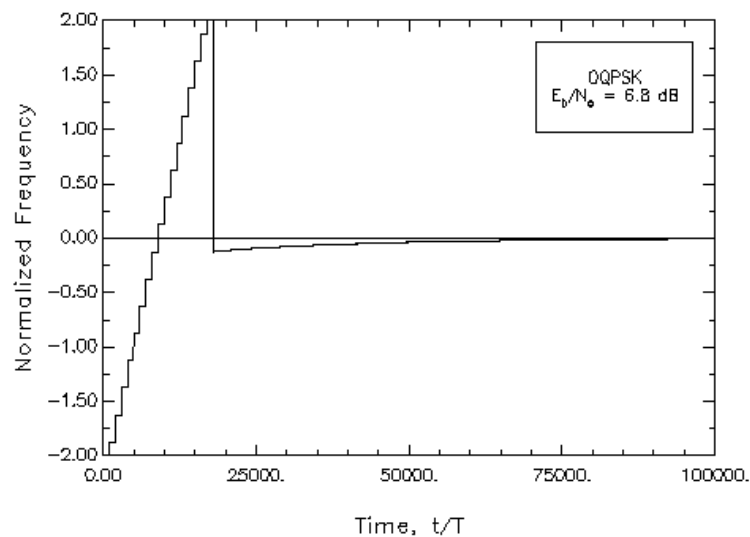


Fig.VIII.21

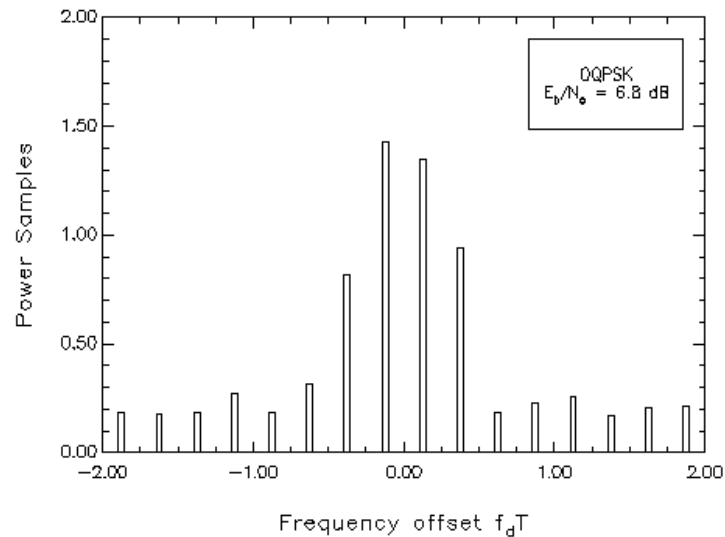


Fig.VIII.22

IX

Overall Performance

IX. 1 Overall Structure of the Receiver

Collecting all the results and schemes presented in the previous chapters, we obtain the overall scheme of the receiver depicted in fig.IX.1 for the MSK and GMSK modulation formats and in figIX.2 for the OQPSK modulation format. As already stated in the previous chapter, in both structures the purpose of the prefilter is to limit noise power without filtering out the useful signal even in the presence of a strong Doppler shift. It is assumed that the receiver front end is provided with a coarse AGC (not shown in figure) so that the total power at the prefilter output is kept constant. The other subsystems shown in both figures are the following:

-) AFC. Its structure is described in chapter VII. It is made of a VCO, a balanced quadricorrelator (BQ) and a loop filter.
-) IF amplifier with a fine automatic gain control (AGC). The bandwidth of this amplifier equals that of the useful signal so that it limits the noise power after frequency conversion.
-) Detection filter. For the choice of this filter see chapter 2.
-) Lock control circuit. A new acquisition process is started as soon as an out-of-lock condition is sensed (see chapter VII).
-) Clock recovery (digital or analog).

-) A decision-aided phase loop. For the OQPSK modulation format phase correction is performed prior to clock recovery.
-) A threshold decision circuit. Its output feeds the decision-aided phase recovery loop.

Another possible implementation of these receivers is shown in fig.IX.3. Here the reference frequency to the BQ is provided by a fixed frequency quartz oscillator (XO) and the IF filter limits the bandwidth of the converted signal. The decision aided carrier loop, the clock recovery loop, the threshold circuit and the detection filter are inside the block labeled as "I-Q demodulator".

(This space is intentionally left blank)

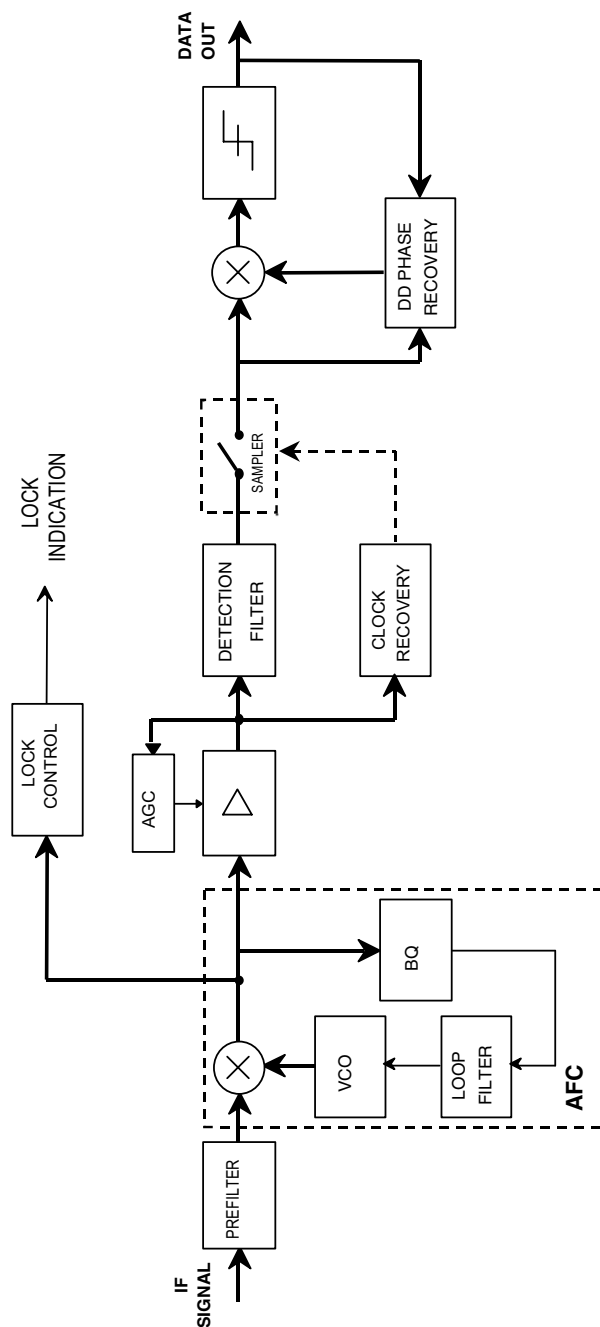


Fig.IX.1

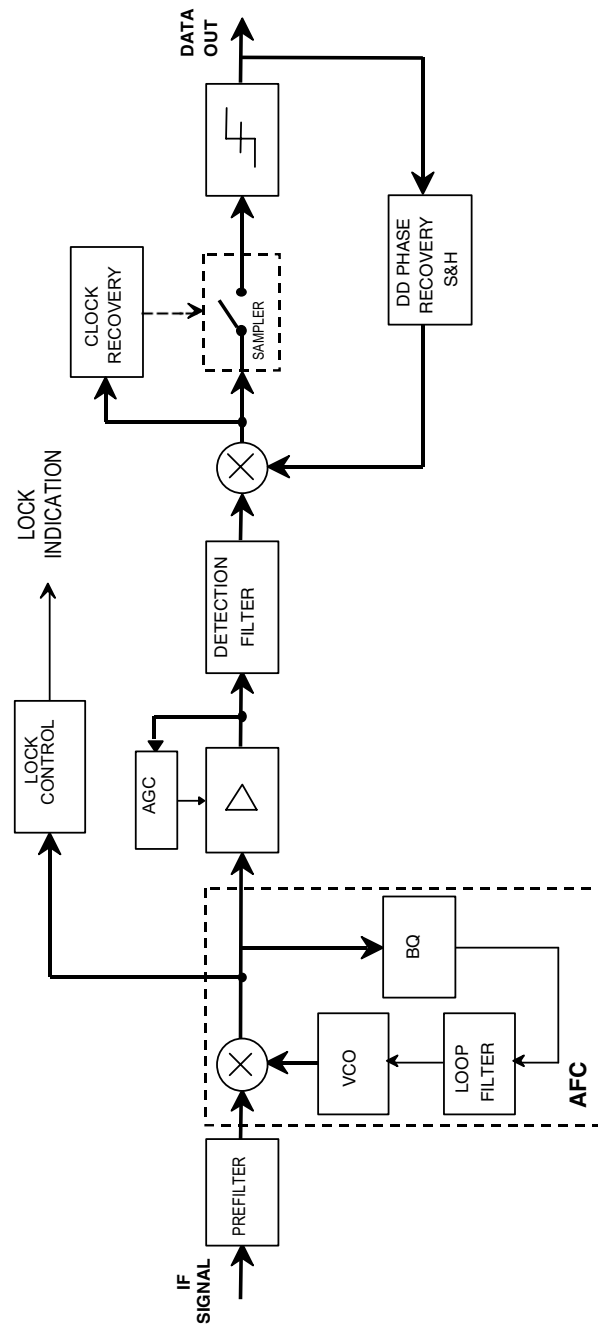


Fig.IX.2

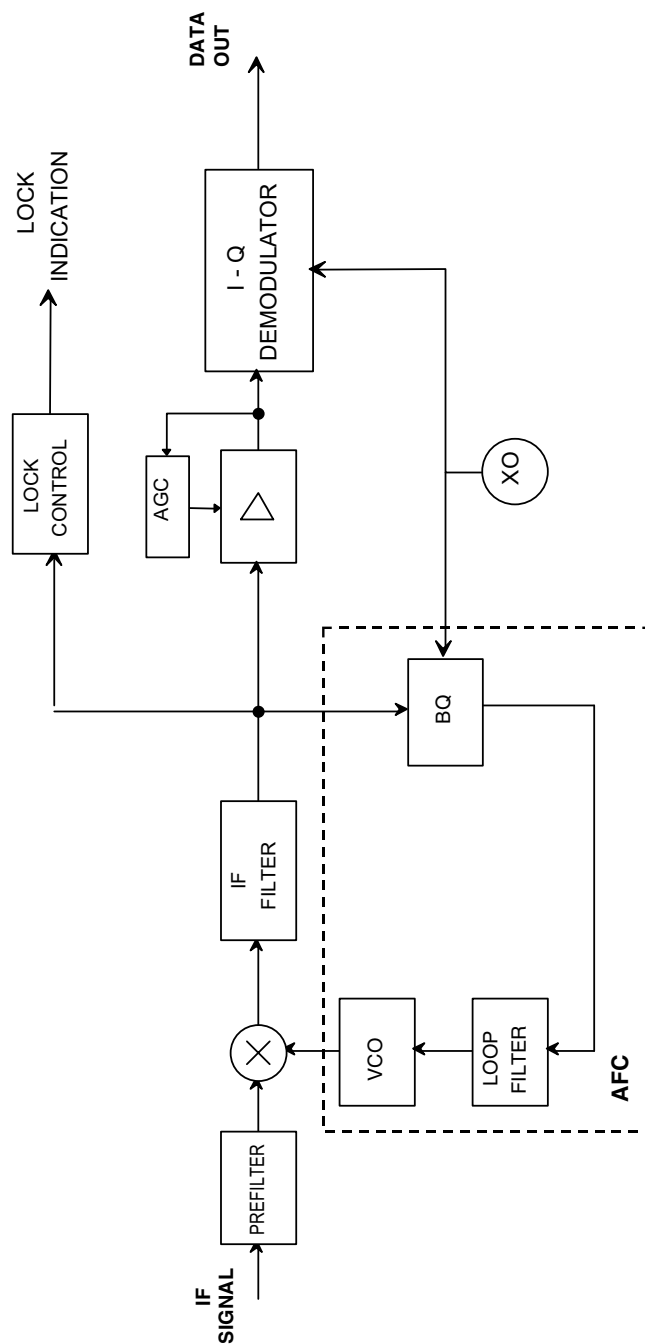


Fig.IX.3

IX. 2 Interaction Between Carrier & Clock Recovery Subsystems

In the preceding Chapters we have seen that a constant phase offset in the received signal does not affect the behavior of the digital clock recovery algorithms for MSK and GMSK, whilst it reduces the amplitude of the timing wave in the case of the square law clock regenerator for OQPSK. However all of these algorithms are sensitive to a frequency offset as we easily show below. To this end, we recall briefly the structure of the SED of the digital clock recovery algorithm #1. The baseband signal is:

$$\tilde{r}_{k,m} \triangleq \tilde{r}(kT + \tau_k + \frac{mT}{2}) \quad m=0,1 \quad (\text{IX.2.1})$$

where τ_k is the current sampling offset. If we let

$$\tilde{\eta}_{k,1} \triangleq (\tilde{r}_{k,1} \tilde{r}_{k-1,1}^*)^2 \quad (\text{IX.2.2})$$

$$\tilde{\eta}_{k,2} \triangleq (\tilde{r}_{k,0} \tilde{r}_{k-1,0}^*)^2 \quad (\text{IX.2.3})$$

the output of the SED at the instant $2kT$ can be written as

$$e_k = \Re [\tilde{\eta}_{k,2} - \tilde{\eta}_{k,1}] \quad (\text{IX.2.4})$$

The S-curve associated with this algorithm is given by

$$S(\tau) = E\{e_k \mid \tau_k \equiv \tau\} \quad (\text{IX.2.5})$$

In the presence of a frequency offset f_d the baseband signal becomes

$$\hat{r}_{k,m} \triangleq \tilde{r}_{k,m} \exp\{j2\pi f_d(kT + \tau_k + mT/2)\} \quad m=0,1 \quad (\text{IX.2.6})$$

Inserting (IX.2.6) in (IX.2.2) and (IX.2.3) we obtain

$$\hat{\eta}_{k,1} \triangleq (\hat{r}_{k,1} \hat{r}_{k-1,1}^*)^2 = (\tilde{r}_{k,1} \tilde{r}_{k-1,1}^*)^2 \exp\{j4\pi f_d T\} =$$

$$= \tilde{\eta}_{k,1} \exp\{j4\pi f_d T\} \quad (\text{IX.2.7})$$

$$\begin{aligned} \hat{\eta}_{k,2} &\triangleq (\hat{r}_{k,0} \hat{r}_{k-1,0}^*)^2 = (\tilde{r}_{k,0} \tilde{r}_{k-1,0}^*)^2 \exp\{j4\pi f_d T\} = \\ &= \tilde{\eta}_{k,2} \exp\{j4\pi f_d T\} \end{aligned} \quad (\text{IX.2.8})$$

so that the error signal becomes

$$e_k = \Re[\hat{\eta}_{k,2} - \hat{\eta}_{k,1}] = \Re[(\tilde{\eta}_{k,2} - \tilde{\eta}_{k,1}) \exp\{j4\pi f_d T\}] \quad (\text{IX.2.9})$$

The corresponding S-curve, say $\hat{S}(\tau)$, is therefore:

$$\begin{aligned} \hat{S}(\tau) &= \Re[\exp\{j4\pi f_d T\} E\{(\tilde{\eta}_{k,2} - \tilde{\eta}_{k,1}) | \tau_k = \tau\}] \\ &= S(\tau) \cos(4\pi f_d T) \end{aligned} \quad (\text{IX.2.10})$$

because $S(\tau) \triangleq E\{(\tilde{\eta}_{k,2} - \tilde{\eta}_{k,1}) | \tau_k = \tau\}$ is a real function. Equation (IX.2.10) proves that frequency offset has the effect of reducing the amplitude of the S-curve. Some form of clock/frequency interaction is therefore to be expected in the acquisition mode.

IX. 3 Tracking Performance - No Doppler Effect

We investigate the behavior of the receiver during tracking mode when the AFC, clock and carrier recovery subsystems are all operating. The noise bandwidths for these three different synchronization subsystems are reported in Table III. Here SLCR means 'Square Law Clock Regenerator' and the bandwidths are all normalized to the bit rate $1/T$. The values listed in the table have already been employed in many simulations whose results are given in the preceding chapters. Fig.IX.4-6 show the SER curves for the three

modulation formats in the absence of Doppler shift (or, equivalently, in the presence of a constant Doppler shift which is entirely compensated for by the AFC). These curves show the good overall performance of the receiver for all values of E_b/N_o .

Modulation Type	Clock Alg.Type	Clock Loop Bandwidth	Phase Tracking Bandwidth	AFC Loop Bandwidth
OQPSK	SLCR	10^{-3}	0.02	$1.25 \cdot 10^{-5}$
MSK	Digital #1	$5 \cdot 10^{-4}$	0.04	$0.625 \cdot 10^{-5}$
GMSK	Digital #1	$5 \cdot 10^{-4}$	0.04	$0.52 \cdot 10^{-5}$

TABLE III

IX. 4 Tracking Performance with Doppler Effect

In order to assess the tracking performance in the presence of a time-varying Doppler shift we consider again the scenario (b) described in chap.VII (characterized by $v=10$ km/sec, $h=200$ km, $R=128$ Kb/sec). The BER curves in this new tracking situation are shown in fig. IX.7-9. It is noted that the Doppler effect causes small additional performance losses in comparison to the corresponding curves shown in the preceding section. This confirms once more that the synchronization subsystems work properly even in a challenging situation.

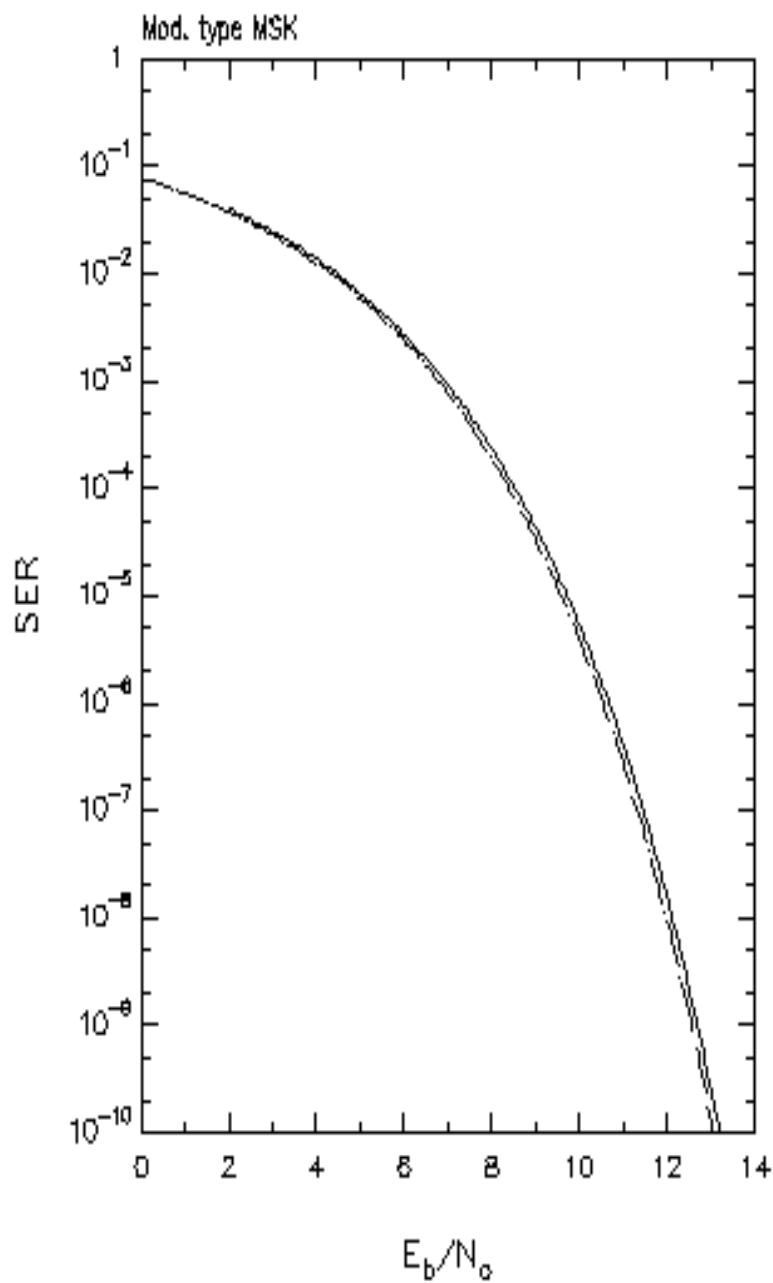


Fig.IX.4

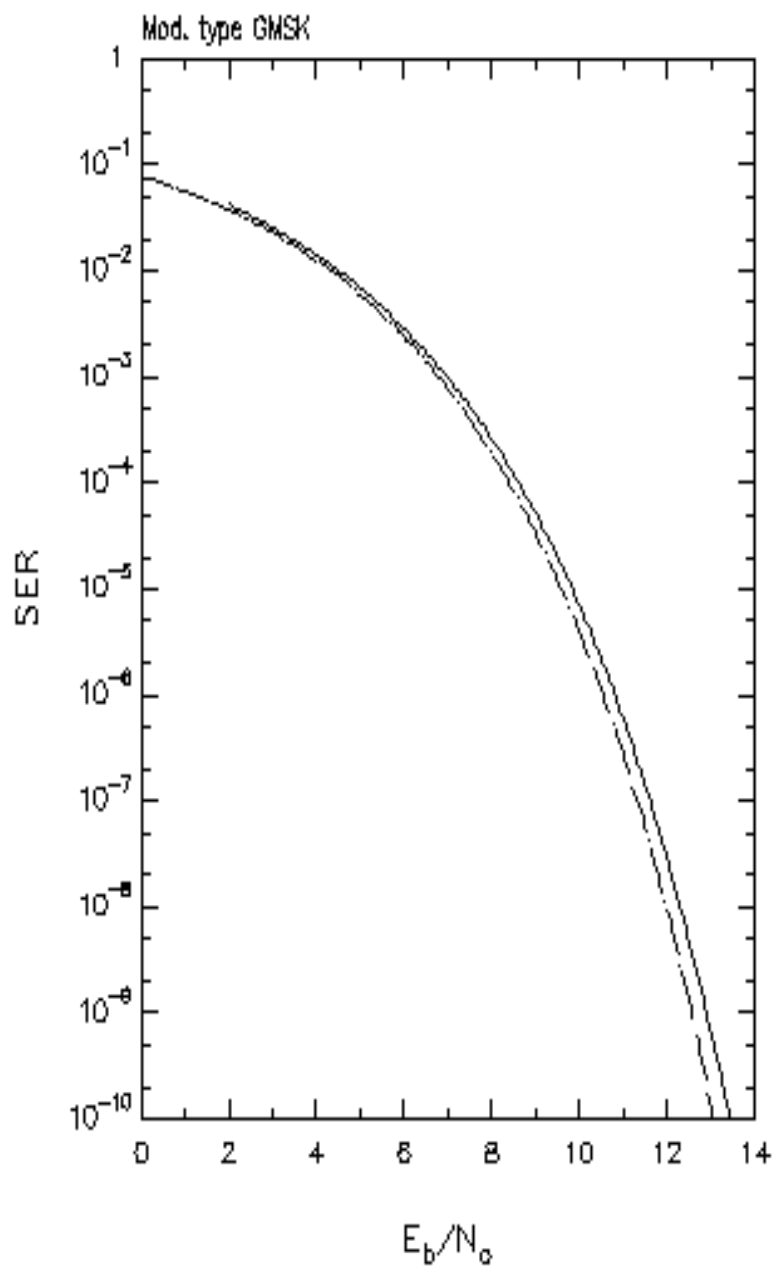


Fig.IX.5

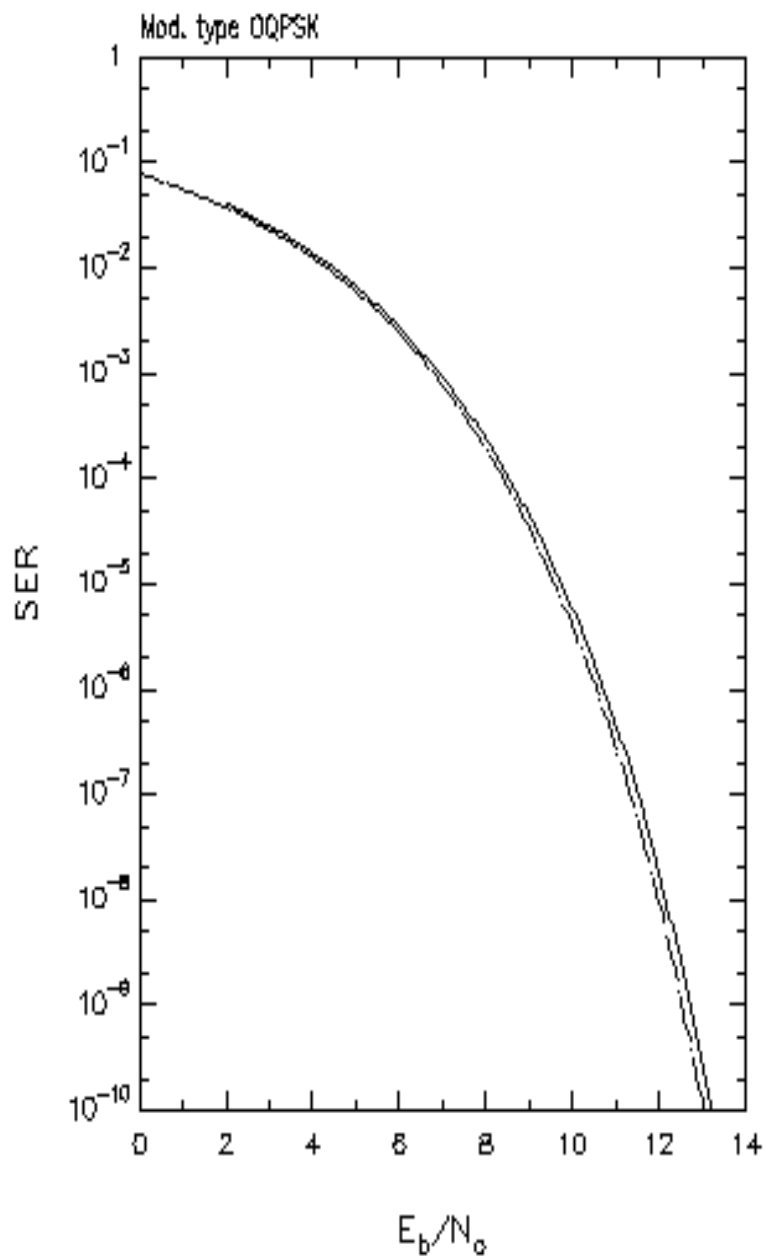


Fig.IX.6

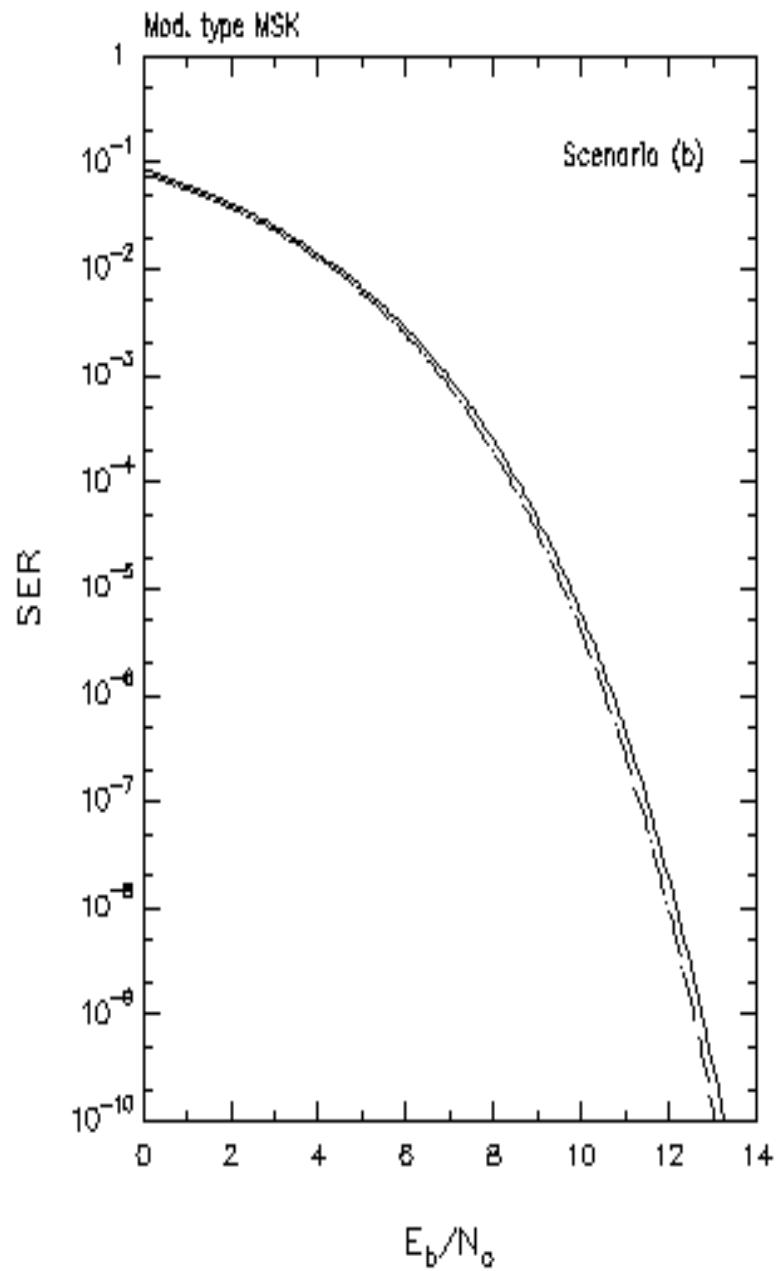


Fig.IX.7

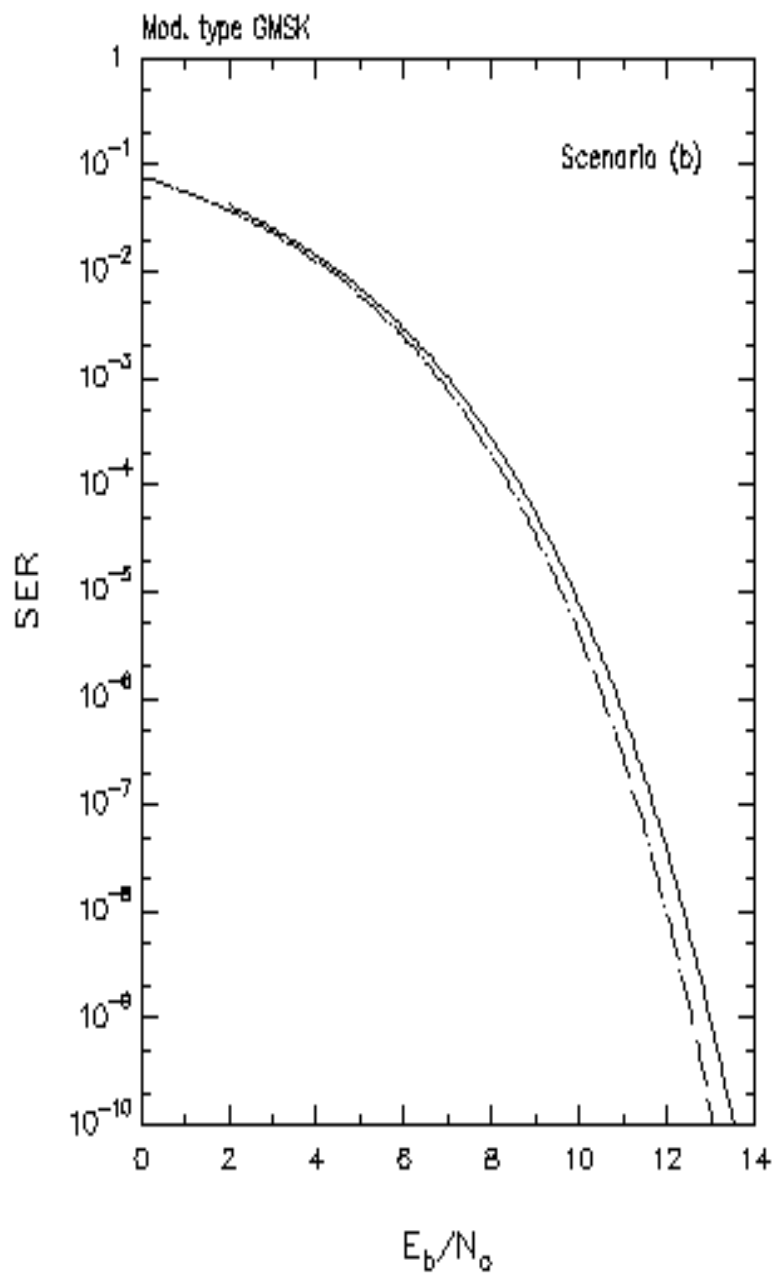


Fig. IX.8

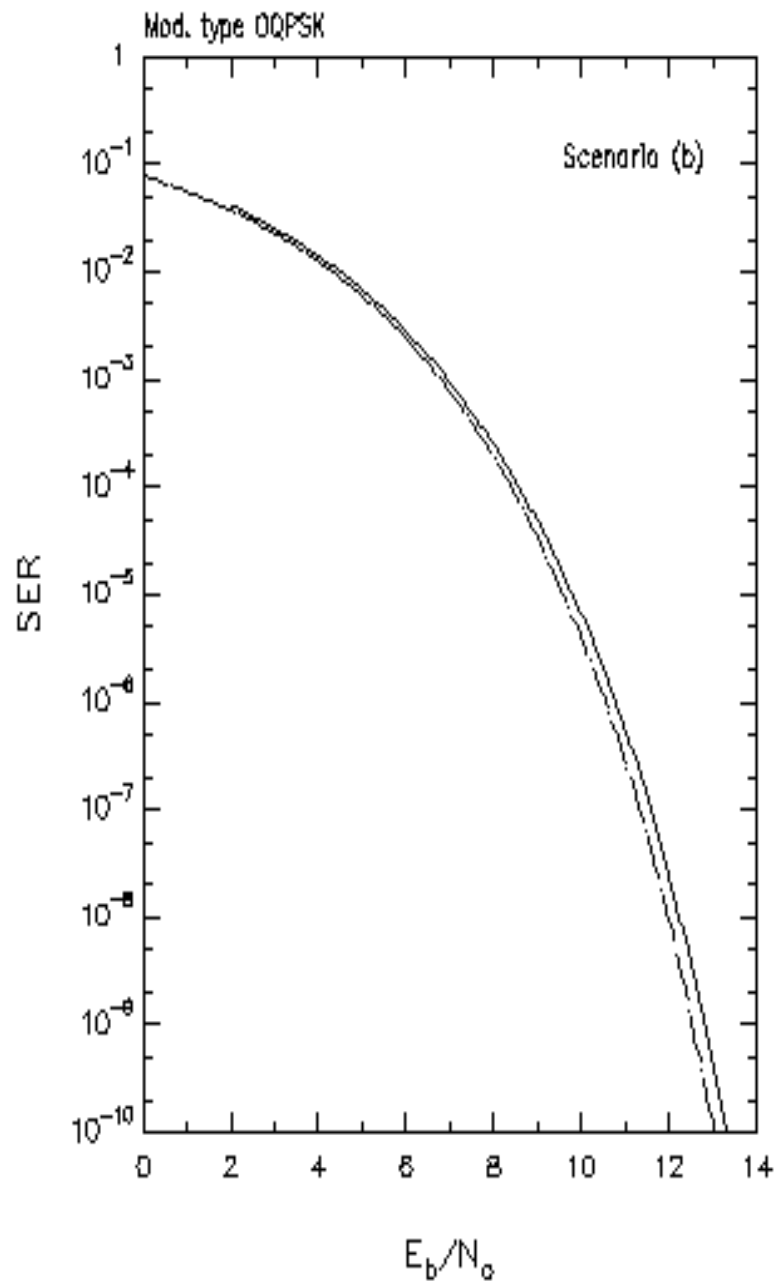


Fig.IX.9

IX. 5 Acquisition Samples

The overall acquisition capability of the receiver was tested by carrying out a set of acquisitions for the three modulation formats under study. In these simulations the transient behavior of the synchronization loops was observed. Figures IX.10-17 show the time diagrams of the normalized frequency error, of the clock sampling instant and of the estimated residual phase error for $E_b/N_0=5$ dB and MSK/GMSK modulations. Figures IX.18-21 show the same diagrams for OQPSK. In all these simulation runs the initial frequency error is set at $f_{d0}T=0.2$ while the clock recovery subsystem starts from the unstable point in the S-curve (worst case condition). It is seen that the carrier phase loop is able to track the rapid phase fluctuations induced by the BQ on the received signal. It is important to notice that, while the carrier phase loop has a fast dynamical behaviour due to its wide bandwidth, clock and frequency subsystems are much slower.

(This space is intentionally left blank)

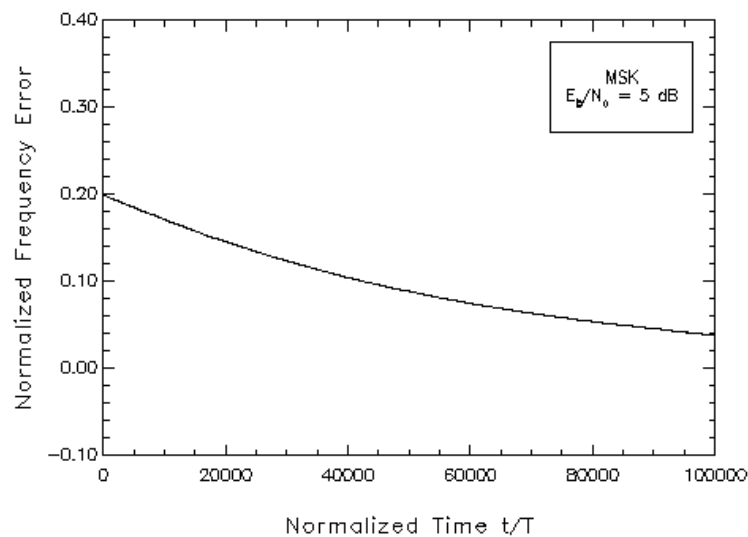


Fig.IX.10

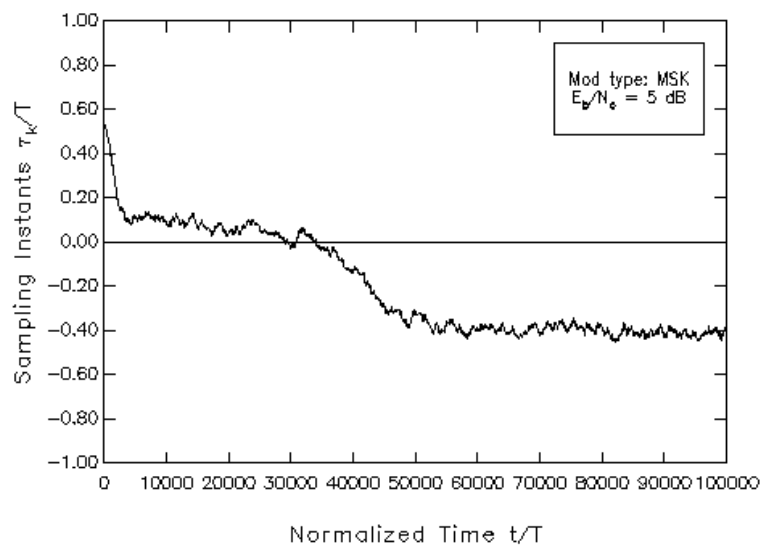


Fig.IX.11

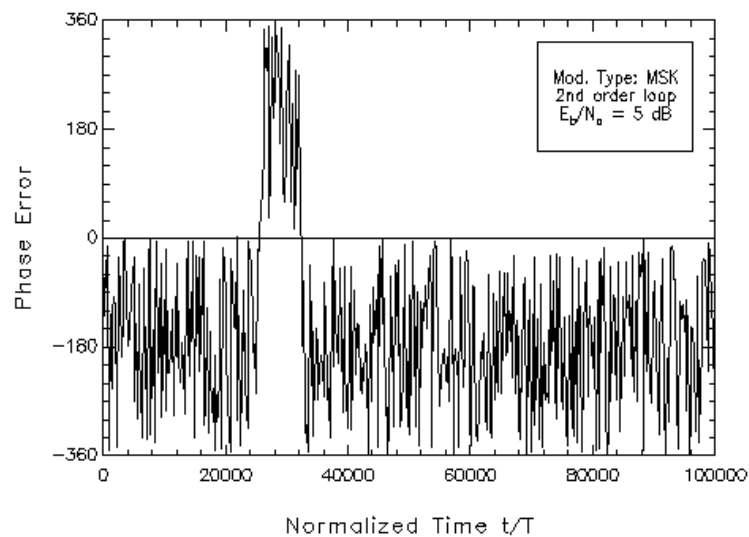


Fig.IX.12

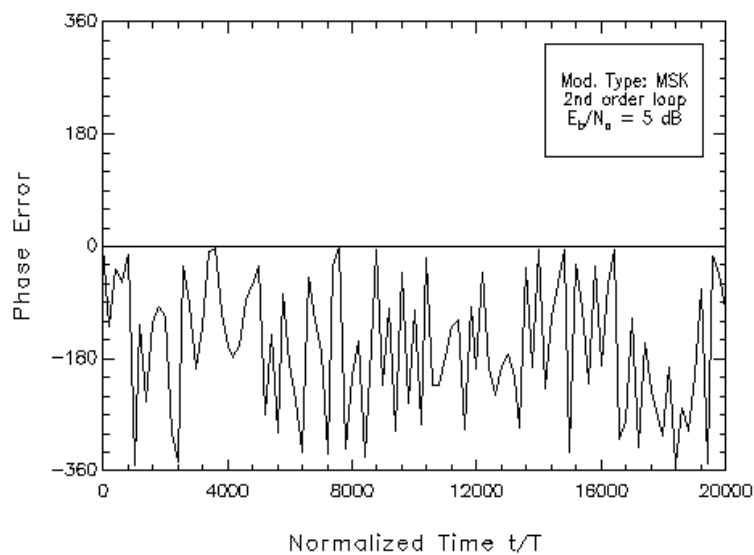


Fig.IX.13

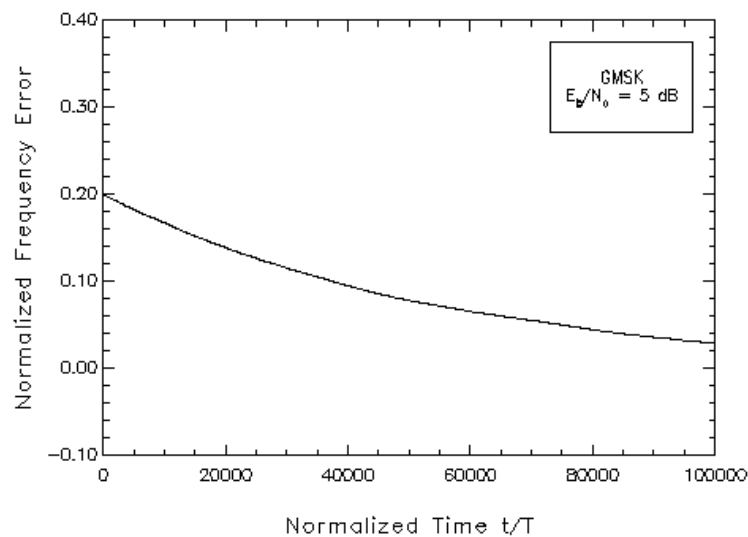


Fig.IX.14

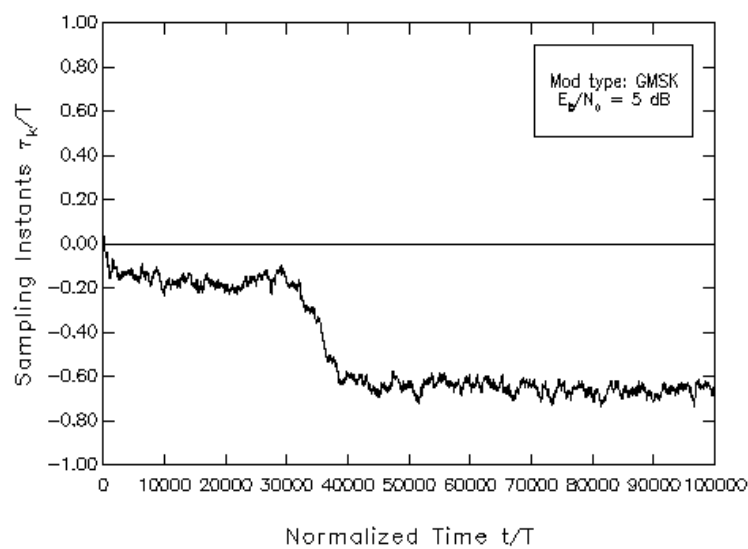


Fig.IX.15

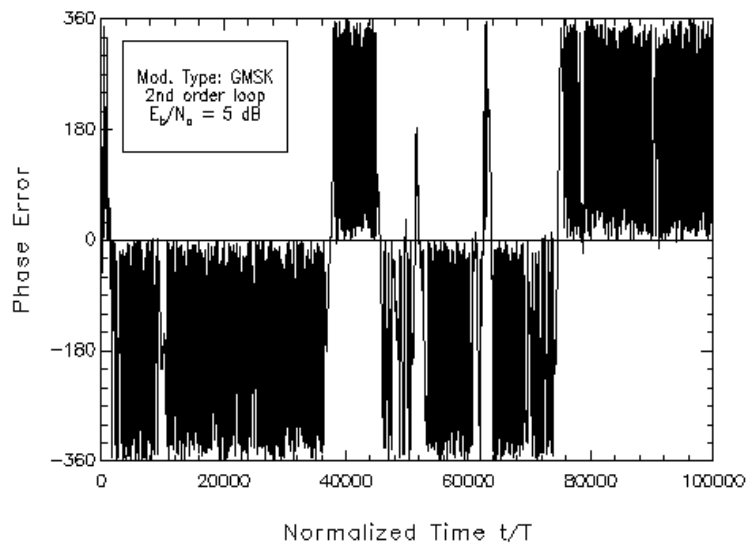


Fig.IX.16

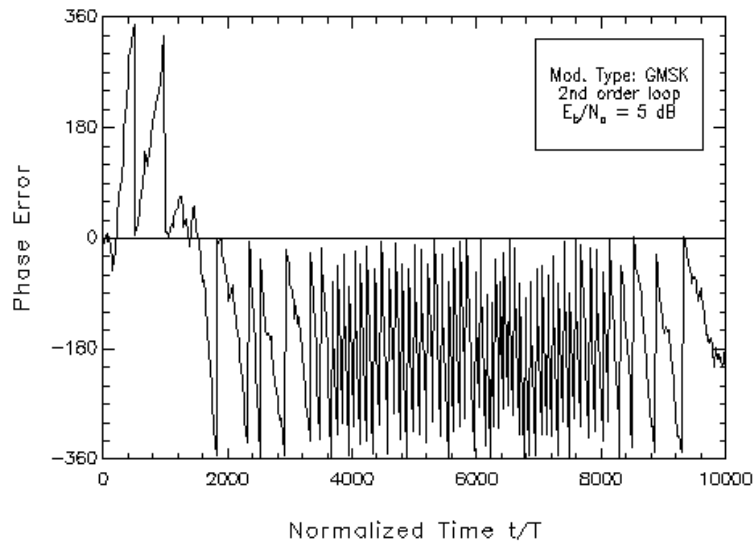


Fig.IX.17

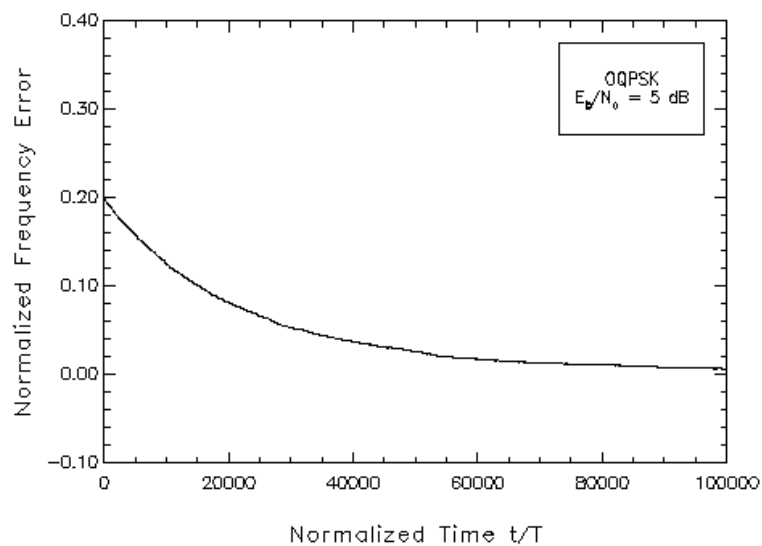


Fig.IX.18

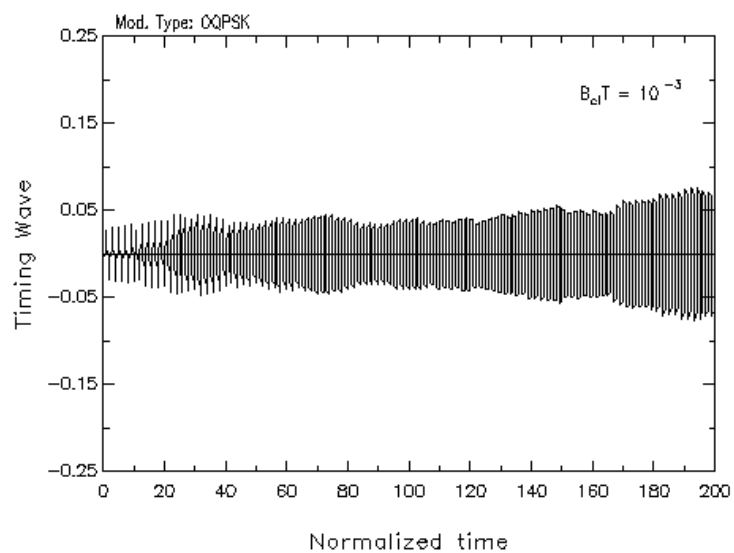


Fig.IX.19

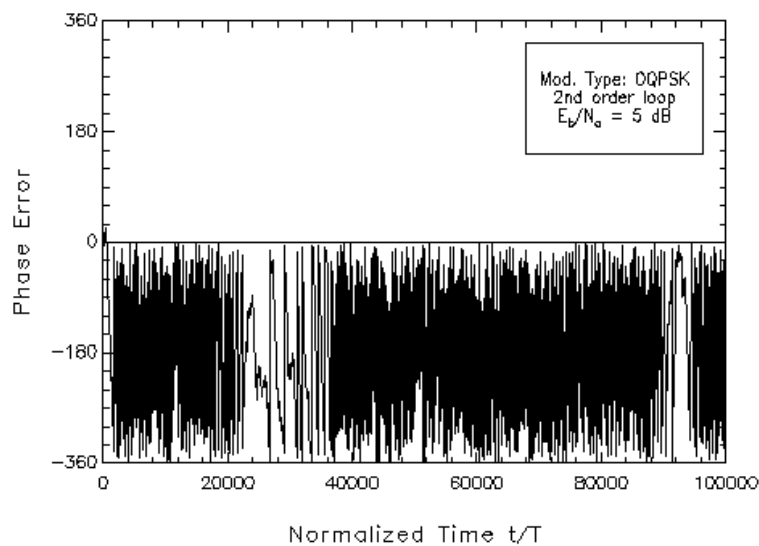


Fig.IX.20

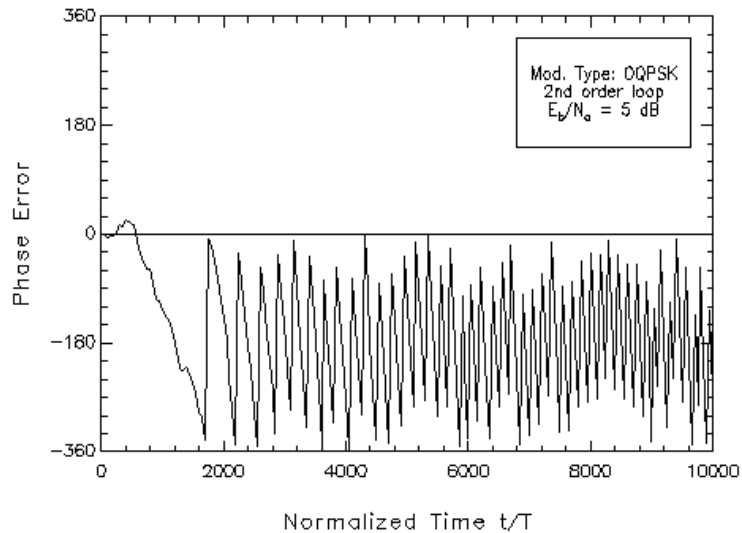


Fig.IX.21

IX. 6 Nonlinear Channels

As already mentioned in sect. II.1, in satellite communications high power amplifiers (HPA's) are to be operated near saturation for power efficiency optimization. As a consequence, undesirable AM-to-PM conversion phenomena arise in signal amplification causing performance degradation, especially for phase-modulated waveforms. This degradation occurs, for instance, for NYQ-OQPSK, while constant-envelope CPM does not suffer from the cited phenomena.

In the following we evaluate the performance loss of NYQ-OQPSK in the presence of the nonlinear channels whose AM/AM and AM/PM characteristics are shown in sect. IV.1, Figs. IV.2-5. In these figures, both input and output power are normalized so as to make the saturation point correspond to 0 dB on both amplitude axes.

In the following we examine separately the behavior of a Solid-State Amplifier (SSA) and that of an L-band TWT Amplifier (TWTA).

A. SSA

The first step in our study was the evaluation (by means of computer simulation) of the 99% normalized bandwidth $B_{99}T$ of the NYQ-OQPSK at the output of the SSA, as a function of the modulation roll-off α and of the Input Back-Off (IBO) on the average input power. The results of our simulations are reported in Fig. IX.22 which shows $B_{99}T$ vs. α for different values of the IBO. This figure allows us to compare the bandwidth occupation of this modulation format (and then its spectrum efficiency), for a fixed value of α , with the bandwidth of MSK and GMSK. The figure shows that, for a fixed roll-off, the bandwidth occupancy decreases as IBO is increased because of a corresponding reduction in the nonlinear distortions.

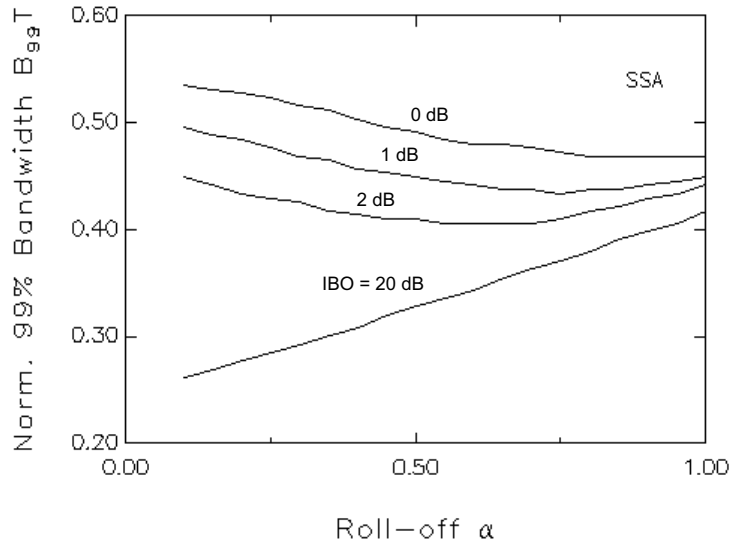


Fig.IX.22

The second step in our study was the evaluation of the Output Back-off (OBO) of the SSA as a function of the IBO, for different values of α . The simulation results are shown in Figs. IX.23-IX.24 for α equal to 0.1 and 1, respectively: from inspection of these figures it can be inferred that the relationship between OBO and IBO does not change appreciably as α varies. These figures are useful to determine the total degradation undergone by NYQ-OQPSK with respect to linear channel operation, when a SSA is used. To this end, we define the Total Power Loss (TPL) as the SNR degradation experienced by NYQ-OQPSK at a fixed BER value, with respect to the ideal case of transmission through a nondistorting power amplifier operated at OBO = 0 dB. For fixed IBO and α , we can compute the TPL as the sum of the following two different contributions:

- 1) The first (indicated as D1 in fig.IX.25) is due to the distortion introduced by the SSA. It can be evaluated by comparing the BER curve obtained

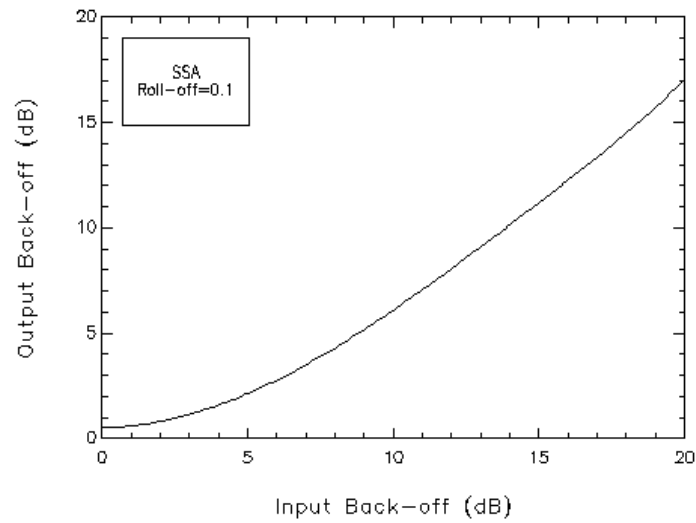


Fig.IX.23

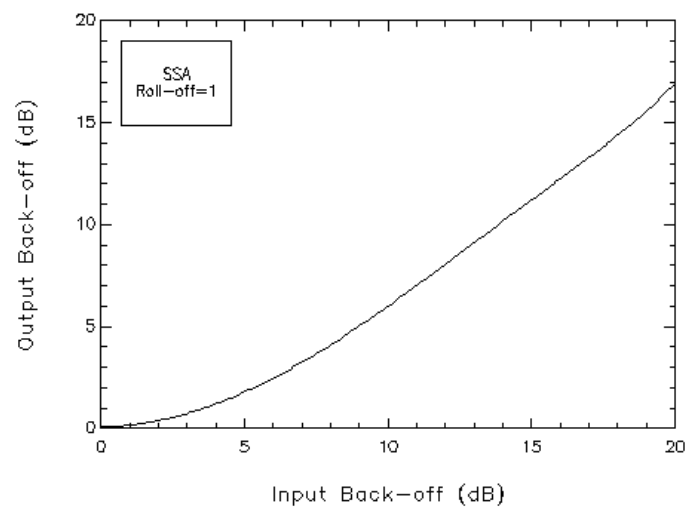


Fig.IX.24

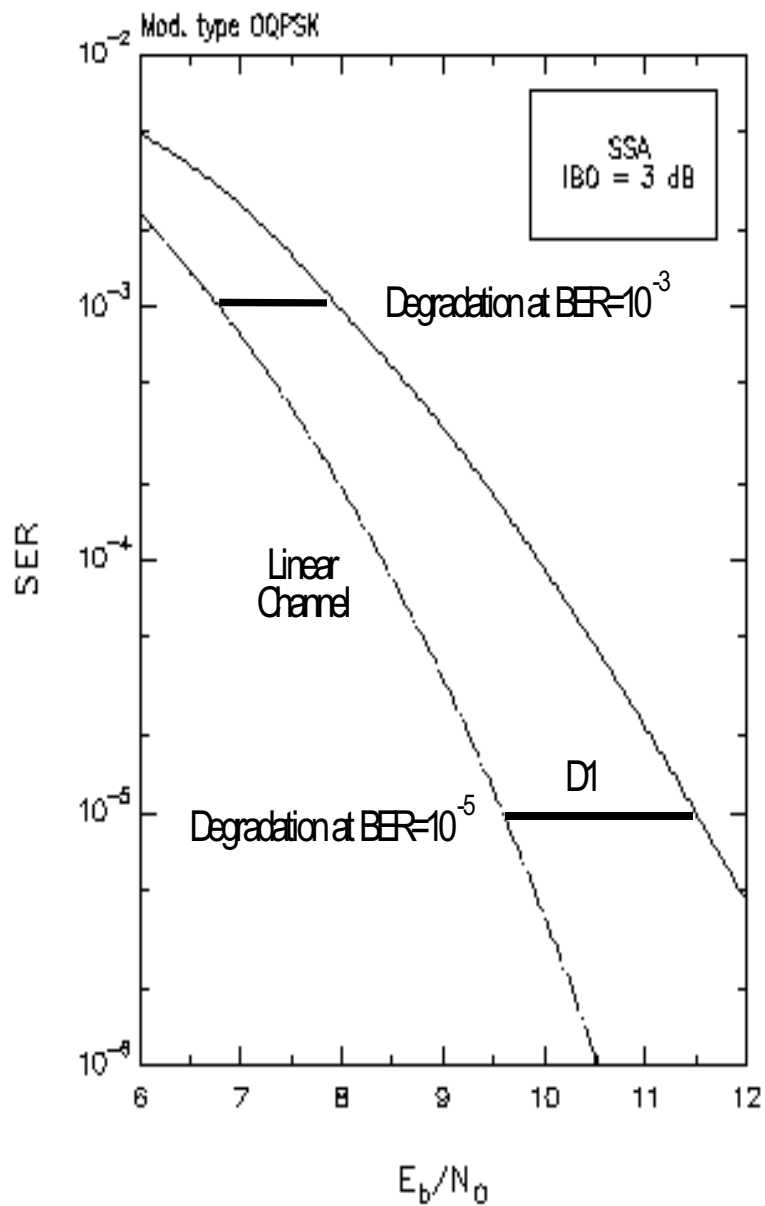


Fig.IX.25

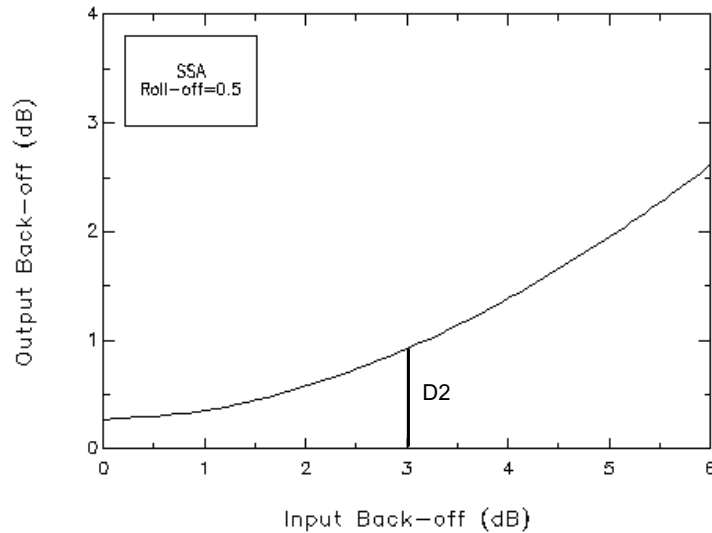


Fig.IX.26

for a fixed value of IBO with the corresponding curve determined in the presence of a linear channel. In the following the degradations are evaluated at $\text{BER}=10^{-3}$ and at $\text{BER}=10^{-5}$. For instance, Fig.IX.25 highlights these losses for $\text{IBO}=3$ dB and $\alpha=0.5$.

2) The second contribution (indicated as D2 in Fig. IX.26) is due to the fact that the operating point of the SSA is normally different from that corresponding to maximum power efficiency ($\text{IBO}=0$ dB).

Figures IX.27-IX.28 show the TPL ($=D1+D2$, in decibels) vs. IBO for $\alpha=0.5$ and $\alpha=1$, respectively. In these figures, the marks represent simulation results which are interpolated by solid-line curves. For any fixed BER, it can be observed that an optimum operating point (i.e. attaining minimum loss) exists which does not necessarily correspond to $\text{IBO}=0$ dB.

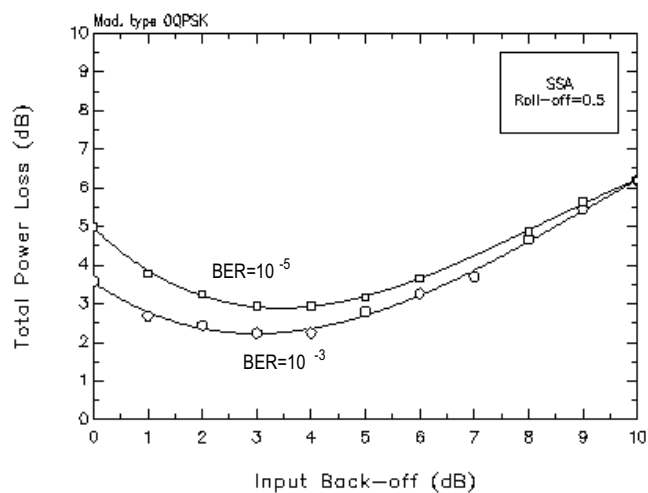


Fig.IX.27

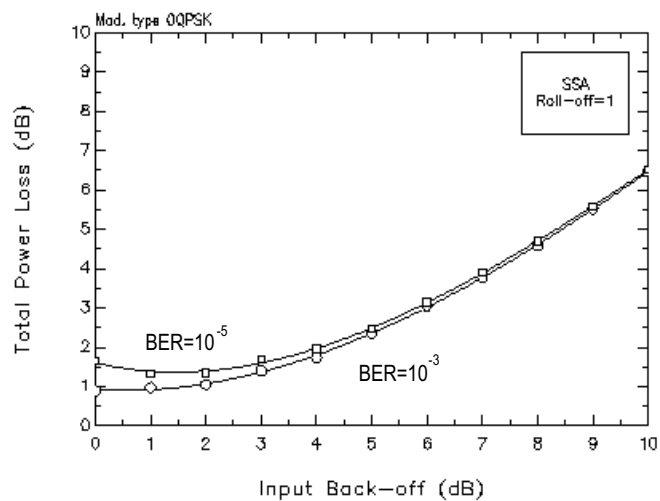


Fig.IX.28

B. TWTA

In this section we examine the system behaviour when a Travelling-Wave Tube Amplifier is employed. We incorporated in our simulation program the AM/AM and AM/PM characteristics of an L-band Hughes TWTA provided by the Contract Technical Manager. The discussion strictly parallels that carried out in the previous section for the SSA. Figure IX.29 is similar to Fig. IX.22 and shows the 99% normalized bandwidth B_{99T} of NYQ-OQPSK at the output of the TWTA vs. the modulation roll-off α , for different values of the IBO. The same considerations made for the SSA also apply to the TWTA. The diagram of the OBO as a function of the IBO for the TWTA is illustrated in Fig. IX.30 for two different values of α . As in the case of the SSA, the relationship between OBO and IBO is hardly affected by variations in α . Finally, for fixed values of IBO and α , the TPL was computed as the sum of the terms D1 and D2 defined in the previous section. Figures IX.31-IX.32 show the TPL vs. IBO for $\alpha=0.5$ and $\alpha=1$, respectively. As with SSA, for any given BER, a value of IBO allowing for minimum loss can be found.

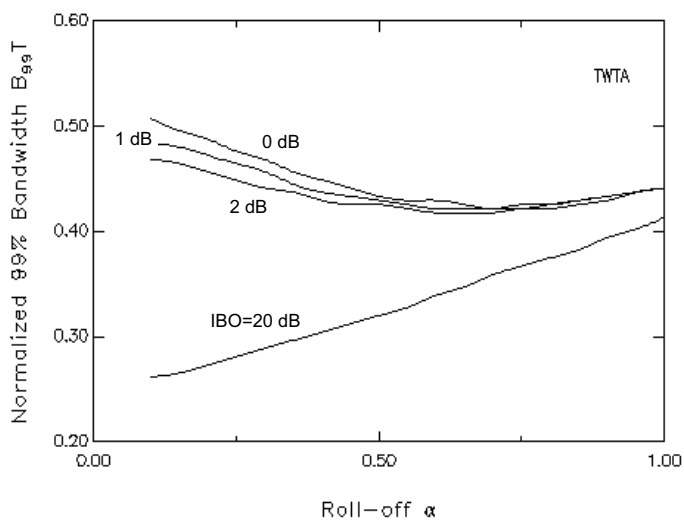


Fig.IX.29

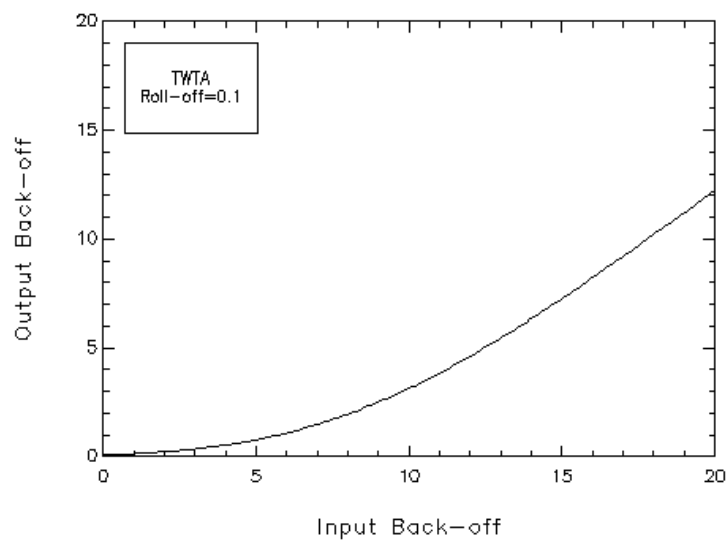


Fig.IX.30

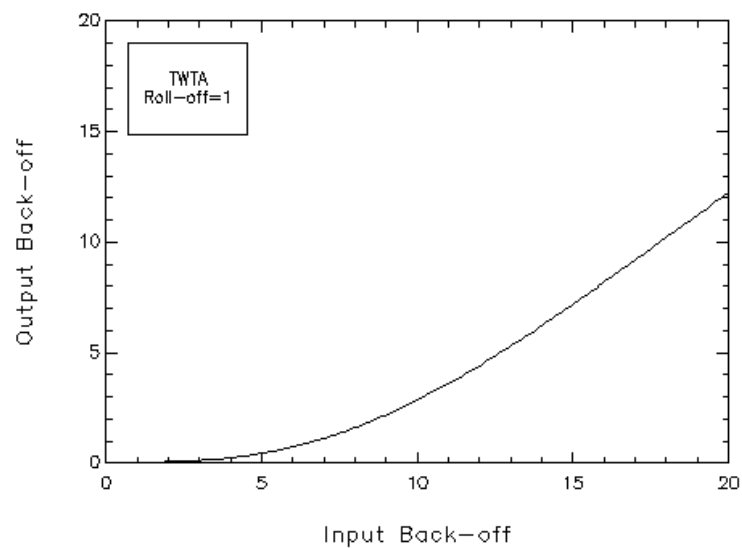


Fig.IX.31

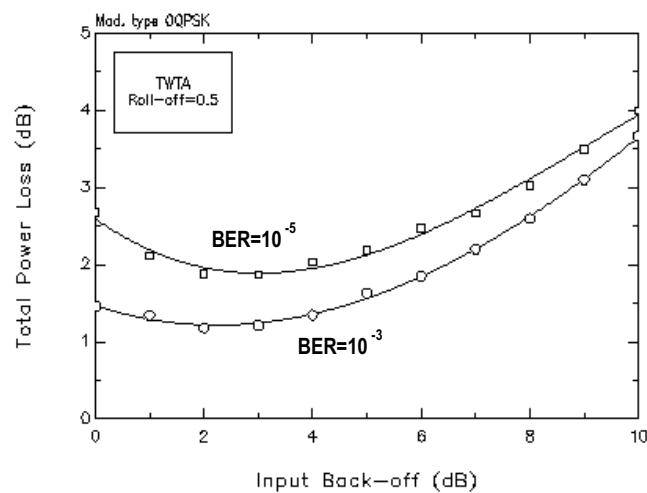


Fig.IX.32

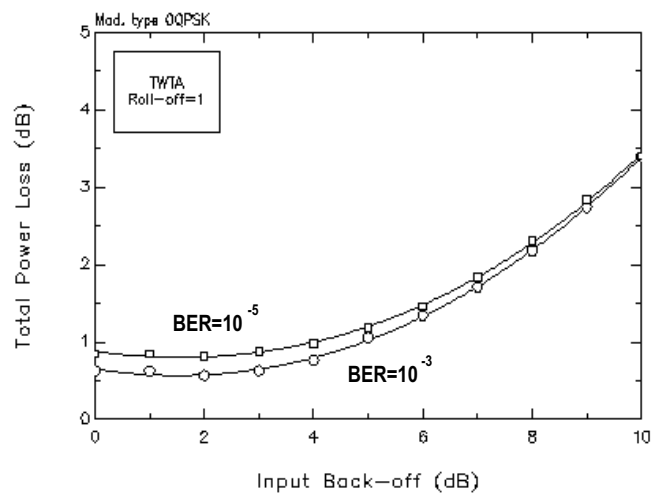


Fig.IX.33

(This space is intentionally left blank)

Final Trade-Off

In this section, the relative merits of the various modulation formats analyzed in the preceding sections are discussed in terms of power and bandwidth efficiency. As far as power efficiency is concerned, the results of our simulations (in the absence of Doppler phenomena) are summarized in Fig. F.1. In this figure, we chose $\alpha=0.5$ and $\text{IBO}=3$ dB (corresponding to minimum TPL) for NYQ-OQPSK.

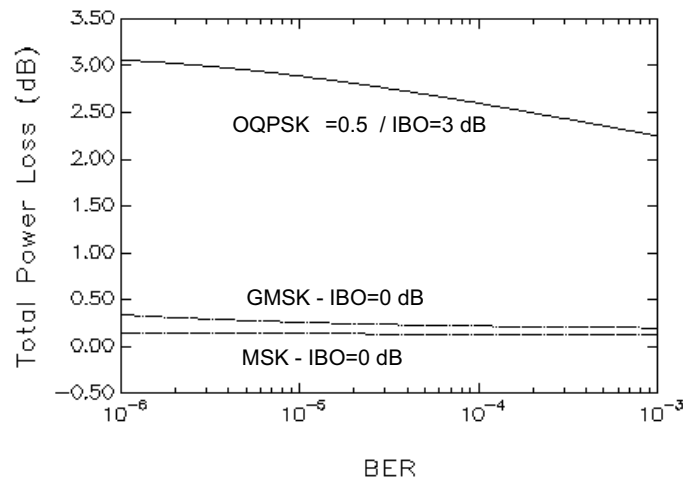


Fig.F.1

As a measure of bandwidth efficiency, we selected the normalized bandwidth $B_{99}T$. Values of $B_{99}T$ for OQPSK, MSK and GMSK are reported in Tab. IV, together with the corresponding TPL's, assuming a SSA is used. It is noted that a slight improvement can be attained in the TPL of OQPSK if a

TWTA is used instead of a SSA.

Modulation Type	Total Power Loss with SSA at 10^{-5} / 10^{-3} BER	Total Power Loss with TWTA at 10^{-5}/10^{-3} BER	99% Normalized Bandwidth
OQPSK $\alpha=0.5$	3.0 / 2.3 dB IBO=3dB	1.9/ 1.2 dB IBO=2dB	0.4
OQPSK $\alpha=1.0$	0.9/ 1.2 dB IBO=1dB	0.6/ 0.8 dB IBO=2dB	0.44
MSK IBO=0 dB	0.1 / 0.1 dB	0.1 / 0.1 dB	0.6
GMSK IBO= 0 dB	0.3 / 0.2 dB	0.3 / 0.2 dB	0.5

TABLE IV

From Tab. IV and from the various discussions of the present study we draw the following conclusions:

-) Continuous-Phase, Constant-Envelope Modulations are particularly suited for the application at hand, especially in view of the use of saturated power amplifiers.
-) Spectrum Efficiency of CPM can be improved through baseband pulse shaping (GMSK).
-) Filtered OQPSK has better spectral efficiency (about 20%) with respect to GMSK, but has 2 to 3 dB of total power degradation in the presence of a Solid

State amplifier (at least for roll-off values less or equal than 0.5) and about 1 dB degradation when a TWT amplifier is employed.

-) Properly designed synchronization subsystems do not introduce significant performance degradations and can track the Doppler shift/accelerations of LEO satellites.
-) Full-Digital modem implementations can be accomplished with minor modifications with respect to the schemes presented in this study.

For the above reasons, we think that the modulation to be recommended for future ESA standards for telemetry links is GMSK since it exhibits good spectral efficiency and also a gain of 2 to 2.7 dB in SNR over filtered OQPSK, in all those situations where a nonlinear solid-state power amplifier must be employed. In our study we selected $B_G T = 0.5$ as the bandwidth of the premodulation filter for GMSK. By narrowing this filter, it is expected that the spectrum efficiency of GMSK may be further improved at the expense of a slight additional power degradation.

References

- [Aga85] O. Agazzi, C.-P.J. Tzeng, D.G. Messerschmitt and D.A. Hodges: *"Timing Recovery in Digital Subscriber Loops"*, IEEE Trans. Commun., vol. COM-33, pp. 558-568, June 1985.
- [Alb89] T. Alberty and V. Hespel: *"A New Pattern Jitter Free Frequency Error Detector"*, IEEE Trans. Commun., Vol. COM-37, pp. 159-163, Feb. 1989.
- [Ana87] F. Ananasso, B. Baccetti, V. Castellani, L. Cellai, A. D'Ambrosio, G. Gallinaro and U. Mengali: *"Study of Reference Recovery for Serial Demodulation of Offset-Binary Modulation Schemes"*, ESA-ESTEC Contract n. 6253/85/NL/DG, Final Report, 1987.
- [And78] J. B. Anderson and D. P. Taylor, *"A Bandwidth-Efficient Class of Signal-Space Codes"*, IEEE Trans. Inform. Theory, vol. IT-24, pp. 703-712, November 1978.
- [And86] J.B. Anderson, T. Aulin and C.E. Sundberg: *"Digital Phase Modulation"*, Plenum Press, New York, 1986.
- [Aul85] T. Aulin: *"Study of a New Trellis Decoding Algorithm and Its Applications"*, ESA-ESTEC Contract n. 6039/84/NL/DG, Final Report, December 1985.
- [Ben87] S. Benedetto, E. Biglieri and V. Castellani: *"Digital Transmission Theory"*, Prentice-Hall, Englewood Cliffs NJ, 1987.

- [Bha81] V.K. Bhargava, D. Haccoun, R. Matyas and P.P. Nuspl: "Digital Communications By Satellite", John Wiley & Sons, New York 1981.
- [Boo78] R.W.D. Booth: "*Carrier Phase and Bit Sync Regeneration for the Coherent Demodulation of MSK*", Proc. IEEE NTC'78, paper n. 6.1.
- [Boo80] R.W.D. Booth: "*Illustration of the MAP Estimation Method for Devising Closed-Loop Phase Tracking Topologies: the MSH Signal Structure*", IEEE Trans. Commun., vol. COM-28, pp. 1137-1142, August 1980.
- [Cah77] C.R.Cahn: "*Improving Frequency Acquisition of a Costas Loop*", IEEE Trans. Commun., Vol. COM-25, pp. 1453-1459, Dec. 1977
- [D'A86] A.N. D'Andrea, U Mengali: "*Jitter Performance Analysis of the Delay-Line Clock Regenerator* ", IEEE Trans. Commun., vol. COM-34, pp. 321-328, April 1986.
- [D'A87] A.N. D'Andrea, U Mengali, R. Reggiannini: "*Carrier Phase and Clock Recovery for Continuous Phase Modulated Signals*", IEEE Trans. Commun., vol. COM-35, pp. 1095-1101, October 1987.
- [D'A90a] A.N. D'Andrea, U Mengali, R. Reggiannini: "*A Digital Approach to Clock Recovery in Generalized MSK*", IEEE Trans. Veh. Tech., vol. VT-10, August 1990.
- [D'A90b] A.N.D'Andrea, U.Mengali: "*Performance of a Quadricorrelator Driven by Modulated Signals*", IEEE Trans. Commun., Vol.COM 38,Nov. 1990.
- [D'A90c] A.N. D'Andrea, U Mengali: "*Design of quadricorrelators for automatic frequency control systems*", submitted to IEEE Trans. Commun. .
-

- [deB72] R. deBuda: *"Coherent Demodulation of Frequency Shift Keying with Low Deviation Ratio"*, IEEE Trans. Commun., vol. COM-20, pp. 429-435, June 1972.
- [DeG89] R. De Gaudenzi: *"QPSK, OQPSK, MSK, GMSK - A Comparative Performance Evaluation for Space Data Transmission Applications"*, ESA Document XRT/89.061/RdG.
- [ESA86] European Space Agency STAB: *"Radio Frequency and Modulation Standard"*, TTAC-A-05 Issue No.2, Jan. 1986.
- [ESA90] European Space Agency Document XRT/396.90/RDG/ce, July 1990.
- [Feh87] K. Feher (Ed.): *"Advanced Digital Communication Systems and Signal Processing Techniques"*, Prentice-Hall, Englewood Cliffs NJ 1987.
- [Fra80] L.E. Franks: *"Carrier and Bit Synchronization in Data Communication - A Tutorial Review"*, IEEE Trans. Commun., vol. COM-28, pp. 1107-1121, August 1980.
- [Gal85] P. Galko and S. Pasupathy, *"Linear Receivers for Correlatively Coded MSK"*, IEEE Trans. Commun., vol. COM-33, April 1985, pp. 338-347.
- [Gar77] F.M. Gardner: *"Hang-up in Phase-Lock Loops"*, IEEE Trans. Commun., vol. COM-25, pp. 1210-1214, Oct. 1977.
- [Gar83] F.M. Gardner: *"Multipath Link and Modem Design for Satellite-Mobile Communications"*, ESA Final Report, ESTEC contract No5146/82/NL/GM(SC), Aug. 1983.
- [Gar85] F.M. Gardner : *"Properties of Frequency Difference Detectors"*, IEEE Trans. Commun., Vol. COM-33, pp. 131-138, Feb. 1985.

- [Gar86] F.M. Gardner: *"A BPSK/QPSK Timing-Error Detector for Sampled Receivers"*, IEEE Trans. Commun., vol. COM-34, pp. 423-429, May 1986.
- [Gar88] F.M. Gardner: *"Demodulator Reference Recovery Techniques Suited for Digital Implementation"*, ESA-ESTEC Contract n. 6847/86/NL/DG, Final Report, August 1988.
- [Gar90] F.M. Gardner: *"Frequency Detectors for Digital Demodulators Via Maximum Likelihood Derivation"*, ESA Final Report: Part II, ESTEC contract No 8022/88/NL/DG, March 1990.
- [God78] D.N. Godard: *"Passband Timing Recovery in an All-Digital Modem Receiver"*, IEEE Trans. Commun., vol. COM-26, pp. 517-523, May 1978.
- [Har83] R.A. Harris: *"Offset Binary Modulation Schemes and Their Application to Satellite Communications"*, 2nd Int. Conf. on New Systems & Services in Telecommun., Liege 1983.
- [Jer84] M.C. Jeruchim: *"Techniques for Estimating the Bit Error Rate in the Simulation of Digital Communication Systems"*, IEEE J. Select. Areas Commun., vol. SAC-2, January 1984.
- [JSAC] IEEE Journal on Selected Areas in Communications - Volume 7, Issue n. 9, December 1989.
- [Lau86] P.A. Laurent, *"Exact and Approximate Construction of Digital Phase Modulations by Superposition of Amplitude Modulated Pulses"*, IEEE Trans. Commun., vol. COM-34, Feb. 1986, pp. 150-160.

- [Lui88] M. Luise: *"Sistemi di Sincronizzazione in un Ricevitore in Tecnologia Digitale per Modulazioni Numeriche Efficienti"*, Dissertazione finale Dottorato di Ricerca II ciclo, Università di Pisa, October 1988 (in Italian).
- [Lui89] M. Luise, U.Mengali: *"OQPSK - Based Approximation to Generalized MSK"*, IEEE Int. Conf. on Commun., Boston 1989.
- [Lui90] M. Luise and U. Mengali: *"A New Interpretation of the Average Matched Filter for MSK-Type Receivers"*, IEEE Trans. Commun., vol. COM-38, December 1990.
- [Mas85] T. Maseng :*"Digital Phase Modulated (DPM) Signals"*, IEEE Trans. Commun., vol. COM-33, pp. 911-918, September 1985.
- [Men77] U. Mengali: *"Joint Phase and Timing Acquisition in Data-Transmission"*, IEEE Trans. Commun., vol. COM-25, pp. 1174-1185, October 1977.
- [Mes79] D. G. Messerschmitt: *"Frequency Detectors for PLL Acquisition in Timing and Carrier Recovery"*, IEEE Trans. Commun., Vol. COM-27, pp.1288-1295, September 1979.
- [Mey90] H. Meyr and G. Ascheid: *"Synchronization in Digital Communications"*, vol. I, John Wiley & Sons, New York 1990.
- [Mue76] K.H. Mueller and M. Muller: *"Timing Recovery in Digital Synchronous Data Receivers"*, IEEE Trans. Commun, vol. COM-24, pp. 516-521, May 1976.
- [Mur81] K. Murota and K. Hirade: *"GMSK Modulation for Digital Mobile Radio Telephony"*, IEEE Trans. Commun., vol. COM-29, pp. 1044-1050, July 1981.

- [Nat84] F.D.Natali, *"AFC Tracking Algorithms"*, IEEE Trans. Commun., Vol. COM-32, pp. 935-947, Aug. 1984.
- [Pas79] S. Pasupathy: *"Minimum Shift Keying: a Spectrally Efficient Modulation"*, IEEE Commun. Magazine, vol. 17, pp. 14-22, July 1979.
- [Piz85] S. V. Pizzi and S. G. Wilson: *"Convolutional Coding Combined with Continuous Phase Modulation"*, IEEE Trans. Commun., Vol. COM-33, pp. 20-29, Jan. 1985.
- [Sar88] H.Sari and S.Moridi, *"New Phase and Frequency Detectors for Carrier Recovery in PSK and QAM Systems"*, IEEE Trans. Commun., Vol. COM-36, pp. 1035-1043, Sept. 1988.
- [Sim] M.K.Simon: *"Discriminator-Aided Acquisition of Suppressed Carrier Signals, parts I and II"*, unpublished work.
- [Tan87] M.S. El-Tanany and S.A. Mahmoud, *"Mean-Square Error Optimization of Quadrature Receivers for CPM with Modulation Index 1/2"*, IEEE Journal on SAC, vol. SAC-5, n. 5, June 1987, pp. 896-905.
- [Tan89] M.S. El-Tanany and S.A. Mahmoud, *"Analysis of Two Loops for Carrier Recovery in CPM with Index 1/2"*, IEEE Trans. Commun., Vol. COM-37, pp. 164-176, Feb. 1989.

(This space is intentionally left blank)

Acknowledgements

We wish to thank Dr. Ing. G. Vitetta of the University of Pisa for his expert contribution to the implementation of the simulation programs. Also, we would like to mention the continuing support and stimulating advice provided by the Technical Manager R. de Gaudenzi throughout this work.

[This page intentionally left blank.]

**REPORT CONCERNING CCSDS RADIO FREQUENCY AND MODULATION
CONSULTATIVE COMMITTEE FOR SPACE DATA SYSTEMS
P1E - RADIO FREQUENCY AND MODULATION**

**ON THE INTRODUCTION OF
BANDWIDTH-EFFICIENT MODULATION METHODS
ON TELEMETRY LINKS**

Reply to AI 98-19

European Space Agency
Jean-Luc Gerner

REPORT CONCERNING CCSDS RADIO FREQUENCY AND MODULATION
CONSULTATIVE COMMITTEE FOR SPACE DATA SYSTEMS
P1E - RADIO FREQUENCY AND MODULATION

1. Scope

At CCSDS P1E meeting of May 1999, two new draft recommendations dealing with bandwidth-efficiency are submitted for discussion:

- Rec 3.1.7A is derived from the SFCG Recommendation 17-2R1 approved at SFCG-18 in September 1998. Rec 3.1.7A recommends to avoid the use of subcarriers and to use filtered suppressed carrier modulations for symbol rates of more than 2 Ms/s. Spectral masks are also provided.
- Rec 3.3.5A recommends the use of filtered OQPSK or of GMSK for symbol rates of more than 2 Ms/s.

This document presents a review of the current use of bandwidth-efficient modulations for commercial applications and assesses the feasibility of applying these modulations in the near future to space science services.

2. Background

The times when the unique driving factor in the design of the space TT&C systems was link performance is gone. Nowadays, frequency bands are getting more and more congested and it is of primary importance to reduce the occupied bandwidth of radiated signals to the minimum necessary compatible with the other mission constraints.

Commercial telecommunication systems, driven by pure financial considerations, have been faced long ago with the problem of packing as many users as possible within a given bandwidth. To this end, huge investments have been made in the search of as bandwidth-efficient as possible modulation methods.

Up to recently, the space science community was not directly concerned with the problem: data rates were low to moderate and, in general, the main determining factor in the assessment of the assigned bandwidth was the maximum Doppler shift rather than the data rate. Several years ago, space agencies, in the frame of CCSDS Subpanel 1E, have started investigating the possibility of introducing more bandwidth efficient modulations for high data rate transmissions. The theoretical work was completed by CCSDS P1E in 1997 and a report of the results was presented at the 1997 Space Frequency Coordination Group meeting, SFCG-17. Based on the CCSDS results, Recommendation 17-2 was drafted and approved as provisional at SFCG-17 and formally approved at SFCG-18, opening the way to CCSDS to adopt bandwidth-efficient modulations for future telemetry systems.

3. A Spectral Mask: Recommendation SFCG 17-2

SFCG Rec17-2R1 recommends spectral emission limits (Fig.1) applicable to space science services

- for transmissions rates of less than 2Ms/s, achievable with the existing CCSDS-recommended modulation schemes
- and for transmission rates of more than 2 Ms/s, for which new modulation methods need to be introduced

This document only addresses modulation methods susceptible to meet the spectral limits for transmission rates in excess of 2 Ms/s.

REPORT CONCERNING CCSDS RADIO FREQUENCY AND MODULATION
CONSULTATIVE COMMITTEE FOR SPACE DATA SYSTEMS
P1E - RADIO FREQUENCY AND MODULATION

(the CCSDS terminology *symbol rate* must be understood as the *rate of the bit stream* (coded or uncoded data) at the input to the modulator. The definition is not applicable to trellis-coded modulation schemes)

It is worthwhile noting that the space links concerned with such data rates are nowadays, and still for a number of years, exclusively links from space to Earth, be they transmitting spacecraft or payload telemetry data. The first applications will most likely be implemented in one of the following bands: 2200-2300 MHz, 8400-8500 MHz, 8025-8400 MHz and at a later stage in the 32 GHz or 37/38 GHz bands.

4. What Modulations Meet the Limits of SF17-2?

References [3] and [4] have performed extensive analyses of all major digital modulation methods susceptible to be introduced in a future CCSDS standard if they present reasonably good bandwidth compactness while still offering satisfactory performances. Their characteristics have been investigated taking into account the specificity of a space telemetry link, such as low E_b/N_0 or channel non-linearities.

Figures 2 to 5 show the spectra of some of the most promising of the modulation methods. Figures 2 and 3 are extracted from [3], figure 4 was produced by E.Vassallo and figure 5 is from [6]. On all these figures the spectral limit as specified in SF17-2 for data rates of more than 2 Mb/s has been added.

The following conclusions can be drawn from these figures:

- Fig.2: Curve 1 shows the theoretical unfiltered QPSK/OQPSK spectrum. Curve 4 is for the filtered (Butterworth, 6 poles, $BT = 1.2$) QPSK/OQPSK spectrum in a linear channel. Curves 2 and 3 present the spectra of the filtered QPSK and OQPSK spectra, respectively, at the output of the non-linear channel (travelling wave tube with 0 dB back-off). These curves confirm the strong sidelobes regrowth in the case of QPSK. Figure 2 shows that the mild Butterworth/ $BT=1.2$ filtering with OQPSK permits to marginally meet the spectral mask requirements. Any smaller value of BT would allow to meet the limit of the mask.
- Fig.3: Curve 1 is the unfiltered 8PSK spectrum in a linear channel. The group 2 of curves displays the 8PSK signal spectrum after filtering through a Butterworth, 6 poles filter with BT products of 1, 1.5 and 2. The same spectra after the signal has been passed through a non-linear channel (TWT with back-off of 0 and 3 dB) appear on the group 3 of curves. With some precaution on the TWT back-off and a BT of 1 or less, the filtered 8PSK modulation can remain within the mask limits.
- Fig.4: The curves shown are for a GMSK signal, with values of BT of 1, 0.5 and 0.25, in a non-linear channel (SSPA, 0dB back-off). It can be seen that in these conditions GMSK does easily comply with the mask for any BT value of 1 or less.
- Fig.5: FQPSK offers spectral roll-off of similar order as GMSK with small values of BT . It is remarkable that, for FQPSK as well as for GMSK, spectral regrowth in a non-linear channel is very moderate.

The list of modulation methods susceptible to comply with the spectral mask is not exhaustive but still demonstrates that the mask of SF17-2 is reasonable and that it can even be envisaged to tighten it in the future if breadboard testing and in-flight demonstration confirm the validity of above figures.

REPORT CONCERNING CCSDS RADIO FREQUENCY AND MODULATION
CONSULTATIVE COMMITTEE FOR SPACE DATA SYSTEMS
P1E - RADIO FREQUENCY AND MODULATION

Above conclusions are summarised in table 1 together with the expected degradation in BER performance of these modulations as compared with an (ideal) unfiltered BPSK signal passed through the same non-linearity.

	BER degrad. 10^{-2}	BER degrad. 10^{-5}	
OQPSK, But/6/BT=1 TWT 0 dB	1.2	1.4	Ref [3], page 56
8PSK SRRC $\alpha=0.5$ SSPA 0 dB	1.6	2.7	Ref [4] (no data available for Butterworth filtering)
GMSK BT=1 TWT 0 dB	0.6	0.6	Ref [3], page 56
FQPSK HPA 0 dB	1.3 (TBC)	1.3 (TBC)	Ref [3], page 56 (data provided by K.Feher)

Table 1: Modulations susceptible to meet the mask of SF17-2. Results from CCSDS studies ([3], [4])

It is interesting at this stage to look at what are the choices made by the commercial telecommunication systems for which bandwidth efficiency is the number one goal.

5. Reuse of Available Technology

Up to now, CCSDS work has been limited to theoretical studies and is lacking the backing of actual hardware testing. The implementation and the testing of a breadboard would allow to verify the expected performances and also to evaluate the feasibility of the technology: implementation of a spaceborne modulator, implementation of a demodulator for the earth station.

In order to gain confidence concerning the feasibility of implementing selected new modulation methods for spacecraft telemetry, it is useful to perform a survey of technologies available in the commercial market. The survey will also help identifying what well-proven technologies for ground applications could be reused for space.

6. Major Digital Modulation Formats

Table 2 covers the current main applications for different modulation formats in both wireless communications and video.

QAM modulation formats are not suitable for space applications: their non-constant envelope property makes them unsuitable for non-linear channels because of high spectral regrowth.

REPORT CONCERNING CCSDS RADIO FREQUENCY AND MODULATION
CONSULTATIVE COMMITTEE FOR SPACE DATA SYSTEMS
P1E - RADIO FREQUENCY AND MODULATION

Modulation Format	Application
MSK, GMSK	GSM, CDPD, DECT, HIPERLAN
BPSK	Space Telemetry, cable modems
QPSK, $\pi/4$ DQPSK	Space telemetry, CDMA, JDC, NADC, TETRA, PHS, PDC, LMDS, DVB-S, cable (return path), cable modems, TFTS
OQPSK	CDMA, space telemetry
FSK, GFSK	Paging, RAM mobile data, AMPS, CT2, ERMES, land mobile, public safety
8PSK	Satellite, aircraft, telemetry pilots for monitoring broadband video systems
16 QAM	Microwave digital radio, modems, DVB-C, DVB-T
32 QAM	Terrestrial microwave, DVB-T
64 QAM	DVB-C, modems, broadband set top boxes, MMDS
256 QAM	Modems, DVB-C (Europe), Digital video (US)

Table 2: Major modulation schemes used in wireless communication and video broadcasting systems

7. Theoretical Bandwidth Efficiency Limits

Bandwidth efficiency describes how efficient the allocated bandwidth is utilised or the ability of a modulation scheme to accommodate data, within a limited bandwidth. Table 3 shows the theoretical bandwidth efficiency limits for the main modulation types. These figures cannot be actually achieved but only approached in practical radios because they require perfect modulators, demodulators, filters and transmission paths.

Modulation Format	Theoretical Bandwidth Efficiency Limits
MSK	1 bit/second/Hz
BPSK	1 bit/second/Hz
QPSK	2 bits/second/Hz
8PSK	3 bits/second/Hz
16 QAM	4 bits/second/Hz
32 QAM	5 bits/second/Hz
64 QAM	6 bits/second/Hz
256 QAM	8 bits/second/Hz

Table 3: Theoretical bandwidth efficiency limits of some popular modulation formats

If the radio has a perfect (rectangular in the frequency domain) filter, then the occupied bandwidth could be made equal to the channel symbol rate¹.

Maximizing of spectral efficiency can be achieved through premodulation filtering so as to reduce the occupied bandwidth. Raised-cosine filters can be used in combination with QPSK or OQPSK or $\pi/4$ DQPSK (e.g. NADC, PDC, PHS systems) and provide among the best spectral efficiency. Another solution is the use of a gaussian premodulation filter in combination with MSK: the GMSK modulation format is used

¹ Channel symbol rate = bit rate / number of bits transmitted with each symbol

REPORT CONCERNING CCSDS RADIO FREQUENCY AND MODULATION
CONSULTATIVE COMMITTEE FOR SPACE DATA SYSTEMS
P1E - RADIO FREQUENCY AND MODULATION

for GSM and was selected for the upcoming DECT and HIPERLAN systems. The Feher-patented FQPSK scheme is claimed to be an even more bandwidth-efficient method.

8. Spectral Efficiency Examples in Practical Radios

The two following examples give an indication of spectral efficiencies that are achieved in practical radio systems.

The TDMA version of the North American Digital Cellular (NADC) system achieves a 48kbps data rate over a 30 kHz bandwidth or 1.6 bits/second/Hz. It is a $\pi/4$ DQPSK based system and transmits two bits per symbol. The theoretical efficiency would be 2 bits/symbol/Hz and in practice it is 1.6 bits/second/Hz.

Some microwave digital radio systems use 16 QAM. This kind of signal is more susceptible to noise and distortion than something simpler such as unfiltered QPSK. This type of signal is usually sent over a direct line-of-sight microwave link or over a wire where there is very little noise and interference. In this microwave digital radio example the bit rate is 140 Mb/s over a bandwidth of 52,5 MHz. The spectral efficiency is 2.7 bits/second/Hz. To implement this, it takes a very clear line-of-sight transmission path and a precise and optimised high-power transceiver.

This second example demonstrates that the designer of a telecommunication system is faced with the need of performing trade-offs between bandwidth-efficiency and link quality (BER for instance). For the above microwave digital radio system, the constraint is the bandwidth: the bandwidth efficiency is paid in power; high transmit power for very high signal-to-noise conditions and power amplifiers of very poor efficiency to ensure high linearity. This is obviously not the choice to make for space telemetry links!

Table 4 is a synthesis of the key features of the modulation methods for some of the major commercial telecommunication systems (from Ref.[6]).

System	Modulation	Freq. Band	Channel symbol rate	Spectral efficiency (bit/s/Hz)
GSM PCS-1900 DCS-1800	GMSK BT=0.3	900 MHz	271 kb/s	1.3
DECT	GMSK BT = 0.5	1.8-1.9 GHz	1.152 Mbps	0.67
HIPERLAN	GMSK	5.1-5.2 GHz	23.5 Mb/s	0.7
NADC JDC	$\pi/4$ DQPSK SRRC $\alpha=0.5$	800-900 MHz 800-900 MHz	48.6 kb/s 42 kb/s	
(non standard)	FQPSK	From 2 to 24 GHz	300kb/s to 10Mb/s	1.3

Table 4: Some of the recent communication systems and their modulation methods
As can be seen, GMSK is the most popular modulation scheme for commercial systems. $\pi/4$ DQPSK is used currently in the US and in Japan but is significantly less

REPORT CONCERNING CCSDS RADIO FREQUENCY AND MODULATION
CONSULTATIVE COMMITTEE FOR SPACE DATA SYSTEMS
P1E - RADIO FREQUENCY AND MODULATION

power-efficient than GMSK or FQPSK and presents more spectral regrowth than GMSK or OQPSK in a non-linear channel.

The list is not exhaustive and the well-known OQPSK modulation with square-root raised cosine (SRRC) Nyquist filtering is another likely candidate. This modulation is widely used by the fixed satellite service with a typical roll-off factor of $\alpha=0.5$. Though less bandwidth-efficient than GMSK or FQPSK, it presents the advantage of the simplicity of implementation of both the modulator and the demodulator, making it more suitable for data rates of tens or hundreds of Mb/s.

6. Conclusion

The analysis contained in this document shows that several modulation schemes which are already used in operational systems are capable to meet the requirements of the spectral mask of provisional recommendation SF17-2 (figure 1). GMSK and FQPSK appear to be the most attractive in terms of spectral efficiency but have never been used operationally at high data rates. FQPSK is a proprietary modulation method; it is covered by a patent and is kept confidential, making an early evaluation impossible and its introduction as a standard somewhat problematic.

The main conclusion from this analysis is that technology for GMSK was developed for a large number of commercial applications. Hence the implementation of a GMSK modulator onboard a spacecraft is unlikely to be too complex or too costly. The best approach is then probably to concentrate on the use of GMSK (BT between 0.5 and 1), or alternatively FQPSK (pending resolution of the patent issue) for high rate space-to-earth telemetry up to a few tens of Mb/s at the input to the modulator. An alternative solution for rates of several hundreds of Mb/s could be OQPSK with a Butterworth filtering of BT=1 or possibly with SRRC filtering with a roll-off factor in the range of 0.5 if GMSK is too difficult to implement at these high rates.

GLOSSARY

AMPS	Advanced Mobile Phone System
CCSDS	Consultative Committee for Space Data Systems
CDMA	Code Division Multiple Access
CT2	Cordless Telephone-2
ERMES	European Radio Message System
GMSK	Gaussian Minimum Shift Keying
GSM	Global System for Mobile communications
JDC	Japanese Digital Cellular
MMDS	Multichannel Multipoint Distribution System
MSK	Minimum Shift Keying
NADC	North American Digital Cellular

REPORT CONCERNING CCSDS RADIO FREQUENCY AND MODULATION
CONSULTATIVE COMMITTEE FOR SPACE DATA SYSTEMS
P1E - RADIO FREQUENCY AND MODULATION

OQPSK	Offset Quadriphase Shift Keying
PDC	Pacific Digital Cellular
PHS	Personal Handy phone System
QPSK	Quadriphase Shift Keying
SFCG	Space Frequency Co-ordination Group
SRRC	Square-Root Raised Cosine

REPORT CONCERNING CCSDS RADIO FREQUENCY AND MODULATION
CONSULTATIVE COMMITTEE FOR SPACE DATA SYSTEMS
P1E - RADIO FREQUENCY AND MODULATION

References:

- 1 Digital Modulation in Communications Systems, HP AN No1298
- 2 Wireless Digital Communications, K. Feher, Prentice Hall, 1995
- 3 Advanced Spectrum Shaping for Efficient Bandwidth Utilisation, A.Southern, M.Otter, M.Reichel, ESA Co 11605/96/F/TB, Sept. 97
- 4 Efficient Modulation Methods Study, W.Martin, T-Y Yan, L.V.Lam, NASA/JPL, Sept.97
- 5 "FIRST: DoD's Range Radio Data Link Standard. Synergy with Commercial Wireless Applications" Proceedings of the WIRELESS'97 Symposium, K.F.Eggertsen, A.Cirineo, A.G.Cameron, K.Feher, Feb. 10-14, 1997, Santa Clara Convention Center, Santa Clara, CA, USA.
- 6 Efficient FQPSK Modulation – Integrated Transceiver Developments, K.Feher, CCSDS meeting, April 1997, ESA Headquarters, Paris, France
- 7 Wireless Communications, T.S. Rappaport, Prentice Hall, 1996

REPORT CONCERNING CCSDS RADIO FREQUENCY AND MODULATION
CONSULTATIVE COMMITTEE FOR SPACE DATA SYSTEMS
P1E - RADIO FREQUENCY AND MODULATION

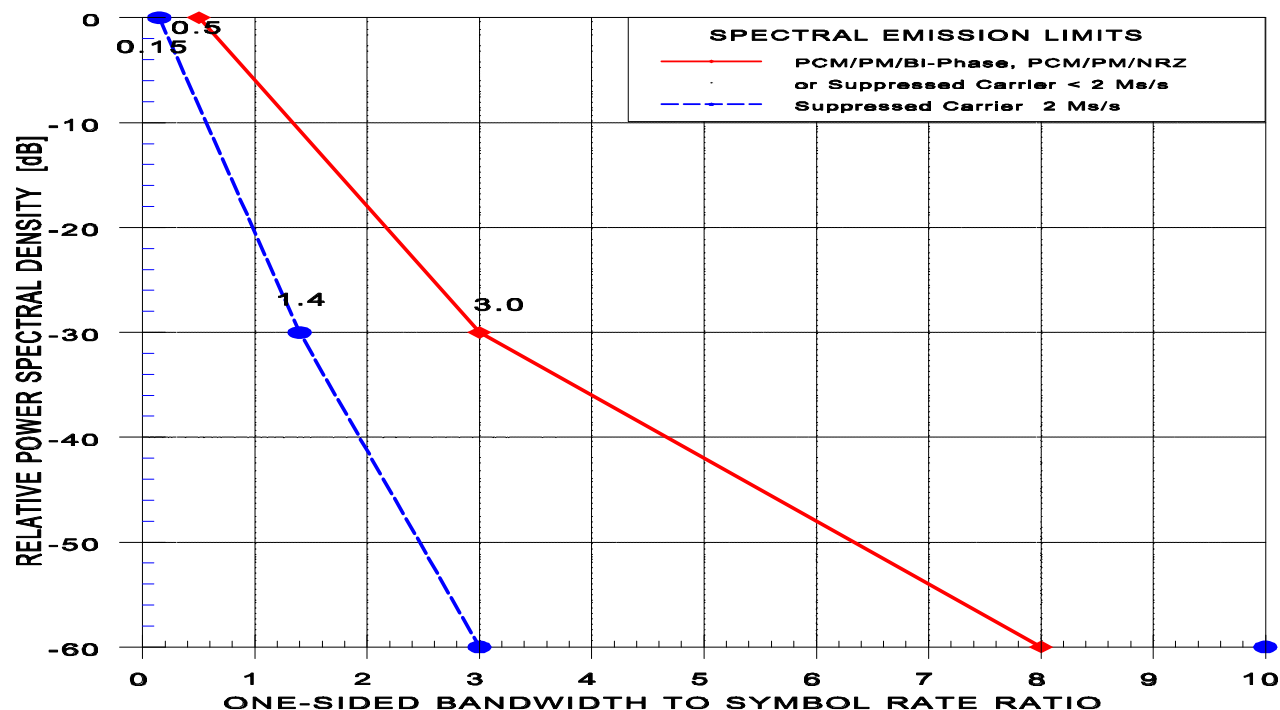


Fig.1: Spectral emissions mask for space science services, telemetry signal
(SFCG provisional Recommendation SF17-2)

Note: On Figure 1, the CCSDS terminology *symbol rate* must be understood as the *data rate* (coded or uncoded data) at the input to the modulator. The definition is not applicable to trellis-coded modulation schemes.

REPORT CONCERNING CCSDS RADIO FREQUENCY AND MODULATION
CONSULTATIVE COMMITTEE FOR SPACE DATA SYSTEMS
P1E - RADIO FREQUENCY AND MODULATION

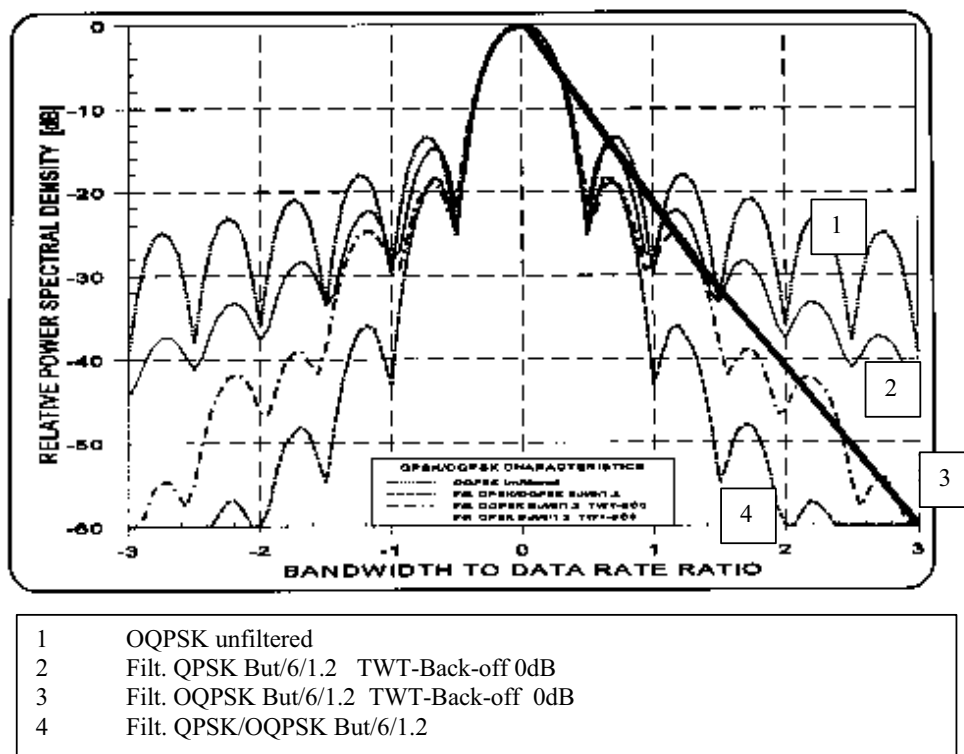
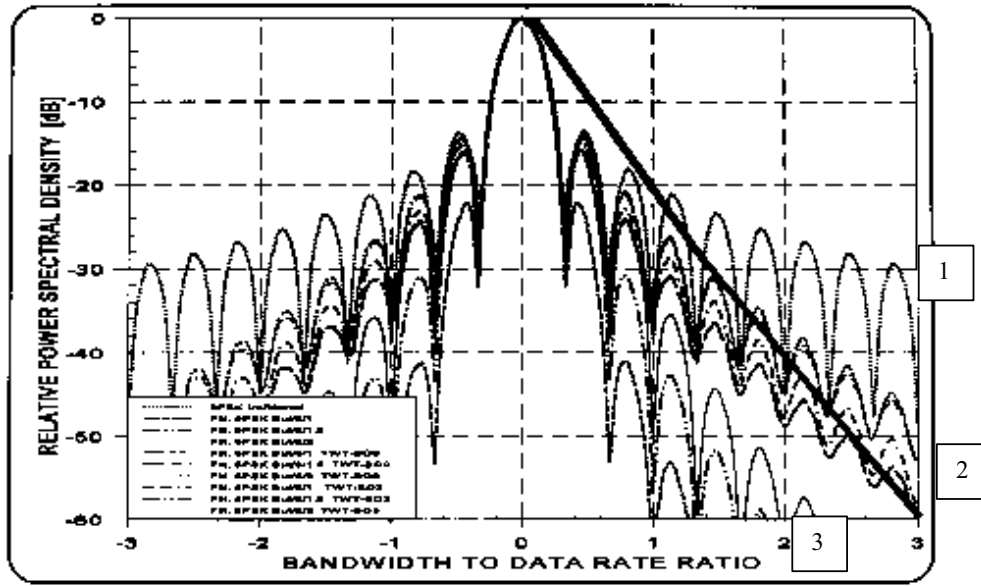


Fig.2: Filtered QPSK/OQPSK in a non-linear channel (Butterworth 6 poles, BT=1.2) ([3], figure 34)

REPORT CONCERNING CCSDS RADIO FREQUENCY AND MODULATION
CONSULTATIVE COMMITTEE FOR SPACE DATA SYSTEMS
P1E - RADIO FREQUENCY AND MODULATION



- | | |
|---|---------------------------------------|
| 1 | 8PSK unfiltered |
| 2 | Filt. 8PSK But/6/1 TWT-Back-off 3dB |
| | Filt. 8PSK But/6/1.5 TWT-Back-off 3dB |
| | Filt. 8PSK But/6/2 TWT-Back-off 3dB |
| | Filt. 8PSK But/6/1 TWT-Back-off 0dB |
| | Filt. 8PSK But/6/1.5 TWT-Back-off 0dB |
| | Filt. 8PSK But/6/2 TWT-Back-off 0dB |
| 3 | Filt. 8PSK But/6/1 |
| | Filt. 8PSK But/6/1.5 |
| | Filt. 8PSK But/6/2 |

Fig.3: Filtered 8PSK in a non-linear channel (Butterworth 6 poles, BT = 1, 1.5, 2) ([3] fig.40)

REPORT CONCERNING CCSDS RADIO FREQUENCY AND MODULATION
CONSULTATIVE COMMITTEE FOR SPACE DATA SYSTEMS
P1E - RADIO FREQUENCY AND MODULATION

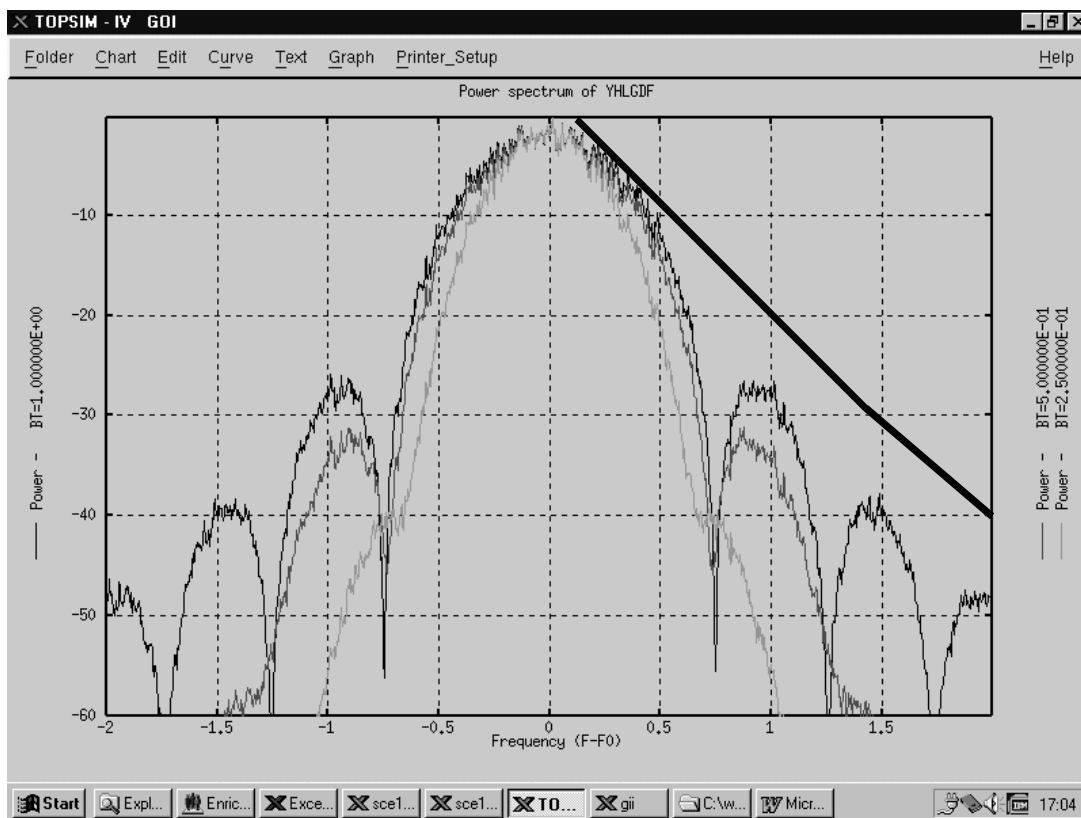


Fig.4: GMSK spectrum, non-linear channel, SSPA at 0dB back-off,
for BT = 1, 0.5, 0.25 (courtesy of E.Vassallo)

REPORT CONCERNING CCSDS RADIO FREQUENCY AND MODULATION
CONSULTATIVE COMMITTEE FOR SPACE DATA SYSTEMS
P1E - RADIO FREQUENCY AND MODULATION

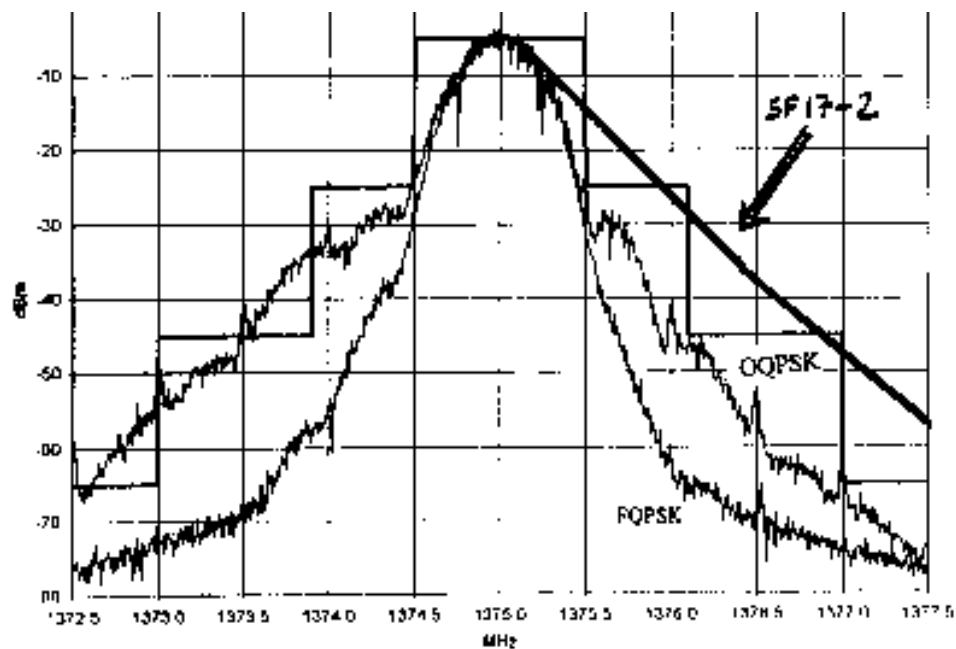


Fig.5: FQPSK and filtered OQPSK spectra, 1.375 GHz, at the output of a non-linear amplifier. The stair-shaped mask is DoD's FIRST mask (draft) [5] ([6] page 6.18)

**REPORT CONCERNING CCSDS RADIO FREQUENCY AND MODULATION
CONSULTATIVE COMMITTEE FOR SPACE DATA SYSTEMS
P1E - RADIO FREQUENCY AND MODULATION**

ANNEX 1

SFCG RECOMMENDATION 17-2R1

REPORT CONCERNING CCSDS RADIO FREQUENCY AND MODULATION
CONSULTATIVE COMMITTEE FOR SPACE DATA SYSTEMS
P1E - RADIO FREQUENCY AND MODULATION

***SPACE FREQUENCY
COORDINATION GROUP***

Recommendation 17-2R1

**EFFICIENT SPECTRUM UTILISATION FOR SPACE SCIENCE SERVICES
ON SPACE-TO-EARTH LINKS**

The SFCG,

CONSIDERING

- a) that frequency bands allocated to the space science services are becoming more congested as space missions multiply, data rates increase, and other services enter these bands;
- b) that usage of spectrum beyond what is actually required increases the potential for interference to other users and at the same time may result in a higher susceptibility to interference from other users of the band;
- c) that notified bandwidth requirements beyond the amount of spectrum actually required generally increases the coordination burden;
- d) that subcarrier modulation techniques require substantially more spectrum compared to suppressed carrier modulation techniques;
- e) that the required bandwidth with subcarrier modulation is a function of the subcarrier frequency and the subcarrier-to-symbol rate ratio;
- f) that, for telemetry subcarrier frequencies above 60 kHz, a subcarrier frequency-to- highest symbol rate ratio not exceeding 4 (for Cat. A missions) or 5 (for Cat. B missions) is generally sufficient to obtain acceptable performance;
- g) that the presence of telecommand feed-through and/or ranging signals may require the selection of a slightly higher value of subcarrier frequency-to-highest symbol rate ratio²;
- h) that subcarriers are not required any longer to separate telemetry data streams because several channels can be present simultaneously on a single RF carrier if virtual channels are used;³
- i) that there are no technical reasons which would require the use of subcarrier modulation for symbol rates above approximately 60 kilosymbol/second (ks/s)⁴;
- j) that the use of PCM/PM/Bi-phase or PCM/PM/NRZ modulation is only

² CCSDS Recommendations 401.0 (2.4.14A)B-1 and 401.0 (2.4.14B)B-1

³ CCSDS Recommendation for Packet Telemetry (CCSDS 102.0-B-2)

⁴ For purposes of this Recommendation, the symbol rate is defined as the baseband bit rate following error correcting coding (if applicable) and Bi- ϕ encoding (if used) but excluding any other spectrum modifying modulation.

REPORT CONCERNING CCSDS RADIO FREQUENCY AND MODULATION
CONSULTATIVE COMMITTEE FOR SPACE DATA SYSTEMS
P1E - RADIO FREQUENCY AND MODULATION

justified when a distinct carrier component is required and for symbol rates below 2 Ms/s;

- k) that filtered modulation schemes have bandwidth characteristics which generally reduce coordination burdens;
- l) that spectrum shaping can be used to significantly reduce the occupied bandwidth;

RECOMMENDS

1. that, with immediate applicability to all space science service bands, space agencies use the most bandwidth efficient modulation schemes practicable for their missions;
2. that, with immediate applicability to all space science service bands, subcarrier modulation shall not be used except where absolutely required and then only for symbol rates below or equal to 60 ks/s;
3. that, with immediate applicability to all space science service bands, if a subcarrier is required, it shall comply with the specifications set forth in considerations f) and g);
4. that, with immediate applicability to all space science service bands, PCM/PM/Biphase or PCM/PM/NRZ modulation shall only be used when a carrier component is technically necessary and for symbol rates below 2 Ms/s;
5. that the emitted spectrum⁵ for all Space Science Services projects starting in or after the year 2001, and that will utilize space-to-Earth link frequency assignments in the bands 2200-2290 MHz, 2290-2300 MHz, 8025-8400 MHz, or 8400-8500 MHz, adhere to the spectral emission masks in Figure 1.

⁵ Measured relative to the peak of the telemetry spectrum and excluding all spurious emissions

REPORT CONCERNING CCSDS RADIO FREQUENCY AND MODULATION
CONSULTATIVE COMMITTEE FOR SPACE DATA SYSTEMS
P1E - RADIO FREQUENCY AND MODULATION

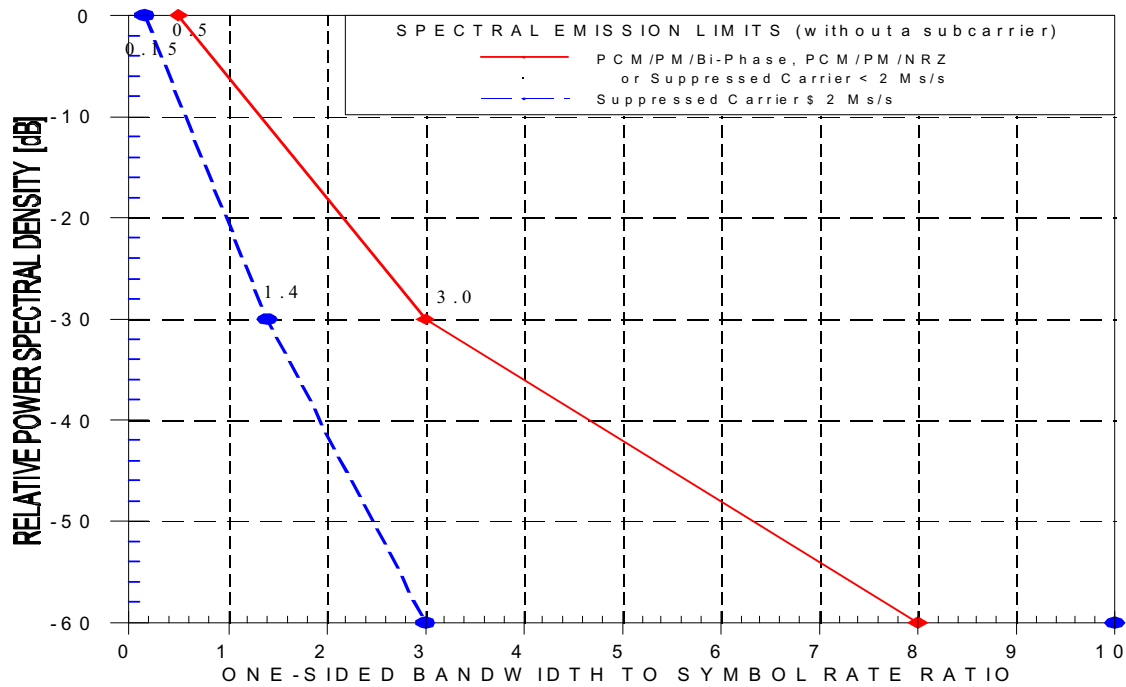


Figure 1

Performance of Selected Bandwidth Efficient Modulations

Dennis Lee and Tsun-Yee Yan
Jet Propulsion Laboratory
California Institute of Technology
Pasadena, CA 91109

October 13, 1999

1 Abstract

This paper presents a comparison between six candidate bandwidth efficient modulations – GMSK $BT_b=0.25$, GMSK $BT_b=0.5$, Square Root Raised Cosine OQPSK $\alpha=0.5$, Butterworth-filtered OQPSK $BT_s=1.0$, FQPSK-B, and T-OQPSK. The comparisons are based on the uncoded -60 dB two-sided bandwidth, the E_b/N_o required to achieve 10^{-3} BER for an uncoded channel with a saturated PA, and the E_b/N_o required to achieve 10^{-6} BER for a coded channel with a saturated PA. Block diagrams of the transmitter and receiver are given for all modulations.

2 Introduction

This paper is a response to action item 99-1E-30 which requested a table synthesizing performances of candidate bandwidth-efficient modulations. The table included many items including maximum rate and hardware validation. However, this report only considers uncoded -60 dB two-sided bandwidth, the E_b/N_o required to achieve 10^{-3} BER in an uncoded channel with a saturated power amplifier, and the E_b/N_o required to achieve 10^{-7} BER in an coded channel with a saturated power amplifier. For the coded bit error probability, 10^{-6} BER in an coded channel was used instead of 10^{-7} due to the length of simulations required to generate enough errors at 10^{-7} BER. However, the coded bit error curve at 10^{-6} BER is fairly linear, and results can easily be extrapolated to 10^{-7} if needed.

The code used in this report consists of a concatenated rate 1/2, k=7 convolution inner code and a (255,223) Reed-Solomon outer code similar to the one used in the Voyager mission. A block interleaver with an interleaving depth of five is inserted between the convolution code and R-S code. Figure 1 shows a block diagram of the coded system for GMSK.

The power amplifier used in this study was a 10W ESA SSPA whose AM/AM and AM/PM characteristics are shown in Figures 2 and 3, respectively. The power amplifier was operated at 0 dB OBO in all cases.

Where possible, exact theoretical expressions for bit error probability for an AWGN channel (linear PA) are given for reference. If exact theoretical equations are not available, bounds on bit error performance are provided instead. For the saturated SSPA, only simulation results are given.

The uncoded BER simulations for all modulations except T-OQPSK include carrier and symbol tracking loops shown in the block diagrams (i.e., Costas loop and MAP symbol synchronizer). For T-OQPSK, ideal carrier and symbol tracking are assumed. The Costas loop bandwidth is adjusted so that the loop SNR is approximately 25 dB. Since no Doppler is assumed (i.e., only a static phase

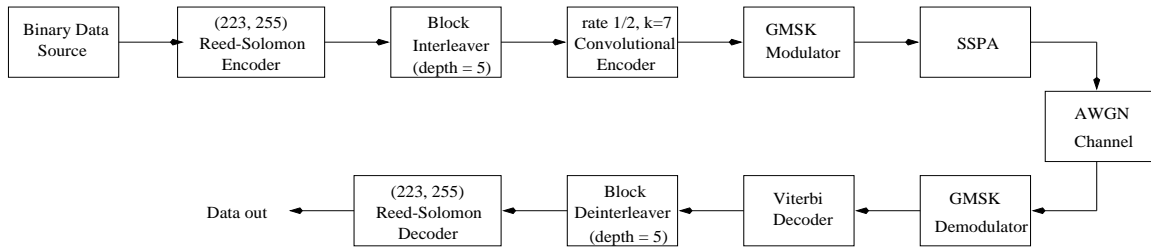


Figure 1: Block diagram of GMSK with concatenated code

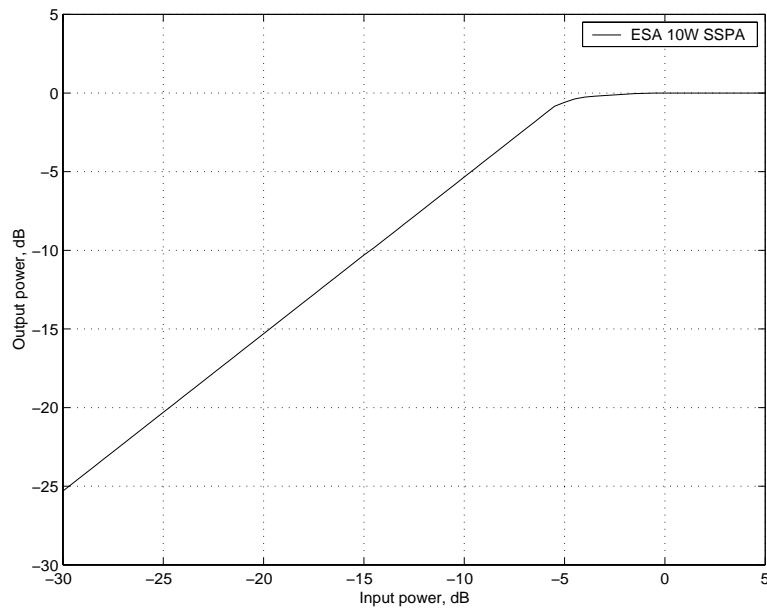


Figure 2: 10W ESA SSPA AM/AM characteristics

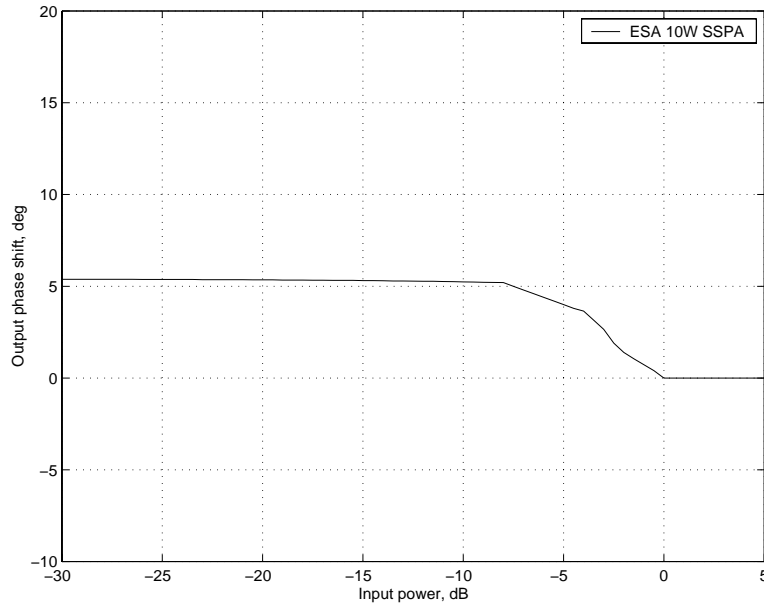


Figure 3: 10W ESA SSPA AM/PM characteristics

error), this value of loop SNR means that there is very little loss due to carrier tracking, as was confirmed by the simulations. For the coded BER simulations, since there was little loss due to non-ideal carrier and symbol tracking, ideal carrier and symbol tracking was assumed in order to reduce simulation time. Investigation on the effects of Doppler on the carrier and symbol tracking loops for these bandwidth efficient modulations is planned.

3 GMSK

Figure 4 shows a block diagram of the GMSK modulator with precoding. The receiver for GMSK used in this study is based on the linear receiver described in [3]. The linear receiver is similar to the standard OQPSK receiver except the detection filter is matched to the first AMP component $h_o(t)$ and cascaded with a Weiner filter. The cascaded filteres can be combined into one equivalent filter. Using this equivalent filter, GMSK can be demodulated using an OQPSK-like receiver.

Figure 5 shows a block diagram of a generic OQPSK receiver which is used for GMSK, filtered OQPSK, and FQPSK-B. For each modulation, the only difference between receivers is the detection filter used. The OQPSK receiver is not optimal in terms of bit error rate for FQPSK-B; however, the optimal FQPSK-B receiver involves sixteen correlators (eight each for the I and Q branches) and a Viterbi algorithm, and was considered too complex to be realistically implemented. For T-OQPSK, the optimal receiver in terms of bit error rate is also different from the generic OQPSK receiver and is shown in Figure 25. However, a simplified T-OQPSK receiver can be implemented using the same generic OQPSK receiver and a Butterworth detection filter.

A BER comparison between theoretical BPSK and GMSK $BT_b = 0.25^1$ and $BT_b = 0.5^2$ using the linear receiver including carrier and symbol tracking is shown in Figure 6. From the figure, the

¹ BT_s is defined as the product of the one-sided 3-dB bandwidth of the baseband filter and the symbol duration

²Using the ESA convention, the bit duration is equal the symbol duration for GMSK. For filtered OQPSK, FQPSK, and T-OQPSK, the bit duration is half the symbol duration

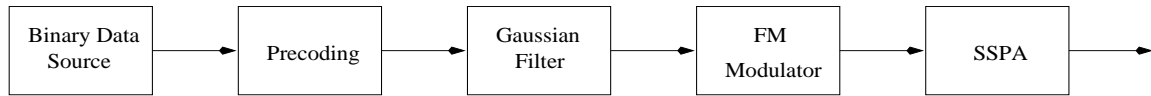


Figure 4: GMSK modulator block diagram

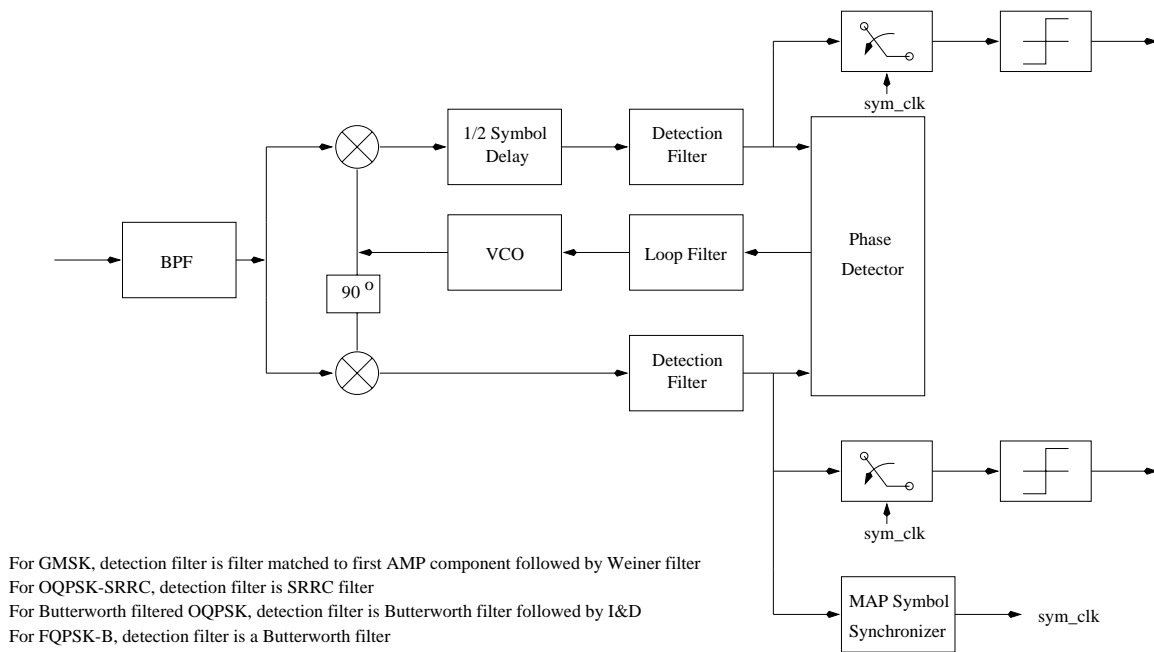


Figure 5: Generic OQPSK receiver block diagram for GMSK, filtered OQPSK, FQPSK-B

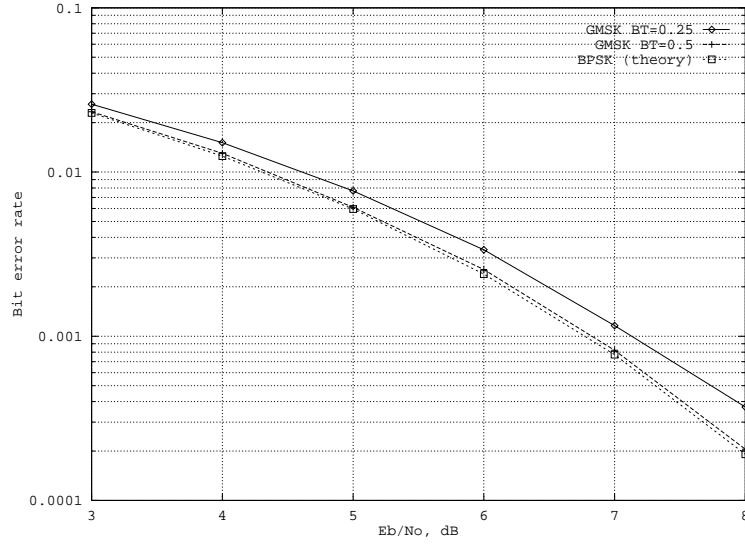


Figure 6: Precoded GMSK BER curve, saturated SSPA channel

E_b/N_o loss with respect to theoretical BPSK for GMSK $BT_b=0.25$ and $BT_b=0.5$ is 0.06 and 0.4 dB, respectively. The BER results were generated with SPW computer simulations using 8 samples per symbol. The number of samples per symbol was minimized in accordance with a more realistic implementation. The transmit and receive filters were implemented using FIR filters with impulse response duration of $10T_b$ (i.e., 80-tap FIR filter).

For the most part, the number of samples per symbol used in the BER simulations were inadequate to produce spectrum plots with frequencies up to $\pm 5f/R_b$ because of the Nyquist sampling theorem. For example, 8 samples per symbol will create frequencies only up to $\pm 2f/R_b$ for OQPSK and $\pm 4f/R_b$ for GMSK. Thus, the sampling frequency had to be increased to generate the spectra, and the filter length was increased by the same factor so that impulse duration of the filter was unchanged (which should also leave the spectra unchanged). For GMSK, 16 samples per symbol were used to generate the spectra; for SRRC-OQPSK, Butterworth filtered OQPSK, FQPSK-B, and T-OQPSK spectra, 32 samples per symbol were used.

The spectrum of GMSK $BT_b = 0.25$ and $BT_b=0.5$ following the SSPA is shown in Figures 7 and 8, respectively. One benefit of GMSK is that its spectrum be the same regardless of power amplifier AM/AM and AM/PM characteristics because of its constant envelope property.

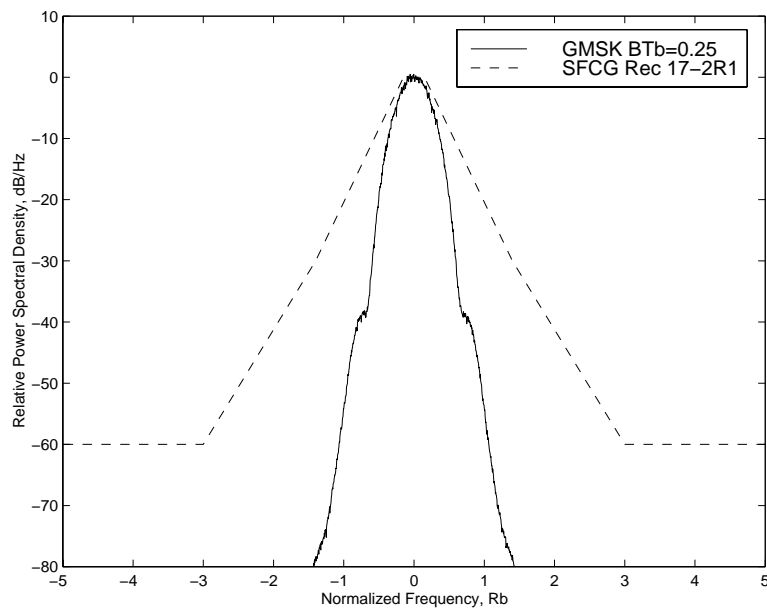
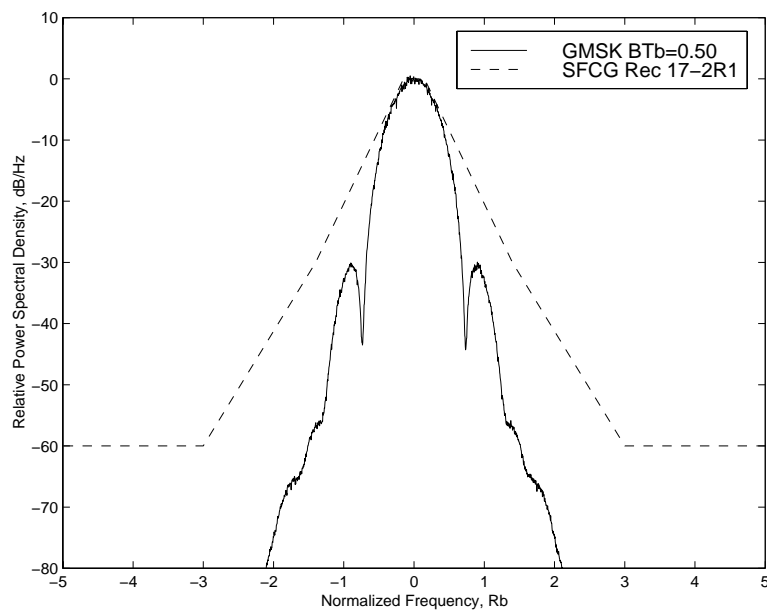
In [3], theoretical upper and lower bounds on the probability of bit error using the linear receiver is given. However, precoding is not considered. With precoding, the bounds are reduced by a factor of two. Hence, the upper bound for precoded GMSK is given by

$$P_e < \frac{1}{2}Q \left(\sqrt{\frac{2E_b}{N_o}} \frac{\gamma_o + \beta_o + \delta}{||h||} \right) + \frac{1}{2}Q \left(\sqrt{\frac{2E_b}{N_o}} \frac{\gamma_o - \beta_o + \delta}{||h||} \right) \quad (1)$$

and the lower bound is given by

$$P_e > \frac{1}{2}Q \left(\sqrt{\frac{2E_b}{N_o}} \frac{\gamma_o + \beta_o - \delta}{||h||} \right) + \frac{1}{2}Q \left(\sqrt{\frac{2E_b}{N_o}} \frac{\gamma_o - \beta_o - \delta}{||h||} \right) \quad (2)$$

where γ_o is the detection filter output due to the current $h_0(t)$ pulse, β_o is the detection filter output due to the current $h_1(t)$ pulse, and δ is the bound on ISI. The tightness of the bounds depends on

Figure 7: GMSK $BT_b=0.25$ Spectrum, saturated SSPA channelFigure 8: GMSK $BT_b=0.5$ Spectrum, saturated SSPA channel

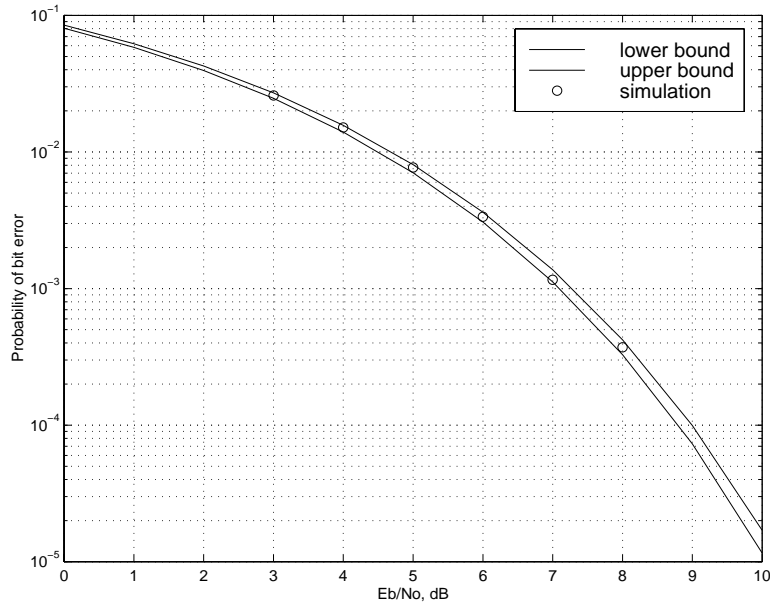


Figure 9: Upper and lower bounds on P_e for precoded GMSK $BT_b = 0.25$

the tightness of the bound on δ , which in turn depends on the BT product. The larger the BT product, the tighter the bound.

Figures 9 and 10 shows a comparison between simulation results and the upper and lower bounds for precoded GMSK $BT_b = 0.25$ and GMSK $BT_b = 0.5$, respectively. As can be seen, the bounds are very tight, and essentially converge for $BT_b \geq 0.5$.

The bit error rate curves for GMSK $BT_b=0.5$ and $BT_b=0.25$ with the concatenated convolutional and R-S code are shown in Figure 11. The bit error rate for BPSK with the same concatenated code is included for comparison. As the figures show, the E_b/N_o loss with respect to coded BPSK at 10^{-6} is 0.02 and 0.13 dB for GMSK $BT_b=0.5$ and $BT_b=0.25$, respectively. The bit error rates for BPSK with a concatenated rate 1/2, k=7 convolution code and (255,223) Reed-Solomon code varies considerably in the literature (e.g., see [1] and [5]). This is most likely due to variations in code parameters such as truncation path length and interleaving depth. Our concatenated BPSK results are generated with SPW and match closely with [1].

4 Square Root Raised Cosine OQPSK

A block diagram of the SRRC-OQPSK modulator is shown in Figure 12. Notice that SRRC-OQPSK (transmission of waveforms with SRRC filter impulse response shape) is not the same as SRRC-filtering of OQPSK (SRRC filtering of NRZ pulses). SRRC-OQPSK is generally generated using a lookup table over several symbols, and satisfies the Nyquist criterion for orthogonality. On the other hand, SRRC filtering of OQPSK requires no special hardware other than a SRRC filter, but is not orthogonal and has ISI. In a AWGN channel with a linear PA, SRRC-OQPSK has no ISI at the maximum eye opening and has the same bit error probability as BPSK; i.e.,

$$P_e = Q\left(\sqrt{\frac{2E_b}{N_o}}\right) \quad (3)$$

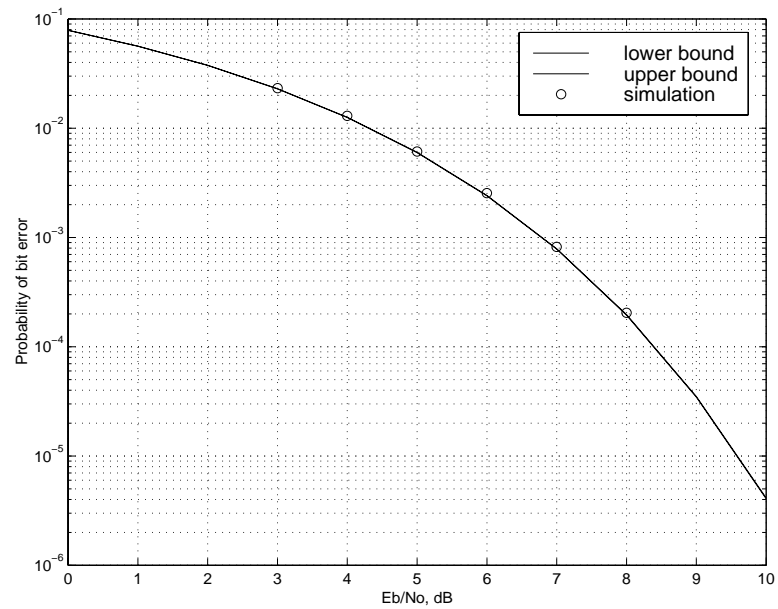


Figure 10: Upper and lower bounds on P_e for precoded GMSK $BT_b = 0.5$

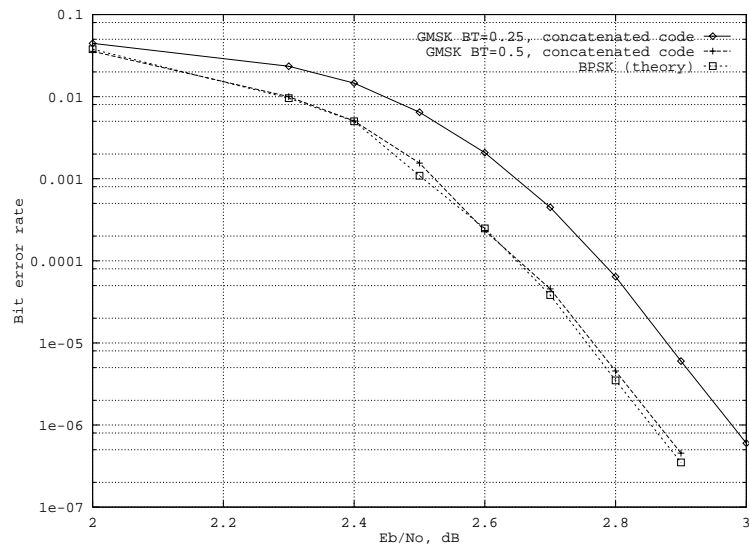


Figure 11: Precoded GMSK with concatenated code, saturated SSPA channel

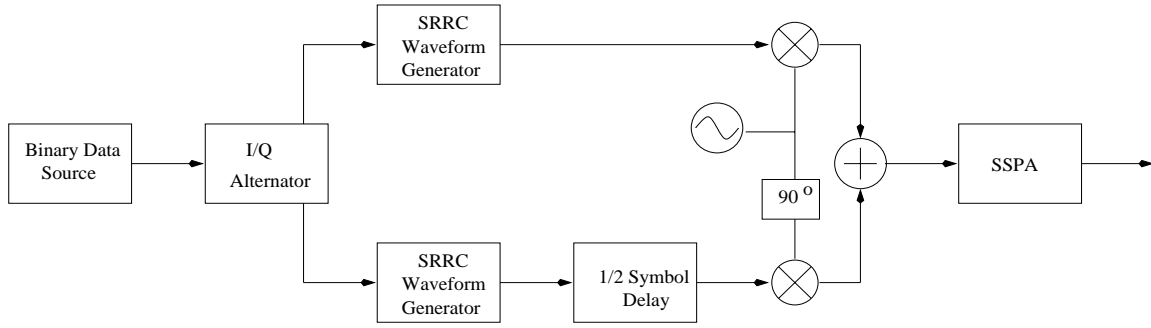
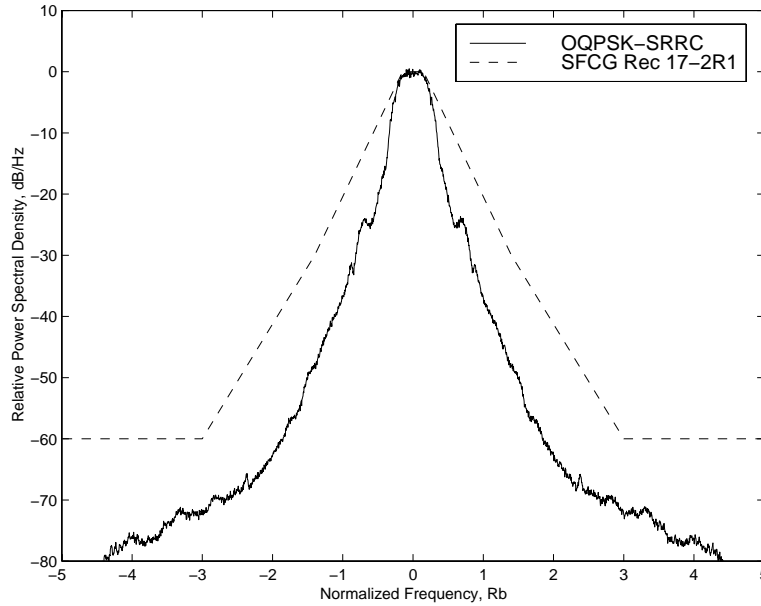


Figure 12: Block diagram of SRRC-OQPSK transmitter


 Figure 13: SRRC Filtered OQPSK ($\alpha=0.5$) Spectrum, saturated SSPA channel

However, with a non-linear PA, SRRC-OQPSK suffers from ISI and spectral sidelobe regrowth because of its non-constant envelope.

The simulated spectrum of SRRC-OQPSK $\alpha = 0.5$ operating with a saturated SSPA is shown in Figure 13. In the BER simulations, eight samples per symbol were used. The parameters of the SRRC filter were $BT_s=1.0$ and roll-off factor $\alpha=0.5$. The filter was implemented as a FIR filter with impulse response duration of $8T_s$ (64 tap filter).

The bit error probability of SRRC-OQPSK operating with a saturated SSPA in an uncoded channel is shown in Figure 14. From the figure, there is a E_b/N_o loss of 0.7 dB with respect to unfiltered BPSK. If an equalizer is used to reduce the ISI, this loss can be reduced. Figure 15 shows the bit error probability of SRRC-OQPSK with a saturated SSPA in coded channel. The figure shows a 0.3 degradation between the coded BER performance of SRRC-OQPSK and BPSK using the same concatenated code.

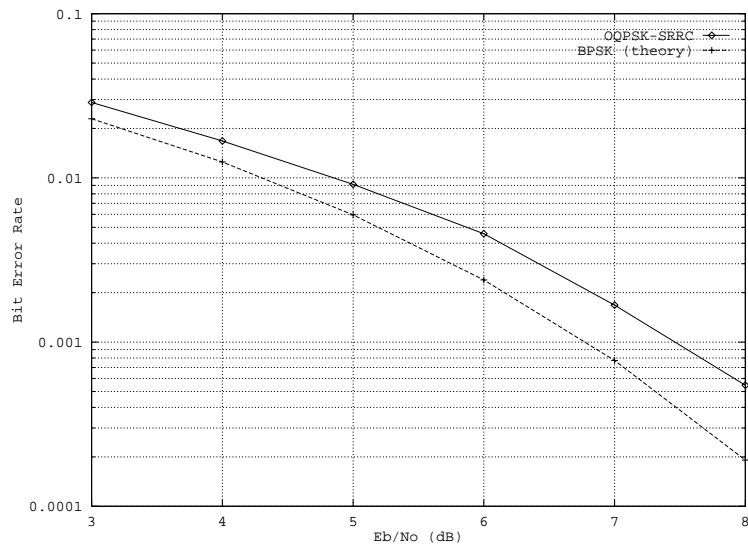


Figure 14: SRRC-OQPSK BER, saturated SSPA channel

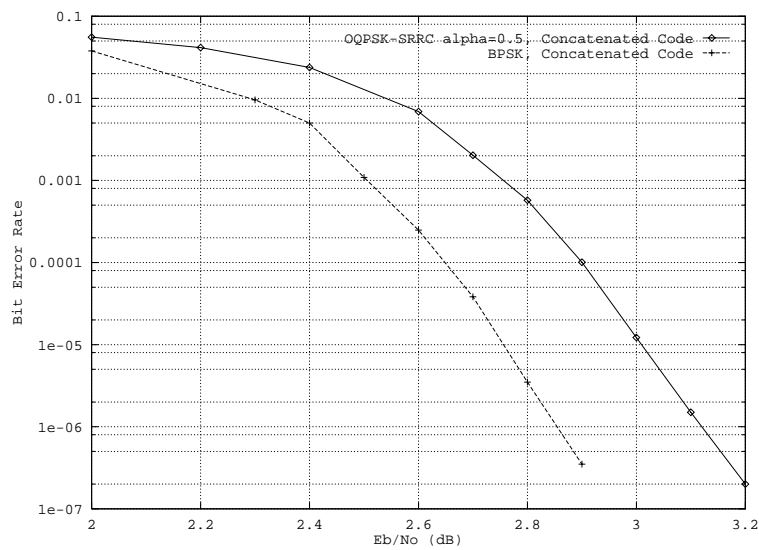


Figure 15: SRRC-OQPSK with Concatenated Code, saturated SSPA channel

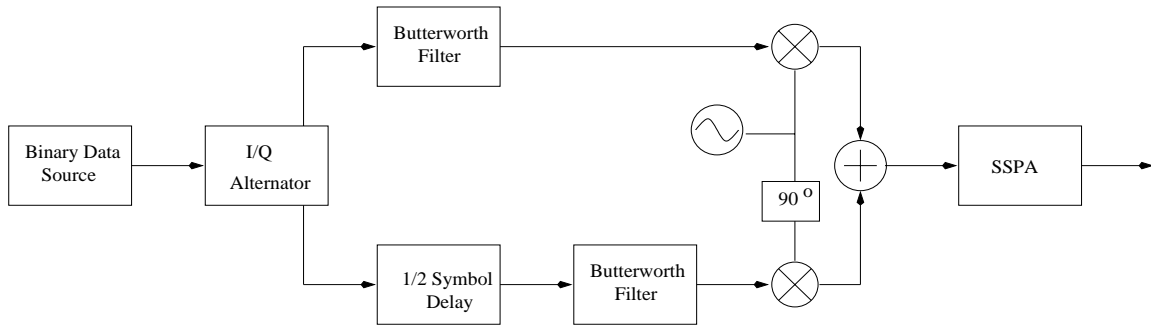
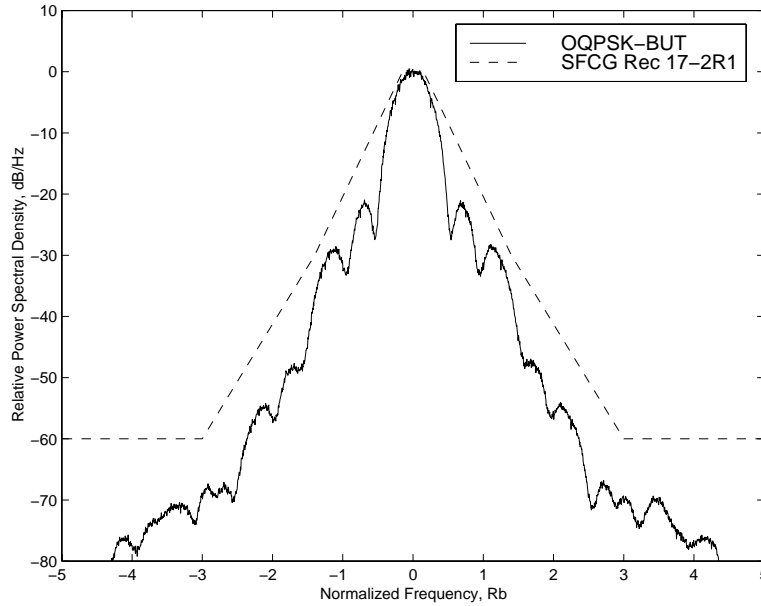


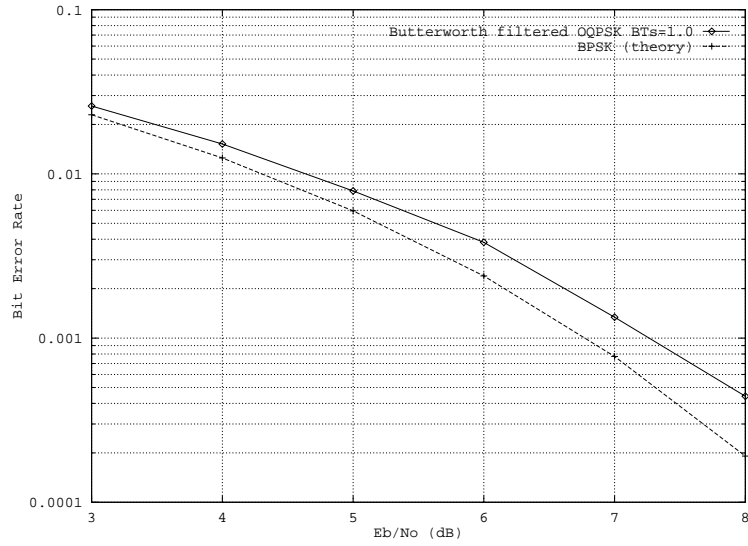
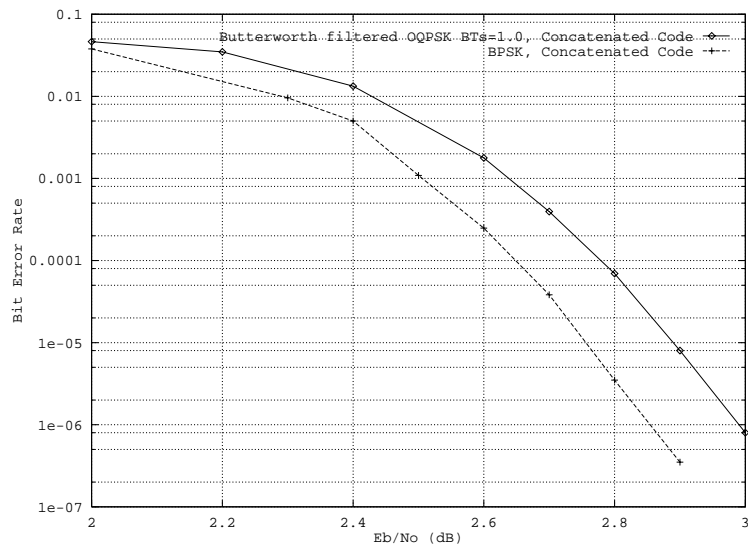
Figure 16: Block diagram of Butterworth filtered OQPSK transmitter


 Figure 17: Butterworth Filtered OQPSK $BT_s=1.0$ Spectrum, saturated SSPA channel

5 Butterworth filtered OQPSK

The modulator block diagram for the Butterworth filtered OQPSK modulator is shown in Figure 16. The Butterworth filter in the diagram is a 3rd order lowpass Butterworth filter with $BT_s=1.0$ (i.e., the filter 3-dB cutoff occurs at the first spectral null of OQPSK). Bit error rate simulations were run with 8 samples per symbol.

Figure 17 shows the simulated spectra of Butterworth filtered OQPSK $BT_s=1.0$ following a saturated 10W ESA SSPA. The bit error rate curve for Butterworth filtered OQPSK operating with a saturated PA is shown in Figure 18. From the figure, Butterworth filtered OQPSK $BT_s=1.0$ with a SSPA suffers a loss of about 0.5 dB with respect to unfiltered BPSK. Figure 19 shows the bit error probability for concatenate coded Butterworth filtered OQPSK with a SSPA at 0 dB OBO. From the figure, coded Butterworth filtered OQPSK has a loss of 0.15 dB with respect to coded BPSK.

Figure 18: Butterworth filtered OQPSK $BT_s=1.0$ BER, saturated SSPA channelFigure 19: OQPSK-BUT $BT_s=1.0$ with Concatenated Code, saturated SSPA channel

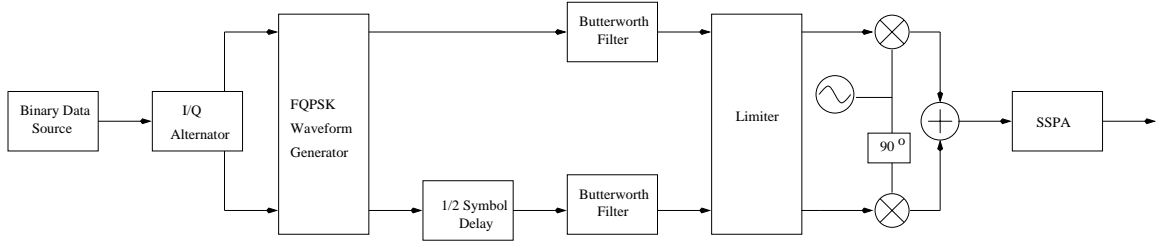


Figure 20: Block diagram of FQPSK-B modulator

6 FQPSK-B

Figure 20 shows a block diagram of the FQPSK-B modulator. For FQPSK-B, both receive and transmit filters were implemented using lowpass Butterworth filters. The envelope of FQPSK-B is quasi-constant (i.e., its envelope has a small amount of fluctuation between uniform sampling instants), so an optional limiter shown in Figure 20 can be added to make the envelope truly constant.

The transmit filter bandwidth represents a tradeoff between occupied bandwidth and bit error probability. The optimum value depends on the application. The receive filter used in this study is a fourth order lowpass Butterworth filter with $BT_s \approx 0.6R_b$ as suggested in [2]. The BER results were generated by SPW simulations using 16 samples per symbol.

Figure 21 shows the spectrum of FQPSK-B following a saturated SSPA. The BER performance of uncoded FQPSK is shown in Figure 22. The bit error rate of coded FQPSK-B using the convolution/Reed-Solomon concatenated code is shown in Figure 23.

It is interesting to note that with coding the E_b/N_o loss of FQPSK-B with respect to BPSK is much less than without coding. With no coding, FQPSK-B is about 1.7 dB worse than BPSK at 10^{-3} BER. With concatenated coding, FQPSK-B is only about 0.5 dB worse than BPSK at 10^{-6} BER. The reason for the difference is that with coding, the FQPSK-B modulator/demodulator inside the concatenated code operates at a very low E_b/N_o in the BER region of interest, on the order of 0 dB E_b/N_o (approximately 3 dB lower than the actual E_b/N_o due to the rate 1/2 code). As shown by Figure 22, the E_b/N_o loss of FQPSK-B compared to BPSK decreases for lower E_b/N_o .

7 T-OQPSK

The block diagram of the T-OQPSK modulator is shown in Figure 24. The corresponding optimal T-OQPSK receiver is shown in Figure 25. As mentioned in the introduction, a simplified receiver can be implemented without the four correlators and the Viterbi algorithm, with decisions based on samples at the end of the waveform and a lowpass filter to bandlimit the noise. This similar to the simplified FQPSK-B receiver using the generic OQPSK structure. However, the optimal receiver for T-OQPSK has significantly fewer elements than the FQPSK-B optimal receiver (4 correlators versus 16 correlators for FQPSK-B), and it can be realistically implemented. Carrier and symbol tracking are more complex due to the Viterbi algorithm, and was not considered in this report.

The theoretical upper and lower bounds for T-OQPSK in a linear AWGN channel are derived in [6], and given below:

$$Q\left(\sqrt{\frac{2E_b}{N_o}}\right) \leq P_e \leq Q\left(\sqrt{\frac{2E_b}{N_o}}\right) \frac{1}{(1 - e^{-E_b/N_o})^2} \quad (4)$$

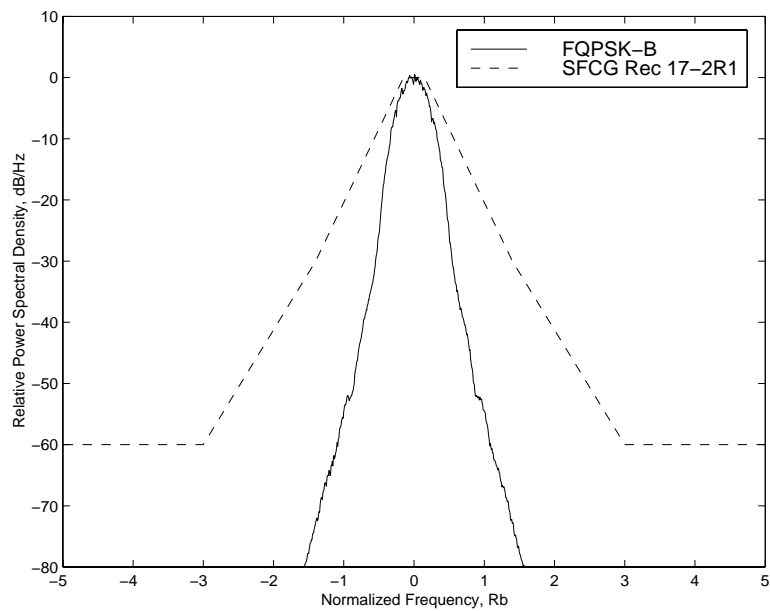


Figure 21: FQPSK-B Spectrum, saturated SSPA channel

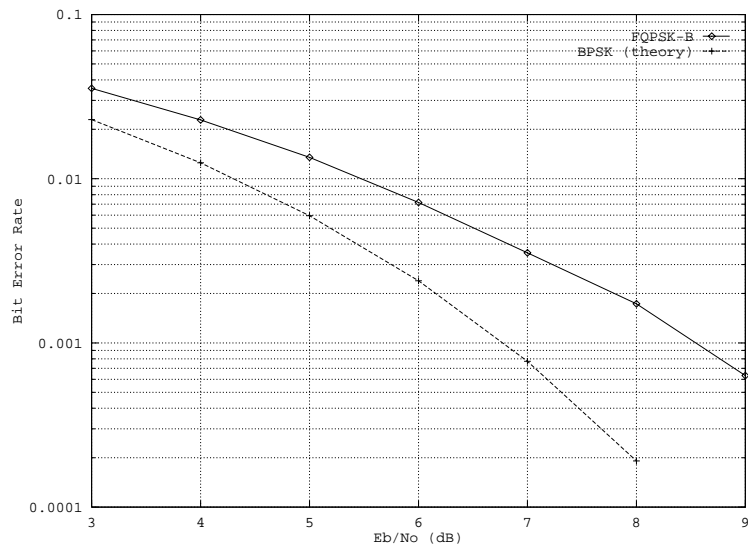


Figure 22: FQPSK BER curve, saturated SSPA channel

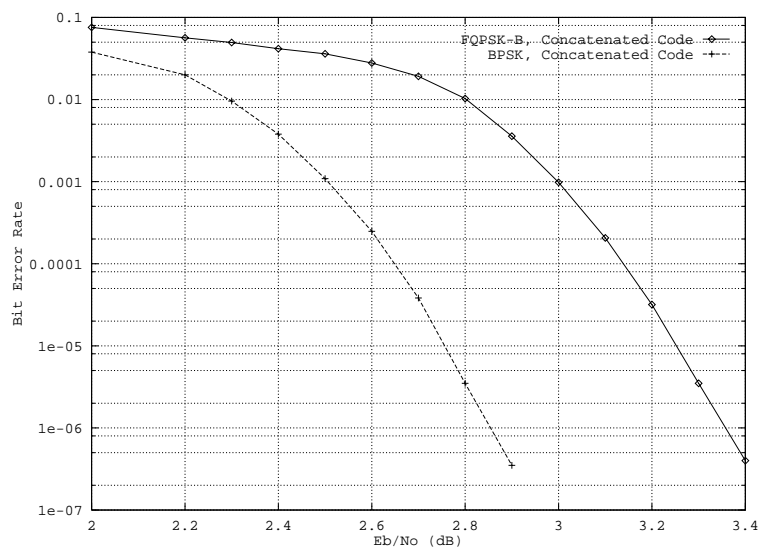


Figure 23: FQPSK-B with Concatenated Code, saturated SSPA channel

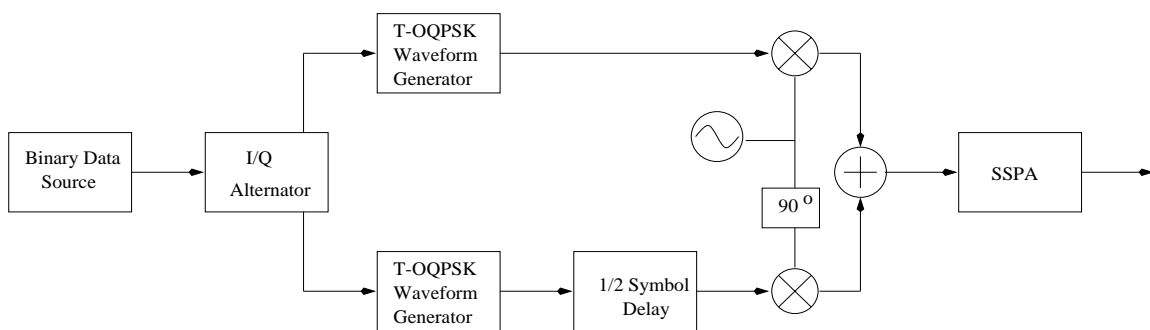


Figure 24: Block diagram of T-OQPSK modulator

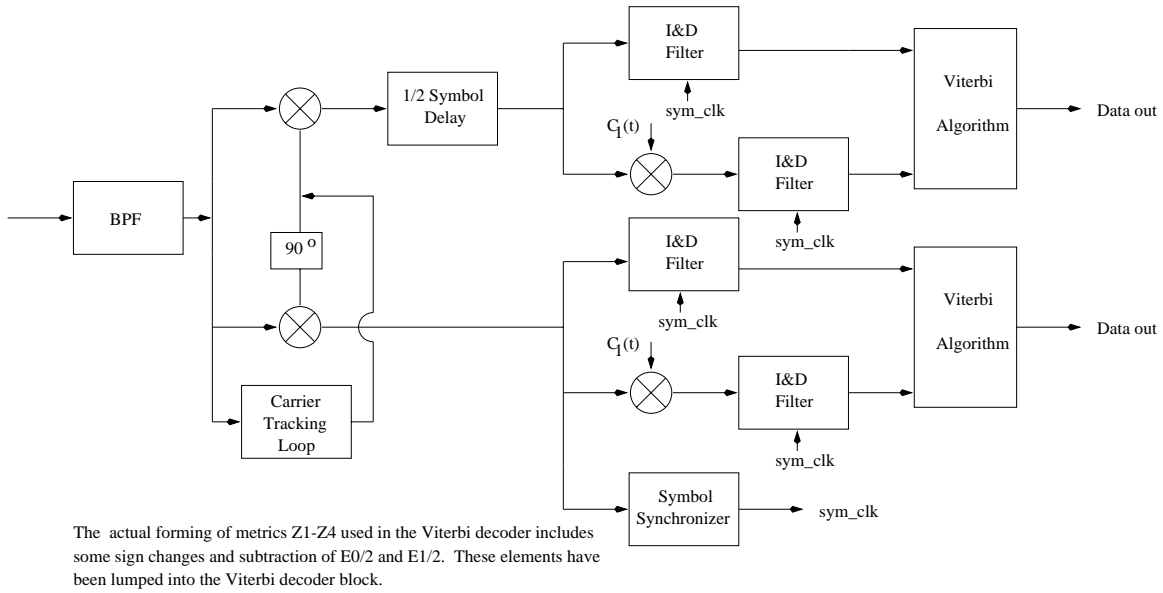


Figure 25: Block diagram of T-OQPSK demodulator

In an uncoded linear AWGN channel, T-OQPSK has virtually the same bit error probability as unfiltered BPSK [6]. However, T-OQPSK is not truly constant envelope and will suffer spectral sidelobe regrowth and BER degradation when passed through a non-linear power amplifier.

The simulated spectrum of T-OQPSK following a saturated 10W ESA SSPA is shown in Figure 26. Figure 27 shows the uncoded bit error probability of T-OQPSK with a saturated SSPA assuming ideal carrier and symbol tracking. As the figure shows, T-OQPSK in an uncoded channel with a saturated SSPA suffers a 0.65 dB degradation with respect to unfiltered BPSK. An equalizer can be added prior to the Viterbi algorithm to reduce the loss due to ISI. In order to generate these BER curves, eight samples per symbol were used.

With a concatenated code, the Viterbi algorithm shown in 24 must be adapted to produce soft-decision outputs as described in [4]. Otherwise, the following Viterbi decoder used for the convolution code can only do hard decision decoding. Combined with burst errors out of the Viterbi algorithm, these two factors will significantly degrade the concatenated code performance. An interleaver can be placed between the Viterbi algorithm and the Viterbi decoder to break up burst errors, with the cost of additional complexity.

The bit error performance of concatenate coded T-OQPSK using the Soft Output Viterbi Algorithm (SOVA) in a linear AWGN channel is given in [8] and results are shown in Table 1. The bit error performance of coded T-OQPSK in a non-linear channel is currently being evaluated.

8 Summary

Table 1 gives a summary of the six modulations discussed above. The bit error rate simulation results have a margin of error of about 0.1 dB E_b/N_o .

As the table shows, all modulations offer over a hundred-fold decrease in uncoded -60 dB bandwidth over unfiltered BPSK. The most bandwidth efficient modulations in terms of uncoded -60 dB bandwidth are GMSK $BT_b = 0.25$ and FQPSK-B. GMSK $BT_b = 0.5$ has about 50% more occupied bandwidth while only offering a 0.1 dB gain over GMSK $BT_b = 0.25$ in a coded channel at

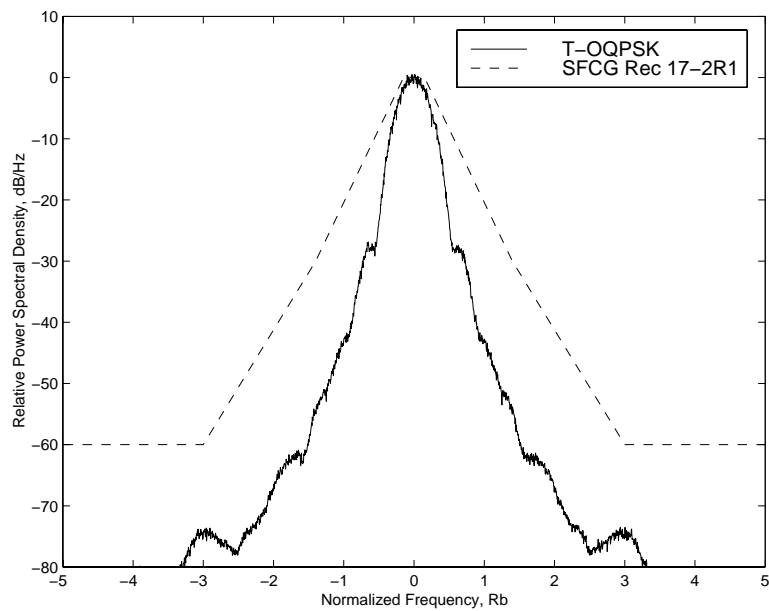


Figure 26: T-OQPSK Spectrum, saturated SSPA channel

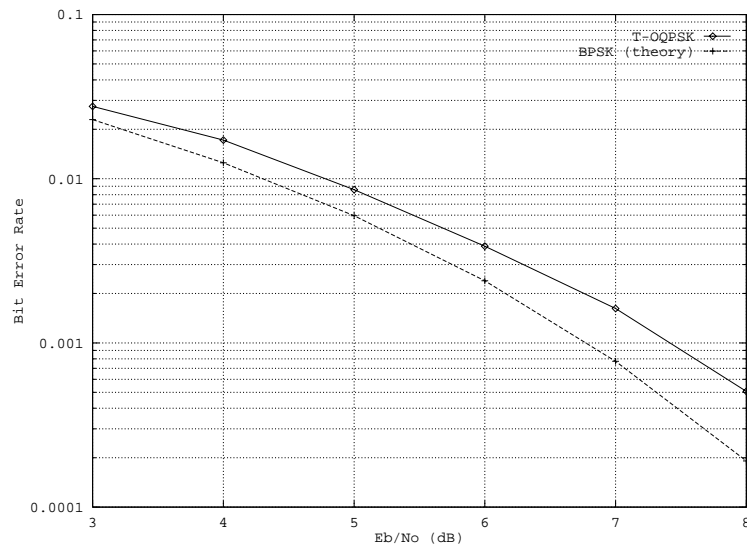


Figure 27: T-OQPSK BER curve, saturated SSPA channel

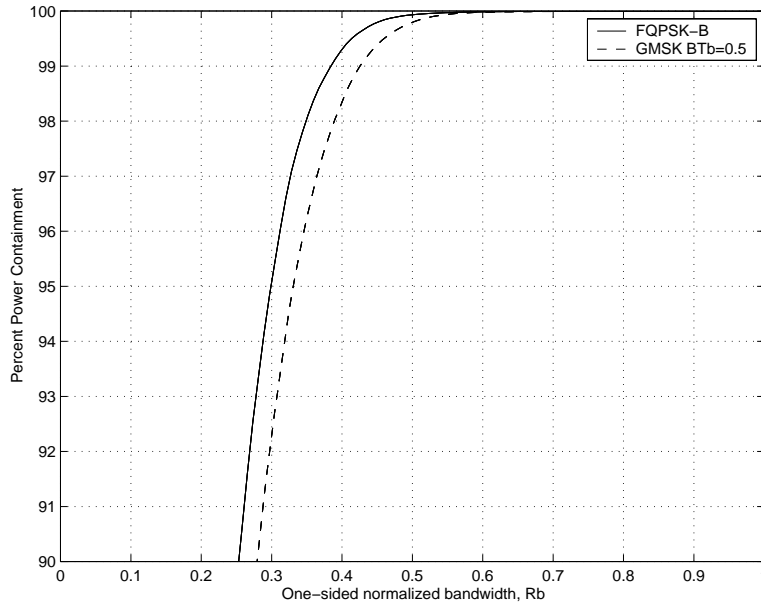


Figure 28: Power containment of GMSK $BT_b=0.25$ and FQPSK-B

$BER=10^{-6}$. Both SRRC-OQPSK and Butterworth filtered OQPSK $BT_s = 1.0$ have roughly 100% to 150% larger bandwidths, respectively, in a saturated SSPA channel than GMSK or FQPSK-B, and do not offer any BER improvement over GMSK and only marginal BER improvement over FQPSK-B in a coded channel. T-OQPSK has roughly the same bandwidth as GMSK $BT_b=0.5$ in a nonlinear channel, while the coded bit error rate in a nonlinear channel is still being evaluated. Due to time constraints, 8-PSK TCM was not included in this study.

While Table 1 shows that GMSK $BT_b = 0.25$ is slightly narrower than FQPSK-B in terms of -60 dB bandwidth, FQPSK-B is narrower than GMSK $BT_b = 0.25$ in terms of 90% and 99% power containment bandwidths. Figure 28 shows a comparison of the two modulations in terms of power containment bandwidths in a saturated SSPA channel. The 90% power containment one-sided bandwidth of FQPSK-B is $0.26 R_b$ while for GMSK $BT_b=0.25$, the 90% power containment bandwidth is $0.28 R_b$. Similarly, the 99% power containment bandwidth is $0.39 R_b$ for FQPSK-B versus $0.42 R_b$ for GMSK. This can be explained by noting that the main lobe of GMSK $BT_b=0.25$ is much wider at the top compared to FQPSK-B (see Figures 7 and 21) even though two spectra reach -60 dB at roughly the same point. Hence, whether GMSK $BT_b=0.25$ or FQPSK-B is more bandwidth efficient depends on how the bandwidth efficiency is defined.

It should be also noted from Table 1 that the E_b/N_o degradation compared to BPSK for all the modulations is considerably less for a coded channel than an uncoded channel, as explained in the section on FQPSK-B. All the coded modulations considered suffer less than 0.5 dB E_b/N_o degradation compared to coded BPSK at 10^{-6} BER, and the E_b/N_o difference between the bandwidth efficient modulations themselves is also reduced.

Table 1: Comparison of Selected Efficient Modulations

Modulation	-60 dB BW ^a	$\frac{E_b}{N_a}$ for 10^{-3} BER, uncoded AWGN		$\frac{E_b}{N_a}$ for 10^{-6} BER, coded AWGN	
		Theory (ref) ^b	Saturated PA ^c	Theory(ref) ^d	Saturated PA ^e
unfiltered BPSK	$635 R_b$	6.79 dB	6.81 dB	2.84 dB	2.84 dB
GMSK $BT_b=0.5$	$3.02 R_b$	6.82 dB	6.84	2.87 dB	2.87 dB
GMSK $BT_b=0.25$	$2.14 R_b$	7.1-7.3 dB ^f	7.14 dB	2.98 dB	2.98 dB
SRRC-OQPSK	$3.76 R_b$	6.79 dB	7.48 dB	2.84 dB	3.14 dB
Butterworth filtered OQPSK $BT_s=1.0$	$4.72 R_b$	7.13 dB ^d	7.28 dB	2.9 dB	3.00 dB
FQPSK-B	$2.18 R_b$	8.5 dB	8.55 dB	3.35 dB	3.35 dB
T-OQPSK	$3.02 R_b$	6.8 dB	7.42 dB ^e	2.9 dB	n/a

^aTwo-sided bandwidth in uncoded saturated SSPA channel^bLinear PA, ideal carrier and symbol tracking^cIncludes Costas carrier tracking loop and MAP symbol synchronizer except for T-OQPSK^dDetermined by SPW simulations in linear channel, with ideal carrier and symbol tracking^eAssumes ideal carrier and symbol tracking^ftheoretical bound

References

- [1] D. Divsalar and J.H. Yuen, "Performance of Concatenated Reed-Solomon/ Viterbi Channel Coding," JPL TMO Progress Report 42-71, July 1982.
- [2] K. Feher, "F-Modulation Amplification," U.S. patent 5,491,457, Feb 1996.
- [3] G.K. Kaleh, "Simple coherent receivers for partial response continuous phase modulations," IEEE Transactions on Select. Areas in Comm., vol. 7, no. 9, December 1989, pp. 1427-1436.
- [4] J. Hagenauer and P. Hoeher, "A Viterbi Algorithm with Soft-Decision Outputs and its Applications," Proc. Globecom '89, Dallas, Texas, November 1989.
- [5] M. Simon, S. Hinedi, and W. Lindsey, *Digital Communication Techniques*. Prentice-Hall, New Jersey, 1995.
- [6] M. Simon, P. Arabshahi, and M. Srinivasan, "Trellis-Coded QPSK with Variable Overlapped Raised-Cosine Pulse Shaping", JPL TMO Progress Report 42-136, February 1999.
- [7] W.C. Lindsey and M.K. Simon, *Telecommunication Systems Engineering*, Dover Publications, New York, 1973.
- [8] T.Y. Yan, "Comparative Study on Efficient Modulation Schemes for Space Applications", internal JPL document, April 1999.

CCSDS Panel 1E

Document 99/40

Comparison of RFI Susceptibility Results – the BPSK Case

(Action Item 99-1E-31)

Gabriella Povero¹ Enrico Vassallo² Monica Visintin³

Nordwijk, October 1999

1 Introduction

Studies of RFI susceptibility of bandwidth-efficient modulation schemes under consideration by CCSDS were presented at the Spring 1999 meeting of subpanel 1E. ESA [1] and NASA [2] contributions were, however, based on different assumptions and it was therefore difficult to compare the results.

In fact, ESA considered only the worst case susceptibility while NASA studied the average case. Moreover, the wideband interference signal was considered by NASA to be an unfiltered BPSK RFI whereas ESA assumed both interfering and victim signal to have the same modulation scheme.

As a consequence, action item 99-1E-31 was placed to try and resolve the apparent differences between the two Agencies.

As first step of the investigation, the benchmark case of unfiltered BPSK in a linear AWGN channel is considered.

In this paper the theoretical behavior of an unfiltered BPSK in the presence of an interferer is studied and compared with simulation results. Both narrow band and wide band interferers are considered. The narrow band interferer is a pure carrier with a uniformly distributed random phase. The wide band interferer is an unfiltered BPSK signal with random phase and timing offset. Both interferers have a frequency offset with respect to the useful signal center frequency. These assumptions are identical to the ones used by NASA [2].

¹ COREP, Politecnico di Torino

² ESOC, European Space Agency

³ Dipartimento di Elettronica, Politecnico di Torino

The case of fixed worst case phase and timing offset is also considered for completeness. This case corresponds to the assumptions of the ESA paper [1] in which, however, the results were presented in a different way.

2 Narrow-band interfering signal

2.1 Random phase

The useful signal is

$$x(t) = \left[\sum_{k=-\infty}^{\infty} \sqrt{E} a_k \psi(t - kT) \right] \sqrt{2} \cos(2\pi f_c t)$$

with $\psi(t) = 1/\sqrt{T} u_T(t)$, while the interferer is

$$x_I(t) = A\sqrt{2} \cos(2\pi f_c t + 2\pi \Delta_f t + \varphi)$$

where φ is a random phase uniformly distributed between $-\pi$ and π and Δ_f is the frequency offset of the interferer with respect to the center frequency of the useful signal.

The signal to interferer power ratio is

$$\eta = \frac{P_s}{P_I} = \frac{E/T}{A^2}$$

The ideal BPSK receiver evaluates the random variable

$$r_k = \int r(t) \sqrt{2} \cos(2\pi f_c t) \psi(t - kT) dt$$

and decides for $\hat{a}_k = 1$ if $r_k > 0$, otherwise it decides for $\hat{a}_k = -1$.

The random variable r_k is the sum of 3 terms:

$$r_k = u_k + i_k + n_k$$

where u_k is the useful part, equal to

$$u_k = \int x(t) \sqrt{2} \cos(2\pi f_c t) \psi(t - kT) dt = \sqrt{E} a_k$$

while n_k is a Gaussian random variable with zero mean and variance equal to $N_0/2$.

The third term, i_k , is due to the interferer and it can be written as

$$\begin{aligned}
 i_k &= \int_{kT}^{kT+T} \frac{2A}{\sqrt{T}} \cos(2\pi f_c t + 2\pi \Delta_f t + \varphi) \cos(2\pi f_c t) dt \\
 &\approx \frac{A}{\sqrt{T}} \int_{kT}^{kT+T} \cos(2\pi \Delta_f t + \varphi) dt \\
 &= \frac{A}{\sqrt{T}} \Re \int_{kT}^{kT+T} e^{j(2\pi \Delta_f t + \varphi)} dt \\
 &= \frac{A}{\sqrt{T}} \Re \left\{ e^{j\varphi} e^{j2\pi \Delta_f kT} \frac{e^{j2\pi \Delta_f T} - 1}{j2\pi \Delta_f} \right\} \\
 &= \frac{A}{\sqrt{T}} \Re \left\{ e^{j\varphi} e^{j2\pi \Delta_f kT} e^{j\pi \Delta_f T} T \sin c(\pi \Delta_f T) \right\} \\
 &= A\sqrt{T} \sin c(\pi \Delta_f T) \cos \left(\varphi + 2\pi \Delta_f \left(k + \frac{1}{2} \right) T \right) \\
 &= \sqrt{\frac{E}{\eta}} \sin c(\pi \Delta_f T) \cos \left(\varphi + 2\pi \Delta_f \left(k + \frac{1}{2} \right) T \right)
 \end{aligned}$$

The error probability is

$$\begin{aligned}
 P(e) &= \frac{1}{2} P(r_k > 0 / a_k = -1) + \frac{1}{2} P(r_k < 0 / a_k = 1) \\
 &= \frac{1}{2} P(n_k > \sqrt{E} - i_k) + \frac{1}{2} P(n_k < -\sqrt{E} - i_k) \\
 &= \frac{1}{2} P(n_k > \sqrt{E} - i_k) + \frac{1}{2} P(n_k > \sqrt{E} + i_k)
 \end{aligned}$$

Since φ is uniformly distributed, also $\xi = \varphi + 2\pi \Delta_f (k + 1/2)T$ is uniformly distributed between $-\pi$ and π and $\cos \xi$ has the same probability density function as $-\cos \xi$. Thus the two probabilities involved in the evaluation of $P(e)$ are equal and $P(e)$ reduces to

$$P(e) = P(n_k > \sqrt{E} + i_k)$$

Define $\zeta = i_k = \sqrt{\frac{E}{\eta}} \sin c(\pi \Delta_f T) \cos(\xi)$ and let $f_\zeta(z)$ be the probability density function of ζ . Then

$$\begin{aligned}
 P(e) &= \int P(n_k > \sqrt{E} + z) f_\zeta(z) dz \\
 &= \int \left(\frac{1}{2} \operatorname{erfc} \frac{\sqrt{E} + z}{\sqrt{N_0}} \right) f_\zeta(z) dz \\
 &= \int \left[\sum_{k=0}^{\infty} z^k \frac{g^{(k)}(0)}{k!} \right] f_\zeta(z) dz
 \end{aligned}$$

where $g(z) = \frac{1}{2} \operatorname{erfc} \left(\frac{\sqrt{E} + z}{\sqrt{N_0}} \right)$ and $g^{(k)}(z)$ is the k -th derivative of $g(z)$.

Being $\frac{1}{2} \operatorname{erfc} \left(\frac{x}{\sqrt{2}\sigma} \right) = \int_x^{\infty} \frac{1}{\sqrt{2\pi}\sigma} e^{-\frac{z^2}{2\sigma^2}} dz = Q \left(\frac{x}{\sigma} \right)$, it is known that

$$\frac{d^k}{dz^k} \operatorname{erfc}(z) = (-1)^k \frac{2}{\sqrt{\pi}} H_{k-1}(z) e^{-z^2}$$

where $H_{k-1}(z)$ is the $(k-1)$ -th order Hermite polynomial evaluated in z .
Thus

$$g^{(k)}(0) = \frac{(-1)^k}{\sqrt{\pi} (\sqrt{N_0})^k} H_{k-1} \left(\sqrt{\frac{E}{N_0}} \right) e^{-E/N_0}$$

and the error probability can be evaluated as

$$P(e) = \sum_{k=0}^{\infty} \frac{g^{(k)}(0)}{k!} E\{\zeta^k\} = \sum_{k=0}^{\infty} \frac{g^{(k)}(0)}{k!} \left[\sqrt{\frac{E}{\eta}} \operatorname{sinc}(\pi \Delta_f T) \right]^k E\{\cos^k(\xi)\}$$

The k -th order moment of $\cos(\xi)$ can be evaluated as follows:

$$\begin{aligned}
 E\{(\cos \xi)^k\} &= E \left\{ \left(\frac{e^{j\xi} + e^{-j\xi}}{2} \right)^k \right\} \\
 &= \left(\frac{1}{2} \right)^k E \left\{ \sum_{n=0}^k \binom{k}{n} e^{j(2n-k)\xi} \right\} \\
 &= \left(\frac{1}{2} \right)^k \sum_{n=0}^k \binom{k}{n} E\{e^{j(2n-k)\xi}\}
 \end{aligned}$$

Since $E\{e^{j(2n-k)\xi}\} = 0$ unless $2n-k = 0$, the k -th order moment reduces to

$$E\{(cos \xi)^k\} = \begin{cases} \left(\frac{1}{2}\right)^k \binom{k}{k/2} & \text{if } k \text{ is even} \\ 0 & \text{if } k \text{ is odd} \end{cases}$$

and finally,

$$\begin{aligned} P(e) &= \sum_{\substack{k=0 \\ k \text{ even}}}^{\infty} \frac{g^{(k)}(0)}{k!} \left[\sqrt{\frac{E}{\eta}} \sin c(\pi \Delta_f T) \right]^k \left(\frac{1}{2}\right)^k \binom{k}{k/2} \\ &= \frac{1}{2} \operatorname{erfc} \sqrt{\frac{E}{N_0}} + \frac{e^{-E/N_0}}{\sqrt{\pi}} \sum_{k=1}^{\infty} H_{2k-1} \left(\sqrt{\frac{E}{N_0}} \right) \frac{1}{(k!)^2} \left[\frac{1}{2} \sqrt{\frac{E}{N_0 \eta}} \sin c(\pi \Delta_f T) \right]^{2k} \end{aligned} \quad (2.1)$$

Table 2.1, Table 2.2, and Table 2.3 show the RFI-induced losses with respect to ideal BPSK for various η (dB), Δ_f and $P(e)$ evaluated using equation (2.1).

Table 2.4, Table 2.5, and Table 2.6 show the RFI-induced losses with respect to ideal BPSK for the same values of η (dB), Δ_f and $P(e)$ evaluated through simulation.

These values are also shown in Figure 2.1, Figure 2.3, Figure 2.5 (theory), and in Figure 2.7, Figure 2.9, Figure 2.11 (simulation), where the losses are plotted as functions of η (dB).

Similarly, these values are also shown in Figure 2.2, Figure 2.4, Figure 2.6 (theory), and in Figure 2.8, Figure 2.10, Figure 2.12 (simulation), where the losses are plotted as function of $R_b = \Delta_f T$.

At $P(e) = 10^{-1}$ some differences exist between the theoretical losses and the simulation results; however, this is due to the difficulty of finding the exact abscissa that gives $P(e) = 10^{-1}$, being the curve very flat.

For smaller values of $P(e)$ simulation and theory are in good agreement, which validates both the theoretical results and the simulation programs. The losses listed in the tables are also in good agreement with the results independently found by Lee in [3] (see Table 2.7).

$\Delta_f T$	$\eta = 0$	$\eta = 3$	$\eta = 6$	$\eta = 9$	$\eta = 12$	$\eta = 15$
0		2.51	1.04	0.48	0.23	0.11
0.25	5.50	1.89	0.82	0.38	0.19	0.09
0.5	1.88	0.82	0.38	0.19	0.09	0.05
0.75	0.34	0.16	0.08	0.04	0.02	0.01

Table 2.1: Losses (dB) at $P(e)=10^{-1}$ w.r.t. ideal BPSK in the presence of narrow-band interference with random phase (theory).

$\Delta_f T$	$\eta = 0$	$\eta = 3$	$\eta = 6$	$\eta = 9$	$\eta = 12$	$\eta = 15$
0		6.37	3.14	1.54	0.76	0.38
0.25	6.00	5.28	2.52	1.24	0.61	0.31
0.5	5.27	2.52	1.24	0.61	0.30	0.15
0.75	1.09	0.54	0.27	0.13	0.07	0.03

Table 2.2: Losses (dB) at $P(e)=10^{-2}$ w.r.t. ideal BPSK in the presence of narrow-band interference with random phase (theory).

$\Delta_f T$	$\eta = 0$	$\eta = 3$	$\eta = 6$	$\eta = 9$	$\eta = 12$	$\eta = 15$
0		8.18	4.17	2.21	1.19	0.63
0.25		6.75	3.39	1.83	0.98	0.51
0.5	6.63	3.38	1.83	0.98	0.51	0.26
0.75	1.64	0.87	0.46	0.24	0.12	0.06

Table 2.3: Losses (dB) at $P(e)=10^{-3}$ w.r.t. ideal BPSK in the presence of narrow-band interference with random phase (theory).

$\Delta_f T$	$\eta = 0$	$\eta = 3$	$\eta = 6$	$\eta = 9$	$\eta = 12$	$\eta = 15$
0		2.41	1.00	0.46	0.22	0.11
0.25	5.01	1.68	0.70	0.31	0.14	0.06
0.5	1.96	0.85	0.40	0.20	0.10	0.05
0.75	0.38	0.19	0.10	0.06	0.03	0.02

Table 2.4: Losses (dB) at $P(e) = 10^{-1}$ w.r.t. ideal BPSK in the presence of narrow-band interference with random phase (simulation).

$\Delta_f T$	$\eta = 0$	$\eta = 3$	$\eta = 6$	$\eta = 9$	$\eta = 12$	$\eta = 15$
0		6.65	3.07	1.50	0.74	0.37
0.25		5.18	2.43	1.17	0.56	0.27
0.5	5.33	2.57	1.28	0.63	0.32	0.16
0.75	1.12	0.56	0.29	0.15	0.08	0.04

Table 2.5: Losses (dB) at $P(e) = 10^{-2}$ w.r.t. ideal BPSK in the presence of narrow-band interference with random phase (simulation).

$\Delta_f T$	$\eta = 0$	$\eta = 3$	$\eta = 6$	$\eta = 9$	$\eta = 12$	$\eta = 15$
0		8.13	4.04	2.16	1.16	0.60
0.25		6.48	3.33	1.80	0.93	0.47
0.5	6.53	3.41	1.85	1.00	0.52	0.27
0.75	1.64	0.88	0.46	0.24	0.12	0.06

Table 2.6: Losses (dB) at $P(e) = 10^{-3}$ w.r.t. ideal BPSK in the presence of narrow-band interference with random phase (simulation).

$\Delta_f T$	$\eta = 9$	$\eta = 12$	$\eta = 15$
0	2.22	1.19	0.61
0.25	1.83	1.00	0.50
0.5	1.00	0.50	0.25

Table 2.7: Losses (dB) at $P(e) = 10^{-3}$ w.r.t. ideal BPSK in the presence of narrow-band interference with random phase (from [3]).

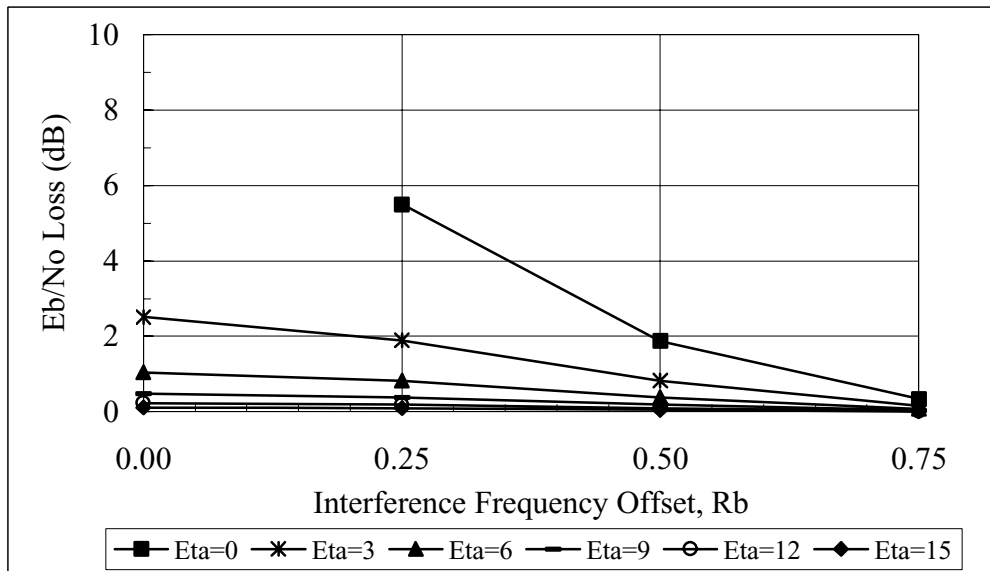


Figure 2.1: Losses (dB) at $P(e) = 10^{-1}$ w.r.t. ideal BPSK as function of $R_b = \Delta_f T$ in the presence of narrow-band interference with random phase (theory).

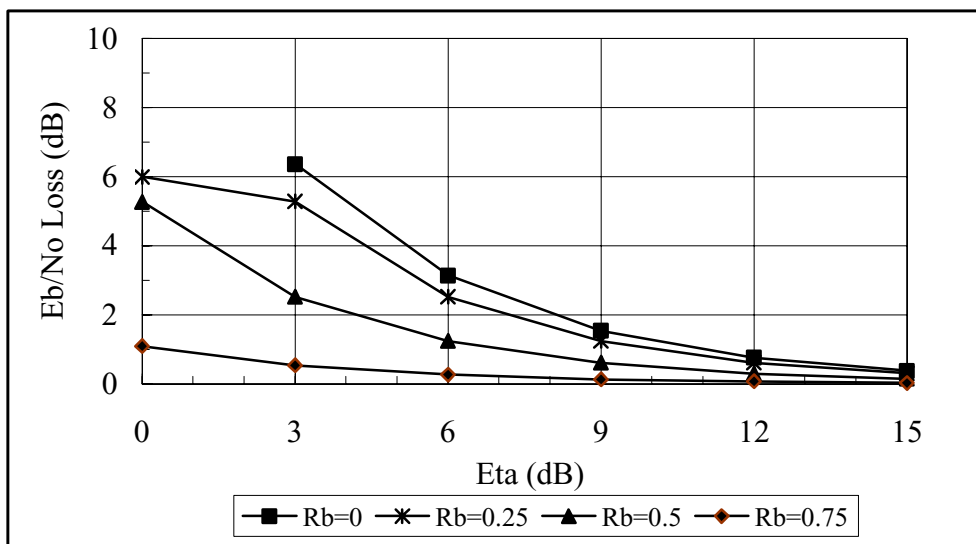


Figure 2.2: Losses (dB) at $P(e) = 10^{-1}$ w.r.t. ideal BPSK as function of η (dB) in the presence of narrow-band interference with random phase (theory).

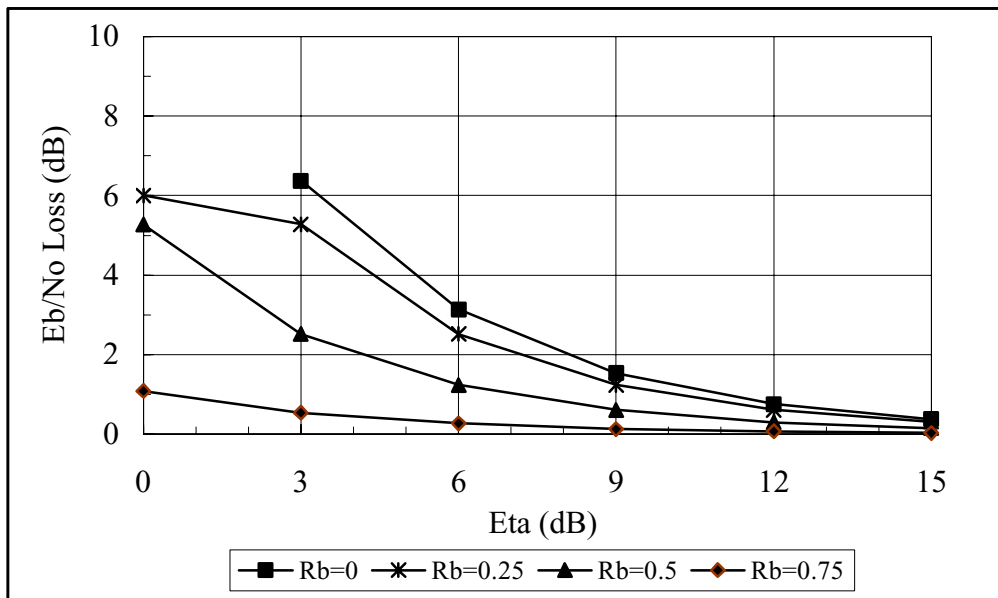


Figure 2.3: Losses (dB) at $P(e) = 10^{-2}$ w.r.t. ideal BPSK as function of η (dB) in the presence of narrow-band interference with random phase (theory).

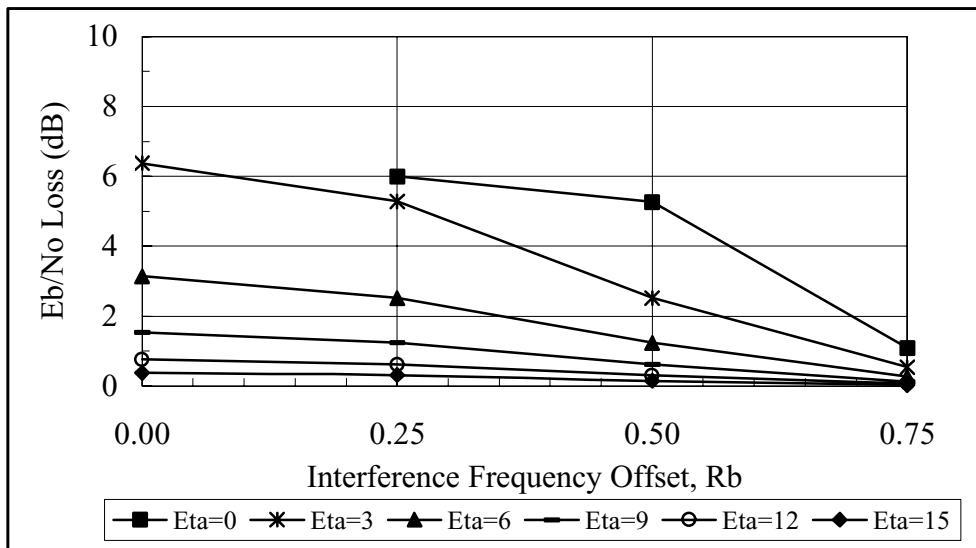


Figure 2.4: Losses (dB) at $P(e) = 10^{-2}$ w.r.t. ideal BPSK as function of $R_b = \Delta_f T$ in the presence of narrow-band interference with random phase (theory).

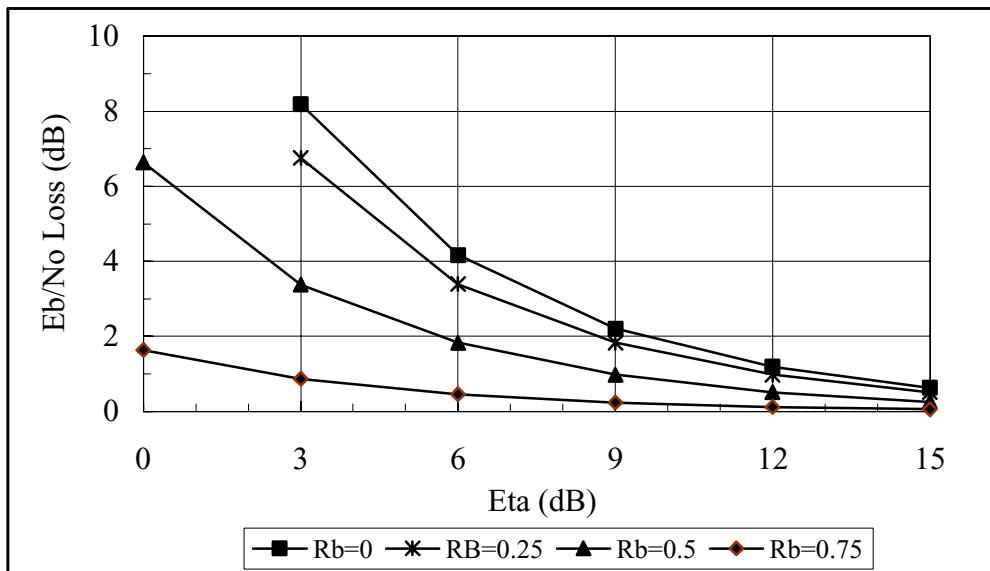


Figure 2.5: Losses (dB) at $P(e) = 10^{-3}$ w.r.t. ideal BPSK as function of η (dB) in the presence of narrow band interference with random phase (theory).

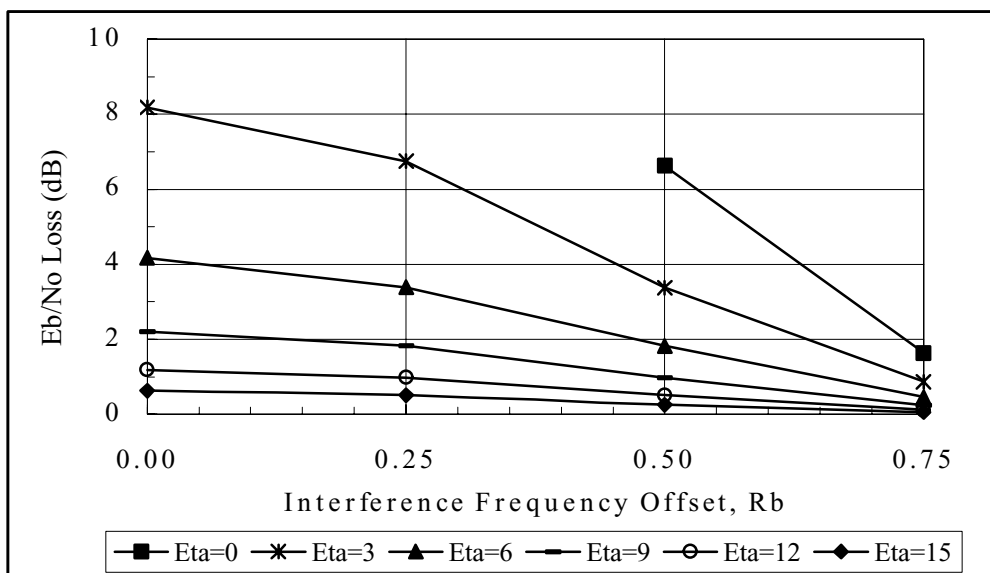


Figure 2.6: Losses (dB) at $P(e) = 10^{-3}$ w.r.t. ideal BPSK as function of $R_b = \Delta_f T$ in the presence of narrow band interference with random phase (theory).

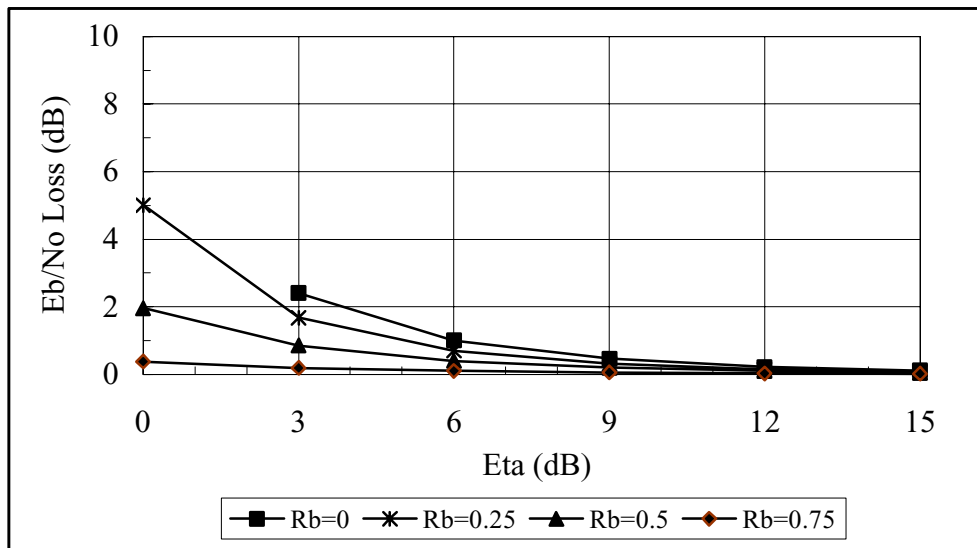


Figure 2.7: Losses (dB) at $P(e) = 10^{-1}$ w.r.t. ideal BPSK as function of η (dB) in the presence of narrow band interference with random phase (simulation).

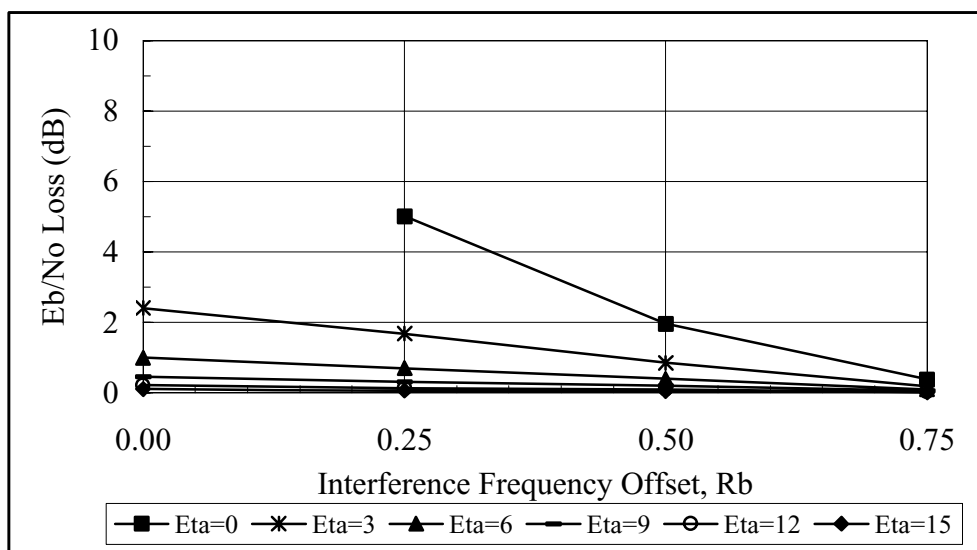


Figure 2.8: Losses (dB) at $P(e) = 10^{-1}$ w.r.t. ideal BPSK as function of $R_b = \Delta_f T$ in the presence of narrow band interference with random phase (simulation).

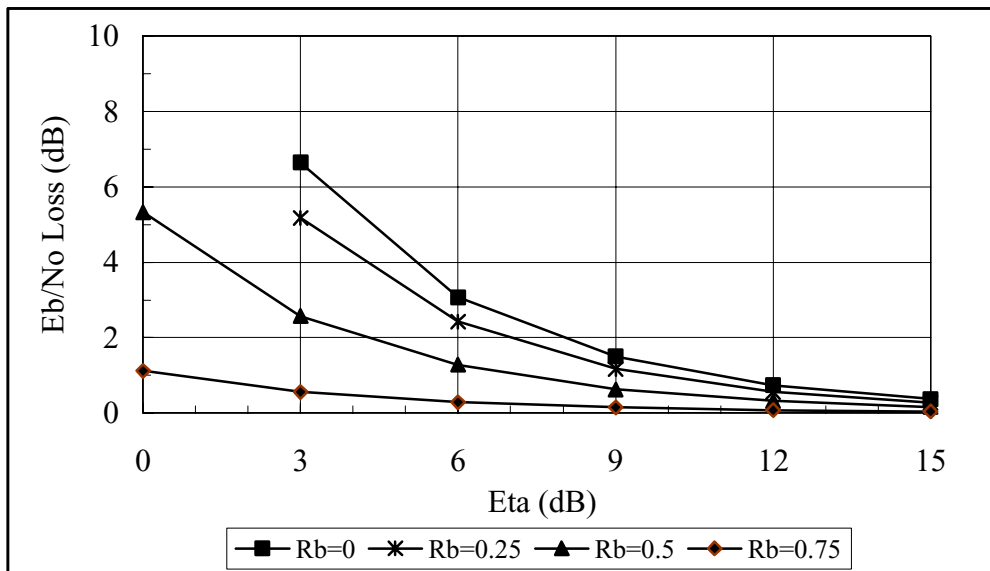


Figure 2.9: Losses (dB) at $P(e) = 10^{-2}$ w.r.t. ideal BPSK as function of η (dB) in the presence of narrow band interference with random phase (simulation).

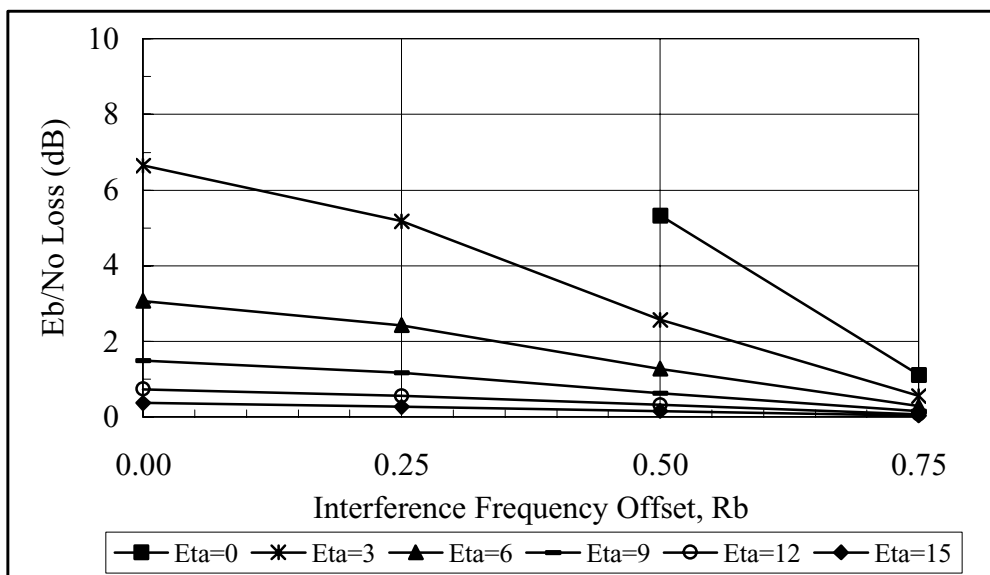


Figure 2.10: Losses (dB) at $P(e) = 10^{-2}$ w.r.t. ideal BPSK as function of $R_b = \Delta_f T$ in the presence of narrow band interference with random phase (simulation).

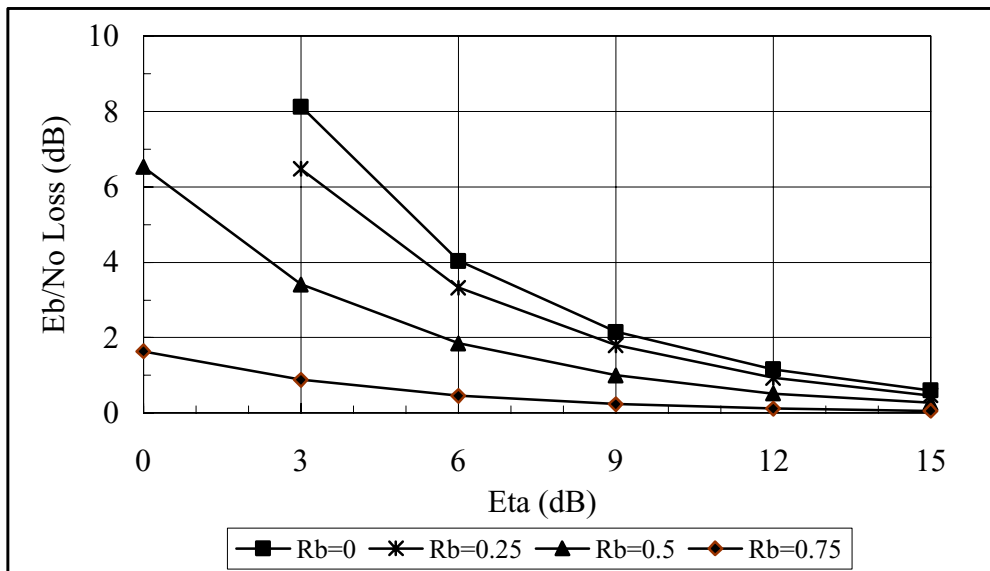


Figure 2.11: Losses (dB) at $P(e) = 10^{-3}$ w.r.t. ideal BPSK as function of η (dB) in the presence of narrow band interference with random phase (simulation).

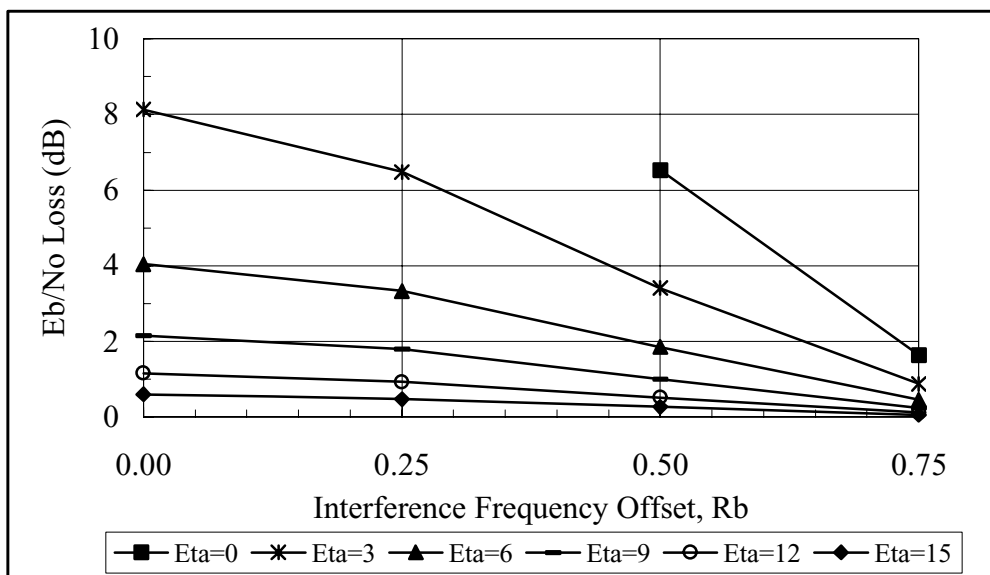


Figure 2.12: Losses (dB) at $P(e) = 10^{-3}$ w.r.t. ideal BPSK as function of $R_b = \Delta_f T$ in the presence of narrow band interference with random phase (simulation).

2.2 Worst case phase

The expressions of the interference term when the frequency offset is equal to 0, $0.25/T_b$, and $0.5/T_b$ are reported in [1].

For $\Delta_f = 0$, the worst case phase value is 0 and the error probability is

$$P(e) = \frac{1}{4} \operatorname{erfc} \left[\sqrt{\frac{E}{N_0}} \left(1 - \frac{1}{\sqrt{\eta}} \right) \right] + \frac{1}{4} \operatorname{erfc} \left[\sqrt{\frac{E}{N_0}} \left(1 + \frac{1}{\sqrt{\eta}} \right) \right] \quad (2.2)$$

For $\Delta_f = 0.25/T_b$, the worst case phase value is $\pi/4$ and the error probability is

$$P(e) = \frac{1}{4} \operatorname{erfc} \sqrt{\frac{E}{N_0}} + \frac{1}{8} \operatorname{erfc} \left[\sqrt{\frac{E}{N_0}} \left(1 + \frac{2\sqrt{2}}{\pi\sqrt{\eta}} \right) \right] + \frac{1}{8} \operatorname{erfc} \left[\sqrt{\frac{E}{N_0}} \left(1 - \frac{2\sqrt{2}}{\pi\sqrt{\eta}} \right) \right] \quad (2.3)$$

For $\Delta_f = 0.5/T_b$, the worst case phase value is $\pi/2$ and the error probability is

$$P(e) = \frac{1}{4} \operatorname{erfc} \left[\sqrt{\frac{E}{N_0}} \left(1 - \frac{2}{\pi\sqrt{\eta}} \right) \right] + \frac{1}{4} \operatorname{erfc} \left[\sqrt{\frac{E}{N_0}} \left(1 + \frac{2}{\pi\sqrt{\eta}} \right) \right] \quad (2.4)$$

Table 2.8, Table 2.9, and Table 2.10 list the losses with respect to ideal BPSK for various η (dB), Δ_f and $P(e)$.

Figure 2.13, Figure 2.14, Figure 2.15, Figure 2.16, Figure 2.17, and Figure 2.18 show the same values as function of η (dB) and of $R_b = \Delta_f T$.

It can be noticed that the losses obtained for a worst case phase and a random phase of the narrow band interferer are similar when the normalized frequency offset $\Delta_f T$ is equal to 0.25, while larger differences are present for the other frequency offsets.

Looking at the value of the interfering term i_k in r_k , it can be seen that it depends on $\varphi + 2\pi\Delta_f Tk$. When $\Delta_f T = 0$ or 0.5 or 1 , etc., i_k depends just on φ : a difference should therefore appear between the cases of random or worst case value for φ . On the contrary, when $\Delta_f T$ takes any other value (included 0.25), i_k depends on k and a sort of time averaging occurs: thus, even if the worst case value of φ is considered, the difference with respect to a random φ becomes negligible.

$\Delta_f T$	$\eta = 0$	$\eta = 3$	$\eta = 6$	$\eta = 9$	$\eta = 12$	$\eta = 15$
0		7.04	2.57	1.06	0.49	0.23
0.25	6.52	1.85	0.81	0.38	0.19	0.09
0.5	5.14	1.92	0.83	0.39	0.19	0.09

Table 2.8: Losses (dB) at $P(e) = 10^{-1}$ w.r.t. ideal BPSK in the presence of narrow-band interference with worst case phase (theory).

$\Delta_f T$	$\eta = 0$	$\eta = 3$	$\eta = 6$	$\eta = 9$	$\eta = 12$	$\eta = 15$
0		9.61	4.96	2.72	1.46	0.74
0.25	>17	6.34	2.82	1.30	0.63	0.31
0.5	7.71	4.12	2.26	1.19	0.60	0.30

Table 2.9: Losses (dB) at $P(e) = 10^{-2}$ w.r.t. ideal BPSK in the presence of narrow-band interference with worst case phase (theory).

$\Delta_f T$	$\eta = 0$	$\eta = 3$	$\eta = 6$	$\eta = 9$	$\eta = 12$	$\eta = 15$
0		10.08	5.43	3.19	1.90	1.10
0.25	18.70	7.49	3.89	2.04	1.05	0.53
0.5	8.18	4.59	2.72	1.61	0.92	0.50

Table 2.10: Losses (dB) at $P(e) = 10^{-3}$ w.r.t. ideal BPSK in the presence of narrow-band interference with worst case phase (theory).

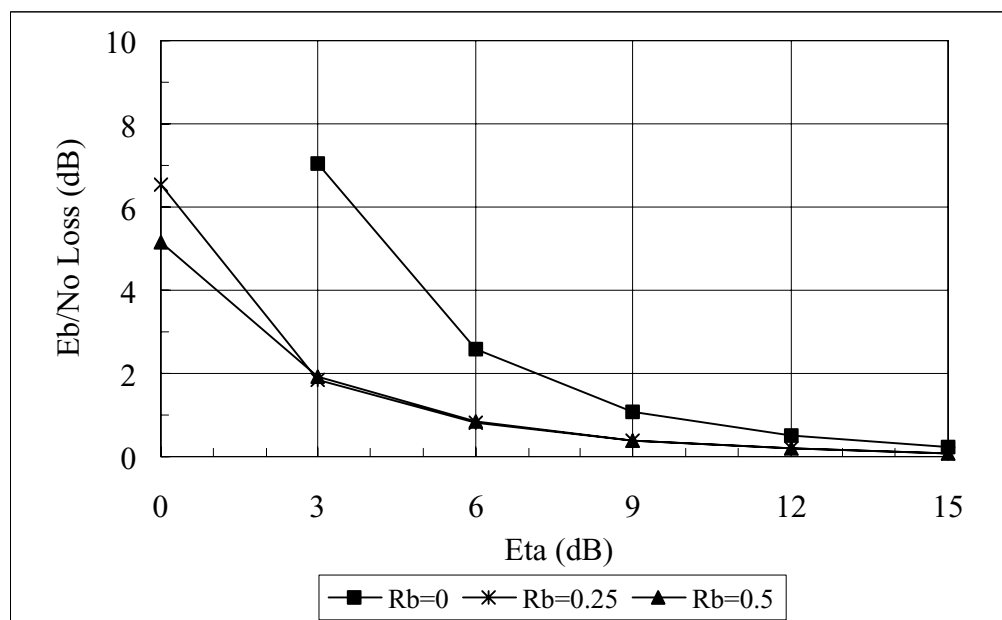


Figure 2.13: Losses (dB) at $P(e) = 10^{-1}$ w.r.t. ideal BPSK as function of η (dB) in the presence of narrow-band interference with worst case phase (theory).

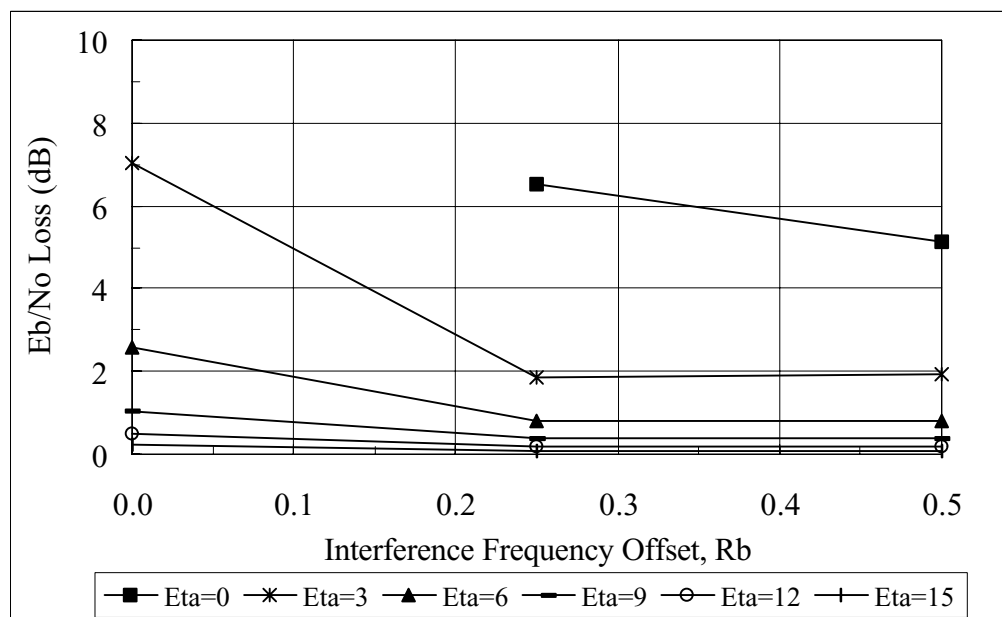


Figure 2.14: Losses (dB) at $P(e) = 10^{-1}$ w.r.t. ideal BPSK as function of $R_b = \Delta_f T$ in the presence of narrow-band interference with worst case phase (theory).

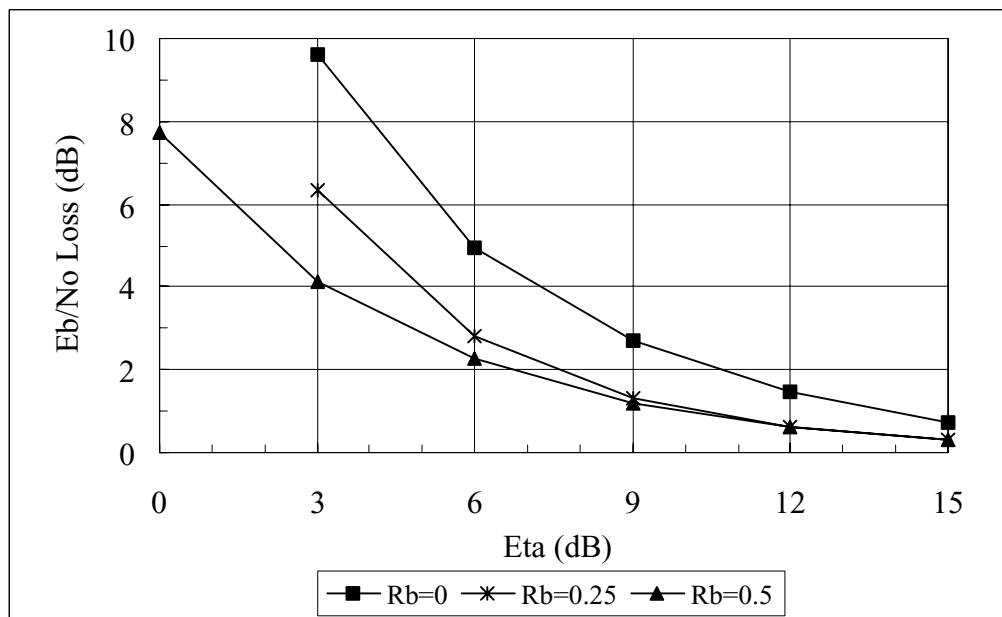


Figure 2.15: Losses (dB) at $P(e) = 10^{-2}$ w.r.t. ideal BPSK as function of η (dB) in the presence of narrow-band interference with worst case phase (theory).

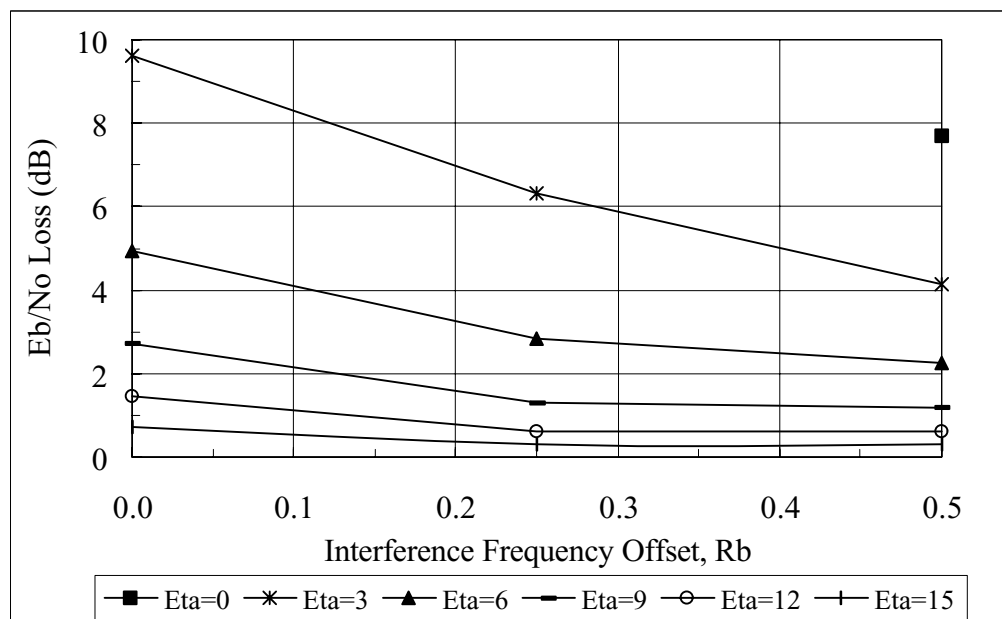


Figure 2.16: Losses (dB) at $P(e) = 10^{-2}$ w.r.t. ideal BPSK as function of $R_b = \Delta_f T$ in the presence of narrow-band interference with worst case phase (theory).

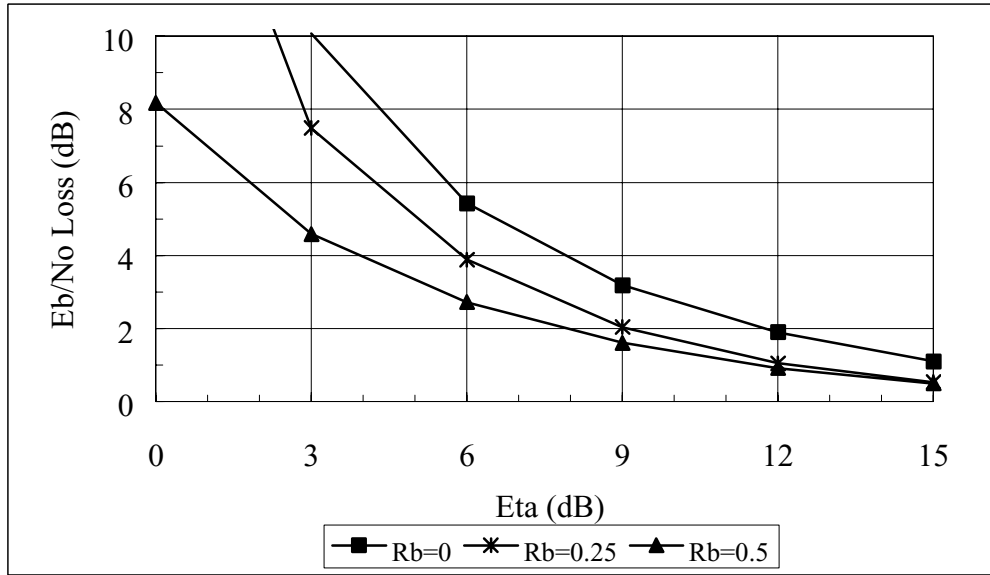


Figure 2.17: Losses (dB) at $P(e) = 10^{-3}$ w.r.t. ideal BPSK as function of η (dB) in the presence of narrow-band interference with worst case phase (theory).

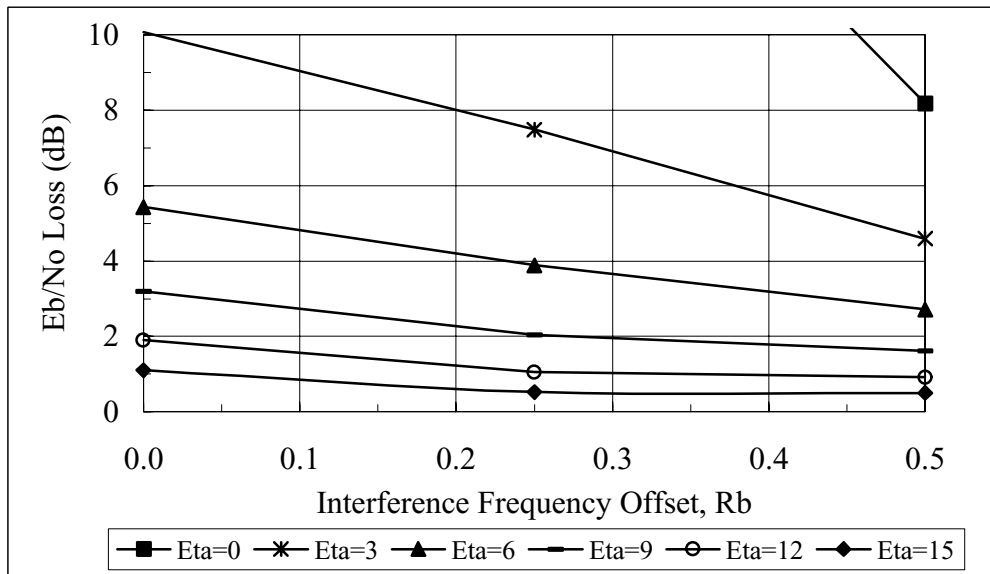


Figure 2.18: Losses (dB) at $P(e) = 10^{-3}$ w.r.t. ideal BPSK as function of $R_b = \Delta_f T$ in the presence of narrow-band interference with worst case phase (theory).

3 Wide band interfering signal

3.1 Random phase and timing offset

The useful signal has the following unfiltered BPSK format:

$$x(t) = \left[\sum_{k=-\infty}^{\infty} \sqrt{E} a_k \psi(t - kT) \right] \sqrt{2} \cos(2\pi f_c t)$$

with $\psi(t) = 1/\sqrt{T} u_T(t)$, while the interferer is also an unfiltered BPSK:

$$x_I(t) = \sum_{k=-\infty}^{\infty} \sqrt{\frac{E}{\eta}} b_k \psi(t - kT - \tau) \sqrt{2} \cos(2\pi f_c t + 2\pi \Delta_f t + \varphi)$$

where φ is a random phase uniformly distributed between $-\pi$ and π , Δ_f is the frequency offset of the interferer with respect to the center frequency of the useful signal, τ is a timing offset and η is the signal to interferer power ratio

$$\eta = \frac{P_s}{P_I} = \frac{E/T}{A^2}.$$

The ideal BPSK receiver evaluates the random variable

$$r_k = \int r(t) \sqrt{2} \cos(2\pi f_c t) \psi(t - kT) dt$$

and decides for $\hat{a}_k = 1$ if $r_k > 0$, otherwise it decides for $\hat{a}_k = -1$.

The random variable r_k is the sum of 3 terms:

$$r_k = u_k + i_k + n_k$$

where u_k is the useful part, equal to

$$u_k = \int x(t) \sqrt{2} \cos(2\pi f_c t) \psi(t - kT) dt = \sqrt{E} a_k$$

while n_k is a Gaussian random variable with zero mean and variance equal to $N_0/2$.

The third term, i_k , is due to the interferer and it can be written as

$$\begin{aligned}
 i_k &= \int x_I(t) \psi(t - kT) \sqrt{2} \cos(2\pi f_c t) dt \\
 &= \sqrt{\frac{E}{\eta}} \sum_n b_n \Re \left\{ e^{j\varphi} \int_{kT}^{kT+T} \psi(t - nT - \tau) \psi(t - kT) e^{j2\pi \Delta_f t} dt \right\} \\
 &= \sqrt{\frac{E}{\eta}} \Re \left\{ e^{j(2\pi \Delta_f kT + \varphi)} \left[\frac{b_k}{T} \int_{\tau}^T e^{j2\pi \Delta_f u} du + \frac{b_{k-1}}{T} \int_0^{\tau} e^{j2\pi \Delta_f u} du \right] \right\}
 \end{aligned}$$

If $b_k = b_{k-1}$, then

$$\begin{aligned}
 i_k &= \sqrt{\frac{E}{\eta}} \Re \left\{ \frac{b_k}{T} e^{j(2\pi \Delta_f kT + \varphi)} \int_0^T e^{j2\pi \Delta_f u} du \right\} \\
 &= \sqrt{\frac{E}{\eta}} b_k \operatorname{sinc}(\pi \Delta_f T) \cos(2\pi \Delta_f kT + \varphi + \pi \Delta_f T) \\
 &= \sqrt{\frac{E}{\eta}} \operatorname{sinc}(\pi \Delta_f T) \cos(\xi) = \zeta_1
 \end{aligned}$$

where ξ is a random variable uniformly distributed between $-\pi$ and π .

If $b_k \neq b_{k-1}$, the interfering term has a more complex expression which depends on τ and φ :

$$i_k = \sqrt{\frac{E}{\eta}} \Re \left\{ e^{j(\varphi + 2\pi \Delta_f kT)} \frac{e^{j2\pi \Delta_f T} - 2e^{j2\pi \Delta_f \tau} + 1}{j2\pi \Delta_f T} \right\} = \zeta_2$$

The error probability conditioned on τ and φ is:

$$\begin{aligned}
 P(e|\varphi, \tau) &= \frac{1}{2} P(e|\varphi, \tau, b_k = b_{k-1}) + \frac{1}{2} P(e|\varphi, \tau, b_k \neq b_{k-1}) \\
 &= \frac{1}{2} P(n_k > \sqrt{E} + \zeta_1) + \frac{1}{2} P(n_k > \sqrt{E} + \zeta_2) \\
 &= \frac{1}{4} \operatorname{erfc}\left(\frac{\sqrt{E} + \zeta_1}{\sqrt{N_0}}\right) + \frac{1}{4} \operatorname{erfc}\left(\frac{\sqrt{E} + \zeta_2}{\sqrt{N_0}}\right)
 \end{aligned}$$

The error probability is the average of $P(e|\varphi, \tau)$ over φ and τ , and can be evaluated using the same power series expansion used for the narrow band case (actually the first probability is exactly equal to that found for the narrow band case):

$$P(e) = \frac{1}{2} \sum_{k=0}^{\infty} \frac{g^{(k)}(0)}{k!} (E \{ \zeta_1^k \} + E \{ \zeta_2^k \})$$

where

$$g(x) = \frac{1}{2} \operatorname{erfc}\left(\frac{\sqrt{E} + x}{\sqrt{N_0}}\right),$$

$$g^{(k)}(0) = \frac{(-1)^k}{\sqrt{\pi} (\sqrt{N_0})^k} H_{k-1} \left(\sqrt{\frac{E}{N_0}} \right) e^{-\frac{E}{N_0}},$$

and $H_n(x)$ is the n -th Hermite polynomial.

As for the k -th moment of ζ_1 , it was evaluated in the case of narrow band interferer, and the result is

$$E\{\zeta_1^k\} = \begin{cases} \left[\frac{1}{2} \sqrt{\frac{E}{\eta}} \operatorname{sinc}(\pi \Delta_f T) \right]^k \binom{k}{k/2} & \text{for } k \text{ even} \\ 0 & \text{for } k \text{ odd} \end{cases}$$

The random variable ζ_2 can be written as:

$$\zeta_2 = \sqrt{\frac{E}{\eta}} \Re \{ \beta e^{j\vartheta} \} = \frac{1}{2} \sqrt{\frac{E}{\eta}} [\beta e^{j\vartheta} + \beta^* e^{-j\vartheta}]$$

where $\beta = (e^{j2\pi \Delta_f T} - 2e^{j2\pi \Delta_f \tau} + 1) / (j2\pi \Delta_f T)$ depends on τ only, and $\vartheta = \varphi + 2\pi \Delta_f kT$ is a random variable uniformly distributed between $-\pi$ and π .

$$\begin{aligned} E\{\zeta_2^k\} &= \frac{1}{2^k} \left(\sqrt{\frac{E}{\eta}} \right)^k \sum_{n=0}^k \binom{k}{n} E \{ e^{jn\vartheta} \beta^n e^{-j(k-n)\vartheta} (\beta^*)^{k-n} \} \\ &= \frac{1}{2^k} \left(\sqrt{\frac{E}{\eta}} \right)^k \sum_{n=0}^k \binom{k}{n} E \{ e^{j(2n-k)\vartheta} \} E \{ \beta^n (\beta^*)^{k-n} \} \\ &= \begin{cases} \frac{1}{2^k} \left(\sqrt{\frac{E}{\eta}} \right)^k \binom{k}{k/2} E \{ |\beta|^k \} & \text{if } k \text{ is even} \\ 0 & \text{if } k \text{ is odd} \end{cases} \end{aligned}$$

Thus, in the overall, the two moments of ζ_1 and ζ_2 are both null for k odd, and thus the error probability can be reduced to

$$P(e) = \frac{1}{2} \sum_{k=0}^{\infty} \frac{g^{(2k)}(0)}{(2k)!} (E\{\zeta_1^{2k}\} + E\{\zeta_2^{2k}\})$$

where

$$E\{\zeta_1^{2k}\} = \left[\frac{1}{2} \sqrt{\frac{E}{\eta}} \right]^{2k} \binom{2k}{k} [\text{sinc}(\pi \Delta_f T)]^{2k}$$

$$E\{\zeta_2^{2k}\} = \left[\frac{1}{2} \sqrt{\frac{E}{\eta}} \right]^{2k} \binom{2k}{k} E\{|\beta|^{2k}\}$$

If $\Delta_f T = 0$, then β reduces to $(1 - 2\tau/T)$, i.e. a random variable uniformly distributed between -1 and 1 ; therefore

$$E\{|\beta|^{2k}\} = \frac{1}{2k+1} \quad (3.1)$$

Thus, if the interferer is isofrequential ($\Delta_f T = 0$), the error probability becomes equal to

$$P(e) = \frac{1}{2} \text{erfc}\left(\sqrt{\frac{E}{N_0}}\right) + \frac{e^{-\frac{E}{N_0}}}{2\sqrt{\pi}} \sum_{k=1}^{\infty} H_{2k-1}\left(\sqrt{\frac{E}{N_0}}\right) \left(\frac{1}{2} \sqrt{\frac{E}{\eta N_0}}\right)^{2k} \frac{1 + 1/(2k+1)}{(k!)^2} \quad (3.2)$$

On the contrary, when $\Delta_f T > 0$,

$$|\beta|^2 = \frac{[a + b \cos \xi]}{(2\pi \Delta_f T)^2}$$

where a and b are equal to $a = 6 + 2 \cos(2\pi \Delta_f T)$, $b = -8 \cos(\pi \Delta_f T)$, and ξ is now a random variable uniformly distributed in the interval $(-\pi \Delta_f T, \pi \Delta_f T)$,

$$\begin{aligned} E\{|\beta|^{2k}\} &= E\{(a + b \cos \xi)^k\} \frac{1}{(2\pi \Delta_f T)^{2k}} \\ &= \sum_{n=0}^k \binom{k}{n} a^{k-n} b^n E\{(\cos \xi)^n\} \frac{1}{(2\pi \Delta_f T)^{2k}} \\ E\{(\cos \xi)^n\} &= \sum_{m=0}^n \binom{n}{m} \frac{1}{2^n} E\{e^{j\xi(2m-n)}\} \\ &= \sum_{m=0}^n \binom{n}{m} \frac{1}{2^n} \text{sinc}(\pi \Delta_f T(2m-n)) \\ E\{|\beta|^{2k}\} &= \sum_{n=0}^k \binom{k}{n} a^{k-n} \frac{b^n}{2^n} \sum_{m=0}^n \binom{n}{m} \text{sinc}(\pi \Delta_f T(2m-n)) \frac{1}{(2\pi \Delta_f T)^{2k}} \quad (3.3) \end{aligned}$$

Adding together all the terms, the final expression for $P(e)$ in the case $\Delta_f T > 0$ is the following:

$$P(e) = \frac{1}{2} \operatorname{erfc} \sqrt{\frac{E}{N_0}} + \frac{e^{-E/N_0}}{2\sqrt{\pi}} \sum_{k=1}^{\infty} H_{2k-1} \left(\sqrt{\frac{E}{N_0}} \right) \frac{1}{(k!)^2} \left[\frac{1}{2} \sqrt{\frac{E}{N_0 \eta}} \right]^{2k} \left\{ [\operatorname{sinc}(\pi \Delta_f T)]^{2k} + E [|\beta|^{2k}] \right\} \quad (3.4)$$

where $E [|\beta|^{2k}]$ is that of equation (3.3).

Tables 3.1-3.6 and figures 3.1-3.15 show the values of the losses with respect to the ideal BPSK evaluated both with formulas 3.2 and 3.4 and the simulation. The correspondence between theory and simulation is good, apart from the cases $\eta = 0$ and $\Delta_f T < 0.5$, where the error probabilities evaluated with formulas 3.2 and 3.4 tend to diverge.

With respect to the results obtained by NASA/JPL and reported in Table 3.7, there is a good agreement, which shows that both ESA and NASA derived the right results.

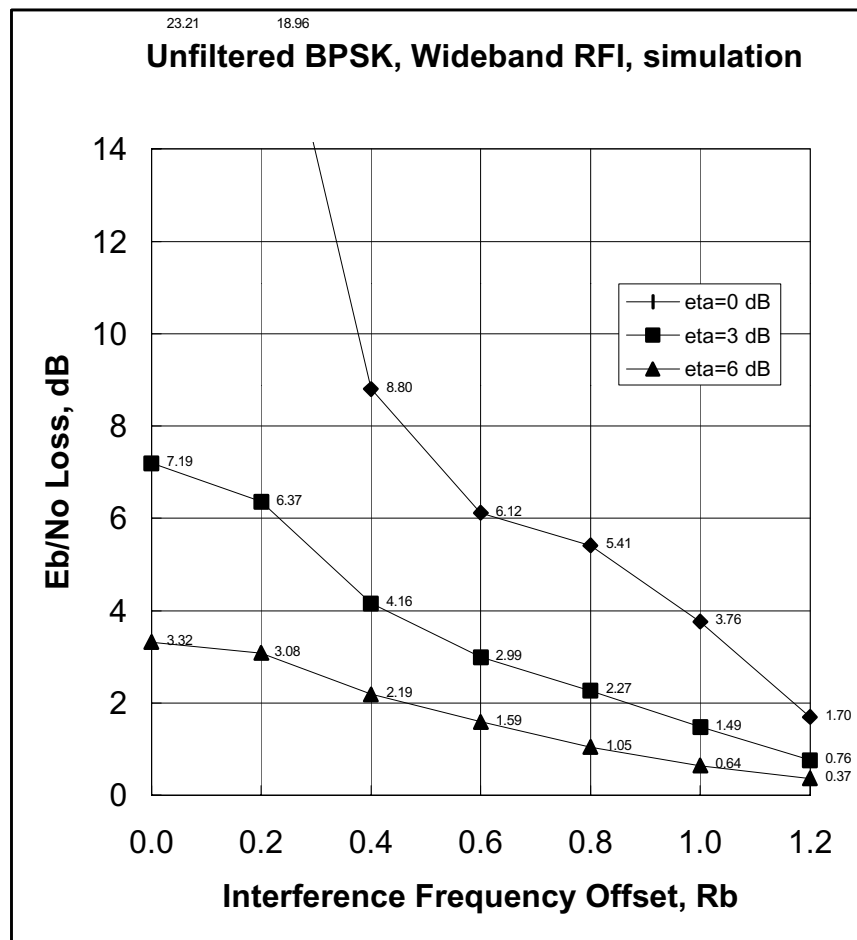


Figure 3.1: Losses (dB) at $P(e)=10^{-3}$ w.r.t. ideal BPSK in the presence of wide-band interferer with random phase and timing offset (simulation).

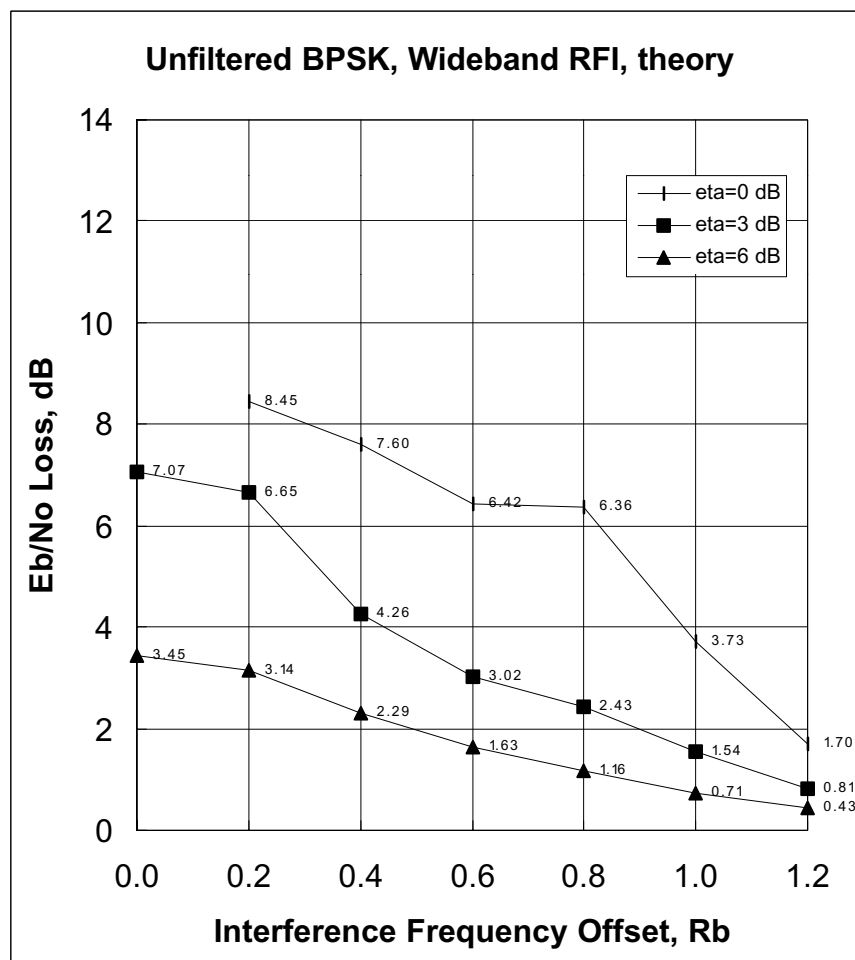


Figure 3.2: Losses (dB) at $P(e)=10^{-3}$ w.r.t. ideal BPSK in the presence of wide-band interferer with random phase and timing (theory).

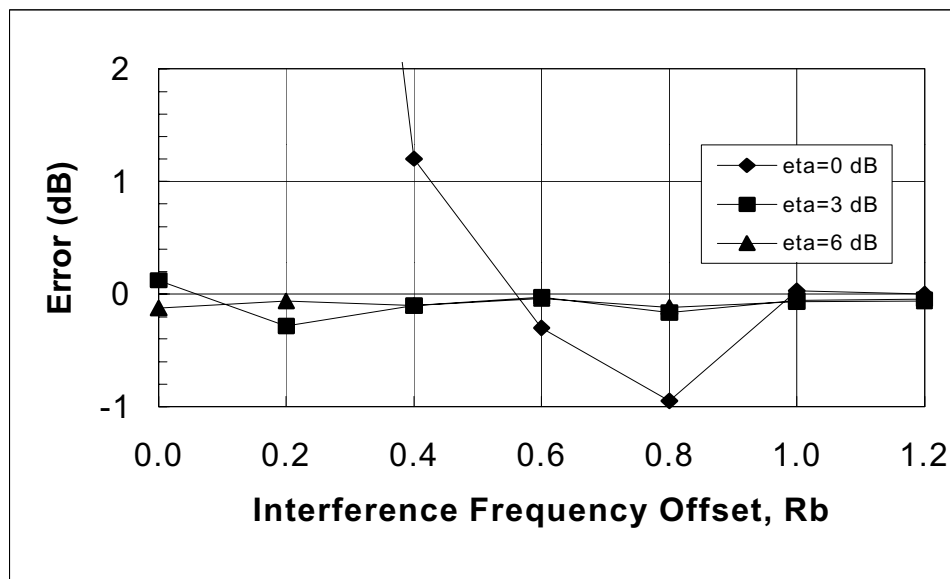


Figure 3.3: Error (dB) at $P(e)=10^{-3}$ between losses obtained with simulation and losses evaluated with theory.

$\Delta_f T$	$\eta = 0$	$\eta = 3$	$\eta = 6$	$\eta = 9$	$\eta = 12$	$\eta = 15$
0	3.830	1.445	0.653	0.313	0.153	0.076
0.25	3.140	1.250	0.570	0.275	0.135	0.067
0.5	1.880	0.817	0.384	0.187	0.090	0.046

Table 3.1: Losses (dB) at $P(e) = 10^{-1}$ w.r.t. ideal BPSK in the presence of wide-band interference with random phase and timing offset (theory).

$\Delta_f T$	$\eta = 0$	$\eta = 3$	$\eta = 6$	$\eta = 9$	$\eta = 12$	$\eta = 15$
0		5.915	2.261	1.056	0.512	0.252
0.25		4.168	1.900	0.914	0.447	0.221
0.5	5.265	2.517	1.240	0.614	0.304	0.151

Table 3.2: Losses (dB) at $P(e) = 10^{-2}$ w.r.t. ideal BPSK in the presence of wide-band interference with random phase and timing offset (theory).

$\Delta_f T$	$\eta = 0$	$\eta = 3$	$\eta = 6$	$\eta = 9$	$\eta = 12$	$\eta = 15$
0		7.069	3.446	1.720	0.866	0.436
0.25		6.133	2.840	1.459	0.749	0.380
0.5	6.630	3.375	1.826	0.977	0.509	0.206

Table 3.3: Losses (dB) at $P(e) = 10^{-3}$ w.r.t. ideal BPSK in the presence of wide-band interference with random phase and timing offset (theory).

$\Delta_f T$	$\eta = 0$	$\eta = 3$	$\eta = 6$	$\eta = 9$	$\eta = 12$	$\eta = 15$
0	3.324	1.238	0.530	0.231	0.097	0.036
0.25	2.918	1.113	0.478	0.208	0.087	0.032
0.5	1.900	0.811	0.375	0.177	0.084	0.039
0.75	0.917	0.445	0.224	0.116	0.061	0.032
1	0.422	0.221	0.118	0.065	0.037	0.021

Table 3.4: Losses (dB) at $P(e) = 10^{-1}$ w.r.t. ideal BPSK in the presence of wide-band interference with random phase and timing offset (simulation).

$\Delta_f T$	$\eta = 0$	$\eta = 3$	$\eta = 6$	$\eta = 9$	$\eta = 12$	$\eta = 15$
0	25.67	5.042	2.117	0.968	0.453	0.212
0.25	12.02	4.147	1.855	0.867	0.409	0.102
0.5	5.336	2.561	1.258	0.617	0.302	0.149
0.75	3.506	1.490	0.704	0.347	0.175	0.089
1	1.649	0.709	0.339	0.171	0.088	0.047

Table 3.5: Losses (dB) at $P(e) = 10^{-2}$ w.r.t. ideal BPSK in the presence of wide-band interference with random phase and timing offset (simulation).

$\Delta_f T$	$\eta = 0$	$\eta = 3$	$\eta = 6$	$\eta = 9$	$\eta = 12$	$\eta = 15$
0	23.21	7.193	3.321	1.636	0.809	0.396
0.25	15.47	5.807	2.836	1.438	0.724	0.357
0.5	6.537	3.410	1.850	0.989	0.513	0.261
0.75	6.147	2.602	1.222	0.598	0.299	0.151
1	3.759	1.485	0.643	0.302	0.149	0.076

Table 3.6: Losses (dB) at $P(e) = 10^{-3}$ w.r.t. ideal BPSK in the presence of wide-band interference with random phase and timing offset (simulation).

$\Delta_f T$	$\eta = 0$	$\eta = 3$	$\eta = 6$	$\eta = 9$	$\eta = 12$	$\eta = 15$
0				1.88	1.00	0.54
0.25		>6	3.00	1.60	0.87	0.48
0.5		3.70	1.90	1.07	0.60	0.13
0.75	5.96	2.48	1.22	0.59	0.33	--
1	3.63	1.44	0.63	0.30	0.15	--

Table 3.7: Losses (dB) at $P(e) = 10^{-3}$ w.r.t. ideal BPSK in the presence of wide-band interference with random phase and timing offset (from [3] and [4]).

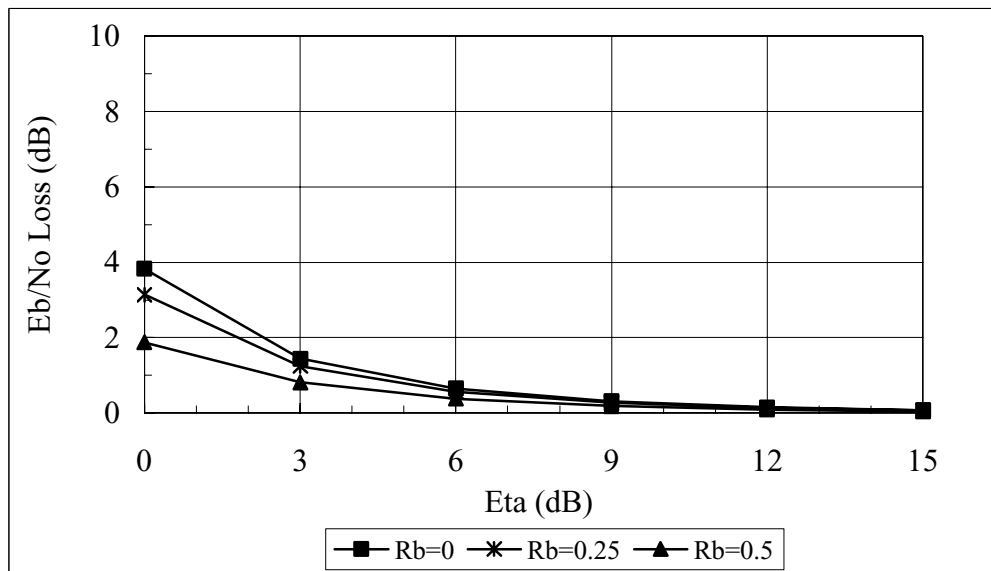


Figure 3.4: Losses (dB) at $P(e) = 10^{-1}$ w.r.t. ideal BPSK as function of η (dB) in the presence of wide-band interference with random phase and timing offset (theory).

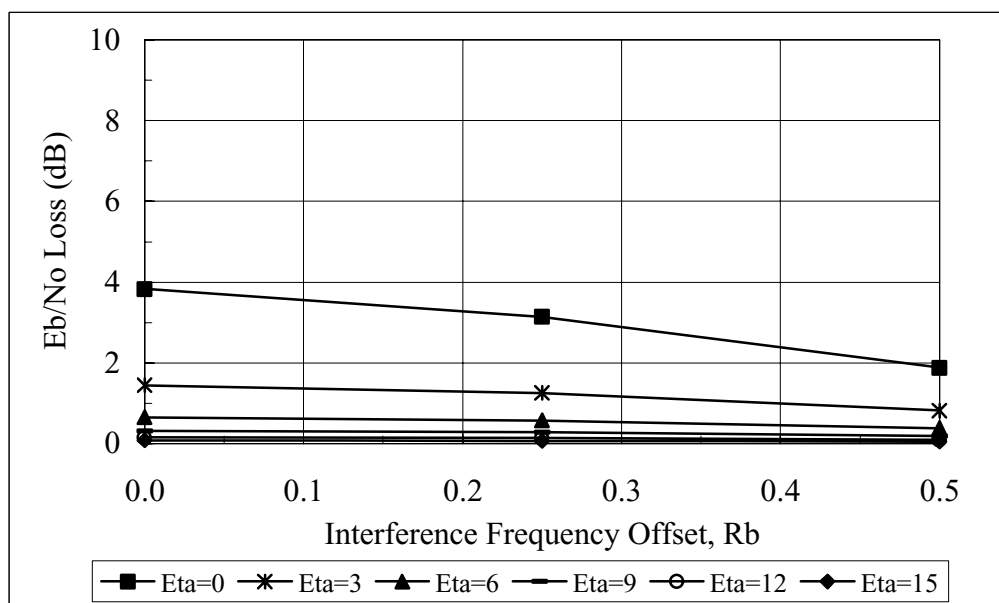


Figure 3.5: Losses (dB) at $P(e) = 10^{-1}$ w.r.t. ideal BPSK as function of $R_b = \Delta_f T$ in the presence of wide-band interference with random phase and timing offset (theory).

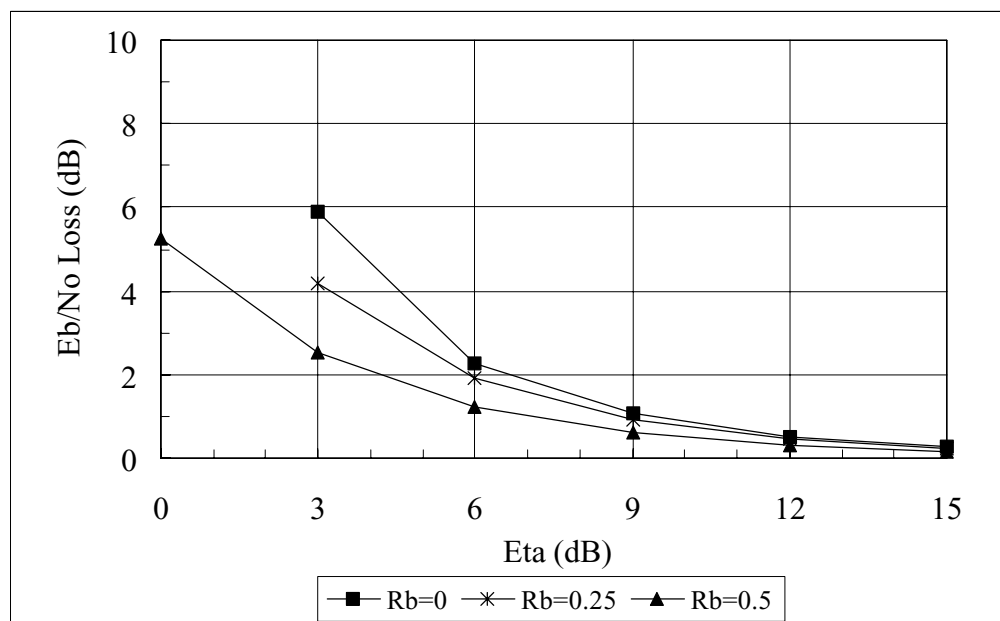


Figure 3.6: Losses (dB) at $P(e) = 10^{-2}$ w.r.t. ideal BPSK as function of η (dB) in the presence of wide-band interference with random phase and timing offset (theory).

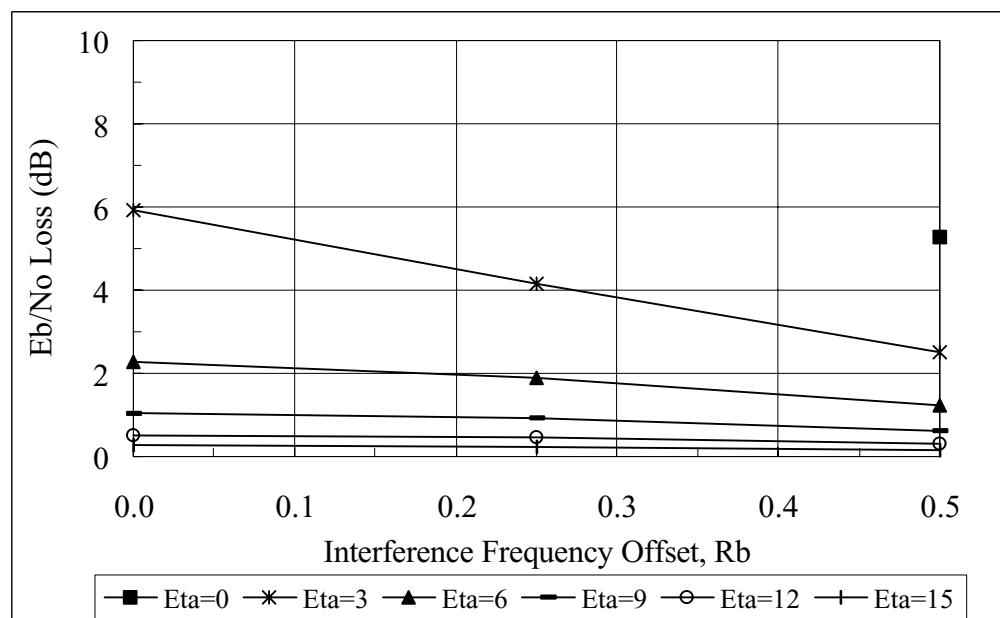


Figure 3.7: Losses (dB) at $P(e) = 10^{-2}$ w.r.t. ideal BPSK as function of $R_b = \Delta_f T$ in the presence of wide-band interference with random phase and timing offset (theory).

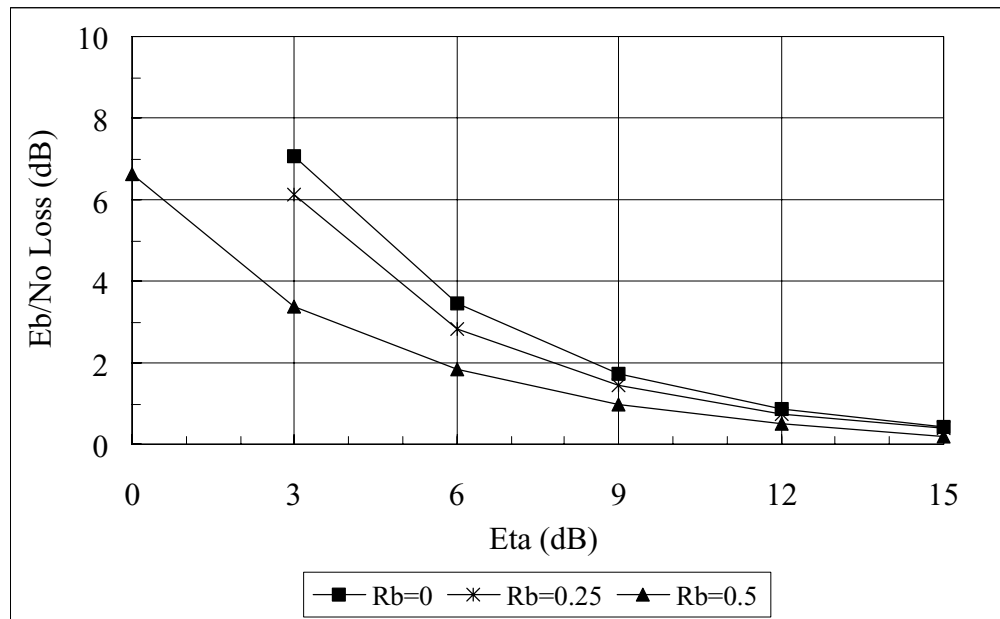


Figure 3.8: Losses (dB) at $P(e) = 10^{-3}$ w.r.t. ideal BPSK as function of η (dB) in the presence of wide-band interference with random phase and timing offset (theory).

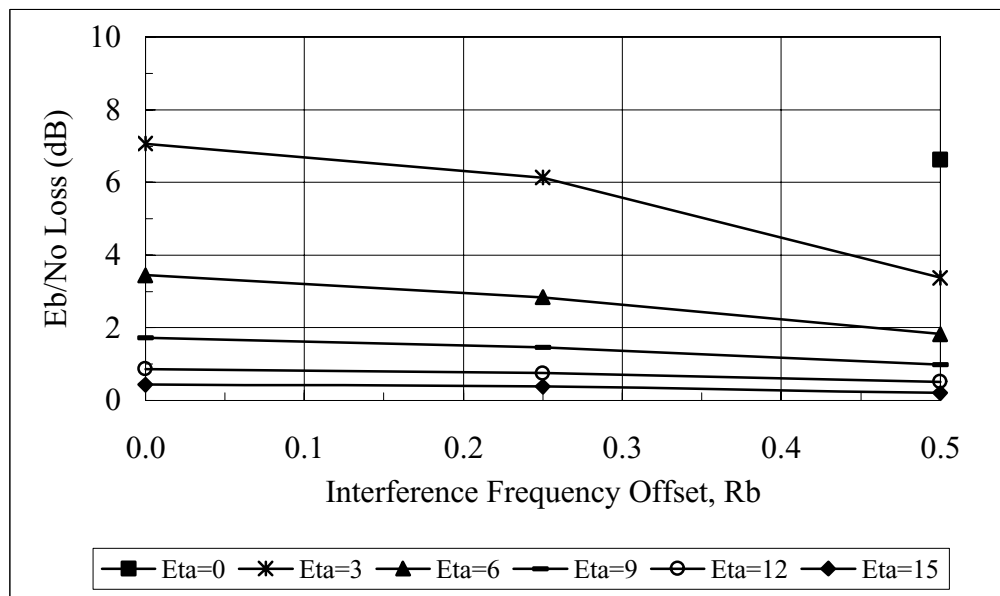


Figure 3.9: Losses (dB) at $P(e) = 10^{-3}$ w.r.t. ideal BPSK as function of $R_b = \Delta_f T$ in the presence of wide-band interference with random phase and timing offset (theory).

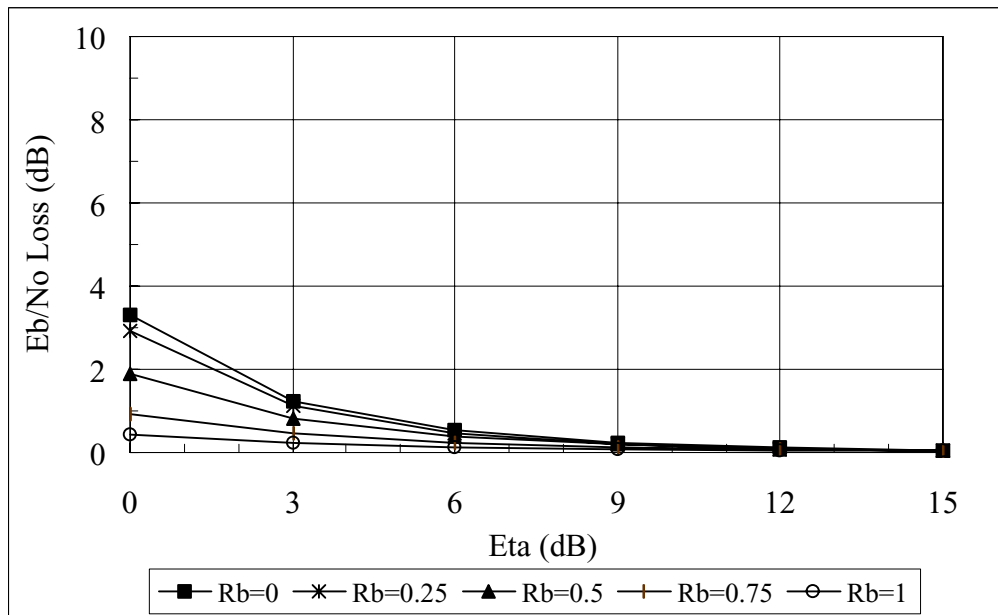


Figure 3.10: Losses (dB) at $P(e) = 10^{-1}$ w.r.t. ideal BPSK as function of η (dB) in the presence of wide-band interference with random phase and timing offset (simulation).

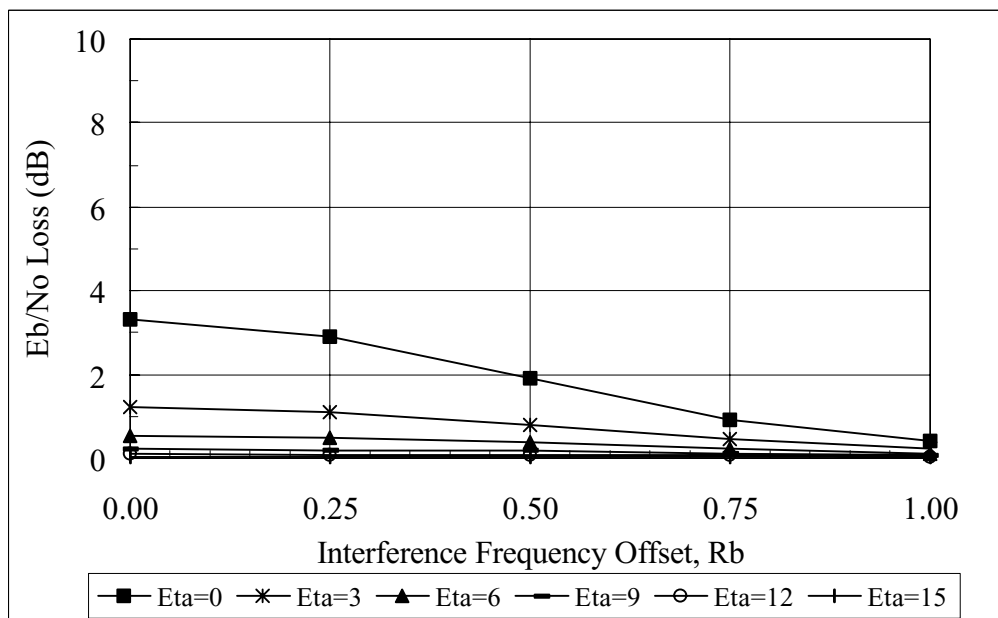


Figure 3.11: Losses (dB) at $P(e) = 10^{-1}$ w.r.t. ideal BPSK as function of $R_b = \Delta_f T$ in the presence of wide-band interference with random phase and timing offset (simulation).

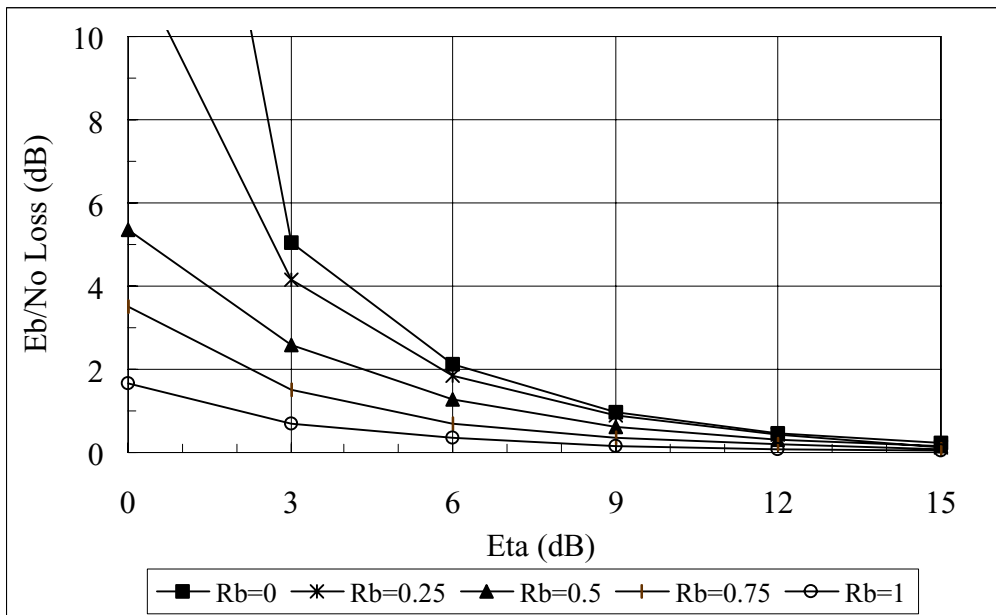


Figure 3.12: Losses (dB) at $P(e) = 10^{-2}$ w.r.t. ideal BPSK as function of η (dB) in the presence of wide-band interference with random phase and timing offset (simulation).

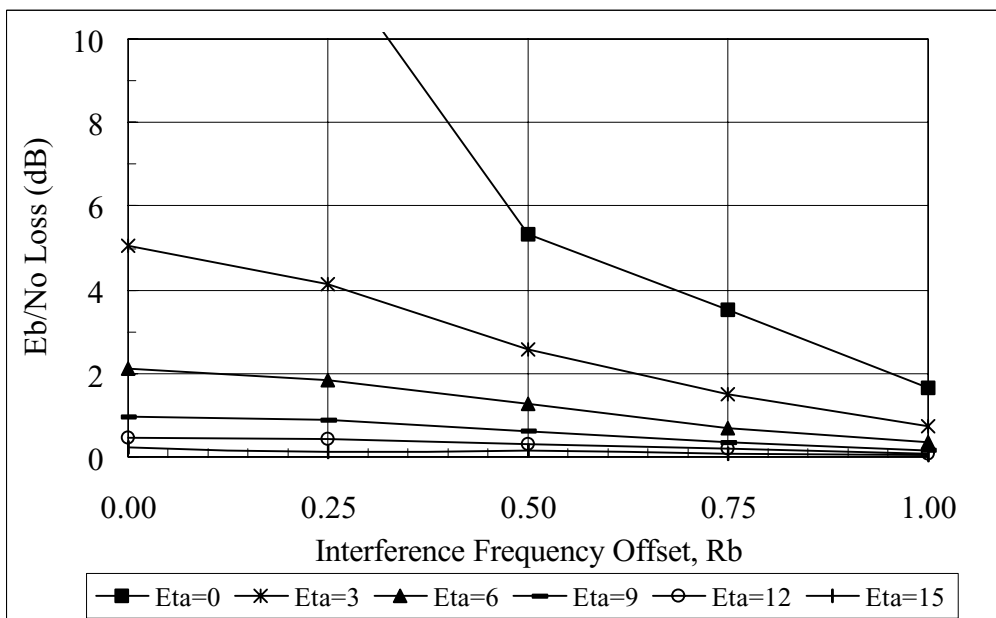


Figure 3.13: Losses (dB) at $P(e) = 10^{-2}$ w.r.t. ideal BPSK as function of $R_b = \Delta_f T$ in the presence of wide-band interference with random phase and timing offset (simulation).

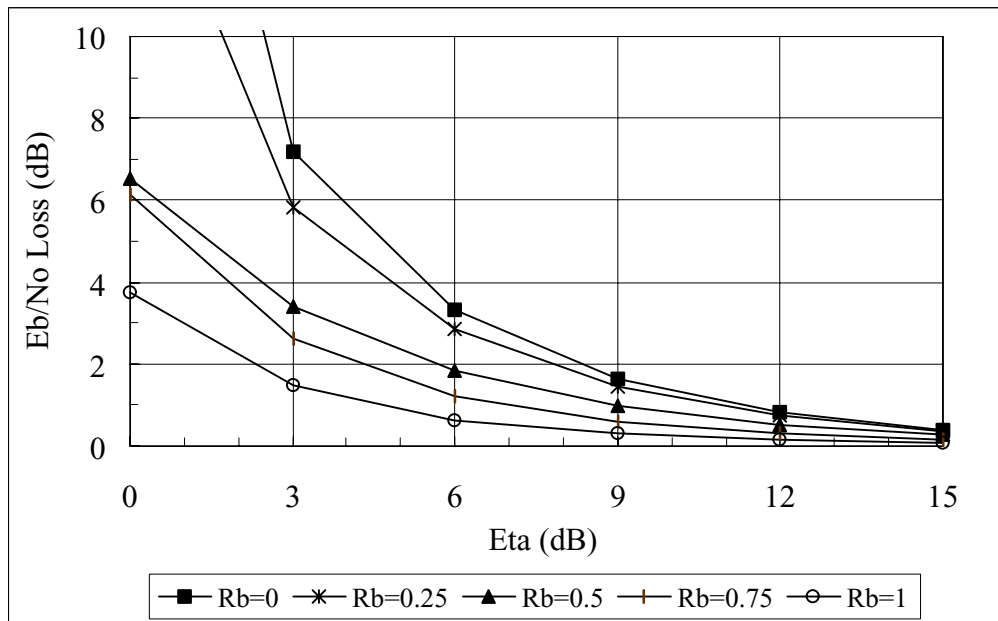


Figure 3.14: Losses (dB) at $P(e) = 10^{-3}$ w.r.t. ideal BPSK as function of η (dB) in the presence of wide-band interference with random phase and timing offset (simulation).

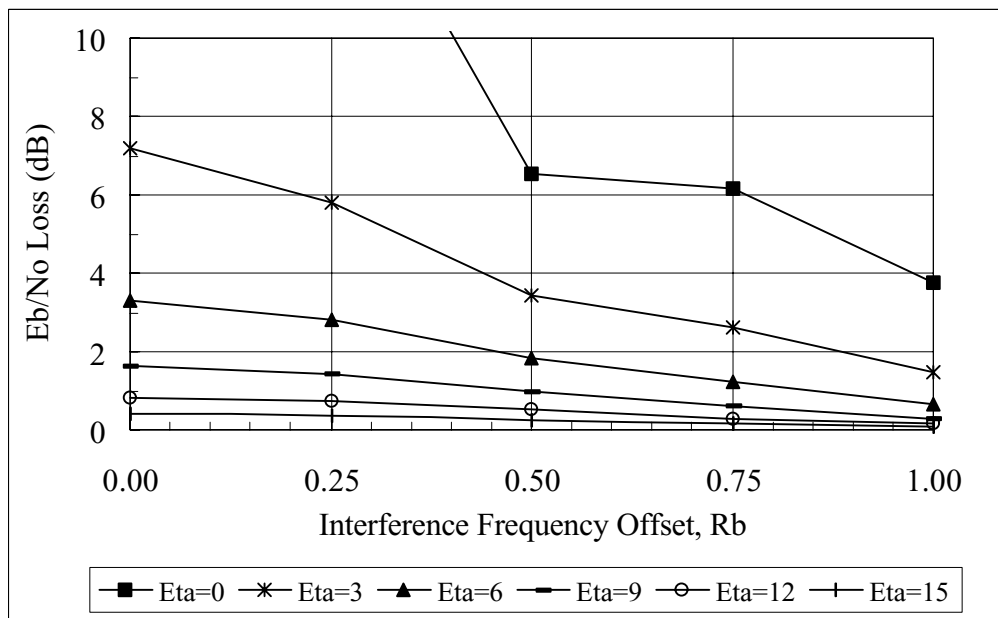


Figure 3.15: Losses (dB) at $P(e) = 10^{-3}$ w.r.t. ideal BPSK as function of $R_b = \Delta_f T$ in the presence of wide-band interference with random phase and timing offset (simulation).

3.2 Worst case phase and timing offset

Starting with the expression of the interfering term i_k , it can be easily shown that,

$$\max(i_k) = \begin{cases} = \sqrt{\frac{E}{\eta}} \left| \text{sinc}(\pi \Delta_f T) \right| & \forall \tau \quad \text{if } b_k = b_{k-1} \\ = \sqrt{\frac{E}{\eta}} \sqrt{a + b \cos[\pi \Delta_f T (2\tau/T - 1)]} & \text{if } b_k \neq b_{k-1} \end{cases}$$

In this second case, $\max(i_k)$ depends on τ and the value of τ which maximizes i_k is that which maximizes

$$m(\tau) = a + b \cos[\pi \Delta_f T (2\tau/T - 1)]$$

where $a = 6 + 2 \cos(2\pi \Delta_f T)$, $b = -8 \cos(\pi \Delta_f T)$.

- if $b > 0$, $\max[m(\tau)] = a + |b|$, for $\tau/T = 1/2 + k/\Delta_f T$; since τ must belong to the interval $[0, T]$, the only solution is $\tau = T/2$. The case $b > 0$ corresponds to the case $\cos(\pi \Delta_f T) < 0$, i.e. $\Delta_f T \in [k + 1/2, k + 3/2]$ for $k = 0, 1, 2, 3, \dots$
- if $b < 0$, $\max[m(\tau)] = a + |b|$, for $\tau/T = 1/2 + (2k + 1)/2\Delta_f T$, thus the minimum positive value for τ is $T/2 + 1/2\Delta_f T$, which is outside the allowed range if $\Delta_f T \leq 0.5$. Thus two cases should be analyzed:
 - ♦ $\Delta_f T \in [k + 3/2, k + 5/2]$ for $k = 0, 1, 2, 3, \dots$: in this case the worst case value of τ is $T/2 + 1/2\Delta_f T$ and $\max[m(\tau)] = a + |b|$
 - ♦ $\Delta_f T \in [0, 1/2]$: in this case the worst case value of τ is 0 and $\max[m(\tau)] = |e^{j2\pi \Delta_f T} - 1| = 2 \sin(\pi \Delta_f T)$.

Therefore,

$$\max(i_k) = \begin{cases} \sqrt{\frac{E}{\eta}} \text{sinc}(\pi \Delta_f T) & \text{if } \Delta_f T \in [0, 0.5] \\ \sqrt{\frac{E}{\eta}} \max\left[\left|\text{sinc}(\pi \Delta_f T)\right|, \frac{a + |b|}{2\pi \Delta_f T}\right] = \sqrt{\frac{E}{\eta}} \frac{a + |b|}{2\pi \Delta_f T} & \text{if } \Delta_f T > 0.5 \end{cases}$$

yielding

$$P(e) < \frac{1}{2} \text{erfc}\left(\sqrt{\frac{E}{N_0}} \left[1 - \sqrt{\frac{1}{\eta}} \max(i_k)\right]\right) \quad (3.5)$$

Figure 3.16 shows $\max(i_k)$ as function of $R_b = \Delta_f T$, while Figure 3.17 shows the asymptotic losses, derived from the expression of $P(e)$ in equation (3.5), for $\eta = 0, 3$, and 6 dB.

Comparing Figure 3.2 with Figure 3.17, it can be noticed that the losses in the presence of a random and a worst case wide-band interferer have a similar pattern; the losses due to a worst case interferer are however 3-6 dB higher.

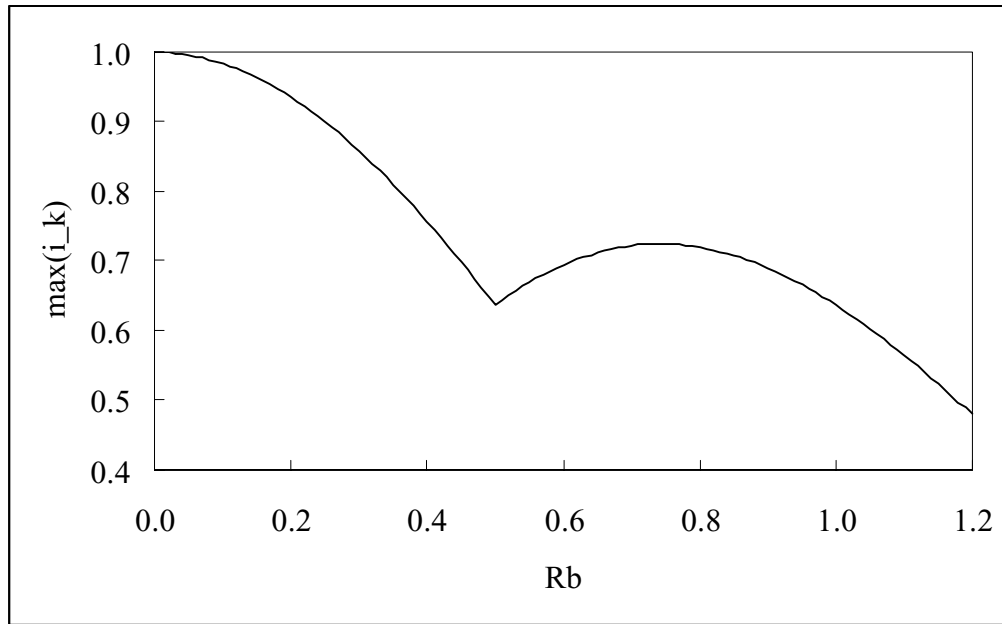


Figure 3.16: $\max(i_k)$ as function of $R_b = \Delta_f T$.

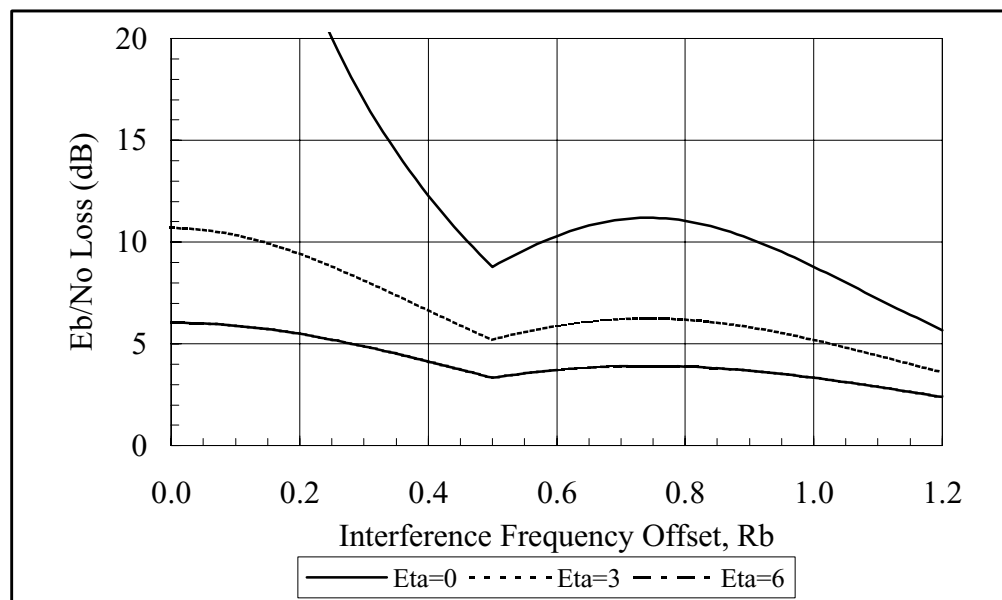


Figure 3.17: Losses (dB) at $P(e)=10^{-3}$ w.r.t. ideal BPSK in the presence of wide band interference with worst case phase and timing offset (theory).

4 Conclusions

With this analysis ESA showed that ESA's and NASA's results presented at the CCSDS Panel 1E Spring 1999 meeting were correct and that the apparent misalignments are easily explainable. It has to be decided whether the worst case or the average interference should be considered in the dimensioning of the transmission system.

5 References

- [1] G.Povero, M.Visintin, E. Vassallo, "Interference Susceptibility of Selected Bandwidth-Efficient Modulation Schemes", CCSDS Panel 1E, May 1999
- [2] W. Martin, T. Yan, D. Lee, M. Srinivasan, "Interference Susceptibility", CCSDS Panel 1E, May 1999
- [3] D. Lee, "BPSK RFI Susceptibility", NASA JPL, July 13, 1999
- [4] W. Martin, T. Yan, A. Gray, D. Lee, "Efficient Modulation Methods Study at NASA/JPL, Phase 4: Interference Susceptibility", CCSDS-SFCG, September 1999`

[This page intentionally left blank.]

Coded Bit Error Performance of Selected Bandwidth Efficient Modulations

Dennis Lee and Tsun-Yee Yan
Jet Propulsion Laboratory
California Institute of Technology
Pasadena, CA 91109

May 4, 2000

1 Abstract

This paper is in response to action item 99-1E-41 concerning the coded bit error curves presented [1] at the CCSDS Panel 1E meeting in October, 1999. The discrepancies between results in [1], [5], and [6] are found to be primarily due to different truncation path lengths and quantization levels in the Viterbi decoder. Simulations of BPSK with standard CCSDS concatenated coding is used to quantify the effects of different truncation path lengths and quantizations. A common set of coding parameters is agreed upon between JPL and ESA for performing CCSDS coding simulations. Using these parameters, the coded bit error probabilities of the six efficient modulations (GMSK $BT_b = 0.5$, GMSK $BT_b = 0.25$, Butterworth filtered OQPSK, Square Root Raised Cosine ($\alpha=0.5$) OQPSK, FQPSK-B, T-OQPSK) are compared.

2 Introduction

At the October 1999 CCSDS Panel 1E meeting, it was noticed that the concatenated coding bit error performance for BPSK presented in [1] was higher than the standard values used by ESA. The performance curves generated by the Denmark Technical University and provided by ESA show that for BPSK with standard CCSDS concatenated coding, $E_b/N_o = 2.56$ dB is required for a bit error probability of 10^{-6} . However, a $E_b/N_o = 2.84$ dB was needed in [1] to produce the same BER.

Upon further examination, the curves in [1] were indeed confirmed as showing the correct bit error probability based on the parameters chosen for the Viterbi decoder (3-bit quantization and a truncation path length of 32 bits). However, as was noted in [1], the BPSK bit error performance with standard CCSDS concatenated coding reported in the literature varies considerably, by as much as 0.5 dB asymptotically. For example, in [6], the E_b/N_o required for a coded bit error probability of 10^{-6} is approximately 2.38 dB. In [4], a E_b/N_o of about 2.85 dB was required for a BER of 10^{-6} based on data from Linkabit. The concatenated coding BER curve in the CCSDS Telemetry Green Book [2] does not extend beyond a bit error probability of 10^{-5} ; however, the required E_b/N_o for a 10^{-5} bit error probability is approximately 2.25 dB, which is about 0.2 dB less than the standard values used by ESA and about 0.4 dB less than the results in [1].

The discrepancies between these results lie primarily in the different parameters chosen for the Viterbi decoder. In particular, the truncation path length (decoding depth) and quantization can

cause a significant difference in bit error probability. Unfortunately, in some cases these parameters are not specified, and lead to seemingly conflicting results. For example, while 3-bit quantization is specified for the concatenated coding bit error rate curve in the CCSDS Telemetry Green Book [2], the truncation path length is left ambiguous. Truncation path length and quantization are not specified in the CCSDS Telemetry Channel Coding Blue Book [3].

Using BPSK as a test case, simulation results are generated to show the effects of different truncation path lengths and number of quantization levels. A common set of parameters for the Viterbi decoder is agreed upon with the group conducting the ESA coded BER study. Coded bit error probabilities for the bandwidth efficient modulations in [1] is updated using these parameters.

3 Truncation Path Length

The standard CCSDS concatenated code consists of a (255,223) Reed-Solomon outer code and a rate 1/2, $k=7$ convolutional inner code with octal generators (133,171). A block interleaver with a depth of five R-S codewords is inserted between the inner and outer codes to break up error burst from the Viterbi decoder.

The BPSK concatenated coding simulation results shown in [1] were produced with a Viterbi decoder using a truncation path length of 32 bits. The standard ESA values from the Denmark Technical University (DTU) are based on a Viterbi decoder with a truncation path length of 128 [5]. Figure 1 shows the bit error probability using different truncation path lengths of 32, 50, 70, and 100 bits and 3-bit quantization. The BER curves are generated using SPW computer simulations. From the figure, there is approximately 0.2 dB E_b/N_o improvement from a truncation path length of 32 to a truncation path length of 70. Increasing the truncation path length above 70 results in minimal BER improvement. Hence, it was agreed with ESA to use a truncation path length of 70 bits for all future CCSDS coded performance studies.

The results in Figure 1 were generated using 3-bit quantization in the Viterbi decoder. The 8 quantization levels defined by the thresholds $\{-1, -0.67, -0.33, 0, 0.33, 0.67, 1.0\}$ with respect to a received signal power normalized to 1. Results from [1] using 3-bit quantization and 32-bit truncation path length had quantization levels that were spaced slightly wider apart, and the BER curves were approximately 0.1 dB worse.

4 Number of Quantization levels

The results in [1] were produced using 3-bit quantization in the Viterbi decoder. Figure 2 compares the bit error performance using 3-bit, 5-bit, and 32-bit quantization and a fixed truncation path length of 70. As the figure shows, a 0.07 dB E_b/N_o improvement in BER performance can be gained by using 5-bit quantization instead of 3-bit quantization. Using 32-bit quantization provides a 0.15 dB improvement over 3-bit quantization. However, since 3-bit quantization is traditionally the most commonly used value, it was agreed upon with ESA to use 3-bit quantization in the Viterbi decoder for future results.

5 Coded Performance of Bandwidth Efficient Modulations

Using these mutually agreed parameters for the Viterbi decoder, the concatenated coding bit error performances of GMSK $BT_b=0.25$, GMSK $BT_b=0.5$, Butterworth filtered ($BT_s = 1$) Offset QPSK, square root raised cosine (SRRC, $\alpha = 0.5$) Offset QPSK, FQPSK-B, and T-OQPSK in a nonlinear satellite channel have been simulated. The AM/AM and AM/PM characteristics of the 10W

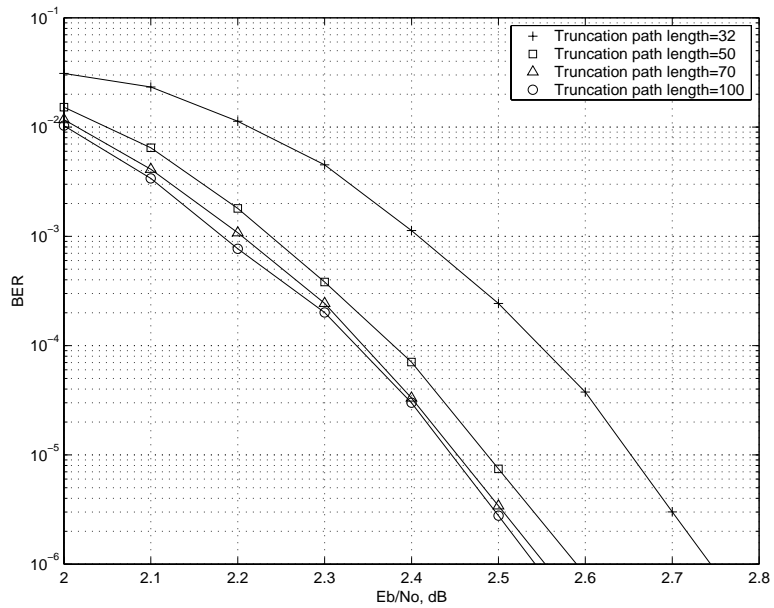


Figure 1: BPSK with standard CCSDS concatenated coding and 3-bit quantization

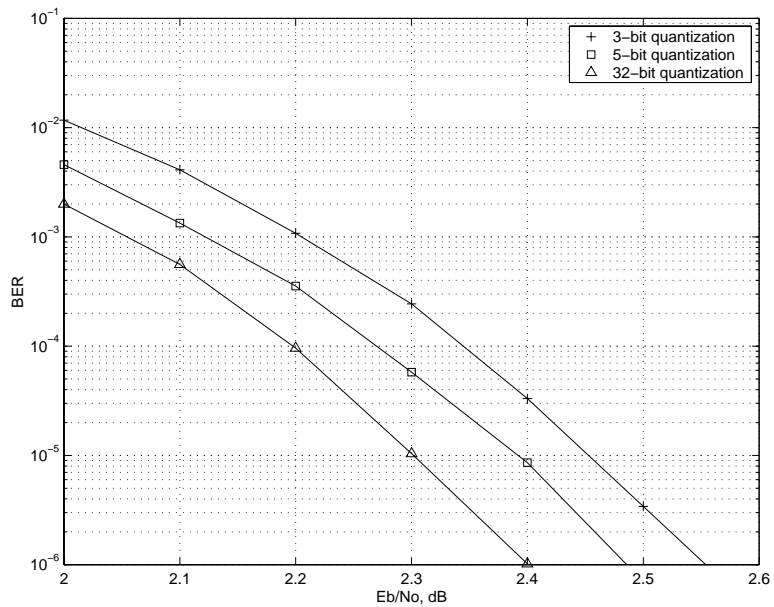


Figure 2: BPSK with standard CCSDS concatenated coding and 70 bit truncation path length

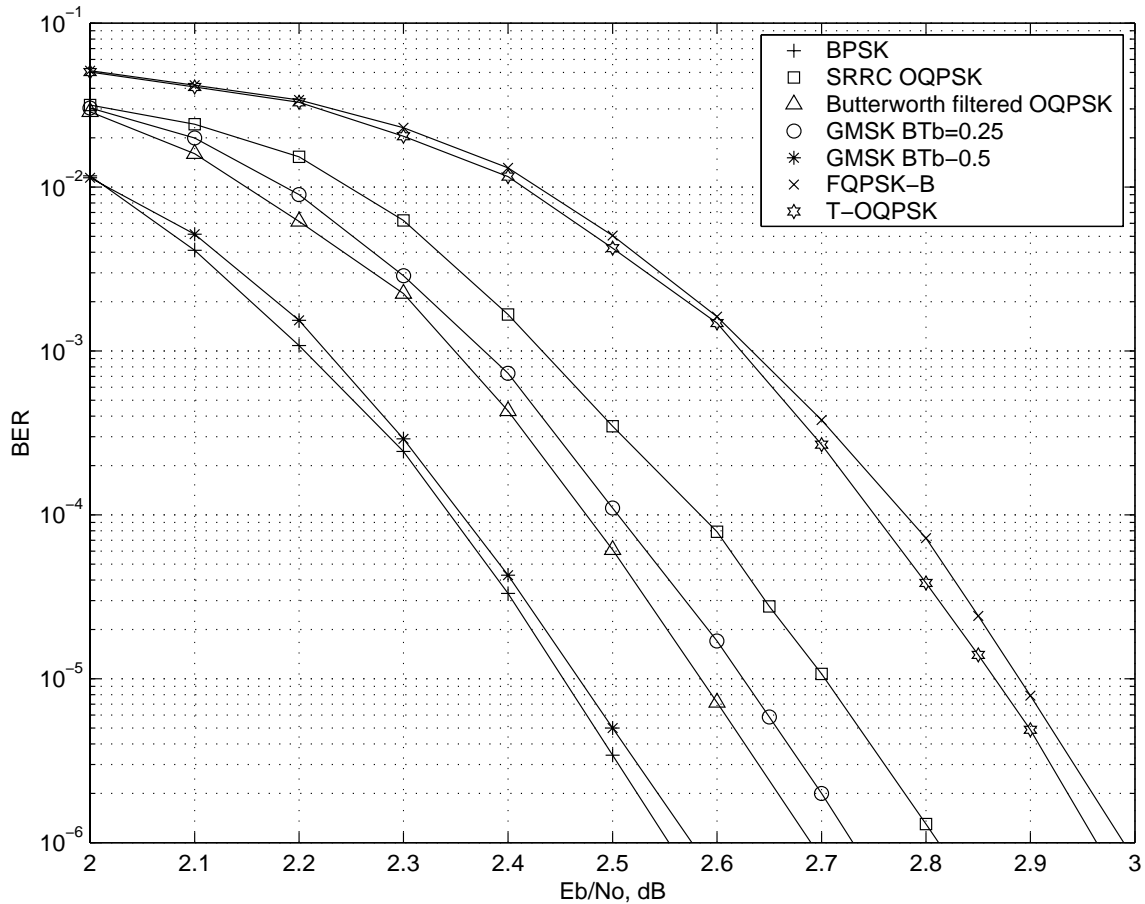


Figure 3: BER of Efficient Modulations using CCSDS concatenated coding

ESA SSPA nonlinearity used in the simulations are shown in [1]. The Viterbi decoder in these simulations used a truncation path length of 70, 3-bit quantization, and quantization levels of $\{-1.0, -0.66, -0.33, 0, 0.33, 0.66, 1.0\}$ for a received signal power normalized to one. Figure 3 compares the new coded bit error performance of six efficient modulations. The bit error probability of BPSK with concatenated coding is included in the figure for comparison.

Action item 99-1E-41 also called for inclusion of the BER performance of T-OQPSK with concatenated coding. The optimal receiver for uncoded T-OQPSK consists of four matched filters followed by a Viterbi algorithm. In order to use this receiver with the CCSDS concatenated code, a Soft Output Viterbi algorithm (SOVA) must be implemented so that the Viterbi algorithm decoding the convolutional code can operate on soft inputs. If hard decisions are used instead, there is approximately a 2 dB degradation in E_b/N_o . On the other hand, a simplified receiver for T-OQPSK consisting of an averaged matched filter can be used instead of the SOVA to generate soft inputs. From simulation results, even though the Viterbi receiver outperforms the average matched filter receiver in the uncoded case, the SOVA receiver does not provide significant BER improvement over the averaged matched filter receiver in the coded case to justify the additional complexity. Hence, the bit error rates for T-QOPSK with concatenated coding shown in Figure 3 was generated using the averaged matched filter receiver.

Table 1 summarizes the E_b/N_o needed for a bit error probability of 10^{-6} for the modulations

Table 1: Required E_b/N_o for 10^{-6} BER with Saturated PA

Modulation	E_b/N_o for 10^{-6} BER
BPSK	2.55 dB
GMSK BT=0.5	2.58 dB
GMSK BT=0.25	2.73 dB
OQPSK-BUT ($BT_s=1$)	2.69 dB
SRRC OQPSK ($BT_s=1$)	2.81 dB
FQPSK-B ($BT_s=1$)	2.99 dB
T-OQPSK ($BT_s=1$)	2.96 dB

shown in Figure 3. The table shows a 0.3 dB E_b/N_o improvement over the results reported in [1] due the different parameters used in the Viterbi decoder; however, the relative performance of the modulations with respect to each other is the virtually unchanged.

6 Summary

This paper responded to two concerns raised in action item 99-1E-41, namely to confirm the BER curves in [1], and to add the BER curve for T-OQPSK with concatenated coding. The discrepancies between the bit error probability for BPSK with standard CCSDS concatenated coding in [1] and results from the DTU were traced back to the different truncation path lengths and quantization levels used in the Viterbi decoding of the convolutional code. A common set of coding parameters (truncation path length of 70 bits and 3-bit quantization) was agreed upon between NASA/JPL and ESA, and bit error probabilities for the six bandwidth efficient modulations were simulated using these parameters. The new parameters resulted in a 0.3 dB E_b/N_o improvement in performance over the previous results reported in [1]; however, the coded performance of the modulations relative to each other was virtually unchanged.

References

- [1] D. Lee and T.-Y. Yan, "Performance of Selected Bandwidth Efficient Modulations", CCSDS Panel 1E meeting, October 1999.
- [2] "CCSDS Telemetry Green Book, Summary of Concept and Rationale", CCSDS 100.0-G-1, December 1987.
- [3] "CCSDS Telemetry Channel Coding Blue Book", CCSDS 101.0-B-4, May 1999.
- [4] D. Divsalar and J.H. Yuen, "Performance of Concatenated Reed-Solomon/ Viterbi Channel Coding," JPL TMO Progress Report 42-71, July 1982.
- [5] G. Povero and M. Visintin, "Results on the BPSK Complete Transmission System", January 2000.
- [6] M. Simon, S. Hinedi, and W. Lindsey, *Digital Communication Techniques*. Prentice-Hall, New Jersey, 1995.

Selected Laboratory Measurements and Results of FQPSK Modems

James Weese and Loc V. Lam
National Aeronautics and Space Administration
Jet Propulsion Laboratory
California Institute of Technology
4800 Oak Grove Dr. MS 238-343
Pasadena, California 91109

A.I. 97-14, 97-15

Abstract

This paper describes laboratory measurements of FQPSK-B modems performed at the Jet Propulsion Laboratory. The bit-error-rate (BER) performance and power spectral density were measured and compared against computer simulation data.

1.0 Introduction

Investigation of FQPSK-B modulation is part of an on-going JPL effort to improve power and bandwidth efficiency for future space communication systems. A major task of this effort is the verification of the performance of bandwidth and power efficient modulations. In late 1997 Dr. Kamilo Feher of the University of California, Davis, provided to members of the Jet Propulsion Laboratory two FQPSK-B modems; a 1 Mbps FQPSK-B modem from *RF Networks* and a 17 Mbps one from *Lockheed*. Subsequently these modems were integrated into JPL's Telecommunication Development Laboratory (TDL) for testing and evaluation. The purpose of the testing was to evaluate and validate the bit-error rate (BER) performance and the spectral efficiency of these modems.

2.0 Testing System Description

The test setups to evaluate the FQPSK-B modems are shown in Figs. 1 and 2 for the 1 Mbps and the 17 Mbps modem respectively. The primary objective is to measure the power spectral density of FQPSK-B modulation over X-Band frequencies with saturated and linearly operated power amplifiers. A second objective is to measure the uncoded BER.

The testing systems for the 1 Mbps and the 17 Mbps consist of the baseband signal generator, the IF modulator, the RF frequency translation network, the RF frequency down-converter and the receiver. The FQPSK-B modulator generates a 70 MHz signal which is then up-converted to the X-Band frequency of 8.450 GHz. Down conversion is achieved through two stages to achieve a 70 MHz signal which is then fed back to the FQPSK modem for demodulation and data detection.

Before the BER can be measured the entire system has to be calibrated for the proper signal-to-noise ratio. This is achieved through the Y-factor calibration system as shown in Figs. 1 and 2. To perform the calibration, the signal path between the output of the FQPSK-B modem and the X-band up-conversion network is severed and the Y-factor is connected to the X-Band network instead. The Y-factor is defined as

(EQ 1)

$$Y = \frac{EB_R}{B_N \sin^2(\theta)} + 1$$

where E is the desired signal-to-noise (E_s/N_o), B_R is the data rate, B_N is a predetermined noise bandwidth, and θ is the modulation index. In FQPSK-B the modulation index is 90° . Once the Y-factor, which is a power quantity, is evaluated for a desired signal SNR (E_s/N_o) and data rate, the power level reads by the power meter in the test system will be adjusted by the attenuators located before the 70 Mhz power amplifier until the power level reads by the power meter match those of the calculated Y-factor.

3.0 Measurement Results

3.1 Power Spectrum Measurements

Figures 3 and 4 show the power spectral density of the 1 Mbps and 17 Mbps FQPSK-B modems taken at the output of the X-Band solid state power amplifier. In an earlier spectral measurement, we observed spurious components in the outer band spectrum of the 17 Mbps modem. These spurious components were eliminated by the bandpass filter located between the FQPSK modem and the X-Band network. In both figures the power spectra change little between the linear and the saturated operating power amplifier. However, the 1 Mbps modem shows 10 dBs more of power spectral density level relative to the 17 Mbps modem. Figure 5 shows the power spectrum measured from generated through computer simulation. The computer-generated spectrum and the 1 Mbps spectrum agrees very well down to -60 dB.

3.2 Bit-Error-Rate Measurements

The BERs measured from the 1 Mbps and the 17 Mbps modems contain bit errors from the differential decoder and the descrambler. These subsystems caused burst errors to occur over several bits. We used the BER counter to determine the burst error and then divided it by the observed BER to obtain the normalized BER. Figure 6 shows the normalized BER of the 1 Mbps and 17 Mbps FQPSK-B modems. Below a BER of 10^{-3} there is little difference in performance between the 1 Mbps and 17 Mbps modems. However above 10^{-3} , the 17 Mbps modem performs better than the 1 Mbps modem. Computer simulated BER of the FQPSK-B using an ideal receiver is also shown in Fig. 6. At BER of 3×10^{-3} and above the hardware measured BER of the 17 Mbps shows better performance than our computer-simulated BER and the 1 Mbps modem BER. This difference is believed to come from a parameter not included in our computer simulation model. At BER of 3×10^{-3} and below the simulated BER and the hardware measured one agree very well.

4.0 Conclusion

The power spectrum and the uncoded BER performance of the FQPSK-B modems were measured at X-band frequencies. At BER above 3×10^{-3} and power spectral density level above -60 dB, both the hardware measured data and the computer simulation data agree very well. In the next phase of measurement, coding will be added to evaluate the BER performance at low symbol SNR.

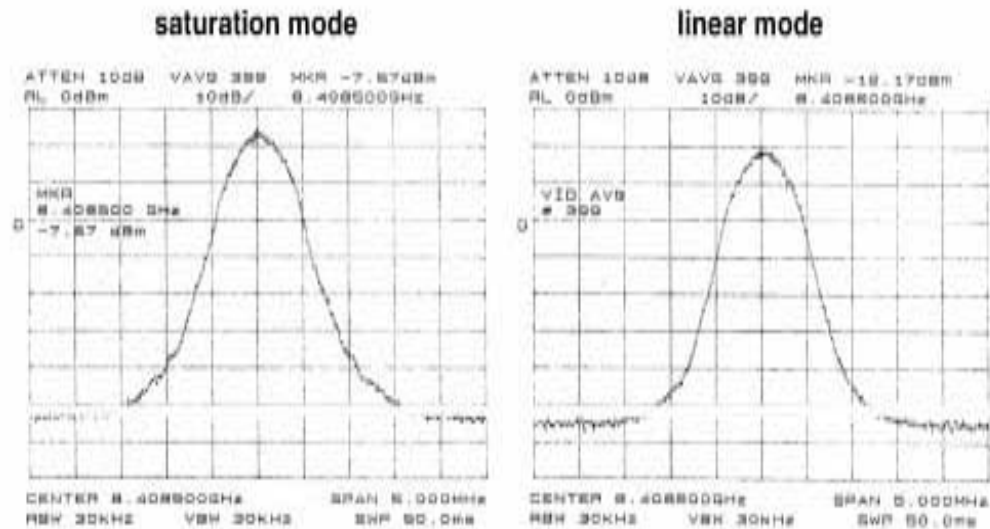


FIGURE 3. FQPSK-B Power Spectrum Measured at X-band (8.45 GHz)

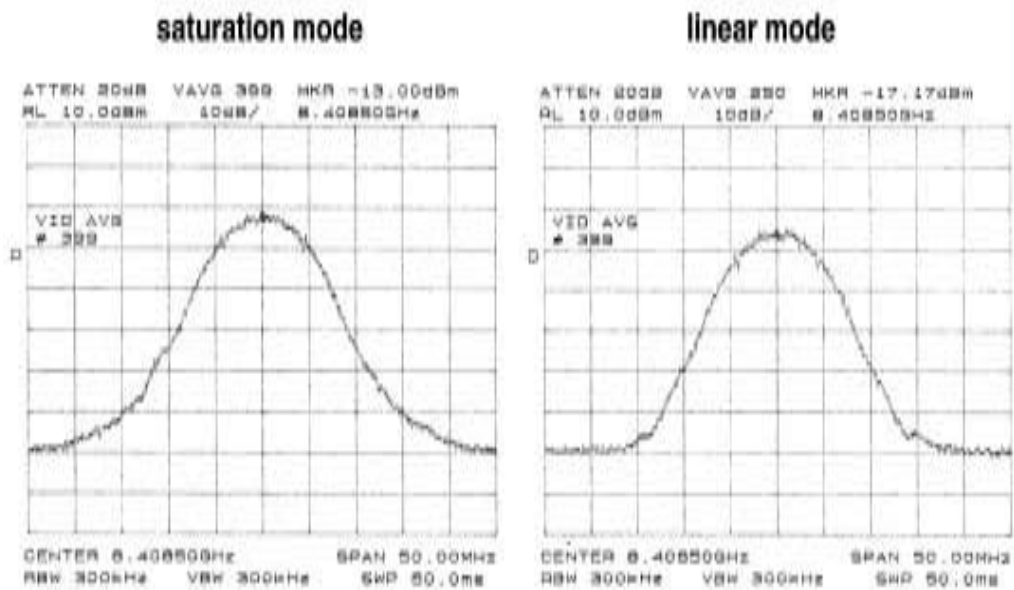


FIGURE 4. FQPSK-B 17 Mbps Modem Power Spectral Measured at X-Band (8.45 GHz)

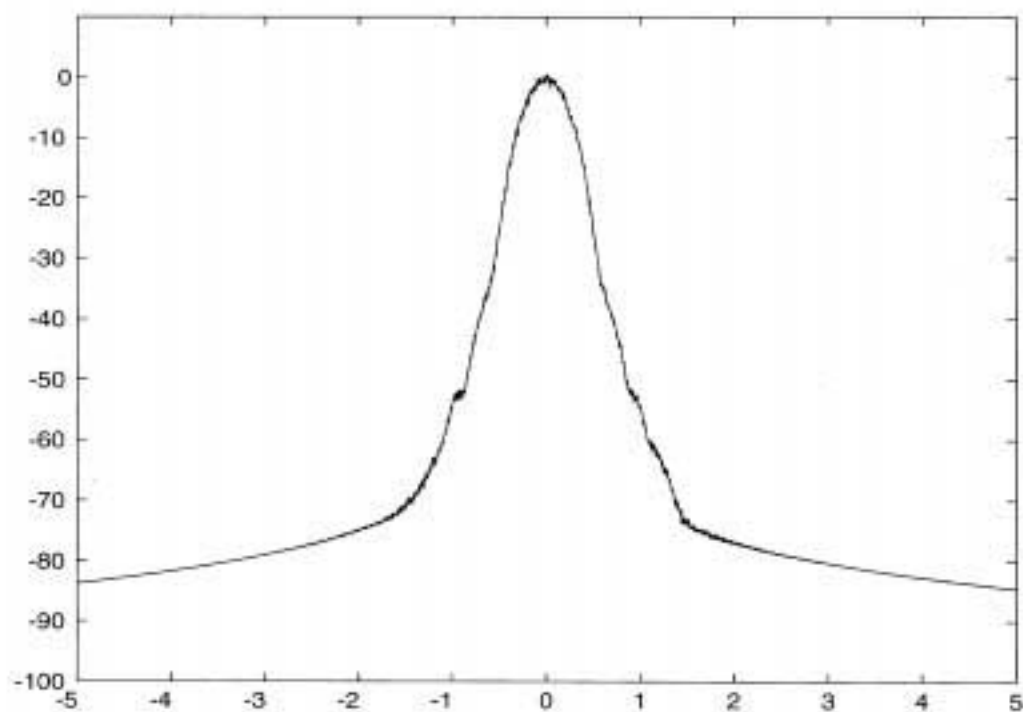


FIGURE 5. FQPSK-B Power Spectrum Measured in Computer Simulation

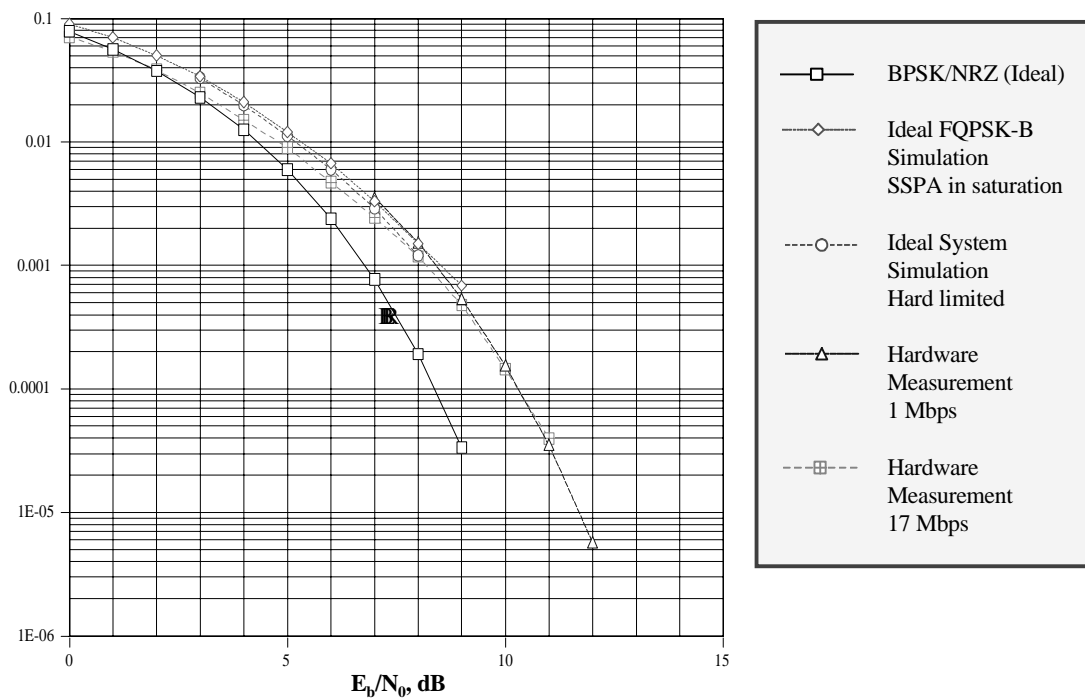


FIGURE 6. FQPSK-B BER Performance

Preliminary Results on Gaussian Minimum Shift Keying Modulation: Spectral Analysis, Error Rates, and Synchronization

Payman Arabshahi and Loc Lam
National Aeronautics and Space Administration
Jet Propulsion Laboratory
California Institute of Technology
4800 Oak Grove Drive, MS 238-344
Pasadena, CA 91109

A.I. 98-X

Abstract

This paper presents recent developments and progress made in the binary Gaussian-Minimum-Shift-Keying (GMSK) modulation. After an overview of GMSK, the algorithm for computing the modulation's power spectral density is discussed; illustrated through numerical simulations; and compared to experimental results. Also presented is the bit-error-rate performance (BER) of an improved GMSK. Additionally, synchronization schemes for GMSK are discussed and results are presented.

1 Introduction

Gaussian Minimum Shift Keying (GMSK) is a modulation scheme in which the phase of the carrier is varied instantaneously by the modulating signal. In contrast to Minimum Shift Keying (MSK), GMSK uses a Gaussian filter of an appropriate bandwidth (defined by the BT product) before the actual modulation. The time domain impulse response of this filter is given by

$$g(t) = \frac{\sqrt{\pi}}{\sqrt{2 \ln 2}} e^{-\pi^2 B^2 t^2 / 2 \ln 2} \quad (1)$$

MSK is essentially binary digital FM with a modulation index of 0.5. It has the following important characteristics: constant envelope, relatively narrow bandwidth, and non-coherent detection capability. The most important characteristic of MSK is that it is a constant-envelope variety of modulation. This makes the modulation scheme more immune to noise than the Amplitude Shift Keying (ASK) scheme. However, MSK does not satisfy the requirements with respect to out-of-band radiation for single-channel-per-carrier (SCPC) mobile radio.

GMSK uses a pre-modulation Gaussian filter which makes the output power spectrum more compact. The pre-modulation Gaussian filter has narrow bandwidth and sharp cutoff properties which are required to suppress the high-frequency components. Moreover, it has a lower overshoot impulse response which allows protection against excessive instantaneous deviation.

This paper is organized as follows. After an overview of the algorithm for computing the GMSK power spectral density in section 2, we present and compare theoretically computed PSD data with computer simulated results. We then present techniques for synchronization of GMSK modulation in section 3, including an optimal carrier tracking loop, and improved bit-error-rate (BER) performance through pre-encoding.

2 GMSK Power Spectral Density

In general the power spectral density of GMSK modulation is given by

$$S(f) = \sum_{k=0}^{2^{L-1}-1} \frac{1}{T} |C_k(f)|^2 \quad (2)$$

where $C_k(f) = \mathcal{F}\{c_k(t)\}$ is the Fourier transform of $c_k(t)$, $-\infty < t < \infty$, and $T = T_b$ is the bit period.

The algorithm for computing the Power Spectral Density of GMSK modulation, due to previous work by [1, 2] and explained in more detail in [3] is outlined in Appendix A. Matlab source files for the algorithm can be found in Appendix B.

The algorithm outlined in Appendix A was computed for values of $L \in \{2, 4, 6, 8, 10\}$, and $BT \in \{0.125, 0.25, 0.5\}$. Plots of power spectral density of GMSK modulation as computed are presented in Figs. 1-3. Note the different vertical scales of the plots. The computed power spectral density was normalized with respect to its DC value prior to plotting.

As can be observed from the plots, the GMSK power spectral density becomes smoother, displaying less and less ripples, as the Gaussian filter truncation length L increases. Presence of periodic behavior in the modulation's spectrum is also evident. There appears to be little benefit in terms of spectral pulse shaping in proceeding beyond $L = 8$.

Figure 4 illustrates a comparison between theoretically computed, and computer simulated GMSK power spectral densities for $L=4$; $BT=0.25$; (left), and $L=2$; $BT=0.5$ (right). Presence of ripples in the theoretically computed results, for low values of L as in this case, is due to the approximation made in deriving the PSD. Namely, that L is sufficiently long such that Eq. (6) (see Appendix A) is satisfied with equality – this is clearly not true for values of L illustrated in Fig. 4. In both comparisons, the two curves are seen to match each other very well for low frequency values, with deviations starting to manifest themselves in the form of ripples as the frequency increases.

3 Synchronization of GMSK Modulation

The traditional Gaussian-Minimum-Shift-Keying scheme with modulation index of 90° is known to have a very narrow power spectrum, as observed from results from the previous section. This in turn results in very low adjacent channel interference as shown in Fig. 5. However, GMSK is often avoided because of synchronization difficulties and the potentially significant receiver loss due in part to synchronization problems and the differential decoder at the receiver.

As a solution to this problem, we present an optimum carrier tracking loop for GMSK along with an open symbol loop. Acquisition performance of the loops is computed and presented as well. In addition, a simple technique to eliminate the differential decoder at the receiver is discussed and shown to improve BER performance.

3.1 GMSK Optimal Carrier Tracking Loop

Since GMSK is a filtered version of MSK and MSK is simply OQPSK with half-sinusoidal pulse shaping it is not surprising to expect that the optimum carrier tracking loop for GMSK will be similar to the carrier tracking loop for OQPSK. The traditional OQPSK carrier loop has been the QPSK Costas loop with a delay of half a symbol time in the Q arm. It has recently been shown [4] that the QPSK Costas

REPORT CONCERNING CCSDS RADIO FREQUENCY AND MODULATION

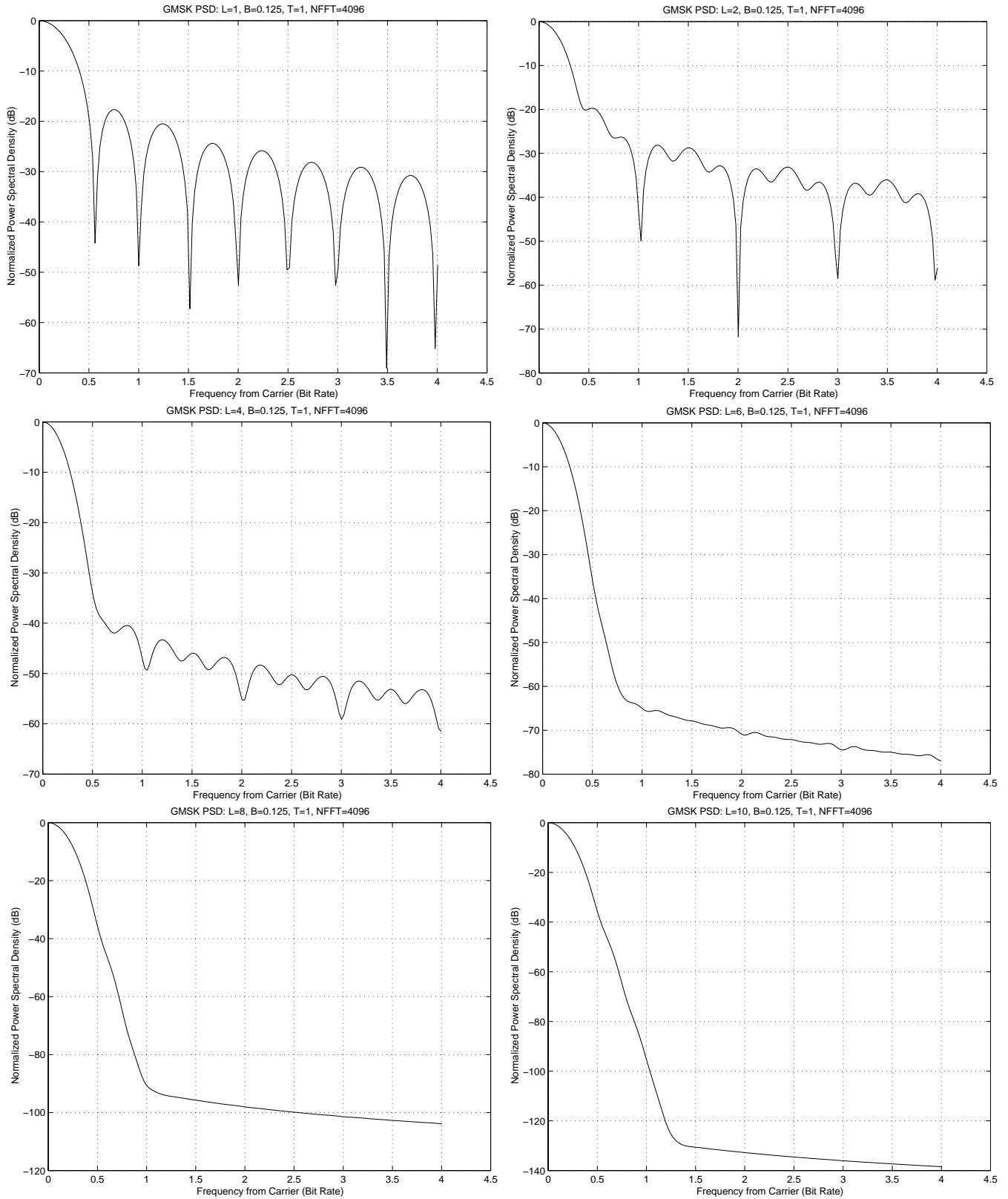


Figure 1: GMSK Power Spectral Density for $L=1,2,4,6,8,10$; $BT=0.125$; $T = 1$; and FFT length 4096.

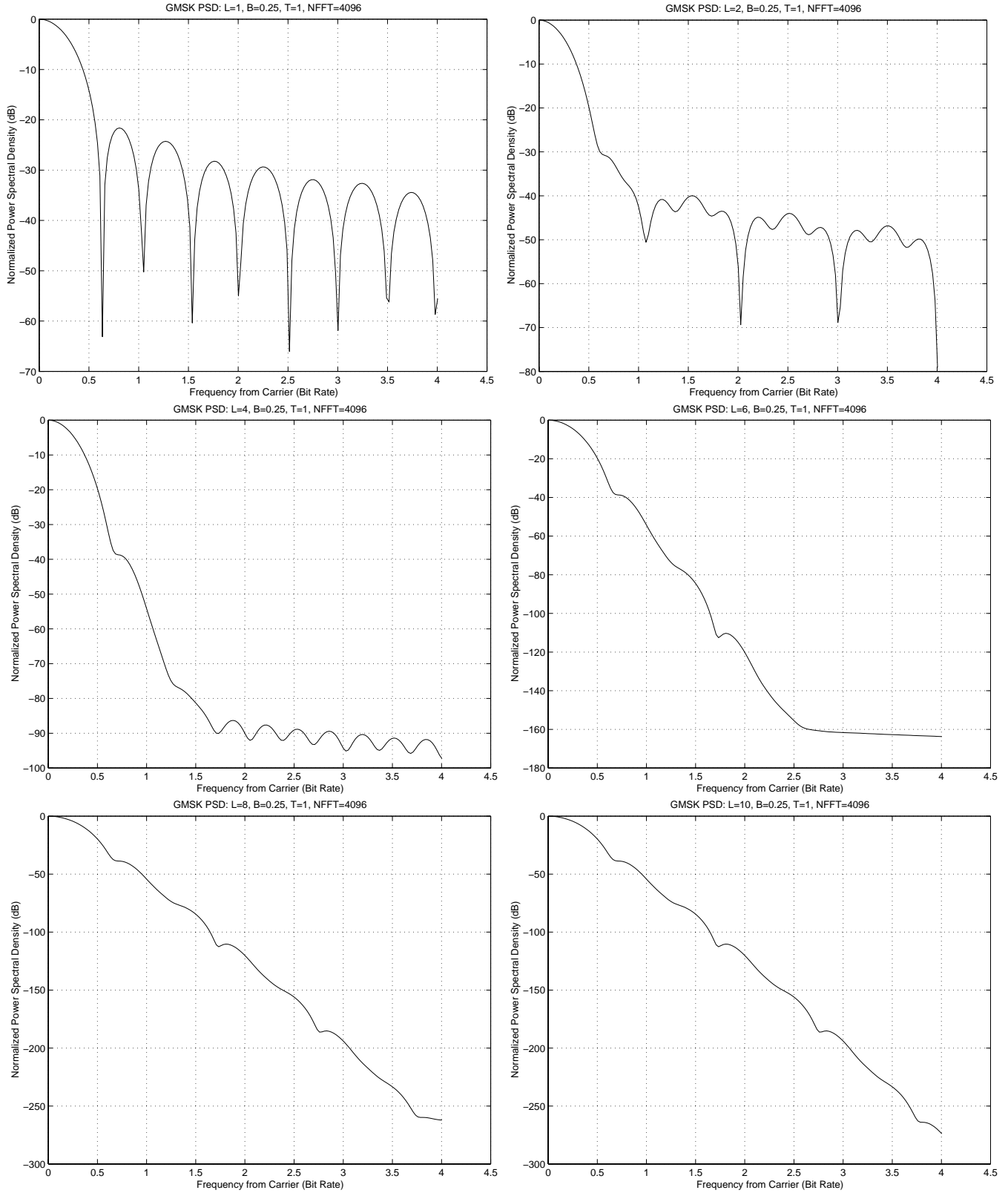


Figure 2: GMSK Power Spectral Density for $L=1,2,4,6,8,10$; $BT=0.25$; $T = 1$; and FFT length 4096.

REPORT CONCERNING CCSDS RADIO FREQUENCY AND MODULATION

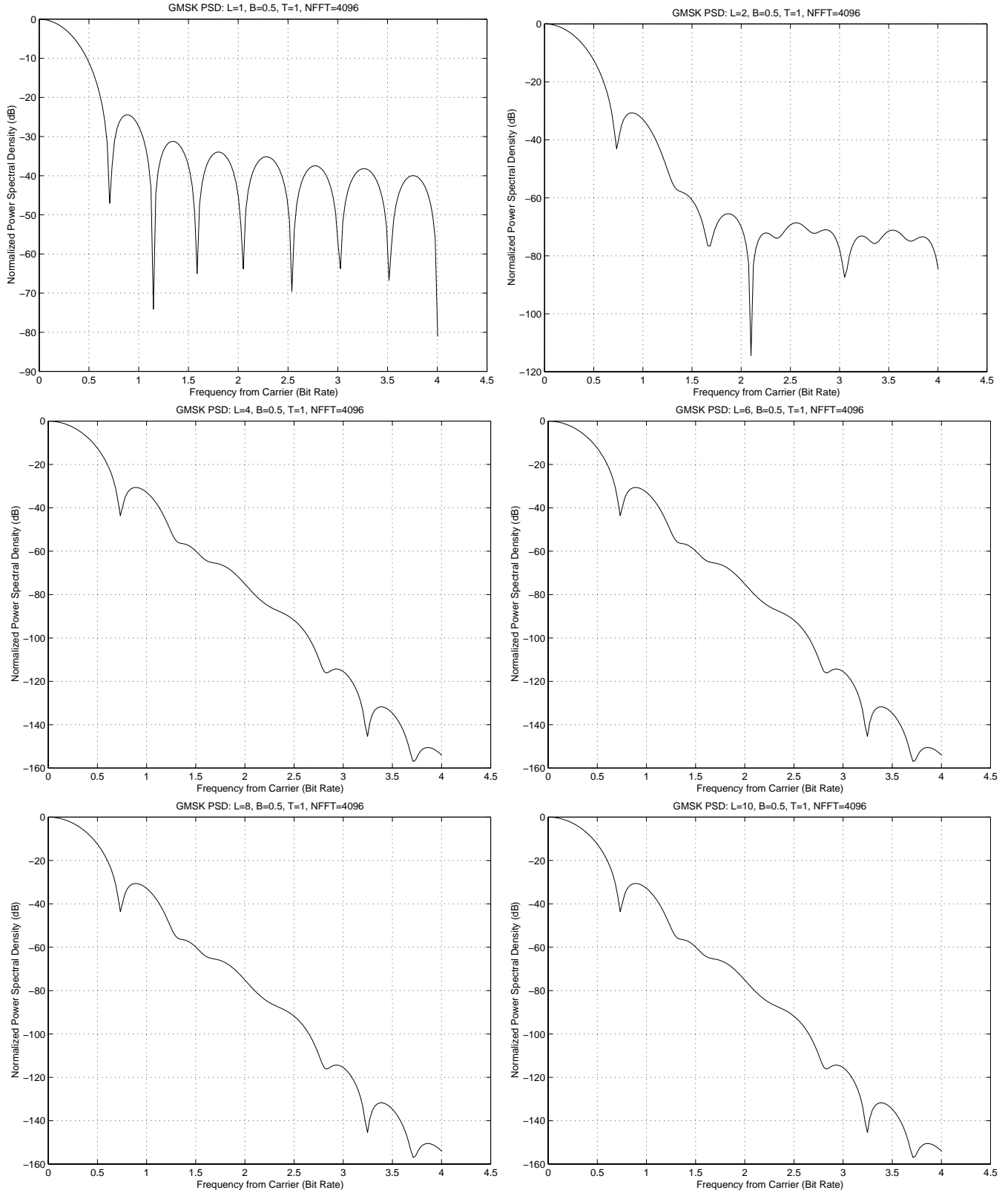


Figure 3: GMSK Power Spectral Density for $L=1,2,4,6,8,10$; $BT=0.5$; $T = 1$; and FFT length 4096.

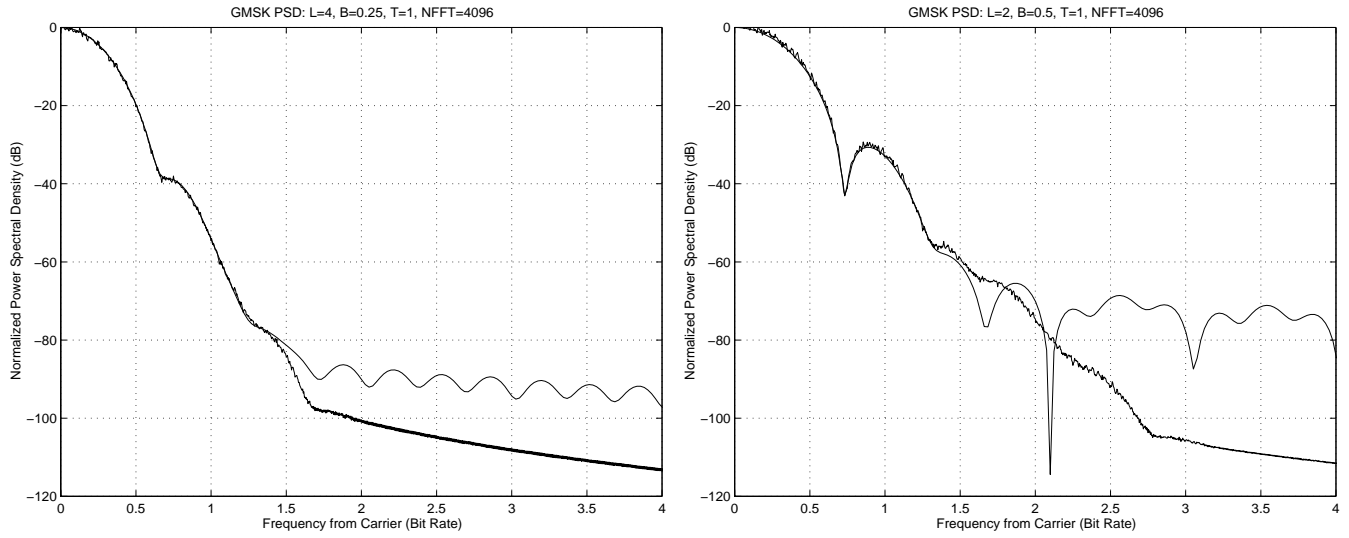


Figure 4: Computed (lighter, with ripples), and simulated (darker, without ripples) GMSK Power Spectral Density for $L=4$; $BT=0.25$; (left), and $L=2$; $BT=0.5$ (right).

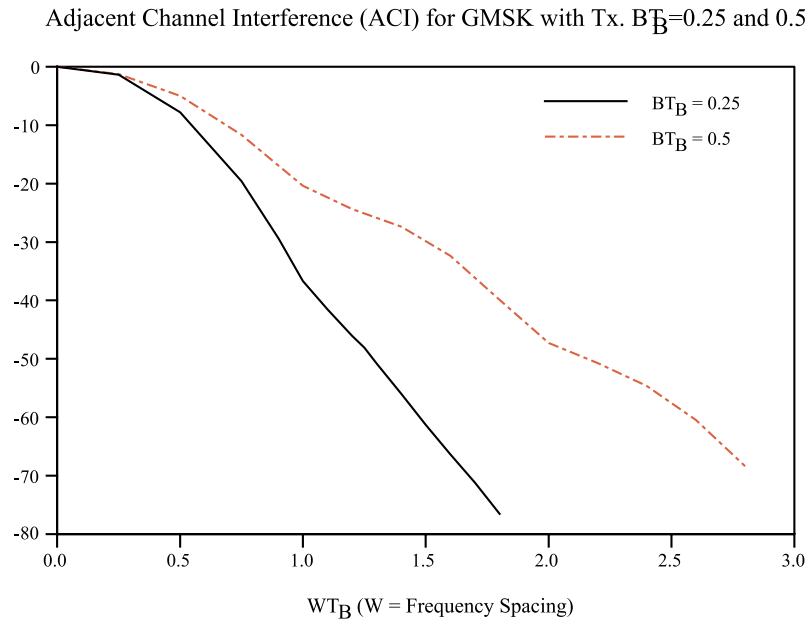


Figure 5: Adjacent channel interference for GMSK, $BT = 0.25, 0.5$.

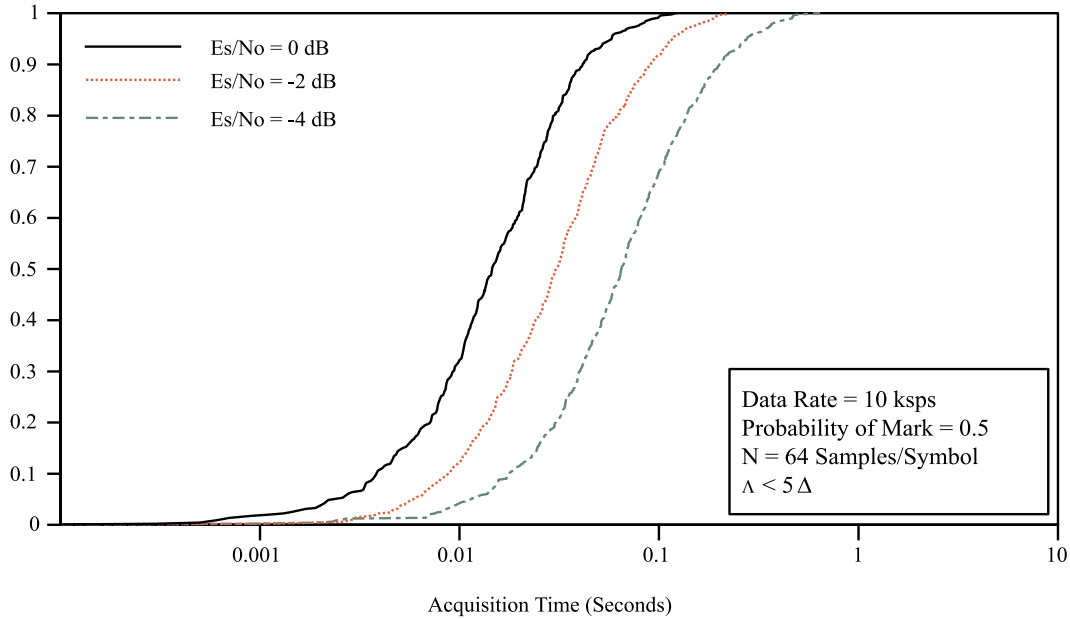


Figure 6: Phase acquisition performance of the open loop with GMSK ($BT = 0.25$) signaling.

loop with a half a symbol delay in the Q arm is not the optimum carrier tracking loop for OQPSK. The optimum carrier tracking loop for OQPSK has been derived and the performance of this loop is being evaluated. In addition, the loop is being modified to receive the GMSK signal. Both acquisition and tracking performances of these loops are being evaluated for unfiltered OQPSK and for GMSK signals.

3.2 GMSK Symbol Loop (An Open Loop Scheme)

In [5] an open-loop symbol scheme based on the maximum a posteriori estimation was discussed. This open loop scheme accommodates arbitrary non-overlapping pulse shapes and data transition densities. It was shown to operate at very low symbol SNRs as low as -10 dB. Since GMSK is an overlapping signaling scheme, the unmodified open symbol loop scheme is not the optimal one for the GMSK signal. However, a computer simulation study was performed to evaluate the acquisition performance of the open symbol loop for GMSK signaling. Figure 6 shows the probability of acquisition performance as a function of time for several bit signal-to-noise ratio. Although the acquisition performance shows that the loop can operate at low bit SNRs, further improvements can be made to improve the performance.

3.3 GMSK with Pre-Encoding

When the modulation index of the traditional GMSK modulator is set at 90° the modulator is inherently a differential modulator. Hence it requires a differential decoder at the receiver to properly recover the transmitted bits. In term of the receiver performance, the differential decoder increases the BER by a factor of two. One way of eliminating the differential decoder in the receiver is to move it to the transmitter prior to the frequency modulator. This is known as pre-encoding the data before the modulation so that the data at the output of the modulator is no longer differentially encoded. Figure 7 shows the computer simulated BER of GMSK ($BT = 0.5$) with the pre-encoder which shows an improvement in the BER

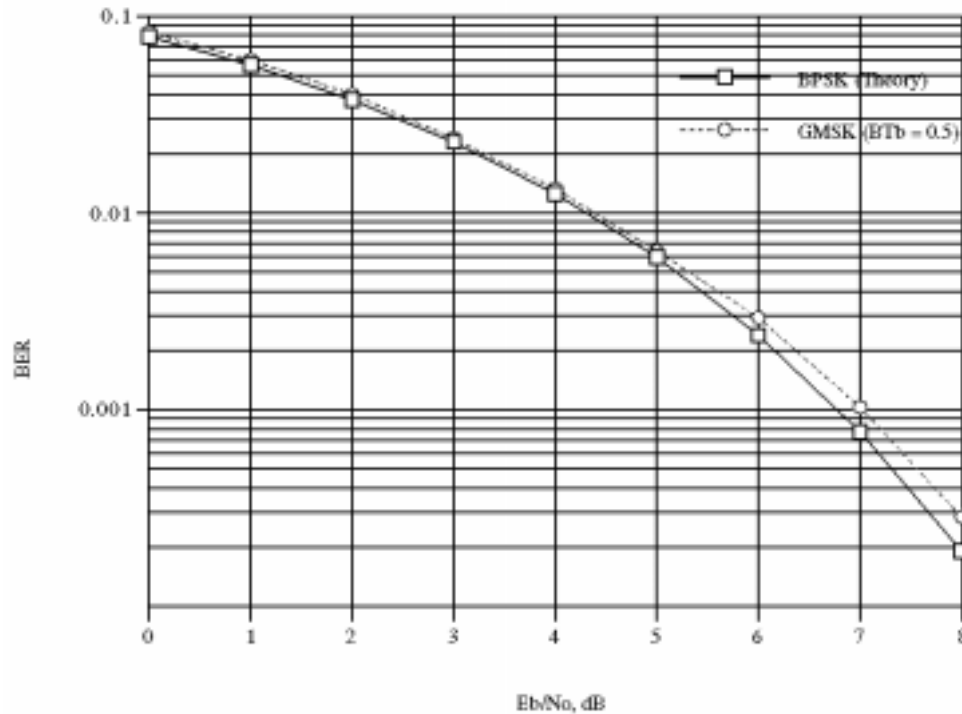


Figure 7: BER of GMSK ($BT = 0.5$) with pre-encoder (ideal transmitter and ideal receiver).

performance by 0.3 dB over the traditional, without pre-encoding, GMSK at $\text{BER} = 10^{-3}$. Both systems employed the linear receiver as discussed in [2]. Figures 8 and 9 show the spectra of the traditional GMSK and the pre-encoded GMSK system. Both spectra appear identical. Pre-encoding improves the BER but does not distort the frequency spectrum.

3.4 Summary

Pre-encoding can significantly improve the receiver performance, especially at low symbol SNR where powerful error-detecting and error-correcting codes are employed. Pre-encoding does not distort the power spectrum – one would get the same spectrum with or without pre-encoding. On the carrier synchronization, an optimal tracking closed loop is being evaluated for acquisition and tracking performance. Likewise, further work is underway to optimize the open and closed loop symbol for GMSK.

References

- [1] P.A. Laurent, "Exact and approximate construction of digital phase modulations by superposition of amplitude modulated pulses," *IEEE Trans. Communications*, vol. 34, no. 2, pp. 150-160, Feb. 1986.
- [2] G.K. Kaleh, "Simple coherent receivers for partial response continuous phase modulation," *IEEE Transactions on Selected Areas in Communications*, vol. 7, no. 9, pp. 1427-1436, Dec. 1989.

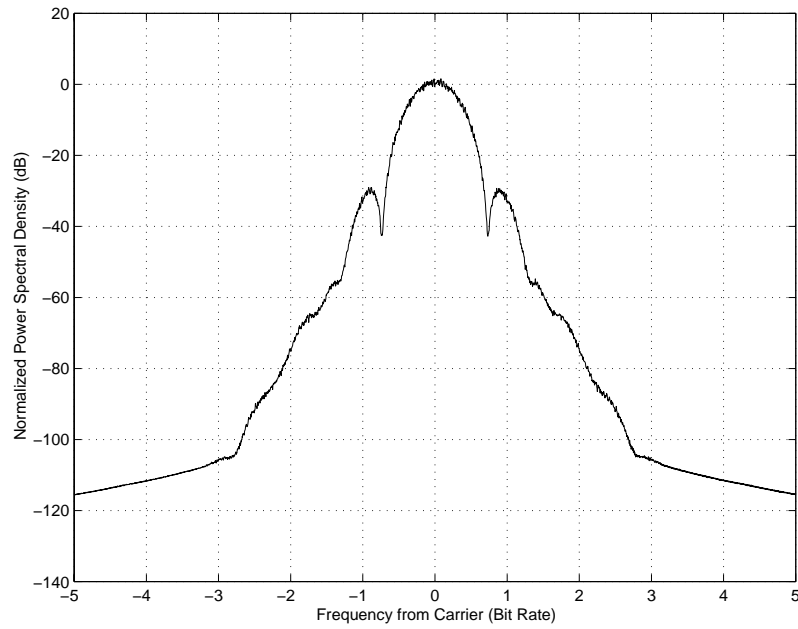


Figure 8: Power spectrum of GMSK ($BT = 0.5, L = 2$) without the pre-encoder.

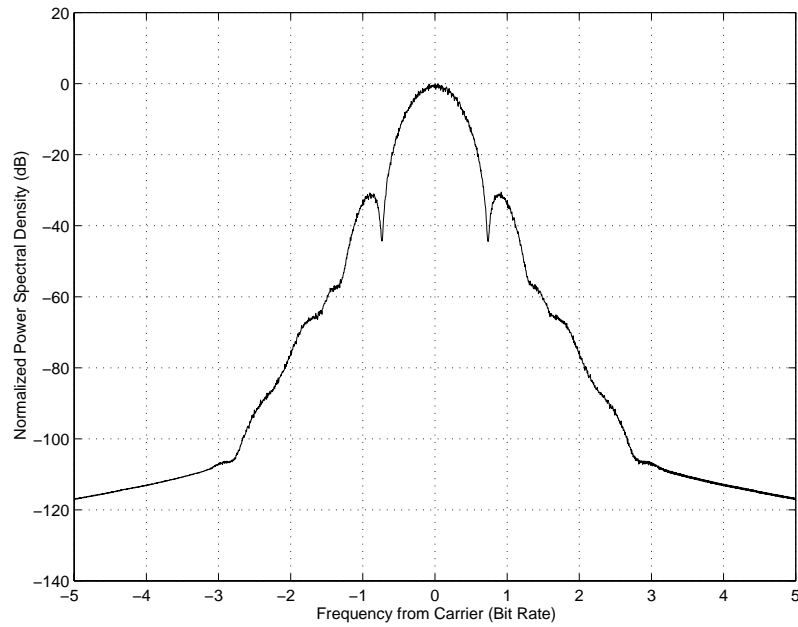


Figure 9: Power spectrum of GMSK ($BT = 0.5, L = 2$) with the pre-encoder. Practically no difference is observed in relation to the case of no pre-encoding.

- [3] M.K. Simon, "On the representation of digital phase modulation by the superposition of amplitude modulated pulses (AMP)," *Internal Report*, Jet Propulsion Laboratory Digital Signal Processing Research Group, April 1998.
- [4] M.K. Simon, "Synchronization of offset QPSK," *TDA Progress Report*, Jet Propulsion Laboratory, May 1998.
- [5] L. Lam, "Acquisition performance of the digital data transition tracking loop," *Position paper 97-3*, CCSDS Meeting, May 1998.

Appendix A: Algorithm for Computing the GMSK PSD

In order to compute the c_k coefficients, and subsequently $S(f)$ we proceed through the following stages:

1. Compute the phase pulse $q(t)$:

The phase pulse $q(t)$ is the integral of the Gaussian frequency pulse $g(t)$:

$$q(t) = \int_{-\infty}^t g(\tau) d\tau \quad (3)$$

This pulse has the property that $q(0) = 0$ and $q(\infty) = 0.5$ in absence of any truncation of $g(t)$.

In presence of truncation of $g(t)$ the expressions for, and relationships between $q(t)$ and the truncated $g(t)$ (denoted by $g_L(t)$) are:

$$g_L(t + LT/2) = \frac{1}{2T} \left[Q\left(\frac{2\pi BT}{\sqrt{\ln 2}} \left(\frac{t}{T} - \frac{1}{2}\right)\right) - Q\left(\frac{2\pi BT}{\sqrt{\ln 2}} \left(\frac{t}{T} + \frac{1}{2}\right)\right) \right] \quad -\frac{LT}{2} \leq t \leq \frac{LT}{2} \quad (4)$$

$$\begin{aligned} q\left(t + \frac{LT}{2}\right) &= \frac{1}{2} + \frac{1}{2} \left[\left(\frac{t}{T} - \frac{1}{2}\right) Q\left(\frac{2\pi BT}{\sqrt{\ln 2}} \left(\frac{t}{T} - \frac{1}{2}\right)\right) - \left(\frac{t}{T} + \frac{1}{2}\right) Q\left(\frac{2\pi BT}{\sqrt{\ln 2}} \left(\frac{t}{T} + \frac{1}{2}\right)\right) \right] \\ &\quad - \frac{1}{2\sqrt{2\pi}} \left(\frac{\sqrt{\ln 2}}{2\pi BT}\right) \left[\exp\left\{-\frac{1}{2} \left[\frac{2\pi BT}{\sqrt{\ln 2}} \left(\frac{t}{T} - \frac{1}{2}\right)\right]^2\right\} - \exp\left\{-\frac{1}{2} \left[\frac{2\pi BT}{\sqrt{\ln 2}} \left(\frac{t}{T} + \frac{1}{2}\right)\right]^2\right\} \right] \end{aligned} \quad (5)$$

where L is the truncation length.

With truncation, $q(t)$ will now satisfy the following property:

$$\int_0^{LT} g(\tau) d\tau < \frac{1}{2} \quad (6)$$

Nonetheless in the development below, we will assume that L is sufficiently long such that Eq. (6) is satisfied with equality. This assumption will lead to deviations from ideal behavior for small L which are currently being investigated, and are not reported in this preliminary study.

2. Compute the generalized phase function:

$$\Psi(t) = \begin{cases} \pi q(t) & 0 \leq t \leq LT \\ \pi/2[1 - 2q(t - LT)] & LT \leq t \leq 2LT \end{cases} \quad (7)$$

As can be seen from the above equation, $\Psi(t)$ will be symmetric around $t = LT$.

3. Compute $S_0(t)$ and its time-shifted versions:

$$\begin{aligned} S_0(t) &= \sin \Psi(t) & 0 \leq t \leq 2LT \\ S_n(t) &= S_0(t + nT) = \sin \Psi(t + nT) & -nT \leq t \leq 2LT - nT \end{aligned} \quad (8)$$

4. Compute $c_k(t)$:

Consider the binary representation of the integer K as

$$K = \sum_{i=1}^{L-1} 2^{i-1} \beta_{K,i} \quad (9)$$

Then, the K th pulse shape is given by

$$c_k(t) = S_0(t) \prod_{i=1}^{L-1} S_{i+L\beta_{K,i}}(t) \quad 0 \leq K \leq 2^{L-1} - 1 \quad 0 \leq t \leq T_K \quad (10)$$

where

$$T_K = T \times \min_{i=1,2,\dots,L-1} [L(2 - \beta_{K,i}) - i]$$

The Power Spectral Density of the modulation can then be found via Eq. (2).

Appendix B: Matlab Source Files for PSD Computation

Matlab codes for gmsk.m, shiftud.m, and Q.m, used in algorithm computation are outlined below.

```
function y=gmsk(T,L,B,N)

% GMSK(T,L,B,N) Computes and plots Gaussian Minimum Shift Keying
% Modulation Power Spectral Density for different values of:
% T = T_b = Bit period, usually set to 1
% L = Truncation Length of the Gaussian Filter >= 1
% B = Bandwidth of Gaussian Filter
% N = FFT size, power of 2
%
% For large values of L (> 11) this routine can take a long
% time to converge. This is due to Matlab trying to compute,
% for instance for L=12, all 2048 C_i functions. Most of the
% C_i's for i greater than a few hundred make a very
% negligible contribution to the PSD, and are the reason why
% matlab gets "hung" trying to compute them.
%
% In this case, an excellent approximation to the PSD is found
% by truncating the number of C_i functions to 512.
%
```



```

%      Last Revision Date: 4/12/98 by payman@jpl.nasa.gov
%

tic      % together with toc at the end of the code, it results in the
        % elapsed time for the computation

%-----BEGIN GMSK.M SOURCE CODE-----

%%%%%%%%%%%%%%%%%%%%%%%%%%%%%%%%%%%%%%%%%%%%%%%%%%%%%%%%%%%%%%%%%%%%%%%%
%
% Compute q(t) with no time shift. Denote this by q0
%
%%%%%%%%%%%%%%%%%%%%%%%%%%%%%%%%%%%%%%%%%%%%%%%%%%%%%%%%%%%%%%%%%%%%%%%%

alpha=0; % Time shift value for q(t), i.e. q(t+\alpha)

t=[-alpha:T./100:L.*T-alpha];

q0=0.5+0.5.*(((t+alpha)./T-L./2-0.5)...
.*Q(((2.*pi*B.*T)./sqrt(log(2))).*(t+alpha)./T-L./2-0.5))...
-((t+alpha)./T-L./2+0.5).*Q(((2.*pi*B.*T)./sqrt(log(2))).
.*((t+alpha)./T-L./2+0.5)))...
-(0.5./sqrt(2.*pi)).*(sqrt(log(2))./(2.*pi*B.*T))).* ...
(exp(-0.5.*(((2.*pi*B.*T)./sqrt(log(2))).*(t+alpha)./T-L./2-0.5)).^2)...
-exp(-0.5.*(((2.*pi*B.*T)./sqrt(log(2))).*(t+alpha)./T-L./2+0.5)).^2));

%%%%%%%%%%%%%%%%%%%%%%%%%%%%%%%%%%%%%%%%%%%%%%%%%%%%%%%%%%%%%%%%%%%%%%%%
%
% Compute q(t) shifted to the right by LT. Denote this by q_LT
%
%%%%%%%%%%%%%%%%%%%%%%%%%%%%%%%%%%%%%%%%%%%%%%%%%%%%%%%%%%%%%%%%%%%%%%%%

alpha=-L.*T;      % Time shift value for q(t), i.e. q(t+\alpha)

t=[-alpha:T./100:L.*T-alpha]; % Re-initialize time to compute q_LT

q_LT=0.5+0.5.*(((t+alpha)./T-L./2-0.5)...
.*Q(((2.*pi*B.*T)./sqrt(log(2))).*(t+alpha)./T-L./2-0.5))...
-((t+alpha)./T-L./2+0.5).*Q(((2.*pi*B.*T)./sqrt(log(2))).
.*((t+alpha)./T-L./2+0.5)))...
-(0.5./sqrt(2.*pi)).*(sqrt(log(2))./(2.*pi*B.*T))).* ...
(exp(-0.5.*(((2.*pi*B.*T)./sqrt(log(2))).*(t+alpha)./T-L./2-0.5)).^2)...
-exp(-0.5.*(((2.*pi*B.*T)./sqrt(log(2))).*(t+alpha)./T-L./2+0.5)).^2));

%%%%%%%%%%%%%%%%%%%%%%%%%%%%%%%%%%%%%%%%%%%%%%%%%%%%%%%%%%%%%%%%%%%%%%%%
%
% Compute Xi(t) which exists over 0 <= t <= 2LT
%
% Xi(t) = pi q(t)                for 0 <= t <= LT

```

```

%      = pi/2 [1 - 2q(t-LT)] for LT<= t <= 2LT
%
% Due to overlap of the two time intervals above at t=LT, we
% don't use the last element of vector q0 (since it is the same
% as the first element of vector q_LT). This is the explanation
% for use of size(q0,2)-1 below. Other than that we just append
% the two parts of Xi(t), in one vector, to form Xi.
%
%%%%%%%%%%%%%%%%%%%%%%%%%%%%%%%%%%%%%%%%%%%%%%%%%%%%%%%%%%%%%%%%%%%%%%%%
t=[0:T./100:2.*L.*T];

Xi=[pi*q0(1:size(q0,2)-1) pi.*0.5.*(1-2.*q_LT)]; % append two segments of Xi

%%%%%%%%%%%%%%%%%%%%%%%%%%%%%%%%%%%%%%%%%%%%%%%%%%%%%%%%%%%%%%%%%%%%%%%%
%
% Compute s0(t)
%
%%%%%%%%%%%%%%%%%%%%%%%%%%%%%%%%%%%%%%%%%%%%%%%%%%%%%%%%%%%%%%%%%%%%%%%%

s0=sin(Xi);

%%%%%%%%%%%%%%%%%%%%%%%%%%%%%%%%%%%%%%%%%%%%%%%%%%%%%%%%%%%%%%%%%%%%%%%%
%
% Case L=1
%
%%%%%%%%%%%%%%%%%%%%%%%%%%%%%%%%%%%%%%%%%%%%%%%%%%%%%%%%%%%%%%%%%%%%%%%%

if L==1
    c0=s0';
    C0=fft(c0,N);
    C0psd=(C0.*conj(C0))/N;
    C0psdnorm=C0psd./C0psd(1);
    C0psddb=10.*log10(C0psdnorm);

    f=100*(0:(164))/N;
    plot(f,C0psddb(1:165));
    grid on
    ylabel('Normalized Power Spectral Density (dB)');
    xlabel('Frequency from Carrier (Bit Rate)');
    title('GMSK PSD: L=1, B=0.125, T=1, NFFT=4096');

%%%%%%%%%%%%%%%%%%%%%%%%%%%%%%%%%%%%%%%%%%%%%%%%%%%%%%%%%%%%%%%%%%%%%%%%
%
% Case L>1
%
%%%%%%%%%%%%%%%%%%%%%%%%%%%%%%%%%%%%%%%%%%%%%%%%%%%%%%%%%%%%%%%%%%%%%%%%

else

```

```

%%%%%%%%%%%%%%%%%%%%%%%%%%%%%%%%%%%%%%%%%%%%%%%%%%%%%%%%%%%%%%%%%%%%%%%%
%
% Compute Matrix of binary coefficients, bvector, \beta_{K,i}
%
%%%%%%%%%%%%%%%%%%%%%%%%%%%%%%%%%%%%%%%%%%%%%%%%%%%%%%%%%%%%%%%%%%%%%%%%

K=[0:2^(L-1)-1];

% Convert ALL K values to binary and write to a string [not a vector]

bstring=dec2bin(K);

%%%%%%%%%%%%%%%%%%%%%%%%%%%%%%%%%%%%%%%%%%%%%%%%%%%%%%%%%%%%%%%%%%%%%%%%
%
% Convert string binary representation to real-binary representation
% using bin2dec so that they can then be stored as a vector (not as a
% string like above). Statement below initializes a vector, bvector, to
% the real-binary representation of the FIRST string out of 2^(L-1) strings.
%
%%%%%%%%%%%%%%%%%%%%%%%%%%%%%%%%%%%%%%%%%%%%%%%%%%%%%%%%%%%%%%%%%%%%%%%%

bvector=bin2dec( bstring(1,:).' );

%%%%%%%%%%%%%%%%%%%%%%%%%%%%%%%%%%%%%%%%%%%%%%%%%%%%%%%%%%%%%%%%%%%%%%%%
%
% We now "fill-up" bvector with the remaining real-binary representations.
% bvector is now really a matrix of 1's and 0's.
%
%%%%%%%%%%%%%%%%%%%%%%%%%%%%%%%%%%%%%%%%%%%%%%%%%%%%%%%%%%%%%%%%%%%%%%%%

for i=1:2^(L-1)-1
    bvector=[bvector bin2dec( bstring(i+1,:).' )];
end

bvectorT=bvector'; % Transposed version of bvector

%%%%%%%%%%%%%%%%%%%%%%%%%%%%%%%%%%%%%%%%%%%%%%%%%%%%%%%%%%%%%%%%%%%%%%%%
%
% Generate coefficients of the S functions all in one "coeff" matrix
% Row 1 of matrix corresponds to S coefficients for c0,
% Row 2 of matrix corresponds to S coefficients for c1, etc
%
%%%%%%%%%%%%%%%%%%%%%%%%%%%%%%%%%%%%%%%%%%%%%%%%%%%%%%%%%%%%%%%%%%%%%%%%

for r=1:2^(L-1) % number of rows
    for c=1:L-1 % number of columns
        coeff(r,c)=(L-c)+L.*bvectorT(r,c);
    end
end
end

```

```

%%%%%%%%%%%%%%%%%%%%%%%%%%%%%%%%%%%%%%%%%%%%%%%%%%%%%%%%%%%%%%%%%%%%%%%%
%
% Generate in one step, all translated versions of S0(t):
% S1(t) = S0(t+1), S2(t) = S0(t+2), etc.
%
% This is done by taking S0(t) (represented by s0), and shifting it
% by the coefficients stored in the "coeff" matrix above. For instance
% if coeff is 3, then the shift in matlab is 100*3 = 300, since the
% sampling time is 1/100 seconds (i.e. 100 ticks per second).
%
% See help for shiftud for explanation of the SHIFTUD function.
%
% At the end of the first pass through the outer loop below, the
% matrix Smatrix will contain L-1 columns, each one representing
% the proper shifted value of s0, i.e. if the first row of the
% coeff matrix is 2 5 7 (for L=4), the the Smatrix's columns 1
% through 3 will contains S2, S5, S7.
%
% At this point (first pass through outer loop), the S functions
% are multiplied by each other to form Sprod and then c0 is
% generated (as column 1 of matrix cmatrix), by multiplying Sprod
% with s0.
%
% During the second pass through outer loop, we proceed through the
% second row of coeff, generating new shifted S functions, and computing
% c1, as the second column of cmatrix. This continues ...
%
% FFT and PSD computations on column of cmatrix then follow.
%
%%%%%%%%%%%%%%%%%%%%%%%%%%%%%%%%%%%%%%%%%%%%%%%%%%%%%%%%%%%%%%%%%%%%%%%%

% Pre-allocate Smatrix to make for-loop run faster, although in practice
% there does not seem to be much difference. Un-comment to enable.
%
%Smatrix=zeros(size(s0,2),(L-1));

if L>10                                % Truncates for-loop below at 512 terms
    M=512;
else
    M=2^(L-1);
end

for m=1:M
    for n=1:L-1
        Smatrix(:,n)=shiftud(s0',-100.*coeff(m,n));
    end
    Spro=prod(Smatrix,2);
    cmatrix(:,m)=s0'.*Spro;
    Cmatrix(:,m)=fft(cmatrix(:,m),N);
    Cpsd(:,m)=(Cmatrix(:,m).*conj(Cmatrix(:,m)))/N;
end

```

```

end

Cpsdfinal=sum(Cpsd,2);
Cpsdfinalnorm=Cpsdfinal./Cpsdfinal(1);           % Normalize PSD
Cpsdfinaldb=10.*log10(Cpsdfinalnorm);

f=100*(0:(164))/N;
plot(f,Cpsdfinaldb(1:165));
grid on
ylabel('Normalized Power Spectral Density (dB)');
xlabel('Frequency from Carrier (Bit Rate)');
title('GMSK PSD: L=12, B=0.125, T=1, NFFT=4096')

end

toc

%-----END GMSK.M SOURCE CODE-----

function y=shiftud(a,n,cs)

%SHIFTUD Shift or circularly shift matrix rows.
% SHIFTUD(A,N) with N>0 shifts the rows of A DOWN N rows.
% The first N rows are replaced by zeros and the last N
% rows of A are deleted.
%
% SHIFTUD(A,N) with N<0 shifts the rows of A UP N rows.
% The last N rows are replaced by zeros and the first N
% rows of A are deleted.
%
% SHIFTUD(A,N,C) where C is nonzero performs a circular
% shift of N rows, where rows circle back to the other
% side of the matrix. No rows are replaced by zeros.
%
% See Mastering Matlab 4.2c by Hanselman and Littlefield,
% page 54

%-----BEGIN SHIFTUD.M SOURCE CODE-----

if nargin<3, cs=0; end           % if no third argument, default is False
cs=cs(1);                       % make sure third argument is a scalar
[r,c]=size(a);                  % get dimensions of input
dn=(n>=0);                      % dn is true if shift is down
n=min(abs(n),r);                % limit shift to less than rows

if n==0 | (cs&n==r)             % simple no shift case
y=a;
elseif ~cs&dn                  % no circular and down
y=[zeros(n,c); a(1:r-n,:)];
elseif ~cs&~dn                 % no circular and up

```

```

y=[a(n+1:r,:); zeros(n,c)];
elseif cs&dn % circular and down
y=[a(r-n+1:r,:); a(1:r-n,:)];
elseif cs&~dn % circular and up
y=[a(n+1:r,:); a(1:n,:)];
end

%-----END SHIFTUD.M SOURCE CODE-----

function x = Q(u)

% Q.m, Q function
% computes the Q function using the complementary error function.

%-----BEGIN Q.M SOURCE CODE-----

if (u >= 0)

x = 0.5*erfc(u/sqrt(2));

else

x = 1 - 0.5*erfc(-u/sqrt(2));

end

%-----END Q.M SOURCE CODE-----

```

[This page intentionally left blank.]

CCSDS Panel 1E
Document 99/36
Questions on GMSK Performances
(Action Item 99-1E-4)

Marco Luise¹ Enrico Vassallo²

1 Introduction

During the CCSDS Spring 1999 meeting, an ESA report on “Advanced Modulation Schemes for Future ESA Standards” [1] was presented.

Two questions were raised on the performance of GMSK ($BT_b=0.5$) as indicated in the BER curve of figure III.4 of such report. The simulation results in this figure show almost negligible end-to-end total power loss for GMSK over the considered non-linear channel (0 dB back-off.)

The first question was:

Are these figures obtained by using a pre-coder at the transmitter?

In fact, NASA's [2] and Aerospace [3] theoretical computations and simulations showed that GMSK is inherently a differential encoding modulation and that double errors appear at the receiver. To compensate for this loss, a pre-coder at the transmitter is recommended.

The second question was:

Are the above results based on a practical implementation of the GMSK demodulator like the so-called average matched receiver or an ideal implementation of GMSK demodulator?

2 Discussion

In the study under consideration, GMSK was treated as a form of OQPSK with particular spectral shaping. This means that the actual non-linearly modulated signal was viewed as resulting out of a linear modulator with staggered I-Q components.

¹ University of Pisa

² ESOC, European Space Agency

Such approach is theoretically correct for MSK, and is approximately valid for GMSK as well, provided that BT_b does not get too small.

The pre-coding is actually a means to directly transfer the input bits to the (non-linear) GMSK modulator onto the I-Q components of the modulated signal.

This "mimics" a linear-modulation arrangement that is in reality impossible, and does not give rise to double-errors.

The receiver used in the study [1] for GMSK is a coherent I-Q demodulator with average matched filters (see Sect. III.1-III.3). No Viterbi detection (as for CPM) is required.

Therefore, the results of the report [1] have to be compared to results obtained by using an averaged matched receiver and a pre-coder in front of the FM modulator.

Such results match very well the simulation results obtained in [4] where a demodulator based on the Laurent decomposition [5] and Viterbi decoding is considered. In fact, the simulated end-to-end losses in [4] for the case $BT_b=0.5$ is 0.03 dB at $BER=10^{-3}$ for the ideal case of perfect synchronization, which is the same assumption of figure III.4 of [1].

Furthermore, table IV of [1] indicates an end-to-end loss of 0.2 dB and 0.3 dB at $BER=10^{-3}$ and $BER=10^{-5}$ respectively, including synchronization losses. This result is based on a joint frequency and phase carrier recovery concept implemented by an automatic frequency control loop followed by a second-order decision-aided carrier phase recovery loop.

3 Conclusions

The results on GMSK performance of the ESA study report [1] have to be compared with results obtained with a pre-coder at the modulator input and an averaged matched receiver as demodulator [2]-[4].

The end-to-end losses in the ideal case of perfect synchronization are identical to the figures independently determined in other CCSDS contributions [4] and have, therefore, to be considered as very reliable estimates.

Moreover, since a practical implementation of the synchronization loops as well as of the demodulation proper was simulated, the low end-to-end losses determined in this report have to be considered representative of a possible and practical hardware implementation.

4 References

- [1] N. A. D'Andrea, M.Luise, U. Mengali, R. Reggiannini, "Advanced Modulation Schemes for Future ESA Standards", ESA Report, March 1991
- [2] M. K. Simon, "MAP-Motivated Carrier Synchronization of GMSK Based on the Laurent AMP Representation", CCSDS P1E Meeting, April 1999
- [3] G.L. Lui, "GMSK Modulation: Description of Waveform, Receiver, and Performance", CCSDS Panel 1E, Houston, May 1998.
- [4] G. Povero, E. Vassallo, M. Visintin, "End-to-End Losses of Selected Bandwidth-Efficient Modulation Schemes", CCSDS P1E Meeting, October 1999
- [5] P.A.Laurent, "Exact and Approximate Construction of Digital Phase Modulations by Superposition of Amplitude Modulated Pulses (AMP)", IEEE Trans. Commun., Vol. COM-34, No. 2, Feb. 1986, pp. 150--160.

[This page intentionally left blank.]



CCSDS P1E 99/42

GMSK Status Report by

Don Olsen
The Aerospace Corp.

For the
CCSDS Meeting Oct. 12-16, 1999

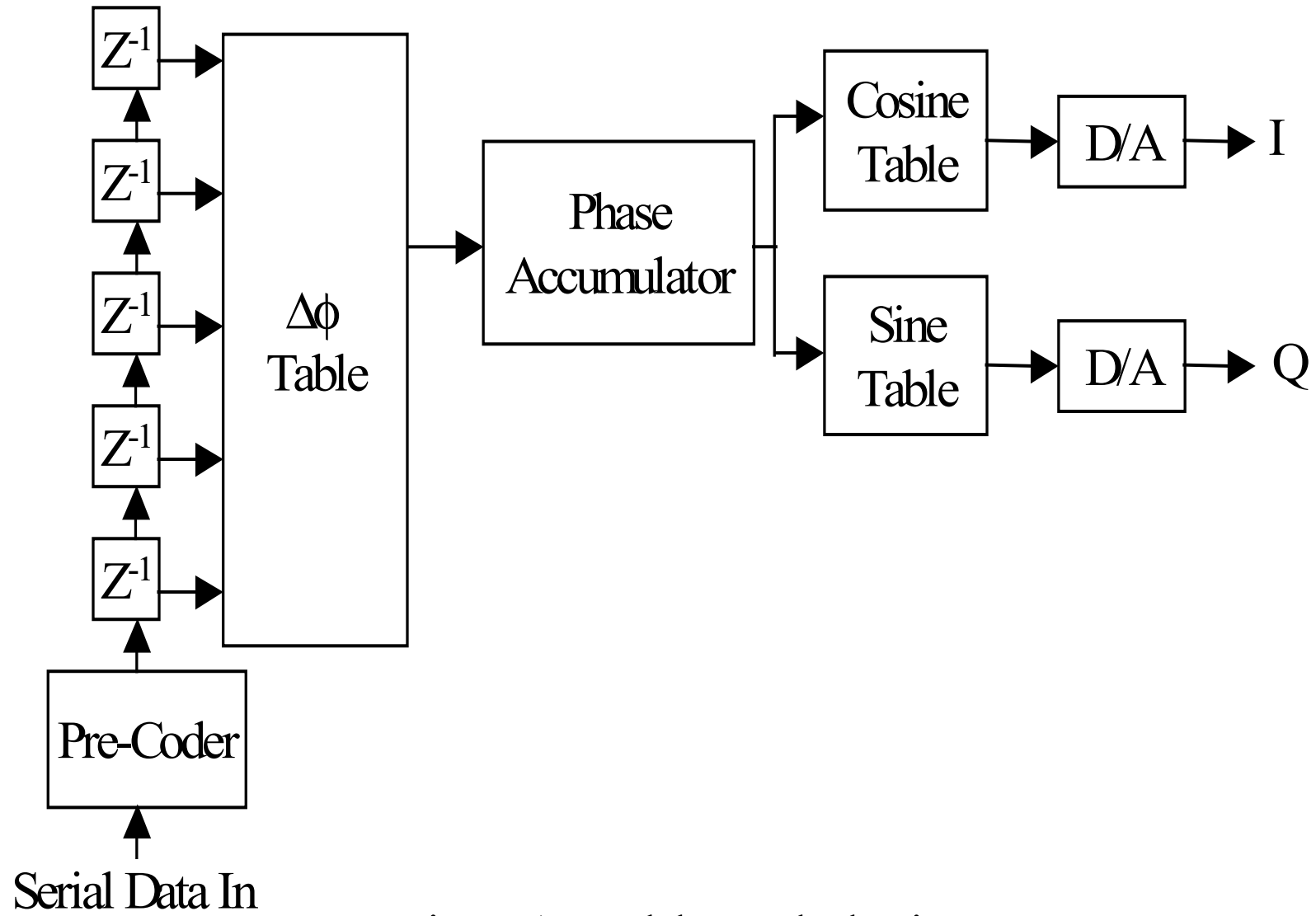


Figure 1, Modulator Block Diagram

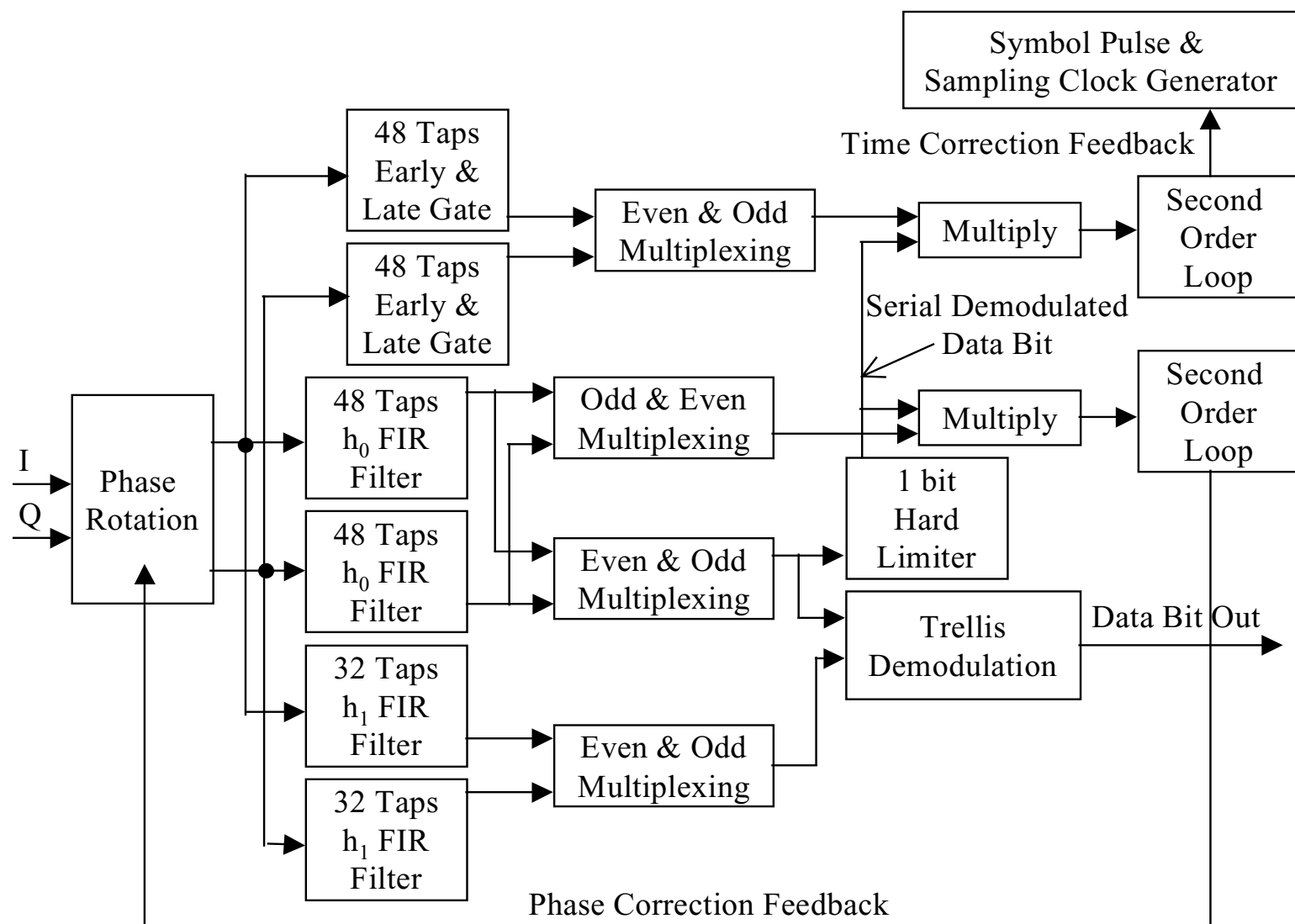
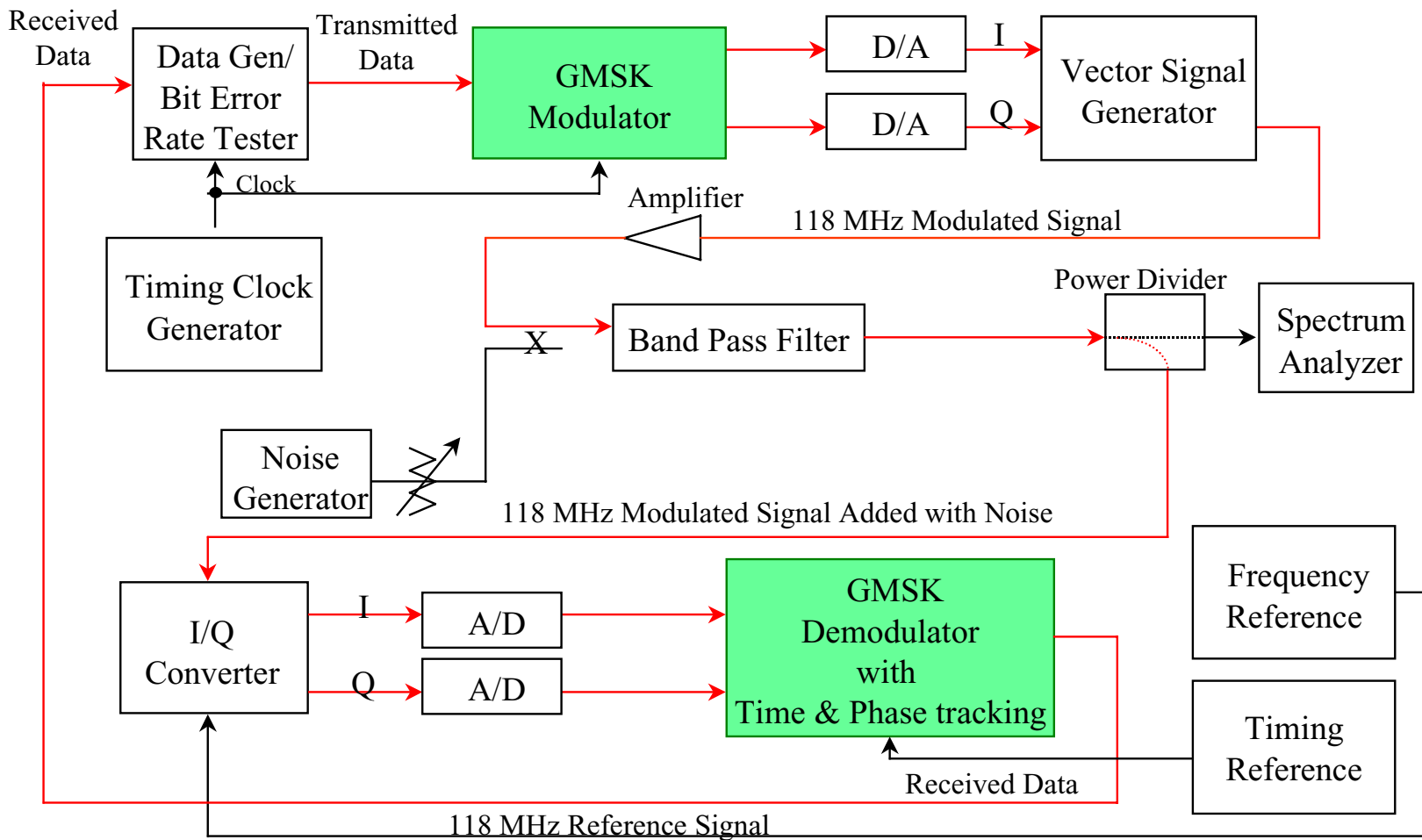


Figure 2, Demodulator Block Diagram

GMSK Modulator and Demodulator with Time and Phase Tracking



Spectral Power Density Glossary

The following chart is the measured spectrum using the preceeding GMSK test set up.

The verticle scale of the chart is 10 dB/division

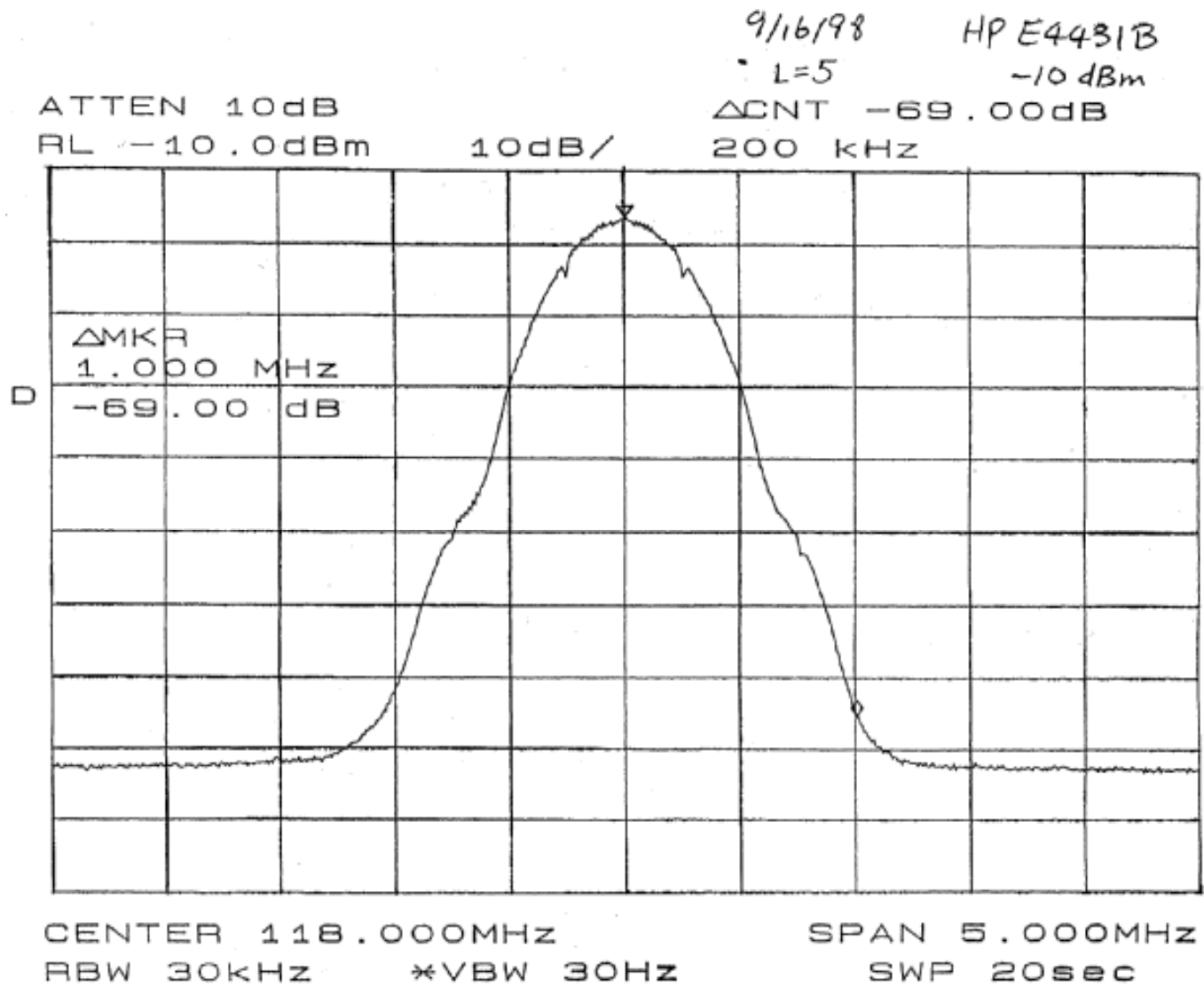
The horizontal scale is 0.5 MHz/division

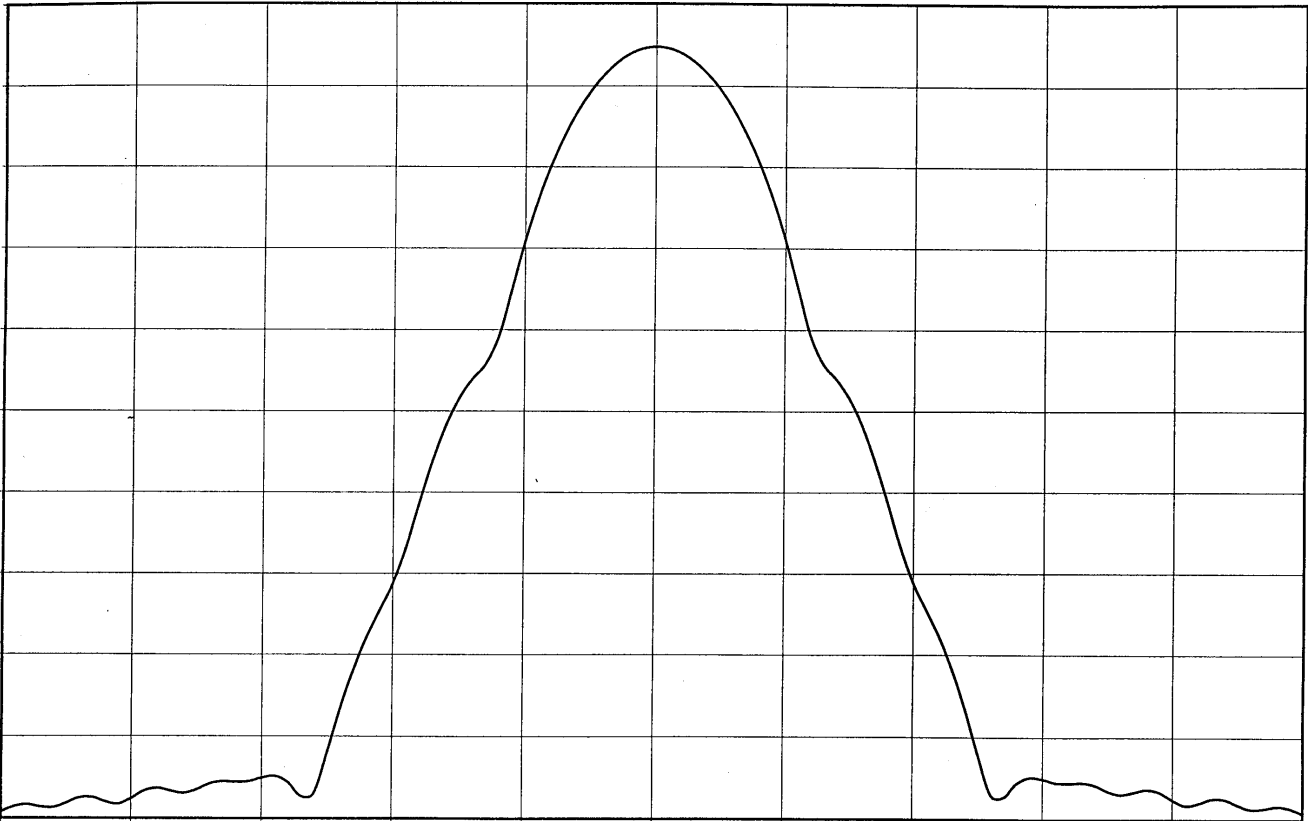
SWP is the spectrum analyzer sweep rate

RBW is the resolution bandwidth

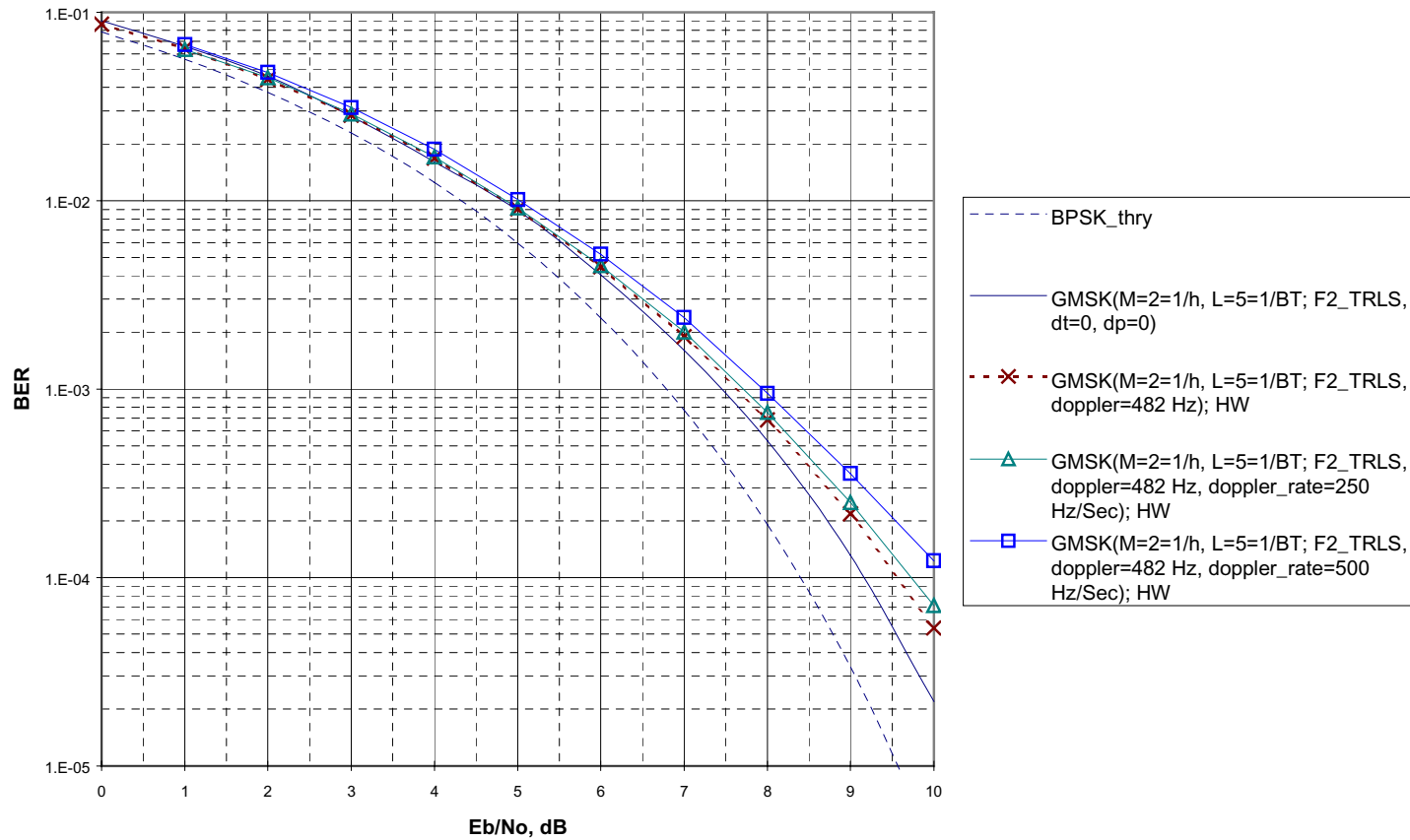
VBW is the video post detection bandwidth

SWP is the time to sweep 5 MHz





GMSK Performance for Various Signal Conditions Using $M=2$, $h=.5$, $BT=1.5=1/L$, with a Two filter Trellis Demodulator and a 4-state 32-path memory





Simulated Performances of FQPSK-1 and FQPSK-KF (or XPSK) Modulations

**André Ribes
CNES / Toulouse**

Member, CCSDS Subpanel 1E (RF & Modulation)

Paper 99/43



Outline

- Introduction
- FQPSK-1 Performance analysis
- BER results for FQPSK-1 vs. BT_b parameter
- FQPSK-1: Comparison with Feher results (H/L w & w/o synchronization)
- Simulation of Spectral density for FQPSK-1
- FQPSK-KF Performance analysis
- BER results for FQPSK-KF vs. BT_b parameter
- SPW Simulations: comparison of BER for FQPSK-1 and FQPSK-KF modulations
- Spectrum comparison between FQPK-1 and FQPSK-KF
- Spectrum Comparison for H/L FQPSK-1 and H/L GMSK ($BT_b=0,5$ & $BT_b = 0,3$)
- Comparison of BER between FQPSK-1 & KF and GMSK
- Conclusion



Introduction

- **This work was performed at CNES-Signal Processing Department by Jean Pierre ROUZAUD, in order to improve our understanding of FQPSK modulations and principles**
- **All practical results presented hereafter was obtained from simulations developped with SPW software**
- **Comparison of performances with results obtained by K.Feher on FQPSK and simulations of GMSK are presented**
- **Concerning Feher modulation, only FQPSK-1 and FQPSK-KF are investigated in this work**

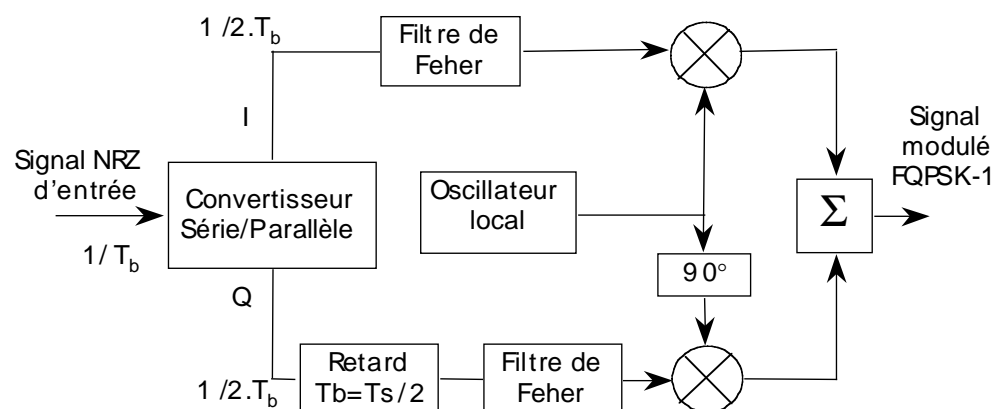


FQPSK-1 Performance analysis

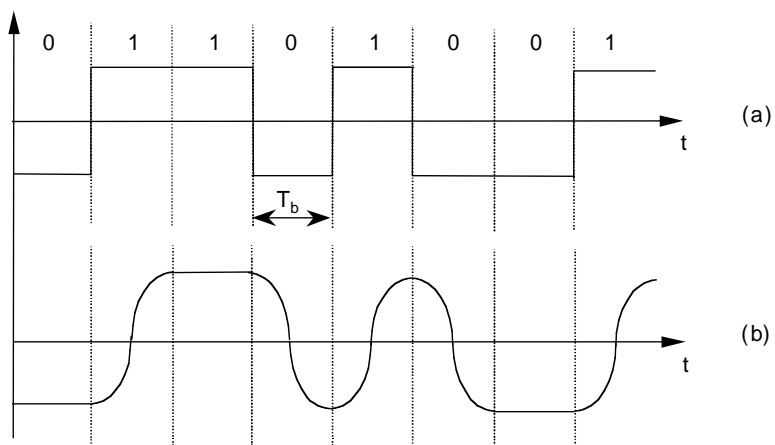
The conditions for Simulation of FQPSK-1 modulation with SPW software are:

- simulation of a full transmitting chain including transmitter and receiver part with AWGN**
 - at Transmitter end: Hard Limiter of the modulated waveform**
 - at Receiver end, two cases for demodulation and data recovery:**
 - Case 1: simple receiver simulation without carrier and clock recovery; predetection ("Matched Filter") filter mechanized with a 4th order Butterworth filter characterized with parameter BT_b**
 - Case 2: full receiver simulation with carrier and clock recovery; predetection ("Matched Filter") filter mechanized with a 4th order Butterworth filter characterized with parameter BT_b .**
- Carrier recovery uses a Costas Loop while clock recovery is based on the "delay & non-linearity" principle.**

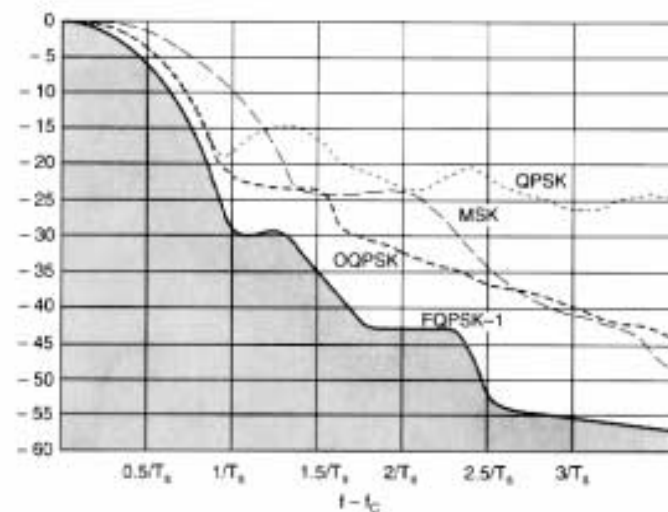
Modulation principle for FQPSK-1



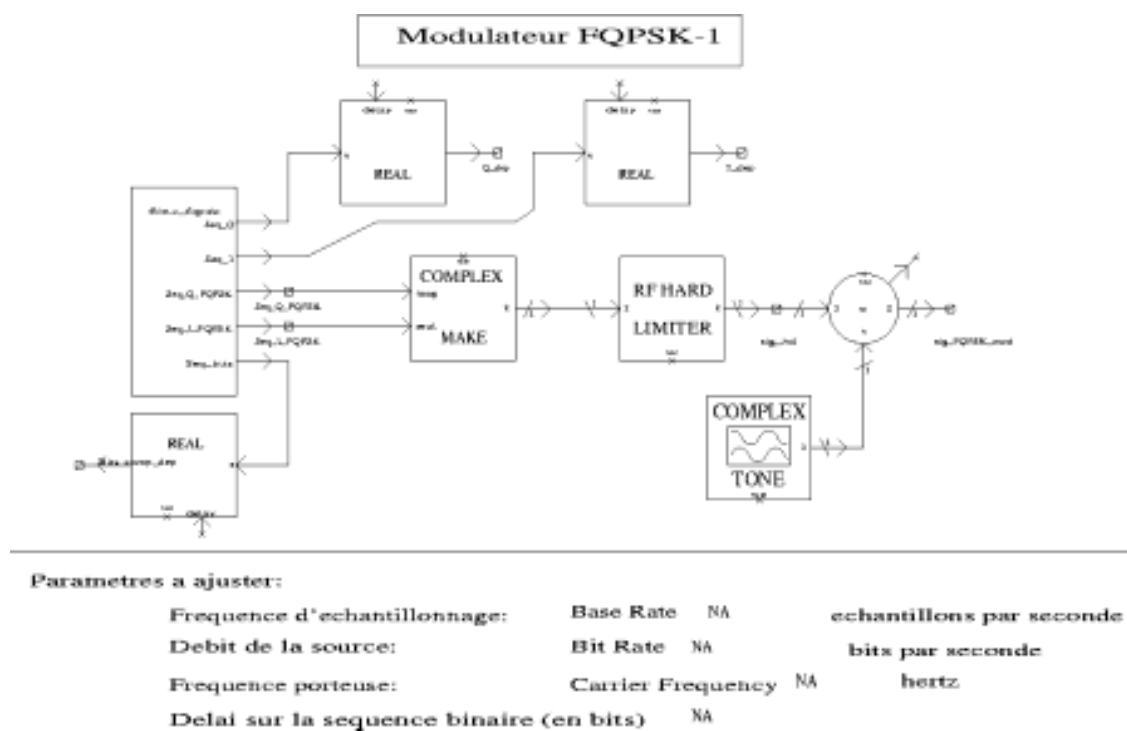
Time signals



Spectrum comparison with H/L

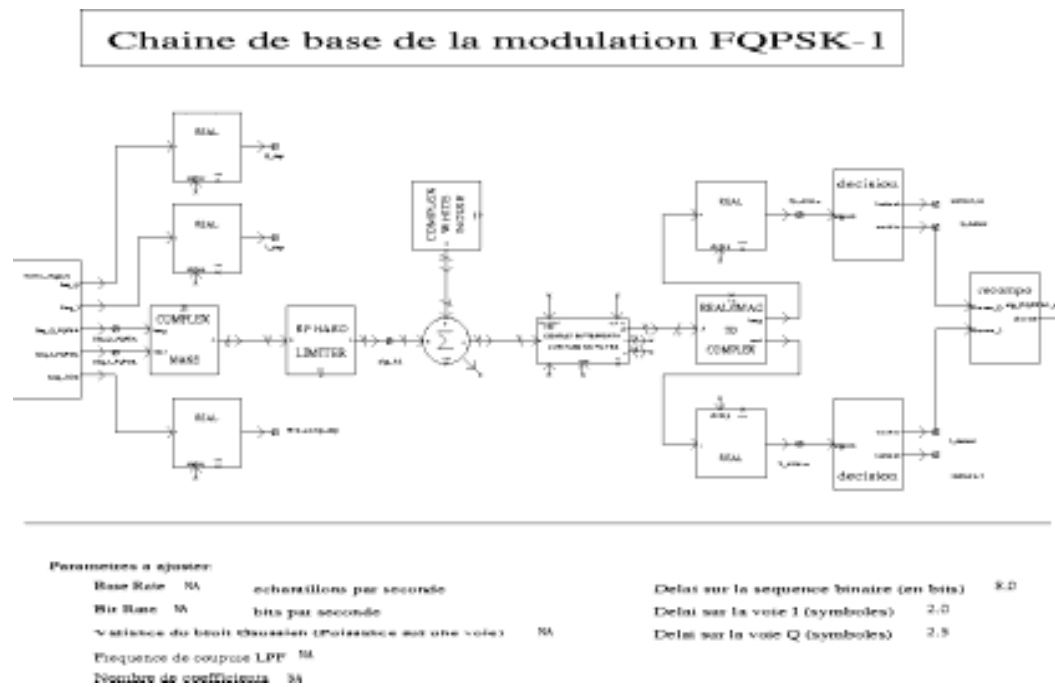


Simulation of FQPSK-1 Modulator in the chain



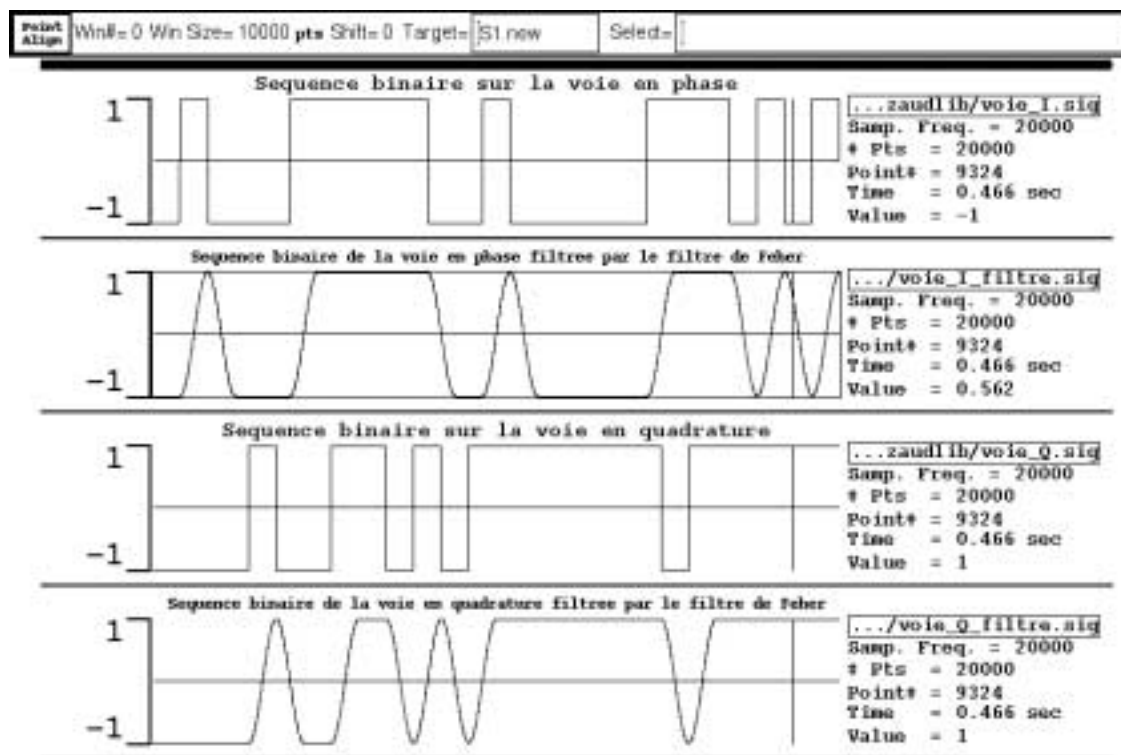


Case 1: Simple receiver simulation for FQPSK-1





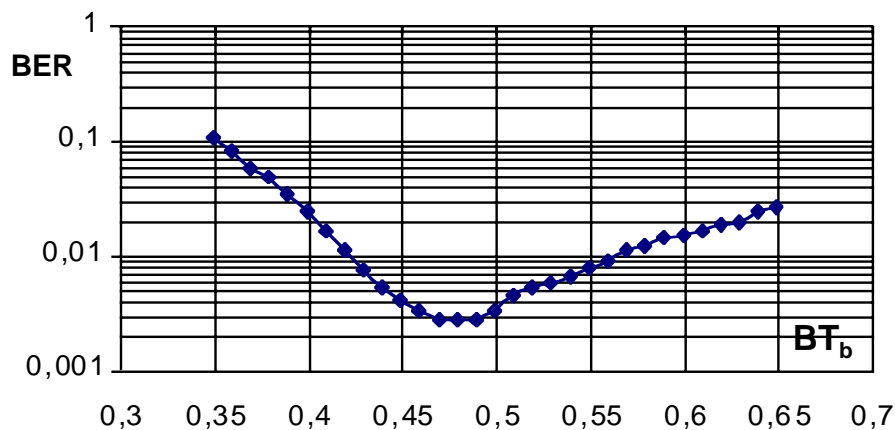
SPW simulation of FQPSK-1 I/Q data stream



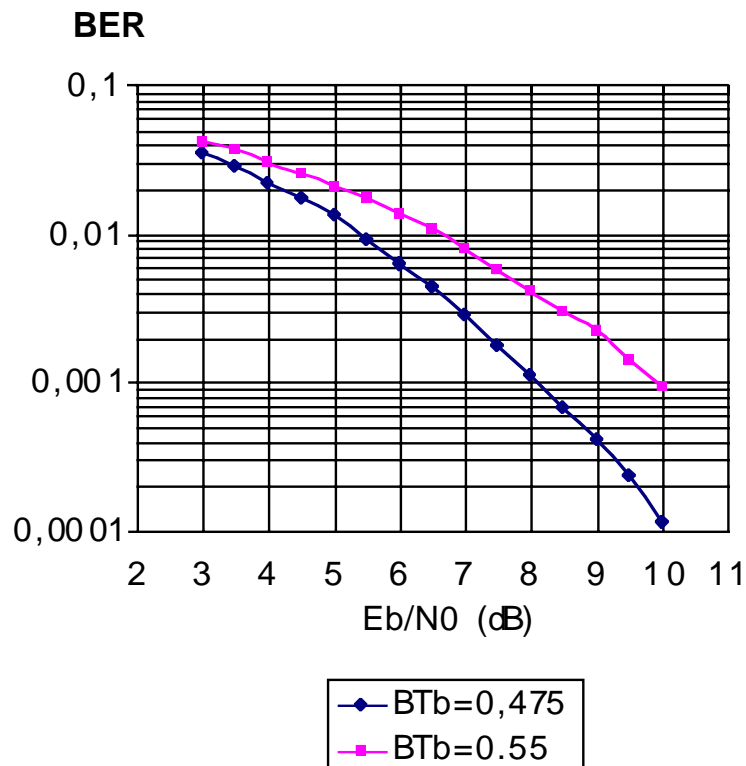
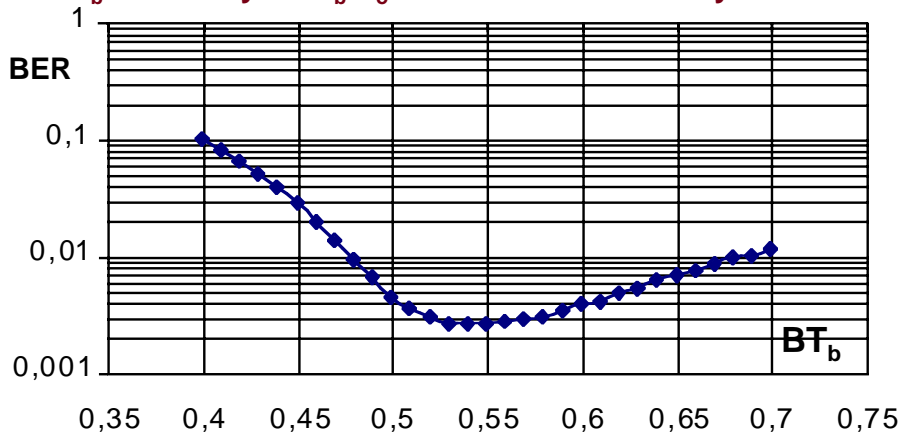


BER results for FQPSK-1 vs. BT_b parameter

BT_b sensitivity for $E_b/N_0 = 7\text{dB}$ with H/L but w/o synchronization

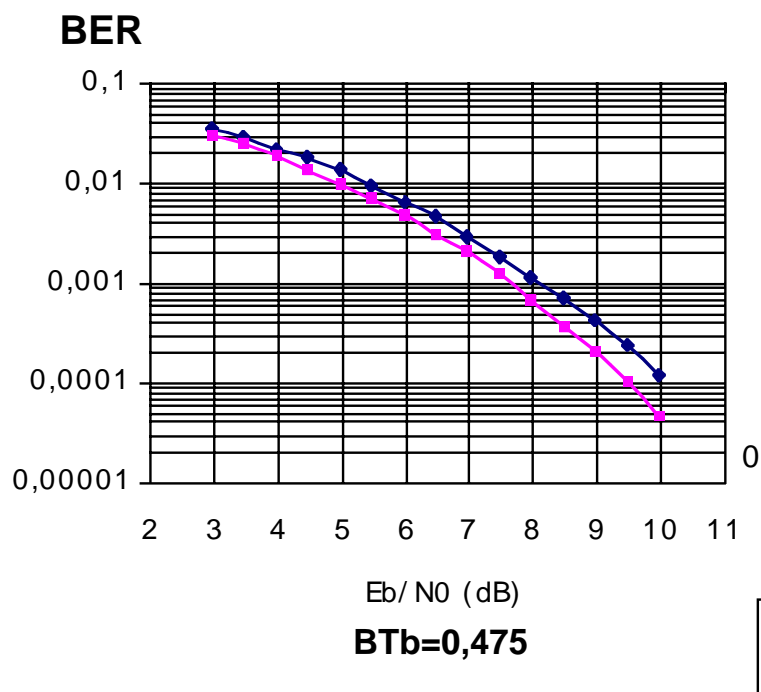


BT_b sensitivity for $E_b/N_0 = 7\text{dB}$ with H/L but w synchronization

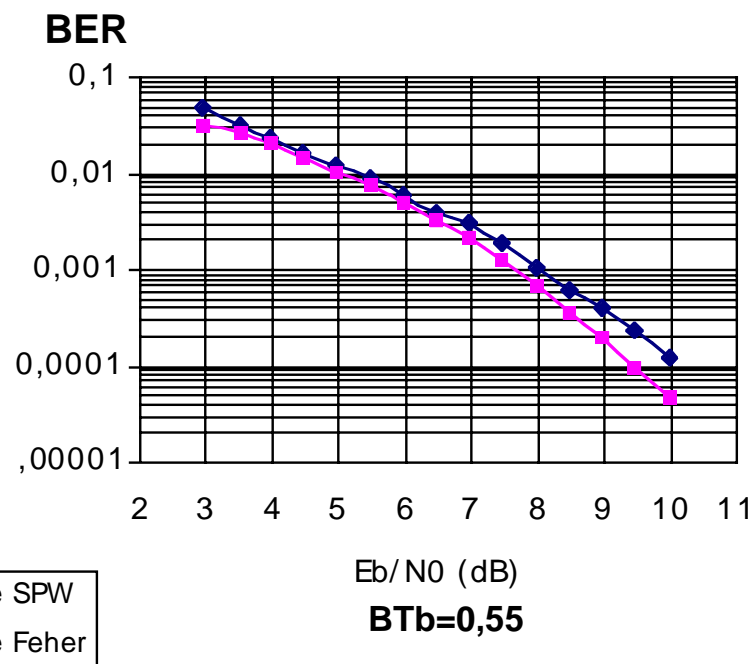




FQPSK-1: Comparison with Feher results (H/L w & w/o synchronization)



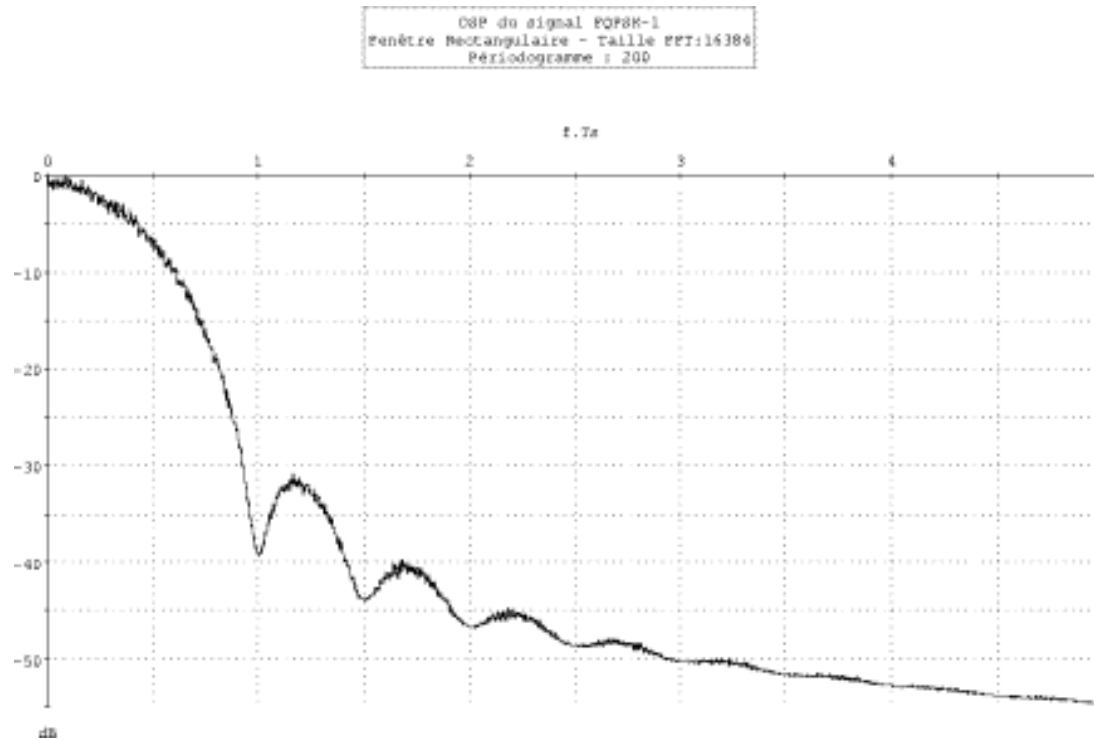
w/o Carrier and clock sync



with Carrier and clock sync



Simulation of Spectral density for FQPSK-1 (1)

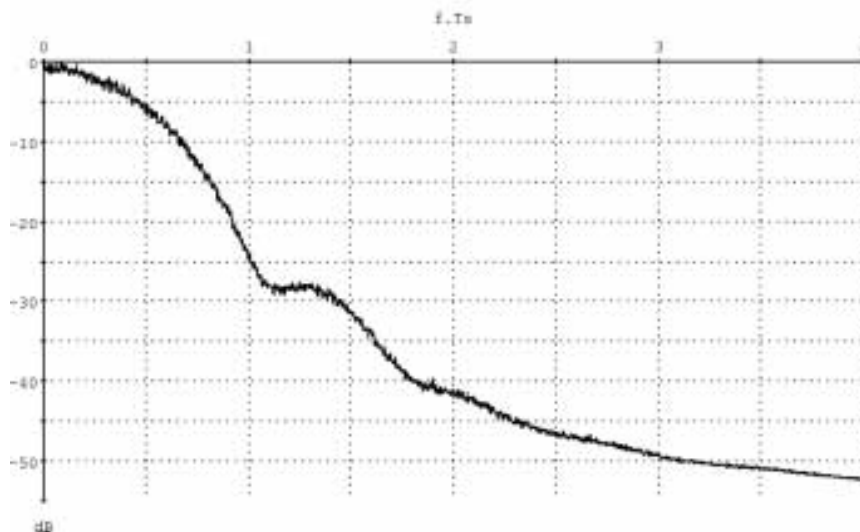


Spectrum w/o H/L - Rectangular Window - FFT Size: 16384



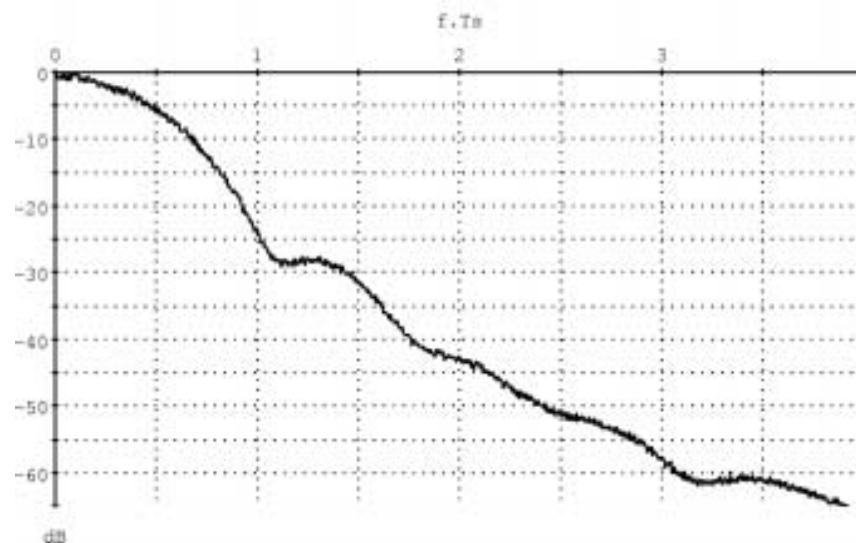
SPW Simulation of Spectral density for FQPSK-1 (2)

DSP du signal FQPSK-1 hard limited
Fenêtre Rectangulaire, Taille FFT: 16384
Périodogramme: 200



Spectrum w H/L - Rectangular Window -
FFT Size: 16384

DSP du signal FQPSK-1 hard limited
Fenêtre de Hamming, Taille FFT: 16384
Périodogramme: 200



Spectrum w H/L - Hamming Window -
FFT Size: 16384



FQPSK-KF Performance analysis

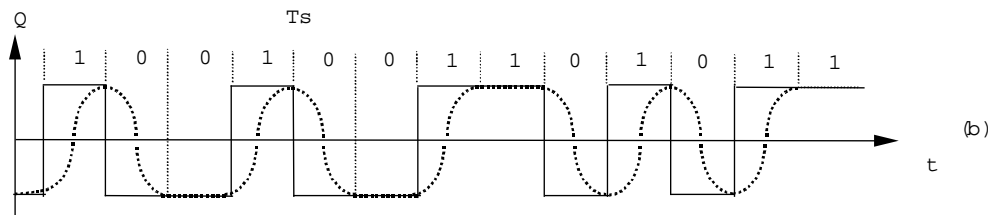
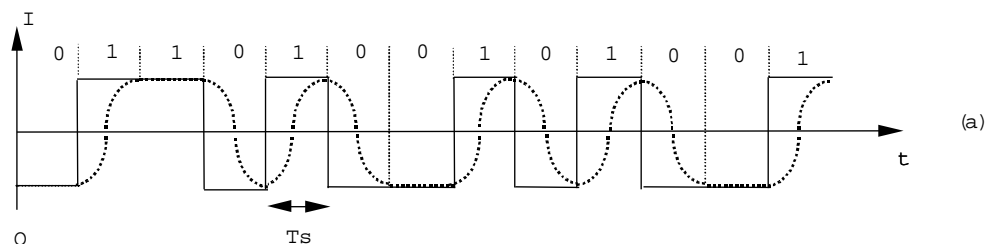
The conditions for Simulation of FQPSK-KF modulation with SPW software are:

- simulation of a full transmitting chain including transmitter and receiver part with AWGN
 - at Transmitter end: Hard Limiter of the modulated waveform
 - at Receiver end, two cases for demodulation and data recovery:
 - Case 1: simple receiver simulation without carrier and clock recovery; predetection ("Matched Filter") filter mechanized with a 4th order Butterworth filter characterized with parameter BT_b
 - Case 2: full receiver simulation with carrier and clock recovery; predetection ("Matched Filter") filter mechanized with a 4th order Butterworth filter characterized with parameter BT_b .
- Carrier recovery uses a Costas Loop while clock recovery is based on the "delay & non-linearity" principle.

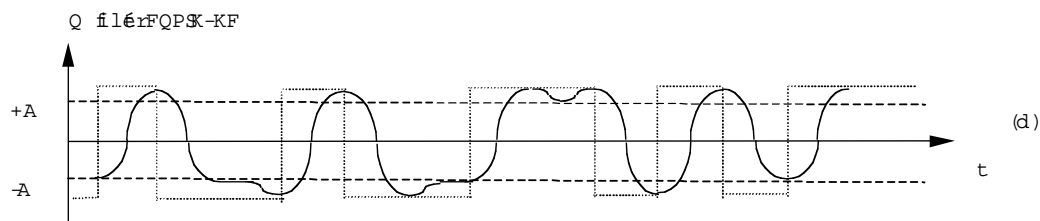
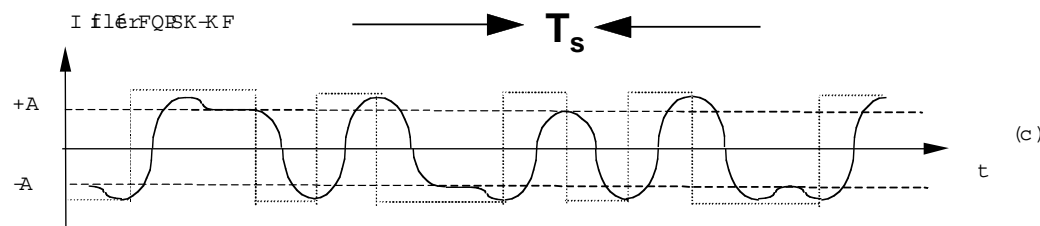


Time representation for I & Q channels in FQPSK-1 and FQPSK-KF

FQPSK-1



FQPSK-KF





Waveform assignation for FQPSK-KF in SPW simulations

Signal	Expression $G(t)=$	Signal	Expression $G(t)=$
S1(t)	$\sin\left(\frac{\pi t}{T_s}\right)$	S8(t)	$-A \cos\left(\frac{\pi t}{T_s}\right)$
S2(t)	$-\sin\left(\frac{\pi t}{T_s}\right)$	S9(t)	$1 - K \cos^2\left(\frac{\pi t}{T_s}\right)$
S3(t)	$\cos\left(\frac{\pi t}{T_s}\right)$	S10(t)	$1 - K \sin^2\left(\frac{\pi t}{T_s}\right)$
S4(t)	$-\cos\left(\frac{\pi t}{T_s}\right)$	S11(t)	$-1 + K \cos^2\left(\frac{\pi t}{T_s}\right)$
S5(t)	$A \sin\left(\frac{\pi t}{T_s}\right)$	S12(t)	$-1 + K \sin^2\left(\frac{\pi t}{T_s}\right)$
S6(t)	$-A \sin\left(\frac{\pi t}{T_s}\right)$	S13(t)	A
S7(t)	$A \cos\left(\frac{\pi t}{T_s}\right)$	S14(t)	$-A$

$$K=1-A$$

A = fixed parameter which influence the amplitude modulation



Truth Table for signal assignation for Simulations of FQPSK-KF

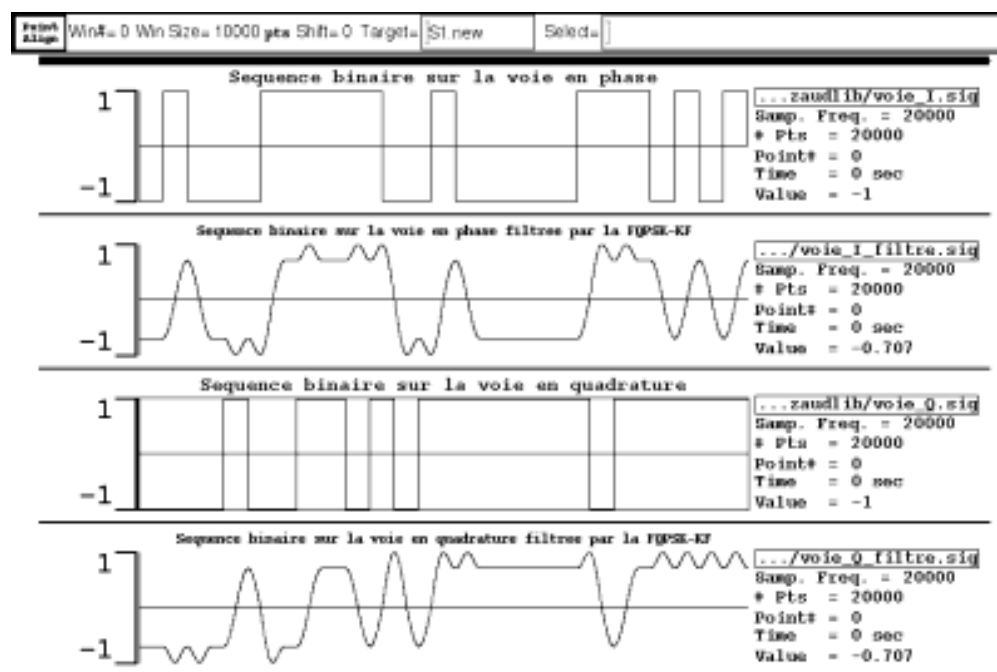
Signal	I_0	I_1	I_2	Q_0	Q_1	Q_2
$S_1(t)$	1	1	0	1	0	0
$S_2(t)$	0	0	1	0	1	1
$S_3(t)$	0	1	1	1	1	0
$S_4(t)$	1	0	0	0	0	1
$S_5(t)$	1	1	0	0	0	0
$S_6(t)$	0	0	1	1	1	1
$S_7(t)$	0	1	1	1	1	1

Signal	I_0	I_1	I_2	Q_0	Q_1	Q_2
$S_8(t)$	1	0	0	1	1	1
$S_9(t)$	1	1	1	1	0	0
$S_{10}(t)$	1	1	1	0	0	1
$S_{11}(t)$	0	0	0	1	0	0
$S_{12}(t)$	0	0	0	0	1	1
$S_{13}(t)$	1	1	1	0	0	0
$S_{14}(t)$	0	0	0	0	0	1

	$Q_0 Q_1 Q_2$							
	000	001	011	010	110	111	101	100
$I_0 I_1 I_2$	000	14	12	11		12	14	11
	001	6		2		6		2
	011	7	3			3	7	
	010							
	110	5		1		5		1
	111	13	10	9		10	13	9
	101							
	100	8	4			4	8	



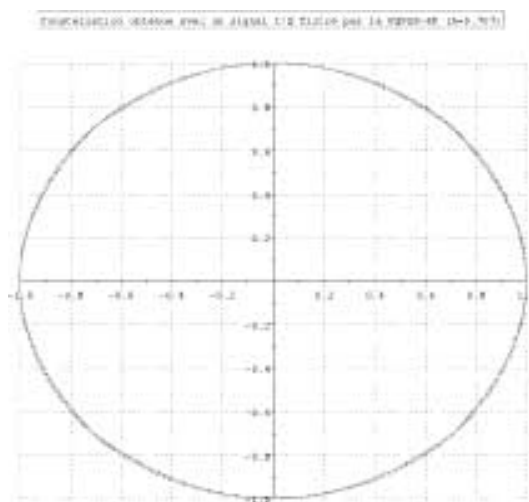
SPW Waveform simulation results for FQPSK-KF



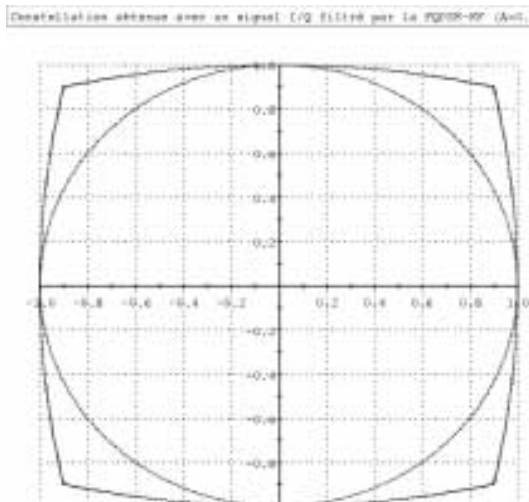


Simulated Performances of FQPSK1 and FQPSK-KF Modulations

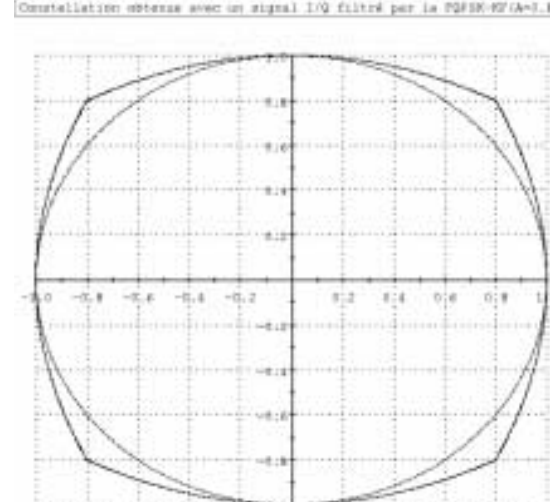
Amplitude diagram for FQPSK-1 and FQPSK-KF (vs. A)



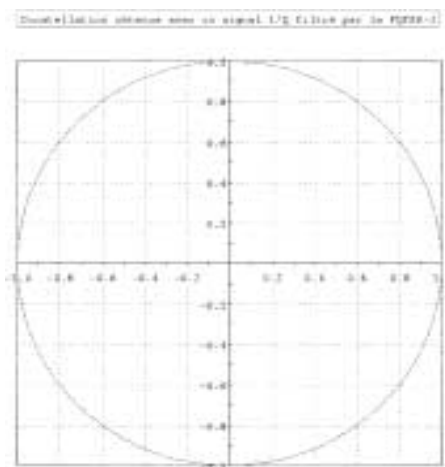
FQPSK-KF w. $A=0,707$



FQPSK-KF w. $A=0,9$



FQPSK-KF w. $A=0,8$

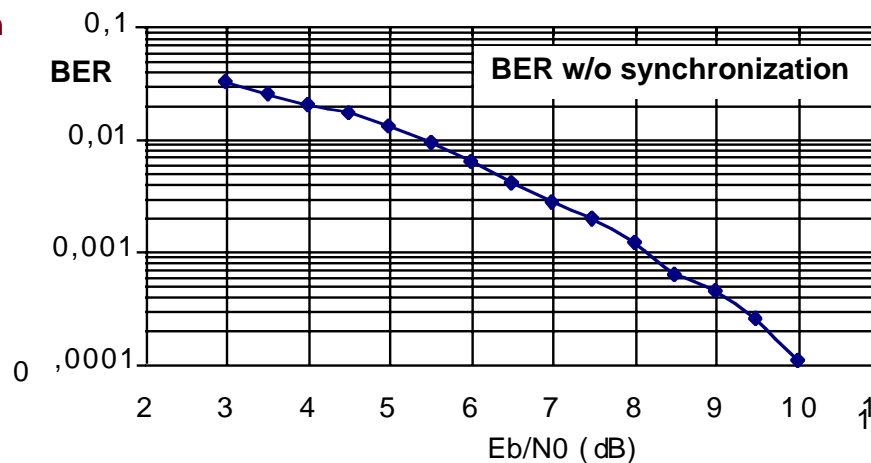
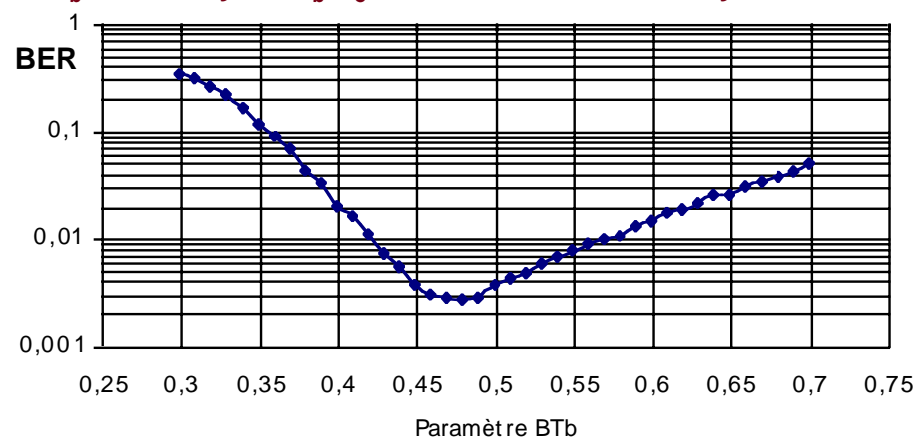


FQPSK-1

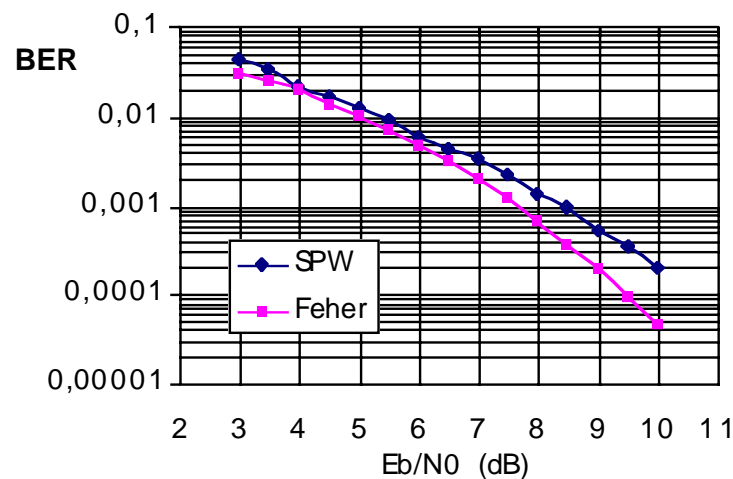
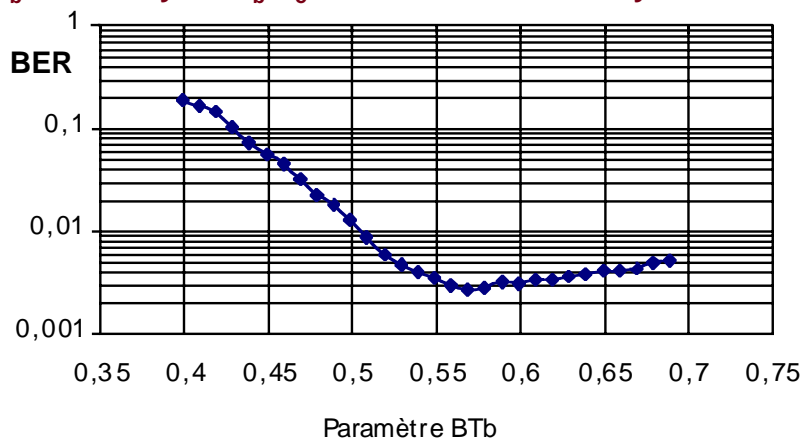


BER results for FQPSK-KF vs. BT_b parameter

BT_b sensitivity for $E_b/N_0 = 7\text{dB}$ with H/L but w/o synchronization



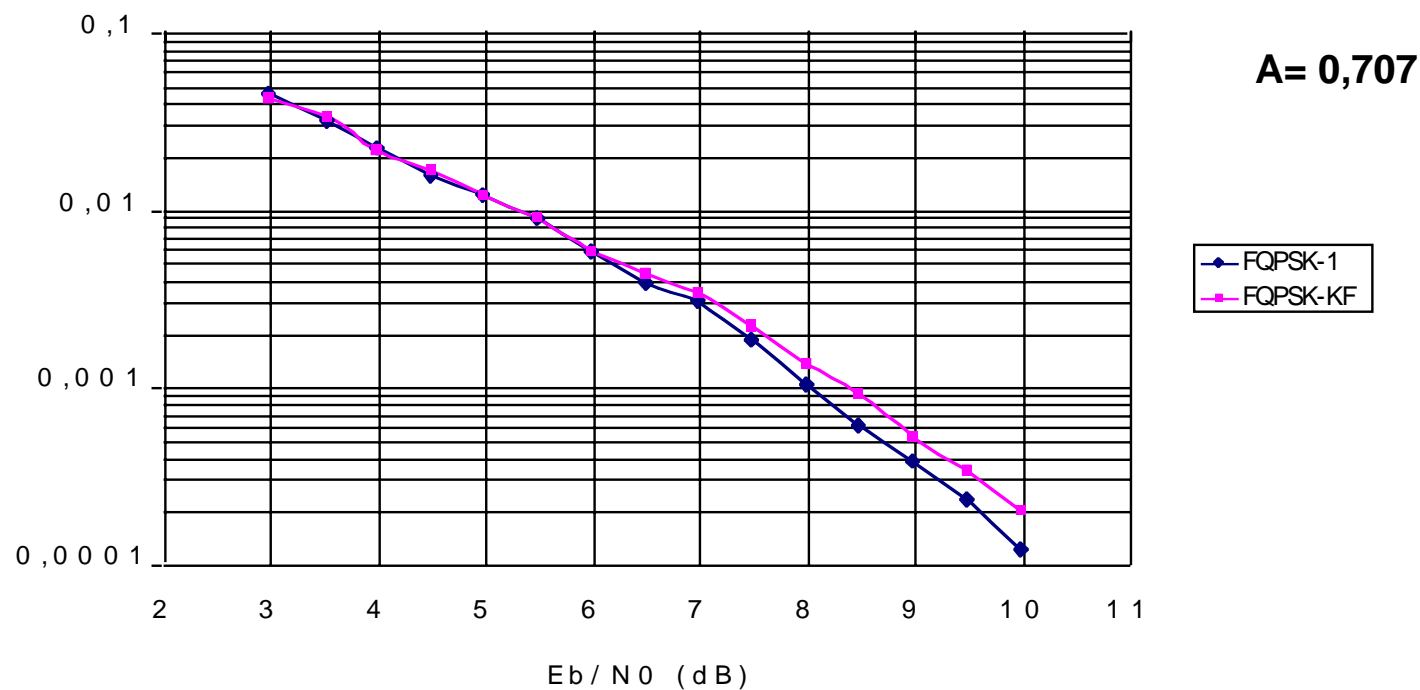
BT_b sensitivity for $E_b/N_0 = 7\text{dB}$ with H/L but w synchronization



FQPSK-KF ($A=0,707$) with H/L and synchro

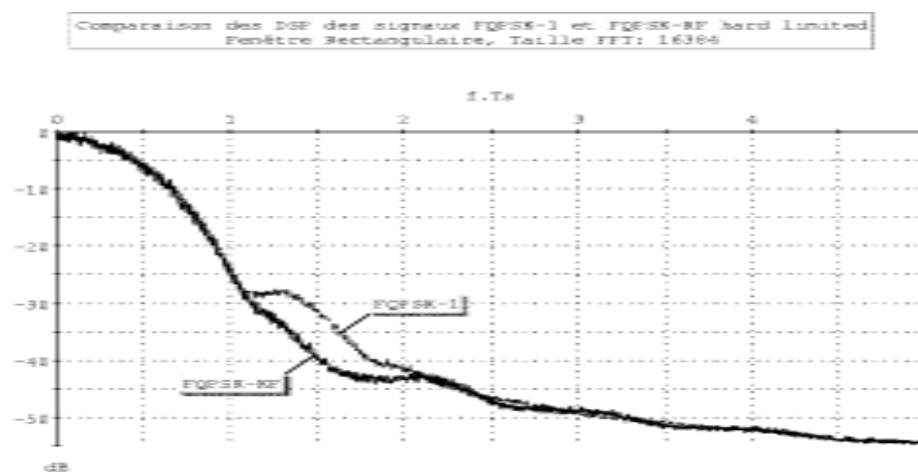
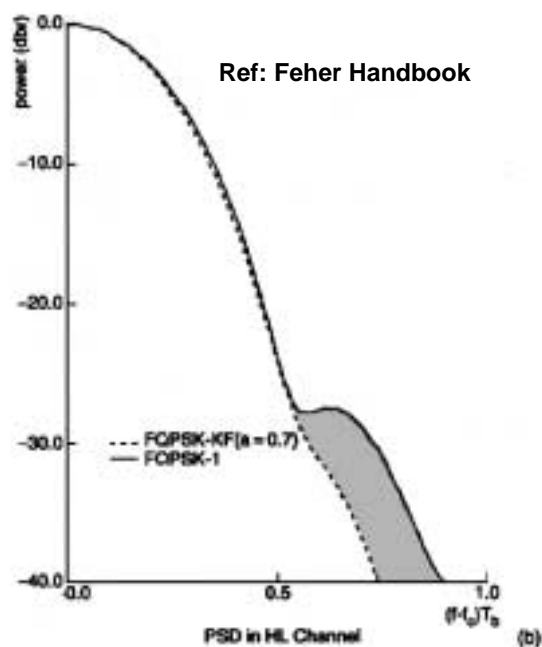


SPW Simulations: comparison of BER for FQPSK-1 and FQPSK-KF modulations



FQPSK-KF modulation presents reduced performances in comparison to FQPSK-1 modulation

Spectrum comparison between FQPK-1 and FQPSK-KF

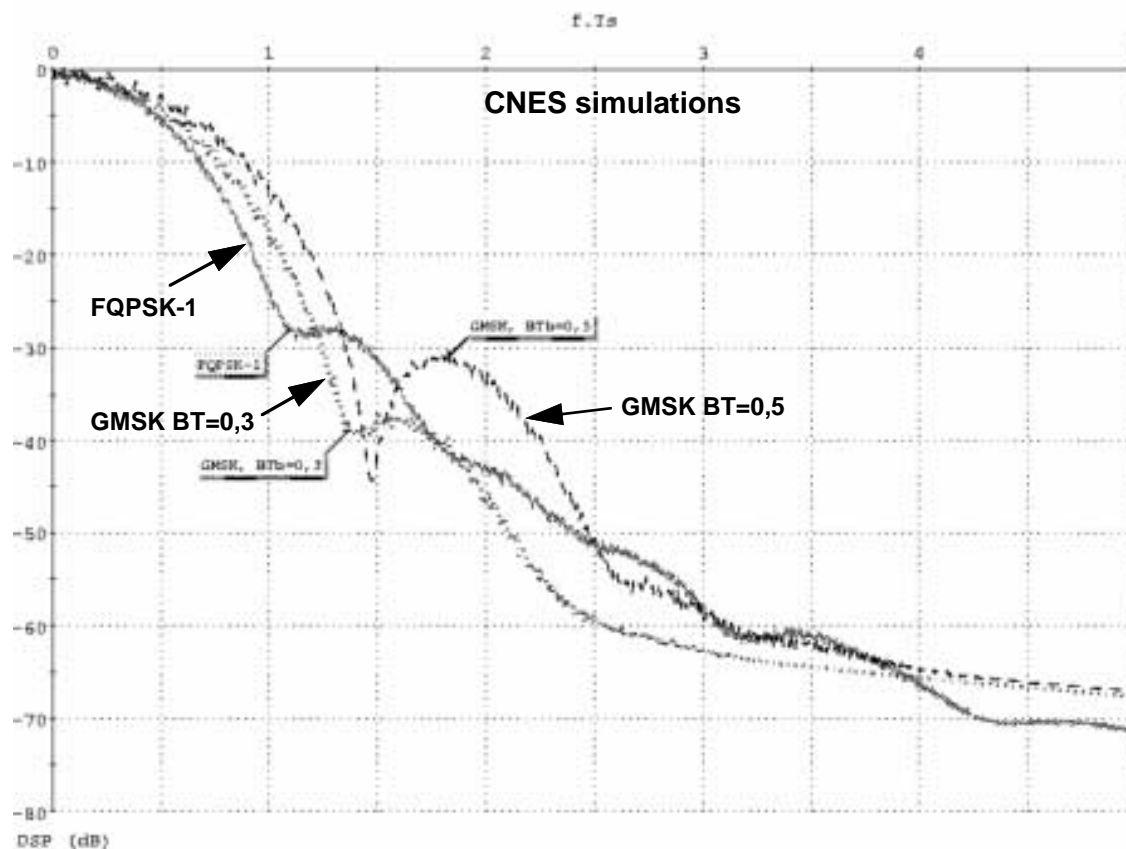
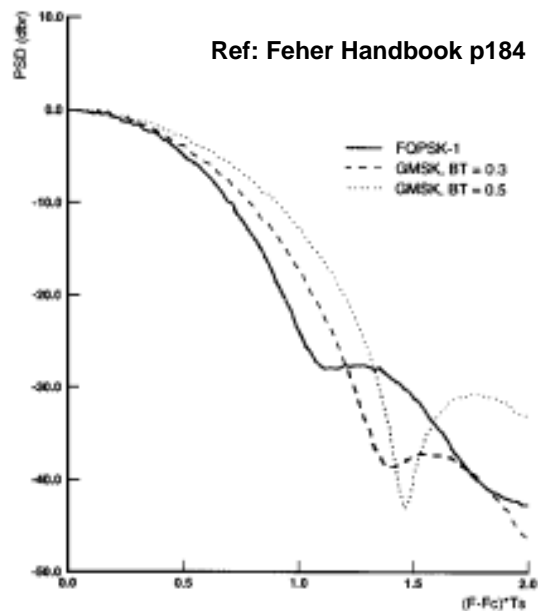




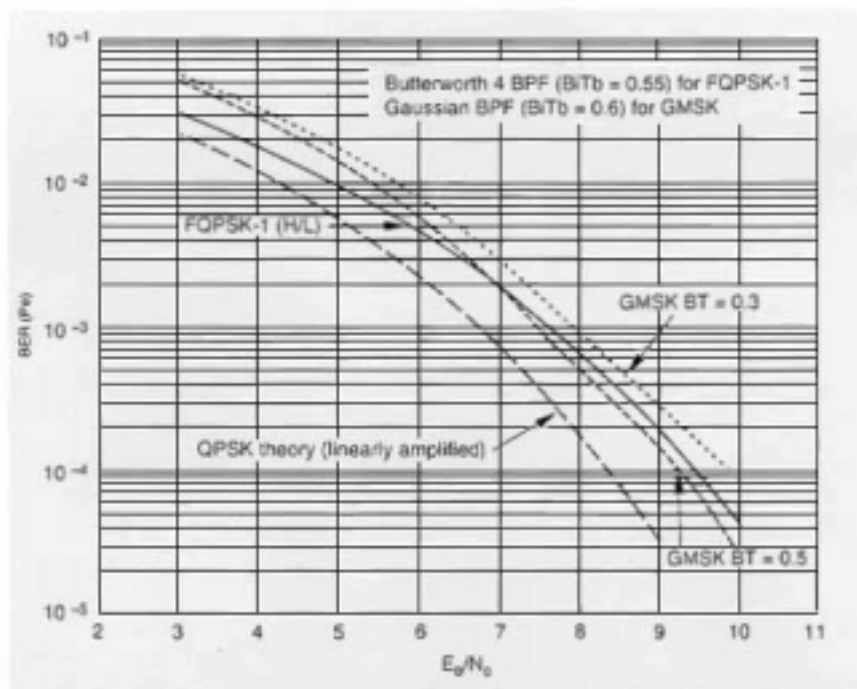
Simulated Performances of FQPSK1 and FQPSK-KF Modulations

Spectrum Comparison for H/L FQPSK-1 and H/L GMSK ($BT_b=0,5$ & $BT_b = 0,3$)

Comparaison des densités spectrales de puissance
des signaux amplifiés non linéairement
(hard limited) FQPSK-1 et GMSK ($BT_b=0,3$ ou $0,5$)

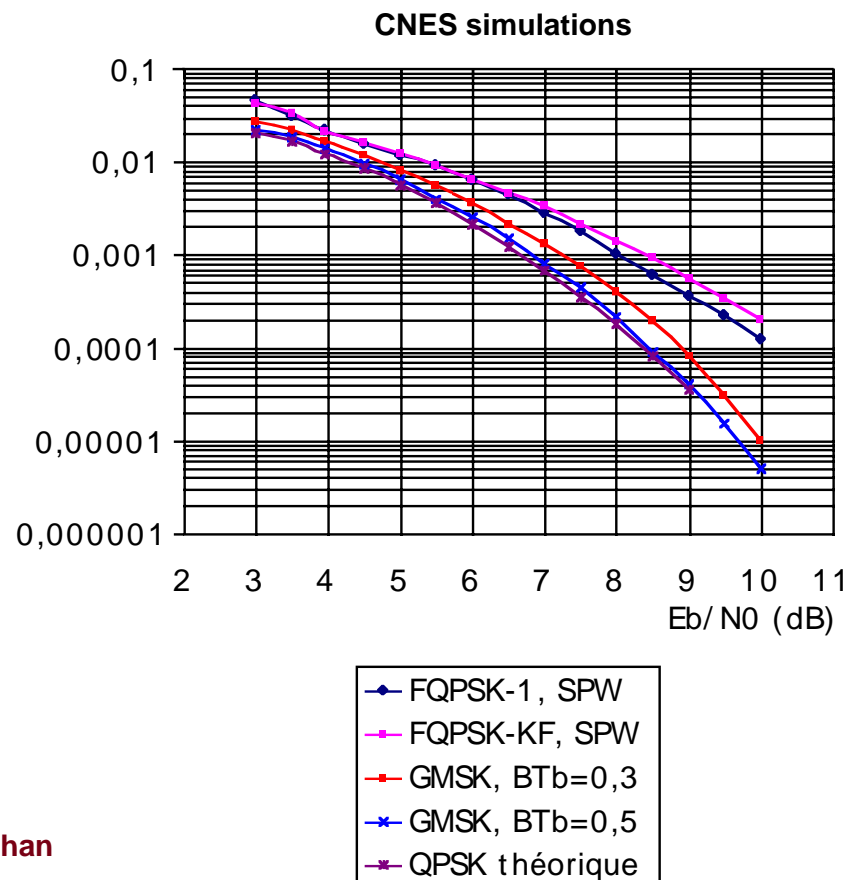


Comparison of BER between FQPSK-1 & KF and GMSK



From Feher Handbook: Wireless Digital Communications: Modulation and Spread spectrum Applications p187 - 1995

Note: For CNES simulations, FQPSK modulations are worst than GMSK modulations in terms of BER.





Conclusion

- Concerning the spectrum occupancy comparison, simulations performed in this work are in good accordance with the results given by Feher in the litterature for the FQPSK-1 and KF and also for GMSK ($BT=0,3$ or $0,5$), under non-linear amplification (Hard Limiter transmitter).
- The difference in spectrum occupancy between FQPSK-1 and FQPSK-KF under Hard Limiter conditions, is mainly visible on a normalized frequency range located between 1 and 2 ($=f.T_s$). The increased complexity of the modulator for FQPSK-KF appears to be not justified in regards of this quite low improvement.
- Concerning the BER comparison between FQPSK-1 and GMSK, there is a difference between the results obtained with SPW in this work and the results presented by Feher in the litterature; GMSK with $BT = 0,3$ or $0,5$ has allways better performances compared to FQPSK-1 in our simulations.
- Concerning FQPSK-KF, the results of BER obtained with SPW and based on a classical receiver (OQPSK receiver) are in accordance with the results presented in TMO Progress Report 42-137 for "Average Matched Filter receiver of FQPSK".

Performance Evaluation and Interpretation of Unfiltered Feher-Patented Quadrature- Phase-Shift Keying (FQPSK)

M. K. Simon¹ and T.-Y. Yan¹

A new interpretation of unfiltered Feher-patented quadrature-phase-shift keying (FQPSK) is presented that readily identifies a means for spectral enhancement of the transmitted waveform as well as an improved method of reception. The key to these successes is the replacement of the half-symbol-by-half-symbol mapping originally used to describe FQPSK by a symbol-by-symbol mapping operation combined with memory. The advantages of such an interpretation are twofold. In particular, the original FQPSK scheme can be modified such that the potential of a waveform slope discontinuity at the boundary between half symbols is avoided without sacrificing the “constant” envelope property of the transmitted waveform, and, furthermore, a memory receiver can be employed to improve error-probability performance relative to previously proposed symbol-by-symbol detection methods. The analysis presented in this article does not include other versions of FQPSK such as FQPSK-B, which currently is being considered for military application.

I. Introduction

JPL has been conducting evaluations of efficient modulation technologies for space agencies under the auspices of the Consultative Committee for Space Data Systems (CCSDS) subpanel 1E, RF and Modulation. One of the technologies pursued is the proprietary Feher-patented quadrature-phase-shift keying (FQPSK) modulation format provided to JPL under the Technology Cooperation Agreement between JPL and Digcom Inc. In its generic form, FQPSK as patented [1] and reported in the recent literature [2,3] is *conceptually* the same as the cross-correlated phase-shift-keying (XPSK) modulation technique introduced in 1983 by Kato and Feher [4].² This technique was in turn a modification of the previously introduced (by Feher et al. [6]) interference- and jitter-free QPSK (IJF-QPSK) with the express purpose of reducing the 3-dB envelope fluctuation characteristic of IJF-QPSK to 0 dB, thus making it appear constant envelope,³ which is beneficial in nonlinear radio systems. (It is further noted that, using a constant waveshape for the even pulse and a sinusoidal waveshape for the odd pulse, IJF-QPSK becomes

¹ Communications Systems and Research Section.

² Other versions of FQPSK referred to as FQPSK-B [5] include proprietary designed filtering for additional spectrum containment. Such filtering is not germane to our discussions in this article and will not be considered.

³ The reduction of the envelope from 3 dB to 0 dB occurs only at the uniform sampling instants on the in-phase (I) and quadrature-phase (Q) channels. It is for this reason that XPSK is referred to as being “pseudo”—or “quasi”—constant envelope, i.e., its envelope has a small amount of fluctuation between the uniform sampling instants.

identical to the staggered quadrature overlapped raised-cosine (SQORC) scheme introduced by Austin and Chang [7]). The means by which Kato and Feher achieved their 3-dB envelope reduction was the introduction of an intentional but controlled amount of cross-correlation between the in-phase (I) and quadrature-phase (Q) channels. This cross-correlation operation was applied to the IJF-QPSK (SQORC) baseband signal prior to its modulation onto the I and Q carriers (see Fig. 1). Specifically, this operation was described by mapping *in each half symbol* the 16 possible combinations of I- and Q-channel waveforms present in the SQORC signal into a new⁴ set of 16 waveform combinations chosen in such a way that the cross-correlator output is time continuous and has unit (normalized) envelope⁵ at all I and Q uniform sampling instants. By virtue of the fact that the cross-correlation mapping is based on a half-symbol characterization of the SQORC signal, there is no guarantee that the *slope* of the cross-correlator output waveform is continuous at the half-symbol transition points. In fact, we shall show that for a random data input sequence such a discontinuity in slope occurs one quarter of the time.

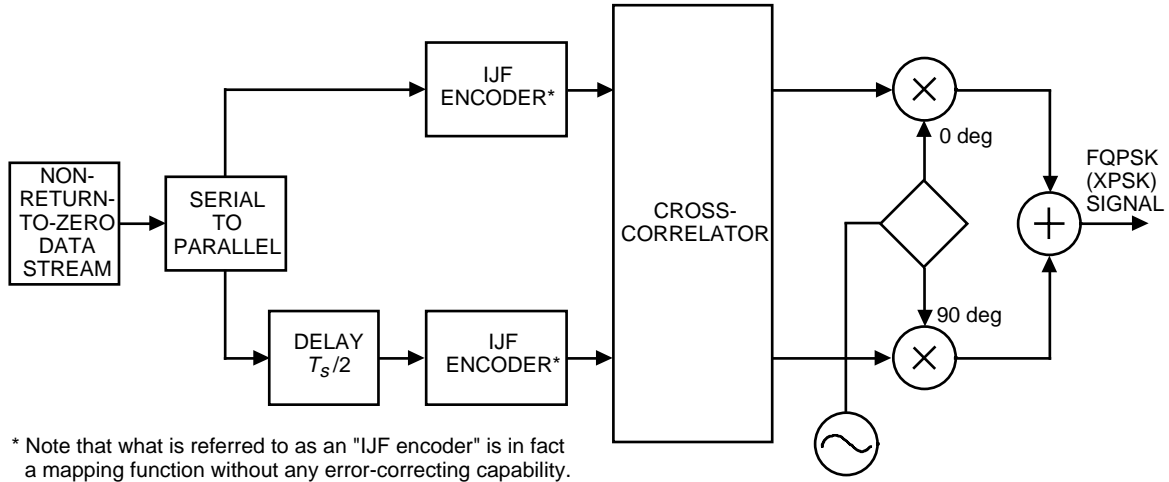


Fig. 1. The conceptual block diagram of FQPSK (XPSK).

It is well-known that the rate at which the side lobes of a modulation's power spectral density (PSD) roll off with frequency is related to the smoothness of the underlying waveforms that generate it. That is, the more derivatives of a waveform that are continuous, the faster its Fourier transform decays with frequency. Thus, since the first derivative of the FQPSK waveform is discontinuous (at half-symbol transition instants) on the average of one-quarter of the time, one can anticipate that an improvement in PSD roll-off could be had if the FQPSK cross-correlation mapping could be modified so that the first derivative is always continuous. By restructuring the cross-correlation mapping into a symbol-by-symbol representation, the slope discontinuity referred to above will be placed in evidence and will be particularly helpful in suggesting a means to eliminate it. This representation also has the advantage that it can be described directly in terms of the data transitions on the I and Q channels and, thus, the combination of IJF encoder and cross-correlator can be replaced simply by a single modified cross-correlator. The replacement of the conventional FQPSK cross-correlator by this modified cross-correlator that eliminates the slope discontinuity leads to what we shall refer to as enhanced FQPSK. We shall show that not only does enhanced FQPSK have a better PSD (in the sense of reduced out-of-band energy) than conventional FQPSK has but, from a modulation symmetry standpoint, it is a more logical choice.

⁴ Of the 16 possible cross-correlator output combinations, only 12 of them are in fact new, i.e., for 4 of the input I and Q combinations, the cross-correlator outputs the identical combination.

⁵ Actually, in the operation's generic form, Kato and Feher allow (through the introduction of a transition parameter, $k = 1 - A$) for a controlled amount of envelope fluctuation. For quasi-constant envelope, one should choose $A = 1/\sqrt{2}$.

A further and more important advantage of the reformulation as a symbol-by-symbol mapping is the ability to design a receiver of FQPSK or enhanced FQPSK (EFQPSK) that specifically exploits the correlation introduced into the modulation scheme to significantly improve power efficiency or, equivalently, error-probability performance. Such a receiver, which takes a form analogous to those used for trellis-coded modulations, will be shown to yield significant performance improvement over receivers that employ symbol-by-symbol detection, thus ignoring the inherent memory of the modulation.

II. Review of IJF-QPSK and SQORC

The IJF-QPSK scheme (alternatively called FQPSK-1) is based on defining waveforms $s_o(t)$ and $s_e(t)$, which are respectively odd and even functions of time over the symbol interval $-T_s/2 \leq t \leq T_s/2$, and then using these and their negatives, $-s_o(t)$ and $-s_e(t)$, as a 4-ary signal set for transmission in accordance with the values of successive pairs of data symbols in each of the I and Q arms. Specifically, if d_{In} denotes the I-channel data symbols in the interval $(n - [1/2])T_s \leq t \leq (n + [1/2])T_s$, then the transmitted waveform $x_I(t)$ in this same interval would be determined as follows:

$$\left. \begin{aligned} x_I(t) &= s_e(t - nT_s) \triangleq s_0(t - nT_s) & \text{if } d_{I,n-1} = 1, d_{I,n} = 1 \\ x_I(t) &= -s_e(t - nT_s) \triangleq s_1(t - nT_s) & \text{if } d_{I,n-1} = -1, d_{I,n} = -1 \\ x_I(t) &= s_o(t - nT_s) \triangleq s_2(t - nT_s) & \text{if } d_{I,n-1} = -1, d_{I,n} = 1 \\ x_I(t) &= -s_o(t - nT_s) \triangleq s_3(t - nT_s) & \text{if } d_{I,n-1} = 1, d_{I,n} = -1 \end{aligned} \right\} \quad (1)$$

The Q-channel waveform, $x_Q(t)$, would be generated by the same mapping as in Eq. (1), using instead the Q-channel data symbols, $\{d_{Qn}\}$, and then delaying the resulting waveform by one-half of a symbol. If the odd and even waveforms $s_o(t)$ and $s_e(t)$ are defined by

$$\left. \begin{aligned} s_e(t) &= 1, & -\frac{T_s}{2} \leq t \leq \frac{T_s}{2} \\ s_o(t) &= \sin \frac{\pi t}{T_s}, & -\frac{T_s}{2} \leq t \leq \frac{T_s}{2} \end{aligned} \right\} \quad (2)$$

then typical waveforms for the I and Q IJF encoder outputs are as illustrated in Fig. 2.

A modulation identical to $x_I(t)$ [and likewise for $x_Q(t)$] generated from the combination of Eqs. (1) and (2) can be obtained directly from the binary data sequence $\{d_{In}\}$ itself without the need for defining a 4-ary mapping based on the transition properties of the sequence. In particular, if we define the two-symbol-wide raised-cosine pulse shape

$$p(t) = \sin^2 \left(\frac{\pi \left(t + \frac{T_s}{2} \right)}{2T_s} \right), \quad -\frac{T_s}{2} \leq t \leq \frac{3T_s}{2} \quad (3)$$

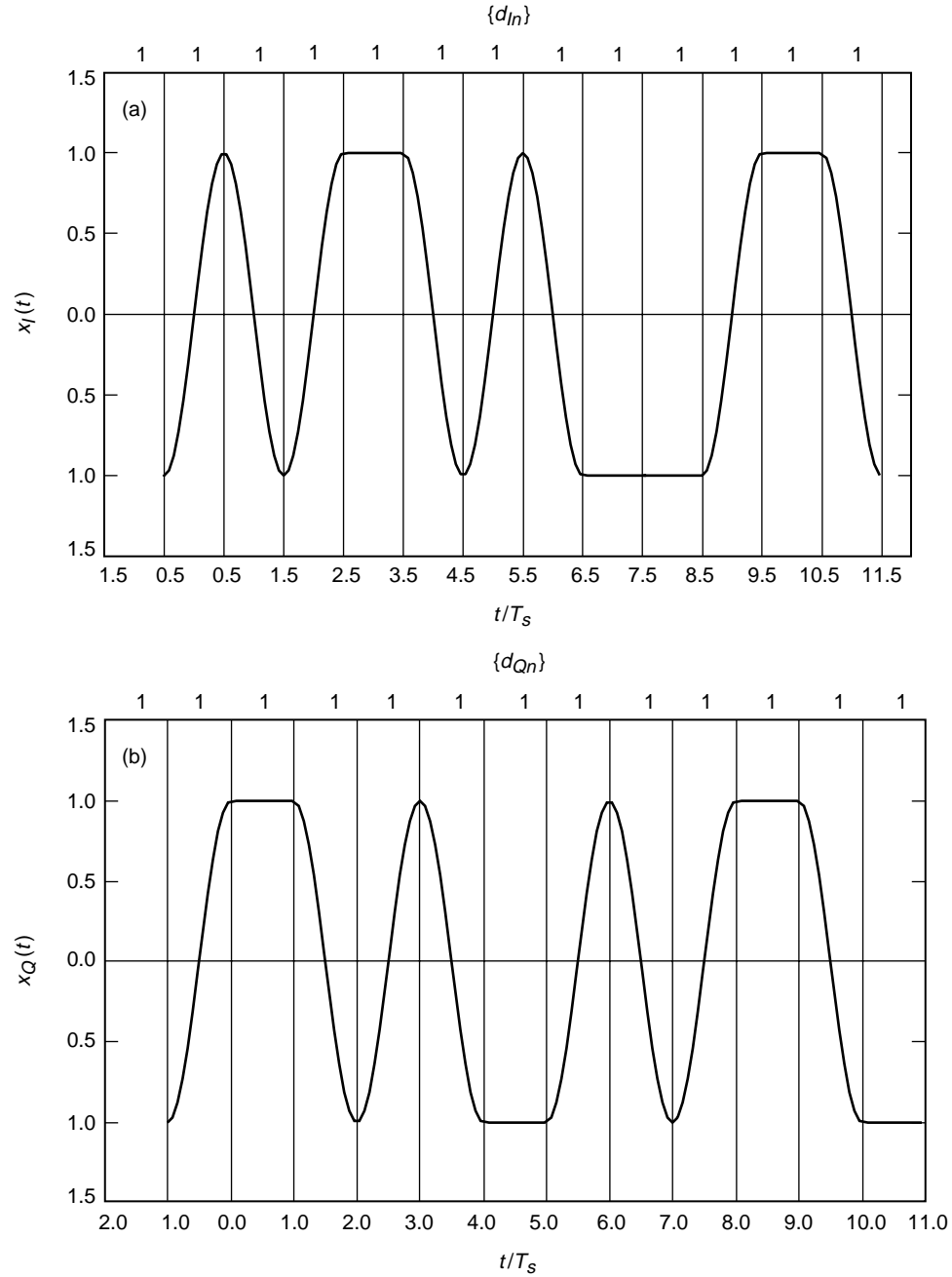


Fig. 2. IJF encoder output: (a) in-phase and (b) quadrature-phase.

then the I modulation

$$x_I(t) = \sum_{n=-\infty}^{\infty} d_{In} p(t - nT_s) \quad (4)$$

will be identical to that generated by the above IJF scheme. Similarly,

$$x_Q(t) = \sum_{n=-\infty}^{\infty} d_{Qn} p\left(t - \left(n + \frac{1}{2}\right) T_s\right) \quad (5)$$

also would be identical to that generated by the above IJF scheme. A quadrature modulation scheme formed from $x_I(t)$ of Eq. (4) and $x_Q(t)$ of Eq. (5) is precisely what Austin and Chang [7] referred to as SQORC modulation, namely, independent I and Q modulations with overlapping raised-cosine pulses on each channel. The resulting carrier modulated waveform is described by

$$x(t) = x_I(t) \cos \omega_c t + x_Q(t) \sin \omega_c t \quad (6)$$

III. A Symbol-by-Symbol Cross-Correlator Mapping for FQPSK

Before revealing the modification of FQPSK that results in a transmitted signal having a continuous first derivative, we first recast the original characterization of FQPSK in terms of a cross-correlation operation performed on the pair of IJF encoder outputs every half-symbol interval into a mapping performed directly on the input I and Q data sequences every full-symbol interval. To do this, we define 16 waveforms, $s_i(t)$; $i = 0, 1, 2, \dots, 15$, over the interval $-T_s/2 \leq t \leq T_s/2$, which collectively form a transmitted signaling set for the I and Q channels. The particular I and Q waveforms chosen for any particular T_s -s signaling interval on each channel depends on the most recent data transition on that channel as well as the two most recent successive transitions on the other channel. The specifics are as follows. Define (see Fig. 3)

$$\left. \begin{aligned} s_0(t) &= A, \quad -\frac{T_s}{2} \leq t \leq \frac{T_s}{2}, \quad s_8(t) = -s_0(t) \\ s_1(t) &= \begin{cases} A, & -\frac{T_s}{2} \leq t \leq 0 \\ 1 - (1 - A) \cos^2 \frac{\pi t}{T_s}, & 0 \leq t \leq \frac{T_s}{2} \end{cases} \quad s_9(t) = -s_1(t) \\ s_2(t) &= \begin{cases} 1 - (1 - A) \cos^2 \frac{\pi t}{T_s}, & -\frac{T_s}{2} \leq t \leq 0 \\ A, & 0 \leq t \leq \frac{T_s}{2} \end{cases} \quad s_{10}(t) = -s_2(t) \\ s_3(t) &= 1 - (1 - A) \cos^2 \frac{\pi t}{T_s}, \quad -\frac{T_s}{2} \leq t \leq \frac{T_s}{2}, \quad s_{11}(t) = -s_3(t) \end{aligned} \right\} \quad (7a)$$

and

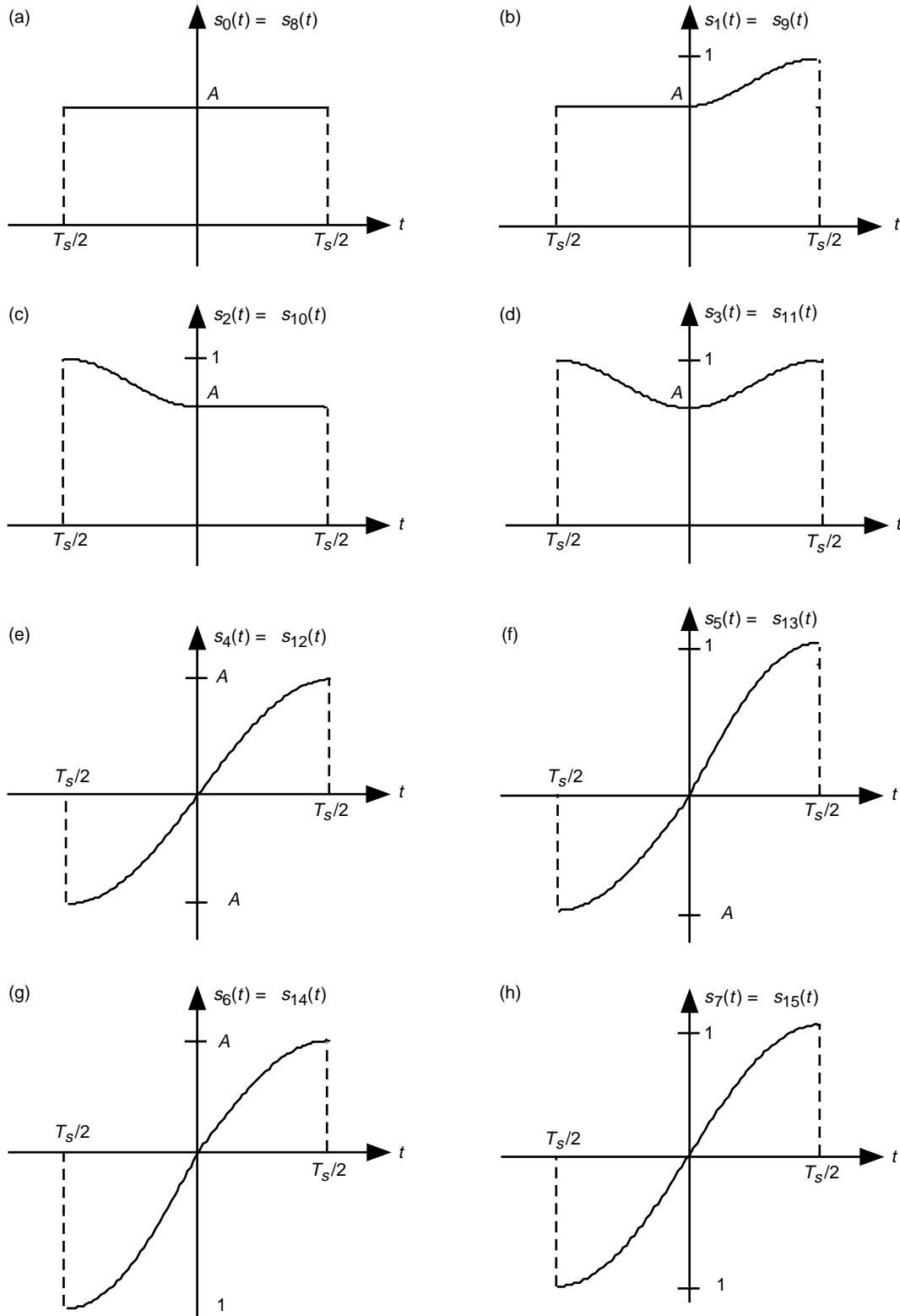


Fig. 3. FQPSK full-symbol waveforms: (a) $s_0(t) = s_8(t)$ vs t , (b) $s_1(t) = s_9(t)$ vs t , (c) $s_2(t) = s_{10}(t)$ vs t , (d) $s_3(t) = s_{11}(t)$ vs t , (e) $s_4(t) = s_{12}(t)$ vs t , (f) $s_5(t) = s_{13}(t)$ vs t , (g) $s_6(t) = s_{14}(t)$ vs t , and (h) $s_7(t) = s_{15}(t)$ vs t .

$$\left. \begin{aligned}
 s_4(t) &= A \sin \frac{\pi t}{T_s}, \quad -\frac{T_s}{2} \leq t \leq \frac{T_s}{2}, \quad s_{12}(t) = -s_4(t) \\
 s_5(t) &= \begin{cases} A \sin \frac{\pi t}{T_s}, & -\frac{T_s}{2} \leq t \leq 0 \\ \sin \frac{\pi t}{T_s}, & 0 \leq t \leq \frac{T_s}{2} \end{cases} \quad s_{13}(t) = -s_5(t) \\
 s_6(t) &= \begin{cases} \sin \frac{\pi t}{T_s}, & -\frac{T_s}{2} \leq t \leq 0 \\ A \sin \frac{\pi t}{T_s}, & 0 \leq t \leq \frac{T_s}{2} \end{cases} \quad s_{14}(t) = -s_6(t) \\
 s_7(t) &= \sin \frac{\pi t}{T_s}, \quad -\frac{T_s}{2} \leq t \leq \frac{T_s}{2}, \quad s_{15}(t) = -s_7(t)
 \end{aligned} \right\} \quad (7b)$$

Note that for any value of A other than unity, $s_6(t)$ and $s_7(t)$ as well as their negatives, $s_{13}(t)$ and $s_{14}(t)$, will have a discontinuous slope at their midpoints (i.e., at $t = 0$), whereas the remaining 12 waveforms all have a continuous slope throughout their defining intervals. Also, all 16 waveforms have zero slope at their end points and, thus, concatenation of any pair of these will not result in a slope discontinuity.

Next, define the following mapping function for the baseband I-channel transmitted waveform $y_I(t) = s_I(t)$ in the n th signaling interval $(n - [1/2])T_s \leq t \leq (n + [1/2])T_s$ in terms of the transition properties of the I and Q data symbol sequences $\{d_{In}\}$ and $\{d_{Qn}\}$, respectively.

- (1) If $d_{I,n-1} = 1, d_{I,n} = 1$ (no transition on the I sequence, both data bits positive), then
 - (a) $y_I(t) = s_0(t - nT_s)$ if $d_{Q,n-2}, d_{Q,n-1}$ results in no transition and $d_{Q,n-1}, d_{Q,n}$ results in no transition.
 - (b) $y_I(t) = s_1(t - nT_s)$ if $d_{Q,n-2}, d_{Q,n-1}$ results in no transition and $d_{Q,n-1}, d_{Q,n}$ results in a transition (positive or negative).
 - (c) $y_I(t) = s_2(t - nT_s)$ if $d_{Q,n-2}, d_{Q,n-1}$ results in a transition (positive or negative) and $d_{Q,n-1}, d_{Q,n}$ results in no transition.
 - (d) $y_I(t) = s_3(t - nT_s)$ if $d_{Q,n-2}, d_{Q,n-1}$ results in a transition (positive or negative) and $d_{Q,n-1}, d_{Q,n}$ results in a transition (positive or negative).
- (2) If $d_{I,n-1} = -1, d_{I,n} = 1$ (a positive going transition on the I sequence), then
 - (a) $y_I(t) = s_4(t - nT_s)$ if $d_{Q,n-2}, d_{Q,n-1}$ results in no transition and $d_{Q,n-1}, d_{Q,n}$ results in no transition.
 - (b) $y_I(t) = s_5(t - nT_s)$ if $d_{Q,n-2}, d_{Q,n-1}$ results in no transition and $d_{Q,n-1}, d_{Q,n}$ results in a transition (positive or negative).
 - (c) $y_I(t) = s_6(t - nT_s)$ if $d_{Q,n-2}, d_{Q,n-1}$ results in a transition (positive or negative) and $d_{Q,n-1}, d_{Q,n}$ results in no transition.

- (d) $y_I(t) = s_7(t - nT_s)$ if $d_{Q,n-2}, d_{Q,n-1}$ results in a transition (positive or negative) and $d_{Q,n-1}, d_{Q,n}$ results in a transition (positive or negative).
- (3) If $d_{I,n-1} = -1, d_{I,n} = -1$ (no transition on the I sequence, both data bits negative), then
- (a) $y_I(t) = s_8(t - nT_s)$ if $d_{Q,n-2}, d_{Q,n-1}$ results in no transition and $d_{Q,n-1}, d_{Q,n}$ results in no transition.
- (b) $y_I(t) = s_9(t - nT_s)$ if $d_{Q,n-2}, d_{Q,n-1}$ results in no transition and $d_{Q,n-1}, d_{Q,n}$ results in a transition (positive or negative).
- (c) $y_I(t) = s_{10}(t - nT_s)$ if $d_{Q,n-2}, d_{Q,n-1}$ results in a transition (positive or negative) and $d_{Q,n-1}, d_{Q,n}$ results in no transition.
- (d) $y_I(t) = s_{11}(t - nT_s)$ if $d_{Q,n-2}, d_{Q,n-1}$ results in a transition (positive or negative) and $d_{Q,n-1}, d_{Q,n}$ results in a transition (positive or negative).
- (4) If $d_{I,n-1} = 1, d_{I,n} = -1$ (a negative going transition on the I sequence), then
- (a) $y_I(t) = s_{12}(t - nT_s)$ if $d_{Q,n-2}, d_{Q,n-1}$ results in no transition and $d_{Q,n-1}, d_{Q,n}$ results in no transition.
- (b) $y_I(t) = s_{13}(t - nT_s)$ if $d_{Q,n-2}, d_{Q,n-1}$ results in no transition and $d_{Q,n-1}, d_{Q,n}$ results in a transition (positive or negative).
- (c) $y_I(t) = s_{14}(t - nT_s)$ if $d_{Q,n-2}, d_{Q,n-1}$ results in a transition (positive or negative) and $d_{Q,n-1}, d_{Q,n}$ results in no transition.
- (d) $y_I(t) = s_{15}(t - nT_s)$ if $d_{Q,n-2}, d_{Q,n-1}$ results in a transition (positive or negative) and $d_{Q,n-1}, d_{Q,n}$ results in a transition (positive or negative).

Making use of the signal properties in Eqs. (7a) and (7b), the mapping conditions in (1) through (4) for the I-channel baseband output can be summarized in a concise form described by Table 1. A similar construction for the baseband Q-channel transmitted waveform $y_Q(t) = s_Q(t - T_s/2)$ in the n th signaling interval $nT_s \leq t \leq (n+1)T_s$ in terms of the transition properties of the I and Q data symbol sequences, $\{d_{In}\}$ and $\{d_{Qn}\}$, respectively, can be obtained analogously to (1) through (4) above. The results can once again be summarized in the form of a table, as in Table 2.

Table 1. Mapping for I-channel baseband signal $y_I(t)$ in the interval $(n - [1/2])T_s \leq t \leq (n + [1/2])T_s$.

$\left \frac{d_{In} - d_{I,n-1}}{2} \right $	$\left \frac{d_{Q,n-1} - d_{Q,n-2}}{2} \right $	$\left \frac{d_{Q,n} - d_{Q,n-1}}{2} \right $	$s_I(t)$
0	0	0	$d_{In}s_0(t - nT_s)$
0	0	1	$d_{In}s_1(t - nT_s)$
0	1	0	$d_{In}s_2(t - nT_s)$
0	1	1	$d_{In}s_3(t - nT_s)$
1	0	0	$d_{In}s_4(t - nT_s)$
1	0	1	$d_{In}s_5(t - nT_s)$
1	1	0	$d_{In}s_6(t - nT_s)$
1	1	1	$d_{In}s_7(t - nT_s)$

Table 2. Mapping for Q-channel baseband signal $y_Q(t)$ in the interval $nT_s \leq t \leq (n+1)T_s$.^a

$\left\lfloor \frac{d_{Q,n} - d_{Q,n-1}}{2} \right\rfloor$	$\left\lfloor \frac{d_{I,n} - d_{I,n-1}}{2} \right\rfloor$	$\left\lfloor \frac{d_{I,n+1} - d_{I,n}}{2} \right\rfloor$	$s_I(t)$
0	0	0	$d_{Q,n}s_0(t - nT_s)$
0	0	1	$d_{Q,n}s_1(t - nT_s)$
0	1	0	$d_{Q,n}s_2(t - nT_s)$
0	1	1	$d_{Q,n}s_3(t - nT_s)$
1	0	0	$d_{Q,n}s_4(t - nT_s)$
1	0	1	$d_{Q,n}s_5(t - nT_s)$
1	1	0	$d_{Q,n}s_6(t - nT_s)$
1	1	1	$d_{Q,n}s_7(t - nT_s)$

^aNote that the subscript i of the transmitted signal $s_i(t - nT_s)$ or $s_i(t - (n + [1/2])T_s)$ as appropriate is the binary coded decimal (BCD) equivalent of the three transitions!

Applying the mappings in Tables 1 and 2 to the I and Q data sequences of Fig. 2 produces the identical I and Q baseband transmitted signals to those that would be produced by passing the I and Q IJF encoder outputs of this figure through the cross-correlator (half-symbol mapping) of the FQPSK (XPSP) scheme as described in [4] (see Fig. 4). Thus, we conclude that *for arbitrary I and Q input sequences, FQPSK can alternatively be generated by the symbol-by-symbol mappings of Tables 1 and 2 as applied to these sequences.*

IV. A New and Improved FQPSK

As discussed above, the symbol-by-symbol mapping representation of FQPSK identifies the fact that 4 out of the 16 possible transmitted waveforms, namely, $s_5(t)$, $s_6(t)$, $s_{13}(t)$, and $s_{14}(t)$, have a slope discontinuity at their midpoints. Thus, for random I and Q data symbol sequences, the transmitted FQPSK waveform on the average likewise will have a slope discontinuity at one-quarter of the uniform-sampling time instants. To prevent this from occurring, we now redefine these four transmitted signals in a manner analogous to $s_1(t)$, $s_2(t)$, $s_9(t)$, and $s_{10}(t)$, namely,

$$\left. \begin{aligned} s_5(t) &= \begin{cases} \sin \frac{\pi t}{T_s} + (1-A) \sin^2 \frac{\pi t}{T_s}, & -\frac{T_s}{2} \leq t \leq 0 \\ \sin \frac{\pi t}{T_s}, & 0 \leq t \leq \frac{T_s}{2} \end{cases} & s_{13}(t) = -s_5(t) \\ s_6(t) &= \begin{cases} \sin \frac{\pi t}{T_s}, & -\frac{T_s}{2} \leq t \leq 0 \\ \sin \frac{\pi t}{T_s} - (1-A) \sin^2 \frac{\pi t}{T_s}, & 0 \leq t \leq \frac{T_s}{2} \end{cases} & s_{14}(t) = -s_6(t) \end{aligned} \right\} \quad (8)$$

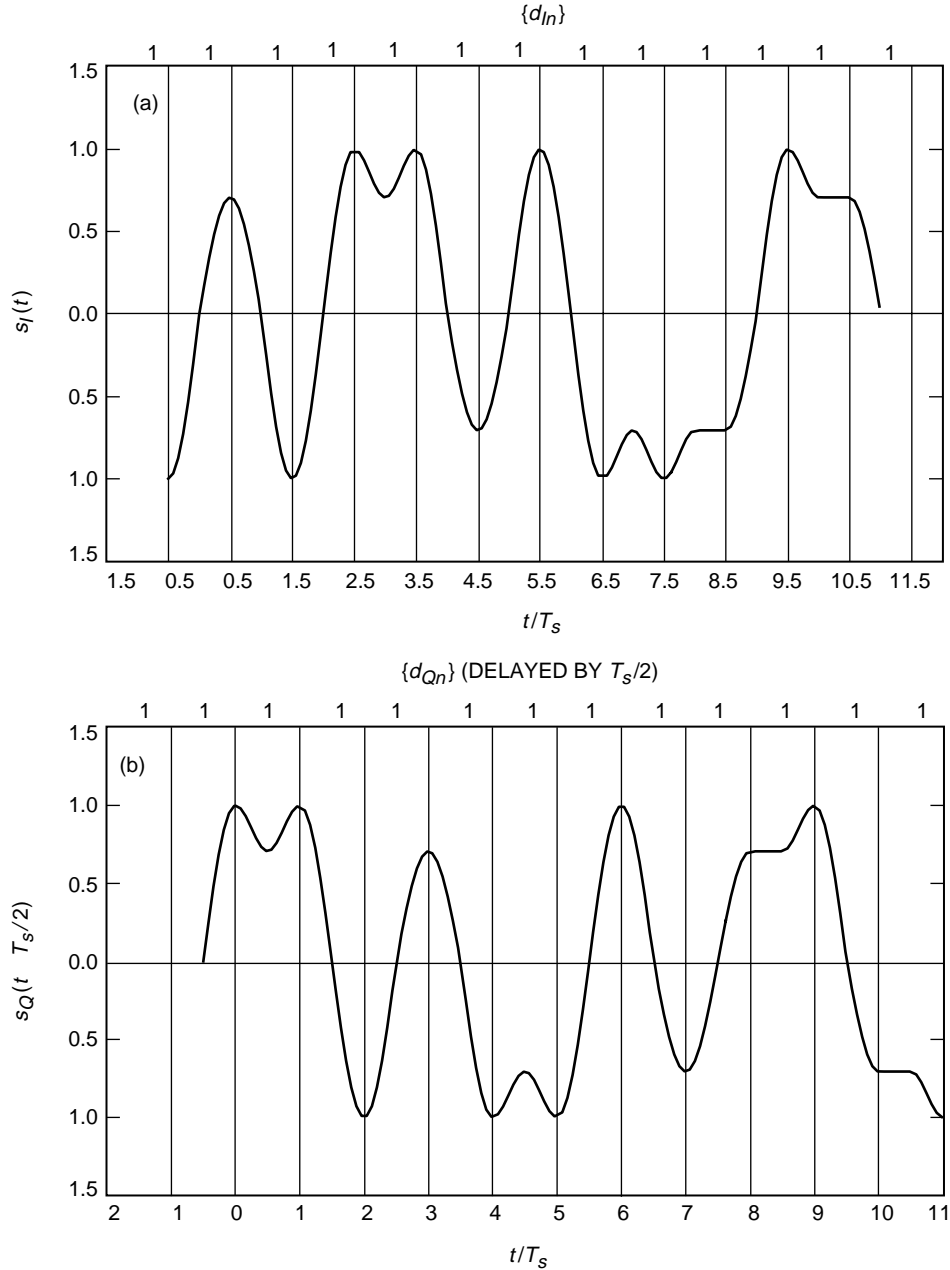


Fig. 4. FQPSK (XPSK) output: (a) in-phase and (b) quadrature-phase.

Note that the signals $s_5(t)$, $s_6(t)$, $s_{13}(t)$, and $s_{14}(t)$, as defined in Eq. (8), do *not* have a slope discontinuity at their midpoints nor for that matter anywhere else in the defining intervals. Also, the zero slopes at their end points have been preserved. Thus, using Eq. (8) in place of the corresponding signals of Eq. (7b) will result in a modified FQPSK signal that has no slope discontinuity anywhere in time *regardless of the value of A* . Figure 5 illustrates a comparison of the signal $s_6(t)$ of Eq. (8) with that of Eq. (7b) for a value of $A = 1/\sqrt{2}$. Figure 6 illustrates the power spectral density of conventional FQPSK and its enhancement, EFQPSK, obtained by using the waveforms of Eq. (8) as replacements for those in Eq. (7b). The significant improvement in spectral roll-off rate is clear from a comparison of the two.

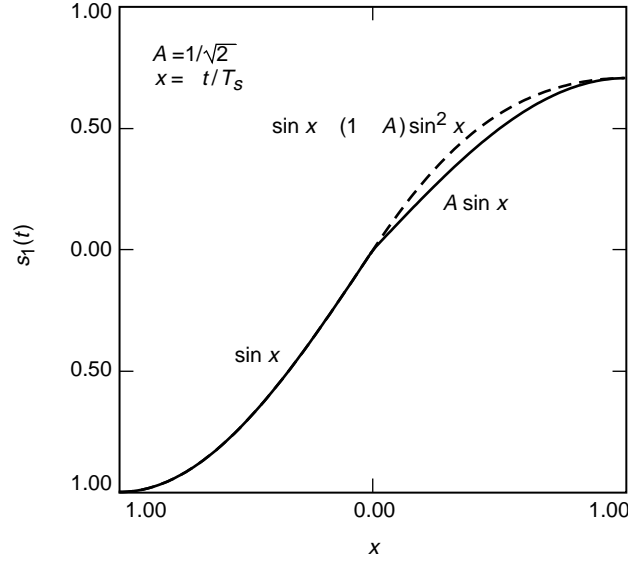


Fig. 5. Original and new FQPSK pulse shapes.

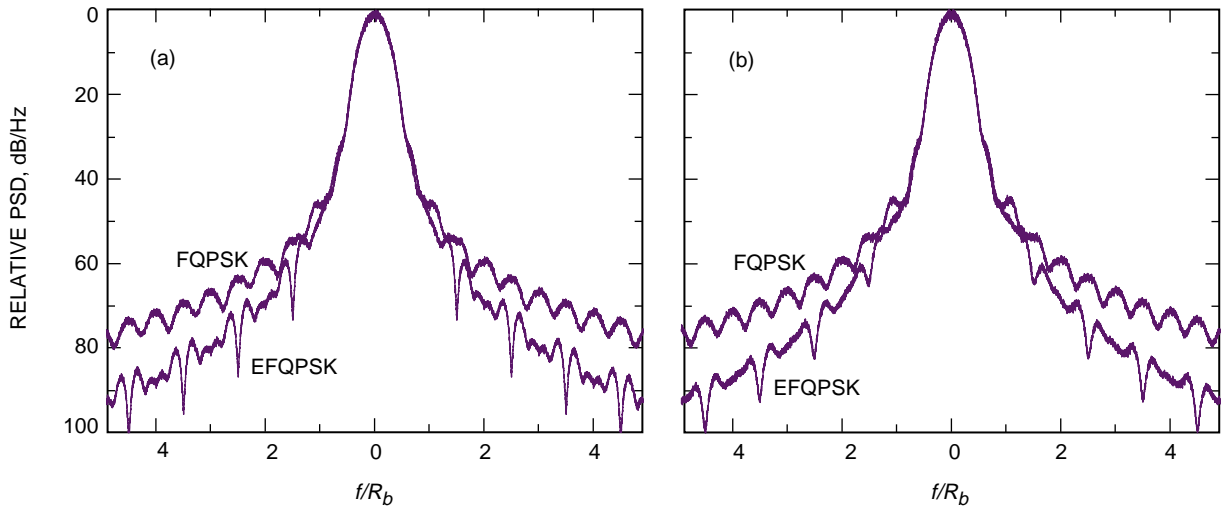


Fig. 6. Power spectra of conventional and enhanced FQPSK: (a) without SSPA and (b) with SSPA.

As it currently stands, the signal set chosen for EFQPSK has a symmetry property for $s_0(t)$, $s_1(t)$, $s_2(t)$, and $s_3(t)$ that is not present for $s_4(t)$, $s_5(t)$, $s_6(t)$, and $s_7(t)$. In particular, $s_1(t)$ and $s_2(t)$ are each composed of one-half of $s_0(t)$ and one-half of $s_3(t)$, i.e., the portion of $s_1(t)$ from $t = -T_s/2$ to $t = 0$ is the same as that of $s_0(t)$, whereas the portion of $s_1(t)$ from $t = 0$ to $t = T_s/2$ is the same as that of $s_3(t)$ and vice versa for $s_2(t)$. To achieve the same symmetry property for $s_4(t) - s_7(t)$, one would have to reassign $s_4(t)$ as

$$s_4(t) = \begin{cases} \sin \frac{\pi t}{T_s} + (1 - A) \sin^2 \frac{\pi t}{T_s}, & -\frac{T_s}{2} \leq t \leq 0 \\ \sin \frac{\pi t}{T_s} - (1 - A) \sin^2 \frac{\pi t}{T_s}, & 0 \leq t \leq \frac{T_s}{2} \end{cases} \quad s_{12}(t) = -s_4(t) \quad (9)$$

This minor change, which produces a complete symmetry in the waveform set, has an advantage from the standpoint of hardware implementation and produces a negligible change in spectral properties of the transmitted waveform. Nevertheless, for the remainder of the discussion, we shall ignore this minor change and assume the version of enhanced FQPSK first introduced in this section.

V. Interpretation of FQPSK as a Trellis-Coded Modulation

The I and Q mappings given in Tables 1 and 2 can alternatively be described in terms of the (0,1) representation of the I and Q data symbols and their transitions. Specifically, define

$$\left. \begin{aligned} D_{In} &\triangleq \frac{1 - d_{In}}{2} \\ D_{Qn} &\triangleq \frac{1 - d_{Qn}}{2} \end{aligned} \right\} \quad (10)$$

which both range over the set (0,1). Then, defining the binary-coded decimal (BCD) representation of the indices i and j by

$$\left. \begin{aligned} i &= I_3 \times 2^3 + I_2 \times 2^2 + I_1 \times 2^1 + I_0 \times 2^0 \\ j &= Q_3 \times 2^3 + Q_2 \times 2^2 + Q_1 \times 2^1 + Q_0 \times 2^0 \end{aligned} \right\} \quad (11)$$

with

$$\left. \begin{aligned} I_0 &= D_{Qn} \oplus D_{Q,n-1}, & Q_0 &= D_{I,n+1} \oplus D_{In} \\ I_1 &= D_{Q,n-1} \oplus D_{Q,n-2}, & Q_1 &= D_{In} \oplus D_{I,n-1} = I_2 \\ I_2 &= D_{In} \oplus D_{I,n-1}, & Q_2 &= D_{Qn} \oplus D_{Q,n-1} = I_0 \\ I_3 &= D_{In}, & Q_3 &= D_{Qn} \end{aligned} \right\} \quad (12)$$

we have $y_I(t) = s_i(t - nT_s)$ and $y_Q(t) = s_j(t - (n + [1/2])T_s)$. That is, in each symbol interval $[(n - [1/2])T_s \leq t \leq (n + [1/2])T_s]$ for $y_I(t)$ and $nT_s \leq t \leq (n + 1)T_s$ for $y_Q(t)$, the I- and Q-channel baseband signals are each chosen from a set of 16 signals, $s_i(t)$, $i = 0, 1, \dots, 15$, in accordance with the 4-bit BCD representations of their indices defined by Eq. (11) together with Eq. (12). A graphical illustration of the implementation of this mapping is given in Fig. 7.

Another interpretation of the mapping in Fig. 7 is as a 16-state trellis code with two binary (0,1) inputs, $D_{I,n+1}$ and D_{Qn} , and two waveform outputs, $s_i(t)$ and $s_j(t)$, where the state is defined by the 4-bit sequence $D_{In}, D_{I,n-1}, D_{Q,n-1}, D_{Q,n-2}$. The trellis is illustrated in Fig. 8, and the transition mapping is given in Table 3. In this table, the entries in the column labeled “input” correspond to the values of the two input bits $D_{I,n+1}$ and D_{Qn} that result in the transition, while the entries in the “output” column correspond to the subscripts i and j of the pair of symbol waveforms $s_i(t)$ and $s_j(t)$ that are output.

To compute the performance of this trellis-coded modulation (TCM), we need to determine the minimum Euclidean distance between pairs of error-event paths that leave a given state and first return to

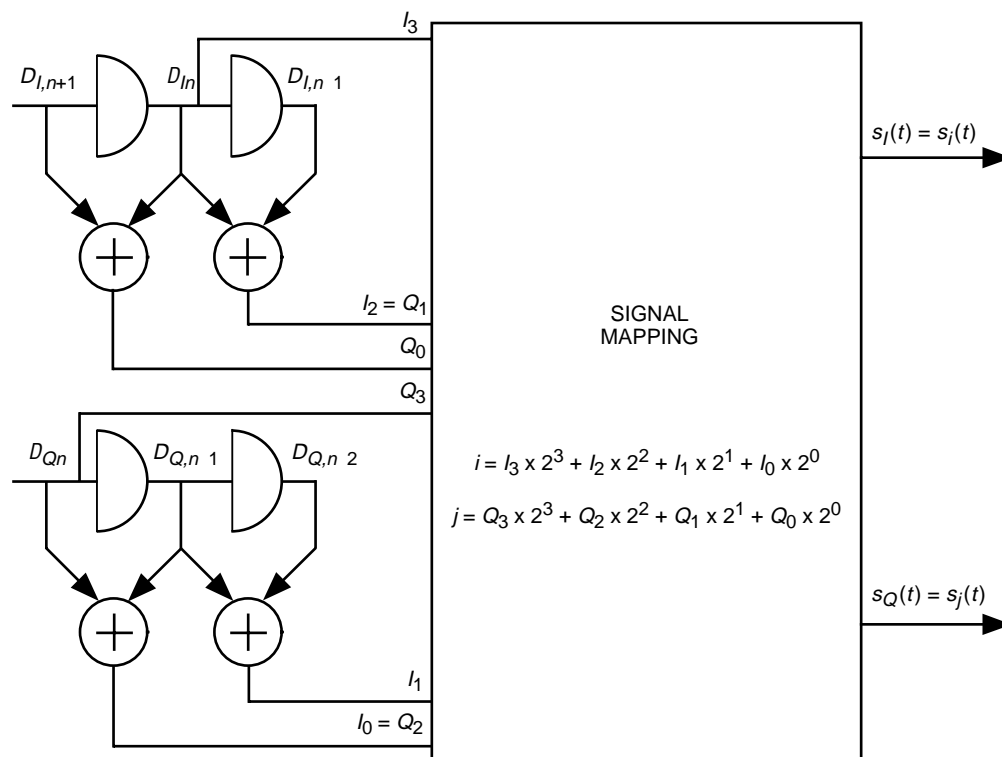


Fig. 7. Alternate implementation of FQPSK baseband signals.

Table 3. Trellis state transitions.

Current state	Input	Output	Next state
0 0 0 0	0 0	0 0	0 0 0 0
0 0 0 0	0 1	1 12	0 0 1 0
0 0 0 0	1 0	0 1	1 0 0 0
0 0 0 0	1 1	1 13	1 0 1 0
0 0 1 0	0 0	3 4	0 0 0 1
0 0 1 0	0 1	2 8	0 0 1 1
0 0 1 0	1 0	3 5	1 0 0 1
0 0 1 0	1 1	2 9	1 0 1 1
1 0 0 0	0 0	12 3	0 1 0 0
1 0 0 0	0 1	13 15	0 1 1 0
1 0 0 0	1 0	12 2	1 1 0 0
1 0 0 0	1 1	13 14	1 1 1 0
1 0 1 0	0 0	15 7	0 1 0 1
1 0 1 0	0 1	14 11	0 1 1 1
1 0 1 0	1 0	15 6	1 1 0 1
1 0 1 0	1 1	14 10	1 1 1 1
0 0 0 1	0 0	2 0	0 0 0 0
0 0 0 1	0 1	3 12	0 0 1 0
0 0 0 1	1 0	2 1	1 0 0 0
0 0 0 1	1 1	3 13	1 0 1 0

Table 3 (contd). Trellis state transitions.

Current state	Input	Output	Next state
0 0 1 1	0 0	1 4	0 0 0 1
0 0 1 1	0 1	0 8	0 0 1 1
0 0 1 1	1 0	1 5	1 0 0 1
0 0 1 1	1 1	0 9	1 0 1 1
1 0 0 1	0 0	14 3	0 1 0 0
1 0 0 1	0 1	15 15	0 1 1 0
1 0 0 1	1 0	14 2	1 1 0 0
1 0 0 1	1 1	15 14	1 1 1 0
1 0 1 1	0 0	13 7	0 1 0 1
1 0 1 1	0 1	12 11	0 1 1 1
1 0 1 1	1 0	13 6	1 1 0 1
1 0 1 1	1 1	12 10	1 1 1 1
0 1 0 0	0 0	4 2	0 0 0 0
0 1 0 0	0 1	5 14	0 0 1 0
0 1 0 0	1 0	4 3	1 0 0 0
0 1 0 0	1 1	5 15	1 0 1 0
0 1 1 0	0 0	7 6	0 0 0 1
0 1 1 0	0 1	6 10	0 0 1 1
0 1 1 0	1 0	7 7	1 0 0 1
0 1 1 0	1 1	6 11	1 0 1 1
1 1 0 0	0 0	8 1	0 1 0 0
1 1 0 0	0 1	9 13	0 1 1 0
1 1 0 0	1 0	8 0	1 1 0 0
1 1 0 0	1 1	9 12	1 1 1 0
1 1 1 0	0 0	11 5	0 1 0 1
1 1 1 0	0 1	10 9	0 1 1 1
1 1 1 0	1 0	11 4	1 1 0 1
1 1 1 0	1 1	10 8	1 1 1 1
0 1 0 1	0 0	6 2	0 0 0 0
0 1 0 1	0 1	7 14	0 0 1 0
0 1 0 1	1 0	6 3	1 0 0 0
0 1 0 1	1 1	7 15	1 0 1 0
0 1 1 1	0 0	5 6	0 0 0 1
0 1 1 1	0 1	4 10	0 0 1 1
0 1 1 1	1 0	5 7	1 0 0 1
0 1 1 1	1 1	4 11	1 0 1 1
1 1 0 1	0 0	10 1	0 1 0 0
1 1 0 1	0 1	11 13	0 1 1 0
1 1 0 1	1 0	10 0	1 1 0 0
1 1 0 1	1 1	11 12	1 1 1 0
1 1 1 1	0 0	9 5	0 1 0 1
1 1 1 1	0 1	8 9	0 1 1 1
1 1 1 1	1 0	9 4	1 1 0 1
1 1 1 1	1 1	8 8	1 1 1 1

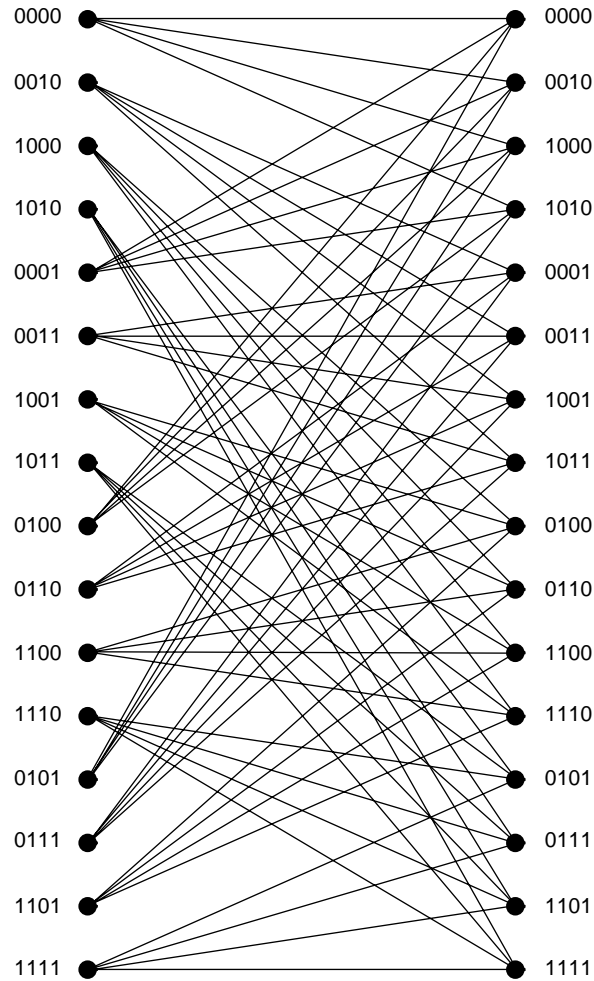


Fig. 8. The 16-state trellis diagram for FQPSK.

that or another state a number of branches later. The smallest-length error event for which there are at least two paths that start in one state and remerge in the same or another state is 3 branches. For each of the 16 starting states, there are exactly 4 such error-event paths that remerge in each of the 16 end states. Figures 9(a) and 9(b) are examples of these error-event paths corresponding to the first two states, respectively, for the case when the start and end states are the same. The remaining length-3 error-event paths for states 9 through 16 are the mirror images of the ones for states 1 through 8 [see, for example, Fig. 9(c), which should be compared with Fig. 9(a)]. Also, the paths for states 9 through 16 will have Euclidean distance properties identical to those for states 1 through 8 since the output symbols along their branches will be the negatives of those along their mirror images. Figures 10(a) and 10(b) are examples of the groups of 4 error-event paths that start in a given state and remerge in another state. A similar mirror-image symmetry exists for these groups of paths and, thus, once again it is sufficient to consider only the first 8 starting states.

It is important to note that the trellis code defined by the mapping in Table 3 is not uniform, e.g., it is not sufficient to consider only the all-zeros path as the transmitted path in computing the minimum Euclidean distance. Rather, one must consider all possible pairs of error-event paths starting from each of the 16 states (8 states is sufficient in view of the above-mentioned distance symmetry properties) and ending in each of the 16 states and determine the pair having the minimum Euclidean distance. The following example illustrates the procedure for the groups of paths that start and end in the same state.

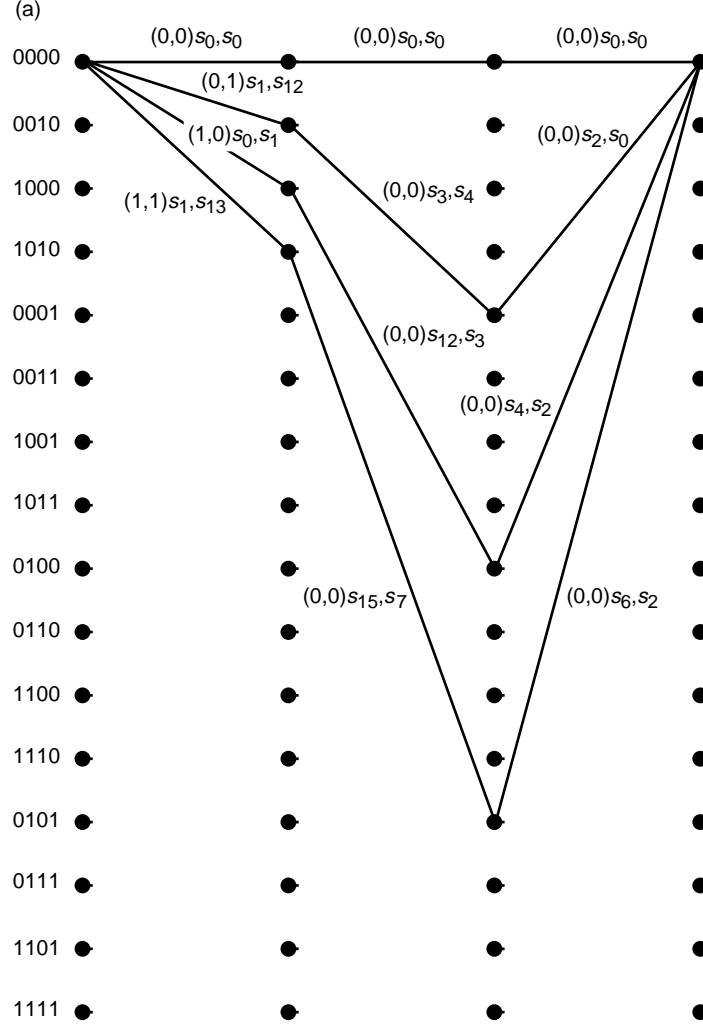


Fig. 9. Paths of length-3 branches starting and ending in (a) state 1, (b) state 2, and (c) state 16.

Upon examination of the squared Euclidean distance between all pairs of paths in the above-mentioned figures, it can be shown that the minimum of this distance, i.e., d_{\min}^2 , occurs between the first and third paths of Fig. 9(b).⁶ Thus, based on the output symbols that occur along this pair of paths, we have

$$\begin{aligned}
 d_{\min}^2 = & \int_{-T_s/2}^{T_s/2} \left[(s_3(t) - s_3(t))^2 + (s_4(t) - s_5(t))^2 + (s_2(t) - s_{14}(t))^2 + (s_0(t) - s_3(t))^2 \right. \\
 & \left. + (s_1(t) - s_5(t))^2 + (s_{12}(t) - s_{14}(t))^2 \right] dt
 \end{aligned} \tag{13}$$

Evaluation of the squared Euclidean distances between the pairs of waveforms required in Eq. (13) using Eqs. (7a) and (7b) for their definitions results, after much algebra, in

⁶ It also occurs between several other pairs of paths starting and ending in the same state.

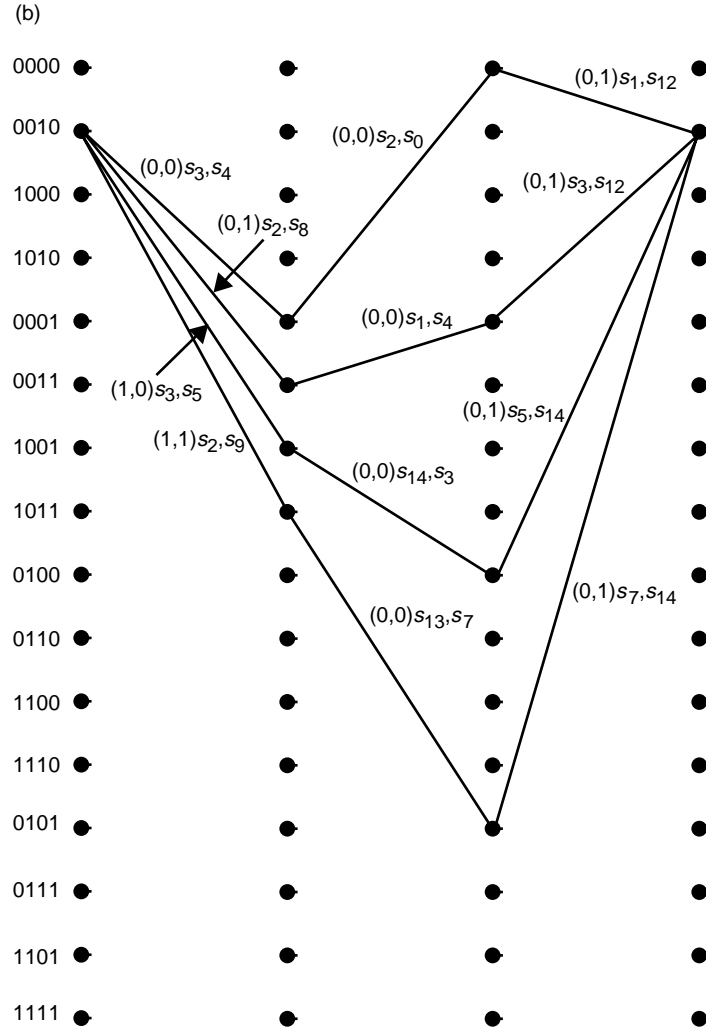


Fig. 9 (contd). Paths of length-3 branches starting and ending in (a) state 1, (b) state 2, and (c) state 16.

$$d_{\min}^2 = \left[\frac{7}{4} - \frac{8}{3\pi} - A \left(\frac{3}{2} + \frac{4}{3\pi} \right) + A^2 \left(\frac{11}{4} + \frac{4}{\pi} \right) \right] T_s = 1.552T_s \quad (14)$$

The average signal ($I + Q$) energy is obtained from

$$E_{av} = \frac{1}{256} \sum_{i=0}^{15} \sum_{j=0}^{15} \int_{-T_s/2}^{T_s/2} [s_i^2(t) + s_j^2(t)] dt = 2 \left[\frac{1}{16} \sum_{i=0}^{15} \int_{-T_s/2}^{T_s/2} s_i^2(t) dt \right] = \frac{1}{4} \sum_{i=0}^7 \int_{-T_s/2}^{T_s/2} s_i^2(t) dt \quad (15)$$

which, again using Eqs. (7a) and (b), evaluates to

$$E_{av} = \left(\frac{7 + 2A + 15A^2}{16} \right) T_s = 0.9946T_s \quad (16)$$

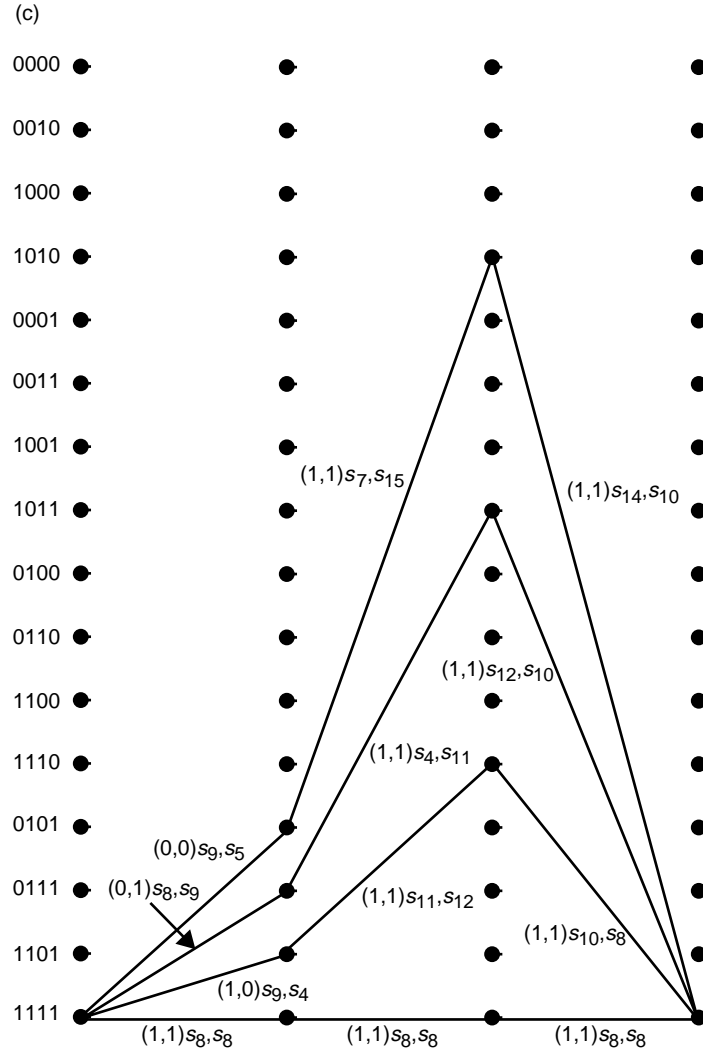


Fig. 9 (contd). Paths of length-3 branches starting and ending in (a) state 1, (b) state 2, and (c) state 16.

Since the average signal (symbol) energy is twice the average energy per bit, \bar{E}_b , then the normalized minimum squared Euclidean distance for the paths corresponding to starting and ending in the same state is

$$\frac{d_{\min}^2}{2\bar{E}_b} = \frac{16 \left[\frac{7}{4} - \frac{8}{3\pi} - A \left(\frac{3}{2} + \frac{4}{3\pi} \right) + A^2 \left(\frac{11}{4} + \frac{4}{\pi} \right) \right]}{(7 + 2A + 15A^2)} = 1.56 \quad (17)$$

Upon examination of all length-3 error-event paths that begin in one state and end in another, e.g., Figs. 10(a) and 10(b), no pair of paths with smaller normalized minimum squared Euclidean distance was found. Furthermore, by exhaustive search, it can be shown that the minimum squared Euclidean distance of Eq. (17) is the smallest over all pairs of paths that start in any state and end in any state regardless of the length of the path. Thus, *the normalized minimum squared Euclidean distance for the FQPSK scheme is given by Eq. (17).*

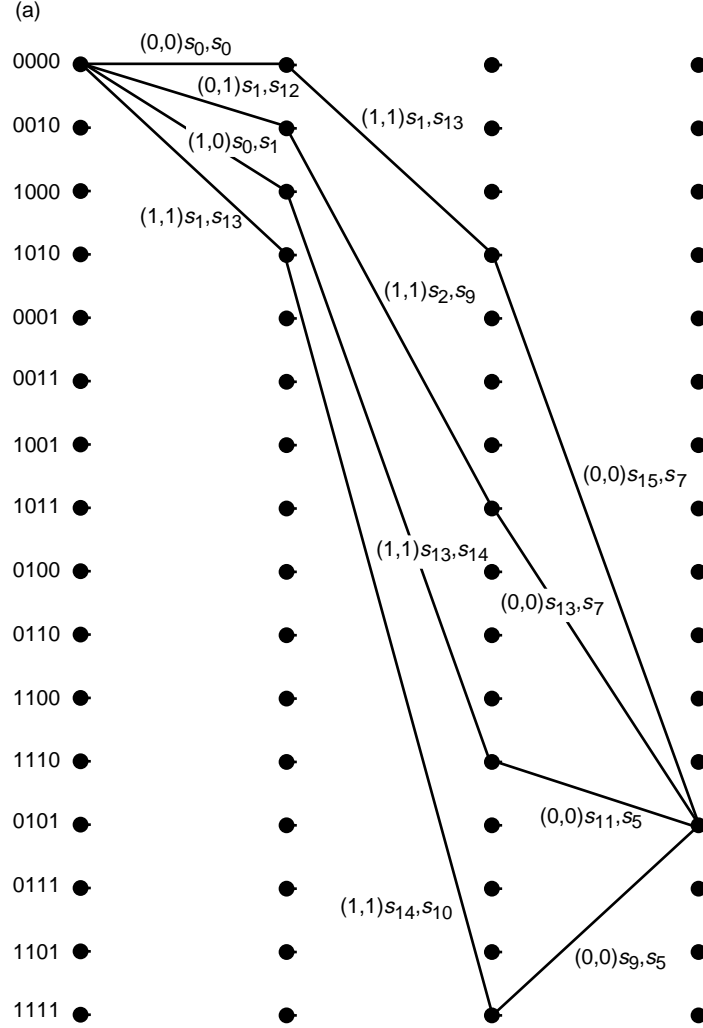


Fig. 10. Paths of length-3 branches starting in state 1 and ending in (a) state 13 and (b) state 2.

For the spectrally enhanced FQPSK using the waveforms of Eq. (8) as replacements for their equivalents in Eq. (7b), the minimum squared Euclidean distance over all length-3 trellis paths occurs, for example, between the first and second paths, starting and ending in state “0000” and is given by [see Fig. 9(a)]

$$d_{\min}^2 = \int_{-T_s/2}^{T_s/2} \left[(s_0(t) - s_1(t))^2 + (s_0(t) - s_{12}(t))^2 + (s_0(t) - s_3(t))^2 + (s_0(t) - s_4(t))^2 \right. \\ \left. + (s_0(t) - s_2(t))^2 + (s_0(t) - s_0(t))^2 \right] dt \quad (18)$$

Once again, evaluation of the squared Euclidean distances between the pairs of waveforms required in Eq. (18), using Eqs. (7a) and (7b) together now with Eq. (8) for their definitions, results, after much algebra, in

$$d_{\min}^2 = \left[\frac{3 - 6A + 15A^2}{4} \right] T_s = 1.564T_s \quad (19)$$

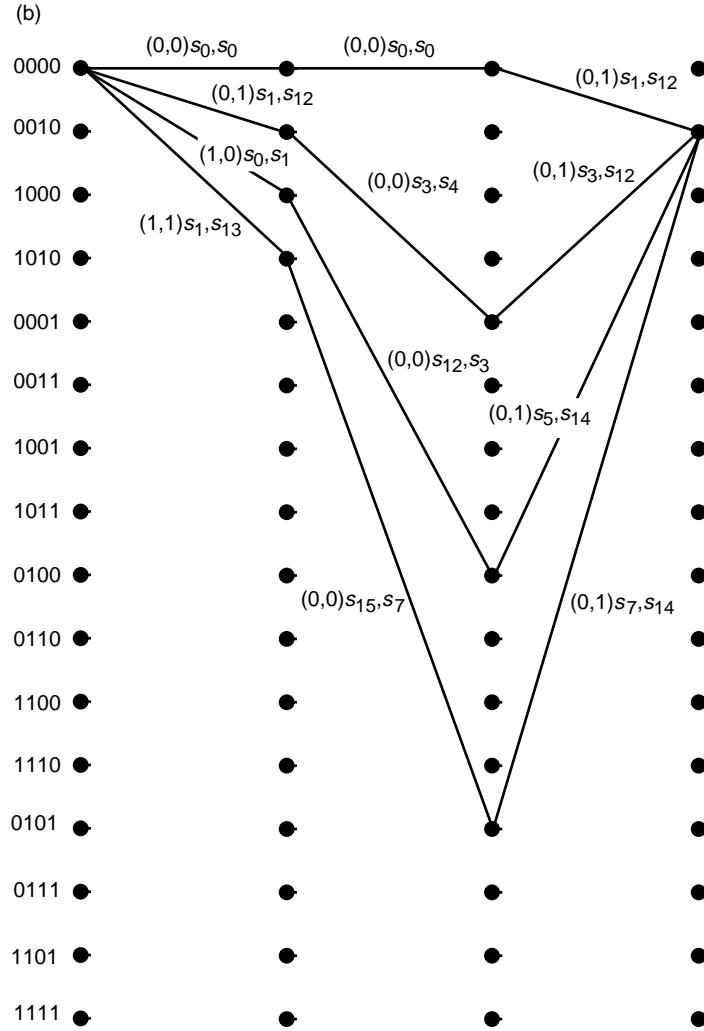


Fig. 10 (contd). Paths of length-3 branches starting in state 1 and ending in (a) state 13 and (b) state 2.

Likewise, the average signal energy is now

$$E_{av} = \left(\frac{\frac{21}{8} - \frac{8}{3\pi} - A \left(\frac{1}{4} - \frac{8}{3\pi} \right) + \frac{29}{8} A^2}{4} \right) T_s = 1.003 T_s \quad (20)$$

Thus, the normalized minimum squared Euclidean distance is

$$\frac{d_{\min}^2}{2E_b} = \frac{(3 - 6A + 15A^2)}{\frac{21}{8} - \frac{8}{3\pi} - A \left(\frac{1}{4} - \frac{8}{3\pi} \right) + \frac{29}{8} A^2} = 1.56 \quad (21)$$

which coincidentally is identical to that for FQPSK. Again there is no other pair of paths starting in any state and ending in any other that produces a smaller normalized minimum squared Euclidean distance.

Thus, we conclude that *the enhancement of FQPSK provided by using the waveforms of Eq. (8) as replacements for their equivalents in Eq. (7b) is significantly beneficial from a spectral standpoint with no penalty in receiver performance.*

In accordance with the foregoing representation of FQPSK as a trellis-coded modulation with 16 states, the optimum receiver (employing a Viterbi algorithm) for FQPSK is illustrated in Fig. 11. Later on, in Section VII, we shall illustrate average bit-error probability (BEP) results obtained from a simulation of this receiver. For the moment, we shall just compare its asymptotic (limit of infinite energy-to-noise ratio) performance with that of the optimum receiver for conventional uncoded offset QPSK (OQPSK). Since for the latter $d_{\min}^2/2\bar{E}_b = 2$, which is the same as that for BPSK [8], then we see that as a trade against the significantly improved power spectrum afforded by FQPSK and its enhanced version relative to that of OQPSK, *an asymptotic loss of only $10 \log(1/1.56) = 1.07$ dB is experienced.*⁷

VI. Symbol-by-Symbol Detection of FQPSK

In this section, we examine the performance of FQPSK when the detector makes decisions on a symbol-by-symbol basis, i.e., the inherent memory introduced by the trellis coding is ignored at the receiver. In order to understand how this can be accomplished, we first will establish the fact that, in any typical transmission interval, there exists a fixed number (in particular, eight) of possible waveforms (pulse shapes) that represent the FQPSK signal and each of these occurs with equal probability. As such, from symbol to symbol, the FQPSK signal appears as an equiprobable M -ary signaling set (with $M = 8$) and thus can be detected accordingly. With this in mind, we shall investigate two possible simple structures, both of which are suboptimum relative to the trellis-coded receiver previously discussed, that exploit the memory inherent in the modulation. The first structure is a standard offset QPSK receiver that employs simple integrate and dumps (I&Ds) as detectors and as such ignores the pulse shaping associated with the above-mentioned M -ary symbol-by-symbol representation. The second structure, which shall be referred to as an average matched-filter receiver, improves on the first one by replacing the I&Ds with matched filters, where the match is made to the *average* of the waveshapes in the M -ary signal set representation. Without loss in generality, the following description shall consider the case $n = 0$ corresponding to the I-channel interval $-T_s/2 \leq t \leq T_s/2$ and the Q-channel interval $0 \leq t \leq T_s$. We shall focus our attention on only the I channel and, as such, our initial goal will be to determine the eight equally likely waveforms that typify an FQPSK waveform in the interval $0 \leq t \leq T_s$. To avoid confusion with the previously defined signals, such as those defined, for example, in Eqs. (7a) and (7b), we shall use upper case notation, i.e., $S_i(t)$, $i = 0, 1, \dots, 7$ to describe these new waveforms. As we shall see, each of these new waveforms shall be composed of the latter half (i.e., that which occurs in the interval $0 \leq t \leq T_s/2$) of the I-channel waveform transmitted in the interval $-T_s/2 \leq t \leq T_s/2$ followed by the first half (i.e., that which occurs in the interval $T_s/2 \leq t \leq T_s$) of the I-channel waveform transmitted in the interval $T_s/2 \leq t \leq 3T_s/2$. As stated above, it will be shown that only eight such possible combinations can exist, and all are equiprobable.

A. Signal Representation

Let $d_{I0} = 1$, or equivalently from Eq. (10), $D_{I0} = 0$. Then, from Table 1, corresponding to $d_{I,-1} = 1$ (which results in $|(d_{I0} - d_{I,-1})/2| = 0$), there are four possible waveforms, $(s_0(t), s_1(t), s_2(t), \text{ and } s_3(t))$ that can be transmitted. Likewise corresponding to $d_{I,-1} = -1$ (which results in $|(d_{I0} - d_{I,-1})/2| = 1$), there are four possible waveforms, $(s_4(t), s_5(t), s_6(t), \text{ and } s_7(t))$, that can be transmitted. In each case, which of the four possible waveforms is transmitted depends on the difference values associated with $d_{Q,-2}, d_{Q,-1}$, and d_{Q0} in accordance with the second and third columns of Table 1. While, in principle, for each possible waveform $s_i(t)$ transmitted in $-T_s/2 \leq t \leq T_s/2$ there are eight possible waveforms that can be transmitted in $T_s/2 \leq t \leq 3T_s/2$, it is straightforward to show that only four

⁷ Needless to say, at smaller (finite) signal-to-noise ratios (SNRs), the loss between uncoded OQPSK and trellis-decoded FQPSK will be even less.

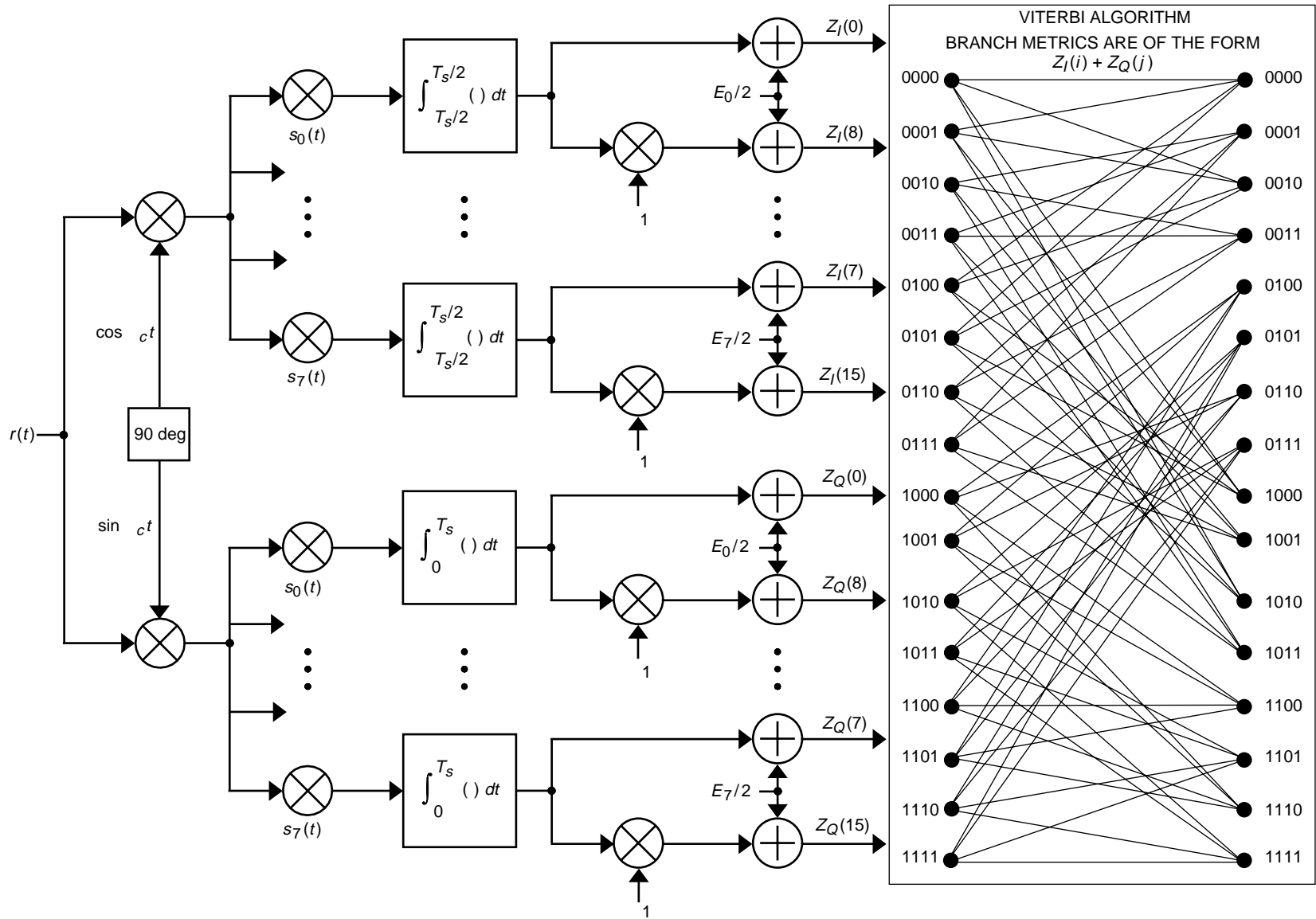


Fig. 11. The optimum trellis-coded receiver for FQPSK.

of these eight are unique. For example, if $s_0(t)$ is transmitted in $-T_s/2 \leq t \leq T_s/2$ (corresponding, as above, to $d_{I,-1} = 1$), then the four possible waveforms that can occur in $T_s/2 \leq t \leq 3T_s/2$ are $s_0(t)$, $s_1(t)$, $s_{12}(t)$, and $s_{13}(t)$. Thus, corresponding to the I-channel signal $s_I(t) = s_0(t)$ in the interval $-T_s/2 \leq t \leq T_s/2$, the transmitted signal $S_i(t)$ for the interval $0 \leq t \leq T_s$ is composed of the latter half of $s_0(t)$ followed by the first half of either $s_0(t)$, $s_1(t)$, $s_{12}(t)$, or $s_{13}(t)$. Looking at the definitions of $s_0(t)$, $s_1(t)$, $s_{12}(t)$, and $s_{13}(t)$ in Eqs. (7a) and (7b), we see that this yields only two distinct possibilities for $S_i(t)$, namely,

$$\left. \begin{aligned} S_0(t) &= A, \quad 0 \leq t \leq T_s \\ S_1(t) &= \begin{cases} A, & 0 \leq t \leq \frac{T_s}{2} \\ \sin \frac{\pi t}{2T_s}, & \frac{T_s}{2} \leq t \leq T_s \end{cases} \end{aligned} \right\} \quad (22a)$$

both of which are equally likely. Thus, in summary, for $d_{I0} = 1$ and $s_I(t) = s_0(t)$ in the interval $-T_s/2 \leq t \leq T_s/2$, there are only two waveforms that can occur in $0 \leq t \leq T_s$, namely, $S_0(t)$ and $S_1(t)$ of Eq. (22a).

Following a similar procedure (still for $d_{I0} = 1$), it can be shown that, for each of the other possible waveforms in $-T_s/2 \leq t \leq T_s/2$, i.e., $s_1(t)$, $s_2(t)$, $s_3(t)$, $s_4(t)$, $s_5(t)$, $s_6(t)$, and $s_7(t)$, there are four waveforms that can occur in the succeeding interval $T_s/2 \leq t \leq 3T_s/2$ but only two possible distinct waveforms in $0 \leq t \leq T_s$. These possibilities are summarized in Table 4.

The signals $S_2(t)$, $S_3(t)$, $S_4(t)$, $S_5(t)$, $S_6(t)$, and $S_7(t)$ are defined as

$$\left. \begin{aligned} S_2(t) &= 1 - (1 - A) \cos^2 \frac{\pi t}{T_s}, \quad 0 \leq t \leq T_s \\ S_3(t) &= \begin{cases} 1 - (1 - A) \cos^2 \frac{\pi t}{T_s}, & 0 \leq t \leq \frac{T_s}{2} \\ \sin \frac{\pi t}{2T_s}, & \frac{T_s}{2} \leq t \leq T_s \end{cases} \\ S_4(t) &= \begin{cases} A \sin \frac{\pi t}{2T_s}, & 0 \leq t \leq \frac{T_s}{2} \\ A, & \frac{T_s}{2} \leq t \leq T_s \end{cases} \\ S_5(t) &= A \sin \frac{\pi t}{2T_s}, \quad 0 \leq t \leq T_s \\ S_6(t) &= \begin{cases} \sin \frac{\pi t}{2T_s}, & 0 \leq t \leq \frac{T_s}{2} \\ 1 - (1 - A) \cos^2 \frac{\pi t}{T_s}, & \frac{T_s}{2} \leq t \leq T_s \end{cases} \\ S_7(t) &= \sin \frac{\pi t}{2T_s}, \quad 0 \leq t \leq T_s \end{aligned} \right\} \quad (22b)$$

Table 4. Possible $S_i(t)$'s for successive combinations of $s_i(t)$.

Signal in $-T_s/2 \leq t \leq T_s/2$	Signal in $T_s/2 \leq t \leq 3T_s/2$	Signal in $0 \leq t \leq T_s$
$s_1(t)$	$s_2(t), s_3(t), s_{14}(t), s_{15}(t)$	$S_2(t), S_3(t)$
$s_2(t)$	$s_0(t), s_1(t), s_{12}(t), s_{13}(t)$	$S_0(t), S_1(t)$
$s_3(t)$	$s_2(t), s_3(t), s_{14}(t), s_{15}(t)$	$S_2(t), S_3(t)$
$s_4(t)$	$s_0(t), s_1(t), s_{12}(t), s_{13}(t)$	$S_4(t), S_5(t)$
$s_5(t)$	$s_2(t), s_3(t), s_{14}(t), s_{15}(t)$	$S_6(t), S_7(t)$
$s_6(t)$	$s_0(t), s_1(t), s_{12}(t), s_{13}(t)$	$S_4(t), S_5(t)$
$s_7(t)$	$s_2(t), s_3(t), s_{14}(t), s_{15}(t)$	$S_6(t), S_7(t)$

In comparing the performances of the suboptimum receivers of FQPSK with that of uncoded OQPSK, we shall reference them all to the same average transmitted power, \bar{P} , or, equivalently, the same average energy-per-bit-to-noise spectral density ratio, $\bar{E}_b/N_0 = \bar{P}T_b/N_0$. In order to do this, we first must compute the energy $E_i = \int_0^{T_s} S_i^2(t) dt$ of each of the waveforms in Eqs. (22a) and (22b) and take their average. The results are summarized below:

$$\left. \begin{aligned} E_0 &= A^2 T_s \\ E_1 &= \frac{3}{4} A^2 T_s \\ E_2 &= \left(\frac{3}{8} + \frac{1}{4} A + \frac{3}{8} A^2 \right) T_s \\ E_3 &= \left(\frac{7}{16} + \frac{1}{8} A + \frac{3}{16} A^2 \right) T_s \\ E_4 &= \frac{3}{4} A^2 T_s \\ E_5 &= \frac{1}{2} A^2 T_s \\ E_6 &= \left(\frac{7}{16} + \frac{1}{8} A + \frac{3}{16} A^2 \right) T_s \\ E_7 &= \frac{1}{2} T_s \end{aligned} \right\} \quad (23)$$

and

$$\bar{E} = \frac{1}{8} \sum_{i=0}^7 E_i = \left(\frac{7 + 2A + 15A^2}{32} \right) T_s \quad (24)$$

Since the average power transmitted in the I channel is one-half the total $(I + Q)$ average transmitted power, \bar{P} , then we have

$$\frac{\bar{P}}{2} = \frac{\bar{E}}{T_s} = \frac{7 + 2A + 15A^2}{32} \quad (25)$$

or, equivalently, the average energy per symbol is given by

$$\bar{P}T_s \triangleq \bar{E}_s = 2\bar{E}_b = \frac{7 + 2A + 15A^2}{16}T_s \quad (26)$$

Comparing Eq. (26) with Eq. (16), we see that the evaluation of average energy per symbol based on the symbol-by-symbol M -ary representation of FQPSK is identical to that obtained from the representation as a trellis-coded modulation. Also note that for $A = 1$, which corresponds to SQORC modulation, we have $\bar{E}_s = (4/3)T_s$, which is consistent with the original discussions of this modulation in [7].

B. Suboptimum Receivers

In accordance with our discussion at the beginning of Section VI, we shall consider two suboptimum receivers for symbol-by-symbol detection of FQPSK, the difference being the manner in which the detector is matched to the received signal. For the average matched-filter case, the detector is implemented as a multiplication of the received signal by $\bar{S}(t) \triangleq (1/8) \sum_{i=0}^7 S_i(t)$, followed by an I&D filter and binary hard-decision device (see Fig. 11). For the OQPSK receiver, the detector is purely I&D (i.e., matched to a rectangular pulse), which is tantamount to assuming $\bar{S}(t) = 1$. Thus, we can cover both cases at the same time, leaving $\bar{S}(t)$ as an arbitrary premultiplication pulse shape, and later substitute the appropriate waveform.

Assuming the M -ary symbol-by-symbol representation of FQPSK just described, then the decision variable Z in Fig. 12 is given by

$$Z = \int_0^{T_s} S(t) \bar{S}(t) dt + \int_0^{T_s} n(t) \bar{S}(t) dt \triangleq \bar{Z} + N \quad (27)$$

where $S(t)$ is the transmitted waveform in $0 \leq t \leq T_s$ and ranges over the set of eight waveforms in Eqs. (22a) and (22b) with equal probability. The random variable N is zero-mean Gaussian with variance $\sigma_N^2 = N_0 E_{\bar{S}}/2$, where $E_{\bar{S}} \triangleq \int_0^{T_s} \bar{S}^2(t) dt$. Thus, the I-channel symbol-error probability (same as the Q-channel symbol-error probability) conditioned on the particular $S(t) = S_i(t)$ corresponding to the transmitted symbol $d_{I0} = 1$ is easily shown to be

$$P_{si}(E) = \frac{1}{2} \operatorname{erfc} \left(\sqrt{\frac{1}{N_0} \frac{\left(\int_0^{T_s} S_i(t) \bar{S}(t) dt \right)^2}{E_{\bar{S}}}} \right) \quad (28)$$

and, hence, the average symbol-error probability is given by

$$P_s(E) \triangleq \frac{1}{8} \sum_{i=0}^7 P_{si}(E) \quad (29)$$

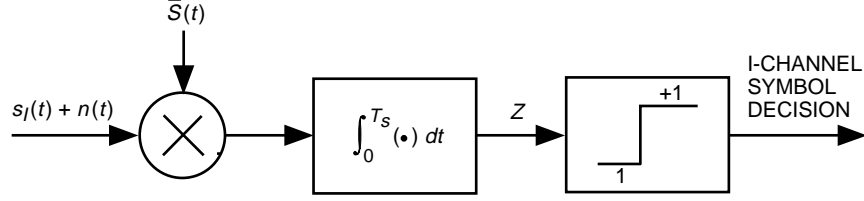


Fig. 12. The suboptimum receiver for FQPSK based on symbol-by-symbol detection.

1. Conventional OQPSK Receiver. For the conventional OQPSK receiver, we set $\bar{S}(t) = 1$, or, equivalently, $E_{\bar{S}} = T_s$ in Eq. (28), resulting in

$$P_{si}(E) = \frac{1}{2} \operatorname{erfc} \left(\sqrt{\frac{T_s}{N_0} \left(\frac{1}{T_s} \int_0^{T_s} S_i(t) dt \right)^2} \right) = \frac{1}{2} \operatorname{erfc} \left(\sqrt{\left(\frac{32}{7 + 2A + 15A^2} \right) \frac{\bar{E}_b}{N_0} \left(\frac{E_i}{T_s} \right)^2} \right) \quad (30)$$

Substituting the average energies from Eq. (23) in Eq. (30) for each signal and then performing the average as in Eq. (29) gives the final desired result for average symbol-error probability, namely,

$$\begin{aligned} P_{si}(E) = & \frac{1}{16} \operatorname{erfc} \left(\sqrt{\left(\frac{32A^4}{7 + 2A + 15A^2} \right) \frac{\bar{E}_b}{N_0}} \right) + \frac{1}{8} \operatorname{erfc} \left(\sqrt{\left(\frac{18A^4}{7 + 2A + 15A^2} \right) \frac{\bar{E}_b}{N_0}} \right) \\ & + \frac{1}{16} \operatorname{erfc} \left(\sqrt{\left(\frac{(3 + 2A + 3A^2)^2}{2(7 + 2A + 15A^2)} \right) \frac{\bar{E}_b}{N_0}} \right) + \frac{1}{8} \operatorname{erfc} \left(\sqrt{\left(\frac{(7 + 2A + 3A^2)^2}{8(7 + 2A + 15A^2)} \right) \frac{\bar{E}_b}{N_0}} \right) \\ & + \frac{1}{16} \operatorname{erfc} \left(\sqrt{\left(\frac{8A^4}{7 + 2A + 15A^2} \right) \frac{\bar{E}_b}{N_0}} \right) + \frac{1}{16} \operatorname{erfc} \left(\sqrt{\left(\frac{8}{7 + 2A + 15A^2} \right) \frac{\bar{E}_b}{N_0}} \right) \end{aligned} \quad (31)$$

2. Average Matched-Filter Receiver. For the average matched filter, we need to compute the correlations of each of the pulse shapes in Eqs. (22a) and (22b) with the average pulse shape $\bar{S}(t)$ and also the energy $E_{\bar{S}}$ of the average pulse shape. Rewriting Eq. (28) in a form analogous to Eq. (30), namely,

$$P_{si}(E) = \frac{1}{2} \operatorname{erfc} \left(\sqrt{\left(\frac{32}{7 + 2A + 15A^2} \right) \frac{\bar{E}_b}{N_0} \frac{\left(\frac{1}{T_s} \int_0^{T_s} S_i(t) \bar{S}(t) dt \right)^2}{\frac{1}{T_s} E_{\bar{S}}}} \right) \quad (32)$$

then the results necessary to evaluate Eq. (32) are tabulated below:

$$\left. \begin{aligned}
 \frac{1}{T_s} \int_0^{T_s} S_0(t) \bar{S}(t) dt &= \frac{A}{4} \left[\frac{1}{2} + \frac{2}{\pi} + A \left(\frac{3}{2} + \frac{2}{\pi} \right) \right] \\
 \frac{1}{T_s} \int_0^{T_s} S_1(t) \bar{S}(t) dt &= \frac{1}{T_s} \int_0^{T_s} S_4(t) \bar{S}(t) dt = \frac{A}{4} \left[\frac{1}{2} + \frac{5}{3\pi} + A \left(1 + \frac{7}{3\pi} \right) \right] \\
 \frac{1}{T_s} \int_0^{T_s} S_2(t) \bar{S}(t) dt &= \frac{1}{4} \left[\frac{3}{8} + \frac{4}{3\pi} + A \left(\frac{3}{4} + \frac{2}{\pi} \right) + A^2 \left(\frac{7}{8} + \frac{2}{3\pi} \right) \right] \\
 \frac{1}{T_s} \int_0^{T_s} S_3(t) \bar{S}(t) dt &= \frac{1}{T_s} \int_0^{T_s} S_6(t) \bar{S}(t) dt = \frac{1}{4} \left[\frac{7}{16} + \frac{4}{3\pi} + A \left(\frac{5}{8} + \frac{7}{3\pi} \right) + A^2 \left(\frac{7}{16} + \frac{1}{3\pi} \right) \right] \\
 \frac{1}{T_s} \int_0^{T_s} S_5(t) \bar{S}(t) dt &= \frac{A}{2} \left[\frac{1}{4} + \frac{2}{3\pi} + A \left(\frac{1}{4} + \frac{4}{3\pi} \right) \right] \\
 \frac{1}{T_s} \int_0^{T_s} S_7(t) \bar{S}(t) dt &= \frac{1}{2} \left[\frac{1}{4} + \frac{2}{3\pi} + A \left(\frac{1}{4} + \frac{4}{3\pi} \right) \right]
 \end{aligned} \right\} \quad (33)$$

and

$$\frac{1}{T_s} E_{\bar{S}} = \frac{1}{16} \left[(1+A)^2 \left(\frac{3}{2} + \frac{4}{\pi} \right) + \frac{3}{8} (1-A)^2 - 2(1-A^2) \left(\frac{1}{2} + \frac{2}{3\pi} \right) \right] \quad (34)$$

Finally, substituting Eqs. (33) and (34) into Eq. (32) and averaging as in Eq. (29) gives the desired result, which we shall not explicitly write in closed form.

VII. Average Bit-Error Probability Performance

The average BEP of the two suboptimum receivers discussed in Section VI is illustrated in Fig. 13 for the case $A = 1/\sqrt{2}$, which is the usual value chosen for implementation of FQPSK. These results are obtained directly from Eq. (31) for the OQPSK receiver and from Eq. (29) in combination with Eqs. (32) through (34) for the average matched-filter receiver. Also included in this figure is the performance corresponding to the optimum uncoded OQPSK receiver (same performance as for uncoded BPSK), i.e., $P_b(E) = 1/2 \operatorname{erfc} \sqrt{E_b/N_0}$, as well as simulation results obtained for the optimum trellis-coded receiver of Fig. 11. We observe, as one might expect, that the average matched-filter receiver outperforms the OQPSK receiver, since an attempt to match the transmitted pulse shape (even on an average basis) is better than no attempt at all. We also observe that the trellis-coded receiver at $P_b(E) = 10^{-4}$ is more than 1-dB better than the average matched-filter receiver, granted that the latter is considerably simpler in implementation. Finally, for the same average BEP, the trellis-coded receiver of FQPSK is only about 0.6-dB inferior to uncoded OQPSK performance, which is a relatively small penalty paid for the vast improvement in PSD afforded by the former relative to the latter.

VIII. Conclusion

By offering a new interpretation of unfiltered FQPSK in terms of a full (as opposed to a half) symbol mapping of an I and Q error-correction coded modulation, we have been able to provide methods for enhancing its spectral properties as well as its error-probability performance. Similar methods can be applied to filtered versions of FQPSK.

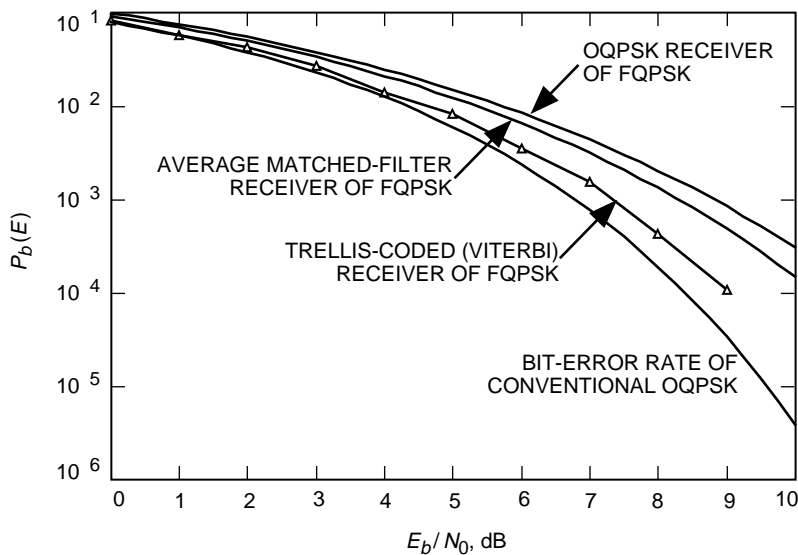


Fig. 13. Bit-error performance of various receivers of FQPSK modulation (the reference curve is the bit-error rate of OQPSK).

Acknowledgment

The authors wish to gratefully acknowledge Meera Srinivasan for simulating the optimum trellis-coded receiver of FQPSK (Fig. 11) and supplying the accompanying numerical results shown in Fig. 13. Additional thanks also are due to Meera for having spent considerable time independently verifying much of what is presented here, which is immeasurably important in establishing the credence of our results.

References

- [1] K. Feher and S. Kato, U.S. Patent 4,567,602; K. Feher, U.S. Patent 5,491,457; and K. Feher, U.S. Patent 5,784,402.
- [2] K. Feher, *Wireless Digital Communications: Modulation and Spread Spectrum Applications*, Englewood Cliffs, New Jersey: Prentice-Hall, 1995.
- [3] K. Feher, "FQPSK Doubles Spectral Efficiency of Operational Telemetry Systems," European Telemetry Conference, ETC '98, Garmish-Partenkirchen, Germany, May 5–8, 1998.
- [4] S. Kato and K. Feher, "XPSK: A New Cross-Correlated Phase-Shift-Keying Modulation Technique," *IEEE Transactions on Communications*, vol. 31, no. 5, pp. 701–707, May 1983.
- [5] W. L. Martin, T-Y. Yan, and L. V. Lam, "CCSDS-SFCG: Efficient Modulation Methods Study at NASA/JPL, Phase 3: End-to-End Performance," SFCG Meeting, Galveston, Texas, September 1997.

- [6] T. Le-Ngoc, K. Feher, and H. Pham Van, “New Modulation Techniques for Low-Cost Power and Bandwidth Efficient Satellite Earth Stations,” *IEEE Transactions on Communications*, vol. 30, no. 1, pp. 275–283, January 1982.
- [7] M. C. Austin and M. V. Chang, “Quadrature Overlapped Raised-Cosine Modulation,” *IEEE Transactions on Communications*, vol. 29, no. 3, pp. 237–249, March 1981.
- [8] J. B. Anderson, T. Aulin, and C.-E. Sundberg, *Digital Phase Modulation*, New York: Plenum Press, p. 29, 1986.

[This page intentionally left blank.]

CCSDS Panel 1E

Document 00/26

Improved GMSK ($BT_b=0.25$) Demodulation PerformanceEnrico Vassallo¹, Monica Visintin²

Abstract

The use of a Soft-Output-Viterbi detector for the GMSK $BT_b=0.25$ modulation is investigated. The overall CCSDS encoding scheme (Reed-Solomon and convolutional codes) is considered, and the bit error rate is evaluated and compared to those of the other transmission schemes analyzed in previous work.

1. Introduction

Some bandwidth efficient modulation schemes have been deeply analyzed in previous work [1, 2, 3, 4, 5, 9], as candidates for adoption by CCSDS space research missions. Among the considered modulations, GMSK turned out to be a good choice, since it is the less sensitive to the presence of narrow or wide band interference, and it does not suffer from the presence of nonlinear amplifiers. Moreover, a complete simulation of the overall transmission system, including the concatenated (Reed-Solomon and convolutional) co-decoders, showed that GMSK with $BT_b=0.5$ has a performance similar to that of an ideal unfiltered BPSK modulation (the estimated loss is equal to 0.01 dB at a bit error rate equal to $1.e-6$), with a 21-fold reduction in bandwidth occupancy. GMSK with $BT_b=0.25$ has an even smaller bandwidth occupancy (25-fold reduction with respect to BPSK), but showed a slightly higher loss (0.16 dB at $BER=1.e-6$) with respect to BPSK. However, in [3, 5] the receiver for the GMSK modulator with $BT_b=0.25$ was not the optimum one, and a question was left regarding the gain that an optimum receiver could produce. This paper analyzes the performance of the overall transmission system, including the optimum but more complex receiver, and compares it to the performance of the systems considered in [3, 5, 9].

2. System description

It was shown in [2] that three types of receiver can be used with a GMSK modulator:

- **type 1 receiver:** a filter with impulse response $C_0(-t)$, a sampler and a zero-threshold detector
- **type 2 receiver:** a filter with impulse response $C_0(-t)$, a Wiener filter which reduces the intersymbol interference, a sampler and a zero-threshold detector
- **type 3 receiver:** two parallel filters with impulse responses $C_0(-t)$ and $C_1(-t)$, respectively, a sampler and a 4-state Viterbi detector

being $C_0(t)$ and $C_1(t)$ the two main pulses in the Laurent's decomposition of the GMSK signal [8]. It was also shown that the type 1 receiver is adequate for the case of a GMSK signal with bandwidth-bit time product $BT_b=0.5$, since in this case pulse $C_0(t)$ conveys practically all the signal energy and substantially no intersymbol interference arises. In the case $BT_b=0.25$, a type 1 receiver gives a poor performance, while a type 3 receiver is optimum; a type 2 receiver gives a performance which stands halfway between that of the other two receivers (see figure 1 taken from [2]).

¹ ESOC, European Space Agency

² Dipartimento di Elettronica, Politecnico di Torino

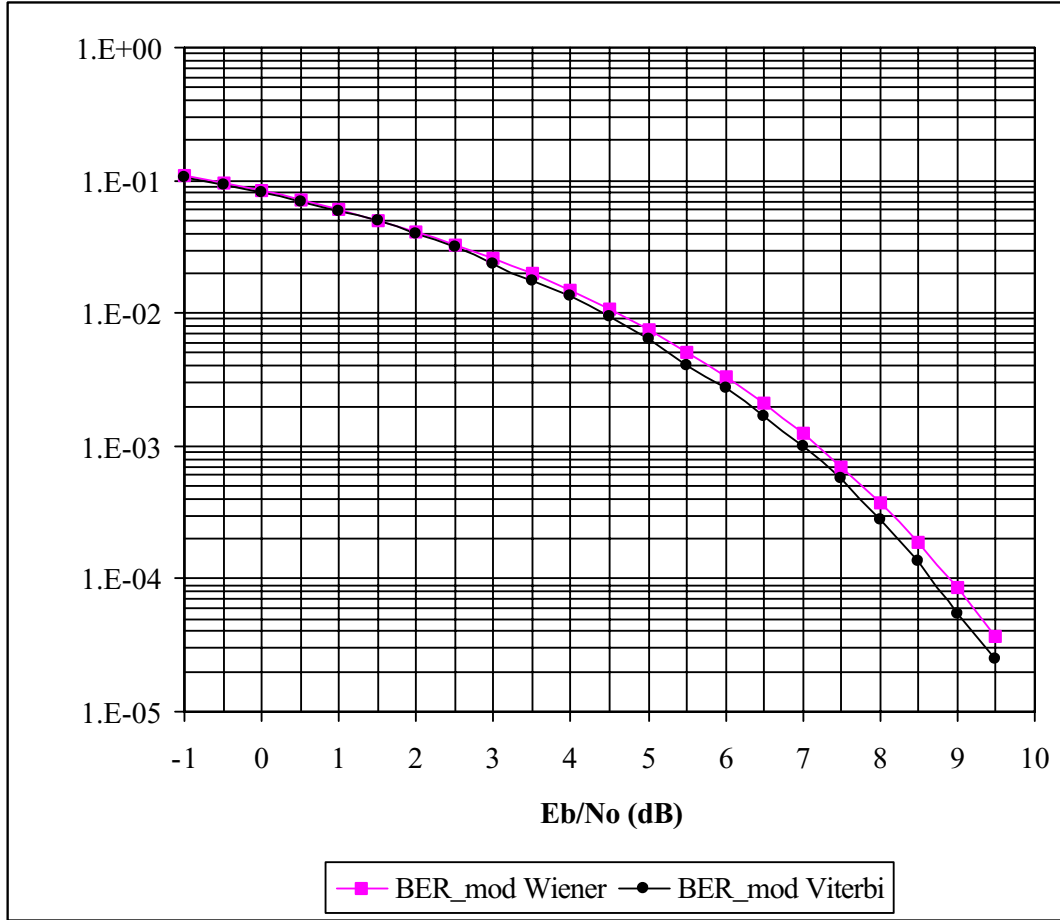


Figure 1: Measured BER at the output of $BT_b=0.25$ GMSK receivers of type 2 (with the Wiener filter) and of type 3 (with the Viterbi detector).

When the overall transmission scheme was considered in [3, 5], a type 2 receiver was used since it is simple (with respect to a type 1 receiver it requires two 3-taps digital filters in addition), and gives a reasonable overall performance; moreover a type 2 receiver naturally gives a soft input to the subsequent Viterbi decoder, as required by CCSDS standards. However a type 3 receiver should guarantee a better overall performance.

The type 3 receiver Viterbi detector is described in the literature [7] as a hard detector, i.e. it delivers the decided bits to the subsequent stage without further information about their reliability. On the other hand, the transmission system under analysis assumes that a 3-bit soft Viterbi decoder is used at the output of the GMSK detector. Therefore the GMSK Viterbi detector described in [7] was modified to produce a soft output, with the use of a Soft-Output Viterbi Algorithm (SOVA) as described in [6]. Due to the fact that the Viterbi detector tends to generate bursts of errors, a block interleaver was placed between the convolutional encoder and the GMSK modulator, and a corresponding de-interleaver was placed between the GMSK SOVA detector and the Viterbi decoder for the convolutional encoding. The resulting overall transmission scheme is depicted in figure 2.

3. Simulation results

Figure 3 and table 1 show the simulation results: the bit error rates measured at the output of a type 2 and type 3 receivers (BER_{mod}) are substantially equal in the considered E_b/N_0 range, while the bit

error rates at the output of the Viterbi convolutional decoder (BER_{vit}) are lower for a type 3 receiver; in the case of the type 3 receiver, BER at the output of the Reed-Solomon decoder was estimated using the approximate relationship between BER and BER_{vit} described in [3, Chapter 4] and in [5]. Note that E_b is the energy of one information bit.

Figure 4 shows the BER curves for all the mo-demodulation schemes considered in [3, 5], and the new BER curve for the $BT_b=0.25$ GMSK modulator, with the type 3 receiver considered in the present work. Table 2 recaps the end-to-end losses over a saturated channel relative to ideal unfiltered BPSK at the required BER of $1.e-6$. It is the same table contained in [5] complemented by the type 3 receiver data for the $BT_b=0.25$ GMSK modulation.

It is apparent that the $BT_b=0.5$ GMSK modulator with a type 1 receiver is still the best choice in terms of BER. However, for applications requiring the smallest occupied bandwidth, $BT_b=0.25$ GMSK with the type 3 receiver has a residual loss of only 0.11 dB with respect to ideal unfiltered BPSK.

E_b/N_0 (dB)	BER_{mod} SOVA	BER_{vit} SOVA	BER SOVA	BER_{mod} Wiener	BER_{vit} Wiener	BER Wiener
2.0	0.122	2.77E-2	3.60E-2	0.123	3.10E-2	4.50E-2
2.1	0.119	2.26E-2	1.73E-2	0.121	2.59E-2	2.77E-2
2.2	0.116	1.91E-2	6.69E-3	0.118	2.13E-2	1.28E-2
2.3	0.114	1.56E-2	1.53E-3	0.115	1.79E-2	4.02E-3
2.4	0.111	1.29E-2	2.88E-4	0.113	1.45E-2	8.13E-4
2.5	0.109	1.06E-2	4.90E-5	0.110	1.19E-2	1.65E-4
2.6	0.106	8.41E-3	5.95E-6	0.107	9.60E-3	1.65E-5
2.7	0.103	6.50E-3	6.55E-7	0.105	7.79E-3	2.15E-6
2.75				0.104	6.95E-3	6.43E-7

Table 1: Simulation results for a type 3 (SOVA) and a type 2 (Wiener) receiver; the shadowed BER values were analytically evaluated from the corresponding values of BER_{vit} .

modulation scheme	E_b/N_0 at $BER=10^{-6}$	Loss (dB)at $BER=10^{-6}$
Unfiltered BPSK	2.57	0.00
Butt. OQPSK	2.92	0.35
SRRC-a OQPSK	2.75	0.18
SRRC-b OQPSK	3.14	0.57
GMSK $BT_b=0.5$ (type 1 rx)	2.58	0.01
GMSK $BT_b=0.25$ (type 2 rx)	2.73	0.16
GMSK $BT_b=0.25$ (type 3 rx)	2.68	0.11

Table 2: Comparison of end-to-end losses

4. Conclusions

The use of a more complex receiver (type 3) allows for a decrease of the end-to-end loss of the $BT_b=0.25$ GMSK modulation relative to ideal unfiltered BPSK from 0.16 dB (type 2 receiver) to 0.11 dB at the required BER of $1.e-6$, an almost negligible value even for systems with the most stringent bandwidth requirements. Receiver complexity is doubled with respect to the simpler receiver previously proposed (type 2), however, it still can be accommodated in today's FPGA (and obviously ASIC) technology.

GMSK with $BT_b=0.5$ has 0.01 dB end-to-end losses in BER performance even with the reduced complexity of the simplified type 1 receiver, but has a larger bandwidth occupancy. It is therefore deemed a promising choice for Deep Space missions.

References

- [1] G. Povero, M. Visintin, *Interference Susceptibility of Selected Bandwidth-Efficient Modulation Schemes, ESA Internal Report, Part I* Support of ESA/ESOC activities in SFCG/CCSDS on advanced modulation schemes, April 1999.
- [2] G. Povero, M. Visintin, *Interference Susceptibility of Selected Bandwidth-Efficient Modulation Schemes, ESA Internal Report, Part II*, Support of ESA/ESOC activities in SFCG/CCSDS on advanced modulation schemes, April 2000.
- [3] G. Povero, M. Visintin, *Interference Susceptibility of Selected Bandwidth-Efficient Modulation Schemes, ESA Internal Report, Part III*, Support of ESA/ESOC activities in SFCG/CCSDS on advanced modulation schemes, April 2000.
- [4] G. Povero, E. Vassallo, M. Visintin, *End-to-End Losses of Selected Bandwidth-Efficient Modulation Schemes*, CCSDS Panel 1E Doc. 99/45, Noordwijk, October 1999
- [5] G. Povero, E. Vassallo, M. Visintin, *End-to-End Performance of Selected Modulation Schemes, Part II: Coded Channels*, CCSDS Panel 1E Doc. 00/11, Annapolis, May 2000
- [6] J. Hagenauer, P. Hoerer, "A Viterbi Algorithm with Soft-Decision Outputs and its *Proceedings of GLOBECOM 1989*, pp. 1680-1686
- [7] G. K. Kaleh, *Simple Coherent Receivers for Partial Response Continuous Phase Modulation*, IEEE JSAC Vol. 7, N. 9, Dec. 1989, pp. 1427-1436
- [8] P. A. Laurent, *Exact and Approximate Construction of Digital Phase Modulations by Superposition of Amplitude Modulated Pulses (AMP)*, IEEE Trans. Commun., Vol. COM-34, N. 2, Feb. 1986, pp. 150-160
- [9] D. Lee, T.-Y. Yan, *Performance of Selected Bandwidth Efficient Modulations*, CCSDS Panel 1E Doc. 99/34, Noordwijk, October 1999.

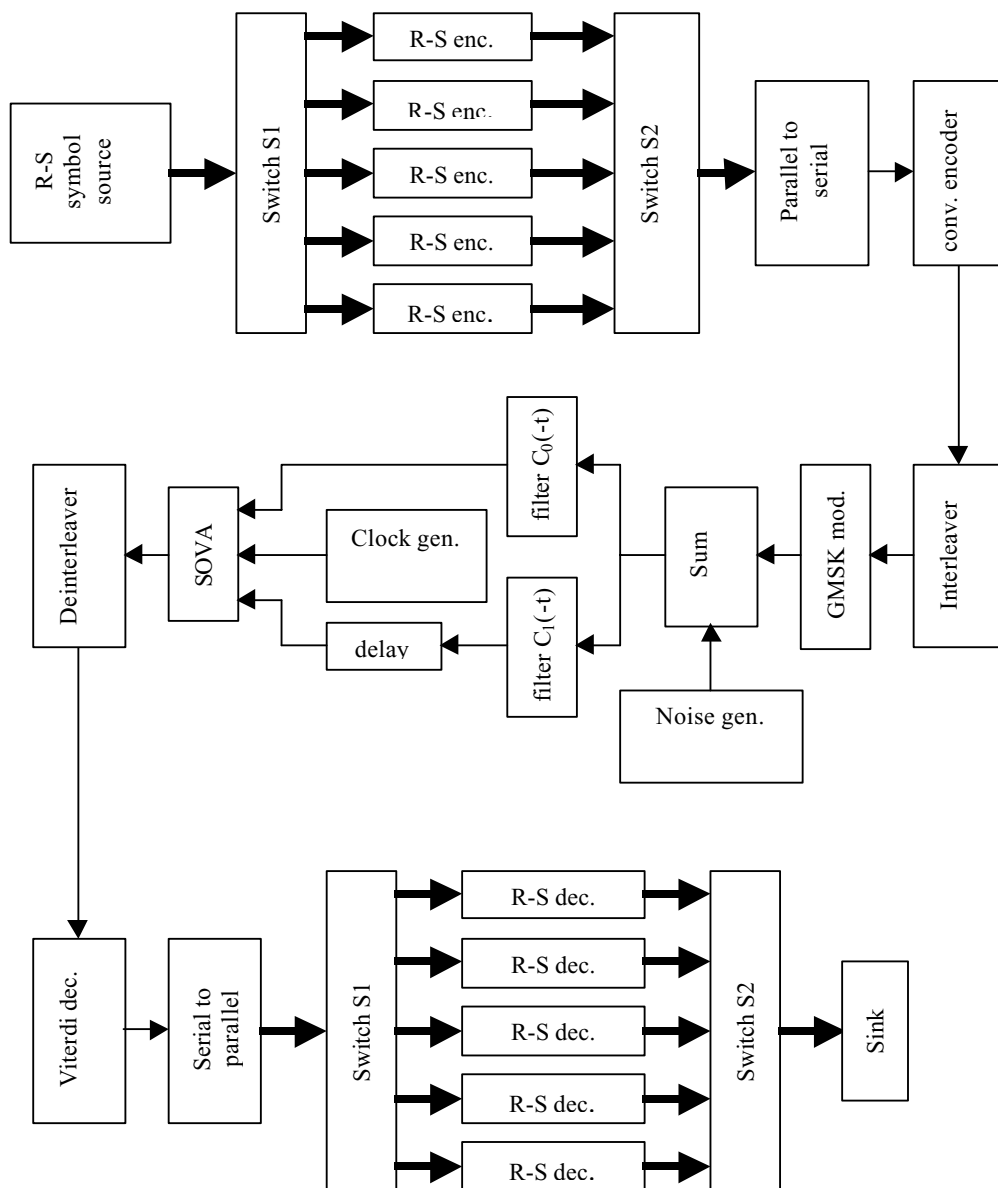


Figure 2: The transmission scheme

Note: SSPA/TWTA after GMSK modulator not shown;
differential pre-coder included in GMSK modulator.

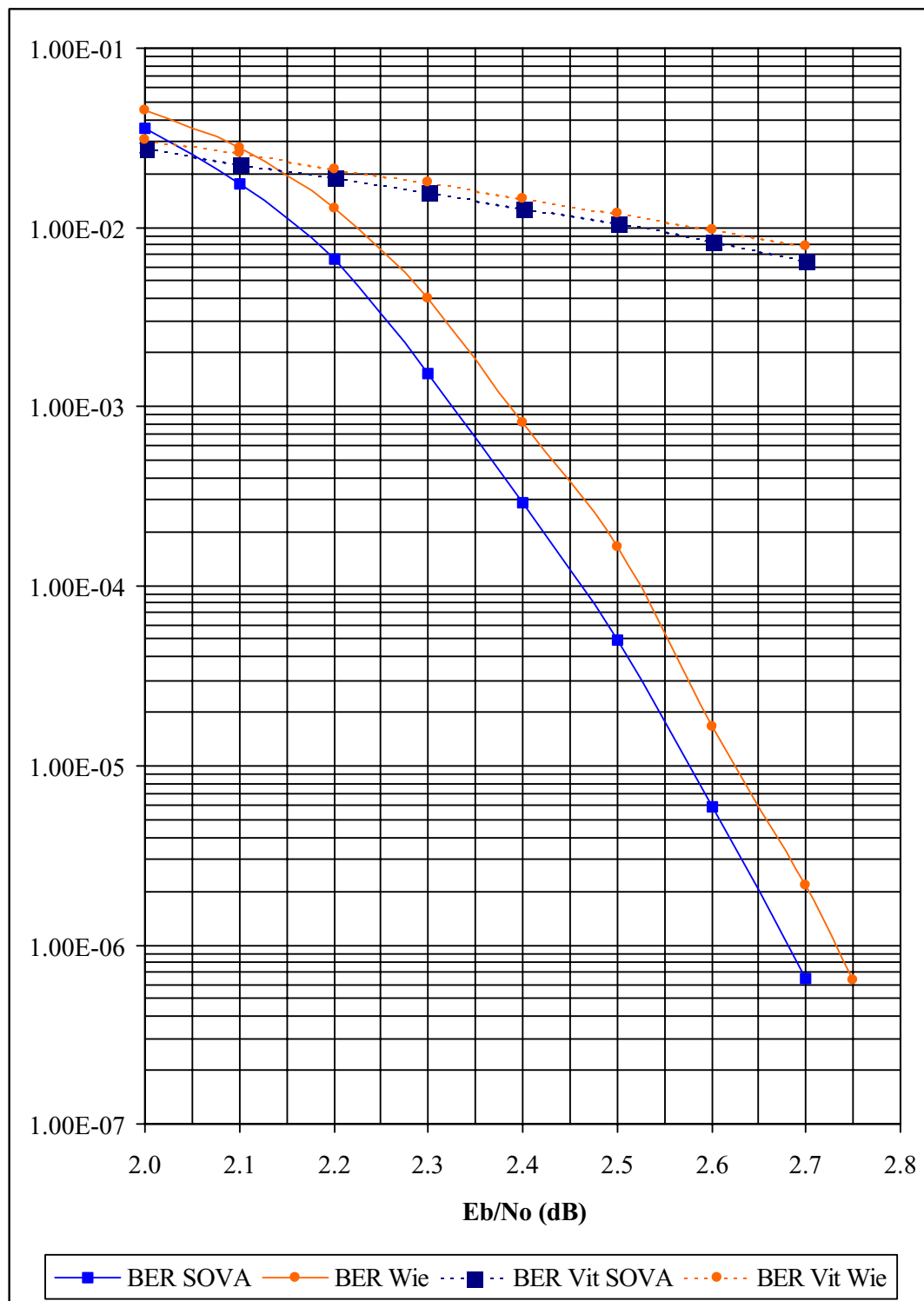


Figure 3: Comparison of BER and BER_{vit} for a type 3 (SOVA) and a type 2 (Wiener) receivers for the GMSK encoded system with $BT_b=0.25$.

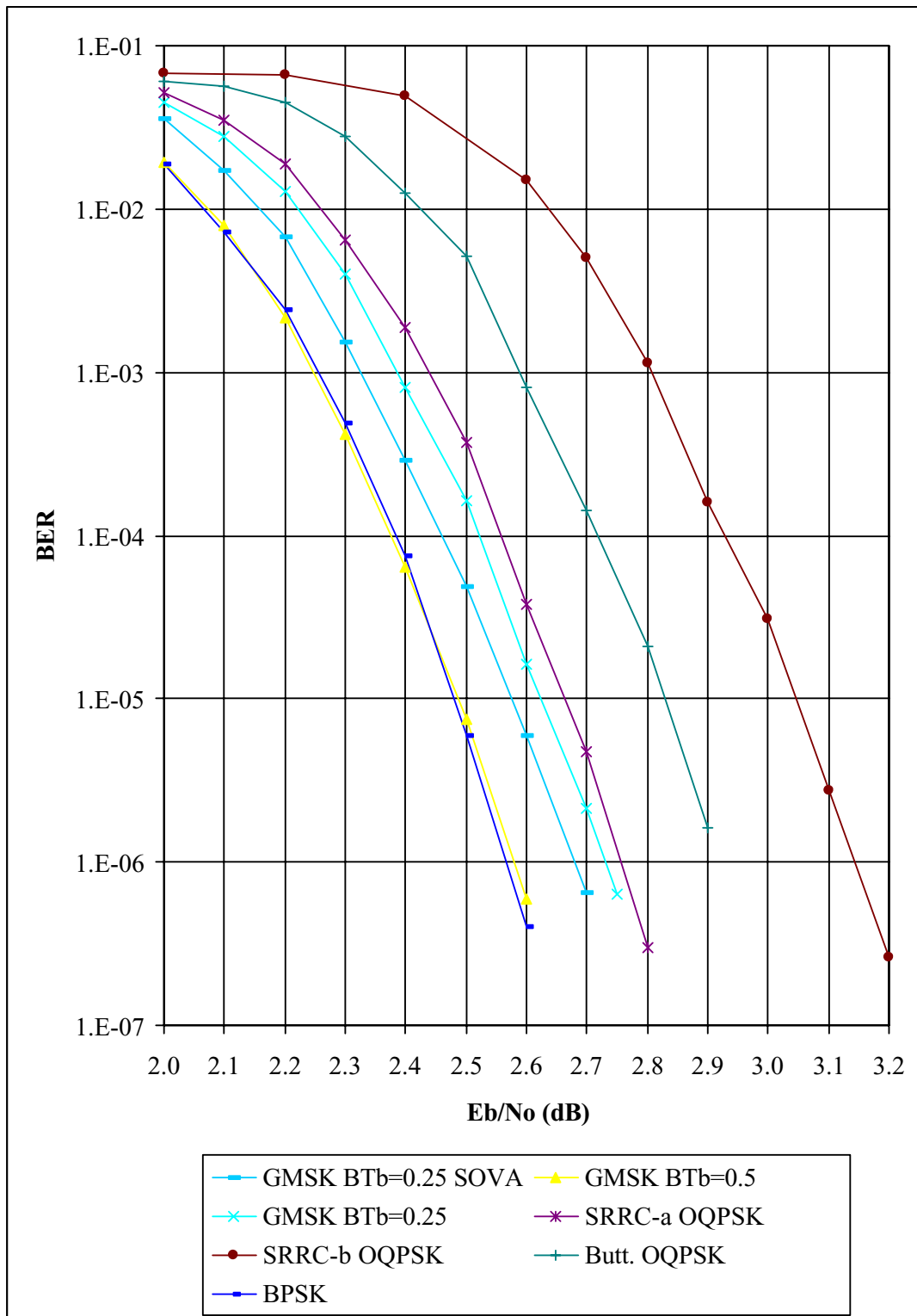


Figure 4: Comparison among all the considered modulation schemes in terms of BER at the output of the Reed-Solomon decoder.

[This page intentionally left blank.]

Coded Bit Error Performance of FQPSK and GMSK with Combined Trellis Decoding

Dennis Lee and Tsun-Yee Yan
Jet Propulsion Laboratory
California Institute of Technology
Pasadena, CA 91109

October 18, 2000

1 Abstract

A new decoding scheme for coded FQPSK and GMSK is presented in which the modulation trellis is combined with the convolutional code trellis. Combining the trellises actually results in simplification of the encoder, and improved bit error performance at the decoder over symbol-by-symbol detection followed by a Viterbi decoder at the cost of a larger number of states. Using a Viterbi receiver, the performance of FQPSK with the combined trellis is within 0.1 dB E_b/N_o of convolutional coded BPSK, and is 0.4 dB better than symbol-by-symbol detection. A simplified combined trellis Viterbi receiver is also simulated with a 0.1 dB improvement over symbol-by-symbol detection. Finally, a combined trellis decoder is devised for GMSK $BT_b = 0.25$, and its simulated BER performance is also within 0.1 dB of convolutional coded BPSK.

2 Introduction

At the May 2000 CCSDS meeting, a full and simplified Viterbi receiver for FQPSK-B with improved BER performance over conventional receivers was introduced [1]. The complex and simplified Viterbi receiver had a 1.2 dB and 0.9 dB E_b/N_o gain, respectively, compared to symbol-by-symbol detection used by commercial receivers at 10^{-5} BER. However, the Viterbi receiver only output hard decisions which made it unsuitable for convolutionally coded FQPSK. Hence, the coded results for FQPSK presented in [2] only used symbol-by-symbol detection.

In the case of two concatenated convolutional codes, a Soft Output Viterbi Algorithm (SOVA) [3] is typically used to generate soft inputs for the outer code. A block diagram of the SOVA with the FQPSK Viterbi receiver is shown in Figure 1. This method has several disadvantages. First, an interleaver is required to break up burst errors from the inner decoder. This requires increased memory requirements as well as decoding delay. Second, the SOVA is suboptimal in that the log likelihood ratios which form the reliability values are computed using only the two best paths entering each state. Other paths which enter the state have been discarded at a previous time in the trellis even though they still contain reliability information on the selected path. This is especially important if the globally second best path had met the globally best path at some previous point in the trellis and was discarded. Moreover, the SOVA is also not suitable for FQPSK because the FQPSK trellis has two output bits per state transition. Since the reliability value is computed jointly for each state transition, there is no way of telling if both the output bits are reliable, or one is very reliable and the other one only marginally so.

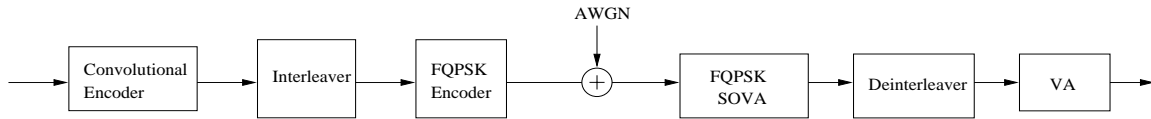


Figure 1: Coded FQPSK using SOV A

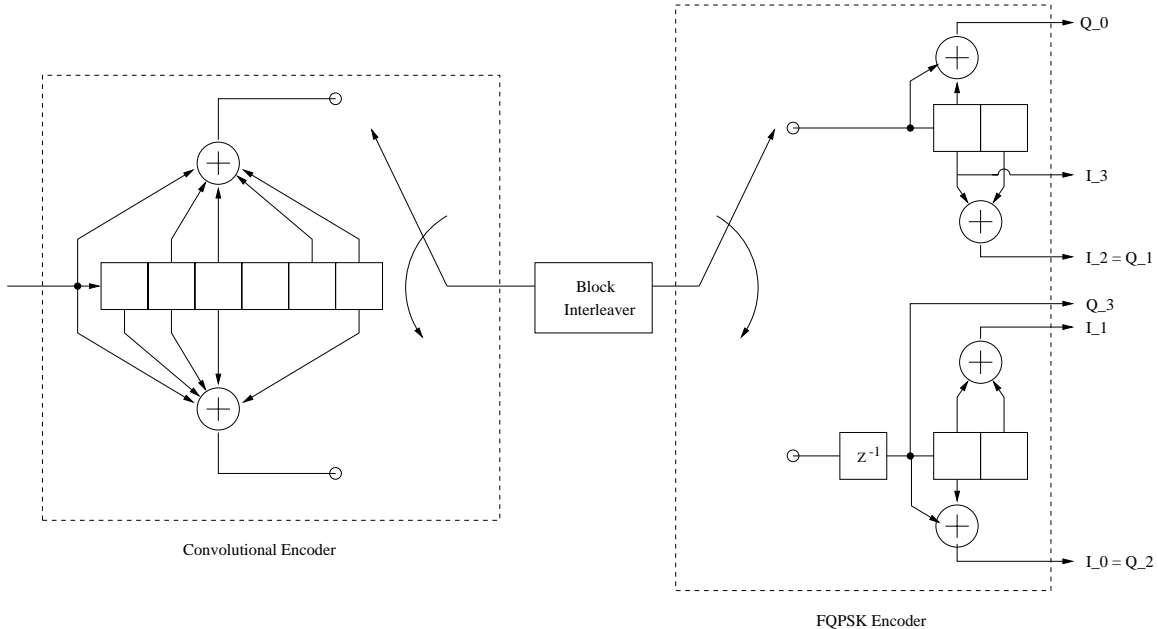


Figure 2: F QPSK encoder with Convolutional Encoding

3 FQPSK combined trellis decoding

Instead of using a SOV A followed by the FQPSK Viterbi decoder, we propose merging the FQPSK and convolutional code trellises together and using only a single Viterbi decoder. As will be shown, this results in a simpler encoder and decoder structure with a slight increase in computation complexity in the VA. Since the log likelihood ratios in the SOVA can never be estimated exactly, using combined trellis decoding may also improve BER performance since the no soft output estimations are passed between decoders (as there is only one decoder).

In general, when two code trellises are combined, decoding of the resulting trellis is much more difficult than the two trellises considered separately. For example, if the inner code has m states and the outer code has n states, the combined trellis of the inner and outer codes can have up to mn states. With two separate Viterbi algorithms, the total number of states is only $m + n$.

The FQPSK trellis has 16 states with 4 transitions to each state [5]. Considering that the CCSDS standard rate $1/2$, $k=7$ convolutional code has 64 states with 2 transitions per state, that implies that the FQPSK combined trellis has 1024 states. Fortunately there are a few simplifications which reduce the number of states.

Figure 2 shows a F QPSK encoder with the standard rate $1/2$ convolutional code. As can be seen from figure, the states of the I and Q FQPSK encoders are simply the delayed outputs of the rate $1/2$ encoder. Thus knowledge of the previous two states of the rate $1/2$ encoder determines

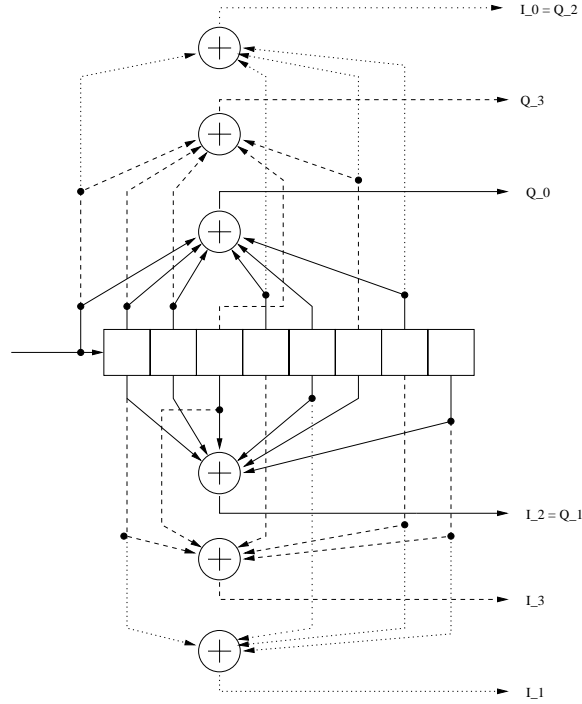


Figure 3: Equivalent FQPSK combined trellis encoder

the current state of the F QPSK encoder. The entire FQPSK encoder can be replaced by adding two more delay units to convolutional code shift register and adding the appropriate taps. This reduces the number of states by a factor of 4 (i.e., from 1024 states to 256 states). Noting the associative property of the XOR function and that $a_k \oplus a_k = 0$, the generators for the outputs can further be simplified to:

$$\begin{aligned}
 Q_3 &= a_k \oplus a_{k-1} \oplus a_{k-2} \oplus a_{k-3} \oplus a_{k-6} \\
 Q_2 &= a_k \oplus a_{k-4} \oplus a_{k-6} \oplus a_{k-7} \\
 Q_1 &= a_{k-1} \oplus a_{k-2} \oplus a_{k-3} \oplus a_{k-5} \oplus a_{k-6} \oplus a_{k-8} \\
 Q_0 &= a_k \oplus a_{k-1} \oplus a_{k-2} \oplus a_{k-4} \oplus a_{k-5} \oplus a_{k-7} \\
 I_3 &= a_{k-1} \oplus a_{k-3} \oplus a_{k-4} \oplus a_{k-6} \oplus a_{k-7} \\
 I_2 &= Q_1 \\
 I_1 &= a_{k-1} \oplus a_{k-5} \oplus a_{k-7} \oplus a_{k-8} \\
 I_0 &= Q_2
 \end{aligned} \tag{1}$$

where a_k is the current input bit to the encoder. Hence the six unique octal generators are $\langle 744, 426, 355, 732, 262, 213 \rangle$ for $Q_3, Q_2, Q_1, Q_0, I_3, I_1$, respectively. These values are used to map to the FQPSK waveforms.

The combined trellis encoder is shown in Figure 3. The combined FQPSK trellis now has 256 states with only 2 transitions to each state. The code rate remains unchanged at rate 1/2. The transmitted inphase FQPSK waveform is $s_I(t)$ where $I = 8I_3 + 4I_2 + 2I_1 + I_0$ and the transmitted quadrature waveform is $s_Q(t)$ where $Q = 8Q_3 + 4Q_2 + 2Q_1 + Q_0$. The FQPSK waveforms are shown

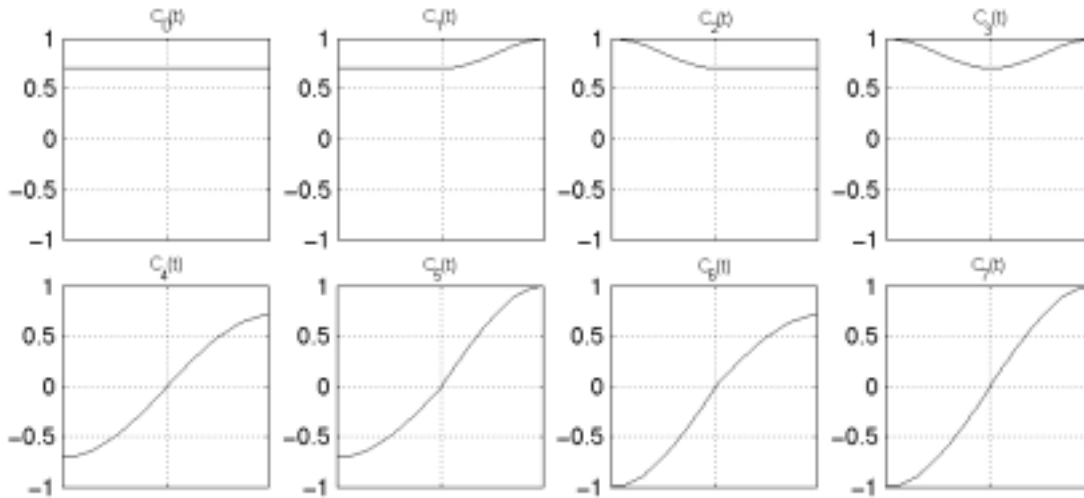


Figure 4: FQPSK Waveforms

in Figure 4.

In general for separate I and Q encoders, the combined trellis will have a number of states in the combined trellis equal to the number of states in the outer code times the number of states in either the I or Q encoders, whichever is greater. With the advent of faster processors and parallel computing techniques, the decoding of large constraint length codes have been made possible for high data rates. Alternatively, a shorter constraint length convolutional code could have been used.

3.1 Simulation Results

The performance of the convolutionally coded FQPSK-B using the combined trellis V A decoder was simulated using Signal Processing WorkSystem (SPW) software. The V A used a truncation path length of 90 bits. The simulated channel consisted of a saturated SSPA and additive white Gaussian noise. No quantization is assumed (i.e., floating point operation). For comparison, the bit error performance of convolutionally coded FQPSK-B using symbol-by-symbol detection and a Viterbi decoder was also simulated over the same channel.

The simulated bit error performance is shown in Figure 5. The combined trellis V A is within 0.1 dB of convolutionally coded BPSK, and provides a 0.4 dB gain over symbol-by-symbol detection.

Using the CCSDS concatenated code¹, the E_b/N_o degradation of FQPSK with combined trellis V A is slightly less. Figure 6 shows the bit error probability of the combined trellis V A with the CCSDS concatenated code assuming no quantization.

4 Simplified FQPSK Viterbi Receiver

In [1], a simplified FQPSK trellis was introduced which reduced the number of states compared the full trellis. For the simplified trellis, there are only 2 states in either the I or Q encoders. When combined with the 64 state trellis, the total number of states in the simplified combined FQPSK trellis is 128 states.

¹(255,223) Reed-Solomon outer code and rate 1/2, k=7 convolution inner code

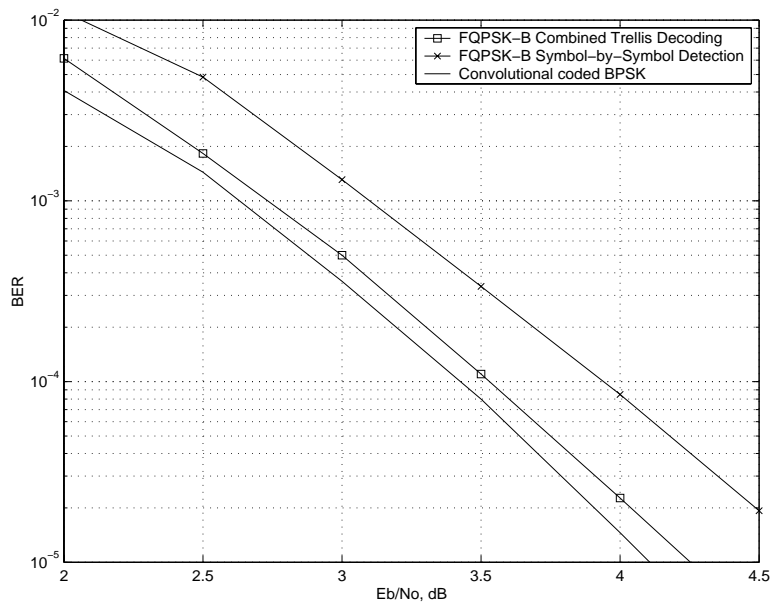


Figure 5: Bit error performance of FQPSK combined trellis VA

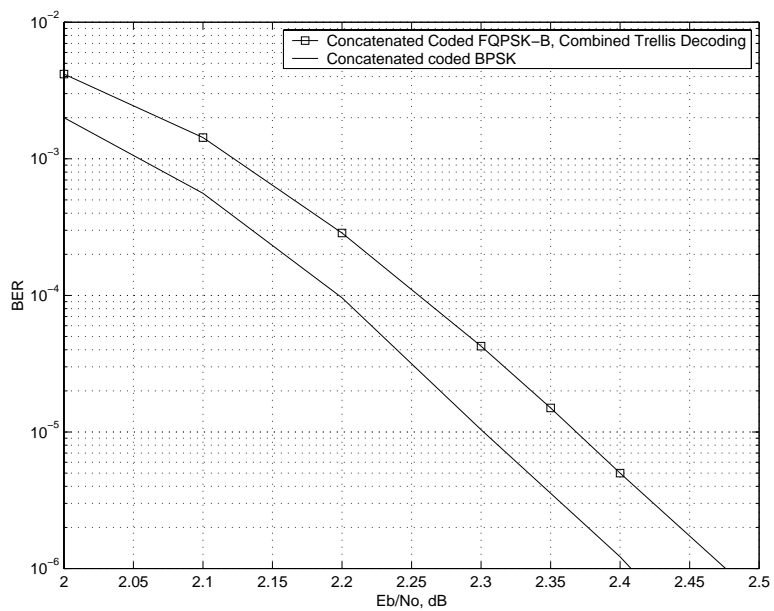


Figure 6: BER of FQPSK with CCSDS concatenated code and combined trellis decoding

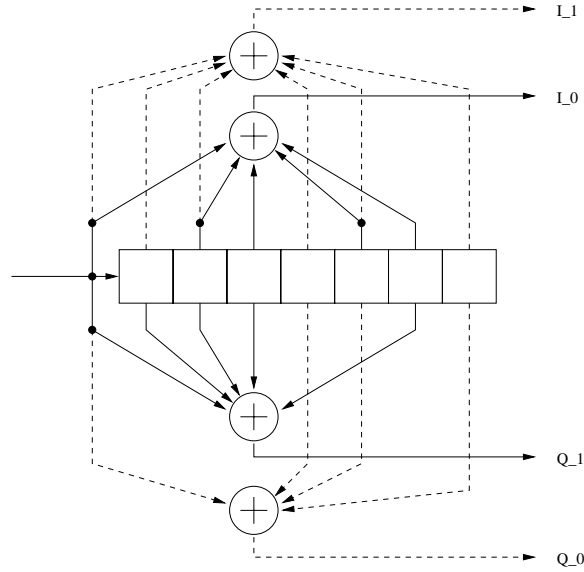


Figure 7: Simplified FQPSK combined trellis encoder

The block diagram of the simplified FQPSK combined trellis encoder is shown in Figure 7. It should be noted that FQPSK is still being transmitted since the actual encoder is still the one shown in Figure 2, but that the decoding is done using a trellis based on the encoder shown in Figure 7. This mismatch between encoded and decoded trellis is made possible by grouping together similar FQPSK waveforms with little loss in BER performance [1].

The BER of the simplified combined trellis decoder is shown in Figure 8. The simplified combined trellis is about 0.1 dB better than symbol-by-symbol detection, but 0.3 dB worse than the full combined trellis. The simplified combined trellis has half the number of states of the full trellis (128 states versus 256 states).

5 GMSK Combined Trellis

Using the 4-state Viterbi receiver for GMSK $BT_b = 0.25$ described in [4], the 4-state GMSK trellis was combined with the standard rate 1/2 convolution code trellis. In precoded form, the coefficients a_n and b_n are determined by:

$$\begin{aligned} a_n &= d_n \\ b_n &= d_n d_{n-1} d_{n-2} \end{aligned}$$

where d_n are the input data and the GMSK signal $s(t)$ is given by:

$$s(t) = \sum_{n \text{ odd}} a_n h_0(t - nT_s) - b_n h_1(t - nT_s - T_s/2) + j \sum_{n \text{ even}} a_n h_0(t - nT_s - T_s/2) - b_n h_1(t - nT_s)$$

The encoding of b_n would imply a single shift register of two bits. However, for quadrature modulation with data split into I and Q streams, this serial shift register can be split into two parallel shift registers of only one bit each. Hence when combined with the 64 state convolutional code, the combined GMSK trellis has only 128 states. Figure 9 shows a block diagram of the GMSK combined trellis encoder after further simplification of the taps.

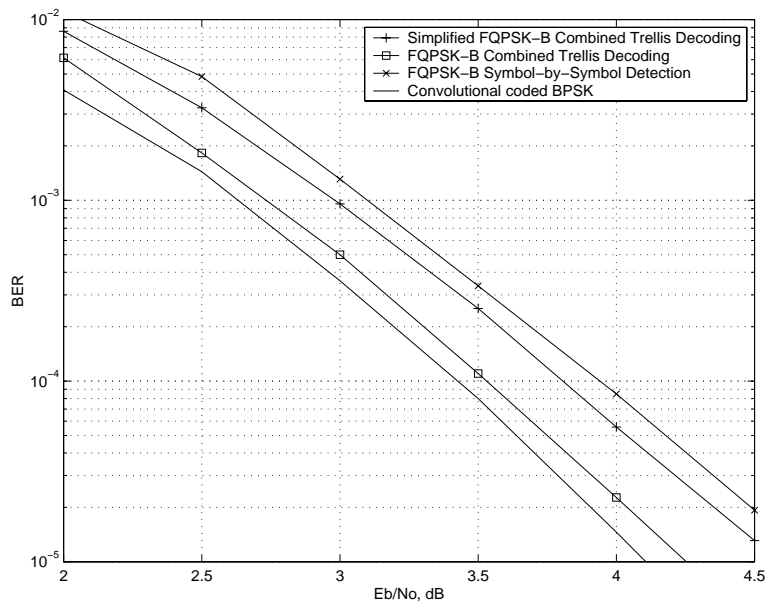


Figure 8: BER using simplified combined FQPSK trellis decoder

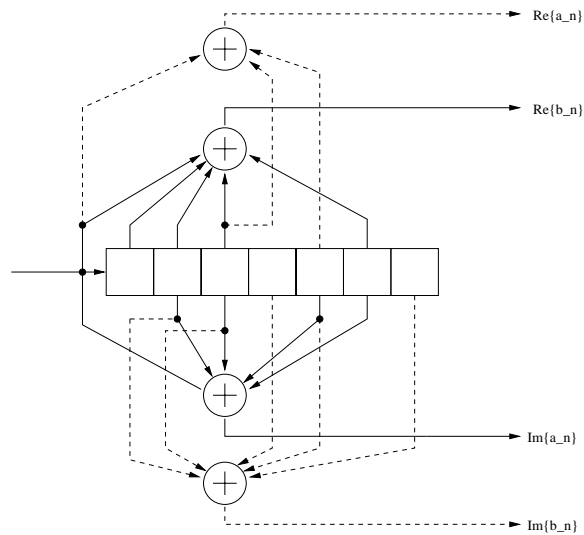


Figure 9: Equivalent convolutional coded GMSK encoder

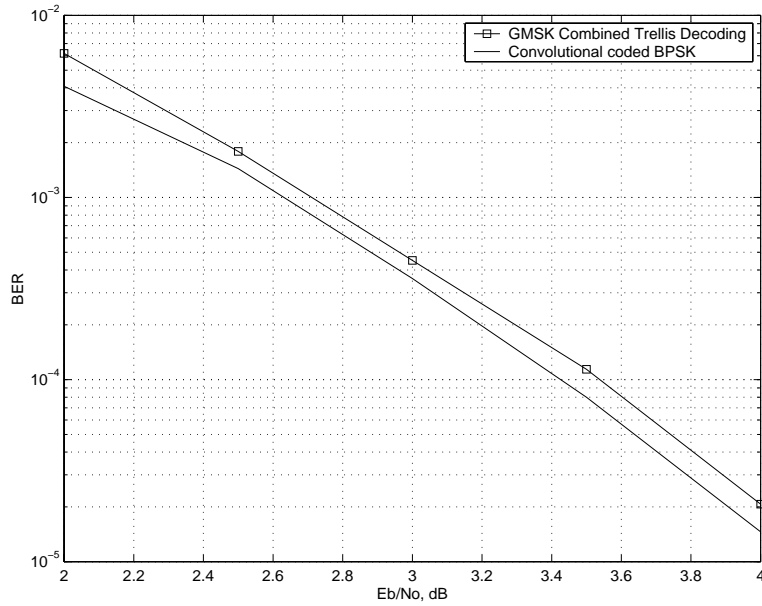


Figure 10: Convolutional coded GMSK with combined trellis decoding

Figure 10 shows the simulated bit error performance of GMSK combined trellis decoding. The BER is within 0.1 dB of BPSK with the same convolutional code.

6 Summary

A combined trellis FQPSK and GMSK decoder is introduced, and its bit error performance simulated. By combining the trellis, simplifications in the encoder structure can be made. In addition, the interleaved separate SOV A and F QPSK/GMSK Viterbi decoders is no longer needed with a combined trellis. The computation and storage of reliability values performed in the SOV A are also no longer necessary. These simplifications come at the cost of a greater number of states in the combined trellis, which means a more slower Viterbi decoder. The bit error performance of F QPSK-B and GMSK $BT_b = 0.25$ with a combined trellis is within 0.1 dB of BPSK with the same rate 1/2 convolutional code.

References

- [1] D. Lee, M.K. Simon, and T.-Y. Yan, "Performance of Near-Optimal and Simplified FQPSK-B Receivers", CCSDS Panel 1E meeting, May 2000.
- [2] D. Lee and T.-Y. Yan, "Coded Bit Error Performance of Selected Bandwidth Efficient Modulations", CCSDS Panel 1E meeting, May 2000.
- [3] J. Hagenauer and P. Hoeher, "A Viterbi Algorithm with Soft-Decision Outputs and its Applications," Proc. Globecom '89, Dallas, Texas, November 1989.
- [4] G.K. Kaleh, "Simple coherent receivers for partial response continuous phase modulations," IEEE Transactions on Select. Areas in Comm., vol. 7, no. 9, December 1989, pp. 1427-1436.
- [5] Simon, M.K. and Yan, T.-Y., "Performance Evaluation and Interpretation of Unfiltered Filtered Quadrature Phase Shift Keying (FQPSK)", JPL TMO Progress Report 42-137, May 1999.

[This page intentionally left blank.]

**NASA GSFC Bandwidth Efficient Modulation Studies:
Response to May, 2000 CCSDS P1E Action Items Including a
Report on Testing of FQPSK Through NASA's Tracking and
Data Relay Satellite System (TDRSS)**

Badri Younes
Goddard Space Flight Center
National Aeronautics and Space Administration
Greenbelt, MD USA

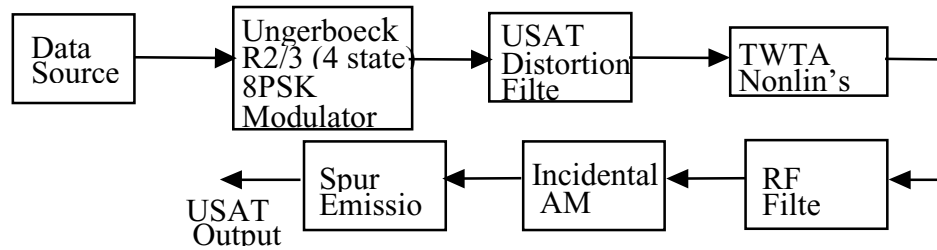
James Brase, Mark Burns
ITT Industries
Advanced Engineering & Sciences Division
Reston, VA USA

ABSTRACT:

NASA Goddard Space Flight Center is currently engaged in a variety of studies and tests to assess the suitability of various spectrally efficient modulation techniques for future near-Earth missions. The results and status of many of these efforts have been presented at recent CCSDS meetings, and have resulted in requests for some additional detailed technical information. This paper is intended to answer a number of CCSDS Panel 1E action items assigned specifically to GSFC at the May, 2000 meeting relating to the provision of additional information on previously documented monodimensional 8 PSK TCM and SRRC-filtered QPSK studies. This paper also answers an action item assigned to all parties concerning existing ground station capabilities and modulation compatibility tests by reporting new results of high rate FQPSK-B testing over the SN.

ACTION ITEMS 00-1E-02 and 00-1E-03:

NASA GSFC was requested to provide additional information on an analysis of the spectral and bit error rate performance of bandlimited monodimensional 8 PSK TCM modulation in NASA Ka-band SN and GN channels. This analysis, documented in the Panel 1E Paper 00/12, employed a User Satellite (USAT) model as depicted in Figure 1 to generate a 1020 Mbps signal RF filtered to the TDRSS KaSAR bandwidth of 650 MHz.

Figure 1: User Satellite Model from Monodimensional 8 PSK TCM Analysis

Several specific data items were requested, including the USAT TWTA AM/AM and AM/PM curves and the frequency response of the USAT Distortions Filter. The distortion characteristics of these components are provided in Table 1. The requested curves are presented in Figures 2 – 4. Note that the TWTA operating point is clearly indicated on the distortions curves.

Table 1: User Satellite Distortions Parameters

Component	Parameter	Value	Comment
Data Source / 8PSK TCM Modulator	Data Rate	1020	Mbps
	Data Asymmetry	0.0	Percent, peak
	Data Jitter	0.0	
USAT Distortions Filter	Gain Flatness	0.6	dB, peak-to-peak
	Gain Slope	0.1	dB/MHz
	Phase Non-linearity	6.0	deg, peak-to-peak
	Roll-off	0.574	dB / MHz
	Bandwidth	867.67	MHz
TWTA Nonlinearity	AM/AM	1.0	dB / dB
	AM/PM	2.5	deg / dB
RF Output Filter	Gain Flatness	0.0	dB, peak-to-peak
	Gain Slope	0.0	dB/MHz
	Phase Nonlinearity	0.0	deg, peak-to-peak
	Rolloff	0.574	dB / MHz
	Bandwidth	650	MHz
Others	Incidental AM	5.0	Percent
	Spurious PM	2.0	deg RMS at 510 MHz
	Spurious Emissions	-30 / -15	dBc, in-band / out-of-band

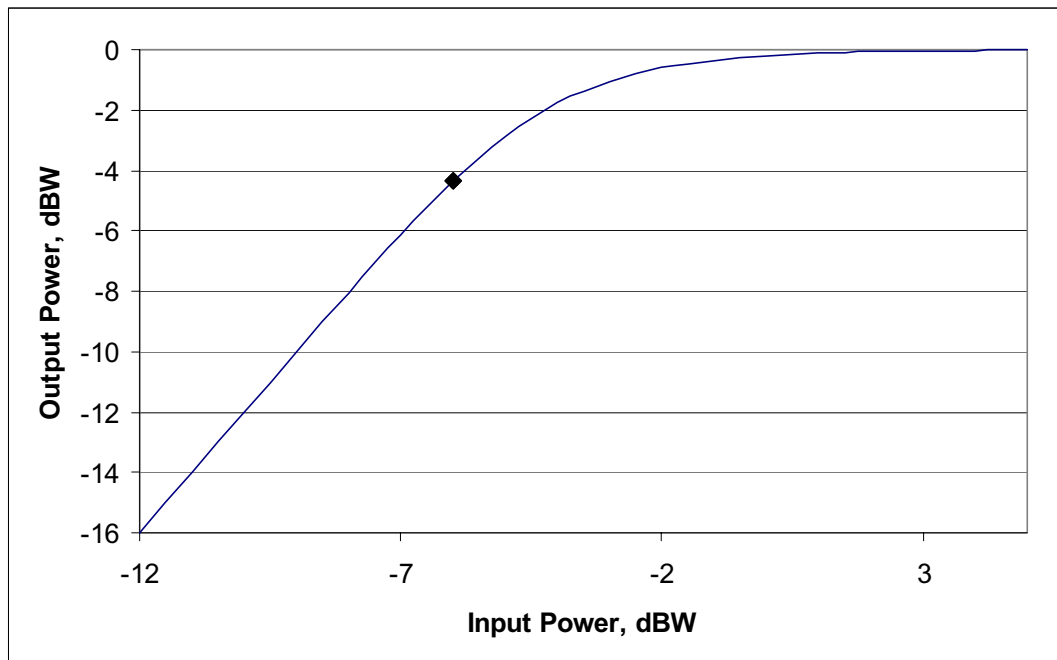
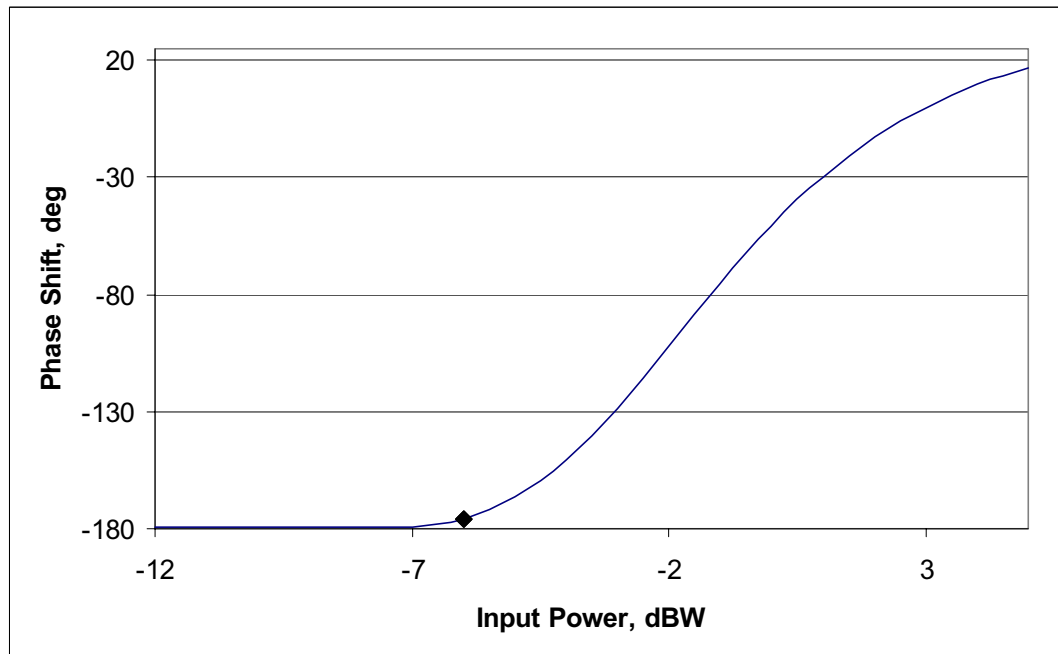
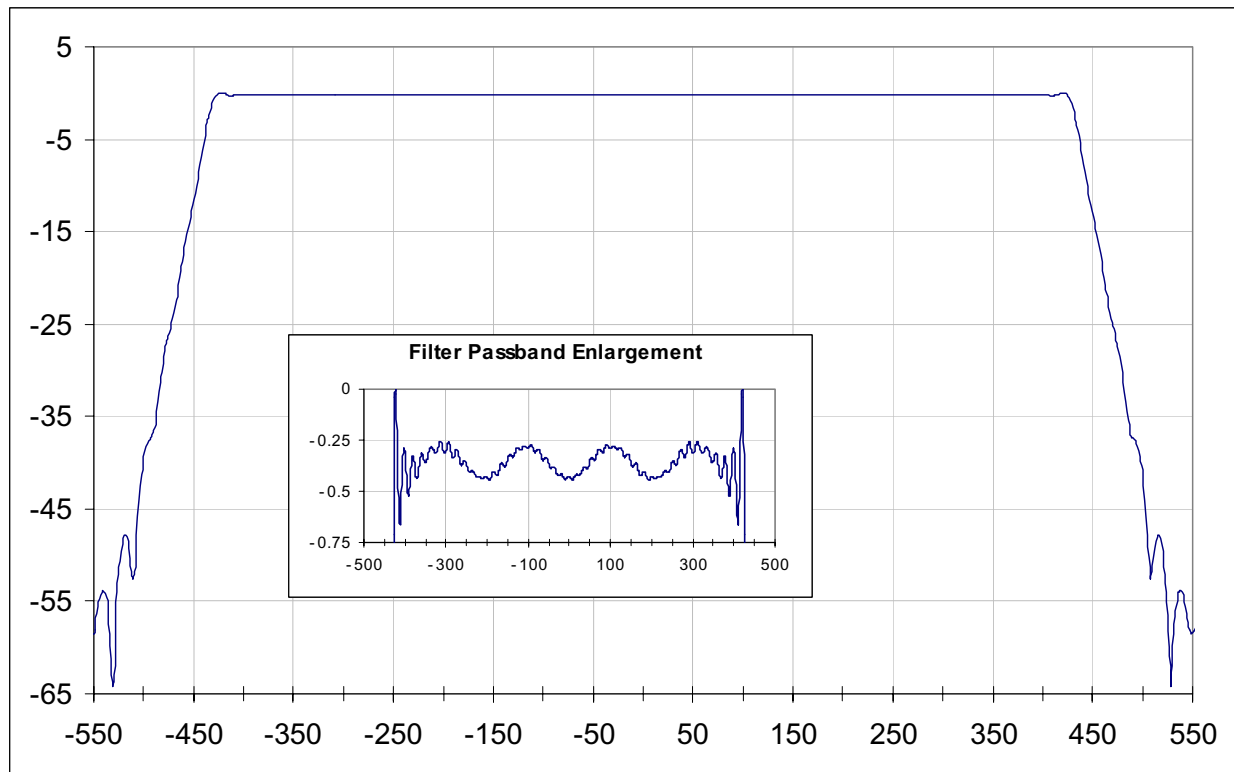
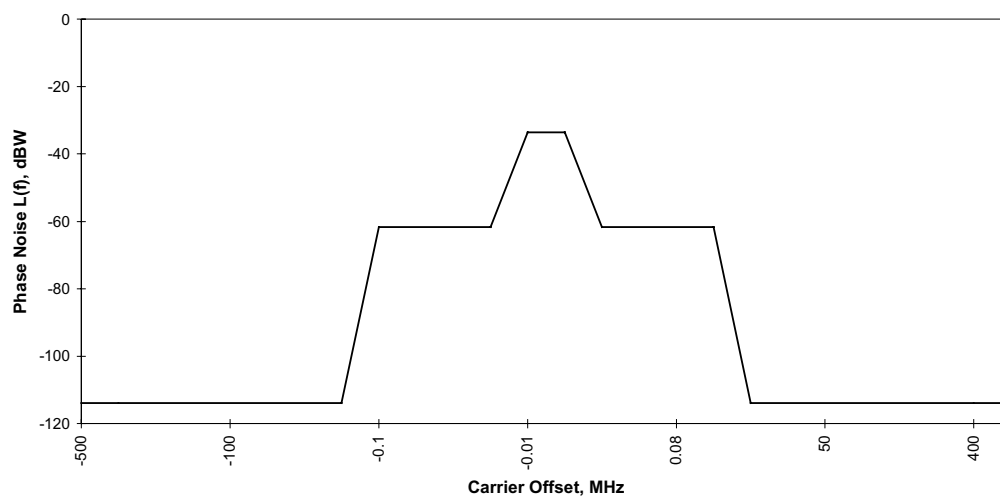
Figure 2: User Satellite TWTA AM / AM Curve**Figure 3: User Satellite TWTA AM / PM Curve**

Figure 4: 8 PSK TCM USAT Distortions Filter Frequency Response

Also requested for this analysis was the Power Spectral Density of the Phase Noise which was included in the BER simulation analysis. This information is provided in Figure 5.

Figure 5: Phase Noise Power Spectral Density

ACTION ITEM 00-1E-07:

GSFC was also requested to provide the TWTA curves used in the SRRC Filtered QPSK analysis. Since both analyses utilized the same TWTA model, the curves provided in Figures 2 and 3 apply.

ACTION ITEM 00-1E-11:

All CCSDS member agencies were requested to document which modulations are supported (now or in the near future) by existing ground stations, and to provide any available information on analyses of the BER performance of any of the CCSDS Efficient Modulation Recommendation candidate modulation techniques when received using modulators designed for alternative techniques.

The NASA Ground Network consists of approximately 15 ground stations with varying support capabilities. Most support carrier and subcarrier modulations for command and low / medium rate telemetry links at S-Band. Maximum S-band command data rates at range from 8 kbps to 216 kbps. Maximum S-Band telemetry rates range from 1 Mbps to 10 Mbps. Limited VHF and L-Band command and telemetry services are also provided.

All S-band GN command and telemetry links employing a subcarrier use BPSK for the subcarrier modulation. Carrier modulations supported include BPSK, QPSK, FM, PM, and AM. High rate (up to 150 Mbps) telemetry service at X-band is available at several GN stations using carrier modulation only. Modulation formats supported include QPSK, SQPSK, UQPSK, AQPSK.

Note that not all modulation formats are supported at all ground stations. For detailed information, refer to the NASA GN Users Guide, available online at <http://www.wff.nasa.gov/~code452/>.

The Space Network currently provides S-band and Ku-band forward and return services. The next generation TDRS satellites currently being deployed will also feature Ka-band links. At S-band, services can be provided in Single Access mode through the steerable SSL dish antennas or in Multiple Access mode through the phased array antenna.

Modulation formats supported by the Space Network include BPSK, QPSK, SQPSK, and SQPN. Note that not all formats are available for all services. For details, refer to the NASA Space Network User's Guide available online at <http://tip.gsfc.nasa.gov/code/530doc.htm>.

Finally, in response to the request for information on cross-support performance analyses of candidate modulation techniques, GSFC submits a copy of a paper generated for the upcoming SFCG meeting which documents the results of testing performed on a high rate FQPSK-B modulator in the TDRS KuSAR channel.

REPORT CONCERNING CCSDS RADIO FREQUENCY AND MODULATION

SFCG-20
7-16 November, 2000
Port Douglas

SF20-5
October 9, 2000

Testing of FQPSK Through NASA's Tracking and Data Relay Satellite System (TDRSS)

National Aeronautics and Space Administration

Introduction

FQPSK modulation is a family of quasi-constant envelope spectrally efficient QPSK variants patented by Kamilo Feher and licensed through Digcom, Inc. FQPSK operates by mapping Pulse Code Modulation (PCM) data into combinations of 16 component waveforms in such a way as to provide phase continuity at the symbol transition points. The resulting smoothness of the time-domain waveforms causes the frequency spectrum of the modulated signal to rolloff much more quickly than standard PSK signals. The FQPSK mapping also introduces a cross-correlation between the I and Q channels to realize a minimal envelope fluctuation of only 0.2 dB. This latter property is key to minimizing the spectral regrowth that is common in satellite communications systems due to high power amplifier saturation. FQPSK-B is an improved version of the original FQPSK which achieves an even greater reduction in spectral sidelobes. Like all versions of FQPSK, an FQPSK-B modulated signal can be detected using a standard OQPSK demodulator with some degree of implementation loss. For instance, in an AWGN channel, the required E_b/N_0 to achieve a 10^{-3} BER is approximately 2.3 dB higher with FQPSK modulation than with unfiltered OQPSK modulation.

Over the past several years, NASA has been evaluating bandwidth efficient modulation techniques for the Ground Network. (GN) [1,2] Goddard Space Flight Center (GSFC) is just beginning to evaluate bandwidth efficient modulation techniques for the Space Network. (SN) The SN consists of a number of geosynchronous Tracking and Data Relay Satellites (TDRS) which support “bent-pipe” relay communications between user satellites and the NASA White Sands Complex (WSC) ground station. For the SN space-to-space link, TDRS users utilize the S-Band (2025 – 2110 MHz, 2200 – 2290 MHz) Single Access (SSA) channel for low data rates (up to 300 kbps forward, 6 Mbps return), or the Ku-band (13.75 – 14.0 GHz, 14.8 – 15.35 GHz) Single Access (KuSA) channel for high rates up to 25 Mbps forward or 300 Mbps return. For the space-to-ground link, (SGL) the TDRS satellite amplifies and shifts the user signals to/from the Ku-band SGL frequencies (14.6 – 15.25 GHz uplink, 13.04 – 14.05 downlink GHz) for transmission to/from WSC. Any analysis evaluating the impacts and benefits of using bandwidth efficient modulation techniques in the Space Network must consider the multiple frequency translations, filtering in the transponder, saturated power amplification, and all signal distortions present in the signal path. This is especially important because missions typically operate through the SN with very low link margins and these missions often therefore cannot incur much additional degradation.

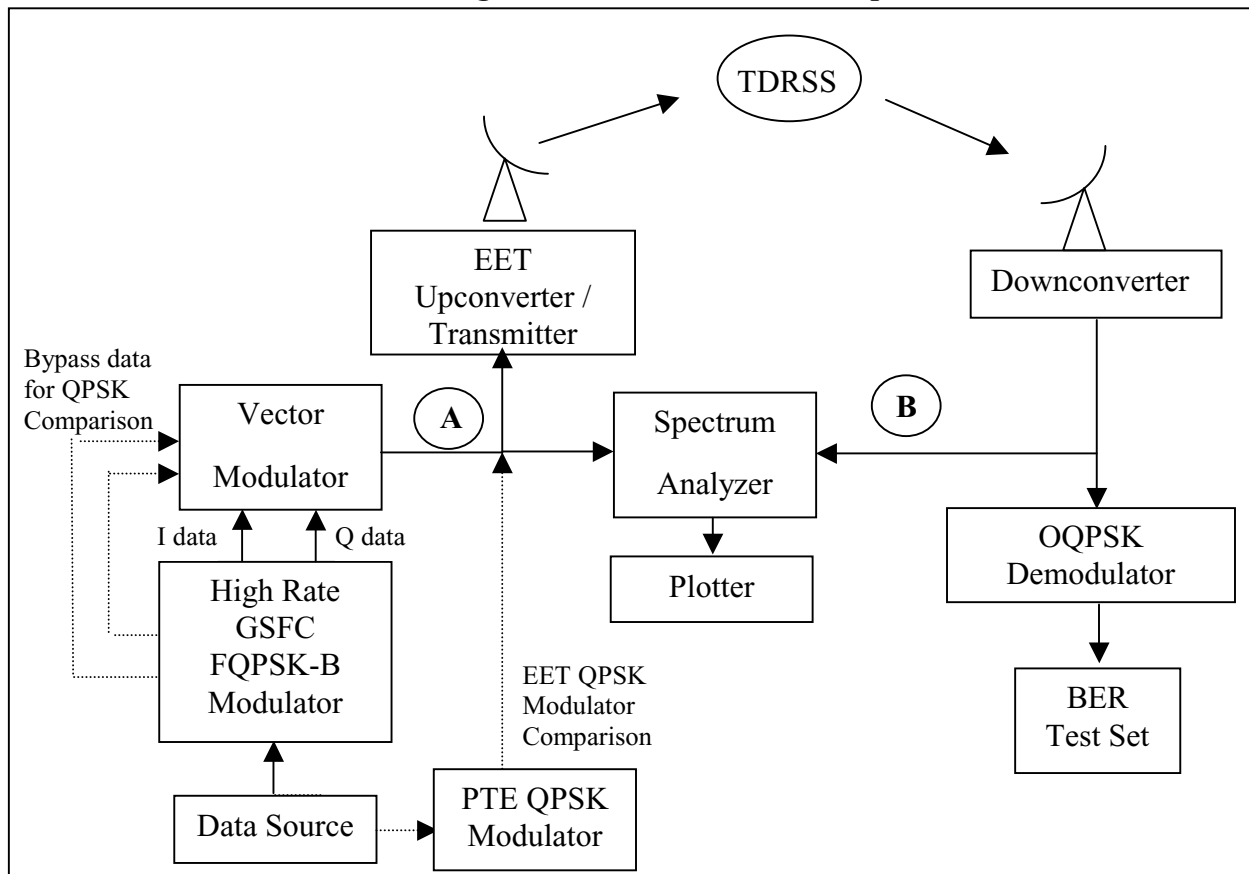
GSFC has developed a prototype high rate FQPSK-B modulator. This prototype, which supports data rates up to 300 Mbps, generates FQPSK I and Q-channel baseband waveforms which can be used as inputs to a vector (or I-Q) modulator. It is being used to assess the suitability of FQPSK-B for future high rate NASA missions. A series of tests were conducted at WSC on September 26 – 27, 2000 to evaluate the performance of this modulator in the SN. This paper documents the results of these tests.

Test Setup

Hardware tests over the SN are conducted using the TDRS Performance Test Equipment (PTE) and the WSC End-to-End Test (EET) system. The WSC EET system and PTE are designed to simulate a user satellite using the TDRS SSA and KSA return services. In the normal test mode, the PTE equipment generates a test data stream, QPSK modulates it, and upconverts the signal to the WSC 370 MHz Intermediate Frequency (IF). The EET amplifies the modulated signal and transmits the signal to the TDRS satellite. The TDRS satellite treats the EET signal just like any signal from a user spacecraft; it amplifies the received signal and multiplexes it onto the SGL. At the WSC, the received SGL signal is downconverted to a 370 MHz IF and routed to the EET QPSK/SQPSK receiver.

For the FQPSK-B modulation tests, a 300 Mbps NRZ data sequence was generated and input to the high rate FQPSK-B modulator. The resulting 150 Mbps I and Q channel waveforms were input to an HP8780A Vector Modulator, which modulated the signal onto a 370 MHz IF carrier. This signal was injected directly into the EET upconverter / transmitter chain, bypassing the normal PTE modulator, and transmitted to a TDRS. The TDRS relayed the signal back to WSC, which downconverted it back to the IF frequency. An OQPSK demodulator was used to detect the data. An OQPSK demodulator was used to detect the data.

Figure 1: SN FQPSK Test Setup



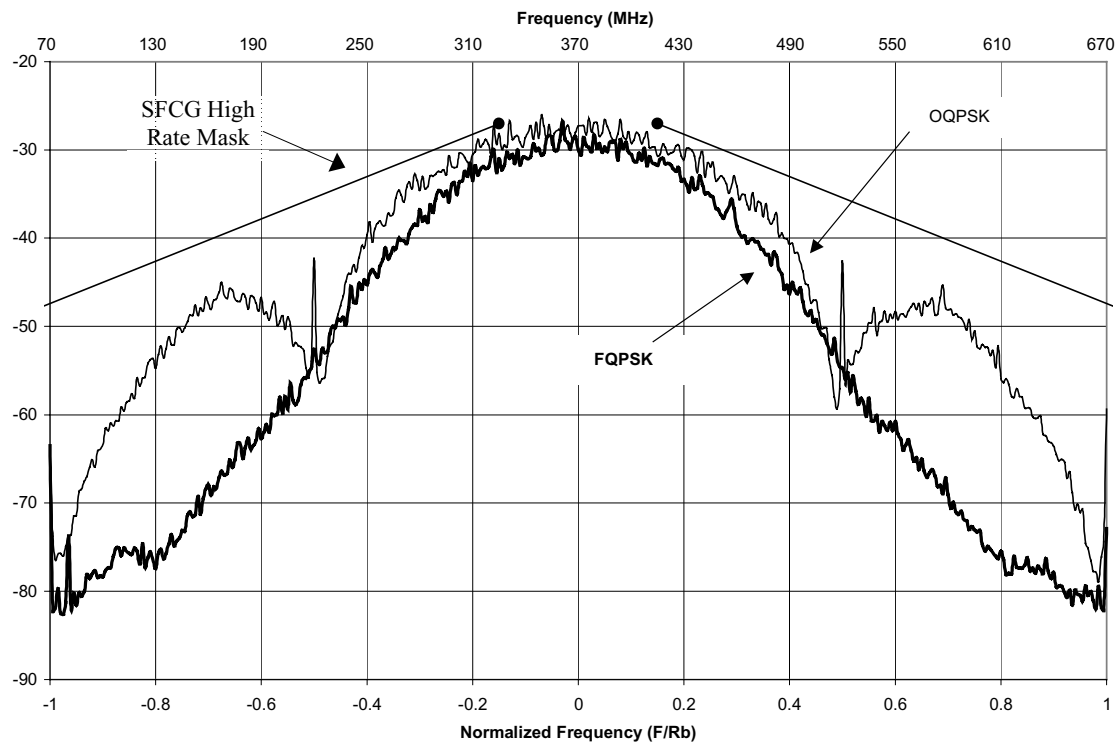
The tests also considered OQPSK modulation using two separate configurations as illustrated in Figure 1. In the bypass mode, the NRZ data was input directly to the vector modulator to produce the 300 Mbps unfiltered OQPSK signal. This signal was then input directly to the EET upconverter.

In the second configuration, the same 300 Mbps NRZ data sequence was input to the WSC PTE QPSK modulator, which OQPSK-modulated the data sequence onto the 370 MHz IF carrier. This configuration was used during BER measurements, but not for the spectral roll-off measurement results presented herein.

Results

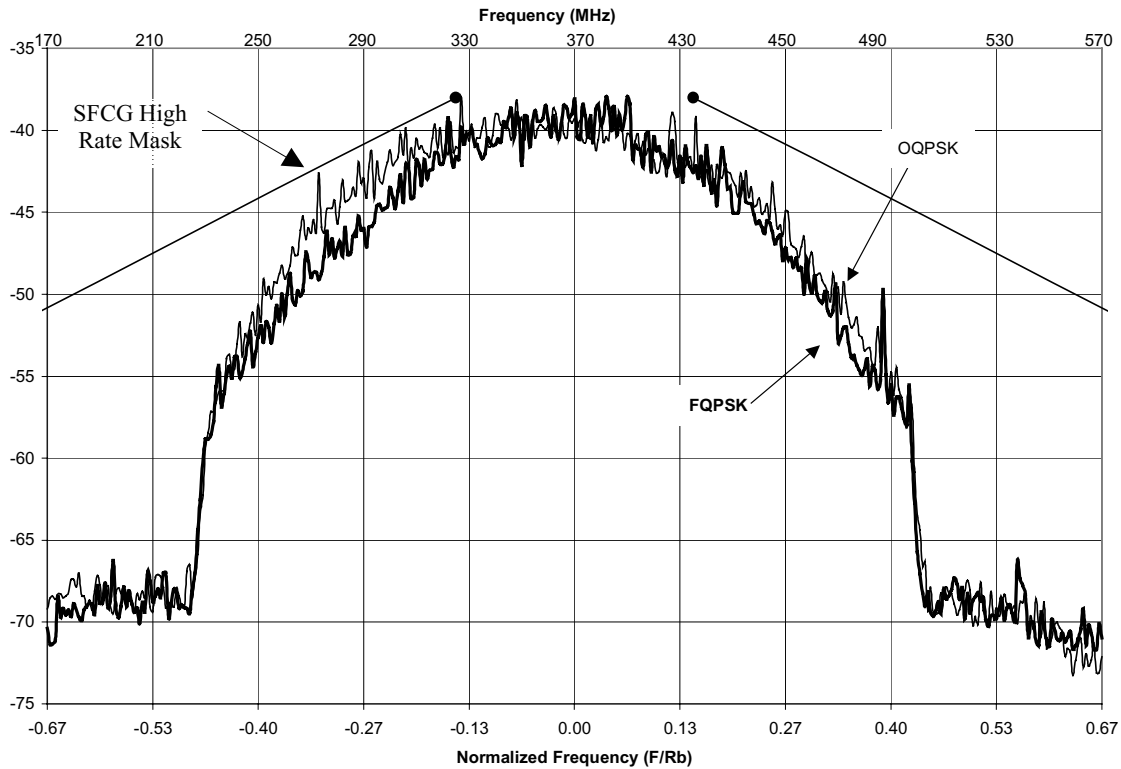
The Power Spectral Densities (PSDs) of the high rate FQPSK-B modulator and the vector modulator in OQPSK mode were measured with an HP 8560E spectrum analyzer. Measurements performed at the modulator output (see point A, Figure 1) are depicted in Figure 2. The corresponding PSDs of the FQPSK and OQPSK signals at the receiver input (see point B, Figure 1) are depicted in Figure 3.

Figure 2: GSFC FQPSK and HP Vector Modulator OQPSK Power Spectral Densities (PSDs) at Modulator Output



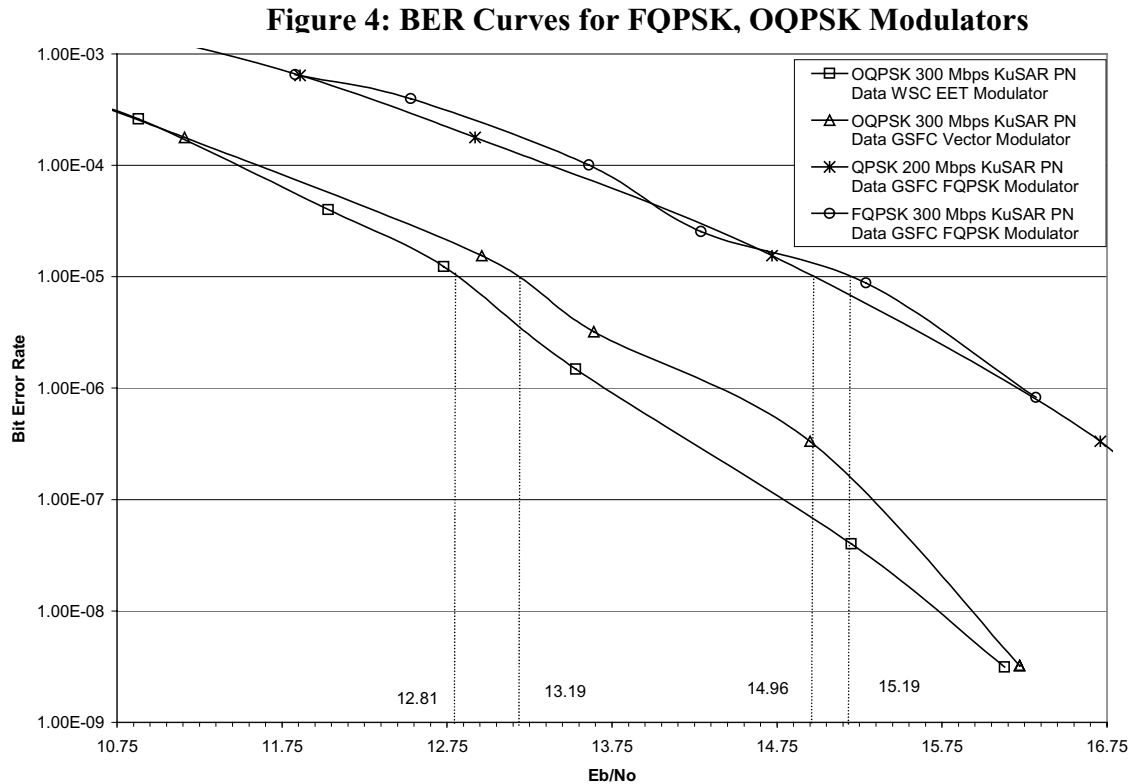
The measured FQPSK-B modulated signal in Figure 2 agrees closely with theoretical and simulated results. Note that although the HP Vector OQPSK modulator is not specifically designed to incorporate baseband or IF filtering, the practical frequency response limitations of the device at very high data rates cause some filtering. Note also that in these results, the modulated signal *is measured at the modulator output, not at the output of the power amplifier*. Some regeneration of power in the PSD sidelobes of the OQPSK signal will occur in the power amplifier due to the non-constant envelope. Furthermore, Figure 2 only spans the mainlobe and the first sidelobe. The signal spectrum within these lobes for both the FQPSK-B and the filtered OQPSK fall well within the SFCG High Rate Spectral Mask. However, it is impossible to draw conclusions about whether the OQPSK and FQPSK-B signals can meet the SFCG high rate mask outside this region and after the power amplifier.

Figure 3: GSFC FQPSK and HP Vector Modulator OQPSK PSDs at Receiver Input



In Figure 3, the TDRS KuSAR channel, with a bandwidth of approximately 225 MHz, filters out all sidelobes as well as a portion of the PSD main lobe of the 300 Mbps signals. As a result, the two modulated signals have very similar PSDs measured at the receiver input.

The bit error rate (BER) was measured for the high rate FQPSK modulator, the vector modulator in OQPSK mode, and the WSC EET OQPSK modulator using the BER test set by varying the uplink (SSL) carrier power and measuring the link C/N₀ and BER. The results of these tests for all three modulators are depicted in Figure 4.



For a data rate of 300 Mbps, the WSC OQPSK modulator achieves a BER of 10^{-5} at 12.81 dB in the 225 MHz KuSAR channel, equating to a 3.21 dB loss as compared to ideal OQPSK performance. A significant portion of this loss is probably attributable to the severe bandlimiting in the TDRS. (See Figures 2 and 3 above). The HP Vector Modulator OQPSK-modulated signal achieves a 10^{-5} BER at 13.19 dB, representing only a 0.38 dB degradation as compared to the WSC OQPSK modulator. Some additional hardware loss is expected in this implementation, as compared to the WSC equipment, because the vector modulator is not a precisely tuned and integrated component of the EET system.

The GSFC FQPSK-B Modulator at 300 Mbps achieves a BER of 10^{-5} at 15.19 dB in the 225 MHz channel. At 200 Mbps, the E_b/N_0 at which a 10^{-5} BER was measured was 14.96 dB. Note that the FQPSK-B modulator BER curves for 200 Mbps and 300 Mbps are virtually identical and the difference at 10^{-5} BER may well be within the confidence interval of the measurement.

Conclusions

The measured GSFC FQPSK-B transmitter output PSD was similar to the simulated ideal FQPSK-B spectrum and well within the high-rate SFCG mask at least over the range given by $|F/R_b| < 1.0$. Mask compliance at the output of the power amplifier could not be verified due to the relatively narrow bandwidth of the TDRS KuSAR bandpass filters.

The theoretical implementation loss for FQPSK-B with an integrate-and-dump OQPSK receiver is approximately 2.7 dB as compared to unfiltered OQPSK. However, as demonstrated by Figures 2 and 3, the OQPSK signals at 300 Mbps in this experiment experience some filtering inside the modulator and even more in the KuSAR channel.

The FQPSK-B signal is also filtered; however, because a higher percentage of the spectral energy is concentrated in the center of the main lobe with FQPSK-B than with OQPSK, much less energy is lost due to the filtering. The diminished impact of the 225 MHz channel filtering on the FQPSK-B signal is demonstrated by the similarity of the measured BER performance of the modulator at 200 Mbps to the 300 Mbps results. As a result, the BER performance degradation of FQPSK-B is only 2.0 dB as compared to the measured OQPSK performance.

These tests have demonstrated that spectrally efficient FQPSK modulation techniques can be employed at high rates in the Space Network at the cost of approximately 2.0 dB of additional implementation loss, as compared to OQPSK filtered by the TDRS KuSAR bandpass filters. Since many SN users, particularly those with high rate TDRSS links, may not be able to accept this additional implementation loss, additional studies are warranted to examine the performance of other bandwidth efficient modulation techniques, including filtered OQPSK.

Acknowledgement

The author of this paper wishes to acknowledge the contributions of Dr. Kamilo Feher to this project. Through a licensing agreement with Digcom, Dr. Feher has graciously provided GSFC with the authority and the necessary detailed technical information to develop modulators which implement the patented FQPSK-B technique for test and validation purposes.

References

- [1] *NASA GSFC Efficient Spectrum Utilization Analysis*, Prepared by ITT Industries for Badri Younes/GSFC, April 19, 2000
- [2] *SF17-28/D CCSDS-SFCG Efficient Modulation Methods Study at NASA/JPL Phase 3: End-to-End System Performance*, Warren Martin, Tsun-Yee Yan, and Loc V. Lam, NASA/JPL, September, 1997

- [3] *FQPSK Test Plan*, Victor Sank and Steve Smith, QSS, August 28, 2000
- [4] *Performance Evaluation and Interpretation of Unfiltered Feher-Patented Quadrature Phase Shift Keying (FQPSK)*, Marvin Simon and Tsun-Yee Yan, NASA/JPL, May 15, 1999
- [5] *Performance of Near-Optimal and Simplified FQPSK-B Receivers*, Dennis Lee, Marvin Harrison, and Tsun-Yee Yan, NASA/JPL, May 4, 2000

[This page intentionally left blank.]



Studies and simulation results on a coherent GMSK demodulator

Paper P1E-00/16

Response to Actions 99-1E-34 and 99-1E-35

Emmanuel Bouisson

André Ribes (CCSDS Member. Panel 1E)

CNES Toulouse

Summary of Actions 34 & 35

- Performances of GMSK with $BT_b=0.25$
- Information on CNES Receiver used for simulations of GMSK for $BT_b=0.5$



GMSK Performances Analysis

Summary

- Principle of the CNES GMSK Receiver for the simulations presented in 1999
- GMSK Simulated BER performances for $BT_b = 0,5$ with Viterbi Algorithm
- GMSK Performances extrapolation for $BT_b = 0,25$, with Viterbi Algorithm



GMSK Performances Analysis

Principle of the CNES GMSK Receiver used for the simulations presented in 1999 Performances for different BTb

GMSK: a particular case of CPM signals

The CPM signals can be expressed by :

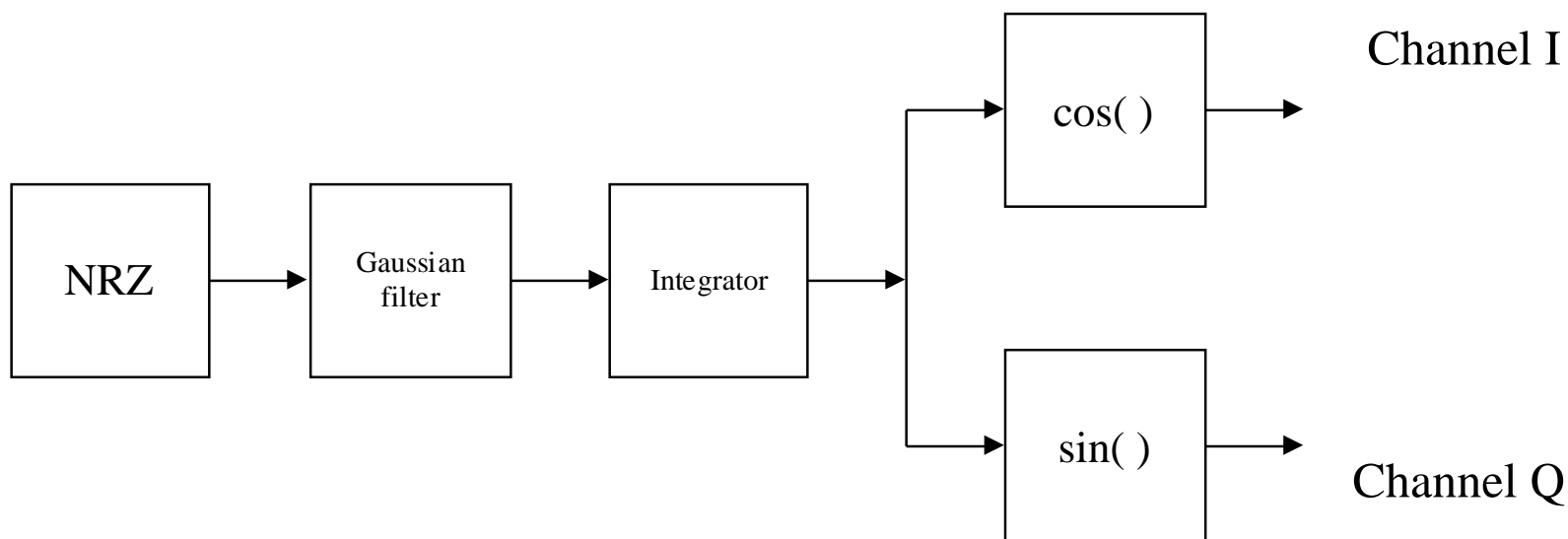
$$s(t) = \sqrt{\frac{2E}{T}} \cos(\omega_0 t + \phi_0 + \phi(t, \alpha))$$

Where the phase is : $\phi(t, \alpha) = 2\pi h \sum_{i=-\infty}^n \alpha_i q(t - iT)$

And
$$S(t) = \cos \left(\omega_0 t + \phi_0 + 2\pi h \sum_{i=-\infty}^n \alpha_i q(t - iT_b) \right)$$

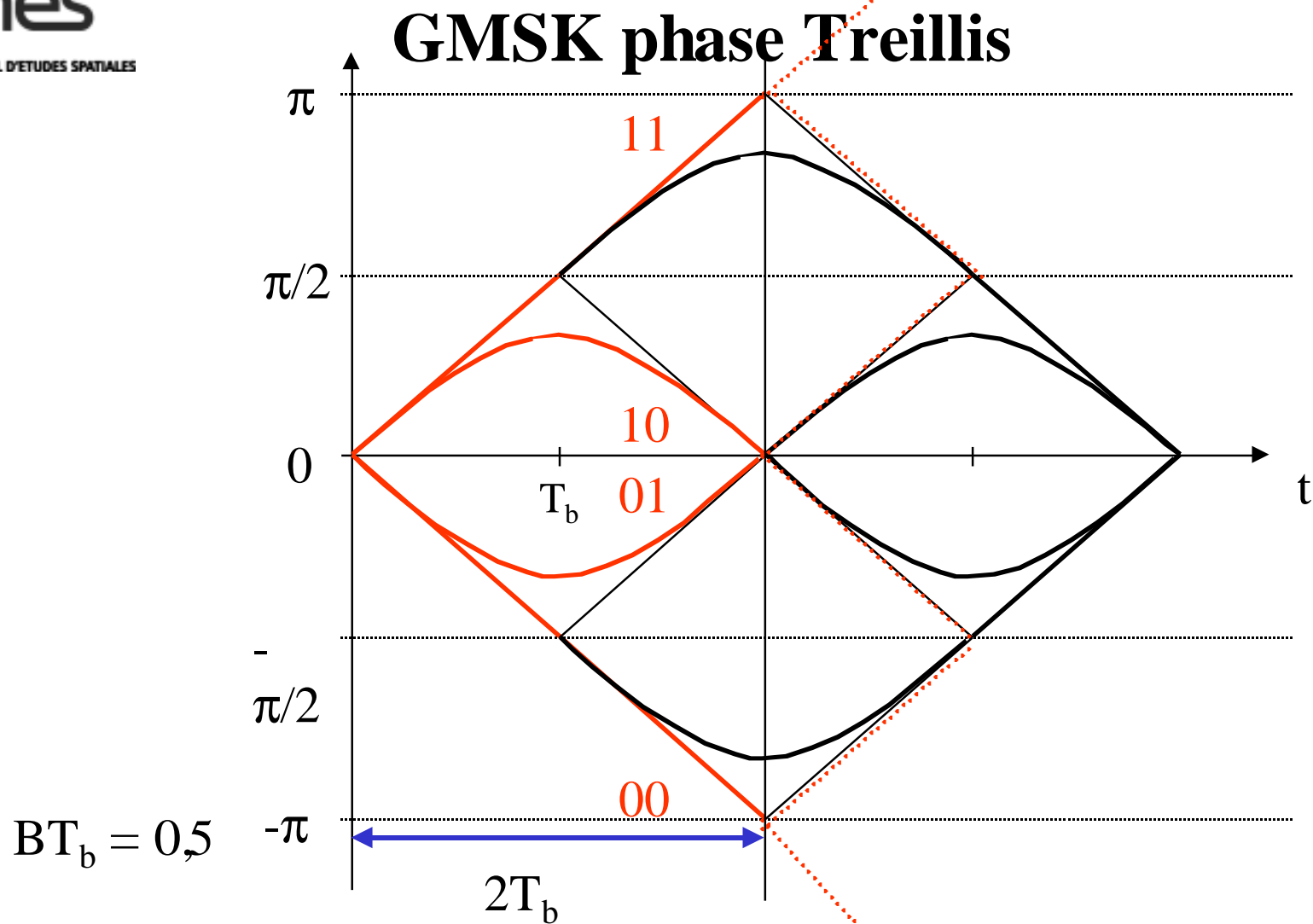
GMSK is a CPM modulation with a particular waveform shaping for $q(t)$ coming from the Gaussian filtering

The IQ baseband modulator



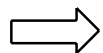
⇒ a FM modulator is also possible

GMSK Performances Analysis

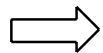


Principle of the algorithm :

For GMSK w. $BT_b = 0,5$



The Euclidean distances for the MSK and GMSK are very close (2 for MSK and 1.95 for GMSK).

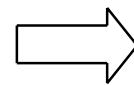


So we use the MSK phase patterns into correlators to perform the symbols recovery.

Correlators used in the simulations

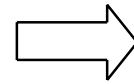
- Working on I and Q both channels
- The correlation signals are :

$$\delta_k = \cos \frac{k\pi T_e}{2T_b}$$



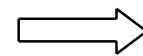
On channel I: 4 correlators
on a 4 symbol length ($S_1(t)$,
 $S_2(t)$, $S_3(t)$ and $S_4(t)$ signals).

$$\lambda_k = \sin \frac{k\pi T_e}{2T_b}$$



On channel Q: 2 correlators
to recover the rotation path
($S_5(t)$ and $S_6(t)$ signals).

Phase pattern for the correlators



MSK phase patterns

Multi-symbol detector used in the simulations

- Multiple hypothesis tests are performed:

$$r(t) = s_i(t) + n(t) \quad t \in [nT_b - T_b, (n+2)T_b + T_b]$$

- Corresponding to algebraic criteria :

$$(r/s_i) + \frac{1}{2} (N_0 \ln(p_i) - E_i) = \sup_j (r/s_j) + (N_0 \ln(p_j) - E_j)$$

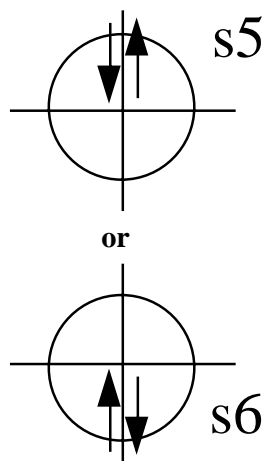
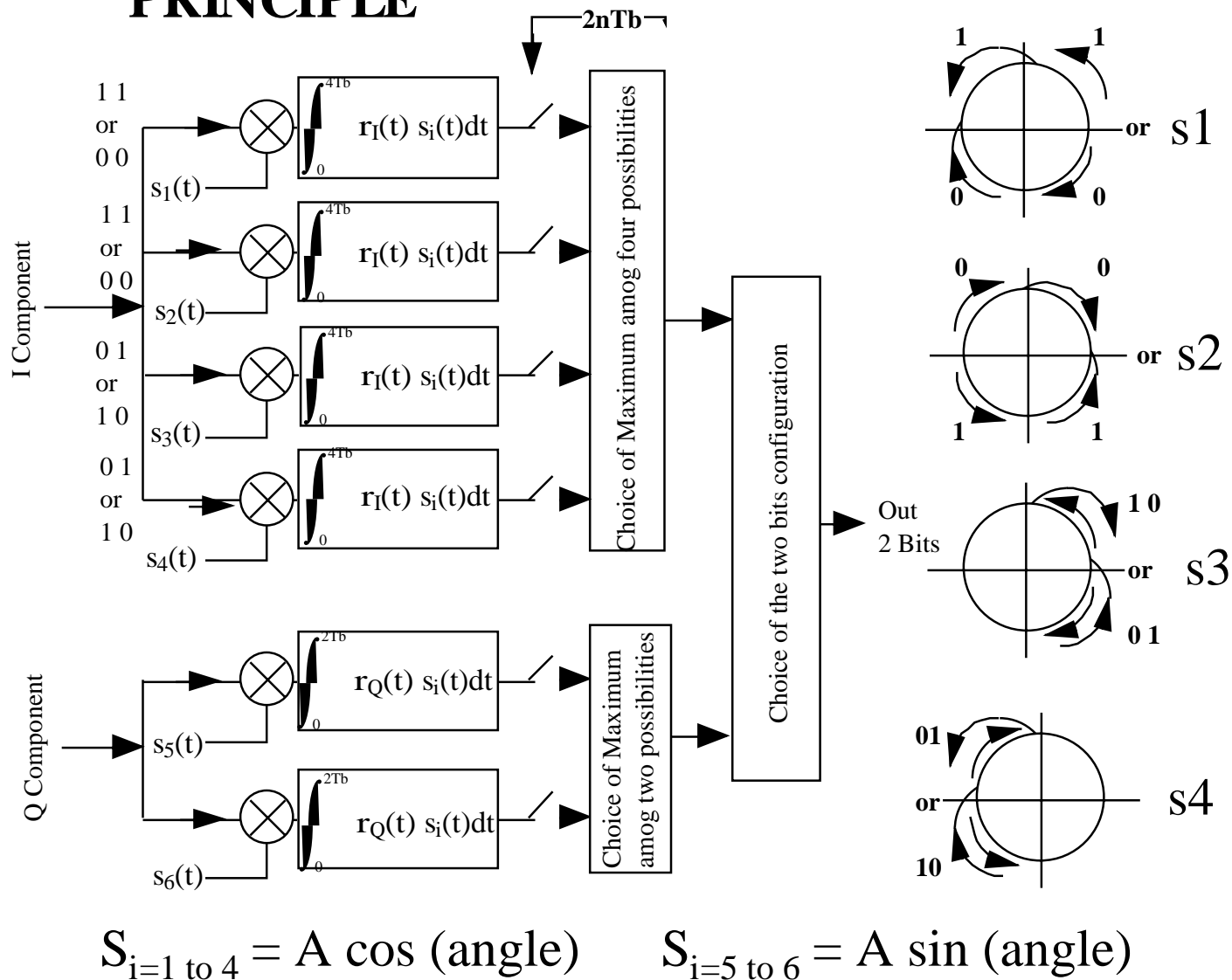
$$(r/s_i) + \frac{1}{2} (N_0 \ln(p_i) - E_i) = \sup_j (r/s_j) + (N_0 \ln(p_j) - E_j)$$



CENTRE NATIONAL D'ETUDES SPATIALES

DEMODULATOR PRINCIPLE

GMSK Performances Analysis



CCSDS- P1E

Annapolis-May 2000

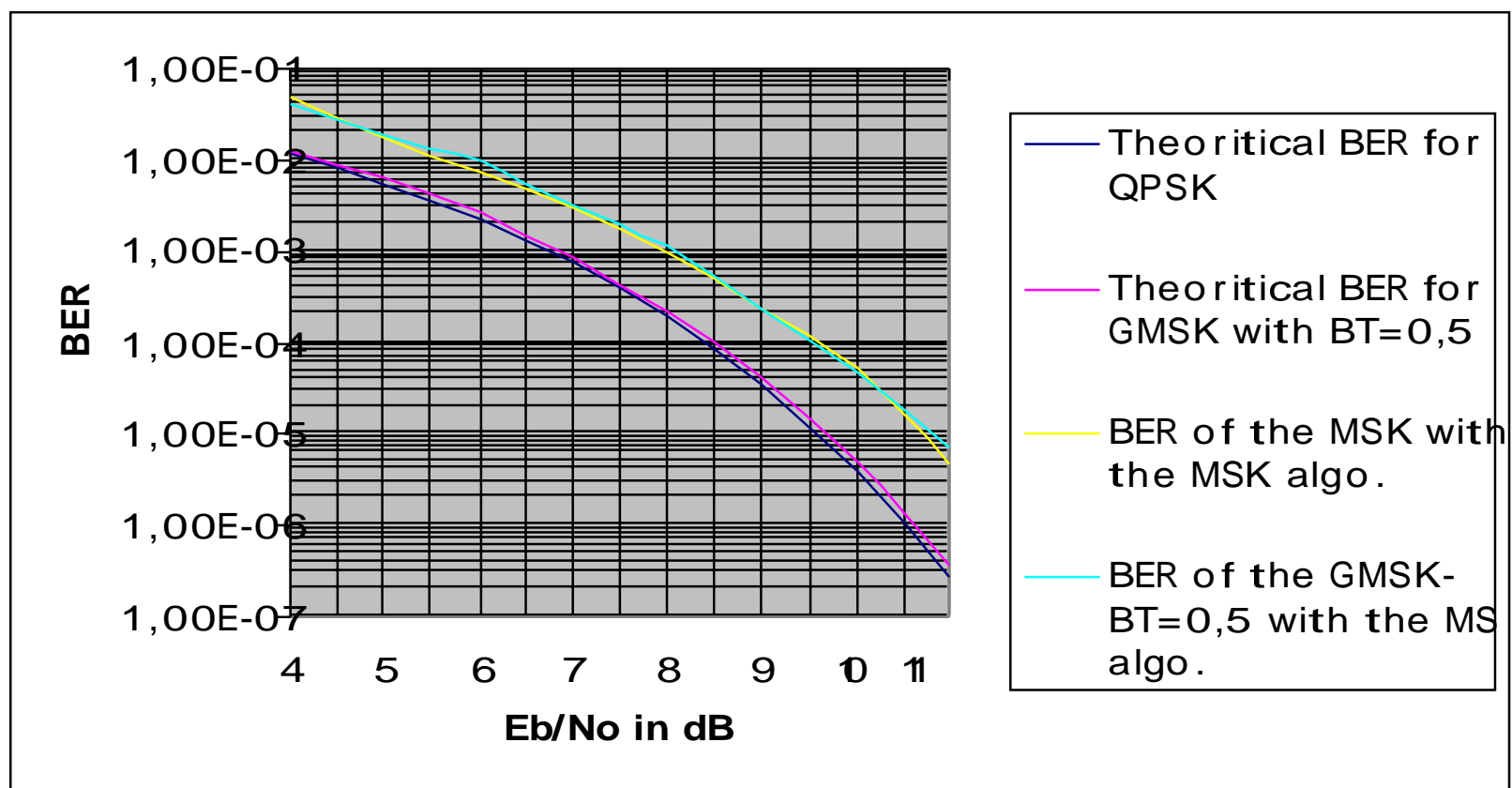
AR/S11



CENTRE NATIONAL D'ETUDES SPATIALES

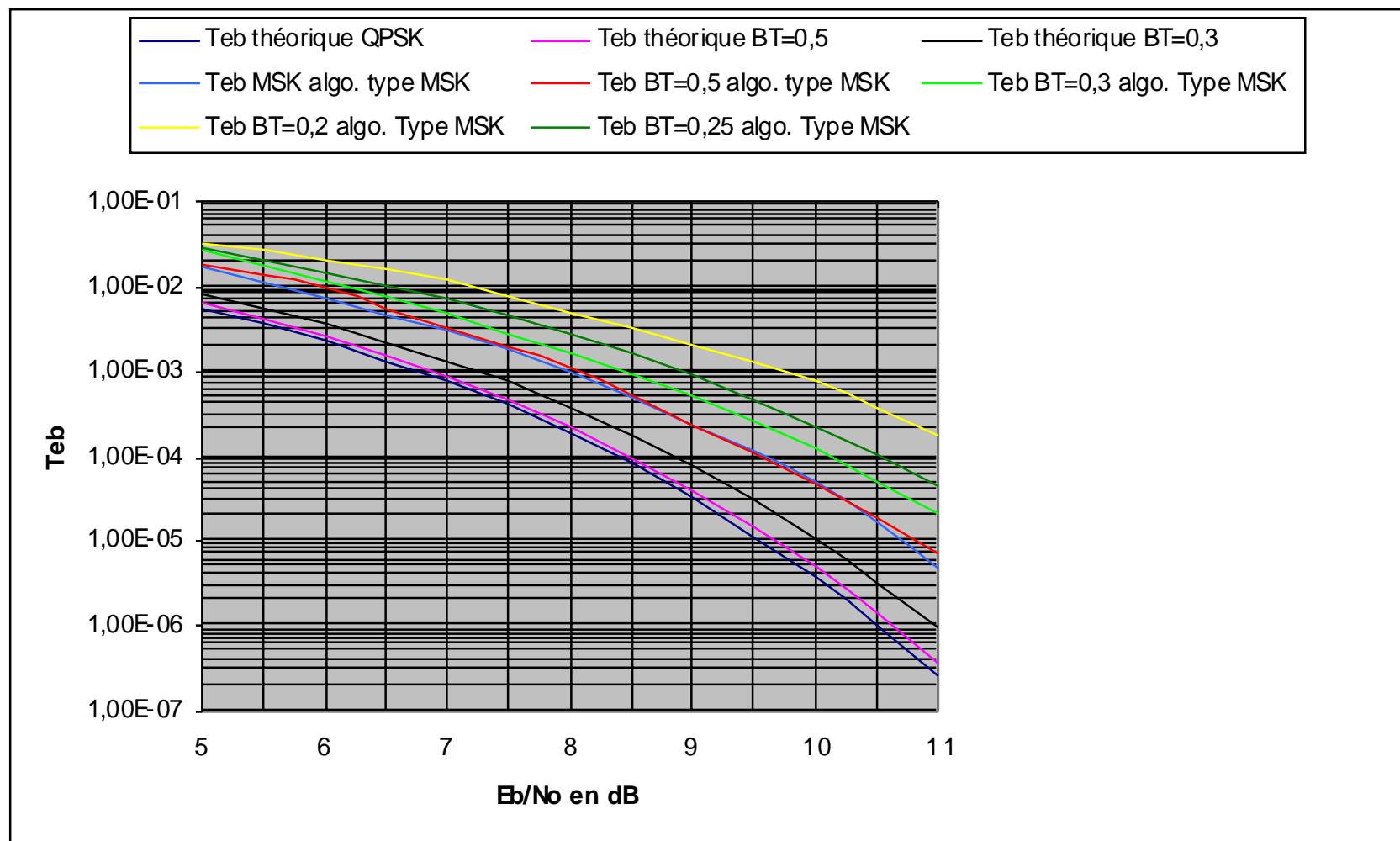
GMSK Performances Analysis

BER results for the GMSK $BT_b=0.5$



GMSK Performances Analysis

Results for different BT_b with the same algorithm



Conclusions:

- The performances of MSK and GMSK- $BT_b=0,5$ are very close, we find an implementation losses of about 1dB.
- The algorithm does not matched very well with the other GMSK BT_b products.
- When the BT_b product decrease the eye diagram is decreasing also, the MSK phase pattern are not matched.
- The solution is to implement the optimum demodulation and detection of CPM signal.



GMSK Performances Analysis

GMSK Simulated BER performances for $BT_b = 0,5$ with Viterbi Algorithm



CENTRE NATIONAL D'ETUDES SPATIALES

GMSK Performances Analysis

Optimal demodulation and detection of CPM signals

- To increase the performances the Viterbi algorithm must be used to take into account the memory of the modulation.
- Any CPM can be describe by a phase treillis. The maximum likelihood sequence detector that searches the paths through the state treillis for the minimum Euclidean distance path can be achieve by the Viterbi algorithm.

Optimal demodulation and detection of CPM signals

$$S(t) = \cos \left(\omega_0 t + \varphi_0 + 2\pi h \sum_{i=-\infty}^n \alpha_i q(t - iT_b) \right)$$

$$\phi(t, \alpha) = \pi h \sum_{i=-\infty}^{n-L} \alpha_i + 2\pi h \sum_{i=n-L+1}^n \alpha_i q(t - iT)$$

$$\phi(t, \alpha) = \Theta_n(t; \alpha)$$

Optimal demodulation and detection of CPM signals

$$\theta(t, \alpha) = 2\pi h \underbrace{\sum_{i=n-L+1}^{n-1} \alpha_i q(t - iT)}_{\text{Correlative state vector}} + 2\pi h \underbrace{\alpha_n q(t - nT)}_{\text{Contribution from the most recent bit}}$$

$$\phi(t, \alpha) = \theta_n + 2\pi h \sum_{i=n-L+1}^{n-1} \alpha_i q(t - iT) + 2\pi h \alpha_n q(t - nT)$$



CENTRE NATIONAL D'ETUDES SPATIALES

GMSK Performances Analysis

Optimal demodulation and detection of CPM signals

- The state of the CPM signal at time $t=nT$ may be expressed as the combined phase state and correlative state denoted as (for a partial response signal pulse of length LT , $L>1$):

$$S_n = \{\theta_n ; \alpha_{n-1} ;; \alpha_{n-L+1}\}$$

Optimal demodulation and detection of CPM signals (1)

- In this case, the number of states of the treillis is:

$$N_s = \gamma M^{L-1} \quad \text{When } \mu \text{ is even}$$

$$N_s = 2\gamma M^{L-1} \quad \text{When } \mu \text{ is odd}$$

for a M-ary modulation with the modulation index $h = \mu / \gamma$

Optimal demodulation and detection of CPM signals (2)

Metric computations:

$$CM_n(\alpha) = \int_{-\infty}^{(n+1)T_b} r(t) \cos(\omega_0 t + \phi(t; \alpha)) dt$$

$$CM_n(\alpha) = CM_{n-1} + \int_{nT_b}^{(n+1)T_b} r(t) \cos(\omega_0 t + \phi(t; \alpha)) dt$$



Optimal demodulation and detection of CPM signals (3)

$$\Rightarrow S_n = \{\theta_n; \alpha_{n-1}\}$$

For the GMSK-BT_b=0.5, L=2.0

$$\Rightarrow N_s = 8$$

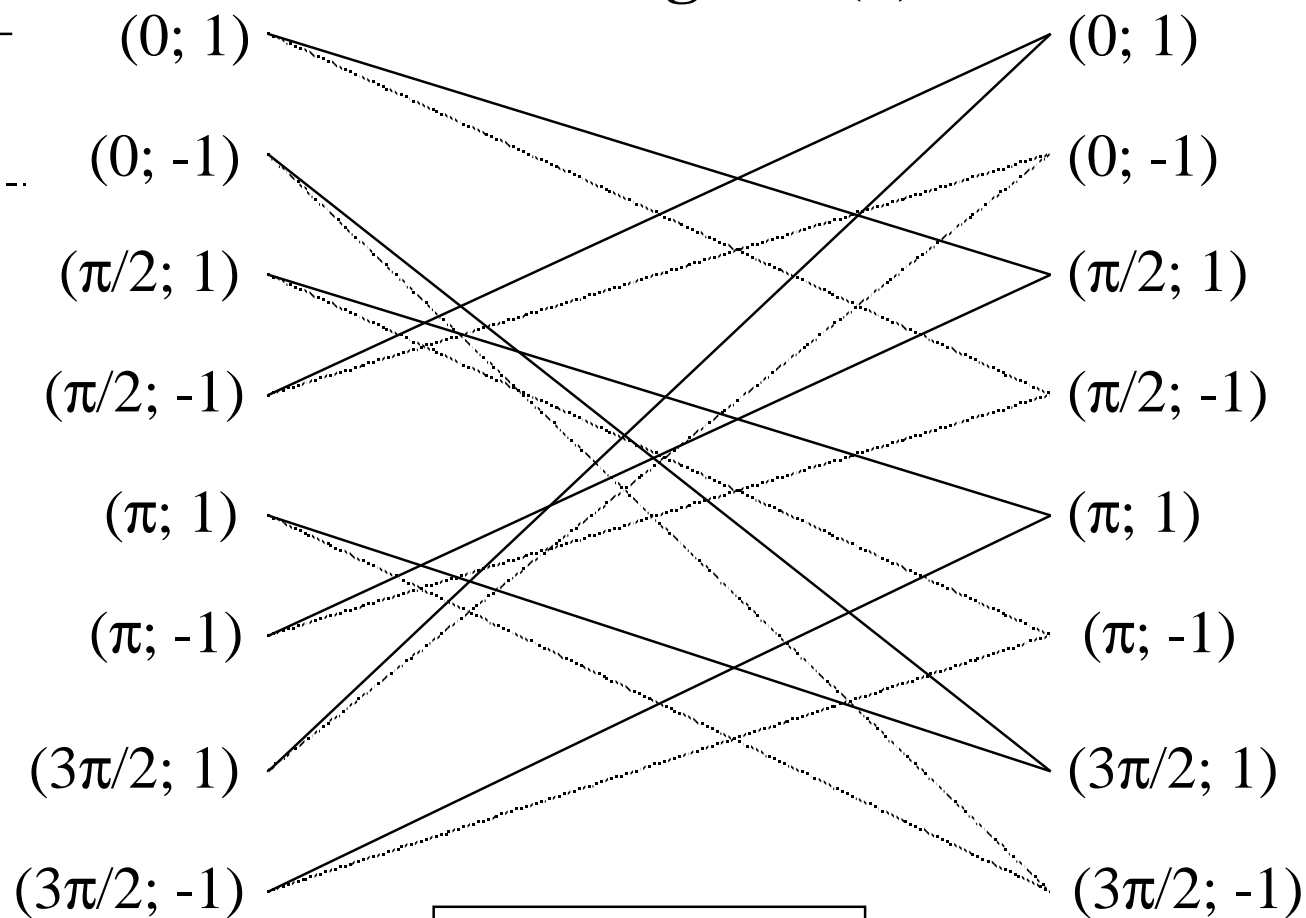
Viterbi Algorithm Characteristics

- ACS on the 16 parallel branch (BT_b=0.5 Case) and choice of 8 survival paths
- BMC on 31 successive bits
- 16 Correlations performed with the actual form of q(t) (optimum pulse shaping)
- No quantification is applied for BMC

Optimal demodulation and detection of CPM signals (4)

$\alpha_i = 1$

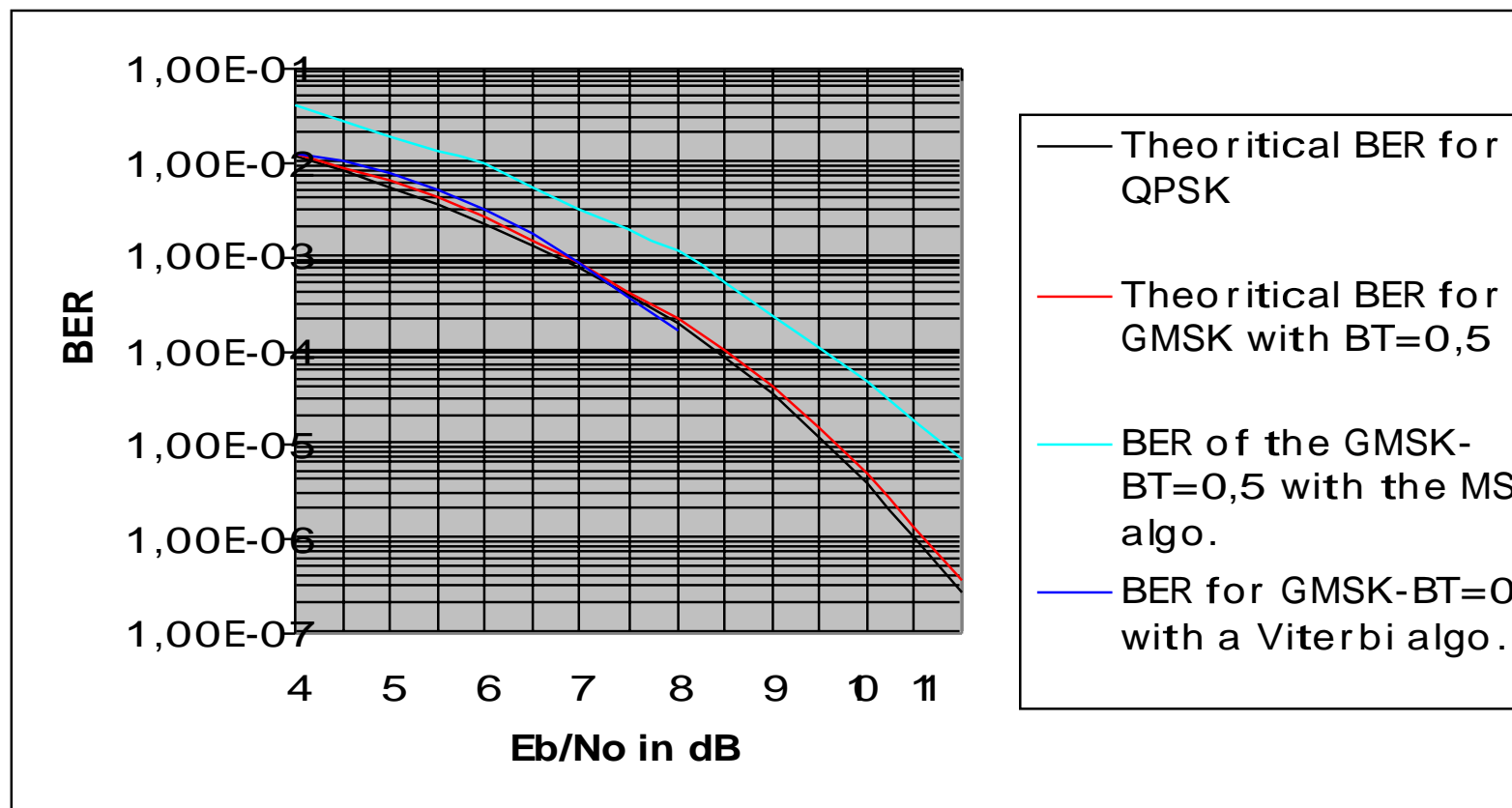
 $\alpha_i = -1$



Viterbi butterfly

GMSK Performances Analysis

BER simulation results for $BT_b = 0.5$ (Carrier and Timing recovery are perfect)



BER simulation results (carrier and timing recovery are perfect)

Conclusions for $BT_b = 0.5$:

-GMSK with $BT_b=0.5$ has a minimum Euclidian distance $E_d=1.95$ (ref 1) while $E_d=2$ for QPSK.

-The theoritical losses regarding the performances of QPSK are 0.11 dB. The simulated results with Viterbi algorithm are in accordance with this value (the point at $E_b/N_o=8$ dB is not very accurate due to a non sufficient number of errors)

Ref 1: Murata & Hirade (IEEE COM 29-July 81)



GMSK Performances Analysis

GMSK Performances extrapolation for $BT_b=0,25$, with Viterbi Algorithm

GMSK Performances Analysis

BER estimation for $BT_b = 0.25$ (Detection based on Viterbi Algorithm)

- For GMS K with a $BT_b < 0.5$ the detection algorithm is the same, but the Viterbi butterfly has more state number.
- Example: for GMSK- $BT_b=0.25$, $L=4$ and the Node number $N_s=32$
- The theoretical performances will be reached with the Viterbi Algorithm, as it is observed for GMSK with $BT_b=0.5$
- The minimum “Euclidian distance” E_d for $BT_b=0.25$ is 1,7 (Ref:1) instead of $E_d=1.95$ for $BT_b=0.5$
- The loss in comparison to QPSK ($E_d=2$) is 0.7 dB
- Unless any “Implementation Losses”, the ultimate performances of GMSK with $BT_b=0.25$ will be given by:

$$BER = \frac{1}{2} \left(1 - \operatorname{erf} \sqrt{\frac{1.7 E_b}{2 N_0}} \right)$$

[This page intentionally left blank.]

CCSDS Panel 1E

Document 99/37

Comparison of results on losses of SRRC-OQPSK in a non-linear channel

Marco Luise¹ Gabriella Povero² Enrico Vassallo³ Monica Visintin⁴

Nordwijk, October 1999

1 Introduction

In the CCSDS meeting held in Newport B., CA, in April 1999, a question arose about the validity of some results related to the following transmission system:

- OQPSK modulator;
- baseband filtering with a square root raised cosine filter (roll-off factor 0.5);
- TWT amplifier, driven at 0 dB back-off;
- ideal receiver with matched filter and threshold detector.

While Politecnico di Torino [1]–[2] and CNES [4] reported an overall end-to-end loss of less than 1 dB with respect to ideal BPSK at a bit error rate equal to 10^{-3} , University of Pisa [3] indicated a loss of about 3.5 dB.

An investigation was therefore necessary to try and explain the differences between these results.

¹ University of PISA

² COREP, Politecnico di Torino

³ ESOC, European Space Agency

⁴ Dipartimento di Elettronica, Politecnico di Torino

2 The measurements

A first difference in the work carried out in [1]-[2] and [3] lies in the definition of loss with respect to an ideal BPSK system, and in the method of measuring it.

The definition used in [1]-[2] is as follows: being E_b/N_0 (dB) the signal to noise ratio necessary to get the given BER for the ideal BPSK system, the loss is the difference between $E_{b,sat}/N_0$ (dB) and E_b/N_0 (dB), where $E_{b,sat}$ is the energy of the signal at the output of the amplifier driven at 0 dB back-off by an unmodulated carrier in the bit time interval T_b , and $N_0/2$ is the noise power spectral density which allows to measure the given error probability in the presence of the nonlinearity.

Notice that, if the amplifier is driven at an input backoff (IBO) different from zero, the value of $E_{b,sat}$ does not change, while N_0 changes; if IBO is high, the received signal is weak and $E_{b,sat}/N_0$ increases; if IBO is low, the received power is high but intersymbol interference (ISI) is heavy and $E_{b,sat}/N_0$ is high again; in-between an optimum backoff exists that minimizes $E_{b,sat}/N_0$.

From a simulation point of view, it is sufficient to define the value of the energy $E_{b,sat}$ (generally the TWTA has a normalized maximum output power equal to 0 dB, so that $E_{b,sat}=T_b$), and generate an additive white Gaussian noise with a suitable power spectrum $N_0/2$ so that the measured BER is as required; then the signal to noise ratio is $E_{b,sat}/N_0$ (the true signal energy E_b' at the receiver, which depends on IBO, is never measured).

In PISA's report [3], instead, the overall loss (dB) is given as the sum of two terms D1 and D2 where:

- D1 (dB) is the loss due to the distortion introduced by the nonlinearity in its operating point (because of ISI, only);
D1 can be measured by comparing the ratios E_b/N_0 (dB) and E_b'/N_0 (dB) necessary to measure the given BER in the ideal system and in the nonlinear system, where E_b' is the received energy in the nonlinear system (it depends on IBO, and it must be measured).
- D2 (dB) is the loss due to the fact that the operating point of the amplifier is different from the maximum power efficiency (IBO=0 dB) and that the nonlinearity compresses the modulated signal, thus reducing its power;
D2 can be measured by comparing the maximum output power of the amplifier (driven by a pure carrier) and the power of the modulated signal at the output of the amplifier working at the assumed operating point.

From a simulation point of view, it is necessary to measure the signal power at the output of the nonlinearity, to determine D2 and E_b' , and run different simulations until the value of N_0 is found which gives the required BER.

If correctly used, the two definitions give the same results, the second having the advantage of separating the term due to ISI alone, and the term due to the power loss. The first definition corresponds to an easier simulation and a more direct measure, which leads to fewer errors.

3 Comparison

University of Pisa provided Politecnico di Torino with the AM/AM and AM/PM curves of the nonlinear amplifier (TWTA1) that presumably had been used to derive the results given in [3].

However that nonlinearity turned out to give values of D1 and D2 different from those reported in [3]. While a difference in the value of D1 (loss due to ISI) could be explained with the fact that a real synchronizer had been used in [3], the difference in D2 (power efficiency loss) can only be explained by assuming that a different nonlinearity had actually been considered in [3].

Unfortunately, University of Pisa could not recover the original simulation programs ran for the report, about 10 years ago. Politecnico compared the values of D1 and D2 obtained with TWTA1, with those reported in [3], and with those obtained with the TWT amplifier (TWTA0) used in the current CCSDS analysis, and with another TWTA of the TOPSIM library (TWTA2), which was in use in 1990.

The simulations were performed considering 32 samples per OQPSK symbol and an SRRC FIR filter with impulse response lasting 10 symbols.

The transmitter used a carrier with phase equal to zero. The TWT amplifier phase shift at each IBO (which can be read from the AM/PM curve) was compensated, the carrier used at the receiver had a fixed phase equal to zero, the clock used at the receiver sampled the signal at the maximum eye opening.

The losses were measured using a semi-analytical technique (noise was not simulated, and the error probability curve was measured by averaging the instantaneous error probabilities for the received signal affected by ISI and power loss).

Figure 1 - CCSDS TWTA Characteristics

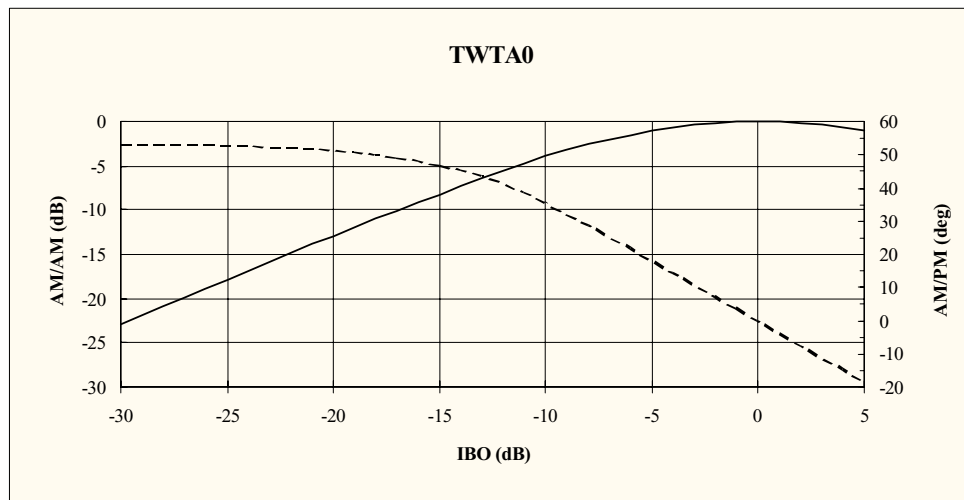


Figure 2 - PISA TWTA Characteristics

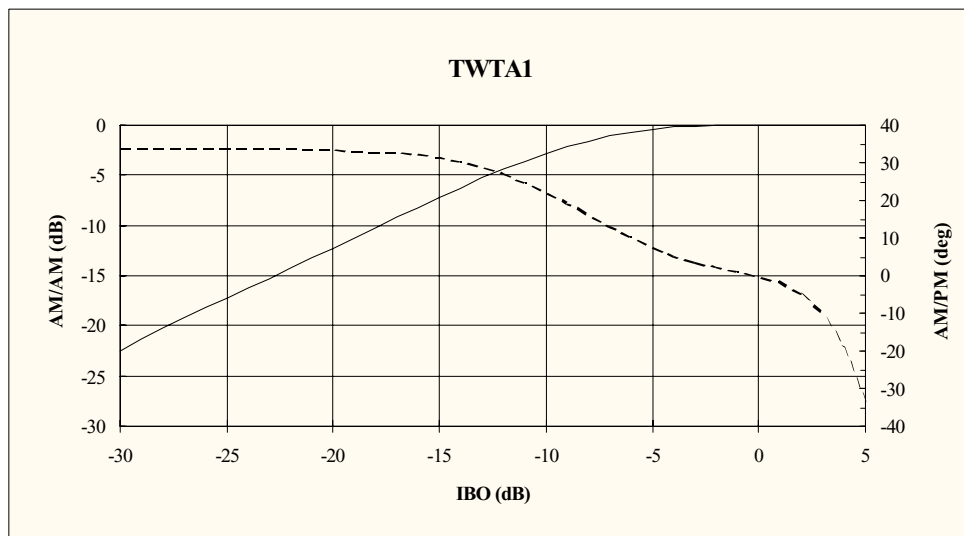


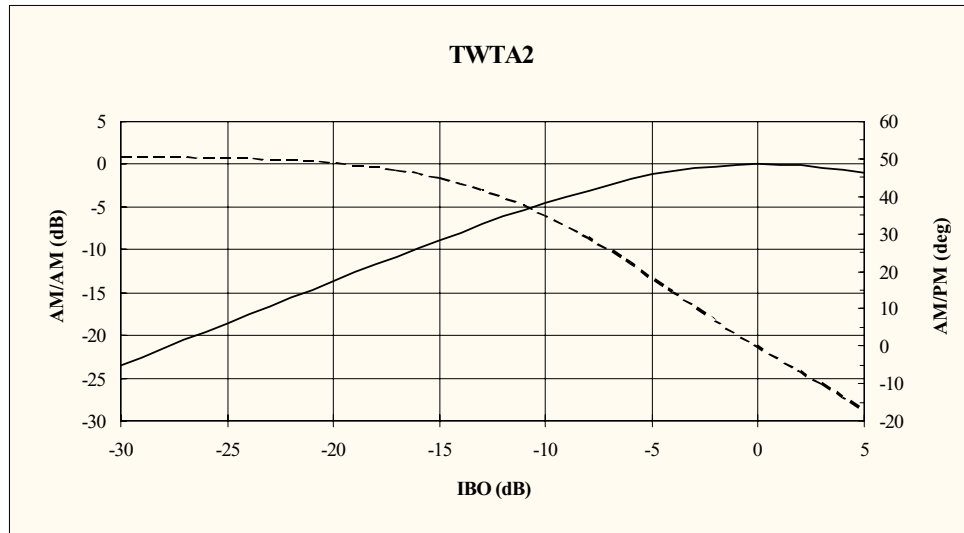
Figure 3 - Topsim Standard TWTA Characteristics

Table 1 shows the measured values of D2 (dB), the power efficiency loss, for different values of input backoff (IBO).

Table 1 – Power Efficiency Losses (D2 [dB])

IBO (dB)	D2 for TWT A0 (CCSDS TWTA)	D2 for TWT A1 (PISA TWTA)	D2 for TWT A2 (TOPSIM TWTA)	D2* in [3]
0	0.119	0.033	0.132	0.2
1	0.183	0.067	0.206	0.4
2	0.327	0.129	0.371	0.6
3	0.548	0.227	0.628	0.9
4	0.845	0.375	0.973	1.4
5	1.213	0.597	1.402	2.0
6	1.647	0.901	1.911	2.4

Table 2 shows instead the values of D1 (dB), the Inter-Symbol Interference Loss, at $\text{BER}=10^{-3}$.

Table 2 – ISI Losses (D1 [dB]) @ $\text{BER}=10^{-3}$

IBO (dB)	D1 for TWTA0 (CCSDS TWTA)	D1 for TWTA1 (PISA TWTA)	D1 for TWTA2 (TOPSIM TWTA)	D1* in [3]
0	0.674	0.611	0.659	3.3
1	0.581	0.566	0.559	2.2
2	0.499	0.536	0.472	1.8
3	0.426	0.493	0.397	1.2
4	0.369	0.430	0.335	0.9
5	0.321	0.363	0.283	0.8
6	0.280	0.303	0.239	0.8

Finally, table 3 shows the total loss (TL) (dB) at $\text{BER}=10^{-3}$; the total loss is here the sum of D1 and D2. The total loss for TWTA0 was also measured with the technique used in [1] and found to be the same.

Table 3 – Total Losses (D1+D2 [dB]) @ $\text{BER}=10^{-3}$

IBO (dB)	TL for TWTA0 (CCSDS TWTA)	TL for TWTA1 (PISA TWTA)	TL for TWTA2 (TOPSIM TWTA)	TL* in [3]
0	0.793	0.644	0.791	3.5
1	0.764	0.633	0.765	2.6
2	0.826	0.665	0.843	2.4
3	0.974	0.720	1.025	2.1
4	1.214	0.805	1.308	2.3
5	1.536	0.960	1.685	2.8
6	1.927	1.204	2.150	3.2

It can be noticed that the main difference between the total losses given in [3] and those measured by Politecnico is due to D1. The values of D2 are different, but they are comparable (notice that D2 of [3] for a given IBO is equal to D2 of TWTA2 for IBO+1 dB), at least for small values of IBO.

Thus it can be argued that the hypothesis about the receiver assumed by Politecnico and by the University of Pisa are different, and this can only be due to a different structure of the synchronization unit.

The presence of a non-ideal synchronizer was not explicitly stated in the chapter of [3] related to the nonlinear amplifiers; however, most of [3] deals with synchronization, so that it is reasonable to assume that a real synchronizer was present also in the non-linear channel simulations.

* These values were taken from the pictures given in [3] and are therefore approximate.

The total losses measured by Politecnico with the 3 different nonlinearities (TWTA0, TWTA1 and TWTA2) are comparable, and the total losses measured with the two different definitions are identical: this assures that the results obtained by Politecnico and CNES related to the CCSDS activities are reliable, as far as the synchronization hypothesis are valid.

4 Conclusions

A comparison of Politecnico's and PISA's results on SRRC-OQPSK losses in a non-linear channel (TWTA) reported at the Spring 1999 CCSDS meeting has been carried out.

The final results are the following:

1. University of Pisa used different AM/AM and AM/PM characteristics for the TWT amplifier being baselined for CCSDS work;
2. University of Pisa simulated the presence of a specific synchronizer (frequency quadricorrelator), different from the Costas loop considered by CCSDS, therefore adding a loss due to imperfect symbol and carrier phase synchronization.

As a consequence the results reported by Pisa cannot be directly compared with those found by Politecnico and CNES but are necessarily higher.

References

- [1] G.Povero, M.Visintin, *Interference Susceptibility of Selected Bandwidth-Efficient Modulation Schemes*, ESA Report , April 1999
- [2] G.Povero, M.Visintin, E. Vassallo, *Interference Susceptibility of Selected Bandwidth-Efficient Modulation Schemes*, CCSDS Panel 1E, May 1999
- [3] N. A. D'Andrea, M.Luise, U. Mengali, R. Reggiannini, *Advanced Modulation Schemes for Future ESA Standards*, ESA Report, March 1991
- [4] A. Ribes et. alii, *8/16 Multi-D Trellis Coded Modulation – an alternative to improve Power/Bandwidth efficiency for high data rate communications*, CCSDS Meeting, April 1999

[This page intentionally left blank.]

CCSDS P1E 99/41

Nonlinearity Effects on Raised Cosine Power Spectrum

T. Eng
9/15/99

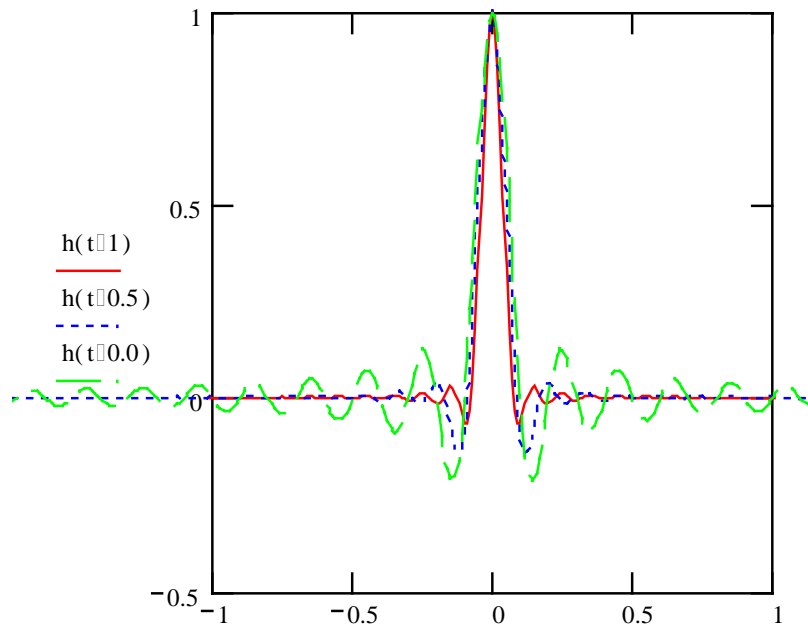
Objective

- Investigate the effect of a nonlinear operation (e.g., TWTAs) on the power spectrum of a bandlimited signal.
 - Input signal consists of a single pulse of the ‘root raised cosine’ impulse response. Parameterized by the roll-off factor ‘r’.
 - Evaluate the power spectrum of the signal at nonlinearity output and compare with that of input signal.

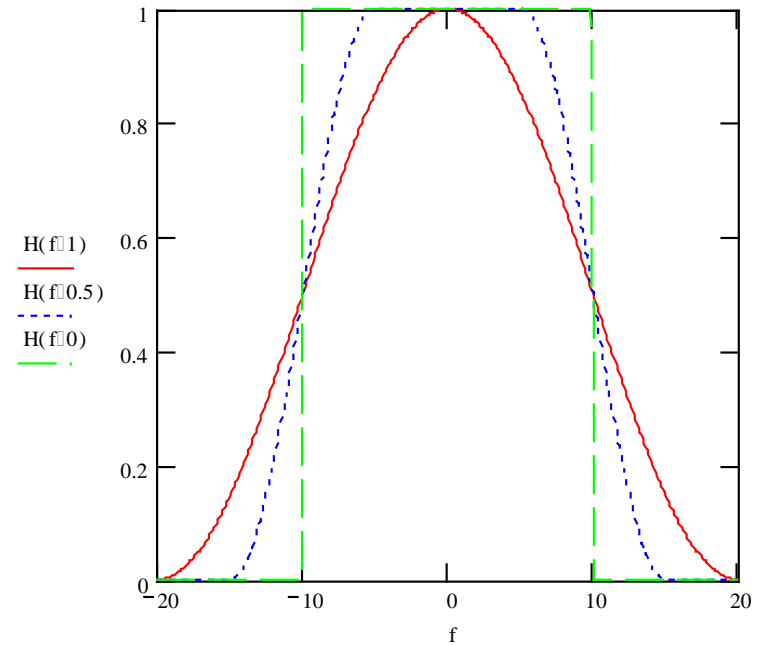
Raised Cosine Signal

$r = 1.0, 0.5, 0.0$

time waveform

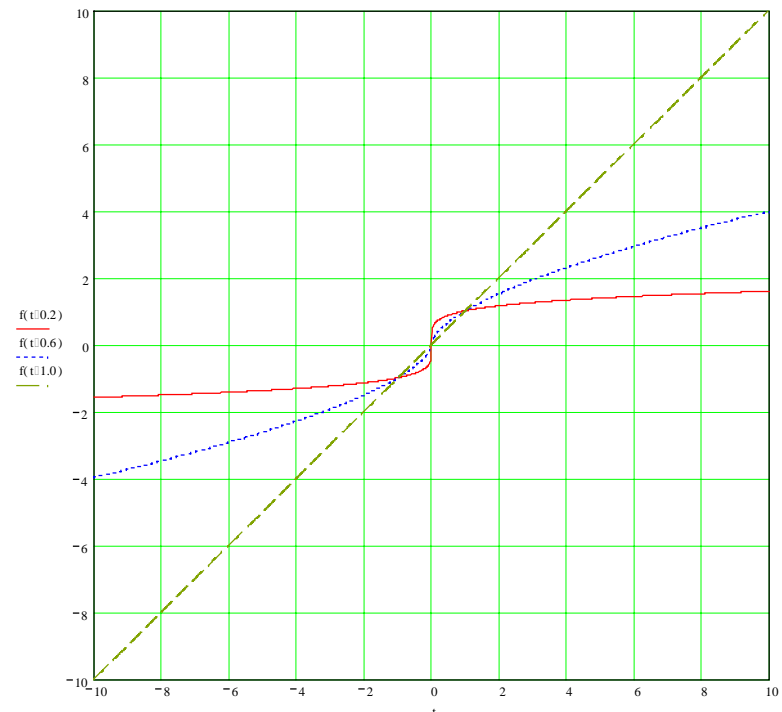


power spectrum



Nonlinearity Model

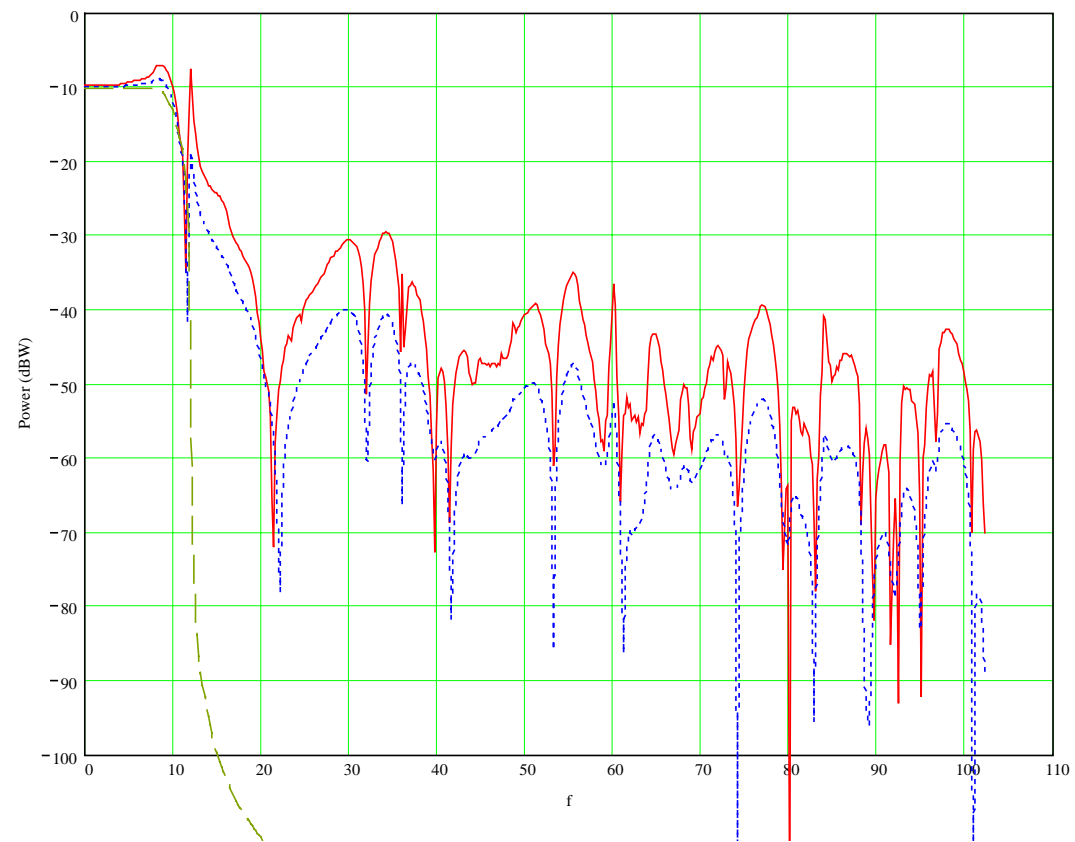
- Modelled as mu-law operator
 - output = μ^{th} power of input
 - $0 < \mu < 1$
 - $\mu = 1$: linear channel
 - $\mu = 0$: hard limiter



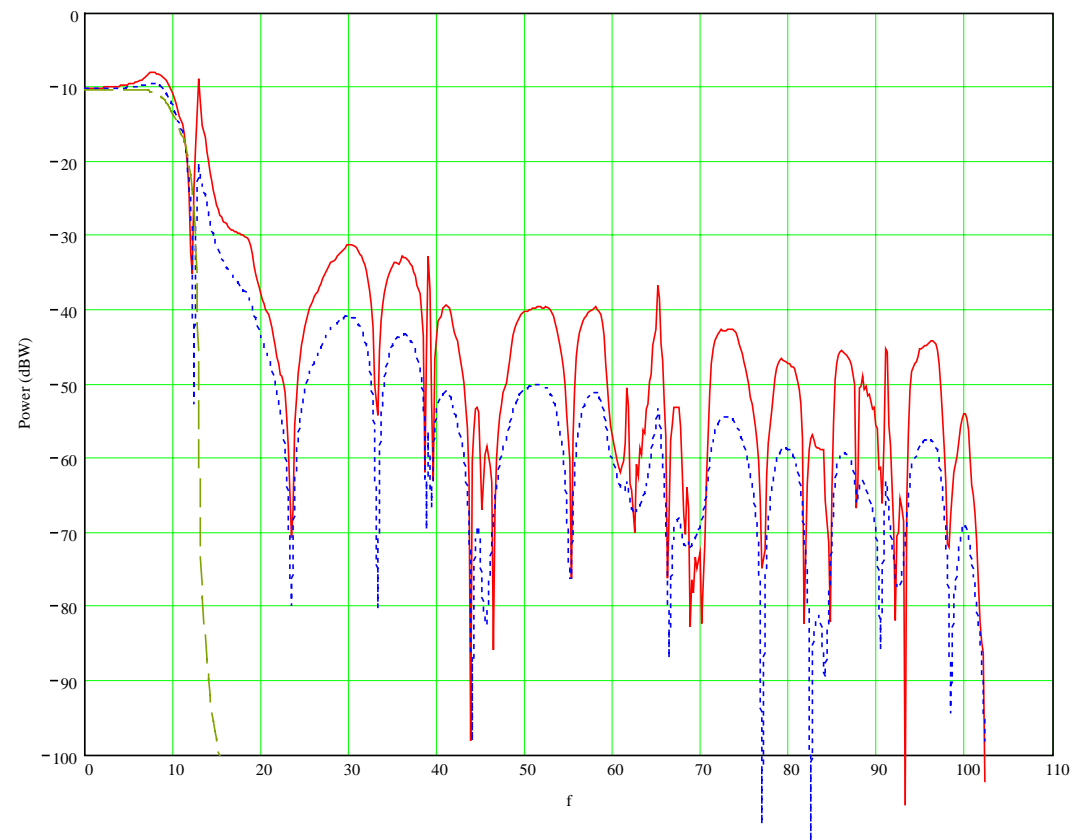
Numerical Results

- Power spectrum calculations done by FFT feature of MathCad.
- Time series of output signal obtained by sampling from $t = -5$ to $t = 5$. Number of samples = 1024.
- Symbol rate set at 10.
- Roll-off factor set at 0.2, 0.3, and 0.5.
- Mu set at 0.6, 0.8, and 1.0.

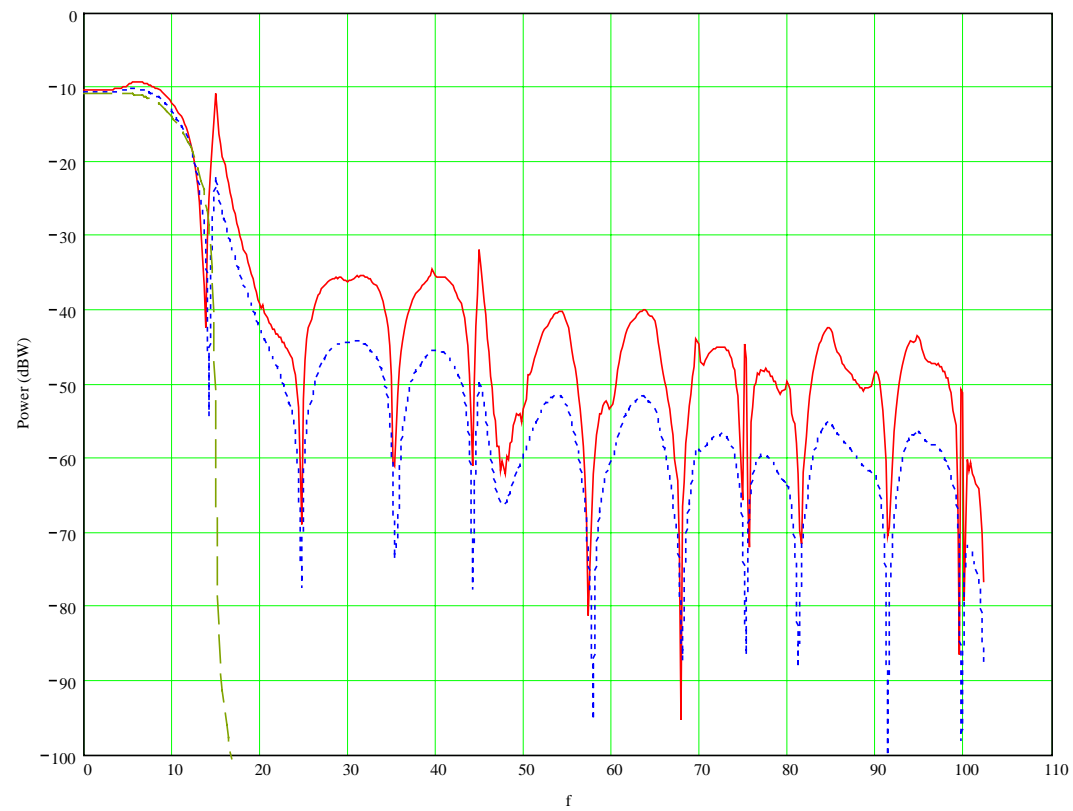
$R_s = 10$, $r = 0.2$, $\mu = 0.6$ (solid), 0.8 (dot), 1.0 (dash).



$R_s = 10$, $r = 0.3$, $\mu = 0.6$ (solid), 0.8 (dot), 1.0 (dash).



$R_s = 10$, $r = 0.5$, $\mu = 0.6$ (solid), 0.8 (dot), 1.0 (dash).



Conclusions

- Significant spectral regrowth is observed when raised cosine pulse is operated on by nonlinearity.
- Regrowth may be mitigated (to some extent) by:
 - increasing excess bandwidth (roll-off factor) of transmitted signal, and/or
 - reducing degree of channel nonlinearity.

[This page intentionally left blank.]

**NASA GSFC Bandwidth Efficient Modulation and Coding Systems Study
QPSK with Square Root Raised Cosine Filtering Evaluation
Follow-up Information for CCSDS Panel 1E Presentation**

D. Zillig

NASA/Goddard Space Flight Center, Greenbelt, MD 20771

Tel: (301) 286-8003; Fax: (301) 286-1724; E-mail: david.j.zillig.1@gsfc.nasa.gov

J. Brase, M. Burns

ITT Advanced Engineering & Sciences, 1761 Business Center Drive, Reston, VA 20190

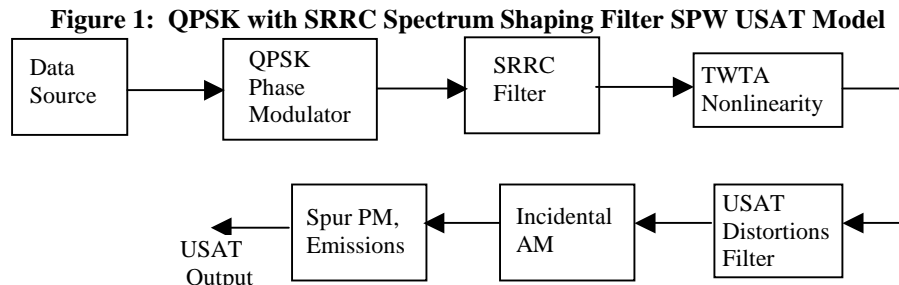
Tel: (703) 438-8198; Fax: (703) 438-8112; E-mail: james.brase@itt.com

1. Introduction

Results from an ongoing NASA GSFC study into the performance of Bandwidth Efficient Modulation and Coding Techniques in Ka-Band Channels were presented to the CCSDS Member Panel on Radio Frequency and Modulation Systems during the Oct 18-22, 1999 meeting. These results included TDRS and direct-to-ground channel Bit Error Rate (BER) performance simulation results and Power Spectral Density (PSD) plots for a QPSK with Square Root Raised Cosine (SRRC) filtering modulation technique. The presentation prompted requests for additional information on the specific implementation of this technique, which were formalized in Action Item 99-1E-39. This paper is intended to answer these questions.

2. Model

Figure 1 depicts the QPSK with SRRC Filtering User Satellite (USAT) SPW model. In this model, the USAT Distortions Filter introduces the gain flatness, gain slope and phase nonlinearity corresponding to the RF/IF components of the satellite (upconverter, LNA, etc.) The TWTA nonlinearity distortions are selected to mirror a Ka-Band TWTA operating in linear mode. The SRRC baseband RF filter was designed to match the filter 3 dB bandwidth to the 650 MHz channel bandwidth.



The RF output filter also serves as an RF Output Filter for spectral containment in this modulation scheme. The final two components in the block diagram model introduce

specified amounts of the Incidental AM, Spurious PM, and Spurious Emissions distortions.

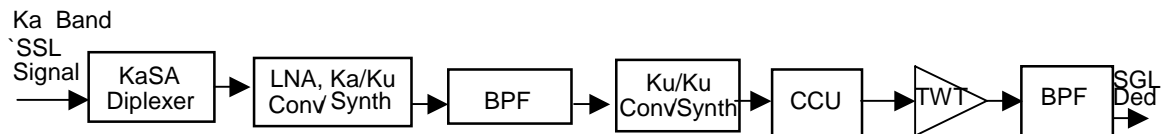
The key parameters for each of these components are provided in Table 1.

Table 1: Model Components and Parameters

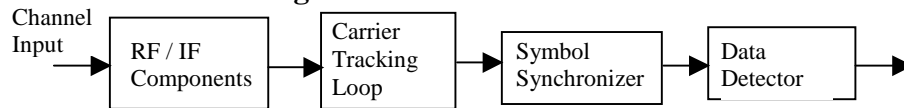
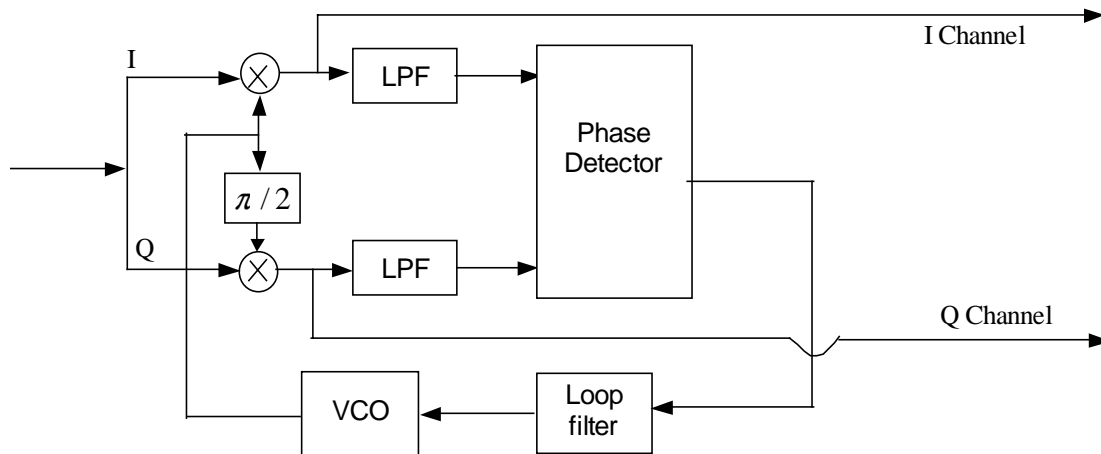
Component	Parameter	Value	Comment
Data Source / QPSK Phase Modulator	Data Rate	1020	Mbps
	Data Asymmetry	5.0	Percent, peak
	Data Jitter	0.1	
SRRC Filter	BW	510 ⁽¹⁾	MHz
	Rolloff	0.63725	
TWTA Nonlinearity	AM/AM	1.0	dB / dB
	AM/PM	2.5	deg / dB
USAT Distortions Filter	Gain Flatness	0.6	dB, peak-to-peak
	Gain Slope	0.1	dB/MHz
	Phase Non-linearity	6.0	deg, peak-to-peak
	Bandwidth	650	MHz
Others	Incidental AM	5.0	Percent
	Spurious PM	2.0	deg RMS at 510 MHz
	Spurious Emissions	-30 / -15	DBc, in-band / out-of-band
(1) Note that PSD plots presented at 10/99 meeting incorrectly used BW=1020 MHz			

Figure 2 depicts the TDRS H, I, J KaSAR Wideband Return Channel model, which was developed using a combination of as-built and CDR subcomponent specification data.

Figure 2: TDRS H, I, J KaSAR Wideband Return Channel Model



The receiver model, which is a modified version of the Second TDRS Ground Terminal high data rate receiver, is depicted in Figure 3. The RF / IF components are modeled as a single bandpass filter with distortions representing the effects of the antenna, waveguide, diplexer, downconverter, etc. The carrier tracking loop is a modified second order Costas loop as illustrated in Figure 4. The symbol synchronizer used in this receiver model is a dual channel data transition tracking loop with a second order closed loop transfer function. Detection is accomplished using a filter matched to the SRRC filter in the modulator. (See Figure 1)

Figure 3: SPW Receiver Model**Figure 4: Modified Second Order Costas Tracking Loop**

The key parameters for the RF / IF components, carrier tracking loop, adaptive equalizer, and symbol synchronizer are summarized in Table 2.

Table 2: Receiver Component Key Parameters

Component	Parameter	Value	Comment
RF / IF Distortions Filter	Gain Flatness	0.6	dB, peak-to-peak
	Gain Slope	0.1	dB/MHz
	Phase Non-linearity	6.0	deg, peak-to-peak
	Roll-off	0.574	dB / MHz
	Bandwidth	693.33	MHz
Carrier Tracking Loop	ARM Filter BW	1020	MHz
	Closed Loop BW	16.32	kHz
	Damping Factor	0.223	
Symbol Synchronizer	Loop Noise BW	207	kHz
	Damping Factor	.707	

3. Power Spectral Density Plots

The PSD plots presented at the October 1999 meeting were measured at the output of the User Satellite (USAT) and were generated using the full scope of distortions and constraints assumed for the study. Inclusion of some of these distortions, including most significantly the Spurious Phase Modulation, resulted in severely distorted modulated spectra which were insufficiently clear for the Panels' considerations.

Furthermore, the PSD plots, which were generated separately from the BER results, were based on an incorrectly-specified SRRC bandwidth value. In the SPW implementation, the SRRC filter is specified by two parameters: BW (corresponding to $1/T_s$) and rolloff. Unfortunately, for the PSD results presented at the October 1999 meeting, BW was incorrectly set to the inverse of the bit period, $1/T_b$, instead of the inverse of the symbol period $1/T_s$.

The incorrect PSD plot provided at the October 1999 meeting is provided as Figure 5. Figure 6 is the corrected PSD plot measured at the output of the USAT. Figure 7 is the same PSD without the Spurious PM and Spurious Emissions distortions. Figure 8 depicts the magnitude response of the SRRC filter. Figure 9 depicts the PSD measured at the output of the filter without any distortions from the TWTA nonlinearity or RF Distortions Filter.

Figure 5: Original Spectrum Shaped QPSK PSD Plot

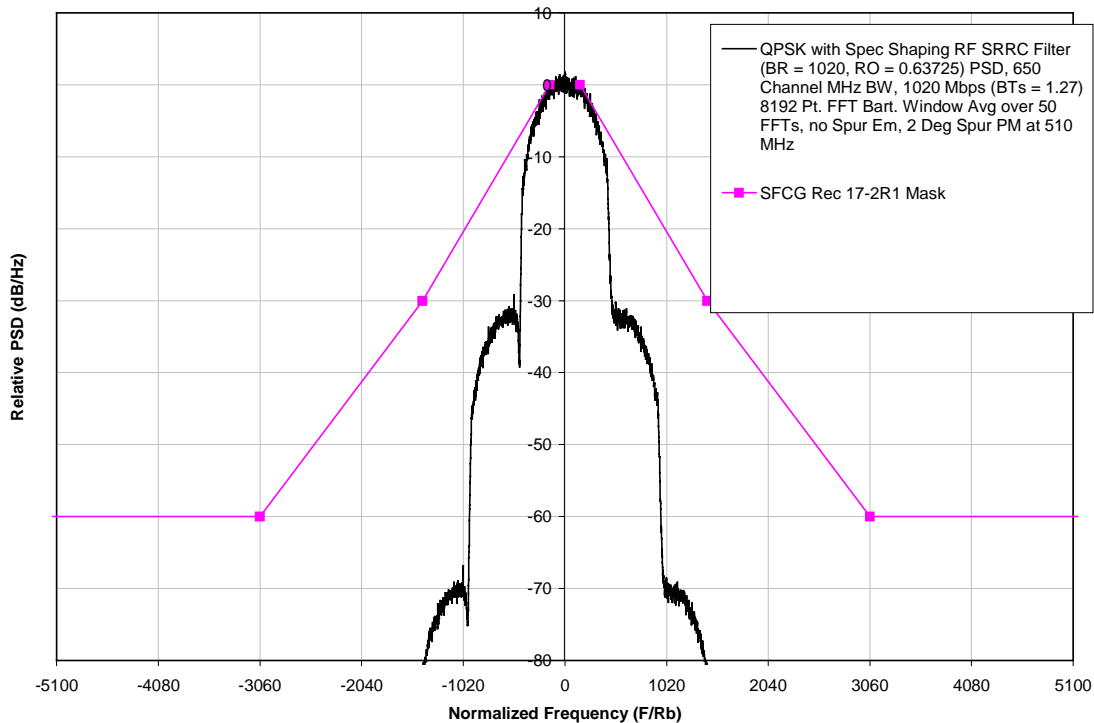


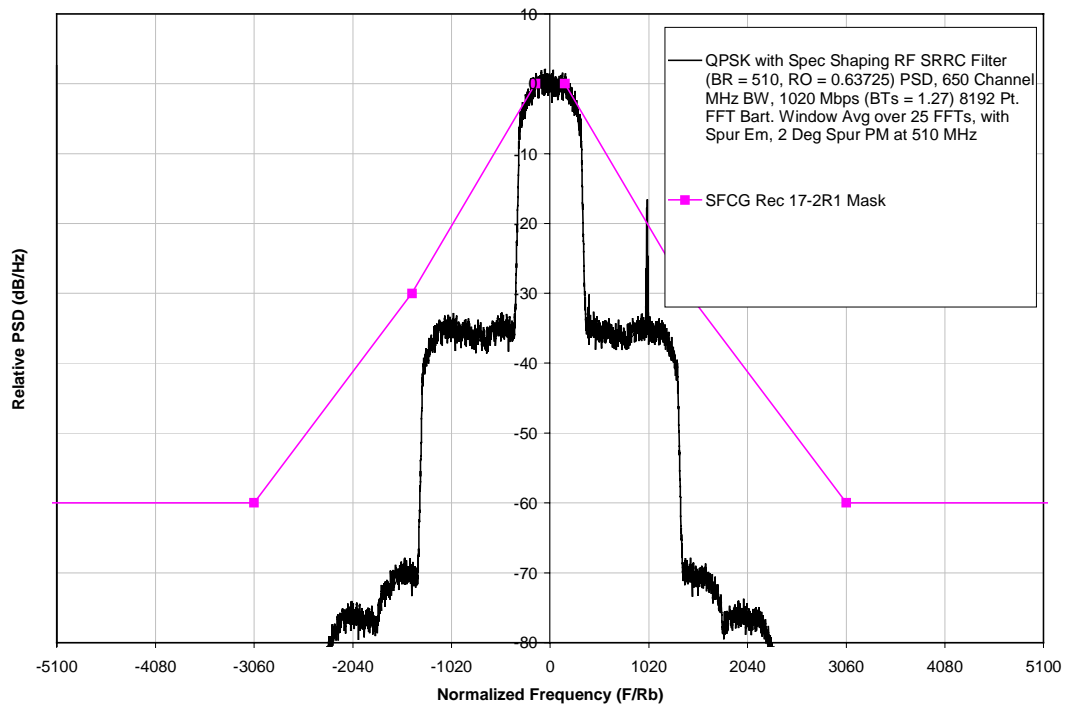
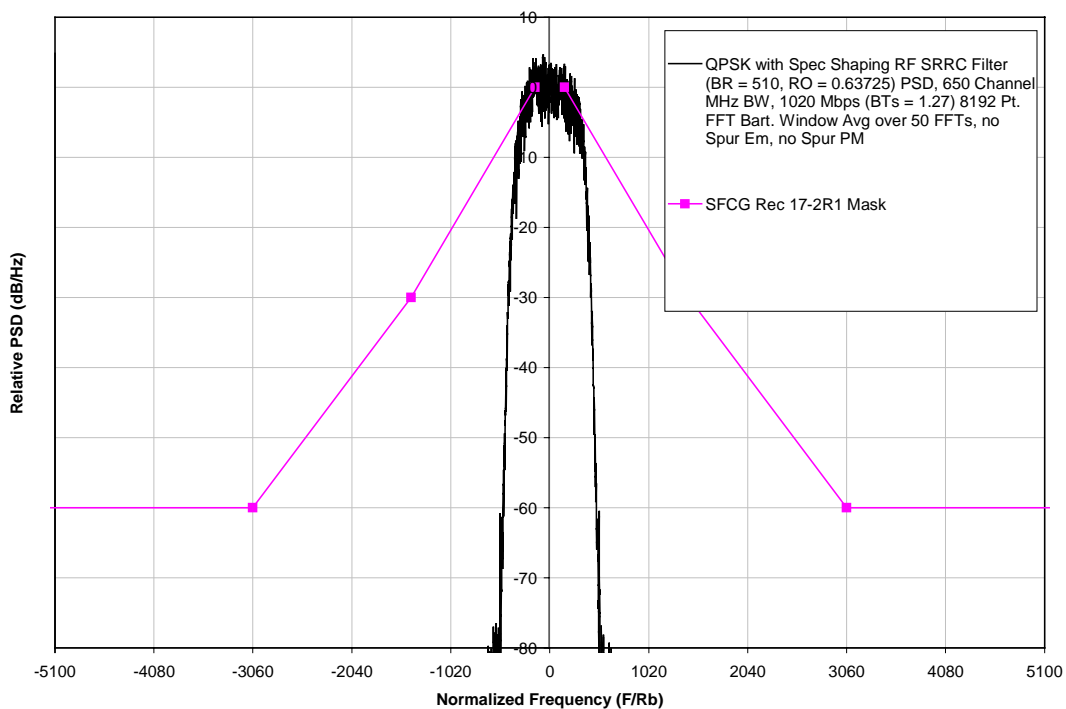
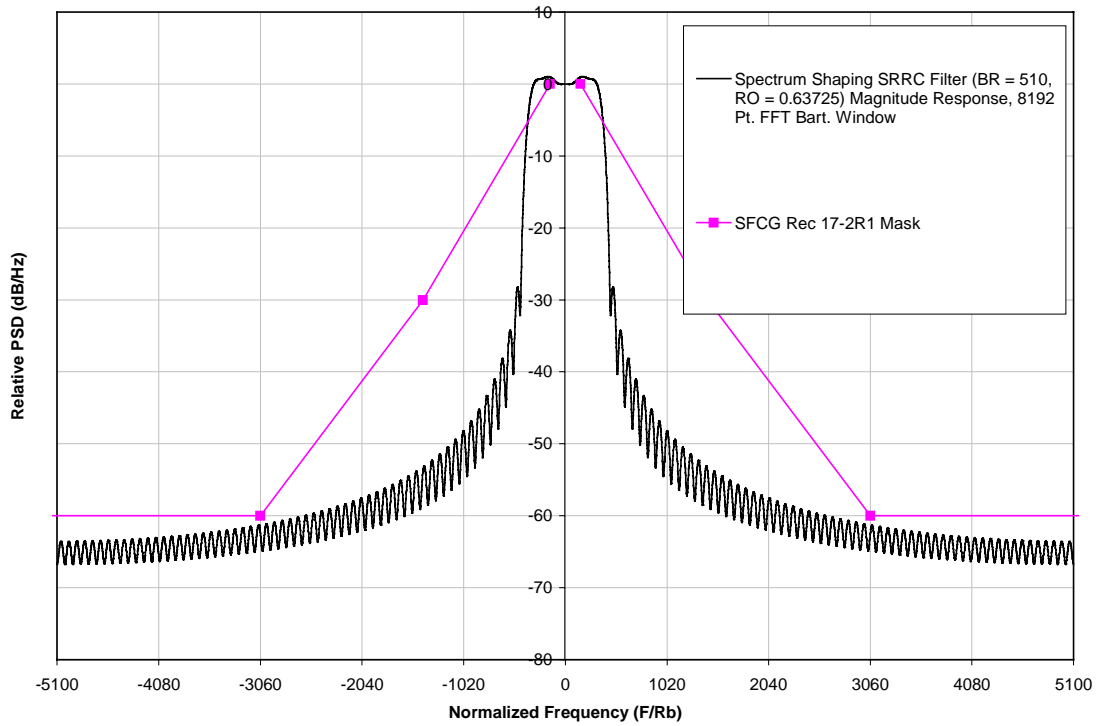
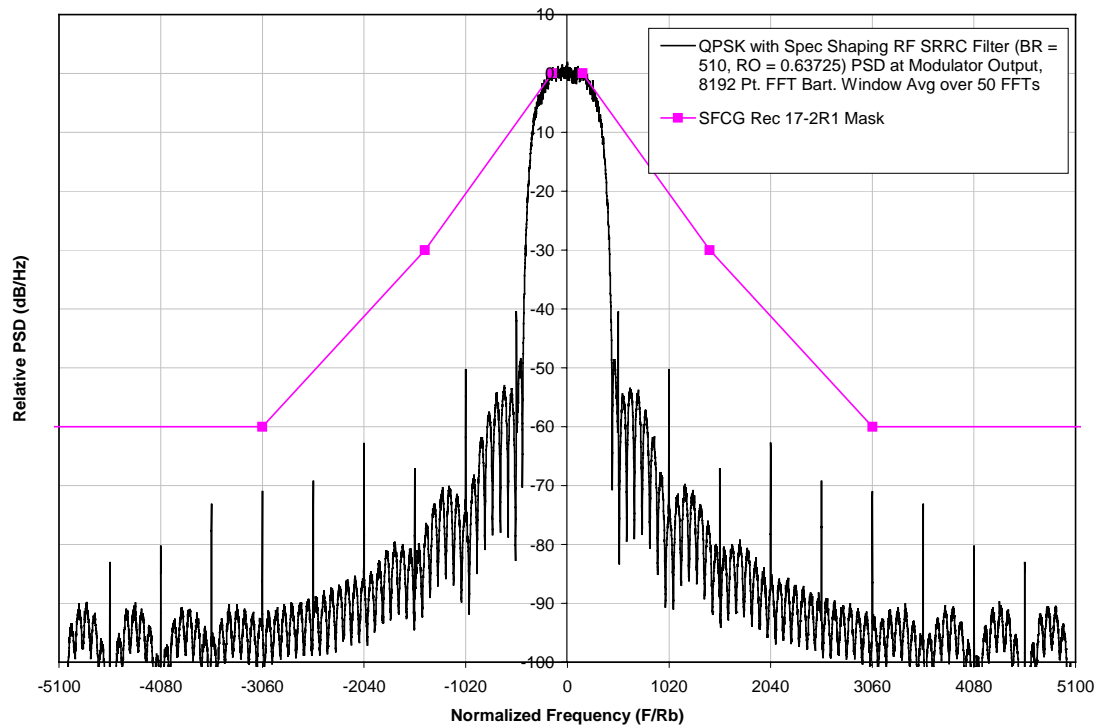
Figure 6: Corrected Spectrum Shaped QPSK Plot with Spur PM / Emissions**Figure 7: Corrected Spectrum Shaped PSD without Spurious PM / Emissions**

Figure 8: SRRC Filter Magnitude Response**Figure 9: Spectrum Shaped QPSK Ideal Modulator / Filter Output**

4. Summary

In response to action item 99-1E-39, this paper provides detailed implementation information on the QPSK with SRRC filtering modulation technique employed in paper 99/47, *Efficient Modulation and Coding Schemes for Future NASA Ka-Band Space Communications*. This paper also corrects an erroneous SRRC-filtered QPSK power spectral density plot presented at the October, 1999 meeting. Note that the bit error rate results from paper 99/47 were generated using the correct SRRC filter parameters, corresponding to the corrected PSD plots supplied herein.

[This page intentionally left blank.]

CCSDS P1E

Bandwidth-Efficient Modulation-Filtered QPSK

Kazuo Nakada

National Space Development Agency of Japan

11 May 2000

1 Introduction

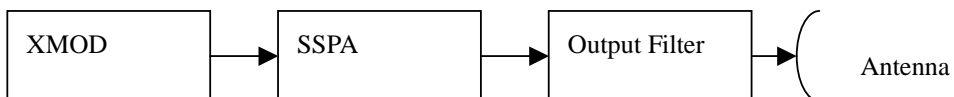
As reply to Action Item 99-1E-40, this document is to report the spectrum of filtered QPSK of ADEOS-II and ALOS satellites and to consider filtered QPSK as Bandwidth-Efficient Modulation.

2 The spectrum of filtered QPSK of NASDA satellites

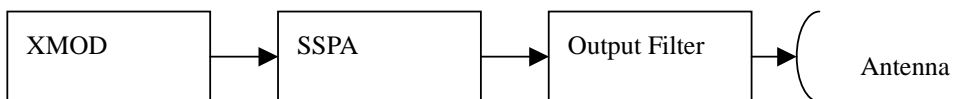
NASDA is developing the earth exploration satellites, ADEOS-II and ALOS. The spectrums of filtered QPSK of ADEOS-II and ALOS are shown in Figure 1-1 and Figure 1-3. These spectrums comply with Recommendation SFCG 17-2R1 spectrum mask (above 2Msps). The frequencies of ADEOS-II and ALOS are close to the frequency band (8450-8500MHz) of the space research service. The transmitters need no baseband filter.

Satellite	ADEOS-II	ALOS
Launch	2001	2002
Life	3 - 5years	3 - 5years
Modulation	QPSK	QPSK
Transmission rate	60Mbps	138.9Mbps
Center frequency	8150MHz	8105MHz
HPA(power)	SSPA(40W)	SSPA(40 W)
Output Back off (Input Back off)	0 dB (0 dB)	0dB (0 dB)
AM/PM	1.0 to 2.5 /dB	The same value as ADEOS-II
Output Filter Characteristics	4pole-Chebyshev Filter, BT=2(Filter characteristics are shown in Fig. 1-2)	4pole-Chebyshev Filter, BT=2(Filter characteristics are shown in Fig. 1-4)
Filter Insertion Loss	0.65dB	0.7 dB(design value)
Eb/No loss (relative to identical BPSK)	approximately 2dB(BER= 10^{-5})	The same value as ADEOS-II

ADEOS-II block diagram



ALOS block diagram



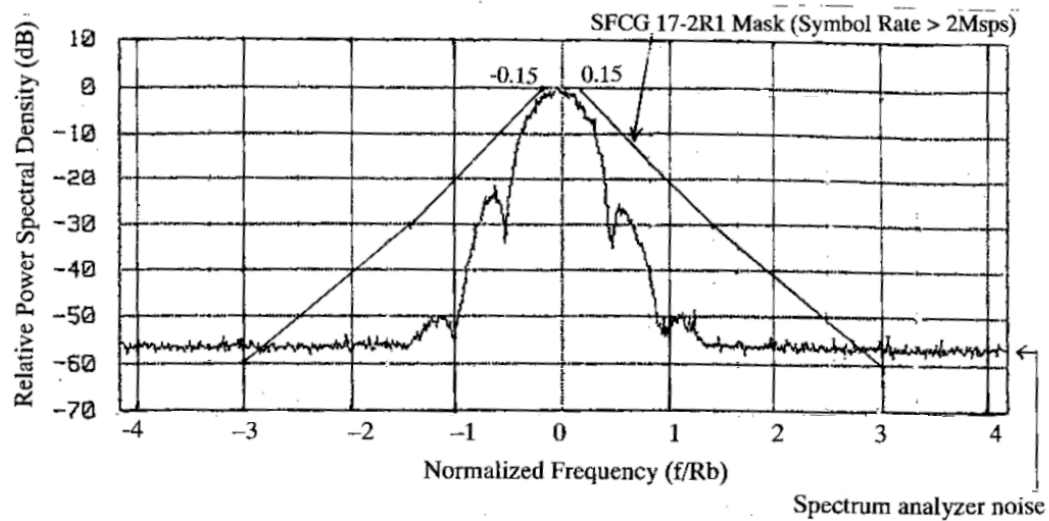


Figure 1-1 Measured Spectrum of ADEOS-II (QPSK, BT=2, 8150MHz, 60Mbps)

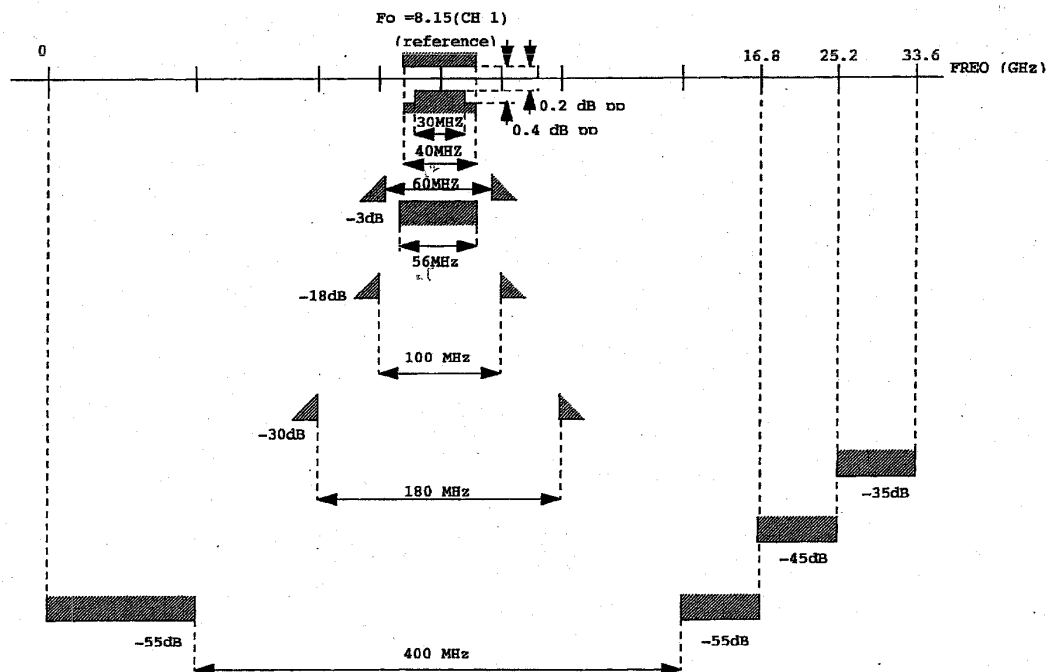


Figure 1-2 ADEOS-II Output Filter characteristics (BT=2)

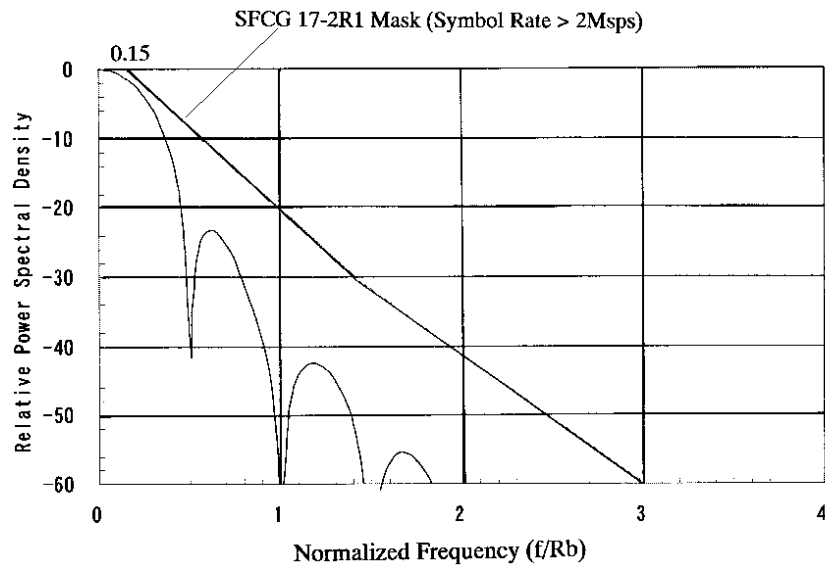


Figure 1-3 Spectrum of ALOS (QPSK, BT=2, 8105MHz, 138MHz)

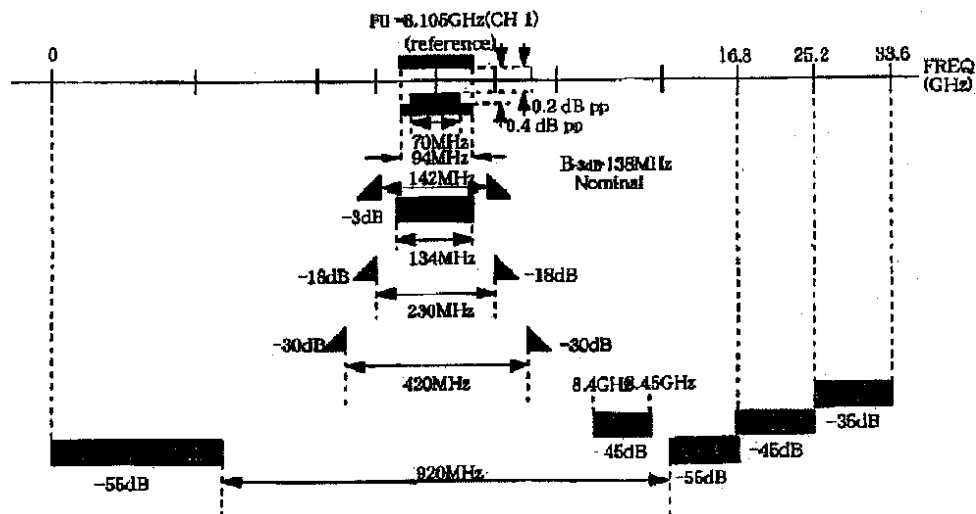


Figure 1-4 ALOS Output filter characteristics (BT=2)

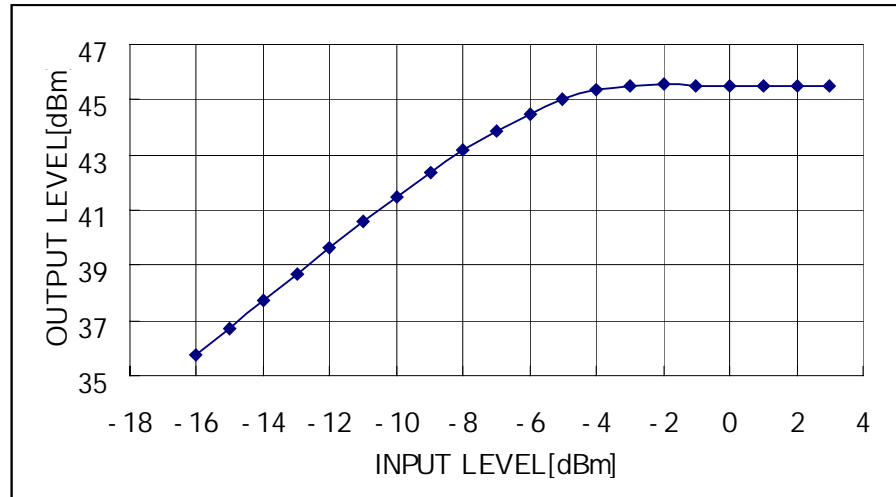


Figure 1-5 ADEOS – II SSPA Characteristics

3 Consideration on filtered QPSK and other bandwidth-efficient modulations

3.1 Transmission rate

For QPSK, the 320Mbps transmitter equipment on satellite have been developed.

For FQPSK and GMSK, the 10Mbps transmitter equipment on airplane have been developed and the above 20Mbps transmitter equipment have not been developed yet. We heard that a breadboard of FQPSK modulator (300Mbps) has been produced and tested. The breadboard cannot guarantee the theoretical performance of FQPSK.

The near future spacecraft needs 20-300 Mbps transmission. In the presence, nobody knows whether FQPSK and GMSK can apply to high rate transmission (above 20Mbps) or not.

Further study about high rate transmission of FQPSK and GMSK is needed for proposing Recommendation of Bandwidth-efficient modulations.

3.2 Patent

Concerning FQPSK patent, FQPSK patent holder has shown the usage condition of FQPSK patent. But, this usage condition of the patent is not sufficient. And it is not appropriate that CCSDS has no Patent policy like ITU-R and ISO. (See Attached paper: “Resolution ITU-R 1-2 Annex 1 Statement on Radiocommunication Sector patent Policy”) It is necessary to select and declare the same statement for Patent as ITU-R and ISO when proposing the draft

recommendation. It is not sufficient to decide the Patent condition for each recommendation like CCSDS.

And we cannot accept CCSDS P1E Doc.00/18 “Feher patented GMSK and FQPSK and FQPSK Patent License and Technology Transfer Agreement for Space Agencies for Scientific Research (DRAFT3)” (Ref.[3]) as follows. Patent lawyer has said that this DRAFT agreement has many problems.

- i) Article 3, 1st paragraph, 3rd sentence “This license does not authorize Licensee to sub-license any Patent covered by this AGREEMENT” : Contractors and subcontractors should be able to use FQPSK patents on the royalty-free condition, when contractors and subcontractor contracted by “Licensee” provide the services with “Licensee”. In this agreement (Draft3), the Patent conditions of Contractors and subcontractors are not regulated.
- ii) Article 4 : In case of using FQPSK, Patent(s) enumerated in ATTACHMENT 1 may not be sufficient for using FQPSK. If the high rate transmitter of FQPSK could be developed in the future, other essential patents about FQPSK may be needed.
- iii) Article 5, the 1st paragraph “quid pro quo basis” : In this Article, nobody knows whether the Space agency has to pay the royalty for using FQPSK patents or not.
- iv) Article 5, the 3rd paragraph “Such publicity or advertising will be in the language and form selected by “Licensor” and “Licensee” agrees to provide “Licensor” with a list of programs and projects, including the specifications and circuit details as well as other design details of the “Licensee” designed hardware and/or software, of laboratory and of over the air satellite or other test results.”: This sentence is not appropriate, because the specifications and circuit details as well as other design details include the know-how and the technology originally developed by “Licensee” and because the sentence for keeping the secret of the know-how and the technology provided by “Licensee” is not regulated in this agreement (Draft3).
- v) Article 5, the 6th paragraph: “If “Licensee”, elects to patent such improved techniques, “Licensor” shall be granted a royalty-free license to use such patents.” : This sentence is not appropriate, because the improved techniques have originally been developed by “Licensee”. We are afraid that this paragraph is against the Anti-monopoly Law.
- vi) Article 9 “SETTLEMENT OF DISPUTES” : The place of arbitration should be regulated in Agreement.

GMSK is said to have many patent problems as seen in Ref.[1].

Filtered QPSK has no patent problem.

3.3 RF output filter

An RF output filter is inserted after HPA and replace a waveguide. For example, the RF output filter for ALOS is compared with the waveguide as the following table.

ALOS is the 3-ton class satellite. ALOS would use 124 kg propellant (nominal) for 5 year attitude control. Comparing with the weight of satellite and propellant, the increased weight (75g) by RF output filter is very small.

	Weight	Size
RF output filter	150g	60 75 60mm ³
Waveguide	75g	40 75 40mm ³

For $\text{BER}=10^{-5}$, the E_b/N_0 Loss of filtered QPSK is approximately 2dB and the insertion loss of RF output filter is 0.65dB. The total loss of filtered QPSK is approximately 2.6dB. This loss is almost the same as the E_b/N_0 loss of EFQPSK (2.6dB), as seen in Ref. [4].

3.4 E_b/N_0 loss

The E_b/N_0 loss relative to ideal BPSK depends on BER. In case of $\text{BER}=10^{-3}$, error correcting code is needed for practical transmission. In case of high rate transmission, error correcting code is almost not used and $\text{BER } 10^{-5}$ is required. So, $\text{BER } 10^{-5}$ is estimated to be appropriate for evaluating modulation method of high rate transmission correctly.

In case of $\text{BER}=10^{-5}$, the E_b/N_0 loss of FQPSK is 2.6dB (Ref. [4]). For ADEOS-II, the total loss of filtered QPSK is approximately 2.6dB. This loss is almost the same as the E_b/N_0 loss of EFQPSK (2.6dB).

3.5 Bandwidth

FQPSK, GMSK, filtered OQPSK and filtered QPSK comply with Recommendation SFCG17-2R1 high rate mask. ($\text{SR}>2\text{Mbps}$) The occupied bandwidth (20dB) of FQPSK, GMSK, filtered OQPSK and filtered QPSK is almost same. (Reference [4], [5] and [6])

As seen in Ref. [4], at the worst case of TWTA, the bandwidths are $3.0R_b$ for OQPSK/PM Butterworth Filter $BT_s=1.0$, $3.1R_b$ for GMSK $BT_s=0.5$ and $3.6R_b$ for Enhanced FQPSK. For Filtered QPSK, the bandwidth is estimated to be $3.6R_b$ at worst TWTA because of RF output filter. The bandwidths of EFQPSK and filtered QPSK are almost same.

To recommend more stringent modulations than Rec.SFCG17-2R1 spectrum mask is against SFCG. The space transmission system by modulations complying with the high rate mask of Rec.SFCG17-2R1 will almost not interfere with other transmission system.

3.6 Interference susceptibility

Reference [7] states that “When comparing interference susceptibility of different modulation

[This page intentionally left blank.]

An Assessment of Shaped Offset QPSK for Use in NASA Space Network and Ground Network Systems

Badri Younes
Goddard Space Flight Center
National Aeronautics and Space Administration
Greenbelt, MD USA

James Brase, Chitra Patel, John Wesdock
ITT Industries
Advanced Engineering & Sciences Division
Reston, VA USA

ABSTRACT:

Shaped Offset QPSK (SOQPSK) describes a family of non-proprietary constant envelope, continuous phase modulation techniques. This paper examines two variants of this technique, SOQPSK-A and B, proposed by Terrance Hill of Nova Engineering, Inc. Both variants are reported to provide spectral containment comparable to that of FQPSK-B and are compatible with the conventional OQPSK demodulators available at existing NASA ground stations. Analyses are performed on both techniques to assess the spectral characteristics and implementation loss performance when used in NASA Space Network (SN) and direct-to-ground channels. High fidelity simulations incorporate effects of hardware distortions typical of NASA transponders and receivers. Recommendations for further study are provided.

INTRODUCTION:

The number of space missions has been steadily increasing over time and this increases the possibility of mutual interference. To promote efficient use of the limited spectrum resources available to space missions, the Space Frequency Coordination Group (SFCG) has recently proposed a very restrictive spectral mask applicable to high data rate ($> 2\text{ Msps}$) spacecraft transmissions in the space-to-Earth direction. A variety of spectrally efficient modulation techniques have been studied within the CCSDS community as a means to achieve compliance with this mask.

The most straightforward technique to implement a spectral mask is to employ an RF output filter after the spacecraft power amplifier. This approach has many drawbacks including a significant insertion loss and large filter volume and mass. Accordingly, CCSDS efforts have focused on the evaluation of advanced baseband filtered or shaped modulations. A number of different techniques have been investigated, including filtered OQPSK, GMSK, and FQPSK. Each of these achieves a rapid rolloff in the magnitude of the spectral sidelobes by replacing the instantaneous phase transitions of OQPSK with a continuous phase trajectory. To avoid

regenerating the sidelobes in a saturated power amplifier, these techniques also feature a constant (or nearly constant) envelope.

The objective of this paper is to assess another modulation technique with similar properties, Shaped Offset QPSK, (SOQPSK). Two variants of this technique, SOQPSK-A and B, which are proposed by Nova Engineering, Inc. [1] are modeled in Signal Processing Worksystem (SPW) and simulations are performed to evaluate their spectral characteristics and bit error rate performance in an SN link through NASA's Tracking and Data Relay Satellite System (TDRSS) and a direct-to-ground link. It should be noted however that because the NASA's Ground Network (GN) incorporates a very large variety of different receivers, the direct-to-ground channel modeled herein is not necessarily representative of all GN links.

As reported in the Hill paper, the measured PSDs of both variants achieve a spectral containment similar to that offered by FQPSK-B and in excess of what is required by the SFCG High Rate Mask. Based on the BER results compiled to date, it appears that both SOQPSK-A and B modulation techniques provide performance comparable to that of other techniques currently under CCSDS consideration when detected using a conventional OQPSK demodulator.

BACKGROUND

Shaped Offset QPSK was initially developed in the early 1980s as an extension of the Shaped BPSK technique used by the US military for transmissions in the UHF SATCOM band. The technique, as documented in MIL-STDs-188-181 and 188-182, replaces the instantaneous phase transitions of SQPSK with a continuous linear phase signal. The resulting phase continuity provides a faster rolloff of the RF spectral sidelobes.

The innovations proposed in the SOQPSK-A and B variants involve the use of shaped phase pulses designed to provide an even greater degree of spectral containment. Each of these variants can be illustrated through representation of QPSK as a frequency modulation.

A QPSK-modulated signal can be represented as:

$$s(t) = \sqrt{2E/(T/2)} \cos(2\pi ft + \phi(t, \bar{\alpha}) + \phi_0)$$

where the input to the phase modulator, $\phi(t, \bar{\alpha})$, is defined as the integral of a sequence of frequency pulses

$$\phi(t, \bar{\alpha}) = 2\pi h \int_{-\infty}^t \sum_{i=-\infty}^{+\infty} \alpha_i g(\tau - iT/2) d\tau \quad -\infty < t < +\infty$$

and where h is the modulation index

For standard OQPSK, $g(t)$ is a unit area delta function and $h = 0.25$. The string of delta functions integrates to sequence of discrete $\pi/2$ phase shifts at the symbol transition instants. The α_i 's are chosen from the set $\{-1, 0, 1\}$ to achieve the appropriate direction for the phase transition.

For MIL-STD SOQPSK, $g(t)$ is a step function and the phase integrates to a constant slope line from one phase point to another during a single bit period. This is similar to MSK; however, unlike MSK the MIL-STD SOQPSK phase can remain constant in the same phase state in successive bit periods, when the phase transition is 0.

The SOQPSK-A and B versions modify the frequency pulse $g(t)$ to incorporate a familiar raised cosine filter shape. The mathematical definition of the SOQPSK-A and SOQPSK-B shapes, $g(t)$, are given by $g(t) = n(t) * w(t)$, where

$$n(t) = \frac{A \cos(\pi \rho B t / T)}{1 - 4(\rho B t / T)^2} * \frac{\sin(\pi B t / T)}{\pi B t / T}$$

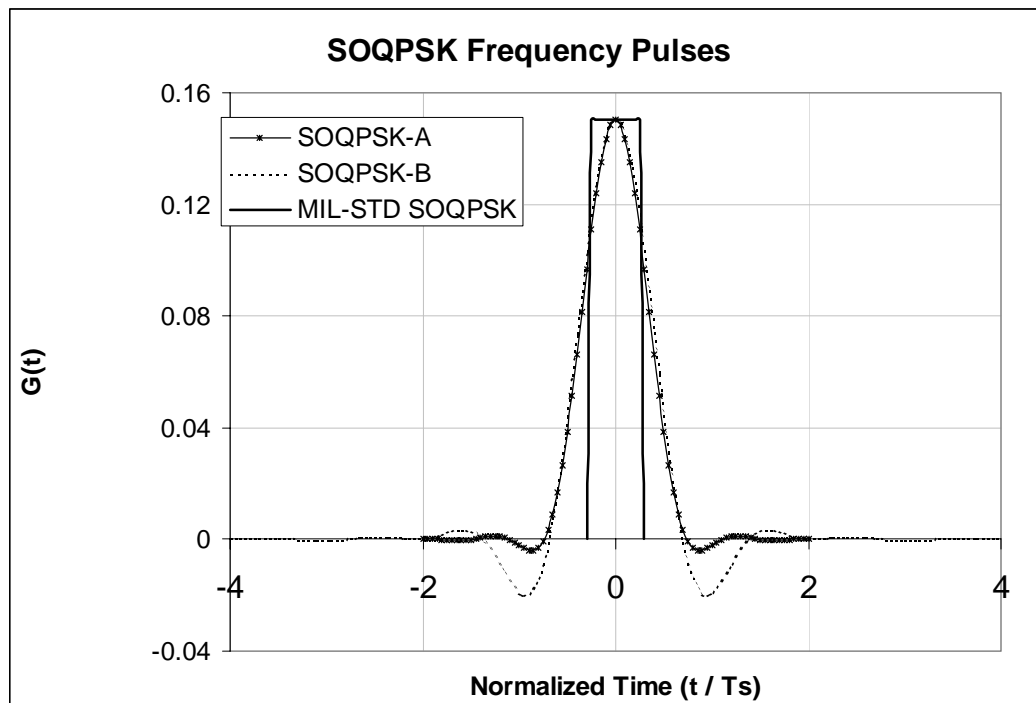
$$w(t) = \begin{cases} 1, & \text{for } |t/T| < T_1 \\ \frac{1}{2} - \frac{1}{2} \cos\left(\frac{(|t/T| - T_1)}{T_2}\right), & \text{for } T_1 \leq |t/T| \leq T_1 + T_2 \\ 0, & \text{for } |t/T| > T_1 + T_2 \end{cases}$$

The specific parameters defining the SOQPSK-A and B variants are listed in Table 1. The resulting frequency pulses are depicted in Figure 1.

Table 1: SOQPSK-A and B Parameters

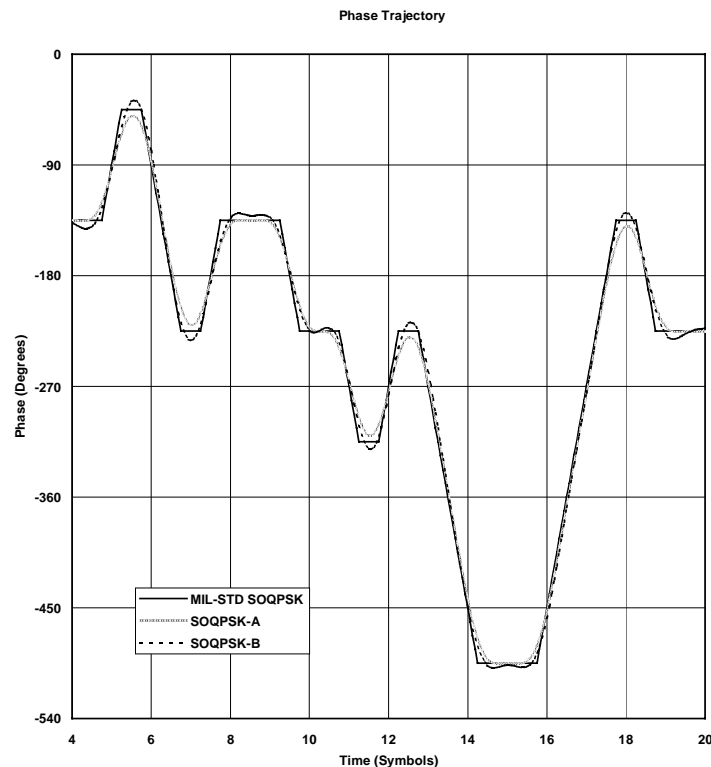
Parameter	SOQPSK-A	SOQPSK-B
	1.0	0.5
B	1.35	1.45
T1	1.4	2.8
T2	0.6	1.2

Figure 1. Frequency pulse shapes for SOQPSK



Note that the SOQPSK-A and B frequency pulses are defined over a time span of 4 and 8 symbol periods (corresponding to 8 and 16 bit periods) respectively. For any given bit period then, the phase transition signal is derived from the integration of 8 or 16 separate $g(t) * (t)$ pairs which are distributed in time by increments of the bit period. The resulting phase trajectory, as depicted in Figure 2, encompasses smooth and continuous transitions over each bit period of magnitude $\pi/2$.

Figure 2. SOQPSK-A and B Phase Trajectories



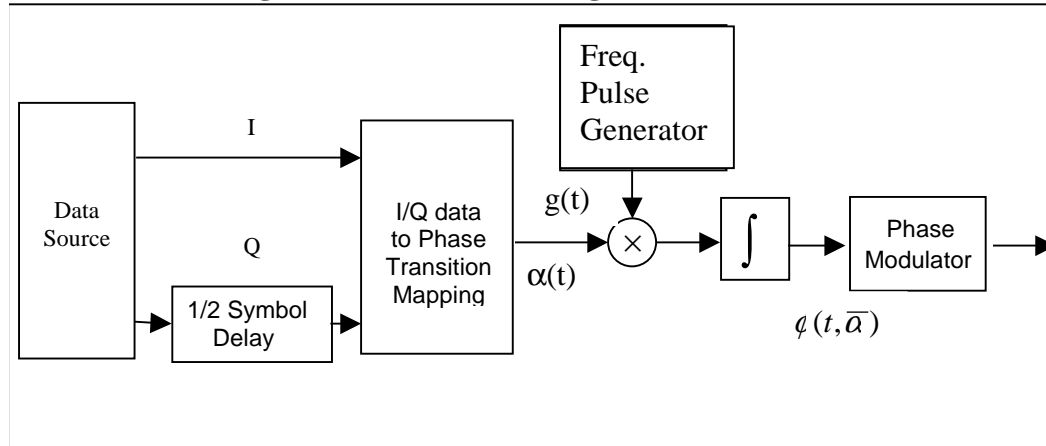
Since the SOQPSK modulated waveform is designed to transition to fixed phase states about the $\pi/2$ distributed QPSK constellation points, the signal can be detected using a conventional OQPSK demodulator. However, close examination of the phase path demonstrates that the terminal phase value in a bit period will be slightly different if the signal is transitioning into that state in that bit period or remaining in the state after a prior transition.

This variation about the optimally-distributed fixed phase constellation points can be expected to result in some implementation loss as compared to unfiltered OQPSK. Based on the continuity of the phase trajectory, however, a narrow modulated signal spectrum can be predicted.

APPROACH

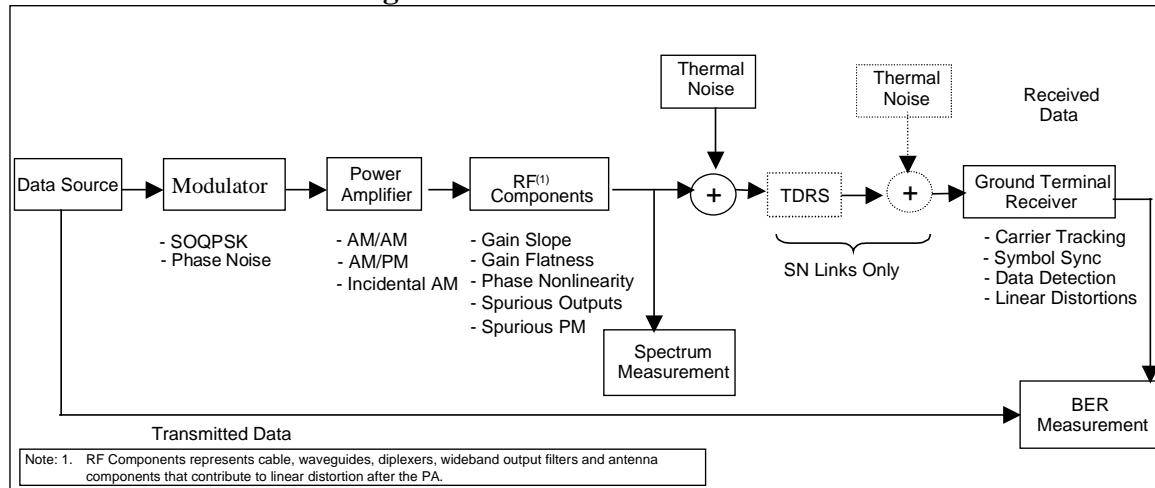
To evaluate the spectral containment and BER performance of the SOQPSK-A and B modulation techniques, an SPW model implementing an SOQPSK modulator was developed and integrated into existing end-to-end systems. The SOQPSK modulator model, as represented in Figure 3, consists of a data source, an I/Q Data to Phase Transition Mapper to generate the $\alpha(t)$ signal, a $g(t)$ pulse generator block and a phase modulator.

Figure 3. SOQPSK Analog Phase Modulator



The modulator simulation model was incorporated into an end-to-end simulation system, depicted in Figure 4, which includes models for the user satellite, TDRS channel, and ground station receiver. The major elements of the system are summarized below.

Figure 4. End-to-End Simulation Model



The user satellite model includes linear and nonlinear distortions intended to be representative of typical NASA S-Band or X-Band spacecraft. The linear distortions used in the simulation model are specified in Table 2.

Table 2. Representative GSFC Flight Project S-Band and X-Band Transmitter Distortion Parameters

Source	Parameter	Value
Data Source	Data Transition Density	50%
	Data Asymmetry, %	Not Simulated
	Data Bit Jitter, %	Not simulated
Modulator	I/Q Power Ratio	1.0:1.0
	I/Q Data Skew, %	0.0
	Frequency Stability, ppm	Not simulated
	Phase Noise, deg. rms	Not Simulated
	Data Transition Time, % of symbol duration	TBD
RF Transmit Components	3 dB Bandwidth, MHz	$9 \times R_b^{(2)}$
	Gain Flatness, dB	0.3 over F MHz ⁽¹⁾
	Gain Slope, dB/MHz	0.1
	Phase Nonlinearity, deg.	3.0 over F MHz ⁽¹⁾
	Spurious PM, deg. rms	2.0
	Spurious Outputs (inband), dBc	30
Notes:		
1. F is defined as 70% of the first null of the transmitted signal spectral density.		
2. Wide bandwidth is used to represent wideband RF transmit components. Typically GSFC flight project transmitters are specified with minimum 3-dB bandwidth of 2x the transmitted symbol rate.		

The non-linear distortions result from the TWTA. For the BER analyses, the TWTA was simulated as operating in saturation and at 1 dB backoff. Note that for the distorted signal PSD results presented below, the TWTA was operated at saturation. The relevant TWTA characteristics at these operating points are summarized in Table 3.

Table 3. Amplifier Operating Point Used in Simulation

Operating point	Input Back-Off	Output Back-Off	AM/AM	AM/PM
1-dB OBO	6.0 dB	1.0 dB	0.47 dB/dB	12.0 /dB
Saturation	0.0 dB	0.0 dB	0.0 dB/dB	15.0 /dB

For BER measurements over the SN link, simulations incorporated the TDRS S-band Single Access Return channel model. The TDRS channel is characterized with another set of linear and non-linear distortion parameters as specified in Table 4.

Table 4. TDRS SSAR Simulation Distortion Parameters

Parameter	Value
AM/AM, dB/dB	0.5
AM/PM, deg./dB	5.5
3 dB Bandwidth, MHz	$1.67 \times R_b$
Roll-off, dB/MHz	8.44
Gain Flatness, dB	0.5
Gain Slope, dB/MHz	0.1
Phase Nonlinearity, deg.	6.0

The ground terminal receiver model includes a second order modified Costas carrier-tracking loop, a dual transition tracking loop symbol synchronizer, an OQPSK demodulator for data detection, and linear distortions due to front-end RF/IF components. The receiver model is depicted in Figure 5. Relevant distortion parameters are provided in Table 5.

Figure 5. Ground Terminal Receiver Block Diagram

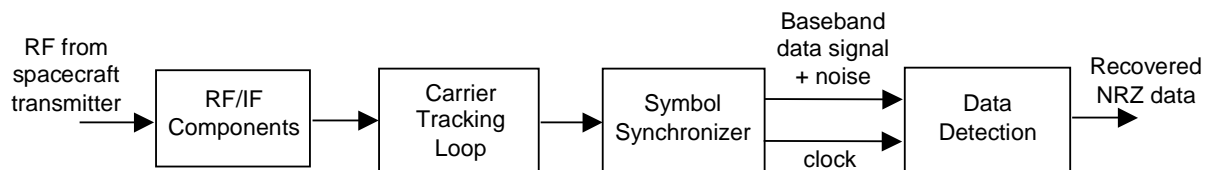


Table 5. Ground Terminal Receiver Linear Distortion Parameters

	Parameter	Value
Channel	3 dB Bandwidth, MHz	3.2 Symbol Rate
	Gain Flatness, dB	0.3
	Gain Slope, dB/MHz	0.1
	Phase Nonlinearity, deg.	5.0
Carrier Tracking Loop	Arm Filter 3-dB Bandwidth(2-sided)	3.07 Symbol Rate
	Closed Loop bandwidth	$1.6 \cdot 10^{-5} \text{ Symbol Rate}$
	Damping Factor	0.707
Symbol Synchronizer	Loop Noise BW, Hz	$2.03 \cdot 10^{-4} \text{ Symbol Rate}$
	Damping Factor	0.707
	Detector Type	Integrate and Dump

RESULTS:

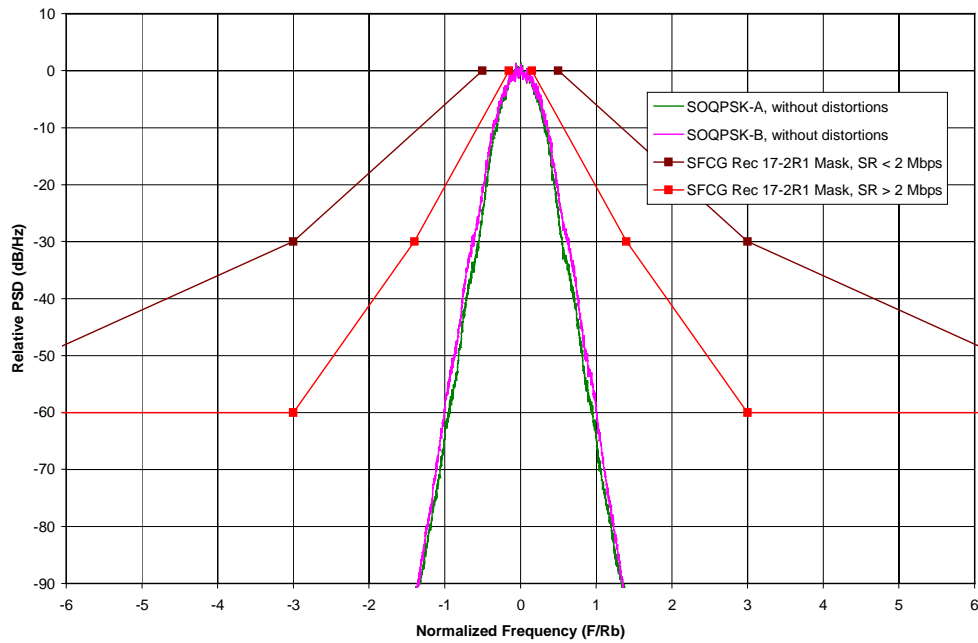
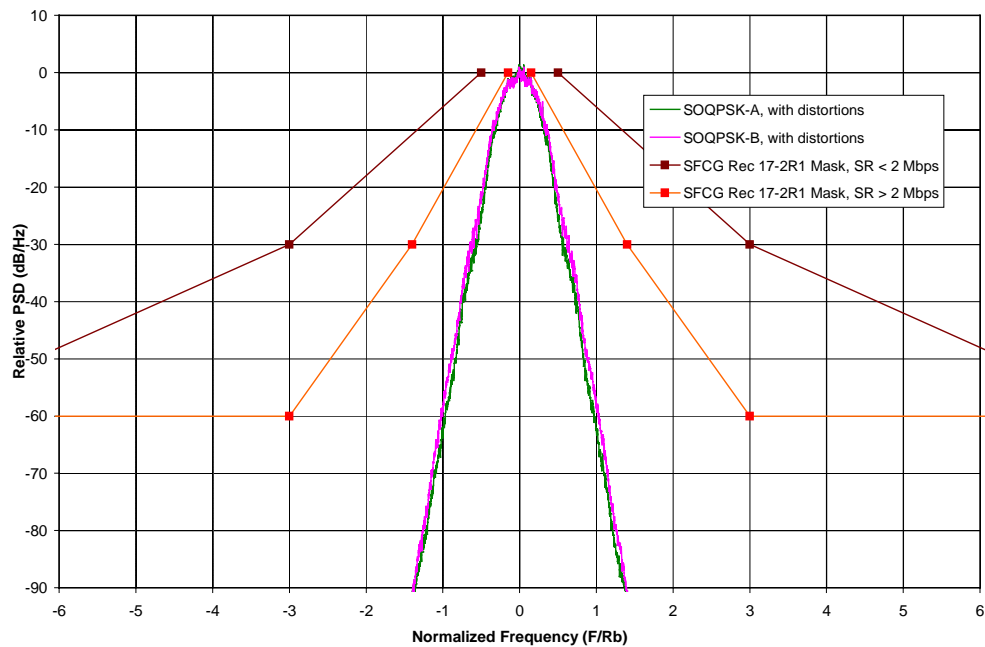
Simulation PSD measurements and other results have been collected for both SOQPSK variants; however, bit error rate analyses are incomplete at this time. The measured 60 dB bandwidth and BER results for SOQPSK-A and B are provided in Table 6, along with the same quantities measured in analyses of other modulation techniques under consideration by CCSDS.

Table 6. Spectrum and BER Performance

Modulation	PA OBO (dB)	Two-sided 60dB Bandwidth	Implementation Loss at 10^{-5} (dB)	
			GN	SN
SOQPSK-A	1.0 dB	$1.90 \times R_b$	3.4	TBD
	0.0 dB	$1.98 \times R_b$	3.4	TBD
SOQPSK-B	1.0 dB	$2.00 \times R_b$	TBD	TBD
	0.0 dB	$2.10 \times R_b$	TBD	TBD
EFQPSK ⁽¹⁾	0.0 dB	$3.60 \times R_b$	3.3	N/A
BB Filtered OQPSK ⁽¹⁾ (Butterworth Filter)	0.0 dB	$4.80 \times R_b$	2.4	N/A
(1) SFCG Efficient Spectrum Utilization Analysis, CCSDS Paper 00/09				

The measured power spectral density plots are provided in Figures 6 – 7. Figure 6 compares the SOQPSK-A and SOQPSK-B PSDs measured without distortions, at the output of the modulator. As indicated in the Hill paper, the SOQPSK-A is slightly narrower than SOQPSK-B at very low power levels. The difference, however, is so negligible as to be virtually undetectable on the plot.

Figure 7 depicts the distorted signal PSDs measured at the user satellite output. From comparison of Figure 6 to Figure 7, we can see that even with a fully saturated power amplifier, no significant spectral regeneration is observed in the distorted signal. Figure 7 also demonstrates that the SOQPSK-modulated user satellite output signal easily meets the high rate SFCG mask.

Figure 6. SOQPSK-A and B Undistorted Power Spectral Density Plots**Figure 7. SOQPSK-A and B Power Spectral Density Plots with Hardware Distortions**

Eye diagrams for SOQPSK-A and B are provided in Figures 8 – 11. Figures 8 and 9 depict the eye diagrams measured without distortions at the output of the modulator.

Figure 8. SOQPSK-A Eye Diagram Without Distortions

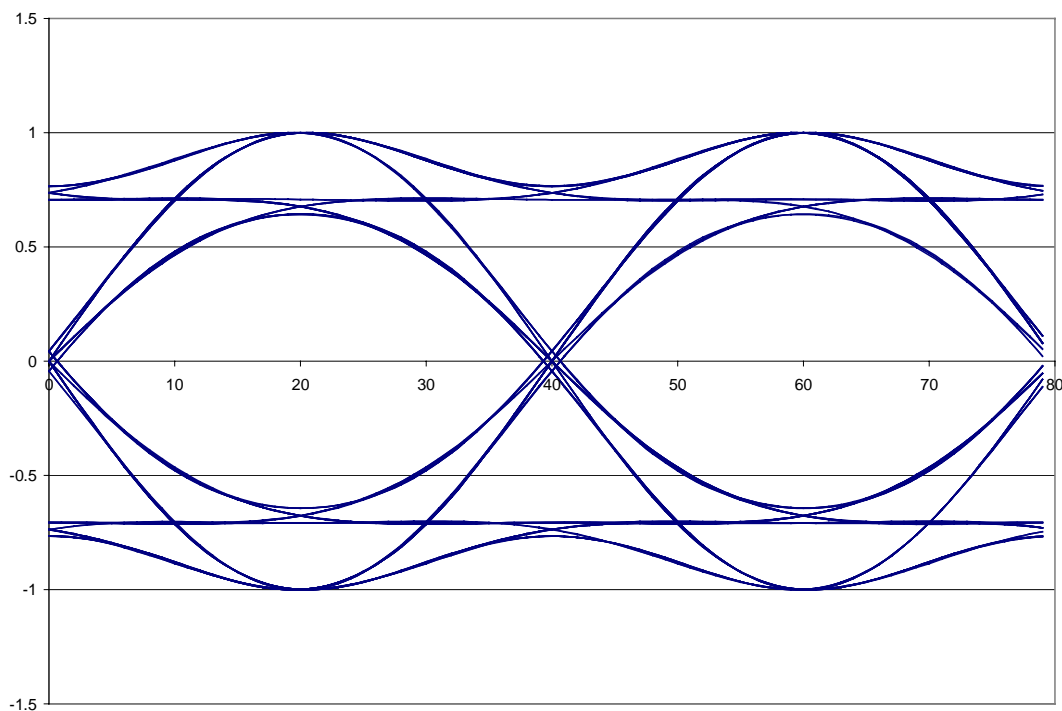


Figure 9. SOQPSK-B Eye Diagram Without Distortions

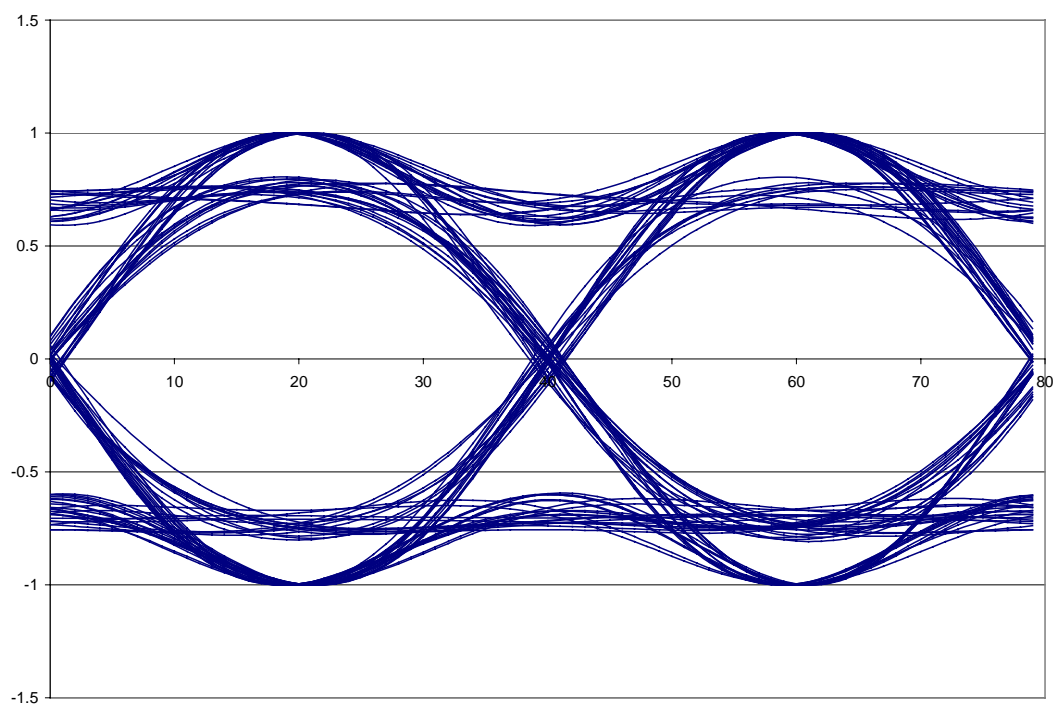


Figure 10. SOQPSK-A Eye Diagram With Distortions

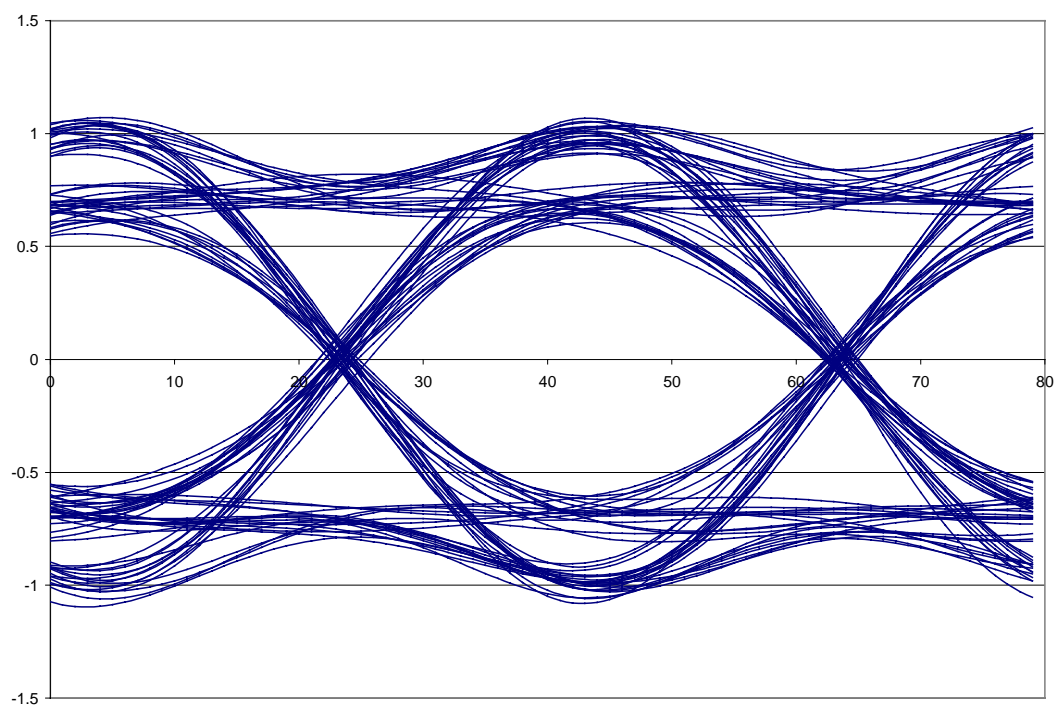
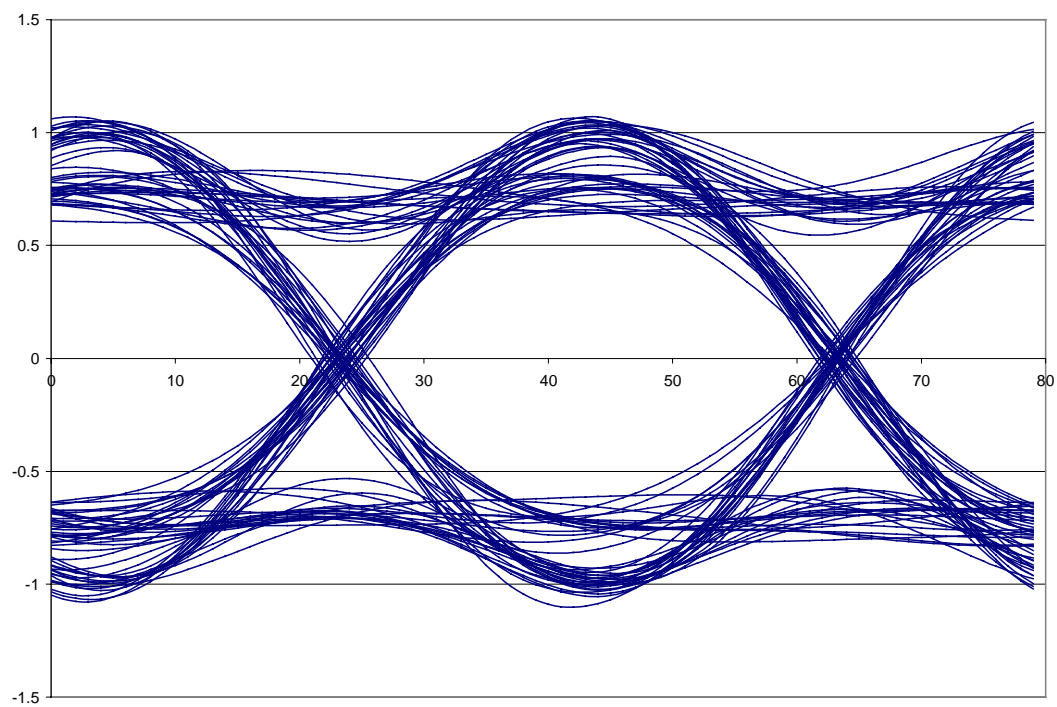


Figure 11. SOQPSK-B Eye Diagram With Distortions



Scatter plots for SOQPSK-A and B are provided in Figures 12 – 15. Figures 12 and 13 are measured without distortions, at the output of the modulator. The measurement is performed at the instant in the symbol period where the eye diagram for the I channel is open widest. Because the modulation is staggered, the Q channel can take on values about ± 1 or near 0 at this point in time.

Figure 12. Scatter Diagram for SOQPSK-A Without Distortions

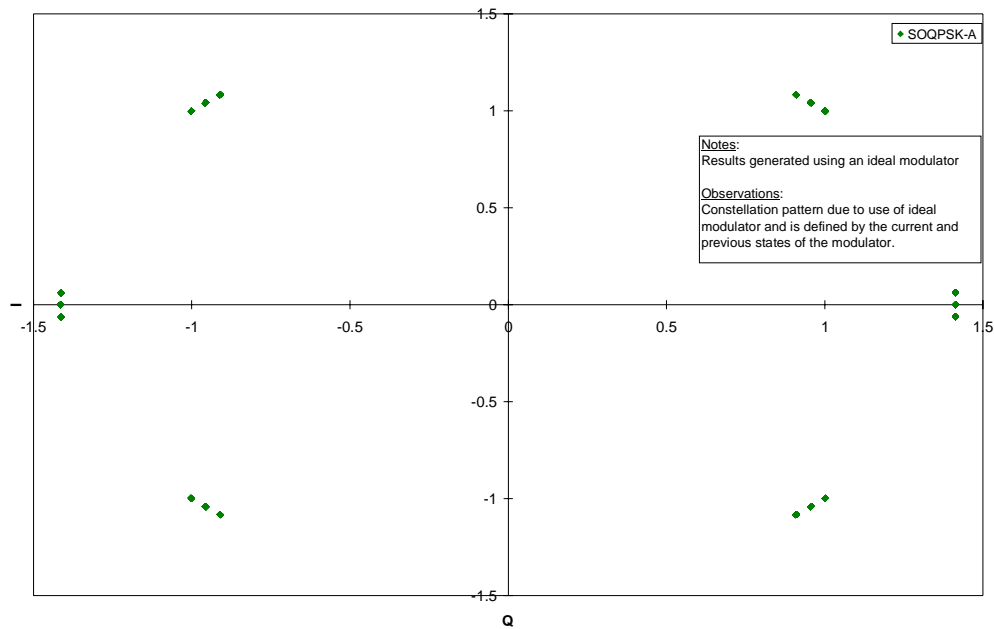
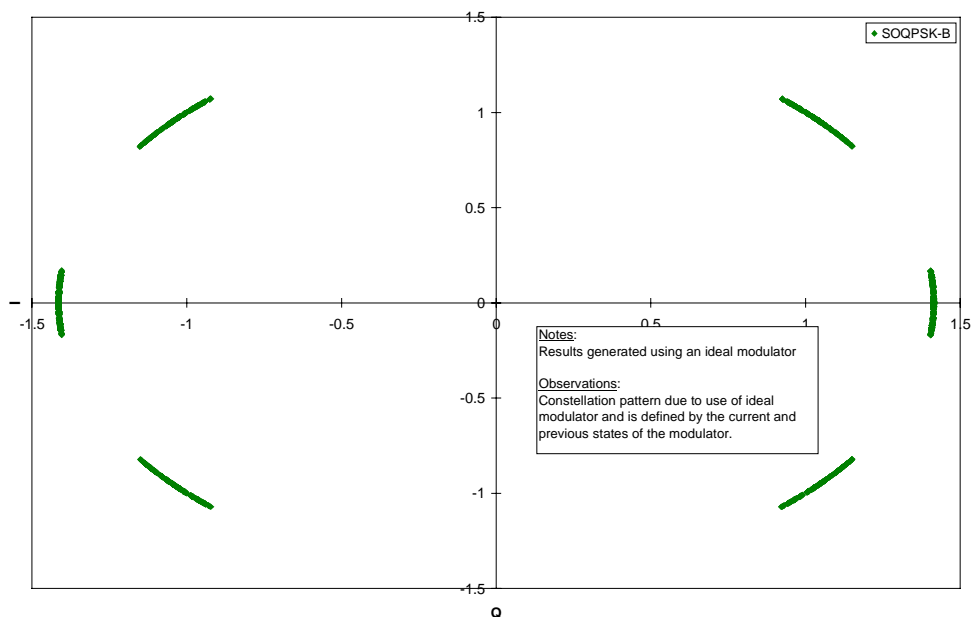


Figure 13. Scatter Diagram for SOQPSK-B Without Distortions



Figures 14 and 15 depict the scatter plots for SOQPSK A and B measured at the output of the user satellite. They demonstrate the effects of the USAT linear and nonlinear distortions. These plots are also collected by sampling the baseband signals at a point in time where the I channel is maximally open.

Figure 14. Scatter Diagram for SOQPSK-A With Distortions

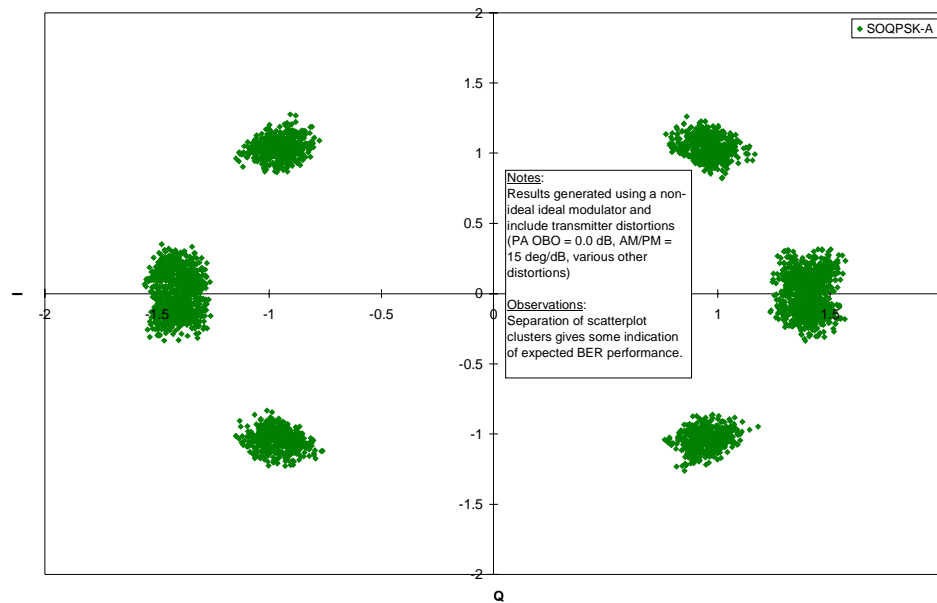


Figure 15. Scatter Diagram for SOQPSK-B With Distortions

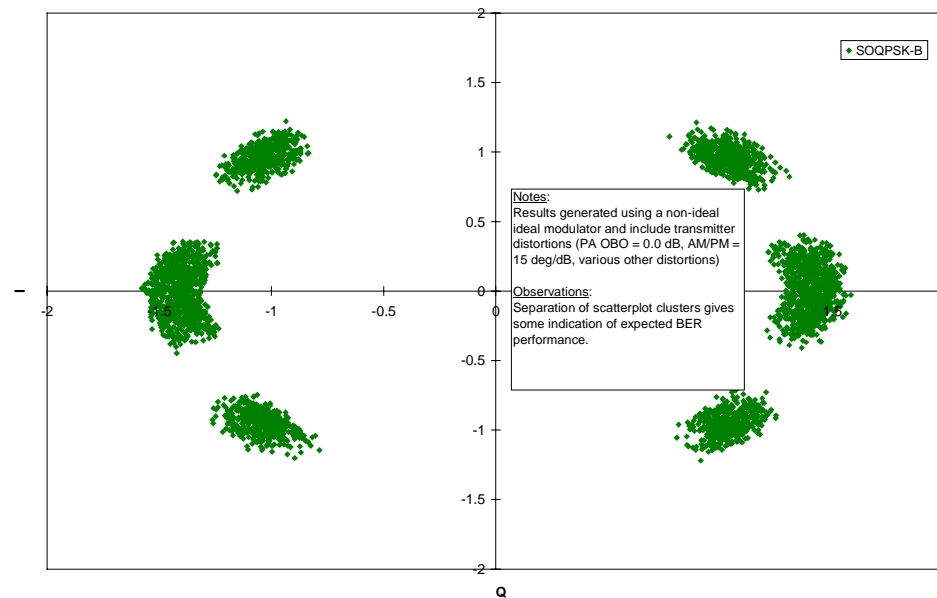
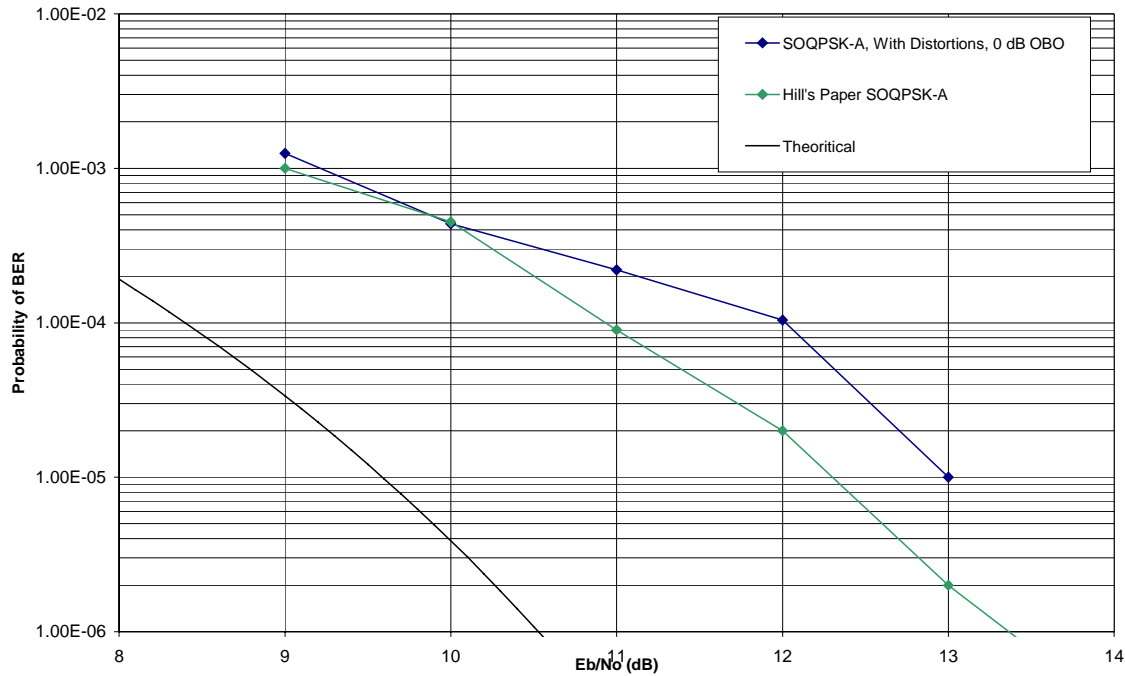


Figure 16 depicts the measured bit error rate for SOQPSK-A through the direct-to-ground channel. The curves for ideal OQPSK and the simulated ideal SOQPSK-A from the Hill paper are also provided as a reference. Note that SOQPSK-A exhibits a loss of approximately 2.8 dB at 10^{-5} as compared to OQPSK. Simulated BER results add an additional 0.6 dB of implementation loss due to the hardware distortions.

Figure 16. Measured SOQPSK-A Bit Error Rate Performance



CONCLUSIONS

Based on the initial results compiled so far, it appears that SOQPSK offers spectral performance and power efficiency comparable to that of FQPSK-B when detected using the conventional OQPSK demodulators utilized by the SN and GN now. SOQPSK also offers the advantage of not being protected by patents. Future analyses will continue to quantify the expected implementation loss in NASA SN and GN systems.

REFERENCES

- [1] *An Enhanced, Constant Envelope, Interoperable Shaped Offset QPSK (SOQPSK) Waveform for Improved Spectral Efficiency*, Terrance J. Hill, Nova Engineering, Cincinnati, OH

Trellis-Coded Quadrature-Phase-Shift Keying (QPSK) With Variable Overlapped Raised-Cosine Pulse Shaping

M. K. Simon,¹ P. Arabshahi,¹ and M. Srinivasan¹

This article introduces the notion of uncoded, partially overlapped, staggered quadrature raised-cosine modulation (SQORC-P) as well as that of a trellis-coded form that is implemented as a specific embodiment of the recently introduced cross-correlated trellis-coded quadrature modulation (XTCQM). Consideration is given to the power spectral density (PSD) of the scheme over both linear and nonlinear channels as well as to its average bit-error probability (BEP) performance on an additive white Gaussian noise (AWGN) channel, the latter being characterized in terms of tight upper and lower bounds. It is shown that a continuously variable trade-off (as a function of the fractional overlap parameter, $0 \leq \alpha \leq 1$) between the rate of spectral roll-off and the amount of envelope fluctuation of the transmitted signal is achievable with a receiver average BEP performance that is virtually independent of the value of α and nominally equivalent to that of uncoded quadrature-phase-shift keying (QPSK).

I. Introduction

Quadrature overlapped raised-cosine (QORC) and staggered QORC (SQORC) modulations were introduced by Austin and Chang in 1981 [1] as schemes that offer a good combination of desirable spectral properties and error-probability performance. These authors analytically described the spectral behavior of these modulations on a linear additive white Gaussian noise (AWGN) channel and, in addition, presented computer simulation results for the same behavior over nonlinear channels characteristic of a traveling-wave tube (TWT) output. Specifically, it was shown that the power spectral density (PSD) of QORC (or SQORC) is equal to the product of that corresponding to minimum-shift keying (MSK) and that of quadrature-phase-shift keying (QPSK) or offset² QPSK (OQPSK) with identical transmitted bit rates. Thus, since the width of the main spectral lobe of MSK is $3/2$ wider than that of QPSK, but its side lobes fall off two orders of magnitude faster (OQPSK varies as f^{-2} and MSK varies as f^{-4}), QORC and SQORC combine the advantageous properties of MSK and QPSK by having a first spectral null at $f = 1/2T_b$ (T_b is the bit duration in seconds) and an asymptotic spectral roll-off that varies as f^{-6} . Also, the QORC or SQORC waveform can be implemented with a transmitter similar to the quadrature form

¹ Communications Systems and Research Section.

² The terms "offset" and "staggered" are used interchangeably in the literature to indicate a modulation in which the in-phase (I) and quadrature-phase (Q) channels are delayed with respect to one another by one-half of a symbol interval. For QPSK modulation, the term "offset" is more common whereas, for QORC, the term "staggered" appears more often.

of modulator used to implement MSK, the difference being the shape of the transmitted pulse on the in-phase (I) and quadrature-phase (Q) channels.

In subsequent years, these schemes were studied further [2–6] both analytically and via simulation with regard to their spectral and error-probability performances over nonlinear band-limited channels. In all cases, the word “overlap” in the title of the acronym used to describe these modulations implied a 100 percent overlap of the two adjacent symbols with the one of interest. As such, QORC and SQORC are not constant-envelope modulations (unlike OQPSK, which is) and, in fact, their envelopes fluctuate as much as 3 dB. Nevertheless, despite the large envelope fluctuation, because of the staggering associated with SQORC, it was still shown in the previously cited references to be a desirable modulation on nonlinear channels from the standpoint of reducing the spectral side-lobe regrowth after bandpass filtering. What would be of interest would be a class of modulations that bridges the gap between OQPSK (constant envelope but slow spectral roll-off) and SQORC (maximum of 3-dB envelope fluctuation and rapid spectral roll-off), thereby allowing a continuous trade-off between these two conflicting properties.

By introducing the notion of partial overlap in the time domain (analogous to the notion of excess bandwidth associated with Nyquist signaling in the frequency domain), we shall describe, using a single fractional overlap parameter, α , a class of modulations referred to as uncoded, partially overlapped, staggered quadrature raised-cosine (SQORC-P) modulation, which at one extreme (no overlap) corresponds to OQPSK and at the other (full overlap) corresponds to SQORC. The parameter, α , therefore allows the system designer to continuously trade off between sharpness of spectral roll-off and degree of envelope fluctuation (which, as mentioned above, on a nonlinear channel is related to the amount of spectral side-lobe regrowth after bandpass filtering). We shall show that this parameterized form of SQORC has a PSD corresponding to the product of the PSD of OQPSK (with a channel—I or Q—rectangular symbol duration of $2T_b$) and the PSD of MSK (with a channel—I or Q— $1/2$ -sinusoidal symbol duration of $2\alpha T_b$). Furthermore, the implementation of SQORC-P can be accomplished in the identical manner as that used to implement conventional SQORC. In particular, the pulse shape for SQORC-P can be obtained by passing a rectangular pulse of duration $2T_b$ through a filter with impulse response equal to that of an MSK pulse of duration $2\alpha T_b$.

Recently, a cross-correlated trellis-coded quadrature-modulation (XTCQM) scheme was introduced³ that focuses on achieving a higher level of spectral containment than that inherent in the bandwidth efficiency of the traditional multilevel modulations, e.g., multiple phase-shift-keying (M -PSK) and quadrature amplitude modulation (QAM), associated with conventional trellis-coded techniques. The emphasis in XTCQM is on maintaining the quadrature identity of the transmitted signal, which is accomplished by applying an M -ary modulation (using different pulse shapes to distinguish among the members of the M -ary set) to each of the I and Q channels, the idea being to simplify the receiver structure (including the various synchronization subsystems). One special case of XTCQM considered in Footnote 3 occurs when there is no cross-correlation between the I and Q channels and either rectangular or purely sinusoidal waveshapes are used as the underlying transmitted waveforms on the I and Q channels in each symbol interval. With a simple rate $1/2$, two-state encoder applied to the input I and Q symbol streams and an appropriate signal (waveshape)-mapping function applied to the encoder outputs, it was shown that the combined I–Q transmitted signal looks like a conventional (fully overlapped) SQORC in that it possesses the identical PSD but has the added advantage of increased power efficiency brought about by the inclusion of the two encoders.

In this article, we show that merely by changing one of the two waveforms assigned to the signal-mapping function, the same special case of XTCQM can be used to generate a transmitted waveform that spectrally resembles SQORC-P but again has the added power efficiency relative to the equivalent uncoded modulation. This class of modulations shall be referred to as trellis-coded OQPSK with variable

³M. K. Simon and T.-Y. Yan, “Cross-Correlated Trellis-Coded Quadrature Modulation (XTCQM),” provisional patent filed, CIT 2885, California Institute of Technology, Pasadena, California, October 5, 1998.

overlapped raised-cosine pulse shaping. While our primary interest is indeed in the trellis-coded case as per the above, we shall begin by first discussing the properties and means of generating an SQORC-P signal. Next we consider the PSD of this signal when transmitted over linear and nonlinear (hard-limited) channels. Following this, we shall present the optimum receiver for the trellis-coded case along with upper and lower bounds on its bit-error probability (BEP). Since the PSD and BEP are both expressed in terms of the overlap parameter, α , we shall be able to demonstrate the continuously variable trade-off (as a function of α) between the corresponding performances of the two extremes corresponding to a transmitted signal having rectangular pulse shaping ($\alpha = 0$) and one having fully overlapped raised-cosine pulse shaping ($\alpha = 1$) typical of OQPSK and SQORC modulations, respectively.

II. The Transmitter Model for Uncoded SQORC-P

Consider a binary source generating a random data sequence $\{d_n\}$ at rate $1/T_b$ b/s. At the transmitter, this data stream is split into even and odd data (symbol) sequences $\{a_n = d_{2n}\}$ and $\{b_n = d_{2n+1}\}$ assigned (arbitrarily) to the I and Q channels. As in all quadrature modulation schemes, each of these symbol sequences occurs at a rate of $1/2T_b = 1/T_s$, and the two are assumed to be synchronous with each other. The I and Q sequences (with rectangular pulses implied) are passed through identical I and Q pulse-shaping filters with impulse response

$$h(t) = \frac{\pi}{4\alpha T_b \sin\left(\frac{\pi}{2\alpha}\right)} \sin\left(\frac{\pi t}{2\alpha T_b}\right), \quad 0 \leq t \leq 2\alpha T_b \quad (1)$$

The response of this pulse-shaping filter to a unit amplitude rectangular pulse of duration $2T_b$ s is a pulse shape $p(t)$ (of duration $4T_b$) that has a raised-cosine roll-off at its edges, is flat in its middle, and has dead zones (zero value) at its beginning and end, i.e., (for convenience of notation, we define the pulse shape shifted to the left by $2T_b$ s so that it is symmetrical around $t = 0$ —see Fig. 1)

$$p(t + 2T_b) = \begin{cases} 1, & 0 \leq |t| \leq (1 - \alpha) T_b \\ \cos^2 \frac{\pi (|t| - (1 - \alpha) T_b)}{4\alpha T_b}, & (1 - \alpha) T_b \leq |t| \leq (1 + \alpha) T_b \\ 0, & (1 + \alpha) T_b \leq |t| \leq 2T_b \end{cases} \quad (2)$$

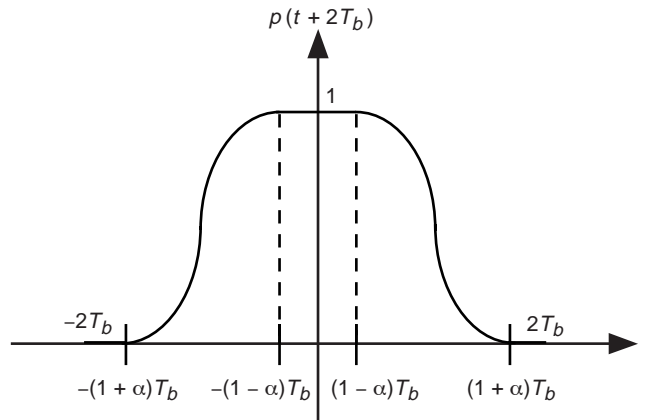


Fig. 1. The pulse shape for SQORC-P.

Thus, the result of passing the I and Q rectangular pulse data streams through the pulse-shaping filters is two streams of partially overlapped raised-cosine pulses. Figure 2 is an illustration of the partially overlapped data stream on the I channel for a typical data sequence and $\alpha = 0.5$ as an example. The partially overlapped I and Q data streams then are delayed with respect to one another by T_b s (as is the case for staggered-modulation schemes), modulated onto quadrature carriers, and then summed, producing the transmitted SQORC-P modulation

$$s(t) = A \sum_{n=-\infty}^{\infty} \{a_n p(t - 2nT_b) \cos \omega_c t + b_n p(t - (2n + 1)T_b) \sin \omega_c t\} \quad (3)$$

where A is an amplitude scaling constant that is related to the average power, S , of $s(t)$ by

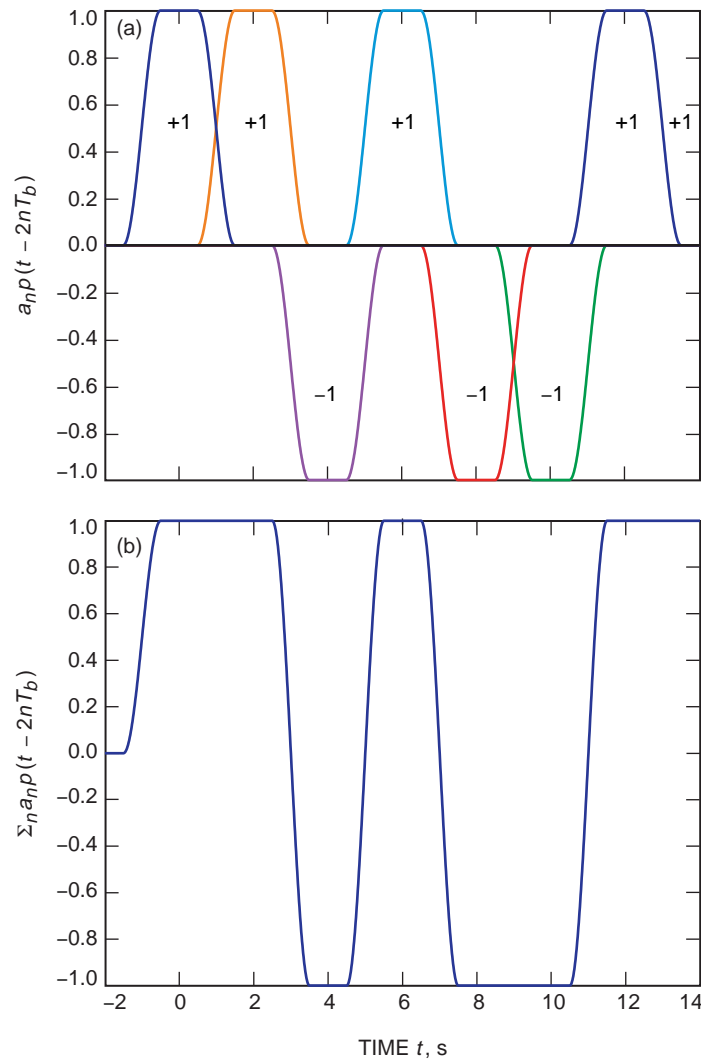


Fig. 2. An illustration of the partially overlapped data stream on the I channel: (a) single raised-cosine pulses for a $+1, +1, -1, +1, -1, -1, +1, +1$ pulse train and (b) the composite waveform ($T_b = 1$) - $\alpha = 0.5$.

$$A = \sqrt{\frac{S}{1 - \frac{\alpha}{4}}} \quad (4)$$

A transmitter for generating the signal of Eq. (3) is illustrated in Fig. 3.

An alternate architecture for generating an SQORC-P signal is given in Fig. 4. Here, once again, the I and Q channel data streams, $\{a_n\}$ and $\{b_n\}$, at rate $1/2T_b$, which were originally obtained by splitting the data sequence $\{d_n\}$ at rate $1/T_b$ into its even and odd indices, now are each split once again into even and odd index subsequences (delayed by $2T_b$ with respect to each other) and occurring at rate $1/4T_b$. These subsequences then are applied to partially overlapped raised-cosine pulses of duration $4T_b$ [as typified by Eq. (2)] and summed back into a single data stream. Pulse-shape filtering here is thus effectively performed through a process of splitting, multiplication by $p(t)$, and recombining.

III. The PSD of SQORC-P Transmitted Over a Linear Channel

Since $p(t)$ is produced by the convolution of a rectangular $2T_b$ s pulse with the impulse response of Eq. (1), then the equivalent normalized (by $2T_b$) low-pass PSD of SQORC-P is easily seen to be (for simplicity, we have normalized A equal to unity)

$$\frac{S_m(f)}{2T_b} = \left| \frac{\sin 2\pi f T_b}{2\pi f T_b} \right|^2 \left| \frac{\cos 2\pi \alpha f T_b}{1 - 16\alpha^2 f^2 T_b^2} \right|^2 \quad (5)$$

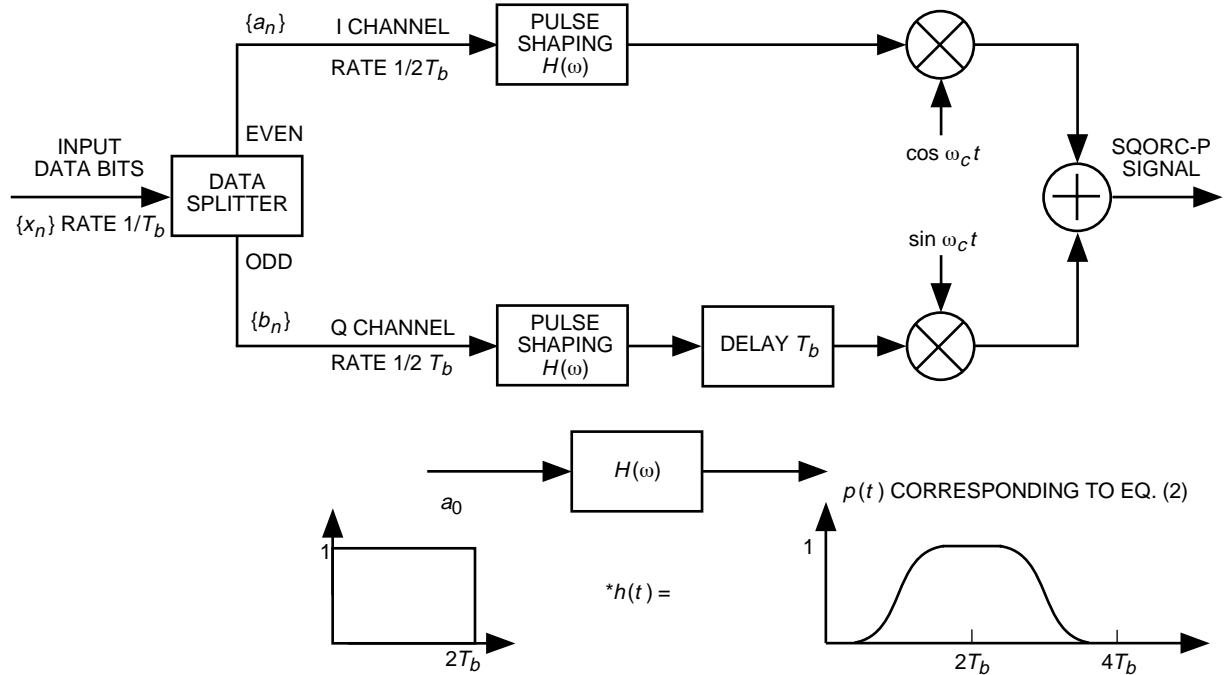


Fig. 3. Generating SQORC-P modulation via filtering.

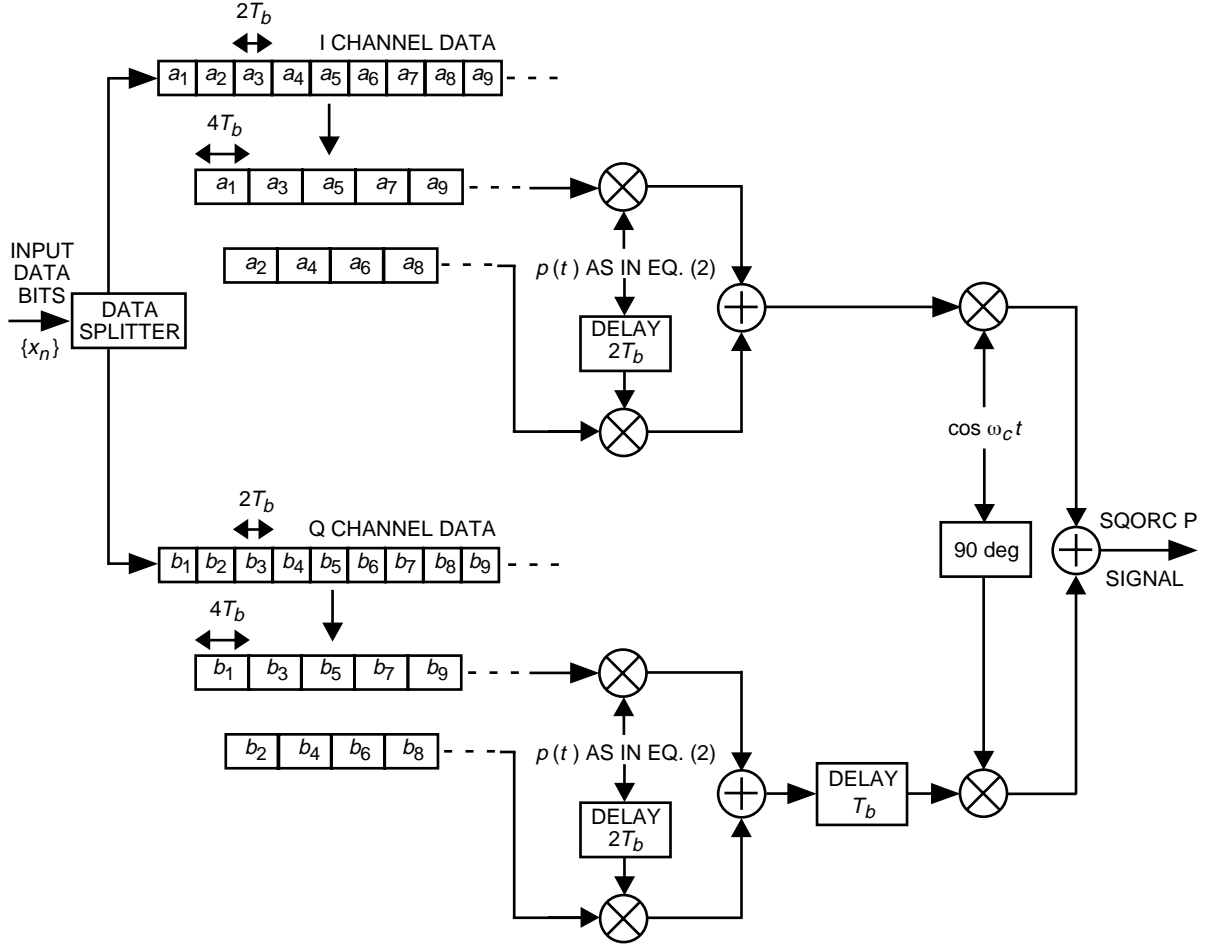


Fig. 4. An alternative architecture for generating SQORC-P modulation using multipliers.

where the first factor represents the PSD of OQPSK (with rectangular pulse shapes of duration $2T_b$ s) and the second factor represents the PSD of the I-Q form of MSK (with a half-sinusoidal pulse shape of duration $2\alpha T_b$ s). Note that, theoretically, for any $\alpha \neq 0$, the PSD of Eq. (4) rolls off asymptotically as f^{-6} , although the rate at which the PSD reaches this asymptote clearly increases as α increases. Figure 5 is an illustration of the PSD of Eq. (4) with α as a parameter varying from zero to one. We observe from this figure the corresponding gradual transition from the PSD of OQPSK to the PSD of SQORC.

IV. The PSD of SQORC-P Transmitted Over a Nonlinear Channel

Following steps analogous to those taken in [3] to determine the PSD of conventional SQORC over a nonlinear channel modeled as a hard limiter, e.g., at the output of a TWT operating in saturation, it can be shown that [3, Eq. (45)] also is applicable to SQORC-P provided that the appropriate pulse shapes are used to characterize the various terms in that expression. In particular, we have

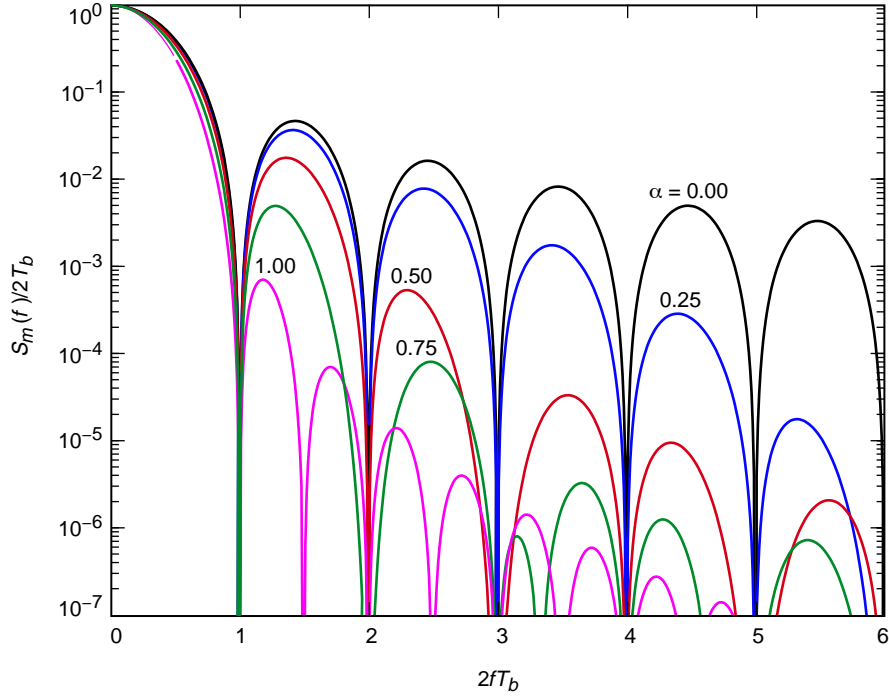


Fig. 5. The power spectral density of SQORC-P over a linear channel with α as a parameter.

$$\begin{aligned}
 \frac{S_m(f)}{2T_b} &= \frac{3}{2} \sum_{k=1}^4 R_k^2 + \frac{1}{2} \sum_{k=1}^4 I_k^2 \\
 &+ \frac{1}{4} \left[\left(\sum_{k=1}^4 R_k \right)^2 + \left(\sum_{k=1}^4 I_k \right)^2 \right] \cos 8\pi f T_b - \frac{1}{2} \left(\sum_{k=1}^4 R_k \right) \left(\sum_{k=1}^4 I_k \right) \sin 8\pi f T_b \\
 &+ (R_1 + R_2 - R_3 - R_4) \left(\sum_{k=1}^4 R_k \cos 4\pi f T_b - \sum_{k=1}^4 I_k \sin 4\pi f T_b \right) \\
 &- R_1 R_3 - R_2 R_4 + I_1 I_3 + I_2 I_4
 \end{aligned} \tag{6}$$

where $R_k \triangleq \text{Re}\{Y_k\}$, $I_k \triangleq \text{Im}\{Y_k\}$, and the Y_k 's are given as follows.

For $0 \leq \alpha \leq 1$,

$$Y_1 = \frac{1}{2\sqrt{2}} \left[\left(\frac{\sin 2\pi f T_b}{2\pi f T_b} \right) - j \left(\frac{\sin^2 \pi f T_b}{\pi f T_b} \right) \right] \tag{7}$$

$$\begin{aligned}
 Y_2 = & \frac{1}{2\pi} \int_0^{\alpha\pi} \frac{\cos 2fT_b z}{\sqrt{1 + \sin^2\left(\frac{z}{2\alpha}\right)}} dz + \frac{1}{2\sqrt{2}} \left[\left(\frac{\sin 2\pi fT_b}{2\pi fT_b} \right) - \alpha \left(\frac{\sin 2\pi\alpha fT_b}{2\pi\alpha fT_b} \right) \right] \\
 & - j \left[\frac{1}{2\pi} \int_0^{\alpha\pi} \frac{\sin 2fT_b z}{\sqrt{1 + \sin^2\left(\frac{z}{2\alpha}\right)}} dz - \frac{1}{2\sqrt{2}} \left[\left(\frac{\cos 2\pi fT_b}{2\pi fT_b} \right) - \alpha \left(\frac{\cos 2\pi\alpha fT_b}{2\pi\alpha fT_b} \right) \right] \right] \quad (8)
 \end{aligned}$$

$$\begin{aligned}
 Y_3 = & -\frac{(1-\alpha)}{2\sqrt{2}} \left(\frac{\sin 2\pi(1-\alpha)fT_b}{2\pi(1-\alpha)fT_b} \right) + \frac{1}{2\pi} \int_{(1-\alpha)\pi}^{\pi} \frac{\sin\left(\frac{z-\pi}{2\alpha}\right) \cos 2fT_b z}{\sqrt{1 + \sin^2\left(\frac{z-\pi}{2\alpha}\right)}} dz \\
 & - j \left[\frac{(1-\alpha)}{2\sqrt{2}} \left(\frac{\cos 2\pi(1-\alpha)fT_b - 1}{2\pi(1-\alpha)fT_b} \right) + \frac{1}{2\pi} \int_{(1-\alpha)\pi}^{\pi} \frac{\sin\left(\frac{z-\pi}{2\alpha}\right) \sin 2fT_b z}{\sqrt{1 + \sin^2\left(\frac{z-\pi}{2\alpha}\right)}} dz \right] \quad (9)
 \end{aligned}$$

For $0 \leq \alpha \leq 0.5$,

$$\begin{aligned}
 Y_4 = & -\frac{1}{2\pi} \int_0^{\alpha\pi} \frac{\cos 2fT_b z}{\sqrt{1 + \sin^2\left(\frac{z}{2\alpha}\right)}} dz - \frac{1}{2\sqrt{2}} \left[(1-\alpha) \left(\frac{\sin 2\pi(1-\alpha)fT_b}{2\pi(1-\alpha)fT_b} \right) - \alpha \left(\frac{\sin 2\pi\alpha fT_b}{2\pi\alpha fT_b} \right) \right] \\
 & + \frac{1}{2\pi} \int_{(1-\alpha)\pi}^{\pi} \frac{\sin\left(\frac{z-\pi}{2\alpha}\right) \cos 2fT_b z}{\sqrt{1 + \sin^2\left(\frac{z-\pi}{2\alpha}\right)}} dz \\
 & + j \left[\frac{1}{2\pi} \int_0^{\alpha\pi} \frac{\sin 2fT_b z}{\sqrt{1 + \sin^2\left(\frac{z}{2\alpha}\right)}} dz - \frac{1}{2\sqrt{2}} \left[(1-\alpha) \left(\frac{\cos 2\pi(1-\alpha)fT_b}{2\pi(1-\alpha)fT_b} \right) - \alpha \left(\frac{\cos 2\pi\alpha fT_b}{2\pi\alpha fT_b} \right) \right] \right] \\
 & - \frac{1}{2\pi} \int_{(1-\alpha)\pi}^{\pi} \frac{\sin\left(\frac{z-\pi}{2\alpha}\right) \sin 2fT_b z}{\sqrt{1 + \sin^2\left(\frac{z-\pi}{2\alpha}\right)}} dz \quad (10a)
 \end{aligned}$$

whereas for $0.5 \leq \alpha \leq 1$,

$$\begin{aligned}
 Y_4 = & -\frac{1}{2\pi} \int_0^{(1-\alpha)\pi} \frac{\cos 2fT_b z}{\sqrt{1 + \sin^2\left(\frac{z}{2\alpha}\right)}} dz + \frac{1}{2\pi} \int_{(1-\alpha)\pi}^{\alpha\pi} \frac{\sin\left(\frac{z-\pi}{2\alpha}\right) \cos 2fT_b z}{\sqrt{\sin^2\left(\frac{z}{2\alpha}\right) + \sin^2\left(\frac{z-\pi}{2\alpha}\right)}} dz \\
 & + \frac{1}{2\pi} \int_{\alpha\pi}^{\pi} \frac{\sin\left(\frac{z-\pi}{2\alpha}\right) \cos 2fT_b z}{\sqrt{1 + \sin^2\left(\frac{z-\pi}{2\alpha}\right)}} dz \\
 & + j \left[\frac{1}{2\pi} \int_0^{(1-\alpha)\pi} \frac{\sin 2fT_b z}{\sqrt{1 + \sin^2\left(\frac{z}{2\alpha}\right)}} dz - \frac{1}{2\pi} \int_{(1-\alpha)\pi}^{\alpha\pi} \frac{\sin\left(\frac{z-\pi}{2\alpha}\right) \sin 2fT_b z}{\sqrt{\sin^2\left(\frac{z}{2\alpha}\right) + \sin^2\left(\frac{z-\pi}{2\alpha}\right)}} dz \right. \\
 & \left. - \frac{1}{2\pi} \int_{\alpha\pi}^{\pi} \frac{\sin\left(\frac{z-\pi}{2\alpha}\right) \sin 2fT_b z}{\sqrt{1 + \sin^2\left(\frac{z-\pi}{2\alpha}\right)}} dz \right] \tag{10b}
 \end{aligned}$$

Evaluating Eqs. (7), (8), (9), and (10b) at $\alpha = 1$ gives results identical to [3, Eq. 45)], corresponding to conventional SQORC. Also, at $\alpha = 0.5$, Eqs. (10a) and (10b) produce the identical result, as should be the case. Figure 6 is a plot of the PSD of Eq. (6) with overlap parameter α as a parameter. Simulation results for the fully overlapped case ($\alpha = 1$) also are indicated for analytical evaluations.

V. The Transmitter Model for Trellis-Coded OQPSK With Partially Overlapped Raised-Cosine Pulse Shaping

In the citation in Footnote 3, a new class of trellis-coded modulations called cross-correlated trellis-coded quadrature modulation (XTCQM) was introduced that combines the bandwidth efficiency of conventional modulation schemes with the power efficiency of error-correction coding, but in a way that maintains the desirable I-Q form of the transmitted signal. Although the generic form of this modulation allows for cross-correlation of the bits generated by the I and Q encoders, i.e., some of the I-encoded bits are used to define the Q-channel waveform and vice versa, specific embodiments also were considered that did not involve such cross-correlation. One of these embodiments with I and Q encoder outputs decoupled implements a signal with spectral properties identical to SQORC but that, from a detection viewpoint, has the properties of trellis-coded OQPSK with fully overlapped raised-cosine pulse shaping. A modulator representing this particular embodiment of XTCQM is illustrated in Fig. 7. Here, the I and Q data sequences, $\{a_n\}$ and $\{b_n\}$, respectively, once again are assumed to be time synchronous, each bit occurring during the interval $(2n-1)T_b \leq t \leq (2n+1)T_b$.⁴ Letting $\{a'_n\}$ and $\{b'_n\}$ denote the (0,1) equivalents of the I and Q data sequences, i.e.,

⁴ Since the choice for the specific time interval occupied by a single bit on the I or Q channel is arbitrary (provided that it is $T_s = 2T_b$ in duration), in this section we make this choice consistent with the notation introduced in the citation in Footnote 3.

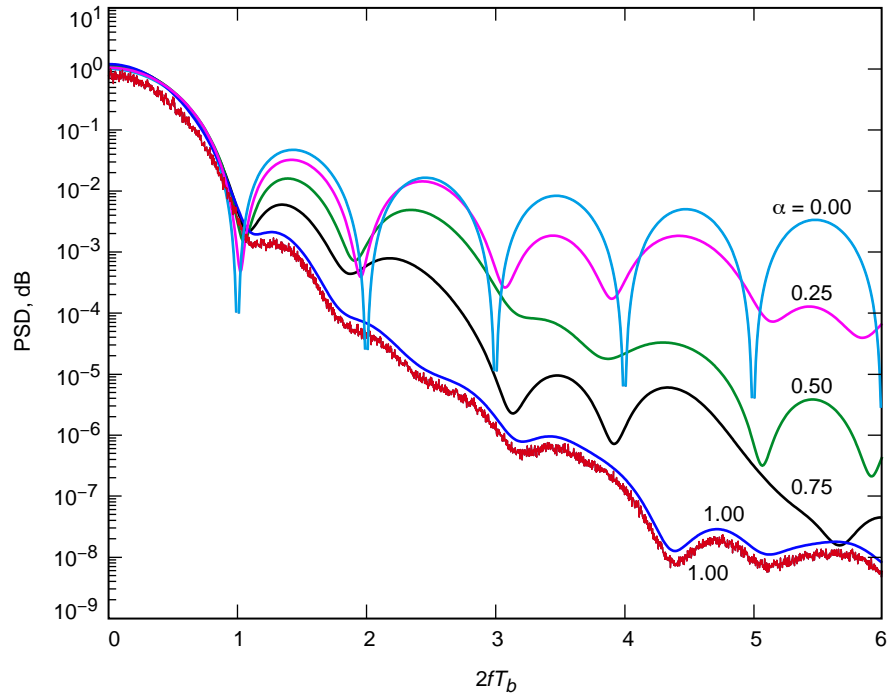


Fig. 6. The power spectral density of bandpass hard-limited SQORC-P (or trellis-coded QPSK with partial overlapping). Simulated results (jagged line) are shown for $\alpha = 1$.

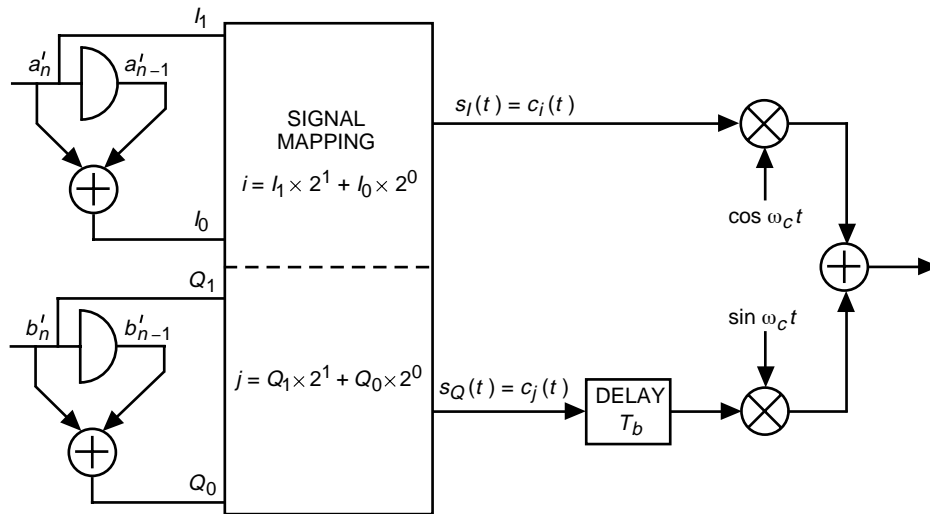


Fig. 7. The trellis-coded QPSK embodiment of the XTCQM transmitter.

$$\left. \begin{aligned} a'_n &\triangleq \frac{1 - a_n}{2} \\ b'_n &\triangleq \frac{1 - b_n}{2} \end{aligned} \right\} \quad (11)$$

then encoding these sequences into the I and Q pairs, I_0, I_1 and Q_0, Q_1 , in accordance with (see Fig. 7)

$$\left. \begin{aligned} I_0 &= a'_n \oplus a'_{n-1}, & I_1 &= a'_n \\ Q_0 &= b'_n \oplus b'_{n-1}, & Q_1 &= b'_n \end{aligned} \right\} \quad (12)$$

and inputting these pairs to a binary-coded decimal (BCD) signal mapper that selects the pair of indices

$$\left. \begin{aligned} i &= I_0 \times 2^0 + I_1 \times 2^1 \\ j &= Q_0 \times 2^0 + Q_1 \times 2^1 \end{aligned} \right\} \quad (13)$$

the transmitted I and Q waveforms are chosen as

$$\left. \begin{aligned} s_I(t) &= c_i(t) \\ s_Q(t) &= c_j(t) \end{aligned} \right\} \quad (14)$$

where the set $c_k(t)$; $k = 0, 1, 2, 3$ is defined by

$$\left. \begin{aligned} c_0(t) &= 1, & -T_b \leq t \leq T_b \\ c_1(t) &= \sin\left(\frac{\pi t}{2T_b}\right), & -T_b \leq t \leq T_b \\ c_2(t) &= -c_0(t) \\ c_3(t) &= -c_1(t) \end{aligned} \right\} \quad (15)$$

That is, for each input pair of data bits a_n and b_n , a pair of indices i and j are selected that designate two of the four possible waveforms in Eq. (15) for transmission as the I and Q signals.

It is a simple matter to modify the XTCQM transmitter embodiment of Fig. 7 so that it generates a waveform whose spectral properties coincide with SQORC-P and whose detection has the characteristics of trellis-coded OQPSK with partially overlapped raised-cosine pulse shaping. In particular, it is straightforward to show that this can be accomplished by simply redefining $c_1(t)$ [and, therefore, its negative, $c_3(t) = -c_1(t)$] as

$$c_1(t) = \begin{cases} \sin\left(\frac{\pi t}{2\alpha T_b}\right), & 0 \leq |t| \leq \alpha T_b \\ 1, & \alpha T_b \leq |t| \leq T_b \end{cases} \quad (16)$$

That is, the form of the transmitter in Fig. 7 is still appropriate with merely a change in the signal set (two of the four) from which the I and Q signals are selected. Clearly in the limit of $\alpha = 1$, $c_1(t)$ of Eq. (16) reduces to its definition in Eq. (15), whereas in the limit of $\alpha = 0$, $c_1(t)$ of Eq. (16) becomes

$$c_1(t) = \text{sgn } t, \quad -T_b \leq t \leq T_b \quad (17)$$

which produces a transmitted waveform with the spectral properties of OQPSK and the detection characteristics of trellis-coded OQPSK (with the usual rectangular pulse shaping). Figure 8 illustrates the two unique waveforms, $c_0(t)$ of Eq. (15) and $c_1(t)$ of Eq. (16), for $\alpha = 0.25, 0.5, 0.75$, and 1.0 , the latter corresponding to $c_1(t)$ of Eq. (15).

The I or Q channel of the transmitted modulation described above has a two-state trellis diagram, which is illustrated in Fig. 9. The dashed line indicates a transition caused by an input “0” to the shift register/XOR gate, and the solid line indicates a transition caused by an input “1.” The branches are labeled with the output signal waveform ($s_I(t)$ or $s_Q(t)$ as appropriate) that results from the transition following the symbol mapping. The optimum receiver for such a trellis diagram and its performance will be discussed in the next section.

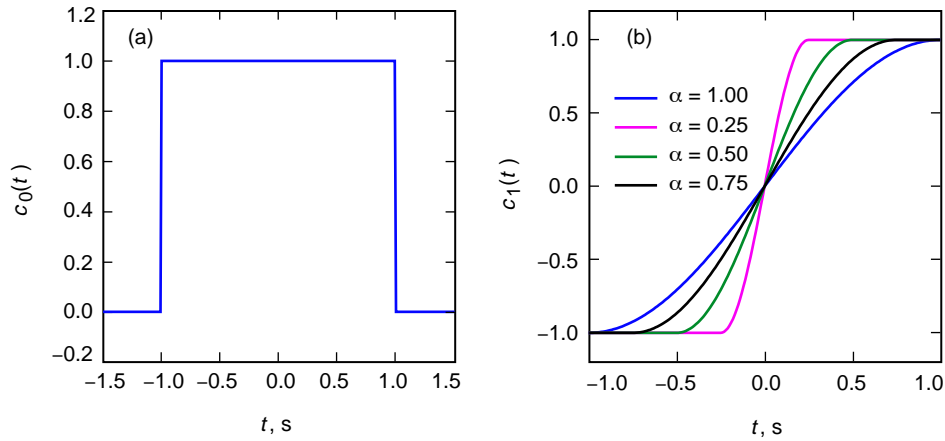


Fig. 8. Trellis-coded OQPSK with raised-cosine pulse-shaping full-symbol waveforms ($T_s = 2T_b = 2$): (a) $c_0(t) = -c_2(t)$ and (b) $c_1(t) = -c_3(t)$.

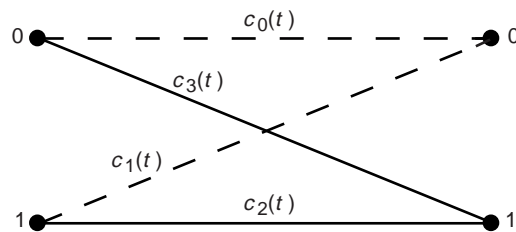


Fig. 9. The two-state trellis diagram for trellis-coded OQPSK with a raised-cosine pulse-shaping modulator.

Finally, the equivalence (in terms of the transmitted waveform) between the embodiment of the XTCQM modulator and the SQORC-P modulator discussed previously can be readily established. Consider the example of Fig. 2, where a sequence $\{a_n\} = \{+1, +1, -1, +1, -1, -1, +1, +1\}$ (or equivalently $\{a'_n\} = \{0, 0, 1, 0, 1, 1, 0, 0\}$) is transmitted in the I arm. From the trellis diagram of Fig. 9, the corresponding transmitted waveform sequence is $\{c_0(t), c_3(t), c_1(t), c_3(t), c_2(t), c_1(t), c_0(t), c_0(t)\}$,⁵ which indeed is identical to the composite waveform in Fig. 2(b).

VI. The Optimum Reception and Bit-Error Probability Performance of Trellis-Coded OQPSK With Partially Overlapped Raised-Cosine Pulse Shaping

The optimum receiver for the waveform generated by the transmitter of Fig. 7 over a linear AWGN channel is discussed in the citation in Footnote 3 and illustrated here in Fig. 10. The input data waveforms are demodulated and then correlated with the two primary waveforms, $c_0(t)$ and $c_1(t)$, which then are passed through integrate-and-dump (I&D) filters (which, combined with the correlators, form matched filters). The structure of this receiver is the same for either fully or partially overlapped raised-cosine pulse shaping, the difference being the assignment of $c_1(t)$ to the correlators in accordance with Eq. (15) or Eq. (16), respectively. Four decision variables, Z_0, Z_1, Z_2 , and Z_3 , are formed, where $Z_2 = -Z_0$ and $Z_3 = -Z_1$ [since $c_2(t) = -c_0(t)$ and $c_3(t) = -c_1(t)$]. Due to the unequal energies of $c_0(t)$ and $c_1(t)$, namely, $E_0 = A^2$ and $E_1 = A^2(1 - \alpha/2)$, biases of $E_0/2$ and $E_1/2$ must be subtracted from the I&D outputs prior to forming the Z_i 's. The decision variables then are fed to a Viterbi algorithm (VA) for final detection.

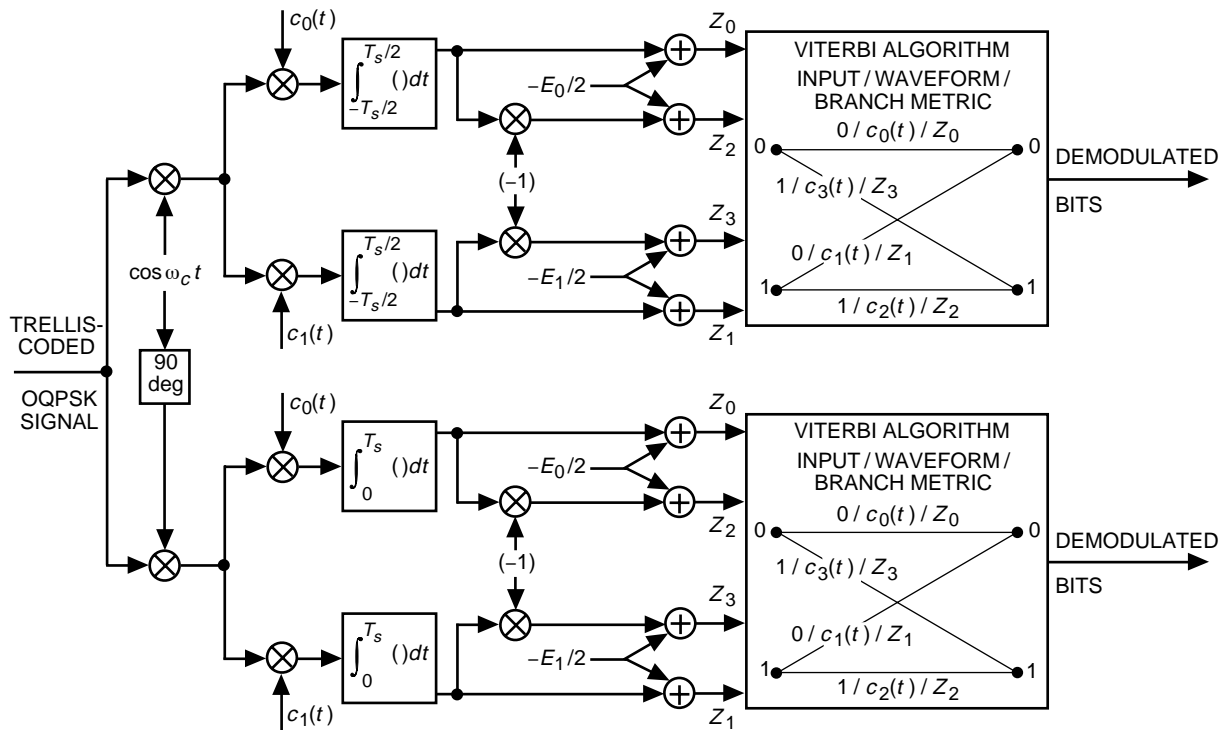


Fig. 10. The optimum receiver structure.

⁵ The first selected waveform, i.e., that corresponding to the interval $0 \leq t \leq 2T_b$, is discarded here since it depends on the initially random state of the shift register. For correspondence with Fig. 2(b), the initial state of the register would have been "1."

The procedure for computing the upper and lower bounds on the average BEP, $P_b(E)$, of the receiver in Fig. 10 is based on the transfer function bound approach outlined in [7]. (Derivations and examples appropriate to the case under consideration here are given on pp. 374–386 of [7] for trellis-coded QPSK.) In particular, the upper bound for the BEP over an AWGN channel is given by [7]

$$P_b \leq \frac{1}{m} Q \left(\sqrt{\frac{d_{\text{free}}^2 \bar{E}_b}{2N_0}} \right) \exp \left(\frac{d_{\text{free}}^2 \bar{E}_b}{4N_0} \right) \frac{\partial T(D, I)}{\partial I} \Big|_{D=\exp(-\bar{E}_b/4N_0), I=1} \quad (18)$$

where d_{free}^2 is the square of the minimum free distance of the code, i.e., the minimum Euclidean distance between a pair of valid, distinct sequences of waveforms, \bar{E}_b is the average energy per bit, N_0 is the single-sided PSD of the AWGN, and $T(D, I)$ is the transfer function associated with the state diagram derived from the trellis diagram. Since, for the case under consideration here, the squared minimum free distance is $d_{\text{free}}^2 = 4$ (independent of α), it is straightforward to show that

$$Q \left(\sqrt{\frac{2\bar{E}_b}{N_0}} \right) \leq P_b(E) \leq Q \left(\sqrt{\frac{2\bar{E}_b}{N_0}} \right) \frac{4}{\left[2 - \exp \left(-\frac{(1 - [\alpha/2]) \bar{E}_b}{(1 - [\alpha/4]) N_0} \right) - \exp \left(-\frac{1}{(1 - [\alpha/4])} \frac{\bar{E}_b}{N_0} \right) \right]^2} \quad (19)$$

where the lower bound is obtained from the single minimum distance path that diverges and remerges with the “0” state after two transitions, which corresponds to a single bit error.

For fully overlapped raised-cosine pulse shaping ($\alpha = 1$), the upper and lower bounds of (19) become

$$Q \left(\sqrt{\frac{2\bar{E}_b}{N_0}} \right) \leq P_b(E) \leq Q \left(\sqrt{\frac{2\bar{E}_b}{N_0}} \right) \frac{4}{\left[2 - \exp \left(-\frac{2\bar{E}_b}{3N_0} \right) - \exp \left(-\frac{4\bar{E}_b}{3N_0} \right) \right]^2} \quad (20)$$

whereas for rectangular pulse shaping ($\alpha = 0$), the upper and lower bounds of (19) become

$$Q \left(\sqrt{\frac{2\bar{E}_b}{N_0}} \right) \leq P_b(E) \leq Q \left(\sqrt{\frac{2\bar{E}_b}{N_0}} \right) \frac{1}{\left[1 - \exp \left(-\frac{\bar{E}_b}{N_0} \right) \right]^2} \quad (21)$$

Asymptotically (\bar{E}_b/N_0 large), the upper and lower bounds of (19) converge toward equality, which indicates that, for any $0 \leq \alpha \leq 1$, the BEP approaches that of uncoded QPSK (or OQPSK), namely, $P_b(E) = Q \left(\sqrt{2\bar{E}_b/N_0} \right)$. For the fully overlapped case, plots of $P_b(E)$ obtained from simulation of the receiver in Fig. 10 and the bounds of (20) are illustrated in Fig. 11. It is observed that over a wide range of \bar{E}_b/N_0 , the lower bound is an excellent approximation of the true performance obtained via computer simulation. Since the lower bound is independent of α , and since the upper bound of (21) (corresponding to $\alpha = 0$) is even tighter than the bounds of (20) (corresponding to $\alpha = 1$), one would anticipate the same degree of tightness for the fit of the lower bound to simulated results here for any partially overlapped case.

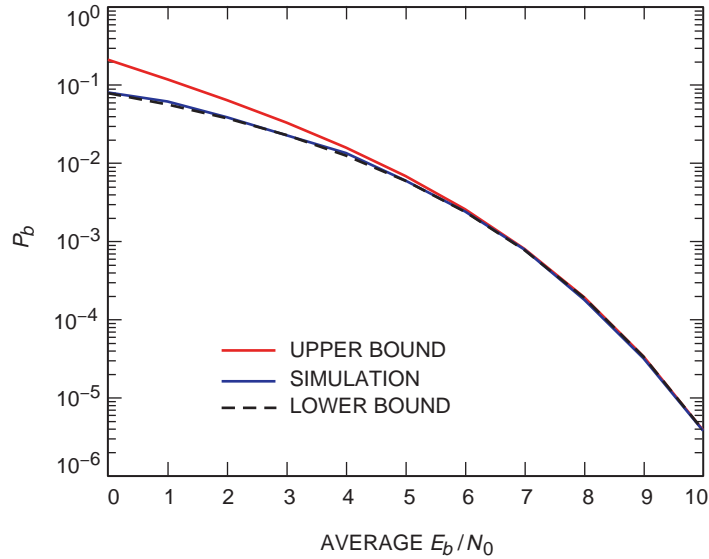


Fig. 11. The simulated BEP and the bounds on the BEP for trellis-coded OQPSK with fully overlapped ($\alpha = 1$) raised-cosine pulse shaping.

VII. Conclusion

In conclusion, trellis-coded OQPSK with partially overlapped raised-cosine pulse shaping offers the system designer the flexibility of a continuously variable trade-off (as α varies between 0 and 1) between the rate of spectral roll-off and the amount of envelope fluctuation of the transmitted signal with a receiver BEP performance that is virtually independent of the value of α and nominally equivalent to that of uncoded QPSK. Furthermore, it should be noted that, if one desires to surround the above trellis-coded modulation scheme with an additional error-correction encoder/decoder, then a soft output Viterbi algorithm (SOVA) [8] would replace the traditional hard decision VA output in Fig. 10.

References

- [1] M. C. Austin and M. U. Chang, "Quadrature Overlapped Raised-Cosine Modulation," *Proc. Int. Conf. Commun.*, pp. 26.7.1–26.7.5, 1980; also *IEEE Trans. Commun.*, vol. COM-29, no. 3, pp. 237–249, March 1981.
- [2] D. Divsalar and M. K. Simon, "Performance of Quadrature Overlapped Raised-Cosine Modulation Over Nonlinear Satellite Channels," *Proc. Int. Conf. Commun.*, Denver, Colorado, pp. 2.3.1–2.3.7, 1981.
- [3] M. K. Simon, J. K. Omura, and D. Divsalar, "Performance of Staggered Quadrature Modulations Over Nonlinear Satellite Channels With Uplink Noise and Intersymbol Interference," *GLOBECOM Conf. Record*, Miami, Florida, pp. 190–197, 1982.
- [4] D. Divsalar and M. K. Simon, "The Power Spectral Density of Digital Modulations Transmitted Over Nonlinear Channels," *IEEE Trans. Commun.*, vol. COM-30, no. 1, pp. 142–151, January 1982.

- [5] X.-H. Chen and J. Oksman, "A Quasi-Constant Envelope Quadrature Overlapped Modulation and Its Performance Over Nonlinear Band Limited Satellite Channels," *Int. Journ. Satellite Comm.*, vol. 14, pp. 351–359, 1996.
- [6] X.-H. Chen and S.-Y. Wong, "Four Novel Quadrature Overlapping Modulations and Their Spectral Efficiency Analysis Over Band-Limited Non-Linear Channels," *Int. Journ. Satellite Comm.*, vol. 15, pp. 117–127, 1997.
- [7] S. B. Wicker, *Error Control Systems for Digital Communication and Storage*, Englewood Cliffs, New Jersey: Prentice-Hall, Inc., 1995.
- [8] J. Hagenauer and P. Hoeher, "A Viterbi Algorithm With Soft-Decision Outputs and Its Applications," *Proc. Globecom '89*, Dallas, Texas, pp. 1680–1686, November 1989.



**8/16 PSK Multi-D Treillis Coded Modulation
an alternative to improve Power/Bandwidth efficiency
for high data rate communications.**

Presentation of a solution for high data rate links

André Ribes

CENTRE NATIONAL D'ETUDES SPATIALES

Toulouse, France



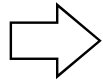
Foreword

- This study was conducted under CNES R&D contract between year 95 and today.
- Responsible of the study at CNES: Guy Lesthievant (Signal Processing Department)
- The following University and Companies was involved in the study and/or development:
 - Basic theoritical works and choices: ENST Paris/Toulouse
(Mrs M.L.Boucheret, JC. Belfiore & X. Giraud)
 - ASICs developement: COMATLAS (G.Lochon, S.Faudeil)
 - SPW Simulations: Europe Informatique/Syntegra (M. Blazy)
 - Experimental CODEC developement: COMATLAS (S. Ilias)
 - Tests and performance evaluation: CNES (G. Lesthievant, E.Peragin, T.Robert)

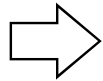


Study Background

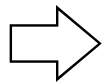
Main objectives of the study:



- Improvement of Satellite to Ground Station links efficiency for high data rate communication



- First application for CNES is for Image Telemetry of Earth Observation projects, like SPOT Follow-On Program



- Purpose of the study: identify the possible use for high data rate links of recent improvements and efficiency applicable to communication channel in terms of:

- capacity in bits/sec/Hz
- reduction of occupied bandwidth
- better use of transmitted power



Possibilities of improvement of channel performances

- Today techniques: use of 4-PSK modulation with or w/o Nyquist filtering and RS coding (SPOT V). The coding is achieved independantly of the modulation.
- The X-Band channel is crowded: reduction of transmitted power and/or improved use of bandwidth is highly wished.
- Reduction of transmitted power: this is possible thanks to the use of channel coding but at the cost of increased bandwidth. For exemple, the L=7, R= 1/2 Convolutional Code provide practically about 4,5 dB of power saving at BER=10⁻⁵ but double the occupied bandwidth !
- Reduction of bandwidth occupancy: is possible thanks to the use of bandwidth-efficient multilevel or multi/phase modulations like M-Ary PSK or QAM modulations.
- M-Ary PSK modulations are prefered to M-Ary QAM Modulations under non-linear amplitude channel conditions.
- Inconvenient of M-Ary PSK (M>4) Modulations: BER Performances are worst than 2 or 4-PSK modulations, at given Eb/No, due to a reduced Euclidian distance. Additional transmitted power is necessary to compensate for these losses
- Possible Solution: introduction of Coded Modulations



Solution to increase power efficiency and/or bandwidth occupancy

•Coded Modulations:

- provide a better use of the spectrum allied to good signal performances, in terms of BER and offer an interesting alternative to classical systems involving coding and modulation separately.

- constitute the solution to improve signal detection performances of multiphase modulations (e.g. 8 or 16-PSK) in a power/bandwidth constrained channel thanks to the increase of Euclidean distance between "signal points"

- Coded Modulations are characterized by an increase of the "number of signals points" in comparison to the corresponding uncoded system to compensate for the increase of bandwidth due to the redundancy introduced by the code.

- 8-PSK Coded modulation offers performance gain in terms of BER vs E_b/N_0 in comparison to uncoded 4-PSK modulation, for the same channel efficiency expressed in Bit/Hz (a maximum of 2 Bit/Hz in this case)

- 16-PSK Coded Modulation offers a reduction of bandwidth occupancy with quite good signal performances, in comparison with 4-PSK uncoded modulation. A better use of the channel in Bit/Hz is observed in this case (up to 3 bits/Hz)



Recall of uncoded M-Ary PSK Modulation principle and performances

- **Occupied bandwidth**
- **Spectral efficiency**
- **Euclidian distance**
- **Spectral density**
- **SER & BER Performances w/o coding**
- **Performances with convolutional coding**



Occupied bandwidth, Spectral efficiency and Euclidian distance for M-Ary PSK Modulations

Occupied Bandwidth and Data rate

$$B = R_S (1+\alpha)$$

R_S = Symbol (or signal) rate

α = Roll-off of SRC Nyquist filter (baseband shaping at transmitter end)

Data rate for M-Ary Modulation in bits/sec:

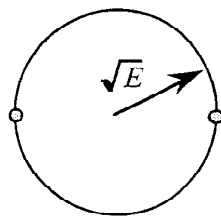
$$D = R_S \log_2 (M)$$

Spectral efficiency

$$\eta = \frac{D}{B} = \frac{\log_2 (M)}{(1+\alpha)}$$

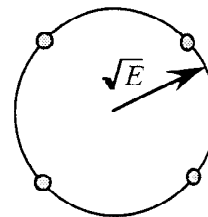
Euclidian Distance

For any M $\Rightarrow d_{\min} = 2\sqrt{E} \sin\left(\frac{\pi}{M}\right)$



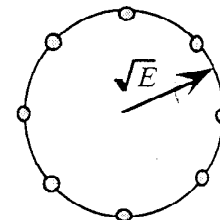
MDP-2

$$d_{\min} = 2\sqrt{E}$$



MDP-4

$$d_{\min} = \sqrt{2E}$$

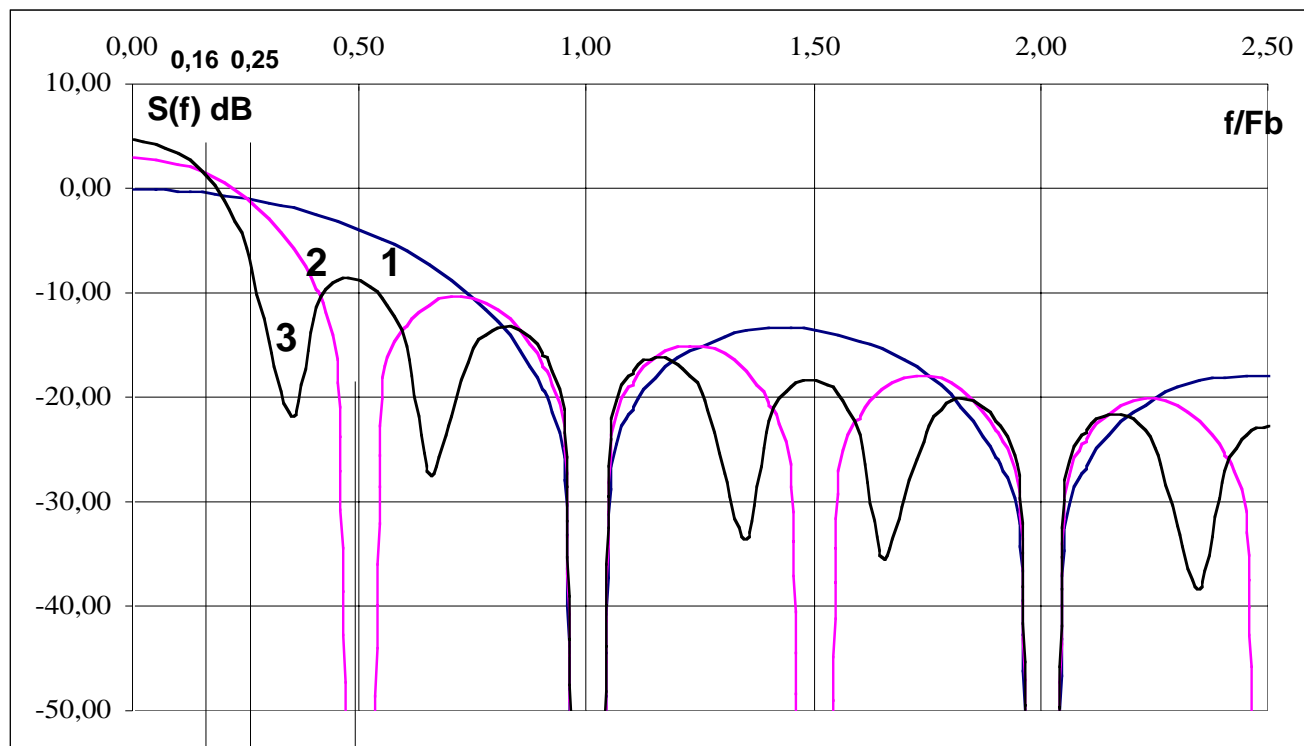


MDP-8

$$d_{\min} = 2\sqrt{E} \sin \pi / 8$$



Spectral density of M-Ary PSK Modulations



3 2 1
Ideal Nyquist bandwidth

Curve 1: 2-PSK (1 Bit/s/Hz)

Curve 2: 4-PSK (2 Bit/s/Hz)

Curve 3: 8-PSK (3 Bit/s/Hz)



Performances of M-Ary PSK uncoded Modulations

P_M : Probability of symbol error for M-Ary PSK modulations (Proakis p.262):

$$P_M = 1 - \int_{-\pi/M}^{\pi/M} p(\theta) d\theta \quad \text{with} \quad p(\theta) = \frac{1}{2\pi} e^{-\gamma} \left(1 + \sqrt{4\pi\gamma} \cos \theta e^{\gamma \cos^2 \theta} \frac{1}{\sqrt{2\pi}} \int_{-\infty}^{\sqrt{2\gamma} \cos \theta} e^{-x^2/2} dx \right)$$

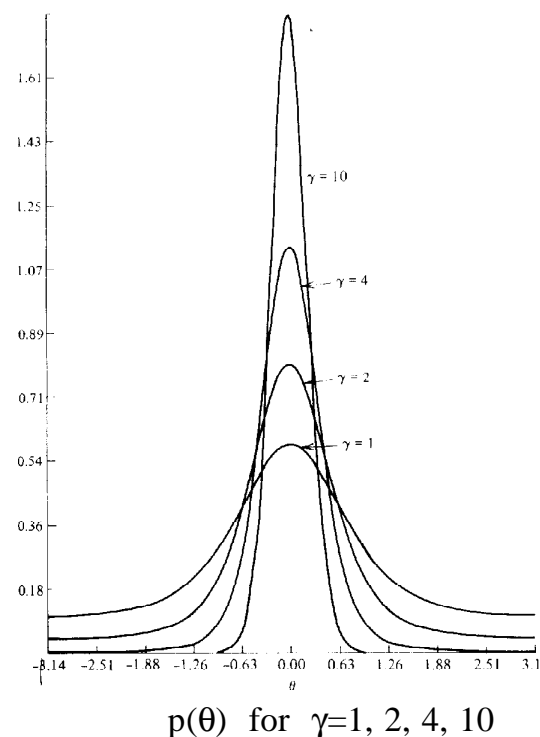
for $\gamma \gg 1$ and $|\theta| < \pi/2$ with $M = 2^k$

$$P_M \approx \text{erfc} \left[\sqrt{\gamma} \sin \left(\frac{\pi}{M} \right) \right] = \text{erfc} \left[\sqrt{k\gamma_b} \sin \left(\frac{\pi}{2^k} \right) \right]$$

$$\gamma = k\gamma_b \quad \text{with} \quad \gamma_b = \frac{E_b}{N_0} \quad (\text{SNR per bit})$$

The bit error rate (Gray code mapping) is

$$P_b \approx \frac{P_M}{k}$$





SER & BER for uncoded 2, 4, 8, 16-PSK and for 2 and 4-PSK with CC

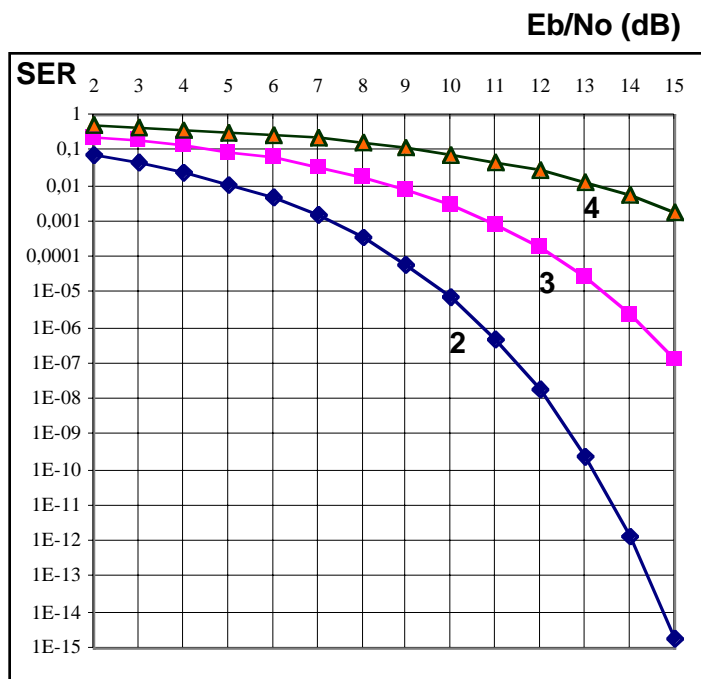


Fig 1: 2 & 4-PSK w CC 7-1/2

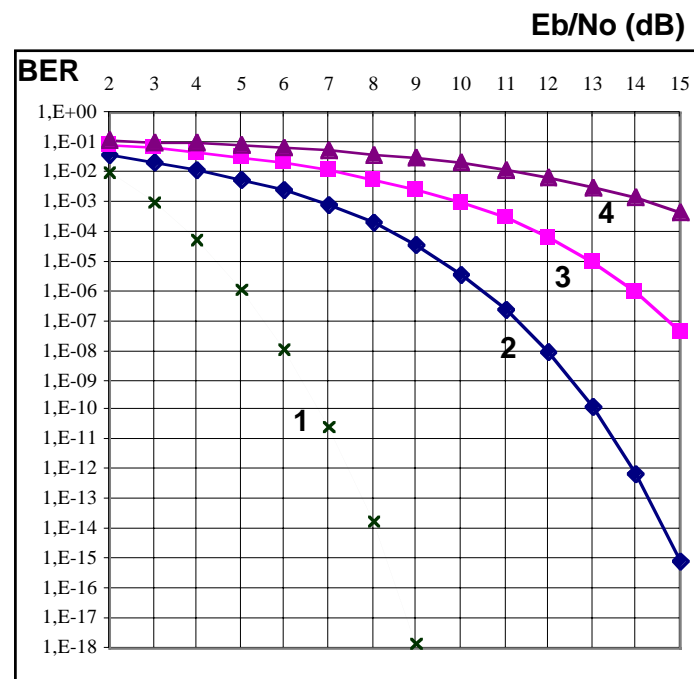


Fig 2: 2 & 4-PSK w/o CC

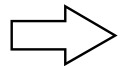
Fig 3: 8-PSK w/o CC

Fig 4: 16-PSK w/o CC

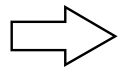


Strategies for Coding and Modulation

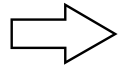
- **Exemple:** association of 4-PSK modulation (intrinsic efficiency = 2 Bit/sec/Hz, assuming a roll-off $r=0$) with a convolutional code with rate $R=2/3$
- **Two possibilities for the modulation:**
 - use of 4-PSK modulation with the coded stream: improvement of performances but the channel efficiency is now $4/3$ Bit/sec/Hz
 - use of 8-PSK modulation: improvement of performances and the channel efficiency reach again 2 Bit/sec/Hz



• For 8-PSK modulation, the coding gain must be sufficient to compensate for the loss due to a reduced Euclidian distance between the signal points.



• For the treillis coded modulation, the coding process increase the Euclidian distance between adjacent paths



• The code performances (number of states) are mandatory and drive the choice of the number of treillis states and consequently the decoding complexity.



Performances of M-Ary modulations with convolutional coding

- The coding is introduced on the data stream
- Each signal point of the M-Ary constellation is represented by a coded pattern z_k of two or more bits (coordinate of the point), related to one given branch of the treillis of the code.
- The signal points of the constellation are not independant
- The valid sequence $\{z_k\}$ are the coded sequences. The other one are "forbidden sequences"
- For a maximum likelihood decoder, the performances of transmission are a function of minimum Euclidian distance, named "free euclidian distance", D_{fed}^2 between the possible coded sequences

$$D_{fed}^2 = \min_{\{z_i\}, \{z_j\}} |\{z_i\} - \{z_j\}|^2$$



Coding gain improvement

- One defines the probability of "error event" as the probability of decoding a coded sequence not identical to the transmitted sequence.
- This probability is well approximated by:

$$P_{\text{eve}} = N_{\text{fed}} \left[\frac{1}{2} \operatorname{erfc} \left\{ \sqrt{\frac{D_{\text{fed}}^2}{4N_o}} \right\} \right]$$

N_{fed} = mean value of the number of coded sequences located at the minimum distance D_{fed}^2 of the transmitted sequence

Coding gain for high SNR $\Rightarrow G_{\text{dB}} = 10 \operatorname{Log}_{10} \left(\frac{D_{\text{fed}}}{d_{\text{min}}} \right)^2$

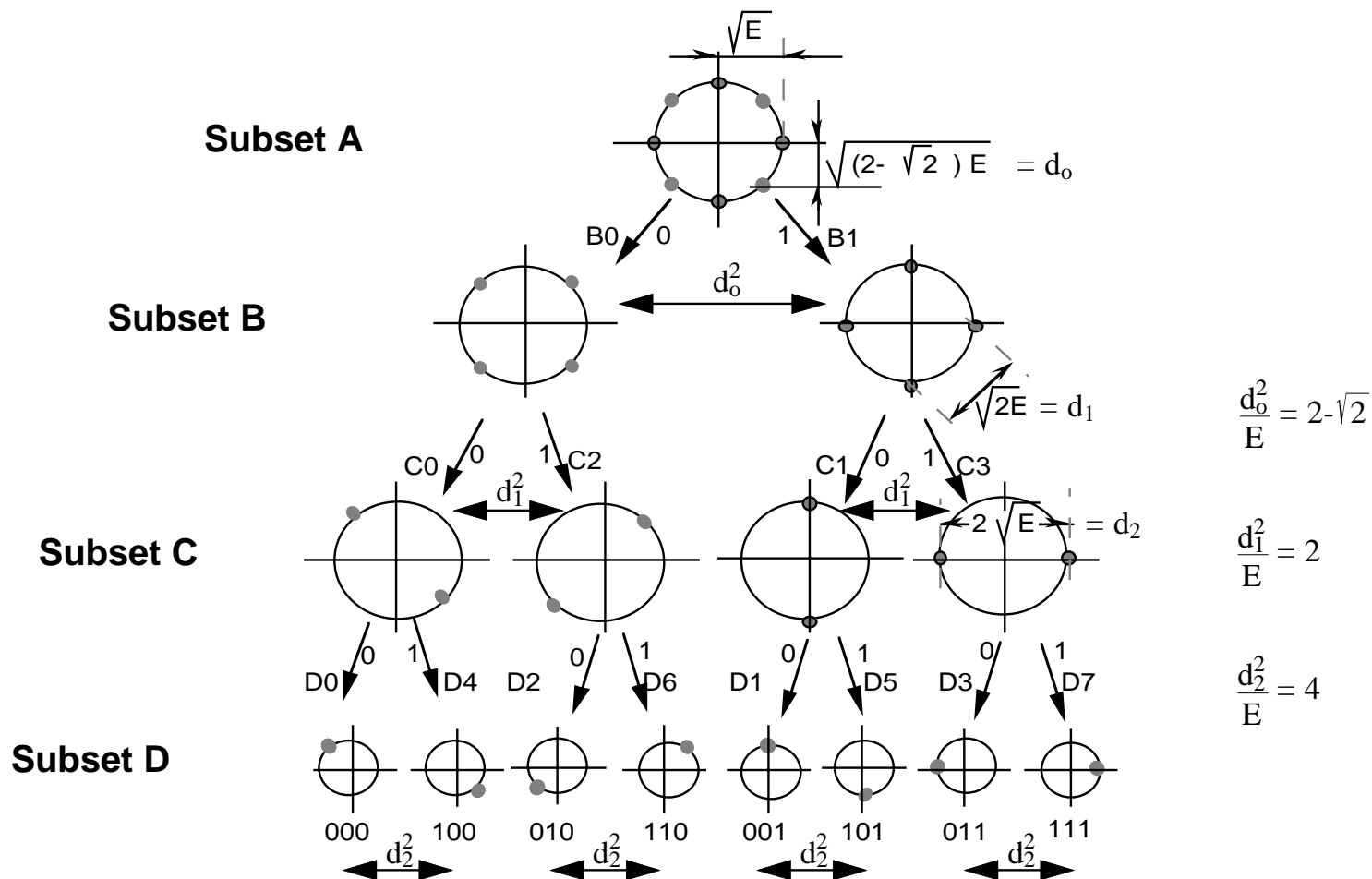
d_{min} = minimum Euclidian distance of the constellation without coding

- ➡ • Maximisation of free Hamming distance of convolutional code does not corresponds to the maximization of Euclidian distance, unless for 2-PSK or 4-PSK modulations.
- ➡ • The only way to optimize M-PSK performances ($M \geq 8$) is to mix coding and modulation in a unique function, the main goal being the maximization of Euclidian distance between coded sequences: this approach was proposed by Ungerboeck in 1976 to give the "Treillis Coded Modulations".



Principle of coded modulations (1)

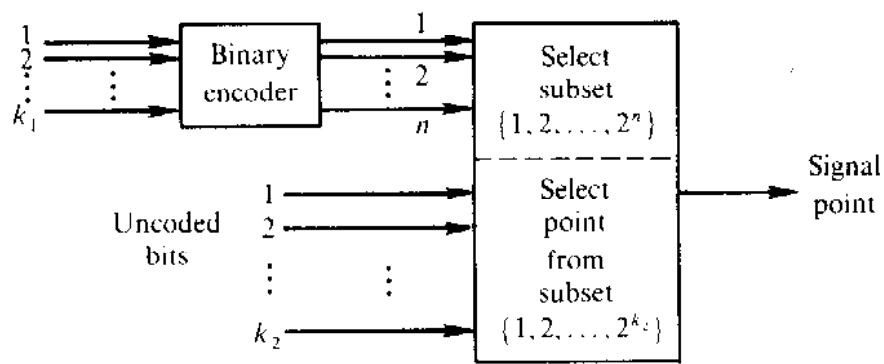
Partitioning exemple of an 8-PSK signal set (Proakis p. 490) - Natural mapping



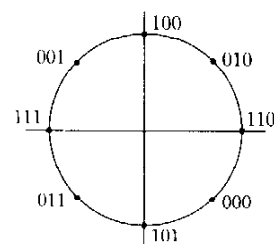
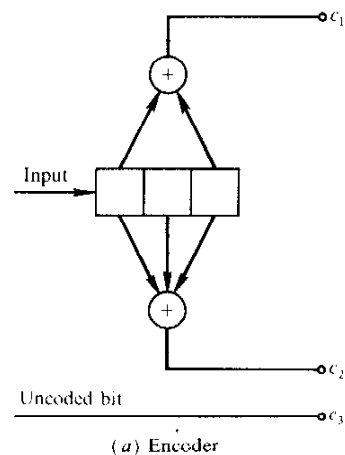


Principle of coded modulations (2)

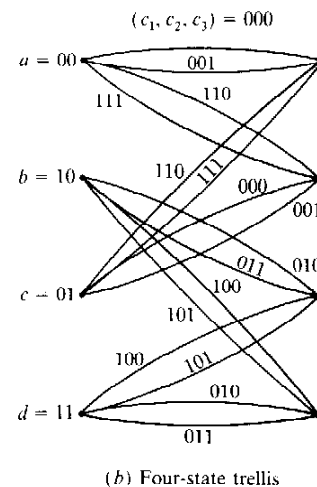
Principle of signal point determination



General structure of combined encoder/modulator.



(c) Mapping of coded bits (c_1, c_2, c_3) to signal points

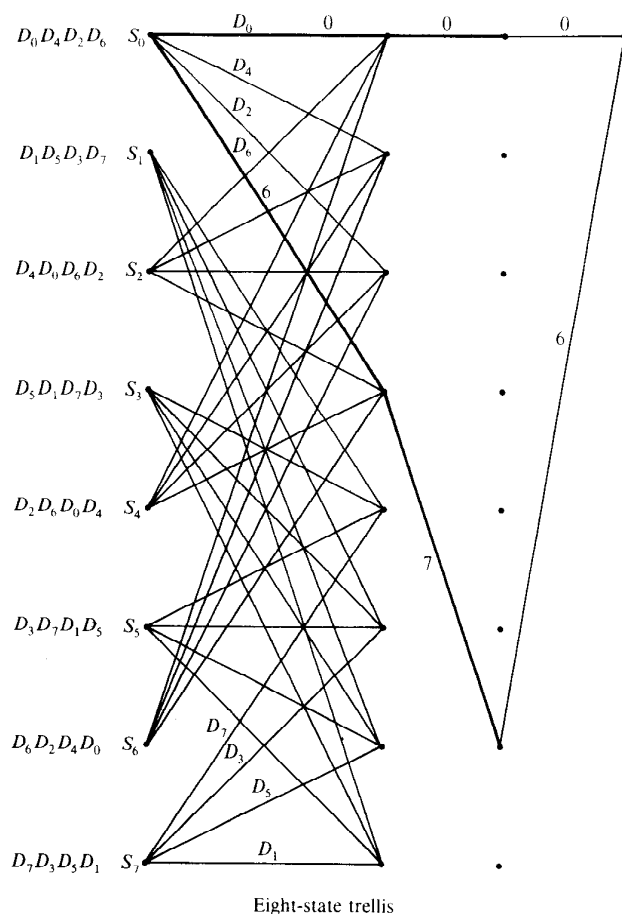


(b) Four-state trellis

Exemple of four States treillis coded 8-PSK Modulation



Determination of Free minimum Euclidian Distance



Eight-state trellis

Eight-state trellis code for coded 8-PSK modulation.

Ungerboek treillis (1982) for 8-PSK Modulation

State transition D0 to D6: d_1^2

State transition D0 to D7: d_0^2

State transition D0 to D6: d_1^2

Free Minimum Euclidian Distance for 8-PSK TCM

$$D_{\text{fed}}^2 = d_0^2 + 2d_1^2 = 4,585 \text{ E}$$

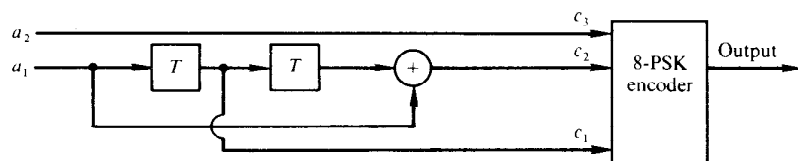
Free Minimum Euclidian Distance for 4-PSK (uncoded)

$$D_{\text{fed}}^2 = d_0^2 = 2 \text{ E}$$

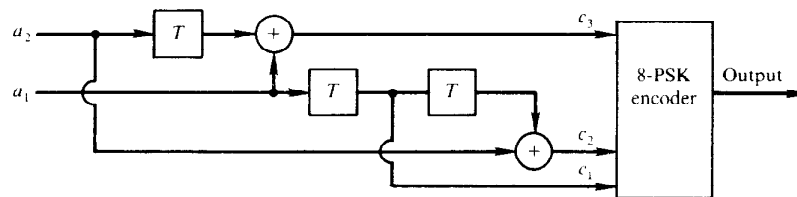
Asymptotic gain: $G = 2,29$ or $3,6$ dB



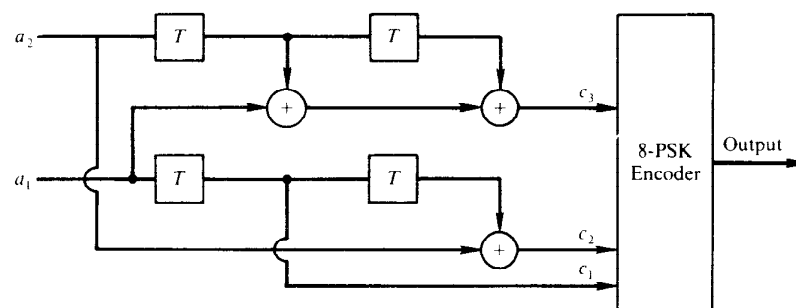
4, 8 and 16 stages convolutional encoders for 8-PSK TCM



(a) 4-state encoder



(b) 8-state encoder



(c) 16-state encoder

From Ungerboeck works (1982)



Coding gain for Treillis Coded 8 and 16-PSK Modulations

From Ungerboeck works (1982-1987)

Coding gain for Treillis coded 8-PSK modulation

Number of states	k ₁	Code rate $k_1/(1+k_1)$	$d_{\text{free}}^2 / \Delta_1^2$	m=2 Coding gain (dB) vs Uncoded 4-PSK
4	1	1/2	2.000	3
8	2	2/3	2.293	3.6
16	2	2/3	2.586	4.1
32	2	2/3	2.879	4.6
64	2	2/3	3.000	4.8
128	2	2/3	3.172	5.0
256	2	2/3	3.465	5.4
512	2	2/3	3.758	5.7
1024	2	2/3	3.758	5.7

Coding gain for Treillis coded 16-PSK modulation

Number of states	k ₁	Code rate $k_1/(1+k_1)$	$d_{\text{free}}^2 / \Delta_1^2$	m=3 Coding gain (dB) vs Uncoded 8-PSK
4	1	1/2	2.259	3.54
8	1	1/2	2.517	4.01
16	1	1/2	2.779	4.44
32	1	1/2	3.258	5.13
64	1	1/2	3.411	5.33
128	1	1/2	3.411	5.33
256	2	2/3	3.556	5.51



Exemple of Monodimensional TCM: Q1875 Codec

Manufacturer:

Qualcomm

Modulation:

Rate 2/3 (8-PSK) and rate 3/4 (16-PSK)

Coding:

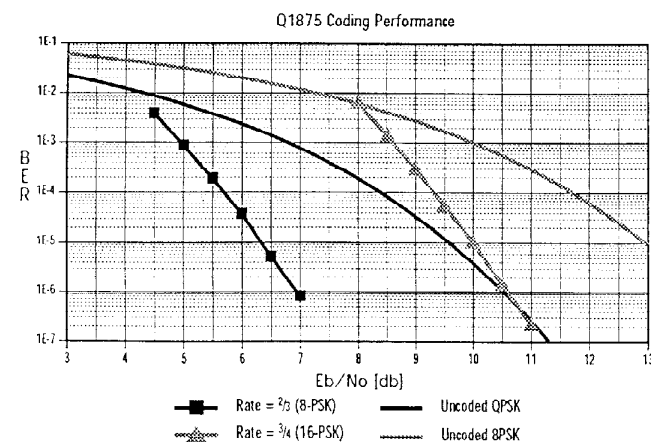
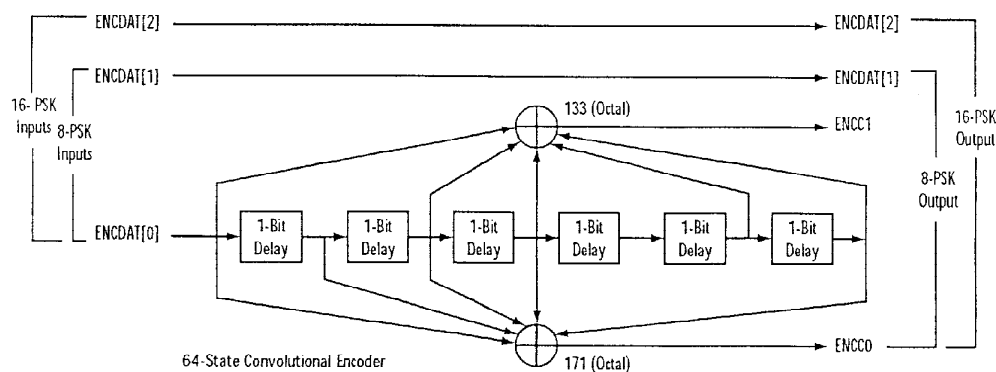
Pragmatic CC L=7, R=1/2

Decoding:

Pragmatic Treillis-Coded modulation decoder

Phase ambiguity resolution:

no self resolution of phase ambiguity





Multi-D Treillis Coded Modulation with concatenated RS code

Presentation of CODEC developped under CNES contract



Multidimensional Treillis Coded Modulations Basics

- **Principle of "k-Dimension - L PSK" TCM:**
 - Transmission of km information bits and 1 redundant bit every kT seconds (T = signaling rate of the modulation)
 - Transmission of k consecutive L-PSK constellations
- **Advantage of Multidimensional vs Monodimensional Treillis Coded Modulations:**
 - Augmentation of Free Euclidian Distance (D_{fed}): improvement of the power gain
 - Reduction of rate processing with a factor k in comparison with monodimensional TCM: possible use of standard technologies for higher information rate
 - Possible introduction of differential coding to suppress phase ambiguity.
- **Constraints of Multidimensional Modulations**
 - Augmentation of "computational complexity" at coding and decoding end



Characteristics of Multi-D TCM/RS - CNES Modem

Modulation:	8-PSK and 16-PSK (Multidimensional TCM: $k=4$)
Transmission efficiency:	2, 2.5, 3 and 3.5 Bit/s/Hz
Inner code:	Dedicated Convolutional $R=3/4$, 64 states ($L=7$)
Outer code	Reed Solomon (255, 239,8) (from DVB-S Standard)
block length	255 bytes
rate K/N	239/255
correction capabilities	8 bytes per block of 255
Channel filtering (waveform shaping):	Selectable SRC (roll-off= 0,35 or 0,5) or NRZ
Channel power amplifier:	Non linear (TWT like or SSPA)
Coding and Multi-D TCM Mapping	FPGA circuits



Spectrum filtering (NRZ and Nyquist)

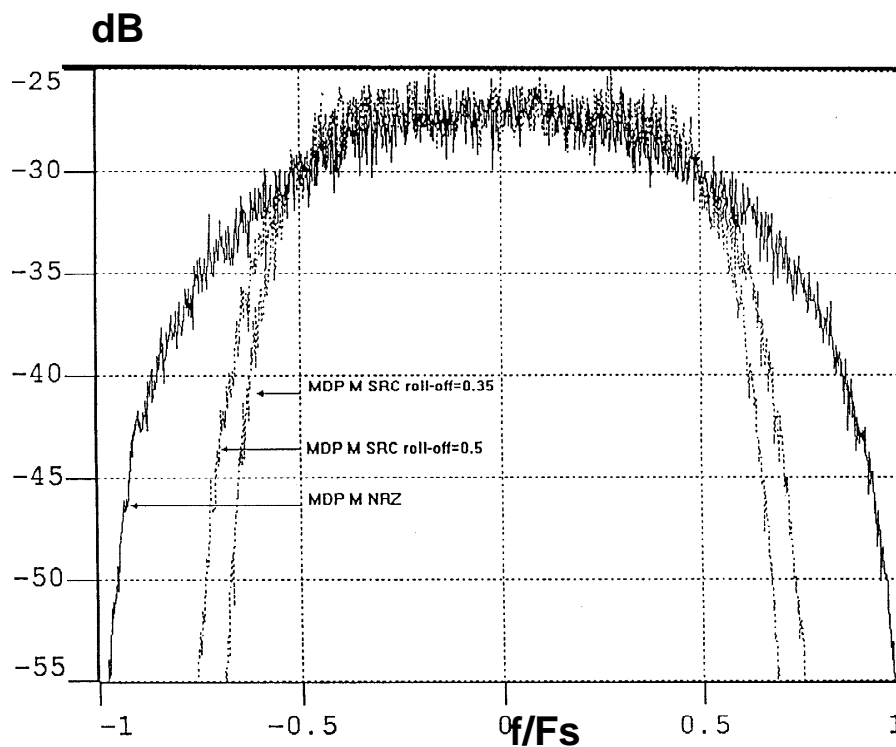
$$H(f) = 1 \quad \text{for } |f| < f_N(1 - \alpha)$$

$$H(f) = \left\{ \frac{1}{2} + \frac{1}{2} \sin \frac{\pi}{2f_N} \left[\frac{f_N - |f|}{\alpha} \right] \right\}^{\frac{1}{2}} \quad \text{for } f_N(1 - \alpha) \leq |f| \leq f_N(1 + \alpha)$$

$$H(f) = 0 \quad \text{for } |f| > f_N(1 + \alpha),$$

where:

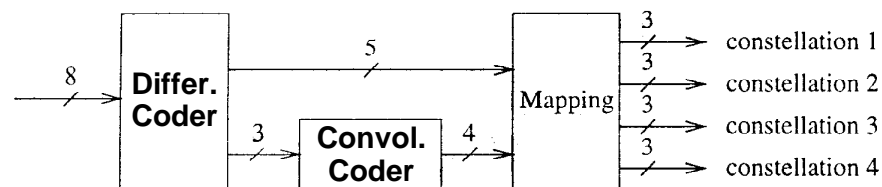
$$f_N = \frac{1}{2T_s} = \frac{R_s}{2} \quad \text{is the Nyquist frequency and } \alpha \text{ is the roll-off factor.}$$



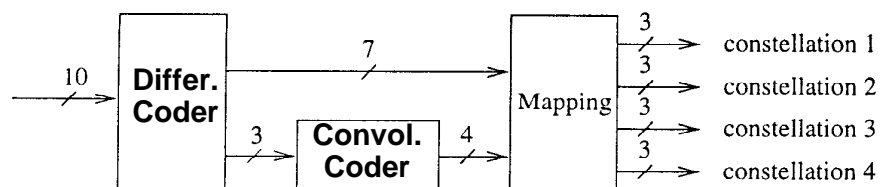
Spectrum shaping with Nyquist (Roll-Off 0.35 or 0.5) or NRZ



Coding and Mapping possibilities

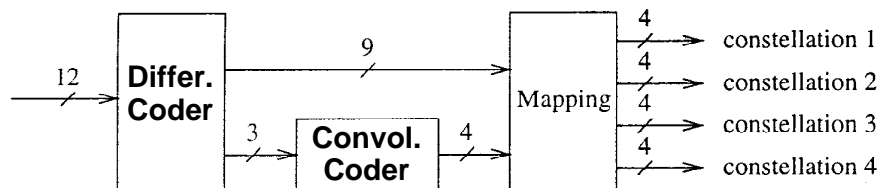


Coding and Mapping for 4D-8PSK 2 B/s/Hz

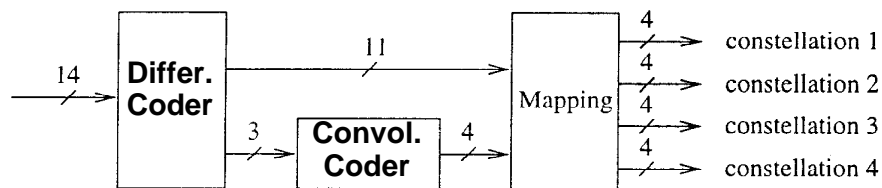


Coding and Mapping for 4D-8PSK 2.5 B/s/Hz

Coding and Mapping for 4D-16PSK 3 B/s/Hz



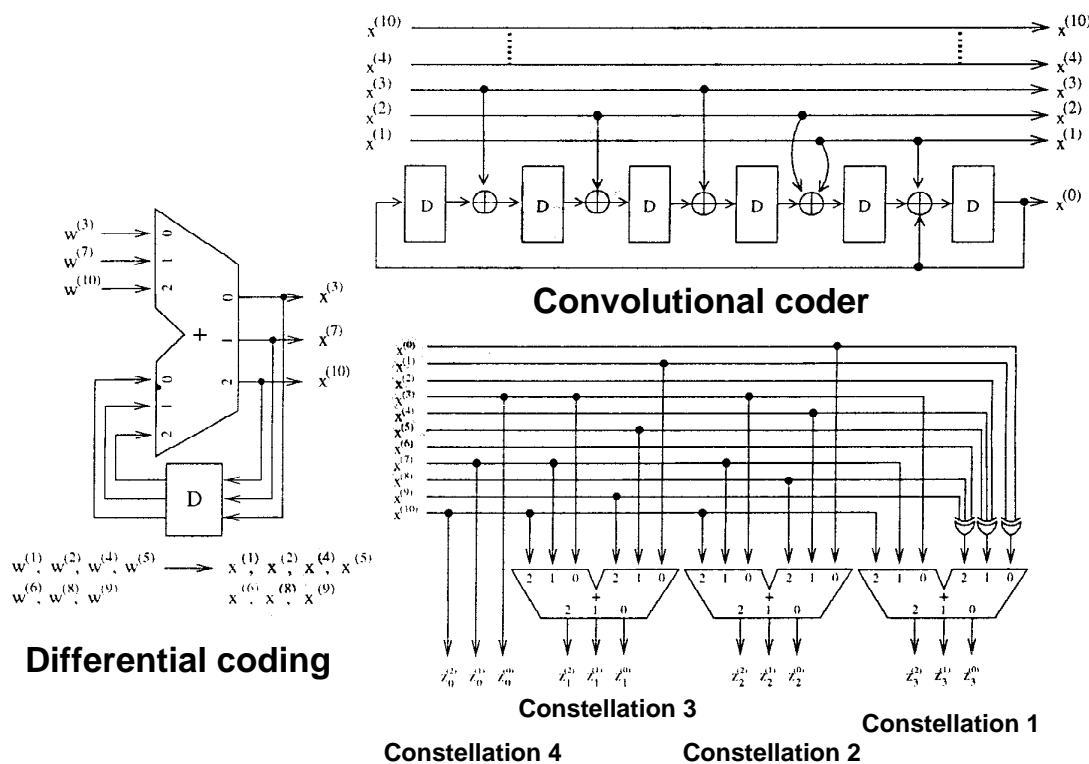
Coding and Mapping for 4D-16PSK 3.5 B/s/Hz



Convolutional code: $R=3/4$, 64 states ($L=7$)

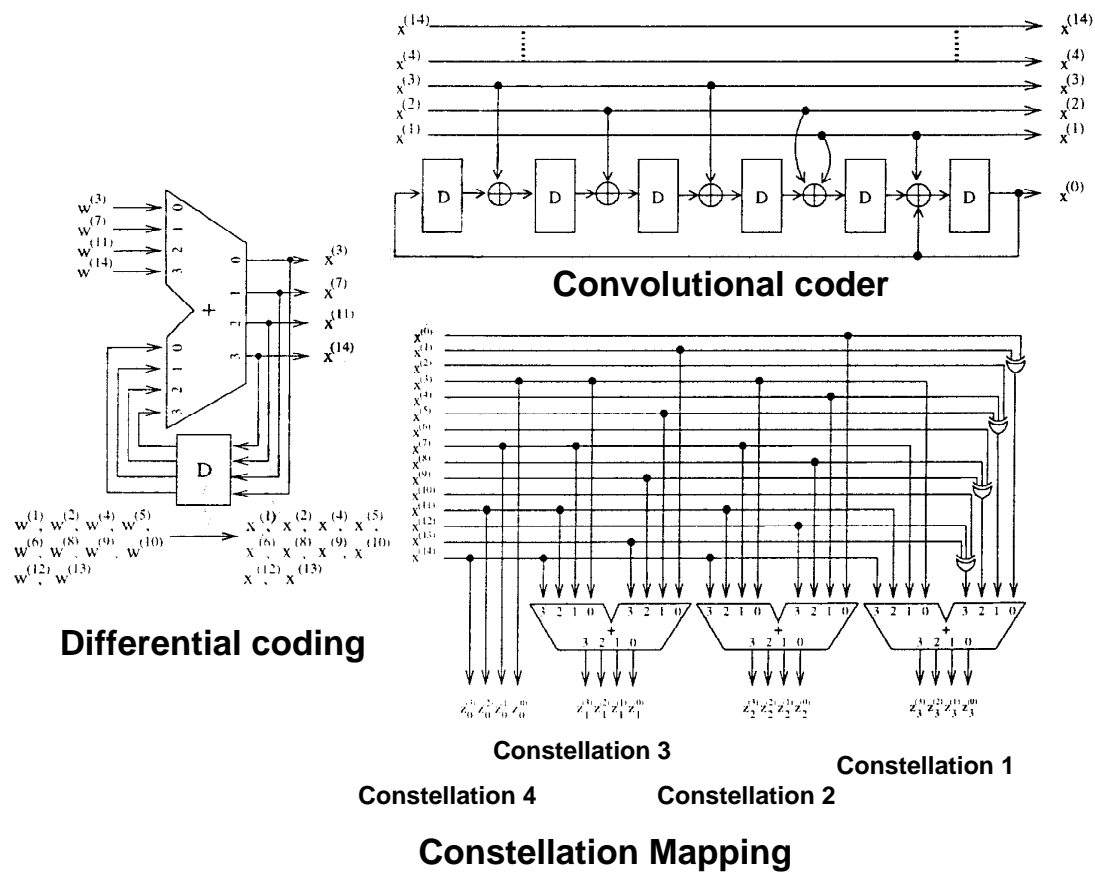


Exemple of Coding and Mapping for 4-8PSK @ 2.5 B/s/Hz





Exemple of Coding and Mapping for 4-16PSK @ 3.5 B/s





Multidimensional Decoder characteristics

Multi-D TCM Decoder

Technology

Maximum Rate of TCM decoder:

Inner code:

Inner code polynom:

Ambiguity resolution capabilities:

Power consumption:

Digital Demodulator:

RS Decoding

CAS 7023 (developped by Comatlas under CNES contract)

CMOS 0.6 μ from VLSI (VSC 6531) /70000 gates

100, 125, 150, 175 Mb/s (depending of efficiency))

Specific $R=3/4$, 64 states Convolutional Code

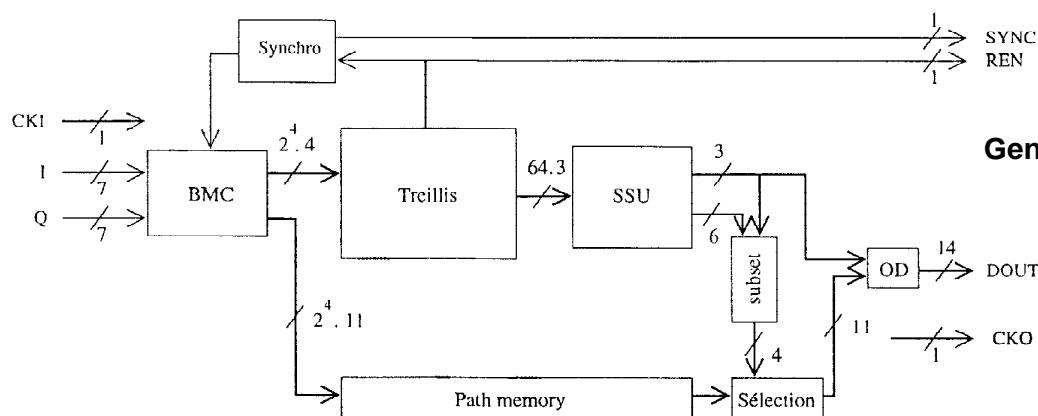
$h^3=050$, $h^2=024$, $h^1=006$, $h^0=103$

22.5°

around 1.2 W (at max Symb rate)

CAS 4153 (2, 4, 8 & 16 PSK) from DVB-S Industry

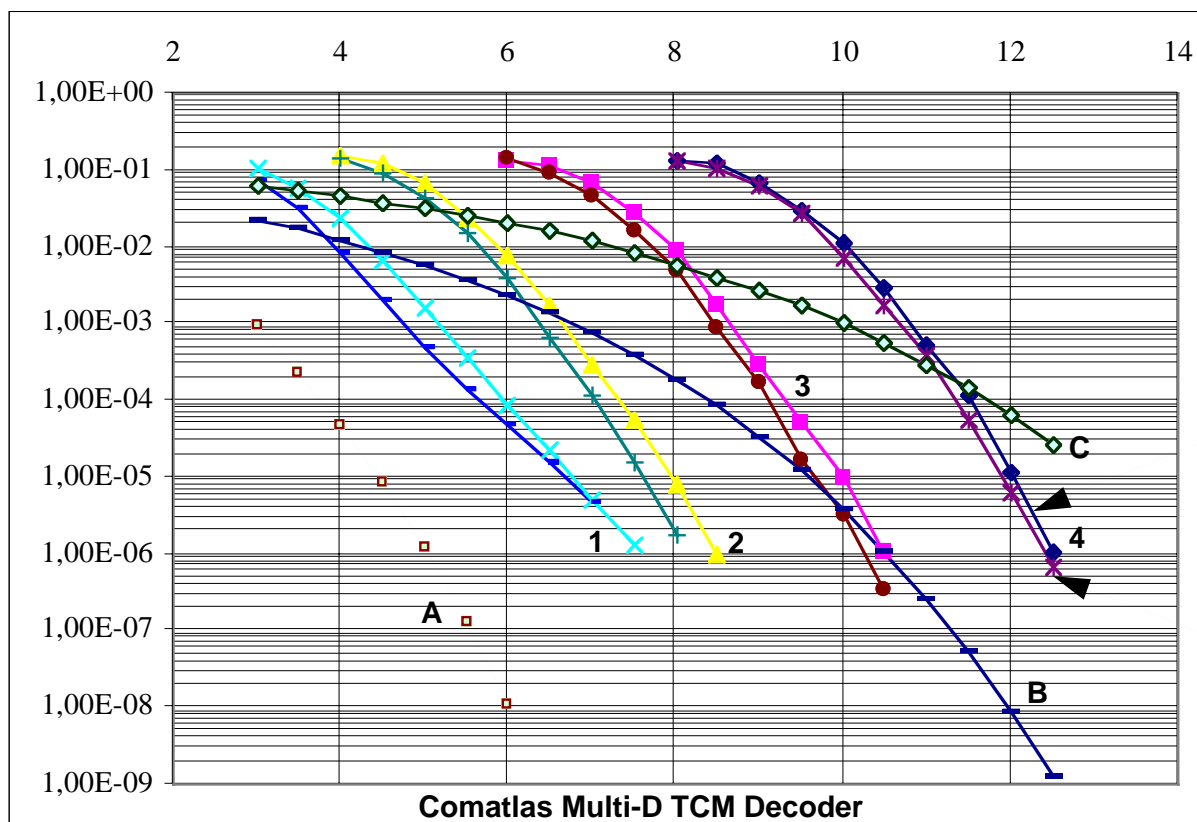
CAS 5203 (DVB-S Standard developped by Comatlas)



General diagram of TCM decoder



BER Performances of TCM decoder ASIC



A: QPSK with CC R=1/2, 64 states

B: QPSK uncoded

C: 8-PSK uncoded

1: 4D-8PSK 2 B/sec/Hz

2: 4D-8PSK 2,5 B/sec/Hz

3: 4D-16PSK 3 B/sec/Hz

4: 4D-16PSK 3,5 B/sec/Hz

Ideal curves: 32 bits Quantification

Real curves: 4 bits quantification (Euclidian Dist.) and 6 bits (cumulated metrics)

Real curve

Ideal curve

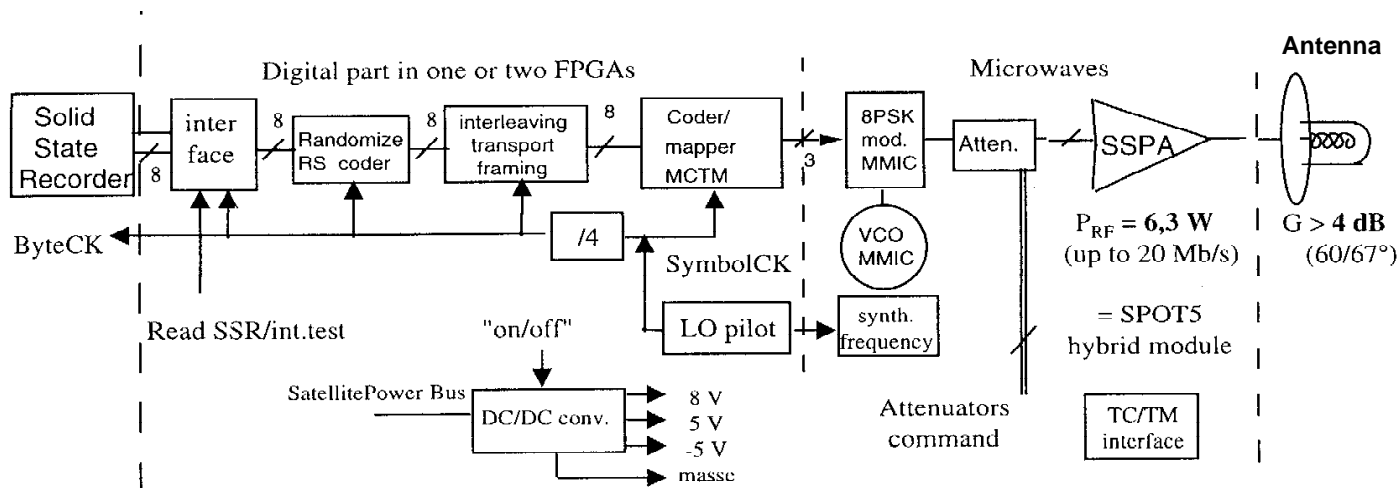


Transmitter/Receiver Demonstrator

- The transmitting section includes:
 - input data randomizer and RS coder
 - interleaving
 - 4D-8/16 PSK TCM Mapper based on FPGAuse
 - Waveform shapping: SRC ($r=0,35$ or $0,5$) or NRZ
 - 8 or 16 PSK MMIC modulator
 - SSPA power amplifier at X-Band
- The receiving section includes:
 - receiver at X-Band (8 GHz)
 - IQ mixer operating at $IF = 720$ MHz
 - 2, 4 ,8 ,16 phase Digital demodulator based on CAS 4153 ASIC
 - Clock regenerator
 - MultiD-TCM decoder based on CAS 7023 ASIC
 - Matrix uninterleaver
 - RS Decoder based on CAS 5203 ASIC
 - Descrambler

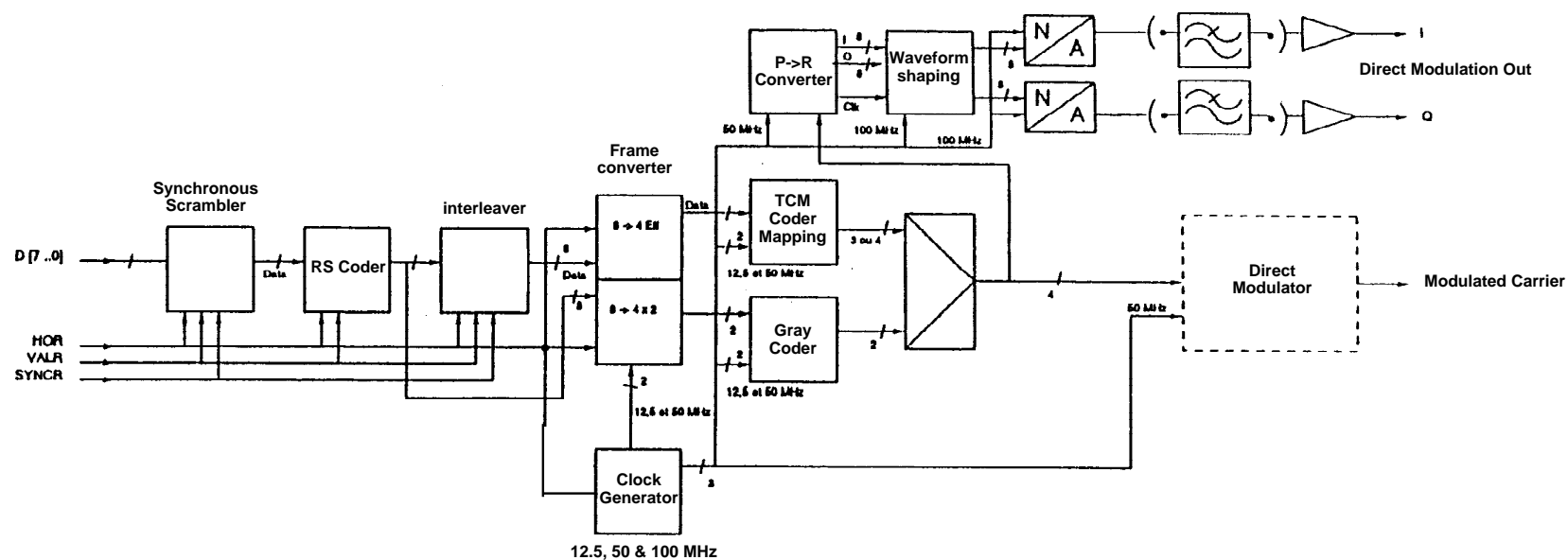


Transmitting Section



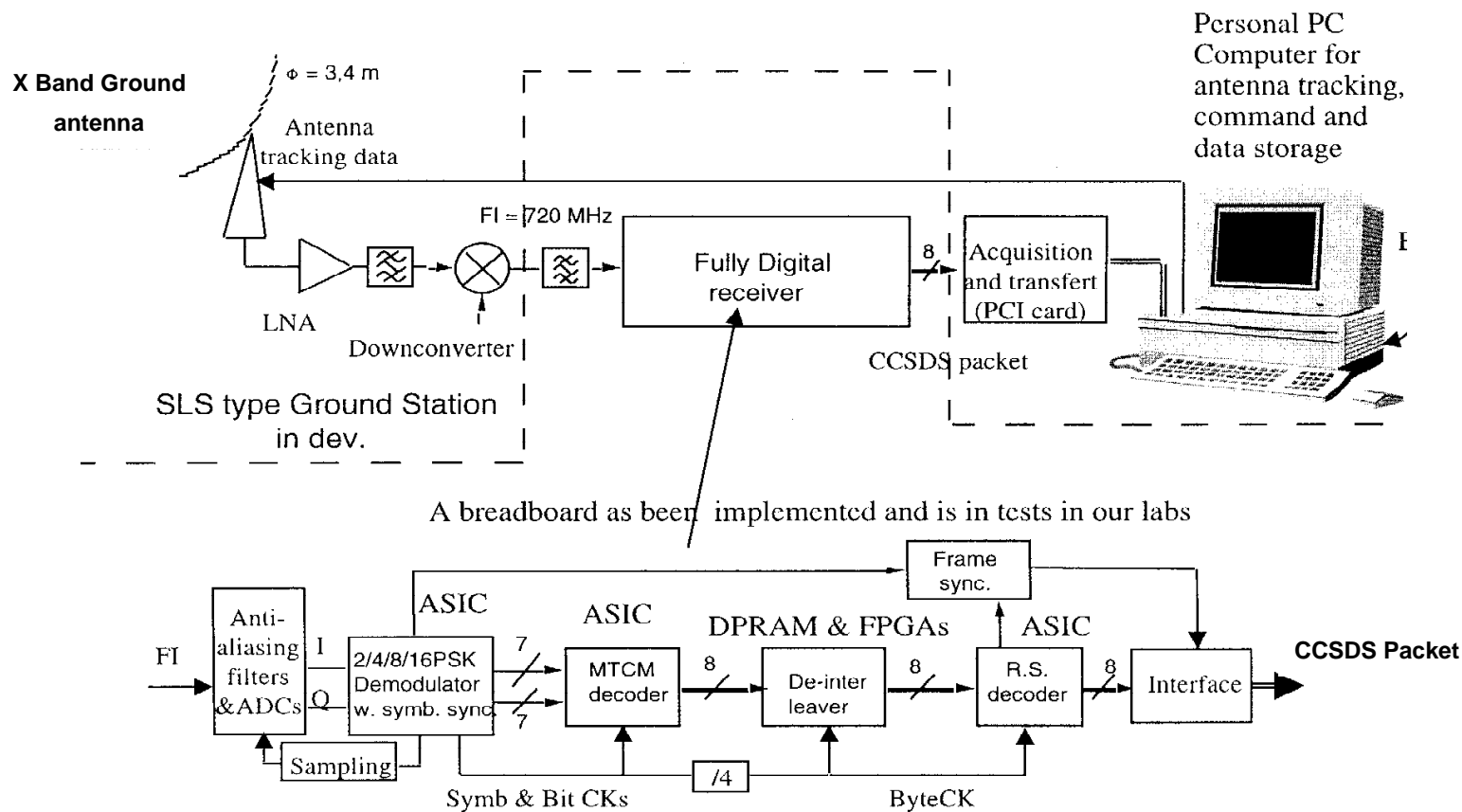


Transmitting board Principle



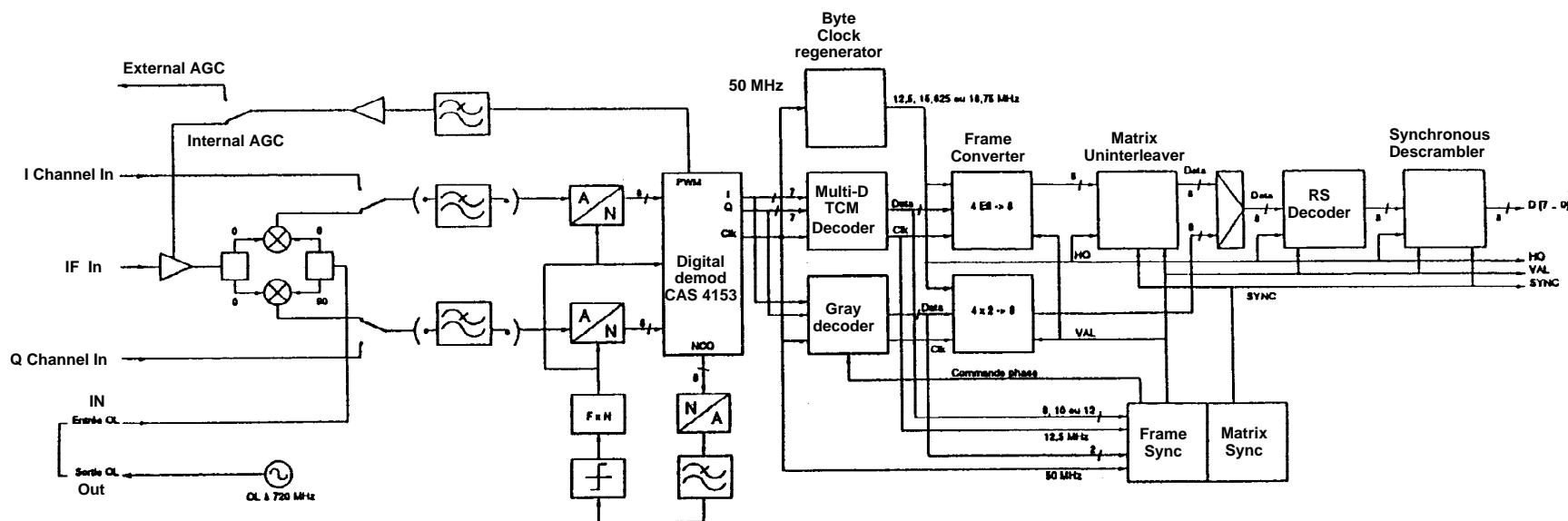


Receiving Section



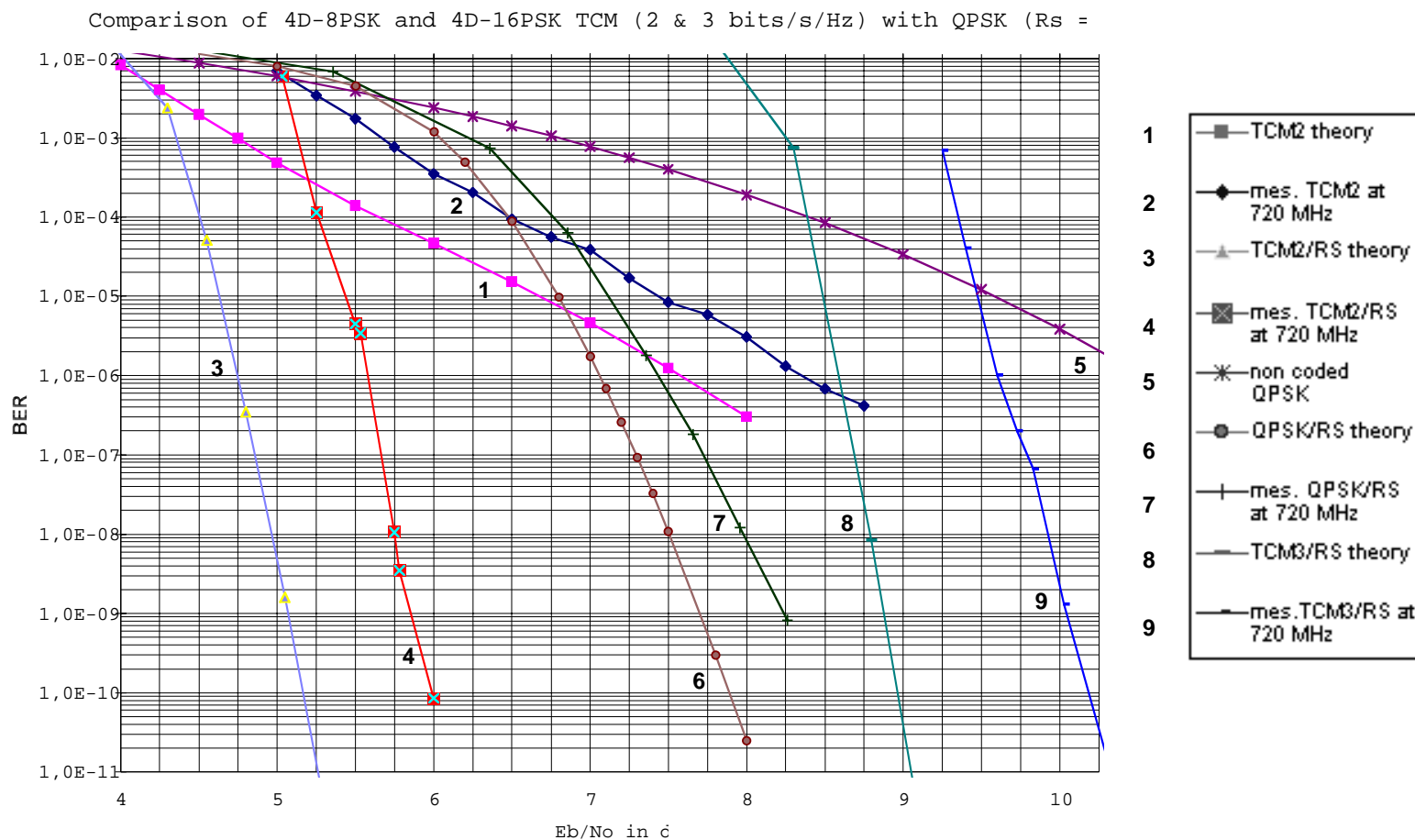


Receiving board Principle





Measured Performances at 50 Mbaud/s at IF= 720 MHz including RS coding





Comparison between available MODEM

TCM MODEM	Efficiency	Number of States	E_b/N_0 (10^{-3})	E_b/N_0 (10^{-6})	Maximum Rate	Power Consum.	Technology
Q1875	2 b/s/Hz	64	5 dB	6,9 dB	50 Mb/s	0,8 W	CMOS ?
	3 b/s/Hz	64	8,6 dB	10,6 dB	75 Mb/s	0,8 W	
dec COMSAT	2,33 b/s/Hz	16	7,3 dB	10,2 dB	233 Mb/s	4,5 W	ECL 1,5 μ m
	2,67 b/s/Hz	16	8,3 dB	11,4 dB	267 Mb/s	4,5 W	
CNES Modem CAS7023	2 b/s/Hz	64	5,2 dB	7,5 dB	100 Mb/s	0,9 W	CMOS 0,6 μ m
	2,5 b/s/Hz	64	6,7 dB	8,5 dB	125 Mb/s	0,95 W	
	3 b/s/Hz	64	8,7 dB	10,5 dB	150 Mb/s	1 W	
	3,5 b/s/Hz	64	10,8 dB	12,5 dB	175 Mb/s	1,1 W	
Newtec 155 MB/s SDH Modem	2,66 b/s/Hz	64	7dB	9,4 dB	170 Mb/s	?	CMOS or ECL?



8/16 PSK Treillis Coded Modulation

Performance comparison

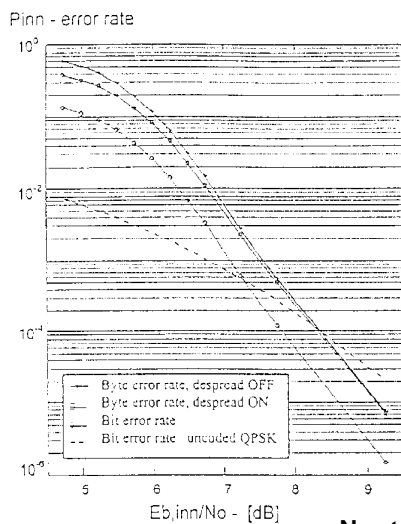
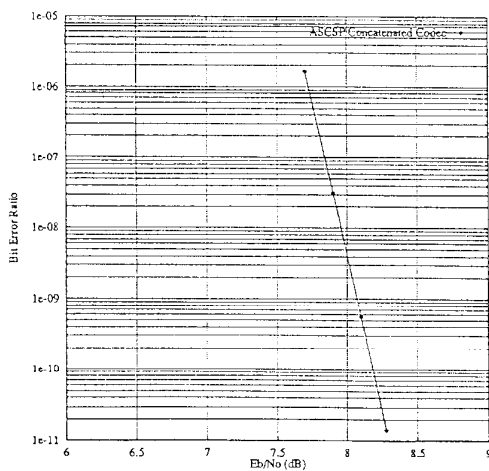


Fig. 3 : Inner code performance
(see text for explanation of $E_{b,inn}/N_0$)



BER vs E_b/N_0 for Concatenated Codec, Ideal AWGN Channel

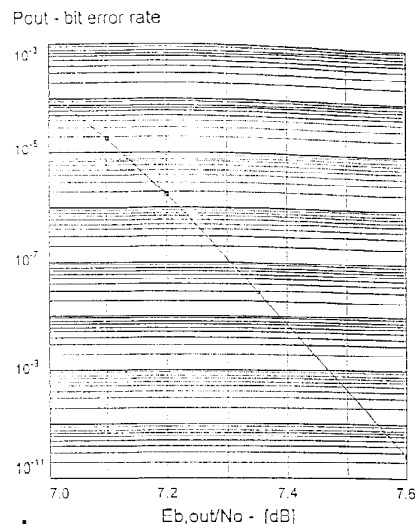
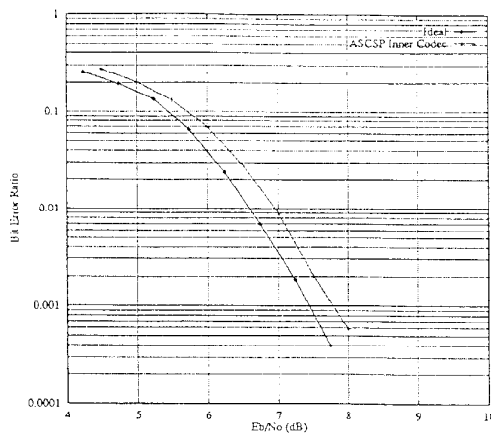
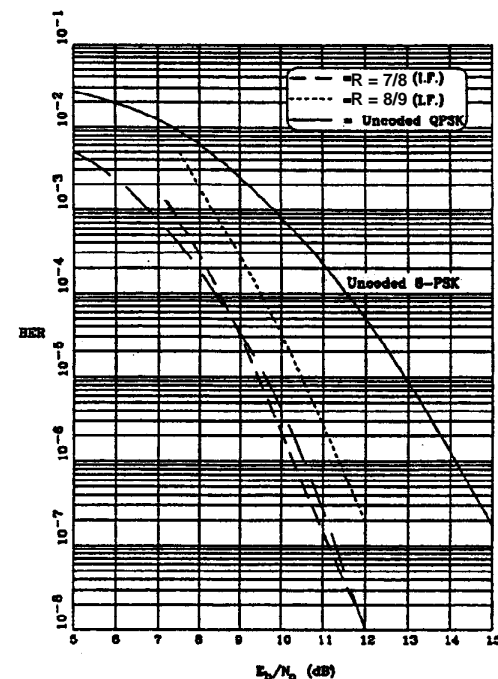


Fig. 5 : concatenated code performance :
- ideal modem and channel
- codec implementation losses included



BER vs E_b/N_0 for Inner Codec, Ideal AWGN Channel



Nominal IF Performance

COMSAT Modem (ECL)

Techsearch/ASCSP
155 Mbit/s FEC CODEC



A basis for a new standard ?

- Based on the work developped, it is possible to propose the frame of a new standard for power/bandwidth efficient phase modulation: use of 4D- 8 or 16 PSK TCM with RS outer code
- Interest of the proposal:
 - good BER performances with self phase ambiguity resolution
 - availability of four selectable channel efficiency: 2, 2.5, 3, 3.5 B/s/Hz
- Convolutional Code: a Pragmatic Solution is proposed, based on the Industry standard Convolutional Coder with rate 1/2 - 64 states, already standardized by CCSDS, but with introduction of puncturing (2/3 and 3/4) as, for exemple, the ETSI recommendation for DVB-S
- RS outer coding: use of the already CCSDS standardised RS code (255,239)

Punctured code definition

Original code			Code rates									
			1/2		2/3		3/4		5/6		7/8	
K	G ₁ (X)	G ₂ (Y)	P	d _{free}	P	d _{free}	P	d _{free}	P	d _{free}	P	d _{free}
7	171 _{OCT}	133 _{OCT}	X: 1 Y: 1	10	X: 1 0 Y: 1 1	6	X: 1 0 1 Y: 1 1 0	5	X: 1 0 1 0 1 Y: 1 1 0 1 0	4	X: 1 0 0 0 1 0 1 Y: 1 1 1 1 0 1 0	3
			C1 = X ₁ C2 = Y ₁		C1 = X ₁ Y ₂ Y ₃ C2 = Y ₁ X ₃ Y ₄		C1 = X ₁ Y ₂ C2 = Y ₁ X ₃		C1 = X ₁ Y ₂ Y ₄ C2 = Y ₁ X ₃ X ₅		C1 = X ₁ Y ₂ Y ₄ Y ₆ C2 = Y ₁ Y ₃ X ₅ X ₇	
NOTE: 1 = transmitted bit 0 = non transmitted bit <div>Polynom: G1 = 171 (X), G2 = 133 (Y)</div>												

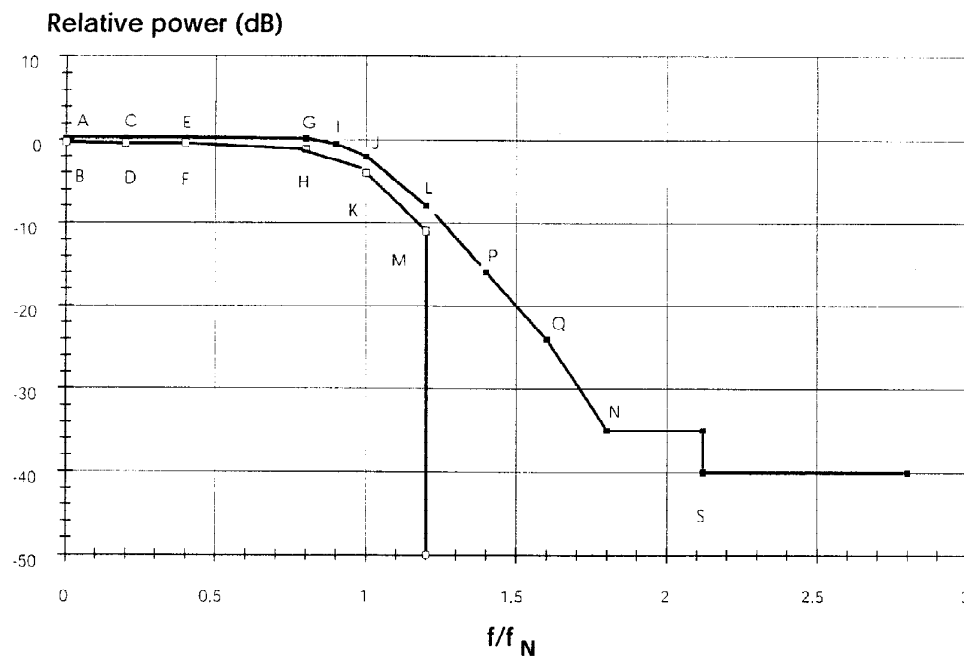


A basis for a new standard ? (con't)

- **Modulation Mapper:** same principle as the one used in the CNES Modem for the four selectable efficiency, including automatic phase ambiguity resolution
- **Possible implementation of:**
 - **Monodimensional 8-PSK TCM** with efficiency of 2 B/s/Hz with CC $R=2/3$
 - **Monodimensional 16-PSK TCM** with efficiency of 3 B/s/Hz with CC $R=3/4$
 - **4D-8PSK TCM** with efficiency of 2 or 2.5 B/s/Hz with CC $R=3/4$
 - **4D-16PSK TCM** with efficiency of 3 or 3.5 B/s/Hz with CC $R=3/4$
- **Possible use of standard CMOS technology** for up to 100 to 175 Mb/s (depending of efficiency): interest for use with high data rate transmission (application to Earth Observation telemetry for exemple)
- **Bandwidth occupancy:** waveform shaping based on Nyquist SRC filtering (roll-off of 0.25, or 0.35 or 0.5 ?)
- **Compatibility with non linear power channel amplifier** like SSPA or TWT
- **Additional studies and/or simulations and/or tests** are necessary to check for the performances of this modulations with a punctured "pragmatic" 7-1/2 convolutional coder/decoder



Exemple of ETSI spectrum template for multi-phase modulations



Template for the signal spectrum mask at the modulator output represented in the
baseband frequency domain (roll-off factor $\alpha = 0,35$)

f_N = Nyquist frequency



ETSI Performance table

Table 5: IF-Loop performance of the System

Modulation	Inner code rate	Spectral efficiency (bit/symbol)	Modem implementation margin (dB)	Required E_b/N_0 (note 1) for BER = 2×10^{-4} before RS QEF after RS (dB)
QPSK	1/2	0,92	0,8	4,5
	2/3	1,23	0,8	5,0
	3/4	1,38	0,8	5,5
	5/6	1,53	0,8	6,0
	7/8	1,61	0,8	6,4
8PSK (optional)	2/3	1,84	1,0	6,9
	5/6	2,30	1,4	8,9
	8/9 (note 3)	2,46	1,5	9,4
16QAM (optional)	3/4 (note 3)	2,76	1,5	9,0
	7/8	3,22	2,1	10,7

NOTE 1: The figures of E_b/N_0 are referred to the useful bit-rate R_u (188 byte format, before RS coding) (so takes account of the factor $10 \log 188/204 \approx 0,36$ dB due to the Reed-Solomon outer code) and include the modem implementation margins. For QPSK the figures are derived from EN 300 421 [3].
For 8PSK and 16QAM, modem implementation margins which increase with the spectrum efficiency are adopted, to cope with the larger sensitivity associated with these schemes.

NOTE 2: Quasi-Error-Free (QEF) means approximately less than one uncorrected error event per hour at the input of the MPEG-2 demultiplexer. Other residual error rate targets could be defined for "contribution quality" transmissions. The bit error ratio (BER) of 2×10^{-4} before RS decoding corresponds approximately to a byte error ratio between 7×10^{-4} and 2×10^{-3} depending on the coding scheme.

NOTE 3: 8PSK 8/9 is suitable for satellite transponders driven near saturation, while 16QAM 3/4 offers better spectrum efficiency for quasi-linear transponders, in FDMA configuration.



References

Channel coding with Multilevel/Phase signals (G. Ungerboeck). IEE Trans on IT (Vol IT-28. No1. January 1982)

Trellis coded Multidimensional Phase Modulation. (S. Pietrobon et al) IEE Trans on IT (Vol IT-28. No36. January 1990)

Digital Communications (J.G. Proakis). Handbook. Mac Graw Hill Cy

Definition study of 2 TCM scheme and synchronization algorithm for carrier and clock. ENST Paris (ML. Boucheret & JC Belfiore)

Comatlas: Final report. Contract 962/CNES/95/1628/00 (Developement of Decoder ASIC for coded modulations)

Several documents related to theoritical & technical concerns about CNES Multi-D TCM Modem: (G. Lesthievent, J.P. Panisset) Internal CNES Documents.

Techsearch: Development of a 155 MB/s FEC Codec (contract INTEL-1163) 1993

Q1875 Pragmatic Treillis Decoder 30, 75 MB/s data rates. Qualcomm Technical data Sheet

Newtec: Development of a 155 MB/s SDH Satellite Modem. Final Report. ESTEC Contract 11486/95/NL/DS

ETSI Standard for DVB-S (EN 301 210 V1.1.1 (1999-03)

[This page intentionally left blank.]

Performance Comparison of 4D 8-PSK TCM and FQPSK-B in a Non-linear Satellite Channel

Dennis Lee, Tsun-Yee Yan, and Warren L. Martin
Jet Propulsion Laboratory
California Institute of Technology
Pasadena, CA 91109

1 Abstract

This paper presents a performance comparison of FQPSK-B and 4-dimensional trellis-coded 8-PSK (4D 8-PSK TCM¹) with square root raised cosine (SRRC) filtering in a non-linear satellite channel. FQPSK-B and 4D 8-PSK TCM have emerged as two bandwidth efficient modulation candidates for the Earth Exploration Satellite Service (EESS) 8025-8400 MHz band. Due to high downlink data rates characteristic of the EESS band, bandwidth efficient modulations must be considered to avoid excessive adjacent channel interference as the number of satellites in the frequency band increases. The comparison between FQPSK-B and 4D 8-PSK TCM is based on spectral occupancy, bit error performance, and computational complexity. Our results show that with a punctured convolutional code, FQPSK-B achieves better bit error performance with a narrower spectrum and less computational complexity than 4D 8-PSK TCM in a non-linear channel.

2 Introduction

Future space science missions will face limited and increasingly congested downlink channels due to escalating return link data rate requirements. In response, the SFCG has recommended that space science projects starting after the year 2001 comply with an emitted spectrum mask for space-to-earth data transmission in the 2200-2290 MHz, 2290-2300 MHz, 8025-8400 MHz, and 8400-8500 MHz bands. At the 1999 CCSDS Panel 1E meeting, a draft recommendation was prepared recommending GMSK or FQPSK-B for future high data rate missions in the 2200-2290 MHz, 2290-2300 MHz, and 8400-8500 MHz bands. However, the 8025-8400 MHz band was not addressed. Recently, SRRC filtered ($\alpha = 0.35$) 4D trellis-coded 8-PSK has been proposed as a basis for a new standard in the 8025-8400 MHz band.

Satellites in the 8025-8400 band typically have low (500-990 km), highly inclined, and circular orbits. Downlinks consist typically of imaging data at high data rates with bit error rate requirements on the order of 10^{-5} for uncompressed images. At the 1999 CCSDS Panel 1E meeting, 4D trellis-coded 8-PSK was shown to operate at high data rates (up to 125 Mbps in a single channel) with good bit error performance for $E_b/N_o > 7$ dB. With SRRC pulse shaping and a post power-amplifier (PA) filter, the spectrum of 4D 8-PSK TCM met the SFCG spectral mask requirement.

A comparison of 4D 8-PSK TCM with unfiltered FQPSK was given in [2], where 4D 8-PSK TCM was shown to be narrower in spectrum with better bit error performance. However, there are

¹The signal set consists of four 2-dimensional 8-PSK constellations which is actually 8-dimensional as referred to in [5]. However, to be consistent with [2], the 4D notation is used.

several concerns regarding this comparison. First, unfiltered FQPSK was used in the comparison instead of FQPSK-B which has a considerably narrower spectrum. Since 4D 8-PSK TCM in [2] utilized a baseband SRRC filter, results for FQPSK should have included a pre-modulation filter as well (FQPSK-B is essentially baseband filtered FQPSK). Second, the spectrum of 4D 8-PSK TCM shown in [2] was generated with a post PA filter and PA output backoff (OBO), neither of which are desirable in generating a standard as some missions may not want or be able to accommodate either one. The advantages of a modulation with constant or nearly constant envelope like FQPSK-B in this regard are obvious. The -40 dB bandwidth of 8-PSK TCM without the post PA filter and PA OBO is considerably wider than FQPSK-B. Finally, the comparison in [2] does not take into consideration the transmitter and receiver complexity inherent in 4D 8-PSK TCM. This computational complexity will eventually limit the data rate, as well as increase cost in terms of the number of gates and size of the digital receiver. We will show that if comparable coding complexity is added to FQPSK-B, it will have better BER performance and a narrower spectrum than SRRC ($\alpha=0.35$) 4D 8-PSK TCM in a nonlinear satellite channel. This is true even taking into account the bandwidth expansion that the coding adds to FQPSK-B.

3 4D trellis-coded 8-PSK

The basic advantage of trellis-coded modulation is that coding gains can be achieved without expanding the bandwidth relative to the uncoded signal set. Multidimensional trellis-coded modulation (MTCM) described in [5] is an extension of TCM. The idea of MTCM is to create a larger signal set by forming the Cartesian product of L two-dimensional MPSK signal sets. The MTCM signal is transmitted over a channel by sending L consecutive signals of a MPSK signal set. Multidimensional TCM allows for higher rate codes, flexibility in achieving a variety of fractional information rates, codes that are transparent to discrete phase rotations of the signal set, and an increase in coding gain over traditional TCM given the same constraint length and coding rate. The disadvantage is in the increased computational complexity for the encoding and decoding process.

A block diagram of the 4D trellis-coded 8-PSK encoder presented at the 1999 CCSDS meeting [1] is replicated in Figure 1. Ten input bits (labeled w^1 to w^{10} in the figure) are fed in parallel into the encoder. The output has twelve bits which are mapped onto four 8-PSK symbols. Hence, each 8-PSK symbol contains 2.5 input bits (referred to as 2.5 bits/Hz). Figure 2 shows the mapping of the three coded bits onto the 8-PSK signal set. The differential encoding shown in Figure 1 provides invariance to 45 degree rotations of the 8-PSK signal set.

Different data rates can be achieved by setting the q least significant bits of the mapping to zero. For example, 4D 8-PSK TCM with 2.0 bits/Hz can be implemented using the same encoder in Figure 1 simply by setting the 2 LSB's of the encoder to zero. Although this flexibility in providing multiple data rates with the same encoder structure is desirable, the resulting encoder does not produce the best asymptotic coding gain (see [5]). However, the difference in performance for values of E_b/N_o under consideration is small. As done in [2], two different rates, 2.0 bits/Hz and 2.5 bits/Hz, are considered in this paper using the encoder structure shown in Figure 1.

The encoder in Figure 1 has $2^6 = 64$ possible states. The decoder finds the minimum distance path using the Viterbi algorithm. Each state has a possible transition to $2^3 = 8$ other states depending on the three bits fed into the convolutional encoder (bits w^1 , w^2 , and w^3 shown in Fig 1). However, the n bits not convolutionally coded create 2^n parallel paths between each state transition. For example, the 2.5 bits/Hz 4D 8-PSK TCM system has 7 such bits (bits w^4 through w^{10}) which create 128 parallel paths for each of the 8 possible transitions to a particular state. To find the minimum distance path to a particular state, the Viterbi algorithm must search through

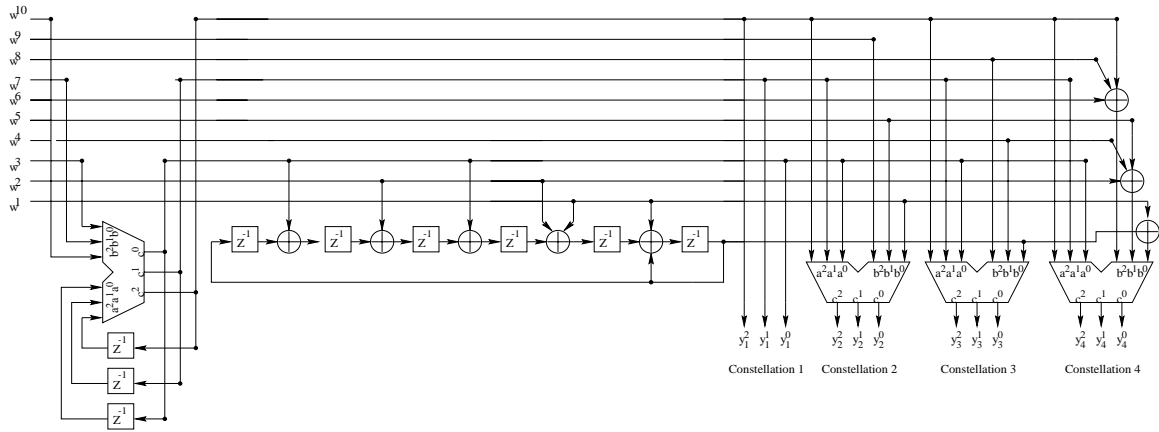


Figure 1: 4D 8-PSK TCM encoder

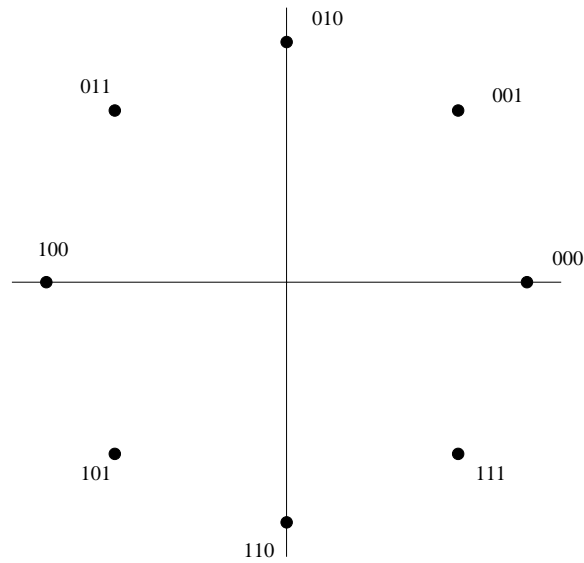


Figure 2: 4D 8-PSK TCM signal mapping for $y_i^2 y_i^1 y_i^0$, $i = 1, \dots, 4$

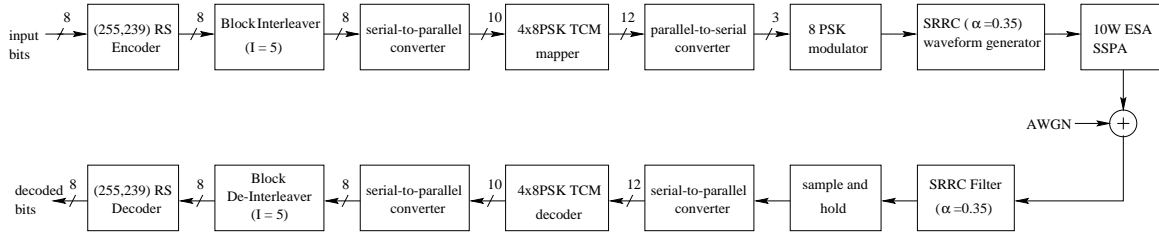


Figure 3: Block diagram of 4D 8-PSK TCM system

the 128 parallel paths from each of the 8 possible state transitions to each of the 64 states. For 2.0 bits/Hz system, there are 32 parallel paths for the each state transitions. As each parallel path causes the decoder to output a different set of bits, each parallel branch must be evaluated.

By comparison, the standard $k=7$, rate $1/2$ convolutional code used in the coded FQPSK-B system has 64 possible states, with each state having only 2 possible transistions and no parallel paths. Of course, to make a fair comparison, the number of possible transistions must be normalized by the number of output bits per decoder iteration. Each decoded transition for 2.5 bits/Hz 4D 8-PSK TCM will result in 10 output bits, and there are 8 output bits for the 2.0 bits/Hz system. Conversely, there is only 1 output bit per decoder iteration of the standard rate $1/2$ convolutional code. In addition, two methods are given in [5] to reduce the number of computations required to process the parallel branches; one involves a separate finite-length Viterbi algorithm to decode the parallel transistions and the other involves large lookup tables. Even taking these factors into account, the Viterbi algorithm for 4D 8-PSK TCM will have at least an order of magnitude more computations per decoded bit than for a standard rate $1/2$ convolutional decoder due to the greater number of state transistions and the parallel paths.

As the spectrum of unfiltered 8-PSK does not comply with the SFCG high rate spectral mask, SRRC pulse shaping with a roll-off factor of $\alpha = 0.35$ is used to reduce the spectral sidelobes. However, after SRRC pulse shaping, the 8-PSK envelope is no longer constant. If a highly non-linear amplifier is used, spectral regrowth causes the sidelobes to exceed the mask. Hence, either significant power amplifier backoff, a post-PA filter, or even both are required to attenuate these sidelobes. Neither of these methods are efficient. Post PA filtering is undesirable [3] because of insertion losses, high Q factors required for lower data rates, and the difficulty in replacing filters when frequencies and data rates change. In general, post-PA filters add weight, size, and cost to a mission. In contrast, pre-modulation filtering operates at baseband and can be implemented digitally which is inexpensive and efficient. While post-PA filtering may be required in certain circumstances, a modulation recommendation for all missions should not be based on assuming a post-PA filter and/or power amplifier OBO. Power amplifier output backoff results in less transmitted power. While OBO is feasible with satellites that have excess transmit power, missions without this luxury must operate near or at amplifier saturation. For this reason, our results are generated using a SSPA with no output backoff.

A block diagram of the SRRC-filtered 4D 8-PSK TCM system under consideration is shown in Fig 3. To match the system studied in [2], a (255,239) Reed-Solomon code and an interleaver/deinterleaver is added to the 4D 8-PSK TCM transmitter and receiver as shown in Fig 3.

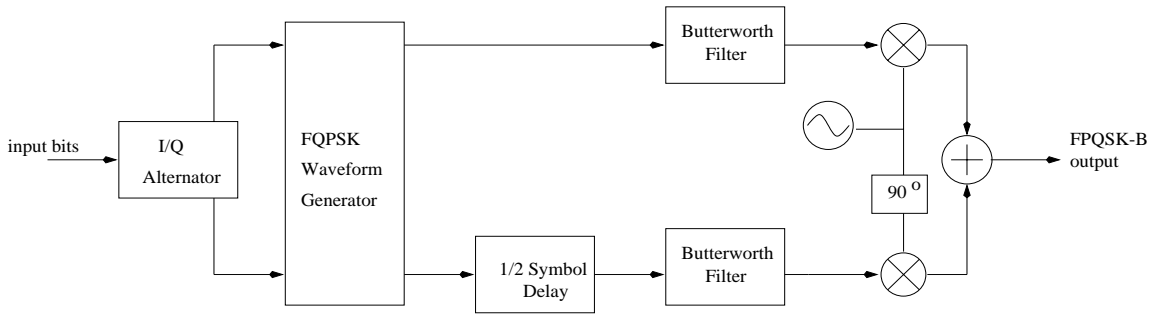


Figure 4: Block diagram of coded FQPSK-B modulator

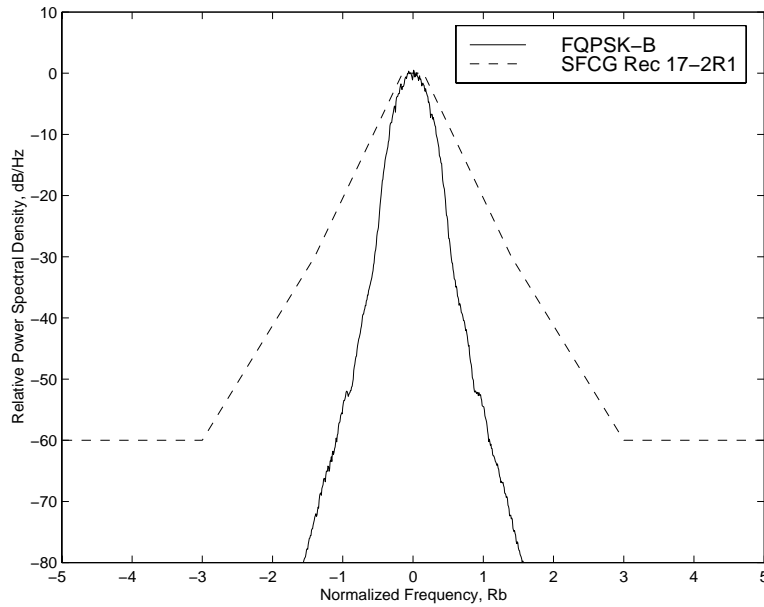


Figure 5: FQPSK-B spectrum, saturated 10W ESA SSPA

4 FQPSK-B

FQPSK-B is a baseband filtered version of FQPSK patented by Dr. Kamilo Feher [4]. A block diagram of the FQPSK-B modulator is shown in Fig 4. The waveform generator produces one of a possible sixteen waveforms (8 different waveforms and their negatives). The pulse shapes are designed to minimize spectral sidelobes and envelope fluctuation. Baseband filtering additionally attenuates the sidelobe levels. Cross-correlation between the I and Q waveforms is introduced to minimize envelope variation to about 2% which is slightly higher than the envelope fluctuation of unfiltered FQPSK. An optional limiter is added to remove the remaining fluctuation. Hence, FQPSK-B has a very compact spectrum as shown in Figure 5 and virtually no spectral regrowth when passed through a non-linear power amplifier.

Another advantage of FQPSK-B is that a simple receiver can be implemented using a sample-and-hold circuit with a Butterworth detection filter. Although this receiver does not produce optimal BER performance, we will show that by adding comparable complexity, it can still outperform

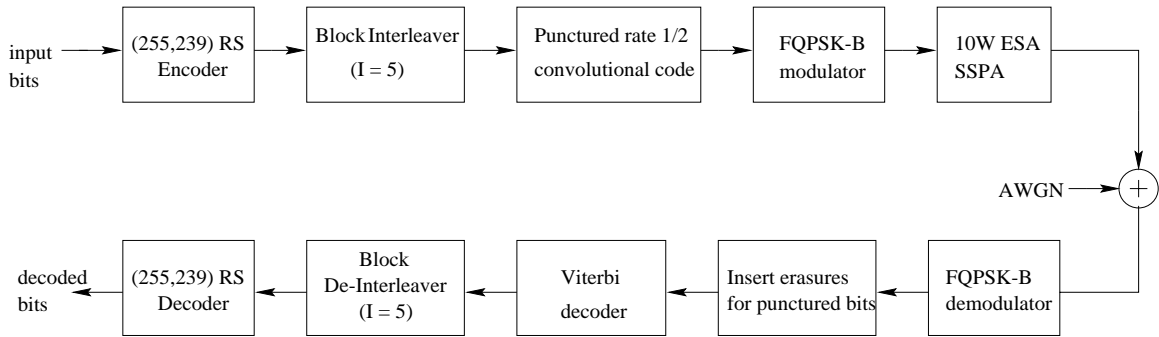


Figure 6: Block diagram of coded FQPSK-B system

the 4D 8-PSK TCM system shown in Fig 3. For a fair comparison, a convolutional code is added to FQPSK-B so that the two modulations have roughly equal receiver and transmitter complexity. This is reasonable since 8-PSK TCM already has a convolutional code built into the modulation. Although the coding will expand the bandwidth of FQPSK-B while it is already accounted for in the trellis-coded modulation, the bandwidth of FQPSK-B is still narrower than SRRC 8-PSK TCM in a non-linear channel even with moderate coding bandwidth expansion.

For comparison purposes in this study, the coded FQPSK-B system uses a standard rate $1/2$, $k=7$ code with puncturing [8]. Punctured codes do not provide maximum coding gain for a given constraint length and coding rate, but it has the advantages of flexibility and low cost in implementing high rate codes. A block diagram of the coded FQPSK-B system used for comparison with 4D 8PSK TCM is shown in Fig 6. As the 4D 8-PSK TCM system studied included a (255,239) Reed-Solomon code and an interleaver, the same is added to the convolutionally coded FQPSK-B system.

Puncturing does not increase the number of possible state transitions or induce any parallel paths between states. Hence, the Viterbi algorithm (VA) for the coded FQPSK-B receiver is identical to VA for the standard rate $1/2$, $k = 7$ convolutional code with erasures inserted in place of the punctured bits. The VA searches through 64 possible states, with 2 possible state transitions to each state and no parallel paths. Note that the VA for the coded FQPSK-B system is still computationally less intensive than 4D 8-PSK TCM as there are fewer possible state transitions to each state and no parallel paths between states.

The coding in FQPSK-B will produce a bandwidth expansion equal to the coding rate. The punctured code rate is chosen such that the occupied bandwidth of coded FQPSK-B is close to the comparable 4D 8-PSK TCM system. In this paper, a punctured rate $3/4$ code is used to compare with 4D 8PSK TCM with 2 bits/Hz, and a punctured rate $7/8$ convolutional code is used to compare with 4D 8PSK TCM with 2.5 bits/Hz.

The power amplifier used for simulations in this study is a 10W ESA SSPA whose AM/AM and AM/PM characteristics are shown in Figures 7 and 8, respectively. This SSPA is consistent with previous CCSDS modulation studies [3]. Note that the AM/PM characteristics of this PA has a maximum output phase swing of less than 6 degrees, and are comparable to some power amplifiers operating with several dB backoff. A comparison using a TWTA or a less favorable SSPA will only benefit FQPSK-B when compared to 4D 8PSK TCM because of FQPSK-B's nearly constant envelope. As explained previously, bit error rate simulations and spectra in this study are determined based on power amplifiers operating in full saturation.

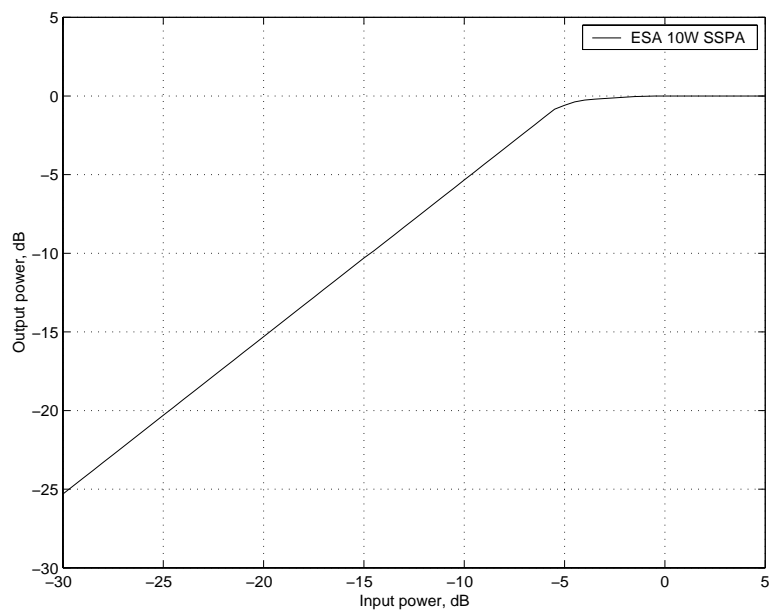


Figure 7: 10W ESA SSPA AM/AM characteristics

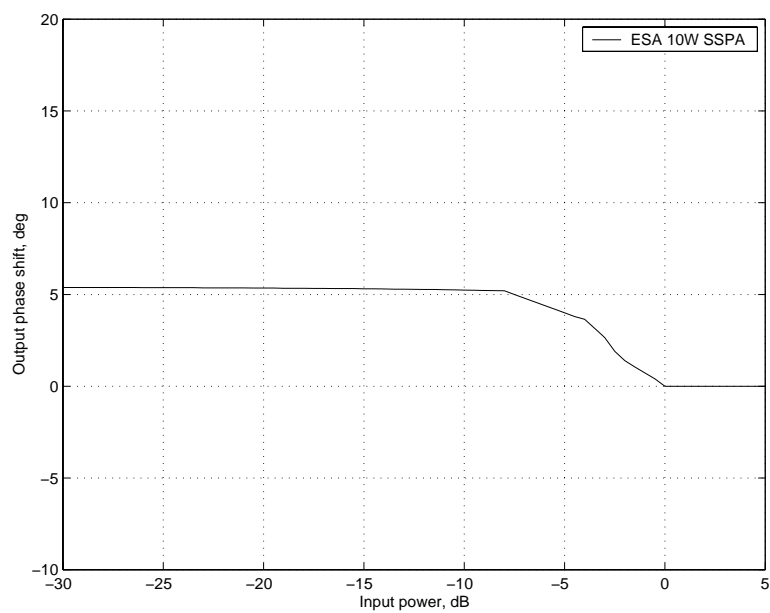


Figure 8: 10W ESA SSPA AM/PM characteristics

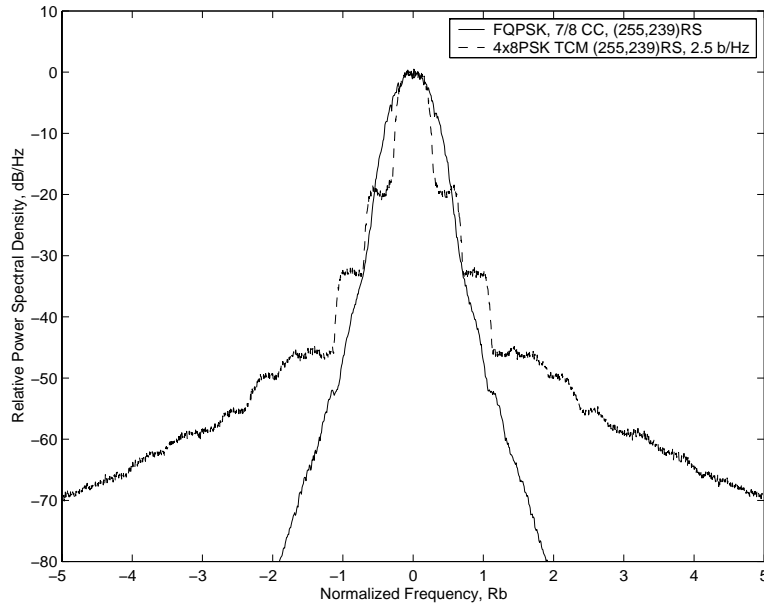


Figure 9: 4D 8-PSK TCM 2.5 bits/Hz vs Rate 7/8 coded FQPSK-B Spectrum

5 FQPSK-B vs 4D 8-PSK TCM Comparison

Tables 1 and 2 summarize the comparison of coded FQPSK-B and 4D 8PSK TCM based on occupied bandwidth, bit error rate performance, and complexity. Two different systems are compared: (255,239) RS coded SRRC-filtered 4D 8PSK TCM 2.5 bits/Hz with (255,239) RS coded, rate 7/8 convolutional code FPQSK-B, and (255,239) RS coded SRRC-filtered 4D 8PSK TCM 2 bits/Hz with (255,239) RS coded, rate 3/4 convolutional code FPQSK-B. The spectrum and BER curves presented are generated using SPW computer simulations and a fully saturated power amplifier model whose characteristics match the 10W ESA SSPA.

Figure 9 compares the spectrum of 4D 8-PSK TCM 2.5 bits/Hz with rate 7/8 coded² FPQSK-B. The frequency has been normalized to the bit rate. As the figure shows, the spectrum of rate 7/8 coded FQPSK-B in a non-linear channel is equal to or narrower than the 4D 8-PSK TCM spectrum below the -20 dB PSD level. The -40 dB two-sided bandwidth for rate 7/8 coded FQPSK-B is approximately $1.8 R_b$, and $2.2 R_b$ for 4D 8-PSK TCM 2.5 bits/Hz. Thus, the -40 dB two-sided bandwidth of rate 7/8 coded FQPSK-B is $0.4 R_b$ narrower than 4D 8-PSK TCM 2.5 bits/Hz, or about 15%. At the -60 dB two-sided bandwidth, rate 7/8 coded FQPSK-B is $4 R_b$, which is about 60% narrower than the comparable 4D 8-PSK TCM system. The bit error probabilities for the two systems is shown in Figure 10. As the figure shows, rate 7/8 coded FQPSK-B requires less E_b/N_o for a given bit error probability. This translates to a reduction in required transmit power. At the bit error rates of interest for uncompressed images ($\approx 10^{-5}$), rate 7/8 coded FQPSK offers a 0.8 dB E_b/N_o gain over 4D 8-PSK TCM 2.5 bits/Hz.

Figure 11 compares the spectrum of 4D 8-PSK TCM 2.0 bits/Hz with rate 3/4 coded FQPSK-B. A slightly lower rate code was used with FQPSK-B to match the reduction in coding rate in the

²The rate 7/8 code is actually $7/8 \cdot 239/255$ because of the Reed-Solomon code. To simplify notation, we simply refer to it as a rate 7/8 code. The same applies for the rate 3/4 code. Note that the results for 4D 8-PSK TCM 2.5 bits/Hz and 2.0 bits/Hz also include the R-S code, and are actually $2.5 \cdot 239/255$ bits/Hz and $2.0 \cdot 239/255$ bits/Hz, respectively.

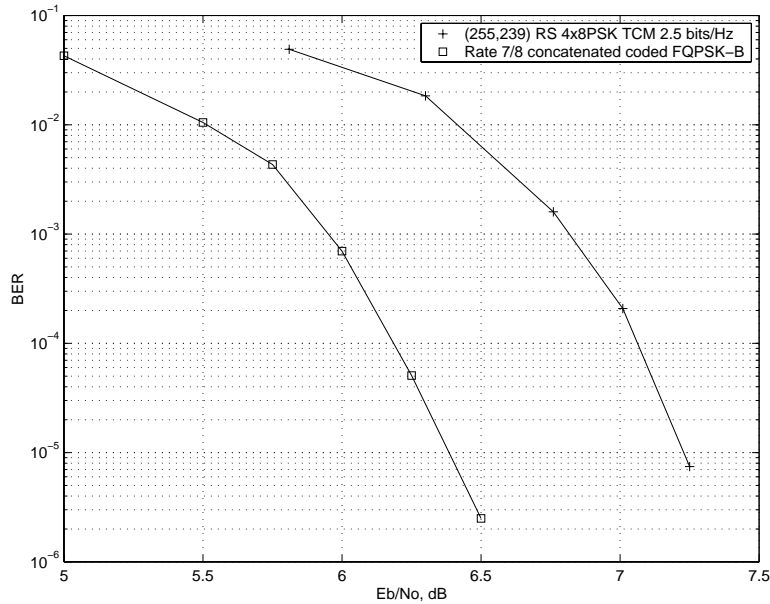


Figure 10: 4D 8-PSK TCM 2.5 bits/Hz vs Rate 7/8 coded FQPSK-B BER

trellis coded system. Even with a lower rate code and consequently more bandwidth expansion, rate 3/4 coded FQPSK-B has a narrower spectrum below the -20 dB PSD level. The -40 dB double-sided bandwidth of rate 3/4 coded FQPSK-B is about $2.0 R_b$, and $2.8 R_b$ for the 8-PSK TCM system. Thus, the -40 bandwidth of rate 3/4 coded FQPSK-B is 25% narrower than 4D 8-PSK TCM 2.0 bits/Hz at the -40 dB PSD level, and about 60% narrower at the -60 dB level. Comparing the corresponding BER curves in Figure 12, the rate 3/4 coded FQPSK-B system also provides better bit error performance. For the bit error rate of 10^{-5} , the rate 3/4 coded FQPSK-B performs approximately 0.5 dB better than 4D 8-PSK TCM 2.0 bits/Hz.

Figure 13 shows the out-of-band power of 4D 8-PSK TCM versus coded FQPSK-B. Note that the -20 dB out-of-band power corresponds to 99% power containment, and -30 dB corresponds to 99.9% power containment. The two-sided 99% power containment bandwidth of 4D 8-PSK TCM 2 bits/Hz is $1.26 R_b$ while the 99% power containment bandwidth of rate 3/4 coded FQPSK-B is $1.07 R_b$, or 15% less. For 4D 8-PSK TCM 2.5 bits/Hz, the 99% power containment bandwidth is $1.01 R_b$. For rate 7/8 coded FQPSK-B, it is 9% less at $0.92 R_b$.

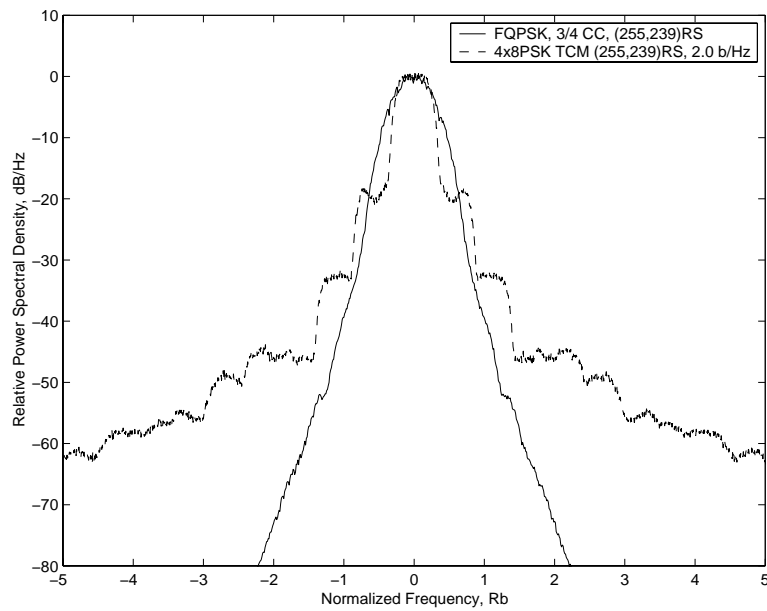


Figure 11: 4D 8-PSK TCM 2 bits/Hz vs Rate 3/4 coded FQPSK-B Spectrum

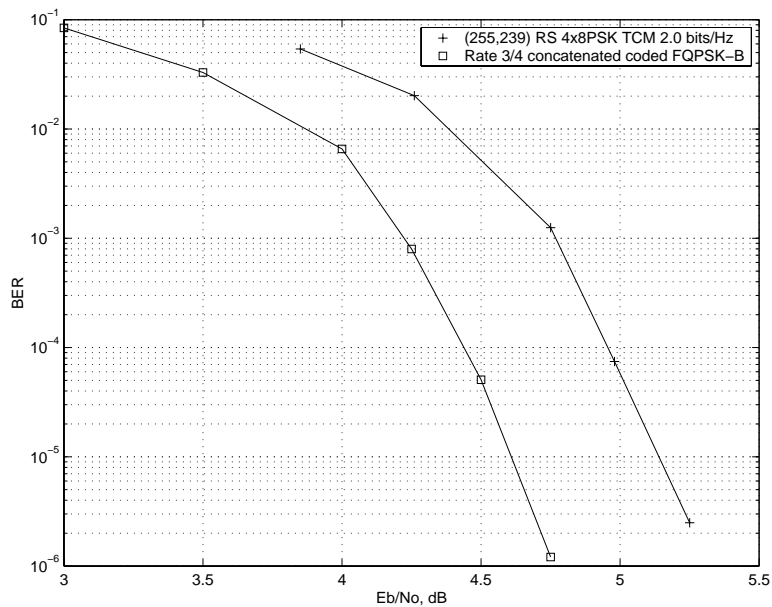


Figure 12: 4D 8-PSK TCM 2 bits/Hz vs Rate 3/4 coded FQPSK-B BER

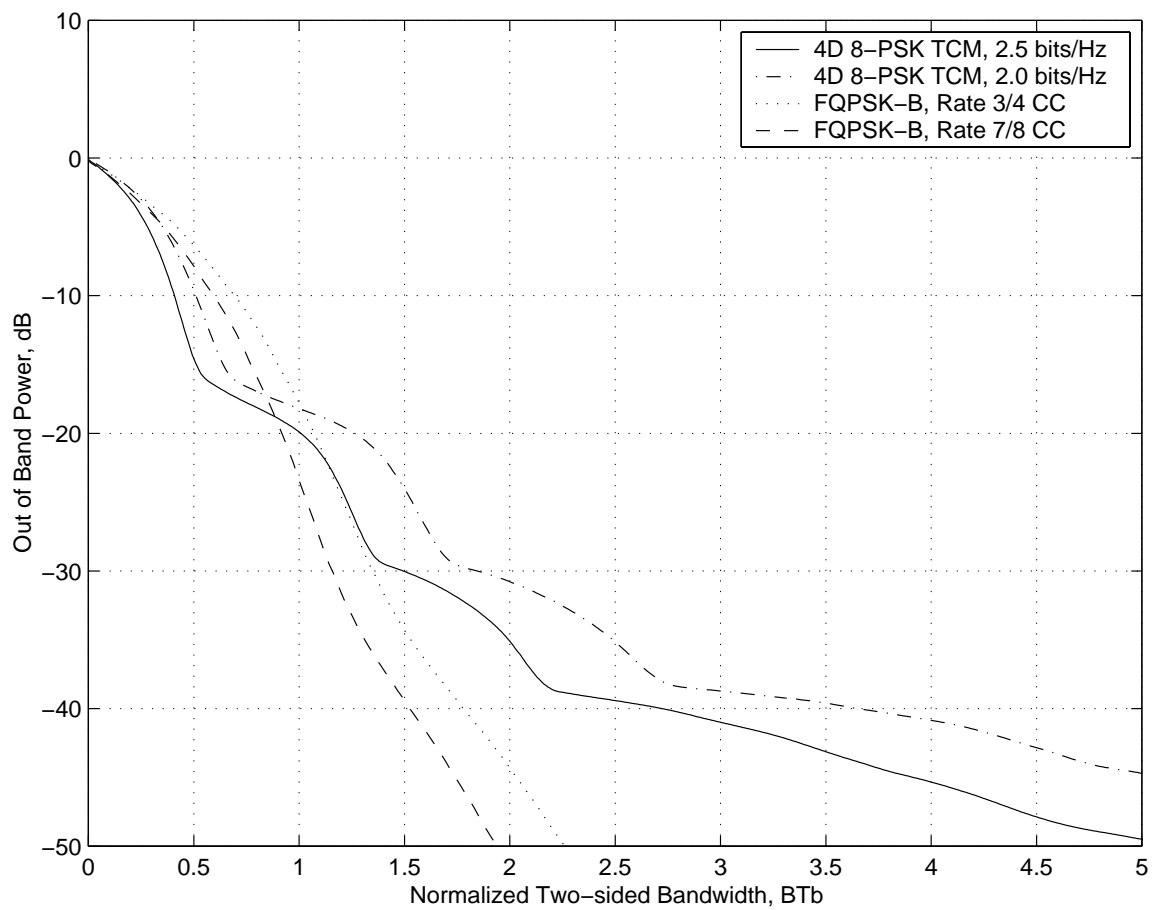


Figure 13: 4D 8-PSK TCM and coded FQPSK-B out-of-band power

Table 1: Comparison of 4D 8-PSK TCM 2.5 bits/Hz and rate 7/8 coded FQPSK-B

	-40 dB 2-sided BW	2-sided 99% power containment BW	E_b/N_0 for 10^{-5} BER	Viterbi decoder complexity
Rate 7/8 coded FQPSK-B	$1.8 R_b$	$0.92 R_b$	6.4 dB	64 states, 2 possible transi- tions per state, no parallel paths
4D 8-PSK TCM 2.5 bits/Hz	$2.2 R_b$	$1.01 R_b$	7.2 dB	64 states, 8 possible transi- tions per state, 128 parallel paths per transistion

Table 2: Comparison of 4D 8-PSK TCM 2.0 bits/Hz and rate 3/4 coded FQPSK-B

	-40 dB 2-sided BW	2-sided 99% power containment BW	E_b/N_0 for 10^{-5} BER	Viterbi decoder complexity
Rate 3/4 coded FQPSK-B	$2.0 R_b$	$1.07 R_b$	4.6 dB	64 states, 2 possible transi- tions per state, no parallel paths
4D 8-PSK TCM 2.0 bits/Hz	$2.8 R_b$	$1.26 R_b$	5.1 dB	64 states, 8 possible transi- tions per state, 32 parallel paths per transistion

6 Additional Issues in Comparison

6.1 Carrier Tracking

In general, suppressed carrier tracking loops for 8-PSK modulations suffer higher squaring losses compared to OQPSK-type modulations such as FQPSK-B. In addition, an 8-PSK carrier tracking loop has twice as many false lock points. Essentially, 8-PSK suppressed carrier tracking loops must track an 8ϕ process versus a 4ϕ process for FQPSK-B, where ϕ is the noisy phase that the loop is tracking³. The BER simulations did not take into account carrier tracking losses, which for the same loop bandwidth will be greater for 8-PSK TCM than FQPSK-B. While the differential encoding in Figure 1 provides phase invariance to the lock point chosen, it will not reduce the squaring losses or eliminate errors that occur when the loop shifts from one lock point to another.

6.2 Maximum Data Rate

An advantage of 8-PSK is that more bits can be transmitted for a given maximum achievable baud rate. In [2], a 4D 8-PSK TCM hardware system was shown which had a maximum bit rate of 125 Mbits/s. Three such channels were combined to give an overall bit rate of 375 Mbits/s. However, due to lower implementational and computational complexity in the transmitter and receiver, FQPSK-B may be able to operate at a higher maximum data rate than 4D 8-PSK TCM despite only getting 2 bits/Hz. Currently, there is development at NASA of a FQPSK-B transmitter

³With the optimal OQPSK carrier tracking loop [7] instead of the more commonly used Costas crossover loop, there are only 2 lock points, a 2ϕ process, and consequently even less squaring loss.

which can transmit 300 Mbit/s over a single channel, more than double the 4D 8-PSK TCM maximum bit rate in a single channel. Multiplexing three FQPSK-B channels will produce 900 Mbits/s. Even with a rate $3/4$ code, the maximum data rate over a single channel will be 225 Mbits/s. With a rate $7/8$ code, the maximum data rate will be 262 Mbits/s on a single channel. To complement the high rate transmitter, a FQPSK-B digital receiver has been already been built that can demodulate up to 600 Mbits/s.

7 Summary

In this paper, the bit error performance and spectrum of SRRC-filtered 4D 8-PSK TCM and FQPSK-B are simulated and compared. Since FQPSK-B has spectral and complexity advantages over 4D 8-PSK TCM while 4D 8-PSK TCM has a BER advantage over FQPSK-B, some of the spectral efficiency and computational simplicity of FQPSK-B is traded for BER improvement using a punctured rate $1/2$ convolutional code. Simulation results show that even with bandwidth expansion due to coding, a coded FQPSK-B system has a narrower spectrum below the -20 dB PSD level in a non-linear satellite channel while providing better bit error performance and lower computational complexity than the comparable 4D 8-PSK TCM system.

References

- [1] A. Ribes, "8/16 PSK Multi-D Trellis Coded Modulation: An alternative to improve Power/Bandwidth Efficiency for High Data Rate Communications", Presented at May 1999 CCSDS Panel 1E meeting.
- [2] A. Ribes, "Experimental Performances of 4D 8-PSK Trellis Coded Modulation", Presented at Oct 1999 CCSDS Panel 1E meeting.
- [3] W.L. Martin, T.-Y. Yan, L. Lam, "Efficient Modulation Methods Study at NASA/JPL: Phase 3: End-to-End System Performance, September 1999.
- [4] S. Kato and K. Feher, "Correlated Signal Processor", U.S. Patent 4,567,602, Jan 1986.
- [5] S. Pietrobon, A. Lafanechere, G. Ungerboeck, D. Costello, "Trellis-Coded Multidimensional Phase Modulation", IEEE Transactions on Information Theory, vol. 36, pp. 63-89, January 1990.
- [6] M. Simon and T.-Y. Yan, "Performance Evaluation and Interpretation of Unfiltered Feher-Patented Quadrature-Phase-Shift Keying (FQPSK)", TMO Progress Report 42-137, May 1999.
- [7] M. Simon, "Carrier Synchronization of Offset Quadrature Phase-Shift Keying", TMO Progress Report 42-133, May 1998.
- [8] Y. Yasuda, K. Kashiki, Y. Hirata, "High-Rate Punctured Convolutional Codes for Soft Decision Viterbi Decoding", IEEE Transactions on Communications, vol. 32, pp. 315-319, March 1984.

**NASA GSFC Bandwidth Efficient Modulation and Coding Systems Study
Monodimensional 8 PSK TCM Evaluation
Follow-up Information for CCSDS Panel 1E Presentation**

D. Zillig

NASA/Goddard Space Flight Center, Greenbelt, MD 20771

Tel: (301) 286-8003; Fax: (301) 286-1724; E-mail: david.j.zillig.1@gsfc.nasa.gov

J. Brase, M. Burns

ITT Advanced Engineering & Sciences, 1761 Business Center Drive, Reston, VA 20190

Tel: (703) 438-8198; Fax: (703) 438-8112; E-mail: james.brase@itt.com

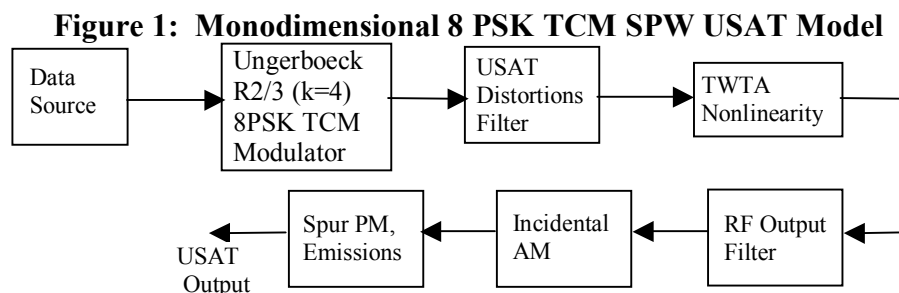
1. Introduction

NASA GSFC presented the results of ongoing studies in paper 99/47, *Efficient Modulation and Coding Schemes for Future NASA Ka-Band Space Communications*, at the October, 1999 meeting of the CCSDS Member Panel on Radio Frequency and Modulation Systems. These results included TDRS and direct-to-ground channel Bit Error Rate (BER) performance simulation measurements and Power Spectral Density (PSD) plots for a monodimensional 8 PSK TCM modulation technique.

Also presented at the October 1999 meeting was paper 99/49, *Performance of Trellis Code Modulation*. This paper, presented by Mr. Andre Ribes of CNES, detailed a family of 4-dimensional 8 PSK TCM schemes and provided results of benchtop testing. In response to action item 99-1E-38, this paper has been prepared to exchange detailed information on the implementation and performance of the monodimensional 8 PSK TCM technique employed in paper 99/47.

2. Model

Figure 1 depicts the monodimensional 8 PSK TCM User Satellite (USAT) SPW model. In this model, the USAT Distortions Filter introduces the gain flatness, gain slope and phase nonlinearity corresponding to the RF/IF components of the satellite (upconverter, LNA, etc.) The modulator reclocks the input data (eliminating Data Asymmetry and Data Jitter) and implements a Rate 2/3 $k=4$ monodimensional Ungerboeck 8 PSK TCM.

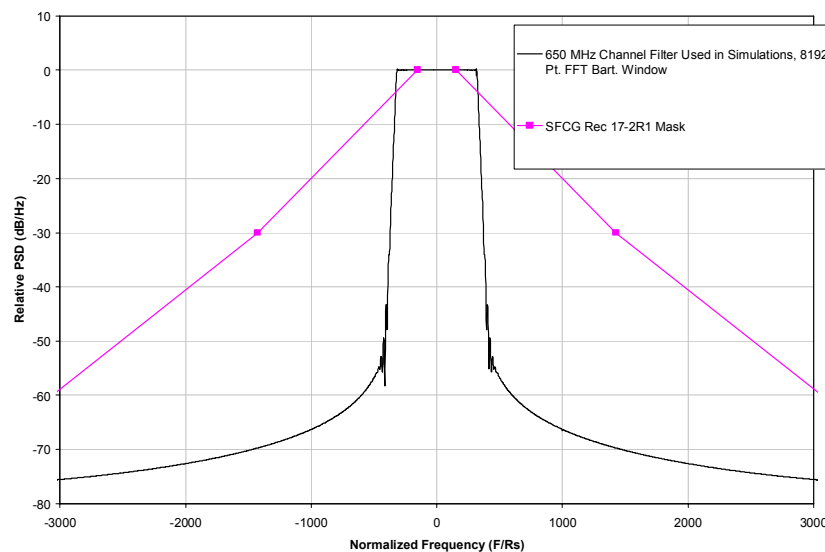


The transition matrix for the modulator is given in Table 1.

Table1: 8 PSK TCM State Transition Matrix

State at t	Input	State at t+1	Real Output	Imag Output
0	0	0	+0.923879532	-0.382683432
0	1	0	-0.923879532	+0.382683432
0	2	1	+0.382683432	+0.923879532
0	3	1	-0.382683432	-0.923879532
1	0	2	+0.923879532	+0.382683432
1	1	2	-0.923879532	-0.382683432
1	2	3	-0.382683432	+0.923879532
1	3	3	+0.382683432	-0.923879532
2	0	1	+0.923879532	-0.382683432
2	1	1	-0.923879532	+0.382683432
2	2	0	+0.382683432	+0.923879532
2	3	0	-0.382683432	-0.923879532
3	0	3	+0.923879532	+0.382683432
3	1	3	-0.923879532	-0.382683432
3	2	2	-0.382683432	+0.923879532
3	3	2	+0.382683432	-0.923879532

The TWTA nonlinearity distortions are selected to mirror a Ka-Band TWTA operating in linear mode. The RF output filter is implemented in SPW as a functional filter through specification of filter bandwidth, roll off, gain flatness, phase nonlinearity, etc. Since this filter was primarily included to provide for bandlimiting for the direct-to-ground



simulations and was not intended to represent an existing or practical component, it was modeled as being distortionless with a relatively fast cutoff. The magnitude response of the filter is provided in Figure 2.

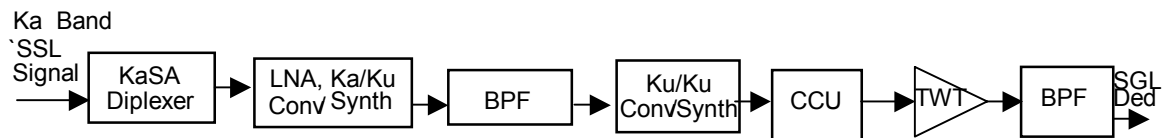
Figure 2: RF Channel Filter Magnitude Response

A comparison of this idealized filter magnitude response to that of an existing Ku-band wideband filter suggests that the rapid roll-off at multi-GHz frequencies is not grossly unrealistic. The final two components in the block diagram model introduce specified amounts of the Incidental AM, Spurious PM, and Spurious Emissions distortions. The key parameters for each of these components are provided in Table 2.

Table 2: Model Components and Parameters

Component	Parameter	Value	Comment
Data Source / 8PSK TCM Modulator	Data Rate	1020	Mbps
	Data Asymmetry	0.0	Percent, peak
	Data Jitter	0.0	
USAT Distortions Filter	Gain Flatness	0.6	dB, peak-to-peak
	Gain Slope	0.1	dB/MHz
	Phase Non-linearity	6.0	deg, peak-to-peak
	Roll-off	0.574	dB / MHz
	Bandwidth	867.67	MHz
TWTA Nonlinearity	AM/AM	1.0	dB / dB
	AM/PM	2.5	deg / dB
RF Output Filter	Gain Flatness	0.0	dB, peak-to-peak
	Gain Slope	0.0	dB/MHz
	Phase Nonlinearity	0.0	deg, peak-to-peak
	Rolloff	0.574	dB / MHz
	Bandwidth	650	MHz
Others	Incidental AM	5.0	Percent
	Spurious PM	2.0	deg RMS at 510 MHz
	Spurious Emissions	-30 / -15	dBc, in-band / out-of-band

Figure 3 depicts the TDRS H, I, J KaSAR Wideband Return Channel model, which was developed using a combination of as-built and CDR subcomponent specification data.

Figure 3: TDRS H, I, J KaSAR Wideband Return Channel Model

The receiver model, which is a modified version of the Second TDRS Ground Terminal high data rate receiver, is depicted in Figure 4. The RF / IF components are modeled as a single bandpass filter with distortions representing the effects of the antenna, waveguide, diplexer, downconverter, etc. The carrier tracking loop is a modified second order Costas loop as illustrated in Figure 5. Note that the phase detector is modified to remove the hard-decision detected 8 PSK symbol data, yielding the phase error estimate. The

symbol synchronizer used in this receiver model is a dual channel data transition tracking loop with a second order closed loop transfer function.

Figure 4: SPW Receiver Model

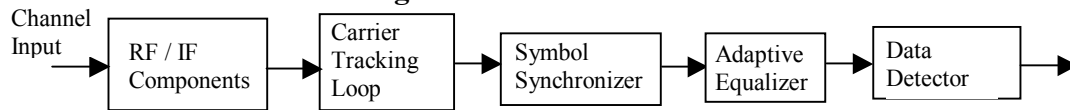
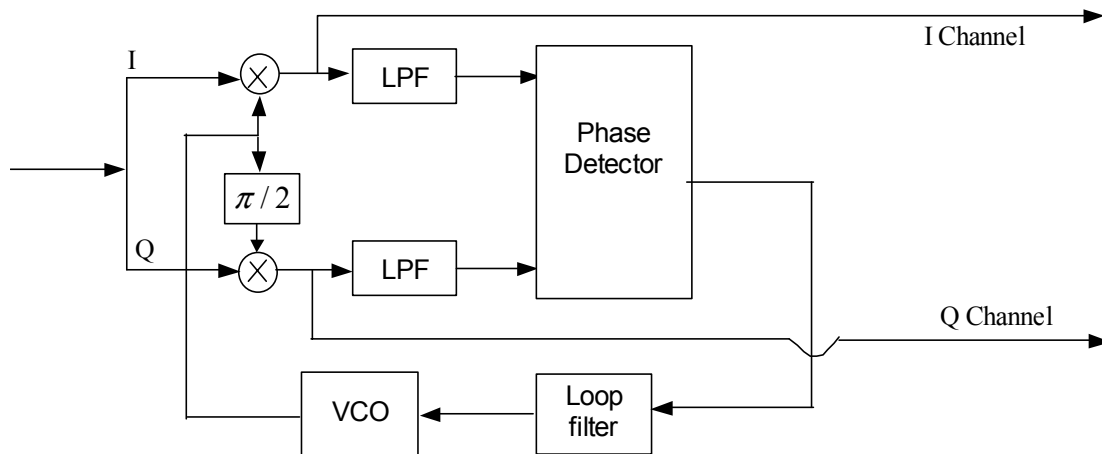
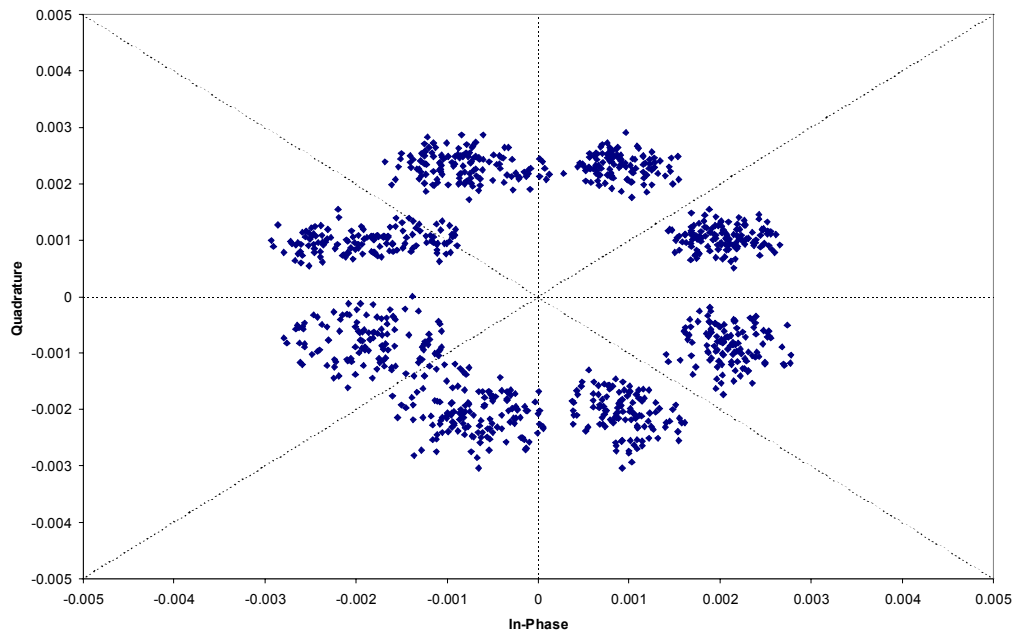
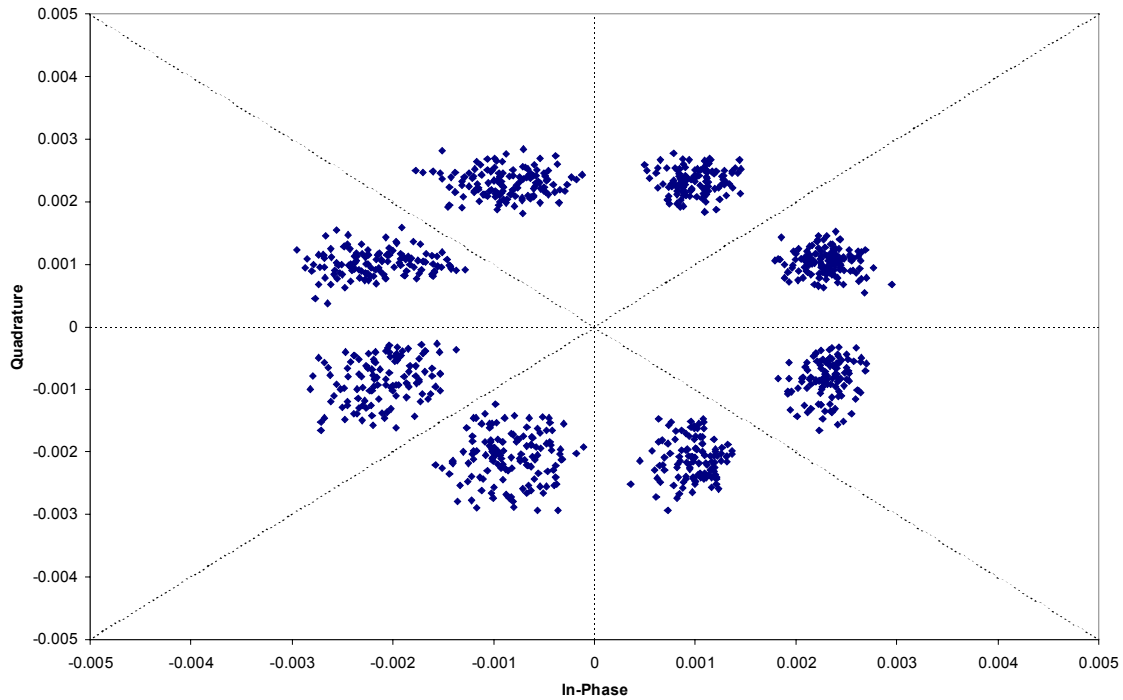


Figure 5: Modified Second Order Costas Tracking Loop



Adaptive equalization is achieved with a general fractionally spaced decision feedback equalizer. Figures 6 and 7 depict the received 8 PSK TCM constellation with and without equalization.

Figure 6: Scatter Plot of 8 PSK TCM Receiver Input without Equalization**Figure 7: Scatter Plot of 8 PSK TCM Receiver Input with Equalization**

The key parameters for the RF / IF components, carrier tracking loop, adaptive equalizer, and symbol synchronizer are summarized in Table 3. Detection is accomplished using the SPW-provided TCM demodulator, which combines the functions of an 8 PSK slicer and a Viterbi sequence estimator.

Table 3: Receiver Component Key Parameters

Component	Parameter	Value	Comment
RF / IF Distortions Filter	Gain Flatness	0.6	dB, peak-to-peak
	Gain Slope	0.1	dB/MHz
	Phase Non-linearity	6.0	deg, peak-to-peak
	Roll-off	0.574	dB / MHz
	Bandwidth	693.33	MHz
Carrier Tracking Loop	ARM Filter BW	1020	MHz
	Closed Loop BW	16.32	kHz
	Damping Factor	0.223	
Symbol Synchronizer	Loop Noise BW	207	kHz
	Damping Factor	.707	

3. Power Spectral Density Plots

The PSD plots presented were measured at the output of the User Satellite (USAT) and were generated using the full scope of distortions and constraints assumed for the study. Inclusion of some of these assumptions, including most significantly the narrowband (650 MHz) RF filter and the Spurious Phase Modulation and Spurious Emissions resulted in severely distorted modulated spectra which were insufficiently clear for the Panels' considerations. A specific request was received for a frequency response generated without the distortion effects of Spurious PM and Spurious Emissions so that a clearer picture of the filtered 8 PSK TCM Spectrum could be evaluated.

Figure 8 depicts the 8 PSK TCM signal at the output of the User Satellite (USAT) without the deleterious effects of spurious PM and spurious emissions. Note that most of the features of the modulated signal spectrum are suppressed due to the channel filtering.

Figure 9 depicts the 8 PSK TCM signal Power Spectral Density (PSD) at various stages throughout the USAT, facilitating an evaluation of the 8 PSK TCM spectrum. Note that the unfiltered signal waveform in this figure demonstrates a characteristic PSK PSD shape with discrete frequency spikes at multiples of the channel symbol (baud) rate of 510 Msps resulting from data asymmetry. Also note it's characteristic $\sin(x)/x$ side lobe amplitude decay which appears to break down for the outermost frequency lobes due to spectral leakage from the FFT.

Also in Figure 9 is the 8 PSK TCM PSD waveform at the output of the TWTA. The USAT model includes an 867 MHz filter between the modulator and the TWTA representing the frequency characteristics of the upconverters, low noise amplifiers and

switches/diplexers. The effects of this filter and the spectrum regrowth from the TWTA can be seen in this waveform.

Figure 8: 8 PSK TCM PSD at Output of USAT Model – no Spur PM / Emissions

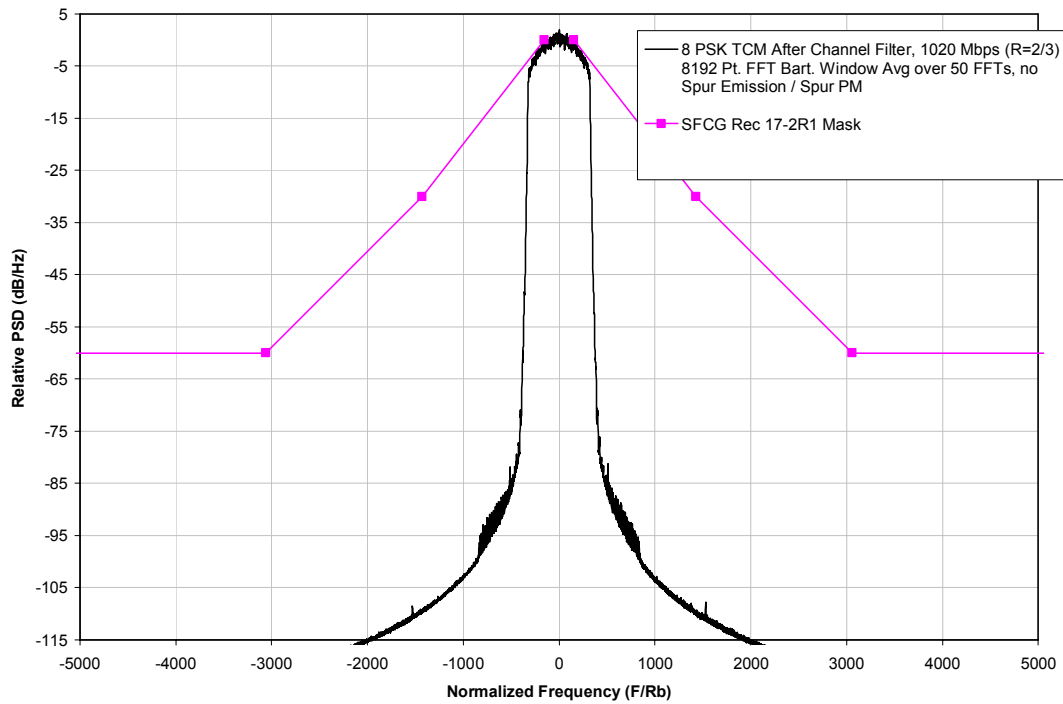
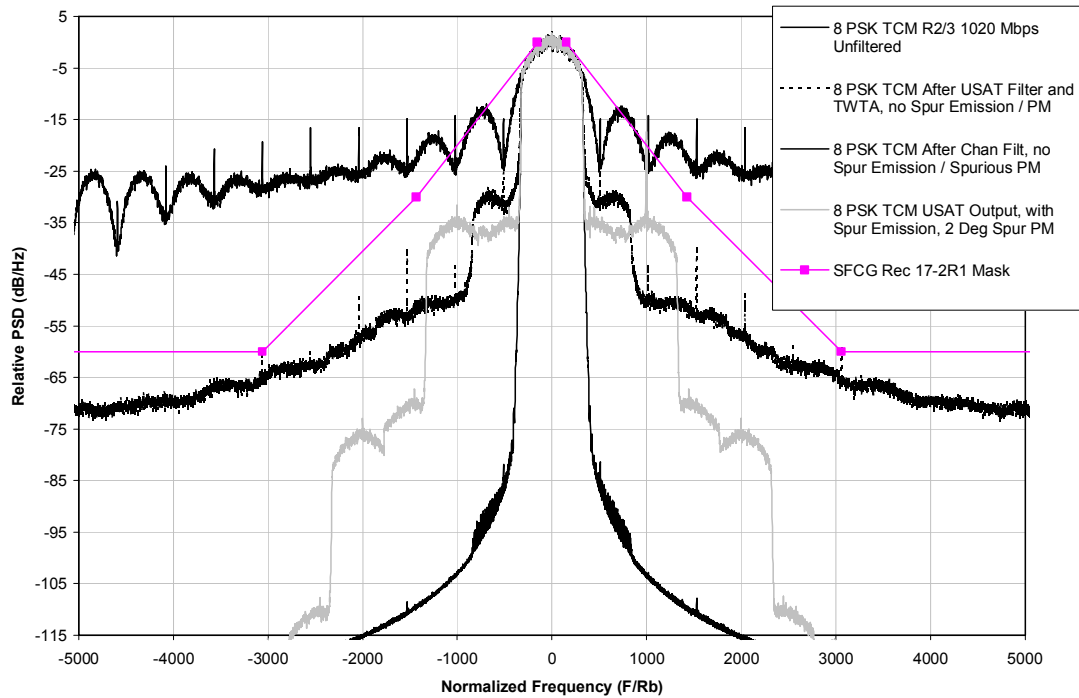


Figure 9: 8 PSK TCM PSD at Various Stages Throughout the USAT



4. Comparison to Multidimensional 8 PSK TCM

A request was also made to compare these results to the multidimensional 8 PSK TCM results presented at the conference by CNES' A. Ribes. Unfortunately, the differences in the schemes and setup implemented by Mr. Ribes from those in this study make direct comparison impossible. A summary of the major differences is given below:

1. CNES results employ two multi-dimensional (4D) pragmatic 8 PSK TCM modulations. The 2.0 B/Sec/Hz version takes 8 input bits, separates them into one group of 5 bits which is fed directly into a mapper and another group of 3 bits which is rate $\frac{3}{4}$ coded into 4 bits which are also fed into the mapper. The mapper combines the 9 input bits, introducing some further redundancy producing four 8PSK symbols (equivalent to 12 bits). The symbol rate R_s is therefore half the bit rate R_b . The 2.5 B/Sec/Hz variety of multidimensional 8 PSK TCM works similarly except it splits 10 input bits into groups of 7 and 3 bits (encoded into 4 symbols prior to the mapper) with a resulting symbol rate $R_s = 0.4 R_b$. These modulations differ in many key ways with the monodimensional Ungerboeck TCM modulation we employed. Although the details of the multidimensional TCM mapping are not specified, it appears to function like a second (concatenated) coding. Because of these fundamental differences, the multidimensional 8 PSK TCM modulations implemented by CNES are not comparable with the results presented in paper 99/47.
2. CNES generated 8 PSK TCM spectrums for 3 modes of operation. The first and third incorporated pulse shaping Square Root Raised Cosine filters which were not used for our 8 PSK TCM modulation. The second mode of operation employed a "nonlinear distributed" modulator. Insufficient detailed information on the characteristics of this modulator is available to permit a comparison.
3. The CNES results were collected at X-Band (8.2 GHz) Any phase noise experienced at this frequency would be proportionally lower than the simulated phase noise experienced in Ka-band simulated results.
4. The CNES results were generated with a proportional channel bandwidth of $BT_s = 1.6$. (Corresponding to a bandwidth of 80 MHz) This value is significantly higher than the $BT_s = 1.27$ (corresponding to a 650 MHz bandwidth) which were employed in the monodimensional 8 PSK TCM analysis.
5. No information was provided on the phase tracking and symbol timing recovery employed by the receiver in the CNES tests.

Implementation of the modulation scheme used in the CNES tests and performance of simulations under similar operating conditions would be possible if the necessary additional information identified above were available.

5. Summary

In response to action item 99-1E-38, this paper provides detailed implementation information on the monodimensional 8 PSK TCM technique employed in paper 99/47, *Efficient Modulation and Coding Schemes for Future NASA Ka-Band Space Communications*. This paper also documents problems inherent in comparing these results to multidimensional 8 PSK TCM results documented in paper 99/49.



4 Dimensional 8PSK-Trellis Coded Modulations for Medium and High Data Rate Links

André Ribes

CCSDS Member - Panel 1E

CNES - Toulouse, France



Summary

- Rationale
- Hardware Implementation
- Spectrum occupancy
- Bit error rate
- Conclusion



Proposal for the use of a new modulation scheme for medium or high data rate telecommunication channels

- For EOS, the X-Band channel is crowded and a reduction of transmitted power and/or improved use of bandwidth is highly wished.
- Today techniques used for EOS (4PSK modulation w or w.o. separate coding) are limited and cannot offer sufficient resources to match the needs for the next years
- Improvement of power efficiency is possible with the coding but at the cost of increasing bandwidth occupation with the actual techniques (coding achieved independantly of the modulation).
- Reduction of bandwidth is possible thanks to the use of bandwidth-efficient multi/phase modulations like M-Ary PSK under non linear channel conditions, but the BER Performances are worst than 2 or 4-PSK modulations, at given E_b/N_0 , due to a reduced Euclidian distance. Additional transmitted power is necessary to compensate for these losses
- Possible Solution: introduction of Treillis Coded Modulations mapped to M-Ary PSK constellations (with $M \geq 8$)



Proposal for a complement to RF and Modulation CCSDS Standard

- **Proposal:** for Medium and High Data Rate Services (e.g. Earth Observation...), a power/bandwidth efficient phase modulation based on the use of 4Dimensional-8PSK Treillis Coded Modulation (with or without RS outer code, considered as an option)
- This modulation is based on the G.Ungerboeck, S.Pietrobon et.al. works in the years 80 and 90
- The proposal provides a possible access to 4Dimensional-16 PSK TCM in the future
- **Benefits of this modulation:**
 - Good BER performances
 - Availability of two selectable channel efficiency for 4D-8PSK TCM: 2 and 2.5 B/s/Hz (theoretical at Nyquist bandwidth), for power / bandwidth adaptation
 - Self phase ambiguity resolution at receiver end (rotationally invariant modulation) with differential coding
 - Power and Bandwidth efficient modulation
 - Reduced processing rate obtained with multidimensional constellations (1/4 rate)



Recall of Multidimensional Treillis Coded Modulation Basics

•Principle of "k-Dimension - MPSK" TCM:

- Transmission of k information bits and 1 redundant bit every kT seconds (T = signaling rate of the modulation)
- Transmission of k consecutive M-PSK constellations

•Advantage of Multidimensional vs Monodimensional Treillis Coded Modulations:

- Augmentation of Free Euclidian Distance (D_{fed}): improvement of the power gain
- Reduction of rate processing with a factor k in comparison with monodimensional TCM: possible use of standard technologies for higher information rate
- Availability of specific convolutional codes and possible introduction of differential coding to suppress phase ambiguity, at the cost of a reduction of the power gain.

•Constraints of Multidimensional Modulations

- Augmentation of "hardware complexity" at coding and decoding end



Coding Options

•Convolutional Code proposed for the treillis: two solutions:

- ➔ •A dedicated solution to improve performances: rate $3/4$ - 64 states code
 - This solution was implemented and tested at CNES
- ➔ •A Pragmatic Solution, based on the CCSDS Convolutional Coder (rate $1/2$ - 64 states), with introduction of puncturing to obtain $R=2/3$ and $3/4$ rate), but:
 - The performances are under analysis today.
 - Self Phase ambiguity resolution must be demonstrated.

•RS Outer Coding:

- Optional (not formally included in this proposal)
- Possible use of the CCSDS standardised RS code (255,223,E=16)
- Or Reed Solomon (254, 239,E=8), derived from DVB-S Standard RS(255,239,16) code, with:
 - block length: 255 bytes
 - rate K/N : 239/255
 - correction capabilities: 8 bytes per block of 255



Coding options: puncturing Matrix for the convolutional code

Punctured code definition

Original code			Code rates									
			1/2		2/3		3/4		5/6		7/8	
K	G ₁ (X)	G ₂ (Y)	P	d _{free}	P	d _{free}	P	d _{free}	P	d _{free}	P	d _{free}
7	171 _{OCT}	133 _{OCT}	X: 1 Y: 1	10	X: 1 0 Y: 1 1	6	X: 1 0 1 Y: 1 1 0	5	X: 1 0 1 0 1 Y: 1 1 0 1 0	4	X: 1 0 0 0 1 0 1 Y: 1 1 1 1 0 1 0	3
			C1 = X ₁ C2 = Y ₁		C1 = X ₁ Y ₂ Y ₃ C2 = Y ₁ X ₃ Y ₄		C1 = X ₁ Y ₂ C2 = Y ₁ X ₃		C1 = X ₁ Y ₂ Y ₄ C2 = Y ₁ X ₃ X ₅		C1 = X ₁ Y ₂ Y ₄ Y ₆ C2 = Y ₁ Y ₃ X ₅ X ₇	
NOTE: 1 = transmitted bit 0 = non transmitted bit												
Polynom: G1 = 171 (X), G2 = 133 (Y)												

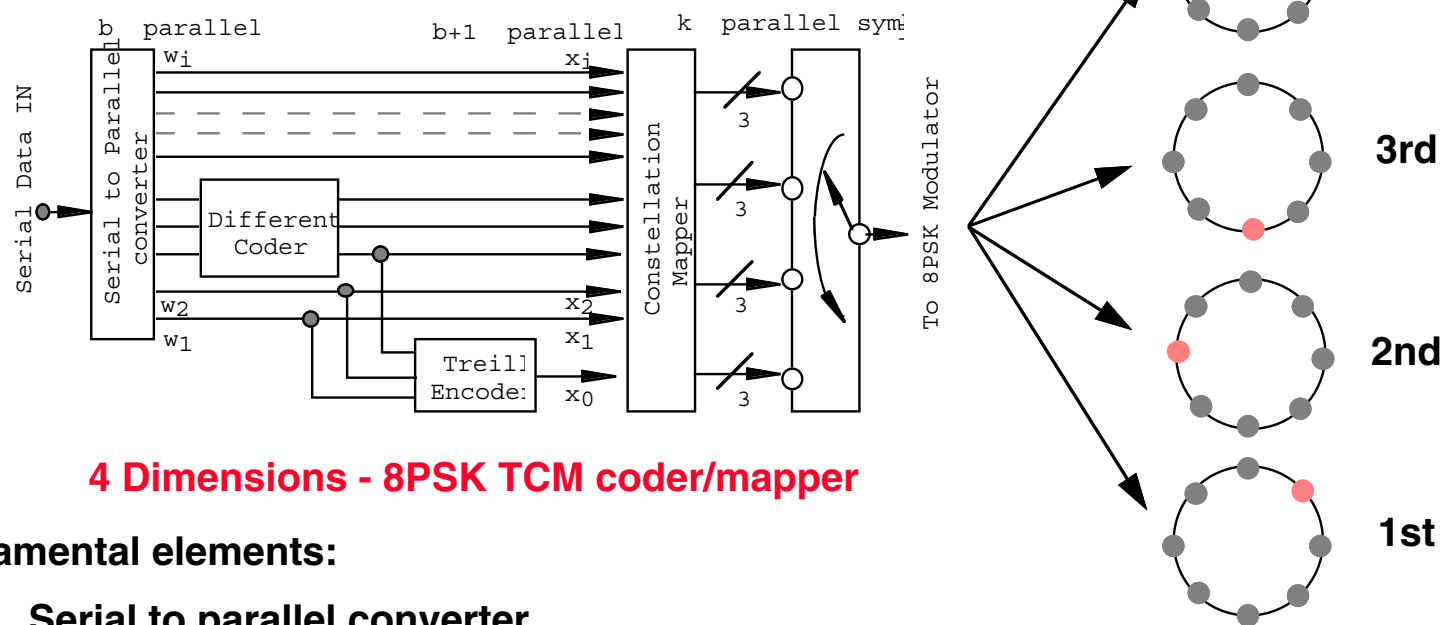
- This matrix corresponds to the DVD-S Standard
- The convolutional code is the same as the CCDS one, unless for the inverter in arm G2

These puncturing matrix are proposed to match with the DVB industry standard and take opportunity of component availability



8 PSK Treillis Coded Modulation

General Principle of the Modulator for 4D-8PSK TCM





Possibility of several efficiencies with 4 Dimensions-8PSK TCM

The following efficiencies are achievable with the four successive constellations:

- 2 bits /Hz** (8 significant bits and one redundant bit)
- 2.25 bits/Hz (9 significant bits and one redundant bit)
- 2.5 bits/Hz** (10 significant bits and one redundant bit)
- 2.75 bits/Hz (11 significant bits and one redundant bit)

Two efficiencies are proposed for the standard: **2 and 2.5 bits/Hz**

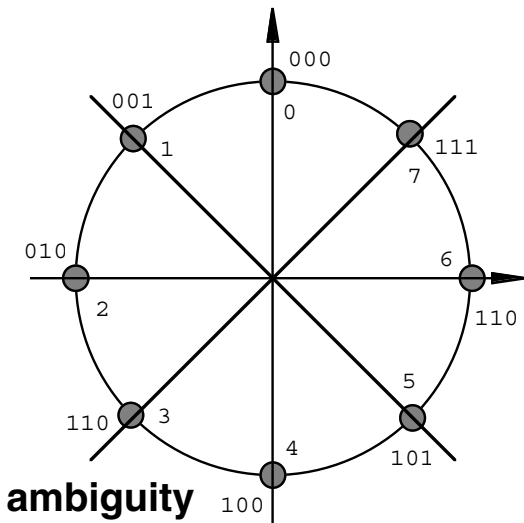
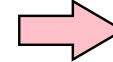


Summary of Characteristics of the proposed 4-D 8PSK-TCM

Carrier Modulation:	8-PSK (Multidimensional TCM: $k=4$)
Transmission efficiency:	2 and 2.5 Bit/s/Hz (selectable)
Trellis code:	Dedicated Convolutional $R=3/4$, 64 states ($L=7$) Or Pragmatic solution based on 7-1/2 CCSDS Convolutional code with puncturing 3/4
Outer code (optional)	Reed Solomon (255, 239, $E=8$) (from DVB-S Standard) or CCSDS RS code (255, 223, $E=16$)
Channel filtering (waveform shaping):	Selectable SRC (roll-off= 0,35 or 0,25-TBD) or NRZ with output filter
Channel power amplifier:	Linear or Non linear amplifier (TWT like or SSPA)
Coding and Multi-D TCM Mapping	FPGA circuits

Characteristics of the two modulations

Natural Mapping for the 8PSK constellations



Convolutional code with differential coding remove 45° phase ambiguity

Same number of coded bits is involved for both cases:

- 3 bits used for coding computations, 5 uncoded bits and one redundant bit for 4D-8PSK @ 2 Bits/Hz
- 3 coded bits for coding computations, 7 uncoded bits and one redundant bit for 4D-8PSK @ 2.5 Bits/Hz
- The same 3 bits are used for convolutional coding for the two efficiencies (simplification of the hardware)

➡ The same decoding treillis (i.e. Viterbi algorithm) is used in both cases at demodulation



Hardware involved for the coder



Signal Set Mapper Equation for 4D-8PSK-TCM @ 2 bits/Hz

$x^{(i)}$ = data line at the input of the mapper

$$\begin{bmatrix} z^{(0)} \\ z^{(1)} \\ z^{(2)} \\ z^{(3)} \end{bmatrix} = \left\{ x^{(8)} \begin{bmatrix} 8 \\ 8 \\ 8 \\ 8 \end{bmatrix} + x^{(7)} \begin{bmatrix} 0 \\ 8 \\ 0 \\ 8 \end{bmatrix} + x^{(6)} \begin{bmatrix} 0 \\ 0 \\ 8 \\ 8 \end{bmatrix} + x^{(5)} \begin{bmatrix} 4 \\ 4 \\ 4 \\ 4 \end{bmatrix} + x^{(4)} \begin{bmatrix} 0 \\ 0 \\ 0 \\ 8 \end{bmatrix} + x^{(3)} \begin{bmatrix} 0 \\ 4 \\ 0 \\ 4 \end{bmatrix} + x^{(2)} \begin{bmatrix} 0 \\ 0 \\ 4 \\ 4 \end{bmatrix} + x^{(1)} \begin{bmatrix} 2 \\ 2 \\ 2 \\ 2 \end{bmatrix} + x^{(0)} \begin{bmatrix} 0 \\ 0 \\ 0 \\ 4 \end{bmatrix} \right\} \text{Mod } 16$$

Generator vectors

$z^{(i)}$ = signals to the 8PSK modulator (four constellations)

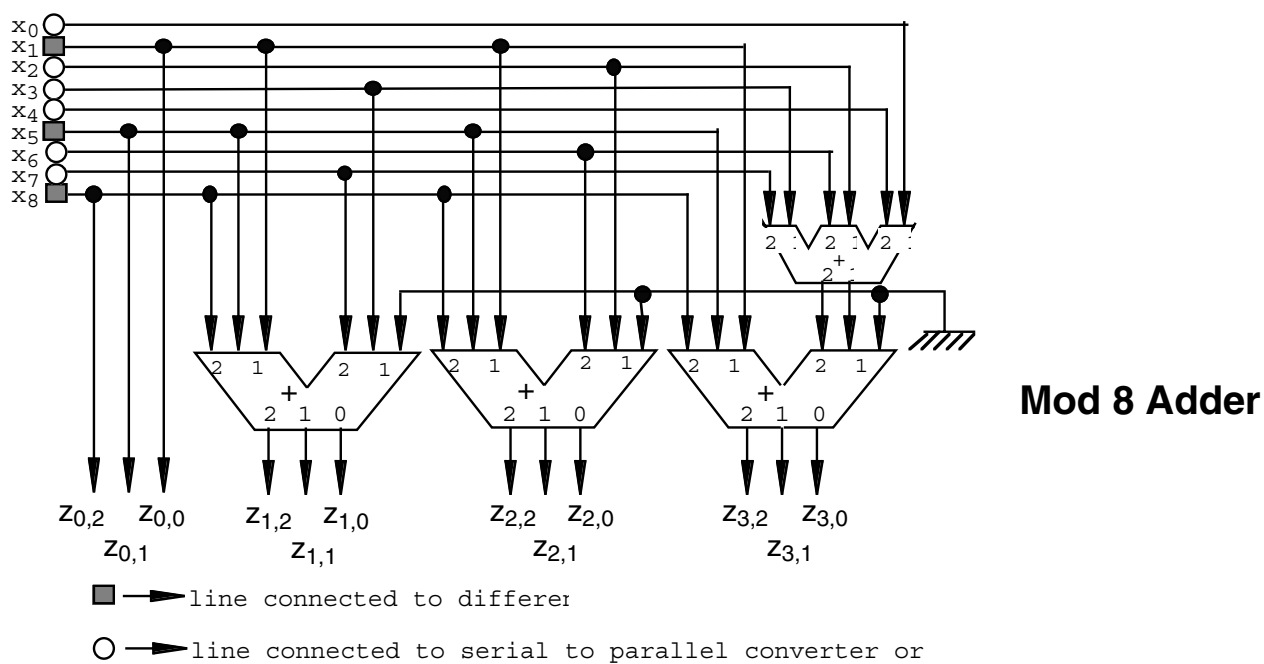
or

$$\begin{bmatrix} z^{(0)} \\ z^{(1)} \\ z^{(2)} \\ z^{(3)} \end{bmatrix} = \left(8 x^{(8)} + 4 x^{(5)} + 2 x^{(1)} \right) \cdot \begin{bmatrix} 1 \\ 1 \\ 1 \\ 1 \end{bmatrix} + 8 \cdot \begin{bmatrix} 0 \\ x^{(7)} \\ x^{(6)} \\ x^{(7)} \oplus x^{(6)} \oplus x^{(4)} \end{bmatrix} + 4 \cdot \begin{bmatrix} 0 \\ x^{(3)} \\ x^{(2)} \\ x^{(3)} \oplus x^{(2)} \oplus x^{(0)} \end{bmatrix} \right) \text{Mod } 16$$

Bits 1, 5 and 8 are sensitive to carrier phase shift



Modulation Mapper @ 2 bits/Hz





Signal Set Mapper Equation for 4D-8PSK-TCM @ 2.5 bits/Hz

$x^{(i)}$ = data line at the input of the mapper

$$\begin{bmatrix} z^{(0)} \\ z^{(1)} \\ z^{(2)} \\ z^{(3)} \end{bmatrix} = \left(x^{(10)} \begin{bmatrix} 8 \\ 8 \\ 8 \\ 8 \end{bmatrix} + x^{(9)} \begin{bmatrix} 0 \\ 8 \\ 0 \\ 8 \end{bmatrix} + x^{(8)} \begin{bmatrix} 0 \\ 8 \\ 8 \\ 2 \end{bmatrix} + x^{(7)} \begin{bmatrix} 4 \\ 4 \\ 4 \\ 2 \end{bmatrix} + x^{(6)} \begin{bmatrix} 0 \\ 0 \\ 0 \\ 8 \end{bmatrix} + x^{(5)} \begin{bmatrix} 0 \\ 4 \\ 0 \\ 4 \end{bmatrix} + x^{(4)} \begin{bmatrix} 0 \\ 0 \\ 4 \\ 4 \end{bmatrix} + x^{(3)} \begin{bmatrix} 0 \\ 8 \\ 2 \\ 2 \end{bmatrix} + x^{(2)} \begin{bmatrix} 4 \\ 4 \\ 0 \\ 2 \end{bmatrix} + x^{(1)} \begin{bmatrix} 0 \\ 0 \\ 2 \\ 2 \end{bmatrix} + x^{(0)} \begin{bmatrix} 0 \\ 0 \\ 2 \\ 2 \end{bmatrix} \right) \text{Mod } 16$$

Generator vectors

$z^{(i)}$ = signals to the 8PSK modulator (four constellations)

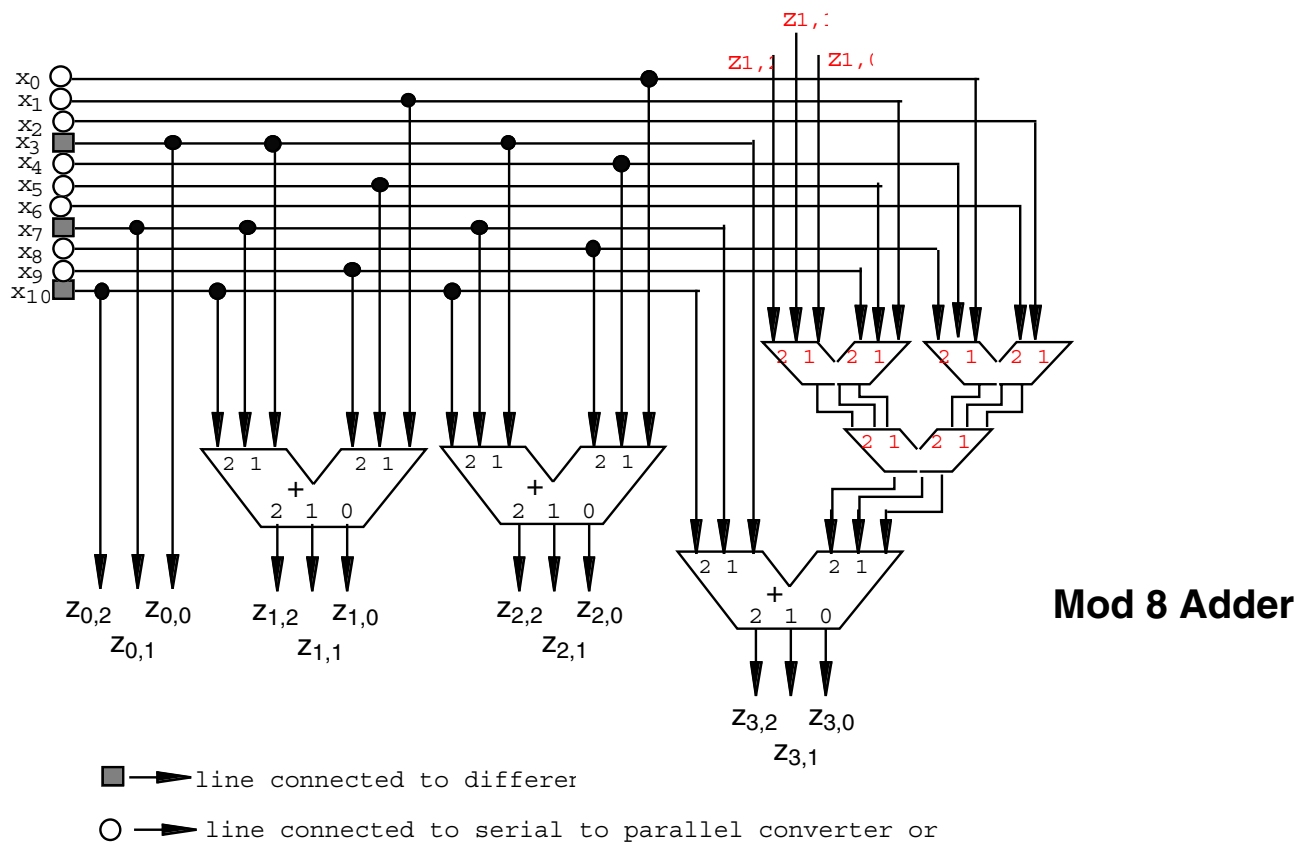
or, after simplification

$$\begin{bmatrix} z^{(0)} \\ z^{(1)} \\ z^{(2)} \\ z^{(3)} \end{bmatrix} = \left(8 x^{(10)} + 4 x^{(7)} + 2 x^{(3)} \cdot \begin{bmatrix} 1 \\ 1 \\ 1 \\ 1 \end{bmatrix} + 8 \cdot \begin{bmatrix} 0 \\ x^{(9)} \\ x^{(8)} \\ x^{(9)} \oplus x^{(8)} \oplus x^{(6)} \end{bmatrix} + 4 \cdot \begin{bmatrix} 0 \\ x^{(5)} \\ x^{(4)} \\ x^{(5)} \oplus x^{(4)} \oplus x^{(2)} \end{bmatrix} + 2 \cdot \begin{bmatrix} 0 \\ x^{(1)} \\ x^{(0)} \\ x^{(1)} \oplus x^{(0)} \end{bmatrix} \right) \text{Mod } 16$$

Bits 3, 7 and 10 are sensitive to carrier phase shift

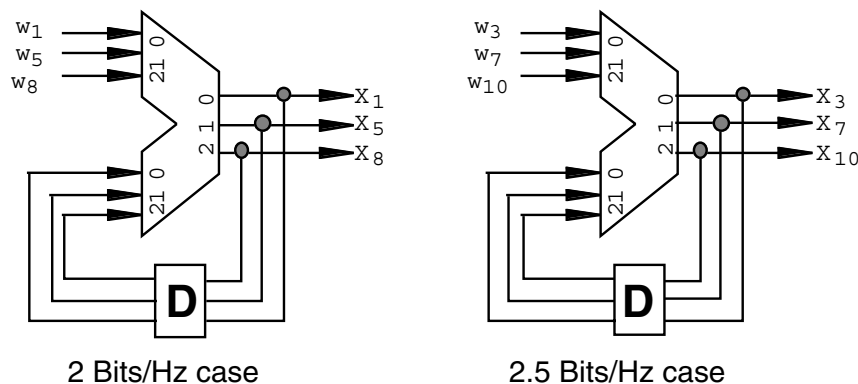


Modulation Mapper @ 2.5 Bits/Hz



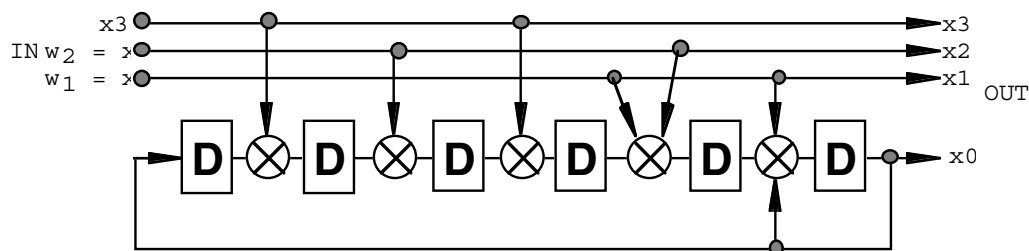


Differential and Convolutional coder



Differential coder

$D = 4T_s$
 $T_s = \text{Symbol period}$



**Convolutional systematic
 coder ($R=3/4$ - 64 States)**

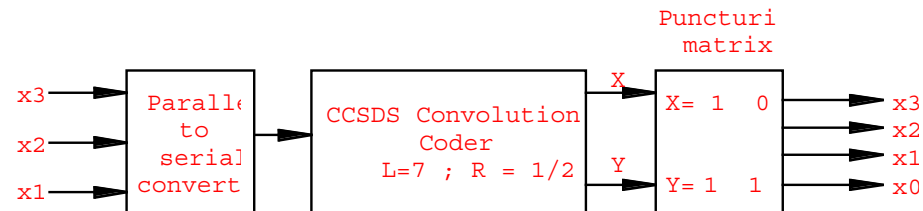
Coder Polynom
 $h^3=050, h^2=024, h^1=006, h^0=103$

The processing speed of the coder is $R_{\text{coder}} = \frac{R_s}{4}$

➔ With $R_s = \frac{R_b}{2}$ at 2 Bits/symbol or $R_s = \frac{2R_b}{5}$ at 2.5 Bits/symbol



Convolutional coder : Pragmatic solution



Basic principle of the proposed solution

The coder corresponds to the CCSDS Standard, unless for the inverter in arm G2

The rate is 3/4 with puncturing according to the proposed matrix (DVB-DSNG standard)

This solution is under validation (simulations) at CNES today.

The processing speed of the coder is: $R_{\text{coder}} = \frac{3R_s}{4}$

With $R_s = \frac{R_b}{2}$ at 2 Bits/symbol or $R_s = \frac{2R_b}{5}$ at 2.5 Bits/symbol

with R_b = bit rate of information data



Modulator Implementation

Application to 4D-8PSK @ 2 Bits/Hz

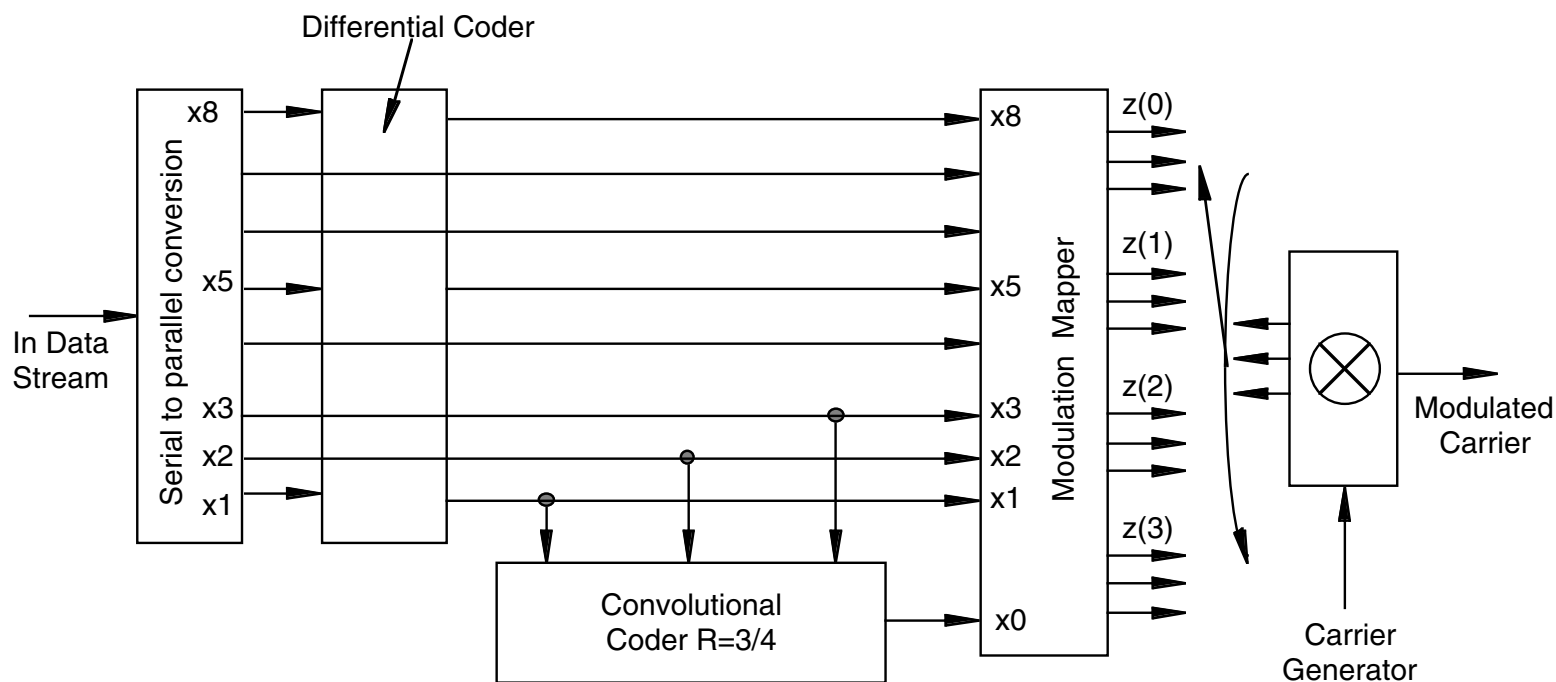


Diagram with 7-3/4 dedicated code



Modulator Implementation

Application to 4D-8PSK @ 2.5 Bits/Hz

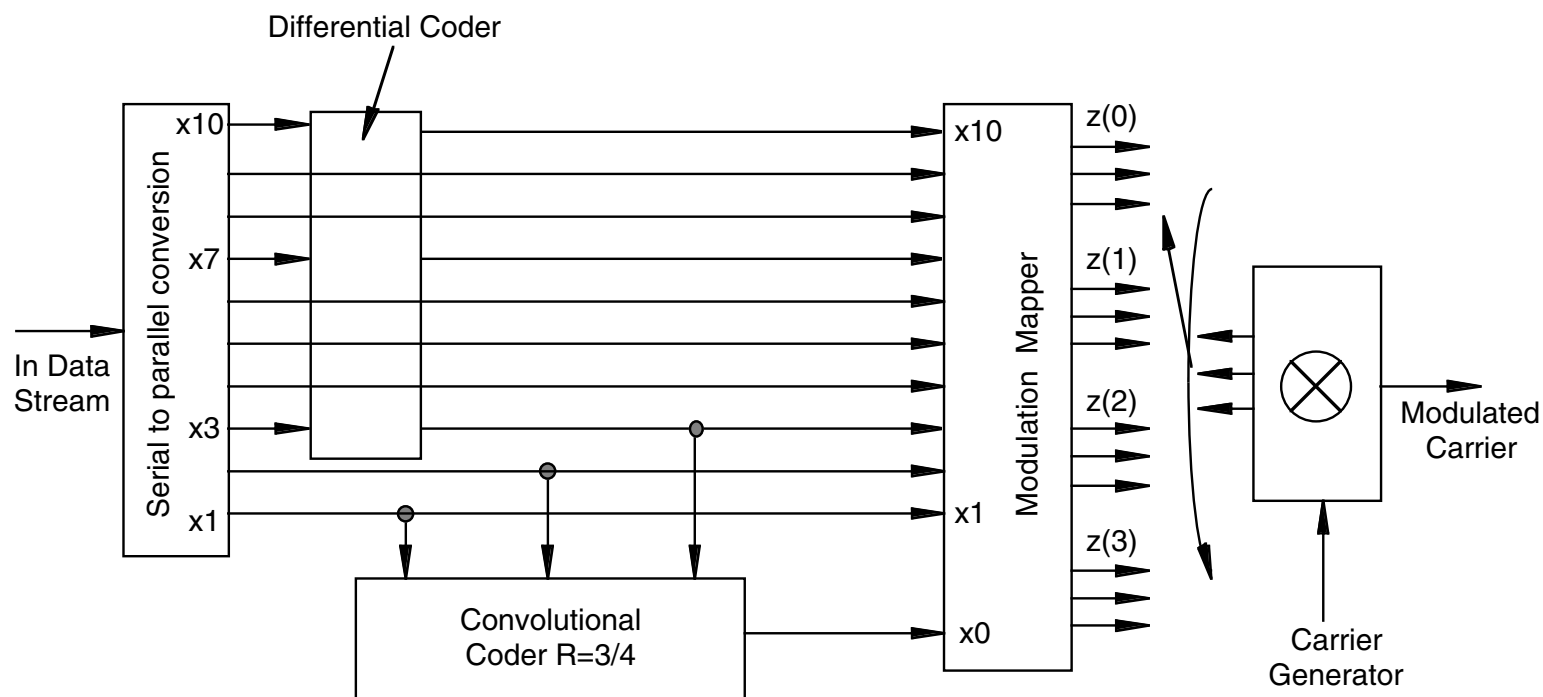
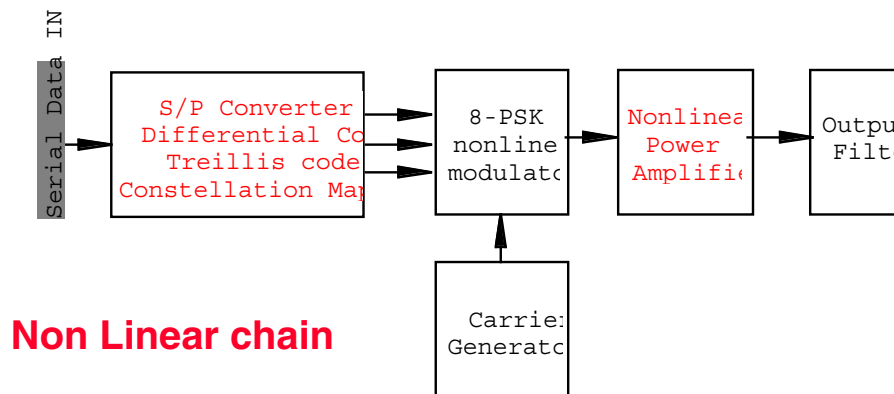
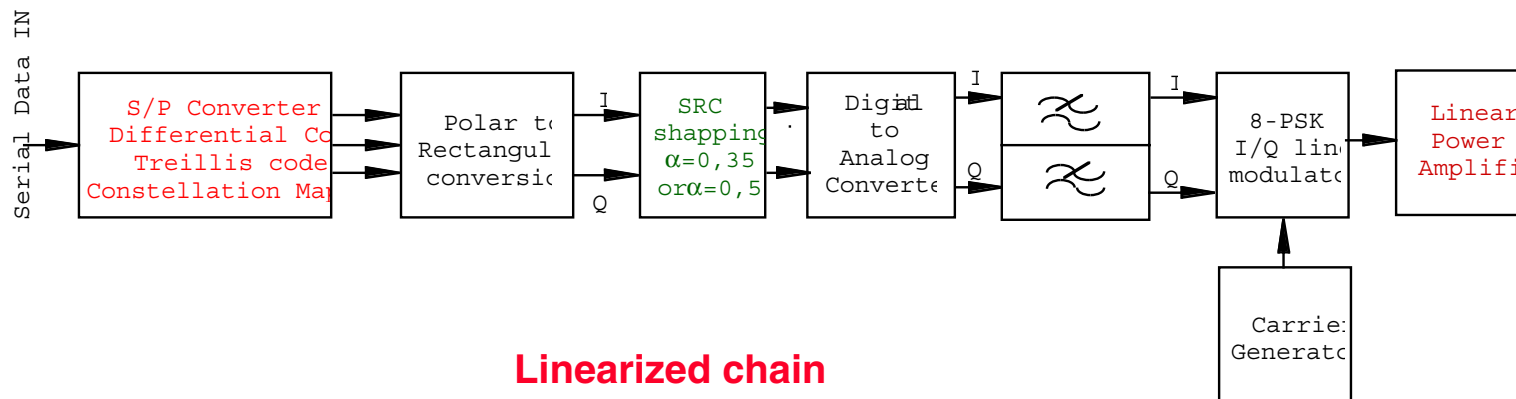


Diagram with 7-3/4 dedicated code



General principle of the transmitting end





Channel Filtering and Waveform shapping



Channel Filtering and Power Amplification

•For Low Data Rate:

- Premodulation waveform shapping adapted to SRRC equivalent filtering with a linear phase modulator (Roll-Off of 0.35 or 0.5)
- A linear (or quasi linear) amplifier is preferred in this case. A reduced back-off can be necessary.
- Predetection filter (matched filter)at receiver end: SRRC with Roll-Off of 0.35 or 0.5, according to the Roll-Off used at the transmitter end

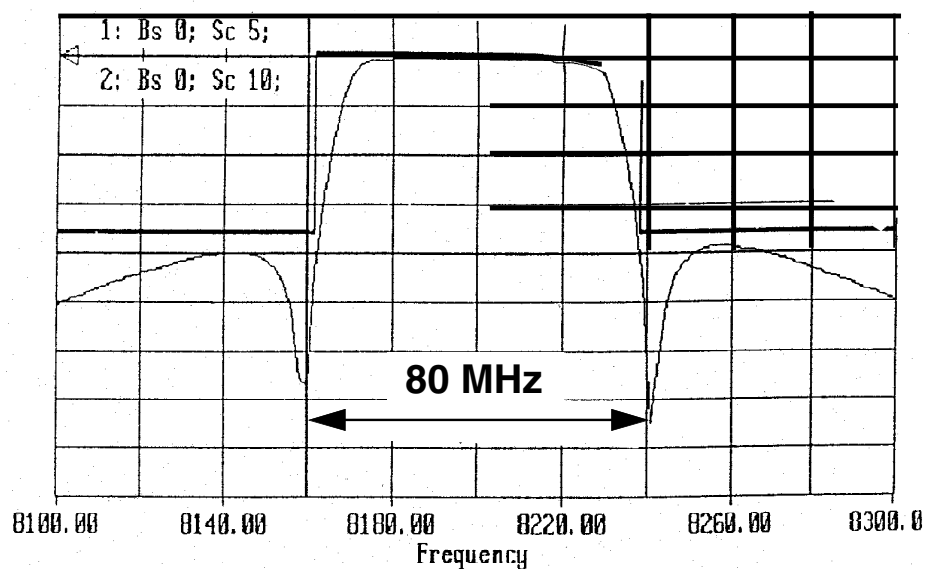
•For High Data Rate:

- "NRZ like" waveform shapping used in conjunction with a non linear modulator and amplifier (TWT or SSPA).
- Power amplifier: non linear amplifier like SSPA or TWTA driven at or near saturation.
- Output OMUX filter needed after the power amplifier to reduce the spectrum regrowth, depending of the non linear amplifier characteristic and the choice concerning the trade off between the spectrum occupancy and the losses on the performances (BER).

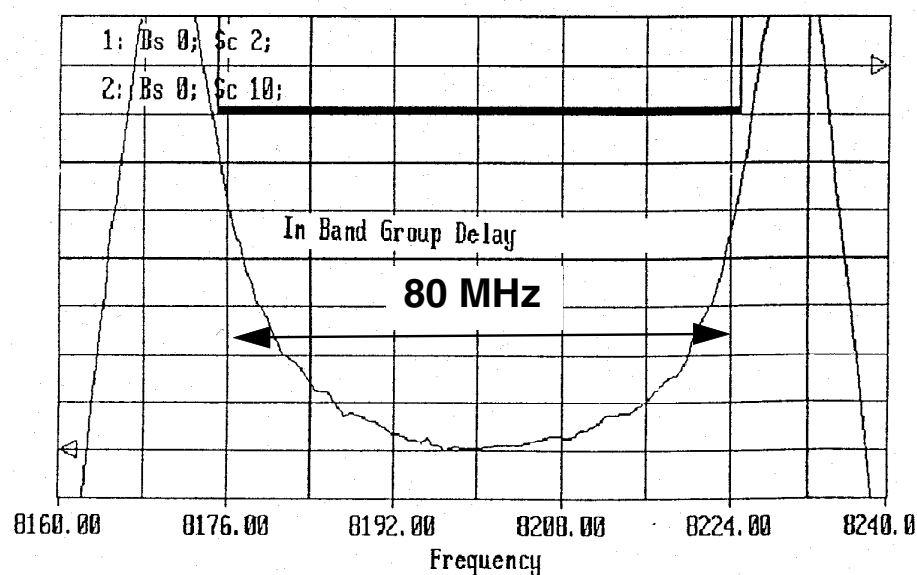


Exemple of Output Filter characteristics (center frequency: 8.2 GHz)

Amplitude in dB



Group Delay in ns

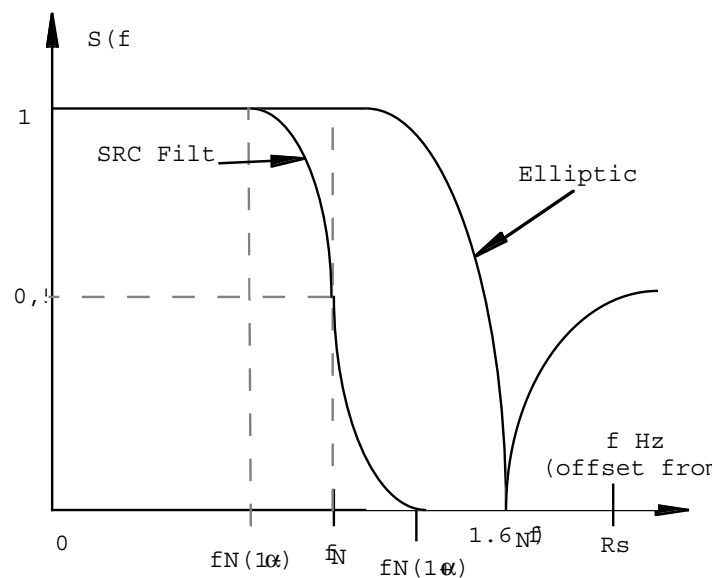


Transfer function adapted to the symbol rate $R_s = 50$ Mbauds



Characteristics of the OMUX Filter

This filter was used during the performance tests



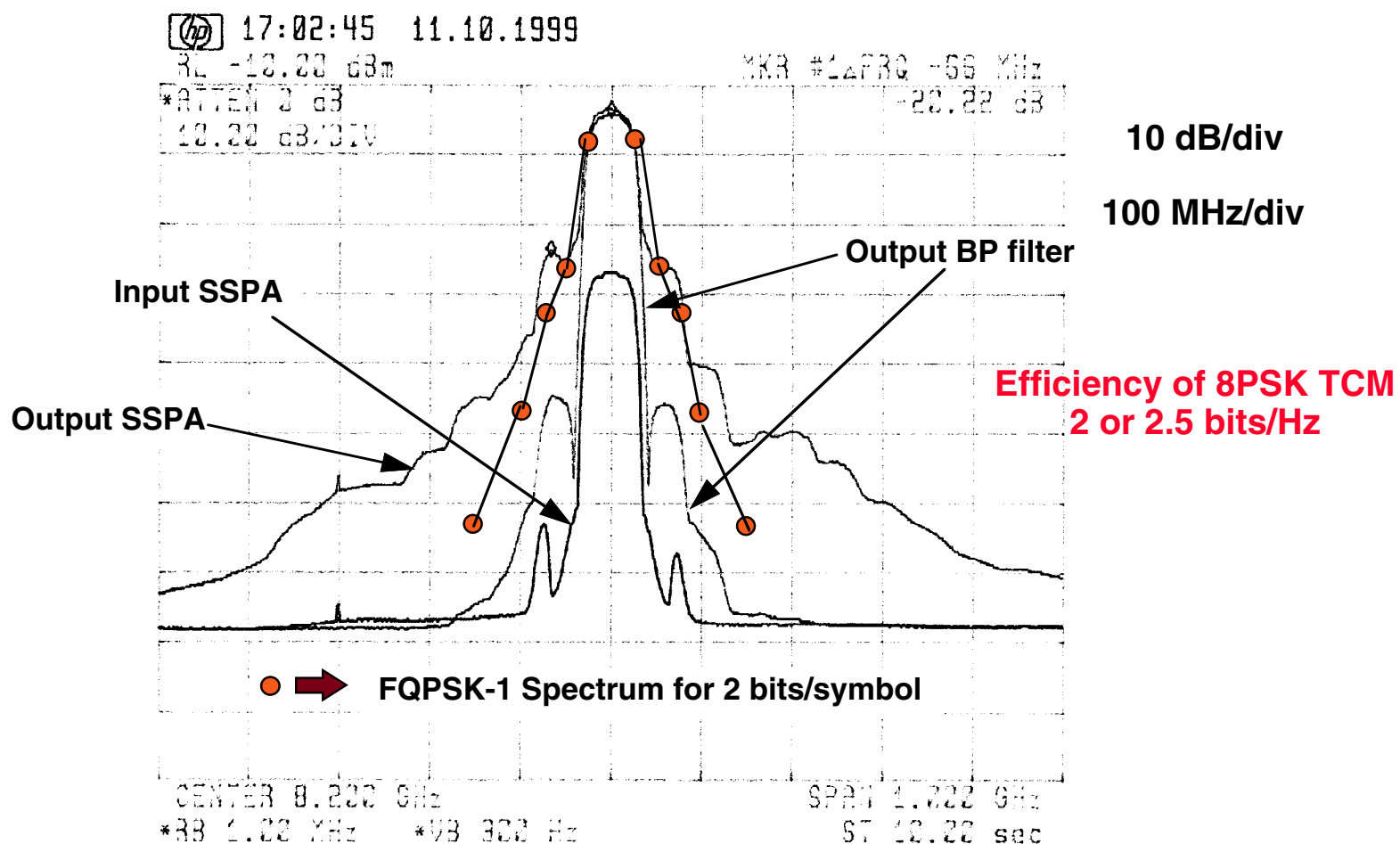
R_s = 8PSK Symbol rate
 $R_s = R_b/2$ or $2R_b/5$

$$f_n = R_s/2$$



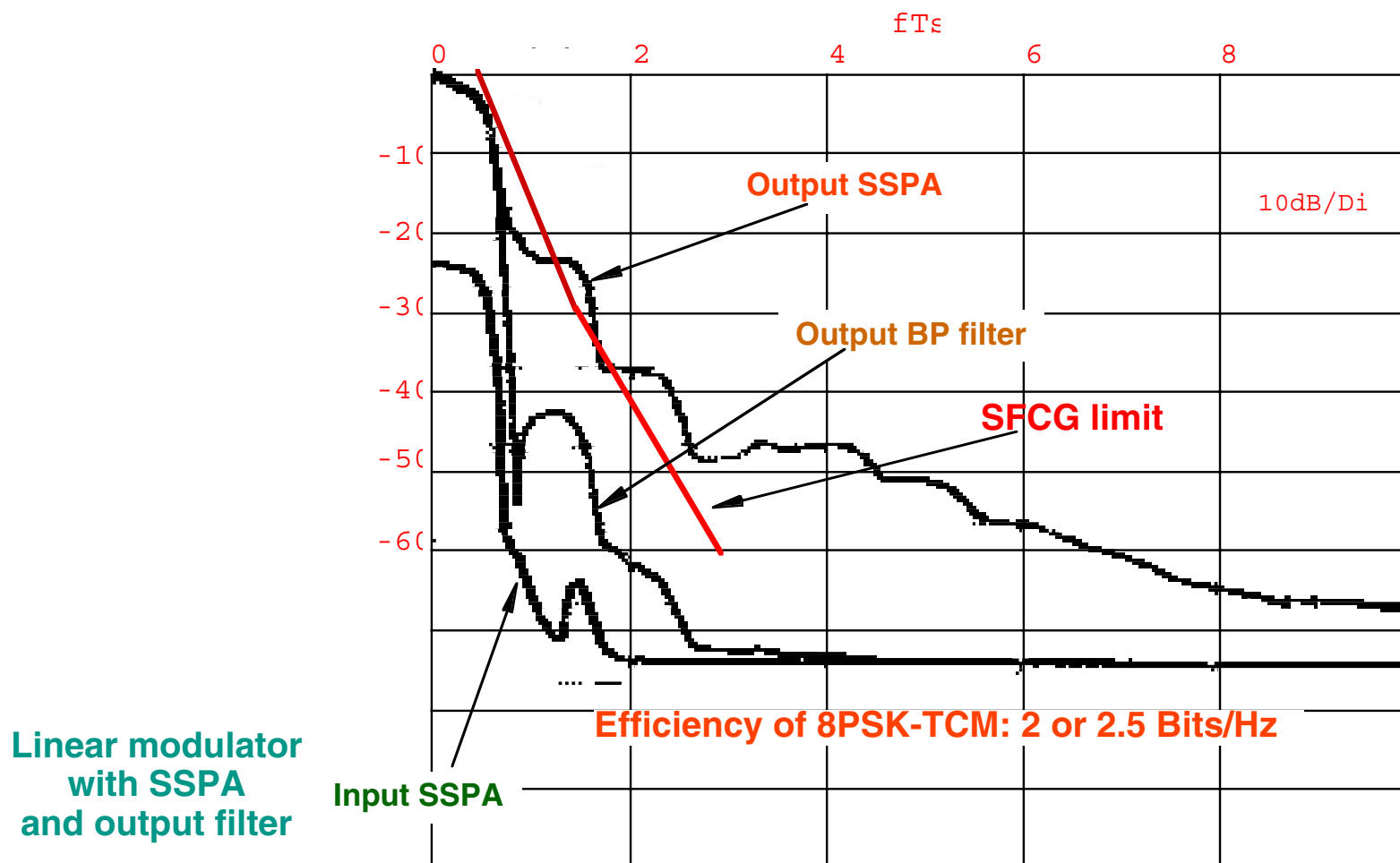
Spectrum obtained with a linear Modulator

Waveform shaping in baseband : SRC/0,35





4D-8PSK-TCM: Spectrum considerations

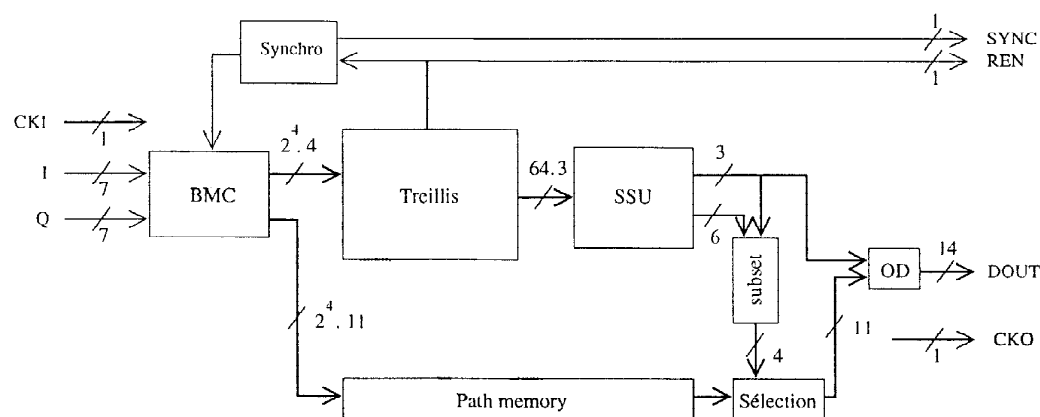




Receiver characteristics

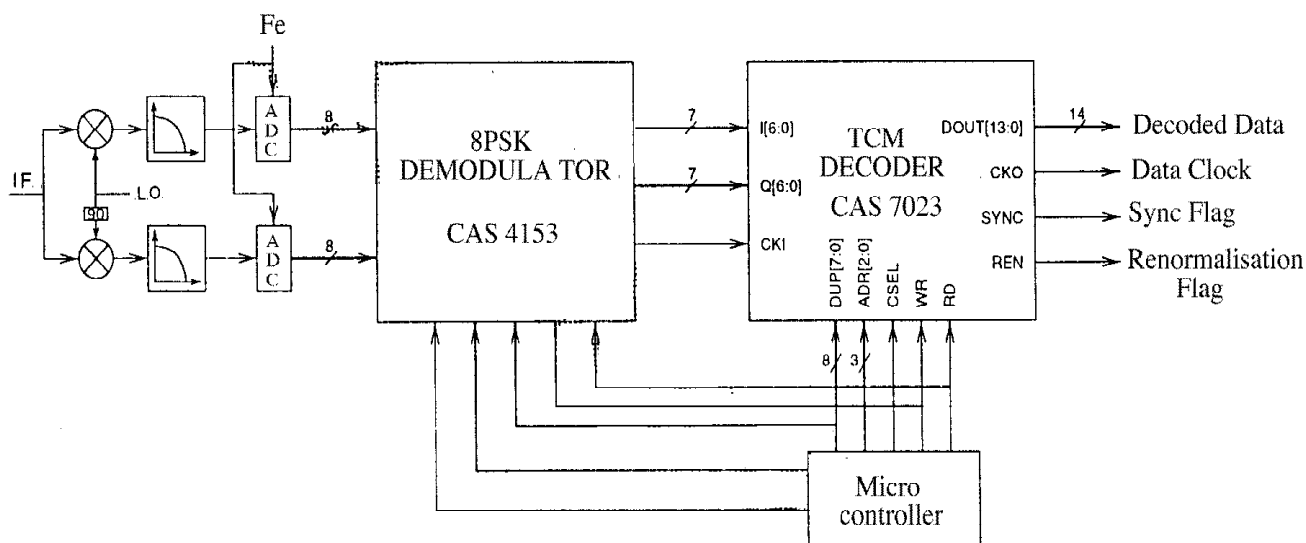


TCM decoder principle



- Quantification of I & Q inputs with 7 bits
- Quantification of Euclidian distances with 7 bits
- Quantification of branch metrics with 7 bits
- Quantification of cumulated metrics with 7 bits

Receiver Application



This is a typical application using two ASICs:

- The 8PSK demodulator is derived of the DVB development with additional capabilities to process the 8PSK and also 16PSK cases
- The TCM decoder was developed for the circumstance in 0.6 μ technology
- This design was used to perform the tests

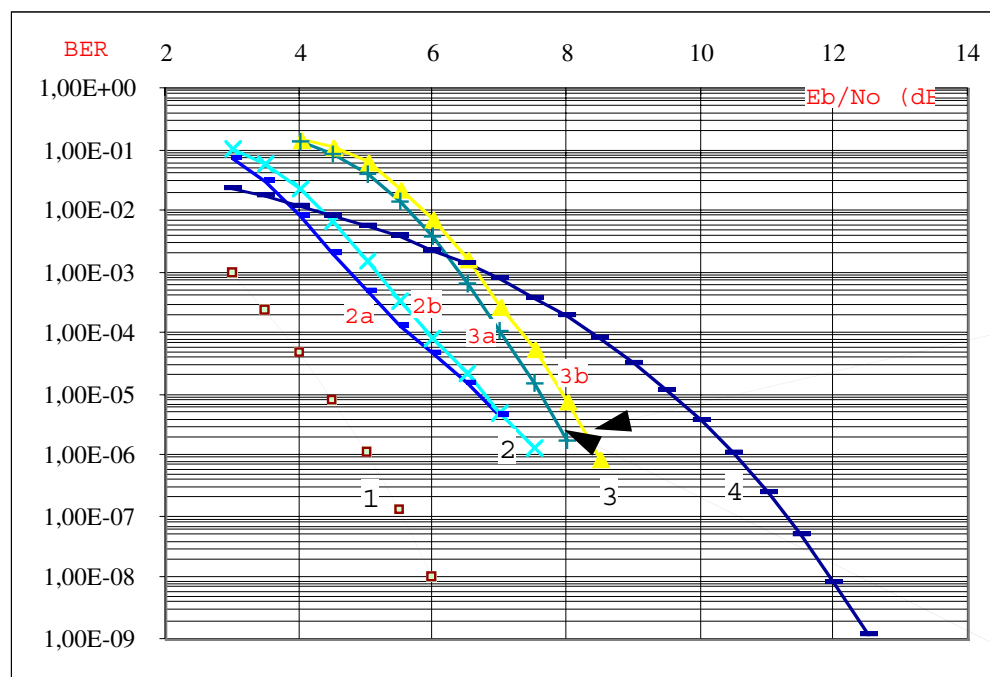


BER Performance summary

- BER Performances of TCM decoder ASIC
- Measured Performances at 50 Mbaud/s at IF= 720 MHz including RS coding
- BER performances with the global chain, including power amplification and output filtering



BER Performances of TCM decoder ASIC



Real curve

Ideal curve

1: QPSK with CC R=1/2, 64 states
4: QPSK uncoded

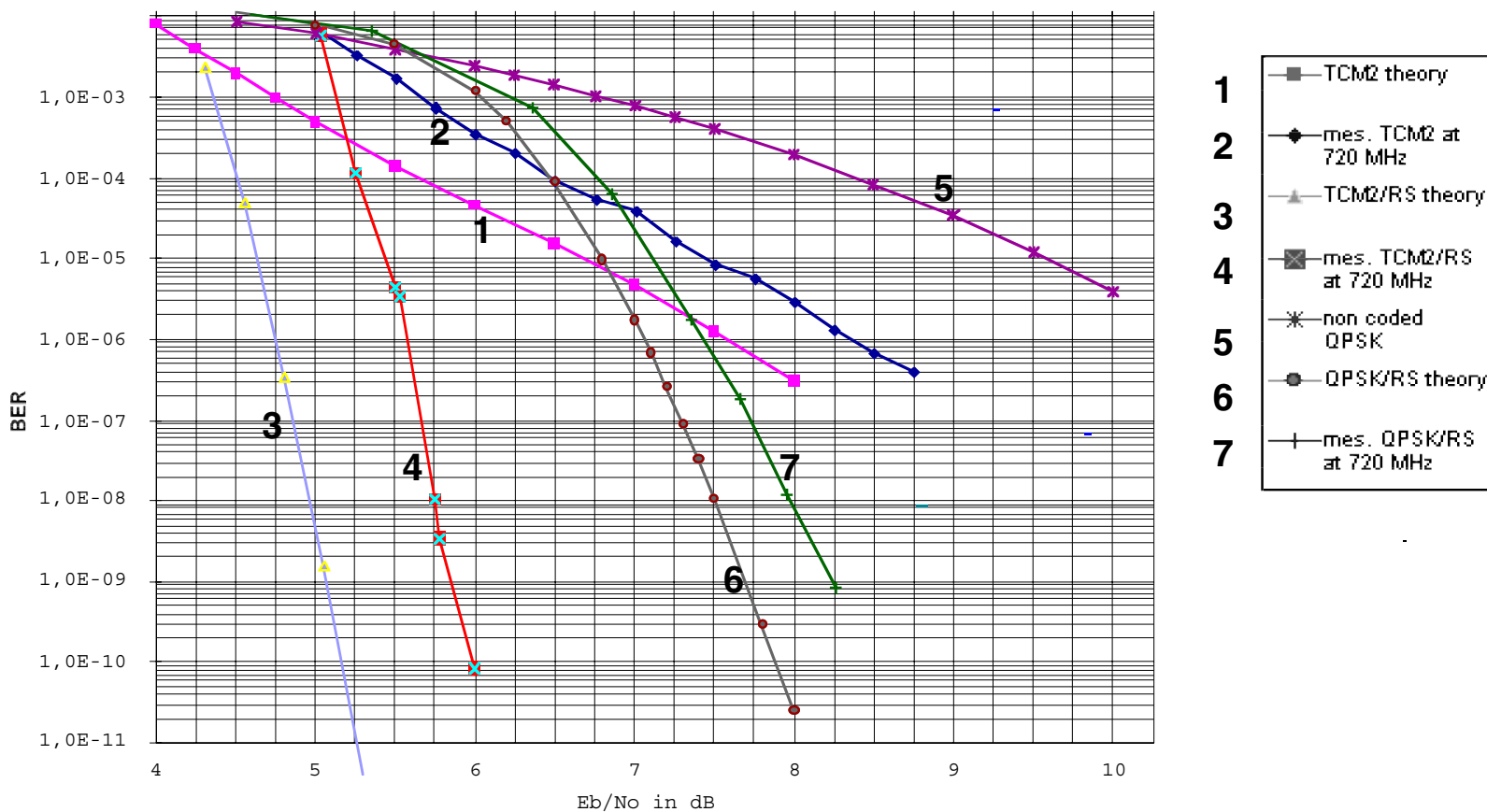
2: 4D-8PSK 2 B/sec/Hz
3: 4D-8PSK 2,5 B/sec/Hz

Ideal curves: 32 bits Quantification

Real curves: 4 bits quantification (Euclidian Dist.) and 6 bits (cumulated metrics)



Measured Performances at 50 Mbaud/s at IF= 720 MHz including RS coding





Global performances

Parameters influencing the losses on BER

The choice of the matched filter at receiver end is in all cases is the Nyquist SRC/0.35 filtering.

The E_b/N_0 is referenced at the output of the Band Pass filter or SSPA

The following additional losses are to be taken into account:

- Output Back Off for the SSPA (between 0.5 to 1.5 dB) (see BER curves)**
- Band Pass filter losses composed of:**
 - insertion losses : in the order of 0.2 dB for the microwave elliptic filter**
 - filtering losses : in the order of 0.5 to 1 dB, depending of the working point of the SSPA (OBO)**



BER Measurement principle and convention

The BER measurement is conducted on the modulated signal obtained at the output of Band Pass filter at 8,2 GHz

The reference of effective signal power for E_b/N_0 is the total signal power measured at the output of the SSPA or the Band Pass Filter at 8.2 GHz, depending of the modulation configuration.

The Noise Spectral Density is calculated by a NoiseCom equipment taking into account:

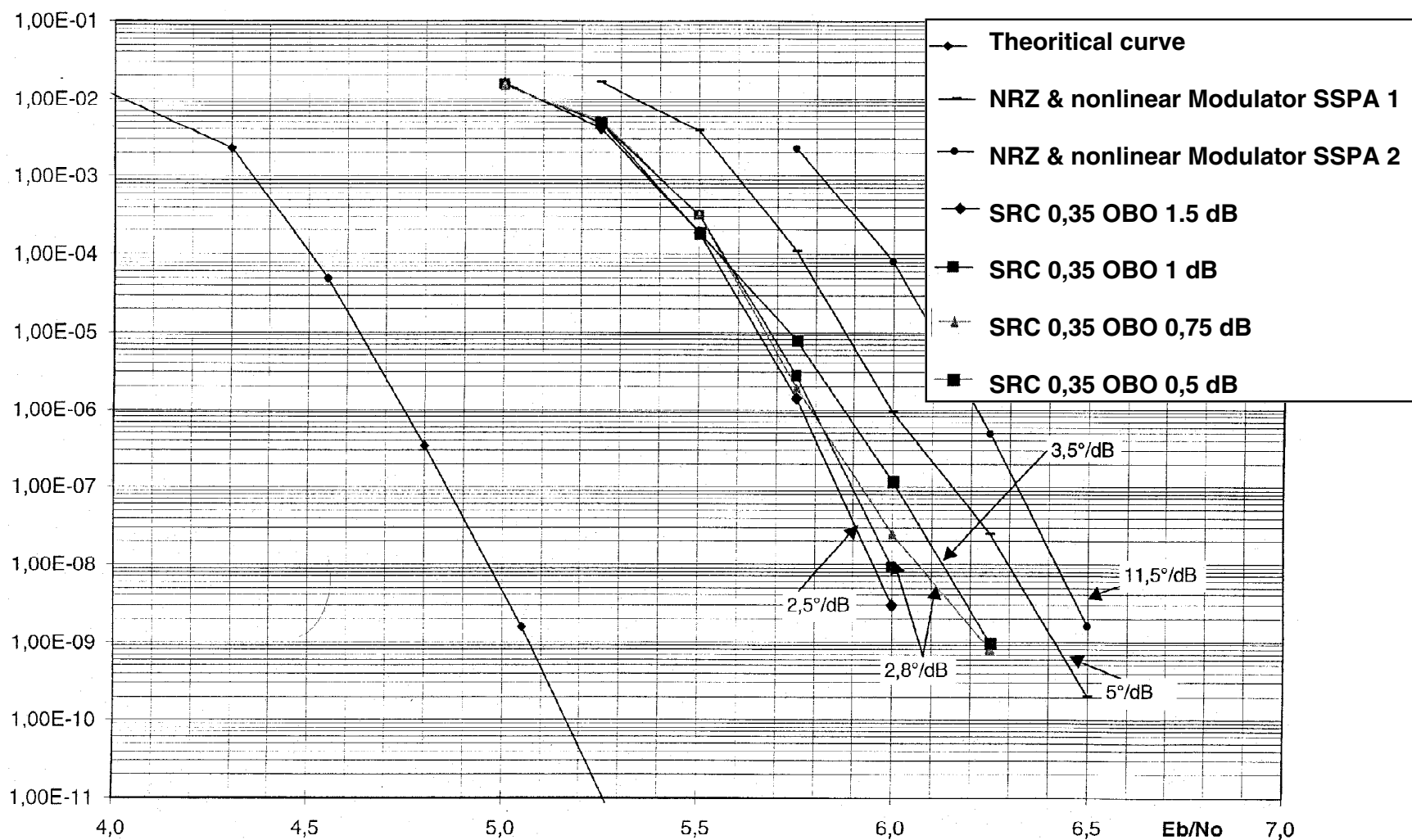
- the usable signal power at the output of the SSPA or the Band Pass Filter at 8.2 GHz**
- the fixed bit rate for the link**

The final BER performances are finally obtained by including the losses of the Band Pass filter in X Band (insertion losses and filtering losses) and the SSPA OBO value fixed for each test.



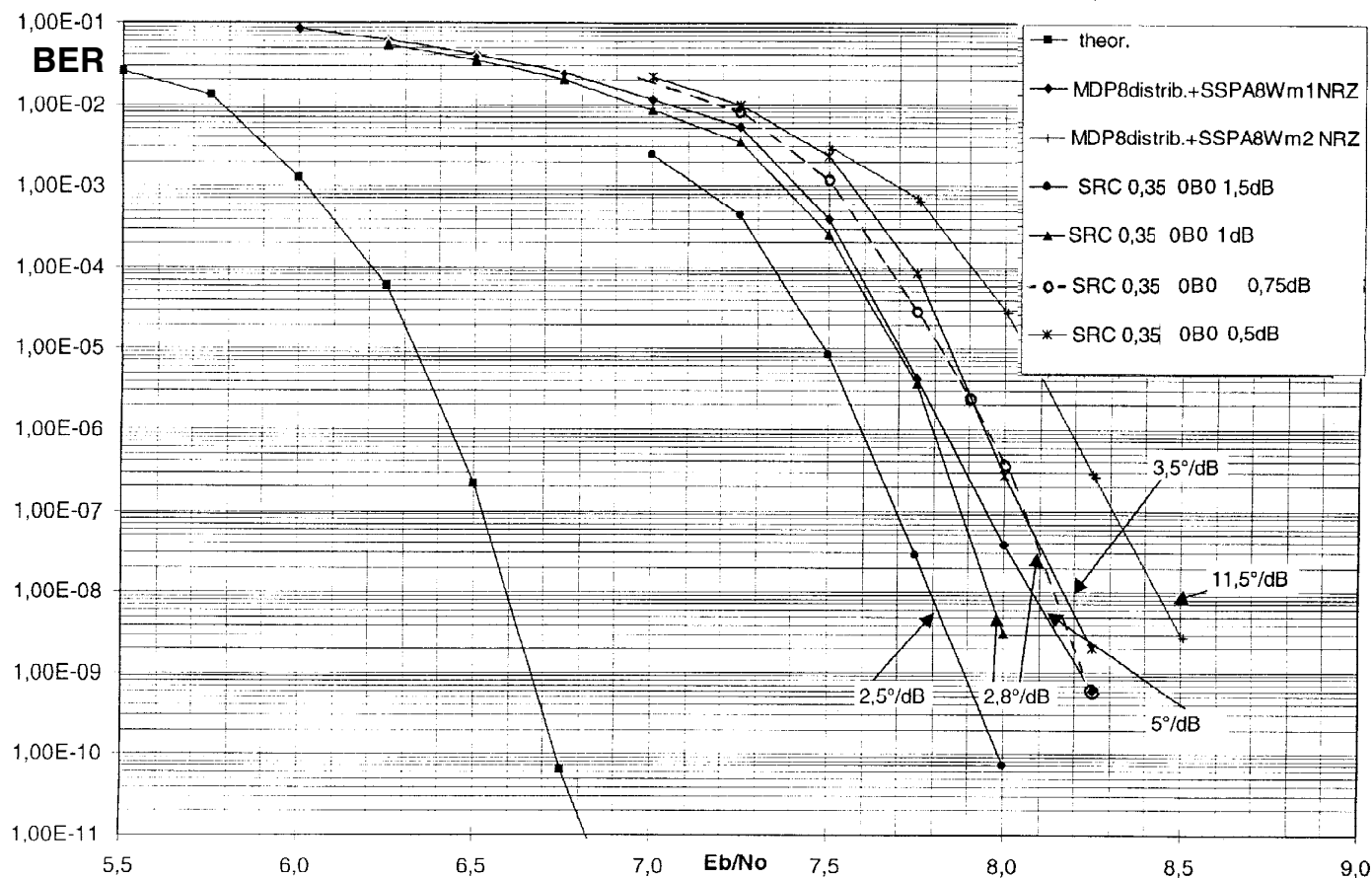
8 PSK Treillis Coded Modulation

AM/PM effect on BER for 4D/8-PSK TCM/RS @ 2b/s/Hz





AM/PM effect on BER for 4D/8-PSK TCM with RS code @ 2.5b/s/Hz





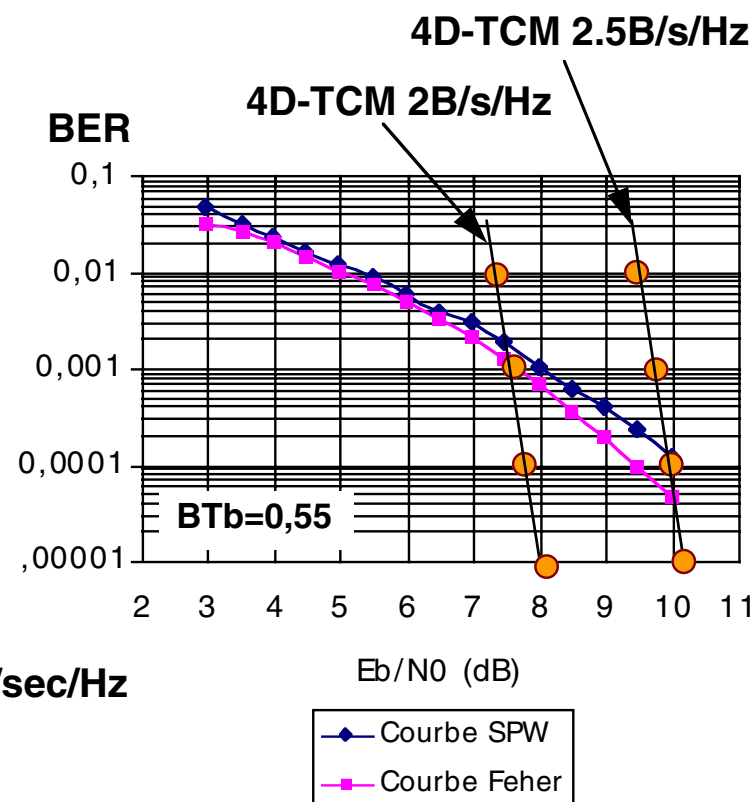
BER Performances of 4D-TCM/RS at 2 and 2.5 B/s/Hz Comparison with FQPSK-1 simulated results

TCM Modulation characteristics

- efficiency : 2 B/s/Hz or 2.5 B/sec/Hz
- waveform shaping: SRC /0,35
- OBO = 1 dB
- Output Filter with 1,2 dB total losses

FQPSK-1 Characteristics

- efficiency : 2 Bit/s/Hz
- BTb = 0,55
- Simulated BER or Feher results



➡ The gain of TCM modulation at 2 B/sec/Hz is significant under 10^{-3} for BER

➡ TCM performances take into account the OBO of the SSPA, the losses of output filter and an operational implementation



CONCLUSION (1)

- **The proposed modulation has been experimented at CNES these last years in the framework of an R&D action.**
- **The results and performances come from simulations and practical tests conducted on hardware developed for the circumstance. TCM ASIC was developed in 0.6 μ technology. The mapping on an updated technology is necessary.**
- **The proposed solution is based on a dedicated coder (optimum regarding the theoretical works of G.Ungerboeck, S.Pietrobon et.al.) but a pragmatic solution based on the CCSDS standard seems possible**
- **This modulation will be tested on the experimental satellite DEMETER in the next years for which a development is undertaken in the industry since the beginning of year 2000.**



Conclusion (2)

The proposed modulation:

- Allows the implementation of 4D-8PSK TCM with two efficiency at 2 or 2.5 B/symbol with CC R=3/4
- Provide good performances in terms fo BER
- Insure phase ambiguity resolution without the need of any "synchronisation word", as it is done in the DVB-DSNG Standard.
- Provides a good bandwidth efficiency based on Nyquist SRC filtering (roll-off of 0.35, or 0.25) for waveform shapping which remains compatible with the techniques used with QPSK modulation today
- Insures compatibility with non linear power channel amplifier like SSPA or TWT
- Insures compatibility with the SFCG template applicable to modulations higher than 2 Mbs/sec. This compatibility was verified with electrical tests
- Allows possible use of standard CMOS technology for up to 100 to 125 Mb/s (depending of efficiency)
- Is compatible with an RS outer code which significantly improve the performances of the link at the cost of a reasonable loss of efficiency.



Conclusion (3)

- **Complementary simulations and/or tests are necessary to check for the performances of this modulations with the punctured "pragmatic" 7-1/2 convolutional coder/decoder in lieu of the dedicated solution. This work is engaged at CNES today. Results will be available in the next months.**
- **The pragmatic solution will give probably good results in terms of BER performances, but the rotational invariance capability must be demonstrated.**
- **A "Very Preliminary" Draft White Book describing this technique is proposed to the CCSDS for standardisation with the two options concerning the convolutional code.**

[This page intentionally left blank.]

Spectral Regrowth Test Data for SRRC 8 PSK Modulation Passed Through an SSPA in Saturation

Don Olsen and Jerry Michaelson

The Aerospace Corporation
Communication Systems Subdivision

Presented to CCSDS P1E
Modulation and Frequency Subpanel

11 May 2000

Objective

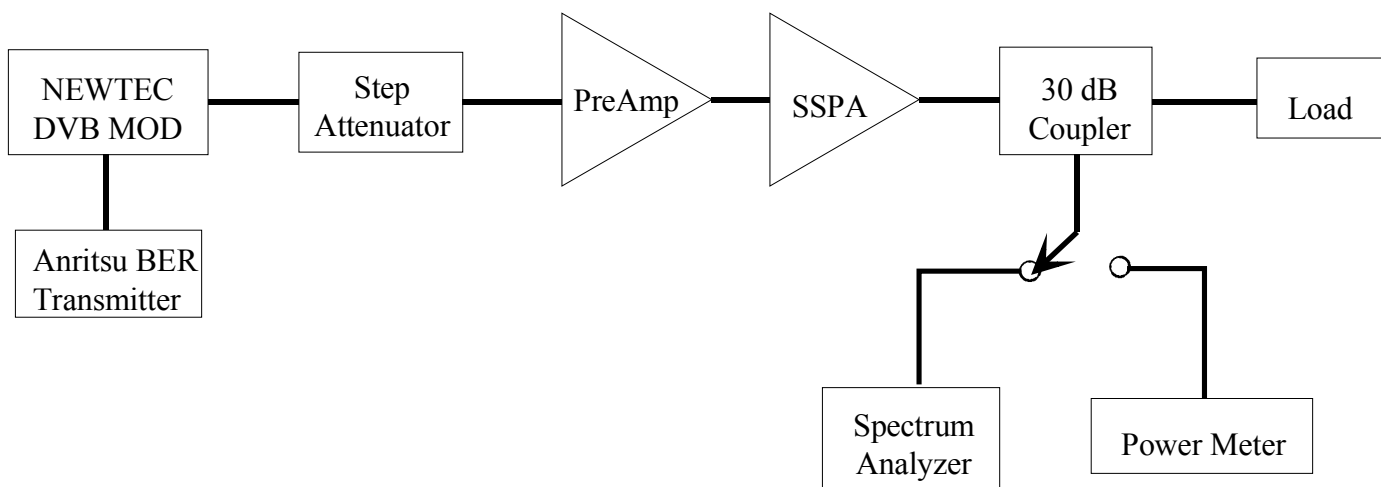
- Investigate the impacts of a non-linear power amplifier on the spectral regrowth of filtered 8-PSK using Square-Root Raised Cosine (SRRC) as the shaping filter:
 - Roll-off factor = 0.25 (Satellite News Gathering (SNG)¹ Standard Waveform uses 0.20)
 - Roll-off factor = 0.35 (Standard DVB² Waveform)

- 1 European Telecommunications Standards Institute (ETS) EN 301 210
- 2 ETS 300 421

Test Conditions

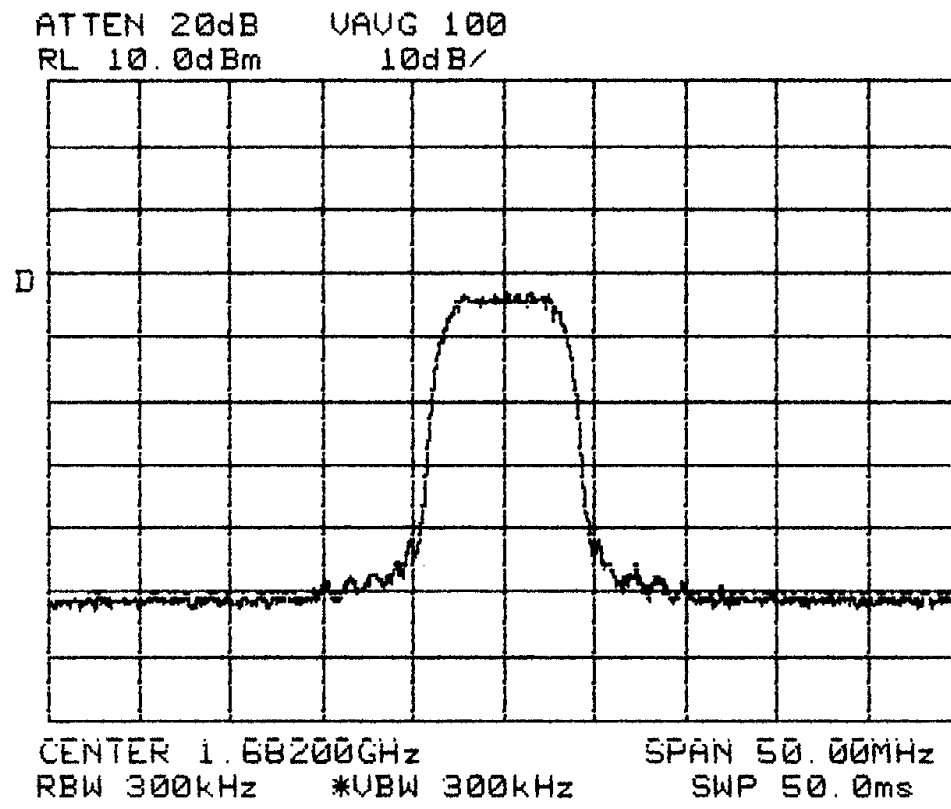
- **Signal Source: Newtec Model NTC/2080 Modulator**
- **Carrier Frequency: 1682 MHz**
- **Symbol Rate = 6.136 Ms/s**
- **Modulation: DVB 8-PSK Waveform with SRRC shaping filter:**
 - Roll-off factor=0.25 and 0.35 (DVB standard)
 - Coding: concatenated coding scheme:
 - Inner code: Convolutional code, rate=8/9
 - Outer code: Reed-Solomon code: RS(188/204)
- **High Power Amplifier(HPA): Solid State Power Amplifier(SSPA):**
 - 1 Watt MiniCircuits ZHL42 driven by Minicircuits ZFL2000

8 PSK Spectral Regrowth Test Configuration

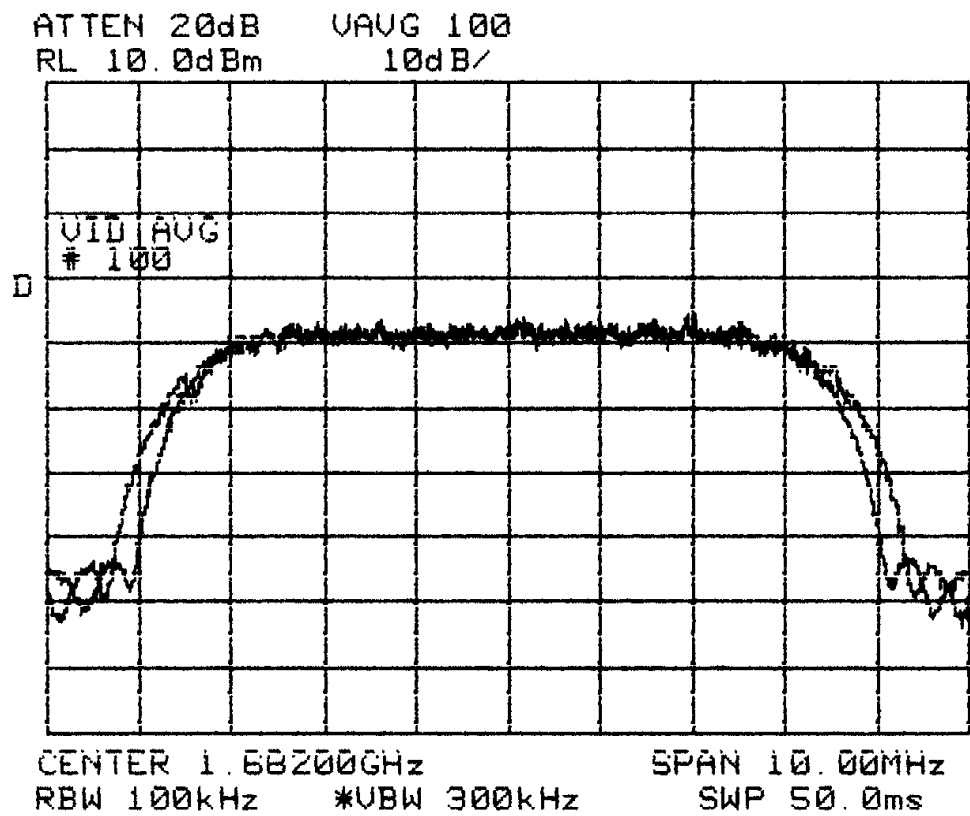


Test Cases

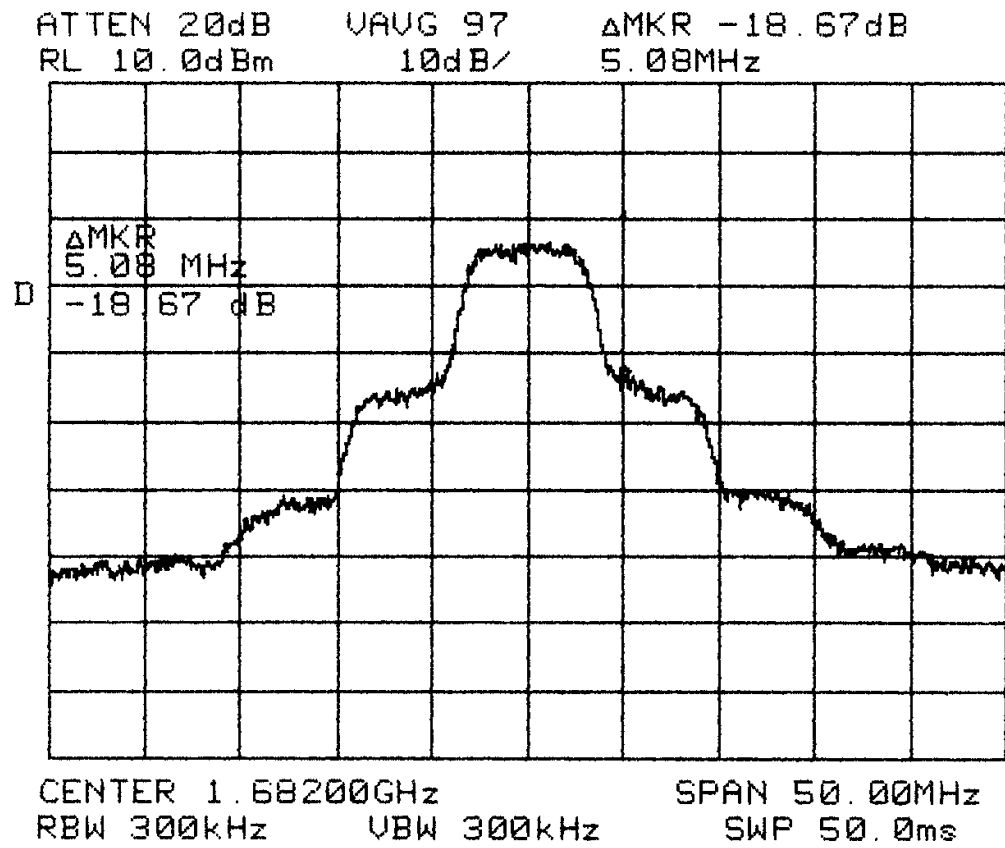
- **Saturated HPA:**
 - Roll-off Factor=0.25
 - Roll-off Factor=0.35
- **Back-off HPA for roll-off factors of 0.25 and 0.35:**
 - 1 dB back-off
 - 2 dB back-off
 - 3 dB Back-off
 - 10 dB back-off
- **Scales for spectrum plots**
 - X-Axis: Frequency in MHz, 5 MHz/division
 - Y-Axis: Power in dBm, 10dB/division



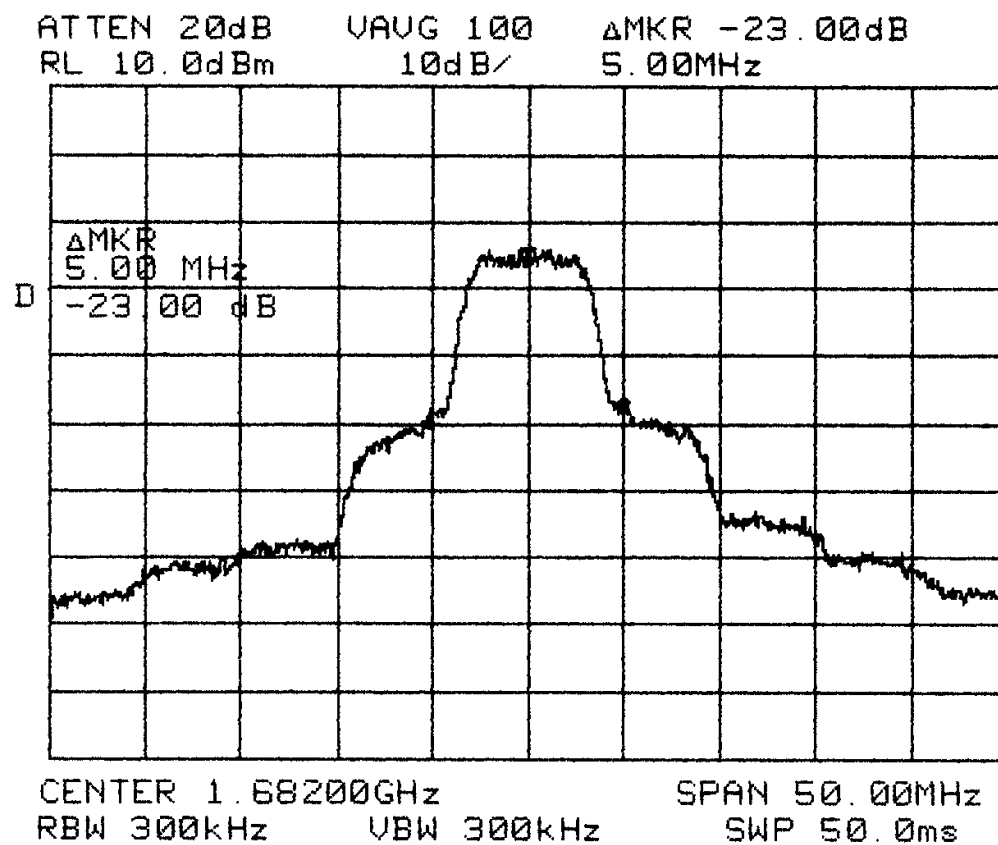
Input Spectrum Roll-off = 0.35



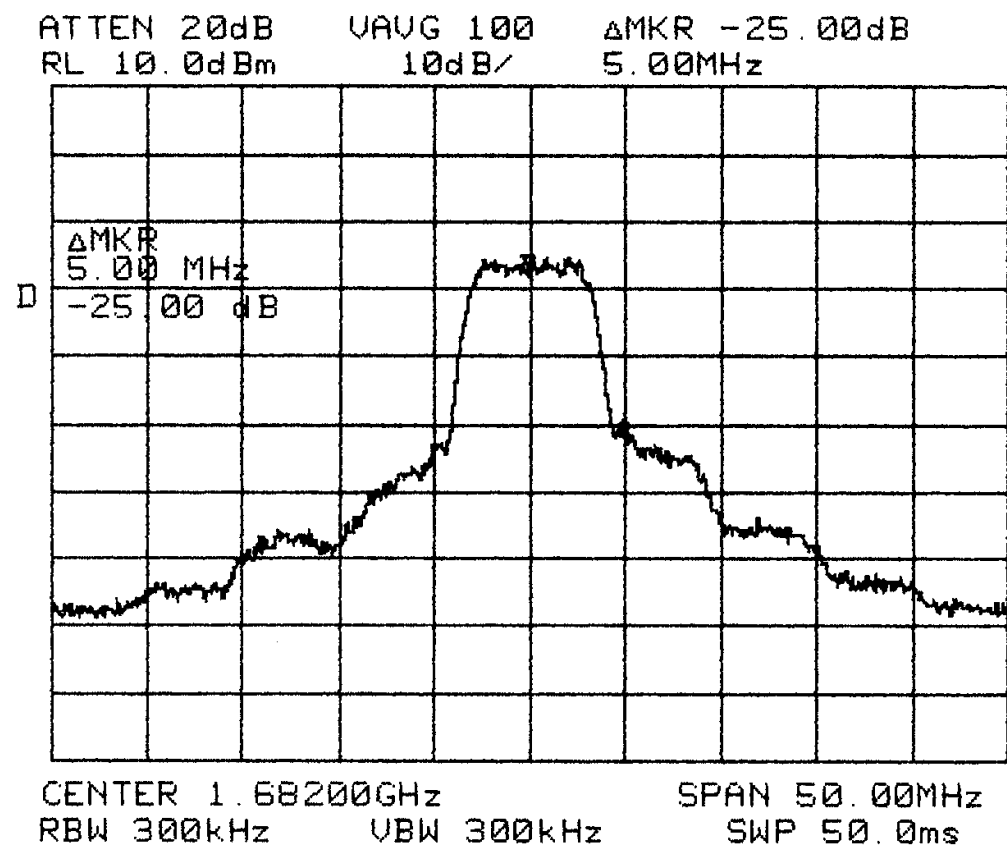
Input Spectrum 0.25 and 0.35 Roll-off



Saturated Amplifier Roll-off = 0.25



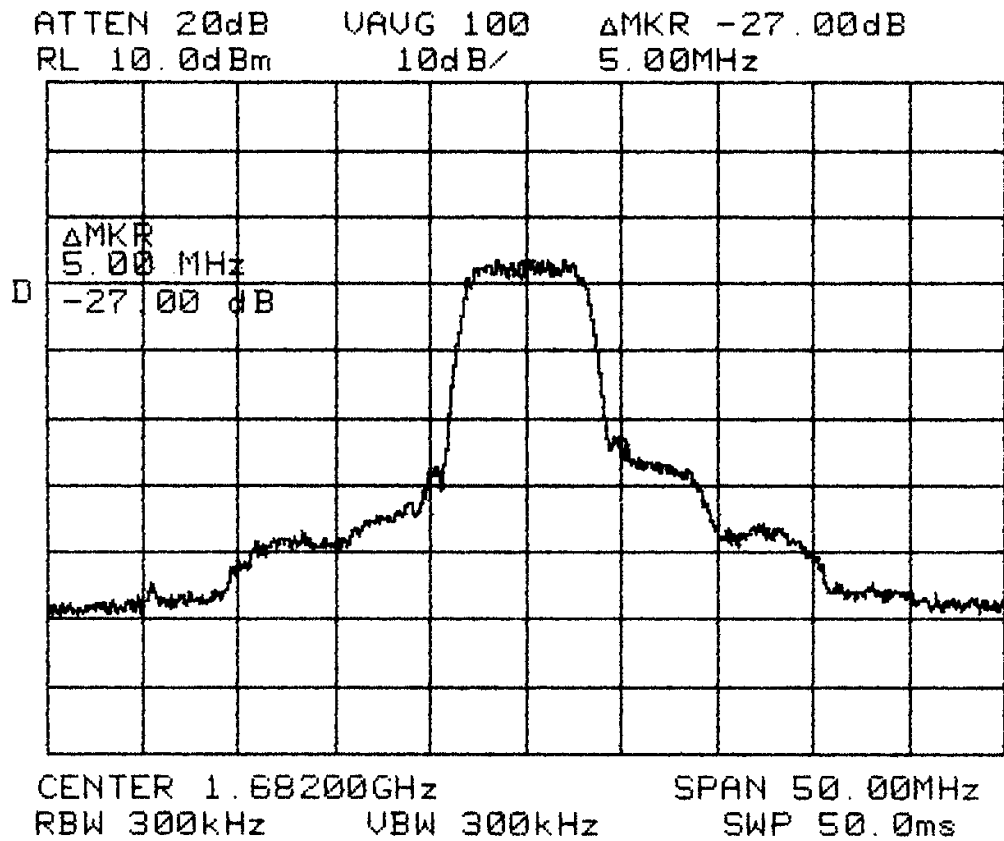
1 dB Backoff Roll-off = 0.25



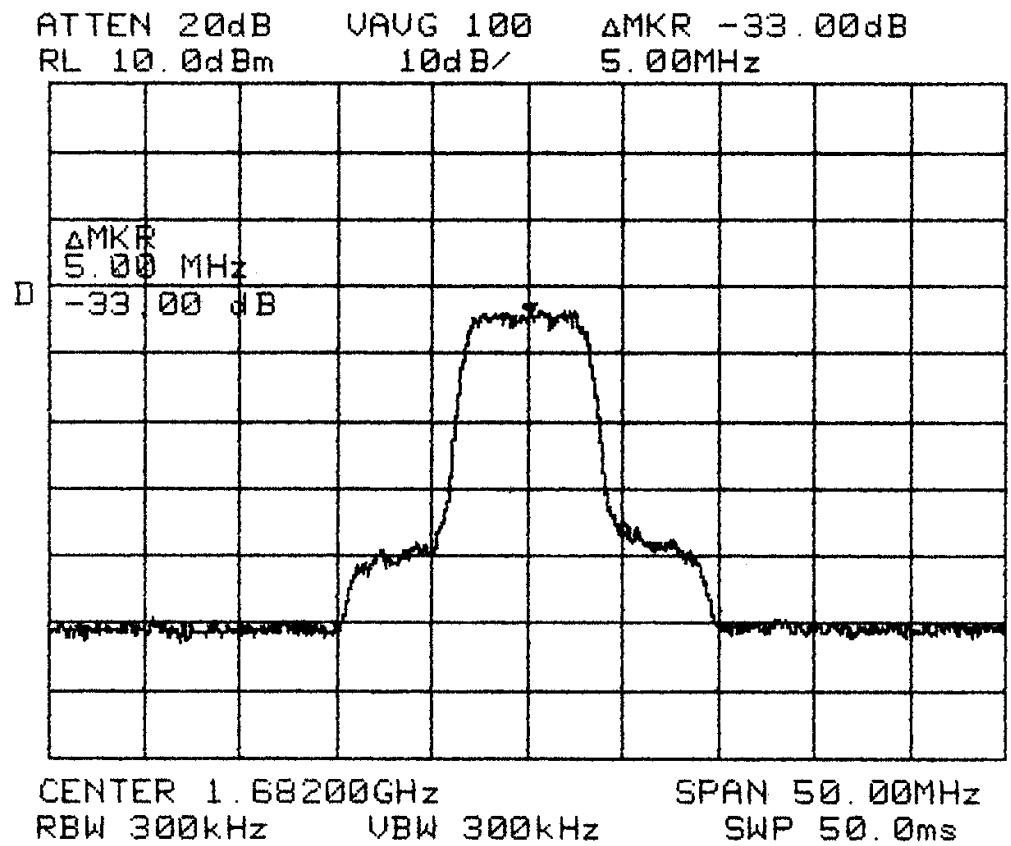
88

2 dB Backoff Roll-off = 0.25

88

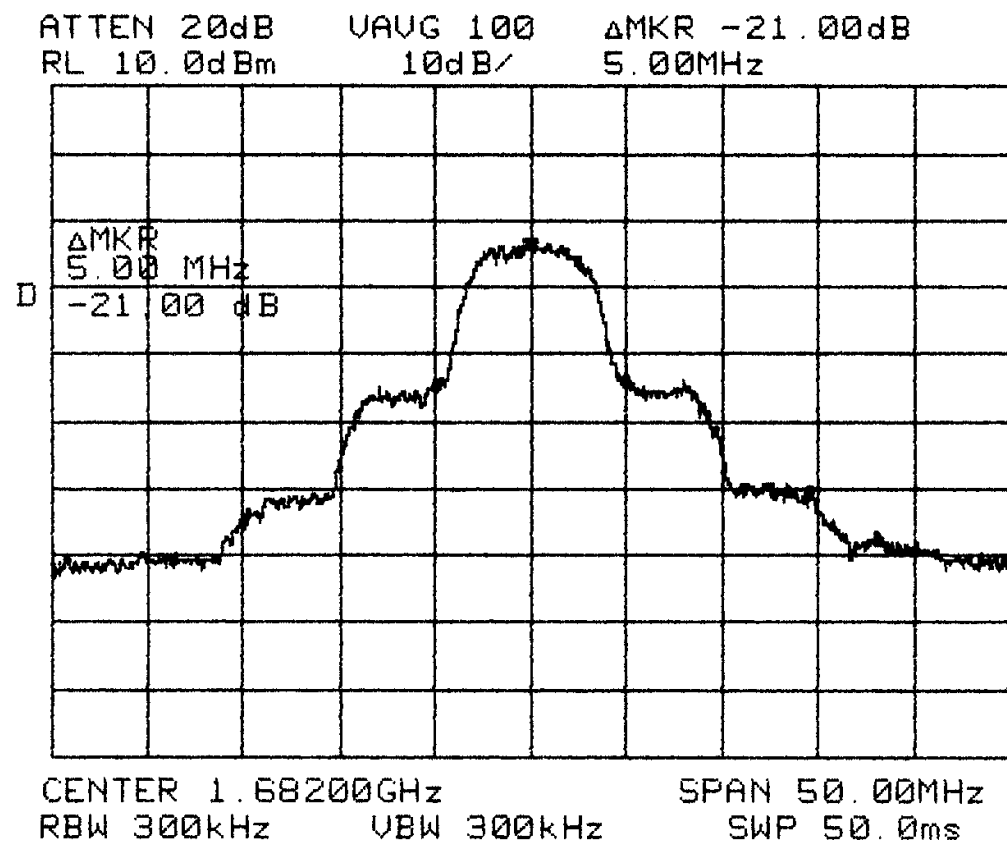


3 dB Backoff Roll-off = 0.25



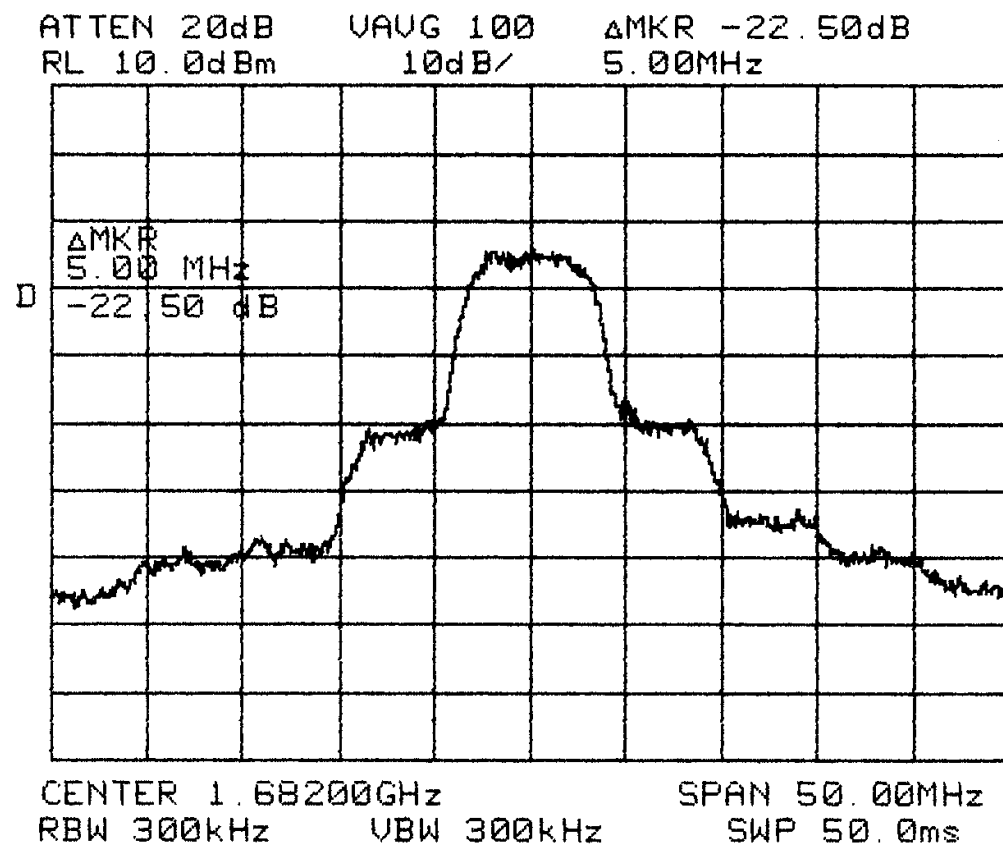
88

10 dB Backoff Roll-off = 0.25



88

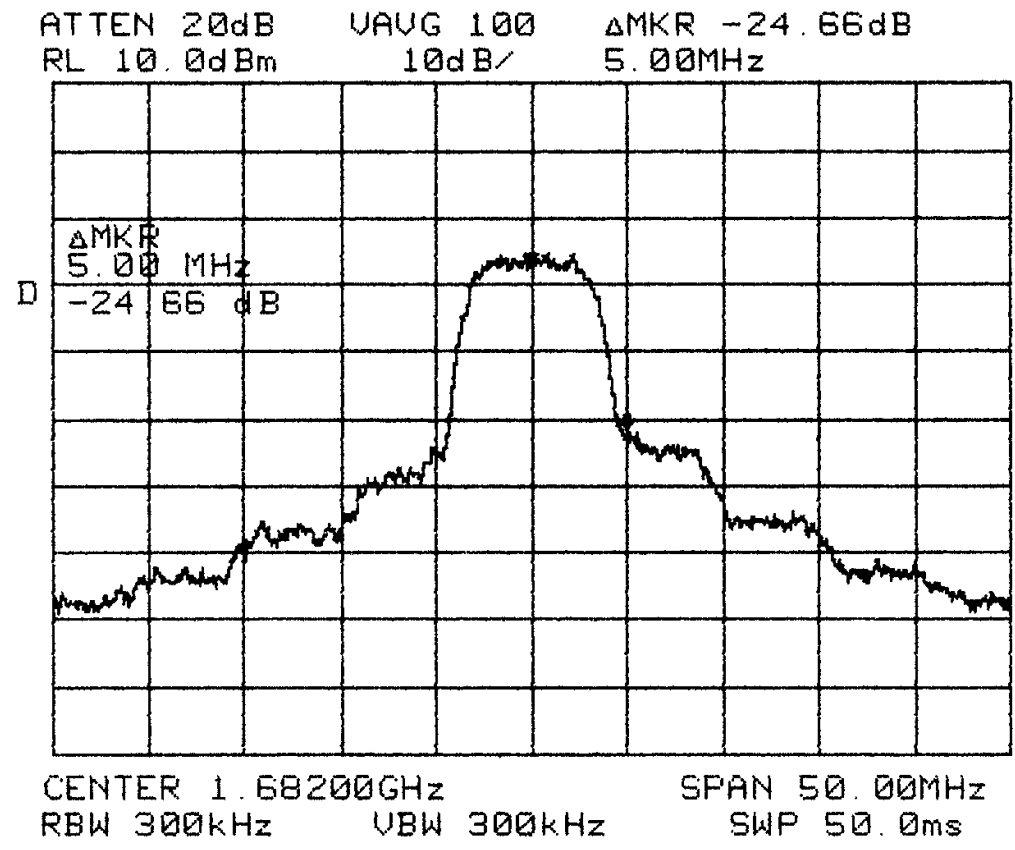
Saturated Amplifier Roll-off = 0.35



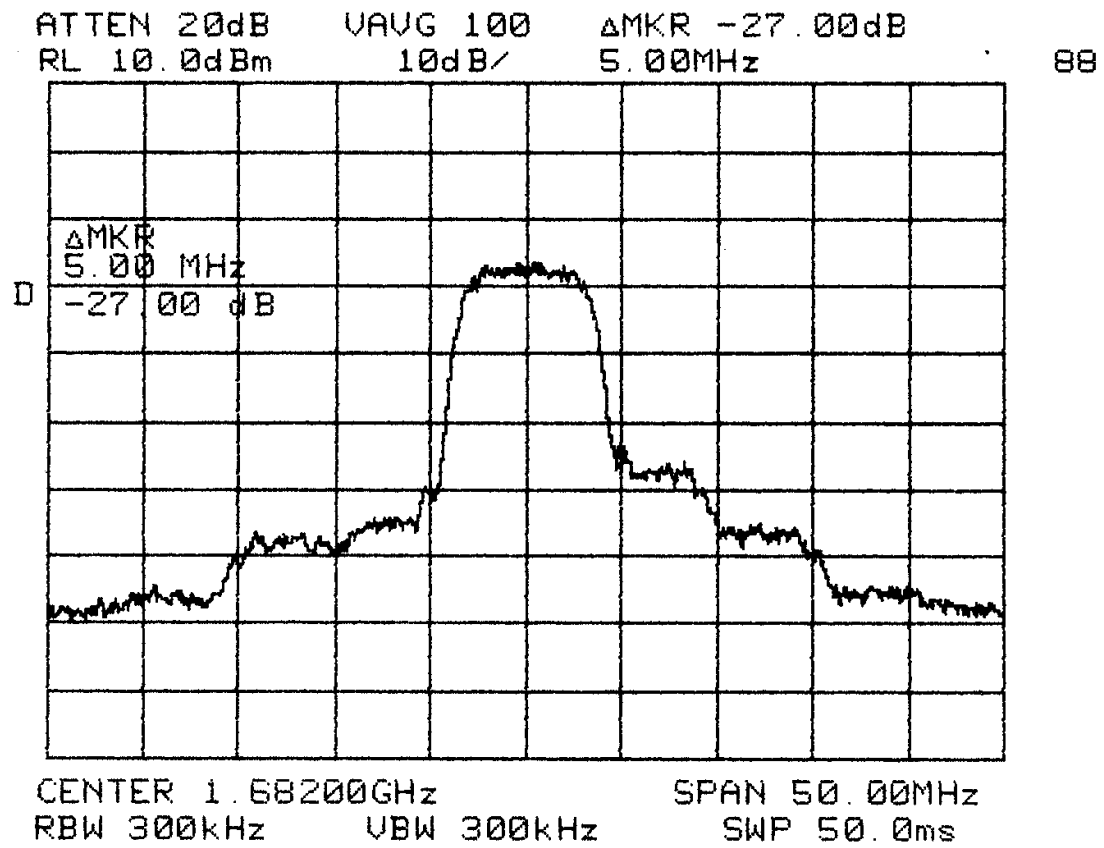
88

1 dB Backoff Roll-off = 0.35

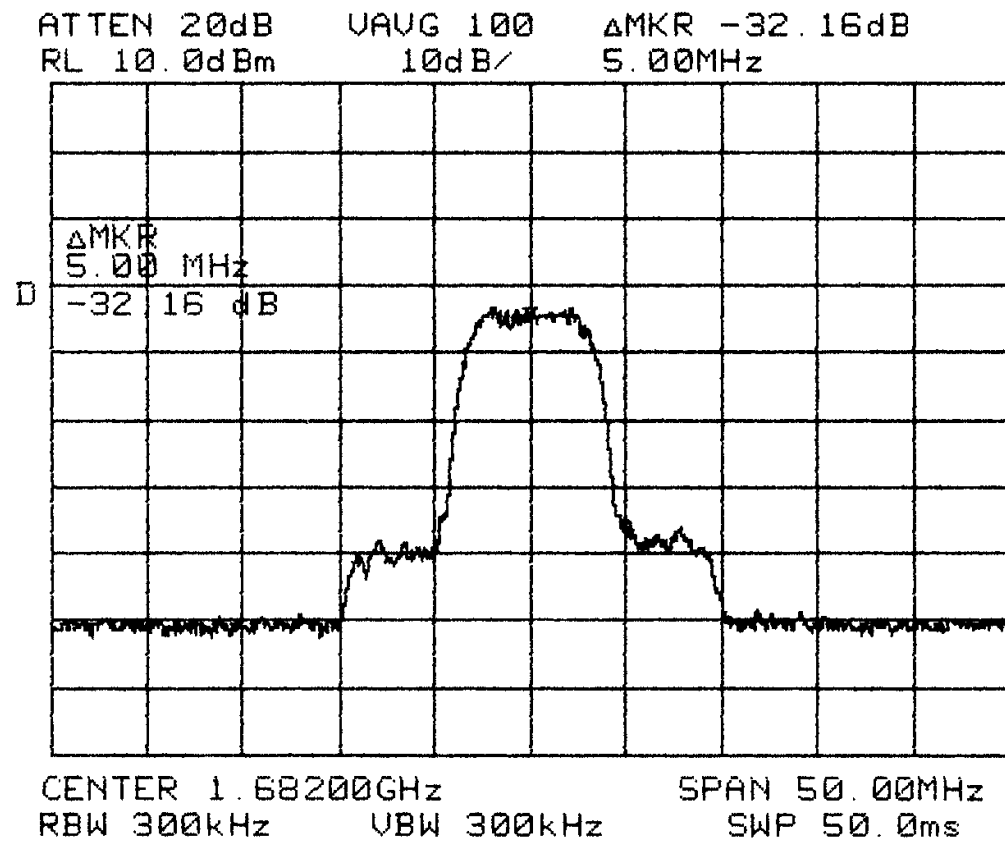
88



2 dB Backoff Roll-off = 0.35

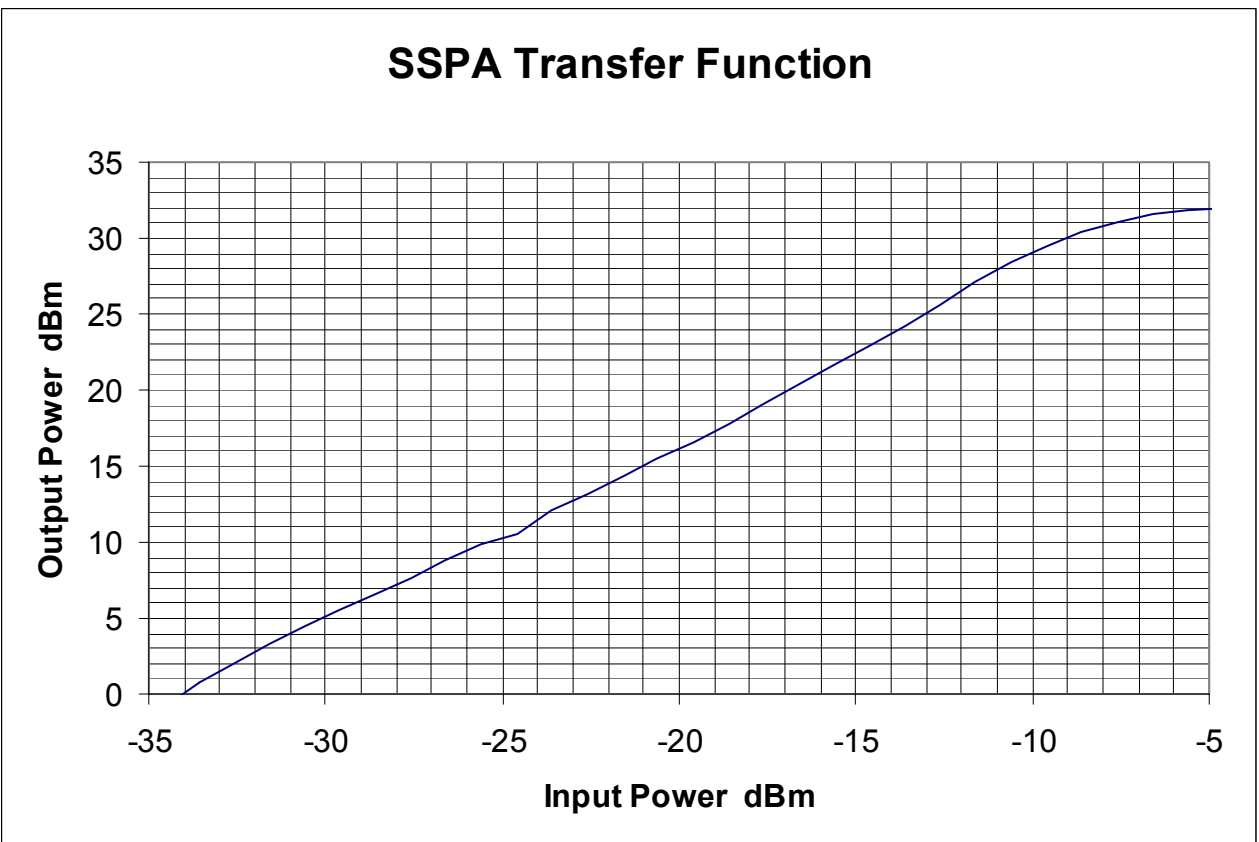


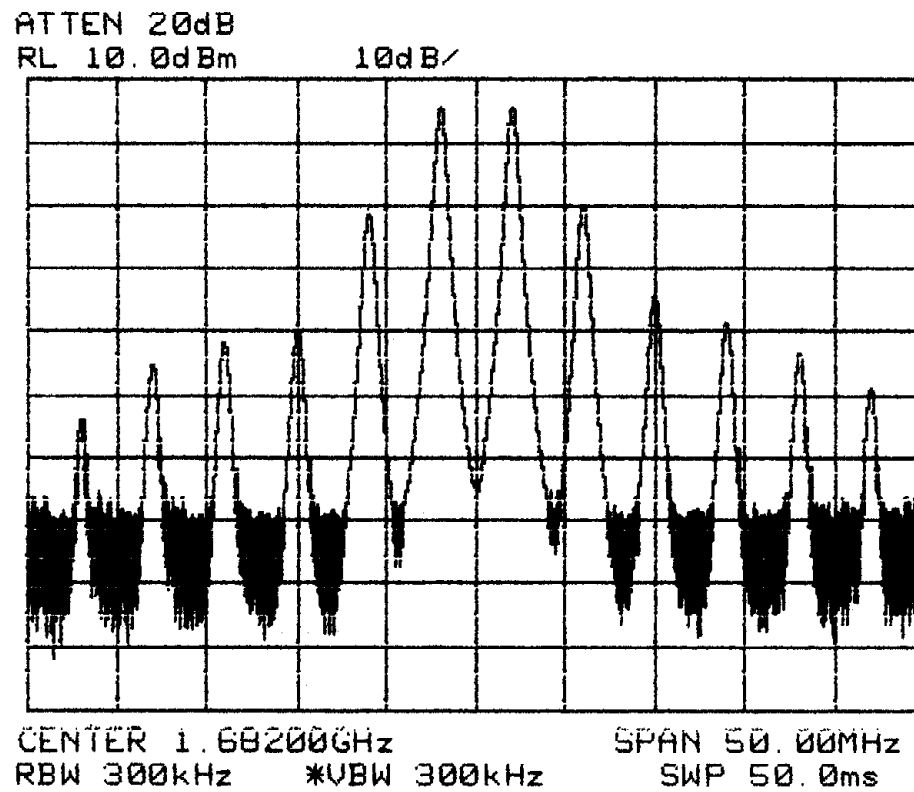
3 dB Backoff Roll-off = 0.35



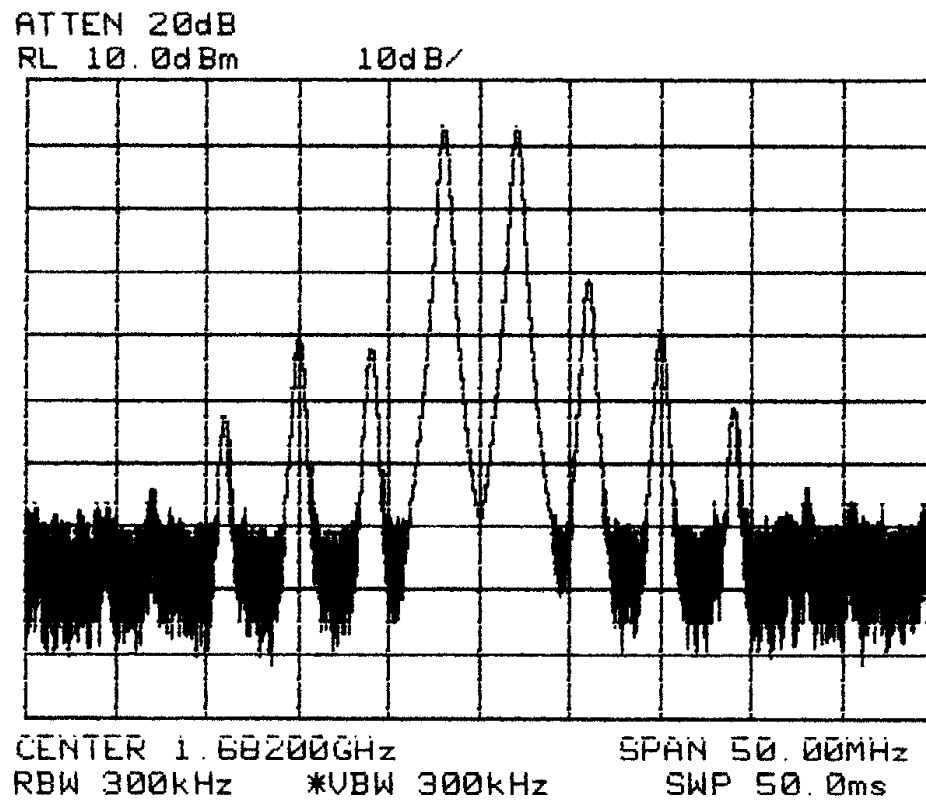
88

10 dB Backoff Roll-off = 0.35





2-Tone Intermodulation Products Saturated Amplifier



2-Tone Intermodulation Products
3 dB Backoff

Summary

- **HPA Back-off reduces spectral regrowth at 5.08 MHz from center frequency**
 - **For 0.35 SRRC filter: Saturated spectral level is 21.0 dB below peak**
 - 1 dB back-off: Spectral regrowth reduced by 1.5 dB
 - 2 dB back-off: Spectral regrowth reduced by 3.7 dB
 - 3 dB back-off: Spectral regrowth reduced by 6.0 dB
 - 10 dB back-off: Spectral regrowth reduced by 11.2 dB
- **Severe filtering produces larger spectral regrowth**
 - **For 0.25 SRRC filter: Saturated spectral level is 18.7 dB below peak**
 - 2.3 dB more regrowth than with 0.35 SRRC filter

Conclusions

- **Saturated amplification of amplitude variations of SRRC leads to raised sidebands**
- **3 dB backoff is needed for 35 dB sideband control**
- **Large dynamic range of adjacent signals may require greater backoff**
- **SRRC 8-ary PSK modulation can be effective in maximizing bandwidth efficiency**
- **When class C power efficient power amplifiers are used for space applications SRRC 8-ary PSK modulation is not recommended**

Spectral Regrowth Test Data for SRRC 8 PSK Modulation Passed Through an SSPA in Saturation

Don Olsen , Albert Leong and Walter Johnson

**The Aerospace Corporation
Communication Systems Subdivision**

**Presented to CCSDS P1E
Modulation and Frequency Subpanel**

**October 2000 Meeting
Toulouse France**

Subjects for this Presentation

- **Improved Amplifier Configuration over April 2000 briefing**
- **Reduced Saturated Gain Transfer Characteristic anomalies**
- **Provides Power Spectral Density Measurements**

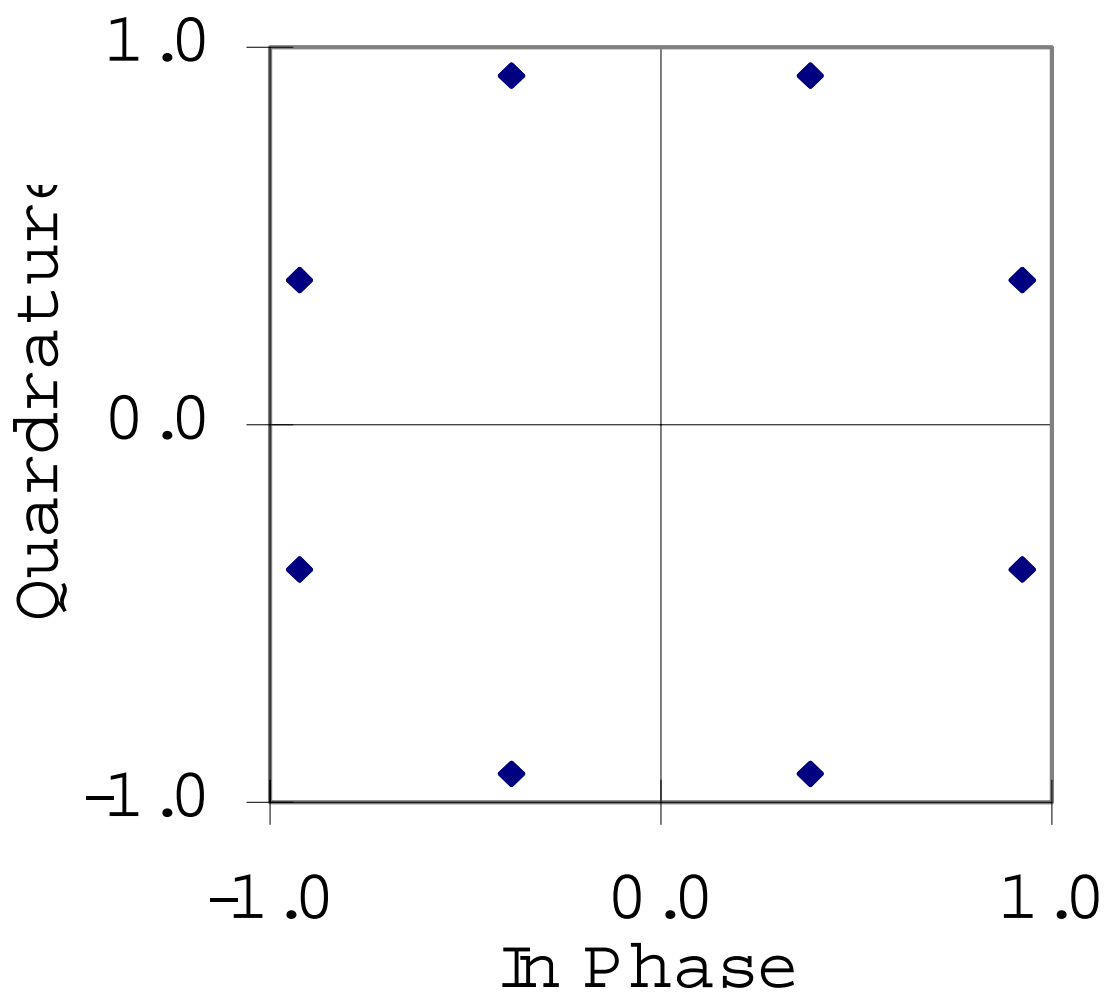
SRRC Filter Properties

- **Square Root Raised Cosine waveforms**
 - Near Nyquist pulse shaping
 - 6 tap FIR approximation to a truncated $\sin(X)/X$ shape
 - Linear modulated prior to carrier modulation
- **Approximates a brick wall bandpass filter**
 - Limit due to demodulator eye closure and tracking difficulties
- **width of transition region controlled by α factor**
 - $\alpha = 0.35$ and 0.55 used herein
- **Center to center channel spacing**
 $(1+\alpha)R_d / m$
- **R_d is the coded data rate (as applicable)**

SRRC 8-ary PSK Properties

- **m = 3 modulation bits per symbol**
- **Nyquist pulse shaping provides steepest spectrum transition**
- **Has a non-constant envelope waveform because of the SRRC filter and thus requires linear amplifiers thereafter to avoid spectral regrowth**

8-ary PSK Constellation

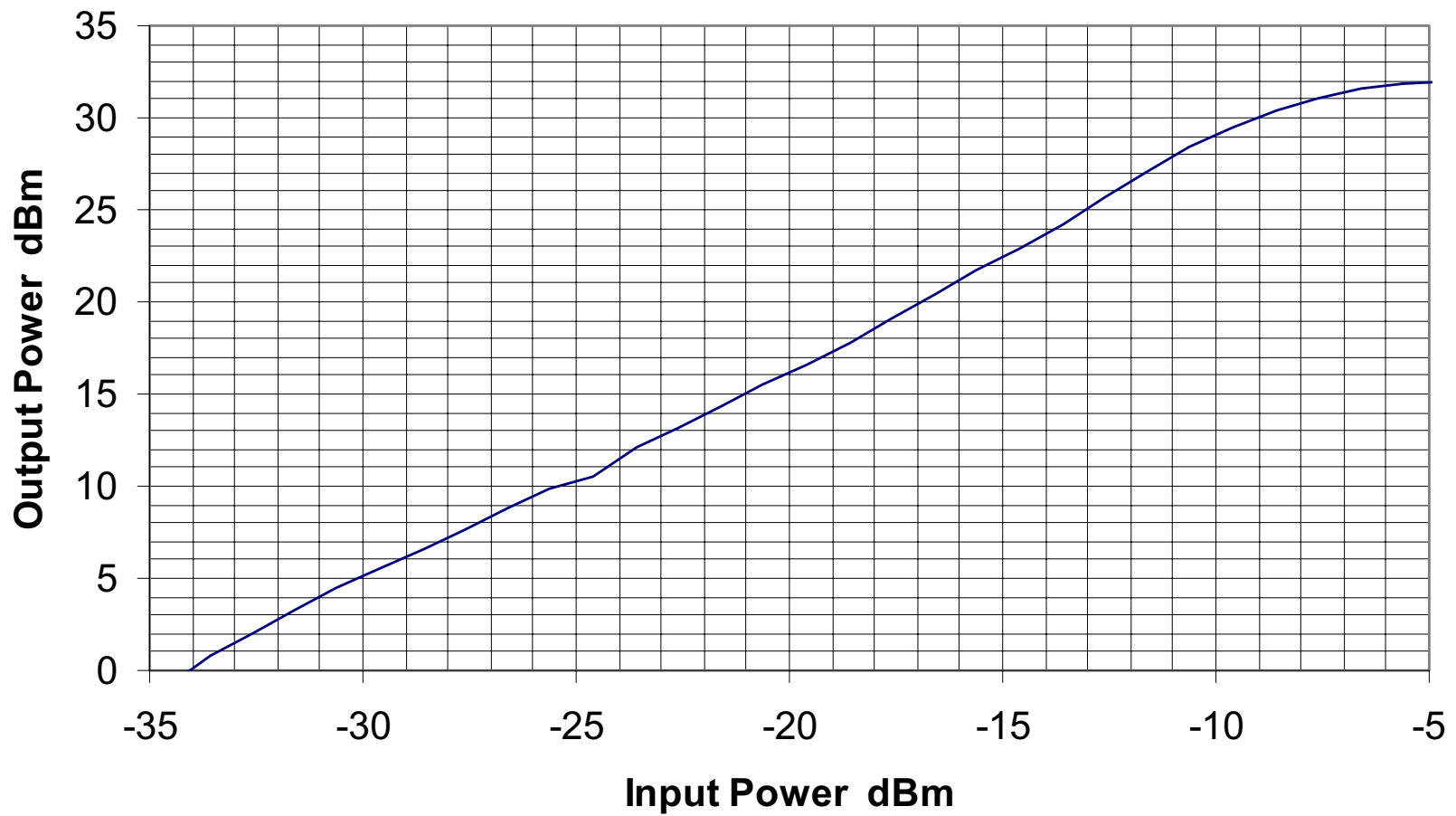


Measured Data

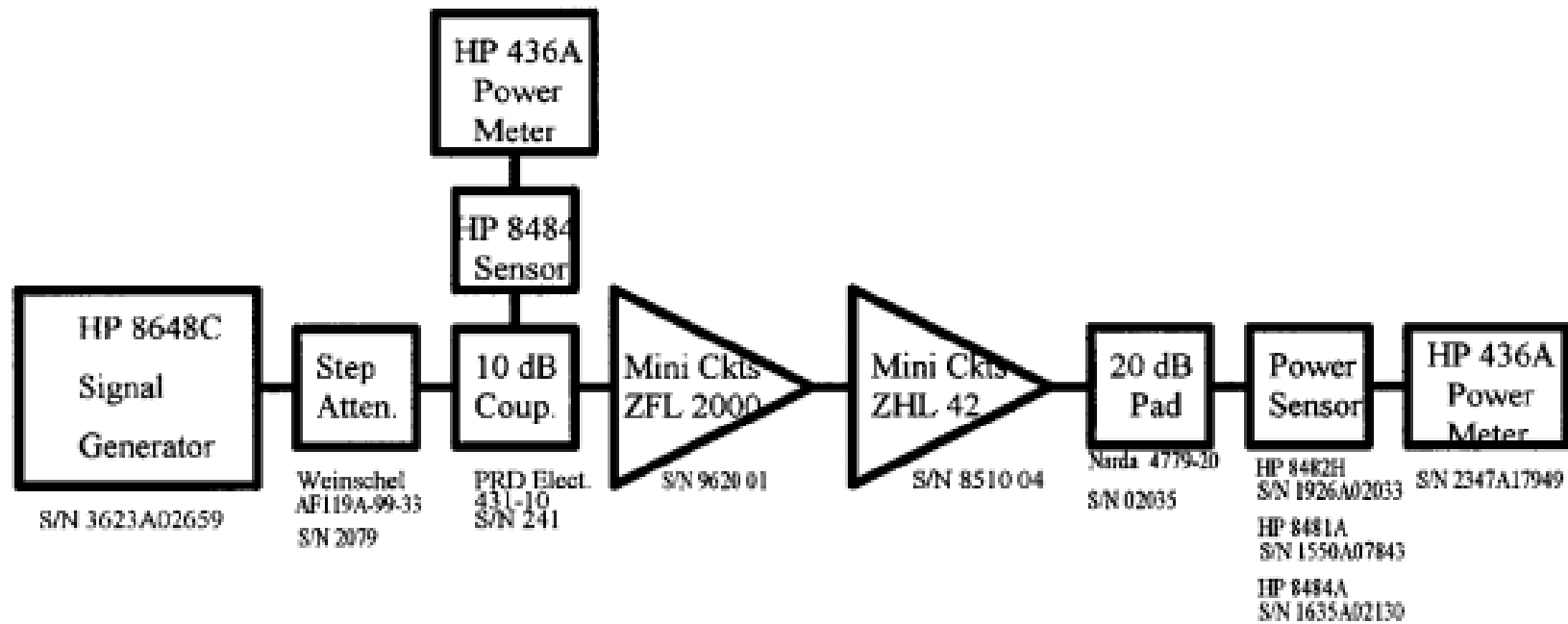
Amplifier Setup Improvements

- **Amplifier input continuously monitored through a 10 dB coupler for accuracy**
- **20 dB pad isolates the amplifier output from the power and spectral measuring equipment**
- **Power meter scale change errors compensated**
- **Preamplifier operating points set well within their saturation levels**

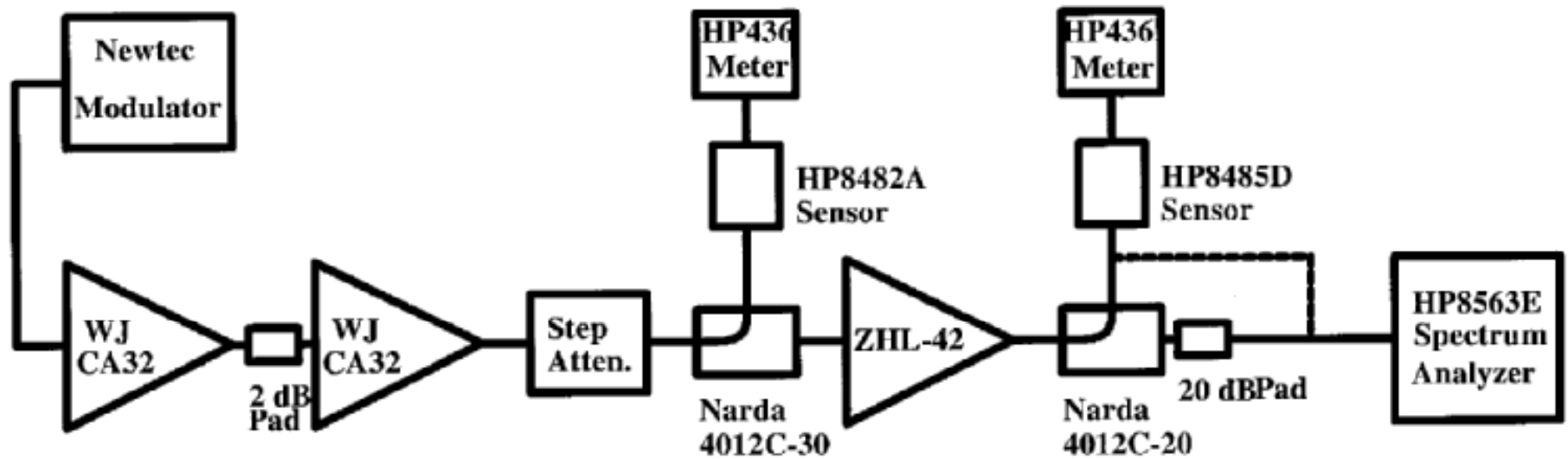
Former SSPA Transfer Function



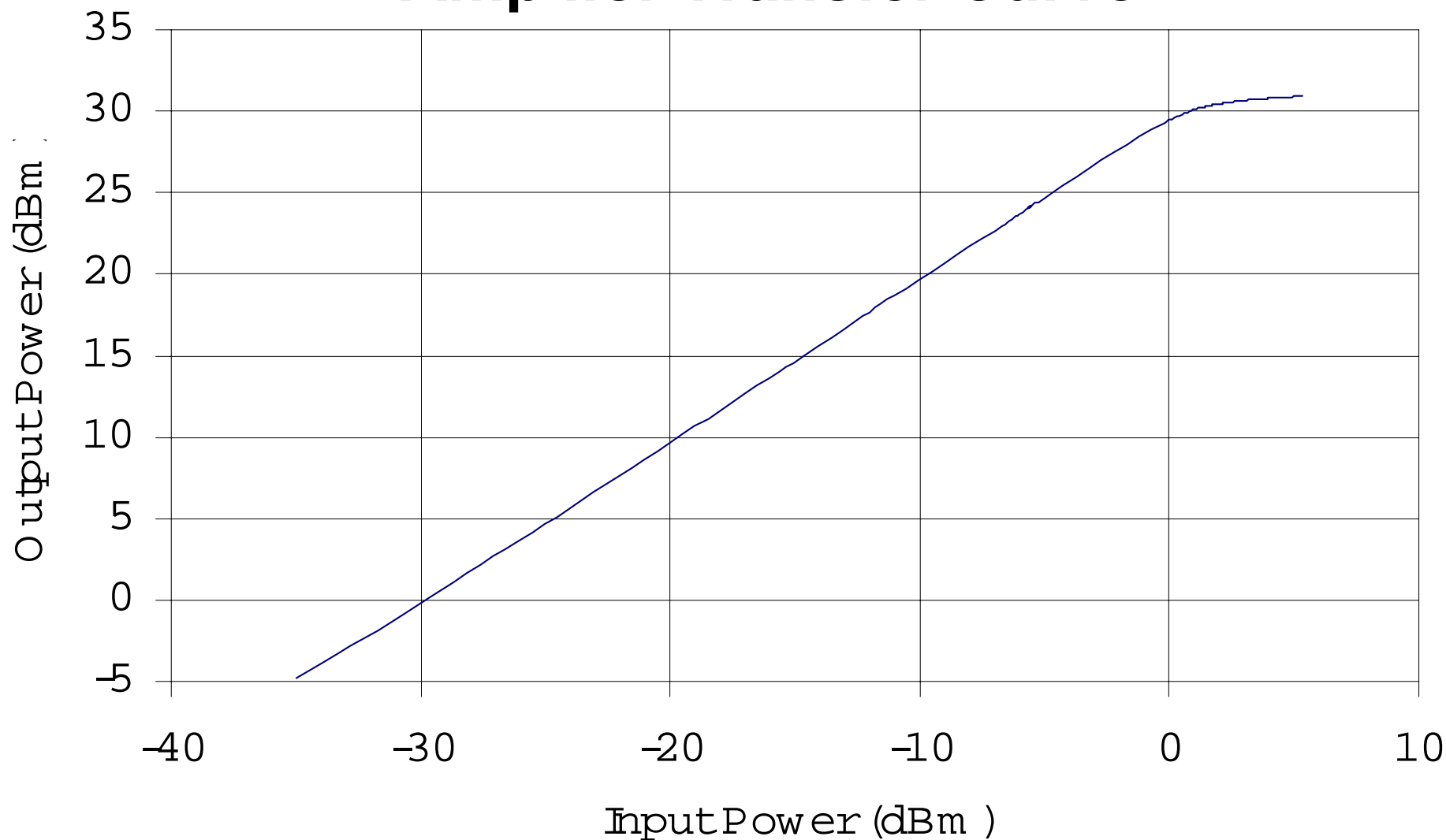
Gain Transfer Test Configuration



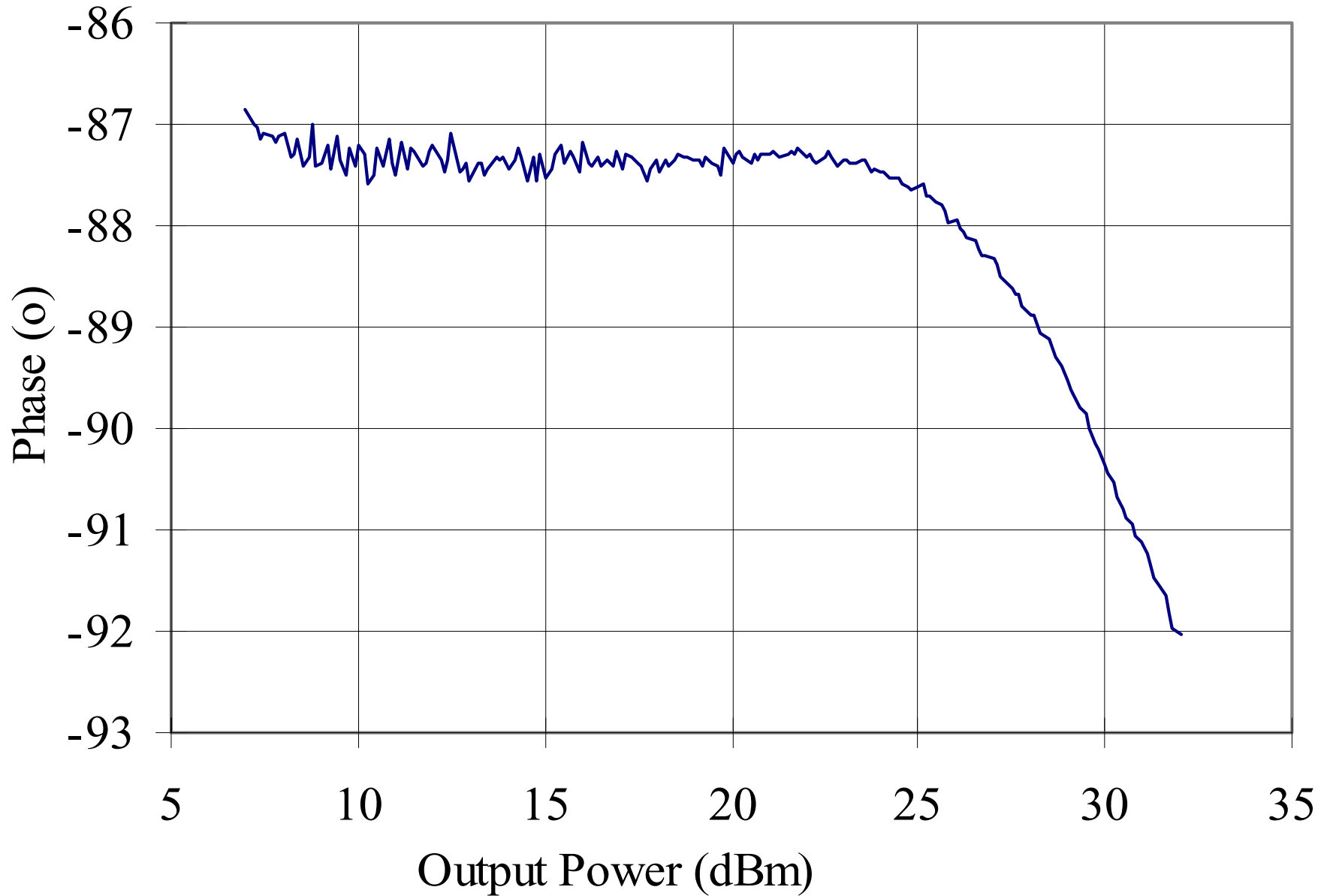
8PSK Spectral Regrowth Test Configuration



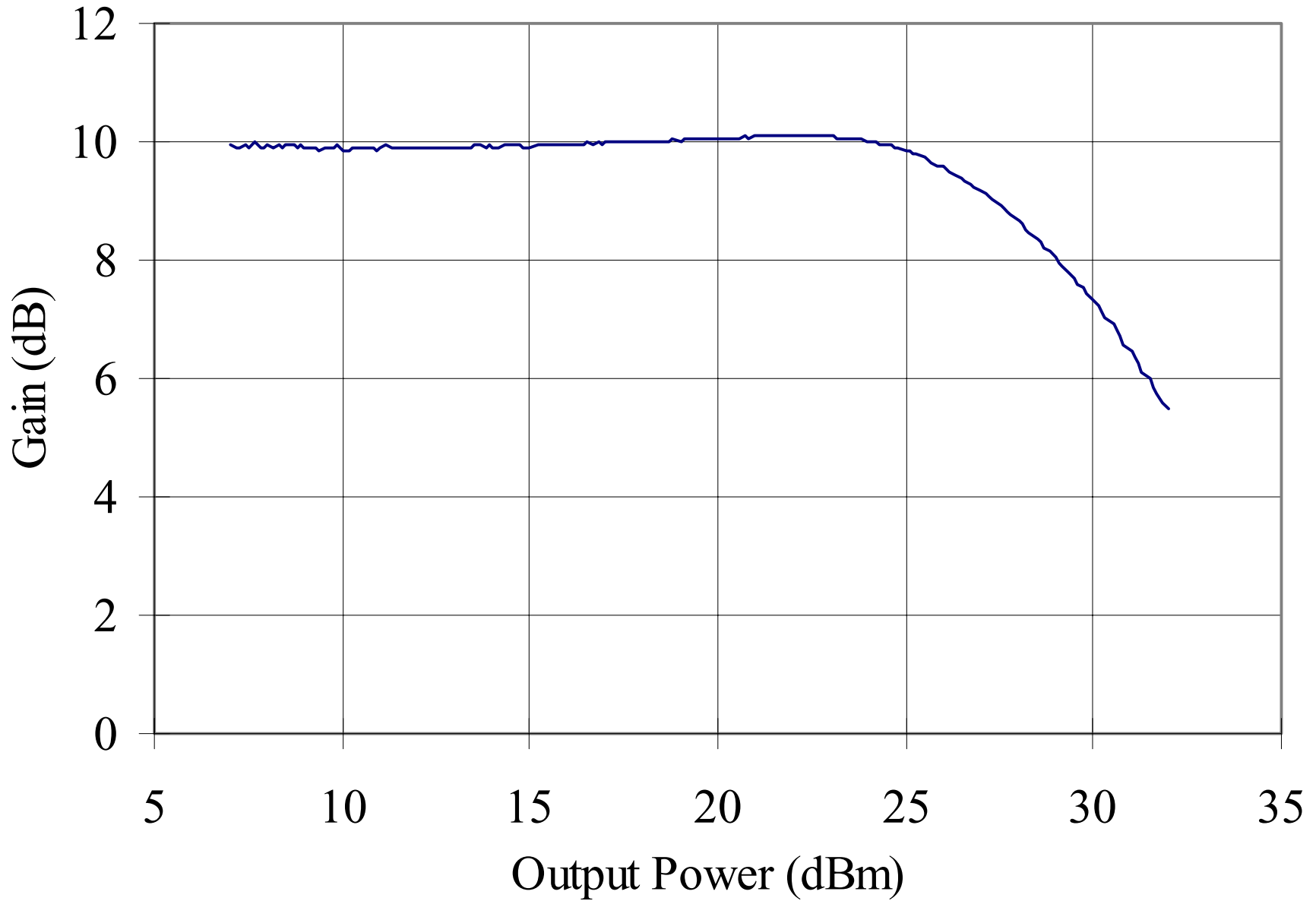
MiniCircuits ZHL-42 Nominal 1.0 W Amplifier Transfer Curve



SSPA Saturation Characteristic AM to PM



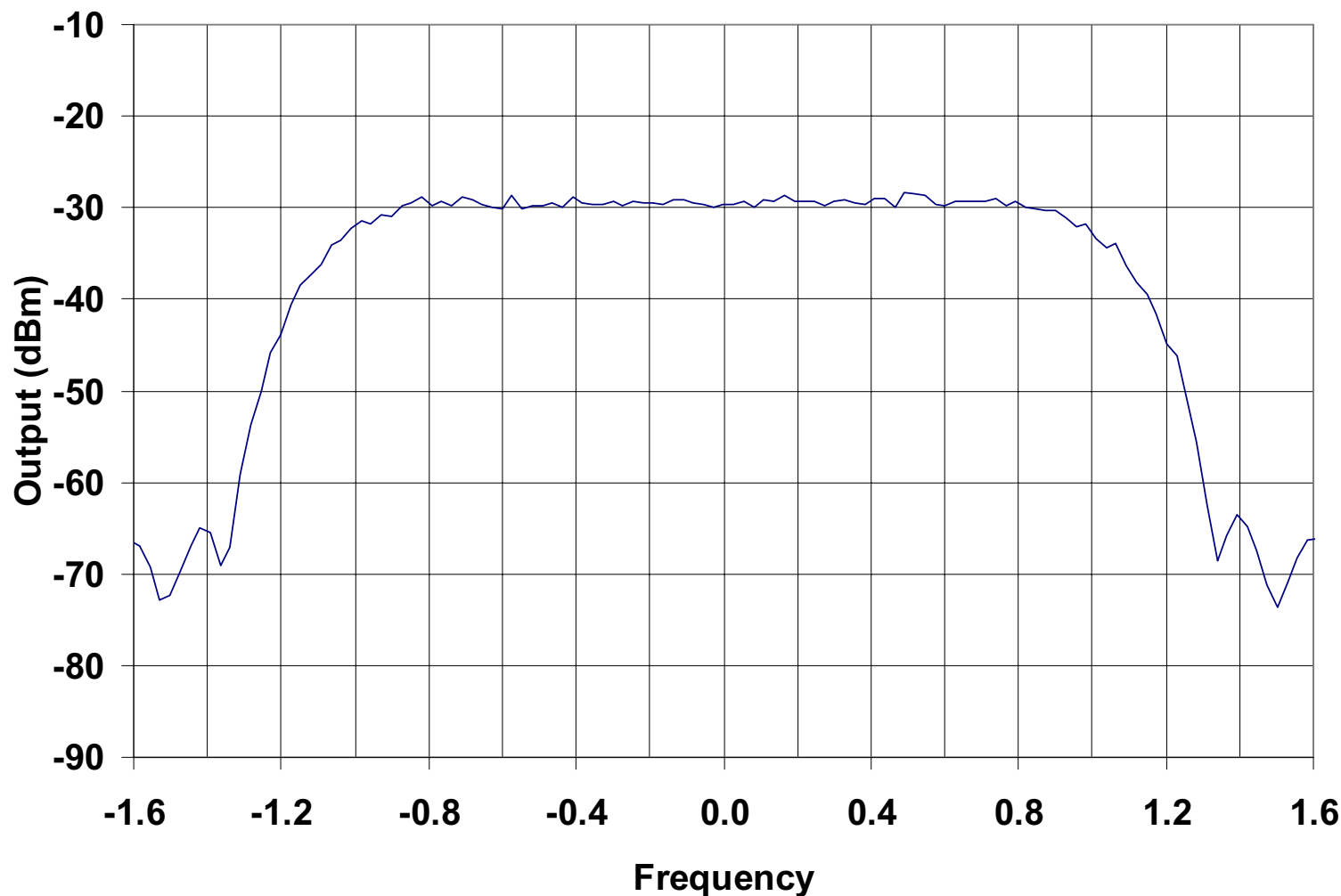
SSPA Saturation Characteristic AM to AM



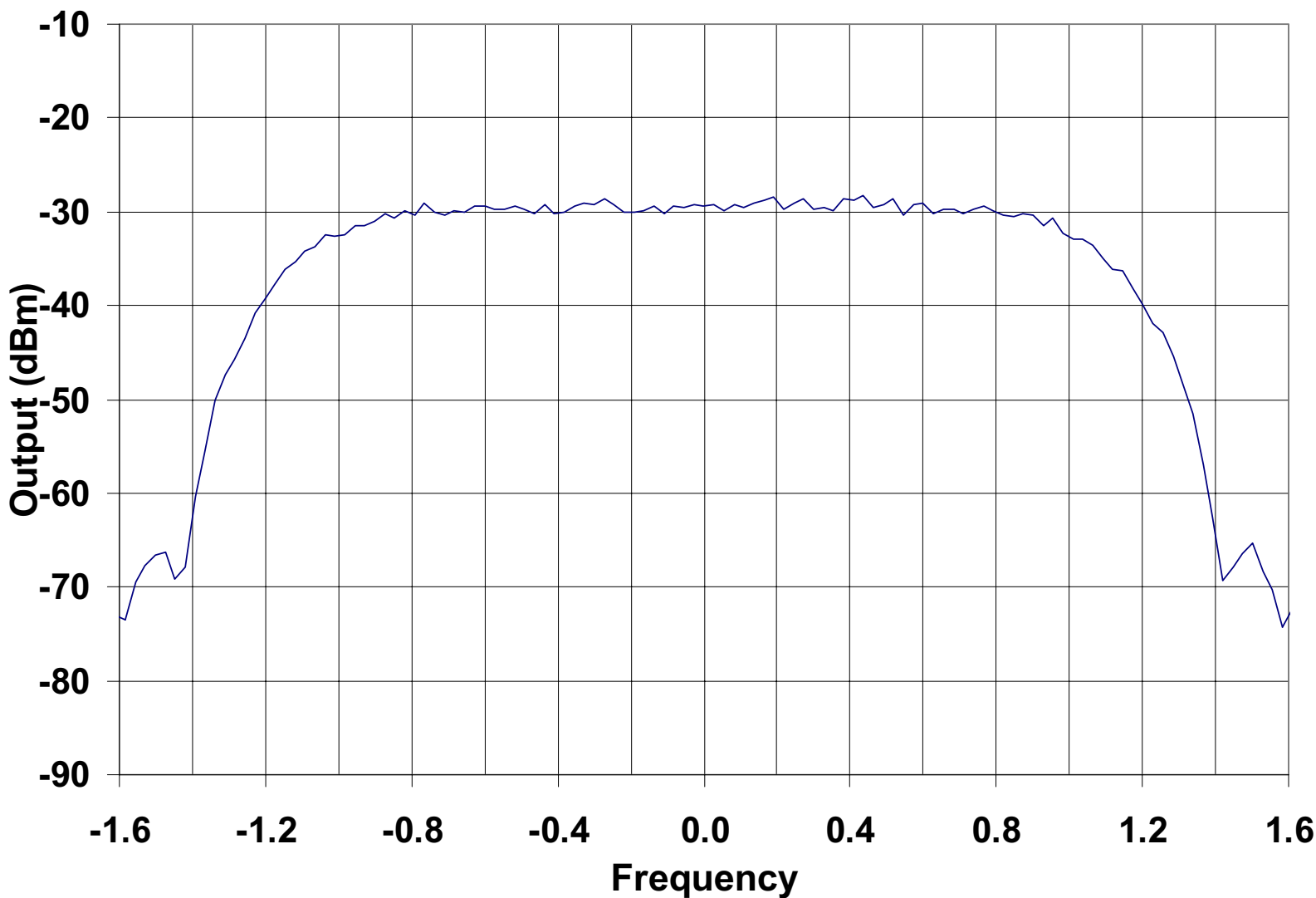
Power Spectral Density Charts

- **Newtec parameters (concatenated code used)**
 - 15 Mbps user data rate, 8-ary PSK modulation
 - α values of 0.35 and 0.55 used
 - These correspond to Newtec modes of 0.25 and 0.35 bandwidth expansion for 26 dB down points
- **Power Amplifier output set relative to saturated level**
- **First chart of the series for each α value shows modulator output with full saturation**
- **The other cases for output power are at levels of**
 - -1, -2, -3, -4, -5, -6, -7, -8, -9, and -10 dB down from saturation

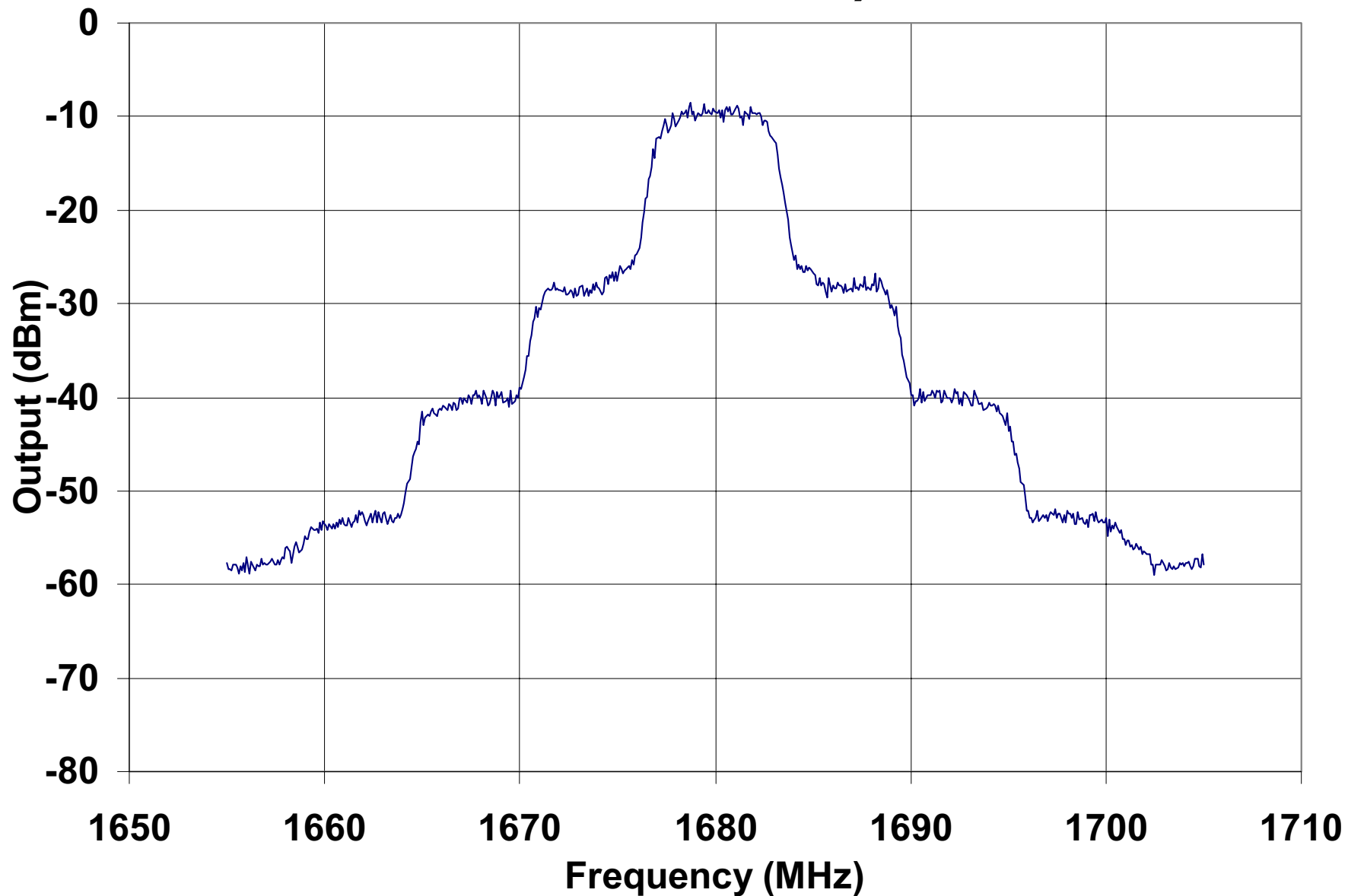
Newtec Output Power Spectral Density for “ α ” = 0.35 Normalized by Twice the Channel Symbol Rate



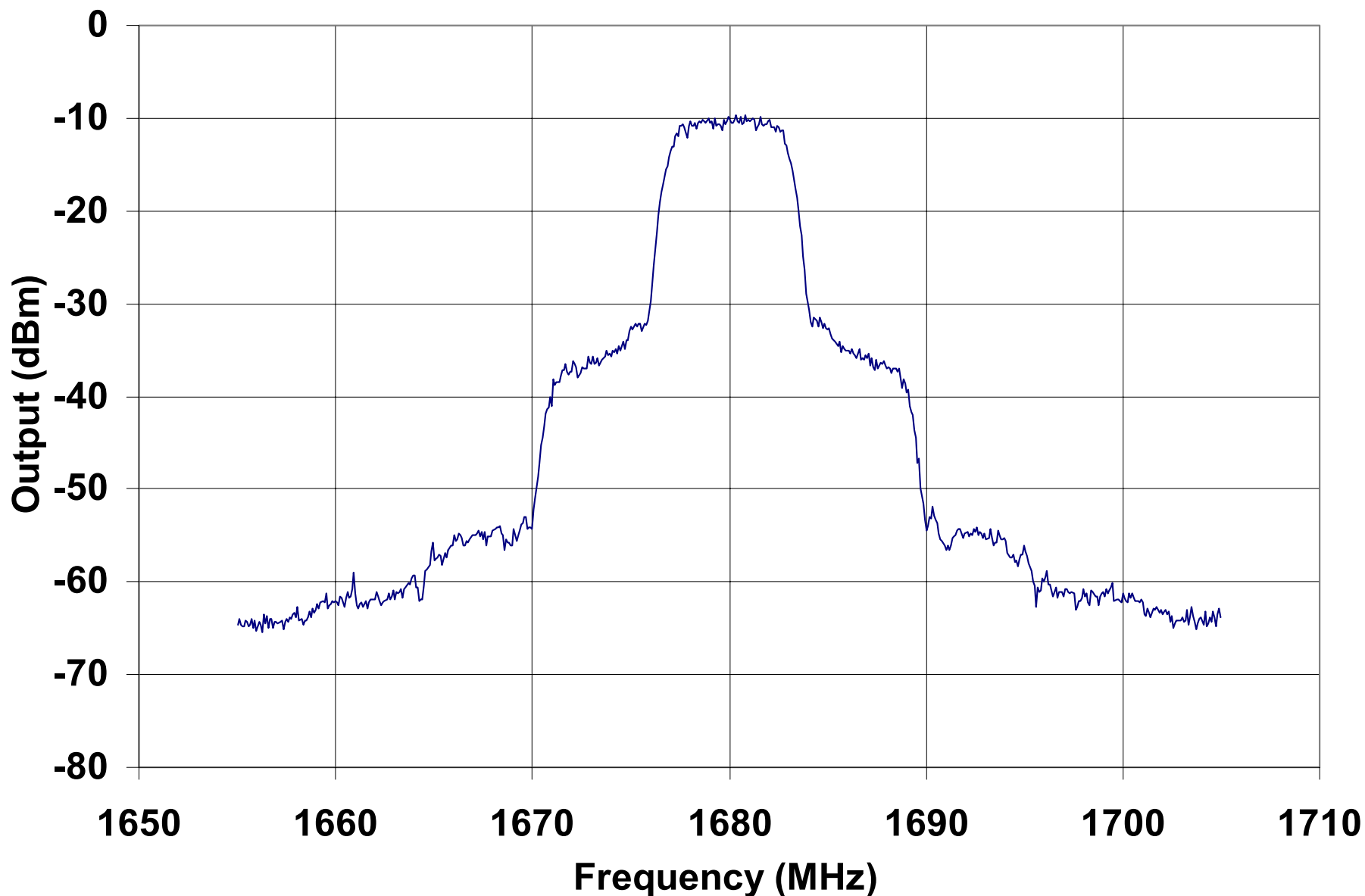
Newtec Output Power Spectral Density for “ α ” = 0.55 Normalized by Twice the Channel Symbol Rate



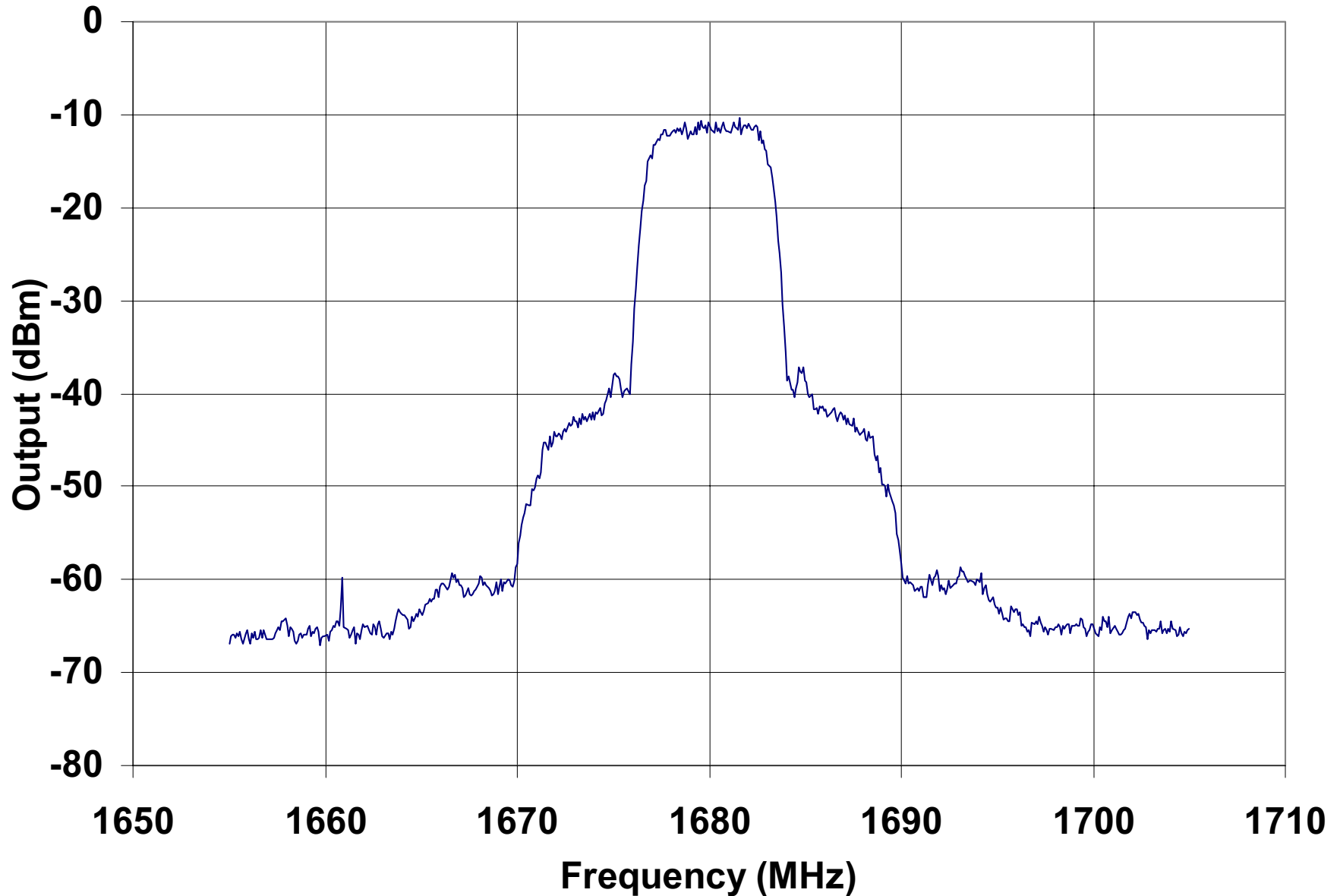
Spectral Density at Saturation for $\alpha = 0.35$)



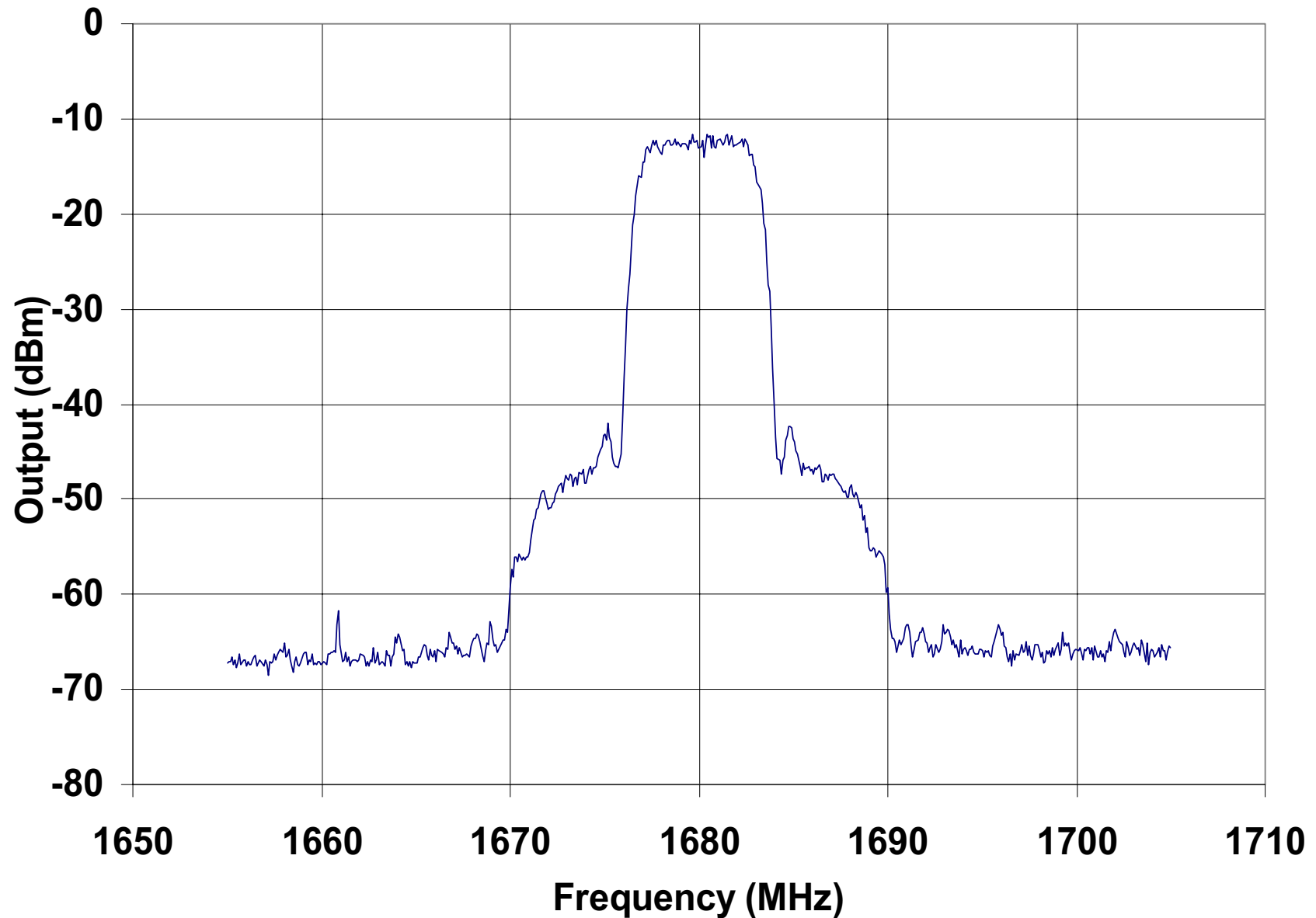
Spectral Density for PA Output at 1 dB Below Saturation $\alpha = 0.35$



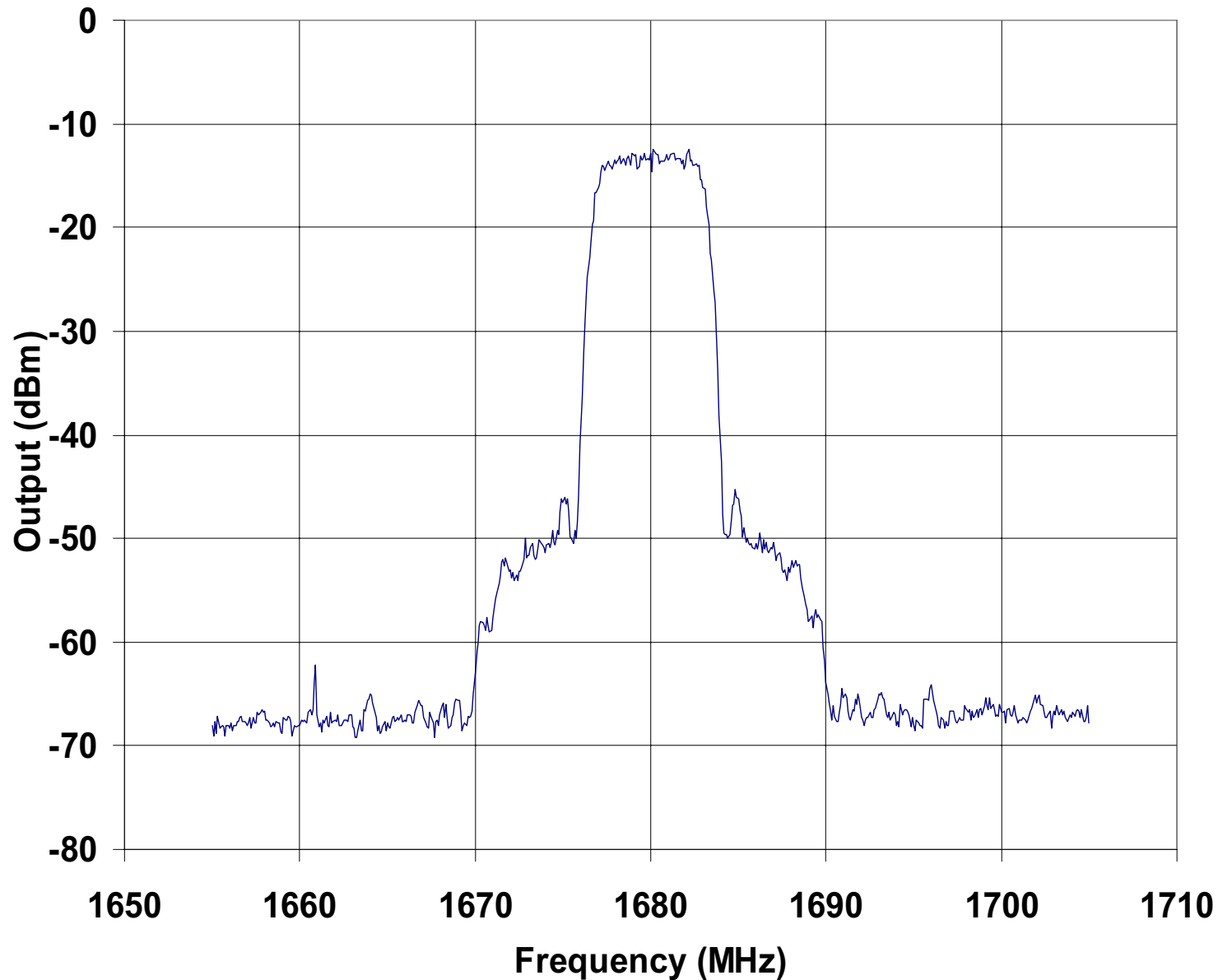
Spectral Density for PA Output at 2 dB Below Saturation $\alpha = 0.35$



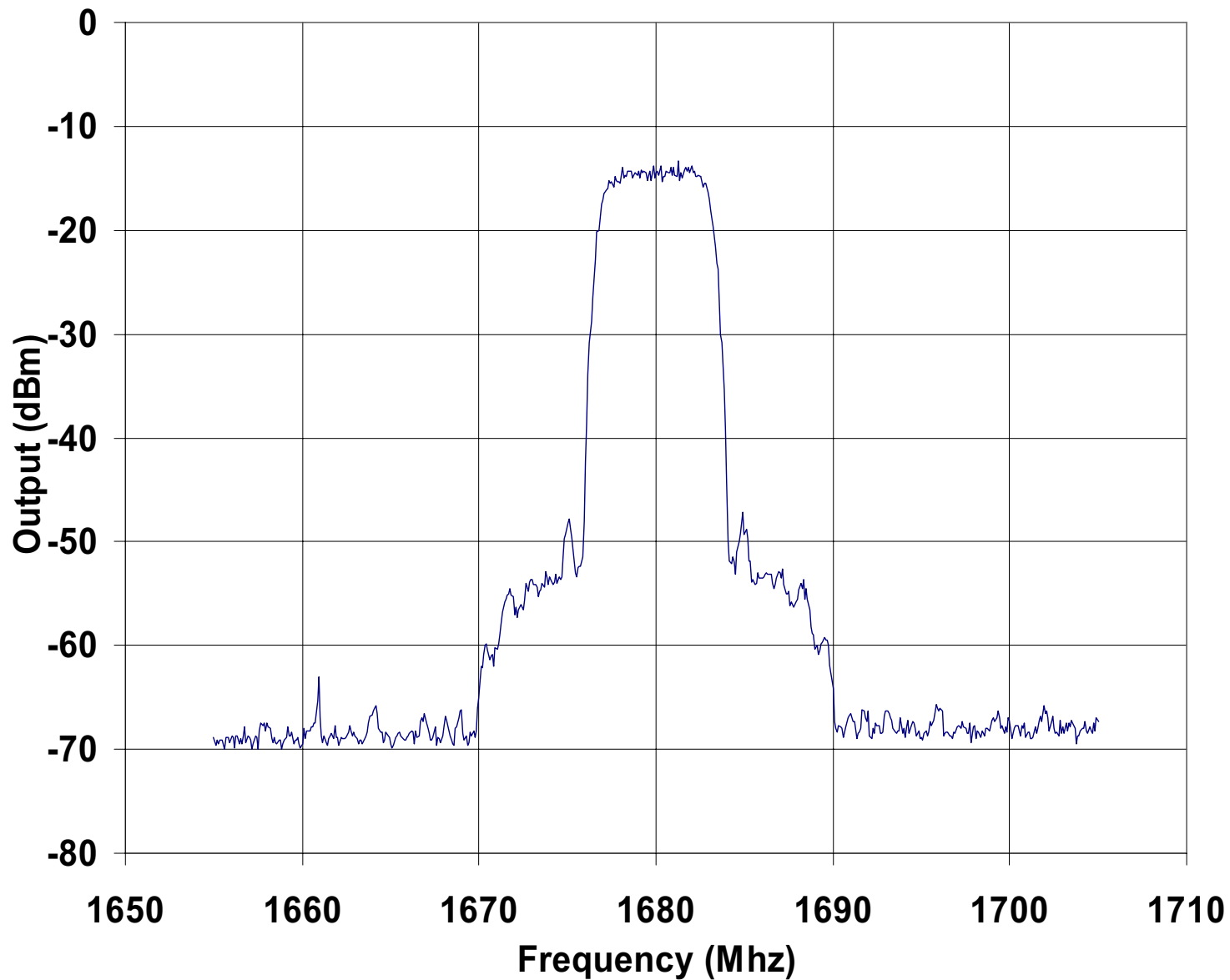
Spectral Density for PA Output at 3 dB Below Saturation $\alpha = 0.35$



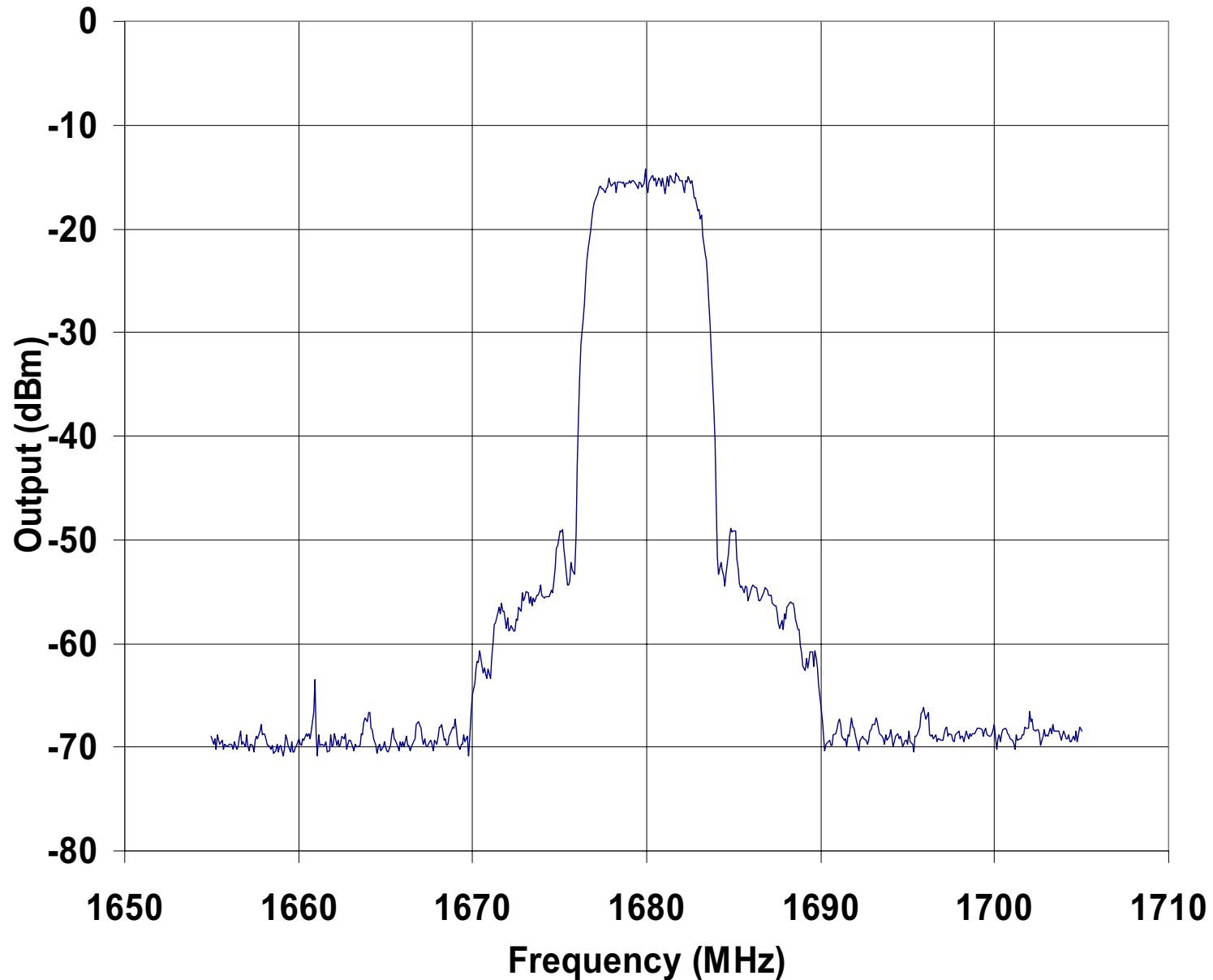
Spectral Density for PA Output at 4 dB Below Saturation $\alpha = 0.35$



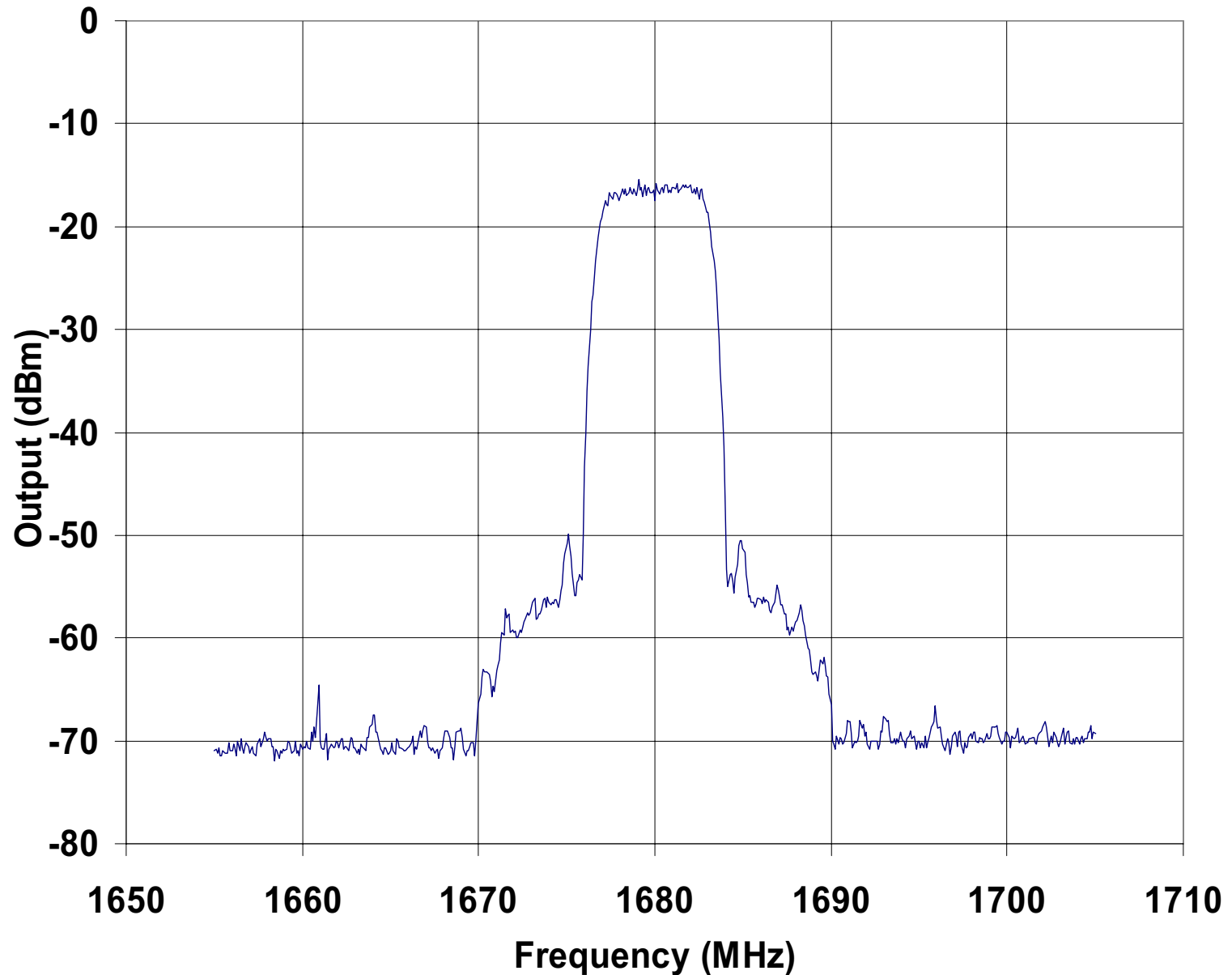
Spectral Density for PA Output at 5 dB Below Saturation $\alpha = 0.35$



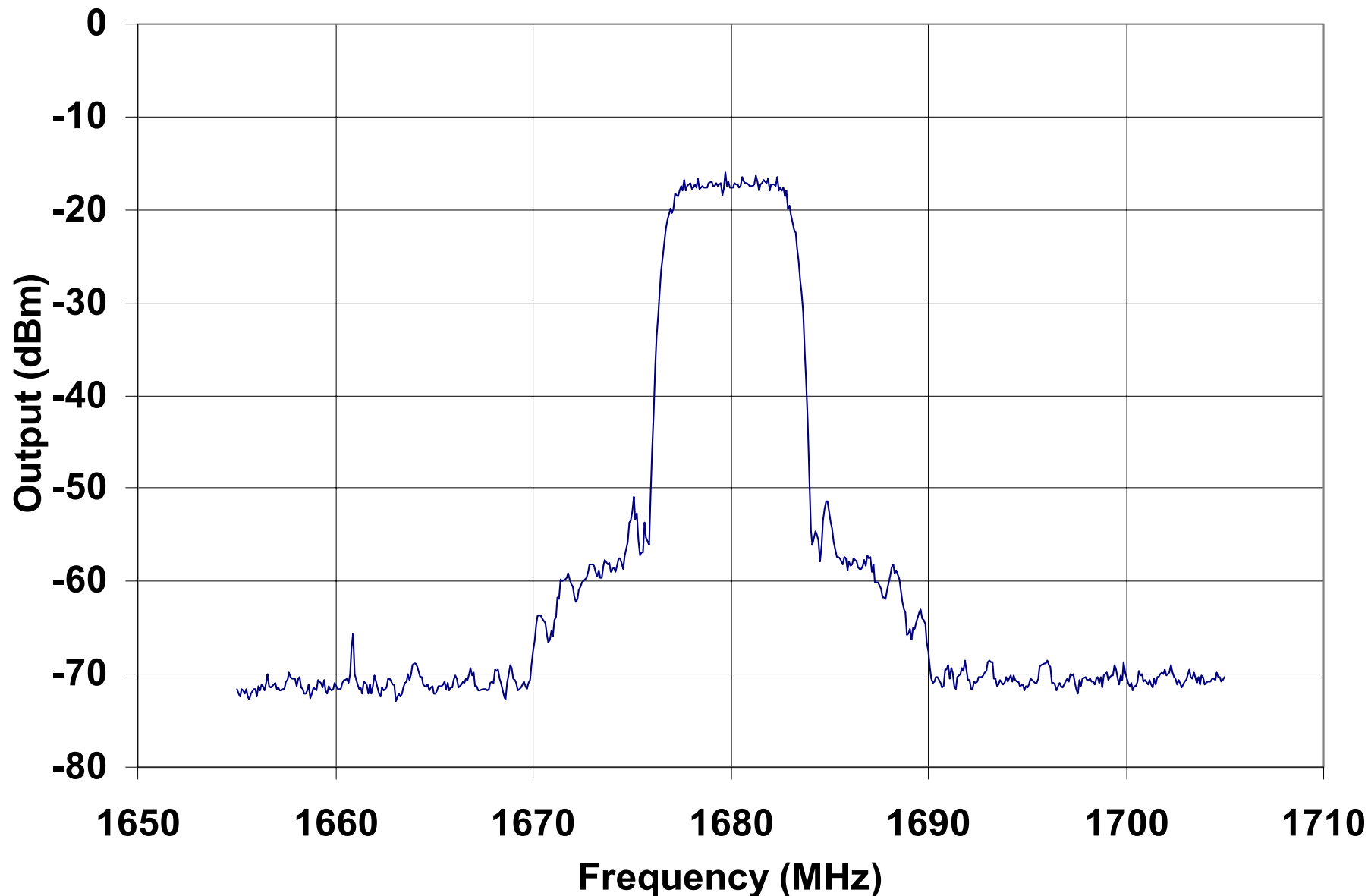
Spectral Density for PA Output at 6 dB Below Saturation $\alpha = 0.35$



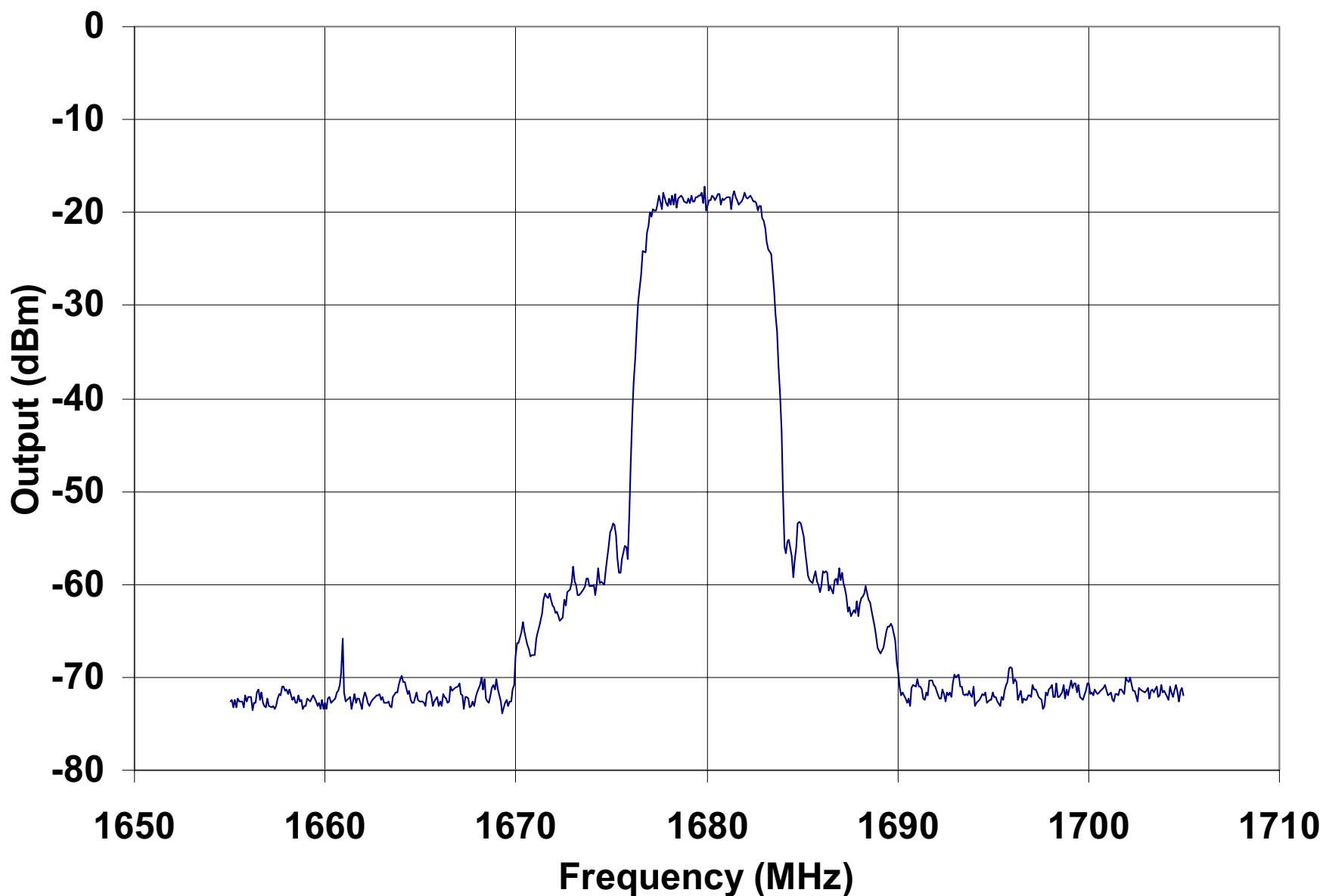
Spectral Density for PA Output at 7 dB Below Saturation $\alpha = 0.35$



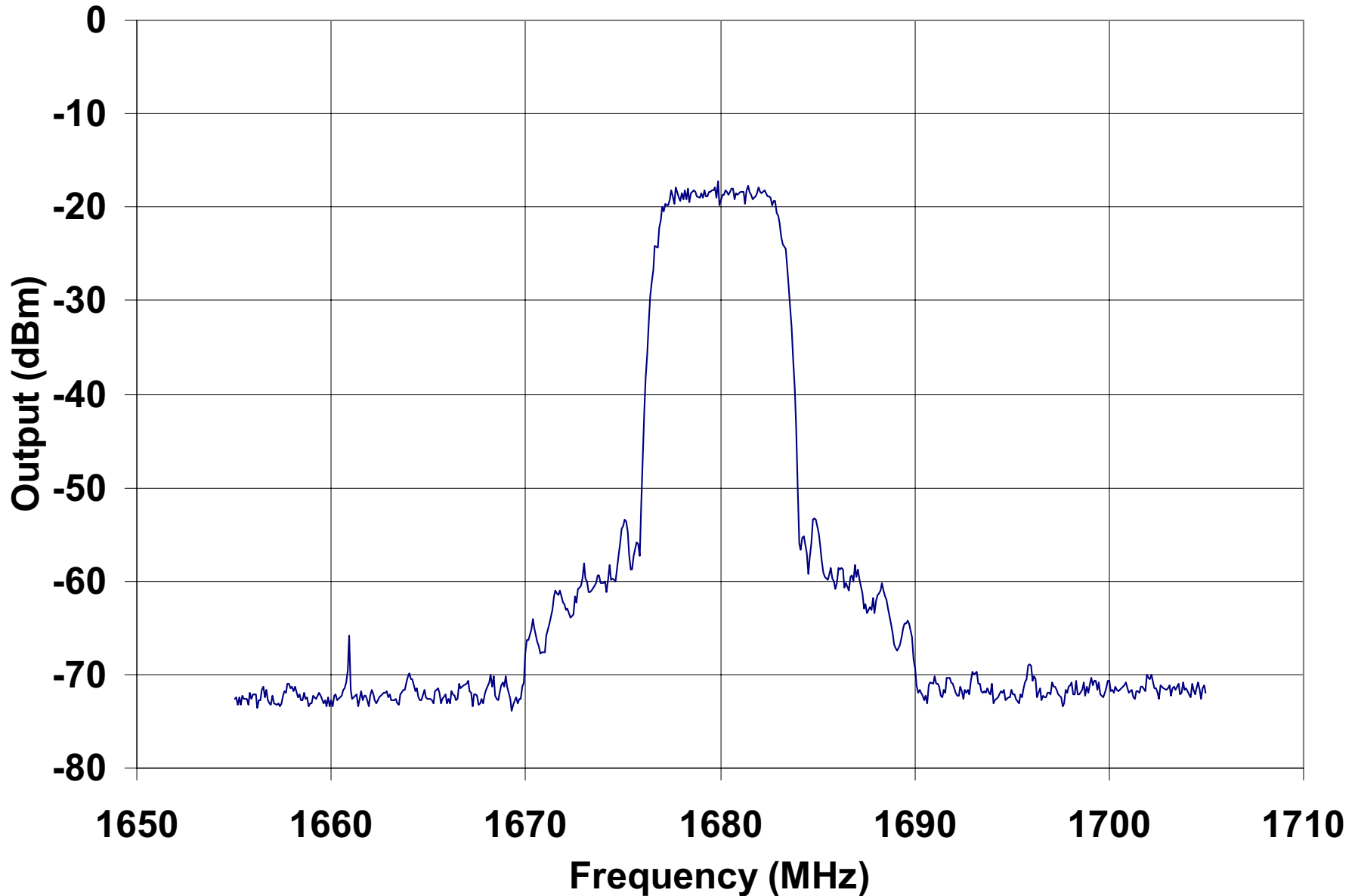
Spectral Density for PA Output at 8 dB Below Saturation $\alpha = 0.35$



Spectral Density for PA Output at 9 dB Below Saturation $\alpha = 0.35$

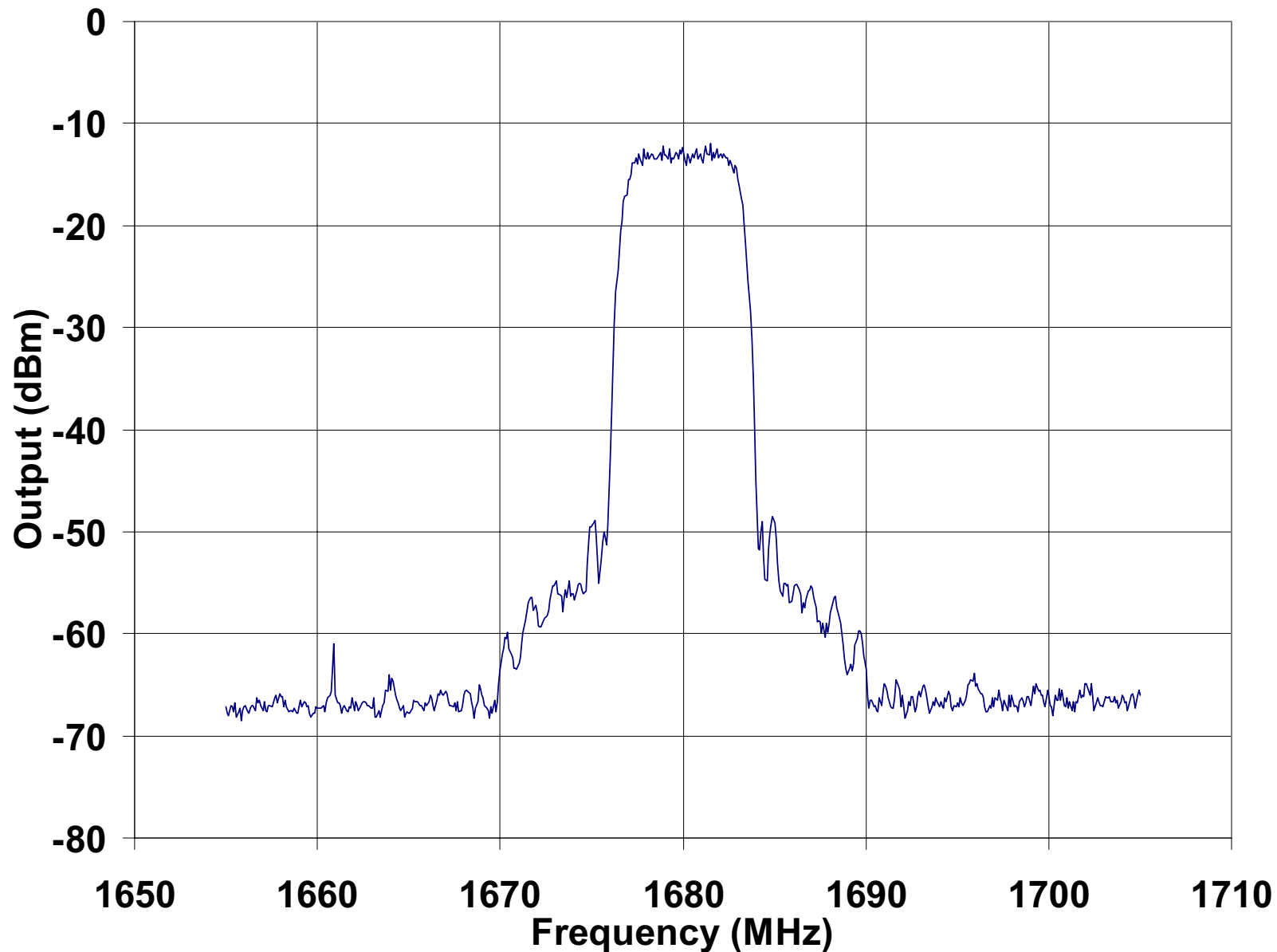


Spectral Density for PA Output at 10 dB Below Saturation $\alpha = 0.35$

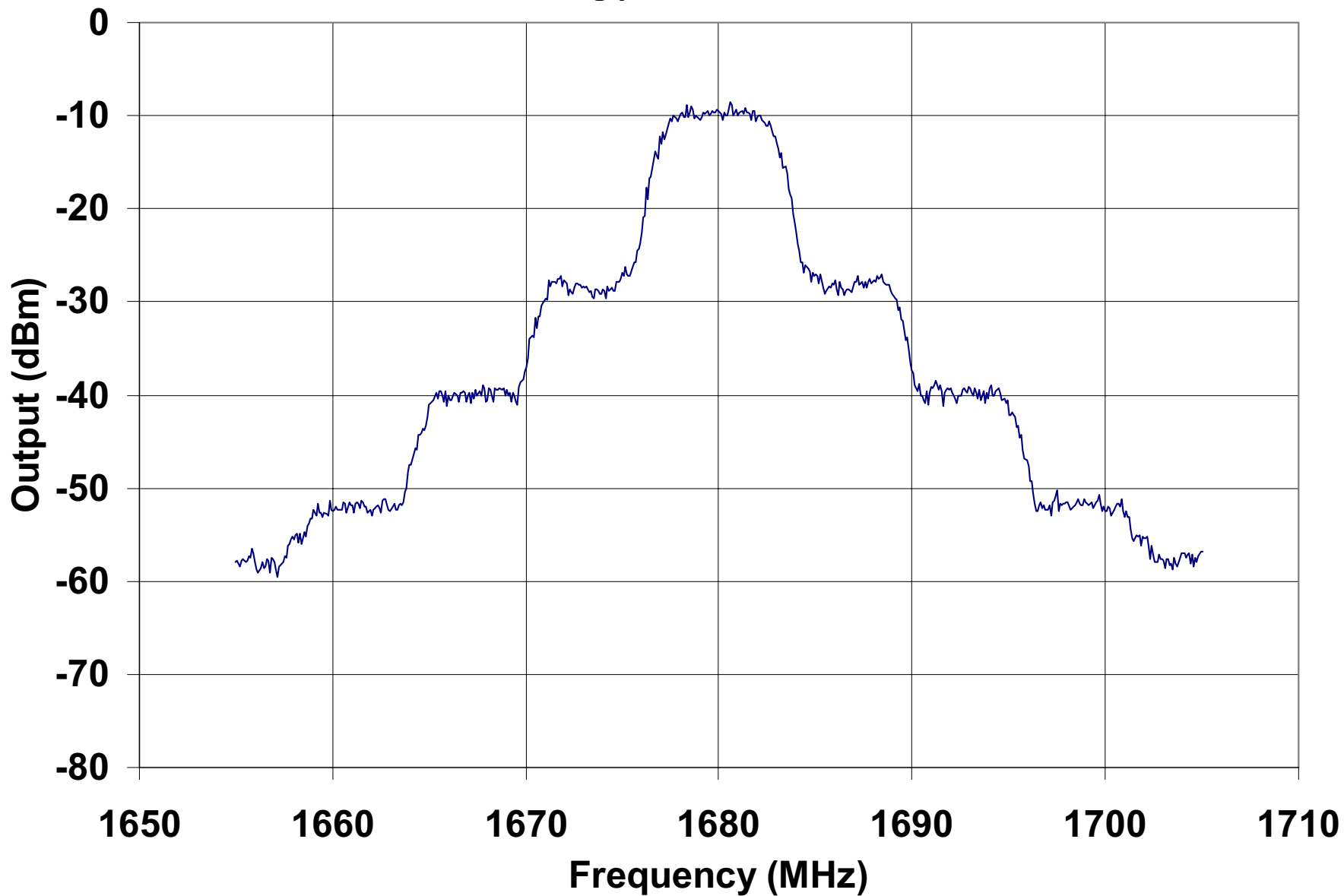


Spectral Density for Driver Output

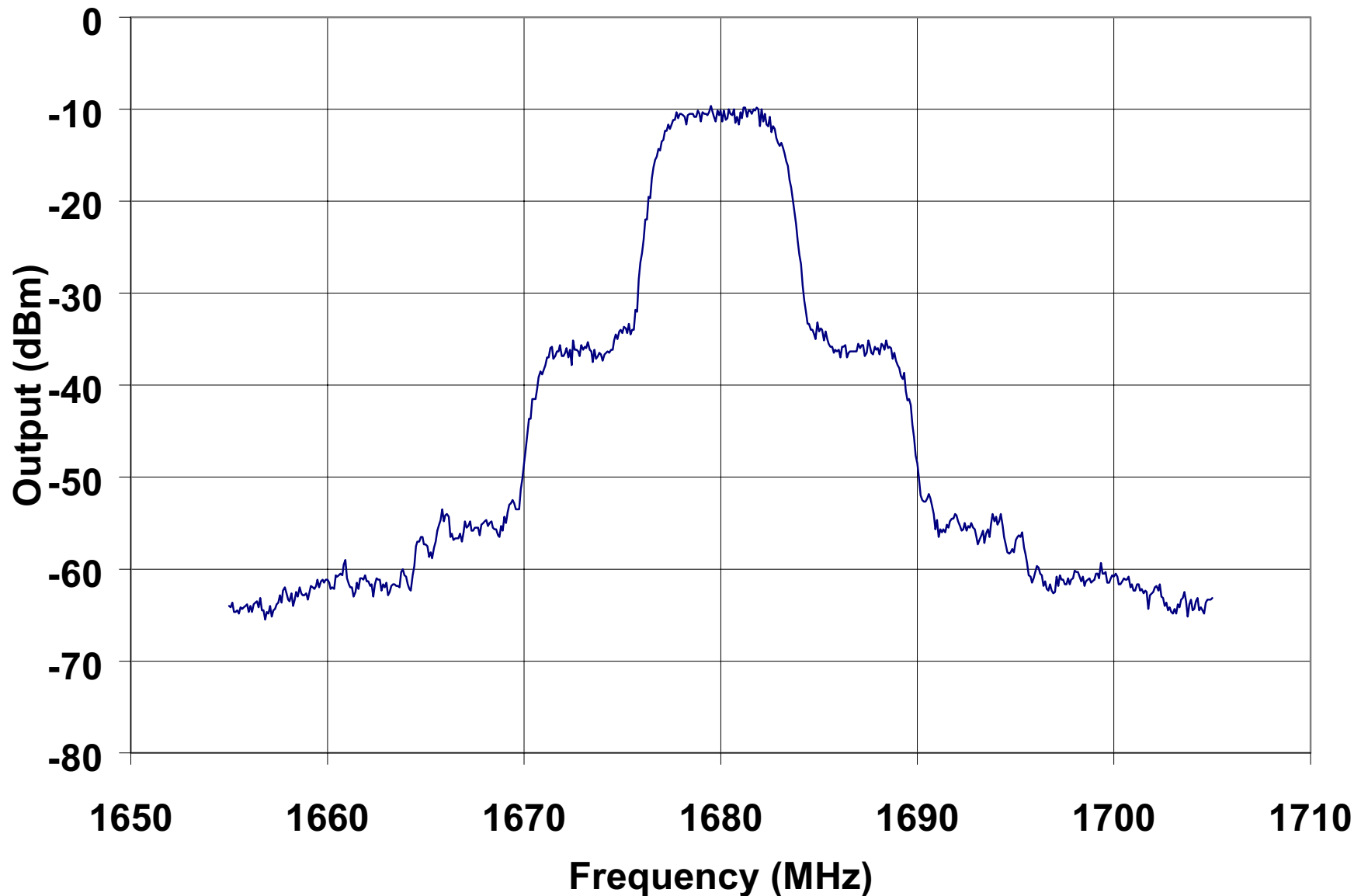
$\alpha = 0.35$



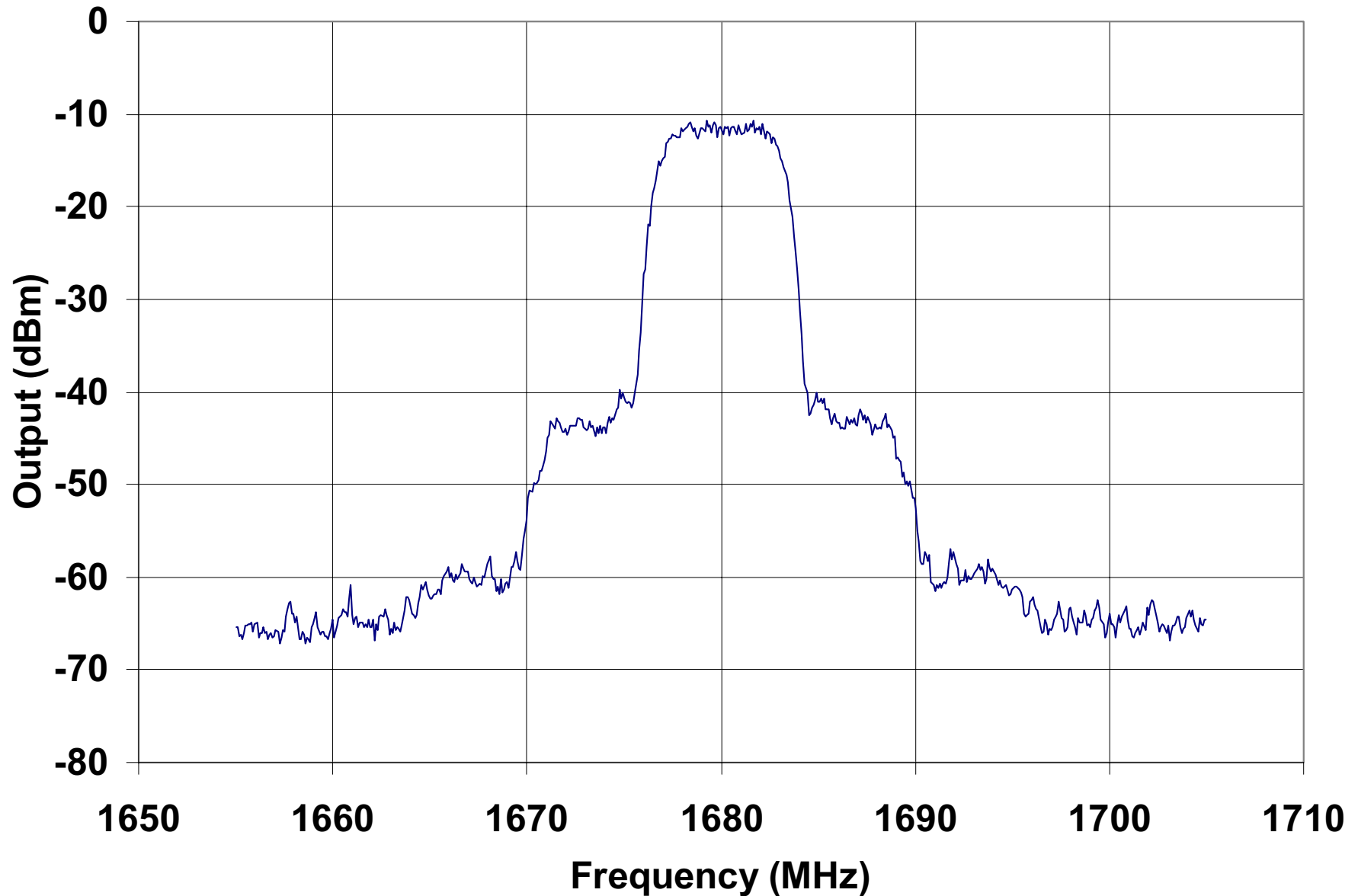
Spectral Density at Saturation for $\alpha = 0.55$



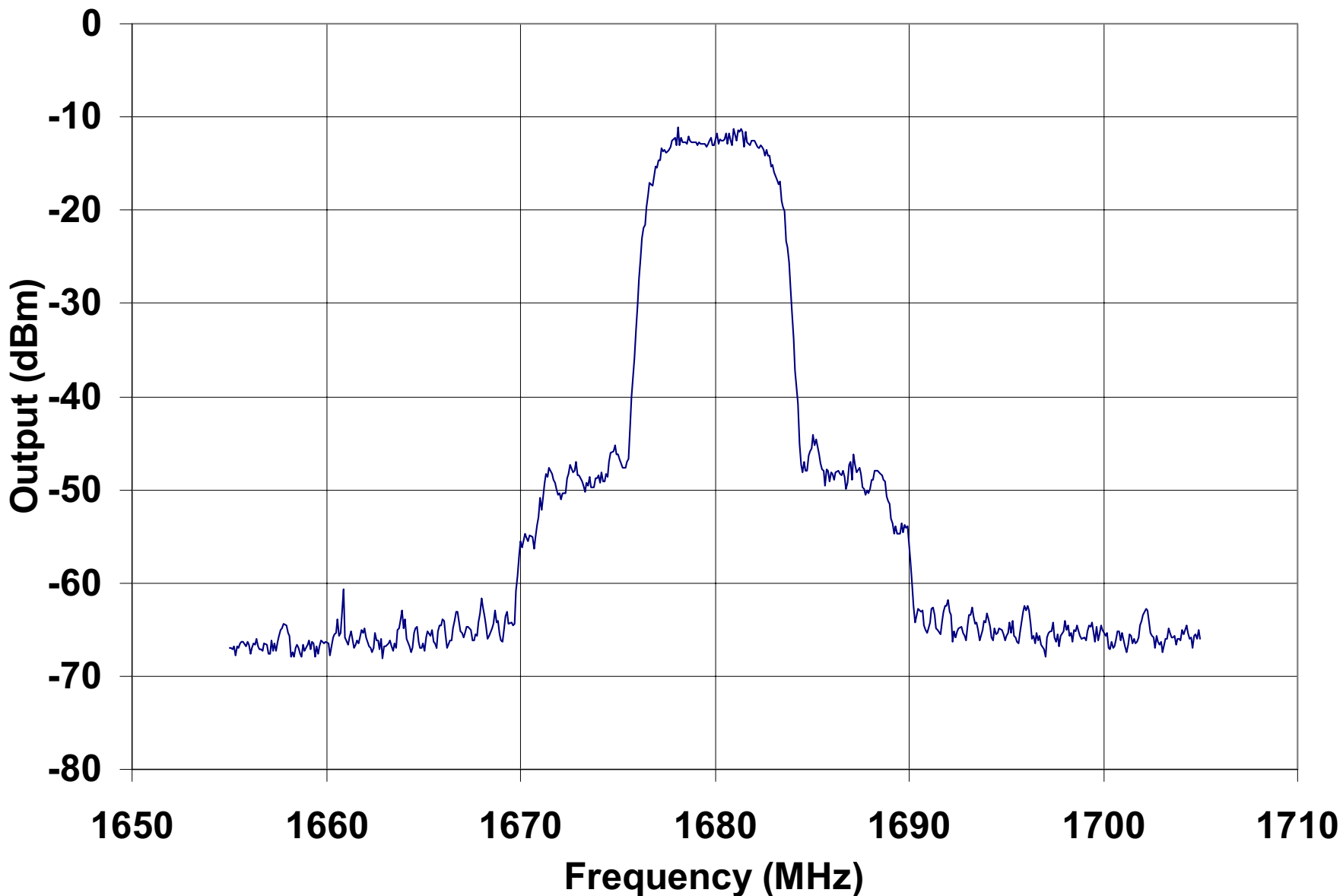
Spectral Density for PA Output at 1 dB Below Saturation $\alpha = 0.55$



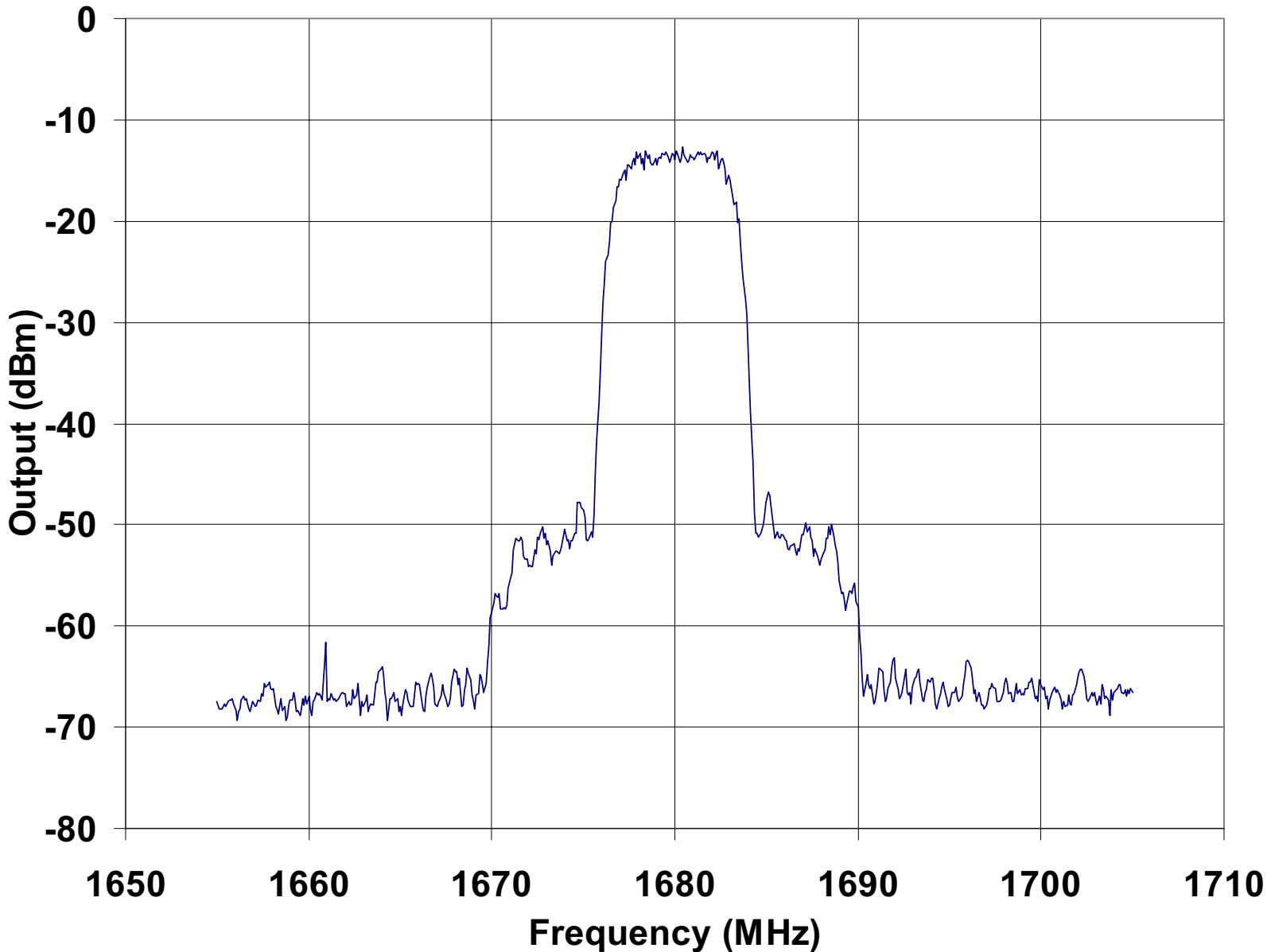
Spectral Density for PA Output at 2 dB Below Saturation $\alpha = 0.55$



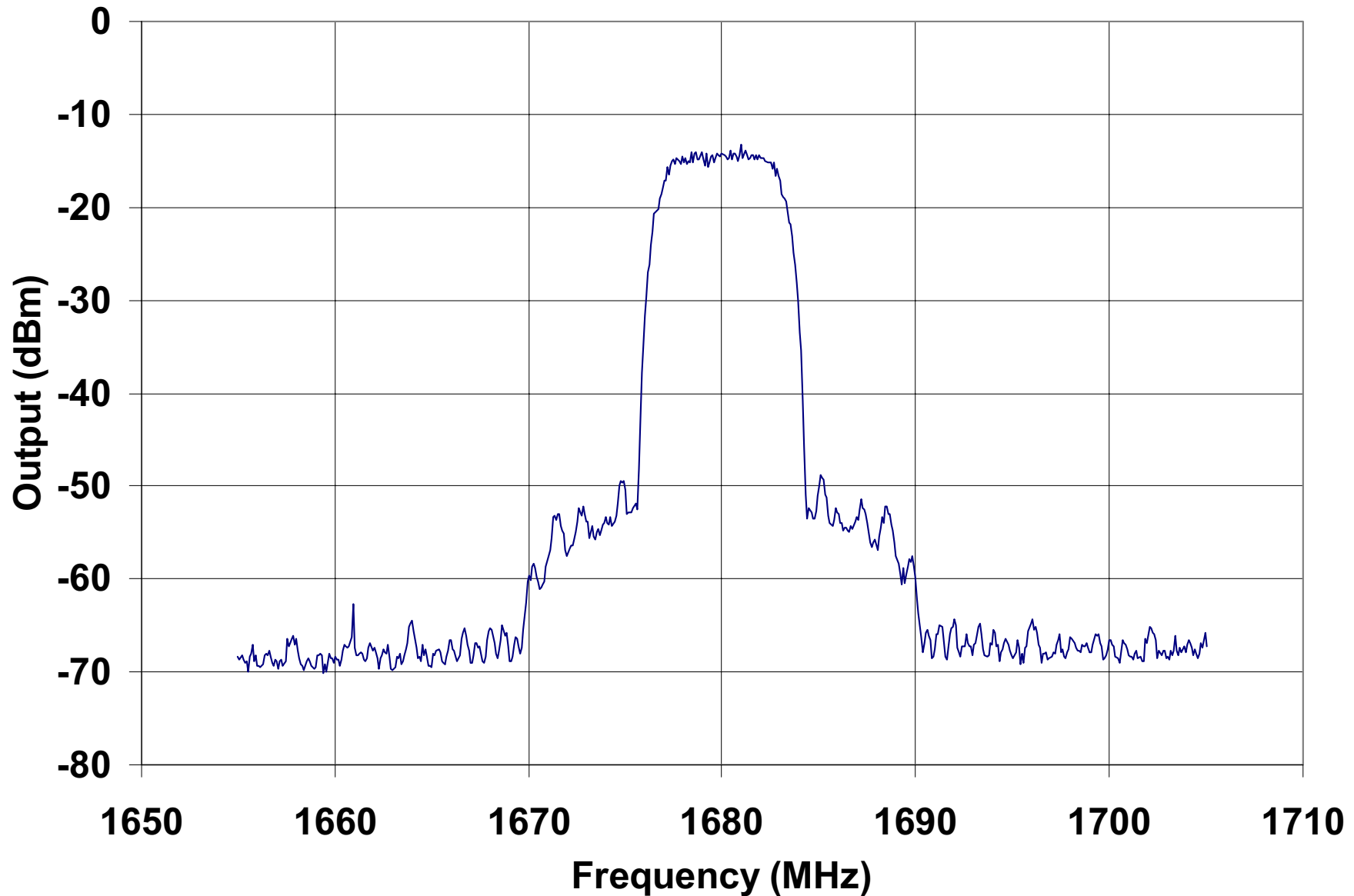
Spectral Density for PA Output at 3 dB Below Saturation $\alpha = 0.55$



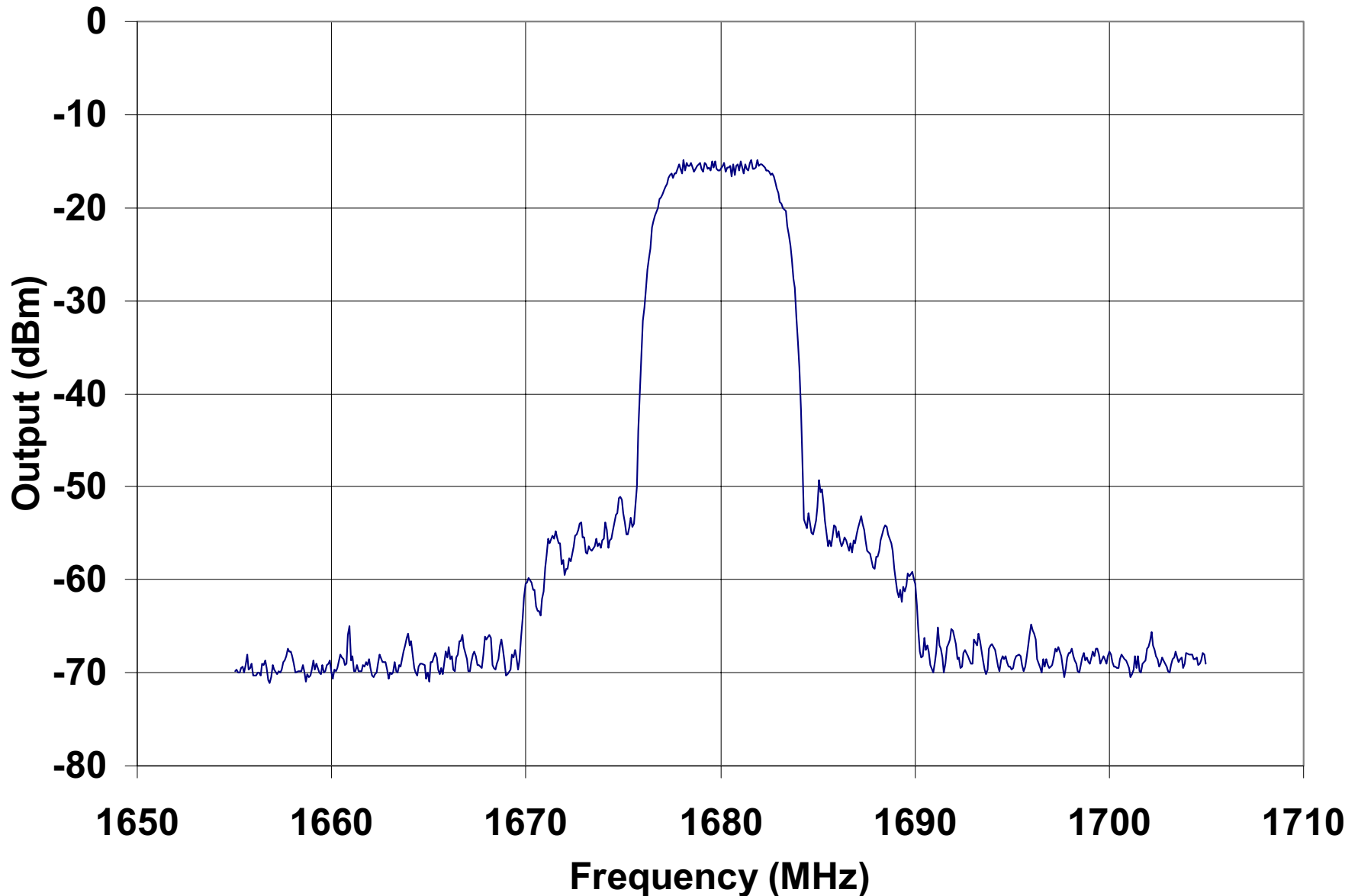
Spectral Density for PA Output at 4 dB Below Saturation $\alpha = 0.55$



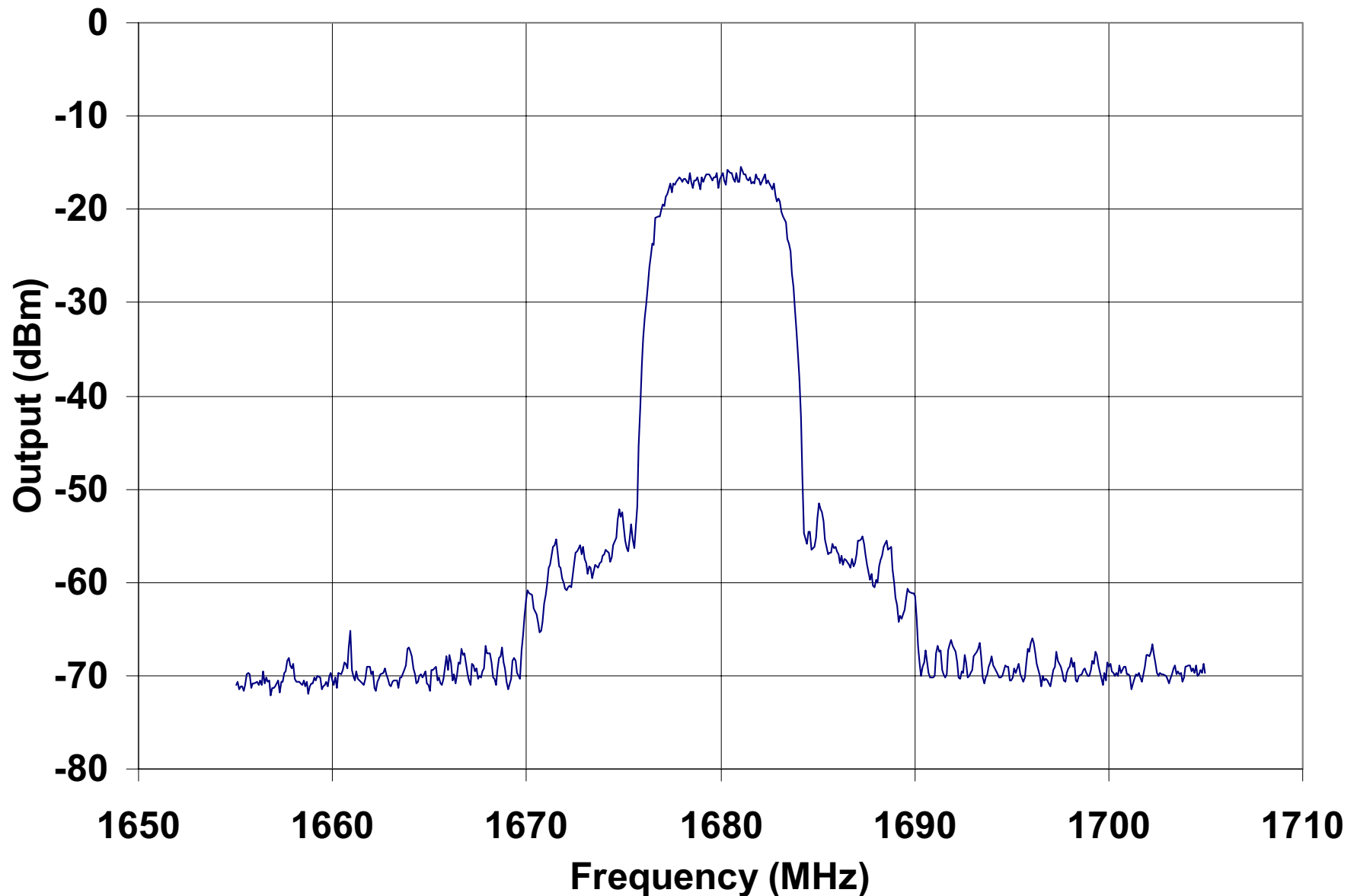
Spectral Density for PA Output at 5 dB Below Saturation $\alpha = 0.55$



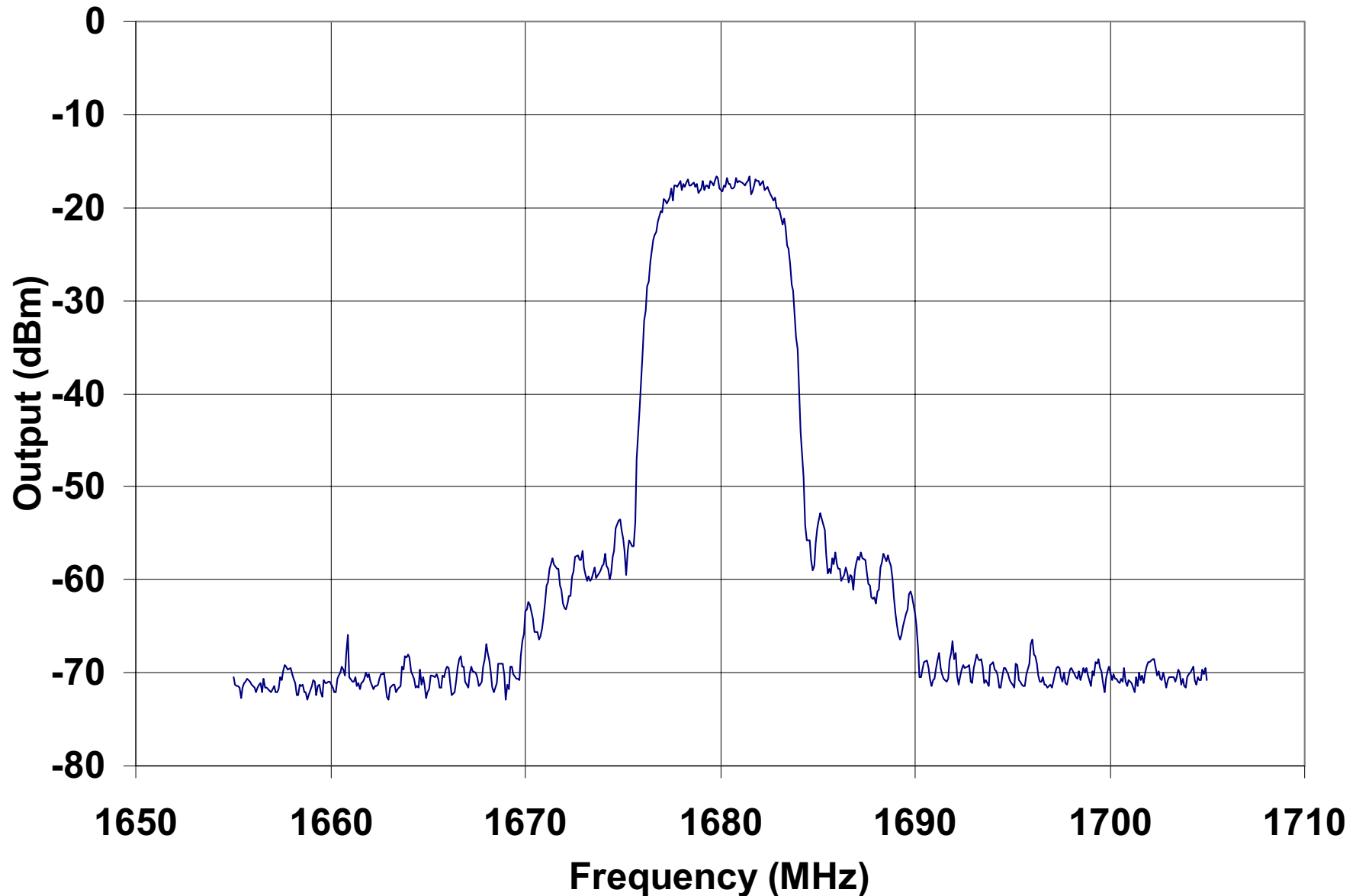
Spectral Density for PA Output at 6 dB Below Saturation $\alpha = 0.55$



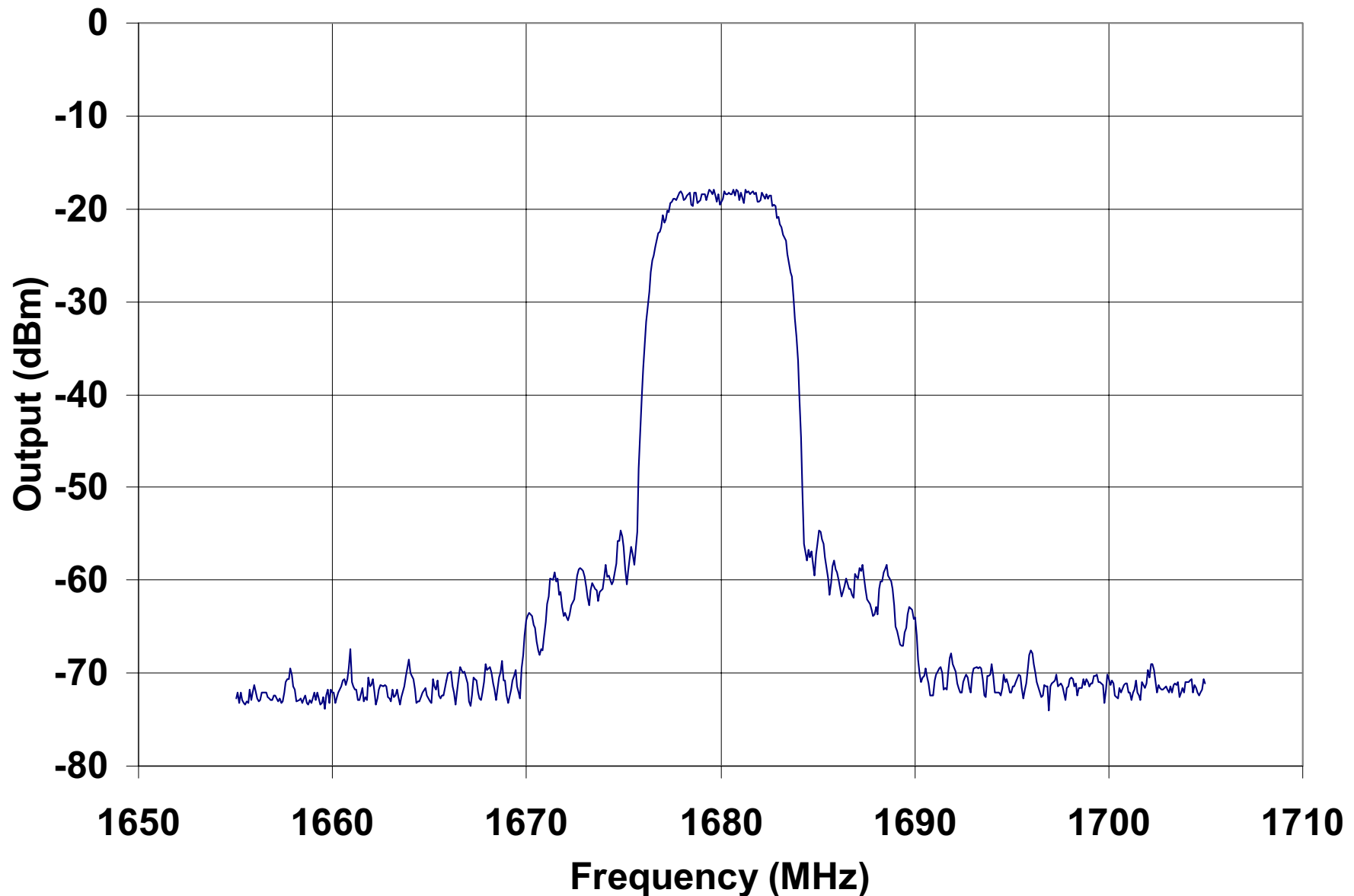
Spectral Density for PA Output at 7 dB Below Saturation $\alpha = 0.55$



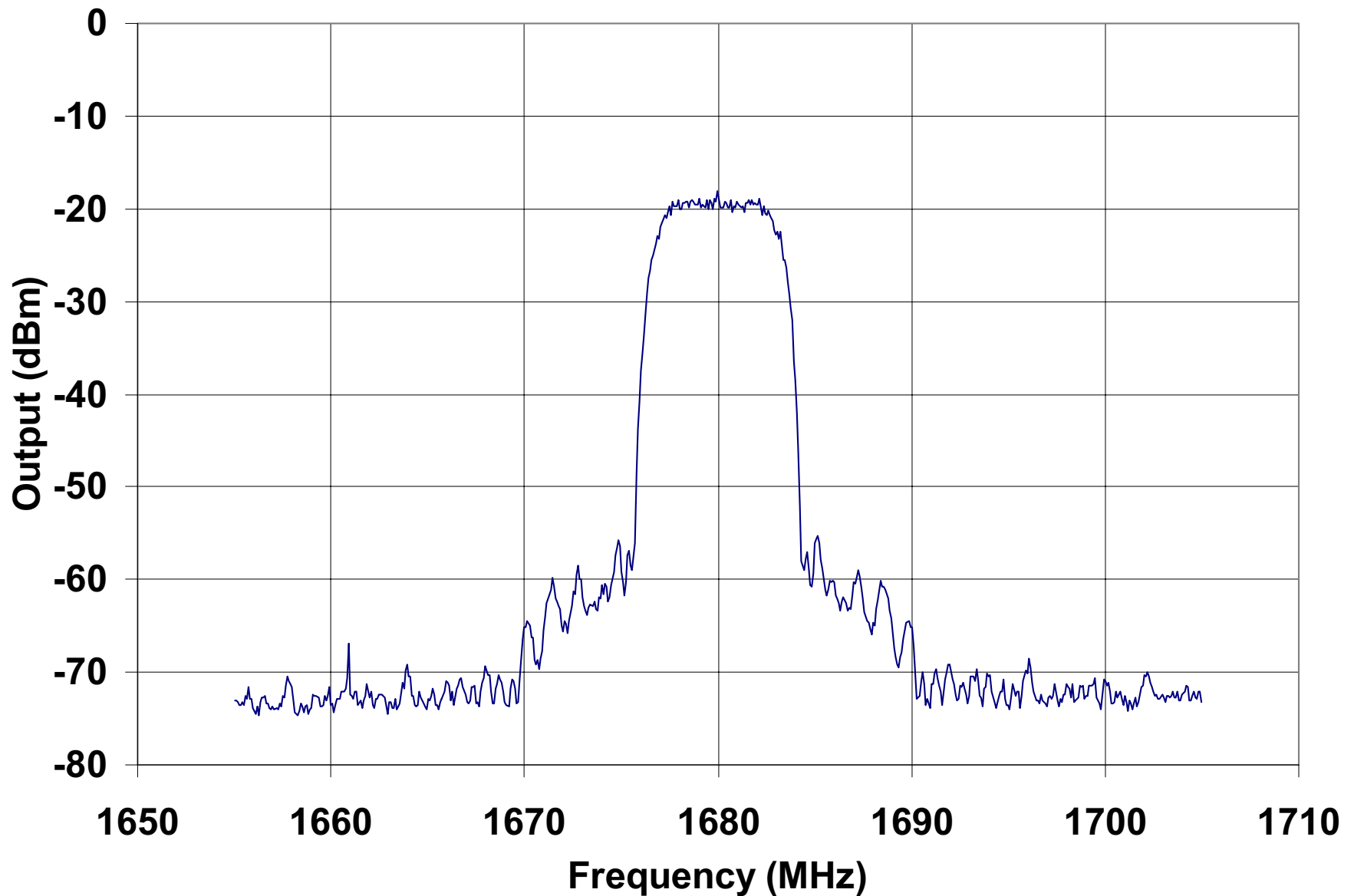
Spectral Density for PA Output at 8 dB Below Saturation $\alpha = 0.55$



Spectral Density for PA Output at 9 dB Below Saturation $\alpha = 0.55$

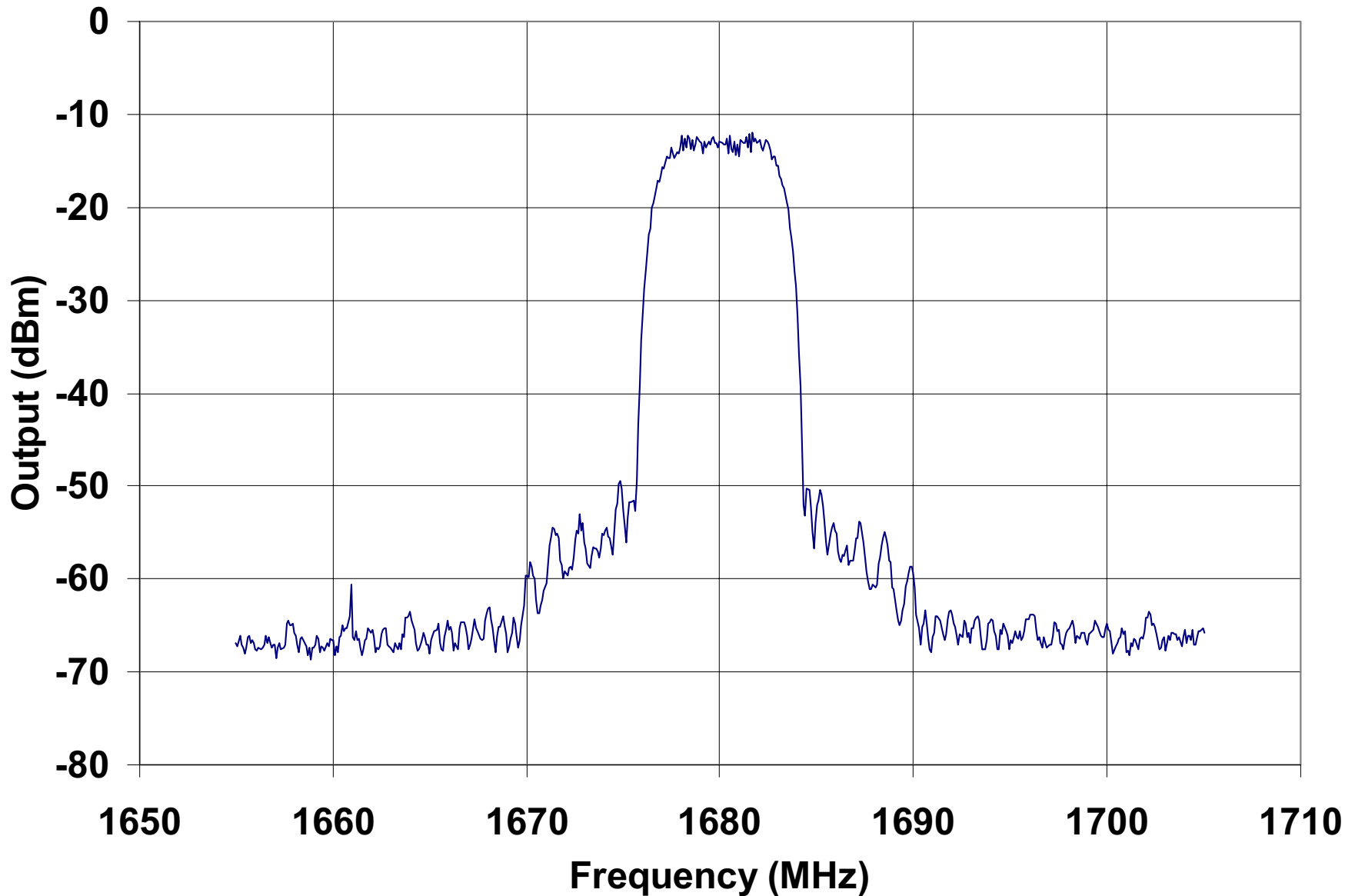


Spectral Density for PA Output at 10 dB Below Saturation $\alpha = 0.55$



Spectral Density for Driver Output

$\alpha = 0.55$



Conclusions

- **The new amplifier transfer function data showed greatly increased linearity in the middle of the range.**
- **SSPA output Sideband levels at -32 dB demonstrated with 3 dB backoff (greatly improved over the April data)**
- **We estimate ~2 dB back off needed when using an appropriate linearizer**

[This page intentionally left blank.]

Acquisition Performance Comparison of the Generalized Maximum A Posteriori Symbol Synchronizer Versus the Data-Transition Tracking Loop

L. V. Lam,¹ T.-Y. Yan,¹ M. K. Simon,¹ and W. L. Martin²

A generalized maximum a posteriori (MAP) symbol synchronizer for arbitrary nonoverlapping pulse shape and data-transition density is derived, and a simplified realization is presented. Acquisition performance at low to very low symbol signal-to-noise ratios (SNRs) is investigated and compared against the conventional data-transition tracking loop (DTTL). Simulation results show that the MAP symbol synchronizer can operate at very low symbol SNRs where the DTTL fails. Furthermore, the new symbol synchronizer reduces the initial acquisition time by at least one order of magnitude as compared with the DTTL. It also has been shown that the new symbol synchronizer is suitable for minimum-shift-keying (MSK) signaling waveforms.

I. Introduction

Recent interest in employing powerful codes, such as turbo codes, for deep-space downlink communications motivates development of receivers operating at low symbol signal-to-noise ratios (SNRs), perhaps as low as -10 dB. At these values of symbol SNRs, traditional receivers using the data-transition tracking loop (DTTL) may experience difficulties in terms of symbol acquisition and tracking. The traditional DTTL is a suboptimal closed-loop implementation derived from the maximum a posteriori (MAP) estimation of the symbol epoch of a rectangular pulse stream in an additive white Gaussian noise (AWGN) environment.

A closed-loop symbol synchronizer, such as the DTTL, is obtained by using the first derivative of the log-likelihood function of the symbol epoch to approximate an error signal. When a rectangular pulse waveform is used, the derivative of the log-likelihood function does not exist; hence, strictly speaking, a closed-loop estimator does not exist for the rectangular pulse. Since the conventional DTTL approximates the first derivative of the rectangular pulse shape by a narrow pulse at its edges, it is pulse shape dependent. If a waveform other than the rectangular pulse is used for transmission, the conventional DTTL suffers a degradation during tracking and acquiring. Furthermore, the conventional DTTL was derived based on the assumption of a high SNR. Its performance will be degraded for low SNR applications [1].

¹ Communications Systems and Research Section.

² Future Missions Planning Office.

The generalized MAP symbol synchronizer described in this article is the optimal estimator for generating the time epochs. It received little attention in the past, mainly because it had been thought of as a “one-shot” estimator. The advent of powerful codes and the need to operate the receiver at low symbol SNRs, together with advances in digital signal-processing electronics, make this estimator an attractive choice for modern digital receiver implementations. In addition, it can be shown that the new symbol synchronizer not only can continuously update the estimate every symbol time, as does the closed-loop scheme, but also is less complex in implementation as compared with the conventional DTTL. This article quantifies the acquisition time performance of the MAP symbol synchronizer based on computer simulations. Several authors have presented performance bounds for the mean-square performance [2–6].³ However, exact theoretical evaluation of the acquisition performance of the MAP estimator is mathematically difficult.

This article is organized into three sections. Section II derives the new symbol synchronizer for an arbitrary data-transition density. Section III presents computer simulation results for both the new estimator and the DTTL. Section IV provides the conclusion.

II. Theoretical Derivation

Consider the received baseband signal written in sample (discrete-time) form as

$$y(n) = \sqrt{S_T} \sum_k a_k p(n - kN - \varepsilon) + v(n) \quad (1)$$

where $n, k = 0, 1, \dots, \infty$, ε is the unknown symbol epoch, $p(n)$ is the nonoverlapping symbol pulse shape of duration T_s seconds, a_k is the k th binary symbol, N is the number of samples per symbol, S_T is the transmitted power, and $v(n)$ is the AWGN with a two-sided power spectral density level of $N_0/2$ W/Hz. Letting \underline{y}_k denote the N -dimensional observation column vector of the signal in the k th symbol interval and $\underline{p}_k(\varepsilon), \underline{v}_k$ the corresponding nonoverlapping pulse shape and noise vectors, then

$$\underline{y}_k = \sqrt{S_T} a_k \underline{p}_k(\varepsilon) + \underline{v}_k \quad (2)$$

Letting \underline{Y}_K be the observation vector over $K + 1$ symbols, then

$$\underline{Y}_K = \begin{bmatrix} \underline{y}_0 \\ \vdots \\ \underline{y}_K \end{bmatrix} = \sqrt{S_T} \begin{bmatrix} a_0 \underline{p}_0(\varepsilon) \\ \vdots \\ a_K \underline{p}_K(\varepsilon) \end{bmatrix} + \begin{bmatrix} \underline{v}_0 \\ \vdots \\ \underline{v}_K \end{bmatrix} \quad (3)$$

Hence, the a posteriori probability density function of the symbol epoch, ε , given the received signal vector, \underline{Y}_K , is

$$P(\varepsilon | \underline{Y}_K) = \frac{P(\varepsilon)}{P(\underline{Y}_K)} \overline{P(\underline{Y}_K | \varepsilon, \underline{a}_K)}^{\underline{a}_K} \quad (4)$$

where the overline denotes statistical averaging over all possible values of the K -symbol data vector \underline{a}_K and ε is assumed to be constant over K symbol intervals. Assuming an independent, identically

³ M. K. Simon, “Maximum Likelihood Sliding Window Estimation of Timing for NRZ Data Streams,” JPL Interoffice Memorandum (internal document), Jet Propulsion Laboratory, Pasadena, California, October 1997.

distributed (i.i.d.) data stream, \underline{v}_K and \underline{a}_K are uncorrelated, and \underline{v}_K has zero mean and a variance of $N_0/2$ W/Hz. Then Eq. (3) can be rewritten as

$$P(\varepsilon|\underline{Y}_K) = \frac{P(\varepsilon)}{P(\underline{Y}_K)} \prod_{k=0}^K \sum_{a_k} P(\underline{y}_k|\varepsilon, a_k) P(a_k) \quad (5)$$

where $P(\underline{y}_k|\varepsilon, a_k)$ is conditionally Gaussian distributed as

$$P(\underline{y}_k|\varepsilon, a_k) = \frac{1}{\left(2\pi \frac{N_0}{2}\right)^{N/2}} \exp \left(-\frac{\left(\underline{y}_k - \sqrt{S_T} a_k \underline{p}_k(\varepsilon)\right)^T \left(\underline{y}_k - \sqrt{S_T} a_k \underline{p}_k(\varepsilon)\right)}{2 \frac{N_0}{2}} \right) \quad (6)$$

where T denotes the transpose operation. For binary communication where a_k takes on values ± 1 and assuming ε is uniformly distributed over $\{0, 1, \dots, N-1\}$, Eq. (5) can be reduced to

$$P(\varepsilon|\underline{Y}_K) = C \prod_{k=0}^K \left(2\alpha \sinh \left(2 \frac{\sqrt{S_T}}{N_0} \underline{y}_k^T \underline{p}_k(\varepsilon) \right) + \exp \left(-2 \frac{\sqrt{S_T}}{N_0} \underline{y}_k^T \underline{p}_k(\varepsilon) \right) \right) \quad (7)$$

where all the constant terms have been combined into C and α denotes the probability that $a_k = +1$. Since $P(\varepsilon|\underline{Y}_K)$ is a product of $K+1$ terms, it is easier to work with the logarithm of $P(\varepsilon|\underline{Y}_K)$. Taking the natural logarithm of Eq. (7) leads to the log-likelihood function

$$\Lambda(\varepsilon|\underline{Y}_K) = C_1 + \sum_{k=0}^K \ln \left(2\alpha \sinh \left(2 \frac{\sqrt{S_T}}{N_0} \underline{y}_k^T \underline{p}_k(\varepsilon) \right) + \exp \left(-2 \frac{\sqrt{S_T}}{N_0} \underline{y}_k^T \underline{p}_k(\varepsilon) \right) \right) \quad (8)$$

where $C_1 \equiv \ln(C)$. Since we are interested in maximizing $\Lambda(\varepsilon|\underline{Y}_K)$ with respect to ε , we can ignore the constant C_1 . Letting $\alpha = 0.5$, Eq. (8) reduces to [1]⁴

$$\Lambda(\varepsilon|\underline{Y}_K) = \sum_{k=0}^K \ln \left(\cosh \left(2 \frac{\sqrt{S_T}}{N_0} \underline{y}_k^T \underline{p}_k(\varepsilon) \right) \right) \quad (9)$$

The generalized MAP estimate of the epoch is the estimate, $\hat{\varepsilon}$, which maximizes the log-likelihood function of Eq. (9). That is,

$$\Lambda(\hat{\varepsilon}|\underline{Y}_K) = \max_{i=0,1,\dots,N-1} \{\Lambda(\varepsilon_i|\underline{Y}_K)\} \quad (10)$$

where

$$\varepsilon_i \in \{0, 1, \dots, N-1\} \quad (11)$$

⁴ Ibid.

The argument in Eq. (9) can now be rewritten as the discrete convolution

$$\underline{y}_k^T \underline{p}_k(\varepsilon_i) = \sum_{n=(k-1)N+i}^{kN+i-1} y(n)p(n - (k-1)N) \quad (12)$$

Hence, Eqs. (9) and (12) specify a realization of the generalized MAP symbol synchronizer. It involves discretely correlating the symbol pulse waveform with all possible shifted received signals. Equation (9) can be rewritten in the recursive form:

$$\Lambda(\varepsilon|\underline{Y}_K) = \Lambda(\varepsilon|\underline{Y}_{K-1}) + \ln \left(\cosh \left(2 \frac{\sqrt{S_T}}{N_0} \underline{y}_K^T \underline{p}_K(\varepsilon) \right) \right) \quad (13)$$

From Eqs. (12) and (13), a recursive implementation of the MAP symbol synchronizer is realized and shown in Fig. 1 [1].⁵

For practical implementation, one can simplify the estimator, as shown in Fig. 2, where the coefficients of the finite impulse response (FIR) filter correspond to N samples of the digitized symbol pulse waveform. The look-up table performs the operation shown in Figs. 1(b) or 1(c). Resetting the accumulator can be accomplished by the preprogram clock with period K or by using the reset signal generator circuitry shown in Fig. 2(b). Note that it is difficult to determine the appropriate value of period K when the symbol SNR is not known. The circuit shown in Fig. 2(b) automatically provides the reset timing needed to reset the accumulator.

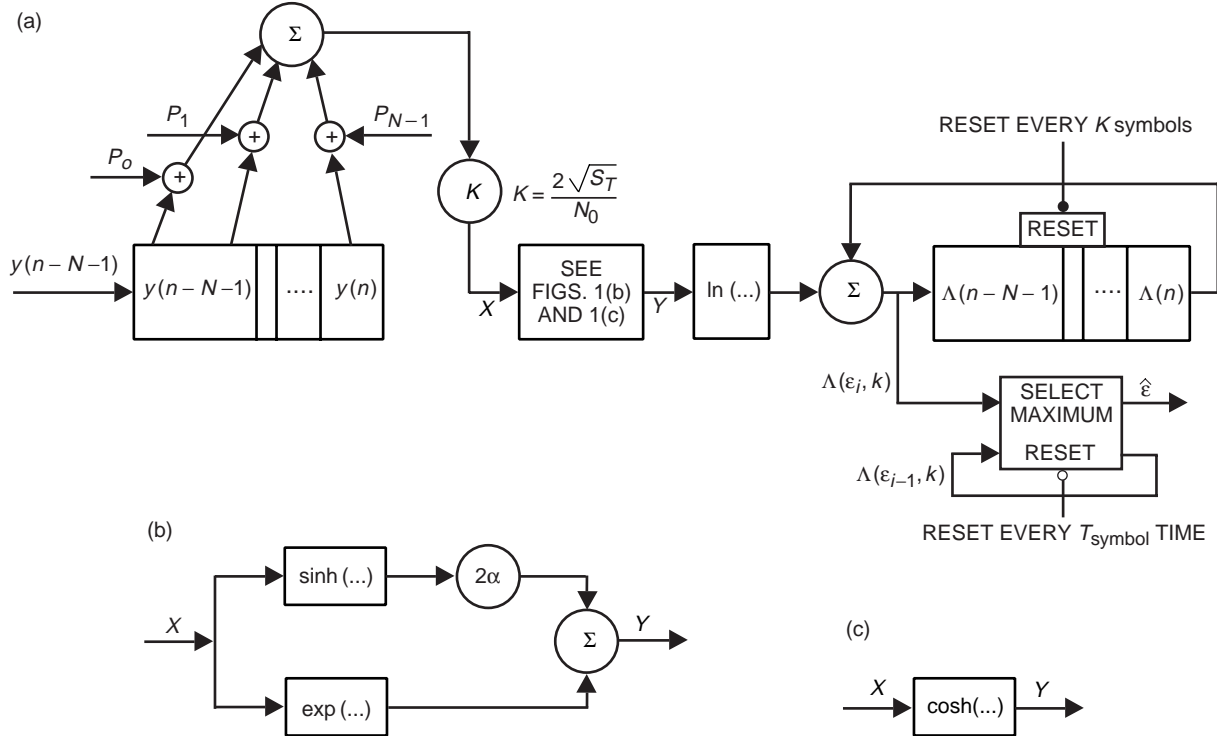


Fig. 1. The recursive MAP symbol synchronizer: (a) implementation, (b) implementation when the probability of mark (α) $\neq 0.5$, and (c) implementation when the probability of mark = 0.5.

⁵ Ibid.

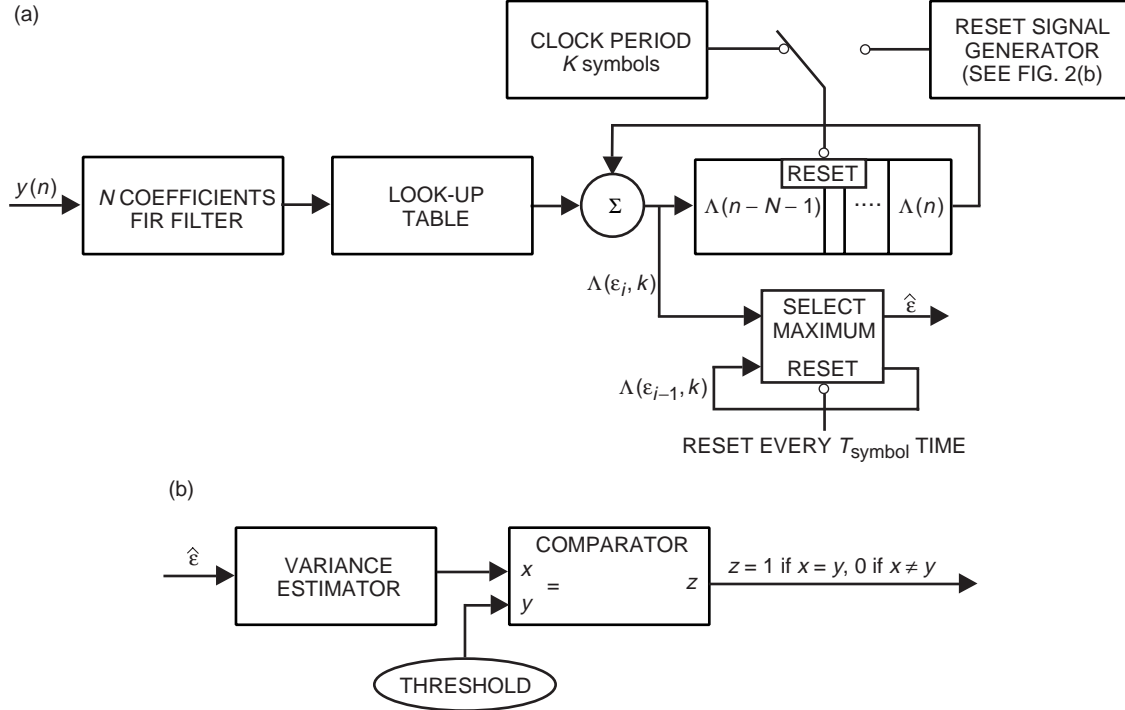


Fig. 2. The simplified estimator: (a) the simplified recursive MAP symbol synchronizer and (b) the reset signal generator.

III. Computer Simulation

Figure 3 shows the communication simulation system in order to compare the acquisition performance of the two symbol synchronizers using the Signal Processing Worksystem (SPW) software from Cadence Design Systems. Table 1 summarizes the simulation parameters.

A. Acquisition Performance of the MAP Symbol Synchronizer

Figure 4(a) shows the probability of acquisition as a function of acquisition time parameterized by the symbol SNR. Each acquisition curve is obtained from 500 simulation runs. For each run, a random epoch is chosen for the symbol synchronizer to acquire. The epoch is assumed to be uniformly distributed over the discrete symbol interval $\{0, 1, \dots, N - 1\}$. The MAP symbol-synchronizer acquisition time is the time at which the synchronizer declares lock and the normalized error between the estimate and the actual epoch is equal to or less than a prescribed value for at least 5 seconds. The normalized error is defined as

$$\lambda = \frac{|\epsilon - \hat{\epsilon}_k|}{T_s} \quad (14)$$

where $\hat{\epsilon}_K$ is the estimate of the symbol epoch made after observing K data symbols. Note that $\hat{\epsilon}_K$ is discrete, with values in the range of $(0, 1, \dots, N - 1)$, while the unknown symbol epoch, ϵ , is continuous. Hence, when ϵ is not an integer multiple of $1/N$, the estimate, $\hat{\epsilon}_K$, will have an irreducible error component of magnitude $|\Delta| < 1/N$. The error component is inversely proportional to the sampling frequency: the higher the sampling frequency (larger N), the smaller the error component, Δ . In this article, ϵ always is an integer multiple of Δ .

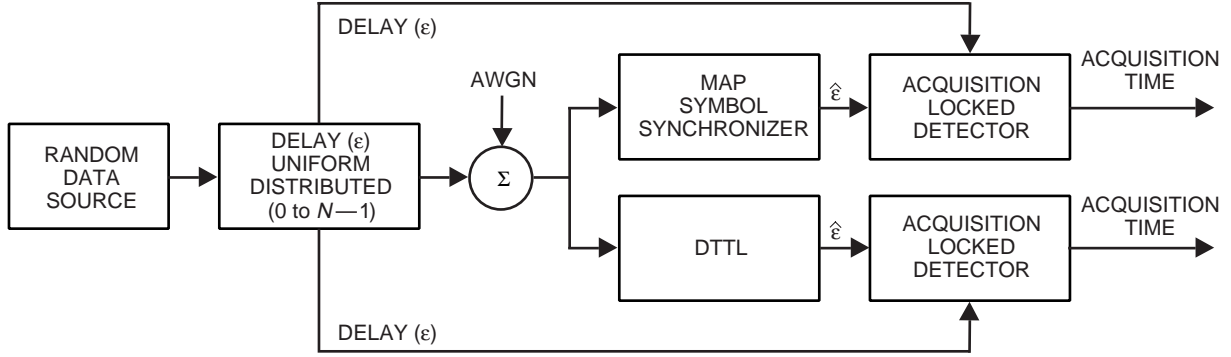


Fig. 3. The computer simulation model for evaluating the acquisition performance of the MAP symbol synchronizer and the DTTL.

Table 1. Simulation parameters.

Parameter	Value
Sampling frequency, f_s	500 kHz
Symbol rate, R_s	10 kHz
No. samples/symbol, N	50

Figure 4(a) shows the probability of acquisition curves when the prescribed value of the normalized error, λ , is set to less than Δ . Figure 4(b) shows the probability of acquisition curves with the normalized error, λ , set to less than Δ and 2Δ . As expected, the acquisition time decreases because larger errors can be tolerated. Note that λ is a function of the variable N .

It often is practical to have small N to minimize processing power and hardware complexity. Reducing N means increasing the irreducible error component Δ . However, the estimate could reach the steady state in a shorter period of time. Figure 4(c) shows the probability of acquisition as a function of acquisition time for various values of N . Here the normalized error, λ , is set to less than Δ , and ε is an integer multiple of Δ .

The MAP estimator shown in Fig. 1 can accommodate data unbalance (i.e., a data-transition density not equal to 0.5). Figure 1(b) shows the implementation for arbitrary α , and Fig. 1(c) shows the case for $\alpha = 0.5$. Since α is not known a priori, Fig. 1(c) represents a suboptimal implementation when α is unequal to 0.5. Figure 5 shows the probability of acquisition versus acquisition time curves for $\alpha = 0.7$. The solid curves result from using the nonlinearity in Fig. 1(b), and the dashed curves result from using the nonlinearity shown in Fig. 1(c). Note that using the correct nonlinearity [i.e., Fig. 1(b)] improves the acquisition probability, but not significantly. The following simulations will not consider transition unbalance in the data probabilities.

The generalized MAP symbol synchronizer shown in Fig. 1 is applicable to any symbol pulse shape, provided that the coefficients of the FIR filter contain the samples of the pulse shape waveform. In this experiment, the half-sinusoidal waveform of the minimum-shift-keying (MSK) signaling was digitized into 50 samples ($N = 50$) and chosen as the FIR filter coefficients. Figure 6(a) shows the probability of acquisition as a function of time for the MSK waveform. Note that $\lambda < 2\Delta$ is used in Fig. 6(a).

Although the generalized MAP symbol synchronizer was designed for nonoverlapping pulse shapes [i.e., zero intersymbol interference (ISI)], simulation results show that it does work with overlapping

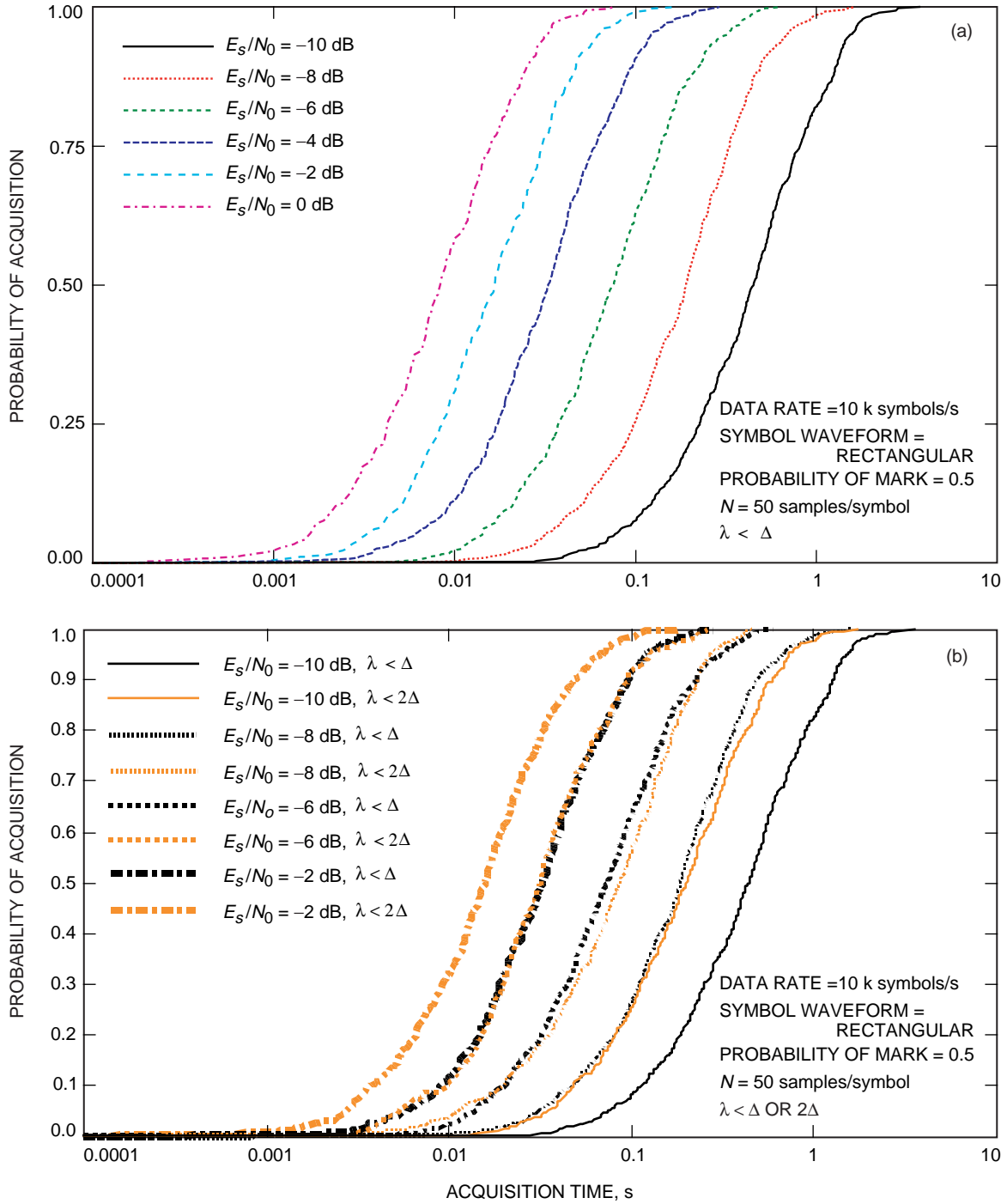


Fig. 4. The acquisition performance of the MAP symbol synchronizer parameterized by: (a) the symbol SNR, (b) the symbol SNR and normalized estimation error, λ , and (c) the number of samples/symbol, N .

pulse shapes that produce ISI. Figure 6(b) shows the probability of acquisition versus acquisition time for a Gaussian-minimum-shift-keying (GMSK) pulse shape with a Gaussian filter bandwidth-to-bit time product ($BT_B = 0.25$). Note that in order for the generalized MAP symbol synchronizer to work properly with ISI pulses, one must allow sufficiently large values of λ to discount the effects of ISI.

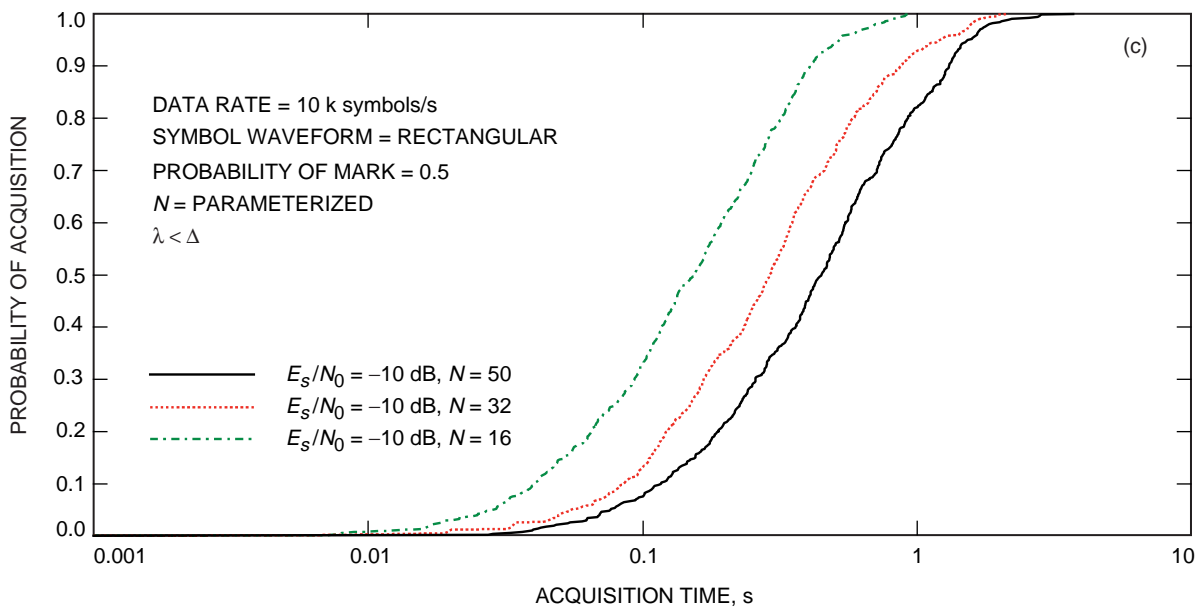


Fig. 4 (cont'd). The acquisition performance of the MAP symbol synchronizer parameterized by: (a) the symbol SNR, (b) the symbol SNR and normalized estimation error, λ , and (c) the number of samples/symbol, N .

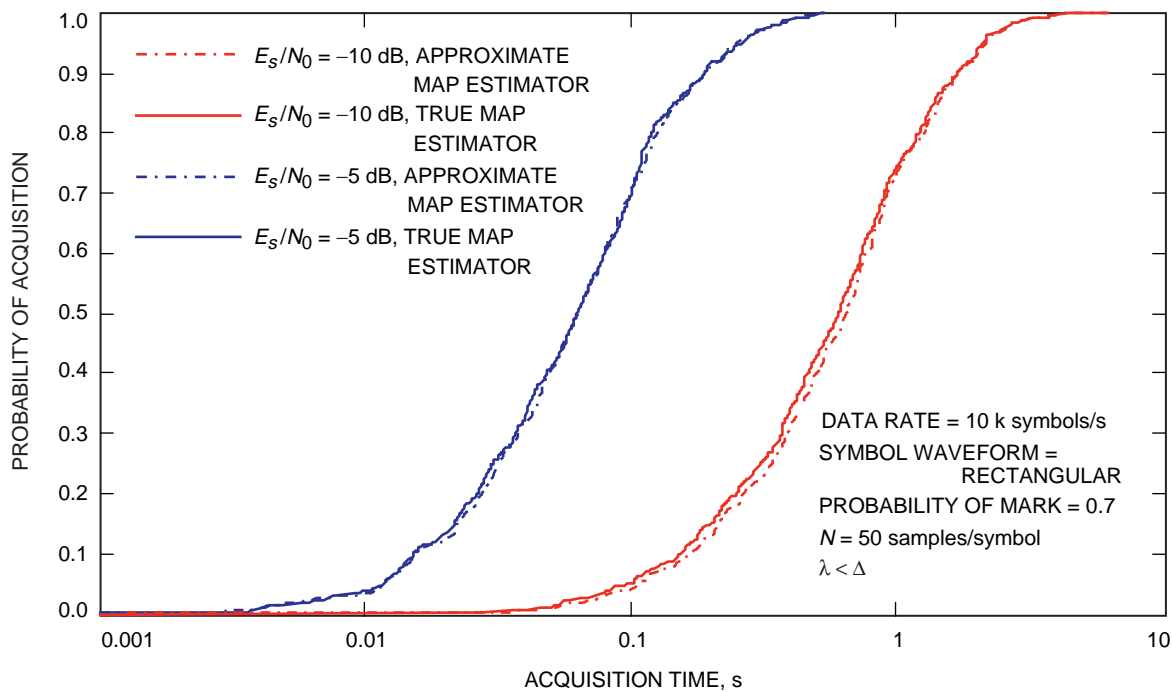


Fig. 5. The acquisition performance of the MAP symbol synchronizer for the approximate and true MAP estimators.

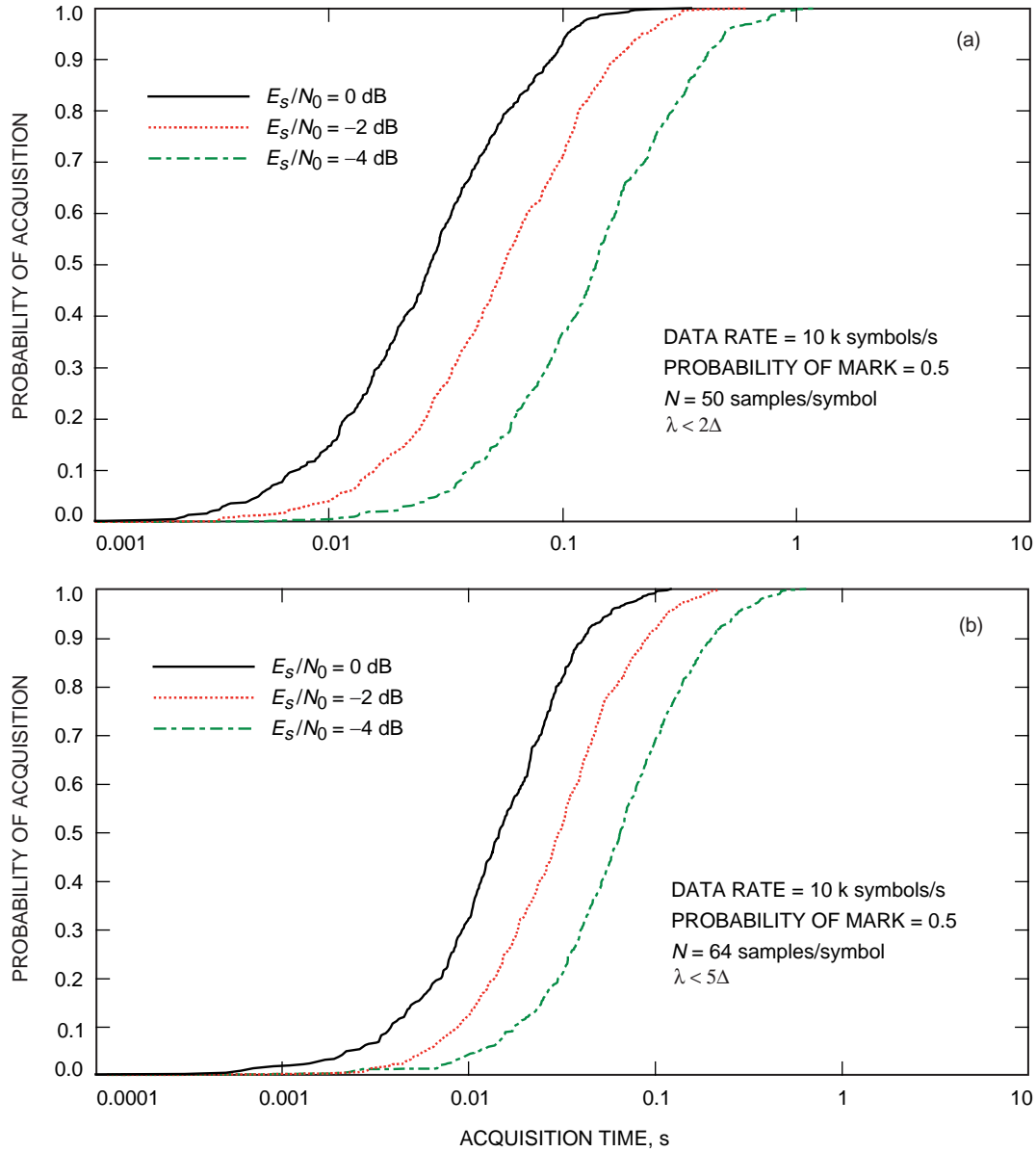


Fig. 6. The acquisition performance of the MAP symbol synchronizer for (a) an MSK waveform and (b) a GMSK ($BT_B = 0.25$) waveform.

B. Acquisition Performance of the DTTL Tracking Loop

The acquisition and tracking performance of the DTTL has been studied extensively⁶ [1,7–9] at medium-to-high symbol SNRs. Since the DTTL was developed for this SNR range, one would expect sub-optimal performance for low symbol SNR applications. Figure 7(a) shows the probability of acquisition as a function of time for the DTTL at various symbol SNRs.

Similarly to those described in Section II.A, each probability of acquisition curve was generated from 500 simulation runs. Acquisition is declared when the phase error (λ_{DTTL}) stays less than or equal to a

⁶ H. Tsou and S. Hinedi, “SPW Simulation for Clock Stability Effects on Acquisition Performance of the Data Transition Tracking Loop,” CCSDS Action Item A-E-93-37 (internal document), Jet Propulsion Laboratory, Pasadena, California, June 1994.

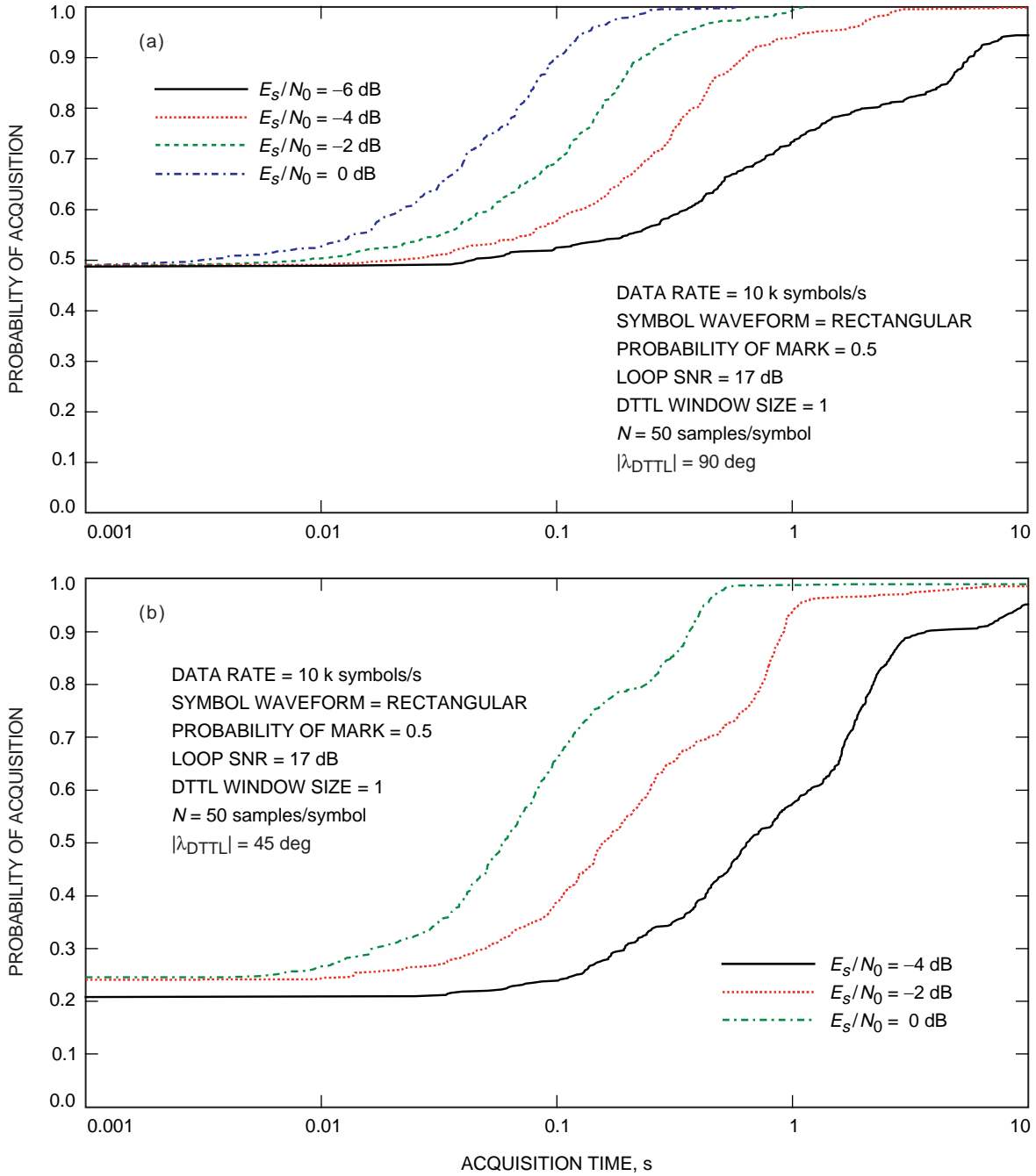


Fig. 7. The acquisition performance of the DTTL parameterized by symbol SNR with: (a) loop SNR = 17 dB and prescribed phase error = 90 deg, (b) loop SNR = 17 dB and prescribed phase error = 45 deg, and (c) loop SNR = 10 dB and prescribed phase error = 90 deg.

prescribed value for at least $10/B_L$ seconds, where B_L is the DTTL's loop filter bandwidth. With the loop SNR set to 17 dB, the normalized window size = 1 (full window), and the prescribed phase error set to 90 deg (the pull-in range of the DTTL), Fig. 7(a) shows the probability of acquisition versus acquisition time. Note that these curves show that the acquisition performance of the DTTL degrades significantly as symbol SNR becomes smaller. At symbol SNRs below -5 dB, the DTTL sometimes fails to acquire within the allotted time. For example, at a symbol SNR = -6 dB, the DTTL failed to acquire after 418 seconds in some simulations. The probability of acquisition curves for symbol SNRs below -6 dB are

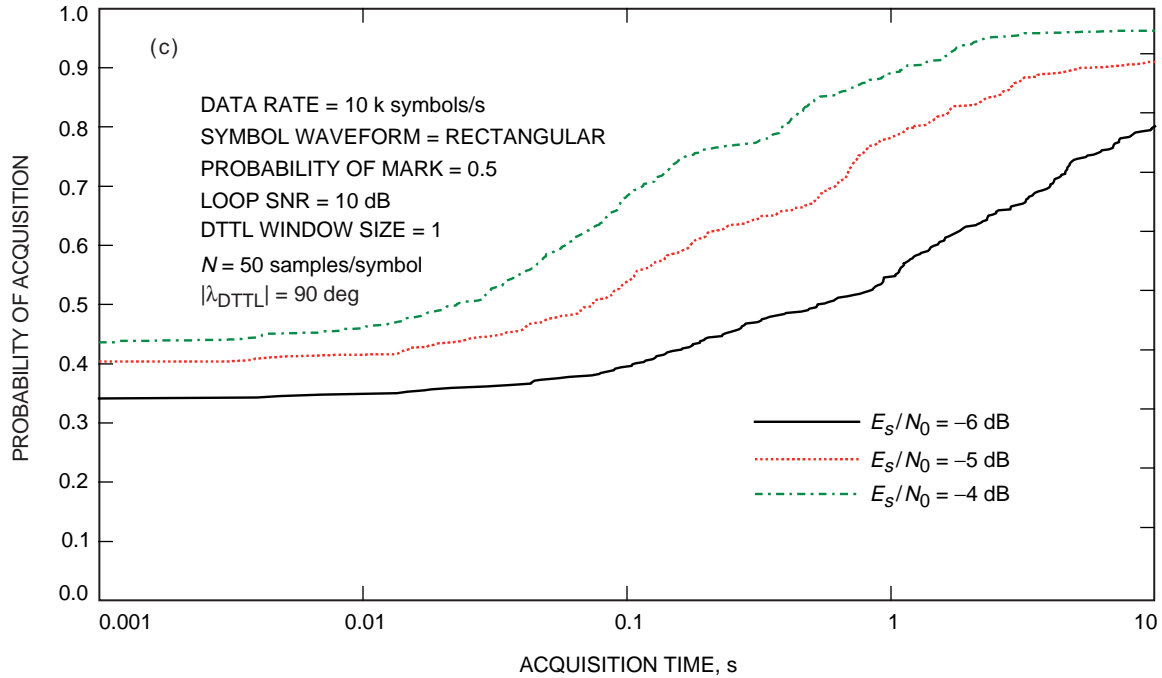


Fig. 7 (con't). The acquisition performance of the DTTL parameterized by symbol SNR with: (a) loop SNR = 17 dB and prescribed phase error = 90 deg, (b) loop SNR = 17 dB and prescribed phase error = 45 deg, and (c) loop SNR = 10 dB and prescribed phase error = 90 deg.

not available, due mainly to the fact that, in this range of SNRs, either the DTTL often does not lock or it would take an extremely long time to generate one of these curves even if the DTTL could acquire at these low SNRs. In Fig. 7(b), the acquisition probability curves were obtained with the prescribed phase error reduced to 45 deg.

Acquisition time of the DTTL is a function of the bandwidth of the loop filter and the window size. Aung et al. [9] have discussed the optimization of these parameters. Increasing the loop bandwidth (i.e., decreasing the loop SNR) is equivalent to increasing the update rate; hence, the acquisition time *could* become smaller. However, increasing the loop bandwidth also means increasing the noise power in the loop; hence, the loop could become unstable, especially at low symbol SNRs. Figure 7(c) shows the acquisition probability curves as a result of widening the bandwidth of the loop filter (i.e., decreasing the loop SNR from 17 dB down to 10 dB). Comparing Fig. 7(a) with Fig. 7(c) shows that the acquisition performance becomes worse for lower loop SNRs (i.e., for larger bandwidths of the loop filter).

C. A Comparison of the Acquisition Performance of the MAP Symbol Synchronizer and the DTTL

A comparison of Figs. 4(a) and 4(b) with Figs. 7(a) and 7(b) clearly shows the advantages of the new symbol synchronizer compared with the DTTL in terms of acquisition time. For a given probability of acquisition, the new symbol synchronizer provides faster acquisition time even under a more stringent criterion, namely smaller phase error. Note that the new symbol synchronizer can acquire, with 100 percent probability, a signal with an SNR as low as -10 dB, provided that the symbol epoch remains unchanged. This was not true for the DTTL. Figure 8 summarizes the performance difference between the new symbol synchronizer and the DTTL by showing the acquisition time as a function of symbol SNR for an acquisition probability of 90 percent. Acquisition time of the new symbol synchronizer (Fig. 8) ranges from a 10-dB improvement at symbol SNRs less than -5 dB to a 3-dB improvement for a symbol SNR about 0 dB, when compared with the DTTL. Note that it is not surprising to see that the acquisition time of the new symbol synchronizer decreases linearly with increasing symbol SNR, as shown in Fig. 8

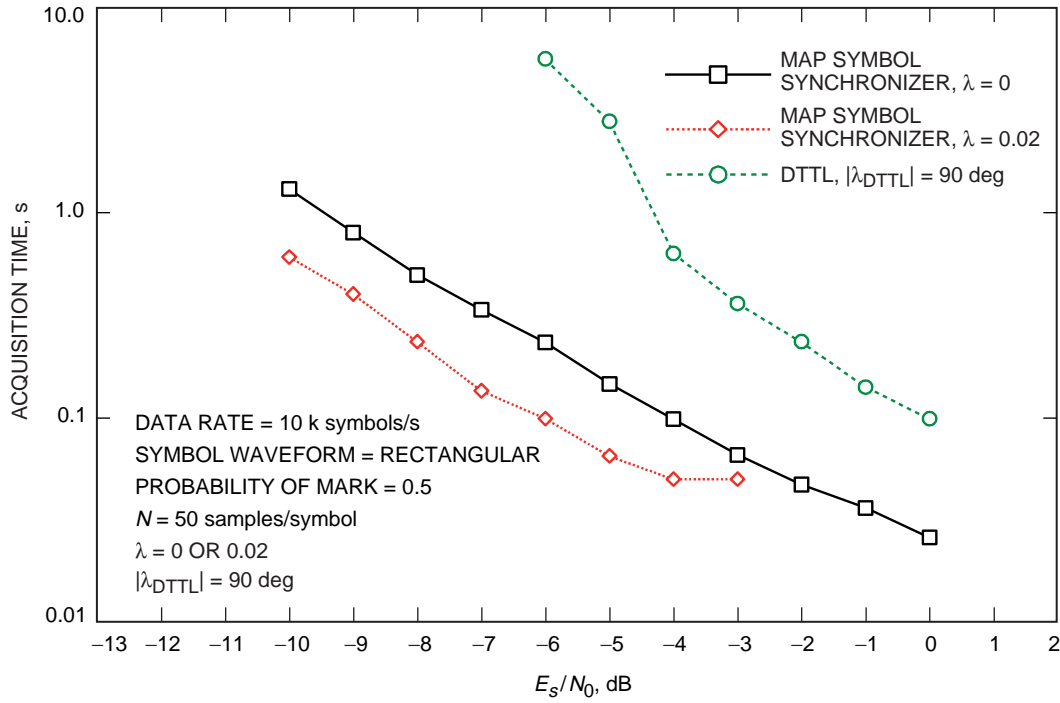


Fig. 8. The acquisition time as a function of symbol SNR for a probability of acquisition = 0.9.

($\lambda < \Delta$). For the AWGN channel, the noise power decreases linearly as a function of the observation time. Hence, increasing the symbol SNR linearly is equivalent to decreasing the observation time linearly (i.e., shortening the acquisition time).

IV. Conclusion

In this article, the generalized MAP symbol synchronizer for arbitrary data-transition density was derived and, based on computer simulation, shown to provide orders of magnitude improvement over the conventional DTTL in terms of acquisition time, particularly at low symbol SNRs. In addition, with the recursive implementation, the MAP symbol synchronizer can continuously update (at the symbol rate) the estimate, as shown in Fig. 1. For example, as shown in Figs. 4 through 6, at symbol SNR = -10 dB, one can update the estimate at least once every 4 seconds with a 90 percent probability that the new estimate has zero tracking phase error. The DTTL will take an order of magnitude longer, provided that it can acquire at a symbol SNR of -10 dB with reasonable phase error.

References

- [1] W. C. Lindsey and M. K. Simon, *Telecommunication Systems Engineering*, Chapter 9, Englewood Cliffs, New Jersey: Prentice-Hall, 1973.
- [2] J. Ziv and M. Zakai, "Some Lower Bounds on Signal Parameter Estimation," *IEEE Trans. on Inform. Theory*, vol. IT-15, pp. 386-391, May 1969.
- [3] D. Chasan, M. Zakai, and I. Ziv., "Improved Lower Bounds on Signal Parameter Estimation," *IEEE Trans. on Inform. Theory*, vol. IT-21, pp. 90-93, January 1975.

- [4] I. Ibragimov and R. Khas'minskii, "Parameter Estimation for a Discontinuous Signal in White Gaussian Noise," *Problemy Peredachi Informatsii*, vol. 11, no. 3, pp. 31–43, July–September 1975, as translated in *Problems of Information Transmission*, pp. 203–212, September 1976.
- [5] A. Terent'yev, "Distribution of the Time of Absolute Maximum at the Output of a Matched Filter," *Radio Engineering and Electronic Physics*, vol. 13, no. 4, pp. 569–573, 1968.
- [6] K. Kosbar, *Open and Closed Loop Delay Estimation with Applications to Pseudonoise Code Tracking*, Ph.D. Dissertation, University of Southern California, Los Angeles, California, July 1988.
- [7] C.-S. Tsang and C. M. Chie, "Effect of Signal Transition Variation on Bit Synchronizer Performance," *IEEE Trans. on Communications*, vol. COM-41, no. 5, pp. 673–677, May 1993.
- [8] S. Million and S. M. Hinedi, "Effects of Symbol Transition Density on Tracking and Acquisition Performance of the Data Transition Tracking Loop at Low Signal-to-Noise Ratios," *The Telecommunications and Data Acquisition Progress Report 42-128, October–December 1996*, Jet Propulsion Laboratory, Pasadena, California, pp. 1–9, February 15, 1997.
http://tda.jpl.nasa.gov/tda/progress_report/42-128/128A.pdf
- [9] M. Aung, W. J. Hurd, C. M. Buu, J. B. Berner, S. A. Stephens, and J. M. Gevargiz, "The Block V Receiver Fast Acquisition Algorithm for the Galileo S-Band Mission," *The Telecommunications and Data Acquisition Progress Report 42-118, April–June 1994*, Jet Propulsion Laboratory, Pasadena, California, pp. 83–114, August 15, 1994.
http://tda.jpl.nasa.gov/tda/progress_report/42-118/118I.pdf

[This page intentionally left blank.]

MAP-Motivated Carrier Synchronization of GMSK Based on the Laurent AMP Representation¹

Marvin K. Simon

Jet Propulsion Laboratory, Mail Station 238-343

4800 Oak Grove Drive, Pasadena, CA 91109

Voice: (818)354-3955, Fax: (818)393-1717

e-mail: marvin.k.simon@jpl.nasa.gov

Topics of interest: Mobile Radio Communications, Synchronization

Abstract

Using the MAP estimation approach to carrier synchronization of digital modulations containing ISI together with a two pulse stream AMP representation of GMSK, it is possible to obtain an optimum closed loop configuration in the same manner as has been previously proposed for other conventional modulations with no ISI. We anticipate that this scheme will outperform other GMSK carrier sync schemes that are derived in a more ad hoc fashion. In view of the fact that the second pulse has significantly less energy than the first, it is also possible that a single pulse stream AMP representation of GMSK is sufficient for satisfactory carrier sync performance thereby reducing the implementation complexity.

¹ The work of Marvin K. Simon was performed at the Jet Propulsion Laboratory, California Institute of Technology under a contract with the National Aeronautics and Space Administration. The author is with the Jet Propulsion Laboratory.

MAP-Motivated Carrier Synchronization of GMSK Based on the Laurent AMP Representation

Marvin K. Simon

1. Introduction

More than a decade ago Laurent [1] described an exact representation for constant envelope digital phase modulations, more commonly known as *continuous phase frequency modulation (CPFM)* or simply *continuous phase modulation (CPM)*, in the form of a superposition of a number of time/phase shifted amplitude-modulation pulse (AMP) streams. The number of such streams was dependent on the *partial response* nature of the modulation as described by the duration, L (in symbols), of the frequency pulse that characterizes the CPM. The primary focus of this work was on *binary* modulation² because of its relative simplicity of implementation and as such the number of pulse streams in the AMP representation is 2^{L-1} . Laurent's motivation for presenting such a representation was two-fold. First, it allowed for easier evaluation of the autocorrelation and power spectral density (PSD) of such modulations, in particular, simple results were specifically obtained for half-integer index modulations, i.e., ones whose frequency modulation index was of the form $h = n + 1/2$, n integer. Second, it allowed for approximation (with reasonably good accuracy) of CPM by a single pulse stream with one optimized pulse shape (called the "main pulse") and as such offered a synthesis means no more complicated, in principle, than *minimum-shift-keying (MSK)*, which itself is a special case of CPM with a rectangular frequency pulse shape and a modulation index $h = 0.5$.

Three years later, Kaleh [3] exploited Laurent's representation of CPM to allow for simple implementation of coherent receivers of such modulations, in particular, for the case of *Gaussian MSK (GMSK)*. Two forms of such receivers were considered, namely, a simplification of the optimum maximum-likelihood sequence estimation (MLSE) receiver and a linear MSK-type receiver, both which yielded small degradation relative to the true optimum MLSE receiver. In addition, Kaleh explicitly showed that for GMSK with a bandwidth-bit time product $BT_b = 0.25$ and a $4T_b$ -wide approximation of the Gaussian pulse, i.e., $L = 4$, a two (rather than $2^{L-1} = 8$) pulse stream approximation is for all practical purposes (the fraction of energy in the neglected six pulse streams is 2.63×10^{-5}) exact. The effective pulse shapes on each of the AMP streams have different shapes and are of different durations (one is $3T_b$ wide and one is

²The work was later extended to the M -ary case by Mengali and Morelli [2].

$5T_b$ wide). As such, both pulse shapes exceed the baud interval and hence each of the AMP pulse streams contains ISI.

In addition to the above advantages of the AMP representation insofar as spectrum evaluation and ideal receiver implementation, there is yet another advantage having to do with carrier synchronization of the receiver. Mengali and Andrea [4] discuss the use of the Laurent representation for CPM primarily in the context of the single pulse stream approximation and as such arrive at decision-directed phase estimation structures that are analogous to those used for MSK.

In this paper, we carry the carrier synchronization problem two steps further with the goal of achieving a more optimum solution. First, we consider the two-pulse stream approximation suggested by Kaleh rather than the single (main) pulse approximation. Second, using the maximum a posteriori (MAP) approach for carrier phase estimation as applied to pulse stream modulations with ISI [5,6], we arrive at a closed loop structure that is not limited to a decision-directed form and moreover accounts for the ISI directly within its implementation. The focus of the presentation here will be on first restating the two pulse stream AMP representation of GMSK in a form that is amenable to MAP estimation of carrier phase and then deriving the optimum structure.³ The performance of this structure and its comparison with other GMSK carrier sync schemes previously reported is currently under investigation and is the subject of a future report.

2. Classical Representation of GMSK

We begin by stating the classical representation of GMSK, namely, a continuous phase frequency modulation of a constant amplitude carrier with a digital pulse stream, i.e.,

$$s(t) = \sqrt{\frac{2E_b}{T_b}} \cos\left(\omega_c t + \int_{-\infty}^t \omega(\tau, \alpha) d\tau + \phi_0\right), \quad nT_b \leq t \leq (n+1)T_b \quad (1)$$

where E_b and T_b respectively denote the energy and duration of a bit ($P = E_b / T_b$ is the signal power), $\omega_c = 2\pi f_c$ is the radian carrier frequency, and $\omega(t, \alpha)$ is the frequency modulation (FM) process which is expressible in the form of a digital pulse stream

$$\omega(t, \alpha) = \pi \sum_{i \leq n} \alpha_i g(t - iT) \quad (2)$$

³By optimum we mean that closed loop structure whose error signal is motivated by the derivative of the log-likelihood ratio associated with the MAP estimation of carrier phase.

where $\alpha = (\alpha_K, \alpha_{-2}, \alpha_{-1}, \alpha_0, \alpha_1, \alpha_2, \alpha_K)$ is the independent identically distributed (i.i.d.) binary data sequence with each element taking on values ± 1 , h is the modulation index assumed to be fixed for all signaling intervals, and $g(t)$ is the normalized *instantaneous frequency pulse* (relative to the nominal carrier frequency f_0) in the zeroth signaling interval which for GMSK is approximated by [3]⁴

$$g\left(t + \frac{LT_b}{2}\right) = \frac{1}{2T} \left[Q\left(\frac{2\pi B}{\sqrt{\ln 2}}\left(t - \frac{T_b}{2}\right)\right) - Q\left(\frac{2\pi B}{\sqrt{\ln 2}}\left(t + \frac{T_b}{2}\right)\right) \right], \quad 0 \leq t \leq LT_b \quad (3)$$

where $Q(x)$ is the Gaussian probability integral, B is the 3 dB bandwidth of Gaussian transmit filter used to shape the pulse, and the value of L used for the approximation is a function of the BT_b product. For $BT_b = .25$ (typical of current applications in that it represents a good tradeoff between bandwidth compression and error probability performance), a value of $L = 4$ is sufficient, i.e., a total of $2^{L-1} = 8$ PAM components is what will be needed to completely represent the signal in AMP form.

It is more common in the literature to express (1) in the form of an equivalent phase modulation (PM), namely,

$$s(t) = \sqrt{\frac{2E_b}{T_b}} \cos(\omega_c t + \phi(t, \alpha) + \phi_0), \quad nT_b \leq t \leq (n+1)T_b \quad (4)$$

where now $\phi(t, \alpha)$ is the equivalent phase modulation process which is also expressible in the form a digital pulse stream

$$\phi(t, \alpha) = \pi \sum_{i \leq n} \alpha_i q(t - iT_b) \quad (5)$$

and $q(t) = \int_{-\infty}^t g(\tau) d\tau$ is the *normalized phase smoothing response* that defines how the underlying phase $\pi\alpha_i$ evolves with time. In general, $q(t)$ extends over infinite time and satisfies the following:

$$q(t) = \begin{cases} 0, & t \leq 0 \\ \frac{1}{2}, & t \geq LT_b \end{cases} \quad (5)$$

For GMSK, this normalized phase smoothing response is obtained from the integral of (3), namely,

⁴The true frequency pulse for GMSK extends over all time.

$$q\left(t + \frac{LT_b}{2}\right) = \frac{1}{2} + \frac{1}{2T} \left[\left(t - \frac{T_b}{2}\right) Q\left(\frac{2\pi B}{\sqrt{\ln 2}} \left(t - \frac{T_b}{2}\right)\right) - \left(t + \frac{T_b}{2}\right) Q\left(\frac{2\pi B}{\sqrt{\ln 2}} \left(t + \frac{T_b}{2}\right)\right) \right] \\ - \frac{1}{\sqrt{2\pi}} \left(\frac{\sqrt{\ln 2}}{2\pi B}\right) \left[\exp\left\{-\frac{1}{2} \left[\frac{2\pi B}{\sqrt{\ln 2}} \left(t - \frac{T_b}{2}\right)\right]^2\right\} - \exp\left\{-\frac{1}{2} \left[\frac{2\pi B}{\sqrt{\ln 2}} \left(t + \frac{T_b}{2}\right)\right]^2\right\} \right], \\ 0 \leq t \leq LT \quad (6)$$

3. AMP Representation of GMSK

In what follows it will be convenient to deal with the normalized (unit amplitude) complex envelope of $s(t)$, i.e., the complex baseband signal $\tilde{S}(t)$ defined by the relation

$$\tilde{S}(t) = \exp\{j\phi(t, \boldsymbol{\alpha})\}, \quad nT_b \leq t \leq (n+1)T_b \quad (7)$$

Define the *generalized* phase pulse function by

$$\Psi(t) = \begin{cases} \pi q(t), & 0 \leq t \leq LT_b \\ \frac{\pi}{2} [1 - 2q(t - LT_b)], & LT_b \leq t \end{cases} \quad (8)$$

which is obtained by taking the nonconstant part of $q(t)$, i.e., the part that exists in the interval $0 \leq t \leq LT$ and reflecting it about the $t = LT$ axis. Thus, in view of (8), $\Psi(t)$ is a waveform that is nonzero in the interval $0 \leq t \leq 2LT_b$ and symmetric around $t = LT_b$. The importance of $\Psi(t)$ is that it allows definition of the following functions which becomes an integral part of the AMP representation of GMSK:

$$S_0(t) = \sin \Psi(t), \quad S_n(t) = S_0(t + nT_b) = \sin \Psi(t + nT_b) \quad (9)$$

Next define the $2^{L-1} = 8$ distinct pulse shapes [1, Eq. (11)]

$$\begin{aligned} C_0(t) &= S_0(t)S_1(t)S_2(t)S_3(t), & 0 \leq t \leq 5T_b \\ C_1(t) &= S_0(t)S_2(t)S_3(t)S_5(t), & 0 \leq t \leq 3T_b \\ C_2(t) &= S_0(t)S_1(t)S_3(t)S_6(t), & 0 \leq t \leq 2T_b \\ C_3(t) &= S_0(t)S_3(t)S_5(t)S_6(t), & 0 \leq t \leq 2T_b \\ C_4(t) &= S_0(t)S_1(t)S_2(t)S_7(t), & 0 \leq t \leq T_b \\ C_5(t) &= S_0(t)S_2(t)S_5(t)S_7(t), & 0 \leq t \leq T_b \\ C_6(t) &= S_0(t)S_1(t)S_6(t)S_7(t), & 0 \leq t \leq T_b \\ C_7(t) &= S_0(t)S_5(t)S_6(t)S_7(t), & 0 \leq t \leq T_b \end{aligned} \quad (10)$$

each of which is a product of the basic generalized pulse shape $S_0(t)$ and $L-1 = 3$

other time shifts of $S_0(t)$. Finally, then the generic AMP form for the complex envelope of GMSK is [1]

$$\tilde{S}(t) = \sum_{K=0}^7 \left[\sum_{n=-\infty}^{\infty} e^{j(\pi/2)A_{K,n}} C_K(t - nT_b) \right] \triangleq \sum_{K=0}^7 \left[\sum_{n=-\infty}^{\infty} \tilde{a}_{K,n} C_K(t - nT_b) \right] \quad (11)$$

which results in the real GMSK signal

$$s(t) = \sqrt{\frac{2E_b}{T_b}} \operatorname{Re}\{\tilde{S}(t)\} = \sqrt{\frac{2E_b}{T_b}} \sum_{K=0}^7 \left[\sum_{n=-\infty}^{\infty} C_K(t - nT_b) \cos\left(\omega_c t + \frac{\pi}{2} A_{K,n}\right) \right] \quad (12)$$

i.e., a superposition of eight amplitude/phase modulated pulse streams. By virtue of the fact that some of the $C_K(t)$'s extend beyond T_b sec (in particular the first four in the set, i.e., the ones with the most energy), as previously stated the corresponding pulse streams consist of overlapping pulses and hence contribute ISI. Also in (11) $\tilde{a}_{K,n} \triangleq e^{j(\pi/2)A_{K,n}}$ is the equivalent complex (unit amplitude) data symbol for the n th transmitted pulse in the K th stream whose phase $(\pi/2)A_{K,n}$ depends solely on the past information data sequence α [1].

In the AMP representation of (11) or (12), the dominant term is the pulse stream corresponding to $C_0(t)$ (for a full response ($L = 1$) CPM, e.g., MSK, it would be the only one) since its duration is the longest (at least $2T_b$ longer than any other pulse component) and it also conveys the most significant part of the total energy of the signal. The next most significant term would be the pulse stream corresponding to $C_1(t)$ which contains virtually all the remaining signal energy. Thus, as previously alluded to, it is sufficient to consider only the first two pulse streams in (11) and hence for all practical purposes we may “exactly” describe GMSK by the complex signal

$$\tilde{S}(t) = \sum_{n=-\infty}^{\infty} \tilde{a}_{0,n} C_0(t - nT_b) + \sum_{n=-\infty}^{\infty} \tilde{a}_{1,n} C_1(t - nT_b) \quad (13)$$

where it can be shown that the equivalent complex data symbols satisfy the relations [3]

$$\begin{aligned} \tilde{a}_{0,n} &\triangleq e^{j\frac{\pi}{2}A_{0,n}} = j\alpha_n \tilde{a}_{0,n-1} \Rightarrow \tilde{a}_{0,2n} \in \{j, -j\}, \quad \tilde{a}_{0,2n+1} \in \{1, -1\} \\ \tilde{a}_{1,n} &\triangleq e^{j\frac{\pi}{2}A_{1,n}} = j\alpha_n \tilde{a}_{0,n-2} \Rightarrow \tilde{a}_{1,2n} \in \{1, -1\}, \quad \tilde{a}_{1,2n+1} \in \{j, -j\} \end{aligned} \quad (14)$$

Note that the symbols in the two data streams alternate (from bit to bit) between purely real and purely imaginary unit amplitude values. Thus, in terms of the real GMSK signal $s(t)$, we can view it as being composed of the sum of two pulse-shaped offset QPSK-type signals with pulse shapes corresponding to $C_0(t)$ and $C_1(t)$ and I, Q

± 1 data symbol ($T_s = 2T_b$ in duration) sequences respectively corresponding to

$$\begin{aligned} a_{0,2n} &= \text{Im}\{\tilde{a}_{0,2n}\}, & b_{0,2n+1} &= \text{Re}\{\tilde{a}_{0,2n+1}\} \\ a_{1,2n} &= \text{Re}\{\tilde{a}_{1,2n}\}, & b_{1,2n+1} &= \text{Im}\{\tilde{a}_{1,2n+1}\} \end{aligned} \quad (15)$$

That is,

$$\begin{aligned} s(t) = \sqrt{\frac{2E_b}{T_b}} & \left[\sum_{n=-\infty}^{\infty} a_{0,2n+1} C_0(t - (2n+1)T_b) \cos \omega_c t - \sum_{n=-\infty}^{\infty} b_{0,2n} C_0(t - 2nT_b) \sin \omega_c t \right. \\ & \left. + \sum_{n=-\infty}^{\infty} a_{1,2n} C_1(t - 2nT_b) \cos \omega_c t - \sum_{n=-\infty}^{\infty} b_{1,2n+1} C_0(t - (2n+1)T_b) \sin \omega_c t \right] \end{aligned} \quad (16)$$

Kaleh [3] also shows that the effective data sequences for the two symbol streams as defined in (14) each have uncorrelated symbols and furthermore the two sequences are uncorrelated with each other. It is possible to show a stronger condition on these sequences, namely, that they are each independent identically distributed (i.i.d.) and independent of each other. This property will be important in applying the average likelihood approach for obtaining the carrier phase estimate. To see these independence properties, it is interesting to interpret the equivalent I and Q data sequences in (16) in terms of the differentially encoded version of the true information sequence α [1]. In particular, it is straightforward to show from the properties in (14) that for the first pulse stream the equivalent I, Q data sequences $\{a_{0,2n+1}\}, \{b_{0,2n}\}$ correspond to the odd/even split of the differentially encoded version of α with the additional constraint that every other symbol be inverted. In mathematical terms, if $v_k = \alpha_k v_{k-1}$ represents the differentially encoded version of α_k , then

$$a_{0,2k+1} = (-1)^k v_{2k-1}, \quad b_{0,2k} = (-1)^k v_{2k} \quad (17)$$

It should be noted that the relation in (17) is precisely the same equivalence between the frequency modulation representation of MSK and its offset QPSK equivalent. For the second pulse stream, the equivalent I, Q data sequences $\{a_{1,2n+1}\}, \{b_{1,2n}\}$ are obtained by first multiplying the differential encoder output by the information bit delayed by one bit interval before performing the odd/even split and alternate symbol inversion, i.e.,

$$a_{1,2k} = (-1)^k v_{2k} \alpha_{k-1} \triangleq (-1)^k w_{2k}, \quad b_{1,2k+1} = (-1)^k v_{2k+1} \alpha_{k-1} \triangleq (-1)^k w_{2k+1} \quad (18)$$

This equivalence can be seen by rewriting the second relation in (14) as

$$\tilde{a}_{1,n} = j\alpha_n \tilde{a}_{0,n-2} = j\alpha_n \tilde{a}_{0,n-1} \tilde{a}_{0,n-1} \tilde{a}_{0,n-2} = \tilde{a}_{0,n} \alpha_{n-1} \quad (19)$$

Finally, since for an i.i.d. information sequence α the differentially encoded version of this sequence is also i.i.d. and since multiplication by a one-bit delayed version of the input does not destroy the i.i.d. property, we reach the conclusions regarding the independence properties of the symbol stream sequences given above. Based on the entirety of the above, we conclude that GMSK can be implemented with the superimposed offset QPSK transmitter illustrated in Fig. 1. The two pulse shapes $C_0(t)$ and $C_1(t)$ as defined by (10) together with (6) and (8) are illustrated in Fig. 2.

4. MAP Estimation of Carrier Phase

Consider now the received signal $y(t)$ composed of the sum of $s(t;\theta)$ and additive white Gaussian noise (AWGN) $n(t)$ where $s(t;\theta)$ is given by (16) with the addition of a uniformly distributed phase θ included in each carrier component. Based on an observation of $y(t)$ over the interval $0 \leq t \leq T_0$ where we arbitrary assume that T_0 is an even integer multiple (say K) of the bit time T_b , we wish to find the MAP estimate of θ , i.e., the value of θ that maximizes the a posteriori probability $p(\theta|y(t))$ or since θ is assumed to be uniformly distributed, the value of θ that maximizes the conditional probability $p(y(t)|\theta)$. For an AWGN channel with single-sided noise power spectral density N_0 watts/Hertz, $p(y(t)|\theta)$ has the form

$$p(y(t)|\mathbf{a}_0, \mathbf{b}_0, \mathbf{a}_1, \mathbf{b}_1, \theta) = C \exp\left(-\frac{1}{N_0} \int_0^{T_0} (y(t) - s(t;\theta))^2 dt\right) \quad (20)$$

where C is a normalization constant and we have added to the conditioning notation the implicit dependence of $s(t;\theta)$ on the i.i.d. I and Q data sequences of the two pulse streams. For a constant envelope (energy) signal such as GMSK, it is sufficient to consider only the term involving the correlation of $y(t)$ and $s(t;\theta)$ and lump the remaining terms into the normalization constant.⁴ Thus, we rewrite (20) as

$$p(y(t)|\mathbf{a}_0, \mathbf{b}_0, \mathbf{a}_1, \mathbf{b}_1, \theta) = C \exp\left(\frac{2}{N_0} \int_0^{T_0} y(t)s(t;\theta) dt\right) \quad (21)$$

⁴We note that for the general ISI problem as treated in [5,6], the energy-dependent exponential term $\exp\left\{-(1/N_0) \int_0^{T_0} s^2(t;\theta) dt\right\}$ is not constant and in fact depends on the data sequence. However, for the “exact” representation of GMSK by the two pulse stream AMP form, we can make the constant envelope assumption and hence ignore the energy-dependent term.

where for convenience we still use C to denote the normalization constant.

Evaluation of (21) for $s(t; \theta)$ corresponding to a single binary pulse stream, e.g., BPSK, with ISI was considered in [5,6]. Extension of the result to an $s(t; \theta)$ corresponding to a single pair of quadrature binary pulse streams (such as QPSK) with identical ISI on the I and Q channels is straightforward and was somewhat discussed in [5]. What we have for the AMP representation of GMSK in (16) is two pairs of offset quadrature binary pulse streams each pair having different amounts of ISI. (Recall that $C_0(t)$ is a pulse of width $5T_b$ and $C_1(t)$ is a completely different pulse of width $3T_b$.) Evaluation of (21) for such a received signal has not been previously considered. Without belaboring the details, following substitution of (16) into (21) and considerable manipulation it can be shown that

$$\begin{aligned}
 p(y(t)|\mathbf{a}_0, \mathbf{b}_0, \mathbf{a}_1, \mathbf{b}_1, \theta) = & C \prod_{\substack{k=-3 \\ k \text{ odd}}}^{K-1} \exp\{a_{0k} I_c(k, 0, \theta)\} \prod_{\substack{k=-4 \\ k \text{ even}}}^{K-2} \exp\{b_{0k} I_s(k, 0, \theta)\} \\
 & \times \prod_{\substack{k=-2 \\ k \text{ even}}}^{K-2} \exp\{a_{1k} I_c(k, 1, \theta)\} \prod_{\substack{k=-1 \\ k \text{ odd}}}^{K-1} \exp\{b_{1k} I_s(k, 1, \theta)\}
 \end{aligned} \tag{22}$$

where

$$\begin{aligned}
 I_c(k, l, \theta) & \triangleq \frac{2\sqrt{2E_b/T_b}}{N_0} \int_0^{KT_b} r(t) \cos(\omega_c t + \theta) C_l(t - kT_b) dt \\
 I_s(k, l, \theta) & \triangleq \frac{2\sqrt{2E_b/T_b}}{N_0} \int_0^{KT_b} r(t) \sin(\omega_c t + \theta) C_l(t - kT_b) dt
 \end{aligned} \tag{23}$$

Note that the conditional (on the data sequences) likelihood function in (22) partitions into a symbol-by-symbol product of conditional likelihood functions; however, because of the presence of ISI in each of the component pulse streams, each argument of the exponential terms involves integration over the entire observation interval $0 \leq t \leq KT_b$ rather than just integration over a single bit interval as is customary in such problems when ISI is absent. (Actually the finite duration of $C_0(t - kT_b)$ and $C_1(t - kT_b)$ will truncate these integrations to an interval (depending on the value of k) smaller than the observation time interval but still larger than the baud interval.)

The average likelihood ratio $p(y(t)|\theta)$ is obtained by averaging (22) over the four i.i.d. component data sequences $\mathbf{a}_0, \mathbf{b}_0, \mathbf{a}_1, \mathbf{b}_1$, namely,

$$\begin{aligned}
p(y(t)|\theta) = & C \prod_{\substack{k=-3 \\ k \text{ odd}}}^{K-1} \cosh\{I_c(k,0,\theta)\} \prod_{\substack{k=-4 \\ k \text{ even}}}^{K-2} \cosh\{I_s(k,0,\theta)\} \\
& \times \prod_{\substack{k=-2 \\ k \text{ even}}}^{K-2} \cosh\{I_c(k,1,\theta)\} \prod_{\substack{k=-1 \\ k \text{ odd}}}^{K-1} \cosh\{I_s(k,1,\theta)\}
\end{aligned} \tag{24}$$

Finally, the MAP estimate of θ , i.e., θ_{MAP} is the value of θ that maximizes (24).

5. Closed Loop Carrier Synchronization of GMSK

As has been done many times in the past to arrive at closed loop carrier synchronizers based on open loop MAP estimates, one takes the natural logarithm of the likelihood ratio, differentiates it with respect to θ and then uses this as the error signal, $e(\theta)$, in a closed loop configuration. The reasoning behind this approach is that $e(\theta)$ will be equal to zero when $\theta = \theta_{MAP}$ and thus the closed loop will null at the point corresponding to the open MAP phase estimate. Thus, proceeding in this fashion, we first obtain

$$\begin{aligned}
\ln p(y(t)|\theta) = & \ln C + \sum_{\substack{k=-3 \\ k \text{ odd}}}^{K-1} \ln \cosh\{I_c(k,0,\theta)\} + \sum_{\substack{k=-4 \\ k \text{ even}}}^{K-2} \ln \cosh\{I_s(k,0,\theta)\} \\
& + \sum_{\substack{k=-2 \\ k \text{ even}}}^{K-2} \ln \cosh\{I_c(k,1,\theta)\} + \sum_{\substack{k=-1 \\ k \text{ odd}}}^{K-1} \ln \cosh\{I_s(k,1,\theta)\}
\end{aligned} \tag{25}$$

Differentiating (25) with respect to θ gives

$$\begin{aligned}
e(\theta) \triangleq \frac{d}{d\theta} \ln p(y(t)|\theta) = & \sum_{\substack{k=-3 \\ k \text{ odd}}}^{K-1} I_s(k,0,\theta) \tanh\{I_c(k,0,\theta)\} - \sum_{\substack{k=-4 \\ k \text{ even}}}^{K-2} I_c(k,0,\theta) \tanh\{I_s(k,0,\theta)\} \\
& + \sum_{\substack{k=-2 \\ k \text{ even}}}^{K-2} I_s(k,1,\theta) \tanh\{I_c(k,1,\theta)\} - \sum_{\substack{k=-1 \\ k \text{ odd}}}^{K-1} I_c(k,1,\theta) \tanh\{I_s(k,1,\theta)\} \\
\triangleq & e_0(\theta) + e_1(\theta)
\end{aligned} \tag{26}$$

where have made use of the fact that from (23) $I_c(k,l,\theta)$ and $I_s(k,l,\theta)$ are derivatives of each other.

The result in (26) suggests a superposition of two loops each contributing a component to the error signal corresponding to associated pulse stream in the two pulse stream AMP representation of GMSK. Fig. 3a and 3b illustrate the two loop

components that must be superimposed to arrive at the closed loop GMSK carrier synchronizer suggested by the error signal in (26).⁶ We offer this scheme as the “optimum” (in the sense of being MAP-motivated) GMSK carrier synchronizer. As is customary, the “tanh” nonlinearity can be approximated by a linear or hard limiter device for low and high SNR applications, respectively. The rate at which the loop updates its carrier phase estimate can vary from every T_b to every KT_b seconds. In the case of the latter extreme, the observation intervals used for each carrier phase estimate do not overlap and as such the loop represents a sequential block-by-block implementation of the MAP open loop estimator. In the case of the former extreme, the observation intervals used for each carrier phase estimate overlap by $(K-1)T_b$ seconds and as such the loop represents a sliding window MAP phase estimator.

6. Conclusions

Using the MAP estimation approach to carrier synchronization of digital modulations containing ISI together with a two pulse stream AMP representation of GMSK, it is possible to obtain an optimum closed loop configuration in the same manner as has been previously proposed for other conventional modulations with no ISI. We anticipate that this scheme will outperform other GMSK carrier sync schemes that are derived in a more ad hoc fashion. The actual performance of our scheme is currently under investigation and will be reported on in the future. In view of the fact that the second pulse has significantly less energy than the first, the outcome of these evaluations might further demonstrate that a single pulse stream AMP representation of GMSK is sufficient for satisfactory carrier sync performance thereby reducing the implementation complexity by a factor of two.

References

- [1] P. A. Laurent, “Exact and approximate construction of digital phase modulations by superposition of amplitude modulated pulses,” *IEEE Transactions on Communications*, vol. COM-34, no. 2, February 1986, pp. 150–160.
- [2] U. Mengali and M. Morelli, “Decomposition of M-ary CPM signals into PAM waveforms,” *IEEE Transactions on Information Theory*, vol. 41, no. 5, September 1995, pp. 1265–1275.

⁶A value of $K = 6$ (for any larger value the noise-free (signal) components of $I_c(k, l, \theta)$ and $I_s(k, l, \theta)$ would not change due to the truncation of the integral caused by the time limitation of $C_0(t - kT_b)$ and $C_1(t - kT_b)$) is no doubt sufficient for these figures.

- [3] G. K. Kaleh, "Simple coherent receivers for partial response continuous phase modulation," *IEEE Transactions on Selected Areas in Communications*, vol. 7, no. 9, December 1989, pp. 1427–1436.
- [4] U. Mengali and A. N. D'Andrea, *Synchronization Techniques for Digital Receivers*, Plenum Press, NewYork and London, 1997.
- [5] S. M. Hinedi, "Carrier synchronization in bandlimited channels," PhD Dissertation, University of Southern California, 1987.
- [6] M. K. Simon and S. Hinedi, "Suppressed carrier synchronizers for ISI channels," GLOBECOM '96 Conference Record, London, England, November 1996.

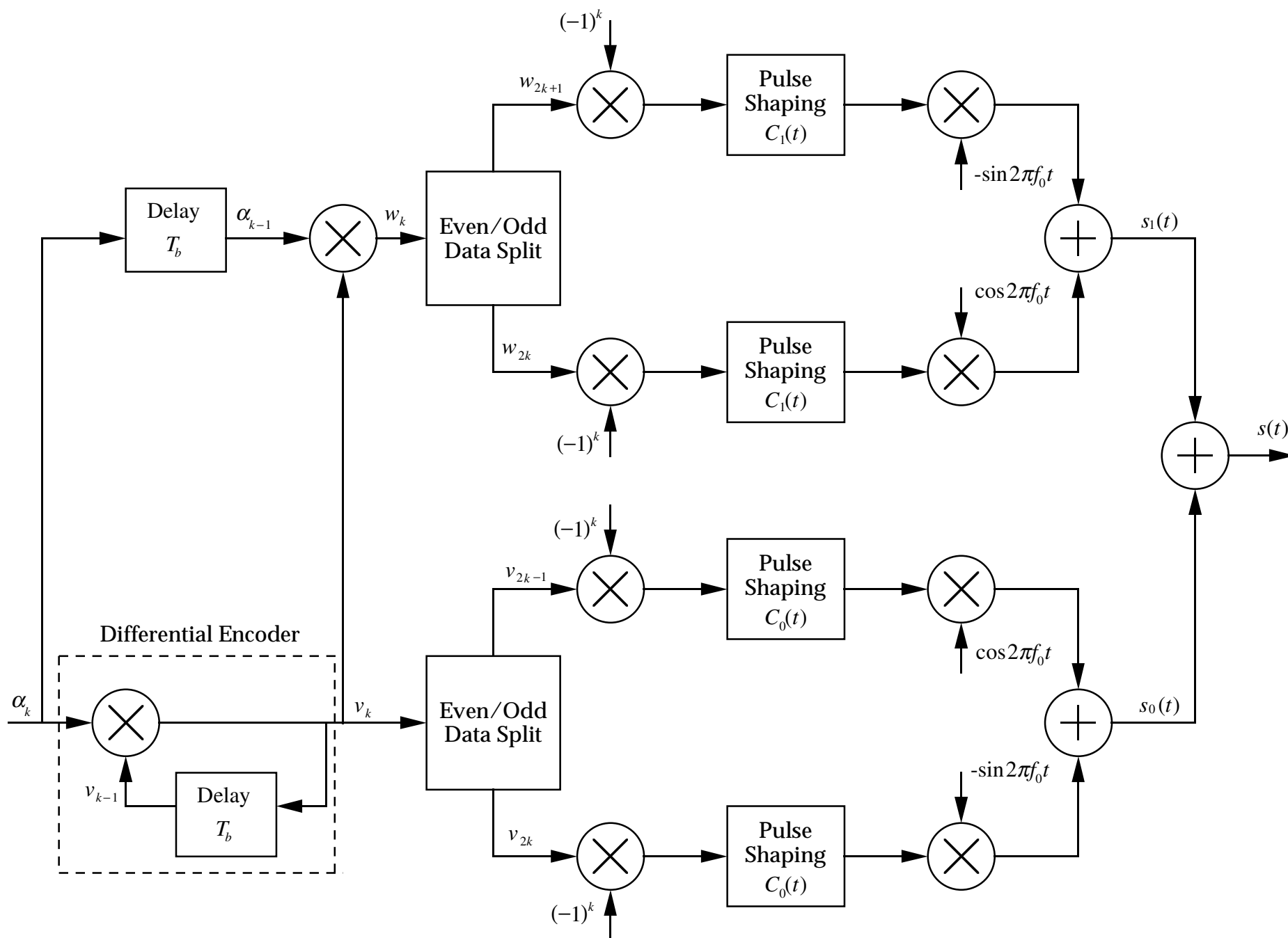
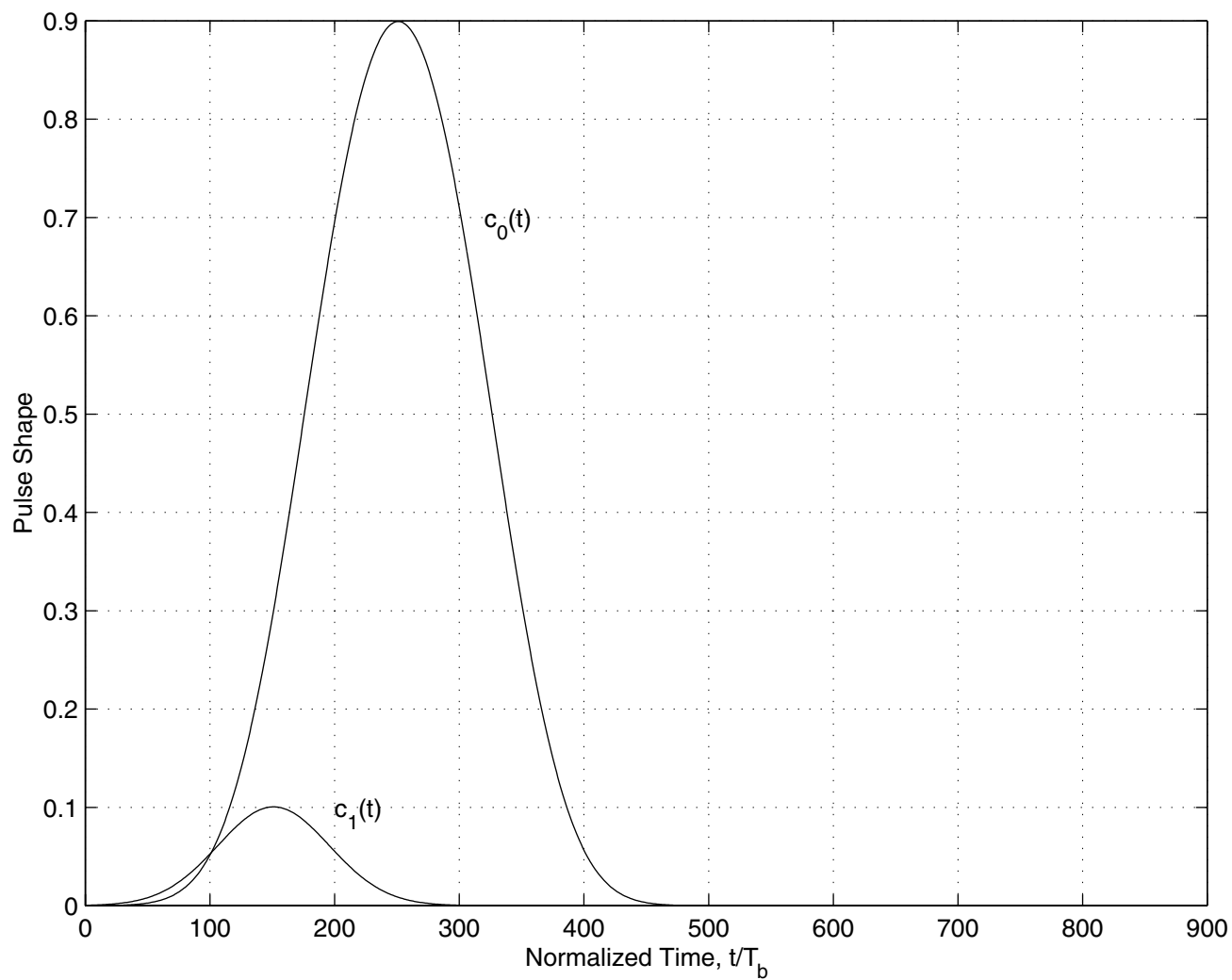


Fig. 1. GMSK Transmitter Implementation Based on AMP Representation



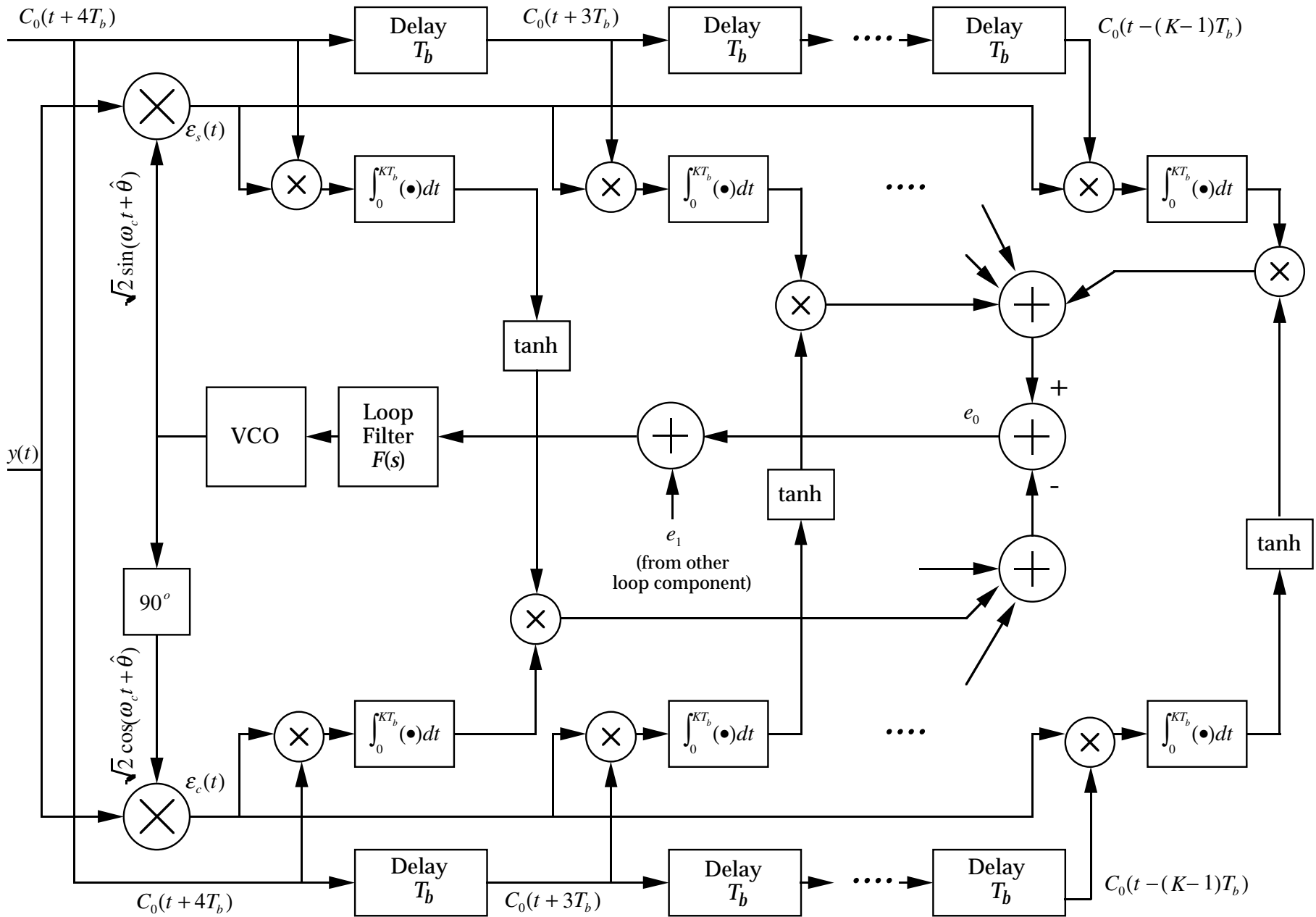


Fig. 3a. Block Diagram of Suboptimum ISI-Compensated MAP Estimation Loop for GMSK (First Signal Component)

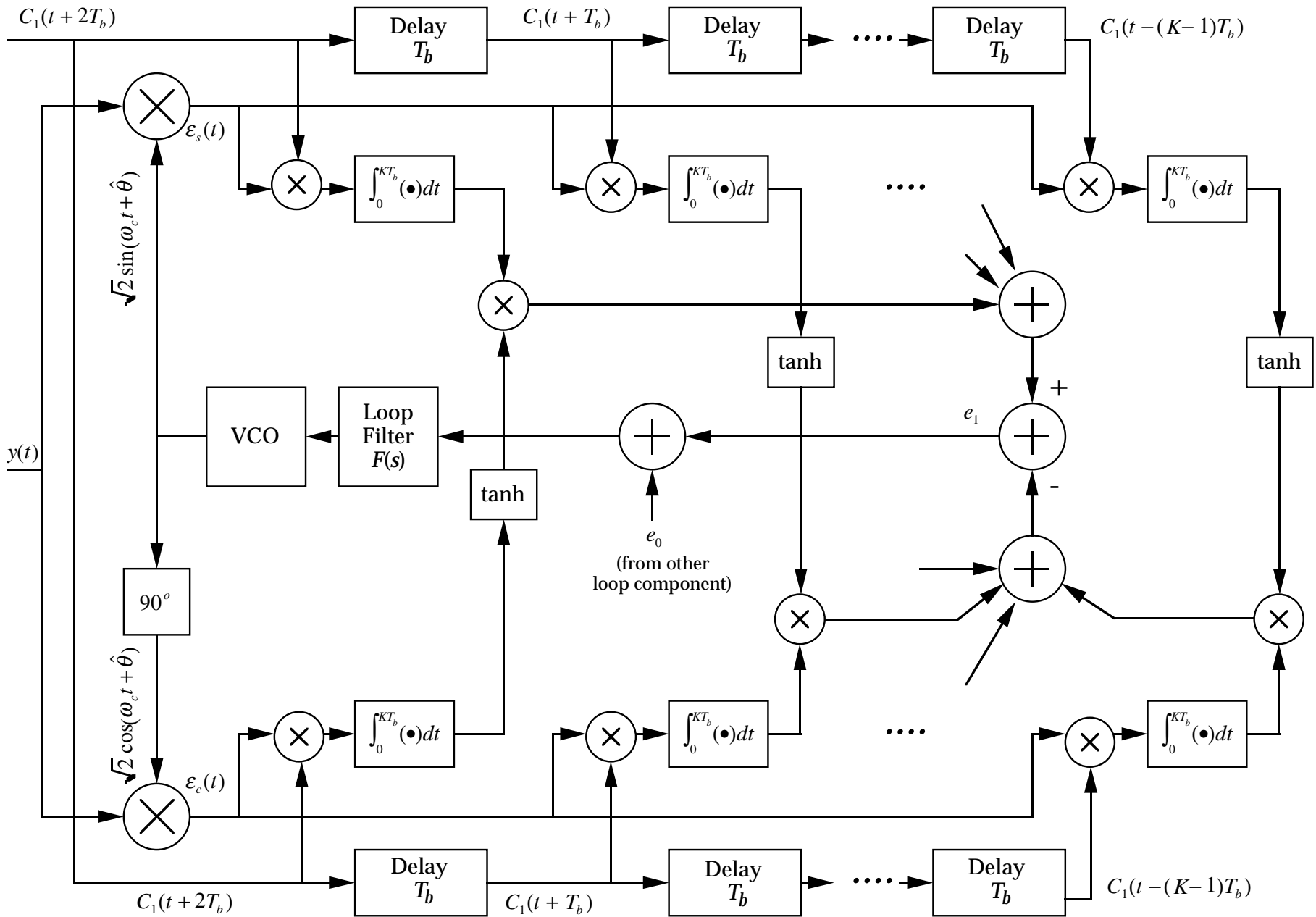


Fig. 3b. Block Diagram of Suboptimum ISI-Compensated MAP Estimation Loop for GMSK (Second Signal Component)

ON THE FEASIBILITY OF USING THE BLOCK V RECEIVER TO SUPPORT 8-PSK MODULATION SCHEME

AI-97-25

Haiping Tsou and Caroline Racho

**National Aeronautics and Space Administration
Jet Propulsion Laboratory
California Institute of Technology
4800 Oak Grove Drive
Pasadena, CA 91109**

ABSTRACT

The DSN's modern deep space receiver, known as the Block V Receiver (BVR), is capable to perform carrier tracking for the residual carrier as well as the suppressed carrier for both BPSK and QPSK signals. With recent studies on various bandwidth efficient modulation schemes, the question arises on the feasibility of using this receiver to support 8-PSK modulation without resorting to costly modification. This report summarizes the simulated carrier tracking performance of a proposed augmented BVR. The simulation results indicate that, despite the significant loss incurred in the augmented BVR by the squaring operation and inter-symbol interference, carrier tracking of an 8-PSK signal using the BVR's cross-over Costas loop is still feasible for near-Earth missions, provided that a sufficient signal-to-noise ratio can be maintained.

1. Introduction

Recently, 8-PSK signaling has been proposed [1] along with other modulation schemes for more efficient utilization of frequency spectrum in non-linear satellite channels. Although no foreseeable future deep space mission plans to use 8-PSK modulation, it is still interesting to find out the feasibility of using a NASA's modern deep space receiver, known as the Block V Receiver (BVR), to support this modulation scheme.

The BVR has been widely deployed in NASA's Deep Space Network (DSN) as a primary receiver for the deep space missions. The major portion of the BVR consists of several application-specific integrated circuits (ASICs) that are designed to perform telemetry demodulation involving carrier, subcarrier and symbol tracking. It supports both residual and suppressed carrier tracking for BPSK and QPSK signals (with Costas loop and cross-over Costas loop, respectively). Currently, no capability of supporting general MPSK modulation other than BPSK and QPSK is considered to be incorporated into its original design.

Because of the ASIC implementation of BVR's high-speed digital signal processing hardware, it is highly desired to avoid any major ASIC modification when making the BVR to support 8-PSK signaling. A possible and, in our opinion, the easiest way to augment the BVR to support 8-PSK signaling has been proposed and its carrier tracking performance has been preliminarily studied in [2]. This report here is intended to summarize the results from a further investigation on the carrier tracking performance of this augmented BVR, including the effects of using a band-pass filter before the nonlinear operation and the imperfect symbol synchronization caused by the use of the data transition tracking loop (DTTL).

2. The Augmented BVR

The carrier tracking and symbol demodulation of the proposed augmented BVR are performed by the functional system blocks shown in Figure 1. A squaring device preceded the cross-over Costas loop can reduce the eight possible signal phases of an 8-PSK signal into four, rendering a signal that is effectively the same as a QPSK signal but at twice of the original carrier frequency and phase. The resulting QPSK signal can be tracked by the BVR's cross-over Costas loop as usual except that the estimated carrier frequency and phase from the numerically controlled oscillator (NCO) needs to be divided by 2, providing the correct carrier phase as the reference to the 8-PSK demodulator. Although this augmented BVR design seems to be a viable solution without resorting to costly ASIC redesign, the way to realize an effective QPSK signal for carrier tracking by a squaring device inevitably results in significant signal-to-noise ratio (SNR) loss. As shown later in this report, it is crucial to insert a band-pass filter in front of the squaring device so that the impact of additional noise caused by squaring the digital signal samples at intermediate frequency can be greatly reduced.

3. Carrier Tracking Performance

Based upon the 8-PSK signaling scheme studied in [1], three binary data streams of NRZ format are fed into a Gray code encoder, mapping the triplet to one of eight equally-spaced phases between 0° and 360° . The resulting eight-level baseband

waveform is passed through a pulse shaping filter which is chosen to be a 5th-order Butterworth filter with unity bandwidth-time product. The baseband filtering is intended to increase the frequency utilization ratio, however, at the cost of increased inter-symbol interference (ISI). A phase modulator then follows the filter to form a constant envelope signal for transmission.

The carrier tracking performance is simulated by the SPW software package with the following parameters:

Sampling Rate $f_s = 600$ Hz

Carrier Frequency $f_c = 100$ Hz

Symbol Rate $R_s = \left(\frac{1}{3}\right)R_b = 10$ symbols/sec

Loop Bandwidth $B_L = 0.05$ Hz

In the simulation, a 2nd-order Butterworth band-pass filter with a 3-dB bandwidth of 60 Hz is chosen to be in front of the squaring device. With the assumption that the symbol timing is perfectly known¹, the carrier tracking performance is simulated for both the cases with or without band-pass filtering, with selected total-power-to-noise-power-spectral-level ratios (P_T/N_0) from a range between 20 and 50 dB-Hz. In order to understand the effect of ISI caused by the baseband filtering, their no-ISI counterparts with baseband filtering removed are also simulated.

Figure 2 shows the carrier tracking performance of these four cases as well as the theoretical QPSK cross-over Costas loop tracking performance [3]. It is noted that the background thermal noise is dominant in the relatively low P_T/N_0 region, so that the performance there is highly dependent on the existence of a band-pass filter which is intended to reduce the squaring loss. In fact, the phenomena of cycle slips and loss of lock begin to emerge around $P_T/N_0 = 26$ dB-Hz for the cases without band-pass filtering (either with or without ISI), while the cases with band-pass filtering are still able to maintain a good carrier tracking with loop SNRs higher than 25 dB. On the other hand, the ISI becomes dominant in high P_T/N_0 region, rendering a divergent performance between the cases with or without baseband filtering. The existence of band-pass filtering makes little difference in this high SNR region.

In order to assess the impact of ISI and squaring loss to the symbol tracking, more simulations using a DTTL to replace the assumed perfect symbol timing are carried out. Figure 3 gives a comparison between the cases with DTTL and with perfect symbol timing when ISI and band-pass filtering are present. It is interesting to find

¹ The delay introduced by the band-pass filter can be estimated and, therefore, properly compensated for this purpose. It is important to note that the ISI introduced by filtering the eight-level baseband waveform is not treated as a source of delay and not a subject for compensation.

a cross-over in the two curves, indicating that the imperfect symbol timing provided by DTTL is actually better than the perfect symbol timing assumed in high P_T/N_0 region. It is alleged that this phenomenon may be caused by a significant shift of symbol timing resulting from the dominant ISI in the high P_T/N_0 region, such that the assumed perfect symbol timing becomes even worse than that provided by a DTTL. Further study on this interesting finding is undergoing in order to verify this allegation.

It is expected that the case with band-pass filtering protection but no ISI has the best carrier tracking performance among the four plotted in Figure 2. However, this best case still has a loop SNR which is consistently 15 dB lower than that from the tracking of an ideal QPSK signal throughout the selected P_T/N_0 range, indicating that it is the penalty paid to square an 8-PSK signal. As shown in Figure 3, a loop SNR degradation of around 20 dB appears when a DTTL is used to track the ISI-affected symbol timing.

4. Conclusion

In this report, a possible and the easiest way to extend the BVR's ability to support 8-PSK signals is presented. The proposed augmented BVR does not require costly redesign of its ASIC hardware. Despite this significant degradation incurred in this design due to the squaring loss and inter-symbol interference, the simulated carrier tracking performance results obtained so far actually suggest that, for near-Earth missions with reasonably high P_T/N_0 , the proposed augmented BVR provides a viable way to enable the BVR to support 8-PSK modulation format.

References

- [1] Rubén Caballero and Sheila Horan, "8-PSK Signaling over Non-linear Satellite Channels," Draft version, New Mexico State University.
- [2] Haiping Tsou and Caroline Racho, "Preliminary Study on the Feasibility of Using the Block V Receiver to Support 8-PSK Modulation Scheme," position paper presented in the Consultative Committee for Space Data Systems RF and Modulation Subpanel 1E Meeting, Paris, April 1997
- [3] Joseph H. Yuen, *Deep Space Telecommunications Systems Engineering*, New York: Plenum Press, 1983

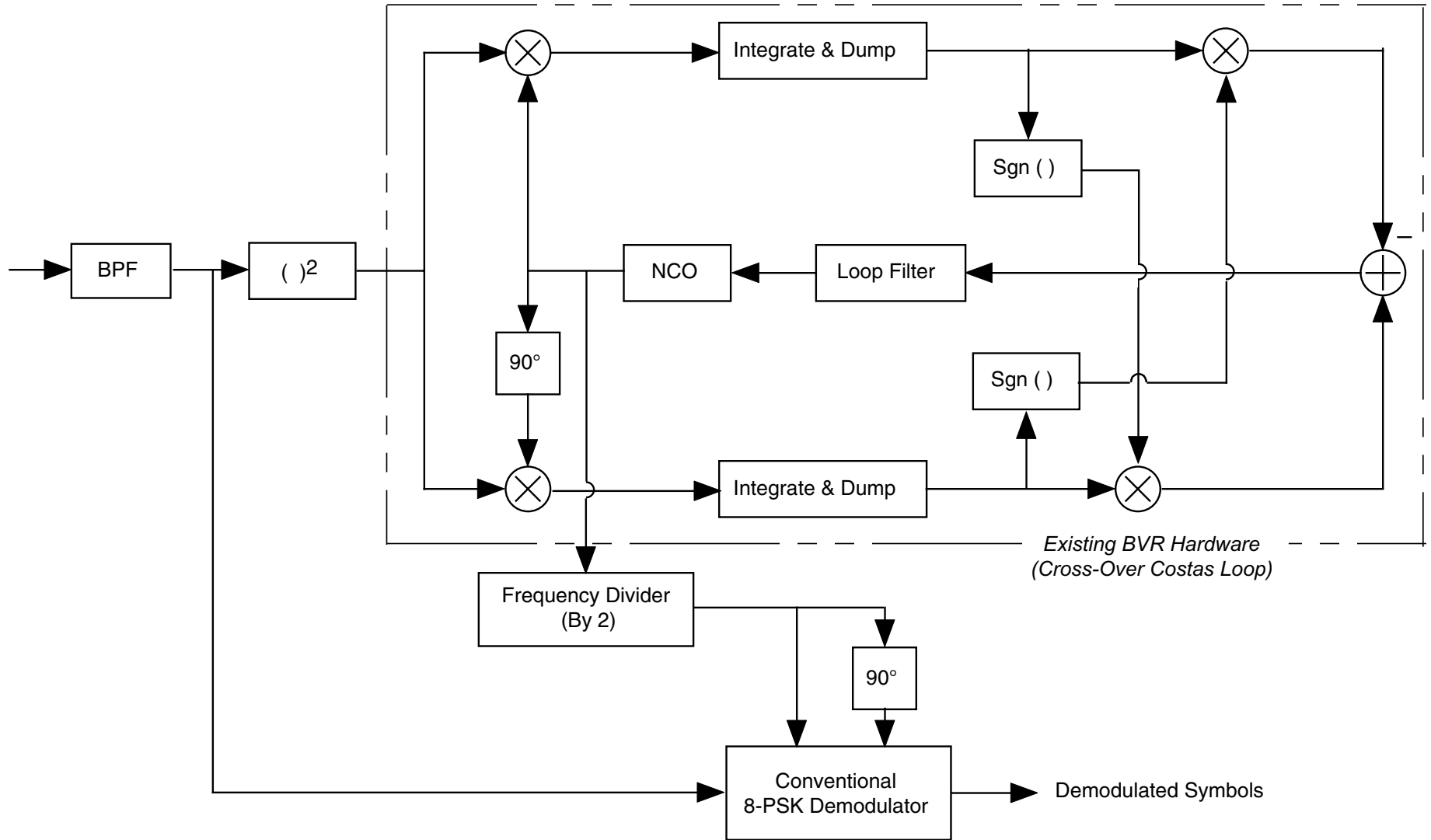


Figure 1 The 8-PSK signal processing unit of the augmented Block V Receiver

Figure 2 Carrier Tracking Performance of the Augmented BVR

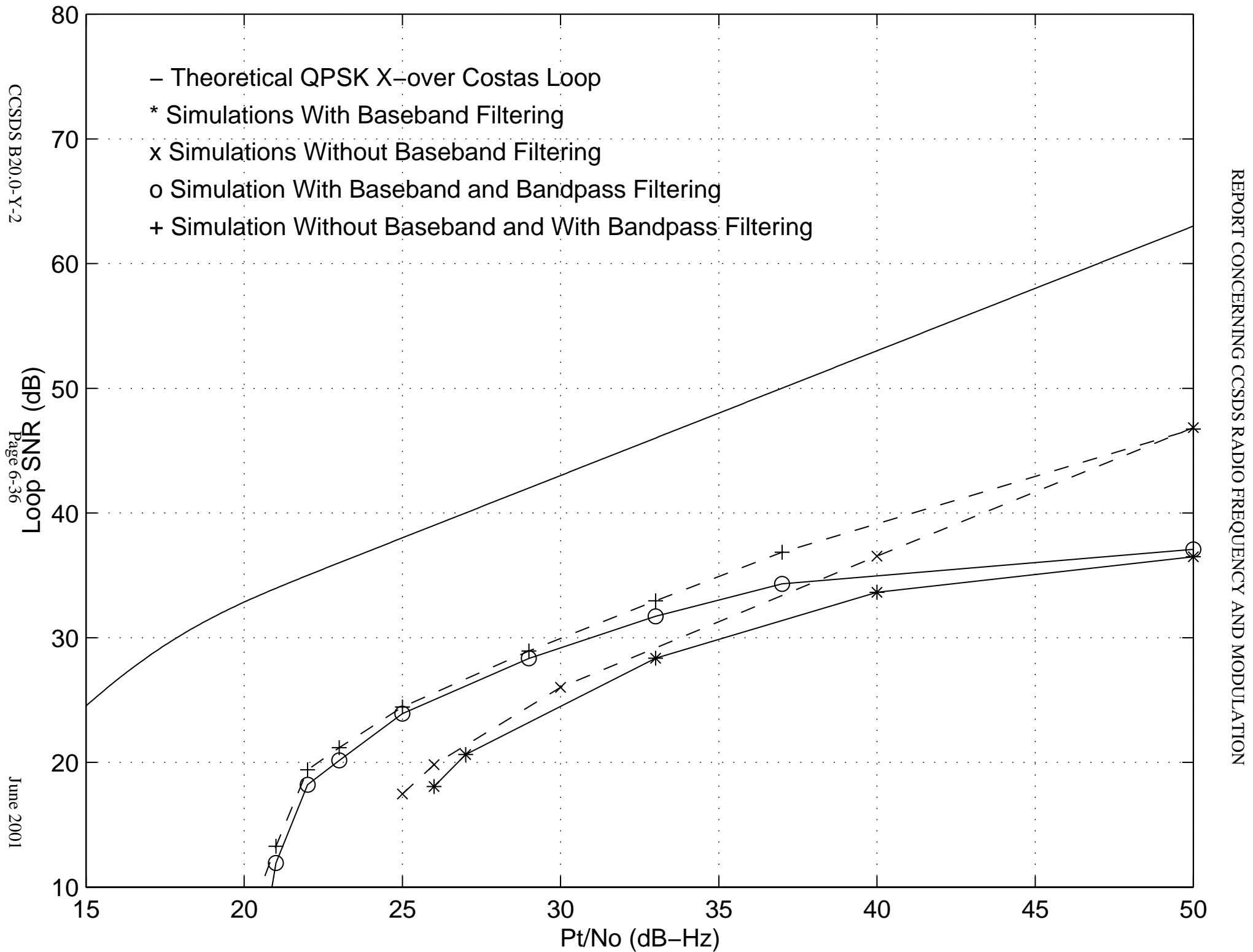
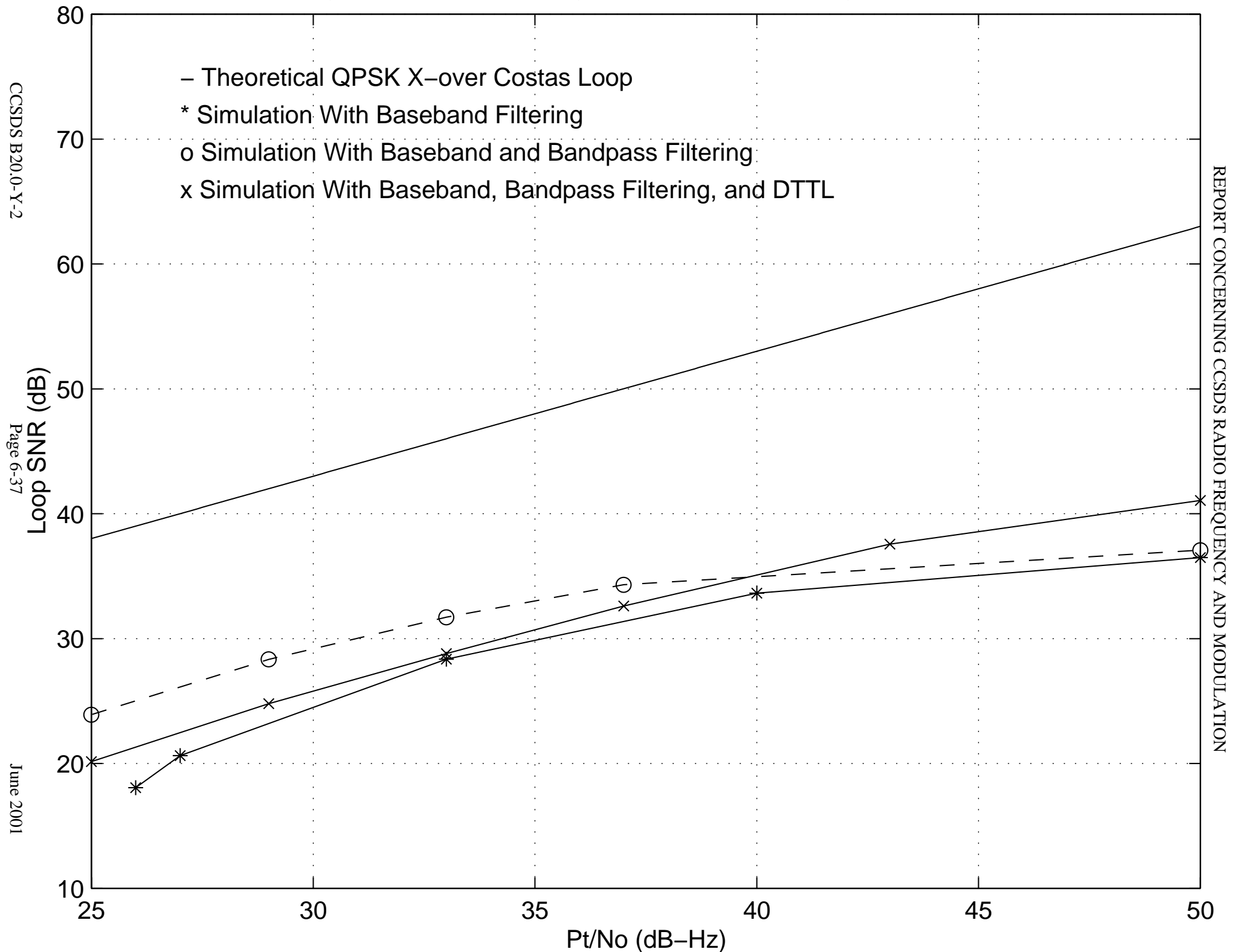


Figure 3 Carrier Tracking Performance of the Augmented BVR



[This page intentionally left blank.]

Power Spectrum of MSK-Type Modulations in the Presence of Data Imbalance

M. K. Simon,¹ P. Arabshahi,¹ L. Lam,¹ and T.-Y. Yan¹

Using the amplitude-modulation pulse (AMP) representation of continuous-phase modulation (CPM) introduced more than a decade ago by Laurent, the power spectral density (PSD) of minimum-shift-keying (MSK)-type modulations (modulation index equal to one-half) is computed in the presence of data imbalance. The advantage of this technique is that closed-form expressions can be obtained that clearly elucidate the partitioning of the spectrum into components due to the effective AMP pulse shapes and those due to the AMP sequence correlations. As such, these expressions give insight into the nature of the PSD distortion produced by the imbalance, i.e., a tilt in the main lobe and a relative unbalance between the upper and lower side-lobe levels caused by the correlation between the in-phase (I) and quadrature-phase (Q) components of the complex AMP data sequences and the correlation between the sequences themselves. It is demonstrated that data imbalance does not change the rate at which the side lobes roll off. It also is shown that, for all practical purposes, the PSD can be computed based on a two-pulse stream AMP approximation.

I. Introduction

It is well-known that continuous-phase modulation (CPM) is a modulation scheme that in addition to being bandwidth efficient offers the advantage of being constant envelope, the latter being significant in systems employing nonlinear amplification. One class of CPM is the group of so-called minimum-shift-keying (MSK)-type modulations that all have modulation index $h = 0.5$ and are distinguished from one another by the shape of the frequency pulse that modulates the transmitted carrier. MSK itself corresponds to a rectangular frequency pulse of duration equal to a bit time, T_b . The reason this group is of interest is that it lends itself to an in-phase-quadrature-phase (I-Q) form of receiver implementation. The evaluation of the power spectral density (PSD) of conventional (corresponding to a balanced random binary data input) angle and frequency modulations has been described in many places in the literature, e.g., [1–6], and specific results have been documented for a variety of popular full- and partial-response MSK-type schemes, including MSK itself, Gaussian MSK (GMSK), and tamed-frequency modulation (TFM).

In addition to pulse shaping, the presence of data imbalance (unequal probabilities for the +1's and -1's) can have a profound effect on the PSD of digital modulations, so much so that standards committees such as the Consultative Committee for Space Data Systems (CCSDS) have included in their specifications

¹ Communications Systems and Research Section.

a limit on the amount of imbalance that can be tolerated [12]. For linear modulations such as amplitude modulation of a binary pulse stream on a carrier, the effect of data imbalance on the PSD is well documented, e.g., [7, Chapter 2], manifesting itself in the addition of a discrete spectral component to the overall PSD with no effect on the *shape* of the continuous component [7]. For phase (or frequency) modulation, the evaluation of the PSD is considerably more complex, and the effect of data imbalance is quite different in terms of its impact on both the discrete and continuous spectral components of the modulator output. Because of these important differences and their significance in relation to the specification on the tolerable amount of data imbalance, a study of the PSD of MSK-type modulations (including GMSK as a specific case of high interest) in the presence of such imbalance is warranted.

Of the many techniques available for evaluating the power spectral density of CPM schemes [1–4], the one deemed most convenient by the authors, particularly for MSK-type modulations with data imbalance, is that which results from a CPM signal representation introduced more than a decade ago by Laurent [4]. In particular, Laurent described an exact representation for CPM in the form of a superposition of a number of time-/phase-shifted amplitude-modulation pulse (AMP) streams. The number of such streams was dependent on the partial-response nature of the modulation as described by the duration, L (in symbols), of the frequency pulse that characterizes the CPM. For binary pulse streams,² the number of pulse streams in the AMP representation is 2^{L-1} . Laurent’s primary motivation for presenting such a representation was that it allowed for easy evaluation of the autocorrelation and PSD of such modulations, particularly for half-integer index modulations, i.e., ones whose frequency-modulation index was of the form $h = n + 1/2$, n integer, which includes the case of interest here (i.e., $n = 0$). Specifically, when the input binary data were random and balanced, the complex data sequences that characterize each of the 2^{L-1} AMP components are themselves uncorrelated and, furthermore, are uncorrelated with each other. As such, the PSD of the composite CPM waveform is equal to the sum of the PSDs of the AMP components, each of which is computed by conventional PSD evaluation techniques for binary amplitude (unit magnitude) modulation of a carrier with a complex independent identically distributed (i.i.d.) data sequence.

In this article, we expand upon the PSD evaluation found in Laurent to include the case of input data imbalance. Specifically, we shall show that, because of the presence of data imbalance, the effective complex data sequences that typify each AMP pulse stream are now themselves correlated and, furthermore, are correlated with each other. The correlation properties of each of these sequences resemble those of a first-order Markov process and, hence, the PSD for each contains a factor due to the pulse shape as well as a factor due to the sequence correlation. Likewise, the cross-correlation properties of the sequences contain pulse shape and correlation factors.

We begin the article by reviewing the Laurent representation for MSK-type modulations. Following this, we present the generic result for the PSD of a modulation composed of a group of correlated data pulse trains each of which contains its own real pulse shape and complex data stream. Next, we apply this generic PSD formula first to MSK and then to GMSK. Since MSK is a full-response scheme, its Laurent representation has only a single pulse stream and, thus, the PSD has no cross-correlation components. Since GMSK can be approximated by a $4T_b$ -wide frequency pulse at the output of the Gaussian filter, it is a partial-response scheme with a Laurent representation having $2^{L-1} = 8$ pulse streams. However, Kaleb [9] explicitly showed that, for GMSK with a bandwidth-bit time product $BT_b = 0.25$ and a $4T_b$ -wide approximation of the Gaussian pulse, i.e., $L = 4$, a two-pulse-stream approximation is for all practical purposes (the fraction of energy in the neglected six pulse streams is 2.63×10^{-5}) exact. Thus, in evaluating the PSD of GMSK, we shall employ this two-pulse-stream approximation of the Laurent representation.

² The work later was extended to the M -ary case by Mengali and Morelli [8].

II. Laurent Representation of MSK-Type Modulations

The classical representation of an MSK-type of CPM modulation has the form

$$s(t) = \sqrt{\frac{2E_b}{T_b}} \cos(\omega_c t + \phi(t, \boldsymbol{\alpha}) + \phi_0), \quad nT_b \leq t \leq (n+1)T_b \quad (1)$$

where E_b and T_b , respectively, denote the energy and duration of a bit ($P = E_b/T_b$ is the signal power), $\omega_c = 2\pi f_c$ is the radian carrier frequency, $\boldsymbol{\alpha} = (\dots, \alpha_{-2}, \alpha_{-1}, \alpha_0, \alpha_1, \alpha_2, \dots)$ is the i.i.d. binary (± 1) data sequence, $\phi(t, \boldsymbol{\alpha})$ is the equivalent phase-modulation process, which is expressible in the form of a digital pulse stream,

$$\phi(t, \boldsymbol{\alpha}) = \pi \sum_{i \leq n} \alpha_i q(t - iT_b) \quad (2)$$

and $q(t) = \int_{-\infty}^t g(\tau) d\tau$ is the *normalized phase-smoothing response* that defines how the underlying phase, $\pi\alpha_i$, evolves with time. In general, $q(t)$ extends over infinite time and satisfies the following:

$$q(t) = \begin{cases} 0, & t \leq 0 \\ \frac{1}{2}, & t \geq LT_b \end{cases} \quad (3)$$

In what follows, it will be convenient to deal with the normalized (unit-amplitude) complex envelope of $s(t)$, i.e., the complex baseband signal $\tilde{S}(t)$ defined by the relation

$$\tilde{S}(t) = \exp\{j\phi(t, \boldsymbol{\alpha})\}, \quad nT_b \leq t \leq (n+1)T_b \quad (4)$$

Define the generalized phase-pulse function by

$$\Psi(t) = \begin{cases} \pi q(t), & 0 \leq t \leq LT_b \\ \frac{\pi}{2} [1 - 2q(t - LT_b)], & LT_b \leq t \end{cases} \quad (5)$$

which is obtained by taking the nonconstant part of $q(t)$, i.e., the part that exists in the interval $0 \leq t \leq LT_b$, and reflecting it about the $t = LT_b$ axis. Thus, in view of Eq. (5), $\Psi(t)$ is a waveform that is nonzero in the interval $0 \leq t \leq 2LT_b$ and symmetric around $t = LT_b$. The importance of $\Psi(t)$ is that it allows definition of the following functions, which become an integral part of the AMP representation of GMSK:

$$S_0(t) = \sin \Psi(t) \quad (6)$$

$$S_n(t) = S_0(t + nT_b) = \sin \Psi(t + nT_b) \quad (7)$$

Next one defines a series of pulse shapes $C_i(t)$, $i = 1, 2, \dots, 2^{L-1}$, each made up of L -fold distinct products of the $S_n(t)$'s. For example, for GMSK with $L = 4$, the $2^{L-1} = 8$ distinct pulse shapes are [4, Eq. (11)]

$$\left. \begin{aligned}
 C_0(t) &= S_0(t)S_1(t)S_2(t)S_3(t), & 0 \leq t \leq 5T_b \\
 C_1(t) &= S_0(t)S_2(t)S_3(t)S_5(t), & 0 \leq t \leq 3T_b \\
 C_2(t) &= S_0(t)S_1(t)S_3(t)S_6(t), & 0 \leq t \leq 2T_b \\
 C_3(t) &= S_0(t)S_3(t)S_5(t)S_6(t), & 0 \leq t \leq 2T_b \\
 C_4(t) &= S_0(t)S_1(t)S_2(t)S_7(t), & 0 \leq t \leq T_b \\
 C_5(t) &= S_0(t)S_2(t)S_5(t)S_7(t), & 0 \leq t \leq T_b \\
 C_6(t) &= S_0(t)S_1(t)S_6(t)S_7(t), & 0 \leq t \leq T_b \\
 C_7(t) &= S_0(t)S_5(t)S_6(t)S_7(t), & 0 \leq t \leq T_b
 \end{aligned} \right\} \quad (8)$$

each of which is a product of the basic generalized pulse shape $S_0(t)$ and $L - 1 = 3$ other time shifts of $S_0(t)$. Finally, then the generic AMP form for the complex envelope of MSK-type signals is [4]

$$\tilde{S}(t) = \sum_{K=0}^{2^{L-1}-1} \left[\sum_{n=-\infty}^{\infty} j^{A_{K,n}} C_K(t - nT_b) \right] \triangleq \sum_{K=0}^{2^{L-1}-1} \left[\sum_{n=-\infty}^{\infty} \tilde{a}_{K,n} C_K(t - nT_b) \right] \quad (9)$$

which results in the real signal

$$s(t) = \sqrt{\frac{2E_b}{T_b}} \operatorname{Re} \left\{ \tilde{S}(t) \right\} = \sqrt{\frac{2E_b}{T_b}} \sum_{K=0}^{2^{L-1}-1} \left[\sum_{n=-\infty}^{\infty} C_K(t - nT_b) \cos \left(\omega_c t + \frac{\pi}{2} A_{K,n} \right) \right] \quad (10)$$

i.e., a superposition of 2^{L-1} amplitude-/phase-modulated pulse streams, some of which contain overlapping pulses. Also in Eq. (10), $\tilde{a}_{K,n} \triangleq j^{A_{K,n}} = e^{j(\pi/2)A_{K,n}}$ is the equivalent complex (unit-amplitude) data symbol for the n th transmitted pulse in the K th stream whose phase $(\pi/2) A_{K,n}$ depends solely on the past information data sequence α in a manner described in [4], namely,

$$A_{K,n} = \sum_{l=-\infty}^n \alpha_l - \sum_{i=1}^{L-1} \alpha_{n-i} \beta_{K,i} \quad (11)$$

where $\{\beta_{K,i}\}$ are the L coefficients (0, 1) in the binary representation of the integer K ($0 \leq K \leq 2^{L-1} - 1$). Since, from Eq. (11), $A_{K,n}$ alternates (with n) between even and odd integer values, then $\tilde{a}_{K,n}$ likewise alternates between being purely real (± 1) and purely imaginary ($\pm j$) values. Thus, as previously mentioned, for each K , $\{\tilde{a}_{K,n}\}$ is a binary amplitude complex data sequence with unit magnitude.

For MSK modulation ($L = 1$), there is only a single pulse stream with pulse shape and data phase

$$\left. \begin{aligned} C_0(t) &= S_0(t) = \sin \frac{\pi t}{2T_b}, \quad 0 \leq t \leq 2T_b \\ A_{0,n} &= \sum_{l=-\infty}^n \alpha_l \end{aligned} \right\} \quad (12)$$

Thus, the equivalent data symbol $\{\tilde{a}_{0,n}\}$ satisfies the differential encoding relationship

$$\tilde{a}_{0,n} \triangleq e^{j(\pi/2)A_{0,n}} = j\alpha_n \tilde{a}_{0,n-1} \Rightarrow \tilde{a}_{0,2n} \in \{j, -j\}, \quad \tilde{a}_{0,2n+1} \in \{1, -1\} \quad (13)$$

For GMSK, the dominant term is the pulse stream corresponding to $C_0(t)$ since its duration is the longest (at least $2T_b$ longer than any other pulse component) and it also conveys the most significant part of the total energy of the signal. The next most significant term would be the pulse stream corresponding to $C_1(t)$, which contains virtually all the remaining signal energy. Thus, as previously alluded to, it is sufficient to consider only the first two pulse streams in Eq. (9) and, hence, for all practical purposes, we may “exactly” describe GMSK by the complex signal

$$\tilde{S}(t) = \sum_{n=-\infty}^{\infty} \tilde{a}_{0,n} C_0(t - nT_b) + \sum_{n=-\infty}^{\infty} \tilde{a}_{1,n} C_1(t - nT_b) \quad (14)$$

where it can be shown that the equivalent complex data symbols satisfy the relations [9]³

$$\left. \begin{aligned} \tilde{a}_{0,n} &\triangleq e^{j(\pi/2)A_{0,n}} = j\alpha_n \tilde{a}_{0,n-1} \Rightarrow \tilde{a}_{0,2n} \in \{j, -j\}, \quad \tilde{a}_{0,2n+1} \in \{1, -1\} \\ \tilde{a}_{1,n} &\triangleq e^{j(\pi/2)A_{1,n}} = j\alpha_n \tilde{a}_{0,n-2} \Rightarrow \tilde{a}_{1,2n} \in \{1, -1\}, \quad \tilde{a}_{1,2n+1} \in \{j, -j\} \end{aligned} \right\} \quad (15)$$

Thus, in terms of the real GMSK signal $s(t)$, we can view it as being composed of the sum of two pulse-shaped offset QPSK-type signals with pulse shapes corresponding to $C_0(t)$ and $C_1(t)$ and I, Q ± 1 data-symbol ($T_s = 2T_b$ in duration) sequences, respectively, corresponding to

$$\left. \begin{aligned} a_{0,2n} &= \text{Im} \{\tilde{a}_{0,2n}\}, \quad b_{0,2n+1} = \text{Re} \{\tilde{a}_{0,2n+1}\} \\ a_{1,2n} &= \text{Re} \{\tilde{a}_{1,2n}\}, \quad b_{1,2n+1} = \text{Im} \{\tilde{a}_{1,2n+1}\} \end{aligned} \right\} \quad (16)$$

That is,

$$\begin{aligned} s(t) &= \sqrt{\frac{2E_b}{T_b}} \left[\sum_{n=-\infty}^{\infty} a_{0,2n+1} C_0(t - (2n+1)T_b) \cos \omega_c t - \sum_{n=-\infty}^{\infty} b_{0,2n} C_0(t - 2nT_b) \sin \omega_c t \right. \\ &\quad \left. + \sum_{n=-\infty}^{\infty} a_{1,2n} C_1(t - 2nT_b) \cos \omega_c t - \sum_{n=-\infty}^{\infty} b_{1,2n+1} C_1(t - (2n+1)T_b) \sin \omega_c t \right] \end{aligned} \quad (17)$$

³ Note that the sequence properties of the first sequence in Eq. (15) are identical to those of MSK.

For random i.i.d. balanced input data, α , Kaleb [9] shows that the effective data sequences for the two symbol streams as defined in Eq. (16) each has uncorrelated symbols and, furthermore, the two sequences are uncorrelated with each other. As we shall see in a later section, when the data are random i.i.d. but unbalanced, these uncorrelated properties no longer hold.

III. A Generic Expression for the PSD of a Sum of Random Pulse Trains With Complex Data Symbols

Consider finding the PSD of a complex signal $\tilde{S}(t)$ of the form in Eq. (9). The traditional method of evaluating such a PSD is first to find the autocorrelation function of $\tilde{S}(t)$, namely, $R_{\tilde{S}}(t, t + \tau) = E \left\{ \tilde{S}(t) \tilde{S}^*(t + \tau) \right\}$, then to time average to remove the cyclostationary property, and finally to take the Fourier transform of the result, i.e.,

$$S_{\tilde{S}}(f) = \mathcal{F} \{ \langle R_{\tilde{S}}(t, t + \tau) \rangle \} \quad (18)$$

By a straightforward extension of the results in [7, Chapter 2], the following result can be obtained:

$$S_{\tilde{S}}(f) = \sum_{i=0}^{2^{L-1}-1} S_{ii}(f) + \sum_{i=0}^{2^{L-1}-1} \sum_{i < j}^{2^{L-1}-1} S_{ji}(f) \quad (19)$$

where

$$S_{ii}(f) = S_{\tilde{a}_i}(f) S_{p_i}(f) \quad (20)$$

with

$$\left. \begin{aligned} S_{\tilde{a}_i}(f) &= \sum_{l=-\infty}^{\infty} R_{\tilde{a}_i}(l) e^{-j2\pi f l T_b}, & R_{\tilde{a}_i}(l) &= E \{ \tilde{a}_{i,k} \tilde{a}_{i,k+l}^* \} \\ S_{p_i}(f) &= \frac{1}{T_b} |P_i(f)|^2, & P_i(f) &\triangleq \mathcal{F} \{ C_i(t) \} \end{aligned} \right\} \quad (21)$$

and

$$S_{ji}(f) = 2 \operatorname{Re} \{ S_{\tilde{a}_{ji}}(f) S_{p_{ji}}(f) \} \quad (22)$$

with

$$\left. \begin{aligned} S_{\tilde{a}_{ji}}(f) &= \sum_{l=-\infty}^{\infty} R_{\tilde{a}_{ji}}(l) e^{-j2\pi f l T_b}, & R_{\tilde{a}_{ji}}(l) &= E \{ \tilde{a}_{j,k} \tilde{a}_{i,k+l}^* \} \\ S_{p_{ji}}(f) &= \frac{1}{T_b} P_i(f) P_j^*(f), & P_i(f) &\triangleq \mathcal{F} \{ C_i(t) \} \end{aligned} \right\} \quad (23)$$

Clearly then, the evaluation of the PSD involves finding the Fourier transform of the various pulse shapes in the AMP representation and both the autocorrelation and cross-correlation of the equivalent complex data sequences.

IV. Cross-Correlation Properties of the Equivalent Complex Data Symbols and Evaluation of the PSD

A. MSK Modulation

For MSK, the equivalent complex data symbols $\{\tilde{a}_{0,n}\}$ are defined in terms of the actual input data symbols $\{\alpha_n\}$ by the iterative relation in Eq. (13). Suppose that $\{\alpha_n\}$ characterizes a random i.i.d. unbalanced source, where

$$\left. \begin{aligned} \Pr\{\alpha_n = 1\} &= 1 - p \\ \Pr\{\alpha_n = -1\} &= p \end{aligned} \right\} \quad (24)$$

with $0 \leq p \leq 1$. Then, it is straightforward to show that $\{\tilde{a}_{0,n}\}$ is a first-order Markov source, and as such, it is balanced, i.e.,

$$\left. \begin{aligned} \Pr\{\tilde{a}_{0,n} = j\} &= \frac{1}{2}, \quad \Pr\{\tilde{a}_{0,n} = -j\} = \frac{1}{2} \quad \text{for } n \text{ even} \\ \Pr\{\tilde{a}_{0,n} = 1\} &= \frac{1}{2}, \quad \Pr\{\tilde{a}_{0,n} = -1\} = \frac{1}{2} \quad \text{for } n \text{ odd} \end{aligned} \right\} \quad (25)$$

and thus $E\{\tilde{a}_{0,n}\} = 0$. However, while the differential encoding operation converts the unbalanced random i.i.d. source to a balanced source,⁴ the symbols of the latter are now correlated. Using the defining relation for $\{\tilde{a}_{0,n}\}$, it is straightforward to show that

$$R_{\tilde{a}_0}(l) \triangleq E\{\tilde{a}_{0,n}\tilde{a}_{0,n+l}^*\} = [-j(1-2p)]^l, \quad l \text{ integer}, \quad R_{\tilde{a}_0}(-l) = R_{\tilde{a}_0}^*(l) \quad (26)$$

i.e., $\{\tilde{a}_{0,n}\}$ behaves analogously to a first-order Markov source with transition probability equal to p . The discrete Fourier transform of Eq. (26) as needed in Eq. (21) is obtained as

$$\begin{aligned} S_{\tilde{a}_0}(f) &= \sum_{l=-\infty}^{\infty} R_{\tilde{a}_0}(l) e^{-j2\pi f l T_b} = \sum_{l=-\infty}^{\infty} [-j(1-2p)]^l e^{-j2\pi f l T_b} \\ &= 1 + 2 \sum_{l=-\infty}^{\infty} (1-2p)^l e^{-j2\pi l(fT_b + 1/4)} \end{aligned} \quad (27)$$

Using a well-known result [10] for the series in Eq. (27), namely,

$$\sum_{k=1}^{\infty} a^k \cos k\theta = \frac{a \cos \theta - a^2}{1 - 2a \cos \theta + a^2} \quad (28)$$

⁴ The implication of a balanced equivalent complex symbol stream for AMP representation of MSK is that no discrete spectrum will be generated.

we obtain the closed-form result

$$S_{\tilde{a}_0}(f) = \frac{4p(1-p)}{2(1-2p)(1 + \sin 2\pi f T_b) + 4p^2} \quad (29)$$

Finally, taking the Fourier transform of the pulse shape in Eq. (12) and substituting its squared magnitude in Eq. (21), the complex baseband PSD of MSK with unbalanced data input becomes

$$S_{\tilde{m}}(f; p) = T_b \frac{16}{\pi^2} \frac{\cos^2 2\pi f T_b}{(1 - 16f^2 T_b^2)^2} \left[\frac{4p(1-p)}{2(1-2p)(1 + \sin 2\pi f T_b) + 4p^2} \right] \quad (30)$$

Note that because of the presence of the term $\sin 2\pi f T_b$ in the denominator of Eq. (29), the equivalent baseband spectrum of Eq. (30) is not symmetric around $f = 0$. Since the PSD of the true MSK signal as described by Eq. (1) is related to the equivalent baseband PSD by

$$S_s(f; p) = \frac{1}{4} [S_{\tilde{m}}(f + f_c; p) + S_{\tilde{m}}(-f + f_c; p)] \quad (31)$$

then, equivalently, the PSD of Eq. (31) will have a tilt around the carrier. And since, also from Eq. (30), we have

$$S_{\tilde{m}}(f; 1-p) = S_{\tilde{m}}(-f; p) \quad (32)$$

then the tilt of the PSD of Eq. (31) reverses when the probability distribution of the input data is reversed.

Finally, for $p = 1/2$, i.e., balanced random data input, the factor in brackets in Eq. (30) becomes equal to unity, and one obtains the well-known PSD of conventional MSK, namely,

$$S_{MSK}(f) = T_b \frac{16}{\pi^2} \frac{\cos^2 2\pi f T_b}{(1 - 16f^2 T_b^2)^2} \quad (33)$$

which is symmetrical around the origin.

B. GMSK Modulation

For GMSK, the equivalent complex data symbols $\{\tilde{a}_{0,n}\}$ are defined in terms of the actual input data symbols $\{\alpha_n\}$ by the iterative relations in Eq. (15). Suppose that $\{\alpha_n\}$ again characterizes a random i.i.d. unbalanced source as described by Eq. (24); then the autocorrelation function of the first equivalent symbol stream is given by Eq. (26) and its associated discrete Fourier transform by Eq. (29). Thus, the PSD of the first component of the AMP representation of GMSK is

$$S_{00}(f; p) = \frac{1}{T_b} |P_0(f)|^2 \left[\frac{4p(1-p)}{2(1-2p)(1 + \sin 2\pi f T_b) + 4p^2} \right], \quad P_0(f) \triangleq \mathcal{F}\{C_0(t)\} \quad (34)$$

with $C_0(t)$ defined in Eq. (8) and evaluated from Eqs. (5), (6), and (7) using for the phase pulse shape

$$\begin{aligned}
 q\left(t + \frac{LT_b}{2}\right) &= \frac{1}{2} + \frac{1}{2T} \left[\left(t - \frac{T_b}{2}\right) Q\left(\frac{2\pi B}{\sqrt{\ln 2}} \left(t - \frac{T_b}{2}\right)\right) - \left(t + \frac{T_b}{2}\right) Q\left(\frac{2\pi B}{\sqrt{\ln 2}} \left(t + \frac{T_b}{2}\right)\right) \right] \\
 &\quad - \frac{1}{\sqrt{2\pi}} \left(\frac{\sqrt{\ln 2}}{2\pi B}\right) \left[\exp\left\{-\frac{1}{2} \left[\frac{2\pi B}{\sqrt{\ln 2}} \left(t - \frac{T_b}{2}\right)\right]^2\right\} - \exp\left\{-\frac{1}{2} \left[\frac{2\pi B}{\sqrt{\ln 2}} \left(t + \frac{T_b}{2}\right)\right]^2\right\} \right], \\
 &\quad 0 \leq t \leq LT_b \quad (35)
 \end{aligned}$$

As mentioned in the introduction, the case of interest here is where $BT_b = 0.25$ and $L = 4$ so that a two-pulse-stream approximation is sufficient.

Following a procedure similar to that used to derive Eq. (26), it can be shown that the autocorrelation function of the second equivalent symbol stream (which is also balanced and, therefore, has zero mean) is given by

$$R_{\tilde{a}_1}(l) \triangleq E\{\tilde{a}_{1,n}\tilde{a}_{1,n+l}^*\} = \begin{cases} 1, & l = 0 \\ -j(1-2p)^3, & l = 1 \\ [-j(1-2p)]^l, & l \geq 2 \end{cases} \quad R_{\tilde{a}_1}(-l) = R_{\tilde{a}_1}^*(l) \quad (36)$$

with discrete Fourier transform

$$S_{\tilde{a}_1}(f) = \sum_{l=-\infty}^{\infty} R_{\tilde{a}_1}(l) e^{-j2\pi f l T_b} = S_{\tilde{a}_0}(f) + 8p(1-2p)(1-p) \sin 2\pi f T_b \quad (37)$$

Thus, the PSD of the second component of the AMP representation of GMSK is

$$\left. \begin{aligned} S_{11}(f; p) &= \frac{1}{T_b} |P_1(f)|^2 4p(1-p) \left[\frac{1}{2(1-2p)(1 + \sin 2\pi f T_b) + 4p^2} - 2(1-2p) \sin 2\pi f T_b \right] \\ P_1(f) &\triangleq \mathcal{F}\{C_1(t)\} \end{aligned} \right\} \quad (38)$$

Note again that, because of the presence of the term $\sin 2\pi f T_b$ in the denominator of Eq. (38), the equivalent baseband spectrum is not symmetric around $f = 0$.

What remains is to compute the cross-correlation function of the two equivalent complex symbol streams. Following the same procedure as that for obtaining the autocorrelation function of the individual pulse streams, we obtain

$$R_{\tilde{a}_{10}}(l) \triangleq E\{\tilde{a}_{1,n}\tilde{a}_{0,n+l}^*\} = \begin{cases} [-j(1-2p)]^{l+1}, & l \geq 0 \\ (1-2p)^2, & l = -1, \\ [j(1-2p)]^{-(l+1)}, & l \leq -2 \end{cases} \quad R_{\tilde{a}_{10}}(-l) = R_{\tilde{a}_{10}}^*(l) \quad (39)$$

with discrete Fourier transform

$$S_{\tilde{a}_{10}}(f) = \sum_{l=-\infty}^{\infty} R_{\tilde{a}_{10}}(l) e^{-j2\pi f l T_b} = e^{j2\pi f T_b} [S_{\tilde{a}_0}(f) - 4p(1-p)] \quad (40)$$

Thus, the cross-spectrum of $\tilde{m}(t)$ is, from Eq. (22),

$$S_{10}(f; p) = 8p(1-p) \operatorname{Re} \left\{ \left[\frac{1}{2(1-2p)(1+\sin 2\pi f T_b) + 4p^2} - 1 \right] e^{j2\pi f T_b} \frac{1}{T_b} P_0(f) P_1^*(f) \right\} \quad (41)$$

which is also not symmetric around $f = 0$. Finally, the complex baseband PSD of GMSK (based on the two-pulse-stream AMP approximation) with unbalanced data input becomes

$$S_{\tilde{m}}(f; p) = S_{00}(f; p) + S_{11}(f; p) + S_{10}(f; p) \quad (42)$$

where $S_{00}(f; p)$, $S_{11}(f; p)$ and $S_{10}(f; p)$ are defined in Eq. (34) and Eqs. (38) and (41), respectively.

C. Other Pulse Shapes (Raised-Cosine Modulation)

As previously implied, one of the nice features about using the Laurent AMP representation of MSK-type CPM to evaluate its PSD is that this representation clearly allows for isolation of the spectral factor due to pulse shaping and of that due to data-symbol correlation. In fact, the results of Section IV.B are really quite general in that they apply to any partial-response modulation with $L = 4$ if one does not restrict oneself to the phase pulse shape of Eq. (35). In fact, the restriction on the duration of the frequency pulse, i.e., the value of L , also is not an issue. The reason behind this already was intimated when we pointed out the fact that the first AMP equivalent data-symbol sequence for GMSK had identical correlation properties to the single-data-symbol sequence that represents MSK. In a more general context, the following statements can be made about the correlation properties of the equivalent data-symbol sequences in the AMP representation.

Consider two CPM modulation schemes with different amounts of partial response, i.e., one is characterized by a frequency pulse of duration $L_1 T_b$ and the other by a frequency pulse of duration $L_2 T_b$ (assume $L_2 > L_1$ for convenience). Note that the CPM schemes need not have the same frequency pulse *shape*. Then, from the construction procedure used to derive the equivalent data-symbol sequences of the AMP representation from the true input-data sequence, it is straightforward to show that the first 2^{L_1-1} of the 2^{L_2-1} sequences that represent the second modulation have properties identical to those of the 2^{L_1-1} that completely represent the first modulation. This nicety allows one to consider, for example, a particular class of MSK-type modulations, all having the same frequency-pulse shape but different durations (i.e., different amounts of partial response) and, assuming that a small subset of the total number of AMP pulse streams is sufficient to characterize the PSD, to have to compute the spectral shaping due to the sequence correlation only one time.

A popular class of MSK-type CPM modulations is that corresponding to a raised-cosine (RC) frequency pulse. For this class (originally referred to as sinusoidal-frequency-shift keying (SFSK) by Amoroso [11]), the frequency pulse is given by

$$g(t) = \begin{cases} \frac{1}{2LT_b} \left[1 - \cos \left(\frac{2\pi t}{LT_b} \right) \right], & 0 \leq t \leq LT_b \\ 0, & \text{otherwise} \end{cases} \quad (43)$$

and for $L = 1$ has a spectral roll-off that varies as f^{-6} (as opposed to an f^{-4} spectral roll-off for MSK). Assuming a two-AMP pulse representation, the PSD for this class (L as a parameter) of modulations would be approximately given by the combination of Eqs. (34), (38), (41), and (42) for $L \geq 2$ or exactly by Eq. (34) for $L = 1$.

Before proceeding with numerical results, we point out that, with some additional computation (which would be warranted if one were interested in very low PSD levels), the PSD evaluation procedure discussed above can be extended to include more than just the first two (dominant) AMP pulse streams. In fact, the results of Section III are quite general and, analogous to Eqs. (26), (36), and (39), all one needs to compute are the autocorrelation and cross-correlation functions of the remainder of the equivalent data symbol streams. For $L = 4$, these remaining six pulse streams are characterized by [9]

$$\left. \begin{aligned} \tilde{a}_{2,n} &\triangleq (j\alpha_{n-1})(j\alpha_n)\tilde{a}_{0,n-3} \\ \tilde{a}_{3,n} &\triangleq j\alpha_n\tilde{a}_{0,n-3} \\ \tilde{a}_{4,n} &\triangleq (j\alpha_{n-2})(j\alpha_{n-1})(j\alpha_n)\tilde{a}_{0,n-4} \\ \tilde{a}_{5,n} &\triangleq (j\alpha_{n-2})(j\alpha_n)\tilde{a}_{0,n-4} \\ \tilde{a}_{6,n} &\triangleq (j\alpha_{n-1})(j\alpha_n)\tilde{a}_{0,n-4} \\ \tilde{a}_{7,n} &\triangleq j\alpha_n\tilde{a}_{0,n-4} \end{aligned} \right\} \quad (44)$$

V. Precoded MSK-Type Modulations

Conventional I-Q-type receivers for MSK-type modulations suffer a small performance penalty due to the inherent differential encoding operation (see, for example, Eq. (13) for MSK itself) performed at the transmitter and the attendant requirement for differential decoding at the receiver. A simple fix to this problem is to *precode* the input data with a *differential decoder* [7, Chapter 10], which in effect cancels the differential encoding operation at the transmitter and eliminates the need for differential decoding at the receiver. From a spectral standpoint, this precoding operation has no effect on the PSD of the transmitted signal when the input data are balanced. However, when the input data are unbalanced, as in the case of interest in this article, the precoder has a definite effect on the transmitted signal PSD. To see how this comes about, we first shall consider the simple case of MSK itself.

Suppose that prior to phase modulation of the carrier the input data stream $\alpha = (\dots, \alpha_{-2}, \alpha_{-1}, \alpha_0, \alpha_1, \alpha_2, \dots)$ first is converted to a complex data stream via

$$\alpha'_n = \alpha_n j^n \quad (45)$$

and then passed through a differential decoder that satisfies the recursion relation

$$\beta_n = -j\alpha'_n (\alpha'_{n-1})^* \quad (46)$$

where β_n denotes the complex binary output of the decoder (input to the MSK modulator) in the n th bit interval. Substituting Eq. (45) into Eq. (46), we see that

$$\beta_n = -j(\alpha_n j^n) (\alpha_{n-1} (-j)^{n-1}) = \alpha_n \alpha_{n-1} \quad (47)$$

which is a conventional differential decoding of the true input data bits. Since the cascade of the differential encoder of Eq. (13) and the differential decoder of Eq. (46) produces a unity gain transmission path, i.e.,

$$\beta_n = -j\tilde{a}_{0,n}\tilde{a}_{0,n-1}^* = -j(j\alpha_n\tilde{a}_{0,n-1})\tilde{a}_{0,n-1}^* = \alpha_n |\tilde{a}_{0,n-1}|^2 = \alpha_n \quad (48)$$

then one can deduce that, for an input binary complex i.i.d. bit sequence $\boldsymbol{\alpha}' = (\dots, \alpha'_{-2}, \alpha'_{-1}, \alpha'_0, \alpha'_1, \alpha'_2, \dots)$ as in Eq. (45), precoded MSK using the precoder (differential decoder) in Eq. (46) is exactly the same as a Laurent representation of MSK [a single complex symbol-pulse stream with half-sinusoidal pulse shape as in Eq. (13)] with the same input data sequence, i.e., $\{\tilde{a}_{0,n}\} = \boldsymbol{\alpha}'$. This equivalence is illustrated in Fig. 1.

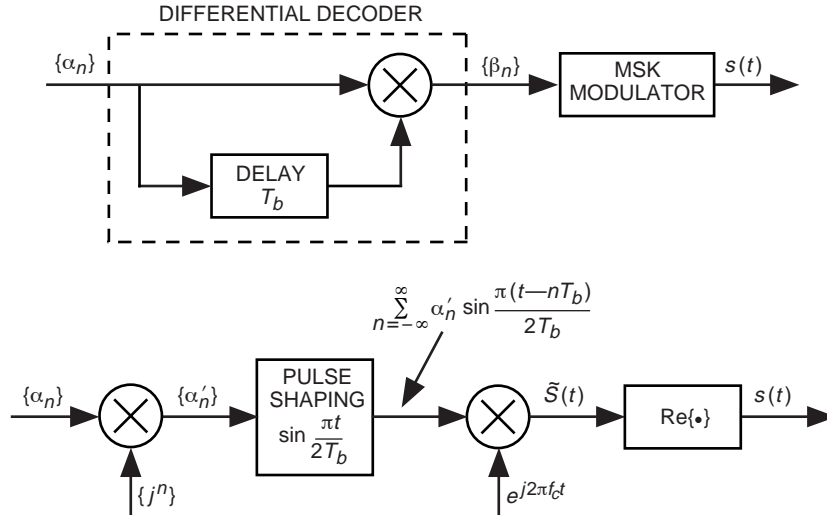


Fig. 1. Equivalent real forms of precoded MSK transmitters.

The upshot of the above equivalence is that, since the conversion from $\boldsymbol{\alpha}$ to $\boldsymbol{\alpha}'$ does not change the statistical (correlation) properties of the sequence, then, based on the Laurent AMP representation, we conclude that the PSD of precoded MSK is that of a linear modulation with an i.i.d. *uncorrelated* complex unbalanced data source and, as such, has a continuous component given by [see Eq. (33)]

$$S_{P-MSK}(f)|_{cont} = 4p(1-p)T_b \frac{16}{\pi^2} \frac{\cos^2 2\pi f T_b}{(1 - 16f^2 T_b^2)^2} \quad (49)$$

and a discrete component derived analogously to [9, Chapter 2] as

$$S_{P-MSK}(f)|_{discr} = (1-2p)^2 \sum_{k=-\infty}^{\infty} \frac{4}{\pi^2} \frac{1}{(1-4k^2)^2} \delta\left(f - \frac{k}{2T_b}\right) \quad (50)$$

where $P-MSK$ denotes precoded MSK. Thus, in summary, the addition of a precoder to the input of an MSK modulator with unbalanced data input removes the tilt of the MSK spectrum due to the unbalance and replaces it with a discrete spectral component as is typical of linear modulations.

For GMSK, since each AMP data stream has its own form of “differential encoding” in terms of the relation between its equivalent symbols and the input bits, any precoder that would be used prior

to the GMSK modulator would not compensate all of the data streams. However, since, as previously mentioned, the first data stream [whose equivalent data symbols are a true complex differential encoding of the input bits as per the first of the two equations in Eq. (15)] is the dominant contributor to the overall representation, it seems fortuitous to employ the same precoder as that used for MSK. When this is done, the first data stream in the AMP representation will now have uncorrelated complex symbols, but the second (and, for that matter, the other six) components still will have correlated symbols. However, because of the dominance of the first pulse stream over the others, one would anticipate, analogously to the MSK behavior described above, the presence of a discrete component in the spectrum and a major reduction in the tilt of the continuous component due to the input data unbalance.

VI. Numerical Evaluations and Simulation Results

Using MATLAB software to evaluate the analytical results, Figs. 2(a) and 2(b) illustrate the complex baseband PSD of unbalanced MSK [see Eq. (30)] for $p = 0.45$ (10 percent unbalance), a typical value

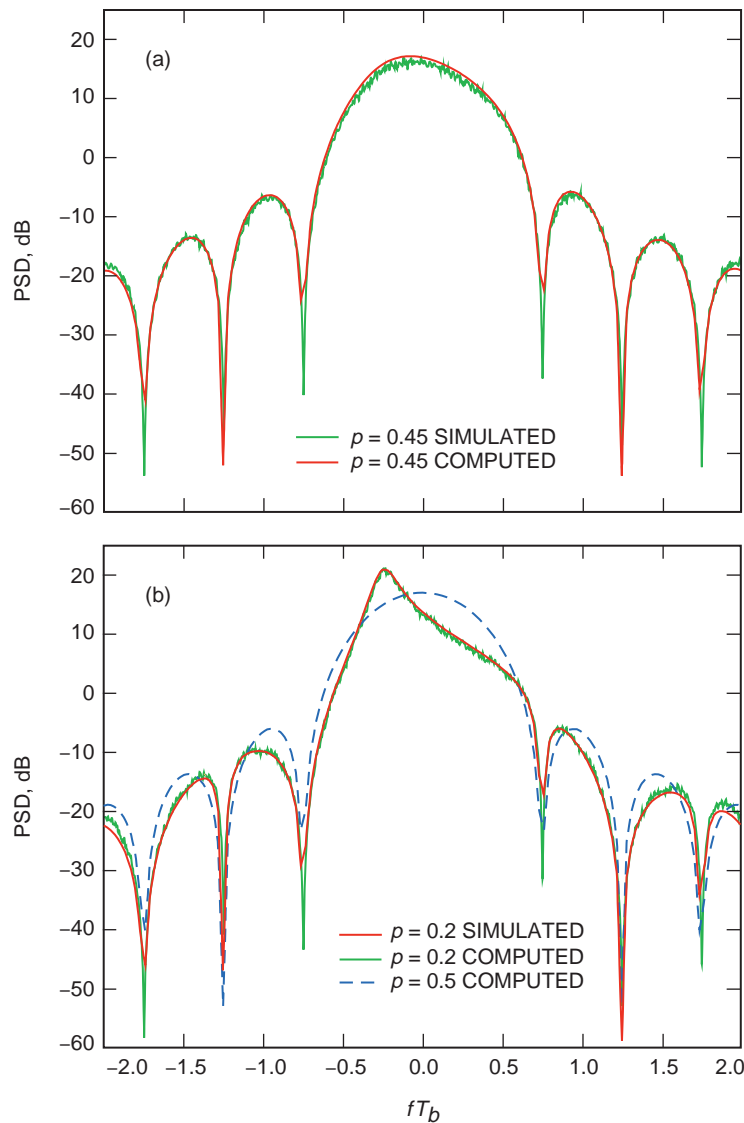


Fig. 2. The complex baseband power spectral density of unbalanced MSK: (a) $p = 0.45$ and (b) $p = 0.2$.

of a standard specification [12], and $p = 0.20$ (60 percent unbalance), which clearly is an extreme case. The PSD for the conventional balanced-data ($p = 0.5$) MSK case [see Eq. (33)] is included for comparison in the latter of the two figures. Superimposed on the calculated PSD curves are numerical results (jagged curve) obtained from a computer simulation of the true GMSK spectrum, which is tantamount to considering all eight AMP components. The GMSK transmitter was simulated using the Signal Processing Worksystems (SPW) software from Cadence Design Systems Inc. and is illustrated in block diagram form in Fig. 3. Evaluation of the simulated PSDs involves two steps. First, 100 blocks of data, each with 256 symbols, were formed, and a Bartlett window was applied to each block. The Bartlett window was chosen because of its low noise floor and the fact that it contributes negligible distortion to the evaluation of the PSDs. Second, a fast Fourier transform (FFT) was performed on each windowed block, and all 100 FFTs were summed and normalized to produce the final PSD result.

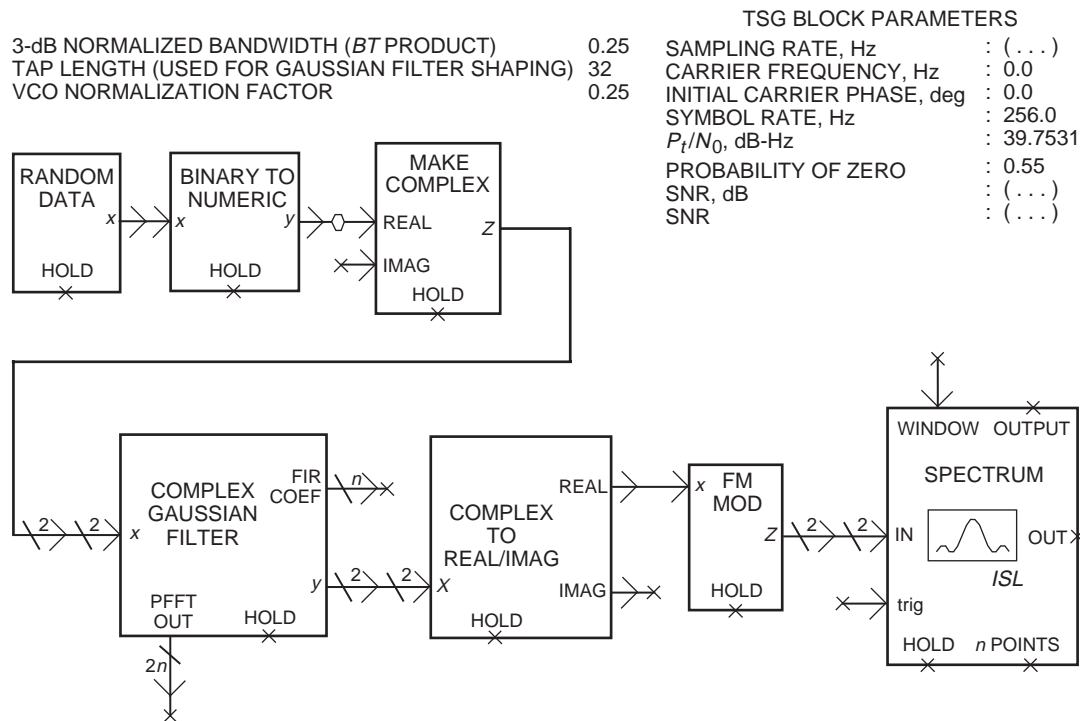


Fig. 3. Computer simulation block diagram of the GMSK transmitter.

We observe from the results in Figs. 2(a) and 2(b) that the asymmetry is such as to increase the side lobes on one side of the spectrum center and decrease them on the other. However, the *rate* at which the side lobes roll off apparently is not changed by the unbalance in the data. The primary effect of the data unbalance on the PSD is to cause a tilt in its main lobe. Also, for the complementary values $p = 0.55$ and $p = 0.80$, the illustrations in Fig. 2(a) and 2(b) simply would be reversed with respect to the frequency axis, i.e., the tilt flips with respect to $f = 0$. Finally, the PSD for the real MSK bandpass waveform would tilt in one direction around $f = f_c$ and in the exact opposite direction around $f = -f_c$. The tilt for the upper side band around $f = f_c$ would be the reverse of that for the complex baseband spectrum because of the reversal of the frequency axis in the relation between these two spectra, as per Eq. (31).

Before showing the PSD of unbalanced GMSK, we first attempt to justify the assumption of using only the first two terms in the Laurent AMP representation to model the transmitted signal. Figure 4 illustrates the PSD of GMSK for $L = 4$ and $BT_b = 0.25$ computed from all $2^{L-1} = 8$ AMP components as well as from only the first two components. As can be seen from the results, the two are virtually identical down to a level of about -70 dB. Thus, we suspect that, for unbalanced GMSK, one can anticipate a

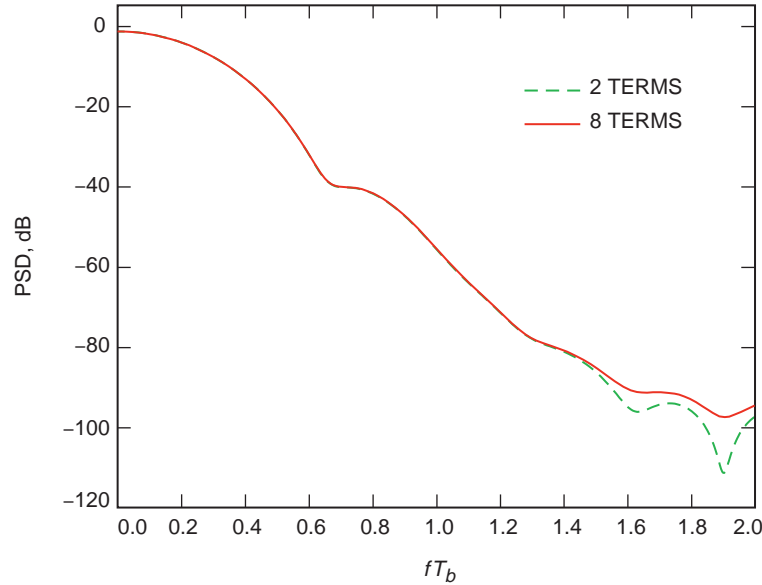


Fig. 4. A comparison of the complex baseband power spectral density of balanced GMSK for two and all eight AMP components.

similar behavior. To guarantee this assumption, we computed the autocorrelation and cross-correlation properties of the next (third) pulse sequence, $\{\tilde{a}_{2,n}\}$, as defined in the first equation of Eq. (44) as well as the corresponding terms that would contribute to the PSD. These results are given in the Appendix and will be used to identify the level above which the PSD computed from only the first two pulse streams is sufficient.

Illustrated in Figs. 5(a) and 5(b) is the complex baseband PSD of unbalanced GMSK [see Eqs. (34), (38), (41), and (42)] for $p = 0.45$ and $p = 0.20$ as well as computer simulation results based on a true GMSK signal. Here again we see that the dominant effect of the data unbalance occurs in the region of the main lobe. In the limit as $p \rightarrow 1$, the power spectrum would become a pair of delta functions at $f = \pm 1/4T_b$, each containing one half the total power. Using the results from the Appendix, the PSD of Fig. 5(b) was recomputed taking into account the addition of the third pulse stream. The comparison of these results is illustrated in Fig. 6. As previously anticipated, above a PSD level of -70 dB, the difference between the two results is undetected.

For the case of unbalanced precoded MSK, the PSD as computed from the superposition (sum) of Eqs. (49) and (50) is illustrated in Fig. 7(a) for $p = 0.55$ and in Fig. 7(b) for $p = 0.10$. Once again, results obtained from computer simulation are superimposed on these figures and indicate excellent agreement with the theory.

VII. Conclusion

The Laurent AMP representation of MSK-type modulations is particularly helpful in the evaluation of the power spectrum of such modulations in the presence of data imbalance. Specifically, the representation allows obtaining closed-form expressions for the power spectrum that clearly elucidate its partitioning into components due to the effective AMP pulse shapes and those due to the AMP sequence correlations. Furthermore, the nature of the PSD distortion produced by the imbalance, i.e., a tilt in the main lobe and a relative unbalance between the upper and lower side-lobe levels, is easily identifiable from the mathematical form of the results.

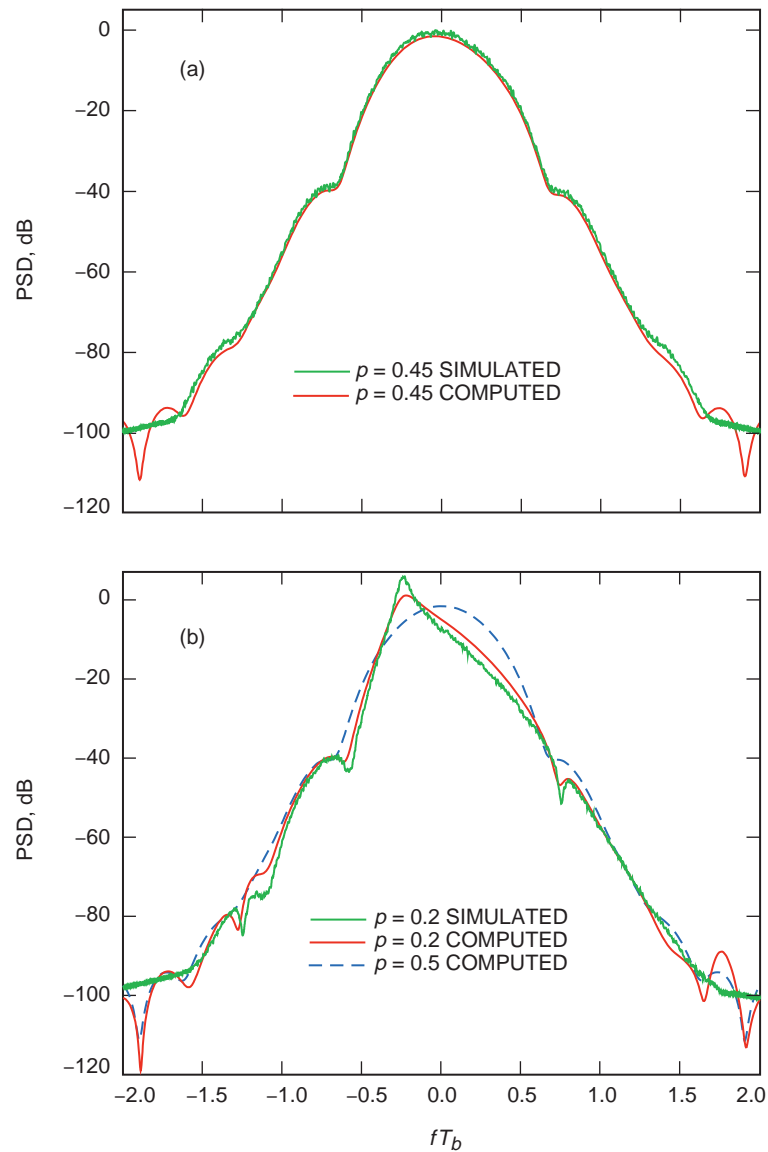


Fig. 5. The complex baseband power spectral density of unbalanced GMSK: (a) $p = 0.45$ and (b) $p = 0.2$.

References

- [1] J. B. Anderson, T. Aulin, and C.-E. Sundberg, *Digital Phase Modulation*, New York and London: Plenum Press, 1986.
- [2] J. Proakis, *Digital Communications*, New York: McGraw-Hill, 3rd ed., 1995.
- [3] B. E. Rimoldi, "A Decomposition Approach to CPM," *IEEE Transactions on Information Theory*, vol. 34, no. 3, pp. 260–270, March 1988.
- [4] P. A. Laurent, "Exact and Approximate Construction of Digital Phase Modulations by Superposition of Amplitude Modulated Pulses," *IEEE Transactions on Communications*, vol. COM-34, no. 2, pp. 150–160, February 1986.

- [5] V. K. Prabhu and H. E. Rowe, "Spectra of Digital Phase Modulation by Matrix Methods," *Bell System Technical Journal*, vol. 53, no. 5, pp. 899–934, May–June 1974.
- [6] V. K. Prabhu and H. E. Rowe, "Power Spectrum of a Digital, Frequency Modulation Signal," *Bell System Technical Journal*, vol. 54, no. 6, pp. 1095–1125, July–August 1975.
- [7] M. K. Simon, S. M. Hinedi, and W. C. Lindsey, *Digital Communication Techniques: Signal Design and Detection*, Englewood Cliffs, New Jersey: PTR Prentice-Hall, 1995.
- [8] U. Mengali and M. Morelli, "Decomposition of M -ary CPM Signals Into PAM Waveforms," *IEEE Transactions on Information Theory*, vol. 41, no. 5, pp. 1265–1275, September 1995.
- [9] G. K. Kaleh, "Simple Coherent Receivers for Partial Response Continuous Phase Modulation," *IEEE Transactions on Selected Areas in Communications*, vol. 7, no. 9, pp. 1427–1436, December 1989.
- [10] L. B. W. Jolley, *Summation of Series*, New York: Dover Publications, 1961.
- [11] F. Amoroso, "Pulse and Spectrum Manipulation in the Minimum (Frequency Shift Keying (MSK) Format," *IEEE Transactions on Communications*, vol. COM-24, no. 3, pp. 381–384, March 1976.
- [12] W. L. Martin, T.-Y. Yan, and L. Lam, *CCSDS-SFCG Efficient Modulation Methods Study: A Comparison of Modulation Schemes, Part 3: End-to-End System Performance*, SF17-28/D, SFCG Meeting, Galveston, Texas, September 16–25, 1997.

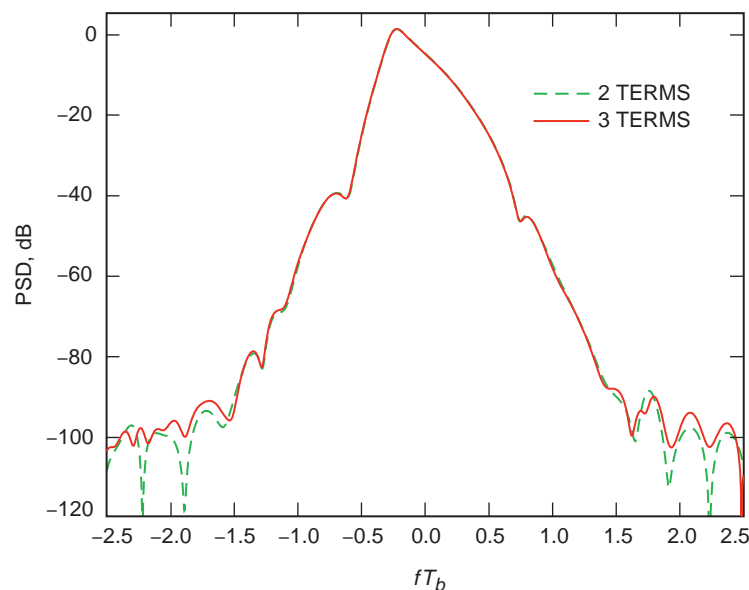


Fig. 6. A comparison of the complex baseband power spectral density of unbalanced GMSK for two and three AMP components, with $p = 0.2$.

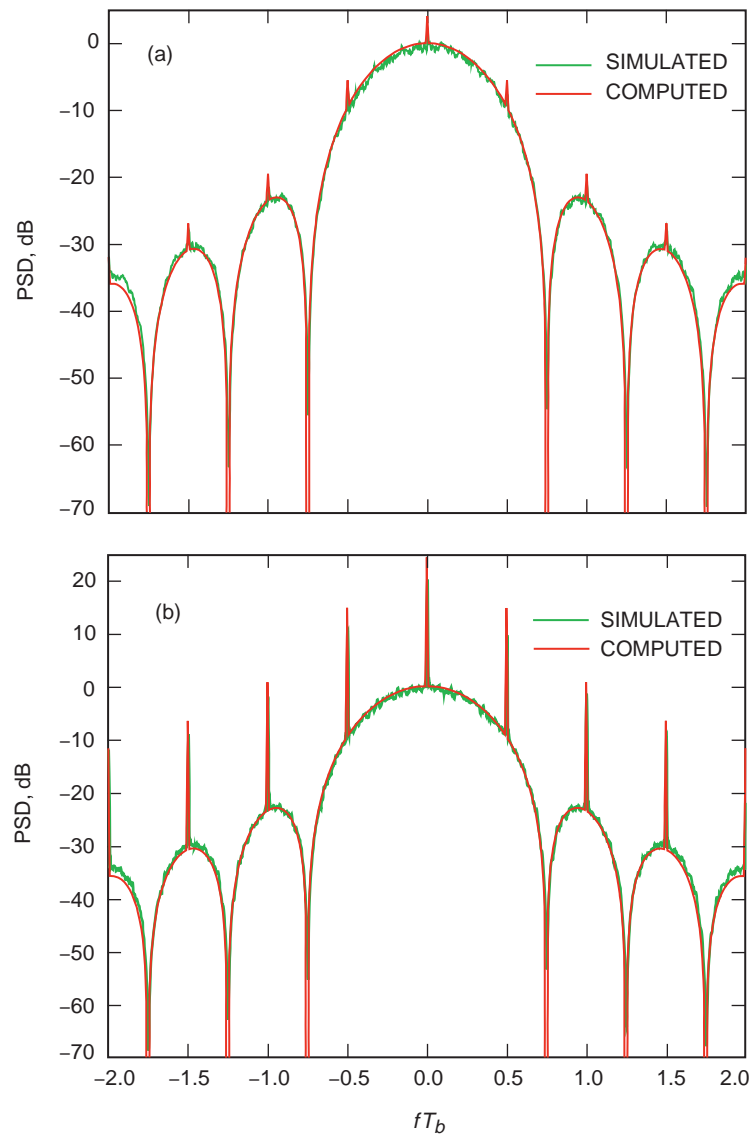


Fig. 7. The complex baseband power spectral density of unbalanced precoded MSK: (a) $p = 0.55$ and (b) $p = 0.1$.

Appendix

Correlation and Spectral Properties of the Third Pulse Stream in the AMP Representation of GMSK

From the defining recursion relation for the third pulse stream, $\{\tilde{a}_{2,n}\}$, as given in Eq. (42) together with the analogous relation for the first and second pulse streams, $\{\tilde{a}_{0,n}\}$ and $\{\tilde{a}_{1,n}\}$, as given in Eq. (15), it is straightforward to show that

$$R_{\tilde{a}_2}(l) \triangleq E \{ \tilde{a}_{2,n} \tilde{a}_{2,n+l}^* \} = \begin{cases} 1, & l = 0 \\ -j(1-2p)^3, & l = 1 \\ -(1-2p)^4, & l = 2 \\ [-j(1-2p)]^l, & l \geq 3 \end{cases}, \quad R_{\tilde{a}_1}(-l) = R_{\tilde{a}_1}^*(l) \quad (\text{A-1})$$

and

$$R_{\tilde{a}_{20}}(l) \triangleq E \{ \tilde{a}_{2,n} \tilde{a}_{0,n+l}^* \} = \begin{cases} [-j(1-2p)]^{l+1}, & l \geq 0 \\ (1-2p)^2, & l = -1 \\ j(1-2p)^2, & l = -2 \\ [j(1-2p)]^{-(l+1)}, & l \leq -3 \end{cases}, \quad R_{\tilde{a}_{02}}(-l) = R_{\tilde{a}_{20}}^*(l) \quad (\text{A-2})$$

$$R_{\tilde{a}_{21}}(l) \triangleq E \{ \tilde{a}_{2,n} \tilde{a}_{1,n+l}^* \} = \begin{cases} [-j(1-2p)]^l, & l \geq 2 \\ -j(1-2p)^3, & l = 1 \\ (1-2p)^2, & l = 0 \\ j(1-2p), & l = -1 \\ -(1-2p)^4, & l = -2 \\ [j(1-2p)]^{-l}, & l \leq -3 \end{cases}, \quad R_{\tilde{a}_{12}}(-l) = R_{\tilde{a}_{21}}^*(l) \quad (\text{A-3})$$

The corresponding components needed to compute the PSD given in Section III are as follows:

$$S_{22}(f; p) = \frac{1}{T_b} |P_2(f)|^2 4p(1-p) \left[\frac{1}{2(1-2p)(1 + \sin 2\pi f T_b) + 4p^2} \right. \\ \left. + 2(1-2p) \sin 2\pi f T_b + 2(1-2p)^2 \cos 4\pi f T_b \right], \quad P_2(f) \triangleq \mathcal{F} \{ C_2(t) \} \quad (\text{A-4})$$

$$S_{20}(f; p) = 8p(1-p) \operatorname{Re} \left\{ \left[\left(\frac{1}{2(1-2p)(1+\sin 2\pi f T_b) + 4p^2} - 1 \right) e^{j2\pi f T_b} - j(1-2p)e^{j4\pi f T_b} \right] \frac{1}{T_b} P_0(f) P_2^*(f) \right\} \quad (\text{A-5})$$

$$S_{21}(f; p) = 8p(1-p) \operatorname{Re} \left\{ \left[[j(1-2p)] e^{-j2\pi f T_b} + \frac{1}{2(1-2p)(1+\sin 2\pi f T_b) + 4p^2} - 1 + (1-2p)^2 e^{j4\pi f T_b} \right] \frac{1}{T_b} P_1(f) P_2^*(f) \right\} \quad (\text{A-6})$$

Selected Laboratory Measurements of the Maximum-A-Posterior Symbol Synchronizer

Andrew Gray, Loc Lam, Tsun-Yee Yan, Warren Martin
Jet Propulsion Laboratory
4800 Oak Grove Dr., M/S 238-343
Pasadena, CA 91109

AI 98-17

AI 98-28

March 29, 1999

1 Introduction

The Maximum-A-Posteriori (MAP) symbol synchronizer development is part of an ongoing research effort at the Jet Propulsion Laboratory (JPL) to improve power and bandwidth efficiency of communication systems. Considerable progress has been made recently in the study of bandwidth efficient modulation techniques [1-3]. Furthermore, issue of receiver concept and performance for bandwidth efficient modulations have been discussed and evaluated [4-5]. In the report, it was illustrated that receivers using the conventional digital-data-transition tracking loop (DTTL) for data synchronization will not be able to function properly at very low symbol SNRs. In addition, the DTTL is not designed for handling pulse shapes other than rectangular. A new symbol synchronizer based on the Maximum-A-Posteriori estimation method has been developed[4,5]. Extensive computer simulations have been performed to evaluate the performance and it has been shown that the MAP symbol synchronizer can be operated at very low symbol SNRs with symbol pulse waveforms other than rectangular [5]. This paper describes the hardware validation of the MAP symbol synchronizer at JPL and demonstrate its performances.

2 MAP Symbol Synchronizer

2.1 System Description

The MAP symbol synchronizer is a maximum-a-posteriori estimator [4,5]. Consider a baseband signal with an unknown delay, ϵ , i.e.

$$y(n) = \sqrt{S_T} \sum_{k=1}^{\infty} a_k p(n - kN - \epsilon) + v(n) \quad (1)$$

where $n = 0, 1, \dots, \infty$, S_T is the transmitted power, ϵ is the unknown symbol delay (epoch), a_k is the k^{th} binary symbol, N is the number of samples per data symbol, $v(n)$ is the AWGN with two-sided power spectral density level of $N_0/2$ Watts/Hz, and $p(t)$ is the arbitrary signal pulse shape. The maximum-a-posteriori function of ϵ , in recursive form, is [4,5]

$$\Lambda(\epsilon | \underline{Y}_K) = \Lambda(\epsilon | \underline{Y}_{K-1}) + \ln(\cosh(2 \frac{\sqrt{S_T}}{N_0} \underline{y}_K^T \underline{p}_K(\epsilon))) \quad (2)$$

where $\underline{Y}_K = (\underline{y}_1, \underline{y}_2, \dots, \underline{y}_K)$ is the observed vector over $K+1$ symbols, \underline{y}_K^T is the N -dimensional observation column vector of the signal in the K^{th} symbol interval, and T denotes the transpose operation. The maximum-a-posteriori estimate of the epoch is the estimate, $\hat{\epsilon}$, which maximizes the function

$$\Lambda(\hat{\epsilon} | \underline{Y}_K) = \max_{i=0,1,\dots,N-1} \{\Lambda(\epsilon_i | \underline{Y}_K)\} \quad (3)$$

In addition, the estimated symbol is also derived from the estimate $\hat{\epsilon}$. To reduce hardware complexity, the nonlinear functions $\ln(\cosh(.))$ is replaced by the absolute value function (i.e. $|\cdot|$). The hardware block diagram of the MAP symbol synchronizer is shown in Figure 1.

2.2 Hardware Design

For design validation purposes, the MAP symbol synchronizer was implemented in an ALTERA FLEX 10KA Field Programmable Gate Array (FPGA) which has 100,000 gates and can operate at clock speed of over 40 Mhz. The FPGA is mounted on the Constellation FLEX 10K board developed by Nova Engineering, Inc. The Constellation board has an on-board 40 Mhz CMOS oscillator and 238 I/O pins. The Constellation FLEX 10K board can be used as a stand-alone board, as part of a larger system or inserted into an ISA slot. Currently, it is installed in a ISA slot of a 300 Mhz Compaq Deskpro Computer. One disadvantage of using the ISA bus is that the data and data clock going to the FPGA through the ISA bus are relatively slow. Figure 2 shows the Constellation FLEX 10K board which contains the MAP symbol synchronizer. Testing the design involves sending the signal sample through an 8-bit bus (bidirectional) to the MAP symbol synchronizer in the FPGA. Synchronized symbol clock and hard decision of the estimated symbol are sent out via the I/O pins which can then be displayed on an oscilloscope. The test signal, which is signal plus noise described in EQ (1), was generated in software using the Signal Processing Worksystem (SPW). The signal is then converted to an 8-bit number and store in a data file. During the test, these files provide the input signal to the MAP symbol synchronizer. Currently, the FPGA is clocked through the ISA bus at a clock speed of 465.1 KHz ($2.15 \mu\text{sec}$). With the sampling rate equal to 16 times the symbol rate (i.e. $N = 16$ Samples per symbol) each sample is read into the FPGA at a rate of 465.1 Kilo samples per second ($2.15 \mu\text{sec}$ per sample) or equivalently, 29.1 Kilo symbols per second. Note that this is the fastest speed that data can be sent through the ISA bus even though the design and the FPGA can handle data rates up to 40 Mhz.

3 Measurement Results

Figures (3-4) shows the captured image from the oscilloscope illustrating the acquisition performances of the MAP symbol synchronizer for various signal delays and signal-to-noise ratio (SNRs). The trace on top shows the system symbol clock for reference and the trace on the bottom shows the estimated symbol clock. Figure (3a-3c) shows acquisition performances for signals with SNR = 0dB, -5dB, and -10 dB respectively with 3 sample delay ($6.45 \mu\text{secs}$) in the channel. The MAP symbol synchronizer acquired in all three SNR cases with the estimated symbol clock (bottom plot) showing between 6.2 and $6.4 \mu\text{secs}$ delay relative to the system symbol clock. Figure (4a-4b) show the acquisition performance at symbol SNR = -10 dB for 5 sample ($10.75 \mu\text{secs}$) and 7 sample ($15.1 \mu\text{secs}$) delay in the channel. The MAP symbol synchronizer acquired both signals at $10.8 \mu\text{secs}$ and $15.2 \mu\text{secs}$ respectively. To measure acquisition time, the estimated clock is recorded in a file from the start to the end of each test run. At 0 dB, -5 dB, and -10 dB, the MAP symbol synchronizer acquired these signals after 24 data symbols, 396 data symbols, and 1903 data symbols.

4 Summary

The MAP symbol synchronizer achieved a very precise phase lock to the noisy input signal in all the test cases. Further tests and measurements are in progress. Additional measurements will be made to quantify the average acquisition time as a function of symbol SNR. Acquisition performance as a function of phase noise, Doppler frequency, and Doppler frequency rate will be measured. Performance for other waveforms such as MSK, FQPSK [6], and GMSK will also be determined. Finally, the MAP symbol synchronizer will be tested at high data rates from approximately 100 Kilo symbols per second to 1 Mega Symbols per second. This requires sampling data from a function generator with an analog-to-digital converter and inputting these samples directly to the symbol synchronizer, bypassing the ISA bus.

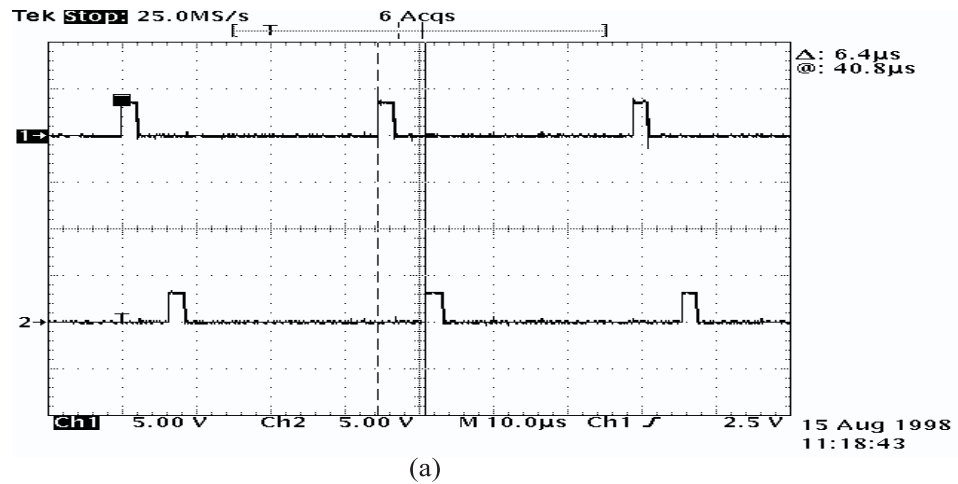
References

1. W. Martin, T-Y. Yan, L. Lam: "CCSDS Phase 3 Study Update," *Report for Consultative Committee for Space Data Systems (CCSDS)*; Jet Propulsion Laboratory (JPL), California Institute of Technology, Pasadena, CA; May 4-8, 1998.
2. A. Southern, M. Otter, M. Teichel: "Advanced Spectrum Shaping for Efficient Bandwidth Utilisation," *ESA Contract 11605/96/F/TB Final Report*; RSI Space Operations Ground Segment Studies and Consultancy., Griesheim, Germany; September 1997.
3. K. Feher: "Efficient FQPSK Modulation-Integrated Transceiver Developments," *Submitted to Consultative Committee for Space Data Systems (CCSDS)*; Digicom Inc., El Macero, CA; April 4, 1997.
4. M. K. Simon, "Maximum Likelihood Sliding Window Estimation of Timming for NRZ Data Streams," *JPL Interoffice Memorandum (internal document)*, Jet Propulsion Laboratory, Pasadena, California, October 1997.
5. L. V. Lam, T.-Y. Yan, M. K. Simon, and W. L. Martin, "Acquisition Performance Comparison of the Generalized Maximum-A-Posteriori Symbol Synchronizer Versus the Data-Transition Tracking Loop," *The Telecommunications and Data Acquisition Progress Report 42-132*, Jet Propulsion Laboratory, Pasadena, California, pp. 1-13, February 1998.
6. Kato, S., and K. Feher, *Correlated Signal Processor*, U.S. Patent 4,567,602, issued 28 January 1986, Canada Paten 1211517, issued 16 September 1986.

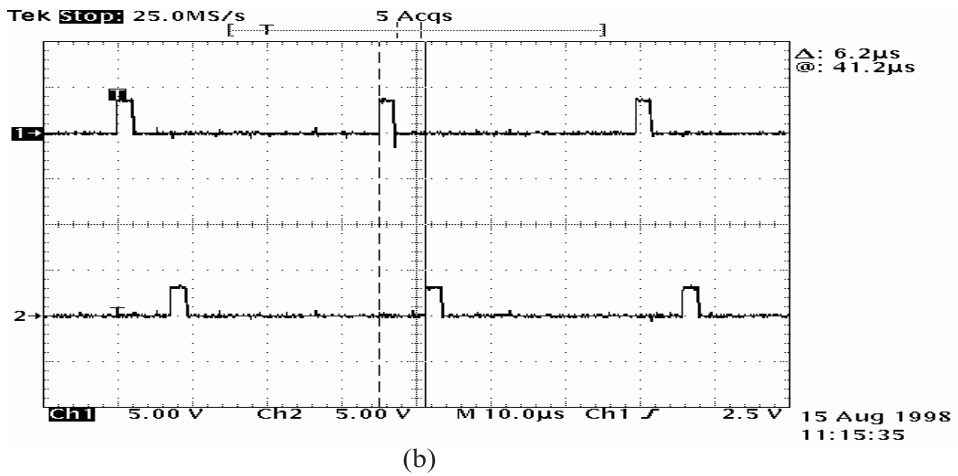
5



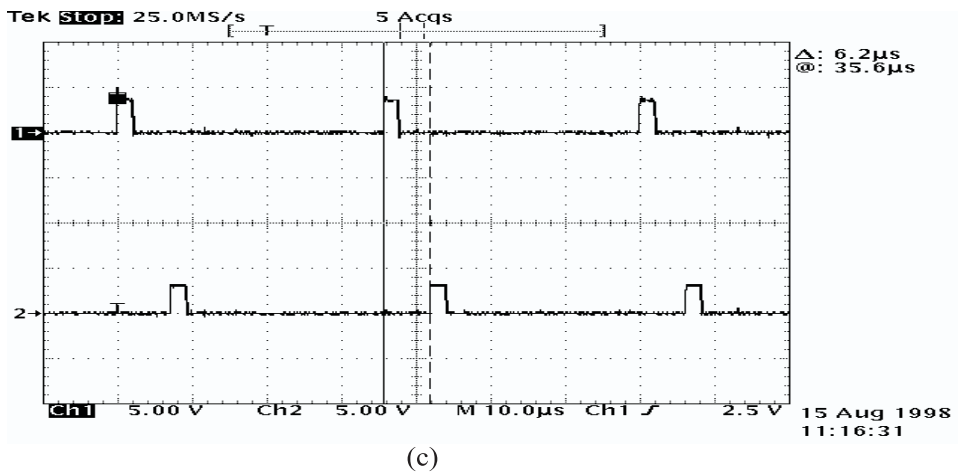
Figure 2: Hardware Block Diagram of the MAP Symbol Synchronizer



(a)

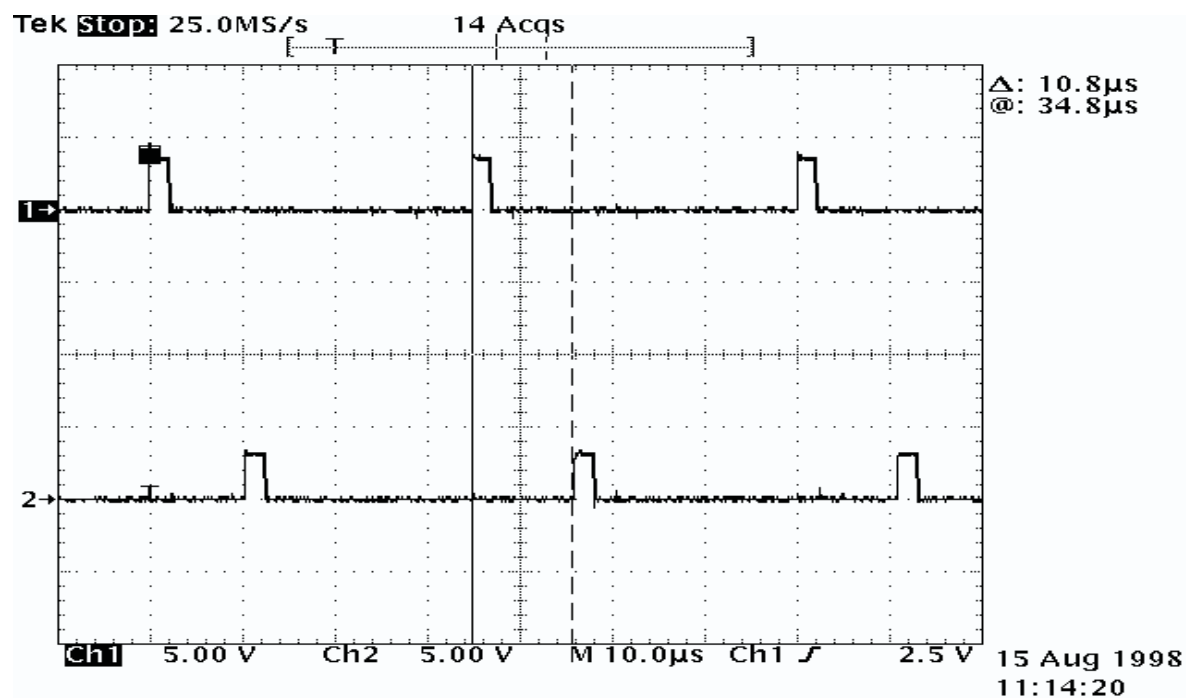


(b)

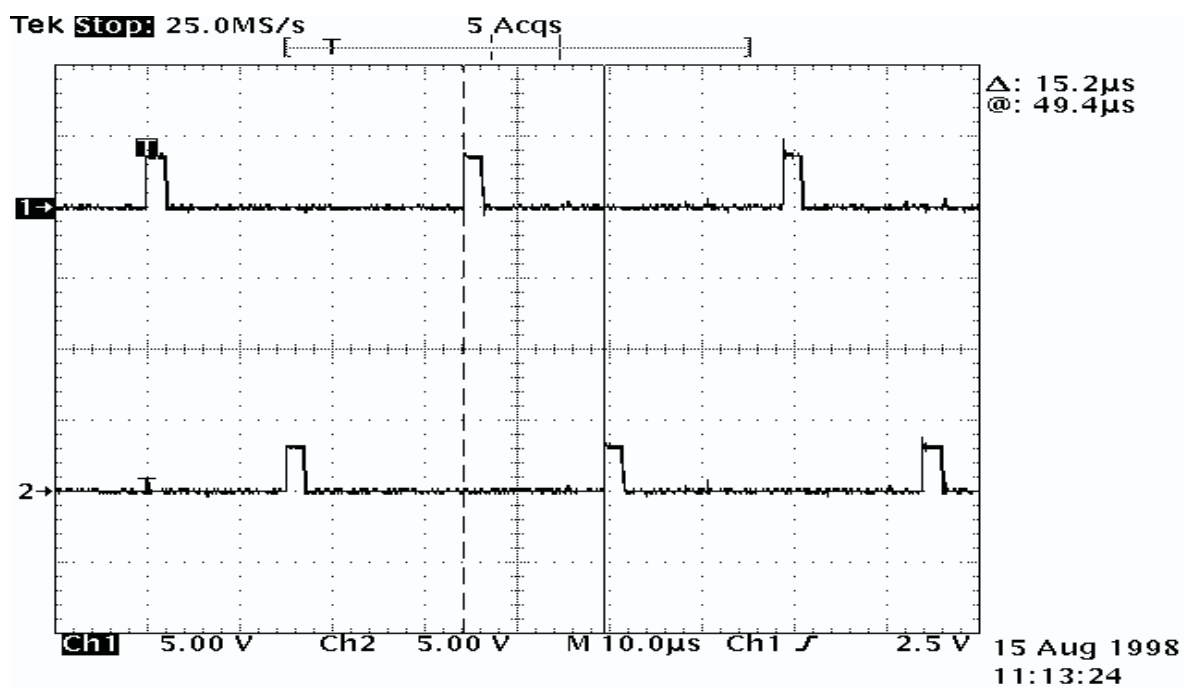


(c)

Figure 3: Acquisition Performance of the Hardware MAP Symbol Synchronizer for $\epsilon = 6.45 \mu\text{sec}$ at symbol(a) SNR = 0dB, (b) SNR = -5, dB, (c) SNR = -10 dB



(a)



(b)

Figure 4: Acquisition Performance of the Hardware MAP Symbol Synchronizer at symbol SNR = -10dB for (a) $\epsilon = 10.75 \mu\text{sec}$ (b) $\epsilon = 15.1 \mu\text{sec}$

Occupied Bandwidth of MSK and GMSK in the Presence of Data Imbalance

Dennis Lee
 Jet Propulsion Laboratory
 California Institute of Technology
 Pasadena, CA 91109

October 13, 1999

1 Abstract

This paper computes the spectral power containment of MSK and GMSK $BT_b=0.25$ (without precoding) and precoded MSK with data imbalance using theoretical expressions derived in [2]. In addition, a theoretical expression for the spectrum of precoded GMSK with data imbalance is derived. The equation is verified through simulations and used to generate the power containment curve for precoded GMSK with data imbalance.

2 Introduction

The spectrum of MSK (both with and without precoding) and GMSK (without precoding only) with data imbalance was computed in [2]. The spectrum in [2] showed considerable effects due to data imbalance, and action item 99-1E-1 was issued to determine the effects of data imbalance on the spectral power containment. In response to the action item, this paper computes the spectral power containment of GMSK $BT_b=0.25$ and MSK in the presence of data imbalance. A new expression for the spectrum of precoded GMSK with data imbalance is derived.

3 MSK/GMSK Spectrum without Precoding

3.1 MSK without precoding

The power spectral density for MSK is derived in [2], and is given below:

$$S(f; p) = T_b \frac{16}{\pi^2} \frac{\cos^2 2\pi f T_b}{(1 - 16f^2 T_b^2)^2} \left[\frac{2p(1-p)}{(1-2p)(1 + \sin \pi f T_b) + 2p^2} \right] \quad (1)$$

where p is the probability that the input bit is a "1". When $p=0.45$, there is 10% data imbalance. Likewise, when $p=0.2$, there is 60% data imbalance.

Figures 1 and 2 show the spectrum of MSK with 10% data imbalance and 60% data imbalance, respectively. The MSK spectrum with no data imbalance is included in the figures for reference. While a CCSDS recommendation limits data imbalance to 10%, the case of 60% data imbalance was included to show the effects of severe data imbalance.

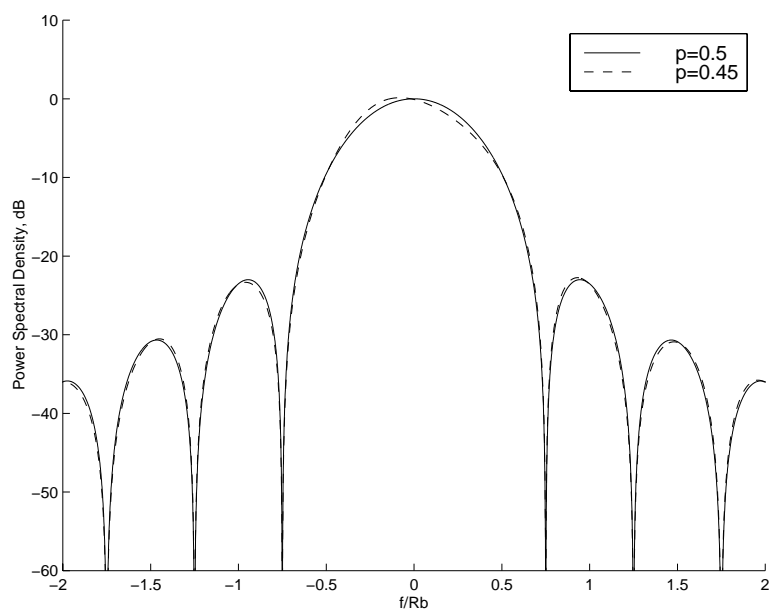


Figure 1: MSK Spectrum without precoding, 10% data imbalance

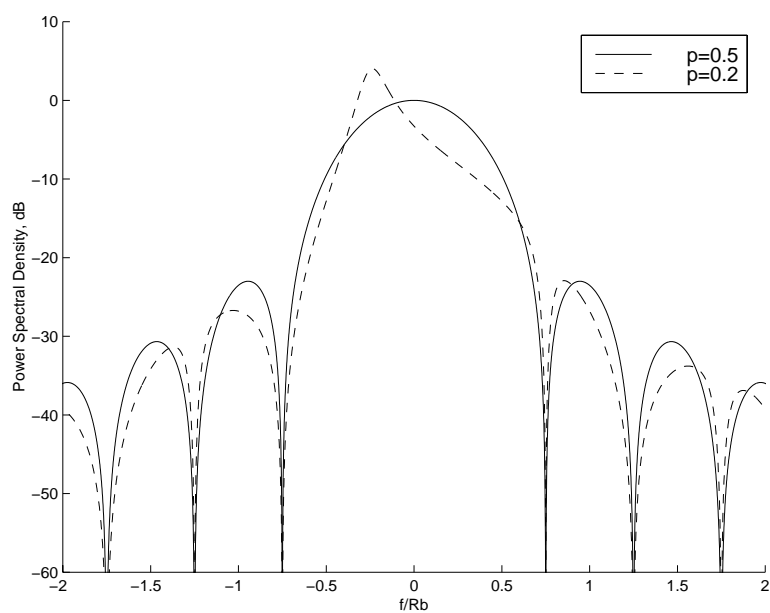
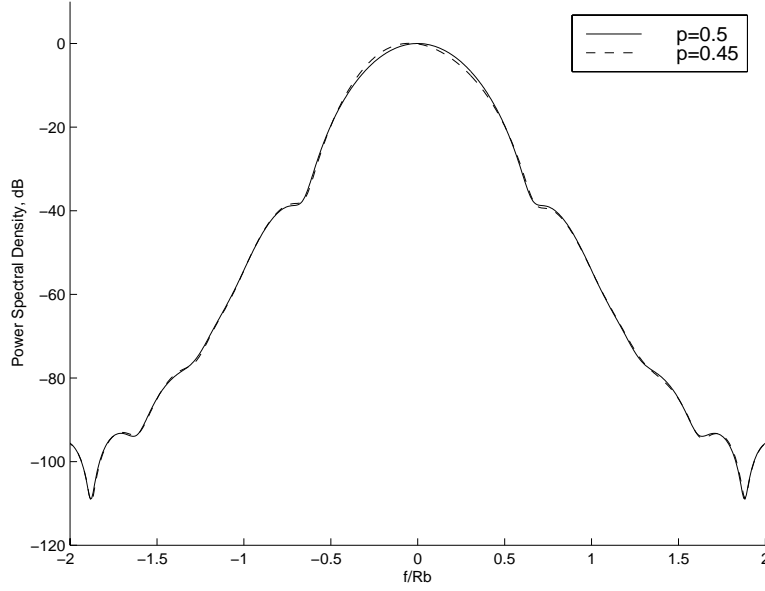


Figure 2: MSK Spectrum without precoding, 60% data imbalance


 Figure 3: GMSK $BT_b=0.25$ Spectrum, 10% data imbalance

3.2 GMSK without precoding

As shown in [3], GMSK can be represented as a sum of amplitude modulated pulses (AMP). It was also shown that a good approximation of GMSK $BT_b=0.25$ can be obtained using only the two largest pulses, $h_0(t)$ and $h_1(t)$. Denoting $S_{00}(f; p)$ as the PSD of the first pulse, $S_{11}(f; p)$ as the PSD of second pulse, and $S_{10}(f; p)$ as the cross-spectrum of the two pulses, the spectrum of GMSK $BT_b=0.25$ is given by [2]

$$S(f; p) = S_{00}(f; p) + S_{11}(f; p) + 2\text{Re}\{S_{10}(f; p)\} \quad (2)$$

where

$$S_{00}(f; p) = \frac{1}{T_b} |H_0(f)|^2 \left[\frac{2p(1-p)}{(1-2p)(1 + \sin \pi f T_b) + 2p^2} \right] \quad (3)$$

$$S_{11}(f; p) = \frac{1}{T_b} |H_1(f)|^2 4p(1-p) \left[\frac{1}{2(1-2p)(1 + \sin \pi f T_b) + 4p^2} + 2(1-2p) \sin 2\pi f T_b \right] \quad (4)$$

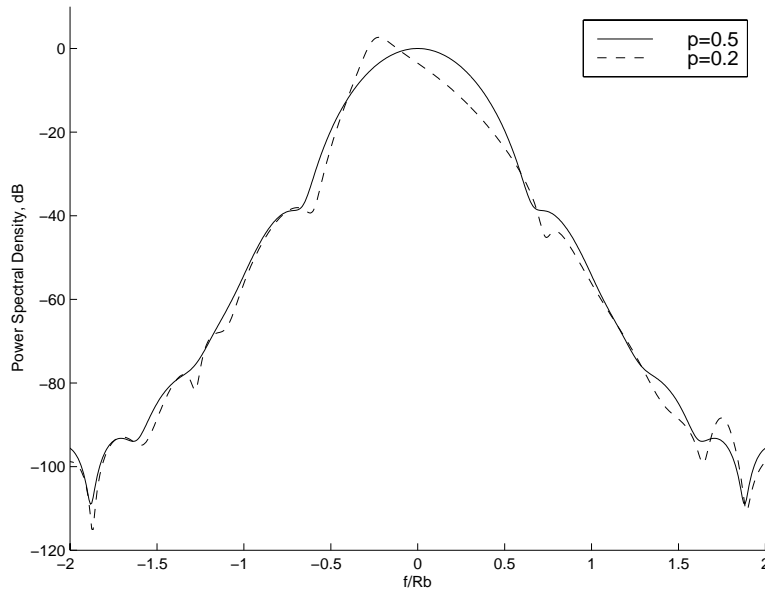
$$S_{10}(f; p) = \frac{1}{T_b} 4p(1-p) \left[\frac{1}{2(1-2p)(1 + \sin \pi f T_b) + 4p^2} - 1 \right] e^{j2\pi f T_b} H_0(f) H_1^*(f) \quad (5)$$

and

$$H_0(f) = F\{h_0(t)\}$$

$$H_1(f) = F\{h_1(t)\}$$

It should be noted that the equation for $S_{11}(f; p)$ in [2] has a typographical error. The correct version is given in Eq. 4. Figure 3 and 4 show the GMSK $BT_b=0.25$ spectrum with 10% data imbalance and 60% data imbalance, respectively.

Figure 4: GMSK $BT_b=0.25$ Spectrum, 60% data imbalance

3.3 Power containment of MSK/GMSK $BT_b=0.25$ without precoding

The power containment is calculated by integrating from $-BW$ to BW , where BW is the one-sided bandwidth normalized by the bit rate R_b . Figure 5 and 6 show the power containment curves as a function of the normalized one-sided bandwidth of MSK with 10% and 60% data imbalance, respectively. The power containment of MSK with 10% data imbalance for a given bandwidth is virtually the same as the power containment without data imbalance. The MSK power containment with 60% data imbalance is less than the MSK with 0% data imbalance for normalized bandwidths less than approximately $0.3 R_b$, but higher for bandwidths greater than $0.3 R_b$. This can be explained by noting that the spectrum of MSK with 60% data imbalance has its power highly concentrated in one peak located at about $0.3 R_b$ (see Figure 2). For small values of the normalized bandwidth, the power containment will not include the peak, and MSK with 0% data imbalance will have higher power containment. However, for normalized bandwidths greater than $0.3 R_b$, the peak is included and consequently, the power containment of MSK with 60% data imbalance is higher.

Figures 7 and 8 show the power containment curves of GMSK $BT_b=0.25$ with 10% and 60% data imbalance, respectively. Again, the power containment of GMSK $BT_b=0.25$ with 10% data imbalance is almost indiscernible from no data imbalance. And for similar reasons given above for MSK with 60% data imbalance, the power containment of GMSK $BT_b=0.25$ with 60% data imbalance is higher for certain bandwidths and lower for other bandwidths than the 0% data imbalance case.

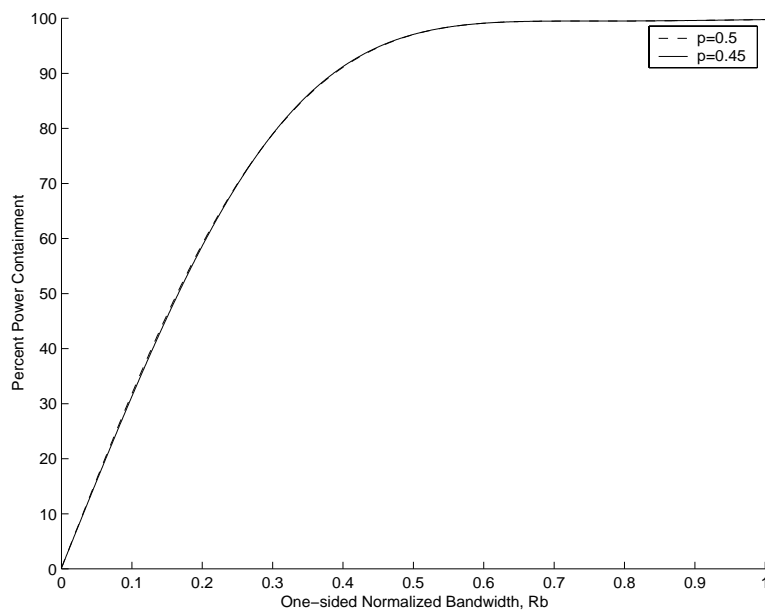


Figure 5: MSK spectral power containment, 10% data imbalance

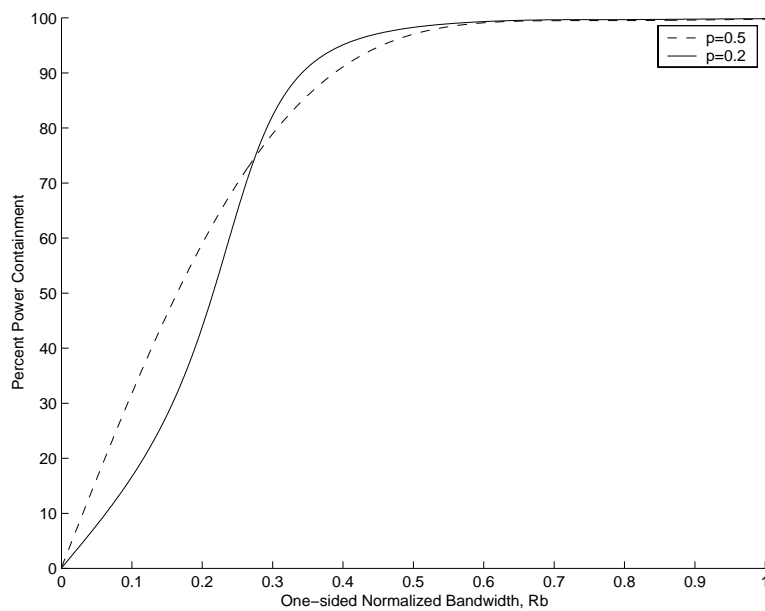


Figure 6: MSK spectral power containment, 60% data imbalance

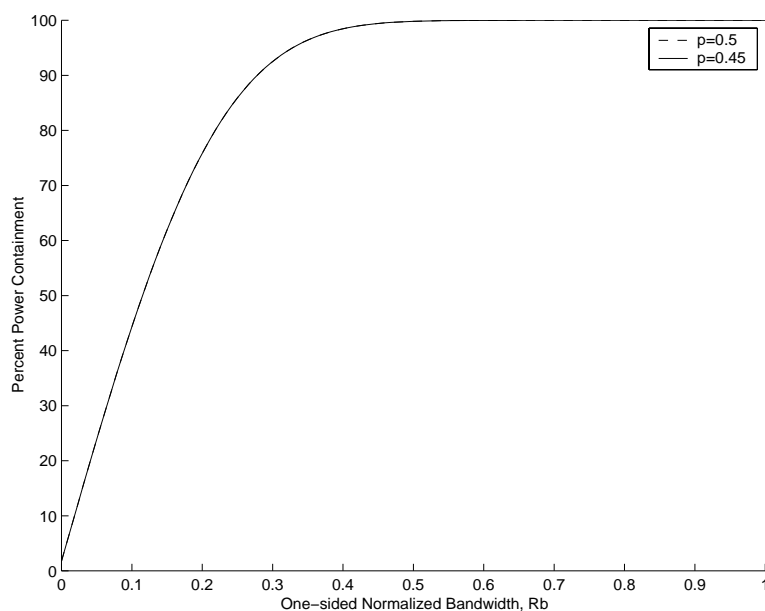


Figure 7: GMSK $BT_b=0.25$ spectral power containment, 10% data imbalance

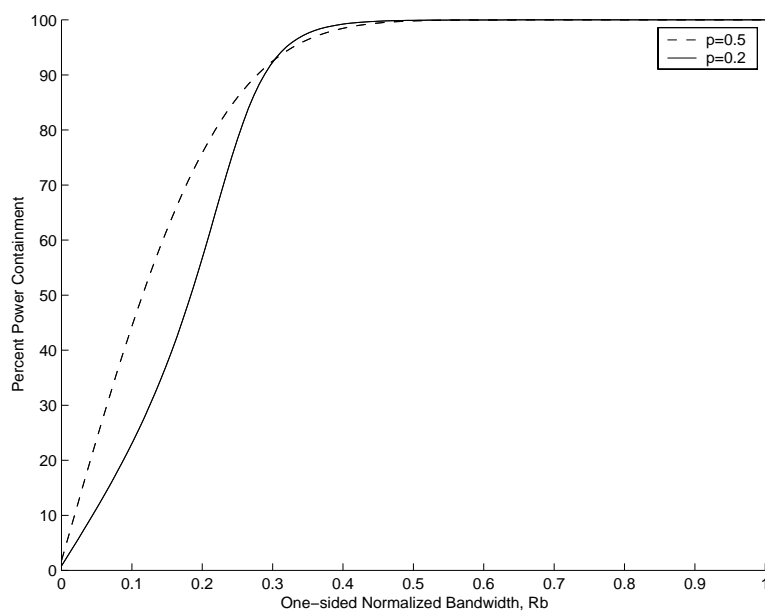


Figure 8: GMSK $BT_b=0.25$ spectral power containment, 60% data imbalance

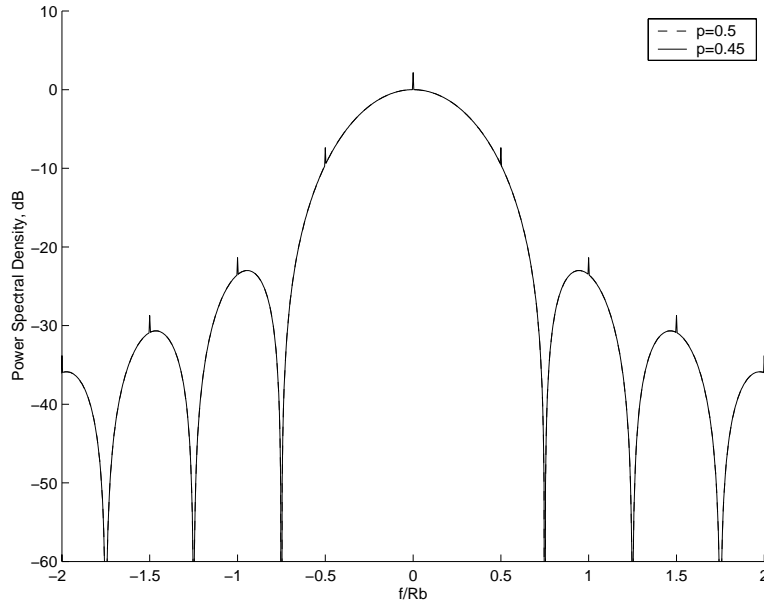


Figure 9: MSK Spectrum with precoding, 10% data imbalance

4 MSK/GMSK Spectrum with Precoding

4.1 Precoded MSK

Without precoding, the equivalent symbols in the AMP representation of MSK/GMSK are differentially encoded. Because of this differential encoding, the equivalent AMP symbols are balanced even though the original data bits are unbalanced. However, differential encoding introduces correlation between the AMP pulses, which accounts for the tilt in the spectrum.

Precoding essentially removes the differential encoding in the AMP representation. As such, the equivalent AMP symbols become uncorrelated, but the data imbalance is no longer removed. For an unbalanced but uncorrelated data source, discrete spectral spikes appear at multiples of the symbol rate. From [2], the spectrum of precoded MSK is

$$S(f; p) = T_b \frac{16}{\pi^2} 4p(1-p) \frac{\cos^2 2\pi f T_b}{(1 - 16f^2 T_b^2)^2} + (1 - 2p)^2 \sum_{k=-\infty}^{\infty} \frac{4}{\pi^2 (1 - 4k^2)^2} \delta\left(f - \frac{k}{2T_b}\right) \quad (6)$$

Figures 9 and 10 show the precoded MSK spectrum with 10% and 60% data imbalance. Note that the continuous part of the MSK spectrum for unbalanced data is the same as for balanced data, but discrete spectral spikes appear at multiples of the symbol rate when there is data imbalance. The amplitude of the spikes depends on the amount of data imbalance.

4.2 Precoded GMSK

The spectrum for GMSK with precoding and data imbalance was not derived in [2]. In this section, we will derive the spectrum of precoded GMSK.

The generic expression for the PSD of a sum of random pulse trains is given by [2]

$$S(f) = \sum_{i=0}^{2^{L-1}-1} S_{ii}(f) + \sum_{i=0}^{2^{L-1}-1} \sum_{j=0}^{2^{L-1}-1} 2\text{Re}\{S_{ji}(f)\} \quad (7)$$

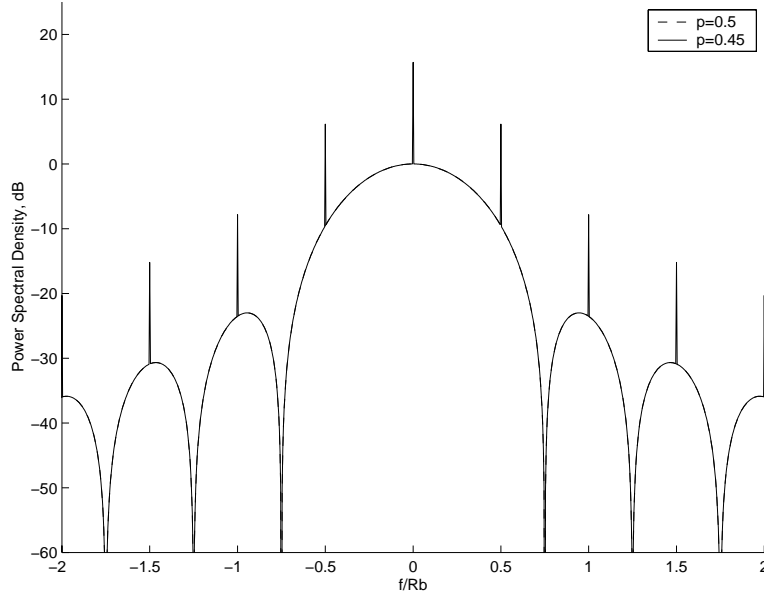


Figure 10: MSK Spectrum with precoding, 60% data imbalance

Approximating GMSK with only the first two AMP components $h_0(t)$ and $h_1(t)$, Eq. 7 simplifies to

$$S(f) = S_{00}(f) + S_{11}(f) + 2\text{Re}\{S_{10}(f)\} \quad (8)$$

Using the notation in [2], the equivalent AMP data symbols for the $h_0(t)$ and $h_1(t)$ pulse streams is

$$\begin{aligned} a_{0,n} &= j\alpha_n a_{0,n-1} \\ a_{1,n} &= j\alpha_n a_{0,n-2} \end{aligned} \quad (9)$$

where α_n is the original i.i.d. unbalanced data sequence.

Let $\beta_{0,n}$ and $\beta_{1,n}$ represent the equivalent AMP data symbols for the $h_0(t)$ and $h_1(t)$ pulse streams after precoding, respectively. Then for $\beta_{0,n}$,

$$\begin{aligned} \beta_{0,n} &= -ja_{0,n}a_{0,n-1}^* \\ &= -j(j\alpha_n a_{0,n-1})a_{0,n-1}^* \\ &= \alpha_n |a_{0,n-1}|^2 \\ &= \alpha_n \end{aligned} \quad (10)$$

Since α_n is i.i.d. but unbalanced, the equivalent AMP data sequence after precoding $\beta_{0,n}$ is uncorrelated but unbalanced. The nonzero mean of $\beta_{0,n}$ means that there will be a discrete component in the spectrum.

For an arbitrary wide-sense stationary, nonzero mean pulse stream $\sum_n a_n p(t - nT)$, the continuous and discrete portions of the spectrum are given by [1]

$$S_{cont}(f) = S_p(f)S_{A_n}(f) \quad (11)$$

$$S_{disc}(f) = \frac{\overline{a_n^2}}{T^2} \sum_k \left| S_p\left(\frac{k}{T}\right) \right|^2 \delta\left(f - \frac{k}{T}\right) \quad (12)$$

where $A_n = a_n - \overline{a_n}$ is the data sequence with the mean removed, T is the symbol duration, $S_p(f)$ is the PSD of the pulse $p(t)$.

Denoting $B_{0,n} = \beta_{0,n} - \overline{\beta_{0,n}}$, we find that

$$\begin{aligned}\overline{\beta_{0,n}} &= (1 - 2p) \\ R_{B_{0,n}}(l) &= E[(\beta_{0,n} - (1 - 2p))(\beta_{0,n+l} - (1 - 2p))^*] \\ &= \begin{cases} (1 - 2p)^2 & l = 0 \\ 0 & \text{otherwise} \end{cases} \\ S_{B_{0,n}}(f) &= 4p(1 - p)\end{aligned}$$

Hence the continuous and discrete parts of the PSD of the first AMP component for precoded GMSK is

$$S_{00,cont}(f; p) = 4p(1 - p)|H_0(f)|^2 \quad (13)$$

$$S_{00,disc}(f; p) = \frac{(1 - 2p)^2}{4T_b^2} \sum_k \left| H_0\left(\frac{k}{2T_b}\right) \right|^2 \delta\left(f - \frac{k}{2T_b}\right) \quad (14)$$

where $|H_0(f)|^2$ is the PSD of $h_0(t)$, and $T = 2T_b$.

Similarly, for the second AMP component $\beta_{1,n}$,

$$\begin{aligned}\beta_{1,n} &= -ja_{1,n}a_{1,n-1}^* \\ &= -j(j\alpha_n a_{0,n-2})(j\alpha_{n-1} a_{0,n-3})^* \\ &= \alpha_n(j\alpha_{n-2} a_{0,n-3})(-j\alpha_{n-1} a_{0,n-3}^*) \\ &= \alpha_n \alpha_{n-1} \alpha_{n-2}\end{aligned} \quad (15)$$

Denoting $B_{1,n} = \beta_{1,n} - \overline{\beta_{1,n}}$, we find that

$$\begin{aligned}\overline{\beta_{1,n}} &= (1 - 2p)^3 \\ R_{B_{1,n}}(l) &= E[(\beta_{1,n} - (1 - 2p)^3)(\beta_{1,n+l} - (1 - 2p)^3)^*] \\ &= \begin{cases} 1 - (1 - 2p)^6 & l = 0 \\ (1 - 2p)^2[1 - (1 - 2p)^4] & l = 1 \\ (1 - 2p)^4[1 - (1 - 2p)^2] & l = 2 \\ 0 & l > 2 \end{cases} \quad R_{B_{1,n}}(-l) = R_{B_{1,n}}^*(l) \\ S_{B_{1,n}}(f) &= 1 - (1 - 2p)^6 + 2[(1 - 2p)^2 - (1 - 2p)^6] \cos(2\pi f T_b) \\ &\quad + 2[(1 - 2p)^4 - (1 - 2p)^6] \cos(4\pi f T_b)\end{aligned} \quad (16)$$

The continuous and discrete parts of the PSD of the second AMP component are given by

$$S_{11,cont}(f; p) = S_{B_{1,n}}(f)|H_1(f)|^2 \quad (17)$$

$$S_{11,disc}(f; p) = \frac{(1 - 2p)^6}{4T_b^2} \sum_k \left| H_1\left(\frac{k}{2T_b}\right) \right|^2 \delta\left(f - \frac{k}{2T_b}\right) \quad (18)$$

where $|H_1(f)|^2$ is the PSD of $h_1(t)$ and $S_{B_{1,n}}(f)$ is given by Eq. 16.

Now we turn our attention to the cross-spectrum $S_{10}(f)$.

$$S_{10}(f) = S_{B_1 B_0}(f) S_{h_1 h_0}(f) \quad (19)$$

where $S_{h_1h_0}(f) = H_0(f)H_1^*(f)$.

Finding $S_{B_1B_0}(f)$,

$$\begin{aligned} R_{B_1B_0}(l) &= E[(\beta_{1,n} - (2p - 1)^3)(\beta_{0,n+l} - (2p - 1))^*] \\ &= \begin{cases} (1 - 2p)^2 - (1 - 2p)^4 & l = 0, 1, 2 \\ 0 & l > 2 \end{cases} \quad R_{B_1,n}(-l) = R_{B_1,n}^*(l) \\ S_{B_1B_0}(f) &= ((1 - 2p)^2 - (1 - 2p)^4)(1 + 2 \cos(2\pi f T_b) + 2 \cos(4\pi f T_b)) \end{aligned} \quad (20)$$

Hence, the continuous and discrete parts of the cross-spectrum are

$$S_{10,cont}(f; p) = ((1 - 2p)^2 - (1 - 2p)^4)(1 + 2 \cos(2\pi f T_b) + 2 \cos(4\pi f T_b))H_0(f)H_1^*(f) \quad (21)$$

$$S_{10,disc}(f; p) = \frac{(1 - 2p)^4}{4T_b^2} \sum_k H_0\left(\frac{k}{2T_b}\right) H_1^*\left(\frac{k}{2T_b}\right) \delta\left(f - \frac{k}{2T_b}\right) \quad (22)$$

The spectrum of precoded GMSK $BT_b=0.25$ is a sum of the discrete and continuous parts of $S_{00}(f)$, $S_{11}(f)$, and $S_{10}(f)$.

$$\begin{aligned} S(f; p) &= 4p(1 - p)|H_0(f)|^2 + 1 - (1 - 2p)^6 + 2[(1 - 2p)^2 - (1 - 2p)^6] \cos(2\pi f T_b) \\ &+ 2[(1 - 2p)^4 - (1 - 2p)^6] \cos(4\pi f T_b)|H_1(f)|^2 \\ &+ 2((1 - 2p)^2 - (1 - 2p)^4)(1 + 2 \cos(2\pi f T_b) + 2 \cos(4\pi f T_b))\text{Re}\{H_0(f)H_1^*(f)\} \\ &+ \left[\frac{(1 - 2p)^2}{4T_b^2} \sum_k \left| H_0\left(\frac{k}{2T_b}\right) \right|^2 + \frac{(1 - 2p)^6}{4T_b^2} \sum_k \left| H_1\left(\frac{k}{2T_b}\right) \right|^2 \right. \\ &\left. + 2 \frac{(1 - 2p)^4}{4T_b^2} \sum_k \text{Re} \left\{ H_0\left(\frac{k}{2T_b}\right) H_1^*\left(\frac{k}{2T_b}\right) \right\} \right] \delta\left(f - \frac{k}{2T_b}\right) \end{aligned} \quad (23)$$

Figure 11 shows a comparison between the theoretical spectrum of precoded GMSK $BT_b=0.25$ with 10% data imbalance and simulation results generated by SPW. Figure 12 shows the same comparison for 60% data imbalance. As the figures show, the theory matches very closely with the simulation results. While only GMSK $BT_b = 0.25$ is considered, Eqn. 23 applies to any value of BT_b , which only affects $H_0(f)$ and $H_1(f)$.

4.3 Power Containment of precoded MSK/GMSK

Figures 13 and 14 show the power containment curves of precoded MSK with 10% and 60% data imbalance, respectively. With 10% data imbalance, the power containment curve of precoded MSK is virtually the same as with no data imbalance. For precoded MSK with 60% data imbalance, the power containment curve is initially higher due to the large spectral spike at 0 R_b . At $0.5R_b$, there is another discrete spike in the spectrum which produces a discontinuity in the power containment curve at $0.5R_b$. Figure 15 shows an enlarged view of the power containment which focuses on the percent power containment values of interest (90% and 99%). As the figure shows, the 90% power containment bandwidth is narrower for 0% data imbalance, but the 99% power containment bandwidth is slightly narrower for 60% data imbalance.

Figures 16 and 17 show the power containment curves of precoded GMSK $BT_b=0.25$ with 10% and 60% data imbalance, respectively. With 10% data imbalance, the power containment curve of precoded GMSK $BT_b=0.25$ is virtually the same as with no data imbalance. Figure 18 is an enlarged view of Figure 17 which focuses on the percent power containment values of interest (90% and 99%). As the figure shows, precoded GMSK with 60% data imbalance has a slightly narrower 90% power containment bandwidth, but a wider 99% power containment bandwidth compared to precoded GMSK with 0% data imbalance.

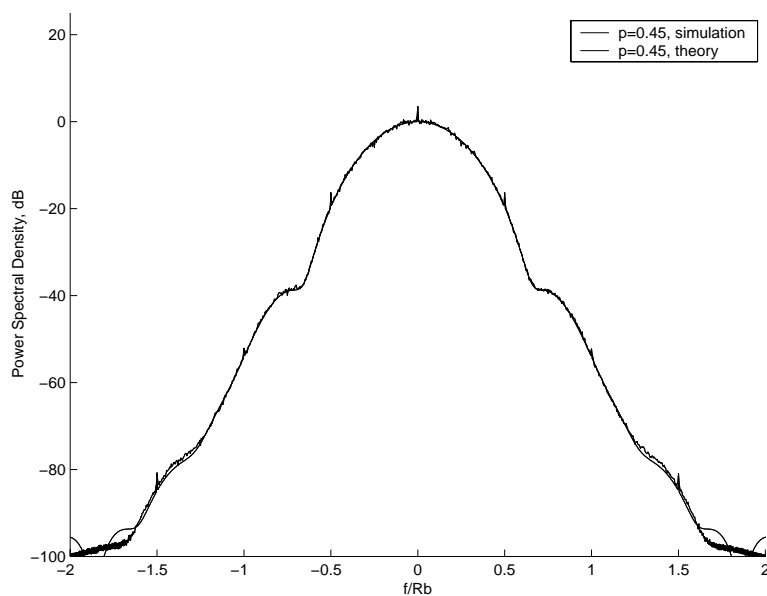


Figure 11: GMSK Spectrum with precoding, 10% data imbalance

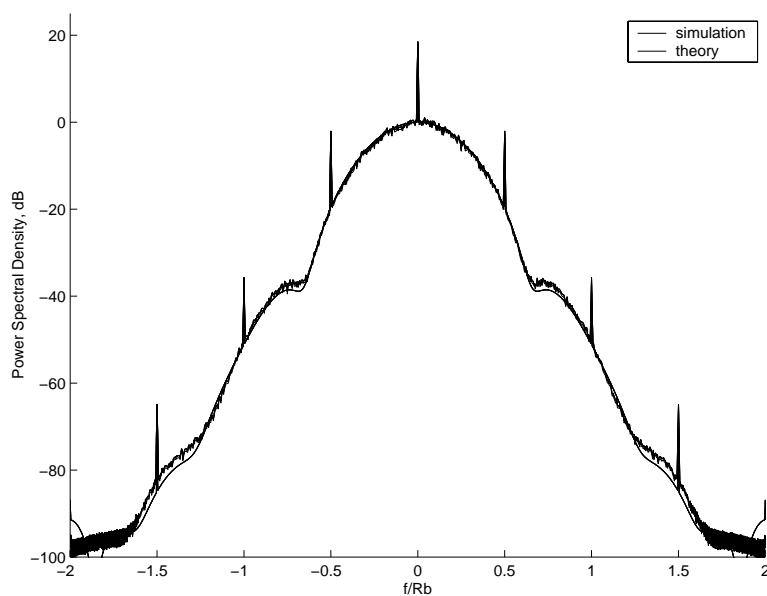


Figure 12: GMSK Spectrum with precoding, 60% data imbalance

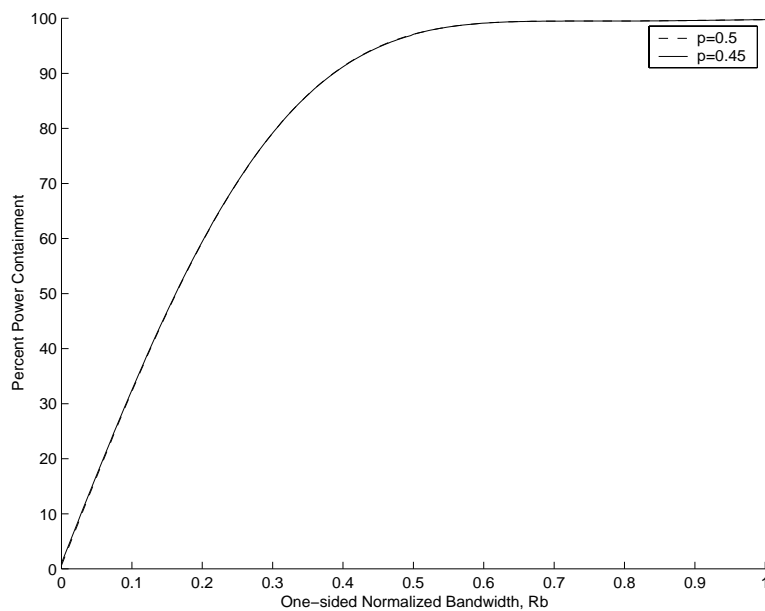


Figure 13: Precoded MSK spectral power containment, 10% data imbalance

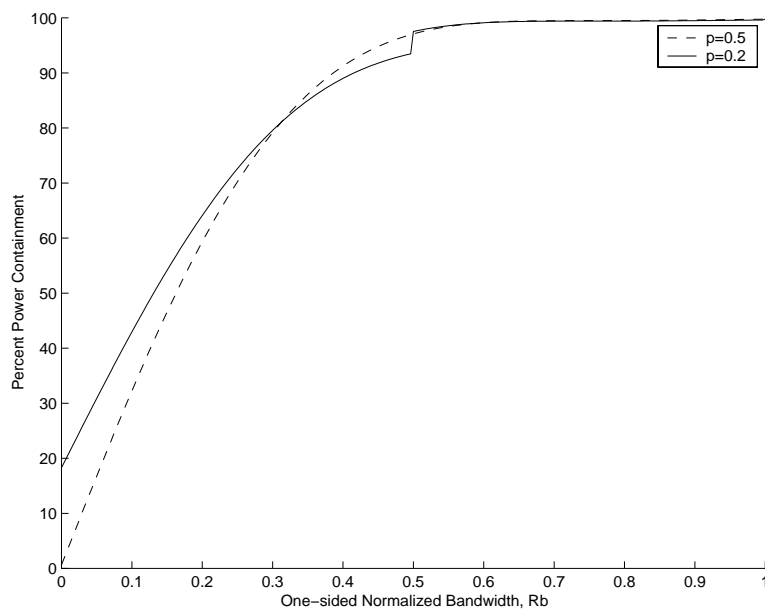


Figure 14: Precoded MSK spectral power containment, 60% data imbalance

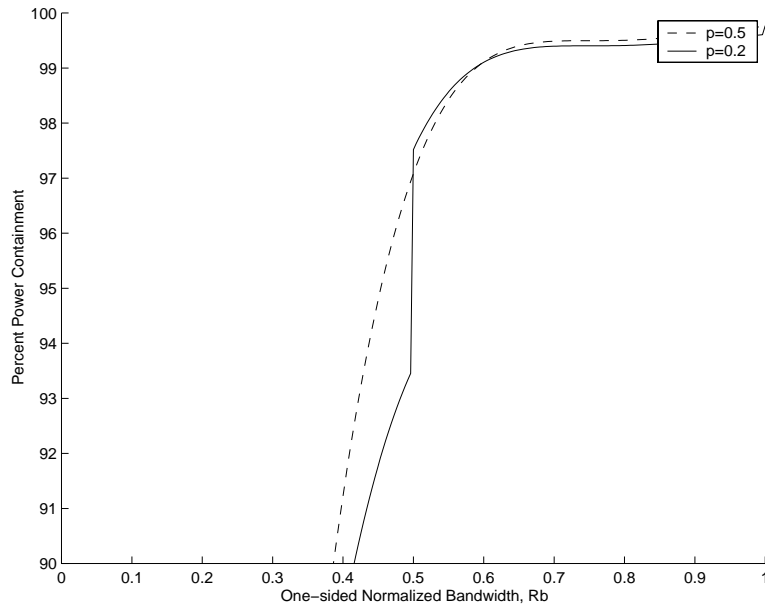


Figure 15: Precoded MSK spectral power containment, 60% data imbalance (enlarged view)

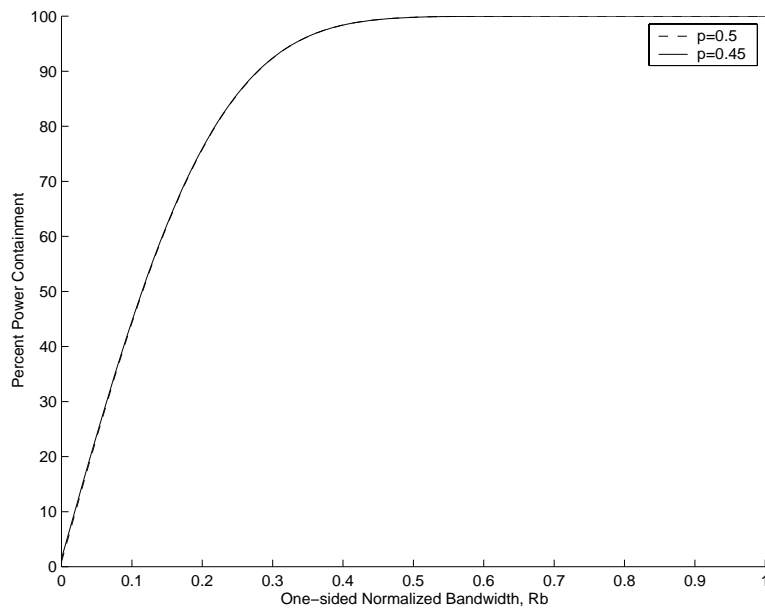


Figure 16: Precoded GMSK $BT_b=0.25$ spectral power containment, 10% data imbalance

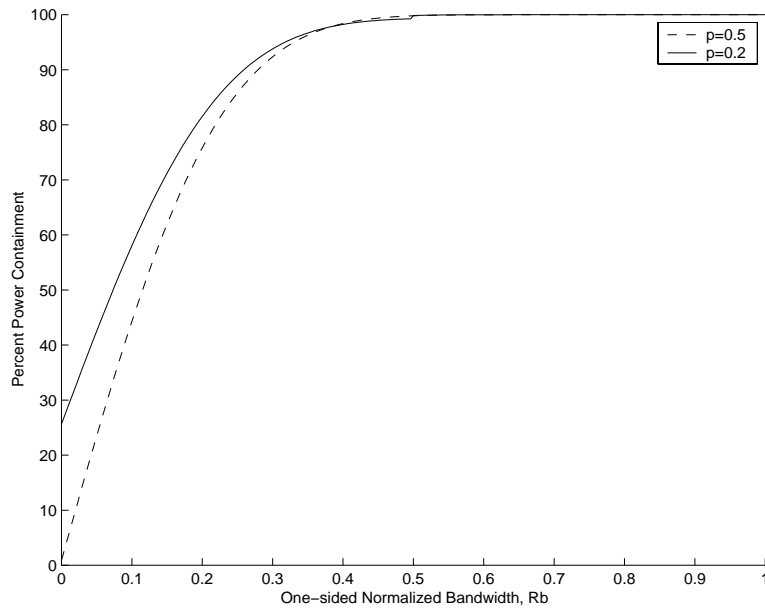


Figure 17: Precoded GMSK $BT_b=0.25$ spectral power containment, 60% data imbalance

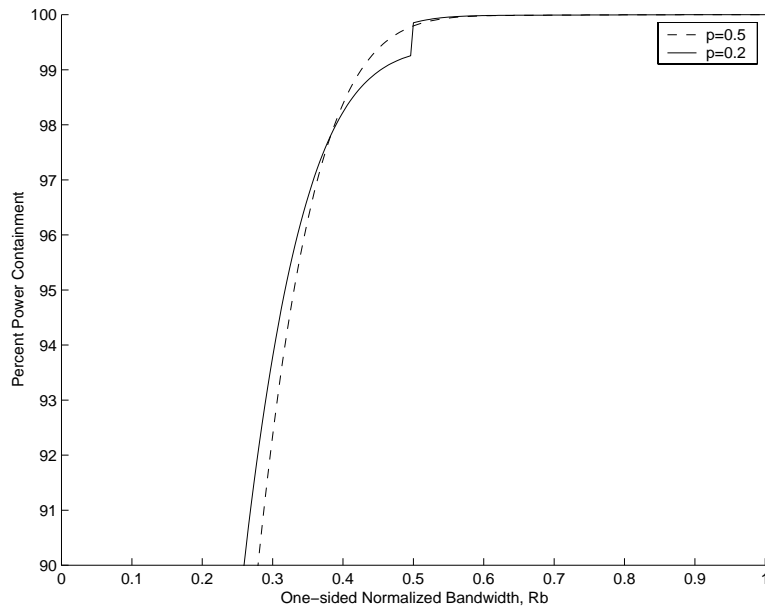


Figure 18: Precoded GMSK $BT_b=0.25$ spectral power containment, 60% data imbalance (enlarged view)

Table 1: 90% Power Containment Normalized Bandwidth for MSK and GMSK

Modulation	0% data imbalance	10% data imbalance	60% data imbalance
MSK	$0.39 R_b$	$0.39 R_b$	$0.34 R_b$
precoded MSK	$0.39 R_b$	$0.39 R_b$	$0.42 R_b$
GMSK $BT_b=0.25$	$0.28 R_b$	$0.28 R_b$	$0.29 R_b$
precoded GMSK $BT_b=0.25$	$0.28 R_b$	$0.28 R_b$	$0.26 R_b$

Table 2: 99% Power Containment Normalized Bandwidth for MSK and GMSK

Modulation	0% data imbalance	10% data imbalance	60% data imbalance
MSK	$0.59 R_b$	$0.59 R_b$	$0.56 R_b$
precoded MSK	$0.60 R_b$	$0.60 R_b$	$0.59 R_b$
GMSK $BT_b=0.25$	$0.44 R_b$	$0.44 R_b$	$0.40 R_b$
precoded GMSK $BT_b=0.25$	$0.42 R_b$	$0.42 R_b$	$0.46 R_b$

5 Summary

Tables 1 and 2 show the one-sided 90% power containment and 99% power containment bandwidth, respectively, for GMSK and MSK, both with and without precoding. As the two tables show, the 90% power containment and 99% power containment bandwidths are unchanged for 10% data imbalance compared to 0% data imbalance. Even with 60% data imbalance, the 90% and 99% power containment bandwidths are not significantly different from the 0% data imbalance case.

The reason is that while data imbalance tilts the spectrum significantly for MSK/GMSK without precoding, integrating over $-B$ to B tends to level out the asymmetry, thus leaving the power containment relatively unchanged. With precoding, data imbalance introduces spectral spikes but does not change the continuous part of the spectrum. The spikes introduce discontinuities at multiples of half the bit rate. These spectral spikes only marginally change the 90% and 99% power containment bandwidths, but it should be noted that the spikes will have a large effect on the -60 dB bandwidth.

References

- [1] M. Simon, S. Hinedi, and W. Lindsey, *Digital Communication Techniques*. Prentice-Hall, New Jersey, 1995.
- [2] M. Simon, P. Arabshahi, L. Lam, and T.-Y. Yan, "Power Spectrum of MSK-Type Modulations in the Presence of Data Imbalance", TMO Progress Report 42-134, August 1998.
- [3] G.K. Kaleh, "Simple coherent receivers for partial response continuous phase modulations," IEEE Transactions on Select. Areas in Comm., vol. 7, no. 9, December 1989, pp. 1427-1436.

GMSK Modulator

DATE : 15/10/99

ISSUE : DRAFT

PAGE : 1 /22

Study of GMSK modulator

Rédigé par/ <i>Written by</i>	Responsabilité-Société/ <i>Responsability-Company</i>	Date	Signature
Catherine Barrieres	Alcatel Space Industries		
Vérifié par/ <i>Verified by</i>			
Emile Tonello	Alcatel Space Industries		
Approbation/ <i>Approved</i>			
Jean-Luc Gerner	ESA		
	Conformité Documentaire/ <i>Documentation Manager</i>		



GMSK Modulator

DATE : 15/10/99

ISSUE : PAGE : 2

ENREGISTREMENT DES EVOLUTIONS / *CHANGE RECORDS*

ISSUE	DATE	§ : DESCRIPTION DES EVOLUTIONS § : <i>CHANGE RECORD</i>	REDACTEUR <i>AUTHOR</i>

GMSK Modulator

DATE : 15/10/99

ISSUE : PAGE : 3

TABLE DES MATIÈRES / TABLE OF CONTENTS

1. INTRODUCTION.....	5
2. SPECIFICATION ANALYSIS.....	6
3. GENERAL CONSIDERATIONS ON GMSK MODULATION	7
3.1 GMSK MODULATION	7
3.2 GENERAL ARCHITECTURE FOR A GMSK MODULATOR.....	8
3.3 IDENTIFICATION OF BER DEGRADATION SOURCES	8
3.3.1 Noise Quantification	9
3.3.2 Phase imperfections	9
3.3.3 Amplitude Imperfections.....	11
3.3.4 Phase Noise	13
4. GMSK MODULATOR CONCEPT ALTERNATIVES.....	14
4.1 DIGITAL MODULATOR.....	14
4.1.1 Description.....	14
4.1.2 Performances	17
4.2 DIGITAL AND ANALOG MODULATOR	17
4.2.1 Description.....	17
4.2.2 Performances	20
4.3 ANALOG MODULATOR	20
5. COMPARISON OF THE DIFFERENT CONCEPTS.....	21
6. CONCLUSION.....	22

GMSK Modulator

DATE : 15/10/99

ISSUE :

PAGE : 4

LISTE DES FIGURES / LIST OF FIGURES

Figure 1 - General architecture of a GMSK modulator	8
Figure 2 - BER degradation due to quantification noise.....	9
Figure 3 - Phase imbalances.....	10
Figure 4 - BER degradation due to phase imbalance	11
Figure 5 - Simulated BER degradation for $\delta = 10$ degrees.....	11
Figure 6 - Amplitude imbalances	12
Figure 7 - Theoretical BER degradation due to α_1	12
Figure 8 - Theoretical BER degradation due to α_2	13
Figure 9 - Third architecture for the GMSK modulator.....	14
Figure 10 - ASIC architecture for the GMSK modulator.....	15
Figure 11 - Second architecture for the GMSK modulator.....	18
Figure 12 - FPGA architecture	19

GMSK Modulator

DATE : 15/10/99

ISSUE : PAGE : 5

1. INTRODUCTION

The purpose of the study is to assess the feasibility, the complexity and the performances of a Gaussian filtered Minimum Shift Keying (GMSK) modulator for on-board applications. The modulator shall have the potential to be used for future space program.

The requirements of the GMSK modulator are summarized in the next table.

Data Rate	from 100kbps to 10Mbps
Selected BT_B	1 ; 0.5 ; 0.25
Spectral emission limits	
BER degradation from theory due to shaping	<0.2 dB

The results of this study will be presented as following:

- Specifications analysis,
- General considerations on GMSK modulation,
- GMSK modulator concept alternatives,
- Comparison of the different alternatives,
- Conclusion.

GMSK Modulator

DATE : 15/10/99

ISSUE :

PAGE : 6

2. SPECIFICATION ANALYSIS

TO BE COMPLETED

GMSK Modulator

3. GENERAL CONSIDERATIONS ON GMSK MODULATION

3.1 GMSK MODULATION

GMSK stands for Gaussian Minimum Shift Keying. This is a modulation scheme in which the phase of the carrier is instantaneously varied by the « modulating » signal (i.e. the information to transmit). GMSK differs from MSK (Minimum Shift Keying) in that a Gaussian filter of an appropriate bandwidth (defined by the BT_B product) is used before the modulation stage. The time-domain impulse response of the filter is described in the equation (1).

$$h(t) = \frac{kB}{\sqrt{\pi}} \exp^{-k^2 B^2 t^2} \quad \text{with } k = \frac{\pi}{\sqrt{2 \ln 2}} \quad (1)$$

MSK can be viewed as either a special case of continuous phase frequency shift (CPFSK) or a special case of OQPSK with sinusoidal symbol weighting.

When viewed as CPFSK, the MSK form can be expressed as :

$$\begin{cases} s(t) = A \times \cos(2\pi f_0 t + d_k \frac{\pi}{2T_B} t + x_k) \\ x_k = x_{k-1} + \frac{\pi k}{2} \times (d_k - d_{k-1}) \mod 2\pi \end{cases} \quad (2)$$

where f_0 is the carrier frequency and $d_k = \pm 1$ represents the bipolar data being transmitted at a rate $R_B = 1/T_B$.

When viewed as OQPSK, the MSK wave form can be expressed as :

$$\begin{cases} s(t) = a_k \cos\left(\frac{\pi}{2T_B} t\right) \cos(2\pi f_0 t) - b_k \sin\left(\frac{\pi}{2T_B} t\right) \sin(2\pi f_0 t) \\ a_k = \cos(x_k) = \pm 1 \\ b_k = d_k \cos(x_k) = \pm 1 \end{cases} \quad (3)$$

The main characteristics of MSK are constant envelope, relatively narrow bandwidth and coherent detection capability. The most important characteristic of MSK is that it is a constant envelope variety modulation. This make the modulation scheme more immune to noise than the ASK (Amplitude Shift Keying) scheme. However, the MSK has not good enough performances relative to the out-of-band radiation. GMSK uses a pre-modulation Gaussian filter which makes the output power spectrum more compact. The pre-modulation Gaussian filter has narrow bandwidth and sharp cut-off properties which are required to suppress high-frequency components. Moreover, it has a lower overshoot impulse response which allows to protect against instantaneous deviation.

GMSK Modulator

DATE : 15/10/99

ISSUE :

PAGE : 8

3.2 GENERAL ARCHITECTURE FOR A GMSK MODULATOR

An algorithm of a GMSK modulator is described below :

- Creation of a NRZ sequence $(-1,1)$ from a binary input sequence $(0,1)$,
- The NRZ sequence is up sampled,
- Integration of the up sampled NRZ sequence,
- Convolution with a Gaussian function,
- Computation of the I and Q components. At this stage, we have the quadrature components of the base-band equivalent signal.
- Transposition of the base-band equivalent signal to the carrier frequency.

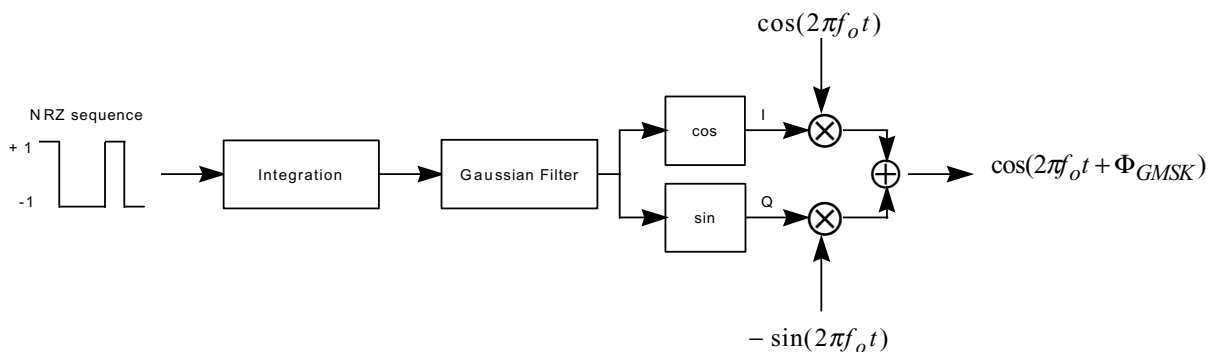


Figure 1 - General architecture of a GMSK modulator

3.3 IDENTIFICATION OF BER DEGRADATION SOURCES

The BER degradation sources in the modulator are :

- noise quantification inasmuch as a digital circuit would be used in the modulator,
- phase imperfections,
- amplitude imperfections,
- phase noise.

In the following the different degradation sources will be studied. In each case, the theoretical BER degradation (that should be observed using the demodulator described in the previous part) will be compared to the simulated results.

GMSK Modulator

3.3.1 Quantification Noise

The quantification noise has to be considered as degradation sources if the GMSK modulator includes a digital circuit.

The quantification noise has been defined as :

$$\sigma_Q = \frac{q^2}{12} \quad \text{with} \quad \begin{cases} q = 2^{-(r-1)} \\ r: \text{number of bits used for quantification} \end{cases} \quad (4)$$

The BER degradation due to the quantification noise is described by the following equation:

$$\Delta_{QUANTIF} = 10 \times \log_{10} \left(1 - \frac{\sigma_Q^2}{\sigma^2} \right) \quad \text{with} \quad \begin{cases} \sigma_Q^2 \text{ represents the quantification noise power} \\ \sigma^2 \text{ represents the noise power in the sampling bandwidth} \end{cases} \quad (5)$$

The figure 2 represents the theoretical BER degradation relative to the number of bits used for quantification.

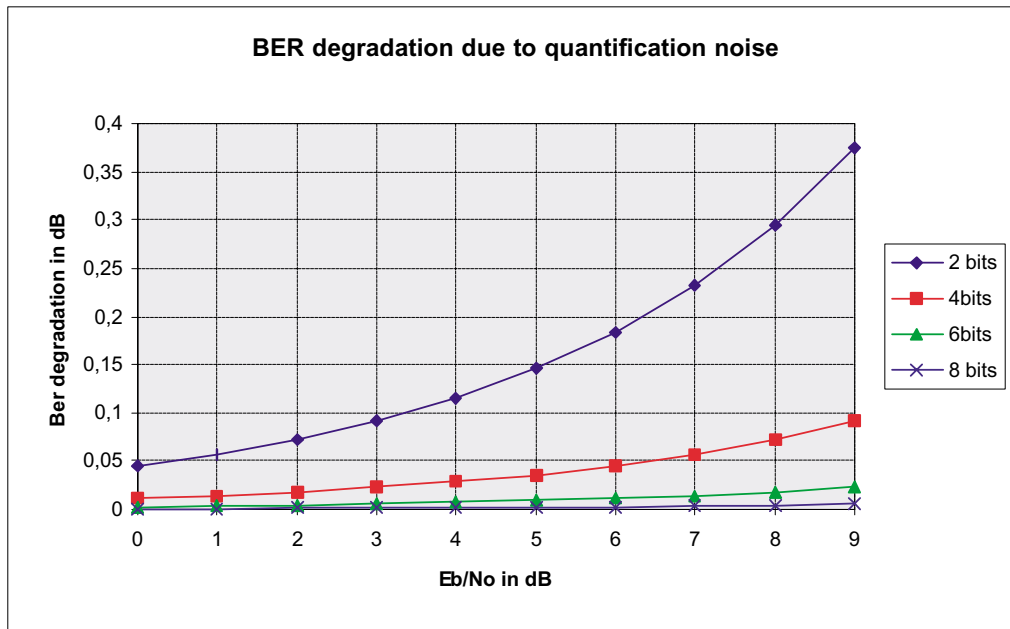


Figure 2 - BER degradation due to quantification noise

To fit with the modulator specifications, the phase has to be quantified at least over 4 bits.

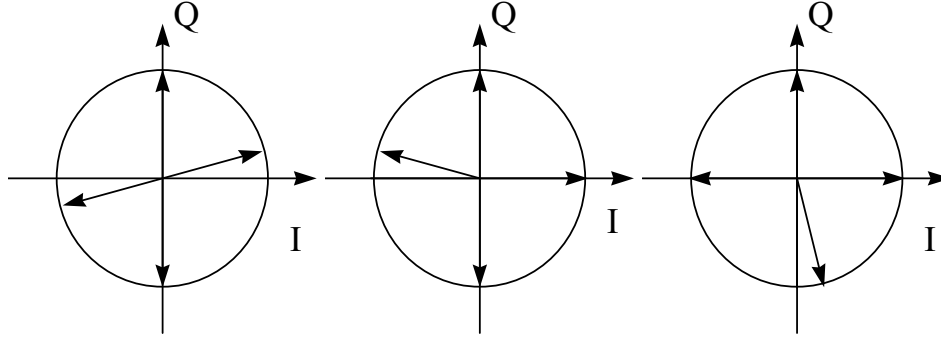
3.3.2 Phase imperfections

As can be shown on the next figure, there could be several phase imbalances between :

- the I and Q components,

GMSK Modulator

- the positive and the negative values of the I component,
- the positive and the negative values of the Q component.

**Figure 3 - Phase imbalances**

1. Phase imbalance between the I and Q components :

Instead of having the expression of the equation (3), the wave form of the signal can be expressed as:

$$s(t) = a_k \cos\left(\frac{\pi}{2T_B} t\right) \cos(2\pi f_0 t + \delta_1) - b_k \sin\left(\frac{\pi}{2T_B} t\right) \sin(2\pi f_0 t) \quad (6)$$

2. Amplitude imbalance between the negative and the positive values of the I component :

$$s(t) = \begin{cases} a_k \cos\left(\frac{\pi}{2T_B} t\right) \cos(2\pi f_0 t) - b_k \sin\left(\frac{\pi}{2T_B} t\right) \sin(2\pi f_0 t) & \text{if } I \geq 0 \\ a_k \cos\left(\frac{\pi}{2T_B} t\right) \cos(2\pi f_0 t + \delta_2) - b_k \sin\left(\frac{\pi}{2T_B} t\right) \sin(2\pi f_0 t) & \text{if } I < 0 \end{cases} \quad (7)$$

3. Amplitude imbalance between the negative and the positive values of the Q component :

$$s(t) = \begin{cases} a_k \cos\left(\frac{\pi}{2T_B} t\right) \cos(2\pi f_0 t) - b_k \sin\left(\frac{\pi}{2T_B} t\right) \sin(2\pi f_0 t) & \text{if } Q \geq 0 \\ a_k \cos\left(\frac{\pi}{2T_B} t\right) \cos(2\pi f_0 t) - b_k \sin\left(\frac{\pi}{2T_B} t\right) \sin(2\pi f_0 t + \delta_3) & \text{if } Q < 0 \end{cases} \quad (8)$$

The BER degradation due to δ_1 , δ_2 or δ_3 are the same :

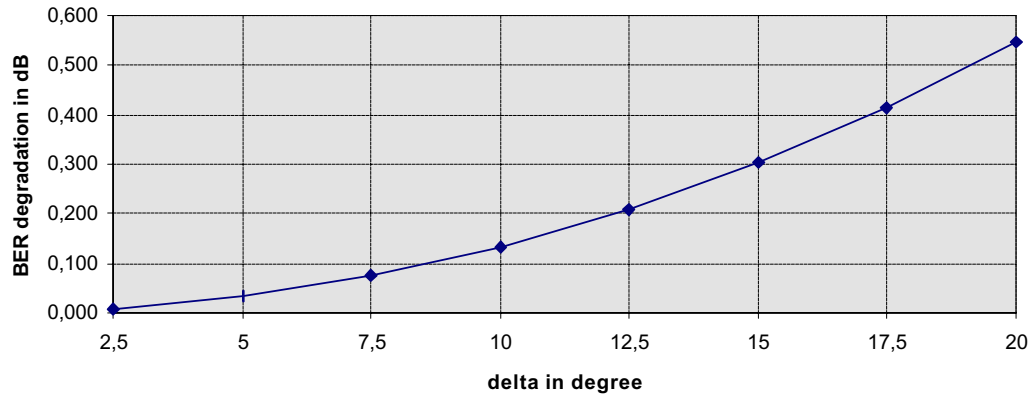
$$\Delta_{\delta_2} = 20 \times \log_{10} \left(1 - \frac{\delta^2}{2} \right) \quad (9)$$

GMSK Modulator

DATE : 15/10/99

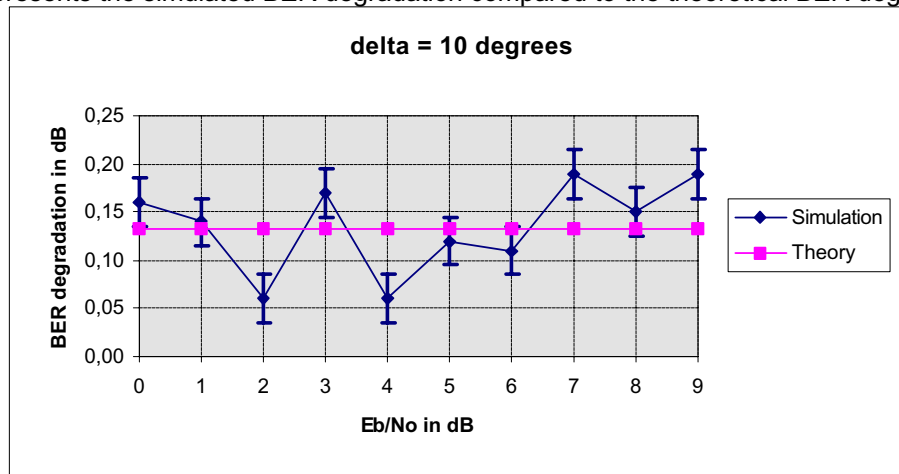
ISSUE :

PAGE : 11

BER degradation due to delta**Figure 4 - BER degradation due to phase imbalance**

To fit with the modulator specifications, the phase imbalance has to be less than 12 degrees (assuming no other contribution to BER degradation).

The figure 6 represents the simulated BER degradation compared to the theoretical BER degradation.

**Figure 5 - Simulated BER degradation for $\delta = 10$ degrees**

3.3.3 Amplitude Imperfections

As previously, there could be several amplitude imbalances between :

- the I and Q components,
- the positive and the negative values of the I component,
- the positive and the negative values of the Q component.

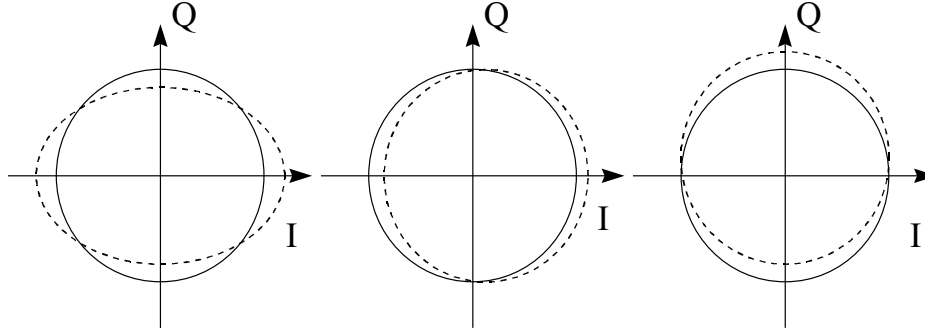
GMSK Modulator

DATE : 15/10/99

ISSUE :

PAGE : 12

These different amplitude imbalances are described on the next figure :

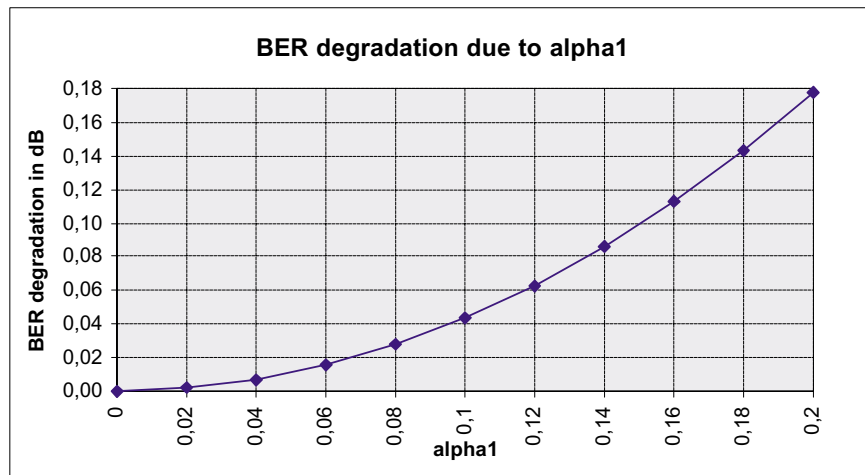
**Figure 6 - Amplitude imbalances**

1. Amplitude imbalance between the I and Q components :

$$s(t) = I \times (1 + \alpha_1) \cos(2\pi f_0 t) - Q \times (1 - \alpha_1) \sin(2\pi f_0 t) \quad (10)$$

The theoretical degradation due to α_1 is:

$$\Delta_{\alpha_1} = 20 \times \log_{10}(1 - \alpha_1^2) \quad (11)$$

**Figure 7 - Theoretical BER degradation due to α_1**

To fit the modulator specifications, α_1 has to be less than 0.2.

2. Amplitude imbalance between the negative and the positive values of the I component :

GMSK Modulator

DATE : 15/10/99

ISSUE :

PAGE : 13

$$s(t) = \begin{cases} I \times (1 + \alpha_2) \cos(2\pi f_0 t) - Q \sin(2\pi f_0 t) & \text{if } I \geq 0 \\ I \times (1 - \alpha_2) \cos(2\pi f_0 t) - Q \sin(2\pi f_0 t) & \text{if } I < 0 \end{cases} \quad (12)$$

3. Amplitude imbalance between the negative and the positive values of the Q component :

$$s(t) = \begin{cases} I \cos(2\pi f_0 t) - Q \times (1 + \alpha_3) \sin(2\pi f_0 t) & \text{if } Q \geq 0 \\ I \cos(2\pi f_0 t) - Q \times (1 - \alpha_3) \sin(2\pi f_0 t) & \text{if } Q < 0 \end{cases} \quad (13)$$

The BER degradation due to α_2 or α_3 are the same. The following figure gives the theoretical BER degradation relative to α_2 .

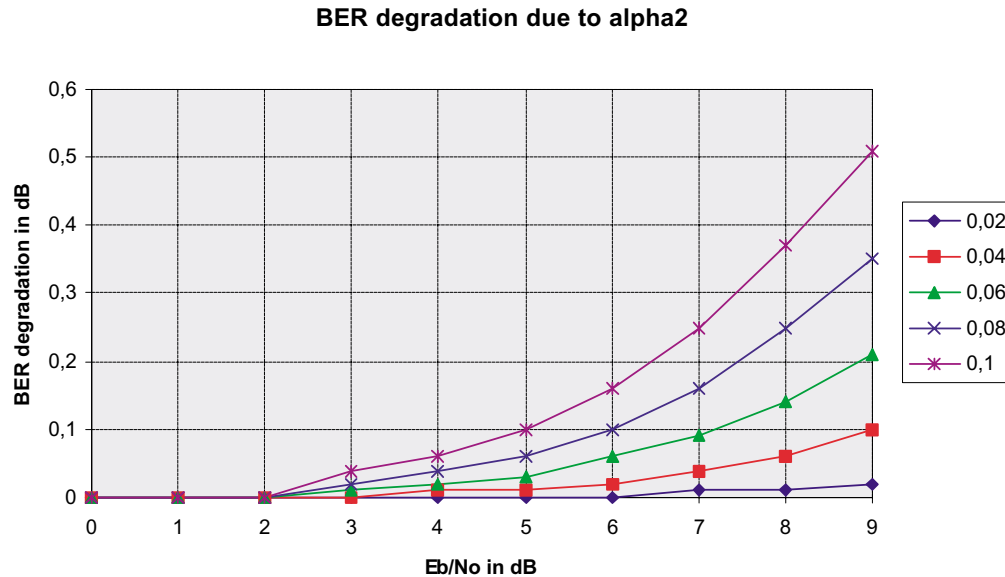


Figure 8 - Theoretical BER degradation due to α_2

To fit with the modulator specifications at any Eb/No up to 9 dB, α_2 has to be less than 0.06.

3.3.4 Phase Noise

The phase noise is related to the local oscillator (LO) that generates the frequency of the carrier. Whatever the architecture of the modulator is, the LO will have the same properties. As a consequence, it will not be considered as being a part of the modulator and the effect of the phase noise on the BER will not be evaluated in the frame of this study.

GMSK Modulator

DATE : 15/10/99

ISSUE :

PAGE : 14

4. GMSK MODULATOR CONCEPT ALTERNATIVES

This part aims to present three different architectures for the GMSK modulator.

The first architecture to be proposed is composed of a digital modulator followed by an Image Rejection Mixer (IRM) to transpose the signal at the transmit frequency.

The second architecture consists in generating an equivalent GMSK base-band signal using a digital circuit and then transposing it to the carrier frequency using an analog modulator.

Finally, the third architecture is completely composed of analog components.

4.1 DIGITAL MODULATOR

4.1.1 Description

This architecture consists in modulating the signal using an ASIC. The figure 12 described the global architecture of the GMSK modulator.

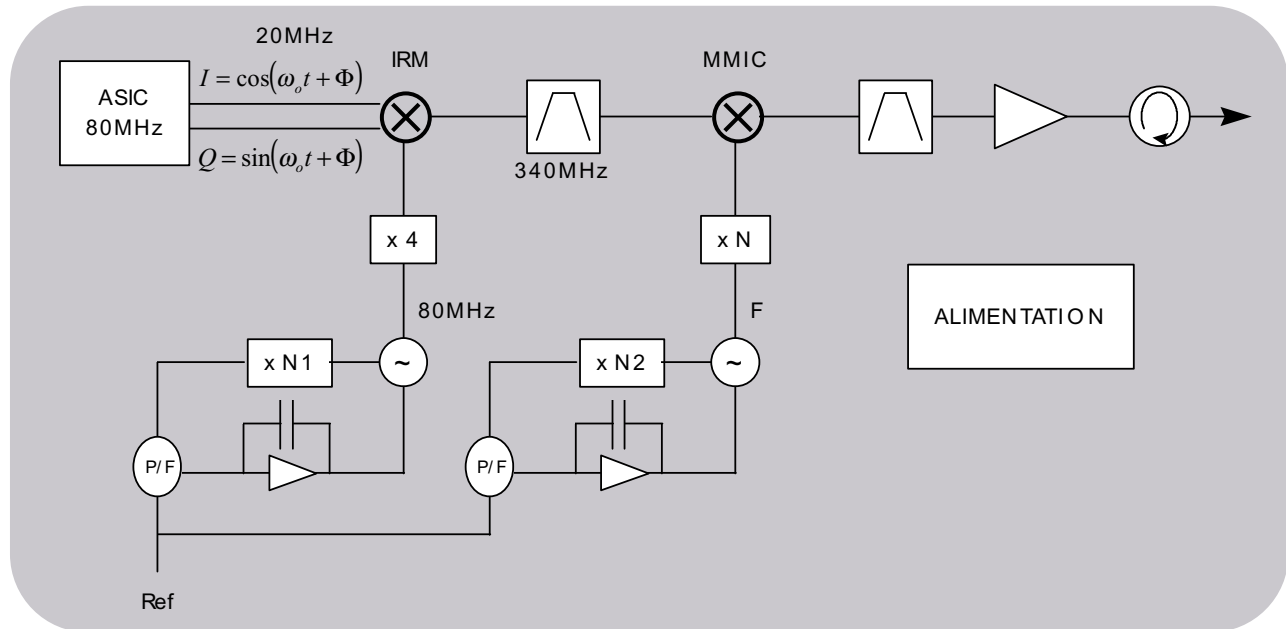


Figure 9 - Third architecture for the GMSK modulator

To transmit at S band (2.25GHz), the parameters N and F are :

$$\begin{cases} N = 1 \\ F = \frac{2.25 - 0.35}{N} = 1.9GHz \end{cases}$$

To transmit at Ka band (34.5GHz), the parameters N and F are :

$$\begin{cases} N = 2 \\ F = \frac{8.45 - 0.35}{N} = 4.05GHz \end{cases}$$

GMSK Modulator

DATE : 15/10/99

ISSUE :

PAGE : 15

To transmit at X band (8.45GHz), the parameters N and F are :

$$\begin{cases} N = 8 \\ F = \frac{34.5 - 0.35}{N} = 4.27 \text{ GHz} \end{cases}$$

In the following, the feasibility of a modulator using an ASIC will be studied whatever the data rate R_b is in the specified range. The worst case is reached for maximum value of the data rate i.e. 10Mbps.

The figure 13 describes the preliminary architecture of the ASIC.

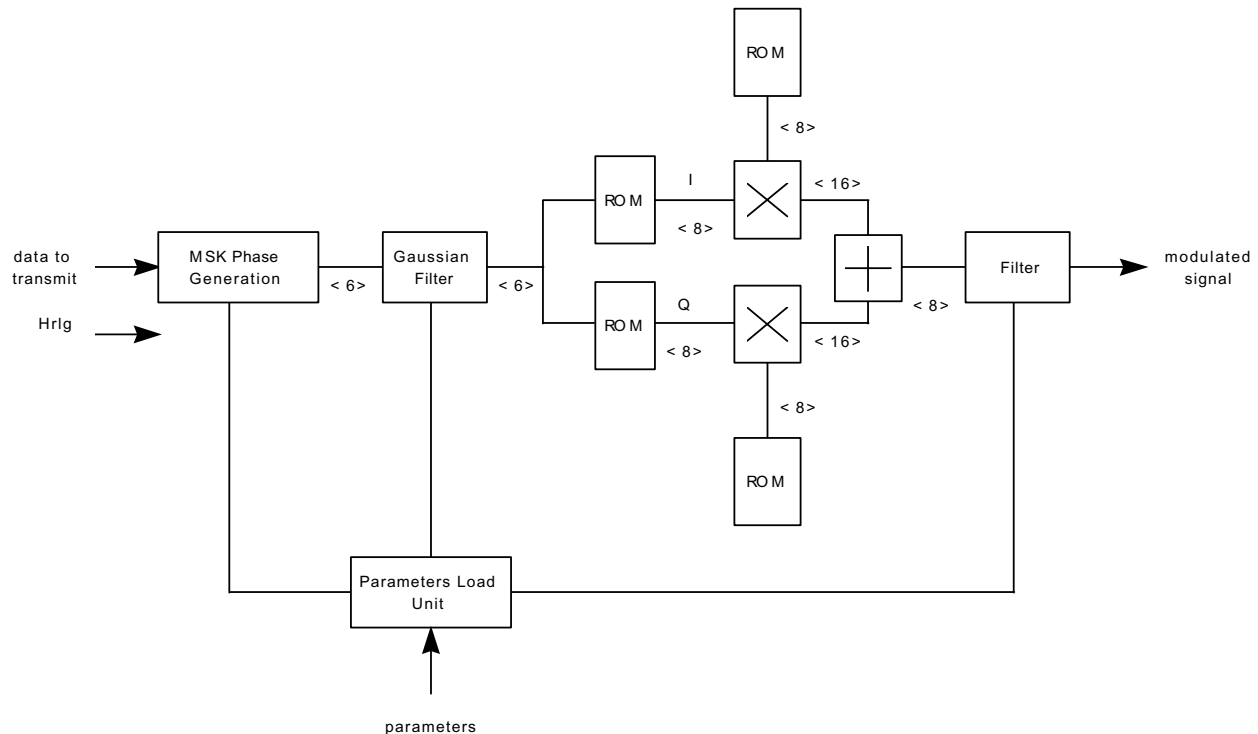


Figure 10 - ASIC architecture for the GMSK modulator

Considering R_b to be equal to 10Mbps, the modulation frequency has to be at least 20MHz ($2 \times R_b$) and the sampling frequency has to be at least 80MHz (Shannon).

With present space qualified technology, it is possible to implement the multiplication function used for transposition at sampling rates up to 40 MHz, thus for values of R_b of up to 5 Mbps. Today's non space-qualified technology can easily operate at the rate of 80 MHz necessary for a bit rate R_b of 10 Mbps and it is expected that this will also be the case with space technology in a relative near future. Note that 80 MHz rate multiplication can also be achieved with two 40 MHz multipliers operating in parallel, at the expense of an increase in complexity but with no extra power consumption.

Since the sampling frequency of the signal and the internal frequency of the ASIC are the same, it is not possible to optimize the complexity of the ASIC (no possibility for resources reuse). Then the function described on the figure 8 will be implemented using:

- 4 ROM (64 x 8),

GMSK Modulator

DATE : 15/10/99

ISSUE :

PAGE : 16

- 2 filters of 32 coefficients each,
- 1 accumulator to generate the MSK phase,
- a transposition unit composed by 2 multipliers (8 x 8) and 1 adder (16x16),
- 1 parameters load unit (PLU).

The number of coefficients used to compute the Gaussian filter depends on the BT_B product. The lower it is, the more coefficients are needed. When $BT_B = 0.25$, the impulse response corresponding to a 32 coefficients FIR is most probably sufficient.

The PLU introduces flexibility in the ASIC design with changeable data rate, BT product and filters coefficients.

The next table summarizes the estimation of the complexity of the ASIC.

	Complexity in number of gates
4 ROM	5200
Gaussian filter	47600
Output filter	57000
Transposition unit	2500
Parameters load unit	7000
Generation of the MSK phase	300
Other	5400
Total	125000

The complexity of the ASIC assumes that the quantification of the ASIC is the one described on the figure 8.

The complexity of the ASIC has been estimated with the 8 bits quantified phase instead of 6. This makes the complexity increasing to 150000.

The secondary power consumption of the ASIC is around:

- 4.5 Watts for the maximum data rate $R_B = 10\text{Mbps}$,
- 1.2 Watts for $R_B = 2\text{Mbps}$.

GMSK Modulator

DATE : 15/10/99

ISSUE : PAGE : 17

4.1.2 Performances

The performances of the modulator relative to the BER degradation are summarized in the following table.

	Imperfections	BER degradation
Quantification Noise	6 bits	< 0.05 dB
Amplitude imperfection	± 0.04	0.01 dB
Phase imperfection	$\pm 2^\circ$	0.01 dB
Total		< 0.2 dB

4.2 DIGITAL AND ANALOG MODULATOR

4.2.1 Description

In this architecture, we propose to generate a GMSK base-band equivalent signal and then to transpose it using an analog modulator.

Whatever the carrier frequency is, we propose to use a S-band modulator (i.e. 2.25GHz). An Image Rejection Mixer (IRM) will be added after the modulator to transmit the signal at higher frequencies.

The architecture of the GMSK modulator is described on the figure 12.

DATE : 15/10/99

PAGE : 18


$$\text{To transmit at Ka band (34.5GHz), the parameters N and F are : } \begin{cases} N = 8 \\ F = \frac{34.5 - 2.25}{N} = 4.03 \text{GHz} \end{cases}$$

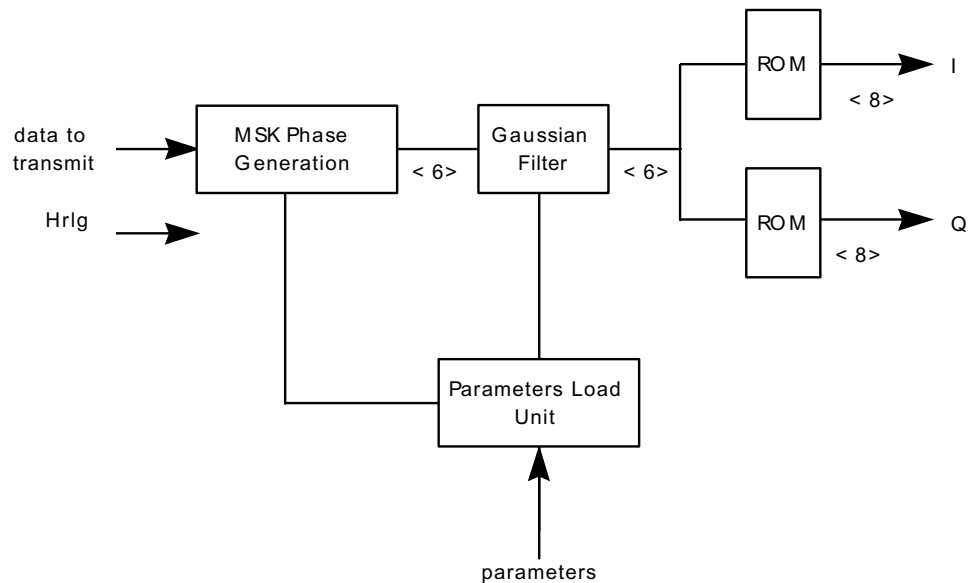
June 2001

GMSK Modulator

DATE : 15/10/99

ISSUE :

PAGE : 19

**Figure 12 - FPGA architecture**

The sampling frequency of the signal and the FPGA frequency are the same and are equal to 80MHz.

As for the previous architecture, nowadays, there is no space qualified technology to develop a FPGA working at this frequency , however it is possible to do it using a non space qualified technology.

The estimation of the complexity of the FPGA is given in the next table. This estimation assumes that the quantification of the FPGA is the one described on the figure 15.

GMSK Modulator

DATE : 15/10/99

ISSUE : PAGE : 20

	Complexity in number of gates
2 ROM	5200
Gaussian filter	47600
Parameters load unit	4000
Generation of the MSK phase	300
Other	2900
Total	60000

The PLU introduces flexibility in the FPGA design with changeable data rate, BT product and filter coefficients.

The secondary power consumption of the ASIC is around 6,2 Watts.

4.2.2 Performances

The performances of the modulator relative to the BER degradation are summarized in the next tab.

	Imperfection	BER degradation
Quantification Noise	6 bits	<0.05 dB
Amplitude Imperfection	± 1 dB i.e. ± 0.12	0.06 dB
Phase Imperfection	$\pm 5^\circ$	0.04 dB
Total		<0.2 dB

4.3 ANALOG MODULATOR***TO BE COMPLETED***

GMSK Modulator

DATE : 15/10/99

ISSUE : PAGE : 21

5. COMPARISON OF THE DIFFERENT CONCEPTS

TO BE COMPLETED

GMSK Modulator

DATE : 15/10/99

ISSUE : PAGE : 22

6. CONCLUSION

TO BE COMPLETED

**FIN DE DOCUMENT
END OF DOCUMENT**

Performance of Near-Optimal and Simplified FQPSK-B Receivers

Dennis Lee, Marvin Simon, and Tsun-Yee Yan
Jet Propulsion Laboratory
California Institute of Technology
Pasadena, CA 91109

May 4, 2000

1 Abstract

Commercial FQPSK-B receivers use symbol-by-symbol detection and suffer a 2 dB E_b/N_o loss at a BER of 10^{-5} relative to BPSK. This paper describes the performance of an FQPSK-B receiver using a Viterbi algorithm (VA) that takes advantage of the FQPSK trellis-coded structure to obtain a 1.2 dB E_b/N_o gain at 10^{-5} BER. However, the complexity of the full FQPSK-B Viterbi receiver requires over an order of magnitude increase in complexity compared to the symbol-by-symbol receiver. A simplified Viterbi receiver with four times less complexity relative to the full FQPSK-B Viterbi receiver is introduced, and shown to have only a 0.3 dB degradation compared to the full Viterbi receiver at 10^{-5} BER. A theoretical bit error probability expression for the symbol-by-symbol FQPSK-B receiver is given in the Appendix.

2 Introduction

Feher-patented QPSK (FQPSK) is a spectrally efficient form of offset QPSK modulation. One of 16 shaped waveforms (8 unique waveforms shown in Figure 1 and their negatives) are transmitted based on a trellis-coded structure described in [2]. The waveforms are designed to have a narrow spectrum and smooth transitions between waveforms. Cross-correlation between the inphase and quadrature phase waveforms is introduced to obtain a nearly constant envelope with less than 0.2 dB envelope fluctuation. The narrow spectrum and quasi-constant envelope of FQPSK makes it very desirable for high data rate missions in a nonlinear satellite channel where bandwidth is a constraint.

A baseband filtered version of FQPSK called FQPSK-B was patented by Dr. Feher in 1986 [1]. The spectral sidelobes of FQPSK-B are significantly lower than FQPSK due to the baseband filtering with sidelobes 70 dB below the peak power spectral density at 1.5 times the data rate away from the center frequency. A comparison of the FQPSK and the FQPSK-B spectra is shown in Figure 2 along with the SFCG high data rate mask. Due to the spectral efficiency of FQPSK-B, it has been recommended for high data rate systems by the CCSDS and IRIG Telemetry Standard 106-00.

The narrow bandwidth of FQPSK-B comes at the cost of an E_b/N_o degradation in bit error rate (BER) performance relative to ideal QPSK, approximately 1.4 dB at 10^{-3} BER using the symbol-by-symbol FQPSK-B receiver. However, the trellis coding inherent in the generation of FQPSK described in [2] allows for improved BER performance using a more complex Viterbi receiver. This

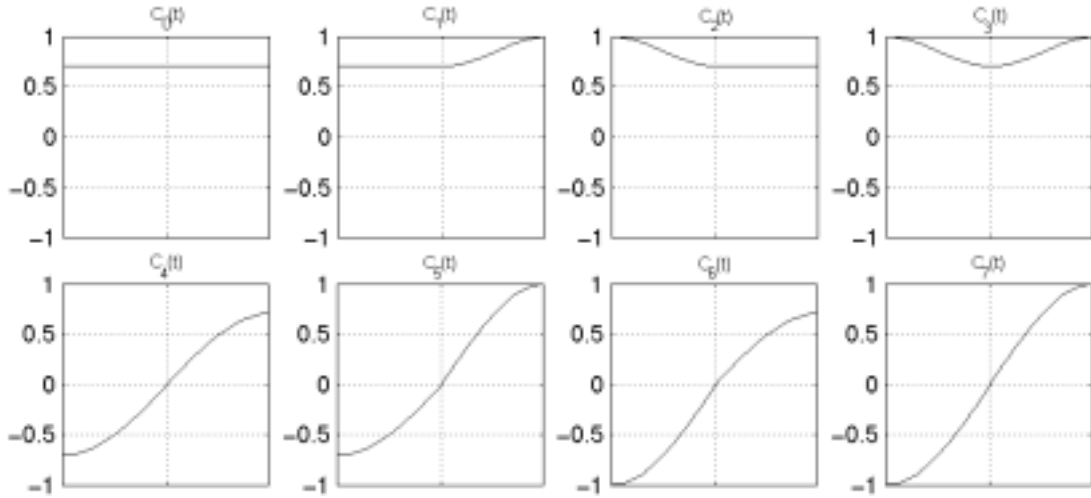


Figure 1: FQPSK waveforms; $C_i(t) = -C_{i-8}(t)$, $i = 8, \dots, 15$

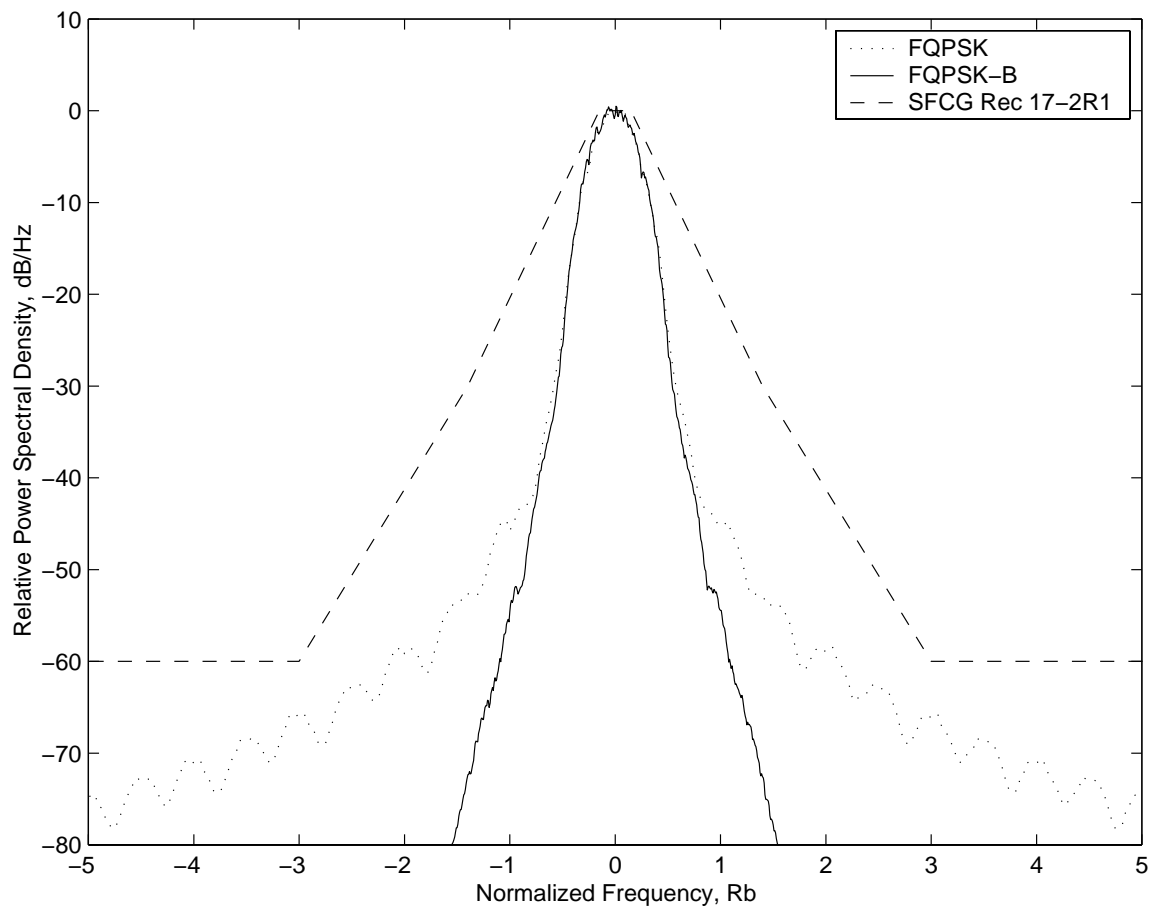


Figure 2: Spectral comparison of FQPSK and FQPSK-B

Viterbi receiver has 16 correlators, and a 16 state Viterbi algorithm which finds the maximum-likelihood path through the FQPSK trellis. The bit error performance of unfiltered FQPSK using the Viterbi receiver was given in [3]; however, the performance of the more spectrally efficient FQPSK-B was not addressed. In this paper, the performance of the FQPSK Viterbi receiver on FQPSK-B is given, and a simplified FQPSK-B Viterbi receiver that requires only 4 correlators and a pair of 2 state Viterbi algorithms is introduced.

3 FQPSK-B Viterbi Receiver

The FQPSK-B receiver most commonly used commercially is a simple sample-and-hold (S&H) receiver. The received signal is demodulated and then filtered using a detection filter whose bandwidth-symbol period (BT_s) is approximately 0.55. The output of the detection filter is then sampled at the maximum eye opening. The S&H receiver uses symbol-by-symbol detection and does not utilize the trellis-coded structure inherent in FQPSK. Improved BER performance can be obtained by using a Viterbi receiver that utilizes the trellis-coded structure to provide coding gain.

A block diagram of the full FQPSK-B Viterbi receiver is shown in Figure 3. The received signal is first demodulated and then correlated against the FQPSK waveforms. Since there are only eight unique waveforms, only eight correlators are needed for each channel (I and Q channels), resulting in sixteen total correlators¹. Instead of correlating against the unfiltered FQPSK waveforms, correlating against the filtered FQPSK waveforms using the FQPSK-B baseband filter may provide improved BER performance. However, the baseband filter is significantly wideband compared to the bandwidth of the waveforms, and any improvement is likely to be small. The correlation values are fed into the Viterbi algorithm which has 16 states with 4 possible transitions to each state. The Viterbi receiver then finds the trellis path with the maximum metric. The branch metrics, Z_j , are computed as follows:

$$Z_j = R_j - \frac{E_j}{2} \quad ; j = 0, \dots, 15 \quad (1)$$

where R_j is the correlation of the received signal and the j^{th} waveform and E_j is the energy in the j^{th} waveform. The correlation values R_8 through R_{15} are obtained by taking the negatives of R_0 through R_7 (i.e., $R_0 = -R_8$, $R_1 = -R_9$, $R_2 = -R_{10}$, etc.).

Using SPW computer simulations, the bit error performance of the full FQPSK-B Viterbi receiver is shown in Figure 4. The simulated channel includes a 10W ESA SSPA operating in full saturation. The BER curves of the FQPSK-B S&H receiver and that of ideal QPSK are included in Figure 4 for comparison. The FQPSK-B Viterbi receiver requires 7.4 dB E_b/N_o for a bit error probability of 10^{-3} , which is 0.6 dB worse than QPSK and 0.8 dB better than the S&H receiver. For 10^{-5} bit error probability, the FQPSK-B Viterbi receiver requires an E_b/N_o of 10.4 dB which is about 0.8 dB worse than ideal QPSK and 1.2 dB better than the S&H receiver.

4 Simplified FQPSK-B Viterbi receiver

The large number of correlators needed for the FQPSK-B Viterbi receiver may be unacceptable in some cases. By grouping the waveforms, a reduction in the number of correlators and the number of states in the Viterbi algorithm can be achieved with only a slight degradation in bit error performance.

The sixteen FQPSK waveforms shown in Figure 1 are separated into 4 different groups. The first group consists of waveforms C_0 through C_3 ; the second group consists of waveforms C_4 through

¹Since the $C_0(t)$ waveform is a constant, the correlator just consists of an integrator

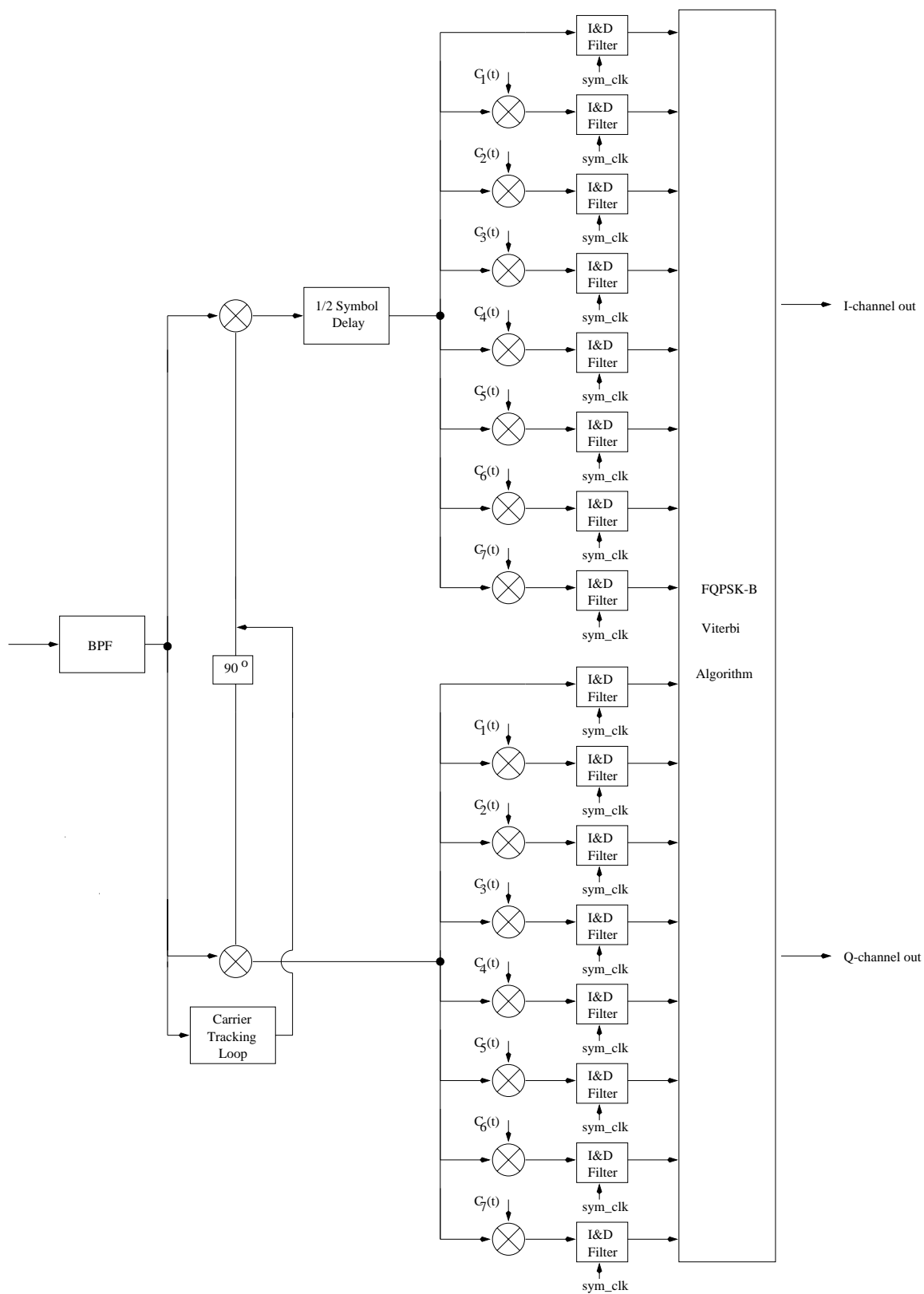


Figure 3: Block diagram of FQPSK-B Viterbi Receiver

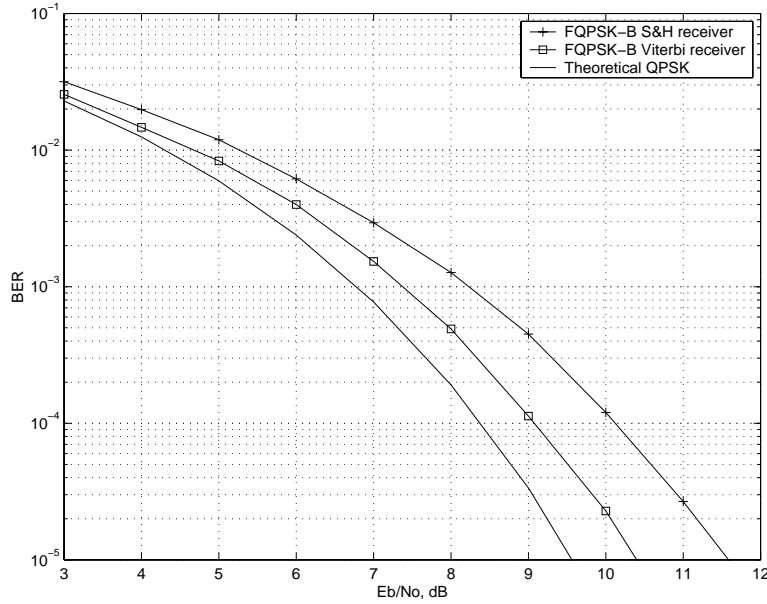


Figure 4: BER of FQPSK-B Viterbi receiver, Saturated SSPA

C_7 ; the third group consists of waveforms C_8 through C_{11} ; and the fourth group consists of waveforms C_{12} through C_{15} . With this grouping, the trellis coded structure of FQPSK splits into two independent I and Q trellises with the T-OQPSK [3] trellis coded structure. Thus with a few modifications, a T-OQPSK Viterbi receiver can be used to detect FQPSK-B signals.

A block diagram of the simplified FQPSK-B receiver is shown in Figure 5. The received FQPSK-B signal is demodulated and then correlated against the average of the waveforms in each group, $q_i(t)$, given below:

$$\begin{aligned} q_0(t) &= \frac{1}{4} \sum_{i=0}^3 C_i(t) \\ q_1(t) &= \frac{1}{4} \sum_{i=4}^7 C_i(t) \\ q_2(t) &= -q_0(t) \\ q_3(t) &= -q_1(t) \end{aligned}$$

Since $q_2(t)$ and $q_3(t)$ are the negatives of $q_0(t)$ and $q_1(t)$, only two correlators are needed for each channel. The VA metrics are again formed as in Eq. (1) except E_j is now the energy in $q_j(t)$. The trellis of the grouped signals is identical to the T-OQPSK trellis. Thus the simplified FQPSK-B Viterbi receiver consists of 4 correlators (two each for the I and Q channels) and a Viterbi algorithm based on the T-OQPSK trellis which has only 2 states and 2 possible transitions to each state. However, since the grouping has decoupled the inphase and quadrature phase waveforms, a separate Viterbi algorithm is needed for each channel as shown in Figure 5.

The bit error rate performance of the simplified FQPSK-B Viterbi receiver is shown in Figure 6. The BER curves of the full FQPSK-B Viterbi receiver, the FQPSK-B S&H receiver, and ideal QPSK are shown for comparison. For a 10^{-3} BER, the simplified FQPSK-B Viterbi receiver requires an E_b/N_o of 7.65 dB, which is about 0.85 dB worse than ideal QPSK but 0.55 dB better than the

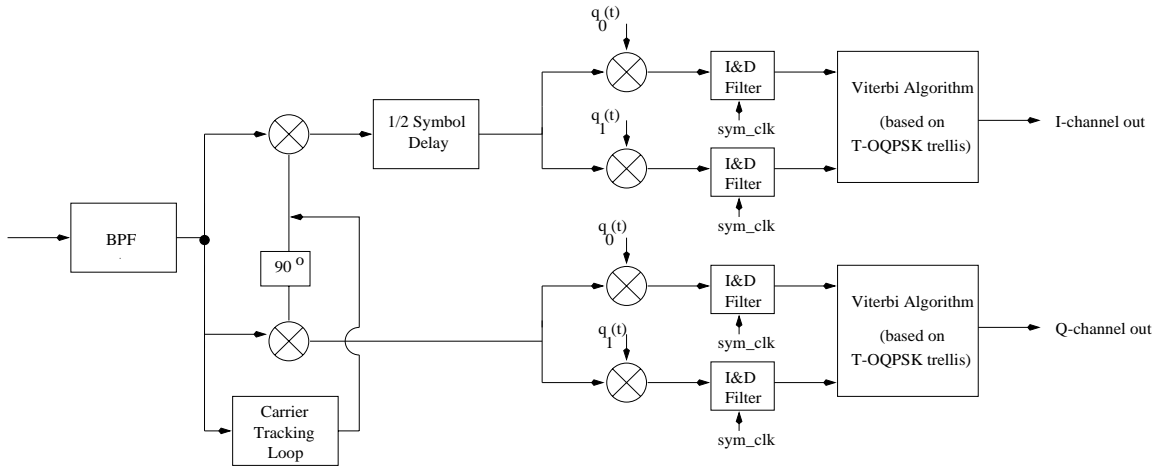


Figure 5: Block diagram of Simplified FQPSK-B Viterbi receiver

S&H FQPSK-B receiver. At 10^{-5} BER, the simplified FQPSK-B Viterbi receiver requires 10.7 dB E_b/N_o , which represents a loss of 1.1 dB compared to ideal QPSK but still manages a 0.9 dB E_b/N_o gain over the S&H receiver.

The computational complexity of the two 2-state Viterbi algorithms can be roughly approximated by a single 4-state Viterbi algorithm with 2 possible transitions per state and 2 output bits per decoding iteration. Thus the simplified FQPSK-B Viterbi algorithm only has to search through 4 branches per output bit compared to 32 branches per output bit for the full FQPSK-B Viterbi decoder. In addition, the full FQPSK-B Viterbi receiver requires 16 correlators versus only 4 correlators for the simplified Viterbi receiver. Thus, the simplified FQPSK-B Viterbi receiver has an 8-fold reduction in the number of branches the VA must search through per decoded bit, and a 4-fold reduction in the number of correlators required. The tradeoff is that the simplified FQPSK-B Viterbi receiver has approximately 0.3 dB E_b/N_o degradation compared to the full Viterbi receiver at 10^{-5} BER.

5 Summary

This paper shows that the BER improvement offered by the unfiltered FQPSK Viterbi receiver in [3] also applies to FQPSK-B, which has a narrower spectrum. Using the FQPSK Viterbi receiver on FQPSK-B, a 1.2 dB gain at 10^{-5} BER over the commonly used sample-and-hold FQPSK-B receiver is achieved. A simplified FQPSK-B Viterbi receiver is introduced by appropriately grouping the symbols and using the T-OQPSK trellis. This simplified receiver has roughly an eight-fold reduction in computational complexity of the Viterbi algorithm and a four-fold reduction in the number of correlators needed compared to the full FQPSK-B Viterbi receiver, yet still maintains a 0.9 dB improvement at 10^{-5} BER over the sample-and-hold FQPSK-B receiver.

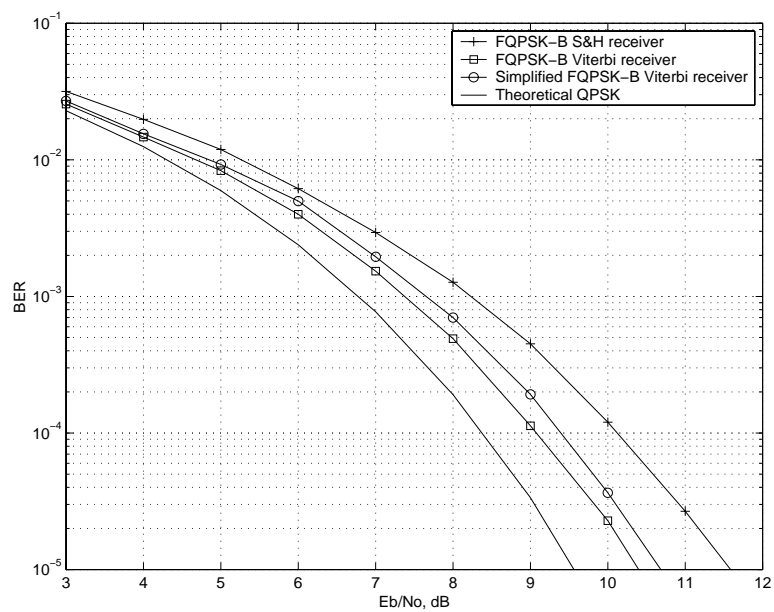


Figure 6: BER performance of simplified FQPSK-B Viterbi receiver

6 Appendix. Theoretical bit error probability of S&H FQPSK-B receiver

The FQPSK waveforms can be rearranged as follows so that fewer ISI symbols need to be considered:

$$\begin{aligned}
s_0(t) &= A, & -\frac{T_s}{2} \leq t \leq \frac{T_s}{2} \\
s_1(t) &= \begin{cases} A, & -\frac{T_s}{2} \leq t \leq 0 \\ A \cos \frac{\pi t}{T_s}, & 0 < t \leq \frac{T_s}{2} \end{cases} \\
s_2(t) &= 1 - (1 - A) \sin^2 \frac{\pi t}{T_s}, & -\frac{T_s}{2} \leq t \leq \frac{T_s}{2} \\
s_3(t) &= \begin{cases} 1 - (1 - A) \sin^2 \frac{\pi t}{T_s}, & -\frac{T_s}{2} \leq t \leq 0 \\ \cos \frac{\pi t}{T_s}, & 0 < t \leq \frac{T_s}{2} \end{cases} \\
s_4(t) &= A \cos \frac{\pi t}{T_s}, & -\frac{T_s}{2} \leq t \leq \frac{T_s}{2} \\
s_5(t) &= \begin{cases} A \cos \frac{\pi t}{T_s}, & -\frac{T_s}{2} \leq t \leq 0 \\ A, & 0 < t \leq \frac{T_s}{2} \end{cases} \\
s_6(t) &= \cos \frac{\pi t}{T_s}, & -\frac{T_s}{2} \leq t \leq \frac{T_s}{2} \\
s_7(t) &= \begin{cases} \cos \frac{\pi t}{T_s}, & -\frac{T_s}{2} \leq t \leq 0 \\ 1 - (1 - A) \sin^2 \frac{\pi t}{T_s}, & 0 < t \leq \frac{T_s}{2} \end{cases} \\
s_8(t) &= -s_0(t) \\
s_9(t) &= -s_1(t) \\
s_{10}(t) &= -s_2(t) \\
s_{11}(t) &= -s_3(t) \\
s_{12}(t) &= -s_4(t) \\
s_{13}(t) &= -s_5(t) \\
s_{14}(t) &= -s_6(t) \\
s_{15}(t) &= -s_7(t)
\end{aligned} \tag{2}$$

Let $h(t) = h_t(t) * h_r(t)$ denote the impulse response of the cascaded baseband FQPSK-B transmit filter $h_t(t)$ and receive filter $h_r(t)$. The filtered waveforms after the receive filter, $r_i(t)$, are given by:

$$r_i(t) = h(t) * s_i(t)$$

Denote t_o as the time of the maximum eye opening. Then the sampled values of the filtered waveforms, $r_{i,k}$, are given by:

$$r_{i,k} = r_i(t_o + kT_s)$$

Assuming that only the $-L_1 \leq k \leq L_2, k \neq 0$ symbols have a significant ISI contribution to the decision made on the $k = 0$ symbol, the decision variable $z_{i,p,q}$ for the $k = 0$ symbol given $s_i(t)$ was transmitted is given by:

$$z_{i,p,q} = r_{i,0} + \sum_{k=1}^{L_2} r_{g_k(i,p),-k} + \sum_{m=1}^{L_1} r_{h_m(i,q),m} + n$$

where the g_k 's are the possible waveforms k symbols later and the h_m 's are the possible waveforms m symbols before, and are defined recursively as follow:

$$\begin{aligned} g_k(i, p) &= F(g_{k-1}(i, p) + 1, j_{k-1} + 1), & g_0(i, p) &= i \\ h_m(i, q) &= B(h_{m-1}(i, q) + 1, c_{m-1} + 1), & h_0(i, q) &= i \end{aligned}$$

where $p = 1, \dots, 4^{L_2} - 1$ represent the different forward paths through the trellis starting with the i^{th} waveform and $q = 1, \dots, 4^{L_1} - 1$ represent the different backwards paths through the trellis starting with the i^{th} waveform. The j_k 's are defined by $p = j_0 + 4j_1 + \dots + 4^{L_2-1}j_{L_2-1}$ and the c_k 's are defined by $q = c_0 + 4c_1 + \dots + 4^{L_1-1}c_{L_1-1}$. $F(x, y)$ is the element in the x^{th} row and y^{th} column in the forward trellis matrix, \mathbf{F} ,

$$\mathbf{F} = \begin{bmatrix} 0 & 1 & 2 & 3 \\ 12 & 13 & 14 & 15 \\ 0 & 1 & 2 & 3 \\ 12 & 13 & 14 & 15 \\ 12 & 13 & 14 & 15 \\ 0 & 1 & 2 & 3 \\ 12 & 13 & 14 & 15 \\ 0 & 1 & 2 & 3 \\ 8 & 9 & 10 & 11 \\ 4 & 5 & 6 & 7 \\ 8 & 9 & 10 & 11 \\ 4 & 5 & 6 & 7 \\ 4 & 5 & 6 & 7 \\ 8 & 9 & 10 & 11 \\ 4 & 5 & 6 & 7 \\ 8 & 9 & 10 & 11 \end{bmatrix} \quad (3)$$

and $B(x, y)$ is the element in the x^{th} row and y^{th} column in the backwards trellis matrix, \mathbf{B} ,

$$\mathbf{B} = \begin{bmatrix} 0 & 2 & 5 & 7 \\ 0 & 2 & 5 & 7 \\ 0 & 2 & 5 & 7 \\ 0 & 2 & 5 & 7 \\ 9 & 11 & 12 & 14 \\ 9 & 11 & 12 & 14 \\ 9 & 11 & 12 & 14 \\ 9 & 11 & 12 & 14 \\ 8 & 10 & 13 & 15 \\ 8 & 10 & 13 & 15 \\ 8 & 10 & 13 & 15 \\ 8 & 10 & 13 & 15 \\ 8 & 10 & 13 & 15 \\ 1 & 3 & 4 & 6 \\ 1 & 3 & 4 & 6 \\ 1 & 3 & 4 & 6 \\ 1 & 3 & 4 & 6 \end{bmatrix} \quad (4)$$

The random variable n is filtered Gaussian noise with variance

$$\sigma_n^2 = \frac{N_o}{2} ||h||^2$$

where $\|h\|^2 = \int_{-\infty}^{\infty} |h^2(t)|dt$. The \mathbf{F} and \mathbf{B} matrices are constructed so that the current waveform is defined by the row number minus one (e.g., row one corresponds to $s_0(t)$), and the elements of the row contain the possible previous symbols in the case of the backwards trellis matrix \mathbf{B} or the possible following symbols in the case of \mathbf{F} . There are only four possible waveform transitions for each waveform which are equiprobable.

Only the probability of error for waveforms $s_0(t)$ through $s_7(t)$ need to be considered as the probability of error for $s_8(t)$ through $s_{15}(t)$ will be the same. Thus the average probability of a bit error is given by:

$$P_e = \frac{1}{2(4^{L_1+L_2+1})} \sum_{i=0}^7 \sum_{p=0}^{4^{L_2}-1} \sum_{q=0}^{4^{L_1}-1} Q\left(\frac{z_{i,p,q}}{\sigma_n}\right) \quad (5)$$

Note that the energy per bit, E_b , is not simply the average of the individual waveform energies because of ISI. Rather, E_b is given by:

$$E_b = \frac{1}{2(4^{L_1+L_2+1})} \sum_{i=0}^7 \sum_{p=0}^{4^{L_2}-1} \sum_{q=0}^{4^{L_1}-1} \int_{-T_s/2}^{T_s/2} \left(h_t(t) * (s_i(t) + \sum_{k=1}^{L_2} s_{g_k(i,p)}(t - kT_s) + \sum_{m=1}^{L_1} s_{h_m(i,q)}(t + mT_s)) \right)^2 dt$$

Therefore,

$$P_e = \frac{1}{2(4^{L_1+L_2+1})} \sum_{i=0}^7 \sum_{p=0}^{4^{L_2}-1} \sum_{q=0}^{4^{L_1}-1} Q\left(\sqrt{\frac{2E_b}{N_o} \frac{(z'_{i,p,q})^2}{\|h\|^2}}\right) \quad (6)$$

where $z'_{i,p,q} = z_{i,p,q}/\sqrt{E_b}$.

The number of terms in Eq. (6) can be quite large for $L_1, L_2 > 2$; however, the $z_{i,p,q}$ terms are just sums of $r_{i,k}$ terms which only need to be computed once. In addition, for the case of FQPSK-B transmit and receive filters, a good approximation to the bit error probability can be found by considering only the ISI from the previous symbol (i.e., $L_1 = 1$ and $L_2=0$). Using this approximation, the probability of error expression reduces to

$$P_e = \frac{1}{32} \sum_{i=0}^7 \sum_{q=0}^3 Q\left(\sqrt{\frac{2E_b}{N_o} \frac{(z'_{i,q})^2}{\|h\|^2}}\right) \quad (7)$$

where

$$z_{i,q} = r_{i,0} + \sum_{m=1}^{L_1} r_{h_m(i,q),m}$$

In this case, only 32 terms need to be computed. Figure 7 shows a comparison of Eq. (7) and the simulated BER of the FQPSK-B S&H receiver. As the figure shows, the 32-term approximation matches closely with the simulation results.

The advantage of theoretical expressions is that the bit error performance of the receiver can be evaluated at extremely low probabilities of error without prohibitively long computer simulations. For example, data containing compressed images may require a bit error rate on the order of 10^{-10} depending on the amount of compression. Figure 8 shows the bit error performance of the FQPSK S&H receiver using the 32-term theoretical approximation at low bit error rates. The FQPSK-B S&H receiver requires about 15.4 dB E_b/N_o for a 10^{-10} BER. For very large E_b/N_o , the asymptotic loss of the S&H receiver with respect to ideal QPSK is approximately 3 dB.

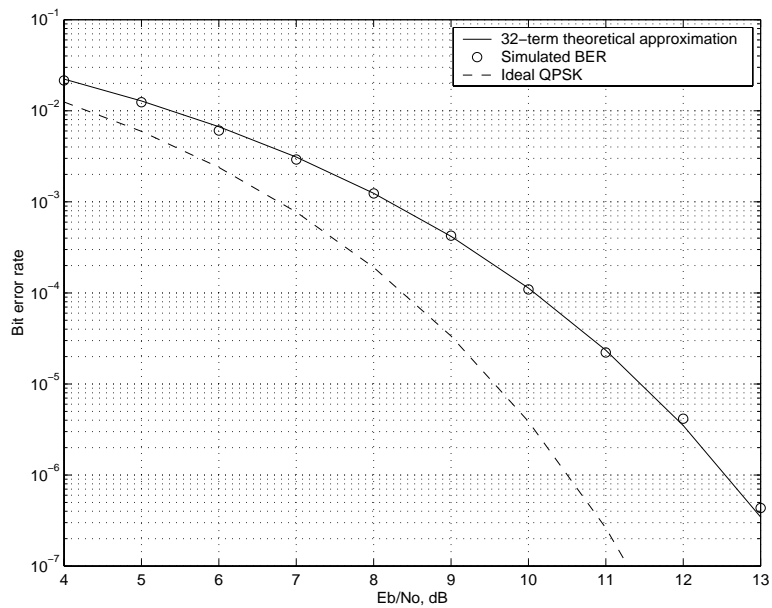


Figure 7: BER of FQPSK-B S&H receiver

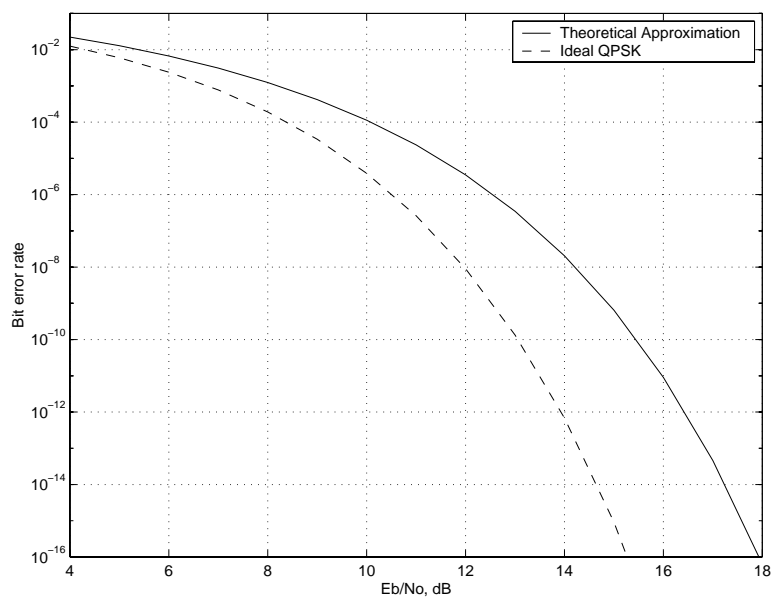


Figure 8: Bit error probability of FQPSK-B S&H receiver at low BER

References

- [1] S. Kato and K. Feher, "Correlated Signal Processor", U.S. Patent 4,567,602, January 1986.
- [2] M.K. Simon and T.-Y. Yan, "Performance Evaluation and Interpretation of Unfiltered Feher-patented Quadrature Phase Shift Keying (FQPSK)", JPL TMO Progress Report 42-137, May 1999.
- [3] M.K. Simon, P. Arabshahi, and M. Srinivasan, "Trellis-Coded Quadrature Phase Shift Keying (QPSK) with Variable Overlapped Raised-Cosine Pulse Shaping", JPL TMO Progress Report 42-136, February 1999.

Prototyping Parallel Algorithms for High Rate FQPSK Waveforms

Edward Kang, Dennis Lee, Norman Lay

I. Introduction

The ability to transmit and receive ever-increasing amounts of extremely high rate data is an enduring challenge in the arena of near-earth, spaceborne science missions. Reliable and efficient transmission of information at these data rates requires the use of integrated power and bandwidth efficient modulation and coding waveforms that exhibit low transmitter, receiver and decoder complexity. Conventional high rate approaches for achieving spectral limiting typically employ sharp post amplifier filtering at the transmitter to limit the interference to the adjacent bands. However, the use of analog filtering alone can produce substantial intersymbol interference and other distortions that substantially affect the detection performance of the signal. In contrast, various theoretical classes of modulation waveforms can be tailored to provide varying degrees of bandwidth and power efficiency or robustness to non-linear transmitter distortions while incurring little or no performance losses. In order to realize many of these signal types, precise amplitude and phase control over the synthesis of these signals is required, typically necessitating the use of digital signal processing for the generation of these modulations.

Serial methods of performing precise digital waveform generation are costly and become computationally limited for GHz processing rates. The design approach described in this paper replaces expensive, high power consumption analog or digital GaAs signal processing technology for high rate applications with low power, high density and relatively inexpensive CMOS technology based on parallel processing methods. This effort is structured to result in hardware algorithms, designs and prototypes to generate different bandwidth efficient modulations for Gbps applications. The combination of parallel architectures and novel waveform generation is intended to provide a full measure of flexibility in performance and bandwidth efficiency in a cost-effective fashion.

The first target waveform to be considered is FQPSK -- a near constant envelope signal whose filtered version has been recommended by CCSDS as a spectrally efficient modulation for high rate near earth communications. FQPSK exhibits substantial robustness to channel non-linearities that are typically encountered through the use of saturated amplifiers for efficient signal transmission. In this paper, we discuss the structure of the waveform, the design approach for its implementation and expansion to high rates in field programmable gate array (FPGA) logic and results of preliminary laboratory testing.

II. The FQPSK Waveform Structure

Feher-patented QPSK, or FQPSK, is a spectrally efficient form of offset QPSK modulation patented by Kamilo Feher in 1986 [1]. In 1998, a trellis-coded interpretation of FQPSK was discovered by Simon and Yan [2] that allowed for a simpler transmitter structure and a receiver with improved bit error performance when utilizing an optimal detector. Using this interpretation for both in-phase and

quadrature channels, one of sixteen spectrally shaped waveforms (the eight unique waveforms shown in Figure 1 and their inverses) is transmitted based on a trellis-coded combination of present and previous data bits. The generation of this waveform may also be viewed as a finite memory bit sequence mapping to select the transmitted, full response, pulse shape from the eight possibilities shown in Figure 1 with the most recent bit determining the polarity of the signal.

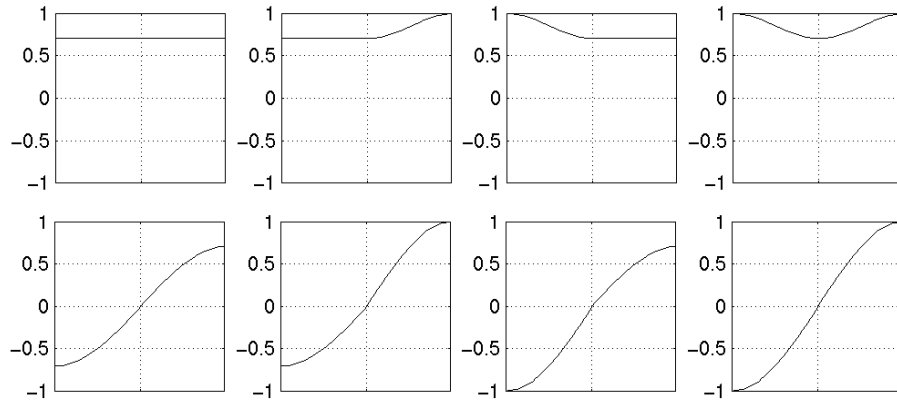


Figure 1. FQPSK waveforms

The FQPSK waveforms are designed to minimize spectral sidelobes and envelope fluctuation. Cross-correlation is introduced between the transmitted in-phase and quadrature waveforms to produce a quasi-constant envelope with less than 0.2 dB envelope fluctuation. Due to its quasi-constant envelope property, FQPSK can pass through a nonlinear power amplifier in full saturation with minimal spectral regrowth. Overall, the spectrum of FQPSK is substantially bandlimited with a 99% power containment bandwidth more than 6 times smaller than QPSK. Figure 2 shows a computer-generated plot of the FQPSK spectrum with the frequency axis normalized to the information data rate (twice the transmit symbol rate).

A baseband-filtered version of FQPSK, known as FQPSK-B, has an even narrower spectrum with sidelobe suppression of -70 dB at approximately 1.5 times the data rate away from the center frequency. FQPSK-B has been recommended by CCSDS and IRIG standards for use in systems that require high data rate, bandwidth efficient communications.

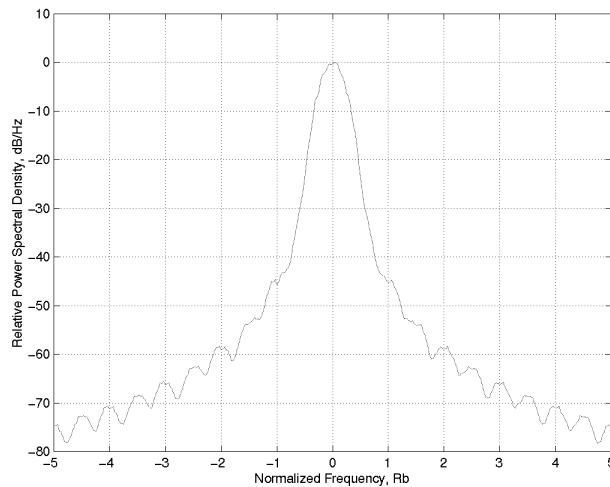


Figure 2. FQPSK Spectrum

III. Digital Modulator Circuit Architecture and Design

Due to their reconfigurability, constantly increasing capacities and availability of radiation tolerant components [3, 4], commercial FPGAs represent an ideal technology in which to validate the concept of low cost, parallel, high rate communications signal processing for potential space-based applications. In this section, we discuss the FPGA circuit architecture used to synthesize the FQPSK complex baseband waveform as synchronous digital samples. The initial effort produced a design for a single processing element whose core could be re-used in a parallel, time-multiplexed fashion to achieve high rate throughput. A high level view of the functional signal flow for the FPGA is shown in Figure 3. Serial input data is initially de-multiplexed into alternating data streams from which pulse shape lookup addresses are computed as depicted in Figure 4, according to the rules given in [2]. The state address and the value of the most recent information bit then provide the selection of the complex FQPSK pulse shape during that symbol interval. The state and bit information are then routed to identical lookup tables that store eight ten-bit samples for each pulse shape. These samples are synchronously read out over a symbol interval with a half symbol delay implemented between inphase and quadrature sample streams.

In terms of implementation details, the modulator's digital design was realized in an Altera Flex 10K family FPGA (EPF10K100ARC240-3). This part is representative of a modest capacity device (approximately 100,000 equivalent gates, 189 user I/Os). A preliminary design for the Trellis-Offset QPSK (T-OQPSK) waveform was written and simulated in VHDL and tested with the digital-to-analog converter (DAC) evaluation board to verify basic system operation. As more sophisticated tools were made available, the subsequent design of FQPSK was done in Verilog for compatibility with related projects and verified using a ModelTech simulation tool. Test inputs consisted of known input bit patterns and digital waveform outputs were compared to a discrete time MATLAB simulation. These inputs and outputs, in turn, respectively formed the test stimulus and response for verifying modulator operation when fully integrated into the test configuration described in the following section.

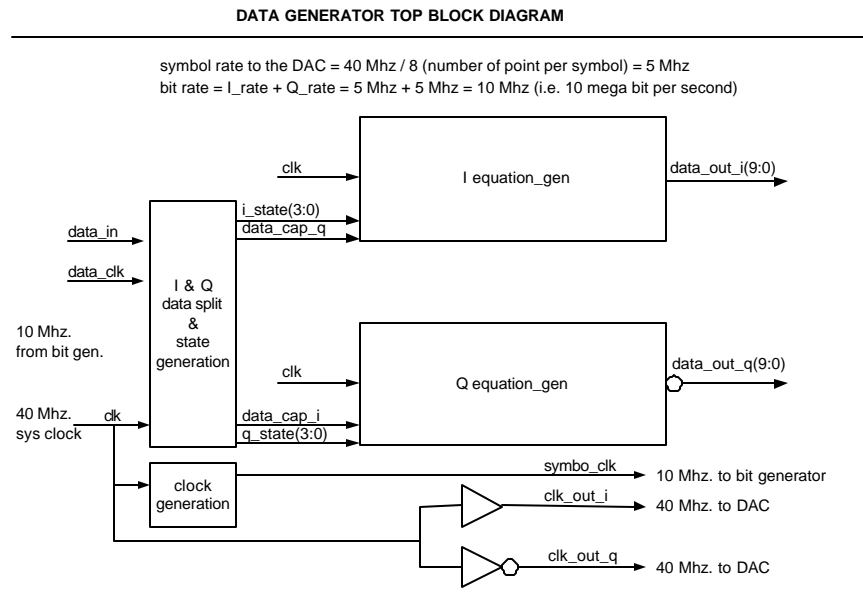


Figure 3. Single Processing Element Configuration

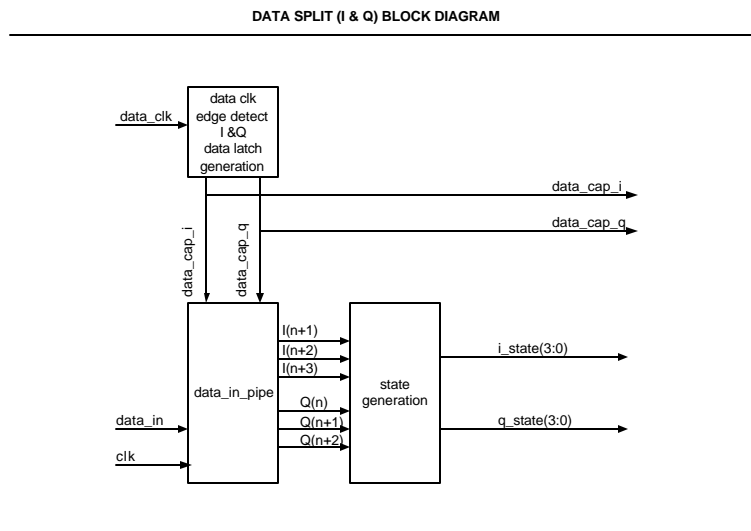


Figure 4. Serial Data Input and State Generation for Waveform Selection

The migration of the single processing element design to multiple parallel processors is depicted in Figure 5 for a dual element configuration. Many aspects of the pulse shape lookup table and state generation remain identical to those present in the initial design. A high rate (80 MHz) 8x10 bit block register is added to the table lookup equation generator and a sample multiplexer is added to the modulator in order to select between the correct symbol output. This approach is sufficient to add low numbers of additional channels within the confines of the FPGA. However, it can quickly become

limited when the high-speed portions of the design outstrip the maximum clock frequencies supported by a particular FPGA technology (typically in the 80 – 150 MHz range). At that point, the incorporation of additional parallel channels can be accommodated by expanding the width of the output words so that many parallel samples are simultaneously output from the FPGA at a lower frequency while retaining a high throughput sample rate. Such configurations then rely on external high speed multiplexing circuitry that is typically rendered in GaAs for the serial sample stream generation. Preliminary analyses have indicated that the number of parallel elements supportable by the Altera FPGA is not circuit area limited but rather I/O pin limited. Depending upon the number of bits in the output samples to the DAC, between seven and nine parallel elements can be accommodated within this part. For substantially larger parts, up to 30 parallel processors can be implemented.

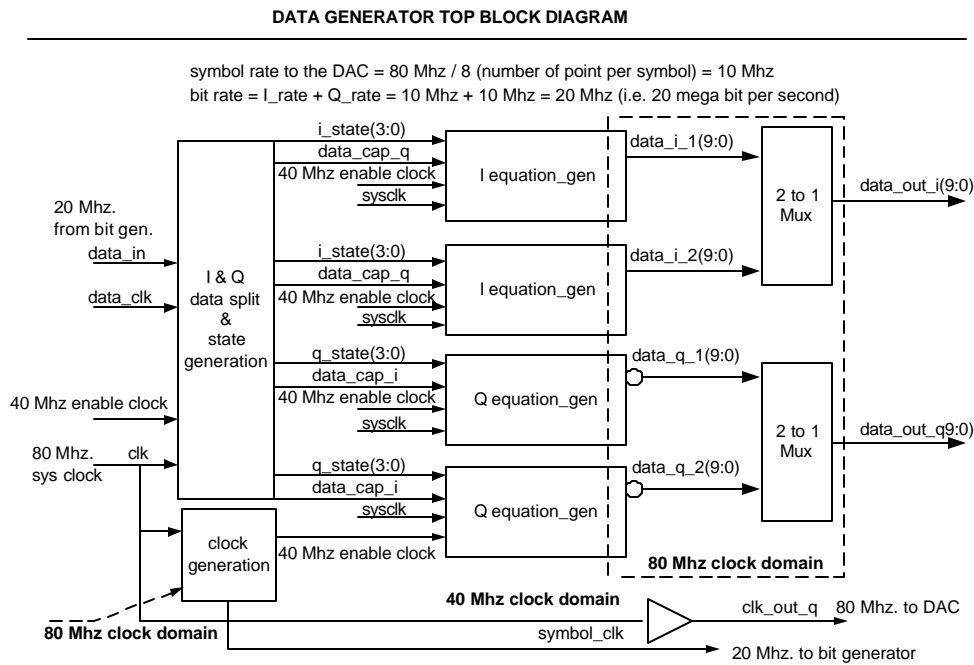


Figure 4. Dual Processing Element Configuration

IV. Laboratory Configuration and Modulator Performance

The initial prototyping effort focused on validating the complex baseband waveform generation of the FQPSK signal. In order to rapidly demonstrate this capability while retaining sufficient flexibility to implement simple parallel processing structures, stand-alone evaluation boards for the FPGA and the dual DACs were integrated into a single chassis and interconnected with test equipment in the configuration shown in Figure 7. A complex upconverter suitable for modulation at UHF carrier frequencies was also used to evaluate the spectral occupancy of the FQPSK signal. An external synthesizer provides a local oscillator input to the upconverter at a frequency of 437.1 MHz. User programmable serial data input into the FPGA was provided by a BitAlyzer 25 bit error rate tester (BERT). The FPGA was programmed to provide the input data clock to the BERT for purposes of maintaining coherent throughput from input data to output waveform samples. The data generator was

used both in known data pattern and random PN sequence generation modes to verify the complex baseband output waveforms.

In Figure 8, eye pattern diagrams taken from oscilloscope measurements are shown for pre- and post-filtered digital-to-analog converter (DAC) output. The eight samples per symbol resolution of the complex baseband modulator is clearly depicted in the unfiltered eye patterns. These results correspond to a sample rate of 40 MHz in both quadrature channels. Since the dual DAC device operates of a single power supply, it produces analog waveforms that include a DC offset component. This constant offset will need to be taken into account in any complex upconversion process so as not to produce an undesired spectral line at the carrier frequency. A quick means of eliminating this component was used for purposes of observing both the filtered baseband signals and the modulated spectrum. At the output of the DAC, a tunable filter [5] was applied with AC coupling to remove the signal-offset characteristic. The 3-dB lowpass corner of the filter was set to 10 MHz. This arrangement is applicable only for purposes of testing on random bit streams, as it will effectively filter out long or endless runs of constant data to the modulator. The filtering applied to the baseband waveforms is sufficient to eliminate higher frequency images associated with the DAC zero order hold and in fact induces some minimal intersymbol interference on the signal.

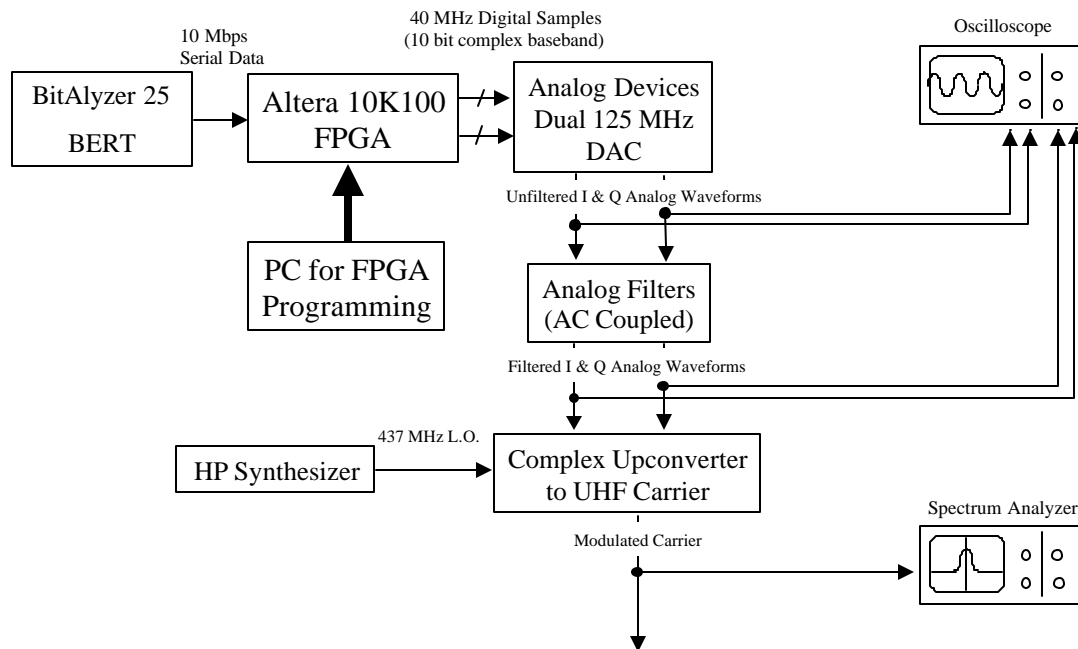


Figure 7. Laboratory test configuration

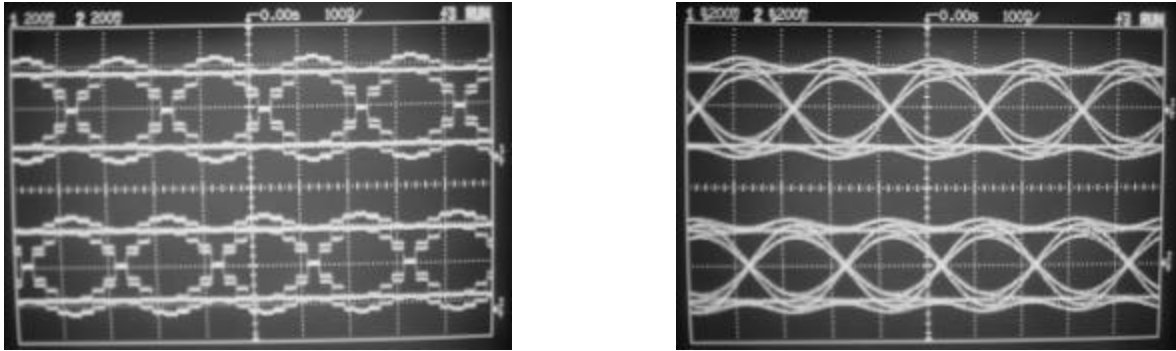


Figure 8. Pre- and post-filtered inphase and quadrature 10 Mbps FQPSK baseband waveforms

The modulated signal spectra shown in Figure 9 respectively correspond to the upconverted FQPSK waveform with and without analog filtering following the baseband DAC outputs. The unmodulated carrier due to the DAC DC offsets is clearly evident in the first spectral plot. With AC coupling and nominal lowpass filtering, the carrier component is removed in the second spectrum analyzer display. In both figures, the spectral containment of the signal agrees very well with the computer-simulated plot of Figure 2 up through the first nulls (-45 dB down from the signal peak), which occur at ± 10 MHz from the carrier frequency. The remainder of the out of band spectral roll-off is not as pronounced as that observed in the simulated performance and is likely the result of reaching the dynamic range of the 10 bit digital-to-analog converters to accurately reproduce an un-quantized waveform. For very high rate systems requiring substantial attenuation at frequency separations greater than one or two sidelobes beyond the main lobe, this is most likely achieved with the aid of relaxed analog filtering.

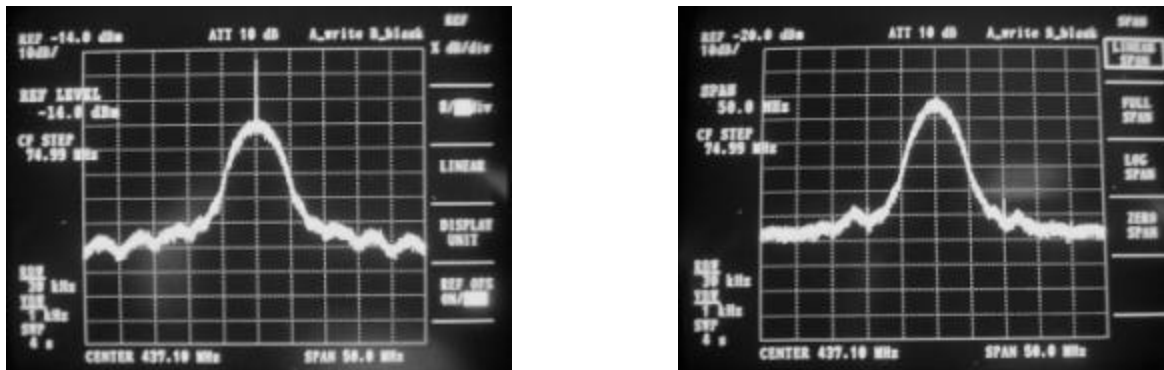


Figure 9. Spectra of 10 Mbps FQPSK UHF Carrier, with and without baseband lowpass filtering

V. Summary

A prototyping effort to implement a 10 Mbps FQPSK modulator using basic commercial FPGA technology was completed in a time period of approximately two months. The designs resulting from this effort help form the algorithmic foundation for the design and implementation of a parallel circuit, low

cost, very high rate, space-based modulator capable of generating a variety of power and bandwidth efficient communications waveforms.

VI. References

1. S. Kato and K. Feher, "Correlated Signal Processor", U.S. Patent 4,567,602, Jan 1986.
2. M.K. Simon and T.-Y. Yan, "Performance Evaluation and Interpretation of Unfiltered Feher-patented Quadrature Phase Shift Keying (FQPSK)", JPL TMO Progress Report 42-137, May 1999.
3. http://www.xilinx.com/products/hirel_qml.htm, Xilinx web site describing aerospace and defense products, as of April 24, 2000.
4. <http://nppp.jpl.nasa.gov/data/xilinx.htm>, JPL parts and reliability web site describing Xilinx parts inventory/availability, as of April 24, 2000.
5. <http://www.krohn-hite.com>, Krohn-Hite web site describing their active filter products, as of April 24, 2000.

An Off-line Coherent FQPSK-B Software Reference Receiver*

Haiping Tsou, Scott Darden, and Tsun-Yee Yan

Jet Propulsion Laboratory
California Institute of Technology
Pasadena, California, USA

ABSTRACT

Using Feher patented Quadrature Phase Shift Keying provides improved spectrum efficiency for high rate telemetry systems. This paper presents an off-line coherent FQPSK-B software reference receiver developed for hardware calibration under contract from the Advanced Range Telemetry (ARTM) program. This receiver is developed in Matlab/Simulink to be consistent with the software capacity available across a number of computing platforms at both ARTM and the Jet Propulsion Laboratory. It also offers a cost-effective approach to demonstrate the advance technologies. The functionality and key features of this receiver (including its internal software transmitter) will be addressed in this paper. Results from end-to-end system simulations are included as examples.

INTRODUCTION

Using Feher patented Quadrature Phase Shift Keying (Feher patented QPSK or FQPSK) improves spectrum efficiency for high rate telemetry systems. An off-line coherent software receiver has been developed for FQPSK-B modulation, a variant in the FQPSK family which includes proprietary designed filtering for additional spectrum containment [1]-[2]. It is intended to be used as (i) a stand-alone receiver offering a platform on which advanced technologies enabling further performance enhancement can be cost-effectively demonstrated, and (ii) a software tool that can be customized for testing and validating various hardware FQPSK-B transceivers under procurement consideration. Because of the testing requirements, the receiver has its own internal reference transmitter and a simple additive white Gaussian noise (AWGN) channel model and, therefore, is capable of performing end-to-end FQPSK-B system simulation and performance evaluation.

The software receiver consists of many functional modules developed in Matlab/Simulink, including differential encoding, FQPSK waveform generation, modulation, channel model, carrier and symbol synchronization, coherent demodulation and detection, differential decoding, and some real-time performance monitors and post-processing test result generators. These modules can be configured differently to carry out specific tasks in each of the receiver's four operating modes. For example, as a stand-alone receiver, it provides off-line demodulation, detection, and decoding of a sampled and digitized FQPSK-B signal from an external source, presumably a hardware transmitter,

* The research described in this paper was carried out by the Jet Propulsion Laboratory, California Institute of Technology under contract with the National Aeronautic and Space Administration.

to get the detected bit stream. Both demodulation and detection are performed coherently, which relies on the receiver's carrier and symbol synchronization loops to generate correct carrier phase reference and symbol timing. The bit error rate (BER) can be measured and compared to that of hardware receiver when the transmitted bit stream is available for BER calculation. The second mode is for hardware transmitter validation in which the software receiver is able to compare the demodulated hardware-generated signal with a reference signal realized by passing an internally generated baseband signal through the same receiver. The resulting error vector magnitude (EVM) measurement indicates hardware problems in the transmitter under test. The third and the fourth modes are for internal testing in which the software receiver functions as an end-to-end simulation system conducting BER and/or EVM tests under a set of user-specified conditions, including modulator imbalances and different filter designs. They can be used for trade-off studies on design parameters to realize a specification that meets certain design goals.

The FQPSK-B software receiver is developed on a Sun Workstation by using Matlab version 5.3 with Simulink toolboxes such as Communication Toolbox, DSP Toolbox, and Real Time Workshop. Because of the cross-platform compatibility of Matlab/Simulink, it can run on computers using operating systems such as UNIX, Window, and MacOS as long as a proper version of Matlab/Simulink is installed. It is also interesting to note that, because of the similarity between FQPSK and other conventional schemes in the QPSK family, the software receiver is flexible in handling many other types of QPSK signal or their derivatives with simple modifications.

The functionality and features of this Matlab/Simulink-based software receiver will be described in the next section, followed by a description of each of the four operation modes and their specific configurations for different applications. In addition, results from end-to-end system simulations using the internal reference transmitter are provided as examples, followed by a discussion of future works at the end of this paper.

FUNCTIONAL DESCRIPTION

The software receiver includes two major functional units: the internal transmitter and the coherent receiver. The functional block diagram of the internal transmitter is shown in Fig. 1, including a

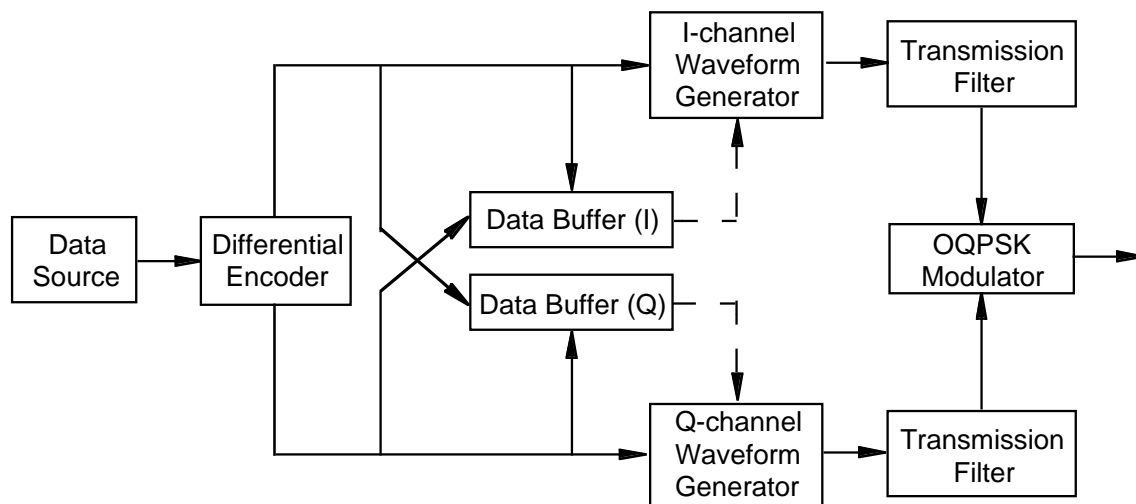


Figure 1 FQPSK-B Software Transmitter

data source (either a random or a fixed known sequence), a differential encoder, an FQPSK waveform generator (including data buffers facilitating cross-correlation between I-channel and Q-channel symbols), transmission filters and an offset QPSK (OQPSK) modulator. The functional block diagram of the coherent receiver is shown in Fig. 2, including an OQPSK carrier tracking loop, a symbol synchronizer providing correct timing for coherent detection, and a differential decoder.

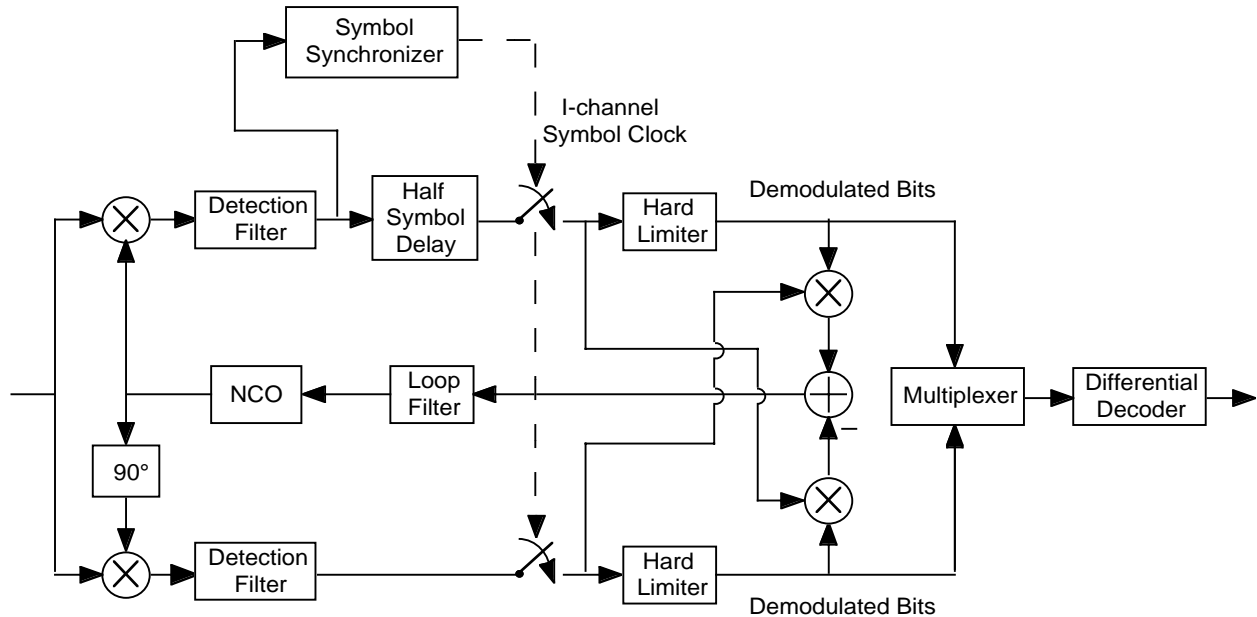


Figure 2 Coherent FQPSK-B Software Receiver

The receiver is developed based upon the assumption that the input signal is an FQPSK-B signal sampled at a fixed (known) rate that is high enough to avoid significant aliasing. The internal transmitter is able to generate such a sampled signal at either baseband or IF with floating-point values. On the other hand, the input from external hardware transmitters has to be a pre-recorded file consists of samples organized according to the Matlab standard I/O format. Typically, these samples are provided by the receiver's hardware front-end¹ that down-converts the received signal from RF to IF and then samples it to produce finite-bit quantized samples. These integer-valued samples will be internally converted to floating-point ones with average signal power normalized to one before being processed by the receiver.

Following are the description of the key functions of the transmitter and receiver.

Differential Encoding and Decoding

Differential coding is provided in the software transmitter according to the telemetry standards specified in IRIG 106-00 [3]. Its use is to resolve phase ambiguity associated with QPSK-based modulations.

In the software transmitter, the binary source data stream, consisting of 0's and 1's with a bit duration of T_b seconds, is first differentially encoded. In particular, the k^{th} coded bit, denoted by

¹ This is normally a hardware digital oscilloscope capable of down-conversion and sampling.

B_k , is a function of the current source bit and the one before that, denoted by b_k and b_{k-1} , at the encoder input and the $(k-2)^{th}$ coded bit, B_{k-2} , at the encoder output. This function is written in the recursive formula as follows

$$B_k = \overline{b_k \oplus b_{k-1}} \oplus B_{k-2}, \quad k \in N = \{0, 1, 2, \dots\}$$

where the symbol \oplus denotes the exclusive-or operator, the over-line represents the logical ‘not’ or inversion operator. The coded bit is then converted from binary format to a non-return-to-zero and leveled (NRZ-L) format by

$$\begin{aligned} 0 &\mapsto -1 \\ 1 &\mapsto +1 \end{aligned}$$

The coded NRZ-L bit stream is split into two, with even-numbered bits to be sent through the in-phase (I) channel and odd-numbered bits through the quadrature (Q) channel. On each channel, the coded bit has a duration that is twice of the source bit duration because of the split of coded bit stream. It is referred to as the symbol duration, $T_{sym} = 2T_b$, since a QPSK symbol represents two bits, one from each channel.

In the receiver, the decoding is performed after demodulation and data detection, rendering the following recursive relationship between coded and source bits.

$$b_k = \overline{B_k \oplus B_{k-2}} \oplus b_{k-1}, \quad k \in N$$

Waveform Generation

The generation of baseband FQPSK signal in the internal software transmitter is based upon a method of performing a symbol-by-symbol cross-correlative mapping on selected I- and Q-channel symbols with a specific set of full-symbol waveforms (wavelets) [4]. To generate FQPSK-B signal requires additional filtering of the FQPSK signal. In the internal software transmitter, a low-pass filter is provided on each of the I- and Q-channel to serve as the transmission filter. The type of this filter and its order and cut-off frequency are user-specified parameters.

Modulation and Demodulation

The internal software transmitter can generate both baseband and modulated FQPSK-B signals. According to IRIG 106-00, the Q-channel signal is delayed with respect to the I-channel signal by one source bit, or equivalently a half symbol, resulting in a wavelet-coded baseband OQPSK signal which can be put onto a carrier to produce a modulated FQPSK-B signals at a user-specified frequency. The mapping between a transmitted symbol and the resultant phase is as follows:

I - channel Symbol	Q - channel Symbol	Corresponding Symbol Phase
+1	+1	45°
-1	+1	135°
-1	-1	225°
+1	-1	315°

In addition, the transmitter is capable of emulating an imperfect phase modulator with user-specified modulator imbalances defined as follows [5]

$$S(t) = [w_1(t) + a_1] \cos(2\pi f_c t + \theta_c) + G[w_2(t) + a_2] \sin(2\pi f_c t + \theta_c + \Delta\theta)$$

where G is the inter-channel amplitude imbalance, $\Delta\theta$ is the inter-channel phase imbalance, and a_1 and a_2 are I-channel and Q-channel dc biases, respectively. In this modulator imbalance model, $w_1(t)$ and $w_2(t)$ represent I-channel and Q-channel signals, f_c is the carrier frequency, and θ_c is a random carrier phase.

On the receiver side, coherent demodulation requires a carrier reference established from the received signal. In particular, the carrier frequency f_c has to be estimated and the carrier phase θ_c has to be continuously tracked. The procedure to get an initial estimate of the carrier frequency and phase is referred to as carrier acquisition. It is done by first creating a carrier component from the received FQPSK-B signal with a hard-limiter, and then performing a discrete Fourier transform (DFT) on the hard-limited signal to have its frequency domain representation. A simple interpolation on the peak value and two values from adjacent bins on both sides of the bin containing the peak value produces the estimated frequency. Here, the non-linearity of a hard-limiter is essential in creating the odd-order harmonics from a fully modulated carrier, including the desired component at the fundamental (carrier) frequency [6].

The tracking of carrier phase is provided by a carrier tracking loop, as shown in Fig. 2, which results from a slight modification of a conventional QPSK cross-over Costas loop [7] by adding a half-symbol delay to its I-arm to compensate for the offset introduced between I- and Q-channel. Immediately after the carrier is acquired, carrier tracking commences with an initialization of the loop's numerically controlled oscillator (NCO) by using the estimated carrier frequency and phase. There are two user-specified low-pass arm filters serving as the detection filters for processing of the FQPSK-B signal. The loop filter implemented is a discrete-time low-pass filter with the following transfer function [8]

$$F(z) = G_1 + \frac{G_2}{1 - z^{-1}} + \frac{G_3}{(1 - z^{-1})^2}$$

where

$$G_1 = rd/T_u$$

$$G_2 = rd^2/T_u$$

$$G_3 = krd^3/T_u$$

and

$$d = \frac{4B_L T_u (r - k)}{r(r - k + 1)}$$

with T_u being the loop update interval in seconds, B_L being the loop bandwidth² in Hz, $r = 4\xi^2$ where ξ is the damping ratio, and k being the type III loop gain (e.g., $k = 0$ for a type II loop) with typical values ranging from 0.25 to 0.5. By specifying these parameters, a tracking loop with desired loop bandwidth can be exactly realized.

Coherent Detection

The software receiver performs coherent symbol-by-symbol hard decision separately on demodulated I-channel and Q-channel symbols. As shown in Fig. 2, this is done by sampling the

² This is the loop bandwidth by design. The actual loop bandwidth may be larger than this designed value depending on the product $B_L T_u$. Generally speaking, for $B_L T_u < 0.05$, the actual loop bandwidth is very close to the designed value.

detection filter output at proper times, presumably once at the mid-point of every symbol. Hence, the symbol clock epochs need to be established from the received signal, which is referred to as symbol synchronization. The software receiver uses a data transition tracking loop (DTTL) [9] to provide the estimated symbol timing. It takes the I-arm detection filter output as the input to its two-arm structure, with a full-symbol integration on a symbol and another full- or partial symbol integration centered at the symbol boundary. The latter provides an error signal to drive the estimated clock moving forwards or backwards when the integration window is not centered exactly at a symbol transition. The resulting I-channel symbol clock is at the mid-point of every Q-channel symbol because of the half-symbol inter-channel delay in the FQPSKB signal. It also enables mid-point sampling of I-channel symbols since these symbols get an additional half-symbol delay in the receiver.

SYSTEM OPERATION

The software receiver is composed of four different set-ups, each being represented by an operating mode in which specific application of the software receiver is addressed with its own configuration. This section provides a description of these four operation modes, namely the receiver mode, the EVM mode, and internal end-to-end BER and EVM modes.

The Receiver Mode

This is the mode in which the software receiver functions as an offline coherent receiver that demodulates, detects, and decodes the received signal. In this mode the receiver accepts input from external source without using either of its internal software transmitters. Depending upon whether the recorded input is on a carrier, the operator can turn on or off the carrier acquisition and tracking subsystems. Other receiver parameters the operator can specify include

- data (bit) rate,
- window, DFT size, and zero-padding (if used) for DFT-based carrier acquisition,
- type, order, and BT_b -product of the detection filters,
- order, damping ratio, update interval, and loop bandwidth for carrier tracking loop,
- order, damping ratio, update interval, and loop bandwidth for symbol tracking loop.

During the real-time processing, the operator can monitor the progress by looking at a sample counter showing the number of samples being processed so far, and the tracking performance by bringing up the plots of residual phase and tracking variance versus time for carrier and/or symbol tracking. Besides these real-time indicators, the receiver will store the following data:

- detected soft I-channel samples (I/Q not aligned),
- detected soft Q-channel samples (I/Q not aligned),
- detected soft I-channel samples (I/Q aligned),
- detected soft Q-channel samples (I/Q aligned), and
- decoded bits,

into separate files for post processing. The detected I/Q-channel samples are the samples obtained by sampling the demodulated I/Q signal at the estimated symbol clock epochs provided by the symbol tracking. They are ‘soft’ since they are not passed through the hard decision yet. These sample files can be used to plot phasor diagrams for demodulated symbols before or after the one-bit I/Q-channel offset is removed. The decoded bit stream is the primary product of this mode. BER calculation can be performed on it if the transmitted bit stream is available for comparison,

which requires a correlative matching process between the decoded and the source bit streams in the post processing to make them aligned.

The EVM Mode

This is the mode for hardware transmitter validation in which the signal from external hardware transmitter is demodulated, detected, and compared to the reference signal from the internal *continuous-time domain* software transmitter. The resulting error vectors provide indication of hardware problems in the transmitter under test. The set-up for EVM is divided into two sides. The reference side is a baseband end-to-end simulation system using the continuous-time domain transmitter to generate baseband FQPSK-B signal from a given periodic source bit stream used also on the test unit side. This baseband signal is then filtered by the detection filter of the software receiver, producing output samples to be saved into a reference sample file for later comparison³. On the test unit side, the same software receiver used on the reference side coherently demodulates the recorded IF signal from the hardware transmitter under test, rendering a test sample file at its detection filter output. This test samples are aligned with the reference samples by performing a correlative matching process between them. The EVM takes place at ideal symbol clock epochs that are readily available from the reference side by simply counting samples in the reference sample file.

The operator is able to specify receiver parameters other than those of detection filter, which remain fixed for both sides of EVM set-up, and get real-time performance monitoring as in the receiver mode. Two data files containing

- entire I-channel samples
- entire Q-channel samples

after the one-bit I/Q-channel offset is removed will be saved for post processing.

The EVM is done in the post processing, in which a correlative matching is performed to align the I/Q-channel sample files with the reference sample files using either I-channel or Q-channel samples and the aligned files are sampled at ideal detection times established by a sample count on the reference side to get the detected symbols. A resulting EVM file will be created, from which EVM statistics, including mean and standard deviation on magnitude and phase for all error vectors and for error vectors associated with individual symbols, are calculated and the following EVM plots:

- Constellation plot -- a plot of error vectors on the signal constellation
- Normalized plot -- a scatter plot of error vectors in the vector space
- I/Q-channel magnitude errors vs. time

can be produced. In addition to EVM, phasor diagram (only with I/Q samples aligned) is also available in the post processing,

The Internal BER Mode

This is the mode for internal BER test in which the software transmitter-receiver pair functions as an end-to-end simulation system conducting BER test under a set of user-specified conditions. It

³ Getting a valid comparison requires the reference sample file to be generated by the internal software transmitter with parameters matching those used in the hardware transmitter under test. In addition, the detection filter has to be specified for this and will also be used on the reference side.

differs from the receiver mode in the choice of signal source. In this mode, the internal discrete-time domain software transmitter is used to provide FQPSK-B signal either on a carrier or on baseband. A channel model is included in this end-to-end system. Currently, only an AWGN channel with a user-specified bit signal-to-noise ratio (SNR), denoted by E_b/N_o , is provided. More sophisticated channel models, including frequency selective multiple-way fading channel, can be easily added later.

The operator can specify transmitter parameters such as

- data (bit) rate -- may include an offset,
- carrier frequency -- may include an offset,
- carrier phase,
- type, order, and BT_b -product of the transmission filters,
- source bit stream from a file or a noise seed if internal binary random number generator is used to generate source bit stream,

the channel parameter, E_b/N_o , and the receiver parameters such as

- data (bit) rate,
- window, DFT size, and zero-padding (if used) for DFT-based carrier acquisition,
- type, order, and BT_b -product of the detection filters,
- order, damping ratio, update interval, and loop bandwidth for carrier tracking loop,
- order, damping ratio, update interval, and loop bandwidth for symbol tracking loop.

Furthermore, the discrete-time domain transmitter is capable of accommodating modulator imbalances such as inter-channel amplitude and phase imbalances and I- and Q-channel dc biases, which allows the effect of modulator imbalances to be included with an end-to-end simulation.

The operation in this mode is all real-time. As previous two modes, an operator is able to get real-time performance monitoring, including a BER counter showing coded and uncoded error performance.

The Internal EVM Mode

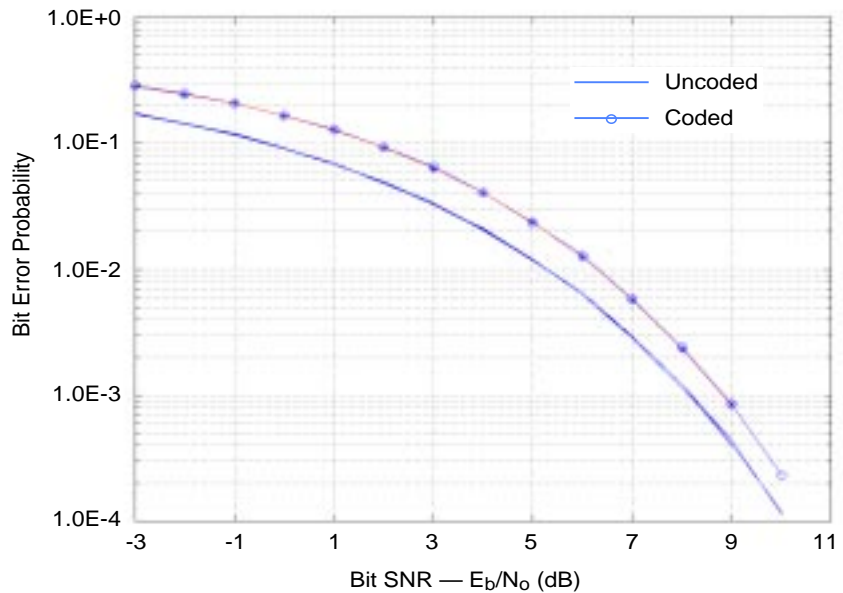
This is the mode for internal EVM test in which two software transmitter-receiver pairs form an end-to-end simulation system conducting EVM test under a set of user-specified conditions. Like the EVM test for external hardware transmitters, the two software transmitter-receiver pairs in the internal EVM test set-up constitute two sides: one for the reference and the other for the test unit. However, in this internal mode, the discrete-time domain software transmitter provides both the baseband signal for the reference side and the modulated signal for the test unit side. Both sides are synchronized so that EVM calculation can be performed in real-time without the need of a post-processing correlation to align signals from both sides. This set-up is intended for simulations to see the effect of (i) user-specified modulator imbalances added to the test unit, (ii) mismatched transmission filters, and (iii) receiver's demodulation and synchronization processing on the EVM results.

During the simulation an operator is able to get real-time performance monitoring, including selected EVM plots. The EVM statistics will be reported at the end of simulation.

EXAMPLES

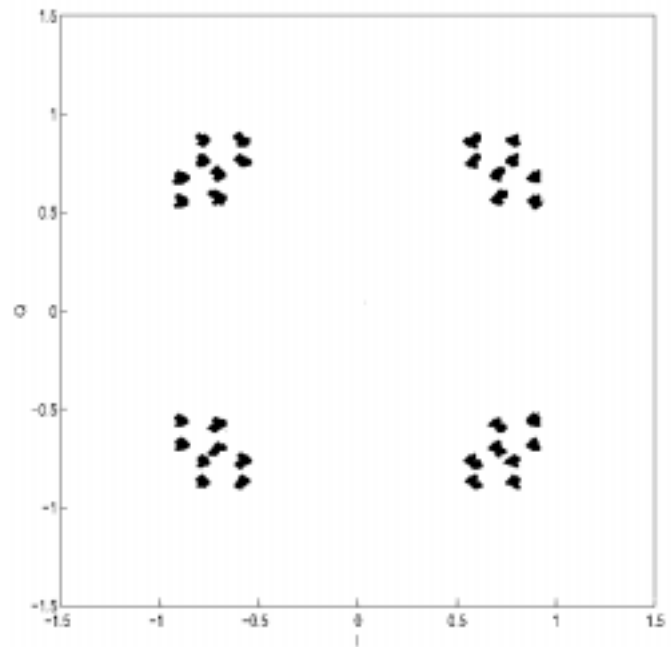
The Bit Error Performance

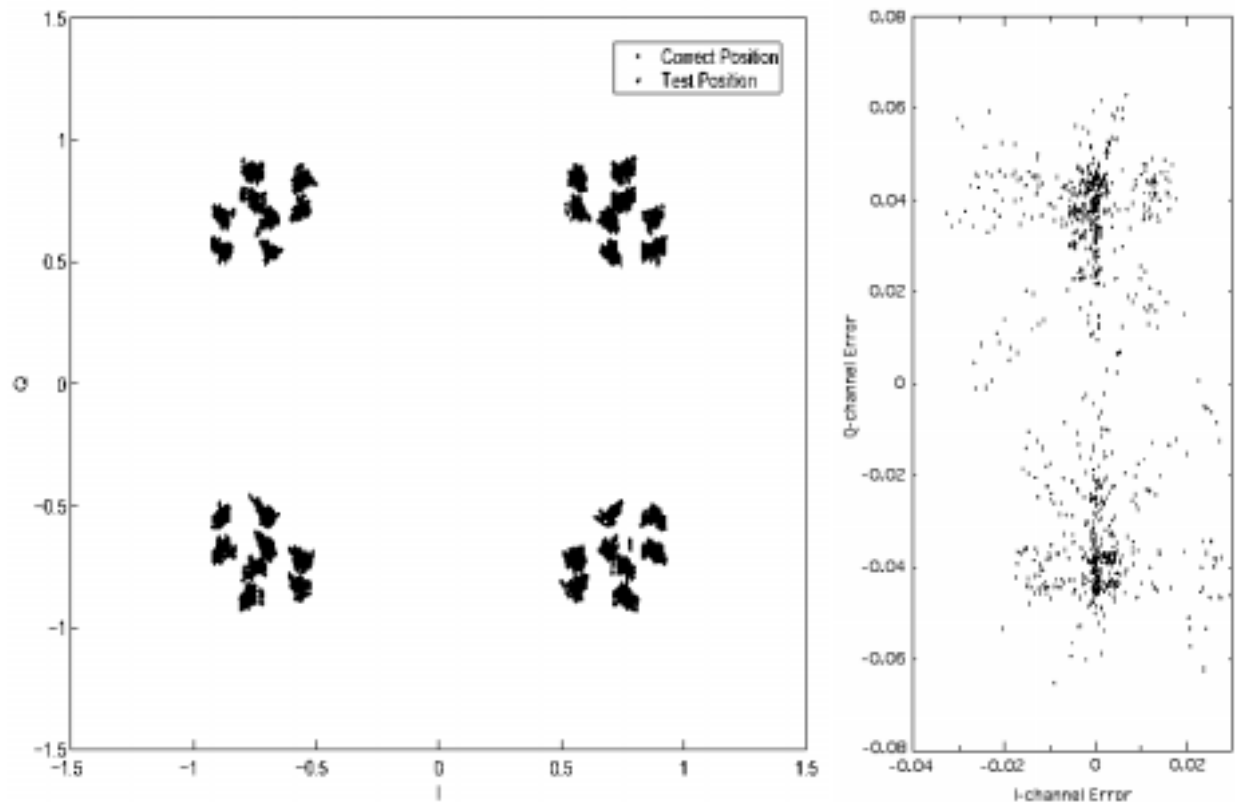
This example shows the bit error performance for a baseband end-to-end system operated in the internal BER mode. Both coded and uncoded BER curves are shown here for bit SNR, E_b/N_o , from -3 to 10 dB. The uncoded BER curve agrees well with the one reported in [10]. As shown here, the degradation caused by differential encoding/decoding is about 0.63 dB at $\text{BER}=0.001$. Simulation results obtained for systems including carrier and symbol tracking show no significant differences compared to these baseband curves, as long as sufficient loop SNRs are maintained.



The EVM test

This example shows the results of an internal EVM test. The phasor diagram to the right is a constellation plot of the perfectly detected (reference) symbols from the receiver after the one-bit I/Q-channel offset is removed. In each quadrant, the corresponding FQPSK-B symbols form a distinct eight-cluster pattern. In the test unit, an amplitude imbalance is deliberately introduced to the Q-channel, making the amplitude of Q-channel symbols 5% smaller than that of I-channel symbols. After demodulation and detection, the error vectors are calculated by comparing both symbol streams symbol by symbol. In the following, two EVM plots are presented as an example. The constellation plot is the figure to the left in which each error vector is represented by an arrow pointing out from its corresponding reference symbol in the phasor diagram, while the normalized plot is the figure to the right that shows a scatter plot of end point of each error vector in a vector space. It is clearly indicated in these EVM plots that the amplitude imbalance exists in the transmitter under test by showing most arrows pointing roughly along the Q-channel direction in the constellation plot and a two-cluster distribution with an average separation approximately equal to 0.04 in the normalized plot.





CONCLUSION

This paper presents the design and development of an off-line coherent FQPSK-B software reference receiver capable of being used for hardware validation and for advance technology development and demonstration. This Matlab/Simulink-based software receiver also includes end-to-end simulations that help a system design to meet certain performance goals. Because of its ease of use and versatility in flexible configurations for various tasks and even for other types of QPSK modulation, this software receiver provides a cost-effective approach with cross-platform compatibility for study, design and development of a quadrature-modulated communication system.

Currently, the software receiver is being modified to accommodate future studies include a frequency selective dynamic fading channel model and various equalizer techniques for mitigating the mobile fading effects.

REFERENCES

- [1] K. Feher et al.: US Patents 4,567,602; 4,644,565; 5,491,457; and 5,784,402, post-patent improvements and other U.S. and international patents pending.
- [2] "FQPSK-B, Revision A1," Digcom-Feher Patented Technology Transfer Document, Digcom Inc., January 15, 1999.
- [3] "IRIG Standard 106-00: Telemetry Standards," Telemetry Group, Range Commanders Council, U.S. Army White Sands Missile Range, New Mexico, January 2000.

- [4] M. K. Simon and T.-Y. Yan, "Cross-correlated Trellis Coded Quadrature Modulation," U.S. patents pending.
- [5] H. Tsou, "The Combined Effect of Modulator Imbalances and Amplifier Nonlinearity on the Performance of Offset Quadrature-Phase-Shift-Keyed (OQPSK) Systems," *The TMO Progress Report 42-137*, Jet Propulsion Laboratory, Pasadena, California, May 15, 1999.
- [6] W. B. Davenport, Jr. and W. L. Root, *An Introduction to the theory of Random Signals and Noise*, McGraw-Hill, New York, 1958.
- [7] M. K. Simon, "On the Optimality of the MAP estimation Loop for Carrier Phase Tracking BPSK and QPSK Signals," *IEEE Trans. on Communications*, vol. COM-27, No. 1, January 1979.
- [8] A. Blanchard, *Phase-Locked Loops: Application to Coherent Receiver Design*, John Wiley & Sons, Inc., New York, 1976.
- [9] W. C. Lindsey and M. K. Simon, *Telecommunication Systems Engineering*, Prentice-Hall, Englewood Cliffs, New Jersey, 1973.
- [10] T.-Y. Yan, *Advanced Range Telemetry Task Interim Report*, Jet Propulsion Laboratory, Pasadena, California, February 1999.

[This page intentionally left blank.]

Bit Error Performance of GMSK, FQPSK-B, SRRC OQPSK, and Butterworth Filtered OQPSK with Block V Receiver

Dennis Lee, Jim Weese, Warren Martin, and Tsun-Yee Yan
Jet Propulsion Laboratory
California Institute of Technology
Pasadena, CA 91109

October 18, 2000

1 Abstract

In response to action item 00-1E-11, this paper examines the bit error performance of four selected bandwidth efficient modulations (BEMs) using an existing DSN demodulatorL. The BEMs, namely GMSK¹, Square Root Raised Cosine OQPSK², FQPSK-B³, and filtered OQPSK⁴, are generated at 10 Mbps using an FPGA. The modulations are upconverted 70 MHz IF and then to 8430 MHz RF where it is amplified by an X-band SSPA. The RF signal is then downconverted and demodulated with the Block V receiver (BVR) which is currently used in the majority of Deep Space ground stations. The spectra of the linearly amplified BEMs at 70 MHz IF and at RF after the SSPA are shown along with the bit error rate measurements obtained with the BVR. In addition, simulated cross-modulation BER performance curves using receivers optimized for each of the modulations are also given.

2 Introduction

At the May 2000 CCSDS Panel 1E meeting, action item 00-1E-11 was issued to investigate the bit error performance of existing demodulators when supporting GMSK, filtered OQPSK, SRRC OQPSK, and FQPSK-B. The aim of this action item was to determine which, if any, of these BEMs are compatible with existing ground station receivers, thus reducing the cost of supporting these modulations.

This study was divided into three parts. First, computer simulations were performed to see if using an OQPSK receiver to demodulate these modulation was possible. Secondly, a modulator had to be built which could output GMSK, FQPSK, SRRC OQPSK, and filtered OQPSK at a sufficiently high rates. Finally, a receiver similar to ones used at the Deep Space ground station had to be obtained and bit error measurements conducted using the BEM modulator.

¹Pre-coded GMSK $BT_b=0.25$

²roll-off factor $\alpha = 0.5$

³Feher-patented QPSK

⁴4th order Butterworth filter, $BT_s=1.0$

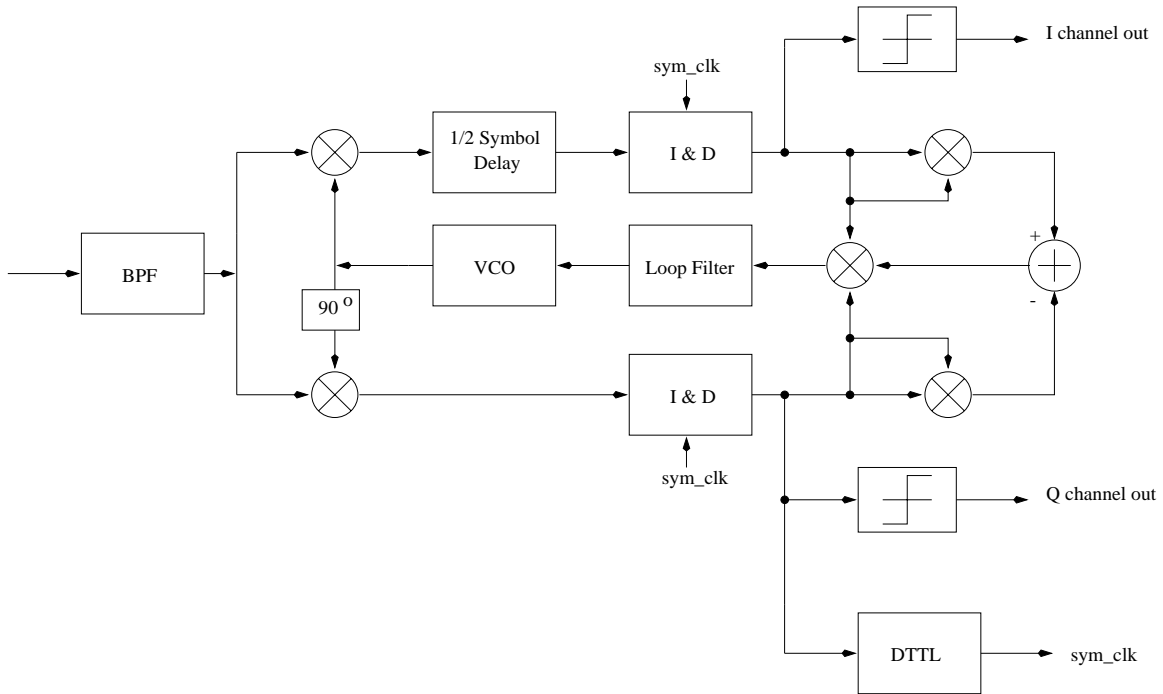


Figure 1: Block diagram of simulated OQPSK receiver

3 Simulation Results

Computer simulations were performed using a conventional OQPSK receiver to demodulate GMSK, SRRC OQPSK, FQPSK-B and Butterworth filtered OQPSK. A block diagram of the simulated receiver is shown in Figure 1. The carrier tracking is done with a crossover Costas loop, and the symbol tracking is done with a DTTL. The simulations were performed using Signal Processing WorkSystem (SPW) software.

Figure 2 shows the simulated bit error rates for the four BEMs over a fully saturated SSPA using the receiver shown in Figure 1. At 10^{-3} BER, Butterworth filtered OQPSK with $BT_s = 1.0$ has the least degradation using an OQPSK receiver, approximately 0.6 dB E_b/N_o with respect to ideal BPSK. GMSK $BT_b = 0.25$ is 1.2 dB from ideal BPSK at the same BER, and FQPSK-B is a 2.4 dB away at 10^{-3} BER using an OQPSK receiver. However, by modifying the detection filter, the performance of GMSK and FQPSK-B can be improved by 0.9 dB and 1.4 dB, respectively, at 10^{-3} BER. SRRC OQPSK has a 1.1 dB E_b/N_o loss with respect to ideal BPSK.

Additional simulations were run using receivers optimized for each of the modulations to determine if they could also support the other modulations. The simulation results, which shown in the Appendix, indicate that these receivers can also support the other modulations.

4 Design of Modulator

In order to generate bit error rate measurements, a modulator had to be built which could generate each of the efficient modulations. A simple solution was created which could produce all four modulation types at up to 10 Mbps, and possibly even 20 Mbps. A field programmable gate array (FPGA) device was programmed to generate different baseband waveforms using a lookup table.

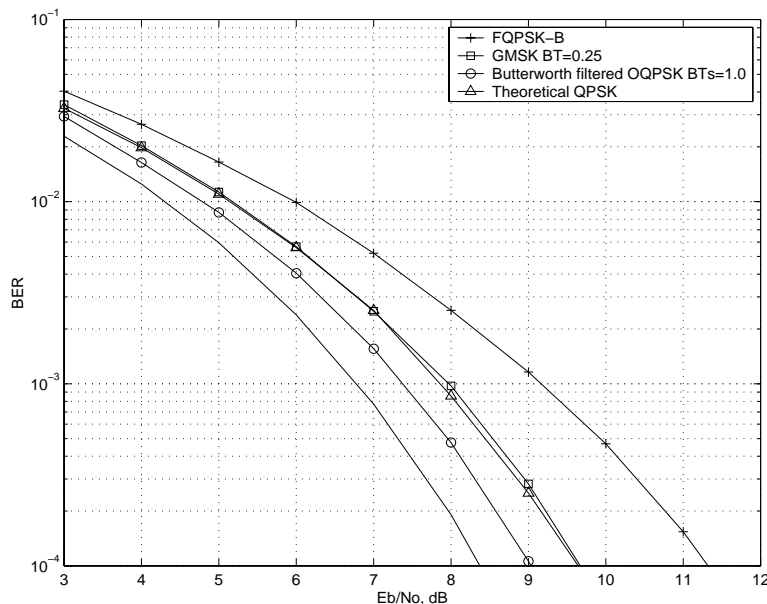


Figure 2: Simulated BER using OQPSK receiver

Figure 3 shows a block diagram of the waveform generator design, in this case for GMSK.

A shift register is used to store the incoming data bits. The values of the preceding and following bits are used to determine the total ISI contribution. The length of the shift register and the number of stored waveforms depended on the number of ISI bits that needed to generate a sufficiently close approximation to the actual signal. Since both the Gaussian filter and SRRC filter have an infinite impulse response, an infinite number of waveforms are needed to exactly duplicate the original signal. However, a close approximation can be obtained considering only 5 bits (the current bit and the two preceding bits and two following bits). The difference between the finite impulse response approximation and the actual GMSK and SRRC OQPSK signal is small, and vanishes if both signals are quantized. The two lookup tables are actually identical, with one whose values are shifted by 4 samples. If space is a premium on the FPGA, only one table is needed if a delayed version of the 3-bit sample counter is used for the Q channel outputs. For SRRC OQPSK and Butterworth filtered OQPSK, the I and Q channel outputs are independent, so two separate parallel shift registers were used.

Butterworth filtered OQPSK required only distinct two waveforms (i.e., plain OQPSK) since the Butterworth filtering could be performed by the filter after the DAC which is needed to smooth the waveforms and remove aliasing. FQPSK-B required 16 waveforms, while GMSK and SRRC OQPSK both required 32 waveforms. These numbers could have been cut in half by noting the symmetry of the waveforms about zero and storing just the positive signed waveforms. Another reduction by a factor of two could have been made by storing only the first half of the waveform, taking advantage of the symmetry in time. However, since there was plenty of room in the FPGA (Altera FLEX10k100A has 100,000 gates), all the possible waveforms were stored. Figure 4 shows the values of the quantized waveforms used for GMSK.

The GMSK modulator in Figure 3 is slightly different from the Gaussian filter/accumulator/VCO approach [5] or the Gaussian filter/accumulator/cosine-sine table approach [1] commonly used. It only uses a lookup table with no preprocessing other than a shift register to store previous values.

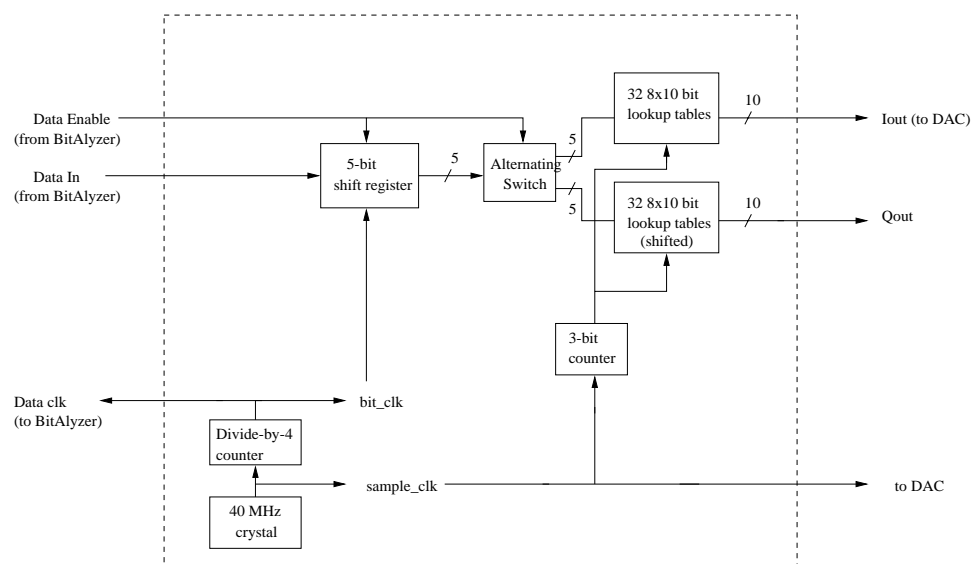


Figure 3: FPGA block diagram for GMSK waveform generator

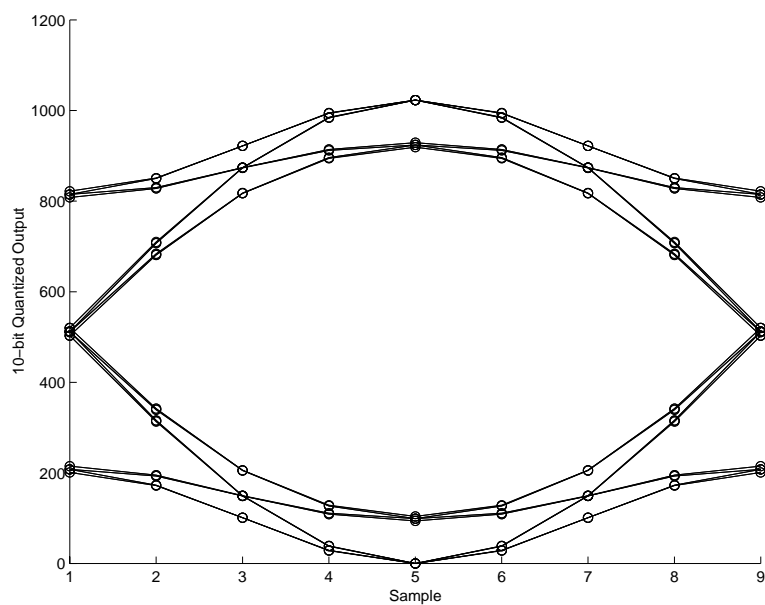


Figure 4: GMSK waveforms

Precoding has also been accounted for in the waveforms. There is no need for accumulators or digital filtering. This should lead to a smaller, more efficient implementation of GMSK with potentially higher maximum data rates for values of BT_b greater than 0.25. For very small values of BT , the number of waveforms starts to become prohibitive. In addition, a large number of quantization levels are required.

The output of the FPGA consisted of two 10-bit values of the I and Q channel waveform samples. Ten bit quantization was used because of the DAC which was readily available. In reality, a 8-bit DAC and possibly smaller could be used without adversely affecting performance. With coarser quantization, memory requirements would be reduced.

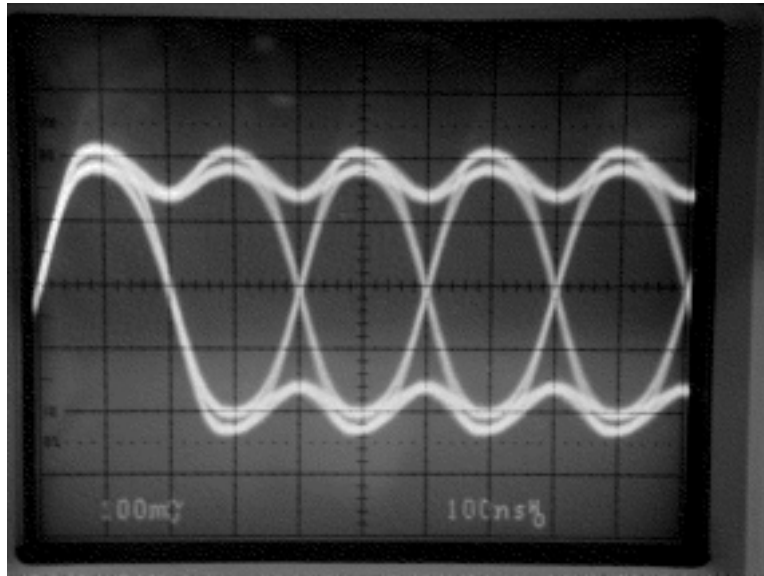


Figure 5: GMSK eye diagram

4.1 Measured Eye Diagrams

The FPGA was clocked at 40 MHz, with 8 samples per symbol. The I and Q channels each produced 5 Msym/s for a total of 10 Mbps. Further tests may be performed using only 4 samples per symbol which would double the maximum rate to 20 Mbps and halve the lookup table size. A 4th order Butterworth low pass filter was placed after the DAC to smooth the output of the DAC and to remove aliasing. Figures 5, 6, 7, and 8 show the eye diagrams of GMSK, FQPSK-B, SRRC OQPSK, and Butterworth filtered OQPSK, respectively, after the low pass filter.

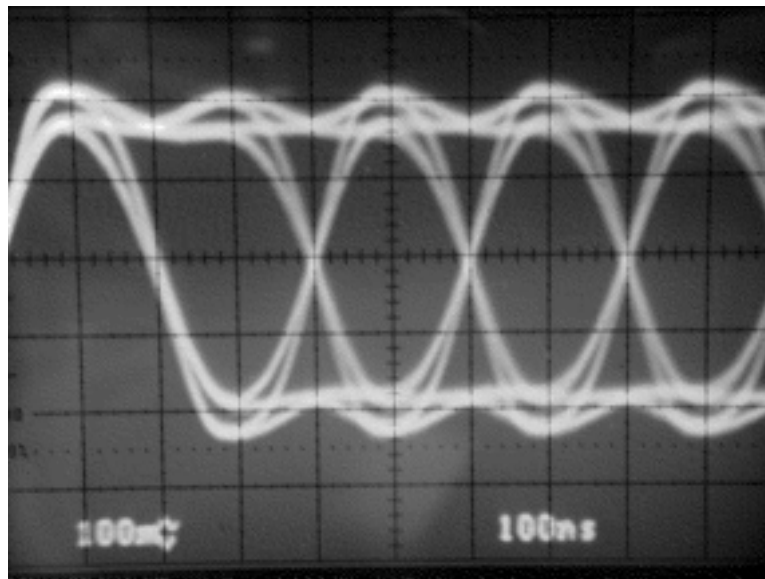


Figure 6: FQPSK-B eye diagram

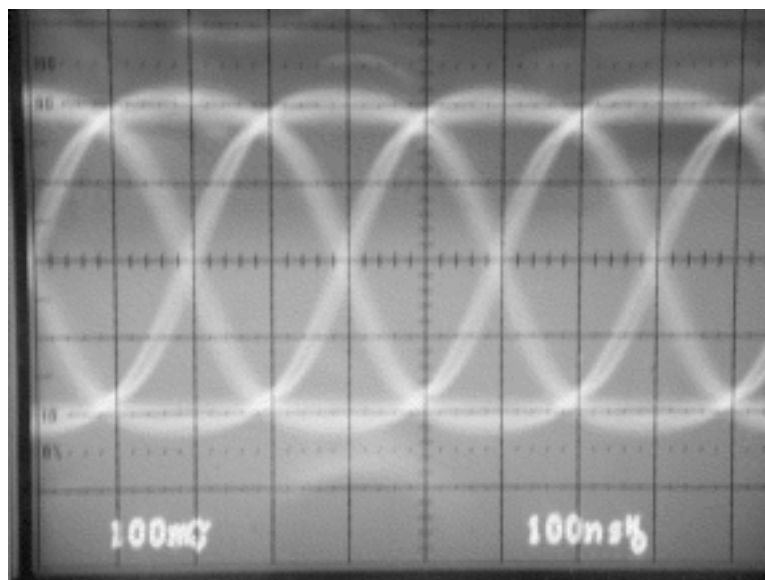


Figure 7: SRRC OQPSK eye diagram

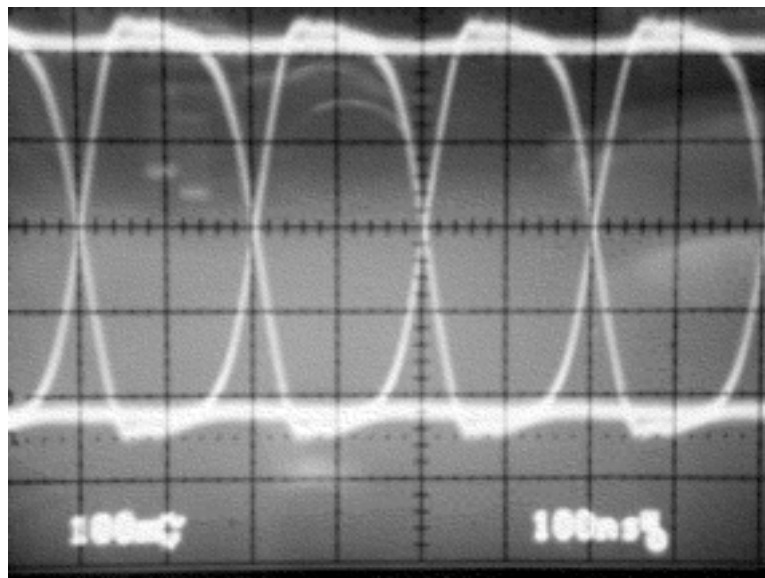


Figure 8: Butterworth filtered OQPSK eye diagram

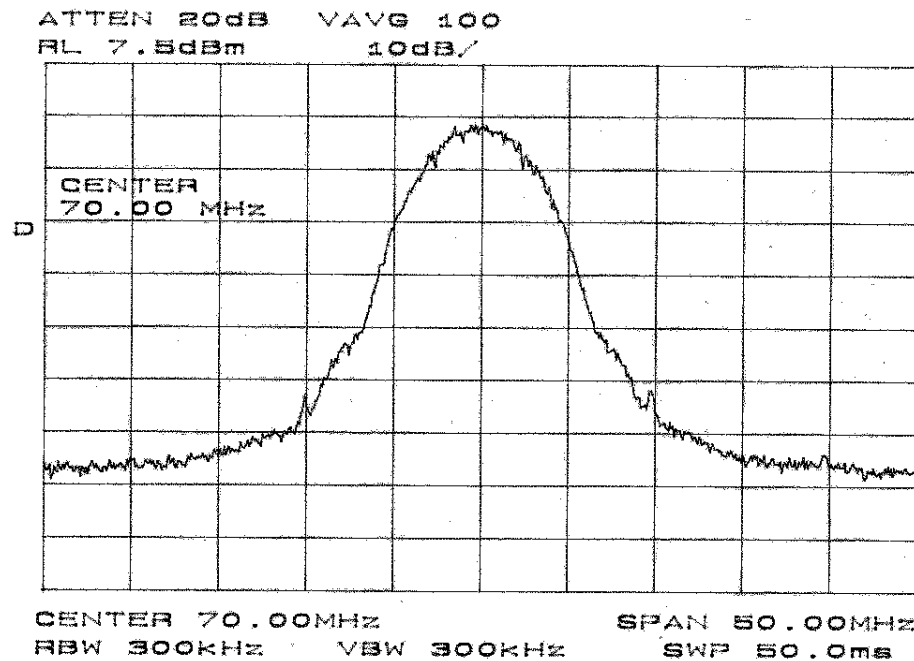


Figure 10: GMSK spectrum, linear

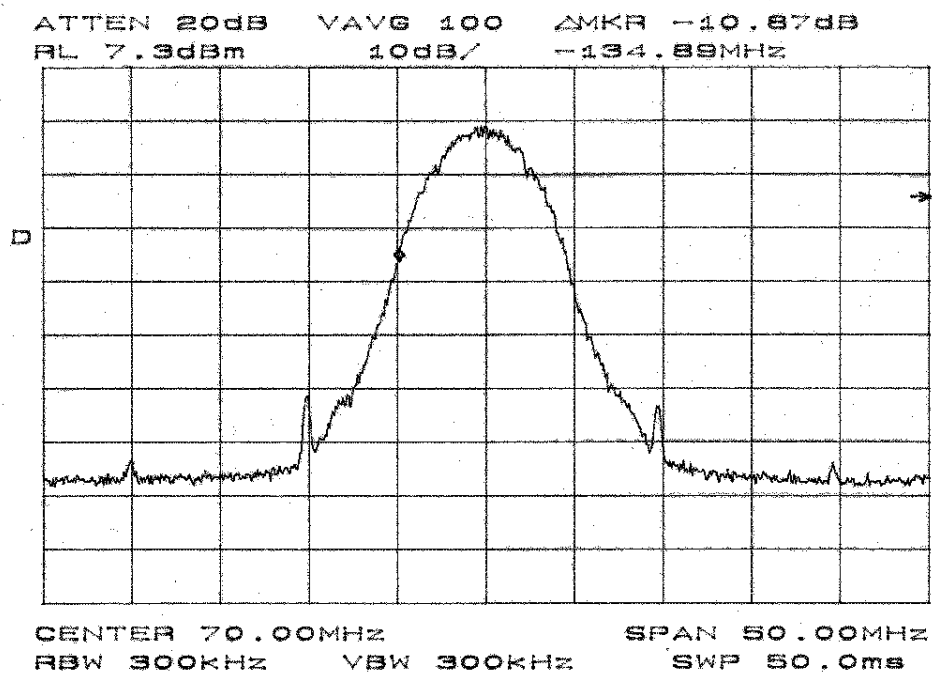


Figure 11: FQPSK-B spectrum, linear

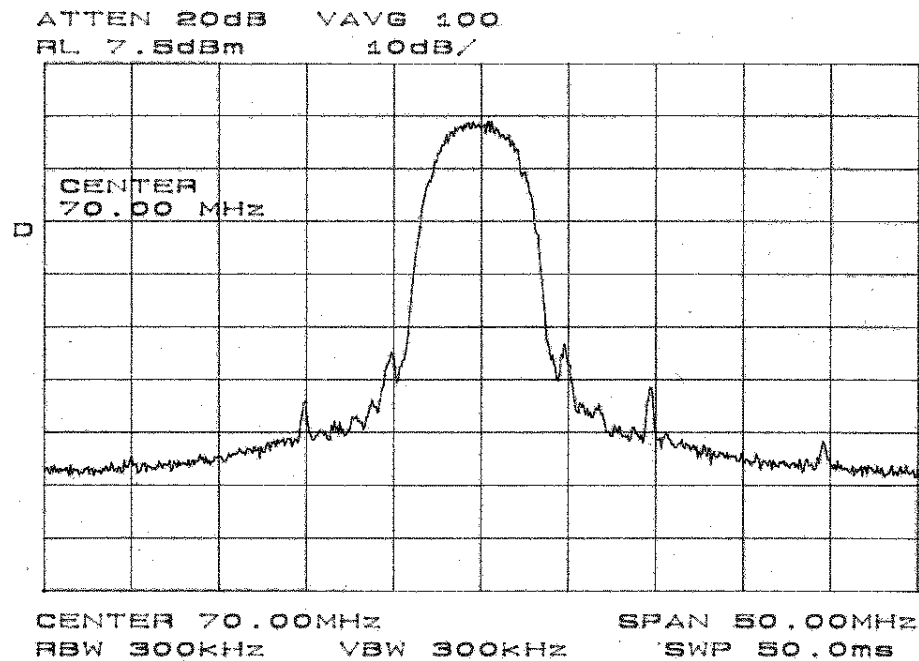


Figure 12: SRRC OQPSK spectrum, linear

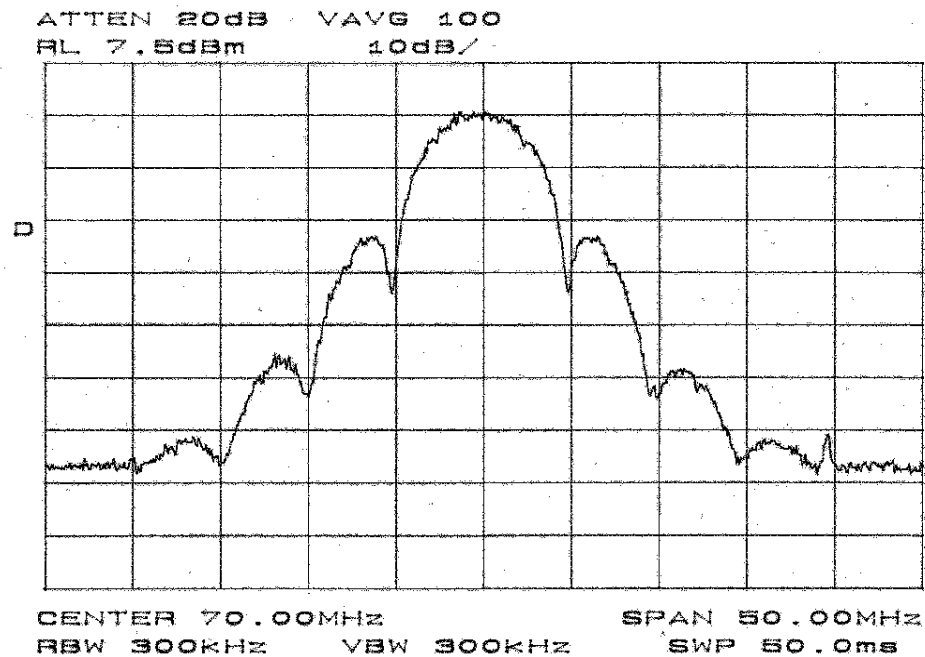


Figure 13: Butterworth filtered OQPSK spectrum, linear

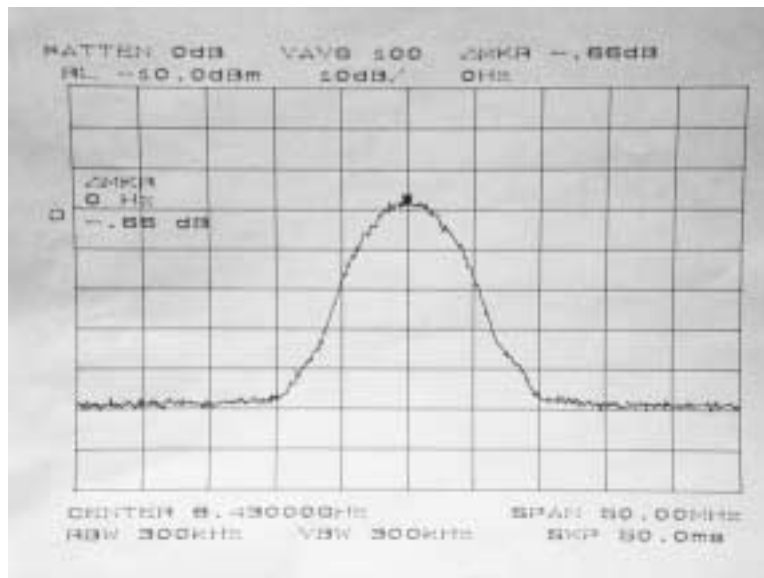


Figure 14: GMSK spectrum following saturated SSPA

4.3 Measured Non-Linearly Amplified Spectrum

The spectrum of the signals after the X-band power amplifier was also measured. Figures 14, 15, 16, and 17 show the spectra of non-linearly amplified GMSK, FQPSK-B, SRRC OQPSK, and Butterworth filtered OQPSK, respectively. Note that Butterworth filtered OQPSK and SRRC OQPSK have considerable spectral regrowth even at the 1 dB compression point while FQPSK-B and GMSK have minimal regrowth.

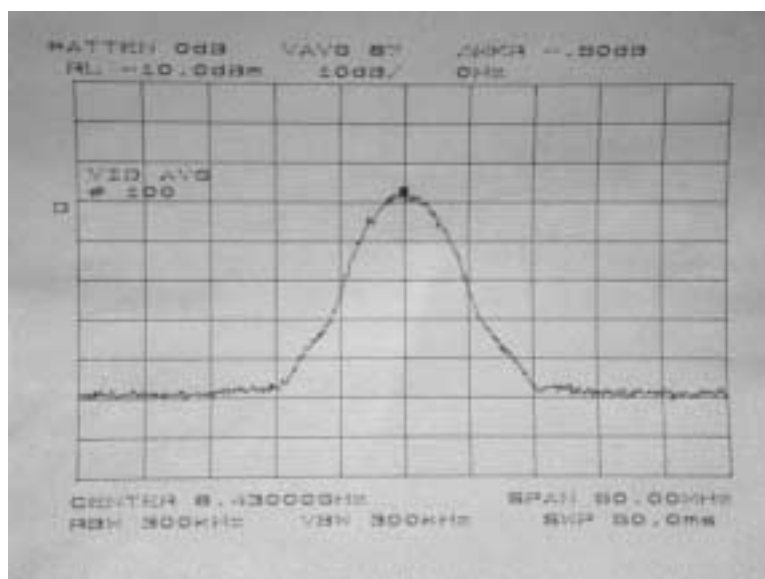


Figure 15: FQPSK-B spectrum following saturated SSPA

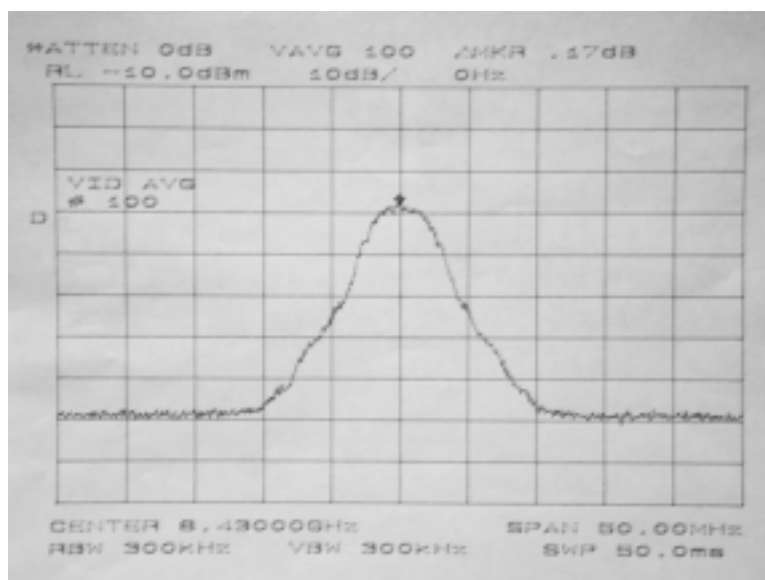


Figure 16: SRRC OQPSK spectrum following saturated SSPA

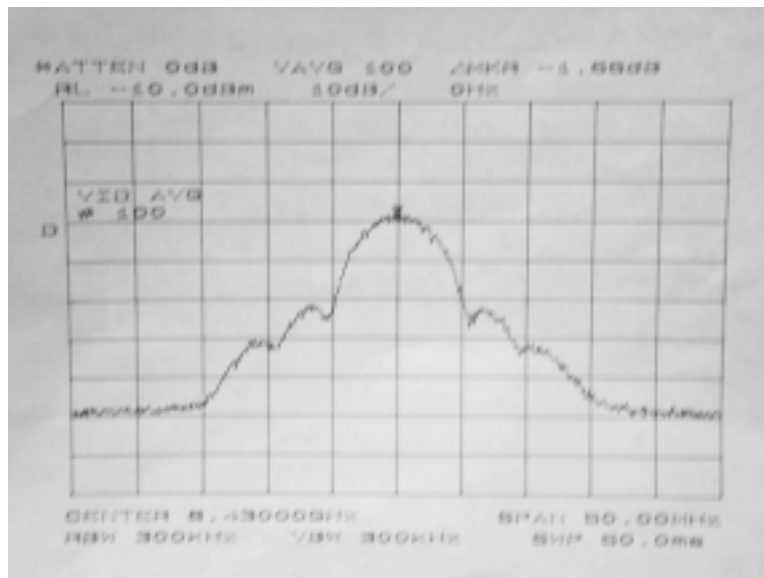


Figure 17: Butterworth filtered OQPSK spectrum following saturated SSPA

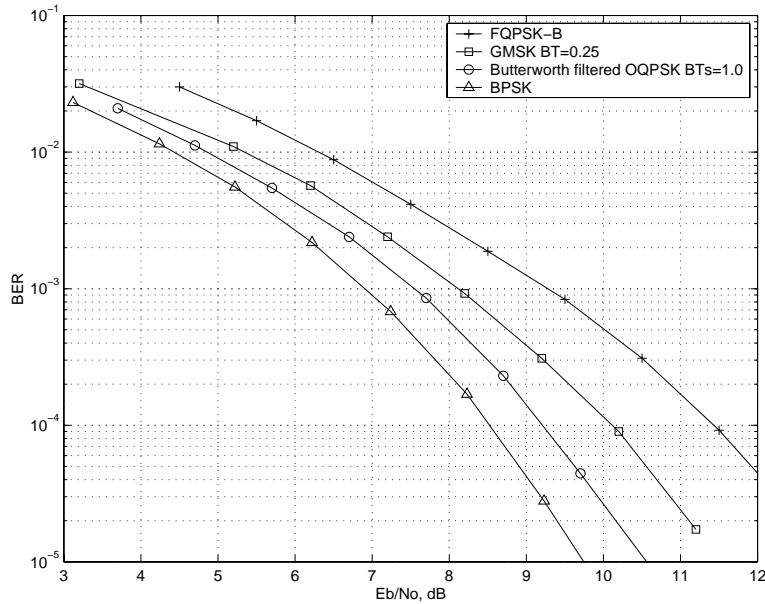


Figure 18: Measured BER using BVR

5 Bit error measurements using Block V Receiver

The majority of Deep Space ground stations currently use the Block V receiver (BVR). The BVR [3] is capable of demodulating BPSK, QPSK, and OQPSK signals and supports fully suppressed carrier modulations. As the BEMs under consideration are inherently OQPSK modulations (i.e., offset I and Q modulations), the ability to demodulate OQPSK is necessary. The BVR is a custom digital design which can handle data rates up to 26 Msps and provide very narrow carrier and symbol tracking loop bandwidths. Carrier acquisition is performed using an FFT. Further tests will be conducted using a commercial OQPSK receiver from Microdyne to determine if other OQPSK receivers can also demodulate these efficient modulations.

Figure 18 shows the measured BER using the Block V receiver to demodulate GMSK, FQPSK-B, SRRC OQPSK, and filtered OQPSK. The measured BER performance of BPSK using the BVR is also shown as a reference. The measured results in the Figure are very close to the simulation results, within 0.2 dB. This is partly because of the narrow loop bandwidths (30 Hz for the carrier tracking loop and 100 Hz for the symbol tracking loop) made possible by the digital implementation of the Block V carrier tracking loop, and the absence of Doppler and other channel imperfections. Additional tests are needed to quantify the effects of a real channel. Butterworth filtered OQPSK had the least BER degradation using the BVR, approximately 0.6 dB E_b/N_o from measured BPSK at 10^{-3} BER. GMSK is approximately 1.25 dB worse than measured BPSK at 10^{-3} BER, while FQPSK-B is 2.4 dB worse using the BVR.

6 Summary

A modulator was built using an FPGA to generate baseband waveforms of GMSK, FQPSK-B, SRRC OQPSK, and Butterworth filtered OQPSK at 10 Mbps. Spectrum measurements of the generated BEMs were taken before and after non-linear amplification. The generated signals were

transmitted at 8430 MHz and demodulated using the JPL Block V receiver which is used in the majority of Deep Space ground stations. Measured bit error rates indicate that GMSK, FQPSK-B, and Butterworth filtered OQPSK can all be received with an OQPSK receiver. Additional tests are planned using a commercially available receiver.

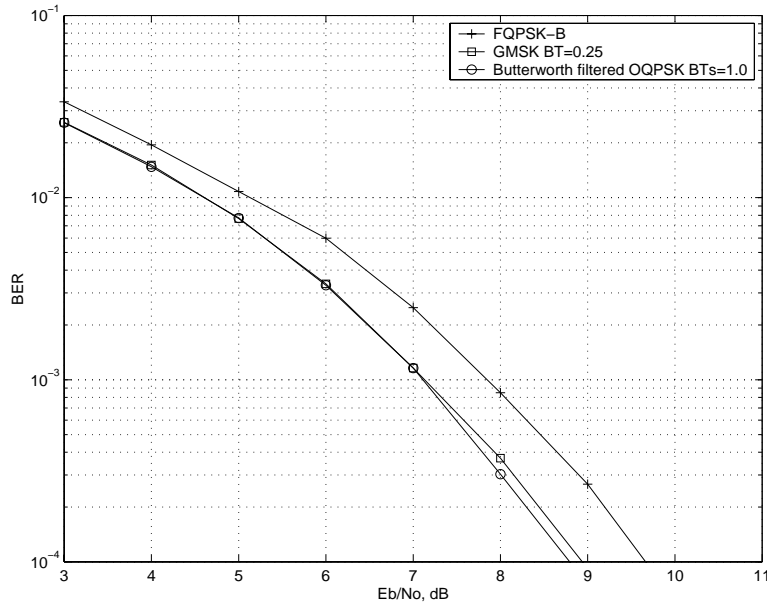


Figure 19: Simulated BER using GMSK receiver

7 Appendix

Computer simulations were also performed to determine if receivers with detection filters optimized for one of the BEMs would also be support the other modulations. The receiver used in the simulations is identical to the one shown in Figure 1 except the integrate-and-dump filter is replaced by a filter optimized to the modulation waveform [2]. These detection filters are chosen to give near optimal performance for symbol-by-symbol detection (i.e., no Viterbi-type receivers). For GMSK, the detection filter is matched to the first component of the Laurent decomposition of GMSK cascaded with a 3-tap Wiener filter [4]. For FQPSK-B, the proprietary FQPSK-B filter is used. For Butterworth filtered OQPSK, the detection filter is a Butterworth filter followed by an integrate-and-dump.

The simulations are performed over a saturated SSPA using SPW software. Figure 19 shows the bit error rates using the GMSK receiver to demodulate the efficient modulations. An interesting point is that the FQPSK-B performs better using the GMSK detection filter than with the proprietary FQPSK-B filter. This is due to the Wiener filter in the GMSK detection filter which serves to cancel some of the ISI even in some of the other modulations.

Figure 20 shows the simulated results using a FQPSK-B receiver to demodulate the other modulations. Simulated results using a Butterworth filtered OQPSK receiver are shown in Figure 21.

Table 1 is a crosstable summarizing the simulated E_b/N_o required for 10^{-3} BER using GMSK, FQPSK-B, and Butterworth filtered OQPSK with a receiver optimized to one of the efficient modulations. In the table, the receiver type is given by the first column and the transmitted modulation is given by the first row.

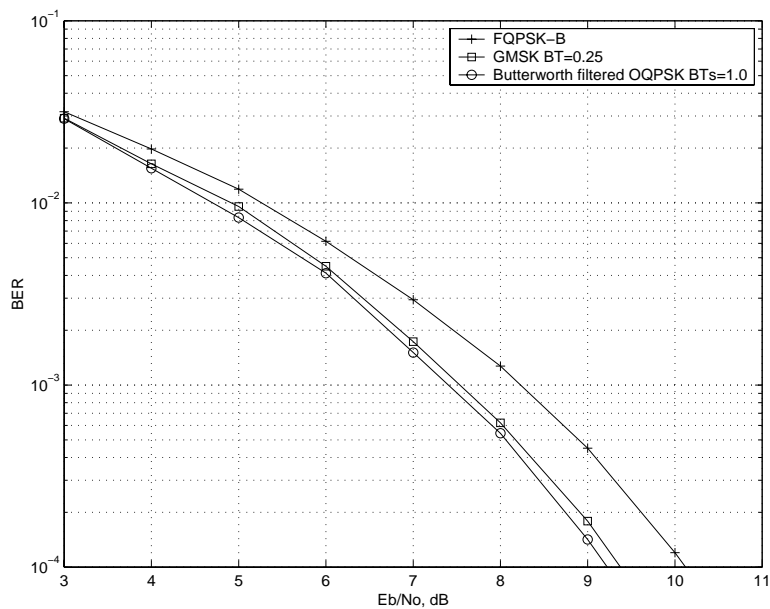


Figure 20: Simulated BER using FQPSK-B receiver

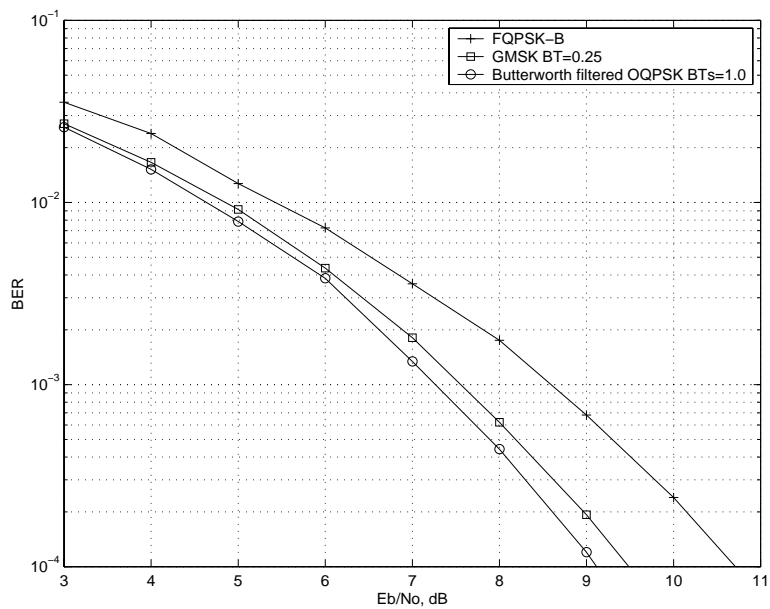


Figure 21: Simulated BER using Butterworth filtered OQPSK receiver

Table 1: Required E_b/N_o for 10^{-3} BER

Receive	Transmit		
	GMSK	FQPSK-B	Filtered OQPSK
GMSK	7.1 dB	7.8 dB	7.1 dB
FQPSK-B	7.5 dB	8.2 dB	7.5 dB
Filtered OQPSK	7.5 dB	8.6 dB	7.3 dB
OQPSK	8.0 dB	9.2 dB	7.4 dB

References

- [1] C. Barrieres and E. Tonello, "Study of GMSK modulator", presented at Oct 1999 CCSDS Panel 1E meeting.
- [2] D. Lee and T.-Y. Yan, "Performance of Selected Bandwidth Efficient Modulations", CCSDS Panel 1E meeting, October 1999.
- [3] P.W. Kinman, "TLM-21 DSN Telemetry System, Block-V Receiver", 810-5 Rev. D, vol 1, December 1996.
- [4] G.K. Kaleh, "Simple coherent receivers for partial response continuous phase modulations," IEEE Transactions on Select. Areas in Comm., vol. 7, no. 9, December 1989, pp. 1427-1436.
- [5] K. Murota and K. Hirade, "GMSK Modulation for Digital Mobile Radio Telephony", IEEE Transactions on Communications, Vol. Com-29, No. 7, July 1981.

CCSDS Panel 1E**Document 99/48****NASA GSFC STUDY
ON THE IMPACT OF SFCG REC17-2R1 SPECTRUM MASK
ON SPACE SCIENCE SERVICES SPACE-TO-EARTH LINKS****National Aeronautics and Space Administration
(NASA)****1. Introduction**

The SFCG has recommended that space science projects starting after the year 2001 comply with an emitted spectrum mask for space-to-earth data transmission in the bands 2200-2290 MHz, 2290-2300 MHz, 8025-8400 MHz, and 8400-8500 MHz. In order to comply with the recommendation, transmitters must limit out-of-band emissions. Two methods of accomplishing this are post power amplifier output filtering and use of a bandwidth efficient modulation technique. SFCG has conducted several studies to assess the spectrum and power requirements for several candidate modulation methods [1, 2, 3]. In these studies it was determined that post power amplifier output filtering was impractical because of the size and insertion loss associated with RF output filtering. Several bandwidth efficient modulation techniques were studied in [1, 2, 3]. Typically, these techniques allow transmission with a more narrow spectrum at the cost of additional transmit power required to achieve the same BER performance.

At SFCG 18, recommendation 17-2R1 was adopted. Action item 18-17 was assigned to J-L. Gerner of ESA with contributions from NASA and others to perform additional studies on the candidate modulation methods to determine the interference susceptibility. There is also a desire by NASA GSFC to more accurately characterize the power requirements for Earth Science and Space science missions by accounting for the impact of transmitter distortions on end-to-end performance. The purpose of this study is to assess the additional power required for several bandwidth efficient modulation techniques while accounting for signal distortions caused by the transmitter hardware. The results of this study can then be used to assess the impact of compliance with SFCG Rec 17-2R1 to GSFC missions. SFCG Rec. 17-2R1 recommends two spectral masks one for symbol rates lower than 2 Mbps and a tighter mask for symbol rates higher than 2 Mbps. Rec 17-2R1 states that the masks are not applicable to spurious emissions[1]. However, it is not clear whether the masks are applicable to the spectral line components due to the modulation process, such as line components due to data asymmetry. In

this study, the continuous spectrum and line components are compared with the masks separately.

This study will compute the emitted spectrum, implementation loss and interference susceptibility for filtered OQPSK and GMSK modulation techniques. Implementation loss will be determined by BER simulations that include the transmitter model, an additive white Gaussian noise channel and a ground terminal receiver model. The simulation will estimate the BER vs. E_b/N_0 performance. The implementation loss is defined as the difference between the E_b/N_0 required for 10^{-3} and 10^{-5} BER in the simulation and the theoretical required E_b/N_0 . The implementation loss translates into additional transmit power required to achieve the desired BER. The difference between the implementation loss for each modulation technique and that for BPSK will demonstrate the link budget cost of compliance with SFCG Rec 17-2R1.

Interference susceptibility will be determined by BER simulations similar to implementation loss simulations with the addition of an interference signal added to the desired signal plus thermal noise. The simulations will determine the interference signal level required to cause an additional 1-dB degradation in BER vs E_b/N_0 performance. Two types of interference will be analyzed: narrowband, modeled as a tone, and wideband, modeled as bandlimited noise.

The study will include transmitter distortions typical to X-band and S-band space-to-ground transmitters used for GSFC missions.

Filtered OQPSK modulations will include Butterworth and Square Root Raised Cosine (SRRC) filters with various bandwidths. Bandwidth will be defined relative to the channel symbol rate using the parameter BT s, where B is the filter two-sided bandwidth and T_s is the channel symbol period. Two implementations of OQPSK modulation will be studied: OQPSK with an I/Q modulator and OQPSK with a linear phase modulator, referred to as OQPSK/PM. Filtered OQPSK with an I/Q modulator filters the I and Q channel NRZ data signals and multiplies the filtered signals with in-phase and quadrature carrier signals. The OQPSK/PM signal is formed by mapping the I and Q NRZ data to a QPSK phase signal, filtering the phase signal and phase modulating a carrier with the filtered phase signal. GMSK modulation will be assessed with $BT = 0.5$ and $BT = 1.0$.

Interference susceptibility will be assessed for narrowband interference centered at two fixed frequencies and wideband interference.

The study will address performance with three transmitter power amplifier operating points: saturation, 1-dB output back-off, and linear operation. The operation with PA in saturation is typically the most power efficient and for this reason is most desirable by mission designers. Additional implementation loss will require additional transmit EIRP. For a non-saturated power amplifier additional DC power is required to achieve the EIRP. These factors contribute to the cost of the spacecraft of complying with the SFCG spectral mask. Additional cost may also be needed to modify the ground terminal receiver. The ground terminal receiver used in this study is an OQPSK type demodulator with integrate and dump, symbol by symbol detection. This receiver is optimum for unfiltered OQPSK but is not optimized for filtered OQPSK or GMSK. To optimize the receiver for these modulation techniques, detection filters must be matched to the transmitted signal pulse shape. The implementation loss and interference susceptibility results apply to the suboptimum receiver. The results represent the performance achievable with ground equipment of the same complexity of that currently used in NASA ground terminals.

The standard OQPSK demodulator must be modified to receive GMSK signal properly but still used an integrate and dump detector. It is recognized that performance can be improved from that presented in this study by using a receiver that is optimized for the transmitted waveform; however, the intent of this study was to determine system performance using existing NASA ground station equipment, or equipment of similar design.

Simulation models were developed and simulations are performed to evaluate transmit signal spectrum, implementation loss, and interference susceptibility.

2. Results Summary

For each modulation technique, the transmitted power spectrum was determined via simulation and compared to the SFCG spectral mask. BER implementation loss was determined via simulation for 10^{-3} and 10^{-5} BER. The results were obtained with three transmitter PA operating points: 6.7-dB Output Back-Off (OBO) which results in a nearly linear amplifier characteristic; 1-dB OBO; 0-dB OBO which represents operating at the saturation point. For the modulation techniques that meet the spectral mask and incurred reasonable implementation loss, interference susceptibility was assessed for wideband and narrowband interference. The results are summarized in Table 1.

Table 1. Summary of Study Results

Modulation Technique	Trans-mitter PA OBO	Compliance With Rec. 17-2R1 Spectral Mask	Implementation Loss		Interference Susceptibility I/N for 1 dB Degradation at BER = 10^{-3}			Recommended
		SR > 2 Msps / SR < 2 Msps	BER = 10^{-3}	BER = 10^{-5}	WB	NB (f=0.0)	NB (f=0.5xRs)	
Unfiltered OQPSK	1.0 dB	No/No	0.5 dB	0.9 dB	-5.8 dB ⁽⁴⁾	-9.0 dB ⁽⁴⁾	-5.0 dB ⁽⁴⁾	No
OQPSK Butterworth Filter, BTs=1.0	1.0 dB	Yes/Yes	13 dB	> 15 dB ⁽¹⁾	NA	NA	NA	No
	0.0 dB	No ⁽⁸⁾ /Yes	NA	NA	NA	NA	NA	No
OQPSK Butterworth Filter, BTs=2.0	1.0 dB	Yes ⁽⁶⁾ /Yes	0.9 dB	1.6 dB	-5.8 dB	-9.7 dB	-7.5 dB	Yes
	0.0 dB	Yes/Yes	1.5 dB	3.0 dB	-5.8 dB	-9.6 dB	-6.7 dB	Yes
OQPSK Butterworth Filter, BTs=3.0	1.0 dB	No/Yes ^(6,9)	0.7 dB	1.3 dB	NA	NA	NA	No
	0.0 dB	No/Yes ^(6,9)	NA	NA	NA	NA	NA	No
OQPSK SRRC Filter, BTs=1.0,	1.0 dB	Yes/Yes ⁽⁹⁾	4.4 dB	8.8 dB	NA	NA	NA	No
	0.0 dB	No/Yes ⁽⁹⁾	NA	NA	NA	NA	NA	No
OQPSK SRRC Filter, BTs=2.0	1.0 dB	Yes ⁽⁶⁾ /Yes ⁽⁹⁾	1.0 dB	1.6 dB	NA	NA	NA	Yes
	0.0 dB	No ⁽⁸⁾ /Yes ⁽⁹⁾	1.4 dB	3.3 dB	NA	NA	NA	Yes
OQPSK SRRC Filter, BTs=3.0	1.0 dB	No/Yes ^{(6) (9)}	0.6 dB	1.1 dB	NA	NA	NA	No
	0.0 dB	No/No ⁽⁹⁾	NA	NA	NA	NA	NA	No
Unfiltered OQPSK/PM	1.0 dB	No/No	0.5 dB	1.0 dB	NA	NA	NA	No
OQPSK/PM Butterworth Filter, BTs=2.0	1.0 dB	Yes/Yes	0.7 dB	1.4 dB	NA	NA	NA	Yes
	0.0 dB	Yes/Yes	0.7 dB	1.4 dB	NA	NA	NA	Yes
GMSK, BTs = 2.0 (BT = 0.5 ⁽²⁾)	1.0 dB	No/Yes ⁽⁷⁾	1.3 dB ⁽³⁾	1.2 dB ⁽³⁾	NA	NA	NA	Yes
	0.0 dB	No/Yes ⁽⁷⁾	1.3 dB ⁽³⁾	1.2 dB ⁽³⁾	-5.8 dB	-11.3 dB	-7.3 dB	Yes
GMSK, BTs = 4.0 (BT=1.0 ⁽²⁾)	1.0 dB	No/Yes ⁽⁷⁾	1.4 dB ⁽³⁾	1.2 dB ⁽³⁾	NA	NA	NA	Yes
	0.0 dB	No/Yes ⁽⁷⁾	1.4 dB ⁽³⁾	1.2 dB ⁽³⁾	-5.8 dB	-10.2 dB	-6.6 dB	Yes
<ol style="list-style-type: none"> Not explicitly simulated. Estimated from BER vs. Eb/No curves. For GMSK, BT is the product of the one-sided bandwidth of the Gaussian filter and the bit duration. For filtered OQPSK and GMSK, BTs is defined as the product of the two-sided filter bandwidth and the duration of transmitted pulses which is 2x the bit duration. GMSK simulation results for BT=1.0 and BT=0.5 were nearly identical. Interference susceptibility for unfiltered OQPSK obtained via closed form analysis using ideal user transmitter. NA - Not Analyzed. The continuous component of the spectrum complies with the mask, but the line components exceed the mask. The spectrum complies with the mask outside of the necessary bandwidth ($\pm 0.5 \times \text{SR}$), but exceeds the mask within the necessary bandwidth. PSD does not comply at frequencies near 3 x symbol rate, but does comply at all other frequencies. Based on Ref. [1]. The PSD's are to be recomputed using a more accurate PSD estimation technique. 								

Based on the results, the following recommendations are provided.

1. Consider relaxing the portion of the SFCG spectral mask within 1x symbol rate to allow GMSK modulation with transmitter distortions. This may also allow other bandwidth efficient modulation techniques and will not affect adjacent channel interference. The mask should not be applied in this region.
2. NASA GSFC missions planning to use S-Band or X-band space-ground links and attempting to meet the SFCG spectral mask should consider filtered OQPSK, including Butterworth and SRRC filtering. The phase modulator implementation of OQPSK (OQPSK/PM) provides a constant envelope signal. These modulation techniques provide a good balance between spectral efficiency and power efficiency and can be implemented without major modifications to NASA GSFC ground stations.. Constant envelope modulation techniques generate less out of band emission when amplified by a PA operating in saturation, allowing for operation with the maximum DC power efficiency.
3. Recommend to study FQPSK and XTCQM as these are constant envelope modulation techniques that can have implementation advantages over GMSK.
4. Further study of the modulation techniques should include: assessment of the impact of a non-ideal symbol synchronizer for GMSK modulation, assessment of OQPSK and GMSK with wider carrier tracking loop bandwidths which may affect the performance, assess impact of a non-ideal phase modulator for OQPSK/PM modulation.
5. Consider filtering to reduce spectrum line components due to data asymmetry.

3. Approach and Simulation Model

The performance of the modulation techniques was assessed using time domain simulation of the transmitter and of the receiver. The simulations were implemented using Signal Processing Worksystem (SPW) software. Simulation models were developed to assess the transmit spectrum, the implementation loss and interference susceptibility of filtered OQPSK and GMSK modulation. The goal of the simulation model is to accurately reflect the performance of the user transmitter hardware including linear and nonlinear distortions. The simulation produces power spectral density of the transmitted signals and bit error rate performance in the presence of transmitter distortions, receiver imperfections and interference.

Figure 1 shows an overview of the simulation models used in the study. The user transmitter generates the user signal with the specified modulation format and distortions. The space-ground channel adds thermal noise and an interference signal. The ground terminal includes linear distortions due to front end filtering, carrier tracking, symbol synchronization and data detection. BER is measured by comparing the received data bits with the transmitted data bits. The transmitted signal spectrum is monitored at the user transmitter output.

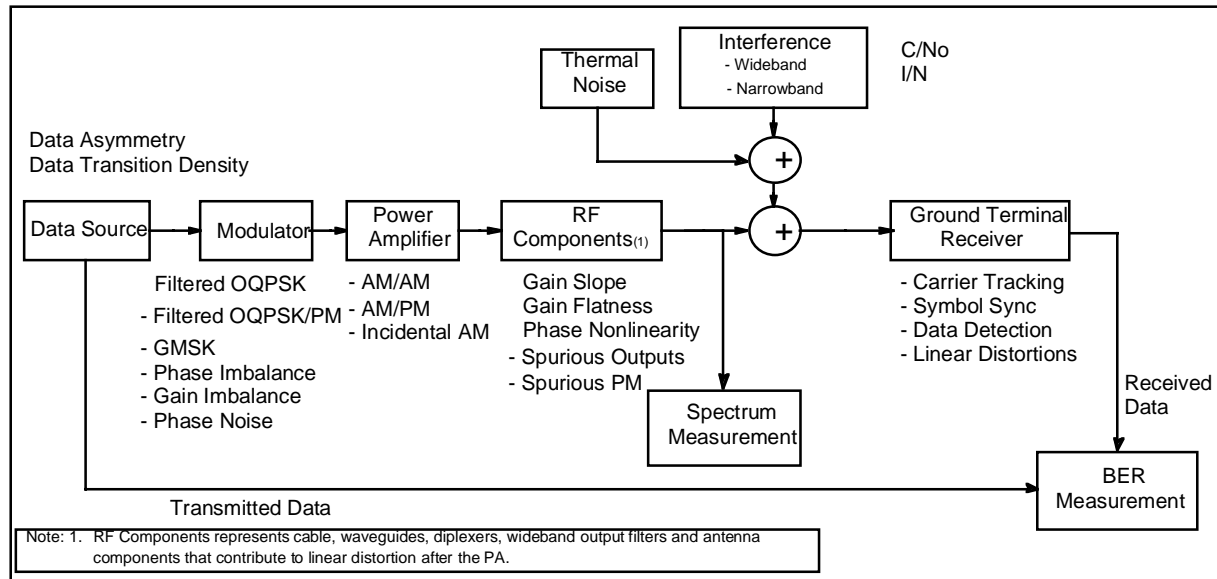


Figure 1. Simulation Model

3.1. Transmitter

The transmitter model produces the waveforms under study and also implements transmitter distortions which are typically specified for NASA GSFC transmitters. The sources of these distortions are indicated in Figure 1. The parameter values used in the simulation are listed in Appendix 2.

The user transmitter includes a data source, modulator (Filtered OQPSK, OQPSK/PM, GMSK), power amplifier, and RF components. The data source represents the spacecraft on-board data system which provides NRZ data to the transmitter and may include data asymmetry.

For filtered OQPSK, two modulator implementations are studied. The first implementation uses an I/Q modulator as shown in Figure 2. The second implementation, referred to as OQPSK/PM, uses a linear phase modulator.

The OQPSK modulator includes a baseband pulse shaping filter which is either a Butterworth or Square Root Raised Cosine (SRRC) filter. Modulation is accomplished with an I/Q modulator as shown in Figure 2. Note that the baseband filtering produces amplitude variations in the NRZ data stream. Because of the I/Q modulator implementation, these amplitude variations are also present in the modulator output signal.

The SRRC filter is typically defined relative to a specified symbol rate so that the half power frequency of the filter response occurs at a frequency which is 1/2 of the symbol rate. Therefore the SRRC filter is typically specified with $BT_s = 1.0$ where B is the two-sided, half-power bandwidth of the SRRC filter and T_s is the symbol rate on each QPSK channel. In this study we use the SRRC filter with $BT_s = 1.0, 2.0$ and 3.0 . With these parameters, the half-power frequency response of the SRRC filter occurs at 0.5, 1 and 1.5 times the symbol rate, respectively.

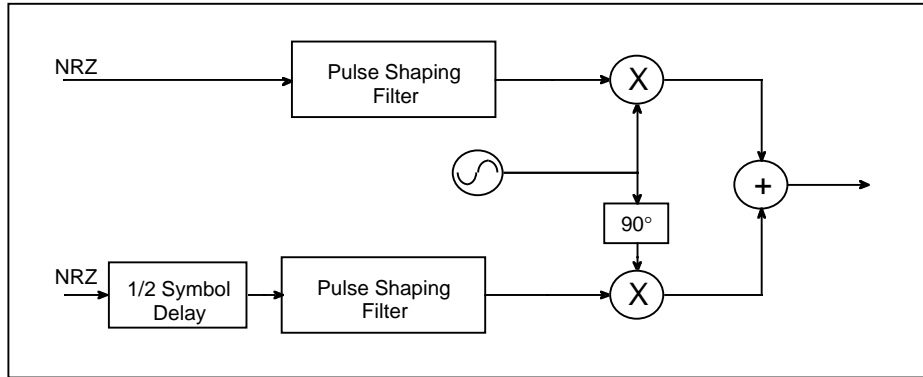


Figure 2. Filtered OQPSK With I/Q Modulator

The output of the filtered OQPSK modulator is:

$$s(t) = y_i(t) \cdot \sin(\omega_c t + \phi) + y_q(t) \cdot \cos(\omega_c t + \phi)$$

where, $y_i(t), y_q(t) = \text{filtered NRZ data}$

$\omega_c = \text{carrier frequency, rad/s}$

$\phi = \text{oscillator phase at } t = 0$

OQPSK/PM uses a linear phase modulator to modulate the carrier as shown in Figure 3.

OQPSK/PM signal is formed by mapping the I and Q channel NRZ data to a QPSK phase signal, filtering the phase signal and then phase modulating a carrier with filtered phase signal.

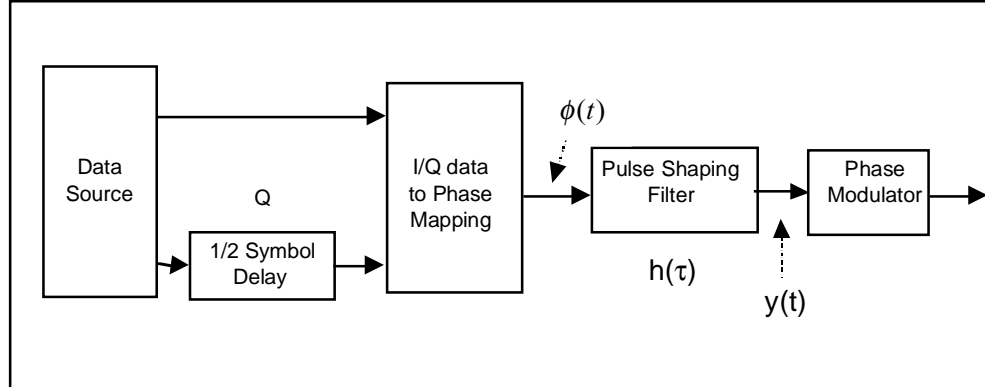


Figure 3. Filtered OQPSK With Analog Phase Modulator (OQPSK/PM)

The output of the modulator is:

$$s(t) = A \cos(\omega_c t + \phi(t) * h(t))$$

where, $\omega_c = \text{carrier frequency, rad/s}$. Filtering used in OQPSK/PM is Butterworth and SRRC as described above for the OQPSK implementation. In the filtered OQPSK/PM modulator, the output signal has a constant envelope. The mapping is performed so that in the absence of filtering, the modulator output is identical to that of an OQPSK modulator.

The GMSK modulator shown in Figure 4 includes a Gaussian filter and a FM modulator.

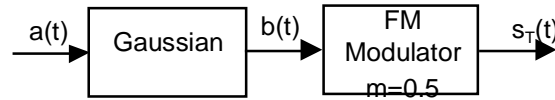


Figure 4. Configuration of the GMSK Modulator

When the data sequence is $\{a_n\}$, a waveform of the transmitted bit sequence can be expressed as:

$$a(t) = \sum_{k=-\infty}^{\infty} b_k u(t - kT_b)$$

$$b_k = \begin{cases} 1; & a_k = 1 \\ -1; & a_k = 0 \end{cases}$$

$$u(t) = \begin{cases} 1; & 0 \leq t < T_b \\ 0; & \text{otherwise} \end{cases}$$

When $a(t)$ is filtered by a Gaussian LPF with its 3-dB, one-sided bandwidth of B_b , the filter output is given by:

$$b(t) = a(t) \otimes c_b(t)$$

$$c_b(t) = \sqrt{\frac{2\pi}{\ln 2}} B_b \exp\left(-\frac{2\pi^2}{\ln 2} B_b^2 t^2\right)$$

$b(t)$ is then fed to the FM modulator with its modulation index of 0.5 to obtain the transmitted signal expressed as:

$$s_T(t) = A \cdot \cos(2\pi f_c t + \phi(t) + \theta_0)$$

$$\phi(t) = \frac{\pi}{2T_b} \int_{-\infty}^t b(\tau) d\tau$$

The transmitter model includes a non-linear power amplifier. The characteristics of the amplifier is provided in Appendix 1. The study evaluates performance of these modulation techniques with the spacecraft transmitter power amplifier operating with the following three Output Back-Off (OBO) points:

- Saturation (0 dB OBO).
- 1 dB OBO.
- Linear (6.7 dB OBO).

The gain transfer for the power amplifier model is based on a TWTA. The phase characteristic is parametric and is designed to provide AM/PM of 12°/dB at the 1 dB OBO operating point. This is the worst case AM/PM allowed by NASA specifications. At this point the maximum phase variation due to AM is 25°. At the 0 dB OBO operating point, the AM/PM is 15°/dB and the maximum phase variation due to AM is 60° (assuming maximum AM variation of 4 dB due to data transitions). Investigation of performance with lower AM/PM is the subject of a future effort. The saturation point has the best DC power efficiency, and thus is the most desirable.

Table 2 lists the AM/AM and AM/PM for the amplifier at the three operating points.

Table 2. Amplifier Operating Points Used in Simulation

Operating Point	Input Back-Off	Output Back-Off	AM/AM	AM/PM
Linear	14 dB	6.7 dB	0.9 dB/dB	0.0 °/dB
1-dB OBO	6 dB	1 dB	0.47 dB/dB	12 °/dB
Saturation	0 dB	0 dB	0.0 dB/dB	15 °/dB

The RF components are modeled by a linear filter that produces gain and phase distortions.

3.2. Ground Terminal Receiver

The ground terminal receiver includes a carrier tracking loop, symbol synchronizer, and data detector. The receiver model also includes linear distortions due to front end RF/IF components.

RF/IF components convert the received RF signal to an intermediate frequency suitable to the receiver. The aggregate linear distortions of these components are modeled as a composite linear filter implemented prior to the receiver input.

The carrier tracking loop acquires the carrier, detects and tracks the phase of the signal. It is a modified second order Costas loop. For OQPSK, the design of carrier tracking loop is based on High Data Rate Receiver at NASA's White Sands Complex. For GMSK, the design is based on reference [5].

The symbol synchronizer recovers the symbol timing of the demodulated signal and provides clock signals synchronized with the data for use in data detection. In GMSK, the clock is also used for the phase detector of carrier tracking loop. The symbol synchronizer design for OQPSK is a data transition tracking loop based on equipment at NASA's White Sands Complex; for GMSK a perfect symbol timing signal is used.

Both OQPSK and GMSK data detectors are coherent, hard decision, symbol by symbol integrate and dump detectors. These are optimum detectors for unfiltered BPSK and QPSK modulation but are suboptimum for filtered OQPSK and GMSK. These detectors represent a the level of complexity employed in receivers currently used in NASA ground terminals. It is recognized that BER performance and interference susceptibility for some modulation techniques could be improved by the use of optimum receivers. Performance with optimum receiver structures is a subject for future study.

3.3. Interference Model

To assess the interference susceptibility of the bandwidth efficient modulation, an interference model is used that adds either a wideband or a narrowband interference signal to the transmitted desired signal. The interference assessment includes wideband and narrowband interference. Wideband interference is modeled as Additive White Gaussian Noise (AWGN) with uniform power spectral density over the desired signal bandwidth and narrowband interference is modeled as a CW tone at a constant frequency.

The interference model generates zero-mean Gaussian noise with the variance required to meet a given signal-to-noise ratio. It also generates either narrowband or wideband interference with power required to meet a given I/N as well. Simulation is performed to obtain the value of I/N which results in 1-dB BER degradation.

4. Results and Discussion

The simulation model described in section 3 was used to generate performance results for filtered OQPSK, filtered OQPSK/PM and GMSK modulation techniques. Performance results include: the transmitted signal spectrum compared to the SFCG Rec. 17-2R1 mask, implementation loss and interference susceptibility.

4.1. Filtered OQPSK Results

4.1.1. Transmit Signal Power Spectrum

The user transmitter simulation model was used to generate power spectral density plots for unfiltered OQPSK, Butterworth filtered OQPSK, and SRRC filtered OQPSK. Reference [1] provides results for several cases of Power Amplifier OBO. The key findings are highlighted here. Figures 5 and 6 provide the PSD plot for Butterworth filtered OQPSK with , PA OBO = 0 dB and $BT_s = 1.0$ and 2.0 , respectively. Figure 7 provides the PSD plot for Butterworth filtered OQPSK with $BT_s = 2.0$ and PA OBO = 1 dB. Also provided in the Figures is the spectral mask recommended by SFCG Rec 17-2R1 for comparison.

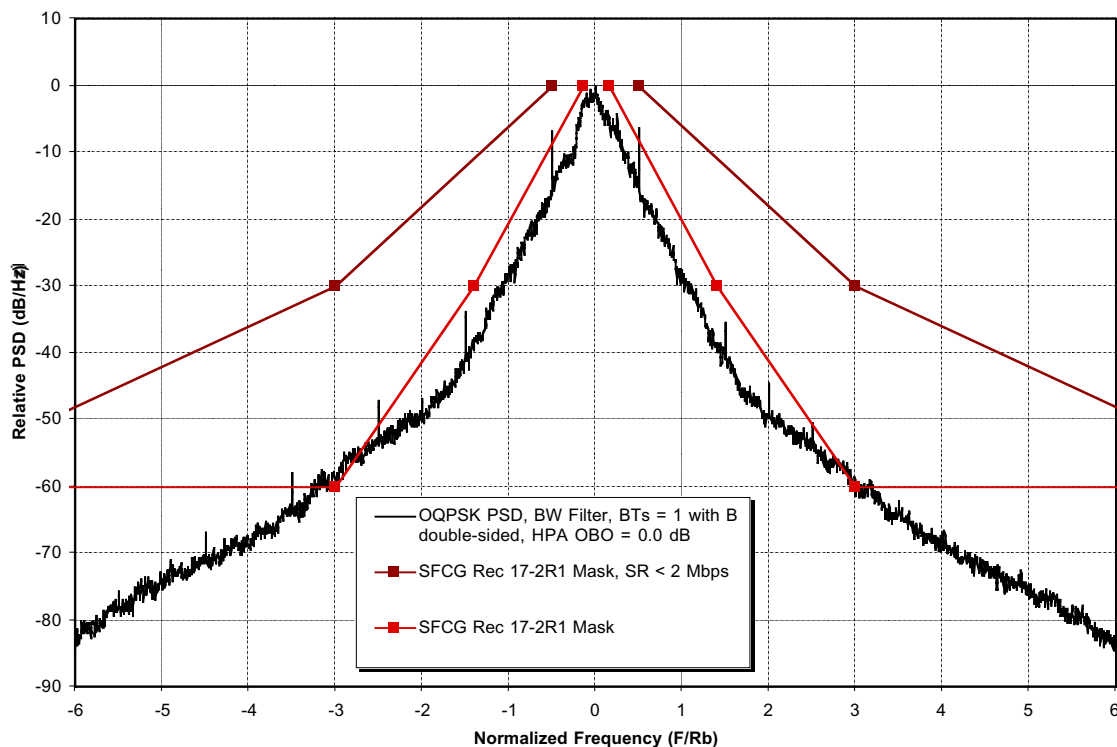


Figure 5. Filtered OQPSK Spectrum
(6-Pole Butterworth Filter $BT_s=1.0$, PA OBO = 0 dB)

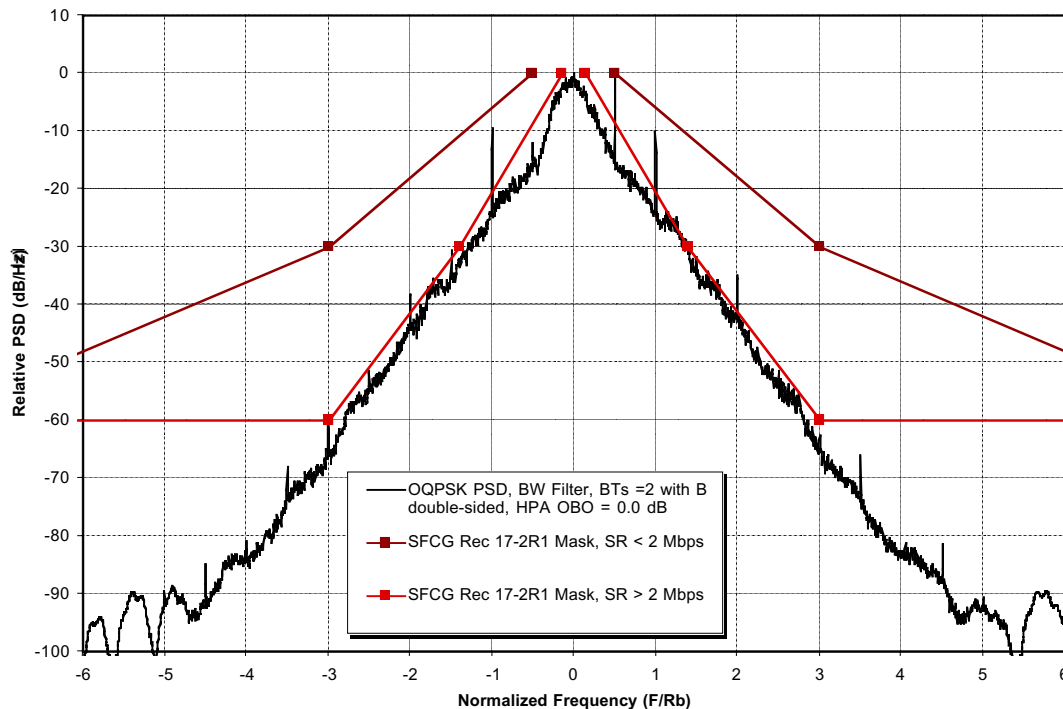


Figure 6. Filtered OQPSK Spectrum
(6-Pole Butterworth Filter $BT_s=2.0$, PA $OBO=0$ dB)

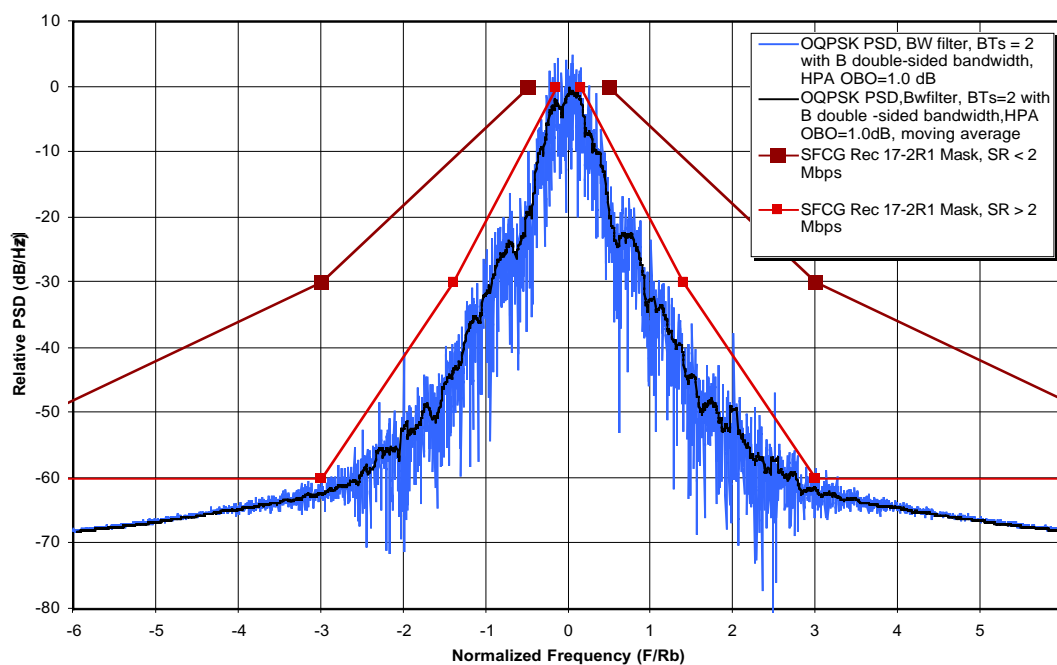


Figure 7. Filtered OQPSK Spectrum
(6-Pole Butterworth Filter $BT_s=2.0$, PA $OBO=1$ dB)

Several cases with various filtering and PA output backoff were simulated, the PSDs were generated and compared with the SFCG Rec 17-2R1 spectral mask. The results are summarized in Table 1. This paper presents a subset of the PSD plots; the complete set of PSD plots are provided in reference [1]. The observations from Figures 5, 6, 7 and the OQPSK PSDs presented in Reference [1] follow.

The PSD for unfiltered OQPSK has significant sidelobes that exceed the SFCG mask. The PSD exceeds the SFCG mask after the third sidelobe. Line spectra due to data asymmetry are evident at multiples of the symbol rate.

For filtered OQPSK with both Butterworth and SRRC filters with $BT=1.0$, the PSD is below the SFCG mask for PA OBO = 1 dB. The PSD exceeds the SFCG mask for PA OBO = 0 dB with sidelobes exceeding the mask after normalized frequency of 4.0 for Butterworth filtering and 3.0 for SRRC filtering. Line spectra due to data asymmetry are reduced in both cases as compared to unfiltered OQPSK.

For both OQPSK with Butterworth (shown in Figure 6) and SRRC filters $BT=2.0$, the PSD is under the mask for PA OBO = 1 dB. The PSD exceeds the mask for PA OBO = 0 dB with $BTs = 1.0$ as shown in Figure 5A with sidelobes exceeding the mask after normalized frequency of 3.0. In both cases, line spectra due to data asymmetry exceed the mask.

For OQPSK with Butterworth or SRRC filter $BT=3.0$, the sidelobes exceed the SFCG mask beginning with the first sidelobe. The PSD for OQPSK with Butterworth or SRRC filter $BT=3.0$ complies with the SFCG mask only for the linear PA case.

In comparing the line components present in each case, it is observed that filtering reduces the spectrum line components due to data asymmetry. For $BTs = 1.0$, spectral line components are not discernable in the PSD plots.

A summary table of filtered PSD vs. the high data rate and low data rate spectral masks of SFCG Rec 17-2R1 is presented in Table 3, below.

Table 3. Filtered OQPSK PSD vs. SFCG Rec 17-2R1 Spectral Mask

Pulse Shaping Filter	PA OBO	BTs = 1	BTs = 2	BTs = 3
Butterworth Filter	6.7 dB (Linear PA)	Yes/Yes	Yes/Yes	Yes/Yes
	1 dB	Yes/Yes	Yes ^[3] /Yes	No/Yes ^[3] ^[5]
	0 dB	No ^[4] /Yes	Yes/Yes	No/Yes ^[3]
SRRC Filter	6.7 dB (Linear PA)	Yes/Yes	Yes/Yes	Yes/Yes
	1 dB	Yes/Yes ^[5]	Yes ^[3] /Yes ^[5]	No/Yes ^[3] ^[5]
	0 dB	No/Yes ^[5]	No/Yes ^[5]	No/No
1. B is double-sided filter bandwidth. 2. Yes/Yes means the PSD is under the high symbol rate/low symbol rate SFCG spectral mask. 3. Line components exceed the mask. 4. PSD exceeds the mask at frequencies near 3 x symbol rate; PSD is within the mask at all other frequencies. 5. Based on Ref. [1]. Results to be recomputed using a more accurate PSD estimation technique				

4.1.2. Implementation Loss

The simulation model described in Figure 1 was used to generate BER vs. E_b/N_0 curves for Butterworth filtered and SRRC filtered QPSK with BTs = 1.0, 2.0 and 3.0. Implementation loss is computed as the additional E_b/N_0 required to achieve 10^{-3} and 10^{-5} BER relative to the E_b/N_0 theoretically required for unfiltered OQPSK modulation. Figure 8 provides the BER curves for Butterworth filter and Table 4 summarizes the BPSK/OQPSK implementation losses for various cases.

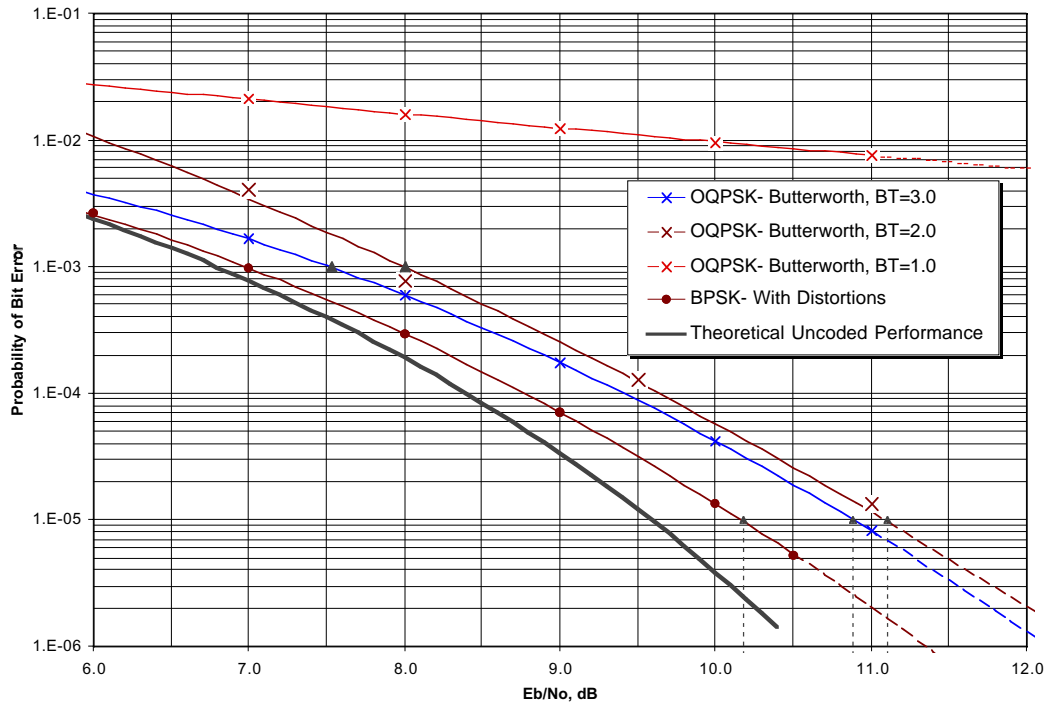


Figure 8. Probability of Error vs. E_b/N_0 for BPSK and Filtered OQPSK Modulation – 6-pole Butterworth Filter

The BER simulations were performed using integrate and dump detectors that are optimum for unfiltered OQPSK modulation. For filtered OQPSK BT=1.0, the implementation loss is significantly higher than for BPSK. The SRRC filter provides better performance than the Butterworth filter. For BT=2.0 or higher, the implementation loss is reasonable even with the suboptimum integrate and dump detectors. At 0 dB PA output backoff, both filter types produced worse results than at 1 dB output backoff.

Table 3 and Table 4 indicate that among the six filtered OQPSK modulations considered, for data rates above 2 Mbps, Butterworth filtering with BTs = 2.0 and 1 dB OBO provides the best link performance while complying with the SFCG mask. For data rates below 2 Mbps, Butterworth filtering with BTs = 3.0 and 0 dB OBO provides the best link performance while complying with the SFCG mask. Both the Butterworth and SRRC filtered OQPSK with BTs = 1.0 exhibited a large implementation loss. This may be able to be reduced by the use of a receive filter matched to the transmit filter instead of the integrate and dump detector.

Table 4. BPSK/QPSK Implementation Loss

Modulation	PA Output Back-Off	Transmitter Distortions	Implementation Loss		
			@BER = 10^{-3}	@BER = 10^{-5}	@BER = 10^{-5} (Relative to BPSK)
BPSK, unfiltered	6.7 dB	None	< 0.1 dB	< 0.1 dB	NA
BSPK, unfiltered	1 dB	Yes*	0.2 dB	0.6 dB	0.0 dB
OQPSK, unfiltered	1 dB	Yes*	0.5 dB	0.9 dB	0.3 dB
OQPSK- 6-pole Butterworth Filter (BT=1.0)	1 dB	Yes*	> 13 dB (est.)	> 15 dB (est.)	> 14.4 dB (est.)
OQPSK- 6-pole Butterworth Filter (BT=2.0)	1 dB	Yes**	0.9dB	1.6 dB	1.0 dB
OQPSK 6-pole Butterworth Filter (BT=2.0)	0dB	Yes*	1.5 dB	3 dB	2.4 dB
OQPSK- 6-pole Butterworth Filter (BT=3.0)	1 dB	Yes*	0.7 dB	1.3 dB	0.7 dB
OQPSK- SRRC Filter (BT=1.0)	1 dB	Yes*	4.4 dB	8.8 dB (est.)	> 8.2 dB (est.)
OQPSK- SRRC Filter (BT=2.0)	1 dB	Yes**	1.0 dB	1.6 dB	1.0 dB
OQPSK- SRRC Filter (BT=2.0)	0dB	Yes*	1.4 dB	3.3 dB	2.7 dB
OQPSK- SRRC Filter (BT=3.0)	1 dB	Yes*	0.6 dB	1.1 dB	0.5 dB
* without phase noise.					
** with phase noise 3.6° rms is also simulated, resulted in less than 0.1 dB additional degradation.					

4.1.3. Interference Susceptibility

The interference model described in Section 3.3 was used to combine the transmitter, noise, and ground terminal models in an end-to-end simulation model as illustrated in Figure 1. The interference is defined by the interference power to noise power ratio I/N . For narrowband interference, the interference center frequency is also specified. Wideband interference and narrowband interference with center frequencies at 0 and 0.5Rs were used to determine I/N for 1-dB degradation relative to baseline performance (no interference) for the Butterworth pulse shaping filter with $BTs = 2$.

The simulation results are compared with theory. Theoretically, the effect of interference can be related to the BER degradation by the following equations. These equations do not account for

distortions. BER degradation is defined as the additional SNR required to achieve the BER performance without interference.

For wideband interference, the interfering signal results in an increase in the noise floor, therefore, the BER degradation due to interference is represented as[1].

$$\text{deg.} = 10 \log(1 + I / N) \text{ in dB}$$

For narrowband interference, the BER is related to interference power by the following equation[1].

$$\bar{P}_e = \frac{I}{2\pi} \int_0^{2\pi} Q \left\{ \sqrt{\frac{2E_b}{N_o}} \left[I - \frac{\sqrt{2}}{\sqrt{\frac{S}{2I}} \Delta\omega T} \sqrt{1 - \cos(\Delta\omega T)} \cos(\theta) \right] \right\} d\theta$$

Where; \bar{P}_e is the average BER over all θ .

θ is a uniform random variable over $0 \sim 2\pi$

E_b is the energy per bit in each I and Q channel

N_o is the one sided noise power spectral density

S is signal power

I is the power of the CW interference

$\Delta\omega$ is interference frequency offset with respect to carrier

By numerically solving this equation, the BER degradation vs. I/N can be obtained.

BER degradation vs. I/N curves are provided by Figure 7 and Figure 8 for Butterworth filtered OQPSK BT= 2 with PA OBO of 0.0 and 1.0 dB, respectively. Both theory and simulation results are provided.

Figures 9 and 10 indicate that BER performance is least susceptible to wideband noise and most susceptible to narrowband interference at zero offset from carrier frequency. These results show that Butterworth filtered OQPSK is not significantly more susceptible to interference than unfiltered OQPSK.

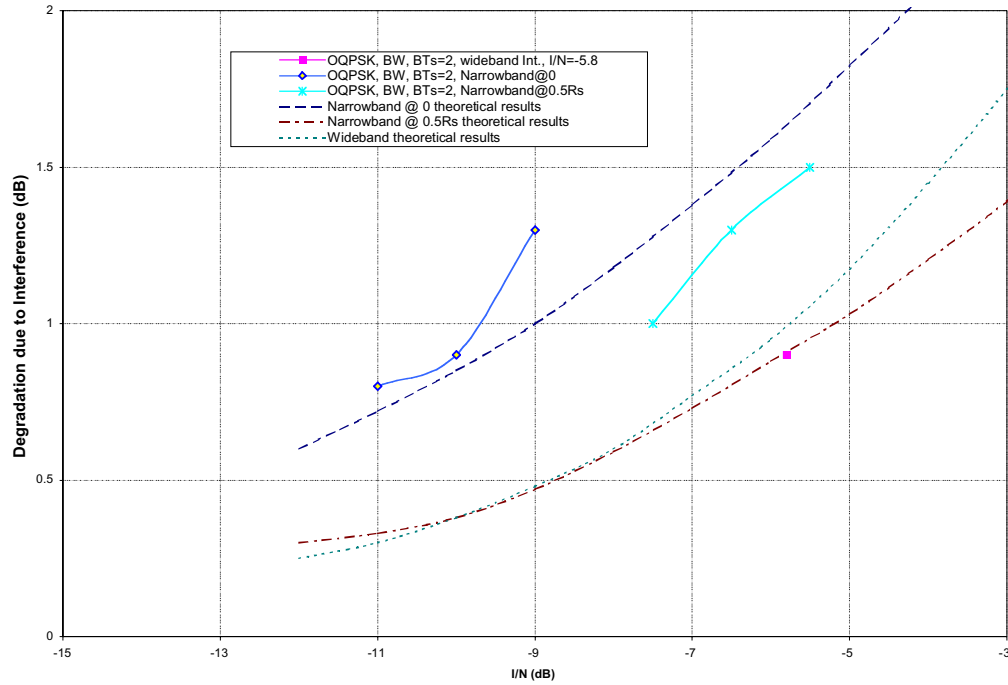


**Figure 9. BER Degradation vs. I/N ,
Butterworth Filtered OQPSK, PA OBO = 1 dB**

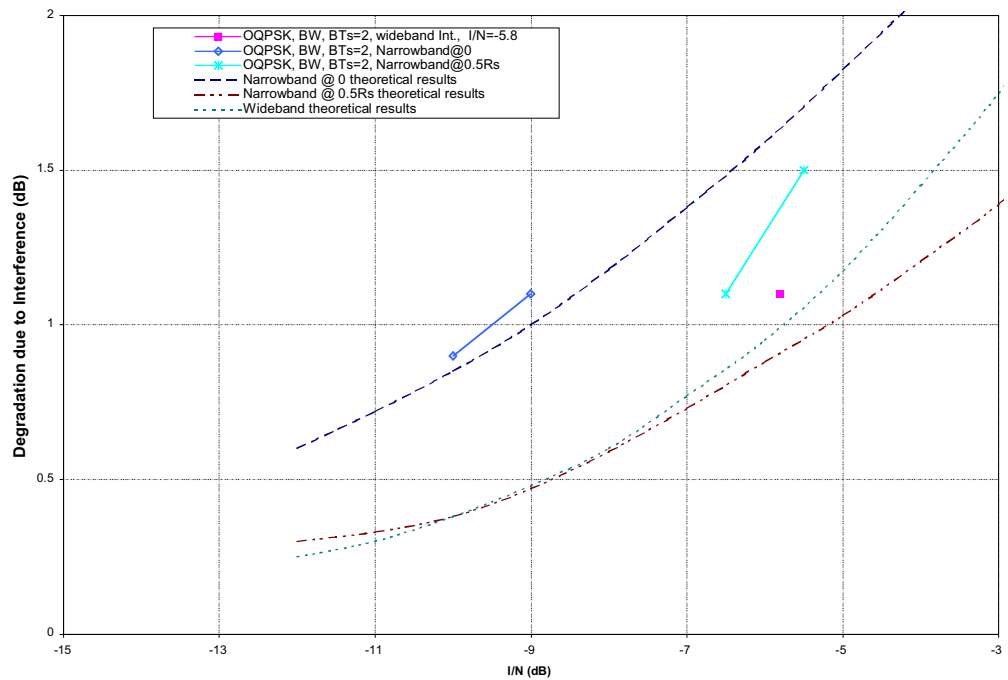


**Figure 10. BER Degradation vs. I/N ,
Butterworth Filtered OQPSK, PA OBO = 0 dB**

4.2. OQPSK/PM Results

4.2.1. Transmit Signal Power Spectrum

Power spectral density was generated for Butterworth filtered OQPSK/PM with $BT_s=2$. The power spectral density for OQPSK/PM with $BT_s=2$ and transmitter PA in saturation is shown in Figure 11 and compared to the spectral mask recommended by SFCG Rec 17-2R1.

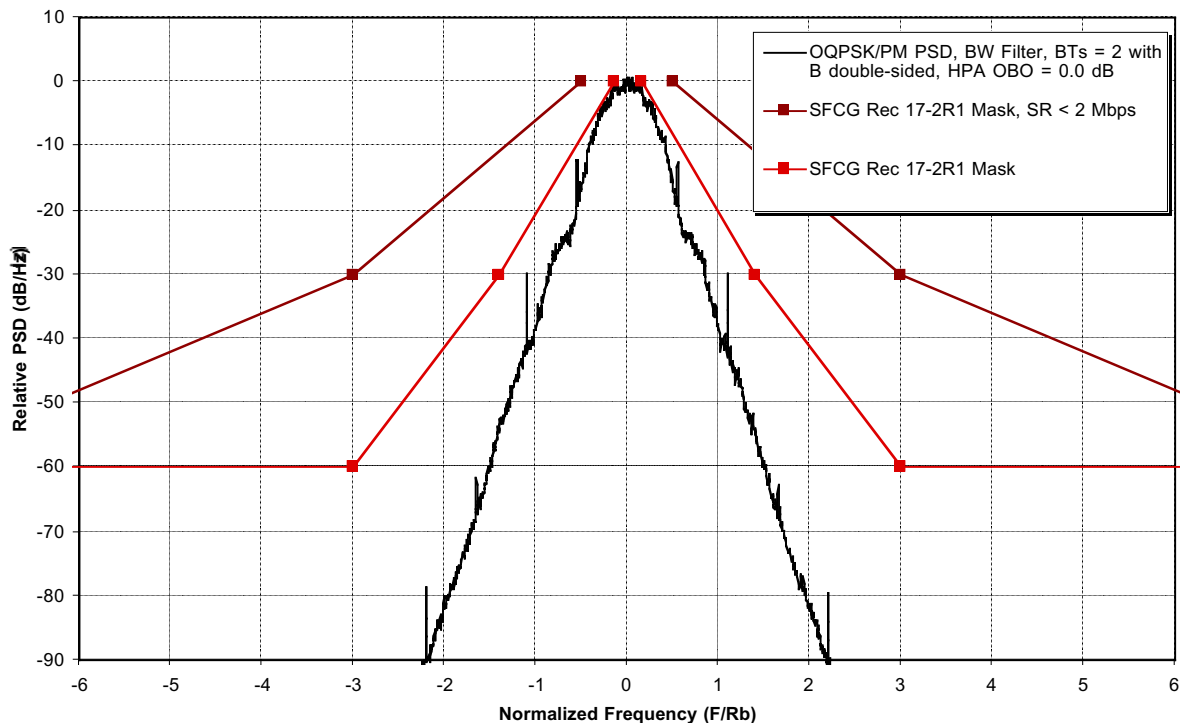


Figure 11. Filtered OQPSK/PM Spectrum
(6-Pole Butterworth Filter $BT_s=2$, PA OBO=0 dB)

For both PA OBO = 0.0 and 1.0 dB, the PSDs for Butterworth filtered OQPSK/PM $BT=2.0$ meet the mask. The line spectra are significantly reduced compared with Butterworth filtered OQPSK.

Since filtered OQPSK/PM is a constant envelope modulation, the PA operating point has little effect on the PSD.

4.2.2. Implementation Loss

BER simulations for filtered OQPSK/PM were performed using the simulation model described in Figure 1. The transmitter included the distortions provided in Appendix 2. The receiver was an integrate and dump, symbol-by-symbol receiver. Table 5 summarizes the implementation loss results.

Table 5. OQPSK/PM Implementation Loss

Modulation	PA Output Back-Off	Transmitter Distortions	Implementation Loss		
			@BER = 10^{-3}	@BER = 10^{-5}	@BER = 10^{-5} (Relative to BPSK)
OQPSK/PM, unfiltered	1 dB	Yes*	0.5 dB	1.0 dB	0.4 dB
OQPSK/PM, BW, BTs = 2	1 dB	Yes*	0.7 dB	1.4 dB	0.8 dB
OQPSK/PM, BW, BTs = 2	0 dB	Yes*	0.7 dB	1.4 dB	0.8 dB
* Without phase noise					

For Butterworth BT=2.0, the implementation loss is about 0.8 dB higher than that for unfiltered BPSK. This approach has significant performance advantages over OQPSK with an I/Q modulator. The implementation loss could be further reduced by the use of a matched filter receiver.

4.3. GMSK Results

4.3.1. Transmit Signal Power Spectrum

The GMSK transmitter model described in Section 3 was used to generate power spectral density plots. Figure 12 presents the PSD for the GMSK transmit signal for BT = 0.5 (BTs = 2.0) with an ideal transmitter and linear power amplifier. Figure 13 presents the PSD for the GMSK transmit signal for BT=0.5 with transmitter distortions and transmitter PA in saturation. In both figures the PSD's are compared with the SFCG Rec 17-2R1 spectral mask. The main lobe of the GMSK emitted spectrum is wider than the main lobe for filtered OQPSK and filtered OQPSK/PM. For the ideal transmitter, the spectrum barely complies with the SFCG spectral mask. For the case with transmitter distortions, the width of the main lobe is increased resulting in non-compliance with the high data rate SFCG spectral mask for frequencies within about 0.5x symbol rate. Outside of 0.5 x symbol rate, the PSD complies with the spectral mask and exhibits no line spectra. In the course of this study, it was observed that data asymmetry has the effect of a long term frequency shift and short term frequency variations in the transmitted signal.

Table 6 summarizes compliance of the GMSK PSD with the SFCG Rec 17-2R1 spectral mask.

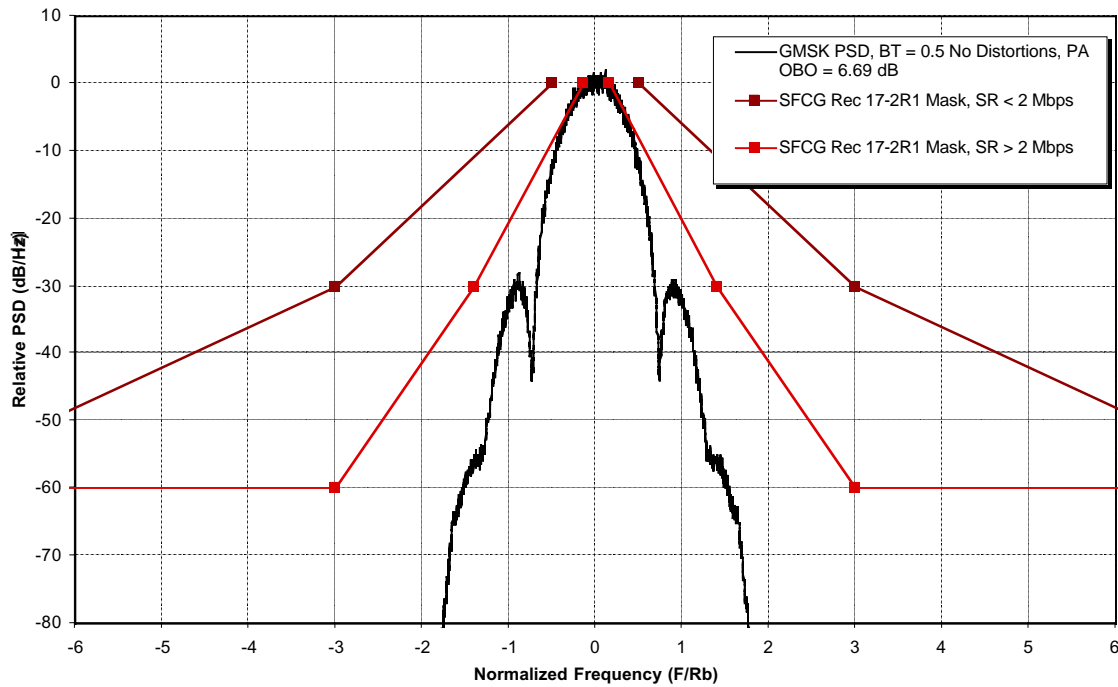


**Figure 12. GMSK Spectrum ($BT=0.5$, Linear PA)
Ideal Transmitter**

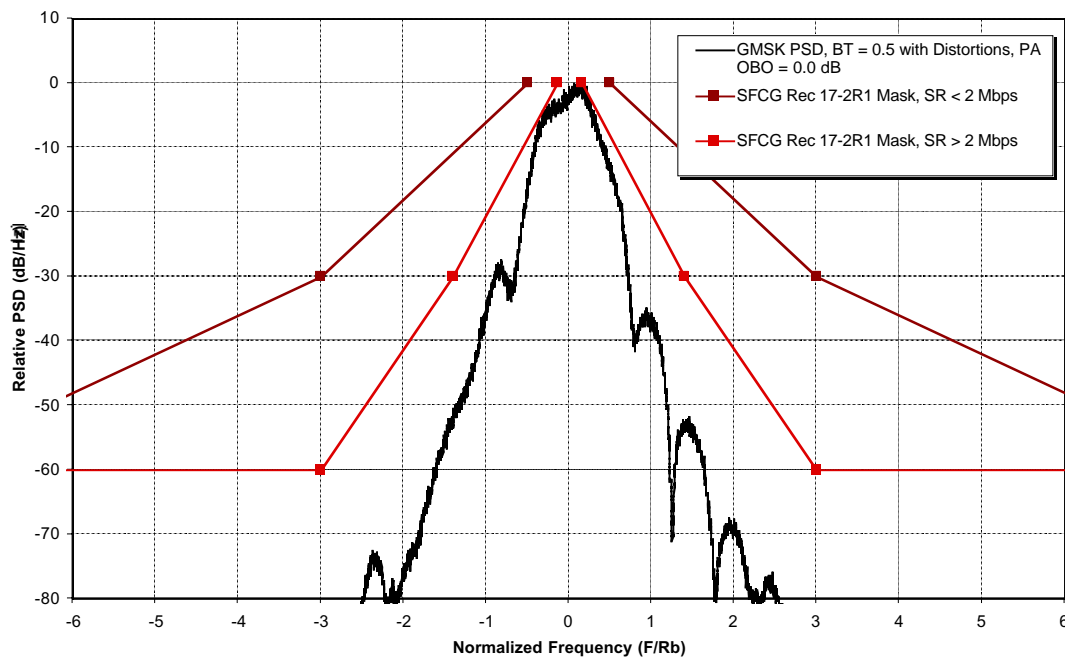


**Figure 13. GMSK Spectrum ($BT=0.5$, PA OBO = 0 dB)
With Transmitter Distortions**

**Table 6. GMSK PSD Compliance With
SFCG Rec 17-2R1 Spectral Mask**

Gaussian Filter Bandwidth	Linear PA (w/o Dist.)	HPA OBO=1dB	HPA OBO=0dB
BT=0.5	Yes/Yes	No/Yes	No/Yes
BT=1.0	Yes/Yes	No/Yes	No/Yes
Note: Yes/Yes means PSD complies with the high symbol rate/low symbol rate SFCG spectral mask.			

Transmitter distortions result in wider sidelobes. Only the PSD without transmitter distortions meets the mask. Unlike filtered OQPSK, the data asymmetry does not cause spectrum line components in GMSK power spectrum. Instead, data asymmetry causes a constant shift in the GMSK signal carrier frequency and short term variations.

The PA operating point does not significantly affect the PSD due to the GMSK constant envelope. Therefore the PA may operate at the saturation point (0dB back off) to achieve the highest DC power efficiency.

4.3.2. Implementation Loss

BER simulations for GMSK were performed using the simulation model described in Figure 1. The transmitter included the distortions provided in Appendix 2. The receiver was an integrate and dump, symbol-by-symbol OQPSK type receiver modified to recover the GMSK data. The transmitter did not include pre-coding prior to the GMSK transmitter. Table 7 provides a summary of GMSK implementation loss. Implementation loss could be reduced by pre-coding the data prior to the modulator and by using a matched filter receiver.

Table 7. GMSK Implementation Loss

Modulation	PA Output Back-Off	Transmitter Distortions	Implementation Loss		
			@BER = 10⁻³	@BER = 10⁻⁵	@BER = 10⁻⁵ (Relative to BPSK)
BSPK, unfiltered,	1 dB	Yes	0.2 dB	0.6 dB	0.0 dB
GMSK, BT = 0.5	6.7 dB	None	1.0 dB	0.8 dB	0.2 dB
GMSK, BT = 0.5	1 dB	Yes	1.3 dB	1.2 dB	0.6 dB
GMSK, BT = 0.5	0 dB	Yes	1.3 dB	1.2 dB	0.6 dB
GMSK, BT = 1.0	6.7 dB	None	1.1 dB	0.8 dB	0.2 dB
GMSK, BT = 1.0	1 dB	Yes	1.4 dB	1.2 dB	0.6 dB
GMSK, BT = 1.0	0 dB	Yes	1.4 dB	1.2 dB	0.6 dB

The implementation loss is nearly identical for BT=1.0 and BT=0.5 and is approximately 1.0 dB higher than that for BPSK. This result is true for PA operating at 1 dB OBO and 0 dB OBO.

These results combined with the spectrum results indicate that GMSK provides a good trade-off of spectral efficiency and power efficiency. Although the GMSK spectrum does not comply with the high data rate SFCG spectral mask within 0.5x symbol rate; the out-of-band roll off is well below the mask.

4.3.3. Interference Susceptibility

The simulation model of Figure 1 was used to assess the interference susceptibility of GMSK modulation received with an integrate and dump symbol-by-symbol detector. Interference susceptibility is characterized by the value of I/N which results in 1-dB BER degradation. Interference susceptibility was assessed for both wideband and narrowband interference. Interference susceptibility was also computed for an ideal transmitter and integrate and dump receiver.

The theoretical equation relating wideband interference with degradation is same as that for OQPSK. For narrowband interference, the BER is related to interference power by the following equation[1].

$$\bar{P}_e = 2 \cdot \frac{1}{2\pi} \int_0^{2\pi} Q \left\{ \sqrt{\frac{2E_b}{N_o}} \left[I - \frac{\sqrt{2}}{\sqrt{\frac{S}{2I} \Delta\omega T}} \sqrt{1 - \cos(\Delta\omega T)} \cos(\theta) \right] \right\} d\theta$$

Where; \bar{P}_e is the average BER over all θ .

θ is a uniform random variable over $0 \sim 2\pi$

E_b is the energy per bit in each I and Q channel

N_o is the one sided noise power spectral density

S is signal power

I is the interference CW tone's power

$\Delta\omega$ is interference frequency offset with respect to carrier

By numerically solving this equation, the BER degradation vs. I/N can be obtained for a BER of 10^{-5} .

Degradation vs. I/N curves are provided by Figure 14 and Figure 15 for $BT=0.5$ and $B=1.0$ with wideband and narrowband interference. Table 1 summarizes the interference susceptibility results.

The simulation results for wideband interference fall close to the theoretical results. For narrowband interference, the simulation results show approximately 1 to 2 dB more sensitivity than the theoretical results. In both the simulation and theoretical results, the difference between narrowband interference at the center frequency and narrowband interference at 1/2 the channel symbol rate is approximately 3.9 dB. This is expected since the power of interference at output

of the receiver integrate and dump detector is proportional to $\frac{\sin^2(\pi f_i T_s)}{(\pi f_i T_s)^2}$ which has 3.9 dB difference between $f_i = 0$ and $f_i = 0.5R_s = 1/2T_s$. I/N differences of 4.0 dB and 3.6 dB are obtained for BT=0.5 and BT=1.0 respectively. The simulation results agree with the theory. Figures 14 and 15 show that GMSK received using an integrate and dump detector is not significantly more susceptible to interference than OQPSK. The BER performance is least susceptible to wideband noise and most susceptible to narrowband interference at zero offset frequency with respect to carrier.

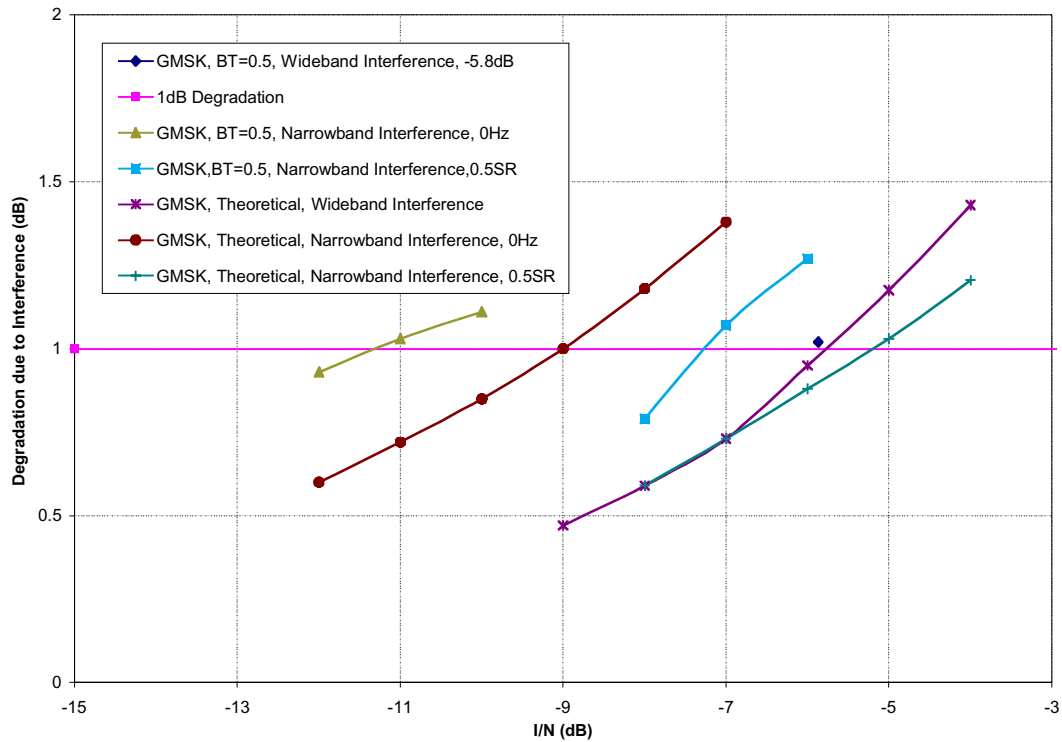


Figure 14. Degradation vs. I/N for GMSK BT=0.5

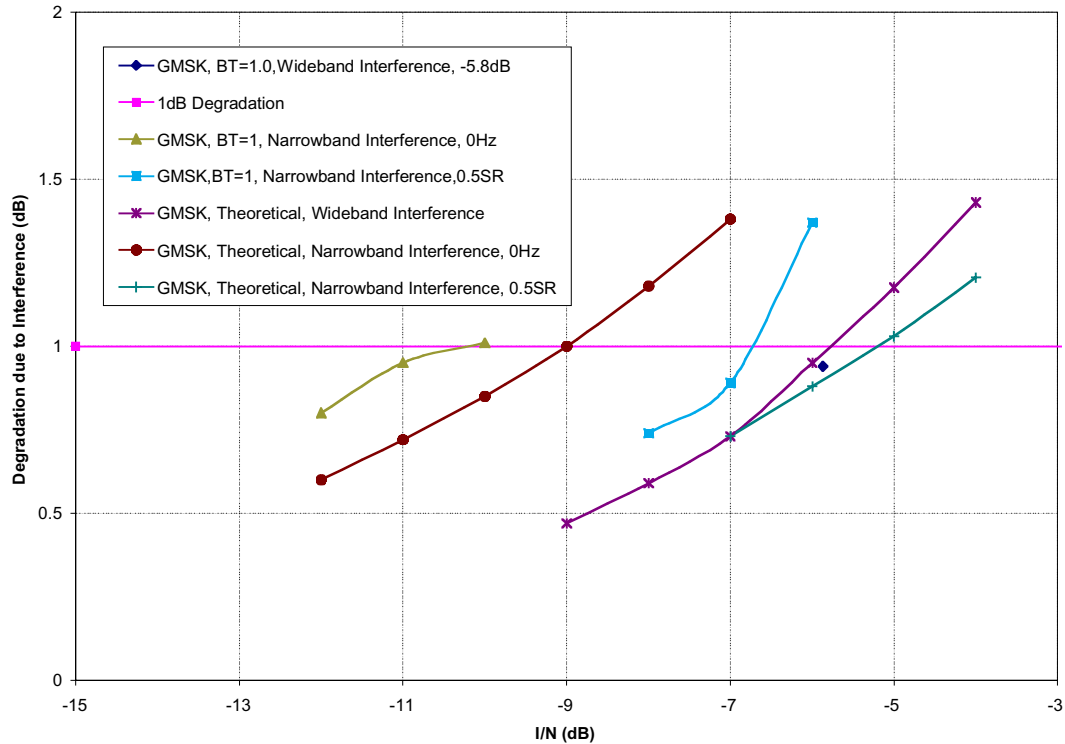


Figure 15. Degradation vs. I/N for GMSK BT=1.0

5. Conclusions

This paper has assessed the spectrum and power efficiency for several variations of filtered OQPSK and GMSK modulation. The assessment included spectrum compliance with the SFCG mask, implementation loss, and interference susceptibility while including distortions caused by the transmitter hardware that are typically specified for NASA/GSFC flight project transmitters.

Both OQPSK/PM and GMSK produce constant envelope signals and employ baseband filtering. This combination seems to allow the best trade-off of bandwidth occupancy and required power.

Filtered OQPSK/PM was the only modulation technique studied that complied with the high data rate SFCG spectral mask when using a transmitter power amplifier operating in saturation. GMSK modulation ($BT = 0.5, 1.0$) complied with the mask for frequencies offset from the carrier greater than $0.5 \times$ symbol rate, but did not comply for frequencies within $0.5 \times$ symbol rate. The portion of the spectral mask within $0.5 \times$ symbol rate is overly restrictive since it prohibits the use of modulation techniques that are otherwise compliant with the mask. GMSK incurs less than 1.0 dB of additional implementation loss compared to BPSK, even with 0-dB OBO. For GMSK, neither the $BT = 0.5$ or $BT = 1.0$ meet the spectral mask with the PA OBO 1 dB or 0.0 dB; however, GMSK is a reasonable technique for reducing the emitted signal bandwidth.

For filtered OQPSK, compliance with the spectral mask is achieved with BT of 2.0 or less and with PA output back-off of 1 dB or more. The filtered OQPSK with $BT=2.0$ has less than 1.0dB additional implementation loss due to filtering when transmitted via a PA with 1dB OBO. Lower BT values comply with mask but incur significant implementation loss with the integrate and dump detector. Performance may be improved by the use of matched filters in the ground terminal receivers. BT values higher than $BT = 2$, provide minimal decrease to implementation loss, but do not comply with the spectral mask. The implementation loss for OQPSK/PM with $BT = 2$ is comparable to that for OQPSK with PA OBO = 1 dB. OQPSK/PM has the advantage of providing the same spectral performance and implementation loss performance as filtered OQPSK with a PA at 1 dB OBO but with a saturated power amplifier.

References

- [1] SFCG Efficient Spectrum utilization Analysis, ETS-450-99114, NASA GSFC/STel/, June 11, 1999.
- [2] CCSDS - SFCG Efficient Modulation Methods Study: A comparison of Modulation Schemes, Phase 1: Bandwidth Utilization, SFCG Action Item 12/32, Warren L. Martin, Tien M. Nguyen, September 1993.
- [3] CCSDS - SFCG Efficient Modulation Methods Study: A Comparison of Modulation Schemes, Phase 2: Spectrum Shaping, SFCG Action Item 12/32, Warren L. Martin, Tien M. Nguyen, August 1994.
- [4] CCSDS - SFCG Efficient Modulation Methods Study at NASA/JPL, Phase 3: End-to-End System Performance, SFCG Action Item 12/32, SF17-28/D, September 1997.
- [5] Efficient Spectrum Utilisation for Space Science Services on Space-to-Earth Links, SFCG Recommendation 17-2R1, 17 September, 1998
- [6] Applications of Digital Wireless Technologies to Global Wireless Communications, Seiichi Sampei, Feher/Prentice Hall, 1997
- [7] Telecommunication Systems Engineer, W. Lindsey and M. Simon, Englewood Cliffs, N.J., Prentice-Hall, 1973.
- [8] Study of Narrow Band Interference into Wide band Digital Links, Phase I: Analytic Model Development, T.W. Benjamin, J.A. Gibble, R.A. Combs, M.J. Kelley, Session 14 of Third Ka Band Utilization Conference, September 15-18, 1997, Sorrento, Italy.

Appendix 1

Power Amplifier Characteristics

The transmitter model used in the simulation includes a non linear power amplifier. The amplifier is modeled as AM/AM and AM/PM lookup table with the characteristics shown in the following table.

Pin (dB)	Pout (dB)	Phase (deg)
-20	-12.39	-104.9
-19	-11.39	-104.9
-18	-10.4	-104.9
-17	-9.44	-104.9
-16	-8.5	-104.9
-15	-7.59	-104.9
-14	-6.69	-104.9
-13	-5.82	-104.9
-12	-5	-104.9
-11	-4.22	-104.895
-10	-3.49	-104.853
-9	-2.81	-104.554
-8	-2.2	-103.016
-7	-1.66	-97.8059
-6	-1.19	-87.5222

Pin (dB)	Pout (dB)	Phase (deg)
-5	-0.81	-74.1438
-4	-0.5	-59.6483
-3	-0.27	-44.8103
-2	-0.12	-29.8658
-1	-0.03	-14.8861
0	-0.02	0.105938
1	-0.09	15.10267
2	-0.19	30.10125
3	-0.33	45.10061
4	-0.48	60.10031
5	-0.65	75.10016
6	-0.85	90.10009
7	-1.08	105.10005
8	-1.33	120.10003

Appendix 2

User Transmitter Distortion Parameters

The transmitter model used in the simulation includes linear and nonlinear distortions due to amplifiers, filters and other RF components. The column labeled Set 1 in the table below provides the parameter values used in the study except data asymmetry was set to 10%.

Source	Parameter	Set 1	Set 2	Phase 3 Study [4]
Data Source	Data Transition Density	0.50	0.50	0.45
	Data Asymmetry, % (OQPSK only)	3.0	5.0	0.0
	Data Bit Jitter, %	Not simulated	Not simulated	Not Simulated
Modulator	I/Q Power Ratio (OQPSK only)	1.0:1.0	1.0:1.0	1.0:1.0
	I/Q Data Skew, %	0.0	0.0	0.0
	Frequency Stability, ppm	Not simulated	Not simulated	Not Simulated
	Phase Noise, deg. rms	3.6	3.6	Not Simulated
	Gain Imbalance, dB (OQPSK only)	0.25	0.5	Universal Phase Modulator ⁽²⁾
	Phase Imbalance, deg. (OQPSK only)	± 2.0	± 5.0	Universal Phase Modulator ⁽²⁾
	Data Transition Time, % of symbol duration (OQPSK only)	See Table 3-2 ⁽⁵⁾	See Table 3-2 ⁽⁵⁾	TBD
Power Amplifier	AM/AM, dB/dB	0.9, 0.47, 0.0	0.47, 0.0	ESA SSPA ⁽³⁾
	AM/PM, deg./dB	0.0, 12.0, 15.0	12.0	ESA SSPA ⁽³⁾
	Incidental AM, %	5.0	5.0	Not Simulated
	Data Transition Induced PM, deg. Rms (OQPSK only)	See Table 3-3 ⁽⁵⁾	See Table 3-3 ⁽⁵⁾	Not Simulated
RF Transmit Components	3 dB Bandwidth, MHz	2,000.0 ⁽⁴⁾	2,000.0 ⁽⁴⁾	Not Simulated
	Gain Flatness, dB	± 0.3 over $\pm F$ MHz ⁽¹⁾	± 0.6 over $\pm F$ MHz⁽¹⁾	Not Simulated
	Gain Slope, dB/MHz	0.1	0.1	Not Simulated
	Phase Nonlinearity, deg.	± 3.0 over $\pm F$ MHz ⁽¹⁾	± 6.0 over $\pm F$ MHz⁽¹⁾	Not Simulated
	Spurious PM, deg. rms	2.0	2.0	Not Simulated
	Spurious Outputs (inband), dBc	30	30	Not Simulated

Notes:

1. F is defined as 70% of the first null of the transmitted signal spectral density.
2. Analog phase modulator was used instead of a QPSK modulator. Gain and phase response of the universal phase modulator is provided in ref [3].
3. Characteristics of ESA SSPA operating in saturation were used.
4. Wide bandwidth is used to represent wideband RF transmit components. Typically GSFC flight project transmitters are specified with minimum 3-dB bandwidth of 2x the transmitted symbol rate.
5. Measured from simulation. These parameters are determined by other specified parameters. The filtering in particular will determine the data transition time; therefore, these parameters are a function of the modulation scheme.